



CITY UNIVERSITY  
LONDON



**Sponsored by:**



UNDERSTANDING, ACCELERATED

Proceedings of the 25<sup>th</sup> ILASS-Europe

Editing: Prof Manolis Gavaises

Cover Page: Artemis Livadarou

**ISBN: 978-960-7365-30-9**



# **The Committees**

## **Conference Chair**

Prof. Manolis Gavaises

Delphi Chair in Fluid Dynamics  
Director, Energy & Transport Research Centre  
City University London

## **Programme Committee**

- Prof J. Nouri, City University London, UK
- Dr N. Mitroglou, City University London, UK
- Mr N. Chatziarsenis, City University London, UK
- Dr N. Nikolopoulos. CERTH/ITESK, Greece
- Dr C. Habchi, IFP, France
- Dr L. Zigan, Erlangen University, Germany

## **Scientific Committee**

- Professor Dr. Günter Brenn, Graz University of Technology Institute of Fluid Mechanics and Heat Transfer, Austria
- Dr. Gilles Bruneaux, Institut Français du Pétrole, France
- Dr. Guillaume Castanet, LEMTA, Nancy University, CNRS, France
- Dr. Humberto Chaves, Technische Universität Bergakademie Freiberg, Germany
- Professor Dr. Gianpietro Elvio Cossali, Facoltà di Ingegneria, Università di Bergamo, Italy
- Professor Dr.-Ing. Joachim Domnick, Esslingen University of Applied Sciences, Germany
- Professor Dr. Klaus Dullenkopf, Universität Karlsruhe, Germany
- Dr. Christophe Dumouchel, URM 6614 - CORIA - Université et INSA de Rouen Technopole du Madrillet, France
- Professor Dr.-Ing. Udo Fritsching, Universität Bremen, Fachgebiet Verfahrenstechnik, Germany
- Dr. Iskender Gökalp, Institut de Combustion, Aérothermique, Réactivité et Environnement-CNRS, France
- Professor Dr. Eva Gutheil, Interdisziplinäres Zentrum für Wissenschaftliches Rechnen (IWR), Universität Heidelberg, Germany
- Dr.-Ing. Oskar Haidn, German Aerospace Center (DLR) Langer Grund, 74239 Lampoldshausen, Germany
- Professor Dr. Yannis Hardalupas, Department of Mechanical Engineering, Imperial College London, UK

- Professor Dr. Morgan Heikal, University of Brighton, UK
- PD Dr. habil Ilia Roisman, CSI - Technische Universität Darmstadt, Germany
- Professor Dr. Arvind Jasuja, School of Mechanical Engineering, Cranfield University, UK
- Dr. Ing. Jan Jedelsky, Thermo-fluidmechanic and Heat Transfer (TFHT) Group, Brno University of Technology, Czech Republic
- Dr. Fabrice Lemoine, LEMTA, Nancy University, CNRS, France
- Dr. Antonio Lozano, LITEC Laboratorio de Investigación en Tecnologías de la Combustion, Spain
- Professor Marco Marengo, Facoltà di Ingegneria, Università di Bergamo, Italy
- Professor Jose Pastor, CMT—Motores Térmicos, Universidad Politécnica de Valencia, Spain
- Dr. Graham Pitcher, Lotus Cars Ltd.Potash Lane, Hethel, UK
- Dr. Leif Rackwitz, Rolls-Royce Deutschland Ltd & Co KG, Combustion & Turbine Dept., Germany
- Dr. Raffaele Ragucci, Istituto Ricerche Combustione, CNR, Italy
- Dr. Norbert Roth, ITLR - University of Stuttgart, Germany
- Professor Dr. Eran Sher, Ben-Gurion University of the Negev, Israel
- Professor Dr. Ilai Sher, Cranfield University, UK
- Professor Dr. Cameron Tropea, CSI - Technische Universität Darmstadt, Germany
- Professor Dr. Bianca Vaglieco, Istituto Motori, CNR, Naples, Italy
- Professor Dr. Stephane Zaleski, Université Pierre et Marie Curie, France
- Professor Jorge Martins Barata, Universidade da Beira Interior, Portugal
- Prof Manolis Gavaises, City University London, UK

# Table of Contents

<b>Modelling</b>	9
Joint Gas Velocity – Mixture Fraction Probability Density Function Modeling of Turbulent Methanol Spray Flows	10
Numerical Investigation of PVP/Water Spray Flows in an Eulerian Framework	17
Direct Quadrature based Sectional Method of Moments for the Simulation of Evaporating Polydisperse Sprays	24
Trajectory and break-up of a liquid jet in a centrifugal field – influenced by a gas flow	31
Modelling of freezing processes in super-cooled droplets on sub-grid scale	39
Numerical and Experimental Study of Mannitol/Water Droplet Evaporation and Drying	47
Deformation and Acceleration of Drop	55
Quantum mechanical effects in n-alkane droplets	62
Theoretical and Numerical Study of Evaporation Effects in Laminar Counter flow Spray Flames	69
Simulations and Experiments on Shape Oscillations of Newtonian and Non-Newtonian Liquid Droplets	76
<b>Experimental Techniques</b>	83
Detection of a position touched by a single-tip optical fibre probe in a micro-droplet measurement	84
Validation of the Multi-Wavelength Light Extinction technique for the characterization of solid nanoparticles	91
Gas-Based Calibration of a Liquid Dispensing Device	98
Velocity measurement in scattering medium using laser correlation velocimetry	108
Real-time Determination of Interfacial Tension from the Shape of a Pendant Drop Based on Embedded Image Processing	115
Visualizing Edge-Conforming Discrete Field Quantities in Electromagnetic Field Problems with Interfaces	122
The Time-shift technique for characterization of non-transparent, spherical particles	130
Multi-scale velocity measurements for high-resolution spray kinematics	136
Experimental studies on behaviour of bubble plume	141
Scale formation Mechanism and Removal Using High Pressure Water Spray Jets	145
Investigation of some primary atomization aspects using double exposure and double view processes	151
PIV Investigation on Flows Induced by Fuel Sprays from an Outwards Opening Pintle Injector for GDI engines	158
Measurement of a wavy and thin liquid film in a small two-fluid nozzle via a single-tip optical fibre probe	167
Planar droplets sizing of a hollow-cone spray using SLIPI-LIF/MIE	173
Two-pulse SLIPI	180
<b>DNS Simulations &amp; Interface Modelling</b>	187
Effect of Reynolds number on the primary jet breakup of inelastic Non-Newtonian fluids from a duplex nozzle using Direct Numerical Simulation (DNS)	188
Embedded DNS of the primary breakup of a prefilming airblast atomizer at aircraft engine operating conditions	195
Direct numerical simulation of liquid sheet atomization in HIT flow: Density ratio and Weber number influences	202
Improving primary atomization modelling through DNS of two-phase flows	209
VOF multi-scale modelling of phase inversion and liquid atomization	218
Collision of Droplets: An Experimental, Numerical and Analytical Approach	225
Numerical Simulations of pinning droplets	232
Numerical Investigation of High Pressure Evaporation of a Resting Acetone Droplet in Nitrogen Environment	239
Coupled modelling impact of liquid interface and dispersed sprays	246
Numerical simulation of primary atomization of a sheared liquid sheet. Part 1: model and numerical method description	254
Numerical simulation of primary atomization of a sheared liquid sheet. Part 2: Comparison with experimental results	261

<b>Atomization</b>	268
Flashing behaviour of rocket engines propellants	269
Temperature and droplet size measurements in a flashing ethanol jet using the global rainbow thermometry	277
Analysis of Multi-hole GDI Injectors under Flash Boiling Conditions	284
Mapping of Pure R-22 Spray Characteristics under Homogeneous Flash Boiling	291
Design of an injection system under low pressure and temperature conditions in liquid fuelled micro UAV's	296
Polymerization in a spray dryer – combining a pre-reaction and a reaction in the spray	304
Measurements on droplet dynamics in the spray transport zone from a Rotary Bell Atomizer	314
Adapted Spray Generation in FSP-processes for Nanoparticle Generation at Large Production Rates	321
Experimental Investigation of Airblast Atomization by Variation of Dynamic Pressure and a Geometrical Scaling Factor	329
Experimental study on the influence of the liquid and air thicknesses on a planar air-blasted liquid sheet	337
Fitting of Different Drop Size Distribution Functions to Spray Data from a Y-jet Type Airblast Atomizer	344
Compressed Gas Aerosol Insert Design	351
Spike Design Nozzle for Reduced VOC Aerosols	358
Effects of acoustic radiation on air-assisted jets in a transverse high-frequency acoustic field	367
Use of ultrasonic atomizers in screening experiments of herbicides	374
Impact of oil content on effervescent atomization of oil-in-water emulsions	381
Deviation and Atomization of a Dielectric Liquid Sheet under Electrohydrodynamic Excitation	387
Influence of pressure surge on bubble generation and spray steadiness in an effervescent atomizer	394
Jet formation from laminar two-phase-flow in a tapered channel	400
Influence of mixing chamber length and liquid viscosity on the effervescent atomization of maltodextrin solutions	408
Spray characteristics from a dodecane internal steam-assisted atomizer with gas-to-liquid ratios varying from 0 to 0.18	415
Effect of air-induction on agricultural flat fan sprays	423
Investigation on Pressure Swirl Nozzles with Coandă Deflection Outlets	430
Fuel Influence on Hollow-Cone Sprays	438
Optimization of Pressure-Swirl Atomizer for a Burner Retrofit	446
Effect of Cone Angle on Droplet Size Classes for Pressure Swirl Atomizers	454
<b>IC Engine Sprays</b>	461
Comparison of experiments and numerical simulations of high pressure transparent injection nozzles	462
String Cavitation in Fuel Injector Nozzle	469
Experimental measurement of jets formed after the impact onto static and onto moving water films	475
A Gibbs free Energy Relaxation Model for Cavitation Simulation in Diesel injectors	482
Diesel Spray Breakup at Pressure	489
Image-Based Analysis of Evaporating Diesel Sprays in the Near-Nozzle Region	496
Zooming into the primary breakup region of engine-related sprays	503
On the use of 3D spray impulse topography for analyzing the effects of nozzle geometry on spray breakup	510
Influence of nozzle hole eccentricity on spray morphology	517
Effects of the Nozzle Geometry on Fuel Dispersion in Non-Evaporative and Evaporative Conditions for a Diesel Injector	525
Optical Analysis of High-pressure Injections in Transparent Diesel Engine	532
Effect of Geometric Shapes of Nozzle Hole for Direct Injection Diesel Engine on Spray Characteristics	541
Analysis of spray evolution from both piezo and solenoid injectors in single cylinder research engine	548
Boundary condition and fuel composition effects on injection processes of diesel sprays at the microscopic level	556
Evaluation of high speed measurements on the spray/wall interaction for diesel injections	571
Study on Cyclic Variation in near-Nozzle Region of Diesel Spray by L2F	579
Transition of Fuel Components into Supercritical State under Diesel Process Conditions	587
Diesel spray interaction with porous structure: space- and time-dependent analysis of fuel distribution in space and its vaporization	594

Combustion of diesel spray in 3D-highly porous reactors under CR-Diesel injection conditions -----	601
Comparison of the Spray Evaporation and Inflammation of Alternative Fuels for Late Injection Timing Mode -----	608
Tomographical Reconstruction of the Radial Fuel Distribution of a DISI Gasoline Spray using Mie Scattering and Laser Induced Fluorescence -----	616
High-speed imaging of the sooting combustion of ethanol-gasoline blended fuel sprays under DISI cold start conditions -----	622
Near-Nozzle Instabilities in Gasoline Direct Injection Sprays -----	629
Investigation of the interaction of in-cylinder flow and fuel injection in an optically accessible direct injection gasoline engine-----	637
Experimental Study on Characteristics of Laser-induced Ignition in Liquid Fuel Spray -----	644
<b>Wall Impingement -----</b>	<b>648</b>
Experimental study of evaporating sessile liquid droplets on a heated horizontal surface -----	649
Mapping Drop Impact Regimes on a Heated Surface -----	656
Wetting Dynamics of Dilute Polymer Solution Drops Impacting on Hydrophobic Surfaces -----	663
A study of liquid spray, droplet impingement and heat transfer -----	670
Phenomenology of Two-Component Droplet-Wall Film-Interaction -----	677
Local heat flux investigation during single drop impingement onto a heated wall -----	684
Droplet impacts of non-Newtonian fluids for bioengineering applications -----	691
Numerical study on air entrapment in droplets under impact onto a solid surface-----	698
Numerical Investigation of Drop Impact onto Hot Surfaces-----	706
A new model for droplet – solid surface interaction. Impingement onto hydrophilic and superhydrophobic surfaces -----	713
Selected Results of the Collaborative Research Center: Droplet Dynamics under Extreme Boundary Conditions SFB-TRR/75-----	721
<b>CFD &amp; LES Simulations -----</b>	<b>729</b>
Liquid-Fuel Ejector Pump under Multi-Phase Flow Conditions -----	730
Gasoline direct injection internal injector flow CFD simulations for various bioethanol blends-----	737
Towards More Realistic Fuel Injector Simulations -----	744
CFD Simulation of a Tapered Swirl Injector Spray in Cross Air-Flow-----	751
Coupled Simulation of Spray Process for Metal Matrix Composite Powder Production-----	760
Numerical computation of ice particle accretion in aircraft engines or on heated surfaces -----	772
Numerical Analysis of a Partially Pre-Vaporized Turbulent Spray Flame using LES and FGM -----	779
Large Eddy Simulation of a lab-scale spray burner -----	786
A new model for marine Heavy Fuel Oil thermophysical properties:validation in a constant volume spray chamber -----	794
Investigation of Fuel Injection Strategies for Partially Premixed Compression Ignition Combustion in Two-Stroke Marine Diesel Engines-----	804
Detailed Investigation of Multi-Component Spray Model Capabilities for Diesel Engine Simulation -----	811
Investigation of Spray Combustion with Fuel-Water Emulsification under Exhaust Gas Recirculation using Detailed Visualization and Spray Modelling -----	818
A multi-coupled Eulerian-Lagrangian solver for airblast injectors including liquid film evolution and primary breakup – Numerical model -----	826
A multi-coupled Eulerian-Lagrangian solver for airblast injectors including liquid film evolution and primary breakup – Application -----	834
Validation of Eulerian-Eulerian Approach for Diesel Sprays, and 3D Coupling with Lagrangian Spray Approach -----	841
Model of Two-Phase Flowfield around Shattering Drop-----	848
Primary Breakup Modelling Within the LES Framework -----	855
Mixing model effects on LES-PDF-PBE simulations of DBP droplets in a turbulent jet -----	863
Large Eddy Simulation of a prefilming airblast atomizer-----	870
VoF-LES Studies of GDi Multi-Hole Nozzle Plume Primary Breakup and Comparison with Imaging Data-----	878
Multi-Scale Analysis of Liquid Atomization Processes and Sprays -----	886
Modelling of Unsteady Effects on Jet Breakup -----	893
Numerical modelling of liquid jets atomization due to leakage of liquefied gas storage -----	901

A New Atomization Model for High Speed Liquid Jets using a Turbulent, Compressible, Two-Phase Flow Model and a Surface Density Approach -----	912
<b>Phase change, combustion and particle phenomena-----</b>	<b>920</b>
Implementation and Calibration of the Icing and Contamination Research Facility (iCORE) -----	921
Assessing icephobicity of superhydrophobic surfaces as passive coating icing mitigation strategy on helicopter blades -----	929
Biodiesel fuel droplets: transport and thermodynamic properties -----	936
Biodiesel Fuel Droplets: Modelling of Heating and Evaporation Processes -----	944
Modelling of Heating and Evaporation of Gasoline Fuel: Effects of Input Parameters -----	952
Experimental study on the regimes of W/O interface in the presence of vertical electric field -----	959
Experimental studies on internal circulation during droplet evaporation -----	966
Turbulence Induced Droplet Breakup -----	972
Droplet entrainment from a single wave propagating in a stratified air-water pipe flow -----	978
The Effect of Superheat on the Performance Characteristics of a Flash Atomized Spray -----	985
Acetone Photophysics Investigations for the Application of PLIFP to Droplet Evaporation Measurements under Supercritical Conditions -----	992
Influence of fluid media on flow pattern and spray break-up applying cylindrical nozzles for the atomization of superheated liquids -----	1000
Phase Doppler characterization of burning sprays from an auxiliary emission control fuel nozzle of a lean two-stage low-NOx combustor for an aero-engine at a simulated aircraft approach condition -----	1006
Experimental Study on Flame Spread of Droplet-cloud Elements with Two-droplet Interaction in Microgravity -----	1014
Study of reactive spray using global rainbow refractometry -----	1019
Generation of Fine Particles with Specified Characteristics -----	1027
Spray drying of particles with narrow PSD by LAMROT atomizer and optimized gas distributor -----	1035
Influence of particles on ligament stretching and fragmentation of suspensions -----	1043
Atomization and spray formation for PVP powder production -----	1050

**Session:**

# **Modelling**

## Joint Gas Velocity – Mixture Fraction Probability Density Function Modeling of Turbulent Methanol Spray Flows

Yong Hu and Eva Gutheil

Interdisciplinary Center for Scientific Computing, University of Heidelberg, Germany

### Abstract

Liquid spray dynamics play a crucial role in analyzing the combustion dynamics in industrial applications such as Diesel engines, liquid rocket propulsion, and industrial furnaces. In these combustion systems, a broad range of spatial and temporal scales and strong non-linear coupling associated with liquid breakup and atomization, turbulent dispersion, and droplet evaporation as well as fuel-air mixing are involved and make spray modeling a challenging task.

In this study, a one-point one-time statistical description of a joint gas velocity - mixture fraction probability density function (PDF) model for the gas phase is derived and modeled. For closure of the PDF transport equation, the simplified Langevin model and the interaction-by-exchange-with-the-mean (IEM) model are extended to account for spray evaporation. For the dispersed liquid phase, the Abramzon - Sirignano model is used for the characterization of droplet heating, vaporization, and motion. The liquid-phase equations are solved by a Lagrangian droplet parcel method using the point source approximation. The application of this framework to a steady, two-dimensional, axi-symmetric, turbulent methanol/air dilute non-reacting spray flow without swirl shows good results compared to experimental data provided by McDonell and Samulsen, and the present PDF approach improves the numerical results obtained using a RANS simulation with an extended  $k$ - $\varepsilon$  model. The analysis of the joint PDF of gas velocity and mixture fraction implies that a linear relation between the gas phase velocity and mixture fraction exists near the centerline, whereas in other regions, the correlation of these variables is considerably weaker, but the general assumption of statistical independence fails.

---

### Introduction

The transported probability density function method for turbulent reactive gas flows has become very popular since Pope's work [1], and it has been shown to be a successful tool for the simulation of turbulent gas flows, in particular for reactive flows. Using the concept of one-point one-time Eulerian PDF, a complete description of turbulent gas flows with increased information of statistical information is obtained, where all moments of the dependent quantities may be evaluated from this joint PDF. The major advantages of the PDF method are exact treatment of convection, body force, mean pressure gradient and chemical reactions. Moreover, the Lagrangian PDF takes full account of long memory of the turbulence. The past history of all the fluid particles' properties can be completely described by the multi-time Lagrangian PDF [1].

PDF methods have been applied to simulate multi-phase flows since the 1990's. Durand et al. [2] describe the gas phase in turbulent two-phase flows with a PDF transport equation. Pai and Subramaniam [3] deduce a unified joint PDF transport equation of all liquid-phase and gas-phase dependent variables. Garg et al. [4] develop accurate numerical methods to solve these PDF equations. Naud [5] and Beishuizen and Roekaerts [6] deal with the joint PDF transport equation of the properties of droplets and gas eddies seen by droplets. Ge and Gutheil [7] deduce and solve the transport equation of the PDF of mixture fraction in turbulent spray flows, and they suggest an extended presumed PDF for turbulent mixing in evaporating sprays. Ge and Gutheil [8] and Ge et al. [9] further develop a joint mixture fraction – gas enthalpy PDF model to simulate spray flames. Kung and Haworth [10] apply a transported PDF method to internal combustion engines. Anand and Jenny [11] use a joint gas phase velocity- composition-frequency PDF for an evaporating spray, where the droplet-seen gas velocity is included in the droplet density function, and the equations are solved with a modified simplified Langevin model. These publications demonstrate that the transported PDF is an excellent method to simulate turbulent multi-phase flows, though there are still some modeling problems such as the correct closure of the influence of droplet evaporation on gas-phase composition PDF [5].

In the present work, a joint gas velocity-mixture fraction PDF is introduced for the modeling turbulent evaporating spray flows. By neglecting fluctuations in spray source terms and liquid void fraction, the joint PDF transport equation of gas velocity and mixture fraction is modeled and solved [12]. The numerical results are compared with experimental data of McDonell and Samulsen [13] and with previous numerical results of a moment closure method using an extended  $k$ - $\varepsilon$  model [14] to account for the spray source term.



### Experimental Setup

A steady, two-dimensional, axi-symmetric, non-reacting turbulent liquid methanol jet without swirl is modeled. The experiments have been performed by McDonell and Samuelsen [13], and the results are available for comparison with the simulations.

The geometry of the liquid injector [13] is shown in Fig. 1. The position of the fuel injector's exit is marked as  $x = 0$  mm. The gas and droplet velocities, droplet size distribution, liquid flux and concentration of methanol vapor are measured at the axial positions of  $x = 7.5$  mm, 25 mm, 50 mm, 75 mm, and 100 mm downstream the nozzle exit. The data at  $x = 7.5$  mm are taken as inlet profiles for the simulations and the results are compared at higher distances. The mass flow rate of the liquid fuel is 1.32 g/s. The airflow results in a pressure drop of 3.73 kPa.

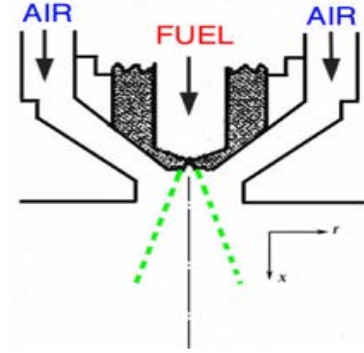


**Figure 1.** Schematic of the geometry of the liquid fuel injector.

### Mathematical Modeling

With the assumption of point particle [2], the void fraction of the liquid phase is neglected. This assumption is valid for dilute sprays. The conservation equations for the gas phase of the turbulent spray flow can then be written as

$$\frac{\partial \rho}{\partial t} + \frac{\partial(\rho U_j)}{\partial x_j} = \dot{S}_{l,1} \quad (1)$$

$$\frac{\partial(\rho U_i)}{\partial t} + \frac{\partial(\rho U_i U_j)}{\partial x_j} = -\frac{\partial p}{\partial x_i} + \frac{\partial \tau_{ij}}{\partial x_j} + \rho g_i + \dot{S}_{l,U_i} \quad (2)$$

$$\frac{\partial(\rho h)}{\partial t} + \frac{\partial(\rho h U_j)}{\partial x_j} = \frac{\partial p}{\partial t} + \frac{\partial}{\partial x_j} \left( \rho D_h \frac{\partial h}{\partial x_j} \right) + \dot{S}_{l,h} \quad (3)$$

$$\frac{\partial(\rho \xi_C)}{\partial t} + \frac{\partial(\rho \xi_C U_j)}{\partial x_j} = \frac{\partial}{\partial x_j} \left( \rho D_M \frac{\partial \xi_C}{\partial x_j} \right) + \dot{S}_{l,1}, \quad (4)$$

where  $\tau_{ij}$  is the viscous stress tensor, and  $\dot{S}_{l,1}$ ,  $\dot{S}_{l,U_i}$ , and  $\dot{S}_{l,h}$  are the spray source terms in the continuity, momentum, and energy equation, respectively; they describe the interaction between the gas and the liquid phases. The definition of the mixture fraction,  $\xi_C$ , used in the present approach is based on the chemical element carbon,  $j = C$ ,

$$\xi_C = \frac{Z_C - Z_{C,min}}{Z_{C,max} - Z_{C,min}} \quad (5)$$

where  $Z_j$  is the mass fraction of element  $j$  in the mixture, which is defined as

$$Z_j = \sum_{i=1}^N \frac{\alpha_{ij} M_j}{M_i} Y_i. \quad (6)$$

Here  $i$  denotes the species in the mixture,  $N$  is the total number of species, and  $\alpha_{ij}$  is the number of element  $j$  in species  $i$ .

A fine-grained, one-point one-time Eulerian joint velocity-mixture fraction probability density function,  $f^*(V, \zeta_C; \mathbf{x}, t)$ , is defined for the gas phase of the turbulent spray flow [12]

$$f^*(V, \zeta_C; \mathbf{x}, t) = \delta(U(\mathbf{x}, t) - V) \delta(\xi_C(\mathbf{x}, t) - \zeta_C). \quad (7)$$

With this definition, the joint velocity – mixture fraction PDF yields

$$\begin{aligned} \frac{\partial F}{\partial t} + \frac{\partial(V_j F)}{\partial x_j} - \frac{\langle \dot{S}_{l,1} \rangle}{\rho} F + \left( g_j - \frac{1}{\rho} \frac{\partial \langle p \rangle}{\partial x_j} + \frac{1}{\rho} \langle \dot{S}_{l,U_i} - U_i \dot{S}_{l,1} \rangle \right) \frac{\partial F}{\partial V_j} + \frac{1}{\rho} \langle (1 - \xi_C) \dot{S}_{l,1} \rangle \frac{\partial F}{\partial \zeta_C} = \\ \left\langle \frac{\dot{S}'_{l,1}}{\rho} \middle| \mathbf{V}, \zeta_C \right\rangle F + \frac{\partial}{\partial \mathbf{V}} \left( \frac{1}{\rho} \left\langle -\frac{\partial \tau_{ji}}{\partial x_i} + \frac{\partial p'}{\partial x_j} - \dot{S}'_{l,U_i} + U_i \dot{S}_{l,1} - \langle U_i \dot{S}_{l,1} \rangle \middle| \mathbf{V}, \zeta_C \right\rangle F \right) - \\ \frac{\partial}{\partial \zeta_C} \left( \frac{1}{\rho} \left\langle \frac{\partial}{\partial x_j} \left( \rho D_M \frac{\partial \xi_C}{\partial x_j} \right) + (1 - \xi_C) \dot{S}_{l,1} - \langle (1 - \xi_C) \dot{S}_{l,1} \rangle \middle| \mathbf{V}, \zeta_C \right\rangle F \right). \end{aligned} \quad (8)$$

The terms on the left-hand-side appear in closed form. They include the terms of convection, body force, mean pressure gradient, and mean spray source terms  $\langle \dot{S}_{l,1} \rangle$ ,  $\langle \dot{S}_{l,U_i} \rangle$  for the transfer of mass and momentum between

the liquid and the gas. The terms on the right hand side of Eq. (8) must be modeled. They include the fluctuating spray source terms, which are neglected in the present study, the viscous stress tensor, the fluctuating pressure gradient, and the molecular diffusion fluxes.

A Lagrangian Monte-Carlo particle method is used to solve the joint PDF transport equation. The flow is discretized into a large number of particles [1], each of which has a set of properties  $\{m^*, x^*, U^*, \xi_C^*\}$  (superscript star denotes the particle property). The PDF transport equation is transformed into a set of stochastic differential equations (SDE), which describe the evolution of the particle properties. The Lagrangian tracking of each computational particle in physical space is governed by

$$dX_i^* = U_i^* dt \quad (9)$$

and its evolution in the velocity-sample space is described using the modified simplified Langevin model [12], which accounts for spray evaporation

$$dU_i^*(t) = \frac{1}{\langle \rho \rangle} \left( \langle \rho \rangle g_i - \frac{\partial \langle p \rangle}{\partial x_i} + \langle \dot{S}_{l,U_i} \rangle - \langle U_i \rangle \langle \dot{S}_{l,1} \rangle \right) dt - \left( \frac{1}{2} + \frac{3}{4} C_0 \right) (U_i^*(t) - \tilde{U}_i) \frac{\tilde{\xi}}{k} dt + \sqrt{C_0 \tilde{\epsilon}} dW_i. \quad (10)$$

Note that Eq. (10) includes extra terms to account for the spray source terms. The diffusion process is represented by a Wiener process  $W(t)$ , where  $dW_i = W_i(t+dt) - W_i(t)$ , which is Gaussian distributed with  $\langle dW_i(t) \rangle = 0$  and  $\langle dW_i(t) dW_j(t) \rangle = dt \delta_{ij}$ . Molecular diffusion is modeled using the extended interaction-by-exchange- with-the-mean (IEM) model [12,7]. Hence, the mixture fraction evolves as

$$\frac{d\xi_C^*(t)}{dt} = -\frac{1}{2} \frac{\tilde{\xi}}{k} C_\phi [\xi_C^*(t) - \tilde{\xi}_C] + [1 - \xi_C^*(t)] \frac{\langle \dot{S}_{l,1} \rangle}{\langle \rho \rangle}, \quad (11)$$

where  $\tilde{\xi}_C$  denotes the estimated mean mixture fraction, and standard constants are used [1]. A more detailed description of the derivation of the present joint PDF equation is given by Ge *et al.* [12].

For the closure of the joint PDF transport equation, the conservation equations of the gas flow including the extended  $k$ - $\epsilon$  model [8] are solved. Spray source terms are described using the particle-source in-cell model [14]. The Abramzon-Sirignano model [15] is used to calculate droplet heating and evaporation in a convective flow field.

At the inlet, a top-hat profile is prescribed for the inlet gas phase mixture fraction, and a Gaussian profile is assumed for the gas velocity. For the Monte Carlo method with a finite number of computational particles  $N$ , the statistical error is of order  $N^{-1/2}$ , and approximately  $1.5 \cdot 10^6$  particles are used to simulate the present evaporating spray flow. At each time step, a number of new particles are injected at the inlet plane based on the inlet mass flux. Along the axis of symmetry, particles that cross the boundary are reflected back into the domain to be consistent with the zero-flux boundary condition. An explicit time marching scheme [1] is used in the Monte Carlo calculation with the method of fractional steps to solve equations (9)-(11). An iterative time-averaging scheme is implemented for this stationary situation.

## Results and Discussion

Figure 2 shows a contour plot of the methanol vapor. Figure 2 reveals that most of the evaporation occurs near the centerline of the jet, and the methanol spray evaporation reduces in both axial and radial directions away from the injection nozzle.

The marked points A through D are the monitor positions for joint PDF analysis with the coordinates A (25,3), B (25,8), C (100,3), and D (100,8), respectively, given in mm. The locations are chosen in such a way that two positions are located at the same axial position, A and C are located in the fuel region for the jet whereas B and D are located in the boundary layer of the fuel jet. First, radial profiles of gas velocity and methanol mass fraction are compared with experimental results.

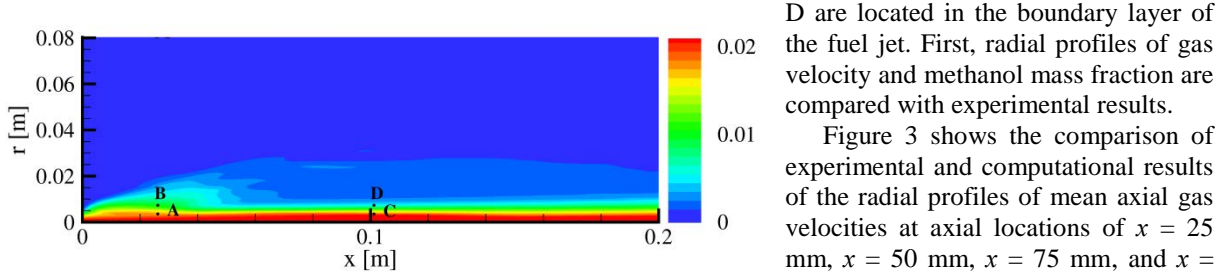
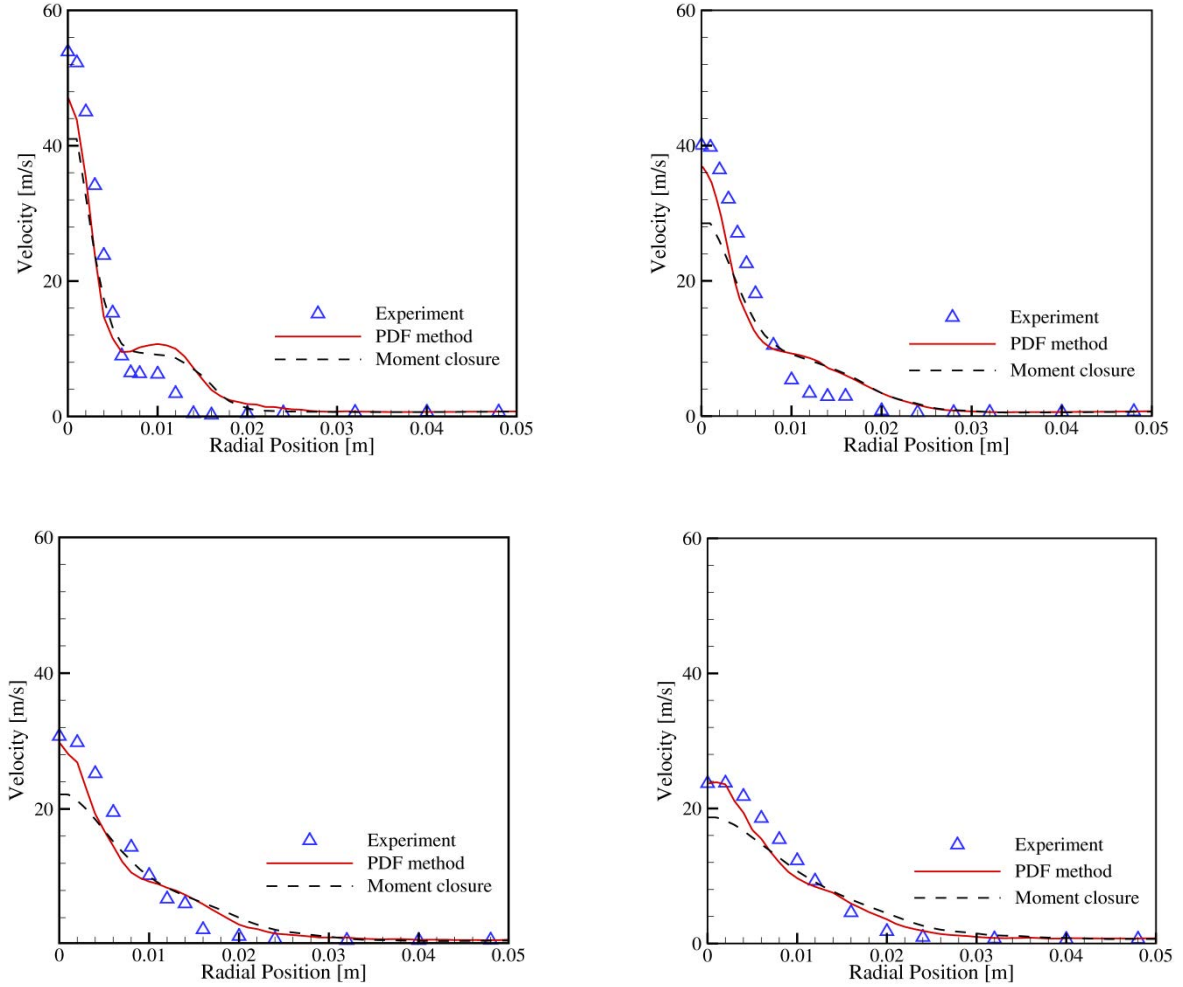


Figure 2. Contour plot of methanol vapor.

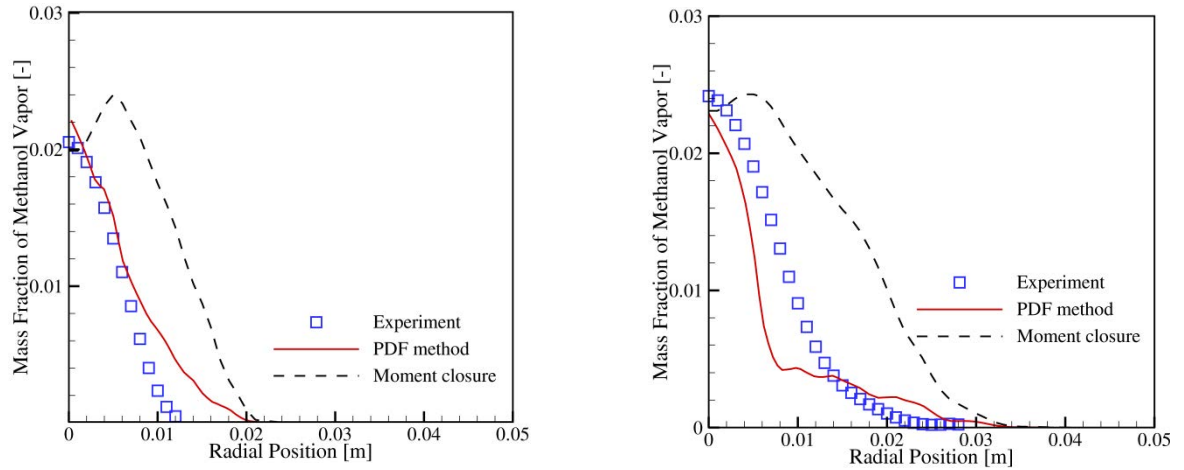
First, radial profiles of gas velocity and methanol mass fraction are compared with experimental results.

Figure 3 shows the comparison of experimental and computational results of the radial profiles of mean axial gas velocities at axial locations of  $x = 25$  mm,  $x = 50$  mm,  $x = 75$  mm, and  $x = 100$  mm, respectively. Symbols denote experimental data [13].



**Figure 3.** Radial profiles of the gas-phase mean axial velocity at  $x = 25$  mm (top left),  $x = 50$  mm (top right),  $x = 75$  mm

Solid lines result from the present joint PDF, dashed lines show former results using the extended  $k-\varepsilon$  model [14]. The results of the joint PDF method are in very good agreement with experimental data, in particular, the shape of the experimental profiles is well captured, and they improve the results of the moment closure model. Generally, numerical results under-predict the experimental data near the centerline, whereas they over-predict experimental results at higher distance from the axis of symmetry. In both regimes, the joint PDF method performs much better than the moment closure model. The current simplified Langevin model neglects the effects of mean velocity gradient and the spray source fluctuating terms, which may be the main source of the



**Figure 4.** Radial profiles of the mass fraction of methanol vapor at  $x = 25$  mm (left) and  $x = 50$  mm (right).

discrepancies found upstream. Excellent agreement is found further downstream at  $x = 75$  mm and  $x = 100$  mm, where the mean velocity gradient is comparatively small. Thus, the joint PDF results greatly improve the agreement with experiment compared to the simulations with the extended  $k-\varepsilon$  model.

Figure 4 shows the radial profiles of the mean mass fraction of methanol vapor at  $x = 25$  mm and 50 mm. The moment closure modeling over-predicts the vapor mass fraction at these two locations, whereas the joint PDF method predicts the same trend as the measurements, although it tends to under-predict the vapor mass fraction at the location of 50 mm. Major differences between the models occur at 0.006 m from the axis where the moment closure modeling results reveal a sharp peak in methanol vapor mass fraction, which over-predicts the maximum peak value of experimental results at the corresponding axial location.

Figure 5 displays the contour plots of joint velocity-mixture fraction PDF at four different positions marked in Fig. 1. It can be seen from the figure, the gas velocity and mixture fraction are statistically dependent at positions A and C near the centerline, where an almost linear relation exists. At these two points, the convective transport in axial direction is the dominant physical process. Comparatively, at positions B and D, the samples show a strong statistical correlation only at the point D downstream, which can be attributed to the fact that the spray evaporation is much more dominant at location B.

The radial profile of the Sauter mean radius, which is not shown here and can be found in [12], shows that the PDF method and the moment closure method produce almost the same results, and they are in qualitative agreement with the measurements. For the non-reactive case, both the temperature and the concentration gradients in flow field are very small. The influence of the gas phase on the liquid phase is not very strong, and the droplet evolution is dominated by inertial motion.

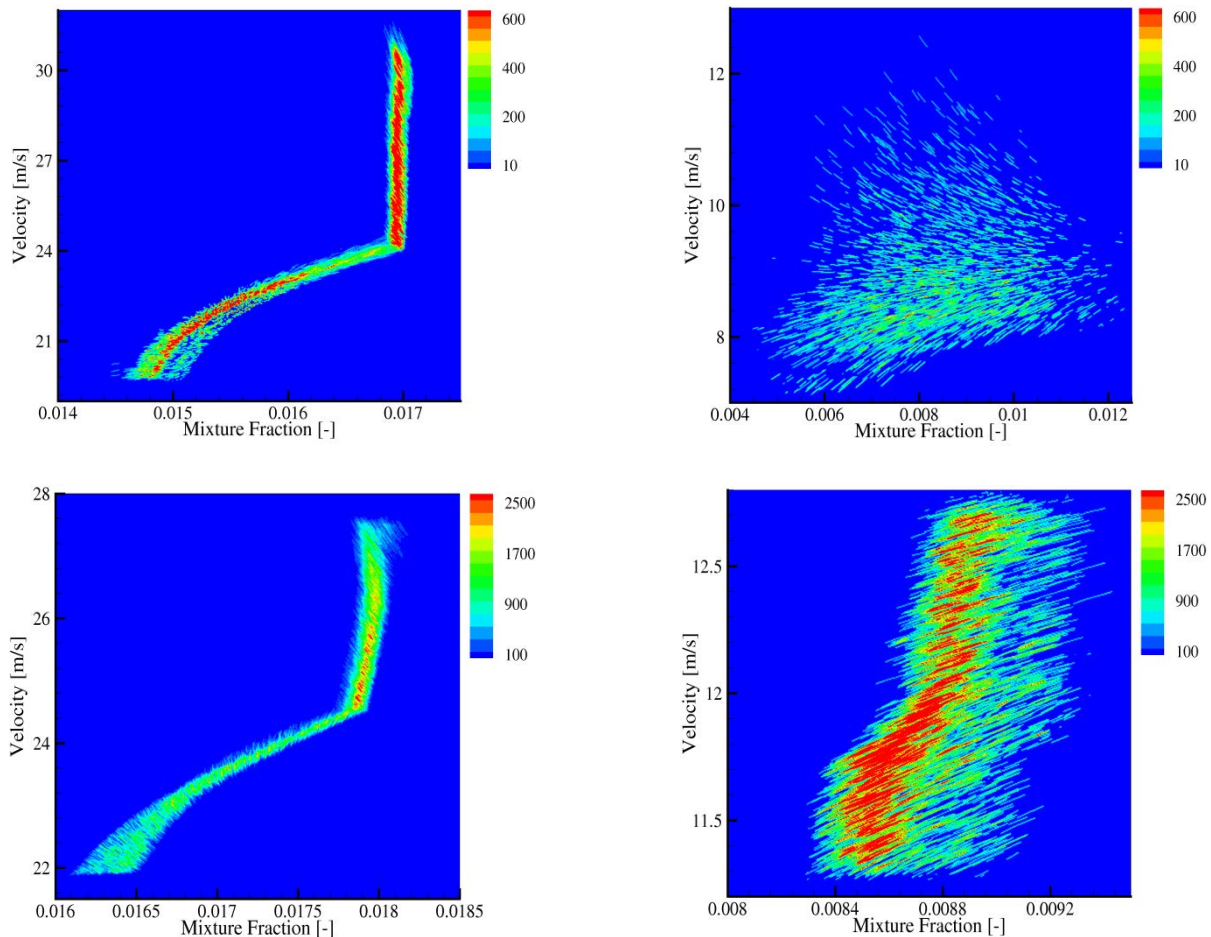


**Figure 5.** Contour plot of joint velocity-mixture fraction PDF. Top left: position A. Top right: position B. Bottom left: position C. Bottom right: position D.

## Conclusions

A joint gas velocity-mixture fraction PDF is introduced for the simulation of turbulent spray flows. The velocity is modeled through a simplified Langevin model, and molecular mixing is described through an IEM model. The PDF transport equation is solved by a Lagrangian Monte-Carlo particle method. The droplet characteristics including heating, vaporization, and motion are solved by a Lagrangian droplet parcel method. Closure of the PDF transport equation and droplet evolution equation is achieved through the mean conservation equations of the gas flow. A steady, two-dimensional, axi-symmetric, turbulent methanol/air dilute non-reactive spray flow without swirl is simulated.

The results of the gas velocities and the mass fraction of methanol vapor are in very good agreement with experimental data, and the PDF results greatly improve the simulations obtained by the moment closure method. The correlation of the gas velocity and the mixture fraction is analyzed at several positions in the flow field, and it is found that the range of correlations range from statistical independence over light correlation to linear dependence. Thus, the assumption of statistical independence is a weak approximation.

## Acknowledgements

The authors acknowledge financial support of Deutsche Forschungsgemeinschaft (DFG). Y. Hu acknowledges financial support through CSC.

## Nomenclature

$C_d$	drag coefficient [-]
$C_{p,l}$	specific heat capacity of liquid [J kg <sup>-1</sup> K <sup>-1</sup> ]
$C_{p,F}$	specific heat capacity of fuel vapor [J kg <sup>-1</sup> K <sup>-1</sup> ]
$D_M$	molecular diffusion coefficient [m <sup>2</sup> s <sup>-1</sup> ]
$f^*$	fine-grained PDF
$\mathbf{F}$	mass density function
$g$	acceleration due to gravity [m s <sup>-2</sup> ]
$h$	enthalpy [J kg <sup>-1</sup> ]
$k$	turbulent kinetic energy [m <sup>2</sup> s <sup>-2</sup> ]
$L_V$	latent heat of vaporization [J kg <sup>-1</sup> ]
$M_i$	molar mass of species $i$ [kg mol <sup>-1</sup> ]
$m^*$	mass of gas particles [kg]
$\dot{m}_d$	droplet vaporization rate [kg s <sup>-1</sup> ]
$p$	gas phase pressure [Pa]
$p'$	fluctuating gas phase pressure [Pa]
$r_d$	droplet radius [m]
$\dot{S}_{l,1}$	spray source term for gas phase continuity equations [kg m <sup>-3</sup> s <sup>-1</sup> ]
$\dot{S}_{l,u_i}$	spray source term for gas phase momentum equations [kg m <sup>-2</sup> s <sup>-2</sup> ]
$\dot{S}_{l,h}$	spray source term for gas phase energy equations [J m <sup>-3</sup> s <sup>-1</sup> ]
$\dot{S}_{l,\emptyset}$	fluctuating spray source terms for gas phase variable $\emptyset$
$t$	time [s]
$\mathbf{V}$	gas velocity in sample space [m s <sup>-1</sup> ]
$\mathbf{U}_i$	gas velocity [m s <sup>-1</sup> ]
$\mathbf{x}$	physical space coordinates [m]
$Y_i$	mass fraction of species $i$ [-]
$Z_i$	mass fraction of element $i$ in the mixture [-]

## Greek symbols

$\xi_C$	mixture fraction [-]
$\zeta_C$	mixture fraction in the sample space [-]
$\epsilon$	turbulent kinetic energy dissipation rate [m <sup>2</sup> s <sup>-3</sup> ]
$\tau_{ij}$	viscous stress tensor [J m <sup>-3</sup> ]
$\rho$	density [kg m <sup>-3</sup> ]
$\alpha_{ij}$	number of element $j$ in species $i$ [-]

### Subscripts

C	carbon
d	droplet
l	liquid
s	surface
x	axial direction

### References

- [1] Pope. S. B., PDF Methods for Turbulent Reactive Flows. *Prog. Energy Combust. Sci.*, Vol. 11, 119-192 (1985).
- [2] Durand. P, Gorokhovski. M, and Borghi. R., An application of the probability density function model to diesel engine combustion. *Combust. Sci. Technol.*, Vol. 144, 47-78 (1999).
- [3] Pai. G. M and Subramaniam. S., A comprehensive probability density function formalism for multiphase flows. *J. Fluid Mech.*, Vol. 628, 181-228 (2009).
- [4] Garg. R, Narayanan. C, Subramaniam. S., A numerically convergent Lagrangian-Eulerian simulation method for dispersed two-phase flows. *Int. J. Multiphase Flow*, Vol. 35, 376-388 (2009).
- [5] Naud. B., PDF modeling of turbulent sprays and flames using a particle stochastic approach. PhD Thesis, TU Delft, (2003).
- [6] Beishuizen. N.A., Roekaerts. D in: *Experiments and Numerical Simulations of Diluted Spray Turbulent Combustion* (B. Merci, D. Roekaerts, A. Sadiki, Eds.), Springer 2011.
- [7] Ge. H.W., and Gutheil. E., PDF simulation of turbulent spray flows. *Atomiz. Sprays*, Vol. 16, 531-542 (2006).
- [8] Ge. H.W. and Gutheil. E., Simulation of a turbulent spray flame using coupled PDF gas phase and spray flamelet modeling. *Combust. Flame*, Vol. 153, 173-185 (2008).
- [9] Ge. H.W., Düwel. I, Kronemayer. H, Dibble. R.W., Gutheil. E, Schulz. C, Wolfrum. J., Laser based experimental and Monte Carlo PDF numerical investigation of an ethanol/air spray flame. *Combust. Sci. Technol.*, Vol. 180, 1529-1547 (2008)
- [10] Kung. E.H. and Haworth. D.H., Transported probability density function (tPDF) modeling for direct-injection internal combustion engines. *SAE Int. J. Engines*, Vol. 1, 591-606 (2008).
- [11] Anand. G and Jenny. P., Stochastic modeling of evaporating sprays within a consistent hybrid joint PDF framework. *J. Comp. Phys.*, Vol. 228, 2063-2081 (2009).
- [12] Ge. H.W., Hu. Y, and Gutheil. E., Joint gas-phase velocity-scalar PDF modeling for turbulent evaporating spray flows, *Combust. Sci. Tech.* Vol. 184(10-11), 1664-1679, (2012).
- [13] McDonell. V.G. and Samuelsen. G.S., An Experimental Data Base for Computational Fluid Dynamics of Reacting and Non-reacting Methanol Sprays. *J. Fluids Eng.*, Vol. 117, 145-153 (1995).
- [14] Hollmann. C and Gutheil. E., Modeling of Turbulent Spray Diffusion Flames Including Detailed Chemistry. *Proc. Combust. Inst.*, Vol. 26, 1731-1738 (1996).
- [15] Abramzon. B and Sirignano. W.A., Droplet Vaporization Model for Spray Combustion Calculation. *Int. J. Heat Mass Transfer*, Vol. 9, 1605-1618 (1989).

## Numerical Investigation of PVP/Water Spray Flows in an Eulerian Framework

Srikanth Reddy Gopireddy and Eva Gutheil

Interdisciplinary Center for Scientific Computing (IWR),  
Heidelberg University, Germany

### Abstract

The direct quadrature method of moments (DQMOM) for an axisymmetric, two-dimensional configuration is extended to model evaporating water and PVP/water spray flows injected into a vertical spray chamber, where the spray is carried by air. The DQMOM constitutes an Euler – Euler formulation, and the present spray flows are modeled accounting for droplet size and velocity distributions. The different physical processes in spray flows are considered through detailed models for convective evaporation and drying of bi-component Polyvinylpyrrolidone (PVP)/water droplets. The Abramzon & Sirignano model with proper extensions to include the effects of polymer presence and resistance from solid layer is implemented, and droplet motion is included through considering drag force and gravity. Moreover, droplet coalescence is included in the present formulation. Appropriate initial and boundary conditions as well as the starting values for simulations are generated from experimental data, which have been carried out at TU Graz, Austria by the group of Prof. G. Brenn. The measurements were performed with phase Doppler anemometry (PDA). The experiment provides the droplet size and velocity distributions at different cross sections away from nozzle exit. The simulation results are compared with experimental data at these cross sections, and very good agreement with experiment is observed. DQMOM shows a much better performance than Lagrangian - Eulerian formulations with respect to computational cost with similar agreement between simulations and experiment, which makes the DQMOM method highly attractive for future applications.

---

### Introduction

Spray drying processes aim to produce particles with prescribed properties including the particle structure, geometric properties, bulk density and chemical structure. First, a spray is generated, which in the course of the process, evaporates and dries. The droplet size distribution and interaction of the liquid phase and the gas flow are key features in the modeling of evaporating spray flows, which are important because of their vast range of industrial and engineering applications. Two-phase effects and poly-dispersion of droplet size distributions dominate the structure of any spray and related applications such as spray flames, end products or spray drying processes, or medical applications. An improved understanding of the physical processes that influence the spray characteristics is essential due to the complexity of the corresponding mathematical problem. The spray dynamics depend on various physical processes such as droplet inertia, evaporation, and gas phase characteristics. Thus, it is important to have reliable models and numerical techniques in order to be able to describe the physics of two-phase flows where the dispersed phase is constituted of droplets of various sizes that may evaporate, coalesce, breakup as well as have their own inertia and size-conditioned dynamics.

There are several Euler - Euler methods that have been developed based upon Williams' spray equation [1] and applied extensively in recent years. For instance, in multi-fluid methods [2], the distribution function is discretized using a finite volume technique that yields conservation equations for mass and momentum of droplets in fixed size intervals called sections or fluids [3]. This approach has recently been extended to higher order of accuracy [4], but discretization of droplet size phase space is still a problem that must be addressed. The efficiency and the applicability of moment based methods [5,6] for multivariate poly-disperse systems have remained a question of interest [7]. In order to address these issues, direct quadrature method of moments (DQMOM) has turned out to be an attractive and suitable alternative [8].

The present work focuses on description of water and Polyvinylpyrrolidone (PVP)/water spray flow by means of DQMOM [8,9], where droplet motion evolves due to interactive drag with ambient gas and gravity. Moreover, droplet collisions are considered. Evaporation of water from bi-component PVP/water droplets is computed by applying a two-film convective droplet evaporation model of Abramzon & Sirignano [10], with extensions to include the effects of non-ideality induced by the polymer presence and added resistance to evaporation rate and droplet heating from solid layer formation at the droplet surface [11]. The initial data for computations are generated using the experimental data, which are provided by the group of Prof. G. Brenn at TU Graz, Austria. The numerical results are compared with experimental data at various cross sections downstream the nozzle exit.

The experimental configuration is explained in the next section followed by the mathematical formulation of DQMOM. Finally, the results are presented and discussed.



## Experiment

The group of Prof. G. Brenn, TU Graz, carried out experimental study with different flow rates of water and PVP/water and various atomizers with different dimensions of swirl chambers and exit diameters are used. The droplet sizes and velocities are recorded at various cross sections for different liquid inflow rates using phase Doppler anemometry (PDA) providing both droplet size and velocity distributions. Figure 1 shows the schematic of the experimental setup.

The present simulations concern the experimental data of water and PVP/water (20% PVP +80% water by mass) sprays generated using the Delavan SDX-SD-90 and SDX-SB-50 hollow-cone nozzles respectively, with liquid inflow rates of 80 kg/h for water and 112 kg/h for PVP/water spray. The liquid is injected into a rectangular spray box, which is designed in such a way that the recirculation of gas, droplets and backpressure are prevented with a blower fitted at the end of the spray box. The spray contains still air at room temperature and atmospheric pressure. Measurements of droplet size and velocity in both radial and axial directions are recorded at cross sections of 0.08 m, 0.12 m, and 0.16 m. The data at 0.08 m are taken as starting values for initial data generation for computations, and results are compared at higher cross sections.

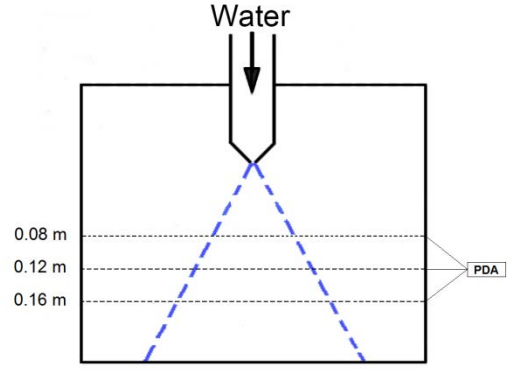


Figure 1: Schematic of experimental setup

## Mathematical modeling

In the present work, DQMOM is extended to model the spray flow in an axisymmetric two-dimensional geometrical configuration, as shown in Fig. 1. The present DQMOM formulation accounts for droplet number density, droplet size and velocity, where evaporation and droplet motion are taken into account. Droplet coalescence is also implemented in the present DQMOM formulation. The gas phase transport equations are not yet coupled to DQMOM rather the inlet gas flow properties are used.

The DQMOM transport equations are derived from Williams' spray equation [1] given by

$$\frac{\partial f}{\partial t} + \frac{\partial(\mathbf{u}f)}{\partial \mathbf{x}} = -\frac{\partial(Rf)}{\partial r} - \frac{\partial(\mathbf{F}f)}{\partial \mathbf{u}} + Q_f + \Gamma_f \quad (1)$$

The equation describes the transport of the number density function  $f(r, \mathbf{u}; \mathbf{x}, t)$  in terms of time,  $t$ , and Euclidean space,  $\mathbf{x}$ . In Eq. (1),  $\mathbf{u}$  and  $\mathbf{F}$  denote droplet velocity and drag force per unit mass, and  $R$  is the change of the droplet radius with time,  $R = dr/dt$ , where  $r$  is the droplet radius. The last two terms in Eq. (1) refer to the droplet interactions.  $Q_f$  denotes the increase in  $f$  with time due to droplet formation or destruction by processes such as nucleation or breakup, whereas  $\Gamma_f$  denotes the rate of change of  $f$  caused by collisions with other droplets.

In this study, a joint radius-velocity number density function is considered, which is approximated by DQMOM as sum of the product of weighted Dirac-delta functions [12] of radii and velocities [8]

$$f(r, \mathbf{u}; \mathbf{x}, t) = \sum_{n=1}^N w_n \delta(r - r_n) \delta(\mathbf{u} - \mathbf{u}_n), \quad (2)$$

where  $w_n$  and  $r_n$  are chosen as  $N$  representative quantities of weights and radii, and  $\mathbf{u}_n$  are the corresponding velocities. The DQMOM formulation results in closed transport equations for droplet weights, i.e. number density, radii and velocities, respectively, which are written in Cartesian coordinates as,

$$\frac{\partial w_n}{\partial t} + \frac{\partial(w_n \mathbf{u}_n)}{\partial \mathbf{x}} = a_n, \quad (3)$$

$$\frac{\partial(w_n \rho_l r_n)}{\partial t} + \frac{\partial(w_n \rho_l r_n \mathbf{u}_n)}{\partial \mathbf{x}} = \rho_l b_n, \quad (4)$$

and

$$\frac{\partial(w_n \rho_l r_n \mathbf{u}_n)}{\partial t} + \frac{\partial(w_n \rho_l r_n \mathbf{u}_n \mathbf{u}_n)}{\partial \mathbf{x}} = \rho_l \mathbf{c}_n, \quad (5)$$

where  $a_n$ ,  $b_n$  and  $\mathbf{c}_n$  are the source terms that account for evaporation, drag force, gravity and coalescence.

Equations (3) - (5) are closed by description of the source terms i.e.,  $a_n$ ,  $b_n$  and  $\mathbf{c}_n$ , using the physical models to



account for effect of droplet evaporation, drag force and coalescence. These source terms are calculated through moment transformation of phase-space terms, which yields the following linear system

$$P_{k,l} = \int \int r^k \mathbf{u}^l \left[ -\frac{\partial(Rf)}{\partial r} - \frac{\partial(\mathbf{F}f)}{\partial \mathbf{u}} + \Gamma_f \right] dr d\mathbf{u} \quad (6)$$

Convective droplet evaporation [10] is accounted for by considering the rate of change of droplet mass and it is computed as [11]

$$\dot{m} = \frac{\sum_{i=1}^N 2\pi R_i \rho_f D_f \widetilde{\text{Sh}} \ln(1+B_{M,i})}{1+\widetilde{\text{Sh}} D_f \delta / [2D_s(R-\delta)]}, \quad (7)$$

which includes the effects of changing droplet size through volume equivalent partial radius, variable film properties, and added resistance from solid layer formation. The solid layer formation may not occur with room temperature evaporation conditions but in higher temperature ambience as in spray drying. The drying temperature plays a major role in final particle characteristics. Here, subscript  $f$  refers to properties in the film,  $\widetilde{\text{Sh}}$  is the modified Sherwood number,  $\delta$  is solid layer thickness,  $D_s$  is the vapor diffusivity through solid layer and  $B_{M,i}$  is the Spalding mass transfer number of evaporating component  $i$ , which is calculated as

$$B_{M,i} = \frac{Y_{i,s} - Y_{i,\infty}}{1 - Y_{i,s}}, \quad (8)$$

where  $Y_{i,s}$  and  $Y_{i,\infty}$  are mass fractions of the component  $i$  in the film at droplet surface and in the bulk of surrounding gas, respectively.  $Y_{i,s}$  is computed from the vapor-liquid equilibrium through the vapor pressure of water ( $i = 1$ ) where the non-ideal behavior of two-component (PVP and water) liquid solution is considered through the calculation of activity coefficient of water. More details of development and application of the evaporation and drying model can found in [11]. The evaporative flux in DQMOM is computed using the ratio constraints of weights, radii and velocities as introduced by Fox *et al.*, [12].

Although the initial temperatures of gas and the droplet are equal and are at room temperature, the droplet temperature is subject to change due to evaporation, and its time evolution is computed using the uniform temperature model [10], with modifications in order to account for solid layer formation, similar to evaporation rate Eq. (7), and it can be written as

$$m C_{pL} \frac{dT_s}{dt} = \frac{Q_L + \dot{m} L_V(T_s)}{1 + \widetilde{\text{Nu}} k_{gf} \delta / [2k_s(R-\delta)]} - \dot{m} L_V(T_s) \quad (9)$$

where  $C_{pL}$  is the specific heat capacity of the liquid,  $T_s$  is the temperature at droplet surface,  $T_g$  is temperature of the surrounding gas and  $L_V(T_s)$  is the temperature dependent latent heat of vaporization at  $T_s$ .  $k_{gf}$  is the thermal conductivity of gas in film,  $k_s$  is the solid layer thermal conductivity and  $\widetilde{\text{Nu}}$  is the modified Nusselt number.  $Q_L$  is the net heat transferred to droplet given by

$$Q_L = \dot{m} \left[ \frac{C_{pLf}(T_\infty - T_s)}{B_T} - L_V(T_s) \right] \quad (10)$$

where  $B_T$  is the Spalding heat transfer number and it is given in terms of Spalding mass transfer [10] as

$$B_T = (1 + B_M)^\phi - 1, \quad (11)$$

and the exponent is given by [10]

$$\phi = \frac{C_{pL}}{C_{pg}} \frac{\widetilde{\text{Sh}}}{\widetilde{\text{Nu}}} \frac{1}{\text{Le}}. \quad (12)$$

Assuming the droplet velocity to evolve by interactive drag exerted by the surrounding gas and gravity, the following relation [13] is used to express the equation of droplet motion

$$\mathbf{F} = \frac{3}{8} \frac{\rho_g}{\rho_l} \frac{1}{r} (\mathbf{u}_g - \mathbf{u}) |\mathbf{u}_g - \mathbf{u}| C_D + \mathbf{g}, \quad (13)$$

where  $\rho_g$  and  $\mathbf{u}_g$  are the density and velocity of the surrounding gas, while  $\mathbf{u}$ ,  $C_D$  and  $\mathbf{g}$  are droplet velocity, drag coefficient, and gravitational acceleration, respectively. The drag coefficient,  $C_D$  is calculated as a function of the droplet Reynolds number,  $\text{Re}_d = 2r\rho_g|\mathbf{u}_g - \mathbf{u}|/\mu_f$ , where  $\mu_f$  is the mean dynamic viscosity in the film, as [14]

$$C_{D,SN} = \begin{cases} C_{D,st}(1 + 0.15\text{Re}_d^{0.687}) & \text{if } \text{Re}_d < 10^3 \\ 0.44 & \text{if } \text{Re}_d \geq 10^3 \end{cases} \quad (14)$$

with  $C_{D,st} = 24/Re_d$ .

Droplet collisions are taken into account through the Eulerian coalescence operator as given in [3,8,15]. In the present work, the process of coalescence [3] is considered while the breakup is currently neglected. In the coalescence modeling, it is assumed that only binary collisions occur, each collision leads to coalescence ( $E_c = 1$ ) or rebound ( $E_c = 0$ ). Mass and momentum before and after the collision are conserved. In addition, the mean collision time is assumed to be smaller than the inter-collision time. Thus, the coalescence function can be written as

$$\Gamma_f = Q_c^+ + Q_c^-, \quad (15)$$

where  $Q_c^-$  and  $Q_c^+$  are computed as

$$Q_c^- = - \int_{-\infty}^{\infty} \int_0^{\infty} f(t, \mathbf{x}; r, \mathbf{u}) f(t, \mathbf{x}; r_1, \mathbf{u}_1) B(|\mathbf{u} - \mathbf{u}_1|, r, r_1) dr_1 d\mathbf{u}_1 \quad (16)$$

and

$$Q_c^+ = \frac{1}{2} \int_{-\infty}^{\infty} \int_0^r f(t, \mathbf{x}; r_1, \mathbf{u}_1) f(t, \mathbf{x}; r_2, \mathbf{u}_2) B(|\mathbf{u}_2 - \mathbf{u}_1|, r_1, r_2) dr_1 d\mathbf{u}_1, \quad (17)$$

where

$$B(|\mathbf{u}_2 - \mathbf{u}_1|, r_1, r_2) = \pi(r_1 + r_2)^2 |\mathbf{u}_2 - \mathbf{u}_1| E_c. \quad (18)$$

In the above equations,  $(r_1, \mathbf{u}_1)$  and  $(r_2, \mathbf{u}_2)$  refer to pre-collision properties of colliding droplets, and the post-collision properties  $(r, \mathbf{u})$  are estimated from pre-collision properties through the relations

$$\mathbf{u} = \frac{r_1^3 \mathbf{u}_1 + r_2^3 \mathbf{u}_2}{r_1^3 + r_2^3}, \quad (19)$$

and

$$r^3 = r_1^3 + r_2^3. \quad (20)$$

Thus, a closed system of equations is described. Eqs. (3) - (5) are solved simultaneously using an explicit finite difference method with appropriate initial and boundary conditions to find  $w_n(\mathbf{x}, t)$ ,  $r_n(\mathbf{x}, t)$  and  $\mathbf{u}_n(\mathbf{x}, t)$ , which assume that the droplet radii, velocities and their corresponding number densities at the inlet plane are set to their initial values generated from experimental data, whereas a free boundary is assumed for the wall and exit plane. At the axis of symmetry, droplets are reflected.

The exact form of the DQMOM linear system relies on the choice of moments. To obtain a solution, the moments are chosen such that the resulting coefficient matrix is regular. In the present work,  $N$  is set to 3 and the corresponding moment set is chosen as  $k \in \{1, 2, \dots, 2N\}$  and  $l \in \{0, 1\}$  [12].

An equidistant rectangular grid is adopted, where the size of each grid cell is  $1.5 \times 10^{-3}$  m in radial direction and  $10^{-4}$  m in axial direction, resulting in a maximum grid of about 100 times 1000 grid nodes. Initial data generation is explained in the next section.

### Initial data generation for the computations

The experimental data at the closest position to the nozzle is used to generate initial data for the numerical computations. The nearest experimental position is 80 mm from nozzle, where the measurements are available at radial positions separated by  $1.5 \times 10^{-3}$  m distance. The PDA data at every radial position consists of droplet radii, velocities in axial and radial directions and the time elapsed for each measurement, which gives the total time carried out over a period. These data is grouped into 100 equal droplet size classes. The effective cross-sectional area of the probe volume is computed. The result of the calculation for a water flow rate of 80 kg/h, at a position of 66 mm from the center is shown in Fig. 2. The trajectory length exhibits strong fluctuations, which increase with the droplet size. Furthermore, the number of droplets in the size classes for the larger diameters is typically much lower than in the smaller size classes.

Therefore, the properties such as droplet trajectory lengths through the probe volume are statistically unreliable for droplets with sizes greater than a certain threshold value [16]. In particular, the decrease of the effective

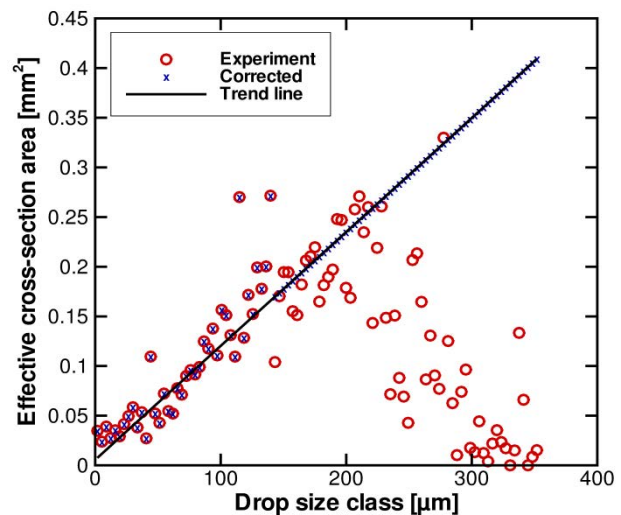


**Figure 2:** Profile of effective cross-section area of the probe volume for measured droplet size

probe volume size with increasing drop size from about 200  $\mu\text{m}$  as shown in Fig. 2 is unphysical. The effective cross-section area is therefore calculated using a linear trend line from a threshold diameter. In the first step, the linear trend line is calculated using a linear regression scheme based on the data in the drop size classes up to 60% of the maximum droplet size. In the second step, for all drop size classes from 40% of the maximum drop size class for this experimental position on, the values of the effective cross section area are obtained as values of the linear trend line. There is, therefore, an overlap of the size class ranges used for computing the trend line and those whose probe volume cross-section areas are calculated using the trend line.

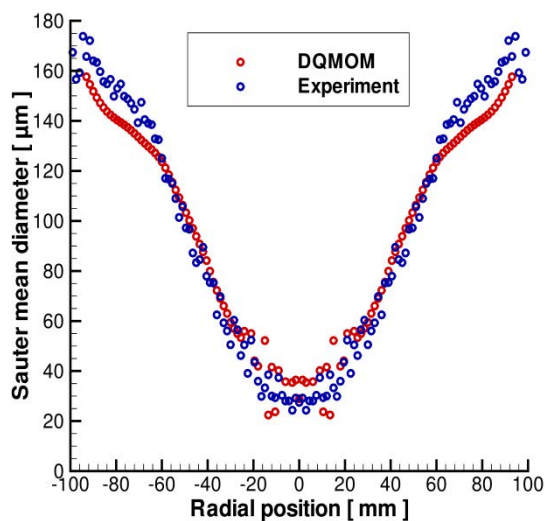
Once the effective cross-sectional area probe volume is corrected, the number density is corrected correspondingly. Then, the moment sets of droplet size and velocities are computed, which are used to calculate the initial weights (number densities), radii and velocities using a product - difference algorithm [17]. In the present study, DQMOM approximates the spray distribution by a 3-node closure, which implies that the required number of moments is 12 (3 each: weights, droplet radii, axial and radial velocities). The same procedure is followed at every radial position for the cross-section of 80 mm.

## Results and discussion

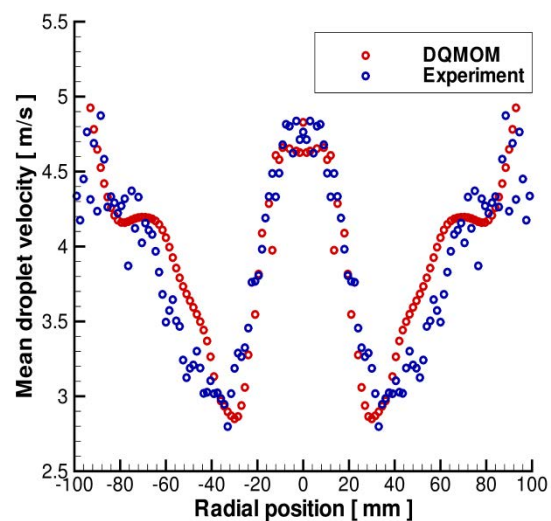
Droplet properties including size and velocity are computed using DQMOM and the results are compared with the experimental data at the cross sections of 0.12 m and 0.16 m away from the nozzle exit. Initially, simulations are carried out with water spray experimental data in order to check the applicability and predictability of DQMOM to spray flows and later it is applied to PVP/water spray flows (20% PVP + 80% water by mass).

Figure 3 shows the computed and experimental profiles of the Sauter mean diameter of water spray at cross sections 0.12 m away from nozzle exit for water inflow rate of 80 kg/h. The results show a typical hollow-cone spray distribution, i.e., the larger size droplets are moving at the periphery of the spray whereas the smaller ones are closer to the axis of symmetry. Comparison of experiment with simulation reveals that DQMOM captures the overall shape of the spray distribution very well, and the numerical results are in good agreement with experiment. A closer look shows that DQMOM results have some scattering near the centerline, and towards the periphery of the spray, they under-predict the experimental results. This discrepancy may result from the numerical scheme, for which an explicit finite difference method is employed to solve Eqs. (3) - (5). The present results may be improved by implementing an implicit method.

The radial profiles of mean droplet velocity of water spray at 0.12 m away from nozzle exit for water flow rate of 80 kg/h are displayed in Fig. 4. It can be seen that the droplet velocity is higher for larger size droplets, which move away from centerline of the spray as anticipated. Interestingly, the small size droplets near to the centerline of the spray also move at a higher velocity as observed in the experiment and thus making the velocity profile bimodal, which is predicted quite nicely by DQMOM. The width of the jet, the local minimum and maximum are captured by the DQMOM and at the spray edge, the experiment shows some scattering behavior whereas DQMOM results show an increasing trend. Further downstream (not shown here), the droplet velocity decreases significantly in larger size droplets due to strong deceleration by the dynamic interaction with the surrounding gas. The air around the spray stagnates and driven into motion at the expense of droplet momentum loss.



**Figure 3:** Profiles of Sauter mean diameter of water spray at 0.12 m away from the nozzle



**Figure 4:** Profiles of mean droplet velocity of water spray at 0.12 m away from the nozzle

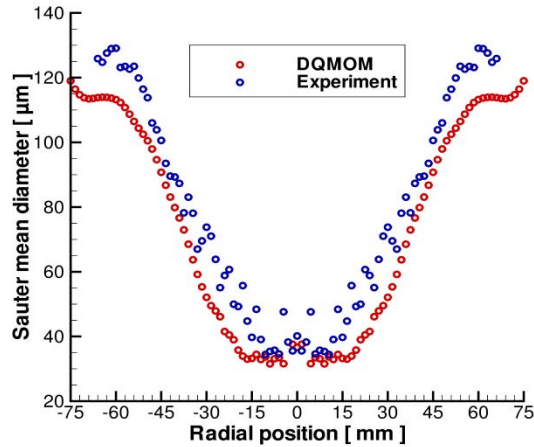


**Figure 5:** Profiles of Sauter mean diameter of PVP/water spray at 0.12 m away from the nozzle

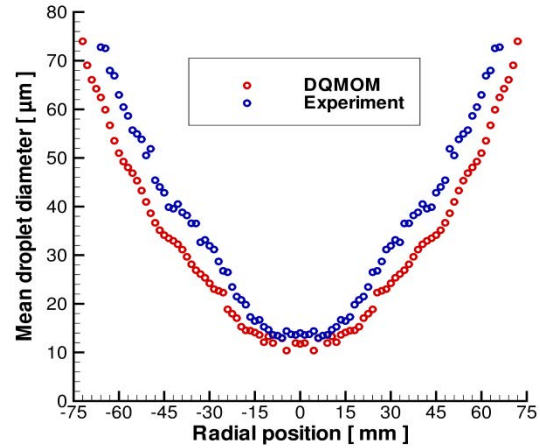


**Figure 6:** Profiles of mean droplet diameter of PVP/water spray at 0.12 m away from the nozzle

In Figs. 5 and 6, the numerical and experimental profiles of Sauter mean diameter and mean droplet diameter of PVP/water spray with liquid inflow rate of 112 kg/h at 0.12 m away from nozzle are shown. An increased liquid flow rate causes a decreased droplet size as anticipated (compare Figs. 3 and 5) and similar to the water spray, in overall, the spray distribution assumes a hollow-cone shape and is nicely predicted by DQMOM. In both figures, a closer look reveals that across all the radial positions the DQMOM under predicts the experimental results and towards the periphery of the spray some deviation is observed particularly in profiles of Sauter mean diameter as compared to experiment. This can possibly be explained by the fact that the DQMOM predicts the global droplet distribution, but there could be local discrepancies induced by the gas phase, which is not resolved in the present study. Coupling of DQMOM with the gas phase and implementing higher order explicit method or implicit numerical scheme to solve DQMOM transport equations would eventually improve the simulation results.

The mean droplet velocity of PVP/water spray with 112 kg/h liquid inflow rate at 0.12 m away from nozzle is shown in Fig. 7. Increased liquid flow rate leads to higher droplet velocity (compare Figs. 4 and 7). The smaller size droplets that lie closer to centerline of the spray are moving at higher velocity than the larger size droplets, which is in quite contrast with that of water spray (see Fig. 4) where both the larger and smaller size droplets move with higher velocity. This may be because initially the gas around the spray is stagnant and the droplets decelerate by aerodynamic drag. The surrounding gas acquires the momentum lost by the droplets, and this creates flow field in which gas is continually entrained into the spray. As the entrained gas enters the spray, it drags small liquid drops at the outer regions of the spray inward and the momentum lost by the droplets at periphery of the spray is larger than the ones the lie closer to axis of symmetry, which explains the smaller velocity of larger droplets [18,19].

Similar behavior is observed in water spray at further downstream as this effect is dependent on initial liquid flow rate, where low liquid flow rate leads to larger droplets which take more time to follow the streamlines of gas than the smaller size droplets. The simulation results are in good agreement with the experiment, particularly in smaller size droplets region whereas towards spray edge there is deviation, which can be attributed to the post-processing of the experimental data as illustrated in the section of initial data generation. Another reason for the discrepancies in the DQMOM results is the non-resolved gas phase.

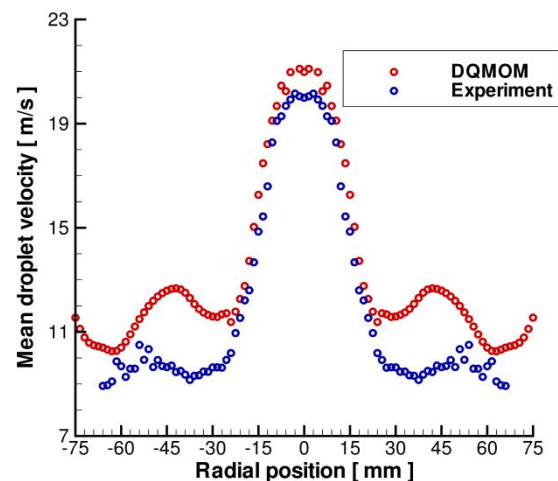


**Figure 7:** Profiles of mean droplet velocity of PVP/water spray 0.12 m away from nozzle

## Conclusions

DQMOM is developed to model water and PVP/water sprays in air, and the results are compared with experimental data. The mathematical formulation of DQMOM is derived accounting for droplet size and velocity, where convective evaporation and heating of bi-component droplet as well as motion are modeled. Moreover, droplet coalescence is included. The droplet size and velocity distributions are analyzed and compared with experimental data.

Numerical and experimental results are compared at different cross sections, where the experimental data of the cross section closest to the nozzle exit are used for the generation of initial conditions for the simulations. The numerical results are found to be in good agreement with experiment. Some deviations between DQMOM and experiment are observed that might result from the present DQMOM formulation, which is not yet fully coupled with the gas phase equations. Moreover, the numerical technique employed uses an explicit finite difference method to solve the DQMOM transport equations – an implicit scheme may lead to considerable improvement. Concerning the experimental data, a post-processing of the raw data has been performed in order to correct the number frequency of large droplets with respect to the effective cross section area, leading to different correction factors for different droplet positions in experimental data away from the centerline, which may also lead to discrepancy between numerical and experimental results.

## Acknowledgements

The authors thank Prof. G. Brenn and E. Wimmer from TU Graz, Austria for providing the experimental data and for many discussions on experimental data processing. They gratefully acknowledge the financial support from Deutsche Forschungsgemeinschaft (DFG) under the program SPP 1423 and through Heidelberg Graduate School for Mathematics and Computational Sciences at IWR.

## References

- [1] F. A. Williams, *Physics of Fluids* 1, 541 (1958).
- [2] F. Laurent, M. Massot, *Combustion Theory and Modeling* 5(4), 537 (2001).
- [3] F. Laurent *et al.*, *Journal of Computational Physics*, 194(2), 505 (2004).
- [4] G. Dufour, P. Villidieu, *Mathematical Modeling and Numerical Analysis (M2NA)*, 39(5), 931 (2005).
- [5] D. L. Marchisio *et al.*, *AIChE Journal* 49, 1266 (2003).
- [6] R. McGraw, *Aerosol Science and Technology* 27(2), 255 (1997).
- [7] D. L. Marchisio *et al.*, *Journal of Colloid Interface Science* 258(2), 322 (2003a).
- [8] D. L. Marchisio, R. O. Fox, *Journal of Aerosol Science* 36, 43 (2005).
- [9] S. R. Gopireddy *et al.*, *Chemie Ingenieur Technik* 84(3), 349 (2012).
- [10] B. Abramzon, W. A. Sirignano, *International Journal of Heat and Mass Transfer* 32(9), 1605 (1989).
- [11] S. R. Gopireddy, E. Gutheil, in *Proceedings of ICLASS*, September 2-6, 2012, Heidelberg, Germany.
- [12] R. O. Fox *et al.*, *Journal of Computational Physics*, 227(6), 3058 (2008).
- [13] G. K. Batchelor, *An Introduction to Fluid Dynamics*, Cambridge University Press London (1967).
- [14] L. Schiller, A. Z. Neumann, *VDI Zeitschrift* 77, 318 (1933).
- [15] J. Hylkema, P. Villidieu, *C.R.A.S. de Paris*, t.325 série, I, 323 (1997).
- [16] H. E. Albrecht *et al.*, *Laser Doppler and phase Doppler measurement techniques*, Springer-Verlag, Berlin (2003).
- [17] R. G. Gordon, *J. Math. Phys.*, 9, 655 (1968).
- [18] S. Ghosh, J. C. R. Hunt, *Proceedings of Royal Society London, A* 444, 105 (1994).
- [19] A. C. S. B. Silva *et al.*, *Building Services Engineering Research and Technology* 25(4), 351 (2004).

## Direct Quadrature based Sectional Method of Moments for the Simulation of Evaporating Polydisperse Sprays

Werner Gumprich and Amsini Sadiki

Department of Energy and Power Plant Technology,  
Technische Universität Darmstadt, Germany

### Abstract

The objective of this work is the validation of the Direct Quadrature based Sectional Method of Moments (DQbSMOM), a new hybrid approach for the numerical modeling of polydisperse sprays in an Eulerian framework, recently proposed by the authors [1]. The DQbSMOM combines the Direct Quadrature Method of Moments (DQMOM) with a Sectional Method (SM) in order to allow an increase in the total amount of DQMOM quadrature points without jeopardizing the well conditioning of the solver matrices. An increase in the total amount of quadrature points, as well as an optimal discretization of the droplet size domain into sections, results in a considerably higher accuracy regarding convective transport and drag. In comparison to the standard DQMOM, a higher accuracy is also achieved regarding the prediction of the evaporative flux, which is calculated with the Eulerian Multi-Size Moment model (EMSM), proposed by Massot et al. [2]. The EMSM model not only accurately describes the evaporating droplet polydispersity but also allows DQMOM to be coupled with a SM, since the moment flux between two sections can be calculated. Moreover, a realistic evaporation model, namely the Abramzon-Sirignano [3] model, has been coupled to the DQbSMOM.

---

### Introduction

The increasing fuel prices and stronger emissions regulations have made combustion one of the most economically important applications of sprays. In combustion processes involving a liquid fuel, the mixing of oxidizer and fuel vapor is strongly influenced by the polydisperse character of the injected fuel, which considerably affects the structure of the flame and, consequently, the combustion efficiency and emissions in gas turbines and IC-engines. Therefore, there is a significant demand for reliable numerical tools to accurately describe and optimize the dense spray behavior in modern engines.

On a mesoscopic level, numerical tools for the spray simulation are based on a kinetic description given in terms of a probability density function. The evolution of this probability density function, also referred to as number density function (NDF), is described by the Williams spray equation [4]. There are two general approaches to solve the Williams equation: the stochastic Lagrangian and the Eulerian moment methods. The stochastic Lagrangian methods approximate the solution of the Williams equation by individually tracking numerical particles (parcels) with a Lagrangian approach. They are considered the most robust, reliable and accurate methods for the spray simulation, allowing a straightforward description of the occurring physical phenomena. Also, each parcel often represents several real droplets of same properties in the spray system, maintaining the computational cost practicable. However, some major drawbacks are associated to the stochastic Lagrangian methods. First, even though a parcel approach is considered, the computational cost is high and strongly dependent on the unsteadiness of the flow and mass loading of the system. In order to avoid a high level of statistical noise and achieve an accurate and smooth continuous field of droplet averaged properties, a sufficient amount of sampled parcels is required within each relevant grid cell during each numerical time-step. This necessary amount of parcels increases significantly for unsteady simulations with fine time and spatial discretization. Especially in the case of Large Eddy Simulation (LES), the necessary amount of sampled parcels is considerably higher in comparison to RANS models. Indeed, LES requires a strong coupling between continuous and disperse phases, significantly increasing the implementation complexity of the Lagrangian method [5]. Nevertheless, a RANS-approach is followed in this paper. Finally, since most parcels are located in a small region of the computational domain, an optimal parallelization of the solver is hardly possible.

Due to the drawbacks associated to the Lagrangian approach, a great interest for alternative methods has emerged. Recently, the Eulerian moment methods have gained special attention. Their general strategy is to calculate the evolution of the moments of the NDF with a set of Navier-Stokes-like transport equations. These transport equations are directly derived from the Williams equation. Their structure and, consequently, their computational cost, do not depend on the droplet mass loading or the unsteadiness of the system. Since the equations of both disperse and continuous phase share the same structure, the coupling between both phases is straightforward and solver parallelization can be optimized. Therefore, the Eulerian moment methods are promising alternatives to the Lagrangian approach.

Numerous Eulerian approaches and their variations have been proposed, each of them with their advantages and drawbacks. Among prominent methods are the Quadrature Method of Moments (QMOM) [6], the Direct



Quadrature Method of Moments (DQMOM) [7,8] and the Sectional Methods (SM) [9,10,11].

The DQMOM is a robust approach for describing the transport in phase space. However, a major challenge involves the accurate description of convective transport and drag effects. The general DQMOM approach is to approximate the NDF by a few quadrature points and assume that all droplets of a certain size locally share the same velocity (mono-kinetic assumption). Hence, regarding convective transport and drag, these quadrature points are handled as ordinary disperse phases of a multi-fluid method. Indeed, the range of droplet sizes and velocities is wide in most spray systems. Thus, a significant error associated to convective transport and drag is observed if only a few droplet size classes are considered. This issue has been recently tackled by Vié et al. [12], who proposed a new model called Coupled Size-Velocity Moments (CSVM) model, which addresses droplet size-velocity correlations in drag and convective transport processes within a moment method framework. Within a DQMOM framework, the most immediate strategy to reduce the error related to convective transport and drag is to increase the amount of quadrature points. However, the amount of quadrature points cannot be arbitrarily increased without jeopardizing the well conditioning of the DQMOM solver. Another challenge associated to DQMOM is the accurate prediction of the evaporative flux, since the NDF is not known.

Recently, the authors have introduced a novel hybrid method, referred to as the Direct Quadrature based Sectional Method of Moments (DQbSMOM) [13,14], which combines the DQMOM with a SM. The general strategy is to split the droplet size domain into sub-intervals, known as sections, and to approximate the NDF with weighted Dirac-delta functions over each section. This results in a set of multi-fluid transport equations, plus scalar transport equations for droplet diameter and temperature. Spray evaporation is calculated with the Eulerian Multi-Size Moment (EMSM) method, proposed by Massot et al. [2], while the evaporation of a single droplet is described with the Abramzon-Sirignano model [3].

In this work, the proposed method is validated for dilute evaporating spray systems. The configuration investigated concerns a non-reacting acetone spray jet. The experimental measurements have been conducted by Gounder [16].

### Numerical model

The proposed method relies on the Williams spray equation [4], a kinetic Boltzmann type equation that describes the evolution of  $f(\phi, \mathbf{u}, T; \mathbf{x}, t)$ , a joint NDF of droplet size, velocity and temperature. The droplet size can be described by different quantities, such as volume ( $v$ ), surface ( $s$ ) or diameter ( $d$ ). For the derivation of the Eulerian transport equations,  $\phi = v$  is considered. The Williams equation is then expressed by:

$$\partial_t f + \partial_{x_i} (u_i f) + \partial_v (R_v f) + \partial_T (\Theta f) + \partial_{u_i} (F_i f) = \Gamma, \quad (1)$$

where  $R_v$  denotes the evaporation rate,  $\Theta$  describes heat transfer,  $F_i$  are the forces acting on the droplet, such as drag and gravitation, and  $\Gamma$  accounts for additional phenomena (i.e. droplet coalescence); in this work,  $\Gamma = 0$ .

### Operator Splitting

The physical phenomena described in the Williams equation are handled separately by considering an operator splitting approach. Thus, physical space transport is de-coupled from the phenomena governing phase space transport, such as droplet evaporation and heat transfer, and the Williams equation (1) is split into the following system:

$$\partial_t f + \partial_{x_i} (u_i f) = -\partial_{u_i} (F_i f) \quad (2)$$

$$\partial_t f = -\partial_v (R_v f) \quad (3)$$

$$\partial_t f = -\partial_T (\Theta f) \quad (4)$$

The solution of the full problem is then approximated by alternatively solving equations (2) to (4). Please refer to Kah [11] for additional details.

It is important to remark that, even though the equation (2) is referred to as *physical space transport*, its right-hand side (RHS) contains a term that describes the drift velocities in the velocity phase space. This splitting strategy results in a straightforward coupling between the DQbSMOM and a multi-fluid method.

### Direct Quadrature based Sectional Method of Moments

In an Eulerian framework, the Williams equation (1) is solved using the DQbSMOM, which combines the DQMOM [8] with a SM [11]. Thus, the droplet size space is discretized into  $N_s$  fixed intervals  $I_k = [v_{k-1}, v_k)$  ( $k = 1, \dots, N_s-1$ ),  $v_0 = 0$ ,  $I_{N_s} = [v_{N_s-1}, \infty)$ , also known as sections, and the NDF is approximated by weighted Dirac-delta functions over each section  $k$ :

$$f_k(v, \mathbf{u}, T) \approx \sum_{n=1}^N w_{k,n} \delta(v - v_{k,n}) \delta(\mathbf{u} - \mathbf{u}_{k,n}) \delta(T - T_{k,n}), \quad (5)$$

where  $v_{k,n}$ ,  $\mathbf{u}_{k,n}$  and  $T_{k,n}$  are the volume, velocity and temperature abscissas, respectively,  $N$  is the number of quadrature points per section  $k$ ,  $w_{k,n}$  are the weights, defined as number of droplets per volume unit, and  $\delta(\mathbf{u} - \mathbf{u}_{k,n})$

$= \delta(u_1 - u_{1,k,n}) \delta(u_2 - u_{2,k,n}) \delta(u_3 - u_{3,k,n})$ . The weighted quadrature points are optimally determined from a set of moments using the Product-Difference (PD) algorithm [17].

The general approach is to derive transport equations for the number density, mass density, momentum density and droplet temperature, respectively:

$$\partial_t (w_{k,n}) + \partial_{x_i} (w_{k,n} u_{i,k,n}) = a_{k,n} \quad (6)$$

$$\partial_t (\rho w_{k,n} v_{k,n}) + \partial_{x_i} (\rho w_{k,n} v_{k,n} u_{i,k,n}) = \rho b_{k,n} \quad (7)$$

$$\partial_t (\rho w_{k,n} v_{k,n} u_{j,k,n}) + \partial_{x_i} (\rho w_{k,n} v_{k,n} u_{j,k,n} u_{i,k,n}) = \rho c_{j,k,n} \quad (8)$$

$$\partial_t (\rho w_{k,n} v_{k,n} T_{k,n}) + \partial_{x_i} (\rho w_{k,n} v_{k,n} T_{k,n} u_{i,k,n}) = \rho d_{k,n} \quad (9)$$

where  $a_{k,n}$ ,  $b_{k,n}$ ,  $c_{j,k,n}$  and  $d_{k,n}$  are source terms related to the drift velocities in phase space. The strategy of the standard DQMOM for closing these source terms is to solve a linear system of equations, which is derived after inserting the approximation (5) into the Williams equation and applying moment transforms to both sides of equation (1):

$$\iiint v^q u_1^l u_2^m u_3^p T^\theta (\partial_t f + \partial_{x_i} (u_i f)) dv d\mathbf{u} dT = \iiint v^q u_1^l u_2^m u_3^p T^\theta (-\partial_v (R_v f) - \partial_T (\Theta f) - \partial_{u_i} (F_i f)) dv d\mathbf{u} dT \quad (10)$$

A choice of  $6N$  moments is then required to build the system; for details on the choice of moments, please refer to Fox et al. [8]. It is important to remark that, in order to be consistent with the mono-kinetic assumption, only moments of order 0 and 1 are considered for the velocity components. Hence, the source terms related to the drift velocities in the velocity phase space can be determined directly, without the need to numerically solve the DQMOM system. Since this same choice of moments is also considered for the temperature, the drift velocities in the temperature phase space can also be determined directly, such that the following holds:

$$\partial_t (T_{k,n}) = \Theta(v_{k,n}, \mathbf{u}_{k,n}, T_{k,n}) \quad (11)$$

Moreover, although the same general DQMOM approach is also considered for the evaporation term, the moment fluxes through the section boundaries are handled in a different way using the EMSM method. Therefore, a numerical solution of the DQMOM system is not necessary regarding the physical phenomena handled in this work.

### Coupling to a multi-fluid method

A linear system of equations, written in the same form as equations (6-9), is derived from equation (2). The source terms found on the RHS of this system are then related to the drift velocities in velocity phase space only (without the effects of evaporation and heat transfer). Note that the LHS of equations (7) and (8) have the same structure as the LHS of the continuity and momentum transport equations of a multi-fluid method, respectively:

$$\partial_t (\rho \alpha_{k,n}) + \partial_{x_i} (\rho \alpha_{k,n} u_{i,k,n}) = 0 \quad (12)$$

$$\partial_t (\rho \alpha_{k,n} u_{j,k,n}) + \partial_{x_i} (\rho \alpha_{k,n} u_{j,k,n} u_{i,k,n}) = RHS \quad (13)$$

where the volume fraction is defined as  $\alpha_{k,n} = w_{k,n} v_{k,n}$ . Thus, each abscissa  $n$  of each section  $k$  represents a disperse phase in the multi-fluid system, composed by  $N \cdot N_s$  disperse phases. It is then assumed that the RHS of equation (13) includes the same terms found in a standard multi-fluid method, such as drag, gravitation and turbulence diffusion (please refer to [18]). This results in a straightforward coupling between the DQbSMOM and a multi-fluid method. Different authors have achieved satisfactory results by following this assumption [19,20,21]. Regarding turbulence, the mathematical correctness of this coupling approach has been recently demonstrated by Belt & Simonin [22].

The turbulence of the continuous gas phase is described with the standard  $k$ - $\varepsilon$  model, while the turbulence of the disperse phase is related to the one of the gas phase, based on the model of Simonin & Viollet [15]. Thus,  $k$  and  $\varepsilon$  equations, extended to account for interphase interaction terms, are solved for the gas phase only. Moreover, the model of Simonin & Viollet follows a two-step averaging procedure, with a phase-weighted average for the turbulence [21], such that no additional terms are present in the averaged continuity equations.

In addition to the multi-fluid equations (12) and (13), scalar transport equations for the diameter and temperature abscissas, respectively, are solved:

$$\partial_t (\rho \alpha_{k,n} d_{k,n}) + \partial_{x_i} (\rho \alpha_{k,n} d_{k,n} u_{i,k,n}) = 0 \quad (14)$$

$$\partial_t (\rho \alpha_{k,n} T_{k,n}) + \partial_{x_i} (\rho \alpha_{k,n} T_{k,n} u_{i,k,n}) = 0 \quad (15)$$

Then, instead of solving transport equations for the DQMOM weights, transport equations for the diameter abscissas, derived from equations (6) and (7), are solved. This strategy is pursued in order to achieve a higher



stability of the solver; a smooth droplet size field is achieved even in regions where the droplet concentration is close to zero.

### Spray evaporation

The evolution of the DQMOM weights and abscissas (or moments), due to droplet evaporation, is calculated with the Eulerian Multi-Size Moment (EMSM) method, proposed by Massot et al. [2]. In order to illustrate the general idea of this method, let a constant evaporation rate  $R_\phi$  be considered. Then, if only evaporation is taken into account, the Williams equation is reduced to:

$$\partial_t f = -\partial_\phi (R_\phi f) \quad (16)$$

for a NDF  $f(t, \phi)$ , where  $\phi$  is the droplet size and  $R_\phi = d\phi/dt$ . Note that  $R_\phi < 0$ . Hence, an analytical solution of equation (16) is given by:

$$f(t, \phi) = \psi(t) \delta(\phi) + f^0(\phi - R_\phi t) \quad (17)$$

with a positive initial NDF  $f^0(\phi)$  on  $[0, \infty)$ . Note that the NDF is simply shifted over the  $\phi$ -axis, maintaining its shape for positive  $\phi$ , while the amount of droplets that have disappeared after a time  $t$  is described by:

$$\psi(t) = \int_0^{-R_\phi t} f^0(\phi) d\phi \quad (18)$$

It can also be shown that, if the evaporative flux  $\psi(\Delta t) = 0$ , applying DQMOM to equation (16) results in a translation of the size abscissas:

$$\phi_{k,n}(t + \Delta t) = R_\phi \Delta t + \phi_{k,n}(t) \quad (19)$$

after a time-step  $\Delta t$ , due to evaporation (see Fox et al. [8]). Thus, the strategy of the EMSM method is to combine the efficiency of DQMOM with an accurate approach to predict the evaporative/moment flux. The moment flux is then calculated by numerically integrating a reconstruction/approximation of the NDF. The Maximum Entropy (ME) method [23] is used to reconstruct the NDF from its moments.

### EMSM algorithm

In order to be consistent with the single-droplet evaporation model described below,  $\phi = s$  is considered for the EMSM method. Hence, the  $N_s$  fixed sections are described in terms of droplet surface by:  $I_k = [s_{k-1}, s_k]$  ( $k = 1, \dots, N_s-1$ ),  $s_0 = 0$ ,  $I_{N_s} = [s_{N_s-1}, \infty)$ , and the EMSM algorithm is given as follows:

For each grid cell, and each time-step  $\Delta t$ :

Loop over all sections  $k$ , from  $k = N_s$  to  $k = 1$ :

1. Calculate the vector of surface moments ( $\mathbf{M}_{s,k}$ ) from the weights  $w_{k,n}$  and abscissas  $d_{k,n}$
2. Calculate the evaporation rate ( $R_s$ ) at the lower boundary of section  $k$  and determine  $s_{\Delta t} = -R_s \Delta t + s_{k-1}$
3. Reconstruct the NDF from the moments  $\mathbf{M}_{s,k}$ , using the ME method, and numerically integrate the moment flux vector:

$$\Psi_{k-1}(\Delta t) = \int_{s_{k-1}}^{s_{\Delta t}} f_{\mathbf{M}_{s,k}}^{ME}(s) \begin{bmatrix} 1 \\ s \\ \vdots \\ s^{2N} \end{bmatrix} ds \quad (20)$$

4. Calculate the modified moment vector:

$$\mathbf{M}^* = \mathbf{M}_{s,k} - \Psi_{k-1} + \Psi_k, \text{ with } \Psi_{N_s} = 0$$

5. Using the PD algorithm, calculate the weights  $w_{k,n}$  and abscissas  $s_{k,n}$  related to  $\mathbf{M}^*$
6. Calculate the evaporation rate and the rate of heat transfer ( $\Theta = dT/dt$ ) for each abscissa  $s_{k,n}$  with  $T_{k,n}$
7. Shift the abscissas:  $s_{k,n}(t + \Delta t) = R_s \Delta t + s_{k,n}(t)$  and  $T_{k,n}(t + \Delta t) = \Theta \Delta t + T_{k,n}(t)$   
Note that, regarding the droplet temperature, this is compatible to equation (11).
8. Calculate  $d_{k,n}$  from  $s_{k,n}$

### Single-droplet evaporation

The evaporation of a single droplet is described with the Abramzon-Sirignano model [3], which is a variation of the classical d<sup>2</sup>-law that incorporates the effects of Stefan flow on heat and mass transfer. The model assumes a uniform droplet temperature and thermal equilibrium on the droplet surface. The evaporation rate and the droplet temperature variation are described by:

$$\frac{dm_d}{dt} = -\frac{Sh^*}{3Sc_G} \left( \frac{m_d}{\tau_d} \right) H_M \quad (21)$$

$$\frac{dT}{dt} = -\frac{\dot{m}_d}{m_d} \frac{1}{c_{p,L}} \left( c_{p,G} \frac{(T_G - T)}{B'_T} - h_{vap} \right) \quad (22)$$

where  $\dot{m}_d = dm_d/dt$ ,  $m_d$  is the droplet mass,  $T_G$  is the temperature of the carrier gas phase,  $c_{p,L}$  and  $c_{p,G}$  represent the constant pressure heat capacity of the liquid and gas phases, respectively,  $h_{vap}$  describes the latent heat of evaporation and  $Sc_G = \mu_G/(\rho_G D_G)$  is the gas phase Schmidt number, with  $D_G$  denoting the binary diffusion coefficient of the gas. In equation (21),  $\tau_d = \rho_L d^2/(18\mu_G)$  is the particle relaxation time for Stokes flow, where  $d$  describes the droplet diameter.  $H_M = \ln(1+B_{M,eq})$  is the specific mass transfer potential, and the Spalding transfer numbers for mass ( $B_{M,eq}$ ) and energy ( $B'_T$ ) are defined as:

$$B_{M,eq} = \frac{Y_{s,eq} - Y_\infty}{1 - Y_{s,eq}}, \quad B'_T = (T_G - T) \frac{c_{p,vap}}{h_{vap}} \quad (23)$$

where  $Y_\infty$  describes the vapor mass fraction away from the droplet surface and  $c_{p,vap}$  denotes the constant pressure heat capacity of the vapor. The vapor mass fraction at the droplet surface ( $Y_{s,eq}$ ) is calculated from the vapor mole fraction, which is related to the saturation pressure through the Clausius-Clapeyron equation.

The heat transfer is then modified by modifying the transfer number for energy:

$$B'_T = (1 + B_{M,eq})^\varphi - 1, \quad \varphi = \frac{c_{p,vap}}{\bar{c}_p} \frac{Sh^*}{Nu^*} \frac{1}{Le} \quad (24)$$

where  $Le = Sc/Pr$  describes the Lewis number, with the Prandtl number defined as:  $Pr = \mu c_p/\lambda$ . The overbar denotes properties that are evaluated using reference values for temperature and vapor mass fraction, which are calculated according to the “1/3 rule” (see Miller et al. [24]). The modified forms of the Sherwood and Nusselt numbers are given by:

$$Sh^* = 2 + \frac{Sh - 2}{F_M} \quad \text{and} \quad Nu^* = 2 + \frac{Nu - 2}{F_T}, \quad \text{with} \quad F_M = \frac{(1 + B_{M,eq})^{0.7}}{B_{M,eq}} \ln(1 + B_{M,eq}), \quad F_T = \frac{(1 + B'_T)^{0.7}}{B'_T} \ln(1 + B'_T) \quad (25)$$

These equations must be solved iteratively, while the Ranz and Marshall correlations [25,26] for the non-modified Sherwood and Nusselt numbers are considered [24]. For more details, please refer to [3,24].

Note that the droplet evaporation rate, given in equation (21), can be expressed in terms of a time derivative of droplet surface:

$$R_s = \frac{ds}{dt} = -Sh^* \frac{\rho_G}{\rho_L} D 4\pi H_M \quad (26)$$

This is consistent with the EMSM algorithm presented above.

## Experimental and numerical configuration

The configuration under study consists of a burner geometry in which the spray is generated by an ultrasonic nebulizer, as experimentally investigated by Gounder [16]. The nozzle of the burner has 10.5 mm of diameter. It is surrounded by a co-flow with 104 mm of diameter. A dilute and non-reacting spray regime is investigated. The liquid is acetone and the air has an ambient temperature of about 293 K.

The velocity and droplet size distribution were measured using Laser Doppler Velocimetry (LDV) and Phase Doppler Particle Anemometry (PDPA). Measurements were conducted at seven locations from 3.15 mm ( $x/D = 0.3$ ) to 315 mm ( $x/D = 30$ ) downstream from the nozzle exit plane. At the exit plane of the burner, the axial mean velocity and turbulence of the gas phase were measured with LDV. For additional details, please refer to Gounder [16].

The computational domain is a cylinder with 100 mm of diameter and 500 mm of length. Its inlet is located at the first measurement location ( $x/D = 0.3$ ) and the experimental data were considered for determining the inlet boundary conditions. The boundary condition for the surface around the cylinder is defined as slip wall, and the axial velocity at the wall is set equal to the one of the co-flow. A 3D block-structured grid with about 350,000 cells was used. Near the inlet plane and center-line of the cylinder, the grid is finer and the smallest cells have a length of about 0.5 mm in each coordinate direction.

For the simulation results presented for this configuration, the droplet diameter domain was discretized in 3 sections  $I_k$ , with  $I_1 = [0, 2e-5 \text{ m}]$ ,  $I_2 = [2e-5 \text{ m}, 4.5e-5 \text{ m}]$  and  $I_3 = [4.5e-5 \text{ m}, \infty)$ , and 2 DQMOM points were considered per section.

Transient simulations with a time-step of  $1.5e-5$  seconds were performed until a stationary state was achieved. The calculation of spray evaporation was sub-iterated 5 times. That is, for each time-step  $\Delta t$ , considered for the transport in physical space, five time-steps of  $\Delta t/5$  were calculated for the EMSM method. This strategy was pursued to achieve time-step independent results regarding evaporation.

## Results and discussion

In order to validate the proposed numerical tool, simulation results and experimental measurements are compared. Figure 1 (left) and (middle) illustrate the Sauter mean diameter (SMD) and the arithmetic mean diameter on different locations of the computational domain. In general, the patterns of the experimental data are well predicted, and satisfactory results are achieved for the investigated flow conditions. However, some deviations to experimental measurements are observed. The droplet mean diameters are under-predicted in a region closer to the inlet plane and farther from the center-line of the spray. These deviations increase along with an increase in the order of moment (SMD). Considering the fact that the influence of larger droplets on a moment of the droplet size distribution function is augmented as the order of moment increases, it can be concluded that the concentration of larger droplets is under-predicted in this region, due to a poor dispersion of larger droplets.

In Figure 1 (right), a good agreement between simulation results and experimental data is observed for the droplet number concentration. Accurate results are also delivered for the droplet volume flux and droplet mean axial velocity, as seen in Figure 2 (left) and (middle).

Figure 2 (right) illustrates the droplet mean radial velocity. It shows that the mean radial velocity is considerably under-predicted. This is usually the case for the standard  $k-\epsilon$  model, and may have a considerable influence on the radial dispersion of droplets.

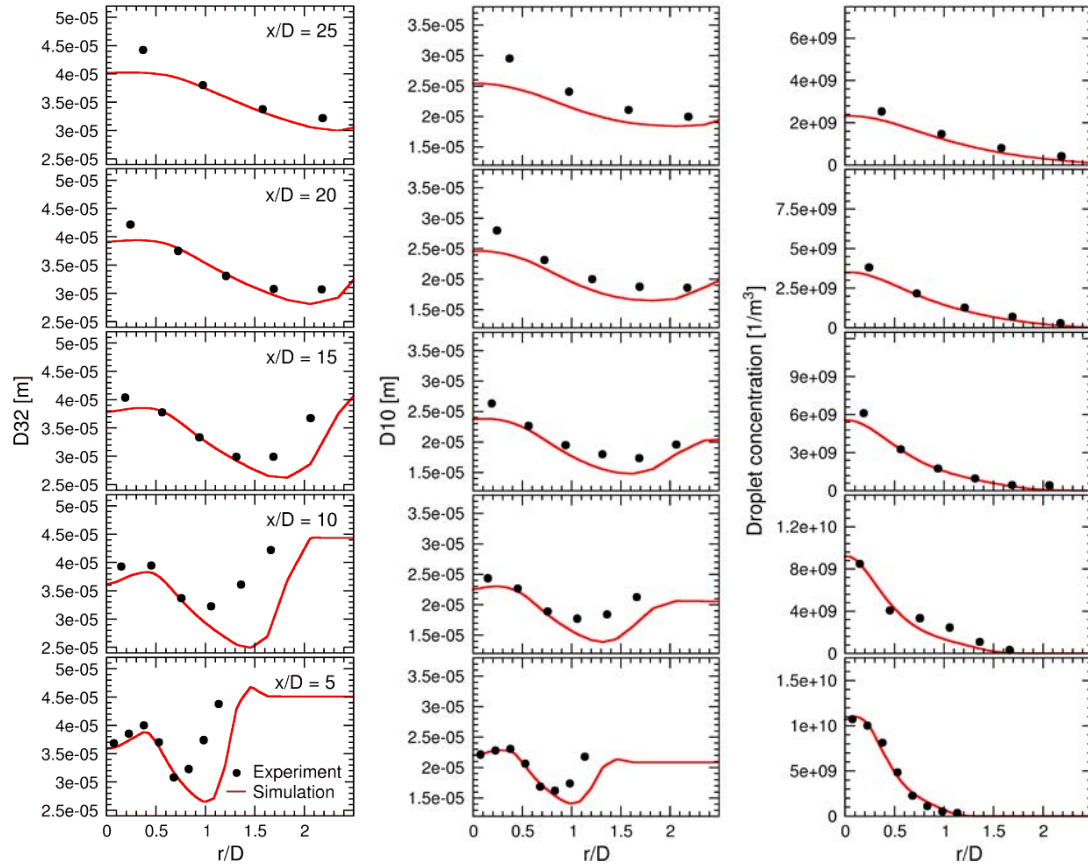


**Figure 1.** Sauter mean diameter (left), arithmetic mean diameter (middle) and droplet number concentration (right) on different measurement locations.

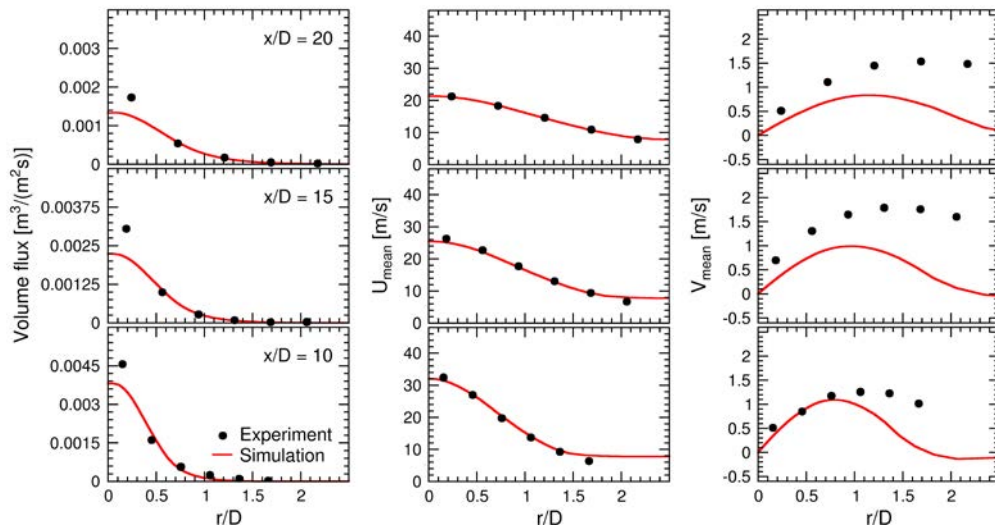


**Figure 2.** Droplet volume flux (left), droplet mean axial velocity (middle) and droplet mean radial velocity (right) on different measurement locations.

## Conclusions

The DQbSMOM, recently proposed by the authors, and the EMSM method have been validated with regard to a dilute evaporating spray under low ambient temperature. A realistic evaporation model, namely the Abramzon-Sirignano model, has been included in the EMSM method. This required the knowledge of droplet temperature. Thus, the designed method has been extended to account for heat transfer as well as a joint NDF of droplet size, velocity and temperature. The proposed tool is probably the first DQMOM-based method to account for droplet temperature, resulting in additional transport equations for temperature abscissas.

Satisfactory simulation results were achieved, showing that the designed numerical tool is able to capture the droplet evaporation process and to describe the spray polydisperse character.

## References

- [1] Gumprich, W., Sadiki, A., Proc. 12th ICLASS, Heidelberg, Germany (2012).
- [2] Massot, M., Laurent, F., Kah, D., de Chaisemartin, S., SIAM J. Appl. Math., Vol. 70, 3203-3234 (2010).
- [3] Abramzon, B., Sirignano, W. A., Int. J. Heat Mass Transfer, Vol. 32, 1605-1618 (1989).
- [4] Williams, F. A., Physics of Fluids, Vol. 1, 541-545 (1958).
- [5] Riber, E., Moureau, V., Garcia, M., Poinso, T., Simonin, O., J. Comp. Physics, Vol. 228, 539-564 (2009).
- [6] McGraw, R., Aerosol Science and Technology, Vol. 27, 225-265 (1997).
- [7] Marchisio, D. L., Fox, R. O., Journal of Aerosol Science, Vol. 36, 43-73 (2005).
- [8] Fox, R. O., Laurent, F., Massot, M., Journal of Computational Physics, Vol. 227, 3058-3088 (2008).
- [9] Schneider, L., A Concise Moment Method for Unsteady Polydisperse Sprays, PhD Thesis, Technische Universität Darmstadt (2009).
- [10] Dufour, G., Villedieu, P., Mathematical Modelling and Numerical Analysis, Vol. 39, 931-963 (2005).
- [11] Kah, D., Prise en compte des aspects polydispersés pour la modélisation d'un jet de carburant dans les moteurs à combustion interne, PhD Thesis, École Centrale Paris (2010).
- [12] Vié, A., Laurent, F., Massot, M., Journal of Computational Physics, Vol. 237, 177-210 (2013).
- [13] Gumprich, W., Sadiki, A., Proc. 12th ICLASS, Heidelberg, Germany (2012).
- [14] Gumprich, W., Sadiki, A., Proc. 8th ICMF, Jeju, Korea (2013).
- [15] Simonin, O., Viollet, P. L., Proc. Numerical Methods for Multiphase Flows, ASME FED 91, 73-82 (1990).
- [16] Gounder, J.D., PhD Thesis, University of Sydney, Australia (2009).
- [17] Gordon, R., Journal of Mathematical Physics, Vol. 9, 655-663 (1968).
- [18] Hill, D.P., The Computer Simulation of Dispersed Two-Phase Flows, PhD Thesis, Univ. of London (1998).
- [19] Choi, D., Schneider, L., Spyrou, N., Sadiki, A., Janicka, J., Proc. 7th ICMF, Tampa, USA (2010).
- [20] Friedrich, M., Weigand, B., Proc. 10th ICLASS, Kyoto, Japan (2006).
- [21] Madsen, J., Computational and Experimental Study of Sprays from the Breakup of Water Sheets, PhD Thesis, Esbjerg Institute of Technology (2006).
- [22] Belt, R., Simonin, O., Proc. ASME FEDSM 2009, FEDSM2009-78095 (2009).
- [23] Mead, L.R., Papanicolaou, N., Journal of Mathematical Physics, Vol. 25, 2404-2417 (1984).
- [24] Miller, R.S., Harstad, K., Bellan, J., International Journal of Multiphase Flow, Vol. 24, 1025-1055 (1998).
- [25] Ranz, W. E. & Marshall, W. R., Chemical Engineering Progress, Vol. 48, 141-146 (1952).
- [26] Ranz, W. E. & Marshall, W. R., Chemical Engineering Progress, Vol. 48, 173-180 (1952).

## Trajectory and break-up of a liquid jet in a centrifugal field – influenced by a gas flow

T. Kalmbach, M. Hauber, M. Liebing and M. Piesche

Institute of Mechanical Process Engineering, University of Stuttgart, Germany

### Abstract

The present work introduces experimental and theoretical studies in spray technology. The motion and the break-up behaviour of jets emerging from rotary cups are examined. In a lot of industrial applications a gas flow normal to the rotation plane is present. Therefore, this work is focusing on the influence of an impressed gas stream on the disintegration of liquid jets in the range of Rayleigh type disintegration. In this work the gas flow is directed parallel to the axis of rotation. A physical-mathematical model was developed to describe and to determine the jet behaviour under these boundary conditions. The modelling is separated into two parts. Calculating the time steady base flow provides information about 3D jet motion and its average contour as a function of jet length. The stability behaviour of the jets is examined by a perturbation analysis. A linear stability analysis is used for describing the disintegration process including the growth of small wavelike disturbances and the drop formation. Temporal and spatial evolutions of disturbances are investigated. In addition to theoretical studies, we built up a test rig. The experimental set up is used to compare and to validate the calculation results under various operating conditions. Shadow imaging provides information about jet motion by means of the jet length and curvature. In addition, drop sizes and average jet diameter, depending on the distance to the orifice, are determined through shadowgraphy.

---

### Introduction

Dispersing of materials is one of the basic operations in mechanical process engineering. Atomization of liquids is required in a lot of industrial applications like spray drying, prilling or coating technologies. The main advantage is based on an increase of the specific surface which leads to a better heat and mass transfer. Atomization devices have to fulfil demanding requirements for these applications. High throughputs must be guaranteed even when applying complex fluids. Additionally, good wear and anti-blocking properties should be maintained. Furthermore, small and uniform droplets are often required. The reasons are a high and constant product quality of spray dried products or the uniform coat thicknesses at coating processes. If rotary atomizers are run in the operating range where Rayleigh Jet Break-up takes place, they are very well suited for these challenges. These rotating devices are often connected with gas streams, which are used to intensify heat and mass transfer and to control the direction of motion of the spray. The gas flow limits the radial fluid propagation resulting in reduced space requirements. At coating technologies the gas flow is used to focus the spray on the components which have to be coated. Besides the influence of the gas stream on the liquid motion and on the heat and mass transfers, it affects the break-up behaviour of the jets.

Laminar jet break-up has been discussed by several authors before. Already in 1878 Lord Rayleigh [1] studied this topic with an energy balance and a linear temporal stability analysis. As a result of his examination he claimed a relation between the diameter of the orifice and the wave length of the most unstable disturbance of a non-viscous, straight, cylindrical liquid jet. Thereby the diameter of the grown drops can be calculated. Later Weber [2] also focussed on this topic using a temporal linear stability analysis. In addition, he took viscous fluids into account. Besides his relation for the critical wave length of viscous liquids he also claimed a correlation for the break-up length which was completed and validated with experimental results of Haenlein [3]. There have also been examinations with linear spatial stability analyses for non-viscous [4] and viscous [5] liquids. But with all these linear analyses it is only possible to calculate the mean drop size and therefore non-linear stability analyses were executed to obtain information about the so called satellite drops. One example for these investigations is the work of Bogoy [6].

The mentioned publications have in common that only cylindrical jets were considered. In most applications jets are elongated. This is also the case in the present work. The elongation is often used to reduce the jet diameter and therefore to decrease the resulting drops. Dilatation caused by gravity was treated, among others, by [7-10]. Through his research Nonnenmacher [9] extended Weber's [2] correlation for the break-up length to gravity-elongated jets. Elongation caused by centrifugal forces like in the present work was examined by a lot of authors, too. For example [11-18] considered jets in the centrifugal field. Except Părău et al. [14] all of them used linear stability analyses. Whereas [11] and [13-16] considered non-viscous or Newtonian fluids [12], [17] and [18] focussed on complex fluids. Piesche [12] and Hawkins et al. [17] analysed non-Newtonian fluids and Gramlich [18] examined particle laden liquid jets. Gramlich [18] transferred Nonnenmacher's [9] correlation to the centrifugal field. In addition, he extended the equation with respect to the influence of the relative gas motion due to the rotation of the atomizer. The extended correlation was used as a boundary condition for his

modelling. His calculation results were in good agreement with experimental results. Considering both, gravity and the centrifugal field, Decent et al. [19] modelled non-viscous jets. Chicheportiche et al. [20] showed the influence of an impressed oscillation on the break-up of dilated liquid jets in the centrifugal field. He demonstrated the possibility to produce uniform droplets at the centrifugal field in a certain range of viscosity.

An impressed gas flow and its influence on the break-up behaviour of liquid jets investigated [21-24], for example. Kitamura and Takahashi [21] examined the impact of a gas stream normal to the direction of their orifice. They assumed to have undilated jets and showed a strong decrease of the break-up length by increasing the gas velocity. Mescher [22] conducted in his similarity trials extensive experimental studies for jets under the influence of gravity and of a gas flow normal to the direction of his orifices. He also found a strong decrease of the jet length due to the relative gas motion. Furthermore, he showed an increase of the span [22] by rising the gas velocity. As a result of his investigations, he claimed correlations for the span, the break-up length and the mean drop size as a function of the relevant dimensionless numbers. He concluded that relative gas motion should be reduced in the case of laminar jet break-up to decrease span. A gas distributor for rotary atomizers was introduced to reach this aim in the case of rotary atomization. Gramlich et al. [23] developed a physical-mathematical model describing jet break-up for the experimental set up of Mescher [22]. The calculation results were in good agreement with their experimental results. Kalmbach and Piesche [24] introduced a physical-mathematical model for particle laden liquid jets in the centrifugal field. Gravity, the centrifugal forces and the influence of an impressed gas flow were taken into account for their 3D-modelling.

The objective of the present work is to develop a model describing Rayleigh Jet Break-up [1] for liquid jets in the centrifugal field including gravity, the centrifugal forces and the effects of an impressed gas flow directed parallel to the rotation axis of the atomizer. Aiming to predict drop sizes, the modelling contains spatial and temporal stability analyses and a model for the time steady jet motion in 3D space. Simultaneously a test rig was built. The experimental investigations serve for comparison and validation and provide us information about the break-up length which serves as a boundary condition for the calculation.

### Physical model

The present modelling is an extension of the 2D-models of [16] and [18]. As mentioned before, these experimentally validated calculation models only include the influences of the centrifugal force and the relative gas motion due to the fluid flow and the rotation of the atomizer. The motion of the jet parallel to the rotation axis was neglected. The present 3D physical-mathematical modelling additionally considers gravity as well as a gas stream normal to the rotation plane. It provides a description of the spatial jet motion and its break-up behaviour and is based on a decomposition of the fluid flow. Separating fluid movement, we are considering the time steady jet motion and superimposed small wavelike disturbances.

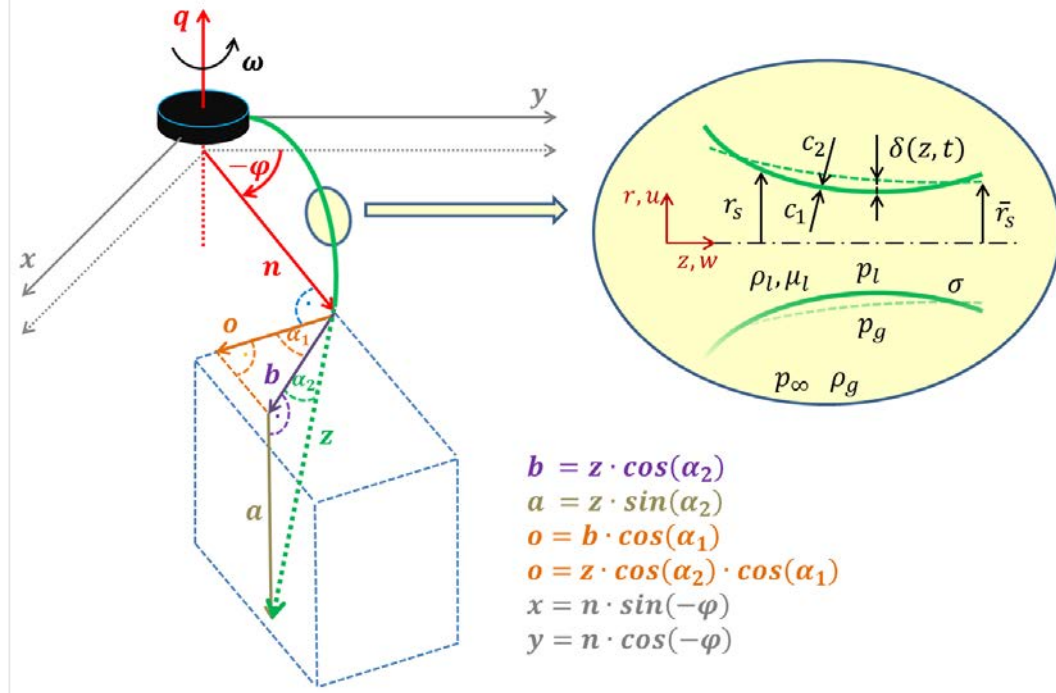


Figure 1. Jet path and contour.

Figure 1 illustrates the spiral jet path in our rotating cylindrical coordinate system  $(n, \varphi, q)$ . A small enlarged part of the jet shows its time-dependent radius  $r_s$  and its time steady radius  $\bar{r}_s$  in the cylindrical jet

coordinate system  $(r, \Phi, z)$ , which is moving with the jet. Assuming rotational symmetry, we neglect the angle  $\Phi$  and any dependency on it in the following. There exists a difference between the two radii due to the small wavelike disturbances. The axisymmetric oscillating radial deviation, which is increasing along the jet, has the amount  $\delta$ . Local jet surface is characterised by the radii of curvature  $c_1$  and  $c_2$ .  $u_j$  and  $w_j$  are the radial and axial velocities. The index  $j = l$  indicates the liquid phase and  $j = g$  the gas phase, respectively. The physical properties of the fluids are the dynamic viscosity  $\mu_j$ , the density  $\rho_j$  and the surface tension  $\sigma$ .  $p_j$  represents the pressure in a particular phase and  $p_\infty$  is the constant ambient gas pressure. The operating conditions are characterised by the angular velocity of the atomizer  $\omega$ , the axial liquid velocity  $w_0$  at the orifice and the velocity of the impressed gas flow parallel to the rotation axis  $v_g$ . Geometrical boundary conditions are the radius of the orifice  $r_0$  and the radius of the atomizer  $n_0$ .

### Time Steady base flow

Due to the decomposition of the fluid flow, the pressures and the velocities can be treated similar to the radius. This means that they are separated into a time steady and an oscillating time-dependent part. Our model describing the time steady jet motion will be presented in the following. It is based on a force and mass balance at an infinitesimal element of the jet. The time steady quantities of the base flow are indicated by an overbar. We chose the subsequent assumptions, limiting computing time and complexity:

- All physical properties are constant.
- The base flow is an uniaxial elongational flow. No shear stresses are considered.
- The relative gas movement results from the jet motion, the induced gas flow of the rotating atomizer and the impressed gas flow normal to the rotation plane.
- The calculation of the spatial curvature of the jet is split into two parts: the determination of the curvature in the plane of the atomizer and the curvature in the plane in which the jet descends.

Considering the balances and the assumptions mentioned above, four equations for the calculation of the time steady base flow can be derived. The dimensionless equation of motion in the axial direction is:

$$\bar{W} \frac{d\bar{W}}{dZ} = \frac{1}{We} \cdot \frac{1}{\bar{R}_s^2} \cdot \left[ \frac{d\bar{R}_s}{dZ} \right] + \frac{3}{Re} \cdot \frac{1}{\bar{R}_s^2} \cdot \frac{d}{dZ} \left[ \bar{R}_s^2 \frac{d\bar{W}}{dZ} \right] + \frac{1}{Fr} \cdot \sin(\alpha_2) + Ro \cdot N \cdot \sin(\alpha_1) \cdot \cos(\alpha_2) - \frac{\rho_g}{\rho_l} \cdot \frac{1}{\pi \bar{R}_s} \cdot c_D \cdot \bar{V}_{rel}^2 \cdot \cos(\theta_1)$$

Due to the split calculation of the spatial curvature, two equations have to be solved for its determination. One provides the dimensionless radius of curvature in the plane of the atomizer  $C_{n\phi}$  and the other supplies the radius of curvature in the  $b$ - $a$ -plane  $C_{bq}$ . The subscription “ $bq$ ” takes into account that a movement in positive  $a$ -direction results in a movement in negative  $q$ -direction of same amount.

$$\frac{(\bar{W} \cdot \cos(\alpha_2))^2}{C_{n\phi}} = -Ro \cdot N \cdot \cos(\alpha_1) + 2 \cdot \left( \frac{Ro}{D} \right)^{0.5} \cdot \bar{W} \cdot \cos(\alpha_2) + \frac{\rho_g}{\rho_l} \cdot \frac{1}{\pi \bar{R}_s} \cdot c_D \cdot \bar{V}_{rel}^2 \cdot \sin(\theta_1) \cdot \sin(\theta_2)$$

$$\frac{\bar{W}^2}{C_{bq}} = -Ro \cdot N \cdot \sin(\alpha_1) \cdot \sin(\alpha_2) + \frac{1}{Fr} \cdot \cos(\alpha_2) + \frac{\rho_g}{\rho_l} \cdot \frac{1}{\pi \bar{R}_s} \cdot c_D \cdot \bar{V}_{rel}^2 \cdot \sin(\theta_1) \cdot \cos(\theta_2)$$

In combination with the integral conservation of mass

$$\bar{W} \bar{R}_s^2 = 1$$

and the following geometrical relations

$$\begin{aligned} \frac{d\phi}{dZ} &= -\frac{\cos(\alpha_1) \cdot \cos(\alpha_2)}{N \cdot D}; & \frac{dN}{dZ} &= \frac{\sin(\alpha_1) \cdot \cos(\alpha_2)}{D}; & \frac{dQ}{dZ} &= -\sin(\alpha_2); \\ \frac{d\alpha_1}{dZ} &= \frac{\cos(\alpha_1) \cdot \cos(\alpha_2)}{N \cdot D} - \frac{\cos(\alpha_2)}{C_{n\phi}}; & \frac{d\alpha_2}{dZ} &= \frac{1}{C_{bq}} \end{aligned}$$

a system of differential equations results for the calculation of the liquid base flow including jet path and its time steady contour. The fact that only one boundary condition for the axial velocity is known (the velocity at the orifice) requires a special solution method. Applying the modified backward integration of [18], the problem can be solved after combining equations (1) and (2) and a subsequent conversion.

In the equations shown above the dimensionless variables and values are formed with the quantities at the orifice and the physical properties of the liquid. The radii  $C_{bq}$ ,  $C_{n\phi}$  and  $\bar{R}_s$  and the coordinates  $Z$  and  $Q$  are related to the radius of the orifice  $r_0$ .  $N$  represents the ratio of the local coordinate  $n$  to the radius of the atomizer  $n_0$ . Therefore the Cartesian coordinates  $X$  and  $Y$  are also related to  $n_0$ . The axial velocity  $\bar{W}$  as well as the relative gas velocity  $\bar{V}_{rel}$  are referred to the liquid velocity at the orifice  $w_0$ . Furthermore, the present equations



additionally depend on the dimensionless numbers Weber number  $We = \rho_l r_0 w_0^2 / \sigma$ , Reynolds number  $Re = \rho_l r_0 w_0 / \mu_l$ , Rotation number  $Ro = \omega^2 n_0 r_0 / w_0^2$  and Froude number  $Fr = w_0^2 / r_0 g$ . Further unknown quantities are the angles of inclination  $\alpha_1$  and  $\alpha_2$  as well as the ratios of the radii  $D = n_0 / r_0$  and the densities  $\rho_g / \rho_l$ .  $\theta_1$  is the angel between the direction of the relative gas movement and the jet.  $\theta_2$  splits the radial part of the drag force into the both directions of curvature. The rotation of the atomizer induces an azimuthal gas motion with the velocity  $v_A$  which is simplified to a potential vortex according to [18]. There exists a velocity difference between the local azimuthal velocity  $v_{rot} = \omega n$  and  $v_A$  causing an azimuthal relative motion of the gas which is expressed by  $(v_{rot} - v_A) / w_0$ . This relative velocity as well as the axial velocity of the liquid jet  $\bar{W}$  and the velocity of the impressed gas flow parallel to the rotation axis  $V_g = v_g / w_0$  compose the relative motion between gas phase and jet. The drag coefficient  $c_D$  is calculated with the correlation of [18].

### Perturbation analysis

A linear stability analysis according to [16] is used for the examination of the growth and decay of superimposed small wavelike disturbances. Based on Rayleigh's assumption [1] the most amplified disturbance leads to the jet break-up. Its wave length is directly correlated with the drop formation and enables the calculation of the drop size. In the following, disturbances of the form

$$\Delta = \Delta_0 \cdot \exp[i(K(Z) - \Omega(T))]$$

are analyzed regarding their temporal and spatial evolution along the jet. All of them have a constant amplitude at the orifice  $\Delta_0 = \delta_0 / r_0$  and depend on the complex functions  $\Omega(T) = \Omega_r + i\Omega_i$  and  $K(Z) = K_r + iK_i$ . These wave functions describe the temporal and spatial amplification and periodicity of the disturbances. Here, the dimensionless time is defined as  $T = tw_0 / r_0$ . In the following, the indices  $Z$  and  $T$  indicate local and temporal derivations, respectively. We are examining a purely temporal and a purely spatial evolution of the disturbances in the present work. This means that we either reduce  $\Omega(T)$  or  $K(Z)$  to a real function for our calculations. Due to this reduction  $\Omega_r$  or  $K_r$  can be locally calculated with Gramlich and Piesche's dispersion relation [16]. Therefore, constant real values for  $K_Z$  or  $\Omega_T$  have to be assumed. If  $\Omega_T$  is calculated, constant real values for  $K_Z$  are applied and vice versa. Integrating  $\Omega_{T,i}$  over break-up time and  $K_{Z,i}$  over jet length the temporal and the spatial amplification of a disturbance is determined, respectively. According to Rayleigh [1] in both cases the most amplified disturbance is chosen. Its wave length is the critical wave length  $\lambda_{crit} = 2\pi r_0 / K_{r,Z,crit}$ . With the relation from [18]

$$\frac{d_D}{2r_0} = \frac{1}{2} \left( \frac{12\pi}{K_{r,Z,crit}|_{Z=L}} (\bar{R}_s|_{Z=L})^2 \right)^{\frac{1}{3}}$$

the drop diameter  $d_D$  results if the dimensionless break-up length  $L = l / r_0$  is known. The dispersion relation derived in [16]

$$\begin{aligned} & -\frac{\rho_g}{\rho_l} \cdot \frac{K_1(K_Z \bar{R}_s)}{K_Z K_0(K_Z \bar{R}_s) + \frac{1}{\bar{R}_s} K_1(K_Z \bar{R}_s)} \cdot \left\{ \Omega_T - \frac{2}{\bar{R}_s} \bar{U}_{rel} - K_Z \bar{W}_{rel} \right\}^2 - \frac{1}{We} \cdot \left[ \frac{1}{\bar{R}_s^2} - K_Z^2 \right] \\ & + \frac{2}{Re} \cdot i(\bar{W} K_Z - \Omega_T) \cdot \left\{ \frac{S^2 + K_Z^2}{S^2 - K_Z^2} \cdot \left( K_Z \frac{I_0(K_Z \bar{R}_s)}{I_1(K_Z \bar{R}_s)} - \frac{1}{\bar{R}_s} \right) - \frac{2K_Z^2}{S^2 - K_Z^2} \cdot \left( S \frac{I_0(S \bar{R}_s)}{I_1(S \bar{R}_s)} - \frac{1}{\bar{R}_s} \right) \right\} \\ & = \frac{(\bar{W} K_Z - \Omega_T)^2}{K_Z} \cdot \frac{S^2 + K_Z^2}{S^2 - K_Z^2} \cdot \frac{I_0(K_Z \bar{R}_s)}{I_1(K_Z \bar{R}_s)} \end{aligned}$$

is gained from a pressure balance at the interface of the jet and is based on the Navier-Stokes equation and the equation of continuity for the liquid phase. The gas phase is treated potential-theoretically. Equation (8) contains the substitution  $S^2 = K_Z^2 + iRe(\bar{W} K_Z - \Omega_T)$  and the modified Bessel Functions  $I_0$ ,  $I_1$ ,  $K_0$  and  $K_1$ . Depending on  $\bar{R}_s(Z)$ ,  $\bar{W}(Z)$  as well as on the radial and axial relative gas velocities  $\bar{U}_{rel} = |\bar{V}_{rel} \cdot \sin(\theta_1)|$  and  $\bar{W}_{rel} = |\bar{V}_{rel} \cdot \cos(\theta_1)|$  the stability analysis is directly connected to the calculation results of the time steady base flow.

### Experiments

Besides the theoretical modelling, we built a test rig. Using a rotary cup atomizer with the radius  $n_0 = 60 \text{ mm}$  we examined two different orifices with the radii  $r_0 = 0.5 \text{ mm}$  and  $r_0 = 1 \text{ mm}$ . Emerging liquid is directed normal to the lateral area of the cylindrical atomizer. The angular velocity  $\omega$  was varied between 30 and 60 *rad/s*. Water and aqueous solutions of glycerine with viscosities up 0.11 *Pas* served as test liquids. The liquid circuit was provided by a gear pump varying  $w_0$  between 0.5 and 2 *m/s*. With a radial fan and several



flow installations the emerged liquid jet was blown normal to the direction of the orifice with velocities  $v_g$  between 0 and 5 m/s. Using high speed imaging and shadowgraphy we analysed the break-up behaviour of the liquid jets. The experimental results for the drop size, the radius and the path of the jet are for comparison and validation with our physical-mathematical modelling. Information about the break-up length serves as a boundary condition for the integration in the stability analysis.

## Results and Discussion

In the following, we present preliminary results. Figures 2 and 3 compare experimental data gained by shadow imaging with calculation results. Figures 2(a) and 2(b) show information about the time steady base flow. Here, lines represent the solutions of the model equations and symbols those of our experiments. The results of the stability analyses are illustrated in form of drop sizes in Figure 3(a) and 3(b). In Figure 3 dashed (upper) lines represent drop sizes calculated by the spatial stability analysis and the solid (lower) lines represent those of the temporal stability analysis.

Dilation of jets for two different gas velocities  $V_g$  is presented in Figure 2(a). Experimental results and calculated  $\bar{R}_s(Z)$  are in good agreement. Decrease of radius along a jet is only negligibly influenced by the examined gas streams. The same tendency is observed for the influence of an impressed gas flow on the jet path in the plane of the atomizer, see Figure 2(b). The path of the blown jet is a little more curved than the one for  $V_g = 0$ . Only small deviation between numerical results and the data gained by shadow imaging can be noticed. Furthermore, both figures show the fact that the break-up length of jets is reduced by increasing gas velocity.

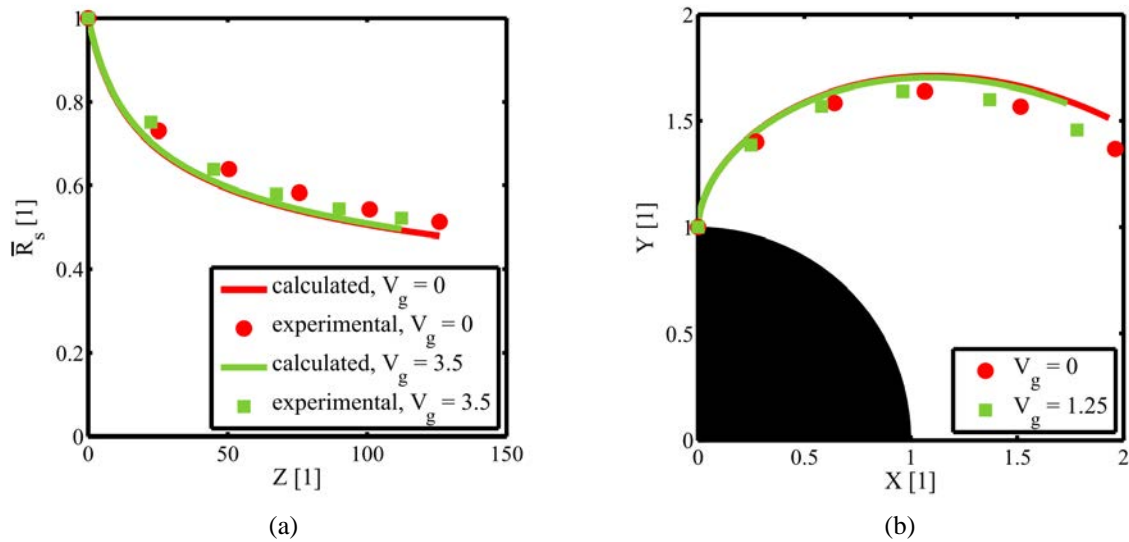


**Figure 2.** Comparison between jets with and without impressed gas streams for experimental (symbols) and calculation results (solid lines). (a): Radius of jet as a function of jet coordinate for  $Re = 1343$ ,  $We = 19.9$ ,  $D = 60$ ,  $Ro = 0.067$ ,  $Fr = 146.8$  and  $\rho_g/\rho_l = 0.0012$ . (b): Jet paths in the plane of the atomizer for  $Re = 62.5$ ,  $We = 34.3$ ,  $D = 120$ ,  $Ro = 0.027$ ,  $Fr = 815.5$  and  $\rho_g/\rho_l = 0.001$ .

Figure 3(a) shows the drop sizes as a function of the rotation number for three different gas velocities. The experimental results lie between the solutions of the spatial and the temporal stability analysis. The spatial stability analysis leads to bigger drop sizes whereas the temporal analysis leads to smaller drops. While only negligible influence of the strength of the impressed gas flow is noticed, increasing the rotation number clearly results in smaller drops. Figure 3 (b) shows drop sizes as a function of gas velocity for two slightly different rotation numbers. The nearly constant courses confirm that the gas velocity has only little influence on the average drop size in the investigated area of gas flows. This phenomenon was reported before by Gramlich et al. [23] for gravity elongated jets. They described this as a consequence of two opposing factors. On the one hand the impressed gas flow reduces the break-up length of jets, which leads to bigger jet diameters at the break-up point. On the other hand, relative gas motion influences the wave length of disturbances causing smaller critical wave lengths. According to equation (7) an increasing break-up diameter and a decreasing wave length have opposite effects. In the examined parameter area both influences seem to counteract.

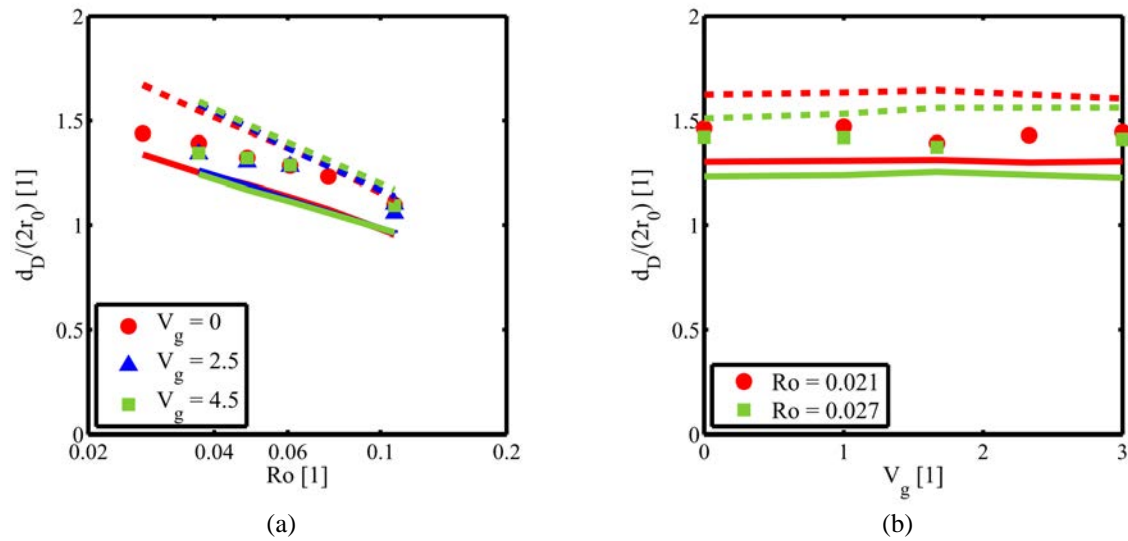


**Figure 3.** Drop diameter as a function of rotation number (a) and gas velocity (b). Dashed (upper) lines represent the results of the spatial stability analysis and solid (lower) lines represent the results of the temporal stability analysis. The symbols are experimental results. Conditions at (a):  $Re = 204.6$ ,  $We = 7.6$ ,  $D = 120$ ,  $Fr = 203.9$  and  $\rho_g/\rho_l = 0.0011$ . Conditions at (b):  $Re = 330.4$ ,  $We = 17$ ,  $D = 120$ ,  $Fr = 458.7$  and  $\rho_g/\rho_l = 0.0011$ .

## Conclusions

We presented a physical-mathematical model for the motion of a liquid jet emerging from a rotary cup atomizer and its break-up behaviour under special boundary conditions. The investigation includes the influences of gravity, centrifugal acceleration and an impressed gas stream directed parallel to the axis of rotation of the atomizer. Both, the effect on the spatial jet motion and the effect on the break-up behaviour of laminar jets were examined. Comparing experimental and theoretical results regarding the path in the plane of the atomizer and the radius along the jet axis, we find good agreement. The measured drop sizes lie between the results of the spatial and the temporal stability analysis. In the investigated area no significant influence of the impressed gas flow on the average drop size was found. Subsequently, we will extend our experimental parameter area. The experimental data will be used to extend the correlation for the break-up length of Gramlich [18], accounting the influence of impressed gas streams. Furthermore, the influence of particles in suspensions on the break-up behaviour will be examined model-theoretically and experimentally.

## Acknowledgements

This project is part of the SPP1423 “Process Spray” of the German Research Foundation DFG. The support from the DFG is gratefully acknowledged.

## Nomenclature

Roman symbols		$L$	Break-up length (1)	$\Phi$	Azimuthal coordinate (rad)
$a$	Substitution ( $m$ )	$N$	Radial coordinate (1)	$\Omega(T)$	Temporal wave function (1)
$b$	Substitution ( $m$ )	$Q$	Axial coordinate (1)		
$c$	Radius of curvature ( $m$ )	$R$	Radial coord., radius (1)	Indices	
$d$	Diameter ( $m$ )	$Re$	Reynolds number (1)	0	Condition at the orifice
$i$	Imaginary unit	$Ro$	Rotation number (1)	1	first
$l$	Break-up length ( $m$ )	$S$	Substitution (1)	2	second
$n$	Radial coordinate ( $m$ )	$U$	Radial velocity (1)	$b$	Direction of b
$o$	Substitution ( $m$ )	$V$	Velocity (1)	$crit$	Critical

$p$	Pressure ( $Pa$ )	$W$	Axial velocity (1)	$g$	Gas, impressed gas flow
$q$	Axial coordinate ( $m$ )	$We$	Weber number (1)	$i$	Imaginary
$r$	Radial coord., radius ( $m$ )	$X$	Cartesian coordinate (1)	$j$	Substitution
$t$	Time ( $s$ )	$Y$	Cartesian coordinate (1)	$l$	Liquid
$u$	Radial velocity ( $m/s$ )	$Z$	Axial coordinate (1)	$n$	Radial direction
$v$	Velocity ( $m/s$ )			$q$	Axial direction
$w$	Axial velocity ( $m/s$ )	<i>Greek symbols</i>		$r$	Real
$x$	Cartesian coordinate ( $m$ )	$\alpha$	Inclination angle ( $rad$ )	$rel$	Relative
$y$	Cartesian coordinate ( $m$ )	$\delta$	Radial deviation ( $m$ )	$rot$	Rotation of the atomizer
$z$	Axial coordinate ( $m$ )	$\theta$	Angle of incidence ( $rad$ )	$s$	Jet
$c_D$	Drag coefficient (1)	$\lambda$	Wave length ( $m$ )	$A$	Azimuthal gas motion
$C$	Radius of curvature (1)	$\mu$	Dynamic viscosity ( $Pas$ )	$D$	Drop
$D$	Radius ratio (1)	$\rho$	Density ( $kg/m^3$ )	$T$	Temporal derivation
$Fr$	Froude number (1)	$\sigma$	Surface tension ( $N/m$ )	$Z$	Local axial derivation
$I_0, I_1$	Mod. Bes. Functions (1)	$\varphi$	Azimuthal coordinate ( $rad$ )	$\varphi$	Azimuthal direction
$K_0, K_1$	Mod. Bes. Functions (1)	$\omega$	Angular velocity ( $rad/s$ )	$\infty$	Far field boundary cond.
$K(Z)$	Spatial wave function (1)	$\Delta$	Radial deviation (1)	$-$	Time steady base flow

## References

- [1] L. Rayleigh, *Proc. London Math. Soc.*, **10**, 4–12 (1878).
- [2] C. Weber, *ZAMM*, **11**(2), 136-154 (1931).
- [3] A. Haenlein, *Forschung auf dem Gebiet des Ingenieurwesens*, **2**(4), 139-149 (1931).
- [4] J. B. Keller, S. I. Rubinow, Y. O. Tu, *Phys. Fluids*, **16**(2), 2052-2055 (1973).
- [5] S. J. Leib, M. E. Goldstein, *Phys. Fluids*, **29**(4), 952-954 (1986).
- [6] D. B. Bogy, *Phys. Fluids*, **22**(2), 224–230 (1979).
- [7] K. Adachi, K. Tagashira, Y. Banba, H. Tatsumi, H. Machida, N. Yoshioka, *AIChE Journal*, **36**(5), 738-745 (1990).
- [8] S. Schneider, Erzeugung und Zerfall gedehnter Laminarstrahlen im Schwerfeld, Dissertation, Universität Dortmund (2002).
- [9] S. Nonnenmacher, Numerische und experimentelle Untersuchungen zur Restentgasung in statischen Entgasungsapparaten, Dissertation, Universität Stuttgart (2003).
- [10] S. Sauter, Globale Stabilität schlanker schweregetriebener hochviskoser und viskoelastischer Flüssigkeitsstränge, Dissertation, Universität Karlsruhe (2005).
- [11] Y. Kitamura, K. Egawa, T. Takahashi, *Jour. Chem. Eng. Japan*, **10**, 1–5 (1977).
- [12] M. Piesche, *Chem. Ing. Tech.*, **60**(3), 212-213 (1988).
- [13] I. M. Wallwork, S. P. Decent, A. C. King, R. M. S. M. Schulkes, *J. Fluid Mech.*, **459**, 43-65 (2002).
- [14] E. I. Părău, S. P. Decent, M. J. H. Simmons, D. C. Y. Wong, A. C. King, *J. Eng. Math.*, **57**, 159-179, (2007).
- [15] S. P. Decent, A. C. King, M. J. H. Simmons, E. I. Părău, I. M. Wallwork, C. J. Gurney, J. Uddin, *Appl. Math. Modelling*, **33**, 4283-4302 (2009).
- [16] S. Gramlich, M. Piesche, *SPRAY 2010 – 9. Workshop über Sprays, Techniken der Fluidzerstäubung und Untersuchungen von Sprühvorgängen*, Heidelberg, Germany, 03. – 05. May 2010.
- [17] V. L. Hawkins, C. J. Gurney, S. P. Decent, M. J. H. Simmons, J. Uddin, *J. Phys. A: Math. Theor.*, **43**, 1-18 (2010).
- [18] S. Gramlich, Numerische und experimentelle Untersuchungen zum Zerfall feststoffbeladener Flüssigkeitsstrahlen im Zentrifugalfeld, Dissertation, Universität Stuttgart (2011).
- [19] S. P. Decent, A. C. King, I. M. Wallwork, *J. Eng. Math.*, **42**, 265-282 (2002).
- [20] J. M. Chicheportiche, J. B. Zainoun, J. P. Renaudeaux, M. Jenger, G. Liu, *24th European Conference on Liquid Atomization and Spray Systems, ILASS*, Estoril, Portugal, 05. – 07. September 2011.

- [21] Y. Kitamura, T. Takahashi, *Jour. Chem. Eng. Japan*, **9**, 282-286 (1976).
- [22] A. Mescher, Einfluss der Gasführung in Sprühtrocknern auf den Fadenzerfall an Rotationszerstäubern - Analyse und Optimierung, Dissertation, Technische Universität Dortmund (2012).
- [23] S. Gramlich, A. Mescher, M. Piesche, P. Walzel, *Chem. Eng. Technol.*, **34**(6), 921–926 (2011).
- [24] T. Kalmbach, M. Piesche, *SPRAY 2012 – 10. Workshop über Sprays, Techniken der Fluidzerstäubung und Untersuchungen von Sprühvorgängen*, Berlin, Germany, 21. – 22. May 2012.

## Modelling of freezing processes in super-cooled droplets on sub-grid scale

K. Eisenschmidt<sup>1</sup>, P. Rauschenberger<sup>1</sup>, C. Rohde<sup>2</sup> and B. Weigand<sup>1</sup>

1: Institute of Aerospace Thermodynamics, University of Stuttgart, Germany

2: Institute for Applied Analysis and Numerical Simulation, University of Stuttgart, Germany

### Abstract

We present a closed form analytical approximate solution for radial symmetric ice growth in a super-cooled droplet, as they exist in clouds. The solution is used as a sub-grid model for direct numerical simulations of the freezing process of the super-cooled droplet including effects like the formation of dendrites. The sub-grid model must predict the temperature fields in the water and the ice phase as well as the time-dependent growth of the ice-water interface. The analytical approach bases on perturbation methods and uses small Stefan numbers as perturbation parameter. It accounts for heat conduction in the ice and the water phase, which is finite, as well as for the Gibbs-Thomson effect, which lowers the melting temperature of the ice particle due to its curved surface.

The analytical results are compared with a numerical solution of the underlying partial differential equations for this specific problem and it can be seen that both are in very good agreement.

### Introduction

Freezing processes in super-cooled droplets in the atmosphere are of critical relevance for precipitation. As these freezing phenomena are not understood well so far, we intend to investigate these freezing processes with Direct Numerical Simulations (DNS) to provide knowledge of the basic principles.

The freezing of a super-cooled droplet, which itself has typically a radius of several microns, starts with the agglomeration of molecules on nanometre scale. Due to the limitation in computational power, several orders of magnitude cannot be resolved on one grid nowadays. The gap between the start of the freezing process and the droplet scale is bridged by the use of sub grid models. A nucleation model predicts the time and location of a nucleation event as well as the critical cluster radius, which is the initial radius for the growth of the ice particle. The initial growth of the ice particle is stable and spherical as instabilities are damped. That allows an analytical description - as long as the assumption of a radial symmetric problem holds - from the initial nucleus radius  $R_c$  up to the radius that limits the stable growth,  $R_{stable}$  [1], as Fig. 1 illustrates.

The ice particle of size  $R_{stable}$  is then resolved on the numerical grid to simulate the unstable, dendritic ice growth with the DNS in-house code FS3D [2]. The analytically calculated temperature in the ice and in the water is an initial condition for the simulation.

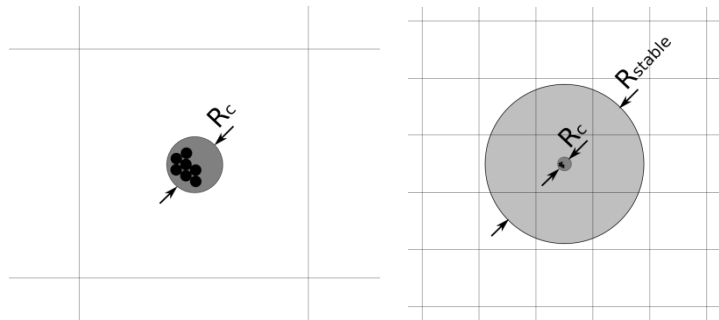


**Figure 1.** Analytical calculation of the spherical growth from the initial nucleus up to the stable radius

The paper presents an analytical solution of the spherical ice growth in the super-cooled droplet. The ice growth is represented by the Stefan problem, which is a free-boundary problem as the ice-water interface moves with time. The movement of the interface itself is described by the Stefan condition, which couples the energy equations in the water and in the ice phase. As the surface of the ice particle is spherical, the lowering of the melting temperature due to the curvature, which is described by the Gibbs-Thomson effect [3], has to be taken into account. Our suggested solution bases on perturbation methods [4], [5]. The Stefan number, which is a characteristic number for the problem, can be used as perturbation parameter as long as it is small. Analytical solutions for the Stefan problem can be found in literature for different special cases and with the use of different methods. [6] and [7] presented solutions for planar or cylindrical problems. Other authors like [8]-[15] described the spherical problem, but accounted only for one phase, or they considered a semi-infinite region, or they did not account for the Gibbs-Thomson effect. In [16] and [17] a semi-analytical approach is presented, where the interface position is calculated numerically. After deducing the perturbation solution for the time-dependent movement of the phase front and of the temperature fields in the water and in the ice phase, we show a comparison between the analytical solution and a

numerical one and discuss the influence of heat conduction in the ice phase.

### Mathematical

### modelling

The spherical growth of the ice-water phase front  $R(t)$  is illustrated in Fig. 2. The initial ice nucleus with radius  $R_c$  that is predicted by a nucleation model starts to grow inside the super-cooled droplet of radius  $R_D$ . The temperature fields in the ice,  $T_i$ , and in the water phase,  $T_w$ , are described by

$$\frac{\partial T_i}{\partial t} = a_i \left( \frac{2}{r} \frac{\partial T_i}{\partial r} + \frac{\partial^2 T_i}{\partial r^2} \right), \quad 0 \leq r \leq R(t) \quad (1)$$

and

$$\frac{\partial T_w}{\partial t} = a_w \left( \frac{2}{r} \frac{\partial T_w}{\partial r} + \frac{\partial^2 T_w}{\partial r^2} \right), \quad R(t) \leq r \leq R_D. \quad (2)$$

The Stefan condition predicts the velocity of the phase front as

$$\rho L \frac{dR}{dt} = -\lambda_w \frac{\partial T_w}{\partial r} \Big|_{R(t)} + \lambda_i \frac{\partial T_i}{\partial r} \Big|_{R(t)}. \quad (3)$$

It states, that the velocity of the interface is limited by the conduction of the latent heat, which is emitted due to the phase change, into the ice and the water phase. The melting temperature at the interface is reduced due to the surface tension  $\sigma$  as the interface is non-planar [3]

$$T_{GT}(r) = T_m \left( 1 - \frac{2\sigma}{\rho L r} \right) \quad (4)$$

and called Gibbs-Thomson temperature. It is the boundary condition of the solid and the liquid phase on their common interface

$$T_w(t, R(t)) = T_i(t, R(t)) = T_{GT}(R(t)). \quad (5)$$

We assume and proof for each case, that the droplet is large enough so that the temperature reaches the ambient temperature at the outer radius

$$T_w(t, R_D) = T_\infty \quad (6)$$

For  $r = 0$  the temperature of the ice must be finite

$$T_i(t, 0) \text{ is finite.} \quad (7)$$

According to the nucleation model, the nucleation rate is evaluated for a constant temperature, which is the ambient temperature  $T_\infty$ . Therefore, the initial condition for the temperature in both phases is the ambient temperature as well

$$T_w(0, r) = T_i(0, r) = T_\infty. \quad (8)$$

The Gibbs-Thomson temperature is set as initial temperature on the ice-water interface. Introducing the dimensionless quantities  $\Theta_{w/i} = (T_{w/i} - T_m) / (T_\infty - T_m)$ ,  $r' = r / R_D$ ,  $R'(t') = R(t) / R_D$  and  $t' = a_w t / R_D^2$  as well as the Stefan number  $St = c_w (T_m - T_\infty) / L$ , which represents the ratio of sensible to latent heat that is present in phase change, and transforming the problem to a planar one by using the transformation  $u = \Theta_w r'$  and  $v = \Theta_i r'$  results in

$$\frac{\partial u}{\partial t'} = \frac{\partial^2 u}{\partial r'^2}, \quad 0 \leq r' \leq R'(t') \quad (9)$$

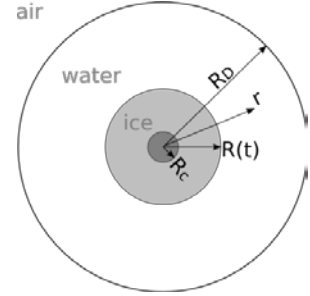


Figure 2. Geometry

$$\frac{\partial v}{\partial t'} = \frac{a_i}{a_w} \frac{\partial^2 v}{\partial r'^2}, \quad R'(t) \leq r' \leq 1 \quad (10)$$

with

$$\begin{aligned} u(t', R') = v(t', R') = \alpha, \quad u(t', 1) = 1, \quad v(t', 0) = 0, \\ u(0, r') = v(0, r') = r' \end{aligned} \quad (11)$$

where

$$\alpha = \frac{2\sigma T_m}{(T_m - T_\infty)\rho L R_D}. \quad (12)$$

The Stefan condition at the interface then reads

$$\frac{dR'}{dt'} = St \left( \left[ \frac{1}{R'} \frac{\partial u}{\partial r'} \right]_{R'} - \frac{u(R')}{R'^2} + \frac{\lambda_i}{\lambda_w} \left[ \frac{1}{R'} \frac{\partial v}{\partial r'} \right]_{R'} - \frac{v(R')}{R'^2} \right). \quad (13)$$

The transformations  $\varsigma = r' / R'(t')$  and  $\eta = (r' - R') / (1 - R')$  fix the phase front. The resulting equations are

$$-\varsigma \frac{dR'}{dt'} R' \frac{\partial v}{\partial \varsigma} + R'^2 \frac{\partial v}{\partial t'} = \frac{a_i}{a_w} \frac{\partial^2 v}{\partial \varsigma^2}, \quad 0 \leq \varsigma \leq 1 \quad (14)$$

$$\frac{dR'}{dt'} (1 - R') (\eta - 1) \frac{\partial u}{\partial \eta} + (1 - R')^2 \frac{\partial u}{\partial t'} = \frac{\partial^2 u}{\partial \eta^2}, \quad 0 \leq \eta \leq 1 \quad (15)$$

with

$$\begin{aligned} u(t', 0) = v(t', 1) = \alpha, \quad u(t', 1) = 1, \quad v(t', 0) = 0, \\ u(0, \eta) = \eta \left( 1 - \frac{R_c}{R_D} \right) + \frac{R_c}{R_D}, \quad v(0, \varsigma) = \varsigma \frac{R_c}{R_D}. \end{aligned} \quad (16)$$

The Stefan condition results in

$$\frac{dR'}{dt'} = St \left( \left[ \frac{1}{R'(1 - R')} \frac{\partial u}{\partial \eta} \right]_0 - \frac{u(0)}{R'^2} + \frac{\lambda_i}{\lambda_w} \left[ \frac{1}{R'^2} \frac{\partial v}{\partial \varsigma} \right]_1 - \frac{v(1)}{R'^2} \right). \quad (17)$$

These coupled, non-linear partial differential equations can be linearized by introducing a perturbation parameter, which is the Stefan number in our case [4], [5]. The approach for the linearization therefore is

$$\begin{aligned} R'(t') &= R_0 + St^n R_1 + St^{2n} R_2 + \dots \\ v(t', \varsigma) &= v_0 + St^n v_1 + St^{2n} v_2 + \dots \\ u(t', \eta) &= u_0 + St^n u_1 + St^{2n} u_2 + \dots \end{aligned} \quad (18)$$

After inserting the perturbation ansatz (18) into eqs. (14), (15) and (17) the terms that are multiplied by the same order of the perturbation parameter are compared and solutions for  $v$ ,  $u$  and  $R'$  for these orders are deduced. The exponent  $n$  has to be chosen so that the equations and the according boundary conditions can be fulfilled. According to [7] we introduce another time scale, which represents the long-term behaviour of our problem and does not have to fulfil the initial condition. But it satisfies the nonlinear interface condition independently from the exponent  $n$ . The long-time scale shrinks the time  $t'$  by multiplying by the Stefan number

$$\tau = t' St. \quad (19)$$

The temperatures  $\hat{v}$  and  $\hat{u}$  are therefore described by

$$St \left( \hat{R}'^2 \frac{\partial \hat{v}}{\partial \tau} - \frac{d\hat{R}'}{d\tau} \hat{R}' \hat{\varsigma} \frac{\partial \hat{v}}{\partial \hat{\varsigma}} \right) = \frac{a_i}{a_w} \frac{\partial^2 \hat{v}}{\partial \hat{\varsigma}^2}, \quad 0 \leq \hat{\varsigma} \leq 1 \quad (20)$$

$$St \left( \frac{d\hat{R}'}{d\tau} (1 - \hat{R}') (\hat{\eta} - 1) \frac{\partial \hat{u}}{\partial \hat{\eta}} + (1 - \hat{R}') \frac{\partial \hat{u}}{\partial \tau} \right) = \frac{\partial^2 \hat{u}}{\partial \hat{\eta}^2}, \quad 0 \leq \hat{\eta} \leq 1. \quad (21)$$

The circumflex indicates that the variables are expressed on the long-time scale. As the left-hand side of eqs. (20) and (21) is multiplied by the perturbation parameter already, the introduction of the perturbation ansatz yields a quasi-stationary temperature field

$$\hat{v} = \alpha \hat{\zeta} \quad (22)$$

$$\hat{u} = (1 - \alpha) \hat{\eta} + \alpha. \quad (23)$$

As mentioned above, the long-term solution cannot and must not fulfil the initial condition. Inserting the perturbation approach into the Stefan condition yields

$$\hat{R}'^2 (1 - \hat{R}') \frac{d\hat{R}'}{d\tau} = \left( \left| \hat{R}' \frac{\partial \hat{u}}{\partial \hat{\eta}} \right|_0 - \alpha (1 - \hat{R}') \right) + \frac{\lambda_i}{\lambda_w} \left( (1 - \hat{R}') \frac{\partial \hat{v}}{\partial \hat{\zeta}} \right)_1 - \alpha (1 - \hat{R}') \quad (24)$$

The resulting 0<sup>th</sup>-order term is independently from the exponent  $n$  and reads

$$\hat{R}_0'^2 (1 - \hat{R}_0') \frac{d\hat{R}_0'}{d\tau} = |\hat{R}_0' - \alpha|. \quad (25)$$

Assuming  $\hat{R}_0' > \alpha$  and integrating, we gain

$$-\frac{1}{3} (\hat{R}_0' - \alpha)^3 + \frac{1}{2} (1 - 3\alpha) (\hat{R}_0' - \alpha)^2 + \alpha (2 - 3\alpha) (\hat{R}_0' - \alpha) + \alpha^2 (1 - \alpha) \ln(\hat{R}_0' - \alpha) = \tau + C_o \quad (26)$$

The position of the ice front is a function of  $\tau^{1/3}$ . As the long-term and the short-time scale have to be matchable at the upper end of the short-time scale and the lower end of the long-time scale, the solution on the short-time scale must show a similar behaviour as the long-time solution. Therefore we set  $n = 1/3$  for the solution on the short-time scale and obtain the phase front as function of  $t'^{1/3}$

$$R_0' = 0 \quad (27)$$

$$R_1'(t') = (3\alpha t' + C_i)^{1/3}. \quad (28)$$

The constant from integration  $C_i$  can be determined from the initial condition that has to be fulfilled by  $R_1$ ,

$$R_1'(t' = 0) = \frac{R_c}{R_D}. \quad (29)$$

Therefore  $C_i$  reads

$$C_i = \frac{1}{St} \left( \frac{R_c}{R_D} \right)^3. \quad (30)$$

As the 0<sup>th</sup>-order of the radius equals zero, we again get a quasi-steady temperature in the ice phase

$$v = \alpha \zeta, \quad (31)$$

and transformed back into  $r'$ -coordinate

$$v = \alpha \frac{r'}{R'(t')}. \quad (32)$$

Using the prescribed method we cannot describe a transient temperature field in the ice phase; the temperature changes only due to the change in the Gibbs-Thomson temperature, which increases with the growing ice particle, and equals the Gibbs-Thomson temperature. As there is no temperature gradient into the ice phase, there is no conduction of the latent heat into the ice phase according to the Stefan condition. We will discuss the influence of the ice phase in the next section.



The 0<sup>th</sup>-order solution in the water phase is given by

$$u_0 = (1 - \alpha)\eta + \alpha + 2 \left( \frac{R_c}{R_D} - \alpha \right) \sum_{n=1}^{\infty} \frac{1}{n\pi} \sin(n\pi\eta) \exp(-(n\pi)^2 t'), \quad (33)$$

and written in  $r'$ -coordinate

$$u_0 = (1 - \alpha) \frac{r' - R'(t')}{1 - R'(t')} + \alpha + 2 \left( \frac{R_c}{R_D} - \alpha \right) \sum_{n=1}^{\infty} \frac{1}{n\pi} \sin \left( n\pi \frac{r' - R'(t')}{1 - R'(t')} \right) \exp(-(n\pi)^2 t'). \quad (34)$$

With knowing the temperature profile we can calculate the 2<sup>nd</sup>-order solution for the radius as

$$R_2'(t') = \frac{1}{(3\alpha t' + C_i)^{2/3}} \int (3\alpha t' + C_i)^{1/3} \left( 1 + \alpha + 2 \left( \frac{R_c}{R_D} - \alpha \right) \sum_{n=1}^{\infty} \exp(-(n\pi)^2 t') \right) dt'. \quad (35)$$

We want to simplify this expression to be able to give an explicit solution. A numerical estimation of the integral with trapezoidal rule shows that the assumption

$$2 \left( \frac{R_c}{R_D} - \alpha \right) \int (3\alpha t' + C_i)^{1/3} \sum_{n=1}^{\infty} \exp(-(n\pi)^2 t') dt' = 0 \quad (36)$$

causes an error of only 1.5% up to the time  $t_{stable}$  that corresponds to the maximum size of the spherical ice particle  $R_{stable}$ . That term is therefore negligible and we can write

$$R_2'(t') = \frac{1 + \alpha}{4\alpha} (3\alpha t' + C_i)^{2/3} + D_i. \quad (37)$$

As

$$R_2'(t' = 0) = 0, \quad (38)$$

the constant  $D_i$  can be determined as

$$D_i = -\frac{1 + \alpha}{4\alpha} C_i^{2/3}. \quad (39)$$

Therefore we gain as function for the ice-water phase front

$$R'(t') = St^{1/3} (3\alpha t' + C_i)^{1/3} + St^{2/3} \frac{1 + \alpha}{4\alpha} (3\alpha t' + C_i)^{2/3}. \quad (40)$$

## Results and Discussion

### Comparison with numerical calculation

The presented analytical solution shall be compared with numerical calculations. Therefore a code for solving the energy equations in the ice and in the water phase has been written in FORTRAN90. The interface position is iterated for each time step. The equations are discretized implicitly via finite differences, first order in time and second order in space. As the numerical procedure for solving the spherical problem can easily be transformed into the planar problem, an existing exact solution for the planar problem [18] has been used to validate the code. The resulting deviation between the analytical and the numerical results for the planar problem is less than 1%.

Figure 3 shows the comparison between the analytical and the numerical solution for the movement of the phase front where  $R_c / R_D = 5.1e - 04$  and  $St = 0.171$ . The assumption of spherical ice growth holds up to  $R'_{stable} = 0.0093$ . The relative error in the time that corresponds with  $R'_{stable}$ ,  $t'_{stable}$ , is about 4%.

The temperature field is also of importance, as it is an initial condition for the simulation of the dendritic growth of the ice particle with the DNS code FS3D. Figures 4 and 5 show the ice and water temperature as comparison between the analytical and the numerical calculation at  $t_{stable}$ . As the transformation back into  $T_i$  would cause a singularity at  $T_i(r = 0)$  in the numerical solution, the results are shown as  $v(r')$  and  $u(r')$ . However, to estimate the relative error, the deviations in  $v(r')$  and  $u(r')$  are expressed in  $T_i(r)$  and  $T_w(r)$  as these temperatures are used as input for the simulation with FS3D. The maximum relative error in the ice phase as well in the water phase is much smaller than 1%.

### Discussion about heat conduction into the ice phase

The deduction of the analytical solution with perturbation methods results in a quasi-steady solution for the temperature field in the ice phase as already mentioned. The comparison with the temperature field from the numerical calculation as shown above confirms the quasi-steady behaviour. The movement of the ice-water phase front is not influenced by the ice phase in the quasi-steady case. The comparison of the numerical calculation that accounts for heat conduction in the ice and in the water phase with one, which only accounts for the heat conduction in the water phase, shows that the maximum relative error in the duration until  $R_{stable}$  is reached is about 0.3%. It seems that the ice particle is that small, that the heat conduction in the ice phase happens much faster than the movement of the phase front, which induces the temperature change. So the information about a change in temperature spreads through the whole ice particle nearly instantaneously.

### Conclusions

A closed form analytical approximate solution has been obtained for the ice-water interface as function of time as well as for the temperature fields in the ice and in the water phase as function of time and space. It has been shown that the ice-water interface moves with the cube root of time and that the temperature in the ice phase is quasi-steady. By comparing the analytical solution with a numerical solution of the underlying partial differential equations for this specific problem, it can be seen that both are in very good agreement for small perturbation parameters, i.e. small Stefan numbers. This is exactly the case under investigation for ice-crystal growth in clouds. It can be concluded, that the spherical ice growth inside a super-cooled droplet can be described with analytical methods. These analytical calculations are used as a sub-grid model for Direct Numerical Simulations on dendritic ice growth. Further investigations will focus on increasing the range of validity of the analytical solution for higher Stefan numbers - which correspond with a higher sub-cooling - as perturbation parameter by the use of Shanks transformation or similar methods.

### Acknowledgement

The authors greatly acknowledge financial support of this project from DFG for the Collaborative Research Center SFB-TRR 75.

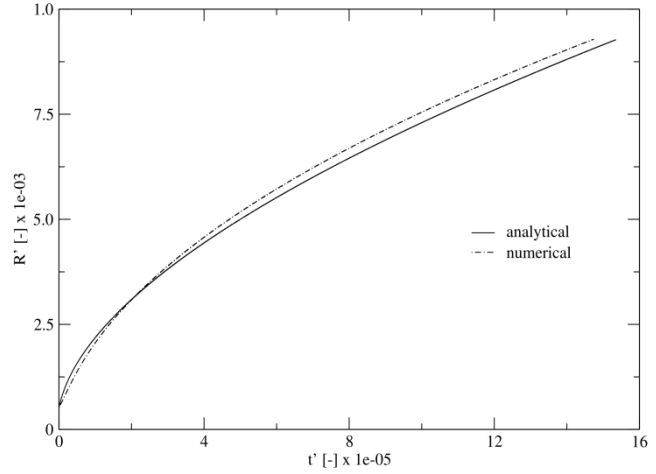


**Figure 3.** Comparison of the analytical and numerical calculation of the phase front growth

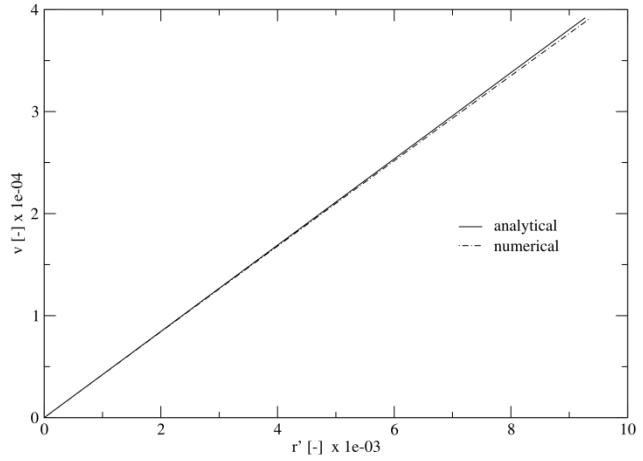


**Figure 4.** Comparison of the analytical and numerical calculation of the temperature field in the ice phase at  $t_{stable}$

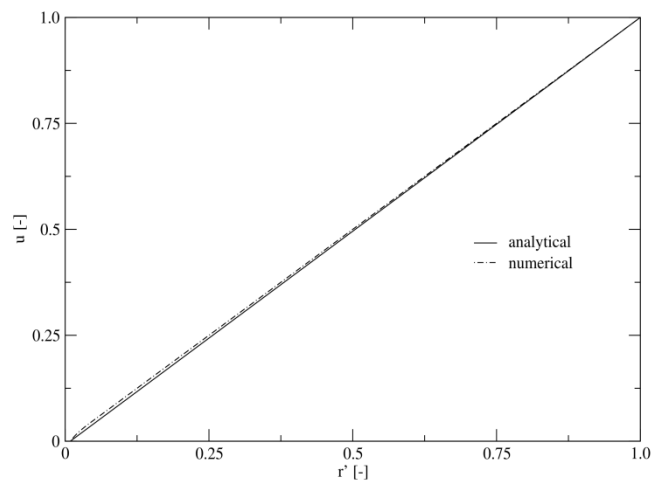


**Figure 5.** Comparison of the analytical and numerical calculation of the temperature field in the water phase at  $t_{stable}$

## Nomenclature

latin			letters	greek letters	
$a$	$[m^2/s]$	thermal diffusivity	$\alpha$	$[-]$	surface tension expression
$c$	$[J/(kgK)]$	specific heat capacity	$\eta$	$[-]$	coordinate in the water phase
$C_i$	$[-]$	constant	$\lambda$	$[N/(sK)]$	heat conductivity
$D_i$	$[-]$	constant	$\rho$	$[kg/m^3]$	density
$n$	$[-]$	exponent of perturbation parameter	$\sigma$	$[N/m]$	surface tension
$r$	$[m]$	radial coordinate	$\zeta$	$[-]$	coordinate in the ice phase
$R$	$[m]$	phase front position	$\tau$	$[-]$	time
$R_c$	$[m]$	initial nucleus radius	$\Theta$	$[-]$	temperature
$R_D$	$[m]$	droplet radius			
$R_{stable}$	$[m]$	maximum spherical ice particle radius	<i>subscripts</i>		<i>superscripts</i>
$St$	$[-]$	Stefan number	$i$	ice	‘ dimensionless
$t$	$[s]$	time	$w$	water	^ long-term scale
$t_{stable}$	$[s]$	duration for reaching $R_{stable}$	$m$	melt	
$T$	$[K]$	temperature	$\infty$	ambient	
$T_{GT}$	$[K]$	Gibbs-Thomson temperature	0	0 <sup>th</sup> -order	
$u$	$[-]$	temperature in the water phase	1	1 <sup>st</sup> -order	
$v$	$[-]$	temperature in the ice phase	2	2 <sup>nd</sup> -order	

## References

- [1] Mullins, W. W. und Sekerka, R. F. Morphological Stability of a particle Growing by Diffusion or Heat Flow. *Journal of Applied Physics*. 1963, Vol. 34, pp. 323-329.
- [2] Rauschenberger, P., et al., et al. Comparative assessment of Volume-of-Fluid and Level-Set methods by relevance to dendritic ice growth in supercooled water. *Computers and Fluids*. 2013, Vol. 79, pp. 44-52.
- [3] McDonald, J. E. Homogenous Nucleation of Supercooled water Drops. *Journal of Meteorology*. 1953, Vol. 10, pp. 416-433.
- [4] Aziz, A. und Na, T. Y. *Perturbation methods in heat transfer*. s.l. : Hemisphere Publishing, 1984.
- [5] Nayfeh, A. H. *Perturbation Methods*. s.l. : John Wiley, 1973.
- [6] Jiji, L. M. On the Application of Perturbation to Free-Boundary Problems in Radial Systems. *Journal of The Franklin Institute*. 1970, Vol. 289, pp. 281-291.
- [7] Weinbaum, S. and Jiji, L. M. Singular Perturbation Theory for Melting or Freezing in Finite Domains Initially Not at the Fusion Temperature. *Journal of Applied Mechanics*. 1977, pp. 25-30.
- [8] Wu, T. and Chen, Y.-Z. Analytical studies of Gibbs-Thomson effect on the diffusion controlled spherical phase growth in a subcooled medium. *Int. J. Heat Mass Transfer*. 2003, Vol. 39, pp. 665-674.
- [9] Stephan, K. und Holzknecht, B. Perturbation solutions for solidification problems. *Int. J. Heat Mass Transfer*. 1976, Vol. 19, pp. 597-602.
- [10] Langer, J. S. Instabilities and pattern formation in crystal growth. *Reviews of Modern Physics*. 1980, Vol. 52.
- [11] Pedroso, R. I. und Domoto, G. A. Perturbation solutions for spherical solidification of saturated liquids. *Journal of Heat Transfer*. 1973, Vol. 95, pp. 42-46.
- [12] Pedroso, R. I. und Domoto, G. A. Inwards spherical solidification - solution by the method of strained coordinates. *Int. J. Heat Mass Transfer*. 1973, Vol. 16, pp. 1037-1043.
- [13] Davis, G. B. und Hill, J. M. A Moving Boundary Problem for the Sphere. *Journal of Applied Mathematics*. 1982, Vol. 29, pp. 99-111.
- [14] Caldwell, J. und Kwan, Y.-Y. On the perturbation method for the Stefan problem with time-dependent boundary conditions. *Int. J. Heat Mass Transfer*. 2003, Vol. 46, pp. 1497-1501.
- [15] Mc Cue, S. W., Wu, B. und Hill, J. M. Classical two-phase Stefan problem for spheres. *Proceedings of The Royal Society A*. 2012, Vol. 464, pp. 2055-2076.

- [16] Case, E. und Tausch, J. An integral equation method for spherical Stefan problems. *Applied Mathematics and Computation*. 2012, Vol. 218, pp. 11451-11460.
- [17] Das, S. und Rajeev. An approximate analytical solution of one-dimensional phase change problems in a finite domain. *Applied Mathematics and Computation*. 2011, Vol. 217, pp. 6040-6046.
- [18] Carslaw, H. S. und Jaeger, J. C. *Conduction of Heat in Solids*. s.l. : Oxford University Press, 1959.

## Numerical and Experimental Study of Mannitol/Water Droplet Evaporation and Drying

Srikanth Reddy Gopireddy<sup>1</sup>, Martin Koester<sup>2</sup>, Eva Littringer<sup>2</sup>, Axel Mescher<sup>3</sup>, Peter Walzel<sup>3</sup>, Nora Urbanetz<sup>2</sup> and Eva Gutheil<sup>1</sup>

1: Interdisciplinary Center for Scientific Computing, University of Heidelberg, Germany

2: Research Center Pharmaceutical Engineering GmbH, Graz, Austria

3: Department of Biochemical and Chemical Engineering, TU Dortmund, Germany

### Abstract

This paper presents a model to describe the evaporation and drying behavior of a single quiescent spherical bi-component mannitol/water droplet, since the models available in literature for droplet evaporation and drying are very simplified and none of them studied the system of a sugar dissolved in water droplets. The water evaporation and solid layer formation in the bi-component droplet is computed using a modification of Brenn's bi-component vaporization model. Non-ideal behavior of the mannitol/water solution is considered through the ASOG method to calculate the activity coefficient of water. The system under consideration is governed by the continuity (diffusion) and energy equations, which are solved using a finite difference method. The simulation results reveal that, as the water evaporates, the droplet starts to shrink and a concentration gradient develops inside the droplet. When the solute concentration further increases at the surface, a thin solid layer forms. This solid surface hampers the further solvent evaporation causing the droplet temperature to rise. The effect of drying conditions such as gas velocity, temperature, and relative humidity on evaporation and drying is studied and simulation results are compared with experiment. The present model effectively captures the initial stages of single droplet drying.

---

### Introduction

For many years active pharmaceutical ingredients (APIs) are delivered to the lung via inhalation aerosols. Dry powder inhalers (DPI) are commonly used to achieve aerosols of a micronized solid API. To guarantee a reliable and constant dosing, the flow properties of the formulation are of high interest. Since the micronized API with a particle size of 1  $\mu\text{m}$  - 5  $\mu\text{m}$  [1] exhibits poor flowability, carriers consisting of larger particles are added to the formulation in order to carry the API particles on their surface. Due to the sufficiently large size of the carrier particles, the adhesive mixtures exhibit adequate flowability. In addition to the flowability the surface structure of the carrier is crucial to the formulation performance [2] and has to be controlled during development. In the last decade, mannitol was identified as a possible carrier for DPIs [3] and efforts were made to tailor the surface structure [4-6]. Spray dried mannitol particles in general have a spherical shape and can consist of two major polymorphs [4, 7]. Recent studies [8-9] reveal that process parameters like droplet size, gas temperature and relative humidity exhibit strong correlation with the final powder characteristics.

In this paper the drying of an aqueous mannitol solution during spray drying is simulated. Many studies present the evaporation phenomena associated with pure and multi-component droplets, but there is a lack of a mathematical model which can predict evaporation and drying behavior of a droplet containing a sugar dissolved in water because of the unknown physical behavior, unavailability of experimental results and complexity of the problem. Mezhericher *et al.* [10] provide a detailed review of all existing theoretical models of evaporation and drying of single droplets containing dissolved and insoluble solids.

Experiments are carried out to evaluate the effect of gas temperature, velocity and humidity as well as mannitol concentration on the drying of mannitol/water droplets. The numerical results are compared to the crystallization of mannitol under controlled conditions and in a pilot scale sized spray dryer.

### Experimental test-rig

#### Spray drying:

Aqueous solutions of 15% (in mass) mannitol (Pearlitol® 200SD, Roquette, F-Lestrem) were spray dried in a pilot scale spray dryer equipped with a LAMROT atomizer as described by Littringer *et al.* [8]. The spray dryer had a total height of 3.7 m (2.2 m conical part) and a radius of 1.35 m. The rotation speed of the LAMROT atomizer was set to 7200 rpm to achieve droplet sizes resulting in particles within a commonly used carrier size range. A feed rate of 10 l/h was used. Two different drying temperatures (70°C and 100°C outlet temperature) were chosen to evaluate the differences in drying behavior. The acquired samples were characterized with respect to particle size, size distribution, surface structure and density.

#### Droplet size distribution:

The droplet size distribution of the sprays generated by the LAMROT atomizer was measured using a Spraytec (Malvern, UK-Worcestershire) as described by Littringer *et al.* [8]. The distance between the measurement zone and the atomizer was fixed to a value of 28 cm and the atomizer's rotation speed was varied from 5000 rpm to 12000 rpm to mimic the conditions inside of the pilot spray dryer. The mannitol content of the sprayed solution was varied between 15 and 30% (in mass).

#### Particle size distribution:

Laser light diffraction (Helos/KF-Magic, Sympatec, D-Clausthal-Zellerfeld) including a dry dispersing system (Rodos, Sympatec, D-Clausthal-Zellerfeld) was used to determine particle size distributions of the spray dried mannitol samples at a dispersion pressure of 0.3 bar as described by Littringer *et al.* [8].

#### Particle surface investigations:

Mannitol samples were examined using a scanning electron microscope (Hitachi H-S4500 FEG, Hitachi High-Technologies Europe, D-Krefeld; Particles were not sputtered) operating at 1 kV as given in the work of Littringer *et al.* [8]. Representative images were chosen for further studies.

#### Density measurements:

The samples' density was measured by helium pycnometry (AccuPycII1340, Micromeritics, D-Aachen) as well as by mercury intrusion pycnometry following the study of Littringer *et al.* [11]. The porosity was determined with a low-pressure (Pascal 140, Thermo Fisher Scientific, I-Milano) and a high-pressure unit (Porosimeter 2000, Carlo Erba, I-Milano). Measurements were performed up to a pressure of 2000 bar.

#### Mathematical modeling

The problem under consideration is the evaporation and drying of an isolated single spherical droplet consisting of a binary mixture of a liquid and a dissolved solid material with low or zero vapor pressure. During the evaporation and drying of the bi-component droplet, there are four stages, which the droplet undergoes as explained by Nesic and Vodnik [12], see Fig. 1. In the initial stage, the droplet temperature quickly rises to an equilibrium temperature, which is most often near to the wet bulb temperature of the drying conditions with some solvent evaporation. In the second stage, the droplet starts to shrink as solvent evaporates and solute mass fraction increases at the surface;

this leads to slight raise in the droplet temperature. The increase in solute mass fraction at the droplet surface hinders further evaporation as vapor pressure of the solvent at the surface drops. The third stage of drying starts when the solute mass fraction at the surface rises to a threshold value, which most often is equal to the saturation of the solute in the solvent, whereupon the solid/crust formation begins. The solid layer thickens with time and develops into the droplet interior as depicted in Fig. 1, and a rapid fall in evaporation rate is observed. In this period, the heat penetrated into the liquid is used for heating the droplet causing the droplet temperature to rise rapidly. Further drying of the droplet depends on the vapor diffusivity through the solid layer. In the final stage of particle drying, solvent boils, leading to dried product formation. The phenomena of evaporation and drying of single droplets can be well defined using the diffusion and heat conduction equations in spherical coordinates. The diffusion equation for the substance  $i$  in the droplet is formulated in terms of mass fraction  $Y_i$ , reads

$$\frac{\partial Y_i}{\partial t} = \frac{D_{12}}{r^2} \left[ \frac{\partial}{\partial r} \left( r^2 \frac{\partial Y_i}{\partial r} \right) \right], \quad (1)$$

where  $D_{12}$  is the binary diffusion coefficient in the liquid. In this equation  $i = 1$  denotes the solvent (water) and  $i = 2$  denotes the solute (mannitol). Initially, the droplet is a homogenous mixture,  $Y_i = Y_{i0}$  at  $t = 0$ . At the droplet center,  $r = 0$ , the regularity condition,  $\partial Y_i / \partial r = 0|_{r=0}$ , must be satisfied at any time. The boundary condition at the droplet surface accounts for the change in droplet size,

$$-D_{12} \frac{\partial Y_i}{\partial r} - Y_i \frac{\partial R}{\partial t} = \frac{\dot{m}_i}{A \rho_l} \quad (2)$$

at  $r = R(t)$ . Here  $\dot{m}$  is the mass evaporation rate of substance  $i$  across the droplet surface,  $R(t)$  and  $A$  are time dependent droplet radius and surface area, respectively, and  $\rho_l$  is the liquid density.  $\dot{m}$  is zero for non-

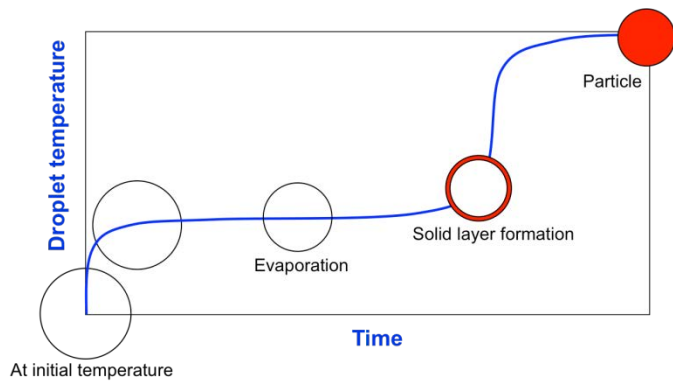


Figure 1. Schematic diagram of different stages in single droplet

evaporating solute (mannitol),  $i = 2$ . The diffusion process described through Eq. (1) provides the mass fraction profiles inside the droplet. For solving this equation, the evaporation rate from the droplet surface,  $\dot{m}$  is needed, which appears in Eq. (2). This rate of evaporation is determined based on Sherwood analogy of Abramzon and Sirignano's model [13], and in the present study, it is used in the extended form for a bi-component liquid mixture as modified by Brenn *et al.* [14],

$$\dot{m} = \sum_{i=1}^N 2\pi R_i \rho_f D_f \widetilde{\text{Sh}} \ln(1 + B_{M,i}), \quad (3)$$

where  $R_i$  is volume equivalent partial radius of component  $i$ , based on its corresponding volume fraction, computed as  $R_i = R(\frac{V_i}{V})^{\frac{1}{3}}$ ,  $\widetilde{\text{Sh}}$  is the modified Sherwood number and  $D_f$  is water diffusivity in film.  $B_{M,i}$  is the Spalding mass transfer number [13, 15] for component  $i$ .

Nesic and Vodnik [3] implemented a similar approach, but they do not account for the volume fraction based radius in the calculation of the evaporation rate, i.e., droplet radius  $R$  is used instead of  $R_i$  in computing  $\dot{m}$ . Since the solute vapor pressure is low or zero and the droplet's solute evaporation rate is zero or very small, negligence of the volume correction (using  $R$  in the place of  $R_i$ ) may lead to an artificial increase in evaporation rate. In the present situation, the summation in Eq. (3) is only over component 1, because solute (mannitol) does not evaporate, but for the sake of generality, the summation is kept. The evaporation rate retardation due to solid layer resistance may be considered through modification of Eq. (3) following the work of Nesic and Vodnik [3]

$$\dot{m} = \frac{\sum_{i=1}^N 2\pi R_i \rho_f D_f \widetilde{\text{Sh}} \ln(1 + B_{M,i})}{1 + \widetilde{\text{Sh}} D_f \delta / [2D_s(R - \delta)]}, \quad (4)$$

where  $\delta$  is the solid layer thickness at the droplet surface and  $D_s$  is the diffusivity of vapor in the solid layer. When the solute mass fraction at the droplet surface reaches a threshold value, which is most often near saturation solubility level, there is initiation of solid layer. This solid layer on the droplet surface offers significant resistance to evaporation and is evident from the second term in the denominator of Eq. (4).

The heat conduction equation, describing the conductive heat transfer within the droplet, is written as

$$\frac{\partial T}{\partial t} = \frac{\alpha}{r^2} \left[ \frac{\partial}{\partial r} \left( r^2 \frac{\partial T}{\partial r} \right) \right], \quad (5)$$

where  $T$  is the liquid temperature,  $\alpha$  denotes the thermal diffusivity,  $r$  is the radial coordinate, and  $t$  stands for time. The above equation is solved with the following initial and boundary conditions: At  $t = 0$  s, the droplet is at uniform temperature,  $T = T_0$ . At the droplet center,  $r = 0$ , zero gradient condition prevails at any time,  $\partial T / \partial r = 0|_{r=0}$ . The energy balance at the droplet surface is given through the boundary condition

$$k_l \frac{\partial T}{\partial r} = h(T_g - T_s) + L_V(T_s) \rho_l \frac{\partial R}{\partial t} \quad (6)$$

at  $r = R$ , where  $R$  is the droplet radius. In Eq. (7),  $T_s$  denotes droplet surface temperature,  $T_g$  stands for gas temperature in the bulk, and  $L_V(T_s)$  is the latent heat of vaporization at the surface temperature,  $T_s$ . In this work, first Eq. (5) is solved numerically with initial and boundary condition as defined above using a finite difference method. It is observed that the gradient in droplet temperature from the center to the droplet surface is very small as the computed Biot number ( $\text{Bi} = h/k_s R = k_g/(2k_s) \text{Nu}$ ) always remains below 0.5. Therefore, in the remaining simulations, uniform temperature within the droplet is assumed, which is a valid assumption as per the revelations made by Mezhericher *et al.* [16]. The droplet temperature continuously changes due to heat transfer from ambient gas to the binary liquid droplet, and it is computed using the energy balance across the droplet, which gives the net heat transferred into the droplet [13], as

$$m C_{pL} \frac{dT_s}{dt} = \dot{m} \left[ \frac{C_{pLf}(T_\infty - T_s)}{B_T} - L_V(T_s) \right], \quad (7)$$

where  $B_T$  is the Spalding heat transfer number. Equation (7) needs modification in order to account for the solid layer formation at droplet surface, and this is achieved through the equation written in terms of the solid layer thickness,  $\delta$ , as

$$m C_{pL} \frac{dT_s}{dt} = \frac{Q_L + \dot{m} L_V(T_s)}{1 + \widetilde{\text{Nu}} k_{gf} \delta / [2k_s(R - \delta)]} - \dot{m} L_V(T_s), \quad (8)$$

where  $\widetilde{\text{Nu}}$  is the modified Nusselt number. Similar to Eq. (4), the second term in denominator inside the bracket of Eq. (8) denotes the resistance due to solid formation at the droplet surface, and its effect becomes significant only when the solid layer thickness,  $\delta$ , is positive. The difference between heat transfer and mass transfer resistance is that the ratio of diffusion coefficients  $D_{12}/D_s$  is larger than the ratio  $k_g/k_s$  [3]. The modified Sherwood and Nusselt numbers are computed as given by Abramzon and Sirignano [13].

The presence of mannitol with water inside the droplet leads to non-ideal liquid behavior, which must be accounted for in calculating the mole fraction of water vapor at the droplet surface. In this work, the liquid mixture is treated as real or non-ideal by determining the influence of individual components on each other through their activity coefficients. The activity coefficient of water in mannitol/water solution is computed using analytical solution of groups (ASOG) contribution method [17]. The effect of temperature on the water activity in mannitol/water solutions for a temperature of 94.5°C and at 160°C computed using ASOG method is shown in Fig. 2.

In the present formulation, the activity coefficient,  $\gamma_i$ , is only required for  $i = 1$ , which enters the calculation of Spalding's mass transfer number,  $B_{M,1}$ , c.f. Eq. (4), in which the mass fraction,  $Y_{1,s}$ , of the evaporating component appears. This mass fraction is calculated from the mole fraction,  $X_1$ , of the evaporating component water, in terms of the activity coefficient,

$$X_1 = \frac{p_{\text{vap},1}}{p_m} \gamma_1 X_{L,1}, \quad (9)$$

where  $p_{\text{vap},1}$  is the vapor pressure of pure water and  $p_m$  is the total mixture pressure, which is equal to the ambient gas pressure, in the present study it equals the atmospheric pressure.

### Numerical solution procedure

The partial differential equation, Eq. (1), with initial and boundary conditions, is solved numerically at every time and spatial location using second order explicit finite difference method. The energy equation, Eq. (8), is an ordinary differential equation, solved using a Runge-Kutta 4<sup>th</sup> order method. The droplet is discretized into equal distant grid points at any given time, and grid independency of the numerical method is tested using different grid sizes with the number of grid points varying from 10 to 100. The value of 50 grid nodes is found to perform well.

### Results and discussion

The simulation of evaporation and drying of single droplets containing mannitol in water is carried out under various drying conditions such as surrounding gas temperature, gas velocity, relative humidity and different initial mannitol mass fraction in water to investigate their effect on drying characteristics. The droplet is assumed to be spherical during the evaporation and drying processes. The thermal properties of mannitol and mass diffusivity of mannitol are given by Grigoriev and Meylikhov [18], and the critical temperature and pressure of mannitol are taken from Daubert and Danner [19]. The vapor diffusion coefficient through the solid layer of mannitol,  $D_s$  and solid thermal conductivity,  $k_s$  are unavailable in literature, therefore, they are computed following the work of Nescic and Vodnik [12]. Physical and thermal properties in the film are estimated at the reference composition using the 1/3<sup>rd</sup> rule [20]. The physical and thermal properties of mannitol/water are computed with the standard rules of mixing. The increase of solubility of mannitol in water with temperature is taken from measurements, and is shown in Fig. 3. The crust/solid layer at the droplet surface is presumed to develop when the mannitol mass fraction becomes 0.9, which is much more than the saturation, in order to avoid re-dissolution of solid layer with increased temperature as the experiment shows strong increase of solubility with temperature. This assumption may need further investigation in future.

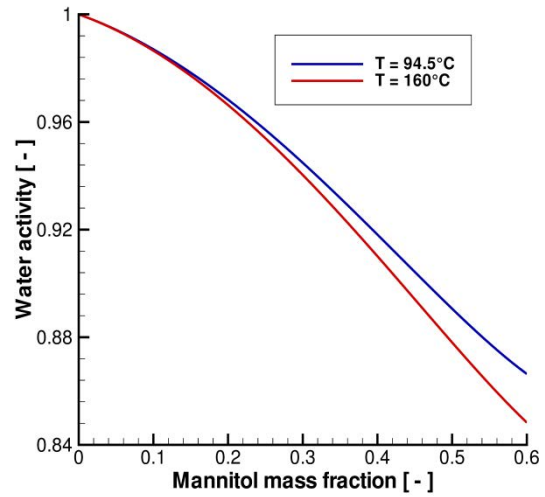


Figure 2. Numerical results of water activity in mannitol/water solution at 94.5 and 160°C

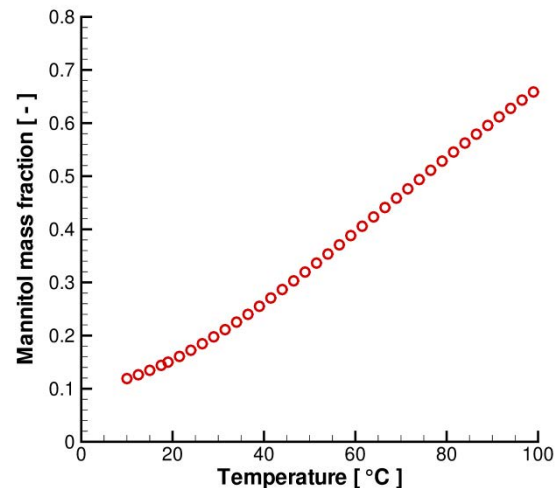
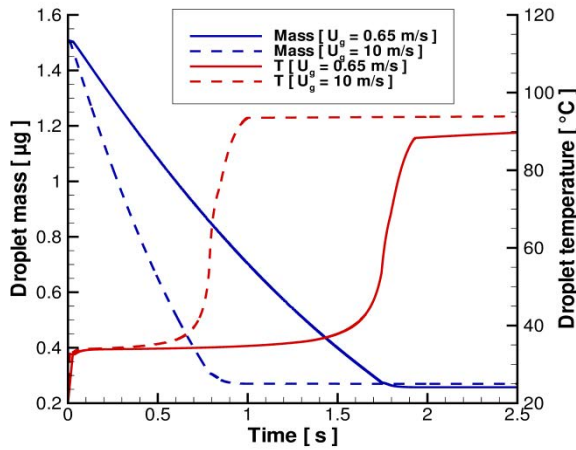
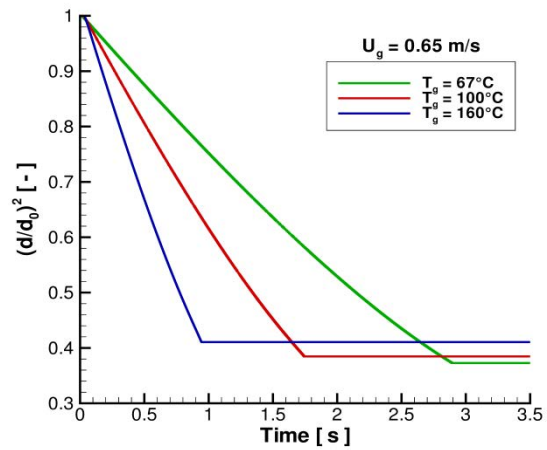


Figure 3. Experimental data of mannitol solubility in water





**Figure 4.** Effect of gas velocity on the temporal evolution of droplet mass and temperature



**Figure 5.** Effect of gas temperature on the droplet surface area

The present simulation results refer to an initial droplet of radius of 70  $\mu\text{m}$  at 20°C containing 0.15 mannitol mass fraction subjected to air with 0.5% R.H. (relative humidity) flowing at 0.65 m/s [8] with 100°C initial gas temperature (standard case). The drying conditions for the numerical simulations are taken from the experiment. Figure 4 shows the change of mannitol/water droplet mass and surface temperature with time for the standard case and for increased initial gas velocity of  $U_g = 10$  m/s. Initially, the droplet temperature rises quickly to an equilibrium value for the given drying conditions and whereupon there is no significant increase in droplet temperature, and droplet mass reduces due to continuous water evaporation. After an initial heating period, the droplet temperature rises very quickly indicating the formation of a solid layer where upon the rate of evaporation is reduced due to added resistance coming from the solid layer, which is reflected in the droplet mass profile. The increased gas flow rate increases convection and thereby the water evaporation, hence there is quicker development of solid layer. The solid layer forms in about 1.7 s with 0.65 m/s, whereas with 10 m/s, the solid layer forms in about 0.75 s. A closer look reveals that there is higher droplet mass at a given time after solid layer formation when compared with lower gas velocity situation, which means that increased gas velocity would lead to larger particle with higher porosity (see Fig. 7).

Figure 5 shows the effect of gas temperature on mannitol/water droplet normalized surface area. Elevated gas temperature leads to higher energy transfer from the gas to the droplet, and thereby, to an increase in the rate of droplet evaporation and drying. Regarding the drying process in general, the surface area continuously decreases due to water evaporation until the beginning of solid layer formation whereupon particle radius remains constant. The higher the gas temperature the shorter the time taken to solid layer formation: In case of 67°C the solid layer develops in about 2.9 s and with 100°C the solid layer forms in 1.7 s, whereas with 160°C, the same is observed in about 0.9 s. The surface area at the time of solid layer formation is larger with higher gas temperature, which means that elevated gas temperatures would result in larger particles at the end of the drying process (see Fig. 7).

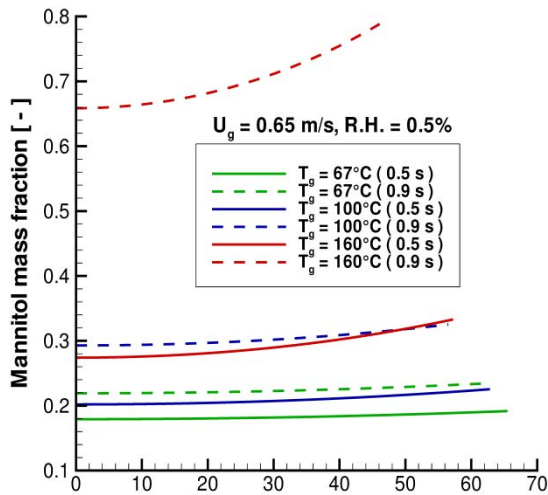


**Figure 6.** Effect of temperature on the profiles of mannitol mass fraction inside the droplet

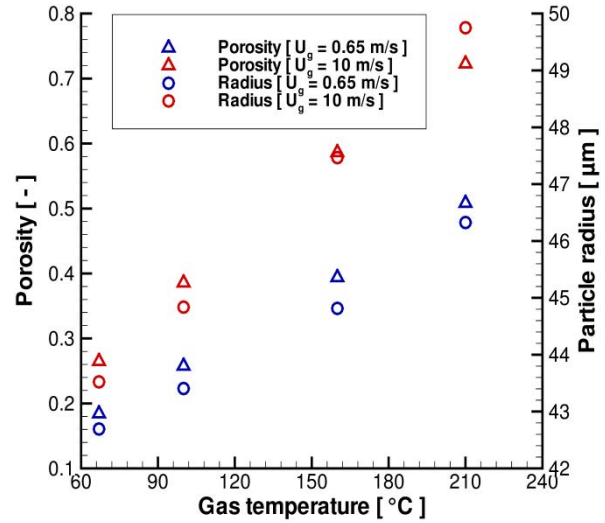


**Figure 7.** Effect of gas temperature and velocity on the particle porosity and final particle size

The effect of gas temperature on the development of mannitol mass fraction profiles inside the droplet of initial radius 70  $\mu\text{m}$  subjected to drying air with 0.5% R.H., flowing at 0.65 m/s with temperatures of 67, 100 and 160°C is shown in Fig. 6 at 0.5 s (solid lines) and at 0.9 s (dashed lines). Initially, the droplet interior has a homogeneous mannitol mass fraction of 0.15 (not shown) and with time, mannitol mass fraction gradients develop inside the droplet, and the droplet size reduces due to continuous water evaporation. For 100°C initial gas temperature, the droplet radius is 63  $\mu\text{m}$  at 0.5 s whereas at 0.9 s it is 56  $\mu\text{m}$ , which is seen in Fig. 6. Increased initial gas temperatures yield higher mass fraction gradients inside the droplet mainly due to the decreased activity coefficient of water in mannitol (see Fig. 2) and enhanced heat transfer. The activity coefficient decreases not only with increase in temperature but also with mannitol mass fraction, which is quite clearly seen at later times i.e., at 0.9 s. The effect of elevated gas velocity and temperature on the final particle porosity and particle radius is shown in Fig. 7. The porosity, defined as the ratio of the volume occupied by water at the instance of solid layer formation over that of the whole particle volume, increases with higher gas temperature and velocity because of quicker solid layer formation thereby yielding larger particles, which is also shown in Fig. 7. The computed porosity of a mannitol particle exposed to 160°C gas temperature (which corresponds to 70°C outlet gas temperature in the experiment) and 0.65 m/s gas velocity is 0.39, and the corresponding experimental value is found to be 0.41 [8]. In the present computations it is assumed that the initial gas temperature equals that of the heater [8], so that the “real” initial gas temperature may be about 15 K lower. Under the same conditions, the final particle radius after spray drying is 42  $\mu\text{m}$  in the experiment (see Fig. 8(a)), which can be compared to the corresponding computed value of 44.8  $\mu\text{m}$ , showing a very good agreement. In the experiment it is found that increased gas temperature leads to less porous particles with shriveled or non-spherical shape (see Figs. 8(a), (b) and (c)) and thereby denser particles are produced i.e., particle densities range between 830  $\text{kg/m}^3$  to 1,100  $\text{kg/m}^3$  for outlet gas temperatures of 70°C to 100°C [8]. In the computations particle shape is assumed to be spherical throughout the evaporation and drying, and therefore, the present numerical results show an increase in porosity with temperature as anticipated. This behavior will change when the final drying step is added to the present model, and if non-spherical particle formation will be considered.

Experimental data on the drying of mannitol droplets in spray drying supports the assumption of spherical particles for lower drying temperatures. Figure 8 shows samples of the mannitol dried under different drying

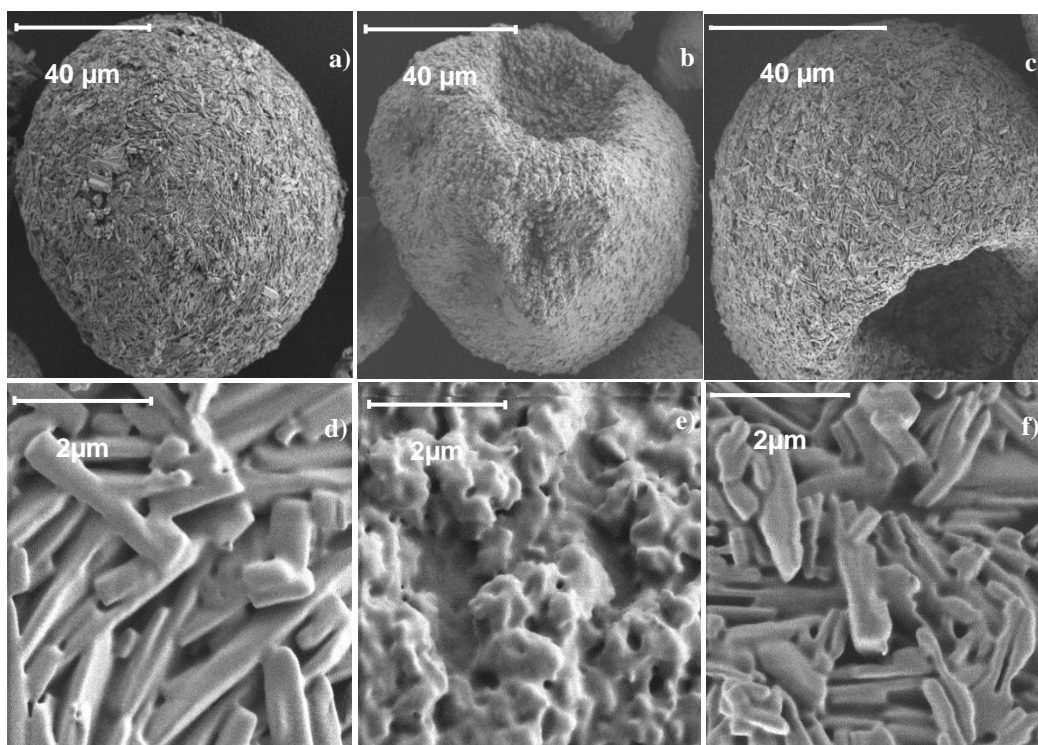


**Figure 8.** SEM images of mannitol samples spray dried at 70°C (a), 100°C (b) and 90°C (c). Zoomed images of the surface structures of these particles at 70°C (d), 100°C (e) and 90°C (f)

temperatures. For the outlet temperature of 70°C, a spherical mannitol particle is obtained, see Fig. 8(a). For the higher outlet temperature of 100°C the particle shape changes from spherical to a 'raisin like' structure, c.f. Fig. 8 (b), that may occur due to inflation of a drying shell and this transition is observed at 90°C, see Fig. 8(c). Higher temperatures lead to faster evaporation of the water, leading to less time to form a stable structure on the droplets surface. From the high porosity in combination with cuts of spray dried mannitol particles in previous studies [8] the formation of a hollow particle with an outer shell is evident. This is in good accordance with the simulations performed so far. The particle surface consists of small, needle shaped structures in case of low drying temperatures as shown in Fig. 8(d) and smaller, non-needle shaped structures for higher drying temperatures, c.f. Fig. 8(e), and the shift from needle shape to non-needle structures is seen in Fig. 8(f). The differences in the dried particle shapes will be addressed after the final drying step will have been included in the model.

## Conclusions

A model to describe the evaporation and the initial stages of drying of the mannitol in water is developed. The system under consideration is governed by the continuity (diffusion) and energy equations. Brenn's model [13] for bi-component droplet evaporation is modified to treat resistance from the solid layer during droplet heating and evaporation, and this extended model is used to compute the initial stages of mannitol/water droplet drying. The time dependent temperature inside the droplet appears to be uniform, and the change in droplet temperature due to heat exchange between the droplet surface and the surrounding gas is calculated with similar modifications used for mass evaporation rate, and resistance from the solid layer is formulated following Nesic and Vodnik [12], where variable physical and thermal properties and the volume fraction based radius are introduced. The mannitol/water liquid mixture is treated as non-ideal with the activity coefficient calculation using the ASOG contribution method.

The effect of various drying conditions on the evolution of particle characteristics is analyzed and the results are compared with experimental data. These drying conditions include the effect of gas temperature, gas velocity, initial mannitol mass fraction and relative humidity, which are found to have significant effect on the evaporation and drying characteristics of mannitol/water droplets. The study reveals that an increase in gas velocity and temperature both cause earlier formation of the solid layer and faster drying, leading to larger particles with higher porosity. Humidity leads to smaller size particles with less porosity, and a lower initial mannitol mass fraction implies that there is more water to evaporate leading to smaller size particles with longer drying times. Experimental and computed porosity and final particle size agree very well.

## Acknowledgements

The authors gratefully acknowledge the financial support of DFG through SPP 1423 and HGS MathComp.

## References

- [1] A. J. Hickey, *Aerosol Science and Technology* 18, 290 (1993/01/01, 1993).
- [2] A. H. d. B. Henderik Willem Frijlink, in *Pulmonary drug delivery - Basics, Application and Opportunities for Small Molecules and Biopharmaceutics*, C. V. f. M. u. N. GmbH, Ed. (2007).
- [3] S. K. Tee *et al.*, *International Journal of Pharmaceutics* 208, 111 (2000).
- [4] S. G. Maas *et al.*, *Atomization and Sprays* 20, 763 (2010).
- [5] W. Kaialy *et al.*, *Colloids and Surfaces B: Biointerfaces* 79, 345 (2010).
- [6] G. Pilcer, K. Amighi, *International Journal of Pharmaceutics* 392, 1 (2010).
- [7] D. E. Braun *et al.*, *International Journal of Pharmaceutics* 385, 29 (2010).
- [8] E. M. Littringer *et al.*, *Drying Technology* 30, 114 (2012/01/01, 2011).
- [9] S. G. Maas *et al.*, *Powder Technology* 213, 27 (2011).
- [10] M. Mezhericher *et al.*, *Drying Technology* 28, 278 (2010).
- [11] E. M. Littringer *et al.*, *Powder Technology* 246, 193 (2013).
- [12] S. Nesic, J. Vodnik, *Chemical Engineering Science* 46, 527 (1991).
- [13] B. Abramzon, W. A. Sirignano, *International Journal of Heat Mass Transfer* 32, 1605 (1989).
- [14] G. Brenn *et al.*, in *Proceedings of ICLASS*, Sorrento, Italy (2003).
- [15] O. Kastner, *Ph.D dissertation*, Friedrich-Alexander University of Erlangen-Nürnberg, Germany (2001).
- [16] M. Mezhericher *et al.*, *Drying Technology* 25, 1035 (2007).
- [17] A. Correa *et al.*, *International Journal of Food Science and Technology* 29(3), 331 (1994).
- [18] I. S. Grigoriev, E. Z. Meylikhov, (Eds.) *Physical Values Handbook*, EnergoAtomIzdat: Moscow (1991).
- [19] T. E. Daubert, R. P. Danner, *Data compilation of properties of pure compounds*, DIPPR Project, AIChE: New York (1992).
- [20] G. L. Hubbard *et al.*, *International Journal of Heat and Mass Transfer* 18, 1003 (1975).

## Deformation and Acceleration of Drop

A. G. Girin

Odessa National Maritime University, Odessa, Ukraine

### Abstract

The influence of drop internal deformation motion on fragmentation at low Weber numbers is studied. The selection mechanism between “bag” and “claviform” breakup modes is thus revealed. The system of equations of accelerating and deforming drop motion is derived. Pressure and surface tension force distributions along ellipsoidal drop surface as well as the utmost gas velocity increasing at drop equator due to drop flattening are taken into account. The obtained numerically solutions are used for analyzing the inertial forces field inside accelerating and deforming drop in the absolute motion.

Two stages of mass forces field formation are established. The conclusion is made that during the first stage the internal deformation flow is prevailing over the drop aerodynamic entrainment. So, the great transiency and non-uniformity of mass forces field, which are caused by internal deformation flow, prevent “bag” early performance over the range  $We > 30$  and provide “claviform” and “multimode” modes. Two necessary conditions are formulated and applied to analyzing the possibility of breakup modes in the Weber number range  $We < 80$ .

### Introduction

When the liquid drop is inserted into a gas stream, it is compelled to the action of various forces, the outer (aerodynamic pressure and viscous friction of gas stream, surface tension) as well as the inner (pressure field in liquid, inertia forces, liquid viscosity). In general, the drop participates in two component motions: transportation acceleration with its mass centre due to aerodynamic entrainment and relative internal deformation flow with respect to the mass centre. Both motions are important for quantitative determination of the phenomena the drop participates in, and are interrelated: acceleration onsets the field of inertia forces and thus affects the pressure inside drop, while the deformation changes the gas pressure and surface tension distributions along drop surface.

The deformation motion inside drop and its influence on fragmentation have been never investigated before. Various papers were aimed to build the deforming drop model in which the pressure values only at a drop equator  $p_2$ , and also in windward  $p_1$  and leeward  $p_3$  stagnation points on drop surface have been taken into account. Burgers (see [1]) established the drop early deformation law:  $d - d_0 = 2(p_1 - p_2)t^2 / 3d_0\rho_l$  ( $d$  – lateral drop diameter). Gordon [2] considered disturbing and stabilizing effects for drop deformation: pressure, inertia, internal circulation, surface tension forces and viscosity. Mitrofanov [3] elaborated the model, which accounts integrally for liquid viscosity and surface tension, is able to implement the drop ablation law and is suitable for potential flow as well as for supersonic one with a separation. The shortcoming of Mitrofanov’s model is the constant values of pressure coefficients  $c_{p1}, c_{p2}, c_{p3}$  which are independent on the degree of drop deformation.

If we take Mitrofanov’s pressure coefficient values,  $c_{p2} = -0.1, c_{p3} = -0.27$ , then it follows from Burgers’ solution that the drop mass centre initial acceleration is only 35% of the stagnation point  $I$  acceleration. The rest of stagnation point acceleration is due to drop deformation motion with respect to drop mass centre. This means that we must clearly distinct the motions of drop mass centre and of its stagnation point because namely the latter is usually fixed in observations. It is more important, that over the range of Weber number  $We < 100$  the mass forces play the key role in the drop breakup, namely, the “bag” and “claviform” generation is the result of the acceleration inertia forces action by means of aperiodic unstable waves, as was shown in [4]. Thus, the inertial forces of deformation motion must be accounted for in the total mass forces balance inside drop, because the fastest unstable wave might has been affected by the deformation inertia. Such evaluation of the deformation inertia role in the mass forces balance is done in present paper.

The specifics of the inner deformation flow are that it has the opposite, co- and counter-flow, directions at the windward and leeward drop surfaces. Then it follows that the deformation-induced inertia generates the non-uniform mass forces field inside the drop. The latter significantly influence on the fastest unstable wave, which parameters determine the kinetics of “bag” and “claviform” breakup modes [4], [5]. This requires examining of the inertia forces induced by the deformation flow inside drop, in order to estimate correctly the wavelength  $\lambda_m$  and period  $t_m$  of  $e$ -fold amplitude growth of fastest unstable disturbance. The deformation motion studying requires, in turn, the mathematical model, which is elaborated in present paper via the drop dynamic equations derivation. Eventually, analysis reveals the two stages: 1) initial dynamics of the fast drop deforming when the strong transiency and non-uniformity prevent the instability performance; 2) at the later stage the mass forces

field is almost uniform and the instability may be realized due to the increasing drop acceleration.

The analyzing of the suffice data obtained here gives the possibility to establish the selection mechanism between “bag” and “claviform” modes, because the question has remained after the paper [4], why within the empirical range  $30 < We < 60$  of “claviform” formation the “bag” mode itself does not occur, although the necessary lateral deformation for “bag” is thrice less than for “claviform”. The conclusion is drawn below that this problem is being solved at the first stage when transiency and non-uniformity of mass forces field prevent the “bag” performance; when the transiency diminishes, the only conditions for “claviform” exist already.

All over the further content the processes are considered until dimensionless time  $T=2$  because after the “bag” or “claviform” formation has begun, the drop is involved into the other mechanisms and forces action.

### Mathematical modeling

As was pointed out by Gordon, [2], an exact mathematical solution would require a complete knowledge of the aerodynamic pressures on the drop as a function of space and time. The pressure distribution depends upon drop shape, which shape is, in turn, governed in part by the external pressure distribution. Because of drop deformation the surface tension is varied from point to point on the drop surface. The surrounding flowfield, the velocity and pressure distributions depend strongly on the drop deformation degree. For example, within the frames of potential solution [6] already at  $D \equiv d/d_0 = 1.71$  the velocity at the equator is  $V_2 = 4V_\infty$  and pressure coefficient is  $c_{p2} = -15$ . These values differ cardinally from those for the sphere, which are often used. At a large drop flattening the pressure significantly decreases only on the narrow strip along drop equator, but on the greater part of drop surface it increases due to deforming, as the data [6] show. This means that the model is required which would adequately reflect the pressure and surface tension temporal redistributions.

The liquid drop dynamics modeling with accounting for acceleration, flattening and peculiarities of gas flow past deformed drop, is hard to be done without simplifying. The results listed below were obtained under assumptions, which are suitable over the range of Weber number considered: fluids are inviscid, incompressible; there is no boundary layer on a drop surface; at some point  $x_{sp}$  the separation of gas flow from drop surface occurs, and after this point the constant “bottom” pressure  $p_b$  settles up until leeward stagnation point. Due to large drop deformations the regime of gas flow past drop may be modified within the same flow, in particular, the bottom pressure and the utmost gas velocity at drop equator depend on a drop flattening degree. The deforming drop aerodynamic drag coefficient is not thus constant. Although other shapes were experimentally observed, we adopt ellipsoidal drop shape as the simplest and appropriate one; it was considered in [3, 6].

The shortcomings of [4] were the suggestions about fixed values of dimensionless drop acceleration and of the utmost deformation, which were set  $k=2.0$  and  $D^*=3.0$ . These deficiencies are overcome below via modelling.

### Equation of drop mass centre motion

To derive the drop motion equation let's apply the theorem of mass centre motion to the cut elementary segment of ellipsoid (fig. 1) in projection on axial direction  $x$ :

$$m_s \frac{d^2 x_c}{dt^2} = F_{px}, \quad (1)$$

where  $m_s = 2/3 a^2 b \Delta \varphi \rho_l$  is segment mass,  $a, b$  – ellipsoid semi-axes,  $\rho_l$  – liquid density,  $F_p$  – the resultant

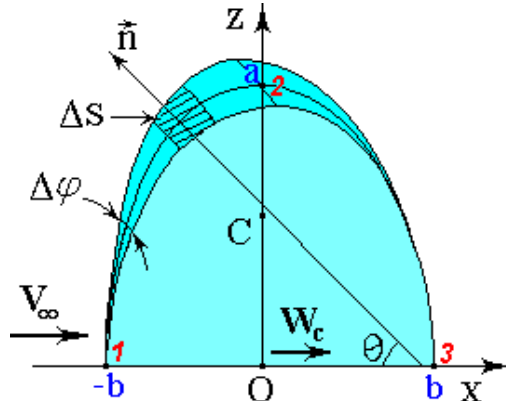


Figure 1. The cut elementary volume of

drop

gas pressure force, which can be obtained by integrating its elementary value  $dF_{px} = -p'_x n_x dS$  along ellipsoid surface,

$$dS = \sqrt{1 + (dz/dx)^2} z dx \Delta \varphi, \quad (x/b)^2 + (z/a)^2 = 1.$$

To obtain the pressure distribution along ellipsoid surface a hypothesis was adopted here that gas velocity at the arbitrary ground  $dS$  is defined by the angle  $\theta$  between the normal to surface vector  $\vec{n}$  and  $x$ -axis, and also by the utmost velocity value  $V_2(l)$  at drop equator  $\theta = \pi/2$ ; here  $l = a/b$  – drop flattening. For the sphere  $\theta$  coincides with a polar angle. Then the formula can be written in the form:  $V = V_2(l) \sin \theta$ , which meets the requirement to be fitted to the case of a sphere.

The legitimacy is confirmed by fair agreement with graphs of  $V(l, \theta)$ , which are listed in [6] for the potential flowfield around ellipsoid; the agreement is taking place when  $V_2 = V_\infty(1 + 0.5l)$ . But for real flows with viscous effects and the gas flow separation from drop surface the dependence must be corrected experimentally and the universal pressure distribution  $c_p = c_p(\theta)$  must be established. Engel [1] has used the approximation of Fage's experimental data in the form  $c_p(\theta) = 1 - 2\sin^2\theta$  till the point of separation,  $\theta_{sp} \approx 60^\circ$ . Collecting the items, the expression for pressure coefficient along drop surface can be written in the form:

$$c_p(x'; l) \equiv \frac{p - p_\infty}{0.5\rho_\infty V_\infty^2} = 1 - 2\sin^2\theta = \frac{(l^2 - 1 + A)x'^2 + 1 - A}{(l^2 - 1)x'^2 + 1}, \text{ for } \theta \leq \theta_{sp}; \quad c_p = c_{p.b.} = \text{const}, \text{ for } \theta_{sp} < \theta < \pi \quad (2)$$

where  $x' = x/b$ ,  $A = (1 + 0.5l)^2$ . The integration along ellipsoid surface from  $x' = -1$  to  $x'_{sp} = x'(\theta_{sp})$  yields

$$F_{p,x} = -\frac{a^2 \Delta \varphi}{2} \left( \int_{-1}^{x'_{sp}} \frac{(l^2 - 1 + A)x'^2 + 1 - A}{(l^2 - 1)x'^2 + 1} dx'^2 + (1 - x'^2_{sp}) c_{p.b.} \right) \cdot \frac{1}{2} \rho_\infty (V_\infty - w_c)^2, \quad (3)$$

where  $V_\infty$  and  $w_c = dx_c/dt$  – gas stream and drop mass centre velocities. Substituting (3) into (1) gives the differential equation of transportation motion with drop mass centre. Due to the symmetry with respect to  $x=0$  plane the resultant surface tension force in projection on  $x$ -direction equals to zero:  $F_{s,t,x} = 0$ .

### Equation of drop deformation

In order to obtain the equation of liquid drop deformation let's apply the theorem of mass centre motion to the cut segment in radial  $z$  direction:

$$m_s \frac{d^2 z_c}{dt^2} = F_{p,z} + F_{s,t,z} + F_{p.liq,z}, \quad (4)$$

where  $z_c = 3\pi a/16$ ,  $F_{s,t}$  is resultant surface tension force,  $F_{p.liq}$  – resultant liquid pressure force which acts at the plane cut lateral segment surfaces. Integrating  $dF_{p,z} = -p' n_z dS$  with the use of distribution (2) we obtain

$$F_{p,z} = -\frac{a^2 \Delta \varphi}{2} \left( \int_{-1}^{x'_{sp}} \frac{(l^2 - 1 + A)x'^2 + 1 - A}{(l^2 - 1)x'^2 + 1} \sqrt{1 - x'^2} dx'^2 + (1 - x'^2_{sp}) c_{p.b.} \right) \cdot \frac{1}{2} \rho_\infty (V_\infty - w_c)^2. \quad (5)$$

Accounting for the symmetry with respect to  $x=0$  plane and integrating the elementary value  $dF_{s,t,z} = -1/2(k_1 + k_2)\sigma n_z dS$ , where  $k_1(x'; l), k_2(x'; l)$  are the principal curvatures,  $\sigma$  is surface tension coefficient, we obtain:

$$F_{s,t,z} = -b\sigma \Delta \varphi \int_{-1}^0 \left( \frac{l^2}{((l^2 - 1)x'^2 + 1)^{3/2}} + \frac{1}{((l^2 - 1)x'^2 + 1)^{1/2}} \right) \sqrt{1 - x'^2} dx'. \quad (6)$$

The pressure force which acts at the segment plane lateral surfaces  $\varphi = \pm \Delta \varphi/2$  is the liquid force due to internal deformation flow. To obtain the resultant  $F_{p.liq,z}$ , let's write down the velocity potential  $\psi$  [1]:

$$\psi = \frac{\dot{b}}{b} \left( \frac{x^2}{2} - \frac{z^2}{4} \right), \quad u_x = \frac{\dot{b}}{b} x, \quad u_z = -\frac{1}{2} \frac{\dot{b}}{b} z, \quad (7)$$

dot means time derivative. Applying the Cauchy – Lagrange integral, we obtain the pressure distribution inside deforming drop:

$$\frac{p'_{liq}}{\rho_{liq}} = \frac{1}{2} b \ddot{b} - \frac{x^2}{2} \frac{\ddot{b}}{b} + \frac{z^2}{4} \left( \frac{\ddot{b}}{b} - \frac{3}{2} \frac{\dot{b}^2}{b^2} \right) - (b + x) \dot{w}_c + \frac{p'_{liql}}{\rho_{liq}}, \quad (8)$$

where  $p' = p - p_\infty$ , and the liquid and gas pressures at windward stagnation point  $l$  are connected:  $p_{liql} = p_1 + \sigma b/a^2$ . Then, integrating the elementary value  $dF_{p.liq,z} = p'_{liq} n_z dS = p'_{liq} \sin(\Delta \varphi/2) dx dz$  over the cut plane  $\varphi = \Delta \varphi/2$ , we obtain:



$$F_{p,liq,z} = \pi ab \rho_{liq} \Delta \varphi \left( \frac{3}{16} b \ddot{b} + \frac{1}{32} \frac{a^2}{b} \ddot{b} - \frac{3}{64} \frac{a^2}{b^2} \dot{b}^2 - \frac{1}{2} \left( b \dot{w}_c - \frac{p'_{liq1}}{\rho_{liq}} \right) \right). \quad (9)$$

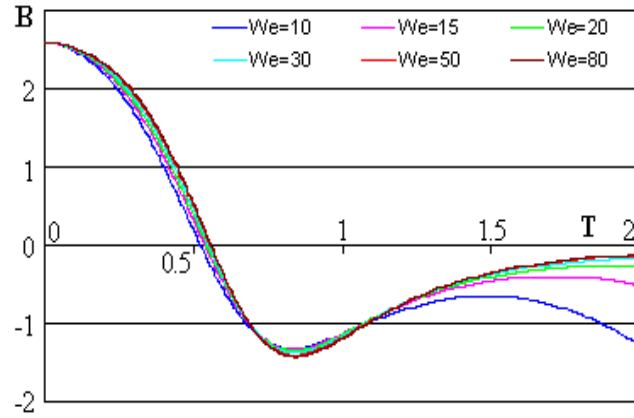
Substituting (5), (6), (9) into (4) and making it solvable for  $\ddot{b}$  we obtain the differential equation of ellipsoidal drop deformation:

$$\ddot{\beta} \left( 1 + \frac{1}{2\beta^3} \right) - \frac{3}{4} \frac{\dot{\beta}^2}{\beta^4} = - \frac{32}{3\alpha\beta^2} (\tilde{F}_{pz} + \tilde{F}_{s,t,z}) - \frac{16}{3} \left( c_{p1} \frac{(1-W_c)^2}{\beta} + \frac{4\beta}{We} - \frac{1}{\sqrt{\rho_g/\rho_{liq}}} \dot{W}_c \right), \quad (10)$$

where  $\alpha = a/r_0$ ,  $\beta = b/r_0$ ,  $r_0$  – initial drop radius,  $\tilde{F} = F/\pi \Delta \varphi r_0^2 \cdot 0.5 \rho_\infty V_\infty^2$ . Since the left-hand side of (10) coincides with that of Mitrofanov's equation [3], the influence of liquid viscosity and mass loss law can be accounted for by adding the same terms as in Mitrofanov's model.

## Results and Discussion

There are three empirical parameters incorporated into presented model:  $c_{p,b}$ ,  $\theta_{sp}$  and  $A$ , which are dependent on the flow-past-drop regime. The peculiarities of drop acceleration and deformation are sensitive to these values, but the reliable empirical data are limited. Engel [1] has used Fage's data for a sphere in speedy flows,  $Re = 1.1 \cdot 10^4$ , with  $c_{p,b} = -0.4$ ,  $\theta_{sp} = 60^\circ$ . Mitrofanov [3] mentioned about the values



$c_{p2} = -0.1$ ,  $c_{p,b} = -0.27$ ,  $\theta_{sp} \approx \pi/2$  in speedy flows. Under the assumption that flow is potential the theoretical data of Ranger and Nicholls [6] show a great influence of  $V_2$  and  $c_{p2}$  on drop deformation, meanwhile detailed calculations with accounting for real gas properties [7] showed much less dependence of  $V_2$ ,  $\theta_{sp}$  and  $c_{p,b}$ . Accounting for the low Weber numbers range considered here, present calculations were carried

**Figure 2.** Dependencies  $B(T)$  over the range  $10 < We < 80$ .

out with some intermediate values  $\theta_{sp} = \pi/2$  ( $x_{sp} = 0$ ),  $V_2 = V_\infty(1 + 0.5l)$ , and  $c_{p,b} = -0.2l^{0.5}$ ,  $A = (1 + 0.5l)$ .

The system of drop dynamics equations (1), (10) was integrated numerically with a help of Runge – Kutta method of fourth-order accuracy. The significant role of deformation flow at the early stage of the mass forces field formation inside drop was revealed. The windward stagnation point acceleration  $B = -\ddot{\beta}$  is the characteristic one in a deformation flow. The dependencies  $B(T)$  for various Weber number values are given in fig. 2 which show that the deformation motion is significant only at the initial stage  $T < 1.5$  and its strength (rate and acceleration) diminishes to time moment  $T = 2.0$  (here  $T = t/t_{ch}$ ,  $t_{ch} = d_0/\sqrt{\rho_\infty/\rho_{liq}} V_\infty$ ). The stagnation points' accelerations are always utmost at the beginning,  $T = 0$ , and they are directed initially to the drop centre at both windward and leeward drop sides. When the acceleration sign alters at  $T = (0.5 - 0.7)$ , the sign of inertial forces of deformation alters too, and the inertial forces become directed out of the drop centre at both windward and leeward sides of the drop, stabilizing thus the drop surface.

The derived equations (1), (10) permit to calculate with a help of (7) the field of total mass forces of inertia inside drop, which in the absolute motion is the superposition of liquid drop motion with mass centre and deformation motion with respect to mass centre. The typical sequence of events is shown in fig. 3 for the case  $We = 10$  in the form of toned pictures. In the absolute coordinate system the leeward surface (right drop side) has the acceleration directed to the drop centre (in the counter-flow direction) until  $T \approx 0.4$ , and zero-acceleration plane exists therefore inside drop (white line, fig. 3). The leeward surface is thus unstable being accelerated from less to more dense fluid, and unstable disturbance might has been developed there, but this disturbance counteracts alongside white line against the similar one at the windward surface, which develops in opposite, co-flow direction. Obviously, they greatly neutralize each other and instability can't be realized.



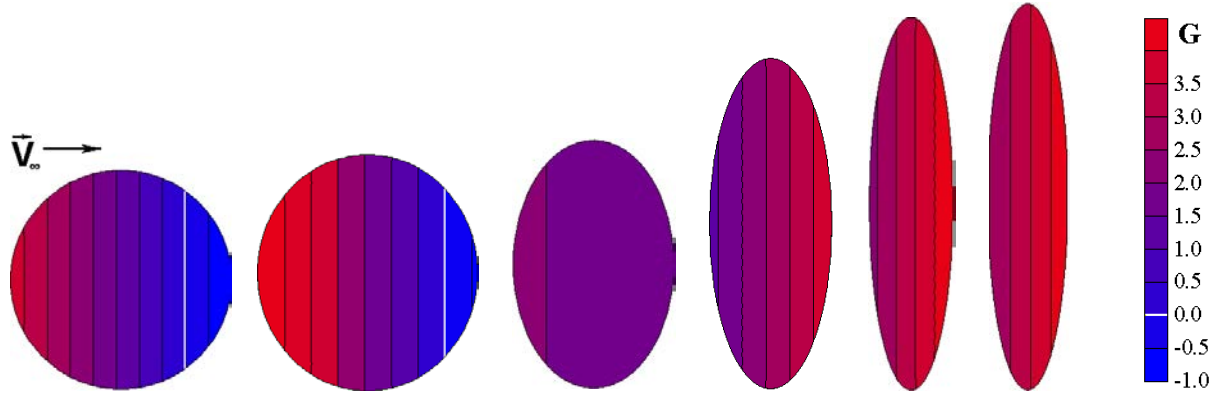


**Figure 3.** Axial mass forces field  $g_x$  inside deforming and accelerating drop in moments  $T=0.0$ ,  $T=0.2$ ,  $T=0.5$ ,  $T=0.8$ ,  $T=1.1$ ,  $T=1.5$ .  $We=10$ ,  $d_0=1mm$ ; dimensionless acceleration  $G=2g_x\rho_l d_0/\rho_g V_\infty^2$ .

The leeward surface becomes stable to time moment  $T \approx 0.5$ , acceleration field inside drop – more uniform, and to the moment  $T \approx (1.0-1.1)$  the value of the absolute acceleration at the unstable windward surface is sufficient already for the instability mechanism of inertia forces to proceed. It is important that the acceleration increasing at the second stage is caused by the growth of drop deformation, as can be seen in fig. 4. Therefore at  $T > 0.8$  the fastest wave length decreases and it could become less than the lateral drop deformation, as it will follow from the analysis of fig. 6. Beginning from  $T=(0.8-0.9)$ , the lateral drop deformation provides a mass centre acceleration  $\ddot{x}_c$  rising.

### The Selection Mechanism

After the period of improper instability development was established, the analysis helps us to reveal the breakup modes selection mechanism in the range of low Weber numbers. The constant drop acceleration value, which is engaged usually at Rayleigh – Taylor instability applications to drop breakup phenomena, doesn't reflect the variation of mass forces inside drop, neither temporal nor spatial. Apparently, in the fast-varied mass forces environment the Rayleigh – Taylor instability mechanism is unable to work. The feasibility of aperiodic instability to perform depends on the duration of the period  $t_{st}$  of stable existence of mass forces field inside drop. The instability is unable to work, if in time period  $t_{in}$  of characteristic  $e$ -fold amplitude growth the fastest unstable wave length is changed significantly due to mass force field changing. Hence, the first necessary condition for the proper instability development is  $t_{in} < t_{st}$ . For the considered usually disturbance of the form  $A=A_0 \exp(ihx + \omega t)$  the former is expressed as  $t_{in} = A(dA/dt)^{-1} \equiv \omega^{-1}(l, G)$ . Similarly, the period of acceleration stable existence can be estimated as  $t_{st} = G(dG/dt)^{-1}$ , where  $G(t)$  is the average liquid acceleration within the ellipsoid thickness. The typical graphs of calculated values  $T_{in}$  and  $T_{st}$  are shown in fig. 5 in the case  $We=15$ .

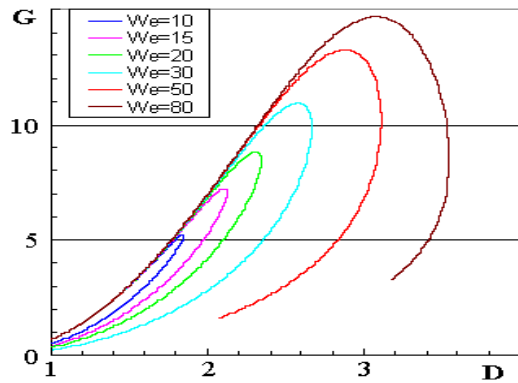


**Figure 4.** Dependencies  $G(D)$  for various  $We$ .

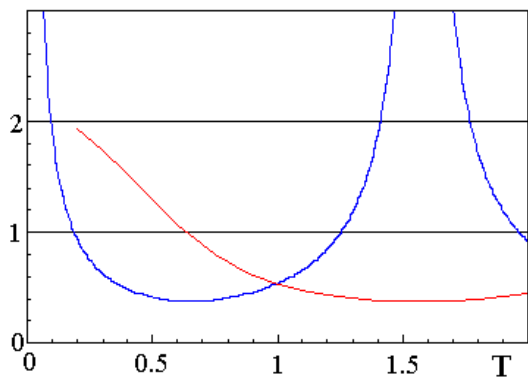


**Figure 5.** Graphs  $T_{in}(T)$  (red) and  $T_{st}(T)$  (blue).

It shows that the first necessary condition only satisfies at  $T > 1.0$ . Thus, during the period  $T < 1.0$  of mass forces field non-uniformity and transiency the performance of aperiodic instability is impossible.

The second necessary condition for aperiodic instability to work at a deformed drop was formulated in [4] at the explanation of “bag” and “claviform” breakup mechanisms, where it was shown that in the range  $We < 100$  the relation between drop deformation  $D = d/d_0$  and the fastest wave length  $L = \lambda_m/d_0$  determines these breakup modes performance. The second necessary condition consists in the requirement that the lateral drop deformation must exceed the current value of the fastest wave half-length,  $d > \lambda_m/2$ , in the case of “bag”, and three half-wavelengths,  $d > 3\lambda_m/2$ , in the case of “claviform” mode. This requirement agrees with observations [5, 8, 9]. The calculated here histories of drop lateral deformation  $D(T)$  and of the fastest wave length  $L(T)$  are shown in fig. 6, *a-d*, and the dependencies  $T_{in}(T)$  are given in fig. 7 for various  $We$ ; the methodical routine [4] was used for  $L(T)$  and  $T_{in}(T)$  calculus.

At  $We=10$  the second necessary condition is only satisfies at  $T=1.5$  in a short time interval, which is much less than  $T_{in} \approx 0.65$ . It means that breakup process is unable to occur. At  $We=15$  the second condition fulfils after the moment  $T_1=1.0$ , for  $\lambda_m/2 < d$ ; thus, bag formation is possible at  $T > T_1 + T_{in} = 1.7$ . Apparently, the critical Weber number value for “bag” mode lies within the interval  $10 < We_{cr}^{bag} < 15$ , being nearest to  $We=10$ . Figure 6, *c* shows that at  $We=30$  the same condition satisfies immediately after transiency terminates at  $T_1=0.9$ , so, the bag formation is possible at  $T > T_1 + T_{in} = (1.4-1.5)$ . It must be noted, however, that up till the moment  $T=1.4$  the drop acceleration grows up, therefore the fastest wave length current value at that moment satisfies to the condition  $3\lambda_m/2 < d$  already (green line), and this means that claviform formation is possible at  $We > 30$ . Nevertheless, the exact value of critical Weber number  $We_{cr}^{cl}$  is the question of mathematical model accuracy, because the time interval for the three half-wavelength formation has no reserve, in contradistinction to the time for one half-wavelengths formation. All the same, we can state that the critical value is nearest to, but some greater than  $We_{cr}^{cl}=30$ .

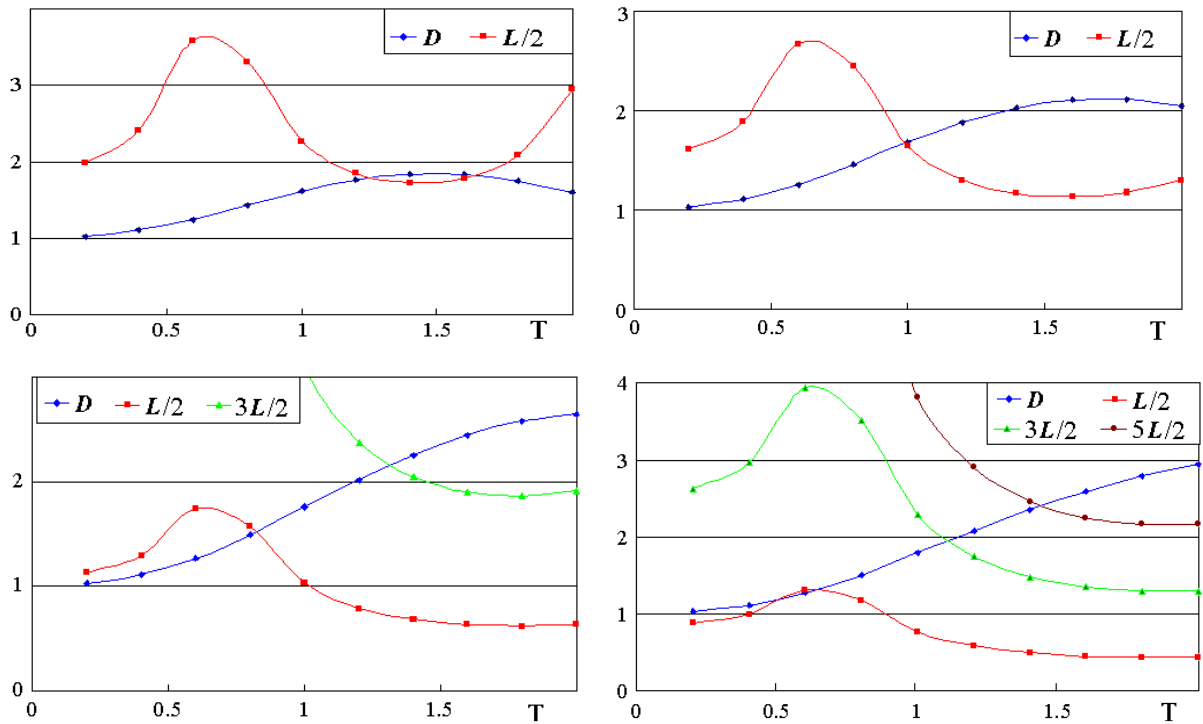


**Figure 6.** *a)* –  $We=10$ ; *b)* –  $We=15$ ; *c)* –  $We=30$ ; *d)* –  $We=50$ . Blue – deformation curve  $D(T)$ , red –  $\lambda_m/2d_0$ , light-green –  $3\lambda_m/2d_0$ , brown –  $5\lambda_m/2d_0$ .

Now we can give the answer to the question quoted in the Introduction: there is no preference in the “claviform” formation before “bag” one at  $We > We_{cr}^{cl}$ , but due to the existence of mass forces transiency period  $T < T_{tr}$ , the condition  $3\lambda_m/2 < d$  for the “claviform” performance already satisfies at the moment  $T_1 + T_{in}$  of the fastest wave transition to non-linear stage.

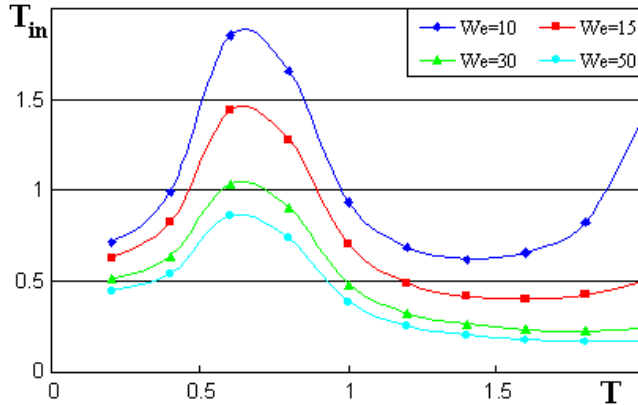


Figure 7. Dependencies  $T_{in}(T)$  for various  $We$ .

The same concerns help us to conclude that at  $We=50$  the condition  $\lambda_m/2 < d$  satisfies before the transiency terminates at  $T_{tr}=(0.9-1.0)$ , and the condition  $3\lambda_m/2 < d$  satisfies immediately after  $T=1.1$ , but to the end of the linear stage of the fastest wave development,  $T=T_1+T_{in} \approx 1.4$ , the fastest wave length almost has the value  $5\lambda_m/2 < d$ . So, at  $We \approx 60$  the formation of several bags (bubbles) is possible at the cross-diameter of deformed drop, which bubbles comprises the multimodal (“chaotic”) mode [4].

## Conclusions

The deformation motion greatly distorts the inertial force field inside drop in the early stage of its interaction with a gas stream. The constant inertial force values of drop mass centre acceleration that are applied usually at drop instability considerations are far from real transient, non-uniform internal mass force fields.

The breakup modes selection mechanism in the range of low Weber numbers is revealed. In particular, the performance of “claviform” mode of drop breakup becomes possible due to the effect of transient non-uniform deformation flow inside drop, which makes unable the instability development at  $T < (0.9-1.0)$ . When the period of transiency terminates at  $T \approx 1.0$ , the fastest wave of length  $\lambda_m/2 < d$  at  $We > 15$ ,  $3\lambda_m/2 < d$  at  $We > 30$ , and  $5\lambda_m/2 < d$  at  $We > 60$  is already in action, which provides “bag”, “claviform” or “multimode” modes of drop breakup in that order. The presented model confirms the results and conclusions of the paper [4] in more details and on more reliable basic model. Obtained here results give the possibility to get more reliable input data for the bag film disintegration calculation within the frames of mathematical model [10].

The simplest theory presented in this paper is based on the mathematical model of accelerating and deforming drop, which simplifies some effects and has therefore the internal inaccuracy. Nevertheless, its quantitative character gives here the possibility to formulate the important questions regarding shattering mechanism, and to elaborate the investigation scheme in order to answer them. Inaccuracy in the description therefore means the necessity to introduce more clarity into the elaborated model. The presented model has wider possibilities for the investigation of a particular drop respond on some aerodynamic effects, for example, when the small (but negative) value of the bottom pressure  $C_{p,b} = -0.05$  was introduced into numerical simulation the drop had the initial motion in opposite, with respect to oncoming gas flow, direction.

## References

- [1] Engel, O. G., *Journal of the Researches of the National Bureau of Standards* **60**: 245-280 (1958).
- [2] Gordon, G. D., *Journal of Applied Physics* **30**: 1759-1761 (1959).
- [3] Mitrofanov, V. V., *Dynamics of fluids* **39**: 76-87 (1979).
- [4] Girin, A. G., *Atomization & Sprays* **22**: 921-934 (2012).
- [5] Joseph, D.D, Belanger, J. and Beavers, G.S., *International Journal of Multiphase Flow* **25**: 1263-1303 (1999).
- [6] Ranger, A. A. and Nicholls, J. A., *AIJA Journal* **9**: 1720-1722 (1970).
- [7] Belotzerkovski, O. M. et alii, *The flow past blunt bodies in supersonic gas streams. Theoretical and experimental investigation*, Moscow: Proceedings of Computational Centre of USSR Academy of Sciences, 1967.
- [8] Theofanous, T.G. and Li, G.J., *Physics of Fluids* **20**: 1-14 (2008).
- [9] Zhao, H., Liu, H.-F., Li, W.-F. and Xu, J.-L., *Physics Fluids* **22**: 114103-114103-8 (2010).
- [10] Girin, A. G. and Ivanchenko, Ye. A., *Atomization & Sprays* **22**: 935-949 (2012).

## Quantum mechanical effects in *n*-alkane droplets

Rasoul Nasiri<sup>1</sup>, Vladimir M Gun'ko<sup>2</sup>, Sergei S Sazhin<sup>1</sup>

<sup>1</sup>Sir Harry Ricardo Laboratories, School of Computing, Engineering and Mathematics,  
University of Brighton, Brighton BN2 4GJ, UK

<sup>2</sup>Chuiko Institute of Surface Chemistry, 17 General Naumov Street, Kiev 03164, Ukraine

### Abstract

According to quantum chemical (QC) calculations of a series of *n*-alkanes ( $C_nH_{2n+2}$  at  $n = 1-8$ ) the gap  $\Delta_{HL}$  between the highest occupied molecular orbital (HOMO) and the lowest unoccupied molecular orbital (LUMO) decreases with increasing methylene group ( $-CH_2-$ ) number in the *n*-alkane chain. While the LUMO level appears to be relatively unchanged, in good agreement with experimental results, the HOMO level is unstabilized and  $\Delta_{HL}$  decreases from approximately 11 eV (methane) to 6.5 eV (*n*-octane). Comparative *ab initio* calculations show not only the quantum confinement effects (QCE) in *n*-alkanes in the gas phase due to the reduction of the  $\Delta_{HL}$  value, but also enabled selection of cost-effective methodologies for modelling long-chain *n*-alkanes ( $n > 8$ ). The used methodologies include 'Local Spin Density Approximation', combining special exchange functional with suitable correlation functional. Electronic structures and energetics of *n*-pentane ( $C_5H_{12}$ ) in the evaporation/condensation processes are studied to understand the molecular mechanism for these processes. Two main step processes, liquid (L)  $\xrightleftharpoons{1}$  liquid-gas (L-G) interface  $\xrightleftharpoons{2}$  gas (G), are analysed. While phase transformations between L and L-G is estimated as activation processes, it is found that there is no energy barrier in the transitions between L-G and G.

### Introduction

*N*-alkanes ( $C_nH_{2n+2}$  at  $n > 4$ ) are the main compounds in Diesel and petrol fuels. Due to a wide range of applicability of *n*-alkanes in science (1) and engineering (2), many groups have tried to develop or refine various molecular models for studying alkanes in the gas and liquid states using quantum chemistry (QC) (3, 4), all atom force field (AAFF) (5-7), united-atom force field (UAFF) (8, 9) and coarse-graining force field (CGFF) (10) methods. The resolutions of these approaches change from electronic structures (QC) to beads (a set of united atoms) in CGFF. Both QC and classical models are powerful methods for investigations of alkane chemistry and physics at molecular level. They can deal with various timescales, system sizes and related quantum effects. While advanced QC methods are based on *many-body* interactions of electrons and nuclei, classical force fields can describe interaction of particles (atoms, united atoms and beads) via *pair-wise* electrostatic, hydrogen bonding, and van der Waals potentials. Note that pure QC methods can give ground state properties ( $T = 0$  K), and the temperature dependent properties such as enthalpy of vaporization can be estimated using the quantum thermo-chemical (QTC) calculations. An alternative approach can be based on Molecular Dynamics/Monte Carlo (MD/MC) (with (QC) or without (FF) consideration of electrons and nuclei) simulation algorithms in which thermal effects are taken into account.

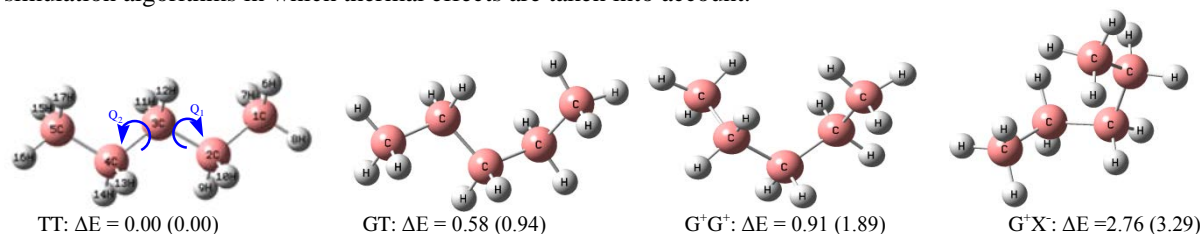


**Figure 1** Structures and relative energies (kcal/mol) of four isomers of *n*-pentane obtained using QC and FF methods. T refers to the trans conformer with dihedral angles  $\varphi_{1,2} = \pm 180^\circ$ , G refers to gauche torsion with  $\varphi_{1,2} = \pm 60^\circ$ , X refers to  $\varphi_{1,2} = \pm 90^\circ$ .  $\varphi_1$  refers to the angle between the planes 1C-2C-3C and 2C-3C-4C;  $\varphi_2$  refers to the angle between the planes 2C-3C-4C and 3C-4C-5C (see the left-hand side scheme).

Traditionally evaporation and condensation of *n*-alkane droplets have been investigated using MD/UAFF simulations (11, 12). In these processes it is essential to take into account the influence of conformational changes caused by temperature and dynamical interactions. Since the energy difference between most conformers of *n*-alkanes is about 1-3 kcal/mol, capturing these conformers by UAFFs or even AAFFs would be challenging. Energies of four isomers of  $C_5H_{12}$  (Figure 1) calculated using Coupled-Cluster with Single and Double Excitations /correlation consistent-polarized Valence Triple Zeta (CCSD (T)/cc-pVTZ) (13) and AAFF (Optimized Potentials for Liquid Simulations - All Atom (OPLS-AA)) (5) (shown in the brackets) are essentially different in QC and force field methods.

For OPLS-AA-FF energies the relative errors are in the range from 20 to 100%. While QC calculations show the values of mole fractions of 0.282, 0.673, 0.034 and 0.011 for conformers of TT, GT, G<sup>+</sup>G<sup>+</sup> and G<sup>+</sup>X<sup>+</sup> respectively (14), the calculations based on the molecular mechanics (MM) method for the same conformers at 300 K lead to rather different values: 0.491, 0.436, 0.064 and 0.009 (15). Using OPLS-AA-FF, Jorgensen's group (5) identified C<sub>22</sub>H<sub>46</sub> as the smallest and most stable *n*-alkane with hairpin (folded) geometry, while Suhm et al. (16) showed, using QC methods and Raman spectroscopy techniques, that C<sub>17</sub>H<sub>36</sub> is the starting point for *n*-alkanes with the folded structure. There is balance between intra- and intermolecular interactions in these molecules (16). These conflicting results have stimulated our interest in finding a suitable method to study the effects of conformational changes or isomerizations of alkanes. We believe that analysis of these effects is important for clarifying the molecular mechanism of the evaporation/condensation processes.

An MC statistical mechanics simulation has shown that *n*-alkanes (from C<sub>4</sub>H<sub>10</sub> to C<sub>12</sub>H<sub>26</sub>) stay in anti-conformations with two gauche bonds per molecule in the gas phase and pure liquid (5). In this study OPLS-AA was applied to a series of these alkanes. Obtained results are in excellent agreement with experimental data. Enthalpy of evaporation of *n*-dodecane obtained using MC simulation and experimental methods were reported to be 16.28 and 14.65 kcal/mol, respectively. Siu et al. (6) developed a revised version of OPLS-AA for long chain hydrocarbon molecules using MD simulation techniques, called L-OPLS-AA, in which intra-molecular parameters of the force field are refitted using high level *ab initio* calculations. The results were in better agreement with experimental data in comparison with the results reported in (5): 22.27 and 14.59 kcal/mol for enthalpy of vaporization of *n*-dodecane by OPLS-AA and L-OPLS-AA, respectively.

None of these force fields are suitable for modelling of *n*-alkanes at high temperatures (internal combustion engine conditions) since those have been developed for simulation of biomolecules. Siepmann's group developed a series of novel FFs named TraPPE (Transferable Potentials for Phase Equilibria) for modelling the vapour-liquid equilibrium of hydrocarbons (alkanes, cycloalkanes, alkylbenzenes, polycyclics and their mixtures) (9, 17-25). These FFs were parameterized to the experimental values of heat of evaporation and density in both gas and liquid phases. Although the TraPPE FFs could provide significant progress in modelling of *n*-alkanes over a wide range of thermodynamic conditions (temperature and pressure) using various resolutions (AA, UA and CG) (19, 20, 24), they could not take into account the effects of the detailed electronic structures of *n*-alkanes during such processes as evaporation/condensation. Knowledge of electronic structures allows one to find an answer to the questions: why does the HOMO-LUMO gap in alkanes decrease when their backbone becomes longer? What are the changes in energies and structures of alkanes during evaporation/condensation from the liquid (L) into the gas (G) state and what are the features of the processes at the liquid-gas (L-G) interface? Part of the second question might be answered using classical FFs such as TraPPE but without consideration of quantum effects caused by changes in the electronic structure. Therefore, in this study, we focus on the electronic structures of *n*-alkanes.

The focus of the paper is on comparative quantum chemical (QC) calculations for *n*-alkanes. In the first part of the paper, a series of short *n*-alkanes (*n* = 1-8) in the gas phase is considered in order to respond to the question Why does the HOMO-LUMO gap decrease as the number of carbons (*n*) in the chain of alkanes increases? In the second part, we will try to extend our calculations to *n*-pentane molecule in the liquid phase to find out whether transformation of the molecule from the liquid phase to the gas phase, or the inverse of this, is a single step process or whether it includes several steps for evaporation/condensation from/to a droplet. These results will provide new insight into the evaporation/condensation of droplets taking into account changes in the *n*-alkane electronic structures during evaporation/condensation. The results will be shown to be in good agreement with experimental observations (25-27).

### Method of analysis and computational scheme

All calculations were performed using Gaussian 09 (28), WinGAMESS (version 11 Aug 2011 (R1)) (29) and GaussView program for visualization (30). Several QC approaches, such as the second-order Møller-Plesset (MP2) perturbation theory, Density Functional Theory (DFT), Semiempirical Quantum Chemical (SQC) and Hartree Fock (HF) methods, were applied to the analysis of alkanes in the gas phase (Figure 2). QC calculations in the liquid phase were performed using an improved SQC potential called the Pairwise Distance Directed Gaussian (PDDG) function (31). In order to find out the relationship between the HOMO-LUMO gap and electronic structures of several conformers in *n*-alkanes, a setup was prepared to evaluate the effect of conformational changes (rotation of the atoms or united atoms around the single C-C bonds) on the molecular orbital bands (MOBs). Two torsion angles  $\phi_1$  and  $\phi_2$  (Figure 1) in the backbone of *n*-pentane molecule were scanned in 10 degree increments using the PDDG/PM3 potential. This gave 36×36 stationary points for *n*-pentane molecule over the potential energy hypersurface. While these dihedral angles were constrained for each point, other remaining internal parameters were optimized. This allowed us to identify the locations of all minima, transition states and even second-order saddle points over the PES (Figure 3).

Using the same potential, a relaxed SCAN on the PES was also used for the analysis of attachment/detachment of *n*-pentane molecule from/to the slab (18C<sub>5</sub>H<sub>12</sub>) (see Figure 4a) to identify of the reactants and products

corresponding to each TS structure during the evaporation. The profile energy is presented in Figure 4b. Note the SQC is not considered to be reliable for quantitative determination of the activation barriers, providing only useful qualitative information on the PES (position of stationary points on the PES). Our conformational analyses are limited to SQCs.

For validation of the PDDG/PM3 function and selection of the best potential, inter- and intra-molecular interactions were compared with CCSD (T)/cc-pVTZ results. The results of comparison of intermolecular interactions  $C_3$ - $C_{12}$  are shown in Table 2. The relative errors in the electronic energies of *n*-pentane molecule as a function of two torsion angles using PDDG/PM3 are shown in Figure 4. We followed this strategy to find out which would be a cost effective QC potential/method for studying the evaporation/condensation dynamics at the level of electronic structures.

## Results

This section shows energies and structures of alkanes in both gas and liquid phases. First, the structures of a series of the *n*-alkanes ( $n=1-8$ ) were fully optimized in the gas phase for evaluation of the HOMO-LUMO gap using various QC methods and basis sets. It is shown in Figure 2 that the HOMO-LUMO gap decreases by about 5 eV when the length of the *n*-alkane chain increases. To find out the reason for this we have investigated the relationship between conformational changes of *n*-alkanes and their MOBs. We started with QC calculations for selected *n*-alkanes in the gas phase.

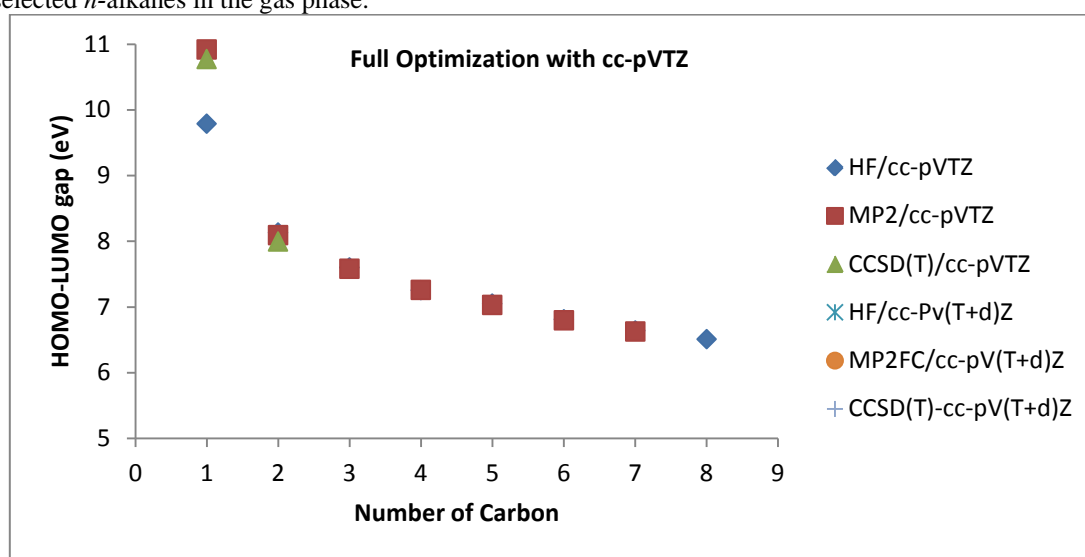


**Figure 2.** The values of the HOMO-LUMO gap versus the number of carbon atoms in *n*-alkanes (C1-C8).

## QC calculations in the gas phase

Using the results discussed above, a setup was prepared for studying inter- and intra-molecular interactions in alkanes. We compared them with high level *ab initio* potentials (MP2 and CCSD (T)) to find the best potential for studying of evaporation of *n*-alkanes. Firstly we calculated the interaction energies between two identical molecules ( $C_3$ - $C_{12}$ ). The results are shown in Table 1. In contrast to the semiempirical potentials of PM6 and AM1, the PDDG/PM3 potential has a good agreement with MP2 results. The HF methods and some conventional DFT were also unable to produce accurate results. Therefore, PDDG/PM3 could be considered reliable for estimating the inter-molecular interactions between *n*-alkane molecules only for the trans-conformer which is the most stable conformer among others (see conformer TT in Figure 1 and compare it with other cases).

In our analysis, we relied on the most stable conformation of *n*-alkanes (all-trans) for studying inter-molecular interactions and considered the effects of other conformers in the following part of the study in which intra-molecular interactions are discussed in detail. Recent QC studies of *n*-butane, *n*-pentane, and *n*-hexane molecules showed that the contribution of trans-conformers rapidly decreases with increasing temperature and the contribution of others increases with increasing temperatures from 100 to 500 K (33-36). The same authors established experimentally and theoretically that conformational changes strongly affect MOBs of *n*-alkanes. This encouraged us to search for all conformers of one of the *n*-alkanes using the PDDG/PM3 semiempirical potential in QC calculations.

The range of variations of electronic energies was determined for all stationary points of *n*-pentane molecule, as a representative of *n*-alkanes, using the PDDG/PM3 potential. We found four minima, six transition states that connect minima and four second-order saddle points that connect all TSs. This could be a hint for clarification of the conformational energy-dependent HOMO-LUMO gap. As can be seen from Figure 3a, the value of the



relative electronic energy increased up to 17 kcal/mol which corresponds to the energy of the second-order saddle point conformer. This value would be larger for longer alkanes since the number of conformers dramatically increases with increasing length of the backbone of *n*-alkanes (the number of nonequivalent minima conformers for C<sub>5</sub>H<sub>12</sub>, C<sub>6</sub>H<sub>14</sub>, C<sub>7</sub>H<sub>16</sub> and C<sub>8</sub>H<sub>18</sub> are 4, 12, 30 and 95 respectively). The relative values of energy for one of the stable conformers increase from 2.76 kcal/mol for G<sup>+</sup>X<sup>-</sup> isomer of *n*-pentane to 4.92 kcal/mol for X<sup>-</sup>G<sup>+</sup>X<sup>-</sup> isomer of *n*-hexane and to 8.08 kcal/mol for L<sup>+</sup>G<sup>+</sup>X<sup>-</sup>G<sup>+</sup>X<sup>-</sup> isomer of *n*-octane (37). Moreover, since the LUMO level was shown to be relatively unchanged, in good agreement with experimental results (25-27), it can be concluded that conformer isomerization (*conformerization*) can lead to a decreasing HOMO-LUMO gap.

**Table 1.** Comparison of inter-molecular interaction energies (kcal/mol) in *n*-alkanes

Molecule	PDDG/PM3	MP2/cc-pVTZ*	PM6	AM1	HF/6-31G**	DFT_B97D/6-31G**	OPBE/6-31G**	OPBESOL/6-31G*)
C12	-10.2	-10.5	-2.7	0.0	-0.2	-8.3	-0.6	-1.9
C11	-9.3	-9.6						
C10	-9.7	-8.75						
C9	-7.3	-7.75						
C8	-5.9	-6.68						
C7	-5.5	-5.96						
C6	-4.5	-4.91						
C5	-3.6	-3.92						
C4	-3.1	-2.97						
C3	-2.0	-2.08						

\*Data collected from [32]. MP2 results were in good agreement with CCSD (T)/cc-pVTZ (see [32]).

For validation of the PDDG/PM3 potential, we compared intra-molecular interactions of *n*-pentane with high level *ab initio* calculations to find out whether the calculated values of energy can be reliable. The results showed that PDDG/PM3 fails in reproducing CCSD (T)/cc-pVTZ results since relative errors reached  $\pm 3$  kcal/mol (see Figure 3b). This issue is related to all SQC methods; these cannot locate TSs correctly on the potential energy hypersurface. The main reasons for this are related to the unusual nature of the TS structures and also their properties which are not available from experiments. Moreover, according to (38), none of the semiempirical potentials can model activation barriers accurately since estimation of the barriers requires a high degree of accuracy in basis sets (SQC are in the lowest levels of the basis sets). An error of  $\sim 1.5$  kcal/mol in the estimation of interaction energies led us to more than one order of magnitude overestimation in the rate of evaporation (39). The intra-molecular interactions have significant effects on the evaluation of activation energies during the evaporation process.

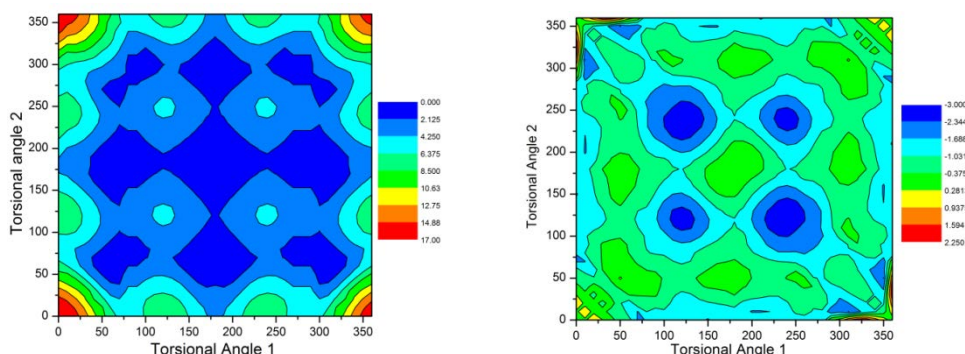


**Figure 3** (a-left hand side) Contours of relative energies (kcal/mol) of *n*-pentane molecule obtained using the PDDG function; (b-right hand side) relative errors (kcal/mol) of the PDDG/PM3 potential in the PES of *n*-pentane molecule.

Martine's group recently developed a double-hybrid DFT in which exchange and correlation effects are taken into account along with spin component contributions and dispersion effects (40). This potential could reproduce inter- and intra-molecular interaction energy values in good agreement with high level *ab initio* methods; the reported errors were less than 0.2 kcal/mol which is better than the chemical accuracy (13). The essential point for our modelling is applicability of a suitable potential that can model conformational changes

properly. We find that DSD-PBEP86-D<sub>2</sub> has these specifications for our molecules (see (41-44) for details). Therefore, DSD-PBEP86-D<sub>2</sub> is suggested as a cost-effective potential for studying alkanes in both gas and liquid phases at a reasonable computational cost.

### Liquid phase

In this part of the paper, we describe structurally and energetically the removal of *n*-pentane molecule from a slab of 18 *n*-pentane molecules (Figure 4). Before starting QC calculations, we optimized the structure of the slab using OPLS-AA force field. This gave us an initial conformer in which molecules were in a zigzag shape (all-trans form) and the distances between their centres of mass were about 0.4 nm. This structure is labelled **Re** in Figure 4.

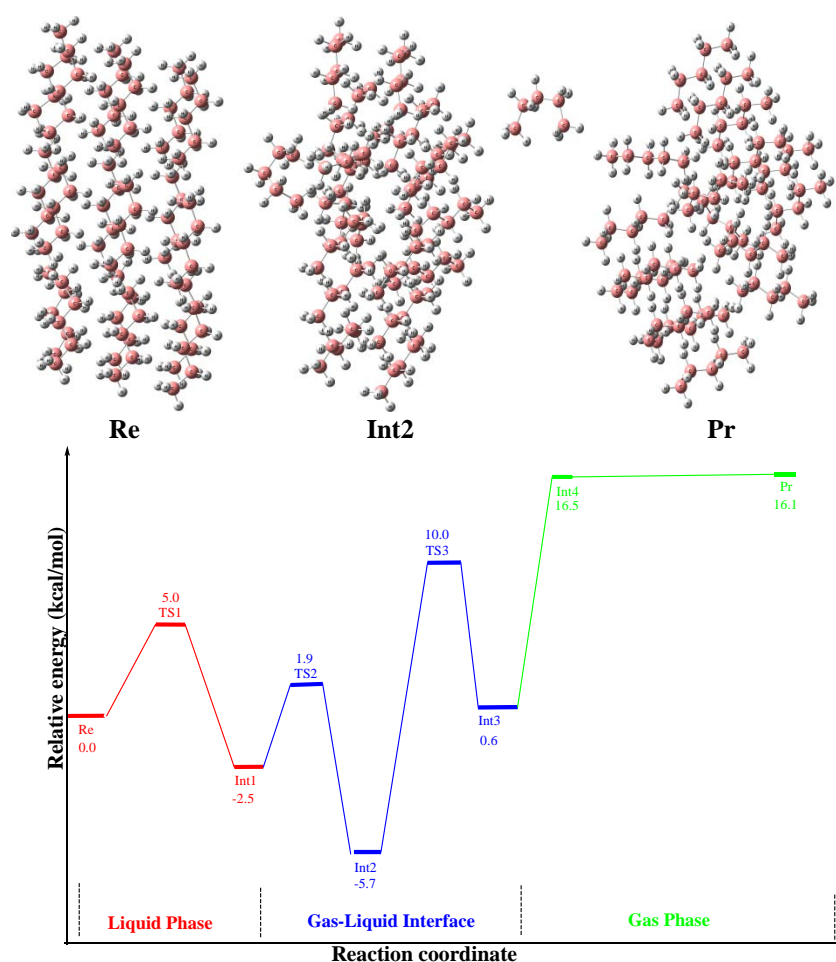


**Figure 4:** (a) Structures of the initial (**Re**), the most stable intermediate (**Int2**) and final products (**Pr**) of *n*-pentane slab in L, L-G and G, respectively. (b) Energy profile of removal of *n*-pentane molecule from the slab (all values of energies were calculated based on the PDDG/PM3 potential, kcal/mol).

A specific technique was applied for obtaining energies and structures of alkanes during the evaporation in the liquid phase (L), liquid-gas (L-G) interface and gas phase (G). A reaction coordinate was defined as a distance along the normal to the plane formed by the centres-of-mass of *n*-pentane. This allowed us to find electronic energies along with relevant structures when the distance between the central molecule in the slab (hereafter denoted *RM*) and the centre of mass (COM) of the slab changed with a step of 0.005 nm. The evaporation starts with the rotation of the methyl group (-CH<sub>3</sub>) around single bonds of C-C in the backbone of the *n*-pentane. At this stage of the process, the dihedral angle of  $\phi_1$  in *RM* changes from 178° in **Re** to 118° in **TS1** and 92° in **Int1**. This means that the structure of *RM* has changed from TT in **Re** in the L phase to GT in **Int1** in the L-G interface. The energy barrier was calculated to be 5 kcal/mol (Figure 4b). The torsion angle  $\phi_1$  in **Int2** reached 73° in **Int3**. This single bond rotation, via **TS2**, leads to the formation of the most stable conformer along the reaction pathway (**Int2**). The presence of the **Int2** shows the concept of surface tension in the L-G interface at the site of evaporation. This downhill process ( $\Delta E = -2.8$  kcal/mol) proceeds with relatively small barriers ( $\Delta E^\ddagger = 4.4$  kcal/mol). For the subsequent step, while  $\phi_1$  remains almost constant (70-80°),  $\phi_2$  changes from 174° in **Int2** to 94° in **Int3**. This endothermic step (6.3 kcal/mol) occurs with a barrier of 15.7 kcal/mol (**TS3**) in the



interface of L-G showing its rate-limiting step in the evaporation process (Figure 4b). At the last step **Pr** was produced. At this stage **RM** was removed from the slab (its distance was 1.8 nm). It was as stable as **Int4** but much more unstable than **Int3** (Figure 4b) showing a barrier-less step in the evaporation/condensation processes. The energy gap between **Int3** and **Int4** or **Pr** shows that **RM** is near the surface and needs sufficient kinetic energy to be evaporated. Therefore, it can be concluded that evaporation/condensation is not an activated process.

This multi-step process leading to accurate estimation of the evaporation coefficient cannot be limited by only one value even under constant thermodynamic conditions. We aim to extend this work in the future by studying the dynamics of these processes with reliable QC potentials. These QC results are expected to enable us to estimate the evaporation/condensation coefficients more accurately than was done earlier (11-12).

## Conclusion

Our QC calculations in the gas phase show that *conformerization* energies in *n*-alkanes are mainly responsible for the reduction of the HOMO-LUMO gap since their contribution increases dramatically with increasing chain length of *n*-alkane molecules. We have found that evaporation of *n*-alkanes is a multi-step complex process for which the transformation of a molecule from L to L-G is considered as an activation process and a barrier-less process occurs during the transition from L-G to G. While phase transformations between L and L-G are estimated as activation processes, it is found that there is no energy barrier in the transition between L-G and G. A double hybrid DFT as a cost-effective potential is suggested for studying the dynamics of evaporation of *n*-alkanes. In this approach all important processes are taken into account (effects of exchange, correlation, dispersion and also spin component contributions of electrons).

## Acknowledgements

The authors are grateful to EPSRC (Grant EP/J006793/1) for the financial support of this work.

## References

- [1] V. Formisano, S. Atreya, Detection of methane in the atmosphere of Mars. *Science*. 306, 1758 (2004).
- [2] S. S. Sazhin, J.-F. Xie, A kinetic model of droplet heating and evaporation: Effects of inelastic collisions and a non-unity evaporation coefficient. *Int. J Heat Mass Transfer*. 56, 525–537 (2013).
- [3] I. Cacelli, G. Prampolini, Parameterization and validation of intramolecular force fields derived from DFT calculations. *J. Chem. Theory Comput*. 3, 1803-1817 (2007).
- [4] B. Eckl, J. Vrabec, Set of molecular models based on quantum mechanical *ab initio* calculations and thermodynamic data. *J. Phys. Chem. B* 112, 12710-12721 (2008).
- [5] L. L. Thomas, T. J. Christakis, Conformation of alkanes in the gas phase and pure liquids. *J. Phys. Chem. B*. 110, 21198 (2006).
- [6] S. W. L. Siu, K. Pluhackova, Optimization of the OPLS-AA force field for long hydrocarbons *J. Chem. Theory Comput*. 8, 1459-1470 (2012).
- [7] W. L. Jorgensen, J. D. Madura, Optimized intermolecular potential functions for liquid hydrocarbons. *J. Am. Chem. Soc.* 106, 813 (1984).
- [8] W. L. Jorgensen, J. D. Madura, Development and testing of the OPLS all-atom force field on conformational energetics and properties of organic liquids *J. Am. Chem. Soc.* 118, 11225-11236 (1996).
- [9] J. I. Siepmann, S. Karaborni, Simulating the critical behaviour of complex fluids. *Nature*. 365, 330 (1993).
- [10] D. H. de Jong, G. Singh, Improved parameters for the Martini coarse-grained protein force field. *J. Chem. Theor. Comp*. 9:687-697 (2013).
- [11] B. -Y. Cao, J.-F. Xie, Molecular dynamics study on evaporation and condensation of *n*-dodecane at liquid–vapor phase Equilibria. *J. Chem. Phys.* 134, 164309 (2011).
- [12] J.-F. Xie, S. S. Sazhin, Molecular dynamics study of the processes in the vicinity of the *n*-dodecane vapour/liquid interface. *Phys. Fluid*. 23, 112104 (2011).
- [13] J. M. L. Martin, What can we learn about dispersion from the conformer surface of *n*-pentane? *J Phys. Chem. A*. 117:3118-32 (2013).
- [14] A. Salam, M. S. Deleuze, High-level theoretical study of the conformational equilibrium of *n*-pentane. *J. Chem. Phys.* 116, 1296–1302 (2002).
- [15] P. Mencarelli, The conformational behaviour of *n*-pentane: A molecular mechanics and molecular dynamics experiment. *J. Chem. Educ.* 72, 511 (1995).
- [16] Nils O. B. Luettschwager, The last globally stable extended alkane. *Angewandte Chemie-International Edition*. 52, 463-466 (2013).
- [17] B. Smit, S. Karaborni, Computer simulation of vapor-liquid phase equilibria of *n*-alkanes. *J. Chem. Phys.* 102, 2126-2140 (1995).
- [18] B. Smit, S. Karaborni, 'Erratum' Computer simulation of vapor-liquid phase equilibria of *n*-alkanes. *J. Chem. Phys.* 109, 352 (1998).

- [19] M. G. Martin, J. I. Siepmann, Transferable potentials for phase equilibria. 1. United-atom description of *n*-alkanes. *J. Phys. Chem. B.* 102, 2569-2577 (1998).
- [20] A. Katie, J. Ilja Siepmann, Transferable potentials for phase equilibria-coarse-grain description for linear alkanes. *J. Phys. Chem. B.* 115, 3452–3465 (2011).
- [21] B. Chen, J. I. Siepmann, Transferable potentials for phase equilibria. 3. Explicit-hydrogen description of *n*-alkanes, *J. Phys. Chem. B.*, 103, 5370-5379 (1999).
- [22] N. Rai, J. I. Siepmann, Transferable potentials for phase equilibria. 10. Explicit-hydrogen description of substituted benzenes and polycyclic aromatic compounds, *J. Phys. Chem. B.*, 117, 273-288 (2013).
- [23] C. D. Wick, M. G. Martin, Transferable potentials for phase equilibria. 4. United-atom description of linear and branched alkenes and of alkylbenzenes, *J. Phys. Chem. B.*, 104, 8008-8016 (2000).
- [24] M. G. Martin, J. I. Siepmann, Novel configurational-bias Monte Carlo method for branched molecules. Transferable potentials for phase equilibria. 2. United-atom description of branched alkanes, *J. Phys. Chem. B.*, 103, 4508-4517 (1999).
- [25] J. W. Au, G. Cooper, The valence shell photo absorption of the linear alkanes,  $C_nH_{2n+2}$  ( $n=1-8$ ): absolute oscillator strengths (7-220eV). *Chem. Phys.* 173, 209-239 (1993).
- [26] B. A. Lombos, P. Sauvageau, The electronic spectra of *n*-alkanes. *J. Mol. Spect.* 24, 253-269 (1967).
- [27] B. A. Lombos, P. Sauvageau, The electronic spectra of normal paraffine hydrocarbons. *Chem. Phys. Let.* 7, 42-43 (1967).
- [28] M. J. Frisch, G. W. Trucks, Gaussian 09 Revision A.02 Gaussian, Inc.: Wallingford, CT, 2009.
- [29] M. S. Gordon, M. W. Schmidt, In: C. E. Dykstra, G. Frenking, K. S. Kim, G. E. Scuseria, editors, *Theory and Applications of Computational Chemistry, the First Forty Years* Amsterdam: Elsevier. pp. 1167-1189 (2005).
- [30] R. Dennington, R. GaussView, version 3.07 ed.; Semichem, Inc.: Shawnee Mission, KS, 2003.
- [31] M. P. Repasky, J. Chandrasekhar, PDDG/PM3 and PDDG/MNDO: Improved semiempirical methods. *Journal of Computational Chemistry.* 23, 1601-1622 (2002).
- [32] S. Tsuzuki, K. Honda, Estimated MP2 and CCSD (T) interaction energies of *n*-alkane dimers at the basis set limit: Comparison of the methods of Helgaker et al. and Feller. *J. Chem. Phys.* 124, 114304 (2006).
- [33] F. Morini, S. Knippenberg, Quantum chemical study of conformational fingerprints in the photoelectron spectra and (*e*, 2*e*) electron momentum distributions of *n*-hexane. *J. Phys. Chem. A.* 114, 4400–4417 (2010).
- [34] S. Knippenberg, Y. R. Huang, Probing molecular conformations in momentum space: The case of *n*-pentane. *J. Chem. Phys.* 127, 174306 (2007).
- [35] M. S. Deleuze, W. N. Pang, Probing molecular conformations with electron momentum spectroscopy: The case of *n*-butane. *J. Am. Chem. Soc.* 123, 4049-4061 (2001).
- [36] W. N. Pang, J. F. Gao, Valence electron momentum spectroscopy of *n*-butane. *J. Chem. Phys.* 112, 8043-8052 (2000).
- [37] D. Gruzman, A. Karton, *J. Phys. Chem. A.* Performance of *ab initio* and density functional methods for conformational equilibria of  $C_nH_{2n+2}$  alkane isomers ( $n = 2-8$ ). 113, 11974 (2009).
- [38] J. J. P. Stewart, Optimization of parameters for semiempirical methods VI: more modifications to the NDDO approximations and re-optimization of parameters. *J Mol Model.* 19:1–32 (2013).
- [39] F. Gharib, R. Nasiri, *Fundamentals of chemical kinetics* by S. R. Logan, chap. 4. Prentice Hall (1996).
- [40] S. Kozuch, J. M. Martin, DSD-PBEP86: in search of the best double-hybrid DFT with spin-component scaled MP2 and dispersion corrections. *Phys. Chem. Chem. Phys.* 13, 20104-20107 (2011).
- [41] A. Karton, A. Tarnopolsky, Highly accurate first-principles benchmark datasets for the parameterization and validation of density functional and other approximate methods. Derivation of a robust, generally applicable, double-hybrid functional for thermochemistry and thermochemical kinetics. *Journal of Physical Chemistry A* 112, 12868–12886 (2008).
- [42] A. Tarnopolsky, A. Karton, Double-hybrid functionals for thermochemical kinetics. *Journal of Physical Chemistry A Letters* 112, 3–8 (2008).
- [43] A. Karton, J. M. L. Martin, Basis set convergence of explicitly correlated double-hybrid density functional theory calculations. *Journal of Chemical Physics* 135, 144119, pp 1–7 (2011).

## Theoretical and Numerical Study of Evaporation Effects in Laminar Counterflow Spray Flames

H. Olguin and E. Gutheil

Interdisciplinary Center for Scientific Computing, University of Heidelberg, Germany

### Abstract

Laminar spray flame structures strongly differ from their gaseous counterpart. Despite this fact, most simulations of turbulent spray flames are based on flamelet models using laminar gas flame structures, so that important spray evaporation effects are not taken into account. In this work, the importance of evaporation effects neglected by gas flamelet models is evaluated. A set of spray flamelet equations is derived, which explicitly includes evaporation. Two new terms accounting for pure evaporation and for combined mixing and evaporation are identified, and the flamelet equations for pure gas combustion are retrieved if no evaporation occurs. Numerical simulations of an axisymmetric laminar ethanol/air counterflow spray flame at different strain rates are carried out. Based on the results, the different terms of the derived spray flamelet equations are evaluated and compared. The results show that evaporation effects are dominant in all the situations studied, even for non-evaporating species and therefore, they must be always considered. Finally, a new flamelet model formulation is suggested, which overcomes the deficiencies of gas flamelet formulations.

---

### Introduction

Turbulent spray flames are relevant in many technical applications such as internal combustion engines, industrial furnaces, household burners, turbines and liquid-fueled rocket engines. The consideration of detailed chemical reaction mechanisms in the simulation of these devices is of vital interest for the investigation and reduction of pollutant emissions during their operation. Unfortunately, a direct inclusion of detailed chemistry dramatically increases the computational cost of the numerical simulations and it is prohibitive in practical cases.

Flamelet models represent a very promising approach for the inclusion of detailed chemical reaction mechanisms in the simulation of turbulent spray flames. Although originally developed for pure premixed or non-premixed turbulent gas flames [1,2,3,4], efforts have been made recently to extend them to more complex multi-regime turbulent flames [5,6,7,8]. In general, multi-regime flamelet models are a combination of mono-regime flamelet approaches, which are selectively applied depending on the locally dominant combustion regime. For instance, in turbulent multi-regime gas flames, a combination of pure premixed and pure non-premixed flamelet models is used to describe the complete flame structure. However, it has been shown that spray flames exhibit a third kind of combustion regime, which is dominated by spray evaporation [9,10]. Flamelet models using flamelet libraries based on gas flame structures are not adequate for the simulation of these zones [11,12]. If multi-regime flamelet models are to be applied to turbulent spray flames, the evaporation-controlled regime must be included in order to properly handle these regions.

Hollmann and Gutheil [12] and Gutheil [13] have proposed an extension of the classical non-premixed flamelet model [1] for spray flames, which consistently uses a library based on laminar spray structures. This approach has been successfully applied to the simulation of turbulent methanol/air [12] and ethanol/air [14,15] spray flames. However, since laminar spray flames cannot be uniquely characterized by the mixture fraction and its scalar dissipation rate, the inclusion of three additional parameters is required [12], which results in a high dimensional library. Although the relevance of evaporation on flamelet structures is very well known [9,10,12,13,16,17,18,19,20], currently, most numerical studies of turbulent spray flames use laminar gas flamelet structures [8,21,22].

The aim of this work is the evaluation of the importance of evaporation effects in the flamelet model for turbulent spray flames, which are neglected by gas flamelet models. For this purpose, the spray flamelet equations are derived under the assumption of a mixing controlled flame structure. Numerical simulations of an axisymmetric laminar ethanol/air counterflow spray flame at different strain rates are carried out. Based on the results, the different terms in the derived spray flamelet equations are evaluated and discussed for different species. Additionally, a new formulation of the spray flamelet model for turbulent spray combustion is suggested.

### Mathematical model

An axisymmetric two-dimensional fuel/air spray flame in the counterflow configuration is considered. An Eulerian-Lagrangian formulation is chosen, where a dilute spray is considered through source terms in the gas phase equations. The spray is modeled through equations accounting for droplet heating, evaporation, and

motion. The two-dimensional equations for low Mach number are formulated using the boundary layer approximation [9,10]. Without loss of generality [16], mono-disperse spray flames are considered. A similarity transformation is applied, which transfers the two-dimensional problem into a one-dimensional formulation [9]. This transformation and its application to viscous flows allow for the inclusion of detailed chemical reaction mechanisms [10,16]. A chemical reaction mechanism for ethanol/air consisting of 38 species and 337 elementary reactions is implemented [16,23]. A single component, spherically symmetric, unsteady droplet model in a convective flow field [24] is employed. The general equations and the numerical solution procedure of the problem can be found in previous publications [10,16].

### Derivation of spray flamelet equations

The flamelet equations derived by Peters [1] are appropriate for pure gas combustion, but they need reconsideration for spray flames. This section provides the derivation of spray flamelet equations, which include spray evaporation. It is assumed that the flame structure varies with the local mixture fraction, i.e. in one dimension. The aim of this work is the formulation of an extended flamelet model for spray flames, which incorporates the effect of droplet evaporation on the laminar counterflow spray flame. Following the methodology employed by Peters [1], a mixture fraction is chosen. In general, the mixture fraction may be based on any element A and it can be defined as

$$\xi_A = \frac{Z_A - Z_{A,\min}}{Z_{A,\max} - Z_{A,\min}}. \quad (1)$$

$Z_A$  is the mass fraction of element A in the mixture. The subscripts ‘min’ and ‘max’ refer to the possible minimum and maximum values of fuel mass in the oxidizer and fuel stream, respectively.  $Z_A$  can be expressed as

$$Z_A = \sum_{k=1}^N \left( \frac{a_{kA} M_A}{M_k} \right) Y_k. \quad (2)$$

$Y_k$  denotes the mass fraction of species  $k$ , and  $a_{kA}$  is the number of moles of element A in species  $k$ .  $N$  is the total number of species, and  $M_k$  and  $M_A$  are the molecular weights of species  $k$  and element A, respectively. In the present work, without loss of generality, the mixture fraction is based on the element C and is denoted as  $\xi$ .

The general three-dimensional transport equation for the mass fraction of a chemical species including Fick’s diffusion law yields

$$\rho \frac{\partial Y_k}{\partial t} + \rho u_i \frac{\partial Y_k}{\partial x_i} = \frac{\partial}{\partial x_i} \left( \rho D_k \frac{\partial Y_k}{\partial x_i} \right) + \dot{w}_k + S_v (\delta_{Fk} - Y_k), \quad (3)$$

where  $S_v$  denotes the mass spray evaporation rate,  $\delta$  is the Dirac-delta function,  $F$  is fuel and  $\dot{w}_k$  denotes the specific chemical reaction rate of species  $k$  for  $k = 1, \dots, N$ . Multiplication of Eq. (3) by  $a_{kA} M_A / M_k$  and summation over all species  $N$  yields a transport equation for the mass fraction of element A. With the assumption of  $Le = 1$  and considering Eq. (1), the transport equation for the mixture fraction,  $\xi$ , is obtained

$$\rho \frac{\partial \xi}{\partial t} + \rho u_i \frac{\partial \xi}{\partial x_i} - \frac{\partial}{\partial x_i} \left( \rho D_k \frac{\partial \xi}{\partial x_i} \right) = S_v (1 - \xi), \quad (4)$$

where the spray source term appears on the RHS of the equation, which is zero in pure gas phase systems. Assuming that combustion takes place in a very thin layer, i.e. flamelet, in the vicinity of the surface of the stoichiometric mixture fraction and that the structure of the flamelets varies only in normal direction to this surface, a coordinate system based on the mixture fraction,  $\xi$ , may be introduced, where all the scalar variables can be expressed as a function of the mixture fraction and the transformed time  $\tau$ . Following the method suggested by Peters [1], Eq. (3) can be transformed from the physical space  $(x_1, x_2, x_3)$  and time,  $t$ , into a new system of coordinates, i.e. the mixture fraction space  $\xi$  and time  $\tau$ . With the transformation rules

$$\frac{\partial}{\partial t} = \frac{\partial}{\partial \tau} + \frac{\partial \xi}{\partial \tau} \frac{\partial}{\partial \xi} \quad \text{and} \quad \frac{\partial}{\partial x_i} = \frac{\partial \xi}{\partial x_i} \frac{\partial}{\partial \xi}, \quad (5)$$

the species transport equations can be rewritten as

$$\rho \frac{\partial Y_k}{\partial \tau} = \left( \rho \frac{\partial \xi}{\partial t} + \rho u_i \frac{\partial \xi}{\partial x_i} - \frac{\partial}{\partial x_i} \left[ \rho D_k \frac{\partial \xi}{\partial x_i} \right] \right) \frac{\partial Y_k}{\partial \xi} + \rho D_k \left( \frac{\partial \xi}{\partial x_i} \right)^2 \frac{\partial^2 Y_k}{\partial \xi^2} + S_v(\delta_{Fk} - Y_k) + \dot{w}_k. \quad (6)$$

With the assumption of equal diffusion coefficients,  $D = D_i$ ,  $i = 1, \dots, N$ , for all species and the introduction of the scalar dissipation rate  $\chi = 2D \left( \frac{\partial \xi}{\partial x_i} \right)^2$ , Eq. (6) becomes

$$\rho \frac{\partial Y_k}{\partial \tau} = \underbrace{\rho \frac{\chi}{2} \frac{\partial^2 Y_k}{\partial \xi^2}}_{\text{Dissipation}} + \dot{w}_k + \underbrace{S_v(\xi - 1) \frac{\partial Y_k}{\partial \xi}}_{\text{Mixing/Evaporation}} + \underbrace{S_v(\delta_{Fk} - Y_k)}_{\text{Evaporation}}, \quad (7)$$

where Eq. (4) is used. In Eq. (7), the first three terms are identical to the flamelet equation for gas flames, and the last two terms are new, and they represent the effect of the spray evaporation on the flame structure. Thus, the flamelet formulation for spray flames does not only depend on the mixture fraction and its scalar dissipation rate, but additionally on the spray evaporation source term,  $S_v$ .

This revised spray flamelet formulation suggests that the structure of the laminar spray flamelet depends on the three parameters mixture fraction, its scalar dissipation rate and the spray evaporation rate. With this formulation, the spray flamelet formulation suggested by Hollmann and Gutheil [12] given as

$$\tilde{\phi} = \int_{-\infty}^{\infty} \int_0^{\infty} \int_0^{\infty} \int_0^1 \phi \tilde{P}(\xi, \chi, E, R_0, v_0) d\xi d\chi dE dR_0 dv_0 \quad (8)$$

may be replaced by the formulation

$$\tilde{\phi} = \int_{-\infty}^{\infty} \int_0^{\infty} \int_0^1 \phi \tilde{P}(\xi, \chi, S_v) d\xi d\chi dS_v, \quad (9)$$

where  $\tilde{\phi}$  denotes the Favre-averaged value of a variable, for instance, the mass fraction of any chemical species, in the turbulent spray flame. This new formulation provides a lower dimensional dependence, which requires a lower dimensional probability density function, whereas the variables equivalence ratio, initial droplet size and velocity might be more straight forward to be determined for the laminar flamelet computations. The major difference is that the former formulation requires consideration of input parameters into the laminar flame computation whereas the evaporation rate in the new formulation is a result from the laminar flame simulation. The effect of the new terms appearing in Eq. (7) will be evaluated in the next section together with the results of the numerical simulations.

## Results and discussion

In this section, the relevance of the new spray flamelet formulation with respect to the contribution of evaporation source terms is evaluated. For this purpose, numerical simulations of two mono-disperse ethanol/air spray flames are performed at low (55/s) and high (950/s) strain rates at the spray side of the configuration, extinction occurs at 1.035/s. An initial droplet radius of 25  $\mu\text{m}$  is considered. The equivalence ratio is unity for all the simulations performed. Figure 1 shows the outer flame structures at low (left) and high (right) strain rate in physical space. In both situations, the spray penetrates deep into the reaction zone, and for elevated strain rate, droplet oscillation around the stagnation plane at axial position 0 mm occurs. In the latter situation, the spray is no longer mono-disperse as seen in Fig. 1 (right part). Two reaction zones prevail for the low strain situation, where the local minimum is caused by spray evaporation, and the reaction zones merge in case of the higher strain rate [10]. The chemical species show typical characteristics of gas-phase combustion such as CO formation prior to  $\text{CO}_2$  formation. The profiles of the spray evaporation rate and the spray evaporation rate multiplied by the gas velocity,  $u_g$ , the mixture fraction and its scalar dissipation rate are displayed in Fig. 2 for the low (left) and high (right) strain rate situations. In laminar gas diffusion flames, the profile of the scalar dissipation rate,  $\chi$ , attains only one maximum value, which is located at the gas stagnation plane. In spray flames, see Fig. 2, two local maxima exist the location of which is dominated by the evaporation process as discussed earlier for methanol/air spray flames [12]. The present simulations for the fuel ethanol confirm this finding, and the profiles of the product of the gas velocity and the evaporation rate,  $u_g S_v$ , shows this influence. This confirmed finding supports the present revision of the spray flamelet equations.

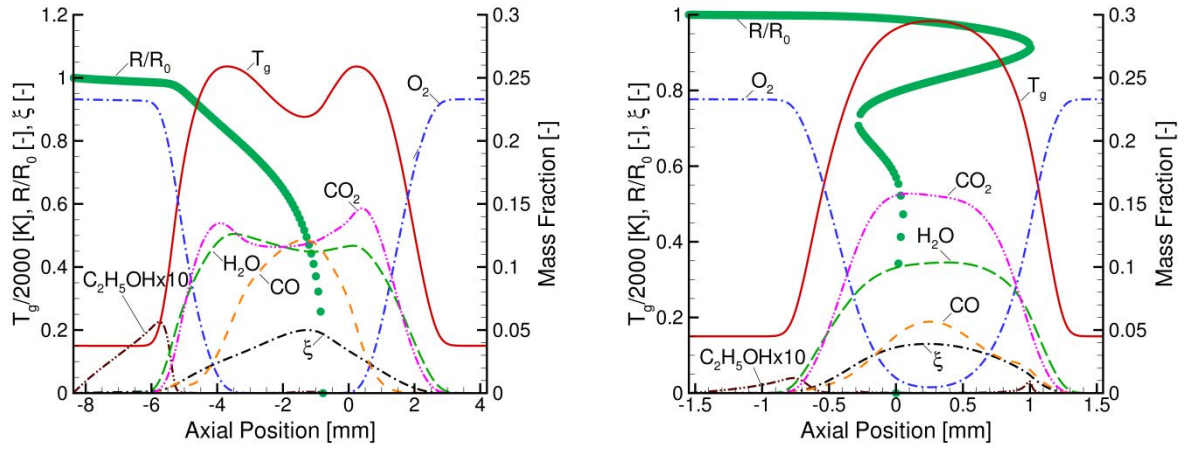


**Figure 1.** Outer ethanol/air spray flame structure  $a = 55/s$  (left) and  $a = 950/s$  (right)

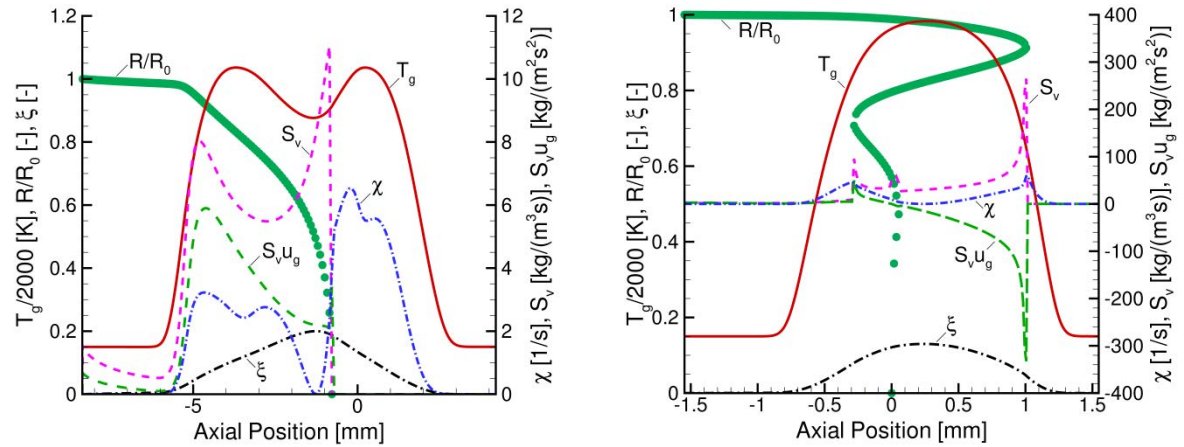


**Figure 2.** Profiles of scalar dissipation rate and evaporation rate,  $a = 55/s$  (left) and  $a = 950/s$  (right)

In order to study the influence of spray evaporation on the flamelet formulation given in Eq. (7), the flame structures are presented and evaluated for different species in the mixture fraction space. Figure 3 shows the contribution of the dissipation, mixing/evaporation and evaporation terms to the mass fraction of ethanol vapor for the low strain situation, where the left part shows the spray side and the right part the gas side of the configuration. This distinction is necessary because of the non-monotonicity of mixture fraction with space shown in Figs. 1 and 2. For the plots presented in Figs. 3-6, the local maximum of the mixture fraction is used to separate the flame structures. The results shown for the spray side of the configuration therefore show an increasing scale of the mixture fraction whereas the gas-sided structures show a decrease of mixture fraction on the abscissa. Figure 3 shows that on the spray side of the configuration, the dominating term in the spray flamelet equation of the ethanol vapor mass fraction in Eq. (7) is found to be the pure evaporation term. The dissipation term is relevant at the beginning of the reaction zone at low values of the mixture fraction. Here, the slope of the ethanol vapor mass fraction changes due to evaporation (leading to an increase in fuel vapor mass fraction) and initiating chemical reactions (decreasing fuel vapor mass fraction). At higher values of mixture fraction, the evaporation term dominates the flamelet equation. The mixing/evaporation term plays a minor role. The droplet completely evaporates at high values of the mixture fraction, which leads to a dominance of the evaporation term just where evaporation is completed. Since there is hardly any evaporated fuel left, all contributions are about zero on the gas side of the configuration.

Corresponding results for the high strain rate are shown in Fig. 4 for the ethanol vapor. At this condition, the evaporation is dominant again, and the dissipation term becomes somewhat relevant in the first droplet reversal point, but the pure evaporation term strongly dominates the structure. The gas side evaluation shows that the

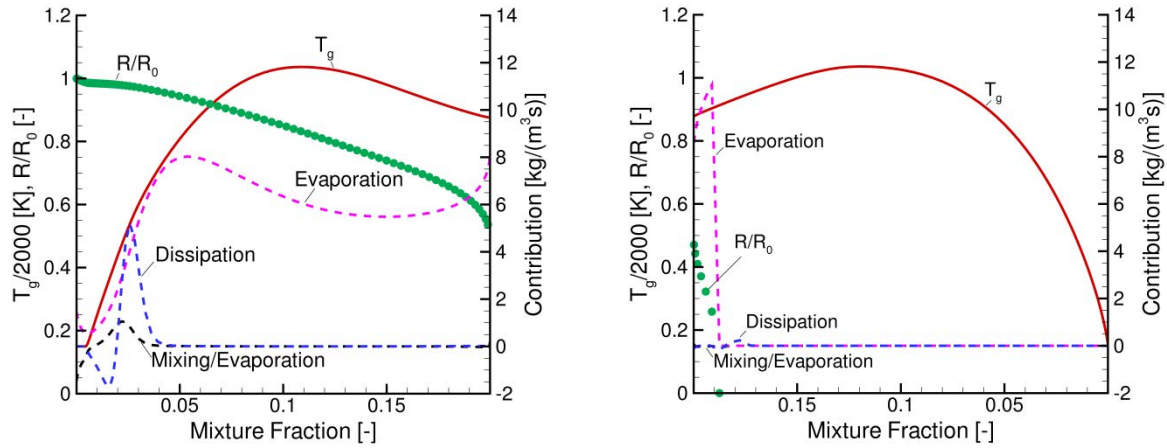


**Figure 3.** Contributions for ethanol, spray side (left) and gas side (right),  $a = 55/s$

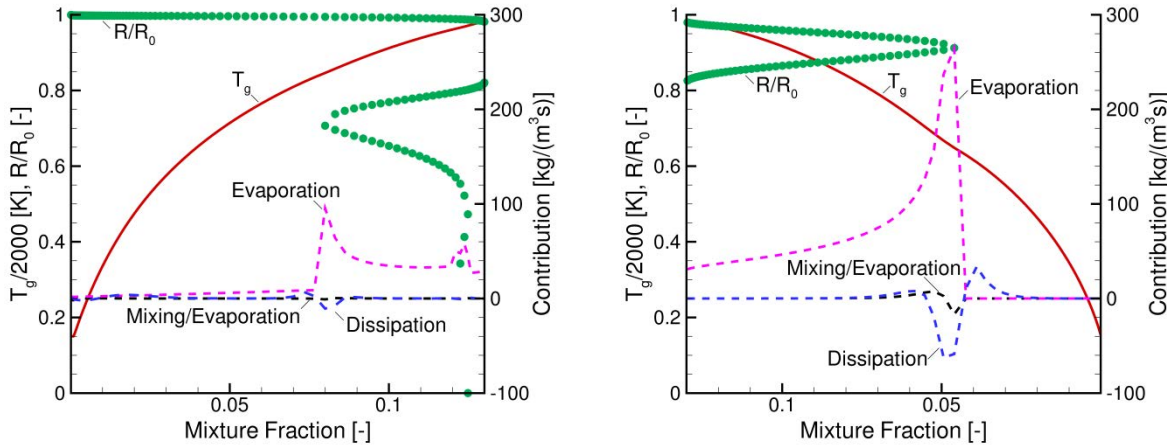


**Figure 4.** Contributions for ethanol, spray side (left) and gas side (right),  $a = 950/s$

presence of droplets change the findings for the low strain situation in such a way that the evaporation again shows significant influence on the flamelet equation of the mass fraction of fuel vapor, whereas the pure dissipation term plays a minor role.

Overall, it can be stated that the flamelet equation for the fuel vapor is dominated by the evaporation term of the flamelet equation, and this explains why approaches neglecting this term are not suitable to represent the flamelet structure of laminar spray flames with gas flamelet models, and evaporation must be taken into account in spray flamelet computations of turbulent spray flames.

Figures 5 and 6 show the low strain and high strain results for the flamelet equation of  $O_2$ . In both strain-rate situations, the mixing/evaporation term dominates the flamelet equation on the spray side of the configuration, and the dissipation term also shows a considerable contribution. Pure evaporation is not relevant, because oxygen is not an evaporating component. Even though this is the case, it can be seen, that the evaporation may not be neglected, and it has a pronounced influence. For the low strain situation shown in Fig. 5, the droplets do not cross the stagnation plane, and dissipation determines the flamelet equation for oxygen on the gas side of the configuration; note that the pure gas combustion situation is recovered. For high strain, see Fig. 6, the droplets cross the stagnation plane, and the mixing/evaporation term again dominates the equation with considerable contribution also of dissipation. The analysis of the spray flamelet equation for the product  $CO_2$  (not shown) reveals similar results as discussed for oxygen. Thus, the present results show that terms attributable to spray processes are important under all conditions, and they must be always considered.

The spray flamelet equations derived and evaluated in the present paper are suitable to describe spray diffusion flames in the counterflow configuration. Spray evaporation is taken into account and dominating



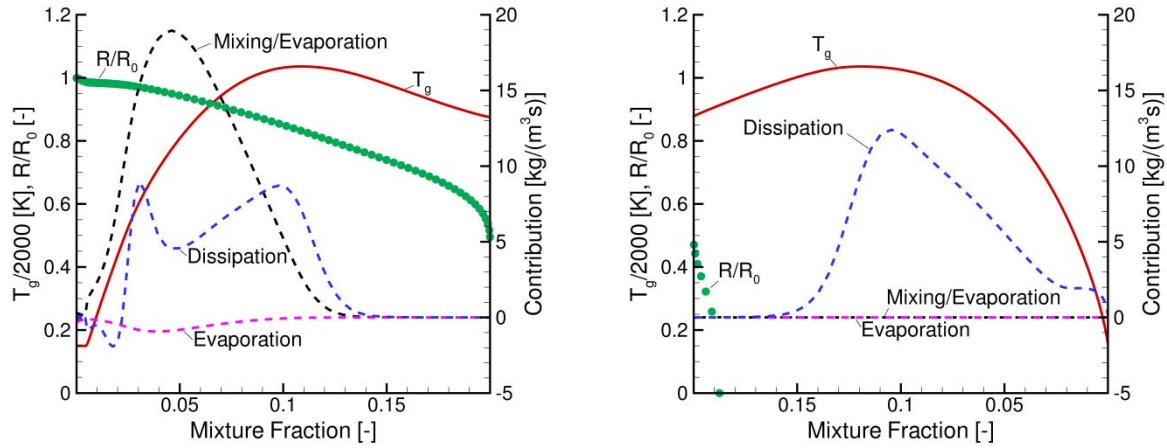


**Figure 5.** Contributions for O<sub>2</sub>, spray side (left) and gas side (right),  $a = 55/s$

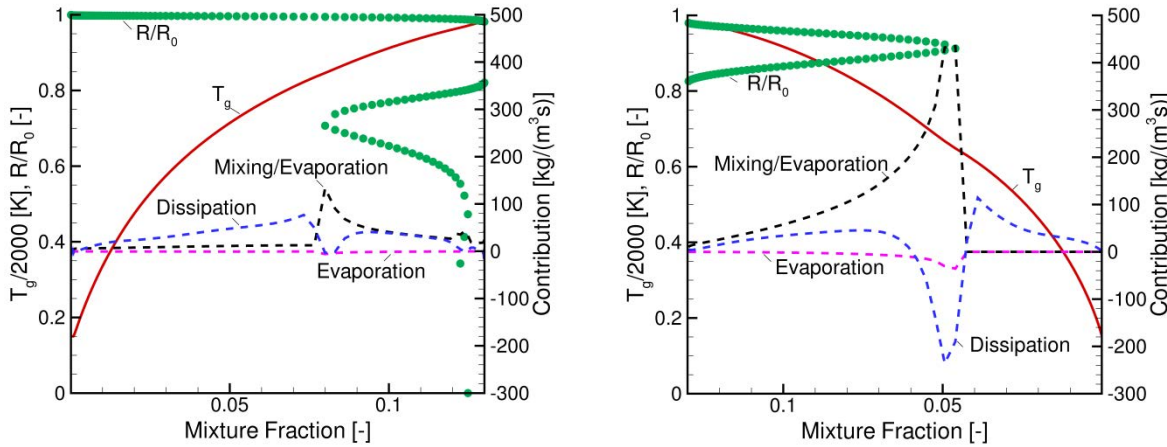


**Figure 6.** Contributions for O<sub>2</sub>, spray side (left) and gas side (right),  $a = 950/s$

evaporation effects are found for the evaporating component and mixing/evaporation effects for non-evaporating components with contribution of the dissipation term. If droplet oscillation occurs, the gas side of the configuration is dominated by the same terms. In situations without droplet oscillation, the standard formulation of the flamelet formulation of pure gas flames is recovered. Thus, the present formulation is an appropriate extension of the classical flamelet formulation for gas flames to spray flames.

## Conclusions

A new set of spray flamelet equations is derived in order to properly account for the evaporation process in these flames. Two new terms appear, which describe spray evaporation and combined mixing and evaporation, the standard gas flamelet equations are retrieved as a special case.

The importance of the new terms is analyzed by means of numerical simulations of an axisymmetric ethanol/air spray flame both at low and high strain rate. It is found that in most situations, the combustion regime is dominated by evaporation or combined mixing/evaporation, which cannot be characterized by gas flamelet formulations. The spray flamelet equation for fuel vapor shows that both the new terms play a significant role, where the pure evaporation term dominates the structure in regions with spray evaporation. For the non-evaporating species oxygen, the combined mixing/evaporation term is of significant importance and may not be neglected. Thus, spray evaporation strongly affects the spray flamelet equations for all chemical species, and therefore it must be included in revised multi-regime flamelet methods.

The present results suggest a revised flamelet model for use in turbulent spray flame computations, where the mixture fraction, its scalar dissipation rate and the spray mass evaporation term act as dependent variables to



determine the spray flamelet structure. This formulation includes the need of the determination of a joint probability density function depending on these variables.

### Acknowledgements

H.O thanks the DAAD for financial support through a research fellowship. Financial support of the German Science Foundation through the Heidelberg Graduate School of Mathematical and Computational Methods for the Sciences “MathComp” of IWR is gratefully acknowledged.

### References

- [1] Peters, N., *Prog. Energy Combust. Sci.* Vol 10 (1984), 319-339
- [2] Pitsch, H., Peters, N., *Combust. and Flame* 114 (1998), 26-40
- [3] Gicquel, O., Darabiha, N., Thévenin, D., *Proc. Combust. Inst.* 28 (2000), 1901-1908
- [4] Van Oijen, J. A., Lammers, F. A., De Goey, L. P. H., *Combust. Flame* 127 (2001), 2124-2134
- [5] Knudsen, E., Pitsch, H., *Combust. Flame* 156 (2009), 678-696
- [6] Nguyen, P., Vervish, L., Subramanian, V., Domingo, P., *Combust. Flame* 157 (2010), 43-61
- [7] Fiorina, B., Darabiha, N., *Combust. Flame* 140 (2005), 147-160
- [8] Franzelli, B., Fiorina, B., Darabiha, N., *Proc. Combust. Inst.* 34 (2012), 2755-2762
- [9] Continillo, G., Sirignano, W. A., *Combust. Flame* 81(1990), 325-340
- [10] Gutheil, E., Sirignano, W. A., *Combust. Flame* 113 (1998), 92-105
- [11] Hollmann, C., Gutheil, E., *Proc. Combust. Inst.* 26 (1996), 1731-1738
- [12] Hollmann, C., Gutheil, E., *Combust. Sci. Technol.* 135 (1998), 175-192
- [13] Gutheil, E., *Prog. Comput. Fluid Dyn.* 5 (7) (2005), 414-419
- [14] Ge, H.-W., Düwel, I., Kronmayer, H., Dibble, R. W., Gutheil, E., Schulz, C., Wolfrum, J., *Combust. Sci. Technol.* 180 (2008) 1529-1547
- [15] Ge, H.-W., Gutheil, E., *Combust. Flame* 153 (2008), 173-185
- [16] Gutheil, E., *Combust. Theory and Model.* 5 (2) (2001), 131-145
- [17] Chen, N. H., Rogg, B., Bray, K. N. C., *Proc. Combust. Inst.* 24 (1992), 1513-1521
- [18] Chen, Z. H., Lin, T. H., Sohrab, S. H., *Combust. Sci. Technol.* 135 (1998), 175-192
- [19] Li, S. C., *Prog. Energy Combust. Sci.* 23 (1997), 303-347
- [20] Greenberg, J. B., Sarig, N., *Combust. Flame* (1996) 431-459
- [21] Dhuchakallaya, I., Rattanadecho, P., Watkis, P., *Appl. Therm. Eng.* 52 (2013), 420-427
- [22] Hasse, C., Peters, N., *Proc. Combust. Inst.* 30 (2005), 2755-2762
- [23] Chevalier, C., *Ph.D. Thesis, Universität Stuttgart, Stuttgart* (1993)
- [24] Abramzon, B., Sirignano, W. A., *Int. J. Heat Mass Transf.* 32 (9) (1989), 1605-1618

## Simulations and Experiments on Shape Oscillations of Newtonian and Non-Newtonian Liquid Droplets

Moritz Ertl<sup>1</sup>, Norbert Roth<sup>1</sup>, Günter Brenn<sup>2</sup>, Hassan Gomaa<sup>1</sup> and Bernhard Weigand<sup>1</sup>

1: Institute of Aerospace Thermodynamics (ITLR), University of Stuttgart, Germany

2: Institute of Fluid Mechanics and Heat Transfer (ISW), Graz University of Technology, Austria

### Abstract

Free shape oscillations of non-Newtonian liquid droplets are studied experimentally and numerically. The liquids are aqueous polyacrylamide solutions, and in the experiment individual droplets are placed in an acoustic levitator. A direct numerical simulation uses the Volume-of-Fluid method. The shear-thinning liquid behaviour is represented by the Carreau-Yasuda model. Numerical results are validated against oscillation frequencies and drop shapes from the experiments. Further numerical simulations reveal the impact of the non-Newtonian liquid behaviour on the oscillations by comparison with Newtonian drops with the same (zero-shear) viscosity. An equivalent Ohnesorge number for the non-Newtonian droplets is calculated from the spatial averaged viscosity. The role of the aperiodic limit in the form of a critical Ohnesorge number is shown. The structure of the spatial distribution of the dynamic viscosity in a non-Newtonian droplet is shown and discussed.

### Introduction

Sprays of droplets have wide applications in industry, from fuel injection in engines to process engineering. Many applications rely on transfer processes across the liquid-gas interface. These processes may be influenced by shape oscillations of the drops. For this and for reasons of scientific interest, drop shape oscillations have been studied since more than a century [1]. The understanding about Newtonian liquid drop shape oscillations is well developed [2-4]. Our knowledge on non-Newtonian liquid drop shape oscillations, however, is still sparse. For interest of applications in process engineering, we study shape oscillations of shear-thinning liquid droplets in a gaseous environment both numerically and experimentally. We first introduce the numerical procedure and the experimental technique. We then validate the numerical results by comparison with results from the experiment and simulate the shear-thinning drop behaviour in free damped drop shape oscillations. Our paper ends with the conclusions.

### Numerical simulations

The oscillating drops are simulated with the ITLR in-house 3D CFD code Free Surface 3D (FS3D). The simulations are direct numerical simulations (DNS), solving the incompressible Navier-Stokes equations with variable dynamic viscosity. The underlying equations of change read for mass conservation

$$\nabla \cdot \mathbf{u} = 0$$

and for momentum conservation

$$\partial(\rho \mathbf{u}) / \partial t + \nabla \cdot [\rho \mathbf{u} \mathbf{u}] = -\nabla p + \nabla \cdot \left[ \mu \left( \nabla \mathbf{u} + (\nabla \mathbf{u})^T \right) \right], \quad (1)$$

where  $\mathbf{u}$  denotes the velocity vector and  $p$  the pressure. Body forces are irrelevant for the simulated flow. The density  $\rho$  is a constant, while the dynamic viscosity  $\mu$  is constant only for Newtonian liquids, and depends on the shear rate  $\dot{\gamma}$  for shear-thinning and shear-thickening non-Newtonian liquids. The shear-thinning liquids of our study are represented by the Carreau-Yasuda model [5]

$$\left( \mu(\dot{\gamma}) - \mu_\infty \right) / \left( \mu_0 - \mu_\infty \right) = \left[ 1 + (\tau \dot{\gamma})^a \right]^{(n-1)/a}, \quad (2)$$

where  $\mu_0$  and  $\mu_\infty$  are the viscosities at zero and very large shear rates, respectively, and  $\tau$ ,  $a$  and  $n$  are parameters specifying the transition between the two viscosities. The values of  $\mu_0$ ,  $\tau$ ,  $a$  and  $n$  are determined from a shear rheometric characterisation of the liquids, and  $\mu_\infty$  is set to a value in the order of the solvent water [5].

The Volume-of-Fluid (VOF) method is used to capture the liquid interface [6]. The field variable  $f$  represents the volume fraction of liquid in a cell, where  $f = 0$  in the gaseous, and  $f = 1$  in the liquid phase. The variable  $f$  is advected according to the equation

$$\partial f / \partial t + \nabla \cdot (\mathbf{u} f) = 0. \quad (3)$$

The interface is reconstructed from the  $f$  field using the method of Piecewise Linear Interface Calculation (PLIC), as proposed in [7]. With the information about the interface shape, capillary stresses can be calculated with a balanced continuum surface force model [8]. A more detailed description of the code can be found in [9].

The simulations are carried out on a cubic computational domain with a Cartesian grid of 128 cells with a length of  $6.25 \times 10^{-5}$  m in each spatial direction, resulting in a total of about 2 million cells. The gravity is set to zero and continuous boundary conditions are selected for all sides. The droplet is initialized quiescent at the centre of the domain as an oblate ellipsoid with an aspect ratio of 5/2 and a volume corresponding to the sphere diameter  $D_0 = 2$  mm. The surrounding medium is air with density  $1.1894 \text{ kg/m}^3$  and dynamic viscosity  $1.82 \times 10^{-5} \text{ Pa s}$ .

### Experimental Technique

Experiments on oscillating drops were carried out at the ISW using polymer solutions for their shear-thinning behaviour. For the experiments, the polyacrylamides Praestol 2500 and 2540 (Stockhausen Inc., Krefeld, Germany) were used. The polymers exhibit a wide spectrum of the molecular weight and differ in their degree of hydrolysis. Praestol 2500 is a non-ionic flexible polymer, while Praestol 2540 is anionic and rigid rod-like. The substances are industrially used as flocculants in waste-water treatment. The solutions were prepared by dissolving the polymer powder in demineralised water and stirring until a clear solution was achieved. After that, the solutions were allowed to age for 24 hours and then characterised with a shear rheometer. The solutions of the two polymers were prepared at two different concentrations so as to have zero-shear viscosities of the two liquids in approximately the same order of magnitude. The solutions were then characterised by a shear rheometer. The elastic properties of the solutions are not considered in the present study. The shear-thinning behaviour of the solutions is well described by the Carreau-Yasuda model. The characterisation results together with the fit by the Carreau-Yasuda model are shown in figure 1. Praestol 2540 0.05% starts out with a higher zero-shear viscosity followed by a steeper decline in viscosity, reaching a lower viscosity at higher shear rates than Praestol 2500 0.8%. Praestol 2540 0.05% has the more pronounced shear-thinning behaviour. The parameter values are listed in Table 1. The liquids were used to form drops with equivalent diameters  $O(2 \text{ mm})$  with an insulin syringe. The drops were placed at a position in space using an acoustic levitator [10]. Shape oscillations of the drops were excited by modulation of the levitating ultrasound. The resonance frequency of the levitated drop was determined by an excitation frequency sweep revealing the response with the largest amplitude. The drop was then excited at that resonance frequency  $O(130 \text{ Hz})$ , which belongs to the lowest-order, quadrupole mode forming oblate and prolate spheroidal drop shapes. At some time during the oscillatory motion, the modulation was switched off and the recording of images of the oscillating drops with a high-speed camera at 2000 fps was started. The results are movies of damped shape oscillations of the polymer solution drops, from which both the frequency and the damping rate were determined by image processing using the software ImageJ.

	$\rho [\text{kg/m}^3]$	$\mu_0 [\text{Pa s}]$	$\sigma [\text{mN/m}]$	$n [1]$	$a [1]$	$\tau [\text{s}]$	$\mu_\infty [\text{Pa s}]$
Praestol 2500 0.8%	1000.9	0.7588	75.55	0.515	1.0	1.4	0.001
Praestol 2540 0.05%	998.8	1.5208	76.51	0.267	3.4	9.5	0.0052

**Table 1.** Material properties of the two polymer solutions (polymer contents in mass %).

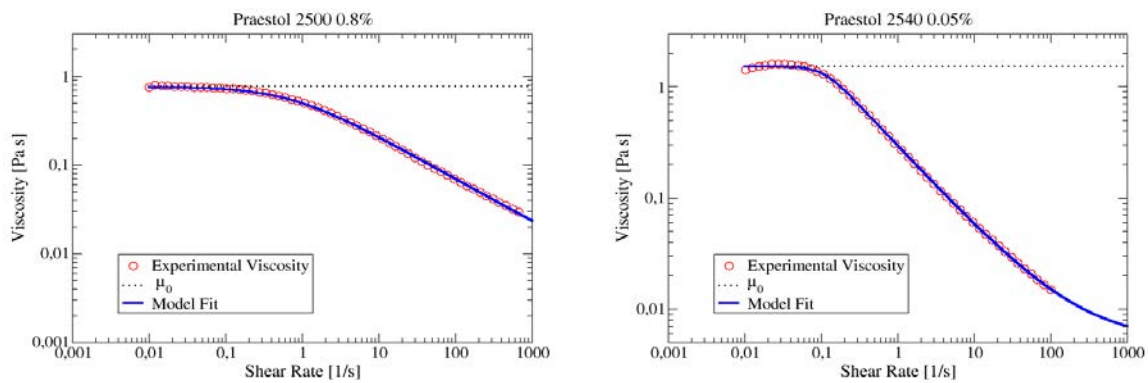


**Figure 1.** Dynamic viscosity versus shear rate for the two polymer solutions studied, both from experiment and the Carreau-Yasuda model. The zero-shear viscosity is shown as a dotted line.

### Validation of the Numerical Approach

The numerical approach is validated against data from the above described experiments. The case of Praestol 2540 0.05% is selected, since it shows the stronger shear-thinning effect. The oscillations of both the experiment as well as the simulation are analysed for frequency and time-dependent deformations. A meridional section, or

side view, of the drop is described in an  $x, z$  coordinate system, where the abscissa displays the  $x$  coordinate. The results are shown in figure 2. The graph on the left shows the oscillations with the peaks selected for the analysis. The graph on the right shows the result of the analysis plotting the peaks in a graph of frequency over dimensionless amplitude  $\varepsilon = a_{max}/a_{mean}$ , where  $a_{max}$  is the amplitude of the analysed maximum and  $a_{mean}$  is the mean amplitude averaged over all oscillations, shown as horizontal lines in the graph on the left in figure 2.

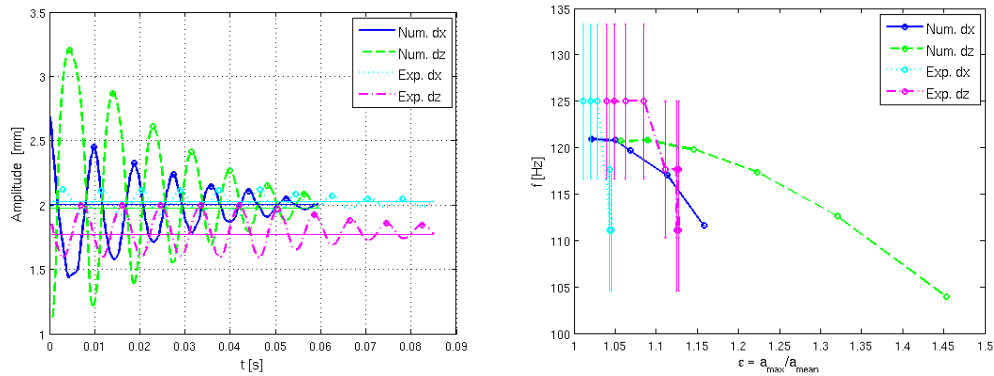


**Figure 2.** Left: Shape oscillations in  $x$  and  $z$  direction for the experiment and the simulation. The peaks for the frequency analysis are marked with a dot. Right: Frequency versus non-dimensional amplitude for the selected maxima

In the range  $\varepsilon > 1.1$ , the experiment and the simulation show rather different amplitudes and frequencies due to the different initial conditions of the process. The experiment uses the acoustic levitator to excite the droplet to its resonance frequency impressing a smaller amplitude but having the droplet in motion. The numerical simulation displaces the droplet to a large amplitude, but quiescent. For both the experiment as well as the simulation, however, the amplitudes converge towards values of  $1 < \varepsilon < 1.1$  after five to six oscillations. The numerical data converges towards a frequency of  $f_{num} \approx 121$  Hz, while the experimental data converge to  $f_{ex} \approx 125$  Hz. The error bars in the figure suggest that this value is well within the error achieved at the sampling rate of 2 kHz. It can be concluded that, once the range of similar amplitudes is reached, the experiment and the simulation are in good agreement within the margin of error.

An additional visual comparison is shown in figure 3. A front view of the droplet is shown, starting from the peak of the sixth oscillation at  $t_{ex} = 0.0505$  s and  $t_{num} = 0.0482$  s in the experiment and the simulation, respectively. The pictures are taken after equal time steps. A similar change in droplet shape can be observed for both the experiment and the simulation.

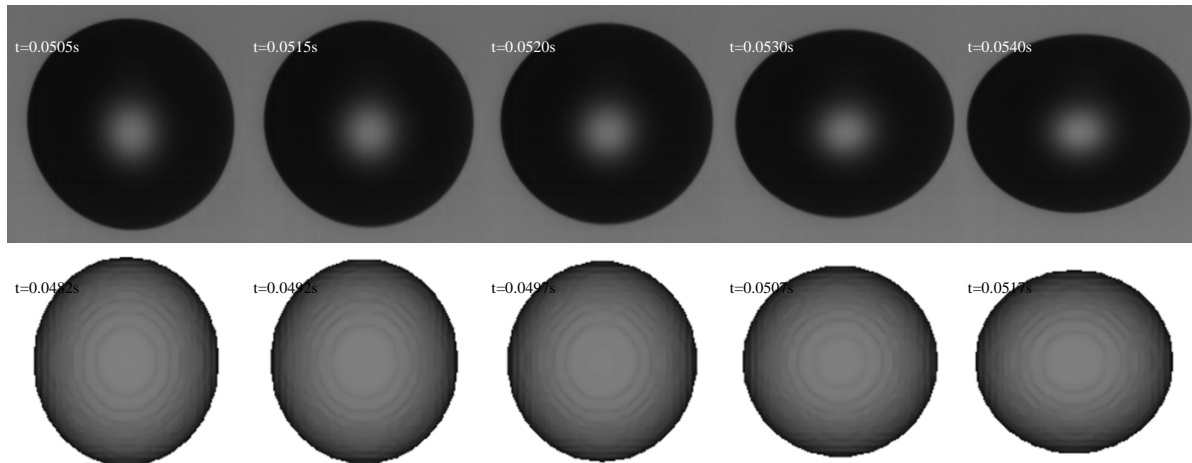


**Figure 3.** Comparison of the front views of an oscillating Praestol 2540 0.05% droplet from the experiment (top row) and the numerical simulation (bottom row). The first pictures are each at maximum amplitude of a similar magnitude. The time steps between the following pictures are identical.

### Non-Newtonian Influence on Drop Shape Oscillations – Results and Discussion

The influence of the non-Newtonian fluid properties on drop shape oscillations is investigated. For this purpose, droplets of Praestol 2500 0.8% (P2500) and Praestol 2540 0.05% (P2540) were simulated. For comparison,

Newtonian droplets with the constant dynamic viscosity  $\mu = \mu_0$  were simulated with the same approach. The development of the drop surface area with time is shown in figure 4 for both the Newtonian and the non-Newtonian liquids. The surface area is rendered non-dimensional with the surface area  $A_0 = \pi D_0^2$  of the sphere

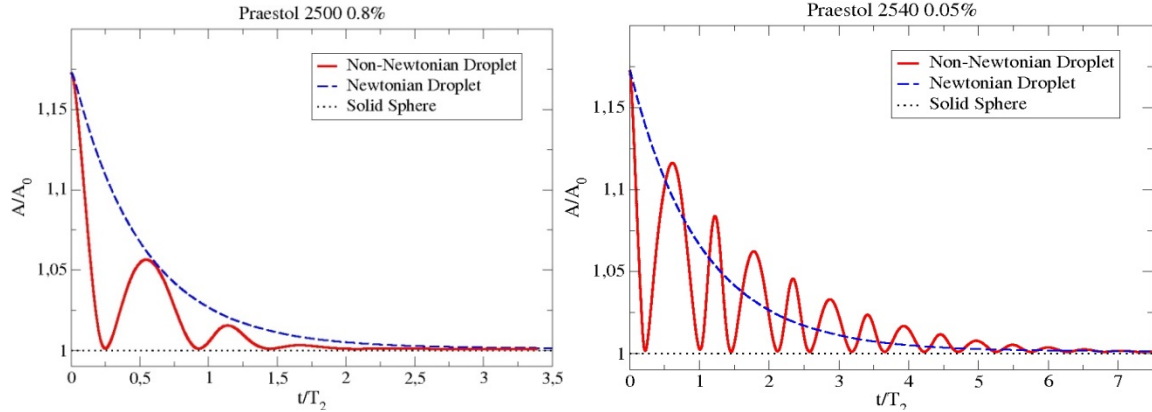


**Figure 4.** Simulated normalized drop surface  $A/A_0$  versus non-dimensional time. Comparison of a Newtonian with a non-Newtonian droplet with a constant viscosity  $\mu_0$ .

with the same volume. Time  $t^* = t/T_2$  is rendered non-dimensional with the period  $T_2$  of a free shape oscillation in the quadrupole mode [1]

$$T_2 = (2\pi/8) \left( \rho D_0^3 / \sigma \right)^{1/2}. \quad (4)$$

The Ohnesorge number

$$Oh = \mu / (\sigma D_0 \rho)^{1/2} \quad (5)$$

is a non-dimensional number quantifying the relative influences of viscous forces to inertial and capillary forces on a liquid system with a free surface. Deformed droplets above a critical Ohnesorge number  $Oh_{ap} = 0.4$  do not perform oscillations, but rather return to the equilibrium shape in an aperiodic way [3]. This value of the Ohnesorge number marks the state of the droplet at which its frequency of oscillation becomes zero. The Ohnesorge number for the Newtonian droplets with the constant viscosity  $\mu = \mu_0$  assumes the values 1.95 and 3.89 for the properties of the P2500 and P2540 solutions, respectively. These droplet states are, therefore, well above the aperiodic limit. The curves for the Newtonian droplets in figure 4 clearly show this expected behaviour. The non-Newtonian droplets with the same zero-shear viscosity, in contrast, exhibit a very different behaviour, showing damped shape oscillations after the start of the motion. In the case of the non-Newtonian droplets, the influence of the decreased viscosity in regions of high shear rates allows for the periodic oscillations observed.

A difference in the behaviours of the two non-Newtonian droplets is also seen in figure 4. While both droplets oscillate, the P2500 solution droplet is dampened such that the amplitude of the oscillations at no time exceeds the value of the Newtonian droplet. The P2540 solution droplet, in contrast, is less dampened and exhibits a higher oscillation frequency than the P2500 solution droplet. Also, it exhibits amplitudes exceeding the corresponding values of the Newtonian droplet. This behaviour is enabled by the steep decrease of the shear-viscosity of the P2540 solution droplet with increasing shear rate. Generally the oscillation frequency tends to increase with decreasing Ohnesorge number of the drop [3].

In order to further analyse the non-Newtonian effects on the liquid motion in the oscillating drop, the viscosity of the liquid is averaged over the drop volume at each time step. With this spatially averaged viscosity, an equivalent Ohnesorge number for a non-Newtonian droplet may be calculated. The development of this Ohnesorge number with time is shown in figure 5 for the two non-Newtonian droplets of the P2500 and P2540 solutions. The shape oscillations are represented in these results as well, with local maxima occurring at the extreme states of prolate and oblate deformation, where the shear rates come to a minimum. The dampening of

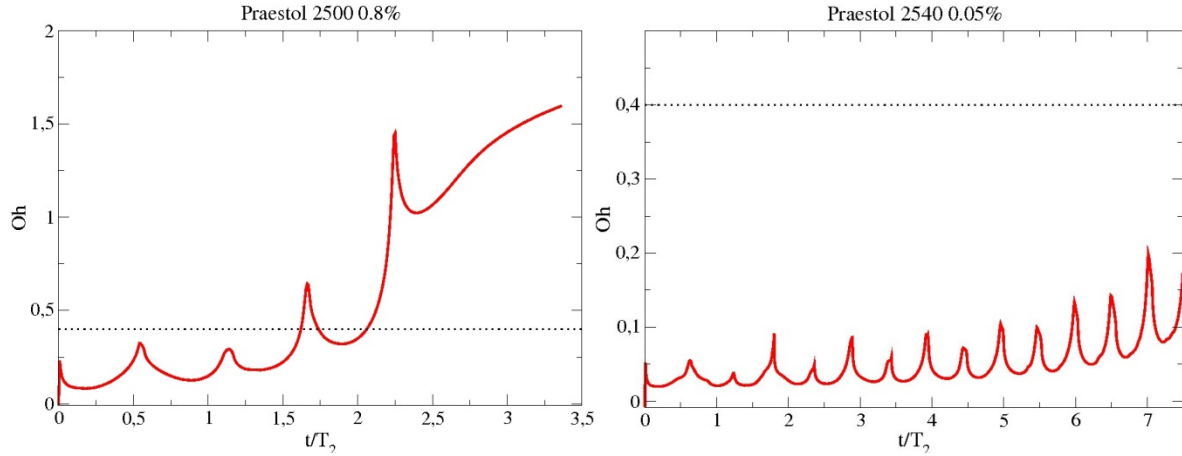


**Figure 5.** Ohnesorge number calculated with an equivalent spatially average viscosity, versus non-dimensional time. The aperiodic limit  $Oh_{ap} = 0.4$  is shown as a dotted line.

the amplitude of the oscillations can also be observed in both graphs, since the smaller amplitudes lead to smaller shear rates and therefore to increasing equivalent volume-averaged Ohnesorge numbers.

An interesting behaviour can be observed when relating the graphs to the aperiodic limit shown in figure 5 as a dotted line. In the case of the P2500 solution, the equivalent Ohnesorge number first exceeds the aperiodic limit at  $t^* \approx 1.6$ . A comparison with figure 4 indicates that, at this time, the droplet just passed the last clearly visible peak. The oscillation corresponding to the last peak of the equivalent Ohnesorge number somewhat after  $t^* \approx 2.2$  can only be observed in an enlarged plot of the surface area, shown in figure 6. The droplet then transits into the aperiodic mode.

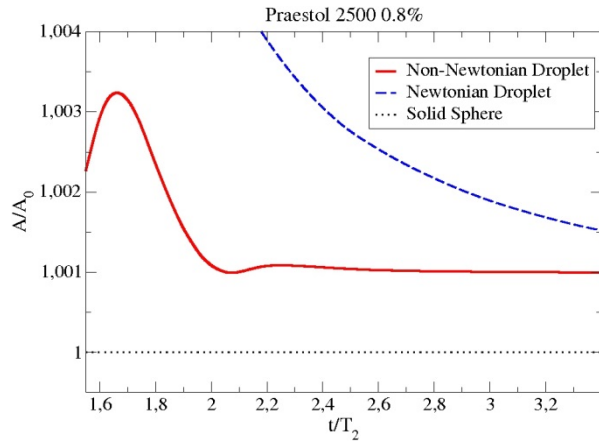


**Figure 6.** Enlarged view of droplet surface area versus time from figure 4 left showing the last oscillation.

For the P2450 solution droplet, the volume-average Ohnesorge number does not reach the aperiodic limit in the computed period of time. The oscillations of the non-Newtonian droplet do not end within the time of the computation. The possible relationship between the equivalent Ohnesorge number exceeding the aperiodic limit and the droplet starting the aperiodic motion is interesting to note and will be studied further in the future.

It is worth noting that the present results were achieved treating the drop oscillations as the solution of an initial-value problem. The drop is initially deformed from the spherical state, and the motion starts from rest. The temporal evolution of the drop shape is then described as the solution of an integro-differential equation in the expansion coefficients  $a_m$  in the axially symmetric drop shape for mode  $m$

$$r(t, \theta) = R + a_m(t) P_m(\theta) \quad (6)$$

which was given for Newtonian fluids by Prosperetti [3]. The equation turns into purely differential for short times after the start of motion, since then vorticity has not had enough time to propagate away from the interface. In contrast, for long times  $t \rightarrow \infty$ , the integral term in the integro-differential equation turns the solution into the one obtained by the normal-mode analysis. The solution of the initial-value problem, therefore, in general differs from the one obtained by normal-mode analysis. The solution of the drop oscillation problem for an initially irrotational state predicts a cut-off Ohnesorge number of

$$Oh_{ap} = \frac{1}{(2m+1)\sqrt{2}} \sqrt{\frac{m(m+2)}{m-1}} \quad (7)$$



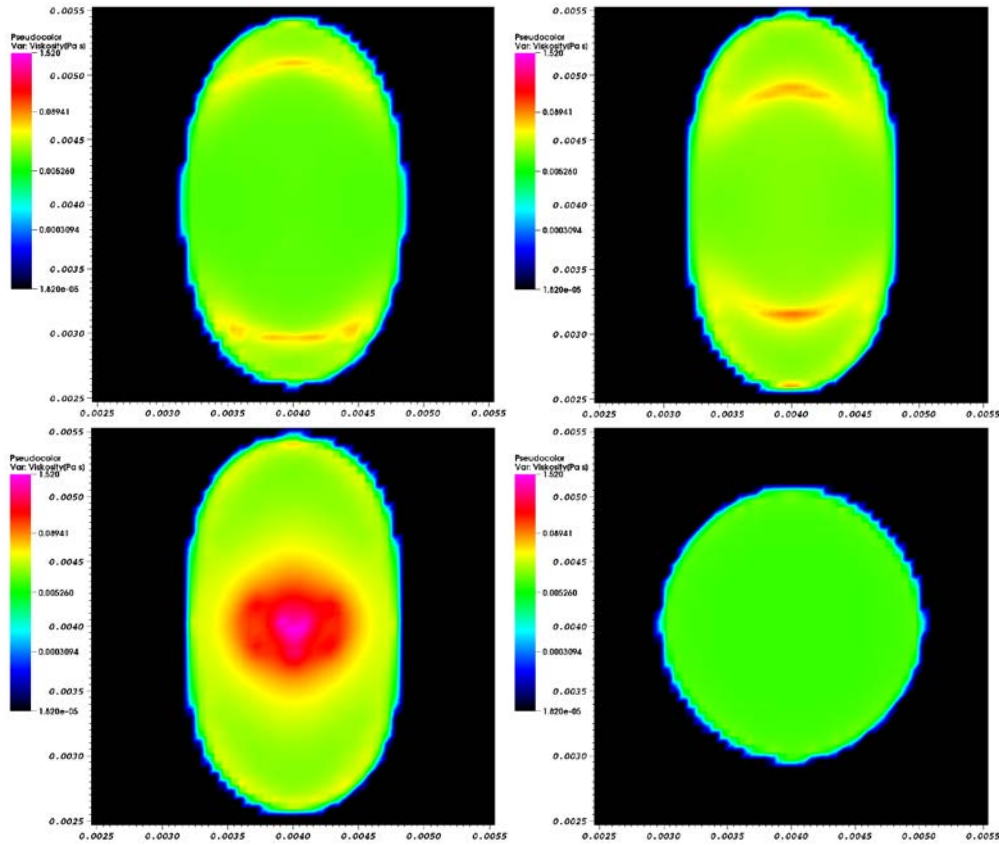


**Figure 7.** Meridional section of a Praestol 2540 0.05% droplet at different times, visualizing the local dynamic viscosity in [Pa s] on a logarithmic scale. Times  $t^*$  are: top left 1.65, top right: 1.73, bottom left: 1.80, bottom right: 2.11.

which for the spheroidal mode  $m=2$  assumes the value of  $2/5 = 0.4$ . In contrast to this, the normal-mode analysis predicts 0.542. It is interesting to note that the Ohnesorge number of 0.4, computed with the volume-average dynamic viscosity, turns out significant for the present shear-thinning liquid drops as well as it was for Newtonian liquids.

The spatial distribution of the viscosity is now analysed. Figure 7 shows profiles of the liquid dynamic viscosity in a meridional section through the centre of a Praestol 2540 0.05% solution droplet at different times. The figure on the top left shows the droplet in a prolate spheroidal shape. A disc-shaped structure can be identified near the ends of both major semi-axes, indicating a spheroidal shell region of higher viscosity throughout the droplet. In the top right figure, the outward expansion of the drop continues, while the regions of higher viscosity retract towards the centre of the droplet. In the figure on the bottom left, the droplet has reached the maximum prolate deformation. At this instant of time, the shear rate in the central region of the droplet goes to zero. A spherical region with  $\mu \approx \mu_0$  develops, contributing to the peaks in the equivalent Ohnesorge number seen in figure 5. The last figure on the bottom right illustrates the opposite case. Here the droplet is a sphere, right at the transition from the prolate to the oblate spheroidal shape. At this instant, shear rates are high and, consequently, the dynamic viscosity is low at an evenly distributed value. The consequence is that the Ohnesorge number reaches a minimum at this time.

## Conclusions

Experiments and numerical simulations on shape oscillations of non-Newtonian, shear-thinning liquids were carried out. The direct numerical simulations are validated against damping rate and frequency of drop shape oscillations from the experiment. The shear-thinning droplets are validated against a corresponding Newtonian case with the same (constant) zero-shear viscosity. The comparison allows the influences from the non-Newtonian liquid behaviour on the shape oscillations to be identified and quantified. An equivalent Ohnesorge number calculated with the spatially average dynamic viscosity of the non-Newtonian liquids was used to gain understanding of the influence of the aperiodic limit of  $Oh$  on non-Newtonian droplet oscillations. It turns out that the spatially average  $Oh$  number of the drop is significant for concluding about the periodic or aperiodic

behaviour of the drop. This is shown in the late stages of the free damped drop oscillations, where the transition to the aperiodic state takes place as the value of  $Oh_{ap}$  is exceeded. Furthermore, the value of  $Oh_{ap}$  which is significant here was obtained by Prosperetti [3] in solving the initial-value problem of drop oscillations. This finding shows that Prosperetti's findings for Newtonian liquids apply for shear-thinning drops also, provided that the Ohnesorge number is computed with a spatially average dynamic viscosity. Visualization of the spatial viscosity profiles in a non-Newtonian droplet was used to identify the regions of the droplet contributing to high values of the average viscosity. It is seen that, in states of high velocities in the drop liquid, which are associated with high shear rates, the dynamic viscosity is low throughout the drop, while it is high in regions of the drop with low shear rates for states near maximum deformation.

### Nomenclature

$a$	Large semi axis [m]	$t^*$	Non-dimensional time [1]
$A$	Surface area [m <sup>2</sup> ]	$u$	Velocity vector [m/s]
$A_0$	Surface of equivalent sphere [m <sup>2</sup> ]		
$D_0$	Equivalent sphere diameter [m]	$\dot{\gamma}$	Shear rate [1/s]
$f$	VOF Variable [1]	$\varepsilon$	Non-dimensional amplitude [1]
$f$	Frequency [Hz]	$\mu$	Dynamic viscosity [Pa s]
$m$	Mode number ( $\geq 2$ )	$\mu_0$	Zero-shear viscosity [Pa s]
$Oh$	Ohnesorge number [1]	$\mu_\infty$	Second Newtonian plateau viscosity [Pa s]
$Oh_{ap}$	Aperiodic limit of Oh [1]	$\rho$	Density [kg/m <sup>3</sup> ]
$p$	Pressure [Pa]	$\tau, a, n$	Carreau-Yasuda model parameters [s], [1], [1]
$t$	Time [s]		

### References

- [1] Lord Rayleigh, J.W.S., On the capillary phenomena of jets. Proc. R. Soc. London A, 1879. 29: 71-97.
- [2] Chandrasekhar, S., The oscillations of a viscous liquid globe. Proc. London Math. Soc., 1959. 9: 141-149.
- [3] Prosperetti, A., Free oscillations of drops and bubbles: the initial-value problem. J. Fluid Mech., 1980. 100: 333-347.
- [4] Shi, T., Apfel, R.E., Oscillations of a deformed liquid drop in an acoustic field. Phys. Fluids, 1995. 7: 1545-1552.
- [5] Tanner, R.I., Engineering Rheology. 2nd ed. 2000, New York: Oxford University Press.
- [6] Hirt, C.W., Nichols, B.D., Volume of fluid (VOF) method for the dynamics of free boundaries. J. Comp. Phys., 1981. 39: 201-225.
- [7] Kothe, D.B., Rider, W.J., Mosso, S.J., Brock, J.S., Hochstein, J.I., Volume tracking of interfaces having surface tension in two and three dimensions. AIAA 96-0859, 1996.
- [8] Brackbill, J.U., Kothe, D.B., Zemach, C. A continuum method for modeling surface tension. J. Comp. Phys., 1992. 100: 335-354.
- [9] Rieber, M., Numerische Modellierung der Dynamik freier Grenzflächen in Zweiphasenströmungen. PhD Thesis Institut für Thermodynamik der Luft- und Raumfahrt. 2004, University of Stuttgart: Stuttgart.
- [10] Yarin, A.L., Brenn, G., Kastner, O., Rensink, D., Tropea, C. Evaporation of acoustically levitated droplets. J. Fluid Mech., 1999. 399: 151-204.



# Session:

# **Experimental Techniques**

## Detection of a position touched by a single-tip optical fibre probe in a micro-droplet measurement

Yuki Mizushima<sup>1</sup> and Takayuki Saito<sup>2</sup>

1: Graduate School of Science and Technology, Shizuoka University, Japan

2: Research Institute of Green Science and Technology, Shizuoka University, Japan

### Abstract

This paper describes a planar technique to measure droplet size and velocity aiming at practical applications to droplet flow-fields. An optical fibre probe is a useful device that gives the sizes and velocities of droplets in real time. This measurement is an intrusive technique; however it successfully detects droplets even though in high number density of droplets. To measure a sub-millimetre-size or micrometre-size droplet, we already developed a Single-Tip Optical fibre Probe (S-TOP). In the present study, we rapidly improve the measurement accuracy of the S-TOP. The accuracy is deeply correlated with pierced positions of individual droplets. For instance, the droplet sizes are evaluated from the dwelling time of the S-TOP (chord length); when the S-TOP touches spherical droplet nearly at its equator, the pierced chord length is shorter than the length of the minor axis. Conventional optical fibre probing has difficulties in evaluating the diameter accurately due to the random touch of an optical fibre probe to a droplet in droplet flows. In the present technique, we propose a new technique of using an informative peak in the S-TOP signal, i.e. post-signal. The post-signal appears before the S-TOP pierces the droplet rear surface around its pole. Utilizing this phenomenon, we established detection method for a position touched by the S-TOP in a droplet measurement, and eliminated the random error. Consequently, the difference in the results of the droplet size between S-TOP and visualization decreased to 10 % or less. This method is widely applied to measurement of arbitrary spherical droplets.

---

### Introduction

Spray atomization is one of important processes in engineering: diesel engine performance, decontamination within healthcare environments, cleaning processes, and so on. To investigate such dispersed two-phase flows, researcher needs information on the sizes and velocities of droplets. Phase Doppler Anemometry (PDA), which is an extension of Laser Doppler Anemometry (LDA), can provide the size and velocity vector of a single droplet at a point [1]. PDA has been applied to various kinds of flow field by many investigators in order to obtain the accurate size and velocity [2]. To obtain spatial distribution of the droplet size and velocity, interferometric laser imaging for droplet sizing technique (ILIDS) is invented and developed [3-5]. However, it is very difficult to find real-time and high-accuracy measurement techniques to satisfy industrial needs. An optical fibre probe is applied to the measurement of gas-liquid two-phase flows. This measurement is an intrusive technique; however it successfully detects droplets even though in high number density. Hence, it is applicable to not only laboratory conditions but also practical equipment. Much research into this technique has been conducted. For medium-size (i.e. 1 mm to 4 mm in equivalent diameter) bubbles/droplets, a multi-tip optical fibre probe is very useful [6]. However, simultaneous measurement of their diameters and velocities has been thought to need at least two optical fibre probes due to its measurement principle. Catellier et al. studied simultaneous measurement technique of a velocity, diameter and void fraction of a bubble/droplet via mono fibre optical probe [7].

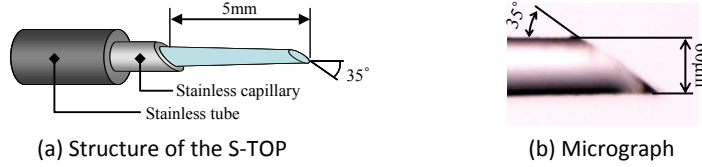
Recently, particular demands for measuring properties of micro droplets have increased in research in multi-phase flows. For the measurement of tiny droplets via optical fibre probe, a multi-tip probe is not applicable, because the multi-tip optical fibre probe is too large to surely pierce them. In order to solve this problem, the authors newly developed a Single-Tip Optical fibre Probe (S-TOP) which realizes the simultaneous measurement of a diameter and velocity of a tiny droplet [8, 9]. While the structural refinement succeeded, inevitable problem of detection of a position pierced by the S-TOP on the droplet is getting more obvious. For example, the droplet size (chord length) is evaluated from dwelling time of the S-TOP in the droplet; when the S-TOP touches a spherical droplet's surface around its equator, the pierced chord length is shorter than the length of the minor axis. The droplet diameter is usually calculated with the chord length, as if it equals to the minor axis. Conventional optical fibre probing has difficulties in evaluating the diameter accurately due to the random touch of an optical fibre probe to a droplet in droplet flows.

In the present technique, we skilfully used informative peaks, so named post-signals, in the S-TOP signals. The post-signal appears before the S-TOP pierces the droplet rear surface around its pole. Uniquely utilizing this phenomenon, we established detection method for a position touched by the S-TOP in a droplet measurement, and eliminate the random error. First, in order to quantify the relationship between the pierced positions and post-signal intensity, we consider the results of medium-size/micro droplet measurement via the S-TOP. Second, the output signals are analysed with the visualization results of the droplets by using a high-speed video

camera. Third, newly developed post-signal method for detection of the pierced positions is proposed. Finally, we discuss the effectiveness of this method.

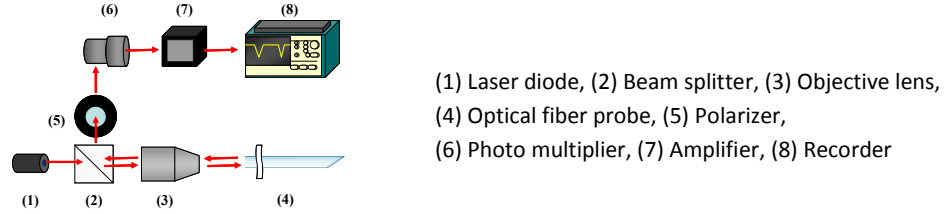
### Single-Tip Optical fibre Probe (S-TOP)

Figure 1 shows the structure of the S-TOP used in the present study. The S-TOP was made up of a synthetic silica optical fibre (external diameter, 230  $\mu\text{m}$ ; core diameter, 190  $\mu\text{m}$ ; jacket thickness, 15  $\mu\text{m}$ ; refractive index, 1.46). The silica optical fibre was fine-drawn using a micropipette puller (P-2000, Sutter Instrument Company). After that, the tip was ground at an angle of 35° to the fibre axis by a micropipette beveller (BV-10, Sutter Instrument Company). The tip diameter was 60  $\mu\text{m}$ . This fibre was inserted and fixed in a stainless capillary.



**Figure 1.** Configuration of the S-TOP

The optics is outlined in Figure 2. The beams from a laser diode (1) (wavelength 635nm) was split by beam splitter (2), and focused on the fibre edge by objective lens (3). A part of the laser beam propagated through the optical fibre was reflected at the other tip (sensing side) of the optical fibre probe, and was propagated back again through the same fibre; then it was input into a photo multiplier (6) through a polarizer (5) cutting direct laser beam from the laser diode. The converted electrical signal was amplified by amplifier (7). The electrical signal was stored in digital oscilloscope (8).



**Figure 2.** Optics

### Signal processing

A typical signal in droplet measurement via S-TOP is plotted in Figure 3 (a). First, the gas phase level  $V_{Gas}$  and the liquid phase level  $V_{Liquid}$  were determined. Second, the high threshold level  $V_{thh}$  and the low threshold level  $V_{thl}$  were decided [10]. In this study, the high threshold level  $V_{thh}$  was 60 % of the mode signal amplitude, and the low threshold level  $V_{thl}$  was 30 % of the mode signal amplitude. Finally, the gradient of the leading edge through the  $V_{thh}$  ( $P_1$ ) and  $V_{thl}$  ( $P_2$ ) were calculated by equation (1).

$$g_{rd} = \frac{dV}{dt} \times \frac{1}{(V_{Gas} - V_{Liquid})}, \quad (1)$$

Droplet velocity  $U_D$  (in a strict sense, average interface velocity of a droplet) was calculated from equation (2).

$$U_D = \alpha \times g_{rd}, \quad (2)$$

where  $\alpha$  is proportionality coefficient between the interface velocity and  $g_{rd}$  (Fig. 3 (b), obtained by preliminary penetration experiments). The chord length  $L_D$  was calculated from equation (3),

$$L_D = U_D \times (t_f - t_s), \quad (3)$$

where  $t_s$  and  $t_f$  are the starting and finishing time of contact between the S-TOP and droplet. The event time  $t_s$  is defined as an intersection point of the straight line (i.e. the gradient is  $g_{rd}$ ) and the gas phase level at leading edge. The  $t_f$  is defined as the time at which a “post-signal” takes the maximum value.

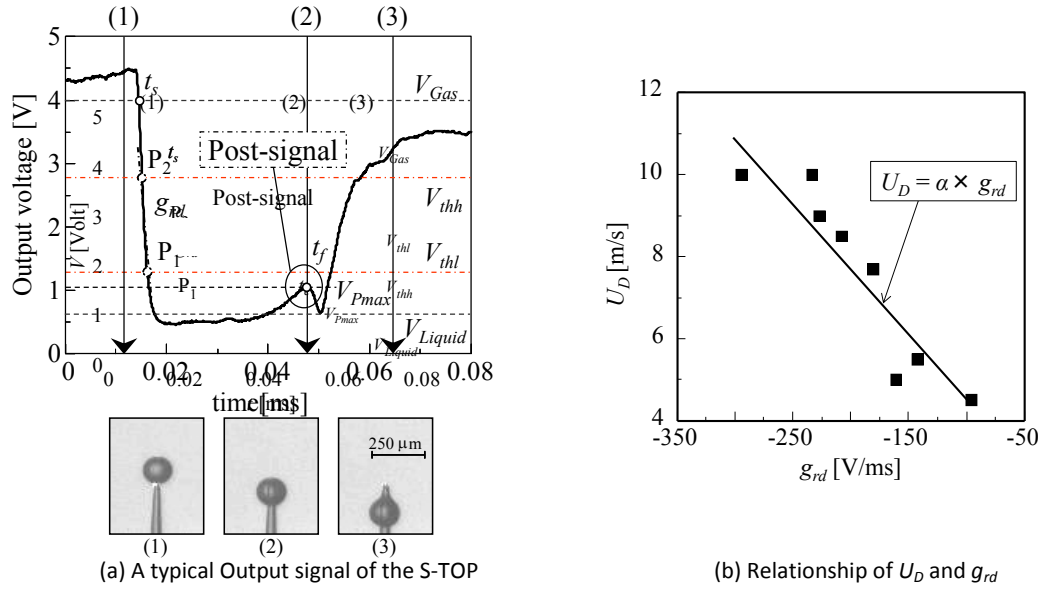


Figure 3. Processing of the S-TOP signal

### Basis of the post-signal

Sakamoto and Saito found that the post-signal results from surface reflection [11]. They rationally calculated S-TOP signals by using ray tracing computation, and concluded that in the case of the S-TOP piercing the interface from the water phase to the air phase, most rays which are discharged from the outlet tip re-enter and return to the inlet tip due to the different refractive indices of phases. In the droplet measurement, it occurs after the S-TOP pierces a droplet, namely before the S-TOP pierces the droplet rear surface; hence, we call this a post-signal. The post-signal has fruitful information for signal processing of optical fibre probing. It appears shortly before the S-TOP tip pierces an interface from the water phase to the air phase, and peaks when the tip is in touch with the interface. Hence, the time of its peak indicates the finishing time of a droplet measurement (Figure 4).

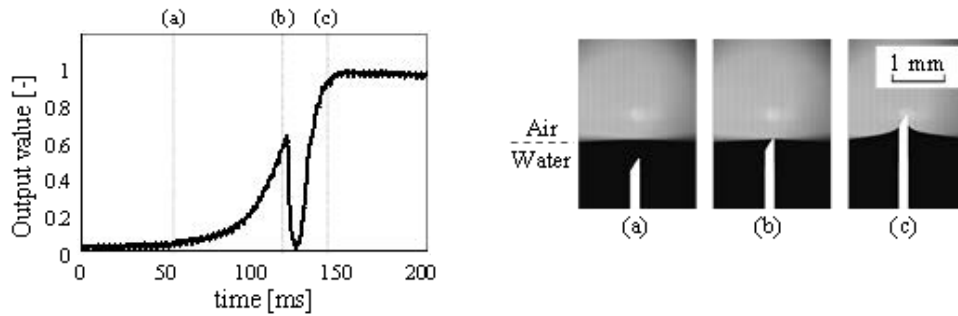


Figure 4. Quasi-piercing experiment of the S-TOP

The post-signal gives us information about not only the event time but also a contact position of the S-TOP on the droplet. According to Eq. (3), the chord length obtained by the probe is very similar to the droplet's minor axis when the probe pierces the centre region of the droplet. In the measurements of a droplet, if  $L_{probe}$  (the distance from the minor axis of the droplet) is limited within an area of  $L_{probe}/L_{major} < 0.3$  ( $L_{major}$ : the length of the major axis of the droplet), i.e. within the centre region, the difference between the measured chord length  $L_D$  and the length of the minor axis of the droplet  $L_{minor}$  (the length of the minor axis of the droplet) is small ( $0.90 < L_D/L_{minor} < 1.00$ ). When the probe pierces droplets in the centre region of a droplet, highly accurate measurement is achieved. However, the difference between the minor axis and measured chord length is a kind

of random difference (it depends on a contact position of a droplet); therefore, it is very difficult to remove the random differences from the measurement results.

To overcome this difficulty, the post-signal is very useful. It takes the largest value in all of the contact conditions when the interface against the S-TOP tip is “microscopically flat” i.e., the centre region of the spherical droplet. We empirically quantified the relationship between the S-TOP contact position and intensity of the post-signal.

### Description of experiments

Figure 5 shows a schematic diagram of the experimental setup used in demonstration of medium-size droplets measurement via the S-TOP. The droplets were launched from a micro capillary (h) (140  $\mu\text{m}$  in inner diameter) placed over the probe (a). The equivalent diameter of the droplets was about 2.0 mm, and their velocities were about 1.5 m/s. We visualized the process of the droplets pierced with the S-TOP using a high-speed video camera (e) (frame rate 10000 fps, exposure time 50  $\mu\text{s}$ , resolution 1024 $\times$ 512 pixels, and spatial resolution 8.33  $\mu\text{m}/\text{pixel}$ ) and a halogen light (g).

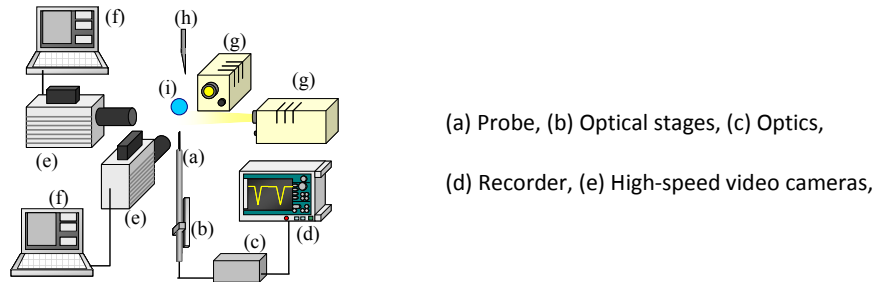


Figure 5. Experimental setup for measurement of medium size droplet

Figure 6 shows a schematic diagram of the experimental setup used in demonstration of micro droplets measurement via the S-TOP. Ion-exchange water in the water tank (b) was pressurized by air (a) (gage pressure  $P = 100$  kPa), and the pressurized water was ejected from nozzle (nozzle diameter  $D = 100$   $\mu\text{m}$ ) (e). The average diameter of the droplets was about 500  $\mu\text{m}$ , and the average velocity was about 10 m/s. The probe was mounted on a three-degree-of-freedom precision micro stage (h) driven by micro stepping motors. The probe position was adjusted precisely through the micro stage as the probe struck the micro droplets. The process of piercing the droplets with the probe was simultaneously visualized, using two high-speed video cameras (j) and (k) (frame rate: 200000 fps, exposure time: 2  $\mu\text{s}$ , resolution: 144  $\times$  64 pixels, and spatial resolution: 8.33  $\mu\text{m}/\text{pixel}$ ), and a halogen light (l).

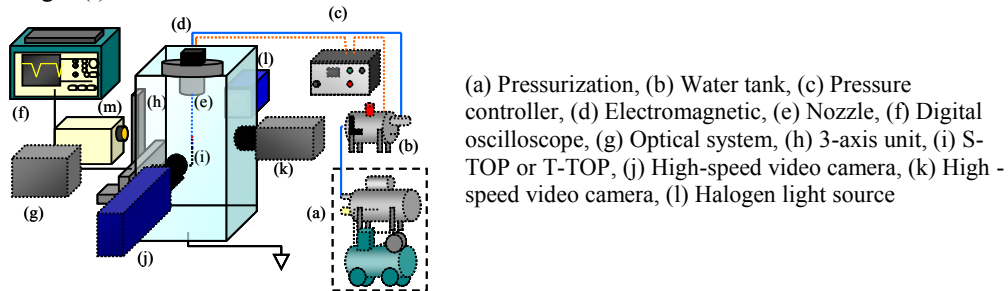


Figure 6. Experimental setup for measurement of micro droplet

### Results and Discussion

Figure 7 shows typical output signals obtained from the measurement of medium-size and micro-size droplets, and the corresponding images. In outer region (Fig. 7 (c), (f)), the signal was V-shaped, because the whole of the S-TOP tip was not covered with water. The other signals formed a shape like an inverse trapezoid (Fig. 7 (a), (b), (d), (e)). These were limitations of the existing methods for detection of the pierced positions (whether the penetration is perfect or not). In this way, the difference between the measured chord length and the length of the minor axis of a droplet is very large ( $L_D/L_{minor} < 0.60$ ). In addition, this kind of a random error is especially difficult to estimate because it entirely depends on droplet flow fields. Although a statistical method was introduced, this random error had never been eliminated in previous studies [12].

Taking the post-signal into consideration, however, the random error can be easily eliminated. The post-signal clearly appears before the S-TOP finishes the dwelling in a droplet at its centre region (Fig. 7 (a), (d)). On the other hand, any post-signals are not detected in the other conditions. By using this, we can identify whether

the S-TOP has touched the droplet at a region near the pole or not (post-signal method). If the post-signal appears, we know that the S-TOP has touched the droplet at the vicinity of its pole. If no post-signals exist within an S-TOP signal, we know the signal is obtained under an imperfect piercing condition. Hence, we calculate the properties of the droplet in consideration of the selected signals. In this newly developed method, the difference in the measured length and the length of the minor axis can be very small ( $0.90 < L_D/L_{minor} < 1.00$ ). The reason why the post-signal intensively appears only when the S-TOP touches the centre region of droplets is explained geometrically. Figure 8 (a) is a visualized image of the discharged beams from the S-TOP tip to the surrounding water by using fluorescent substance, Rhodamine B. In this picture, the discharged beams have directional characteristics along the S-TOP axis. When the interface against the tip is flat (Figure 8 (b)), beams reflected at the interface are effectively collected. On the other hand, the beams are immediately reflected to the other than the S-TOP axis when the interface is inclined (the pierced position moves from the centre region) (Figure 8 (c)). These tendencies are the same in arbitrary spherical droplets as shown by the experimental results.

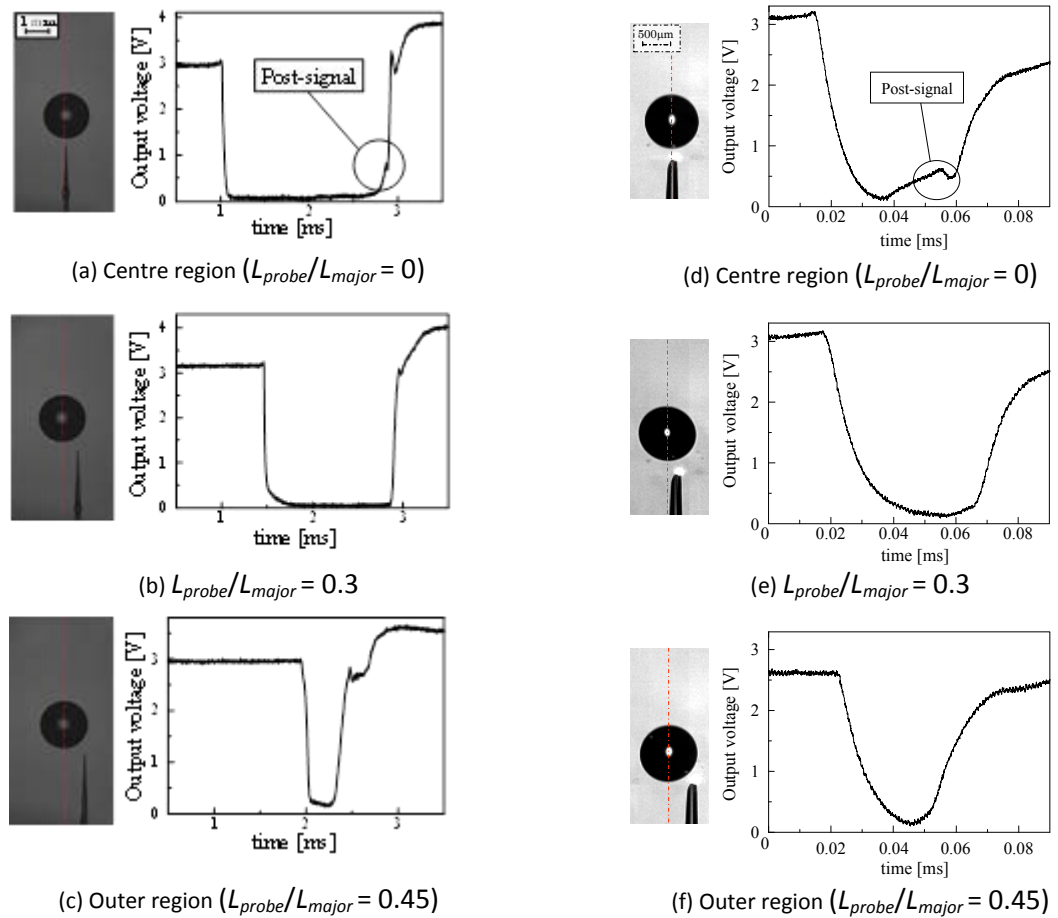


**Figure 7.** Output signals from the droplet measurement

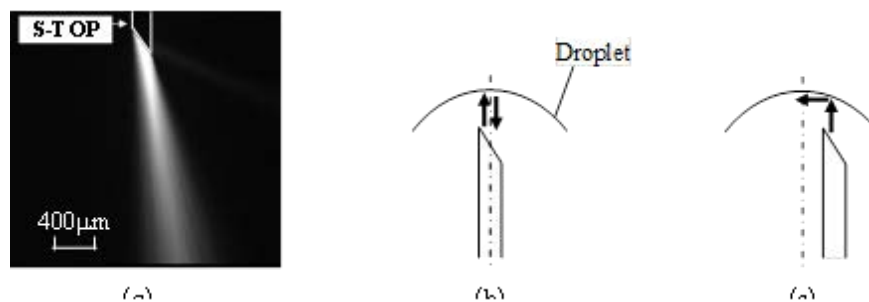


**Figure 8.** Effect of the interface curvature on the post-signal

## Conclusions

In this study, we aimed at improving the measurement accuracy of the S-TOP. We focused on the relationship between the intensities of the post-signal and the S-TOP's contact positions. Its intensity took the maximum value when the S-TOP touched the centre region of a droplet. While, the post-signal disappeared when the S-TOP touched the outer region of a droplet. To use this interesting characteristics, we established the post-signal method for signal processing, continuously we improved the S-TOP's measurement accuracy, i.e., we identified whether the S-TOP had touched a droplet at the vicinity of its pole or not. This newly developed method successfully reduced the difference between the measured chord length and the length of the minor axis of a droplet ( $0.90 < L_D/L_{minor} < 1.00$ ). This method will be applied to arbitrary spherical droplets. As the prospect, we will conduct the S-TOP measurements in a droplet flow, and we will confirm the effectiveness of the post-signal method.

## Acknowledgements

The present study was promoted and financially supported by Category “A” of the Grants-in-Aid for Scientific Research, Japan Society for the Promotion of Science. We thank JSPS for its help in the financial support.

## Nomenclature

$V_s$	output voltage level [V]
$g_{rd}$	gradient of downslope of output signal [V/ms]
$U$	velocity
$\alpha$	proportionality coefficient [m/V]
$t$	time [ms]
$L$	distance or length [mm]

### Subscripts

Gas	gas phase
Liquid	liquid phase
thh	high threshold
thl	low threshold
D	droplet
s	start of penetration
f	finishing of penetration
Pmax	maximum value of post-signal
probe	position of S-TOP
major	major axis of droplet
minor	minor axis of droplet

## References

- [1] Durst, F. and Zaré, M. “Laser Doppler measurement in two phase flows”, *Proceedings of the Laser Doppler anemometry symposium*, Copenhagen, Denmark, pp. 403–429, (1975)
- [2] Stewart, J. A., et al. “Radial Analysis of Fine Sprays Using Phase Doppler Anemometry (PDA)”, ILASS-Europe 2010.
- [3] Hesselbacher, K.H., et al. “Experimental investigation of Gaussian beam effects on the accuracy of a droplet sizing method”, *Appl. Opt.*, Vol. 30, pp. 4930–4935. (1991)
- [4] Glover, A.R., et al. “Interferometric laser imaging for droplet sizing: a method for droplet-size measurement in sparse spray systems”, *Appl. Opt.*, Vol. 34 pp. 8409–8421, (1995)
- [5] Kawaguchi, T., et al. “Dynamic ILIDS measurement by means of high-speed Nd:YLF laser”, ILASS-Europe 2010.
- [6] Hong, M., Cartellier, A. and Hopfinger, E.J. “Characterization of phase detection optical probes for the measurement of the dispersed phase parameters in sprays”, *Int. J. Multiph. Flow*, Vol. 30 pp. 615–648 (2004)
- [7] Cartellier, A. “Simultaneous void fraction measurement, bubble velocity, and size estimate using a single optical probe in gas-liquid two-phase flows”, *Rev. Sci. Instrum.*, Vol. 63 5442, (1992)
- [8] Saito, T., et al. “Measurement of tiny droplets using a newly developed optical fibre probe micro-fabricated by a femtosecond pulse laser”, *Meas. Sci. Technol.*, Vol. 20 114002, (2009)
- [9] Mizushima, Y. and Saito, T. “Detection method of a position pierced by a single-tip optical fibre probe in bubble measurement”, *Meas. Sci. Technol.*, Vol. 23 085308, (2012)

- [10] Sakamoto, A. and Saito, T. “Robust algorithms for quantifying noisy signals of optical fiber probes employed in industrial-scale practical bubbly flows”, *Int. J. Multiph. Flow*, Vol. 41 pp. 77–90 (2012)
- [11] Sakamoto, A. and Saito, T. “Computational analysis of responses of a wedge-shaped-tip optical fiber probe in bubble measurement”, *Rev. Sci. Instrum.*, Vol. 83 075107, (2012)
- [12] Clark, N.N. and Turton, R. “Chord length distributions related to bubble size distributions in multiphase flow”, *Int. J. Multiph. Flow*, Vol. 14 pp. 413–424, (1988)



## Validation of the Multi-Wavelength Light Extinction technique for the characterization of solid nanoparticles

I. T. Horváth<sup>1</sup>, P. Colinet<sup>2</sup> and M. R. Vetrano<sup>1</sup>

1: Environmental and Applied Fluid Dynamics Department, von Kármán Institute for Fluid Dynamics, Belgium

2: Transfers, Interfaces and Processes Department, Université Libre de Bruxelles, Belgium

### Abstract

The present paper describes the on going work about the development of the Multi Wavelength Light Extinction (MWLE) technique for the characterisation of submicron particles. The MWLE technique retrieves the particle size distribution function from the Ultraviolet Near-Infrared light transmittance spectrum of a particle cloud. This is done using a proper data inversion algorithm based on a mathematical model of light extinction. In this work the model chosen is the Mie theory, which assumes that the measured particles are spherical and homogeneous. The data inversion algorithm is based on the Tikhonov regularisation and it is optimised by the L-curve method. In this work, the experimental validation of the MWLE technique for solid KCl (potassium chloride) particles is also presented. The test aerosol is produced by the atomisation and drying of an aqueous KCl solution. The shape and morphology of the produced particles are evaluated using both available literature and a simple analytical model for evaporating solution droplets. The measurement results are compared to Scanning Mobility Particle Sizing (SMPS) measurements. The latter are obtained by using a commercial instrument, which has allowed the measurements simultaneously with the MWLE technique. The comparison resulted in a good quantitative agreement of the measured total concentrations and particle size distribution functions.

### Introduction

The characterisation of sub-micron sized particles became an important subject of research during the past decades. Such particles are used at numerous fields of science and industry e.g. food and pharmaceutical industry, material science, biotechnology. The online and non-intrusive characterisation of particles of such small size still represents a challenge.

The MWLE technique is a non-intrusive optical measurement technique, which is capable to carry out simultaneous size and concentration measurements of small particles. The technique has numerous advantages, such as the minimal required optical access, the possibly large stand-off distance, the simple optical setup, the short measurement time and the immediate retrieval of the particle size statistics. These advantages could make it widely applicable for both industrial and scientific problems.

The main goal of the present work is to experimentally validate the MWLE technique, using an established commercially available instrument as the reference. First, the theoretical background of the MWLE technique is described including the inversion algorithm, which solves the arising ill-conditioned inverse light scattering problem. The capabilities of the inversion method have been evaluated through simulation studies from which, a representative case is shown. Afterwards the test particle generation method is described and the shape and morphology of the resulting solid particles are predicted based on the related literature and a simple model for the evaporation of solution droplets. The experimental setup is presented in details. It allows the simultaneous characterisation of the same particles by the MWLE and SMPS techniques, thus eliminating the need to precisely control the particle properties. Finally, the comparison of the measurement results is presented for a typical case. The comparison is evaluated on the basis of the obtained particle size distribution (PSD) function, total concentration and volumetric mean diameter.

The data inversion leads to the solution of a Fredholm integral equation of the first kind, which turns out to be a severely ill-conditioned problem. [1–3] highlighted the difficulties of the data inversion process and investigated their effect on the accuracy of the technique. In the present work an inversion algorithm was applied, which is based on the optimised Tikhonov algorithm and the Non-Negative Least Squares (NNLS) method.

### The Multi Wavelength Light Extinction Technique

The MWLE technique uses the measured ultraviolet (UV) to near infrared (NIR) spectrum of transmittance ( $Tr(\lambda) = I/I_0$ ) for the reconstruction of the particle properties. In the definition of  $Tr(\lambda)$ ,  $I_0$  refers to the light intensity incident to the investigated particle cloud and  $I$  to the attenuated intensity at the detector side of the particle cloud. The MWLE technique attempts to find the best fit to a measured transmittance spectrum by means of a modeled one. The fixed parameters of the model are the particle shape, morphology, complex refractive index of the particles and the size parameter  $x$  ( $x = D\pi/\lambda$ , where  $D$  is the particle diameter and  $\lambda$  is the

wavelength of the illuminating light). The variable parameters of the model are the sought particle properties (PSD, concentration). Assuming the material (KCl), shape and morphology of the particles - in our case spherical shape and homogeneity – the transmittance spectrum of a hypothetical particle size distribution function can be modelled. The latter is called the forward problem. Conversely, using the same assumptions and attempting to fit a measured transmittance spectrum with the modelled one through varying the particle size distribution function constitutes the inverse problem.

According to the Lambert-Beer law [4],

$$Tr(\lambda) = e^{-\tau L} \quad \text{Eq. 1}$$

where  $\tau$  is the optical density of the investigated medium and  $L$  the path length that the light travels through the particle cloud. The optical density of a particle cloud is a function of the wavelength ( $\lambda$ ) of the illuminating light and the complex refractive index ( $m$ ) of the particles. It can be expressed in the following form:

$$\tau(\lambda, m) = \int_{D_{min}}^{D_{max}} Q_{ext}(D, \lambda, m) \frac{D^2 \pi}{4} N(D) dD. \quad \text{Eq. 2}$$

$Q_{ext}(D, \lambda, m)$  is called the extinction efficiency factor, which is the function of particle size ( $D$ ), wavelength ( $\lambda$ ) and complex refractive index ( $m$ ). Assuming spherical and homogeneous particles,  $Q_{ext}$  can be calculated using the Mie theory.  $N(D)$  is the number concentration of particles with diameter  $D$ . Combining **Eq. 1** and **Eq. 2** and changing to volumetric particle size distribution function, the following relation is obtained:

$$-\ln(Tr(\lambda)) \frac{2}{3L} = \int_{D_{min}}^{D_{max}} Q_{ext}(D, \lambda, m) \frac{V(D)}{D} dD. \quad \text{Eq. 3}$$

The discretized form of Eq 3 can be obtained using linear quadratures for both  $D$  and  $\lambda$  leading to a linear algebraic equation:

$$T = S \cdot V \quad \text{Eq. 4}$$

where  $T$  is the discretized form of the left hand side of **Eq. 3**,  $S$  is a matrix related to the extinction efficiency factors and vector  $V$  is the unknown volumetric particle size distribution function. In order to retrieve the volumetric PSD function  $V(D)$ , **Eq. 4** should be inverted. Unfortunately, due to the smoothing effect of matrix  $S$  the above system is ill-conditioned and numerically unstable.

In the present study **Eq. 4** is solved by the non-negative Tikhonov regularization, which is optimized by the L-curve method [5]. The fundamental idea of the Tikhonov regularization is the stabilization of the solution by applying a priori assumptions. In general form, the regularized solution can be obtained by means of a minimization problem:

$$V_{reg} = \min\{\|S \cdot V - T\|_2^2 + \gamma^2 \|L \cdot V\|_2^2\}. \quad \text{Eq. 5}$$

If the original ill-conditioned problem was given in the form of **Eq. 4**, with  $V$  being the unknown vector. The quantity  $\gamma$  is called the regularization parameter, which controls the weight given to the minimization of the norm of the side constraint ( $\|L \cdot V\|_2^2$ ) relative to the minimization of the residual norm ( $\|S \cdot V - T\|_2^2$ ). The choice of the regularization parameter is essential for a successful regularization. In the present method the regularization parameter is optimized in every inversion using the L-curve optimization [6].

In **Eq. 5** matrix  $L$  is the regularization matrix, which formulates the criteria to be minimized, thus representing the a priori knowledge about the nature of the solution. In [7] the role of the regularization matrix is extensively explained, while examples are also given. In the present study the 0<sup>th</sup> order difference matrix was used to stabilize the solution. Consequently, the side constraint was the minimization of the 0<sup>th</sup> order derivative of the solution. This is reasonable since PSD functions take very small values outside a finite interval.

Because of the non-negativity of a particle size distribution function it is advantageous to complement the Tikhonov regularization with a non-negativity constraint. Using the formulation of **Eq. 6**, the problem can be solved by the Non-Negative Least Squares (NNLS) algorithm.

$$\min_{x \geq 0} \|(S^T S + \gamma^2 \cdot L^T L)V - S^T T\|_{2-LSQ}^2 \quad \text{Eq. 6}$$

Summarizing, the Tikhonov method does not seek the solution with the smallest residual norm, but allows small deviations from that, in order to find a solution with smaller overall norm, which satisfies the side constraints, too. Consequently, the inversion process should be validated numerically and experimentally before applying the MWLE technique as a particle characterization tool.

## Numerical validation

The numerical validation of the inversion algorithm is not presented here in details. Instead, only one representative example is shown. A solid particle aerosol consisting of KCl particles have been modelled with a lognormal particle size distribution function with mean diameter 200nm and dispersion factor 0,3. The transmittance function of this distribution has been modelled on the 200nm...1000nm wavelength interval. The model aerosol exhibited a minimal transmittance of 0.89 at the wavelength 228nm. The modelled transmittance spectrum has been disturbed by normally distributed random error with amplitude 1% of the actual transmittance value. The inversion of the hypothetical data has been performed for 50 different random errors using the 0<sup>th</sup> order regularization matrix. The mean value of the results has been calculated at each diameter. The comparison of the generated and the retrieved mean distribution functions is shown on **Figure 1**. The comparison displays the satisfactory reconstruction of the hypothetic PSD function. The peak of the function is slightly underestimated but the mean value and standard deviation are well captured.

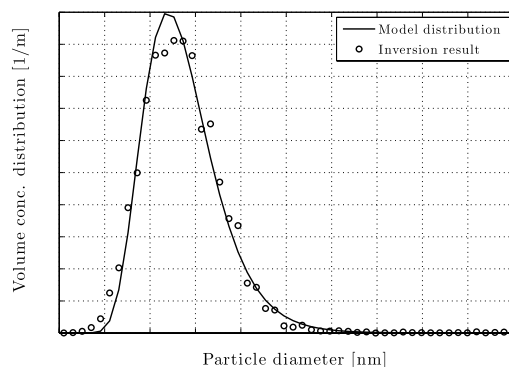


**Figure 1** - Comparison of modelled and retrieved particle size distribution functions

## Particle generation

The test particles have been generated by atomizing an aqueous KCl solution and evaporating the water content of the resulting droplets. In this process a pneumatic atomizer is fed with pressurized air, whose flow rate and pressure are measured by a rotameter and a manometer respectively. A valve controls the latter parameters. The KCl aerosol is produced of 1 wt% aqueous solution of KCl. After the atomization of the liquid, the droplets pass through a diffusion dryer column, which is filled with silica gel. Silica gel is a hygroscopic material with porous structure that is able to accumulate a large quantity of water molecules due to its large specific surface area. When the relative humidity of the atmosphere increases due to the presence of liquid droplets, water vapor molecules diffuse fast into the silica gel. The adsorption of water molecules increases the moisture content of the silica gel until it reaches saturation. Color indicators can be used for indicating the latter state. When saturation is reached, the silica gel can be regenerated by exposing it to a low relative humidity environment on an elevated temperature. The resulting size of the dried solid particles directly depends on the initial droplet size and the solute concentration inside the droplets. The control of the latter parameter provides a simple way to adjust the size and volumetric concentration of the solid particles.

## Shape and morphology of the test particles

According to the corresponding literature, various particle shapes and morphologies can result from the above-described process. [8–10] has reported that the general shape of the particles is spherical due to the spherical shape of the precursor droplets. Mainly full and hollow spheres were reported together with cubes and less organized structures occurring in some cases. [11] has suggested that the resulting morphology of a spherical particle is function of the solute concentration profile inside the particle at the moment of solute crystallization on the droplet surface. The latter initiates when the solute concentration reaches the Critical Super Saturation (CSS). Two different situations can be distinguished. Full particles are formed when the entire concentration profile lies above the Equilibrium Saturation (solubility, ES). In this case crystallization occurs in the complete volume of the droplet, after being triggered by crystallization on the surface. Hollow particles are formed, when a part of the concentration profile lies below the ES. In such a situation crystallization occurs only in the outer shell of the droplet.

The solute concentration profile inside the droplet is a function of time and can be obtained by numerically solving the appropriate differential equations as described by [11]. In our simple approach, we assume that the evaporation of the droplets is limited by the rate of diffusion of the water vapor molecules away from the liquid-gas interface. Furthermore, we assume that the vapor pressure on the interface is equal to the equilibrium vapor pressure (local equilibrium on the interface) and it can be calculated from Raoult's law (shouldn't you put a

reference or just write the equation??) as a function of solute concentration. The concentration boundary layer - where an increase of concentration is expected due to the difference between the solute diffusion rate and the droplet shrinkage rate - has a thickness, which can be estimated from:

$$\delta \sim \frac{D_l}{|\dot{a}|} \quad \text{Eq. 7}$$

where  $D_l$  is the diffusion coefficient of the solvent and  $|\dot{a}|$  is the absolute value of the droplet radius time derivative (i.e. the interface velocity). In the simplest case one can assume that the solute concentration is constant outside the concentration boundary layer (i.e. in the bulk of the droplet) and equal to the initial concentration. A solute mass balance then yields an estimate of the concentration inside the boundary layer, i.e. close to the surface. Here, we shall content ourselves with an estimation of the thickness of the boundary layer however, using **Eq. 7**. Assuming diffusion limited evaporation process, the rate of change of droplet radius remains proportional to the diffusion coefficient of the surrounding gas ( $D_g$ ) and the difference of vapor pressure between the droplet surface and far away from it ( $p_{v,i} - p_{v,\infty}$ ).  $p_{v,i}$  can be calculated from Raoult's law, once the molar fraction of the solute ( $X_\Sigma$ ) in the solution at the interface is known:  $p_{v,i} = p_{sat}(1 - X_\Sigma)$  with  $p_{sat}$  being the equilibrium vapor pressure of the pure solvent. The rate of change of droplet radius then reads:

$$\dot{a} = - \frac{D_g}{\rho_l R T} \cdot \frac{p_{sat}(1 - X_\Sigma) - p_{v,\infty}}{a}, \quad \text{Eq. 8}$$

where  $\rho_l$  is the density of the liquid,  $R$  is the specific gas constant of air and  $T$  is the ambient temperature. The resulting particle morphology can be predicted based on the value of  $\delta/a$  (readily found by inserting **Eq. 8** in **Eq. 7**) in the moment when crystallization occurs on the droplet surface. At this moment the solute concentration at the surface is equal to CSS. If  $\delta/a \gg 1$  the process favors the formation of full particles and if  $\delta/a \ll 1$  the occurrence of hollow particles is more probable. The mentioned ratio can be evaluated once the value of CSS is known. Assuming the homogeneous nucleation of crystallization cores, it can be calculated by the method proposed by [12]. In the present case the CSS was found to be 2.64, meaning that crystallization starts at a concentration 2.64 times larger than the solubility (or ES) of the solute (344 g/L at 293K temperature). Based on this value,  $\delta/a$  was found to be 11.8, suggesting that volume precipitation is the favored way of crystallization, hence resulting in full particles.

## Experimental setup

The experimental setup used for validating the MWLE technique by comparison with the SMPS measurements is constituted by an aerosol generator, suitable test sections for both of the instruments and the instruments themselves. **Figure 2** shows the sketch of the experimental setup.

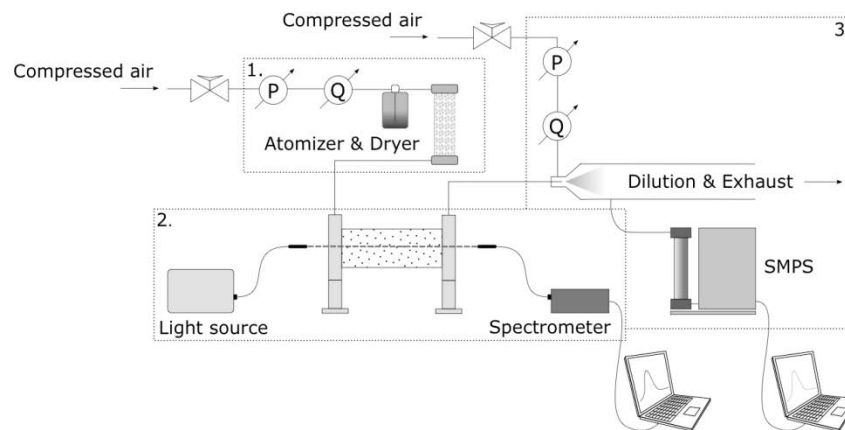


**Figure 2:** Experimental setup for simultaneous measurements of solid KCl nanoparticles with the MWLE and SMPS techniques

Solid KCL nanoparticles are generated by an aerosol generator (subsystem 1). The synthesized solid KCL particles enter the test section, which is a cylindrical Plexiglas reservoir. The MWLE measurements are performed inside this reservoir (subsystem 2). The particles enter at one side of the reservoir from 4 inlets equally distributed around the perimeter. The extraction is performed similarly at the other end of the reservoir.

A collimated, white light beam passes through the test chamber along its longitudinal axis. After passing through the particle cloud, the light is received and analyzed by a spectrometer and a personal computer. The length of the cylindrical reservoir corresponds to the path length ( $L$ ) travelled by the light beam inside the particle cloud. In order to avoid the sedimentation of the particles inside the reservoir, a continuous flow is maintained by the constant particle production and an ejector (indicated as Dilution & Exhaust on **Figure 2** which is installed downstream the test chamber. The pressure and flow rate of the ejector feed air are measured with a manometer and a rotameter, respectively. Since the ejector mixes the primary flow (with particles) with a large flow rate of secondary air (clean), it also serves as an aerosol dilutor, thus equilibrating the large difference of concentration range between the MWLE and SMPS techniques. The measurement of the secondary air flow rate allows the calculation of the dilution ratios, which are generally between 100 and 300. The sampling tube of the SMPS instrument is connected downstream the ejector, providing the sampling of the diluted aerosol. The SMPS system and the corresponding aerosol dilutor are indicated as subsystem 3.

The SMPS instrument is able to measure particles in the size range 10nm...1000nm. It consists of two main units. The first unit is called Differential Mobility Analyzer (DMA). It classifies the investigated particles into narrow size ranges within the measurement range, according to their electrical mobility. The classified particles proceed to the second unit, which is called Condensation Particle Counter (CPC). In this unit the particles are enlarged to approx. 10 $\mu$ m by condensing butanol on their surface. The enlarged particles are then counted by an optical method. The SMPS instrument performs the measurement of the different size channels one after the other. The total concentration of the particles below 1000nm can be obtained by integrating the obtained PSD function. The scanning of the complete size range takes approx. 5 minutes. The instrument can be used without the DMA unit, too. In this case the total concentration of the particles can be effectively determined, also including particles larger than 1000nm.

### Experimental conditions

In order to perform the valid comparison of the measurement techniques, an experimental PSD had to be obtained, which falls within the measurement ranges of both techniques. This has been achieved by atomizing a KCl solution with 1 wt% concentration at 2.2 bar atomization pressure. A dilution ratio of 1:205.8 has been necessary for the SMPS measurements. The MWLE measurements have been performed on the wavelength range spanning from 230nm to 1000nm. The complex refractive index function presented in [13] has been used for the light scattering modeling.

### Comparison of measurement results

The comparison of the MWLE and SMPS measurement results is displayed on **Figure 3**. The distribution curves agree in terms of mean value and standard deviation, too. It is noted that a small secondary mode centred at 700nm is equally identified by both techniques. The comparison of the measured total concentrations and volumetric mean diameters ( $D_{4,3}$ ) is presented in **Table 1**. The comparison concludes a remarkable agreement between the two measurement techniques that rely on entirely different principles. The agreement also confirms the validity of the assumptions made about shape and morphology of the test particles, namely that they are spherical and homogeneous.

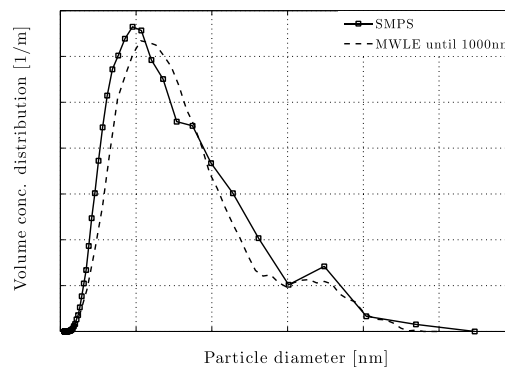


**Figure 3** – Comparison of PSD functions obtained by the SMPS and MWLE techniques

**Table 1** - Comparison of total concentrations and mean diameters obtained by the SMPS and MWLE techniques

	Total volume concentration [-]	$D_{4,3}$ [nm]
SMPS	$2,42 \cdot 10^{-8}$	333,5
MWLE	$2.22 \cdot 10^{-8}$	333,5

## Conclusions

In the present work the Multi Wavelength Light Extinction technique has been introduced. The Mie theory has been used for modeling the light extinction of the investigated particles. The latter required assuming the particles to be spherical and homogeneous. These assumptions have been evaluated using a simple analytical model that is capable to predict the morphology of the solid particles obtained from evaporating solution droplets. The data inversion has been performed with the optimized non-negative Tikhonov regularization. The inversion algorithm has been tested numerically using hypothetical lognormal PSD functions. The presented example showed the satisfactory accuracy of the inversion. The MWLE technique has been experimentally validated by comparing the inversion results to Scanning Mobility Particle Sizing measurements. The reference measurements have been carried out using a commercial instrument. The comparison of the retrieved particle size distribution functions displayed satisfactory agreement. Accordingly, the obtained total concentration and volumetric mean diameter values also showed a good agreement.

The present study has concluded that the MWLE technique can be used as an accurate sub-micron particle characterization technique and in the future it will be used to investigate different solid particle systems.

## Acknowledgements

The presented work has been financed by the Walloon Region under the NANOTECH convention C6405 and the Fonds de la Recherche Scientifique (FNRS).

## Nomenclature

$Tr$	<i>Transmittance</i>
$I$	<i>Attenuated intensity</i>
$I_0$	<i>Incident intensity</i>
$\lambda$	<i>Wavelength</i>
$x$	<i>Size parameter</i>
$D$	<i>Particle diameter</i>
$\tau$	<i>Optical density</i>
$L$	<i>Path length of light</i>
$m$	<i>Complex refractive index</i>
$Q_{ext}$	<i>Extinction efficiency factor</i>
$N(D)$	<i>Number size distribution function</i>
$D_{min}$	<i>Smallest diameter occurring in a particle ensemble</i>
$D_{max}$	<i>Largest diameter occurring in a particle ensemble</i>
$V(D)$	<i>Volumetric particle size distribution function</i>
$T$	<i>Constant of the resulting linear system of equations</i>
$S$	<i>Coefficient matrix</i>
$V_{reg}$	<i>Regularized solution</i>
$\gamma$	<i>Regularization parameter</i>
$L$	<i>Regularization matrix</i>
$\delta$	<i>Concentration boundary layer to particle radius ratio</i>
$D_l$	<i>Diffusion coefficient of solvent</i>
$a$	<i>Particle radius</i>
$D_g$	<i>Diffusion coefficient of gas</i>
$p_{v,i}$	<i>Vapor pressure on the liquid-gas interface</i>
$p_{v,\infty}$	<i>Ambient vapor pressure</i>
$p_{sat}$	<i>Equilibrium vapor pressure</i>
$X_\Sigma$	<i>Molar fraction of solute in the conc. boundary layer</i>
$\rho_l$	<i>Density of the liquid</i>
$R$	<i>Specific gas constant</i>
$T$	<i>Absolute ambient temperature</i>
$D_{4,3}$	<i>Volumetric mean diameter</i>

## References

- [1] G. Viera and M. A. Box, “Information content analysis of aerosol remote-sensing experiments using an analytic eigenfunction theory: anomalous diffraction approximation,” *Applied Optics*, vol. 24, no. 24, pp. 4525–4533, 1985.
- [2] T. Kourti, J. F. Macgregor, and A. E. Hamielec, “Turbidimetric Techniques Capability To Provide the Full Particle Size Distribution,” in *Particle Size Distribution II*, 1991, pp. 2–19.
- [3] C. Dellago and H. Horvath, “On the accuracy of the size distribution information obtained from light extinction and scattering measurements - I. Basic considerations and models,” *Journal of Aerosol Science*, vol. 24, no. 2, pp. 129–141, 1993.
- [4] H. C. van de Hulst, *Light scattering by small particles*. Dover publications, 1981, p. 470.
- [5] P. C. Hansen, *Rank-Deficient and Discrete Ill-Posed Problems*. SIAM, 1998, p. 246.
- [6] P. C. Hansen and D. P. O’Leary, “The use of the L-curve in the regularization of discrete ill-posed problems,” *SIAM Journal on Scientific Computing*, vol. 14, no. 6, pp. 1487–1503, 1993.
- [7] W. H. Press, S. A. Teukolsky, W. T. Vetterling, and B. P. Flannery, *Numerical recipes*, 3rd ed. Cambridge, 2007, p. 1235.
- [8] K. H. Leong, “Morphology of aerosol particles generated from the evaporation of solution drops,” *Journal of Aerosol Science*, vol. 12, no. 5, pp. 417–435, Jan. 1981.
- [9] K. H. Leong, “Morphological control of particles generated from the evaporation of solution droplets: Experiment,” *Journal of Aerosol Science*, vol. 18, no. 5, pp. 525–552, 1987.
- [10] M. Eslamian and N. Ashgriz, “Spray Drying, Spray Pyrolysis and Spray Freeze Drying,” in *Handbook of atomization and sprays*, N. Ashgriz, Ed. Boston, MA: Springer US, 2011, pp. 849–860.
- [11] G. V. Jayanthi, S. C. Zhang, and G. L. Messing, “Modeling of Solid Particle Formation During Solution Aerosol Thermolysis,” *Aerosol Science and Technology*, vol. 19, no. 4, pp. 478–490, 1993.
- [12] G. He, V. Bhamidi, R. B. H. Tan, P. J. A. Kenis, and C. F. Zukoski, “Determination of Critical Supersaturation from Microdroplet Evaporation Experiments,” *Crystal growth & design*, vol. 6, no. 5, pp. 1175–1180, 2006.
- [13] H. H. Li, “Refractive Index of Alkali Halides and Its Wavelength and Temperature Derivatives,” *Journal of Physical Chemistry Reference Data*, vol. 5, no. 2, pp. 329–526, 1976.

## Gas-Based Calibration of a Liquid Dispensing Device

Keskinen, Karri and Kaario, Ossi

Thermodynamics and Combustion Technology Research Group, Aalto University, Finland

### Abstract

In analysis techniques requiring accurate liquid dosing, dispensing valves yielding discrete liquid quantities are utilized. However, potential valve defects and unitary variation may mandate calibration of each dispensing unit in the assembly stage. In dispensing applications where liquid calibration is costly or hazardous, an optional method is preferable. The current study focused on the feasibility of performing valve anomaly recognition and output calibration using pressurized air as the dispensed substance. The valves involved were a micro-dispensing single-orifice valve and an automotive port fuel injection 12-orifice valve. Both types operate via solenoid actuation. Three different, Newtonian low-viscosity liquids were used in the study. System liquid calibration was based on measurement of vaporized liquid concentration with known injection settings and a known gas stream. Conversely, the proposed gas calibration used the decline of reservoir air pressure in estimation of valve properties. Determining valve properties from a pressure decline measurement is an inverse problem. However, this study focused on a forward problem where measured pressure decline was numerically reproduced via zero-dimensional (0-D) flow models. Due to gas compressibility and liquid incompressibility, flow rate expressions differ significantly between the two fluid types. Experiments were conducted to determine whether the gaseous 0-D model was sufficient in description of the dispensing system. In order to estimate the Reynolds number in liquid flow cases, previously unknown liquid viscosity values were measured. While liquid and gas discharge coefficients were not equal, an evident correlation existed. With different valve and liquid types,  $C_{D,l}(\text{Re}_{D,l}) \approx 2/3 \cdot C_{D,g}(\text{Re}_{D,g})$ . Statistical valve series averages in terms of discharge properties were defined as nominal valves. These nominal valves then served as a basis of comparison in tests where anomaly recognition and calibration were investigated. Geometric anomalies could clearly be detected by the gas dispensing routine in an altered test valve. Control system calibration was considered successful with the micro-dispensing valve type.

### Introduction

A range of applications, e.g. in the field of transportation, utilize a gas stream fed with a stream of volatile liquid, subsequently combining into a gas mixture via evaporation of the liquid. A prime example of this principle is the fuel-air mixture formation process in a liquid-fueled Otto engine. A correct dispensed amount is paramount in achieving acceptable gas mixtures in these applications. A common method for controlling dispensed amount is to implement a closed-loop control system, in which inputs are adjusted according to feedback obtained from another part of the system. Fuel injection using a lambda sensor is a common example of this principle. Conversely, no feedback is present in an open-loop control system, where sufficient prior knowledge of the dispensing equipment and its properties is assumed. Using this knowledge, a correct dispensing setting is predicted with a model.

If an application is safety-critical, redundant hardware is a requirement [1]. When employing a closed-loop control system, one relies heavily on the sensor providing feedback to the controller. Upon detection of a failure in the sensor, a fault detection and isolation (FDI) routine is initiated. A common configuration is to have a closed-loop system with an open-loop-operated FDI [2], in which the parallel systems form a redundancy. However, use of this also demands that the predictive component is well-defined, i.e. the relationship between system inputs and outputs are well known. With solenoid-operated dispensing valves, the primary control inputs are signal duration and frequency. In addition, properties of the fluid and those of the valve affect the output, i.e. dispensed mass or volume. In the prediction-based system, valve properties must hold with regard to its model within the control system. In practice, this means that the electrical actuation functions normally, valve flow rate-influencing structures contain no geometric anomalies and valve sealing is sufficient.

In a gas stream dispensing application, depending on component criticality, each valve unit may require a checkup of these properties before completion on the assembly line. If a particularly accurate output, within defined rejection intervals, is required from the predictive control routine, each dispensing unit may be subjected to control system calibration, where predictive model parameters are altered to reflect the minute differences between the current dispensing system and its nominal counterpart.



The direct method for both anomaly recognition and fine-tuned calibration would be to measure a steady-state liquid flow rate through the valve at a certain nominal condition (injection pressure). However, this is often inconvenient, particularly if the dispensing valve is to be separate from the rest of the device assembly during testing. Moreover, potentially harmful substances may mandate special safety measures. These factors and their effect on production cost motivate development of optional methods in verifying unitary dispensing valve properties.

The purpose of this study is to determine whether a gas-based calibration and anomaly detection algorithm can be feasibly implemented in a dispensing system where volatile liquid is fed to a stream of gas. Focally, two different types of dispensing valves, and three liquids are involved.

## Experimental setup

Figure 1 displays the testing arrangement used in the study. The liquid dispensing setup (left) was used in portrayal of valve flow properties with the target liquids. It included a liquid reservoir pressurized with air. In the experiments, liquid was periodically dispensed into a known gas stream through a solenoid valve. The gas stream was slow enough to induce a minimal drop in static pressure downstream of the valve. Once injected, the liquid entered a mixing volume where vaporization of the liquid was ensured, along with the homogenization of the gas mixture. The exiting gas mixture was then subjected to vapour concentration measurement using Fourier transform infrared spectroscopy (FTIR). Injected mass, and liquid flow rate, were subsequently derived from a series of these measurements.

The gas dispensing test rig (right) was similar to that of the liquid, with the exception that the pressurizing air was itself the dispensed substance. Furthermore, no passing gas stream was included, and no concentration measurements were made. The solenoid valve was actuated for a specified voltage pulse width, at a specified frequency. Pulse width was chosen so that the effect of valve opening and closing was diminished. Within the test rig, initial pressurization was set at varying points between 50 and 150 kPa. Once dispensing commenced, reservoir pressure was measured at a frequency of 10 Hz. Gaseous flow rate was derived from this measurement.

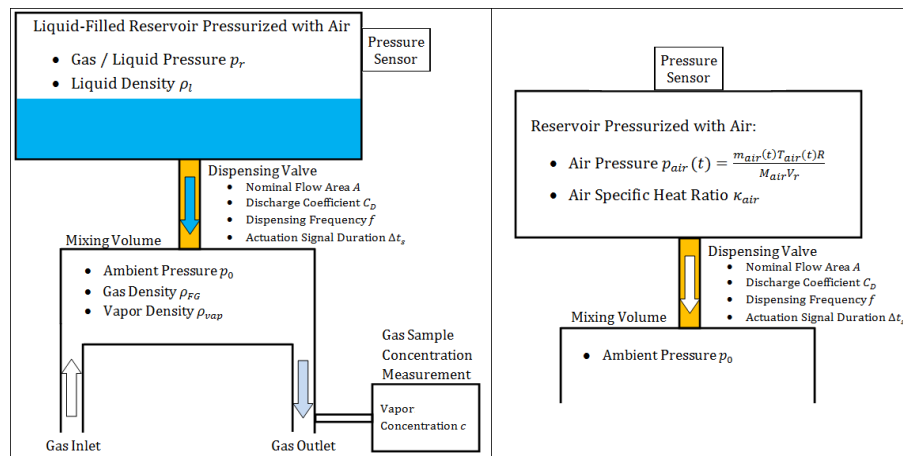


**Figure 1.** Schematics of liquid (left) and gas (right) dispensing arrangements

Valves involved in the study consisted of a 10 unit series of 12-orifice port fuel injection (PFI) valves, and a 4 unit series of single-orifice micro-dispensing (MD) valves. Both types operate by direct solenoid actuation. The liquids tested with the arrangement were three volatile organic compounds (named henceforth C1, C2 and C3) with known density, but previously unknown viscosity. For the purposes of the study, dynamic liquid viscosities were measured with a rotational viscometer in ambient conditions, resulting in 1.31, 1.21, and 0.99 mPa · s for C1, C2 and C3, respectively. These viscosity values are very close to that of liquid water. No viscosity-temperature dependence was accounted for in the study.

## Mathematical modelling

Within the context of this study, all injection valves were treated as a single flow restriction. For a single restriction, liquid mass flow rate  $dm_l/dt$  can be derived from Bernoulli's principle for incompressible flows:

$$\frac{dm_l}{dt} = C_D A_n \sqrt{2\rho_l \Delta p} \quad (1)$$

where  $C_D$  is the flow discharge coefficient,  $A_n$  is total orifice flow area,  $\rho_l$  is liquid density and  $\Delta p$  is injection pressure drop, i.e. the difference between reservoir pressure and ambient pressure. A single injected dose  $m_l$  can be computed as:

$$m_l = \frac{1}{f_{inj}} \frac{dm_s}{dt} \frac{F_{m,l}}{1 - F_{m,l}} \quad (2)$$

where  $f_{inj}$  is (constant) injection frequency,  $dm_s/dt$  is the mass flow rate of the surrounding gas stream, and  $F_{m,l}$  is the mass fraction of the vaporized liquid, derived from the FTIR concentration measurement. When making measurements from various solenoid actuation durations, injected mass could be plotted as a function of valve actuation time (Figure 2). From this data, instantaneous liquid mass flow rate was estimated as the slope of the measurements (red line). Using the inaccuracies of individual measurements, sensible error margins were also obtained.

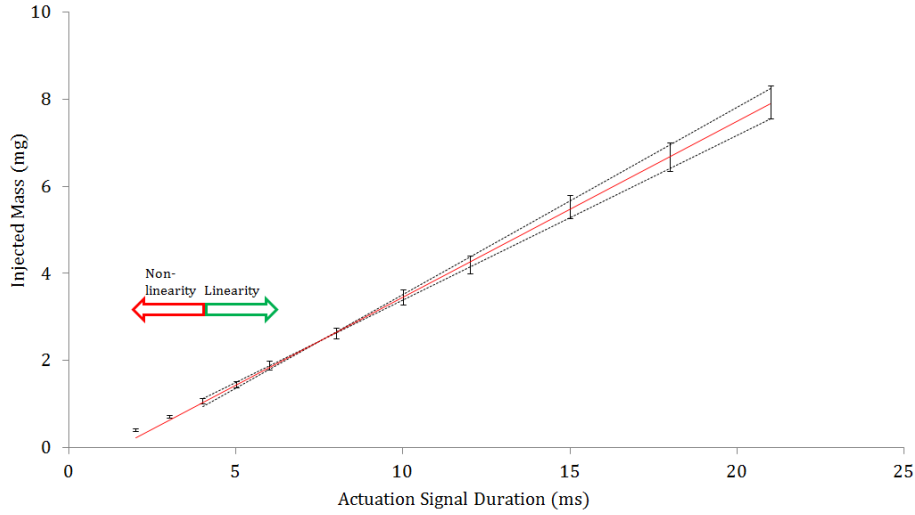


**Figure 2.** Injected mass measurements at different signal durations, along with a linearity trend describing instantaneous mass flow rate

Understandably, this is only one of a variety of methods in liquid-operated valve flow rate measurement. Unlike common high pressure injector measurements [3], this method does not provide accurate transient data, but an estimate on the average mass flow rate with a fully open valve.

Gaseous dispensing was described with the following model. Instantaneous gaseous mass flow rate  $dm_g/dt$  through an orifice can be described with a pair of equations, depending on the pressure ratio  $p^* = p_{amb}/p_r$ :

$$\frac{dm_g}{dt} = \begin{cases} C_D \beta A_n \sqrt{2 \left( \frac{p_r}{RT} \right)_g \Delta p}, & p^* \geq p^*_{crit} \\ C_D A_n p_r \sqrt{2 \left( \frac{\kappa}{RT} \right)_g \left( \frac{2}{\kappa_g + 1} \right)^{\frac{\kappa_g + 1}{2(\kappa_g - 1)}}}, & p^* < p^*_{crit} \end{cases} \quad (3)$$

where  $R_g$  is the specific gas constant,  $T_g$  is gas temperature, here assumed similar to ambient room temperature,  $p_{crit}^*$  is the critical pressure ratio for sonic flow, and  $\kappa_g$  is the gas specific heat ratio. Furthermore, factor  $\beta$  is defined as:

$$\beta = \sqrt{p^{*\frac{2}{\kappa_g}} \left( \frac{\kappa_g}{\kappa_g - 1} \right) \left( \frac{1 - p^{*\frac{\kappa_g - 1}{\kappa_g}}}{1 - p^*} \right)} \quad (4)$$

The change in pressure in the system ( $dp_r/dt$ ) then follows:

$$\frac{dp_r}{dt} = f_{inj} \Delta t_s \frac{p_r}{m_{g,t=0}} - \frac{dm_g}{dt} \quad (5)$$

where  $\Delta t_s$  is solenoid actuation duration (in seconds) and  $m_{g,t=0}$  is the initial mass of gas within the reservoir.

Now, this is an ordinary differential equation (ODE) with reservoir pressure  $p_r(t)$  as the unknown function. When observing the gaseous mass flow rate expression, where reservoir pressure lies in several inner functions, it can be stated that the ODE is very convoluted in terms of direct (analytical) solution. Within a numerical framework, however, the matter is simpler, and explicit Eulerian time integration yields:

$$p_r(t + \Delta t) \approx p_r(t) + \frac{dp_r}{dt} \Delta t \quad (6)$$

When using an explicit Eulerian scheme (instead of e.g. a Runge-Kutta scheme), it is important that the system is sufficiently monotonic and without large gradients. While we have now described system behaviour for both liquid and gas arrangements, one crucial component is missing from our analysis, that is, the expression of discharge coefficient  $C_D$ . This signifies the ratio of actual mass flow rate to that directly implied by the conditions in equation (3), i.e. losses occurring in the valve flow. According a methodology developed by Giffen and Muraszew [4], previously utilized in e.g. [5] [6], orifice flow discharge can be described as follows:

$$C_D = a_0 + a_1 \sqrt{\text{Re}_D} \quad (7)$$

where  $a_0, a_1$  are constants.  $C_D \in [0,1]$  and flow Reynolds number  $\text{Re}_D$  is defined as:

$$\text{Re}_D = \frac{\rho U D}{\mu} \quad (8)$$

Here,  $\rho$  is fluid density,  $U$  is fluid mean velocity,  $D$  is orifice hydraulic diameter, and  $\mu$  is fluid dynamic viscosity. Equation (7) is thought to hold when the flow is laminar. It was observed that Reynolds numbers in the current cases were smaller than what is implied as a minimal condition for pipe flow turbulence [7]. The Reynolds number definition brings an additional dose in complexity for description of the gaseous dispensing model. Fluid mass flow rate, and therefore mean velocity  $U$ , is dependent on  $C_D$  in eq. (3). Moreover,  $C_D$  is dependent on  $\text{Re}_D$ , which is, in turn, dependent on  $U$ . Thus, the definition of  $C_D$  is implicit in the mathematical system. In a discrete system, it is possible to effortlessly circumvent this issue. For each discrete time step  $t_k$ , we have the Reynolds number  $\text{Re}_{D,k}$ . Selecting  $k = k_0$ , we can plug in an initial guess for  $\text{Re}_{D,k_0}$ . Following this, we can define:

$$\text{Re}_{D,k} = \begin{cases} \frac{4}{\pi\mu D} \frac{dm_g}{dt}_{k+1}, & k < k_0 \\ \frac{4}{\pi\mu D} \frac{dm_g}{dt}_{k-1}, & k > k_0 \end{cases} \quad (9)$$

This means that Reynolds number values were imported into the computation from neighbouring time steps. Meanwhile, other relevant measures were computed according to information on the current time step. It was found that, in the context of the current process type, this approach was sufficient. When the time step difference  $|k - k_0|$  increased, Reynolds numbers converged towards the solution of the implicit equation. Another option would have been to iteratively solve the implicit equation for each time step.

Let us initialize  $a_0, a_1$  with some feasible values. This initialization inevitably led to a degree of discrepancy between the experimental and computational results. This is exemplified by the left frame in Figure 3. Therefore, optimization of  $a_0, a_1$  was performed in a manner leading to minimization of the total squared discrepancy  $\tau$ :

$$\tau = \sum_{t_k} (p_{r,sim} - p_{r,ex})^2 \quad (10)$$

Optimization was carried out with a generic software-based algorithm. The outcome with optimized values of  $a_0, a_1$  proved very close to the measurement (Figure 3, right).

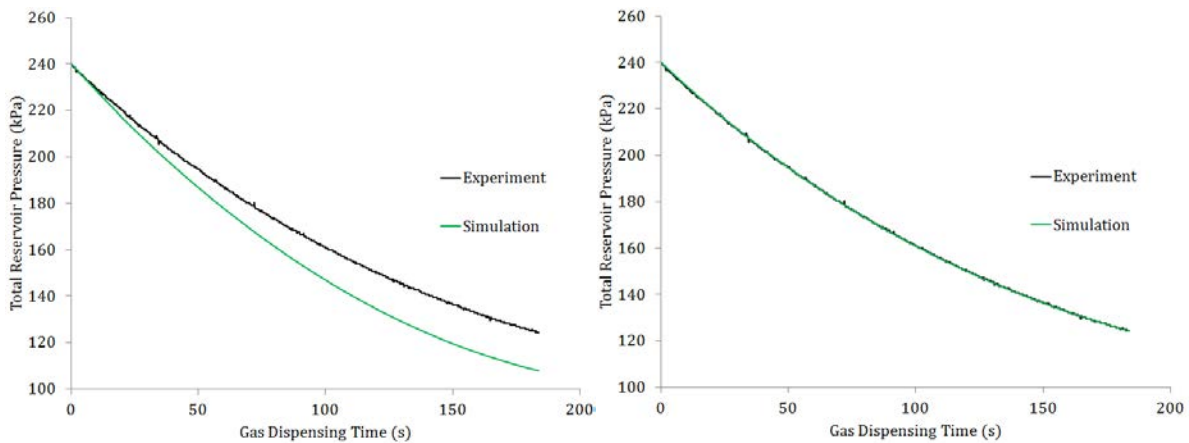


**Figure 3.** Example of experimental and simulated reservoir pressure development, dispensing through a micro-dispensing valve. Initial guess case (left) and least-squares optimized case (right)

## Results and Discussion

As an outcome of the discharge model optimization, the function  $C_{D,g}(\text{Re}_{D,g})$  was obtained. From the perspective of geometric anomaly recognition and dispensing system calibration, it was interesting to assess the relationship between gas and liquid discharge properties. However, making a large number of liquid measurements would have been impractical in terms of workload. Since each liquid measurement point constituted a large number of individual concentration measurements (Figure 2), the number of points per valve unit was kept low. The authors recognize the effect of this hindrance to describing the relationship with a complicated function. However, for practical purposes, this ambiguity was neglected. In an attempt to describe the relationship via a coefficient, we were striving to find  $Z$  that satisfies the equation:

$$C_{D,g}(\text{Re}_{D,g}) = Z C_{D,l}(\text{Re}_{D,l}) \quad (11)$$

For gas, a complete description for  $C_D(\text{Re}_D)$  was obtained with a single experiment. For the entire valve series, a nominal valve was formed by averaging individual  $a_0, a_1$  values. For liquid, discrete  $C_D$  values were

obtained through the methodology presented in (1), (2), and Figure 2. Figure 4 shows two individual cases where both gas and liquid  $C_D$  are plotted. The solid curve displaying gaseous  $C_D$  describes the measurement (Figure 3), whereas  $C_D$  points for compounds C1 and C2 have been computed from measurements. Meanwhile, the dashed curve is simply the gaseous  $C_D$  multiplied with the constant  $Z$ .

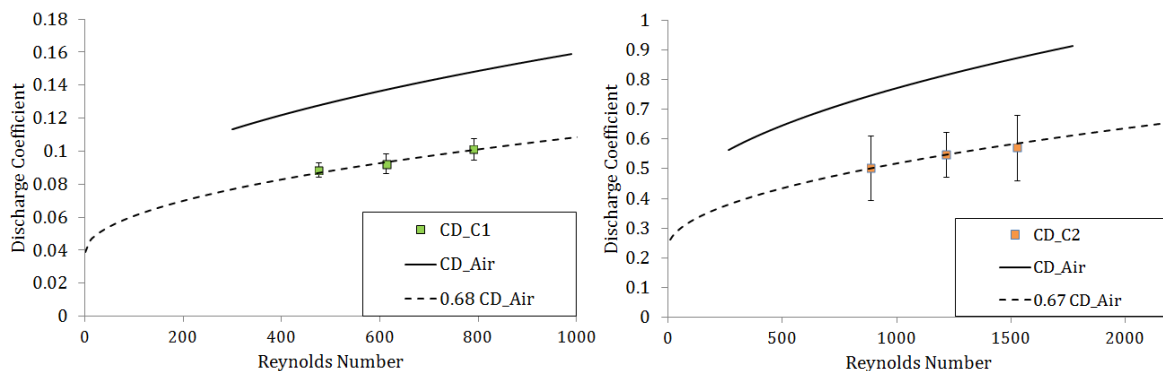


**Figure 4.** Gaseous  $C_D$  values (solid curve), liquid  $C_D$  measurements (markers) and permuted gaseous  $C_D$  (dashed curve). MD valve (left) and PFI valve (right)

Several matters became evident from the results in Figure 4. First, liquid flow discharge coefficients seemed to differ significantly from gaseous coefficients. Second, both gas and liquid followed the same trend of increasing  $C_D$  upon increasing Reynolds number. Third, while valve geometries in the MD and PFI cases were distinctly different, liquid measurement results scaled to the gaseous result similarly. Finally, uncertainties in the liquid measurement differed significantly. While  $C_D$  could be defined within very stringent limits for the MD valve, the large doses of the PFI valve combined with the measurement capabilities of the used FTIR system resulted in significantly higher uncertainty. Results similar to Figure 4 are shown in Tables 1 and 2. These tables show the optimized gaseous flow parameter pair  $a_0, a_1$  for each valve unit, and the experimentally perceived liquid-to-gas discharge coefficient ratio  $Z$ .

**Table 1.** Collation of gaseous flow discharge parameters  $a_0, a_1$ , and best-fit liquid-to-gas discharge ratio  $Z$  for varying MD valve unit – liquid compound combinations

Valve ID	Compound	$a_0$	$a_1$	$Z$
MD01	C2	0.0557	0.00337	0.695
MD01	C1	0.0557	0.00337	0.680
MD02	C2	0.0557	0.00332	0.685
MD03	C1	0.0570	0.00324	0.670
MD03	C3	0.0570	0.00324	0.630
MD04	C3	0.0537	0.00330	0.590

**Table 2.** Collation of gaseous flow discharge parameters  $a_0$ ,  $a_1$ , and best-fit liquid-to-gas discharge ratio  $Z$  for varying PFI valve unit - liquid compound combinations

Valve ID	Compound	$a_0$	$a_1$	$Z$
PFI05	C2	0.365	0.0128	0.670
PFI07	C3	0.386	0.0138	0.670
PFI08	C1	0.414	0.0132	0.720
PFI09	C3	0.384	0.0140	0.640
PFI10	C2	0.390	0.0140	0.695
PFI11	C1	0.407	0.0129	0.680
PFI12	C3	0.380	0.0138	0.635
PFI13	C2	0.423	0.0123	0.670
PFI14	C1	0.386	0.0137	0.740

Results in Table 1 show the similarity of the MD valves in terms of gaseous dispensing, as  $a_0$ ,  $a_1$  values were very close to each other. For the PFI valve (Table 2), more significant differences existed, as values for both parameters varied by ca. 10 % of parameter magnitude. However, in general, values of  $Z$  were close to 2/3.

As for liquid-gas discharge matching, compounds C1 and C2 produced  $Z$  values generally close to each other. With C3, this coefficient was lower with both valve types. Due to the high volatility of C3, experiments could only be conducted at the high reservoir pressure range (ca. 140 kPa). While this was a potential detriment to result quality, it can also be hypothesized that the high volatility combined with the sudden pressure drop causes cavitation and orifice flow restriction.

Geometric anomaly recognition was tested with the PFI valve by sealing 2 of the 12 nozzle orifices. The point of interest was to see how both gas and liquid dispensing altered when conditions resembling a blockage occur. Figure 5 shows results derived from this comparison. Black curves and orange markers are derived from the non-sealed nozzle, whereas red curves and the magenta marker are from the sealed nozzle. Sealed valve  $C_D$  values are noted as ‘indicated’ since they are computed according to an erroneously presumed non-sealed state. As in Figure 4, dashed lines are computed from the solid curves merely by using a coefficient.

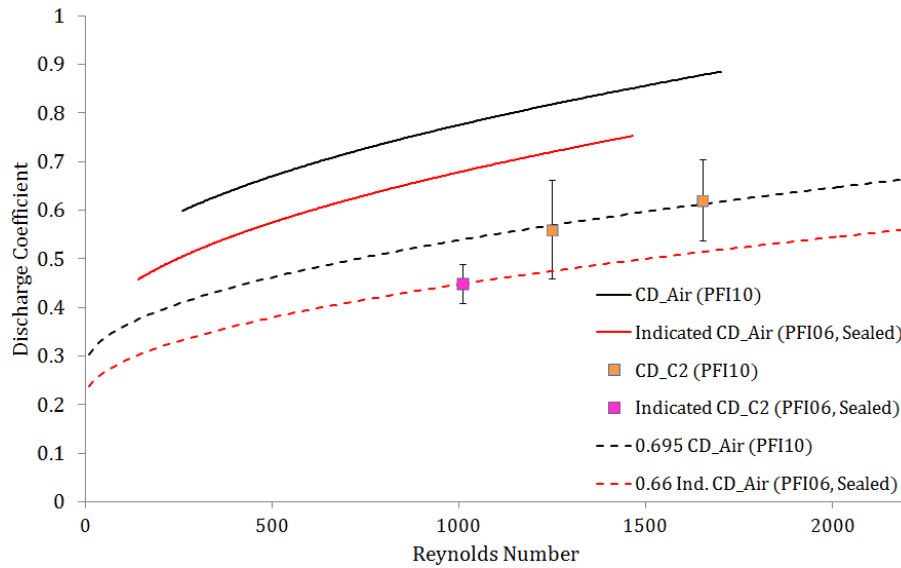


**Figure 5.** Experimental and simulated reservoir pressure development, dispensing through a micro-dispensing valve. Initial guess case (left) and optimized case (right)

The solid lines in Figure 5 display the clear difference between the non-sealed and sealed cases. Curve shapes were similar, and they could be related almost exactly by the ratio of open orifices (10/12). Furthermore, both gaseous results scaled towards the liquid result with reasonably similar Z values (0.660 and 0.695). These results yielded us two matters of interest. First, geometric changes in valve geometry were very accurately noticeable via the gas dispensing experiment, and second, the geometric changes were noticeable in a similar fashion in both gas and liquid dispensing cases.

Finally, implementation experiments were carried out for both the MD and PFI valves, consisting of 20 test cases for each valve type. These experiments utilized nominal (averaged) valve definitions as a baseline. A unitary gas dispensing experiment was compared with this definition; data was used to calibrate the open-loop control system. The tests were carried out in various conditions for injection frequency and pulse width, with pressurization between 64 and 143 kPa. As an important remark, valve-independent error sources also existed in the experiment, and instead of the result quantities, attention should be directed at result differences.

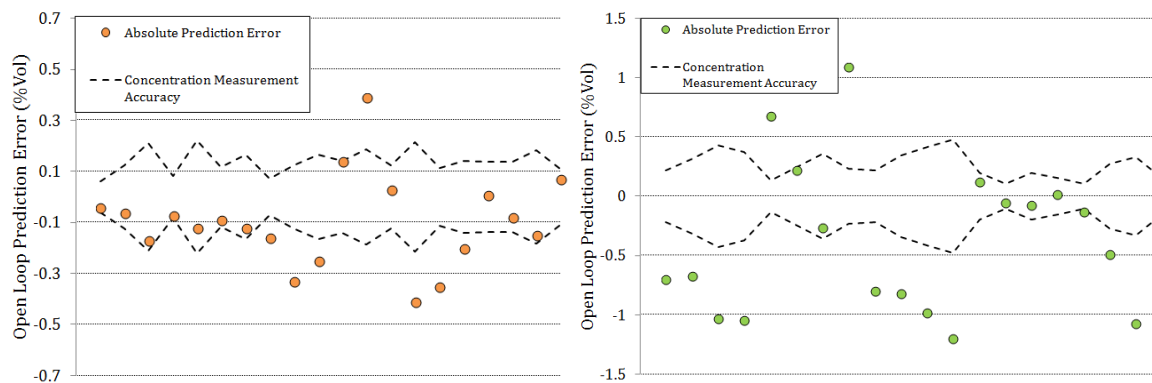


**Figure 6.** Implementation test, open-loop control system. MD valve and C2 (left), PFI valve and C1 (right)

The focal point in figure 6 is the relationship of the prediction error to the measurement accuracy. With the MD valve, the majority of error points lied within sensor tolerance. The opposite was true for the PFI valve, where errors were, at a number of points, over twice the sensor tolerance. An explanation to this phenomenon is supplied by results in Tables 1 and 2: Perceived valve discharge characteristics  $a_0, a_1$  varied significantly more with the PFI valve, leading to an inaccurate definition of the nominal valve. Furthermore, dispensing pulse widths (5-15 ms) were generally lower than with the MD valve (4-32 ms), potentially leading to more variance due to the higher importance of valve opening and closing processes. This characteristic is unfavourable if the valve is to be used in dispensing system calibration.

## Conclusions

This study focused on utilizing gaseous dispensing in the verification and calibration of a liquid dispensing system. For series of both MD and PFI valves, liquid flow characteristics were defined via experiments, while a computational model was constructed to describe the gaseous dispensing system. Via this model, gaseous discharge characteristics were accessed and compared with liquid discharge characteristics. A clear correlation was found with liquid-to-gas discharge ratios close to 2/3, as a function of orifice flow Reynolds number. It was found that the gas dispensing routine was sufficiently accurate for correctly perceiving geometric anomalies. The MD valve showed potential in open-loop control system calibration, while dispensing inconsistencies with the PFI valve implied dubious applicability for calibration.

## Nomenclature

0-D	Zero-dimensional
C1, C2, C3	Newtonian, low-viscosity test liquids 1, 2, 3
FDI	Fault detection and isolation
FTIR	Fourier transform infrared spectrometry
MD	Micro-dispensing
PFI	Port fuel injection
$a_0, a_1$	Parameters for Reynolds number based Giffen-Muraszew flow model
$A_n$	Total orifice flow area
$C_D$	Discharge coefficient (subscript $g$ = gas, $l$ = liquid)
$f_{inj}$	Dispensing frequency
$dm_g/dt$	Gas mass flow rate
$dm_l/dt$	Liquid mass flow rate
$dm_s/dt$	Surrounding gas stream mass flow rate
$dp_r/dt$	Rate of reservoir pressure drop
$F_{m,l}$	Mass fraction of vapour originating from liquid injection
$k$	Time step index
$k_0$	Cut-off time step index
$m_{g,t=0}$	Initial reservoir gas mass
$m_l$	Liquid dose per injection
$p_r$	Reservoir gas pressure (subscript $ex$ = experiment, $sim$ = simulation)
$p_{amb}$	Ambient pressure
$p^*$	Downstream-upstream pressure ratio
$p^*_{crit}$	Critical pressure for choked (locally sonic) flow
$\Delta p$	Injection pressure drop
$R_g$	Specific gas constant
$Re_D$	Pipe Flow Reynolds number (subscript $g$ = gas, $l$ = liquid)
$t$	Time
$\Delta t$	Time step
$\Delta t_s$	Solenoid actuation duration
$T_g$	Gas temperature
$U$	Mean orifice flow velocity
$Z$	Liquid-gas discharge coefficient ratio
$\beta$	Isentropic expansion factor for gaseous flow
$\kappa_g$	Gas specific heat ratio
$\mu$	Fluid dynamic viscosity
$\rho_l$	Liquid density
$\tau$	Total squared discrepancy



## References

- [1] Blanke, M., M. Staroswiecki, and N.E. Wu. *Concepts and Methods in Fault-tolerant Control*. in *American Control Conference*. 2001.
- [2] Patton, R.J., *Fault-tolerant control: The 1997 situation*. 1997, Proceedings of the 3rd IFAC symposium on fault detection, supervision and safety for technical processes. p. 1033-1055.
- [3] Bower, G.R. and D.E. Foster, *A Comparison of the Bosch and Zuech Rate of Injection Meters*. SAE Technical Paper Series, 1991.
- [4] Giffen, E. and A. Muraszew, *The Atomization of Liquid Fuels*. 1953, London: Chapman & Hall Ltd. 246.
- [5] Kiijärvi, J., *Diesel Fuel Injection System Simulation*, in *Internal Combustion Engine Laboratory*. 2003, Helsinki University of Technology: Espoo, Finland. p. 125.
- [6] Keskinen, K., et al., *Improving the Accuracy of 1-D Fuel Injection Modeling*. SAE Technical Paper Series, 2012.
- [7] Avila, K., et al., *The Onset of Turbulence in Pipe Flow*. Science, 2011. **333**(6039): p. 192-196.

## Velocity measurement in scattering medium using laser correlation velocimetry

T. Lacroix, S. Idlahcen, J-B. Blaisot and C. Rozé

CORIA, UMR 6614 CNRS, University & National Institute of Applied Sciences  
Rouen, France

### Abstract

Characterizing atomization of fuel in the near field of a diesel injector remains of great interest for the optimization of combustion engines in the context of fuel consumption efficiency enhancement and pollutant emission reduction. Due to the high liquid droplets concentration inducing multiple scattering, most of optical techniques fail to provide valid information. Nevertheless, the laser correlation velocimetry technique (LCV) has proved to be efficient in such conditions to determine spray drops velocity. The potential of the technique to perform measurement in dense scattering medium is addressed in this paper. The limits in terms of particle size and concentration of the scattering medium are highlighted.

---

### Introduction

Nowadays the environmental standards are more and more drastic, the aim being to reduce pollutant emissions. The standards EURO5, is effective for any vehicle registered from January 2011, allowed up to 180 mg/km emission of nitric oxide (NO<sub>x</sub>). EURO6 standard is planned for September 2014 for the commissioning of motor vehicles. The mass tolerance limit for NO<sub>x</sub> will be then 80 mg/km. Furthermore, a notion of “particle number limit” will come into effect besides the mass limit.

The steady evolution of these standards leads manufacturers to optimize the automotive injectors ensuring better mixing within the combustion chamber. This optimization involves the study and understanding of fuel sprays in order to improve the atomization process, but also the two-phase combustion. In direct injection applications, the properties of fuel jet near the injector outlet are difficult to characterize, numerically or experimentally. To characterize the jet, it is essential to know the spatial and temporal variations of the liquid near the injector outlet. Measurement techniques as Laser Doppler Anemometry [1] or Particle Image Velocimetry [2, 3], are commonly used in sparsely areas, sufficiently far from the nozzle exit. Those techniques become unusable near the injector outlet, where the spray is optically too dense and liquid elements have a random shape.

Ongoing studies are conducted in our team to establish initial conditions for atomization simulation [4-8]. Chaves et al. developed laser correlation velocimetry (LCV) to measure the axial velocities in the dense liquid phase very close to the nozzle exit [9]. This technique is an application to dense liquid sprays of the time-of-flight measurement principle. A photomultiplier receive the light from two measurement volumes inside the spray. The light intensity collected varies over time, depending on the density of the spray and on the size and shapes of the particles crossing the measurement volumes. The signal recorded by the first measurement volume will be similar to the signal recorded by the second (located slightly downstream to the first one), but with a time delay. The time delay between the two signals corresponds to the time-of-flight set by a liquid structure between the two measurement volumes. The velocity is then derived by the ratio of the distance between the two measurement volumes to this time delay.

Despite the many advantages of this technique, which requires a relatively simple installation, the relationship between the real velocity and the measured velocity is not straightforward, particularly in tough conditions as those near the nozzle exit. The objective of this study is to improve the interpretation of LCV signals, especially in the vicinity of the nozzle outlet where the liquid is not yet fragmented. For this, we use an environment in which the optical density was controlled. The laser passes through a thin cell filled with water. A solution of glass microspheres of known concentration is added into the cell in order to vary the optical depth of the medium. The amplitude of the laser light will be affected by the density of the cell as well as the correlation coefficient between the recorded signals.

A brief overview of the LCV as well as correlation calculation is established in the first part. The experimental setup and the glass microspheres used will be presented in a second paragraph. It will be shown that the quality of the measurement, evaluated through the value of the correlation coefficient, is related to the quality of the recorded signal and thus depends on the optical thickness of the scattering medium. To conclude this work, a quality criterion for the measurement of the velocity will be proposed and some perspectives will be given.

## Experimental setup

The objective of this work is to determine the limits of application of LCV on a dense medium, but also to see if this limit depends on the size of the structures in the medium.

### a. LCV system configuration

The light source is composed of a continuous laser (800 mW at 532 nm) (1), and a power adjustment device (polarizer and a half-wave plate) (2). The test object in the present study is a 50  $\mu\text{m}$  diameter fiber, fixed on a rotating disc (3) and placed in the object plane. A cell (4) of thickness 10 mm is juxtaposed to the object. This cell contains the scattering medium whose particle size and concentration vary. A converging lens (5) with a focal length of 150 mm, projects the region of interest strongly magnified ( $\gamma=12$ ) on the imaging plane. Two light fibers (6) stacked vertically with a diameter of 1 mm ( $\Delta f = 1000 \mu\text{m}$ ) are placed in the imaging plane, and each one is associated to a photomultiplier. These fibers define the two measurement volumes in the object plane. The measurement volumes have the shape of a cylinder parallel to the optical axis of the laser. Their diameter is proportional to the diameter of the optical fibers and inversely proportional to the magnification of the optical system. As any element that crosses the laser beam modifies the signal, i.e. the measure is not local in the laser beam direction. Thus, the spray has to be as thin as possible in order to prevent erroneous velocity measurement [8].

The vertical distance  $\Delta x$  between the center of the two measurement volumes is determined by the relative distance  $\Delta f$  between the two fiber in the image plane, and the magnification of the imaging system,  $\Delta x = \Delta f/\gamma = 83,3 \mu\text{m}$ . A spatial filter is placed at the focal point of the lens to filter the multiple scattering.

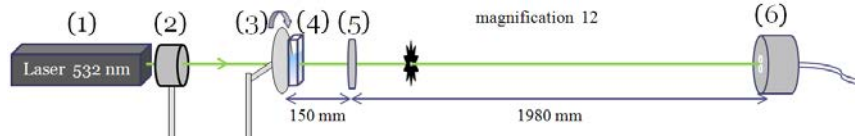


Figure 1. Laser Correlation Velocimetry (LCV) experimental setup.

### b. calculation correlation and velocity

The two signals are recorded on an oscilloscope (Lecroy Waverunner) with an 8-bit dynamic range at a sampling frequency of 100 MHz on a total time of 5 ms. With these parameters, 500 000 points are recorded on each channel.

The data sets are split into smaller data windows of 50 000 points (500  $\mu\text{s}$ ) with an offset of 5 000 points (50  $\mu\text{s}$ ). A moving object passing through the first measurement volume will block a part of the light sent to the first detector. This variation of light intensity will reach the second detector located slightly downstream, with a temporal shift. The correlation calculation between the two signals denoted  $x_i$  and  $y_i$  is given by:

$$R(\tau) = \frac{\sum_{i=1}^N (x_i - \bar{x}) \cdot \sum_{i=1}^N (y_{i-\tau} - \bar{y})}{\sqrt{\sum_{i=1}^N (x_i - \bar{x})^2} \cdot \sqrt{\sum_{i=1}^N (y_{i-\tau} - \bar{y})^2}} \quad (1)$$

The correlation coefficient  $R(\tau)$  ranges between -1 and +1, and has a maximum for a time delay corresponding to the time-of-flight of the object. This time delay ( $\Delta t$ ) and the distance  $\Delta x$  are used to deduce the velocity of the liquid structure passing in the measurement volume.

The relative uncertainty for the magnification of the setup and the one for the determination of  $\Delta t$  lead to an overall uncertainty for the measured velocity of about 9,5%. In addition, the trajectory plays a role on the relative uncertainty as mentioned by Leick [10]. Indeed, a structure passing the two measurement volumes with an angle  $\theta$  will give an anomaly large velocity. As shown in the figure 2, the distance  $\Delta x'$  is then shorter than  $\Delta x$ . The estimated velocity can thus be as high as 1.4 times the real velocity for a trajectory angle of 45°[8]. The maximum trajectory angle of around 10° of our configuration, leads to a velocity estimation error below 2,5%.

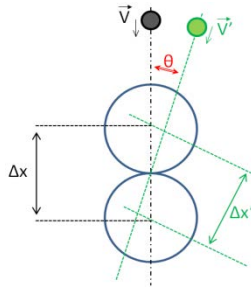


**Figure 2.** Overestimation of the velocity in the case of a trajectory with a relative angle  $\theta$ . The estimation error coefficient is given by  $1/\cos(\theta)$

### c. Characteristics of the microspheres

The characteristics of the silica particles placed in water to create the scattering media are given in table 1. The diameter indicated in table 1 are values provided by the manufacturer.

Diameter	Volume of a sphere (m <sup>3</sup> )	Density	Mass of a sphere (Kg)	Concentration (particles/m <sup>3</sup> )
2 μm	$4,1889 \cdot 10^{-18}$	2500 Kg / m <sup>3</sup>	$1,047 \cdot 10^{-14}$	$9549,30 \cdot 10^{12}$
5,4 μm	$8,2449 \cdot 10^{-17}$		$2,061 \cdot 10^{-13}$	$485,15 \cdot 10^{12}$
9,9 μm	$5,0805 \cdot 10^{-16}$		$1,270 \cdot 10^{-12}$	$78,73 \cdot 10^{12}$
19,3 μm	$3,7642 \cdot 10^{-15}$		$0,941 \cdot 10^{-11}$	$10,62 \cdot 10^{12}$

**Table 1.** Properties of the microspheres

For each test condition, a measurement with an empty cell is made to serve as a reference and the concentration is increased step by step by adding 0.1 ml of a solute of water and microspheres of fixed concentration.

The optical depth (Z) of the medium is determined by the equation (2) where ( $\Phi_b$ ) is the transmitted flux and ( $\Phi_0$ ) is the incident flux[11].

$$Z = -\ln(\tau_{\text{part}}) = -\ln\left(\frac{\Phi_b}{\Phi_0}\right) \quad (2)$$

## Results and discussions

The measurements are performed for the four microspheres diameters separately. For each measurement point, 0.1 ml of the solute is added in the cell. The quality of LCV signals recorded is strongly dependent on the concentration of particles. The figure 3 shows an example of two LCV signals at a concentration of  $5,32 \cdot 10^{13}$  particles/m<sup>3</sup> on the left, and at a concentration of  $42,56 \cdot 10^{13}$  particles/m<sup>3</sup> on the right figure.

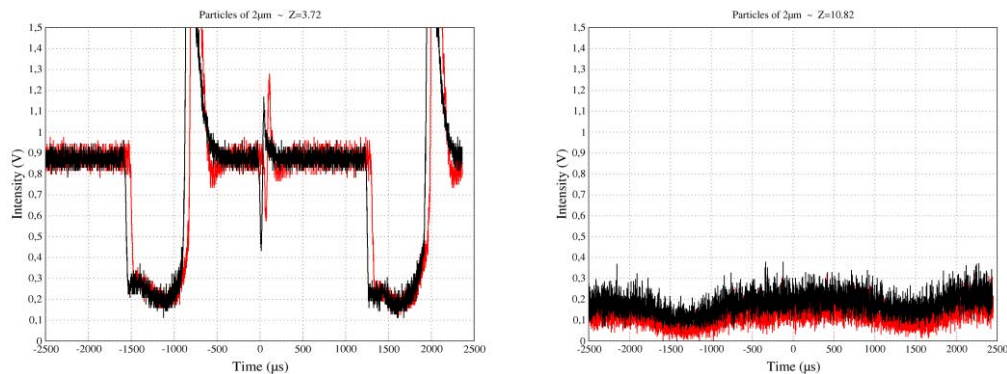


**Figure 3.** Example of LVC signals for two different concentrations.

In the figure 3, the signal is centered on the disturbance generated by the fiber fixed on the disk. The velocity information is altered by the noise induced by the addition of diffusing particles in the optical path.

The decrease of the signal-to-noise ratio (SNR) is presented in figure 4 as a function of the optical thickness that increases by addition of scattering particles in the cell. The SNR (in decibels) is defined as the power ratio between the signal (Us) and the background noise (Un).

$$\text{SNR}_{(\text{dB})} = 20 \log \left( \frac{U_s}{U_n} \right) \quad (3)$$

Each point on the figure represents the averaged value of SNR over 30 measurement points. The dash line represents the non-linear regression for the global evolution of the SNR.

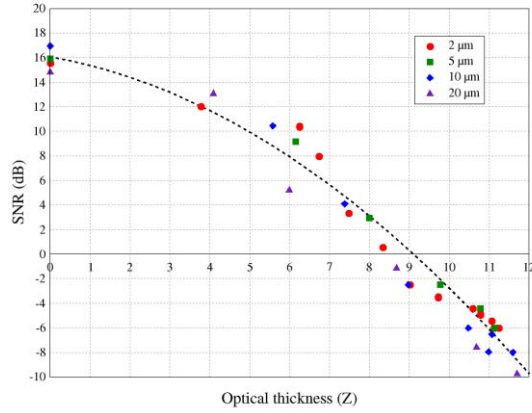


**Figure 4.** Variation of the signal-to-noise ratio as a function of the optical thickness.

As stated by Bushberg et al [12], it will be difficult to recognize the information in the signal due to excessive noise, for SNR lower than 7 dB. This corresponds, in this work to an optical thickness greater than 6.5. The plot on the left of figure 5 shows the average of the correlation coefficient variation as a function of the optical thickness within the cell. With the augmentation of the optical thickness, the correlation coefficient decreases as the light intensity received by the optical fibers.

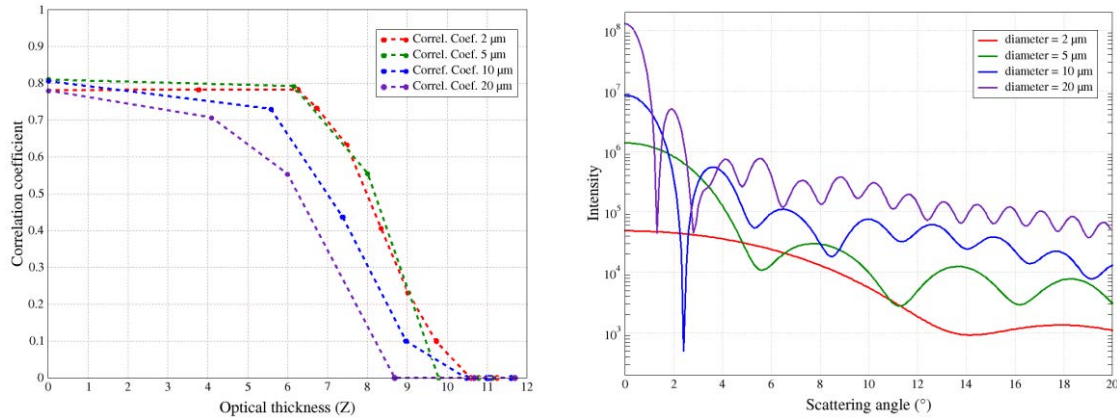


**Figure 5.** Correlation coefficient as a function of optical thickness for four sizes (left)  
Intensity as a function of the scattering angle for different sizes of particles (right)

Variation of the correlation coefficient for scattering particles of diameter of 2μm and 5μm are very similar. With the increase of the particle size, the correlation coefficient curves decline faster. For particles with a very small diameter, the light is scattered more uniformly on a wide range of angles, causing a homogeneous distribution of light in the forward direction as can be seen on Mie scattering intensity as a function of the scattering angle presented on the right plot of figure 5. The forward scattering for particles of large diameter is more intense and will reduce the quality of the collected signal, and increase the noise.

The velocity of the disk determined by the LCV for different optical thicknesses with 2μm diameter microspheres is presented in figure 6. A reference velocity (black points) is determined from the rotational speed of the disk, derived from the time period of LCV signal, and averaged over ten records. The orange points are the velocities calculated by the LCV technique for different acquisitions.

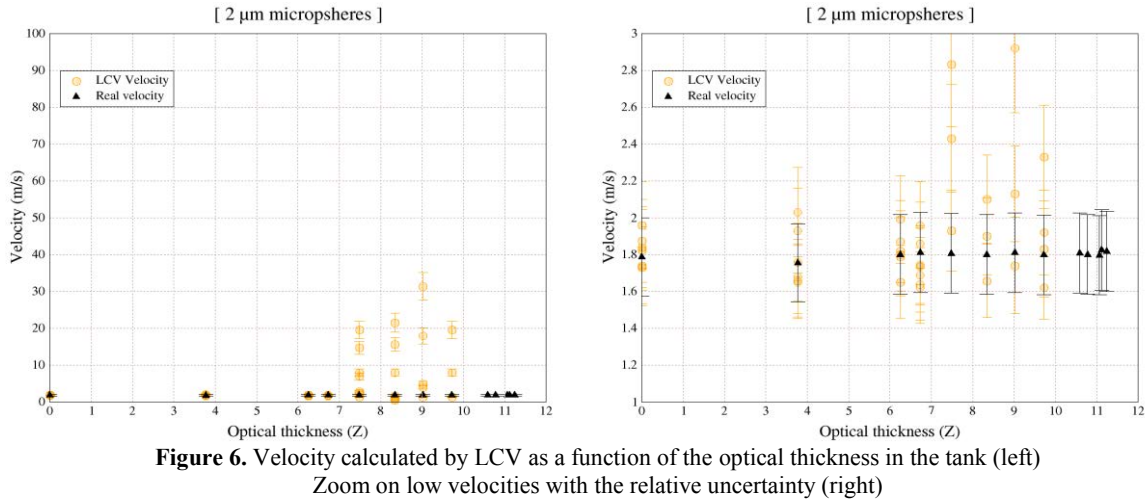


**Figure 6.** Velocity calculated by LCV as a function of the optical thickness in the tank (left)  
Zoom on low velocities with the relative uncertainty (right)

When the density increases, the signals, and thus the correlation calculation are disturbed by a higher noise. A correlation calculation performed on the noise gives a very small time delay, i.e. a very high velocity. Therefore, as soon as SNR reduces, noise becomes predominant in the signal and in the computation of the correlation coefficient. This results in an overestimation of the velocity. Correlation coefficient and velocity measured by LCV are shown in figure 7 for the four sets of scattering particles.

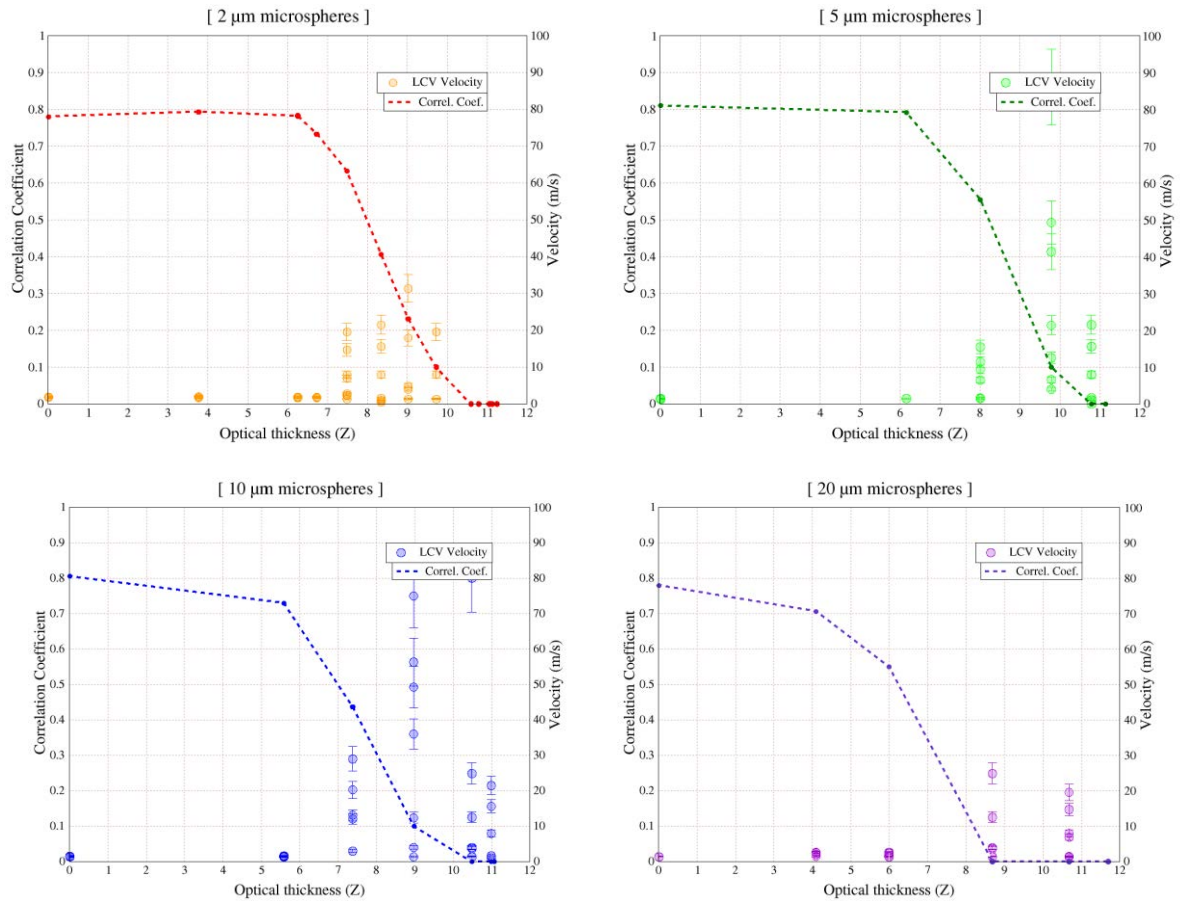


**Figure 7.** Correlation coefficient and velocities as a function of optical thickness

Whatever the size of the microspheres, when the optical thickness is greater than 7, the amplitude of the LCV signal becomes too weak, the signal-to-noise ratio decreases drastically and the correlation is no more reliable. Then, the velocity deduced from the time delay can suffer from noise perturbations and move away from the real velocity, obtained from the rotation speed of the disc. An optical thickness of 7 seems to be a maximum limit above which LCV measurements are not reliable. The low reliability is not due to a loss of correlation between the two signals, but rather to a correlation of noisy parts of the signal that leads to an overestimation of the velocity.

## Conclusion

The LCV technique is a non-intrusive measurement technique that can be applied in the near nozzle region of the injector where the spray is dense and that do not require particular assumptions about the shape of the liquid elements passing through the measurement volume.

To determine the limits of this technique, we have tested the ability of measuring velocity through a scattering medium of controlled optical thickness. The scattering medium was obtained by adding calibrated micro-sphere to a small cell filled with water. The concentration and the diameter of the particles were varied.

Tests were performed on the measurement of the velocity of a glass fiber attached to a rotating disk.

The increase of the concentration of particles increases the optical thickness of the medium. It was shown that whatever the size of the scattering particles, velocity measurements could be performed up to optical thickness of 7. Correlation computation is still possible for higher optical thicknesses. However, the velocity values obtained for an optical thickness above 7 are not in agreement with the real velocity. Beyond this value, the correlation coefficient is less than 0,700. This is due to the fact that in the case of a high particle concentration, or a high optical thickness, correlations are done on noisy signals. Correlation on noise leads to very short time delay estimations and thus to overestimated velocities.

## Nomenclature

$LCV$	<i>Laser Correlation Velocimetry</i>
$R(\tau)$	<i>Correlation coefficient</i>
$\Delta f$	<i>Distance between the center of the optical fibers</i>
$\Delta x$	<i>Distance between the center of the two measurement volumes</i>
$\Delta t$	<i>Time delay</i>
$\gamma$	<i>Optical magnification</i>
$Z$	<i>Optical thickness</i>
$\Phi_b$	<i>Transmitted flux</i>
$\Phi_0$	<i>Incident flux</i>
$U_s$	<i>Signal power</i>
$U_n$	<i>Background noise power</i>

## References:

- [1] Sasaki, O., et al., *Laser Doppler velocimeter that selectively measures a specified velocity vector*. Appl. Opt., 1980. **19**(2): p. 289-292.
- [2] Yildiz, D., J.P.A.J. van Beeck, and M.L. Riethmuller, *Feasibility Exploration of Laser-based Techniques for Characterization of a Flashing Jet*. Particle & Particle Systems Characterization, 2004. **21**(5): p. 390-402.
- [3] Lourenco, L.M., *Velocity bias technique for particle image velocimetry measurements of high-speed flows*. Appl. Opt., 1993. **32**(12): p. 2159-2162.
- [4] Yon, J., J.-B. Blaisot, and M. Ledoux, *Unusual laser-sheet tomography coupled with backlight imaging configurations to study the diesel jet structure at the nozzle outlet for high injection*. 2002. **9**(1): p. 19.
- [5] Idlahcen, S., et al., *Time gate, optical layout, and wavelength effects on ballistic imaging*. J. Opt. Soc. Am. A, 2009. **26**(9): p. 1995-2004.
- [6] Idlahcen, S., et al., *Sub-picosecond ballistic imaging of a liquid jet*. Experiments in Fluids, 2012. **52**(2): p. 289-298.
- [7] Sedarsky, D., et al., *Velocity measurements in the near field of a diesel fuel injector by ultrafast imagery*. Experiments in Fluids, 2013. **54**(2): p. 1-12.

- [8] Hespel, C., et al., *Laser correlation velocimetry performance in diesel applications: spatial selectivity and velocity sensitivity*. Experiments in Fluids, 2012. **53**(1): p. 245-264.
- [9] Chaves, H., et al., *High-speed flow measurements within an injection nozzle*. 1993: p. 265-272.
- [10] Leick, P., *Quantitative Untersuchungen zum Einfluss von Düsengeometrie und Gasdichte auf den Primärzerfallsbereich von Dieselsprays*. Ph.D theses, Technical University of Darmstadt, Germany, 2008.
- [11] Calba, C., et al., *Ultrashort pulse propagation through a strongly scattering medium: simulation and experiments*. J. Opt. Soc. Am. A, 2008. **25**(7): p. 1541-1550.
- [12] Bushberg, J.T., et al., *The essential physics of medical imaging*. Lippincott Williams & Wilkins, 2001.



## Real-time Determination of Interfacial Tension from the Shape of a Pendant Drop Based on Embedded Image Processing

M. Najmabadi <sup>1</sup>, F. Tamm <sup>2</sup>, M. Klaiber <sup>1</sup>, Y. Baroud <sup>1</sup>, S. Drusch <sup>2</sup> and S. Simon <sup>1</sup>

1: Institute of Parallel and Distributed Systems, University of Stuttgart, Germany

2: Department of Food Technology and Food Material Science,  
Technical University of Berlin, Germany

### Abstract

The pendant drop method for measuring the interfacial tension leads to a significant time delay due to the software processing speed to compute the interfacial tension from the respective shadow image sequence even with multicore CPUs. Recent progress in embedded image processing hardware especially in the performance of field programmable gate arrays (FPGA) makes it possible to perform the required image processing tasks with significant speed up compared to CPU based software. In this work, an embedded image processing architecture and hardware platform is proposed to process the pendant drop profile extraction in real-time. The proposed architecture is based on a single pass algorithm to process a very high speed line wise pixel stream instead of a full image buffer random memory access. The experimental results prove that the realized hardware-platform can provide real-time results, independent of the image sensor frame rates. The accuracy of the algorithm is more than 97 percent compared to pendant drop software based on the Young-Laplace equation method and can be enhance if required.

Key Words: interfacial tension; pendant-drop method; parallel image processing architecture; FPGA

---

### Introduction

Interfacial tension is of great importance for several applications, e.g. oil recovery in the petrol industry [1], the ink and paint industry [2] and characterisation of the properties of foams and emulsions. The emulsifiers used to stabilise foams and emulsions require a high surface activity [3]. The surface activity is expressed by the rate of interfacial tension decrease within a certain period caused by adsorption of a surface-active agent to the interface [4]. A rapid initial decrease in interfacial tension reflects a fast stabilisation of the interface, thus preventing coalescence e.g. in a foaming process [5].

Spray-drying is another process in which the dynamics of adsorption of surface-active agents to an interface are relevant. Due to the short lifetime of a droplet during spray-drying between 0.1 and 1 ms and a residence time within the drying process of 0.1 to 10 s [6], a high resolution observation of the change in surface tension is needed. A recently established method allows analysis of the alteration in surface tension within a time scale relevant for processes like spray drying, making use of a modified pendant drop tensiometer [7]. By injection of emulsifier solution into a drop of water, i.e. an initially empty surface not containing any surface active substance, its adsorption behaviour can be analysed.

Interfacial tension and its dynamic development can be analysed by various methods. One of these methods is based on the analysis of the shape of a pendant droplet containing the surface-active agent and the density difference between the two adjacent phases, according to the Young-Laplace-equation [8]. The high amount of data being created within a few seconds makes real-time observation of the alteration of interfacial tension difficult. The long time required for data analysis is one of the most significant drawbacks of this method. In order to reduce the processing time and accelerate computing applications, the field-programmable gate array (FPGA) was proposed [9]. Accordingly, Laackmann et al. [10] proposed reconfigurable embedded image system in spray processing application, to obtain significant hardware acceleration compared to a CPU for real time analysis. Additionally, in order to avoid the need for buffering the image, Klaiber et al. [11] proposed a raster scan processing on the image pixels such that only several image lines instead of full images have to be stored.

In this work the focus is mainly on designing real-time architecture as a solution for processing high amount of data which is generated by a high-frame rate camera.

The reminder of this paper is organized as follows: at the beginning the theoretical method for deriving the interfacial tension is explained, in third section the hardware architecture is described. This is followed by the results in section 4 and a conclusion in the last section.

## Theoretical Background

The theoretical background of interfacial tension calculation has been given in e.g. [8, 12, and 13], which is based on a special form of the Young-Laplace equation. The interfacial tension,  $\sigma$ , is derived from the following equation:

$$\sigma = \Delta\rho \frac{R_1 R_2}{R_1 + R_2} , \quad (1)$$

where  $\Delta\rho$  is the density difference between the two phases,  $R_1$  and  $R_2$  represent the two principle radii of curvature. It has been proven that the equation (1) in axisymmetric interface can be represented as the following system of ordinary differential equations as a function of the arc length,  $S$ , in a dimensionless form [8]:

$$\frac{d\phi}{dS} = \frac{2}{B} - Z - \frac{\sin\phi}{X} , \quad (2)$$

$$dX = \cos\phi \, dS , \quad (3)$$

$$dZ = \sin\phi \, dS , \quad (4)$$

$X$ ,  $Z$  and  $S$  are dimensionless parameters generated by multiplication of  $x$ ,  $z$  and  $s$  by  $\tau$ . The coordinates  $x$ ,  $z$ ,  $s$  and  $\phi$  are illustrated in Figure 1 and  $\tau$  can be derived by following equation:

$$\tau = \frac{\sqrt{\Delta\rho \, g}}{\sigma} . \quad (5)$$

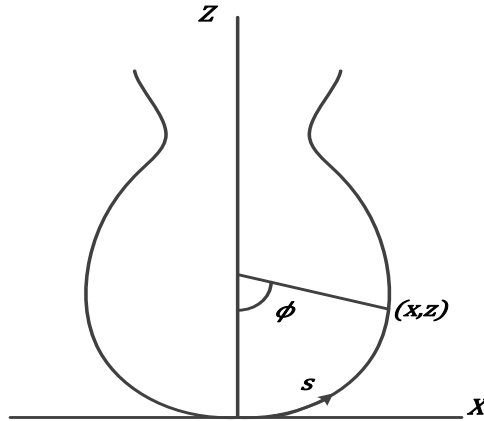


**Figure 1:** Geometry and notation of symbols of a pendant-drop profile.

Fourth order Runge-Kutta solver was used to numerically solve the set of differential equations, (2, 3, 4), that would give the interfacial tension. Since solving the differential equations numerically is computationally intensive, as reviewed by Arashiro et al., 1999 [14] they proposed a simplified table based method in which interfacial tension,  $\sigma$ , is derived from the following equation:

$$\sigma = \frac{\Delta\rho \, g \, De^2}{H} , \quad (6)$$

where  $De$  is the equatorial diameter of the drop,  $g$  is the gravitational constant and  $H$  is a correction factor, related to the shape factor of the pendant drop,  $S$ , defined as:

$$H = \frac{1}{S} , \quad (7)$$

$$S = \frac{Ds}{De} . \quad (8)$$

In equation (8),  $D_s$  is the diameter at a horizontal plane distant  $De$  from the apex point of the drop defined as in Figure 2. The correlation between  $H$  and  $S$  was already determined experimentally [14], and a set of  $1/H$  values versus  $S$  is available. So, determining  $De$  and  $D_s$  from the drop profile are the key elements of this work, which are explained in the next section.

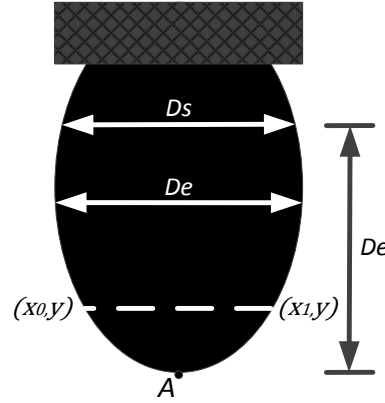


**Figure 2:** The pendant drop geometry.

### Algorithm for Efficient Embedded Image Processing

In order to obtain an acceleration based on embedded image processing with field programmable gate arrays (FPGA) an algorithm based on equation (6) is chosen. The algorithm consisted of five steps, which are mapped to the five pipelined processing units of the final hardware architecture described in the results section. These steps are described as follows:

#### 1. Sub-pixel thresholding:

The objective of sub-pixel thresholding is to detect sudden changes in droplet edges and determining the position of the droplet boundary.

The first processing unit, PU 1, captures the raw data and applies the thresholding filter in sub-pixel manners, by performing a comparison of each pixel intensity with respect to a threshold value. This sub-pixel thresholding operation can be expressed as:

$$pp(x,y) = \begin{cases} 0 & \text{if } pi(x,y) < threshold \\ \frac{pi(x,y)}{255} + x & \text{Otherwise} \end{cases} \quad . \quad (9)$$

Where  $pi$  stands for pixel intensity and  $pp$  stands for pixel position.

In fact by using the sub-pixel method the digitization resolution on the edge of the droplet has been increased. It has been proved that the accuracy of the method is mainly dependent on the precision of the determination of the drop edges [15].

#### 2. Apex point detection:

The goal of the second step is detecting the apex point of the droplet, which is marked as point  $A$  in Figure 2.

The first droplet pixel, which is detected in raster scan by the image sensor, will be considered as an apex point. Accordingly, the camera is rotated 180 degree to capture the apex point of the droplet before other parts of the droplet. The coordination of the apex point will be used in the fourth processing unit.

#### 3. Droplet diameter detection:

Within this step, the diameter of the drop is measured. The first and the last pixel of the drop in one row are shown in Figure 2. Measuring the diameter is done by subtracting the pixel position of the first and last drop in one row:

$$drop\ diameter = pp(x_1,y) - pp(x_0,y) \quad . \quad (10)$$

This processing unit does not stop processing until the end of the image. The reason is that it measures the diameter of the drop and saves only the largest diameter in a register. As a result, the value which remains in the register is called  $D_e$ .

#### 4. Droplet diameter detection at a certain distance:

The fourth processing unit requires the largest diameter of the drop as an input parameter and measures the drop diameter at a distance  $D_e$  away from the point  $A$ . Since  $D_e$  may change during the third processing unit, this unit also continues processing until end of the image.

#### 5. Needle diameter detection:

The last processing unit measures the needle diameter by subtracting the pixel value of the first and last needle pixels in one row. The needle diameter is required for the scaling factor, which can be determined by following equation:

$$\text{Scaling Factor} = \frac{\text{needle diameter (mm)}}{\text{needle diameter (pixel)}} \quad (11)$$

After processing the five steps in embedded hardware,  $D_s$ ,  $D_e$  and the needle diameter are transferred to the computer. As a result, when the last pixels of the image are transferred from the image sensor, all required variables are extracted without buffering the whole drop image.

### Experimental System

The protein used was a whey protein hydrolysate with a degree of hydrolysis of 9,7 % and a protein content of 94,9 % (dry matter). The analysed solution ( $\omega = 2,0$  wt%) was prepared with distilled water at least 12 hours before analysis and stirred at 300 rpm overnight to ensure complete rehydration of the protein. The experimental setup is schematically represented in Figure 3. Inside a temperature controlled chamber a droplet of distilled water is created through the large opening ( $d = 1.65$  mm) of the double channel needle system, with air as surrounding phase. Subsequently  $2 \mu\text{l}$  of protein solution is injected through the small opening ( $d = 0,51$  mm) with the automatic dosing unit of the apparatus. The camera of the system was replaced by a high performance FPGA camera with a resolution of  $2048 \times 1088$  pixels and up to 300 frames per second, the high-performance 6x par focal zoom lens with integrated continuous fine focus and a controller module for adjusting the syringe position.

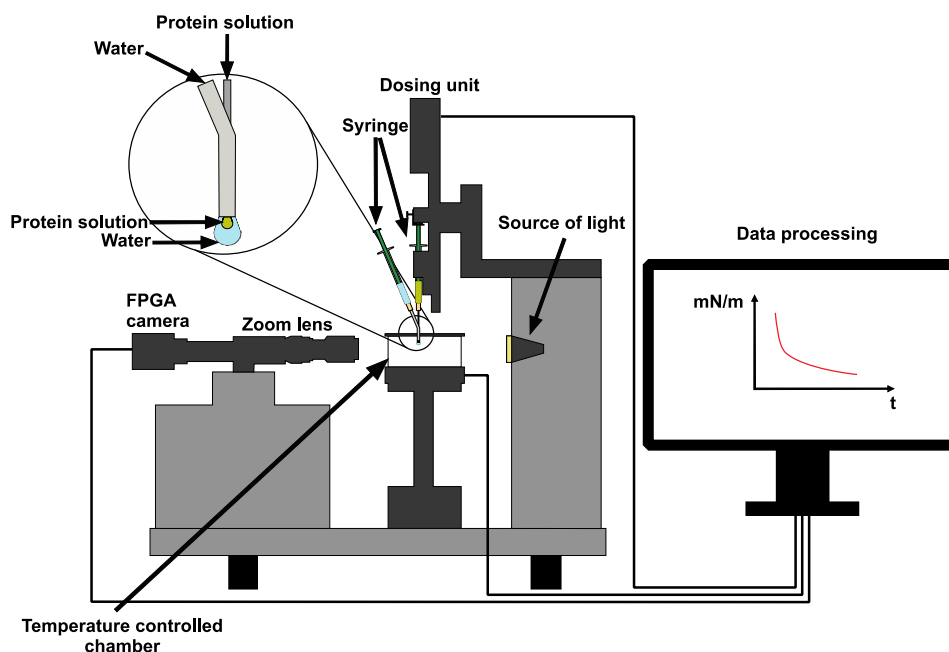
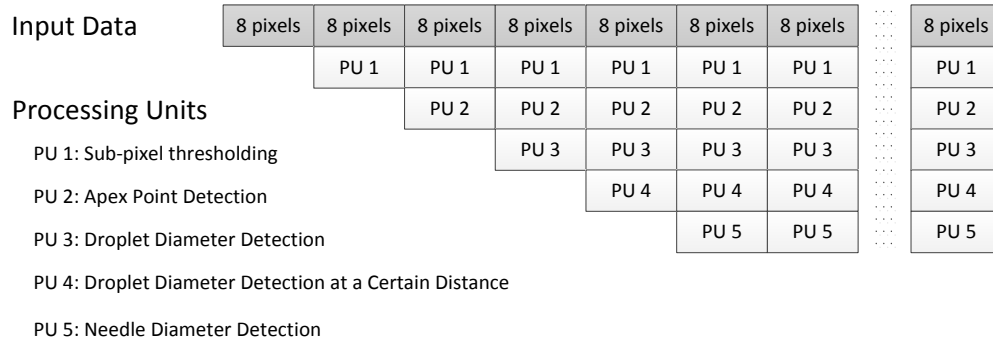


Figure 3: Pendant drop tensiometer with modified dosing system [16].

### Results and Discussion

An embedded image processing system has been proposed here for real-time determination of interfacial tension. The system is composed of a high-speed image sensor and a high performance field programmable gate

array (FPGA). In such a system, which is called FPGA camera, the pixel data is transferred from image sensor directly to the FPGA for further processing. Generally, buffering all pixels of the image into the FPGA buffers is a bottleneck, which is avoided in our design. For that, only eight pixels of the image are buffered and processed at a time in a pipeline manner as it is shown in Figure 4. The pipeline processing refers to the parallel processing unit where the output of one processing unit is the input of the next processing unit.



**Figure 4:** Five-stage pipelined architecture.

As it is shown in Figure 4 from raw pixel data acquisition to the final measurement all steps are pipelined and single-pass mechanism was used, which applies real-time determination of  $D_s$ ,  $D_e$  and interfacial tension. As a result, the acceleration factor of the proposed algorithm on the realized hardware-platform can reach up to 100 compared to a software implementation on a fast CPU.

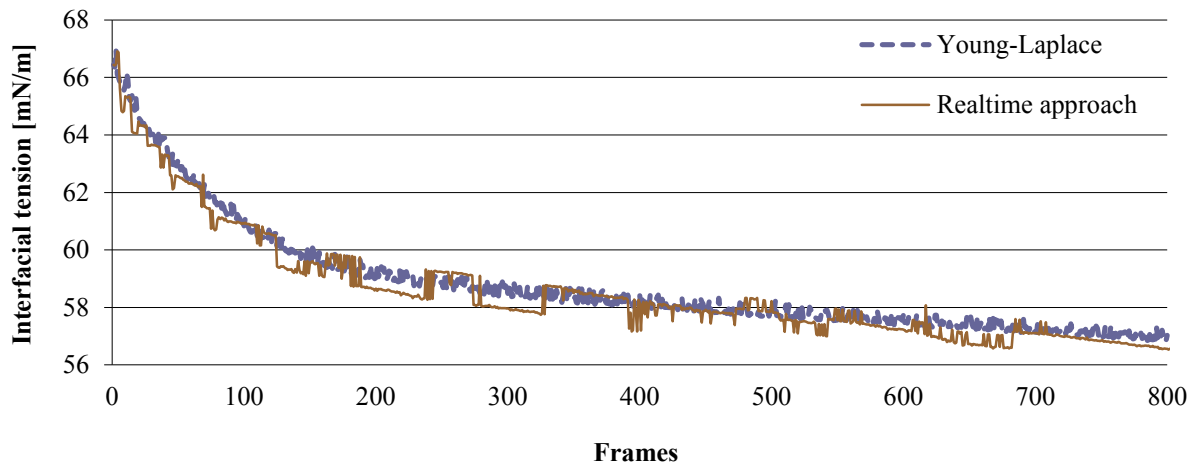


**Figure 5:** Interfacial tension values within 800 frames.

With respect to the accuracy, Figure 5 shows the evolution of the interfacial tension as a function of time. The purpose of this test is to determine the accuracy of the algorithm within one frame per second. It can be seen in the most frames, the computed values, which were obtained experimentally, have a maximum deviation of three percent compared to Young-Laplace equation method which was solved by Fourth order Runge-Kutta solver. This deviation is unavoidable due to different reason. The main reason is that, the real-time approach uses only few parameters to obtain interfacial tension in contrary to the Young-Laplace equation method which uses the whole drop profile to calculate interfacial tension. Nevertheless, Table 1 shows sensitivity of the algorithm to one pixel deviation in  $D_s$  and  $D_e$ . In this theoretical example, the interfacial tension is derived from the equation (6). From Table 1, it can be concluded that one pixel deviation in measurement leads to almost one percent deviation in final result.

**Table 1:** Computed interfacial tension.

<i>De</i>	<i>Ds</i>	<i>Needle</i>	<i>Interfacial Tension</i>
390	270	226	65.51
390	271	226	64.87
389	270	226	64.74

## Conclusions

A parallel architecture for a reconfigurable embedded image processing system is proposed to calculate the interfacial tension from the shape of a pendant drop online. The proposed architecture is suited for a single pass algorithm to determine the interfacial tension based on the equatorial diameter of the drop. The architecture consists of five pipelined processing units leading to memory-less pixel stream processing to determine the interfacial tension in real-time. In order to increase the accuracy of the chosen algorithm, sub-pixel thresholding was introduced to calculate the equatorial diameter of the droplet from a shadow image with high accuracy. Based on the equatorial diameter, the interfacial tension is computed by a method derived from the Young-Laplace equation. The experimental results show that the realized embedded image processing hardware accelerates the computation by a factor of 100 compared to a widely used commercial software on a multicore CPU. This software to determine the interfacial tension is based on a differential equation derived from the Young-Laplace equation. The interfacial tension calculated on the embedded image processing system deviates less than three percent compared that software being the chosen reference. If required, the deviation can be further reduced by a more sophisticated algorithm and architecture of the reconfigurable embedded image processing system.

## Acknowledgements

We would like to acknowledge the support provided by the German Research Foundation (DFG). This work has been carried out within the research project Si 586 7/1 which belongs to the priority program DFG-SPP 1423 “Prozess Spray”.

## Nomenclature

<i>De</i>	diameter of the drop at the equator
<i>Ds</i>	diameter of the drop measured horizontally at a distance <i>De</i> , from the vertex
$\Delta\rho$	density difference,
<i>g</i>	gravitational constant
<i>H</i>	correction factor
<i>R</i> <sub>1</sub>	first primary radius of curvature
<i>R</i> <sub>2</sub>	second primary radius of curvature
<i>s</i>	arc length of drop interface
<i>S</i>	non-dimensionalized arc length of drop interface
<i>x</i>	horizontal distance
<i>X</i>	non-dimensionalized horizontal distance
<i>z</i>	vertical distance
<i>Z</i>	non-dimensionalized vertical distance

## References

1. Zhang, J., Li, G., Yang, F., Xu, N., Fan, H., Yuan, T., & Chen, L. “Hydrophobically modified sodium humate surfactant: Ultra-low interfacial tension at the oil/water interface” *Applied Surface Science*, 259, 774–779, (2012).
2. Holme, I., “Advances in the science and technology of paints, inks and related coatings” 2005. *Surface Coatings International Part B: Coatings Transactions*, 88(4), 285–299, (2005).
3. Kim, Y., Koczko, K., & Wasan, D., “Dynamic Film and Interfacial Tensions in Emulsion and Foam Systems”, *Journal of colloid and interface science*, 187(1), 29–44, (1997).

4. Minones Conde, J., Escobar, M. D. M. Y., Pedroche Jiménez, J. J., Rodriguez, F. M., & Rodriguez Patino, J. M., “Effect of enzymatic treatment of extracted sunflower proteins on solubility, amino acid composition, and surface activity” *Journal of agricultural and food chemistry*, 53(20), 8038–45, (2005).
5. Marinova, K. G., Basheva, E. S., Nenova, B., Temelska, M., Mirarefi, A. Y., Campbell, B., & Ivanov, I. B. “Physico-chemical factors controlling the foamability and foam stability of milk proteins: Sodium caseinate and whey protein concentrates”, *Food Hydrocolloids*, 23(7), 1864–1876, (2009).
6. Elversson, J., & Millqvist-Fureby, A., “Particle size and density in spray drying-effects of carbohydrate properties” *Journal of pharmaceutical sciences*, 94(9), 2049–60, (2005).
7. Drusch, S., Hamann, S., Berger, A., Serfert, Y., & Schwarz, K., “Surface accumulation of milk proteins and milk protein hydrolysates at the air–water interface on a time-scale relevant for spray-drying”, *Food Research International*, 1–6, (2011).
8. T. Runke, B. Song, J. Springer, “Surface –and Interfacial Tensions of Liquid Crystalline Polymers”, *Phys. Chem.* 98, 508-511, (1994).
9. André D., “The Density Advantage of Configurable Computing”, *IEEE Computer*, 33(4):41--49, (2000).
10. J. Laackmann, S. Ahmed, R. Sedelmayer, M. Klaiber, W. Pauer, S. Simon, H-U. Moritz, “Investigation of polymerization and drying of polyvinylpyrrolidone in an acoustic levitator using a smart camera for online process measurement”, *ICLASS 2012, 12th Triennial International Conference on Liquid Atomization and Spray Systems*, Heidelberg, Germany, Sept. (2012).
11. M. Klaiber , S. Ahmed, Z. Wang, L. Rockstroh, Y. Gera, S. Simon, “Online Imaging Analysis of Spray Processes Based on a Reconfigurable Embedded System”, in *10 Workshop über Sprays, Techniken der Fluidzerstäubung und Untersuchungen von Sprühvorgängen*, Berlin, Germany, May, (2012).
12. Anatsiadis, S. H., Chen, J.-K., Koberstein, J. T., Siegel, A. F., Sohn, J. E., and Emerson, J. A., “The determination of interfacial tension by video image processing of pendant fluid drops”, *Colloid Interface Sci.* 119, 55, (1987).
13. Hartland, S., and Hartland, R. W., “Axisymmetrical Fluid–Liquid Interfaces.” *Elsevier*, Amsterdam, (1976).
14. Arashiro, E. Y., & Demarquette, N. R., "Use of the pendant drop method to measure interfacial tension between molten polymers". *Materials Research*, 2(1), 23–32, (1999).
15. Song, B., Springer, J., ” Determination of Interfacial Tension from the Profile of a Pendant Drop Using Computer-Aided Image Processing”, *Journal of Colloid and Interface Science* Volume 184, Issue 1, 1 December, Pages 64–76, (1996).
16. Tamm, F., Sauer, G., Scampicchio, M., & Drusch, S., “Pendant drop tensiometry for the evaluation of the foaming properties of milk-derived proteins”, *Food Hydrocolloids*, 27(2), 371–377, (2012).

## Visualizing Edge-Conforming Discrete Field Quantities in Electromagnetic Field Problems with Interfaces

G. K. Karch<sup>1</sup>, F. Sadlo<sup>1</sup>, H. Songoro<sup>2</sup>, E. Gjonaj<sup>2</sup>, T. Weiland<sup>2</sup>, T. Ertl<sup>1</sup>

1: Visualization Research Center, University of Stuttgart, Germany

2: Technische Universität Darmstadt, Institut fuer Theorie Elektromagnetischer Felder, Germany

### Abstract

Finite element-based electromagnetic field simulation strongly benefits from using edge-conforming representations of the electric field. In this paper we address the visualization of discrete field data resulting from such simulations on 10-node quadratic tetrahedral grids. The use of higher-order grids enables, on the one hand, the accurate approximation of curved interfaces between electromagnetic materials, and on the other hand, it allows for a more accurate computation of derived quantities such as Coulomb forces and related surface tensions. However, a major drawback so far has been the lack of appropriate visualization techniques—common visualization systems do not support this type of data—necessitating a resampling step with all the involved drawbacks, including artifacts in the form of imposed continuity across material boundaries. We introduce a visualization framework implemented as a set of ParaView plugins that evaluates edge-conforming data by means of vector basis functions. Based on this framework we present different visualization approaches for the investigation of the electric field at material boundaries. We demonstrate their utility using electro-hydrodynamics simulations of water droplet on the surface of high voltage insulator, representing a two-phase flow problem driven by strong electric fields.

---

### Introduction

The investigation of electromagnetic fields on material boundaries is of special interest in the development of structures that are exposed to the influence of strong electromagnetic fields. While the electric field at the interfaces is continuous parallel to the material surface, it commonly exhibits strong discontinuities in normal direction. These discontinuities pose problems in numerical simulations with finite element methods. The traditional approach, based on node-based elements, imposes continuity at boundaries due to the component-wise interpolation, resulting in an undesired smooth representation of quantities across the interface. Therefore, edge-based representation of vector quantities was introduced into the finite element methods. In the resulting approach, the simulated quantity is interpolated by means of vector shape functions that have several characteristics important for the representation of the electric field at material boundaries. Since neighboring elements share tangent components on the edges, the tangential field is continuous across those elements. On the other hand, the shape functions cause the tangential component to vanish at the element faces opposite to an edge (see Figure 2a) and 2b) for illustration), thus allowing for discontinuities in the normal component, which in turn enables correct representation of the electric field at interfaces. Additionally, the introduction of nonlinear elements, such as quadratic tetrahedra, enables more accurate approximation of curved surfaces, which has particular importance for the computation of the electric field, as the sharp, piecewise linear representation would artificially amplify the electric field. Consequently, the nonlinear elements significantly reduce the required number of tetrahedra for the approximation of curved boundaries.

Current visualization frameworks, however, do not allow for correct representation of the electric field from edge-based elements—due to their component-wise interpolation they miss field discontinuities across the interfaces. Thus, in this paper we present a framework that is able to correctly visualize the simulated field at material boundaries. The field is directly evaluated from the vector shape functions, taking higher-order elements (quadratic tetrahedra) into account, thus providing visualizations consistent with the simulation model. We exemplify the utility of our approach using electro-hydrodynamics simulations of water droplet on the surface of high voltage insulator.

### Related Work

Edge elements were introduced into the finite element method in [8] and [7]. Bossavit [7] identified Whitney elements [9], which are widely used in finite element simulations, as a natural discretization method for eddy currents. The basis functions of edge elements were generalized to arbitrary order for the finite element method, and the resulting convergence was analyzed in [10]. The advantages and disadvantages of edge elements as well as their applications are discussed in [11] and [12]. Isoparametric elements described in [18] represent an alternative that allows for efficient and accurate higher-order computations.



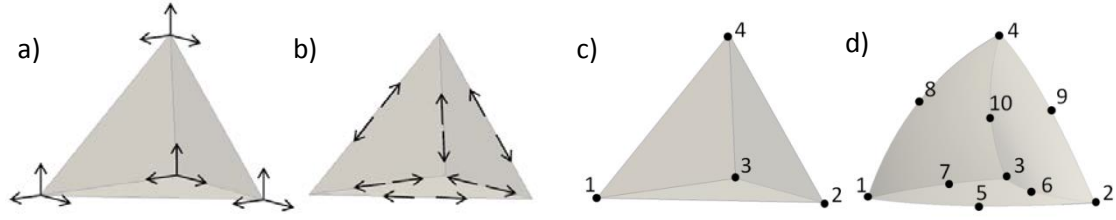


**Figure 1.** Data representation on tetrahedral elements. a) Node-based data representation, b) edge-based data representation b), c) linear tetrahedron, d) quadratic tetrahedron with additional mid-edge points.

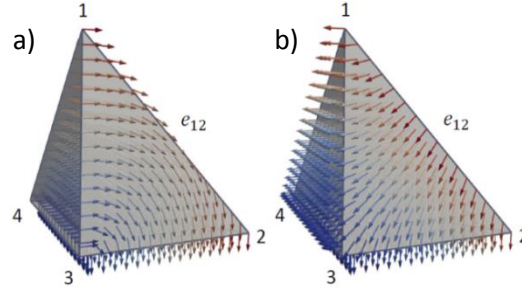


**Figure 2.** Vector basis functions on tetrahedra. a) First order basis function  $\vec{N}_{1,2}^1$  on edge  $e_{1,2}$  and b), second order basis function  $\vec{N}_{1,2}^{13}$  on edge  $e_{1,2}$ .

In the field of visualization, several techniques have been developed to address appropriate representation of higher-order elements. Wiley et al. [1] developed a technique for direct ray casting of curved quadratic elements without prior tessellation into linear elements. For cell-based polynomial fields, isosurface extraction from higher order finite elements was proposed in [2], where adaptive mesh refinement is employed for accurate representation of isosurfaces, which can also be applied to discontinuous elements. A technique for isosurface extraction providing a trade-off between rendering speed and quality was suggested by Pagot et al. [17], based on a particle motion along the gradient field, and ray casting in the neighborhood of final location of the particles. Schroeder et al. [3] addressed the complexity of higher-order basis functions from p- and hp-adaptive methods by employing an automatic tessellation technique with recursive edge-based subdivision. Visualization of discontinuous Galerkin simulations was presented in [4], where an adaptive sampling technique is used for high quality volume rendering, and utilization of a GPU cluster allows for interactivity. Parallel vectors feature extraction from discontinuous Galerkin simulations was proposed in [16]. A solution for the visualization of non-conforming meshes, based on point-based rendering, was developed by Zhou and Garland [5]. Isosurfaces from higher-order elements can be also visualized in a point-based manner [6], in which case the costly inverse mapping to evaluate the basis functions is avoided. Most recent works in the field of higher-order finite element visualization include a ray casting method with pre-computation of world-element space transformation [14], as well as ray casting with depth peeling [15]. It is worth noting that edge elements have not been introduced into visualization so far, and it is thus the aim of this paper to do so.

### Quadratic Tetrahedra

Quadratic tetrahedra are particularly suitable for finite element-based simulations involving electromagnetic field problems with interfaces, since they allow for curved edges and faces. Considering that the elements can adapt to relatively strong deformations, mesh refinement can be avoided for many problems. This at the same time allows for a significant reduction of the required number of elements—curved parts of the simulation domain no longer require strong refinement for accurate computation of the electric field. These elements, however, are more difficult to implement, and the mesh formation takes significantly longer than for linear elements [19]. Quadratic tetrahedra have variable metric, i.e., the Jacobian determinant is not constant over tetrahedron. This further complicates computations, e.g., point location inside tetrahedra.

A quadratic tetrahedron is illustrated in Figure 1d) (cf. Figure 1c) for comparison with a linear tetrahedron). The element is defined by 10 nodes, each carrying three components of the vector field, resulting in 30 degrees of freedom. The shape functions for quadratic tetrahedra are defined as:

$$N_l = L_l(2L_l - 1), \text{ for } l = 1, \dots, 4 \quad (1)$$

$$N_5 = 4L_1L_2, N_6 = 4L_2L_3, N_7 = 4L_1L_3, N_8 = 4L_1L_4, N_9 = 4L_2L_4, N_{10} = 4L_3L_4. \quad (2)$$

The world coordinates ( $x_1, x_2, x_3$ ) of a point inside a quadratic tetrahedron can be obtained from barycentric coordinates ( $L_1, L_2, L_3, L_4$ ) using:

$$x_i = \sum_{l=1}^{10} x_{il} N_l \quad (3)$$

where  $x_i$  represents the  $i$ -th world coordinate of the sought point, and  $x_{ij}$  represent the  $i$ -th coordinate of the  $j$ -th node of the tetrahedron. Since the computation of barycentric coordinates from world coordinates is nontrivial for quadratic tetrahedra, iterative methods, such as Newton-Raphson iterations, are commonly used.

### Edge-Conforming Data Representation

In the node-based finite element method, the data are stored on the nodes of the elements. As illustrated in Figure 1a), for a linear tetrahedral element there are four nodes, each carrying three components of the vector field. In edge-based representation, on the other hand, the data are attached to the edges of an element, as shown in Figure 1b). Here, each edge stores two tangential components of the vector field. In both representations there are in total twelve degrees of freedom for a linear tetrahedron. It is worth noting, however, that incomplete degrees are widely used in simulations of the electromagnetic field with interfaces in order to handle discontinuities at material boundaries. To compute the electric field in the edge-based element, the Whitney vector basis functions are employed. The first order incomplete Whitney shape functions are defined as

$$\vec{N}_{i,j}^l = L_i \nabla L_j - L_j \nabla L_i, \text{ for } l = 1, \dots, 6, \quad (4)$$

where  $i$  and  $j$  are nodes defining the edge  $e$ ,  $L_i$  and  $L_j$  are barycentric coordinates of nodes  $i$  and  $j$ , and  $\nabla L_i$  and  $\nabla L_j$  are the constant gradients of the barycentric coordinates. The basis functions are then used to interpolate the electric field  $\vec{E}$  from the tangential components  $c$ :

$$\vec{E} = \sum_{l=1}^6 c_l \vec{N}^l. \quad (5)$$

To extend the element to the complete first order, additional edge functions are used:

$$\vec{N}_{i,j}^l = L_i \nabla L_j + L_j \nabla L_i, \text{ for } l = 7, \dots, 12. \quad (6)$$

The second order basis functions are defined for edges:

$$\vec{N}_{i,j}^l = L_j(2L_i - L_j) \nabla L_i + L_i(L_i - 2L_j) \nabla L_j, \text{ for } l = 13, \dots, 18 \quad (7)$$

and faces:

$$\vec{N}_{i,j}^l = L_i L_j \nabla L_k - L_i L_k \nabla L_j, \text{ for } l = 19, \dots, 22 \quad (8)$$

$$\vec{N}_{i,j}^l = L_j L_k \nabla L_i - L_j L_i \nabla L_k, \text{ for } l = 23, \dots, 26 \quad (9)$$

$$\vec{N}_{i,j}^l = L_i L_k \nabla L_i + L_i L_k \nabla L_j + L_i L_j \nabla L_k, \text{ for } l = 27, \dots, 30. \quad (10)$$

In Figure 2 two edge functions are shown. Both basis functions have non-zero tangential component along the edge  $e_{12}$  and zero tangential component on the faces (1,3,4) and (2,3,4). The edge-conforming representation has thus several characteristics that are particularly useful in electromagnetic simulations. First and foremost, they do not impose continuity more than required by physics of the given phenomena. This means they can handle discontinuities of the normal component at the interfaces while ensuring continuity of the tangential field component. It is worth noting that continuity across the interfaces must be accomplished explicitly. Additionally, they allow comparably simple local p-adaptation, and are well suited for the solution of partial differential equations for the field intensities derived from Maxwell's equations.

### Transformation from Node-based to Edge-based Representation

In our visualization framework, we need to evaluate Equation 5 to visualize the electric field inside a quadratic tetrahedron. Hence, the tangential components must be either provided directly from the simulation or computed in the pre-processing step from the node-based representation. In the latter case, the electric field must be stored on each of the 10 nodes of a quadratic tetrahedron, such that two tetrahedra may share node coordinates, but their electric field data is defined separately for each node. For example, if there are three elements sharing one node, the node position might be defined once, but the electric field components three times, once for each tetrahedron. This allows us to compute the tangential components by finding the solution to the following system of linear equations:

$$(11)$$

$$\mathbf{A}\mathbf{c} = \mathbf{b}.$$

$\mathbf{A}$  is assembled from local matrices of each tetrahedron, and the local matrix elements are defined as:

$$a_{l,m} = \sum_{q=1}^Q (\vec{N}^l \cdot \vec{N}^m) w_q \det(J_q), \quad (12)$$

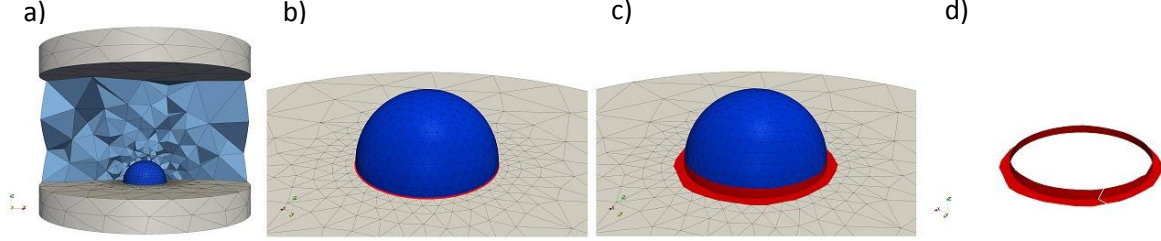


**Figure 3.** Stages for the visualization of electric field on the contact line. a) Simulation domain with three materials: air (light blue), water drop (dark blue), and insulator (gray). b) The contact line (red) between drop and insulator is extracted. c) The drop cells and insulator cells adjacent to the contact line are extracted. d) The extracted contact region is cut before the “unrolling” stage illustrated in Figure 4.



**Figure 4.** The process of Laplacian smoothing for the contact region (from left to right). The cut points from each side are positioned away from each other (left). Iterative smoothing applied to the rest of the mesh points (middle). Final rectification applied to the points, so that they lie on a plane (right).

where  $Q$  is the number of quadrature points,  $w_q$  is the weight of quadrature point  $q$ , and  $\det(J_q)$  is the Jacobian determinant at point  $q$ , with respect to barycentric coordinates. The full expression for the Jacobian determinant in quadratic tetrahedra can be found in [19]. Vector  $\mathbf{b}$  is assembled from

$$b_l = \sum_{q=1}^Q \sum_{k=1}^3 (\vec{N}^l \cdot \vec{E}_q) w_q \det(J_q), \quad (13)$$

where the electric field  $\vec{E}_q$  at point  $q$  is computed from Equation 3.  $l$  and  $m$  are local basis function indices which must be transformed to global indices  $i$  and  $j$  to assemble the matrix  $\mathbf{A}$  and vector  $\mathbf{b}$ :

$$A_{i,j} = a_{l,m}, b_i = b_l. \quad (14)$$

After the assembly, the system can be solved for  $\mathbf{c}$  using a linear algebra package (we used PETSc).

## Visualization

We implemented our visualization methods as plugins in ParaView [20]. The data is read either in node-based form or edge-based form using our custom reader plugin. In the former case, we transform the data to edge representation, as described in the previous section. This was done for the simulation results visualized in this paper, as they were converted to node-based representation at simulation output. Note that the mapping between local and global indices is also used later in Equation 5 to find the global tangential components for the local indices of the shape functions.

We have developed two visualization methods using our framework. In the first one, we evaluate and visualize the electric field on the material interface—in our case, on the interface between air and the droplet in a strong electric field (Figure 3a)). In the second one, we visualize the time-dependent electric field within a region near the contact line between droplet and the insulator on which the droplet is located. To facilitate the analysis of this region, which is important for the investigation of the dynamics, including static discharges [21], we “unroll” the region of the droplet interface and insulator surface near the contact line to create a rectangular strip, and stack the resulting strips from consecutive time steps to a space-time representation in order to provide an appropriate visualization of the space-time dynamics. The details are given in the next two sections.

### Electric Field on the Interface

For the visualization of the electric field on the air-drop interface, the quadratic tetrahedra adjacent to the interface between the two materials  $M_1$  (air) and  $M_2$  (water) must be found from the material information provided with the simulation data. For each tetrahedron, we check if it belongs to  $M_1$ , and if so, we determine if it faces a tetrahedron of material  $M_2$ . If this is the case, we store the indices of both elements inside a list. Subsequently, a triangular mesh that represents the interface is extracted from the shared faces of the quadratic tetrahedra stored in the list. Please note that for the visualization we approximate curved tetrahedral faces from the simulation by linear triangles. Each triangle in the mesh is then subdivided into smaller coplanar triangles.

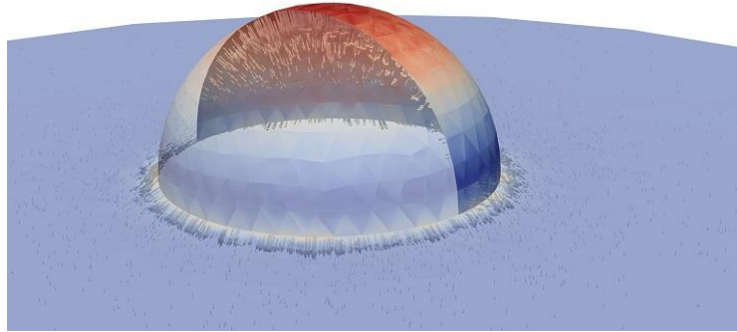


**Figure 5.** Visualization of a droplet on an insulator in the presence of strong electric field. The insulator and droplet are made partially transparent to reveal the electric field direction (glyphs with size scaled according to the field strength). The electric field is strongest at the top of the droplet (red) as well as at the interface.

For each resulting triangle we compute the middle point, and evaluate its barycentric coordinates in the original triangle. Since the coordinates are computed on tetrahedral faces (i.e.,  $L_i = 0$  on the face opposite to node  $i$ ), it is not necessary to employ computationally expensive point location algorithms. The shape functions are then evaluated using Equations 4 and 6-10, and finally the electric field is evaluated using Equation 5 and stored on the resulting mesh. See Figure 5 for a result. The whole procedure was implemented as a ParaView plugin.

### Space-Time Visualization of Electric Field around Contact Line

To extract the contact line between air, water, and insulator (Figure 3b)), we first extract two interfaces: interface  $I_1$  between  $M_1$ (air) and  $M_2$  (water), and interface  $I_2$  between  $M_1$  and  $M_3$  (insulator). From those interfaces we take only those triangles that share at least one point with a triangle from the other interface. The resulting triangular mesh is shown in Figure 3c). In the next step we cut the mesh (Figure 4) and duplicate the cut points so that on each side of the cut the triangles are topologically disconnected. The cut points from one side are then positioned away from the other cut points (Figure 4, left). An iterative Laplacian smoothing, illustrated in the rest of Figure 4, is performed on the other points of the mesh strip, placing each point to the average of the direct neighbors at each iteration. Only neighbors on the perimeter are taken into account for the points lying on it, otherwise the whole mesh would collapse into one line. The extracted contact region, shown in Figure 3d), and the smoothed counterpart (Figure 4, right) are subdivided into fine triangular meshes, such that for each cell in the original geometry there is a corresponding cell in the smoothed one. Finally, we sample the data on the original subdivided mesh, as described in the previous section, and assign the values to the smoothed mesh.

To obtain a space-time representation, a 3D rectilinear grid is created such that the resolution in  $T$  direction corresponds to time (i.e., number of simulation time steps), while the  $x$ - $z$  plane is aligned with the “unrolled” contact line strips. For the simulation data we used a 1024 x 51 x 25 grid (i.e., with 51 time steps and 1024 x 25 samples per strip). We then sample the smoothed (triangulated) strip for each time step in the  $x$ - $z$  plane of the 3D grid at the respective  $T$  (time step) position. As a result, the strips from consecutive time steps are sampled and then stacked on each other, resulting in a 3D grid.

To reveal the temporal variation of the electric field, isosurface extraction and volume rendering are employed on the space-time stack. The isosurface extraction (see Figure 6) is done with the Marching Cubes algorithm using the “Contour” plugin from ParaView. Volume rendering (see Figure 7) displays 3D scalar data in a transparent form, where opacity and color is defined for each scalar value using a so-called transfer function. The final image is achieved by a compositing technique, based on the rendering equation of the

emission-absorption light model, using the “Volume” data representation from ParaView. For the space-time stacking and 3D mesh generation we developed our ParaView plugin.

## Results and Discussion

The basic visualization of electro-hydrodynamic simulations of a droplet in the presence of strong electric fields is illustrated in Figure 5. The simulation was obtained by coupled fluid dynamics and electrical field solver: the finite element method step determines the electric field, which is then used to compute the dynamics of the droplet with the finite volume method according to the induced flow. The solution of the fluid dynamics stage is fed back to find the electric field in the domain. The process is repeated for each simulations step. Figure 5 shows one time step from the simulation. The droplet is positioned on an insulator, within a strong, vertical electric field. The electric field lines (not shown in the figure) are vertical. As can be seen, the electric field is strongest at the top of the droplet. What is more interesting, however, is that the field strength on the contact line

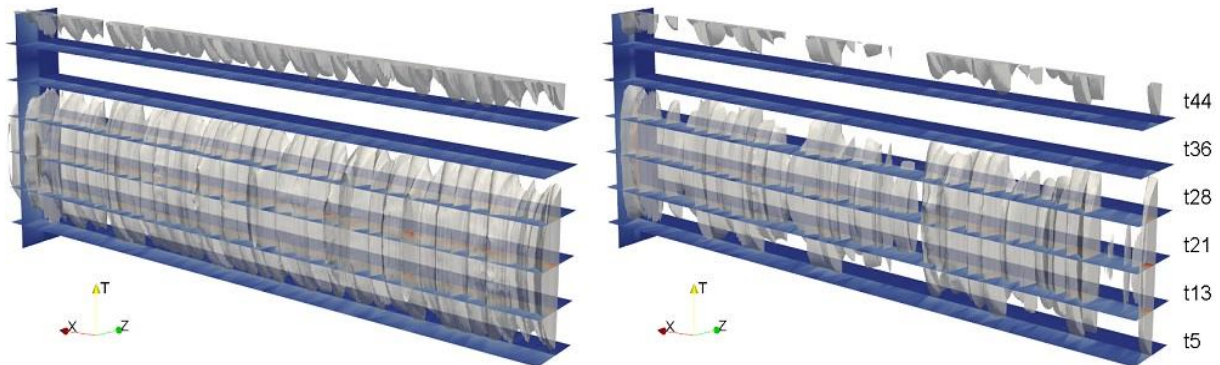


**Figure 6.** Visualization of the time-dependent electric field a) tangent and b) normal to the interface around the contact line, visualized here as cross sections (horizontal rectangles) obtained by Laplacian smoothing. Time evolution from bottom to top (T-axis, respective time steps on the right). Air-insulator interface is at the front, drop-air interface in the back. The transparent isosurfaces and the vertical plane show the temporal variation of the electric field. Interestingly, the normal component varies stronger than the tangent one.

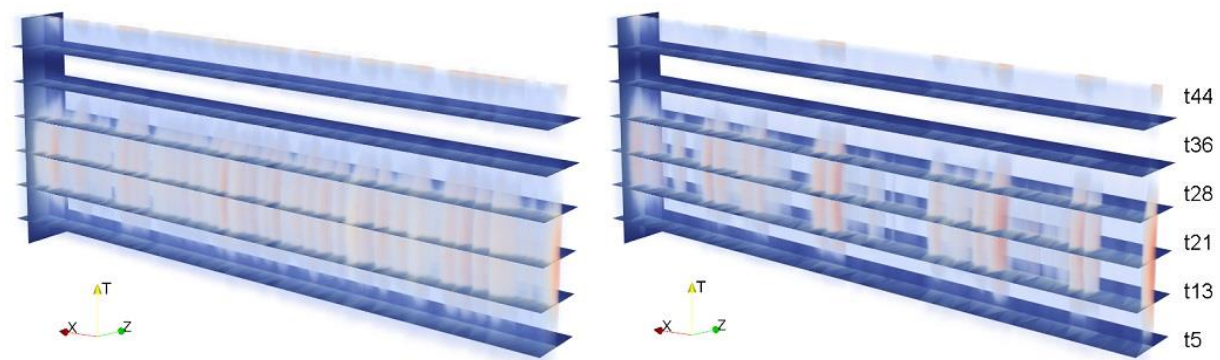


**Figure 7.** Space-time visualization of the time-dependent electric field, as in Figure 6. Volume rendering is shown instead of isosurfaces. The magnitude of the electric field is considerably lower for the drop-air interface (back side of the planes).

is amplified due to the sharp corner formed by the droplet-insulator contact region. Since this region is of particular interest for the domain experts, the next visualization technique facilitates the investigation of the time-dependent electric field near the contact line.

In Figures 6 and 7, the space-time visualization of the electric field in the contact region is presented. The images on the left show the electric field tangent to the drop (insulator) surface, while the images on the right show the field normal to the interface. Six simulation time steps are displayed (see previous section) and a vertical color-coded cross section shows the time development of the field at one position in the contact region. The air-insulator interface is oriented to the front. Figure 6 additionally shows a transparent isosurface of the magnitude of the tangent (normal) field component, while Figure 7 displays the magnitude by volume rendering. The visualization shows interesting characteristics of the time-dependent vector field. It exhibits periodic intervals, as indicated by the isosurface: the high magnitude regions disappear before time step 36 to appear



again after time step 44. Volume rendering reveals that the tangential field has uniform distribution along the contact line, while the normal field is characterized by stronger spatial variation. It is also evident that the electric field magnitude is considerably weaker on the drop boundary. The static representation of temporal process enables insights into the overall behavior of the electric field along the drop-insulator contact region.

## Conclusion

We presented methods for the visualization of electromagnetic field simulations with interfaces. Our framework is tailored towards the edge-based representation for correct visualization of the vector quantities at the material boundaries. We exemplified the benefits of our methods using data from electro-hydrodynamic simulations of a droplet in the presence of strong electric fields. Since the contact line between the droplet and the insulator is of particular importance for the investigation of the dynamics, including static discharges, we have provided a space-time visualization of the electric field along the circular contact region which avoids occlusion and provides a static representation of time dependent process. As future work we would like to address the performance of our method—in our prototype we have used only one processor for the evaluation of the tangential components. The utilization of multithreading would significantly speed up the computation. GPU parallelization of the most demanding stages would also be a promising approach. Additionally, we would like to generalize our framework to other electromagnetic field problems with interfaces.

## Acknowledgements

The authors would like to thank the Deutsche Forschungsgemeinschaft (DFG) for support within the Collaborative Research Center SFB-TRR 75.

## References

- [1] Wiley, D. F., Childs, H., Harmann, B., Joy, K.: Ray Casting Curved-Quadratic Elements. In *Proceedings of the Sixth Joint Eurographics - IEEE TCVG conference on Visualization*, (2004), pp.201-210.
- [2] Remacle, J.-F., Chevaugnon, N., Marchandise, É., Geuzaine, C.: Efficient visualization of high-order finite elements. *International Journal for Numerical Methods in Engineering* 69, 4 (2007), pp.750-771
- [3] Schroeder, W. J., Bertel, F., Malaterre, M., Thompson, D., Pebay, P. P., O'Bara, R., Tendulkar, S.: Methods and Framework for Visualizing Higher-Order Finite Elements. *IEEE Transactions on Visualization and Computer Graphics* 12, 4 (2006), pp.446-460
- [4] Üffinger, M., Frey, S., Ertl, T.: Interactive High-Quality Visualization of Higher-Order Finite Elements. *Computer Graphics Forum* 29, 2 (2010), pp. 337-346
- [5] Zhou, Y., Garland, M.: Interactive Point-Based Rendering of Higher-Order Tetrahedral Data. *IEEE Transactions on Visualization and Computer Graphics* 12, 5 (2006), pp.1229-1236
- [6] Meyer, M., Nelson, B., Kirby, R. M., Whitaker, R.: Particle Systems for Efficient and Accurate High-Order Finite Element Visualization. *IEEE Transactions on Visualization and Computer Graphics* 13, 5 (2007), pp.1015-1026
- [7] Bossavit, A.: A rationale for 'edge-elements' in 3-D fields computations. *IEEE Transactions on Magnetics* 24, 1 (1988), pp.74-79
- [8] Nedelec, J. C.: Mixed finite elements in R3. *Numerische Mathematik* 35, 3 (1980), pp.315-341
- [9] Whitney, H.: Geometric integration theory. *Dover Books on Mathematics Series*, Dover Publications, (2005)
- [10] Webb, J.P.: Hierarchical vector basis functions of arbitrary order for triangular and tetrahedral finite elements. *IEEE Transactions on Antennas and Propagation* 47, 8 (1999), pp.1244-1253
- [11] Webb, J.P.: Edge elements and what they can do for you. *IEEE Transactions on Magnetics* 29, 2 (1993), pp.1460-1465
- [12] Mur, G.: Edge elements, their advantages and their disadvantages. *IEEE Transactions on Magnetics* 30, 5 (1994), pp.3552-3557
- [13] Irons, B.M., Zienkiewicz, O.C.: The Isoparametric Finite Element System: A New Concept in Finite Element Analysis. Royal Aeronautical Society, (1969)
- [14] Bock, A., Sunden, E., Liu B., Wunsche, B., Ropinski, T.: Coherency-Based Curve Compression for High-Order Finite Element Model Visualization. *IEEE Transactions on Visualization and Computer Graphics* 18, 12 (2012), pp. 2315-2324
- [15] Liu, B., Bock, A., Ropinski, T., Nash, M., Nielsen, P., Wüsche, B. C.: GPU-accelerated direct volume rendering of finite element data sets. In *Proceedings of the 27th Conference on Image and Vision Computing New Zealand*, (2012), pp. 109-114
- [16] Pagot, C., Osmari, D., Sadlo, F., Weiskopf, D., Ertl, T., Comba, J.: Efficient Parallel Vectors Feature Extraction from Higher-Order Data. *Computer Graphics Forum* 30, 3 (2011), pp.751-760

- [17] Pagot, C., Vollrath, J., Sadlo, F., Weiskopf, D., Ertl, T., Comba, J. L. D.: Interactive Isocontouring of High-Order Surfaces. *Scientific Visualization: Interactions, Features, Metaphors, Dagstuhl Follow-Ups 2*, (2011), pp.276-291
- [18] Irons, B.M., Zienkiewicz, O.C.: The Isoparametric Finite Element System: A New Concept in Finite Element Analysis. Royal Aeronautical Society, (1969)
- [19] Advanced Finite Element Methods (ASEN 6367), Department of Aerospace Engineering Sciences,
- [20] University of Colorado at Boulder  
(<http://www.colorado.edu/engineering/CAS/courses.d/AFEM.d/AFEM.Ch10.d/AFEM.Ch10.pdf>)
- [21] ParaView - Open Source Scientific Visualization. (<http://www.paraview.org/>)
- [22] Songoro, H., Gjonaj, E., Weiland, T.: Computational modeling of water droplet deformation in strong electric fields. In *International Conference on Electromagnetics in Advanced Applications (ICEAA)*, (2012), pp.333-336

## The Time-shift technique for characterization of non-transparent, spherical particles

C. Tropea and W. Schäfer

Institute of Fluid Mechanics and Aerodynamics, Center of Smart Interfaces,  
Technische Universität Darmstadt,

### Abstract

The time-shift technique, also known as the pulsed-displacement technique, is re-visited as a means of measuring size, velocity and relative refractive index of spherical, non-transparent particles. Building on the basic measurement principle, several new innovations are introduced, making the technique significantly more attractive for use outside of the laboratory. These include validation criteria for two-detector arrangements, and approaches for achieving higher size bandwidths, in particular lower measurable sizes. However, the main novelty introduced in this contribution is the ability to measure non-transparent droplets. Such droplets are quite common, for example in spray drying processing or in paint sprays.

In this contribution the basic working principle of the time-shift techniques will be reviewed, followed by guidelines for the optical layout. Example measurements are presented.

---

### Introduction

The characterization of spherical, transparent particles in terms of size, velocity and possibly relative refractive index is of major interest in a variety of applications, but especially when investigating sprays of pure liquids. Counting techniques, i.e. techniques which measure and count individual droplets, are often desirable over integrating techniques such as the laser diffraction technique (LDT), since the velocity information, together with the counts can yield flux densities and concentration estimates. Several techniques fulfill these expectations, in particular direct imaging and interferometric techniques, such as the phase Doppler technique, holography, rainbow refractometry or interferometric particle imaging. Available techniques for this purpose have been recently summarized in a review article (1).

However also the time-shift (TS) technique is an interesting candidate in this respect, and for several reasons there are very good grounds to re-visit this technique with the intention of making it more suitable for practical applications. One motivation is that the TS technique does not require coherent light and can therefore take advantage of low-cost, high power light sources which have recently become available. Furthermore, the TS technique can be optically configured to work in the near backscatter, allowing transmitting and receiving optics to be aligned through a single optical access to the measurement position. This immediately opens the possibility of a probe construction, i.e. all optical components in a single housing; hence achieving a higher degree of robustness.

The time shift technique itself is not new, its origins go back to the Ph.D. thesis of Semidetnov in 1985 (2). Hess and Wood (3) presented several different optical configurations of the time-shift technique, all operating in forward scatter, i.e. employing scattered light from reflection and first-order refraction. One focus of their development was to enlarge the measurable size range, especially for smaller droplets. In their instrument velocity was measured using the laser Doppler or the time-of-flight technique. In their study they called this technique the pulse displacement technique. Lin et al. (4) also worked in forward scatter and employed three illuminating light sheets, extending the measurement capability to include relative refractive index. In Damaschke et al. (5) and Albrecht et al (6) configurations suitable for backscatter detection were introduced, enabling more compact optical arrangements and easier optical access to the measurement position, while at the same time enabling size and refractive index to be obtained using only one illuminating beam. The laser Doppler technique was used for velocity measurement. Damaschke et al. also examined the sensitivity of the time-shift technique to non-sphericity of the scattering particle as well as limitations for small particle sizing.

It can be noted that the distinguishing feature of the time-shift technique compared to other techniques for size and velocity measurements of particles is the fact that the time-shift technique uses a shaped beam, meaning that the intensity variation of the beam varies considerably over the diameter of the particle to be measured. Hence, the time-shift technique utilizes a fundamentally different measurement principle than for instance the grating anemometer introduced by Semiat and Dukler (7) or Cartellier (8). The condition of a shaped beam can naturally arise, especially with larger particles and/or bubbles, and a technique closely related to the time-shift technique has been introduced by Brankovic et al. (9), known also as the triple-peak technique (Yu and Varty (10)). These realizations have also relied on the laser Doppler technique for velocity measurement. Indeed, these and several other variations of this technique (11) can be considered special cases of the time-shift technique. All of these techniques assume sphericity of the particle.



However, general principles for optically configuring the time-shift instrument for a given application remain lacking as do validation strategies for enabling the technique to be used in situations with higher particle densities. Furthermore, the use of the laser Doppler technique or the time-of-flight approach for the particle velocity measurements add complexity and cost to the time-shift technique. The present work attempts to alleviate some of these shortcomings.

### Measurement Principle

The measurement principle of the time-shift technique is only briefly summarized here, since adequate descriptions can be found elsewhere (Albrecht et al. (2003)). The measurement principle of the time-shift technique is based on the light scattering of a single particle from a shaped light beam. Whether the intensity variation is Gaussian, as would be the case for a laser beam in TEM<sub>00</sub> mode, or any other form, is not important in principle. However some advantages can be recognized for the subsequent signal processing if a Gaussian beam is used.

The light scattered from a single particle can be interpreted as the sum of all scattering orders present at the detector location. This decomposition of scattered light into various scattering orders is well described by the Debye series (12) expansion of the Mie (13) scattering functions, or by using a geometric optics (14) approach to compute the scattered field. Considering the propagation of individual rays of light through the particle, as depicted in Figure 1, the point at which the incident ray intersects the particle surface is known as the incident point. The angle of an incident point is called the incident angle  $\theta_i$ . The point where the light ray exits a particle after reflection or a number of refractions is called a glare point (15).

If the illuminating beam is ‘shaped’, effectively a different measurement volume is realized for each received scattering order, and each measurement volume is displaced in space from one another. This is in contrast to illumination by a homogeneous plane wave, for which all scattering orders are received with the same incident intensity, regardless of the particle position. The magnitude of the displacement between the illuminated volume and the measurement volume depends on the particle size, refractive index, scattering order and the scattering angle. The displacement in space translates through the particle velocity component in the direction of measurement volume separation into a temporal separation of the received signals; hence the two different designations of this technique: the pulse displacement technique or the time-shift technique.

When a particle passes through these different measurement volumes, the measurement volume displacement appears as a time shift of the signal on any one single detector. The number and relative position of the measurement volumes in space are related to the relative position of the respective incident points of the scattering orders and their modes of the received light. The position of these incident points depend in turn on scattering angle and relative refractive index, and can be calculated by ray tracing methods. In order to achieve adequate separation of the different measurement volumes in space, the particle size must be larger than the size of the shaped light beam. The size ratio which is adequate for reliable measurements will depend to some extent on the exact optical configuration; in general forward scattering arrangements can size smaller particles.

An example time-shift signal originating from a water droplet passing through a Gaussian shaped beam and collected at a scattering angle of 150deg from forward scatter is illustrated in Figure 2, in which signal components are observable from the following scattering orders: surface wave long path, reflection ( $p=0$ ), second-order refraction mode 1 ( $p=2.1$ ), second-order refraction mode 2 ( $p=2.2$ ) and surface wave short path. The time between individual peaks in the time-shift signal  $S(t)$  will depend on the detection angle, the relative refractive index, the particle velocity normal to the illuminating beam, and the particle size. If the first two parameters are known and the particle velocity is measured, e.g. using a laser Doppler or time-of-flight technique, then the particle size can be deduced from the time shift between two of the signal peaks. In the example shown in Figure 2 three main signal peaks are obtained; hence two independent measures of particle size would be possible, e.g.  $t_{p=0} - t_{p=2.1}$  or  $t_{p=0} - t_{p=2.2}$ .

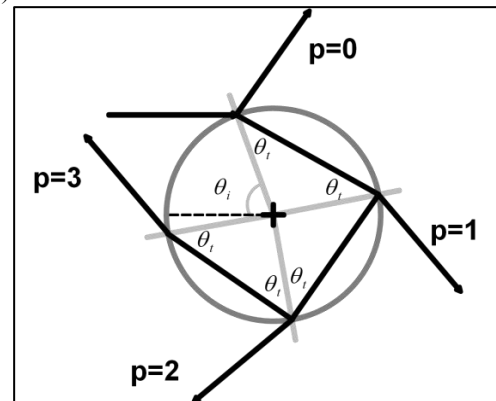


**Figure 1:** Schematic illustration of the scattering orders according to geometrical optics. Abbreviations: GP - glare point;  $p=0$ , reflection;  $p=1$ , first-order refraction;  $p=2$ , second-order refraction;  $p=3$ , third-order refraction;  $\theta_i$ , incident angle

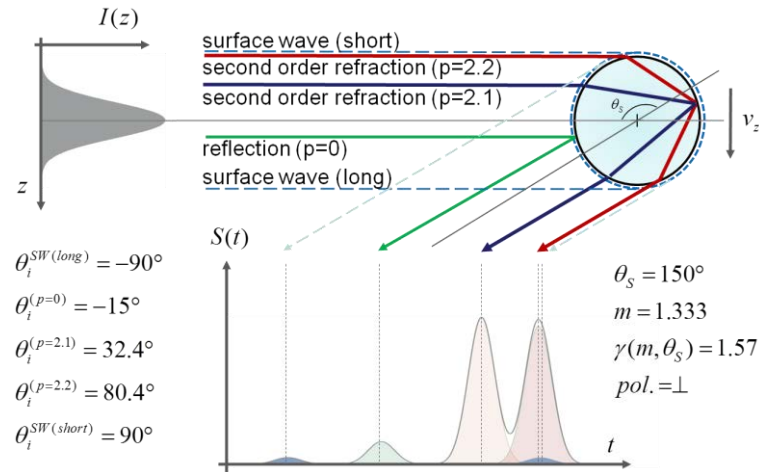


**Figure 2:** Time-shift signal originating from a water droplet passing through a Gaussian beam and with a detector placed at a scattering angle of 150deg from forward scatter.

### Measurement System for Non-Transparent Particles

For non-transparent particles such as emulsions, suspensions or dispersions, as one would expect in a spray dryer or with painting applications, the light scattering properties of single droplets are expected to change significantly. In particular, the transmission of light through the particle is expected to be greatly reduced and scattering from internal scattering centers can be expected. This changed situation is depicted graphically in Figure 3. Therefore, the signal obtained at a given detector will comprise reflective scattering and scattering from within the droplet. Direct detection of higher order refractive components ( $p > 0$ ) can only be expected for very dilute droplet mixtures.

A suitable optical configuration for the size measurement of such droplets is shown in Figure 4, in which two detectors are used in a near backscatter arrangement. This configuration can be extended by employing a Doppler or time-of-flight measurement of droplet velocity. Two detectors are used at different scattering angles, since the arrival time of the reflective signal obtained from the droplet will depend now on scattering angle, droplet velocity and droplet size (no longer relative refractive index.) Knowing the scattering angle of each detector (shown symmetric in Figure 4) and the droplet velocity from the time-of-flight measurement, allows the drop size to be computed from the time shift between the reflected peaks of the time-shift signal.

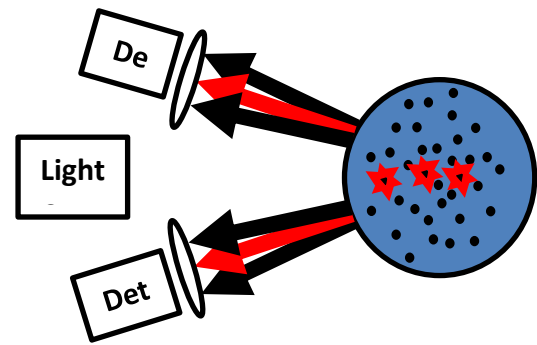


**Figure 3:** Schematic illustration of light scattering from a non-transparent droplet.

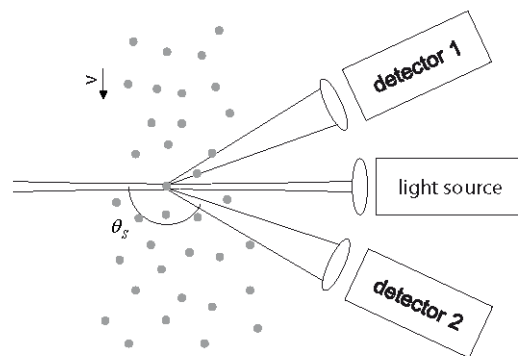


**Figure 4:** Optical configuration for a two-detector time-shift device operated in backscatter.

The signals expected from each detector arising from a single illuminated volume are depicted in Figure 5. This signal exhibits two main features: the first is a baseline signal arising from the internal scattering in the particle and extending over a residence time  $d/v$ , i.e. the particle diameter divided by the velocity of the particle normal to the illuminating beam. The second feature is the reflective peak, appearing at different times for each detector, the arrival time being dependent on the respective detection angle, the particle velocity and the droplet diameter. Knowing the geometric parameters of the optical configuration, the time shift between the two reflective peaks is linearly related to the particle diameter, if the droplet velocity is known.

Any one signal from each detector can be expressed analytically as:

$$S(t) = \underbrace{C_0 w_0 (d^2 - 4v^2(t - t_0)^2)}_{\text{baseline}} + \underbrace{\sum \frac{A_p}{C_p} \exp\left\{-\frac{2((t - t_0) - t_{p=0})^2}{\sigma^2}\right\}}_{\text{refraction}} - \underbrace{A_0 \exp\left\{-\frac{2((t - t_0) - t_{p=0})^2}{\sigma^2}\right\}}_{\text{reflection}} \quad (1)$$

which exhibits three components. The first component corresponds to the baseline signal, whose amplitude will somehow be related to the scattering center concentration in the droplet  $C$ . This component has been approximated by a width of  $(d/v)$ , where  $d$  is the particle diameter and  $v$  the particle velocity. The second component is related to higher-order refractive components, but will be neglected for all but the most dilute particles (non-transparency). The last component corresponds to the reflective scattering and is represented here by a Gaussian shape of width  $\sigma$ , assuming that the illuminating beam also exhibits a Gaussian intensity profile.

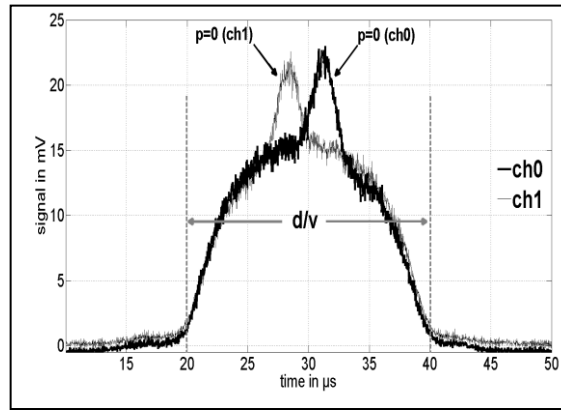


**Figure 5:** Typical signals expected from a two-detector time-shift measurement system.

Note that the velocity of the particle can also be deduced from the width of this reflective peak, if the width of the illuminating beam ( $b$ ) has been measured beforehand using, for instance, a beam scan device. Then the velocity is given as:  $v = b / \sigma$ . To make use of Eq. (1), the acquired signal is fit to the analytic expression (1) by adjusting the parameters  $C$ ,  $A_0$ ,  $t_0$ , and  $t_{p=0}$ . The quantities  $t_0$  and  $t_{p=0}$  refer to the arrival time of the particle in the illuminating volume and the time shift of the reflective peak for the particular detector. Such a fitting procedure (model parameter estimation) can be accomplished using different methods; in the present study a least squares regression has been used.

### Signal Validation and Example Measurements

In practice the signals shown in the previous section contain noise and can also be distorted when multiple particles traverse the measurement volumes simultaneously. This experience is illustrated in Figure 6a, where signals arising from other particles being in the measurement volume are shown, as opposed to signals suitable for further processing, shown in Figure 6b. To distinguish between suitable signals and non-suitable signals, the baseline portion of the signal is examined in more detail. Specifically, the amplitude of each baseline signal from detectors 1 and 2 must coincide within pre-determined bounds. Otherwise, the signals are rejected from further statistics.

Further signal validation is conceivable. From the previous section it is clear that the particle velocity can be estimated from the width of the reflective peaks, knowing the width of the illuminating Gaussian beam beforehand. However the velocity can also be estimated from the time-of-flight between signals on a single detector, knowing the separation of the illuminating volumes. This validation is only applicable if the time-of-flight technique is used for the velocity measurement. Each of these estimates can be performed with each detector; hence redundancy is available, which can be used for validation purposes.

Also the particle size can be estimated twofold. The main approach is to use the time-shift between reflective peaks of different detectors. However the particle size will also directly influence the width of the baseline signal. This is indicated in Figure 5 with the quotient  $d/v$ . Hence, if the velocity is known, for example

from the Doppler or time-of-flight measurement, then a further estimate of particle size can be performed. This may be of special interest for non-spherical particles, e.g. for ice crystals.

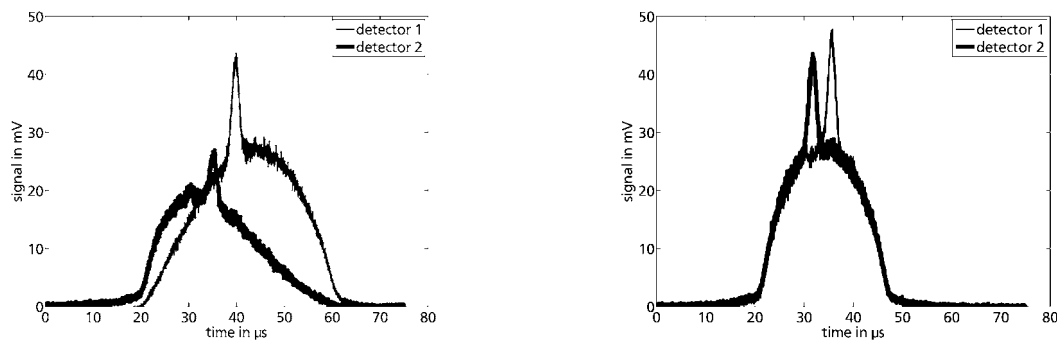


**Figure 6:** Example time-shift signals. a) Signals with multiple particle in measurement volume simultaneously; b) signals suitable for further processing

The measurement system and signal processing procedure described above has been used to perform measurements in a milk spray. A simple pressure atomizer was used (Lechler 632.363) at various pressures. The time-shift signal used a laser source at wavelength 405nm. For velocity measurement the time-of-flight technique has been used. The scattering angles of detectors were 147deg for detector 1 and 160deg for detector 2 and a detection volume has been used of 1mm, determined by the aperture used in front of the detector.

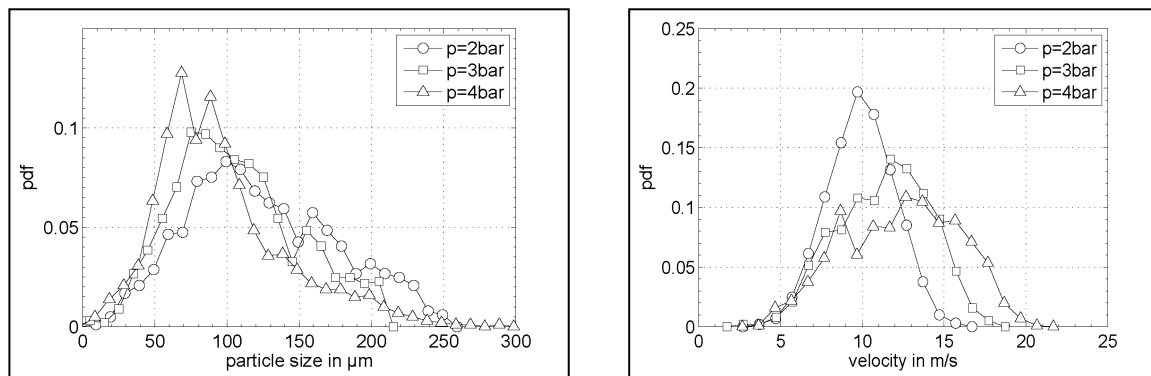


**Figure 7:** Measured milk droplet size and velocity at different atomizer pressures

The results of these measurements are presented in Figure 7. Figure 7a shows the probability density function of the droplet sizes for three different nozzle pressures. The higher pressure resulted in a smaller mean droplet diameter. Figure 7b shows the corresponding velocities of the particles. With increasing nozzle pressure the mean velocity increases.

## Conclusions

The suitability of the time-shift technique for the size measurement of non-transparent droplets has been discussed. For such droplets, reflected scattered light is used. Scattered light arising from internal scattering within the droplet contribute to the obtained signals in the form of a baseline signal, which also exhibits dependencies on particle size and velocity. A measurement system has been introduced, operating in backscatter and using two detectors and two illuminating beams. The velocity measurement is performed using the time-of-flight principle; the size measurement is derived from the time shift between reflective components of the signal on different detectors. Overall considerable redundancy is available in both the size and velocity measurement, offering numerous possibilities for signal validation.

The feasibility of this technique for measuring non-transparent particles has been demonstrated with the measurement of a milk spray from a simple pressure driven atomizer.

## Acknowledgements

This work was financially supported by the Deutsche Forschungsgemeinschaft through the Research Training Group GRK 1114 "Optical measurement techniques for characterizing interfacial transport phenomena".

## References

- [1] Tropea, Cameron. Optical particle characterization in flows. *Ann Rev Fluid Mech.* 2011, S. 43:399-426.
- [2] Semidetnov, Nikolai. *Investigation of laser Doppler anemometer as instrument for two-phase flow measurements (in Russian)*. Leningrad : Ph.D. Thesis, Leningrad Institut for Precision Mechanics and Optics, 1985.
- [3] Hess, Cecil F und Wood, C. P. The pulse displacement technique – a single particle counter with a size range larger than 1000:1. *Part.Part.Syst.Charat.* 1994, S. 11:107-113.
- [4] Lin, S. M., Waterman, D. R. und Lettington, A. H. Measurement of droplet velocity, size and refractive index using the pulse displacement technique. *Meas. Sci. Techn.* 2000, S. 11:L1-L4.
- [5] Damaschke, Nils, et al. Optical particle sizing in backscatter. *Appl Optics.* 2002, S. 41:5713-5727.
- [6] Albrecht, Hans-Ernst, et al. *Laser Doppler and Phase Doppler Measurement Techniques*. Heidelberg : Springer-Verlag, 2003.
- [7] Semiat, R und Dukler, A E. Simultaneous measurements of size and velocity of bubbles and drops: a new optical technique. *AIChE J.* 1983, S. 27:148.
- [8] Cartellier, Alain. Grating anemometer for local velocity measurements of large bubbles and drops: theoretical analysis. *Applied Optics.* 1986, S. 25:2815-2820.
- [9] Brankovic, A, Currie, Iain G und Martin, William W. Laser Doppler measurements of bubble dynamics. *Phys Fluids.* 1984, S. 27:348-350.
- [10] Yu, P Y.W und Varty, Robert L. Laser-Doppler measurement of the velocity and diameter of bubbles using the triple-peak technique. *Int J Multiphase Flow.* 1988, S. 765-776.
- [11] Wunderlich, Bernd, et al. *Verfahren zur Bestimmung der Geschwindigkeit und der Größe von Teilchen mittels einer für die Laser-Doppler-Velocimetrie geeigneten Anordnung.* 102007052795 02. 11 2007.
- [12] Debye, Peter. Der Lichtdruck auf Kugeln von beliebigem Material. *Annalen der Physik.* 1909.
- [13] Mie, Gustav. Beiträge zur Optik trüber Medien, speziell kolloidaler Metallösungen. *Annalen der Physik.* 1908.
- [14] Glantschnig, W J und Chen, S H. Licht scattering from water droplets in the geometrical optics approximation. *Appl Optics.* 1981, S. 20:2499-2509.
- [15] van de Hulst, H C und Wang, R T. Glare points. *Appl Optics.* 1991, S. 30:4755-4763.

## Multi-scale velocity measurements for high-resolution spray kinematics

D. Sedarsky, S. Idlahcen, C. Rozé, J.B. Blaisot

CORIA/CNRS UMR-6614, Université et INSA de Rouen, France

### Abstract

Ultrafast shadow imaging (USI) is a transillumination measurement and filtering approach which allows in-focus structure to be resolved within an object plane along the line-of-sight of the imaging system. Using a laser pulse and optics which image the center of the jet results in a signal field which is dominated by spatially resolved features which appear superimposed on the (unfocused) line-of-sight intensity background. In the present work, this spatially resolved image information is exploited to observe and track the velocity and morphology of select structure within the spray volume. A set of four different spatial and temporal scales relevant to liquid breakup and spray formation are isolated in USI measurements of a high-pressure diesel spray and image correlation velocimetry analysis is implemented to target the selected spray structure. The analysis is applied to single-shot images of diesel injection events, forming a time-resolved data set for each identified scale which characterizes the spray from start of injection to fully developed spray conditions.

---

### Introduction

The complex fluid dynamics interactions which drive the formation of high-pressure sprays remains a topic of intense scientific as well as practical interest. At present, the turbulent multiphase breakup processes which are essential to the function of atomizer nozzles used in fuel injection, cooling, and industrial manufacturing are to a large degree designed through empirical testing and much about their function is not well understood. The turbulent forces and momentum exchange active at the edges of transient liquid jets is of particular interest, as these disturbances define the character of the spray which develops as this liquid core disintegrates.

From a measurement standpoint, the rapidly evolving multiphase environment, intense scattering, and chaotic small-scale motion of a turbulent fuel spray presents challenging conditions for optical diagnostics. Shadowgraphy is one optical diagnostic which has been successfully applied to observe the line-of-sight macrostructure of a wide variety of sprays. The forward-scatter collection geometry and variable sensitivity of shadowgraphy makes it less susceptible to some of the multiple-scattering interference which hinders diagnostics in turbid media. In regions where spray features can be reliably separated from the background, image correlation velocimetry (ICV) can be applied to follow the spray formation process, and track the evolution of fluid structures [1, 2, 3]. In this work, ultrafast shadow imaging (USI), a variant of shadowgraphy that incorporates pulsed ultrashort coherent illumination and imaging optics is applied to a diesel spray, allowing the detection of spatially resolved spray structure. The resulting time-resolved images are then processed and analyzed to determine liquid structure velocities, where special care is taken to account for the spatial filtering of the sampling and correlation procedure used to calculate velocity information.

### Experiment Setup

The USI system used for the single-shot measurements discussed here can be viewed essentially as a focused shadowgraphy system [4], where signal from a collimated source light is collected by a lens after interaction with the region of interest and imaged to a detector (see Fig. 1a). In the present study, intense coherent laser pulses were used to illuminate the near field of a single-hole test injector. The light transmitted through the jet and spray formation region was collected by imaging optics and directed to the detector forming images at approximately 1:1 magnification. The source light was generated by a specialized system consisting of two matched regenerative amplifiers seeded by a single Ti:Sapphire laser oscillator. This arrangement is capable of illuminating the spray with a pair of synchronized ultrashort ( $\sim 120$  fs) laser pulses with precisely controlled inter-pulse timing, at a repetition rate of 1 kHz. The intense peak energy and precise timing of the source laser pulses ensure that the system can make full use of dynamic range and response of the detection system. In addition, the ultrashort source light serves to precisely freeze the spray motion as well as the optical seeing conditions in the imaging path. This results in sharp spray edges and well-resolved features in regions where the object plane, positioned at the center of the spray, intersects the periphery of the liquid column.

By combining this source and optical arrangement with a double-exposure CCD camera, the system is capable of recording time-correlated image-pairs with a minimum interframe time separation of 120 ns, where the minimum separation in time is limited by the switching and setup constraints of the camera electronics. Post-

processing and analysis of these image-pairs, as discussed in the following section, can subsequently be applied to yield dynamic information on the character of the spray.

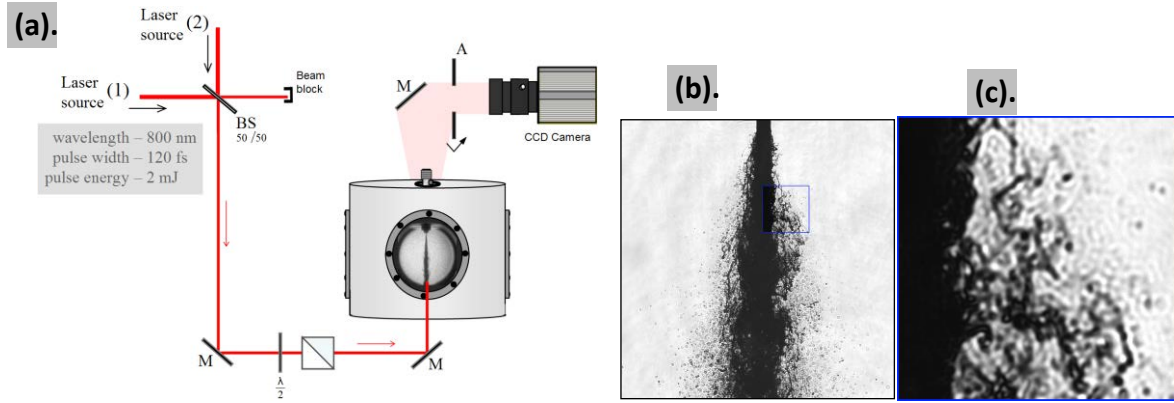


**Figure 1:** (a) Ultrafast shadow imaging (USI) system used to capture image-pairs. (b) Single-shot fuel spray image ( $P_{inj} = 40$  MPa, nozzle dia. =  $113 \mu\text{m}$ ). (c) detail view of inset from (b).

The injector used in this work was mounted on a three-way translation stage housed in an enclosure with four windows, providing line-of-sight optical access in two directions (see Fig. 1a). The measurements were carried out using a calibration liquid (ISO 4113) with properties similar to Diesel fuel with precisely controlled viscosity, density, and surface tension specifications (see Table 1). The single-orifice injector with a hole diameter of  $113 \mu\text{m}$  was supplied with fuel through a Common Rail accumulator, allowing adjustable injection pressures from 40 to 100 MPa. Each injection event was triggered electronically by two current levels of  $400 \mu\text{s}$  duration, at a repetition rate of 1 Hz, where the reference clock for the complete system was set by the period of the laser oscillator (80 MHz).

**Table 1.** Properties of ISO 4113 calibration oil.

Density	Viscosity	Surface Tension
$821 \text{ kg/m}^3$	$0.0032 \text{ kg/(m}\cdot\text{s)}$	$0.02547 \text{ N/m}$

In this arrangement the temporal response of the injector control assembly contributes timing jitter on the order of  $1 \mu\text{s}$  to the onset of each injection event. This systematic error was reduced by noting that jet penetration length for a high pressure Diesel injection is a linear function of time at early injection times. For each separate time delay case, the hydrodynamic starting time of the injection was extrapolated from the average jet penetration length, determined from sets of 200 images.

### Velocity by correlation

To produce reliable velocity information, it is important that the tracked structure in the time-correlated data be spatially resolved, i.e. reliably confined to a suitable spatial region, such that the intensity change in the images can be related to the real-world motion or morphology of the observed structure. The imaging approach used in this work allows in-focus structure to be resolved within an object plane along the line-of-sight of the measurement volume. Here, the laser source pulse and imaging optics which efficiently gather light from the center of the jet produce an imaged field which is dominated by the in-focus edges and droplets of the diesel spray (see Fig. 1b and c). These spatially resolved features appear superimposed on the (unfocused) line-of-sight intensity background. Thus, the optical transfer function of the optical arrangement makes it possible to differentiate resolved (in-focus) structure from the unresolved intensity contributions.

A variety of methods can be used to estimate the motion of resolved structure, and hence velocity, from successive time-resolved images. The results shown in this work are based on a region-matching approach which employs the normalized image cross-correlation given by:

$$\frac{1}{n-1} \sum_{y,z} \frac{1}{\sigma_I \sigma_T} (I(y,z) - \bar{I}) \cdot (T(y,z) - \bar{T}) \quad (1)$$

Here, ‘search field’ and ‘template’ image sub-regions,  $I(y,z)$  and  $T(y,z)$ , are chosen from images produced by consecutive laser pulses which are spaced appropriately in time to produce time-correlated image data.

Along with the desired features of droplets and the spray periphery, the images acquired by the optical system contain unfocused structure and regions which do not provide data suitable for correlation analysis. In order to generate clean velocity information the focused image features must be identified and separated from this unfocused background. For the results discussed here the in-focus regions are identified by keying on high frequency information in the shadow image spatial intensity allowing focused image regions to contribute to the region-matching analysis and discriminating against regions which lack high spatial frequency content.

Prior to analysis, the image data are normalized to the measured background intensity. The image from the first pulse is taken at time  $t_1$ ; the second pulse produces an image at time,  $t_2 = t_1 + \Delta t$ , where  $\Delta t$  is given by the time delay between each pair of laser pulses. A set of rectangular image regions are selected from the  $t_1$  image, and cross-correlated with a set of rectangular regions selected from the  $t_2$  image, to yield the  $dy/dt$  and  $dz/dt$  components representing velocity of resolved features confined to the object plane. Selection of appropriately located  $t_1$  image region windows is accomplished by applying edge detection to the shadow image intensity data to identify candidate regions which should be allowed to contribute to the dynamic analysis. Edge pixels selected by the detection scheme are randomly sampled to form template and search field image sub-regions which are processed to obtain correlation matchings. Here, the displacements of image spatial intensity indicated by the matching is assumed to be equivalent to liquid structure motion in the measurement volume.

In the next step of the analysis, the matching results and their associated image sub-regions are validated by a set of criteria which examine the spatial variance and texture energy of the image regions, as well as the correlation strength and bounds constraints of the matching results. With the exception of the bounds constraints, each of these validation criteria amount to a test of spatial information content for the tested region, with an associated threshold level which further discriminates image regions selected to participate in the analysis.

This velocity analysis is related to the correlation matching of particle image velocimetry (PIV) [5] and laser speckle imaging (LSI) [6]; however there are important differences which necessarily impact both the implementation of the analysis and the interpretation of the velocity results. One major aspect which differentiates ICV from PIV is the spatial form of the intensity data which is correlated. PIV takes advantage of a well-structured distribution of point features generated by seeding the region of interest. In contrast, the intensity fields matched in ICV often exhibit wide variation and correspond to non-point structure. In most cases, these spatial data exhibit distinct macrostructure and intrinsic scale information related to the dynamics of the fluid motion. Thus, ICV intensity fields generally include spatial information which is filtered by the procedure used to select and match data in the analysis. The work presented in the following section takes advantage of this aspect of ICV to generate velocity information specific to the motion of select spatial scales in the measured images.

### Spatial frequency response

The action of the image correlation process includes the explicit application of region selection criteria, as defined by the extent, shape, and position biases used to form the match template and search field correlation windows. The shape and size of these regions limit the range of the velocity results and applies an implicit weighting function to the spatial frequencies present in the image intensity data.

The effect of this weighting function is somewhat analogous to the low-pass filter action of an interval sampling function (box filter). For example, if a voltage signal is integrated over a small sampling interval, the resulting signal is a *sinc*-function-like low-pass response caused by the systematic cancelling of the positive and negative fluctuations of the voltage within the interval. In this case, if the sampling interval exactly matches one complete cycle of a sinusoidal signal, there is zero response.

The normalized cross-correlation of the matching procedure (Eqn. 1) measures contrasting intensity in a 2-D region, not absolute response as in the voltage measurement. However, if one computes the contrast of a full cycle of a black/white line-pair pattern at a spatial frequency that exactly matches the sampling interval (window size), the result is a full correlation response. If the line-pair in the  $t_2$  image is shifted, this response decreases. Smaller line-pairs (corresponding to higher spatial frequencies) placed within the window will contribute to the correlation response as well, but with a strength that is proportionate to their area with respect to the window size. Thus, the chosen regions contribute a band-pass weighting effect, with a naturally limited



correlation response to high-frequency content and a maximum low-frequency response set by the extent of the correlation windows. Larger windows allow lower spatial frequencies to affect the correlation, and minimize the effects of smaller variations in the image field. This weighted response can be further tailored by applying a blurring filter to the image data which further minimizes the influence of small-scale structure on the correlation results.

For measurements of small features or large sensor pixels, it is also important to note how the image data is discretized at the sensor pixel level, where each individual photo-active site represents a spatial domain sample of the imaged intensity signal. If the signal contains more than one half-cycle variation over the pixel size, the sampling of the sensor will cause frequency domain aliasing. This causes intensity from higher spatial frequency components of the signal to appear at inverted locations in the spatial frequency domain, reflected around the Nyquist frequency determined by the pixel size and separation [7].

Figures 2 and 3 show velocity vectors derived from liquid structures on the periphery of a fuel injection spray at four different normalized cross-correlation process sampling (windowing) conditions. In each of the four cases, the size of the search fields and match templates are increased while maintaining their relative sizes at a 3:1 ratio. The increasing correlation window sizes select resolved structure motion at different scales, resulting in significant variations in the vector magnitude statistics. Resulting in different views of velocity throughout the spray as the correlation process is optimized for different structure. In each case, a representative set of ~1k vectors are calculated using the same single-shot diesel spray image-pair, and shown together with the normalized velocity magnitude histogram constructed from the full 200 image dataset.

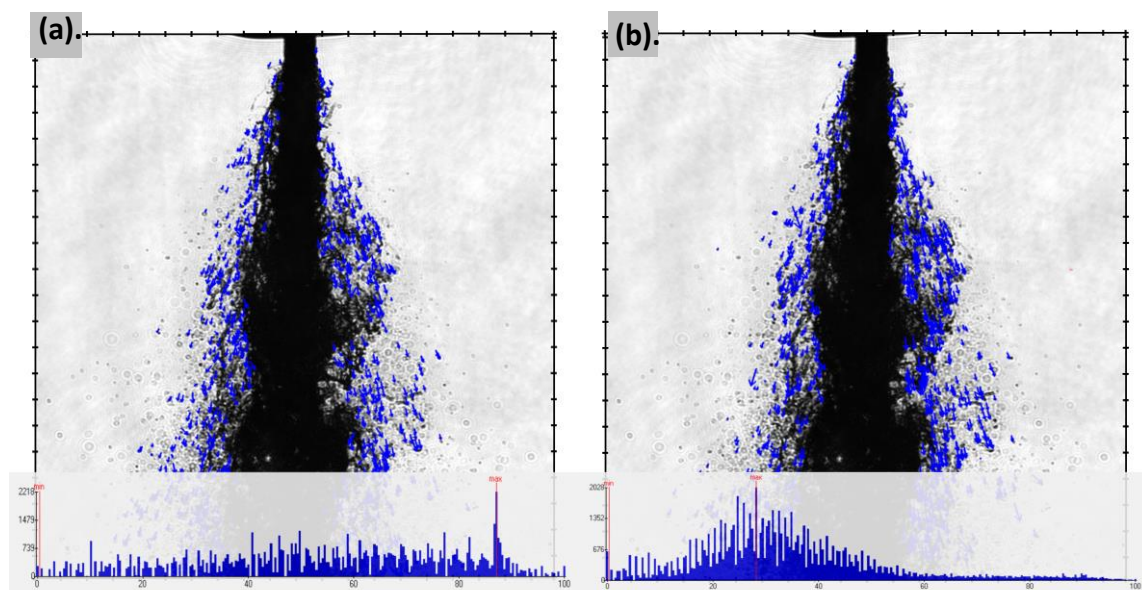


**Figure 2.** (a) USI result and velocity vectors computed using 20x20 pixel template regions correlated in a 60x60 search field. Histogram shows the range-normalized vector magnitude distribution derived from 200 images. (b) USI result and vectors computed using 40x40 pixel template regions correlated in an 80x80 search field, with vector magnitude histogram computed from 200 single-shot image-pairs.

The vector results shown in Fig. 1(a) were calculated with 20x20 match template windows correlated within 60x60 search field regions, corresponding to fluid structures in the 18  $\mu\text{m}$  range. Here the velocity vectors present a broad histogram, reflecting the relatively chaotic movement of small features and droplets dominated by the effects of turbulent energy exchange and small scale instabilities, as well as the rapid dispersion of small outlying droplets in the object plane at the spray periphery. By contrast, the statistics of Fig. 1(b) show a more regular histogram with a wide dominant mode. In this case, the vector results were calculated with 40x40 template regions correlated within 120x120 search field regions, corresponding to 36  $\mu\text{m}$  liquid features. The larger drops and short, or partially formed ligaments that dominate this range exhibit less fluctuation than the smaller features of Fig. 1(a), but still contain significant rapidly evolving structure as evidenced by the heavy tail of the magnitude distribution.

The vector results shown in Fig. 2(a) were calculated with 80x80 template regions correlated within 240x240 search fields. These features correspond to fluid structures as large as 72  $\mu\text{m}$ , and thus represent more general motion of edge regions and large ligaments in the spray. Here, the mode of the distribution is more narrowly distributed at lower magnitudes corresponding to the bulk motions of the spray column as it spreads downstream of the nozzle. The results of Fig. 2(b), which show vectors calculated with 100x100 pixel template windows in 300x300 pixel search fields, are even more narrowly distributed. Here the dominant features are as large as 90  $\mu\text{m}$  and the computed vectors reflect the steadier progression and movement of the large-scale spray structure.

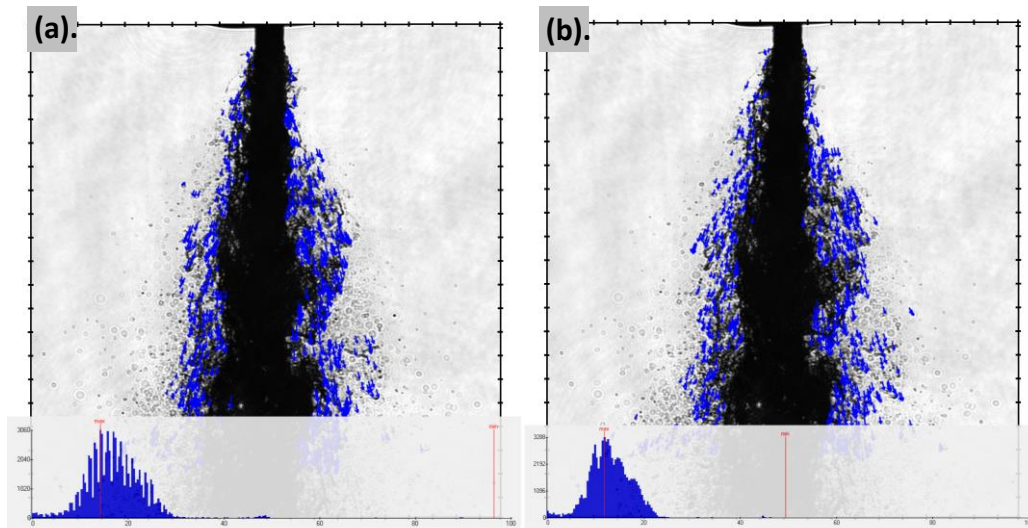


**Figure 3.** (a) USI result and velocity vectors computed using 80x80 pixel template regions correlated in a 240x240 search field. Histogram shows the range-normalized vector magnitude distribution derived from 200 images. (b) USI result and vectors computed using 100x100 pixel template regions correlated in a 300x300 search field, with vector magnitude histogram computed from 200 single-shot image-pairs.

## References

- [1] Tokumaru, P., Dimotakis, P., Image correlation velocimetry, *Experiments in Fluids*, 19:1-15, 1995.
- [2] Sedarsky, D., Idlahcen, S., Rozé, C., Blaisot J-B., Velocity measurements in the near field of a diesel fuel injector by ultrafast imagery, *Experiments in Fluids*, 54(2):1-12, 2013
- [3] Sedarsky, D., Idlahcen, S., Blaisot J-B., Rozé, C., Planar velocity analysis of diesel spray shadow images, *arXiv:1203.5347 (physics.flu-dyn)*, 2012.
- [4] Settles, G., *Schlieren and Shadowgraph Techniques*, Springer-Verlag, Heidelberg, Germany, 2001.
- [5] Adrian, R.J., Westerweel, J., *Particle Image Velocimetry*, 2010.
- [6] Zakharov, P., Völker, A.C., et al., Dynamic laser speckle imaging of cerebral blood flow, *Optics Express* 17(16):13904-17 (2009).
- [7] Goodman, J., *Introduction to Fourier Optics*, 3<sup>rd</sup> Ed., Roberts and Co., Englewood, Colorado, 2005.

## Experimental studies on behaviour of bubble plume

Prasad. C, Shamit Bakshi and Dhiman Chatterjee

Department of Mechanical Engineering, IIT Madras, India

### Abstract

In this work experiments are conducted to study in details the behaviour of bubble plumes under different parametric conditions. Through visual observation, the transition behaviour of the bubble plume under different parametric conditions like source width, gas flow rate and free surface height of water are studied. The bubble plume is generated by electrolysis process since uniform size of bubbles can be generated by this process and is suited for transition studies. A descriptive detail of the plume transition based on the combined effect of gas flow rate and source width, free surface height is presented. With the increase in gas flow rate, earlier transition of bubble plume is observed. And the source width also has a distinct effect on the transition of the plume. The present experimental results are also compared with the existing literature.

---

### Introduction

A bubble plume is defined as a continuous flow of rising bubbles by buoyant force. Such plumes are commonly employed in wastewater treatment, mixing of hot and toxic liquids and destratification of lakes and reservoirs. The general flow patterns of the bubble plume in a liquid medium can be categorised in three different regimes as homogeneous, transition and heterogeneous[1, 2]. Homogeneous regime is characterized by uniformly sized small bubbles travelling vertically with minor transverse and axial oscillations. In the transition regime, the bubble does not rise vertically, and they begin to coalesce and break up at a certain height. Heterogeneous regime is one where the bulk liquid circulation, coalescence and break up of bubble occur. However their hydrodynamic characteristics and inherent nature can be studied through experiments.

### Experimental test-rig

A schematic representation of the experimental setup is shown in Figure 1. It consists of a tank with square base, electrode arrangements, laser lighting arrangement and a CCD camera. The DC power supply of 0-30V, 0-5 amps with a resolution of 100mV and 10mA is used to vary the current across the electrodes. The electrode arrangement consists of anode made of copper clad laminate (110mm X 30mm), a cathode made of copper sheet embedded in the perspex. The length of the cathode is kept constant as 125mm and the widths are varied as 0.04mm, 0.1mm, 0.5mm respectively. Both the anode and cathode are flush mounted in the electrode holder which is located at the centre of the tank. The anode is kept upside down in order to prevent the rising oxygen bubbles so as to study the hydrogen bubble plume alone. For transition studies a light sheet using a continuous wave laser (5mW power 532 nm wavelength) is used. The images were taken using CCD camera with a 16 mm focal length lens and a frame speed of 60. Bubble plume is generated by passing current across the electrode from DC power supply (electrolysis of water). Experiments were conducted for different gas flow rates (0.0205, 0.0381, 0.04119, 0.0514, 0.0614, 0.0719, 0.0822 and 0.0925 mm<sup>3</sup>/s/mm), for three different source widths (0.04 mm, 0.1mm and 0.5 mm). The flow rate of the plume is controlled by adjusting the current and is calculated using Faradays law of electrolysis. All the experiments are performed under atmospheric conditions.

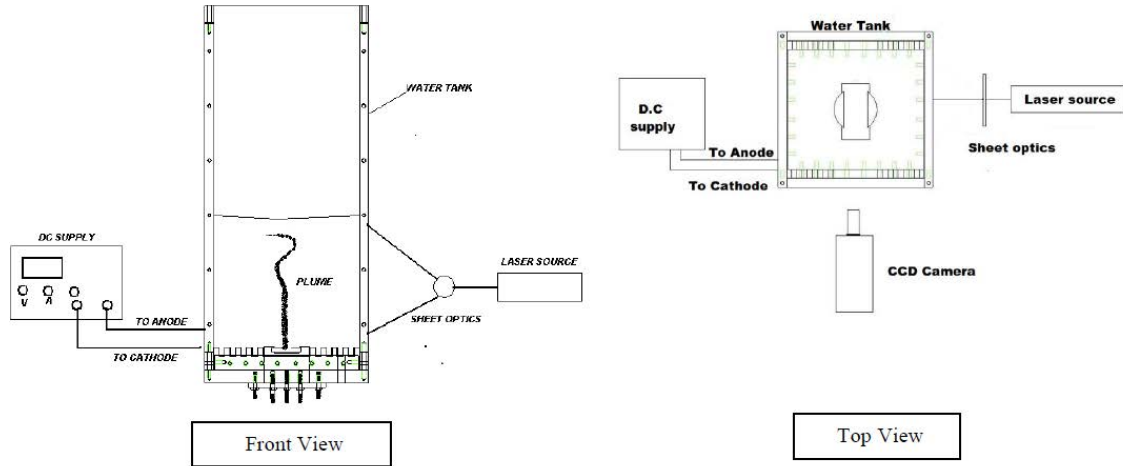


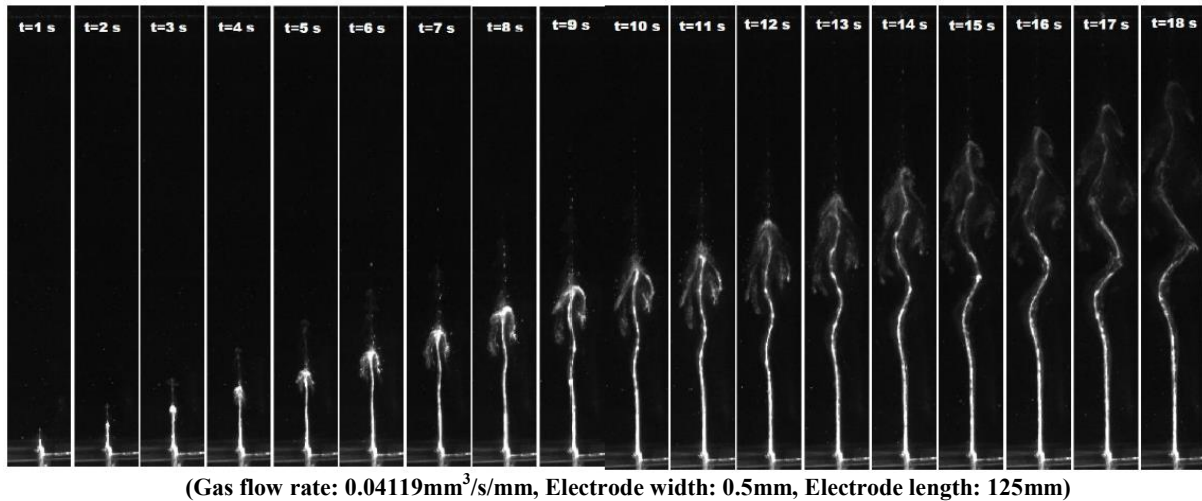
Figure 1: Schematic of experimental setup

## Results and Discussion

### Transition studies

The snapshots of the images taken after the inception of bubble plume for the flow rate of  $0.0411 \text{ mm}^3/\text{s}/\text{mm}$  is shown in figure 2. It is noted that, the plume has a tendency to lose its structure at certain height after some time period in the water tank (i.e., the steady nature of the plume was disturbed). In other words, the height at which complete dispersion of the bubble plume occurs can phenomenally said to be the transition of the plume from the source, considering that there is no further relaminarization of the bubble plume. The parameters such as gas flow rate, source width and the free surface height of water that influences the transition were studied from the present experimental observations.

Figure 2: Sequence of images of bubble plume after inception



The transition height for all the cases were calculated by analyzing a sequence of images over a time period and averaged, since it is difficult to obtain the transition height from a single image as the plume oscillates from time to time. The combined effect of free surface height and the gas flow rate is shown in Figure 3. For a free surface height of the 15 cm, we observe no transition of the plume for lower flow rates. It is observed that, as the gas flow rate is increased the transition of the bubble plume occurs earlier. It is seen that the free surface height does not significantly affect the transition for 0.5mm source width except for lower gas flow rates. However, for 0.04mm source width, difference in transition height is observed.

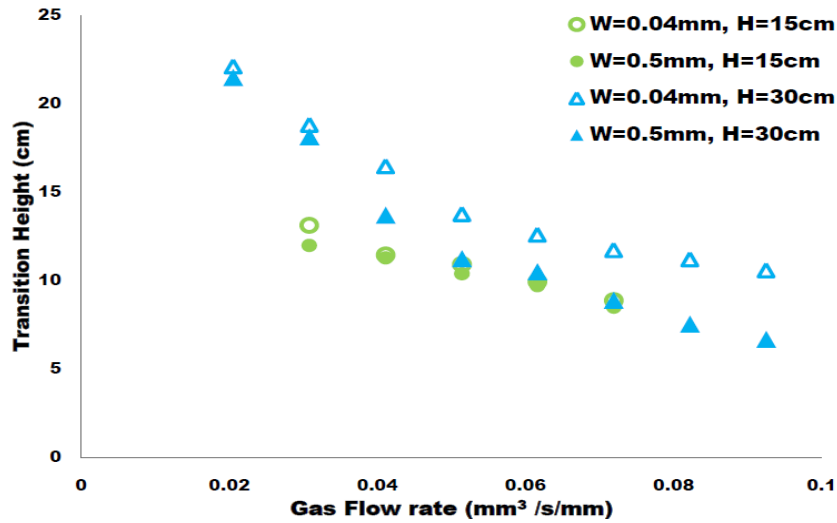


Figure 3: Effect of gas flow rate and free surface height on transition of bubble plume

The present experimental results were non-dimensionalized, normalized and compared with the data from the literature [3]. By dimensional analysis, the Grashof number based on source width is defined as [3] ( $Gr_0 = (gW^3/\nu^2) * \epsilon_0$ ). For the present experimental studies the bubble size is taken as  $150 \mu m$  [3]. Figure 4 shows the correlation of non dimensional transition height with source Grashof number for the present studies along with the literature data. It is noted that the transition of the bubble plume are in good agreement with the the data in literature and the correlation can be extended to much lower Grashof numbers.

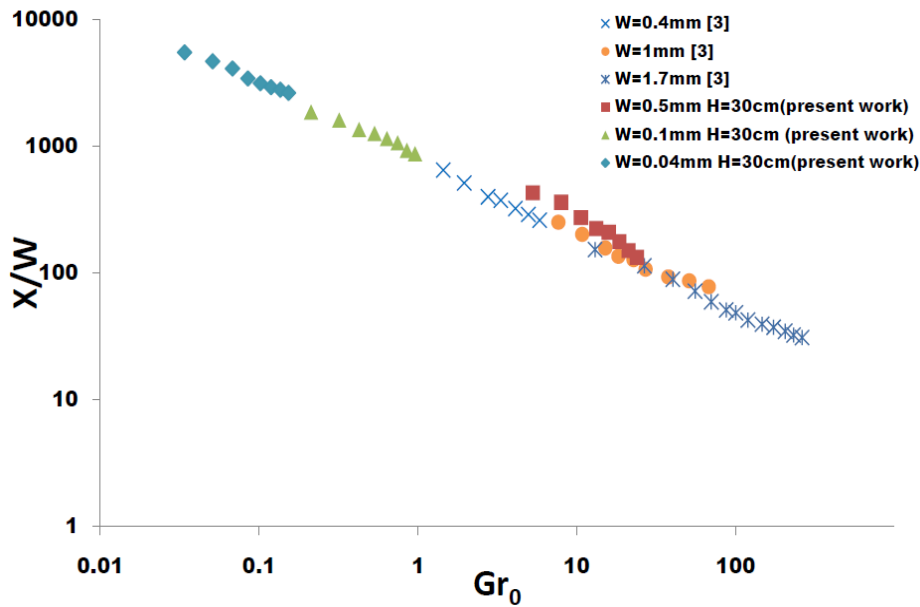


Figure 4: Non-dimensional correlation of transition height with source Grashof number.

## Conclusions

Experimental results for transition of bubble plumes are presented in this document. The transition height is seen to decrease with increasing gas flow rate. The correlation for transition height with Grashof number as proposed in earlier literature [3] is seen to extend to lower Grashof numbers.

## Nomenclature

$Q_g$  = Gas flow rate ( $\text{mm}^3/\text{s}/\text{mm}$ )  
 $W$  = Width of the source (mm)  
 $X$  = Transition height (cm)  
 $H$  = Free surface height (cm)  
 $Gr_0$  = Source Grashof number  
 $\varepsilon_0$  = Void fraction

## References

- [1] Díaz, M.E., F.J. Montes, and M.A. Galán, *Experimental study of the transition between unsteady flow regimes in a partially aerated two-dimensional bubble column*. Chemical Engineering and Processing: Process Intensification, 2008. **47**(9-10): p. 1867-1876.
- [2] Shaikh, A. and M.H. Al-Dahhan, *A review on flow regime transition in bubble columns*. International Journal of Chemical Reactor Engineering, 2007. **5**(1).
- [3] Alam, M. and V.H. Arakeri, *Observations on transition in plane bubble plumes*. Journal of Fluid Mechanics, 1993. **254**: p. 363-374.
- [4] Rensen, J. and V. Roig, *Experimental study of the unsteady structure of a confined bubble plume*. International Journal of Multiphase Flow, 2001. **27**(8): p. 1431-1449.

## Scale formation Mechanism and Removal Using High Pressure Water Spray Jets

A.J.Abbas, G.G.Nasr, A.Nourian and G.C.Enyi

Spray Research Group, School of Computing, Science and Engineering,  
University of Salford, Manchester, M5 4WT

### Abstract

Scale formation along oil and gas production tubing has been one of the greatest challenges encountered during oil and gas production, which results in the partial or total blockage in cross sectional area of flow, and high pressure drop, thereby reducing the production rate to nearly zero in some cases, causing huge loss due to decline production rates. Several attempts have been made by various researchers and companies involved, with either mechanical cleaning as an option or chemical/acid addition as inhibitors and dissolvers, until recently, the use of high pressure jetting technique was chosen for reduced residual effects to the mechanical integrity of the tubing, as well as environmental benefits.

However, this research work investigate the mechanism of scale formation to ascertain the scale prediction and timely removal using high pressure jets , with scale precipitation test based on temperature, PH as well as salinity effects. Calcium carbonate (hard scale) subjected to 100°C and varying salinity level, 50.8g of the scale was formed within 48hours of settlement and deposition, which was removed completely. Also a paraffin scale as often formed in gas production, formed through solidification wax subjected to jet pressure from 60bar (6MPa) to 140bar (14MPa), with most of the scales removed only from 100bar(10MPa) above. Also, the scale cleaning set up was used to investigate the angular orientation of nozzles at 60 and 90° to horizontal, at range of pressure from 60bar (6MPa), 100bar (10MPa) and 140bar (14MPa). Findings from these experiments confirm 90° nozzle scale cleaning to be efficiently higher than the 60° orientation, also that timely scale removal is the most efficient approach using high pressure spray jets as the scale mechanical properties changes with time due to stronger bond formation when left for long, and will be difficult to remove.

---

### Introduction

The production rates of oil and gas wells tend to decline as time progresses. The major cause of this decline is as a result of natural or induced mechanism being imposed during the production of Oil and Gas from the reservoir to surface facilities [1]. Natural influences are as a result of change in physical and chemical characteristics in situ in the presence of produced water. While, induced mechanism can be as a result of well completions, production activities and secondary recovery techniques like water injection which can lead to scale formation as incompatible waters meet [2].

Over decades, scale formation has been as a major predicament in the decline of production rate in Oil and Gas wells. These scales are experienced from the reservoir to downstream facilities and majorly in wellbores [6]. Scales occupy significant portions of these facilities from subsurface to surface thereby restricting the optimum retrieval of hydrocarbon and causing hundred to millions of dollars to be lost by production companies yearly [5].

In recovering oil and gas, millions of dollars have been spent in exploring, drilling, developing and producing hydrocarbon. Oil companies' work toward maximizing profit by gaining back their initial investment and realizing a positive cash flow as time progresses, but the dilemma being faced due to scale formation could reduce company's investment and assets. Various inhibiting and removal techniques have proven to be quite effective [3;4], though some of these removal techniques still initiate some problems in terms of reduction in the value of production equipment, hence other scale removal techniques are analysed and discussed in this work which aids optimised recovery of hydrocarbon without damage to facilities and hence efficient recovery of company's investment.



## Experimental Set-up

### (A) Scale Formation Mechanism Experiment

Long tubing of 2-inches internal diameter was prepared for this experiment. The laboratory oven was pre-heated at 100°C before the start of the experiment. The weighing balance was put on and allowed to attain its sensitivity of 0.0gram. The weight of the empty tubing was then measured. Tubing containing 1.6g CaCO<sub>3</sub> repeated with 1.6g CaCO<sub>3</sub> together with 10g NaCl, and also 1.6g CaCO<sub>3</sub> together with 50g NaCl. The weight of the NaCl and CaCO<sub>3</sub> samples used for the experiment was measured. 400ml of distilled water at 100°C was measured in a measuring cylinder. 400ml water was poured into a beaker and the salt was mixed thoroughly in the water with a spatula bit by bit until the first undissolved particle appeared in solution. 1Molar solution of NaOH was prepared using 4g in 100ml of water. The pH of the NaOH solution and mixed calcium carbonate samples were measured. The pH of each carbonate sample was increased to about 10, with the NaOH solution. Each mixture was poured into the appropriate closed tubing. The solution was left in the tubing inside the pre-heated oven for 24 hours, till well dried. The weight of the tubing was taken after 24hours. The difference in the weight of the tubing before and after the experiment indicates the approximate weight of scale form

### (B) Scale Cleaning Experiment

To prepare the candle wax for the experiment; the candle wax was first heated in a steel rectangle pan in order for it to take the shape of the pan. After cooling, the scale sample was placed and secured in the upper transparent Perspex tube of the simulated experimental apparatus. This was adopted only for the candle wax, as part of initial preparation for the volume scale removal trials.

The connections of all experimental components are appropriately situated as in Fig. 3 and 4, i.e. spray head, water tank and water pump, the scale sample was then placed on the aluminium base flange and secured in position, the spray head adjusted to the 25mm required downstream distance from the scale sample, the scale sample with the aluminium base assembly was correctly placed to coincide with the vertical axis of the atomiser, fitted to the spray head, the water pump was bled with the hydraulic line to release air bubbles by turning on the pump and this was carried out to remark any occurring cavitation. The inter connection of the hydraulic hose from the water pump to the spray head and to the water tank back to the pump is connected properly and tight firmly. Image of each scale sample was taken, using still canon camera, before and after each test run. The water pump was turned on first, at an initial spray at low flow rate 8.7 l/min. and pressure 60bar (6.0 MPa), and then adjust until the desired flow and pressure were obtained. After 5 minutes with the aid of a stopwatch switch off the water pump and then collect the particles of scale removed from the scale sample through a sieve positioned on top of the water tank. The particles of scale sample collected by the sieve were dried and weighed with a weighing scale (range  $\pm$  (0.1g)). Image of the scale sample was taken again after test run. The procedure was then repeated the above for desired pressures using one flat fan spray nozzle respectively for 5minutes. Record the different reading of each test run of the experiment for further analysis. Repeat and apply all the above procedures on different scale samples Repeat and apply all the above procedures on the Candle Wax Scale Sample by applying different angles (60° and 90°).

## Results and Discussion

### (a) Scale Formation Mechanism

This experiment indicated the effect of Temperature, pH and NaCl on formation of CaCO<sub>3</sub> scale. Fine powder of CaCO<sub>3</sub> was used for the experiment to allow for the precipitation of CaCO<sub>3</sub> from solution. The same quantities of fine CaCO<sub>3</sub> samples were used in different tubing to analyse the effect of temperature, pH and various quantities of NaCl which aid in the formation of calcium carbonate scales.

Table 1 can show that, the formation of scales increased as a result of increase in the amount of dissolved NaCl in solution with dissolved CaCO<sub>3</sub> samples under relatively high temperature of 100°C with a pH of about 10, this is better analysed using Fig. 1 and 2 from which is a positive linear relation of scale deposited against NaCl in solution, this shows the effect of NaCl on scale deposition indicating the relationship of proportional increase of NaCl in solution with increase in scale deposition. The formation of calcium carbonate scale is dependent on the quantity of NaCl in solution, further increase in the quantity of the NaCl also lead to more rough and difficult scale on pipe surface. The reverse is the case when comparing the effect of NaCl on already formed CaCO<sub>3</sub> and on CaCO<sub>3</sub> in solution at 100°C. Hence, comparing this with the former, the scale formed in increasing order.



**Table 1:** Scale formation test

Sample	Weight(g)						
	NaCl (g)	CaCO <sub>3</sub> (g)	Empty Tubing	Tubing 48hrs after (g)	Tubing with sample(g)	Evaporated Water (g)	Scale formed (g)
A	0	1.6	2242.60	2243.60	2609.41	366.81	1.00
B	10	1.6	2086.70	2097.70	2474.7	388.00	11.00
C	50	1.6	2499.10	2549.9	2907.9	408.80	50.80



**Figure 1** Tubing sample before the experiment



**Figure 2** Tubing sample after the experiment

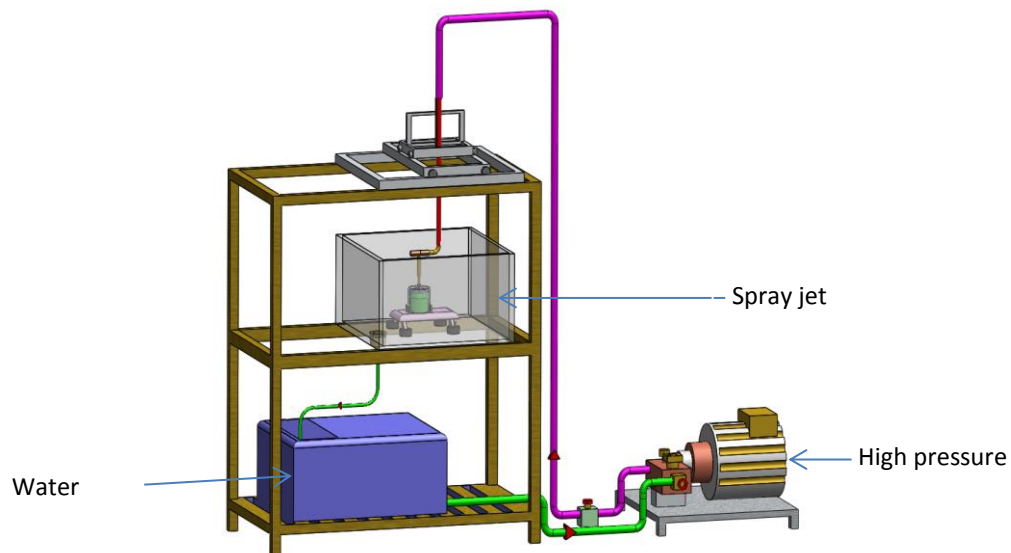


**Figure 3** Experiental rig

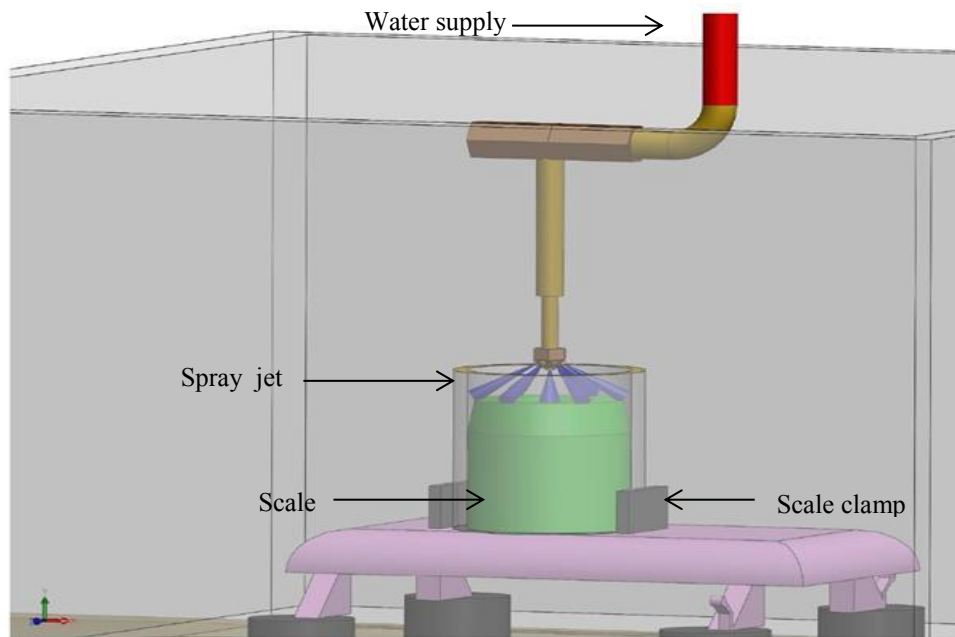


**Figure 4.** Spray Chamber

**Table 2** Scale cleaned at 90° at various pressures

Pressure (bar)	Nozzle height	Duration (min)	Angle(Degrees)	Volume of scale removed(cm <sup>3</sup> )
60	25	5	90	0.2
100	25	5	90	1.9
140	25	5	90	12.3

**Table 3** Scale cleaned at 60° at various pressures

Pressure (bar)	Nozzle height	Duration (min)	Angle(Degrees)	Volume of scale removed(cm <sup>3</sup> )
60	25	5	60	0.5
100	25	5	60	1.2
140	25	5	60	2.2

**Table 4** Scale removed at 60bar for various cleaning times

Pressure (bar)	Nozzle height	Duration (min)	Angle(Degrees)	Volume of scale removed(cm <sup>3</sup> )
60	25	5	90	0.5
60	25	7.5	90	0.6
60	25	10	90	1.1

**Table 5** Scale removed at 100bar at various cleaning times

Pressure (bar)	Nozzle height	Duration (min)	Angle(degrees)	Volume of scale removed(cm <sup>3</sup> )
100	25	5	90	1.9
100	25	7.5	90	12.8
100	25	10	90	16.1

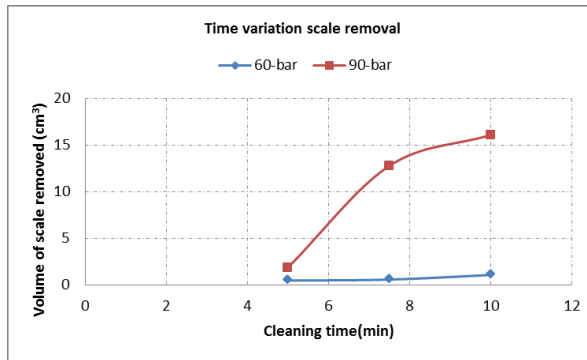


**Figure 5** Scale removed versus time

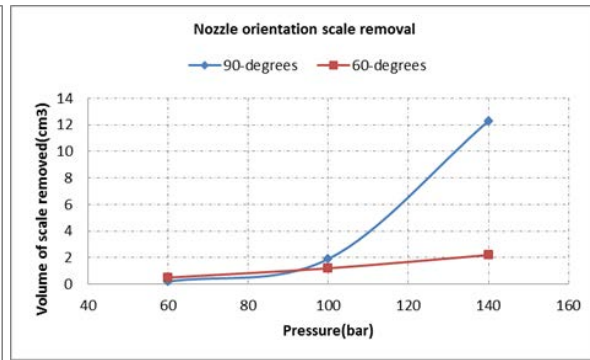


**Figure 6** Scale removed versus pressures

Fig 5 shows the compare of the 60bar and 100bar in 90 degrees positionat 25mm from the nozzle. With respect the wax, improve the pressure is the most direct factor of descaling effect. The 100bar in 7.5min is about twenty (20) times than 60bar in 7.5min, and 100bar in 10min is sixteen(16) times than 60bar in 10min. Improve a bit of pressure are able to reach an increase of the original 16-20 times cleaning efficiency, and if calculate the cost, 100bar should use more power and more water, but the descaling efficiency of 100bar is about ten times of 60bar.

Fig 6 shows the 90 degrees and 60 degrees at 25mm from the nozzle in different pressure. From the 60bar and 100bar, there are mostly same between the 60 degrees and 90 degrees. When the pressure increase to 140bar, there is higher cleaning efficiency at 90 degrees because a scale collapsed violently.

When the experiments in 90 degrees at 25mm do from the nozzle and the time is 5 min appear a scale collapse violently, but in 60 degrees is not. If the reasons for these causes is material itself such as uneven destiny of the all wax and the part of wax may has some voids or impurities due to fracture mechanics, hence may why has a scale was removed violently when the pressure is not reached enough damage wax. Although the surface of the wax is not smooth because the certain parts of the contraction the by the wax cooling process. The high pressure water is difficult to act in one point when wax surface smooth enough. When the surface is not smooth, it is easy to act at a point.

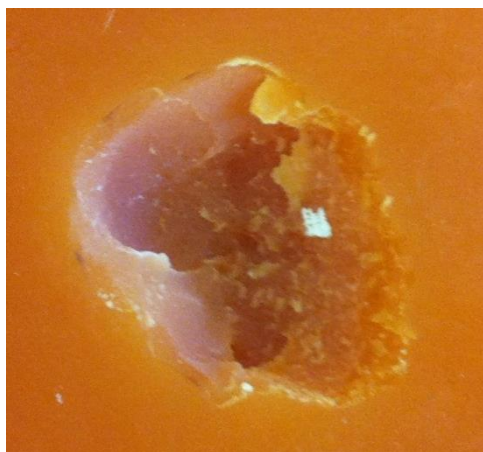


**Figure 7** Smooth scale surface



**Figure 8** Rough scale surface

The Fig.7 is shows on a smooth surface and it is clearly to see the bottom of the hole is very coarse and it is explanation the high pressure water can not concentrated in one point. The Fig. 8 is shows rough surface and the bottom of the hole is very smooth and has a little deeper than Fig. 7. Regardless of any type of scale, increase cleaning time or to increase the pressure both can achieve the purpose of descaling the Scale deposition. Research may find the critical point as certain action to improve the cleaning time can cause a lot of waste of water resources. If continuously improve pressure will not improve the cleaning efficiency, when the pressure has reaches a certain level. How to find the balance between the time and pressure cannot be ignored. From the experiment of the pressure is 60bar in 90 degrees at 25mm from the nozzle. The efficiency of 100bar in 5min is more higher than 60bar in 10min. According to the fouling characteristics depending on how much pressure. If scaling hardness such as crystallization scaling may require higher cleaning pressure and optimum nozzle design and orientation.

## Conclusions

Findings from the investigation confirmed that the scale growth and hardening are subject to PH and salt concentrations, which varies from one oil reservoir to another. Also scale cleaning processes seems more efficient for soft scale such as wax hydrocarbon when the nozzle is placed at 90° to the horizontal instead of 60°, although future research is recommend to check their combination

## Acknowledgements

The author wishes to thank the Spray Research Group (SRG), and the Petroleum Technology Development Fund (PTDF) for their technical and financial support for this investigation.

## Nomenclature

$CaCO_3$	Calcium carbonate
C	Centrigrade
g	gramme
l/min	Litres per minute
M	Molar
mm	millimetre
min	Minute
NaCl	Sodium Chloride
NaOH	Sodium Hydroxide
pH	Power of Hydrohen

## References

- [1] Yuping, Z. et al (2001) The Kinetics of carbonate scaling – application for the prediction of down hole Carbonate scaling, *Journal of Petroleum Science and Engineering* 29, 85-95.
- [2] Nasr, G.G., Burby M, and Giri, S. (2007), Descaling of Well head Production Tubing using High Pressure Water Atomisers, Spray Research Group, Institute of Materials Research (IMR), School of Computing, Science and Engineering (CSE), University of Salford, Manchester.
- [3] Collins I.R. and M.M.Jordan, M.M. (2003) Occurrence, Prediction, and Prevention of Zinc Sulfide Scale Within Gulf Coast and North Sea High-Temperature and High-Salinity Fields, *Society of Petroleum Engineers*, Volume 18, No.2, August, pp. 200-209.
- [4] Fan C., et al, (2012) Ultra high-Temperature / Ultra high -Pressure Scale Control for Deepwater Oil and Gas Production, *SPE Journal*, Vol. 17, no.1, March, pp. 177-186.
- [5] Akanji, L. (2012), Petroleum Geology Slide, Geology, Exploration, Drilling and Production, School of Computing Science and Engineering, University of Salford, Manchester.
- [6] Ramstad K., Tydal T., Askvik K.M., Fotland P., (2005) Predicting Carbonate Scales in Oil Producers from High-Temperature Reservoirs, *SPE Journal*, Vol.10, No.4, December, pp. 363-373.

## Investigation of some primary atomization aspects using double exposure and double view processes

S. Makhoul<sup>1</sup>, J. H  lie<sup>1</sup> and J. Cousin<sup>2</sup>

1: Continental Automotive SAS, Toulouse, France

2: CORIA laboratory, Rouen, France

### Abstract

A close-up imagery technique based on a double exposure coupled with a double view is presented. A 3-hole sharp edge inlet injector is used to atomize n-heptane. Low pressure gasoline primary breakup is investigated in the present work. The spray is photographed from two different axes thanks to a semi-transparent mirror that divides the light beam. A couple nanolite spark lamps are installed as sources of two superimposed flashes with a controllable delay that suits the spray displacement. Images are post treated in three different manners and the results discussed in this work concern the spray angles, the particle relative displacement, the droplet size as well as the continuous liquid interface. Spray angle results prove that the jet is symmetric. However, the dispersed phase results present a difference between both sides of the continuous liquid core. This shows the effect of the pre-developed cavitation on the primary breakup process. The continuous core progresses in conical shape with rotational motion until 10 orifice diameters where it starts to tear into ligaments and releases droplets.

### Introduction

In order to improve the understanding of spray atomization, in the case of high pressure gasoline multi-hole injectors, the primary breakup is one of the most important points to investigate. In the present study, the spray is analyzed in a close view by direct imaging shadowgraphy. A two-color double pulse technique used to follow the spray motion in a small time interval. This technique has been developed a long time ago using laser sheet illumination. It was first performed aiming to study spray plume propagation in diesel fuel injection [1]. It has also been applied to look at the flow through a turbine cascade [2] and at a jet produced by an air assist piezoelectric atomizer [3]. In this technique a particle-laden flow-field is doubly exposed with coincident two color laser sheets. There are many laser techniques used to measure droplets velocity. However, some do not provide velocity and size simultaneously such as laser diffraction and scattering measurements [4]. But most importantly is that laser techniques like PDA are not suitable for near nozzle continuous liquid core behavior studies. Therefore, we opted to use two nanolite spark lamps from HSPS Company in Germany instead of laser sheets. Marmottant et al. [5] used a couple of xenon flash lamps to investigate the spray formation. In the present work the development of a doubly exposed and doubly photographed near nozzle jet system, as well as shadowgraph images post-treatment analysis are reported with the aim of studying the spray primary atomization of the continuous liquid core. Imaging techniques offer many advantages, such as the capability of analyzing droplets independently of their size and identifying liquid core edges simultaneously, the easier optics alignment – in comparison to laser techniques – which will be presented in the experimental set-up section. Meanwhile shadowgraphy imaging techniques may also introduce some errors due to particle volume projection for instance and uncertainty in distinguishing overlapped particle images from a single one, which are not taken into consideration in this work.

### Experimental test-rig

The experimental close-up bench used in this study is the same as the one used in former work [6], although it is equipped with a box that contains two nanolite lamps rather than one. As shown in figure 1, the box package delivers two light beams geometrically superposed. In front of each nanolite, a color filter is added to distinguish each light beam. A blue filter that allows lower light wavelength to travel is installed in front of lamp 1, while an orange filter cutting wavelengths under 550 nm is inserted in front of the second lamp. Having the control over both flashes, we can choose the initial time and the interval that separates them in a way that suits the injection duration and the injection velocity. In

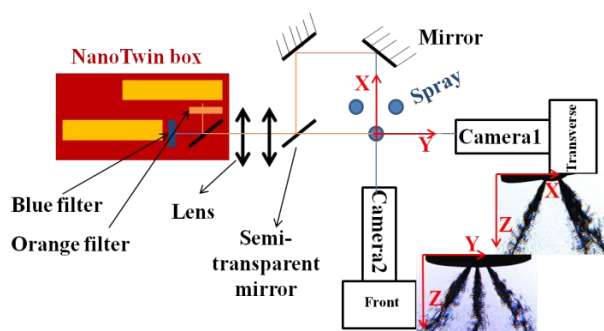


Figure 1 : Experimental set-up for double view axis and double color exposure.



order to visualize the spray on both cameras placed on two axes at 90°, a semi-transparent mirror is used to divide the light beam at the exit of the box into two beams. One of them continues straight forward in the direction of axis 1 (injector – camera1), while the second beam is switched towards two other mirrors that conducts it into the direction of axis 2 (injector – camera2). Identical RGB 3x8bits cameras - CMOS Nikon D300s - equipped with a lens of 105 mm focal distance are used. The resolution is 2  $\mu\text{m}$  per pixel for an image size of 4288x2848 pixels. Flash duration is short enough to freeze the flow on the recorded images. The first flash comes from the (nanolite – orange filter) pair at  $t_0$ . The second flash comes from the (nanolite – blue filter) pair at  $t_0 + \Delta t$ . It allows us to obtain a doubly exposed jet image on the same frame on each camera. This means that a “blue jet” precedes the “orange one” contrary to the flash delay order. This reversal in color order is due to the fact that flashes are crossed in shadows as shown in figure 2. The injector used in this study has sharp edge nozzle inlets,  $L/D$  ratio of 2.2, three holes of 0.2 mm in diameter  $D$  and 30° angle between hole direction and its central axis. At 5 bar, the injector discharge coefficient and mass flow rate are 0.7 and 1.53 g/s respectively. Its central axis is inclined of 8° in respect to the vertical line of the transverse view in order to get a sharp caption of the middle jet in the front view. Note that this injector axis position is 1° inclined in respect to the vertical line of the front view. This inclination could not be seen before image post-treatment. N-heptane of vapor pressure  $P_v$  equal to 0.047 bar at 20°C is injected at 5 bar only. Aiming for droplet sizing, the light beam should be parallel all the way through the injector tip and camera lens. Therefore, two lenses were installed before the semi-transparent mirror to obtain a cylindrical light beam of 1 cm in diameter to enlighten the injector tip identically from both axes.

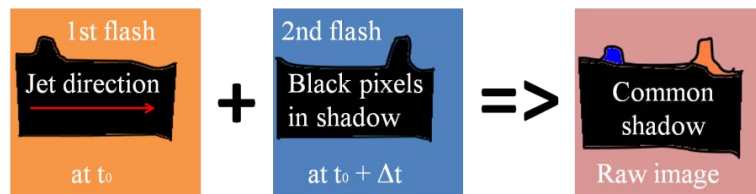


Figure 2: Raw image construction.

### Droplet and ligament phenomenology

Figure 3 is a post treated raw image showing a portion of the spray at two different instant. This portion is from 2.8 to 4 mm underneath the injector. The blue liquid patterns correspond to the initial time  $t_0$ . In red, the same patterns are frozen as they look like 12  $\mu\text{s}$  later on. The delay choice is such as the ligament breakup occurs between the two flashes. As shown here, particles released from the primary atomization are not always well shaped circular droplets. As the jet propagates in the axial direction  $Z$ , crests are developed transversally and elongated into ligaments. As the ligament expands, its width decreases until it tears in many smaller particles of different shapes. This is what can be seen in case number 1 on top of figure 3. A ligament can also have a different fate such as the one shown in figure 3 second case. In this case the ligament is not fragmented into several smaller ligaments and particles, but rather keeps its shape unchanged while releasing a single droplet. The radial kinetic energy of the jet stores a liquid volume at the far end of the ligament which becomes a free droplet due to its momentum which is large enough to overcome the capillary forces.

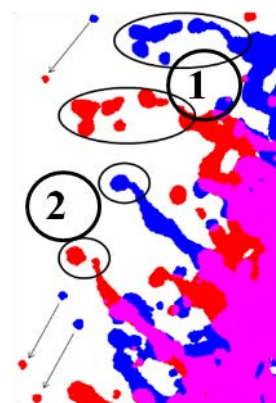


Figure 3: Post-treated raw image (transverse view, delay 12  $\mu\text{s}$ ).

### Image Analysis

As presented in figure 1, raw images given by both cameras are identical, although those coming from camera number two are less contrasted because of the light intensity loss after reflection over mirrors. Therefore, the light sensitivity of the second camera was increased. The emission-spectrometer of nanolites is presented in figure 4 by a cloud of dots. The (nanolite – blue filter) pair spectrometer is presented on the same graph in blue dashed line. While the (nanolite – orange filter) curve which reaches an intensity peak of 1.2 at 600 nm is in orange straight line. An interval from 500 to 580 nm of light wavelength is common for both spectra. When we split the raw image in its three grey color channels, we obtain the red liquid in the blue channel grey image, and the blue liquid in the red channel grey image. The green one is useless as its grey image shows both liquids. Since then, for each shot we obtain two grey images from each view and each image corresponds to the jet at a given instant. This post-treatment was applied on images from a

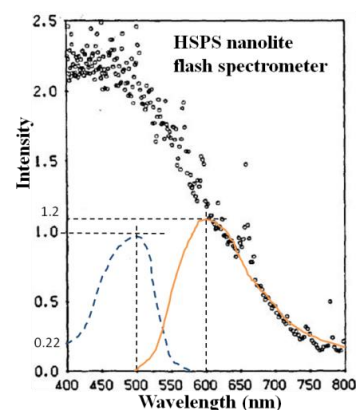


Figure 4: Emission-Spectrometer.

doubly exposed calibration target installed in place of the injector in order to apply the calibration procedure as presented by Blaisot et al. [7, 8]. This target contains particles with diameters that vary from 10 to 90  $\mu\text{m}$  and the process was conducted by ensuring that they are on the camera focus plane. Once the position of the sharpest image is found for both cameras, an evaluation of droplet sizing was obtained for both light beams and results are presented in figure 5. It compares the results of the droplet sizing measurement accuracy for a standard nanolite as well as for the 2 pairs of nanolite-filter used in this experiment. The  $x$  axis contains the real diameter  $D_r$  of particles on the calibration target. The  $y$  axis shows the ratio of the measured diameter over the real one. As we can see the bigger the real diameter is, the more accurate the measurements are. The worst scenario is for droplets of a diameter smaller than 10  $\mu\text{m}$  where the blue liquid overestimates the real droplet size by less than 10%. The post treatment conducted on flow images in the present study can be organized in three stages. First, a post treatment similar to the one detailed in a previous article [6] that allows to measure different spray direction angle definitions. Second, a post treatment splits each shot-to-shot binarized image to separate its dispersed phase from its continuous liquid phase as explained in [6]. Each phase is then analyzed separately. Finally a PIV analysis is conducted on the dispersed phase using DirectPIV software provided by R&D vision [9].

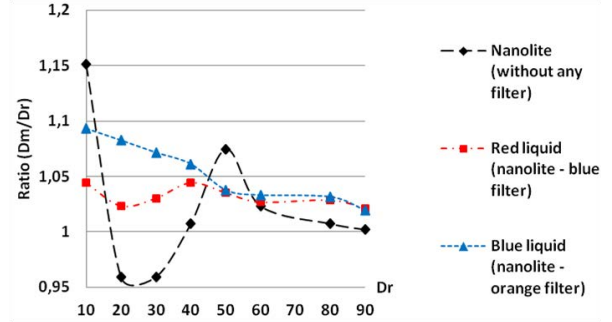


Figure 5: Calibration process accuracy.

### Theoretical velocity estimation at nozzle outlet

Applying Bernoulli's equation between the orifice inlet and outlet sections yields to the theoretical liquid velocity  $u_t$  at nozzle outlet (Eq1). The discharge coefficient  $C_D$  is the ratio between the measured mass flow  $\dot{m}_f$  and the theoretical one (Eq2). It can also be written as the product of the velocity coefficient  $C_v$  that takes into account the loss in velocity and the outlet area ratio  $C_a$  that incorporates the loss of liquid area at the nozzle exit section as demonstrated by Payri et al. [10, 11] (Eq3).

$$u_t = \sqrt{2(P_i - P_b)/\rho_l} = \sqrt{2\Delta P/\rho_l} \quad (\text{Eq 1}).$$

$$C_D = \dot{m}_f / A \cdot u_t \cdot \rho_l = C_v \cdot C_a \quad (\text{Eq 2}).$$

$$C_v = u_{eff}/u_t, C_a = A_{eff}/A \quad (\text{Eq 3}).$$

Where  $P_i, P_b, \rho_l, A, u_{eff}, A_{eff}$ , are the inlet pressure, the back pressure, the liquid density, the nozzle section, the effective liquid velocity at nozzle outlet and the effective outlet section occupied by liquid phase only. In this study, n-heptane is injected at a pressure drop  $\Delta P$  of 4 bar. The cavitation number  $K$  is defined as the ratio of the difference between fuel inlet pressure and its vapor pressure over the in-nozzle pressure drop. The experiment conditions of this study yields to a cavitation number of 1.24. The injector critical cavitation point is at a back pressure of 28.8 bar for 100 bar inlet pressure which yields to a critical cavitation number  $K_{crit}$  of 1.4. Payri in his cited articles refers to Lichtarowicz et al. [12] indicating that for  $K$  values bigger than the critical cavitation number the flow will only be under the liquid phase depending mainly on the Reynolds number. This is not the case here, and at 5 bar inlet pressure cavitation starts taking place inside the nozzle when back pressure is less than 1.39 bar. At atmospheric conditions and with a relatively long nozzle injector, as it is the case in our study we can consider that the cavitation is not fully developed and the flow boundary layer is reattached to the nozzle surface before its outlet section. Therefore, the area contraction ratio  $C_a$  is considered equal to 1. Combining the equations above yields to the conclusion that liquid phase velocity at nozzle outlet is  $u_{eff} = 22.4 \text{ m/s}$ ; It corresponds to Reynolds and liquid Weber numbers around 7430 and 3388 respectively.

## Results and Discussion

### 6-1 Spray angle results

The spray mean directions and the standard deviations from both sides are measured using the analysis approach introduced in former work [6] on all raw recorded images.

$$\bar{\beta} = \sum_{i,j} \beta_{i,j} \cdot P_{i,j} / \sum_{i,j} P_{i,j} \quad \text{and} \quad std_{ext} = \sqrt{\sum_{i,j} (\beta_{i,j} - \bar{\beta})^2 \cdot P_{i,j} / \sum_{i,j} P_{i,j}} \quad \text{if } \beta_{i,j} < \bar{\beta}; \quad std_{int} \text{ if } \beta_{i,j} > \bar{\beta}$$

Where  $\bar{\beta}$ ,  $\beta_{i,j}$  and  $P_{i,j}$  are the spray mean direction angle with the vertical frame line, the angle formed between the vertical frame line and the line joining the orifice centre and the pixel  $(i,j)$ , the probability of liquid existence

at pixel  $(i,j)$ . From the transverse view  $std_{ext}$ ,  $std_{int}$  are the standard deviations of  $\bar{\beta}$  at the injector external side (towards negative  $X$ ) and its internal or central side. From the front view  $std_{ext}$ ,  $std_{int}$  are respectively at the left (towards negative  $Y$ ) and right sides of the dense liquid core.

View	$\bar{\beta}$ (red)	$\bar{\beta}$ (blue)	$std_{ext}$ (red)	$std_{ext}$ (blue)	$std_{int}$ (red)	$std_{int}$ (blue)	Dense spray (red)	Dense spray (blue)	Dense spray std
Transverse	-23.04	-22.91	11.76	12.97	12.94	13.93	-23.6	-23.6	0.2
Front	1.45	1.42	11.43	12.05	11.13	11.54	2.65	2.65	0.59

**Table 1:** Spray angle values.

The dense spray mean direction is obtained by binarization with adequate threshold as detailed in the previous work. As injection pressure used here is 5 bar only, the dense spray is a continuous liquid core volume projection with ligaments around rather than a very dense spray of droplets as for high pressures. In the transverse view case, the spray mean direction angle  $\bar{\beta}$  is very close to the dense spray mean direction angle.  $std_{ext}$  is also close to  $std_{int}$ . These results prove that the jet is symmetric and that cavitation is not having an important influence on the spray atomization process unlike lower  $L/D$  injectors [6]. The same result is seen in the front view case where the spray is slightly inclined towards the positive  $Y$  due to 1° inclination of injector.

### 6-2 Dispersed phase of the spray

In this section the dispersed phase of the spray is investigated on each side of the continuous liquid core.  $N$  represents the mean number of particles per image,  $D_{32}$  the Sauter Mean Diameter,  $DV_{90}$  the particle diameter such that 90% of the total liquid volume is contained in drops with smaller diameter and  $Ecc$  the mean particle eccentricity defined as being the ratio of the distance from the center of a conic section to either of its two foci to its semi major axis. On the transverse view, the internal side which is the in-nozzle non cavitating side is forming 62.7% of the total particle number. Although the important standard deviation of this value shows that this comparison is not reliable in terms of particle formation. On the front view, this value is more balanced. All other values are very similar, despite slightly bigger particles on the front view. Eccentricity values and their standard deviations mean particle shapes are rather elliptical with an important variety range. Sauter mean diameter of particles is still around 60  $\mu\text{m}$  which gives a gaseous Weber number of 1.5 for a droplet velocity of 22.4 m/s indicating that no secondary atomization occurs in the present study.

	Side	$N$	Std of $N$	$D_{32}$ (m)	$DV_{90}$ (m)	$Ecc$	Std of $Ecc$
Transverse view	Internal	81.98	33.76	$5.98 \cdot 10^{-5}$	$1.05 \cdot 10^{-4}$	0.588	0.207
	External	48.79	11.65	$5.85 \cdot 10^{-5}$	$1.04 \cdot 10^{-4}$	0.577	0.203
Front view	Right (int)	66.6	19.52	$6.21 \cdot 10^{-5}$	$1.07 \cdot 10^{-4}$	0.614	0.236
	Left (ext)	46.21	27.49	$6.2 \cdot 10^{-5}$	$1.06 \cdot 10^{-4}$	0.611	0.237

**Table 2:** Mean values of particle properties measured for 358 images at instant  $t_0$ .

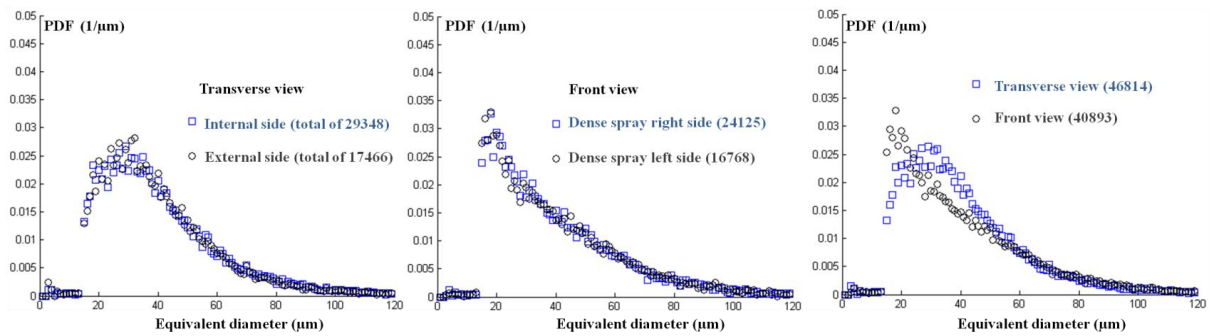


**Figure 6:** Droplet sizing PDFs for both views.

Figure 6 compares the droplet sizing PDFs between both views. Comparing both sides of the continuous liquid core for each view apart, we can see that the difference is negligible. PDF curves have the same shape and droplet size values as show the left hand side and the middle graphs. The right hand side graph shows on the transverse view PDF that an important number of particles are gathered between 20 and 40  $\mu\text{m}$  equivalent diameters which is not the case for the front view.



### 6-3 PIV results

Images post treated by DirectPIV were organized, for each view, in 8 groups of 50 pairs. The groups correspond to delays  $\Delta t$  of the second flash from 2 to 16  $\mu\text{s}$  by steps of 2  $\mu\text{s}$ . The delay precision is around 50 ns due to the nanolite drivers and other electronic devices. The first flash is always taken at  $t_0 = 2$  ms after start of injection with a 3 ms injection duration, to make sure that steady state conditions are reached. Considering velocity as calculated earlier, the particle displacement at high delay values such as 14 and 16  $\mu\text{s}$  is about 150 and 170 pixels in the vertical direction. That large displacement may affect the cross-correlation of the PIV software analysis which needs an image mesh size of at least 4 times the particle displacement. The same behavior happens with extremely small displacements, smaller than the size of particles, such as the 2  $\mu\text{s}$  delay case.

The results obtained for each view are very coherent especially at 4 and 6  $\mu\text{s}$  delays. The most important values of relative errors between those two delays are at the top of the jet and at its sides. Very near the injector, until 10 orifice diameters and due to the small number of droplets in this region, velocity vectors are less consistent in numbers, norms and angles. While at a distance of 20 diameters, only vectors at the farthest radial positions on both sides of the jet are different than the packet in the middle which looks very consistent and stable in norm at 22 m/s with an accuracy of 6%.

Figure 7 and 8 present the mean values of velocity vector properties at delays 4 and 6  $\mu\text{s}$  in a transverse view region where the average particle existence probability is above 80%. The bold numbers on figure 7 and 8 correspond to the relative values of velocity vector properties with respect to those of the continuous liquid core represented at its spatial position by thick lines. The continuous liquid core travels with a velocity direction inclination of  $-23.6^\circ$  to the vertical line in the transverse view. Its theoretical velocity norm is considered equal to 22.4 m/s in the region of the frame. From the right hand side graph of figure 7, one can deduce that the velocity norm values increase with the increase of particle distance to injector (at least until 5 mm). This could be due to the increasing development of instabilities on the continuous liquid core with the increase of distance Z. Figure 8 can explain in details what is happening to the young particles. The theoretical continuous jet

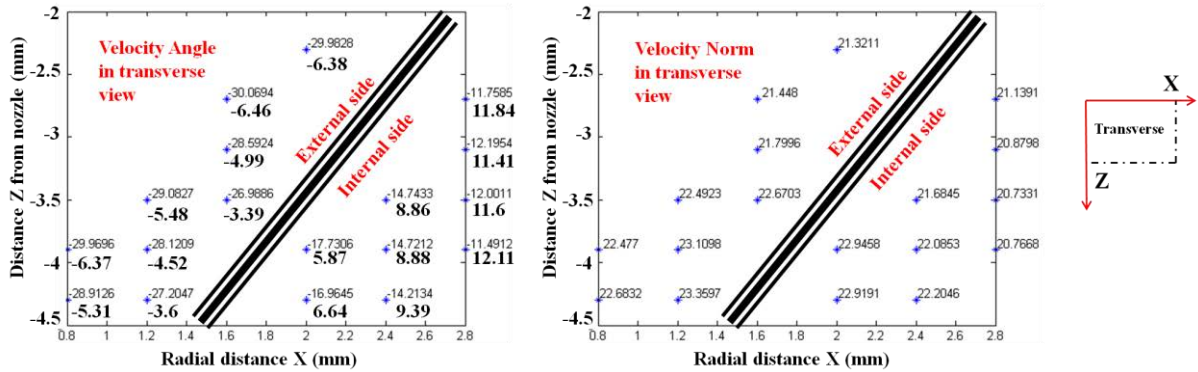


Figure 7: Mean values of velocity vector angle and norm in region of 80% particle existence.

velocity components are  $V_x = -8.75$  m/s and  $V_z = 20.62$  m/s. From the particle relative velocities we deduce that the farther the relative radial position of the particle is, the bigger its relative radial velocity component is. Comparing the internal side particles with the external side ones, in terms of relative radial velocity, we reach the conclusion that values on the internal side are generally bigger than those on the external side which is the in-nozzle cavitation side. Note that this difference in measurements was proven to be above the precision error. The vertical velocity component  $V_z$  on the external side shows that particles are slower relatively to the continuous jet while it is the opposite at the internal side. This result is similar to what Sou et al. showed in [13] about the slower spray side that corresponds to the in-nozzle cavitation side. The radial relative velocity of particles is similar in front view to the one of the transverse view. Hence, the cylindrical continuous jet is

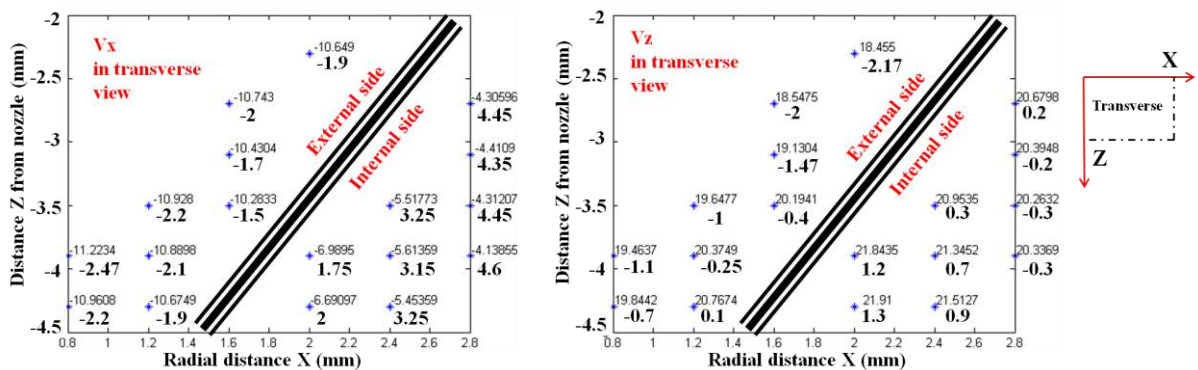


Figure 8: Mean values of velocity vector components in region of 80% particle existence.

rotating around itself helicoidally. This explains why the further is the particle in the  $(X,Y)$  plane from the central cylindrical jet, the faster it is released.

#### 6-4 Continuous phase of the spray

To investigate the continuous liquid phase of the spray, image pairs were analyzed by measuring the wrinkling and the jet radial size in bands iterated from the orifice outlet until the frame lowest point. The wrinkling is defined to be the interface density  $S/V$ , where  $S$  is the interface surface and  $V$  the liquid volume. Due to the spatial projection, it is substituted by a length density  $L/S$ . Considering that the biggest ligament that the spray could produce should be smaller in width than the orifice diameter, the chosen width size of the bands is  $D$ . To follow a ligament from a band to the next one it should not travel a distance bigger than  $D$ . With a velocity norm of 22.4 m/s, the 8  $\mu$ s delay looks like the best compromise as the displacement of pixels is 10% smaller than  $D$ . Results are presented in figure 9 where zero corresponds to the injector outlet. The first value is at  $D$  distance underneath the injector on axis  $Z$ . The curves corresponding to the jet at 8  $\mu$ s delay are translated by one step towards zero in order to compare, in each band step, the change occurred on the ligament pattern between the two flashes. Left hand side of figure 9 shows a little difference in terms of jet average wrinkling until the jet reaches 2 mm underneath the injector. Once this position is reached, the wrinkling curves increase and the values from the second flash are almost always on top. This means that the same ligament pattern, when its vertical position is closer than 2 mm underneath the injector, did not experience a lot of change in its shape between the two flashes. But once this pattern is further downstream than 2 mm, its shape starts to gain in terms of wrinkling values after 8  $\mu$ s delay. Graph at the right hand side of figure 9 shows that the jet radial size is increasing following a slope with the increase of the distance to injector tip. This slope bends at the exact position where wrinkling starts to increase and reaches a maximum soon after this position. At 2 mm, the liquid core shape deformation starts, the wrinkling increases and the radial size decreases. The jet tears into sheets and ligaments in both visualized directions as the same results were also observed on the front view at the same primary breakup position (figure 10). The important error bars on the graphs, especially after 2 mm of axial position, mean that the values are not reliable quantitatively but prove qualitatively that the spray ligament shapes and sizes can vary so much after this position.

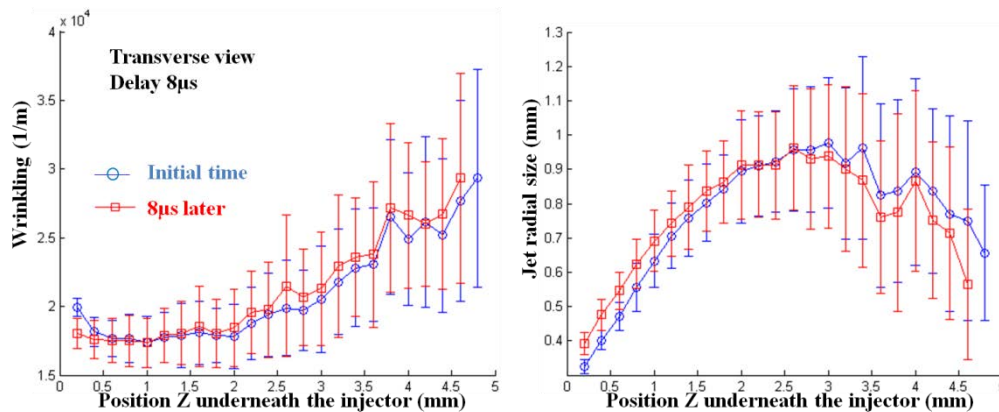


Figure 9: Continuous jet wrinkling (on the left hand side) and radial size.

Figure 10 compares the continuous jet radial size of both views. Again, they both similarly follow the same slope until slightly before reaching 2 mm underneath the injector tip. After 2 mm, the jet still is getting wider in the radial direction but loses its original shape as explained above because the slope starts to bend and decreases shortly afterwards. Combined with PIV results, this proves that the jet progresses in a conical shape with rotational motion as part of its kinetic energy is transformed into the radial direction and releases particles with non-negligible radial velocity. It also explains why the probability of finding particles newly released by the young spray do not reach 80% before crossing a 2 mm distance underneath the injector as seen in PIV results.

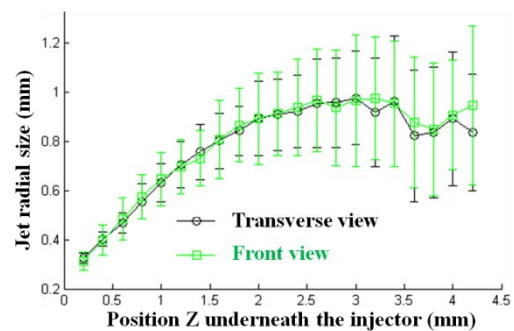


Figure 10: Jet radial size from both views.

## Conclusions

The spray injected at 5 bar was visualized by a close-up doubly exposed and doubly viewed techniques in order to investigate its dispersed and continuous phases simultaneously. In the investigated range of injection pressure, this preliminary work shows the pertinence of such a methodology to characterize the primary breakup experimentally. On one hand, the particle properties such as the velocity field and the distribution size were obtained in two planes ( $X,Z$ ) and ( $Y,Z$ ). On the other hand, the spray mean angles and the liquid/gas interface evolution in time were also analyzed in those two planes. The main results presented in this work can be summarized in the following points:

- At low pressure, the sprays resulting from injectors with  $L/D$  ratio higher than 1 are weakly influenced by the in-nozzle shear cavitation as the flow boundary layer could be reattached to the nozzle surface unlike the case studied in previous work [6].
- In the first 5 mm underneath the injector, droplets with diameters smaller than 15  $\mu\text{m}$  are very rare.
- Particle relative velocity (in comparison to liquid core velocity) is more important on the internal side than on the external side (in-nozzle cavitating side). This result shows the effect of cavitation on the primary breakup process.
- Liquid core interface wrinkling starts increasing at 2 mm underneath the injector tip. This is where the increasing slope of the liquid core radial size starts to incline due to the breakup process.
- Experiments showed that in the first 2 mm the liquid jet takes a conical shape with a swirling motion. Further downstream, the jet starts losing its original shape as its radial kinetic energy tears it into ligaments and particles are released with non-negligible radial velocity.
- This experimental technique allows investigating the droplet formation and the liquid/gas interface evolution simultaneously.

## References

- [1] G.J. Smallwood, W.S. Neill, D.R. Snelling (1985), 'Diesel engine combustion program at the Defence Research Establishment Ottawa', DREO Report No. 926.
- [2] L.P. Goss, M.E. Post, D.D. Trump, B. Sarka, C.D. MacArthur, G.E. Dunning (1989), 'A novel technique for blade-to-blade velocity measurements in a turbine cascade', AIAA-89-2691.
- [3] G.J. Smallwood, D.R. Snelling (1990), 'A two-colour technique for two-dimensional particle image velocimetry', NATO Advanced Study Institute on Combusting-Flow Diagnostics, Portugal.
- [4] A. Lecuona, P.A. Sosa, P.A. Rodriguez, R.I. Zequeira, 'Volumetric characterization of dispersed two-phase flows by digital image analysis', Meas. Sci. Technol. 11 (2000) 1152-1161.
- [5] P. Marmottant, E. Villermaux, 'On spray formation', J. Fluid Mech. (2004), vol. 498, pp. 73-111.
- [6] S. Makhlouf, J. Hélie, O. Grimoux, J. Cousin, L. Gestri, A. Wood, G. Wigley, 'Spray resulting from high pressure atomization with low  $L$  over  $D$  multihole injectors and the role of the cavitation', Iclass2012, Heidelberg, Germany, Sept 2-6, 2012.
- [7] J.B. Blaisot, N. Fdida, 'Drop size distribution measured by imaging: determination of the measurement volume by the calibration of the point spread function', Meas. Sci. Technol. 21 (2010) 025501.
- [8] J.B. Blaisot, J. Yon, 'Droplet size and morphology characterization for dense sprays by image processing: application to the diesel spray', Experiments in Fluids (2005) 39: 977-994.
- [9] A. Susset, J.M. Most, D. Honoré, 'A novel architecture for a super-resolution PIV algorithm developed for the improvement of the resolution of large velocity gradient measurements', Exp. Fluids (2005).
- [10] R. Payri, J.M. Garcia, F.J. Salvador, J. Gimeno, 'Using spray momentum flux measurements to understand the influence of diesel nozzle geometry on spray characteristics', Fuel 84 (2005) 551-561.
- [11] J.M. Desantes, R. Payri, F.J. Salvador, J. Gimeno, 'Measurements of spray momentum for the study of cavitation in diesel injection nozzles', SAE paper 2003-01-0703.
- [12] A.K. Lichtarowicz, R.K. Duggins, E. Markland, 'Discharge coefficients for incompressible non-cavitating flow through long orifices', J. Mech. Eng. Sci., 7 (2), 1965.
- [13] A. Sou, R.H. Pratama, R. Ohashi, R. Sugimura, 'Cavitation in a nozzle with asymmetric inflow and its effects on liquid jet', Ilass – Europe 2011, Estoril, Portugal.

## PIV Investigation on Flows Induced by Fuel Sprays from an Outwards Opening Pintle Injector for GDI engines

Andrea Marchi<sup>1,2</sup>, Youyou Yan<sup>1</sup>, Jamshid M. Nouri<sup>1</sup> and C Arcoumanis<sup>1</sup>

1: School of Engineering and Mathematical Sciences, City University London, UK

2: Ricardo, Germany

### Abstract

Pintle-type outwards opening injectors actuated by piezoelectric technique have demonstrated the ability to meet the challenging requirements in spray-guided gasoline direct injection engines. Previous studies carried out by spray visualisation showed that the spray had a stable spray cone angle against elevated in-cylinder back pressures, which have been determined by the integral spray images using continuous or flash white light illumination. However the fuel cloud structure at the end of injection was not well defined when the injection was completed in the white light Mie scattering visualisation. In order to show the details of the spray cloud structure, two dimensional flow visualisation illuminated by a laser sheet was used under the atmospheric condition. The results showed complex multiple vortices forming a recirculation zone inside the fuel cloud. To further study the structure of such vortices, a double pulsed laser sheet illumination was employed to obtain the instantaneous velocity fields of fuel droplets using the Particle Image Velocimetry (PIV) technique. The PIV system was also used to study air motion induced by the spray near the injector nozzle; a good agreement was found in the air entrainment velocities when compared to the LDV measurements.

### Introduction

This experimental work is concerned about the characterisation of the fuel spray structure and of the induced air-entrainment near nozzle exit using a pintle-type injector. Pintle-type outwards opening injectors are actuated by piezoelectric technique and have advantageous features such as the enhanced atomization by high injection pressures up to 200 bar and increased surface contact area between fuel cone spray and the surrounding air; stable spray structures within the range of engine cylinder pressures from the intake stroke to the late compression stroke; and short injection durations comparing to other types of injectors with fast responses at the opening and closing of the pintle valves. The spray exiting the conical ring nozzle of a pintle piezoelectric injector exhibited a string formed hollow conical structure [1-5]. The conical structure is formed by the conical design of the fuel exit passage of the injector. Enlarged injector model tests showed that the string formation on the conical surface is due to either fuel cavitation or air entrainment taking place from outside into the region inside, but close to the injector nozzle exit[6]. Further investigations of spray stabilities were carried out on three prototype injectors operating in a direct injection optical engine by the integral Mie scattering spray visualization [7]. The spray was identified having a stable spray cone angle at the injector nozzle exit and a recirculation zone at the front of the spray. The stability of the spray cone angle was assessed by statistical analysis of the cone angle in terms of the mean cone angle and the standard deviation of the measured cone angles, therefore the stability of injector performances was compared under test conditions including the injection pressure, the in-cylinder backpressure, the injector needle lift and the engine speed. In this paper, the spray cloud structure after the end of injection was investigated by the two-dimensional Mie scattering imaging and the PIV technique; also air motion induced by the spray was measured by both PIV and LDV techniques under the atmospheric condition.

### Experimental Setup

The experiment was carried out in atmosphere using the fuel injection system equipped with a constant volume chamber[1]. A pintle-type outwards opening injector was connected to a common rail. A three-piston-type pump driven by an electric motor delivered high-pressure fuel of Iso-octane to the common rail. Fuel temperature was kept at room temperature using a water-cooled heat exchanger in the fuel circulation from the fuel tank to the common rail, then back to the fuel tank.

Figure 1 shows the optical setup of the PIV measurement. The TSI PIV system consists of a Pegasus-PIV laser, a set of laser sheet formation optics, a Photon FASTCAM-APX RS high-speed video camera system and INSIGHT 3G PIV image analysis software. The double-head Nd:YLF laser produces green light at a wavelength of 527 nm with a beam diameter of 1.5 mm. It has the ability to operate at the repetition rate of 10 kHz with a total power of 10 watts per head. Energy per pulse is 10 mJ and the laser pulse width is less than 180 ns at 1 kHz repetition rate per head. The energy stability is high with the rms of less than 1% in the laser power.

The double cavities of the Pegasus-PIV laser are triggered independently by a laser pulse synchronizer, therefore the time delay between the two double pulses can be set much smaller than that of the repetition rate. Synchronised with the Pegasus-PIV laser was a Photon FASTCAM-APX RS high-speed video camera system capable of recording up to 3000 fps with the full resolution of 1024 x 1024 pixels per frame.

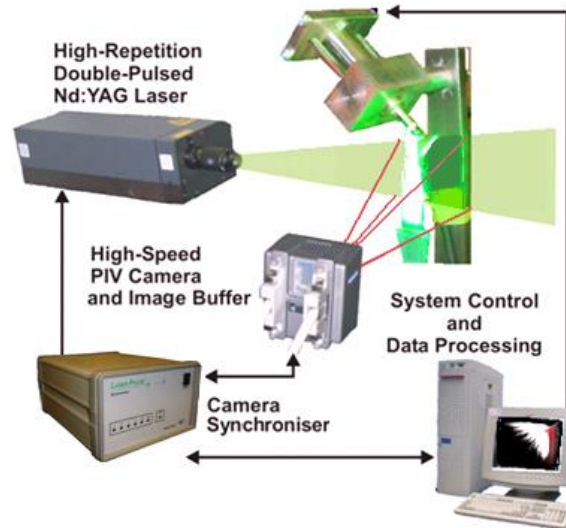


**Figure 1:** Experimental setup of the high-speed PIV system

In the two-dimensional spray visualisation study, the diode pumped Nd:YLF laser was replaced by a 1.5W Argon-Ion laser which provided continuous illumination for spray visualisation. The same Argon-Ion laser was part of the DANTEC PDA system, which was used for the LDV measurement in this study.

## Results and Discussion

Vortex structures demonstrated by the fuel droplet movement and re-distribution are revealed after the end of a fuel injection by the 2D Mie scattering visualisation with an aid of a high speed camera. The light sheet, shown in Figure 2, was located at the symmetrical plane of the conical spray. The camera was perpendicular to the light sheet and the speed of imaging was 7200 fps with an exposure time of 90  $\mu$ s.

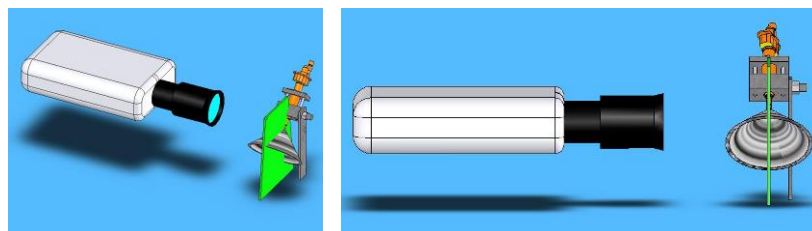


**Figure 2:** Setup of Vertical Mie-scattering Visualisation

Figure 3 shows the evolution of a spray. The nominal cone angle of the spray of this injector was close to 90°. The axis of the injector was tilted 45° to the gravitational vertical so that the in-plane spray cone edges are in horizontal and vertical directions. Previous studies of conventional spray visualisation have shown that the hollow cone of the spray following the annulus nozzle passage was disintegrated into a string structure. The string structure of the spray is evident in the images in Figure 3 between 0.11 ms and 0.53 ms. This was during the spray injection with the injection duration of 0.6 ms; the light scattered by the fuel droplets in liquid phase acted as a secondary illumination, so that the front surface of the spray can be unintentionally visualised and the string structure can be identified. At 0.53 ms, a recirculation ring was observed outside the spray. The recirculation area grew with time and formed a ring of vortex outside of the conical spray, as shown in the image of 1.09 ms; referred to as outer vortex. This ring of vortex has a counter rotating ring of vortex inside the spray; referred to as inner vortex. The inner ring of vortex became clear in the image at 1.64 ms. As the injector needle was closed, fuel droplets from upstream near the injector nozzle were observed drawn into these rings of



vortices. Those fuel droplets became the tracing particles for flow visualisation and for the PIV measurements later on. Although the vortices at the two sides of the injector axis are not exactly symmetrical, but the centres of the two main vortex rings in the visualisation plane are symmetrical about the injector axis, indicating that the two counter rotating vortex rings were formed simultaneously inside and outside following the conical shape of the spray. In the images from 1.09 ms onwards, the vortices grew in size with time showing the dissipation of the vortices and at the same time, the flow was losing its tracing particles as fuel droplets evaporated. It should be pointed out that the circular structures of fuel distribution with dark centres in a single image do not represent vortices at the time, as they could be formed at an earlier stage of the injection due to either the instability of the spray or the spray induced vortices. The two main vortex rings marked in Figure 3 are the result of the observation of consecutive images of the recording.

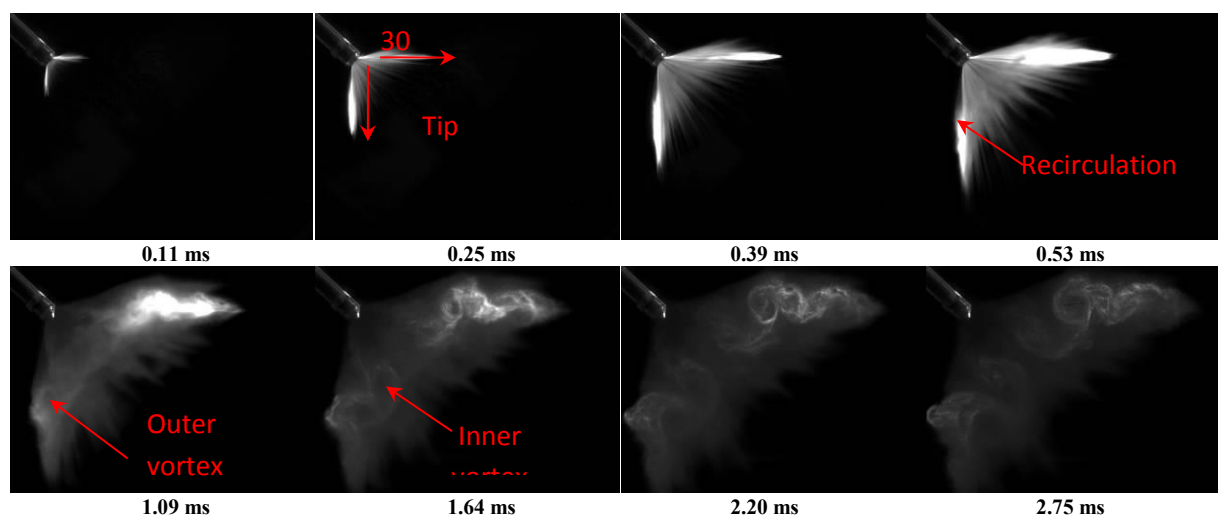


**Figure 3:** 2D Mie Scattering Images of Spray Evolution  
(Injection Pressure 200bar and Injection Duration 0.6 ms)

In Figure 4, the injection pressure was kept constant at 200 bar and injection durations were 0.6 ms, 1 ms and 2 ms. Figure 4(a) shows the raw images of the sprays at around 1.1 ms ASOI. This particular imaging time was chosen to show clear differences between the three injection durations. At this time, injection was definitely completed for the injection duration of 0.6 ms and it was in the middle of the injection for the injection duration of 2 ms. As for the injection duration of 1 ms, the injector needle was just closed, but the string structure of the spray was still visible. The three images of injection durations of 0.6, 1 and 2ms show clear geometrical similarities in terms of the location of the recirculation and the spray tip penetration.

Figure 4(b) shows the spray tip penetration as illustrated in Figure 3 at 0.25 ms. The tip penetration is defined as the furthest distance of the spray from the injector exit. In each image, a vertical penetration and a horizontal penetration distance were measured by a computer program with a fixed threshold for all three cases of injection durations. The horizontal and the vertical penetration were found advancing at the same rate at the beginning until the penetration of the spray reached around 35 mm, shown as the initial linear part of the graph. The averaged penetration speeds over the two sides and the three cases is 115 m/s with 2% variation in the injection durations of 0.6, 1, and 2 ms. After the linear part, both horizontal and vertical penetrations were slowed down considerably with the horizontal penetration advanced further compared to the vertical side. Comparing the vertical penetrations of the three injection durations, marked by hollow symbols in Figure 4(b), no clear difference in the vertical penetrations was found in the three injection durations. Spray droplets after EOI in a shorter injection duration of 0.6 ms or 1 ms carried on moving away from the injector at a same speed as those in the injection duration of 2 ms, which were in the middle of injection until 2 ms. There was a slight difference in the horizontal penetrations, marked by solid symbols in Figure 4, the increase in the injection duration resulted a higher penetration length after the linear part of the graph, however the limits of the penetrations were not changed much in the three cases. The results also show that at the end of injection the average penetration speeds in vertical direction for three injection durations were found between 10 to 12 m/s, whereas in the horizontal direction the penetration speeds were in the range between 14 to 21 m/s for the three injection durations. Penetrations on both sides show a massive reduction in droplets momentum compare to those in the beginning of the injection which is due to considerable secondary breakup taken place in the early part of injection producing smaller droplets and therefore their loss of momentum and penetration; more details can be

found in [8] where the variation of Webber number,  $We$ , with distance from injector are discussed and shows massive reduction in  $We$  within the first 10 mm from the injector.

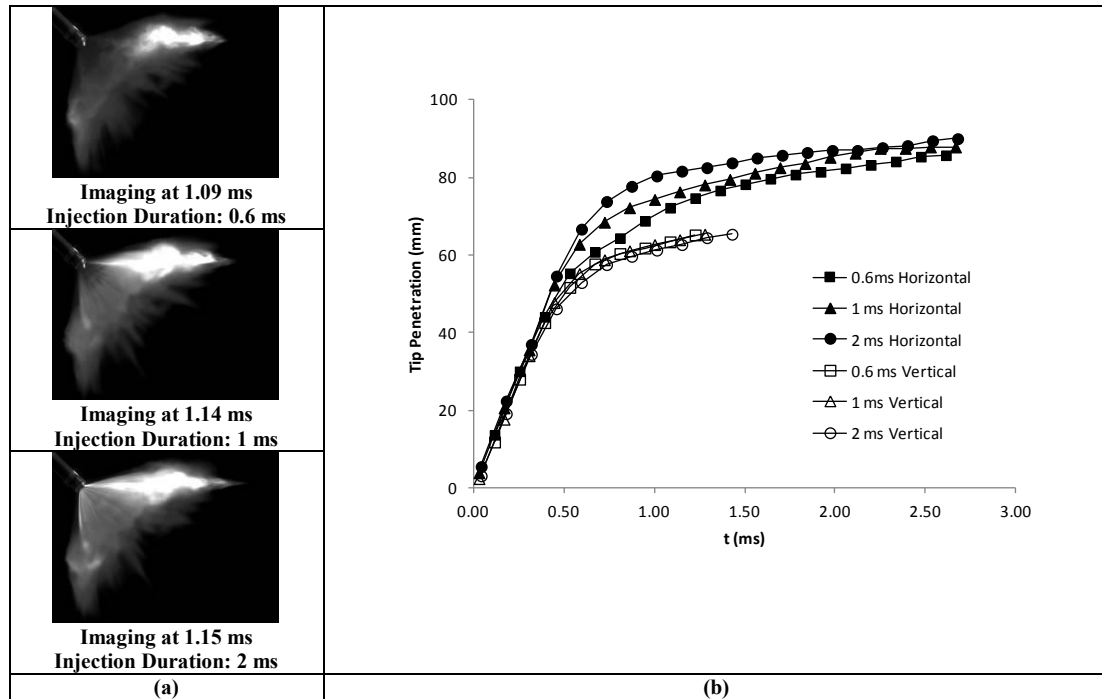
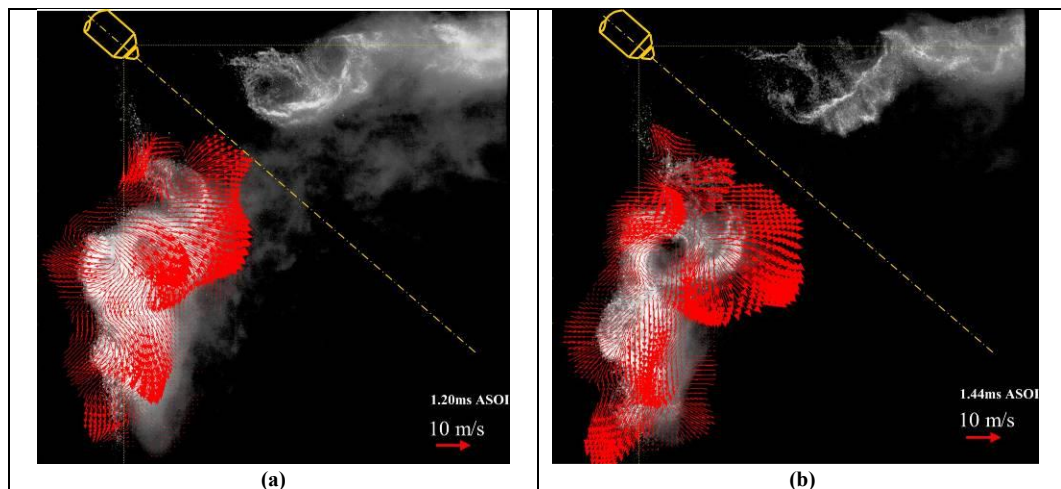
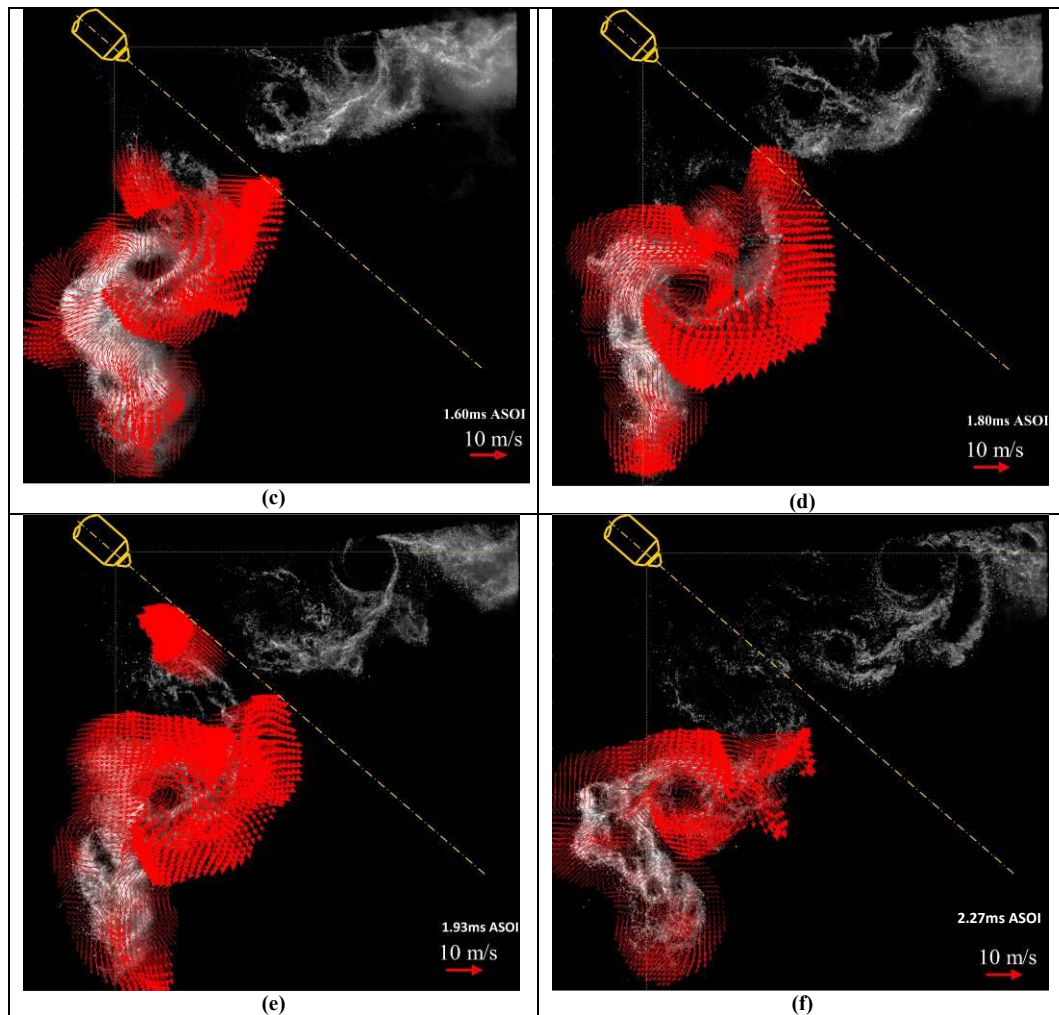


Figure 4: (a) Spray Visualisation (b) Spray Penetration (Injection pressure 200 bar)

As mentioned earlier, a static image of the 2D Mie scattering of fuel droplets is unable to show the velocity field of the vortices in the wake of an injection. This information was obtained by the PIV technique using the floating fuel droplets as tracing particles for the air/fuel droplet two-phase flow. Figure 5 shows the instantaneous velocities in the wake of sprays, which are superimposed on one of the two processed PIV images used for obtaining the velocity vectors. The laser sheet was projected towards the spray from left to right in the images. In the areas where no sufficient scattered light existed, the PIV measurements were not available and only one half of the images were processed and presented for the PIV measurements. Due to the restriction of the PIV sampling rate, maximum 1500 pairs per second with the full spatial resolution, the PIV results in Figure 5 are snap shots of different injections.





**Figure 5:** PIV Measurement of Recirculation Zones  
(Injection Pressure 200bar and Injection Duration 0.6 ms)

The velocity fields presented in Figure 5 show the effect of the mutual interaction of the two counter rotating vortices, generating a flow directed into the spray cone. The sequence of images show the expansion of the vortices radially toward the axis of the injector at 1.20 ms ASOI and onwards, which can be verified by what was observed in the 2D Mie scattering visualisation. In the 2D Mie scattering visualisation, focus of the study was on the formation of vortices shown in the images, whereas the PIV results show that the radial expansion is the dominant feature of the velocity field.

In addition to radial expansion of the vortices, the rotation of the vortices was also superimposed on translation movement of the vortices, especially before 1.60ms ASOI. When a translation velocity is superimposed on the relative rotational velocity field, it shifts the location of the zero velocity perpendicularly to the translation velocity. The translation velocity decreased with time as that of the spray tip penetration. At 1.60ms ASOI, it can be observed that the centre of velocity field of the outer vortex did not coincide with the centre of the background image. It was estimated the outer vortex moved towards the injection jet direction with a sliding velocity of around 10 m/s.

Because of the rotation of the inner vortex ring, an upward flow was built up in the upper central region of the spray cone. In the image at 1.93ms ASOI, fuel droplets were found moving up towards the injector tip with velocities about 15 m/s, indicating a strong upward flow in this region. Finally, at 2.27ms ASOI the centre of the velocity field is almost overlapped to the fuel distribution vortex image, which means that the translating speed was significantly reduced or in other words the vortex at this stage did not move any further.

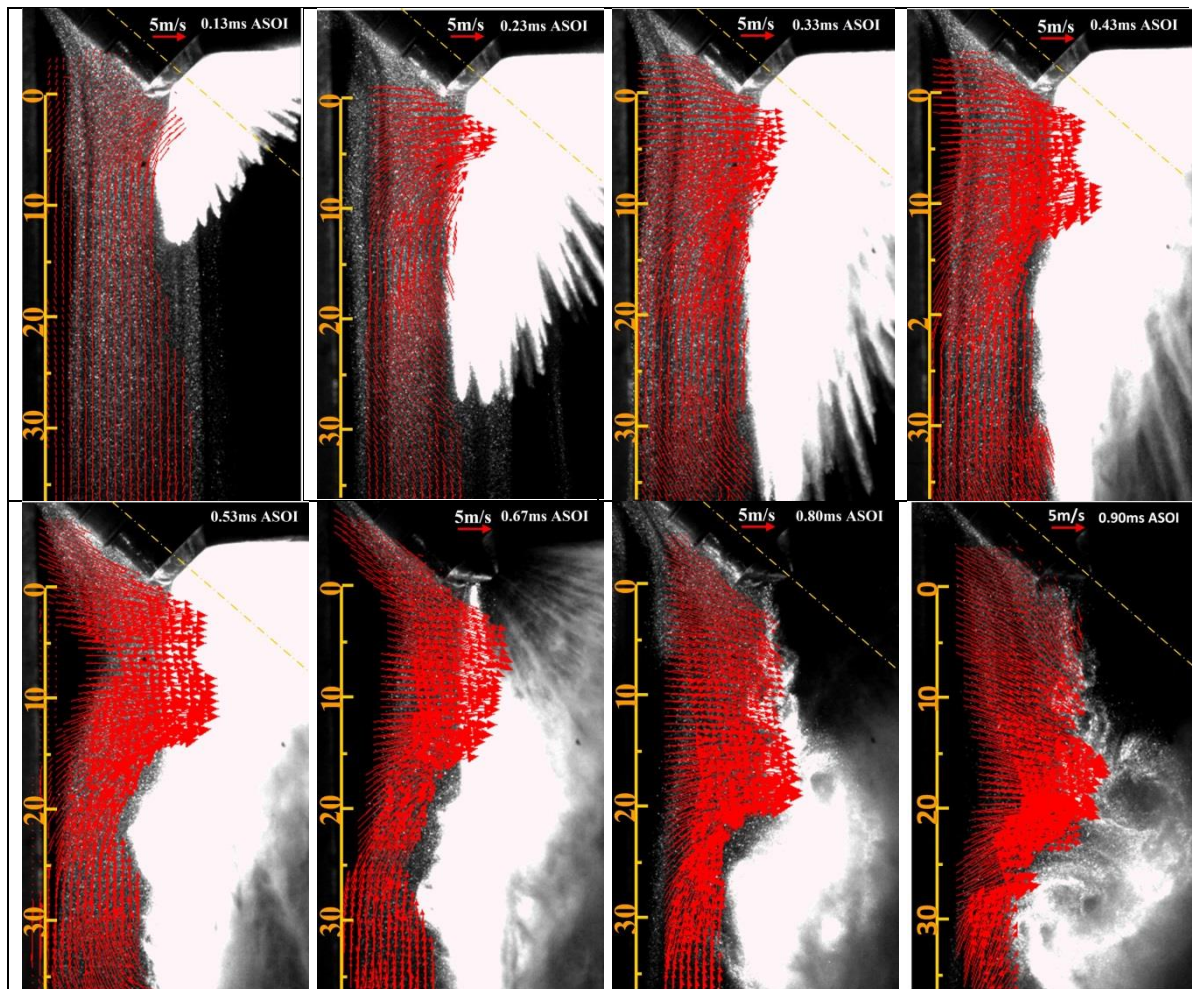
The instability in the spray has been demonstrated in terms of the breakdown of annular spray film into a number of strings, a wavy surface along a string, flapping in spray cone angle, formation of recirculation around the spray and variation in the spray front penetration[7]. Figure 5 shows the instantaneous velocity distributions



of fuel droplets. Although a pair of vortices is clearly identified after the end of injection, the original start of the outer ring of vortex can be traced back to the recirculation developed at the out surface of the spray during an injection. Individual snap shots of the flow field show the repeatability in the occurrence of vortices generated by the spray. However the repeatability in the formation of vortices is much less evident due to the instability in both spray dynamics and aerodynamics. No attempt was made to obtain an ensemble average over a number of sprays in this study.

In the application of the gasoline direct injection engines, in-cylinder air flow and fuel droplet distribution are the main factors which affect the air/fuel mixture formation for achieving repeatable and reliable combustion in every single engine combustion cycle under a wide range of engine operation condition of load and speed. Results of instantaneous velocity distributions will be useful for understanding the time averaged flow measurements by other laser diagnostic techniques, such as LDV or PDA, as well as for interpreting CFD results. In addition, a single shot image of a flow field gives the information on what happened in a real flow.

The PIV analysis using fuel droplets as tracing particles was successful where the interrogation area was away from the injector nozzle and when it was after EOI. In the vicinity of the injector tip, no fuel droplets were present for PIV analysis, whereas during a spray injection, fuel droplets were too dense to be distinguished by an imaging based optical technique. Extra seeding particles were introduced in order to overcome the lack of tracers of naturally existing fuel droplets. For the same experimental setup, shown in Figure 1, the area around a spray was seeded with atomised water droplets with sizes of order of  $2\ \mu\text{m}$  and a mean velocity of  $0.3 \pm 1.3\ \text{m/s}$ , measured by LDV. The air flow is now visible with the seeding droplets, as shown in Figure 6 so it is possible to study air flow during injections. Air flow surrounding the spray is important, especially the velocity component of the air flow towards the spray, as the air entrainment influences the fuel droplet evaporation.

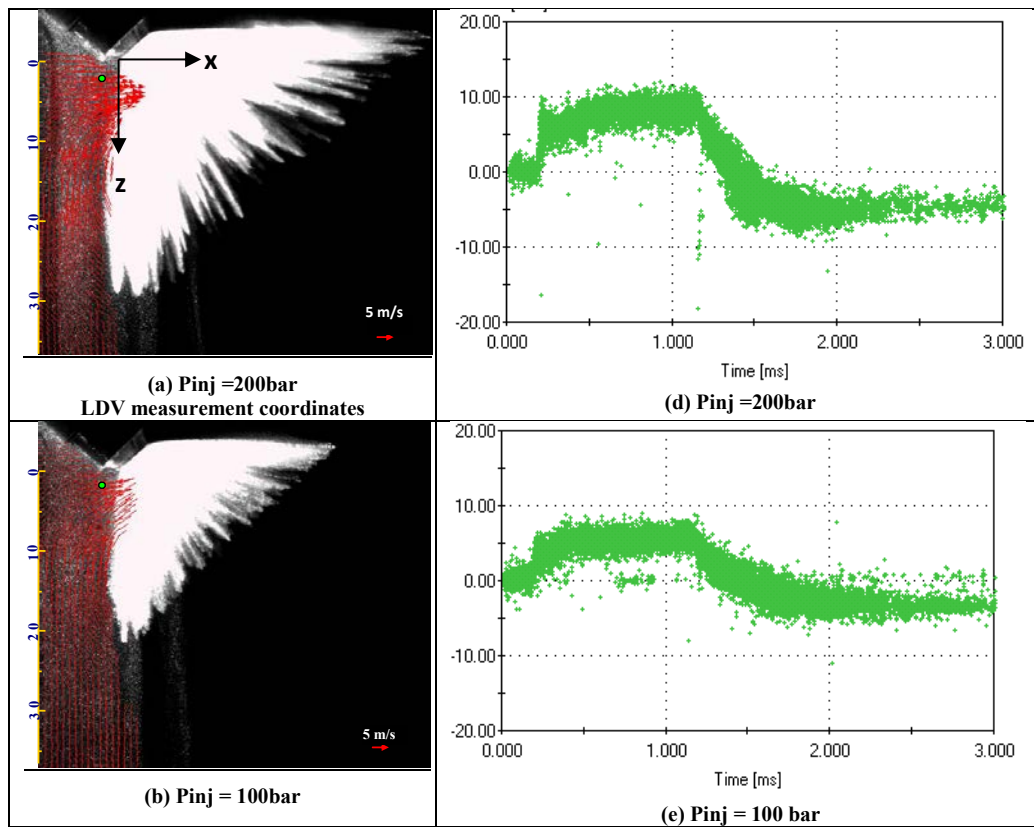


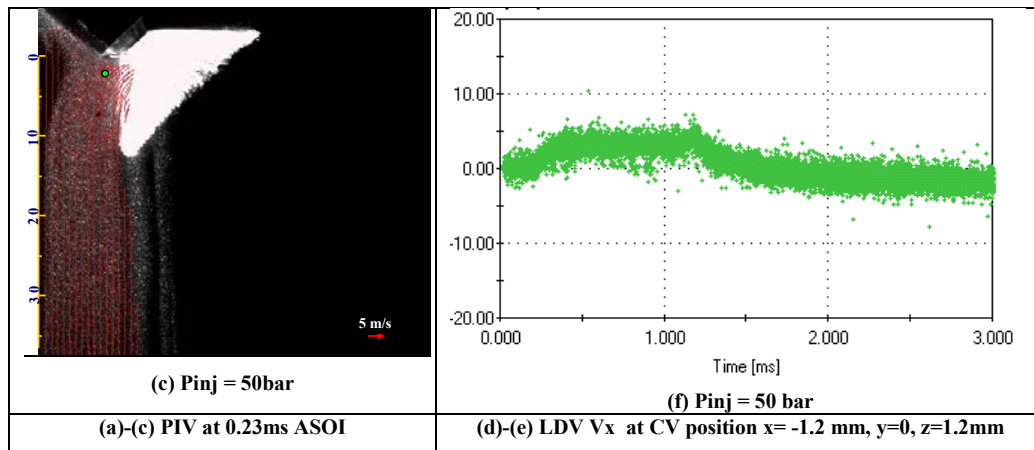
**Figure 6:** Air Entrainment  
(Injection Pressure 200bar and Injection Duration 0.6 ms)

Figure 6 shows air entrainment as sprays evolved. At 0.23 ms ASOI, the air entrainment exhibited a jet like profile with a peak jet velocity at a distance of about 4 mm from the injector exit and the direction of air flow of at the peak velocity was almost normal to the spray flow. As the spray evolved the horizontal component of the air velocity increased in intensity with values up to 10m/s and hit the spray in the same near nozzle area, but with an expanded effected area on the spray further downstream, so that at 0.33ms ASOI the air entrainment in the form of an air jet was found in the area up to 8mm away from the nozzle exit. At 0.43ms ASOI, the onset of the outer recirculation can be seen at a distance of about 10-15mm from the nozzle; in fact, the faint bump on the spray profile represents the initiation of the outer vortex that was discussed in the previous section. At this stage, the air velocity profile becomes wider and takes a shape of double peak jet progressively extending downstream. A broader air jet towards the spray was found at 0.53ms ASOI comparing to that at 0.43ms ASOI.

From 0.67 ms ASOI onward the PIV images clearly show how the air entrainment follows the evolving outer vortex ring promoting its formation with a horizontal velocity of about 10m/s preceding its motion. Finally, at 0.30ms after the end of the injection (or 0.90 ms ASOI), the spray starts losing its density and therefore it is possible to visualise the internal cross-section of the spray and the full set of counter rotating vortices as was previously shown in Figure 5. The last image at 0.9ms ASOI, also reveals how the air entrainment is interacting on the wakes of sprays and more specifically on the inner vortex, which explains its displacement toward the injector axis at a later stage shown in Figure 5.

The PIV measurement was validated by a LDV measurement. The measurement location, the control volume of the beam crossing, was set close to the injector nozzle exit. Due to the restriction of access, the air flow speed in the direction towards the spray was measured at a location above the spray. Its axial symmetrical location in the area of the vertical side of the spray is marked as the green dot in Figure 7(a). The velocity component towards the spray is marked as in x direction. The asymmetrical features of the spray and surrounding air flow exist, but it is of a secondary importance and not considered in Figure 7. Figure 7 compares velocity fields at the vertical side of the spray at a fixed imaging time of 0.23 ms ASOI and temporal velocity variations at one point, of which the relative position to the spray is shown in the graph.





**Figure 7:** PIV and LDV Measurements of Air Entrainment

The velocity of the air entrainment was assessed at three injection rail pressures of 200bar, 100bar and 50bar and the results are presented in Figure 7. Each of the three rows in Figure 7 corresponds to an injection pressure. The first column of images represents the PIV velocity field measurements and the second column of graphs shows the temporal variations of LDV measurements for the normal velocity components towards the spray. PIV measurements show the velocity component in the direction towards the spray increased with the injection pressure. At 50 bar injection pressure the velocity was about 2 m/s which increased to 4 and 7 m/s at injection pressures of 100 and 200 bar respectively. The trend of increase in air entrainment velocity with the injection pressure matches with the LDV measurements. The LDV results show the air entrained flow motion exhibited a steady and relatively strong velocity field near the nozzle exit. A step increase in air motion was observed at injection pressures of 100 and 200 bar, whereas the air motion was gradually built up at 50 bar injection pressure. At the injection pressure of 200 bar, instantaneous velocities were found in the range between 5 to 10 m/s. This range was reduced to 3 to 8 m/s at the injection pressure of 100 bar and was decreased further to 1 to 5 m/s at 50 bar of injection pressure.

The agreement in the PIV and LDV measurements verified that the setup of the PIV technique, including the seeding density in the range of 20-30 per interrogation area, was adequate in the study of air entrainment. In the spray recirculation measurements the particle density depended on the number of spray droplets, which was around 10 droplets per interrogation area to produce a valid result. The maximum displacement of particle images was set to be about one eighth of the interrogation window size to reduce the measurement uncertainties caused by particles leaving/entering the interrogation area and sub-pixel values were used in the cross-correlation to increase the measurement accuracy.

## Conclusions

An experimental investigation was carried out to characterise the fuel spray structure at the end of injection and the induced air-entrainment near nozzle exit of a pintle-type injector using two-dimensional Mie scattering imaging, PIV and LDV techniques. The followings are the most important findings:

- A pair of count rotating vortices was identified by the two-dimensional Mie scattering after the end of injection. The recirculation zone formed by vortices trapped fuel droplets to propagate further away from the injector tip.
- Using the fuel droplets as the natural seeding for Particle Image Velocimetry (PIV), velocity fields were obtained to provide the speeds of fuel droplets in the vortices in the recirculation zone. The results provided an overview of quantitative instantaneous velocity fields and flow stream patterns, which will be useful for understanding the fuel transportation, as well as for CFD validations in the prediction of spray characteristics of the outwards opening pintle-type Injectors.
- PIV and LDV measurements of air motion induced by the spray show the degree of air entrainment which is vital for the phase change of fuel evaporation.

## Acknowledgements

The financial and technical support provided by BMW AG is gratefully acknowledged. The authors would also like to thank Tom Fleming and Jim Ford from City University London for their valuable technical support during the experimental programme.

## References

- [1] .Nouri, J.M., Hamid, M.A., Yan, Y. and Arcoumanis, C., *Spray characterization of a piezo pintle-type injector for gasoline direct injection engines* Journal of Physics: Conference Series, 2007. **85**(ICOLAD 2007).
- [2] Befrui, B., Corbinelli, G., Robart, D., Reckers, W. and Weller, H., *LES simulation of the internal flow and near-field spray structure of an outward-opening GDI injector and comparison with imaging data*. SAE paper, 2008: p. 01-0137.
- [3] Wigley, G., Pitcher, G., Nuglisch, H., Helie, J. and Ladommatos, N. *Fuel spray formation and gasoline direct injection*. in *8th International Symposium on Internal combustion diagnostics (AVL)*. 2008. Baden-Baden, Germany.
- [4] Zigan, L., Schmitz, I., Flügel, A., Wensing, M., & Leipertz, A. , *Structure of evaporating single-and multicomponent fuel sprays for 2nd generation gasoline direct injection*. Fuel, 2011. **90**(1): p. 348-363
- [5] .Martin, D., P. Pischke, and R. Kneer., *Investigation of the influence of multiple gasoline direct injections on macroscopic spray quantities at different boundary conditions by means of visualization techniques*. International Journal of Engine Research, 2010. **11**(6): p. 439-454.
- [6] Marchi, A., Nouri, J. M., Yan, Y. and Arcoumanis, C., *Internal flow and spray characteristics of pintle-type outwards opening piezo injectors for gasoline direct-injection engines*. SAE Trans. J. Engines, 2007. **116**(3): p. 01-1406.
- [7] Marchi, A., Nouri, J., Yan, Y. and Arcoumanis, C., *Spray stability of outwards opening pintle injectors for stratified direct injection spark ignition engine operation*. International Journal of Engine Research, 2010. **11**(6): p. 413-437.
- [8] Marchi, A., *Internal flow and spray characteristics of an outwards opening pintle-type gasoline-injector*. 2009, City University London.

## Measurement of a wavy and thin liquid film in a small two-fluid nozzle via a single-tip optical fibre probe

Hajime Furuichi<sup>1</sup> and Takayuki Saito<sup>2</sup>

1: Graduate School of Engineering, Shizuoka University, Japan

2: Research Institute of Green Science and Technology, Shizuoka University, Japan

### Abstract

In the present study, we developed a new measurement technique for a liquid film thickness by using a single-tip optical fibre probe (S-TOP). The S-TOP with a cone-shaped tip was employed, and was fixed parallel to the main stream in a transparent duct. First, we simultaneously obtained probing signals, and wavy surface images filmed by high-speed video camera. Processing the probing signals, a fraction of the liquid phase at every installation position of the S-TOP was calculated and compared with the visualized results. Second, we calibrated the OFP signals via our original 3D-numerical simulation. The simulator traced an enormous number of ray-segment trajectories in rigorous consideration of the polarization and energy of every ray. We provided a reconstructed wavy surface of the liquid film from visualized results, and the hypothetical S-TOP, to the computation. Traversing the 3D-modeled hypothetical S-TOP in the vertical direction against the pipe wall, we interpolated and corrected the experimental results. Finally, we found out that the installation position of the S-TOP equals the average thickness of the liquid film when the fraction of the liquid phase was 52%. In addition, we applied our new technique to the measurement of the liquid film inside a small-diameter two-fluid nozzle. As a result, the average thickness and maximum amplitude were 61  $\mu\text{m}$  and 28  $\mu\text{m}$ , respectively. Hence, the S-TOP technique was considered to possess high measurement accuracy and appropriateness satisfactorily for practical measurement of a thin and wavy liquid film.

---

### Introduction

An optical fibre probe (OFP) is one of useful techniques to measure a bubble or droplet in a gas-liquid two-phase flow; i.e. simultaneous measurement of bubble/droplet velocity, diameter and number density [1-4]. The measurement principle of the OFP is very simple. A sensing tip of the OFP detects a gas-liquid interface due to a difference of the refraction indices. In past studies regarding the OFP, it was forced to have limitations on spatial resolution, because at least two probes were needed to calculate parameters of a bubble/droplet. One of the authors developed a single-tip optical fibre probe (S-TOP) which can measure a bubble/droplet only with a single probe [4-6]. Since a diameter of the S-TOP's sensing-tip was small enough, highly spatial resolution was certainly fulfilled (less than 50  $\mu\text{m}$ ).

In the present study, we applied the S-TOP to measurement of a wavy liquid film thickness. Although measuring a liquid film flow is very necessary for improvement of safety and efficiency in industrial plants, no researchers realized the direct measurement method inside the practical equipment [7-10]. Moreover, it is difficult to accurately measure the liquid-film thickness, because the flow is wavy and a thin liquid film forms. We measured the liquid-film thickness by using an S-TOP with a cone-shaped tip (6- $\mu\text{m}$  diameter) that was set parallel to a pipe wall and traversed precisely. First, in the experiment, we detected output signals from the S-TOP, and captured wavy surface images by using a high-speed camera simultaneously. Through the image processing, time-series wave-heights of the liquid film were obtained, and the average thickness and maximum amplitude were obtained. From the probing signals, a fraction of liquid phase at every installation position of the S-TOP was calculated and compared with the visualization results of the liquid-film parameters. Second, we analysed optical probing signals by using our original 3D-ray-tracing simulator under the same conditions as the experiments in order to calibrate the experimental results. In this simulator, an enormous number of ray-segment trajectories were traced in the system composed of the S-TOP and liquid film by rendering complicated optical boundary conditions [11]. The output signals from a hypothetical S-TOP and the fraction of the liquid phase were computed by interpolating the installation positions where the actual S-TOP was fixed in the experiment. Further, a relationship between the installation position and the fraction was obviously obtained. Finally, appropriateness and applicability of the S-TOP were demonstrated in practical measurement. We found out the installation position of the S-TOP equals the average thickness of the liquid film when the fraction of the liquid phase was 0.52. Our new technique was demonstrated in measurement of a wavy and thin liquid film inside a small-diameter two-fluid nozzle. The average thickness and maximum amplitude were 61  $\mu\text{m}$  and 28  $\mu\text{m}$ , respectively. These results accorded with the corresponding visualization results.



### Basics of optical fibre probing

An OFP detects gas-liquid interface with its sensing tip [12]. Figure 1 shows a micrograph of the S-TOP's sensing-tip used in this study. The optical fibre was a step-index and multimode quartz fibre (core diameter: 100  $\mu\text{m}$ , clad thickness: 5  $\mu\text{m}$ ). Its end was fine-drawn into cone-shape by laser-processing, and a diameter of the sensing tip was 6  $\mu\text{m}$ . Figure 2 shows an optical setup of the OFP measurement system used in the present study. The laser beams from a LD (a) are focused on the other fibre end (inlet tip) (c) by an objective lens (b). Some of the incident laser beams reach the sensing tip by the total reflection in the fibre. They are reflected or refracted at the tip surface, depending on the phase around the sensing tip. Some of the returned laser beams in the optical fibre are extracted by a beam splitter (d) and polarizer (f). Finally, they are converted to electrical signals through a photomultiplier (f). The electrical output-signals are recorded in a digital oscilloscope (h). Consequently, the phases passing through the OFP tip can be detected based on the intensities of the returned laser beams.

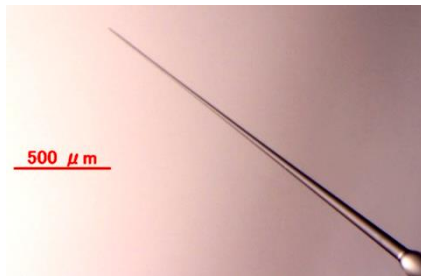


Figure 1. A cone-shaped tip of the S-TOP.

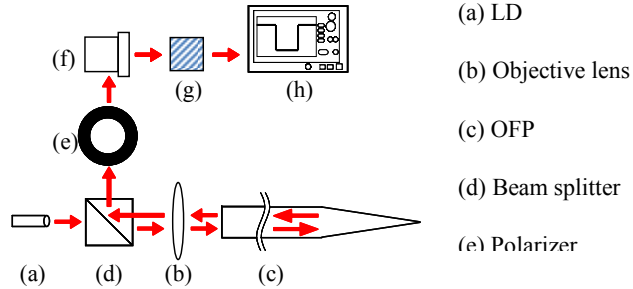
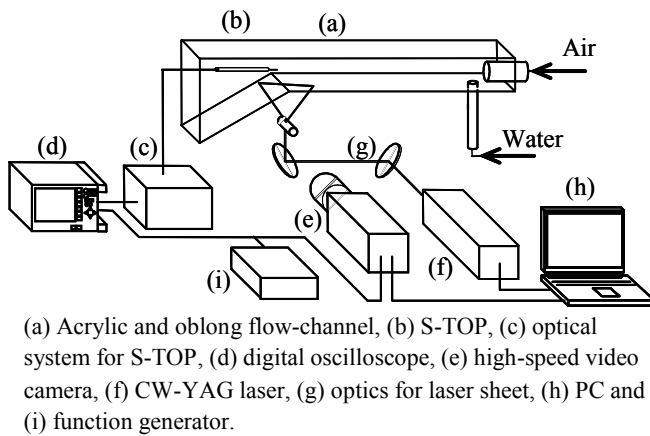


Figure 2. Optical setup of the OFP technique.

### Experimental setup

To establish our new technique, we executed preliminary experiment. We simultaneously measured a quasi-liquid-film generated in a transparent oblong duct by using the S-TOP and high-speed visualization (LIF method).

The experimental setup is illustrated in Figure 3. An acrylic and oblong duct (a) was horizontally fixed. Water (150 L/min) and compressed air (0.12 L/min) were injected from an inlet of the flow channel. The S-TOP (b) was horizontally fixed and traversed in the vertical direction. Its position was precisely controlled through a precisely linear stage. The fixed positions of the S-TOP from the duct bottom are listed in Table 1. The output signals of the S-TOP at every position were recorded in a digital oscilloscope (d). In addition, a high-speed video camera (4000 fps, 576×576 pixels, 6.7  $\mu\text{m}/\text{pixel}$ ) (e) was employed in order to visualize a measurement area of the S-TOP. A YAG-laser (wavelength: 632 nm) (f) was sheeted and irradiated from the duct bottom. The laser sheet of a 1-mm width excited Rhodamine B (excitation wavelength: 635 nm, fluorescence wavelength: 675 nm) that was dissolved in the water. Furthermore, the output signals from the S-TOP and the camera were perfectly synchronized by using a function generator (i).



(a) Acrylic and oblong flow-channel, (b) S-TOP, (c) optical system for S-TOP, (d) digital oscilloscope, (e) high-speed video camera, (f) CW-YAG laser, (g) optics for laser sheet, (h) PC and (i) function generator.

Table 1. Fixed positions of the OFP.

$L_p$ [ $\mu\text{m}$ ]						
63	163	263	313	363	413	463
513	563	663	763	863	963	1063

Figure 3. A schematic of the experimental setup.

## Signal processing

Intensity of the returned laser beams from the sensing tip changed, depending on the phase (i.e. air or water) around the sensing tip. Hence, an ON/OFF signal was obtained from the S-TOP. A typical and processed output signal is shown in Figure 4. The difference in refraction indices between the air phase and the optical fibre (quartz glass) is large while the sensing tip is positioned in the air phase ((1), (2)). Thus, the output voltage becomes high ( $V_{gas}$ ). On the other hand, the difference in the refraction indices is small while the tip is dipped in the liquid film (water). Thus, the output voltage becomes low ( $V_{liquid}$ ) owing to a decrease in the intensity (3). To determine the phase around the tip through the signal processing, the threshold  $V_{th}$  was used. We calculated the threshold via the histogram method. In the S-TOP measurement, the output signals were detected at every fixed position. A fraction of the liquid phase  $\alpha$  was calculated from each raw-signal by the following equation:

$$\alpha = \frac{\sum_{i=1}^n T_i}{T_{all}} \quad (1)$$

where  $T_i$  and  $T_{all}$  are the discrete time interval during the tip's immersion in the liquid phase, and the total measurement time, respectively. A summation of  $T_i$  was calculated by the signal-processing with the threshold voltage  $V_{th}$ . According to Eq. (1), the tip was immersed in the liquid film in the total measurement time when the fraction  $\alpha$  equals 1. On the other hand, the tip was in the air phase when the fraction  $\alpha$  equals 0.

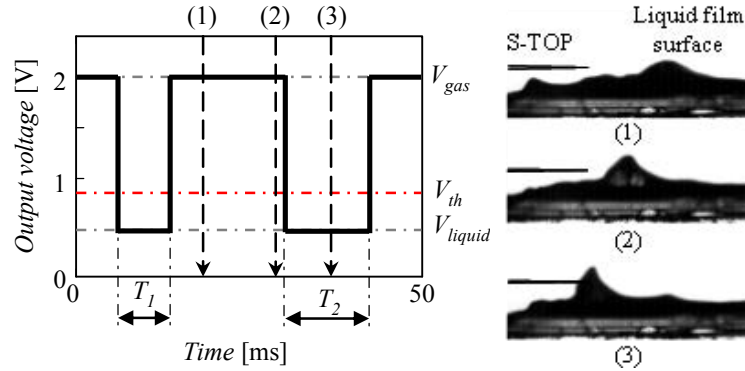
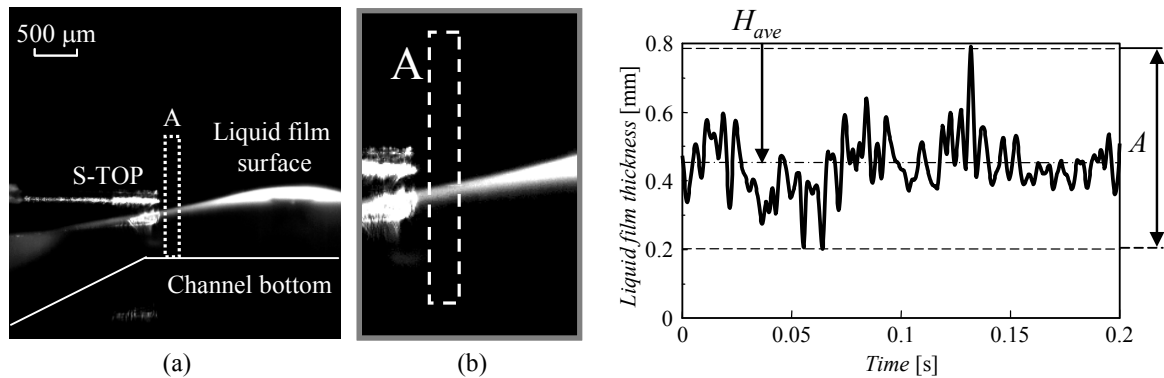


**Figure 4.** A calculation for a fraction of liquid phase.

## Visualization Results

Figure 5 shows a typical image captured via the high-speed video camera. We visualized liquid-film surfaces excited by the sheeted YAG-laser. In Fig. 5, the fluorescent surface was sharp enough to detect the edge. To obtain the parameters of the liquid film, an interrogation area “A” was selected immediately upstream of the S-TOP’s sensing-tip. We calculated the average wave-height in “A”, and processed every image. Thus, the time-series wave-height was obtained and a typical result is plotted in Figure 6. Further, we estimated the average thickness  $H_{ave}$  and maximum amplitude  $A$  of the liquid film as references for the results through the S-TOP.



(a) A typical image captured by the visualization. (2) A close-up image of the extracted area.

**Figure 6.** A time-series wave-height calculated from the image processing in the interrogation area.

**Figure 5.** An image processing of the visualization result.

It was to be desired that the interrogation area was positioned in the exactly-same area as the sensing-tip (“C” in Figure 7 (a)). However, in the area “C”, the fluorescence of the wavy surface was not sharp enough to be detected, because the laser beams emitted from the S-TOP were scattered. Further, the liquid film was basically considered as an unsteady flow [13, 14]. Hence, we had to quantify a difference of the time-series wave-forms that was caused by determination of an interrogation area. We calculated a correlation coefficient between the wave-form derived from the interrogation area “A” and that derived from “B”. “B” was a mobile area in the  $x$ -direction from  $X_0$  to  $X_1$  (a 100-pixel difference between  $X_0$  and  $X_1$ ) as shown in Fig. 7 (a). Comparing the average wave-height in every mobile area “B” to that in the fixed area “A”, the correlation coefficient was approximately equal to 1 as plotted in Fig. 7 (b). As a result, the wave-forms were independent of the interrogation area. Therefore, the wave-form calculated in “A” was assumed to be same as that in “C”.

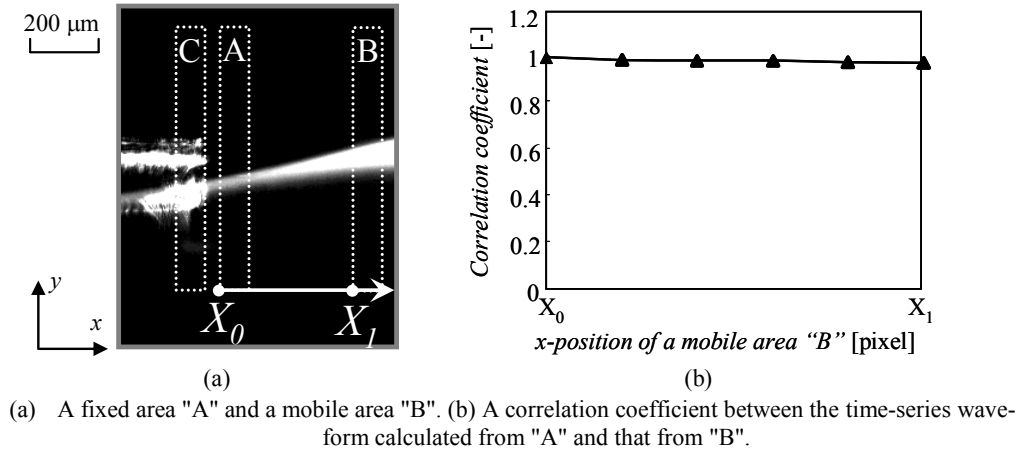


**Figure 7.** An influence of a determination of the time-series wave-height.

### Results of liquid-phase fraction

To compare the results measured through the S-TOP with the reference results through the visualization, we considered a relationship between the liquid-phase fraction  $\alpha$  and a relative height of the S-TOP. The experimental results are plotted in Figure 8 (a) and (b) (circles). The horizontal axis represents the liquid-phase fraction  $\alpha$ . The vertical axis represents the relative position (dimensionless installation position of the S-TOP) given by

$$R_p = \frac{L_p - H_{ave}}{A} \quad (2)$$

The reference results via the visualization were substituted into  $H_{ave}$  and  $A$  in Eq. (2), respectively. The relative position  $R_p$  equals 0 when the S-TOP position equals the average thickness  $H_{ave}$ . Thus, in the practical measurement without the visualization (only with the S-TOP), the liquid-film parameters were able to be estimated by using only the fraction  $\alpha$ .

We interpolated and corrected the experimental results in consideration of numerical results from a 3D-ray-tracing simulation [8], to accurately obtain the relationship between the fraction  $\alpha$  and the relative position  $R_p$ . In the simulator, the light waves were transposed to ray segments, and the light diffraction was negligible. 3D-reflection/refraction of the incident laser beams was numerically computed based on the Snell’s law. In addition, the complicated probing signal from a hypothetical S-TOP was output by computing the polarization and energy of every ray through the Fresnel’s equation. To simulate the probing signal, the incident/reflection angles and the energy of refraction/reflection were quantified on the interfaces. We rendered 3D-curved surfaces of the liquid film flow which were referred from the time-series wave heights in Fig. 6. The installation positions of the actual S-TOP were interpolated by traversing the hypothetical S-TOP. Therefore, the computational fraction and an interpolation of the experimental plots were obtained as shown in Fig. 8 (b) (dotted line). Furthermore, we successfully corrected the interpolated line as drawn in Fig. 8 (b) (solid line). The correction was achieved by using the least square method and by parallel-shifting the interpolated line. The correction was considered to be needed owing to an asymmetrical tip of the actual S-TOP. Although the fibre-tip was fine-drawn by laser-processing, the cone-shaped tip was slightly strained. Hence, the sensing tip was not exactly on the central axis of the actual S-TOP. On the other hand, the 3D model of the hypothetical S-TOP had an exactly circular-cone-shaped tip. The relationship between the interpolated line and the corrected line was represented by a diameter of the S-TOP as below,

$$TH_a = TH_n - 0.233r \quad , \quad (3)$$



where  $TH_a$ ,  $TH_n$  and  $r$  were interpolated values of the fraction  $\alpha$ , a corrected value of the fraction  $\alpha$  and the diameter of the OFP, respectively. Eq. (3) is applicable to a cone-shaped tip of an S-TOP. For other shapes of the tip, we need to find out the specific coefficient of  $r$ . Therefore, based on the numerical simulation of the S-TOP, the calibration enables us to correctly calculate the relationship between the fraction  $\alpha$  and  $R_p$ .

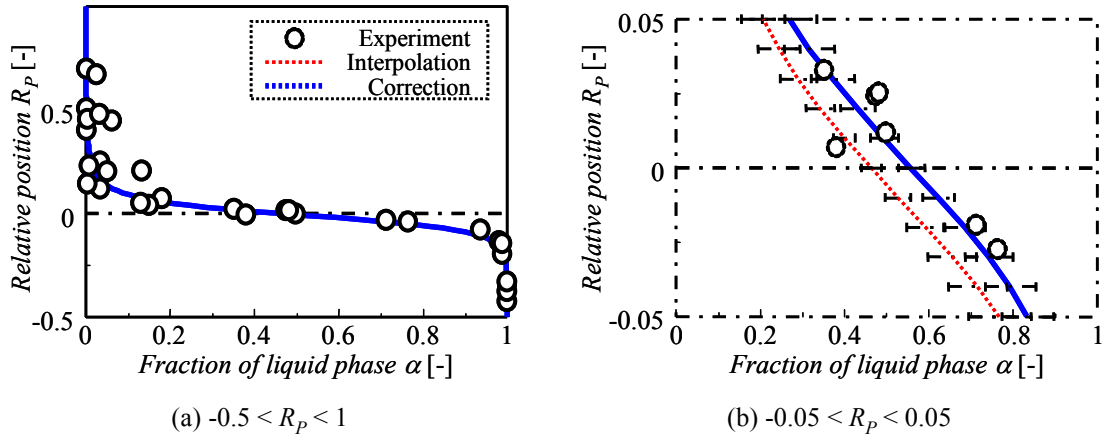


Figure 8. Results of the liquid-phase fraction from the S-TOP.

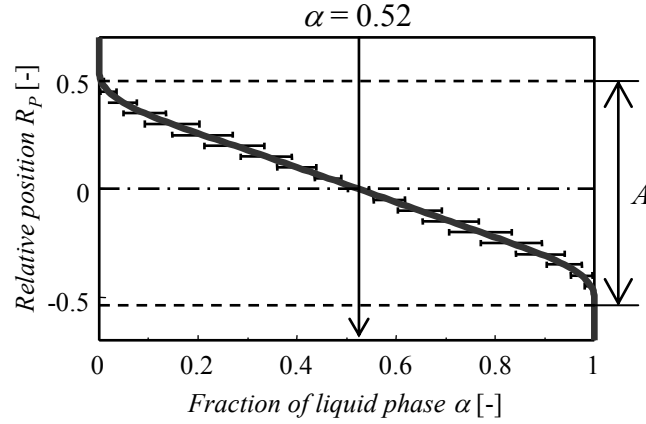


Figure 9. Results of the numerical simulation with the 100-times-iterated random-wave.

### Measurement results in a small-bore two-fluid nozzle

In a practical measurement with the S-TOP, we need to measure average liquid-film-thickness only by using the liquid-phase fraction  $\alpha$ . We generalized this measurement technique to a liquid film flow by computing random waves. A random wave was derived from a superposition method of linear progressive waves with different amplitude, period, length and random phase difference. By computing a hypothetical S-TOP with the 100-times-iterated waves, a result of the relationship between the fraction  $\alpha$  and the relative position  $R_p$  was obtained. The result almost accorded with Eq. (3). In Figure 9,  $R_p$  equals 0 with a standard deviation of 0.02 when  $\alpha$  is equal to 0.52. Moreover, a margin of  $R_p$  in the  $\alpha$  range between 0 and 1 equals the maximum amplitude  $A$ .

We applied those results to a practical measurement of an annular flow inside a steam-water two-fluid nozzle (inlet diameter: 13.0 mm, outlet diameter: 6.0 mm) [15]. In consideration of the calibrated results of the previous experiment, the average thickness  $H_{ave}$  and maximum amplitude  $A$  of the liquid film were estimated in the condition of  $R_p = 0.52$  and  $0 \sim 1$ .  $H_{ave}$  and  $A$  resulted in  $61 \pm 6.2 \mu\text{m}$  and  $28 \pm 6.2 \mu\text{m}$ , respectively. Thus, our new technique using the S-TOP had high effectiveness for practical measurement of an annular-liquid-film flow, and it was applicable in measurement of thin and wavy liquid films of several tens micrometres.

### Conclusion

The objective of this study was to newly establish a liquid-film measurement method using the S-TOP (Single-Tip Optical-fibre Probe). First, we simultaneously obtained the output signals from the S-TOP and visualization images. The relationship between the liquid phase fraction  $\alpha$  and the relative position of the S-TOP  $R_p$  was obtained from the signals and visualization. Second, we rendered a hypothetical S-TOP touching a 3D-

wave-surface using the ray tracing simulator. We successfully interpolated and corrected the experimental results. Finally, we found out the installation position of the S-TOP was equal to the average thickness  $H_{ave}$  when the fraction  $\alpha$  was 0.52. Furthermore, the breadth of  $R_p$  in the  $\alpha$  range between 0 and 1 was equal to the maximum amplitude  $A$ . In the demonstration, we measured the annular liquid-film flow inside a small two-fluid nozzle via the S-TOP.  $H_{ave}$  and  $A$  were 61  $\mu\text{m}$  and 28  $\mu\text{m}$ , respectively. Hence, our new method using an S-TOP possesses high measurement accuracy and appropriateness in practical measurement for a thin and wavy liquid film.

## Acknowledgements

The present study was promoted and financially supported by Category “A” of the Grants-in-Aid for Scientific Research, Japan Society for the Promotion of Science. We thank JSPS for its help in the financial support.

## Nomenclature

$V_s$	output voltage level [V]	$T_s$	time interval [sec]
$\alpha$	fraction of liquid phase [-]	$R_s$	relative position [ $\mu\text{m}$ ]
$L_s$	installation position [ $\mu\text{m}$ ]	$H_s$	liquid film thickness [mm]
$A$	maximum amplitude of liquid film [mm]		
$r$	diameter of S-TOP		

### Subscripts

gas	gas phase	liquid	liquid phase
th	threshold	P	S-TOP (probe)
total	total measurement	ave	average

## References

- [1] Miller, N. and Mitchie, R. E., Measurement of local voidage in liquid/gas two-phase flow systems using a universal probe, *J. Brit. Nucl. Energy Soc.*, 2, pp. 94-100, (1970).
- [2] Cartellier, A. and Achard, J. L., Local phase detection probes in fluid/fluid two-phase flows, *Rev. Sci. Instrum.* 62, pp. 279-303, (1991).
- [3] Mudde, R. F. and Saito, T., Hydrodynamical similarities between bubble column and bubbly pipe flow, *J. Fluid Mech.*, 437, pp. 203-228, (2001).
- [4] Saito, T. et al., Measurement of tiny-droplets using a newly developed optical fibre probe microfabricated by femtosecond pulse laser, *Meas. Sci. Technol.*, 20, 114002, (2009).
- [5] Mizushima, Y. and Saito, T., Detection method of a position pierced by a single-tip optical fibre probe in bubble measurement, *Meas. Sci. Technol.*, 23, 085308, (2012).
- [6] Mizushima, Y. and Saito, T., Measurement technique of bubble velocity and diameter in a bubble column via single-tip optical-fiber probing with judgment of the pierced position and angle, *Chem. Eng. Sci.*, In Press, (2013).
- [7] Hazuku, T. et al., Measurement of liquid film in microchannels using a laser focus displacement meter, *Experiments in Fluids*, 38, pp. 780–788, (2005).
- [8] Takamasa, T. and Kobayashi, K., Measuring interfacial waves on film flowing down tube inner wall using laser focus displacement meter, *Int. J. Multiphase Flow*, 26, pp. 1493-1507, (2000).
- [9] Alekseenko, S. V. et al, Measurements of the liquid-film thickness by a fiber-optic probe, *Instruments and Experimental Techniques*, 46 (2), pp. 260–264, (2003).
- [10] Zaitsev, D.V. et al., Measurement of locally heated liquid film thickness by a double-fiber optical probe, *Experiments in Fluids*, 34, pp. 748–754, (2003).
- [11] Sakamoto, A. and Saito, T., Computational analysis of responses of a wedge-shaped-tip optical fiber probe in bubble measurement, *Rev. Sci. Instrum.*, 83 (7), 075107, (2012).
- [12] Sakamoto, A. and Saito, T., “Robust algorithms for quantifying noisy signals of optical fiber probes employed in industrial-scale practical bubbly flows”, *Int. J. Multiph. Flow*, Vol. 41 pp. 77–90 (2012).
- [13] Giroud-Garapon, S., Heid, G., Laverne G., Simonin O., Experimental and numerical study of thin wall liquid film spreading on a heating surface, *ILASS Europe 2002*, Saragossa, Spain, (2002).
- [14] Fukano, T. and Ousaka, A., Prediction of the circumferential distribution of film thickness in horizontal and near-horizontal gas-liquid annular flows, *Int. J. Multiphase Flow*, 15 (3), pp. 403-419, (1989).
- [15] Sanada, T., Mitsuhashi, Y., Mizutani, H. and Saito, T., Flow structure of steam–water mixed spray, *Nucl. Eng. Des.* 240 (12), pp. 3974–3983 (2009).

## Planar droplets sizing of a hollow-cone spray using SLIPI-LIF/MIE

Y.N. Mishra, E. Kristensson, S.G. Pettersson and E. Berrocal

Division of Combustion Physics, Lund University, SE-22100, Lund, Sweden

### Abstract

In this work, we report an original experimental approach for measuring the two-dimensional distribution of the droplets Sauter Mean Diameter (SMD) using the SLIPI-LIF/MIE technique. A hollow-cone spray is formed by continuously injecting water mixed with a non-toxic fluorescing dye at 20 bars injection pressure. The spray is illuminated using a continuous wave laser. The illumination wavelength (here, 447 nm) is carefully chosen to excite the injected dye/water mixture, which generates a significant Laser Induced Fluorescence (LIF) signal peaking at 514 nm. The LIF and Mie signals are simultaneously recorded using two CCD cameras and their intensity ratio is used to extract a two-dimensional distribution of the droplets SMD. In this article, we show that even for the case of a dilute hollow-cone spray, where single scattering events are in majority, the LIF/Mie measurement of droplets SMD still remains strongly affected by multiple light scattering. We demonstrate, then, that the use of SLIPI is unavoidable to obtain trustable SMD measurements based on the LIF/Mie ratio, even for optically dilute sprays.

---

### 1. Introduction

The practical demands of high performance of liquid atomizer based combustion devices have necessitated improving the atomization process since it is directly linked to the efficiency of the device. The performance of a spray is judged by its ability to disintegrate the bulk liquid into micrometric droplets which transport and evaporate prior to combustion. This characteristic of a spray decides the efficiency as well as features of any liquid driven combustion system. It is therefore significant to investigate the spray structure with both high temporal and spatial resolution. Droplets sizing is a key component for determining the spatial distribution of spray morphology and for quantitative characterization of spray.

In the past, various optical measurement techniques have been developed to determine droplet size distributions. One of the first optical approaches for drop-sizing was reported in 1976 and is known as ensemble light scattering [1]. The ensemble light scattering (ELS) is a line-of-sight technique, which detects forward scattered light from the particles in a light path formed by collimated laser beam. Prior to its arrival at the detector, the non-scattered signal from the droplets passes through a Fourier Transform lens to generate a diffraction pattern. For each spherical particle, this diffraction pattern represents a concentric laser light ring. Widely spaced rings represents small spherical particles whereas, a large spherical particle represents closely spaced rings. Apart from these features, the ELS measurement provides a poor spatial resolution and is very sensitive to multiple light scattering issues. In the early eighties, Phase Doppler anemometry (PDA) [2-3] was introduced as a point measurement technique for measuring the spray droplet diameters. Today, the technique is used as a standard tool for simultaneous real time measurement of the geometric size of droplets and velocity. Even though, it is a well-established and accurate tool for droplet characterization, the PDA measurements can take several hours due to point by point scanning over the wide-spread spray. Also, the technique fails to give any data in optically dense media.

In the year 1993, planar drop-sizing (PDS) was first time implemented in a transient spray as an imaging tool for instantaneous two-dimensional mapping of the droplets distribution [4]. In PDS, the LIF and Mie signals from a light sheet illuminated media are simultaneously recorded and the intensity ratio of the LIF and Mie signal yields relative SMD of spray droplets [4-7]. As an advanced technique, PDS has two main advantages over PDA, first, improved spatial resolution and second, the faster measurement over a wider section of a spray. However, discrepancies in PDS measurements remained prominent mainly due to the multiple light scattering and the SMD measurements were not reliable. Later, polarization ratio method (PRM) was developed for measuring the relative SMD [8]. In PRM, a 45<sup>0</sup> polarized laser beam crosses a spray and the vertical and horizontal components of Mie signal are simultaneously recorded with two cameras. The ratio of the vertical and horizontal components is used to deduce the geometrical mean diameter. PRM technique has not been explored much due to the multiple light scattering issues. Therefore, all the above mentioned techniques are efficiently applicable only in low droplets densities to avoid signal perturbations introduced by multiple light scattering. In optically dense sprays, measurements are “paralyzed” by both multiple light scattering and light extinction. A detailed study has been reported in reference [9], on the account for light extinction and multiple scattering in PDS of dense sprays. Recent results [10] from planar droplet sizing have shown that multiple light scattering contributions are not the same between the LIF and Mie signals and cannot, therefore, be simply removed from the LIF/Mie ratio. The intensity contribution from multiple scattering needs to be suppressed on both the LIF and Mie signals for accurate SMD measurements.

Structured Laser Planar Illumination Imaging (SLIPI) has been established as a recognized diagnostics for efficiently removing the multiple light scattering contributions in optically dense sprays [11]. In reference [10], the SLIPI approach has been used for the first time in combination with the LIF/Mie ratio for mapping the droplets SMD in a non-combusting diesel spray. It has been shown that SLIPI was leading to consequent improvement in measuring the SMD for the case of optically dense media such as diesel sprays. However, the necessity of using SLIPI-LIF/Mie in the case of dilute sprays has not been shown yet. Using the SLIPI as a tool for mitigating multiple light scattering, it is of relevance to investigate PDS approach on a standard hollow-cone water spray. Here in this report, we have applied the SLIPI-LIF/Mie drop-sizing technique to determine the SMD of a hollow-cone water spray droplets. Since, a large number of applications are based on the use of hollow-cone sprays, the presented results will be of interest to researchers spanning from academic to industrial areas.

## 2. Description of SLIPI-LIF / Mie Technique

### 2.1 SLIPI

SLIPI stands for **Structured Laser Illumination Planar Imaging**. It works on the principle of combining structured illumination with planar laser imaging. The main goal of the SLIPI technique is to preserve all the singly scattered photons while removing most of the multiply scattered photons. A Ronchi grating is usually used to create the modulated light sheet. An image of a sample illuminated with a sinusoidal modulated intensity is described by:

$$I(x, y) = I_C(x, y) + I_S(x, y) \cos(2\pi x v + \varphi) \quad (1)$$

where  $v$  represent the modulation frequency, and  $\varphi$  the spatial phase. Here,  $I_C(x, y)$  is the intensity of singly and multiply scattered photons and  $I_S(x, y)$  represents the amplitude of singly scattered photons only. SLIPI extract and preserve  $I_S(x, y)$  while removing  $I_C(x, y)$  and  $\cos(2\pi x v + \varphi)$  from the image after post processing. While crossing a scattering medium like a spray, multiply scattered photons lose the modulated signature while singly scattered photons preserve it. Thus the amount of single light scattering represents the local undisturbed amplitude of modulation. To extract this information, experimentally, a minimum of the three intensity modulated images are recorded with a spatial phase corresponding to  $0^\circ$ ,  $120^\circ$  and  $240^\circ$ . To produce a SLIPI image, the root-mean square of the three recorded images is calculated as:

$$I_S \frac{\sqrt{2}}{3} [(I_0 - I_{120})^2 + (I_0 - I_{240})^2 + (I_{120} - I_{240})^2]^{1/2} \quad (2)$$

A conventional image can be constructed from the simple averaging of the three images as:

$$I_C = \frac{I_0 + I_{120} + I_{240}}{3} \quad (3)$$

Thanks to the recently published thesis on SLIPI [12], the technique and its applicability have been reviewed and discussed in details.

### 2.2 LIF / Mie droplet sizing

The SMD of spray droplets is possible to determine by taking the ratio of a signal proportional to droplet volume (LIF) and a signal proportional to droplets surface area (Mie) [4]. For each pixel of a camera, the SMD corresponding to a distribution of droplets is expressed as:

$$SMD = \frac{K_{LIF}}{K_{Mie} \cdot Q_s} \frac{\int_{D=0}^{\infty} D^3 \cdot dN(D)}{\int_{D=0}^{\infty} D^2 \cdot dN(D)} \quad (4)$$

where  $dN(D)$  is the droplet probability distribution and  $Q_s$  is related to incident ray detection angle.  $K_{LIF}$  and  $K_{Mie}$  include experimental components such as scattering efficiency, detector response, signal collection angle, laser power etc. Some publications [13-14] which focus on the accuracy of the LIF/Mie ratio for SMD calculations have found that the ratio of  $K_{LIF}/(K_{Mie} \cdot Q_s)$  should not be considered as a constant (especially at  $90^\circ$  detection [10]) as it has been assumed in earlier papers [4, 5, 6]. Therefore, in SMD measurements several experimental complications remain in addition to numerically calculated uncertainties. To be able to extract the absolute SMD using SLIPI LIF/Mie approach, a number of assumptions and procedures must be considered as reported in reference [10]. In this study, only the relative SMD is considered in the two-dimensional distribution of the hollow-cone water spray droplets.

### 3. Description of the experiment

### 3.1 Experimental set-up

A hollow-cone water spray is investigated at ambient temperature, atmospheric pressure and with a liquid injection pressure set to 20 bars. In order to achieve a broad band LIF signal, the injected water is seeded with translucent fluorescing dye from yellow highlighter's ink. While exiting the nozzle, the dyed water solution forms a liquid sheet which quickly disintegrates into ligaments and fine droplets. A portable SLIPI setup has been designed and a schematic of the optical arrangement is shown in figure 1. The center of the spray is illuminated at  $\lambda = 447 \text{ nm}$  (CW: DPSS solid-state laser) at a height of 1 cm below the nozzle tip. The vertically modulated laser sheet of height 5.8 cm excites the seeded dye present in the spray droplets. This results to a LIF emission peaking at 514 nm. The Mie and LIF signals are specifically detected using two high efficiency optical filters. For the LIF signal a long pass filter with a cut-off wavelength at 490 nm is used, whereas, for the Mie signal, a band-pass filter with transmission centered at 438 nm ( $\pm 12 \text{ nm}$ ) is used (optical density 6 in blocking). The SLIPI LIF and Mie images are simultaneously recorded using the standard detection scheme (two cameras of same dynamic range positioned orthogonal to each other) at  $90^\circ$  from the illuminated plane. This scheme allows detecting the LIF and Mie signals simultaneously once the perfect overlapping in between the two images is obtained to ensure the actual spray symmetry deduced from the ratio. For the perfect overlapping, the LIF and Mie images must be warp in order to have the same field of view at the pixel scale. This warping process is performed from a calibration procedure and using an adequate test pattern. However, in order to obtained good statistics of the spray development over time, the LIF and Mie images were recorded with a relatively long exposure time. The LIF signal was recorded at camera exposure time of 200 ms with 200 accumulations, and the Mie signal was recorded at exposure time of 5 ms with 300 accumulations.

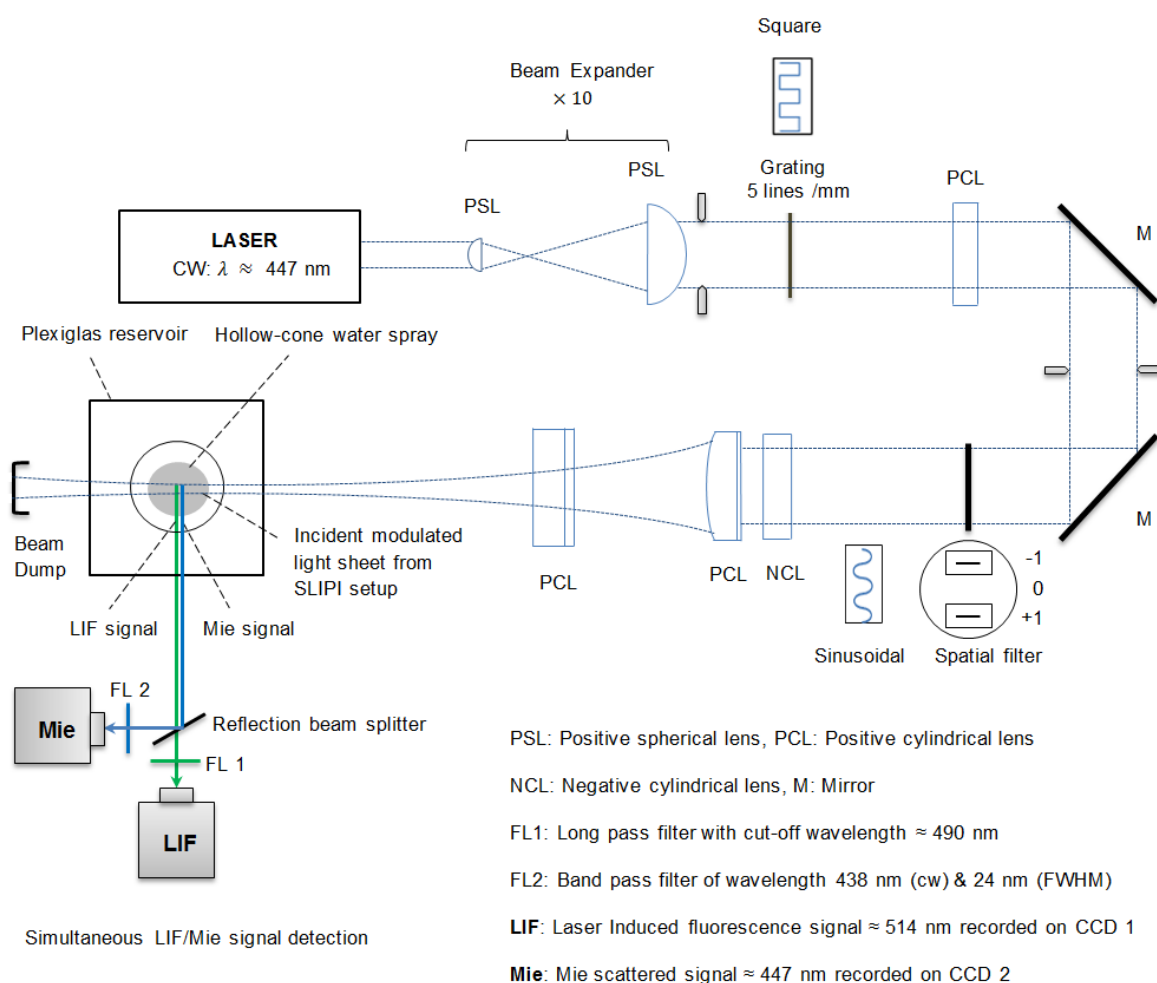


**Figure 1: Top-view of the experimental setup**

The exposure time was adjusted to avoid image saturation while optimizing the camera dynamic range. The CCD cameras used for this experiment are two 14 bit electrons multiplying CCDs (EMCCD Luca R from

ANDOR), providing images of  $1004 \times 1002$  pixels. While the incident laser power was equal to 900 mW, the final averaged power of the laser sheet was equal to 45 mW. The f-number of the collecting lens was adjusted to  $f_{\#}=8$ .

### 3.2 Transmission measurements

Transmission measurements have also been performed in order to deduce the optical thickness of the spray. These measurements were based on SLIPI using a glass cuvette filled with the fluorescing water solution used in the spray. The incident profile of the light sheet was deduced by imaging the cuvette when no spray was running, while the final light sheet intensity profile was deduced by imaging the cuvette while the spray was running.

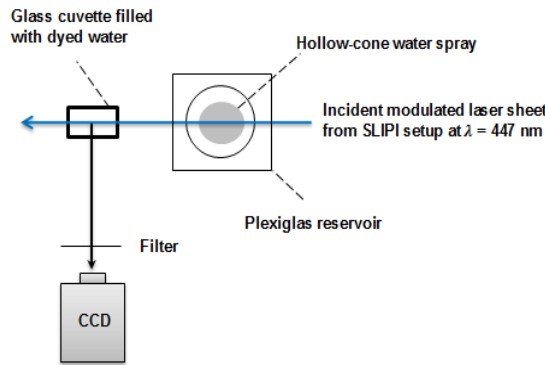
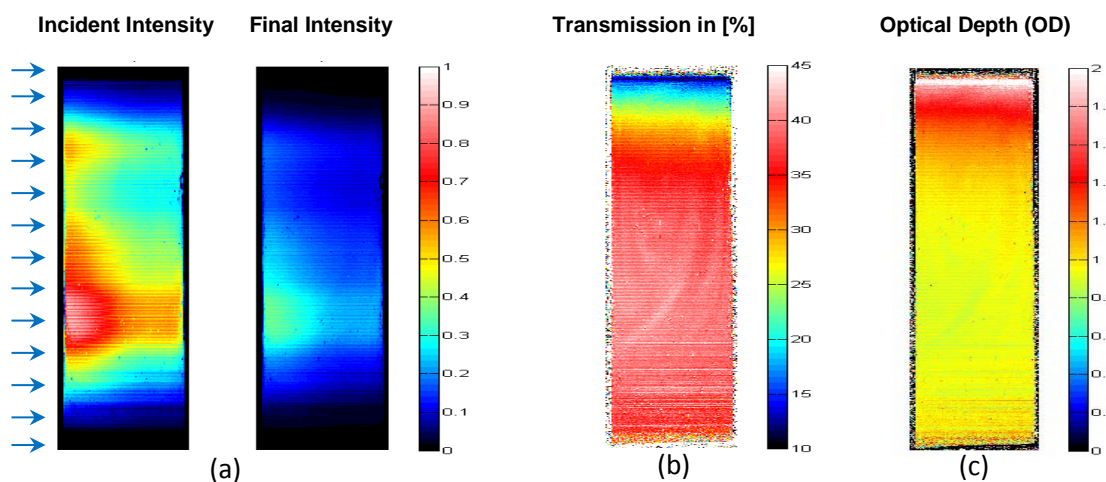


**Figure 2:** Top-view of the transmission setup. A glass cuvette filled with the fluorescing water was imaged to obtain an image of the laser sheet profile. For recording the incident and final intensity profiles, the spray is turned off and on respectively.

## 4. Results and discussions

### 4.1 Transmission measurements in the hollow-cone water spray

The incident and final intensity profiles are shown in figure 3 (a). The averaged transmission profile is shown in figure 3(b). These results show that while crossing the spray, light intensity has reduced to approximately 35-40%. The averaged transmission is calculated by taking the ratio of the final and incident profile images. The Optical Depth (OD) of the hollow-cone water spray is shown in figure 3(c). The OD is calculated based on the Beer-Lambert law [15] and corresponds here to an averaged value of  $OD \sim 1$ . Therefore, most of the incident light is interacting only once with the droplets. From this measurement it is evident that the hollow-cone spray used in our experimental study is dilute.



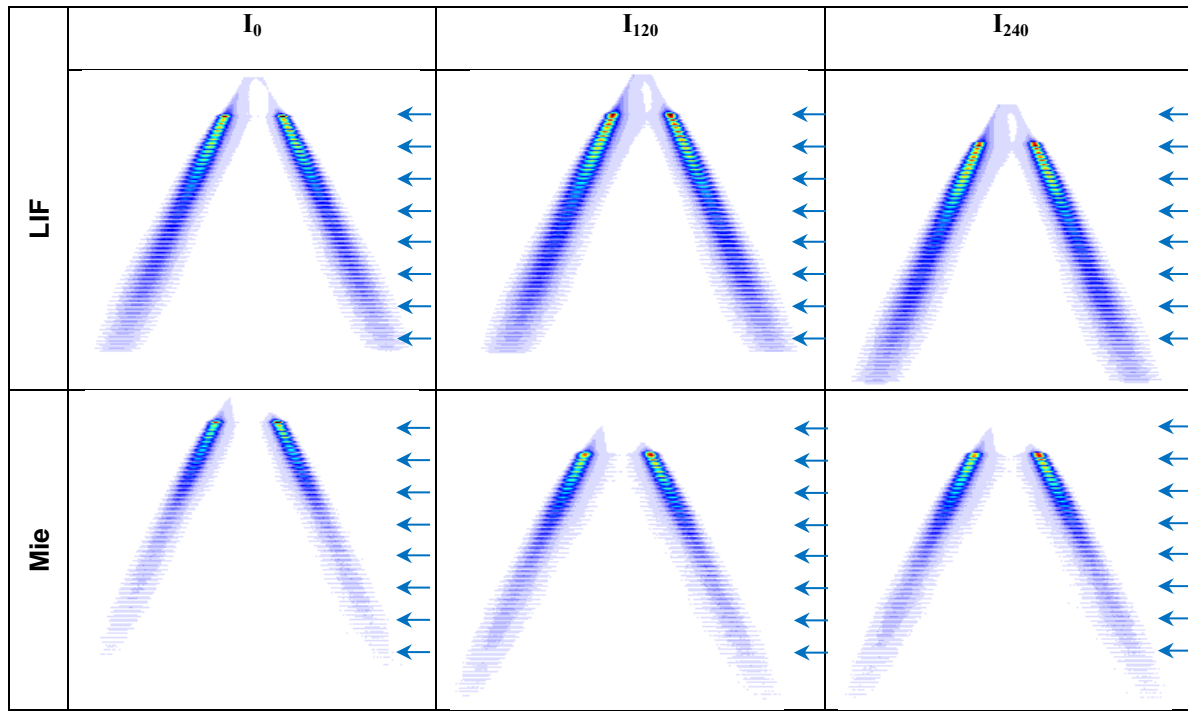
**Figure 3:** Incident and final intensity profile of the laser sheet. The measurement is performed using a rectangular glass cuvette containing the fluorescing water solution (see figure 2 for experimental description). Based on these measurements the light transmission could be deduced together with the optical depth of the spray along the vertical axis of the laser sheet (see figure 3(b) and (c)).

Figure 3(b) represents the light transmission along the vertical axis of the light sheet crossing the spray. These results are obtained by dividing the final intensity profile by the incident intensity profile shown in figure 3(a). Figure 3(c) shows the deduced optical depth. In this case, the OD is mostly close to  $\sim 1$  which confirms that the spray is dilute.

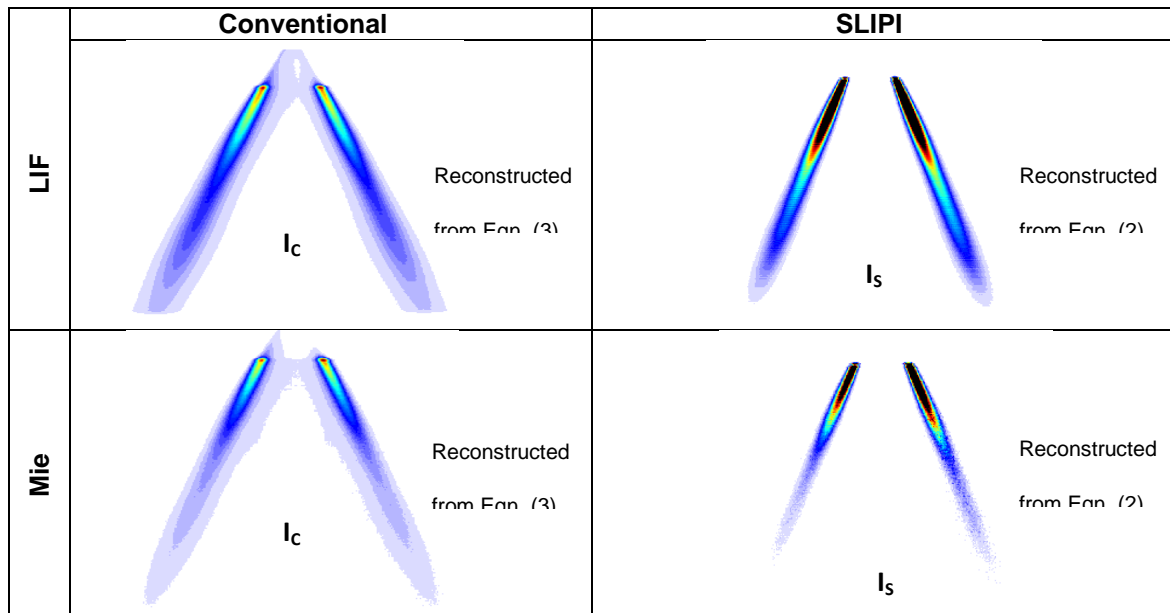
#### 4.1 Creation of conventional and SLIPI LIF/Mie images from three modulated images

Figure 4 shows the conventional LIF/Mie and the SLIPI LIF/Mie images generated by recording the three modulated images of LIF and Mie signals from the hollow-cone spray. The three modulated LIF and Mie images recorded with a phase difference of  $120^\circ$  degrees are shown in figures 4(a). The corresponding conventional LIF/Mie images are created by following equation (3) while SLIPI-LIF/Mie images are created by using equation (2) as shown in figure 4(b). The incident light is illuminating the hollow-cone spray from the right direction is represented by arrows.

(a)



(b)



**Figure 4:** The Conventional LIF/Mie and the SLIPI LIF/Mie images of the hollow-cone spray are generated by recording the three modulated images of LIF and Mie signals as shown in figure 4(a). Images showing the three modulated images of LIF and Mie signals are recorded with a phase difference of  $120^\circ$ . The conventional LIF/Mie images created by averaging the three modulated images and the SLIPI LIF/Mie images generated by taking the root-mean square of the three modulated images are shown in figure 4(b).



Comparing the conventional and the SLIPI images in figure 4(b), it is evident that in the SLIPI-LIF /Mie images the signal intensity at right shoulder of the hollow-cone spray is higher as compared to its left shoulder (due to light extinction), whereas, in the conventional LIF/Mie images, the light intensity from the two shoulders of the hollow-cone spray has not reduced much. This is due to the presence of the cumulative contribution of multiple light scattering in case of conventional LIF/Mie images.

Therefore, the issues of multiple light scattering are apparent in conventional LIF/Mie images of the hollow-cone spray and images are affected by blurring effects. On the other hand, those effects are not visible in the SLIPI images because the SLIPI technique removes most of the multiply scattered photons. This result is consistent with the application of SLIPI approach in a hollow-cone water spray in previous paper [11].

#### 4.2 Relative SMD mapping

The relative SMD of droplets distribution is shown in figure 5 from the LIF/Mie image ratios. A good symmetry of the hollow-cone spray can be observed on these images, both for the conventional and the SLIPI images. Color bars with black and white background have both been used on the same SMD images for comparison purposes. The Conventional LIF/Mie and the SLIPI-LIF/Mie images are presented in figure 5(a-c) and in figure 5(b-d) respectively. From the conventional SMD part, we could easily see the presence of blurring effects around the central part of the spray. This contributes to dislocation of local signature of droplets distributions.

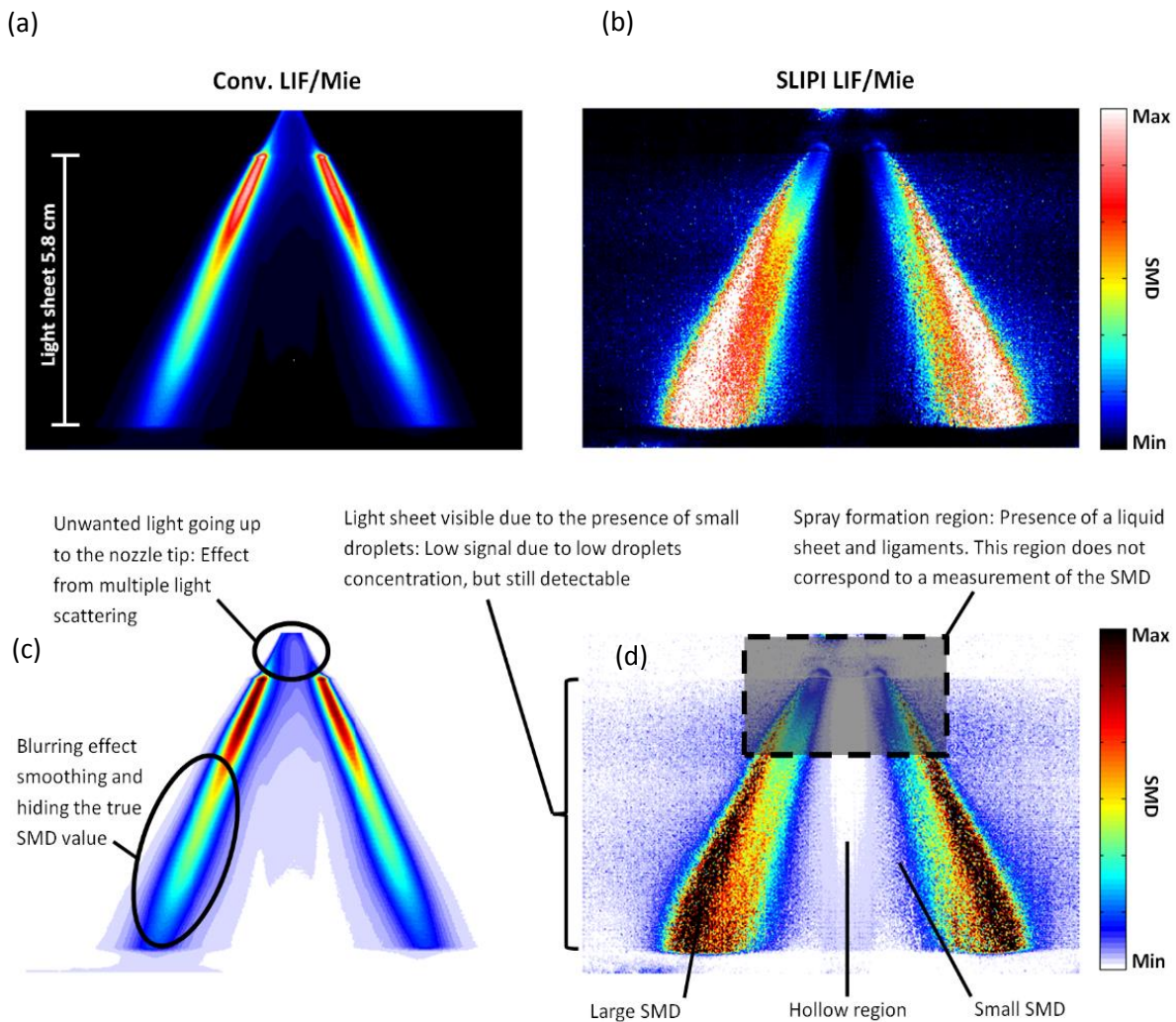


**Figure 5:** Comparison between the conventional and the SLIPI SMD images. Figures 5(a) and 5(c) represent the conventional LIF/Mie images with black and white background, respectively. The SLIPI LIF/Mie images with black and white background are shown in figures 5(b) and 5(d). This comparison concludes that the conventional SMD images suffers from multiple light scattering ; whereas, the SLIPI SMD images yield a faithful description of relative SMD distribution in the hollow-cone spray.

In conventional images, such issues are mostly apparent around the spray edges and towards the spray forming tails. In figure 5(c), the marked area refers to those effects; hiding the true value of SMD due to smoothing and unwanted light going up to the nozzle exit. On the other hand, the SLIPI-SMD images given in figure 5(b) and 5(d) are corrected from the multiple light scattering contributions and, therefore, reproduce a faithful two dimensional distributions of droplets SMD. However, the droplets SMD cannot be considered in rectangular marked area in figure 5(d) due the presence of a liquid sheet and ligaments. The spray droplets with large and low SMD can be easily distinguishable along with the hollow region as shown in figure 5(d). The global blurring effect from the center of the hollow-cone spray is completely removed. Also in figure 5(d), one could identify the presence of small droplets evaporating around the hollow-cone spray. Signal from these small droplets is low due to low droplets concentration but still detectable with SLIPI-LIF/Mie. It is also important to highlight that since the SLIPI-LIF/Mie images are free from the multiple light scattering contributions, the spray symmetry in SMD is achieved by taking the ratio of LIF and Mie images. More specifically, with the SLIPI approach, the influence of the light extinction is cancelled out by dividing the LIF/Mie signals of the two shoulders of the hollow-cone spray. Therefore, the SLIPI-SMD on the two sides of the hollow-cone spray represents a very good symmetry which was not possible to achieve with the earlier measurements performed using the PSD drop-sizing technique reported in reference [6].

## 5. Conclusions

The LIF/ Mie planar drop sizing approach was merged together with SLIPI, to extract the two-dimensional distribution of droplets SMD in a hollow-cone water spray. Results of two-dimensional SMD mapping were presented and compared for conventional and SLIPI images. However, the SLIPI-SMD results need to be calibrated with a PDA system for knowing the size of droplets which is currently in progress. The transmission measurements confirmed the dilute nature of the spray. It was found that even in this case, the multiple light scattering effects impose large errors on the SMD measurement. Therefore, for faithful SMD mapping it is important to use SLIPI-LIF/Mie over the conventional LIF/Mie approach to mitigate the multiple light scattering issues. The LIF/Mie signal detection strategy with one camera instead of two cameras can also be an important factor to consider for such measurements. In future studies, it would be very useful to verify the presented approach at different liquid pressures of injection, different incident laser power, different dye concentration and different camera  $f_{\#}$ . Such study would demonstrate the robustness of the technique. A second future work should focus on the calibration procedure to obtain the absolute SMD mapping.

## Acknowledgements

The authors gratefully acknowledge the Swedish Research Council, for providing the financial support for the Project 2011-4272. Funding from Linne centre (within the Lund Laser Centre), the CECOST (through SSF and STEM), and the ERC Advance Grant DALDECS is highly appreciated.

## References

- [1] P.N. Wild et al., Appl. Opt. 25(19) (1986) 3520-3526.
- [2] W. D. Bachalo et al., J. Eng. Pow. 102 (1980) 798.
- [3] L.G. Dodge et al., Appl. Opt. 26 (1987) 2144-2154.
- [4] C.N. Yeh et al., 1 (1996) 297-308.
- [5] P. L. Gal et al., Opt. Laser Technol. 31 (1999) 75- 83.
- [6] B.D. Stojkovic et al., Appl. Phys. B 73 (2001) 75-83.
- [7] R. Domann et al., Par. Part. Syst. Charact. 20 (3) (2003) 209-218.
- [8] D. L. Hofeldt et al., Appl. Opt. 32 (1993) 7551-7558.
- [9] D. Stepowski et al., 13th Int. symp Lisbon, Proceed. paper 1061 (2006).
- [10] E. Berrocal et al., Appl. Phys. B 109 (2012) 683- 694.
- [11] E. Berrocal et al., Opt. Express 16 (2008) 17870-17881.
- [12] E. Kristensson, Ph.D. thesis, Lund University (2012).
- [13] G. Charalampous et al., Appl. Opt 50(9) (2011) 1197-1209
- [14] G. Charalampous et al., Appl. Opt 50(20) (2011) 3622-3637.
- [15] H. C. van de Hulst, Dover (1981).

## Two-pulse SLIPI

Elias Kristensson

Combustion Physics, Lund University, Sweden

### Abstract

Structured Laser Illumination Planar Imaging (SLIPI) is a laser sheet imaging technique that is capable of suppressing the intensity contribution arising from multiply scattered light, which contains misleading information. The SLIPI technique has so far been applied mostly for averaged imaging of sprays, as it requires three acquisitions (laser pulses) to reconstruct the full spray structure. Operating SLIPI with fewer acquisitions generates errors in the form of lines that stretch across the image. The need for three laser pulses makes “single-shot” imaging using SLIPI both a very experimentally complicated and expensive approach. Here a novel SLIPI approach, which circumvents this limiting factor, is presented and demonstrated. By taking advantage of a loophole in the theory of structured illumination it is possible to extract a SLIPI image from two acquisitions only, which, in turn, both simplifies the optical arrangement and reduces the end cost significantly. This development will allow standard off-the-shelf PIV lasers and interline transfer CCD or CMOS cameras to be used to acquire temporally frozen SLIPI images of sprays. The principle of the method is explained and exemplified here using averaged data, where the two-pulse approach is compared with traditional (three-pulse) SLIPI. From the comparison it can be concluded that the new method can, under certain conditions, provide practically identical results. The key factor is the choice of the modulation frequency – the narrower the superimposed intensity modulation, the better the results agree. Finally, the single-shot capability of the technique is demonstrated on a steady-state hollow-cone water spray operating at 60 bars.

### Introduction

It is common knowledge within the spray community that photons do not always propagate along a straight, unperturbed path through an optically dense spray [1]. In fact, the phrase *optically dense* implies that the majority of photons interact with the droplets via scattering. Some photons experience a multiple number of interaction events, which leads to problems as one attempts to form an image of the spray via means of optical techniques. The most noticeable error when detecting such multiply scattered photons is a reduced image contrast (blur). The intensity contribution from these photons may also render analytical errors [2]. Issues like these motivated the development of advanced optical techniques such as Ballistic Imaging (BI) [3] and X-ray radiography [4, 5], both designed to address the multiple light scattering problem. BI is based on illuminating the spray with an ultra-short laser pulse and use a time-gating scheme to inhibit the detection of the late arriving multiply scattered photons. X-ray radiography takes advantage of a reduced scattering cross-section of X-ray and matter, effectively reducing the optical depth (turbidity) of the spray.

Recently a third imaging technique with a similar ability to tackle the multiple light scattering issue was demonstrated. The method, named Structured Laser Illumination Planar Imaging (SLIPI), is based on laser sheet imaging but, unlike this technique, SLIPI differentiates between singly and multiply scattered light [2, 6, 7]. This is made possible by encoding a pattern into the laser sheet intensity profile, the idea being that only the singly scattered photons preserve this structural information. Although several alternative optical arrangements are possible, it is most common to guide the laser beam through a ronchi transmission ruling, which blocks part of the light and thereby generates several parallel dark lines in the laser sheet. If the turbidity of the probed spray is below a certain limit ( $OD \approx 6$ ) these lines are visible in the acquired laser sheet image. Surrounding the lines is a blurry glow that arises from photons having undergone multiple scattering events. Interestingly, displacing the lines along the laser sheet has barely an effect on the surrounding glow. This phenomenon is what allows SLIPI to – through computational means – suppress the diffuse multiply scattered light.

Unfortunately, illuminating the spray with an array of laser lines rather than an ordinary laser sheet, which has a homogeneous intensity profile, has a clear drawback. To extract only the singly scattered light and accurately construct the entire spray image, without leaving any trace of the incident line structure, three acquisitions (subimages) are required, between which the spatial phase of the line structure is shifted 120 degrees. For time-averaged imaging this is mostly a matter of inconvenience, yet for single-shot applications this requirement becomes a limiting factor. Attaining a “single-shot” (temporally frozen) SLIPI image of a spray would require a complicated optical arrangement, comprising three individual pulsed high-power lasers and three ICCD cameras [8]. The cost of this approach would thus greatly exceed that of the time-averaged scheme, which only requires a single camera and laser. The prerequisite for *three* subimages is particularly unfortunate; a setup based on two subimages would yield a considerable reduction of both the overall cost and complexity as this would allow off-

the-shelf PIV lasers and standard interline transfer CCDs or CMOSs to be used. In this paper a novel approach to extract such a SLIPI image from only two subimages is presented and demonstrated.

## Two-pulse SLIPI

The idea of two-pulse SLIPI is to illuminate the spray with two phase-mismatched intensity modulated laser sheets successively and to extract the absolute value of the intensity difference between these two subimages. Doing so will lead to the suppression of the multiply scattered light, whose intensity is distributed identically in both subimages (under ideal conditions). However, even though this approach would, in theory, remove the blurring caused by multiple light scattering, it is not possible to accurately reconstruct the spray image using merely two subimages – traces of the incident line structure *will* remain and distort the reconstructed image. The negative impact of these traces often outweighs the improvement realized by SLIPI, which explains why the two-pulse approach previously has been avoided. However, there is a loophole in the theory of structured illumination that could be exploited to make this approach feasible for spray imaging.

To understand the loophole, it is useful to think of each subimage in reciprocal space (Fourier transform), wherein each element represents a certain spatial frequency component  $\nu$ . Image structures with low spatial frequencies reside close to the origin, while high resolution information resides further away. The highest resolvable frequencies ( $\nu_{\max}$ ) in a given image form a circular region around the origin, no finer image details can be observed beyond this so-called *observable region*. Note that the position of this border is not always dictated by the pixel density of the camera but is also influenced by e.g. the quality of the camera objective, solid angle of collection, various amplification stages, etc. It may also depend on the sample itself, which is especially true for spray visualization where the probed sample inherently acts as a low-pass (smoothing) filter. To avoid these sample/equipment related factors in the discussion it is convenient to normalize the observable frequencies with respect to the highest spatial frequency component, according to:

$$\bar{\nu} = \frac{\nu}{\nu_{\max}} \quad (1)$$

With that representation, the highest resolvable feature ( $\bar{\nu}_{\max}$ ) of an imaging system equals unity, regardless of the number of pixels.

The Fourier transform of a SLIPI subimage contains three prominent points: the dc-offset and the fundamental frequency component – ground-frequency – of the sinus-striped laser sheet, appearing symmetrically around the dc. This is illustrated in Fig. 1a-c for three sinusoidal frequencies that are superimposed on a flat intensity field. Provided below each example is the corresponding two-pulse SLIPI image, i.e. constructed from two phase-mismatched subimages. The apparent stripy residual line structures are caused by a lack of information that ordinarily is provided by the third subimage. Note that these artefacts are unavoidable in a two-pulse SLIPI setup. However, two important features can be observed in the two-pulse SLIPI images. First, the residual lines have exactly twice the frequency of their corresponding ground-frequency<sup>1</sup>. Second, the undesired superimposed fringe pattern becomes less pronounced as the ground-frequency increases (compare Fig. 1d and Fig. 1f). The explanation for this lies in the Fourier transform of each image: as the ground-frequency increases, the residuals are forced towards the border of the observable region and eventually, as the ground-frequency approach  $\bar{\nu} = 0.5$ , they are no longer resolvable. In other words, by simply modulating the laser sheet intensity with a sufficiently high spatial frequency, the artefacts generated in the two-pulse SLIPI approach become so fine that the imaging system “fails” to resolve them. What would remain in a real application is a laser sheet image of the spray, corrected for multiple light scattering. In this way it is possible to extract a SLIPI image from only two subimages.

Depending on the spatial resolution of the imaging system, it can be experimentally difficult to attain  $\bar{\nu} = 0.5^2$ , i.e. the ground-frequency needed to avoid residuals. It is still possible to employ two-pulse SLIPI in such a case, but at the cost of image resolution. This is illustrated by the shaded circles in Fig. 1d-f, which mark the residual-free (low frequency) region of each two-pulse SLIPI image. By rejecting the higher spatial frequencies – using computational means – it is possible to extract a low-resolution two-pulse SLIPI image without any interfering residuals.

<sup>1</sup> Actually, the residuals are even overtones to the ground-frequency.

<sup>2</sup> The problem is mostly associated with the alignment of the optics.

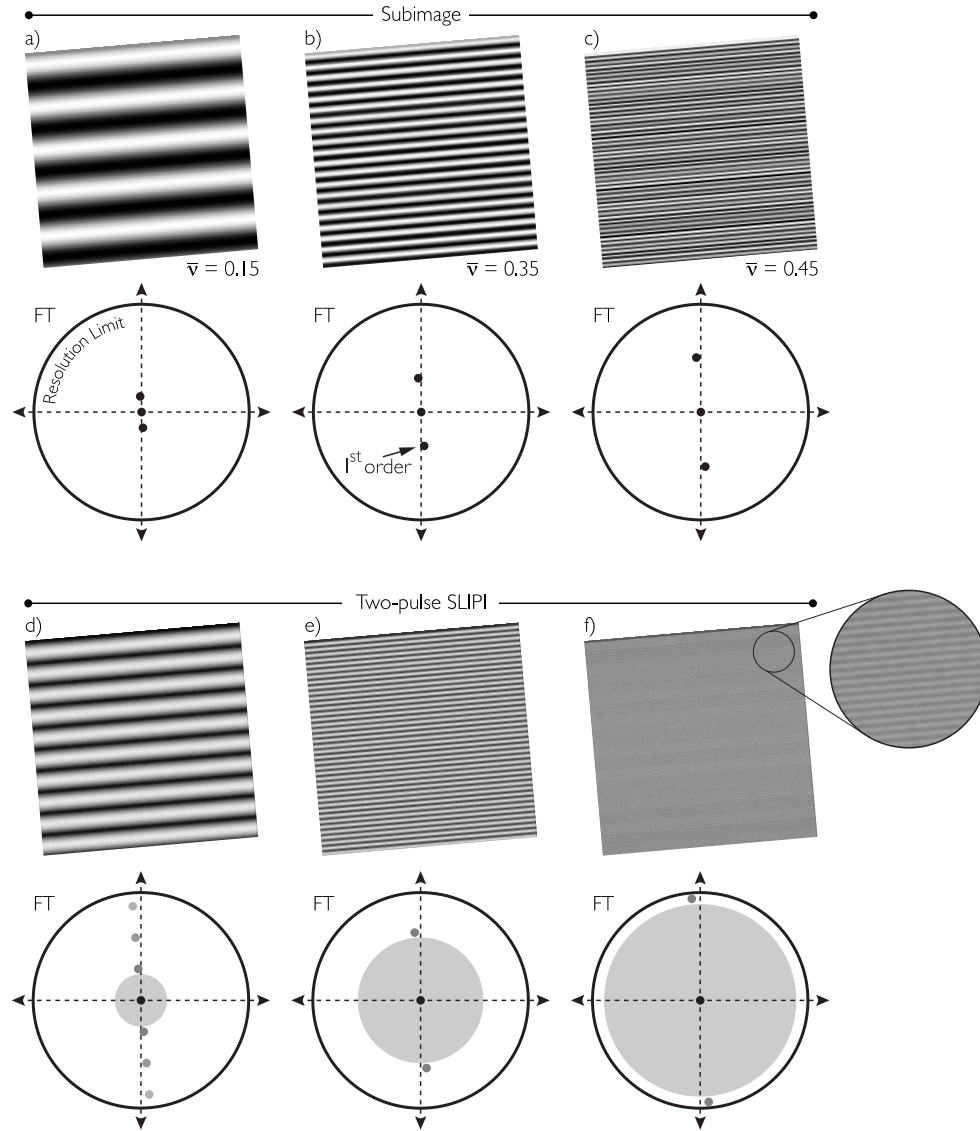


**Figure 1.** Two-pulse SLIPI generates image artefacts with a frequency twice that of the ground-frequency. Thus, by increasing the ground-frequency, the artefacts become less apparent and eventually, they fall outside the observable region. This allows residual-free two-pulse SLIPI images to be extracted. The grey shaded area marks the residual-free region of a two-pulse SLIPI image, which can be accessed through low-pass filtering. Below each image its respective Fourier transform (FT) is provided.

To investigate the potential and limitations of the two-pulse approach and also determine whether it provides useful, trustworthy information, the near nozzle region of a hollow-cone spray was probed. One key factor under investigation is the ground-frequency – a higher frequency is expected to provide better, more detailed results as a larger portion spatial frequencies are retained. Figure 2 shows two two-pulse SLIPI images attained using either a ground-frequency of  $\bar{\nu} = 0.09$  or  $\bar{\nu} = 0.29$ . The unfiltered images ( $f_c = 1$ ) clearly illustrate how the approach generates undesired residual line structures in the SLIPI image. However, as expected, the residuals in the high-frequency case are much less visible as they are manifested as intensity fluctuations at  $\bar{\nu} = 0.58$ . The corresponding value in the low-frequency case is  $\bar{\nu} = 0.18$ . The “low-pass filtered” images show the residual-free portion of each SLIPI image, extracted by applying a low-pass filter on each two-pulse SLIPI image. Although the general spray shape is preserved, the effect of the filter is clearly visible in the low-frequency case, which lacks high spatial frequencies. This is also illustrated in the resolution chart picture, which has been acquired with the same camera system and convolved with the corresponding low-pass filter.

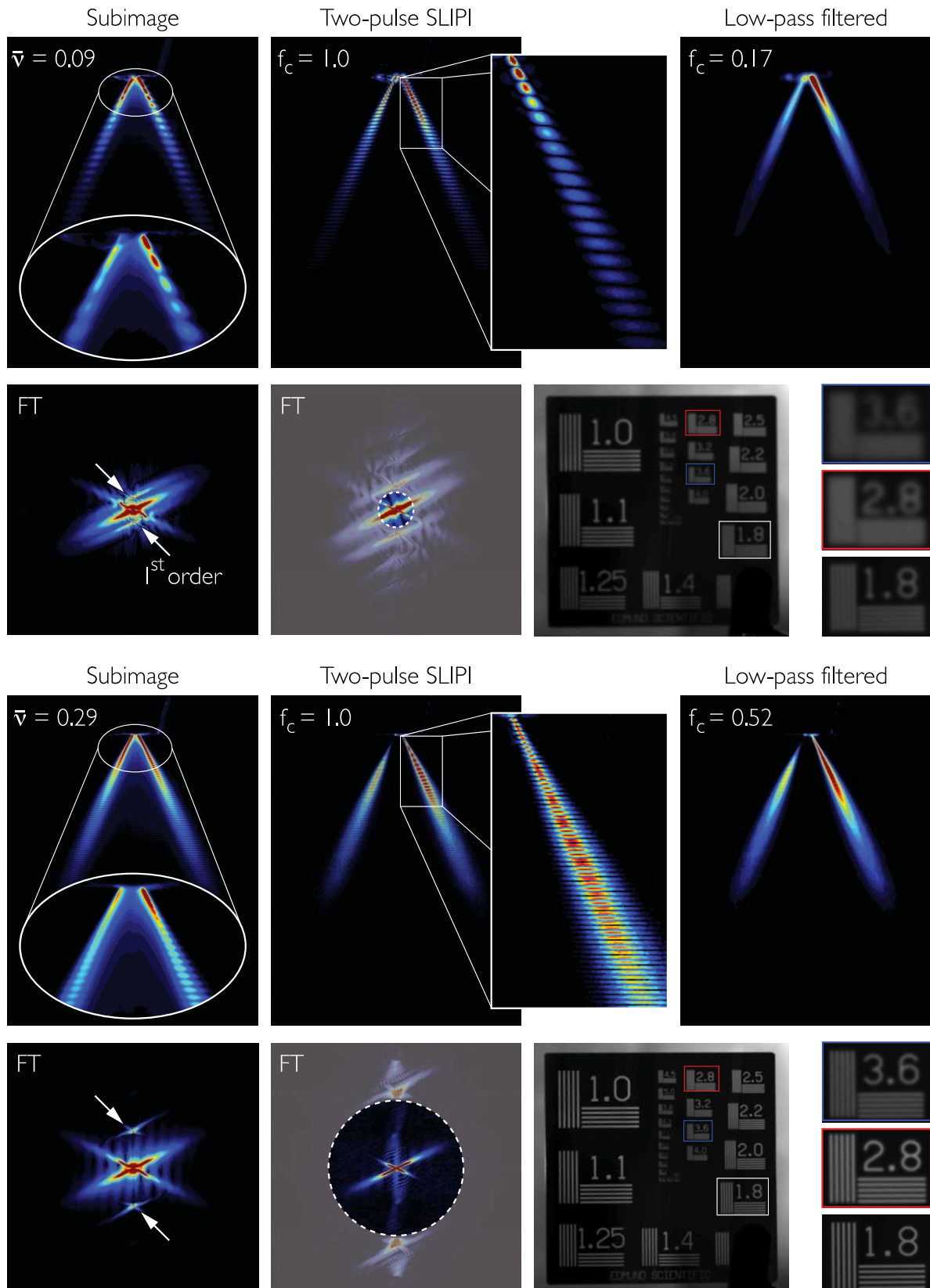


**Figure 2.** The principle of two-pulse SLIP. The lack of information carried by the third, missing subimage generates residual lines that stretch across the SLIP image, where a lower ground-frequency leads to more visible residuals. The “Low-pass filtered” image shows the residual-free part of each two-pulse image ( $f_c$  is the cut-off frequency). The shaded area in the Fourier transform indicates the information that is lost in the process.



## Results and Discussion

Perhaps the most important aspects that need to be investigated are accuracy and precision. In this proof-of-principle study, these factors are studied qualitatively by comparing the results with those obtained using the ordinary (three-pulse) SLIPI method, where no spatial resolution is sacrificed. In the comparison, the near nozzle region of the hollow-cone spray was probed with gradually increasing ground-frequencies, the result of which is shown in Fig. 3. The study reveals that relatively low ground-frequencies provide unsatisfactory results – the loss of high spatial frequencies clearly distorts the shape of the spray. However, the results also show that selecting a sufficiently high ground-frequency (in this case  $\bar{\nu} = 0.29$ ) leads to negligible differences between the two- and three-pulse SLIPI approaches. This implies that this particular spray structure is primarily described by spatial frequencies below  $\bar{\nu} \approx 0.5$  and that rejecting higher frequencies has very little or no effect on the end result. As explained above, a ground-frequency of  $\bar{\nu} = 0.5$  would yield no losses of spatial resolution, yet these test cases show that there is not always a need to select such a high ground-frequency.

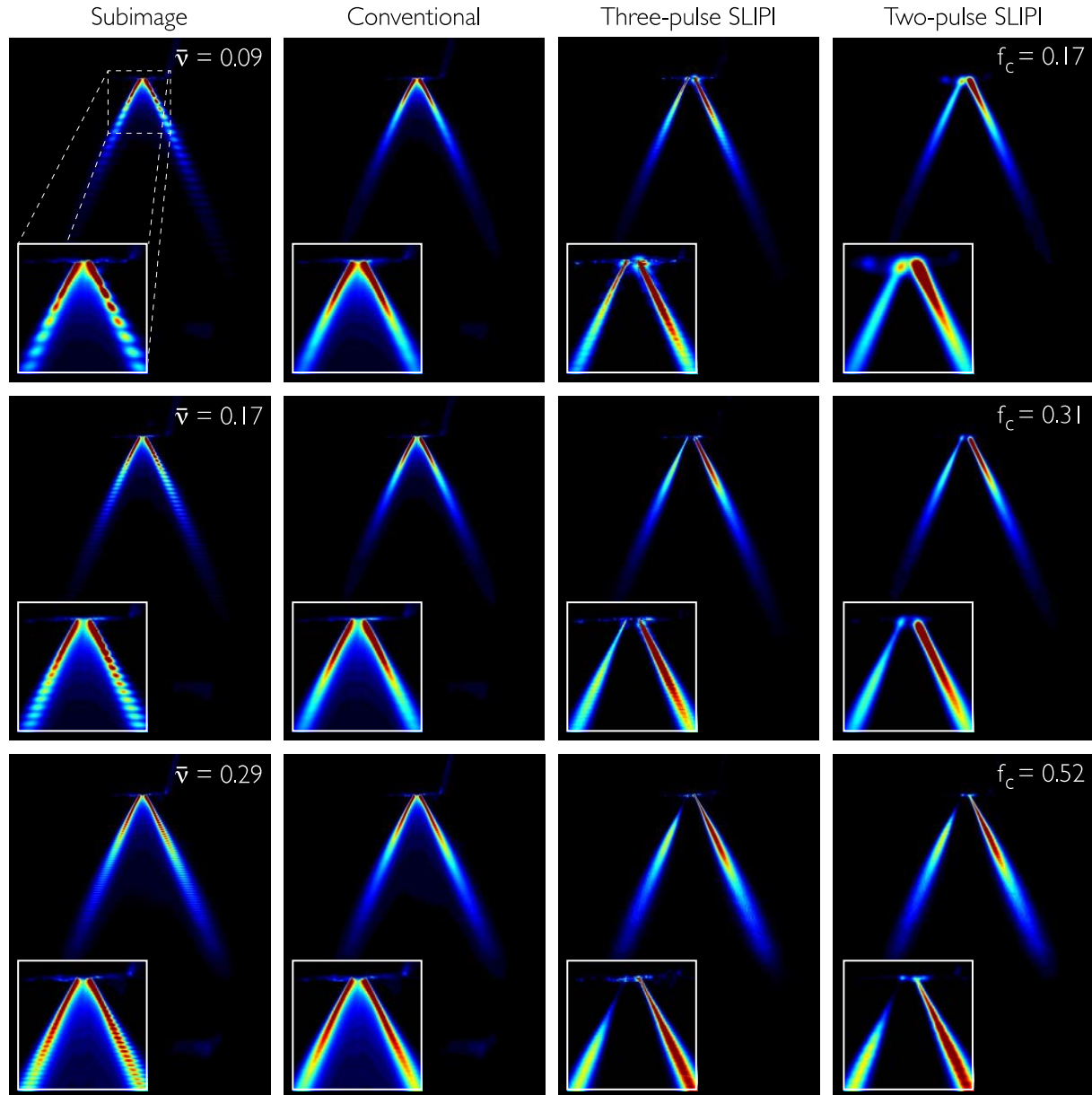
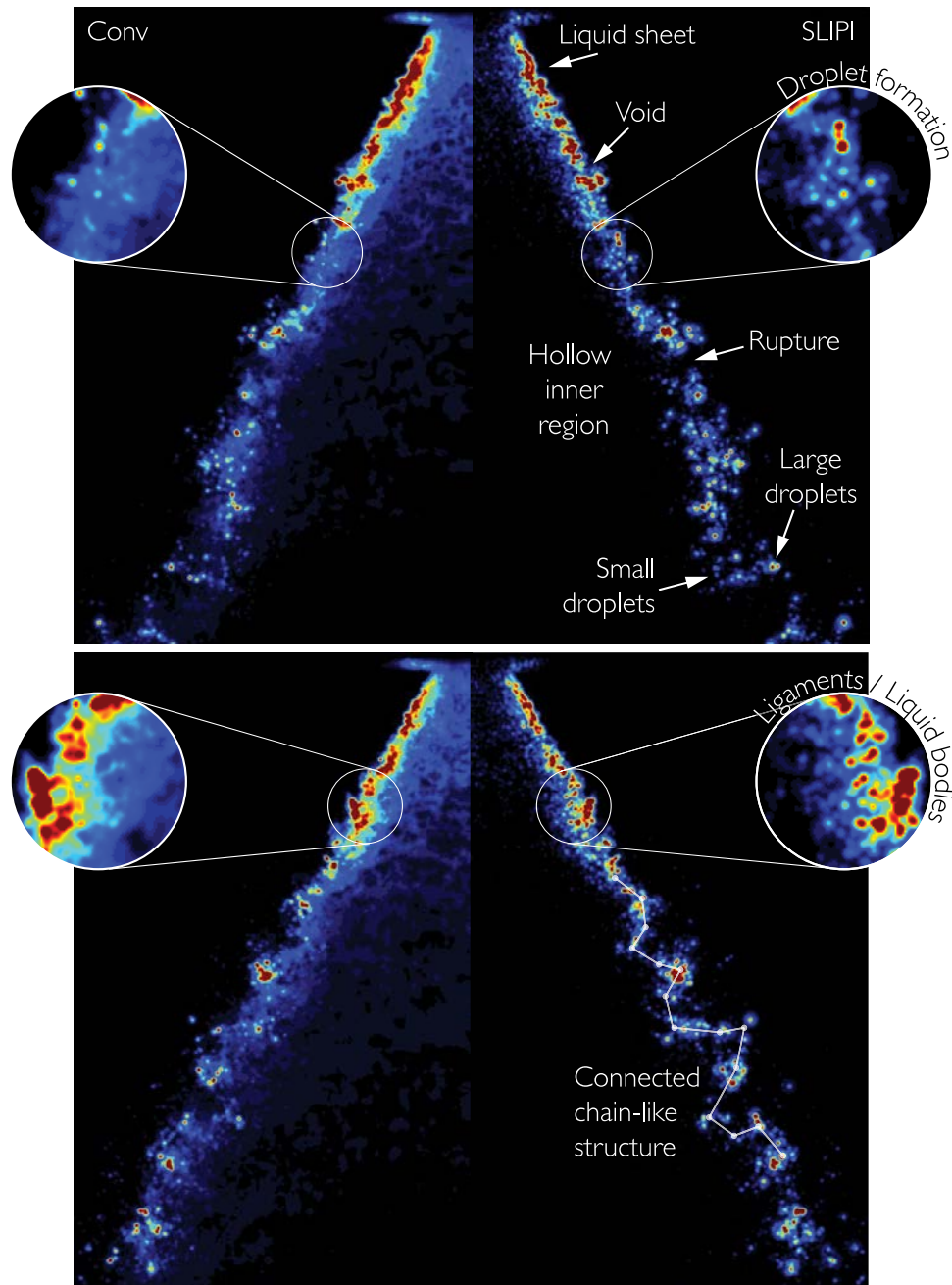


**Figure 3.** Comparison between two- and three-pulse SLIPI. The drawback with the former approach is that spatial resolution is sacrificed, where the ground-frequency of the SLIPI laser sheet determines the magnitude of this loss. The results show that selecting a too low ground-frequency lead to unsatisfactory results, where the spray shape clearly becomes distorted.

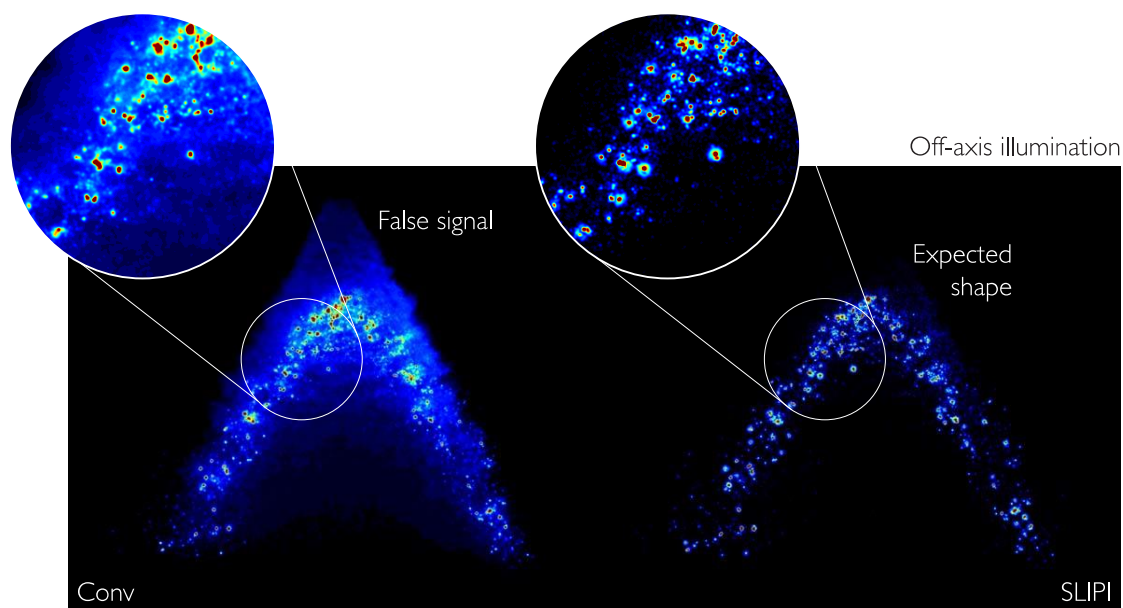
However, above a certain limit, in this case  $\bar{\nu} = 0.29$ , only minor image differences can be detected.



Figure 4 shows snapshots of the hollow-cone spray using either conventional laser sheet imaging or two-pulse SLIPI, recorded simultaneously. The two-pulse SLIPI images were acquired using two individual pulsed Nd:YAG lasers (10 ns pulse length) in combination with a sCMOS (LaVision Imager), allowing a pulses separation of  $\sim 150$  ns. In an ideal case, the injected liquid remains static during this time interval, as all detected movements lead to errors (ghosting) in the processing. Therefore, for higher injection pressures it is advised to reduce this time ever further as this requirement may not be met otherwise (this also depends on the field-of-view). The laser pulses were recombined using a 50:50 beam-splitter in a similar fashion as in reference [8]. Figure 5 shows snapshots of a region behind the central axis off the spray, where the signal from multiple light scattering is clearly visible. Notice how the expected arc-like shape of the spray in this off-axis region is restored when employing two-pulse SLIPI.



**Figure 4.** Comparison between conventional laser sheet imaging and two-pulse SLIPI. The images are acquired simultaneously and show half of the spray. A low-pass filter with a cut-off frequency of  $f_c = 0.45$  is applied on the SLIPI images, yet the loss of high spatial frequencies does not cause any apparent distortion. On the contrary, finer details and sharper image gradients are observed in the SLIPI cases thanks to the removal of the blurring effect caused by the multiply scattered photons.



**Figure 5.** “Single-shot” images of a region behind the central axis of the hollow-cone spray. Due to the detection of multiply scattered light, the conventional laser sheet image shows signal going up to the nozzle orifice, even though this region is not directly illuminated. The expected arc-like shape of the spray is restored with the two-pulse SLIPI approach.

## Conclusions

In conclusion, a SLIPI setup based on two subimages has been developed and demonstrated, both for averaged and “single-shot” applications. The primary benefit of the presented approach is a reduced experimental complexity, especially for “single-shot” studies. Acquiring such temporally frozen data previously would require three individual lasers and cameras – with this new method similar results could, in principle, be obtained with a single (double-pulsed) laser in combination with an interline transfer ICCD or CMOS, thus also reducing the full cost of the arrangement significantly. The presented method takes advantage of a loophole in the theory of structured illumination. It has long been known that attempting to reconstruct a structured illumination image with merely two subimages generates interfering residual line structures. However, these artefacts appear at twice the spatial frequency of the intensity modulation (ground-frequency) and can therefore be rejected, either experimentally or computationally, without sacrificing too much structural information. If a loss of resolution is unacceptable, a ground-frequency of  $\bar{\nu} = 0.5$  should be selected, as this, theoretically, leads to no reduction of the spatial resolution (at the cost of increased experimental complexity). However, it should be noted that a spray system often acts as a low-pass filter and one shall therefore not expect the same spatial resolution when probing a spray as when viewing a resolution chart. A slight loss of resolution is therefore not always noticeable.

## Acknowledgements

Finally, the author wishes to show his appreciation to the Linné Center within the Lund Laser Center (LLC) as well as CECOST through SSF and STEM for financial support. Also the ERC Advanced Grant DALDECS is acknowledged.

## References

- [1] G. J. Smallwood and O. L. Gülder, *Atomization Spray*, 10, 355-386, 2000.
- [2] E. Kristensson, L. Araneo, E. Berrocal, J. Manin, M. Richter, M. Aldén, and M. Linne, *Opt. Express*, 19, 13674-13663, 2011.
- [3] M. Linne, M. Paciaroni, E. Berrocal and D. Sedarsky, *Proceeding of the 32nd International Symposium on Combustion*, 2009.
- [4] C. F. Powell, Y. Yue, R. Poolab, and J. Wanga, *Journal of Synchrotron Radiation*, 7, 356-360, 2000.
- [5] J. Wang, *Journal of Synchrotron Radiation*, 12, 197-207, 2005.
- [6] E. Berrocal, E. Kristensson, M. Richter, M. Linne and M. Aldén, *Opt. Express*, 16, 17870-17881, 2008.
- [7] C. Chartier, J. Sjöholm, E. Kristensson, Ö. Andersson, M. Richter, B. Johansson and M. Aldén, *SAE Technical Paper 2012-01-1718*, 2012.
- [8] E. Kristensson, E. Berrocal, M. Richter and M. Aldén, *Atomization Spray*, 20, 337-343, 2010

# Session:

## **DNS Simulations & Interface Modelling**

## Effect of Reynolds number on the primary jet breakup of inelastic Non-Newtonian fluids from a duplex nozzle using Direct Numerical Simulation (DNS)

Chengxiang Zhu, Moritz Ertl and Bernhard Weigand

Institute of Aerospace Thermodynamics (ITLR), University of Stuttgart, Germany

### Abstract

The phenomena of primary jet breakup for inelastic Non-Newtonian fluids at three different Reynolds numbers ( $Re_0$ ) are compared and discussed in this paper using Direct Numerical Simulation (DNS). For all simulations, the in-house code Free Surface 3D (FS3D) based on the Volume of Fluid (VOF) method is applied. A 20 wt.-% Polyvinylpyrrolidone (PVP) solution is selected as the Non-Newtonian fluid. The shear thinning viscosity of this fluid is resolved by employing a modified power law model. The specific flow features and the surface structures for three different  $Re_0$  are explained in detail. Further insight into the free surface area and the velocity gradient of the jets is illustrated as well. The Non-Newtonian characteristics of the liquid jets are obtained by analyzing both the local Ohnesorge number ( $Oh_{loc}$ ) and the viscosity in the liquid phase. With increasing Reynolds number, the mean value of the liquid viscosity decreases accordingly.

### Introduction

Liquid jets have been widely applied in industry and other applications, like inkjet printing, agricultural irrigation and fuel injection. Scientists all over the world have paid a lot of efforts to analyze the phenomena of jet disintegration both experimentally and numerically, and tried to investigate the influence of different factors on jet sprays. The jet breakup mechanism can normally be classified into three main regimes (Rayleigh breakup, wavy breakup and atomization) according to dimensionless quantities like the Reynolds number  $Re = \rho U_0 D / \mu$  and the Ohnesorge number  $Oh = \mu / (\rho \sigma D)^{0.5}$ . In the current paper, emphasis will be put on the influence of  $Re$  on jet breakup phenomena.

Many investigations in the past have been carried out on this topic. In the following, some of the literature will be discussed. Castrejon-Pita et al. [1] studied the effect of  $Re$  on liquid jets experimentally based on commercial inkjet setups. Their investigated  $Re$  were all below 100. Portillo et al. [2] focused their research on axial instability waves in regions near the nozzle exit with different  $Re$ , experimentally. Different from that in [1], their investigated jet breakup all belonged to the atomization type. Kendil et al. [3] studied a turbulent liquid jet penetrating into a quiescent pool of water under six different  $Re$  both numerically and experimentally. Shinjo and Umemura [4,5] investigated numerically the primary atomization of liquid jets in detail at three different  $Re$ . All these previous studies suggested that  $Re$  has a significant influence on jet breakup phenomena.

However, all previous studies were dealing with Newtonian fluids, and there is no reference in literature for a numerical analysis of Non-Newtonian jet breakup. This is because Non-Newtonian simulations are actually more complicated not only on the accurate capturing of the free surface, but also on the describing of the non-constant viscosity behaviour. Non-Newtonian fluids can be classified into several types. Out of them, power law fluids have only very weak elastic effects which can be neglected [6]. They can further be classified into two regimes based on their viscosity behaviour: shear thinning or shear thickening. The liquid analyzed in the current work, a 20 wt.-% Polyvinylpyrrolidone (PVP) solution, belongs to the shear thinning power law fluids.

In this paper, a specified Reynolds number  $Re_0 = \rho_l U_0 D / \mu_0$ , which is based on the liquid viscosity  $\mu_0$  at zero shear rate, is defined and used. Direct numerical simulations (DNS) of Non-Newtonian primary jet breakup at three different  $Re_0$  are carried out in this work. The emphasis is focused on their influence on flow features and the corresponding Non-Newtonian characteristics.

### Numerical method and setups

The in-house DNS code Free Surface 3D (FS3D), which solves the incompressible Navier-Stokes (NS) equations, is applied for all simulations in this paper. It has been validated by many two-phase applications like droplet collision, splashing, bubble rising and liquid jets. The interface-capturing VOF method [7] is employed

in FS3D to capture the free surface between the two phases. A piecewise linear interface calculation (PLIC) scheme proposed by Rider and Kothe [8] is employed to reconstruct the interface. In order to describe the Non-Newtonian viscosity of the liquid phase, a modified power-law model is applied:

$$\mu_l(\gamma) = \mu_0 / (1 + \mu_0 \gamma^{1-n} / K), \text{ with } \gamma = (\|0.5(\nabla \mathbf{u} + (\nabla \mathbf{u})^T)\|_2)^{0.5}, \quad (1)$$

where  $\mu_l$  denotes the liquid dynamic viscosity,  $\mu_0$  is the viscosity at zero shear rate,  $\gamma$  is the shear rate,  $K$  and  $n$  are model constants which correspond to different fluids and environmental conditions. For the 20 wt.-% PVP solution at 20°C, variables  $K$  and  $n$  are set to  $K=8908$  and  $n=0.126$  according to experimental data from Schröder et al. [9]. This modified power-law model has been validated by Motzigmber et al. [10] for a droplet collision case. Focke and Bothe [11] performed other validation cases like the two phase gap flow and the Bretherton problem. All these studies suggest that the shear rate dependent viscosity in two-phase flows can be described successfully by this model in FS3D.

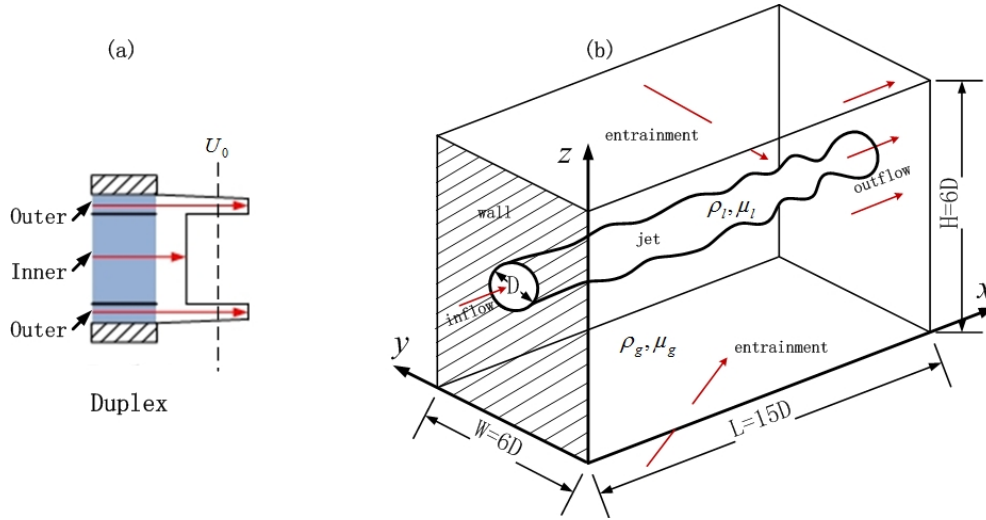


**Figure 1.** Duplex nozzle and the corresponding velocity profile (a). Computational domain (b).

Fluid properties and inflow conditions for the current study are listed in Table 1. It is noticeable that the viscosity here is only the value at zero shear rate. From this table, the density ratio between the liquid and the gas phase is 871, while the viscosity ratio is 1435, which indicate a typical discontinuity in material properties on interfaces. In this work, a circular duplex nozzle, with the velocity profile shown in Fig. 1, is selected. This is due to two main reasons: firstly, the duplex nozzle is applied in industry especially for fluid-mixing, which indicates a wide practical background. Secondly, flow from the duplex nozzle has a larger shear stress compared to other simple nozzle configurations. Thus, the Non-Newtonian characteristics of the liquid phase can be observed easier. The inflow turbulence is superimposed at the inlet by a turbulence generator developed by Huber et al. [12] based on the work of Kornev and Hassel [13]. A 3D rectangular computational domain is employed, the height and the width of which are both set to 6 times the jet diameter, while the length is set to  $15D$ . A rough estimation of the required grid spacing can be obtained by calculating the Kolmogorov length [14], from which the smallest dissipative length scale  $\lambda_k$  is found to be within the range of 4-9  $\mu\text{m}$  :

$$\lambda_k = L_t / Re_t^{0.75}, \text{ with } Re_t = (\rho_l u' L_t) / \mu_l, \quad (2)$$

where  $L_t$  is the turbulent length scale, and  $u'$  is the velocity fluctuation. In the present simulations, 64 cells are used in the jet diameter, which results in a total cell number of 33.5 million and an actual grid spacing of around 6  $\mu\text{m}$ . Therefore, the grid resolution is reasonably satisfied.

**Table 1.** Summary of inflow conditions.

Nozzle diamet er $D$ (m)	Turbulenc e intensity $Tu$	Turbulent length scale $L_t$ (m)	Liquid density $\rho_l$ (kg/m <sup>3</sup> )	Liquid viscosity $\mu_0$ (Pa s)	Gas density $\rho_g$ (kg/m <sup>3</sup> )	Gas viscosity $\mu_g$ (Pa s)	Surface tension $\sigma$ (N/m)	Liquid velocity $U_0$ (m/s)	Reynold s number $Re_0$	Weber number $We$
4.0e-4	15%	4.0e-5	1049 <sup>[9]</sup>	2.559e-2 <sup>[9]</sup>	1.204	1.783e-5	64.37e-3 <sup>[9]</sup>	30	492	5867
								50	820	16296
								80	1312	41719

## Results and Discussion

### 3D Jet Structure

The surface structures of the liquid jet for three different  $Re_0$ , are given in Fig. 2 for  $t^*=6.3$  ( $t^*$  is the dimensionless time, defined as  $t^* = tU_0/D$ ), where  $xz$ -symmetric slices are contoured by the dimensionless normal vorticity field  $\omega_y^* = (\partial u / \partial z - \partial w / \partial x)D / U_0$ . For  $x/D < 1$ , the three jets exhibit a similar surface behavior induced by the inflow turbulence. Interfacial fluctuations with small amplitudes, but in a large number, can be observed. But for  $x/D > 1$ , most of these perturbations vanish with increasing axial position for  $Re_0 = 492$ , while they are enhanced for  $Re_0 = 1312$  due to stronger aerodynamic forces. Near the jet tip at  $x/D = 9$ , one liquid hole can be detected for  $Re_0 = 492$ , while the jet disintegrates more strongly for  $Re_0 = 820$ . For  $Re_0 = 1312$ , the jet tip disintegrates thoroughly, with the formation of numerous ligaments and droplets. Therefore, it can be concluded that with increasing  $Re_0$ , the jet becomes further unstable and disintegrates more easily. It should be pointed out here that the Non-Newtonian behavior of the liquid phase enhances the influence of  $Re_0$ . This will be explained in further details in the Non-Newtonian section of this paper.

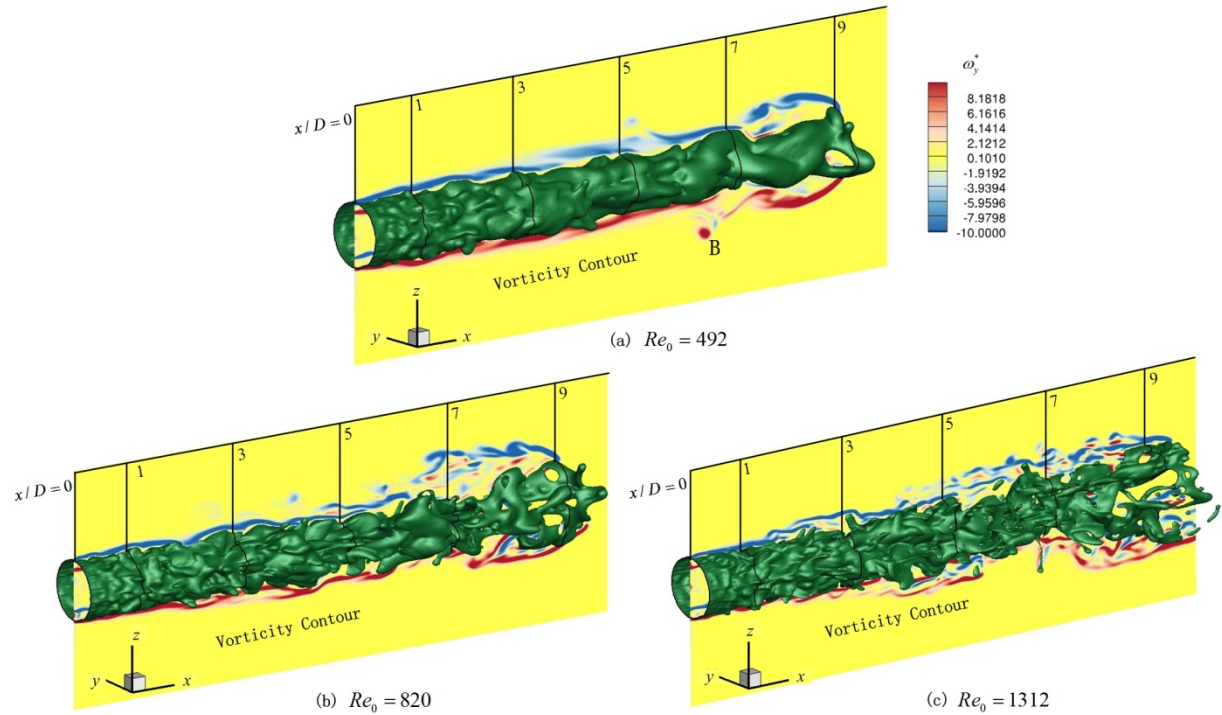


**Figure 2.** 3D view of the jet structures at three  $Re_0$  for  $t^*=6.3$ . The symmetric slices are contoured by the dimensionless normal vorticity field  $\omega_y^*$ .

Regarding the sectional  $xz$ -slices in Fig. 2, two obvious regions with strong vorticity can be detected in the jets. This is due to the existing of interfaces between the outer and the inner flow, which creates a large streamwise velocity gradient ( $\partial u / \partial z$ ). With increasing  $Re_0$ , the vorticity field in the gas phase is further distorted, especially between  $7 < x/D < 9$ . For instance, the highest positive vorticity  $\omega_y^*$  on the upper half of this



slice increases from 14.5 for  $Re_0 = 492$  to 35.3 for  $Re_0 = 1312$ . It is also noticeable that at position  $P$ , a separated circular vorticity region is formed due to local high shear rates.

### Surface Area

The surface area of the liquid jet from a duplex nozzle can be affected by several factors. On one hand, interfacial fluctuations are formed as a consequence of the inflow turbulence, increasing the total surface area. Meanwhile, disintegrations, especially at high  $Re_0$ , have a similar effect. On the other hand, the flow from both channels impact and merge, decreasing the surface area. Therefore, two opposing factors exist, which differ for different  $Re_0$ . To further analyze this behavior, a dimensionless quantity is defined as  $S^* = S / (\pi U_0 D t + \pi (D/2)^2)$ , representing the free surface area of the jet. Here, the actual jet surface area  $S$  is normalized by the ideal surface area of a column jet with a constant inflow velocity  $U_0$ . The term  $\pi U_0 D t$  denotes the lateral area of the column jet increasing with time, while the term  $\pi (D/2)^2$  represents the tip area of the jet.

For  $Re_0 = 492$ , the surface area of the jet increases with time before  $t^* = 1.9$  due to interfacial fluctuations introduced by the inflow turbulence. But from  $t^* = 1.9$  on, the surface area decreases, from 1.94 at  $t^* = 1.9$  to 1.63 at  $t^* = 6.6$ . This is because the small perturbations are smoothed during this period, and the liquids merge. For  $Re_0 = 820$ , the surface area of the liquid jet increases before  $t^* = 3.3$ , with a larger gradient than for  $Re_0 = 492$ . For  $t^* > 3.3$ , however, the surface area remains nearly constant, indicating a balanced effect of the impacting factors. For  $Re_0 = 1312$ , the surface area increases much faster than for the other two jets, to 3.2 at  $t^* = 3.5$ . After that, it remains nearly constant till  $t^* = 5.3$  and increases again afterwards. At  $t^* = 6.6$ , it reaches  $S^* = 3.4$  in this case, which is 2.1 times higher than that for  $Re_0 = 492$  at the same time.

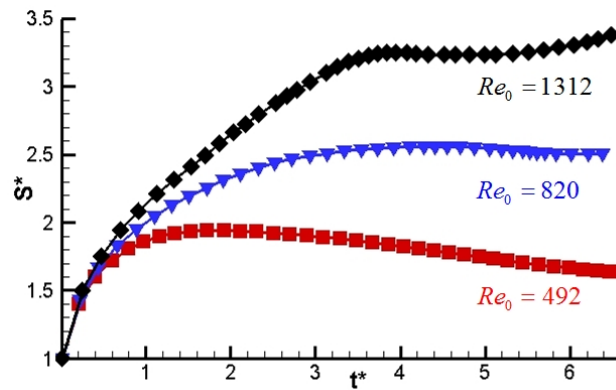


Figure 3. Tendency of the surface area of three liquid jets at different  $Re_0$ .

### Velocity Gradient Profile

For shear thinning Non-Newtonian fluids, the physical property viscosity relates greatly to the flow property velocity. At positions where high shear rates (high velocity gradients) exist, viscosity of the liquid phase decreases accordingly. Therefore, the velocity gradient is the link between the flow and the physical properties. Figure 4 gives the velocity gradient ( $\partial u / \partial z$ ) profiles, which are normalized by  $(U_0 / D)$  at different axial positions for the here investigated jets at  $t^* = 6.3$ . It should be pointed out firstly that  $z / D = 3$  is the jet center.

Regarding the velocity gradient for  $Re_0 = 492$ , the highest absolute value attains 28.9 at position  $B$  (which is near the interface  $z / D = 3.5$  in the axial plane of  $x / D = 1$ ). It is generated because the gas near the liquid surface is accelerated, forming a thin shear layer around the jet. Similar behaviors can also be found for the other two jets. At position  $A$ , an obvious oscillation of the velocity gradient can be observed in the axial plane of  $x / D = 5$ . This is because in this axial position, the gas phase near the jet center ( $z / D = 3$ ) has not been accelerated, while the air close to the outer liquid flow is accelerated. Therefore, high velocity gradients are formed. For  $Re_0 = 820$ , the highest absolute value of the velocity gradient attains 26.9 at position  $D$ . It is also noticeable that at position  $C$ , a high velocity gradient is generated, due to the existence of interfaces between the outer and the inner flow around the radial position of  $z / D = 3.35$  and 2.65. For the other two jets, similar high gradients can also be observed around this position. It can be seen that the amplitudes of this dimensionless velocity gradient are of the same order of magnitude for the three different jets. For  $Re_0 = 1312$ , in spite of the high velocity gradients



around the interface at position  $E$ , a high velocity gradient at position  $F$  can additionally be observed due to the existence of a region with relatively low velocity which has been previously mentioned.

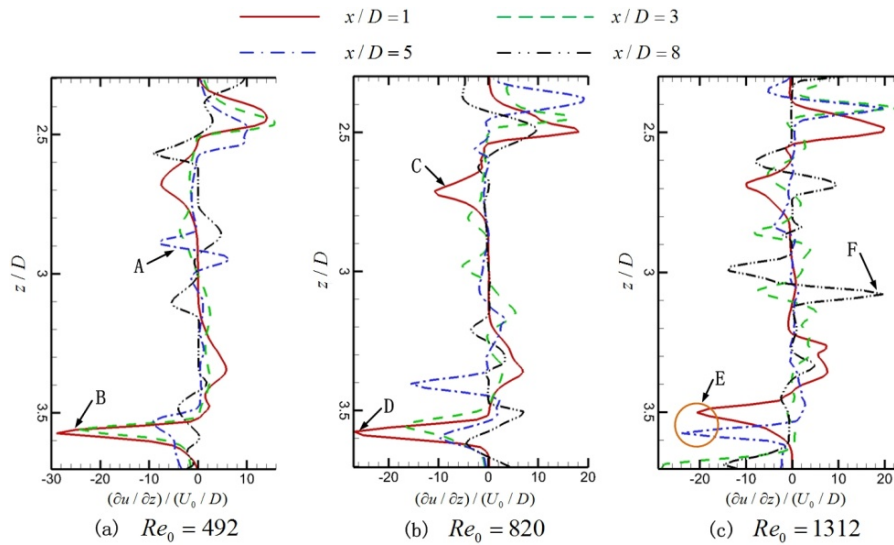


**Figure 4.** Deformation of the velocity gradient profile with increasing axial position in three jets at  $t^* = 6.3$ .

### Non-Newtonian Characteristics

Distribution of the local Ohnesorge ( $Oh_{loc}$ ) number, which is defined as  $Oh_{loc} = \mu_{loc} / (\rho_l \sigma D)^{0.5}$ , is contoured in the  $xz$ -plane of three jets in Fig. 5. It takes the local viscosity  $\mu_{loc}$  into account, and represents the ratio of viscous forces to the surface tension forces. Since  $\rho_l$ ,  $\sigma$  and  $D$  are all constant in the current cases, the variation in  $Oh_{loc}$  only results from  $\mu_{loc}$ . In general, with increasing  $Re_0$ ,  $Oh_{loc}$  decreases accordingly. The arithmetic mean of  $Oh_{loc}$  in the liquid phase is 0.143 for  $Re_0 = 492$ , but decreases by nearly 20%, to 0.116 for  $Re_0 = 1312$ . Therefore, the higher the  $Re_0$ , the stronger the Non-Newtonian characteristics of the jet. From Fig. 5, it can also be observed that the lowest  $Oh_{loc}$  in these symmetric planes are all located in the shear layer between the outer and the inner flow from the nozzle exit. It attains 0.068 for  $Re_0 = 492$ , while is far below 0.06 for  $Re_0 = 1312$ .

Regarding the 2D distribution of  $Oh_{loc}$ , a specific triangle region with high  $Oh_{loc}$  near the nozzle exit can be detected in all three jets. Liquids from the inner channel are injected with a mean velocity of  $0.5U_0$ . But due to the acceleration of flow from the outer channel, more of the inner liquids are sheared with increasing axial position. Hence, the thickness of this region shrinks, resulting in a triangle shape. The length of this triangular region decreases with increasing  $Re_0$  as well, which indicates a stronger shear behavior at high  $Re_0$ . In spite of this region, two more positions are worth to be noticed. Firstly, the jet tip also shows a high  $Oh_{loc}$  for all three jets, but the highest  $Oh_{loc}$  decreases with  $Re_0$ . In addition, the jet tip disintegrates more thoroughly at higher  $Re_0$ . Secondly, it is already hard to tell the coaxial flow feature just from the jet structure for  $Re_0 = 1312$ , but it is still clear to observe two axial flows for  $Re_0 = 492$ . And liquids from the outer channel obtain a high  $Oh_{loc}$  over 0.14 from the axial position  $x/D = 4$  on for  $Re_0 = 492$ .

The local fluid viscosity along the streamwise axes which are dashed in Fig. 5, is normalized by the zero-shear viscosity  $\mu_0$  and illustrated in Fig. 6. Obviously, the variation of the fluid viscosity increases with  $Re_0$ , and the amplitude increases as well. At  $x/D = 0$  for instance, the fluid viscosity is 0.79 for  $Re_0 = 492$ , which decreases to 0.61 for  $Re_0 = 1312$ . Taking only the liquid phase into consideration, the arithmetic mean value of the liquid viscosity  $\mu / \mu_0$  over  $x$  can be calculated to 0.968 for  $Re_0 = 492$ , suggesting a weak shear behavior along the center of this jet. With increasing  $Re_0$ , the average viscosity of the liquid phase decreases. It is 0.903 for  $Re_0 = 820$ , while it is only 0.798 for  $Re_0 = 1312$ .

As previously mentioned, liquid jets become more unstable with increasing  $Re_0$  due to higher inertia energy. For Non-Newtonian shear thinning fluids, this influence is further enhanced. From Fig. 6, the average liquid viscosity decreases with  $Re_0$  and is smaller than the zero-shear value  $\mu_0$ . In case that two jets obtaining the same inertia energy, viscous forces of the shear thinning jet are hence weaker than for the Newtonian jet. Therefore, the Non-Newtonian jet disintegrates more easily. It is also noticeable that with increasing  $Re_0$ , this influence is enhanced further, because the average liquid viscosity decreases accordingly.

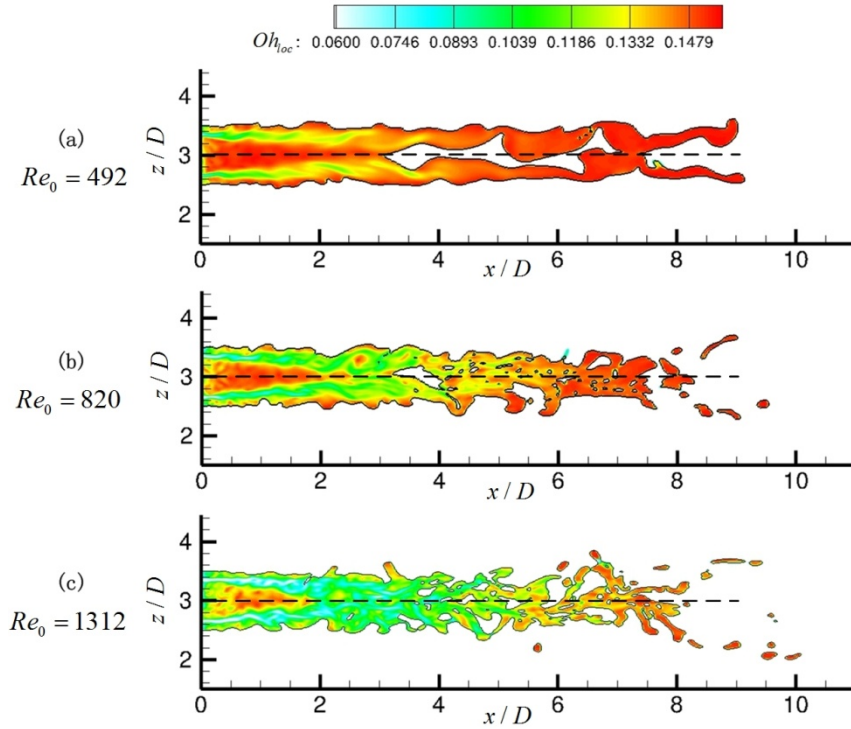


**Figure 5.** Distribution of the local Ohnesorge number in the symmetric  $xz$ -plane with three  $Re_0$  at  $t^*=6.3$ .

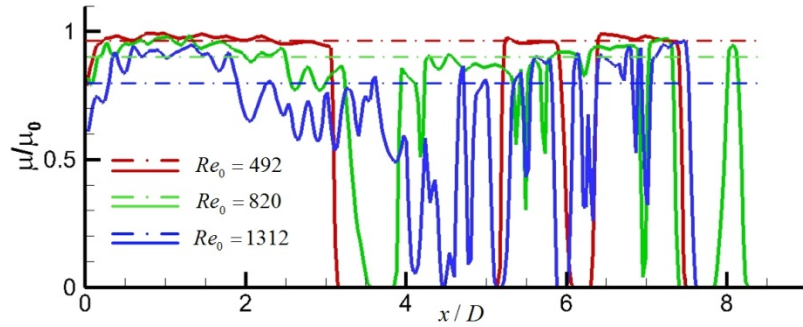


**Figure 6.** Distribution of the local viscosity (solid lines) in three jets along the streamwise axes which are dashed in Fig. 5 at  $t^*=6.3$ . Three dash-dotted lines here correspond to the arithmetic mean viscosity of the liquid phase over  $x$ .

## Conclusions

In the current paper, three different  $Re_0$  are applied at the inlet of liquid jets to investigate their influence on the breakup of an inelastic shear thinning fluid. With increasing  $Re_0$ , the jet becomes more unstable. Interfacial fluctuations vanish with increasing axial position at a small  $Re_0$ , but are enhanced at high ones. The resulting surface area of liquid jets, which is impacted by many factors like perturbations, disintegrations and surface merging, increases with  $Re_0$ . Due to the coaxial flow feature of liquid jets coming out of a duplex nozzle, a high velocity gradient is generated on the interface between the outer and the inner flow. As a consequence, a small liquid viscosity and hence a small  $Oh_{loc}$  are formed around here. And with increasing  $Re_0$ , the arithmetic mean value of the viscosity and  $Oh_{loc}$  decreases accordingly.

## Acknowledgements

The authors gratefully acknowledge the High Performance Computing Center Stuttgart (HLRS) for their support in supplying the computational time on the super computer NEC SX-9 under Grant No. FS3D/11142. We also sincerely acknowledge financial support of this project from DFG for the priority program SPP 1423 “Process Spray”, as well as the financial support from the China Scholarship Council (CSC).

## Nomenclature

$D$	Diameter of the nozzle	$U_0$	Inflow velocity of liquid jets
$K$	Constant for the power law model	$x, y, z$	Coordinates
$L_t$	Turbulent length scale	$\gamma$	Shear rate
$n$	Constant for the power law model	$\lambda_k$	Smallest dissipative length scale
$Oh$	Ohnesorge number	$\mu$	Viscosity
$Re$	Reynolds number	$\mu_0$	Viscosity at zero shear rate
$Re_0$	Reynolds number at zero shear rate	$\rho$	Density
$S$	Free surface area	$\sigma$	Surface tension
$S^*$	Dimensionless free surface area	$\omega$	Vorticity
$t$	Time		
$t^*$	Dimensionless time	<i>Subscript:</i>	
$Tu$	Turbulence intensity	$l$	Liquid phase
$u, v, w$	Velocity components	$g$	Gas phase
$u'$	Velocity fluctuation	$loc$	Local property

## References

- [1] Castrejon-Pita J. R., Hoath S. D. and Hutchings I. M., *Journal of Fluid Engineering* 134: 011201 (2012).
- [2] Portillo J. E., Collicott S. H. and Blaisdell G. A., *Physics of Fluids* 23: 124105 (2011).
- [3] Kendil F. Z., Danciu D. V., Schmidtke M., Salah A. B., Lucas D., Krepper E. and Mataoui A., *Progress in Nuclear Energy* 56: 100-110 (2012).
- [4] Shinjo J. and Umemura A., *International Journal of Multiphase Flow* 36: 513-532 (2010).
- [5] Shinjo J. and Umemura A., *International Journal of Multiphase Flow* 37: 1294-1304 (2011).
- [6] Clasen C, Phillips P. M., Palangetic L. and Vermant J., *AIChE Journal* 58: 3242-3255 (2012).
- [7] Hirt C. W. and Nichols B. D., *Journal of Computational Physics* 39: 201-225 (1981).
- [8] Rider W. J. and Kothe D. B., *Journal of Computational Physics* 141: 112-152 (1998).
- [9] Schröder J., Lederer M. L., Gaukel V. and Schuchmann H. P., *24th ILASS on Liquid Atomization and Spray Systems*, Estoril, Portugal, 2011
- [10] Motzigmamba M., Roth N., Bothe D., Warnecke H. J., Pruss J., Wielage K. and Weigand B., *18th Annual Conference on Liquid Atomization and Spray Systems*, Zaragoza, Spain, 2002.
- [11] Focke C. and Bothe D., *Journal of Non-Newtonian Fluid Mechanics* 166: 799-810 (2011).
- [12] Huber C., Gomaa H. and Weigand B., *High Performance Computing in Science and Engineering* 10 (2011).
- [13] Kornev N. and Hassel E., *Physics of Fluids* 19(6): 068101 (2007).
- [14] Batchelor G. K., *The theory of Homogeneous Turbulence* (1953).

## **Embedded DNS of the primary breakup of a prefilming airblast atomizer at aircraft engine operating conditions**

Benjamin Sauer, Amsini Sadiki and Johannes Janicka

Institute of Energy and Power Plant Technology, Technische Universität Darmstadt, Germany

### **Abstract**

An improved understanding of the breakup processes of two-phase flows is essential to effectively control the fuel atomization. A detailed insight into the phenomena of primary breakup is a major limitation in gaining this knowledge. The embedded DNS concept aims to fill this gap as the DNS is only used in the primary breakup region. In this study the methodology is used to simulate a generic prefilming airblast atomizer at aircraft engine related operating conditions covering a range from high-altitude relight to idle conditions. Qualitatively, different primary breakup mechanisms can be distinguished: the stretched ligament breakup, the torn sheet breakup and the membrane sheet breakup. A quantitative assessment shows a good agreement with prefilmer experiments at atmospheric conditions. The breakup length and frequency, the streamwise deformation velocity and the Sauter diameter are investigated. At high-altitude relight conditions, large structures are found, the breakup length and time scales are long. At idle conditions, the spray is dominated by significantly smaller droplets. The liquid sheet collapses directly ahead of the trailing edge. The eDNS concept is a valuable tool to study the phenomena of primary breakup under realistic aircraft engine operating conditions. The kerosene properties are important in order to control the primary breakup and assure small droplets.

---

### **Introduction**

A detailed understanding of the primary breakup in two-phase flows is still a missing link in effectively control the process of fuel atomization under all possible operating conditions.

The Lean Premixed and Prevaporized (LPP) combustion is the favored concept for future aircraft engine combustors. More than in conventional combustors, the lean burn technology depends highly on the fuel atomization. LPP promises to improve efficiency, ignition behavior and pollutant emissions.

Simulating the primary breakup in two-phase flows is not new it was already performed for diesel jets [e.g. 1] or for a jet in crossflow [e.g. 2]. In both configuration, the liquid jet enters the domain with a high liquid velocity. As a consequence, instabilities are developing at the liquid surface. These instabilities are the source of the subsequent disintegration of the jet. The breakup time and the spatial domain are short as the jet collapses close to the injecting nozzle.

The prefilmer configuration instead is different. Prefilming airblast atomizers are employed in aircraft engines. The liquid enters through a small slit, flows along the prefilmer to the trailing edge. The film is pushed forward by the coflowing air stream from above. Downstream of the trailing edge, the liquid sheet is sandwiched between two coflowing air streams from top and bottom. The transformation process from the liquid wall film to separated structures and droplets takes more time and covers a larger spatial domain. Therefore, numerical and experimental studies require enormous resources and are more challenging than using jet configurations. The impact of the air bulk velocity on the breakup time and length scale was shown applying airblast atomizer experiments [3, 4]. Comparing prefilmer and non-prefilmer configurations, Bhayaraju found that the primary breakup occurs faster for the former [5].

A DNS of the primary breakup of a prefilming airblast atomizer including the liquid wall film along the prefilmer and the collapse of the liquid sheet cannot be found in literature. Non-prefilming airblast atomizers were simulated in 2-D in preliminary parametric studies [6, 7]. This studies focused on the applicability of the numerical methods. Sander and Weigand performed a DNS of a non-prefilming configuration investigating the influence of the inlet boundary conditions on the breakup process [8].

The authors introduced the embedded DNS concept which applies the resources consuming DNS only in the relevant breakup region. The DNS domain is embedded in a LES region where transient inlet conditions for the DNS are extracted in “quasi” DNS quality. An introduction to the eDNS methodology is provided elsewhere [9].

In this study, the eDNS concept is used to simulate the primary breakup of aircraft engine operating conditions. The simulations cover conditions related to high-altitude relight as well as aircraft engine idle conditions as far as the Reynolds number and Weber number range is concerned. First, a brief description of the eDNS concept is provided before the numerical set-up and the condition are introduced. The results are organized into a qualitative assessment discussing the observed primary breakup mechanisms and a quantitative assessment where the simulations are validated against experimental results. The document ends with the main conclusions of this work.

### Embedded DNS concept

Simulating atomization accurately is a tremendous numerical challenge since time and length scales vary over several orders of magnitude, the phase interface is a material discontinuity and surface tension forces are singular. Thus, the DNS of technical atomization processes in complex geometries are not feasible. The embedded DNS is based on the idea of simulating the atomization process accurately using a DNS without taking into account the rather complex geometry of the airblast atomizer itself. Figure 1 illustrates a prefiling airblast atomizer which is used in aircraft engine. The breakup region is small compared to the entire complex geometry.

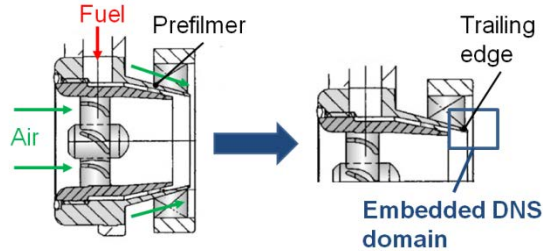


**Figure 1.** From the airblast atomizer to the embedded DNS domain

To get an insight into the fundamentals of primary breakup, the prefiling airblast atomizer geometry is simplified to a generic planar prefilmer as seen in figure 2. This simplification makes it feasible to compare the simulation against experimental data. It has been concluded that a planar liquid sheet shows a behavior equivalent to an annular one [4].

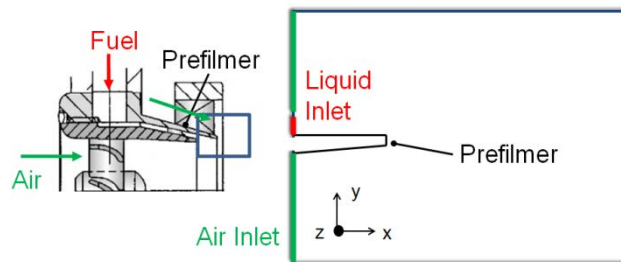


**Figure 2.** From the airblast atomizer to the generic planar geometry

The concept of an eDNS requires the generation of transient inlet boundary conditions. Therefore a LES of the turbulent channel flow is performed prior to the DNS. The velocity fields are applied as transient Dirichlet boundary conditions to the inlet planes of the eDNS domain. A linear interpolation in space and time is conducted as the DNS resolution is higher and the DNS time step is smaller than in the LES of the turbulent channel flow. The DNS of the breakup process is carried out on an equidistant grid. The liquid is injected through a small slit, travels along the prefilmer lip to the trailing edge. A detailed introduction into the eDNS concept by the authors can be found elsewhere [9].

### Numerical Set-Up and flow configuration

This work aims to investigate the appearance of the primary breakup at aircraft engine related operating conditions. Table 1 shows the range of typical operating conditions of an aircraft engine. The data were experimentally obtained in the DLR flow chamber [10] and at the high-altitude relight test rig in Derby [11]. The Reynolds number is based on the channel half height and the Weber number on the liquid slit height. The eDNS concept makes it possible to simulate operating points ranging from high-altitude relight to idle conditions. The  $Re$  and  $We$  range of Start, Take off and Landing is much higher, thus the computational grid would need a further refinement in order to resolve the small turbulent length scales and the smallest droplets resulting from primary breakup in a two-phase DNS.

Table 2 summarizes the flow conditions of the simulations. Two sets of air and liquid parameter are used: air at atmospheric conditions together with kerosene at atmospheric conditions, and air at 3 atmospheres together with kerosene at elevated temperatures (ca. 550 K) corresponding to a significantly smaller surface tension force  $\sigma$ .

**Table 1.** Typical aircraft engine operating conditions (experimental test rig) [10, 11]

Operating points	Start	Idle	Take off	Cruise	Landing	Altitude Relight
$p_{air}$ [bar]	36	4.8	29.6	14.7	18.4	0.2
$T_{air}$ [K]	850	477	809	759	709	265
$u_{air}$ [m/s]	98	74	96.8	93.3	90.3	60
$\rho_{air}$ [kg/m <sup>3</sup> ]	14.76	3.51	12.75	6.75	9.04	0.26
$v_{air}$ [m <sup>2</sup> /s]	2.69e-06	7.72e-06	3.02e-06	5.48e-06	3.92e-06	6.20e-05
$\sigma_{liq}$ [kg/s <sup>2</sup> ]	0.00232	0.0188	0.00448	0.0105	0.00879	0.025
$Re_{air}$	364,200	95,470	320,000	169,700	231,600	9,677
$We_f$	18,327	305	7,994	1,678	2,515	11.2

**Table 2.** Flow conditions of the eDNS

Operating points	1	2	3	4
$u_{air}$ [m/s]	20	50	20	50
$\rho_{air}$ [kg/m <sup>3</sup> ]	1.21	1.21	3.9	3.9
$v_{air}$ [m <sup>2</sup> /s]	1.5e-05	1.5e-05	4.7e-06	4.7e-06
$u_{liq}$ [m/s]	0.5	0.5	0.5	0.5
$\rho_{liq}$ [kg/m <sup>3</sup> ]	742	742	650	650
$v_{liq}$ [m <sup>2</sup> /s]	1.09e-06	1.09e-06	2.9e-07	2.9e-07
$\sigma_{liq}$ [kg/s <sup>2</sup> ]	0.025	0.025	0.0085	0.0085
$Re_{air}$	5,333	13,333	17,021	42,553
$\rho_{liq}/\rho_{air}$	613.2	613.2	166.7	166.7
$We_f$	1.9	11.9	18.4	114.7
$M$	2.6	16.3	9.6	60.0

The eDNS is computed on an equidistant grid with a spacing of 20  $\mu\text{m}$ . No turbulence model is set thus the negative influence of the turbulence model on the near-interface velocities is rejected. The free surface is expected to appear more wrinkled as the transport of surface instabilities are not damped by the effect of a turbulence model [12]. The breakup simulations use the Volume-of-fluid (VOF) method. Second order accurate schemes in space and time are applied: Crank-Nicolson in time, and a Gauss linear convection differencing scheme in space. The PISO-algorithm is implemented to solve the equations.

## Results and Discussion

The results are organized in a qualitative and a quantitative section. The qualitative section covers the appearance of the liquid sheet disintegration. The visualization of the breakup is compared to the known primary atomization mechanisms in order to characterize and classify the breakup process. The quantitative section validates the simulations using data from a prefilmer experiment. Parameters such as breakup length and frequency, the streamwise deformation velocity and the Sauter diameter at the domain outlet are investigated.



### Qualitative results

Under the influence of the accelerated air flow in an airblast atomizer various deformation structures are generated. These structures include sacs (bag-like structures), cells (thin planar liquid structures), ligaments (thin cylindrical structures) and membranes (liquid surfaces with protuberances and ramifications). It is accepted that these structures resulting from primary breakup are still too coarse to be considered as droplets. Droplets are generated during the secondary breakup [13]. The appearance of the primary atomization is categorized in several primary atomization mechanisms (figure 3). All of these mechanisms involve one or several liquid deformations produced by one or several fluid instabilities. These instabilities then disintegrate the liquid sheet.

Figure 3 compares the different primary atomization mechanisms. The breakup illustrations and the experimental snapshots by Fernandez [14] are used as the baseline for this qualitative comparison. The mechanisms are classified using the momentum flux ratio  $M$ . For OP 1 the stretched ligament breakup is found. The air velocity and the air density are considerably small, thus the development of sac structures is facilitated.

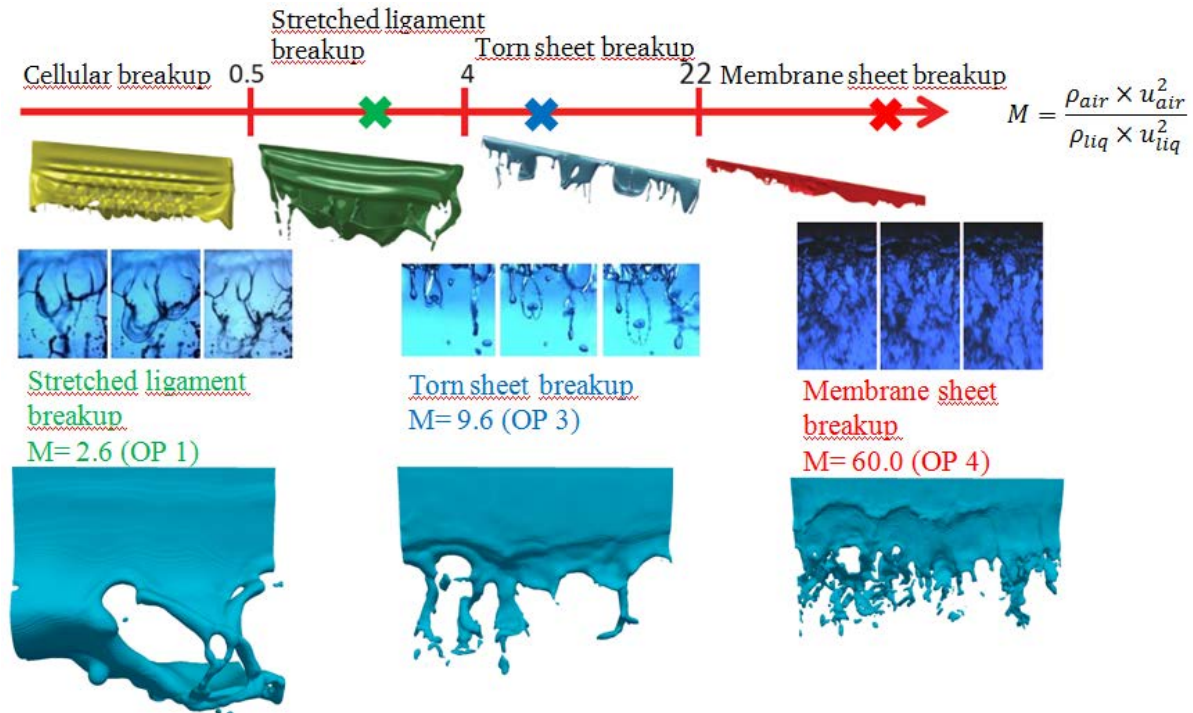


**Figure 3.** Different primary atomization mechanisms: experimental snapshots and illustrations by Fernandez [14]

For OP 3 the air velocity is constant, but the air and liquid properties are changed. As the momentum flux ratio goes beyond 4, the appearance of this regime is dominated by long and thick streamwise ligaments. These ligaments are highly irregular in spacing and frequency. This breakup regime is named torn sheet breakup. The regime starting at a momentum flux ratio of 22 is known as membrane sheet breakup. OP 4 can be grouped into this category. Here, neither streamwise or spanwise ligaments are dominant. Instead, this mechanism is distinguished by the formation of membranes. These membranes consist in liquid ramifications joined by highly fragmented liquid. The liquid has many protuberances. This breakup mechanism forms a more steady, breakup length and frequency than the torn sheet breakup.

Figure 4 illustrates the airblasted sheet evolution during primary breakup for the various operating conditions. The simulations at atmospheric conditions are found in the top row, the one at elevated air pressure and reduced surface tension force are situated in the bottom row. Several major observations can be derived from these snapshots: the breakup length is shortened continuously from OP 1 to OP 4 as three primary breakup mechanisms are passed through. At atmospheric conditions (top row), the phase interface appears very stable. At OP 1, the connected sheet shows sinusoidal oscillations around the prefilmer. Due to the movement inside the air stream, the sheet spans and thins until the air stream finally forces through the sheet. As a follow-up the sheet is stretched and contracted before large structures are finally separated. At OP 2, the air velocity is raised. Due to the higher velocity, the air contact region and the kinetic energy transferred from the air stream to the liquid film increases. Irregular longitudinal structures are visible. These longitudinal ligaments collapse and form separated structures downstream of the connected sheet. For these operating conditions, no surface waves on top of the liquid film are observed while flowing down the prefilmer.



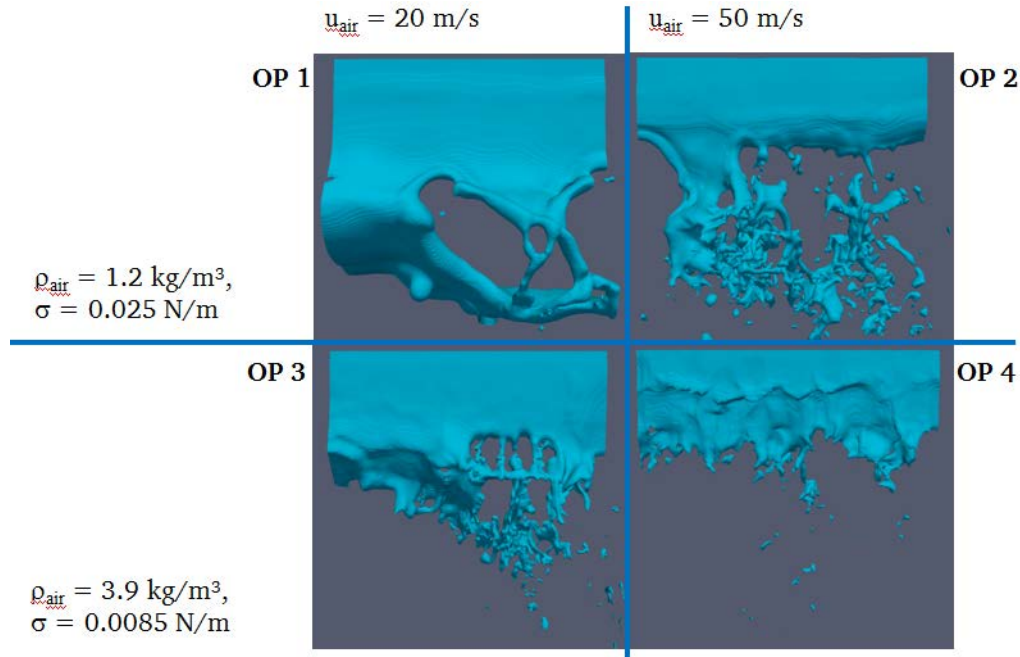


**Figure 4.** Airblasted sheet evolution for the different operating conditions

The bottom row indicates the airblasted sheet evolution for elevated pressure conditions and reduced surface tension force. OP 3 is represented by the torn sheet breakup regime similar to OP 2. Consequently, this atomization mechanism is also dominated by an irregular appearance and the formation of streamwise filaments. The increase in air flow density compensated for the decreased air velocity when contrasting OP 3 with OP 2. For OP 4, the breakup structures seem more regular. The sheet collapses close to the prefilmer trailing edge. Spanwise and streamwise ligaments are generated at the tip of the liquid sheet. Small structures and droplets are formed and transported downstream to the outlet of the eDNS domain. The breakup length is reduced, the breakup frequency is boosted. Surface waves moving in streamwise direction along the prefilmer are observed at OP 4. These disturbances accelerate the liquid sheet breakup downstream the trailing edge when the liquid sheet is sandwiched between both air streams.

#### Quantitative results

A quantitative validation of the primary breakup of a prefilming airblast atomizer configuration is limited to a very few number of experiments. Here, the authors compare the numerical results to the prefilmer experiment by Gepperth et al. [3]. Gepperth et al. used a planar prefilming geometry to investigate the sheet breakup. Different liquid fuels were used. The air stream velocity was varied in a range from 20 m/s to 70 m/s at atmospheric pressure condition. In this study, the properties of Shellsol D40 are applied meaning that the results using this fuel provide the baseline for the quantitative validation.

Similar to the experiment, the same parameters are used to compare the simulations with the experiments. The streamwise deformation velocity  $u_{def, str}$  is the streamwise velocity at the tip of the accumulated sheet (bottom left in figure 5).  $l_b$  represents the breakup length, hence the location where liquid structures are separated from the continuous liquid sheet (top right in figure 5). The breakup frequency  $f_b = u_{def, str}/l_b$  is a measure for the time distance between consecutive atomization events (top left in figure 5). The Sauter diameter ( $D_{32}$ ) of the structures and droplets at the domain outlet is also shown (bottom right in figure 5).

Simulation and experiment are in good agreement for the breakup frequency in figure 5 (top left). As the  $We$  number increases, the time span between two consecutive breakup events is decreased. The breakup length (top right) shows a good qualitative match between experiment and simulation. The increase in breakup length in the experiment between  $We=4$  and  $We=10$  cannot be described physically. Comparing the computations quantitatively, the breakup length is predicted shorter in the simulation than observed in the experiment. The authors believe that this effect is related to the still comparable coarse grid resolution in the eDNS. Thus, liquid bridges between two structures cannot be resolved. As a consequence, these structures already appear as separated from the liquid sheet.

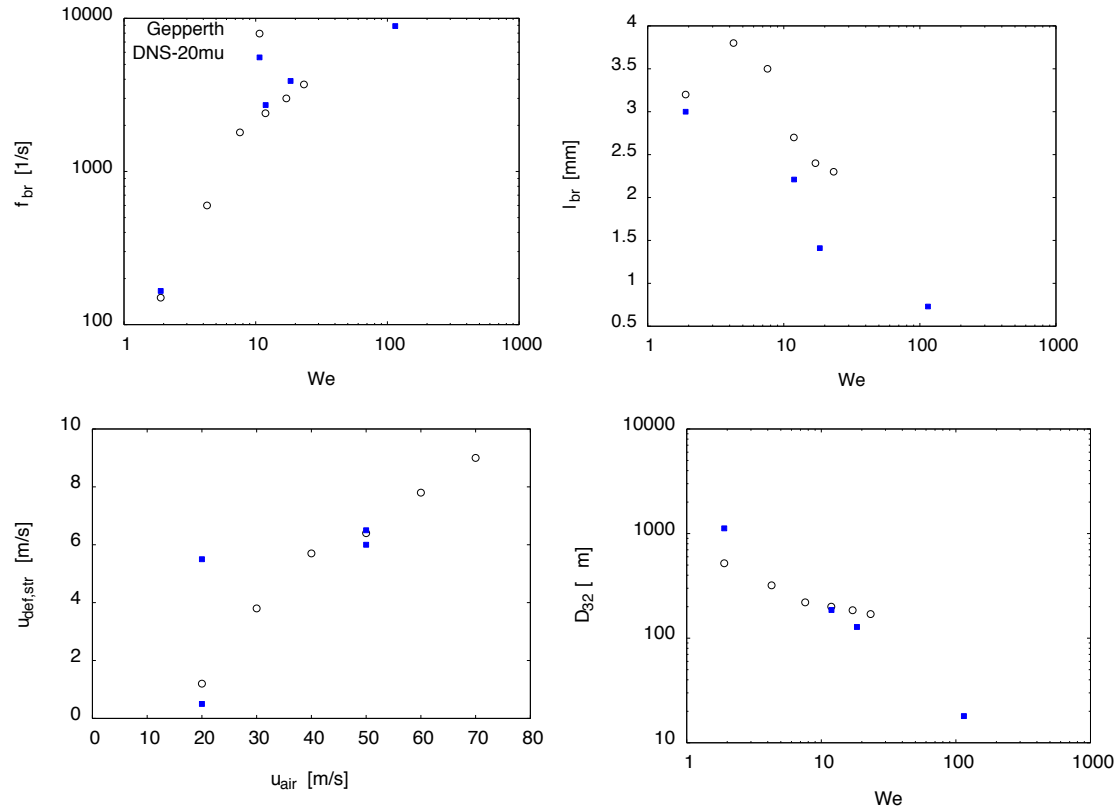


**Figure 5.** Quantitative validation with prefilmer experiment by Gepperth et al. [3]: top left – breakup frequency on film We number; top right – breakup length on film We number; bottom left – streamwise deformation velocity on air stream velocity; bottom right – Sauter diameter on film We number

The bottom left figure illustrates the liquid sheet deformation velocity on the air stream velocity. OP 1 and OP 2 are in good agreement with the experiments. These operating points use the same set of air and liquid properties as in the experiment. In OP 3 and OP 4 the surface tension force is reduced. The phase interface appears increasingly unstable. Thus, the interaction between air stream and liquid surface is intensified meaning that the streamwise deformation velocity is significantly higher at OP 3 compared to OP 1. The bottom right figure shows the Sauter diameter related to the  $We$  number. Simulations and experiments show the same tendency. OP 2 and OP 3 in the torn sheet breakup regime show a good agreement with the experimental results. For the membrane sheet breakup in OP 4, the Sauter diameter is reduced further. Unfortunately, no prefilmer experiment exists applying a momentum flux ratio beyond 22. But as the air stream velocity is increased while maintaining the reduced surface tension force, the breakup length is shortened. As a result, numerous separated structures are formed. These structures interact with the air- stream, the structures break up in smaller structures and droplets while getting accelerated towards the eDNS outlet. For OP 1, the Sauter diameter is overpredicted. As OP 1 represents the stretched ligament breakup regime, the streamwise domain length is not sufficient to form smaller structures. As the collapse of the sheet occurs close to the eDNS outlet, only large structures are detected. These structures are too close to the outlet to perform a further breakup process to smaller structures and droplets. Furthermore, the droplet detection process at the domain outlet assumes spherical droplets. Structures as detected at OP 1 are way too large to fulfill this assumption.

## Conclusions

In this study, the embedded DNS approach was applied to a generic planar prefilming airblast atomizer. Qualitatively, the primary atomization mechanisms can be distinguished with the characterization of the dominant deformation phenomenon in each regime. Quantitatively, the breakup frequency, the breakup length, the liquid sheet deformation velocity and the droplet Sauter diameter at the eDNS domain outlet show a good overall agreement with an experiment applying a planar prefilming airblast atomizer. The authors are planning to compute all operating points on a finer grid (at least 10 μm) to investigate the sensitivity of the quantitative results on the grid resolution. It is expected that especially the breakup length will increase with further refinement of the grid. Also, the refinement will positively influence the formation of small structures.

## Acknowledgements

This work was supported by the Deutsche Forschungsgemeinschaft (DFG) in the framework of GRK 1344 *Unsteady System Modeling of Aircraft Engines*.

## Nomenclature

DNS	Direct Numerical Simulation
eDNS	Embedded DNS
LES	Large Eddy Simulation
LPP	Lean Premixed and Prevaporized
OP	Operating point
VOF	Volume of fluid method

D	Droplet diameter [ $\mu\text{m}$ ]
f	Frequency [1/s]
l	Length [mm]
M	Momentum flux ratio
p	Pressure [bar]
Re	Reynolds number
T	Temperature (K)
u	Velocity (m/s)
We	Weber number

## Greek letters

$\gamma$	Volume fraction
$\nu$	Kinematic viscosity ( $\text{m}^2/\text{s}$ )
$\rho$	Density ( $\text{kg}/\text{m}^3$ )
$\sigma$	Surface tension force (N/m)

## Subscripts

32	Sauter (diameter)
br	Breakup
air	Gaseous phase (air)
def,str	Streamwise deformation
f	Liquid film
liq	Liquid phase

## References

- [1] de Villiers, E., Gosman, A. D., Weller, H. G., *SAE World Congress* (2004).
- [2] Herrmann, M., *ICLASS 11<sup>th</sup> International Conference on Liquid Atomization and Spray Systems*, Vail, USA (2009).
- [3] Gepperth, S., Müller, A., Koch, R., Bauer, H.-J., *ICLASS 12<sup>th</sup> International Conference on Liquid Atomization and Spray Systems*, Heidelberg, Germany (2012).
- [4] Fernandez, V. G., Berthoumie, P., Laverne, G., *C. R. Mécanique* 337:481-491 (2009).
- [5] Bhayaraju, U. C., “Analysis of Liquid Sheet Breakup and Characterisation of Plane Prefilming and Nonprefilming Airblast Atomisers”, Ph.D. Thesis, Technische Universität Darmstadt, Germany, 2007.
- [6] Lozano, A., Call, C. J., Dopazo, C., Garcia-Olivares, A., *Atomization and Sprays* 6:77-94 (1996).
- [7] Couderc, F., Estivalezes, J. L., *ILASS Americas 18<sup>th</sup> Conference on Liquid Atomization and Spray Systems*, Irvine, USA (2005).
- [8] Sander, W., Weigand, B., *Physics of Fluids* 20, 053301 (2008).
- [9] Sauer, B., Sadiki, A., Janicka, J., *ICMF 8<sup>th</sup> International Conference on Multiphase Flow*, Jeju, Korea (2013).
- [10] Behrendt, T., *DLR-Forschungsbericht* 2003-14, ISSN 1434-8454 (2004).
- [11] Moosbach, T., Sadanandan, R., Meier, W., Eggels, R., *ASME Turbo Expo*, Glasgow, UK (2010).
- [12] Frank, T., *NURETH 11<sup>th</sup> International Topical Meeting on Nuclear Reactor Thermal-Hydraulics*, Avignon, France (2005).
- [13] Hsiang, L. P., Faeth, G. M., *International Journal of Multiphase Flow* 21(4): 796-819 (1995).
- [14] Fernandez, V. G., “Experimental Study of a Liquid Sheet Disintegration in a High Pressure Environment”, Ph.D. Thesis, Université de Toulouse, France, 2010.

## Direct numerical simulation of liquid sheet atomization in HIT flow: Density ratio and Weber number influences

J.-L. Estivalezes<sup>1,2</sup> and S. Vincent<sup>3</sup>

1: ONERA, The French Aerospace Lab, France

2: Université de Toulouse, IMFT, France

3: Université de Bordeaux, I2M, France

### Abstract

The atomization of fuel jets in car or plane engines is a complex process handling multiphase motions and turbulent flow regimes in a highly coupled way. This work aims at describing, by Direct Numerical Simulation (DNS) of interfacial flows, the coupling between turbulent flow structures and interface deformations occurring during atomization of a liquid sheet. An incompressible Ghost Fluid solver coupled to a level set interface tracking method are implemented for representing at small scale all the flow and interfacial scales of the problem. The atomization of a liquid sheet by a Homogeneous Isotropic Turbulence (HIT) is studied by DNS and a parametric study is presented according to density and viscosity ratios at the interface as well as surface tension magnitude

### Introduction

The direct numerical simulation of multiphase flows is investigated to characterize the atomization of a liquid sheet by a turbulent gas flow. Applications are ranging from the atomization of a diesel jet in car engines to the atomization a liquid precursor jet in a plasma flame for nano-coating manufacturing. The models and numerical methods rely on the incompressible Navier-Stokes equations, a ghost fluid approach and level set methods for interface tracking. In a previous work [1], we have investigated the influence of the density ratio between the two phases on the spectral behaviour of the turbulent kinetic energy. In the present paper, we carry on this work by a more detailed analysis of the influence of the density ratio on droplet pdf, interface density, kinetic energy evolution in each phase during decay.

### Governing equations and numerical methods

As we are mainly interested by the numerical simulation of the air-assisted disintegration of a sheet at moderate velocities, we will use the incompressible Navier-Stokes equations in both phases :

$$\begin{aligned} \nabla \cdot \mathbf{u} &= 0 \\ \frac{\partial \mathbf{u}}{\partial t} + (\mathbf{u} \cdot \nabla) \mathbf{u} &= -\frac{1}{\rho} (\nabla p + \nabla \cdot (2\mu \mathbf{D})) \end{aligned}$$

Across the interface, the Navier-Stokes equations solution respect the so called kinematic and dynamic boundary conditions ( [.] define the jump across the interface location)

$$\begin{aligned} [\mathbf{u}] \cdot \mathbf{n} &= 0 \\ [p] - \mathbf{n} \cdot [\mu \mathbf{D}] \cdot \mathbf{n} &= \sigma \kappa \\ \mathbf{t} \cdot [\mu \mathbf{D}] \cdot \mathbf{n} &= 0 \end{aligned}$$

Here  $\sigma$  is the surface tension coefficient,  $\kappa$  the local curvature,  $\mathbf{n}$  and  $\mathbf{t}$  are respectively the normal and the tangent at the interface. Classical projection methods are performed to ensure the incompressibility constraint [2] The spatial discretization is based on staggered MAC uniform cartesian grids for the velocity components, all others quantities as density, pressure and level-set are cell-centered. The convection terms in the momentum equations are approximated in a conservative way with fifth order accurate WENO schemes [3]. This particular choice has been motivated by the robustness and low numerical dissipation of such schemes to perform direct numerical simulations [4]. Time integration is performed with a third order accurate TVD Runge-Kutta scheme. It should be pointed that the incompressibility constraint is enforced at each Runge-Kutta sub-step. The Poisson equation for the pressure is solved by a fast multigrid preconditioned conjugated gradient method [5]. A level-set method [6] is used to capture the interface, which is implicitly given by the zero of the smooth function  $\phi(x, t)$ . By convention, the level-set function  $\phi$  will be taken negative in the liquid and positive in the gas and the normal  $\mathbf{n}$  will point towards the positive values of  $\phi$ . Moreover,  $\phi$  is imposed to be the signed distance function to the interface. This particular property of the level-set function is of major importance.

Indeed, this property ensures the level-set to be well behaved at the interface between the two fluids. The evolution of the interface is implicitly captured by the zero-level of  $\phi$  which obeys the following equation

$$\frac{\partial \phi}{\partial t} + \mathbf{u} \cdot \nabla \phi = 0$$

As for the momentum equation, the level-set equation is solved by a fifth order WENO scheme for spatial discretization and a third order TVD Runge-Kutta scheme. While this equation will move the level-set  $\phi(x, t) = 0$  at the correct velocity,  $\phi(x, t)$  will no longer remain a distance function. This can lead to large mass losses or gains as the interface will behave poorly. Consequently, the level-set must be regularly reinitialized to overcome this drawback. This is achieved by solving to the steady state the following Hamilton-Jacobi equation for  $\phi$  [7]

$$\begin{aligned} \partial \phi / \partial t + \text{sign}(\phi_0)(\|\nabla \phi\| - 1) &= 0 \\ \phi(x, 0) &= \phi_0(x) \end{aligned}$$

The jump conditions for pressure and pressure gradient in the Poisson pressure equation as well as jump condition for the viscous terms are taken into account by the ghost fluid method [8]

## Results and Discussion

### Parameters of the simulations

The computational domain is a  $2\pi$  square box with periodic boundary conditions on each side. The spatial grid resolution is  $512^3$ . Simulations are performed at low Reynolds numbers. This field is generated in Fourier space: it fulfills the constraint of incompressibility and follows a prescribed energy spectrum. A complete description of the method to initiate an H.I.T. field can be found in [9]. The initial energy spectral density (energy spectrum) is given by:

$$E(k) = \frac{r^2}{2A} \frac{1}{k_p^{\gamma+1}} k^\gamma e^{(-\frac{\gamma}{2}(\frac{k}{k_p})^2)}$$

$k$  is the wave number, values of the different constants can be found in (Trontin 2008).

$\nu$	$u'$	$\epsilon$	$L_f$	$\lambda$	$\eta$	$T_e$	$R_{L_f}$	$R_\lambda$
0.003	1.0	0.911	0.279	0.222	$1.312 \times 10^{-2}$	0.278	93	74

**Table 1.** Parameters of the initial turbulence field

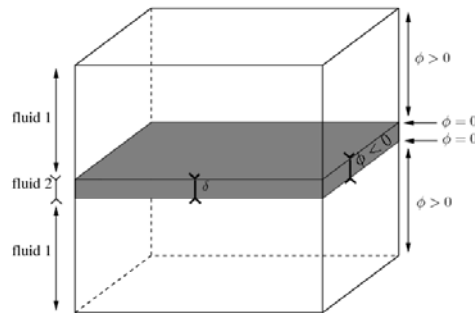


**Figure 1.** Flow field configuration

As shown in Fig. 1, a thin plane layer (or sheet hereafter) is added in the H.I.T. field generated from the energy spectrum given by the previous equation. The sheet is represented by the fluid 2 (which can be seen as the liquid

phase) in Fig. 1. Its thickness is 5 % of the box size and 24 times the Kolmogorov spatial scale of the initial HIT field. This corresponds to a volume liquid fraction of 5 %, whereas previous studies were performed for 95 % volume liquid fraction [1] Three density ratio ( $r = \rho_l/\rho_g$ ) have been studied:  $r=1$ ,  $r=10$  and  $r=50$ . The kinematic viscosity in the two phases is kept the same, in order that the same kinematic turbulence field is experienced by both phases

#### Qualitative behaviour of the flow

In the figure 2, we have plotted the interface location for the 3 Weber numbers studied, i.e.  $We=0.05$ ,  $We=2$  and  $We=110$  for the higher density ratio simulated ( $r=50$ ). The Weber number is defined as follows:  $We = \rho_g u'^2 \delta / \sigma$ , with  $\rho_g$  the gaz density,  $u'^2$  the initial turbulent intensity,  $\delta$  the sheet thickness and  $\sigma$  the surface tension coefficient.

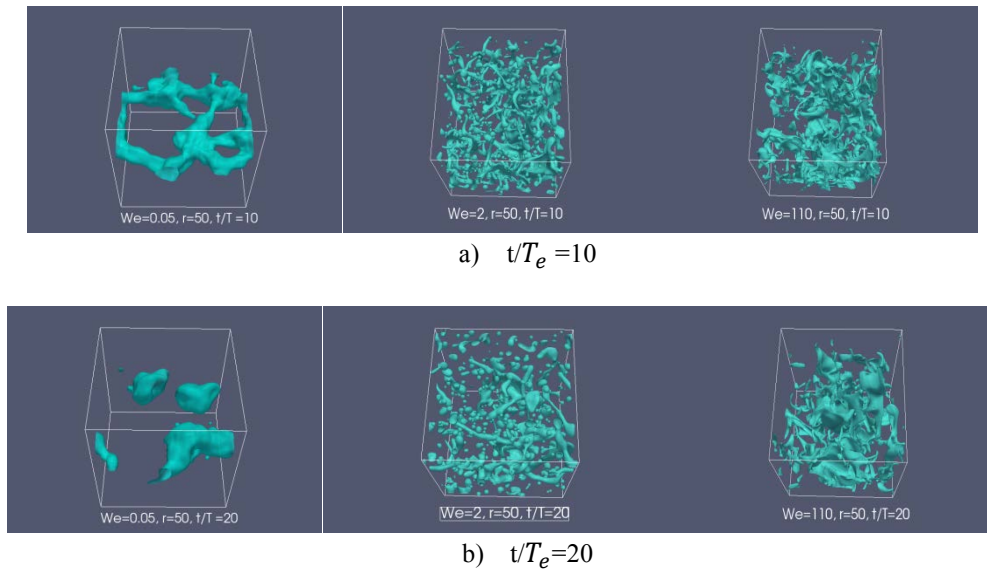


**Figure 2 :** Interface behaviour at different times during decay for  $r=50$

In this figure, one can observe that whatever is the Weber number, fragmentation appears even at early time during decay, which was not the case at least for  $We=0.05$  for  $r=1$  ratio. For the highest Weber number, the fragmentation process gives birth to leaves rather than droplets, which is clearly different from the two others Weber numbers. This particular behaviour is no more observed if the density ratio is lowered as can be seen in figure 3.

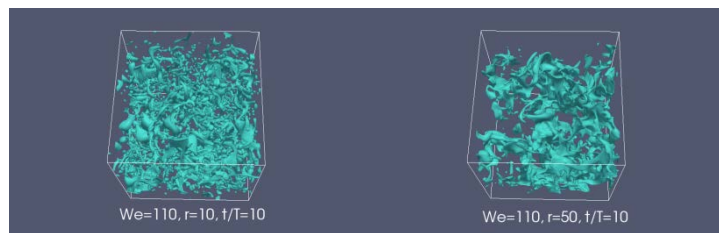


**Figure 3 :** Interface behaviour at  $r=10$  and  $r=50$ ,  $We=110$ ,  $t/T=10$

#### Kinetic energy evolution

We present on the next figures the kinetic evolution during decay for the 2 largest Weber numbers ( $We=2$  and  $We=110$ ) and for the 3 density ratio ( $r=1$ ,  $r=10$ ,  $r=50$ ).

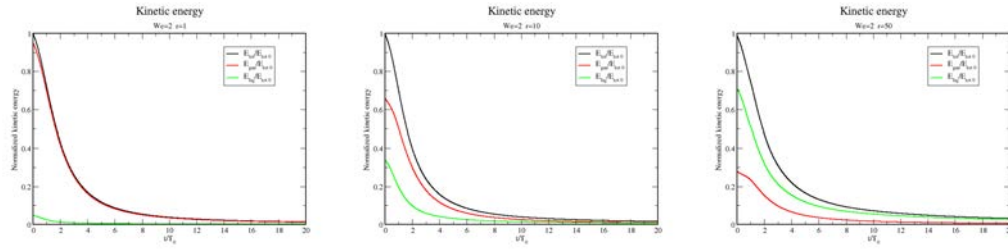


**Figure 4** : Kinetic energy evolution , We=2, r=1, 10, 50

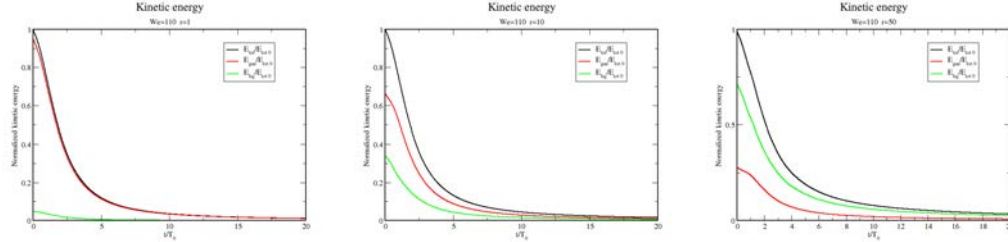
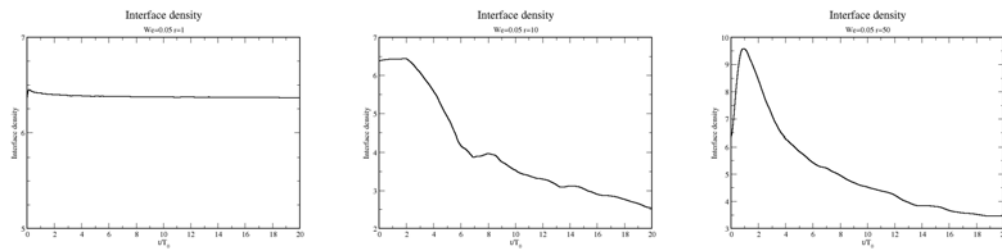


**Figure 5** : Kinetic energy evolution , We=110, r=1, 10, 50

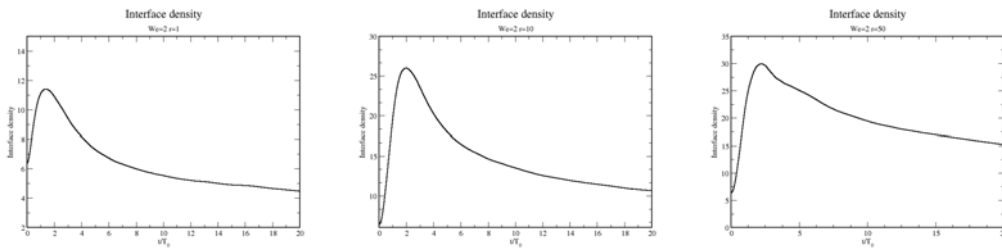
What we observe in this figures, is that the temporal evolutions of the kinetic energy are very similar for both Weber numbers. It should be said that what we look at is the massic kinetic energy ( unweighted by density). For low density ratio, the main part of kinetic energy is contained in the gaz phase, whereas for highest density ratio, it is for the liquid phase. Another feature that is observed from log-log plot of kinetic energy ( not shown here for lake of space) , is that we also see and power law decay for both phases as in single phase decay but with a different exponent which is depending both from the Weber number and the density ratio.

#### Interface density evolution

In order to quantify the way the sheet will disintegrate, it is interesting to study the interface density evolution during decay. This quantity is defined as the ratio of the surface on the interface between the two phases divided by the corresponding volume of the liquid phase. From the level-set function, one can simply evaluate the surface of the interface by taking the smoothed Dirac function of the level-set. The corresponding volume is given by the smoothed Heavyside function. The interface density function is the ratio of them. The following figures show the interface density evolution for the 3 Weber numbers and for the 3 density ratio.



a) We=0.05



b) We=2



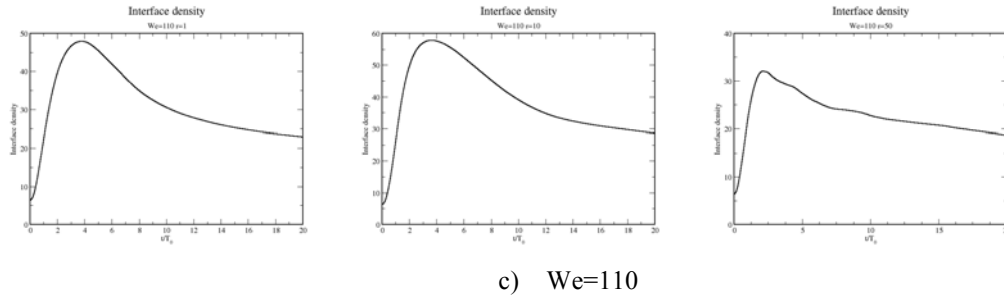


**Figure 6:** Density interface evolution for  $We=0.05, 2, 110$ , and  $r=1, 10, 50$

Except for the smallest Weber number and for density ratio of 1 and 10, we can observe a quite similar evolution. Indeed, an increase of density ratio up to 2 to 4 eddy time turnover appears, followed by a decrease towards asymptotic values. The maximum of the density ratio seems to correspond to the moment when fragmentation of the liquid sheet is maximum. After that, decay due to coalescence between drops and ligaments appears up to a nearly stabilized value which is depending both with the Weber number and the density ratio.

#### *Droplets distribution evolution*

In order to get more insight into the liquid sheet evolution during turbulence decay, we try to extract a droplets distribution at different times. To do that, we develop an post processing algorithm based on simply connected volume, i.e. we detect locally simply connected volume and identify it to an equivalent sphere that will give the diameter of the equivalent droplet. The main shortcoming of this approach is that it does not make any difference between a real sphere and a ligament. So we tend to overestimate real spherical droplets population.

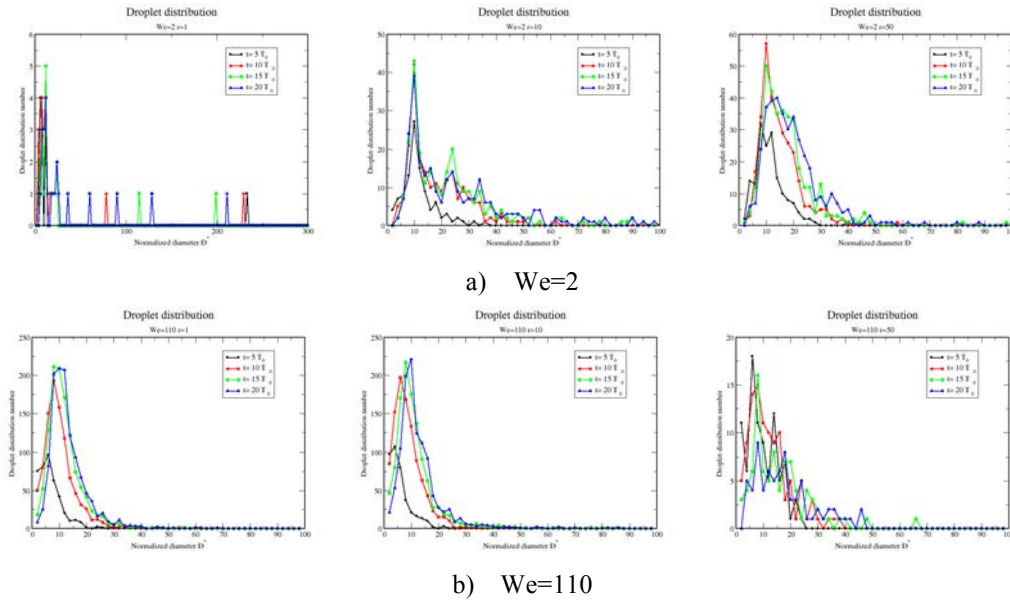


**Figure 7:** Droplets distribution for  $We=2, 110$ , and  $r=1, 10, 50$

The Weber number=0.05 is not shown here as only 3 big blobs appears for the largest density ratio  $r=50$ . The droplet diameter is normalized by the grid size  $\Delta x$ . For  $We=2$  and  $r=1$  the scale for the normalized diameter is stretched as big blobs are observed in the domain which is not more the case for others density ratio and higher Weber numbers. Always for  $We=2$ , for  $r=10$ , after formation of small droplet around  $D^* = 10$ , at early times of decay (around  $t/T_e = 5$ ), we observe at later times droplets coalescence with a maximum of  $D^* = 35$  for  $t/T_e = 20$ . A similar behaviour is also observed for the case  $We=2$  and  $r=50$ , but now the coalescence is more important around  $D^* = 20$  for  $t/T_e = 20$ . For  $We=110$ , the same trends are observed, at least for  $r=1$  and  $r=10$ , the main difference comes from the first fragmentation diameter which is now around  $D^* = 8$ . After coalescence and increase up to  $D^* = 10$  is observed at later time of the turbulent decay. The last case  $We=110$  and  $r=50$  shows a quite different behaviour, with for the later time higher values of  $D^*$ . Indeed, one can see in the figure, that we get local maximum around  $D^* = 20$  and  $D^* = 30$ . In fact, in that case, we don't really have spherical droplet, rather are observed (see figure 4) ligaments and leaves.

### Spectral analysis

In figure 8, are plotted the kinetic energy spectra for the 3 Weber numbers and the 3 density ratio. The first thing to see in this figure, is that whatever are the weber numbers and the density ratio, the same behaviour is observed, i.e. an energy gain at high wave number which is no present in single phase HIT flow. This particular behaviour has also be observed in previous studies for high liquid fraction ( 95 %). This behaviour is characteristic from this type of flow including interface between two fluids. Another typical feature of the spectral behaviour is the formation of a kind of inertial zone which spread over a decade whereas single phase flow on such configuration ( with quite low turbulent Reynolds number) do not show it. If we try to fit a power law in this zone, depending on the Weber number and density ratio, fitted exponent ranges from -3 to -4 which is very different of inertial exponent for single phase HIT flow. As the moment, it is not clear why such behaviour is observed.

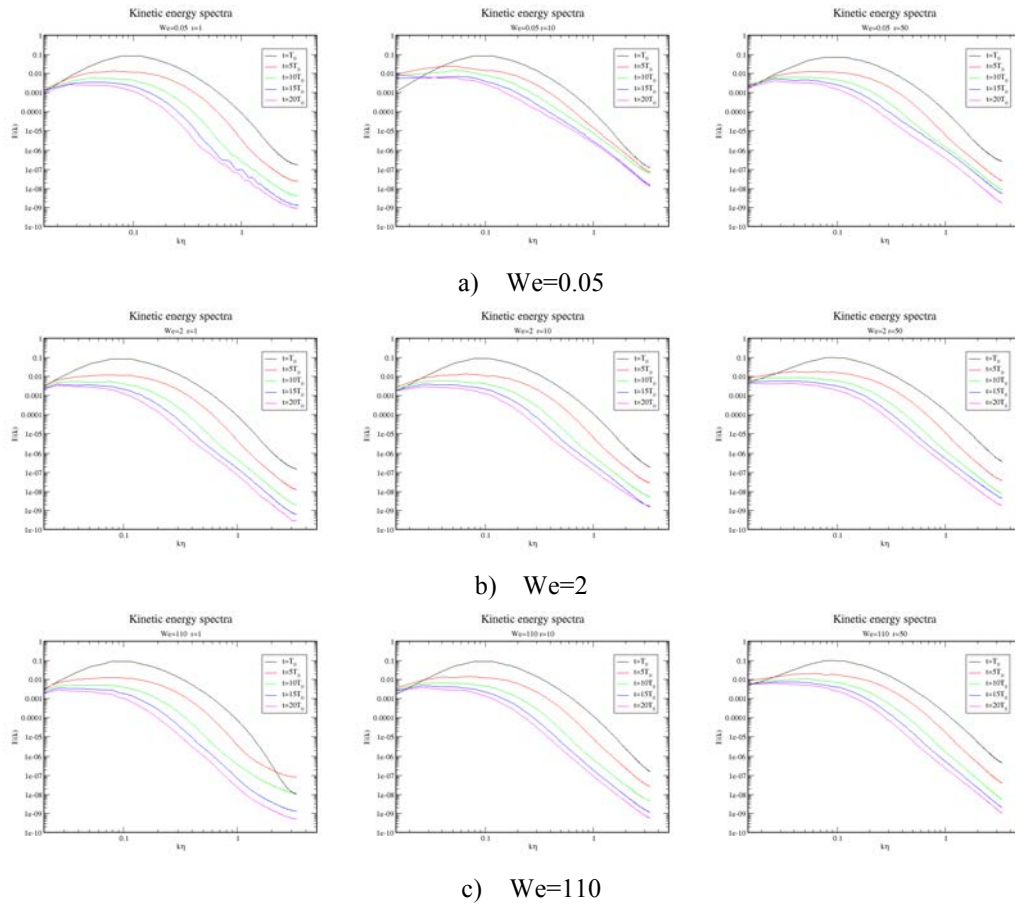


Figure 8: Kinetic energy spectra

### Conclusions

Detailed direct numerical simulation of two-phase interfacial flow in homogeneous isotropic turbulence configuration have been conducted for different turbulent Weber numbers and density. Results on kinetic energy decay show that for each Weber number simulated, increasing density ratio gives high energy in the liquid part of the flow. Moreover, total kinetic energy exhibits power law decay like in single phase HIT flow, but different exponents are found depending on both Weber numbers and density ratio. Concerning interface density evolution, except for the lowest Weber number, we observe a similar behaviour for the different density ratio simulated, with an increase of the interface density at early time around 2 to 4 eddy turnover time, followed by a decrease towards an asymptotic value depending of the turbulent Weber number. This increase indicates the beginning of the liquid sheet fragmentation into smaller droplets. To more precisely quantify droplet formation and evolution during decay, we have analysed the droplets distribution function by extracting from the level-set function simply connected volumes and transform them in equivalent spherical droplets. Smaller droplets are formed at early times ( $t/T_e \sim 5$ ) then coalescence process increases droplets size. This behaviour has been observed for the two larger Weber number, whereas for the smallest one, only few big blobs appear for the

higher density ratio. Finally spectral analysis of kinetic energy has been performed. The same conclusion can be drawn concerning spectral evolution compare to  $r=1$  density ratio. A kind of inertial zone with constant exponent is exhibited over one decade whatever is the density ratio and the turbulent Weber number, the value of the exponent ranges between -3 and -4. This behaviour is quite singular and most likely to surface tension forces that are exciting the flow field at high wave number.

### Acknowledgements

This work was granted access to the HPC resources of [CCRT/CINES] under the allocation 2012- [6430] made by GENCI (Grand Equipement National de Calcul Intensif)

### Nomenclature

Level-set function :  $\phi$   
 Liquid density :  $\rho_l$   
 Gaz density :  $\rho_g$   
 Density ratio :  $r = \frac{\rho_l}{\rho_g}$   
 Liquid sheet thickness:  $\delta$   
 Weber number:  $We = \rho_g u'^2 \delta / \sigma$   
 Surface tension coefficient :  $\sigma$   
 Turbulence intensity :  $u'^2$   
 Eddy turnover time :  $T_e$   
 Spatial Kolmogorov scale:  $\eta$   
 Taylor microscale:  $\lambda$   
 Dissipation:  $\epsilon$   
 Kinematic viscosity:  $\nu$   
 Normalized diameter:  $D^* = \frac{D}{\Delta x}$

### References

- [1] J.-L. Estivalezes , S. B. Rabé, Vincent, J.-P. Caltagirone, P. Trontin : Effects of density ratio during the disintegration of a liquid sheet by a HIT flow, ILASS 2011, Estoril
- [2] A. Chorin Math. Comp, 22:745-762 (1968)
- [3] C.W. Shu, "Essentially non-oscillatory and weighted essentially non-oscillatory schemes for hyperbolic conservation law", ICASE - NASA Report, 1997
- [4] P. Trontin, S. Vincent, J.-L. Estivalezes and J.-P. Caltagirone, Int. J. Numer. Meth. Fluid., 56:1543-1549 (2008).
- [5] O. Tatebe, "MGCG Method, a robust and highly parallel iterative method", University of Tokyo, 1996
- [6] M. Sussman, J. Comput. Phys., 114:144-159 (1994).
- [7] G.S. Jiang and D. Peng, SIAM J. Sci. Comput, 21(6):2126-2143 (2000)
- [8] R. Fedkiw and X. Liu and M. Kan, J. Comput. Phys., 160:151-178 (2000)
- [9] R.S. Rogallo, "Numerical experiments in homogeneous turbulence", NASA report TM 81315, 1981

## Improving primary atomization modelling through DNS of two-phase flows

B. Duret, T. Menard, J. Reveillon and F.X. Demoulin

UMR6614-CORIA, Technopôle du Madrillet, BP 12, Avenue de l'Université,  
76801 Saint-Etienne-du-Rouvray Cedex, France

### Abstract

This study employs DNS of two-phase flows to compare and improve primary atomization models used in RANS and/or LES formalisms. The paper is based on the ELSA model, which was initially proposed in Vallet, A., Borghi, R., 1999. Modélisation eulerienne de l'atomisation d'un jet liquide. Comptes Rendus de l'Académie des Sciences - Series IIB - Mechanics-Physics-Astronomy 327 (10), 1015 – 1020. This model has been used successfully in many studies to describe the complete liquid atomization process from primary atomization to the dispersed spray. A two phase flow homogeneous isotropic turbulence was used for the numerical configuration. A statistical analysis of the equilibrium Weber number was performed with a DNS of two-phase flows to verify the definition given by the ELSA model. This verification was carried out for various liquid volume fractions, mesh resolutions, and surface tensions. An ensemble averaging of the time evolution of the interface density was performed to check the validity of the interface density equation used in the ELSA model. The initial and final equilibrium is shown on Figure 1, illustrating the increase of interface density when the surface tension is reduced. Proposed improvements of the ELSA model were compared with the reference DNS for multiple configurations. The new proposal shows good agreement with DNS data. Afterwards, the proposed formulation of the model is introduced in an implementation of the ELSA approach in OpenFOAM to check the impact of the improved model in a liquid jet configuration. Differences between the original and new approach are discussed.

---

### Introduction

Combustion of liquid fuel remains one of the major source of energy. The injection phase is a critical step for mixture preparation and the induced combustion. Hence, many works have been devoted to the description of the injection process and its influence on the vaporisation and mixing. However, experiments allowing these processes to be studied are difficult in particular close to the dense zone of the spray. The last decade has seen the appearance of numerical method devoted to two-phase flows with an accurate description of the interface. Volume of Fluid method [10], Level Set method [24] and Front-tracking method [26] are the most common strategy used for Direct Numerical Simulation (DNS) of interfacial flows. Discontinuities at the interface have to be treated carefully. To do this, numerical methods like the delta function method [3] and the ghost fluid method [8] were developed. The last one made possible to apply sharp jump conditions at the interface. As far as atomisation is concerned, successful studies have emerged to describe the primary atomisation of liquid jets [18] [21].

Unfortunately, these simulations have shown that, even with a resolution of 0.35 micrometers [21], the finest scales of the flow are not resolved. To optimize the computational cost, some studies use an adaptive mesh refinement [1] [9] but there is still a numerical cut-off scale. It is possible that in few years, improvement of numerical methods and computational efficiency will permit to solve the finest scale of two-phase flows. Furthermore, the finest scale in multiphase flows remains unknown, contrary to the Kolmogorov and the Batchelor scale in single phase flows.

This issue shows that subgrid models are necessary to modelize the physics under this particular scale, like the Large Eddy Simulation (LES) of single phase flows. LES of two phase flows have been investigated in few studies. A first approach consist in keeping interface tracking methods to solve the interface, but without solving the finest scales of wrinkling ( [13] for example). Another approach, more phenomenological, is to describe continuously the transition between a well resolved interface and structures smaller than the cell size. This approach introduces the interface density area, which indicate the quantity of interfacial area in each cell, but without indications on the shape of the structures [4]. This last work adapt the ELSA model (initially proposed by Vallet and Borghi [27] ) to LES modelling. These approaches give interesting statistical results, independent of the mesh size and in accordance with reference two-phase flow.

In order to improve LES modelling, it is useful to study well defined configurations which allows us to solve all relevant scales of the flow. In single-phase flows, DNS of Homogeneous Isotropic Turbulence (HIT) is still used to study turbulence characteristics and scalar mixing. Extension of this configuration to two-phase flows to characterize interface/turbulence interactions is emerging in recent DNS studies : initially with a forced HIT [17], a freely decaying turbulent two-phase flow has been studied also [25], and recently vaporization has been

included [6]. Other applications are with solid particles in an HIT [5], and with a downward turbulent flows for bubbly flows [15].

The aim of this paper is to pursue these studies by analysing statistical quantities extracted from a validated two-phase flows DNS database [6], with a main focus on interfacial quantities. From these results we can extract useful information in order to improve modelling of primary atomisation. In this paper, we focus on the ELSA model, because with this approach in the dense zone of the spray is addressed directly [27] [14]. The reference DNS is based on the well referenced ARCHER code [18]; the interface tracking method used is a coupled Level Set/VOF method. A sufficiently high density ratio between the two phases is chosen to simulate realistic engine conditions. Both quantitative and qualitative aspects are analysed.

In the following part of this work, the constitutive equations and numerical procedures are first described for the DNS and then for the model used. The flow geometry is then depicted. Next, an appropriate definition of the equilibrium Weber number is proposed. Finally, a statistical analysis of the interface density is carried out by studying the time evolution of the interface density between two equilibrium state for different configurations and liquid volume fractions. Corrections on the interface density equation are proposed and tested.

### Governing equation

The joint Level Set/VOF method is coupled with a projection method to carry out the direct numerical simulation of incompressible Navier-Stokes equations :

$$\frac{\partial \mathbf{V}}{\partial t} + (\mathbf{V} \cdot \nabla) \mathbf{V} = -\frac{\nabla p}{\rho} + \frac{1}{\rho} \nabla \cdot (2\mu \mathbf{D}) + \mathbf{f} + \frac{1}{\rho} \sigma \kappa \delta(G) \mathbf{n}$$

where  $p$  is the fluid pressure,  $\mathbf{V}$  the velocity vector,  $\mathbf{g}$  the gravity vector,  $\mu$  the dynamic viscosity, and  $\mathbf{D}$  the viscous deformation tensor. At the interface, the surface tension force can be considered based on the Dirac function  $\delta(G)$ :  $\sigma$  is the surface tension,  $\mathbf{n}$  the normal unit vector,  $\kappa$  is the curvature computed from the Level Set function  $G$ . To maintain the turbulent kinetic energy at a prescribed level, it is necessary to use a forcing method. This is achieved through the source term  $\mathbf{f}$ , which induces a linear forcing [20]. It gives  $\mathbf{f} = A \mathbf{v}'$  where  $A$  is the forcing coefficient,  $\mathbf{v}'$  represent velocity fluctuations. The constant  $A$  is computed at each time step to sustain a prescribe level of velocity fluctuations over the whole domain. This method maintains a statistically stationary homogeneous isotropic turbulence. More details about the forcing method are explained in Duret et al. [6].

To correctly describe the interface, the VOF method is used jointly with the Level Set to enforce mass conservation [18]. For the sake of clarity, the average value of the VOF method scalar in the complete domain is called the liquid volume fraction  $\phi$ , and the local liquid volume fraction within a cell is  $\phi_i$ . They are defined as follows :  $\phi = V_l/V_t$ , where  $V_l$  is the total volume of liquid and  $V_t$  the total volume of the domain.  $\phi_i = V_{li}/V_c$ , where  $V_c$  is the cell volume and  $V_{li}$  is the volume of liquid within a cell.  $\phi_i$  respects the following transport equation:

$$\frac{\partial \phi}{\partial t} + \mathbf{V} \cdot \nabla \phi = 0$$

Finally, to take into account jump conditions at the interface, the Ghost Fluid method is used [8].

### Numerical configuration

The solution is carried out in a three dimensional cubical domain with periodic boundaries similar to the study of Duret et al. [6]. This configuration extends previous numerical studies on mixing in single-phase flows [7] to two-phase flows with a fully resolved liquid-gas formulation. To accurately control the various inputs of the simulation, a three dimensional forced homogeneous turbulence of a gas / liquid flow is considered with a liquid volume fraction ranging between 5% to 95%. The liquid gas interface is represented in Figure 1 to illustrate the numerical configuration for a liquid volume fraction of 5 %.

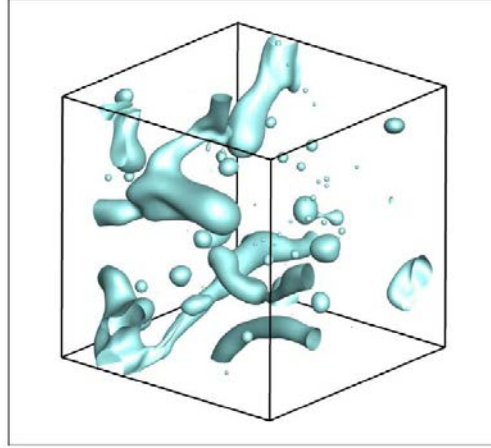


**Figure 1** : Interface visualization, liquid volume fraction  $\phi=5\%$

### Primary atomization modelling

By analogy with the flame surface density, a postulated equation for the mean interface density was proposed by Vallet and Borghi [27]. The mean interface density is defined by the area of liquid-gas surface by unit of volume ( $\bar{\Sigma} = S_L / V$ ). This was the first formulation of the ELSA model, dedicated to the atomisation regime (high Weber and Reynolds number). This equation include appropriate source/sink terms, to take into account effects of surface tension, vaporization, turbulence and coalescence.

The liquid/gas interface density equation have been written in many different ways since the first proposal (for example [11] [12] and [2], in this work the latest equation of the interface density is chosen [14] :

$$\frac{\partial \bar{\Sigma}}{\partial t} + \frac{\partial \bar{\Sigma} \tilde{u}_i}{\partial x_i} = \frac{\partial}{\partial x_i} \left( \frac{\nu_t}{Sc_t} \frac{\partial \bar{\Sigma}}{\partial x_i} \right) + \underbrace{\Phi(S_{init} + S_{turb})}_{dense} + \underbrace{(1 - \Phi)(S_{coll|coal} + S_{2ndBU})}_{dispersed} + S_{vapo}$$

Where  $\bar{\Sigma}$  is the mean interface density,  $\Phi$  is a repartition function used to share out dense ( $\Phi = 1$ ) and dilute source terms ( $\Phi = 0$ ),  $Sc_t$  the turbulent Schmidt number and  $\nu_t$  the turbulent viscosity and  $\tilde{u}$  the Favre averaged mixture velocity. In the present DNS configuration (dense two-phase flows HIT, and no phase change) the interface density equation is reduced to :

$$\frac{\partial \bar{\Sigma}}{\partial t} = S_{turb}$$

The turbulence source term is modelled following Vallet and Borghi [27] and Lebas et al. [14] :

$$S_{turb} = C_\Sigma \frac{\bar{\Sigma}}{\tau_t} \left( 1 - \frac{\bar{\Sigma}}{\bar{\Sigma}^*} \right)$$

Where  $\bar{\Sigma}^*$  is the "equilibrium" interface density,  $\tau_t$  a turbulent timescale and  $C_\Sigma$  has been set to unity due to lack of information. This term corresponds to the production/destruction of liquid-gas interface density due to the turbulent flow stretching, wrinkling and the effects of collision and coalescence in the dense part of the spray. It is assumed to be driven by a turbulent time scale  $\tau_t$ . This production/destruction term is defined in order to reach an equilibrium value of the surface density  $\bar{\Sigma}^*$ . It corresponds to the quantity of surface that would be obtained by keeping constant the total mixture turbulent kinetic energy and the liquid volume fraction.

Usually, an equilibrium Weber number is used in primary atomisation modelling to determine  $\bar{\Sigma}^*$  :

$$We^* = \frac{\phi \tilde{k}}{\sigma \bar{\Sigma}^*}$$

Without any information on this variable, the equilibrium Weber number has been set to unity. This means that the total energy is equally distributed between the kinetic energy and the surface energy. With this Weber number it is then possible to compute  $\bar{\Sigma}^*$  and finally  $S_{turb}$ . In this work, it is possible to extract the equilibrium

surface density and the Weber number from the DNS and verify if this definition is adequate. This is done for two mesh resolutions.

Another comparison is performed by analysing the work of Luret et al. [16] [17] who performed similar simulations but the turbulence was not fully resolved at small scales (contrary to the presented one which was validated [6]), because the main objective in Luret et al. [16] [17] was to study droplets collision.

## Results and discussion

### Equilibrium Weber number

The previous definition of the equilibrium Weber number tends to infinity or zero when  $\phi$  is closed to 0 or 1 (for example very dense two-phase flows).

A new definition of  $We^*$  is proposed to avoid this issue :

$$We^* = \frac{2(\rho_L + \rho_G)\phi(1-\phi)\bar{k}}{\sigma\bar{\Sigma}^*} \quad (1)$$

This definition may looks surprising, it is only an attempt to build a formulation of the Weber number applicable to a wide range of liquid volume fractions encountered in atomisation (from dispersed spray to dense spray).

From the DNS it is possible to compute  $We^*$  and then check if the assumption of the model ( $We^* = 1$ ) is meaningful. Results are shown in Figure 2.  $\bar{\Sigma}^*$  and  $\bar{k}$  are volume averaged in the whole domain and then time averaged over at least 80 eddy turnover times ( $\tau_t = \bar{k}/\varepsilon$ ) for the computation of the Weber number to assure proper statistical convergence. In the following,  $t^*$  is the time normalized by  $\tau_t$ . For the simulation using different surface tension, a different averaging procedure is used, presented in the next section.

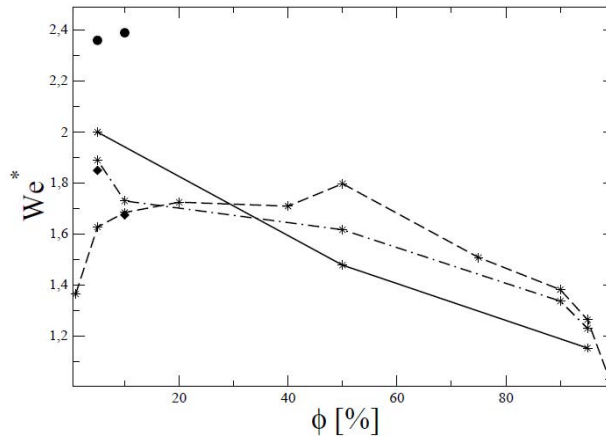


**Figure 2 :** Equilibrium Weber number for various liquid volume fractions. Plain line :  $256^3$  configuration, dashed-dotted line :  $128^3$  configuration, dotted line : Results from Luret et al. [16] [17]. Symbols indicates the surface tension value. \* :  $\sigma_{ref} = 0.0135$ , • :  $\sigma = 0.8\sigma_{ref}$  and ♦ :  $\sigma = 1.4\sigma_{ref}$ .

It is impressive that for these three configurations, the value of the Weber number is always ranged between  $We^* = 1$  and  $We^* = 2.5$  instead of the previous formulation (see Figure 2), even with a coarse grid, a turbulence not fully resolved or different surface tension. This may justify the use of Equation 1. This can be very handy when using primary atomisation model, because all variables are known in except  $\bar{\Sigma}^*$  (see previous section), this last can be computed by assuming a Weber number equal to approximately 1.63 for example which is the mean value of the equilibrium weber number for all simulations. Or, one can interpolate  $We^*$  using the  $256^3$  curve, which is the most resolved case.

However, Figure 2 shows that some limitations may appears when using this approximation when the surface tension is reduced, because it significantly increases the  $We^*$ . This is not the case when the surface tension is increased, results are very similar with those obtained with the reference surface tension. Note that despite the high resolution of this simulation, solving the smallest scale of the flow is still a stiff issue. Thus, when the surface tension is reduced, smaller wrinkling of the interface is expected. An increase of the mesh resolution may be needed in this case, and will be investigated in future works.

*Analysis of  $S_{turb}$*



Previous work assumed that the definition of  $S_{turb}$  is adequate. Unfortunately, this equation was postulated and has not been verified directly experimentally or numerically to the author's knowledge. Here we propose to check this model by changing the surface tension between two computations, to induce a surface density variation.

Starting from a reference case where  $\square = 5\%$ ,  $\overline{\Sigma}_1^* = 13571 \text{ m}^{-1}$  and the total time simulated  $t_{final} = 180 \tau_t$ , the averaging procedure is :

- restart from this reference case each  $5 \tau_t$ , see Figure 3
- change the surface tension by a coefficient  $\alpha$ , consequently  $\sigma_2 = \alpha \sigma_1$
- continue the computation until a new equilibrium  $\overline{\Sigma}_2^*$  is reached
- during the computation, extract the time evolution of the mean interface density  $\overline{\Sigma}_1^*(t)$

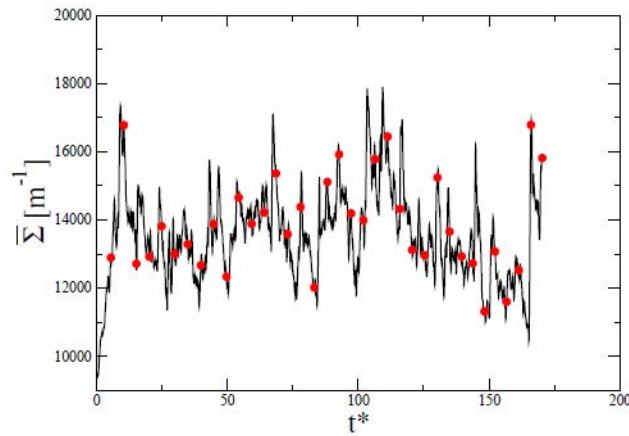


**Figure 3 :** Mean interface density time evolution  $\overline{\Sigma}^*(t)$  for the reference case  $\square = 5\%$ . Restarts points used as an initial condition in red circle, i.e. each point corresponds to the departure of one simulation.

Finally, an ensemble averaging over the 36 simulations is performed to reduce the statistical noise. This procedure is used for two different coefficient : 0.8 and 1.4. The first mimics the breakup regime and the second the coalescence regime. The transient behaviour of the interface density is captured, as well as the final equilibrium state  $\overline{\Sigma}_2^*$ . A three dimensional representation of the interface at two equilibrium (initial  $\overline{\Sigma}_1^*$  and final state  $\overline{\Sigma}_2^*$ ) is shown on Figure 4 for the breakup case. Smaller liquid structures and highly wrinkled interface can be seen on the left figure, showing the increase of the interface density induced by reducing the surface tension.

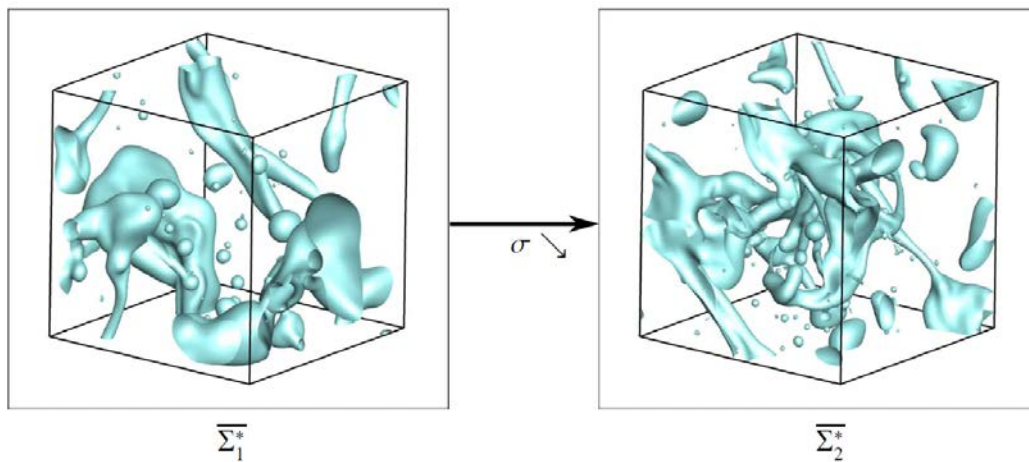


**Figure 4 :** three dimensional representation of the liquid-gas interface from the initial equilibrium  $\overline{\Sigma}_1^*$  to the final one  $\overline{\Sigma}_2^*$  for  $\square = 5\%$  in the breakup regime.

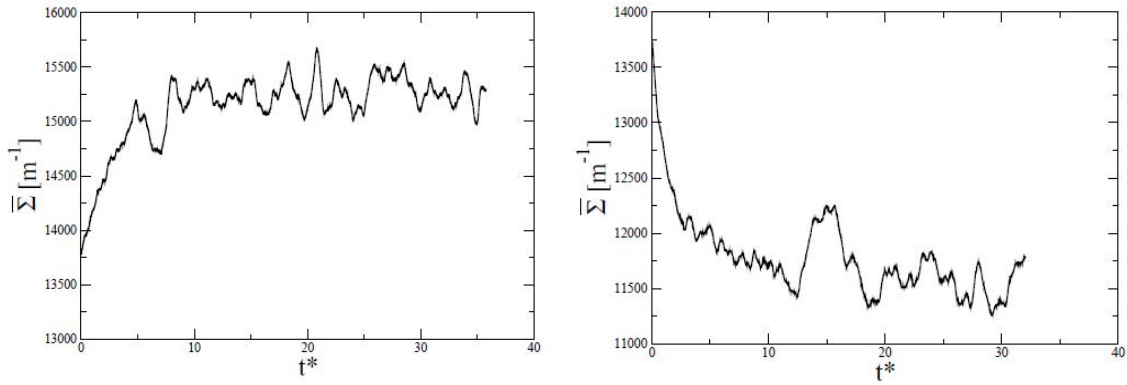


**Figure 5 :**  $\bar{\Sigma}^*(t)$  extract from the DNS for  $\square = 5\%$ . Left : breakup regime, right : coalescence regime.

Results are presented in Figure 5. Some statistical noise remains even with a consequent ensemble averaging, but is negligible compared to the order of the variation of the solution. As expected, the interface density increases with time because of the modified surface tension, the new equilibrium value in this case reach  $\bar{\Sigma}_2^* = 15270 \text{ m}^{-1}$ . For the coalescence case, obviously the interface density decreases, and the new equilibrium value in this case reach  $\bar{\Sigma}_2^* = 11652 \text{ m}^{-1}$ . The transient evolution of the interface density is very fast and seems quite similar in both cases. As mentioned before, the only term remaining in the interface density equation is  $S_{turb}$  in this configuration. Consequently, a verification of this term can be done by comparison with DNS. To focus on the interface density time evolution, the initial condition and final equilibrium value  $\bar{\Sigma}^*$  of the Ordinary Differential Equation (ODE) are those from the DNS. With the initial equation, the equilibrium is reached too quickly (see Figure 6), leading in a overestimation of the interface density value in both cases (breakup and coalescence).

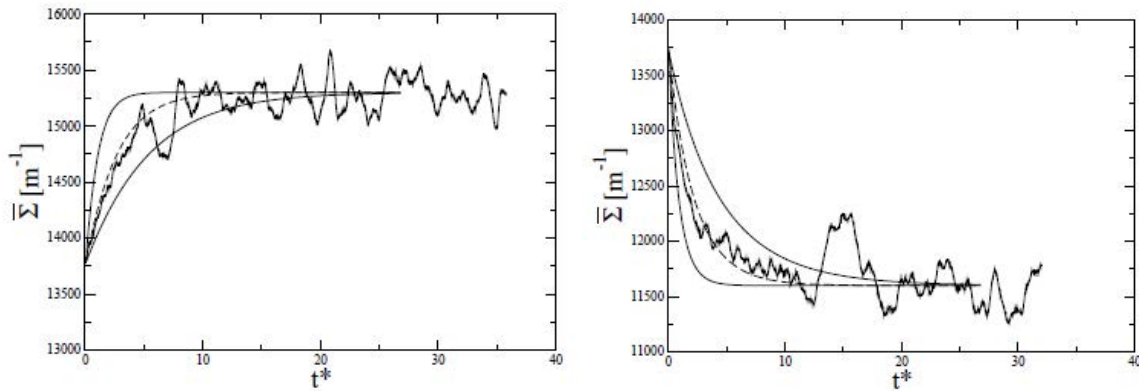


**Figure 6 :**  $\bar{\Sigma}^*(t)$  extract from the DNS (plain line) and from the model (dotted line) where  $C_\Sigma = 0.4$ . The dotted curve is bounded by two curves where the constant  $C_\Sigma = 0.2$  and  $C_\Sigma = 1$  (original value from ELSA model) in plain line. Left : breakup regime, right : coalescence regime.  $\square = 5\%$ .

However, the equation used to define this evolution seems to be adequate, because it already gives a satisfactory approximation, which was not evident before this work. To match correctly DNS results the modelling constant  $C_\Sigma$  has to be adjusted. The best value found for the constant is  $C_\Sigma = 0.4$ , based on DNS results for the breakup case.  $C_\Sigma = 1$  (original value) and  $C_\Sigma = 0.2$  are also indicated to measure the constant's impact on the solution. The constant is also used for the coalescence regime and seems to work even with a very different topology change : the variation of the surface tension is 40% instead of 20% and the regime is totally different.

Moreover, this constant should be independent of the liquid volume fractions studied. To confirm the validity of this constant, the liquid volume fraction is changed to check if the constant remains identical. Results for  $\square = 10\%$  are shown in Figure 7, for breakup and coalescence regime.

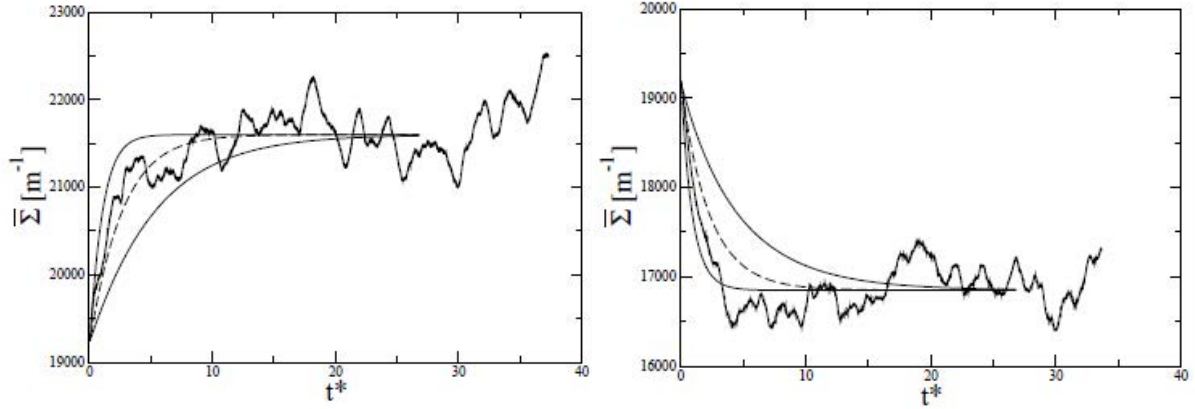


**Figure 7 :**  $\overline{\Sigma}^*(t)$  extract from the DNS (plain line) and from the model (dotted line) where  $C_{\Sigma} = 0.4$ . The dotted curve is bounded by two curves where the constant  $C_{\Sigma} = 0.2$  and  $C_{\Sigma} = 1$  (original value from ELSA model) in plain line. Left : breakup regime, right : coalescence regime.  $\Delta = 10\%$ .

The averaging procedure is the same as before. Satisfying results are found, except a small deviation for the coalescence case at  $\Delta = 10\%$ . However in all cases, the new constant shows better agreement with the DNS than the previous one ( $C_{\Sigma} = 1$ ) and the shape of all curves remains similar.

This analysis confirms the good behaviour of the ELSA model to capture  $\overline{\Sigma}^*(t)$  for these different configurations, but a slight correction of the constant is needed to recover the DNS results.

### Impact of the modelling proposal on ELSA approach applied to atomization

To test the impact of the new modelling proposal on the ELSA approach, this latter has been implemented in the open source software OpenFoam [28]. The ELSA modelling details corresponds exactly to the propose version of the model done by Lebas et al. [14] except for the modelling of the source term in the surface density equation  $S_{turb}$ . As far as this term is concerned the  $S_{turb}$  model is referred as ModL for the model used in [14] and is refereed as ModB for the present proposal. ModB used an equilibrium Weber number defined from equation (1) and the a typical value of  $We^* = 1.5$  (see Fig. 2) is used to computed the equilibrium surface density  $\Sigma^*$ . The constant  $C_{\Sigma}$  takes the previously fitted value  $C_{\Sigma} = 0.4$ . The test case is representative of a Diesel injection with an injector Diameter equal to  $100\mu m$ . The inlet velocity is  $100ms^{-1}$ , the liquid density is set to  $696 kgm^{-3}$  and the gas density is equal to  $50 kgm^{-3}$ .

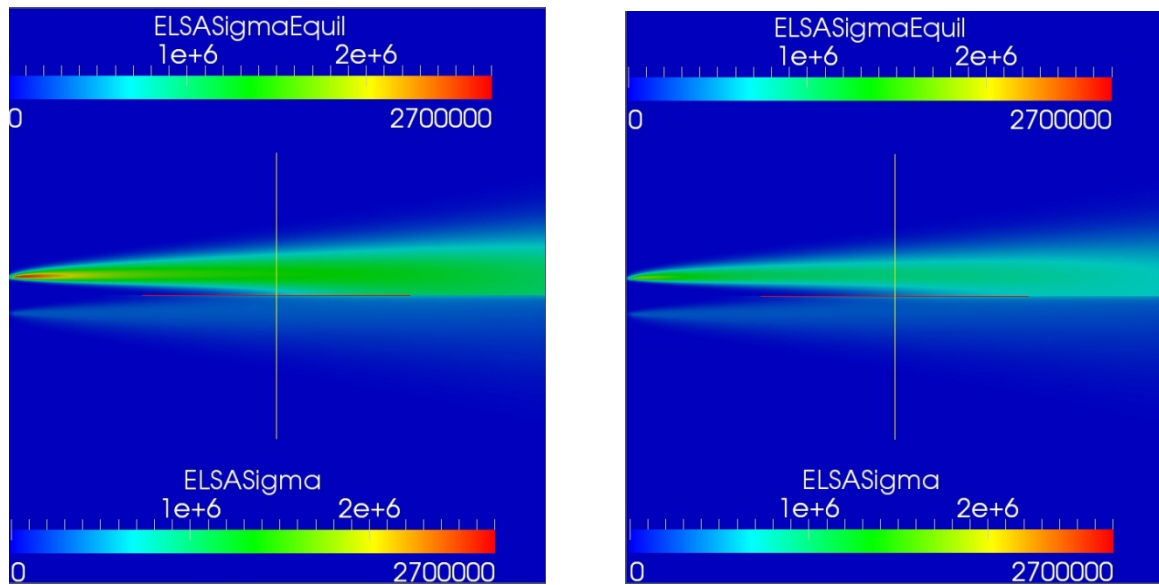


**Figure 8 :** Surface density result of the both modelling approaches ModL (left) and ModD (right). On top is the surface density at the equilibrium  $\Sigma^*$ , the bottom part represents the mean surface density

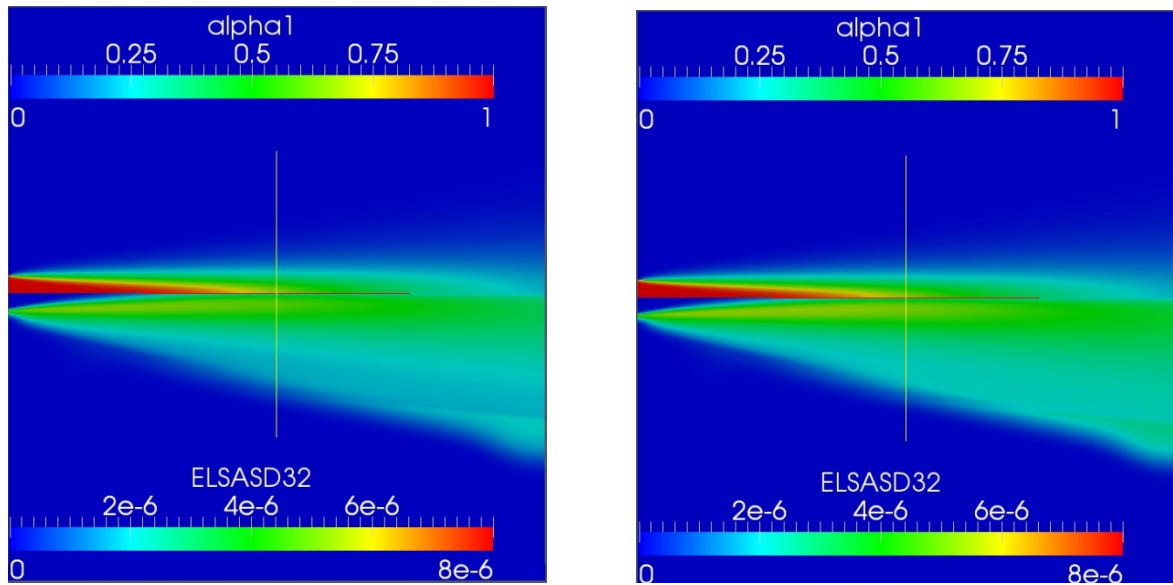


**Figure 9:** Results of ModL (left) and ModD (right). On top is the mean liquid volume fraction, the bottom part represents the Sauter mean Diameter  $D_{32}$ .

The axisymmetric simulation of the jet has been conducted using openFoam V 2.1.0 after that the ELSA model solver was built. Presented results are obtained once the injection is stabilized. This computation used for the turbulence the standard RANS k-epsilon model see ref [14] for more details. Fig. 8 shows an important impact of the modelling of  $S_{turb}$  on the equilibrium surface density. The new proposal ModD leads to a smaller amount of liquid-gas surface at the equilibrium. This effect is also amplified on the mean surface density because the leading constant of the source term  $S_{turb}$  is reduced with the model ModD by comparison to the previous formulation ModL. As a consequence there is less surface for the same amount of liquid, thus the Sauter mean Diameter of the spray increases significantly, see Fig. [9]. The new implementation of the ELSA model has to be validated by comparison of the spray computed to well defined experiments. Such comparisons are under way especially with data obtained on spray A in the context of Engine Combustion Network [29].

## Acknowledgements

This work was granted access to the HPC resources of IDRIS and CINES under the allocation 2012-x2012026153 made by GENCI (Grand Equipement National de Calcul Intensif).

## References

- [1] Agbaglah, G., Delaux, S., Fuster, D., Hoepffner, J., Josserand, C., Popinet, S., Ray, P., Scardovelli, R., Zaleski, S., 2011. Parallel simulation of multiphase flows using octree adaptivity and the volume-of-fluid method. *Comptes Rendus Mécanique* 339 (2-3), 194 – 207, high Performance Computing.
- [2] Beheshti, N., Burluka, A., Fairweather, M., 2007. Assessment of -y liq model predictions for air-assisted atomisation. *Theoretical and Computational Fluid Dynamics* 21, 381–397.
- [3] Brackbill, J. U., Kothe, D. B., Zemach, C., 1992. A continuum method for modelling surface tension. *Journal of Computational Physics* 100 (2), 335 – 354.
- [4] Chesnel, J., Reveillon, J., Menard, T., Demoulin, F.-X., 2011. Large eddy simulation of liquid jet atomisation. *Atomisation and Sprays* 21 (9), 711–736.
- [5] Corre, C., Estivalezes, J., Vincent, S., Olivier, S., 2008. Direct numerical simulation of the motion of particles larger than the kolomogorov scale in a homogeneous isotropic turbulence. In: 2008 ASME Fluids Engineering Conference, 10-14 Aout 2008, Jacksonville, Florida USA.
- [6] Duret, B., Luret, G., Reveillon, J., Menard, T., Berlemont, A., Demoulin, F.-X., 2012. Dns analysis of turbulent mixing in two-phase flows. *International Journal of Multiphase Flow* 40 (0), 93 – 105.

- [7] Eswaran, V., Pope, S. B., 1988. Direct numerical simulations of the turbulent mixing of a passive scalar. *Physics of Fluids* 31 (3), 506–520.
- [8] Fedkiw, R. P., Aslam, T., Merriman, B., Osher, S., 1999. A non-oscillatory eulerian approach to interfaces in multimaterial flows (the ghost fluid method). *Journal of Computational Physics* 152 (2), 457 – 492.
- [9] Fuster, D., Bagué, A., Boeck, T., Moyne, L. L., Leboissetier, A., Popinet, S., Ray, P., Scardovelli, R., Zaleski, S., 2009. Simulation of primary atomisation with an octree adaptive mesh refinement and vof method. *International Journal of Multiphase Flow* 35 (6), 550 – 565.
- [10] Hirt, C. W., Nichols, B. D., 1981. Volume of fluid (vof) method for the dynamics of free boundaries. *Journal of Computational Physics* 39 (1), 201 – 225.
- [11] Iyer, V., Abraham, J., Magi, V., 2002. Exploring injected droplet size effects on steady liquid penetration in a diesel spray with a two-fluid model. *International Journal of Heat and Mass Transfer* 45 (3), 519 – 531.
- [12] Jay, S., Lacas, F., Candel, S., 2006. Combined surface density concepts for dense spray combustion. *Combustion and Flame* 144 (3), 558 – 577.
- [13] Labourasse, E., Lacanette, D., Toutant, A., Lubin, P., Vincent, S., Lebaigue, O., Caltagirone, J.-P., Sagaut, P., 2007. Towards large eddy simulation of isothermal two-phase flows: Governing equations and a priori tests. *International Journal of Multiphase Flow* 33 (1), 1 – 39.
- [14] Lebas, R., Menard, T., Beau, P., Berlemont, A., Demoulin, F., 2009. Numerical simulation of primary break-up and atomisation: Dns and modelling study. *International Journal of Multiphase Flow* 35 (3), 247 – 260.
- [15] Lu, J., Tryggvason, G., 2007. Effect of bubble size in turbulent bubbly downflow in a vertical channel. *Chemical Engineering Science* 62 (11), 3008 – 3018.
- [16] Luret, G., Blokkeel, G., Lebas, R., Ménard, T., Berlemont, A., Demoulin, F., 2008. Spray interactions: modelling of collision/coalescence phenomena. In: 22nd European Conference on Liquid Atomisation and Spray Systems. Como Lake, Italy.
- [17] Luret, G., Menard, T., Blokkeel, G., Berlemont, A., Réveillon, J., Demoulin, F., 2010. Modelling collision outcome in moderately dense spray. *Journal of Atomisation and Spray* 20 (3), 93.
- [18] Menard, T., Tanguy, S., Berlemont, A., 2007. Coupling level set/vof/ghost fluid methods: Validation and application to 3d simulation of the primary break-up of a liquid jet. *International Journal of Multiphase Flow* 33 (5), 510 – 524.
- [19] Morel, C., 2007. On the surface equations in two-phase flows and reacting single-phase flows. *International Journal of Multiphase Flow* 33 (10), 1045 – 1073.
- [20] Rosales, C., Meneveau, C., 2005. Linear forcing in numerical simulations of isotropic turbulence: Physical space implementations and convergence properties. *Physics of Fluids* 17 (9), 095106.
- [21] Shinjo, J., Umemura, A., 2010. Simulation of liquid jet primary breakup: Dynamics of ligament and droplet formation. *International Journal of Multiphase Flow* 36 (7), 513 – 532.
- [22] Sussman, M., Fatemi, E., Smereka, P., Osher, S., 1998. An improved level set method for incompressible two-phase flows. *Computers & Fluids* 27 (5-6), 663 – 680.
- [23] Sussman, M., Puckett, E. G., 2000. A coupled level set and volume-of-fluid method for computing 3d and axisymmetric incompressible two-phase flows. *Journal of Computational Physics* 162 (2), 301 – 337.
- [24] Sussman, M., Smereka, P., Osher, S., 1994. A level set approach for computing solutions to incompressible two-phase flow. *Journal of Computational Physics* 114 (1), 146 – 159.
- [25] Trontin, P., Vincent, S., Estivalezes, J., Caltagirone, J., 2010. Direct numerical simulation of a freely decaying turbulent interfacial flow. *International Journal of Multiphase Flow* 36 (11-12), 891 – 907.
- [26] Unverdi, S. O., Tryggvason, G., 1992. Computations of multi-fluid flows. *Physica D: Nonlinear Phenomena* 60 (1-4), 70 – 83.
- [27] Vallet, A., Borghi, R., 1999. Modélisation eulerienne de l'atomisation d'un jet liquide. *Comptes Rendus de l'Académie des Sciences - Series IIB - Mechanics-Physics-Astronomy* 327 (10), 1015 – 1020.
- [28] Weller, H. G., H. Jasak and C. Fureby. "A tensorial approach to computational continuum mechanics using object-oriented techniques." *Computer in Physics* 12(6), 1998.
- [29] <http://www.sandia.gov/ecn/cvdata/dsearch.php>

## VOF multi-scale modelling of phase inversion and liquid atomization

L. Osmar<sup>1</sup>, S. Vincent<sup>1,\*</sup>, J.-L. Estivalezes<sup>2</sup>, T. Ménard<sup>3</sup>, W. Aniszewski<sup>3</sup> and J.-P. Caltagirone<sup>1</sup>

1: Université de Bordeaux, I2M, France

2: ONERA, The French Aerospace Lab, France

3: Université de Rouen, Coria, France

### Abstract

DNS of fragmentation and atomization of liquid film or jets by Volume of Fluid methods requires developing new characteristics of interface tracking methods in order to be able to provide a physical description of small fluid parcels at a scale smaller than the Eulerian simulation grid. A new Eulerian/Lagrangian VOF approach is proposed in order to describe the large scales of the interface during atomization and at the same time the droplets smaller than the Eulerian grid size in a Lagrangian manner. Specific models are applied to the Lagrangian objects in order to account of drag, lift or buoyancy effects. A specific phase inversion configuration is considered to illustrate the interest of the VOF method to simulate fragmentation and atomization of liquid interfaces.

---

### Introduction

The small scale simulation of jet atomization [1], engine piston cooling [2] or liquid/liquid phase separation [3] with a mesh smaller than the smaller interfacial scale is an almost impossible task in three dimensions. However, the design of car engines or chemical engineering applications require to develop Computational Fluid Dynamic (CFD) tools capable of providing a complete description of two-phase unsteady structures in order to characterize the distribution of droplet size in application problems. The efficiency of combustion or chemical reaction is highly dependent on this two-phase characteristic of the flow.

In the present work, a Volume Of Fluid sub-mesh (VOF-SM) [4] approach is extended to multi-scale modelling of multiphase flow in order to handle fragmentation and atomization of interfacial flows. Applications of the numerical method are fragmentation and atomization of liquid jets, droplet and bubble flows, spray and dispersed motions. Based on the Lagrangian advection of volume markers smaller than the Eulerian Navier-Stokes grid, isolated marker particles are identified and specific sub-grid physical effects are added to account for drag, lift or buoyancy effects. The dense marker parts of the flow are considered as Eulerian and a macroscopic Eulerian VOF function is obtained as the local statistic of the presence of marker volume. In this way, a multi-scale VOF method is obtained which is able to describe at the same time the large scales of the interface and the sub-grid scales of the interface, i.e. the dispersed phase. Finally, resolved particle distribution functions are obtained with an explicit description of fluid parcels smaller than the Eulerian grid size. The VOF-SM results will be compared to simulations using classical interface tracking methods such as VOF-PLIC [5] or Level Set [1] [6] approaches.

The article is structured as follows: the second section is devoted to presenting the mathematical models used to mimic two-phase flows with resolved interfaces at small scales. Section three presents the numerical methods implemented for the simulations. Section four summarizes the Benchmark results obtained by different teams with different CFD codes on two phase inversion problems and finally section five provides some conclusions and perspectives.

### Mathematical modelling

A one-fluid model devoted to incompressible isothermal multiphase and turbulent flows [7] is formulated for small scale representation of interface deformation and rupture. The resulting fragmentation and atomization will be described at each time step of the simulation. The Navier-Stokes equations expressed classically for a single phase flow are also valid for two-phase flows with resolved interfacial scales as soon as an additive surface tension term and an advection equation for an Eulerian indicator function  $C$  are considered. It reads:

$$\rho \left( \frac{\partial \vec{u}}{\partial t} + \vec{u} \cdot \nabla \vec{u} \right) = -\nabla p + \rho \vec{g} + \nabla \cdot \left[ \mu (\nabla \vec{u} + \nabla' \vec{u}) \right] + \sigma \kappa \vec{n} \delta_i \quad (1)$$

$$\nabla \cdot \vec{u} = 0 \quad (2)$$

$$\frac{\partial C}{\partial t} + \vec{u} \cdot \nabla C = 0 \quad (3)$$

In equation (1), the source term  $\sigma \kappa \vec{n} \delta_i$  accounts for the jump of momentum at the interface. This term is localized on the interface thanks to the Dirac delta function and is oriented in the normal direction to the interface. Classically, the curvature and the normal to the interface are obtained as derivatives of the indicator function as follows:

$$\vec{n} \delta_i = \nabla C \quad (4)$$

$$\kappa = \nabla \cdot \left( \frac{\nabla C}{\|\nabla C\|} \right) \quad (5)$$

In the present work, no turbulence modelling is used. It is assumed that all the time and space scales of the flow are resolved so that a Direct Numerical Simulation (DNS) will be investigated by means of the CFD tools.

### Numerical methods

In order to provide a comparison between different numerical approaches and to realize a numerical benchmark devoted to phase inversion and liquid fragmentation and atomization, three different CFD codes are used in the present work: the Thétis code developed at I2M, the DyJeat code developed at ONERA and the Archer code developed at CORIA. All these CFD tools allows for the direct numerical simulation of multiphase flows at small scale. They use structured staggered grids, finite volumes MPI parallel implementations.

Thétis is based on a Volume Of Fluid Sub-Mesh method [4] in which C stands for the volume fraction of a given fluid in each mesh cell. The interface is defined as C=0.5 whereas fluid 2 is located by C=1 and fluid 1 by C=0. The surface tension forces are approximated by means of a continuum surface force [8] and centred schemes are used for both inertial and viscous terms in the momentum equations (1). The advection equation on C is numerically treated on a Lagrangian way by means of volume markers distributed in each cell at the initialisation time. They are tracked by means of an interpolated velocity coming from the solving of (1-2). As soon as markers belonging to phase 1 are isolated, *i.e.* they are inside a cell with C>0.5 and the neighbouring cells are such that C<0.5, the Eulerian volume fraction C of this cell is set to zero during the post-processing of the phase function distribution. In this way, the pdf of the droplet size accounts for these fluid parcels at a subgrid scale by considering each isolated marker as an individual droplet whose size is defined initially as a fraction of the cell volume. The finally obtained pdf provides the large scale droplets detected as C=0.5 isosurfaces (macro-droplets) and also the small scale droplets detected as isolated markers. The first implementation of this method was successfully applied to the atomization of a supercritical jet in [9].

The DyJeat and Archer codes are designed upon a Level Set technique and use WENO schemes for the discretization of the advection term in the advection equation (3). The interest of the WENO schemes is to provide a high order convergence in space while ensuring almost zero oscillations of the solutions which are generally due to the hyperbolic character of the equation. The indicator function C stands for the signed distance to the interface in this case. The interface is located by the zero isosurface of the Level Set function C. In addition to equation (3), a re-distance equation is used to maintain the properties of distance of the Level Set function, *i.e.*  $\|\nabla C\| = 1$ . The related works are [1], [6] and [10]. With DyJeat and Archer, only the macro-droplets are solved explicitly by the CFD codes.

To finish with numerical methods, the approximation of equations (1-2) is treated differently in Thétis on one hand and DyJeat and Archer in the other hand. Thétis is based on an augmented Lagrangian method for ensuring the velocity-pressure coupling and a continuum surface force approximation for the surface tension terms. The implicit discretisation of the momentum equation requires solving a linear system which is fulfilled by means of a BiCGFSTAB II solver preconditioned under a Modified and Incomplete LU solver. The reader can refer to [11] for further details on these techniques. DyJeat and Archer on their parts utilizes a time splitting approach for accounting of incompressibility and momentum conservation while the jump of velocity and momentum at the interface is represented by a Ghost Fluid approach [12]. The capillary force is implicitly tackled with by the ghost fluid method. A BICG Poisson solver preconditioned under a multigrid algorithm allows for the solving of



the projection of the velocity field on a divergence free subspace. These works have been previously published in [1] and [6] for example.

## Results and Discussion

The phase inversion of an oil droplet into a heavier fluid inside a closed box is an interesting problem for leading comparisons of CFD codes devoted to multi-phase flow simulations of fragmentation and atomization. This problem is typical of multi-scale interfacial flows in which large interfacial scales are observed with at the same time small dispersed droplets interacting with the larger drops according to coalescence or rupture of interfaces. The same CFD codes would be possibly used to simulate jet atomization for example. An illustration is given in figure 1 left according to [3] [13]. The initial condition is geometrically simple, the solution at large times is known and a physical parametric study can easily be investigated by changing the density or viscosity ratios at the interface as well as the surface tension coefficient. In addition, a numerical convergence study can be investigated in order to estimate the sensitivity of the results to grid density or numerical methods used. On a numerical point of view, physical parameters can be defined such that a numerical convergence study is realizable for a DNS configuration, *i.e.* all the flow and interfacial time and space scales are solved. Laminar as well as turbulent conditions can be generated. Similarly, strongly dispersed flows as well as large drop topologies can be induced according to the physical characteristics of the two liquids.

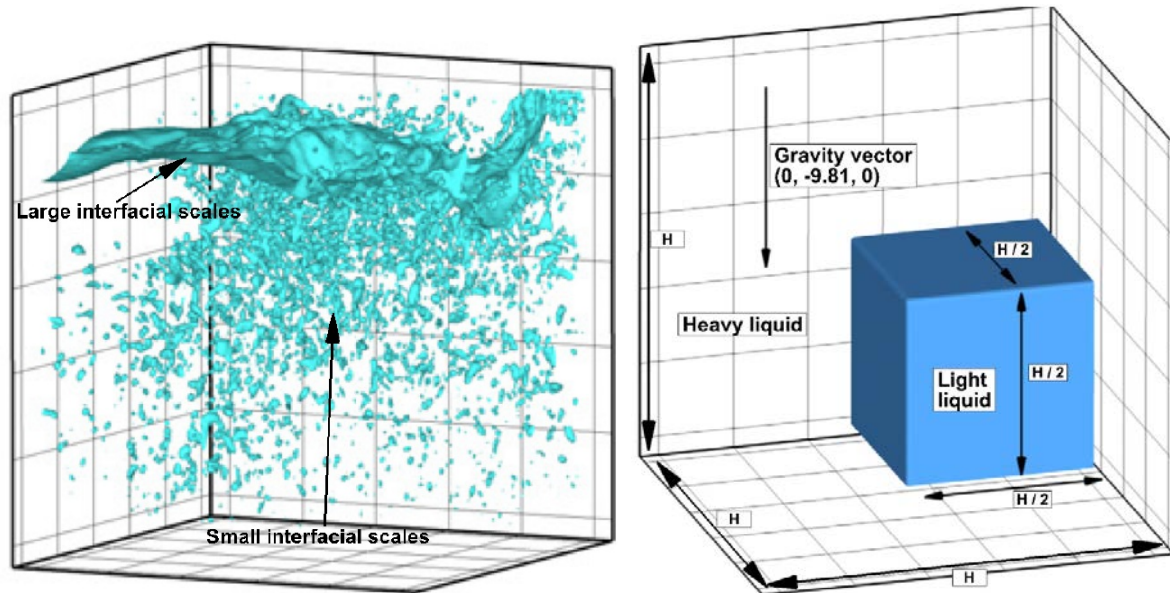


**Figure 1.** Example of phase inversion problem with interface atomization [3] (left) and definition sketch of the phase inversion problem (right).

As described in figure 1 right, an initial cubic drop of light liquid, referred to as fluid 2, is placed in the bottom part of a cubic box full of a heavier liquid called fluid 1. The size of the box is (0:1; 0:1; 0:1) while the one of the drop is (0:05; 0:05; 0:05). The boundary conditions are sliding impermeable walls, modelled by a symmetry condition on the velocity. No wetting properties are specified on the walls explicitly, they are wetting to both fluid 1 and 2. Several characteristics of the fluids are considered, in order to investigate various multi-scale interfacial flow topologies. The properties of the fluids control these conditions, in terms of Reynolds, Ohnesorge and Weber numbers. The dimensionless numbers are defined as

$$\text{Re} = \frac{\rho_1 H U_g}{\mu_1} \quad \text{We} = \frac{\rho_1 H U_g^2}{\sigma} \quad \text{Oh} = \frac{\mu_1}{\sqrt{\sigma \rho_1 H}}$$

where the predicted velocity  $U_g$  is defined according to the density variations at the interface and the buoyancy

forces as  $U_g = \frac{\rho_1 - \rho_2}{\rho_1} \sqrt{\frac{Hg}{2}}$ . The characteristic length  $H$  is chosen to be the size of the cavity equal to

0.1m for case 1 and 1 m for case 2. An integral characteristic time scale can be deduced from  $U_g$  and  $H$  as

$t_c = \frac{H}{U_g} = \frac{\rho_1}{\rho_1 - \rho_2} \sqrt{\frac{2H}{g}}$ . For the sake of simplicity, the characteristics of fluid 2 are assumed constant and

the properties of fluid 1 are changed. The fluid 1 parameters and related dimensionless numbers are given in table 1. The test case 1 is used as a simple configuration with low inertia and large capillary forces whereas case 2 corresponds to larger inertia effects and lower capillary forces. The multi-scale interfacial character of the flow will be predominant for these two configurations.

	Density	Viscosity	Surface tension	Re	We	Oh	H
<b>Case 1</b>							
Fluid 2	1000	0.1	0.045	70	11	0.047	0.1
Fluid 1	900	0.1					
<b>Case 2</b>							
Fluid 2	1000	0.001	0.45	221472	109	0.000047	1
Fluid 1	900	0.1					

**Table 1:** parameters of the two phase inversion problems.

#### Case 1:

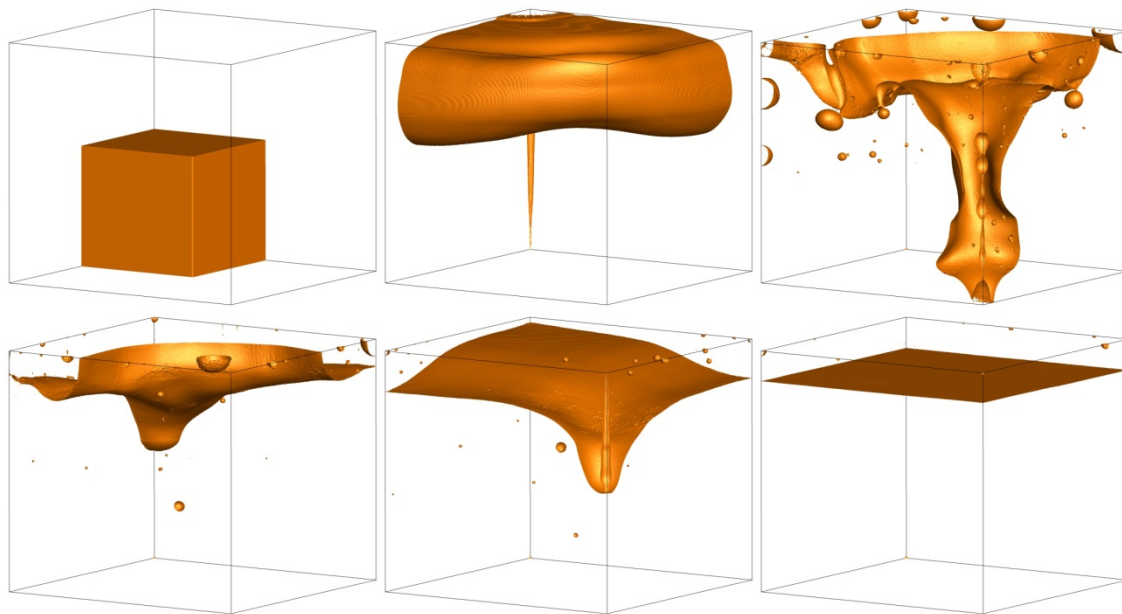


**Figure 2.** Time evolution of the interface between fluid 1 and 2 for the phase inversion case 1 obtained with VOF-SM in Thétis on a  $256^3$  grid.

The numerical simulation of case 1 is described in figure 2 concerning the time evolution of the interface between the two fluids. Almost 100 s are computed in order to satisfy the phase separation completely. For times lower than 1 s (the characteristic time in this configuration), the oil droplet goes to the top part of the cavity under buoyancy effects and hits the top boundary of the cavity. After this impact, the flow becomes very unsteady with a peak of kinetic energy and enstrophy, as described in figure 3. Numerous large droplets are generated and the gravity effects drives back the oil to the top part of the cavity under an oscillating movement of the interface which tends to be almost flat and horizontal over time. For later times, all the oil should be located in the  $1/8H$  top part of the cavity. It can be observed that the dimensionless volume of oil in this part of the simulation domain tends to fill this volume while being subjected to a shaking motion controlled by the width  $H$  of the cavity. This shaking is also observed on the kinetic energy curves and on the enstrophy time history in oil.

A comparison between the Level Set and VOF simulations is also provided in figure 3. The VOF-SM, Level Set with continuum surface force treatment of capillary forces and VOF-PLIC methods of Thétis are compared to the Ghost fluid simulation coming from Archer (or in an equivalent way from DyJeat). The kinetic energy in oil and water and the dimensionless volume of oil in the top  $1/8H$  part of the cavity are in very good agreement and

compare favourably. We can observe that for case 1 a  $256^3$  grid is enough to capture the main features of the flow. The enstrophy curves highlight the same behaviour but a difference is noticed concerning the peak of its magnitude after almost 1s. Simulations driven with DyJeat on a  $1024^3$  grid are under investigation in order to understand if the differences comes from an under resolution of the unsteady character of the flow in oil and

water. The interfacial scales seem to be correctly resolved. However, an estimate of the possible effect of parasitic surface tension currents is also under consideration

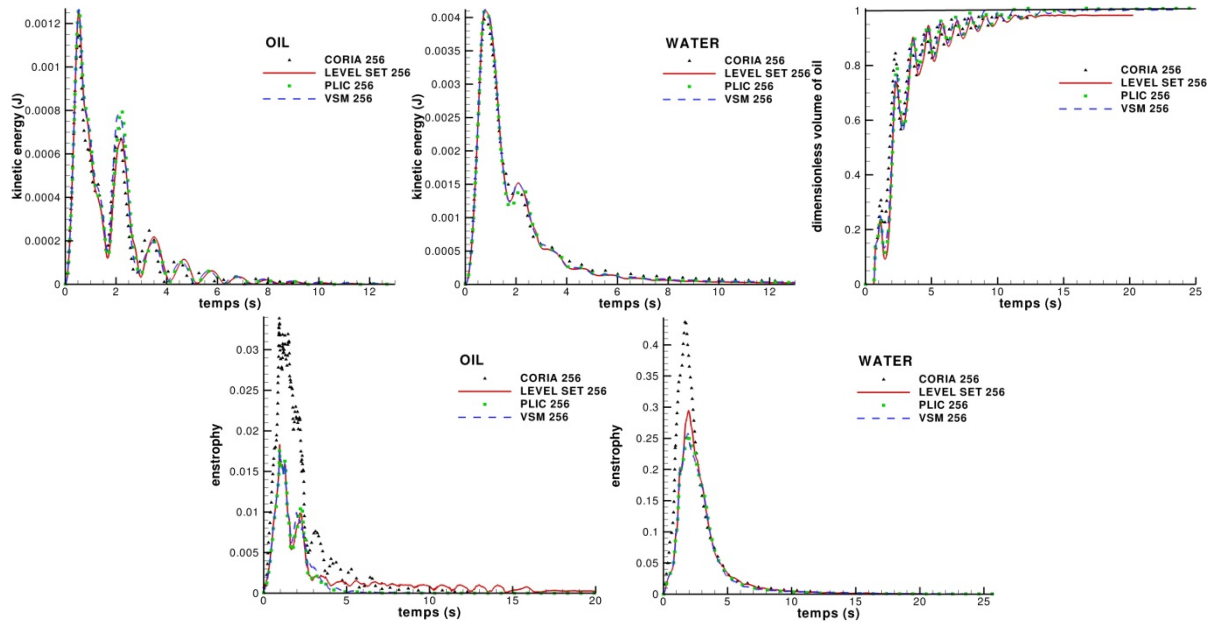


**Figure 3.** Time evolution of kinetic energy, volume of oil in the top 1/8H part of the cavity (volume occupied by oil at the end of phase separation) and enstrophy in oil (fluid 1) and water (fluid 2) – 256<sup>3</sup> grid for Thétis (Level Set, VOF-PLIC and VOF-SM) and 512<sup>3</sup> grid for Archer (CORIA).

## Case 2:

The simulation of case 2 is much more difficult as the flow is very unsteady and provides a large fragmentation/atomization of the initial oil drop. First simulations realized with VOF-SM in Thétis are proposed in figure 4 on a 256<sup>3</sup> grid. This case is under investigation with the different codes and the comparisons are not finished yet. It seems clear that the use of a sub-grid detection of oil droplet with the VOF-SM approach will be necessary. It can be imagined that major differences will arise when the Eulerian interface tracking techniques such as Level Set or VOF-PLIC will be compared to the multi-scale VOF-SM method. The pdf of the droplet sizes will be proposed in order to characterise the topological distribution of atomisation. The results will be presented in an exhaustive way during the oral presentation of the ILASS congress.

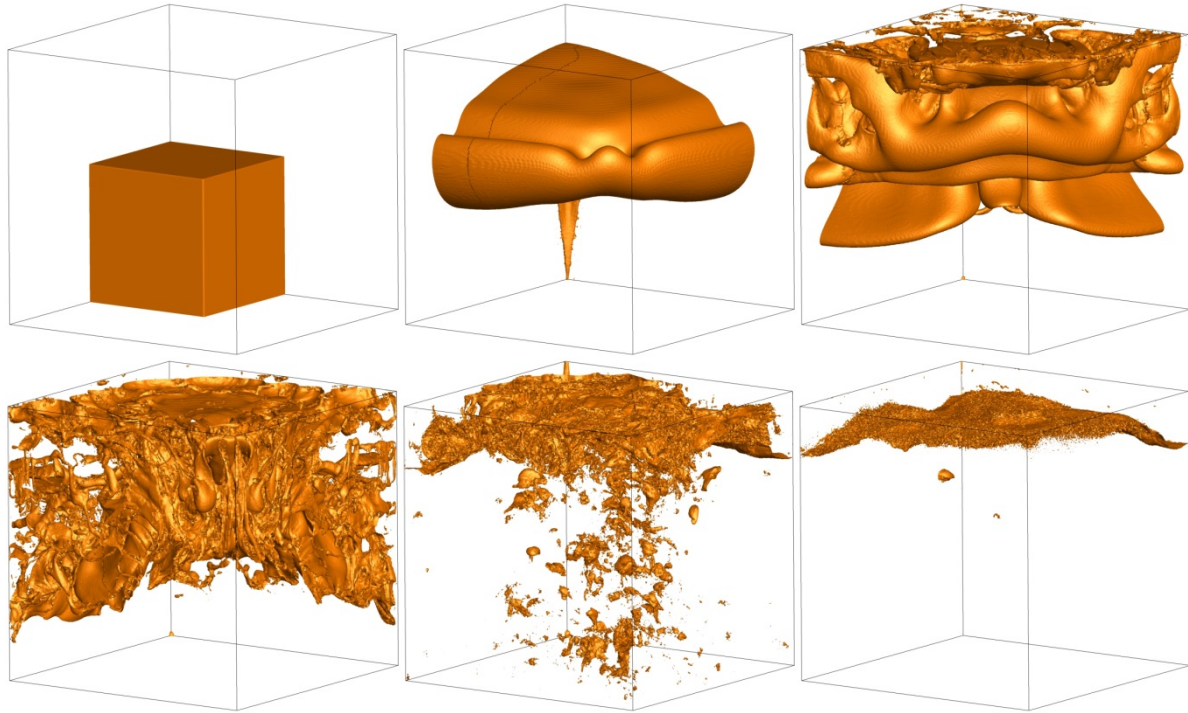


**Figure 4.** Time evolution of the interface between fluid 1 and 2 for the phase inversion case 2 obtained with VOF-SM in Th  tis on a  $256^3$  grid.

## Conclusions

A Phase inversion problem has been investigated numerically by direct numerical simulation of two phase flows solved at small scales by means of different numerical methods and CFD codes so as to provide a Benchmark for atomization simulation. It has been demonstrated that for refine grids, an Eulerian Level Set approach can favourably compare to results obtained on coarser grids with a multi-scale VOF-SM technique.

Further developments of the VOS-SM are under implementation in order to account for subgrid physics of isolated markers including Lagrangian forces such as drag, lift or buoyancy. These results will be presented during the ILASS conference for case 2. In addition, comparisons between VOF-SM simulations and Eulerian Level Set results on refined grids will be proposed.

## Acknowledgements

The authors thank the Aquitaine Regional Council for the financial support dedicated to a 256-processor cluster investment. This work was also granted access to the HPC resources of CCRT, CINES and IDRIS by GENCI (Grand Equipement National de Calcul Intensif) under reference number x2013026115. The present research developments are also under financial support of ANR Modemi.

## Nomenclature

$\delta_i$	Dirac delta function indicating interface	$m^{-1}$
$\kappa$	Local interface curvature	$m^{-1}$
$m$	Dynamic viscosity	Pa.s
$\rho$	Density	$kg.m^{-3}$
$\sigma$	Surface tension coefficient	$N.m^{-1}$
$C$	Interface indicator function	
$g$	Gravity	$m.s^{-2}$
$H$	Characteristic length of the phase inversion	m
$p$	Pressure	Pa
$t$	Time	s
$\vec{u}$	Velocity	$m.s^{-1}$
$U_g$	Characteristic velocity	$m.s^{-1}$

## References

- [1] Ménard T., Tanguy S., Berlemont A., *International Journal of Multiphase Flow*, 33:511-524 (2007).
- [2] Osmar L., Vincent S., Caltagirone J.-P., Reungoat D., Mermaz-Rollet G., *Atomization and Sprays*, 22:185–205 (2012)
- [3] Vincent, S., Larocque, J., Lacanette, D., Toutant, A., Lubin, P., Sagaut, P., *Computers and Fluids*, 37:898-906 (2008).
- [4] Vincent, S., Balmigère, G., Caltagirone, J.-P., Meillot, E., *Journal of Computational Physics*, 229:73-106 (2010).
- [5] Tomar G., Fuster D., Zaleski S., Popinet S., *Computers and Fluids*, 39: 1864-1874 (2010).
- [6] Trontin P., Vincent S., Estivalezes J.-L., Caltagirone J.-P., *International Journal of Multiphase Flow*, 36:891-907 (2010).
- [7] Kataoka I., *International Journal of Multiphase Flow*, 12:745–758 (1986).
- [8] Brackbill J.U., Kothe D.B., Zemach C., *Journal of Computational Physics*, 100:335–54 (1992).
- [9] Ouchène R., Erriguible A., Vincent S., Subra-Parternault P., *Mechanical Research Communications*, under publication, 2013
- [10] Osher, S., Sethian J., *Journal of Computational Physics*, 79:12–49 (1988).
- [11] Vincent S., Sarthou A., Caltagirone J.-P., Sonilhac F., Février P., Mignot C., Pianet G., *Journal of Computational Physics*, 230 :956–983 (2011).
- [12] Fedkiw R., Liu X., Kang M., *Journal of Computational Physics*, 160:151–178 (2000).
- [13] Larocque J., Vincent S., Lubin P., Lacanette D., Caltagirone J.-P., *International Journal of Heat and Fluid Flow*, 31:536-544 (2010).
- [14] Vincent S., Caltagirone J.-P., Jamet D., *Multiphase Science and Technology*, 6:101-104 (2004).

## Collision of Droplets: An Experimental, Numerical and Analytical Approach

Norbert Roth<sup>1</sup>, Camille Mercadé<sup>1</sup>, Hassan Gomaa<sup>1</sup>, Christian Focke<sup>2</sup>, Dieter Bothe<sup>2</sup>,  
Ilia V. Roisman<sup>3</sup> and Bernhard Weigand<sup>1</sup>

1: Institute of Aerospace Thermodynamics, University of Stuttgart, Germany

2: Center of Smart Interfaces, Technische Universität Darmstadt, Germany

3: Fachgebiet Strömungslehre und Aerodynamik, Technische Universität Darmstadt, Germany

### Abstract

Head-on collisions of droplets have been studied experimentally, numerically and analytically. The Weber numbers characterizing the collision process have been chosen, in a way that a pizza shaped disc is formed with a very thin lamella in its center and thicker rim at the outer border. In the experiments no rupture of the lamella and no instabilities at the rim could be observed. Good agreement in the evolution of the disc diameter with time was found for all methods applied. An experimental validation of direct numerical simulation and an analytical model was carried out to identify, which method is suitable for which phase of the collision process.

---

### Introduction

The main purpose of the present work is a hybrid experimental/computational/theoretical approach to the detailed description of a droplet dynamic process. As an example, head-on collisions of droplets in the Weber number range  $200 < We = (\rho v_r^2 D) / \sigma < 1000$  have been chosen, where  $D$  is the diameter of the droplets,  $v_r$  the relative velocity between the droplet,  $\rho$  the density and  $\sigma$  the surface tension of the droplet liquid. By combining the advantages of each method it is possible to obtain a comprehensive understanding and to extend the range of validity for predicting the collision process. In addition focus is set on the detailed description of the collision process. The evaluation of the time evolution of the disc dynamics in the given Weber number range allows a direct quantitative comparison of the different methods in addition. The key points of the individual methods presented here for the purpose of an evaluation and comparison have been described in detail elsewhere [1-5]. Nevertheless, in order to allow a better understanding of the different methods, an overview including some improvements is given below.

### Experimental methods

In the experiments two monodisperse droplet streams are used in order to be able to produce head-on collisions of droplets with sufficiently high Weber numbers. The collision process is observed from two directions perpendicular to each other by shadowgraphy. One direction is perpendicular to the plane, which is defined by the trajectories of the droplets or the droplet streams. The experimental setup is shown in Fig. 1 schematically. The droplet stream generators generate droplets of the same initial size, temperature, velocity, and inter droplet distance. In order to obtain head-on collisions the generators are adjusted, that the trajectories of both droplet streams are in a plane. For the illumination of the shadowgraphs a flash lamp, so-called Nanolite, is used, producing flashes, which are sufficiently short to freeze the droplet motion. By using a beam splitter the light of the flash lamp can be used for both directions I and II of observation. The images are taken by two PIV-Cameras (Camera I: LaVision ImagerPro and Camera II: LaVision ImagerPro X). On each camera several pairs of colliding droplet at different stages of the observation process are imaged. However, on each camera pairs of droplets can be seen, which belong to the identical collision process. On one pair of frames 3-4 different stages of the collision process are imaged. In using the double exposure feature of the PIV-cameras 3-4 additional stages at a later time are obtained. This is illustrated in Fig. 2. Here, for a Weber number of 270, corresponding images are shown. On the left hand side both frames of camera I, and on the right hand side both frames of camera II are shown. In each case the time delay between the first and the second frame is chosen in a way, so that the droplet move half of the inter droplet distance of the droplet stream. In Fig. 2 on each image four different collision processes are imaged numbered 1 - 4. Due to the nature of monodisperse droplet streams the evolution of each process is almost the same. In order to track the whole collision process images are taken in triggering the cameras initially with different delay times with respect to the droplet generation, the time delay between the first and second frame is kept constant. From the images of camera I the droplet diameter  $D$ , the inter droplet distance  $s$  and the angle between the trajectories of the droplet streams can be determined. Knowing the frequency  $f$  of the generation of the droplets the droplet velocity  $v$  can be calculated to  $v = s \cdot f$ .



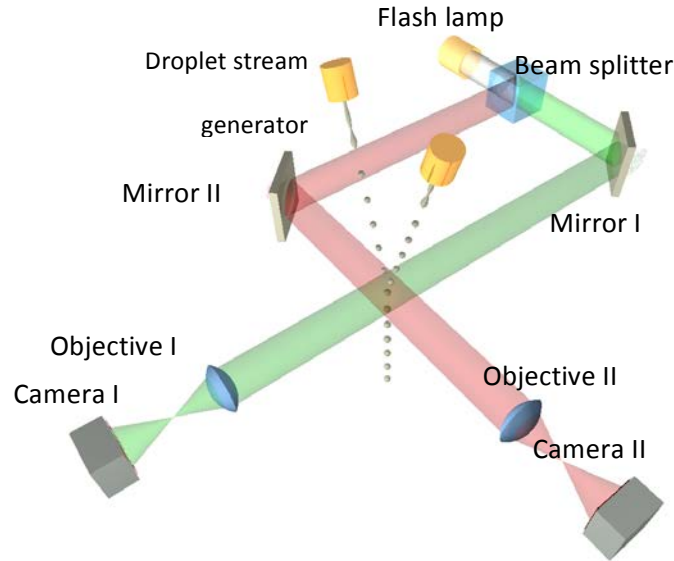


**Figure 1:** Schematic view of the experimental setup. The light paths I and II of the different directions of observation are depicted in different colours.

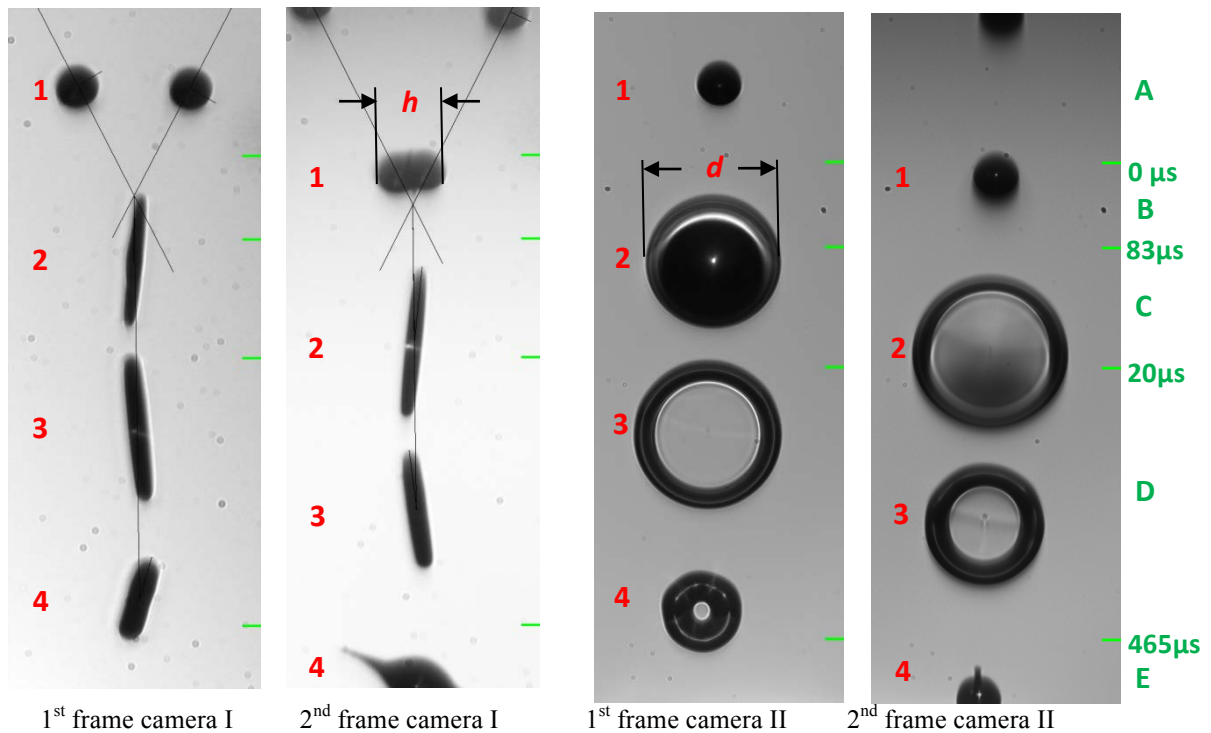


**Figure 2:** Example of images taken by the PIV-cameras I and II showing the collision process for  $We \approx 270$  from two directions at two different times  $t$ . On each image four approximately equal processes, numbered 1- 4, can be seen. At the right image the different phases of the collision process are indicated.

The thickness  $h$  in the centre of the two colliding droplets or let's say the thickness of the lamella in the centre of the developing disc can be determined in the initial phase of the collision process as long as  $h$  is larger than the thickness of the rim of the developing disc.

From the images of camera II the diameter  $d$  of the developing pizza shape disc and the form of this disc can be obtained. The existence of a thin liquid lamella in the centre of the disc can be detected and it can be seen whether disc instabilities develop at the rim.



## Numerical methods

The collision process is simulated using the ITLR in-house code FS3D that is described in detail in [2]. The direct numerical simulation (DNS) code FS3D solves the incompressible 3D Navier-Stokes equations. In order to describe free liquid surfaces the Volume-of-Fluid (VOF) method and a Piecewise Linear Interface Construction (PLIC) is used. In a first approach the collision process is simulated in full three-dimensional (3D) complexity. In the simulation the colliding droplets are initialized each with half of the relative velocity  $v_r$ , however, with opposite directions. With a grid refinement in the plane perpendicular to the trajectory at the location, where the pizza shaped disc develops, the evolution of the disc can be simulated. The lamella in the centre of the disc, however, becomes very thin in reality. For higher Weber numbers a rupture of the lamella is observed in the simulation. This is in contradiction to experimental results (see Fig. 2) and caused by insufficient grid resolution. Therefore the code has been modified in order to stabilize the lamella and prevent its unrealistic rupture. An even finer grid would result in an increase in computational time, which is not feasible.

### Lamella stabilization

A stabilizing algorithm, which is able to prevent the lamella from rupturing, is developed at the Center of Smart Interfaces, Technical University Darmstadt [3]. The simulations give a quantitative prediction of the resulting diameter of the droplet collision complex. The stabilizing algorithm allows for computing collision results for reflexive separations with large Weber numbers. The reason of the rupture can be explained by the surface tension computation, which is incorporated using the continuum surface stress (CSS) model. The algorithm of CSS smoothes the  $f$ -field using a 27 cell stencil. The  $f$ -field indicates, where fluid is liquid,  $f = 1$ , or gaseous,  $f = 0$ . Subsequently a capillary pressure tensor is computed on the smoothed field again using a 27 cell stencil so that the surface tension in one cell is influenced by 125 cells. If a second interface is present in these cells, the surface tension computation is corrupted. The stabilization algorithm corrects the capillary pressure tensor computation by avoiding artificial interactions of the two sides of the lamella. For the computation of the surface tension of one lamella side, a modified  $f$ -field is used which is obtained by “virtually illuminating” the droplet from one side such that only one side of the lamella is visible by the surface tension algorithm, as illustrated in Fig. 3.

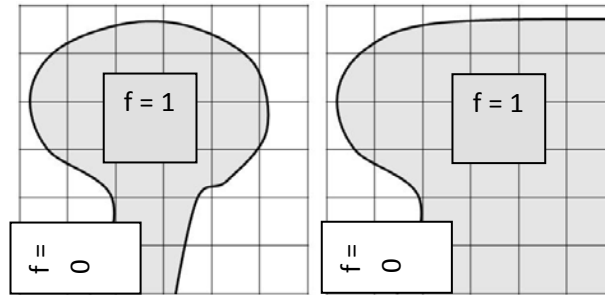


**Figure 3:** Schematics of lamella stabilization, left: original  $f$ -field of rim and lamella, right:  $f$ -field used for surface tension computation of the left lamella side (after “illumination” from the left).

The surface tension of the opposite lamella side is computed in an analogous manner. In the rim area, the original  $f$ -field is used. The surface tension forces are computed for the different fields and afterwards merged in an appropriate way. In order to distinguish both lamella sides and to allow for a correct  $f$ -transport, a minimum lamella thickness of two cells must be kept by filling the lamella with artificial liquid. Special care has to be taken for the amount of additional liquid to avoid considerable effects on the collision dynamics. Comparisons with experiments show that the additional liquid does not lead to deviations if the resolution is high enough. For further details see [3]. Applying the lamella stabilization, the VOF-code is able to predict the correct outcome of such collisions.

### Mechanistic modeling of the collision of viscous droplets

Collision models are the subject of numerous studies for instance [4 - 6]. In the present work, the collision model described in [7] is used as the starting point for our mechanistic modeling. Let us recall the main features of this model.

A main simplification concerns the flow in the lamella which is approximated by an axially symmetric flow of a liquid film [8, 9]. With the assumption that the film is thin and spreads infinitely, together with the approximation of the lamella geometry by a Gaussian bell curve [10], the dimensionless lamella thickness  $h_L =$

$$h/D \text{ develops according to } h_L = \frac{\Theta_1}{(t^* + \tau)^2} \exp\left[-\frac{6\Theta_2 R^2}{(t^* + \tau)^2}\right], \quad (1)$$

with the dimensionless time  $t^* = t v_r / D$  and the dimensionless Radius of the disc  $R = d/2D$ . The model parameters  $\Theta_1$ ,  $\Theta_2$  and  $\tau$  are determined by fitting to experimental or numerical data. To capture the dynamics of the rim, the mass balance of the rim and the momentum balance between the lamella and rim are considered. The momentum balance accounts for the inertia of the rim, the viscous damping of the flow in the lamella, the surface tension force and the inertia of the liquid that flows into the rim. The viscous damping term is derived from an analysis of the flow in the lamella. The balance equation of the momentum leads to an ordinary differential equation for the radius which reads as

$$\frac{V}{4\pi R} \ddot{R} = h_L \left[ \frac{R}{t + \tau} - \dot{R} \right]^2 + \frac{12h_L}{\text{Re}(t + \tau)} - \frac{4}{\text{We}} \quad (2)$$

Eq. (2) can be solved numerically, if appropriate initial conditions are given. The volume of the rim  $V$  can be gained from the mass balance.

#### Model

#### Extension

In order to extend the model from [7] for collisions with a significant viscosity influence, the description of the lamella thickness is modified. The lamella thickness (Eq. 1) is included in the calculation of the collision dynamics. In the original model  $\Theta_1 = \Theta_2$  is used. The model is extended by introducing different  $\Theta_i$  in order to describe the lamella thickness and its temporal evolution separately. The volume of the rim is redefined so that mass conservation is still guaranteed.

#### Application of the Collision Model

To apply the above model, information of the model parameters  $\Theta$  and  $\tau$  needs to be gained. The strategy here is to simulate the first phase of a collision ( $t^* \leq 2$ ) in order to determine  $\Theta_2$  and the initial conditions. The parameters  $\Theta_1$  and  $\tau$  are equal for all collisions. A simulation study with  $\text{Re} = 100, 200, 300$  and  $\text{We} = 100, 200, 300$  yields the constant parameters  $\Theta_1 = 0.299$  and  $\tau = 0.105$ . A least squares fit of Eq.(1) to the lamella geometry gained by the simulation of the first collision phase yields  $\Theta_2$ . The assumption of the original model  $\Theta_1 = \Theta_2$  would lead to an under-prediction of the viscosity influence in binary droplet collisions. Comparison of the model results with a fully resolved simulation shows that the procedure introduced above allows for a quantitative prediction of the temporal evolution of the collision complex diameter.

The simulation the first phase of a collision is necessary to apply the model. The absence of fine structures allows for a coarse resolution in the simulation of the first phase. The model reduces the CPU-time by a factor of 300 compared to the fully resolved simulation of the complete collision.

## Results and Discussion

In this section results of experiments, numerical simulations, and analytical studies are compared and the benefits of each approach are discussed in order to improve the physical understanding of the head-on collision process and to indicate problems to be solved in the future. The process of head-on droplet collisions can be separated in five phases:

- A. Approaching phase until the droplets are in contact ( $t^* < 0$ ).
- B. Development of a pizza shaped disc ( $t^* < 2$ ).
- C. Spreading of the disc until it has reached its maximum diameter.
- D. Collapse of the disc until the thin film in the centre has disappeared.
- E. Further development of the liquid mass.

First an illustration of these five phases is given by means of a direct numerical simulation of the head-on collision process.

Direct numerical simulations (DNS) are performed fully three-dimensional with the program code FS3D without any modifications using a computational domain of  $2100 \mu\text{m} \times 1050 \mu\text{m} \times 2100 \mu\text{m}$  and a resolution of  $256 \times 256 \times 256$  cells. Due to the grid refinement the smallest cell has a dimension of  $8.2 \mu\text{m} \times 0.55 \mu\text{m} \times 8.2 \mu\text{m}$ . Calculations are performed for  $\text{We} = 270$  and  $\text{We} = 500$ . The other parameters for this case and all others cases presented in this study are listed in Table 1.

**Table 1:** Parameters used in this study

Droplet parameters	DNS, Analytic We = 273	Experiment We = 270	DNS, Analytic We = 500	Experiment We = 500
Diameter $D$	232.75 $\mu\text{m}$	$\approx 231.6 \mu\text{m}$	235.94 $\mu\text{m}$	$\approx 235.9 \mu\text{m}$
Velocity (experimental) $v$	-	$\approx 12.4 \text{ m/s}$	-	$\approx 17 \text{ m/s}$
Angle between droplet streams	-	$\approx 53.6^\circ$	-	$\approx 54.2^\circ$
Relative velocity $v_r$	5.656 m/s	$\approx 5.6 \text{ m/s}$	7.74 m/s	$\approx 7.74 \text{ m/s}$
<b>Droplet liquid</b>	iso-Propanol			
Density	784.5 $\text{kg/m}^3$			
Viscosity	$2.39 \cdot 10^{-3} \text{ Pa s}$			
Surface tension	21.4 mN/m			
<b>Ambient gas</b>	Air			
Density	1.20464 $\text{kg/m}^3$			
Viscosity	$1.837 \cdot 10^{-5} \text{ Pa s}$			

In Fig. 4 the topology of the DNS for a Weber number of  $We = 270$  is shown for the five phases. For this Weber number even without stabilization the lamella does not rupture. The topology can be directly compared to the experiments presented in Fig. 2, where in the right figure the beginning and ending of the phases is indicated.

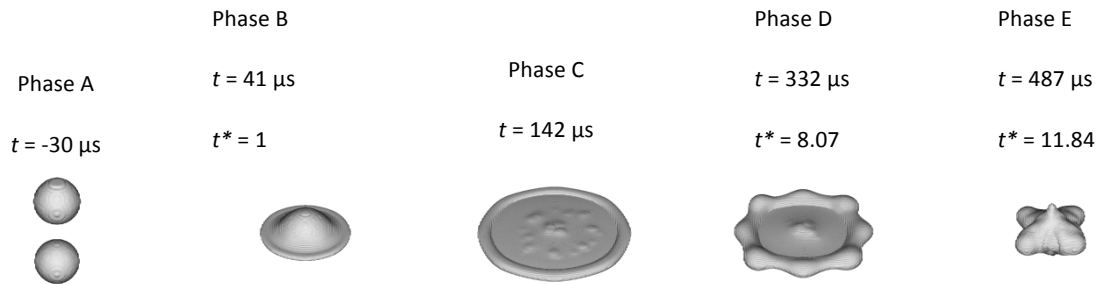


**Figure 4:** Results of a direct numerical simulation for a Weber number of  $We = 270$  without stabilization of the lamella. Shown is the topology of the collision process for the five phases.

Phase A ends, when the droplets get into contact assuming that there is no deformation of the droplets before. At this moment the collision process starts with phase B and with the collision time  $t^* = 0$ . In phase B a pizza shaped disc develops with a rim at the border and a lamella in the centre. According to the mechanistic modelling phase B ends, when the dimensionless time  $t^* = 2$  and it is assumed, that the disc diameter  $d$  increases according to the analytical model. Phase C is characterized by a further increase of the disc diameter until it has reaches its maximum. In phase D the disc diameter decreases until the lamella in its centre disappears. From the velocity field obtained by the DNS it is found, that at least in the beginning of phase D liquid is transported from the lamella into the rim as assumed in the analytical model. This results in a thinning of the lamella, while the disc diameter decreases. In phase E the further development of the liquid may be described. At the beginning of phase E the liquid spreads very fast in the direction perpendicular to the former disc ending in one or more droplets depending on the boundary conditions.

The global parameters as disc diameter  $d$  and thickness  $h$  of the lamella in the disc centre allow to some extent a comparison of the experimental, numerical and analytical models. There are small differences between the parameters of the experiment and the parameters used in the numerical and analytical study because it is very difficult to match all parameters in the experiment. In Fig. 5 the development of the disc diameter, which spans the phases B to D, is depicted for two different Weber numbers  $We \approx 270$  and  $We \approx 500$ . The filled circles show experimental data obtained from pictures shown in Fig. 2 on the right hand side. The solid lines correspond to DNS without the stabilization of the lamella, whereas the open triangles are results with the stabilization of the lamella. For  $We = 500$  the solid line ends before phase D is finished. At this point the lamella ruptures in the simulation without stabilization, whereas in the experiments no rupture could be observed. Therefore in this case the stabilization is necessary as can be seen in the diagram. These simulations with stabilization are performed using a computational domain of  $750 \mu\text{m} \times 750 \mu\text{m} \times 325 \mu\text{m}$  and a resolution of  $256 \times 256 \times 128$  cells with three symmetry planes. The resulting resolution is 80 cells/ $D$ . The mechanistic model for  $We = 270$ , indicated by the dashed line, is in good agreement with the experimental and numerical data. For higher Weber numbers above  $We = 300$  this model is not valid anymore. In Fig. 5 the phases are indicated on the abscissa, however, shown are only the phases for  $We = 270$ . All corresponding data show a good agreement.

In Fig. 6 for the Weber number  $We = 270$  the development of the thickness of the lamella in the centre of the disc is shown. The filled symbols are experimental results. These results are obtained from pictures shown in Fig. 2 on the left. It is clear, that this is only possible if the thickness is larger than the thickness of the rim at the outer border of the disc. Therefore this results end at the beginning of phase C.

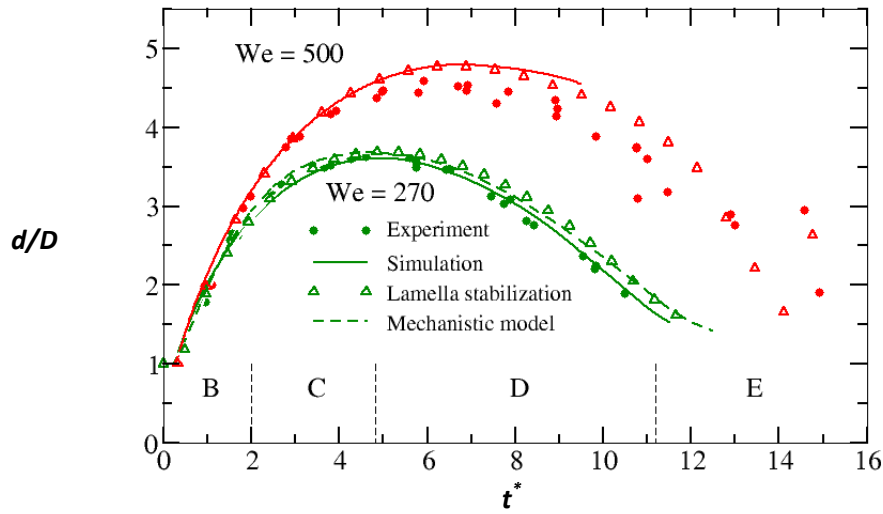


**Figure 5:** Dimensionless disc diameter as a function of dimensionless time for two different Weber numbers. The filled symbols indicate experimental results, the solid line DNS without stabilization of the lamella, the open symbols indicate results with stabilization. The dashed line indicates results of the mechanistic model. In addition the different phases for  $We = 270$  are indicated.

The solid line indicates results obtained from DNS without stabilization. As can be seen in phase D during the contraction of the disc the thickness increases.

This may be caused by small bubbles included in the lamella, as can be seen in Fig. 4 for phase C and D. In phase E after the disc has collapsed a sudden increase in thickness is observed associated with the spreading of the liquid perpendicular to the former disc. In the results of the DNS with stabilization the thickness does not increase during the recoiling of the disc in phase D. The spreading in phase E is different too. Due to the mechanistic model a straight line is obtained, when the inverse of the square root of the thickness is plotted as a function of the dimensionless time. This is performed with the results of the DNS with lamella stabilization.

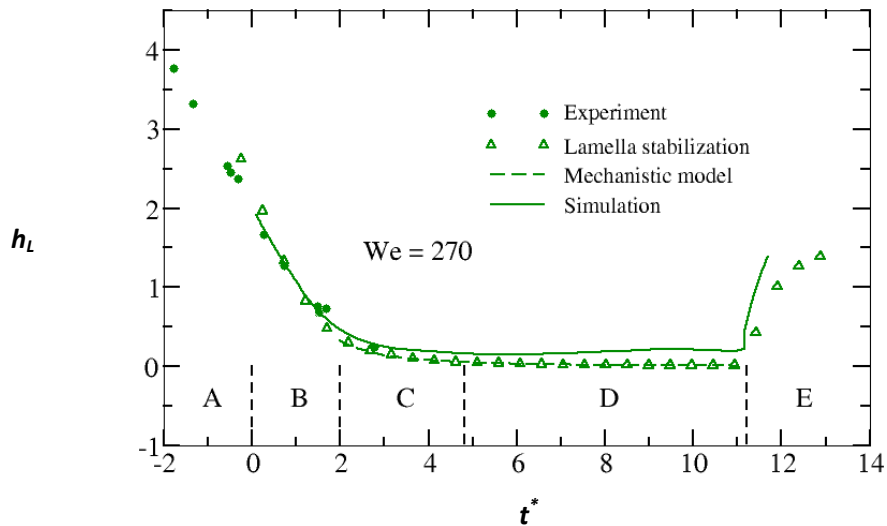


**Figure6:** Dimensionless thickness of the lamella as a function of the dimensionless time. Shown are results for  $We = 270$ . The filled symbols indicate experimental results, the solid line DNS without stabilization of the lamella, the open symbols indicate results with stabilization. The dashed line indicates results of the mechanistic model.

As predicted a linear behaviour for  $t^* > 2$  is found. A linear regression gives the parameter  $\Theta_l$  and  $\tau$  used to obtain the analytical results shown in Fig. 6 as a dashed line. The data obtained by the different methods show good agreement in phases A, B and in the beginning of phase C.

The topology of the collision process can be determined by experimental and numerical methods. A good agreement is obtained in phases A, B and C. The flow field obtained by the DNS should be reliable in these phases. However, in phase D the numerical simulations show non-realistic instabilities of the rim, which are oriented at the numerical grid. Therefore the flow field obtained by the DNS has to be interpreted very carefully. For much larger Weber numbers such instabilities are found in the experiments too.

## Conclusions

Each phase of the collision process can be described at least to some extent by one or more methods described above. In order to summarize it can be said, that in the early phases of the collision process a good agreement between the methods can be identified. The more the collision process proceeds, however, this becomes worse. A further improvement of the numerical simulations, as already performed to stabilize the lamella, will close the gaps, where the DNS still fails. An improvement of the observation and evaluation techniques in the experiments, will allow better validation of the DNS. All these improvements are the basis for the development of better analytical models.

A next step may be to study collision processes at much higher Weber numbers, at which instabilities are observed experimentally at the rim of the disc.

## Acknowledgements

We gratefully acknowledge financial support provided by the Deutsche Forschungsgemeinschaft within the scope of the SFB-TRR 75 and the Priority Program 1423 “Process Sprays”. The authors greatly appreciate the High Performance Computing Center Stuttgart (HLRS) for support and supply of computational time under the Grant No. FS3D/11142.

## References

- [1] N. Roth, H. Gomaa, B. Weigand, B., Droplet Collisions at High Weber Numbers: Experiments and Numerical Simulations. In *Proc. DIPSI Workshop 2010*, ISBN: 978-88-96333-51-8, Bergamo, Italy (2010).
- [2] J. Schlottke, W. Straub, K.-D. Beheng, H. Gomaa, B. Weigand, Numerical Investigation of Collision-Induced Breakup of Raindrops. Part I: Methodology and Dependencies on Collision Energy and Excentricity. *Journal of the Atmospheric Sciences*, **67**(3), 557-575 (2010).
- [3] C. Focke, D. Bothe, Direct Numerical Simulations of Binary Collisions of Shear Thinning Droplets at High Weber Numbers. *Physics of Fluids* **24**(7), 073105 (2012).
- [4] N. Ashgriz, J.Y. Poo, Coalescence and separation in binary collisions of liquid drops. *J. of Fluid Mechanics*, **221**, 183-204 (1990).
- [5] G. H. Ko, H. S. Ryou, Modeling of droplet collision-induced breakup process. *Int. J. of Multiphase Flow*, **31**(6), 723-738 (2005).
- [6] A. Munnannur, R.D. Reitz, A new predictive model for fragmenting and non-fragmenting binary droplet collisions. *Int. J. of Multiphase Flow*, **33**(8), 873-896 (2007).
- [7] I.V. Roisman, C. Planchette, E. Lorenceau, G. Brenn, Binary collisions of drops of immiscible liquids. *J. of Fluid Mechanics*, **690**, 512-535 (2012).
- [8] A. Yarin, *Free Liquid Jets and Films: Hydrodynamics and Rheology*. Interaction of mechanics and mathematics series. Longman Scientific & Technical, 1993.
- [9] A. Yarin, D.A. Weiss, Impact of drops on solid surfaces: self-similar capillary waves, and splashing as a new type of kinematic discontinuity. *J. of Fluid Mechanics*, **283**, 141-173 (1995).
- [10] I. V. Roisman, E. Berberovic, C. Tropea, Inertia dominated drop collisions. I. On the universal flow in the lamella. *Physics of Fluids*, **21**, 052103 (2009).

## Numerical Simulations of pinning droplets

N. Linder<sup>1,2</sup>, I. V. Roisman<sup>2</sup>, H. Marschall<sup>3</sup> and C. Tropea<sup>1,2</sup>

1: Graduate School of Computational Engineering, Technische Universität Darmstadt, Germany

2: Institute of Fluid Mechanics and Aerodynamics, Technische Universität Darmstadt, Germany

3: Institute Mathematical Modeling and Analysis, Center of Smart Interfaces,  
Technische Universität Darmstadt, Germany

### Abstract

Prediction of flows governed by wetting phenomena is a challenging problem, mainly because it requires an accurate description of the moving contact line. In this context, the contact angle hysteresis, which describes propagation and pinning of the contact line as well as the dynamically changing contact angle, is essential for correct prediction of such flows. In existing numerical simulations a dynamic contact angle, which depends on the contact line velocity, is realized by prescribing the gradient of the phase fraction at the wall. This approach fails when the contact line is pinned. In this study we introduce a numerical model that satisfies the boundary conditions (BC) at the wall corresponding to the contact angle hysteresis and accounts for both pinning and sliding phases of the contact line behavior. It combines a Dirichlet and Neumann BC for the phase fraction to prescribe a zero contact line velocity when the contact line is pinned and to allow its propagation if the calculated value of the contact angle is outside the interval between the advancing and receding static contact angles. The numerical code is validated by the simulations of a drop sliding on an inclined solid substrate under the action of the gravity. The theoretical predictions agree well with the experimental data.

---

### Introduction

Liquid wetting or in general flows with a liquid-solid-vapor interface have a broad application in industry and are an important field of research. Coating, complex wetting, sprays, ink-jet printing and liquid cooling are just some examples of their application.

In all of them, the understanding of the behavior of the contact line (where solid, liquid and vapor meet) is essential to analyze the overall characteristics. In high Weber number flows (multiphase flows with high velocities), movement of the contact line can be observed, whereas in low Weber number flows, a contact line tends to rest at its position [1], although external forces act on it. The numerical realization of this behavior is the focus of the present work.

The numerical simulation of multiphase flows is a broad field of research and in applications. In the last decades several methods have been developed, reaching from Molecular Dynamic (MD) simulations [2] and Lattice-Boltzmann methods (LBM) [3] to continuum mechanical descriptions in the Finite-Volume [4] or Finite-Element method [5]. In the last two methods, two main branches to account for multiple phases exist: eulerian methods, where a reconstruction of the interface is necessary and langrangian methods where the grid fits the phase interface [6]. The prominent methods in eulerian schemes are the Volume of Fluid (VoF) [7] and Level-Set (LS) [8] Method.

### Static situations

In a system with a triple line, the interplay between the fluid-fluid interface (cohesion) and the fluid-solid interaction (adhesion) determine a particular state of wetting. It results in a certain contact angle, the angle between the tangent of the liquid interface and the solid wall. It was described by Young as the equilibrium state between the surface tensions of the three interfaces as

$$\sigma_{VS} = \sigma_{SL} + \sigma_{LV} \cos \theta$$

where  $\sigma$  is the surface tension and the indices V, S and L represent vapor, solid and liquid, respectively.

### Dynamic Situations

If a contact line moves, for example on an inclined plate, the value of the contact angle changes dynamically according to the contact line velocity. The greater the velocity, the greater the contact angle. This behavior has been studied by several researchers who introduced various models. They differ slightly depending on the range of Capillary numbers ( $Ca = \mu \mathbf{u}_{cl} / \sigma$  where  $\mathbf{u}_{cl}$  is the contact line velocity and  $\mu$  the viscosity) or applications which they investigated.

According to Kistler [9] the dynamic contact angle can be expressed by:

$$\theta_d = f_H \left( Ca + f_H^{-1}(\theta_e) \right)$$

where the Hoffmann function  $f_H$  is defined as

$$f_H = \cos^{-1} \left\{ 1 - 2 \tanh \left[ 5.16 \left[ \frac{x}{1 + 1.31x^{0.99}} \right]^{0.706} \right] \right\}$$

For small Weber numbers, this model reduces to the so-called Hoffmann's law:

$$\theta_d = 4.54 Ca^{0.535}$$

### Transition

A contact line (e.g. of a drop) can pin, which means it does not move although it is exposed to gravity, cross-flow or inertia. A typical example is a rain drop on the windshield, which remains at its position although the surface is inclined.

The reason for pinning is based on the adhesion of the liquid with the solid. The main mechanisms are adsorption (physiosorption and chemisorption), mechanical interlocking, diffusion and electrostatics. Physiosorption are basically van-der-Waals forces, acid-base interactions and hydrogen bonds as well as the effects of surface roughness are most important in our applications.

From a macroscopic point of view, this phenomena is described by the *contact angle hysteresis*: Within a range of two contact angles, the advancing contact angle  $\theta_A$  and the receding contact angle  $\theta_R$ , the contact line does not move. If these limits are exceeded, the contact line abruptly starts to move and the dynamic contact angle, as described before, can be observed.

These three stages together comprise the contact angle hysteresis that completely describes the relation between the contact line velocity and the contact angle, including the receding and advancing phase with the dynamic contact angle, and the area of zero contact line velocity, the hysteresis. An example of a contact angle hysteresis for  $\theta_A = 120^\circ$  and  $\theta_R = 60^\circ$  is plotted in Fig. 1.

### Numerics

In applications of low Weber number, the influence of the viscous forces and the contact angle hysteresis are dominant. In numerical simulations they therefore need to be accurately accounted for. However, the typical no-slip BC at the wall does not allow movement of the contact line. Consequently, an infinite force would be necessary to move the contact line [10]. A typical approach to circumvent this *force singularity* at the interface is to introduce slip in the vicinity of the contact line [11]. With this approach, the macroscopic observations of a moving contact line can be numerically realized. However, experiments showed that the fluid *rolls* over the solid surface [12]. So the molecular no-slip condition at a wall is still valid, but the movement stems from complex molecular interactions at the interface. Hence, the artificial slip is a strong simplification, but it has yielded reasonable results.

The introduction of slip in the vicinity of the contact line successfully removed the force singularity and enabled a broad range of numerical applications. On the contrary, the natural no-slip completely vanishes and pinning can no longer be realized. Using a pure slip boundary condition, a droplet on an inclined plate will slide down, independent of the static values of the hysteresis.

### Literature

Dynamic contact angle models have been used in several numerical simulations and they improve the agreement between experiments and simulations compared to static contact angle models. An overview of different contact angle models used in numerical simulations is given in [13]. Several studies analyzed the dynamic contact angle of a droplet impact onto a solid dry surface in the VoF Method [14-16] or LS Method [17, 18], as well as coupled VoF-LS approaches [19]. Additionally, using MD simulations the dynamic contact angle was studied on small length scales [11, 20]. In the FE framework, explicit methods with a moving grid [6, 21] were used. LB methods were also applied to account for the dynamic contact angle [22, 23].



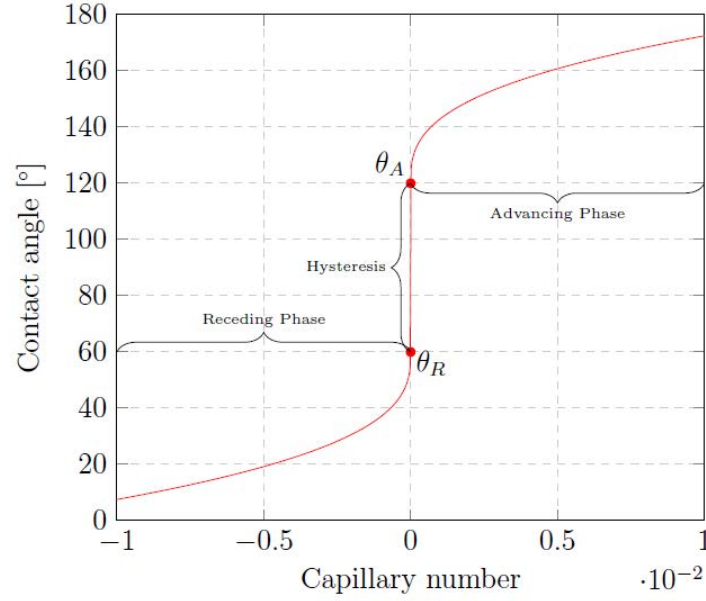


**Figure 1.** Kistler's dynamic contact angle model with respect to  $\theta_A = 120^\circ$  and  $\theta_R = 60^\circ$

Some publications also take the hysteresis into account [17, 24, 25]. In the LB method, Wang et al. [24] realize pinning and the dynamic contact angle from a geometrical consideration where, depending on the current contact angle, an index function to track the interface is adopted. It is unclear, whether the contact angle can change within the hysteresis and during the advancing and receding phase. Spelt [17] imposes a zero contact line velocity within the hysteresis for the redistance step in the level-set approach. Duquenois et al. [25] impose the zero contact line velocity and the contact angle by modifying the first marker at the boundary to satisfy the contact angle hysteresis boundary condition.

The main subject of this work is the introduction of a numerical refinement to account for the full contact angle hysteresis and to allow pinning as well as the transition to the sliding phase of the contact line with a dynamic contact angle model. It uses a Robin BC which combines a no-slip (Dirichlet) BC with a slip (Neumann) BC by a linear combination and reproduces the full contact angle hysteresis in the VOF framework. Its application will improve most numerical wetting simulations, especially at low Weber numbers, and correctly account for the stick-slip phenomena.

### Governing Equations

The numerical simulations in this study are performed using the OpenFOAM-solver *interFOAM*, a solver based on the VoF method utilizing algebraic advection schemes for phase fraction advection. [26-29].

The full incompressible Navier-Stokes equation (conservation for mass and momentum) for one phase read

$$\nabla \cdot \mathbf{U} = 0$$

$$\frac{\partial}{\partial t}(\rho \mathbf{U}) + \nabla \cdot (\rho \mathbf{U} \mathbf{U}) = -\nabla p + \nabla \cdot \boldsymbol{\tau} + \rho \mathbf{f}^{ext}$$

where  $\rho$  is the density,  $\mathbf{U}$  the velocity,  $p$  the pressure,  $\boldsymbol{\tau}$  the stress tensor and  $\mathbf{f}^{ext}$  external forces.

In the VoF scheme an additional equation for the transport of the phase fraction is introduced:

$$\frac{\partial}{\partial t} \alpha + \nabla \cdot (\mathbf{U} \alpha) = 0$$

The momentum equation is modified to account for surface tension by introducing the continuum surface force (CSF) [30] due to density gradient at the interface:

$$\mathbf{F}_\sigma = \sigma \kappa \mathbf{n}_\sigma.$$

$\Sigma$  is the (in our case constant) surface tension.  $\kappa$  the curvature of the interface and  $\mathbf{n}_\sigma$  the normal vector of the interface.  $\kappa$  can be calculated by

$$\kappa = -\nabla \cdot \frac{\nabla \alpha}{|\nabla \alpha|}.$$

To solve this set of equations, they need to be discretized and appropriate boundary conditions applied. As a solution algorithm for transient flows, the pressure implicit with splitting operators (PISO) scheme is used. The spatial domain is discretized into a 3D unstructured grid, dominated by hexahedral cells and refined towards the area of interest.

### Boundary Conditions

In order to numerically solve the set of equations, boundary and initial conditions for each variable need to be provided. The initial conditions describe the initial state of each variable, which is the phase fraction in the computational domain and, if necessary, velocities or pressure. At the boundary of the domain, boundary conditions that represent the physical behavior (e.g. a wall) need to be provided. Accordingly, two types of boundary conditions exist: Neumann and Dirichlet BCs. A Dirichlet BC prescribes a fixed value at the boundary (e.g. used for the velocity at a no-slip wall) whereas a Neumann BC prescribes a gradient at a boundary in normal direction (e.g. to prescribe a heat flux through a wall). As a third type, the Robin BC combines both boundary condition by linear combination. An additional blending factor indicates which boundary condition is locally applied ( $\beta=1$  for Dirichlet BC and  $\beta=0$  for Neumann BC). The simultaneous combination ( $0 < \beta < 1$ ) of both is not used here.

As outlined in the introduction, the force singularity at the contact line has been circumvented by the introduction of slip in the vicinity of the contact line. Additionally the prescription of the direction of the gradient for the phase fraction allows to dynamically change the contact angle. Using a contact angle model as a lookup table, a dynamic contact angle model for the receding and advancing phase can be numerically realized. To do that, for each cell at the boundary, the Capillary number needs to be calculated. In VoF simulations, the extraction of the contact line velocity is not straightforward. We use the following scheme to extract the local contact line velocity:

First, the relative velocity between the cell-centers and the wall is calculated:

$$\mathbf{U}_R = \mathbf{U}_P - \mathbf{U}_b$$

Next, the components parallel to the wall are calculated by

$$\mathbf{U}_R = \mathbf{U}_R - (\mathbf{n}_b \cdot \mathbf{U}_R)\mathbf{n}_b$$

where  $\mathbf{n}_b$  is the normal vector of the wall. Then, the direction of the interface parallel to the wall is found by

$$\mathbf{n}_{\sigma||Wall} = \mathbf{n}_\sigma - (\mathbf{n}_b \cdot \mathbf{n}_\sigma)\mathbf{n}_b$$

and the contact line velocity finally reads

$$\mathbf{U}_{cl} = \mathbf{n}_{\sigma||Wall} \cdot \mathbf{U}_R$$

Now the Capillary number can be calculated and the local contact angle extracted and applied.

This scheme has been used to simulate moving contact line problems [15], but it fails when pinning of the contact line is expected. For this reason, the present study proposes a refinement in the handling of the numerical boundary condition for the phase fraction. It accounts correctly for the hysteresis and allows transition from pinning to the sliding phase. Its realization is explained in the following chapter.

### Robin Boundary Condition for the Phase Fraction

The motivation for this work is a more accurate numerical realization of the contact angle hysteresis. As mentioned before, the pinning of a contact line and its transition to the sliding phase is not properly reproduced by a pure Neumann boundary condition.

Looking at the contact angle model from Fig. 1, the segments of the receding and advancing phases are realized as before - with a Neumann BC prescribing the dynamic contact angle as a function of the contact line velocity. Additionally, within the hysteresis, a Dirichlet BC is applied, that prescribes a constant value of the phase fraction at the wall. Thus, the contact line is fixed and the contact angle can adjust itself. The transition between the two stages depends on the local contact angle of a boundary cell. It is realized by setting the blending factor of the Robin BC accordingly.

With this approach we can realize a full dynamic contact angle model including pinning and sliding of the contact line. Our approach fully reproduces the model of Fig. 1. The workflow is now described more detailed:

### 1. Extract the current contact angle

For each boundary-cell, the current contact angle is calculated by

$$\cos \theta_{Cur} = \frac{\mathbf{n}_b \cdot \nabla \alpha_p}{|\mathbf{n}_b| |\nabla \alpha_p|}$$

where  $\nabla \alpha_p$  is the gradient at the cell center and  $\mathbf{n}_b$  the normal vector of the boundary face of the cell. This contact angle will set the blending factor  $\beta$  accordingly and tell us in a later step whether we are within the hysteresis or not.

### 2. Calculate local Capillary number

The local Capillary number will be calculated which is necessary if the contact line is in motion and a contact angle needs to be calculated.

#### a) Current contact angle is within the hysteresis

If the current contact angle of the cell calculated in Step 1 is within  $\theta_A$  and  $\theta_R$  we prescribe  $\mathbf{u}_{cl} = 0$  by prescribing  $\alpha_b$  as in the timestep before. The value at the boundary has not changed and consequently the contact line did not move. So we locally apply a Dirichlet boundary condition and the contact angle adjusts itself. This additionally makes sure, that the contact angle can exceed  $\theta_A$  or  $\theta_R$  while a Dirichlet BC is applied and switch to a slip BC.

#### b) Current contact angle is beyond the hysteresis

If the current contact angle exceeds the static values of  $\theta_A$  and  $\theta_R$ , a Neumann boundary condition is locally applied and the gradient of  $\alpha$  is prescribed. We take the Capillary number calculated in step 2 and extract a contact angle using a contact angle model (e.g. Kistler). The value of  $\alpha$  at the patch will adjust itself corresponding to the prescribed contact angle (the contact line will move).

### 3. Identify the advancing or receding edge

It is not always sufficient to only check for the local contact angle to decide in which *phase* the contact line currently is. It may happen, that even at the trailing edge the current contact angle is greater than  $\theta_A$ , or at the advancing front the contact angle is smaller than  $\theta_R$ . Therefore, we additionally check the sign of the dot-product between the *averaged drop velocity*  $\mathbf{U}_{Dir}$  with the gradient of the phase fraction.

$$\mathbf{U}_{Dir} = \frac{1}{n_{cells}} \sum_{cells} \alpha_p \left( \frac{\mathbf{U}_p}{|\mathbf{U}_p|} \right)$$

If they point in the same direction, it can be identified as a part of the trailing edge, in opposite directions as leading edge.

If now a cell is identified as a *slip* cell (the current contact angle is beyond the hysteresis), the calculation of the curvature at the boundary yields a given calculated contact angle. In the discretized form, the curvature is calculated as the sum of the gradients on the faces of the cell:

$$\kappa = -(\sum_f \nabla \alpha_f + \sum_b \nabla \alpha_b).$$

Whereas internal values on the faces can be calculated via interpolation with neighboring cells, the gradient at the patch can be prescribed directly. The indices are explained in Fig. 3. For cells that are identified as being in the hysteresis, no correction of the boundary gradient is performed and the value at the boundary remains constant. The contact line pins.

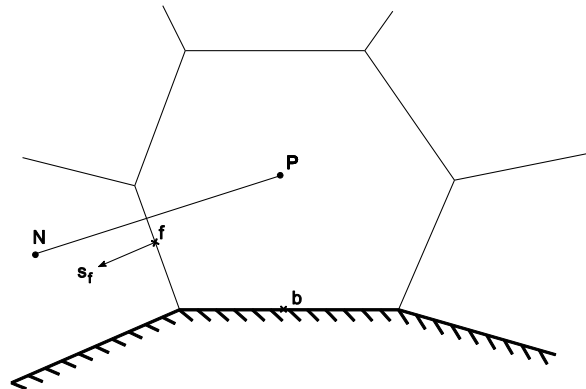


Figure 3. Visualization of the used indices.

## Results and Discussion

To verify the new boundary condition, tilted plate simulations were performed and the critical inclination angle at which a drop starts to slide is compared to the experimental work of Pierce et al. [31]. In their work, they analyzed different drop placement techniques for tilted plate experiments. We use their results of critical inclination angles of droplets with different volumes (from 20  $\mu\text{l}$  to 70  $\mu\text{l}$ ) on two different substrates (Alkyle Ketene Dimmer (AKD) and fluorinated silicon). The parameters of the hysteresis can be found in Tab. 1.

Advancing and receding contact angles (°)			
Experiments	AKD	$163 \pm 5$	$83 \pm 6$
	Fl. silicon	$124 \pm 4$	$112 \pm 3$
Simulations	AKD	168	77
	Fl. silicon	128	109

**Table 1.** Contact angle measurements from the experiments [31] and the contact angles used for the numerical simulation

The simulations were performed using a 3D setup whereas half a droplet was simulated and the other half accounted for by a symmetry plane perpendicular to the solid substrate. In a first stage, a droplet *impact* onto the horizontal surface with a low impact velocity was performed. After a stationary result was obtained, the gravity was set to mimic the inclination of the plate. If a droplet slid out of the domain, the angle of the gravity vector to the solid substrate was identified as the critical inclination angle.

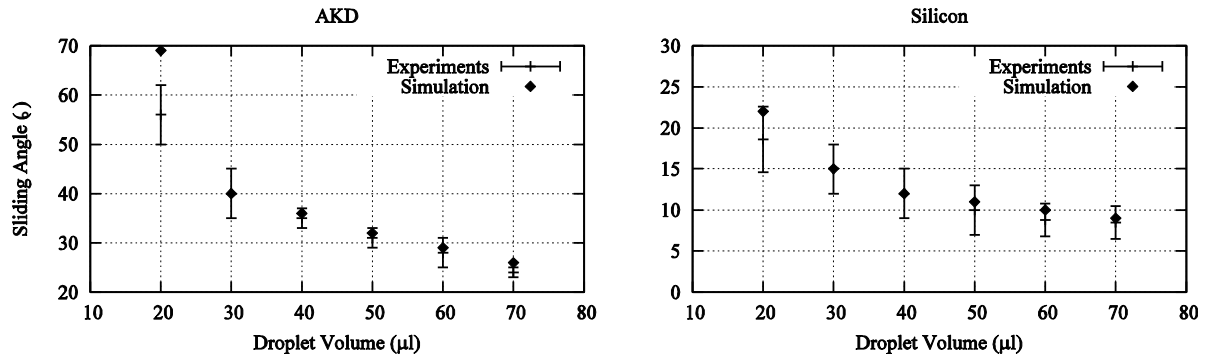


**Figure 4.** Comparison of the critical inclination angle in experiments of [31] and simulations.

The numerical results agree with the experimental data (see Fig. 4). As the mesh was not changed, the resolution for the 20  $\mu\text{l}$  was coarse compared to the others, explaining the slight deviation seen for these results. Using the former, pure gradient BC, the droplet slid even at level surfaces for all droplet volumes.

## Conclusions

We present a numerical approach for a more accurate realization of the contact angle hysteresis in the VOF framework. It numerically accounts for pinning and improves simulations of low Weber number. The results agree well with the experiments of Pierce et al. [31].

## Acknowledgements

The work of N. Linder is supported by the 'Excellence Initiative' of the German Federal and State Governments through the Graduate School of Computational Engineering at the Technische Universität Darmstadt. Additionally, the authors would like to thank A. Amirfazli, A. Criscione and C. Chang for the fruitful discussions.

## References

- [1] 1. Sikalo, S., *Analysis of Droplet Impact onto Horizontal and Inclined Surfaces*. 2002, Technische Universität Darmstadt.
- [2] 2. Allen, M.P. and D.J. Tildesley, *Computer Simulation of Liquids*. 1989: Oxford University Press.

- [3] Chen, S. and G.D. Doolean, *Lattice boltzmann method for fluid flows*. Annual Review Fluid Mechanics, 1998. **30**: p. 329-364.
- [4] Ferziger, J.H. and M. Peric, *Computational Methods for Fluid Dynamics*. 2002: Springer, Berlin.
- [5] Bathe, K.J., *Finite Element Procedures*. 1996: Prentice Hall.
- [6] Fukai, J., Z. Zhao, D. Poulikakos, C.M. Megaridis and O. Miyatake, *Modeling of the Deformation of a Liquid Droplet Impinging Upon a Flat Surface*. Physics of Fluids a-Fluid Dynamics, 1993. **5**(11): p. 2588-2599.
- [7] Hirt, C.W. and B.D. Nichols, *Volume of Fluid (Vof) Method for the Dynamics of Free Boundaries*. Journal of Computational Physics, 1981. **39**(1): p. 201-225.
- [8] Osher, S. and R. Fedkiw, *Level Set Methods and Dynamic Implicit Surfaces*. 2003: Springer, New York.
- [9] Kistler, S.F., *Hydrodynamics of wetting*, in *Wettability*, J.C. Berg, Editor., Marcel Dekker: New York.
- [10] Huh, C. and L.E. Scriven, *Hydrodynamic model of steady movement of a solid/liquid/fluid contact line*. Journal of Colloid and Interface Science, 1970. **35**: p. 85-101.
- [11] Thompson, P.A. and M.O. Robbins, *Simulations of contact-line motion: Slip and the dynamic contact angle*. Phys Rev Lett, 1989. **63**(7): p. 766-769.
- [12] Veretennikov, I., A. Indeikina and H.C. Chang, *Front dynamics and fingering of a driven contact line*. Journal of Fluid Mechanics, 1998. **373**: p. 81-110.
- [13] Saha, A.A. and S.K. Mitra, *Effect of dynamic contact angle in a volume of fluid (vof) model for a micro fluidic capillary flow*. Journal of Colloid and Interface Science, 2009. **339**: p. 461-480.
- [14] Roisman, I.V., L. Opfer, C. Tropea, M. Raessi, J. Mostaghimi and S. Chandra, *Drop impact onto a dry surface: Role of the dynamic contact angle*. Colloids and Surfaces a-Physicochemical and Engineering Aspects, 2008. **322**(1-3): p. 183-191.
- [15] Berberovic, E., *Investigation of Free-surface Flow Associated with Drop Impact: Numerical Simulations and Theoretical Modeling*, in *Technische Universität Darmstadt*. 2010.
- [16] Afkhami, S., S. Zaleski and M. Bussmann, *A mesh-dependent model for applying dynamic contact angles to VOF simulations*. Journal of Computational Physics, 2009. **228**(15): p. 5370-5389.
- [17] Spelt, P.D.M., *A level-set approach for simulations of flows with multiple moving contact lines with hysteresis*. Journal of Computational Physics, 2005. **207**(2): p. 389-404.
- [18] Sussman, M., P. Smereka and P. Osher, *A level set approach for computing solutions to incompressible two-phase flow*. Journal of Computational Physics, 1994. **114**.
- [19] Yokoi, K., D. Vadillo, J. Hinch and I. Hutchings, *Numerical studies of the influence of the dynamic contact angle on a droplet impacting on a dry surface*. Physics of Fluids, 2009. **21**(7).
- [20] Koplik, J., R. Banavar and J.F. Willemsen, *Molecular dynamics of poiseuille flow and moving contact lines*. Physical Review Letters, 1987. **60**(13): p. 1282-1286.
- [21] Bertagnolli, M., M. Marchese and G. Jacucci, *Modeling of Particles Impacting on a Rigid Substrate under Plasma Spraying Conditions*. Journal of Thermal Spray Technology, 1995. **4**(1): p. 41-49.
- [22] Mukherjee, S. and J. Abraham, *Investigation of drop impact on dry walls with a lattice-boltzmann model*. Journal of Colloid and Interface Science, 2007. **312**: p. 314-354.
- [23] Briant, A.J., A.J. Wagner and J.M. Yeomans, *Lattice Boltzmann simulations of contact line motion. I. Liquid-gas systems*. Physical Review E, 2004. **69**(3).
- [24] Wang, L., H.B. Huang and X.Y. Lu, *Scheme for contact angle and its hysteresis in a multiphase lattice Boltzmann method*. Phys Rev E Stat Nonlin Soft Matter Phys, 2013. **87**(1): p. 013301.
- [25] Duquennoy, C., O. Lebaigue and J. Magnaudet, *A numerical model of gas-liquid-solid contact line*. Fluid Mechanics and Its Applications, 2001. **62**: p. 89-98.
- [26] Jasak, H., *Error analysis and estimation in the Finite Volume method with applications to fluid flows*. 1996, Imperial College, University of London.
- [27] Rusche, H., *Computational Fluid Dynamics of Dispersed Two-Phase Flows at High Phase Fractions*. 2002, Imperial College, University of London.
- [28] Ubbink, O., *Numerical Prediction of two fluid systems with sharp interfaces*. 1997, Imperial College, University of London.
- [29] Berberovic, E., N.P. van Hinsberg, S. Jakirlic, I.V. Roisman and C. Tropea, *Drop impact onto a liquid layer of finite thickness: dynamics of the cavity evolution*. Phys Rev E Stat Nonlin Soft Matter Phys, 2009. **79**(3 Pt 2): p. 036306.
- [30] Brackbill, J.U., D.B. Kothe and C. Zemach, *A Continuum Method for Modeling Surface-Tension*. Journal of Computational Physics, 1992. **100**(2): p. 335-354.
- [31] Pierce, E., F.J. Carmona and A. Amirfazli, *Understanding of sliding and contact angle results in tilted plate experiments*. Colloids and Surfaces A: Physicochem. Engineering Aspects, 2007. **323**: p. 73-82.

## Numerical Investigation of High Pressure Evaporation of a Resting Acetone Droplet in Nitrogen Environment

I. Shevchuk, A. Sadiki and J. Janicka

Department of Energy and Power Plant Technology, TU Darmstadt, Germany

### Abstract

A numerical solver, based on the volume of fluid interface capturing method (1), was extended to deal with variable densities and transport properties adopting low Mach number assumptions. Energy and binary species transport equations were included for both liquid and gas phases. Evaporation, solubility effects and temperature and composition dependent variable thermophysical properties were also considered, to make the solver suitable for investigation of transient and fully three-dimensional evaporation processes at subcritical, transcritical and supercritical environmental conditions. Using Peng-Robinson equation of state and empirical correlations to define thermophysical properties, microgravity evaporation of a stagnant droplet in a carrier gas at elevated temperatures and pressures was investigated. First, an n-heptane droplet in nitrogen environment at 10 bar, 20 bar and 50 bar was simulated on a spherically symmetric computational grid. Numerical results were compared with experiments of *Nomura* (2) and simulations performed by *Zhang* (3). Finally, an acetone droplet in nitrogen environment at 10 bar, 20 bar, 30 bar and 60 bar was simulated on the similar grid.

---

### Introduction

Computational fluid dynamics (CFD) plays a great role in the development and efficiency optimization of modern combustion systems, allowing reduction of development times and costs. Since diverse combustion systems, like diesel engines or aircraft engines, operate with non-premixed liquid fuels directly injected in the combustion chamber, spray evaporation has a direct impact on mixture formation and combustion behaviour. Modelling single droplet evaporation, correlating evaporation rates and droplet lifetimes is in turn necessary for modelling of spray evaporation. Especially at high temperatures and pressures, typical for combustion chambers, several assumptions usually made for low-pressure evaporation, e.g. constant density and constant thermophysical properties, chemical equilibrium at the gas-liquid-gas-interface, etc., are not compulsory valid and thus, high temperature and pressure effects have to be taken into consideration. Comprehensive models describing heat and mass transfer for all-pressure and all-temperature regimes can be found in publications by *Harstad and Bellan* (4, 5).

This study concentrates on the evaporation of a single component fuel droplet in a carrier gas environment at low liquid gas relative velocities. The focus is first put on nearcritical and transcritical evaporation, which means that the critical pressure or temperature of the fuel can be approached or exceeded, however staying below the critical point of the fuel carrier gas mixture.

Several experimental studies have been performed on droplet evaporation at such conditions (2, 6, 7). Also, several numerical studies successfully reproduced the experiments (3, 8-13). All of them consider temperature-, pressure- and composition-dependent fluid properties, assume chemical equilibrium on the interface and neglect viscous heating and radiation, as well as Soret and Dufour effects, what justify these assumptions for the particular case of the aforementioned environmental conditions. On the other hand, almost all of these studies, except of (11), use spherically symmetric formulation of governing equations and domain separation for the liquid and the gas phases. The scope of this work was to adopt this approach into the framework of the volume of fluid (VOF) methodology and to implement it using the open source CFD toolbox OpenFOAM, allowing using it for deforming interfaces as well.

Perhaps, the most investigated system for transcritical evaporation is the substance combination of n-heptane and nitrogen. This fact makes it attractive for validation purposes for new numerical solvers. Apart from frequently investigated model fuels, like n-hexane, n-heptane or n-octane, acetone is of particular research interest. Not even being a fuel in a common sense, the interest to acetone is owed to its light absorption and emission properties, that make acetone extraordinary suitable for laser diagnostic applications (14) and thus, allowing contact-free high-resolution measuring of species concentrations during evaporation and mixture formation processes.

As for the mentioned reasons, the substance pairs of n-heptane-nitrogen and acetone-nitrogen were picked up for investigation. Keeping in mind the medium-term goal to develop a numerical tool, suitable for simulation of subcritical, transcritical and supercritical evaporation and surface dynamics of a fuel droplet, a simple mathematical model and the simplest axisymmetric case of transcritical evaporation in microgravity were chosen to begin with.

## Mathematical modelling

### Conservation equations

A similar set of conservation equations to solve was chosen, as proposed in (3). The mathematical model accounts for the conservation of mass, momentum, energy and mass of the minority specie  $k$ :

$$\frac{\partial \rho}{\partial t} + \nabla \cdot (\rho \mathbf{U}) = 0 \quad (1)$$

$$\frac{\partial (\rho \mathbf{U})}{\partial t} + \nabla \cdot (\rho \mathbf{U} \mathbf{U}) - \nabla \cdot \boldsymbol{\tau} = -\nabla p + \rho \mathbf{g} + \int_{S_I} \mathbf{n} \sigma \kappa dS_I \quad (2)$$

$$c_p \frac{\partial (\rho T)}{\partial t} + c_p \nabla \cdot (\rho T \mathbf{U}) - \nabla \cdot \lambda \nabla T - \sum_{k=1}^2 J_k h_k = \int_{S_I} \sum_{k=1}^2 \dot{m}_{k,\text{evap}}'' h_{k,\text{evap}} dS_I \quad (3)$$

$$\frac{\partial (\rho Y_k)}{\partial t} + \nabla \cdot (\rho \mathbf{U} Y_k) - \nabla \cdot (\rho D \nabla Y_k) = 0 \quad (4)$$

with density  $\rho$ , velocity vector  $\mathbf{U}$ , temperature  $T$ , minority specie mass fraction  $Y_k$ , pressure  $p$ , gravitational acceleration vector  $\mathbf{g}$ , surface tension coefficient  $\sigma$ , interface curvature  $\kappa$ , heat capacity  $c_p$ , thermal heat conductivity  $\lambda$ , diffusive mass flux  $J_k$ , partial enthalpy  $h_k$  and specific heat of evaporation  $h_{k,\text{evap}}$  of the specie  $k$  respectively.  $S_I$  stands for interface area,  $\mathbf{n}$  for interface normal unity vector and  $\dot{m}_{k,\text{evap}}''$  for the phase change mass flux of the specie  $k$  per unit area, defined positively in case of evaporation.  $\boldsymbol{\tau}$  is the Newtonian viscous stress tensor:

$$\boldsymbol{\tau} = \mu (\nabla \mathbf{U} + \nabla \mathbf{U}^T) - 2/3 \mu (\nabla \cdot \mathbf{U}) \mathbf{I} \quad (5)$$

with dynamic viscosity  $\mu$  and identity tensor  $\mathbf{I}$ .

### Thermophysical properties

To calculate liquid and gas densities, depending on pressure, temperature and mixture composition, Peng-Robinson thermal equation of state (PR-EOS) was used (15).

$$p = \frac{RT}{V - b} - \frac{a}{V^2 + 2bV - b^2} \quad (6)$$

where  $V$  is the molar volume and  $a$  and  $b$  are parameters. Using a simple quadratic mixing rule,  $a$  and  $b$  become functions, dependent on critical pressure  $p_c$ , critical Temperature  $T_c$  and acentric factors  $\omega$  of each species, mixture temperature and composition, and a binary interaction coefficient  $k_{kl}$  (15). Following pure substance parameters were used for the PR-EOS (**Table 1**). Binary interaction coefficients  $k_{kl}=0.1441$  (16) and  $k_{kl}=0.2086$  (17) were used for n-heptane-nitrogen and for acetone-nitrogen mixtures, respectively.

**Table 1:** Pure substance parameters for PR-EOS

	$T_c$ [K]	$p_c$ [bar]	$\omega$ [-]
n-Heptane	540.0	27.40	0.351
Acetone	508.1	47.01	0.309
Nitrogen	126.2	33.98	0.039

To calculate the mixture enthalpy  $h$ ,  $h$ - $T$ - $p$  relation was evaluated using PR-EOS-based departure functions (18) with empirical correlations for pure substances ideal gas heat capacities (19). The heat of evaporation was than calculated as a difference of partial specific enthalpies of each component in the gaseous and in the liquid phase

$$h_{k,\text{evap}} = h_{k,\text{liquid}} - h_{k,\text{gas}} \quad (7)$$

As proposed in (8), correlations by *Chung et al.* (20, 21) were used to calculate viscosities and thermal conductivities of the mixtures. *Wilke-Chang* method (22) was used to obtain binary mass diffusivities in the liquid phase and *Chapman-Enskog* theory (18) in combination with *Riazi & Whitson* correction for dense fluids (23) were used for the gas phase respectively. Following parameters (**Table 2**) were used in addition to the parameters from **Table 1** to calculate the transport properties:



**Table 2:** Pure substance parameters for calculation of transport properties

	$M$ [kg/kmol]	$\rho_c$ [kmol/m <sup>3</sup> ]	$T_{bp}$ [K]	$V_{bp}$ [m <sup>3</sup> /kmol]	$\Delta h_{ig}^\circ$ [J/kmol]	$\mu$ [D]	$\phi$ [-]
n-Heptane	100.2	2.35	371.6	$164.75 \cdot 10^{-3}$	$-189.9 \cdot 10^6$	0.00	1.0
Acetone	58.08	4.78	329.2	$76.98 \cdot 10^{-3}$	$-218.5 \cdot 10^6$	2.91	1.0
Nitrogen	28.01	11.18	77.4	$31.76 \cdot 10^{-3}$	0.0	0.00	1.0

with molar mass  $M$ , critical density  $\rho_c$ , boiling point temperature  $T_{bp}$ , boiling point volume  $V_{bp}$ , enthalpy of formation of gas at standard conditions  $\Delta h_{ig}^\circ$ , dipole moment  $\mu$  and association factor for solvent  $\phi$ .

### Vapour-liquid equilibria (VLE)

Droplet surface was supposed to be in thermodynamic equilibrium, assuming the equality of temperature, pressure and fugacities of each component at the gas-liquid-interface. Similar to the enthalpy, fugacity can be determined from the PR-EOS using departure functions (18). Isobars of the resulting VLEs are shown in Figure 1 for the investigated pressures.

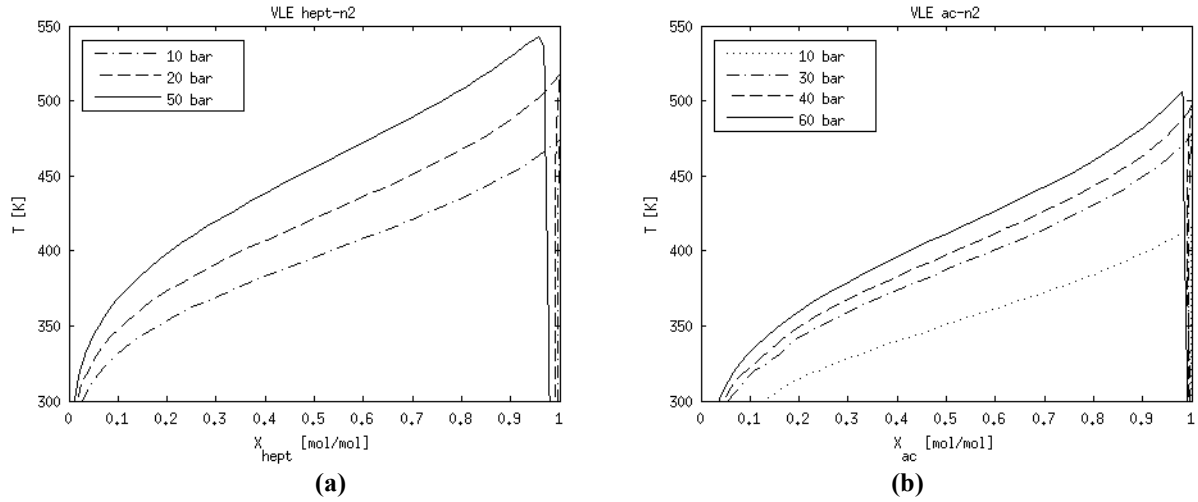


**Figure 1.** Isobars of vapour-liquid-equilibria for systems of n-heptane-nitrogen (a) and acetone-nitrogen (b), computed using the Peng-Robinson equation of state

### Interface capturing and numerical solution procedure

A VOF-based approach was used for capturing the liquid-gas-interface. The main idea of this method is to advect an indicator function  $\alpha_1$ , corresponding to the volume fraction of the disperse phase in a computational cell, through the fluid domain. The values of the indicator function  $\alpha_1$  are 1 inside of the disperse phase (here liquid),  $0 < \alpha_1 < 1$  in cells containing interface and 0 elsewhere. A transport equation for  $\alpha_1$  can be derived from the continuity equation (1), applied on liquid phase (24):

$$\frac{\partial \alpha_1}{\partial t} + \nabla \cdot (\alpha_1 \mathbf{U}) - \nabla \cdot (\alpha_1 (1 - \alpha_1) \mathbf{U}_r) = - \frac{\alpha_1}{\rho_1} \frac{D\rho_1}{Dt} - \int_{S_1} \frac{\dot{m}_{evap}''}{\rho_1} dS_1 \quad (8)$$

A single field formulation is used for the momentum and temperature equations (2,3), what means that they are solved in the entire computational domain, regardless of the phase. Therefore some mixing rules have to be applied on fluid properties in the transition region  $0 < \alpha_1 < 1$ . These are the mass weighted mean for heat capacity and the volume weighted mean for density, viscosity and thermal conductivity, respectively.

In contrast to the equations above and for the sake of accuracy, the species mass transport equation (4) was being solved for every phase separately. The drawback of this method is the need of iterative coupling of the species transport equations explicitly, increasing computation costs. Since no grid boundary align to the interface in the VOF-notation, surface specific species source terms due to evaporation were modelled through the transformation into volumetric ones. For that, numerical relaxation of species mass fractions inside of the transition region, defined by a delta function  $\delta_{evap}$ , onto the equilibrium concentrations with an artificial relaxation time constant  $\tau_{rel}$  ( $\tau_{rel} \ll \tau_{drop\_lifetime}$ ) was applied:

$$\dot{Y}_k = \delta_{evap} (Y_{k,eq} - Y_k) / \tau_{relax} \quad (9)$$

The entire system of equations was solved in a segregated manner within a SIMPLE iteration loop.

### Simulation setup

Not the entire droplet, but just a spherical symmetrical segment of it and its environment were simulated. The initial droplet diameter was 0.72 mm in each case. The initial distance from the free surface to the inlet/outlet boundary condition representing the far field was 24 mm. Grid resolution within the droplet and in the vicinity of the droplet surface was 1.2 to 1.5  $\mu\text{m}$ . The computational domain with boundary conditions is schematically depicted in Figure 2.

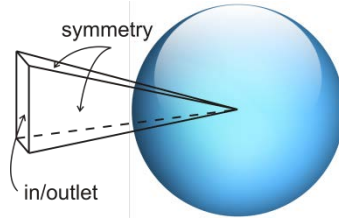


**Figure 2.** Schematically representation of the computational domain

### Results and Discussion

In Figure 3, evolution of the dimensionless droplet diameter is shown for 10 bar and 50 bar respectively, and different initial gas phase temperatures, corresponding to the experiments of *Nomura et al.* (2). Comparison to the experiments shows, that evaporation mass rates are accurately predicted for higher environmental temperatures ( $T_\infty \sim 1.5 T_{c,\text{hept.}}$ ), but are overestimated for “moderate initial gas temperatures ( $T_\infty < T_{c,\text{hept.}}$ ).

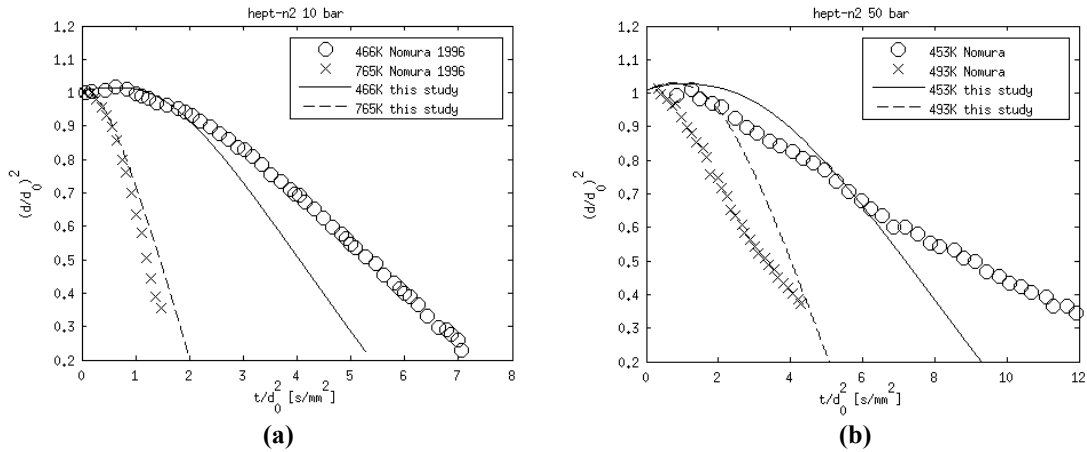


**Figure 3.** Comparison of the experimentally measured droplet diameter evolution (2) to the numerical results at 10 bar (a) and 50 bar (b) environmental pressure.

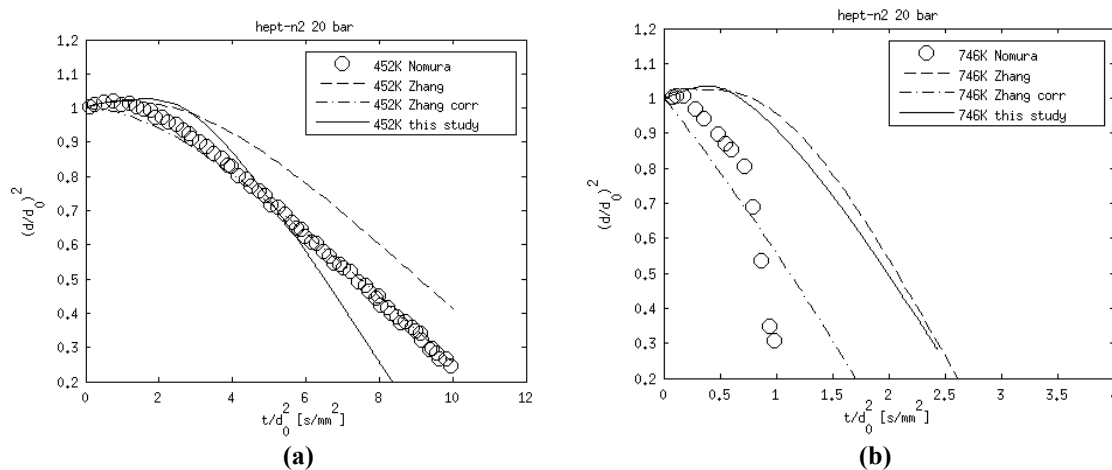


**Figure 4.** Comparison of the experimentally measured droplet diameter evolution (2) to the numerical results of *Zhang* (3) and of the present work at 20 bar and initial gas temperatures of 452 K (a) and 746 K (b).

Figure 4 shows the evolution of the dimensionless droplet diameter at 20 bar environmental pressure and initial gas temperatures of 452 K and 746 K. Numerical results are compared to the experiments of *Nomura et al.* (2) and simulation of *Zhang* (3). Both, numerical results of this study and the results of *Zhang* show much longer

heat-up times (initial period of growing droplet diameter), than observed in the experiments. As a reason for that, *Zhang* assumed that the relative motion of the droplet to the test chamber, while being introduced in the test position, induced circulations inside of the droplet before the begin of the experiment causing a rush heat up of the droplet. Therefore, *Zhang* corrected his model and included initial internal droplet circulation, what significantly improved his results (Figure 4). If this hypothesis is correct, it would also explain the overestimation of the heat-up times in the present study.

One can observe, that during the heat-up time the agreement of the results of this work to the results of *Zhang* is very good. At 20 bar and initial gas temperature of  $T_{\infty} = 746$  K (Figure 4b), also the evaporation rate is comparable to *Zhang's* simulations. At  $T_{\infty} = 452$  K however, the evaporation rate is once again overestimated and thus, the slope of the  $d^2$ -curve becomes steeper. In all probability, this happens because of the overestimation of the droplet surface temperature due to the chosen surface modelling approach without a sharp numerical interface between the gas and the liquid phases. As a result, the heat of evaporation is being distributed over the interface zone, smearing its impact into the temperature field and causing higher temperature in computational cells where the interface temperature was obtained. At higher environmental temperatures, the specific heat of evaporation becomes lower, temperature gradients at the interface become steeper and velocities, caused by evaporation, increase due to higher evaporation rates. As a result, convection and heat conduction processes become dominating the relative impact of the heat of evaporation shrinks.

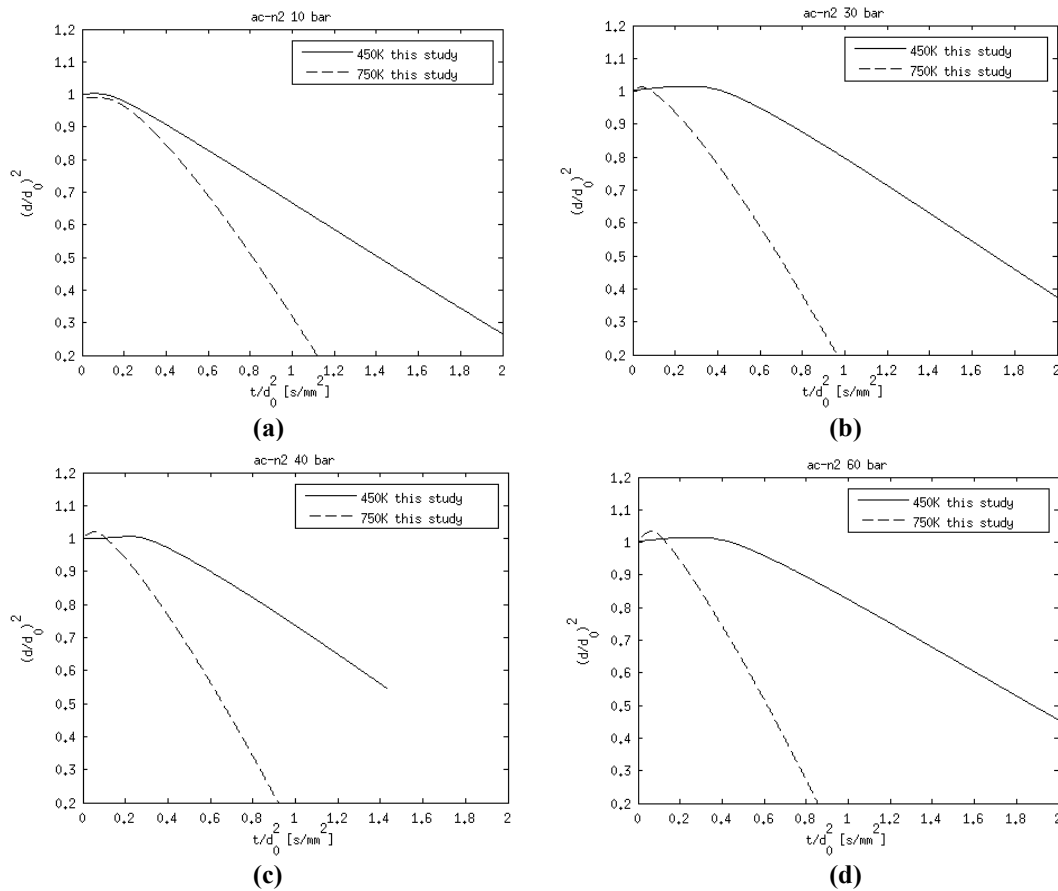


**Figure 5.** Time dependent history of dimensionless droplet diameter of an evaporating acetone droplet in nitrogen environment at environmental pressures of 10 bar (a), 30 bar (b), 40 bar (c) and 50 bar (d), respectively, and initial gas temperatures of 450 K and 750 K.

Numerically obtained dimensionless diameter of an evaporating acetone droplet in nitrogen at different environmental temperatures and pressures are shown in Figure 5. Even if no validation data is available at the moment and the quantitative results might be questionable because of the already mentioned overestimation of the evaporation rates predicted by the numerical model at moderate environmental temperatures, one can clearly see the considerably higher evaporation rates of acetone compared to n-heptane at almost similar conditions. The major reason for this remarkable difference is higher equilibrium concentrations of acetone in the gas phase compared to n-heptane, especially at lower interface temperatures (Figure 1).

## Conclusions

An approach to combine a mathematical model, used by *Zhang* (3) for simulation of transcritical droplet evaporation, with a volume of fluid based method for interface capturing was presented in this paper. Applied to a resting droplet of n-heptane in nitrogen carrier gas, the method shows good accordance to the results obtained by *Zhang* for environment temperatures above the critical temperature of n-heptane. For environment temperatures beneath the critical point of n-heptane, evaporation rates are being overestimated by the proposed method.

Further, this approach was applied on a droplet of acetone, sometimes used as a model fuel for experimental investigations of evaporation and mixture formation processes, evaporating in nitrogen. The study qualitatively shows that at elevated pressures and temperatures the acetone droplet evaporates much faster compared to the n-heptane droplet of the same size and at same conditions. The quantitative correctness of these results, however, is not yet approved.

For the mentioned reasons, further improvements of the numerical method are required to prevent the overestimation of the evaporation rate at environmental temperatures below the critical point of the fuel. Afterwards, the model can be extended to account for the transition over the critical point of the mixture and second order transport effects in the heat and mass transport equations.

## Acknowledgements

This research is conducted at the department of Energy and Power Plant Technology of the Technical University of Darmstadt and is a part of the collaborative research centre SFB Transregio 75. The authors thank DFG for founding and supporting this work.

## Nomenclature

### Roman symbols

$a$	attraction parameter
$b$	van der Waals covolume
$c_p$	specific heat capacity
$D$	Fick's diffusion coefficient
$\mathbf{g}$	gravitational acceleration vector
$h$	specific enthalpy
$\Delta_i h_{ig}^\circ$	enthalpy of formation at standard conditions
$\mathbf{I}$	identity tensor
$J$	diffusive mass flux
$k$	binary interaction parameter
$M$	molar mass
$\dot{m}''$	mass flux through the interface
$p$	pressure
$R$	universal gas constant
$S$	surface
$T$	temperature
$t$	time
$\mathbf{U}$	velocity vector
$V$	molar volume
$X$	mole fraction
$Y$	mass fraction

### Greek symbols

$\alpha$	disperse phase volume fraction
$\delta$	Dirac delta function
$\kappa$	curvature
$\lambda$	thermal heat conductivity
$\mu$	dynamic viscosity
$\mu$	dipole moment
$\rho$	density
$\mathbf{T}$	viscous stress tensor
$\tau$	relaxation time constant
$\sigma$	surface tension coefficient
$\omega$	acentric factor

### Subscripts

$l$	disperse phase
ac	acetone
bp	boiling point
c	critical property
I	interface
eq	phase equilibrium
evap	evaporation
hept	n-heptane
ig	ideal gas
$k, l$	species indices
r	relative
$\infty$	far field

## References

- [1] C. W. Hirt, B. D. Nichols, Volume of fluid (VOF) method for the dynamics of free boundaries. *Journal of Computational Physics* **39**, 201-225 (1981).
- [2] H. Nomura, Y. Ujiie, H. J. Rath, J. Sato, M. Kono, Experimental study on high-pressure droplet evaporation using microgravity conditions. *Twenty-Sixth Symposium (International) on Combustion*, 1267-1273 (1996).
- [3] H. Zhang, Evaporation of a suspended droplet in forced convective high-pressure environments. *Combustion Science and Technology* **175**, 2237-2268 (2003).
- [4] K. G. Harstad, J. Bellan, An all-pressure fluid drop model applied to a binary mixture: heptane in nitrogen. *International Journal of Multiphase Flow* **26**, 1675-1706 (2000).
- [5] K. G. Harstad, J. Bellan, Evaluation of commonly used assumptions for isolated and cluster drops in nitrogen at all pressures. *Combustion and Flame* **127**, 1861-1879 (2001).
- [6] R. L. Matlosz, S. Leipziger, T. P. Torda, Investigation of liquid droplet evaporation in a high temperature and high pressure environment. *International Journal of Heat and Mass Transfer* **15**, 831-852 (1972).
- [7] H. Ghassemi, S. W. Baek, Q. S. Khan, Experimental study on binary droplet evaporation at elevated pressures and temperatures. *Combustion Science and Technology* **178**, 1031-1053 (2006).
- [8] G.-S. Zhu, S. K. Aggarwal, Transient supercritical droplet evaporation with emphasis on the effects of equation of state. *International Journal of Heat and Mass Transfer* **43**, 1157-1171 (2000).
- [9] H. Zhang, Numerical research on a vaporizing fuel droplet in a forced convective environment *International Journal of Multiphase Flow* **30**, 181-198 (2004).
- [10] P. He, Y. Li, L. Zhao, Evaporation of liquid fuel droplet at supercritical conditions. *Science China Technological Sciences* **54**, 369-374 (2011).
- [11] G. Strotos, M. Gavaises, A. Theodorakakos, G. Bergeles, Numerical investigation of the evaporation of two-component droplets. *Fuel* **90**, 1492-1507 (2011).
- [12] B. Balaji, V. Raghavan, K. Ramamurthi, G. Gogos, A numerical study of evaporation characteristics of spherical n-dodecane droplets in high pressure nitrogen environment. *Physics of Fluids* **23**, 14 (2011).
- [13] G. Gogos, S. Soh, D. N. Pope, Effects of gravity and ambient pressure on liquid fuel droplet evaporation. *International Journal of Heat and Mass Transfer* **46**, 283-296 (2003).
- [14] F. Weckenmann, B. Bork, E. Oldenhof, G. Lamanna, B. Weigand, B. Böhm, A. Dreizler, Single acetone droplets at supercritical pressure: droplet generation and characterization of PLIFP. *Zeitschrift für Physikalische Chemie* **225**, 11-12 (2011).
- [15] D.-Y. Peng, D. B. Robinson, A new two-constant equation of state. *Industrial & Engineering Chemistry Fundamentals* **15**, 59-64 (1976).
- [16] H. Knapp, R. Döring, L. Oellrich, U. Plöcker, J. M. Prausnitz, *Vapor-Liquid Equilibria for Mixtures of Low-Boiling Substances*. Dechema Chemistry Data Series (Dechema, 1982).
- [17] T. Windmann, A. Köster, J. Vrabec, Vapor-liquid equilibrium measurements of the binary mixtures nitrogen + acetone and oxygen + acetone. *Journal of Chemical & Engineering Data* **57**, 1672-1677 (2012).
- [18] B. E. Poling, J. M. Prausnitz, J. P. O'Connell, *The Properties of Gases and Liquids*. (The McGraw-Hill, ed. 5th, 2001).
- [19] B. E. Poling, G. H. Thomson, D. G. Friend, R. L. Rowley, W. V. Wilding, *Perry's Chemical Engineers' Handbook*. (The McGraw-Hill, ed. 8th, 2008).
- [20] T.-H. Chung, L. L. Lee, K. E. Starling, Applications of kinetic gas theories and multiparameter correlations for prediction of dilute gas viscosity and thermal conductivity. *Industrial & Engineering Chemistry Fundamentals* **23**, 8-13 (1984).
- [21] T.-H. Chung, M. Ajlan, L. L. Lee, K. E. Starling, Generalized multiparameter correlation for nonpolar and polar fluid transport properties. *Industrial & Engineering Chemistry Research* **27**, 671-679 (1988).
- [22] C. E. Wilke, P. Chang, Correlation of diffusion coefficients in dilute solutions. *AIChE Journal* **1**, 264-270 (1955).
- [23] M. R. Riazi, C. H. Whitson, Estimating diffusion coefficients of dense fluids. *Industrial and Engineering Chemistry Research* **12**, 3081-3088 (1993).
- [24] I. Shevchuk, P. Rauschenberger, J. Janicka, A VOF method for isobaric expandable flows. *Proceedings in Applied Mathematics and Mechanics* **12**, 531-532 (2012).

## Coupled modelling impact of liquid interface and dispersed sprays

N. Hecht, Z. Bouali T. Menard, J. Reveillon and F.X. Demoulin

UMR6614-CORIA, Technopôle du Madrillet, BP 12, Avenue de l'Université, 76801  
Saint-Etienne-du-Rouvray Cedex, France

### Abstract

Injection and atomization of liquid is widely used in many industrial and domestic applications such as, fuel injection in engines or burners, spray painting, medical sprays, spray drying, etc.

Various approaches are used to simulate two-phase flows. Usually, interface tracking (Eulerian approach) is used to simulate the primary atomization (Ménard et al., 2007) while the Lagrangian particle-tracking approach may be used to model the dispersed spray (Reveillon and Demoulin, 2007). However these approaches have never been considered simultaneously, until very recently.

Indeed, to improve simultaneously the accuracy and the numerical costs of the physical outcomes of the simulations, it is necessary to develop coupling procedures between these two approaches (Herrmann, 2010) in order to simulate large scale liquid structures with a CLSVOF method and small scale liquid structures by a Lagrangian particles approach. This procedure allows to follow the evolution of the smallest droplets generated during primary atomization by transforming the 'Eulerian interfacial droplets' into 'Lagrangian droplets' while preserving their position, mass and momentum.

The objective of our work is to study the effects of the numerical switch between the Eulerian and the Lagrangian framework: numerical dispersion, physical and numerical limits of the procedure, numerical cost, etc. Two DNS solvers Archer (LS/VOF) and Asphodel (Lagrangian) are coupled together to simulate the dispersion of droplets in a forced homogeneous turbulence. Triple comparisons (Interfacial / Lagrangian / Interfacial + Lagrangian) will be carried out for several prescribed physical parameters (liquid mass fraction, turbulence intensity, etc) .

---

### Introduction

In order to decrease the fuel consumption and clean emission of automobiles, it is essential to optimize the engine combustion. The performances of diesel engine are largely link to atomization process. A lot of study have been realised to describe the injection process and its influence.

However, experimental atomization process studies are really difficult to capture size drop distribution and the atomization process in the dense zone of the spray. Consequently some numerical approaches have been developed, these approaches used a two-phase flows model to describe the interface gas/liquid like Volume of fluid method (Hirt and al. 1981) , Level Set method (Sussman et al. 1994) and Front-tracking method (Unverdi et al. 1992) . All of these methods are used for Direct numerical simulation ( DNS ), and give good results to describe the primary atomization of liquid jets (Ménard et al. 2007, Desjardins et al. 2008, Shinjo et al. 2010).

However all of these methods have the default to lose mass when the size of structure becomes smaller than the size of the cell mesh. For overcome this default we can use adaptive mesh refinement (Agbaglah and al. 2011, Fuster et al. 2009) but the problem remain same. Another solution is to couple Eulerian approach with a Lagrangian particle-tracking approach (Herrman 2008, 2011). The process of coupling is to transform the Eulerian droplets into Lagrangian droplets when the size of the first is too small. The disadvantage of this method is some conservative quantities can be changed like the turbulent kinetic energy or the momentum or mass.

The aim of this paper is to study the influence of the coupling on the conservative quantities. We will transform a Eulerian droplet into a Lagrangian droplet in a DNS of Homogeneous Isotropic Turbulence (HIT) (Luret and al. 2008,2010 ; Duret and al. 2012). The Eulerian part will be resolved in DNS, the interface tracking method that has been used is a coupled Level Set/VOF method with the ARCHER code ( Ménard et al. 2007)

## Numerical methods

### Navier-Stokes and scalar equations

The joint Level Set/VOF method is coupled with a projection method to carry out the direct numerical simulation of incompressible Navier-Stokes equations :

$$\frac{\partial \mathbf{V}}{\partial t} + (\mathbf{V} \cdot \nabla) \mathbf{V} = -\frac{\nabla p}{\rho} + \frac{1}{\rho} \nabla \cdot (2\mu \mathbf{D}) + \mathbf{g} + \mathbf{f} + \dot{\mathbf{v}} \quad (1)$$

Where  $p$  is the fluid pressure,  $\mathbf{V}$  the velocity vector,  $\mathbf{g}$  the gravity vector,  $\mu$  the dynamic viscosity,  $\mathbf{D}$  the viscous deformation tensor, and  $\dot{\mathbf{v}}$  result from a two-way coupling. At the interface, the surface tension force can be considered based on the Dirac function  $\delta(G)$ :  $\sigma$  is the surface tension,  $\mathbf{n}$  the normal unit vector,  $k$  is the curvature computed from the Level Set function  $G$  (definition of  $k$ ,  $\mathbf{n}$  and  $G$  are given later). To maintain the turbulent kinetic energy at a prescribed level, it is necessary to use a forcing method. This is achieved through the source term  $\mathbf{f}$ , which induces a linear forcing (Rosales & Meneveau 2005). It gives  $\mathbf{f} = A\mathbf{v}'$  where  $A$  is the forcing coefficient,  $\mathbf{v}'$  represent velocity fluctuations. The constant  $A$  is computed at each time step to sustain a prescribe level of velocity fluctuations over the whole domain. This method maintains a statistically stationary homogeneous isotropic turbulence. More details about the forcing method are explained in Duret and al. (2012).

To correctly describe the interface, the VOF method is used jointly with the Level Set to enforce mass conservation (Ménard et al. 2007). For the sake of clarity, the average value of the VOF method scalar in the complete domain is called the liquid volume fraction  $\phi$ , and the local liquid volume fraction within a cell is  $\phi_i$ . They are defined as follows :  $\phi = V_l/V_t$ , where  $V_l$  is the total volume of liquid and  $V_t$  the total volume of the domain.  $\phi_i = V_{lc}/V_c$ , where  $V_c$  is the cell volume and  $V_{lc}$  is the volume of liquid within a cell.  $\phi_i$  respects the following transport equation:

$$\frac{\partial \phi}{\partial t} + \mathbf{V} \cdot \nabla \phi = 0 \quad (2)$$

### Interface tracking method

In the following, the interface tracking method and the treatment of discontinuities are recalled. More details can be found in the work of Ménard et al. (2007). Level Set methods use a continuous function to describe the interface, this function is defined as the signed distance between any points of the domain and the interface. The 0 level curve of that function therefore provides the interface location. The convection equation to describe the motion of the interface in a given velocity field  $\mathbf{V}$  reads:

$$\frac{\partial G}{\partial t} + \mathbf{V} \cdot \nabla G = 0 \quad (3)$$

Eq. (3) is hyperbolic type, and the discretization method must combine a high convergence order and robustness. Thus, for the distance function field, a 5th-order WENO scheme Shu (1997) is used for convective terms. The normal unit vector  $\mathbf{n}$  and the curvature of the interface  $k(G)$  are evaluated thanks to the Level Set function by :

$$\mathbf{n} = \frac{\nabla G}{|\nabla G|} \quad k(G) = \nabla \cdot \mathbf{n} \quad (4)$$

The Level Set method  $G$  no longer remains a distance function when solving Eq. (3) because of the velocity gradients. A redistancing algorithm Sussman et al. (1998) is thus applied to keep  $G$  as the signed distance to the interface. Specific studies have been developed to evaluate some of these methods Menard et al. (2007). It has been found that the Coupled Level Set and Volume-of-Fluid method (CLSVOF, see Sussman & Puckett (2000)) is well adapted to capture atomization processes (See Menard et al. (2007) for details). The main concept of this method is to benefit from the advantage of both level set and VOF strategies: mass loss is limited through the VOF method and a fine description of interface properties is kept with the Level Set.



Fluid dynamics equations are solved in the context of a low mach number approach, thanks to a projection method for the direct numerical simulation of incompressible Navier-Stokes equations. The density and the viscosity depend on the sign of the Level Set function according to each phase (liquid and gas). To finalize the description of the two-phase flow, jump conditions across the interface are taken into account with the Ghost Fluid (GF) method (Liu et al. 2000, Tanguy et Berlemont 2005).

### Dispersed phase Lagrangian description

As described by Reeks, it is possible to take into account many forces to characterize the droplet dynamics. However, the purpose of this text is to present a basis to carry out DNS-DPS of two-phase flows. Thus, because of the high density ratio between liquid and gas phases, the drag force, which is prevalent, has only been selected. Additionally, several usual assumptions have been used: some of them are given in the following, others may be found in the review paper of Sirignano (1983). First, the liquid is supposed dispersed and each droplet is unaware of the existence of the others. Any internal liquid circulation or droplet rotation is neglected and an infinite liquid heat conduction coefficient is assumed. As a consequence, liquid core temperature remains uniform but evolves as a function of time. The spray is supposed to be local sources of mass following the saturation law and modifying momentum and gaseous fuel topology, depending on the local gas temperature, pressure and vapor mass fraction.

By denoting  $\mathbf{V}_k$  and  $\mathbf{X}_k$  the velocity and position vectors of droplet  $k$ , respectively, the following relations:

$$\frac{d\mathbf{V}_k}{dt} = \frac{1}{\beta_k^{(V)}} (\mathbf{U}(\mathbf{X}_k, t) - \mathbf{V}_k) \quad (5)$$

$$\frac{d\mathbf{X}_k}{dt} = \mathbf{V}_k \quad (6)$$

are used to track any  $k$  droplet evolution throughout the computational domain. The vector  $\mathbf{U}(\mathbf{X}_k, t)$  represents the gas velocity at the droplet position  $\mathbf{X}_k$ . The right hand side term of equation (5) stands for a drag force applied to the droplet and  $\beta_k^{(V)}$  is a kinetic relaxation time. It may be obtained from the  $k^{th}$  droplet dynamics:

$$m_k \frac{d\mathbf{V}_k}{dt} = \mathbf{D}_k \quad (7)$$

Where  $\mathbf{D}_k$  is the drag force applied to the  $k^{th}$  droplet considered as a sphere. It directly leads to the kinetic relaxation time for the  $k^{th}$  droplet:

$$\mathbf{D}_k = 3\pi a_k \mu C u_d [\mathbf{U}(\mathbf{X}_k, t) - \mathbf{V}_k] \quad (8)$$

Where  $a_k$  is the droplet diameter,  $\rho_k$  is the liquid density and  $\mu$  is the gas viscosity.  $C u_d = 1 + \text{Re}_d^{2/3} / 6$  is a corrective coefficient to account for the variation of the drag factor according to the droplet Reynolds number .

$$\text{Re}_k = \rho |\mathbf{u}(\mathbf{X}_k - \mathbf{v}_k)| a_k / \mu \quad (9)$$

### Eulerian/Lagrangian coupling

In this section, the Eulerian/Lagrangian coupling procedure for the case of a liquid/gas flow whose phase interface is tracked by a CLSVOF approach is described. Regions of the computational domain where the level set scalar  $G$  is  $G > 0$  are denoted as liquid, whereas regions with  $G < 0$  are denoted as gas. The purpose of the coupling procedure is to identify separated regions  $\Omega_k$  of liquid in gas (or gas in liquid) fulfilling certain criteria, to remove these from the level set tracking representation, and to insert them into a Lagrangian framework, preserving their volume  $V_k$ , center of mass  $\mathbf{X}_k$ , and momentum  $\rho_k \mathbf{U}_k$  :

$$\mathbf{V}_l = \int_{\Omega_k} d\mathbf{x} \quad \mathbf{x}_k = \frac{1}{V_l} \int_{\Omega_k} \mathbf{x} d\mathbf{x} \quad \mathbf{V}_k = \frac{1}{V_l} \int_{\Omega_k} \mathbf{V}(\mathbf{x}) d\mathbf{x} \quad (10)$$

Where  $\rho_k$  is the constant liquid density. Removal criteria considered in this paper are based on the derivation assumptions of typical Lagrangian spray models, i.e that the individual droplets be small and nearly spherical. The size criterion is expressed in terms of a reference volume  $V_{ref}$ , if a liquid structure have a volume  $V_l < V_{ref}$ , it will be candidate for being transform. An other criterion will be expressed in terms of an eccentricity measurement of  $e_{ref}$ , its represents the shape of the liquid structure.

$$\mathbf{e}_k = \frac{R_k}{\max(G_k)} \quad R_k = \sqrt[3]{\frac{3V_l}{4\pi}} \quad (11)$$

Where  $R_k$  is the droplet rayon and  $\max(G_k)$  is the maximum Level Set in the drop. In a perfect drop the eccentricity  $e_k$  will be 1 and the more the drop will be deformed the more the eccentricity  $e_k$  will be high

The algorithm of detection and reconstruction of droplet use a technique to spread the information to the neighbour. To remove a liquid structure into the Eulerian representation the fraction of volume need to be reset and the Level Set function of the structure need to be inversed.

The term  $\dot{\mathbf{v}}$  in the first equation respresent source terms for the gaseous phase momentum due to transfers from liquid phase, *i.e.* exchanges from the Lagrangian quantities to the Eulerian grid. Every Lagrangian source has to be distributed over the Eulerian nodes by adding the volumic contributions from droplets. The expressions of the momentum source term explain in Reveillon (2010) and is:

$$\dot{\mathbf{v}}^{(n)} = -\frac{1}{V} \sum_k \alpha_k^{(n)} \frac{dm_k \mathbf{V}_k}{dt} \quad (12)$$

Where  $V$  is the cell volume,  $m_k$  is the mass of droplet  $k$  and  $\alpha_k^{(n)}$  is the distribution coefficient of the  $k$  droplet source term on the node  $n$ .

## Results and Discussion

### Numerical configuration

Similar to the study of Luret at al. (2008,2010) and Duret et al. (2012), a three dimensional cubical domain with a full periodic boundaries were used in the simulation. The side of the domain is 0.15 mm long. They are discretized by a uniform grid 64x64x64 ( $dx = 2.38 \mu m$ ).

This configuration extends previous numerical studies on mixing in single-phase flows to two-phase flows with a fully resolved liquid-gas formulation. To accurately control the various inputs of the simulation, a three dimensional forced homogeneous turbulence of a gas/ liquid flow is considered with a liquid volume fraction of 5% and an average kinetic energy  $k_c = 3.6 m^2.s^{-2}$ . The density of liquid and gas are 753.6 and 25  $kg.m^{-3}$ , respectively. A surface tension is 0.0135  $N.m^{-1}$  and a dynamic viscosity of liquid and gas are  $5.65.10^{-4}$  and  $1.879.10^{-5}$  Pa.s, respectively.

The liquid gas interface at time  $t = 87 \mu s$  is represented in Figure 1 to illustrate the numerical configuration for a liquid volume fraction of 5 %.

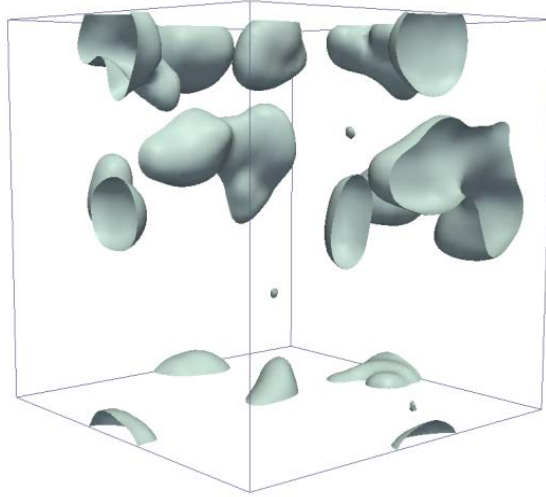


**Figure 1:** Visualisation of interface between liquid and gas. A total volume fraction of liquid is 5%.

### Removal Criteria

The removal criteria have a primary role in our simulations. For example in the case presented in figure 1, we can remove a certain amount of liquid structure.

If removal criteria have been fixed to  $R_k < 2 \cdot dx$  and  $e_k < 2$  nothing will be transformed. Contrary to the reference case, if the reference volume is increased i.e  $R_k < 2.5 \cdot dx$  only one structure will be concerned. This structure will be transformed into a Lagrangian particle and can be seen ( in red ) on Figure 2

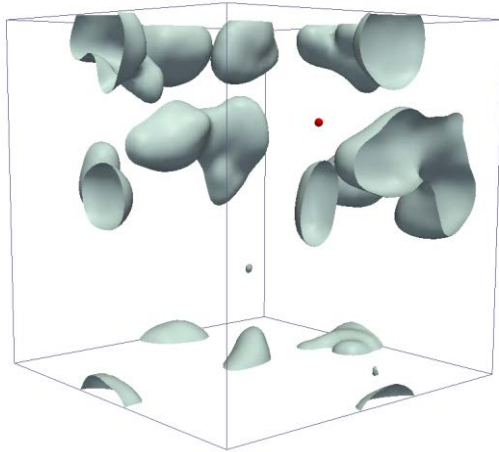


**Figure 2:**Interface visualisation with a transformed droplets. Lagrangian droplets are colored red.

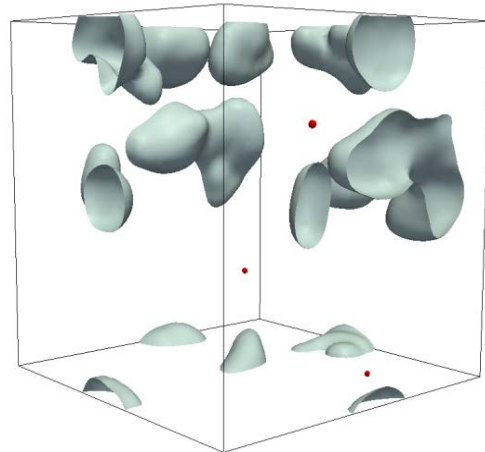


**Figure 3 :** Interface visualisation with three transformed droplets. Lagrangian droplets are colored red

To illustrate another possibility, the reference eccentricity can be increased i.e  $e_k < 2.5$ . Consequently, three structures will be transformed. The result is shown (particle are in red) on Figure 3.

We can note that the two last droplets transformation have a smaller volume than the first droplet transform. Consequently we can think that small droplet can have an eccentricity higher than big droplet. Therefore, the choice of the criteria will be a critical for future simulations.

## Physical quantity

In this section, the influence of droplet transformation for physical quantities will be observed. Evolution of mass, momentum and kinetic energy will be studied before and after droplet transformations. And this only locally, i.e. in cells which contain the liquid transformed structure into a Lagrangian droplet.

In the following, for sake of clarity, figures have been normalized by a reference value of the considered variable.

Figure 4 and 5 represent scatter plots of two physical quantities: mass, momentum for liquid and gas phases, respectively, before and after the transformation of droplets (eulerian to lagrangian description). A ideal transformation implies conservation of these physical quantities.

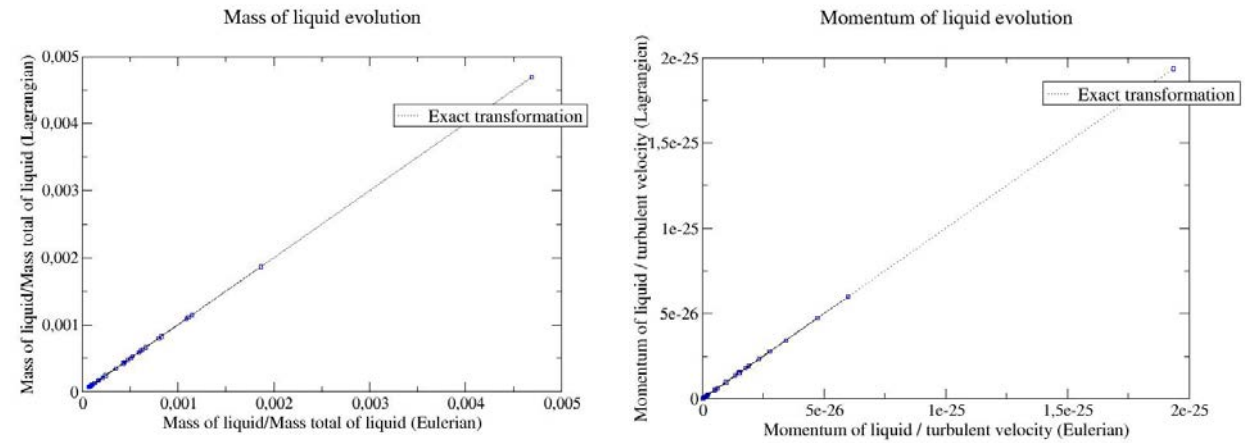


**Figure 4 :** Scatter plots of the evolution of mass (left), momentum (right) of liquid.

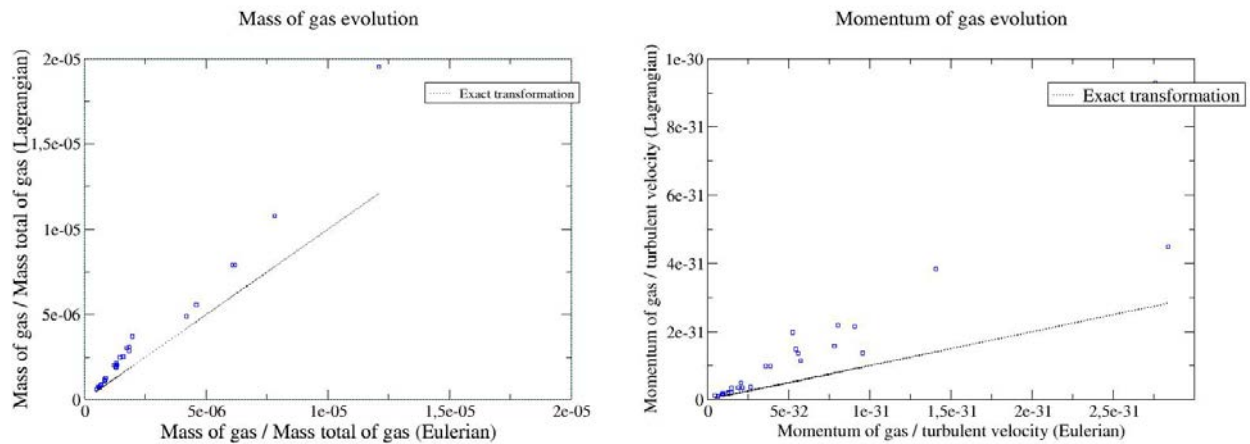


**Figure 5 :** Scatter plots of the evolution of mass (left), momentum (right) of gas.

The figure 4 shows that mass and momentum of liquid are conserved, unlike to the physical quantities of gas plotted in figure 5. The non-conservation of gas quantities is caused by removing eulerian droplet described by some nodes and replacing it with one point (lagrangian description) containing information about position, velocity and diameter of droplet. Then, the area initially occupied by the eulerian droplet conserve the local velocity but its local density becomes the gas density. This is same as adding a quantity of gas with velocity of the removed liquid.

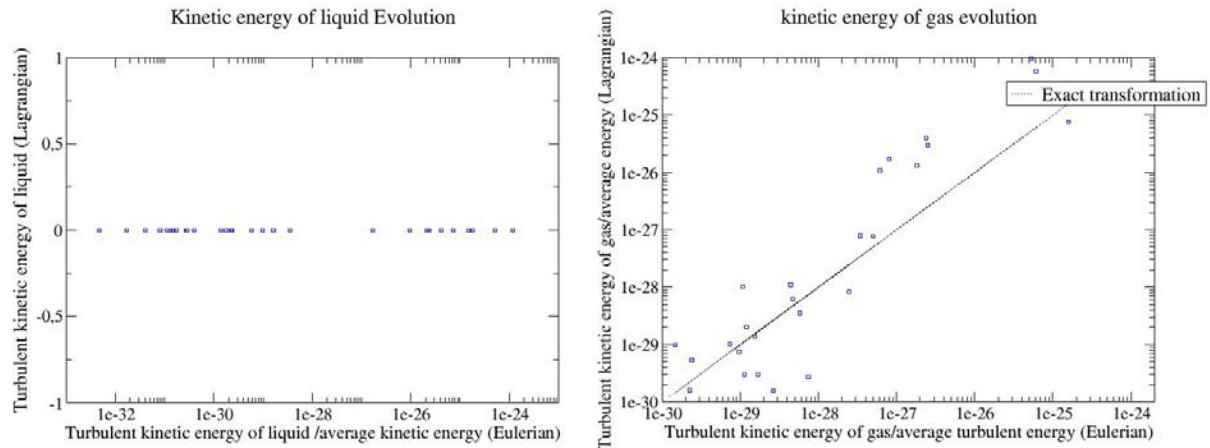


**Figure 6 :** Scatter plots of the evolution of turbulent kinetic energy of liquid (left) and gas (right)

The figure 6 shows that turbulent kinetic energy of liquid and gas are not conserved. In the liquid the turbulent kinetic energy of a drop in lagrangian is nil. And in the gas the turbulent kinetic energy vary because the quantity of gas increase and his average velocity is modified.

**Conclusions** This paper presents a first step to develop a coupling between a eulerian and lagrangian approach in order to be able to carry out a DNS of two-phase flow without mass loss. This step has underlined particular difficulties to conserve physical quantities of gas phase caused by suppression of eulerian droplet and replacement by lagrangian droplet.

The next step will be dedicated to resolve the issue concerning the non-conservative gas quantities and to study the impact of transformation on the path droplet.

## References

- [1] Hirt C. W. and Nichols B. D., "Volume of fluid (vof) method for the dynamics of free boundaries," *Journal of Computational Physics*, vol. 39, no. 1, pp. 201 – 225, 1981.
- [2] Sussman M., Smereka P., and Osher S., "A level set approach for computing solutions to incompressible two-phase flow," *Journal of Computational Physics*, vol. 114, no. 1, pp. 146 – 159, 1994.
- [3] Unverdi S. O. and Tryggvason G., "Computations of multi-fluid flows," *Physica D: Nonlinear Phenomena*, vol. 60, no. 1-4, pp. 70 – 83, 1992.
- [4] Menard T., Tanguy S., and Berlemont A., "Coupling level set/vof/ghost fluid methods: Validation and application to 3d simulation of the primary break-up of a liquid jet," *International Journal of Multiphase Flow*, vol. 33, no. 5, pp. 510 – 524, 2007.
- [5] Desjardins O., Moureau V., and Pitsch H., "An accurate conservative level set/ghost fluid method for simulating turbulent atomization," *Journal of Computational Physics*, vol. 227, no. 18, pp. 8395 – 8416, 2008.
- [6] Shinjo J. and Umemura A., "Simulation of liquid jet primary breakup: Dynamics of ligament and droplet formation," *International Journal of Multiphase Flow*, vol. 36, no. 7, pp. 513 – 532, 2010.
- [7] Agbaglah, G., Delaux, S., Fuster, D., Hoepffner, J., Josserand, C., Popinet, S., Ray, P., Scardovelli, R., and Zaleski, S. (2011) *Comptes Rendus Mecanique* 339(2-3), 194 – 207 *High Performance Computing*.
- [8] Fuster, D., Bague, A., Boeck, T., Moyne, L. L., Leboissetier, A., Popinet, S., Ray, P., Scardovelli, R., and Zaleski, S. (2009) *International Journal of Multiphase Flow* 35(6), 550 – 565.
- [9] Herrmann M. ,A Parallel Eulerian Interface Tracking/Lagrangian Point Particle Multi-Scale Coupling Procedure. *J. Comput. Phys.*, 229, pp. 745-759, 2010
- [10] Herrmann M. ,A balanced force Refined Level Set Grid method for two-phase flows on unstructured flow solver grids . *J. Comput. Phys.*, 227:2674–2706, 2008.
- [11] Luret, G., Blokkeel, G., Lebas, R., Menard, T., Berlemont, A., and Demoulin, F. (2008) In 22nd

European Conference on Liquid Atomization and Spray Systems Como Lake, Italy.

- [12] Luret, G., Menard, T., Blokkeel, G., Berlemont, A., Reveillon, J., and Demoulin, F. (2010) *Journal of Atomization and Spray* 20(3), 93
- [13] Duret, B., Luret, G., Reveillon, J., Menard, T., Berlemont, A., and Demoulin, F.-X. (2012) *International Journal of Multiphase Flow* 40(0), 93 – 105.
- [14] Sirignano W.A. ,Fuel droplet vaporization and spray combustion theory. *Prog. Energy Combust. Sci.*, 8:291–322, 1983.

## Numerical simulation of primary atomization of a sheared liquid sheet. Part 1: model and numerical method description

Ghislain Blanchard, Philippe Villedieu and Davide Zuzio

ONERA (The French Aerospace Lab), France

### Abstract

A compressible two-fluid model has been developed to simulate the primary atomization of a sheared liquid sheet. The numerical approach is based on a partially implicit low-Mach scheme with a compressive MUSCL scheme for unstructured meshes. Details on the physical model and the numerical method are given in this paper. Numerical simulations of academic test cases are presented to show the ability of the present methodology to provide accurate results for interfacial flow problems involving capillary effects. Numerical simulations of primary atomization of a sheared liquid sheet are presented in a second paper [3] and compared with experimental results

### Introduction

In aircraft combustion chambers, the injection of fuel is commonly achieved by air-blast atomizers which create a spray by pulverising a liquid sheet of fuel thanks to strong co-flowing airflows. The simulation of this process is challenging since it involves multi-scale phenomena from the primary atomization of the liquid jet to the formation of small droplets.

In the last decade, several studies have been devoted to the development of numerical simulation methods for dealing with this problem. They are generally based on sharp interface methodologies and aim to describe the whole atomization process from the larger scales to the smaller ones ([7],[8] and [15]). In this work, our objective is not to use such a DNS approach but rather to capture the larger scale phenomena of the liquid sheet fragmentation mechanism. In the future, this macro-scale atomization model will be coupled to both a droplet formation model and a dispersed phase model for computing the spray evolution.

For the sake of clarity, the presentation of our work has been divided into two parts:

- The first part, which is the object of the present paper, is devoted to the description of the two-fluid model and the numerical methods; academic test case results are also shown to assess that this methodology (which is not a sharp interface method but rather an interface capturing one) is able to provide accurate results for free moving interface problems involving capillary effects.
- The second part, which is the object of a second paper [3], is devoted to the validation of this methodology for computing the primary atomization of a sheared liquid sheet; comparisons between numerical and experimental results are presented and analysed.

### Physical model description

The present model is a compressible two fluid model in which both non miscible fluids are assumed to be simultaneously present at any point in space. The two fluids are supposed to be at local mechanical equilibrium: both fluids have locally the same velocity ( $\mathbf{v}=\mathbf{v}_1=\mathbf{v}_2$ ) and the same pressure ( $p=p_1=p_2$ ). The mass and momentum balance equations of the model lead to the system (253):

$$\begin{cases} \frac{\partial \tilde{\rho}}{\partial t} + \text{div}(\tilde{\rho} \otimes \mathbf{v}) = 0 \\ \frac{\partial \rho \mathbf{v}}{\partial t} + \text{div}(\rho \mathbf{v} \otimes \mathbf{v} + p \mathbf{I}) = \text{div}(\boldsymbol{\tau}_c + \boldsymbol{\tau}_v) + \rho \mathbf{g} \end{cases} \quad (1)$$

where  $\tilde{\rho} = [\tilde{\rho}_1, \tilde{\rho}_2] = [\alpha_1 \rho_1, \alpha_2 \rho_2]$  are the fluid bulk densities,  $\alpha_i$  is the volume fraction of the fluid  $i$ ,  $\rho = \tilde{\rho}_1 + \tilde{\rho}_2$  is the fluid mixture bulk density,  $p$  is the fluid mixture pressure,  $\boldsymbol{\tau}_c$  is the capillary stress tensor,  $\boldsymbol{\tau}_v$  is the viscous stress tensor and  $\mathbf{g}$  is the external body force volume density.

In system (253), it is worth noting that both fluids play a symmetric role and that the volume fraction of one of the two-phase, e.g.  $\alpha_1$ , is not a primary unknown (as it is usually the case) but rather an outcome of the model given by the closure relationship (2)

$$\begin{cases} \alpha_1 + \alpha_2 = 1 \\ p = p_1(\tilde{\rho}_1 / \alpha_1) = p_2(\tilde{\rho}_2 / \alpha_2) \end{cases} \quad (2)$$

System (2) is the consequence of the assumption of local mechanical equilibrium between the two non miscible fluids located at the same point (i.e. it applies to each cell in a finite volume framework). In (2), the fluid equations of state are supposed to only depend on the density ( $p_i = p(\rho_i)$ ). This assumption could be released



but here it is not restrictive since, in the intended applications, the Mach number is small enough to assume that dynamical and thermal effects are almost uncoupled. We also refer to [4], [10] and [12].

The fluid mixture is supposed to behave as a Newtonian fluid for which the general form of the viscous stress tensor reads:

$$\boldsymbol{\tau}_v = -\frac{2}{3}\mu \cdot \text{div}(\mathbf{v})\mathbf{I} + \mu(\nabla\mathbf{v} + {}^t\nabla\mathbf{v}) \quad (3)$$

where  $\mu = \alpha_1 \mu_1 + \alpha_2 \mu_2$  is the dynamic viscosity of the two fluids mixture. For low-Mach flows, the first term in the expression (3) of  $\boldsymbol{\tau}_v$  is neglected:

$$\boldsymbol{\tau}_v = \mu(\nabla\mathbf{v} + {}^t\nabla\mathbf{v}) \quad (4)$$

The capillary stress tensor is modelled according to the Continuum Surface Stress (CSS) formulation 0 which is well suited to diffuse interface method and which is conservative by construction.

$$\boldsymbol{\tau}_c = \sigma \left[ \mathbf{I} - \frac{\nabla\alpha_1 \otimes \nabla\alpha_1}{\|\nabla\alpha_1\|^2} \right] \|\nabla\alpha_1\| \quad (5)$$

### Numerical method description

For the intended applications, it is mandatory to minimize artificial viscosity effects while keeping a high robustness to deal with high density ratio in the vicinity of the interface. To reach these objectives two main features have been introduced in the present finite volume scheme:

- The expression of the numerical flux has been adapted to deal with low Mach number flows and to avoid the consequent excessive dissipation inherent to classical upwind schemes [5].
- A MUSCL approach has been used to achieve robust second order space accuracy and a special attention has been paid to the multidimensional slope limitation procedure in order to sharpen the interface

The numerical scheme is based on a partially implicit finite volume scheme on unstructured 3D meshes. An implicit time discretization of the mass conservation equations avoids the acoustic CFL limitation of the time step [5]. The scheme reads for a given cell K:

$$\begin{cases} \tilde{\rho}_K^{n+1} = \tilde{\rho}_K^n - \frac{\Delta t}{|K|} \sum_{e \in \partial K} \left[ \mathbf{G}_{K,Ke}^{\tilde{\rho}} |e| \right] \\ \rho_K^{n+1} \mathbf{v}_K^{n+1} = \rho_K^n \mathbf{v}_K^n - \frac{\Delta t}{|K|} \sum_{e \in \partial K} \left[ \mathbf{G}_{K,Ke}^{\rho v} |e| \right] + \frac{\Delta t}{|K|} \mathbf{S}^g(\tilde{\rho}_K^{n+1}) \end{cases} \quad (6)$$

where  $\mathbf{G}_{K,Ke}^{\tilde{\rho}}$  and  $\mathbf{G}_{K,Ke}^{\rho v}$  are numerical fluxes through a face  $e$  shared by the cell  $K$  and  $Ke$  (notations are illustrated in **Figure 1**).  $\mathbf{S}^g$  is the gravity source term. The superscript  $n$  refers to the time discretization. By convention,  $(\cdot)_K$  refers to the cell-averaged value of the discrete solution in the cell  $K$ ,  $(\cdot)_{e,K}$  refers to the extrapolated face-averaged value of  $(\cdot)_K$  to the centre of the face  $e$ . The extrapolation procedure, which leads to a second order space accurate scheme, will be addressed hereafter.

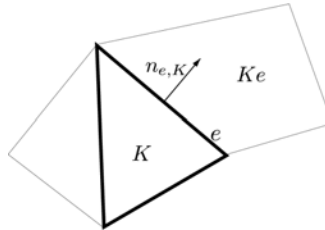


**Figure 1.** Notations for cell K

### Expression of the fluxes

In order to give expressions of the fluxes in (6), we define:

$$p_e^{n+1} = \frac{1}{2} (p_{e,K}^{n+1} + p_{e,Ke}^{n+1}) \quad \mathbf{v}_e^n = \frac{1}{2} (\mathbf{v}_{e,K}^n + \mathbf{v}_{e,Ke}^n) \quad (7),(8)$$

Then, the mass flux is:

$$\mathbf{G}^{\tilde{\rho}} = V_{e,K}^+ \tilde{\rho}_{e,K}^{n+1} + V_{e,K}^- \tilde{\rho}_{e,Ke}^{n+1} \quad (9)$$

Where:

$$V_{e,K}^- = \min(\mathbf{V}_e^n \cdot \mathbf{n}_{e,K}, 0) - \gamma_e \max(p_{Ke}^{n+1} - p_K^{n+1}, 0) \quad (10)$$

$$V_{e,K}^+ = \max(\mathbf{V}_e^n \cdot \mathbf{n}_{e,K}, 0) - \gamma_e \min(p_{Ke}^{n+1} - p_K^{n+1}, 0) \quad (11)$$

In (10) and (11), the positive coefficient  $\gamma_e$ , which is calculated from (12), ensures the stability of the low-Mach numerical scheme under a CFL-like condition [5].

$$\gamma_e = \Delta t \times \max \left( \frac{|\partial K|}{2\rho_K^{n+1}|K|}, \frac{|\partial Ke|}{2\rho_{Ke}^{n+1}|Ke|} \right) \quad (12)$$

The expression of the numerical flux  $\mathbf{G}_{K,Ke}^{\rho v}$  in the momentum equation is given in (13).

$$\mathbf{G}_{K,Ke}^{\rho v} = \mathbf{G}_{K,Ke(Euler)}^{\rho v} + \mathbf{G}_{K,Ke(visc.)}^{\rho v} + \mathbf{G}_{K,Ke(cap.)}^{\rho v} \quad (13)$$

Where :

$$\left\{ \begin{array}{l} \mathbf{G}_{K,Ke(Euler)}^{\rho v} = V_{e,K}^+ \left[ \rho_{e,K}^{n+1} \mathbf{v}_{e,K}^n \right] + V_{e,K}^- \left[ \rho_{e,Ke}^{n+1} \mathbf{v}_{e,Ke}^n \right] + p_e^{n+1} \mathbf{n}_{e,K} \\ \mathbf{G}_{K,Ke(visc.)}^{\rho v} = \mu_e \left[ \left( \nabla \mathbf{v}^n \right)_e + {}^t \left( \nabla \mathbf{v}^n \right)_e \right] \cdot \mathbf{n}_{e,K} \\ \mathbf{G}_{K,Ke(cap.)}^{\rho v} = \sigma_e \left\| \left( \nabla \alpha^{n+1} \right)_e \right\| \left[ \mathbf{I} - \left( \nabla \alpha^{n+1} \right)_e \otimes \left( \nabla \alpha^{n+1} \right)_e / \left\| \left( \nabla \alpha^{n+1} \right)_e \right\|^2 \right] \cdot \mathbf{n}_{e,K} \end{array} \right. \quad (14)$$

### Details on the MUSCL approach

To reach second order space accuracy, a constrained piecewise linear approximation is reconstructed within cells to evaluate face values involved in flux calculation. Both primitive variables  $\mathbf{q} = [\rho_1, \rho_2, \alpha_1, \mathbf{v}]$  and conservative variables  $\mathbf{w} = [\tilde{\rho}_1, \tilde{\rho}_2, \rho \mathbf{v}]$  can be considered for this piecewise linear approximation. In the present study, primitive variables have been chosen. This choice allows to control more precisely how to limit the gradient of  $\alpha_1$  to get a sharp interface. For each cell K of the mesh, the linear reconstruction procedure consists in the following steps:

- 1) Calculate the unconstrained gradient  $\nabla q_{iK}$  of each primitive variable  $q_i = \rho_1, \rho_2, \alpha_1, \mathbf{v}$  within cell K using a linear least-square method.
- 2) Calculate the slope limiter  $\lambda_{iK}$  to ensure that for each face  $e$  of cell K, the extrapolated face value  $q_{ie,K} = q_{iK} + \lambda_{iK} \times \nabla q_{iK} \cdot (\mathbf{x}_e - \mathbf{x}_K)$  is not a new local extremum.
- 3) Calculate extrapolated face value  $\mathbf{q}_{e,K}$
- 4) Calculate the conservative face values  $\mathbf{w}_{e,K}$  from the primitive ones  $\mathbf{q}_{e,K}$
- 5) Compute  $\alpha_{1e,K}$  by solving system (2) with the state  $\mathbf{w}_{e,K}$
- 6) Calculate fluxes

The slope limiter  $\lambda_{iK}$  of step 2, which is necessary to satisfy the discrete local maximum principle under the CFL condition, is calculated with an adapted version of the Barth and Jespersen limiter 0 :

$$\lambda_{iK} = \begin{cases} \beta_1 \times \min \left( \beta_2, \frac{q_{iK} - q_{iK}^{\min}}{q_{iK} - q_{i\partial K}^{\min}}, \frac{q_{iK}^{\max} - q_{iK}}{q_{i\partial K}^{\max} - q_{iK}} \right) & \text{if } \|\nabla q_{iK}\| > 0 \\ 0 & \text{otherwise} \end{cases} \quad (15)$$

$$\text{where : } \begin{cases} q_{iK}^{\min} = \min_{\forall Ke \in \text{neighbors}(K)} (q_{iK}, q_{iKe}) \\ q_{iK}^{\max} = \max_{\forall Ke \in \text{neighbors}(K)} (q_{iK}, q_{iKe}) \end{cases} \quad \text{and,} \quad \begin{cases} q_{i\partial K}^{\max} = \max_{\forall e \in \partial K} (q_{ie,K}) \\ q_{i\partial K}^{\min} = \min_{\forall e \in \partial K} (q_{ie,K}) \end{cases}$$

The limiter (15) is similar to the Barth and Jespersen limiter if  $\beta_1 = \beta_2 = 1$ . In the present study, parameter  $\beta_1$  is set to 0.9 to prevent stability issue. Parameter  $\beta_2$  is set depending on the reconstructed variable. For variables which are assumed to vary smoothly in space, as  $\rho_1$ ,  $\rho_2$  and  $\mathbf{v}$ , the parameter  $\beta_2$  is set to 1 to obtain an almost second order linearity preserving reconstruction. For discontinuous variables, such as volume fraction  $\alpha_1$ , the parameter  $\beta_2$  is set to infinity (in practice it is just removed) to obtain a very compressive limiter which will sharpen the interface. In fact, the limited gradient of discontinuous variables within a cell is maximized so that reconstructed face values are as close as possible to local extreme values.

## Results on academic test cases

Many academic test cases have been simulated to verify and validate the above described numerical methodology by comparing results with analytical solutions, existing DNS results or experiments. Among them, Rayleigh-Taylor instabilities, rising bubbles and binary droplet collisions cases were investigated and are presented here to discuss both strengths and limitations of the present model and numerical methodology.

### Rayleigh-Taylor instability

Rayleigh-Taylor instability can be observed when a horizontal layer of heavy fluid is superimposed over a lighter one. This situation can lead to an unstable equilibrium of the interface between the two immiscible fluids: interface is subject to the destabilising effect of the gravity and the stabilising effect of the surface tension. From a numerical point of view, this phenomenon is a common test case ([9],[11],[16]) which allows quantitative comparison with an analytical solution in the linear regime and qualitative comparison with high-order numerical method in the non-linear regime.

#### Linear regime:

Under the linear theory hypothesis, a small initial sinusoidal perturbation  $a(x)=a_0 \cos(kx)$  of the interface between two inviscid fluids grows in time following an exponential law as  $\exp(n t)$  with  $n$  given by :

$$n^2 = k \cdot g \left( \frac{\rho_h - \rho_l}{\rho_h + \rho_l} - \frac{k^2 \sigma}{g(\rho_h + \rho_l)} \right) \quad (16)$$

where  $\sigma$  is the surface tension,  $g$  is the gravity,  $\rho_h$  and  $\rho_l$  are respectively the heavier fluid density and the lighter fluid density.

In our simulations, the same parameters as in [9] have been used. The computational domain is a 2D rectangular box ( $L_x=2\pi$ ) $\times$ ( $L_y=4\pi$ ), with periodic boundary conditions on vertical walls and slip conditions on the horizontal ones. The physical parameters of the fluids are  $\rho_h=3 \text{ kg.m}^{-3}$ ,  $\rho_l=1 \text{ kg.m}^{-3}$ . Sound celerity in the fluids were set to  $c_l=914 \text{ m.s}^{-1}$  and  $c_h=340 \text{ m.s}^{-1}$ . At initial time, the interface position between the two fluids is given by  $y_{\text{int}}(x,0)=0.5L_y+a_0 \cos(kx)$  with  $a_0=0.002 \times L_x$  and  $k=1$ . With these conditions, the marginal stability ( $n=0$ ) corresponds to  $\sigma_c=20 \text{ N.m}^{-1}$ . Simulations have been carried out with five different values of the surface tension ( $\Phi = \sigma/\sigma_c = 0.1, 0.25, 0.5, 0.8, 0.9$ ) and different mesh sizes ( $16 \times 32, 32 \times 64, 64 \times 128, 128 \times 256$ ). For each case, the numerical growth rate  $n$  is obtained by a linear curve fit in the amplitude range of  $1.5 \leq \ln(a/a_0) \leq 3$  as in [9], see **Figure 3**. Comparisons between numerical results and linear theory on **Figure 4** show that the predicted growth rates are close to the linear theory. However, for small value of  $\sigma$ , the growth rate tends to be underestimated as it was also reported in [9]. Although numerical results are in good agreement with linear theory for value of  $\Phi$  close to unity, **Figure 3** shows that the interface is subject to high frequency oscillations. It could be due to the effect of spurious currents, whose magnitude is higher when  $\sigma$  increases.

#### Non-linear regime:

For this case, parameters are the same as used in [11] and [16] : computational domain size ratio is  $L_y/L_x=4$ , initial interface position is given by  $y_{\text{int}}(x,0)=0.5L_y+0.05\cos(2\pi x/L_x)$  and fluid properties are  $\rho_h=1.225 \text{ kg.m}^{-3}$ ,  $\rho_l=0.1694 \text{ kg.m}^{-3}$ ,  $\mu_l=\mu_h=3.13 \text{ Pa.s}$  and  $\sigma=0$ . Sound celerities were set to  $c_l=914 \text{ m.s}^{-1}$  and  $c_h=340 \text{ m.s}^{-1}$ . Simulation was run on a  $128 \times 512$  grid which is equivalent to the mesh resolution used in [16]. Periodic conditions are used for vertical boundaries and no-slip condition are used for horizontal walls. At the final state  $t=0.9s$ , Figure 2 shows complex interface between fluids remains sharp thanks to the compressive MUSCL approach and results are in good agreement with those provided by the high order sharp interface Level-Set method presented in [16].

### Rising bubble

The rising of a single gas bubble subject to gravity in a 2D water column tank has been studied. This test case is interesting as viscous, capillary and gravity effects are simultaneously involved.

$R$  denotes the bubble radius.  $\rho_L$  and  $\mu_L$  refer to the density and dynamic viscosity of the water, respectively. Characteristic parameters of the flow, such as Reynolds number and Bond number (17), were set to the same values as in [13] to allow comparison between numerical results. The 2D computational domain is a box ( $L_x=6R$ ) $\times$ ( $L_y=10R$ ) with symmetry condition on vertical boundaries and no-slip wall condition on horizontal boundaries. At initial time, the position of the bubble center is  $(x_0, y_0)=(3R, 2R)$ .

$$\text{Re} = \sqrt{(2R)^3 g \rho_L / \mu_L} = 1000, \quad \text{Bo} = 4\rho_L g R^2 / \sigma = 200 \quad (17)$$

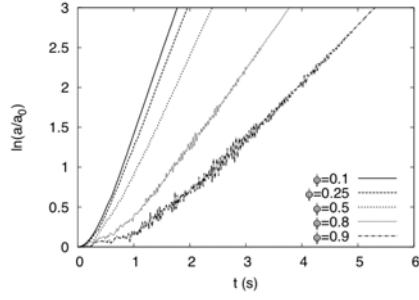


**Figure 3.** Time histories of the Rayleigh-Taylor instability growth.

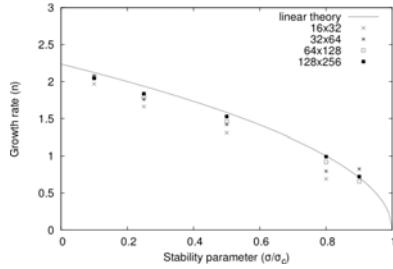


**Figure 4.** Dispersion diagram of the Rayleigh-Taylor instability

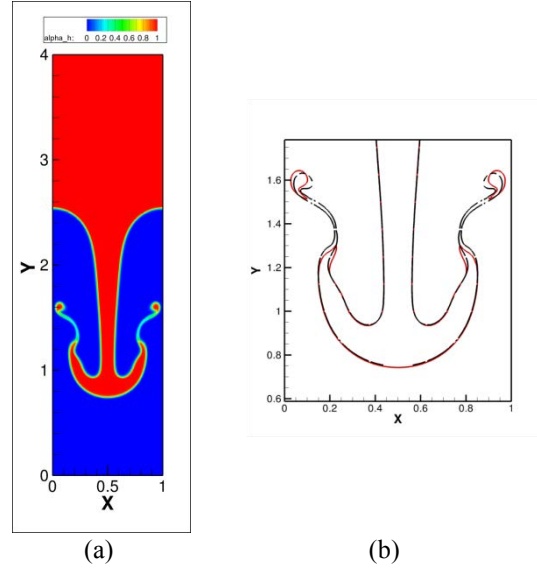


**Figure 2.** Computed Rayleigh-Taylor instability with SLOSH at  $t=0.9s$ . (a): volume fraction of the heavier fluid. (b): comparison between interface position from [16] (black dashed line) and iso-contour from SLOSH (red line) with an equivalent 128x512 mesh.

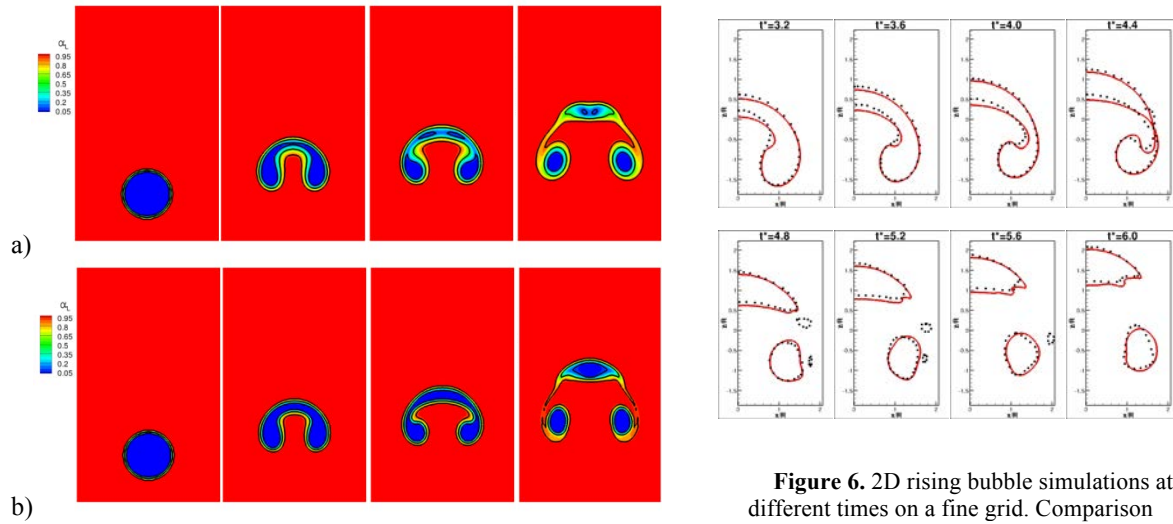


**Figure 5.** Simulations of the rising bubble on a coarse grid (40x133). Black solid line : iso-contour  $\alpha_L = (0.1, 0.5, 0.9)$ . a) Barth limiter 0. b) compressive limiter (15).

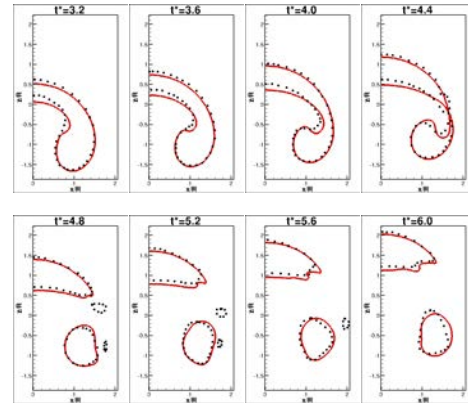


**Figure 6.** 2D rising bubble simulations at different times on a fine grid. Comparison between iso-contour  $\alpha = 0.5$  (red solid line) and Level-Set interface from [11] (black dotted line).  $t^* = t\sqrt{g/R}$

First, numerical simulations were performed on a uniform coarse grid (40x133) to compare results obtained with the classical Barth limiter and results of the proposed compressive limiter (15). In **Figure 5**, results clearly shows the sharpening effect of limiter (15) which drastically reduces the diffusion of the interface and preserves the bubble shape.

Numerical simulations were also performed with the same mesh resolution as in [13]. **Figure 6** shows that present results and Level-Set results [13] are similar. Nevertheless, the formation of small bubbles observed in [13] is not reproduced with our numerical approach. At this point, it is difficult to know what the most realistic results are because experimental data are not available for this 2D planar case.

### Head-on binary droplet collisions

Numerical simulations of head-on binary droplet collisions have been investigated, as in [14], to assess the ability of the present approach to deal with situations where inertial and capillary mechanisms play an important

role. Conditions similar of the experimental study in 0 were used for simulations to allow comparisons. In 0, authors characterize head-on equal size droplet collision regimes according to two non-dimensional numbers: the droplet Weber  $We$  and the Ohnesorge number  $Oh$ . In our simulations, two collision regimes have been investigated at two different droplet Weber numbers,  $We=23$  and  $We=40$ , and a constant Ohnesorge number  $Oh=0.0047$ . To simulate case  $We=23$ , a 3D uniform grid (120x240x120) of eighth of the whole domain is used given symmetry of the problem. To simulate case  $We=40$ , a 2D axisymmetric uniform grid (360x1440) is used to validate both versions of the code. The mesh resolution is equivalent to 96 cells in the droplet diameter for  $We=23$  and 288 cells in the droplet diameter for  $We=40$ . Figure 7 and Figure 8 show that simulation results are in good agreement with experiments 0. Each step of the collision process is qualitatively well reproduced by simulations. In particular, it is observed that the formation of the satellite droplet is well predicted for the case  $We=40$ .

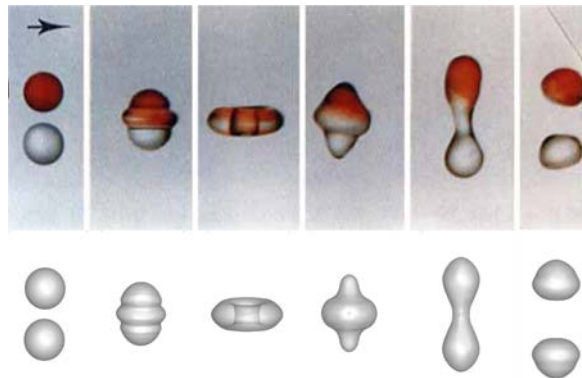


**Figure 7.** Head on binary collision at  $We=23$ . First row: experimental results from 0. Second row: our 3D simulation.

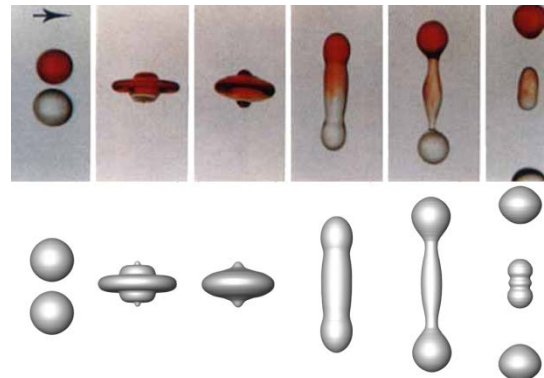


**Figure 8.** Head on binary collision at  $We=40$ . First row: experimental results from 0. Second row: our 2D axisymmetric simulation.

## Conclusions

In this work, the development of a compressible two-fluid model and numerical methods designed to simulate complex interfacial flows on unstructured grids has been addressed. The partially implicit low Mach scheme and the interface sharpening process used in the present methodology have been assessed on simulations of academic test cases and have been validated against theoretical, experimental and numerical data. Results show that the interface remains sharp and its position is well predicted. These conclusions are confirmed by the results presented in the second-part-paper [3] devoted to the simulation of the primary atomization of a sheared liquid sheet.

## Acknowledgement

This work was carried out in the framework of the European project FIRST. The authors would like to thank the EC for its financial support. The first author also gratefully acknowledges the funding support of the French Direction Générale de l'Armement.

## References

- [1] N. Ashgriz, J.Y. Poo. Coalescence and separation in binary collisions of liquid drops. *J. Fluid Mech.* 221,183-204, 1990.
- [2] T.J. Barth, D.C. Jespersen. The design and application of Upwind Schemes on Unstructured Meshes. *AIAA Paper 89-0366*, January 1989.
- [3] G. Blanchard, P. Villedieu, D. Zuzio. Numerical simulation of the primary atomization of a sheared liquid sheet. Part 2: Comparison with experimental results. *Submitted to the 25th European Conference on Liquid Atomization and Spray Systems, Crete, September 2013*
- [4] G. Chanteperdrix, P. Villedieu, J.-P. Villa. A compressible model for separated two-phase flows computations. *Proceedings of the 2002 ASME Fluids Engineering Division Summer Meeting, Montréal, Québec, Canada. FEDSM2002-31141.*
- [5] N. Grenier, J.-P. Vila, P. Villedieu. An accurate low-Mach scheme for a compressible two-fluid model applied to free-surface flow. *Journal of Computational Physics*, 2013, *accepted*

- [6] D. Gueyffier, J. Li, A. Nadim, R. Scardovelli, S. Zaleski. Volume-of-fluid interface tracking with smoothed surface stress methods for three dimensional flows. *Journal of Computational Physics* 152 (1999) 423-456
- [7] M. Herrmann. A parallel Eulerian interface tracking/Lagrangian point particle multi-scale coupling procedure. *Journal of Computational Physics*, Volume 229, Issue 3, 1 February 2010, Pages 745-759.
- [8] T. Ménard, S. Tanguy, A. Berlemont. Coupling level set/VOF/ghost fluid methods: Validation and application to 3D simulation of the primary break-up of a liquid jet, *International Journal of Multiphase Flow*. Volume 33, Issue 5, May 2007, Pages 510-524.
- [9] M. Oevermann, R. Klein, M. Berger, J. Goodman. A projection method for two-phase incompressible flow with surface tension and sharp interface resolution. *Zuse Institute Berlin – Report 17*; 2000.
- [10] L.-R. Plumerault, D. Astruc, P. Villedieu, P. Maron. A numerical model for aerated-water wave breaking. *International Journal for Numerical Methods in Fluids*, 2011
- [11] S. Popinet, and S. Zaleski. A front-tracking algorithm for accurate representation of surface tension. *Int. J. Numer. Meth. Fluids*, 30: 775–793, 1999
- [12] R. Saurel, R. Abgrall. A Multiphase Godunov Method for Compressible Multifluid and Multiphase Flows. *Journal of Computational Physics*, Volume 150, Issue 2, 10 April 1999, Pages 425-467.
- [13] Mark Sussman, Peter Smereka, Stanley Osher. A Level Set Approach for Computing Solutions to Incompressible Two-Phase Flow. *Journal of Computational Physics*, Volume 114, Issue 1, September 1994, Pages 146-159
- [14] S. Tanguy, A. Berlemont. Application of a level set method for simulation of droplet collisions. *International Journal of Multiphase Flow*, Volume 31, Issue 9, September 2005, Pages 1015-1035
- [15] G. Tomar, D. Fuster, S. Zaleski, S. Popinet. Multiscale simulations of primary atomization. *Computers & Fluids*, Volume 39, Issue 10, December 2010, Pages 1864-1874
- [16] D. Zuzio, J.L. Estivalezes. An efficient block parallel AMR method for two phase interfacial flow simulations. *Computers & Fluids*, Volume 44, Issue 1, May 2011, Pages 339-357

## **Numerical simulation of primary atomization of a sheared liquid sheet. Part 2: Comparison with experimental results**

Philippe Villedieu , Ghislain Blanchard and Davide Zuzio

ONERA (The French Aerospace Lab), France

### **Abstract**

Numerical simulations of the primary atomisation of a sheared liquid sheet have been performed using the two-fluid model of SLOSH code described in 0 by the same authors. From a numerical point of view, several experimental configurations investigated in [2] have been considered by varying the flow parameters. Direct comparisons between numerical and experimental results were made to assess the ability of the numerical model to reproduce the main physical mechanisms of the primary atomisation process as they were experimentally observed.

---

### **Introduction**

In aircraft combustion chambers, the injection of fuel is commonly achieved by air-blast atomizers which create a spray by pulverising a fuel liquid sheet thanks to strong co-flowing airflows. During this process, two stages can be distinguished: the primary and the secondary atomization. Recently, numerical strategies based on the coupling of an interfacial flow model dedicated to the primary atomization and a dispersed phase model dedicated to the secondary atomization have been investigated [7] to simulate the complete atomization process. In this work, simulations of primary atomisation have been carried out with SLOSH code (described in [1]) for realistic configurations and the results have been compared to experimental results from [2]. The objective of these computations is to prove the ability of SLOSH methodology (in which the interface is rather captured than exactly tracked as in sharp interface methods) to accurately simulate primary instabilities and large scale features of the primary atomization process.

It is worth pointing out that our objective was not to make a DNS of the full atomization process (from ligament creation to droplet formation) as in [3],[5] and [7] but rather to capture the larger scale phenomena of the liquid sheet fragmentation mechanisms, having in mind that, in a second step, these resolved scales could be used to provide input data (source term location, droplet velocities and sizes) for the coupling with a spray model.

### **Code assessment methodology**

At ONERA, experimental investigations were carried out for liquid sheet atomization. In particular, the study described in [2] has provided a significant database for the primary atomization of a planar sheared liquid sheet by a planar air-blast atomizer (Figure 1). Here, this database is used as a reference and therefore we refer to [2] for the detailed description of the experimental configuration. The liquid sheet is injected through a slit located at the trailing edge of a NACA airfoil. The numerical study has been focused on one specific geometry which is denoted C9 in [2] (see Figure 2).

Two dimensional simulations of the primary atomisation of a planar liquid sheet have been performed in order to assess the ability of the code to accurately reproduce the global scale behaviour of the liquid sheet oscillations and primary atomization (such as the global oscillation frequency and the mean break-up length which are both mostly governed by the growth of 2D longitudinal Kelvin-Helmholtz instabilities). A parametric study has been carried out in which both the influence of the mesh resolution and the effect of some relevant physical parameters (inlet air jet velocity and thickness) have been investigated.

Preliminary 3D simulations have recently been performed in order to confirm the promising 2D results and to assess that the SLOSH numerical approach is also able to reproduce the 3D mechanisms of the primary atomization process.

### **Test case description**

#### **2D case**

The main characteristics of the geometry are shown in Figure 2. For 2D simulations, 2D meshes corresponding to the median plane of the injector were used. In Figure 3, one of the meshes is shown with a colour code to identify boundary conditions. Red line denotes the gas inlet where mass flow rate is specified. Blue line indicates the liquid inlet where a Poiseuille velocity profile is imposed. Green contour shows the pressure outlet boundary condition. Remaining boundary conditions were treated as no-slip walls. For the gas inlet, the mass flow rate was determined by integrating the target gas velocity profiles measured experimentally



close to the injector [2]. Correspondence between experimental gas velocities and mass flow rate at gas inlet are given in Table 1. For liquid inlet, the average flow velocity was always set to  $2.2\text{m.s}^{-1}$  (only gas velocity varies).

Experimental gas velocity $V_g(\text{m.s}^{-1})$ [2]	30	50	80
Equivalent 2D mass flux rate $(\text{kg.s}^{-1}.\text{m}^{-2})$	13.90	19.37	38.86

**Table 1** Mass flow rate at gas inlet.

To simulate accurately the primary atomization of the liquid sheet, special care was paid to the mesh quality and the mesh resolution downstream of the liquid injection. Thus, meshes were built for being similar to a Cartesian uniform grid in the region from the liquid inlet up to 30mm downstream. Two mesh resolutions have been tested in this region. The first one, which is called *mesh<sub>10</sub>*, has 10 cells in the sheet thickness (i.e.  $\Delta x=30\mu\text{m}$ ). The second one, which is named *mesh<sub>20</sub>*, corresponds to 20 cells in the sheet thickness (i.e.  $\Delta x=15\mu\text{m}$ ). The total number of cells is approximately 600000 cells for *mesh<sub>10</sub>* and 900000 cells for *mesh<sub>20</sub>*.

The numerical time steps, which are calculated under CFL conditions, were between  $10^{-8}\text{s}$  and  $10^{-7}\text{s}$  (depending on cases).



**Figure 1** Air-blast atomizer used in [2].

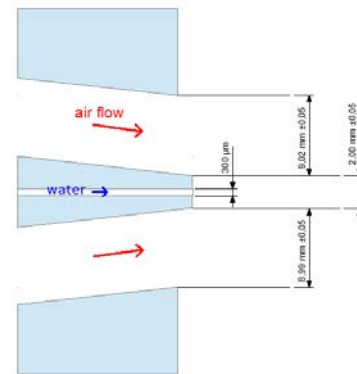


**Figure 2** Injector layout for C9 configuration [2].

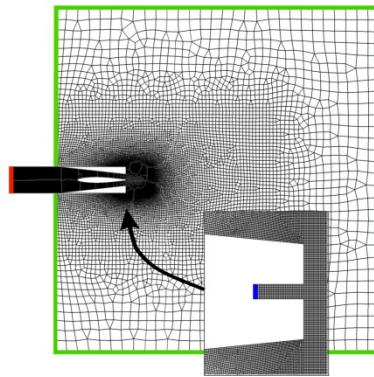


**Figure 3** A 2D mesh of the median plane of the injector

Like in [2], water and air are considered for the liquid and gas phases, respectively. Fluid properties are given in Table 2.

	Density $\rho$ ( $\text{kg.m}^{-3}$ )	Dynamic viscosity $\mu$ ( $\text{Pa.s}$ )	Sound celerity ( $\text{m.s}^{-1}$ )	Surface tension $\sigma$ ( $\text{N.m}^{-1}$ )
air	1.225	$1.91 \times 10^{-5}$	341	0.07
water	1000	$1.0 \times 10^{-3}$	1490	

**Table 2.** Fluids properties

### 3D case

The selected test case corresponds to a kerosene injector under a 11 bar pressure for which experimental measurements have been performed at ONERA [6]. The physical parameters are reported in Table 3. The computational domain has dimensions of  $20\text{ mm} \times 10\text{ mm} \times 5\text{ mm}$ . We used a non uniform Cartesian mesh of

11 million cells, strongly refined in the liquid core region. The cell number in the liquid sheet thickness was equal to 10 which corresponds to a characteristic cell size of 30  $\mu\text{m}$ . The time step was approximately equal to  $10^{-7}\text{s}$ .

	Density $\rho$ ( $\text{kg.m}^{-3}$ )	Dynamic viscosity $\mu$ (Pa.s)	Sound celerity ( $\text{m.s}^{-1}$ )	Surface tension $\sigma$ ( $\text{N.m}^{-1}$ )	Inlet velocity ( $\text{m.s}^{-1}$ )
air	13.2	$1.0 \times 10^{-5}$	108	0.00257	25
kerosene	812	$1.1 \times 10^{-3}$	523		2

**Table 3.** 3D simulation parameters

## Results and Discussion

### One-phase flow 2D simulations

Simulations of the air flow without liquid injection were performed for ensuring that the code is able to accurately compute the air velocity field. This is an essential step before considering two-phase flows.

Figure 4-a shows that results for the vertical profiles of the mean longitudinal gas velocity downstream of the injector nozzle are very close to the experimental ones. A similar comparison is shown in Figure 4-b for the vertical profiles of the mean vertical velocity. The agreement is still correct. Figure 5 shows a comparison between the vertical profiles of the numerical RMS velocity with the corresponding experimental ones. The agreement is clearly not as good as for the mean velocity. While the RMS gas velocity peak positions are qualitatively well predicted, the numerical results tend to overestimate the fluctuation intensity. The same simulations have also been performed with CEDRE ONERA code (<http://cedre.onera.fr/>) and the same conclusions have been obtained. This discrepancy could be due to the fact that, unlike the mean velocity field, the fluctuation velocity field is 3D. This explanation will be explored in a future work.

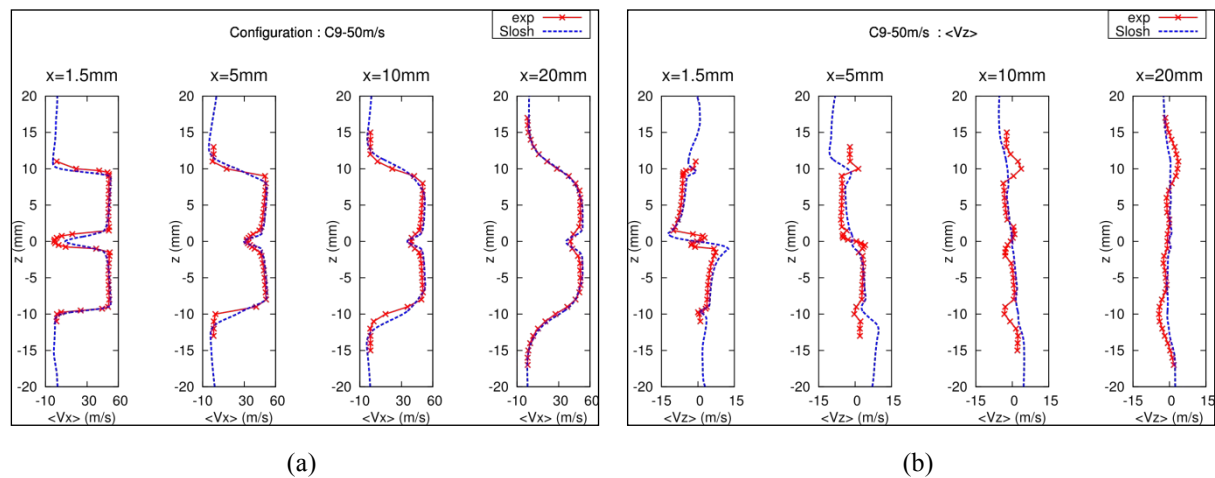


**Figure 4** Vertical profiles of mean gas velocity at different distances from the injector nozzle. Comparison between 2D SLOSH simulations and experiments [3]. (a) longitudinal mean gas velocity  $\langle V_x \rangle$ . (b) vertical mean gas velocity  $\langle V_z \rangle$ .

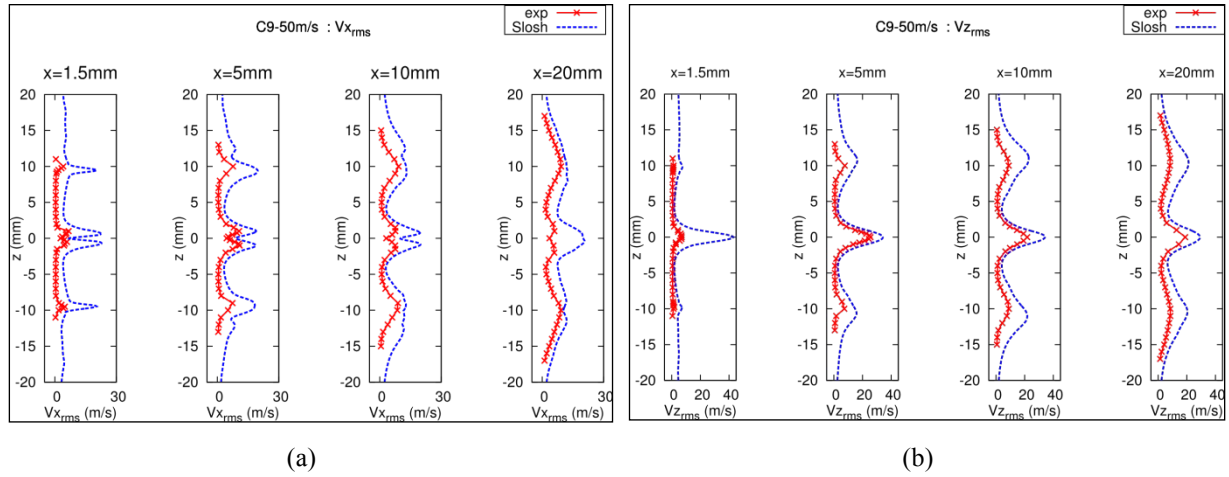


**Figure 5** Vertical profiles of RMS gas velocity at different distances from the injector nozzle. Comparison between 2D SLOSH simulations and experiments [3]. (a) longitudinal RMS gas velocity  $V_{x\text{ RMS}}$ . (b) vertical RMS gas velocity  $V_{y\text{ RMS}}$ .

### Two-phase flow 2D simulations

2D simulations have been carried out with the  $mesh_{10}$  mesh for the three gas velocity given in **Error! Reference source not found.** Figure 6 shows a global visualisation of the liquid sheet for  $V_g=50\text{m/s}$ . It can be observed that the sheet liquid core is well captured by the numerical methodology 0. The interface remains sharp until the liquid sheet breakup occurs, as expected. After break-up, the mesh resolution is too coarse for the numerical solution being able to capture small liquid structures. As a consequence, the interface is smeared and the liquid phase is artificially diffused in the gas flow. It is worth pointing out that this is not a problem since the objective here is only to capture the larger scale phenomena of the liquid sheet fragmentation mechanisms, having in mind that, in a second step, these resolved scales could be used to provide input data for the coupling with a spray model.

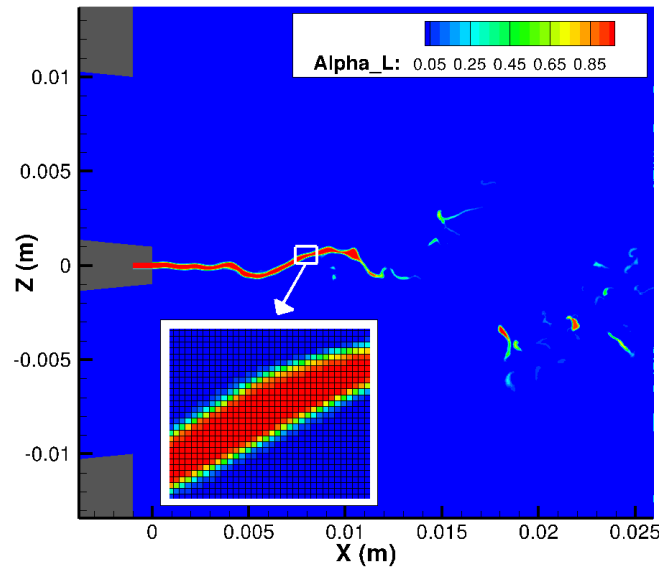


**Figure 6** Global visualisation of the simulated liquid sheet.  $V_g=50\text{m/s}$ . Mesh:  $mesh_{10}$ . Colour scale: liquid volume fraction field.

### Break-up length

From the instantaneous liquid volume fraction fields obtained at time  $t_n=n.T$  (with  $T = 1/10000$  s), the corresponding break-up lengths  $L_b(t_n)$  were determined by using exactly the same numerical algorithm as for

the experimental data which is described in [2]. Figure 7 shows snapshots (at some instants after the transient phase) of the simulated liquid sheet for 3 different inlet air jet velocities. The green line indicates the experimental mean value [2] of the liquid sheet break-up distance from the injector nozzle. Figure 8-a shows a comparison between the numerical and the experimental mean values of the break-up length for the 3 different air flow velocities. It can be observed that the higher the air velocity, the shorter the break-up distance. This tendency is well reproduced in the 2D simulation even if the mean break-up length is underestimated for low gas velocities.

### Flapping frequency

From the instantaneous liquid volume fraction fields obtained at time  $t_n = n.T$  (with  $T = 1/10000$  s), the maximal vertical position of the liquid sheet,  $y_{\max,i}(t_n)$ , was determined for several longitudinal position  $x_i$ . FFT of the discrete signals  $y_{\max,i}(t)$  were performed to get spectra of the liquid oscillatory motion at the different longitudinal positions. From these spectra, the frequency corresponding to the maximal value of the FFT was identified and compared to the experimental value of the flapping frequency obtained with the same procedure. Figure 8-b shows a comparison between the numerical results with the experimental ones. The tendency of the flapping frequency to increase with the air flow velocity is well reproduced but the quantitative agreement is not very good. This discrepancy could be due to 3D effects which are of course not reproduced in our 2D simulations. The influence of the mesh resolution was also suspected but it can be noticed in Figure 8-b that both meshes,  $mesh_{10}$  and  $mesh_{20}$ , lead to similar results as regards the flapping frequency.

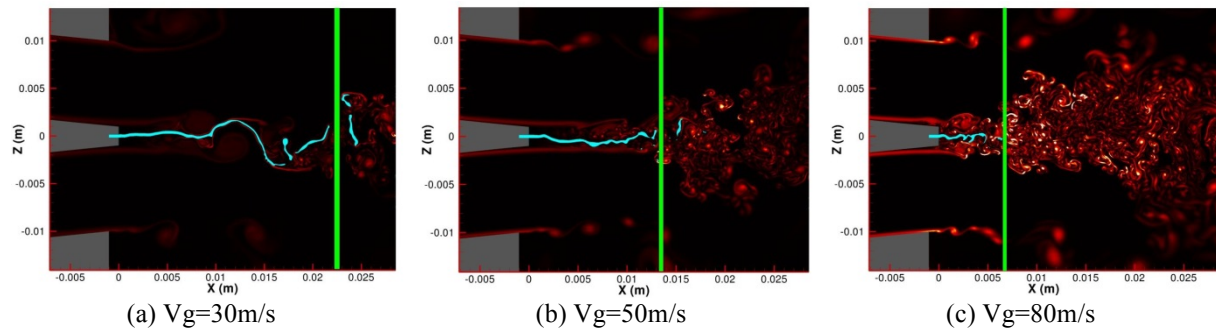


**Figure 7** Influence of the air jet velocity on the break-up length of the liquid sheet. Cyan: snapshot of the simulated liquid sheet. Red scale: vorticity field of the gas phase. Green line: measured mean breakup length from experiments [2].

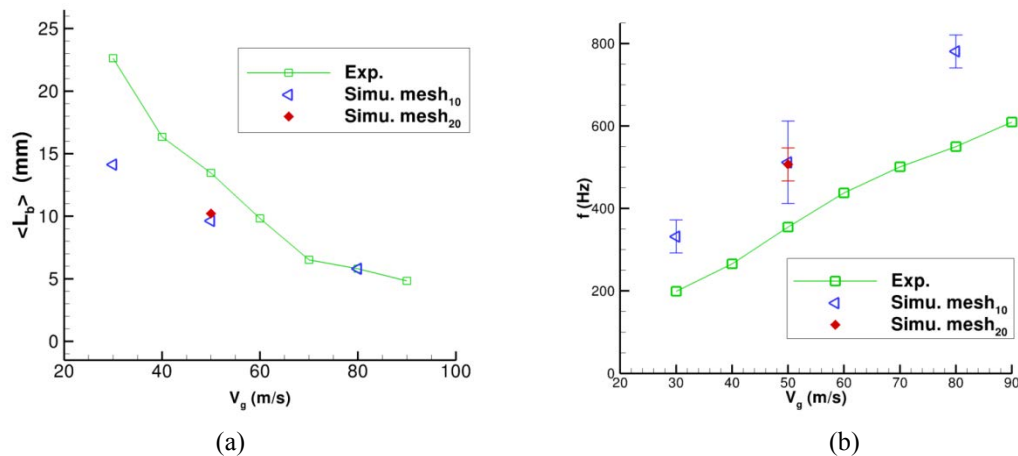


**Figure 8** Comparison between numerical and experimental results for different air velocities. (a) mean break-up length of the liquid sheet. (b) flapping frequency of the liquid sheet.

### Preliminary 3D two-phase flow simulations

Preliminary 3D simulations have been performed in order to assess that SLOSH code is also able to reproduce the 3D mechanisms of the primary atomization process. Figure 9 shows snapshots of the liquid sheet interface (0.5 - iso-surface of the liquid volume fraction). Transverse instabilities which lead to the formation of

ligaments can be observed. It is worth mentioning that no artificial perturbation has been necessary for initiating them. These first results are very encouraging as regards the ability of SLOSH numerical method 0 to simulate primary atomization.

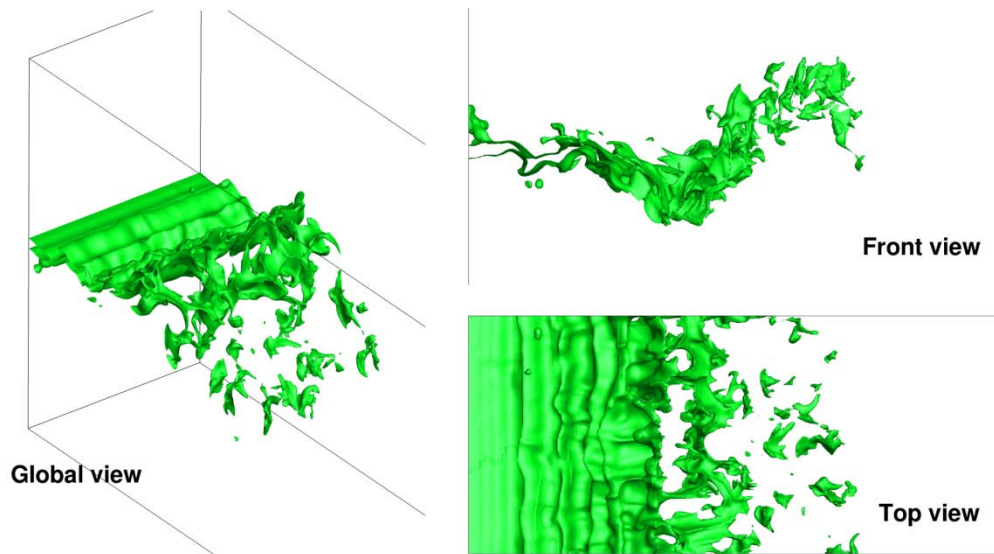


**Figure 9** Simulated 3D liquid sheet.

### Conclusions and way forward

In this work, numerical simulations of the primary atomization of a sheared liquid sheet have been investigated with the two fluid model of SLOSH code. For now, comparisons between numerical results and experimental data suggest that large-scale mechanisms of the primary atomization are well captured by the numerical simulations even if further quantitative validations are still necessary. These promising results are the starting point for the future development of a coupling approach between SLOSH two fluid model of and a dispersed phase model thanks to a droplet formation model, in order to simulate the whole atomization process.

### Acknowledgements

This work was carried out in the framework of the European project FIRST. The authors would like to thank the EC for its financial support. The second author also gratefully acknowledges the funding support of the French Direction Générale de l'Armement.

### References

- [1] G. Blanchard, P. Villedieu, D. Zuzio, Numerical simulation of the primary atomization of a sheared liquid sheet. Part 1: model and numerical method description, *submitted to the 25th European Conference on Liquid Atomization and Spray Systems, Crete, September 2013*.
- [2] B. Déjean, P. Berthoumieu, P. Gajan, Experimental study on the influence of the liquid and air thicknesses on a planar air-blasted liquid sheet, *submitted to the 25th European Conference on Liquid Atomization and Spray Systems, Crete, September 2013*.
- [3] G. Tomar, D. Fuster, S. Zaleski, S. Popinet, Multiscale simulations of primary atomization, *Computers & Fluids*, Volume 39, Issue 10, December 2010, Pages 1864-1874
- [4] M. Herrmann, A parallel Eulerian interface tracking/Lagrangian point particle multi-scale coupling procedure, *Journal of Computational Physics*, Volume 229, Issue 3, 1 February 2010, Pages 745-759.

- [5] T. Ménard, S. Tanguy, A. Berlemont, Coupling level set/VOF/ghost fluid methods: Validation and application to 3D simulation of the primary break-up of a liquid jet, *International Journal of Multiphase Flow*, Volume 33, Issue 5, May 2007, Pages 510-524
- [6] V. Gutierrez Fernandez. Experimental Study of Liquid Sheet Disintegration in a High Pressure Environment. PhD thesis, Université de Toulouse, 2010.
- [7] D. Zuzio et al., Numerical simulation of primary and secondary atomization, , *Comptes Rendus Mécanique*, Volume 341, Issues 1–2, January 2013, Pages 15-25, <http://dx.doi.org/10.1016/j.crme.2012.10.003>

# Session:

# Atomization

## Flashing behaviour of rocket engines propellants

H. Kamoun<sup>1</sup>, G. Lamanna<sup>1,\*</sup>, B. Weigand<sup>1</sup>, C. Manfretti<sup>2</sup>, A. Rees<sup>2</sup>, J. Sender, M. Oschwald<sup>2</sup>  
and J. Steelant<sup>3</sup>

1: Institute of Aerospace Thermodynamics, Universität Stuttgart, Germany

2: Institute of Space Propulsion, German Aerospace Center (DLR), Germany

3: ESTEC-ESA, Noordwijk, The Netherlands

### Abstract

This paper investigates the characteristics and morphology of a flash-atomising jet by means of high-speed shadowgraphy. The study of a flash-disintegrating jet is particularly relevant for the aerospace industry. Therefore, this study includes both storable and cryogenic rocket engine propellants. The experiments are carried out with an inert equivalent of MMH, i.e. ethanol and oxygen. Both are used as propellants for upper stages of the Ariane 5 respectively on the storable EPS engine AESTUS and the cryogenic ESC-A engine HM-7B or the future ESC-B upper stage engine Vinci. A comparison between the flashing behaviour of these two fluids is conducted and shows a similarity in the shape of the spray despite the huge differences in the physical properties of the two fluids. The flashing spray is barrel-shaped and characterized by a large spreading angle. Based on this similarity, the applicability of the onset criterion for fully-flashing, originally derived for storable and retrograde fluids, is verified for cryogenic propellants, showing a satisfactory agreement.

### Introduction

Flash-atomization occurs when a liquid fuel is injected into a chamber where the ambient pressure  $p_\infty$  is lower than the fuel saturation pressure  $p_{sat}(T_{inj})$ . The inception of flashing strongly depends on the level of superheat ( $R_p = p_{sat}(T_{inj})/p_\infty$ ) and on the transient heat conduction process within the jet. If flashing occurs, then bubble bursting induces jet disintegration. This process has a strong impact on the spray morphology and droplet size distribution, and hence on the combustion efficiency of the engine. Due to its relevance for automotive and industrial applications, considerable progress has been made in the modelling (e.g. Senda et al. [1]) and experimental (e.g. Cleary et al. [2] and Yildiz et al. [3]) investigation of a flash-atomising liquid spray at atmospheric conditions. The experimental investigation and modeling of superheated jets at low back pressures have received, instead, less attention, due to the difficulty of maintaining the ambient pressure constant at near vacuum conditions. Kurschat et al. [4] were among the first to investigate the evaporation of highly superheated liquid jets in near vacuum conditions. They modeled the evaporation as a sonic deflagration followed by an axisymmetric supersonic expansion of a two-phase flow. Their analysis has been further extended by Vieira and Moreira [5]. They showed that, at extreme conditions (i.e. very low back pressures), the rapid and intense phase-change process is limited by a maximum mass rate condition. The latter is known as the Chapman- Jouguet point in analogy to a deflagration wave in a combusting gas. These findings are particularly relevant for space propulsion systems, operating at near-vacuum conditions. When expanding high-pressure fluids into near vacuum, e.g. during engine start-up or when venting, a state of high superheat may be attained and the process of mixture formation occurs through flash atomization and vaporization. Hence a prediction of flash atomization and evaporation is of great interest, especially for propellants currently used in rocket engines. As an example the flashing behaviour of MMH and NTO, used as fuel and oxidizer on the Ariane 5 upper stage (EPS) Aestus engine is of importance during start-up in vacuum as it drives the complete ignition process, due to the hypergolic nature of the propellants.

For this purpose a reliable flash-atomisation's experimental database under near vacuum conditions for these fluids, which includes data on spray morphology, droplet size, velocity and temperature distribution should be available. In this paper experiments are carried out with two types of fluids used as propellant in rocket engines: Ethanol and oxygen. Ethanol, a storable fluid, is used as an inert equivalent of MMH which is implemented as propellant on the Aestus engine or various apogee engines for satellites. Cryogenic fluid oxygen (LOx), which is used as propellant in Ariane 5 upper stage (ESC-A) engine HM-7B and in the future Ariane 5ME upper stage (ESC-B) engine Vinci, is also of interest for use in a new generation of cryogenic reaction and control (RCS) engines (8). As a first step, a comparison between the flashing behaviour of these two different types of fluids is conducted for different superheat level by means of high-speed shadowgraphy. Then the different flashing regimes are investigated and a nucleation-based criterion (Lamanna et al. [6]) to predict the transition to flashing is verified for cryogenic propellants. The outline of the paper is as follows. The section "Flashing" reviews briefly the most relevant non-dimensional parameters governing the flash atomization and bubble nucleation processes. The test facilities used to investigate flashing behavior of ethanol and LOx, the optical setup and the post processing are described in the section "Experimental setup and post processing". The experimental results



and the correlations to predict flashing onset are presented in section “Results”. Final conclusions are presented in the last section.

## Flashing

As mentioned in the introduction, the phenomenon of flashing occurs when a fluid is injected in an environment, where the ambient pressure  $p_\infty$  is lower than the saturation pressure of the injected fluid. This is illustrated in Figure 1, where the saturation curve is depicted.

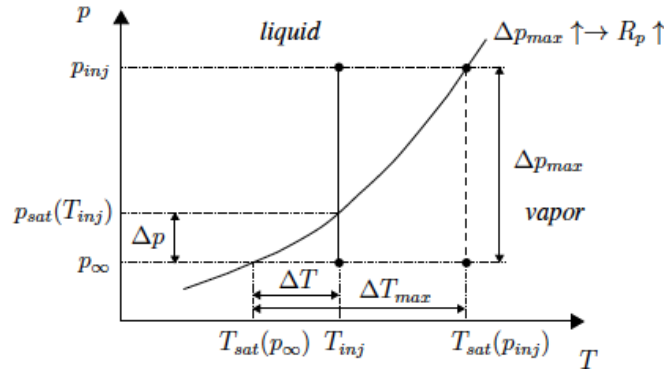


Figure 1. Flashing parameters

As indicated in Figure 1, the superheat level can be described through two parameters. The first parameter ( $\Delta T$  - i.e. the degree of superheat) is defined as the difference between the fuel injection temperature and the saturation temperature at the assigned back-pressure:

$$\Delta T = T_{inj} - T_{sat}(p_\infty) \quad (1)$$

The second parameter  $R_p$  is defined as the ratio between the saturation pressure at the fuel injection temperature and the prescribed back-pressure:

$$R_p = \frac{p_{sat}(T_{inj})}{p_\infty} \quad (2)$$

In a previous work [7] it was shown that the parameter  $R_p$  plays a dominant role in the bubble nucleation process. In fact, with regard to the classical nucleation theory (CNT), the nucleation rate can be expressed as a function of  $R_p$  and the dimensionless surface tension  $\Theta$  defined as:

$$\Theta = \frac{a_0 \sigma}{k_b T_{inj}} \quad (3)$$

where  $k_b$  is the Boltzmann constant,  $\sigma$  the surface tension,  $T_{inj}$  the injection temperature and  $a_0 = (36\pi)^{1/3} (v_m)^{2/3}$  the molecular surface area with  $v_m$  denoting the liquid molecular volume. The nucleation rate can be expressed as:

$$J_{CNT} \propto \sqrt{\frac{2\sigma}{\rho m}} \exp\left(-\frac{\Delta G^*}{k_b T_{inj}}\right) = \sqrt{\frac{2\sigma}{\rho m}} \exp\left(\frac{16\rho\sigma^3}{3(\Delta\mu)^2}\right) = \sqrt{\frac{2\sigma}{\rho m}} \exp\left(-\frac{4}{27} \frac{\Theta^3}{(\ln R_p)^2}\right) \quad (4)$$

where  $\Delta G^*$  represents the formation energy of the critical cluster and  $\Delta\mu$  the chemical potential.

In a previous paper [6], we demonstrated that, for storable and retrograde fluids, the two non-dimensional parameters  $R_p$  and  $\Theta$  can be effectively employed to predict the transition to fully-flashing. The validity of this approach for cryogenic fuels (namely LOx) is verified in the result section.

## Experimental setup and post processing

### Test facility

For the flash atomization experiments two different setups are used: one for the ethanol experiments, installed at ITLR in Stuttgart and one for the LOx experiments, installed at DLR in Lampoldshausen.

The ITLR test bench is designed to investigate the flashing behavior of ethanol at medium vacuum conditions ( $0.02 \text{ bar} < p_{am} < 0.4 \text{ bar}$ ). A schematic layout of the facility is shown in Figure 2. The injector chosen is a standard automotive fuel injector, which has been adapted to low-pressure applications thanks to a special nozzle design. It has a characteristic response time of roughly 0.4 ms and is capable of establishing steady-state conditions within about 1ms. With the present setup, injection times of 50 ms can be achieved with no appreciable change in back pressure. The nozzle has a diameter  $D$  of  $150 \mu\text{m}$  and an exit orifice aspect ratio  $L/D=6$ . Accessibility for optical diagnostics is granted by four circular windows in the vacuum chamber at 90 degree apart from each other. Table 1 summarizes the operating conditions, which can be realized with this

setup. Further information about the test facility can be found in [6].

Parameter	Range
Injection pressure $p_{inj}$	10 bar
Injection temperature $T_{inj}$	293 – 390 K
Back pressure $p_{\infty}$	0.02 – 0.4 bar

**Table 1.** Overview of attained test conditions (ITLR)

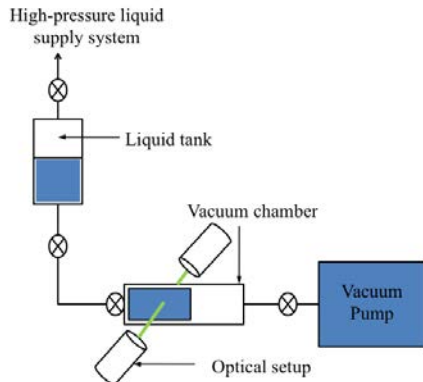


**Figure 2.** Test rig and periphery

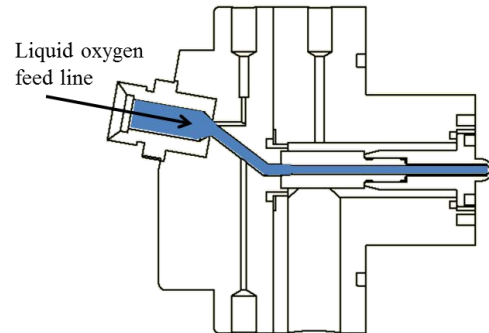


**Figure 3.** Battleship thruster injector head

The DLR experimental set-up for LOx flashing investigations includes a 400N battleship thruster (Figure 3) complete with a vacuum tank and vacuum pump. The chamber (Figure 4) was designed with a contraction ratio typical of reaction and control (RCS) engines in the 400N-thrust class and a quasi-circular cross-section to ensure increasing Mach numbers with axial distance downstream. Optical access to the combustion chamber is provided by two lateral windows, which cover 75% of the chamber length. The back-pressure was varied between 0.035 and 0.3 bar. Two injector configurations were tested: 2.4 mm and 0.3 mm. Table 2 summarizes the characteristics of both configurations.

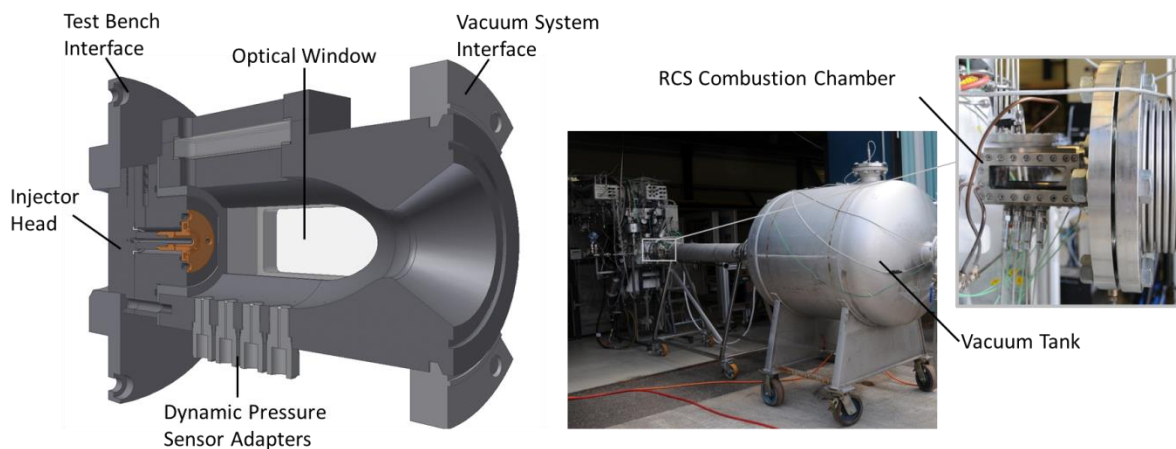


**Figure 4.** Battleship thruster schematics and vacuum equipment

<b>Configuration # 1:</b>	
Oxygen injector diameter	2.4 mm
Feed pressure	2.5 bar
Feed temperature	80 K
<b>Configuration # 2:</b>	
Oxygen injector diameter	0.3 mm
Feed pressure	17 bar
Feed temperature	117 K

**Table 2.** Injector configurations (DLR)

### Optical Setup

A standard Z-set-up was used for shadowgraphy imaging of the spray. The optical setup settings for the different setups are summarised in Table 3.

<b>ITLR</b>		
Camera	Photron Fastcam SA1	
<u>Resolution</u>	<u>Frame rate</u>	<u>Magnification</u>
256 x 784 pixel	22500 fps	1:4
512 x 440 pixel	30000 fps	1:1
<b>DLR</b>		
Camera	SA-X	
<u>Resolution</u>	<u>Frame rate</u>	<u>Configuration</u>
1024 x 368 pixel	19200	Configuration # 1
512 x 256 pixel	50000	Configuration # 2

**Table 3.** Optical setup settings

### Post processing

This section describes the post-processing algorithm, used to extract the spray geometrical data from the high-speed shadowgraph images. The Matlab code was developed by Stotz et al. [9]. For accurate results, the image-processing algorithm must reduce the background noise and enhance the image contrast without altering the spray contour. Then, the spray images are thresholded to separate the spray from the background. Once the spray contour has been defined, its upper and lower branch  $y_i(x)$  are subsequently used to calculate the upper and lower half of the local spreading angles  $\theta_i(x)$  according to

$$\tan [\theta_i(x)] = \frac{y_i(x) - y_i(1)}{\Delta x}, i = \text{upper, lower} \quad (5)$$

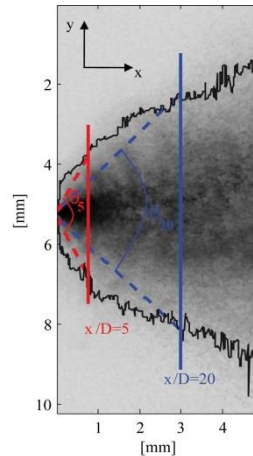


**Figure. 5:** Definition of the local jet spreading angle

The total spray angle, shown in Figure 5, is then calculated at different axial positions ( $x/D=2$ ,  $x/D=5$ ,  $x/D=10$ ,  $x/D=20$ ,  $x/D=60$ ) as:

$$\theta(x) = \theta_{upper}(x) - \theta_{lower}(x) \quad (6)$$

By applying Eq. (6) to all acquired images, temporally and spatially resolved information on the lateral spreading of the jet is gained.

□

### Results

This section summarizes the main findings from the high-speed shadowgraphy campaign on superheated jet atomization. First, based on the shadowgraphs a concise review of the different flash-atomization regimes is provided and the flashing behavior of ethanol and LOx are compared. Second, the transition criterion previously introduced in [6] is briefly described and its applicability to cryogenic propellants verified through comparison with the DLR test campaign.

Figure 6 shows the changes in the ethanol jet morphology with increasing degree of superheat. For sub cooled liquid jets ( $R_p < 1$  or  $\Delta T < 0$ ), mechanical breakup controls the disintegration process. In the present experiments, jet breakup occurs in the Rayleigh regime (Figure 6a -  $R_p = 0.949$ ) due to the low injection velocities. Mechanical breakup prevails also for low degrees of superheat (see Figure 6b -  $R_p = 1.298$ ), since the onset of nucleation

requires a high degree of superheating. By increasing the superheat level ( $R_p$ ), a transition towards the fully flashing regime gradually occurs, as shown in Figure 6c,  $R_p=2.310$ . Within the transition region, the liquid jet still retains a liquid core of finite length. Flash boiling is confined to the periphery of the liquid core and results in a wider angled spray. By further increasing the parameter  $R_p$ , the fully flashing regime sets in, as shown in Figure 6d ( $R_p=37.98$ ). The jet disintegrates directly at the nozzle exit and assumes a barrel shape configuration with a large spreading angle.

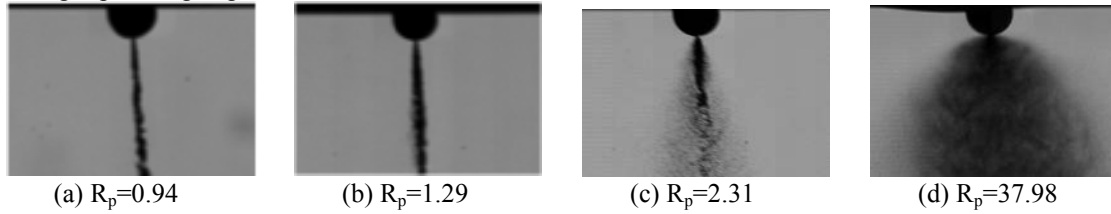


**Figure. 6:** Spray geometry at different superheat level. Fluid: ethanol,  $p_{inj}=10$  bar

The same behavior is observed for the LOx experiments despite the huge differences in the physical properties of ethanol and LOx. The fully flashing LOx jet also exhibits a barrel-shaped, finely atomized spray as shown in Figure 7. With increasing superheat levels, the spray becomes wider while preserving its bell-shape. Right at the nozzle exit plane, the spray angle may reach values as high as 150 degree depending upon the initial degree of superheat  $R_p$ , as illustrated in Figure 7.

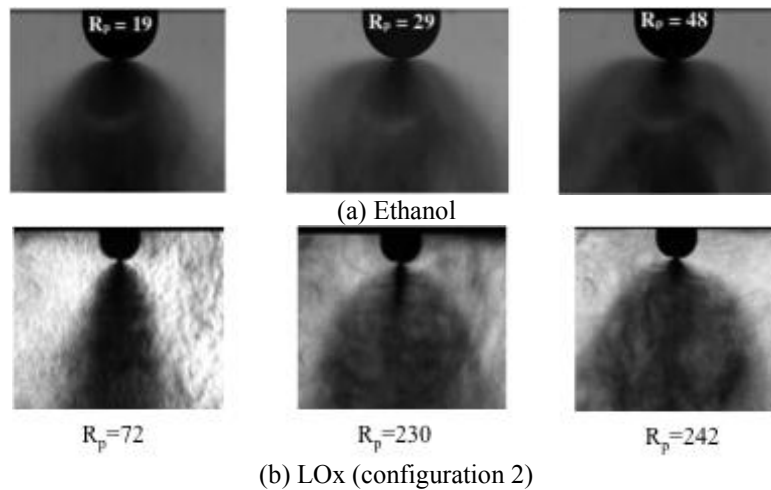


**Figure. 7:** Examples of fully flashing sprays

Using the post-processing Matlab code presented in the previous section, the spray spreading angle is extracted and plotted as a function of the superheat level in Figure 8 for both fluids. The same trend is observed for both fluids, proof that cryogenic fluids behave like storable fluids.

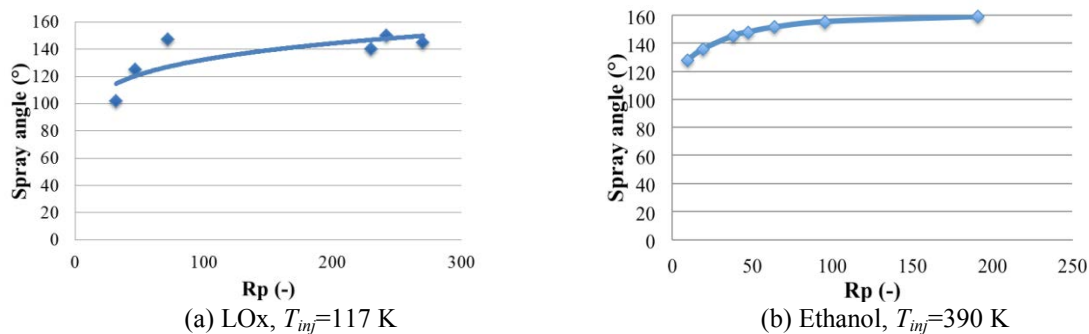


**Figure. 8:** Spray angle as function of initial superheat  $R_p$ . Axial location:  $x/D=5$ .

As shown in Figure 8, the spreading angle increases with increasing superheat. In fact higher  $R_p$  values correspond to higher nucleation rates (Eq. 4), and therefore to an increased number of micro bubbles bursting within the bulk liquid and finer atomization. As soon as a threshold of roughly 150 degree in the opening angle is reached, however, the spray morphology and angle (see Figure 7 and Figure 8) become relatively insensitive to further increase in the initial superheat. As pointed out in [6], this behavior can be explained in light of recent

advances on the theoretical description of nucleation in confined space (Kozisek et al. [10]). The authors demonstrated that the energy barrier to nucleation increases in small volumes. In the fully flashing regime, the high nucleation and bubble growth rate lead to a reduction of the liquid volume and hence to an increase of the nucleation barrier. This prevents any further increase of the nucleation rate at higher  $R_p$  values and, hence, in the spray radial spreading. These findings are consistent with the recent experimental results of Cleary et al. [2] on droplet size measurement using PDA. The authors observed a rapid decrease in the droplet SMD at the onset of flashing, which is consistent with the increase of the nucleation rate with superheat (i.e. finer atomization). Above a certain threshold (e.g. Witlox et al. [11], p. 32), the SMD exhibits an appreciably slower decay till it reaches a constant minimum value for very high initial superheat. This trend in droplet SMD provides an indirect confirmation of the quenching of nucleation rate due to volume depletion effects [10].

In order to further corroborate the similarity in flashing behavior between ethanol (storable) and LOx (cryogenic), the nucleation-based transition criterion [6] is verified for superheated cryogenic jets using LOx shadowgraphs. For clarity, the analysis and results presented in [6] are briefly summarized hereafter. We demonstrated that both the spray lateral spreading and the onset of the fully flashing regime are controlled by bubble nucleation. Specifically, the spray angle is directly related to the population of bubble clusters; while the transition to the fully flashing regime is directly related to the energy barrier to nucleation. Basically, transition will occur when the surplus in chemical potential  $\Delta\mu$  balances the work made by surface tension to form the new phase. In non-dimensional term, this is equivalent to state that the non-dimensional expression for the energy barrier in Eq. (4) must be of order one

$$C = \frac{DG^*}{k_b T_{inj}} = \frac{16\rho S^3}{3(Dm)^2} = \frac{Q^3}{(\ln R_p)^2} = O(1) \quad (7)$$

If  $\chi$  is smaller than one, then the excess in chemical potential is sufficient to overcome the work done to form a new surface and the fully flashing regime sets in. The value of the energy barrier for the different experiments considered in this work is shown in Figure 9. Their classification into the different regimes is based on the spray morphology, derived from the high-speed shadowgraphs. As can be seen, transition occurs for  $\chi=O(1)$  for both fluids and for  $\chi < 1$  all experiments are in the fully flashing region. This finding confirms the applicability of the nucleation-based threshold to cryogenic fluids and shows that, despite the huge difference in the physical properties of storable and cryogenic rocket propellants, they exhibit the same flashing behavior. The reasons for the data scatter observed in the onset region have been extensively discussed in [6] and are related to the need of including surface effects and scaling laws for correcting the temperature dependence of CNT.

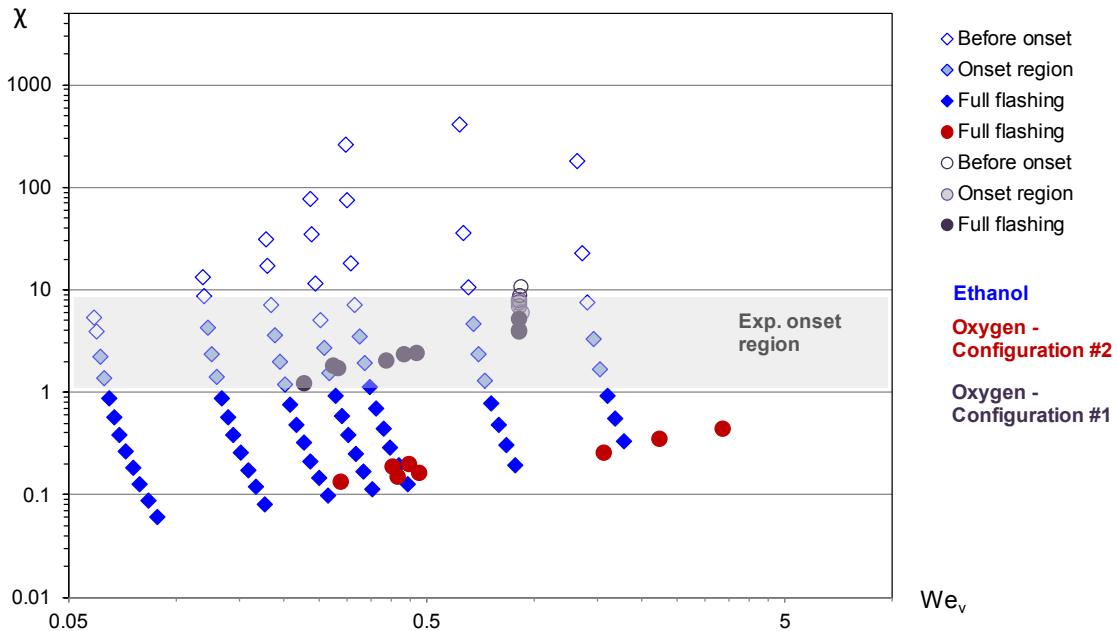


Figure. 9: Transition criterion for the onset of fully flashing regime.

## Conclusions

The disintegration behavior of highly superheated jets has been investigated by means of high-speed shadowgraphy for fluids of interest in the space industry: storable and cryogenic fluids. The experiments have been carried out at low pressure and near vacuum conditions, employing ethanol and liquid oxygen (LOx) as test fluids. For both fluids, in the fully flashing regimes the sprays exhibit a barrel shape. An increase in superheat results in a wider spray until a certain limit is reached.. After that, the spray angle becomes relatively insensitive to further increase in the initial superheat due to the liquid volume reduction, which is responsible for an increase in the nucleation energy barrier. An important finding in this work is that ethanol and LOx show a similar flashing behavior despite the huge difference in their physical properties. The similarity is further corroborated by the applicability of a nucleation-based transition criterion to cryogenic propellants. Note that the criterion had been originally proposed only for storable and retrograde fluids. In this new formulation, transition to the fully flashing regime occurs when the excess in chemical potential, equals the surface energy work. This is equivalent to state that the non-dimensional expression for the energy barrier must be of order one.

## Nomenclature

<b>Symbol</b>	<b>Quantity</b>	<b>SI Unit</b>
$a_0$	the molecular surface area	$m^2$
$D$	nozzle exit diameter	$m$
$J_{CNT}$	Nucleation rate	$1/(m^3s)$
$k_b$	Boltzmann constant	$J/K$
$L$	nozzle length	$m$
$m$	molecular weight	$kg$
$p$	pressure	$pa$
$R_p$	superheat level	-
$T$	Temperature	$K$
$v_m$	liquid molecular volume	$m^3$
$We_v$	Weber number	-
$x$	axial position	$m$
$\Delta G^*$	formation energy of the critical cluster	$J$
$\Delta\mu$	chemical potential	$J$
$\sigma$	surface tension	$N/m^2$
$\Theta$	dimensionless surface tension	-
$\chi$	transition criterion	-
<b>Subscripts</b>	<b>Quantity</b>	
$\infty$	ambient value	
$inj$	injection value	
$sat$	saturation properties	

## References

- [1] J. Senda, Y. Wada, D. Kawano & H. Fujimoto. (2007). Improvement of combustion and emissions in diesel engines by means of enhanced mixture formation based on flash boiling of mixed fuel. *Int. J. Engine Res.* 9, 15–27.
- [2] V. Cleary, P. Bowen & H. Witlox. (2007). Flashing liquid jets and two-phase droplet dispersion. i. experiments for derivation of droplet atomisation correlations. *Journal of Hazardous Materials* 142, 786–796.
- [3] D. Yildiz, P. Rambaud, J. van Beeck & J. Buchlin. (2006). Evolution of the spray characteristics in superheated liquid jet atomization in function of initial flow conditions. In *ICLASS*.
- [4] T. Kurschat, H. Chaves & G.E.A. Meier. (1992). Complete adiabatic evaporation of highly superheated liquid jets. *J. Fluid mech.* 236, 43-59.
- [5] J. R. Simoes-Moreira, M. M. Vieira, and E. Angelo. (2002). Highly expanded flashing liquid jets. *Journal of Thermodynamics and Heat Transfer* 16, 415-424.
- [6] G. Lamanna, H. Kamoun, B. Weigand & J. Steelant. Towards a unified treatment of fully flashing sprays. (submitted to the *Int. J. Multiphase flow*).
- [7] H. Kamoun, G. Lamanna, B. Weigand & J. Steelant. (2010). High-speed shadowgraphy investigations of superheated liquid jet atomisation. In *Proc. 22nd Conf. Liquid Atomization and Spray Systems. Paper ILASS2010-109*, Cincinnati (USA).
- [8] C. Manfletti. Laser Ignition of a Battleship 400N Cryogenic RCS Thruster: Pre-Ignition Conditions. (submitted to the *Journal of Propulsion and Power*)
- [9] I. Stotz, G. Lamanna, B. Weigand, and J. Steelant. (2008). Shock tube study on hydrocarbon free jets using high-speed shadowgraphy. *Proceedings of the 15th AIAA International Space Planes and*

Hypersonic Systems and Technologies Conference , 2008.

- [9] Z. Kozisek, K. Sato, S. Ueno & P. Demo. (2011). Formation of crystal nuclei near critical supersaturation in small volumes. *J. Chem. Phys.* 134 (9), 094508.
- [10] H. Witlox, M. Harper, P. Bowen & V. Cleary. (2007). Flashing liquid jets and two-phase droplet dispersion ii. comparison and validation of droplet size and rainout formulations. *J. Hazardous Materials* 142, 797–809.

## Temperature and droplet size measurements in a flashing ethanol jet using the global rainbow thermometry

H. Kamoun<sup>1</sup>, G. Lamanna<sup>1,\*</sup>, B. Weigand<sup>1</sup>, S. Saengkaew<sup>2</sup>, G. Grehan<sup>2</sup> and J. Steelant<sup>3</sup>

1: Institute of Aerospace Thermodynamics, Universität Stuttgart, Germany

2: UMR 6614 CORIA, France

3: ESTEC-ESA, Noordwijk, The Netherlands

### Abstract

A liquid injected into an environment where the pressure is lower than its saturation pressure can experience flash-atomization. Due to the non-equilibrium nature of the flashing process a non-intrusive technique is used in this work to measure simultaneously the temperature and the droplet size evolution in a flashing ethanol jet: the Global Rainbow Thermometry (GRT). The experiments are carried out with ethanol issuing from a small nozzle into a vacuum chamber at different injection temperature up to 389 K and ambient pressure between 0.04 bar and 0.08 bar. The temperature data are then compared with the data obtained in a previous work using the Differential Infrared Thermography (DIT) to cross validate the applicability of both techniques for flashing phenomenon investigation. Both temperature database measured by GRT and DIT showed a good agreement downstream the nozzle exit. But in the near nozzle region the temperature evolution measured by GRT differs much from DIT measurements, due to the high temperature gradient and multiple scattering effects in this high-density region. The droplet measurement results showed a homogeneous droplet size distribution in the flashing spray due to the explosive disintegration of the superheated liquid jet.

### Introduction

Flash-atomisation occurs when a liquid fuel is injected into an ambient pressure  $p_{am}$  lower than the fuel saturation pressure  $p_{sat}(T_{inj})$ . The superheat level can be described as the ratio between the saturation pressure at the fuel injection temperature and the prescribed back pressure:  $R_p = p_{sat}(T_{inj})/p_{am}$ . Although flash-boiling is considered to be detrimental in many technical applications (e.g. the accidental release of flammable and toxic pressure-liquefied gases in nuclear and chemical industry), it can have some potential benefits in propulsion systems as it is known to produce a fine spray with enhanced atomization.

In superheated liquid jets, the disintegration process is controlled by two concomitant factors: The onset of nucleation and the rate of bubble growth [1]. Depending on the local degree of superheat, the distribution of nucleation sites leading to bubble bursting determines the morphology of the resulting spray. Despite its technical relevance, a comprehensive and verified model for superheated jet disintegration is still not available due to the paucity of reliable experimental data. The review on recent progress on the modeling of superheated (flash) atomization and vaporization revealed that a true verification of the models can be accomplished only if both temperature and droplet size data are available. This knowledge enables the validation of evaporation and atomization models for a superheated jet and/or droplet. In this paper we are interested in the determination of the temperature and the droplet size evolution along a flashing jet.

In the past, many studies have been conducted to measure droplet size distribution along a superheated jet using different optical techniques like photography [2] or phase doppler anemometry [3, 4]. From the experimental data empirical correlations for droplet sizes were established (Witlox et al. [5], Cleary et al. [6], Yildiz et al. [3], Yildiz et al. [7] for studies at atmospheric conditions and Lecourt et al. [4] for near vacuum conditions). The proposed correlations have the merit to lead to an engineering model for the rapid and efficient characterization of a flash-atomizing liquid jet. Unfortunately their range of applicability is rather limited, being restricted to the particular fluids and operating conditions tested. On the contrary to the droplet size distribution in a flashing jet, the temperature distribution inside the jet has rarely been reported in the past despite its relevance for the modeling of a flashing phenomenon. Only intrusive techniques have been used to investigate the thermal behavior of the flashing jet. Touil [8] measured the temperature evolution along the spray centerline using thermocouples. The temperature profile presents an initial decay from the nozzle exit until a certain distance where a minimum value is achieved. The same behavior was observed by Yildiz et al. [9] using a rack of thermocouples. A major drawback of using thermocouples is that the position of the first thermocouple may trigger the inception of flash boiling, thus altering drastically the behavior and evolution of the superheated jet. Due to the non-equilibrium nature of the flashing process accurate measurements are only possible with non-intrusive techniques. Therefore a laser-based technique is used in this work to measure simultaneously the temperature and the droplet size evolution along a flashing ethanol jet: the Global Rainbow Thermometry (GRT). The temperature data along the jet axis are then compared with the data obtained in a previous work using the Differential Infrared Thermography (DIT) [10] to cross validate the applicability of both techniques for



flashing investigation.

The outline of the paper is as follows. The GRT principles and the data evaluation algorithm are described in Section "GRT principles". In the section "Experimental setup and post processing" the test facility used to investigate flashing, the GRT optical setup and the post processing are described. The results of the droplet size and temperature measurement experiments are reported and analyzed in section "Results", where a comparison between the results obtained using GRT and DIT is performed. A droplet size correlation is also developed. Final conclusions are presented in the last section.

### Global rainbow thermometry (GRT) principles

The Global Rainbow Technique (GRT), introduced by van Beeck et al [11], has a large potential of application in realistic sprays. GRT is one of the non-intrusive techniques, which can be used to measure average droplet temperature and droplet size distribution in a spray. For one droplet, the main rainbow is created by the interference between first internal reflected light ( $p=2$ ) and external reflected light ( $p=0$ ) producing a high peak of intensity light, easily identified. The angular location of the rainbow is very sensitive to the droplet refractive index value, then to the temperature. However, the rainbow location is also sensitive to the droplet shape.

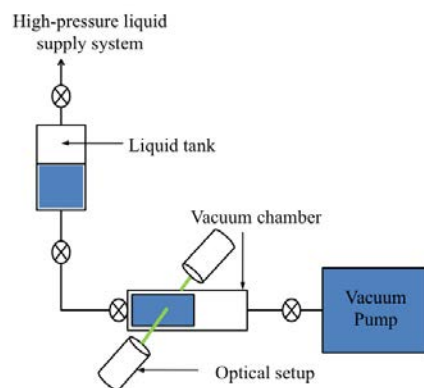
For GRT, the collective rainbow is created by the summation of a large number of individual rainbows scattered by several droplets. Analysing this global rainbow signal permits to extract the average droplet temperature and size distribution simultaneously. The position of the collective rainbow is essentially dependant on the value of the refractive index of the droplet, therefore on the temperature, while the shape of global rainbow distribution depends on the mean diameter and size distribution: the sensitivity to the particle shape is strongly reduced [12].

In literature, different inversion algorithms have been proposed with various degrees of complexity, computational efficiency and underlying simplifying assumptions to extract the droplet refractive index and the size distribution from the GRT optical signal. Van Beeck et al. [11] proposed several inversion algorithms of the GRT experimental signal based on the Airy theory and on the assumption that the size distribution is a lognormal function. More recently, Saengkaew [13] introduced a new methodology to accurately extract the value of the refractive index (temperature) and size distribution from the GRT intensity profile based on Nussenzveig's theory [13]. More specifically, the inversion is carried out in two complementary steps:

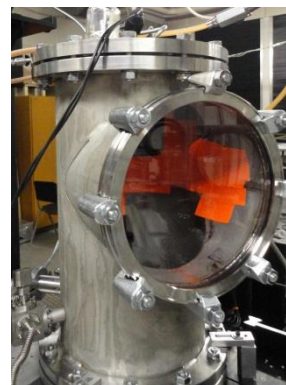
1. By using a Non Negative Last Square method, the best size distribution for a given refractive index value is researched.
2. By minimizing the distance between the measured intensity profile and the computed intensity profile obtained from step1, the refractive index is extracted.

This inversion algorithm is used in this work to measure the temperature and droplet size evolution in an ethanol flashing spray.

### Experimental setup and post processing



(a) Test rig and periphery



(b) Vacuum Chamber

**Figure 1.** Test facility

#### Test facility

The test bench is designed for performing flash atomization and vaporization experiments at medium vacuum conditions ( $0.02 \text{ bar} < p_{\text{am}} < 0.4 \text{ bar}$ ). A schematic layout of the facility is shown in Fig. 1a. The injector chosen is a standard automotive fuel injector, which has been modified for low-pressure applications. The nozzle has a diameter  $D$  of  $150 \mu\text{m}$  and an exit orifice aspect ratio  $L/D = 6$ . One circular big window (Diameter 200 mm) is installed in the vacuum chamber (Fig.1b) allowing capturing the global rainbow signal of the spray. Further operational details and details of instrumentation, as well as more complete schematics can be found in [14]. All

experiments presented in this paper are performed with ethanol under ambient temperature  $T_{am}=297\text{ K}$ .

#### GRT optical setup

The global rainbow optical setup is shown in Fig. 2. The experimental setup consists mainly of two parts: emitting part and receiving part.

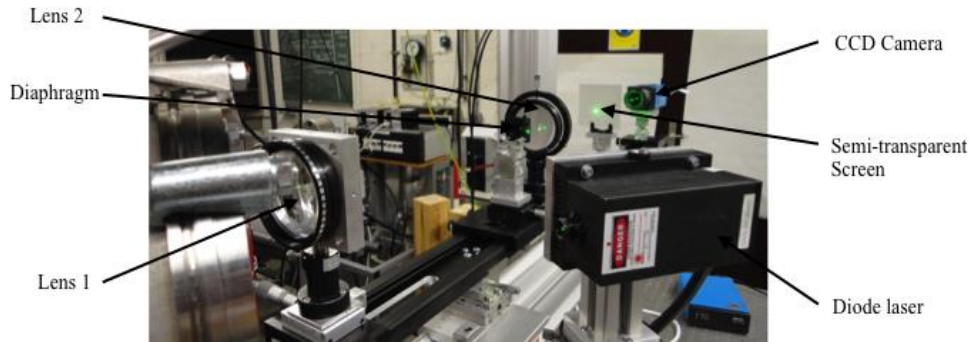


**Figure 2.** GRT optical setup

The emitting part consists of a diode laser ( $\lambda=532\text{nm}$ ,  $P=500\text{mW}$ ). The laser emits a beam with a diameter equal to 1 mm and is directed towards the spray. The light scattered by the ethanol droplets, is collected at an angle of roughly 141 degree from incident beam. The receiving part consists of two spherical lenses, a diaphragm and a CCD camera. Both lenses have a large diameter (80 mm) and a focal length  $f=160\text{ mm}$ . In the image plane of the first lens, a diaphragm (diameter 2 mm) is placed to select and define the measurement volume. This will let only the selected scattered light from the measurement volume pass and lock undesirable ambient light. The second lens projects the scattered light on a semi transparent screen scanned by a CCD Camera (PCO 4000 with a resolution of 4008 x 2672 pixels). The semi-transparent screen is placed at the image plane of the two-lenses system. Since GRT is a point measurement technique, the emitting and receiving parts are mounted on a 2D traverse allowing the horizontal and vertical positioning of the measuring volumes relative to the nozzle exit. The nominal resolution of the traverse is  $10\text{ }\mu\text{m}$ .

As the rainbow technique is based on the measurement of the absolute location of the light scattered around the rainbow angle, it is essentially to know the absolute angular location of each pixel of the camera measured by an additional setup shown in Fig.3.

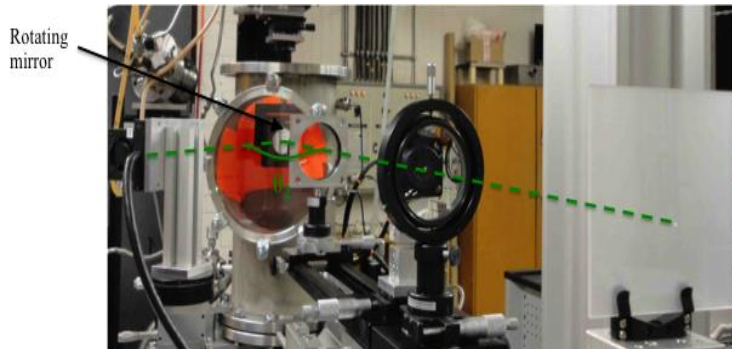


**Figure 3.** Calibration setup

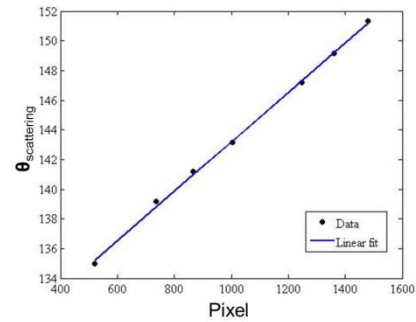


**Figure 4.** Calibration curve

The top of the vacuum chamber is removed and a rotating mirror is placed in the same position as the injector head. By rotating the mirror, the laser beam is reflected resulting in a bright point in the semi-transparent screen and the image taken by the camera. The associated angle  $\theta_2$  (Fig.3) is determined by reading the position of the mirror on the rotation stage. The scattering angle is then given by:

$$q_{\text{scattering}} = 180 - q_2 \quad (1)$$

The correlation giving the relation between the pixel on the camera and the scattering angle is plotted in Fig. 4. The uncertainty in the temperature measurement using this method results from the error on determining the scattering angle. The total error in the scattering angle measurement results in the error in reading the angle on the mirror rotation stage  $\delta_1$ , in reading the pixel corresponding to the scattering angle in the image taken by the camera  $\delta_2$  and the error from the linear fit giving the relationship between pixels and scattering angles  $\delta_3$ .

The error in reading the scattering angle is determined by the resolution of the rotation stage:  $\delta_1=0.008^\circ$ . During the experiments the angular range the camera was acquiring was about  $16.3^\circ$ . This corresponds to a pixel range of 960 pixel. So the error of one pixel corresponds to an error in the angle  $\Delta\delta_2=0.02^\circ$ . The maximum error in the

scattering angle resulting from the use of the linear fit is  $\Delta\delta_3 = \max(\theta_{Data} - \theta_{fit}) = 0.2^\circ$ . So the precision reached with this method is of  $\Delta\delta = \delta_1 + \delta_2 + \delta_3 = 0.228^\circ$  that means a systematic error for temperature measurement for ethanol of ca.  $\pm 4K$ . No influence of the error in the scattering angle on the droplet diameter measurements is expected, since the size measurement depends only on GRT profile shape.

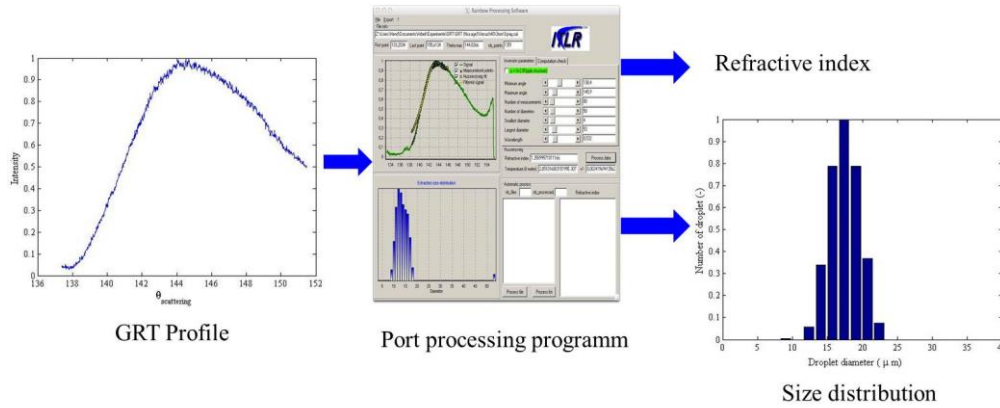


**Figure 5.** Post-processing

#### GRT post processing

The recorded image (Fig. 5) is transformed to an intensity profile versus the absolute scattering angle using the relationship scattering angle/pixel constructed by the calibration. Using the inversion algorithm developed by Saengkaew [13], the refractive index and the size distribution are extracted (Fig. 5). The correlation between ethanol refractive index and temperature need to be known to determine the average temperature of the droplets. A correlation found in [14] is used in this work.

## Results

In the following section, temperature and droplet size measurements results are reported. This section is divided into two parts. In the first part the temperature data obtained by GRT are presented and compared to the data obtained in a previous work [10] using the differential infrared thermography (DIT) to cross-validate both techniques. In the second part the droplet size distribution in a flashing jet is presented and a correlation to predict the droplet size is developed.

#### Temperature results

The axial temperature distributions in an ethanol superheated spray, obtained by using GRT and DIT are compared in Fig. 6a. In Fig 6b the dimensionless axial temperature profiles measured by both methods are plotted together with the theoretical profile for a single phase turbulent jet [15] given by:

$$\frac{T_{axis} - T_{am}}{T_{inj} - T_{am}} = \frac{0.7}{0.14x / D + 0.29} \quad (2)$$

In the downstream region ( $x/D < 25$ ), the GRT measurement points show good agreement with the temperature data obtained using DIT. A maximal discrepancy of 8% is observed. Notice that the relative error in GRT data is about 12%. Both methods showed the same trend predicted by the theory in this region. As expected a decrease of the temperature along the spray axis is observed. The measured temperature values match the theoretical values thus implying that flash-vaporization plays no role in the downstream cooling of the jet.

However near the nozzle exit, the dimensionless axial temperature profile in a flashing spray shows that the axial temperature approaches the ambient temperature much faster in a fully flashing jet. Indeed, from the DIT temperature data, already at  $x/D \approx 4$  the difference ( $T_{axis} - T_{am}$ ) has already reduced by 60% from the initial temperature difference ( $T_{inj} - T_{am}$ ) due to flash boiling. Despite this discrepancy, the temperature measured by the DIT showed the same trend as the theory. But the GRT measurements showed an opposite trend: an increase in the temperature is observed. The same opposite trend in the GRT temperature measurements was also observed by Yildiz et al [16].

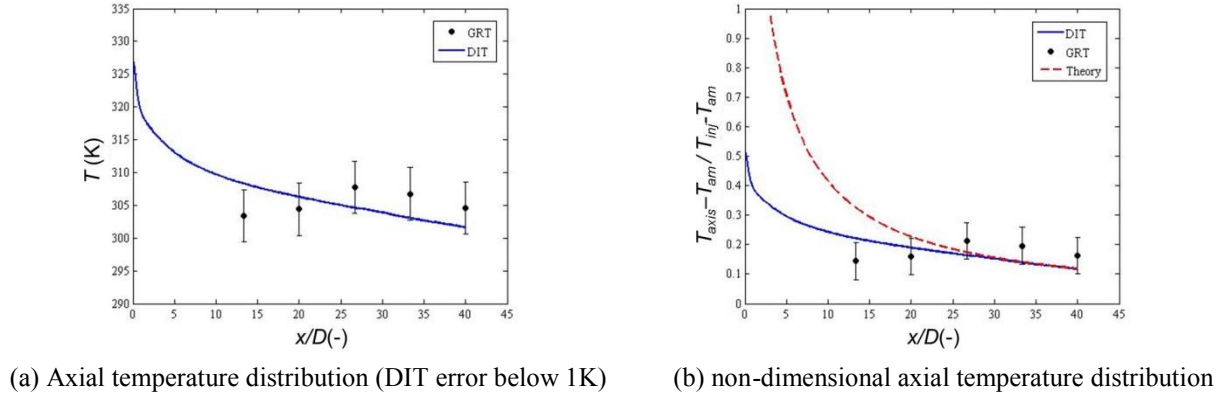


**Figure 6.** DIT vs. GRT. Liquid: Ethanol.  $T_{inj}=358$  K,  $p_{am}=0.06$  bar,  $R_p=16.4$

This behaviour is a consequence of three combined factors. First of all, GRT is sensitive to the internal temperature gradient inside the droplet. This gradient is present especially during the initial rapid cooling phase of the jet in the near nozzle region as showed by the DIT temperature measurements. Moreover due to the high density of the dispersed phase in this region, the global rainbow signal is disturbed or in extreme cases suppressed by multiple scattering. The third disturbing factor is the presence of non-spherical droplets and ligaments near the nozzle exit, which alter the quality of the optical signal. Despite these encountered problems in the near nozzle region for the GRT method, the good agreement between DIT measurements, GRT measurements and the theory in the downstream region validates both methods and proves their applicability to measure the temperature in a flashing spray.

#### Droplet size results

The data inversion algorithm described in a previous section allows the determination of the droplet size distribution as shown in Fig. 5. From this size distribution the mean diameter  $d_{10}$  is calculated. Figure 7a shows the mean diameter evolution along the spray centreline for different injection conditions. The standard deviation of this measurement is below 8%.

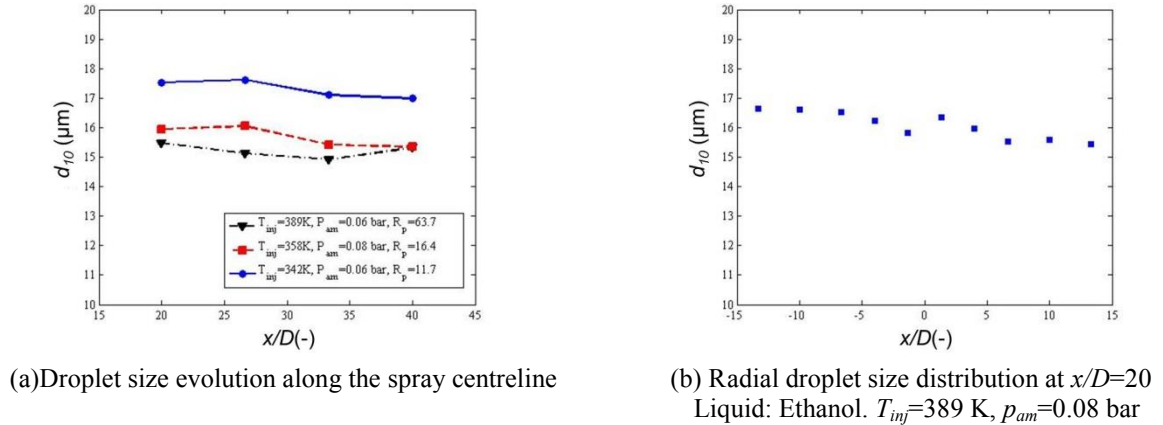


**Figure 7.** Droplet size evolution along the spray centreline

As expected the droplet diameter decreases with increasing superheat level. In fact, a flashing jet is characterized by an abrupt phase transition (liquid to gas) within the liquid jet through nucleation and bubble growth and breakup of the liquid phase. Based on the classical nucleation theory (CNT) the number of stable vapour nuclei generated per unit volume and time  $J$  is proportional to

$$J_{CNT} \propto \sqrt{\frac{2\sigma}{\rho m}} \exp\left\{-\frac{16\rho\sigma^3}{3(k_b T_{inj} \ln(R_p))^2}\right\} \quad (3)$$

where  $m$  is the mass of a liquid molecule  $\sigma$  is the surface tension,  $k_b$  is the Boltzmann constant,  $T_{inj}$  is the injection temperature and  $R_p$  denotes the superheat level. From this equation it is clear that with increasing superheat level the nucleation rate increases too, leading to smaller droplet in the flashing spray after jet disintegration.

The experimental results show that the droplet sizes are homogeneous along the axis. The same is also observed

for the radial evolution of the droplet diameter (Fig. 7b). The fully flashing spray is also characterized by a uniform droplet size distribution. This finding leads to the assumption, that there is only one nucleation event for the flashing spray. This assumption is confirmed by Kožíšek et al. [17]. They determined the conditions under which the first nuclei of a new phase are formed, using the numerical solution of kinetic equations for homogeneous and heterogeneous nucleation. They found that the energy barrier for nucleation is higher in smaller liquid droplet. A higher superheating is also needed to form vapor nuclei in small volumes. However, after the jet disintegration due to bubble bursting, small droplets arise and the degree of superheat decreases. This inhibits the formation of new vapor nuclei in these small liquid droplets. Therefore, the droplet diameter decreases slowly along the spray centerline due only to the evaporation process.

From the experimental data, a correlation to predict the droplet diameter in a flashing spray is developed based on the classical nucleation theory. From a heuristic point of view, the process of flash-atomization and vaporization is clearly described as the subsequent progression of homogeneous (or heterogeneous) nucleation, bubble growth and breakup through bubble disruption. Senda et al [1] assumed that the droplet breaks up into small droplets twice as many as the number of bubbles. As a consequence, the diameter of droplets after breakup can be calculated. The number of droplets is calculated from the nucleation rate:

$$n_d = 2J_{CNT}V_0\Delta t \quad (4)$$

where  $V_0$  is the start volume and  $\Delta t$  is the nucleation time in the range of  $10^{-3}$ s [18]. Since:

$$m_0 = n_d r_l V_d = r_l V_0 \quad (5)$$

and using eq. (4) the droplet diameter is given by:

$$d_{10} = 2 \left( \frac{3}{8\rho J_{CNT}\Delta t} \right)^{1/3} \quad (6)$$

A comparison between the measured and the calculated droplet diameter is reported in Table 1.

$T_{inj}$ (K)	$p_{am}$ (bar)	$R_p$ (-)	Droplet diameter (exp.) ( $\mu m$ )	Droplet diameter (Theory) ( $\mu m$ )	Error (%)
342	0.06	11.7	17.29	18.8	8
358	0.08	16.4	15.64	16.1	2.85
389	0.06	63.7	15.1	15	0.66

**Table1:** Comparison between the measured and the calculated droplet diameter

The good agreement between theory and experiments validates the assumption of a nucleation-controlled shattering of a superheated jet.

## Conclusions

Global Rainbow Technique (GRT) has been successfully used to measure the temperature and droplet size evolution in an ethanol flashing spray.

By comparing the obtained axial temperature profile with the profile obtained in a previous work using the differential infrared thermography (DIT) and with the theory of a single phase turbulent jet, the applicability of both techniques for flashing investigation was validated. However a good agreement between both techniques was only observed in the downstream region of the nozzle exit ( $x/D > 20$ ). In the near nozzle region, the GRT temperature measurements show an opposite trend as the one measured by the DIT and predicted by the theory: the droplet temperature increases. This is due to the high temperature gradient, the presence of ligaments and non-spherical droplets and multiple scattering effects in this high-density region.

The droplet measurement results showed that the droplet diameter decreases with increasing superheat level, since the number of stable vapour nuclei increases too. The fully flashing spray is also characterised by a uniform droplet size distribution. This proves that there is only one nucleation event for the superheated liquid injection. Based on the nucleation theory a correlation is developed to predict the droplet diameter in a flashing spray. The measured and the calculated droplet size showed a good agreement with a max discrepancy of 8% corresponding also to the measurements standard deviation.

## Nomenclature

<i>Symbol</i>	<i>Quantity</i>	<i>SI Unit</i>
$d_{10}$	mean diameter	$m$
$D$	nozzle exit diameter	$m$
$f$	focal length	$m$
$J_{CNT}$	Nucleation rate	$1/(m^3 s)$

$k_b$	Boltzmann constant	J/K
$L$	nozzle length	m
$m$	molecular weight	kg
$n_d$	droplet number	-
$p$	pressure	pa
$P$	Laser power	W
$R_p$	superheat level	-
$T$	Temperature	K
$V$	Volume	m <sup>3</sup>
$x$	axial position	m
$\delta$	error	-
$\Delta t$	nucleation time	s
$\lambda$	wave length	m
$\theta_{\text{scattering}}$	Scattering angle	°
$\rho$	density	kg/m <sup>3</sup>
<b>Subscripts</b>	<b>Quantity</b>	
$axis$	axial value	
$am$	ambient value	
$inj$	injection value	
$l$	liquid properties	
$sat$	saturation properties	
$0$	start condition	

## References

- [1] J. Senda, Y. Wada, D. Kawano & H. Fujimoto. (2007). Improvement of combustion and emissions in diesel engines by means of enhanced mixture formation based on flash boiling of mixed fuel. *Int. J. Engine Res.* 9, 15–27
- [2] R.D. Reitz. (1990). A photographic study of flash boiling, *aerosol Science Technology*, 12, 561-569.
- [3] D. Yildiz, P. Rambaud & J. van Beeck. (2004). Break-up, droplet size and velocity characterizations of a two-phase flashing r134a jet. In 5th Int. Conf. Multiphase Flow.
- [4] R. Lecourt, P. Barricau & J. Steelant. (2009) Spray velocity and drop size measurements in vacuum conditions. *Atomization and Sprays* 19 (2), 103–133
- [5] H. Witlox, M. Harper, P. Bowen & V. Cleary. (2007). Flashing liquid jets and two-phase droplet dispersion ii. comparison and validation of droplet size and rainout formulations. *J. Hazardous Materials* 142, 797–809.
- [6] V. Cleary, P. Bowen & H. Witlox. (2007) Flashing liquid jets and two-phase droplet dispersion. i. experiments for derivation of droplet atomisation correlations. *Journal of Hazardous Materials* 142, 786–796.
- [7] D. Yildiz, P. Rambaud, J. van Beeck & J. Buchlin. (2006). Evolution of the spray characteristics in superheated liquid jet atomization in function of initial flow conditions. In ICLASS.
- [8] A. Touil 2004. Modelisation des Jets Diphasiques Liquide Vapeur et du Rain-Out . PhD Thesis. Ecole Nationale Supérieure des Nines de Saint-Etienne.
- [9] D. Yildiz, P. Rambaud, J. van Beeck & J. Buchlin. (2003). Thermal characterization of a r134a two-phase flashing jet. 6th National Congress on Theoretical and Applied Mechanics, Gent, Belgium, May 26-27.
- [10] H. Kamoun, G. Lamanna, B. Weigand & J. Steelant. (2012) Experimental flashing jet thermal characterization by non intrusive optical technique. In Space propulsion 2012
- [11] J.P.A.J. van Beeck, D. Giannoulis, L. Zimmer and M.L. Riethmuller, *Optics letters*, 24 (1999), 1696-1698.
- [12] S. Saengkaew, G. Godard, J.B. Blaisot and G. Gréhan, Experimental analysis of global rainbow technique: sensitivity of temperature and size distribution measurements to nonspherical droplets. *Experiments in Fluids*, Saengkaew. S PhD
- [13] H. Kamoun, G. Lamanna, B. Weigand & J. Steelant. (2010). High-speed shadowgraphy investigations of superheated liquid jet atomisation. In Proc. 22nd Conf. Liquid Atomization and Spray Systems. Paper ILASS2010-109, Cincinnati (USA).
- [14] D. Bonin. (2006). Thermométrie par arc-en-ciel, Master thesis, CORIA, Rouen
- [15] G.N. Abramovich. (1963). The theory of turbulent jets. The M.I.T Press.
- [16] D. Yildiz, J.P.A.J. van Beeck & M.L. Riethmuller. (2002). Global rainbow thermometry applied to a flashing two-phase R134-A Jet , 11th International Symposium on Application of Laser Techniques to Fluid Mechanics, Lisbon, Portugal, July 8-11, 2002
- [17] Z. Kozisek, K. Sato, S. Ueno & P. Demo 2011 Formation of crystal nuclei near critical supersaturation in small volumes. *J. Chem. Phys.* 134 (9), 094508 (9 pages).
- [18] M. Wilck, K. Hämeri, F. Stratmann and M. Kulmalas. (1998). Determination of homogeneous nucleation rates from laminar-flow diffusion chamber data. *J. Aerosol Sci.* Vol. 29, No. 8.



## Analysis of Multi-hole GDI Injectors under Flash Boiling Conditions

A. Wood<sup>1</sup>, G. Wigley<sup>1</sup> and J. Helie<sup>2</sup>

1: Dept. AAE, Loughborough University, UK

2: Continental Automotive SAS, Toulouse, France

### Abstract

During certain stages of GDI engine operation there is an inevitability of the occurrence of flash boiling due to increased fuel temperature and reduced in-cylinder pressure. This paper describes the application of the phase Doppler technique to investigate the spray from a 6-hole 60° injector under sub-atmospheric conditions and with the addition of heat.

It was found that the level of jet-to-jet interaction, even under non-superheated conditions leads to spray angle decrease and droplet entrainment in the steady state injection period, however, the flashing process lead towards a more pronounced spray collapse occurring earlier after the start of injection.

The nature of the vortex formed on the edge of the spray tip under flashing conditions was also investigated. It was shown that this vortex is relatively strong, drawing into it all droplets with diameter of less than 10µm, and that the lasting legacy of the vortex is that the spray continues to collapse throughout the duration of the injection.

The PDA results confirm, as expected, that the drop size is reduced under flash boiling conditions, and this is most evident in the spray core, the area into which the small droplets and fuel vapour are drawn by a reduction in pressure in this area.

### Introduction

During certain stages of the operation of modern GDI engines, usually low load or with a warm engine, the combination of increased fuel temperature and sub-atmospheric cylinder pressure during injection can lead to a phenomenon known as flash boiling. Put simply flash boiling is the rapid formation and growth of bubbles inside droplets as the level of evaporation promoted by the droplet heating cannot be sustained purely on the droplet surface, which leads to the shattering of the droplets into many smaller droplets as part of a two-phase flow region.

Flash boiling will occur when the ambient pressure into which the fuel is injected is below the saturation pressure. Saturation pressure increases with fuel temperature.

Zeng et al [1] investigated a multi-hole injector under various superheat degrees with a summary of the results shown in Figure 1. A 90° cone angle injector was used for this investigation, whereas a 60° injector will be used for the results presented in this paper. As expected with increased levels of flash boiling the vapour quantity is increased, which will lead to an overall greater likelihood of entrainment. These results suggest that a large degree of superheat is required in order to cause full spray collapse, but even at partial collapse conditions strong vortices appear to be formed on the edge of the spray tip.

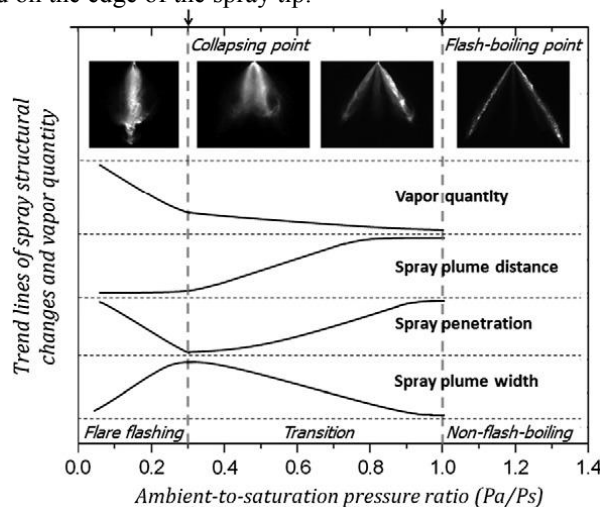
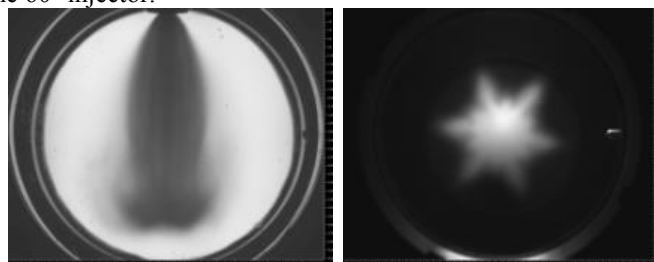


Figure 1. Summary of investigation on flashing alcohols fuels

Numerical work of Khan et al [2] described the formation of jet to jet interaction and the sprays progression. They suggest that the fuel is drawn into the centre of the spray from the original spray streams and is forced out

of this area at a stagnation plane in the spray. This process seems to be experimentally confirmed [3], where interstitial streams under flash boiling conditions in the gaps between the original injection streams seems to be linked to such process.

Previously an investigation was carried out by Mojtabi et al [4] with a multi-hole 60° injector, the XL2 from Continental. This investigation showed that even under a low degree of superheat (or even negative superheat), as shown in Figure 2 which features gasoline as the test fuel with ambient pressure 0.3 bar and fuel temperature 60°C, the spray collapse and formation of interstitial streams occurs. This suggests that the spray collapse and formation of the interstitial streams is partly due to the flash boiling process, but also due to the formation of a blockage to pressure equalisation between the inside and outside of the spray. In the course of this work a comparison was made between a 60° and a 90° injector which showed that the sprays from the 90° injector would only collapse under a high degree of superheat, however, the spray collapse is observed for much a much lower degree of superheat for the 60° injector.



**Figure 2.** Summary of investigation on flashing fuels with a 60° injector

### Experimental test-rig

The investigation featured a multi-hole XL3.0 GDI injector from Continental Automotive. The prototype injector, which was made for research purposes, features a 6 hole nozzle with a total cone angle 60° and 60° circumferentially between the three spray streams. The injector was fuelled with n-heptane with a fuel line pressure of 100 bar.

The spray testing was conducted inside a high pressure/high temperature cell which can operate in the range 0.1-10 bar and fuel temperature 20-100°C. The cell is filled with nitrogen and regularly purged to remove the remnants of previous injections. The injection chamber was constructed with quartz windows at an angle of 110° to allow the 70° scattering angle required for optimal application of the phase Doppler technique. The fuel is heated by heaters placed within the injector holder and measured at the injector tip. The set-up, including the pressure cell and the phase Doppler system, is shown in Figure 3. The whole system is controlled with an in-house LabVIEW system.

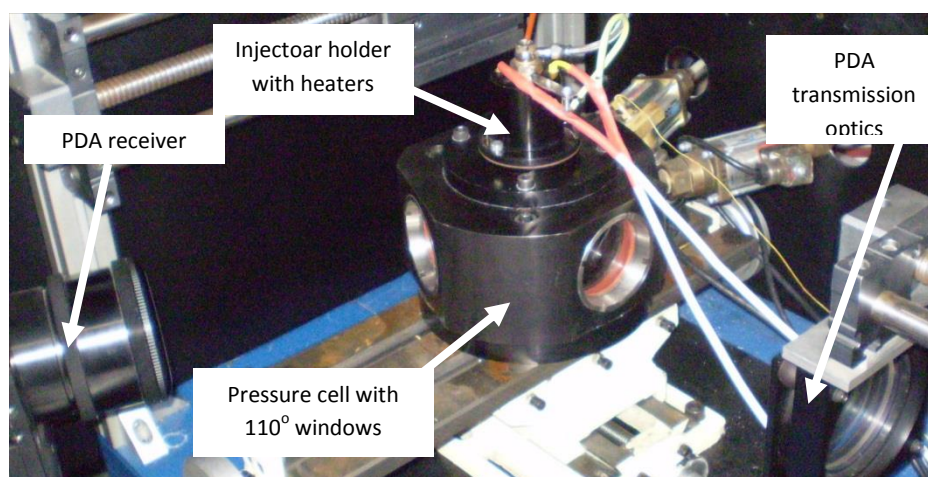


**Figure 3.** High pressure/high temperature cell and PDA transmitter and receiver

The design, construction and application of the two component PDA transmission system to study dense GDI fuel sprays has been well documented, [5]. The configuration for the 488 and 514 nm laser beam wavelengths at the final focussing lens was:- beam diameters of 5 mm, equal beam pair separations of 50 mm, laser powers of 100 and 200 milli-watts per beam with a horizontal polarisation. With a focal length lens of 300 mm this produced coincident measurement volumes of diameters of 37 and 39 microns with fringe spacings of 2.94 and 3.10 microns respectively for the two wavelengths. The 514 nm beam pair were in the vertical plane to measure



the axial droplet velocity and size with the 488 nm beam pair in the orthogonal plane to measure the radial droplet velocity.

The Dantec 57X10 receiver was positioned at a scattering angle of 70 degrees. This optical configuration resulted in an effective measurement volume length of 0.1 mm. In-conjunction with the Dantec processor the transmitter and receiver set up produced a droplet velocity bandwidth of -30 to 110 m/s with a drop size measurement range of up to 100 microns.

Measurements were conducted at four axial positions downstream in radial scans through the spray through both the original spray axis and the interstitial stream, which represents and injector rotation of 30°. Each radial scan traversed from the injector axis to the outer edge of the spray stream. The measurement co-ordinates in the vertical plane were  $Z = 10, 20, 30$  and  $40\text{mm}$  below the nozzle tip. The horizontal traverse was computer controlled and programmed with a radial step increment,  $x$ , of nominally 5-10% of the  $Z$  value in order to resolve local high velocity gradients across the spray stream. Quoted time is after electronic start on injection (AESOI).

## Results and Discussion

As previously mentioned the flash boiling process greatly affects the nature of the spray produced by the multi-hole injectors. The flash boiling process leads to an overall collapsing of the spray and formation of new spray streams in the gaps between the original spray streams, known as interstitial streams.

The analysis presented is acquired at three different pressure levels: 0.9, 0.3 and 0.1 bar and a two temperatures for the lowest pressure of 25 and 45°C. These values were chosen as they represent a non-flashing case, a non-flashing case which exhibits a weak spray collapse, a case with the fuel condition close to the saturation vapour pressure and a fully flashing case respectively. The 4 investigated cases are shown on the saturation pressure curve for n-heptane in Figure 4. As shown in [4], a dramatic increase of temperature would generate a complex coupled faster evaporation, therefore here the pressure dependency has been used and the change in temperature is limited. However, in any flash boiling conditions, evaporation will proceed together with the changed atomisation.

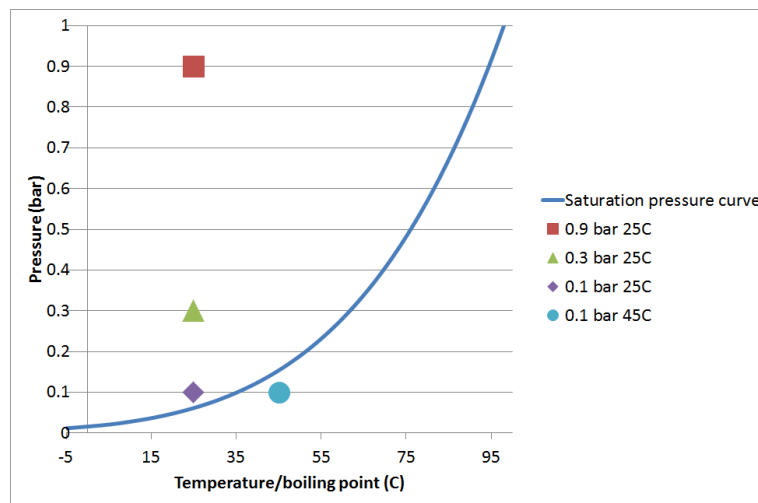


Figure 4. Test sites in relation to the saturation pressure curve

### Behaviour in Main Spray Streams

The velocity vectors for the early injection period for the main streams, shown in Figure 5:

0.9 bar 25°C

- Regular injection stream with jet like profile

0.3 bar 25°C

- Still maintains jet like profile but overall injection width has increased

0.1 bar 25°C

- Wide jet profile again formed
- Some evidence at  $Z=10$  of full cone spray formation beginning due to spray collapsing

0.1 bar 45°C

- Velocity vectors missing in spray centre due to low beam transmission efficiency
- Spray shows no jet like profile, but immediately forms a full cone
- Some evidence of vortices forming on the outer edge at  $Z=30$  and  $40$

Injector axis

→ 50m/s

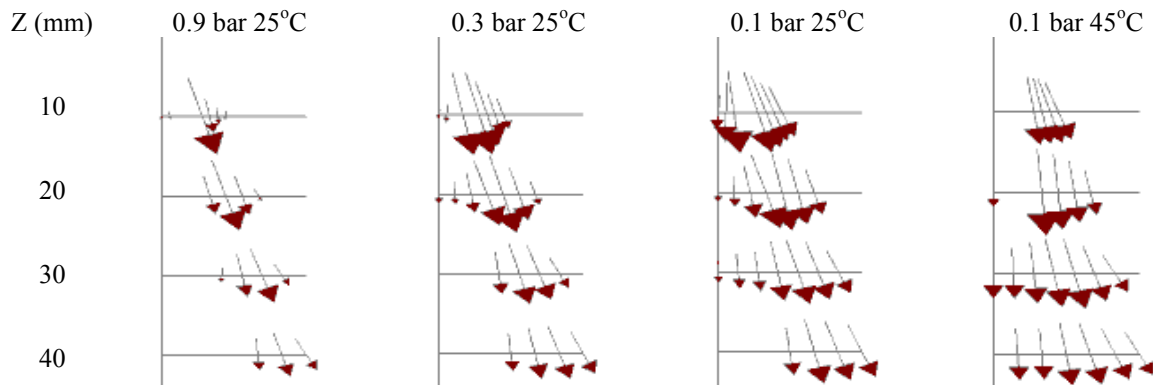


**Figure 5.** Velocity vectors in main spray streams @  $t=0.88\text{ms}$  AESOI – early injection period

The velocity vectors for the steady state injection period for the main streams, shown in Figure 6:

0.9 bar 25°C

- Jet like profile remains, but has moved slightly inboard

0.3 bar 25°C

- Spray has a jet like core, but an overall wide profile and again has moved inboard

0.1 bar 25°C

- Spray has formed a solid cone spray
- Highest velocities are again inboard, but along the same jet axis as for the non-flashing case

0.1 bar 45°C

- Vectors again missing in spray core near the injector due to low beam transmission efficiency
- Solid cone spray formed
- Highest velocities are along the injector axis showing a full spray collapse

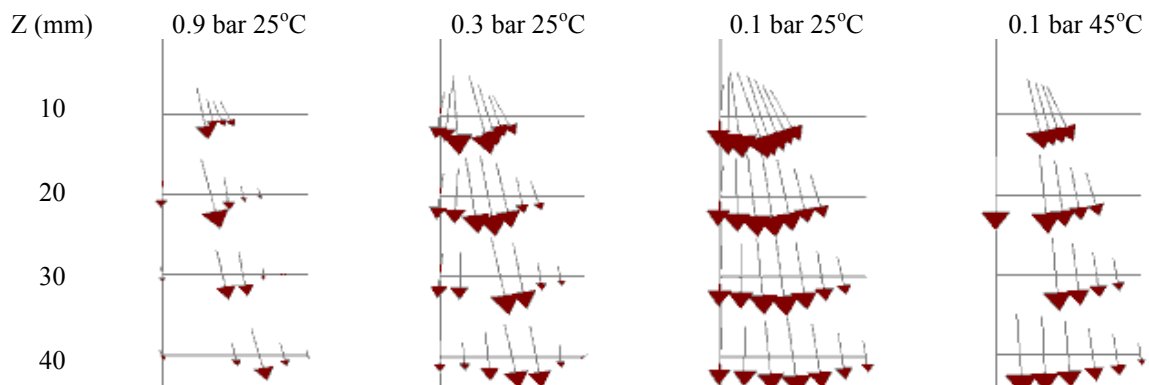


**Figure 6.** Velocity vectors in main spray streams @  $t=2.13\text{ms}$  AESOI – steady state injection period

Initially the reduced pressure and increased temperature both lead to an increase in spray width and this increased spray width correlates to an increased level of spray collapse. The non-flashing cases exhibit jet like profiles at the start of injection and with the reduced pressure levels this jet widens as the injection progresses. The maximum velocity vector is moved slightly inboard for the reduced pressure levels. For the flashing case spray collapse happens immediately after the start of injection due to the small droplets and fuel vapour being drawn into the spray core. The overall width of the spray cone is slightly reduced over the duration of the injection due to an increased level of spray collapse.

#### ***Behaviour in Interstitial Spray Streams***

The velocity vectors for the early injection period for the interstitial streams, shown in Figure 7:

0.9 bar 25°C

- Little spray has migrated into this area due to the strong jet-like nature of the spray in the main stream

0.3 bar 25°C

- A weak jet-like spray is formed possibly due to jet-to-jet interactions
- Some evidence of the start of spray collapse at  $Z=10$

0.1 bar 25°C

- Wider jet-like spray is formed

- Again evidence of the start of spray collapse
- 0.1 bar 45°C
- Fully collapsed spray initially very similar to that observed in the main streams for this condition
  - Strong evidence of vortices propagating downstream at Z=30 and 40 on the edge of spray

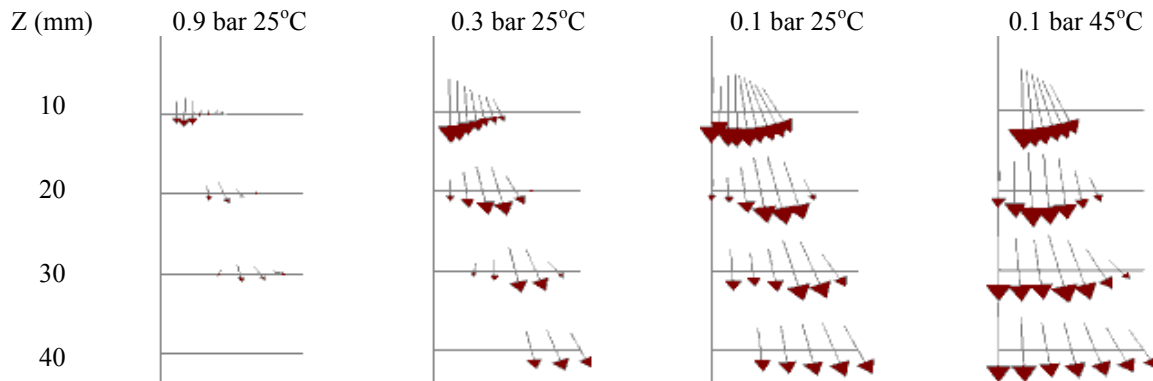


**Figure 7.** Velocity vectors in interstitial spray streams @  $t=0.88\text{ms}$  AESOI – early injection period

The velocity vectors for the steady state injection period for the interstitial streams, shown in Figure 8:

- 0.9 bar 25°C
- Little spray has migrated into this area due to low levels of jet-to-jet interaction
- 0.3 bar 25°C
- A collapsed spray exists around the injector axis
  - Some weak motion exists further from the spray axis, again possibly due to jet-to-jet interactions
- 0.1 bar 25°C
- Fully collapsed spray forming a solid cone spray
  - Similar velocities exhibited across spray
- 0.1 bar 45°C
- Again a fully collapsed spray exists which forms a solid cone spray
  - Highest velocity vectors are close to the injector axis
  - Downstream the spray collapses inwards

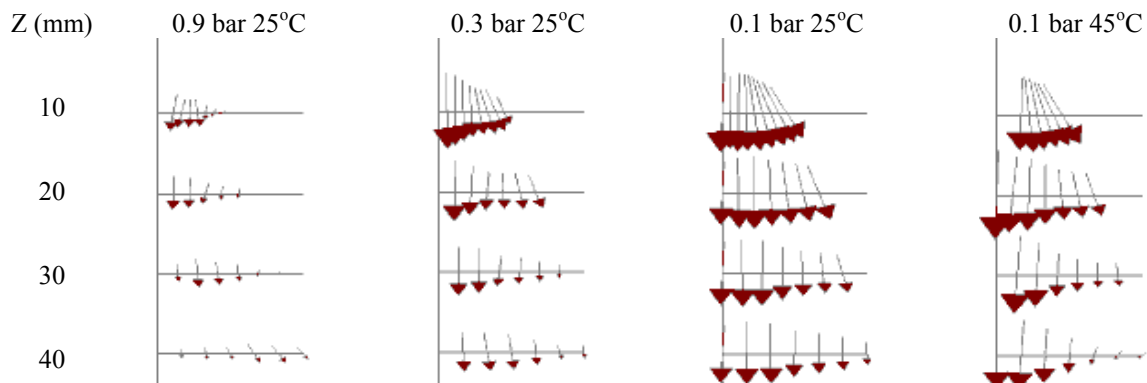


**Figure 8.** Velocity vectors in interstitial spray streams @  $t=2.13\text{ms}$  AESOI – steady state injection period

In the interstitial streams it can be seen that with reduced pressure the level of jet-to-jet interaction is increased. As the streams combine it increases the likelihood of spray collapse as the fuel forms a blockage to air penetrating into the spray core to equalise the pressure outside and inside the cone. These effects are observed even from the start of injection for the flashing case as the many small droplets and fuel vapour are immediately drawn into the central portion of the spray by the low pressure, as the level of jet-to-jet interaction is increased with the flash boiling process.

### ***Spray Collapse***

One point of interest is the time resolved behaviour on the edge of the spray under flashing conditions. The plot in Figure 9 shows the radial velocity of droplets recorded over the injection period for the 0.1 bar 45°C test site at the edge of the spray,  $Z=40\text{mm}$ ,  $x=15\text{mm}$ . Droplets over  $10\mu\text{m}$  are blue and droplets under  $10\mu\text{m}$  yellow.

- Initial droplets are all large and are moving away from the injector axis – this is usual as large drops will always reach the measurement volume first as they have the greatest momentum due to their mass.
- Then a large number of small drops arrive at the measurement volume, nearly all with +ve velocities, away from the injector axis. This could be the lower side of a vortex passing through.
- Suddenly the direction of travel of all small droplets changes. This appears to suggest the upper side of the recirculation is now passing through. The large drops maintain their original trajectory as they are suitably massive to not be entrained.
- After the initial maximum in –ve radial velocity the profile relaxes, but still with all small droplets showing a velocity towards the spray axis, showing the spray continues to collapse inwards. It appears this is as a consequence of the vortex which by this time is far downstream.

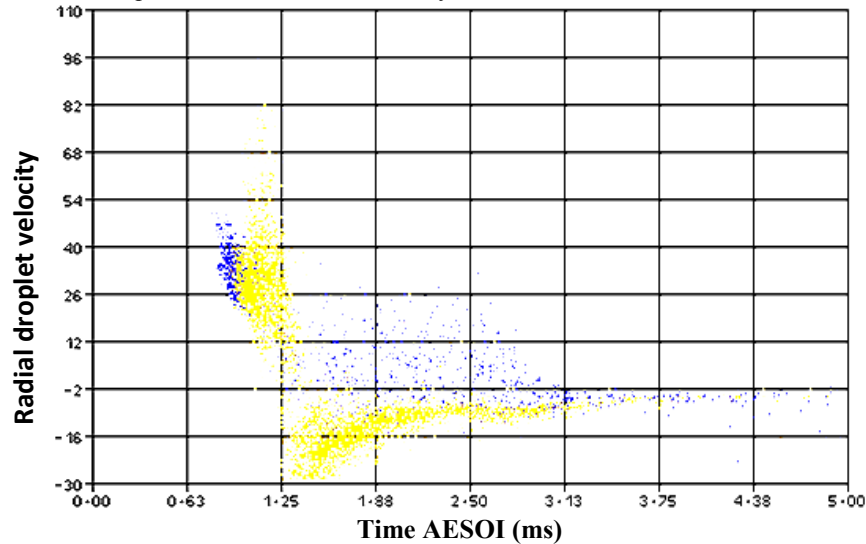


**Figure 9.** Different behaviour of large (blue) and small (yellow) droplets on the outer edge of a flashing spray (0.1 bar 45°C) in the interstitial streams @  $Z=40$ ,  $r=15$ mm

The same sudden changes are observed in the main streams, but the effects are less pronounced. The same is also true for the non-superheated collapsing cases, but again the effects are less pronounced with closer to atmospheric pressure conditions. This shows the spray collapse and subsequent formation of vortices is exaggerated by the flash boiling process, but also occurs in non-flashing cases. The conclusions drawn from this are that the collapsing process is due to the reduced pressure inside the spray cone, and the differences between the flashing and non-flashing case are due to the increased likelihood of entrainment for the smaller droplets produced by the flash boiling process.

### Drop Size

Overall drop size reduction is one of the key advantages previously reported with flashing sprays. The shattering process of droplets caused by bubble growth within droplets will inevitably lead to the formation of a large number of small droplets, but the key droplets from an emissions point of view are the large drops which cause HC and PM emissions due to their fuel volume. For this reason the characteristic used for drop size is  $D_{32}$ .

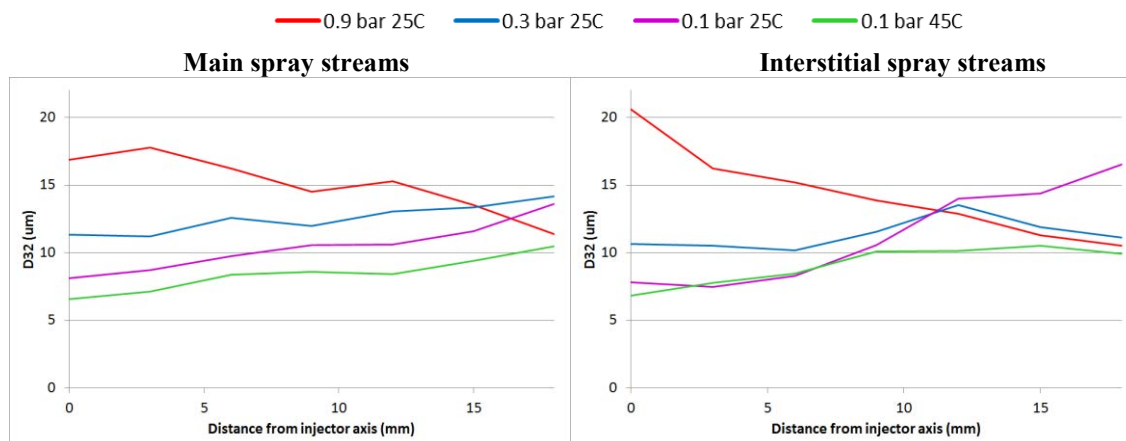


**Figure 10.** Drop size profiles throughout spray at  $Z=40$ mm

The  $D_{32}$  plots for both the main and interstitial streams, Figure 10, show an overall reduction in droplet diameter, most notably close to the injector axis. The reduction in  $D_{32}$  close to the injector axis is due to the spray collapse having a great entrainment effect on the smaller droplets, which have lower momentum, and can be observed for all three of the sub-atmospheric cases. As expected the drop size is smallest for the flashing case and in general for the non-flashing cases a reduction in pressure is associated with a reduction in mean droplet diameter.

## Conclusions

The phase Doppler technique has been successfully applied to a 6-hole 60° GDI injector under a variety of ambient pressure and fuel temperature conditions. Four test conditions were investigated: 0.9 bar, 25°C, which represents a spray which should not collapse, 0.3 bar, 25°C, which represents a spray which will exhibit jet-to-jet interactions and a weak spray collapse, 0.1 bar, 25°C, which represents a spray with large levels of jet-to-jet interactions and a defined spray collapse but under non-superheated conditions and 0.1 bar 45°C which represents a collapsing spray under flash boiling conditions.

The first condition maintains a jet like profile and as expected shows little jet-to-jet interaction. The 0.3 bar condition shows a spray which initially shows a jet like profile, but as the injection proceeds the level of jet-to-jet interaction increases and leads to a weak collapse of the spray. For the 0.1 bar, 25°C the initial spray jet is much wider than the previous two cases and leads to a more pronounced spray collapse due to the formation of a spray blockage between the inside and outside of the spray cone. Finally the superheated case, 0.1 bar, 45°C, shows an immediate spray collapse and evidence of the formation of a vortex on the edge of the spray tip.

The nature of this vortex was investigated. It is shown that the smaller droplets, which are the droplets with low enough momentum to be entrained into vortices of this type, have a high positive radial velocity in the early stages of injection, however, the smaller droplets measured in the next phase of the injection all have a high level of negative radial velocity. This suggests that the upper edge of a vortex is then passing through the measurement volume. Later in the injection on the outer edge of the spray the droplets all travel inwards towards the spray centre with low velocity levels.

Finally the drop size across the spray for the four conditions was analysed. It was shown that the drop size, particularly in the spray centre is lower under sub-atmospheric conditions. This reduction is most pronounced with the addition of heat to the fuel to achieve flash boiling of the fuel due to the shattering of droplets by the flashing process. The reduction in drop size in the centre of the spray is due to the increased likelihood of small droplets to be entrained into that region, and therefore is more pronounced with a reduction in drop size.

## References

- [1] Wei Zeng, Min Xu, Gaoming Zhang, Yuyin Zhang, David J. Cleary: Atomization and vaporization for flash-boiling multi-hole sprays with alcohol fuels; *Fuel* Vol. 95, p287-297, 2012
- [2] M. M. Khan, J. Helie, M. Gorokhovski, A. Wood, G. Wigley, J. Kashdan, J. P. Dumas, M. Mojtabi, P. Guibert: Numerical Analysis of Multihole Gasoline Direct Injection Sprays; ICLASS 2012, Heidelberg, Germany, September 2012
- [3] Min Xu, Yuyin Zhang, Wei Zeng, Gaoming Zhang, Ming Zhang: Flash Boiling: Easy and Better Way to Generate Ideal Sprays than the High Injection Pressure; *SAE Int. J. Fuels Lubricants*. 6(1):137-148, 2013
- [4] M. Mojtabi, N. Chadwick, G. Wigley and J. Helie: The effect of flash boiling on break-up and atomization in GDI sprays; ILASS Europe 2008, Lake Como, September 2008
- [5] G. Wigley, G. Pitcher, H. Nuglisch, J. Helie, N. Ladommatos: Fuel spray formation and gasoline direct injection; AVL 8<sup>th</sup> International Symposium on Combustion Diagnostics, Baden-Baden, 2008

## Mapping of Pure R-22 Spray Characteristics under Homogeneous Flash Boiling

Levy M., Sher E. and Levy Y

Faculty of Aerospace Engineering, Technion - Israel Institute of Technology, Haifa, Israel

### Abstract

Flash-boiling method is one of the most common current atomization methods in household, painting and medicine applications. The nucleation process is the major leading phenomenon that dominates the flash-boiling process, and, therefore, the spray characteristics. Studies dealing with flash boiling atomizers under homogeneous nucleation regime are very rare, although it is anticipated that homogeneous nucleation may result in finer sprays with smaller droplets than that achieved with heterogeneous nucleation. The nucleation rate in the homogeneous case is significantly greater and requires a simpler atomizer structure which may be potentially suitable for applications requiring small droplets, such as fuel injection systems in combustors and engines. In an earlier work (Levy & Sher 2010), we have made an attempt to define the desired conditions for homogeneous nucleation, and proposed a simple visualization technique to determine the border between heterogeneous and homogeneous nucleation regimes in a simple single-orifice atomizer. In the present work, we used a Phase Doppler Particle Analyzer (PDPA) to measure the spray properties during the transitions from heterogeneous to homogeneous nucleation regime.

---

### Introduction

Flash-boiling atomization systems are widely used in household, painting and medicine applications. In most of these spraying systems, the atomization unit consists of an inlet orifice, an expansion chamber and a discharge orifice. Nucleation occurs at the inlet orifice on the walls (heterogeneous nucleation), the bubbles develop in the expansion chamber, and a rapid bubble growth (flash-boiling) occurs when the mixture leaves the discharge orifice. The nucleation process is a major leading phenomenon that dominates the flash-boiling process, thus the spray characteristics. Former studies (Sher & Elata 1977, Park & Lee 1994, Rashkovan et al. 2003, Sher et al. 2008, Bar-Kohany et al. 2004 and Bar-Kohany et al. 2007) showed that the flash-boiling method results in high quality fine sprays, and it is anticipated that homogeneous (rather than heterogeneous) nucleation may result in a much finer spray. Since the time scale of the bubble growth in homogeneous nucleation is much shorter than that in heterogeneous nucleation, using homogeneous nucleation requires a simpler atomization unit construction, and thus may be potentially suitable for fuel injection systems in combustors and engines.

Studies dealing with flash boiling atomizers under homogeneous nucleation regime are very rare, although it is anticipated that homogeneous nucleation may result in even finer sprays with smaller droplets. Under homogeneous regime, the bubbles also form at the mixture bulk rather than only on the orifice walls. Therefore, the nucleation rate in the homogeneous case is significantly greater (Avedisian 1985). Using homogeneous nucleation requires a simpler atomizer structure, and thus may be potentially suitable for applications demanding small droplets, such as fuel injection systems in combustors and engines.

In the current work, we used a Phase Doppler Particle Analyzer (PDPA) to measure spray properties during the transitions from heterogeneous to homogeneous nucleation regime.

### Experimental test-rig

An experimental system was used to form a two phase spray during rapid depressurization, and to measure spray characteristics. The main objective was to observe the evolution of spray characteristics by controlling the initial temperature and pressure under homogeneous nucleation regime. A Chlorodifluoromethane ( $\text{CHClF}_2$ ), or in its commercial name, R-22, has been used as the dispersed fluid.

We used an adjustable system to inject pure R-22 superheated liquid into the surroundings; the system enabled us to control the initial injection temperature and pressure. Depressurization to atmospheric pressure generated the R-22 flash boiling.

Standard commercial tanks usually contain saturated R-22 have a simple mechanism allowing only gas to flow through their valve. By using a controlled refrigerating/heating circulator, the R-22 was cooled down and condensed in the pressure tank. When a prescribed amount of R-22 was accumulated, the tank was heated back to the room temperature. Following, compressed air was used to pressurize the R-22 to the desirable level. The compressed liquid R-22 was forced to pass through a fine dense filter (15 $\mu\text{m}$  mesh), and then through a pipe

wrapped with a controlled heating mantle, allowing warming up the liquid to the desirable temperature. Finally, the compressed heated liquid was injected to the surroundings through a 100 $\mu$ m diameter plain orifice (Figure 1).

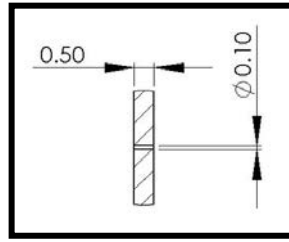


**Figure 1:** Orifice dimensions [mm]

We used TSI's Phase Doppler Particle Analyzer (PDPA) to measure spray characteristics. The PDPA measuring system generated two intersecting laser beams; the spray liquid droplets passed through the beams intersection zone, scattering the light into a multi detector receivers (Figure 2). After feeding R-22 refractive index to the system's software, the signals received in the detectors could be used to analyze the droplets' diameter and velocity. We also used a controlled 3D positioning system to measure the droplets characteristics at a specific downstream distance.

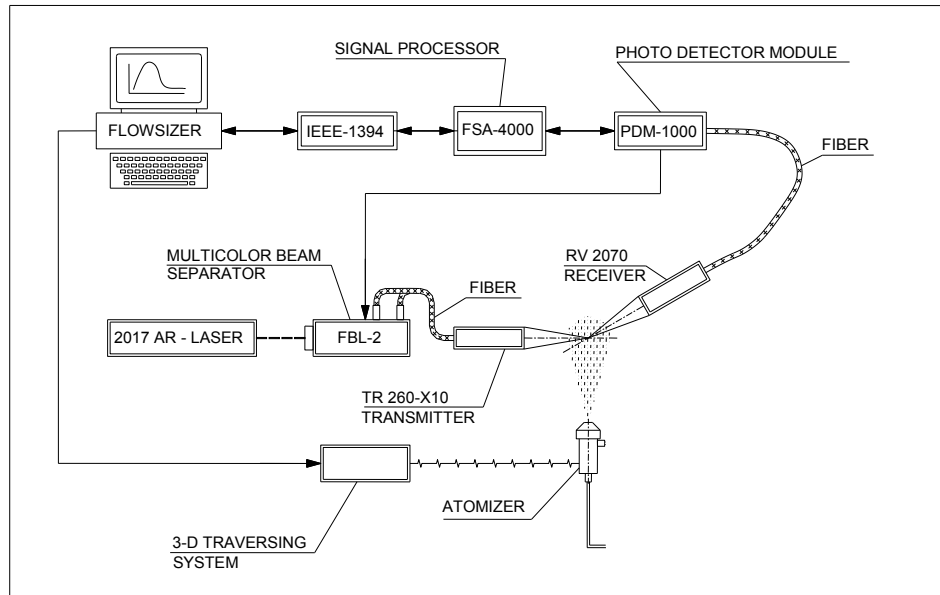


**Figure 2:** The PDPA measuring system

The measuring sequence for each measuring point included six steps: positioning the orifice in a desirable point to measure parameters at a specific distance  $H$  from the orifice; scanning the spray crosswise using the PDPA to detect the symmetric axis of the spray; positioning the system to measure parameters at a specific distance  $R$  from the symmetric axis; adjusting the spray formation system till a desirable initial temperature and pressure was achieved; waiting for the spray to be stabilized; sampling 100,000 droplets using the PDPA measuring system; and analyzing the droplets' characteristics using TSI's FLOWSIZER™ system software.

## Results and Discussion

More than 200 measuring points have been sampled, at different initial temperature and pressure, and at different distances from the orifice and from the spray symmetric axis. We observed a normal velocity distribution for all measuring points; one representative example is shown below (Figure 3), and a clear monotonic decrease in the Sauter mean diameter with temperature increasing at constant pressure (Figure 4).

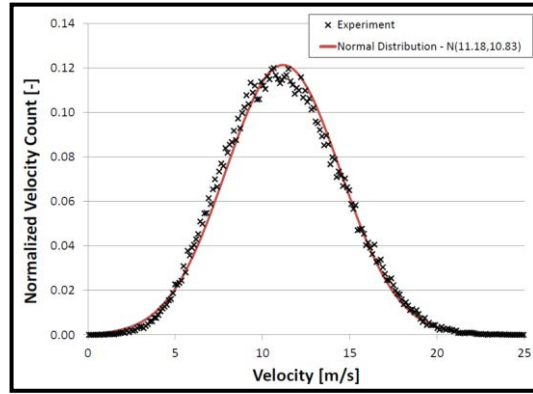


**Figure 3:** Velocity distribution 30mm downstream at the spray axis (Temperature - 45°C, Pressure - 40bar)

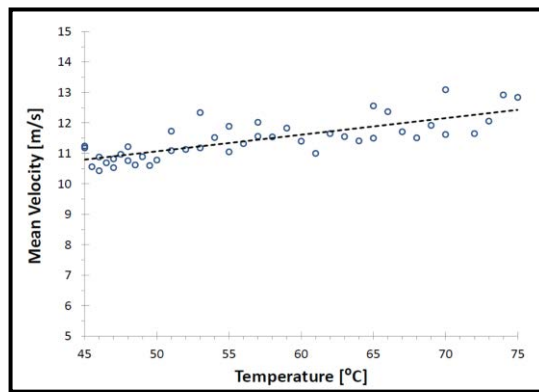


**Figure 4:** Mean Velocity vs. Temperature 30mm downstream at the spray axis (Temperature - 45°C, Pressure - 40bar)

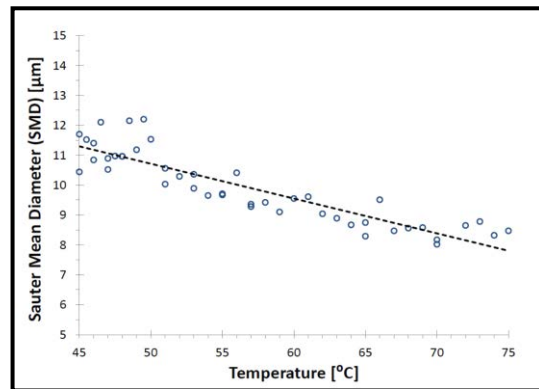


**Figure 5:** Sauter mean diameter vs. Temperature, 30mm downstream at the spray axis (Temperature - 45°C, Pressure - 40bar)

The effect of the temperature on the Sauter mean diameter is shown in Figure 5. We noticed a Rosin-Rammler distribution for all measuring points; one representative example is shown in Figure 6. Diameter decreasing during temperature increasing has been observed at any pressure, distance from the orifice or distance from the symmetric axis; also, the slope was similar in all of those cases. It indicates an increase of the nucleation rate.



According to the classic theory of nucleation, nucleation rate strongly grows while increasing temperature under homogeneous nucleation regime. Therefore, it is expected that spray characteristics under homogeneous flash boiling regime will be significantly affected by temperature. To ensure flash boiling under homogeneous nucleation regime, a pure superheated liquid R-22 was injected to the surrounding at high depressurization rate and high temperatures, close to the critical temperature.

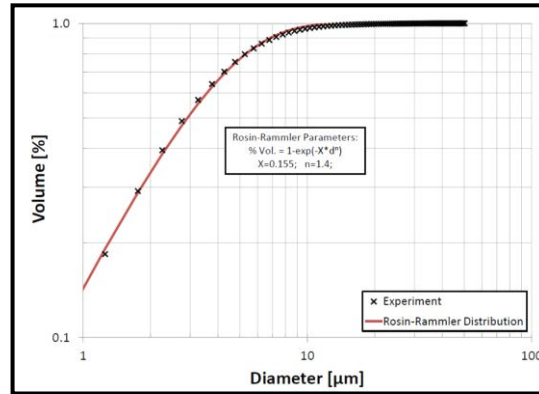


**Figure 6:** Diameter Cumulative Distribution Function, 30mm downstream at the spray axis (Temperature - 45°C, Pressure - 40bar)

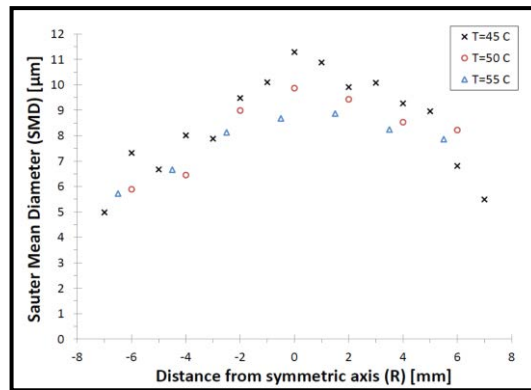


**Figure 7:** SMD ( $D_{32}$ ) vs. Distance from Center of Spray (R), 30mm downstream (Temperature - 45°C, Pressure - 40bar)

From former experimental investigations it was concluded that the superheating limit of pure substance at atmospheric pressure is about 90% of its critical temperature (Blander and Kats 1975); and specific for R-22, the superheat limit temperature, or homogeneous nucleation limit is 327.8 K (Avedisian as cited by Lide, 1995). Consequently, superheated liquid R-22 cannot sustain at atmospheric pressure over temperature of 54.65°C without undergoing phase transition. It is also known, that the nucleation regime is affected by the depressurization rate. Low depressurization rates, are dominated by heterogeneous nucleation; high rates, dominated by homogeneous. It was suggested that for blow-down processes the rate limit is 400MPa/s (Hutcherson et. al, 1983). In the current work, depressurization rate was about 80,000MPa/s, depending on initial injection pressure and temperature; while the initial temperatures range is 45°C to 75°C. Hence, a homogeneous nucleation regime is expected.

The initial injecting temperature had major influence on all droplet mean diameters, and liquid volume flux; about 25% reduction of droplet mean diameter ( $D_{10}$ ) and almost 85% reduction of liquid volume flux, by increasing initial temperature from 45°C to 75°C (at constant initial pressure). It indicates the influential effect of temperature on nucleation rate, as suggested by the classic theory of nucleation. The results confirm that under homogeneous nucleation regime a high quality spray is expected, characterized by small and uniform droplets; and in those terms the initial temperature is the most effective mechanism to reduce droplet diameter.

## Conclusions

The homogeneous nucleation process is extremely affected by the initial liquid temperature, considering a pure substance undergoing flash boiling during rapid depressurization through a simple structure atomizer. The initial pressure has only a minor effect on the nucleation process, negligible comparing to the initial temperature.

The spray shape is not affected by temperature or pressure under homogeneous nucleation regime. The only visible change is in the spray opacity, increasing temperature causes decrease in droplet diameter and liquid volume flux, and thus spray becomes more and more clear.

Finally, using homogeneous nucleation requires a simpler atomization unit construction, and thus may be potentially be suitable for fuel injection systems in combustors and engines.

## References

- [1] Avedisian, C.T. (1985), "The Homogeneous Nucleation Limits of Liquids", *Journal of Physical and Chemical Reference Data*, Vol. 14, 695-729.
- [2] Bar-Kohany, T. and Sher, E. (2004), "Subsonic Effervescent Atomization - A Theoretical Approach", *Atomization and Sprays*, Vol. 14, pp.495-509.
- [3] Bar-Kohany, T., Sher, I., and Sher, E. (2007), "Choked Flow of a Bubbly Mixture Through an Effervescent/Flashing Atomizer: A Theoretical Approach", *Atomization and Sprays*, Vol. 17 pp.431-449.
- [4] Blander, M. and Kats, J.L. (1975), "Bubble Nucleation in Liquids", *AIChE Journal*, Vol. 21 (5), 833-848.
- [5] Hutcherson, M.N, Henry, R.E. and Wollersheim, D.E. (1983), "Two-Phase Vessel Blowdown of an Initially Saturated Liquid – Part 2: Analytical", *J. Heat Transfer*, Vol. 105 (4), 694-699.
- [6] Levy, M. and Sher, E. (2010), "Transition from Heterogeneous to Homogeneous Nucleation in A Simple Structure Flash-Boiling Atomizer", *Atomization and Sprays*, Vol. 20, No. 10, pp.905-907.
- [7] Lide, D.R. (1995), *CRC Handbook of Chemistry and Physics*, 76<sup>th</sup> Ed., CRC Press.
- [8] Park, B.S. and Lee, S.Y. (1994), "An Experimental Investigation of the Flash Atomization Mechanism", *Atomization and Sprays*, Vol. 4, 159-179.
- [9] Rashkovan, A., Rivin, B., Kholmer, V. and Sher, E. (2003), "Flashing Injection of CO<sub>2</sub>-Dissolved Mixture", ICLASS, 13-17 July, Sorrento, Italy.
- [10] Sher, E., Bar-Kohany, T. and Rashkovan, A. (2008), "Flash-boiling atomization", an invited review article - *Prog. Enrgy Combust. Sci.*, Vol. 34, No. 4, pp.417-439.
- [11] Sher, E. and Elata, C. (1977), "Spray Formation from Pressure Cans by Flashing", *I&EC, Process Design and Development*, Vol. 16, 237-242.

## Design of an injection system under low pressure and temperature conditions in liquid fuelled micro UAV's

Jonas Galle and Sebastian Verhelst

Department of Flow, Heat and Combustion mechanics, Ghent University, Belgium

### Abstract

Today, unmanned air vehicles (UAV's) are extensively used for a wide range of applications, from amateur to human to military applications. Electric propulsion is preferred for small UAV's, while piston engines and gas turbines are used for the bigger ones. The proposed engine in this work covers the midscale for restartable, low budget vehicles (<10kg and 30-200N thrust). Simplicity, durability and manufacturability are the main target goals of the design. The liquid fuelled engine is designed to run on gasoline and ethanol as a fuel and a hydrogen peroxide – water solution as oxidizer. The advantage of the high energy density of the liquid reactants is counteracted by the difficulty for the ignition of the reactants at low pressures and temperatures, especially at the starting up process. In this work, different nozzles and injection strategies were tested and evaluated under similar conditions that exist at start up of the engine. It has been found that even for reasonable manufacturing process and precision, good atomization can be obtained if a mixture of gas and liquid is premixed prior to injection. This can be realized by catalytic decomposition of the hydrogen peroxide without the need for an extra gas supply circuit. This exothermal reaction provides the additional advantage of injecting a hot mixture in the cold combustion chamber, allowing easier ignition.

### Introduction

Unmanned air vehicles (or simply UAV's) are found in a wide range of applications, from amateur to human to military applications. A great number of small UAV's use electrical energy for the propulsion, making them flexible, simple, safe and quiet. The main drawback of this propulsion strategy is the low energy density of batteries compared to energy stored in liquid phase (cf. left of Fig.1). In addition, the speed and flight range of the vehicle is limited. This is the point where turbines make their entrance. However, micro turbines used for the somehow bigger UAV's are complex and expensive. The small dimensions require small clearances in order to maintain reasonable efficiency, while the rotating parts should be able to expand due to the high temperature. As the scale of turbo machinery is reduced, the compressor efficiency decreases and, therefore, the total efficiency drops non-linearly with its size when it is used in a micro-propulsion system [1]. This results in an efficiency decrease between 30 to 50% as compared to big turbines.

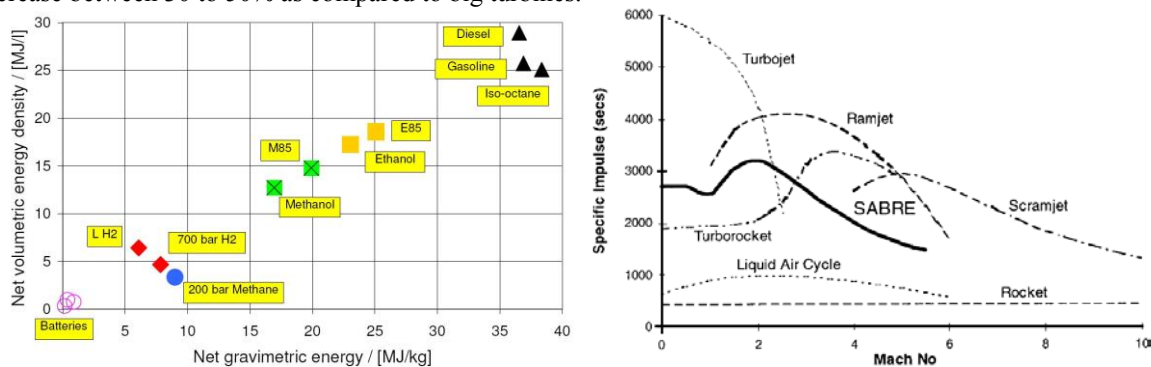


Figure 1. Left: energy densities of common fuels [2]. Right: specific impulse for different jet engines [3].

Rocket engines are the lightest of all jet engines, but the efficiency strongly depends on the design of the nozzle, and the operating range such as altitude differences, chamber design temperatures and pressures. In optimized rocket engines the efficiency can be about 60% [4], for high chamber pressure and temperature, while efficiency for a turbojet usually is around 30-40%.

Another measure to compare jet engines is the specific impulse  $I_{sp}$ , defined as the flow of on-board propellants required to produce a certain amount of thrust. Since rocket type engines carry both the oxidizer and fuel, the specific impulse is significantly lower than that of the turbojet engine [3] (cf. right of Fig.1). But energy is required to power the compressor as for a turbojet which can be very high [5]. For rocket engines, this energy can be stored in a gas tank to pressurize the fuel and liquid.

The scaling of a rocket-type engine suffers from the same problems as a micro-turbine in terms of maximum operating pressure and temperature.

So apart from the drawbacks, the rocket type engine seems the most suitable solution for the considered application -the most important reasons for this choice being the missing moving parts subjected to high temperatures and the high energy density.

The paper is arranged as follows: firstly, the concept of the engine is explained. The focus is drawn to the performance of the start-up and main injectors. Secondly, the test-rig and measurement methods are discussed, followed by an overview of different injection strategies, reactant choice and nozzle types. Some potential systems were tested and evaluated under the start-up conditions for a mixture of a gas and liquid. Based on the results, the chosen nozzle was tested with the hydrogen peroxide. Finally, we draw a number of conclusions and tackle future work.

## Engine concept

Figure 2 shows a cross section of the prototype test engine with its most important parts and features. The engine is designed to meet following needs

- cheap and easy to (mass) produce
- efficient and low weight
- mid-range UAV: 30-200N thrust, <15kg
- restart ability to restart during flight
- low pressure fueling circuit (0.8-1MPa)
- save (no toxic liquids or gases)
- high durability and reliable (little moving parts)

As mentioned in the introduction, small engines require careful design of the heat transfer, manufacturing precision and constructional complexity and weight. Furthermore, most standard available components for systems of this dimension range are limited in handling pressures and temperatures. The considered engine and surrounding components will be limited to pressures up to 1MPa due to mechanical restriction.

Pressurizing of the reactants is realized by a working gas ( $N_2$ ).

The nominal chamber pressure during operation is designed to be 0.5MPa absolute. With a nominal fuel injection pressure of 0.8MPa absolute, this means that only a low pressure drop is available for the fuel injection. Proper injection for these low pressures, conditions and dimensions is not straight forward and is the main focus of this work.

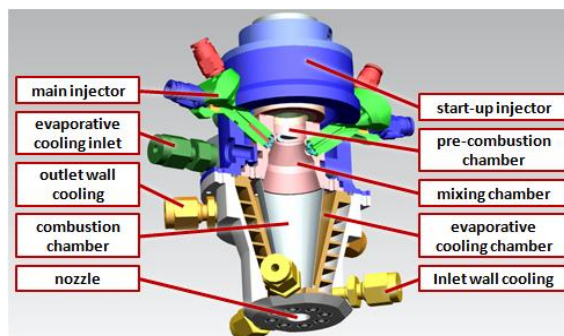


Figure 2. cross section of the prototype engine

## Experimental test-rig

To study the injection strategies and nozzle type performance, an optically accessible setup is initially required rather than a full scaled test engine (cf. Fig. 3). The experiments involve injection at ambient conditions, since this will be the most problematic situation for a system with restart abilities. The setup involves 3 supply lines: a liquid fuel (ethanol or gasoline), a liquid oxidizer (60wt% hydrogen peroxide (HP) - 40wt%water) and a gaseous oxidizer (pressurized air). The HP-solution and fuels are contained in a bladder in such way there is no contact with the working gas. The flow of the HP, fuel and pressurized gas are controlled with pressure based flow controllers (1). One-way valves (2) are implemented for safety and in order to prevent the fluids from flowing to the wrong tank. Solenoid valves (3) activate the injection for the desired fluid. They can be flexibly programmed for tuning and different injection strategies by varying the supply voltages and PWM signal for multiple injection. A pressure driven carburetor (4) can be installed for premixing the fuel with a gas. Finally, the oxidizer (HP) and fuel and/or pressurized gas are supplied to the injector (5). The injector can be changed depending on the injection strategy used, as will be discussed in section "Injection strategies" and section "Nozzle types"

Focused shadowgraph imaging is used as the high speed optical diagnostic to visualize the spray. A green high power led (7) acts as light source and a PCO Dimax (8) captures the images at 10kHz. The solenoid valves (3) and camera (8) are simultaneously triggered, which allows the determination of the hydraulic delay.

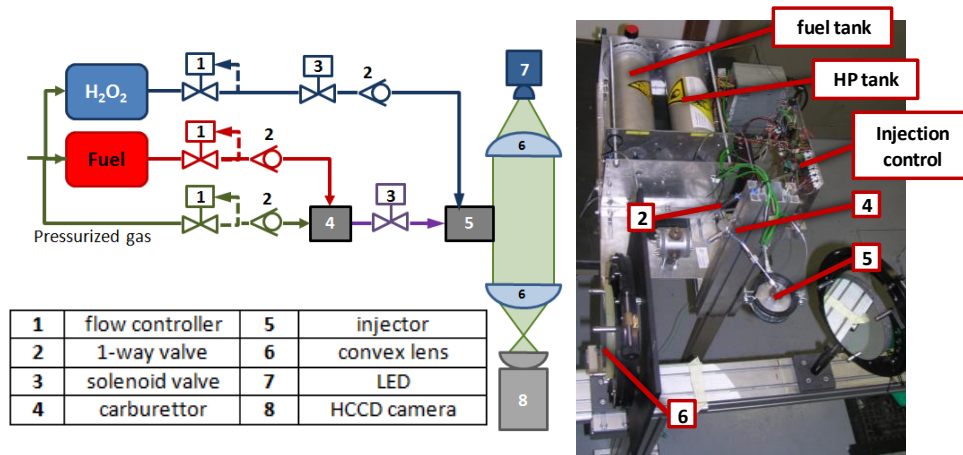


Figure 3. Schematic representation and actual implementation of the experimental setup.

### Injection strategies

The limitations of this type of engine are the low injection pressures and low ambient density and temperature, which makes proper atomization difficult. For this reason, choosing the injection strategy is of extreme importance. The fuel and oxidizer can be injected in 3 different ways:

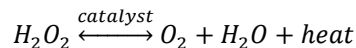
- both as a liquid
- both as a gas
- one as a gas and one as a liquid

For a proper spray combustion, the mixing process of fuel and oxidizer is the most important factor apart from the fuel and oxidizer properties. Despite the easy storage and high energy density, injection of both fuel and oxidizer in liquid phase requires time to mix and evaporate. Atomization of the injection significantly increases the evaporation and mixing rate but is difficult to achieve at such low injection pressures and ambient densities [6]. The mixing process can be enhanced by mixing them beforehand and injecting this mixture through a single injector.

If a gas and liquid are both injected through the same nozzle, the atomization suddenly becomes completely different, as will be demonstrated later on. This type of injection can be most likely a liquid fuel with a gaseous oxidizer or mixture of a liquid fuel & oxidizer with an additional gas. However, the latter strategy might require an additional (large) tank and gas supply circuit which increases the system's complexity and weight.

Finally, the solution to avoid the need for atomization and evaporation is to inject both fuel and oxidizer as a gas. This way, only the right mixture ratio and ignition energy is required. But, the storage of the gases is difficult and requires cryogenic, pressurized or absorption storage technology [4].

A promising compromise for the atomization problem is the use of a hydrogen peroxide (HP). Hydrogen peroxide is considered as a non-toxic, green (mono-) propellant fuel which is usually used in small thrusters in satellites or micro gas turbines [7-10]. Hydrogen peroxide has the advantage that it can be catalytically decomposed by an exothermal reaction with the formation of water vapor and oxygen:



With this property, the liquid oxidizer can be transformed into a gaseous fluid prior to injection, without the use of complex and energy consuming components. Additionally, the internal energy of the injected mass is increased due to the exothermal reaction, allowing easier and earlier ignition.

The most relevant properties HP are shown in table 1 together with the considered fuels for this project. The properties of water are added as well, since HP is commercially available in a water solution.

Some applications use HP as a monopropellant thruster [7], but due to the low heat release of HP compared with the gasoline or ethanol combustion, the supply tanks would become too big to keep the total energy and thrust equal. And since HP comes in a solution with water, the heat of evaporation of the water should be taken into account as well. One of the advantages of HP is its high density, compared to most other fuels and oxidizers [11], which is an important factor for aero application.

### Nozzle types

There are numerous nozzle configurations which can be used for many different spray and combustion applications, such as orifice, swirl, hollow cone, twin, co/counter-flow, air atomizing and spiral nozzles.

Taking the boundary condition into account, some of these nozzle technologies can be ruled out: simple nozzle holes such as used in today's piston engines use high injection pressures (~velocities) and high backpressures to create sufficient atomization and mixing. Aerodynamic forces, turbulence and cavitation. Co-flow injectors are mostly used for gaseous fuelled burners or in applications where the dimensions allow long flame lift-off lengths, such as industrial burners. Hollow cone nozzles have the disadvantage of being difficult to construct for low mass flow rates. They need very small clearance and accurate positioning in order to have a homogeneous flow pattern. In numerous low injection pressure applications swirl and twin nozzles have shown a good atomization pattern and are both easy to manufacture compared to the other types of nozzles. These 2 types of nozzles were preferred for the first design of this application.

	HP	w ater	EtOH	gasoline
density (@313K) [kg/m <sup>3</sup> ]	1450	998	789	740
molar mass [g/mol]	34	18	46	~100
liquid heat capacity [J/kgK]	2620	4182	2720	2220
gaseous heat capacity [J/kgK]	1267	2258	1800	2000
viscosity (@293K) [mPa.s]	1.25	1.00	1.20	1.18
boiling point [K]	423	373	350	300-488
Auto ignition temperature [K]	-	-	662	465-743
heat of evaporation [kJ/kg]	1520	2443	846	180-350
Flammability limits [vol%]	-	-	3.3-19.0	1.3-7.6
heat of decomposition [kJ/kg]	2780	-	-	-
Lower heating value [kJ/kg]	-	-	27000	43000

**Table 1.** Properties of hydrogen peroxide (HP), water, ethanol (EtOH) and gasoline [12, 13].

### The twin nozzle

Figure 4 shows a high speed image recording of a twin nozzle (0.35mm diameter holes, 70° angle between the nozzle channels) fuelled with only a liquid (top) and with a mixture of a liquid and gas (bottom) for different time instances after visible start of injection (AVSOI). It is noted that the terms “gas” and “liquid” are used since the liquid and gas can be both fuel and oxidizer if the injected HP is only partially decomposed. On the right side of Fig.4 a CAD drawing and manufactured nozzle are shown. Although the liquid fuelled nozzle seems to have a good performance with the naked eye, high speed imaging reveals some defects: the fuel that was left in the injector produces a liquid sheet before breaking up (up to 5 - 6mm). During the steady state injection, the breakup length is still too long as indicated by the image scale (distance between the 2 red horizontal lines is 5mm).

In the case where fuel is premixed with a gas (bottom row of Fig.4), the atomization is almost immediate and no liquid sheet exists the nozzle. Slightly bigger droplets are however noticed at the start of injections (cf. 100µs and 850µs AVSOI images in Fig.4). Essentially, no further visible breakup was found, apart from dispersion of the droplets. The breakup mechanism is mainly caused by the friction forces between the fast moving gaseous oxidizer and fuel inside the small nozzle holes.

In order to improve the atomization at start of injection, the gas valve was activated a little earlier than the liquid fuel valve. Nevertheless, no significant difference was detected. This can be explained by the fact that as both valves are energized equally, the gas flow reacts faster than the liquid flow, resulting in a similar effect of an earlier opening gas valve.

Apart from the difference in droplet size, (the) faster penetration can be detected in case of premixed injection, as well as the smaller spray angle (about 66° for the standard twin nozzle and only 57° for the fuel-gas mixture injection); the droplets in the premixed spray are significantly smaller and have a much smaller inertia. When the 2 jets collide, the droplets are much easier deflected. In the ideal case (complete symmetry and same momentum for the 2 jets), all the fuel should flow along the injector axis. A faster penetration is mainly established by the



higher injection velocity, which follows directly from the basic Bernoulli equation when the same injection pressure is used.

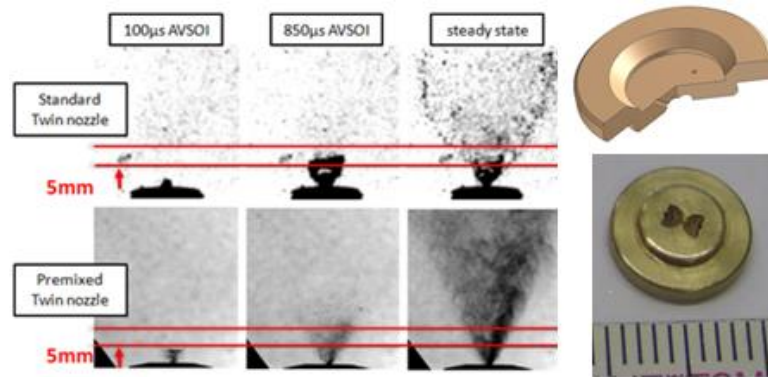


**Figure 4.** Upper row: the standard twin nozzle spray, bottom row: premixed twin nozzle spray at 3 different timings AVSOI. (shadowgraphy @ 10kHz), right: cross sectional and realized image of the nozzle (0.35mm holes, 70° angle between nozzle holes)

The flow rate of the gas and liquid were varied in order to understand the nozzle behavior in the different operation conditions. Low flow conditions for both are not considered since this condition is not relevant for the application, as the injectors will be used near maximum operating pressure. Qualitative results are shown in Fig.5. Similar conclusions as earlier can be drawn: the atomization improves with gas flow, while the spray angle decreases (with the gas flow). From the qualitative spray cross section, it was found that the higher the gas flow, the more the spray approaches a full cone angle which gives the best dispersion for a given spray angle. As the gas flow decreased to zero, the spray pattern tends to form a planar spray and became more sensitive to the machining accuracy. The spray pattern was very similar for all different tested nozzle types operating with a mixture of liquid and high gas flow.

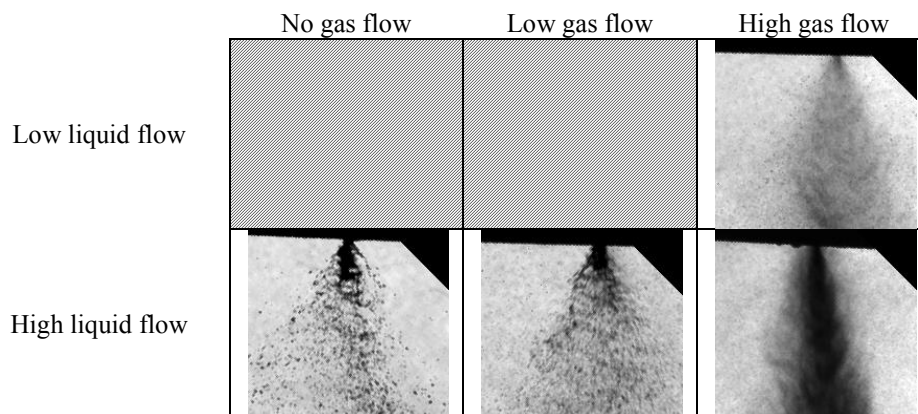


**Figure 5.** Overview of the performance of the twin nozzle injector for different liquid and gas flow rate (distance between red horizontal lines is 5mm, shadowgraphy @ 10kHz)

### ***The triple nozzle***

With the idea to increase the atomization capabilities of the nozzle when using a small or no gas flow, a triple nozzle was manufactured, similar to the twin version. The same total mass flow (or flow area) can be obtained with smaller holes which improves the atomization. However, no additional improvements were noticed and the nozzle was prone to the injector position and manufacturing process, resulting in spray with an important angle offset. This is the main reason why this concept is not further investigated.

### ***The swirl nozzle***

A swirl nozzle was constructed and is visualized at the right of Fig.6. At the left side, high speed images for the single liquid fuel (top) and premixed injection (bottom) are shown, as well as a cross sectional drawing and manufactured nozzle.

The idea of swirl nozzles is to create a rotating fluid motion, turbulence and mixing by injecting the liquid and/or gas into a chamber by eccentric placed holes. Due to this rotating motion the droplets are forced to move outwards by centrifugal forces, resulting in high dispersion. Tests were performed with the swirl nozzle as

shown in figure 6. Two swirl nozzles were tested, one with a nozzle throat diameter of 1mm and the other with 2mm.

Since the length of the swirl chamber was rather long, the spray was much less affected by the manufacturing process and a symmetric spray was noticed under all conditions.

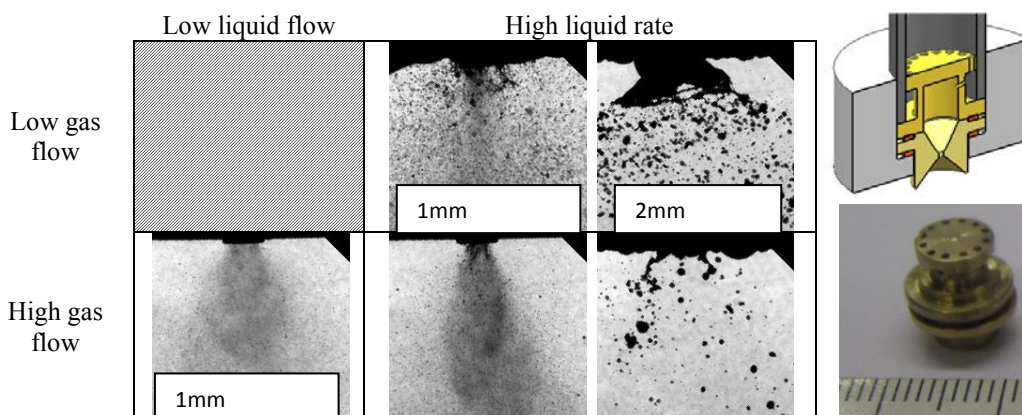


**Figure 6.** Left: overview of the performance of the swirl injector for different liquid and gas flow rate, with “1mm” indicating a throat diameter of 1mm; “2mm” a throat diameter of 2mm (shadowgraphy @ 10kHz), Right: CAD cross section of the used swirl chamber

For most of the conditions, the atomization was poor and decreased with the increasing liquid/gas ratio. For high liquid and low gas flow a liquid sheet was formed, as was the case for the twin nozzle without gas flow. Strong differences exist between the 1mm and 2mm throat diameter. This can be explained by the fact that the atomized liquid droplets, when entering the swirl chamber, will hit the wall of the swirl chamber. Even at high liquid & gas flow rates and throat diameter of 1mm, bigger droplets were noticed at the boundary of the spray, originating from the wall film.

This liquid film is driven towards the throat. The smaller the throat, the higher the gas velocity, which again encourages breakup. As a conclusion, swirl nozzles are not the best solution for a fluid composed of liquid and gas.

### Towards the injector design

As discussed earlier (in this paper), atomization under atmospheric conditions with liquid injection is difficult, but realizable with a proper chosen injection strategy. For the application, catalytically decomposed hydrogen peroxide will be used. The considered concentration of HP in water is 60wt%. The advantage of this choice is that temperatures are low enough for the oxidizer to mix with the fuel inside the injector with chance of auto-ignition, to ensure a high life expectancy of catalytic bed and to keep the combustion temperatures at acceptable levels. Furthermore, this concentration of HP is still commercially widely available.

Due to the small dimensions of the engine (and injectors), it is not expected to have a fully decomposed HP at the exit of the nozzle, but rather a mixture of gas and liquid, as was studied in previous sections.

It has been frequently reported in literature [11] that the design of the catalytic bed is the biggest issue in the injector performance. Many different types of catalysts and catalytic beds were already investigated in the past, ranging from simple and commercially available to exotic and expensive ones [7, 14].

Several options were investigated in the framework of this application, but the optimal configuration for long term use was not yet found. The main problems that arose were the loss of catalytic material and the poor contact surface-to-volume ratio. The other difficulty is the rather high water concentration which lowers the rate of temperature increase at start-up. Examples in literature usually make use of HP concentrations higher than 80wt%, with the HP as the propellant [8, 10, 11]. This way they suffer less from the wet and low temperature issue, but they suffer from a low life-time of the catalytic bed. With a new installed catalytic bed, the MnO<sub>2</sub> granules (about 0.7-1mm) and a MnO<sub>2</sub>-activated ceramic honeycomb-like structure give good performance. A perforated copper plate with holes of 0.6mm in diameter is installed before the nozzle to create a sac volume and to prevent the holes from clogging by the MnO<sub>2</sub> granules. Additionally, this sac volume assures

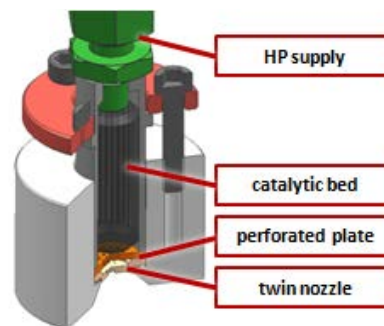


**Figure 8.** Design of the tested HP injector.



an equally distributed mixture over the nozzle holes to avoid asymmetric spray. The cross section of the injector is shown in Fig.8.

A small rocket-type engine with restart ability requires 2 injection strategies:

- injection at start-up conditions: atmospheric pressure and temperature
- injection at nominal conditions: high temperature, higher pressure (5bar in current application)

It is not required that both strategies are realizable with a single injector: the start-up injection does not have to produce thrust, but rather to create a hot, reacting atmosphere for the main injection. Considering this application, separated designs seem to be the most efficient for 2 reasons: only a limited amount of injectors can be installed in the combustion chamber head due to the small dimension and mechanical restrictions. This would imply that the mass flow rate will be high. As for the starting up situation, this would imply a high loss of fuel and oxidizer. The lower the flow, the better the catalytic decomposition and the faster the injectors and chamber heat up, as the catalytic reaction increases with temperature.

As a conclusion, a single centralized injector for low flow rates will be installed for the start-up sequence. The main injectors will be positioned around the center directed towards the start-up injector.

The main differences between the injectors will be the flow rate and the size of the catalytic bed. Low flow rates and highly decomposed HP (so big catalytic bed) are required for the start-up injector.

The performance of the HP injector strongly depends on the conditions of the catalytic bed: a wet and cold catalytic will react slower. Experiments have shown that humidity plays a dominant role. Figure 9 shows the start of the HP injector with a wet body temperature of 40°C. It takes about 500ms before a reasonable atomization is obtained. For a cold but dry catalytic bed, the steady state is almost immediately reached with noticeable droplets and the spray is very similar for the high gas flow situation investigated in previous sections.

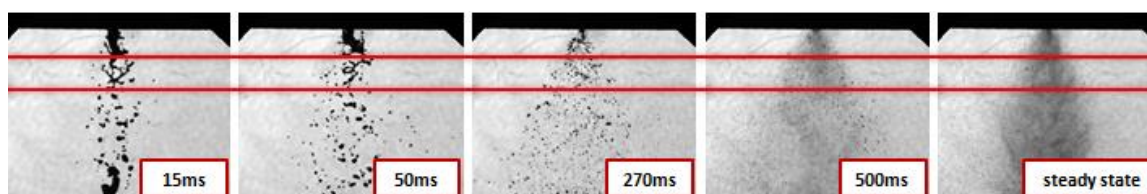


**Figure 9.** start-up of the HP injector (with 0.35mm twin nozzle) with a wet catalyst at 40°C at different time instants after visual start of injection. Distance between the 2 horizontal lines represents 5mm (shadowgraphy @ 10kHz).

## Future perspectives

The proof of concept is shown in this work, but additional work is required in the design of the catalytic bed. Improvement of the surface-to-volume ratio is one of the potential factors where significant improvement is possible. Spray combustion was not yet considered in this paper, but will be intensively studied in terms of ignition and emission formation.

## Conclusions

In this paper, nozzles were studied for use in a small UAV rocket-type engine under low temperature and pressure conditions and with restart ability. Twin, triple and swirl nozzles were selected and investigated by a high-speed shadowgraph diagnostic. Atomization was significantly improved by the injection of a gas-liquid mixture, rather than liquid only. With this observation, catalytically decomposed hydrogen peroxide was proposed as an oxidizer for this engine concept. A prototype injector was constructed and tested in terms of atomization. The following conclusions were drawn:

- Triple nozzles do not offer additional advantages and are more prone to the injector position and manufacturing defects
- Swirl nozzles have a very poor atomization when the gas flow becomes low. Bigger droplets are noticed in all conditions at the outer boundary of the spray
- Due to the gas flow, twin nozzles produce a full cone spray rather than a planar spray, as can be expected from a pure liquid injection
- The HP injector is very sensitive to the catalytic bed that was used: a wet bed significantly decreases the starting capabilities of the injector
- In steady state operation, the HP injector provides spray patterns similar to those resulting from liquid-gas mixture tests.

## Acknowledgements

The company Evonik (Germany) is gratefully thanked for the supply of the hydrogen peroxide HYPROX(R)600 and Aquadosil (Germany) for the MnO<sub>2</sub> granules.

## References

- [1] Jacobson, S.A., Aerothermal Challenges in the Design of a Microfabricated Gas Turbine Engine, in 29th AIAA Fluid Dynamics Conference 1998: Albuquerque, NM.
- [2] Pearson, R.J. and J.W.G. Turner, Gasoline/ethanol/methanol tri-flex-fuel vehicle as a means to expediting sustainable methanol production, in IQPC international conference: automotive fuels 2008.
- [3] Varvill, R. and A. Bond, A comparison of propulsion concepts for SSTO reusable launchers. JBIS, 2003. 56: p. 108-117.
- [4] Sutton, G.P. and O. Biblarz, Rocket propulsion elements. 7th edition ed 2001.
- [5] Schreckling, K., Gas turbine engines for model aircraft 2003.
- [6] Stiesch, G., Modeling engine spray and combustion processes 2003: Springer.
- [7] Cervone, A., et al., Development of hydrogen peroxide monopropellant rockets, in American Institute of Aeronautics and Astronautics.
- [8] Amri, R. and T. Rezoug, Numerical study of liquid propellants combustion for space applications. Acta Astronautica, 2011. 69: p. 485-498.
- [9] Krishnan, S., A. Sang-Hee, and L. Choong-Won, Design and development of a hydrogen-peroxide rocket-engine facility. Jurnal Mekanikal, 2010. 30: p. 24-36.
- [10] Cheung, W.S. and J.R. Tilston, Hydrogen peroxide based propulsion system for micro air vehicle applications, in American Institute of Aeronautics and Astronautics
- [11] Cervone, A., et al., Development of green hydrogen peroxide monopropellant rocket engines and testing of advanced catalytic beds, in 42nd IAAA/ASME/SAE/ASEE joint propulsion Conf. and Exhibit 2006: Sacramento, California, USA.
- [12] Marzzacco, C.J., The enthalpy of decomposition of hydrogen peroxide: a general chemistry calorimetry experiment. Journal of Chemical Education, 1999. 76(11): p. 1517-1518.
- [13] Perry, R. and D.W. Green, Perry's chemical engineers' handbook 1997.
- [14] Pasini, A., et al., Performance characterization of pellet catalytic beds for hydrogen peroxide monopropellant rockets. Journal of propulsion and power, 2011. 27(2): p. 428-436.

## Polymerization in a spray dryer – combining a pre-reaction and a reaction in the spray

Magnus Tewes and Urs A. Peuker

Institute of Mechanical Process Engineering and Mineral Processing,  
Technische Universität Bergakademie Freiberg, Germany

### Abstract

A new process is created if a reactive polymerizing system is sprayed in a common spray dryer. Thus a fourth step, polymerization, is added to the common operations, atomization, drying and solid formation. All of which are in competition and the process becomes complex. But an optimized process has the advantage of generating well defined powder polymers in shape and form within short process time. Because of the kinetics of the reaction the short retention time is a bottle neck of the process. Therefore a fast reaction is needed and the radical polymerization of acrylic acid and its salts are chosen.

To handle the kinetic problem the reaction has to be split in a reaction starting within the nozzle like a plug flow reactor and a progressing reaction in the atomized droplets. The droplets are like small batch reactors, a runaway of the reaction from a safety point of view is of no consequences because of the small volumes. The focus of research is the engineering of the special 3-fluid-nozzle where the educts are mixed together, heated up and atomized finally. In this work the mixing and heating are investigated in an intermediate device before tests in a spray dryer will be continued.

---

### Introduction

Powder polymers are mostly used in a wide application field like pharmaceutical, cosmetics and chemical industries. Especially water soluble or water absorbing polymers are present as additives in drugs, in hair styling products or in cleaning agents. Polymers as powders instead of gels or solutions are in advantage concerning transport and storage or further processing because of their flowing characteristics and stability. But the production of these powders is extensive. After the polymerization in different reaction steps for dissipating the high amount of exothermic heat formation processes are required like drying, milling and agglomeration. The idea to combine all the single steps in a so called one step process is obvious and theoretical described in an U.S. patent from 1993 [1]. Krüger adopted this new process concept, designed a plant and called the process spray polymerization [2]. The plant is a vertical heated pipe reactor with an ultra sonic droplet generator that creates droplets in a row in the sizes of 90–220  $\mu\text{m}$ . He investigated the generation of superabsorbent polymer particles. But he shows that efficiency and yield of the spray polymerization are the key problems. Most of the educts evaporate during the drying and aren't available for the reaction consequently. The modification of the spray polymerization process and a development of an economical concept is the motivation of this research.

The new concept is based on a common spray dryer, the main aggregate, where the liquid is atomized by a high velocity gas and dries by a hot gas in a co-current stream. The dryer itself combines three different sub-processes, atomization of the liquid to small droplets, drying and solid formation of the dispersed droplets. Finally the dried particles get separated from the gas stream. The advantage of a spray dryer is the fast process time ( $< 10$  s) because of the small droplets and the high convective heat transfer by the drying gas. It is used to generate solid particles from a liquid rapidly but gently. A new process will be created if – additional to these three operations – a reactive system is sprayed. In this case polymer reactions are applied, so the idea is a one step process from a liquid monomer solution to a ready powder polymer.

The reaction in a droplet is compared to a small batch reactor, which is heated by the drying gas in the spray dryer. If the monomer is volatile it will evaporate during the heating and the concentration of monomer in solution changes. With the heating the reaction accelerates and the concentration of monomer decreases. Polymer molecules are formed and change the viscosity of the liquid in the droplet. In addition to that the polymer will tend to build a skin on the surface of the droplet and change the heat and mass transfer from the inner droplet to the outside. If the monomer isn't volatile only the solvent evaporates and the concentration increases first, but then the reaction decreases the concentration again. It becomes clear now that the process becomes more complex by the competition of all four sub-processes. The benefit of the reaction in the droplets is that no safety problems will occur because of the small volume. A runaway of the reaction as the worst case will only cause unintended particle morphologies. But the advantage of the small droplets and the fast drying times of a spray dryer is also a bottle neck of the spray polymerisation.

Due to the low retention time in the spray dryer the process requires a very intensive reaction with fast polymerization kinetics. Therefore the polymerization is a radical reaction of acrylic acid and its acrylates. This system is also used by Krüger because of the fast growing rates [2]. The acrylates are nonvolatile and nonflammable compared to the acid and therefore easier to use without taking into account explosion protection.

Although the monomer system is very fast and has been tested for a polymerization in a droplet, first considerations about the reaction kinetics show that the retention time is still too low. A pre-treatment of the reactive liquid has to be done to start and properly progress the reaction before it gets atomized. The focus of this research is on the pre-reaction before the atomization in order to guarantee an effective one step process and production of well defined particles in size and shape. The kinetics of the pre-reaction is also important to figure out the effect of the four different sub-processes in the droplet during the spray drying.

The start of the polymerization is mainly depended on the decomposition kinetics of the starter or of the monomers. The decomposition rate is a function of temperature and concentration of the educts. Radicals activate monomers and macro molecules are formed. These oligomers or molecules with higher polymerization degree effect the atomization. In earlier works the influence of molecular mass of a polymer solution has been investigated [3]. There is a big influence on the atomization if molecular mass is high enough to cause a complex rheology with non-Newtonian viscoelastic behaviour. Then filaments instead of droplets are formed.

The pre-reaction is necessary to overcome the problem of the short retention time. If the start of the reaction is before the atomization the properties of the liquid will change depending on the amount of pre-treatment. Therefore a special 3-fluid nozzle is designed to investigate the effect of the retention time of the reactive liquid within the nozzle. This nozzle is modular designed to change the retention time in the nozzle and to heat the nozzle inside. The next chapter is dealing with the design.

Because of the fact that the rheology has a big influence on the atomization a new approach has been developed to measure the rheokinetics or function of viscosity over the time during the polymerization. In this work results are presented and used to demonstrate the progress of reaction within the nozzle. Finally an intermediate device is built and further results to the inner mixing of the 3-fluid nozzle are presented.

### Introducing the 3-fluid nozzle

The reason for developing a pre-reaction is to enlarge the process time the reactive liquid has to polymerize in. This pre-treatment will be done before the atomization. In order to have a compact process and keep the idea of a one-step-process a new nozzle has to be invented. The new nozzle is therefore a 3-fluid nozzle so that all the educts are able to be fed separately.

Nozzles for different applications are available at the market and even a 3-fluid nozzle has just been patented [4]. But the claim is to combine several options. Figure 1 demonstrates the design and shows the different functions the nozzle has. The liquids, monomer and starter solution, are fed centrally and mixed inside before the outlet. Here the use of a static mixer is an option to improve the mixing of the two feeds. Because of the use of a thermal initiator the temperature has a high impact on the decomposition rate. The temperature can be controlled with a heating fluid that heats the inner pipe of the nozzle by a double jacket. As it is shown in figure 1 the geometry of the nozzle has two lengths to vary. The first length of the inner pipe can be varied in order to change the location where monomer and initiator are mixed together internally. Then the reaction starts and progresses till it is atomized. After the atomization the reaction progresses in the droplet

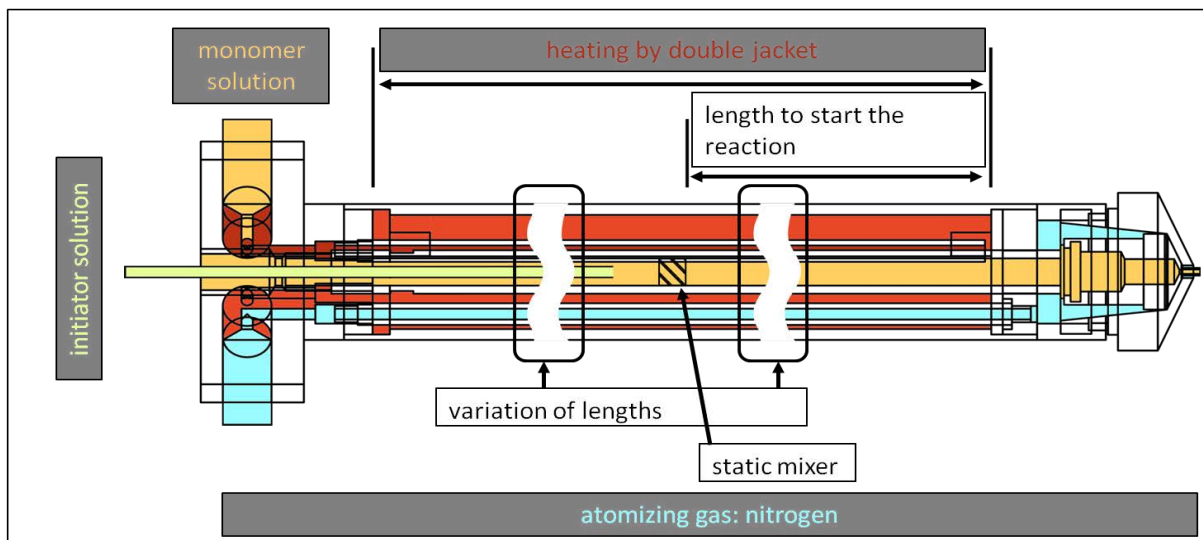


**Figure 1:** Design of a 3-fluid nozzle for starting a pre-reaction before atomization

compared to a small batch reactor, whereby the nozzle is more of a laminar flow reactor. The other variation is the length of the whole nozzle. It can influence the retention time of the two liquids in the nozzle at a constant flow rate. A constant flow rate is set in order to have no effect on the atomization later. The combination of these lengths will guarantee that the inflowing fluids first reach the desired temperature before they are mixed. Then polymerization starts and progresses within the nozzle until the liquid gets atomized. Secondly, a variation of the pre-reaction time is available. An optimum of the geometry will be needed where on the one hand the temperature for reaction is reached and on the other hand the progress of the reaction is sufficient. The more the reaction is progressing the better the efficiency of the spray polymerization, but the higher the degree of polymerization at the nozzle tip. With the length of the polymer chain the viscosity raises, this can hinder the droplet formation or block the nozzle.

For atomization the third fluid, nitrogen, is used at a high pressure. The gas is fed through the double jacket concentric to the tip of the nozzle. Through thin channels and with a tangential direction to the liquid's exit the gas is swirled and expands outside the nozzle. High velocity gas atomizes the reactive liquid compared to standard twin fluid nozzles. Finally the new 3-fluid nozzle is a combination of an external mixing 2-fluid and an internal 2-fluid nozzle.

Another advantage of the nozzle is that its design is like an lance. So every inlet is on the bottom of the nozzle including the outlet of the double jacket and the outlet of the spraying fluids is at the tip of the nozzle. Applying this special nozzle in a common spray dryer can be done without any problems. Because of former investigation of the atomization of polymer solutions the constructed nozzle tip is the same as the 2-fluid nozzle. It is a nozzle of Buchi corporation with a liquid diameter of 0.7 mm and a gas diameter of the annular gap of 1.5 mm. First tests concerning the heating up and the mixing within the nozzle were made and are presented in the following.

### Measuring the effect of the rheokinetics on the radical polymerization

A free radical polymerization is mostly an exothermic reaction because the combination of small monomer molecules to a polymer chain means losing degrees of freedom. The amount of reaction heat becoming free is especially a safety problem if very fast reactions are processed. These fast reactions are used for polymerizations in a spray dryer.

The kinetics of the polymerization is generally described in three different steps; initiation, propagation and termination. Monomers are inactive under certain conditions so an initiator is used. The initiator is decomposed and forms radicals that activate monomers if an initiator radical is connected with a monomer. The polymerization starts and the radical monomers form a polymer chain by connecting more and more monomers. This chain growing step is called propagation. If the growing is interrupted and the chain becomes inactive the reaction is at its last step, the termination. Often the combination or disproportionation of two active polymer chains ends the reaction.

The kinetics of the reaction's beginning is normally described by the following equation. The rate of the propagation reaction rate is described as the change in concentration in the time interval by the use of some simplifications [5].

$$r = \frac{dc_M}{dt} = \sqrt{\frac{k_i}{k_t}} \cdot k_p \cdot \sqrt{c_i} \cdot c_M \quad (1)$$

The indices  $i$ ,  $p$  and  $t$  show the influence of the three different steps. All constants  $k$  are depended on temperature and the material and are described by the Arrhenius law.

In view of the complete transformation of monomers to polymers the radical polymerization is more complex. So the reaction is described by the help of statistic values, like the distribution or mean value of the molecular weight. The molecular weight will be measured with special chromatography. This analyzing technique often uses light scattering or viscosity measurement to determine the volume of the polymer coils. The intrinsic viscosity is measured in dilute solution and is a reciprocal concentration which can determine the mean molecular weight. Equation 2 shows the relation of mean molecular weight  $\bar{M}$ , intrinsic viscosity  $\eta$  and concentration  $c$  and was developed by several scientists; Staudinger, Fikentscher, Houwink, Huggins, Hess and Sakurada [6-10].

$$\eta = K \cdot c^b \cdot \bar{M}^a \quad (2)$$

The idea of measuring the viscosity over time during a polymerization and therefore be able to describe the kinetics is first described in detail by Malkin and Kulichikhin and called rheokinetics. The aspiring target of this method is to generate a semi empirical description. For the initial stage of the radical polymerization of acrylamide in water they find equation 3. This function is developed with the use of equation 1 and 2 and describes the viscosity  $\eta$  over the time  $t$  [11].

$$\eta(t) = K' \cdot c_{M,0}^a \cdot c_{I,0}^{b-a} \left( k_p \sqrt{\frac{k_i}{k_t}} \right)^{a+b} \cdot t^b \quad (3)$$

The parameter  $K'$  takes into account the dependency of the viscosity with change of temperature. It is like the kinetic parameters  $k$  calculated with the Arrhenius law.

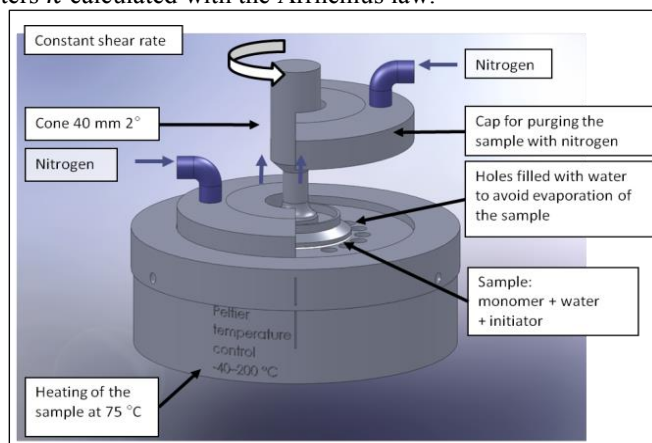


**Figure 2:** Modification of a rheometer to measure the viscosity over time during a polymerization

In addition the knowledge of the function of viscosity over the reaction time is of great benefit because of the atomization. The results of former investigations on the atomization of polymer solutions will be helpful to optimize the retention time of the reactive solution in the nozzle. To measure the rheokinetics a modification of a rheometer is necessary as shown in figure 2.

The standard rheometer is a HR-1 by TA Instruments and has a cone-plate geometry. The 2° cone with 40 mm diameter is connected to a motor and the plate is coupled with a Peltier temperature control. The Peltier element covers a temperature between -40 and 200 °C with a controlled heating rate of up to 10 °C/min.

The modification is done by covering the sample with two semi caps. They are connected to a nitrogen supply and at a certain step the sample gets purged with nitrogen during the measurement. Here the nitrogen is – when turned on – starting the reaction while oxygen that inhibits the polymerization is displaced rapidly. The geometry of the caps fits with no contact to the moveable cone. Through small gaps the gas is forced from the caps over the holes and the sample between caps and cone to the outside. Several holes are drilled in an additional plate and arranged in a circle around the upper cone. This plate is the next modification and has two functions. It fits with the Peltier plate with which it is screwed together. The holes in it are filled with water, so during the measurement the nitrogen flows over the water and is saturated. By this evaporation of the sample is suppressed because of a saturated atmosphere.

With heating up the sample to a temperature of 75 °C the procedure to get the time dependence of the viscosity starts. The sample is a solution of monomer, water and initiator with a volume of 525 µL. A damage of the rheometer because of the high reaction enthalpy is therefore not likely. Then nitrogen is turned on (0.1 L/min) and the lack of an inhibition of the radicals will start the polymerization immediately. Normally an inhibitor is present in monomers to avoid a self ignition, but it works in combination with oxygen only [12]. At a constant shear rate of 300 1/s and a sampling rate of 0.5 Hz the function of viscosity during the polymerization is recognizable.

### Results of the polymerization in the rheometer

The reactive system used is acrylic acid and its acrylates. A work of another researcher shows that a polymerization with this material in a droplet during a free fall has just been successful [2]. The monomer is applied by BASF SE and contains an inhibitor. With a vapour pressure of 4.3 hPa the acid is less volatile than water. But acrylic acid is flammable and explosion protection has to be guaranteed if it is used in spray dryers. That is why the salts of the acrylic acid, acrylates, are less harmful and preferred to use. They are produced by neutralisation of the acid e.g. with sodium hydroxide in a solution.

The results of the rheokinetics have two benefits. On the one hand the viscosity function is measured and an optimizing nozzle design is possible. On the other hand it is an aspiring target to use the method of Kulichikhin and Malkin to get information about the kinetics of the reaction as it is mentioned in equation 3. But this equation has a big disadvantage because of the dimensions. For the initial boundary,  $t = 0$ , the viscosity would also be zero if  $b$  is not equal to zero and is consequently not logical.

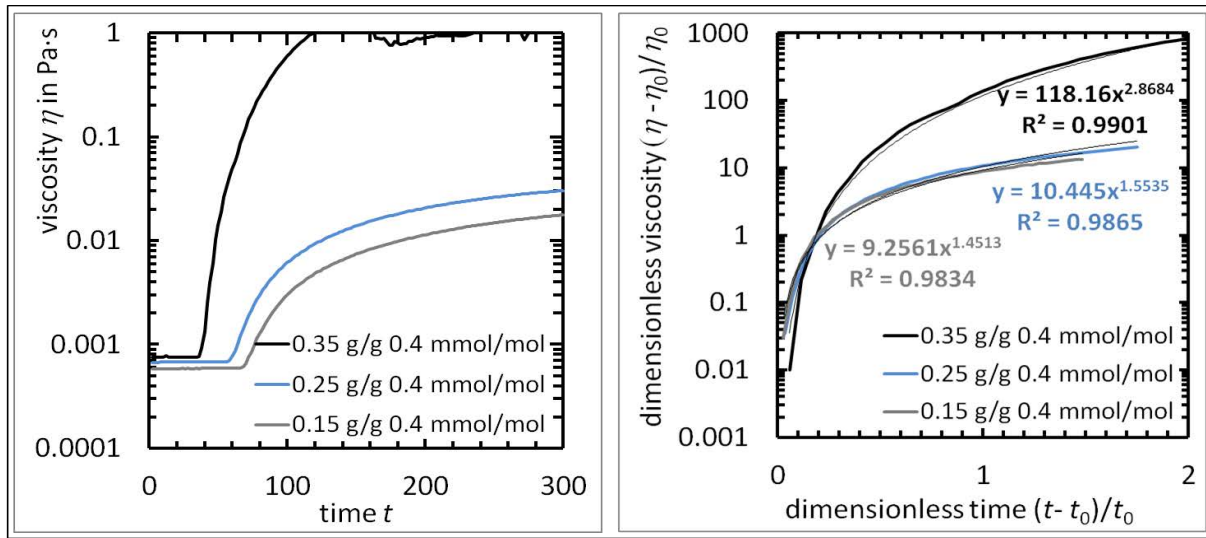


**Figure 3:** Working with rheokinetics – l. data directly by the rheometer, r. dimensionless view for the analyzing

All following results are done with the same testing procedure as described before and with a minimum of two repetitions. In order to explain the analyzing three different measurements of acrylic acid with the same initiator concentration (0.4 mmol/mol) but different mass fractions, 15, 25, 35 g/g%, are used as an example. In figure 3 left the raw data of the measurements are shown in a diagram. The shear viscosity is a function of time and gets a high gradient after a characteristic time. This time – when the viscosity starts to increase rapidly after a plateau – is called the zero time or time of the viscosity's increase  $t_0$ . It can be directly captured by the raw data.

The next information that is necessary to describe the function  $\eta(t)$  is the gradient after passing the zero time. In order to work with the data a transformation to dimensionless quantities is necessary. Therefore the viscosity as well as the time is calculated by the quotient of the differences between start and now related to the starting. Then a regression to a power function is done by fitting the measurement mathematically.

The result of the zero time is presented in figure 4. Here acrylic acid and the first results of sodium acrylate are plotted with a view to the concentration of the initiator in the liquid. Different analyses have shown that only the amount of starter is determining the resulting zero time. And it is obvious, that the more initiator is present the more radicals are getting free during the decomposition and consequently the zero time is decreasing. But the comparison between acrylic acid and sodium acrylate is not significant by now. It seems that the zero time of the acrylate is less than for acrylic acid. For every concentration the zero time can be calculated by using an exponential regression. A first simple rule of optimizing the 3-fluid nozzle is that the retention time has to be

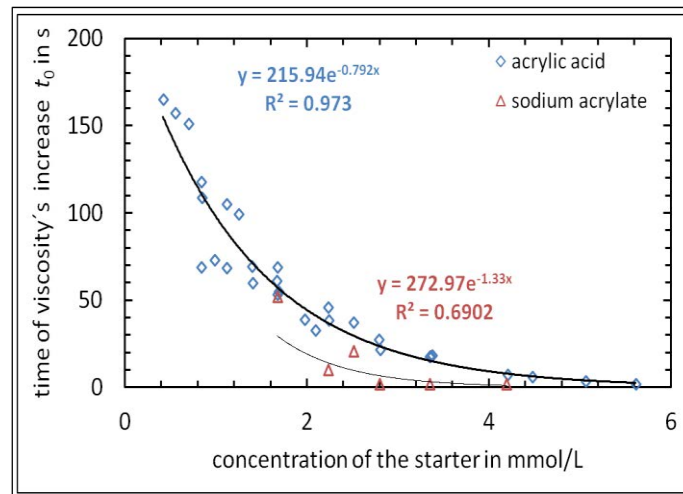


**Figure 4:** Time of the viscosity's increase for acrylic acid and sodium acrylate



smaller or equal to the zero time. Then the viscosity of the liquid is low enough (compared to water) so no problems concerning the atomization will occur. In order to that rule an example of a 50 g/g% solution of acrylic acid should react in a pipe of a maximum length of 200 mm if the concentration of the starter is 0.3 mmol/mol. A length of 400 mm should be applied if the concentration is 0.18 mmol/mol.

By knowing the limiting viscosity for the atomization the first rule has to be extended with the amount of the viscosity's increase during polymerization.

Figure 5 is presenting the missing information to describe the function of viscosity over the whole time. Taking into account the work of Kulichikhin and Malkin the equation 3 is able to be simplified by combining all constants and get a simple equation. This is done in equation 4. Now the viscosity is only a function of time and two constants, a factor  $\beta$  and an exponent  $b$ .

$$\frac{\Delta\eta(t)}{\eta_0} = \beta \cdot \left(\frac{\Delta t}{t_0}\right)^b \quad (4)$$

As it is seen in figure 5 left, the factor  $\beta$  is a function of the molar fraction of the monomer and of the initiator at the beginning when  $t = t_0$ . This dependence is given by a product of two power functions and a factor. The result shows that the influence of monomer molar fraction is very high compared to the amount of the initiator. In addition the range of values is very broad, so it has to be noticed that although the square of the correlation coefficient is near to one the variance of the power function is high. There is a good agreement compared to the power function of equation 3.

But on the right of figure 5 another mathematical correlation is in no agreement with the results of Kulichikhin and Malkin. Here the same power function is correlated with other coefficients. The exponent  $b$  is therefore also depended on the monomer and initiator molar fraction at the reaction start. Here the influence of the monomer is only the power of 2 higher that the influence of the initiator. Thus this result is in contrast to the rheokinetics of equation 3 – meaning that during the polymerization the influence of the monomer and initiator starting concentration is present at all time. And the influence of the monomer is higher at the start of the viscosity's increase than afterwards. The correlation of the exponent is more exact than the factor's because its values are tighter. Although the square of the correlation coefficient is lower than on the left of figure 5 the mean fluctuation is 15 %. On the left the mean fluctuation is 69 %.

The presented results are able to extend the theoretical model of the progress of the polymerization within the nozzle. This model is based on a simplified heat and mass transfer for a plug flow reactor. Now the function of viscosity with time will be integrated. The extended modelling will generate base points for the optimizing. For validation the theoretical model plenty of tests with the nozzle have to be arranged. In an intermediate device, where the nozzle is processed in a dripping mode and no drying is applied, results to the temperature distribution and to the efficiency of the inner mixing are made. Now the focus is on the theoretical model first and the mixing is presented afterwards.

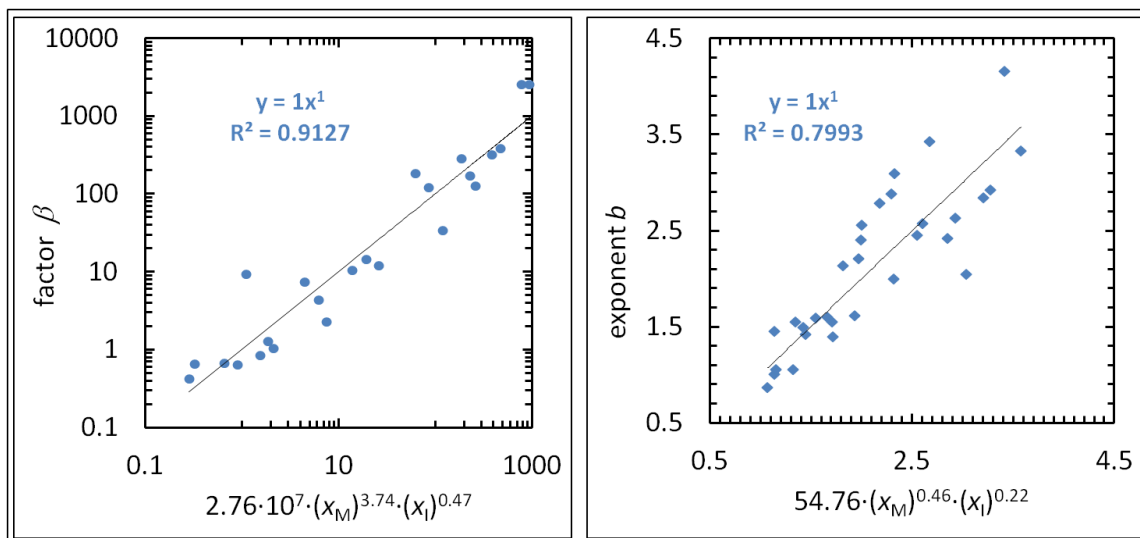
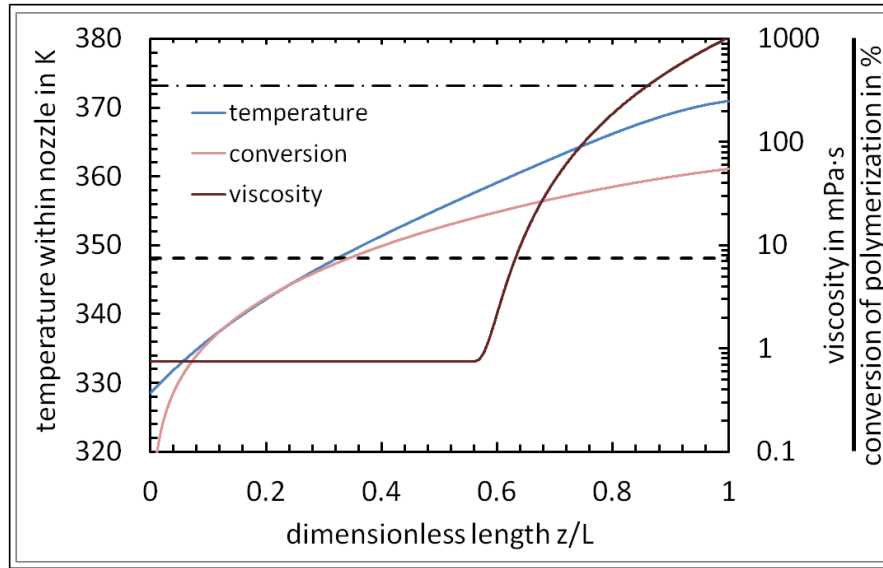


Figure 5: Presenting the values for calculating the viscosity gradient in the nozzle over time





**Figure 6:** Calculating the temperature, conversion and viscosity in the nozzle for 0.4 g/g acrylic acid in water with an initiator ratio of 0.6 mmol<sub>initiator</sub> / mol<sub>monomer</sub> during the pre-reaction

### Modelling the progress of the polymerization within the nozzle during the pre-reaction

Before tests with the reactive system will be done, theoretical considerations are necessary. The first reason for the consideration is that a good model will reduce the number of tests. But the more important reason is the fact that the tests deal with a fast reactive monomer, which will probably cause safety problems. A runaway of the 3-fluid nozzle is possible because the high reaction enthalpy will accelerate the reaction and the pressure within the nozzle will rapidly increase if the nozzle gets blocked because of the resulting viscosity's increase.

The modelling is based on the heat and mass transfer equations. These differential equations are presented in equation 5 and 6. A transformation to a dimensionless form is made. On the one hand the mass transfer is the quotient of the conversion and the change of the dimensionless length  $dz/L$ . It is calculated with the use of the Damköhler number. The rate  $r$  describes the reaction kinetics and was introduced in equation 1. The heat transfer is given as the quotient of the change of the dimensionless temperature and the dimensionless length. The heat transfer is depended on the mass transfer, that is why a simultaneous solution of both equations is necessary.

$$\frac{dU}{dz/L} = \frac{\tau r_0}{c_{10}} \left( \frac{r}{r_0} \right) = Da_0 \left( \frac{r}{r_0} \right) \quad (5)$$

$$\frac{d\vartheta}{dz/L} = Da_0 \left( \frac{r}{r_0} \right) \frac{\Delta T_{ad}}{T_0} - \frac{K_W A_W}{\dot{V} \rho \tilde{c}_p} (\vartheta_W - \vartheta) \quad (6)$$

To solve the problem of the simultaneous solution easily the differential quotients are approximated as difference quotients. By choosing a small increment for the control variable  $z$ , length of the pipe, the solving is done numerical by several iterations.

A result of the calculation is shown in figure 6. Here the temperature and conversion is plotted over the dimensionless length. It is an example for a high conversion within the nozzle when using a 0.4 g/g acrylic acid solution in water with an initiator ratio of 0.6 mmol<sub>initiator</sub> / mol<sub>monomer</sub>. The dashed line marks the reaction temperature of 75°C. As an upper limit the dash-dot line marks the boiling temperature of water at 1 bar because then the solution overcomes the boundaries of constant pressure and single phase; reactive solution. It is shown that the temperature and the conversion increase until the end of nozzle at 400 mm. That is obvious because of the enthalpy of the reaction. After a high rise of the conversion its gradient becomes lower because the polymerization consumes the monomers and the maximum of 100 % is the theoretical limit. The lower gradient of the conversion at the end damps the temperature gradient because of the linking of heat and mass transfer. If only the temperature and the conversion would be considered the safety of the pre-reaction seems to be guaranteed, because the temperature is below the boiling point of water. The high conversion should increase the efficiency of the process very much as no reactive mass is evaporated.

But the result of the viscosity's development is crucial. The function of viscosity is calculated with the results presented before. The start of the function is when the temperature is crossing the first mark at 75°C. After the plateau ending with the zero time the viscosity function is calculated by the use of the power functions.

If the rheokinetics can be transferred to the behavior within the nozzle and a critical viscosity for the atomization is known the model is able to find optimal parameters for a safe reaction. To find the critical viscosity extensive spraying tests are necessary because shear rate and deformation is much higher during atomization. Sometimes non-Newtonian effects are covered [3]. In the example above a viscosity of 1028 mPas would cause the blocking of the nozzle sooner or later. Because it is just a simple model a testing of the forecast is absolutely necessary.

In the intermediate device, where only dripping without drying is applied, tests with different temperatures have been done. The heating on within the 3-fluid nozzle has been measured with thermal elements and finally has validated the model concerning the energy balance. But before the testing of a reactive solution will be done measurements concerning the mixing within the nozzle are necessary. That's why the next and last chapter presents the current work on this topic.

### Presenting the developed device and results of the mixing within the nozzle

The advantage of the 3-fluid nozzle is the mixing of the initiator and monomer solution within the nozzle. The supply vessels for the solutions are stored cooled and dark so a pre-reaction takes only place in the nozzle because of the temperature's increase. But in a pneumatic nozzle the velocity of the liquid is low and the flow laminar. Mixing in a laminar flow where a layer flow is supposed is difficult because only diffusion will create a radial movement. Diffusion is a very slow process that's why the idea is to vary the relative velocity between initiator and monomer solution. Another method is to apply a static mixer in the nozzle.

First of all a measuring technique has been considered in a current work [12]. The decision to use an optical measurement is to have an inline measurement with no interruption of the flows. Tests with a sampling out of the nozzle were not very successful. The present measuring device consists of a light source, a camera, a visible nozzle and two lenses. The nozzle is a PMMA pipe with the same inner diameter of 5mm like the 3-fluid nozzle. The light is emitted by an LED diode with a mean wavelength of 550 nm, green light. With the use of a sum lens and a cylindrical lens the light is nearly parallel after passing the nozzle. It is the principle of a collimator. When the light hits the CMOS sensor of the camera the software generates a gray-scale image. At last a tracer, Allura Red a red dye, is used to color the water flowing through the initiator pipe.

The possibility to measure local concentration with this device can be explained with the Beer–Lambert law, see equation 7.

$$\frac{I}{I_0} = e^{-\varepsilon \cdot l \cdot c} \quad (7)$$

If the light emitted by the LED with intensity  $I_0$  is transmitted though a different medium then the intensity afterwards  $I$  is lower because light is absorbed. The measurement of the intensity quotient, the knowledge of the extinction coefficient  $\varepsilon$  and the distance the light goes through the medium  $l$  determines the concentration  $c$ . Because of the use of a camera the change of the quotient of the gray-values during the experiment and without the dye is measured. The measurement device is demonstrated in figure 7; during a run top left. For calculating a

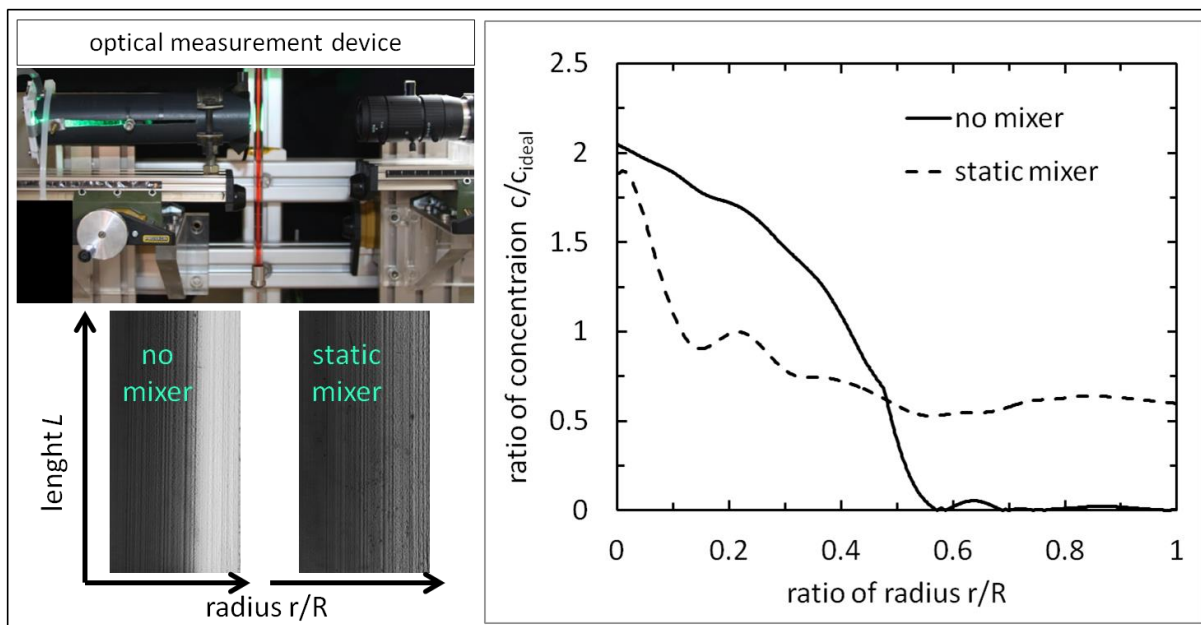


**Figure 7:** Presenting l.: the optical measurement device and r.: first results with a static mixer to improve the mixing within the nozzle [12]

concentration at a certain point in the pipe a self made algorithm is used. First calibration images with a known concentration are used and the quotients of the gray-values are measured. These values are in a known relation with the real quotient of the intensities of the Beer–Lambert law. If then an image is taken during the experiment the concentration is calculated with the help of the algorithm because the gray-values at different concentrations and different positions are known. In addition with the algorithm it is taken into account that during the way through the pipe the light transmits discrete concentric layers with different concentrations. With the calculation is assumed that the layers with the same concentration are axially symmetric. By an integral approach the calculation moves from a homogenous layer at the edge of the pipe to the centre.

Analyzing the results in figure 7 bottom left it is obvious that only by variation of the relative velocity no mixing is applied. Because of the laminar flow and the low turbulence at the geometries no radial velocity induces a mixing effect. But it is also seen that the use of a static mixer right below the end of the initiator pipe, see figure 1, applies a good mixing, optically detected. By now the best result is shown on the right of figure 7. Here the calculated ratio of the concentrations is plotted over the dimensionless radius of the pipe. A ratio of 1 means that the concentration at this point is the same as in an ideal mixture. The diagram in figure 7 shows that the static mixer improves the mixing compared to no mixer within the nozzle. Only a small part in the centre of the nozzle is not mixed well. But with further tests the results will be improved more. Currently the best static mixer is a simple orifice with a diameter of 1.2 mm.

## Conclusions

The presented work shows the development that has been done to design a spray polymerizing process. The focus is on the pre-reaction before the atomization in order to improve the efficiency of the process because only low retention times are present. First a special 3-fluid nozzle has been invented and explained in detail. In order to do first practical tests it was mentioned that there is still a big lack of information concerning the right use of a high reactive radical polymerization. Therefore a new measuring technique is presented to study the influence of the polymerization, especially the influence on the viscosity. The effect is called rheokinetics. Results of acrylic acid and sodium acrylate are presented. A semi empirical function of the viscosity of acrylic acid has been determined and it has been demonstrated that the influence of the concentration of monomer is higher than of the initiator at the start of the reaction.

In addition a modelling of the heat and mass transfer during the pre-reaction in the nozzle is presented. With a model the temperature and conversion distribution along the axis of the nozzle is calculated. The combination of the viscosity function with the model allows finding basic points to plan further experiments with a reactive solution and avoid a runaway of the reaction and consequently risks.

At least an optical measurement device to test the inner mixing of 3-fluid nozzle is mentioned. Here the development of a static mixer shows improved results.

Finally the outlook work is to test the nozzle with a reactive solution in the intermediate device. Then the step to work in a spray dryer with atomization is not very far away.

## Acknowledgements

We would like to thank the German research foundation for the financial support and the BASF SE for donating the materials. A special thank is to all the co-workers in the SPP 1423 and to our team at our institute, especially to my students.

## Nomenclature

### Latin

$a$	exponent of power function
$A$	area of heat transfer
$b$	exponent of power function
$c$	concentration in mol/L
$\tilde{c}_p$	heat capacity at constant pressure in J/(kg·K)
$Da$	Damköhler number
$I$	intensity
$k$	reaction constant in L/(mol·s) or 1/s
$K$	empirical constant
$K$	overall heat transfer coefficient in W/(m <sup>2</sup> ·K)
$l$	length in mm
$L$	length in mm
$M$	molecular mass in g/mol

$r$	rate of polymerization in mol/(L·s)
$r$	radius in mm
$R$	radius of the nozzle's inner pipe in mm
$St$	Stanton number
$t$	time in s
$T$	temperature in K
$U$	conversion
$\dot{V}$	flow rate
$x$	molar fraction
$z$	length in mm

#### Greek

$\beta$	factor of power function
$\beta$	Prater number
$\varepsilon$	extinction coefficient
$\eta$	viscosity in Pa·s
$\rho$	density in g/L
$\vartheta$	dimensionless temperature
$\tau$	retention time in s

#### Indices

0	initial condition
ad	adiabatic
$i$	initiation
$I$	initiator
ideal	ideal
$M$	monomer
$p$	propagation
$t$	termination
$W$	wall

## References

- [1] Y. A. Levendis; T. Panagiotou; R. Flagan, Patent U.S. 5,269,980 (1993-12-14)
- [2] M. Krüger, Hamburg, PhD thesis ( 2003)
- [3] M. Tewes and U. A. Peuker, Proceedings ICLASS 12<sup>th</sup> (2012)
- [4] W. Heßberger; P. Look-Herber; M. Bewersdorf; B. Bertsch-Frank; T. Lieser; C.-J. Klasen; K. Müller, Patent DE 4329204 A1 (1993-08-31)
- [5] M. Stickler, Makromol. Chem., 180, 2615 (1979)
- [6] H. Fikentscher and H. Mark, Kolloid Z., 49, 135 (1929)
- [7] H. Staudinger, Kolloid Z., 51, 71 (1930)
- [8] K. Hess and I. Sakurada, Ber. Dtsch. Chem. Ges., 64, 1183 (1931)
- [9] M. Huggins, J. Phys. Chem., 42, 911 (1938)
- [10] R. Houwink, J. Prakt. Chem., 157, 15 (1940)
- [11] S. G. Kulichikhin and A. Y. Malkin, Polym. Eng. Sci., 37, 1331 (1997)
- [12] H. Becker, Darmstadt, PhD thesis (2003)
- [13] S. Ostmann, Freiberg, Master thesis (2013)

## Measurements on droplet dynamics in the spray transport zone from a Rotary Bell Atomizer

C. Stevenin<sup>1</sup>, Y. Breaux<sup>1</sup>, J. Balcaen<sup>1</sup>, A. Blond<sup>2</sup> and J. Y. Charneau<sup>2</sup>

1 : LAMCOS, UMR 5259 – INSA Lyon, 69621 Villeurbanne, France

2 : IMP, UMR 5223 – INSA Lyon, 69621 Villeurbanne, France

### Abstract

Rotary bell atomizers used in industrial spray painting for automobiles commonly involve high speed air jets, which shape the spray and focus droplets on the part to paint. Previous experimental studies have shown that the quality of the painting process was correlated with droplet size and velocity and that the spray characteristics were strongly affected by the resulting turbulent airflow. Droplet velocity is measured in the transport zone of the spray with a Droplet Tracking Velocimetry method. Joint distributions of droplet size and velocity highlight the impact of droplet size on droplet dynamics. Finally, the droplet mean velocity and the droplet turbulence are investigated with respect to droplet size.

### Introduction

In rotary bell systems, a paint film is atomized under the influence of centrifugal and aerodynamic forces, and a shaping air is applied to confine the spray towards the part to paint. These atomizers, widely used in automobile industry, provide a uniform paint film thickness and good transfer efficiency, which furthermore can be increased if an electrostatic field is applied between the atomizer and the target.

Over the past decade, a number of numerical studies was performed to demonstrate the ability of CFD codes to correctly predict the paint film thickness on plane [1] or curved parts [2]. However, no validation was reported concerning the velocity field of the airflow or the droplet characteristics in the spray and in the vicinity of the target. As pointed out by recent papers [3], the characteristics of the impacting droplets (diameters, velocities or viscosities) play an important role in the paint film formation process and, as a consequence, need to be accurately predicted by numerical models. As a first step towards an experimental validation of numerical modelling for paint spray dispersion, this experimental study aims at providing some preliminary measurements for droplet size and velocity distributions in the transport zone of the spray.

### Materials and methods

In this work, a waterbased metallic paint is atomized in a temperature-controlled environment using a commercial high-speed bell atomizer PPH 308 provided by *SAMES Technologies*. These experiments are carried out at CoatingXpert research facility located in Oyonnax on INSA Lyon's plastics engineering site. Ambient temperature is fixed at 293K. The atomizer is static and oriented in such a way that the bell cup axis of rotation is horizontal. The rotational speed is about 30000 rotations per minute (rpm), which corresponds to a maximal tangential velocity of about 100 m/s at the edge cup for a bell cup diameter of 65mm. A high velocity air flow is used to shape the spray and entrain droplets in the axial direction. This airstream is brought from 36 orifices of 0.8mm diameter located behind the bell. As a first step, no electrostatic field is applied and no workpiece is placed in the flow. Test conditions are reported in Table 1. According to Domnick and Thieme [4], these operating conditions correspond to the jets disintegration regime and droplets result from the fragmentation of individual ligaments on the bell edge.

Parameter	Range
Cup diameter $d_{cup}$	65mm
Paint flow rate $Q_p$	200 cc/min
Shaping air flow rate $Q_a$	230 NL/min
Rotational speed $\Omega$	30 Krpm
Paint density $\rho_L$	1210 kg.m <sup>-3</sup>
Paint surface tension $\sigma$	30x10 <sup>-3</sup> N.m <sup>-1</sup>
Paint dynamic viscosity $\mu_L$	0.15 kg.m <sup>-1</sup> .s <sup>-1</sup>
Reynolds number $Re = \pi * \rho_L * \Omega * d_{cup}^2 / \mu_L$	5.3x10 <sup>4</sup>
Weber number $We = \pi^2 * \rho_L * \Omega^2 * d_{cup}^3 / \sigma$	2.7x10 <sup>7</sup>
Flow number $FN = (2^{1/2} / \pi) * \rho_L^{0.5} * \sigma^{-0.5} * d_{cup}^{-3/2} * Q_p$	1.8x10 <sup>-2</sup>

Table 1: Test conditions

Spray visualization and characterization are performed using shadowgraph imaging system provided by *LaVision*. A 10-bit 1040 x 1376 pixel camera captures the backlit spray with a field of view of 2.1 x 2.7 mm, image resolution being about 2 pixels/μm, and a flash duration of a few nanoseconds. Time interval between two successive frames varies between 2 μs and 30 μs according to the mean droplet velocity. The focal plane is positioned on the cup axis of rotation. Droplet size and velocity measurements are restricted to a zone where droplet trajectories are strongly affected by the air flow (FIG. 1).

Each dataset is composed of 500 image couples, which corresponds in our datasets to a sufficient number of events to build reliable statistics. Thereafter, experimental results regarding mean and standard deviation of droplet velocity distributions are based on 95% confidence intervals and we will not report statistics based on less than 300 detected droplets in a given size class. Number of detected droplets will be reported on FIG. 2.

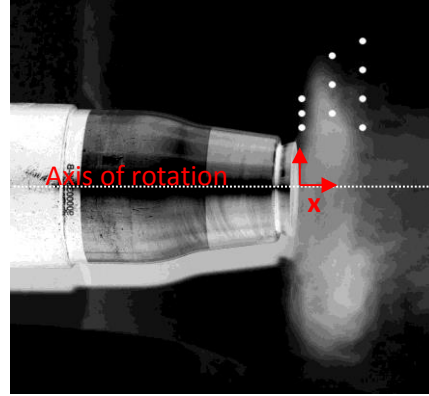


FIG. 1 – Dataset positions

Droplet sizing and tracking algorithms are implemented in *MATLAB* software. Droplet detection is performed by thresholding the wavelet transform of grayscale images, following an original approach proposed by Blaisot and Yon [5] and used by Stevenin [6].

Droplets contours are then determined from intensity pixel values in the neighbourhood of each detected objects using *Image Processing Toolbox* built-in functions. Droplet equivalent diameters  $d$  are computed from the projected areas  $A$  delimited by these contours, by assuming that droplets have a spherical shape:

$$d = \sqrt{\frac{4A}{\pi}}. \quad (1)$$

Number size distributions  $f_N(d)$  are eventually deduced from surface size distributions  $f_S(d)$  by the relation:

$$f_N(d) = \frac{d_{20}^2}{d^2} f_S(d), \quad (2)$$

where  $d_{20}$  is the surface mean diameter, which is the mean diameter of the droplet size distribution directly extracted from images. From equation (2), arithmetic mean diameter and Sauter mean diameter will be respectively defined as:

$$d_{10} = \int_0^\infty d * f_N(d) dd, \quad \text{and} \quad d_{32} = \frac{\int_0^\infty d^3 * f_N(d) dd}{\int_0^\infty d^2 * f_N(d) dd}. \quad (3)$$

Droplets velocity is obtained by matching the detected objects between two successive frames. The point-matching algorithm adopted here is based on the work of Gold *et al.* [7] and was developed to solve combinatorial optimization problems with two-way winner-take-all constraints. In tracking problems, these constraints are that, in an image pair, one droplet in one frame corresponds to one or none droplet in the other frame. This algorithm was successfully applied to estimate droplet velocities in fuel sprays by Malek *et al.* [8]

and Fdida [9]. For our dataset it has shown similar or superior performance in comparison with *Davis* (*LaVision*) commercial software.

## Results and Discussion

In the following section,  $x$  and  $y$  are respectively the Cartesian coordinate components in axial and vertical direction in the Cartesian system reported on FIG. 1.  $u$  and  $w$  denote, respectively, the horizontal and vertical velocity of droplets. Instantaneous droplet velocities are in a classic manner decomposed into mean and fluctuating parts  $u = \langle U \rangle + u'$  and  $w = \langle W \rangle + w'$ , where the brackets  $\langle \cdot \rangle$  indicate statistical averaging over an ensemble of uncorrelated images. Mean and standard deviation are based on a 95% confidence interval and a population of at least 300 droplets.

### Droplet size

For the three axial positions considered ( $x = 5\text{mm}$ ,  $x = 25\text{mm}$  and  $x = 45\text{mm}$ ), arithmetic mean diameter  $d_{10}$  and Sauter mean diameter  $d_{32}$  increase with  $y$  (FIG. 3). At these positions, liquid volume concentrations are lower than  $10^{-4}$  and droplet collisions can be neglected. In all the zone of measurements, the paint spray is very polydispersed, and droplet size ranges from  $5\mu\text{m}$  up to  $130\mu\text{m}$  (FIG. 2 and 3). In this context, Sauter mean diameter profiles result likely from the dispersion of the initial polydispersed droplet population, since large droplets with higher inertia are less entrained by the air flow than small ones.

Sauter mean diameter values are found greater than those predicted from Domnick and Thieme [4] correlation  $d_{32} = 0.6\text{Re}^{0.056}\text{We}^{-0.58}Q_p^{0.41}$ , which gives  $d_{32} = 10\mu\text{m}$ . However, further calibration experiments would be necessary to enforce these experimental mean diameter values, since no depth of field correction was applied to take into account the dependence of the volume of measurements with droplet size [10]. Moreover, in this work droplets are assumed spherical for simplicity although more complex geometrical representations of droplet shapes could be more suited to get a more accurate diameter assessment. Indeed, preliminary results show that ellipsoidal shapes would be more appropriate as mean droplet eccentricity reaches value close to 0.8.

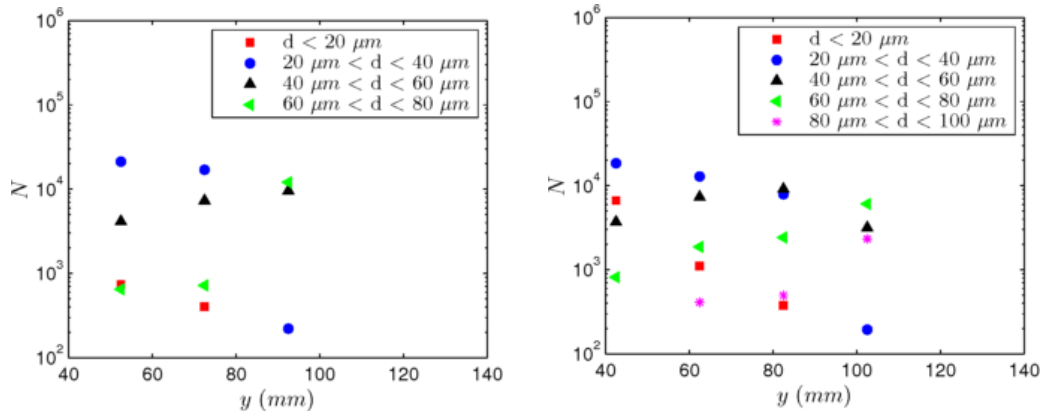


FIG. 2 – Number of detected droplet in each dataset per droplet size class, at  $x=25\text{mm}$  (left) and  $x=45\text{mm}$  (right)

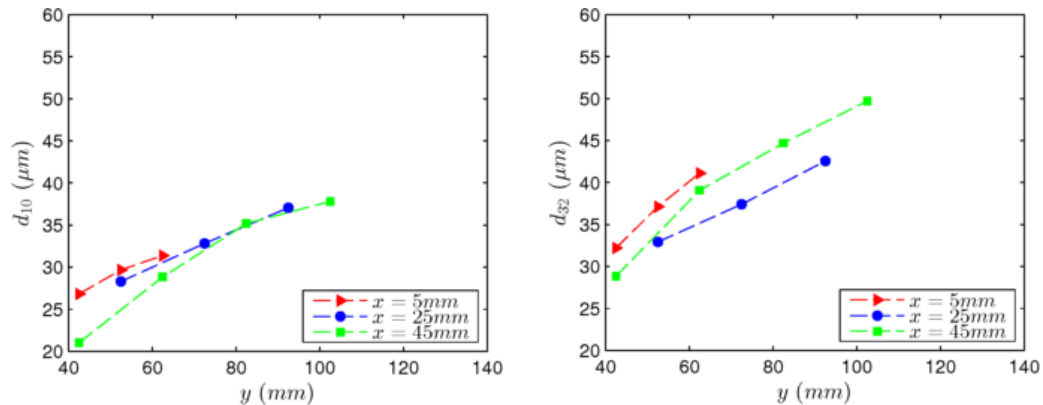


FIG. 3 – Arithmetic mean diameter (left) and Sauter mean diameter (right)



### Droplet dynamics

Droplets leave the bell cup edge under the influence of the centrifugal force with a mean angle of approximately  $70^\circ$  with the bell axis of rotation, which is higher for large droplets and lower for small ones. At  $x=5\text{mm}$ , droplets interact with the shaping air flow and lose a part of their vertical velocity (FIG. 4). Due to inertia and aerodynamic drag effects, small droplets slow more rapidly than large ones and the vertical velocity depends strongly on droplet diameters. On the contrary, droplets are accelerated in the horizontal direction by the air flow and droplet horizontal velocity becomes more correlated with droplet size with increasing distance to the bell.

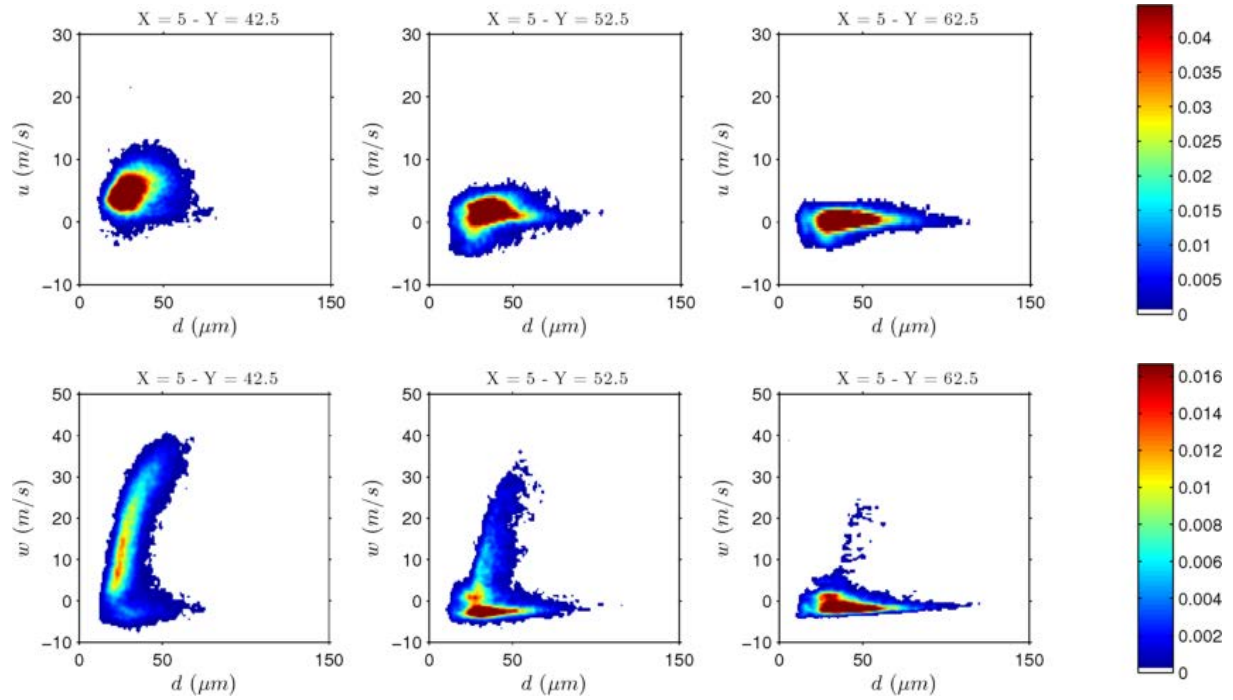


FIG. 4 – Joint distribution of droplet size and (a) droplet horizontal velocity, (b) droplet vertical velocity at  $x=5\text{mm}$

Smaller droplets are more easily entrained by the shaping air flow (FIG. 5). Higher values of horizontal mean droplet velocity are found for  $y < 60\text{mm}$ , which corresponds to positions where air velocity is stronger. At  $x=25\text{mm}$ , droplets still move radially away (FIG. 6), whereas at  $x=45\text{mm}$  most droplets are directed toward the axis under the influence of the air flow. At  $x=45\text{mm}$ , smallest droplets ( $d < 20\mu\text{m}$ ) still have positive vertical mean velocity values. Though this same behaviour is predicted by our tracking algorithm and *Davis LaVision* software, this results must be tempered by the fact that droplet matching is a difficult task in this zone where smallest droplet are very mixed by turbulence and uncertainties are higher than in simpler flow situations. However, in spite of these positive vertical mean velocity values, we must notice that these droplets are in fact directed almost horizontally.

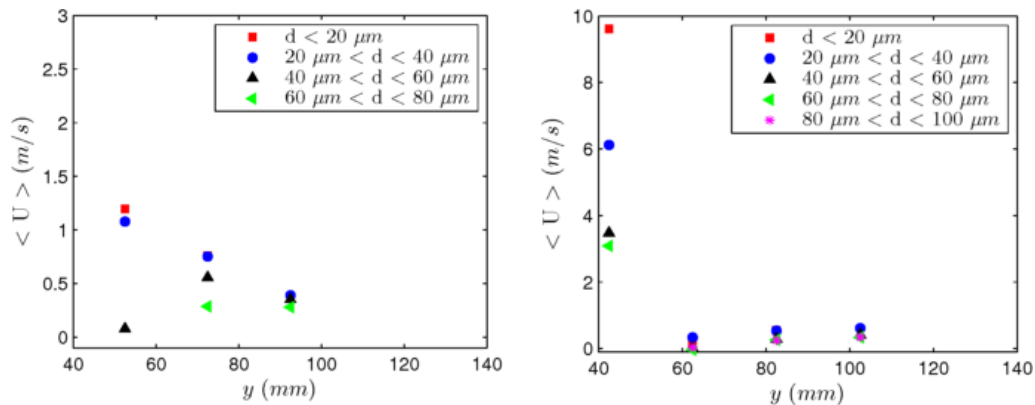


FIG. 5 – Horizontal mean velocity per droplet size class at  $x=25\text{mm}$  (left) and  $x=45\text{mm}$  (right)

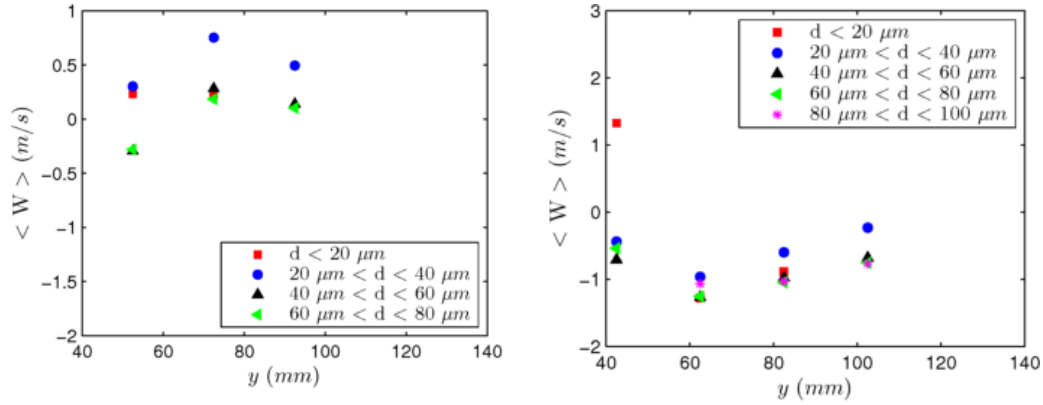


FIG. 6 – Vertical mean velocity per droplet size class at  $x=25$ mm (left) and  $x=45$ mm (right)

Standard deviations of droplet velocity components increase with decreasing droplet size (FIG. 7), as small droplets follow more closely air vortices and are more mixed by turbulence. Droplet velocity fluctuations are higher near the axis where air speed is higher. For all the datasets, standard deviation values are high in comparison with the corresponding mean velocity values: for instance, the ratio of standard deviation to mean horizontal velocity is in a range from 1.1 to 1.7 at  $x=25$ mm and from 0.6 to 0.7 at  $x=45$ mm. It is to be noted that at most points of measurements horizontal mean velocity is weak and negative values of instantaneous horizontal droplet velocity occur. Droplet turbulence seems therefore to play a very important role in droplet dispersion.

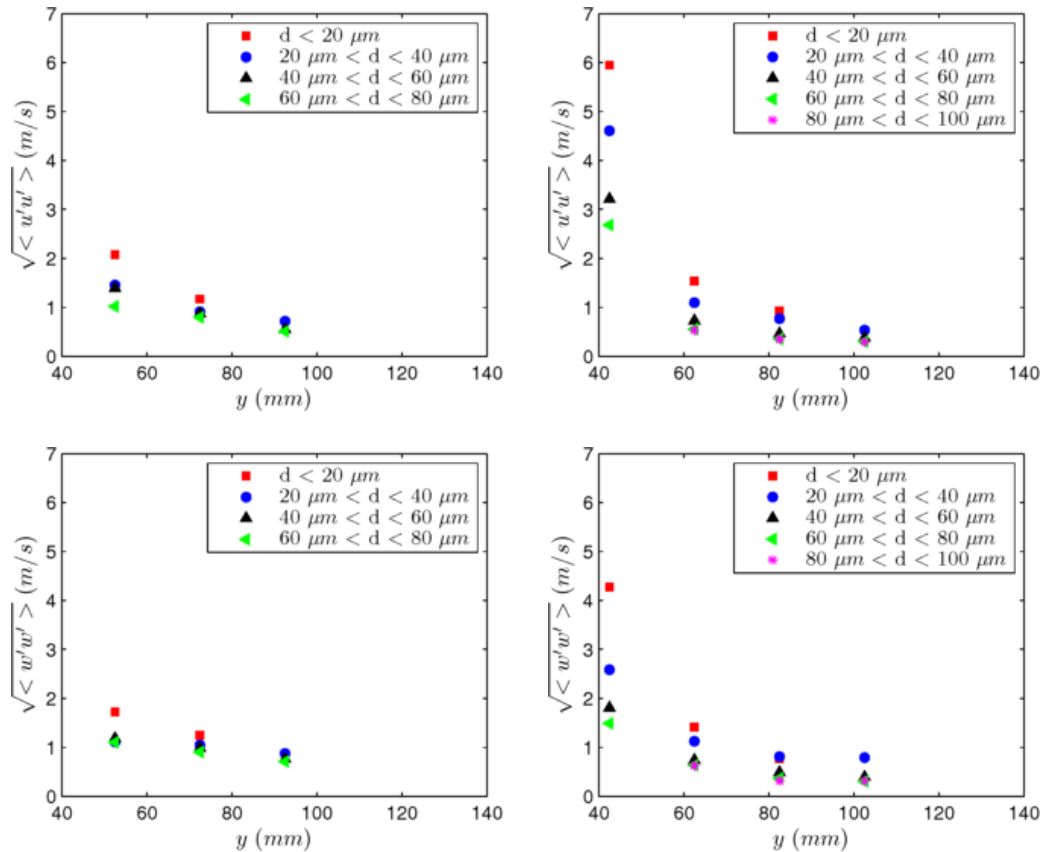


FIG. 7 – Standard deviation of velocity per droplet size class at  $x=25$ mm (left) and  $x=45$ mm (right)

Anisotropy of droplet turbulence increases with  $y$ : near the axis, the anisotropy factor  $a$  defined as  $a = \langle w'w' \rangle / \langle u'u' \rangle$  is lower than unity with values around 0.5 whereas for  $y > 90$ mm  $a$  is around 2 (FIG. 8). With respect to our datasets, anisotropy factors do not seem to be related with droplet size.

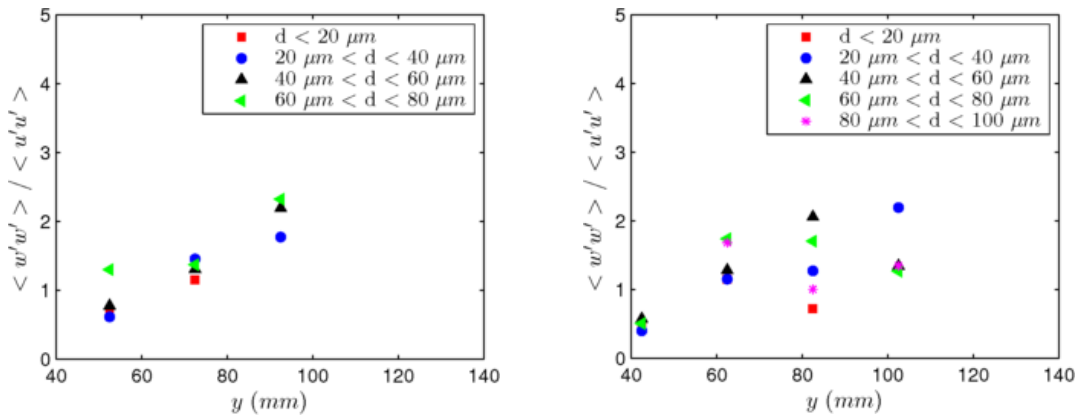


FIG. 8– Anisotropy coefficient per droplet size class at  $x=25\text{mm}$  (left) and  $x=45\text{mm}$  (right)

### Conclusions

Some preliminary results on droplet size and velocity were obtained using a Droplet Tracking Velocimetry method in the transport zone of a paint spray. In all the zone of measurements, the spray is found very polydispersed and results highlight the dependence of droplet velocity with droplet size. As expected, droplets are less influenced by the air flow when increasing droplet size and smaller droplets are more mixed by turbulence than larger ones. Anisotropy of droplet turbulence increases radially and seems independent of droplet size.

These results will be completed in a near future by hot-wire anemometry measurements to improve our knowledge on the spray dispersion dynamics and with regard to the interactions between the turbulent air flow and the spray. A particular attention will be focused on droplet turbulence anisotropy in comparison with air flow turbulence anisotropy. Numerical modelling of the spray dispersion using Eulerian/Lagrangian approaches will be eventually validated from experimental data of droplet and air velocity.

### Acknowledgement

This work is a part of a project supported by the French National Agency for Research (ANR; ANR-11-RMNP-0009) and involving SAMES Technology, Plastic Omnium and academic partners (INSA-Lyon, LRP and ICS).

### Nomenclature

$\langle \cdot \rangle$	Ensemble average
$d$	Droplet equivalent diameter
$d_{10}$	Arithmetic mean diameter
$d_{20}$	Surface mean diameter
$d_{32}$	Sauter mean diameter
$f_N$	Numeric size distribution
$f_S$	Surface size distribution
$u$	Instantaneous horizontal droplet velocity
$w$	Instantaneous vertical droplet velocity

### References

- [1] V. Viti and J. Kulkarni, CFD Analysis of the Electrostatic Spray Painting Process with a Rotating Bell Cup, ILASS Americas, Orlando, Florida, USA, May 2008
- [2] A. Mark, B. Andersson, S. Tafuri, K. Engström, H. Söröd, F. Edelvik and J. S. Carlson, Simulation of electrostatic rotary bell spray painting in automotive paint shops, *Atomization & Sprays*, 23(1):25-45, 2013
- [3] J. Domnick, Effect of Bell Geometry in High-Speed Rotary Bell Atomization, ILASS Europe 2010, Brno, Czech Republic, September 2010
- [4] J. Domnick and M. Thieme, Atomization characteristics of high-speed rotary bell atomizers, *Atomization and Sprays*, 16, 857-874, 2006
- [5] J. B. Blaisot and J. Yon, Droplet size and morphology characterization for dense sprays by image processing: application to the diesel spray, *Experiments in fluids*, 39(6), 977-994, 2005

- [6] C. Stevenin, Etude de l'atomisation d'un jet haute vitesse: Application à l'irrigation par aspersion et à la pulvérisation, Ph.D. Thesis, Ecole Centrale Marseille, France, 2012
- [7] S. Gold, A. Rangarajan, C.-P. Lu, S. Pappu and E. Mjolsness, New algorithms for 2D and 3D point matching : pose estimation and correspondance, *Pattern recognition*, 31(8), 1019-1031, 1998
- [8] M. Malek, D. Allano, S. Coëtmellec, C. Özkul and D. Lebrun, Digital in-line holography for three dimensional-two-components particle tracking velocimetry, *Measurement Science and Technology*, 15(4), 699-705, 2004
- [9] N. Fdida, Développement d'un système de granulométrie par imagerie Application aux sprays larges et hétérogènes, Ph.D. Thesis, Université de Rouen, France, 2008
- [10] C. Stevenin, S. Tomas, A. Vallet, M. Amielh and F. Anselmet, Shadowgraphy investigations of high speed water jet atomization into still air, *ICLASS 2012, Heidelberg, Germany, September 2012*

## Adapted Spray Generation in FSP-processes for Nanoparticle Generation at Large Production Rates

Achelis, Lydia<sup>1</sup>, Li, Xinggang<sup>1</sup>, Meierhofer, Florian<sup>2</sup>, Schreiner, Manuel<sup>1</sup>, Fritsching, Udo<sup>1,2</sup>, Gröhn, Arto<sup>3</sup> and Wegner, Karsten<sup>3</sup>

1: Particles and Process Engineering, University of Bremen, Germany

2: Foundation Institute of Materials Science (IWT), Bremen

3: Institute of Process Engineering, Swiss Federal Institute of Technology (ETH), Switzerland

### Abstract

The development of a new atomizer concept aiming to larger production rates of nano-particles by the Flame Spray Pyrolysis process (FSP) is presented. In the conventional FSP process (external mixing gas/liquid nozzle) production rate may be varied by increasing the precursor feed rate and/or the precursor concentration. However, both measures typically result in the formation of larger nanoparticles. The aim of the new atomizer concept is to address the spray structure in a way that keeps the flame height almost constant and modifies the flame width instead. Therefore, the time scales and residence time-temperature histories of the droplets and particles are expected to be similar while the production rate is increased. The new atomizer concept combines a swirling liquid film generation that is atomized by a swirling gas flow. In the first step a cone of liquid ligaments and primary droplets is generated through a conventional pressure-swirl nozzle. The ligament is atomized in the second step, by the impinging gas from a circular nozzle. A numerical model is used to simulate the gas flow and spray distribution in the adapted atomizer concept. In cold spray experiments, the process parameters such as volumetric flow rate of the liquid (250-400 ml/min), gas flow rate (100-550 l/min) and angle of liquid outlet (30-120°) as well as gas swirl inlet (0-45°) are investigated. An enlarged and steady spray results from an increasing outlet angle of the liquid and increasing gas flow leading to a reduction of the droplet sizes. Fluctuations of the spray are observed during the increase of the gas mass flow rate. However, with a certain inlet angle of the gas and an increased gas mass flow, the desired spray spreading through a strong effect of centrifugal forces is observed.

### Introduction

During the past decades, it has been recognized that nano-sized metal oxide particles and clusters can be effectively adapted in diverse commercial applications and electrical devices, mostly due to their distinctly different properties when compared to bulk. Nowadays, such materials are already utilized in different products such as catalysts, solar cells, advanced batteries, fuel cells, paints, polishing slurries, antimicrobials and others. The large scale manufacturing of such materials is therefore of great interest [1].

Flame Spray Pyrolysis (FSP) is a versatile process for dry synthesis of nanoparticles (NP) from the gas-phase. In this process, low cost metallic precursors (e.g. tin(II) 2-ethylhexanoate) dissolved in liquid fuels (e.g. xylenes) are fed into a nozzle. Dispersion gas, typically pure O<sub>2</sub> leaves the nozzle at speed of sound and atomizes the liquid into fine droplets with mass median diameter ( $d_{50,3}$ ) of approximately 10 µm. The spray is ignited with a premixed oxy-methane support flame. Droplet evaporation, nucleation, cluster formation, coalescence, and finally agglomeration of the product NPs occur as respective process steps in FSP along the spray's trajectory [2]. Organic solvents as well as the precursor itself provide the required combustion enthalpy for the high temperature (> 2000 °C) reactions. Furthermore, it has been shown that almost all periodic table elements can be produced as oxides, salts, or even metal NP in the laboratory-scale reactors with production rates of a milligram to gram/hour [3, 4].

Several scale-up studies of FSP have been carried out [5-10]. Heine et al. showed that SiO<sub>2</sub> production rates up to 1.1 kg/h can be realized [7]. Results showed that for a constant dispersion gas feed rate, an increase in the production rate either by increasing the metal concentration of the precursor or by increasing the precursor feed rate results in increased particle concentration and flame length, thus producing bigger NPs. In contrast, an increase in the dispersion gas flow rate enhances the mixing, accelerates combustion, and decreases the flame length as well as the droplet concentration in the gas flame, all together yielding to production of smaller nanoparticles. This correlation between particle size and production rate can be considered as a trade-off in large scale production facilities.

In common nozzles applied in the FSP process, both the liquid precursor and dispersion gas are introduced as jet flow in the axial direction causing a rather slim and elongated flame shape. However, it is hypothesized that broadening the spray angle may result in a broader flame and could enable higher nanoparticle production rates. Swirl atomizers seem as an ideal solution for this problem, as they are already used in diverse processes such as fuel injection in combustion engines or turbines [11, 12], as well as melt atomization [13, 14]. Based on this

concept a novel FSP nozzle design for higher production rates is suggested in this work. Here, both liquid and dispersion phase are set into a rotational motion to accomplish a wide spray angle as well as a stable spray pattern.

### Experimental Setup

The atomizer concept for formation of a modified spray combines the generation of a liquid film which is atomized with a swirling gas flow. Figure 1 shows a sketch of the atomizer. The liquid flows through a commercial pressure-swirl nozzle (Schlick Atomizing Technology, Hohlkegeldüsen Modell 121-123), leaves it through a small cylindrical hole (1mm) and forms a hollow cone lamella which is atomized into liquid ligaments and primary droplets. These fragments are further atomized by a swirling gas stream generated through a custom-made gas nozzle. The main characteristics of the combined atomizer are analyzed in cold spray experiments with water and air as liquid and gas phases, respectively. The effects of liquid outlet angle, gas swirl inlet angle and gas/liquid flow rates are investigated (Table 1).

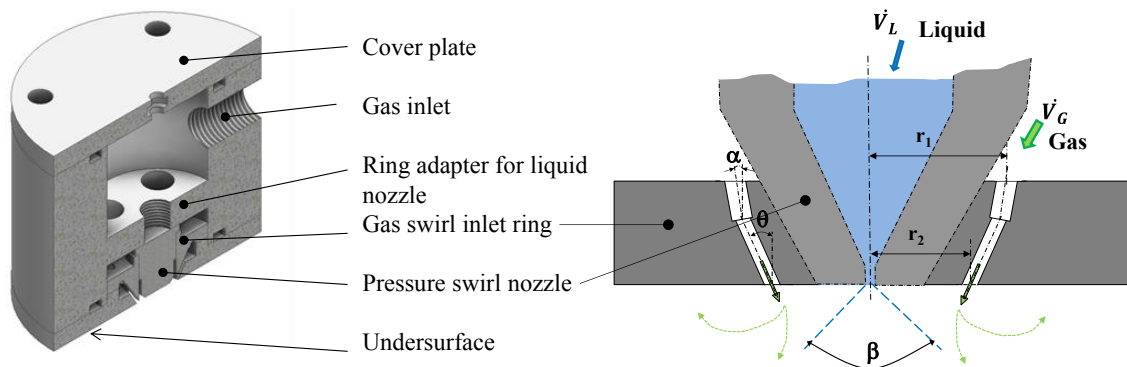


**Figure 1 a.** Schematic of the combined atomizer

**b.** Details of the atomizer – sketch with gas swirl inlet angle ( $\alpha$ ); slit nozzle angle ( $\theta$ ); liquid outlet angle ( $\beta$ )

The spray structure is analyzed with laser-light-sheet illumination photography (camera and macro objective). The angle of the spray cone is measured in 5° steps. Laser diffraction (Sympatec Helos) is used to measure the droplet size distribution in the spray. The gas velocity is calculated by measuring the pressure difference with a pitot tube.

### Mathematical modelling

The swirling gas flow out of the ring slit nozzle is modelled as a 2D axis-symmetric problem by considering only the part after the slit nozzle exit. 2D axis-symmetric problems can be dealt with in OpenFOAM by generating a mesh in 3 dimensions on wedge geometry and applying 'wedge' type boundary condition on any patch in both side plane(s) of the wedge. In Fig. 2 (a) and (b) the computational geometry and mesh are exhibited. The geometry is specified as a wedge of small angle (e.g. < 5°) and one cell thick running along the plane of symmetry. The computational domain is of 100 mm in axial (z) direction and 40 mm in radial (r) direction. The slit width of the nozzle is 1 mm. The mesh consists of 20000 cells.

A transient solver using the PISO (pressure-implicit split-operator) algorithm is employed together with  $k-\omega$  SST turbulence model. Without considering gas compressibility, the velocity at the nozzle exit (inflow) depends on gas volume flow rate ( $\dot{V}_G$ ), gas swirl inlet angle ( $\alpha$ ), slit nozzle angle ( $\theta$ ) and nozzle dimensions. In the present work, the volumetric flow rate is in the range of 100 to 800 l/min and the swirl nozzle angle changes from 0° to 15°. The average gas velocity at the slit nozzle exit can be estimated by the following expressions:

$$\text{axial velocity: } U_z = \frac{\dot{V} \cos \theta}{S_{slit}}; \text{ radial velocity: } U_r = -\frac{\dot{V} \sin \theta}{S_{slit}}$$

**Table 1.** Range of selected process and geometric parameters

Liquid volume flow	$\dot{V}_L$	ml/min	250 – 400
Gas volume flow	$\dot{V}_G$	ln/min	100 – 700
Liquid outlet angle	$\beta$	°	30; 70; 120
Gas swirl inlet angle	$\alpha$	°	5; 15; 30; 45
Slit nozzle angle	$\theta$	°	30

where  $S_{slit}$  represents the section area of slit nozzle exit. Assuming a constant angular momentum of the gas flow in the slit nozzle, the average tangential velocity at nozzle exit can be approximated by the following expression:

$$\text{tangential velocity: } U_t = \frac{r_1}{r_2} \frac{\dot{V} \sin \alpha}{n S_{swirl}},$$

where  $S_{swirl}$  is the cross section area of the inlet at swirl nozzle exit and  $n$ , the number of inlets from swirl nozzle (here four). Here the value of  $r_1/r_2$  is  $\sim 2$ . Fig. 2 (c) exhibits the calculated gas flow field with gas volume flow rate 200 ml/min and swirl angle  $5^\circ$ . The gas flow field is well developed at 50 ms and the results are mirrored on the  $z$  axis. Under these conditions the gas entrainment is obvious inside the swirling flow.

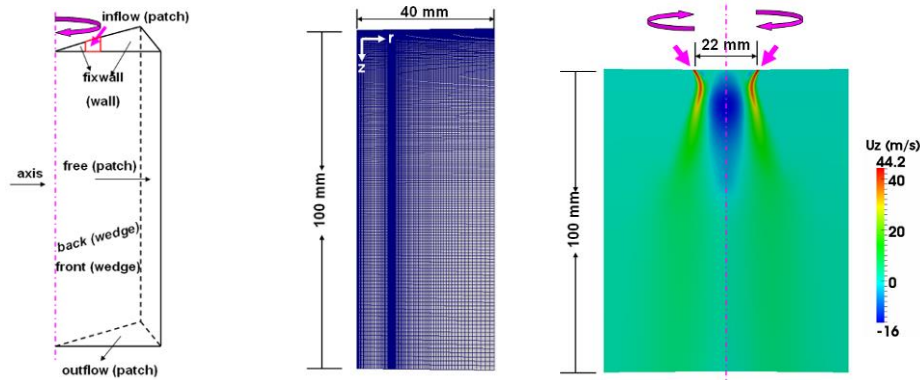


**Figure 2.** a. Schematic of computational domain b. Mesh c. Calculated gas flow field

## Results and Discussion

Experiments with different geometric nozzle parameters (angles of liquid and gas) and process parameters (flow rate of liquid and gas) are carried out to produce a modified, enlarged and steady spray of small droplets. Thereby, the expansion and direction of the gas flow is of interest as well as the interaction between gas and liquid. These characteristics can be observed in the formation of the spray cone. The geometry of the spray cone was investigated by analysing the laser-light-sheet images

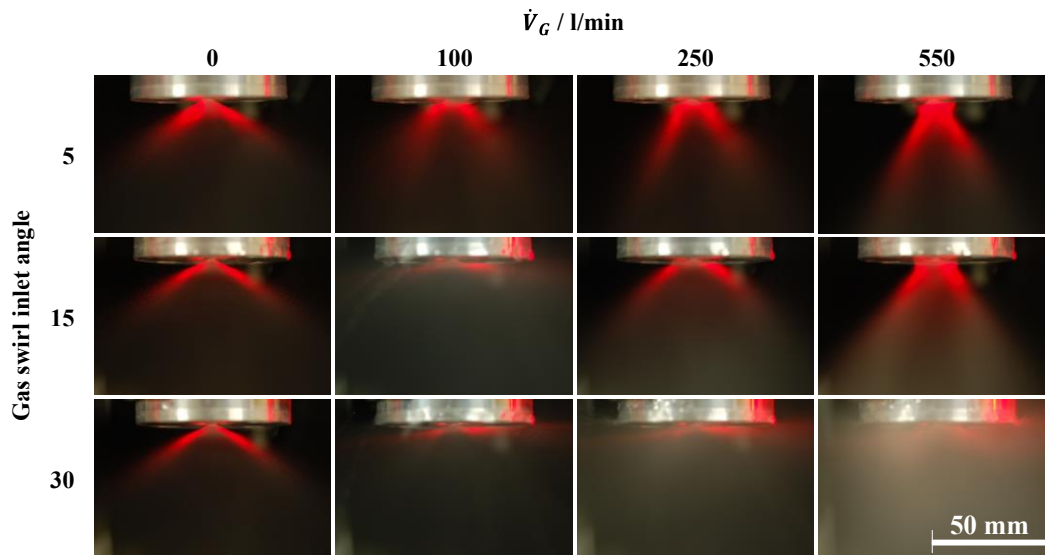


**Figure 3.** Formation of the spray cone by using a liquid outlet angle of  $120^\circ$ , depending on the gas volume flow  $\dot{V}_G$  and gas swirl inlet angle. Flow fluctuations and a horizontal spreading of droplets at specific gas conditions are observed.

The three images in the left column in Fig. 3 display the spray cone without gas flow and therefore secondary atomization. The spray cone angle is formed due to the pressure swirl nozzle depending on the liquid outlet angle of  $120^\circ$  and a liquid volume flow of 250 ml/min. The formation of the spray cone under the effect of the



rotational swirled atomization gas is observed and shown in the images on the right side. For these experiments gas swirl inlet angles from 5-30° and volumetric gas flow rates from 100 up to 550 l/min are used.

Gas recirculation or other negative effects are not observed when using the 5° swirl inlet (upper images). With increased gas flow the spray cone narrows down and an increased local mass concentration of droplets close to the nozzle outlet becomes visible. This gives a qualitative view of the local density of the atomized droplets. By increasing the swirl inlet angle to 15° (second row), the droplets spread in radial direction and splash onto the nozzle. Also spray pulsation is observed with a gas flow of 100 l/min. However, further increase of the gas flow rate stops the fluctuation and the process is stabilized. With larger swirl inlet angles up to 30° strong fluctuations and recirculations are observed again, independent on the gas flow. A high amount of droplets is deposited on the nozzle which is undesirable.

This relationship between spray cone angle and gas flow is demonstrated in Fig. 4. The measured spray cone angles, generated by four different swirl inlet angles (5-45°) versus gas volume flow are shown. Two different trends are visible. The spray cone angle generated with 5° and 15° swirl inlet decreases with increasing gas flow in comparison to nearly constant spray cone angles of approximately 150° with larger swirl inlet angles.

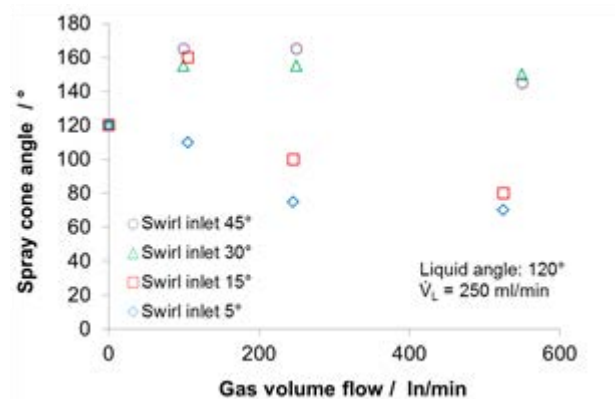
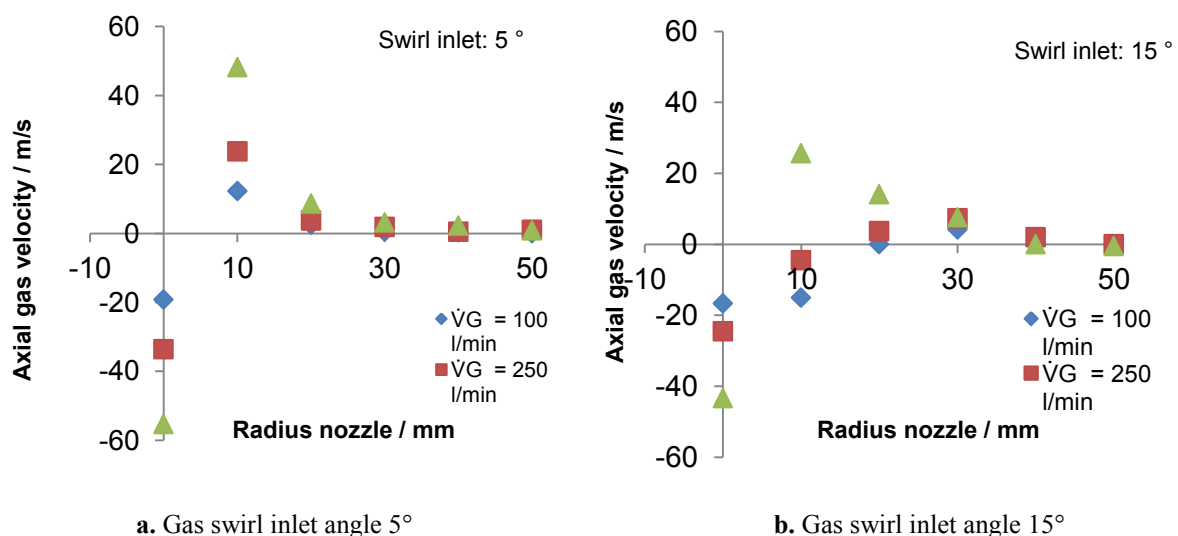


**Figure 4.** Trends of the spray cone angle with increasing gas velocity changing for different swirl inlet angles

The axial gas velocity was measured with a pitot tube and the corresponding data are given in Fig. 5. The tube was positioned 20 mm from the nozzle exit and moved in radial direction from 0 to 50 mm. The swirl inlet angles of 5 and 15° were tested while the gas volume flow was varied. In the centre of the nozzles an area of underpressure is detected (negative velocity). The gas velocity increases from a minimum in the nozzle centre to a maximum at 10 mm. A higher gas velocity follows a higher gas flow. By using the 15° swirl inlet, a smaller maximum velocity is measured and the region of under pressure enlarges. Here, the axial velocity becomes positive even for small flow rates of 100 l/min only at a radial distance of 30 mm to the nozzle center line. The main direction of the velocity is the radial component causing a horizontal spray (parallel to the nozzle plate) which is visible in Fig. 3. By increasing the gas flow for the 15° gas swirl inlet, the axial gas velocity is pronounced but less in comparison to the 5° swirl inlet. Following from these observations, the atomization has to be more effective and the droplet size distribution becomes smaller by a 5° swirl inlet.



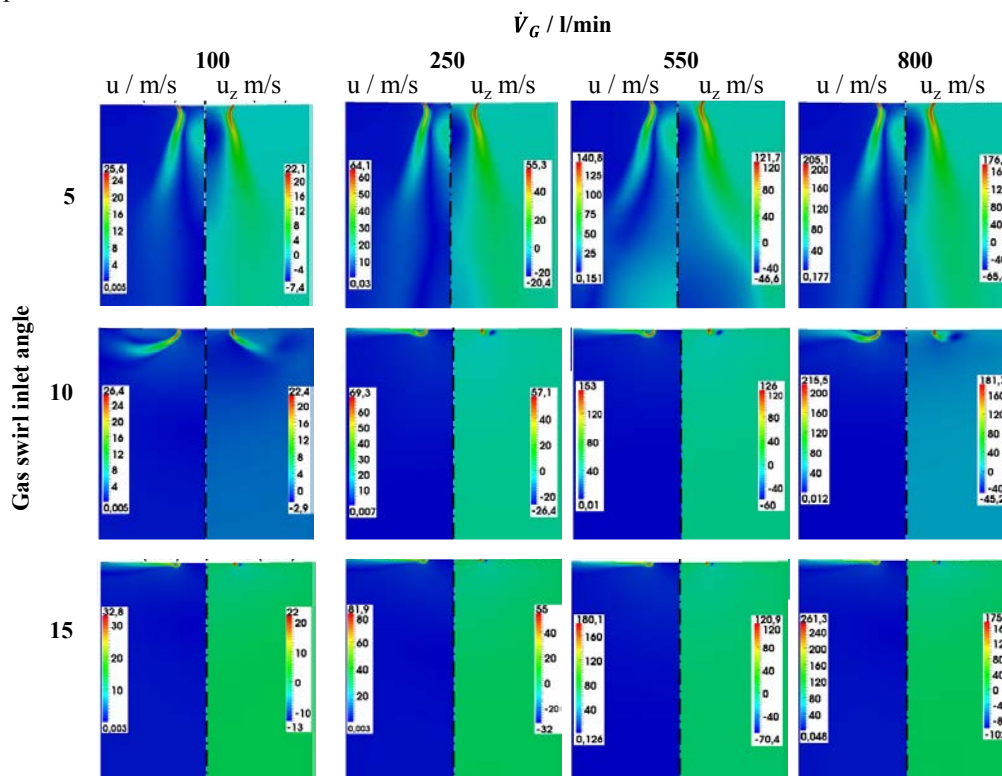
**a.** Gas swirl inlet angle 5°

**b.** Gas swirl inlet angle 15°

**Figure 5.** Higher maximum axial gas velocity by using 5° swirl inlet angle instead of 15° with changed under pressure area

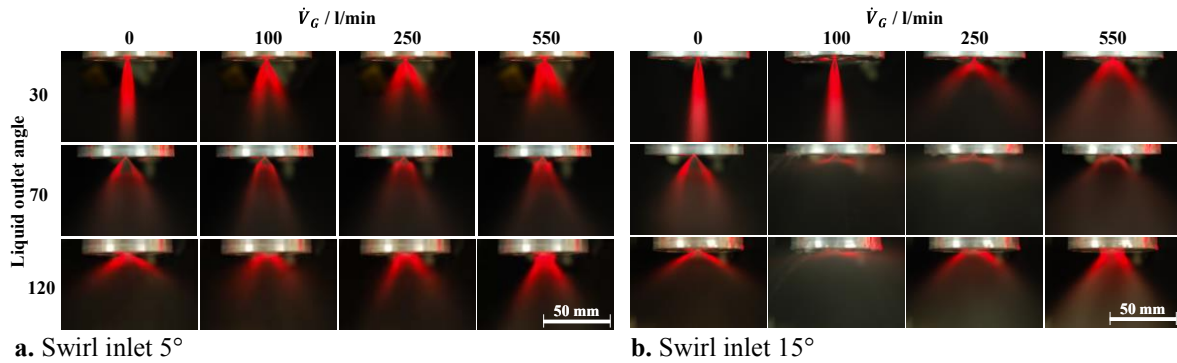
Regarding Fig. 3-5 it can be stated that when using the 5° swirl inlet, small but stable spray cones are produced. By using the nozzle with a swirl inlet angle of 15° or larger, the rotational and radial velocities are promoted and the spray is dispersed. In addition, the emerging recirculation areas close to the nozzle intensified the flow in radial direction, as well as the Coanda effect between gas and nozzle. For gas flow rates > 100 l/min the liquid detaches from the nozzle plate and forms a spray cone again (15° gas swirl inlet).

Fig. 6 shows calculated gas velocity fields (left: total velocity; right axial velocity) under different operation conditions, e.g., under different volume flow rates and swirl angles. With increasing gas volume flow rate also the velocities are higher but the gas flow pattern changes only slightly. The swirl inlet angle  $\alpha$ , which determines the ratio of gas rotational velocity to the normal velocity at slit nozzle exit, has great influence on the gas flow pattern; with increasing swirl inlet angle the main flow is bended outwards in the radial direction, even touching the upper wall, and the recirculation inside the swirling flow is not so significant. For swirl inlet angles > 10°, similar flow patterns are obtained as for swirl angle 15°. The simulation results can well explain why the spray droplets move towards the nozzle in the experiments. However, the effect of increased swirl inlet angle on gas flow profiles cannot be observed.



**Figure 6.** Gas flow patterns under different volume flow rates and swirl inlet angles

In consideration of these results, experiments with two further liquid swirl nozzles at outlet angles of 30 and 70° were carried out, aiming for the generation of a wide and stable spray. Fig. 7 shows the LLS-images of experiments with gas flow up to 550 l/min, liquid outlet angles 30, 70 and 120° and swirl inlet angles of 5 and 15°. All experiments done with the 5° swirl inlet angle are stable and the resulting spray cone angles are in a range of 40°-70°. In contrast, experiments done with 15° swirl inlet causes unstable behaviour (70 and 120° liquid outlet angle). The spray cone resulting with 30° liquid outlet angle and 100 l/min gas flow seems more compressed as the spray cone without gas impact. The gas did not atomize the liquid fragments in a secondary atomization step; it just narrows the liquid cone. With increasing gas flow, the axial direction of the gas stream increases and the liquid is atomized.

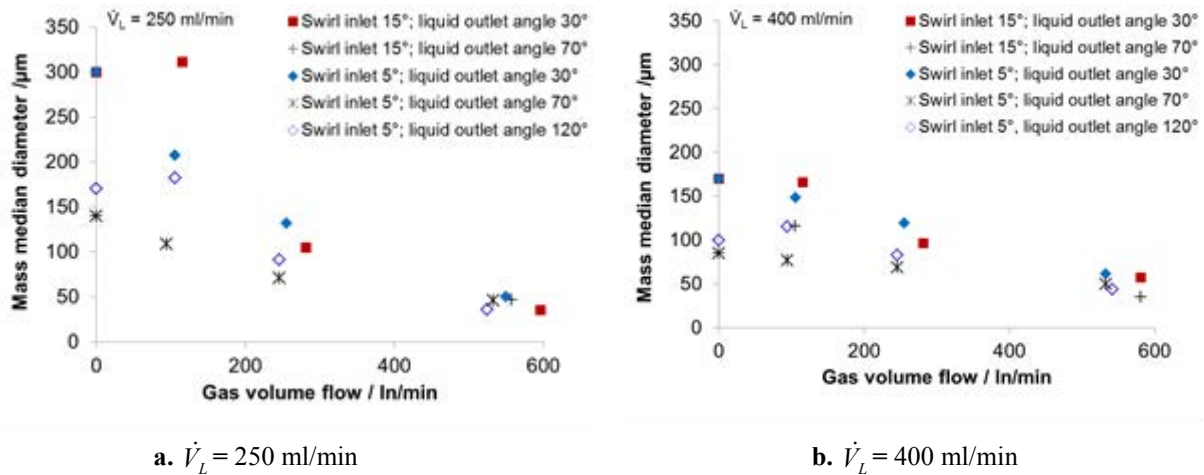


a. Swirl inlet 5°

b. Swirl inlet 15°

**Figure 7.** Formation of the spray cone by using a liquid outlet angle of 30°, 70° and 120°, depending on the gas volume flow  $\dot{V}_G$  and gas swirl inlet angle

The droplet size distribution of experiments with 5 and 15° gas swirl inlet angle and 30, 70 and 120° liquid outlet angle is measured. Spreading of droplets in radial direction cannot be detected, because these droplets deposit onto the lens of the measurement system. The mass median diameter depending on the gas volume flow is presented in Fig. 8. On the left (Fig. 8a), experiments carried out with 250 ml/min liquid flow rate and on the right (Fig. 8b) with 400 ml/min are shown.



a.  $\dot{V}_L = 250$  ml/min

b.  $\dot{V}_L = 400$  ml/min

**Figure 8.** Decreased mass median diameter with increasing gas volume flow. Small mass median diameter by using liquid outlet angle of 70° and swirl inlet angle of 5°

Generally, the droplet size decreases with increasing gas volume flow. Experiments with a 15° swirl inlet lead to larger droplets. The contact point between gas and liquid (the atomization zone) is displaced because of the rotational velocity and a smaller gas impulse. Primary atomization is the dominant mechanism up to a gas flow 100 l/min and causes a smaller mass median diameter for 400 ml/min. However, with increasing the gas flow at a liquid flow rate of 250 ml/min the atomization produces small droplets (35 μm).

The developed atomizer concept and spray conditions have been tested in combustion experiments at ETH Zurich. Fig. 9 shows an ethanol spray flame at a liquid flow rate of 100 ml/min and a gas flow rate of 200 l/min illustrating the potential increase of production rate in the FSP process. These investigations will be continued in future.

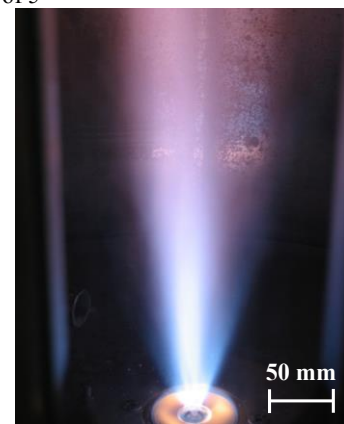


**Figure 9.** Ethanol spray flame at a liquid flow rate of 100 ml/min

## Conclusions

For scale-up of the FSP-process, new atomization concepts need to be developed. Atomization experiments with water (cold spray) were carried out with different nozzle designs and gas-liquid volume flows. The resulting spray cone angles and mass median diameter were measured. Experimental results were also compared to conducted CFD simulations. It was shown that a wider spray cone is produced in comparison to the conventional FSP ( $< 30^\circ$ ). The droplet size decrease depends on the gas volume flow. Using  $70^\circ$  liquid outlet angle in combination with a  $5^\circ$  swirl inlet angle led to a small average ( $40\ \mu\text{m}$ ) droplet size. The performance of the atomization depends on the available kinetic energy, which is provided by using the  $5^\circ$  swirl inlet angle with pronounced axial velocity component. A wider spray cone can be generated by a higher swirl inlet angle depending on the rotational velocity. Fluctuations are observed in a range of 100-250 l/min gas volume flow when using  $>15^\circ$  swirl inlet angle. These conditions are not applicable to the FSP process. The simulation of the gas flow reproduced the main features of the experiments. For the swirl inlet of  $5^\circ$  the gas flow is described well, as well as the gas flow in rotational direction.

In summary, an adapted atomizer to produce wide and stable spray cone is obtained with a  $5^\circ$  swirl inlet angle and  $70^\circ$  liquid outlet angle. A smaller droplet size distribution may be attained with a higher gas momentum for the atomization. This could be realized by employing a shorter distance between liquid and gas exit as well as a higher gas pressure drop and velocity.

## Acknowledgements

The authors would like to acknowledge the EU (Seventh framework program), for their solid financial support of this project (Advanced FSP Project No: CP-FP 228885-2).

## Nomenclature

$d_{50,3}$	$\mu\text{m}$	Mass median diameter
$n$	-	Number of gas swirl inlets
$r_1$	m	Distance center nozzle to center gas swirl inlet
$r_2$	m	Distance center nozzle to gas slit outlet
$S_{\text{Slit}}$	$\text{m}^2$	Section area of slit nozzle exit
$S_{\text{Swirl}}$	$\text{m}^2$	Cross section area of gas inlet
$u_r$	m/s	Radial velocity
$u_t$	m/s	Tangential velocity
$u_z$	m/s	Axial velocity
$\dot{V}_L$	ml/min	Liquid volume flow
$\dot{V}_G$	ln/min	Gas volume flow (norm)
$\alpha$	$^\circ$	Gas swirl inlet angle
$\beta$	$^\circ$	Liquid outlet angle
$\theta$	$^\circ$	Slit nozzle angle

## References

- [1] Holman, M., Novotny, M., Kemsley, J., Nordan, M., Raje, J., Sullivan, T., Pekarskaya, E., Abkemeier, K., Schiamberg, B., Nüssel, B., Krule, E., Mamikunian, V., Hartshorn, C., *The Nanotech Report*, 5th Edition, 2007.
- [2] Wang, C., Friedlander, S.K., Mädler, L., Nanoparticle aerosol science and technology: an overview. *China Particuology*, 2005. 3(5): p. 243-254.
- [3] Teoh, W.Y., Amal, R., Mädler, L., Flame spray pyrolysis: An enabling technology for nanoparticles design and fabrication. *Nanoscale*, 2010. 2(8): p. 1324-1347.
- [4] Wegner, K., Schimmoeller, B., Thiebaut, B., Fernandez, C., Rao, T.N., Pilot Plants for Industrial Nanoparticle Production by Flame Spray Pyrolysis. *KONA Powder and Particle Journal* 2011. No.29
- [5] Bickmore, C.R., Waldner, K.F., Treadwell, D.R., Laine, R.M., Ultrafine Spinel Powders by Flame Spray Pyrolysis of a Magnesium Aluminum Double Alkoxide. *Journal of the American Ceramic Society*, 1996. 79(5): p. 1419-1423.
- [6] Laine, R.M., Hinklin, T., Williams, G., Rand, S.C., Low-Cost Nanopowders for Phosphor and Laser Applications by Flame Spray Pyrolysis. *Materials Science Forum*, 2000. 343-346: p. 500-510
- [7] Mueller, R., Mädler, L., Pratsinis, S.E., Nanoparticle synthesis at high production rates by flame spray pyrolysis. *Chemical Engineering Science*, 2003. 58(10): p. 1969-1976.
- [8] Mueller, R., Jossen, R., Pratsinis, S. E., Watson, M., Akhtar, M. K., Zirconia Nanoparticles Made in Spray Flames at High Production Rates. *Journal of the American Ceramic Society*, 2004. 87(2): p. 197-202.
- [9] Mueller, R., Jossen, R., Kammler, H. K., Pratsinis, S. E., Akhtar, M. K., Growth of zirconia particles made by flame spray pyrolysis. *AIChE Journal*, 2004. 50(12): p. 3085-3094.
- [10] Rosebrock, C., Pokhrel, S., Mädler, L., Fritsching, U., Noriler, D., Meier, H.F., Spray structural parameter influence on the Flame Spray Pyrolysis (FSP) process for nanoparticle production. *ILASS – Europe 2011, 24th European Conference on Liquid Atomization and Spray Systems*, Estoril, Portugal, 2011
- [11] Khavkin, Y.I., *Theory and Practice of Swirl Atomizers*. 2004, Taylor & Francis.
- [12] Yu, G., Yu, G., Li, J. G., Zhao, J. R., Yue, L. J., Chang, X. Y., Sung, C. J., An experimental study of kerosene combustion in a supersonic model combustor using effervescent atomization. *Proceedings of the Combustion Institute*, 2005. 30(2): p. 2859-2866.
- [13] Achelis, L., Uhlenwinkel, V., Characterisation of metal powders generated by a pressure-gas-atomiser. *Materials Science and Engineering: A*, 2008. 477(1-2): p. 15-20.
- [14] Li, X., Heisterüber, L., Achelis, L., Uhlenwinkel, V., Fritsching, U., Spray process modeling in metal matrix composite production. *Atomization and sprays* 2011. 21 (11): p.933-948

## Experimental Investigation of Airblast Atomization by Variation of Dynamic Pressure and a Geometrical Scaling Factor

J. C. Wollgarten<sup>1</sup>, M. Gebretsadik<sup>1</sup>, N. Zarzalis<sup>1</sup>, O. Nuri Sara<sup>2</sup>, F. Turrini<sup>3</sup> and P. Di Martino<sup>3</sup>

1: Karlsruhe Institute of Technology (KIT), Engler-Bunte-Institute (EBI), Engler-Bunte-Ring 1, 76131 Karlsruhe, Germany

2: Department of Chemical Engineering, Cankiri Karatekin University, 18200 Cankiri, Turkey

3: AVIO S.p.A., Via I Maggio 56, 10040 Rivalta di Torino, Italy

### Abstract

Liquid fuel combustion is strongly influenced by the droplet sizes and their distribution. The prediction of the flow field with superimposed combustion requires the knowledge of droplet size distribution. The current investigation involves in studying the droplet size distribution by varying different parameters that influence the spray characteristics, hence, the Sauter mean diameters (SMD) of a swirled prefilming airblast injection system (IS) were varied in this investigation. The varied parameters are the geometry of the IS with a linear scaling factor of two and the aerodynamic conditions. The SMDs of the entire spray were determined by combining the results of two different measurement methods. The first method is based on a particle dynamics analysis (PDA) system and the second is a combination of the SMD determined by the PDA and the mass flux measured by a patternator.

The results show that an increase in air velocity decreases the SMD. Differences in the SMD were observed from the two calculation methods with or without the patternator mass flux. These deviations occur due to the fact, that the PDA system does not detect non-spherical droplets and droplets in the recirculation zone might be detected more than once. On the other side, the patternator itself influences the flow field of the IS. For the scaled-down IS it can be concluded that the similarity of two phase flows is not given by scaling of the IS, because of the change in SMD and the distribution of the liquid mass flux. This also means that the fuel to air distribution and therefore the temperature distribution will change in the case of superimposed combustion.

### Introduction

The current development of propulsion engines focuses on the reduction of nitrogen oxides ( $\text{NO}_x$ ), carbon monoxide (CO) and unburned hydrocarbons (UHC) emissions due to environmental conventions. One of the essential processes in an engine to reach this goal is the fuel atomization. A promising technology for aviation applications is the prefilming airblast atomization investigated by Lefebvre and Miller [1]. This concept generates a broad range of fuel to air ratio with a homogeneous fuel to air distribution which also causes a homogeneous temperature distribution and thus low thermal  $\text{NO}_x$  emissions for combustion mean temperatures below 1900 K. The research work described in the paper was performed within a European Commission (EC) program in cooperation with the industrial partner AVIO. During the NEWAC (New Aero Engine Core Concepts) program of the sixth framework [2] [3], the Karlsruhe Institute of Technology (KIT) and the AVIO group developed a partially evaporating and rapid mixing (PERM) IS. This IS is a prefilming double swirled nozzle operating at lean combustion conditions. The atomization process at the end of the lip is now further investigated in the FIRST (Fuel Injector Research for Sustainable Transport) program of the seventh framework.

Generally, the development of lean injection system airblast nozzle is difficult because of the conflictive behavior of  $\text{NO}_x$  and CO emissions at lean operating conditions. Increase in amount of air raises the CO emissions at conditions close to the weak extinction limit [4]. The interaction of air and fuel is important to guarantee a sufficient atomization of the liquid and therefore a fast evaporation and low-emitting combustion. Experimental effort is necessary to enable the success of CFD calculations of lean IS airblast nozzles, as the CFD simulations are strongly dependent on the droplet distribution and the droplet sizes which are implemented as boundary conditions. The detection of the spray mass flux is still challenging due to the inaccuracies of the measurement systems. Former investigations of Dullenkopf [5] show that the measurement error of the local mass flux measured by a PDA system is about 30% for airblast nozzles and can even be higher for complex flows with recirculation. Therefore the droplets sizes and mass distribution were investigated experimentally by means of PDA and patternator measurements. The global SMD value characterizing the whole spray as a combination of the two experimental methods at different axial distances was built.

The parameters varied by the investigation were the geometry and the aerodynamic conditions. The geometry was varied by the investigation of two similar scaled nozzles with a scaling factor of 2. The variations of the aerodynamic conditions were realized by different pressure drop.



## Experimental test-rig

The experiments were performed at the atmospheric atomization test rig (ATA) at the Engler-Bunte-Institute (EBI) in KIT. The rig is equipped with instruments for measuring liquid pressure, the air and liquid temperature and the pressure drop across the nozzle. The spray is not confined in order to ensure that no distortion of spray takes place due to presence of chamber wall and to ease the optical measurements. Figure 1(a) shows a schematic of the ATA test rig. The PDA system is a Dantec FiberPDA with a BSA P80 signal processor. The focal length of the emitter is 500 mm and the beam space is 38 mm. The scattering mode is refraction, with a scattering angle of 30°. This ensures the detection of droplets with a diameter between 0 µm and 137 µm. The abort criterion during the experiments was the detection of 50000 droplets or 200 s of measurement time. The fundamentals of the Phase Doppler Anemometry are generally known and are explained by Bachalo et al. [6] and Albrecht [7]. The problem in evaluating the global droplet size distribution and therefore the global SMD generated by an IS is the determination of the radial fuel flux distribution. Due to high spray density the Particle-Dynamics Analysis (PDA) measurement techniques can only be applied in a certain distance from the IS exit. The PDA is a point by point measurement technique, so the determined droplet distributions at different radial points of the same axial distance from the IS exit have to be weighed by the mass flux at the corresponding points. The mass fluxes measured by the PDA might not be precise due to non-spherical particles which cannot be captured by PDA and also due to the recirculation of particles in a swirled airblast nozzle that could be detected more than once in the positive flow direction. Particles with negative velocities reduce the volumetric flow flux measured by the system. Therefore, the collection of the spray by a patternator was performed. The patternator is a metal cross partitioned into segments with an area of 5×5 mm<sup>2</sup> (Figure 1(b), (c)). The drain of each segment is collected in Erlenmeyer flasks whose mass were measured before and after the experiment. It is possible to determine the amount of liquid distributed along the radius. Due to the risky application of kerosene in an atmospheric spray test rig, de-mineralized water was used.

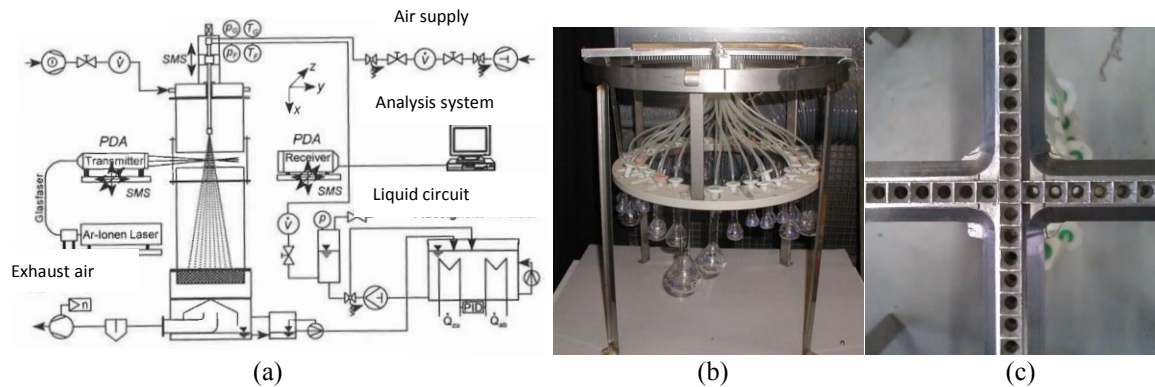


**Figure 1.** (a) Schematic of the atmospheric atomization test rig, (b,c) picture of the patternator

The PERM IS is a lean combustion concept and shown in Figure 2. It consists of a primary (1) and a secondary (2) air jet which are co-swirled and circulate around a lip. In the primary swirler a pressure atomizer induces a fuel film (3) onto the lip which is shear blasted at the end by the two air jets. The swirl generates a vortex breakdown and therefore an inner recirculation zone (IRZ) which stabilizes the combustion process [8]. The two investigated nozzles differ in the size. The scaled version of the IS is scaled down by factor 2. In this document, the IS will be named as “prototype” for the non scaled and as “scaled” for the scaled down. Table 1 shows a survey of the performed experiments and its measurement conditions. The ratio of air to fuel (AFR) is calculated with the massflow of two fluids (liquid and air) and is an important factor in determining whether the combustion is rich or lean.

$$AFR = \frac{\dot{M}_a}{\dot{M}_l} \quad (1)$$

## Mathematical modeling

The atomization process of airblast atomizers and its advantages for combustion are sufficiently explained in the literature by Lefebvre [9, 4] and are not repeated here. The Weber number ( $We$ ) which describes the ratio of the force of inertia to the surface force is given in Eq. (2) with  $u_R$  as the relative velocity between air and liquid,  $L_c$  as the characteristic length and  $\sigma_l$  as the surface tension. The characteristic length is defined as the inner lip radius  $R_0 = D_0/2$ .



**Table 1.** Performed experiments

NOZZLE	n°	z/R <sub>0</sub> [-]	AFR	$\frac{\Delta p}{p_0}$ [%]
Prototype	1	4.15	35	2
	2	4.15	27	3.5
Scaled	3	4.15	27	3.5
	4	4.15	27	6.9

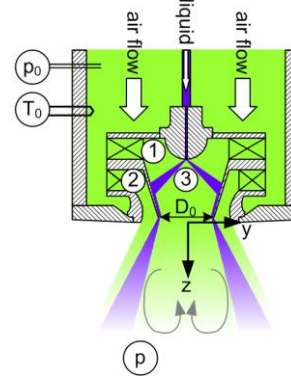


**Figure 2.** Schematic of the IS

$$We = \frac{L_c \cdot \rho_a \cdot u_R^2}{\sigma_l} \quad (2)$$

The calculation of the SMD at each radial measurement position  $j$  is done in the following manner, with  $C$  as the number of captured droplets and  $i$  as the single droplet:

$$D_{32j} = 6 \cdot \left( \frac{\frac{\pi}{6} \sum_{i=1}^{C_j} d_{ij}^3}{\pi \sum_{i=1}^{C_j} d_{ij}^2} \right) = \frac{\sum_{i=1}^{C_j} d_{ij}^3}{\sum_{i=1}^{C_j} d_{ij}^2} \quad (3)$$

Eq. (3) results in a radial SMD distribution. The final step is to combine this distribution with the measured mass flux in order to obtain the global SMD value describing the whole spray at the specific axial position.

$$D_{32} = \frac{\sum_{j=0}^n \left( \dot{N}_j \cdot \frac{\sum_{i=1}^{C_j} d_{ij}^3}{C_j} \right)}{\sum_{j=0}^n \left( \dot{N}_j \cdot \frac{\sum_{i=1}^{C_j} d_{ij}^2}{C_j} \right)} \quad (4)$$

$\dot{N}_j$  is the total number of droplets per second at each radial measurement position  $j$ .

$$\dot{N}_j = \frac{\dot{M}_j}{\rho_l \frac{\pi}{6} \frac{\sum_{i=1}^{C_j} d_{ij}^3}{C_j}} \quad (5)$$

The mass flow  $\dot{M}_j$  in eq. (5) is a result from the patternator measurement at each radial position. In order to consider the fact that measurements have taken place along the diameter, the amount of liquid inside the Erlenmeyer flasks with respect to time is used to calculate the mass flow and is weighed with the particular ring area  $A_r$ .

$$\dot{M}_{Patj} = \frac{M_j}{t} \cdot \frac{A_{rj}}{A_{mj}} \quad (6)$$

To calculate the SMD only with the PDA data, the mass flow is determined with the volumetric flow flux which is directly calculated by the PDA system.

$$\dot{M}_{PDAj} = \dot{V}_j \cdot A_{rj} \cdot \rho_l \quad (7)$$

## Results and Discussion

### Validation Check

Generally the atomization process can be divided into two parts: The primary atomization at the end of the lip and the secondary atomization due to high relative velocities between the droplets and the air. The calculation of a SMD describing the whole spray would be incorrect if the latter occurs. For this purpose, the cumulative size distribution at different axial positions is plotted in Figure 3. The different curves show a good accordance. For  $z/R_0=3.18$  the amount of smaller droplets is bigger than for  $z/R_0=4.15$  and 5.13. It can be assumed that no significant secondary atomization occurs downstream the prefilmer. To minimize the measurement effort due to a broad radial distribution, an axial distance of  $4.15 z/R_0$  was chosen.

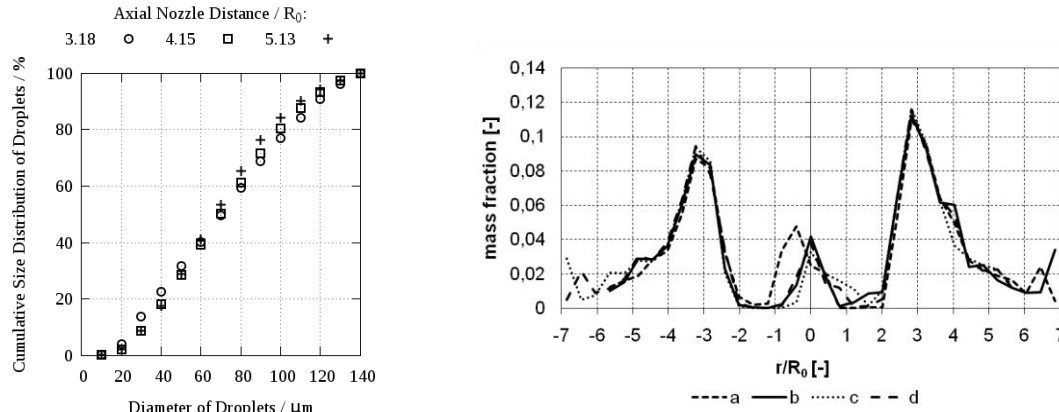


**Figure 3.** (a) Cumulative size distribution for the prototype IS; (b) mass distribution measured with the patternator

### Effect of pressure drop

Increase in pressure drop results in a higher air velocity and thus a bigger We-number. The atomization becomes finer. The diagram on the left in Figure 4 shows the experimentally identified SMD distribution of the scaled IS for a pressure drop of 3.5% and 6.9% (cases 3 and 4). For the latter case it can be assumed that two effects cause very big droplets close to the axis. First, stripping of droplets from the prefilmer can occur due to high shear forces. The second effect is due to the increase in the fuel pressure in the fuel supply line in order to keep the AFR constant by increasing the air mass flux. Increasing the pressure in the fuel line (pressure atomizer) causes an increase of the momentum of the droplets which are generated by the pressure atomizer. In the case of 6.9% pressure loss, some big droplets with increased momentum do not reach the atomization lip and are registered in the centre of the flow field as shown in Figure 6. The data rate in the area close to the axis is very low so that less than 20 droplets could be detected at each measurement position and these effects are neglected.

Figure 4 (b) sketches the relative mass fraction (see Eq. (8)) measured with the patternator.

$$M_j = \frac{m_j}{\sum_{j=0}^n m_j} \quad (8)$$

The results confirm the small amount of liquid mass flux for  $r/R_0$  smaller than 2. Nevertheless, the total mass measured by the patternator is much closer to the axis with 6.9% pressure drop than for 3.5%. This is a result of the higher air velocity and the smaller droplets for  $r/R_0 > 2$ . The inertia of these droplets is smaller and causes a concentration closer to the axis. The resulting difference in the liquid mass flux distribution will also influence the AFR distribution in the case of combustion and has to be considered by the discussion of combustion limits or exhaust gas emissions. This behaviour cannot be observed for nozzles with gaseous fuels (one phase flow) and is a characteristic of combustion with two phase flows.

### Effect of scaling

Scaling down an IS with liquid fuel causes problems because the flow field similarity cannot be maintained. The distribution of droplets inside the flow is different due to the changing ratio of inertial forces between gaseous and liquid phase because the centrifugal forces depends on the radius. With a scaled down geometry and the same pressure drop across the IS, the characteristic length and therefore the We-number decreases. The SMD distribution is not affected by the scaling (Figure 5(a)) but the We-number reduction causes an increase of the global SMD (comparison of cases 2 and 3 in Table 2).

The spray angle is broader due to an increasing of the centrifugal forces by decreasing the ratio and can be seen in the relative mass fraction diagram in Figure 5(b)

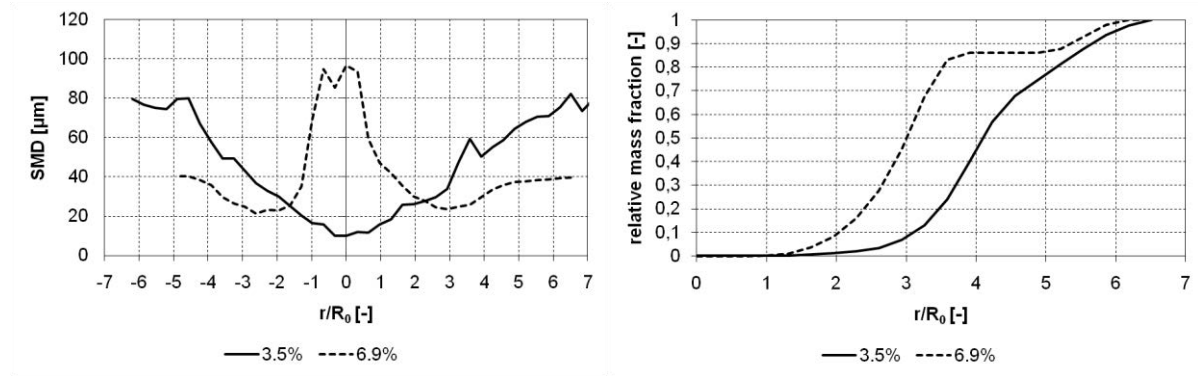


**Figure 4.** (a) Effect of pressure drop for the scaled IS; (b) relative mass fraction

Authors like El-Shanawany and Lefebvre [10] observed that for constant air velocity the SMD decreases with decreasing airblast atomizer diameter. This reveals that the current state of scaling influence on atomization is unclear and further investigation on this topic is necessary.

Additionally experiments with constant We-number were performed to determine the effect of pressure drop which is 3.5% for the prototype IS and 6.9% for the scaled IS (cases 2 and 4). Figure 6(a) compares the SMD distributions for constant We number. For  $r/R_0$  smaller than 2.5 bigger particles are found for the scaled which are the results of the effects which have already been described and which are negligible. The calculated global SMD in Table 2.

For the two cases 2 and 4 demonstrates that the influence of velocity on the We number is much higher than the length scale.

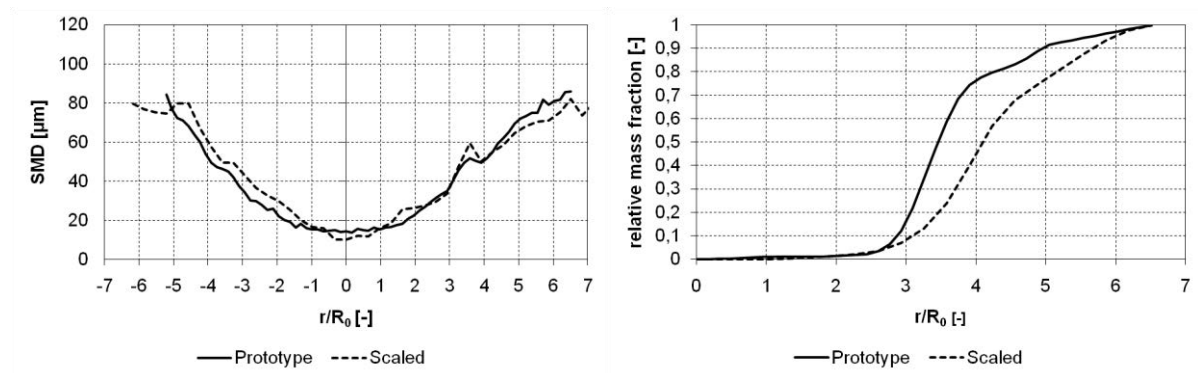


**Figure 5.** (a) Effect of scaling for constant pressure drop on the SMD distribution; (b) relative mass fraction determined with the patternator at  $z/R_0$  4.15

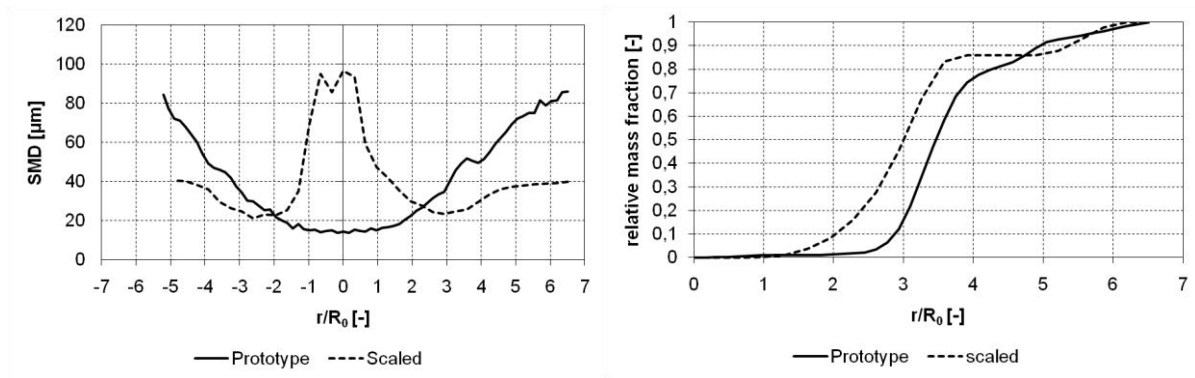


**Figure 6.** (a) Effect of scaling for constant We-number on the SMD distribution; (b) relative mass fraction determined with the patternator at  $z/R_0$  4.15

### PDA and Patternator - mass comparison

This subsection compares the relative mass fraction and the global SMD calculated with PDA and patternator data. Both measurement systems have problems with an accurate determination of the spray. The patternator itself is disturbing the air flow and the measurement procedure is prone to measurement errors caused by the experimental process. Thus, the experiments were repeated several times to evaluate whether the results are reproducible. Four experiments with a similar mass distribution are in the diagram of Figure 3(b). At positions having measurement difficulties, i.e., regions close to the axis and at high radii show bigger deviations. Nevertheless, the results of the patternator show a mass distribution which defines the spray angle.

PDA determined mass fluxes are not precise due to the fact, that only spherical droplets are detected by the system and droplets may be detected more than once in the recirculation zone. Thus, only droplets with a positive axial velocity were considered. Furthermore, droplets with negative velocities are calculated as a negative flow flux. Figure 7 illustrates the differences between the relative mass fraction determined with PDA and patternator for two different experiments. In the left diagram (case 1) the pressure drop across the IS was 2% and the difference between the measurement methods is in the range of measurement errors. Finally, the globally calculated SMD is very similar. In the right diagram (case 4) the pressure drop is 6.9% and the mass detected by the PDA system is shifted to higher radii and leads to a global SMD which is 19% bigger than the calculated with the patternator results. The shift to higher radii could be observed for almost all experiments except for a very low pressure drop. It can be concluded that an increase in pressure drop induces an increase in deviation between the two measurement methods. In order to evaluate the two different calculation procedures we applied them at different axial positions. The results shown in Figure 8 demonstrate that the calculation with the combined method (Patternator, PDA) is a more realistic approach because the calculated SMD remains constant at the different axial positions.

The global calculated SMDs are given in Table 2.

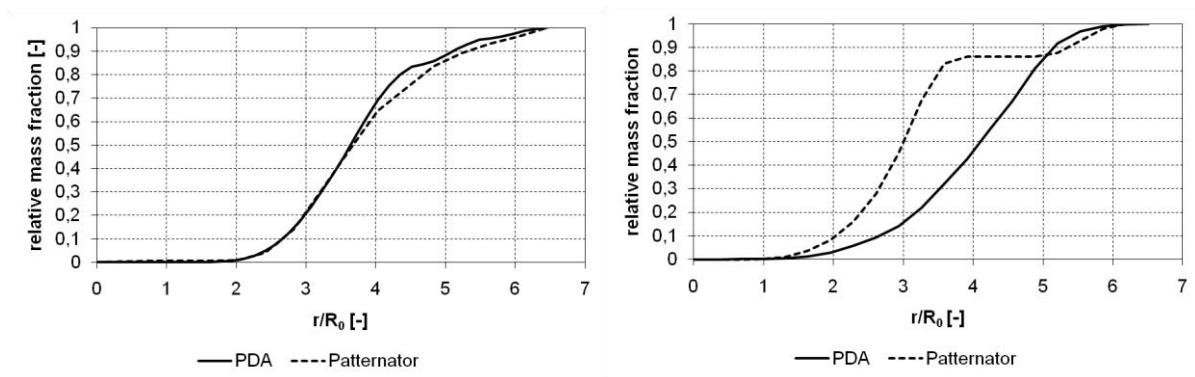


**Figure 7.** (a) PDA and (b) patternator relative mass fraction comparison for experiment n°1 and n°4 at  $z/R_0=4.15$

**Table 2.** Combines global SMD comparison

NOZZLE	n°	SMD; Patternator- PDA	SMD; PDA- PDA	Difference [%]
Prototype	1	56	55	-1.8
	2	48	52	+8.4
Scaled	3	57	59	+3.5
	4	27	32	+18.5

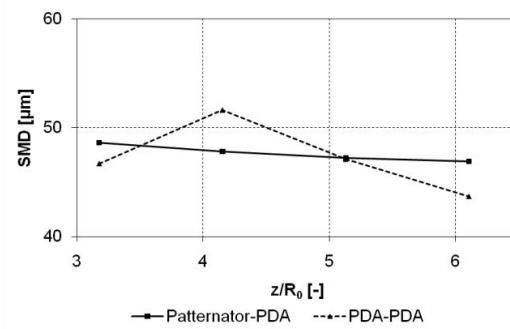


**Figure 8.** global SMD comparison

## Conclusions

The experiments mainly focus on the determination of global SMD and the effect of linear scaling on the atomization and spray using swirled prefilming airblast ISs. Linear scaling of the IS causes a change of the liquid mass flux distribution due to the changes in the centrifugal forces. At the same flow and thermodynamic conditions the SMD of the scaled IS increases. The influence of air velocity in the We number is much bigger than the influence of scaling. Additionally, two different measurement methods to determine the mass distribution of the spray were examined and the global SMD was calculated. The results show that with a combined technique of patternator and PDA the global SMD does not change significantly for different axial measurement positions. This leads to the conclusion that the combined technique is the more realistic approach.

## Acknowledgements

We kindly acknowledge the financial support by the European Commission through project FIRST under Grant Agreement n° ACP0-GA-2010-265848.

## Nomenclature

$A_r$	Ring area	$\dot{N}_j$	Number of droplets per second at position j
$A_m$	Measurement area	NEWAC	New Aero Engine Core Concepts
AFR	Air to fuel ratio in kg-air/kg-fuel	$\text{NO}_x$	Nitrogen oxides
ATA	Atmospheric atomization test rig	p	Pressure
$C_j$	Number of collected droplets	PDA	Particle Dynamics Analysis
CO	Carbon monoxide	PERM	Partially evaporating and rapid mixing
CFD	Computational Fluid Dynamics	r	Radius
d	Diameter	$R_0$	Characteristic nozzle radius
$D_{32}$	Sauter mean diameter	SMD	Sauter Mean Diameter
EBI	Engler-Bunte-Institute	t	Measurement time
FIRST	Fuel Injector Research for Sustainable Transport	UHC	Unburned hydro carbons
IS	Injection system	$u_R$	Relative velocity
IRZ	Inner recirculation zone	$\dot{V}_j$	volumetric flux
KIT	Karlsruher Institute of Technology	We	Weber-number
$L_c$	Characteristic length	y	Radial coordinate
$m_j$	Mass at position j	z	Axial coordinate
$M_j$	Relative mass fraction at position j	$\rho_a$	Density of air
$\dot{M}$	Mass flow rate	$\rho_l$	Density of liquid
n	Number of radial measurement positions	$\sigma_l$	Surface tension of liquid

## References

- [1] A. Lefebvre and D. Miller, *The development of an air blast atomizer for gas turbine application*. College of Aeronautics, 1966.
- [2] S. Marinov, M. Kern, K. Merkle, N. Zarzalis, A. Peschiulli, F. Turrini, and O. Sara, “On swirl stabilized flame characteristics near the weak extinction limit.” ASME, 2010.
- [3] M. Kern, S. Marinov, P. Habisreuther, N. Zarzalis, A. Peschiulli, and F. Turrini, “Characteristics of an ultra-lean swirl combustor flow by les and comparison to measurements.” ASME, 2011.
- [4] A. Lefebvre, *Gas turbine combustion*. CRC, 1999.
- [5] K. Dullenkopf, M. Willmann, S. Wittig, F. Schöne, M. Stieglmeier, C. Tropea, and C. Mundo, “Comparative mass flux measurements in sprays using a patternator and the phase-doppler technique,” *Particle & particle systems characterization*, vol. 15, no. 2, pp. 81–89, 1998.
- [6] W. Bachalo and M. Houser, “Phase/doppler spray analyzer for simultaneous measurements of drop size and velocity distributions,” *Optical Engineering*, vol. 23, no. 5, pp. 583–590, 1984.
- [7] H. Albrecht, *Laser Doppler and phase Doppler measurement techniques*. Springer Verlag, 2003.
- [8] A. K. Gupta, D. Lilley, and N. Syred, *Swirl flows*. Taylor & Francis, 1984.
- [9] A. Lefebvre, *Atomization and sprays*. CRC, 1989.
- [10] M. El-Shanawany and A. Lefebvre, “Airblast atomization-the effect of linear scale on mean drop size,” in *Gas Turbine Conference and Products Show*, vol. 1, 1980.

## Experimental study on the influence of the liquid and air thicknesses on a planar air-blasted liquid sheet

Baptiste Déjean, Pierre Berthoumieu and Pierre Gajan

DMAE, Onera Toulouse, France

### Abstract

This experimental study is devoted to the analysis of an air-blasted atomizer behavior whose air and liquid thicknesses are changed. Variation of liquid thickness is realized by modifying the injector inside; when for air thickness, wedges are introduced in the air flow duct. Using different experimental methods: tomography and shadowgraphy visualizations, oscillation frequency and breakup length are measured and studied. Thickness of each fluid has not the same influence depending on each atomization process parameter. Breakup length is strongly correlated to liquid thickness; when frequency depend more on air thickness. But more than air thickness, for the frequency especially, the flow configuration plays the most significant role, through influence of boundary layer characteristics as wall shear stress. This study highlights the necessity of another non dimensional number than the momentum flux ratio (MFR). This new number could complete the physical description of the phenomenon by taking into consideration some geometrical aspects of the injector and some physical variables characterizing the air flow configuration.

---

### Introduction

Reduction of pollutant emissions and improvement of the aircraft engine efficiency is currently the most important challenges of the aeronautical research. To reach these two goals, an optimization of the combustion processes based on simulations, is needed. Generally, for these simulations, the boundary condition for the liquid fuel is imposed through the numerical injection of droplets parcels. The characteristics of these droplets are deduced from size and velocity distributions measured a few millimeters from the injector. With this approach the great coupling between the gas and liquid phase during the first instants of the liquid injection is not taken into account. In particular, the influence of the flow unsteadiness resulting from this coupling, which directly impacts the flame behavior, is not reproduced in the simulations. In order to improve the quality of these calculations, it is therefore necessary to correctly model all the atomization steps and particularly the primary break-up, where the most part of difficulty reside.

For this purpose, experimental studies were led at Onera on liquid sheet pulverization by high speed air flow corresponding to an air-blast atomizer type (Carentz, 2000), (Larricq, 2006) and (Fernandez, 2010). Precedent studies revealed the influence of liquid thickness on the spray drop size (Lefebvre, 1992), the oscillation frequency (Siegler et al., 2003) and break-up length (Arai & Hashimoto, 1985). Few papers were focused on air thickness variation but the conclusions bring no answer about its influence, (Siegler et al., 2003) or (Lozano et al., 2005). In order to complete the data base and to have a better understanding of the influence of liquid and air thicknesses on the primary atomization process, new experiments were performed. The main results obtained are presented in this paper.

### Experimental test-rig

This study is performed on a simplified 2D liquid sheet sheared on its two faces by a high velocity air stream (Figure 9a). The liquid sheet generator was designed at ONERA in the framework of previous study on this topic (Larricq et al., 2005) and (Fernandez et al., 2009); it is an airfoil with an 89 mm chord and a NACA63-010 profile. A couple of perforations at each injector side allowed the entrance of the liquids. The liquid sheet is formed on the trailing edge of the injector through a 40 mm width slit. A wedge system inside of the airfoil permits to vary the slit thickness. Three values are considered in this study: 300, 450 or 600  $\mu\text{m}$ . A Masterflex pump is used to inject the liquid up to 90 g/s. This device permits to monitor the liquid flow rate that imposes the initial velocity of the liquid film.

The injector is placed on the SHAPE (SHeet Atomisation and Prefilming Experiments) set up shown in figure 1 c. The air flow is obtained from an 80 bars reservoir. Its mass flow rate is controlled by a valve coupled to a Coriolis flow meter. The main feature of this atmospheric injection line was designed in order to obtain uniform, stable and laminar flow from 20 to 100 m/s in a 46 mm square section. In order to modify the air flow thickness at the liquid injection outlet location, wedges with different shapes and width can be inserted in the square pipe. They can be convergent (named C) or divergent (D). These letters C or D are accompanied with a number corresponding to the air flow thickness in order to name each wedge configuration (Figure 9b).



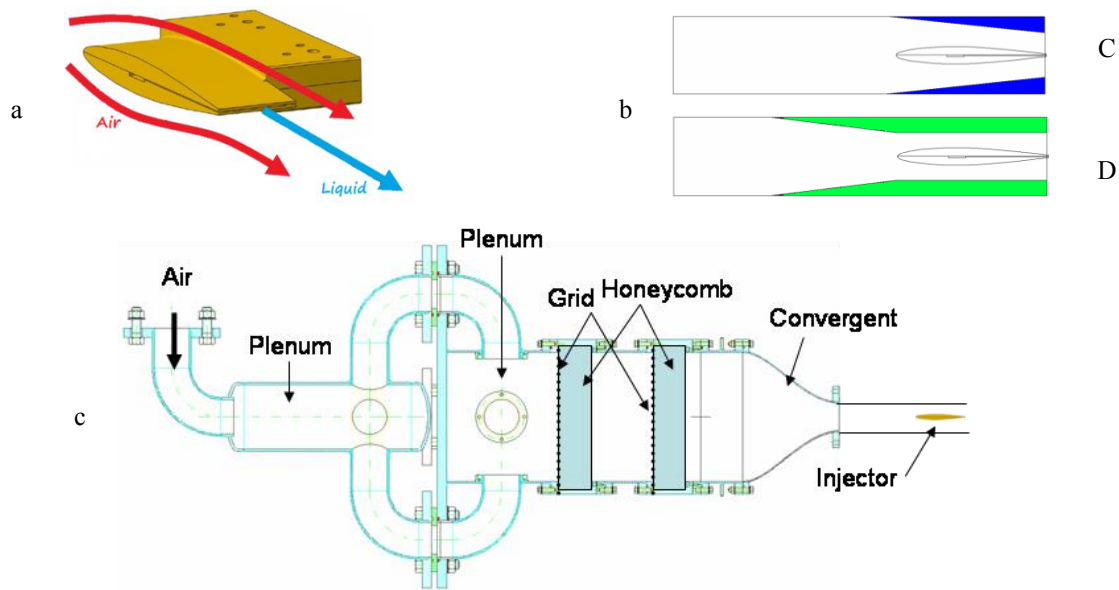


**Figure 1.** Experiment facilities. a: airblast generator, b: obstruction used to modify air flow, up: convergent (C); down: divergent (D), c: SHAPE bench sketch

## Measurement systems

### Boundary layer characterisation

A hot wire probe of 1.25 mm length and 5  $\mu\text{m}$  diameter was used to characterize the air flow at the injector nozzle. Thanks to this device measures can be done at a few micrometres of the injector outlet with a great spatial resolution due to the small probe size. The frequency response of the CTA (Constant Temperature Anemometer) electronic device used permits to reach velocity fluctuations up to 100 kHz.

Before and after each measurement campaign a calibration is performed in comparison with a Pitot probe.

### Visualizations and image processing

The use of imaging techniques allows a better knowledge of the behaviour of the liquid sheet. These techniques, non-intrusive, can also give quantitative information on the breakdown of the sheet. Two main techniques are used: the shadowgraphy and laser tomography. In the two cases, a high speed video camera is preferred in order to follow the liquid sheet displacements. Shadowgraphy technique was used to obtain principally qualitative results (Figure 2) when tomography gives quantitative measures through images processing.

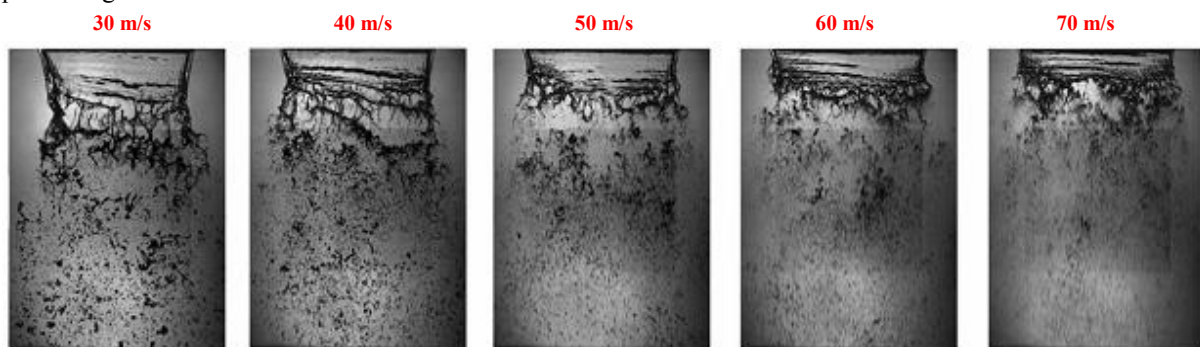


**Figure 2.** Shadowgraph of the liquid sheet

Laser tomography is used to determine breakup length and oscillation frequency of the liquid sheet. A planar laser sheet perpendicular to the liquid plane is used to illuminate a liquid slice in the middle of the liquid layer. In this case, fluorescein is added in the water. This dye absorbs the photon emitted by the laser at 495 nm (blue) and re-emits light at 521 nm (green) (Figure 3). The use of a matched filter on the camera lens eliminates the direct reflection from the incident laser sheet on the surface of the liquid film.

### Breakup length measurements

For these measures, both visualisation techniques are used simultaneously in order to obtain an image where both laser continuity and liquid sheet are visible simultaneously. By this way the threshold used during the image processing is adjusted to reveal the real breakup length (Figure 4). 500 images are taken and for each experiment configuration and the threshold is adapted on the about 50 first images thanks to the shadowgraphy.

### Frequency measurements

From tomography images acquired with high speed camera, the instantaneous transversal location of the liquid sheet is determined at different longitudinal positions. FFT of these displacement signals permit to determine the flapping frequency of the liquid sheet. To have frequency results high speed camera was coupled with a laser sheet to obtain a longitudinal section in the liquid sheet (Figure 5). The purpose was to measure the liquid sheet displacement over time and after apply an FFT analysis on this signal to finally have a measurement of the flapping frequency. This technique allows to check visually the result obtained and also to have a frequency spectrum all along the liquid sheet, from injection point to breakup. For this acquisition 2048 images are taken at a rate of 3400 im/s, for the frequency measurements the resolution becomes 1.7 Hz.

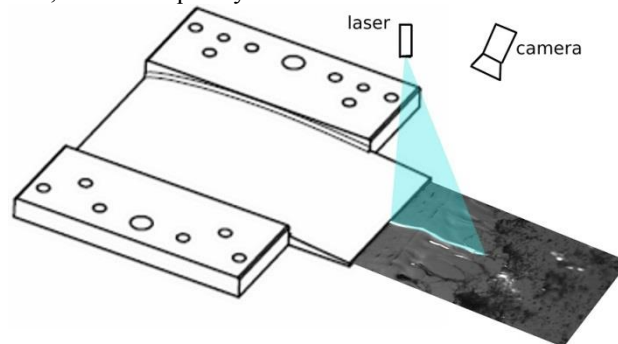


Figure 3. Laser tomography

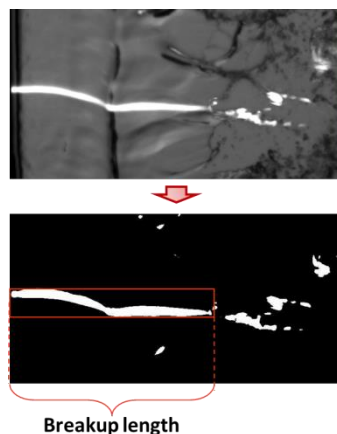


Figure 4. Breakup length measurement

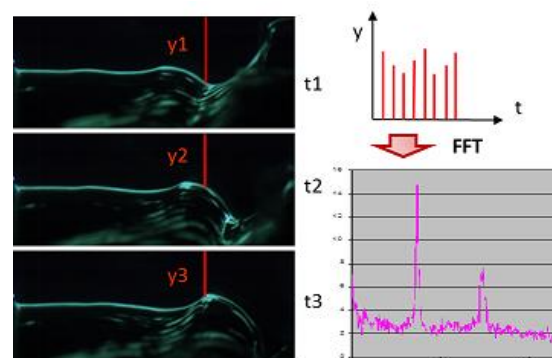
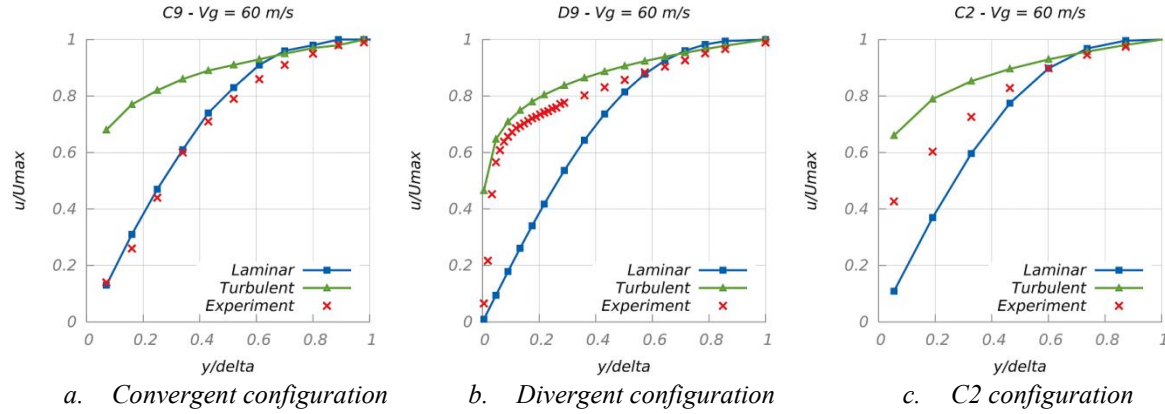


Figure 5. . Frequency from high speed video.

## Results and discussion

### Boundary layer characterisation

Test campaign with a hot wire probe is made at the trailing edge of the injector without water injection. The measurements are done for all the wedges and for air velocity ranging from 30 m/s to 90 m/s. Velocity profiles in Figure 6 are representative of the different boundary layer shapes obtained. To estimate the flow regime, the boundary layer profiles are compared with a 1/7 law corresponding to a turbulent boundary layer and a Pohlhausen law approximating of the exact Blasius theory obtained for a laminar boundary layer (Gosse, 1995). This approximation is valid for a uniform flow parallel to flat plate with no incidence and is considered acceptable for this study.


**Figure 6.** Velocity profile close to the injector lips

With the convergent wedges, the shape of the curve is close to the laminar profile. On the opposite the velocity profile obtained for the divergent configuration is close to a turbulent flow condition. For the C2 configuration a particular behaviour is observed and can be described as a transitory profile due to the low air flow thickness. As a first conclusion on the boundary layer profiles, a configuration difference (convergent / divergent) will lead to a different flow regime (laminar / turbulent) which could explain some behaviour differences between the two configurations. The first element extract from these measurements is the boundary layer thickness which is defined as the distance from the wall where the velocity is 99% of the maximal air velocity. As expected there are large differences between the laminar and turbulent regimes (Table 1).

Boundary layer thickness	Wedges (air thickness)							
	Divergent configuration			Convergent configuration				
Air velocity	D22 22 mm	D14 14 mm	D9 9 mm	C14 14 mm	C9 9 mm	C6 6 mm	C4 4 mm	C2 2 mm
30 m/s	2,67 mm	3,69 mm	4,11 mm	0,73 mm	0,65 mm		0,64 mm	0,53 mm
40 m/s	2,29 mm	3,66 mm	3,98 mm	0,66 mm	0,63 mm	0,61 mm	0,55 mm	0,45 mm
50 m/s	2,10 mm	2,98 mm	3,63 mm	0,64 mm	0,62 mm	0,55 mm	0,52 mm	0,42 mm
60 m/s	2,21 mm	2,56 mm	3,52 mm	0,57 mm	0,55 mm	0,50 mm	0,47 mm	0,37 mm
70 m/s	1,69 mm	2,59 mm	3,31 mm	0,52 mm	0,51 mm	0,47 mm	0,46 mm	0,35 mm
80 m/s	1,67 mm	2,37 mm	3,09 mm	0,48 mm	0,47 mm	0,44 mm	0,42 mm	0,31 mm
90 m/s			2,95 mm	0,45 mm	0,41 mm	0,45 mm	0,39 mm	

**Table 1.** Boundary layer thickness evolution for the different wedges

In the divergent configuration the boundary layer thickness increases as the air thickness decreases due to a change of the expansion ratio, it varies from 1.24, for D22, to 1.9 for the D9 configuration. This larger expansion promotes an earlier detachment. On the other hand, in the convergent case, boundary layer thickness decreases with the air thickness. For the largest air configuration, C14 to C4, boundary layer profiles correspond perfectly to the laminar profile except for the C2 configuration giving a profile between the two used laws (laminar and turbulent Figure 6c). The wall shear stress can be extracted from these measurements by the classical formula (1) by considering the closest position where velocity values are valid in this case 0.2 mm from the wall and assuming that this point was in the viscous sub layer. Values are available in Table 2.

Wall shear stress	Restriction (air thickness)							
	Divergent configuration			Convergent configuration				
Air velocity	D22 22 mm	D14 14 mm	D9 9 mm	C14 14 mm	C9 9 mm	C6 6 mm	C4 4 mm	C2 2 mm
30 m/s	1,83	1,68	1,21	1,27	1,39		1,43	1,61
40 m/s	2,53	2,31	1,80	1,78	1,78	2,11	2,34	2,55
50 m/s	3,26	2,92	2,52	2,12	2,36	2,74	2,69	3,60
60 m/s	4,02	3,57	2,85	3,00	3,29	3,45	3,71	4,94
70 m/s	4,79	4,29	3,53	3,94	4,12	4,29	4,27	6,27
80 m/s	5,62	4,87	3,97	4,86	5,07	4,97	5,13	6,81
90 m/s			4,39	5,84	6,24	5,31	6,08	

**Table 2.** Wall shear stress evolution for the different wedges

$$\tau_p = \mu \frac{\partial U}{\partial y_0} \quad (1)$$

## Frequency

Thanks to the high speed camera records, frequency measurement is done by image processing all along the liquid flow and confirmed by image visualization. This technique corroborates that the flapping phenomena is associated with a continuous frequency increase with air flow velocity for both configurations (convergent and divergent). Nevertheless, a different behaviour can be observed between the two flow configurations. For the divergent case, an increase of the air flow thickness leads to a significant frequency rise (Figure 7). Otherwise, in the convergent case, the air flow thickness seems have a lower influence (Figure 8).

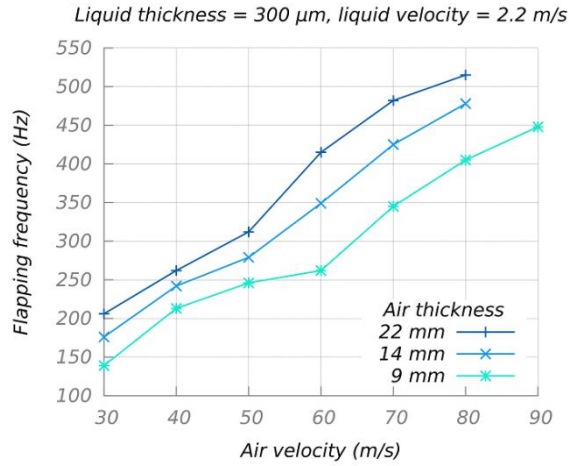


**Figure 7.** Flapping frequency evolution with air velocity – Divergent wedges

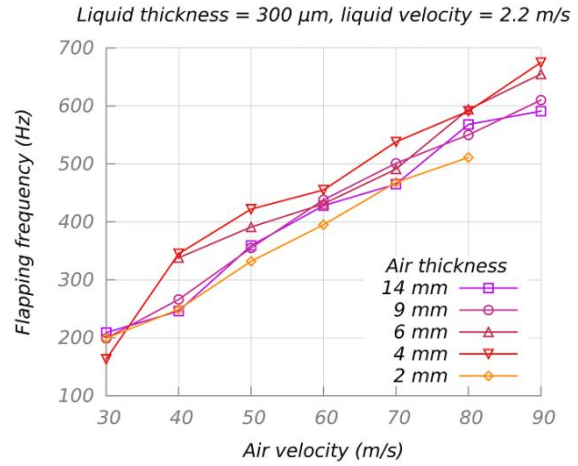


**Figure 8.** Flapping frequency evolution with air velocity – Convergent wedges

For these configurations the flapping frequency is plotted against the air thickness at a given air velocity (Figure 9). Except for the thinner air flow configuration (C2), the flapping frequency decreases when the air thickness increases. This difference obtained with the C2 wedge can be explained by the transitory boundary layer condition revealed from the velocity measurements.

These first results show some differences depending on air flow conditions. Nevertheless they are not directly related to the air thickness or to the boundary layer thickness. So it is important to find parameters which can explain the differences between the configurations. For this purpose, the frequency evolution against the wall shear stress was plotted for all the flow conditions (Figure 10). It can be seen that quite linear curves are obtained. Nevertheless two distinct slopes can be discerned depending on the wedge configuration. Furthermore it can be seen that the smaller convergent configuration (C2) have a behaviour closer to the divergent case than to the other convergent cases. Thus, it seems that the slope depends not only on the shear stress but also on the boundary layer type (laminar or turbulent) so another parameter, not identified yet, has to be considered.

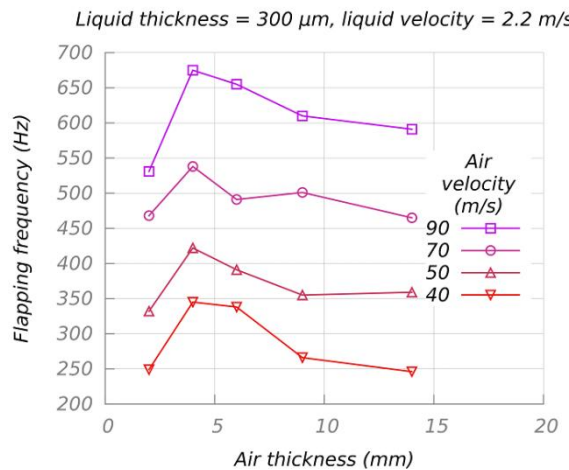


**Figure 9.** Flapping frequency evolution with air thickness – Convergent wedges

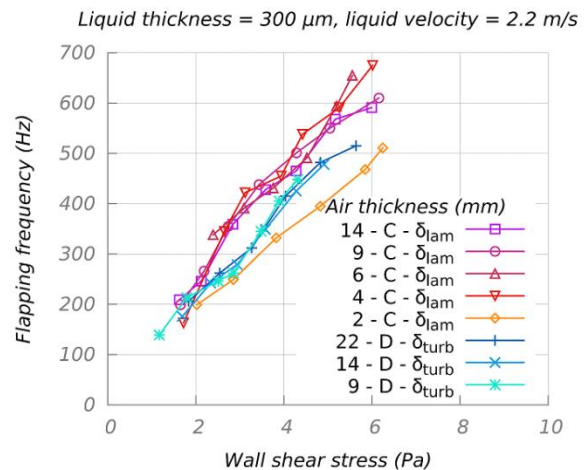


**Figure 10.** Oscillation frequency evolution against wall shear stress for convergent (C) with laminar boundary layer ( $\delta_{lam}$ ) and divergent (D) with turbulent boundary layer ( $\delta_{turb}$ )



### Breakup length

In a second step the influence of the air thickness on the breakup length of the liquid sheet is studied. The experimental determination of this quantity is difficult because the instantaneous breakup position is not fixed; it changes with the flapping of the sheet. To perform these measurements an automatic image analysis was developed in order to process 500 images and obtain a good statistical representation.

This analysis shows expected tendencies as a decrease of the breakup length with the air velocity increase or a liquid velocity decrease. The breakup length is linearly dependent on the liquid velocity (Figure 11). Otherwise, the breakup length decreases with the air speed value following a  $v_{air}^{-1}$  law (Figure 12). Those tendencies are well-known results and this study was made to bring out the air flow configuration influence. As shown on Figure 11 or Figure 12, an air flow thickness augmentation leads to a decrease of the breakup length whatever the convergent or divergent configuration. This decrease is nearly proportional  $t_{air}^{-0.25}$  where  $t_{air}$  is the air flow thickness. At a given air velocity and for a same air thickness, a divergent and a convergent air flow will give approximately the same breakup length. This result indicates that the breakup length depends not only on the air velocity but also on the air momentum flux.

By comparing the results obtained with different liquid thicknesses, it can be seen that this parameter influences the break-up length when the liquid and the gas velocity are kept constant (Figure 13). Nevertheless, if the liquid flow rate is fixed no influence is observed (Figure 14).

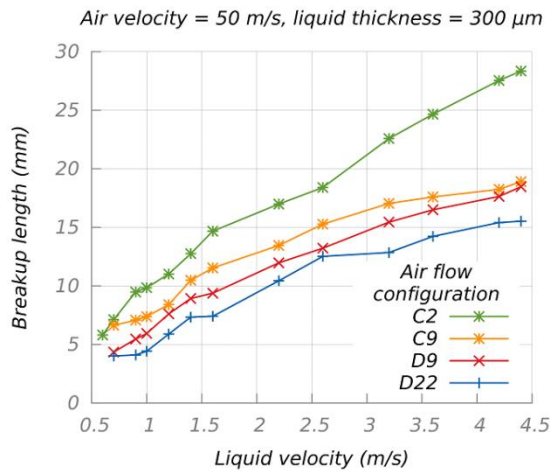


Figure 11. Breakup length according to liquid velocity

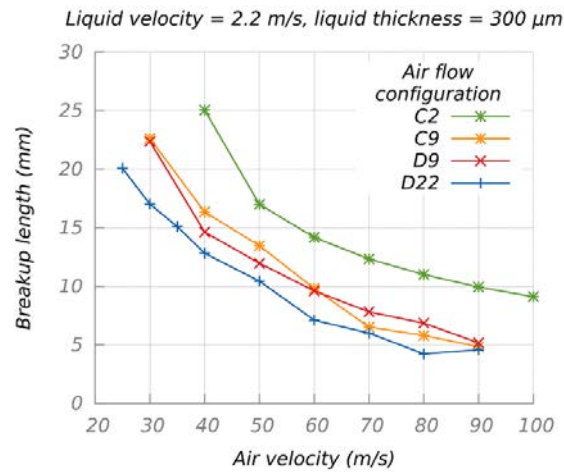


Figure 12. Breakup length according to air velocity

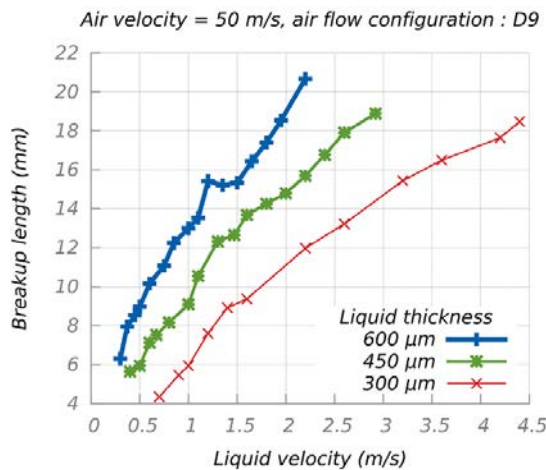


Figure 13. Breakup length according to liquid velocity for different liquid sheet thickness for a constant air velocity (50m/s)

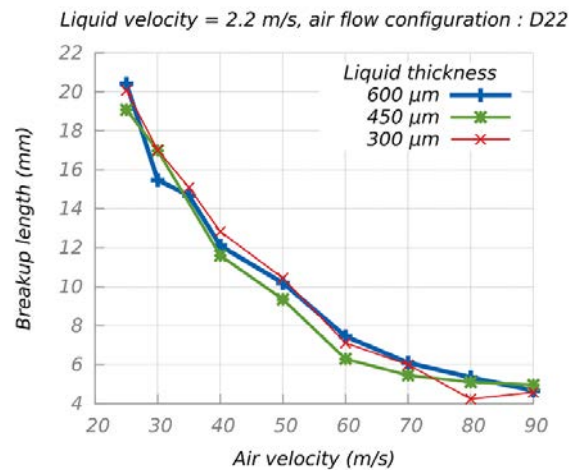


Figure 14. Breakup length according to air velocity for different liquid sheet thickness for the same liquid flow rate

## Conclusion

This study on liquid sheet atomization highlights the influences of liquid and air thicknesses of the different characteristics of atomization process (oscillation frequency, breakup lengths, mean droplet sizes...). Different influences have been shown depending on each fluid flow and break-up characteristics. A direct correlation between liquid flow rate and break-up length is clearly identified. For this parameter, air flow thickness plays a less influent role and configurations none. As for flapping frequency, it is the opposite. Liquid flow thickness influence could not be shown when effect of air flow thickness is obviously highlighted. For this parameter, its evolution depends on the air flow configuration and more especially through the wall shear stress and the air flow boundary layer. The regime of this near wall flow gives different results depending on its laminar, turbulent or transitory behavior. Flapping frequency evolution against wall shear stress gives then a good agreement for each flow regime. These results, on the liquid sheet atomization by an air flow shear, show the importance of fluids thicknesses on different parameters of primary break-up. These influences highlight the need of others parameters as only density and air flow through the momentum flux ratio (MFR) used actually to describe atomization regimes. This goes in the same way as the conclusions of Lozano who has introduced fluids thicknesses in this ratio (Lozano et al., 2005). But as shown on frequency results, flows thicknesses are not enough to determine primary breakup characteristics and other parameters of boundary layer as wall shear stress or vorticity thickness have to be taken into consideration.

## Acknowledgments

This work was carried out in the framework of the European project FIRST. The authors would like to thank the CEE for the financial support.

The French DGA is also gratefully acknowledged for its funding support.

## References

- [1] Arai, T. & Hashimoto, H., 1985. Disintegration of a thin liquid sheet in a cocurrent gas stream. *ICLASS*.
- [2] Carentz, H., 2000. *Étude de la pulvérisation d'une nappe liquide mince*. Thèse. Paris 6.
- [3] Fernandez, V., 2010. *Experimental study of a liquid sheet disintegration in a high pressure environment*. Thèse. Uni. Toulouse - ISAE.
- [4] Fernandez, V., Berthoumieu, P. & Lavergne, G., 2009. Primary atomization in water and kerozene liquid sheets at high pressure. *11th ICLASS*.
- [5] Gosse, J., 1995. Mécanique des fluides. *Techniques de l'Ingénieur*, A 1870, pp.1-57.
- [6] Larricq, C., 2006. *Étude de la pulvérisation assistée en air d'une nappe liquide et influence d'un vent ionique sur les instabilités hydrodynamiques*. Thèse. ENSAE.
- [7] Larricq, C., Lavergne, G., Berthoumieu, P. & Thivet, F., 2005. Improvement of Airblast injectors with electro-aerodynamic actuators. *2nd International Symposium on Non Equilibrium Processes, Combustion and Atmospheric Phenomenon*
- [8] Lefebvre, A., 1992. Twin-fluid atomization: factors influencing mean drop size. *Atomization and Sprays*, 2, pp.101-19
- [9] Lozano, A., Barreras, F., Siegler, C. & Löw, D., 2005. The effects of sheet thickness on the oscillation of an air-blasted liquid sheet. *Experiments in Fluids*, 39, pp.127-39.
- [10] Siegler, C., Lozano, A. & Barreras, F., 2003. Influence of air and liquid channel thickness on the oscillation behavior of an air-blasted liquid sheet. *ICLASS*

## Fitting of Different Drop Size Distribution Functions to Spray Data from a Y-jet Type Airblast Atomizer

Tuomas Paloposki<sup>1</sup> and Takao Inamura<sup>2</sup>

1: Department of Energy Technology, Aalto University, Finland

2: Department of Intelligent Machines and System Engineering, Hirosaki University, Japan

### Abstract

Four different drop size distribution functions were compared with experimental data obtained for a Y-jet type airblast atomizer. The experimental data consisted of 21 different drop size distributions. The  $\chi^2$  statistical test was used to evaluate the goodness-of-fit between the distribution functions and experimental data. It was found that the best fit to the experimental data was obtained with a sum of two log-normal distribution functions, followed by the log-hyperbolic distribution function, the Nukiyama-Tanasawa distribution function and the log-normal distribution function (in that order).

### Introduction

In many spraying processes, e.g., in the combustion of liquid fuels, the size distribution of the drops has a significant effect on the performance of the process. We have studied the possibility of using mathematical functions to describe drop size distributions in sprays. We hope that by using such functions, the task of comparing different drop size distributions with each other can be carried out more easily and systematically than by just comparing the mean sizes or some other representative diameters of the drops. Other possible uses for drop size distribution functions include the mathematical modeling of spraying processes.

### Experimental test-rig

The experimental data were collected during the development of a Y-jet type multi-port airblast atomizer which was equipped with a fluid amplifier. The objective was to develop an atomizer which produces a spray with a constant mean drop size independent of the liquid flow rate. The experimental rig and the measurement techniques have been described by Inamura and Nagai (1995). In an earlier study (Paloposki and Inamura 1996), we already did some work on fitting drop size distribution functions to the experimental data of Inamura and Nagai, but that work has now been updated and expanded.

For the current study, we took the data obtained with three different design configurations of the atomizer as explained in Table 1. The names of the design configurations were chosen to be compatible with Figure 14 of Inamura and Nagai (1995). Since 7 different liquid flow rates had been tested for each configuration, the total number of data sets (measured distributions) was 21. The naming of the data sets is also explained in Table 1.

**Table 1.** Design configurations of the atomizer and the naming of the data sets.

Configuration of the atomizer	Diameter of the larger ports $D_l$ [mm]	Diameter of the smaller ports $D_s$ [mm]	Diameter of the orifice $D_o$ [mm]	Experimental data
(a)	2.0	1.4	1.6	Runs 11 – 17
(c)	1.8	1.4	1.6	Runs 21 – 27
(d)	1.8	1.4	1.0	Runs 01 – 07

Configuration (a) was the best of the tested configurations in the sense that the Sauter mean diameter of the drops remained almost constant even when the liquid flow rate was varied, as shown in Figure 14 (a) of Inamura and Nagai (1995). The other two configurations also seemed to be quite satisfactory, as illustrated in Figures 14 (c) and (d) of Inamura and Nagai (1995).

### Mathematical modelling

For each data set, the following four distribution functions were fitted to the measured drop size distributions: the log-normal distribution function (LN), the Nukiyama-Tanasawa distribution function (NT), the log-



hyperbolic distribution function (LH) and a sum of two log-normal distribution functions (LN2). Thus, there were  $4 \times 21 = 84$  cases to be analyzed.

The goodness-of-fit for each case was evaluated using the  $\chi^2$  statistical test. The theoretical background of the  $\chi^2$  test has been described by, e.g., Cramér (1945), who also presented practical guidelines on how the testing should be carried out. The application of the  $\chi^2$  statistical test to analysis of drop size distributions has been described by Paloposki (1994).

The test procedure can be divided into three parts, the first of which is to arrange the experimental data in tabulated form. The second part is to estimate the values of the parameters of the distribution function to be tested. The theoretical foundations of the  $\chi^2$  test are built upon the assumption that the maximum likelihood method is used in the estimation of the parameter values. However, it has been pointed out by Cramér that estimation of the parameter values by minimizing the value of the test statistic  $\chi_0^2$  is equivalent to the maximum likelihood method if the number of observations is large. As the  $\chi^2$  test itself is only meaningful if the number of observations is large, we may conclude that the estimation method based on the minimization of the test statistic  $\chi_0^2$  is fully applicable in practical work.

The third part is to perform a comparison between the theoretical distribution and the experimental data (the theoretical distribution is the distribution which is obtained when the estimates of the parameter values are inserted into the expression of the distribution function). The comparison is based on the value of the test statistic  $\chi_0^2$  which is defined as

$$\chi_0^2 = \sum_{i=1}^M \frac{(N_{i,theor} - N_{i,obs})^2}{N_{i,theor}}$$

and is approximately distributed as  $\chi^2$  with

$$\nu = M - 1 - k$$

degrees of freedom. Here  $N_{i,theor}$  and  $N_{i,obs}$  are the theoretical and observed number of drops in class interval  $i$ , respectively,  $M$  is the number of class intervals, and  $k$  is the number of adjustable parameters in the expression of the distribution function. For the cases analyzed here,  $M = 18$  and  $k$  varies from 2 (the log-normal distribution function) to 5 (the sum of two log-normal distributions); thus,  $\nu$  varies from 12 (the sum of two log-normal distributions) to 15 (the log-normal distribution function).

Finally, the value of the test statistic  $\chi_0^2$  is converted into a probability value  $P$  by using the equation of the  $\chi^2$  distribution with  $\nu$  degrees of freedom. The  $P$  value is the probability that the differences between the theoretical distribution function and a randomly chosen sample from a population obeying the theoretical distribution function would be equal to or larger than those observed in the case being analyzed. It can be seen that small differences between the theoretical function and experimental data (good fit) lead to low values of  $\chi_0^2$  and high  $P$  values (suggesting that the deviations could well have arisen due to statistical fluctuations); large differences between the theoretical function and experimental data (poor fit) lead to high values of  $\chi_0^2$  and low  $P$  values (suggesting systematic differences between the theoretical distribution and experimental data).

The computation of the  $P$  value is essentially a normalization procedure and is carried out to ensure a fair comparison between different distribution functions. If we only look at the values of the test statistic  $\chi_0^2$ , then we can improve the fit by adding more and more adjustable parameters into the expression of the distribution function, and finally we may even reach one-to-one correspondence between the mathematical function and experimental data, but this will not be very helpful in our trying to understand the situation. When the  $P$  value is computed, then the number of adjustable parameters has an effect via the number of degrees of freedom; in some sense, each adjustable parameter represents a price which must be paid and the  $P$  value tells us whether or not the improvements that we see have been worth the price which we have paid.

## Results and Discussion

Run 01 is first used as an example to illustrate the results. A summary of all results is given later in this section.

The results for Run 01 are presented in Table 2 and in Figure 1. It can be seen that the best fit was obtained with a sum of two log-normal distribution functions, followed by the log-hyperbolic distribution function, the Nukiyama-Tanasawa distribution function and the log-normal distribution function (in that order). For the log-normal and Nukiyama-Tanasawa distribution functions, the  $P$  values were clearly too low to be acceptable. For the log-hyperbolic distribution function and for the sum of two log-normal distribution functions the  $P$  values were much better but still lower than what would be desired.

**Table 2.** The results from the fitting of the different distribution functions to data from Run 01.

Distribution function	Test statistic $\chi^2_o$ [ ]	Number of d.o.f. $\nu$ [ ]	Probability value $P$ [ ]
Log-normal distribution	82.25	15	0.000
Nukiyama-Tanasawa distribution	35.64	14	0.001
Log-hyperbolic distribution	26.35	13	0.015
Sum of two log-normal distributions	22.98	12	0.028

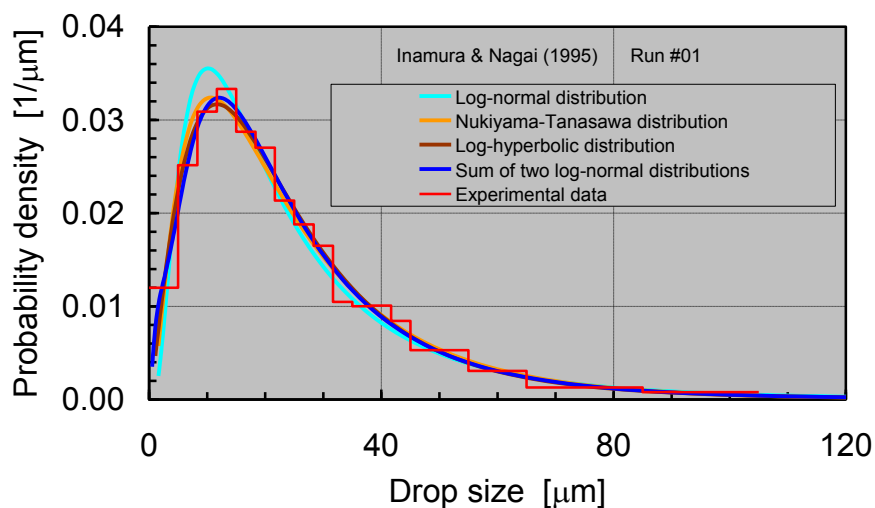


**Figure 1.** Fitting of the different distribution functions to data from Run 01.

It is of interest to note that the poor fit provided by the log-normal distribution function can clearly be seen in Figure 1, but the visual differences between the other three distribution functions seem to be rather small, and this is regardless of the fact that the  $P$  value for the Nukiyama-Tanasawa distribution function was much poorer than the  $P$  values for the log-hyperbolic distribution function and for the sum of two log-normal distribution functions. It has to be emphasized that it would be extremely hazardous to judge the goodness-of-fit on the basis of visual observation alone; quantitative statistical tests are needed to really be able to evaluate the quality of the results.

A summary of all results is given in Table 3 in accordance with what was observed for Run 01, it can be seen that the best results were obtained with a sum of two log-normal distributions, followed by the log-hyperbolic distribution function, the Nukiyama-Tanasawa distribution function and the log-normal distribution function. It is worrisome, however, that even with the sum of two log-normal distributions, which gave the best results, there are still quite a few experiments with very low  $P$  values.

**Table 3.** Summary of  $P$  values for all cases analyzed in this study.

Distribution function	Distribution of $P$ values for the different cases (21 for each distribution function)		
	$P < 0.01$	$0.01 \leq P < 0.05$	$P \geq 0.05$
Log-normal distribution	12	7	2
Nukiyama-Tanasawa distribution	7	7	7
Log-hyperbolic distribution	4	7	10
Sum of two log-normal distributions	3	4	14

The results are also illustrated in Figure 2. It can be seen that for the log-normal distribution function, the  $\chi_0^2$  values are mostly located above the curve  $P = 0.01$  and only two cases actually reach to better than  $P = 0.05$ ; for the other distribution functions, things gradually seem to improve and the range of  $\chi_0^2$  values moves downwards. For the sum of two log-normal distribution functions, the majority of  $\chi_0^2$  values are below the curve  $P = 0.05$ , but even now one third of all cases still fail to reach the region where  $P > 0.05$ . (Note that the visual appearance of the plot is slightly affected by the results from Run 14; this data set proved to be particularly difficult for all four distribution functions, and the  $\chi_0^2$  values were above 48 for all of them).

Similarly to the results as a whole, the fit obtained for Run 01 improves when moving from log-normal to Nukiyama-Tanasawa to log-hyperbolic to a sum of two log-normal distributions. The improvement of the  $\chi_0^2$  values for Run 01 are also shown in Figure 2.

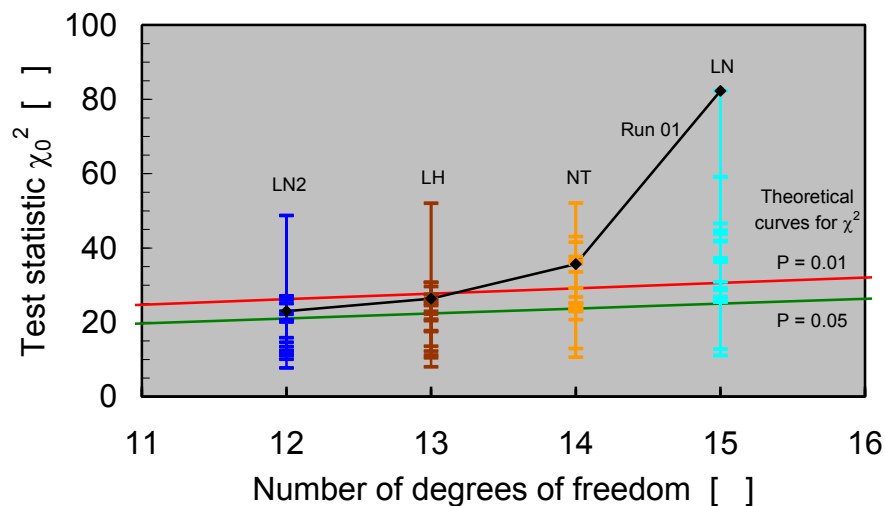


**Figure 2.** Values of the test statistic  $\chi_0^2$  for all 84 cases. The results for Run 01 are also shown.

For the log-normal distribution function, the parameter values appeared to be quite stable and behaved in a logical manner. The results are illustrated in Figure 3. It can be seen that for each design configuration, the logarithmic mean size and the logarithmic standard deviation (parameter  $\sigma$ ) were almost constants regardless of the liquid flow rate; thus, the original design objectives for the atomizer were met. Regression analysis also makes it possible to compute the confidence intervals for the values of the parameters; the results indicated that for configuration (a), the drop mean size appears to be independent of liquid flow rate at a 95 % confidence level, thus confirming the earlier statement that configuration (a) was the best design. However, it is perhaps not advisable to take the confidence intervals too seriously, since the theory is based on the assumption of normality in arrays, and this assumption is clearly not satisfied since the log-normal distribution function performed rather poorly in the  $\chi^2$  statistical test.

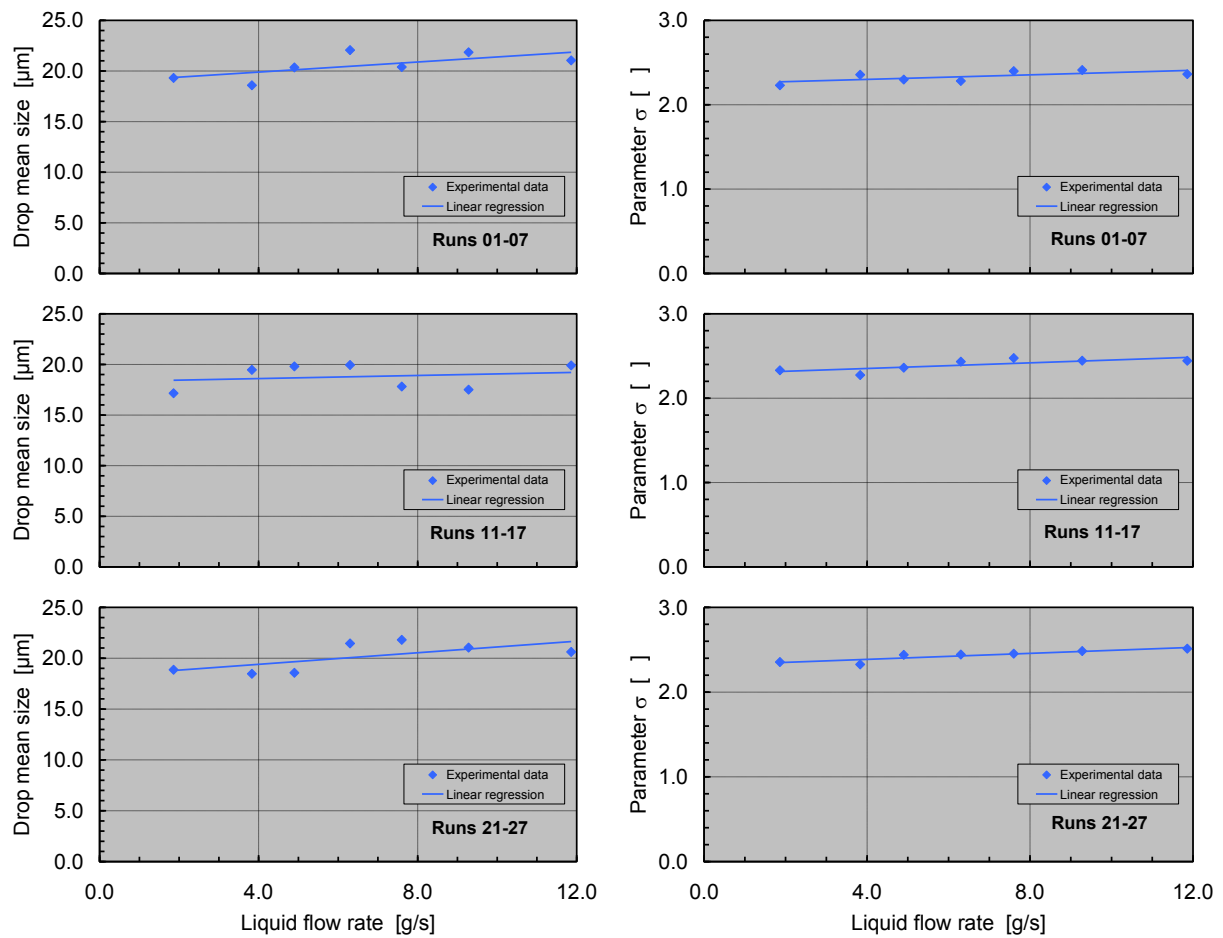


**Figure 3.** The best-fit parameters (logarithmic drop mean size and logarithmic standard deviation  $\sigma$ ) of the log-normal distribution function for all 21 data sets and linear regression lines fitted to the results.

For the Nukiyama-Tanasawa distribution function, the parameters values exhibited a peculiar behavior which is illustrated in Figure 4.

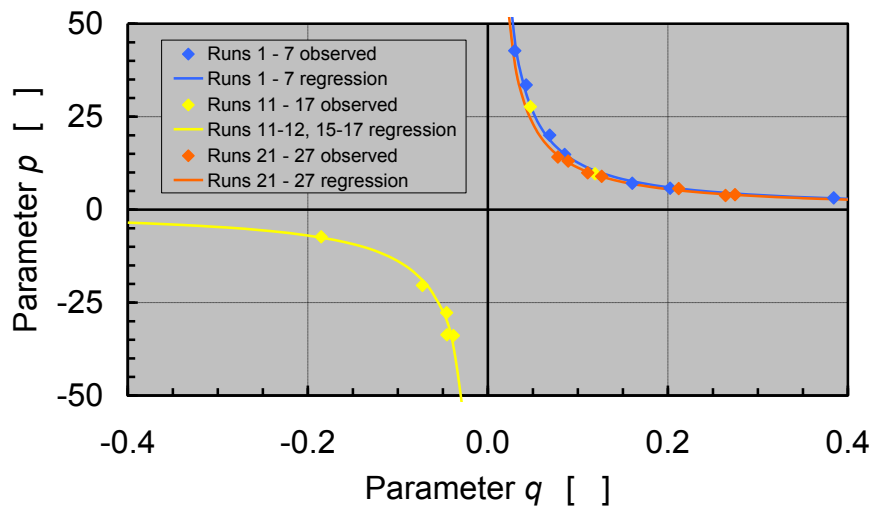


**Figure 4.** The behavior of the parameters  $p$  and  $q$  of the Nukiyama-Tanasawa distribution function.

The values of parameters  $p$  and  $q$  appeared to be strongly correlated, and while there seemed to be slight variations in the individual correlations for Runs 01–07, 11–17 and 21–27, in all cases the relationship between  $p$  and  $q$  could be roughly described with the equation  $p = 1/q$ . It is even more remarkable that this equation seemed to hold both for the cases where  $p$  and  $q$  were both positive (16 of the 21 cases behaved in this manner) and for the cases where  $p$  and  $q$  were both negative (the remaining 5 cases behaved in this manner). Our findings seem to support the earlier observations made by Lecompte and Dumouchel (2008). To be fully accurate, we need to note that Lecompte and Dumouchel actually replaced parameter  $p$  with an alternative parameter  $\alpha = p+1$ , but since the range of  $p$  in our results was from 3 to 43, the difference between  $p$  and  $p+1$  turns out to be almost negligible.

For the log-hyperbolic distribution function, the parameter values varied widely and no clear trends could be detected. Although the log-hyperbolic distribution function provided better results than the log-normal and Nukiyama-Tanasawa distribution functions, it was also more difficult to use and required more computational time.

As stated earlier, the best results were obtained with a sum of two log-normal distribution functions. The fitting of a sum of two log-normal distribution functions to data from Run 01 is illustrated in Figure 5. The dominating component (representing 86 % of the drops in this case) is called Log-normal 2 in the plot and has parameter values fairly close to those obtained for a single log-normal distribution function fitted to the same data. The other component (representing 14 % of the drops in this case) is called Log-normal 1 and has a finer mean size and wider distribution around the mean. It was quite typical for all cases that the sum of two log-normal distribution functions consisted of a dominating component closely resembling the single log-normal distribution which had been calculated separately and another component which seemed to patch the fit wherever needed, usually in the region of the smaller drops. It was not possible to detect any meaningful trends in the values of the parameters of the latter component.

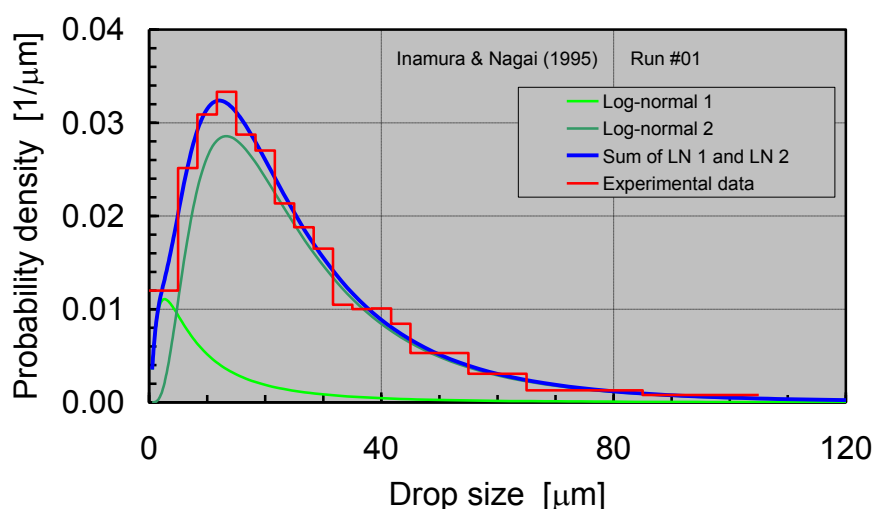


**Figure 5.** Fitting of a sum of two log-normal distribution functions to data from Run 01.

## Conclusions

Four different drop size distribution functions were compared with experimental data obtained for a Y-jet type airblast atomizer. The drop size distribution functions were the log-normal, Nukiyama-Tanasawa and log-hyperbolic distribution functions and a sum of two log-normal distribution functions. The experimental data consisted of 21 different drop size distributions. The  $\chi^2$  statistical test was used to evaluate the goodness-of-fit between the distribution functions and experimental data.

It was found that the best fit to the experimental data was obtained with a sum of two log-normal distribution functions, followed by the log-hyperbolic distribution function, the Nukiyama-Tanasawa distribution function and the log-normal distribution function (in that order). The differences in goodness-of-fit were not very

consistent; although steady improvement was often observed when moving from the log-normal distribution function to the Nukiyama-Tanasawa and log-hyperbolic distribution functions and finally to a sum of two log-normal distribution functions, there were also some measured distributions which could be reasonably well described with all four distribution functions employed in this study, while some others proved to be quite difficult to all four distribution functions.

The parameters of the Nukiyama-Tanasawa distribution function seemed to be strongly correlated to each other. This finding resembles the earlier findings of Lecompte and Dumouchel.

Further work is needed to evaluate the relative merits of different drop size distribution functions. In particular, it has to be noted that in this study, all the measured distributions were fairly similar to each other. It would be useful to carry out a comparative study on experimental data exhibiting larger variations in size distributions.

## **References**

- [1] H. Cramér (1945), *Mathematical methods of statistics*. Princeton University Press.
- [2] T. Inamura, N. Nagai (1995), Control of mean droplet diameter issued from Y-jet type airblast atomizer by using fluid amplifier. *Atomization and Sprays* 5 pp. 243–260.
- [3] M. Lecompte, C. Dumouchel (2008), On the capability of the generalized gamma function to represent spray drop-size distributions. *Part. Part. Syst. Charact.* 25 pp. 154–167.
- [4] T. Paloposki (1994), Drop size distributions in liquid sprays. *Acta Polytechnica Scandinavica, Mechanical Engineering Series* No. 114.
- [5] T. Paloposki, T. Inamura (1996), Drop size distributions in sprays from a Y-jet type airblast atomizer. *Contributed papers of the 12<sup>th</sup> Annual Conference of ILASS-Europe on Liquid Atomization and Spray Systems*, Lund, 19–21 June 1996, pp. 191–196.

## Compressed Gas Aerosol Insert Design

M. Burby<sup>1</sup>, G.G.Nasr<sup>1</sup>, AJ Yule<sup>1</sup> and N Asmuin<sup>2</sup>

<sup>1</sup>: Spray Research Group (SRG), Institute of Materials Research (IMR)  
University of Salford, UK

<sup>2</sup>: Department Civil Engineering, University Tun Hussein Onn, Malaysia

### Abstract

Consumer Aerosols (“package aerosols” or “aerosol cans”) are hand-held devices for spraying air fresheners, hair spray, surface cleaners, polishes and deodorants. Industrial Aerosols are similar devices for spraying: cleaners, lubricants, paints and adhesives. They also have hospital and specific medical uses, spraying coagulants and disinfectants. World-wide around 20 billion devices are manufactured annually. Led by the Californian Air Resources Board (CARB) in 2001, the use of liquefied gas propellants in aerosol cans will eventually be banned. This paper addresses the challenges of replacing hydrocarbon propellant with an inert compressed gas through the use of a novel atomizer insert and valve assembly. The aim is to understand the roles of internal flow turbulence, geometry, bubble generation, and dissolved gas effects, in the production of fine sprays. From this knowledge a range of new atomizer inserts and valves will be developed. The problem of achieving fine atomization without liquefied gas propellant is addressed by bleeding off some can gas (air, nitrogen or carbon dioxide) into the valve so that a bubbly flow is fed to the atomizing “insert”; i.e. giving internal mixing two-fluid atomization. A challenge is that the available atomizing gas/liquid mass ratio is less than 1%. Thus the investigation uses systematic experiments and CFD to establish both suitable designs of gas/liquid preparation arrangements and also the designs of atomizing insert for producing the required combinations of drop size and liquid flow rate, for both water-based and ethanol-based liquid products

### Introduction

One of the major contributing factors to world pollution today is the use of hydrofluorocarbons (HFCs) used in domestic household aerosols. Globally, there are around 20 billion devices manufactured annually and the UK has a foremost share of this market (BAMA report 2006, [1]), manufacturing 5 billion units which is second only to USA.

Propellants used in aerosol cans, comprise of two categories: liquid suspension or emulsion and liquefied propellant in gas or compressed gas. The propellant ingredients in an aerosol can, differ for each product and is dependent on the function of the product being sprayed, for example hairspray, deodorant, air-freshener etc.

One of the first popular volatile organic compound (VOCs) aerosol propellant used in aerosol sprays was chlorofluorocarbons (CFCs), such as, trichlorofluoromethane (F11), dichlorofluoromethane (F12) and dichlorotetrafluoroethane (F14). CFCs were initially used as an aerosol propellant because they are non-flammable, stable, low in toxicity and extremely safe under normal conditions of use. This same stability means that they are not destroyed in the troposphere but instead drift upwards to the stratosphere, where they are broken down by the strong sunlight. This releases chlorine (Cl), which adds to the natural depletion cycle of ozone.

In the mid-1970s, there was concern over the use of fluorocarbons, as it was found to adversely affect the ozone layer. In 1997 the Montreal Protocol called for the elimination of CFCs and today, almost all aerosol cans contain alternative propellants, such as Liquefied Petroleum Gas (LPG), Hydrofluorocarbons (HFCs). Some of the propellants used are butane, methylene chloride, nitrous oxide, o-phenyl phenol, propane, trichloroethane or trichloroethylene.

HFCs (Volatile organic compound) were a replacement for CFCs, as they do not contain any chlorine and so do not deplete ozone. However HFCs do release hydrocarbons, which ultimately contribute to the greenhouse effect. With continued environmental pressures to lower the quantity of green house gases, the use of HFCs in aerosol cans will also be eventually banned and alternative non-volatile organic (non-VOC) propellants will have to be used.

The predicted move to non-VOC propellants represents a number of challenges to the industry, as non-VOC sources, such as compressed air have limited energy when compared to HFCs. Therefore to ensure comparable atomization quality to traditional propellants over the life of the can, novel insert and valve arrangements will have to be designed for the aerosol industry.

Figure 1 compares how can pressure varies over the duration of the can life for a conventional HFC can and a non-VOC can utilising compressed air. As shown in Fig. 1 for the can filled with butane, a relatively constant gas pressure, typically 4 to 5 bar is maintained through the life of the can, thus being able to provide a relatively constant energy source and thus flow rate throughout the can life. The other benefit that arises from using VOC



as a propellant, is the energy content through the flash vaporisation of the liquid propellant as it is exposed to atmospheric pressure, thus aiding the atomization process.

For a non-VOC propellant, such as compressed air, the pressure within the can drops significantly through the life of the can. This is due to the air volume within the can increasing as the product is consumed and thus reducing the pressure within the can. This results in a reduction in the energy and ultimately atomization quality of the spray.

The challenges in designing a compressed aerosol can using a non-VOC propellant, such as compressed air is to maintain adequate pressure within the can for as long as possible. Typically the pressure in the can must remain above 3.5 bar to ensure suitable atomization quality over the life of the spray and to also ensure that there is sufficient gas pressure to empty the can of product.

Additionally, depending on the application of an aerosol spray there are a number of performance criteria to be met, these being:

- flow rate through the life of the can;
- droplet size through the life of the can;
- penetration (throw);
- and cone angle.

At low flow rates (<6g/s) using small orifices (between 0.3 mm and 0.5 mm) very fine sprays can be produced at least as well via turbulence generated in the atomiser, and also by bubble generation by cavitation. This is of fundamental interest for applications that are striving for fine atomization with low energy costs, such as gasoline direct injection and, of principal interest here, household aerosols.

In recent projects [2], [3], [4], [5], [6], [7], [8] the investigators have studied methods of replacing VOC propellants in aerosol cans whilst maintaining spray quality. Some of the results have demonstrated the future capability of providing VOC-free aerosols using inert gas propellant through appropriate design of the internal nozzle and valve. For the work presented within this paper, the product flow rates used in the investigation primarily concentrated around the hairspray, air freshener and polish range (0.4 to 1.2 g/s).

### Aerosol Can

The atomisation process is concerned with the transformation of bulk liquid into a spray or aerosol by creation of new surface. A VOC can is typically divided into three partitions:

- i. Gas propellant exerting pressure;
- ii. Liquefied propellant becoming a gas mixture with product;
- iii. Product concentrates solvent and liquefied propellant;

and as shown in Fig. 2 consists of the following components:

- i. **Aerosol Actuator Cap:** Fits onto the valve stem.
- ii. **Valve Cup:** Typically constructed from tinned steel, or aluminium.
- iii. **Outer Gasket:** This is the seal between the valve cup and the aerosol can.
- iv. **Valve Housing:** It contains the valve stem, spring and inner gasket.
- v. **Valve Stem:** The tap through which the product flows.
- vi. **Inner Gasket:** Covers the hole in the valve stem.
- vii. **Valve Spring:** Usually made up of stainless steel.
- viii. **Dip Tube:** Allows the liquid to enter the valve.

The can contains the formulation to be atomized, the dip tube and valve assembly. The dip tube transmits the liquid from the bottom of the can to the valve assembly, at the outlet of the valve assembly is the stem which the actuator cap sits upon. Within the actuator is an insert, which comprises of swirl passageways and a final exit orifice which emits the spray.

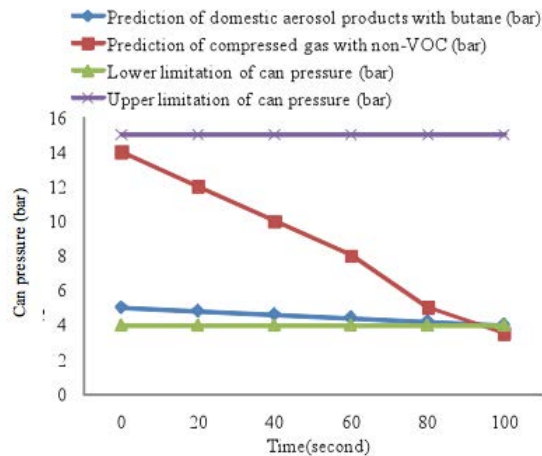


Figure 1: Can pressure over can life

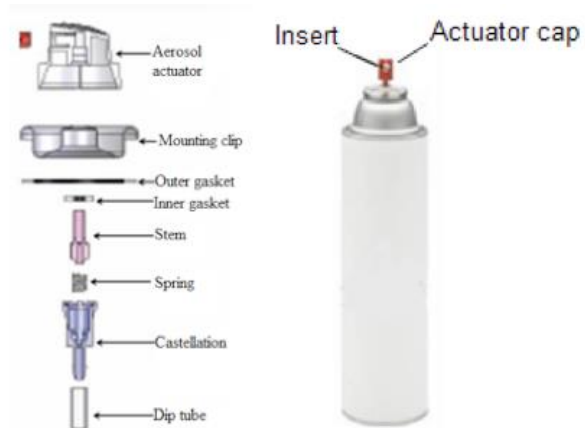


Figure 2: Aerosol can assembly

As shown in Fig. 2, the actuator cap is the unit the user presses to activate the valve assembly to spray the product in the can. The actuator permits easy opening and closing of fluid to the atomiser insert, via the valve. It is through the orifice in the actuator/insert that the product is discharged. As shown in Fig. 3 the design of the inner chamber, between the boss and the insert and size of the exit orifice of the insert contributes to the physical form (mist, coarse spray, solid stream or foam) in which the product is discharged. The type and quantity of propellant used and the dimensions of the actuator/ insert design also effect the particle size of the emitted product.

Figure 4 illustrates a typical actuator which has the swirl vane channels injection molded into the design, in some designs the swirl channels are molded into the boss.

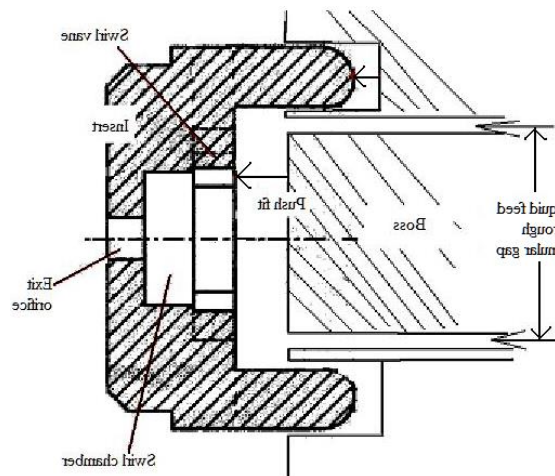


Figure 3: Swirl vane channels injection molded

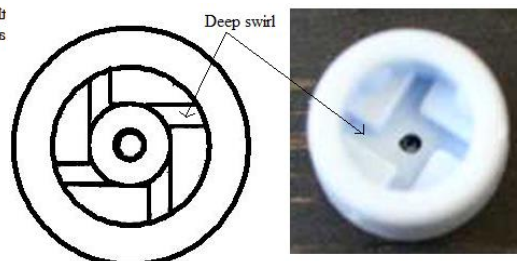


Figure 4: Atomiser insert with deep swirl

As shown in Fig. 3 the boss on the actuator cap sits behind the swirl vanes and liquid is fed into the outer parts of these vanes, before entering the swirl chamber. This imports a vortex flow, leading to a conical liquid sheet at the exit of the orifice, therefore giving a spray.

The aim of the work presented in this paper is to understand how flow conditions, such as; turbulence, bubble generation and dissolved gas effects within the insert can be generated through various geometrical flow features (as described in the next section) to produce a fine spray. From this knowledge a range of new atomizer inserts and valves will be developed that will suited to non-Voc aerosol applications.

## Experimental Set Up

### Insert Design

In this investigation a variety of multiple insert designs were tested. The multiple insert design consisted of a number of individual disc inserts (Fig. 6 ) that had a series of internal flow features to alter the turbulent structure within the insert, with the aim of producing conditions suitable for the generation of a fine spray. The inserts were assembled in varying combinations, as shown in Fig. 6 and for each design droplet size measurements were taken over a range of flow rates and pressures. These insert flow features, as shown in Table 2 will be discussed as follows:

#### Approach chamber (Part A)

Part A (Table 1) is called upper cylinder (UC) or approach cylinder. It is positioned just after the mixing chamber. It is made from brass plate with a 25mm diameter and a thickness of 1.0mm. The plate has a hole at the centre with different Part A's having sizes ranging from 0.9mm to 1.5mm.

#### Throttling hole (Part B)

Part B (Table 1) is the throttling hole, which is used to reduce the effective flow area within the channel and so accelerate the flow. Two types of throttling hole were used in the designs tested:

- i) Straight throttling hole.
- ii) Throttling hole with divergence

The throttling hole was made from a brass plate with a 25mm diameter and 0.5mm wall thickness. It is labeled a throttling hole because of the position after part A (or upper cylinder). The designs for a range of part B's consisted of a number of small holes with varying diameters.

#### Expansion chamber (Part C)

Part C (Table 1) is known as the expansion chamber and is made from a 25mm diameter brass plate. This part was usually located after part B or the throttling hole.

#### Turbulator Chamber (Part D)

Part D (Table 2) is known as the turbulator, and it is made from a brass plate and it is similar to part C. The length of the turbulator is twice that of the expansion chamber. It has 2mm diameter hole drilled in the centre with 1mm depth.

#### Orifice Channel (Part E)

The final component, part E (Table 1) is the orifice channel. It combines a conical protrusion and a final orifice channel. This part is also called an exit orifice or extension orifice. It is located between the aforementioned chamber and final orifice. There are five different sizes of orifice channel and are labelled as: part E, E1, E2, E3 and E4, and are described in the following:

- (i) Part E has a conical protrusion with a divergence angle of  $26^\circ$ . A hole of 1mm depth and 0.5mm in diameter and is drilled through the disc. Part E6 is a reverse of part E, conical protrusion and acts as the final orifice.
- (ii) Part E1 has one hole drilled to a depth of 1mm and 0.3mm in diameter with a conical protrusion inclined at  $26^\circ$  tangentially. The hole continues with a straight hole, 0.3mm in diameter and 1.0mm depth. Part E7 is a reverse of part E1.

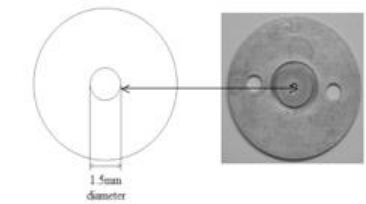
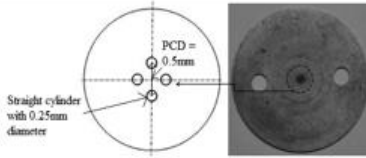
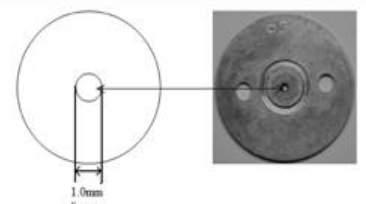
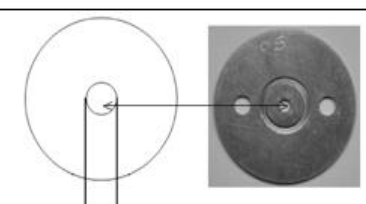
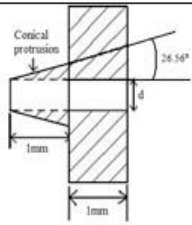
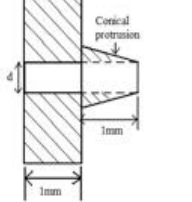
<b>Part A</b>	
<b>Part B</b>	
<b>Part C1 &amp; C2</b>	
<b>Part D</b>	
<b>Part E &amp; E1</b>	
<b>Part E6 &amp; E7</b>	

Table 1: Multiple insert flow features

- (iii) Part E2 has the same characteristics as Part E. The hole is 0.5mm in diameter and to a depth of 0.5mm.
- (iv) Part E3 has a hole drilled as a star shape and at the front there is a conical protrusion that is inclined at 26° tangentially. The hole was drilled to a depth of 1mm and 0.3mm in diameter and then continues with a straight hole 0.3mm diameter and to a depth of 1.0mm.
- (v) Part E4 has an inclined conical protrusion of 26° and a hole of 0.5mm in diameter and a depth of 0.6mm.
- (vi) Part E10 is the reverse form of part E4, with a conical protrusion acting as the final orifice.

### Control Board

The steady spray experimental apparatus enabled the liquid and gas supply to be independently regulated to the insert. As shown by the schematic in Fig. 5, the control system comprised of: a reservoir (1) filled with de-ionised water and pressurised to 12 bar (maximum) by using the regulator on a standard 200 bar compressed air bottle (2). The pressurised liquid is supplied to the insert (4) via 4mm bore nylon tubes. A rotameter for the liquid (6) and an electronic pressure gauge (liquid) (5) were used to measure the flow rate and supply pressure to the insert and the flow rate was regulated via a needle valve (7).

For the two fluid atomiser designs, bourdon pressure gauge (gas) (8) and an electronic pressure gauge (gas) (11) were used to measure the supply pressure. In addition, there was also an electronic flow meter (gas) (9) and rotameter (10) used to measure the supply gas flow rate to the atomiser insert. A needle valve on the gas rotameter was used to control the flow rate of gas.

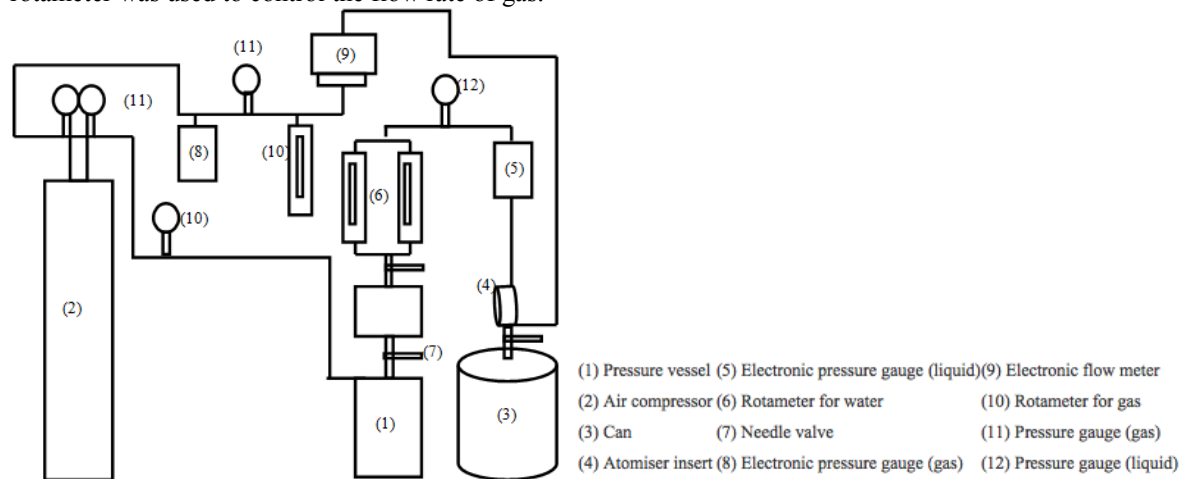


Figure 5: Schematic of the control board

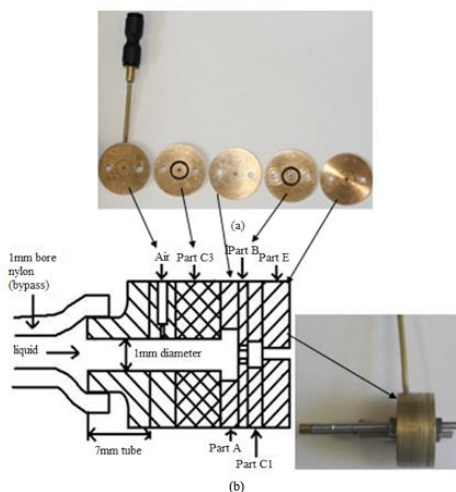


Figure 6: Multiple insert assembly

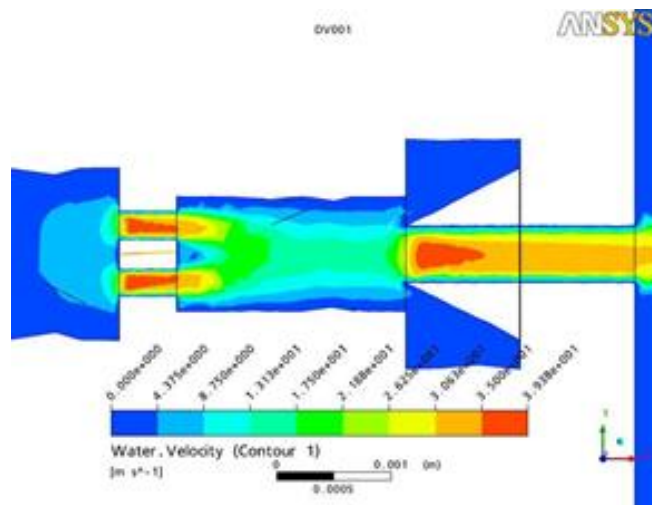


Figure 7: CFD velocity contour plot

## Quantitative Measurements

To analyse the spray structure for the insert designs, a number of quantitative measurements were used. A Malvern Mastersizer-X was used to measure the droplet size of the spray produced at a stand-off distance of 200mm. The Cone angle for the spray was measured from still images of the spray and the flow rate was measured directly from the rotameters on the control board (timed collection techniques were also used).

## Results and Discussion

CFD was used throughout this investigation to analyse the flow structure through the insert arrangement. Figure 7 shows a section view of the insert arrangement of a gas/liquid bubbly flow feeding a multiple insert arrangement via inlet bores (note the downstream plenum of the exit nozzle has not been shown).

From experimental testing and CFD analysis, it became apparent that the inserts altered the flow structure in the following ways. As shown in Fig. 8, liquid would flow through the liquid inlet (a) into the flow channel (b) it is then mixed with gas coming from the compressed air (c) at the mixing chamber. The gas inlet is perpendicular (90°) to the liquid inlet. The mixing of the gas with the liquid in the mixing chamber creates bubbly flow, which passes through a jetting orifice from which the bubbly flow passes through an outlet expansion chamber (d). This produces turbulent bubble-laden jets, which impact on the sharp edges (e) at the outlet of the expansion chamber (d). The throttling hole can be offset away from the centre line rather than might be expected by simply protecting the throttling hole in the orifice channel.

The combination of the bubble-laden jets and their impact on the sharp edge, combine to give flow separation from the interior surface of the orifice channel (f). The length of the orifice channel is such that the flow reattaches to the wall in the downstream region (g), so that a new bubble starts to form before the jet finally discharges at the exit orifice.

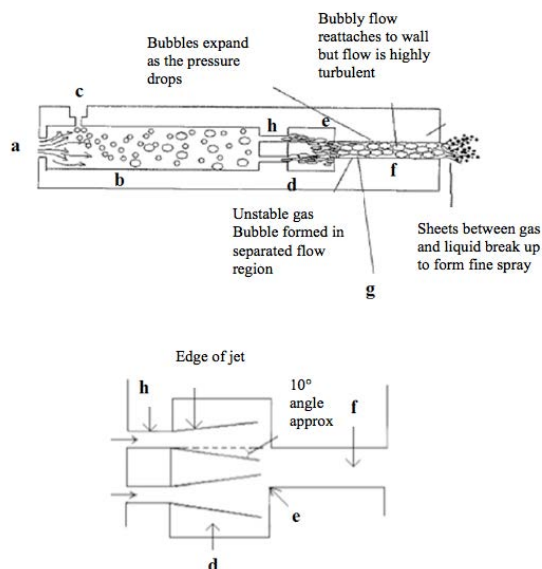


**Figure 8:** Operation of bubbly flow jets from ratio the throttling hole in the atomiser insert

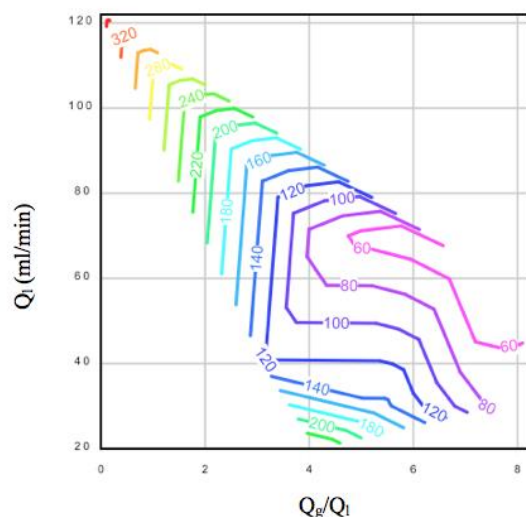


**Figure 9:**  $D_{v,50}$  of liquid flow rate against gas to liquid

## Droplet size

A useful method of processing data from the experiments was the use of iso-contours derived from the data matrices, for example Fig 9, for one geometry, shows drop size contours with variation of water and gas flow rates. The results show the combinations of supply pressure, inlet and outlet insert diameters, swirl and other internal geometry parameters, that can best match the required drop size-liquid flow rate combinations in current liquefied gas propellant aerosols.

As shown in Fig. 10, a typical sample of the numerous geometrical combinations tested at 9 bar have been plotted. This is a typical can starting pressure for a non-VOC propellant. The best devices produced a  $D_{v,0.5}$  spray between 24 $\mu$ m to 45 $\mu$ m, (Fig. 11) which, falls within the depiction fine spray. The rest of the devices produced droplet sizes of which are more suited to larger droplet applications, such as, disinfectant surface treatment and air fresheners. This best gas/liquid ratio that achieved this droplet size was 4/1. It should be noted that at this ratio there would still be sufficient air pressure remaining to atomize the product at the end of the can life.



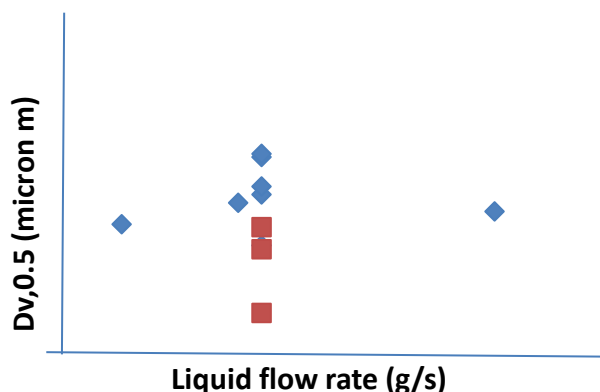


Figure 10: Multiple insert (liquid and gas)

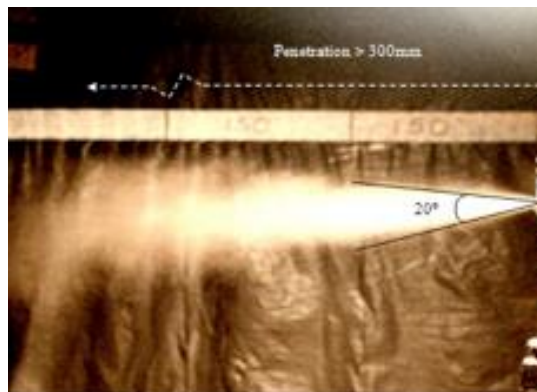


Figure 11: Multiple insert (liquid and gas) 4 g/s

## Conclusions

In this investigation the spray characteristics of two fluid flow insert arrangements have been investigated to establish their potential for producing a fine aerosol spray using compressed air as the propellant. The main finding of the investigation highlight that:

- By using multiple inserts and injecting air upstream of the internal flow features, bubbly flow further reduces the droplet size to that of a fine spray, to between 24- 45 $\mu$ m  $D_{v,50}$ .
- The use of iso-contour plots can aid in the design process and selection of gas/liquid ratio and or product flow rates to achieve a certain droplet size.
- The droplet sizes produced by the two-fluid insert arrangement illustrates that most consumer product aerosol droplet sizes that are currently produced using HFCs can be achieved by using compressed air.
- The adoption of non-VOC aerosol insert technology by aerosol manufacturers would significantly reduce the contribution of greenhouse-causing gases emitted to the atmosphere.

## References

- [1] British Aerosol Manufacturers Association, Smith Square London, Annual Report, 2006.
- [2] Asmuin, N., 2011, *Investigation into Novel Matched Valve Actuator Atomizer Insert Design for Compressed Gas Aerosols*, PhD Thesis, University of Salford.
- [3] Nasr, G. G., Yule, A. J. and Burby, M. L., 2009, *Spray discharge assembly*, Patent No. WO2011/061531, April 2011.
- [4] Nasr, G. G., Yule, A. J. and Burby, M. L., 2009, *Aerosol spray device*, Patent No. WO2011/128607, April 2011.
- [5] Nasr, G. G., Yule, A. J. and Burby, M. L., 2009, *Low loss valve*, Patent No. WO2011/061481, April 2011.
- [6] Nasr, G. G., Yule, A. J. and Burby, M. L., 2009, *Liquid dispensing apparatus*, Patent No. WO2011/042751, April 2011.
- [7] Nasr, G. G., Yule, A. J. and Burby, M. L., 2009, *Liquid dispensing apparatus*, Patent No. WO2011/042752, April 2011.
- [8] A. Nourian., 2013, *Next generation of consumer aerosol valves using inert gases*, PhD Thesis.

## **Spike Design Nozzle for Reduced VOC Aerosols**

Sharief R. A.

Higher Education of Mechanical Engineering, Stockport College, Manchester, SK1 3UQ, England, UK

### **Abstract**

The desire to reduce the level of propellant used in aerosol canisters is topical issue at the moment and is likely to become more important in the future due to legislation planned in certain countries, which proposes to impose restrictions on the amount of propellant that can be used in hand-held aerosol canisters. The reduction in the level of propellant causes a reduction in pressure available drive the fluid through the nozzle arrangement and also results in less propellant being present in the mixture to assist with the droplet break up. Therefore, there is a requirement for different types of designs of nozzle arrangement that is capable of reducing an aerosol spray composed of suitably small droplets at low pressure and at lower manufacturing cost. This paper describes new developments and experiments that have been carried out to explore the effects of spike shape nozzles on the spray quality on reduced volatile organic compounds (VOC) products. This design consists of one piece, which reduces the manufacture cost marginally. The results have shown that the Spike designs have been successful to overcome problems caused by anti-rust formulation in air fresheners without any effect to spray quality. Spike initial, spike and spike advanced designs have all been demonstrated in this paper.

---

### **Introduction**

Because of the ease of atomizing by using a flashing propellant, there has been remarkably little published research on how the internal geometry of the actuator affects performance, where the actuator is the cap of the can, which fits on the valve and contains the exit orifice and an internal flow passage. The exit orifice may be a simple orifice, such as for antiperspirants, or a swirl-insert, for example for polish and paint sprays. Currently the propellants used are blends of liquefied hydrocarbon, mainly butane and these are classified as Volatile Organic Compounds (VOC's). Legislation controlling VOC use is becoming increasingly strict and is already affecting the household aerosol market in California and encouraging research in this area. Figure 1 shows the typical Spike design consisting of 3 exit holes, mounted on a cone shape. The hole sizes determine flow rates and the angle of the cone shape determine the drop sizes. Figure 2 shows flow schematic of atomization.

### **Experimental Test Rig**

Droplet size was measured using a laser diffraction instrument (Malvern and Spray Tec.), an average of three tests had been taken for each data point; flow rate was measured by weighing the can, the spray time was on average of five seconds. Spray distances from the lenses is 500 mm for the air fresheners spray. The actuators in the research programme have been specially machined from Perspex (Plexiglas) and Brass, a method of unit construction has been developed so that combinations of different shapes and sizes of inlets and exists can be used. Internal passages and flow control devices may be tested systematically. Because of variation of temperature difference between summer and winter, all tests must be done at room temperature, 20 centigrade



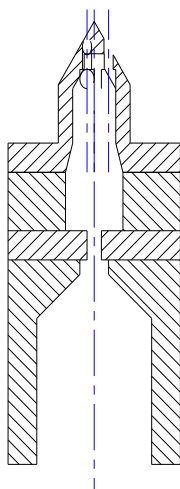


**Fig. 1** The typical Spike design

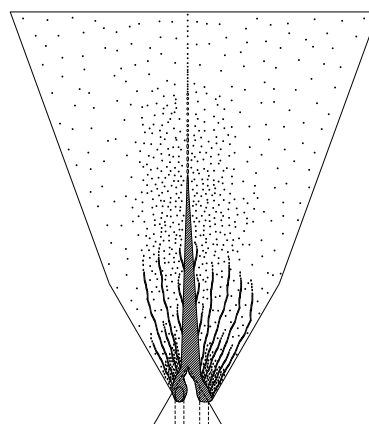


**Fig. 2** Flow Schematic of atomization

## Results and Discussion

Experiments that have been carried out to explore the effects of cyclonic device nozzle on the spray quality causing break on droplets, these designs working well with reduced VOC's products, none viscous products such as air fresheners, also worked remarkably well with air freshener products that contain anti-rust formulation and water.. Several techniques has been used in order to creates more turbulence and breaks up, consequently reduces drop sizes and produce fine droplet.

These designs are simple and capable of producing good spray with low cost of manufacturing. More complex designs of household aerosol can actuators have been made possible by using these designs; this has made feasible the use of various flow control devices with no cost penalty.

Experiments have shown that flow control devices permit control of droplet size, control of flow rate, spray pattern manipulation, the production of narrower droplet size distributions, and reduction of can VOC content.

An experimental research programme has systematically applied these flow control devices in specially made actuator models for the cases of spraying those very different types of products, non viscous, anti-perspirant, hair spray, body spray, air-freshener and viscous products, polish, oil and paint

The Air Freshener Nozzle Performance Tests carried out with the Lionstar AF design with 17% VOC + 5% water formulation against typical market can design & formulation.

As shown in Figure 3 and 4 the spray pattern for Lionstar AF design demonstrates a better coverage with wider spray angle.

Table 1 below shows the general overview performance over can life of a typical market can against Lionstar reduced VOC. These results show an improvement of drop sizes by 10 microns and the flow rate by 50%.

Table 2 shows particle sizes downstream of nozzles from 10 to 70cm, the improvement is obvious when measuring droplets after 50cm downstream, by 15 microns.

Table 3 and 4 show Dv0.5 of Lionstar AF designs throughout spray plume and at different radial angle orientations of nozzle.

General look of the spray plume show that Lionsstar designs have a wider angle and the density looks proportionate at 10cm from nozzle onwards just as the original does. Before the 10cm mark, a “streamer core” is noticeable although it shows to breakup beyond the 10cm. No boulders or spitting occurs from this core. Some residue collects and spits after spray stops, due to larger “dead volume” of nozzle.

Nozzle	Flow Rate (g/s)	Dv05 @500mm (um)	Full Spray angle	Distance from nozzle (cm)	70	50	30	20	10
Typical Market Can	1-0.9	35-50	30	Typical Market Can	55	38	36	29	24
Lionstar Reduced VOC	1.6-1.5	32-40	40	Lionstar Reduced VOC	35	34	32	29	24

**Table 1** General overview performance over can life

**Table 2** Dv0.5 (micron) downstream of nozzle

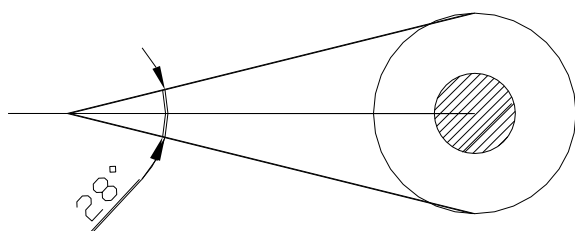


**Fig 3** Typical Market Cap spray pattern at 20cm

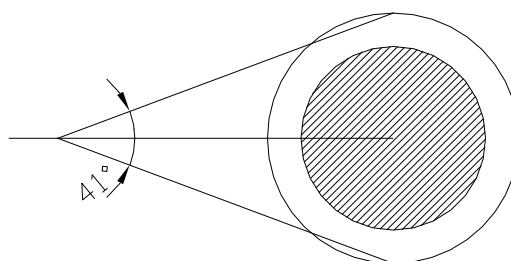


**Fig 4** Lionstar Reduced VOC spray pattern at 20cm

Position within spray plume	Dv05 (um) @50cm
Centre	34
Half way	34
Edge	37

**Table 3** Tests carried out at different AF design throughout spray plume

Nozzle angular position (deg)	Dv05 (um) @50cm
0	35
45	34
90	34
180	35

**Table 4** Tests carried out at different radial angle orientations of nozzle

Systematic tests were undertaken in order to match the spray characterization such as flow rates, drop sizes and spray angles of original market cap design. The advantage of Lionstar design is made from one piece, simple and solves problems of different formulations, such as anti-rust formulations and the standard formulations. The Spike designs were successful with a reduced Volatile Organic Compounds (VOC) at different levels, up to 17% of the original of 29%. As known, when we reduce the VOC in the products, such as air fresheners, the spray quality deteriorates, so it is necessary to keep the quality of spray and other spray characterizations.

All the products are reduced VOC As shown in figures 5 to 18, model designs consist of inlets could take different shapes, horizontal, tangential or vertical inlet. Inlets also could control the flow rate. pre-throttle works with air fresheners as flow control as well as create more fine droplets with no penalty to flow rate, pre-throttle sizes have to be optimized to be effective. Throughout the paper, all spike designs selections include different sae angles, exit diameters, and throttle sizes Systematic tests were undertaken, in order to reduce the drop size diameter of droplets. Spike designs illustrate flow control devices that have been explored.

Systematic tests enabled selection of optimum combinations of exit orifice and throttle sizes and sae angles, with the aim of producing fine sprays but with reduced inhalable fraction of droplets. This is achieved by producing a near-homogeneous two-phase mixture in the pre-chamber which completes atomisation inside and just downstream of the exit orifice. Minimization of liquid film on the exit orifice wall also appears to assist in reducing the width of the size distribution. Applications of spike designs is achievement of a major reduction in hydrocarbon content for air-freshener sprays with no adverse effect on the drop size distribution.

In order to do this hydrocarbon propellant level is reduced in the can during the filling operation, and also the liquid propellant must be replaced by water. This produces problems in obtaining good atomisation for three reasons; (1) the can pressure is reduced, (2) flash vaporization is reduced, and (3) surface tension and viscosity of the liquid phase are increased.

Development work showed that to solve these problems it was considered necessary to (1) ensure significant vapour release occurred within the actuator, (2) produce a highly turbulent flow, but at length scale small compared with the flow geometry, and (3) minimize the size of the exit orifice. Reduction in can VOC content is obtained without worsening the drop size distribution (volume and median diameter is around 40 micron for air fresheners), 30 to 60 microns for different types of reduced VOC.

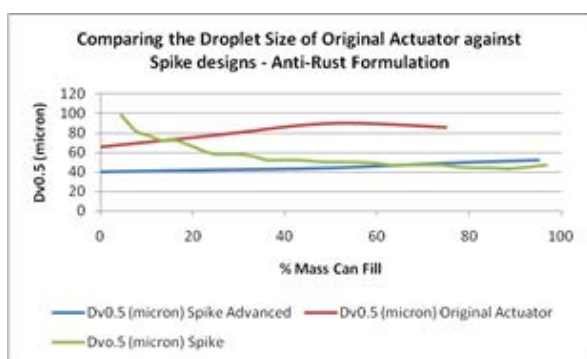
Figures 5 to 10 show results with anti-rust formulation products such as air fresheners at different reduced VOC. All the tests were carried out at 17% reduced VOC, except for figure 5 and 6, which were carried out at 24.5% reduced VOC. Figure 5 and 6 shows droplet size and flow rate of spike designs against original market cap with anti-rust formulation. The spike advance designs show superior to the spike design and the original market cap. The improvement of the drop sizes is very obvious especially when the can is nearly empty, with improvements of more than 50%. This has also kept the flow rates almost constant. The Spike an advanced design is as shown in figure 1 as well as consisting of two throttles hitting each other in the chamber just before the Spike exits.

Figure 7 and 8 compares the droplet size and flow rate of original market caps against the standard Spike designs, showing better performances and consistency. Especially after 50% of can mass fill, by maintaining the flow rate the same as original. Figure 9 and 10 show two of Lionstar designs against an original market cap. The standard Spike still exhibits superior performances compared to original market cap designs, maintaining the flow rates almost equal.

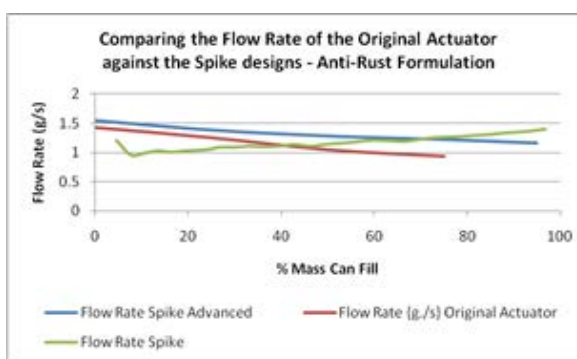
Figure 11 to 18 show results with standard formulation products of air fresheners. Figures 11 and 12 shows three spike designs with different exit sizes. The results show that the bigger the exit size, the higher the flow rate. However the smaller exits produce better droplet sizes. Figure 13 and 14 compares the different degrees of sae, comparing the sae 60, 45 and 30. The wider the sae angle, the more favorably smaller the droplet sizes are, whilst maintaining an almost equal flow rate. This shows that the larger angle, sae60 was the best performing compared to the other angle sizes.

Figure 15 and 16 shows the comparison of two types of angles, sae60 and tetra60, shows that the standard sae60 performed more favorably. Figures 17 and 18 compares droplet size and flow rate of different reduced VOC levels against original full VOC level. This shows that the spike designs maintain the droplet sizes and flow rates despite a reduction of VOC in cans.

Figure 19 Shows a typical air freshener spray of the initial Spike design with figure 20 showing the vertical design of an initial Spike design as well as in a schematic diagram form, Figure 21 and 22 shows spike design and air freshener spray for spike design.



**Fig 5** Graph showing droplet size of spike designs against original with anti-rust formulation at 17% reduced VOC



**Fig 6** Graph showing flow rate of spike designs against original with anti-rust formulation at 17% reduced VOC

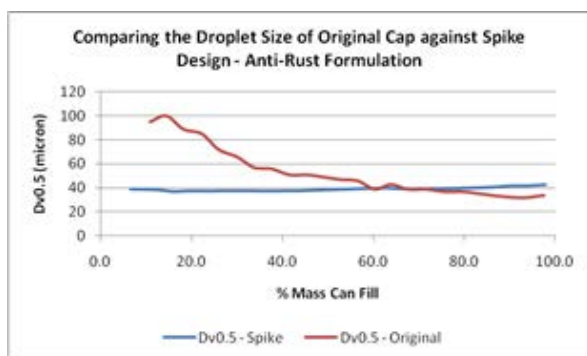


**Fig 7** Graph showing droplet size of spike against original with anti-rust formulation at 24.5% reduced VOC

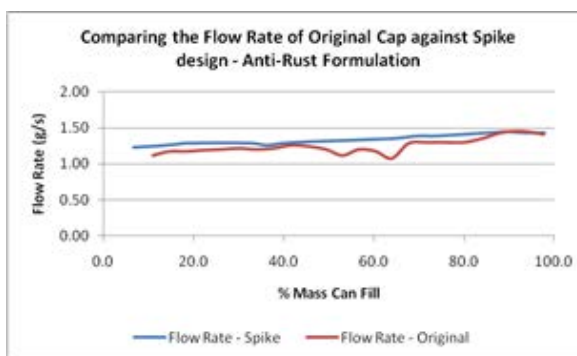


**Fig 8** Graph showing flow rate of spike against original with anti-rust formulation at 24.5% reduced VOC

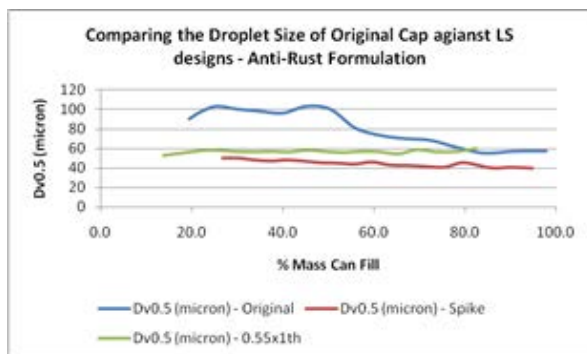


**Fig 9** Graph showing droplet size of Lionstar designs against original with anti-rust formulation at 17% reduced VOC

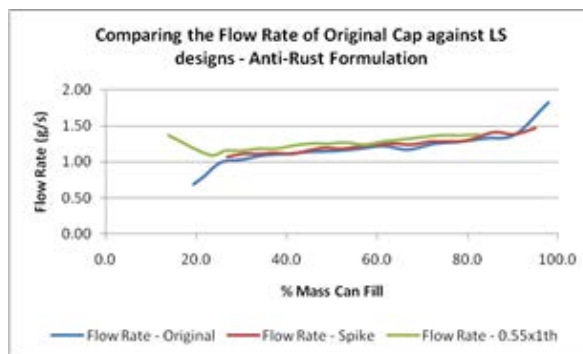


**Fig 10** Graph showing flow rate of Lionstar designs against original with anti-rust formulation at 17% reduced VOC

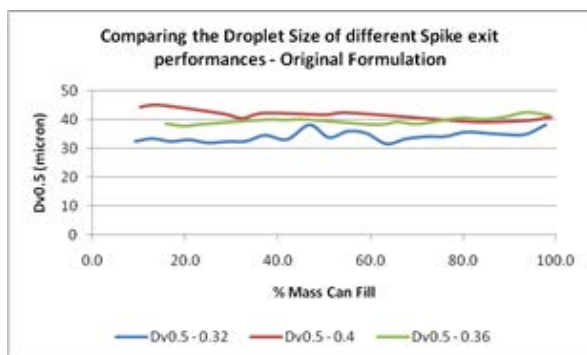


**Fig 11** Graph comparing the droplet size of different spike exits with original formulation at 17% reduced VOC

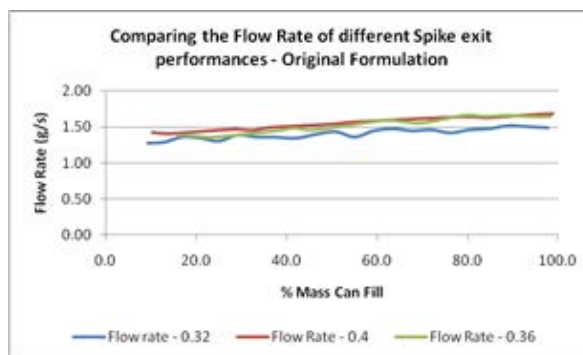


**Fig 12** Graph comparing the flow rate of different spike exits with original formulation at 17% reduced VOC

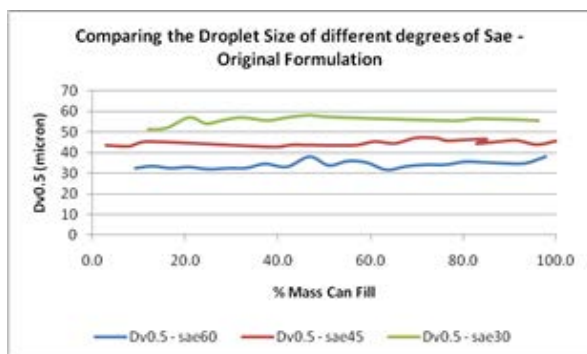


**Fig 13** Graph comparing droplet sizes of different degrees of Sae with original formulation at 17% reduced VOC

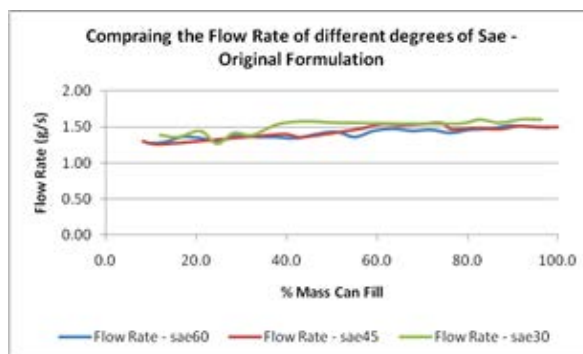


**Fig 14** Graph comparing flow rate of different degrees of Sae with original formulation at 17% reduced VOC

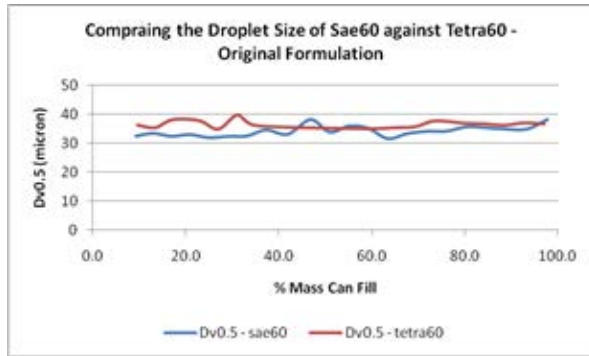


**Fig 15** Graph showing droplet size of Sae60 against Tetra60 with original formulation at 17% reduced VOC

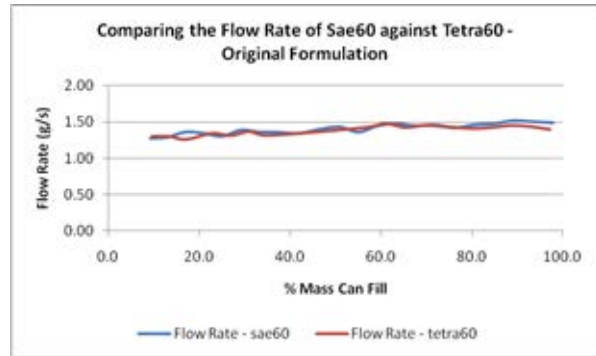


**Fig 16** Graph showing droplet size of Sae60 against Tetra60 with original formulation at 17% reduced VOC

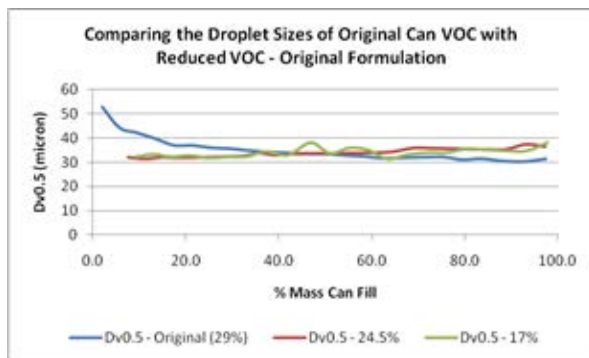


**Fig 17** Graph showing the droplet size of original can VOC against Reduced VOC with original formulation at 17% reduced VOC

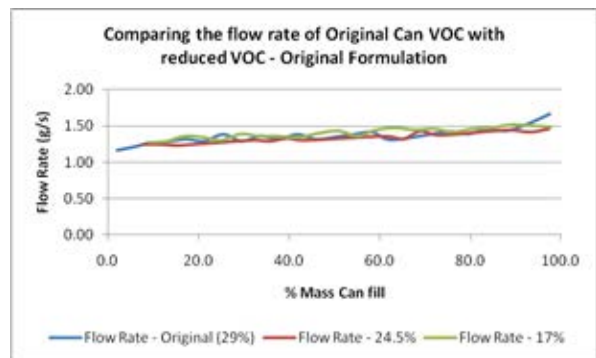


**Fig 18** Graph showing the flow rate of original can VOC against Reduced VOC with original formulation at 17% reduced VOC



**Fig 19** Showing a typical air freshener spray of the initial Spike design

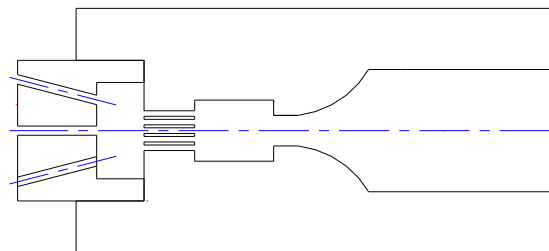
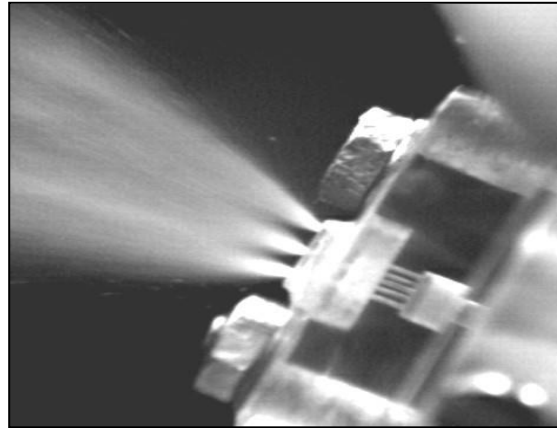


**Fig 20** showing the vertical design of an air freshener, an initial Spike design



**Fig 21** Showing air freshener spray of Spike design



### Detail at Exit Holes

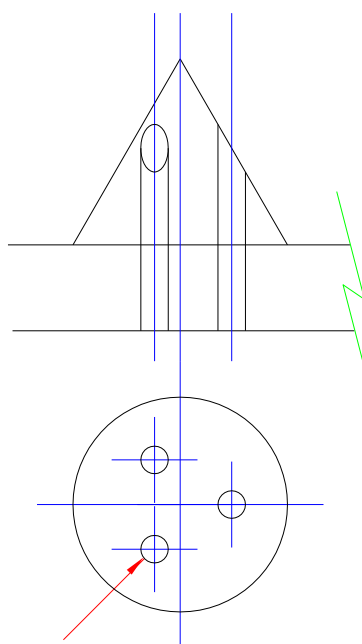


**Fig 22** Showing Spike design

### Conclusions

The series of experiments show that the advanced Spike designs, which consist of the standard Spike design plus two throttles hitting each other at the chamber just before downstream of the exit, performed very well compared to spike design as well as original market cap designs, with concentrated anti-rust formulation. The standard Spike designs also shows much better performance and improvement of drop sizes when comparing to original market cap design, at different reduced VOC. Under all circumstances, such as reduced VOC levels and different formulations, Spike advanced performed much better, yielding smaller droplet sizes as well as maintaining flow rate, compared to other spike design and original market cap. It has also been shown that the  $\theta$  degree of 60 was the best performing amongst the other  $\theta$  angles. The three 0.32 exits performed better than the 0.36 and 0.4 exits, producing smaller droplet sizes, despite the three 0.4 exits showing larger flow rates.

The Spike designs demonstrated its simplicity, low manufacturing costs and superior performances. This Spike design might be able to be used for different applications and products, although more experiments needed to prove this.

### References

- [1] G. Eales and K. Laidler, "A nozzle and a dispenser having such a nozzle, UK patent publication No. WO 2007/017626" world intellectual Property Organisation Application No. PCT/GB2006/002811
- [2] K. Laidler, R. A. Sharief, H. Abduljailil, "Shaped Chamber, Nozzle arrangement, UK patent Publication No. WO2005005053 (A1)" World Intellectual Property organization application No. WO2004GB02848 20040702 (2005-01-20)

## Effects of acoustic radiation on air-assisted jets in a transverse high-frequency acoustic field

F. Baillot<sup>1</sup>, J.B. Blaisot<sup>1</sup>, C. Richard<sup>2</sup> and M. Théron<sup>3</sup>

1: CORIA, UMR 6614, CNRS Université et INSA de Rouen, BP 12, 76801 Saint Etienne du Rouvray, France

2: LMRS, UMR 6085 CNRS-Université de Rouen, BP 12, 76801 Saint Etienne du Rouvray, France

3: CNES Launchers Directorate 52 rue Jacques Hillairet 75612 PARIS Cedex France

### Abstract

High-frequency ( $\geq 1000\text{Hz}$ ) acoustic instabilities have been proven to be extremely harmful to the operation of rocket engines. Indeed, a constructive coupling between heat release rate fluctuations and pressure oscillations associated with the acoustic transverse modes of the combustion chamber may occur. Atomization of the liquid oxidizer is able to drive instabilities which could yield modulations of the instantaneous heat release rate. In this work, influences of a transverse high-frequency acoustic field (1000 Hz) on the atomization of air-assisted jets were investigated experimentally for a wide range of aerodynamic regimes ( $0 \leq We \leq 3300$ ,  $0 \leq Re_l \leq 6000$ ). Jets are placed in a semi-open resonant cavity. Numerical simulations, confirmed by a couple of experimental data, were performed to characterize the acoustic field in the cavity. The acoustic field can be modeled at the main order as a planar standing wave corresponding to the 2nd transverse mode of the cavity. Extremely high acoustic pressure levels ( $\approx 168\text{ dB}$ ) were applied. Direct imaging, including still images but also high-speed video capture (up to 10 kHz), was applied to visualize responses of jets positioned at various specific locations in the acoustic field. Depending on the location of the air-assisted jet in the cavity, the liquid jet can be flattened into a liquid sheet normal to the acoustic axis, or flatten and deviated or not modified at all. The high acoustic level of acoustics is a key parameter to induce physics responsible of the perturbations on the liquid systems. It is shown how non-linear acoustic effects control liquid jet behavior, and how flattening and deviation are related to the action of the radiation pressure and of the resulting force calculated over the liquid-gas interface.

### Introduction

Rocket-engine efficiency strictly depends on their ability to sustain mechanical stress induced by combustion instabilities that can occur in the combustion chamber [1]. High-Frequency thermo-acoustic instabilities are among the most harmful instabilities that can be amplified by coupling acoustic pressure and combustion heat release rate fluctuations, inducing heat transfer fluctuations at the walls. The mechanisms leading to the modulation of the local instantaneous rate of heat release are not yet well understood. Many physical or chemical processes can be responsible of its appearance; here focus is placed on the interaction between acoustics and atomization. Indeed, during transitional regimes of rocket-engines, liquid jets of reactant still remain as well as liquid droplets resulting from their atomization. The dynamics of these liquid jets can be controlled by transverse acoustic modes of the chamber and non-linear effects induced by the very high pressure fluctuations. Unusual responses of the liquid system to these non-linear effects can affect the coupling with the acoustic modes of the chamber, even by a rearrangement between azimuth and longitudinal modes.

In the literature, a few works focused on responses of a free round jet to a transverse acoustic field (ultrasonic and high-frequency waves), and even fewer on those of a coaxial jet (high-frequency waves). Buffum & Williams [2] studied how a transverse acoustic field with an acoustic level greater than 140 dB influenced a non-assisted turbulent liquid jet placed at a pressure node. They found that the jet was displaced in the direction of the transverse acoustic field at the forcing frequency. The amplitude of the displacement increased with the acoustic level and was approximately 10 times greater than what would be predicted when using the steady-flow drag coefficient for a solid cylinder. This phenomenon was interpreted as caused by a drag enhancement resulting from the non-quasi-steady gas flow around the jet. Above 160 dB, the jet began to be atomized at twice the acoustic frequency. Hoover et al. [3] observed a jet flattened like a sheet under the action of high-frequency acoustic perturbations, if the acoustic level was high enough. The flattening occurred perpendicular to the acoustic direction. These authors suggested that the flattening arose from a velocity coupling mechanism similar to the deformation induced by the impact of two opposite transverse steady gas flows on a round jet. However, the range of the Weber number of the supposed mechanism greatly differed from that of their experiments. So, even though the authors found similar tendencies, the results suggested that the physical mechanism involved in the flattening of the jet was actually different in the two experiments. A similar flattening is noted in results reported by Chehroudi & Talley [4] for a free liquid jet of nitrogen introduced into a chamber at room temperature under sub- or supercritical pressures (see also [5]). Even though no physical explanations were given, the authors mentioned that the impact of the acoustic waves on the jet structure was strong at subcritical pressures, strongest at near-critical pressures and weakest at supercritical pressures. To complete this study at a high-pressure, Davis & Chehroudi [6] extended it to a shear coaxial jet still constituted of a central liquid jet of

nitrogen, with the addition of an annular gaseous nitrogen co-flow. But no flattening phenomenon was observed by the authors.

A previous work [7] showed that different non-linear effects occurred on an air-assisted jet positioned either at a pressure anti-node or velocity anti-node in a standing acoustic field. The action of the acoustic field appeared as a consequence of nonlinear acoustic effects, involving the local radiation pressure distribution and/or the resulting radiation pressure force. At a pressure anti-node, the main effect of acoustics on the air-assisted jet was to modulate the longitudinal gaseous flow velocity at the same frequency than the forcing and no modification of the atomization regimes was observed. At a velocity anti-node, when acoustic pressure level exceeded a certain threshold, the liquid jet was submitted to large-scale shape modifications that drastically modified the atomization regime. Indeed, in such a case, the initial cylindrical shape turned into a flattened shape, resulting in the formation of a liquid sheet that further disintegrate not only under the action of usual liquid sheet breakup processes, but also under the action of Faraday instabilities induced by the acoustic field. The change of shape was attributed to a non-uniform distribution of the radiation pressure around the liquid jet. It was also shown that the higher the Weber number of the air-assisted jet, the higher the acoustic pressure level threshold was needed.

In the present study, the effect of the acoustic field is investigated for a single jet placed at various positions in the field and also for three jets the responses of which are studied simultaneously as they are placed at several locations in the acoustic field. Droplet clustering induced by acoustics is thus demonstrated.

### Experimental test-rig

The experimental test rig is composed of an acoustic resonant cavity within which liquid is injected. The cavity (see Figure 1) consists of two parallel and vertical steel plates and PVC roof and floor. The two vertical plates have a thickness of 2 cm that promotes acoustic reflections and are 360 mm apart in order to optimize the acoustic field at the frequency  $f=1000$  Hz. A pair of compression drivers Beyma CP850Nd are placed on each vertical plate, at a distance of 70 mm from the floor, and are as close to each other as possible (i.e. 165 mm between compression driver axes) as shown in figure 1.b. Acoustic pressure level up to 170 dB is reached with this configuration. The acoustic field is measured by Brüel & Kjaer microphones (model 4944) able to hold sound pressure level up to 182 dB. The cavity is placed in acoustically isolated room to prevent noise inconvenience for the surrounding.

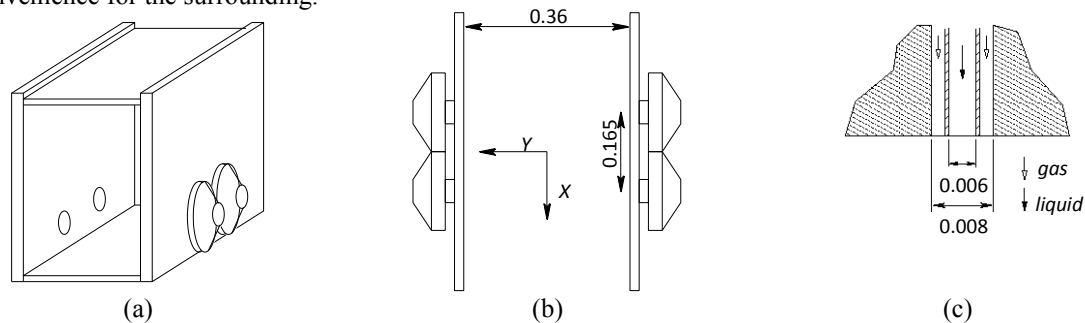


**Figure 1.** Experimental test-rig: a – 3D sketch of the acoustic cavity, b – upper-side view of the cavity, c –Injector nozzle geometry. Dimensions are in meters.

The liquid used is water, and the gas flowing around the liquid jet is air. The experiments are performed at atmospheric pressure. Injectors are mounted such that their exit plane coincides with the inner surface of the roof. The diameter of the central orifice for the liquid flow is  $D_l = 6$  mm and the external diameter for the gas flow is  $D_g = 8$  mm (cf. Fig. 1.c). Up to three injectors can be run simultaneously. For each injector, the maximum flow rates are 100 L/h and 5 g/s for liquid and gas respectively.

Still image visualizations have been performed with a high resolution CCD camera (MatrixVision mvBlue COUGAR-X 125a, 2448x2050 pixels) associated to an objective of focal length  $f=75$ mm, yielding a field of view of 65 x 55 mm. A stroboscope light source (EG&G MVS 2600, flash duration = 10  $\mu$ s) is used with this camera. High-speed visualizations were also performed with a Vision Research Phantom V12 camera associated to an objective of focal length  $f=105$ mm, giving a maximum field of view of 180 x 110 mm. The exposure is controlled by the electronic shutter of the high speed camera that can be as low as 0.3  $\mu$ s. A white continuous light source (Lot-Oriel LSB530, 300W) is used in this case.

### Characterization of the acoustic field

Compression drivers generate progressive acoustic waves, which, under controlled conditions of resonance of the acoustic cavity, lead to the formation of a stationary wave. Numerical simulations of the acoustic response of the cavity were performed with COMSOL Multiphysics commercial software. These simulations were used

to optimize the configuration of the acoustic cavity and the driver placement. The maximal efficiency was obtained numerically for a cavity with a roof and a floor, and 2 x 2 drivers placed near the floor. This was confirmed experimentally. Indeed, in a configuration with 2 x 2 drivers placed near the top of the cavity, without floor, the maximum amplitude peak of the acoustic pressure  $P_{max}$ , measured experimentally was about 5600 Pa ( $\approx 168$ dB). In the configuration with a floor and 2 x2 drivers placed near the bottom of the cavity, the level reached 170 dB and over. Figure 2 shows the numerical acoustic field in the cavity. Particular planes of interest are identified in this stationary acoustic field. They are noted by a black dash line for pressure anti-nodes ( $P_{an}$ ), red dot lines for velocity anti-nodes ( $V_{an}$ ) (or pressure nodes), and white lines for acoustic flux anti-nodes ( $F_{an}$ ). Acoustic flux is defined as the product of pressure and velocity fluctuations  $u'p'$ .

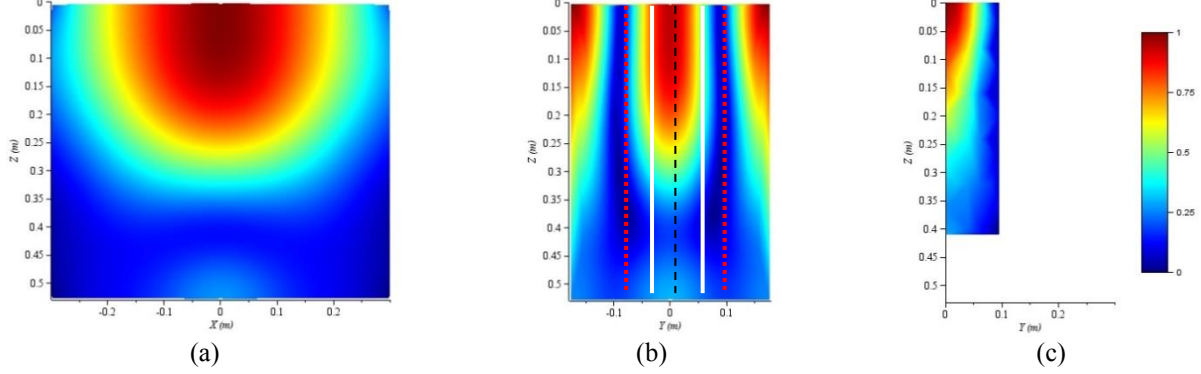


**Figure 2.** Acoustic pressure fields: a, b – numerical simulations, c experimental measurements. Pressure amplitude values are normalized by  $P_{max}$ .

### Jet atomization without acoustics

The gas and liquid flow rates accessible with the experimental setup allow covering air-assisted atomization regimes including Rayleigh, shear, membrane, membrane/fiber and fiber regimes, as identified by Lasheras & Hopfinger [9]. Illustrations of the atomization regimes without acoustics are presented in figures 3 and 5 below.

### Jet atomization regimes with acoustics

Under the action of an intense acoustic field, the atomization of the liquid jet can be deeply modified. The more dramatic changes were observed for jets placed in an acoustic velocity or flux anti-nodes. Morphological transformations of a coaxial jet placed at a velocity anti-node are shown in figure 3. Under these conditions, the cylindrical jet is flattened into a liquid sheet along a plane perpendicular to the acoustic axis. The flattening of the jet results in an apparent thinning on lateral views (see lower row of figure 3). As soon as the liquid sheet is formed, it disintegrates under the action of Faraday's instabilities induced by acoustics on the two plane liquid interfaces. An example of oblique view of this phenomenon is shown in figure 4.

The flattening of the jet is ascribed to the action of non-linear effects of the acoustic field on the liquid-gas interface. This phenomenon results from the action of the acoustic radiation pressure  $P_{rad}$  defined by the difference between the time-averaged volumetric potential and kinetic acoustic energies [10] :

$$P_{rad} = \frac{1}{2\rho_g c^2} \langle p'^2 \rangle - \frac{\rho_g}{2} \langle \vec{u}' \cdot \vec{u}' \rangle.$$

In the presence of an object, the radiation pressure results from the stationary incident field and the acoustic field scattered by this object. The radiation pressure around the jet has been estimated. This computation is based on the analyses of the results concerning the action of the radiation pressure on a rigid sphere by King [11] and on a rigid cylinder by Wu et al. [12]. Radiation pressure is proportional to  $P_{max}^2$ . At a pressure anti-node, the spatial distribution of  $P_{rad}$  is constant and acts as a pressurizing environment ( $P_{rad} > 0$ ). At a velocity anti-node, the distribution is non-uniform and essentially associated to traction effects ( $P_{rad} < 0$ ). The minimum negative value happens in the plane ( $\pi$ ) perpendicular to the acoustic axis. For a non-uniform radiation pressure distribution around the jet, the Laplace's law implies a modification of the local radius of curvature of the interface. The liquid jet is thus deformed, resulting in a stretching in the plane ( $\pi$ ). The flattening phenomenon is first observable at a velocity anti-node where the radiation pressure presents the stronger minimum value. For a jet placed between a velocity anti-node and a pressure anti-node, the non-uniform radiation pressure is still present, but an increase of  $P_{max}$  is needed in order to make the flattening phenomenon occur. This increase has to be greater as the jet location goes closer to the pressure anti-node. At this very position, the phenomenon is in fact no more observable due to the uniform distribution of  $P_{rad}$ .

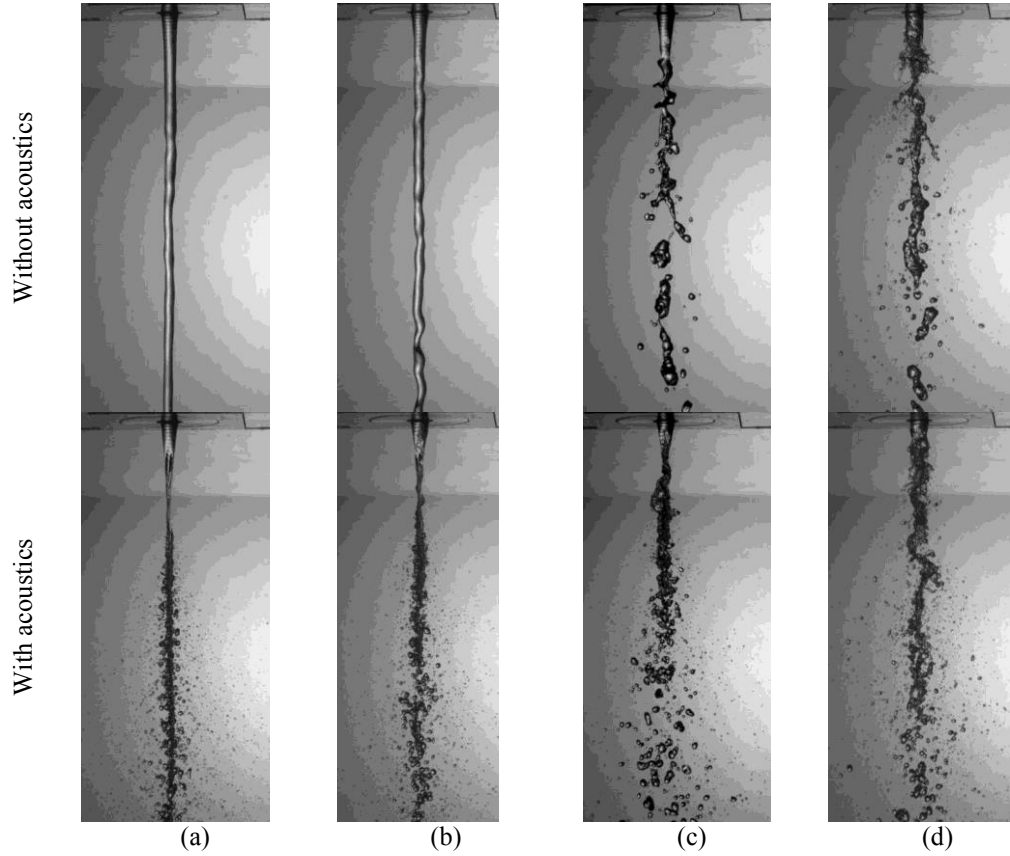


**Figure 3.** Effect of a transverse acoustic field at a velocity anti-node for different atomization regimes:  
 -a- Rayleigh; -b- Shear; -c- Shear Membrane; -d- Membrane.  
 Maximum acoustic pressure level  $P_{max}$  is about 159 dB for these illustrations.

A deviation of the liquid system is also observed for a jet placed in an acoustic flux anti-node, as can be seen in figure 5. This effect is still interpreted as the result of the non-uniform distribution of radiation pressure around the liquid jet. At a pressure anti-node or at a velocity antinode, pressure radiation distribution is symmetrical in a plane perpendicular to the jet axis, around a center point coincident with the center of the jet. Between these two locations, radiation pressure is no more symmetrical, resulting in a non-null net force designated hereafter as the radiation force.

For a perfect reflecting object, the resulting radiation force  $\vec{F}_{rad}$  is expressed by:

$$\vec{F}_{rad} = \iint_{surface} -p_{rad} \vec{n} dS$$

where  $\vec{n}$  is the unit vector positively outside the surface.

For a rigid cylinder Wu et al. [12] obtained  $F_{rad} = \frac{(3-\eta)p_{RMS}^2 \pi k R^2 \sin(2k\delta)}{2(1+\eta)c^2 \rho_g}$  in the case  $\kappa = kR \ll 1$ .

As mentioned above,  $F_{rad}$  is maximum in an acoustic flux anti-node and null at pressure and velocity anti-nodes. In the present application, as  $\eta < 3$ ,  $F_{rad}$  is oriented from a pressure anti-node towards the velocity anti-nodes. The effect of this force is noticeable when it is of the order of magnitude of the weight and the inertia of liquid elements on which it is acting. Moreover, this effect is drastically reduced in the presence of a coaxial gaseous jet surrounding the liquid jet, as soon as the initial gaseous jet impulse  $\rho_g u_g^2$  is high enough to become the dominant effect on the liquid interface deformation through Kelvin Helmholtz instabilities.

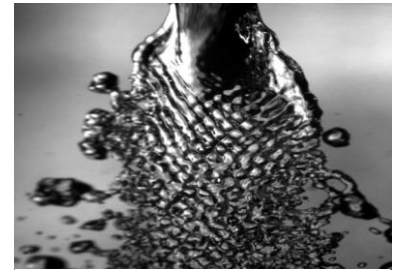


**Figure 4.** Faraday instability on a liquid jet in a transverse acoustic field at a velocity anti-node

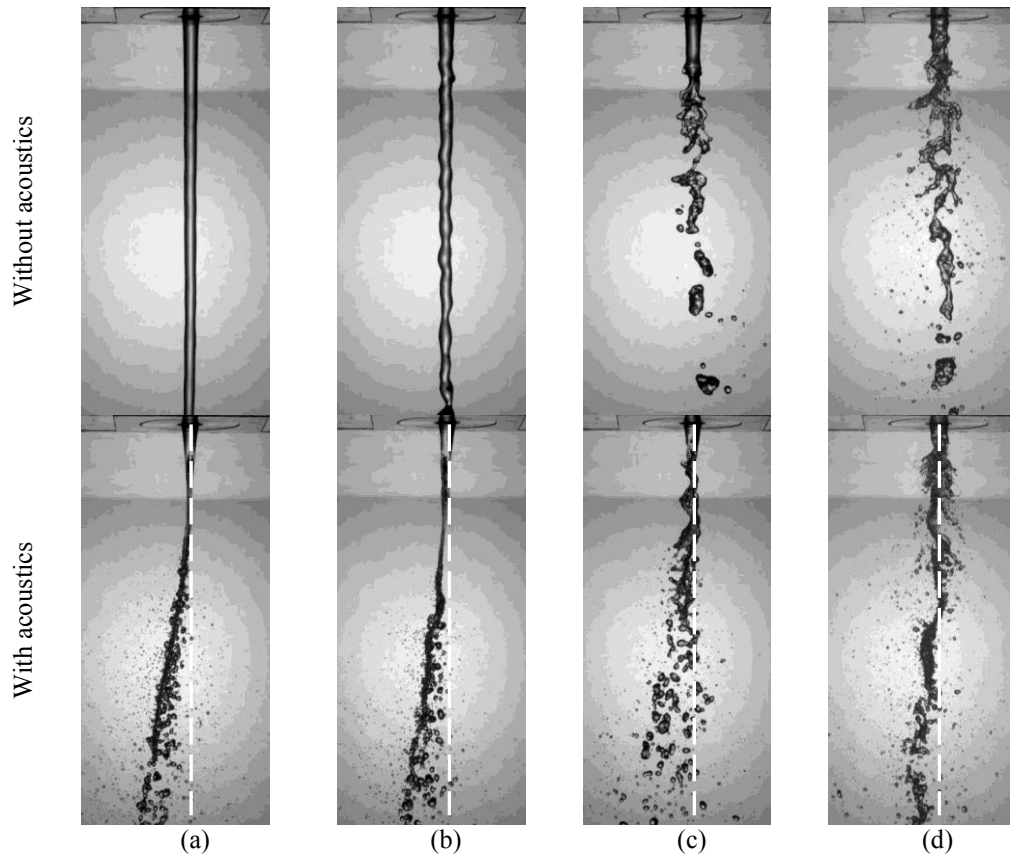


**Figure 5.** Effect of a transverse acoustic field at an acoustic flux anti-node for different atomization regimes:  
-a- Rayleigh; -b- Shear; -c- Shear Membrane; -d- Membrane ( $P_{max} = 161$  dB).

The previous results have been obtained with a single injector. The study has been extended by putting three injectors on the roof of the cavity. Visualizations of two configurations studied here illustrate phenomena observed in figure 6 for the setting-up ( $V_{an} F_{an} P_{an}$ ) and in figure 7 for the setting-up ( $F_{an} P_{an} F_{an}$ ). When several injections take place simultaneously in the acoustic cavity, a drop clustering effect occurs. This effect is consecutive to the atomization of the liquid jet generated by the acoustic field, added to the atomization by the air annular jet. We can note on the figure 6 an accumulation of material in the plane of the velocity anti-node and a desertification in the plane of the pressure anti-node. This phenomenon is accompanied by a large tilting of the fluid system in the neighborhood of the intensity anti-node, which contrasts with the overall vertical displacement of material along vertical descending lines at velocity and pressure anti-nodes (see figures 6 and 7).

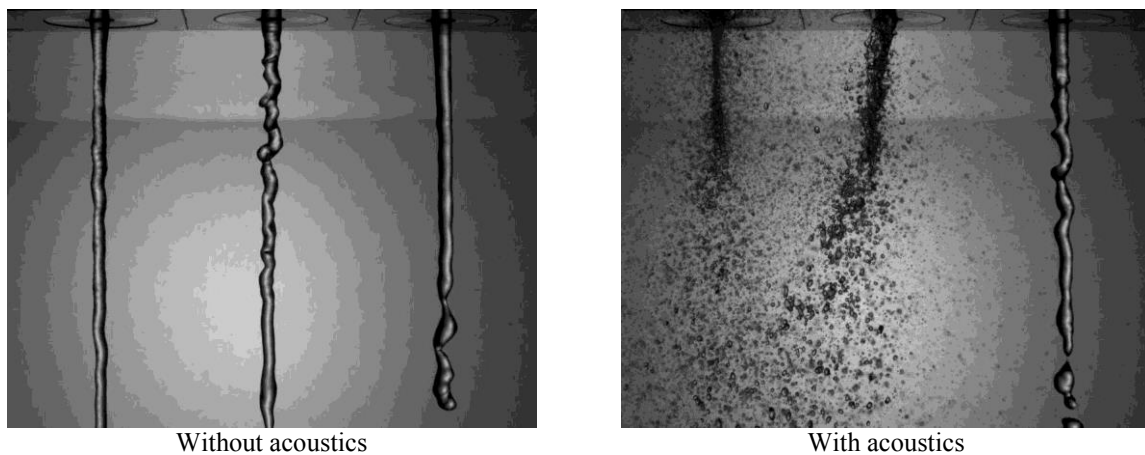


**Figure 6.** Effect of a transverse acoustic field on three jets placed at a velocity anti-node (left), an acoustic flux anti-node (middle) and a pressure anti-node (right). Atomization regime is shear breakup. Maximum acoustic pressure level  $p_{max}$  is 164 dB for these illustrations.

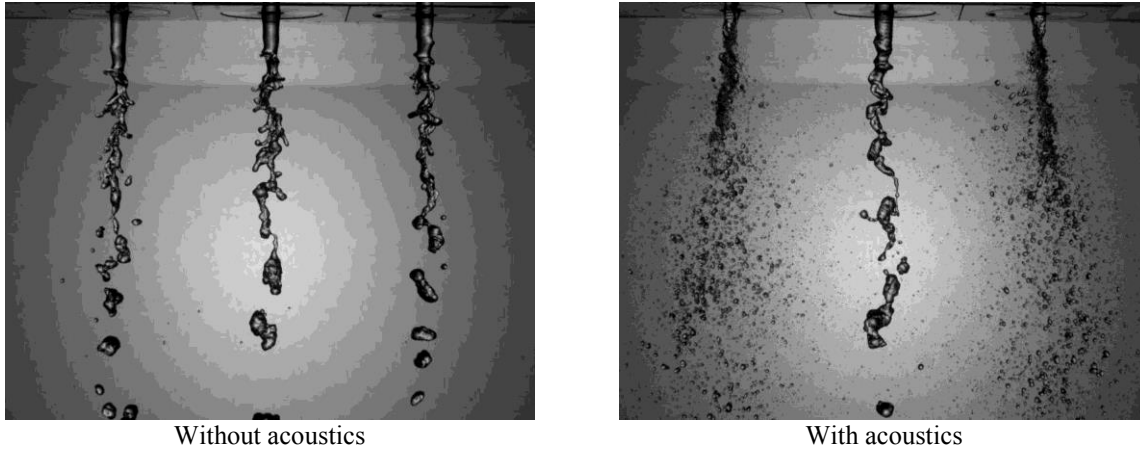


**Figure 7.** Effect of a transverse acoustic field on three jets placed at an acoustic flux anti-node (left and right) and at a pressure anti-node (middle). Atomization regime is shear-membrane.  
Maximum acoustic pressure level  $p_{max}$  is around 161.4 dB for these illustrations.

## Conclusions

The action of a transverse acoustic field on the flow emanating from an air-assisted atomizer has been studied. It was shown that nonlinear acoustic effects modify the behavior of the liquid jet. The more dramatic changes were observed for jets placed in acoustic velocity or flux anti-nodes. The jet placed at a velocity anti-node is flattened and the liquid sheet formed disintegrates under the action of Faraday instabilities. A jet placed at a flux anti-node is flattened and deviated towards the nearest velocity anti-node. These observations show a spatial redistribution of drops under the action of the acoustics.

In the presence of combustion, these effects can produce:

- a longitudinal modulation of the mass-flow rate of the annular jet, generated by the transverse acoustic wave, and a not much perturbed behavior of the liquid jet in the neighborhood of pressure anti-nodes. This can lead to the shedding of periodic vortices of gas, able to generate modulations of the heat release rate liable to feed a thermo-acoustic loop.
- a spatial non-homogeneity of the heat release inside the combustion chamber, and a wall distribution of the thermal flux showing alternate successions of hot spots.

## Acknowledgements

This study was granted by CNES under the program REST.

## Nomenclature

### Non-dimensional numbers

$Re_l = \frac{\rho_l u_l D}{\mu}$  : liquid Reynolds number

$We = \frac{\rho_g u_l^2 D}{\sigma}$  : gaseous Weber number

### Greek symbols

$\delta$  : distance between the axis of the jet and pressure anti-node

$\rho_g$  : gaseous density

$\rho_l$  : liquid density

$\kappa$  : non-dimensional acoustic wave number

$\sigma$  : surface tension

$\mu_l$  : liquid viscosity

$\eta = \rho_g / \rho_l$  : density ratio

### Roman letters

$c$  : speed of sound

$f$  : acoustic excitation frequency

$F_{rad}$  : radiation pressure force

$k$  : acoustic wave number

$P_{max}$  : maximum amplitude of the pressure fluctuation

$P_{rad}$  : radiation pressure

$P_{rms}$  : RMS pressure

$p'(x, y, z, t)$  : local pressure fluctuation

$R$  : radius of the jet

$SPL$  : sound pressure level

$u'(x, y, z, t)$  : local velocity fluctuation



## References

- [1] V. Yang, W. Anderson, Liquid rocket engine combustion instability, *Progress in Astronautics and Aeronautics*, **169**, (AIAA, Washington, DC, 1995).
- [2] G. Buffum, F. A. Williams, Response of Turbulent Jets to Transverse Acoustic Fields. In *Proceedings of the 1967 Heat Transfer and Fluid Mechanics Institute* (ed. P. A. Libby, D. B. Olfe & C. W. Van Atta), pp. 247–276. Stanford University Press, Stanford, CA. 1967.
- [3] D. V. Hoover, H. M. Ryan, S. Pal, C. L. Merkie, H. R. Jacobs, R. J. Santoro, Pressure oscillations effects on the jet breakup. *Heat Mass Transfer Spray Syst.*, **187**, 27–36 (1991).
- [4] B. Chehroudi, D. Tailley, Preliminary visualizations of acoustic waves interacting with subcritical and supercritical cryogenic jets. In *15th Annual Conference on Liquid Atomization and Spray Systems (ILASS Americas)*, Madison, WI. 2002.
- [5] M. Oswald, J. J. Smith, R. Branam, J. Hussong, A. Schik, B. Chehroudi, D. Talley, Injection of fluids into supercritical environments. *Combust. Sci. Technol.*, **178**, 49-100 (2006).
- [6] D. Davis, B. Chehroudi, Shear-coaxial jets from a rocket-like injector in a transverse acoustic field at high pressures. In *44th AIAA Aerospace Sciences Meeting*, Reno, NV. 2006.
- [7] Baillet, J.B. Blaisot, G. Boisdron, C. Dumouchel, Behaviour of an air-assisted jet submitted to a transverse high frequency acoustic field. *J. Fluid Mech.*, **640**, 307-344 (2009).
- [8] Boisdron, Etude de l'atomisation d'un jet liquide assisté par air soumis à une onde acoustique stationnaire transverse haute fréquence, thesis, University of Rouen (2006).
- [9] J.C. Lasheras, E.J. Hopfinger, Liquid jet instability and atomisation in a coaxial gas stream. *Annu. Rev. Fluid Mech.*, **32**, 275–308 (2000).
- [10] L. Landau, E. Lifchitz, *Mécanique des Fluides*. (Ed. MIR, 1989).
- [11] L.V. King, On the acoustic radiation pressure on spheres. *Proc. R. Soc. Lond. A*, **147** (861), 212–240 (1934).
- [12] Wu J. Du G. Work S. Warshaw S. Acoustic radiation pressure on a rigid cylinder : an analytical theory and experiments. *J. Acoust. Soc. Am.*, **87**, 581-586 (1990)

## Use of ultrasonic atomizers in screening experiments of herbicides

J. Domnick<sup>1</sup>, A. Scheibe<sup>1</sup> and Q. Ye<sup>2</sup>

<sup>1</sup>University of Applied Sciences Esslingen, Germany

<sup>2</sup> Fraunhofer Institute for Manufacturing Engineering and Automation, Stuttgart, Germany

### Abstract

Commercially available ultrasonic atomizers have been tested for screening experiments of herbicides applied to different seedlings. As major characteristics, spray cone angle and mass flux distribution of the herbicide droplets have been investigated. Two different modes, i. e. a permanent moving mode of the atomizer across each row, and a stop-and-go mode with the atomizer stopping above each seedling have been considered. It was found, that the original design of the ultrasonic atomizers under optimum parameter settings is able to deliver the required fine spray with the possibility to vary the cone angles in a wide range. However, the low axial momentum of the spray results in a high sensitivity to any changes in the surrounding air flow field, leading to insufficient mass distributions and waste of material. Consequently, numerical simulations have been performed to optimize the auxiliary airflow applied to the ultrasonic atomizers with respect to mass and momentum distribution. First results indicate that it will be very difficult to achieve an appropriate compromise between spray cone stability and maximum air momentum, which is, of course limited by the brittleness and sensitivity of the seedlings. In addition, the different seedling geometries, which, by the way, change over time, are very difficult to handle.

### Introduction

The commercial launch of new herbicides requires an intensive and long phase of screening experiments. In case of active agents, which are absorbed by the leaf surfaces, small seedlings of different species have to be exposed to a well-defined, reproducible spray of the aqueous herbicide solution. Usually, the seedlings are regularly arranged in parallel rows with a typical distance of 10 cm (see Fig. 1). The herbicides are sprayed according to a given schedule and the long-term growth and performance of the plants is monitored. In the standard spaying procedure, a single atomizer with a large spray cone angle is used, resulting in a significant non-uniform agent distribution across the target and significant losses of herbicide material that is not reaching the seedlings.

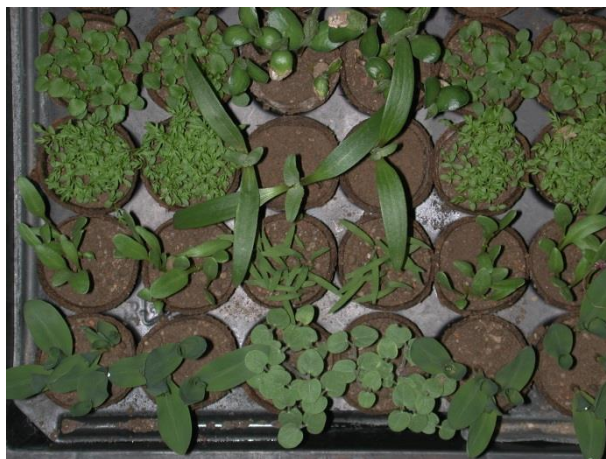


**Figure 1:** Regular arrangement of the different seedlings for herbicide screening tests

In a sophisticated concept, small atomizers with limited spray cone extension should allow a more individual spraying of single seedlings, despite their individual shape and length. More precisely, appropriate atomizers that could be adapted for this application should deliver the required characteristics, i.e.

- An almost constant local liquid flux inside the spray to achieve a corresponding constant agent loading on the leaf surfaces
- A well-defined spray cone angle to avoid uncontrolled agent exposure of neighborhood seedlings
- A high transfer efficiency
- Only moderate air and droplet momentum to avoid mechanical degradation of the seedling, but the

same time achieving a certain penetration depth of the droplets in the region of the leafs  
For this purpose, different ultrasonic atomizers have been experimentally investigated, including their general spray characteristics as well as the impact of the growth performance of the seedling.

### Experimental test-rig and instrumentation

In this contribution, the results of different commercially available ultrasonic atomizers are reported that should allow an individual spraying of single seedlings. Two different operation modes were tested, i. e. a permanent moving mode of the atomizer across each row, and a stop-and-go mode with the atomizer stopping above each seedling for some seconds.

To ensure well-defined environmental conditions, a specific flow chamber has been designed and built, including a controlled vertical airflow in downward direction with filtered inlet. In addition, the chamber prevented uncontrolled emission of herbicide-laden air. Furthermore, removal of overspray droplets was realized applying suction air through a perforated plate underneath the individual seedling trays. The atomizer was mounted on a controlled 3-dimensional linear traversing system. The whole test rig is shown in Fig. 2.



**Figure 2:** Flow chamber with control system (left) and traversing system above the seedling trays (right)

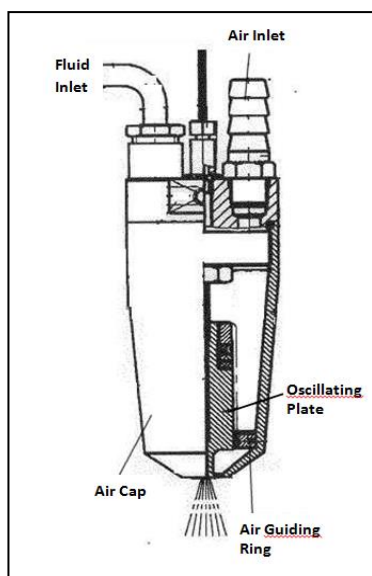


**Figure 3:** Lechler US 1 ultrasonic atomizer

Different commercially available ultrasonic atomizers have been tested, producing very similar results. In Fig. 3, a Lechler US1 atomizer is shown consisting of typical design elements. The central oscillating plate is surrounded by an air chamber forming an annular ring with air guiding elements around the plate. Airflow rate and geometry of the guiding elements and the annular exit are arranged to produce specified characteristics of the spray cone, e. g. spray cone angle. As delivered by the manufacturer, the air-guiding ring consists of regularly spaced grooves with either 30° or 60° inclination to achieve a swirling component of the outlet airflow and consequently a better dispersion of the spray flow. However, additional geometries without swirling have also been tested.

The driving frequency of the oscillator was set constant at 100 KHz with a small variation of input power between 6 and 9 W. Best spray cone stability was found at medium power. As typical for ultrasonic atomizers, useful atomization was limited to fluid viscosities below approximately 20 mPas, which was, by far, sufficient for the solutions used throughout the present

investigations [1]. For fluid dosing a syringe pump has been used. The maximum fluid flow rate has been limited to 0,33 ml/min (20 ml/min). In stop and go mode with 1 s cycle time this corresponds to the amount of solution per seedling.

In general, it was found that applying the operation conditions described above atomization was sufficiently stable yielding a very fine spray as known for ultrasonic atomizers. Therefore, the experimental investigations focus mainly on qualitative properties of the application, such as spray cone angle, spray cone stability, local liquid mass fluxes and transfer efficiencies (amount of solution reaching the target).

## Experimental Results

In preliminary investigations, the operating conditions of the ultrasonic atomizer have been optimized, mainly with respect to the temporal stability of the spray cone. As a first result, the input power was kept constant at 7,5 W. Secondly, the influence of the fluid flow rate had to be considered. In Fig. 4, the relation between fluid flow rate and spray stability is shown.

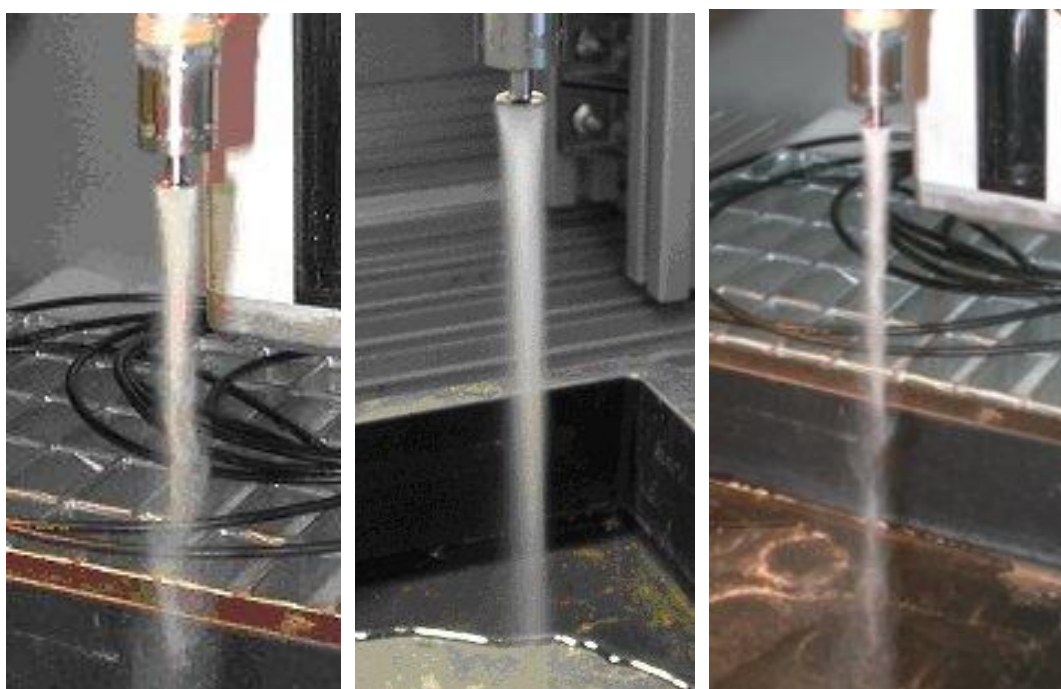


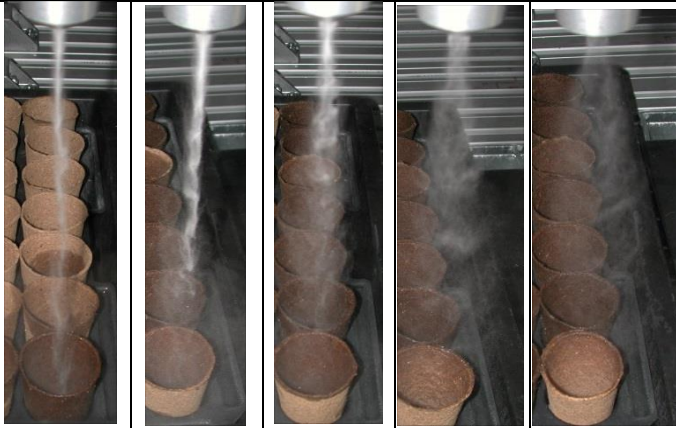
**Figure 4:** Spray cone at 0,17 ml/s (left), 0,23 ml/s (centre) and 0,33 ml/min (right) without air cap

Obviously, at 0,23 ml/s liquid flow rate the spray cone delivers the best stability with respect to geometry and density almost without any intermittent or fluctuating components. Therefore, this liquid flow rate was kept constant throughout all further experiments, although it is directly connected with the speed of the process, i. e. the required spraying time per seedling.

From geometrical considerations, taking into account spacing and diameter (45 mm) of the seedling trays as well as the maximum height of the seedlings, a spray cone angle of approximately 10° and 150 - 200 mm distances between atomizer and support should be optimum. In Tab. 1, the characteristics of the sprays produced at a flow rate of 0,23 ml/s and a distance of 170 mm at various exit air velocities are compared. These results were achieved by using an air-guiding ring with 12 grooves with an inclination angle of 10°. As most important characteristics, spray cone and angle transfer efficiencies are indicated. As expected, the spray cone angle increases with increasing air exit velocity, reaching a maximum value of 40° at 7 m/s air velocity, which is, by far, too large. The corresponding transfer efficiency decreases to 22 % only, mainly due to liquid droplets propagating outside the tray. At optimum spray cone angles between 10° and 15° (0,8 – 2 m/s air outlet velocity), the transfer efficiencies vary between 60 and 75 %, partly due to geometrical overspray, partly due to a rebound effect of the air. Of course, this test only shows the nominal deposition potential, as the real transfer efficiency depends also on the shape of the seedling. Nevertheless, between 40 and 25 % of the solution is lost in the optimum case already.



Despite these results, it should be emphasized, that the ultrasonic atomizer delivers a very fine spray, almost independently of the airflow rate applied. In other words, atomization quality and spray propagation are well separated. In this way, the mechanical impact of the airflow onto very sensitive seedlings can be minimized also. Furthermore, as the air is not participating in the atomization process, switching on and off the atomizer can be done without significant transient effects. Therefore, almost identical results were obtained in stop and go traverse mode, i. e. applying intermittent spraying. In this case, approximately 0,2-0,3 ml solution was applied to each individual seedling.

<b>Air pressure (mbar)</b>	0	<10	10	20	50
<b>Air exit velocity (m/s)</b>	0	0.8	2	5	7
<b>Spray cone angle (°)</b>	<3	10	15	30	40
<b>Spray cone shape</b>					
<b>Transfer efficiency (%)</b>	86	74	61	43	22

**Table 1:** Spray cone shape and application characteristics at different airflow rates (distance 170 mm)

The results shown above apply to the stop and go mode with stationary atomizer during the spraying period, which is, according to the required solution mass per seedling of 0,2 g, around 1 s. Alternatively, the atomizer can be moved continuously across the seedling while spraying. Clearly, the overall performance of the application process will thereby be reduced, however, there might be technological and maintenance advantages due to a less complex control system. At a given spacing of the seedling trays of approximately 50 mm, estimated traversing speed should be around 100 mm/s. The effect of this speed on the spray cone formation is shown in Fig. 5, together with a comparative photo at 300 mm/s. These photos were taken without auxiliary air, i. e. at smallest spray cone angle. The downdraft airflow inside the chamber was approximately 0,2 m/s.

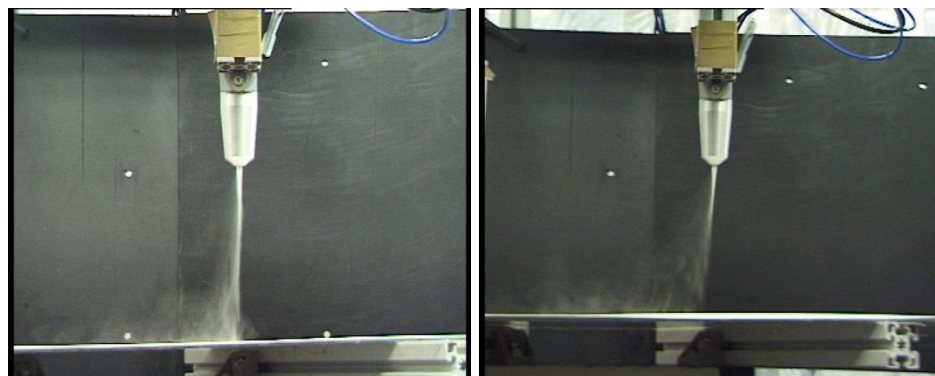


**Figure 5:** Influence of traversing speed on spray cone (left: 100 mm/s, right: 300 mm/s)

The effect of the traversing speed is clearly visible as a deformed spray cone axis and an expanded region of droplets in the wake of the spray. It can be estimated, that at the effects are similar at higher auxiliary airflow

rates with enlarged spray cone angles. Due to the very small droplet diameters and the low initial droplet momentum, the droplets are easily following any superimposed airflow. Hence, it is very difficult to achieve a selective application of solution to specific seedlings or groups of seedlings.



**Figure 6:** Ultrasonic atomizer with HV needle electrodes

In other applications of spray deposition, e.g. painting, it is well known, that the usage of so-called electrostatics may improve transfer efficiencies significantly. Usually, high negative potential is applied to the atomizer, producing both, an appropriate electrical field between atomizer and grounded target as well as negatively charged droplets. In case of conductive liquids, charging must be provided through permanent corona discharge at needle electrodes (external charging) to avoid insulation of the complete liquid feed system. Therefore, a commercially available external charging system normally used for high-speed rotary bell atomizers, consisting of 6 individual needle electrodes, has been adapted to the ultrasonic atomizers, as shown in Fig. 6.

However, first results indicate almost negligible effects on the spray cone formation and more or less unchanged transfer efficiencies. Most likely, the charging of the droplets is too weak due to a significant distance between the spray and the external electrodes. In addition, the atomizer must be properly grounded. Clearly, additional work is necessary to verify any positive influence of electrostatic charging. It should be noted, that applying electrostatic charging to seedlings with different geometries and sizes create additional difficulties due to a corresponding distortion of the electrical field.

### Initial numerical simulations

So far, the liquid mass distributions throughout the spray cones were found to be more or less of Gaussian shape. However, for many seedlings, especially those with larger flat leaves, it would be far better to have a uniform liquid distribution. This is basically related to the uniformity of the agent concentration on the leaves. Based on existing experiences from painting applications with air spray guns, a modified air cap surrounding the ultrasonic atomizer has been constructed. In principle, this air cap consists of a central annular outlet similar to the existing atomizer, but also additional shaping air “horns” to modify the near nozzle velocity field. The air cap geometry is shown in Fig. 7 as 3-D view and as planar cross section.

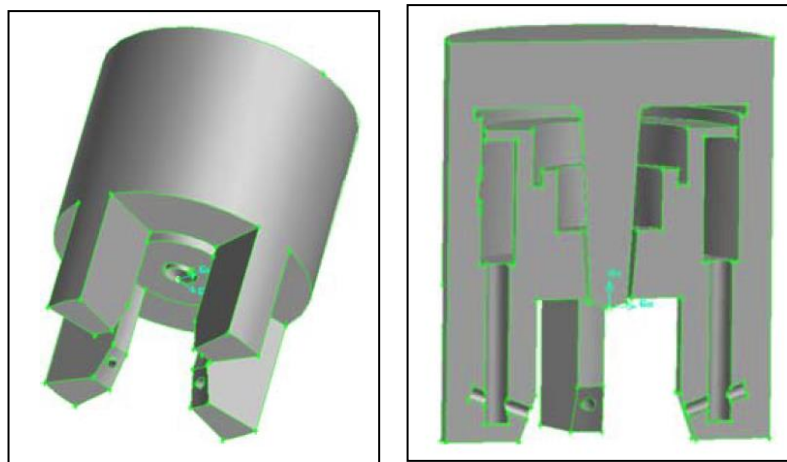


**Figure 7:** Newly designed air Cap

In a first step, single-phase simulations have been performed to investigate the correlation between geometry and airflow rates and the resulting velocity profiles at various distances from the atomizer. The considered 3-D domain, shown in Fig. 8, has a size of 0,4 m x 0,4 m x 0,4 m. The combined structured and unstructured grid with typically 350 000 cells has been appropriately refined in regions inside and near the atomizer region, but also in the region of the wall jet in front of the planar target [2]. The distance between atomizer tip and target

was 200 mm. As inlet conditions, air pressures at the atomizing side and the shaping air side were set individually to deliver specific air outlet velocities. A typical result is shown in Fig. 9.

A final challenge, which has been considered only superficially, so far, is the very different sizes and geometries of the seedlings, as shown in Fig. 1 already. Higher seedlings with long but narrow leaves may be in the same arrangement as smaller but wider ones, which very often expand outside their own tray. As a first step, guiding vanes have been tested that move with the atomizer to erect the seedling leaves and to bring them into the spraying zone. However, leaves lying below may be covered and not receiving enough herbicide solution.

Clearly, the final result of long-term herbicide application should not look like Fig. 10.

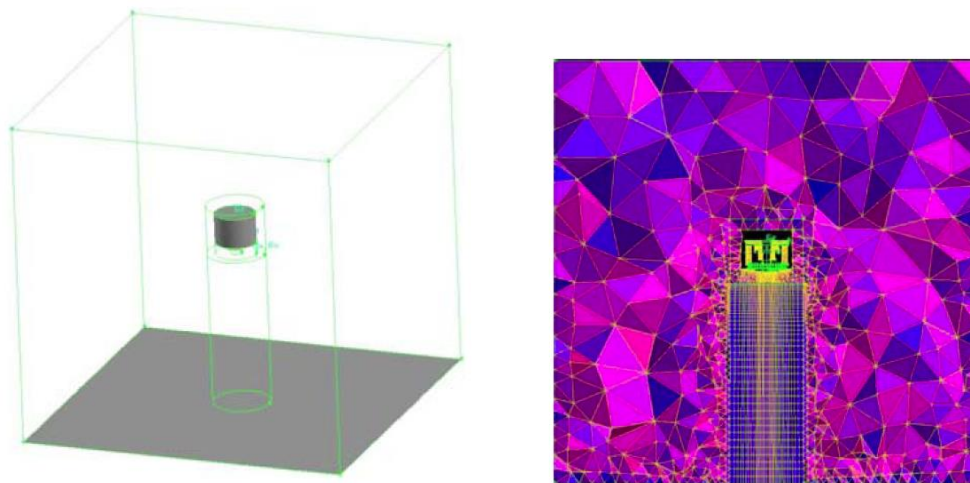


**Figure 8:** Simulation domain and cross section of the applied grid

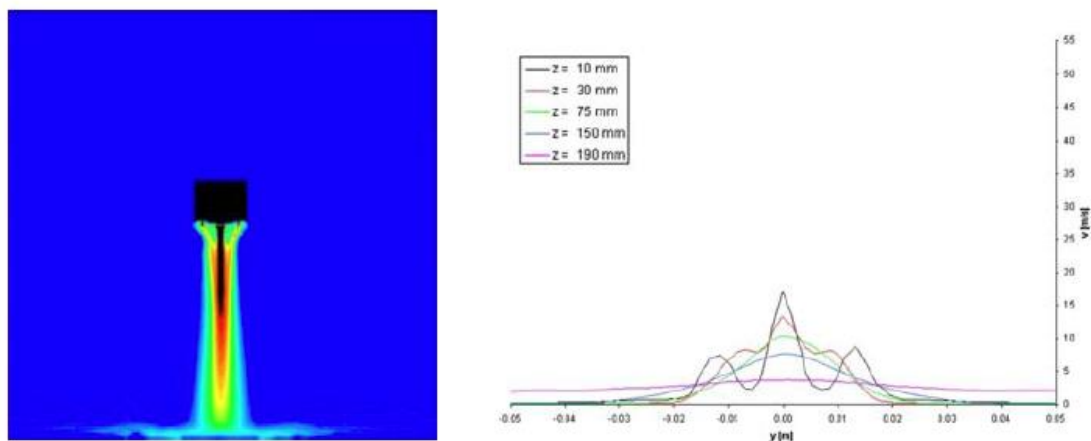


**Figure 9:** Calculated airflow field (left) and velocity profiles at different distances from the atomizer (right)





**Figure 10:** Appearance of seedlings after long-term herbicide application

### Conclusions and Outlook

Under various aspects, the usage of ultrasonic atomizers for the application of herbicides to small seedling is very promising and worth to be investigated. Ultrasonic atomization delivers almost uniquely a complete separation between the atomization process and the further propagation of the droplets. In the present application, a fine spray required for a homogenous agent distribution on the leaves of the seedlings can be achieved without significant air involved. Additional auxiliary air at low pressure that is applied through an air cap around the atomizer can be used to tailor the spray cone and partly adapt the spatial droplet concentration to the seedling size and geometry. Also, the small air velocities produce only minor momentum on the sensitive plants. The corresponding transfer efficiencies measured at empty tray, in stop and go mode at favourable working distances and spray cone angles are between 60 % and 75 %.

On the other hand, the very soft spray cone with low axial momentum is easily influenced by any superimposed airflow, e.g. as existing when working in continuous traversing mode. Hence, the accuracy of application to an individual seedling will decrease and contamination of neighbourhood seedlings will increase. Here, it should be noted that the application frequency might vary from seedling to seedling, even within one tray.

Numerical simulations with a modified air cap have also been started to improve the velocity profile and, hence, the mass flux at working distance, which has so far been mainly Gaussian. However, first results that the constructed air cap, which has been designed similar to existing systems used in air spray painting, needs further design considerations.

Future work will also considering a method to deal with the different sizes and shapes of the seedlings. A first approach was to use guiding vanes that erect the leaves and bring them inside the spray cone.

### References

- [1] A. Lozano, J.A. Garcia, J.L. Navarro, E. Calvo, F. Barreras: Influence of viscosity on droplet size distribution and generation rate in ultrasonic atomization, *Atomization and Sprays*, Vol. 20, No. 11 pp. 923-934 (2000)
- [2] Q. Ye, J. Domnick, E. Khalifa: Simulation of the spray coating process using a pneumatic atomizer, 18th Annual Conference of ILASS-Europe on Liquid Atomization and Spray Systems, September 9-11, 2002, Zaragoza, Spain

## Impact of oil content on effervescent atomization of oil-in-water emulsions

A. Kleinhans, P. Stähle, J. Schröder, V. Gaukel and H.P. Schuchmann

Karlsruhe Institute of Technology, Food Process Engineering, Karlsruhe, Germany

### Abstract

In this study the impact of the oil content of oil-in-water emulsions on the change of the oil drop size distribution during atomization by an effervescent nozzle was investigated.

Many spray dried food powders are oil-in-water emulsions. The oil drop size is the main factor influencing product characteristics of relevance to consumers. The effervescent atomizer used in this study is a special internal mixing pneumatic nozzle not in common use in food industry yet. A model emulsion consisting of vegetable oil, whey protein, maltodextrin and water was used. The viscosity ratio between disperse and continuous phase was set to approximately 1.

It was shown that an increase of ALR led to a decrease in the spray sauter mean diameter as well as a reduction of the oil drop sizes within the spray. Furthermore a lower oil content led to an increase in oil drop breakup at higher ALR. Besides break-up, coagulation and coalescence was found in atomization, also influenced by the amount of oil.

---

### Introduction

Spray drying processes are widely used for the production of dry food powders. These food powders are often dried emulsions like milk based concentrates and dairy products for e.g. coffee instant products. The encapsulation of oil or oil soluble flavors within dry wall matrices is applied to reduce reactions with e.g. light or oxygen, to improve the flow behavior of the powders and to hide a potentially occurring unfavorable taste (1-3). Encapsulation efficiency may be enhanced by choosing a suitable wall or core material (1). The amount of wall material within the feed influences the encapsulation efficiency and the spray drying conditions. The higher the dry matter content in the feed, the less drying energy is required for drying the spray drops.

However, the feed viscosity increases with increasing dry matter content. Atomization of highly viscous liquids is an essential and very demanding process step. For high viscous liquids pneumatic atomizers are widely used in industrial applications, despite the disadvantage of their high atomization gas consumption. A special type of internal mixing pneumatic atomizer with measurably lower atomization gas consumption is the effervescent atomizer (4).

When oil-in-water emulsions are sprayed for drying reasons it is of high relevance to know whether their inner structure (oil droplet size distribution) is maintained as they affect product properties as encapsulation efficiency, mouth feel, instant properties or shelf life stability (2). Stresses applied for atomization also act on oil drops and may thus effect their size distribution. Several research groups observed a decrease in oil drop size with increasing stress in atomization (5-7).

Our study thus concentrated on the effect of process parameters and emulsion composition on the oil droplet size distribution after effervescent atomization.

### Experimental test-rig

#### Atomizer

Several groups have investigated effervescent atomization for e.g. industrial burners (8-11). In contrast to other gas induced atomization like flash or dissolved gas atomization, the atomization gas (compressed air or nitrogen) is injected through injector holes into the feed. In the mixing chamber, it forms a two phase flow prior to the nozzle. According to Sovani (11) and Konstantinov (12), the most favorable state of the two phase flow in the mixing chamber is a bubbly flow. Due to the narrowing in the nozzle orifice, the two phase flow will transform into an annular, slug or plug flow depending on liquid properties and process parameters (13).

One of the most important process parameter for the formation of the flow regimes is the ratio of the atomization gas flow to the liquid flow: air-to-liquid ratio by mass (ALR) - see equation 1 (gas mass flow rate  $\dot{m}_g$ , liquid mass flow rate  $\dot{m}_l$ ) (10, 14).

$$ALR = \frac{\dot{m}_g}{\dot{m}_l} \quad [1]$$

When leaving the nozzle orifice, the atomization gas expands leading to a breakup of thin liquid threads into liquid filaments and further into single spray drops.

In our trials, an effervescent atomizer was used with a constant mixing chamber geometry ( $d_m = 6$  mm,  $l_m = 46,5$  mm) as well as a nozzle orifice diameter  $d_o$  of 1.5 mm and length  $l_o$  of 1.5 mm (see Fig. 1). Figure 1 shows a sketch of the atomizer geometry used for the experiments. The geometry was designed according to Chin and Lefebvre (10) and is associated to a so called outside-in geometry which is also used by several groups (e.g. Jedelsky et. al (8)).

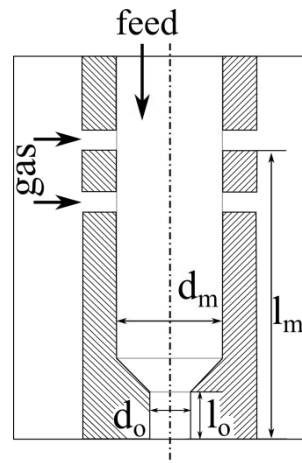


**Figure 1.** Sketch of effervescent atomizer geometry - gas is injected into the feed flow and induces a two phase flow prior the nozzle.

For the atomization of the emulsions, a test rig according to Figure 2 was used. The atomizer was fixed on a slide unit to ensure a horizontal and vertical positioning option. The liquid support is run by an eccentric screw pump and was kept constant at a volume flow of 12 l/h. The atomization gas is supplied by a compressed air unit. During the experiments, the pressure of the liquid and of the atomization gas was measured. Laser diffraction spectroscopy was used for determination of the spray drop size distribution during atomization (Malvern Spraytec).

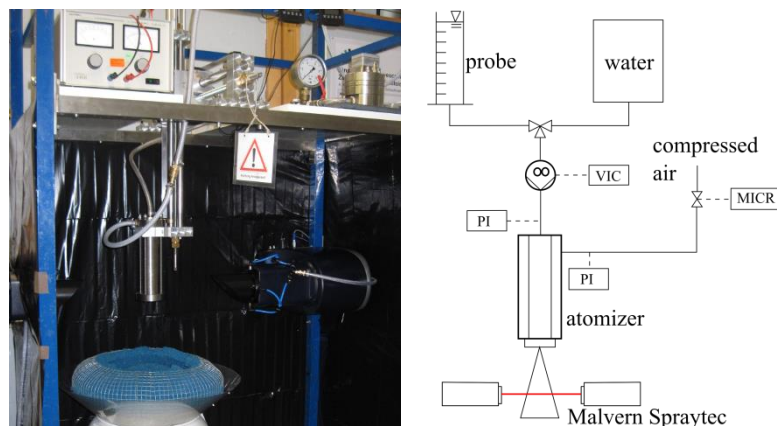


**Figure 2.** Experimental test rig with slide unit, atomizer and laser diffraction spectroscope (left) and schematic representation of the test rig (right).

## Emulsion

As previously reported (7, 15), a model oil-in-water emulsion was used for the experiments. The continuous phase consisted of demineralized water, maltodextrin (C\*Dry MD 01910/ Cargill, Germany) and whey protein

concentrate (Lacprodan 87/Arla Foods GmbH, Germany). Vegetable oil (St. Wendeler Ölsaaten, Germany) was used as disperse phase. Its fraction was varied from 1 to 10 wt-% and the emulsifier concentration was always set to 10 % of the oil mass fraction.

For shear flow in Newtonian liquids, oil drop breakup can be described by the capillary number  $Ca$  (see equation 2 - viscosity of continuous phase  $\eta_c$ , shear rate  $\dot{\gamma}$ , interfacial tension  $\gamma$ , drop diameter  $x$ ):

$$Ca = \frac{\eta_c \cdot \dot{\gamma} \cdot x}{2 \cdot \gamma} \quad [2]$$

The critical capillary number is the value that has to be exceeded for oil drop breakup (16). Grace indicated that the viscosity ratio  $\lambda$  (see equation 3 - viscosity of disperse  $\eta_d$  and continuous phase  $\eta_c$ ) is a crucial factor influencing the critical capillary number. Armbruster (17) and later Jansen et al. (18) showed that for high concentrated systems the viscosity of the emulsion  $\eta_e$  has to be used instead of the viscosity of continuous phase.

$$\lambda = \frac{\eta_d}{\eta_c} \text{ respectively } \lambda = \frac{\eta_d}{\eta_e} \quad [3]$$

Viscosities were measured by rotational rheometry (Anton Paar Physica MCR 101/301) with increasing shear rate from 1 to 1000 s<sup>-1</sup> at 25 °C. As shear rates in the atomization process are expected to be up to 10<sup>6</sup> s<sup>-1</sup>, the viscosities measured at the maximum shear rate of the rotational rheometer (1000 s<sup>-1</sup>) are used to calculate the viscosity ratio.

Samples of the emulsions were taken prior to atomization (untreated) and after atomization (atomized) at different ALR. The oil drop size distribution was measured by laser diffraction spectroscopy (Beckman Coulter LS 13320 and Retsch Horiba LA-950) afterwards. To visualize the occurring drop break up, a ratio of the  $x_{50,3}$  of the atomized and the untreated emulsion is used (see equation 4), further mentioned as normalized median oil drop diameter  $\chi$  (15).

$$\chi = \frac{x_{50,3;\text{atomized}}}{x_{50,3;\text{untreated}}} \quad [4]$$

Previous results depicted that the oil drop breakup during atomization depends on the viscosity ratio (15). There, the results of normalized median oil drop diameter in the model emulsion (same as defined above) with 20 wt-% oil at different viscosity ratios have shown 3 different regions. In the region of high viscosity ratio above 4 the results show clearly that the oil drop breakup increases with higher ALR and decreases with increasing viscosity ratio. The most interesting results are depicted near a viscosity ratio of one. Here, oil drops are broken easily and the dependency on the ALR is changing. In the third region at viscosity ratio below 0.4, there is no significant influence of ALR or viscosity ratio on oil drop breakup visible. This may be due to the high viscosity of the emulsion of 180 mPas and nearly 730 mPas as well as the aggravated spray drop breakup.

Therefore, the region of a viscosity ratio near 1 is investigated in our experiments. The viscosity of the continuous phase of the emulsion (with 1, 3 and 10 wt-% oil) was adjusted by adding maltodextrin at different concentrations (39.6, 38 and 32,6 wt-%) for the target viscosity ratio in our system.

Another key factor for the oil drop breakup during atomization is the oil content, as it influences interactions of drops in breakup leading to e.g. coalescence or aggregation. Investigations into these effects have not been published yet.

## Results and Discussion

### Viscosity

Fig. 3 represents viscosity curves of emulsions with three different oil contents (1, 3, 10 wt.-%) as well as the viscosity of the disperse phase itself ("100 % oil content"). The disperse phase depicts a Newtonian behavior. The emulsions however show an increased viscosity and a slight shear thinning behavior. At 1000 s<sup>-1</sup>, the viscosities of the emulsions are slightly higher as the one of the disperse phase. As intended, up to 10 % of oil content no difference on the viscosity of the emulsion could be found. The viscosity ratio in the model system thus was  $0.85 \pm 0.01$ , which is quite close to 1.

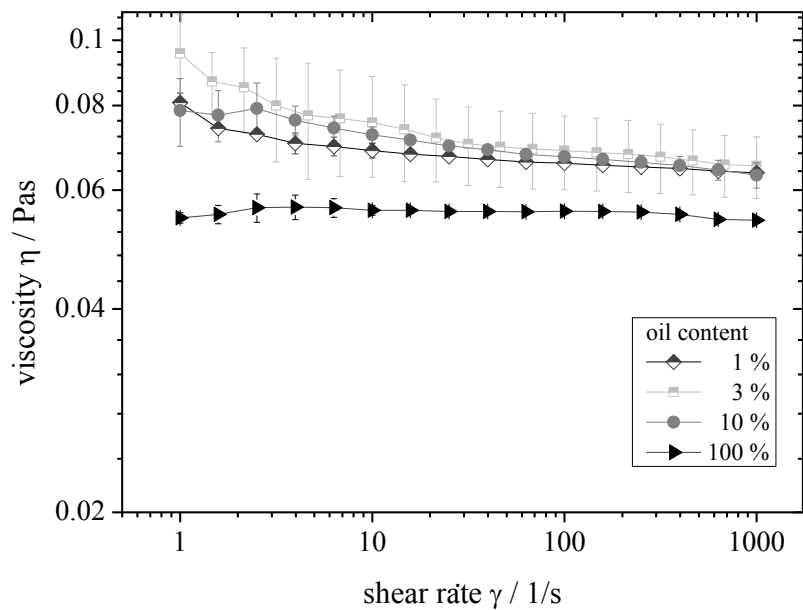


**Figure 3.** Viscosity curves of emulsions with 1, 3 and 10 wt-% oil content as well as of pure oil (disperse phase, 100 %).

### Spray drop sizes

In Fig. 4, the results of the spray drop size measurements are shown. For all oil contents, the characteristic drop size sauter mean diameter  $x_{1,2}$  decrease with increasing ALR. This was expected due to the higher amount of used atomization gas and thus the higher amount of atomization energy available. Furthermore, there is no difference in atomization between the three emulsions visible with fits to the fact that all emulsions have nearly the same viscosity and surface tension (data not shown).

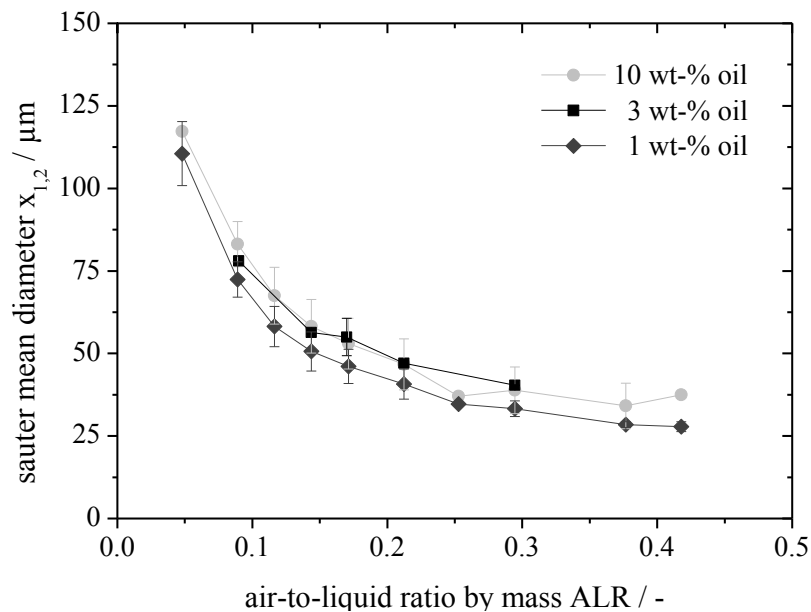


**Figure 4.** Spray sauter mean diameter  $x_{1,2}$  of the atomized emulsions with 10, 3 and 1 wt-% oil for different ALR

### Oil drop breakup

Fig. 5 presents the normalized median oil drop diameter of the emulsions with 1, 3 and 10 wt-% oil for different ALR. As found by Schröder et al. (15) at a viscosity ratio of  $\lambda = 1.3$  and above, an increase in ALR leads to a decrease in oil drop size within the spray for emulsions of oil content  $< 10$  wt.-%. Between these emulsions, there is no difference in oil drop size visible.

At increased oil content (10 wt-% of oil) the oil drop sizes decreases in the range of low ALR, and then increases for higher ALR. A similar behavior was also seen by Schröder et al. (15) at an oil content of 20 wt-% and at a viscosity ratio of 0.67.

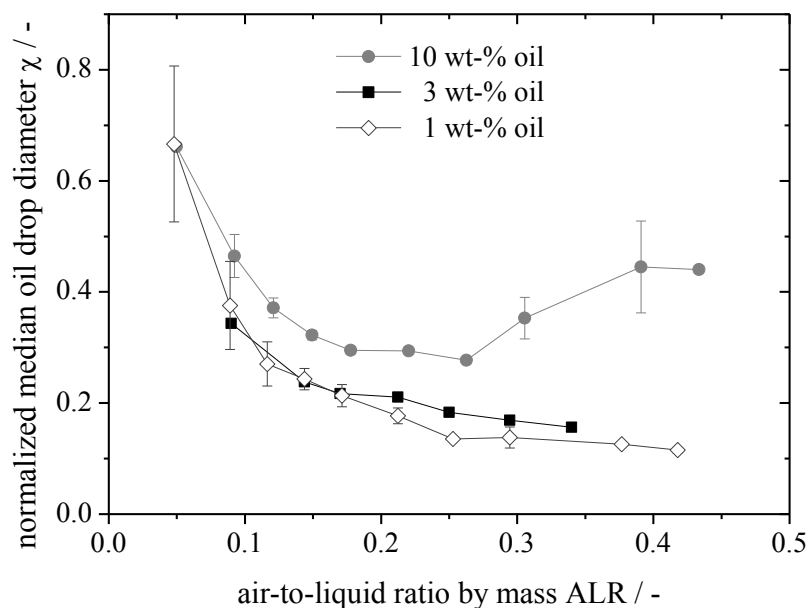


**Figure 5.** Normalized median oil drop diameter of emulsions with 1, 3 and 10 wt-% oil for different ALR.

This effect may be induced by coalescence or coagulation phenomena of the oil drops during atomization. The amount of oil affects the collision probability within spray drops. As shown in Figure 4, the spray drops of all atomized emulsions are of the same sizes at same atomizing conditions. Therefore, each spray drop contains more oil drops when formed of an emulsion higher in dispersed phase content. This in turn may lead to a denser packing of oil drops inside the spray drops and thus to a higher possibility of coalescence of the oil drops.

In addition the amount of emulsifier is increased in the emulsions with increased disperse phase content, whey proteins, used as emulsifier here, are known to enhance the tendency of coagulation (19, 20). In Figure 6, two microscopy images of two different emulsions are shown. On the left-hand side, a representing image of the emulsion with 1 wt-% oil after atomization is depicted. Here, no effect like coagulation of the emulsifier concentration on the emulsion inner structure is visible. At the right, an emulsion with 10 wt-% oil after atomization at higher ALR is shown. It can be clearly seen that some coagulates have formed. The coagulation may lead to the effect in size measurement of the oil drop size distribution shown in Figure 5.

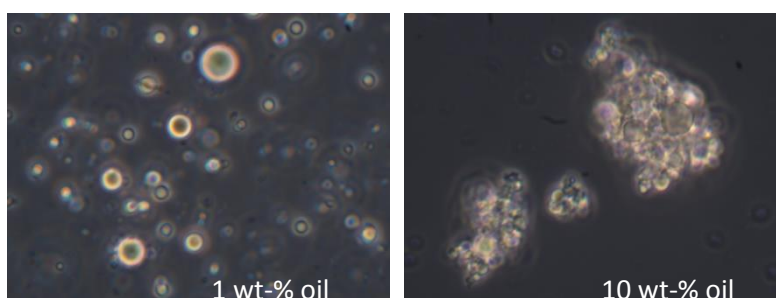


**Figure 6.** Microscopy images of two emulsions after atomization: 1 wt-% no coagulation is visible (left), 10 wt-% coagulation did happen (right)

## Conclusions

In this work, it was shown that oil drops in oil-in-water emulsions are broken up due to the stresses present during effervescent atomization. Besides the viscosity ratio, the oil drop sizes after emulsion atomization is also influenced by the amount of oil in the emulsion. It could be shown that besides break-up of droplets also coagulation is found. The coagulation rate increased with the number of oil droplets within one spray drop, thus with increasing oil and emulsifier content of the emulsion atomized and with increasing break-up efficiency during atomization. In order to investigate oil drop coagulation during emulsion atomization more work will be

done in future. Especially the influence of the type and the amount of emulsifier and its impact on the stability of the emulsion will be investigated more in detail.

## Acknowledgements

The work at the KIT has been carried out with financial support of the German Research Foundation (DFG) within the research program DFG-SPP 1423 “Process-Spray”. We also like to thank the Ministry of Science, Research and Art of Baden-Württemberg for financing the Malvern Spraytec. The authors gratefully acknowledge the skilful help of Andrea Butterbrodt, Julie Gorenflo and Pascal Lang.

## Nomenclature

$\dot{m}$	[kg/s]	mass flow rate
$d$	[mm]	diameter
$l$	[mm]	length
$\eta$	[Pas]	viscosity
$\dot{\gamma}$	[1/s]	shear rate
$\gamma$	[N/m]	interfacial tension
$x$	[ $\mu\text{m}$ ]	drop size

## Indices

$m$	mixing chamber
$o$	orifice
$d$	dispers phase
$c$	continuous phase
$e$	emulsion
50,3	median of volume size distribution
1,2	sauter mean diameter

## Dimensionless Numbers

ALR	[-]	air-to-liquid ratio by mass
Ca	[-]	Capillary number
$\lambda$	[-]	viscosity ratio
$\chi$	[-]	normalized median oil drop diameter

## References

- [1] S. M. Jafari, E. Assadpoor, Y. H. He, B. Bhandari, *Drying Technol.* **26**, 816 (2008).
- [2] K. G. H. Desai, H. J. Park, *Drying Technol.* **23**, 1361 (2005).
- [3] B. F. Gibbs, S. Kermasha, I. Alli, C. N. Mulligan, *International Journal of Food Sciences and Nutrition* **50**, 213 (1999).
- [4] F. J. Petersen, O. Worts, T. Schaefer, P. E. Sojka, *Pharmaceutical development and technology* **6**, 201 (2001).
- [5] C. D. Bolszo, A. A. Narvaez, V. G. McDonell, D. Dunn-Rankin, W. A. Sirignano, *Atomization and Sprays* **20**, 1077 (2010).
- [6] M. L. Vignolles *et al.*, *Journal of Dairy Science* **92**, 58 (2009).
- [7] J. Schröder, F. Werner, V. Gaukel, H. P. Schuchmann, (Cosmosware, Athen, 2011).
- [8] J. Jedelsky, M. Landsmann, M. Jicha, I. Kuritka, 2008).
- [9] J. Jedelsky, M. Jicha, *Atomization and Sprays* **18**, 49 (2008).
- [10] J. S. Chin, A. H. Lefebvre, *Journal of Engineering for Power-Transactions of the Asme* **117**, 266 (1995).
- [11] S. D. Sovani, P. E. Sojka, A. H. Lefebvre, *Progress in Energy and Combustion Science* **27**, 483 (2001).
- [12] D. Konstantinov, R. Marsh, P. Bowen, A. Crayford, *Atomization and Sprays* **20**, 525 (2010).
- [13] O. Baker, *Oil & gas journal: international petroleum news and technology* **53**, 185 (1954).
- [14] B. A. Baker, E. A. Davis, J. Gordon, *Cereal Chemistry* **67**, 451 (1990).
- [15] J. Schröder *et al.*, *J Food Eng* **111**, 265 (2012).
- [16] H. P. Grace, *Chemical Engineering Communications* **14**, 225 (1982).
- [17] H. Armbruster, Universität Karlsruhe (TH) (1990).
- [18] K. M. B. Jansen, W. G. M. Agterof, J. Mellema, *Journal of Rheology* **45**, 227 (2001).
- [19] H. G. Kessler, *Lebensmittel- und Bioverfahrenstechnik - Molkereitechnologie* (Verlag A. Kessler, München, ed. 4. Edition, 1996).
- [20] L. M. Huffman, *Food Technology* 49 (1996).



## Deviation and Atomization of a Dielectric Liquid Sheet under Electrohydrodynamic Excitation

Michel Daaboul<sup>1</sup>, Christophe Louste<sup>2</sup> and Philippe Traore<sup>2</sup>

1: Faculty of Engineering, Mechanical Engineering Department,  
University of Balamand, Al-Kurah, Lebanon

2: PPRIME Institute, Department of Fluid Flow, Heat Transfer and Combustion,  
CNRS – University of Poitiers – ENSMA,  
Bd Marie et Pierre Curie, BP 30179, 86962 Futuroscope Chasseneuil Cedex, France

### Abstract

A new electrohydrodynamic (EHD) actuator based on a dielectric barrier injection system has been developed in order to enhance fuel atomization in air blast atomizers. In industrial air blast atomizers, the fuel is injected at low pressure through an annular slit. The liquid sheet is then atomized by the shear forces exerted by the co-flowing air stream. High air velocities are needed in order to obtain a fine atomization. The objective was to electrically atomize the liquid sheet without the need to an external air flow like the one seen in air blast atomizers. In the proposed EHD actuator, the liquid sheet is atomized only with the help of electric forces and without any mechanical influence.

Experiments have been carried out on 300  $\mu\text{m}$  thin sheets of commercial Diesel oil with a very close flow rate to the ones used in turbo engines. The velocity varies between 0.6 m/s and 2 m/s. Images are recorded with a high speed camera. The liquid sheet could be fully atomized when the actuator is running. In this paper, the effect of the electric signal frequency on the mechanical behaviour of the excited sheet, mainly on the angle of deviation, is presented.

### Introduction

Liquid atomization [1] is very important for efficient combustion in aeronautical engines. In these engines, the fuel sheet is atomized by the use of air blast atomizers. The fuel is injected through an annular slit to get a tubular sheet. It is then atomized by shear forces exerted at the liquid surface by co-flowing air streams. A very high air velocity is required in order to get a fine atomization. Otherwise, the atomization will produce larger droplets and the combustion will be less effective. This is the major drawback of air blast atomizers. In addition, for very low velocities, encountered in daily flights, the liquid sheet is not well sprayed anymore.

Two approaches were developed to avoid these undesired phenomena. Passive methods like the study of break-up and fuel properties are sometimes performed. [2][3][4][5]

More efficient active methods to induce instabilities at the surface of the liquid sheet are also used [6][7]. These active methods involve the use of actuators like the one presented in this paper.

Several studies were carried out on electrically induced fuel spraying [8]. Numerical and experimental approaches were undergone. Very important results were obtained by Shrimpton [9].

It was demonstrated that the injected charge density has a direct relationship with the droplet size. However, the injected charge density could not be increased indefinitely because a Corona discharge would take place. But very high electric fields could be reached within this device without the occurrence of electric breakdown.

In industrial atomizers, fuel is injected through an annular slit which produces a thin tubular sheet of fuel. For research purposes, experiments have been carried out on a plane liquid sheet because it is easier to investigate than a cylindrical one.

In the present work, the dielectric liquid sheet is destabilized by the use of an electrohydrodynamic (EHD) actuator. Such actuators could be used for flow control applications [10].

The objective is to atomize a liquid sheet like in air blast atomizers even in the absence of co-flowing air streams, i.e. with zero air velocity. The liquid sheet is therefore atomized by electric forces only. The sheet is then stable when the actuator is turned off.

The side view of the liquid sheet is mainly studied in this paper. Investigations on the front view were carried out in two previous papers [11] and [12]. The influences of the electric signal frequency and of the liquid sheet velocity on the behaviour of the electrically excited fuel sheet are generally underlined. The atomization of the sheet and its angle of deviation are presented. The primary atomization is only studied, the secondary atomization being neglected.

## Experimental Setup

In this work, experiments were carried out on a plane sheet of fuel. The experimental setup is schematically presented in Figure 1.

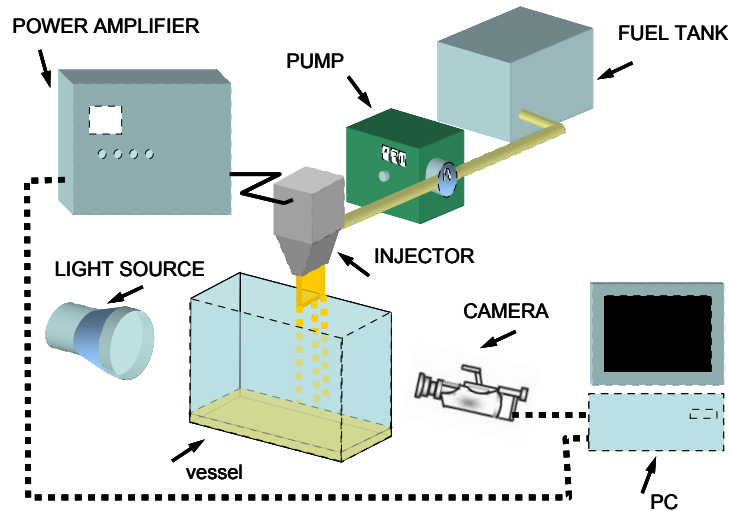


Figure 1. Experimental Setup

The fuel is pumped from a tank to the injector via a gear pump. The flow rate is controlled by the gear pump, allowing therefore controlling the velocity of the liquid sheet. Inside the injector, a surge chamber smoothes out the turbulence of the fuel. The liquid is then pushed through the rectangular slit. The tested liquid is commercial Diesel oil, a dielectric liquid with a slight conductivity. The characteristics of this dielectric liquid at a temperature of 20°C are close to the kerosene ones and are presented in Table 1.

Table 1. Typical Characteristics of the Diesel Oil at 20 °C

Mass density	$\rho$ [kg.m <sup>-3</sup> ]	850
Kinematic viscosity	$\nu$ [m <sup>2</sup> .s <sup>-1</sup> ]	$4.3 \cdot 10^{-6}$
Electrical conductivity	$\sigma$ [S.m <sup>-1</sup> ]	$1.15 \cdot 10^{-9}$
Relative permittivity	$\epsilon_r$	2.2

A schematic view of the fuel injector (Item 3 in Figure 1) is proposed in Figure 2. It is composed of the dielectric body (1). The fuel inlet is located at the top of the injector (2). The carburant turbulence is smoothed through the surge chamber (3) before entering into the rectangular slit (4). Two blades (5-6) are used as lips in order produce a 300  $\mu$ m thick, 6 cm wide plane sheet (7). The actuator is mainly composed of two electrodes. The first one is the grounded blade made of steel (6). The second one is a steel strip (8) embedded into the second blade (5) and connected to the high voltage power supply. The electrode (8) is implanted inside the dielectric material (5) to avoid the formation of an electric arc between both electrodes. Such an electrohydrodynamic actuator is often called a Dielectric Barrier Injector. It was first proposed by [13] and [14]

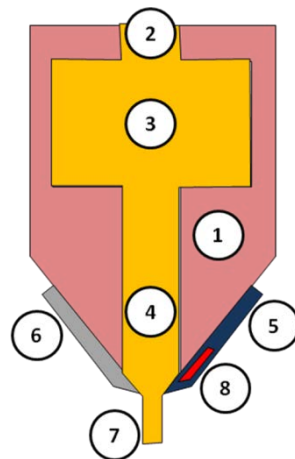
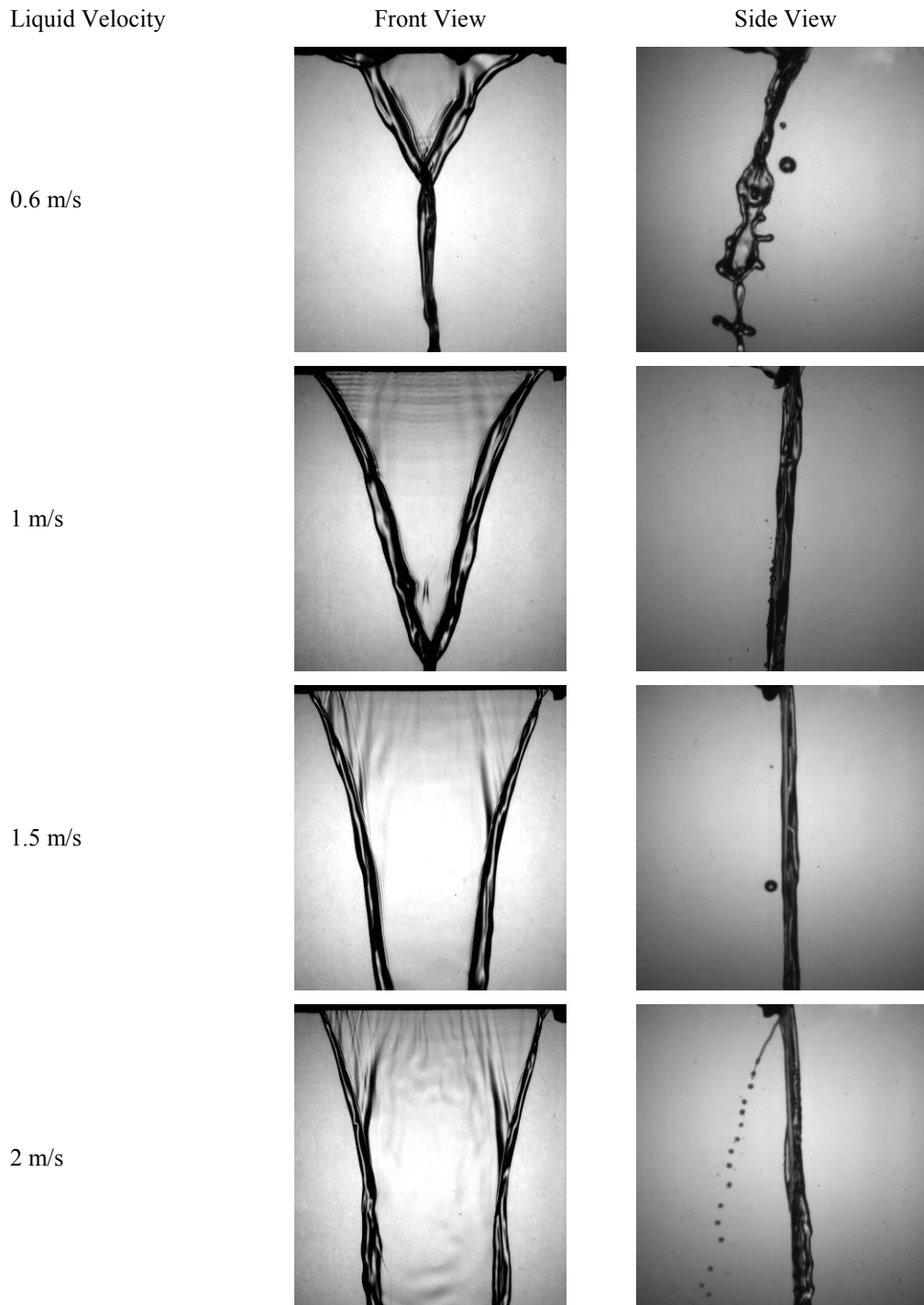


Figure 2. Schematic view of the fuel injector

### High-Speed Camera Images

Images were recorded with the help of a high-speed camera. Figure 3 shows the shadow images of the liquid sheet of Diesel oil obtained at various flow rates in quiescent air. They correspond to a liquid velocity ranging from 0.6 m/s to 2 m/s. Note that in Figure 3, the actuator is off, hence the liquid sheet is stable. In the absence of electric excitation, a typical triangular plane sheet bounded by two cylindrical rims flows out from the slit (mainly visible for 1 m/s velocity). The injector lips are visible as a black line at the top of the images. As a result of the surface tension the edges contract and the rims grow as they accumulate the liquid from the contracted sheet. Very slight disturbances are visible on the liquid sheet but they are not sufficient to induce its breakup. Because of the surface tension, the two rims draw together and impinge to form another sheet at right angle before impinging again and forming a cylindrical jet. Several imaging techniques were used to study the atomization of liquid sheets in [13] and [16]



**Figure 3.** Shadow images of the stable plane sheet at different velocities.

### Influence of the Liquid Sheet Velocity

In Figure 4, one can see that the excited liquid sheet is less deviated from its initial axis (yellow line on images) when its velocity is increased. The spray obtained with 2 m/s velocity is also the least developed.

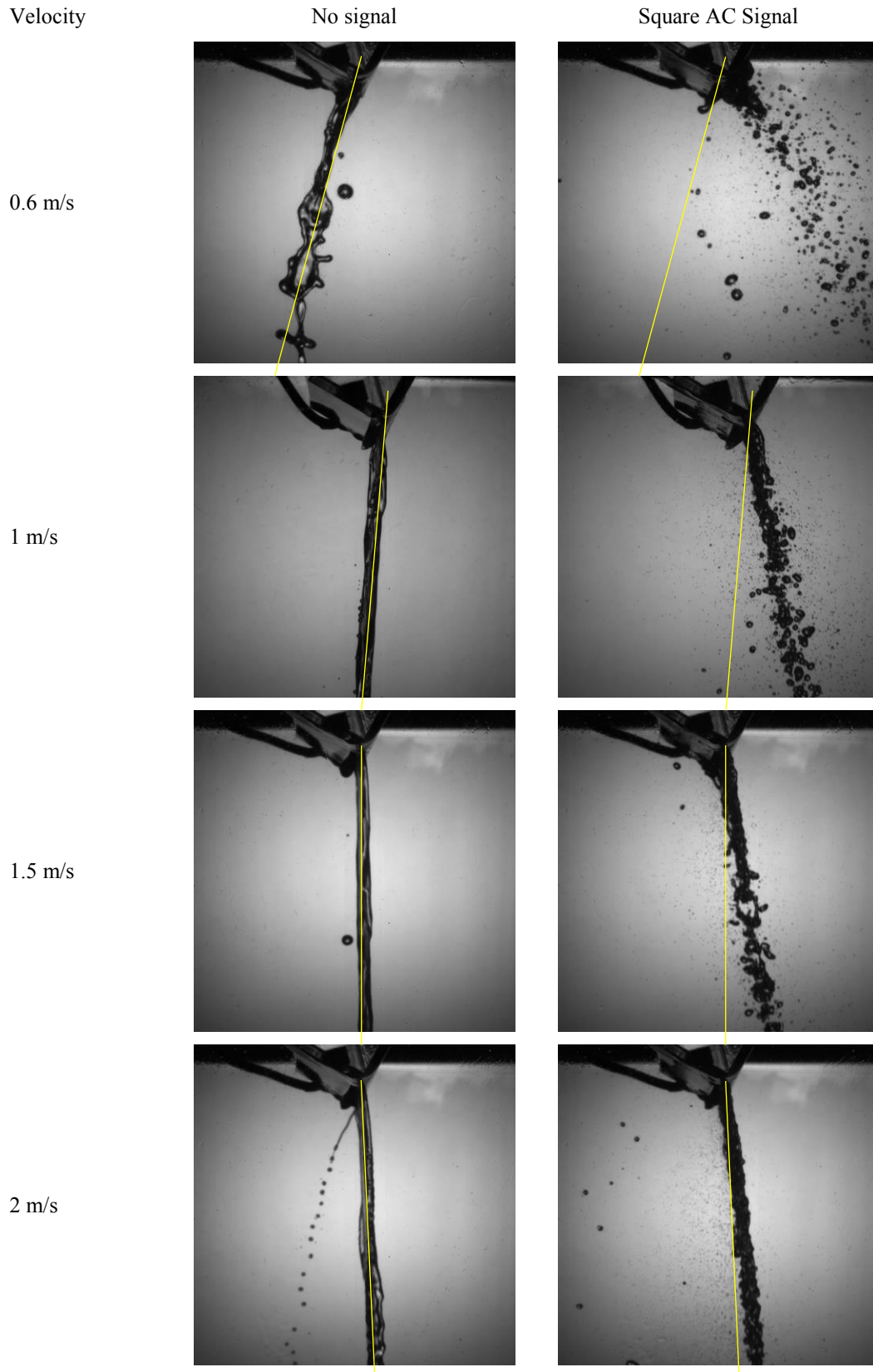


**Figure 4.** Shadow images of the excited plane sheet at different velocities.  
(Square AC signal, 30 kV amplitude, 2 kHz frequency)

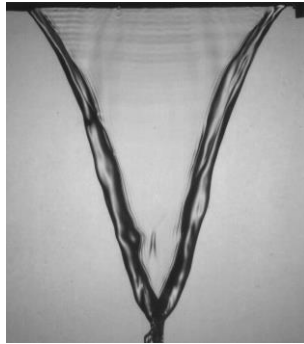
## Influence of the Electric Signal Frequency

Frequency

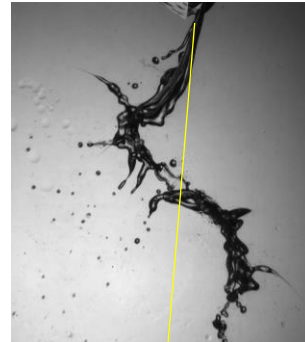
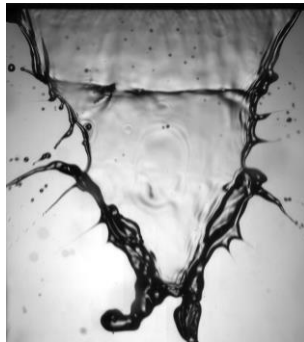
Front view

Side view

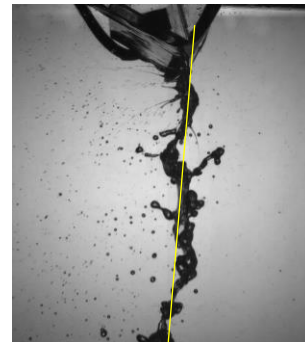
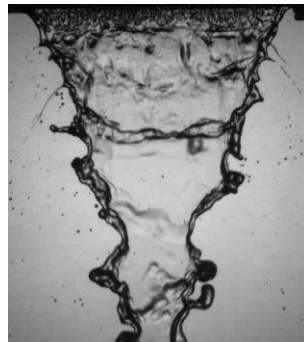
No signal



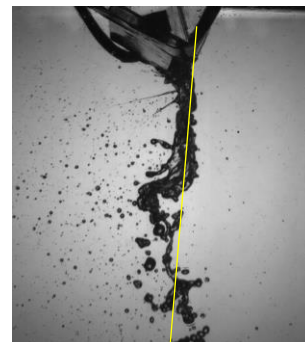
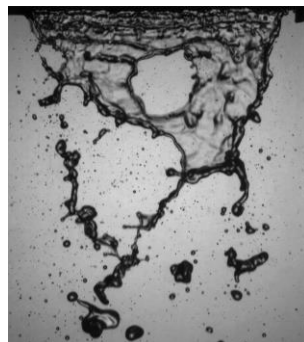
10 Hz



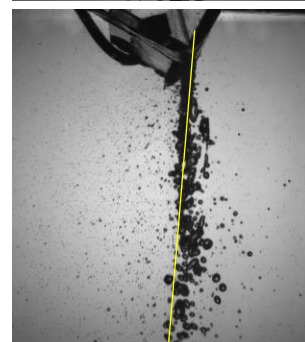
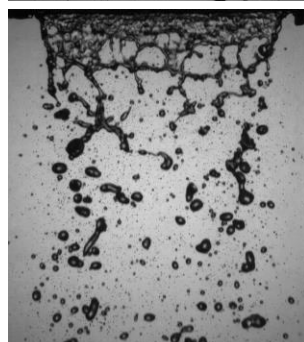
50 Hz



100 Hz



500 Hz



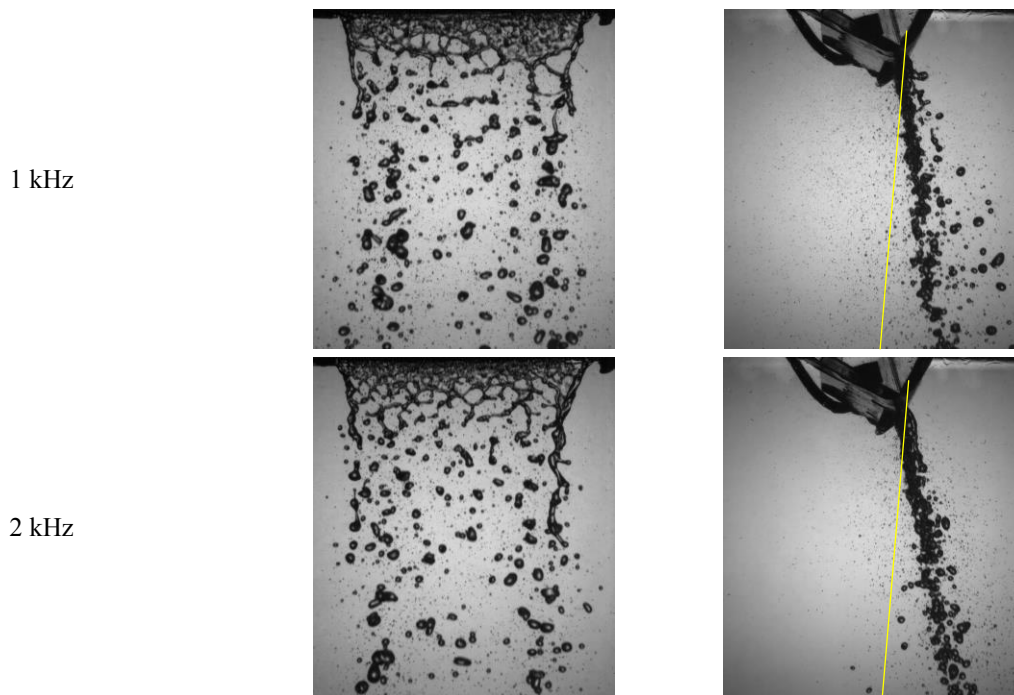


**Figure 5.** Shadow images of the excited plane sheet at different electric signal frequencies.  
(Square AC signal, 30 kV amplitude, 1 m/s liquid sheet velocity)

Figure 5 presents the behaviour of the liquid sheet when electrically excited at different frequencies of a square AC signal with 30 kV amplitude. Below 100 Hz, a longitudinal wave is visible. The frequency of this wave is equal to the electric signal one. The liquid sheet axis is unchanged (yellow line on side view images). Small droplets also appear. These droplets originate from the thin ligaments emerging from the wave. Starting from 500 Hz, the sheet is deviated by an angle from its initial axis and is fully atomized. This angle of deviation increases when the frequency increases up to 2 kHz. However, the spray angle decreases. Note that when the liquid sheet is fully atomized, no ligaments are visible and the droplets are directly issuing from the explosion of the sheet due to the strong instabilities induced by charge injection.

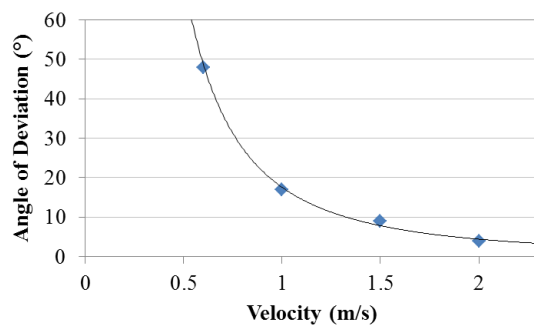


**Figure 6.** Angle of deviation versus liquid velocity.

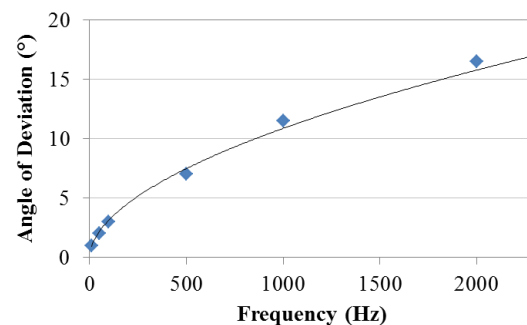


**Figure 7.** Angle of deviation versus signal frequency.

Figures 6 and 7 present the variations of the angle of deviation with the liquid sheet velocity and the electric signal frequency, respectively. It can be seen that the behaviour is asymptotic. When the liquid sheet velocity increases, electric forces are not strong enough to deviate the liquid sheet. Similarly, the angle of deviation increases asymptotically with the frequency until reaching a maximum value.

## Conclusions

This paper presented a new electrohydrodynamic actuator for electrospraying applications. This actuator allowed to electrically destabilize a liquid sheet with the help of a built-in dielectric barrier injection system. Experiments were carried out on a 300  $\mu\text{m}$  thin, 6 cm wide sheet of commercial Diesel oil. The liquid sheet velocity is similar to the ones used in turbo engines. However, the atomization is induced by electric disturbances in contrary with the mechanical instabilities induced in air blast atomizers.



The effects of the liquid sheet velocity and of the electric signal frequency on the atomization of the liquid sheet as well as on its angle of deviation from its initial axis were presented.

It was noticed that when the liquid sheet velocity is low enough, the electric forces are able to deviate the liquid sheet from its initial position by an important angle. This effect is less evident for higher velocities.

Similarly, an asymptotic behaviour with the frequency was also obtained on the angle of deviation. For low frequencies, the liquid sheet was not fully atomized. A longitudinal wave was rather observed. This wave has the same frequency of the applied electric signal. However, at high frequencies, the liquid sheet is fully atomized and small droplets are visible to show a complete and fine atomization. The spray angle also decreases for very high frequencies.

In this study, the primary breakup of liquid sheets of fuel was investigated. A future experimental study on the droplet size should be carried out. Also, a coupling between air blast atomizers and dielectric barrier injection actuator will be investigated to study their combined effect on fuel sheets atomization.

Further experiments on the spray characteristics one will be conducted in the future in order to complete this work and understand all the phenomena involved in EHD spraying.

## References

- [1] Chigier, N. and Dumouchel, C., *Atomization of Liquid Sheets*, Prog. Astronaut Aeronaut 166:241-259 (1996).
- [2] Mansour, A. and Chigier, N., *Disintegration of liquid sheets*. Phys. Fluids A 3: 2971–2980 (1990).
- [3] Mansour, A. and Chigier, N., *Dynamic behavior of liquid sheets*. Phys. Fluids A 2: 706–719 (1991).
- [4] Dumouchel, C., *On the experimental investigation on primary atomization of liquid streams*, Experiments in Fluids 45-3: 371–422 (2008).
- [5] Bremond, N., Clanet, C., and Villermaux, E., *Atomization of undulating liquid sheets*, Journal of Fluid Mechanics 585 (2007).
- [6] Larricq-Fourcade, C., Lavergne, G., Berthoumieu, P., and Thivet, F., *Improvement of Airblast injectors with electro-aerodynamic actuators*, 2nd International Symposium on Non Equilibrium Processes, Combustion and Atmospheric Phenomenon, 41-49 (2005).
- [7] Boukra, M., Cartellier, A., Ducasse, É., Gajan, P., Lalo, M., Noel, T., and Strzelecki, A., *Use of Faraday instabilities to enhance fuel pulverisation in air-blast atomizers*, Comptes Rendus - Mécanique 337-6-7:492-503 (2009).
- [8] Kelly, A.J., *The Electrostatic Atomization of Hydrocarbons*, J. Inst. Energy 57:312–320 (1984).
- [9] Shrimpton, J.S. and Rigit, A.R.H., *Spray characteristics of charge injection atomizers with small orifice diameters*, Atomization and Sprays 16-4:421-442 C (2006).
- [10] Louste, C., Daaboul, M., and Romat, H., *Experimental study of a plane turbulent wall jet induced by a dielectric barrier injection in dielectric liquid*, IEEE International Conference on Dielectric Liquids 16:106-109, Poitiers, France (2008).
- [11] Louste, C., Daaboul, M., Traore, P., and Romat, H., *Experimental Study of electrical primary break-up of a thin sheet of dielectric liquid controlled by an ElectroHydrodynamic actuator*, ILASS – Europe 2010, 23rd Annual Conference on Liquid Atomization and Spray Systems, Brno, Czech Republic (2010).
- [12] Louste, C., Daaboul, M., Traore, P., and Romat, H., *Influence of Signal Properties on ElectroHydroDynamic Primary Break-up of Thin Sheets of Dielectric Liquid*, ICLASS 2012, 12<sup>th</sup> Triennial International Conference on Liquid Atomization and Spray Systems, Heidelberg, Germany (2012).
- [13] Louste, C., Daaboul, M., and Romat, H., *A study of vortex shedding induced by dielectric barrier injection*, Journal of Electrostatics 67-2-3:348–353 (2009).
- [14] Priol, L., Louste, C., and Romat H., *Experimental study of a dielectric barrier injection in Diesel oil. Measurements of liquid velocity by LDV*, ESA/IEEE Electrostatics Joint Conference:95–102 (2006).
- [15] Berthoumieu, P. and Lavergne, G., *Video Techniques Applied to the Characterization of Liquid Sheet Breakup*, Journal of Visualization 4-3:267-275 (2001).
- [16] Dombrowski, N. and Fraser, R.P., *A photographic investigation into the disintegration of liquid sheets*, Phil. Trans. Roy. Soc. London A 247:101-130 (1954).



## **Influence of pressure surge on bubble generation and spray steadiness in an effervescent atomizer**

Debjoyti Sen, Miguel Balzan, Brian A. Fleck and David S. Nobes

Department of Mechanical Engineering, University of Alberta, Canada

### **Abstract**

Bubble formation from a gas jet in a liquid cross-flow inside the mixing conduit of an effervescent atomizer is studied using flow visualization. For a constant liquid cross-flow rate, the injected gas flow rate was adjusted to achieve gas liquid ratio (GLR) of  $3.30 \times 10^{-5}$  to  $13.23 \times 10^{-5}$ . High speed shadowgraph imaging was used to monitor bubble generation and break-up at the location of gas injection and at the nozzle exit of the effervescent atomizer. Intermittent choking at the exit nozzle is shown to have a morphological impact on the bubbly flow. This impact is visible as a pressure wave that propagate upstream from the nozzle exit. This pulse is found to have a strong influence on bubble formation at the gas injection location leading to bubble distortion and break-up. In most cases, a liquid jet is observed to propagate through the centreline of larger bubbles as the pressure pulse passes. Equivalent diameter bubble sizing from image data showed that with increasing GLR a bi-modal distribution of bubble size was developed. A constructive feedback for the generation of large bubbles was developed, progressively developing a more intermittent flow.

---

### **Introduction**

Effervescent atomizers are becoming one of the commonly used atomizers because of their ability to generate a fine spray at low operating pressure. The effervescent atomizer process involves injecting gas and liquid into a mixing chamber and allows the gas- liquid mixture to exit through a small nozzle [1]. Small droplets of liquids are formed when the gas suddenly expands due to large pressure drops across the nozzle [2]. Effervescent atomizers have applications in combustion, upgrading of heavy oil and spray systems [2].

Effervescent atomizers suffer from a major problem of flow unsteadiness and intermittent flow. Intermittent flow reduces the efficiency of the effervescent atomizers. Intermittent flow can also cause non-uniform droplet size distribution [2–4]. A uniform and controlled droplet size distribution of the spray droplet is preferred in most applications [2]. Several factors influence the unsteady behaviour of the effervescent atomizer. Internal two phase flow structures play a key role in the behaviour of the external spray. Catlin and Swithenbank [5] observed that internal flow structures and intermittent large bubbles interacting with the nozzle create instability in the external spray. Similar studies were conducted by Kim and Lee [6] and Huang et al. (7), and both the groups related external spray behaviour with gas to liquid ratio (GLR) values which influences the internal flow regime. Ghaemi et al. [3]. and Mondalo et al. [4]. identified that small dispersed bubbles inside the mixing conduit results in a stable spray. Sen et al. [7] used flow visualization technique and suggested the influence of pressure wave travelling along the length of the mixing chamber could play a role in flow instability.

The present work uses flow visualization techniques to understand interaction between exit orifice and bubbles of different sizes. Image processing techniques were used to compute the size of the bubbles at both upstream and downstream locations. Statistical representation, in form of probability density functions, is used to detail bubble size at different GLR values. The size of the bubbles from statistical distribution was used to establish a connection between bubble size and diameter of exit orifice.

### **Experimental Set Up**

The experimental facility consists of a horizontal channel which replicates the mixing conduit of an effervescent atomizer and is shown in Fig. 1. The channel has a square cross section of side 12.7 mm and the total length of the channel was 1.12 m. The channel has two transparent windows made of polycarbonate. The transparent windows allow viewing and illumination of the channel from either side. The end of the channel is fitted with a replaceable plastic orifice of sloth width,  $D_{eo}$ , equal to 1 mm. The bottom of the channel is fitted with twelve air injection ports located along the length of the channel. The effective length of the mixing conduit can be adjusted by selecting the location of the air injection port. Air is pressurized to 150 psi using a compressor (GX4FF, Atlas Copco), which allows steady supply of air. A mass flow controller (MC-20 SLPM, Alicat Scientific) was used to precisely regulate the flow of air into the channel. Water was used as the working fluid for conducting the experiments. A centrifugal pump provides feed water into the channel and the flow into the channel was regulated by ball valves. The rate of flow of water into the channel was measured using water mass flow meters (MC-205LPM-D, Omega). The experiments are conducted with a constant liquid flow rate,  $Q_L$  of 0.299 L/s. This flow rate results in a mean velocity of 2.98 m/s inside the square conduit and a Reynolds

number of 24,330. The gas flow rates at injection are varied from 0.5 slpm through 2.0 slpm in steps of 0.5 slpm. The above flow rates of air and water results in GLR values ranging from  $3.30 \times 10^{-5}$  to  $13.23 \times 10^{-5}$ .

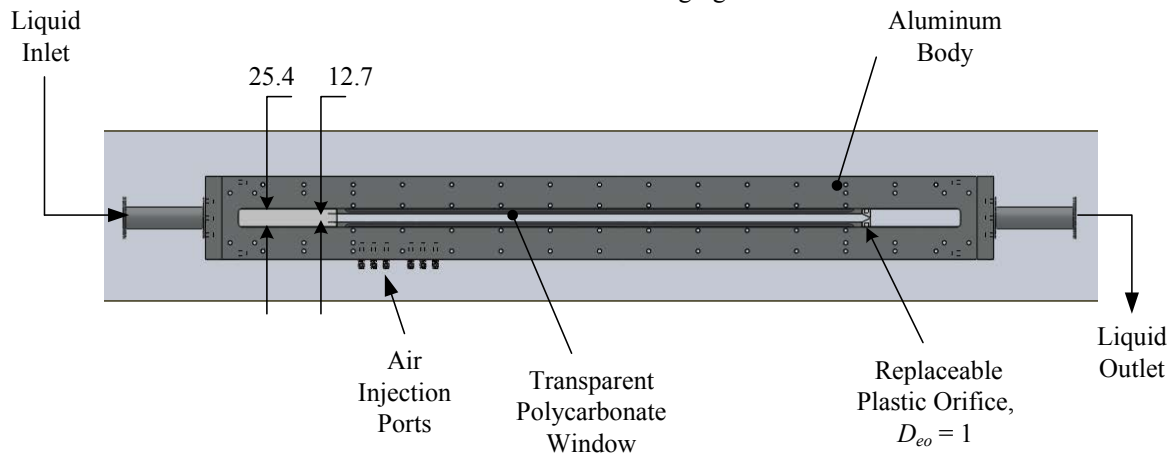


**Figure 1:** Schematic of the flow channel. All dimensions are in mm.

The two phase flow phenomena inside the channel were studied for different GLR values. High speed shadowgraph imaging was used to capture bubble formation, gas jet breakup and interaction of the bubbles with exit orifice. The shadowgraph system consisted of a high speed camera ( Lightning RDT Motion Pro, Redlake Inc.) and a high intensity diffused light source for illumination. The camera was operated at 3000 frames per second which allowed the capture slow motion movies of behaviour of gas jet and air bubbles in liquid cross flow. The raw images obtained from the camera are processed using an image processing technique as described below.

## Image Processing

An example single raw image obtained from the camera is shown in Fig. 2(a). The image has a non-uniformly illuminated background. In the image processing scheme, images are processed to identify the gas jet and the bubbles in the field-of-view. The bubbles shown in the raw image have darker edges compared to the background. The image is inverted based on its intensity, so that the images of the bubbles and the gas jet have higher intensity compared to the background. The inverted image is passed through a non linear morphological subtraction filter which is used to remove the non-uniform background. The contrast of the image is enhanced using an intensity mapping function to obtain distinct structures of the gas bubble and the result of this processing step is shown in Fig. 2(b). A Sobel's method of edge detection was used to identify the edges of the gas bubbles. Once the edge of the bubble is identified, it's size is dilated to prevent any gaps in the outline of the bubble shape. The intensity of all the pixels inside the edge boundary are assigned with a value of 1 and rest of the pixels in the image are assigned a zero value, binarizing the image. The image is subsequently eroded to negate the effect of change in size which occurring during dilation process. The final black and white images are obtained after image processing as shown in Fig. 2(c).

The sizes of the bubbles are detected by determining the number of connected pixels which have an intensity value of 1. The equivalent diameter is calculated by finding out the area of the pixels occupied by a bubble image and equating it to a circle with diameter,  $d_{eq}$  which will occupy the same area as that of the bubble image. The equivalent diameters of the all the bubbles that are obtained in an image are recorded. For each GLR case; 7550 images are obtained at 3000 fps per second. The current results are obtained by scanning through all the images with interval of 50 images (Image 1, Image 50, Image 100...Image7550). This was done to avoid repetition while calculating the bubble diameters. With an interval of 50 images, the same bubble will not appear in the field of view in two consecutive images.

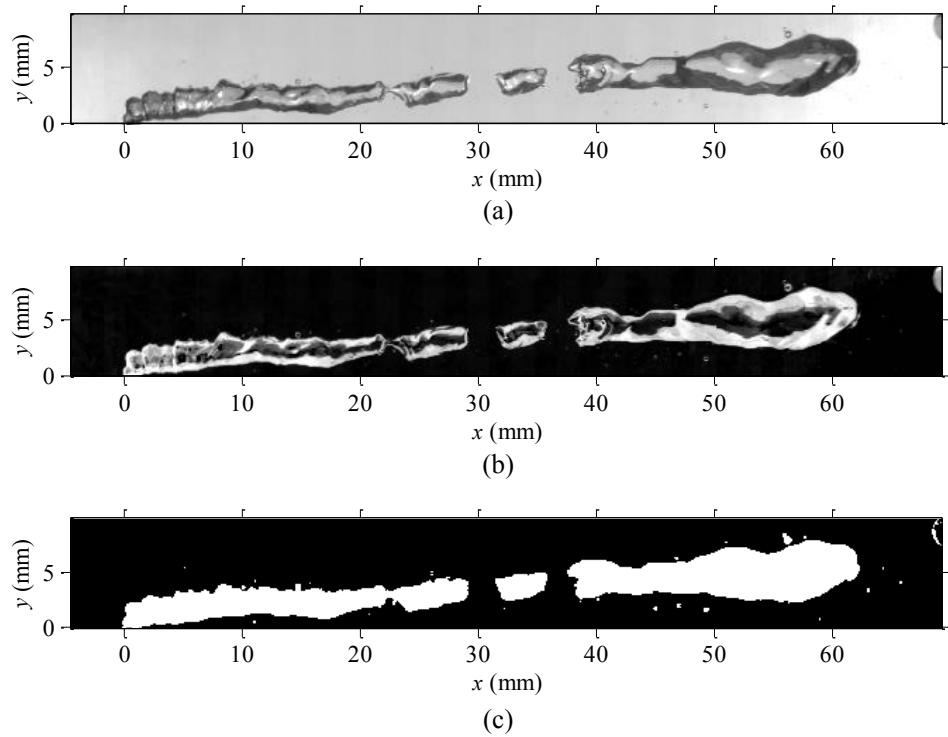


**Figure 2:** Image of a gas jet breaking up into bubbles in liquid cross flow (a) Raw image (b) Image after removal of background and (c) Final processed image

## Results and Discussion

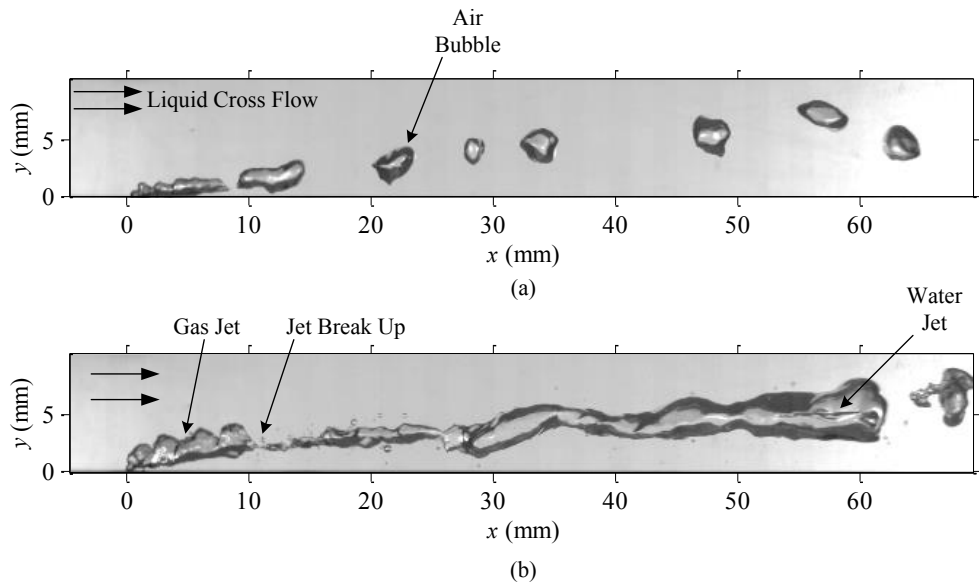


**Figure 3:** Injection of gas into liquid cross flow at two different GLR values (a)  $GLR = 3.30 \times 10^{-5}$  (b)  $GLR = 13.23 \times 10^{-5}$

Figure 3 shows the images of gas injection into liquid cross flow at injection location. Fig 3(a) and Fig. 3(b) show injection of gas at GLR values  $3.3 \times 10^{-5}$  and  $13.32 \times 10^{-5}$  respectively. At lower GLR values small circular gas bubbles are observed to be formed and length of the gas jet is also small (Fig 3(a)). At higher GLR values, a larger gas jet is formed, as well as, the gas jet breaks up into larger bubbles (Fig 3(b)). The bubbles or the gas jet

formed for higher GLR values were observed to undergo deformation in a periodic manner. One such event is captured in the image shown in Fig. 3(b). The end of the gas jet begins to form a large bubble, undergoes a deformation and a water jet appears to travel through the centre of the bubble. This event was observed to regularly coincide with the breakup of the gas jet. From observation of the time series image data, it is believed that a pressure surge travelling in negative  $x$  direction is responsible for such a deformation and water jet phenomenon.

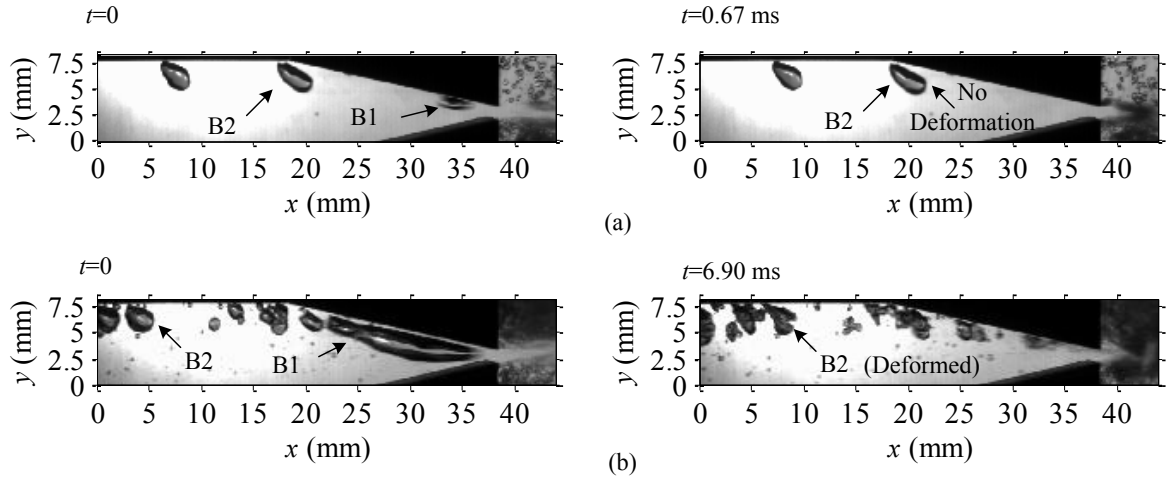


**Figure 4:** Interaction of exit orifice with bubbles at two different GLR values. (a)  $GLR = 3.30 \times 10^{-5}$  (b)  $GLR = 13.23 \times 10^{-5}$

Figure 4 shows the interaction of bubbles with the exit orifice downstream from the gas injection location for the same two GLR's shown in Fig. 3. Fig. 4(a) shows a small bubble denoted by B1 passes through the exit orifice. Small bubbles formed at low GLR values at upstream location travels downstream and interact with the exit orifice. Another bubble B2 which is located further upstream of B1 is observed when B1 passes through the nozzle. In the case of low GLR values, where bubbles with smaller diameter appear at the exit orifice, the shape of bubble B2 remains unaffected. The shape of bubble B2 at left and right of the Fig. 4(a) remains unaltered as the bubble B1 passes through the orifice.

With increase in GLR, the size of the bubbles reaching the downstream nozzle location increases. When bubble B1, a large bubble compared to the exit orifice, passes through the exit, it blocks the small orifice with gas. Water in the main channel accelerates as the less dense and compressible air pass through the nozzle. This is followed by a rapid deceleration and the incompressible water begins to flow through the nozzle. With this deceleration a pressure surge is believed to be generated that propagates upstream. The appearance of the pressure surge can be observed by looking at the deformation of the bubble B2 just after bubble B1 passes through the exit orifice shown in Fig. 4(b). This pressure surge originating at the downstream of the nozzle is believed to be transmitted will upstream and influences gas jet break up and bubble formation. This pressure pulse results in a feedback loop between the generation of the pressure surge by the large bubbles and the large bubble formation process.

A quantitative measurement of the equivalent diameter of the bubbles is undertaken for different GLR values. A statistical representation was carried out in the form of probability density functions (pdf) to show the size distribution of the equivalent bubble diameters at different GLR values. The statistical diameter trends are plotted for injection location as well as for downstream orifice location. The image processing algorithm has successfully detected a large number of small bubbles which have typical size range less than 1.5 mm in equivalent diameter. Due to the high number of these bubbles, the pdf will be biased towards the small bubbles. A cut off range for the statistical analysis was determined and it was found to be 1.5 mm. All bubbles exceeding an equivalent diameter of 1.5 mm are plotted in the pdf shown in Fig. 5.

The diameter trends at the injection location of gas into the bubble chamber are shown in Fig. 5(a). The positive tails of diameter profile increases with increase in GLR values. There is a sharp peak for GLR value  $3.30 \times 10^{-5}$ . This is due to the fact that at low values of GLR; small circular bubbles are generated with steady size distribution which gives the sharp peak. The small bubbles, with such a size distribution, squeeze through the small orifice without blocking it and there is no evidence of a pressure surge. However, with increase in GLR values, the gas jet breaks up into larger bubbles. This is confirmed from flow visualization as well as from the diameter trends displayed in Fig. 5. The large bubbles continuously shreds off small bubbles as they travel

downstream through the channel. The larger bubbles which are formed intermittently are believed to be responsible for the pressure surge. At downstream location for higher GLR value there is a significant number of small bubbles compared to upstream location. This is evident by comparing the diameter trends for GLR value  $13.23 \times 10^{-5}$  in Fig 5 (a) and Fig 5 (b).

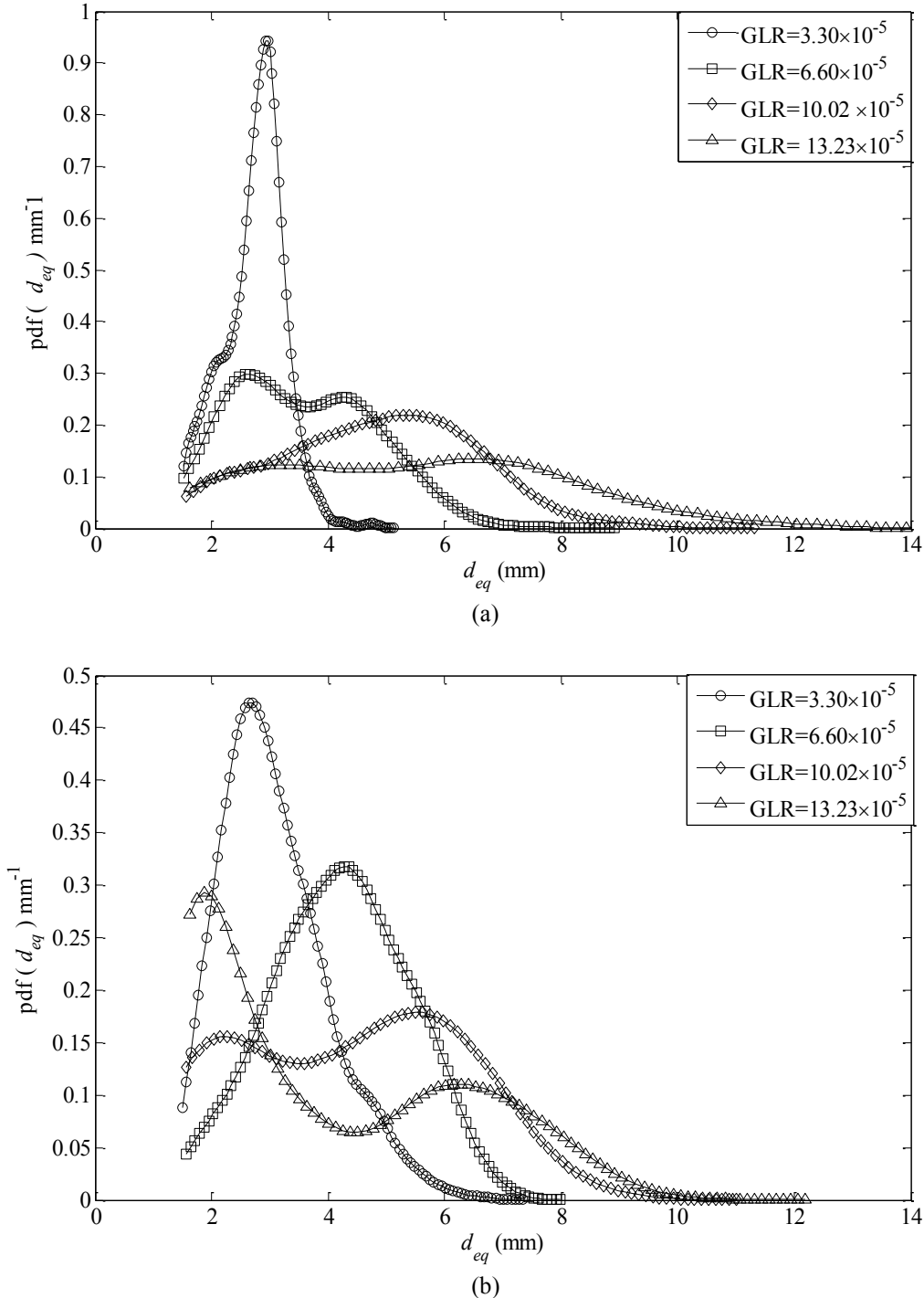


**Figure 5:** Probability distribution of equivalent diameter of gas bubbles at different GLR values.  
 (a) Injection location at upstream of the channel  
 (b) Exit orifice location at downstream of the channel

## Conclusions

In the present work the interaction of bubbles with exit orifice is captured. The bubble size appears to have an influence in generating flow structures resulting from the generation of pressure waves at the exit of the effervescent nozzle. Intermittent choking of the nozzle exit orifice generates a pressure wave which influences two phase flow structure upstream of the channel. Quantitative study along with flow visualization technique shows that for bubble size approximately three times the diameter of the exit orifice can squeeze through the orifice without choking it. Understanding of this phenomenon will lead to design of more stable effervescent spray systems.

## Acknowledgments

The authors acknowledge funding support for this research from Alberta Ingenuity Fund, the Natural Sciences and Research Council (NSERC) of Canada, and the Canadian Foundation of Innovation (CFI).

## References

- [1] T. C. Roesler, A. H. Lefebvre, in *Proc. of the Meeting of the Central States Section of the Combustion Inst.*, (1998).
- [2] D. Konstantinov, R. Marsh, P. J. Bowen, A. Crayford, Effervescent Atomization for Industrial Energy-Technology Review, *Atomization and Sprays* **20**, 525–552 (2010).
- [3] S. Ghaemi, P. Rahimi, D. S. Nobes, Effect of Bubble Generation Characteristics on Effervescent Atomization At Low Gas-Liquid Ratio Operation, *Atomization and Sprays* **20**, 211–225 (2010).
- [4] S. Maldonado *et al.*, Development of an Experimental Method To Evaluate the Stability of Gas-Liquid Sprays, *Atomization and Sprays* **18**, 699–722 (2008).
- [5] C. A. Catlin, J. Swithenbank, Physical Processes Influencing Effervescent Atomizer Performance In The Slug and Annular Flow Regimes, *Atomization And Sprays* **11**, 575–595 (2001).
- [6] J. Y. Kim, S. Y. Lee, Joo Youn Kim and Sang Yong Lee, **11**, 735–756 (2001).
- [7] X. Huang, X. Wang, G. Liao, Visualization of two phase flow inside an effervescent atomizer, *Journal of Visualization* **11**, 299–308 (2008).
- [8] D. Sen, M.A. Balzan, D.S. Nobes and B.A. Fleck, Bubble Formation and Flow Instability In An Effervescent Atmoizer, *Journal of Visualization*, Submitted 2013.

## Jet formation from laminar two-phase-flow in a tapered channel

Alexander Stratmann, Axel Mescher and Peter Walzel

Particle Technology Lab, TU Dortmund, Germany

### Abstract

In the past, laminar and turbulent two-phase flow was investigated for different channel-geometries. This work focuses on the development of a laminar two-phase flow in a channel with triangular cross-section attenuating in downstream direction. Additionally the channel is curved and stable stratified flow is maintained up to the outlet due to the centrifugal effect. Depending on the flow conditions jets of different shapes are formed at the channel orifice. After detachment the coaxial gas flow triggers wind-induced break-up of the liquid jet. Differently viscous liquids, i.e. water and water-glycerol solutions were used at different flow-rates of liquid and air. The jet and drop formation was analyzed by backlight images. It is shown, that the break-up length reaches a maximum value and decreases for further increased gas flow-rates and gas-Weber-numbers respectively. Besides the investigation of jet-formation and break-up length the drop size distribution was measured. Mean drop sizes and *span* values are discussed. The experiments are compared to theoretical models.

---

### Introduction

Gas-liquid flow has been investigated for multiple geometries and flow conditions. The investigations first focused on the behavior of free liquid jets in ambient air [1]. It was shown, that break-up of liquid jets can be separated in different break-up regimes. From low to high liquid velocities the regimes are draining, dripping, laminar break-up, i.e. Rayleigh break-up and atomization. First findings were published by Plateau [2]. Especially laminar jet break-up has a major advantage compared to other liquid break-up mechanisms as e.g. sheet break-up, for example pressure nozzles. Narrow drop size distributions can be achieved at proper flow conditions. However, the drop formation rate is limited and the throughput is low. The jet diameter and the produced drop size are linked as shown by Rayleigh [3]. Jet attenuation can be achieved by acceleration, e.g. with spiraling jets (LAMROT) [4] emerging from rotating systems or by flow focussing by surrounding air stream. Walz [5], Calvo [6] and Groom [7] have studied the influence of a coaxial gas stream surrounding a liquid jet. They were able to attenuate liquid threads leading to smaller drops or fibres, but still saving a narrow drop size distribution. Gordillo et al. [8] investigated an analytical model to describe the break-up length and jet diameter in a coaxial liquid-gas flow.

The present work covers the aspect of thin jet formation from a tapered and simultaneously curved channel. Gas and liquid are supplied to the channel inlet exhibiting a fairly large cross sectional area. Downstream the channel cross section reduces and both phases get accelerated leading to a thin liquid film moving in the groove of the triangular cross-section. At proper flow conditions the thin liquid film detaches as laminar jet. The curvature helps to hold the phases within separate flow domains.

Application of the system could help collecting of broadly distributed aerosols from chaotic gas liquid mixtures and to discharge the liquid with a well specified drop size subsequently allowing for efficient phase separation.

### Experimental test-rig

A tapered channel was fabricated from PMMA, in order to allow for observing the accelerated open channel flow inside the channel together with the investigation of the liquid jet break-up at the outlet. The inlet cross-sectional area of the channel was  $32 \text{ mm}^2$  and the outlet area was  $1.5 \text{ mm}^2$ . A sketch of the channel is shown in figure 1. The channel represents a  $90^\circ$  spherical sector with an outer radius of  $R_a = 35 \text{ mm}$ . The channel has a triangular cross section for flow stabilization reasons.

The experimental test rig is shown in figure 2. The fluid is supplied by a gear pump and fed into the gas stream by a syringe capillary. A thin and stable liquid film is formed due to the small gap between capillary and channel inlet. The ratio between the outer capillary diameter  $D_C = 1.1 \text{ mm}$  and channel inlet diameter  $D_{hy} = 8 \text{ mm}$  is small, allowing for only minor disturbances of the air flow. The air is supplied by the compressed air network of the lab and the gas-pressure is controlled. The volumetric flow-rates of gas and liquid are measured. All experiments were carried out at ambient air pressure. The overpressure of the gas-flow at the channel inlet was varied in the range of  $4 < \Delta p < 17 \text{ mbar}$ . It is measured by a U-tube manometer. Water and aqueous solutions of glycerol were used for variation of viscosity between  $1 < \mu_l < 3 \text{ mPas}$ . This leads to different but



small Ohnesorge numbers based on the nozzle outlet diameter with  $Oh = \mu_l / (D_{hy} g_l \sigma)^{1/2}$ . The liquid to gas ratio  $\rho_l / \rho_g$  was varied between 2 and 100.

For the first experiments the nozzle was installed with  $\alpha = 60^\circ$ -inclination towards the horizontal plane. The inclination angle was not varied during the present study. A backlight imaging equipment was used for flow characterization. In order to improve the contrast of the images and the visibility of jet and drops the fluid was colored with black ink. Due to the low concentration of the ink of 1% (mass), the liquid properties were only slightly influenced.

The images were acquired via a CCD-camera (AVT Stingray F504) at a low shutting rate. Backlight was provided by a pulsed LED-panel and synchronized to the imaging cycle of the camera. The image acquisition rate was 2.5 Hz and a total number of 20 images was taken for each measurement. All images were processed and analyzed by an in-house MATLAB<sup>TM</sup> routine. The jet length, jet diameter and drop size distribution were extracted from the image series. Because of relaxation of the initially triangular flow cross-section at the channel outlet the initial jet diameter could not be measured directly. Therefore the diameter of the jet with circular cross-section is taken at different distances from the outlet and extrapolated towards the channel orifice.

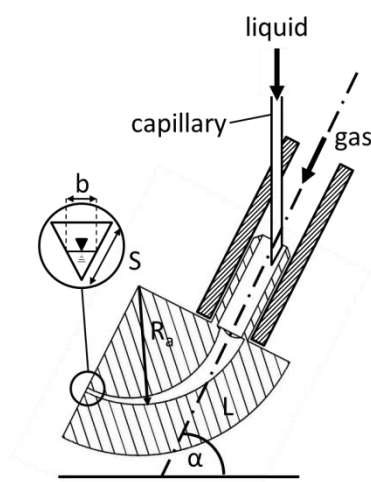


figure 1: scheme of the tapered channel with triangular cross section

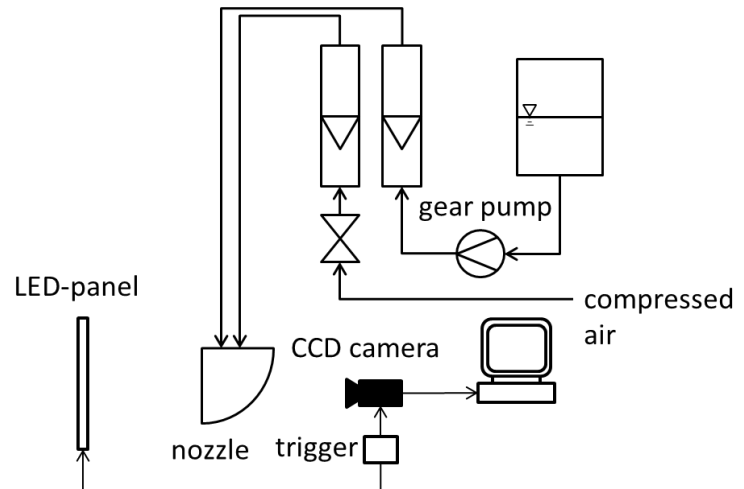


figure 2: experimental test rig

The drop size was analyzed and three representative diameters  $d_{10,3}$ ,  $d_{50,3}$  and  $d_{90,3}$  were calculated according to the 10%, 50 % and 90%-percentile of the accumulated volumetric drop size distribution. The width the drop size distribution can be described by the *span*-value defined in equation (1).

$$span = \frac{d_{90,3} - d_{10,3}}{d_{50,3}} \quad (9)$$

Small *span*-values represent narrow drop size distributions.

### Mathematical modelling

In the present work a straightforward approach for jet diameter estimation was used. For both phases the energy balance of the flow was formulated as shown in equation (10) and (11).

$$\Delta p_l = \frac{\rho_l v_l^2}{2} - \int \lambda_{wl} \rho_l v_l \frac{x}{d_{hy,l}} dx + \int \lambda_{lg} \rho_g v_g \frac{x}{b} dx \quad (10)$$

$$\Delta p_g = \frac{\rho_g v_g^2}{2} - \int \lambda_{wg} \rho_g v_g \frac{x}{d_{hy,g}} dx - \int \lambda_{lg} \rho_g v_g \frac{x}{b} dx \quad (11)$$

The pressure drop of both phases was formulated with respect to the dynamic pressures of both flow components and the characteristic friction coefficients. Both pressure drops depend on the height of the liquid flow, its hydraulic diameter respectively. The friction factors  $\lambda_{wl}$  for the liquid-wall interaction is calculated by Hagen-Poiseuille's law as  $\lambda_{wl} = 64/Re$  considering laminar flow. The gas-wall interaction  $\lambda_{wg}$  is calculated by Blasius' law  $\lambda_{wg} = 0.316 \cdot Re^{-1/4}$ , as the gas-flow has turbulent character. Typical effective *Re*-numbers are 100-700 for the liquid flow and 2000 – 4500 for the gas flow. A liquid-gas friction factor  $\lambda_{lg}$  was fitted to the experimental data. The fitted value is  $\lambda_{lg} = 0.08$ , matching typical values of turbulent flows in channels. The

roughness here is represented by the waviness of the gas-liquid interface. However, this aspect was not examined in detail during the present study.

The hydraulic diameters of both, the gas- as well as the liquid flow was calculated as  $d_{hy} = 4A/S$ , where  $A$  represents the cross-sectional area of the individual phase and  $S$  represents its contact line. As both pressure drops can be assumed to be equal for both phase, the energy balance results in an implicit equation describing the height of the liquid film at the outlet of the tapered channel.

$$h_l = H \left( 1 + \frac{\dot{V}_g}{2\dot{V}_l} \sqrt{\frac{\rho_g}{\rho_l} \frac{1 - \lambda_{gl} \frac{2H}{h_l S} - \lambda_{gL} \frac{(1 + h_l/H) + 1/2}{(H - h_l^2/H)}}{1 - \frac{32\mu_l SL}{\rho_l \dot{V}_l}}} \right)^{-1/2} \quad (4)$$

The experiments have shown a slight decrease in liquid film height along the tapered channel. However, during the present study the hydraulic diameter of the liquid flow was assumed to be constant along the channel for simplification. The model will be further refined and the impact of the decreasing film thickness will also be included.

According to the calculated and/or measured film thickness and by knowledge of the volumetric flow-rate the detachment velocity  $v_l$  of the liquid film can be determined. It corresponds to the initial velocity of the jet. Based on that and by measurement of the initial diameter of the liquid jet  $d_j$ , the Weber-number for the liquid can be calculated.

$$We_l = \frac{d_j v_l^2 \rho_l}{\sigma} \quad (5)$$

Rayleigh [3] formulated a mathematical model to determine the characteristic disturbances of laminar jets with given diameters and liquid properties. For the in-viscid case the diameter of the drops is  $d = 1.89 \cdot d_j$ . Weber [1] also included the effect of the liquid viscosity. Besides the characteristic frequency of the jet break-up a characteristic growth rate and the break-up time respectively, can be estimated. For a given detachment velocity the break-up length of the jet can therefore also be calculated. Viscosity exerts a damping effect on the break-up frequency and leads to higher break-up lengths, see equation (6).

$$l = k \cdot d_j \left( \sqrt{We_l} + 3 \frac{We_l}{Re_j} \right) \quad (6)$$

With  $Re_j = d_j v_l \rho_l / \mu_l$ , the factor  $k$ , representing the influence of the initial amplitude of the jet disturbance, was estimated by Weber as  $k = 12$  for water in a free falling jet [1] based on the experiments of Haenlein [9].

## Results and Discussion

Different volumetric flow-rates of the liquid and the gas phase were investigated. The impact of the gas on the liquid jet was expressed by a gas-Weber number  $We_g = (D_{hy} v_g^2 \rho_g) / \sigma$ . The gas-Weber-number is defined with the hydraulic diameter of the triangular channel outlet  $D_{hy}$ , in order to describe the gas influence on the liquid flow. For a given liquid,  $We_g$  is only influenced by the detachment velocity  $v_l$ . This formulation allows for a better illustration of the experimental results. The liquid flow inside the tapered channel was characterized by a liquid flow-rate-Reynolds number  $Re_l = (\rho_l \dot{V}_l) / (D_{hy} \mu_l)$ . It is as well formed with  $D_{hy}$ .

The experiments were carried out with water and water-glycerol solutions at varying  $Oh$ -numbers. Three flow and break-up regimes were observed. First at low  $We_g$  the liquid forms individual drops at the nozzle orifice. This “dripping” case was not further investigated during the present work. The first data shown in figure 3 correspond to the first occurrence of jets. By increasing the air-flow a jet is formed at the nozzle, being bend downward by gravity. It was observed, that for lower liquid flow-rates, higher initial gas flow-rates are needed to form a liquid jet. This can be explained by the stronger braking effect at low liquid flow-rates. For such flow condition the jet break-up is dominated by the liquid velocity and follows the principles of Rayleigh break-up [3]. By increasing the air-flow, the liquid jet is lifted and the gas-flow surrounds the liquid jet. The jet length increases with higher gas flow-rates towards its maximum value. Afterwards further increased  $We_g$  leads to decreased break-up length and to wind induced jet break-up. The air disturbs the liquid jet, causing shorter and non-axisymmetric jets. In figure 3 a dashed line separates the axisymmetric and wind-induced break-up regimes.

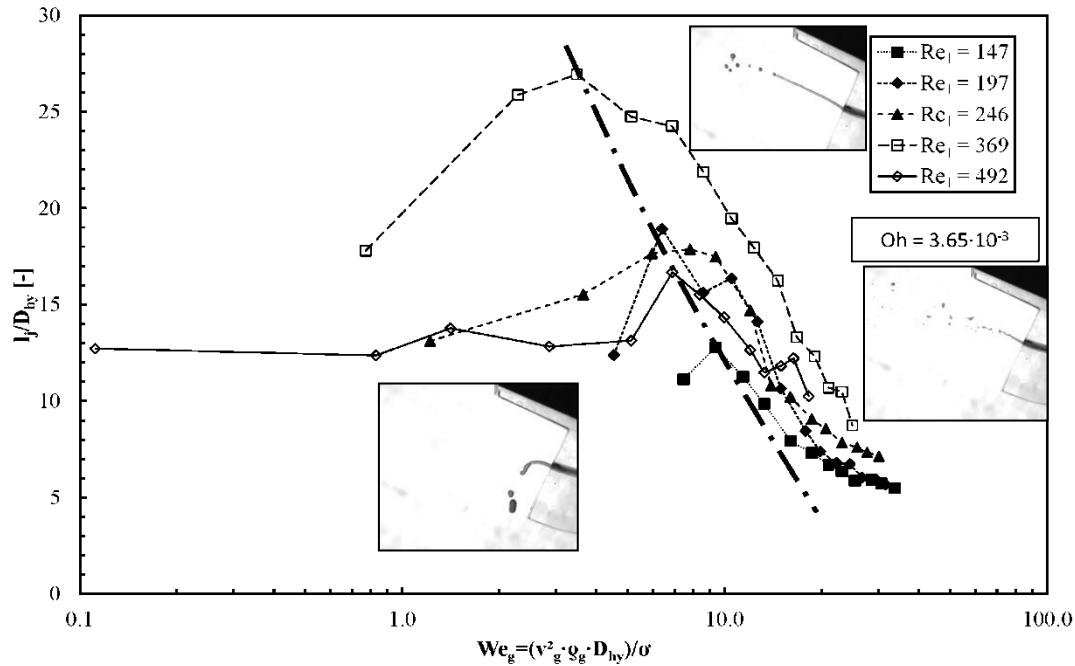


figure3: Related jet length at different  $We_g$  and liquid flow  $Re_l$ -numbers

In further experiments, the viscosity was varied between 1 and 3 mPas. For the viscosities of 1 and 1.5 mPas jet formation could be observed for all investigated liquid flow-rates. At a viscosity of 3 mPas a stable liquid jet could not be produced for all combinations of liquid and gas flow-rates. The flow pattern changes from stratified liquid-gas flow to slug flow inside the tapered channel. The desired stratified gas/liquid flow could be obtained only at higher gas flow-rates. However, as soon as jet formation occurs, wind induced break-up was observed, due to the high gas flow-rate necessary for jet formation.

#### Jet diameter measurement

In figure 4 the jet diameter is shown for different volumetric flow-rates of water expressed by the Reynolds number  $Re_l = (Q_l)/(D_{hy}\mu_l)$ . It decreases corresponding to an increase of the gas pressure Reynolds number  $Re_{p,g} = (\Delta p \rho_g)^{1/2} D_{hy}/\mu_g$  representing the impact of the gas pressure. On the other hand the diameters are increasing for higher volumetric flow-rates of the liquid. Figure 5 shows the impact of viscosity for a liquid flow-rate of  $\dot{V} = 1$  l/h. For  $Re_{p,g}$  smaller than 2200 the jet diameter is larger for a viscosity of 3 mPas compared to the case of 1 mPas. The diameter decreases with rising  $Re_{p,g}$  due to higher gas pressures.

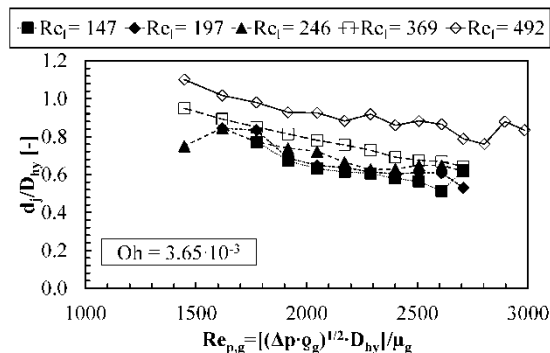


figure 4: Jet diameter related to the hydraulic diameter of the nozzle at different liquid flow-rates for water

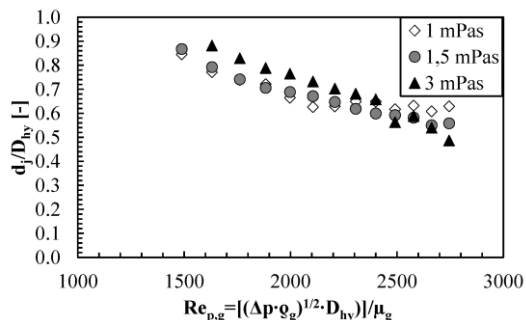


figure 5: Jet diameter related to the hydraulic diameter of the nozzle at different viscosities at a liquid flow-rate of  $\dot{V} = 1$  l/h

In figure 6 a comparison of measured jet diameters and the pressure balance model equation (4) is shown for a flow-rate of  $\dot{V}_l = 1$  l/h and a viscosity of  $\mu = 1$  mPas. The liquid-gas friction factor was fitted to be  $\lambda_{lg} = 0.08$ , matching typical values of flows in hydraulically rough ambience. The roughness here is represented by the waviness of the gas-liquid interface. However, this aspect was not examined in detail during the present

study. For higher viscosities an underestimation of the jet diameter was observed for the chosen friction coefficient. However, in all experiments a good agreement of the numerical and experimental values for  $d_j$  with a deviation of 15% could be found for  $\lambda_{lg} = 0.08$ .

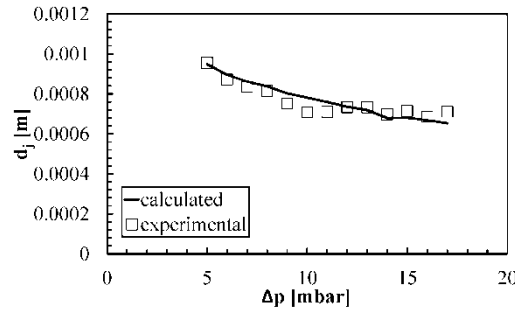


figure 6: calculated and measured jet diameters for a flow-rate of  $\dot{V} = 1 \text{ l/min}$  and a viscosity of  $\mu = 1 \text{ mPas}$

### Jet break-up length measurement

In figure 7 the liquid jet length related to the jet diameter is plotted vs  $We_L = (\rho_L v_L^2 d_j) / \sigma$ . At all viscosities and flow-rates an increase of the  $l_j/d_j$  ratios can be observed. For a higher liquid flow-rate the maximum of  $l_j/d_j$  rises. For increased viscosities the maximum is shifted towards higher  $We_L$ .

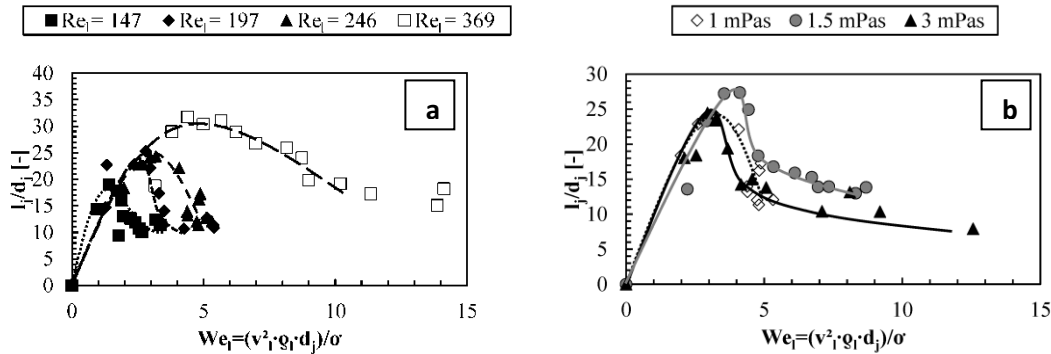


figure 7: experimental data of the jet length according to the liquid Weber number for different liquid flow-rates and  $\mu = 1 \text{ mPas}$  (a) and for a liquid flow-rate of  $\dot{V} = 1 \text{ l/min}$  and different viscosities (b).

The observed break-up lengths were compared to equation 5, even though Weber's law for jet break-up length is not valid for superimposed liquid-gas flow. However, at least at low gas-flow-rates such comparison may be reasonable. For the calculation of the liquid break-up length Weber and Haenlein proposed a k-value of 12 [9]. Due to the different experimental setups a deviation was observed between the proposed value of 12 and the optimum value for fitting the results of the present study. At least for experimental parameter-sets representing low gas-liquid interaction a remarkable coincidence between theory and experiments could be obtained by adjusting  $k = 15$ . The larger value of k suggests higher jet stability due to the elongation effect caused by the fast flowing gas. The predicted values for the liquid jet length and the measured length for different volumetric flow-rates and a viscosity of  $1 \text{ mPas}$  are shown in figure 8.

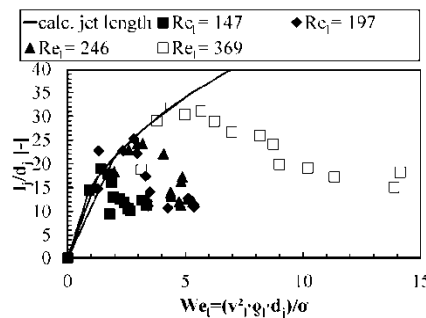


figure 8: Calculated ( $k = 15$ ) and experimental jet length at different liquid flow-rates.

## Drop size distribution

The drop size is measured by shadow imaging of the drops, a subsequent drops count and recalculation into a volumetric size distribution. The mean drop diameter  $d_{50,3}$  for  $Oh = 3.65 \cdot 10^{-3}$  is plotted against  $We_g$  in figure 9. The mean diameter decreases for higher gas flow-rates and increases at higher liquid flow-rates. The same effect is observed at increased viscosities.

In figure 10 the correlation between the jet diameter and the mean drop size is shown for  $Oh = 3.65 \cdot 10^{-3}$  for different gas and liquid flow-rates. At low gas-Weber numbers the drop size is slightly larger than the theoretical drop-to-jet-size-ratio of about 2. Increased gas-Weber-numbers lead to decreased drop sizes and lower values of the drop-to-jet-size-ratio.

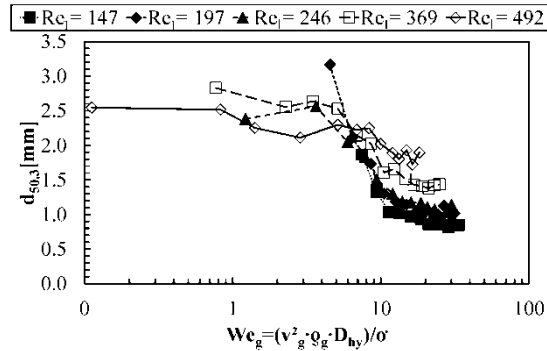


figure 9: mean drop size at different liquid flow-rates for  $\mu = 1 \text{ mPas}$

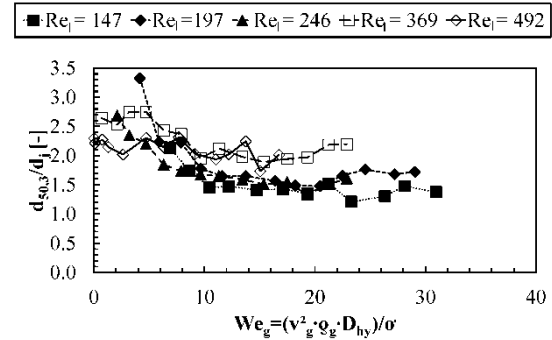


figure 10: Correlation between mean drop size and jet diameter for different liquid flow-rates at  $\mu = 1 \text{ mPas}$

The width of the drop size distribution can be described by the *span* value. Figure 11 shows the *span* for different  $We_g$  and  $Oh = 3.65 \cdot 10^{-3}$ . The *span* value rises with increasing  $We_g$ . For all gas-flow-rates, comparable *span* values below 1 were obtained. Increasing viscosity from 1 to 3 mPas does not change the *span*.

A flow condition was found leading to very low *span* value below 0.1 and nearly mono disperse drops with  $d_{50,3}/d_j = 0.92$  as shown in figure 12. The flow condition is characterized by very short break-up length due to strong gas-liquid interaction. However, the gas liquid interaction, does not lead to broadly distributed drop sizes in the mentioned case. The flow condition shown in figure 12 will be closer observed in future examinations.

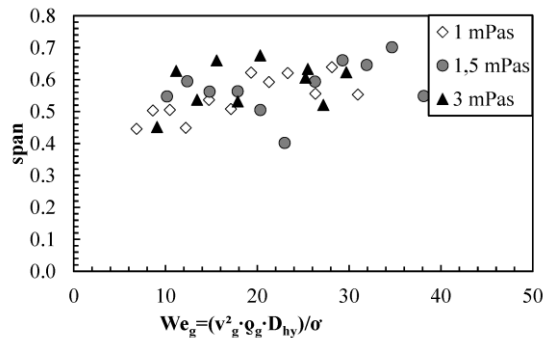


figure 11: *span* values for a liquid flow-rate of  $\dot{V} = 1 \text{ l/h}$  for 3 viscosities

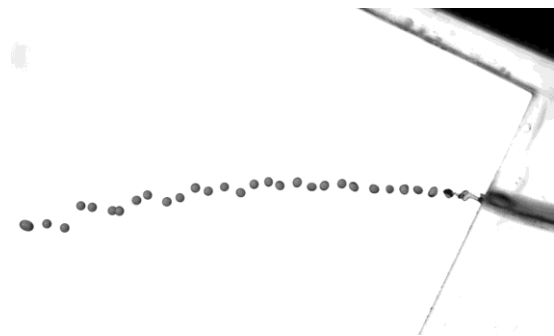


figure 12: image of near mono disperse drops at a viscosity of 3 mPas and a liquid flow-rate of  $\dot{V} = 1 \text{ l/h}$ ,  $\Delta p = 16.5 \text{ mBar}$

## Conclusions

The present work covers the detachment and formation of liquid jets from a stratified air-liquid flow in a tapered and curved channel with triangular cross-section. The behavior of the jet break-up length is comparable to free falling jets as long as the gas-liquid interaction is weak. Two break-up regimes, laminar and wind-

induced break-up could be observed for differently viscous liquids. At a viscosity of 3 mPas the desired stratified liquid-gas flow could not be obtained for higher liquid flow-rates as slug flow occurred. Rising  $Re_{p,g}$  leads to thinner jet diameters. The theoretical model for the jet diameter already fits experimental data in reasonable manner, but will be improved in future work. Largest drop size to jet diameter ratio was observed close to the theoretical value of about 2. However, for low  $We_g$  larger drop sizes were observed. By increasing  $We_g$  the drop size distinctly decreases. The *span* value for all experiments is below 1 except for wind-induced conditions. For special adjustments very low *span* values of about 0.1 could be observed, which will be closer investigated in a more detailed manner during future work.

## Nomenclature

b	side length of the liquid flow with triangular cross-section [m]
$d_{10,3}$	drop size representing the 10%-percentile of the volumetric drop size distribution [m]
$d_{50,3}$	drop size representing the 50%-percentile of the volumetric drop size distribution [m]
$d_{90,3}$	drop size representing the 90%-percentile of the volumetric drop size distribution [m]
$D_{hy}$	hydraulic diameter of the channel outlet [m]
$d_{hy}$	hydraulic diameter of one phase [m]
$d_j$	diameter of the liquid jet [m]
$d_i$	length of the liquid jet [m]
H	height of the channel exit [m]
$h_l$	height of the liquid phase in the channel [m]
L	Length of the channel [m]
$\dot{m}$	mass flow-rate [kg/s]
$Re_j = \frac{d_j v_l \rho_l}{\mu_l}$	jet Reynolds number
$Re_l = \frac{\dot{V}_l \rho_l}{D_{hy} \mu_l}$	liquid Reynolds number
$Re_{p,g} = \frac{\sqrt{\Delta p \rho_g} D_{hy}}{\mu_g}$	gas pressure Reynolds number
S	side length of the channel exit [m]
v	velocity of phases at channel exit [m/s]
V	volumetric flow-rate [m <sup>3</sup> /s]
$We_g = \frac{D_{hy} v_g^2 \rho_g}{\sigma}$	gas Weber number
$We_l = \frac{d_j v_l^2 \rho_l}{\sigma}$	liquid Weber number
$\mu$	dynamic viscosity [Pas]
$\rho$	density [kg/m <sup>3</sup> ]
$\lambda$	friction factor
$\sigma$	surface tension [N/m <sup>2</sup> ]
$l, g$	indices for the gas and liquid phase

## References

- [1] Weber, C.; Zum Zerfall eines Flüssigkeitsstrahles; Zeitschrift für angewandte Mathematik und Mechanik; 1931; (11); p136–154.
- [2] Plateau, J. A. F.; Statique expérimentale et théorique des liquides soumis aux seules forces moléculaires; Gauthier-Villars; 1873; (2).
- [3] Rayleigh, S. J. W.; On the instability of jets; Proc. London Math. Soc.; 1878; (10); p4–13.
- [4] Schröder, T.; Walzel, P.; Design of Laminar Operating Rotary Atomizers under Consideration of the Detachment Geometry; Chem. Eng. Echnol.; 1998; (21); p349–354.
- [5] Walz, A.; Mayer, M.; Theoretische und experimentelle Untersuchung zur Herstellung von Stein- und Glaswolle in Blasdüsen; Glastechnik Berichte; 1966; (8); p359–370.
- [6] Ganán-Calvo, A. M.; Barrero, A.; A novel pneumatic technique to generate steady capillary microjets; J. Aerosol Sci.; 1999; (30); p117–125.
- [7] Groom, S.; Entwicklung und Optimierung pneumatischer Mikrozerstäuber für den verbesserten Probeeintrag in der Plasmaemissionsspektrometrie AES; ().
- [8] Gordillo, J. M.; Pérez-Saborid, M.; Ganán-Calvo, A. M.; Linear stability of co-flowing liquid–gas jets; Journal of Fluid Mechanics; 2001; ().
- [9] Haenlein, A.; Über den Zerfall eines Flüssigkeitsstrahles; Forschung im Ingenieurwesen; 1931; (2); p139–149.



## **Influence of mixing chamber length and liquid viscosity on the effervescent atomization of maltodextrin solutions**

Philipp Stähle, Volker Gaukel and Heike P. Schuchmann

Institute of Process Engineering in Life Sciences, Section I: Food Process Engineering, Karlsruhe Institute of Technology (KIT), Karlsruhe, Germany

### **Abstract**

The effervescent atomizer was invented in the field of combustion technology. It is reported to atomize relatively high viscous liquids into small spray drops at low atomizing gas consumption (1). These findings make the atomizing principle also interesting for applications like spray drying of food based liquids. Therefore, we investigated the influence of the shear viscosity (0.014 to 0.308 Pa s), the gas pressure (0.2 to 0.6 MPa) and the mixing chamber length (0.76 to 96.5 mm) on the effervescent atomization of maltodextrin solutions. The mean spray drop size  $x_{1,2}$  increases with increasing shear viscosity of the liquid. The gas pressure shows a beneficial effect on  $x_{1,2}$  for a low shear viscosity whereas its effect diminishes at higher shear viscosities. At low gas pressures the mixing chamber length shows no influence on  $x_{1,2}$  regardless of the shear viscosity. At the highest gas pressure  $x_{1,2}$  shows a decreasing tendency with a decreasing mixing chamber length. Overall, the air to liquid mass ratio shows the major influence on  $x_{1,2}$  especially for values below 0.2. The findings of this study are of importance if a high viscosity food based liquid has to be atomized in fine spray drops at low gas consumption.

---

### **Introduction**

Spray drying is a typical drying technique in the food industry to enhance the shelf life of water based foodstuffs. In this technique the liquid is atomized at the top of a tower and brought in contact with hot air afterwards. While the drops fall evaporation of the water and particle formation takes place. To ensure a stable process the produced spray drops have to form a dry crust before they get in contact with the dryer walls. If the spray drops are too large drying will be incomplete and the wet particles will deposit on the walls. This in turn is likely to have a negative impact on the product quality as well as on the safety and stability of the process. In an ideal process, all particles can be separated and collected from the air downstream. As in every drying process, the required drying energy is directly linked to the amount of water which has to be removed. Hence, a high dry matter content prior to the spray drying process is favoured. However, for common food based liquids the viscosity increases dramatically with an increase in dry matter content. This in turn is detrimental to the atomization so a stable drying process cannot be guaranteed. The pressure atomizer is a common atomizer in the food industry. However, this atomizing technique requires high pressures up to several 10 MPa to atomize liquids with elevated viscosity adequately. Another possible drawback of pressure atomizers may be the small dimensions of the exit orifice to ensure such high pressures at the desired flow rates of the liquid. Hence, if a suspension is to be atomized a pressure nozzle might get blocked. It is generally agreed that air assisted atomizers are more suitable to atomize liquids with high viscosity in fine spray drops. The main drawback of common air assisted atomizers is the high consumption of atomizing gas. At production scale of food spray dryers, producing several tons of powder per hour, the energy consumption of the air compressors makes the use of common air assisted atomizers uneconomic in most cases.

In the field of combustion technology a new air assisted atomizing technique was established which is reported to be relatively insensitive to liquid viscosity and works at low atomizing gas consumption (1). The effervescent atomizing technique is distinct from other air assisted atomizing principles in the way the atomizing gas and the liquid are brought together. In effervescent atomizers the gas is bubbled into the liquid in a mixing chamber before the liquid is ejected (1). According to Sovani et al. 2001, the atomizing gas has two functions: First, it squeezes the liquid into ligaments with reduced thickness inside the exit nozzle orifice and second, it expands upon exiting the nozzle shattering the liquid (1). The atomizing performance is directly linked to the two-phase flow pattern in the mixing chamber (2). For the construction of an effervescent atomizer, the geometry of the mixing chamber is a critical point since it influences the two-phase flow and hence the spray drop size. The mixing chamber length controls the travelling length and hence the time the two-phase flow is allowed to develop or transform. Results from literature show that the influence of the mixing chamber length on the spray drop size is not completely clear (3). It has been shown in many studies that spray drop size is a non-linear function of the atomizing gas/liquid ratio by mass (ALR). The spray drop size decreases sharply with an increase of ALR from zero to a specific value and thereafter decreasing only moderately with a further increase of ALR (1). According to Konstantinov et al. 2010, this is because of a change in the mechanism of drop formation at different ALRs: At low ALRs individual bubbles expand outside the nozzle and shatter the liquid. At larger ALRs more air is entrained which breaks the liquid into drops via aerodynamically induced shear and

disturbances. The transition from one regime to the other depends on the physical properties of the liquid (4). Another key operating parameter is the pressure drop between the mixing chamber and the surrounding of the atomizer. It is expected that the mixing chamber pressure is only slightly less than the atomizing gas supply pressure (4). Many studies showed that an increased gas pressure is promoting a fine atomization (1). The studies of the group around Lefebvre showed that there is an exception of this general rule for high viscous Newtonian liquids (5). In their work, viscosity and gas pressure was changed in the range of 0.4 to 0.968 Pa s and 1.12 to 2.35 MPa, respectively, and no influence of the gas pressure on the spray drop size was observed. Regarding the physical properties of the liquid the viscosity is believed to have the strongest influence on the atomization (4). Here, literature reveals some contradictorily results: On the one hand, the spray drop size is found to be nearly or completely independent of liquid viscosity (5, 6). On the other hand, an enhanced liquid viscosity was detrimental to the atomization and resulted in bigger spray drops (7).

The majority of the numerous fundamental studies about effervescent atomizers used water or other low viscosity liquids typical for combustion technology. In contrast to this, we investigated the effervescent atomization of a high viscosity food based liquid. Care was taken to meet the physical properties of representative liquids which are commonly spray dried in food industry. Additionally, we studied the influence of gas pressure and mixing chamber length on the effervescent atomization of a food based liquid. The latter two parameters were chosen as they were identified to affect atomizer performance and are important for the construction of an effervescent nozzle.

### Experimental test-rig

As a typical food based liquid with mutable viscosity we dissolved different amounts of powdered maltodextrin (C\*Dry MD 01910, Cargill, Germany) in distilled water. In the calculation of the weight based powder concentrations the water content was considered. We determined the shear viscosity  $\eta$  of the solutions with a rotational rheometer (MCR101 or MCR301, Anton Paar, Ostfildern, Germany) equipped with a coaxial cylinder system (CC-27, Anton Paar). After equilibration to a temperature of 25 °C for 3 min the flow curves of the samples were recorded at a shear rate range of 1 1/s to 1000 1/s. The latter is the upper limit of the rheometer. The density  $\rho$  and the refraction index RI of the liquids were measured with a refractometer (Carl-Zeiss) and a pycnometer, respectively.

To adjust the flow rate of the solutions in the atomizer we changed the motor speed of an excentric screw pump (MD 006-12, Seepex, Bottrop, Germany). Using a gear volume flow indicator (VSI 04/16, VSE, Neuenrande, Germany) the liquid flow rates were set in the range of 6 l/h to 21 l/h with equidistant steps of 3 l/h (SI units:  $1.6671 \cdot 10^{-6} \text{ m}^3/\text{s}$  to  $5.833 \cdot 10^{-6} \text{ m}^3/\text{s}$ , steps  $8.337 \cdot 10^{-7} \text{ m}^3/\text{s}$ ). A schematic drawing of the vertical mounted “outside-in” effervescent atomizer is drawn in Figure 1.

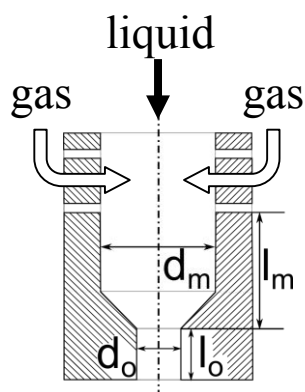


Fig. 1: Schematic drawing of the “outside-in” effervescent atomizer

The liquid enters centered from the top, flows down inside the pipe and gets radial penetrated by the atomizing gas flowing through nine injection holes in total. Each injection hole had a diameter of 0.5 mm. The holes were asymmetrically distributed over the perimeter in two levels with a spacing of 10 mm. We define the mixing chamber length  $l_m$  as the distance between the last gas injection row downstream and the onset of the exit orifice. In this work, we investigated different mixing chamber lengths of 0.76, 36.5 and 96.5 mm whilst keeping the mixing chamber diameter  $d_m$  constant at 6 mm. The restriction between the mixing chamber and the exit orifice had a full angle of 118 °. For all trials the exit orifice diameter  $d_o$  and the length  $l_o$  of the exit orifice was 1.5 mm, respectively. Pressurized gas was taken from the air supply of the building and controlled by a pressure reducer to gas pressures  $p_G$  of 0.2, 0.4 and 0.6 MPa. The resulting gas flow rate was measured for each

setting of gas pressure and liquid flow rate based on the heat capacity of the gas (High-Tech EL-FLOW, Bronkhorst, AK Ruurlo, Netherlands).

After the discharge of the two-phase flow from the exit nozzle orifice we measured the spray drop size at a downstream distance of 250 mm with a laser diffraction spectroscopy (Spraytec, Malvern, Herrenberg, Germany) in the center of the spray. The system was equipped with a 750 mm range lens covering a drop size range of 2 to 2000  $\mu\text{m}$ . The analysis of the scattering data was done by consideration of the respective refractive indexes according to Mie theory. Due to the occurrence of a strong beam steering effect for 30 % maltodextrin the scattering data of the two detectors nearest to the laser axis were not considered for the analysis as proposed by (8). In case of the other maltodextrin solutions the scattering data of all detectors was taken into account. We chose the Sauter mean diameter  $x_{1,2}$  as a representative spray drop size for the hole spray. All data points reported with a standard deviation were repeated at least twice.

## Results and Discussion

### Material characterization

Figure 2 depicts the flow curves of the investigated maltodextrin solutions. All maltodextrin solutions studied show a Newtonian flow behaviour in the inspected shear rate range. The shear viscosity  $\eta$  increases from 0.014 to 0.308 Pa s with an increasing maltodextrin dry matter content from 30 to 50 %, respectively. The viscosity increase for 30 % maltodextrin at shear rates above 100 1/s is attributed to the occurrence of Taylor vortices in the shearing gap of the measurement device and therefore not taken into account. Despite the observed Newtonian flow behaviour of the solutions a shear thinning behaviour beyond the shear rate limit of 1000 1/s cannot be excluded.

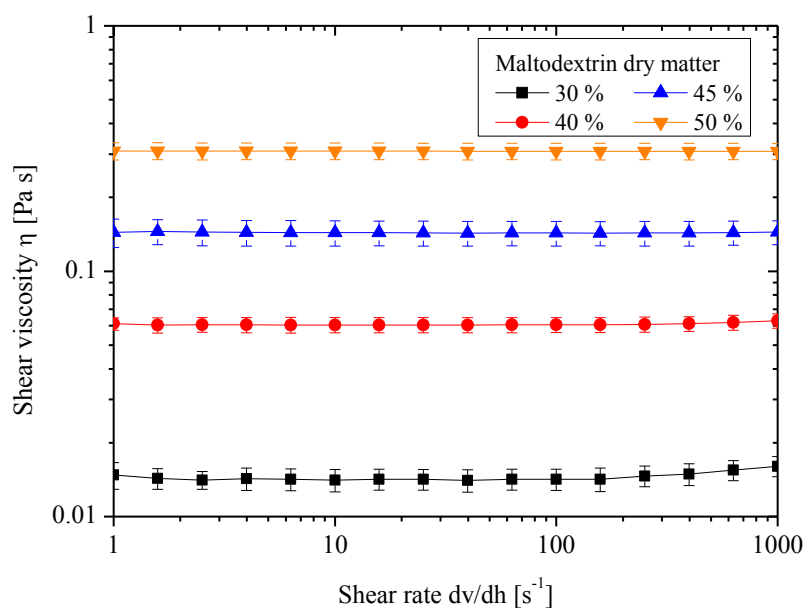


**Fig. 2:** Influence of shear rate on the shear viscosity in dependence of the maltodextrin dry matter concentration

The density  $\rho$  and the refractive index RI of the maltodextrin solutions increase from 1131 to 1242  $\text{kg/m}^3$  and from 1.385 to 1.431 with an increase in dry matter content from 30 to 50 %, respectively. Table 1 summarizes the physical properties of the maltodextrin solutions.

**Tab. 1:** Physical parameters of the maltodextrin solutions

Maltodextrin [wt.-%]	$\eta$ [Pa s]	$\rho$ [kg/m <sup>3</sup> ]	RI [-]
30	$0.014 \pm 0.001$	$1131 \pm 2$	$1.385 \pm 0.001$
40	$0.060 \pm 0.004$	$1185 \pm 1$	$1.406 \pm 0.001$
45	$0.143 \pm 0.016$	$1121 \pm 2$	$1.418 \pm 0.000$
50	$0.308 \pm 0.024$	$1242 \pm 2$	$1.431 \pm 0.007$

#### Influence of liquid shear viscosity on spray drop size

Figure 3 shows the Sauter mean diameter  $x_{1,2}$  as a function of ALR for a constant gas pressure  $p_G$  of 0.6 MPa and a mixing chamber length  $l_m$  of 35.5 mm. In Figure 3 the atomizing performance is shown in dependence of the shear viscosity of the maltodextrin solutions.

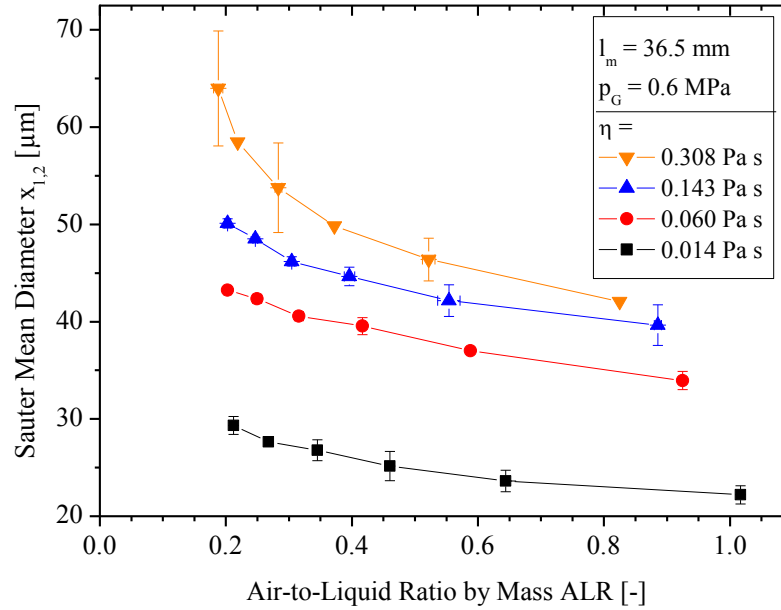


**Fig. 3:** Influence of ALR on the spray drop size in dependence of the shear viscosity

The results show that for all shear viscosities investigated  $x_{1,2}$  decreases with increasing ALR of 0.2 to 0.8 and higher. This effect is more pronounced at the highest shear viscosity. According to Konstantinov et al. 2010, this indicates a change in the drop formation mechanism with increasing ALR for a shear viscosity of 0.308 Pa s (4). On the other hand, for the lower shear viscosities of 0.014, 0.060 and 0.143 Pa s the effect of ALR on  $x_{1,2}$  is quite small indicating the same drop formation mechanism throughout the ALR range investigated. At a constant ALR  $x_{1,2}$  increases with an increasing shear viscosity. This finding is in contradiction to the studies of Buckner et al. (5, 6) but in accordance to the work of Schröder et al. (7).

To study the influence of shear viscosity on  $x_{1,2}$  at an ALR of 0.6 we added simple exponential fits to the data shown in Figure 3. The fits reveal that  $x_{1,2}$  increases from about 24 to about 44  $\mu\text{m}$  with increasing shear viscosity from 0.014 to 0.308 Pa s. The dependence of  $x_{1,2}$  on shear viscosity at investigated parameters (ALR = 0.6,  $p_G$  = 0.6 MPa,  $l_m$  = 36.5 mm) can be expressed with Equation 1:

$$x_{1,2} = c + A \cdot \exp(b \cdot \eta) \quad \text{Eq. 1}$$

The values of  $c$ ,  $A$  and  $b$  in Eq. 1 are  $43.29 \pm 0.81$ ,  $-27.27 \pm 2.04$  and  $-23.82 \pm 4.00$ , respectively, and the accuracy of the fit  $R^2$  is 98.88 %. This finding reveals that the influence of shear viscosity on  $x_{1,2}$  diminishes at higher values of the shear viscosity. A possible explanation for this effect could be a shear thinning behaviour of higher concentrated maltodextrin solutions at the actual shear rate during atomization. This would result in a lower shear viscosity as indicated by the rheometer measurements.

#### Influence of gas pressure on spray drop size

We investigated the effect of gas pressure on  $x_{1,2}$  in dependency of the shear viscosity of different maltodextrin solutions. Figure 4a) depicts the influence of ALR on  $x_{1,2}$  at a mixing chamber length  $l_m$  of 36.5 mm in

dependence of the gas pressure  $p_G$  at a shear viscosity of 0.014 Pa s. Figure 4b) shows the same results at a shear viscosity of 0.308 Pa s.

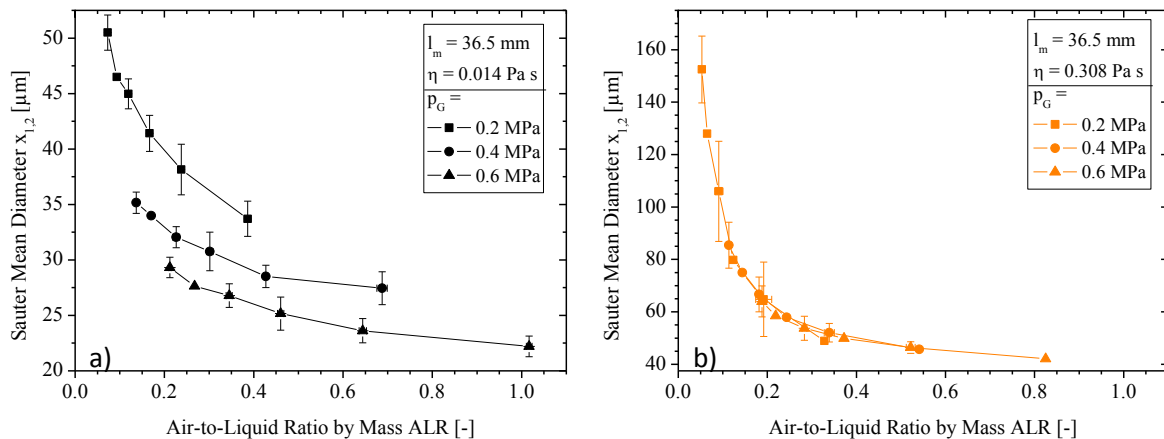


**Fig. 4:** Influence of ALR on the spray drop size in dependence of the gas pressure for a) 0.014 Pa s and b) 0.308 Pa s

The results shown in Figure 4a) reveal the following findings for the atomization of a maltodextrin solution with a low shear viscosity of 0.014 Pa s:

- With increasing ALR  $x_{1,2}$  decreases independently of  $p_G$ .
- The spray drop mean size  $x_{1,2}$  is good reproducible for every  $p_G$  investigated which is indicated by small standard deviations with a maximum value of about  $2 \mu\text{m}$ . These standard deviations were calculated from trails which were repeated four times in total.
- For low gas pressures ( $p_G = 0.2 \text{ MPa}$ )  $x_{1,2}$  decreases sharply from about  $51 \mu\text{m}$  to about  $34 \mu\text{m}$  with increasing ALR from 0.07 to 0.4. For ALRs larger than 0.2 the slope flattens. At the high gas pressure of  $p_G = 0.6 \text{ MPa}$   $x_{1,2}$  decreases only moderately from approximately  $29 \mu\text{m}$  to about  $22 \mu\text{m}$  with increasing ALR from 0.2 to 1.0.
- The biggest change in  $x_{1,2}$  can be achieved at an ALR in the range of 0.07 to 0.2. For higher ALRs smaller drops are attainable but its effect on  $x_{1,2}$  diminishes. These findings indicate a change in the drop formation mechanism at an ALR of 0.2 (4).
- At constant ALR, e.g. 0.2,  $x_{1,2}$  can be lowered from approximately  $38 \mu\text{m}$  to about  $22 \mu\text{m}$  with an increase in  $p_G$  from 0.2 to 0.6 MPa, respectively. This is in accordance to many other studies where the influence of gas pressure on spray drop size was investigated (1).

This means if a maltodextrin solution with low shear viscosity is to be atomized and a minimum spray drop size is desired it is beneficial to use a high gas pressure and a high ALR. However, the effect of ALR on the spray drop size decreases beyond 0.2.

The results shown in Figure 4b) give us the following information about the effervescent atomization of a maltodextrin solution with a high shear viscosity of 0.308 Pa s:

- As for the low shear viscosity  $x_{1,2}$  decreases with increasing ALR independently of  $p_G$ .
- The atomization at a  $p_G = 0.2 \text{ MPa}$  lacks of a good reproducibility as the maximum value of the standard deviation is about  $19 \mu\text{m}$ . With increasing  $p_G$  the reproducibility also increases indicated by a maximum standard deviation of about  $6 \mu\text{m}$  at  $p_G = 0.6 \text{ MPa}$ . Both deviations were calculated from trails repeated four times in total.
- In contradiction to the findings at a low shear viscosity there is no influence of  $p_G$  on  $x_{1,2}$  observable for a high shear viscosity of 0.308 Pa s. These results are in accordance to other findings (5). The beneficial effect of  $p_G$  on  $x_{1,2}$  decreases gradually with increasing shear viscosity (results not shown) from a remarkable effect at 0.014 Pa s to a non observable one at 0.308 Pa s.
- For ALRs in the range of 0.05 to 0.2  $x_{1,2}$  decreases sharply from about  $152 \mu\text{m}$  to about  $65 \mu\text{m}$ . Beyond a ALR of 0.2  $x_{1,2}$  decreases only moderately to approximately  $42 \mu\text{m}$  at an ALR of 0.8. As already discussed, this effect is due to a change in the drop formation mechanism: At ALRs below 0.2 the expansion of the gaseous phase shatters the liquid. At higher ALRs drop formation is dominated by aerodynamically induced shear and disturbances (4).

Similar to the low shear viscosity it is also beneficial to chose a high ALR if a maltodextrin solution with a high shear viscosity is to be atomized. But in contradiction to the findings at low viscosities there is no need to choose a high gas pressure, except for the better reproducibility at gas pressures larger than 0.2 MPa. For all

viscosities studied in this work the change in drop formation mechanism seems to be at an ALR of 0.2. This is also valid for the investigated viscosities not shown in Figure 4.

#### Influence of mixing chamber length on spray drop size

We investigated the influence of the mixing chamber length  $l_m$  for three different lengths. To show the effects of  $p_G$  and shear viscosity the results are presented in two figures. Figure 5a) shows the results at  $p_G = 0.2$  MPa and the lowest and highest shear viscosity available in this study whereas Figure 5b) depicts the same results but at  $p_G = 0.6$  MPa.

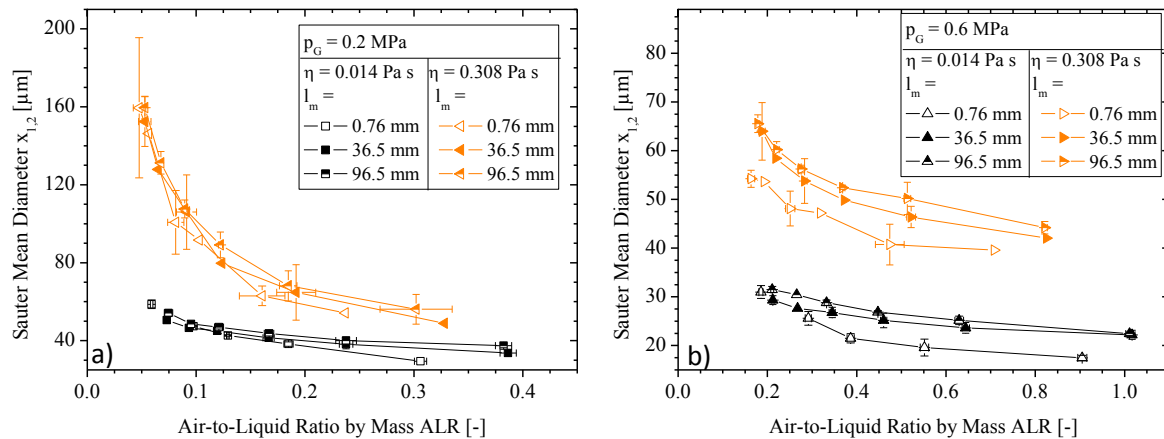


**Fig. 5:** Influence of ALR on the spray drop size in dependence of the mixing chamber length for a) 0.2 MPa and b) 0.6 MPa

The results shown in Figure 5 give us additional information to the already mentioned findings regarding the influence of shear viscosity on  $x_{1,2}$  and the influence of  $p_G$  on the reproducibility at different shear viscosities. For every mixing chamber length investigated  $x_{1,2}$  decreases with increasing ALR. Figure 5a) reveals that for  $p_G = 0.2$  MPa no influence of  $l_m$  on  $x_{1,2}$  is observable regardless of the shear viscosity studied. At a higher gas pressure of 0.6 MPa there seems to be a decreasing trend of  $x_{1,2}$  with decreasing  $l_m$  for a constant ALR (Figure 5b). Unfortunately, at this time the reason for this finding is not fully understood.

#### Conclusions

In this work, we investigated the influence of shear viscosity  $\eta$ , gas pressure  $p_G$  and mixing chamber length  $l_m$  on the effervescent atomization of maltodextrin solutions. In the studied shear rate range the flow behaviour of the solutions is Newtonian. The shear viscosity increases from 0.014 to 0.308 Pa s for an increasing maltodextrin dry matter content from 30 to 50 %, respectively. While the shear viscosity is increased the Sauter mean diameter  $x_{1,2}$  of the drops increases from approximately 23 μm to about 43 μm (ALR = 0.6,  $p_G = 0.6$  MPa,  $l_m = 36.5$  mm). Results indicate that the influence of shear viscosity on  $x_{1,2}$  diminishes at higher values. A possible explanation could be a shear thinning behaviour of the higher concentrated solutions at the shear rates present during atomization. The gas pressure shows a beneficial effect on  $x_{1,2}$  for the low shear viscosity with its effect decreasing with increasing shear viscosity within the inspected pressure range. Further, at higher shear viscosities a higher  $p_G$  results in a more reproducible atomization. For all shear viscosities investigated  $x_{1,2}$  decreases sharply with an increasing ALR up to a value of 0.2 and only moderately if the ALR is increased further. At  $p_G = 0.2$  MPa the mixing chamber length seems to have no influence on the spray drop size. At  $p_G = 0.6$  MPa  $x_{1,2}$  decreases with a decreasing mixing chamber length regardless of the shear viscosity. To understand the effervescent atomization of food based liquid with high shear viscosity more fundamentally further investigations should concentrate on the two-phase flow pattern within the atomizer.

#### Acknowledgements

The authors would like to thank Andrea Butterbrodt and Michael Groß for their technical support. The work has partly been carried out with financial support of the German Research Foundation (DFG) within the research program DFG-SPP 1423 “Prozess-Spray”.

## Nomenclature

### Latin characters

ALR	-	Air-to-Liquid Ratio by Mass
$d_m$	mm	Mixing chamber diameter
$d_o$	mm	Exit orifice diameter
$l_m$	mm	Mixing chamber length
$l_o$	mm	Exit orifice length
$p_G$	MPa	Gas pressure
RI	-	Refraction index
$x_{1,2}$	$\mu\text{m}$	Sauter mean diameter

### Greek characters

$\eta$	Pa s	Shear viscosity of liquid
$\rho$	$\text{kg/m}^3$	Density of liquid

## References

- [1] S. D. Sovani, P. E. Sojka, A. H. Lefebvre, *Progress in Energy and Combustion Science* **27**, 483 (2001).
- [2] J. Y. Kim, S. Y. Lee, *Atomization and Sprays* **11**, 735 (2001).
- [3] J. Jedelsky, M. Jicha, J. Slama, J. Otahal, *Energy & Fuels* **23**, 6121 (2009).
- [4] D. Konstantinov, R. Marsh, P. Bowen, A. Crayford, *Atomization and Sprays* **20**, 525 (2010).
- [5] H. J. Buckner, P. E. Sojka, *Atomization and Sprays* **1**, 239 (1991).
- [6] H. J. Buckner, P. E. Sojka, *Atomization and Sprays* **3**, 157 (1993).
- [7] J. Schröder, M.-L. Lederer, V. Gaukel, H. P. Schuchmann, *ILASS 2011 Conference Proceeding*, (2011).
- [8] A. Mescher, P. Walzel, *Chemie Ingenieur Technik* **82**, 717 (2010).



## Spray characteristics from a dodecane internal steam-assisted atomizer with gas-to-liquid ratios varying from 0 to 0.18

C. Mirat<sup>1,2</sup>, D. Durox<sup>1,2</sup> and T. Sculler<sup>1,2</sup>

1: CNRS, UPR 288 “Laboratoire d’Énergétique Moléculaire et Macroscopique, Combustion”, Grande Voie des Vignes, 92295 Châtenay-Malabry, France

2: Ecole Centrale Paris, Grande Voie des Vignes, 92295 Châtenay-Malabry, France

### Abstract

In thermal power plants, combustion is often realized with liquid fuels injected by twin-fluid atomizers assisted with steam due to its abundance in such systems. The quality of the spray generated at the injection nozzle outlet depends essentially on the gas to liquid mass flow rate ratio (*GLR*), the inlet gauge pressure of gas and liquid and the geometry of the atomizer. Parametric analyses of the influence of the atomizer geometry and *GLR* were generally considered with water and air as the working fluids. Analyses with fuel and steam are more seldom. The objective of this work is to characterize the influence of *GLR* on the structure of the resulting spray in a generic twin-fluid atomizer fed by dodecane and steam. These measurements are the initial data needed to examine the dynamics of a flame stabilized on this device. Two different types of experiments are conducted to characterize a dodecane spray with air or steam as the atomizing assisting fluid. The shape taken by the spray is visualized with a backlight technique by zooming near the injector outlet when the *GLR* is varied. These images are used to qualitatively examine the influence of flow changes on the spray regime. Droplet size and velocity distributions are then characterized by a phase Doppler particle analyzer system. By operating with a constant fuel mass flowrate, measurements on the injector axis far away from the injection plane indicate that droplet velocities increase linearly with the *GLR* with a sudden change in the slope for a certain threshold level of injected steam or air flow rates. This transition was found in the different configurations explored, but the transition appears at different *GLR* values. Conversely, the Sauter mean diameter (*SMD*) of the droplet size distribution first decreases when the *GLR* increases from zero, before reaching a roughly constant value for high *GLR*. The transitions observed on the droplet velocity and droplet size distributions appear for all the geometrical configurations of the atomizer and flow operating conditions tested with cold air or over-heated steam but for different values of *GLR*. Attempts are made to identify the origin of this transition.

---

### Introduction

Twin-fluid atomizers are used in many applications for heavy fuel combustion [1–5]. The quality of the spray generated at the injection nozzle outlet depends essentially on the gas to liquid mass flow rate ratio (*GLR*) [6, 7] and the geometrical configuration of the atomizer.

Parametric analyses of the influence of the atomizer geometry [4, 8], and gas to liquid mass flow rates injected in the system [4, 8, 9] were generally considered with water and air as working fluids. They were shown to have an influence on the two-phase flow regime within the nozzle. These different regimes designated by bubbly, slug, annular and dispersed were mainly studied in horizontal or vertical transparent pipes [10, 11]. Based on these observations, Wallis [12] developed a set of models to determine the pressure drop at the pipe extremities. Generally twin-fluid atomizer operates in the bubbly regime for small values of *GLR* [13–15]. For higher values of *GLR* the bubbly regime vanishes, transitions to a slug regime were identified to finally reach an annular regime at high *GLR*. The objective of this work is to characterize the influence of the *GLR* on the structure of the resulting spray in a generic twin-fluid atomizer fed by dodecane and steam.

The experimental setup used to generate and characterize the spray is presented in the next section. Results for steam and nitrogen atomizing gases are explored by varying also their temperature. The analysis is presented as a function of *GLR* values.

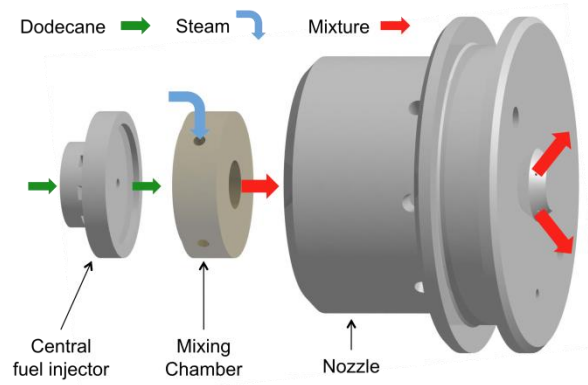


**Figure 1.** Schematic of the main elements of the generic internal steam assisted nozzle.

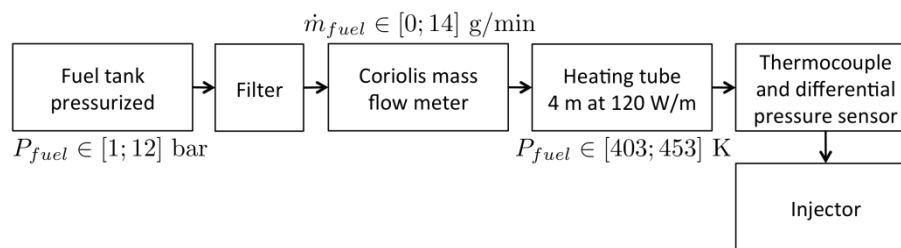


**Figure 2.** Diagram of the fuel supply line.

## Experimental setup

In the present study, a generic internal twin-fluid atomizer was designed. The injector features a simplified geometry and was designed to stabilize flames with a thermal power of 10 kW. It is made of three different pieces that form the injector when assembled. A sketch of this injector is shown in Figure 1. The fuel supply feeds a mixing chamber through a central injection nozzle with a diameter  $d_f = 0.10$  mm. The resulting fuel jet is intersected by four gas jets radially distributed at the inlet of the mixing chamber. These jets penetrate in the mixing chamber by four circular holes, each featuring a diameter  $d_s = 0.10$  mm. This two-phase fluid mixture leaves the mixing chamber through five cylindrical injection holes with diameter  $d_n = 0.20$  mm regularly distributed around the nozzle. The injection axis of the holes makes an angle of  $52.5^\circ$  with the atomizer axis. The atomizer is embedded in a regulated and instrumented experimental setup. Dodecane was used as fuel for the experiments presented in this work. A pressurized tank fed with dodecane feeds a Coriolis mass flow meter with a maximum fuel mass flow rate of  $14 \text{ g min}^{-1}$  at 12 bar. In this study, the fuel mass flow rate is fixed to  $\dot{m}_f = 12.5 \text{ g min}^{-1}$ . The fuel gauge pressure and temperature are recorded continuously during the experiments. The fuel supply line is represented in Figure 2.

Over-heated steam, heated nitrogen or nitrogen at ambient temperature were used to atomize the liquid dodecane. The steam supply line is represented in Figure 3(a). Steam is produced by a Bronkhorst steam generator heated by a 500 W thermal resistance. A water tank pressurized by nitrogen feeds a Coriolis mass flow meter and then the evaporator with a maximum water mass flow rate of  $2 \text{ g min}^{-1}$ . This system provides an overheated steam flow at  $T_1 = 423 \text{ K}$  with a maximum pressure of 5 bar. Downstream the evaporator, a heating tube maintains the steam flow at the same temperature (423 K) and feeds the injector. The nitrogen supply line is represented in Figure 3(b). A nitrogen tank feeds a thermal mass flow meter with a maximum nitrogen mass flow rate of  $2.4 \text{ g min}^{-1}$ . The nitrogen flow can be heated at  $T_2 = 413 \text{ K}$  or supplied at ambient temperature  $T_3 = 293 \text{ K}$ . The atomizing gas temperature before injection in the mixing chamber and the gauge pressure are continuously recorded during these experiments with a thermocouple and a differential pressure sensor installed along the heating line. To avoid condensation when fuel and steam are mixed, a heating tube is used to feed the atomizer and heat the fuel at the same temperature as the atomizing gas. To avoid possible condensation within the system, the whole test rig is thermalized at about 473 K. The gas to liquid mass flow rate ratio ( $GLR$ ) is determined from indications from the mass flow meters. In these experiments, the range of  $GLR$  covered is comprised between 0.01 and 0.18 as in typical industrial applications. Three different types of experiments are conducted to characterize the spray, flow and the pressure in the mixing chamber. The droplet size and velocity

distributions are measured using a Phase Doppler Particle Analyser (PDPA) enabling the determination of two velocity components. A 4 W Argon laser is used to this purpose. The detection unit is placed off the injection axis by an angle of 30° to have the best angle for the light scattered by the dodecane droplets corresponding to a diffusion index  $n = 1.45$ . An achromatic collection lens with a focal length of 300 mm focuses the scattered light on the detection sensors. To ease post-processing of the data, channel 1 of the PDPA was used to measure directly the droplet velocity  $u$  along the jet axis. For this purpose the laser head was rotated by 52.5° with respect to the vertical direction. Figure 4 shows the PDPA with the green and blue laser beams crossing within the spray close to the injection plane when the emission head is inclined relative to the vertical axis. The PDPA was settled to measure droplet sizes with diameters ranging from 1  $\mu\text{m}$  to 129  $\mu\text{m}$  and to measure simultaneously two components of the droplet velocities. In this experiment, the laser and detection units were placed on a micrometric three axes displacement. This system allows an accurate mapping of the jet spray at the atomizer injection outlet.

A backlight technique is used to visualize the spray. In order to freeze images of the spray a Fischer nanolite is used with flash duration about 20 ns. This light is placed behind the jet and an ICCD camera records the shadow of the spray. This technique yields qualitative information of the shape taken by the spray and enables to examine its dynamics to test the influence of geometrical and flow parameters on the spray patterns.

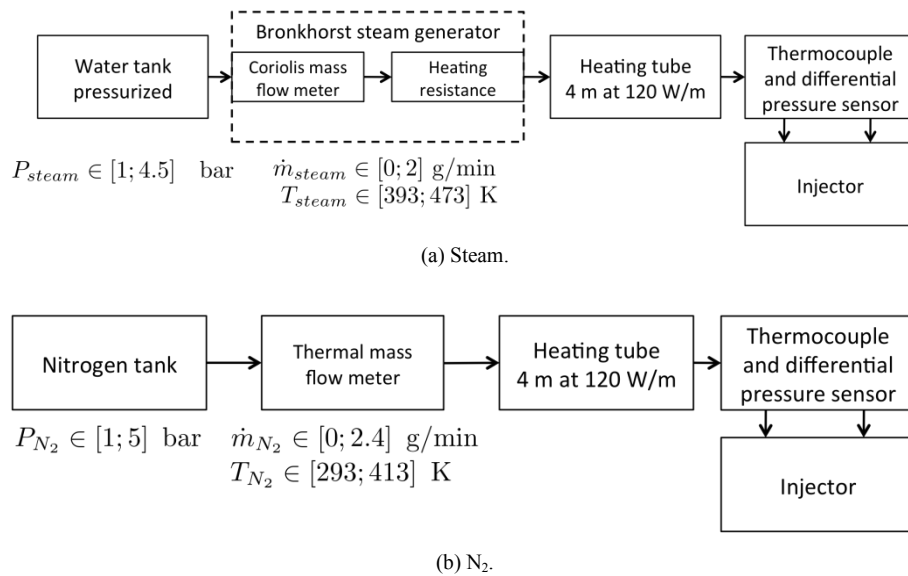


Figure 3. Diagrams of the atomizing gas supply line.

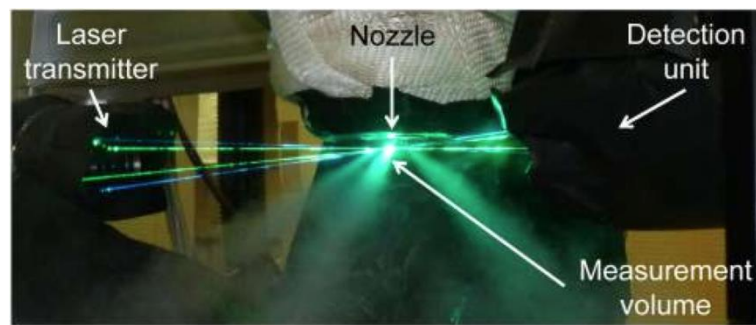
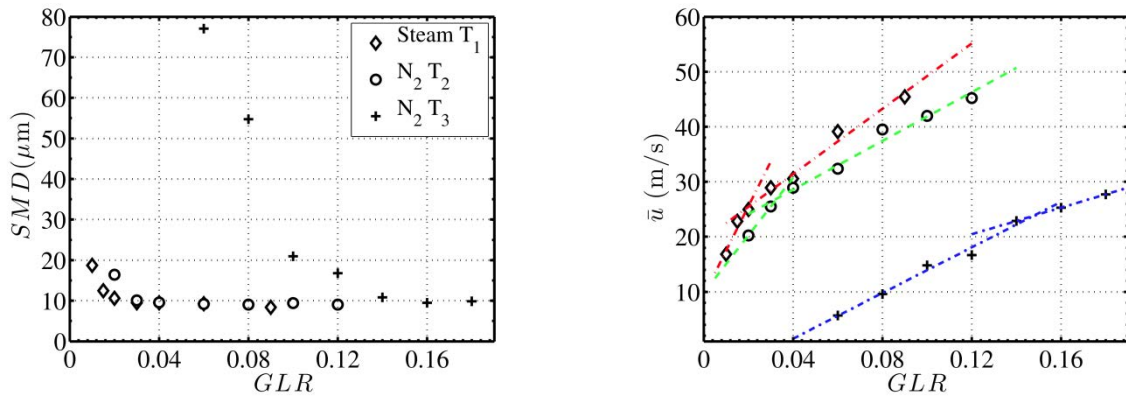


Figure 4. Photo of the injector with the spray and the PDPA.

### Spray characteristics

The evolution of the  $SMD$  as a function of the  $GLR$  is examined on the center of the jet axis 10 mm downstream the injection plane. Figure 5(a) shows this evolution when overheated steam, heated  $N_2$  and  $N_2$  at ambient temperature are used. For the three configurations, the  $SMD$  first decreases when the  $GLR$  increases, before reaching a roughly constant value at 10  $\mu\text{m}$ . It is also worth noting that the plateau value of the  $SMD$  is the same for all atomizing gas conditions. The first regime is the typical evolution for twin-fluid atomizers observed for small values of the  $SMD$  [16–19]. The second regime with a roughly constant value for large values of  $GLR$  was also observed in a few studies [6, 15, 20]. One may also note that the value of  $GLR$  corresponding to the transition between these regimes is a function of the atomizing gas flows. For  $N_2$  at  $T_3 = 293$  K, this transition

occurs at about  $GLR \approx 0.13$ . For over-heated steam, it takes place at about  $GLR \approx 0.02$ , a value close to that found for heated  $N_2$ ,  $GLR \approx 0.03$ .



(a) Sauter mean diameter  $SMD$  evolution as a function of  $GLR$ .

(b) Mean droplet axial velocity  $\bar{u}$  evolution as a function of  $GLR$ .

**Figure 5.** Measurements are made on the center of the jet axis,  $z = 10$  mm downstream the injection plane.  $\blacklozenge$ : Steam at  $T_1 = 423$  K,  $\bullet$ :  $N_2$  at  $T_2 = 413$  K and  $+$ :  $N_2$  at  $T_3 = 293$  K. Dashed lines indicates trends in Figure 5(b).

The droplet velocity was simultaneously measured with the PDPA system. Figure 5(b) shows the mean axial droplet velocity  $\bar{u}$  evolution as a function of the  $GLR$  for the same operating conditions as in Figure 5(a). The droplet velocity increases linearly with the  $GLR$  for small  $GLR$ . When steam is used, a change in the slope appears when the  $GLR$  reaches the value of 0.025. For higher  $GLR$ , the droplet velocity still increases linearly with the  $GLR$  but at a slower rate. This sudden transition was found in the different configurations explored, but the transition appears at different  $GLR$  values depending on the gas atomizing flow. It is also worth noting that the break in the slopes observed on the droplet velocity evolution appears for the same  $GLR$  value as the transition observed on the  $SMD$  to a constant value (Figure 5(a)). According to Ramamurthi *et al.* [15] and Lee *et al.* [21], this transition is related to a change of the flow regime within the nozzle from a slug to an annular regime. The pressure in the mixing chamber has an influence on this transition and the corresponding  $SMD$  value [6]. Ramamurthi *et al.* [15] add that this influence of the pressure within the mixing chamber is characteristic of bubbly or slug flow regimes. It is decided to make a visualization of the flow downstream the nozzle in order to confirm the existence of a multi-phase flow transition within the nozzle.

### Spray visualization

Visualizations of the spray were made with a backlight method. The experiments are conducted with nitrogen at ambient temperature in order to limit the noise on the image generated by steam. The nozzle used for these experiments is composed by only one hole with a diameter  $d_n = 0.45$  mm, which corresponds to the hydraulic diameter of the nozzle equipped with five holes with a diameter  $d_n = 0.20$  mm.

Figures 6 shows images with a reversed gray color colormap of the spray taken by backlight for  $GLR = 0.04$  (Figure 6(a)) and  $GLR = 0.16$  (Figure 6(b)). The left image in Figure 6(a) shows a sudden expansion of an atomizing gas bubble with ligament formation of dodecane. The right image in Figure 6(a) shows the breakup of the ligaments. Downstream these ligaments large droplets are formed in agreement with the trend observed for the evolution of the droplet  $SMD$  as a function of  $GLR$  in Figure 5(a).

The image in Figure 6(b) shows the spray generated by the injector with  $GLR = 0.16$ . Downstream the injector a uniform zone with equal pixel intensities appears which represents a liquid film. Downstream, the liquid film breaks up and generates small droplets uniformly distributed in the space. According to Sovani *et al.* [6] and Ramamurthi *et al.* [15], images in Figure 6(a) are typical of an intermittent flow like in the slug flow whereas the image in Figure 6(b) is a feature of an annular flow. These visualizations confirm the change of the flow regime in the nozzle. The atomizer operates in an intermittent flow regime for small values of  $GLR$  and features a transition to an annular flow regime for higher values of  $GLR$ . These observations are in agreement with the transition observed in the evolution of droplet size and velocity as a function of  $GLR$  in Figures 5(a) and 5(b). It is interesting to determine the critical value of  $GLR$  for the transition of the multi-phase flow within the nozzle. The flow pattern map is used for this purpose.

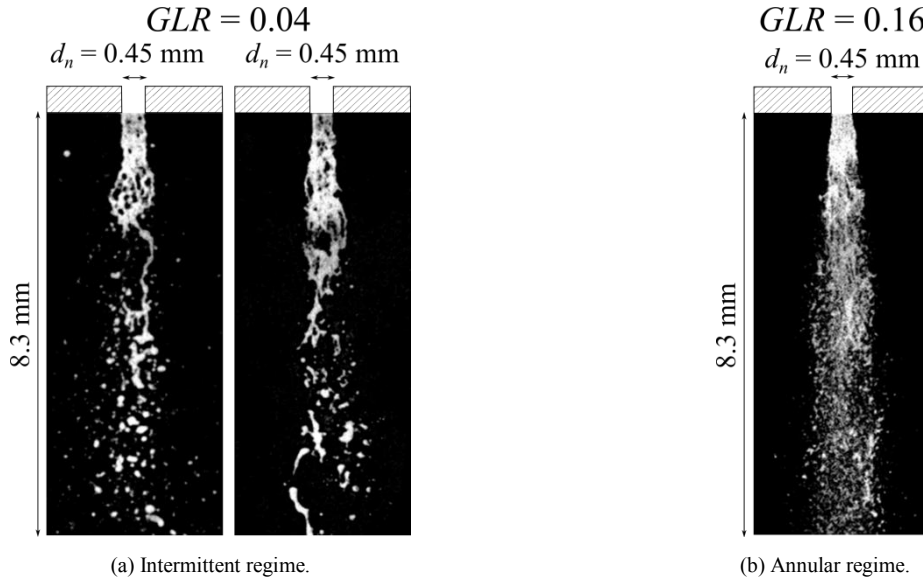


**Figure 6.** Negative pictures of the spray by backlight method for  $GLR = 0.04$  (Figure 6(a)) and  $GLR = 0.16$  (Figure 6(b)). The dodecane spray is assisted by  $N_2$  at ambient temperature  $T_3 = 293$  K.

### Flow pattern in the nozzle

The flow regime within the atomizer depends on geometrical configuration of the atomizer, gas and liquid flow properties. There are different flow pattern maps that may be used to determine the flow regime: the Baker flow pattern map [10] used by Chin *et al.* [13] and Jedelsky *et al.* [14, 22] or the flow pattern map from Taitel and Dukler [11] and from Mandhane [23]. According to Delhaye [23], the two-phase flow regime inside a horizontal pipe can be estimated based on the flow map of Mandhane [23]. This flow map represents the superficial velocities of the liquid phase  $j_f$  as a function of superficial velocity of the gaseous phase  $j_g$ . The superficial velocities are defined as the volumetric flow rate of the phase through the total cross-sectional area of the nozzle:

$$j_g = \frac{\mathcal{Q}_g}{A_n} \quad (1)$$

where  $\mathcal{Q}_g$  is the volumetric flow rate of gas and  $A_n$  is the cross section area of the nozzle. Figure 7 shows the Mandhane flow pattern map modified by Delhaye [23] where lines delineate the regime boundaries. Symbols represent the flow regime inside the nozzle found with the pressure measured inside the mixing chamber and flow parameters calculated for each  $GLR$  and the different atomizing gases. For each configuration, values of  $j_f$  are roughly constant due to the small variation of the fuel density  $\rho_f$  as a function of temperature. The superficial fuel velocity is also independent of  $GLR$ . The gas superficial velocity  $j_g$  increases with increasing values of  $GLR$ . Figure 7 indicates that the two-phase flow within nozzle operates in the slug flow regime for small values of  $GLR$  and becomes annular or mist annular flow when the  $GLR$  increases in agreement with images of the spray in Figure 6. This analysis of the flow regimes in the nozzle may be used to determine values of the  $GLR$  for transitions. These values however do not match those found in Figures 5(a) and 5(b). To further examine the transitions of the multi-phase flow within the nozzle, comparisons between experimental data and two models are conducted in the next section.

### Models of pressure drop

Using indications of flow patterns identified in Figure 7, the measured pressure evolution inside the mixing chamber is compared with two typical models developed by Wallis [12]. The first model considers a homogeneous flow. This model is generally used to represent the evolution of a multi-phase flow in the dispersed regime [12, 24]. The second model investigated considers separated phase flows [12]. Figure 8 shows the ratio between the mean relative static pressure in the mixing chamber and the atmospheric pressure as a function of  $GLR$ . Symbols represent experimental data. The pressure in the mixing chamber for steam and heated  $N_2$  flows increases rapidly with the  $GLR$  with an inflection point for a certain value. For this pressure  $N_2$  at  $T_3 = 293$  K, increases only slowly with the  $GLR$ . In Figure 8, black dashed lines represent the pressure drop

calculated with the homogeneous model [12]. There is a good agreement between homogeneous model predictions and experimental data for overheated steam and  $N_2$  at  $T_2 = 413$  K. However, the model does not predict the correct pressure drop for the last experiment when  $N_2$  is used at ambient temperature.

The separated phase flow model is now used with an interfacial friction factor  $C_f$  defined by Wallis [12]:

$$C_f = 0.005[1 + m(1 - \alpha)] \quad (2)$$

where  $\alpha$  is the void fraction in the mixing chamber and  $m$  is a constant. Wallis [12] gives a value for  $m = 75$ . Lund *et al.* [25] noted that the friction factor is a function of the liquid mass flow rate. In Figure 8, red dashed lines represent the evolution predicted by this separated phase annular flow model as a function of  $GLR$ . The value of the parameter  $m$  in Eq. (2) is chosen here equal to  $m = 15$  to fit model predictions with experimental data. The pressure drop predicted by this model captures well experimental data for the atomizing gas  $N_2$  at  $T_3 = 293$  K for values of  $GLR$  below 0.14. For higher values, the pressure in the mixing chamber increases more rapidly with the  $GLR$ . This value for the  $GLR$  corresponds to the transition observed in droplet diameters in Figure 5(a). This model does enable to capture the pressure drops observed when overheated steam or  $N_2$  at  $T_2$  are used.

Figure 8 thus indicates that the homogeneous flow model matches experimental data for heated gases, whereas the separated phase flow model matches pressure measurements when  $N_2$  is used at ambient temperature. However, the analysis of the pressure evolution in the mixing chamber does not enable to fully explain the regime transition observed in these experiments. Further work is needed.

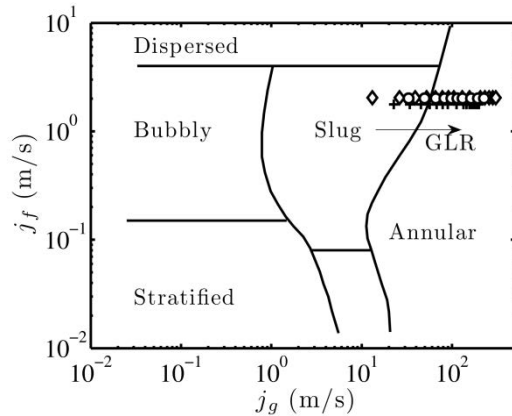


**Figure 7.** Flow pattern map according to Mandhane from Delhaye [23]. Symbols indicate calculated conditions in the nozzle orifice that depend on the  $GLR$  and atomizing gas.  
 ◆: Steam at  $T_1 = 423$  K, ○:  $N_2$  at  $T_2 = 413$  K and □:  $N_2$  at  $T_3 = 293$  K.

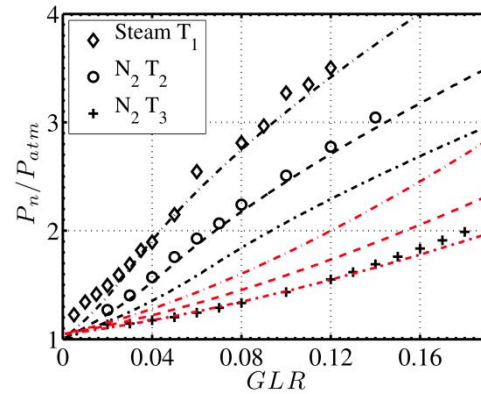


**Figure 8.** Mean pressure measured in the mixing chamber divided by the atmospheric pressure as a function of  $GLR$ .

Black dashed lines represent predictions from the homogeneous model and red dashed lines show those found with the separated phase flow model [12]. Experimental data  
 ◆: Steam at  $T_1 = 423$  K, ○:  $N_2$  at  $T_2 = 413$  K and □:  $N_2$  at  $T_3 = 293$  K.

## Conclusions

An experimental analysis of the evolution of the  $SMD$  and the mean velocity of droplets generated by an internal twin-fluid atomizer fed by dodecane has been carried out as a function of  $GLR$  with two atomizing gases at different temperatures. It was found that the droplet velocity increases linearly with the  $GLR$  with a change in the slope. This sudden transition is found in the different configurations explored, but the transition appears at different  $GLR$  values. The  $SMD$  first decreases when the  $GLR$  increases, before reaching a roughly constant value in all configurations explored. This transition takes place for the same  $GLR$  value as that found in the break of the slope of the jet spray velocity.

To analyze this flow regime transitions, backlight visualization of the spray have been made for two  $GLR$ . It was observed that the two-phase flow pattern within the nozzle is intermittent for small  $GLR$  and becomes annular when the value of the  $GLR$  increases. The Mandhane flow pattern map has been used to determine the value of  $GLR$  for the transition. Using the Mandhane flow pattern map, it was found that a regime transition of the two-

phase flows within the nozzle between slug to annular or mist annular takes place when the value of  $GLR$  increases. The value of  $GLR$  transition for overheated steam is  $GLR \approx 0.02$  and  $GLR \approx 0.05$  for nitrogen at ambient temperature. The corresponding pressure within nozzle was modelled with a homogeneous phase flow model for heated atomizing gases and with a separated phase flow model when nitrogen at ambient temperature is used. Further work is needed to determine a transition criterion.

## Acknowledgements

This work is a collaboration between the Laboratory EM2C and EDF R&D under contract with EDF / CRSA number 5910072747. We also would like to thank the technical staff of the EM2C laboratory for their assistance during the design and construction of the experimental setup.

## Nomenclature

$A$	cross sectionnal area (m <sup>2</sup> )
$C_f$	interfacial friction factor
$d$	diameter (m)
$GLR$	gas-to-liquid ratios
$j$	superficial velocity (m/s)
$m$	coefficient
$n$	diffusion index
$P$	Pressure
$\dot{Q}$	volumetric flow rate
$SMD$	Sauter mean diameter (μm)
$T$	temperature (K)

□

### Greek symbols

$\alpha$	void fraction
$\rho$	density (kg/m <sup>3</sup> )

### Subscripts

$f$	liquid phase
$g$	gas phase

## References

- [1] C. Junqua, *La Technique Moderne* **76**, 23 (1984).
- [2] I.-P. Chung, C. Strupp, J. Karan, *6<sup>th</sup> European conference on Industrial Furnaces and Boilers* (John Zink Company, Lisbon, Portugal, 2002).
- [3] E. Lincheta, J. Barroso, J. Sua ez, F. Barreras, A. Lozano, *18<sup>th</sup> ILASS-Europe* (Zaragoza, Spain, 9 - 11 September 2002).
- [4] F. Barreras, A. Lozano, J. Barroso, *Atomization and Sprays* **16**, 127 (2006).
- [5] D. Konstantinov, R. Marsh, P. Bowen, A. Crayford, *Atomization and Sprays* **20**, 525 (2010).
- [6] S. D. Sovani, P. E. Sojka, A. H. Lefebvre, *Progress in Energy and Combustion Science* **27**, 483 (2001)
- [7] A. H. Lefebvre, *Atomization and Sprays* (Hemisphere Publishing Corp., New York, 1989).
- [8] G.Ferreira, J.A. Garcia, F.Barreras, A.Lozano, E.Lincheta, *Fuel Processing Technology* **90**, 270 (2009).
- [9] S. Lal, A. Kushari, M. Gupta, J. C. Kapoor, S. Maji, *Experimental Thermal and Fluid Science* **34**, 1029 (2010).
- [10] O. Baker, *Oil Gas Journal* **53**, 185 (1954).
- [11] Y. Taitel, A. Dukler, *AIChE Journal* **22**, 47 (1976).
- [12] G. B. Wallis, *One-dimensional Two-phase Flow* (McGraw-Hill, 1969).
- [13] J.S. Chin, A.H. Lefebvre, *Journal of Engineering for Gas Turbines and Power – Transactions of the ASME* **117**, 266 (1995).
- [14] J. Jedelsky, M. Jicha, *12<sup>th</sup> ICLASS* (Heidelberg, Germany, 2–6 September, 2012), pp. 1–9.



- [15] K. Ramamurthi, U. K. Sarkar, B. N. Raghunandan, *Atomization and Sprays* **19**, 41 (2009).
- [16] P. J. Mullinger, N. A. Chigier, *Journal Institute of Fuel* **47**, 251 (1974).
- [17] A. H. Lefebvre, *Particle & Particle Systems Characterization* **13**, 205 (1996).
- [18] D. A. Nguyen, M. J. Rhodes, *Powder Technology* **99**, 285 (1998).
- [19] N. P. Yadav, A. Kushari, *Particle & Particle Systems Characterization* **28**, 25 (2012).
- [20] J. Schröder, A. Kleinhans, Y. Serfert, S. Drusch, H. P. Schuchmann, and V. Gaukel, *Journal of Food Engineering* **111**, 265 (2012).
- [21] S. Y. Lee, J. Y. Kim, *Atomization and Sprays* **11** (2001).
- [22] J. Jedelsky, M. Jicha, 10<sup>th</sup> ICLASS (Kyoto, Japan, 27th August 1st September, 2006).
- [23] J. M. Delhay, *Thermohydraulique des réacteurs*, Génie Atomique (EDP Sciences, 2008).
- [24] J. Jedelsky, M. Jicha, J. Slama, J. Otahal, *Energy & Fuels* **23**, 6121 (2009).
- [25] M. T. Lund, C. Q. Jian, P. E. Sojka, J. P. Gore, M. V. Panchagnula, *Journal of Engineering for Gas Turbines and Power - Transactions of the ASME* **120**, 750 (1998).

## Effect of air-induction on agricultural flat fan sprays

L. Opfer<sup>1</sup>, I. V. Roisman<sup>1</sup>, J. Venzmer<sup>2</sup>, M. Klostermann<sup>2</sup> and C. Tropea<sup>1</sup>

1: Institute of Fluid Mechanics and Aerodynamics, Technische Universität Darmstadt,  
Germany

2: Evonik Industries AG, Essen, Germany

### Abstract

This study is dedicated to the experimental investigation of agricultural air induction flat fan nozzles. In particular, the effect of injecting air bubbles into the inner nozzle flow on the breakup behaviour of the liquid is analysed. For this purpose, standard agricultural flat fan nozzles are operated with open and sealed air inlets. High-speed visualizations of the near nozzle region that reveal the structure of the liquid lamella are recorded. A conductivity based measurement technique is used to obtain quantitative data about the length of the intact lamella. The results show that this length is noticeably decreased by the air bubbles. A phase-Doppler instrument is then employed to measure the volume fraction of potentially drift-prone drops in the final spray.

### Introduction

Spray drift is a common problem during the application of herbicides and pesticides. The use of highly effective agricultural plant protection agents such as glyphosate requires a strict control of the affected area. This is necessary since even very small amounts of drifted spray can cause severe damage to surrounding ecosystems.

The susceptibility of a spray to drift mainly depends on its drop size distribution. The trajectory of small drops is highly affected by wind, whereas bigger drops are much more likely to reach the ground within a small horizontal distance from the spraying nozzle.

Crop protection agents are commonly atomized and applied by flat fan nozzles. Such nozzles are characterized by the ejection of a liquid sheet that breaks up in ligaments. These ligaments are subject to capillary instabilities and are further fragmented in single drops. A detailed analysis of liquid sheet breakup can be found in [1]. In [2] it is shown that the interaction between the lamella and the surrounding air is responsible for the occurrence of instabilities that cause breakup of the liquid sheet.

One approach in minimizing the amount of liquid contained in small drops is the use of air-induction nozzles. Here, air is sucked into the spray nozzle where it mixes with the liquid and forms small bubbles. These bubbles are ejected with the liquid and promote breakup by acting as nuclei in the lamella of the flat fan spray. Due to mass conservation, the lamella of such a flat fan spray becomes thinner with increasing distance from the orifice. When breakup is promoted, which means that the breakup region is shifted towards the orifice, ligaments and drops are formed from a thicker liquid film. This results in larger drops, which are then less prone to drift.

The general technique of manipulating liquid breakup by injecting gas bubbles in the flow is referred to as *effervescent atomization*. A recent study about the effect of effervescent atomization with application to radially expanding liquid sheets can be found in [3] whereas a previous, more general review is given in [4].

Another way of influencing the breakup behaviour of liquid sheets is the use of surface active adjuvants. The effect of some adjuvants on the characteristics of the sprays is described in [5], [6] and [7]. It is found that depending on the adjuvant, the volume fraction of potentially drift-prone liquid may either be increased or decreased. The authors conclude that sprays with added emulsions yield coarser drop size distributions than the ones with surfactant solutions.

### This study

In the present work, the effect of air-induction on liquid breakup and final spray characteristics is studied experimentally. Standard agricultural nozzles are operated with open and sealed air inlets, so that the nozzle performance with and without air induction can be compared. The nozzles are operated at injection pressures in the range of 3 – 8 bars, as recommended by the manufacturer. The following table presents the parameters of the nozzles used in this study.

nozzle	type	spray angle [degree]	volume flux @ 3 bar [liter/min]
N1	Lechler ID 90-01	90	0.39
N2	Lechler ID 90-02	90	0.8
N3	Lechler ID 90-03	90	1.19

### High-speed visualizations of the liquid sheet breakup

A digital high-speed video system is used to record time resolved shadowgraphs of the liquid sheet breakup. The camera (Vision Research Phantom V12) is operated at a frame rate of 6200 images per second and a resolution of 1280 x 800 pixels. Continuous backlighting is achieved using a mercury vapour lamp.

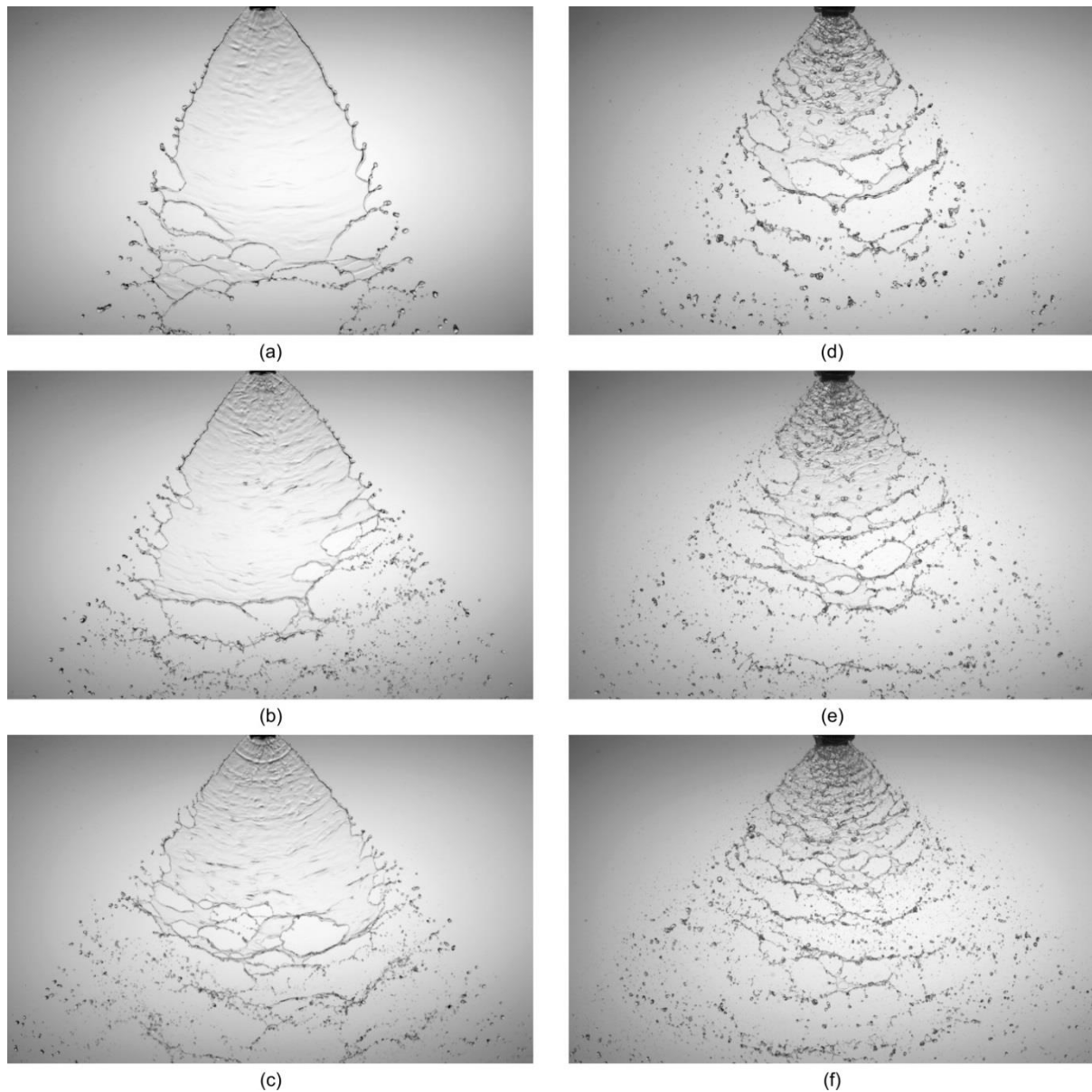


**Figure 1.** Visualizations of liquid breakup (nozzle N2). The left column (a-c) shows the breakup of the sheet originating from a nozzle with sealed air inlets. The right column (d-f) shows the sheet breakup of a nozzle with open air inlets. The injection pressures are 3 bar (a,d), 5.5 bar (b,e) and 8 bar (c,f). The field of view is approximately 85 x 65 mm.

A comparison between the breakup processes of nozzles with open and sealed air inlets is depicted in Figure 1. The liquid surface is much smoother when no air bubbles are present in the flow. However, it can be noted that below the orifice, the surface of the liquid sheet originating from the nozzle with closed air inlets is also slightly disturbed by capillary waves. These capillary waves are produced by the flow inside the nozzle and are a remainder from the air induction mechanism, even if the openings are sealed from the outside.

It can clearly be observed that air bubbles are present in the lamella when the air inlets are open. The diameters of these air bubbles are in the order of several hundred micrometers, which is generally larger than the film thickness of the lamella. This indicates that the bubbles either have a disc-like shape or that they emerge from the liquid film.

Holes in the liquid sheet are generated by bursting bubbles. These holes expand due to surface tension which pulls the hole rim towards the liquid phase. The expansion velocity of the holes can be estimated from the well-known Taylor rim velocity [8]:

$$V_{rim} = \sqrt{\frac{2\sigma}{\rho_l h}},$$

where  $\sigma$  is the surface tension coefficient,  $\rho_l$  is the density of the liquid and  $h$  is the local film thickness of the lamella. The occurrence of the holes leads to a much more jagged morphology of the liquid sheet, compared to the case without bubbles present in the flow. Due to the expanding holes, the lamella is transformed into a web of connected ligaments, which break apart due to capillary instabilities. For all injection pressures, this mechanism reduces the intact length of the liquid sheet. This length, which can be considered as a breakup length, is not constant but changes in time.

While the air induction mechanism causes a severe change to the overall breakup process, only a very minor fraction (below ten per cent) of the bubbles present in the lamella do finally generate a hole in the film. Two mechanisms that prevent the formation of holes from air bubbles can be identified from the high-speed visualizations:

1. A large amount of bubbles is entrained into the rims of expanding holes. When such an entrained bubble bursts, it enlarges the corresponding hole by a small amount, but does not serve as an independent hole nucleus. This effect is shown in Figure 2.
2. Some of the bubbles burst at only one side of the lamella. In most of these cases the liquid film is able to heal itself and no hole is generated. The rupture of a bubble without the occurrence of a hole is followed by a several concentric capillary waves.

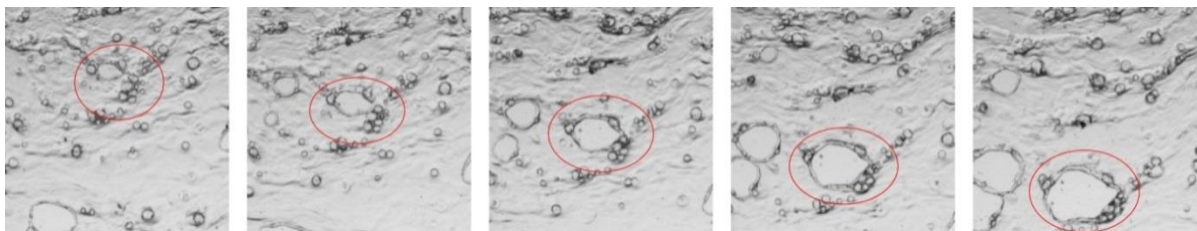


**Figure 2.** Entrainment of air bubbles into the rim of an expanding hole.

## Breakup length of the lamella

### Experimental method

The breakup length of the lamella is measured with a conductivity based technique, as depicted in Figure 3(a). Similar techniques are commonly used for the investigation of diesel sprays, e.g. in [9]. A thin wire (diameter 300  $\mu\text{m}$ ) is connected to one terminal of a voltage supply source ( $U = 18 \text{ V}$ ), with a resistor ( $R = 500 \text{ k}\Omega$ ) connected in series. The other terminal is connected to the electrically conducting nozzle mount.

The vertical distance between the orifice and the wire can be controlled by a traverse; the wire is driven into the lamella from below. Once the lamella provides an electrical connection between the wire and the nozzle mount, a certain current flows through the electrical circuit and the voltage drop over the resistor is measured by a digital oscilloscope. At each position, 100 kSamples are acquired with a sample rate of 50 kHz.

It has to be noted that holes in the liquid film can only be detected when the hole diameter is larger than the diameter of the wire. If a hole with diameter smaller or equal to the wire diameter passes the conductivity probe, an electrical connection between nozzle and wire will always be established. However, the diameter of air bubbles present in the flow are of the same order of magnitude as the wire diameter. Once these bubbles burst, their diameter is rapidly increasing due to the effect of surface tension. Hence, this effect biases the results mainly in the zone where the first holes occur.

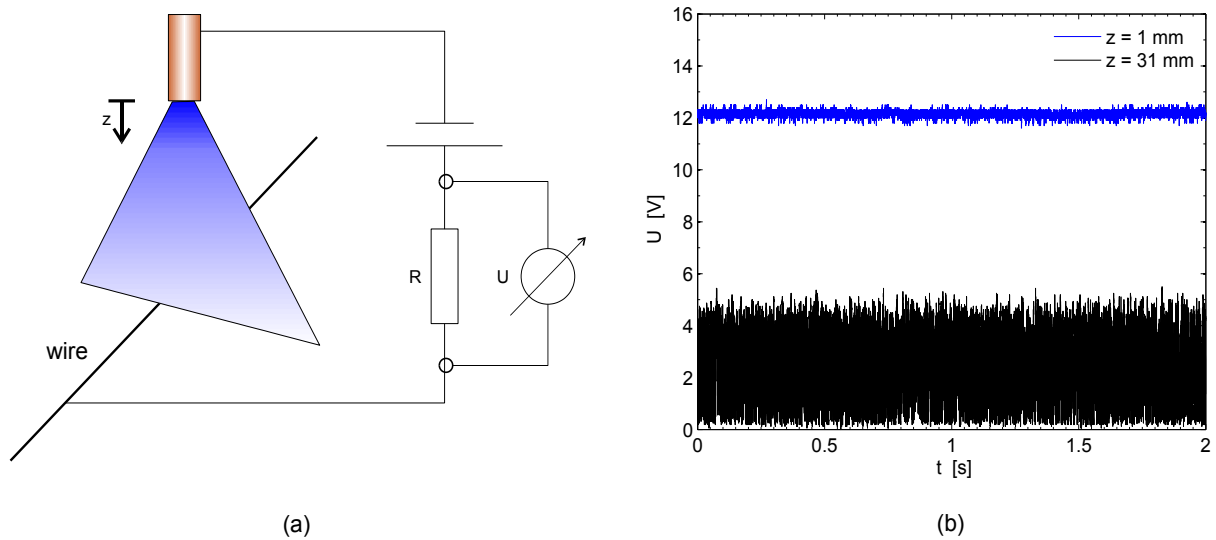


**Figure 3.** (a) Sketch of the electrical circuit used for the breakup length measurements. (b) Exemplary representation of the raw voltage signals.

Examples of the electrical signals are depicted in Figure 3(b). One of the signals shown here is acquired at a distance of 1 mm from the orifice. The lamella is always intact at this position, which is indicated by the constant level of the voltage signal. The noticeable noise in that signal arises from the air induction process. The unsteady suction of ambient air causes a changing amount of air bubbles in the nozzle. This results in a time dependent conductivity of the inner nozzle flow; hence produces a certain noise in the voltage signal.

The strong variations in the signal acquired at a distance of 31 mm from the orifice can directly be related to temporal variations of the lamella length. The voltage lies between a maximum value for a completely intact lamella and zero volts when the wire is outside the liquid sheet. Since the electrical connection between wire and nozzle mount can be established through the web of thin ligaments, values between the minimum and the maximum can also be found.

In order to obtain time averaged information about the state of the lamella at a given position, the raw signal is first binarized. A threshold value of  $U_{Tr} = U_{max}/2$  is used to divide the data points in two classes, where  $N_1$  is the number of data points with  $U \geq U_{max}/2$  and  $N_0$  is the number of data points where  $U < U_{max}/2$ . The ratio

$$P = \frac{N_1}{N_1 + N_0}$$

is a measure for the time averaged integrity of the lamella. The value  $P$  ranges from  $P = 1$  at positions close to the orifice to  $P = 0$  at positions where the liquid breakup is completed. The  $z$ -Position for  $P = 0.5$  can be used as a measure for the breakup length.

## Results

The effect of orifice size and injection pressure on the breakup behaviour is shown in Figure 4. It can be recognized that the breakup length clearly correlates with orifice size. Increasing the orifice size results in a larger breakup length. For the cases with air induction, the breakup length is increased by about 30% from nozzle 1 to nozzle 2. Between nozzle 2 and nozzle 3 an increase of about 10% can be found. The same trend can be seen in the cases without air induction.

A distinct change to the effect of injection pressure is imposed by the air induction mechanism. Without it, an increased injection pressure leads to a smaller breakup length. This is in good agreement with the observations from the high-speed visualizations. However, with air induction the evolution of  $P$  is almost independent of the injection pressure and only a very weak correlation can be found.

In Figure 5, a direct comparison of the breakup behaviour between open and sealed air inlets is shown for nozzle 1 and nozzle 3. It can be seen that the air induction process considerably reduces the breakup length for a given nozzle.

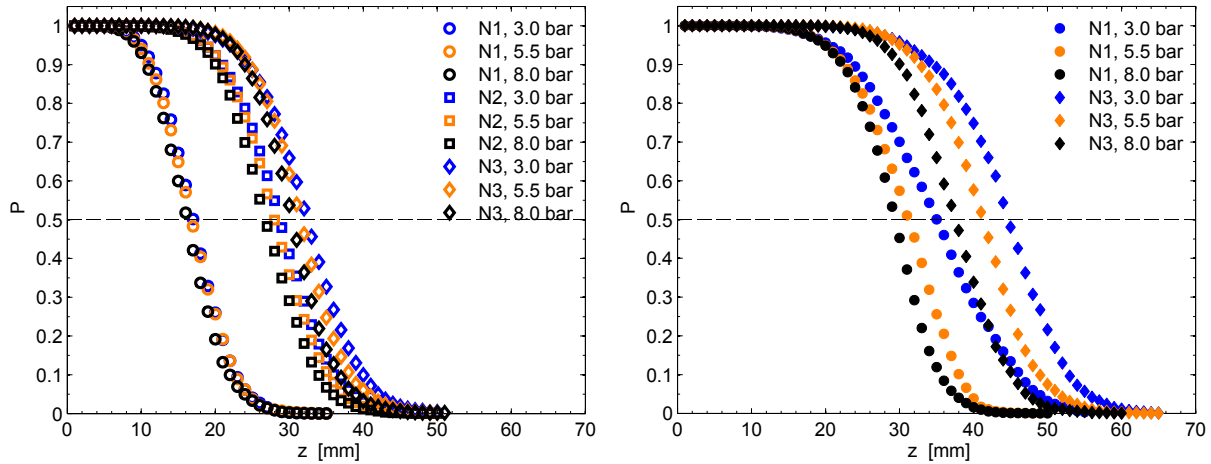


**Figure 4.** Breakup length measurements for various orifice sizes and injection pressures. Results in the left image are obtained with open air inlets, the right image shows results of measurements with sealed air inlets.

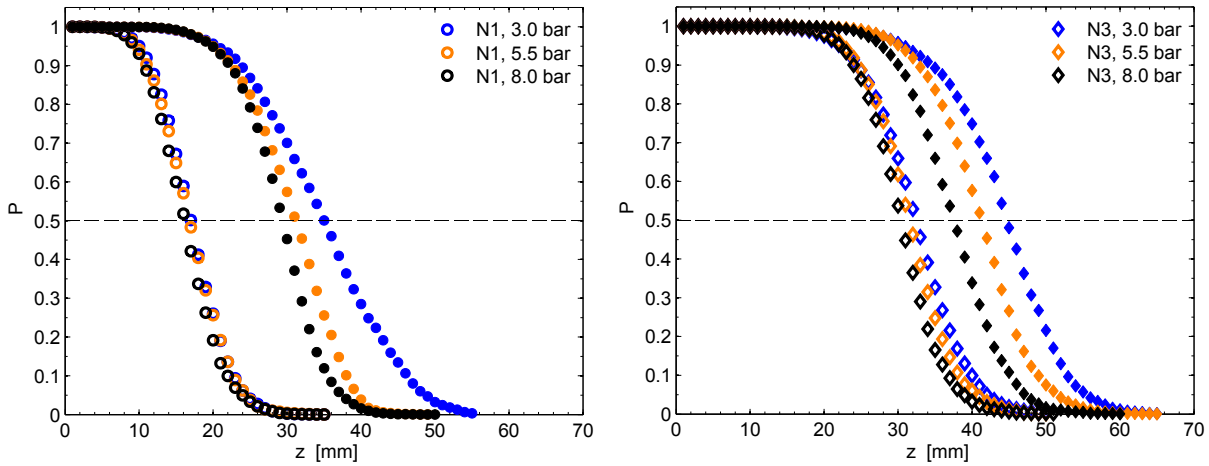


**Figure 5.** Effect of air induction on breakup length for nozzle 1 (left image) and nozzle 3 (right image). Open symbols denote open air inlets, filled symbols denote sealed air inlets.

### Drop Sizes

The final spray is characterized by a phase-Doppler instrument at a distance of 120 mm from the orifice. The phase-Doppler instrument is operated using the parameters as given in the following table.

Laser power	Scattering angle	Focal length of transmitter	Focal length of receiver	Sensitivity	Signal gain
200 mW	40°	600 mm	500 mm	1000 V	20 dB

The phase-Doppler instrument provides an accurate method of measuring the velocities and diameters of spherical drops. However, this technique is rather sensitive to deviations from a spherical drop shape. Even slightly deformed drops can lead to erroneous results. A detailed analysis of this effect can be found in [10].

From Figure 1, it can easily be recognized that a significant number of non-spherical drops are present in the spray. While surface tension tries to restore a spherical shape, the interaction between liquid phase and surrounding air can lead to further deformation or oscillation of the drops. The ratio between deforming aerodynamic forces and surface tension forces is expressed by the Weber number.

$$We = \frac{\rho_a d u^2}{\sigma},$$

where  $\sigma$  is the surface tension coefficient,  $\rho_a$  is the density of the liquid,  $d$  is the drop diameter and  $u$  is the drop velocity. The influence of drop deformation on the phase-Doppler results is shown Figure 6. While a clear correlation between drop size and velocity can be seen for the smaller drops, the diameter measurements of

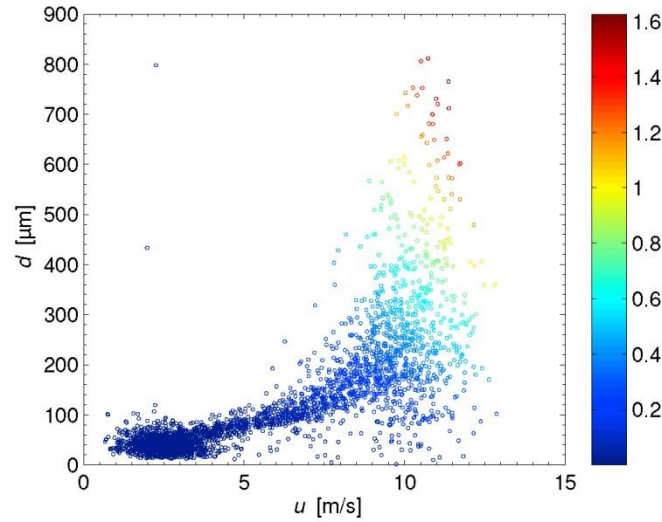


**Figure 6.** Correlation between drop size and velocity at an injection pressure of 5.5 bars. The Weber number of each detected drop is indicated by the marker color.

bigger drops with higher Weber numbers are subject to strong noise and are not reliable any more.

In order to avoid errors due to non-spherical particles, only drops that are prone to drift ( $d < 100 \mu\text{m}$ ) are considered in this study. While the absolute mass distributions can't be obtained since the amount of mass located in drops with  $d > 100 \mu\text{m}$  is not known, relative mass distributions can be used to analyse the effect of air induction on the spray. Drop size data is collected for 180 seconds and the amount of volume located in small drops ( $d < 100 \mu\text{m}$ ) is compared for the case of open air inlets and sealed air inlets.

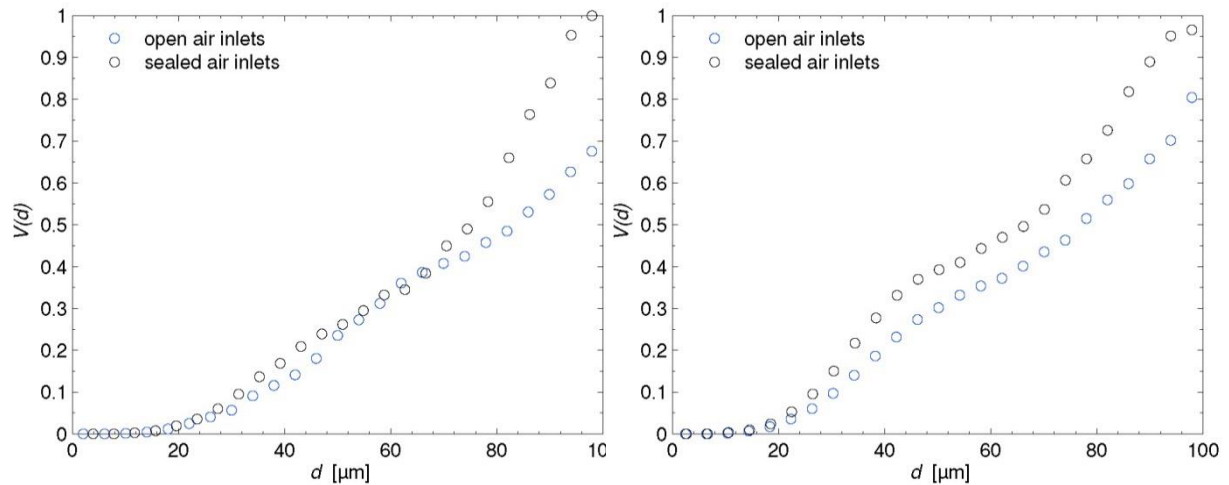


**Figure 7.** Relative volume distributions of small drops. The distributions are normalized by the maximum value at each injection pressure. Nozzle 1, 3 bars (left side) and 8 bar (right side.)

Relative mass distributions are shown in Figure 7. It can be seen that air induction leads to a smaller amount of potentially drift-prone drops. Air induction causes a reduction of volume located in drops smaller than  $100 \mu\text{m}$  of 29% at 3 bars, 30% at 5.5 bars and 32% at 8 bars.



## Conclusions

In the present study, the effect of air induction on agricultural flat fan sprays is analysed. High-speed visualizations reveal the structure of the liquid lamella during breakup. It can clearly be observed how bursting bubbles generate holes in the film, which promote breakup and decrease the length of the intact lamella. Since the thickness of the lamella decreases with distance from the orifice, this effect reduces the amount of liquid that is located in small drops.

Breakup lengths of the liquid sheet are measured using a conductivity probe technique. It is shown that the breakup length decreases with higher injection pressures when no air bubbles are present in the flow. When air bubbles are present in the flow, the breakup length is noticeably shorter and almost independent of the injection pressure.

The amount of liquid that is contained in small drops, that are prone to drift, is measured with a phase-Doppler instrument. While large, non-spherical drops present in the spray prevent an absolute measure of that amount, a relative comparison is made for the respective injection pressures. This analysis reveals that the reduction of liquid volume that is prone to drift is in the order of 30%, compared to the same nozzle with closed air inlets.

## References

- [1] N. Dombrowski and R. Fraser, “A photographic investigation into the disintegration of liquid sheets,” *Philosophical Transactions of the Royal Society of London. Series A, Mathematical and Physical Sciences*, vol. 247, no. 924, pp. 101–130, 1954.
- [2] R. Fraser, P. Eisenklam, N. Dombrowski, “Drop formation from rapidly moving liquid sheets,” *AIChE*, 1962.
- [3] H. Lhuissier and E. Villermaux, “‘Effervescent’ atomization in two dimensions,” *Journal of Fluid Mechanics*, vol. 714, pp. 361–392, Jan. 2013.
- [4] S. Sovani, P. Sojka, and A.H. Lefebvre, *Effervescent atomization*, vol. 27, no. 4. 2001, pp. 483–521.
- [5] M. C. B. Ellis, C. R. Tuck, and P. C. H. Miller, “The effect of some adjuvants on sprays produced by agricultural flat fan nozzles,” *Crop Protection*, vol. 16, no. 1, pp. 41–50, Feb. 1997.
- [6] M. C. Butler Ellis and C. R. Tuck, “How adjuvants influence spray formation with different hydraulic nozzles,” *Crop Protection*, vol. 18, no. 2, pp. 101–109, Mar. 1999.
- [7] M.C. Butler Ellis, C. Tuck and P. C. Miller, “How surface tension of surfactant solutions influences the characteristics of sprays produced by hydraulic nozzles used for pesticide application,” *Colloids and Surfaces A: Physicochemical and Applied Aspects*, vol. 180, no. 3, pp. 267–276, May 2001.
- [8] G. Taylor, “The Dynamics of Thin Sheets of Fluid. II. Waves on Fluid Sheets,” *Proceedings of the Royal Society A: Mathematical, Physical and Engineering Sciences*, vol. 253, no. 1274, pp. 296–312, Dec. 1959.
- [9] D. G. Salters, “A conductivity probe technique for investigating the breakup of diesel sprays,” *Atomization and Sprays*, vol. 4, no. 1, pp. 41–63, 1994.
- [10] N. Damaschke, G. Gouesbet, G. Gréhan, H. Mignon, and C. Tropea, “Response of phase Doppler anemometer systems to nonspherical droplets,” *Applied optics*, vol. 37, no. 10, pp. 1752–61, Apr. 1998.

## Investigation on Pressure Swirl Nozzles with Coandă Deflection Outlets

J. Kamplade, E. Musemic and P. Walzel

Particle Technology Lab, TU Dortmund, Germany

### Abstract

Spray angle deflection by Coandă orifices mounted to swirl nozzles can be characterized by major geometrical parameters as  $R_c/D$  and by the flow- or pressure Reynolds-number. In general at proper conditions it is possible to achieve much higher spray angles than with sharp edged nozzles. Equal Reynolds-numbers show comparable deflection behaviour. Detachment takes place at too small deflection radii. Too high Reynolds numbers leading into a transition region with strongly unstable sheets and finally to the same spray angle as obtained with a sharp edged nozzle. The sheet velocities measured with fiber optical probes at deflected sheets show significant decay when the deflection is operating. As known from basic consideration concerning aerodynamic break-up of sheets, velocity and spray angle simultaneously affect the drop size generated by swirl nozzles.

Drop sizes were measured with water by means of a Laser Diffraction Spectrometer. The effect of higher spray angles caused by deflection orifices is partly compensated by the lower flow velocity. For that reason drop sizes are hardly affected by the Coandă opening when operated at the same pressure and equal orifice size as sharp edged nozzles. The course of the span vs. the Laplace-number does not show significant deviations with or without Coandă deflection body.

### Introduction

Pressure swirl nozzles lead to significant loss in kinetic energy especially at high swirl and when the liquid is viscous. Energy loss means reduced exit velocity of the sheet, increased discharge sheet thickness and reduced spray angle. Even at low viscous liquids spray angles larger than  $\Theta = 110^\circ$  can hardly be achieved at common orifices with higher swirl ratio  $\Delta$  only. For explanation of swirl ratio see e.g. [1, 2]. In technical applications larger spray angles even beyond  $\Theta = 110^\circ$  up to  $180^\circ$  are often desired. Especially in the case of viscous liquids the spray angles are frequently too small due to angular momentum loss within the swirl chamber. However spray angle modification is possible with trumpet openings exploiting the so called Coandă effect [3]. This kind of design is known for long periods and also available from nozzle manufactures.

The flow stability of deflected sheets on Coandă openings was described in [3] analysing the influence of the deflection radius  $R_c$  related to the nozzle diameter  $D$ . The design of sharp edged nozzle orifice compared to Coandă openings, also called trumpet opening, are shown in figure 1

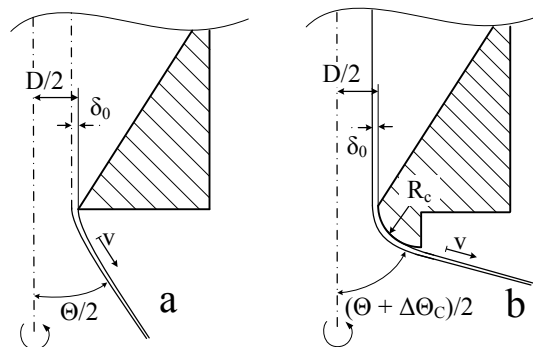


**Figure 1.** With a trumpet opening at a swirl nozzle as in (b), the spray angle can be increased. The sheet is deflected following the convex contour. The smallest cross-section has the diameter  $D$ .

The liquid sheet deflection is effective in a certain range of geometrical parameters and operating conditions. As known from single-phase systems, too small deflection radii lead to premature sheet detachment from the deflection body, which is unwanted for most cases [4, 5].

Despite common application of swirl nozzles with trumped shaped openings, the mechanism behind the deflection of the emerging sheet is not yet understood completely. In general, three major different deflection mechanisms were identified by literature and investigated in this study:

The wetting properties of the deflection body material influence adhesion of the liquid, eventually prevent detachment of the liquid from the body surface, often called “tea pot effect” [6–8]. Different nozzle

materials were tested and practically no effect of the contact angle within the range of  $13^\circ < \Theta_C < 98^\circ$  was visible for technical relevant conditions. Data can be found in [3].

Under-pressure in the gap between the nozzle body and the moving sheet draws the liquid towards the wall. The under pressure is caused by ambient air entrainment into the liquid sheet at the detachment edge [9, 6, 4]. Lower ambient pressures were found to promote proper deflection in cases when the deflection radius is close to its minimum value for given swirl conditions. Lower ambient pressure mean lower gas densities and lower pressures at the detachment edge easing deflection [3].

The boundary layer may also promote a sheet deflection, because of a torque moment caused by the flow profile within the boundary layer [6]. This dominant effect is strongly determined by the Reynolds-number and will be addressed within this paper

The Reynolds-number in general dominates the flow of the sheet around the curved opening. Due to the laborious flow velocity determination (see below), the easy accessible pressure Reynolds-number  $Re_p = D(\Delta p)^{1/2}/\mu$  is used, replacing the actual flow velocity of the emerging sheet in the Reynolds-number by the pressure drop at the nozzle. For definition and explanation of this characteristic number compare also [10, 11]. New surface formation close to the nozzle means only minor energy consumption and can therefore be neglected. At too high Reynolds numbers the sheet cannot be deflected properly and the spray angle recedes to the value of the sharp edged nozzle. This behaviour was examined and quantified in the following trails.

## Experimental test-rig

The test equipment consists of a pumping device, several swirl nozzles, a cooling system to maintain the temperature and various measuring devices. The spray angle were measured with a backlighting photography set up, see also [12]. The sheet velocity was registered by an optical fiber system as explained in [13]. The droplets were measured with a laser diffraction system.

### *Spray angle measurements*

For the spray angle measurement the nozzles had swirl ratios in the range between  $0.5 < \Delta < 7.2$ . Deflection radii ratios, shortly called deflection ratios, were within the range of  $0.22 < R_C/D < 0.7$ . All nozzle had diameters of  $D = 6 \text{ mm}$ . Geometrical parameters are indicated in figure 1. The experimental liquids consisting of glycerol-water mixtures were adjusted such to cover the viscosity range  $1 < \mu < 43.9 \text{ mPas}$ . The overhead pressure was changed between  $0.03$  and  $0.18 \text{ MPa}$ , resulting in pressure Reynolds-numbers from  $2,000$  until  $80,000$ . The spray was discharged into ambient atmosphere.

### *Sheet velocity*

Sheet velocity measurements were performed with the mentioned optical fiber system. A water-glycerol mixture with a viscosity of  $11.2 \text{ mPas}$  and a density of  $1150 \text{ kg/m}^3$  was used as a test liquid. It is sprayed by a swirl nozzle with a swirl ratio of  $\Delta = 4.79$  and an orifice diameter of  $D = 6 \text{ mm}$ . The nozzle was operated at  $0.03$ ,  $0.05$  and  $0.1 \text{ MPa}$ . To verify the sheet deflection influence on the velocity coefficient, four outlet openings are compared. One of them is without a deflection opening and three are with deflection ratios of  $R_C/D = 0.33$ ,  $R_C/D = 0.66$  and  $R_C/D = 1$ .

### *Drop sizes*

The measurement of drop sizes were performed with a MALVERN Spraytec with its laser beam oriented orthogonal to the direction of spray propagation, at a distance of  $460 \text{ mm}$  from the nozzle orifice. The spray width at the measurement point was controlled by a slot to  $150 \text{ mm}$ . During the drop size determination, the laser obscuration is in between  $4$  to  $10 \%$  the distance between the detector and the laser is  $740 \text{ mm}$ . Preventing secondary spray upon impact, the test-rig is layered with foam material and a gas suction of  $0.15 \text{ m}^3/\text{s}$  is operated from the collector bin. A pressure air bleeding and repeated lens cleaning ensures proper measurement conditions.

The same swirl nozzle with an orifice diameter  $D = 6 \text{ mm}$  and swirl ratio of  $\Delta = 4.79$  is operating with water from the tap water connection. The surface tension was determined with  $\sigma = 0.068 \text{ N/m}$ . The atomisation pressure is controlled by a valve and set at  $0.03$ ,  $0.06$ ,  $0.09$  and  $0.12 \text{ MPa}$ . Pressure Reynolds-numbers between  $30,000$  and  $65,000$  are achieved. Within the experiments four orifice openings with different deflections ratios are applied. The deflection ratios are  $R_C/D = 0.33$ ,  $0.66$ ,  $1$  and one opening without deflection body. The spray angle is nearly  $\Theta = 80^\circ$  for common nozzle orifice and nearly  $\Theta_{\max} = 140^\circ$  for the other bodies. The large spray angles indicate sheet attachment to the convex contour of the orifice opening.

## Results and Discussion

### Spray angle measurements

As shown in figure 2 the deflected spray angle is decreasing with increasing pressure Reynolds-number for special combination of geometrical designs and liquid properties in different manner. Starting at lower pressure Reynolds-numbers the sheet is deflected but then the deflection decreases gradually exceeding from a well-defined pressure Reynolds-number within a transient region down to the level of the sharp edged nozzle. Comparable transition behaviors of spray angles were found at 24 geometrical nozzle combinations. Five representative graphs are shown in figure 2. The transition regions are characterized by significantly high standard deviation of the spray angles when evaluating 320 images per sequence. In figure 2 the standard deviation is illustrated by error bars and photos of typical spray pattern are included.

The graph for a viscosity of  $\mu = 1 \text{ mPas}$ , a swirl ratio of  $\Delta = 0.96$  and a deflection ratio of  $R_c/D = 0.42$  shows small relative standard deviation except inside the transient region. The spray angle is deflected for the lowest three pressure Reynolds-numbers ( $\theta \approx 135^\circ$ ). Between  $Re_p \approx 56,800$  and  $Re_p \approx 65,600$ , the spray angle drops and reaches the value of  $80^\circ$ . As well as fully deflected as fully detached spray cones are smooth and illustrate a stable flow (fig. 2 - 1 & 3). However the cone in the transient region is unstable (fig. 2 - 2). It changes the spray angle periodically resulting in an un-uniform spray pattern.

For a viscosity of  $\mu = 1.6 \text{ mPas}$  and a swirl ratio of  $\Delta = 4.23$ , spray angle reduction from  $135^\circ$  to  $92^\circ$  takes place between pressure Reynolds-numbers of 20,000 and 38,000. The standard deviation increases in this region significantly. For  $\Delta = 5.89$  the slope of the spray angle decay inside the transient region increases compared to  $\Delta = 4.23$ .

Further increase of viscosity indicates that the transition is not fully covered in the range of pressure Reynolds-number adjusted within our trials. The standard deviation is between 10 and 20 % for viscosities of  $\mu = 4.2 \text{ mPas}$  and  $\mu = 9.8 \text{ mPas}$ . Also the photos show unstable flow behavior, hence all measured pressure Reynolds-numbers probably lie in the transient region.

In conclusion, the pressure Reynolds-number range between the widened and the detached spray angle increases with increasing viscosities and decreasing swirl ratio. This two parameters influence the sheet velocity and thickness within the orifice. The tangential velocity rises with increasing swirl ratio. In consequence, the air core diameter increases and the sheet become thinner. Friction losses because of higher viscosity lead to an opposite behavior.

According to this relation, thinner sheets seem to be deflectable even at higher pressure Reynolds-numbers. Thicker sheets detach at lower pressure Reynolds-numbers, but the spray angle decreases slower with increasing pressure Reynolds-number. Therefore, a bigger deflection ratio  $R_c/D$  is necessary for the spray angle expansion at higher viscosity. The sheet velocity and thickness are responsible for the sheet momentum. The deflection force has to overcome the inertia forces for proper operation.

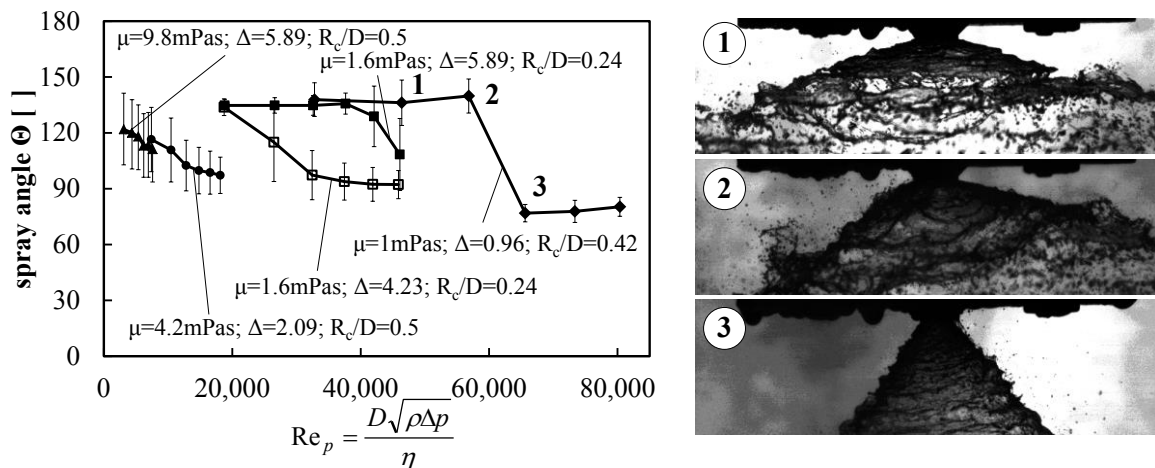


**Figure 2.** Transition between the deflected and the detached sprays is indicated by different spray angles. With increasing pressure Reynolds-number the spray angle decreases at critical deflection ratios  $R_c/D$ . Transient regions can be identified by the increasing standard deviation of the spray cone

Within the same pressure Reynolds-number interval for different viscosities, at a given nozzle and opening geometry equal spray angles are expected, as shown in figure 3. In order to prove this behavior tests were performed with 3 liquids with different viscosities and operated at comparable pressure Reynolds-numbers. This behaviour clarifies that there are no substantial influencing parameters on the spray angle deflection in the

observed range except the nozzle design, the liquid parameters, flow conditions and eventually the environmental gas pressure [3].

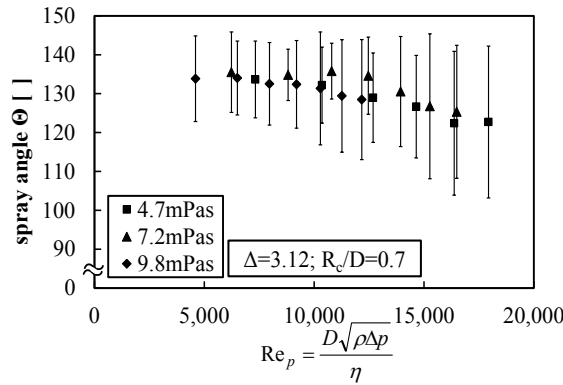


**Figure 3:** Results of spray angle measurements with different viscosities within the same pressure Reynolds-number range are shown. A good agreement in the spray angles can be identified. The spray angle is practically independent of the viscosity for the same Reynolds-number.

### Sheet velocity

Assuming aerodynamic wave breakup regime of the sheet it can be expected that the mean drop size depends on  $\kappa/(2\phi^2\Delta p^*)$  [14]. The velocity coefficient is the ratio of the sheet velocity  $v$  at the detachment point related to the potential velocity  $u = (2\Delta p/\rho)^{1/2}$  [14], the Laplace-number here is defined as  $\Delta p^* = \Delta p D/\sigma$ . The sheet number expresses the sheet attenuation due to the laterally divergent liquid propagation [10]. It relates the sheet thickness parameter  $K = \delta/x$  [15] to the orifice cross section  $A = D^2\pi/4$ , where  $\delta$  is the sheet thickness and  $x$  is distance from the orifice in flow direction.

$$\kappa = \frac{4\delta x}{\pi D^2} = \frac{C_D}{2\pi\phi\sin(\Theta/2)} \quad (1)$$

For swirl nozzles, the sheet number can be expressed with the nozzle discharge coefficient  $C_D$ , the velocity coefficient  $\phi$  and the spray angle  $\Theta$ . The discharge coefficient  $C_D$  in equation 1 relates the volumetric flow rate to the flow rate theoretically given by the Bernoulli equation assuming occupation of the total cross-section and parallel streamlines. Compare also [14, 16, 17]. Considering the given terms with increasing spray angle maintaining the differential pressure and the nozzle internal geometry the mean drop size should be reduced as long as the velocity remains constant. Even though Coandă openings widen spray angles, it must be questioned how the detachment velocities are affected.

In figure 4, the measured velocity coefficients are plotted towards the orifice distance in flow direction for different outlet opening geometries. Exemplary, two pressure Reynolds-numbers are shown in graph (a) and (b). Generally, velocity determination too close to the orifice fails with the optical fiber system because of too small disturbances at the sheet surface. The fiber velocimetry only operates properly, when the sheet oscillation amplitudes are sufficient and the sheet is still intact [18]. Due to these facts, the working range is limited. This is especially valid for the case of premature detached sheet, when the sheet breakup-length decreases stronger compared to the attached sheet.

In case of  $Re_p = 3,150$  (fig. 4a), the velocity coefficient is nearly equal to  $\phi = 1$  at the first suitable distance from the nozzle while operating the swirl nozzle without a deflection body. Increasing the distance from the nozzle the velocity coefficient decreases due to friction losses with the ambient air. It reaches a value of  $\phi = 0.85$ . The deflected sheet velocity coefficient at  $R_c/D = 0.66$  and  $R_c/D = 1$  is significantly smaller compared to the nozzle without deflection body. Increasing the distance of measurement also reveals a velocity decrease.

The deflection radius for  $R_c/D = 0.33$  is too small to promote a proper sheet attachment at this flow conditions. Illustrated by a strobe-light, the sheet is disturbed and the spray angle is fluctuating. The nozzle operates inside the transient region between the deflected and detached sheet. In this case the velocity coefficient is about  $\phi = 0.85$  near the orifice and  $\phi = 0.65$  close to the point of sheet breakup.

Measurement at  $Re_p = 4,050$  in figure 4b show a similar characteristic for deflected sheets and the nozzle without deflection body. Only the orifice with the deflection ratio of  $R_c/D = 0.33$  shows increased velocity coefficients with premature detachment. Because of the disturbed sheet, the velocity determination fails at some distances.

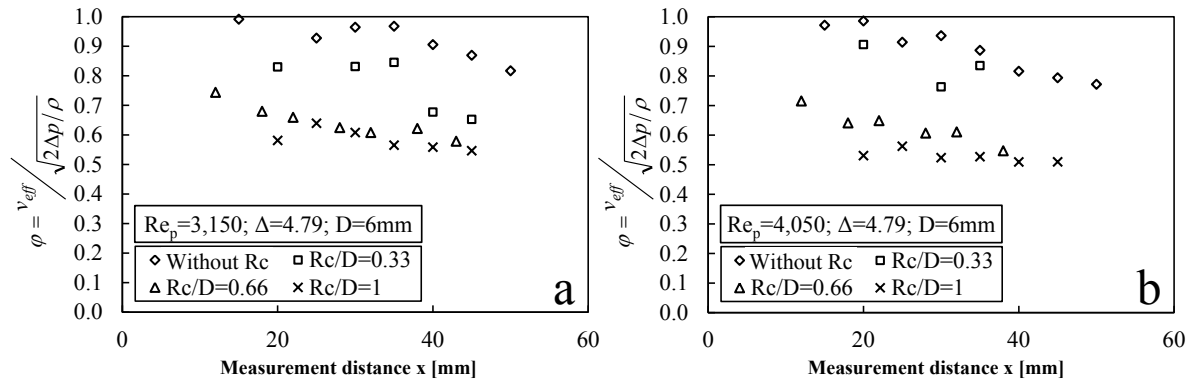


**Figure 4.** Fibre optical measured velocity coefficients depending on the orifice distance are plotted for two pressure Reynolds-numbers. The sheets are deflected for deflection ratios of  $R_c/D = 0.66$  and  $1$ .  $R_c/D = 0$  is used as reference, where there is no deflection body influence on the sheet. The velocity coefficient is clearly influenced by the deflection.

### Drop size measurements at trumpet openings

Three drop size measurements were performed for every adjustment i.e. deflection orifice geometry and atomisation pressure. Each measurement consists of 60 samples. Those have been averaged for analysing the deflection influence. Comparing the results of multiple measurements, the reproducibility is satisfactory. The mean standard deviation is 6 % while the maximum deviation is 11 %.

Tagging the attachment effect on the drop size, the volumetric cumulative distribution, the Sauter mean diameter  $SMD$  of the spray and the *span* value are evaluated.

The drop size distributions at Laplace-numbers of  $\Delta p^* = 5,300$  and  $\Delta p^* = 10,600$  are shown in figure 5 for typical adjustments. The measurements for all Laplace-numbers show similar behavior. In figure 5 the volumetric cumulative distributions, which results from the different nozzle orifices, are plotted.

In case of the smaller Laplace-number, the distributions have nearly the same shape for the different deflection ratios over the whole drop size distribution ( $DSD$ ). Surprisingly there are no remarkable differences between the orifices with and without deflection bodies. The  $DSD$  is even independent of the deflection body geometry. The volume based mean drop size is  $515 \pm 15 \mu m$  and denotes only small variation.

Increasing the Laplace-number, a similar tendency is observed. Certainly, the agreement between der cumulative distributions up to a drop size of  $d = 400 \mu m$  is constantly close. Accordingly, the plots differ slightly and somewhat smaller drops are generated by the orifice with the largest deflection ratio. This deviation accounts for higher variation in volume based mean drop size, compared to the lower Laplace-number. The mean drop size is  $407 \pm 28 \mu m$ . Still the differences are small and no significant trend depending on the deflection body geometry can be identified, no distinct effect on the drop size distribution is visible.

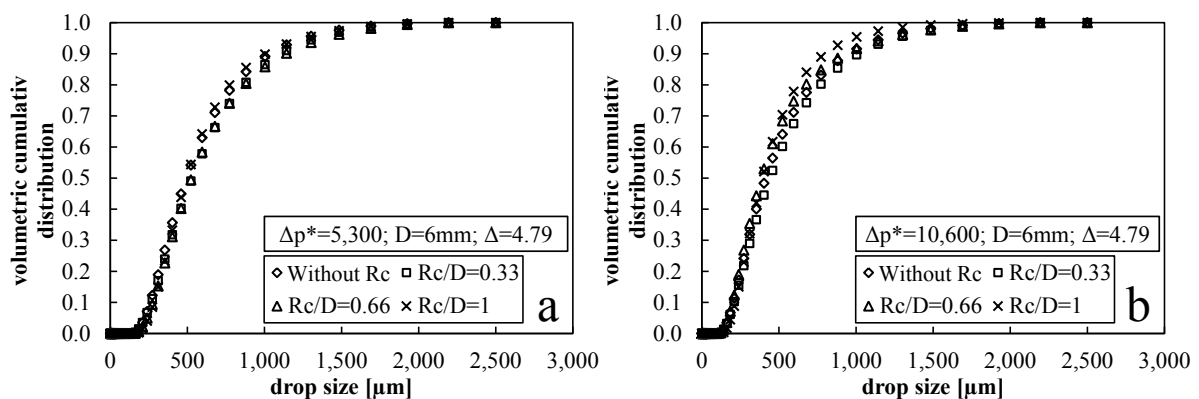


**Figure 5.** Comparison between the  $DSD$  of swirl nozzles with different deflection orifice geometries operating at the same Laplace-number or differential pressures. The courses for a moderate (a) and a high (b) Laplace-number are shown.

The  $SMD$  vs. the Laplace-number for different deflection orifice geometries is plotted in figure 6a. As expected the  $SMD$  decreases with increasing pressure Reynolds-number. The  $SMD$  decreases from about  $700 \mu m$  at  $\Delta p^* = 2,600$  to  $350 \mu m$  at  $\Delta p^* = 10,600$ . In case of the smallest Laplace-number the  $SMD$  is slightly dispersed. Here, the nozzle without deflection body leads to somewhat larger  $SMD$  than the nozzle with sheet deflection.  $SMD$ 's are closer together, but no clear tendency is visible. Increasing Laplace-number, the  $SMD$  for the different orifice geometries also become nearly equal and no significant deviation is noticeable. The results

indicate that the *SMD* reduction through increased spray angles is fully compensated through the sheet retardation obviously caused by the additional contact area between the liquid sheet and the nozzle. Therefore, Coandă nozzles can hardly be used to achieve smaller drops, however higher spray angles as desired for some applications may quite well be achieved.

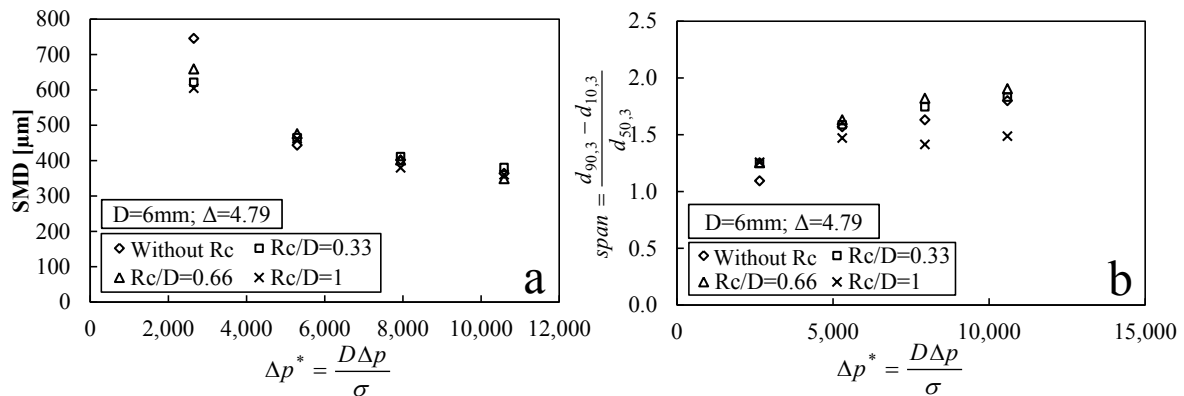


**Figure 6.** *SMD* (a) and span value (b) are plotted towards Laplace-number for swirl nozzles with different deflection orifices.

The *span* value serves as an indicator for the drop size distribution width. In addition to the mean drop size, the distribution width is essential for the spray quality. Drops of equal size have similar characteristic during the spray process, for instance equal penetration depths or trajectories. In figure 6b the measured *span* values are shown contingent upon the deflection body geometry and the Laplace-number.

The *span* value is about 1.1 for the smallest Laplace-number and the sharp edged orifice. In contrast it is about 1.2 applying the nozzle with a deflection orifice. Increasing the Laplace-number the *span* value increases as expected. Here, it reaches the level between 1.5 and 1.9. Even at small deviations, a fixed order of the deflection ratio regarding the span can be noticed for the following Laplace-number. The order starting from the highest *span* is  $R_c/D = 0.66$ ,  $R_c/D = 0.33$ ,  $R_c/D = 0$  and  $R_c/D = 1$ . The *span* caused by the largest deflection ratio is the smallest even smaller than at the sharp edged nozzle. This may be caused by a laminarisation of the flow, however this measurement has to be repeated.

## Conclusions

The spray angle expansion by means of Coandă deflections is depending on the pressure Reynolds-number and the nozzle geometry, i.e. the swirl ratio  $\Delta$  and the deflection ratio  $R_c/D$ . This was proven by observing the deflection behaviour of the sheet and the spray angle at equal pressure Reynolds-number but different liquid viscosities. In general, high pressure Reynolds-numbers promote a premature sheet detachment and therefore an increased deflection ratio  $R_c/D$  is needed, in order to achieve a proper deflection. However, also lower pressure Reynolds-numbers at given swirl ratios may lead to fairly thicker sheets at the orifice and may as well cause inadequate deflection. For high Reynolds-numbers, the transition between a deflected and a premature detached sheet is sudden. In contrast, at low pressure Reynolds-numbers, the spray angle decreases gradually while increasing the Reynolds-number until the level of a conventional sharp edged swirl nozzle is reached. The velocity measurements show a noticeable impact of the Coandă deflection body on the velocity coefficient. Compared to the sharp edged nozzle, the velocity coefficient is reduced by about 30 %, mutually due to the friction losses along the additional contact area between the liquid sheet and the deflection orifice.

From drop size measurements it can be concluded that the drop size reduction through larger spray angles is obviously mostly compensated by the reduced velocity coefficient. Therefore, the *SMD* and *span* achieved with Coandă nozzles are almost the same as in the case of conventional sharp edged nozzles. However, Coandă nozzles are still appropriate for applications when large spray angles are desired.

In future, more experiments have to be performed in order to describe the behavior of the velocity coefficient at different nozzle orifice geometries and liquid viscosities in more detail. Also the impact of the deflection on the drop size distribution at higher viscosities is still to be.

## Acknowledgements

The authors want to express their gratitude to the German research foundation „Deutsche Forschungsgemeinschaft (DFG)“ for their financial support of the project.



## Nomenclature

Symbol	Description	Unit
A	orifice cross section	[mm <sup>2</sup> ]
C <sub>D</sub>	discharge coefficient	[-]
D	orifice diameter	[mm]
d	drop size	[μm]
DSD	drop size distribution	[-]
K	sheet thickness parameter	[mm <sup>2</sup> ]
Δp	atomizing pressure	[MPa]
r	radius	[mm]
R <sub>C</sub>	Coanda deflection radius	[mm]
Re <sub>p</sub>	pressure Reynolds-number	[-]
SMD	Sauter mean diameter	[mm]
u	potential velocity	[m/s]
v	sheet velocity	[m/s]
x	sheet running length	[mm]
δ	sheet thickness	[mm]
σ	surface tension	[N/m]
Θ	spray angle	[°]
Θ <sub>C</sub>	contact angle	[°]
ρ	density	[kg/m <sup>3</sup> ]
κ	sheet number	[-]
μ	dynamic viscosity	[Pas]

Index	Description
0	detachment point
E	Entry
SC	Swirl chamber

### Non-dimensional number

R <sub>C</sub> /D	Deflection ratio
Re <sub>p</sub> = D(ρΔp) <sup>1/2</sup> /μ	Pressure Reynolds-number
Δ = πr <sub>SC,E</sub> D/(2A <sub>E</sub> )	Swirl ratio
Δp* = DΔp/σ	Laplace-number
φ = v/(2Δp/ρ) <sup>1/2</sup>	velocity coefficient

## References

- [1] Dombrowski, N. and Hasson, D. 1969. The flow characteristics of swirl (centrifugal) spray pressure nozzles with low viscosity liquids. *AIChE Journal* 15, 4, 604-611.
- [2] Musemic, E. and Walzel, P. 2011. *Estimation of Drop Sizes Using Pressure Swirl Atomizers*, Estoril, Portugal.
- [3] Musemic, E. and Walzel, P. 2012. *Swirl Atomizers with Coanda Deflection Outlets*, Heidelberg, Germany.
- [4] Newman, B. 1961. The Defelction of Planejets by Adjacentboundaries: Coanda Effect. *Boundary Layer and Flow Control*, 1, 232-264.
- [5] Panitz, T. and Wasan, D. 1972. Flow attachment to solid surfaces: The Coanda effect. *AIChE Journal* 18, 1, 51-57.
- [6] Reiner, M. 1956. The Teapot Effect: ... a problem. *Physics today*, 16-20.
- [7] Kistler, S. and Scriven, L. 1994. The teapot effect: sheet-forming flows with deflection, wetting and hysteresis. *Journal of Fluid Mechanics* 263, 19-62.
- [8] Bocquet, L., Duez, C., and Ybert, C. 2010. Wetting Controls Separation of Inertial Flows from Solid Surfaces. *Physical Review Letters* 104, 8, 84503.
- [9] Squire, M. 1950. Jet Flow and its Effects an Aircraft. *Aircraft Engineering*, 62-66.
- [10] Walzel, P. 1982. Auslegung von Einstoff-Druckdüsen. *Chemie Ingenieur Technik* 54, 4, 313-328.
- [11] 2000. *U mann's Encyc opedia of Industria C emistry*. Wiley-VCH Verlag GmbH & Co. KGaA.
- [12] Musemic, E., Gaspar, M., Weichert, F., Müller, H., and Walzel, P. 2010. *Experimental Examination of the Liquid Sheet Disintegration Process Using Combined Photography and Fiber Based Measuring Techniques*, Brno, Czech Republic.
- [13] Musemic, E., Gaspar, M., Weichert, F., and Walzel, P. 2008. *Analysis of Multiphase Flow during the Process of Sheet disintegration at Hollow Cone Nozzles using multiple one-dimensional Fiber Sensors*, Como Lake, Italy.

- [14] Dombrowski, N., Fraser, R., and Eisenklam, P. 1962. Drop formation from rapidly moving liquid sheets. *AIChE Journal* 8, 5, 672-680.
- [15] Dombrowski, N. and Johns, W. 1963. The aerodynamic instability and disintegration of viscous liquid sheets. *Chemical Engineering Science* 18, 3, 203–214.
- [16] Lefebvre, A. 1989. *Atomization and sprays*. Hemisphere Pub. Corp, New York.
- [17] Musemic, E. 2011. Durchsatzverhalten von Hohlkegeldüsen. *Chemie Ingenieur Technik*, 83, 237-246.
- [18] Musemic, E. 2013. *Experimentelle Untersuchung zum Tropfenbildungsprozess an Hohlkegeldüsen*. Dissertation, TU Dortmund.

## Fuel Influence on Hollow-Cone Sprays

F. Mathieu, J. Palmer, M. A. Reddemann, R. Kneer

Institute of Heat and Mass Transfer, RWTH Aachen University, Germany

### Abstract

In this study the macroscopic spray characteristics of ten different model fuels are examined experimentally by post-processing of images taken with a high-speed camera. The injector employed is designed for gasoline direct-injection engines and features an outwardly opening nozzle forming hollow-cone shaped sprays. The sprays are visualized while propagating in a high pressure chamber which provides engine-relevant conditions in terms of ambient temperature and pressure: these are varied from 300 to 600 K and from 0.5 to 1.5 MPa respectively. The investigated model fuels are Ethanol, 1-Butanol, 1-Decanol, Iso-Octane, Tetrahydrofurfuryl-alcohol (THFA), Ethyl-Levulinate, Butyl-Levulinate, 2-Methylfuran (2-MF) and 2-Methyltetrahydrofuran (2-MTHF). The experiments are carried out at injection pressures of 5, 10 and 20 MPa using a constant energizing duration of 500  $\mu$ s. The comparison of the model fuels reveals significant differences in temporal spray penetration due to varying Reynolds- and Ohnesorge numbers. In particular the penetration length as well as the formation of vortex systems is strongly fuel-dependent. In terms of homogeneous mixture formation especially the furans 2-MTHF and 2-MF turn out to be promising fuel candidates.

### Introduction

The limited availability of fossil energy resources combined with increasing carbon dioxide emissions and a rising energy demand requires the investigation of alternative energy resources: The research project "Tailor-Made Fuels from Biomass" aims for pathways towards new synthetic fuels derived from biomass. For the utilization of these fuels the injection is one important subprocess that controls combustion efficiency and hence influences both, engine performance and emissions. A number of studies, e.g. [1-6], have shown that fuel composition strongly affects specific spray characteristics such as primary break-up, penetration length and secondary droplet sizes. In this study, one focus is on biomass-derived furan-type fuels, which are compared to conventional fuel candidates. For this purpose a parametric study is conducted: Besides the fuel variation, the ambient conditions together with the injection pressure are systematically varied to gain a complete view of the major influences on the temporal spray behavior. In order to judge the alternative fuels' applicability for present DISI engines, Iso-Octane, which is widely used in literature as substitute for standard gasoline, is used as reference fuel. The acquired image series are evaluated both qualitatively and quantitatively with respect to liquid penetration length, overall spray shape, vortex formation and evaporation duration and are then compared to Iso-Octane.

### Materials and Methods

The employed injector together with the pressure system is depicted in Fig.1. The injector has a piezo driven, outwardly opening needle with a design cone angle of  $94^\circ$ , its full needle lift is 35  $\mu$ m and the length of the slightly diverging annular channel between seat and needle is approx. 311  $\mu$ m. Due to the annular channel, the evolving overall spray shape forms as a hollow-cone.

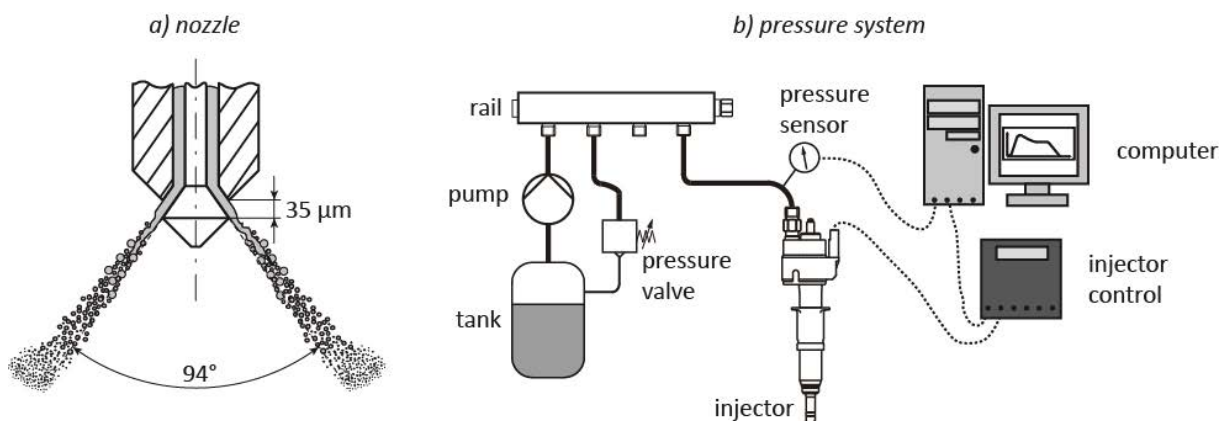
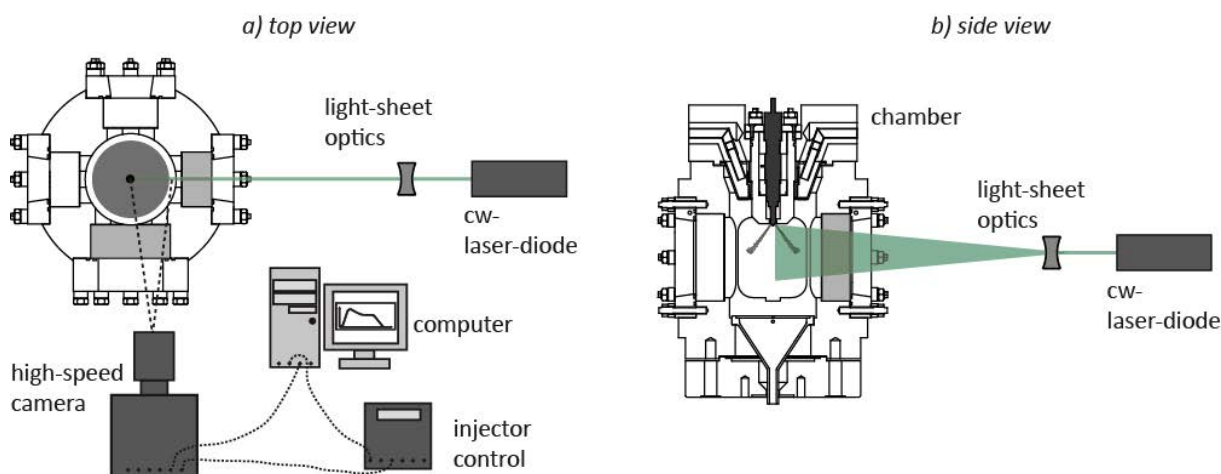


Figure 1. Schematic sketch of a) nozzle design and b) pressure

The experiments are carried out at injection pressures of 5, 10 and 20 MPa and a constant energizing duration of 500  $\mu$ s. Due to the short energizing duration no stationary spray is reached and therefore all target quantities are referred to certain time steps. The injection pressure is provided by an original car manufacturer high pressure pump for DISI engines. The pump is continuously boosting fuel into a rail which is equipped with a pressure control valve. The pressure is monitored by a piezo pressure transducer mounted close to the injector giving insight into the static pressure behavior during injection with high temporal resolution. Injection and pressure recording are triggered by a specific injector control unit provided by Continental.

In order to characterize the spray shape, information e.g. on the thickness of the liquid sheet or the sheet's cone angle are desirable quantities. Due to the nature of the hollow-cone spray simple imaging techniques such as line-of-sight shadowgraphy or stray light visualizations suffer from the limited depth of field of conventional optics, which cannot cover the full cone completely. Insight into the cross section of the hollow-cone is disturbed by droplets moving outside the depth of field. In this study, light-sheet visualizations are used to image the cross section of the hollow-cones, see Fig. 2.



**Figure 2.** Schematic sketch of the light-sheet visualizations set-up.

The beam of a continuous wave (cw) Nd:YAG laser with optical power of 2 W is expanded in one direction by a light-sheet optics to illuminate the spray at its cross section. A high-speed camera (Model: Photron FastCam SAX) is equipped with a Zeiss Makro-Planar lens with 100 mm focal length and takes images with a repetition rate of 40,000 frames per second. The camera's shutter speed was set to 10  $\mu$ s. Camera and lens are adjusted to image only half of the full cone with a field of view of 36 mm x 49 mm (height x width), the image scale is 10.36 pixel/mm. The acquisition duration for each injection event is 160 frames or 4000  $\mu$ s, hence also the spray evaporation after end of injection is covered.

In order to provide engine-relevant conditions in terms of ambient pressure and temperature during injection, the injector is mounted in the head of a specifically designed high-pressure chamber, which provides access for optical measurement techniques. The chamber is continuously flown by air, which can be pressurized and heated as desired. The ambient conditions for this study are chosen as follows: pressures of 0.5, 1.0 and 1.5 MPa and temperatures of 300, 450 and 600 K. This variation leads to 270 different operating points (10 liquids, 9 chamber conditions, 3 injection pressures). Each operating point was repeated 20 times to gain insight into the cyclic variations.

Ten different liquids are investigated: three monohydric alcohols (Ethanol, 1-Butanol and 1-Decanol), two alkanes (n-Dodecane and Iso-Octane), three furan-based liquids with cyclic molecular structure (Tetrahydrofurfuryl-Alcohol (THFA), 2-Methylfuran (2-MF) and 2-Methyltetrahydrofuran (2-MTHF)) and two platform chemicals derived from cellulose (Ethyl- and Butyl-Levulinate). In contrast to combustion-related research, mixture formation is not directly dominated by the liquids chemical composition or functional groups but by their macroscopic properties, e.g. density or viscosity. Table 1 gives the most important macroscopic properties of the liquids at standard conditions, marking THFA and 1-Decanol as the most exotic ones with exceptional high viscosity, surface tension and very low volatility. In terms of a fast evaporating liquid phase, 2-MTHF and 2-MF a priori show promising properties with boiling points well below 100  $^{\circ}$ C, which are even lower than those of conventional fuel substitutes like Ethanol or Iso-Octane.

Besides the liquid fuel properties the atomization process is influenced by plenty other parameters, e.g. the nozzle geometry, the flow velocity at the nozzle exit or the ambient density. A common way to decrease the number of influences is the usage of dimensionless numbers. In terms of atomization there are mainly three numbers used in literature, the Reynolds number ( $Re$ ), the Ohnesorge number ( $Oh$ ) and the density ratio ( $\rho^*$ ):

**Table 1.** Fundamental fuel properties (1 bar and 25 °C,  $\rho$ : liquid density,  $\eta$ : dynamic viscosity,  $\sigma$ : surface tension,  $T_{\text{boil}}$ : boiling point,  $\Delta h_v$ : enthalpy of vaporization, data taken from [7] unless otherwise noted)

	$\rho$ [kg/m <sup>3</sup> ]	$\eta$ [m Pas]	$\sigma$ [m N/m]	$T_{\text{boil}}$ [°C]	$\Delta h_v$ [kJ/kg]
<b>Iso-Octane</b>	689	0.47	18.2	99	300
<b>n-Dodecane</b>	744	1.36	24.8	225	354
<b>Ethanol</b>	784	1.04	21.9	81	920
<b>1-Butanol</b>	804	2.41	24.2	118	708
<b>1-Decanol</b>	824	10.54	28.2	231	511
<b>THFA</b>	1048	4.68	37.1	178	524
<b>2-MF</b> <sup>[8,9]</sup>	910	0.38	25.5 <sup>a)</sup>	64	397
<b>2-MTHF</b> <sup>[10-12]</sup>	849	0.47	24.6	80	395
<b>Ethyl-Levulinate</b> <sup>[13]</sup>	1007	1.94	32.7	196	481
<b>Butyl-Levulinate</b> <sup>[13]</sup>	971	2.54	31.0	236	437

a) taken from <http://www.chemspider.com/Chemical-Structure.10340.html> (May 2013)

$$Re = \frac{\rho \cdot v \cdot 2h}{\eta} \quad Oh = \frac{\eta}{\sqrt{\rho \cdot \sigma \cdot 2h}} \quad \rho^* = \frac{\rho_{\text{air}}}{\rho}$$

The characteristic length used here is the hydraulic diameter of the channel flow which equals twice the channel height perpendicular to the nozzle flow direction:  $h = 35 \mu\text{m} \cdot \sin(94^\circ/2) = 25.6 \mu\text{m}$ . In a prior study [6], the authors have developed a correlation to estimate the nozzle outlet velocity for the present injector. Fig. 3 exemplarily shows the distribution of the investigated fuels within the Reynolds-Ohnesorge diagram.

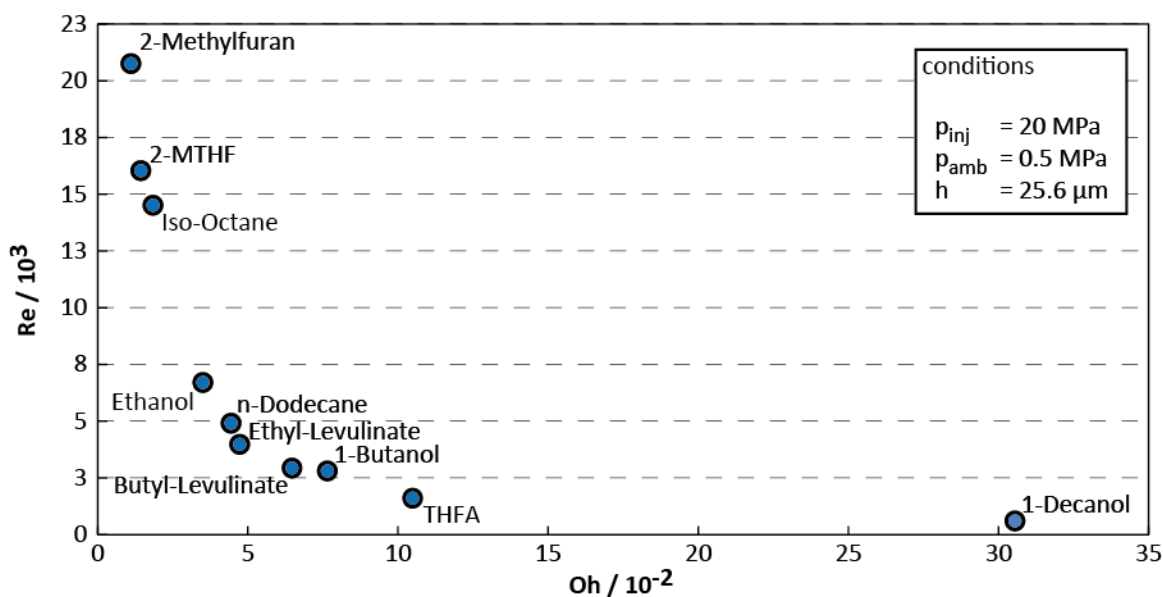


**Figure 3.** Reynolds-Ohnesorge classification of the investigated fuel candidates for standard conditions according to Table 1.

High Reynolds numbers tend to promote sheet breakup due to increased turbulence. High Ohnesorge numbers indicate that viscous forces are predominant for the sheet breakup over surface tension forces. As can be seen, the furans 2-MF and 2-MTHF feature higher Reynolds-Numbers than Iso-Octane at comparable conditions. In contrast 1-Decanol and THFA are expected to show poor breakup of the liquid sheet.

## Image Analysis

To extract quantitative data from images, a common way is the binarization of raw greyscale images. From

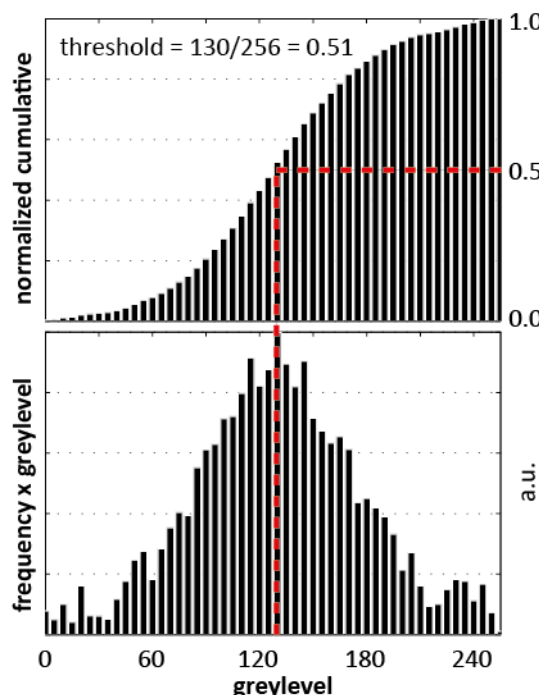


**Figure 4.** Determination of thresholds for image binarization from image histograms

determined, whose cumulative energy first exceeds 50 %. The threshold is then computed as ratio of the 50%-greylevel and the maximum greylevel (256 for 8-bit greyscale). This 50%-criterion has proven to deliver adequate binarization throughout the injection. Note in Fig. 5 a) that the region below the nozzle (illuminated due to multiple scattering) is not converted to the binary image Fig. 5 b). On the other hand the dynamic adjustment of the threshold also allows detecting very dilute (and hence less intense) sprays in the evaporation phase.

The image processing is done with Matlab©: first the raw image is converted into a binary image in the described manner and the nozzle is cut-off to avoid reflections from the nozzle being treated as liquid spray. For the binary image the contour of the spray cloud is computed and the contour is further analyzed in terms of penetration length, cloud thickness, hollow-cone as well as sheet angle and the evaporation duration. All acquired data is accessible with the temporal resolution of the camera, i.e. 25  $\mu$ s, including the averaged values over 20 injections and their standard deviations.

## Results

In order to gain an impression of the overall spray shapes, Fig. 6 shows raw images of the investigated fuels at the end of injection. The fuel influence is obvious: With exception of 1-Decanol all alkanes and monohydric alcohols show a relatively broad and bright spray cloud whereas the alternative fuels form a thinner sheet.

The sheet thickness is an indicator for atomization quality: a thin sheet preserves most of its momentum and air entrainment is reduced. A characteristic toroidal vortex can be identified on most of the images, but its size decreases with decreasing sheet thickness, which is a second indicator for inferior mixture formation at this stage of injection. Another issue of these sprays is visible at the spray tip especially for 2-MF and 2-MTHF: here, small clouds of liquid are separated downstream of the main spray cloud, which is a priori not expectable, since the leading droplets are fully facing the aerodynamic drag and should be decelerated more strongly than

theses binary images the spray contour can be computed and analyzed in terms of thickness, liquid penetration length or other quantities of interest. However, the choice of the binarization level is crucial, since it determines whether a certain pixel of the image is recognized as liquid or not. Hence, the results obtained depend on the selected threshold for binarization. That is why a fixed value for the binarization level has to be pursued; nevertheless, for the described visualization of hollow-cone sprays a specific problem arises: due to multiple scattering not only the cross section of the liquid sheet is illuminated but the complete cone. This can be observed in Fig. 5 a), the raw image shows the cross section as area with mostly saturated pixels, but there is also spray detected vertically below the nozzle, which does not represent the sheet's cross section but the hollow-cone lying outside of the light-sheet. A fixed value for the binarization threshold would lead to a binary image that either covers areas outside the spray cross-section or fails to detect liquid in the later stage of injection. Therefore, an algorithm is developed to compute suitable threshold levels for binarization: for each raw image an energy histogram is evaluated, which gives the energy contained in a certain greylevel bin (frequency of occurrence times greylevel) as function of greylevel, see Fig. 4. These energy levels are then cumulated and normalized to the total energy. Finally the greylevel is



**Figure 5.** Progression of image analysis: the raw image a) is converted into a binary image without the nozzle b), the contour of the spray cloud is detected and target quantities are computed c).

the following drops. This observance might be related to the divergent annular channel of the nozzle, which favors ingestion of air into the channel and causes specific spray features of this type of injector [14]. However, this issue has to be further investigated by microscopic visualizations close to the nozzle.

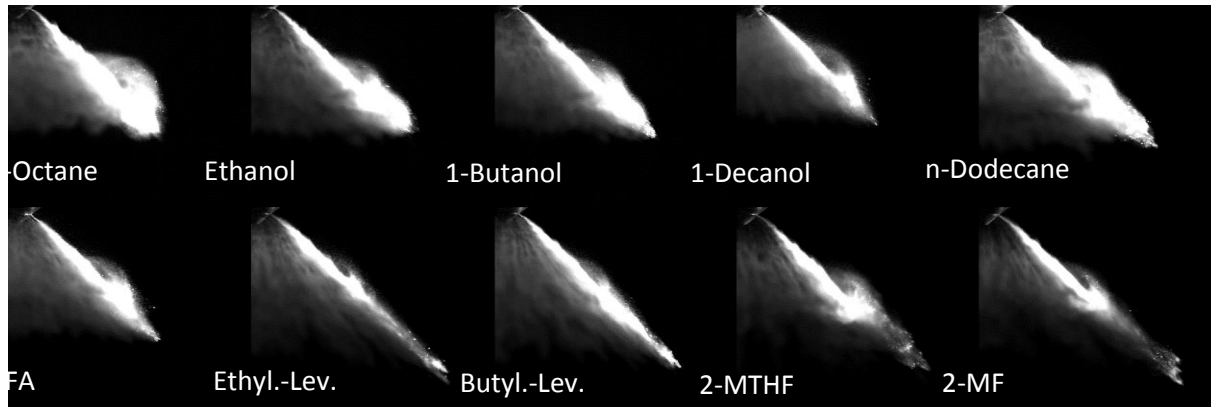


**Figure 6.** Comparison of spray structures. Spray propagation is from top left to bottom right. Ambient pressure: 1 MPa / ambient temperature: 600 K / injection pressure: 20 MPa / shown time step: 650  $\mu$ s after energizing injector (end of injection)

Although the fuel influence is in the focus of this study, varying ambient conditions are also investigated. Fig. 7 gives an overview of those influences on the penetration in spray direction at the end of injection. The penetration increases with injection pressure and decreases with ambient density. Accordingly temperature and pressure have contrary influences on penetration, since density is increased by increasing pressure and decreasing temperature. These findings hold for all fuels investigated.

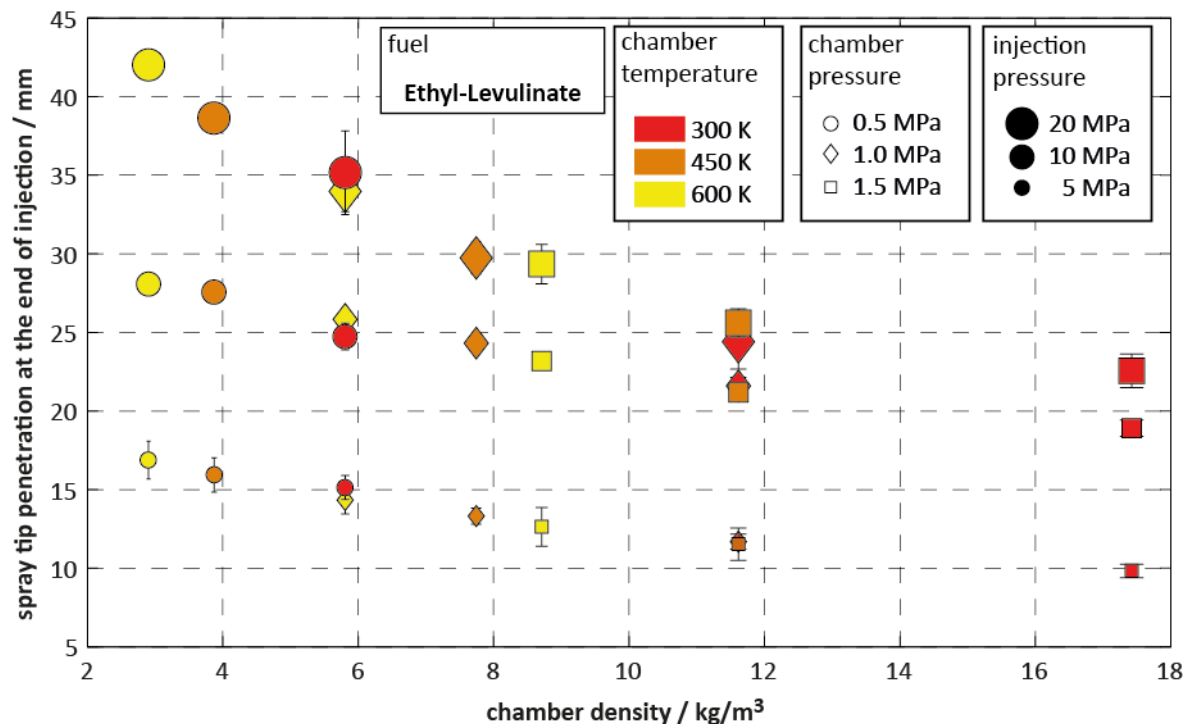


**Figure 7.** Spray penetration of Ethyl-Levulinate at the end of injection (650  $\mu$ s after energizing injector) for various operating conditions

The main focus is on the fuel influence of critical spray parameters at comparable ambient conditions. Fig. 8 compares acquired penetration data for all fuels. Two cases are shown: *i*) the penetration at the moment the injector closes and *ii*) the maximum penetration observed in the investigated period of 4000  $\mu$ s. Considering the end of injection the penetration tends to decrease with increasing Ohnesorge number. This is related to the start of injection, which is delayed for the fuel candidates with higher viscosity (and hence higher Ohnesorge number). The maximum penetration, however, shows only little variation, all fuels reach values around 48 mm



with a deviation of approximately  $\pm 10\%$ . These findings imply that liquid penetration is not the limiting parameter in terms of the fuel's applicability in DISI engines. On the other hand, with increasing viscosity the energizing duration in the engine has to be increased to deliver comparable amounts of fuel mass into the cylinder: this in fact directly increases liquid spray penetration.

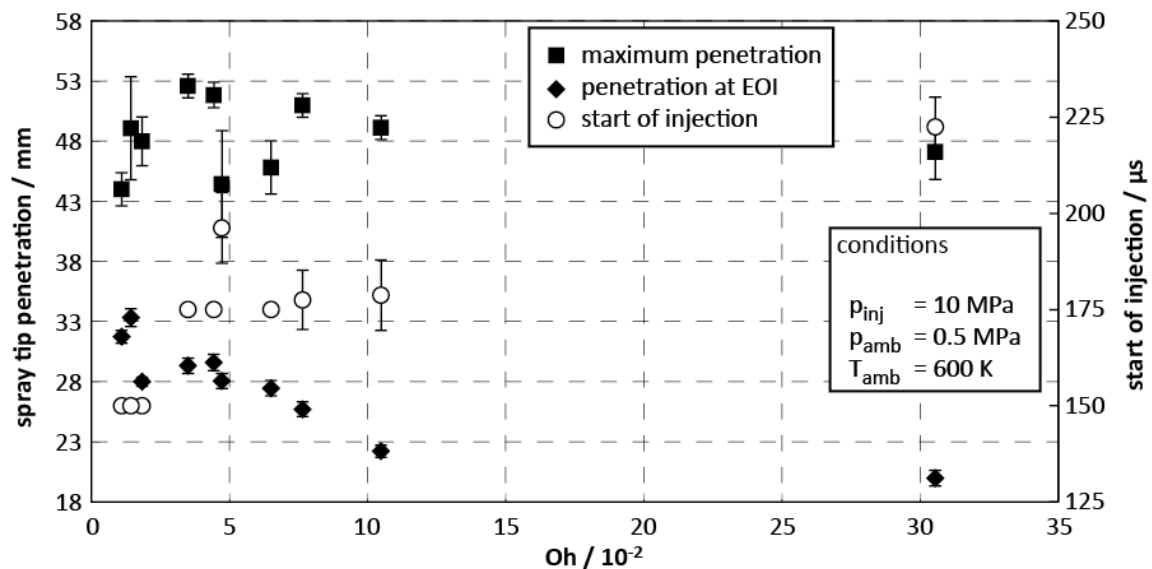


**Figure 8.** Spray penetration and start of injection as function of Ohnesorge number (EOI: end of injection) covering all investigated fuels.

The results for sheet thickness and hence sheet cone angle are skipped at this point, since the present technique cannot deliver trustworthy values for these quantities, in particular the unwanted illumination of the full cone disturbs the analysis of the inner sheet contour, so that significant variations arise due to the binarization. However, an interesting quantity for the engine applicability of the fuel candidates can be extracted from the images: the time until complete evaporation has occurred. Fig. 9 gives an overview of the acquired durations for an ambient temperature of 600 K and different ambient pressures. The fuels are arranged according to their normal boiling point, but the actual evaporation duration depends on a couple of further influences. For THFA and 1-Decanol, for instance, there was still liquid detectable until the end of acquisition, hence the values are put to 4000  $\mu\text{s}$  understanding that their real values are even higher. This exceptional behavior is apparently due to the worse atomization of 1-Decanol and THFA, which have the highest Ohnesorge numbers (lowest Reynolds numbers) in the field.

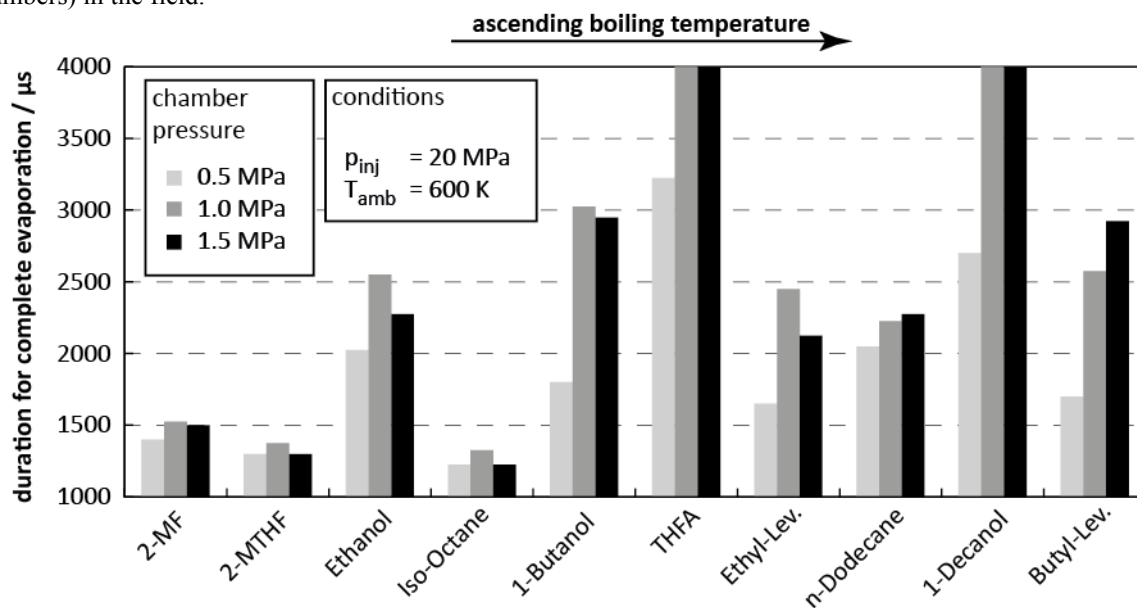


**Figure 9.** Duration for complete evaporation of the investigated fuels. The fuels are sorted according to their normal boiling temperature.

Considering Ethanol, also the influence of enthalpy of vaporization can be observed; although Ethanol features a similar boiling point and Ohnesorge number like 2-MF, 2-MTHF and Iso-Octane, it's evaporation duration is notably higher due to its exceptional high enthalpy of vaporization (refer to Tab. 1). Nonetheless, despite of THFA and 1-Decanol all fuels reveal an acceptable evaporation behavior compared to conventional gasoline fuel substitutes Iso-Octane and Ethanol. In particular the furans 2-MF and 2-MTHF are competitive candidates compared to Iso-Octane.

## Conclusions

Ten different liquids have been investigated by means of high-speed visualizations and post-processing of the acquired images. From the raw images qualitative differences regarding the atomization process and the evolving spray shapes could be pointed out. Considering penetration lengths of the liquid phase, this study distinguished between penetration at the end of injection and the maximum occurring penetration, showing that the fuel influence on maximum penetration was minor, whereas the penetration at the end of injection was related to the fuel's Ohnesorge number. Furthermore, the evaporation behavior of the liquids was discussed revealing that especially the furans 2-MF and 2-MTHF are promising fuel candidates in terms of mixture formation.

One drawback of the light-sheet visualizations applied in this study was the illumination of unwanted areas outside the sprays' cross section due to multiple scattering, which hindered the contour detection notably. Hence, the investigation of these quantities requires more sophisticated techniques, for instance the structured laser illumination planar imaging (SLIPI) [15].

## Acknowledgements

This work was performed as part of the Cluster of Excellence "Tailor-Made Fuels from Biomass", which is funded by the Excellence Initiative of the German federal and state governments to promote science and research at German universities. The authors also thank Continental AG for providing the driver unit of the injector.

## Nomenclature

$\rho$	liquid density	[kg/m <sup>3</sup> ]
$\rho_{air}$	ambient density	[kg/m <sup>3</sup> ]
$\eta$	dynamic viscosity	[m Pa s]
$\sigma$	surface tension	[m N/m]
$T_{boil}$	boiling temperature	[°C]
$\Delta h_v$	enthalpy of vaporization	[kJ/kg]
$v$	outlet velocity	[m/s]
$h$	channel height	[μm]
$Re$	Reynolds number	[-]
$Oh$	Ohnesorge number	[-]
$\rho^*$	density ratio	[-]

## References

- [1] Zigan, L., Schmitz, I., Flügel, A., Wensing, M., Leipertz, A., "Influence of fuel properties on spray formation and evaporation measured on a piezo-electric injector for the 2nd generation gasoline direct injection," *Proceedings of Injection Systems for IC Engines*, London, England, May 2009.
- [2] Higgins, B.S., Mueller, C.J., Siebers, D.L., "Measurements of Fuel Effects on Liquid-Phase Penetration in DI Sprays," *SAE Technical Paper 1999-01-0519*, 1999.
- [3] Ahmed, A., Ejim, C.B., Fleck, B., Amirfazli, A., "Effect of Biodiesel Fuel Properties and Its Blends on Atomization," *SAE Technical Paper 2006-01-0893*, 2006.
- [4] Reddemann, M. A., Mathieu, F., Martin, D., Kneer, R., "Experimental Investigation of Spray Propagation and Mixture Formation of Tailor-Made Fuels under Engine-Relevant Conditions," *ICLASS 2009*, Vail, Colorado USA, July 2009.

- [5] Mathieu, F., Reddemann, M., Martin, D., Kneer, R., “Experimental Investigation of Fuel Influence on Atomization and Spray Propagation Using an Outwardly Opening Injector,” *SAE Technical Paper 2010-01-2275*, 2010.
- [6] Mathieu, F., Cárdenas, M., Reddemann, M. A., Kneer, R., “Fuel Influence on Propagation and Near-Nozzle Velocities of GDI Hollow-Cone Sprays,” *ILASS Europe 2011*, Estoril, Portugal, September 2011.
- [7] Daubert, T. E., Danner, R. P., *Physical and thermodynamic properties of pure chemicals*, Hemisphere Pub. Corp., New York, 1994.
- [8] Loras, S., Aucejo, A., Monton, J. B., Wisniak, J., Segura, H., “Phase Equilibria for 1,1,1,2,3,4,4,5,5,5-Decafluoropentane + 2-Methylfuran + Oxolane and 1,1,1,2,3,4,4,5,5,5-Decafluoropentane + 2-Methylfuran + Oxolane at 35 kPa,” *J. Chem. Eng. Data*, Vol. 47, pp. 1256-1262, 2002.
- [9] Yaws, C. L., “Transport properties of chemicals and hydrocarbons: viscosity, thermal conductivity and diffusivity of C1 to C100 organics and Ac to Zr inorganics,” William Andrew, New York, 2009.
- [10] Villares, A., Sanz, L., Giner, B., Lafuente, C., Lopez, M. C., “Study of the surface tension of Chlorocyclohexane or Bromocyclohexane with some cyclic ethers,” *J. Chem. Eng. Data*, Vol. 50, pp. 1334-1337, 2005.
- [11] Comelli, F., Francesconi, R., Bigi, A., Rubini, K., “Molar heat capacities, densities, viscosities, and refractive indices of Dimethyl Sulfoxide + Tetrahydropyran and + 2-Methyltetrahydrofuran at (293.15, 303.15, and 313.15) K,” *J. Chem. Eng. Data*, Vol. 52, pp. 639-644, 2007.
- [12] Horstmann, S., Gardeler, H., Böls, R., Zudkevitch, D., Gmehling, J., “Vapor-Liquid equilibria and excess enthalpy data for the binary systems 2-Methyltetrahydrofuran with 2,2,4-Trimethylpentane (Isooctane), Ethanol, Toluene, Cyclohexane, and Methylcyclohexane,” *J. Chem. Eng. Data*, Vol. 44, pp. 959-964, 1999.
- [13] Lomba, L., Giner, B., Bandrés, I., Lafuente, C., Pino, M. R., “Physicochemical properties of green solvents derived from biomass,” *Green Chem.*, Vol. 13, pp. 2062-2070, 2011.
- [14] Befrui, B., Corbinelli, G., Robart, D., Reckers, W., Weller, H., “LES Simulation of the Internal Flow and Near-Field Spray Structure of an Outward-Opening GDI Injector and Comparison with Imaging Data,” *SAE Technical Paper 2008-01-0137*, 2008.
- [15] Kristensson, E., Berrocal, E., Richter, M., Aldén, M., “Nanosecond structured laser illumination planar imaging for single-shot imaging of dense sprays,” *Atomization and Sprays*, Vol. 20(4), pp. 337-343, 2010

## Optimization of Pressure-Swirl Atomizer for a Burner Retrofit

Jan Jedelsky<sup>1</sup> and Miroslav Jicha<sup>1</sup>

1: Faculty of Mechanical Engineering, Brno University of Technology, Technická 2896/2, 61669 Brno, Czech Republic

### Abstract

This study documents several ways to reduce drop size in spray of a spill-return type pressure-swirl atomizer (PSA) for a waste oil burner. In the first part, liquid breakup and spray microstructure of PSAs was documented using spray photography and Phase-Doppler Anemometry (PDA) on a cold test bench at different loads.

Then factors that affect the spray characteristics, such as: (1) nozzle design and dimensions, (2) operational conditions and (3) physical properties of atomized liquid, were analysed based on a literature survey. According to the analysis, several geometrical factors were chosen for design of six nozzles with modified geometry that were probed using PDA.

The literature data analysis shows that a modification of rheological properties of fuel used, namely its heating-up, would significantly reduce  $D_{32}$  mainly due to a viscosity change. Our tests show that doubling the inlet pressure with additional reduction of exit orifice size to keep flow rate would drop  $D_{32}$  by 28 – 33%. The simplest and the most cost efficient way is an optimization of the internal nozzle geometry, which according to our tests, leads to a reduction of  $D_{32}$  by about 7%.

### Introduction

Pressure-swirl atomizers (PSAs) are widely used in industrial and domestic burners, gas turbine combustors, rocket engines, and many other engineering areas thanks to their simple design, low power demands and good atomization characteristics. Their research and development, intense in 50ties to 80ties, declined in past decades with more effort put to new concepts with larger potential for spray enhancement (twin-fluid, ultrasound, electrostatic and other atomizers). Old burners and incinerators are forced to modernize their equipment to fulfil today emission requirements. Due to economical limitations, an optimization of individual components is often preferred against investments into fully new technologies.

Characteristics of fuel nozzles, such as the spray cone angle (SCA), drop-size and velocity distribution have a significant effect on the burner performance. Spray quality affects stability limits, combustion efficiency and pollutant emission levels. Good atomization quality promotes the fuel evaporation and decreases the demand of ignition energy [1].

Original spraying devices in old burners, designed according contemporary state of the art, provide a suitable means for optimization using present knowledge. A waste amount of available literature can be found for design and operation of PSAs. The older investigations [2-7] are predominantly experimental or analytical, numerical simulations prevail today [8-13] although also experimental works can be found [14, 15]. The present works are often focused to specific phenomena while older sources, that frequently document correlations amongst operation and design factors and spray quality, are useful in our study.

In this paper we document a strategy to improve spray characteristics of original PSA in a waste oil combustor keeping original oil gun and modifying only inner part of the atomizer. We focus on a reduction of droplet size. A detailed measurement of PSA spray at different loads using PDA and photographic documentation for description of the spray macro and microstructure is made first as a basis and information source for further works and for validation of numerical models. Literature survey related to PSAs have given a number of results describing effect of liquid properties, operation conditions and internal design on the spray, they are however inconsistent or sometimes lead to contradictory recommendations for the spray improvement. We have therefore (1) systematically analysed the published data, (2) selected several most promising geometrical factors to vary, (3) designed and tested several nozzles with modified geometry and (4) analysed their results acquiring an optimized PSA. The combination of published findings with our own experiments reduced the number of required tests so only several nozzle samples were fabricated and tested to keep the innovation cost low. The work, focused on improvement of particular burner, was written from more general perspective to be helpful also in other cases.

### Experimental Facility

The experimental apparatus includes atomizer under test, cold test bench with fluid supply system and Phase-Doppler Analyzer (PDA). A schematic layout of the test bench is shown in Fig. 1 left. It consists of a gear pump (1) that supplies fuel from a main tank (2) through filters (3), control valves (4, 5) and flow meters (6) into the atomizer (7). A chiller (8) controls the fuel temperature and so its viscosity. The spray falls into a collector (9) and then it is returned to the main supply tank by a pump (10). The collector is connected to a fuel mist

separator that keeps the spray zone free of aerosol but does not substantially disturb the spray. The fuel piping is equipped with a hydraulic shock absorber (11) placed in front of the atomizer. Pressure (12) and temperature (13) readings are taken at the atomizer inlet.

Time-resolved size and velocity of droplets were measured using a PDA by Dantec Dynamics. This 1-component PDA system, equipped with a standard optics, was used in the first-order refraction mode with parallel (horizontal) polarization. For detailed description of the PDA see [16]

A set of with spill-return PSAs was used for the research. All the atomizers used a common gun with replaceable inner nozzles (Fig. 1 right). The gun, manufactured for the cold tests, provided an inlet, distribution and return of fuel and gripping to a 3D computer controlled support. It was designed according to a real nozzle body used in a burner. The inner nozzles were of the same geometry with different size of some parameters. Their internal geometric dimensions are listed in Table 2 below. Fuel is fed into a swirl chamber through four tangential ports with square cross-section. The swirl chamber contains a cylindrical entry part (missing in some designs) followed with a conical part and exit orifice with small length-to-diameter ratio. The nozzles were continuously operated with vertical downward position of the main axis. All tests were made with one batch of light heating oil (LHO) which simulates real hydrocarbon fuel (crude or residual oil, waste fuels etc.). Physical properties of the LHO at room temperature are:  $\sigma = 0.0297 \text{ kg/s}^2$ ,  $\rho_l = 874 \text{ kg/m}^3$ ,  $\mu_l = 0.0185 \text{ kg/m}\cdot\text{s}$ .

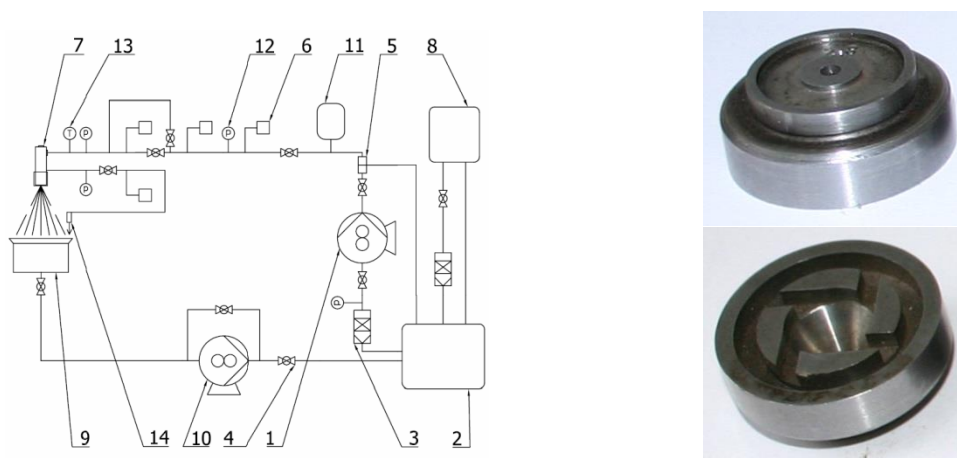


**Figure 1.** Schematic layout of the experimental facility (left), details of the inner nozzle (right).

## Results and Discussion

In the first part liquid breakup and spray microstructure of PSAs is documented with the use of spray photography and PDA measurements at different loads. In next part factors that affect the spray characteristics are described and analysed. Finally several nozzle modifications are tested with aim to reduce the drop size.

### *Spray structure and characteristic spray parameters*

A photographic documentation of the PSA spray for the original nozzle (N0) was performed to observe the breakup process and to acquire overall information on spray macrostructure. The liquid is internally swirled using the tangential ports and spread along the internal surface of the swirl chamber. It is discharged in annular form and flows downstream the exit orifice in the form of a conically shaped film due to the tangential velocity component converted into the radial one. The exit velocity is proportional to a square root of the inlet pressure differential,  $\Delta p_l$ . The film is slightly wrapped and waved due to the remains of the streams from the individual ports and these irregularities grow up with distance from the nozzle due to internal turbulences as well as due to an action of the surrounding air. At low  $\Delta p_l$ , about 0.2 MPa, the liquid film shows an onion stage; the surface tension forces dominate and overcome the radial momentum which causes the film to collapse. The film does not break up until the contact point and poorly atomizes afterwards (Fig. 2). The spray shape changes with increasing  $\Delta p_l$  to a tulip-like one with inferior atomization. Primary atomization of whole the liquid volume completes at  $\Delta p_l > 0.4 \text{ MPa}$  in large distance from the nozzle exit. With further increasing  $\Delta p_l$ , the atomization improves and the breakup point approaches the exit orifice due to the film thickness reduction and increasing relative gas-to-liquid velocity. Also the SCA widens. At common operating pressures, units of MPa, the discharged mass has a form of fully developed hollow cone spray. Further change of  $\Delta p_l$  does not significantly changes the SCA anymore, its value is practically given by the internal nozzle conditions. The observed spray structure and its variation with  $\Delta p_l$  are in accordance with the findings described in [17].

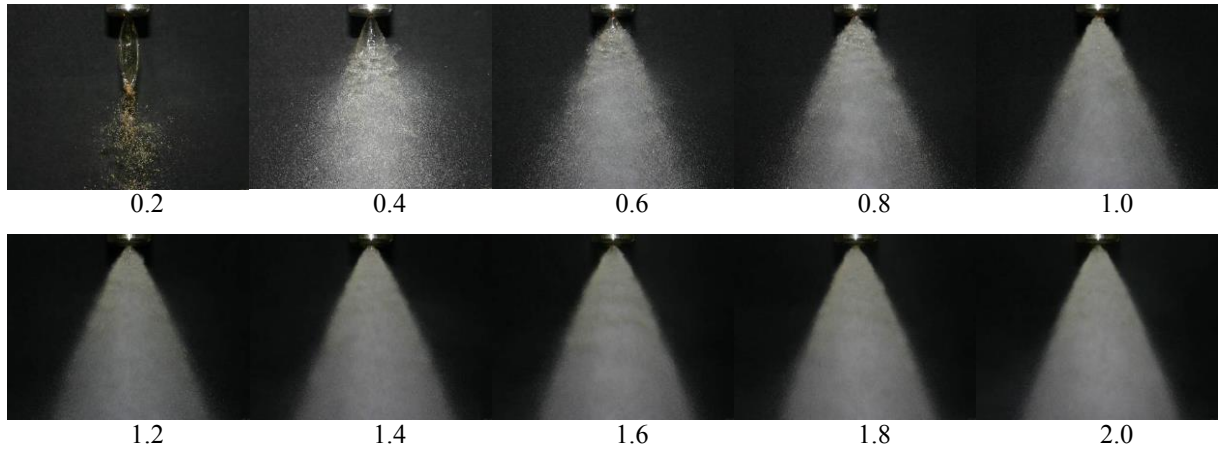


**Figure 2.** Spray structure at varying  $\Delta p_l$  [MPa], return line closed.

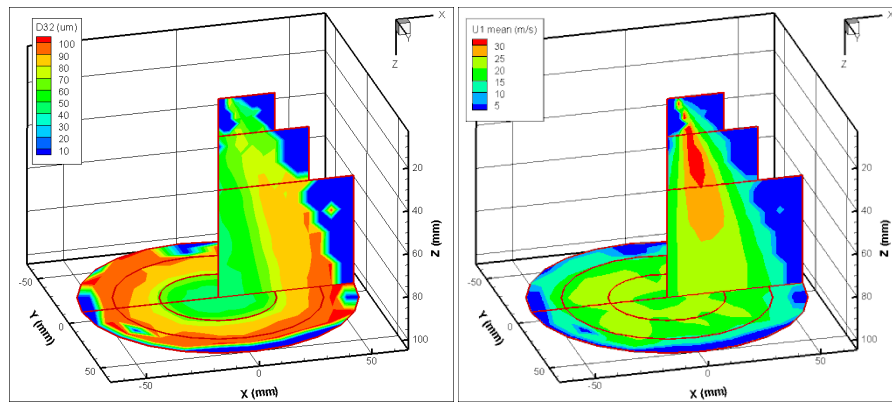


**Figure 3.** Spatial distribution of  $D_{32}$  (left) and  $v_m$  (right), nozzle N0 at  $\Delta p_l = 1$  MPa, return line closed.

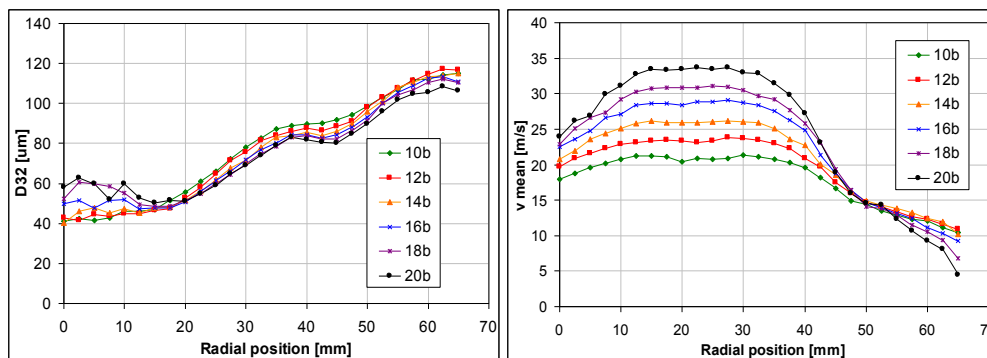


**Figure 4.** Radial distribution of  $D_{32}$  (left) and  $v_m$  (right) at varying  $\Delta p_l$ ,  $z = 100$  mm, N0, return line closed.

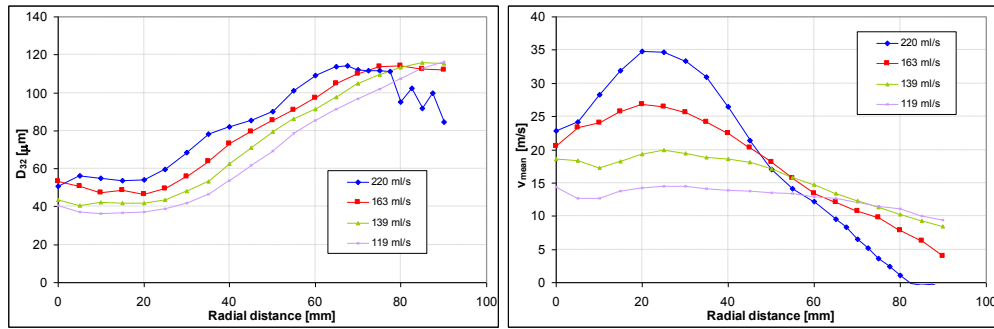


**Figure 5.** Radial distribution of  $D_{32}$  (left) and  $v_m$  (right) at  $z = 100$  mm, N0, return line opened.

Illustrative spatial distribution of mean droplet size, represented by  $D_{32}$ , and mean axial velocity,  $v_m$ , within the spray is documented in Fig. 3. The plots of  $D_{32}$  show very small droplets near the atomizer centreline and larger droplets in the semi-conical part of the spray. Data rate distribution (not shown here) indicates most of the droplets concentrated near the hypothetical conical envelope. Fast moving discharged liquid (see the  $xz$ -plane) keeps its momentum also during breakup within the main stream, slowly decelerates downstream and more easily decelerates on both sides (in the  $x$  direction) due to a drag force acting on the droplets. The  $xy$ -plane shows somehow non-uniform circumferential distribution of  $v_m$ . It is probably caused by streams formed by the four swirl channels and also fabrication imperfections can have an effect.

Radial variation of  $D_{32}$  is well seen in Fig. 4. The size is about  $40 \mu\text{m}$  in the centreline and increases up to almost  $120 \mu\text{m}$  on the spray border at  $\Delta p_l = 1 \text{ MPa}$ . Increase in  $\Delta p_l$  lead to a reduction of the size at radial distances  $r > 15 \text{ mm}$ . The opposite trend near the centreline can be explained by enhanced mixing at larger pressures and transfer of larger droplets into the area. However the spray in  $r < 20 \text{ mm}$  is of low importance as it contain less than 3% of the total liquid mass at all inspected regimes. The profile of  $v_m$  is almost flat within  $10 < r < 30 \text{ mm}$  and gradually decreases out of this area due to droplet deceleration by the surrounding air. Increased inlet pressure energy results in larger  $v_m$  at  $r < 50 \text{ mm}$ . The inverse trend at  $r > 50 \text{ mm}$  is caused with reduced size of droplets at larger pressure, which are more likely to decelerate and probably also by an annular eddy induced in the surrounding air.

Fig. 5 documents an effect of the return line opening. It causes a discharged mass reduction, followed with thinning of the liquid film and reducing  $v_m$  at the nozzle exit. As a consequence drop size decreases. Observed reduction of  $v_m$  is given partially by the already mentioned reduced  $v_m$  at the nozzle exit and partially by droplet deceleration. Another result of the opened return line is an SCA widening due to conserved tangential and reduced axial velocity component.

### Factors Affecting Atomization Quality

Characteristics of PSA sprays depend generally on (1) nozzle design and dimensions, (2) operational conditions and (3) physical properties of atomized liquid. A waste amount of literature sources deals with relations between these factors and atomization quality of PSAs; for their resume see [17, 18]. Empirical relations for  $D_{32}$  are often given in a simple form:

$$D_{32} = a_1 \cdot \sigma^{a_2} \cdot \mu_l^{a_3} \cdot \rho_l^{a_4} \cdot \rho_g^{a_5} \cdot \dot{m}_l^{a_6} \cdot \Delta p_l^{a_7} \quad (1)$$

Values of the coefficients  $a_1$  to  $a_7$  for the most frequent correlations are documented in Table 1. All dimensional quantities are given in SI units.

**Table 1.** Coefficients in Eq. (1).

Reference	$a_1$	$a_2$	$a_3$	$a_4$	$a_5$	$a_6$	$a_7$
Orzechowski [19]	52	—*	0.204	-0.204	—	0.282	-0.397
Radcliffe [6]	7.3	0.6	0.25	-0.25	—	0.25	-0.4
Lefebvre [4]	2.25	0.25	0.25	—	-0.25	0.25	-0.5
Jasuja [20]	4.4	0.6	0.16	-0.16	—	0.22	-0.43
Babu et al. [7] for $\Delta p_l < 2.8 \text{ MPa}$	133	—	—	-0.643	—	0.643	-0.547
Babu et al. [7] for $\Delta p_l > 2.8 \text{ MPa}$	607	—	—	-0.698	—	0.753	-0.576
Wang and Lefebvre [2] $a_8^{**}$	1.35	0.25	0.5	—	-0.25	0.25	-0.625
Wang and Lefebvre [2] $a_9^{**}$	0.011	0.25	—	0.25	-0.25	0.75	-0.625

\*the effect is not considered

\*\*full equation is  $D_{32} = a_8 \cdot d_o^{0.25} + a_9 \cdot d_o^{0.75}$ . It was derived by combining the original formula. in [4] with film thickness calculated according to Simmons and Harding [21].



To evaluate effect of the above factors on atomization quality of PSAs some quantities included in the Eq. (1) have to be found or set. Pressure difference  $\Delta p_l$  is an independent, controlled parameter. Liquid flow rate  $\dot{m}_l$  is given by nozzle construction and vary with  $\Delta p_l$  according to Bernoulli effect:

$$\dot{m}_l = C_D A_o 2 \cdot (\Delta p_l / \rho_l)^{0.5} \quad (2)$$

where discharge coefficient,  $C_D$ , is calculated according Rizk and Lefebvre [3]:

$$C_D = 0.35 (A_p / D_s d_o)^{0.5} (D_s / d_o)^{0.25} \quad (3)$$

Dimensions for the nozzle N0, used here, give  $C_D = 0.51$ . Above documented LHO physical properties and ambient air density  $\rho_g = 1.188 \text{ kg/m}^3$  are used.

### Liquid physical properties

Droplet size depends on physical properties of the atomized liquid,  $\rho_l$ ,  $\sigma_l$  and  $\mu_l$ , as it follows from Eq. (1). Physical properties of hydrocarbon fuels are temperature dependent. They can be controlled using additives.

Density is typically  $\rho_l = 500 - 900 \text{ kg/m}^3$  and can be modified by a blending with another liquid, indexed as 2, of different density  $\rho_{l2}$ :  $\rho_l = \rho_{l1} R(1 + M)/(M + R)$ , where  $R = \rho_{l2}/\rho_{l1}$  and  $M = m_{l2}/m_{l1}$ . However large  $M$  or  $R$  values are required to significantly affect  $\rho_l$ . The correlations in Table 1 are not consistent in the prediction of  $\rho_l$  effect; the exponent  $a_4$  varies from -0.698 [7] to 0.25 [2]. Densities of hydrocarbon fuels depends on temperature,  $t$ , as [22]:

$$\rho_l = -0.000172t^2 - 0.376891t + 881.6 \quad (4)$$

Reduction of  $\sigma_l$  has positive effect on  $D_{32}$  according all authors, with  $0.25 < a_2 < 0.6$ . It can be reduced using a surfactant and varies with  $t$ . For most of organic matters a temperature coefficient of the surface tension can be considered:

$$d\sigma_l/dT = -1 \cdot 10^{-4} \text{ N/m}\cdot\text{K} \quad (5)$$

The effect of the liquid viscosity is given by  $0.16 < a_3 < 0.50$ . Viscosity is highly temperature dependent; the relation of kinematic viscosity on temperature is often found to approximate [23]:

$$\nu_l = A \cdot \exp(Ev/k \cdot T) \quad (6)$$

where  $k$  is Boltzmann's constant, and  $A$  and  $Ev$  constants [2]. For LHO with kinematic viscosity of  $2.12 \text{ e}^{-5} \text{ m}^2/\text{s}$  at  $20^\circ\text{C}$  one can find  $A = 3.41 \text{ e}^{-11} \text{ m}^2/\text{s}$  and  $Ev/k = 3908.7 \text{ K}^{-1}$ . For dynamic viscosity:

$$\mu_l = \rho_l \nu_l \quad (7)$$

Fuel heating would affect all the three physical properties simultaneously. Reduction of  $D_{32}$  by 30 to 60% can be expected according to Table 1 when heating LHO from 20 to  $120^\circ\text{C}$  mainly due to the viscosity change, except [7] who predict 2% increase and [6] who assumes zero effect. This solution would be advantageous also for reduction of the pressure drop in the fuel line.

### Atomizer operation conditions

Operation conditions of PSAs are given by liquid pressure drop  $\Delta p_l$  on the nozzle and by  $\dot{m}_l$ . For particular atomizer those values are dependent each other according Eq. (2). Eq. (1) with Table 1 describe influence of  $\Delta p_l$  on  $D_{32}$  as  $D_{32} \propto \Delta p_l^{a_7}$ , where  $-0.25 < a_7 < -0.55$ . A change of  $\Delta p_l$  from 2 to 4 MPa should reduce  $D_{32}$  by 16 to 32%, however our above results (Fig. 4) show  $D_{32} \propto \Delta p_l^{-0.1}$  only so doubling  $\Delta p_l$  will reduce  $D_{32}$  by 7%. The  $\Delta p_l$  increase would increase  $\dot{m}_l$  as well (see Eq. (2)). Corresponding reduction of nozzle size would be necessary to keep  $\dot{m}_l$  constant. It would additionally reduce  $D_{32}$  by 21 – 26% according a simulation made using correlations in Table 1.

### Internal Geometry of the Atomizer

Nozzle design considerably affects the spray character so the original, several decades old, nozzle N0 was revised based on available literature. The ratio of swirl chamber diameter to final orifice diameter,  $d_s/d_o$ , should, according to Carlisle [24], be  $d_s/d_o < 5$ . Tipler and Wilson [5] recommend  $d_s/d_o = 2.5$ . However our simulation using Eq. (1) with coefficients in Table 1 predict a monotonous decrease of  $D_{32}$  with  $d_s/d_o$  increase; a change from 2 to 4 leads to decrease of  $D_{32}$  by 3 to 10%. Length/diameter ratio of swirl chamber,  $l_s/d_s$ , should be kept short to minimize frictional losses [17]. However sufficient length must be provided for the separate jets issuing

from the swirl port to coalesce into a uniform vortex sheet. Larger  $l_s/d_s$  values up to maximum of 2.75 result in improved atomization according [25]. Lefebvre [17] states that lower value leads to smaller sheet thickness. Present values are already relatively low about 0.6 – 0.7. Length/diameter ratio of final orifice,  $l_o/d_o$  should be as small as possible due to frictional losses. Original value 0.3 – 0.4 was reduced to 0.2 which is a reasonable minimum from manufacturing point of view. Tipler and Wilson [5] recommend that length / diameter ratio of swirl ports should not be less than 1.3 as short slots discharge the liquid in a diffused manner and may result in an uneven spray. It additionally leads to a tendency of radial flow instead of tangential movement. The area of swirl ports,  $A_p$ , influences pressure drop upstream the atomizer and hence amount of pressure accessible for atomization and also for a swirl momentum at the exit. Finally it influences generated sheet thickness. According to [17] smaller area leads to smaller sheet thickness.

The above recommendations for spray improvement can be summarised as: smaller  $d_s/d_o$ , increased  $l_s/d_s$  to 2, reduced  $A_p$ , high enough (more then 1.3) length/diameter ratio of swirl ports and  $l_o/d_o$  reduced to 0.2. To investigate these effects a several modifications against the current nozzle design (N0) were proposed: (a)

**Table 2.** Internal nozzle dimensions and results for  $\Delta p_l = 2$  MPa.

Nozzle	$d_o$ [mm]	$l_o$ [mm]	$d_s$ [mm]	$l_s$ [mm]	$l_o/d_o$ [-]	$A_p$ [mm <sup>2</sup> ]	$\dot{m}_l$ [kg/s]	$\alpha/2$ [deg]	$D_{32}$ [μm]
N0	2.8	1.0	12.0	0	0.36	33.6	0.196	28.4	88.9
N1	2.98	1.25	8.4	0	0.42	33.6	0.305	28.3	83.0
N2	2.96	1.25	12.0	5	0.42	33.6	0.226	27.0	87.9
N3	2.99	1.25	12.0	0	0.42	16.0	0.152	36.9	97.8
N4	2.98	0.5	8.4	0	0.17	33.6	0.316	27.3	83.4
N5	2.96	0.5	12.0	5	0.17	33.6	0.232	29.9	86.3
N6	2.99	0.5	12.0	0	0.17	16.0	0.154	37.1	93.4

reduction of  $d_s/d_o$  from 4.3 to 3.0 (N1), (b) increase of  $l_s/d_s$  from 0 to 0.4 (N2), (c) reduced  $A_p$  from  $4 \times 2.9 \times 2.9$  mm to  $4 \times 2.0 \times 2.0$  mm (N3), (d) reduced  $l_o/d_o$  to 0.2 (N4 – N6). Actual nozzle dimensions are documented in Table 2. As shown, reduction of  $d_s/d_o$  decreases  $D_{32}$ , by 7%. Other modifications,  $l_s/d_s$ ,  $l_o/d_o$ ,  $A_p$ , lead to smaller or even negative effect on drop size. These three effects are independent so their combination should lead to total reduction of drop size by 28 to 48%. This assumption will be confirmed by future measurements.

## Conclusions

Our study shows a number of ways for drop size reduction in PSA sprays. Modification of rheological properties of used fuel, namely its heating-up by several tens of Centigrades, should reduce  $D_{32}$  significantly mainly due to the viscosity change. Doubling the inlet pressure with additional reduction of exit orifice size to keep flow rate will directly drop  $D_{32}$  by 7%, with additional drop by 21 – 26% due to nozzle size reduction. The simplest and the most cost efficient way is an optimization of the internal nozzle geometry. It, according to our tests, leads to a reduction of  $D_{32}$  by about 7%. The way (or a combination of several changes) chosen depend on a configuration of original fuel system and possibilities for its modification with probable additional investments.

## Acknowledgements

Authors greatly acknowledge financial support from project No. 101/11/1264 funded by the Czech Grant Agency and from Operational Programme “Research and Development for Innovations” – “NETME Centre – New Technologies for Mechanical Engineering” Reg. No. CZ.1.05/2.1.00/01.0002.

## Nomenclature

$A$	cross-section area	(m <sup>2</sup> )
$a_i$	coefficients in Eq. (1)	(–)
$C_D$	discharge coefficient	(–)
$D_{32}$	Sauter mean diameter	(μm)
$d$	diameter	(m)
$l$	length	(m)
$M$	mass ratio	(–)
$\dot{m}_l$	liquid mass flow rate through exit orifice	(kg/s)
$R$	density ratio	(–)
$r$	radial distance	(mm)
$T$	thermodynamic temperature	(K)
$t$	temperature	(°C)
$v_m$	mean axial velocity	(m/s)
$x, y, z$	Cartesian coordinates ( $z$ = axial distance)	(mm)

#### Greek symbols

$\alpha$	spray cone angle, SCA	(deg)
$\Delta p_l$	inlet pressure differential	(MPa)
$\mu$	dynamic viscosity	(kg/m·s)
$\nu$	kinematic viscosity	(m <sup>2</sup> /s)
$\rho$	density	(kg/m <sup>3</sup> )
$\sigma$	liquid/gas surface tension	(kg/s <sup>2</sup> )

#### subscripts

$g$	gas, ambient air
$i$	index number
$l$	atomized liquid (light heating oil, LHO)
$m$	mixture
$o$	exit orifice
$p$	swirl ports
$s$	swirl chamber

#### References

- [1] Lefebvre, A.H. and D.R. Ballal, *Gas turbine combustion, alternative fuels and emissions*. 2010, Taylor & Francis, Boca Raton. p. 1 online resource (xix, 537 p.).
- [2] Wang, X.F. and A.H. Lefebvre, *MEAN DROP SIZES FROM PRESSURE-SWIRL NOZZLES*. Journal of Propulsion and Power, 1987. **3**(1): p. 11-18.
- [3] Rizk, N.K. and A.H. Lefebvre, *INTERNAL FLOW CHARACTERISTICS OF SIMPLEX SWIRL ATOMIZERS*. Journal of Propulsion and Power, 1985. **1**(3): p. 193-199.
- [4] Lefebvre, A.H., *Gas turbine combustion*. McGraw-Hill series in energy, combustion, and environment. 1983, Washington: Hemisphere Pub. Corp. xvii, 531 p.
- [5] Tipler, W. and A.W. Wilson, *Combustion in Gas Turbines*, in *CIMAC*. 1959: Paris. p. 897 – 927.
- [6] Radcliffe, A., *Fuel Injection, High Speed Aerodynamics and Jet Propulsion*. 1960.
- [7] Babu, R.K., M.V. Narasimhan, and K. Karayanaswamy, *Prediction of Mean Drop Size of Fuel Sprays from Swirl Spray Atomizers*, in *Proceedings of the second International Conference on Liquid Atomisation and Spray Systems*. 1982: Madison, Wisconsin. p. 99-106.
- [8] Cousin, J., S.J. Yoon, and C. Dumouchel, *Coupling of classical linear theory and maximum entropy formalism for prediction of drop size distribution in sprays: Application to pressure-swirl atomizers*. Atomization and Sprays, 1996. **6**(5): p. 601-622.
- [9] Jeng, S.M., M.A. Jog, and M.A. Benjamin, *Computational and experimental study of liquid sheet emanating from simplex fuel nozzle*. Aiaa Journal, 1998. **36**(2): p. 201-207
- [10] Yeh, C.L., *Turbulent flow simulation of liquid jet emanating from pressure-swirl atomizer*. Heat and Mass Transfer, 2008. **44**(3): p. 275-280.
- [11] Yeh, C.L., *Numerical simulation of a turbulent liquid jet emanating from a plain-orifice atomizer and a pressure-swirl atomizer*. Numerical Heat Transfer Part a-Applications, 2007. **51**(12): p. 1187-1212.
- [12] Xue, J., et al., *Effect of geometric parameters on simplex atomizer performance*. Aiaa Journal, 2004. **42**(12): p. 2408-2415.
- [13] Park, H. and S.D. Heister, *Nonlinear simulation of free surfaces and atomization in pressure swirl atomizers*. Physics of Fluids, 2006. **18**(5).
- [14] Moon, S., E. Abo-Serie, and C. Bae, *Air flow and pressure inside a pressure-swirl spray and their effects on spray development*. Experimental Thermal and Fluid Science, 2009. **33**(2): p. 222-231.
- [15] Chu, C.C., et al., *An experimental investigation of swirl atomizer sprays*. Heat and Mass Transfer, 2008. **45**(1): p. 11-22.
- [16] Jedelsky, J., et al., *Development of an Effervescent Atomizer for Industrial Burners*. Energy & Fuels, 2009. **23**: p. 6121-6130.
- [17] Lefebvre, A.H., *Atomization and sprays*. Combustion, 1989, New York: Hemisphere Pub. Corp. xi, 421 p.
- [18] Bayvel, L. and Z. Orzechowski, *Liquid Atomization*. 1993: Taylor & Francis Inc.
- [19] Orzechowski, Z., *Liquid atomization*. (In Polish) ed. 1976, Warsaw: WNT.
- [20] Jasuja, A.K., *ATOMIZATION OF CRUDE AND RESIDUAL FUEL OILS*. Journal of Engineering for Power-Transactions of the Asme, 1979. **101**(2): p. 250-258.
- [21] Simmons, H.C. and C.F. Harding, *SOME EFFECTS OF USING WATER AS A TEST FLUID IN FUEL*

- NOZZLE SPRAY ANALYSIS*. Journal of Engineering for Power-Transactions of the Asme, 1981. **103**(1): p. 118-123.
- [22] Powley. *Crude oil density versus temperature and pressure*. [cited 2006 19 Oct.]; Available from: <http://www.searchanddiscovery.net/documents/2006/06015powley/images/a09.htm>.
- [23] Summers, H. *Theory of viscosity measurement*. [cited 2006 19 Sept.]; Available from: <http://www.hanssummers.com/electronics/viscometer/theory.htm>.
- [24] Carlisle, D.R., *Communication on the Performance of a Type of Swirl Atomizer*, by A. Radcliffe, in *Proc. Inst. Mech. Eng.* 1955. p. 101.
- [25] Elkotb, M.M., N.M. Rafat, and H.M. A., *The Influence of Swirl Atomizer Geometry on the Atomization Performance*, in *Proceedings of the first ICLASS*. 1978: Tokyo. p. 109 – 115

## Effect of Cone Angle on Droplet Size Classes for Pressure Swirl Atomizers

B. Yazici<sup>1</sup> and O. Uzol<sup>2</sup>

1: Defense Industries Research and Development Institute, Scientific and Technological Research Council of Turkey (TÜBİTAK-SAGE), Ankara, Turkey.

2: Department of Aerospace Engineering, Middle East Technical University, Ankara, Turkey.

### Abstract

The effect of spray cone angle on the break-up point, droplet size classes and flow structure is investigated by using high speed shadowgraphy technique and a 2-D Phase Doppler Particle Analyser system. Two hollow cone pressure swirl type atomizers designed and manufactured such that they have the same Sauter Mean Diameter (SMD) and mass flow rates but with different spray cone angle. The first atomizer has a full cone angle of 70° and the second one has a full cone angle of 120°. Through the design process, empirical correlations in the literature are used to estimate the atomizer parameters. The results obtained from high speed shadowgraphy and Phase Doppler Particle Analyser (PDPA) measurements compared with the empirical calculations. Measured Sauter Mean Diameter values are higher than the ones calculated with empirical formulas as it verifies the findings in the literature. Two different droplet size classes are used to investigate the flow field and droplet velocities. Through the flow field investigation, it can be deduced that the effect of recirculation at the core region of the atomizer is increases with the increasing cone angle of the spray.

### Introduction

Pressure swirl atomizers are found to be the inexpensive and most reliable type of atomizer for fuel injection due to its superior atomization characteristics and relatively simple geometry. The pressure swirl atomizers, in general, produce a hollow cone spray without the presence of liquid jet along the axis of the atomizer. This property of the hollow cone spray has the advantage of recirculating the hot combustion products to the atomizer exit to stabilize the flame [1].

In pressure swirl atomizers the propellant is fed through the tangential inlet passages into the swirl chamber. A liquid vortex with a free surface is formed within the atomizer. The radius of the free surface changes from minimum at the base of the swirl chamber to a larger value at the exit of the nozzle. A thinner liquid film exits through the nozzle and eventually breaks up into fine droplets forming a hollow cone spray.

There are few studies available in the literature on the effect of cone angle on the droplet size classes and velocity field. A unique study performed by SANTOYA et al. [2] on flow field induced by hollow cone pressure swirl atomizers. In these experiments PDPA system is used to measure the velocity field and Sauter Mean Diameter (SMD) variation through the atomizer center line.

In this study, two hollow cone pressure swirl atomizers designed, manufactured and tested by using high speed shadowgraphy system and PDPA system. Water is used as working fluid.

### Atomizer Design Study

In order to investigate the effect of cone angle on atomizer droplet size classes and flow field generated by the momentum transfer from droplets to the flow field, two atomizers designed and manufactured. To make a meaning full comparison of the two atomizers, SMD of the atomizers set to be equal and the mass flow rates chosen to be close to each other.

The Sauter mean diameter (SMD) of the resulting spray can be estimated using the empirical equation of Wang and Lefebvre [3]

$$SMD = 4.52 \left( \frac{\sigma \mu_l^2}{\rho_a \Delta P_l} \right)^{0.25} (t \cos \theta)^{0.25} + 0.39 \left( \frac{\sigma \rho_l}{\rho_a \Delta P_l} \right)^{0.25} (t \cos \theta)^{0.75} \quad (1)$$

In order to calculate the SMD value of the atomizers, spray cone angle has to be calculated. Equation (2), which is proposed by RIZK & LEFEBVRE [4] can be used to estimate this parameter.

$$2\theta = 6 \left[ \frac{D_s d_o}{A_p} \right]^{0.15} \left[ \frac{\Delta P_l d_o^2 \rho_l}{\mu_l^2} \right]^{0.11} \quad (2)$$

Another important parameter to calculate the SMD is the film thickness “t”. GIFFEN&MURASZEW [5] proposed the following equation for the calculation of film thickness.

$$\frac{(1-X)^3}{(1+X)} = 0.09 \left( \frac{A_p}{D_s d_o} \right) \left( \frac{D_s}{d_o} \right)^{0.5} \quad (3)$$

Where X can be calculated as,

$$X = \frac{(d_o - 2t)^2}{d_o^2} \quad (4)$$

By solving the equation (3) one can obtain the film thickness of the atomizer. It is interesting that for that equation, the film thickness is only depends on the geometric parameters of the atomizer. The parameters of the designed pressure swirl atomizers with two different cone angle values are given in **Table 1**. In this table geometric parameters and the results of the calculations performed with the above equations are listed for both atomizers. Also fluid parameters added at the end of the table which are used to calculate the flow properties and SMD. Moreover a cut-away drawing of the atomizers is given in Figure 1.

**Table 1.** Geometric and Flow Properties of Designed Atomizers

		Atomizer-1	Atomizer-2
Geometric Properties	Orifice Diameter	1.4 mm	3.6 mm
	Port Diameter	1.6 mm	1.0 mm
	Number of Ports	2	2
	Swirl Chamber Length	7.0 mm	11.9 mm
	Swirl Chamber Diameter	7.0 mm	11.9 mm
Flow Properties	Cone Angle	70°	120°
	Film Thickness	0.2043 mm	0.1948 mm
	Mass Flow Rate	27.6 g/s	32.6 g/s
	ΔP	7.3 bar	3.14 bar
	SMD	66.52 μm	59.87 μm
Fluid Properties	Density of Water	1000 kg/m <sup>3</sup>	
	Viscosity of Water	0.001 kg/s <sup>2</sup>	
	Density of Air	1.050 kg/m <sup>3</sup>	

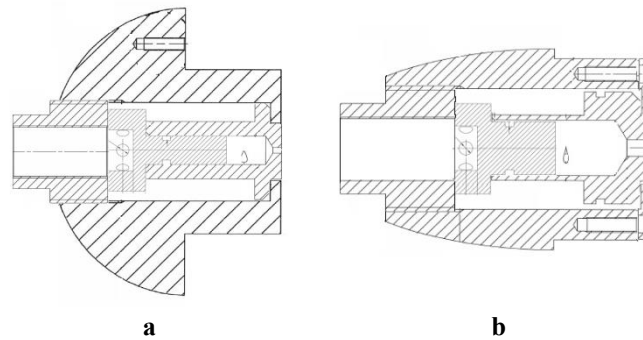


**Figure 1.** Cut-Away Drawings of Designed Atomizers, a) Atomizer-1, b) Atomizer-2

## Experimental Setup

The atomizer test facility consists of a high pressure water tank and pressurizing equipment. Using an industrial type pressure regulator high pressure tank set to test pressure and water fed to the atomizer inlet. Water flow rate is controlled by a needle valve and flow rate measured with a turbine type flow meter.

At the first part of the experiments a high speed camera system is used to visualise the flow field. Break-up length of the atomizers and cone angle is measured by using image processing toolbox of MATLAB.

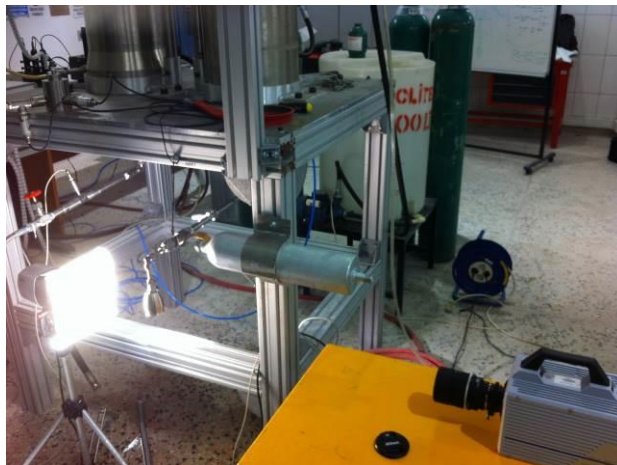


**Figure 2.** High Speed Shadowgraphy Setup

High-speed direct shadowgraph system is used to visualize the resulting hollow cone spray. The backlight illumination of the spray is obtained with a halogen lamp and a diffuser screen. Light source and the camera are aligned at the opposite sides as shown in Figure 2. The effective image area for camera is 384x128 pixels and the frame rate for camera is 90 kHz. The images taken are processed with the image processing toolbox of MATLAB software.

In the second part of the experiments, a 2-D PDPA system (TSI) is used to measure the SMD ( $D_{32}$ ) values and velocities of the droplets generated by two atomizers.



**Figure 3.** Phase Doppler Particle Analyzer.

The radial variation in Sauter mean diameter (SMD) is measured at eight axial location with a commercial Phase Doppler Particle Analyzer (PDPA). The PDPA system is composed of an Ar-Ion laser, a multicolor beam separator, a transmitter, a receiver and a signal processor. The receiver and transmitter are positioned on a 3-axis traverse in a 43° forward scatter configuration. Laser power set to 300mW and 250mm beam separator is used to obtain the droplet sizes.



## Results and Discussion

### Measurement of Spray Cone Angle & Break-Up Distance

The images obtained from the high speed camera system given in Figure 4. The break-up distance and cone angle values for two atomizers obtained by using the image processing toolbox of MATLAB software. A calibration image is taken with a known length captured prior to measurements as a reference length.

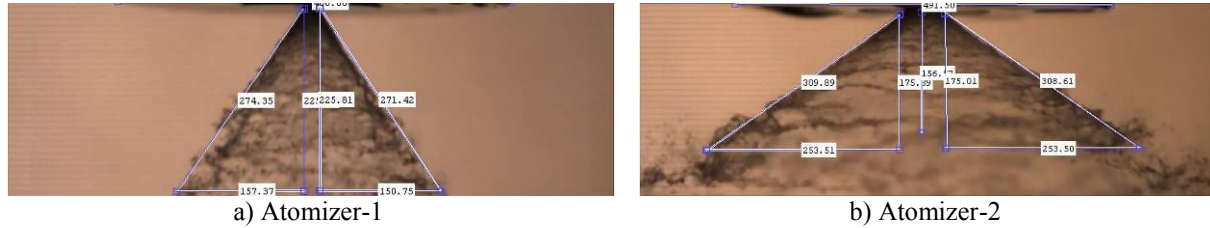


**Figure 4.** Image Processing of Atomizer-1 and Atomizer-2

For Atomizer-1 cone angle is measured as  $68.60^\circ$  and the break-up length is measured as 10.06 mm. For the second atomizer cone angle is measured as  $110.62^\circ$  and the break-up length is measured as 12.70 mm. The break-up length is chosen to be the point where the ligaments disappear and drops appear.

### Measurement of Droplet Size Classes

A TSI 2-D PDPA system is used to measure the droplet size classes and velocity field. Measurements obtained for Atomizer-1 and Atomizer-2 at eight and nine axial locations respectively. The first point for both atomizers is 15 mm downstream of the atomizer exit plane. Due to the fact that Atomizer-1 has a less cone angle to increase the fidelity, measurements made in every 3 mm in radial axis. But for the Atomizer-2 measurements performed in every 5 mm in radial axis. For both atomizers measurements made in every 5 mm in axial axis.

The SMD values of the two atomizers are given in Figure 5 and Figure 6 respectively. SMD values are calculated with the FLOWSIZER software of TSI.

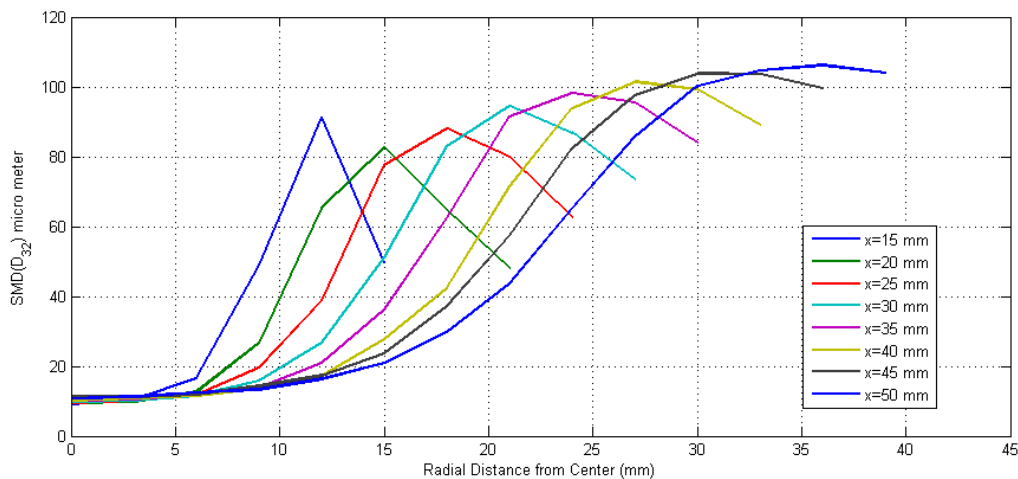


**Figure 5.** SMD Values of Atomizer-1

In Figure 5, it can be seen that the SMD values are smaller at the core region of the atomizer and progressing through the radial axis SMD values are increasing. Also the peak value of the SMD is increasing when moving through the downstream locations except the data taken at  $x=15$  mm. This phenomenon can be attributed to break-up of the liquid sheet is so close to measurement point. After passing the liquid jet SMD decreases rapidly. When moving through the axial axis, rapid decrease in SMD disappears.

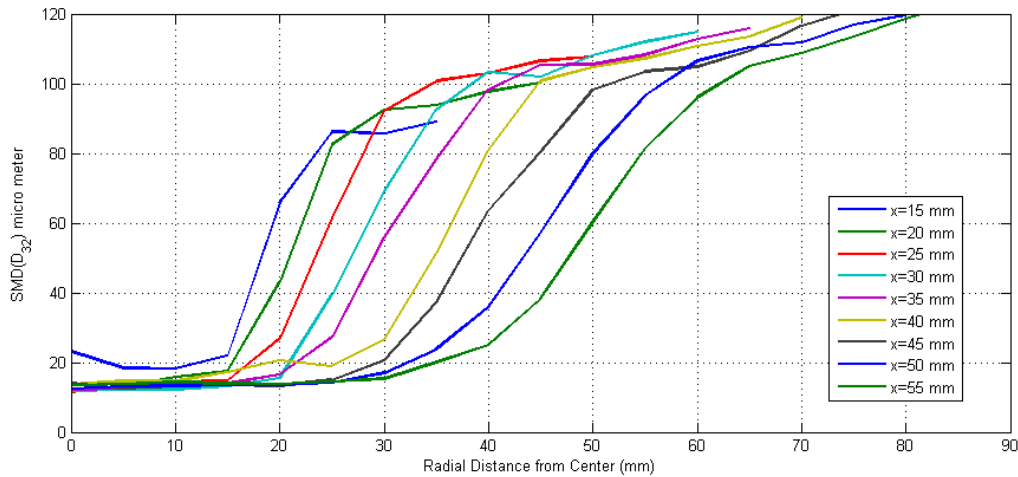


**Figure 6.** SMD Values of Atomizer-2

In Figure 6, measured SMD values for Atomizer-2 are given. Also for this atomizer, SMD values are smaller at the core region of the atomizer flow field. However, with the increases cone angle the SMD values did not decreases after passing the liquid jet region.

#### Flow Field Investigation

Velocity measurements also performed for both atomizers. PDPA system measures the droplet size and velocity of the droplet sequentially. Also it is known that the droplets which have a diameter smaller than  $10\mu\text{m}$  tends to follow the air velocity flow field. While the bigger droplets maintain their momentum to certain distance and keep their direction and velocity. Therefore, in Figure 7 and Figure 8, velocity vectors of two different size classes plotted.

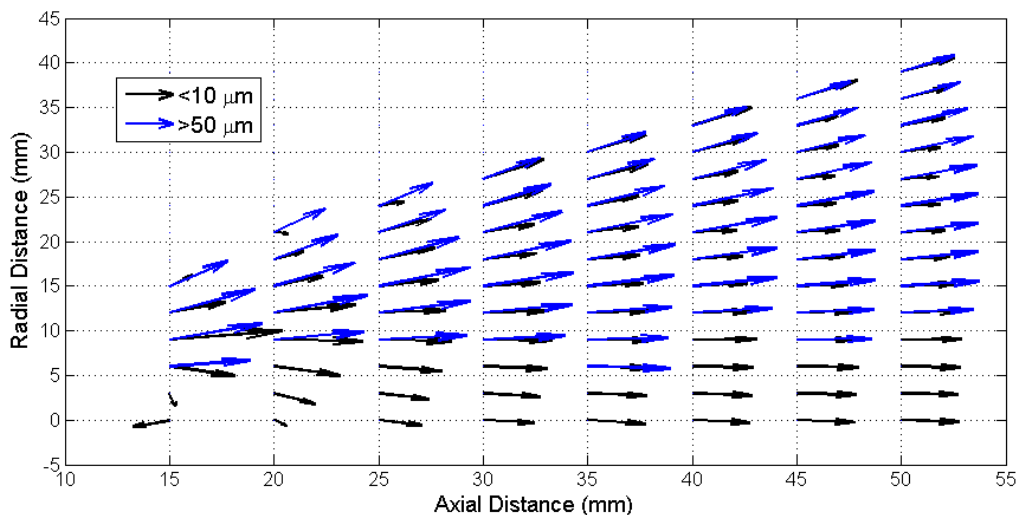


**Figure 7.** Velocity Field for Different Droplet Size Classes of Atomizer-1

InFigure 7, velocity vectors for the droplets having a diameter of less than  $10\mu\text{m}$  and bigger than  $50\mu\text{m}$  are plotted. For the smaller droplets a reverse flow region is appears at the core region of the atomizer but after moving downstream this recirculation disappears. For the bigger droplets it can be seen that they maintain their direction and velocity magnitude through the measurement domain.

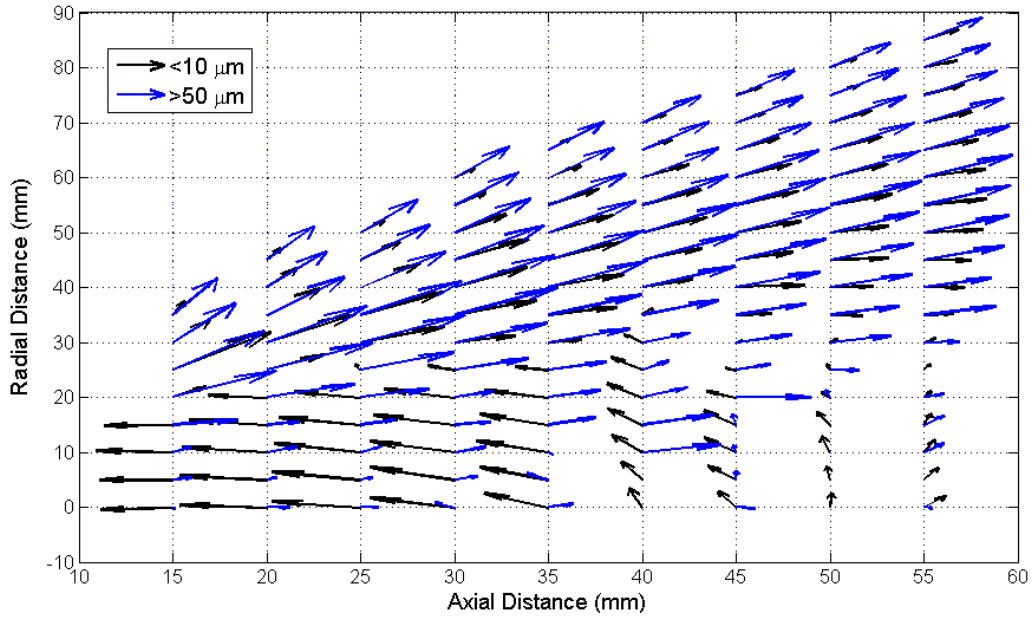


**Figure 8.** Velocity Field for Different Droplet Size Classes of Atomizer-2

For Atomizer-2, the strength of the recirculation is higher than the smaller cone angle case. The smaller droplets pushed through the upstream with the effect of high swirling effect of atomizer jet before break-up. The effect of swirl creates a low pressure region at the centre axis thus the vacuum effect pulls the smaller droplets. Again for this case bigger droplets maintain their momentum through the measurement domain.

## Conclusions

Droplet size classes and induced velocity fields generated by two pressure swirl atomizer having different spray cone angles are investigated using Phase Doppler Particle Analyser. The results shows that, although atomization take place in a quiescent flow field, due to momentum transfer between the droplets and continuum phase, flow field changes dramatically. This effect also induced by the swirling liquid jet emerging from the nozzle exit of the atomizer. As a consequence of increasing swirl velocity to axial velocity ratio in order to increase the cone angle, the swirl strength increases in the core section of the atomizer downstream. This causes a bigger and stronger recirculating flow field downstream of the atomizer.

## Acknowledgements

This study has been supported by TÜBİTAK-SAGE under Project IBTA founded by State Planning Organization of Turkey.

## Nomenclature

- $\theta$  : Spray Half Cone Angle (deg)
- $\mu_l$  : Dynamic Viscosity of Working Fluid (kg/s<sup>2</sup>)
- $\rho_a$  : Density of Surrounding Media (kg/m<sup>3</sup>)
- $\Delta P_l$  : Pressure Drop Across Atomizer (Pa)
- $t$  : Film Thickness (m)
- $\rho_l$  : Density of Working Fluid (kg/m<sup>3</sup>)
- $D_s$  : Diameter of Swirl Chamber (m)
- $d_0$  : Orifice Diameter (m)
- $A_p$  : Port Area (m<sup>2</sup>)

## References

- [1] Lefebvre A.H., *Atomization and Sprays*, CRC Press, Florida, 1989, ISBN 0-891116-603-3, pp 1.
- [2] Santayola J.L. et al., *Analysis by droplet size classes of liquid flow structure in a pressure swirl hollow cone spray*, Chemical Engineering and Processing, Vol. 49, Issue 1, January 2010, Pages 125-131
- [3] Wang X.F., Lefebvre A.H., *Mean Drop Sizes from Pressure-Swirl Nozzles*, AIAA Journal of Propulsion, Vol. 3, No. 1, Jan.-Feb. 1987.
- [4] Rizk and Lefebvre A.H., *Prediction of Velocity Coefficient and Spray Cone Angle for Simplex Swirl Atomizers*, Proceedings of 3<sup>rd</sup> International Conference on Liquid Atomization and Spray Systems, London, 1985
- [5] Giffen E., Muraszew A., *Atomization of Liquid Fuels*, Chapman and Hall, London, 1953

# Session:

## **IC Engine Sprays**

## Comparison of experiments and numerical simulations of high pressure transparent injection nozzles

S. Jollet, A. Heilig, K. Bitner, D. Niemeyer and F. Dinkelacker

Institut für Technische Verbrennung, Leibniz Universität Hannover, Germany

### Abstract

The design of the injection system in direct-injection diesel engines is an important challenge, as the jet breakup, the atomization and the mixture formation in the combustion chamber are closely linked. These factors have a direct impact on emissions, fuel consumption and performance of an engine. The shape of the spray at the outlet is determined by the internal flow of the nozzle. Here, geometrical parameters, the injection pressure, the injection duration and the cavitation phenomena play a major role.

In this work, the flow dependency in transparent single-hole-nozzle models with different sac hole and spray hole geometries are analyzed. The transparent acrylic glass nozzle is placed on the front part of a commercial BOSCH injector (CRI2-18 Gen2) where the tip is removed. On a test bench driven by a common rail injection system, a rail pressure up to 1250 bar can be achieved, being much higher than what is known from literature for transparent nozzles. High-speed shadowgraphic imaging is used to visualize the transient processes inside the transparent nozzle, where especially regions with cavitation can be detected.

A strong influence of the transient needle movement on the cavitation at the needle seat and the spray hole is found during the opening and closing process of the needle. During the steady state phase of injection various cavitation phenomena are visible in the transparent injection hole, being influenced by the nozzle geometry and the fuel pressure. Different characteristics of cavitation in the sac and spray hole can be detected, and the spray formation in the primary breakup zone is influenced.

These experimental studies are combined with transient numerical RANS simulations employing a moving mesh. This allows to study varied multi-phase and cavitation models and to validate them. Some of the simulations already agree quite well with the experimental conditions and show the same behaviour concerning the cavitation phenomena at the needle seat and in the nozzle during the opening and the closing process at least qualitatively.

### Introduction

The injection process of diesel engines influences the pollutant emissions. The spray formation is significantly influenced by the internal flow of the injector. One of the key parameters here is the generation of cavitation caused by the geometry and the needle lift.

In modern diesel engines the injection pressure is established up to 2000 bar. The details of the flow and phase change processes inside the injector are of increasing importance for such injectors. In order to visualize the processes inside the injector, the tip of the injector is made out of transparent acrylic glass, which can be adapted on the real injector. However, the use of acrylic glass has the problem of durability for the desired high injection pressures. In this work, an effort has been made to increase the resistance structurally. Injection pressures up to 1600 bar were reached, before the component failed. With these experimental measurements the validation of multiphase and cavitation models is possible for the high pressure range. Details of the time-dependent geometry like that of the lifting needle are as important as the two phase processes inside the injector. Here, for instance, cavitation effects can occur. Cavitation effects in the injection port area destabilize the emergent fuel jet and improve the jet break-up [1].

### Experimental test-rig

The experimental setup consists of the pressure supply, the optical measurement technique and transparent injector. **Figure 1** shows the schematic structure of the measurement setup that is used for recording the nozzle flow and spray atomization. The test rig is equipped with a control computer which communicates with an interface unit.

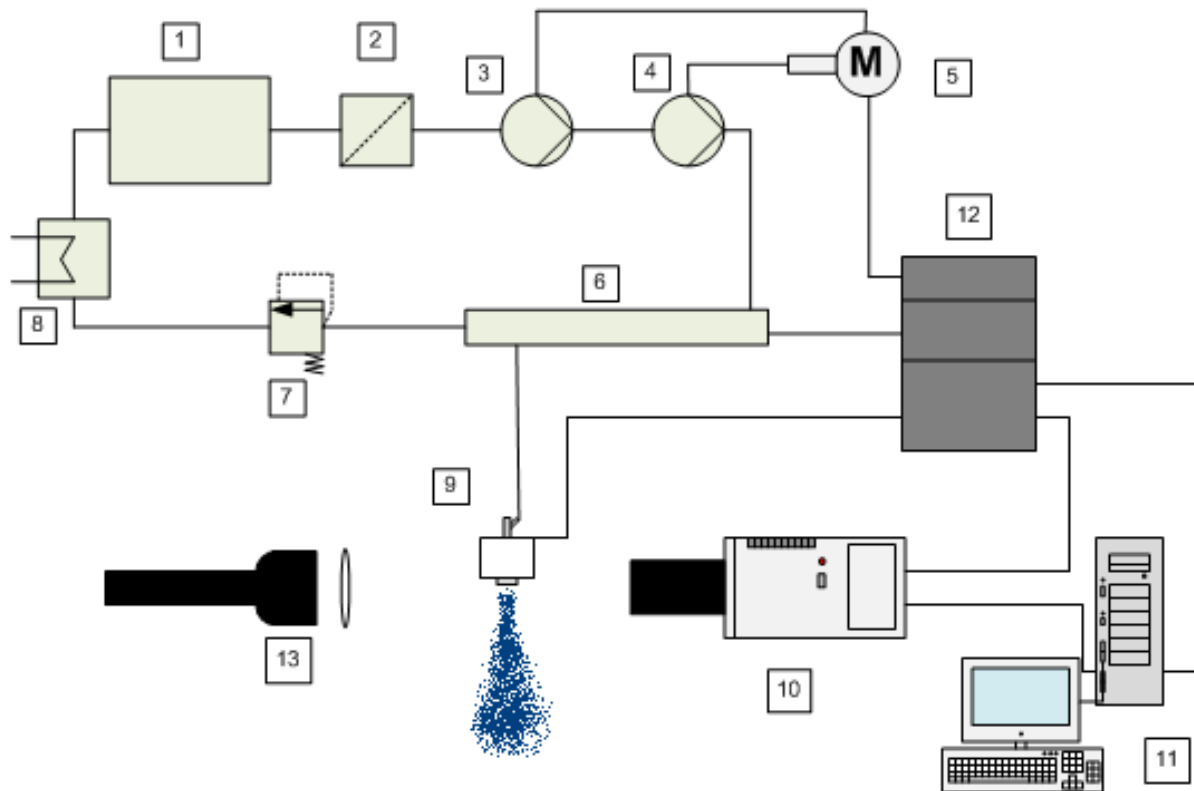


**Figure 1.** Schematic measurement supply of the test-rig for transparent injector. (1) Fuel tank; (2) Fuel filter; (3) Force-feeding pump; (4) High-pressure pump; (5) Electric motor; (6) Rail; (7) Control valve; (8) Heat exchanger; (9) Injector holder with transparent Nozzle; (10) CCD-Camera; (11) Control-PC; (12) Interface; (13) Illumination

A stationary high pressure pump can generate a pressure of 100 bar to 3000 bar. The generated pressure is injected to the rail. The rail is from a 4-cylinder car engine and is equipped with a pressure sensor and an overflow valve. This guarantees injecting on constant pressure levels. The magnetic injector is controlled by an interface. For the measurements with the transparent nozzle, the injector was cut off below the needle seat so that the sealing surface is maintained.

High speed imaging is done with a Phantom v711 camera, supporting a maximum resolution of 1280 x 800 pixel. With reduced resolution frame rates of 290 kHz were reachable. With the minimum exposure time of 1  $\mu$ s the blurriness due the motion can be reduced. For the object lens a focal length of 50 mm with a light intensity of 1:1,4 and two intermediate rings with 20 mm and 12 mm are used. Also an AF-S Teleconverter 2x and a Extension Tube 23 was applied for the measurements.

In this work, the shadow method is used. The sensor of the camera is directly illuminated with parallel light. The insertion of objects into the beam can cause two different types of shadow, which are imaged on the sensor of the camera:

- An opaque body absorbs or reflects the incident light completely, whereby a black shadow is projected.
- Translucent phase boundaries or objects with different refractive index deflect light partially or reflect it out of the beam. From that some areas with lower illumination are generated in the image plane, being grayed out [1]. A refraction will occur, whenever the incident light by the Snellius refraction law is not orthogonal to the phase boundary.

The shadow method is suited to these measurements, because the refractive indices of the used medium, diesel ( $n_{\text{Diesel}} = 1,455$ ) and acrylic glas ( $n_{\text{Acrylic}} = 1,491$ ), have a similar value. A minimal refraction appears only at the phase interface (with  $n_{\text{Liquid}} \neq n_{\text{Vapour}}$ ). The vapour phase of the cavitation area is assumed to have a refractive index of  $n_{\text{Vapour}} \approx 1$ . Thereby the phase boundary creates a dark shadow on the image [2].



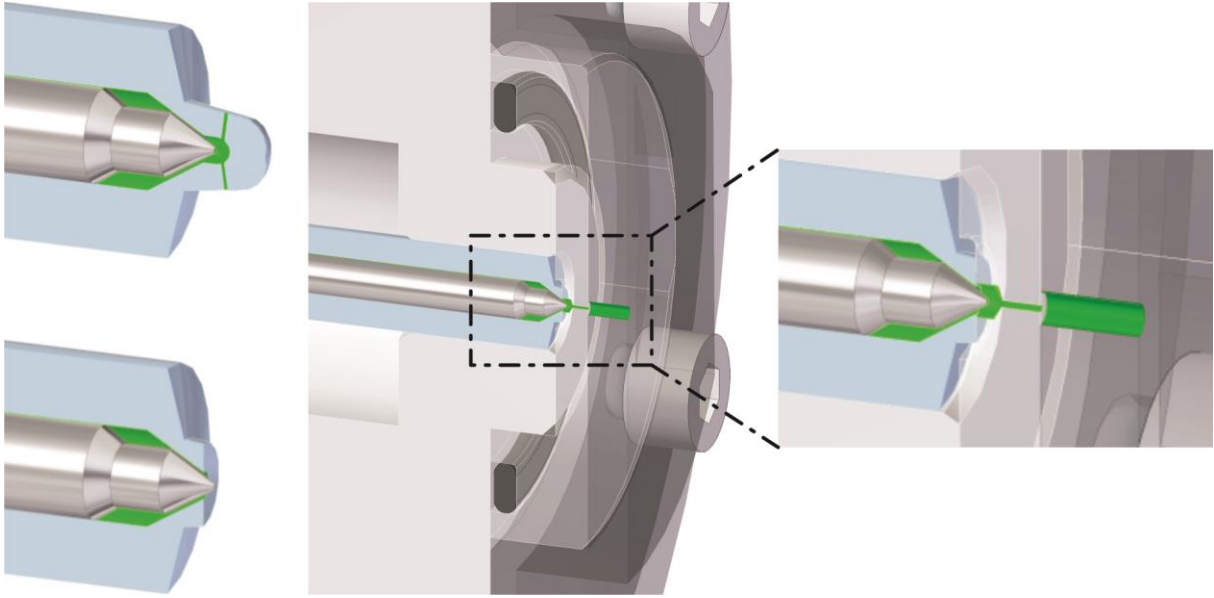


**Figure 2.** Schematic Bosch injector (CRI2-18 Gen2), where the tip is flattened and the transparent acrylic glass nozzle is assembled on the front part.

### Geometry

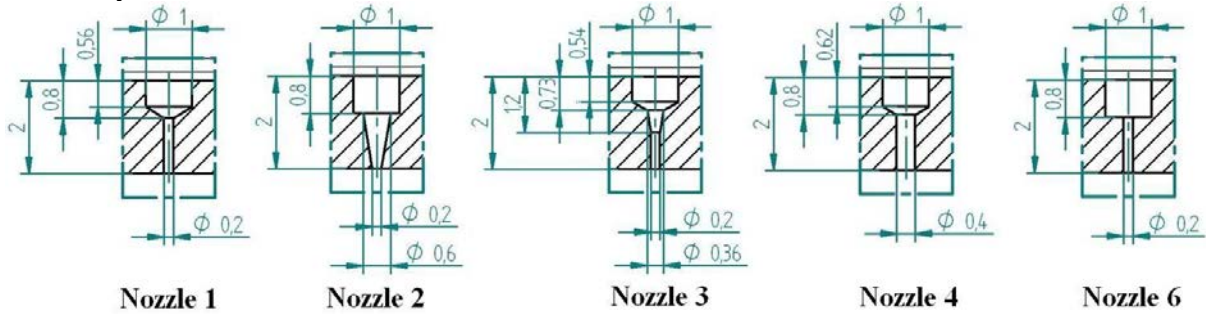


**Figure 3.** Dimensions and profile of the single-hole nozzle geometries (in mm).

For the measurements 5 configurations of single-hole-nozzles were analysed, Figure 3, where the dimensions are given. The diameter is 200  $\mu\text{m}$  and in one case 400  $\mu\text{m}$ . The nozzle geometry is selected to be cylindrically or conically shaped or having a combined shape. Acrylic glass is used as transparent material. Further details are described in [7].

### Mathematical modeling

For this study the “Mixture” multiphase model is used [3][4][6]. The “Mixture” multiphase model describes the multiphase flow by a mixing formulation. The conversion equation is described for the total mixture, instead of an individual phase conversion.

$$\frac{\partial}{\partial t} \left[ \sum_N (\rho_N \alpha_N) \right] + \frac{\partial}{\partial x_i} \left[ \sum_N (\rho_N \alpha_N u_{Ni}) \right] = 0 \quad (1)$$

where the density, mixture fraction  $\alpha_N$  and velocity of the different phases  $N$  is included.

With the mixture  $\rho_{mix} = \sum_N (\alpha_N \rho_N)$ , the velocity  $u_{i,mix} = \sum_N ((\alpha_N \rho_N u_{i,N}) / \rho_{mix})$  and

equation (1), the mixture continuity equation (2) is defined as

$$\frac{\partial}{\partial t}(\rho_{mix}) + \frac{\partial}{\partial x_i}(\rho_{mix}u_i) = 0. \quad (2)$$

The same approach is transferred to the mixture momentum equations (Equation (3)) with the additional body force  $k_i$ , the mixture viscosity  $\eta_{mix}$  and the drift velocity  $u_{i,dr,N} = u_{i,N} - u_{i,mix}$  between the mixture and the phase  $N$ :

$$\begin{aligned} \frac{\partial}{\partial t}(\rho_{mix}u_{i,mix}) + \frac{\partial}{\partial x_i}(\rho_{mix}u_{i,mix}u_{j,mix}) = & \rho_{mix}k_i - \frac{\partial p}{\partial x_i} \\ & + \frac{\partial}{\partial x_j} \left[ \eta_{mix} \left( \frac{\partial u_{i,mix}}{\partial x_j} + \frac{\partial u_{j,mix}}{\partial x_i} \right) \right] \\ & + \frac{\partial}{\partial x_j} \left[ \sum_N (\alpha_N \rho_N u_{i,dr,N} u_{j,dr,N}) \right] \end{aligned} \quad (3)$$

The mixture energy equation (4) is

$$\frac{\partial}{\partial t} \left[ \sum_N (\rho_N \alpha_N e_N) \right] + \frac{\partial}{\partial x_i} \left[ \sum_N (\alpha_N u_{i,N} (\rho_N e_N + p)) \right] = \frac{\partial}{\partial x_i} \left( k_{eff} \frac{\partial T}{\partial x_i} \right) + S_e \quad (4)$$

with the effective thermal conductivity  $k_{eff}$ , the temperature  $T$  and volumetric heat sources  $S_e$  [5].

Cavitation modelling is commonly based on the Rayleigh-Plesset-Equation (5). This equation describes the pressure-dependent dynamics of the growth of bubbles with radius  $R_B$  in a compressible fluid:

$$R_B \ddot{R}_B + \frac{3}{2} \dot{R}_B^2 = \frac{1}{\rho_l} \left[ p_v - p_h - \frac{2\sigma}{R_B} - 4\eta \frac{\dot{R}_B}{R_B} \right] \quad (5)$$

with first and second derivation of the radius, with the density of the liquid  $\rho_l$ , the surface tension  $\sigma$  and the viscosity of the liquid  $\eta_l$ . Simplifying equation (5), the second time derivation  $\ddot{R}_B$ , the surface tension and the viscosity of the liquid is neglected. The growing or contracting rate of the bubble is essentially a function of the difference between the internal bubble pressure  $p_v$  and the hydrostatic liquid pressure  $p_h = p_0 + \rho_l g h$  (with the ambient pressure  $p_0$  and the pressure at the height  $h$ ):

$$\dot{R}_B = \sqrt{\frac{2(p_v - p_h)}{3\rho_l}} \quad (6)$$

For the application in two-phase models essentially the mass transfer rate  $R$  between the liquid and the gas phase is needed.

The Zwart-Gerber-Belamri cavitation model assumes large vapour bubbles of equal size, which do not affect each other [5]. Here the vapour fraction  $\alpha_v = n_B 4/3 \pi R_B^2$  is calculated by the number of bubbles  $n_B$  and the volume of the bubbles.

For the evaporation caused by cavitation, the vapour fraction  $\alpha_v$  will be replaced by  $\alpha_{nuc}(1 - \alpha_v)$ . The  $\alpha_{nuc}$  term describes the density of the nuclei, where vapour bubbles can arise. The term  $\alpha_{nuc}(1 - \alpha_v)$  describes the progression of the nucleus that deactivates due to increasing vapour fraction. Introducing an evaporation coefficient  $F_{vap}$  and a condensation coefficient  $F_{con}$  the transfer rates for cavitation  $R_e$  or condensation  $R_c$  are given for the Zwart-Gerber-Belamri cavitation model with

$$R_e = F_{vap} \frac{3(\alpha_{nuc}(1 - \alpha_v))\rho_v}{R_B} \sqrt{\frac{2(p_v - p_h)}{3\rho_l}} \quad \text{if } p_h \leq p_v \quad (10)$$

$$R_c = F_{con} \frac{3\alpha_{nuc}\rho_v}{R_B} \sqrt{\frac{2(p_v - p_h)}{3\rho_l}} \quad \text{if } p_h \geq p_v \quad (11)$$

## Results and Discussion

A comparison of the cavitation behaviour of the experiment and the simulation was investigated for Nozzle 1. For this simulation the  $k - \varepsilon$  – Turbulence-Model with Enhanced Wall Treatment, EWT approach has been used. For the multiphase flow the “Mixture” model and for the cavitation the “Zwart-Gerber-Belamri” model was used. In **Figure 4** the opening and the closing process at 1300 bar injection pressure is compared with the experiment.

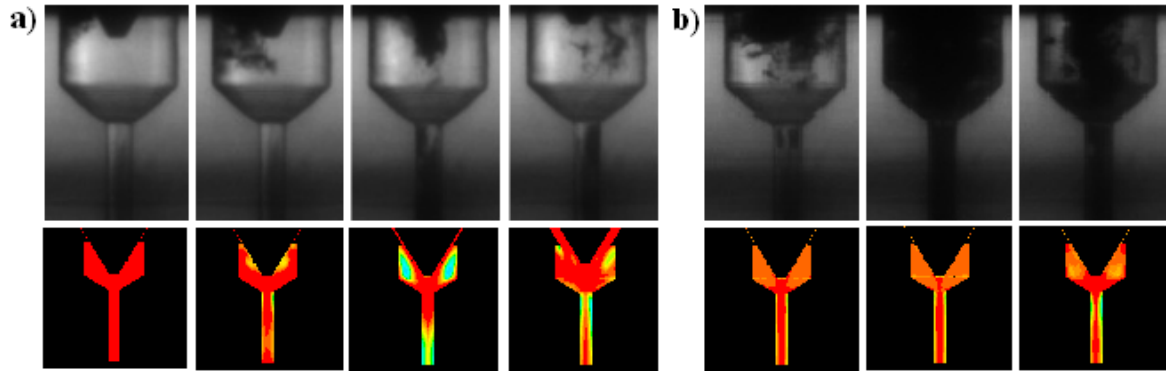


**Figure 4.** Cavitation behaviour in a transparent injector geometry with needle lift influence at 1300 bar injection pressure (Comparison between experiment and numerical simulation) a) Opening process b) Closing process.

In the measurements cavitation regions are characterized by the dark parts of the images. In all measurements two zones of cavitation were detected. One zone is the area in the needle seat, another zone is in the spray hole. When the needle lift begins, small cavitation areas in the needle seat and in the nozzle are formed. The cavitation increases during the needle lift process, both experimentally and in the simulation (Figure 4). When the needle is completely open, the cavitation in the nozzle is fully developed. For the closing process a reverse effect can be observed.

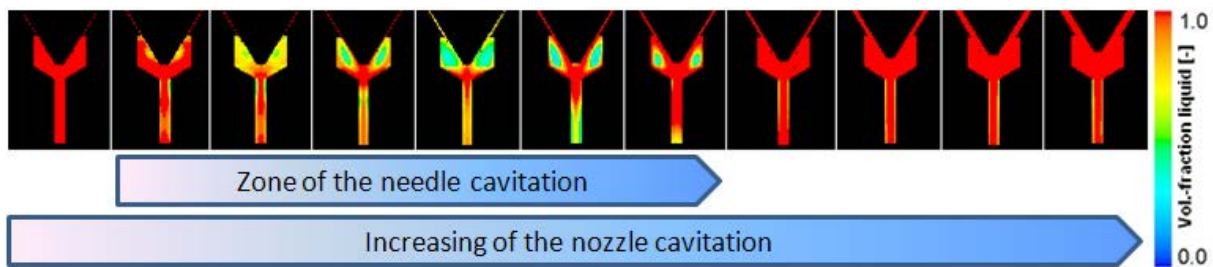


**Figure 5.** Simulation of the cavitation formation during the opening process at 1300 bar (Nozzle 1).

In **Figure 5** the same calculated opening process is shown with shorter time steps. The cavitation in the needle seat begins very early, as soon as the needle lifts and is limited to a quite short period of time. Whereas the cavitation in the nozzle starts strongly fluctuating at the inlet, but increases until the needle is completely open. When the cavitation is fully developed, a stationary behaviour can be observed. The same behaviour is seen in the experiment (Figure 6).

In the experimental measurements the transient behaviour of the transparent nozzle was visualized for different geometries. The vapor phase appears black due to the different refraction indexes. In Figure 6 to Figure 10 the opening process with the moving needle is shown for the different geometries. The needle seat cavitation is caused by the needle lift. The cavitation in this zone decreases with continuous needle lift up to the stationary process. The cavitation stops in the needle seat when the needle is completely open and the stationary process is reached. In contrast to the needle seat cavitation the cavitation in the nozzle is also formed while the needle stays open. Obviously a large volume of the sac hole and the nozzle causes long time periods while cavitation in the needle seat can be observed. Comparing Nozzle 1 (200  $\mu\text{m}$ ) and Nozzle 4 (400  $\mu\text{m}$ ) it can be seen that for the

latter case the stationary cavitation region is formed only close to the outlet of the nozzle. Here, future work is planned to validate also scaling laws.

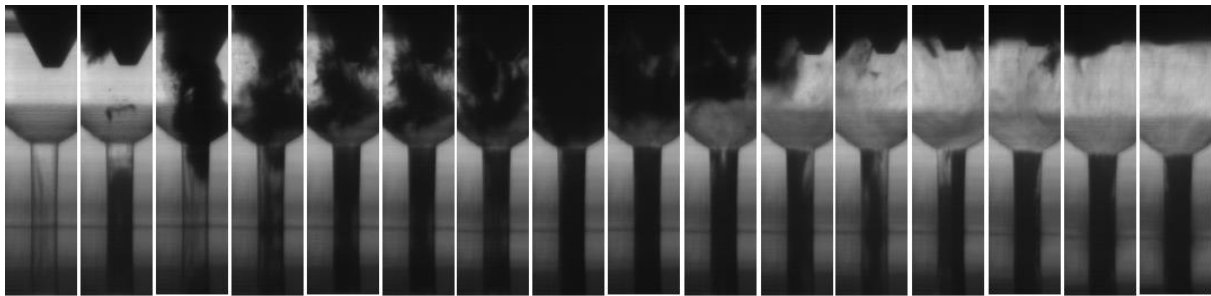


**Figure 6.** Cavitation formation during the opening process at 1300 bar (Nozzle 1) Volume: 0.555 mm<sup>3</sup>.

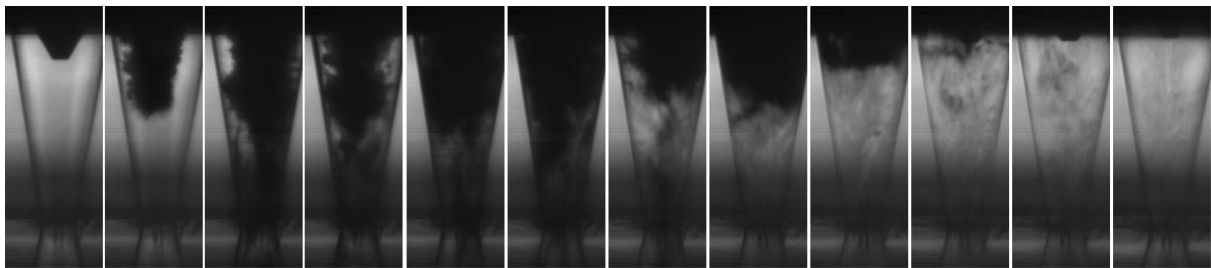


**Figure 7.** Cavitation formation during the opening process at 1400 bar (Nozzle 2) Volume: 0.792 mm<sup>3</sup>.

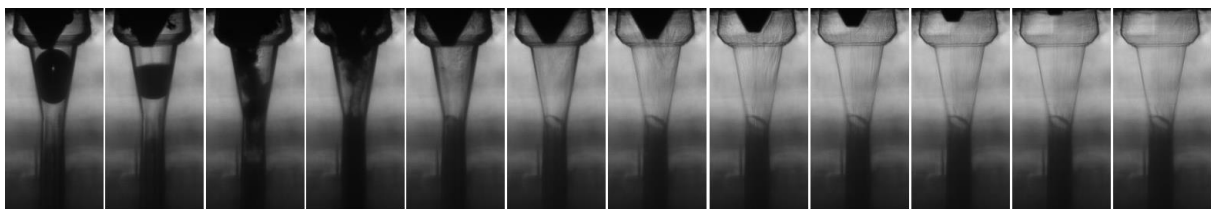


**Figure 8.** Cavitation formation during the opening process at 1100 bar (Nozzle 3) Volume: 0.553 mm<sup>3</sup>.

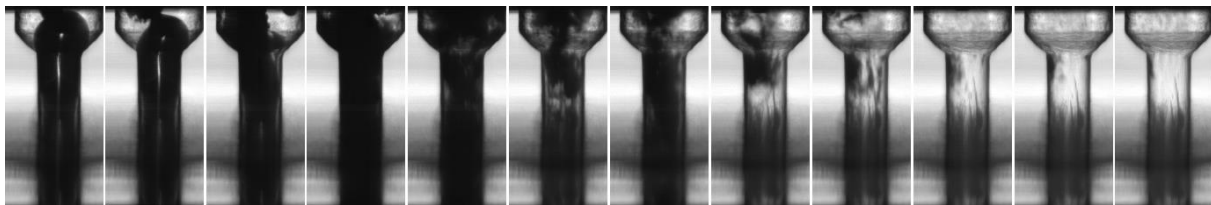


**Figure 9.** Cavitation formation during the opening process at 500 bar (Nozzle 4) Volume: 0.711 mm<sup>3</sup>.

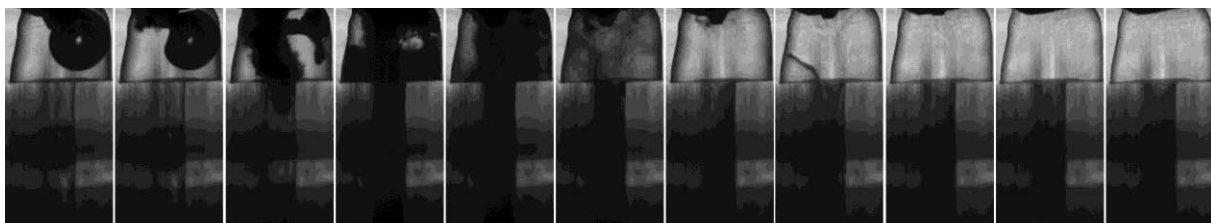


**Figure 10.** Cavitation formation during the opening process at 800 bar (Nozzle 6) Volume: 0.666 mm<sup>3</sup>.

In **Figure 11** (left) the duration of the needle seat cavitation is evaluated for the different geometries as a function of injection pressure. Generally the duration is shorter for higher injection pressure. The absolute values of the duration are sensitive to fine parameters. This is indicated by some measurements done later again, after disassembling and assembling the nozzle head. The general pressure dependent trend is similar, however.

Variation of the injection pressure for the geometries of Nozzle 1 and 2, as shown in **Figure 11** (right), indicates that the duration of the needle seat cavitation decreases only up to appr. 800 bar for increasing injection pressure. At higher pressure levels, the duration of cavitation increases. For these measurements the visualisation in the transparent nozzles up to 1500 bar could be realized – beyond these points the transparent nozzles were destroyed.

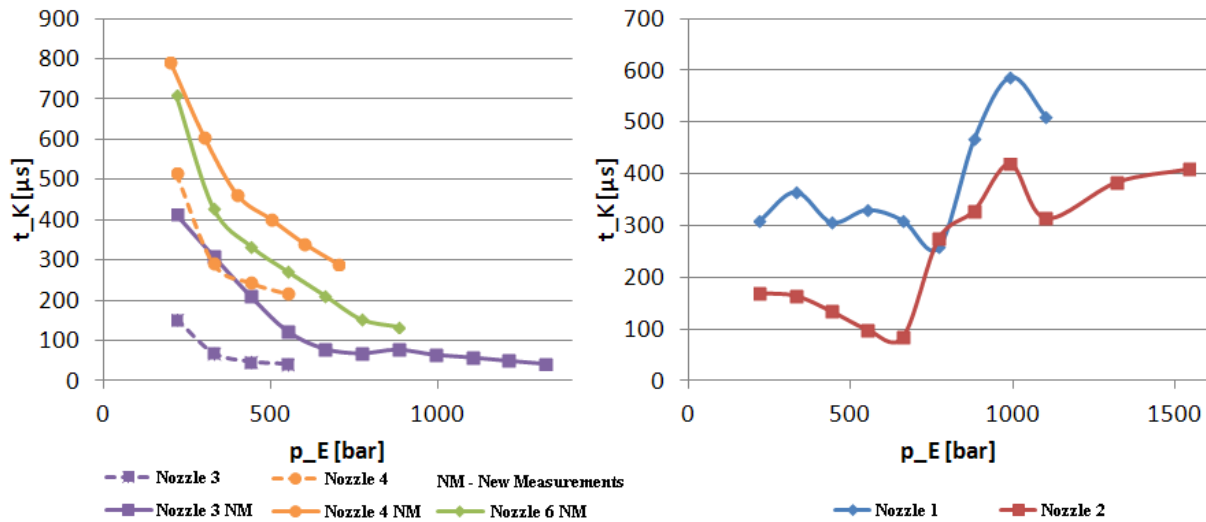


Figure 11. Duration of the needle seat cavitation of different geometries

## Conclusions

The shadow method is qualified for the detection of the cavitation area during the unsteady process of injection. This investigation shows that it is important to understand the transient processes inside the injector, including the needle seat details. The duration of cavitation in the needle seat depends on the geometry and the volume behind the needle seat. A comparison between experiment and simulation is possible, and partly already corresponding behaviour is found. The experimental data is therefore useful to validate simulation models. Cavitation in the nozzle increases while lifting the needle. The comparison of the simulation and the experiment shows the right trend, but it also indicates that there are more influences to be regarded. The investigations show, how important transient effects are, especially during the movement of the needle. Transient numerical RANS simulations, employing a moving mesh, are suitable at least in first order to evaluate generally these transient flow processes. Detailed studies concerning the applicability of different multi-phase and cavitation models are possible with highly resolved experiments. Here more work is planned in the near future. It may be seen also, if fully time dependent calculations, e.g. based on large eddy simulation approaches are even more predictive.

## References

- [1] Walther, J.: Quantitative Untersuchung der Innenströmung in kavitierenden Dieseleinspritzdüsen, TU Darmstadt, Dissertation, 2002.
- [2] Blessing, M.: Untersuchung und Charakterisierung von Zerstäubung, Strahlausbreitung und Gemischbildung aktueller Dieseldirekteinspritzsysteme, Universität Stuttgart, Dissertation, 2004.
- [3] ANSYS, Inc., ANSYS FLUENT Theory Guide, Release 13.0 - 2010.
- [4] Brennen, C. E., Fundamentals of Multiphase Flow, Paperback Edition, Cambridge University Press, 2009.
- [5] Zwart, P.J., Gerber, A.G., Belamri, T.: A Two-Phase Flow Model for Predicting Cavitation Dynamics, In Fifth International Conference on Multiphase Flow, Yokohama, Japan, 2004.
- [6] Jollet, S., Willeke, T., Dinkelacker, F.: Comparison of Various Models for Transient Nozzle Flow Simulations Including Time-Resolved Needle Lift, ICLASS - International Conference on Liquid Atomization and Spray Systems, Heidelberg, Germany, 2012.
- [7] Heilig, A.: Untersuchung des Primärzerfalls von Hochdruckdieselsprays mittels optischer Messtechnik, Universität Hannover, Dissertation, 2013.

## String Cavitation in Fuel Injector Nozzle

Akira Sou, Raditya Hendra Pratama and Yusuke Kibayashi

Graduate School of Maritime Sciences, Kobe University, Japan

### Abstract

String cavitation may take place in a nozzle of fuel injector at low needle lift, which plays an important role in fuel spray characteristics. The mechanism and the condition of string cavitation formation have not been understood yet. In this study cavitation in cylindrical nozzles with 4 mm in diameter  $D$  and 16 mm in length  $L$  ( $L/D = 4$ ) with an asymmetric lateral inflow from upstream together with the discharged liquid are visualized to investigate string cavitation by focusing on the asymmetric lateral inflow velocity, needle lift  $Z$ , and mean liquid velocity  $V$  in the nozzle. As a result, we find that (1) string cavitation takes place at low needle lift ( $Z/D \leq 3$ ) due to the formation of a helical flow in the nozzle, which is triggered by the asymmetric lateral inflow, (2) we presented a string cavitation regime map, (3) the angle  $\theta$  of the discharged hollow-cone liquid skirt or the jet increases with decreasing  $Z/D$  and increasing  $V$ , (4) the diameter of the string cavitation increases with decreasing  $Z/D$ , and (5) string cavitation is unstable near the boundaries of the string cavitation regime.

### Introduction

It was known that cavitation takes place in a nozzle of Diesel fuel injectors and it affects the injected spray characteristics [1-10]. Hiroyasu et al. [2] clarified through a symmetric visualization of a scale-up nozzle of 4 mm in diameter that development of cavitation from the inlet to near the exit of a nozzle, which is often called supercavitation [3], enhances liquid spray atomization. Following the finding, visualizations of cavitation in real size nozzles were carried out [3,9,11,13-15]. One of the present authors conducted a high-speed visualization and LDV (Laser Doppler Velocimetry) measurement of turbulent cavitation flow in two-dimensional (2D) symmetric nozzle [4] and a visualization of a symmetric single cylindrical nozzle [7] to clarified that cavitation clouds are shed from the tail of a recirculation zone filled with a cavitation film, and a strong vortex flow around the cloud is the one to induce a large deformation of the discharged liquid jet. We classify the above cavitations into recirculation flow-induced-cavitation (RIC). To understand more complex cavitation flows in real fuel injectors, observations of cavitation in nozzles with an asymmetric inflow from upstream [8-10], with tilted angles [8-11], with a complex upstream geometry [12], and with real fuel injector geometries [12-15] have been carried out. In some of these experiments [12,14,15], a so-called string cavitation, which we classify into helical flow-induced-cavitation (HIC), has been observed especially at low needle lift. Although string cavitation has a large impact on the injected fuel spray, the mechanism how it takes place and the conditions at which it appears have not been clarified yet. In this study we carry out a visualization of cavitation in single cylindrical nozzles of 4 mm in diameter  $D$  and 16 mm in length  $L$  ( $L/D = 4$ ) with an asymmetric lateral inflow from upstream to investigate string cavitation and the discharged liquid. Transparent injectors with various needle lifts  $Z$  are used, and mean liquid velocity  $V$  in the nozzle are varied to clarify the formation mechanism of string cavitation and the conditions of the string cavitation appearance.

### Experimental setup

Figure 1 shows the schematic of experimental setup. Filtered tap water at 30 °C in temperature  $T$  was pumped through a transparent acrylic nozzle into ambient air at atmospheric pressure and room temperature. Valves were adjusted to control liquid flow rate, which was measured using one of flow meters, by which mean liquid velocity  $V$  in the nozzle was varied. Pressure gauge was installed at the upstream of the nozzle to measure injection pressure. Images of cavitation in the nozzles and the injected liquid jet were taken using a high speed camera (Vision Research, Phantom v211) and a metal-halide lamp (Kyowa Co. Ltd., MID-25FC).

Figure 2 (a) shows the schematic of a Valve-Covered-Orifice (VCO) nozzle, in which liquid fuel flows into a nozzle with an asymmetric transverse inflow through the gap  $Z$  between needle valve and the seat. We made acrylic model injectors as shown in Figures 2 (b) and (c) to examine the effects of the asymmetric inflow on string cavitation and the discharged liquid jet. The cylindrical nozzle is 4 mm in diameter  $D$  and 16 mm in length  $L$  ( $L/D = 4$ ). Front views of cavitation in the injectors with various gaps (needle lift)  $Z$  ( $Z = 2, 4, 8, 12, 16, 20, 24, 28$ , and 32 mm, i.e.,  $Z/D = 0.5, 1, 2, 3, 4, 5, 6, 7$ , and 8) were captured to investigate the effects of the lateral inflow velocity in the upstream on cavitation and the jet. Cavitation in an axisymmetric single-hole nozzle with  $D = 4$  mm,  $L = 16$  mm and upstream diameter  $D_u = 32$  mm [7] was also visualized for reference.



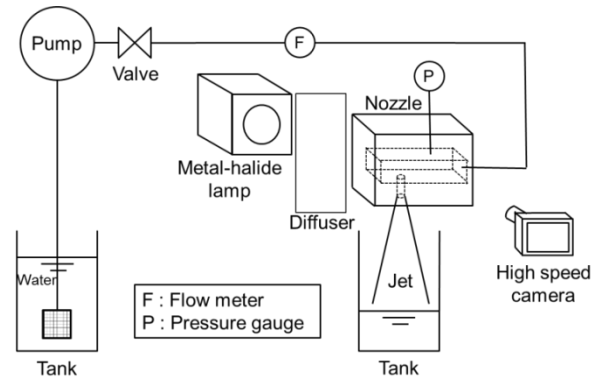


Figure 1. Experimental setup

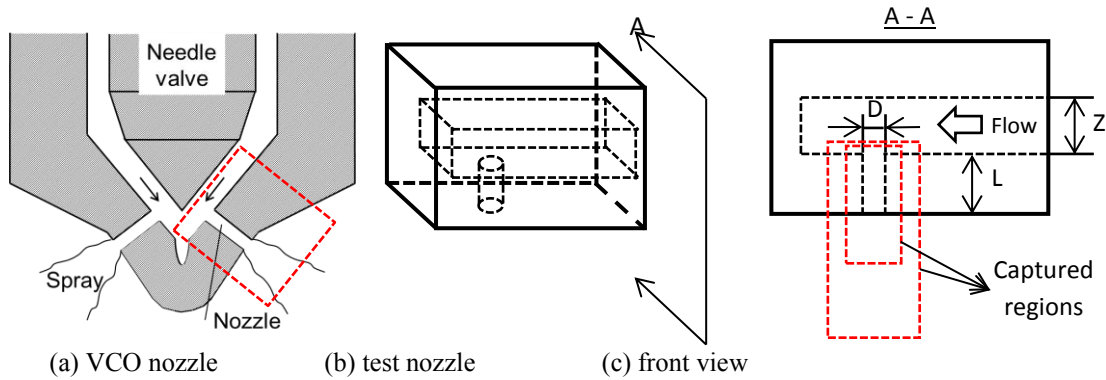


Figure 2. Geometry and dimensions of the test nozzles

## Results and Discussion

Figure 3 shows the images of cavitation in the axisymmetric nozzle and the liquid jets. No cavitation is observed at  $V \leq 6.4$  m/s and a wavy liquid jet is discharged. Tiny cavitation bubbles are seen in vena contracta at  $V = 10.4$  m/s (incipient cavitation) and the liquid jet remains wavy jet. Super cavitation and an atomized liquid jet are formed at  $V = 13.1$  m/s. For  $V \geq 13.5$  m/s, hydraulic flip with a smooth liquid jet appear.

The images for the case of the asymmetric injector with high lift ( $Z/D = 8$ ) are shown in Figure 4. For  $Z/D = 8$  cavitation patterns are almost same as those of the axisymmetric nozzle since the upstream volume is large. Note that imperfect hydraulic flip with a slightly deformed jet is formed for  $V \geq 14.3$  m/s, which is preferable than the smooth jet (total hydraulic flip) in internal combustion engines.

Figures 5 and 6 are the images of nozzles with an axisymmetric inflow and a lateral inflow for high lift ( $Z/D = 8$ ), respectively. In the asymmetric case cavitation near the right wall is slightly longer than that along the left side of the wall, which must be the reason of the larger liquid deformation on the right side of the jet.

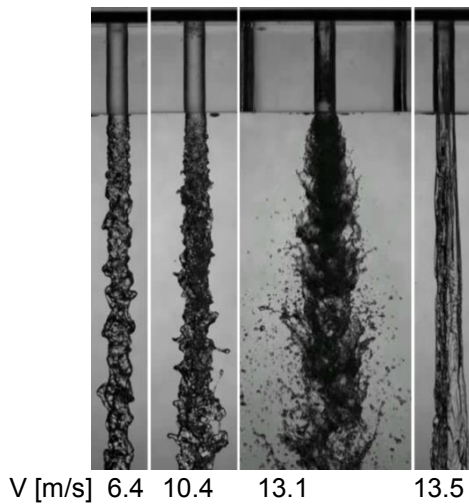


Figure 3. Images for an axisymmetric nozzle

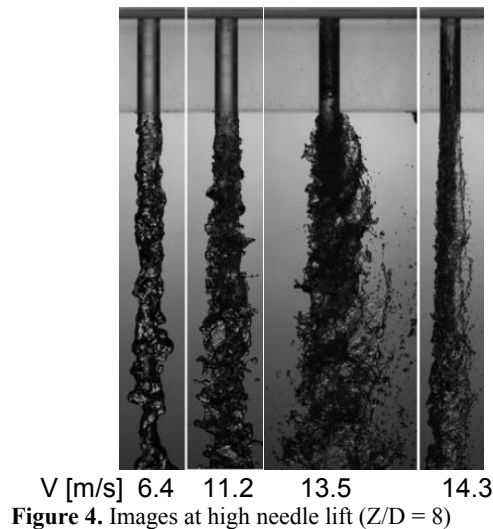
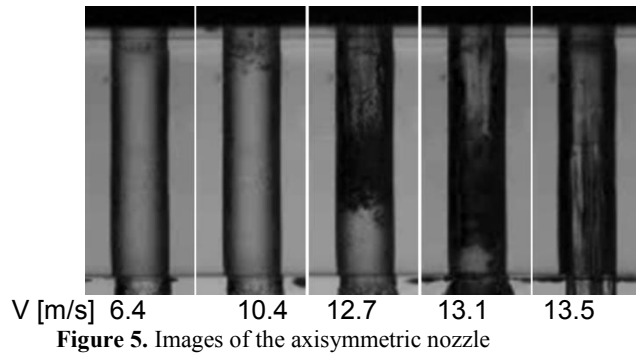
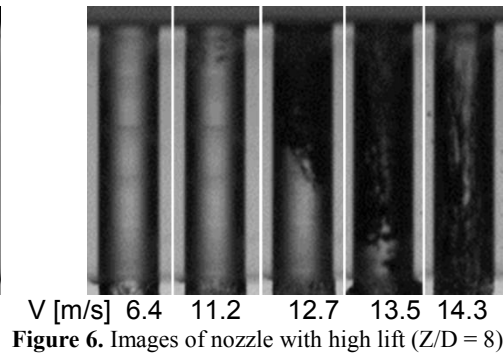


Figure 4. Images at high needle lift ( $Z/D = 8$ )





**Figure 5.** Images of the axisymmetric nozzle



**Figure 6.** Images of nozzle with high lift ( $Z/D = 8$ )

Similar results are observed for  $Z/D \geq 4$ , which are classified as high lift cases. It should be noted that although no cavitation is seen at very low  $V$  for  $Z/D = 4$ , a slightly twisted liquid jet is formed. The twisted jet suggests the formation of a weak helical flow in the nozzle.

Figure 7 shows the images for low needle lift of  $Z/D = 3$ . In low lift cases ( $Z/D \leq 3$ ) a string cavitation is formed at low  $V$ , which results in the formation of a hollow cone liquid skirt. The result suggests that string cavitation can occur even at low Reynolds number, which allows us to perform numerical simulations easily. For higher  $V$  ( $V = 8.0, 11.9$  m/s) a thin string cavitation reaches the upper wall (the bottom of the needle valve). The string is slanted toward the left side due to the major inflow from right side. The larger  $V$  is, the wider the liquid jet angle becomes. These flow phenomena suggest that the string cavitation is caused by the helical inflow, which is triggered by the lateral upstream inflow. As shown in Figure 8, when needle lift is low ( $Z/D = 0.5$ ), the string cavitation and the hollow cone liquid skirt appear at lower  $V$  and the cone angle is larger. It should be noted that the hollow cone liquid skirts are not symmetric. Figure 9 shows the string cavitation in the nozzle with  $Z/D = 3$ . String cavitation is slanted, which is the reason of the above mentioned asymmetric liquid skirt behaviours. At high  $V$  not only string cavitation but also tiny cavitation bubbles appear near the right inlet edge. We may call it hybrid cavitation, however the effects seem to be small.

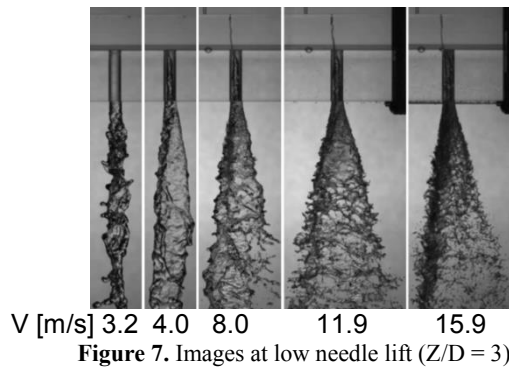


**Figure 7.** Images at low needle lift ( $Z/D = 3$ )

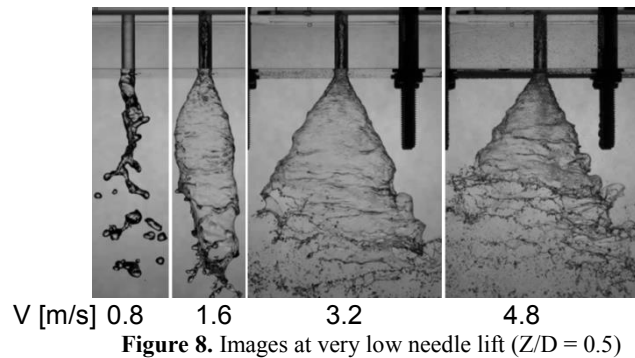


**Figure 8.** Images at very low needle lift ( $Z/D = 0.5$ )

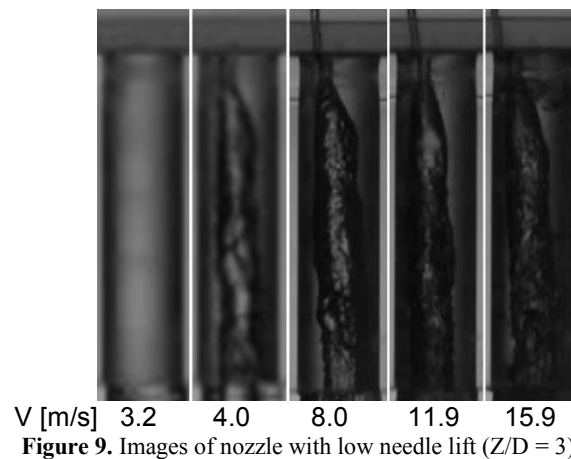


**Figure 9.** Images of nozzle with low needle lift ( $Z/D = 3$ )

A string cavitation regime map for the cylindrical nozzles is shown in Figure 10, where the vertical axis is  $Z/D$  and the horizontal axis is mean liquid velocity  $V$  in the nozzle. At high needle lift of  $Z/D \geq 4$ , the effects of the asymmetric lateral inflow are so small that cavitation regime transits at almost same  $V$ . On the other hand, at low

needle lift of  $Z/D \leq 3$  string cavitation or hybrid cavitation is formed. The onset of string cavitation (incipient string cavitation) takes place at lower  $V$  in lower lift  $Z$ .

It should be noted that the cavitation regime map depends not only on the needle lift  $Z$  and velocity  $V$  but also on upstream geometry, such as upstream width, depth, possible needle angles and so on which are illustrated in Figure 2 (a).

Liquid jet angles are measured at 8D downstream of the nozzle exit. Ten images of liquid jets are analysed for each  $V$  and  $Z/D$  to obtain mean liquid jet angle  $\theta$  and is shown in Figure 11. At high  $Z/D$  jet angle  $\theta$  is small and increases at super cavitation regime. Jet angle  $\theta$  is larger at lower  $Z/D$  and higher  $V$ . For  $Z/D \leq 3$ , the angle  $\theta$  is very large due to the formation of the hollow cone liquid skirt. The lower  $Z/D$  is, the larger the angle  $\theta$  becomes due to the stronger centrifugal force.

Diameters of the string cavitations are measured at 4 mm upstream of the nozzle exit by taking into account the effects of refraction at the cylindrical nozzle wall. Figure 12 shows the mean diameter of the string cavitations normalized by nozzle diameter  $D$ . The diameter is larger at lower  $Z/D$  and is almost independent from  $V$ .

String cavitation is unsteady and unstable near the boundaries of the string cavitation regime. The probability of the occurrence of string cavitation is plotted in Figure 13. The result indicates that string cavitation is not stable near the incipient cavitation condition especially at  $Z/D = 3$ .

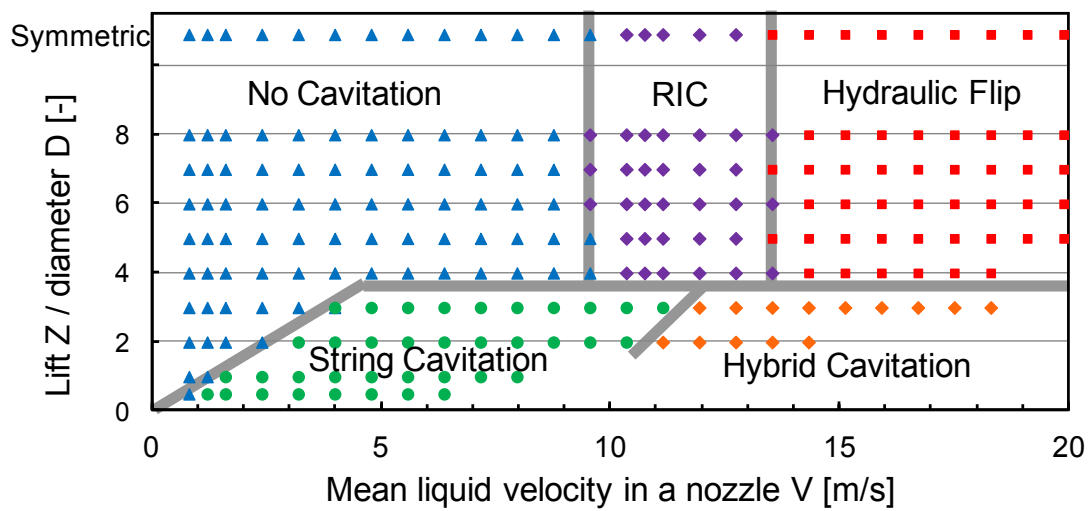


Figure 10. String cavitation regime map

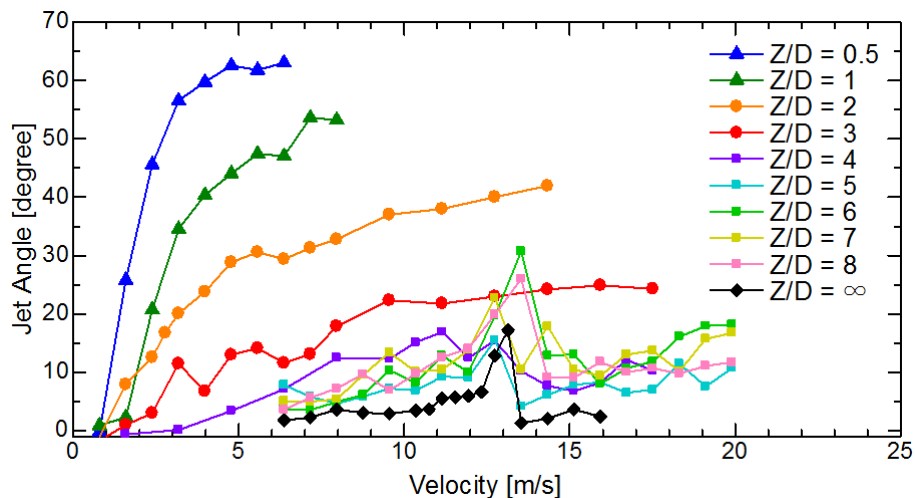


Figure 11. Liquid jet angle

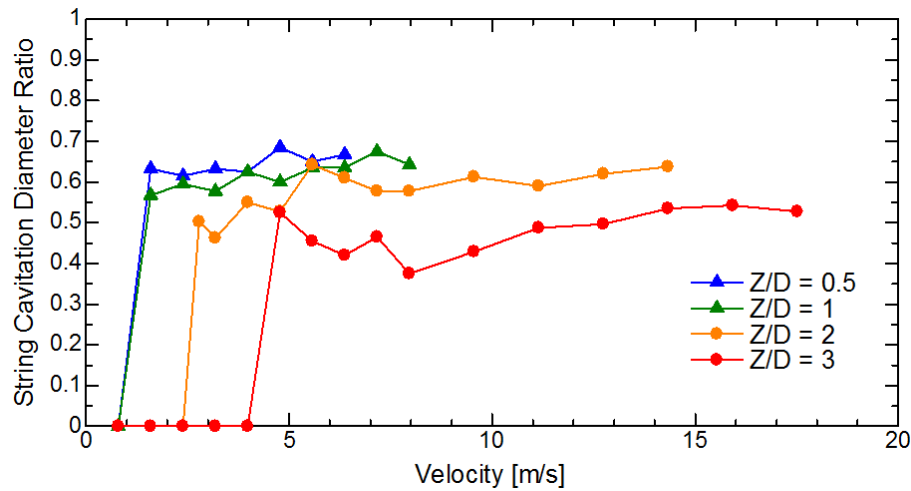


Figure 12. Diameter of string cavitation

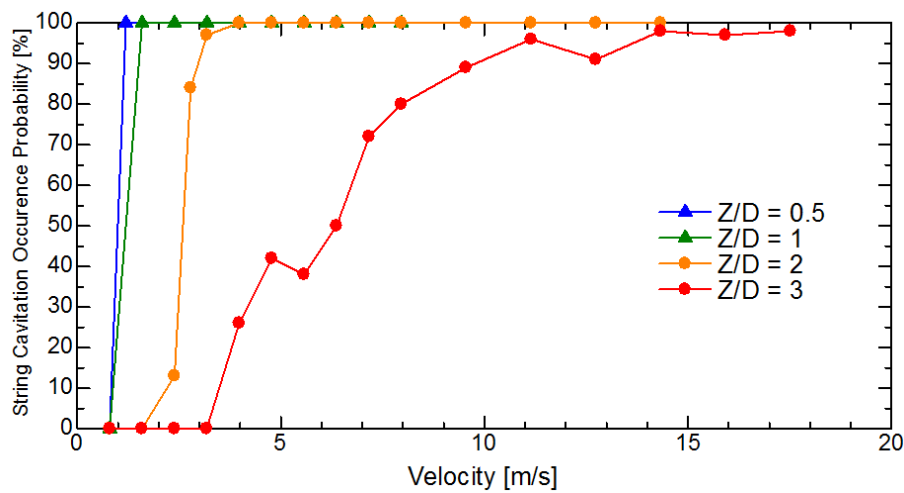


Figure 13. Probability of string cavitation occurrence

## Conclusions

Cavitation in cylindrical nozzles with an asymmetric lateral inflow from upstream as well as the discharged liquid are visualized to investigate string cavitation by focusing on an asymmetric lateral inflow velocity, needle lift  $Z$ , and liquid velocity  $V$  in the nozzle. As a result, the following conclusions are obtained.

- (1) String cavitation takes place at low needle lift ( $Z/D \leq 3$ ) due to the formation of a helical flow in the nozzle, which is triggered by an asymmetric lateral inflow.
- (2) A string cavitation regime map is presented, which is plotted against  $Z/D$  and  $V$ .
- (3) The angle  $\theta$  of the injected hollow-cone liquid skirt or the jet increases with decreasing  $Z/D$  and increasing  $V$ .
- (4) The diameter of the string cavitation increases with decreasing  $Z/D$ .
- (5) String cavitation is unstable near the boundaries of the string cavitation regime.

## Nomenclature

$D$	Nozzle diameter [m]
$L$	Nozzle length [m]
$V$	Mean liquid velocity in a nozzle [m/s]
$t$	Time [s]
$Z$	Needle lift [m]

## References

- [1] Bergwerk, W., 1959, "Flow Pattern in Diesel Nozzle Spray Holes," *Proc. Instn. Mech. Engrs.*, Vol. 173, No. 25, 655–660.
- [2] Hiroyasu, H., Arai, M. and Shimizu, M., 1991, "Break-up Length of a Liquid Jet and Internal Flow in a Nozzle," *Proc. ICLASS-91*, 275–282.
- [3] Chaves, H., Knapp, M., Kubitzek, A., Obermeier, F. and Schneider, T., 1995, "Experimental Study of Cavitation in the Nozzle Hole of Diesel Injectors Using Transparent Nozzles," *SAE Paper*, Paper No. 950290, 199–211.
- [4] Sou, A., Hosokawa, S. Tomiyama, A., 2007, "Effects of Cavitation in a Nozzle on Liquid Jet Atomization", *Int. J. Heat Mass Transfer*, Vol. 50, Iss. 17-18, 3575–3582.
- [5] Sou, A., Hosokawa, S. and Tomiyama, A., 2010, "Cavitation in Nozzles of Plain Orifice Atomizers with Various Length-to-Diameter Ratios," *Atomization and Sprays*, Vol. 20, Iss. 6, 513–524.
- [6] Sou, A., Ilham M. M., Isozaki, K., Hosokawa, H., Tomiyama, A., 2008, "Effects of Nozzle Geometry on Cavitation in Nozzles of Pressure Atomizers", *J. Fluid Sci. Technol.*, Vol. 3, No. 5, pp. 622–632.
- [7] Sou, A., Ilham, M. M., Hosokawa, S. and Tomiyama, A., 2008, "Ligament Formation Induced by Cavitation in a Cylindrical Nozzle," *J. Fluid Sci. Technol.*, Vol. 3, No. 5, 633–644.
- [8] Ganippa, L. C., Bark, G., Andersson, S. and Chomiak, J., 2001, "Comparison of Cavitation Phenomena in Transparent Scale-up Single-Hole Diesel Nozzles," *Proc. CAV2001*, A9.005.
- [9] Miranda, R., Chaves, M., Martin, U. and Obermeier, F., 2003, "Cavitation in a Transparent Real Size VCO Injection Nozzle," *Proc. ICLASS 2003*.
- [10] Sou, A., Raditya, H. P., Ohashi, R. and Sugimura, R., 2011, "Cavitation in a Nozzle with Asymmetric Inflow and its Effects on Liquid Jet", *Proc. ILASS Europe 2011*.
- [11] Collicott, S. and Li, H., 2006, "True-scale True-pressure Internal Flow Visualization for Diesel Injectors," *SAE Paper*, 2006-01-0890.
- [12] Soteriou, C., Andrews, R., Torres, N., Smith, M. and Kunkulagunta, R., 2001, "Through the Diesel Nozzle Hole - A Journey of Discovery II," *Proc. ILASS-Europe 2001*.
- [13] Chaves, H., Miranda, R. and Knake, R., 2007, "Particle Image Velocimetry Measurements of the Cavitating Flow in a Real Size Transparent VCO Nozzle," *Proc. Int. Conf. on Multiphase Flow (ICMF 2007)*, S4\_Mon\_C\_6.
- [14] Andriotis, A., Gavaises, M. and Arcoumanis, C., 2008, "Vortex Flow and Cavitation in Diesel Injector Nozzles," *J. Fluid Mech.*, Vol. 610, 195–215.
- [15] Hayashi, T., Suzuki, M., Ikemoto, M., 2012, "Visualization of Internal Flow and Spray Formation with Real Size Diesel Nozzle", *Proc. ICLASS 2012*, ICLASS 2012-1375.
- [16] Sou, A., Raditya H. P., Tomisaka, T., 2012, "Cavitation in a Nozzle of Fuel Injector", *Proc. CAV 2012*, pp. 483–488.

## Experimental measurement of jets formed after the impact onto static and onto moving water films

Samah K. Alghoul

Power Division, Mechanical and Industrial Engineering Department, Faculty of Engineering,  
the University of Tripoli, Tripoli-Libya

### Abstract

Comparison between jet formation onto static and onto moving water films is conducted from experimental data. The data is acquired using high speed imaging. Similar impact conditions have been chosen for the impact onto moving and static films. The two cases have been compared and differences have been identified and presented in detail. The results show that jets produced from the impact onto static films are much higher than those produced from the impact onto the moving films. Also the film movement is found to reduce the amount of secondary droplets produced after the impact for the cases of normal impact studied in this paper.

### Introduction

The study of the dynamics of droplet impact onto moving films is of significant importance due to its relevance to many industrial applications including lubrication and surface cooling in aeroengines (1, 2). Recent limited research has been focusing on the study of droplet impact onto moving films (3-5). The results of these studies showed that there are some very important differences between droplet impact onto moving films and static films. These differences will have an effect on the modelling of related applications. Although these studies highlighted major aspects of droplet impact onto moving films, there is no direct comparison between the outcomes of the impact onto static and moving films or the transition boundaries between different impact outcomes. In this paper a detailed experimental investigation is conducted in order to compare the jet formed after the impact for impacts onto static and onto moving liquid films.

### Problem definition and important parameters

In this paper comparison between the jet formation from the impact onto static and moving films are presented and discussed in detail in order to identify the main differences between the two cases.

Although the non-symmetrical effects of the impact on moving films are highlighted in previous work (3), the work shown here compares very similar cases, i.e. the film thickness and width is the same with the droplet size and impact Weber number equal for both the impact on static and on moving films.

Figure 1 a & b shows a schematic of the problem where a single droplet impacts static (a) or moving (b) water film. The droplet falls under the effect of gravitational force in still air so the droplet velocity and momentum just before the impact can be changed by changing the height from which the droplet falls and also by changing the droplet diameter. This change in the droplet momentum at the impact leads to a change in the impact outcomes so jets on both static and moving films can be acquired.

As shown in previous work (3, 4, 6-9) the droplet impact Weber number ( $We$ ) is the most important parameter that decides the impact outcome for the impact onto static liquids. Another important parameter that is used to identify the impact outcomes is the  $K$  parameter which is also known as the splash factor (3, 4, 8-15):

$$K = We^{0.375} Re^{0.25} \quad \text{Equation 1}$$

Where  $We$  and  $Re$  are the droplet Weber and Reynolds number just before the impact and are defined as

$$We = v_i^2 \rho d / \sigma \quad \text{Equation 2}$$

$$Re = \rho v_i d / \mu \quad \text{Equation 3}$$

Where  $\rho$ ,  $\mu$ ,  $\sigma$  are the droplet density, viscosity and surface tension respectively.

The moving film has a steady average velocity ( $v_f$ ) and thickness ( $h_f$ ). In some cases where the film thickness is not deep, the thickness has an effect on the impact outcomes and the transition boundary of the impact outcomes may be affected by the film height  $h_f$  or the dimensionless film height  $h_f^*$  where  $h_f^* = h_f / d$ .

For the current work all the above parameters are included in the study. In addition the film Reynolds number ( $Re_f$ ) and Froude number ( $Fr_f$ ) should be taken into consideration as they represent the effect of the film movement and they are defined as

$$Re_f = \rho v_f R_f / \mu \quad \text{Equation 4}$$

$$Fr_f = v_f^2 / h_f g \quad \text{Equation 5}$$

Where  $g$  is the gravitational force and  $R_h$  is the hydraulic radius of the duct ( $R_h = W \cdot h_f / (2h_f + W)$ ),  $h_f$  is the film height and  $W$  is the film/duct width.

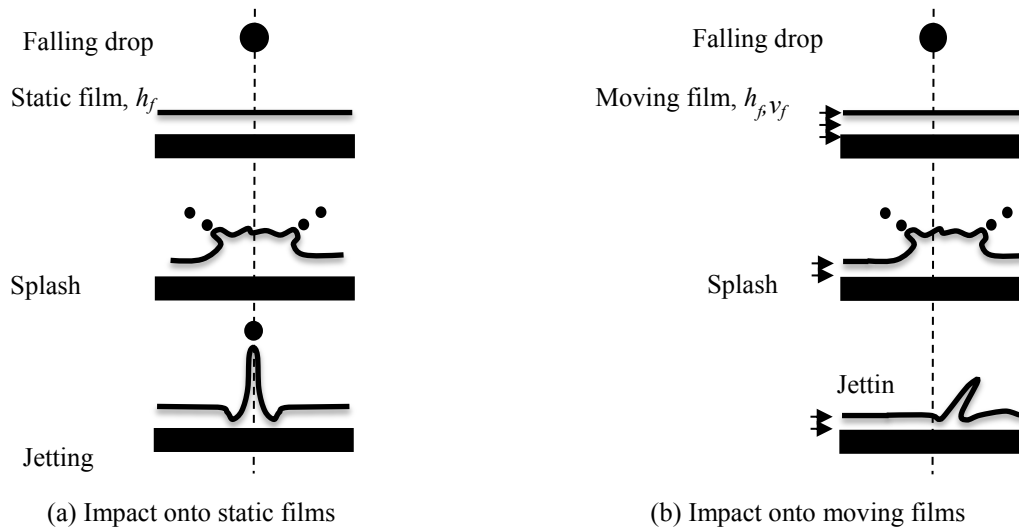


**Figure 1 :** Sketch of single droplet impact onto (a) static and (b) moving liquid films

### Experimental test-rig

Figure 2 shows the rig used in this work. It consists mainly of the droplet production system and the film generation system. The droplets are produced using a syringe pump connected to a capillary tube with changeable needles attached at the end of the capillary. The moving water film flows in a rectangular open duct, the film flow rate can be adjusted using a control valve and it is measured using a rotameter. A high speed imaging system was used to capture the images of the impact outcomes. For more details about the rig see reference (3).

Sets of the impact on static films that have the same condition for the sets of data for the impact on moving films are also recorded and are used in the comparison in this paper.

### Results and discussion

Two different cases (Figure 3 and 4) of impacts are presented to compare the differences in jets formed after the impact. The outcomes of the impacts on a moving film are represented in the left side of the figures, while the right side shows the impact onto a static film with the figures comparing pairs of images at exactly the same time after the impact.

For the first case which is shown in Figure 3, the droplet diameter is 3.8 mm with an impact Weber number of 460 and the film thickness for moving and static films is 4.3mm. The Reynolds number of the moving film is 300 and Froude number is 0.35. The figure shows that the outcomes of the impact on both the static and moving films are *corona splash* at an early stage of the impact. This is illustrated in the figure at 10 ms where the shape of the crown looks similar. The measurement of the mass of the secondary droplets produced from the crown is very difficult to be done. That is because these secondary droplets breakup from the crown and fly in radial direction which makes doubt about seeing all the produced droplets. Moreover, as the secondary droplets move in radial direction they leave the camera focus field very quickly. However, the mass of these droplets are considered very small when compared to the mass of the droplet detached from the tip of the jet.

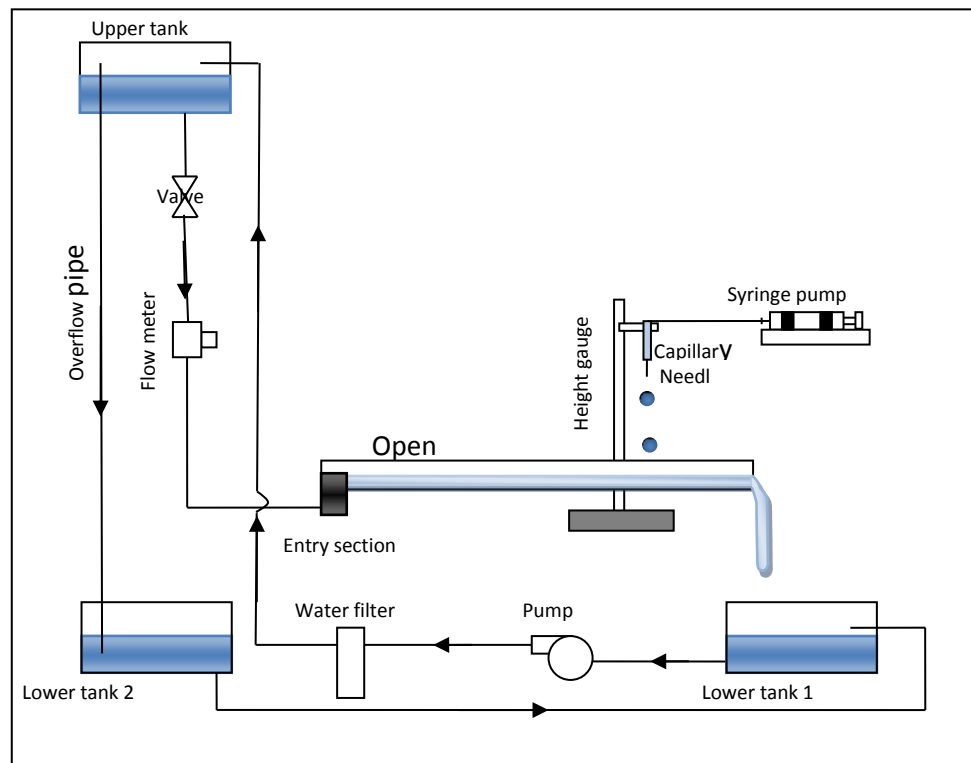


**Figure 2 :** The experimental rig including the film generation system and the droplet production mechanism

At 50 ms in Figure 3 a jet is clearly shown above the surface of the film for the impact onto static case while no jet is formed for the impact on the moving film at this point of time. At a late stage of the impact (50ms to 80 ms) differences can be seen very clearly between the jet formed for the impact on the static and the moving. In the static case, large secondary droplets are produced compared with those produced from the corona splash at 10 ms. On the other hand, the impact on moving films did not produce any secondary droplets. That is because the jet does not reach the necessary length to breakup (16). Again the figure shows jet produced for the impact onto moving film is inclined in the same direction of the film flow while the jet produced from the static impact is normal to the film surface which agrees with the results obtained in previous work (3) .

Time(ms)	Impact on moving film	Impact on static film
0		
10		
20		



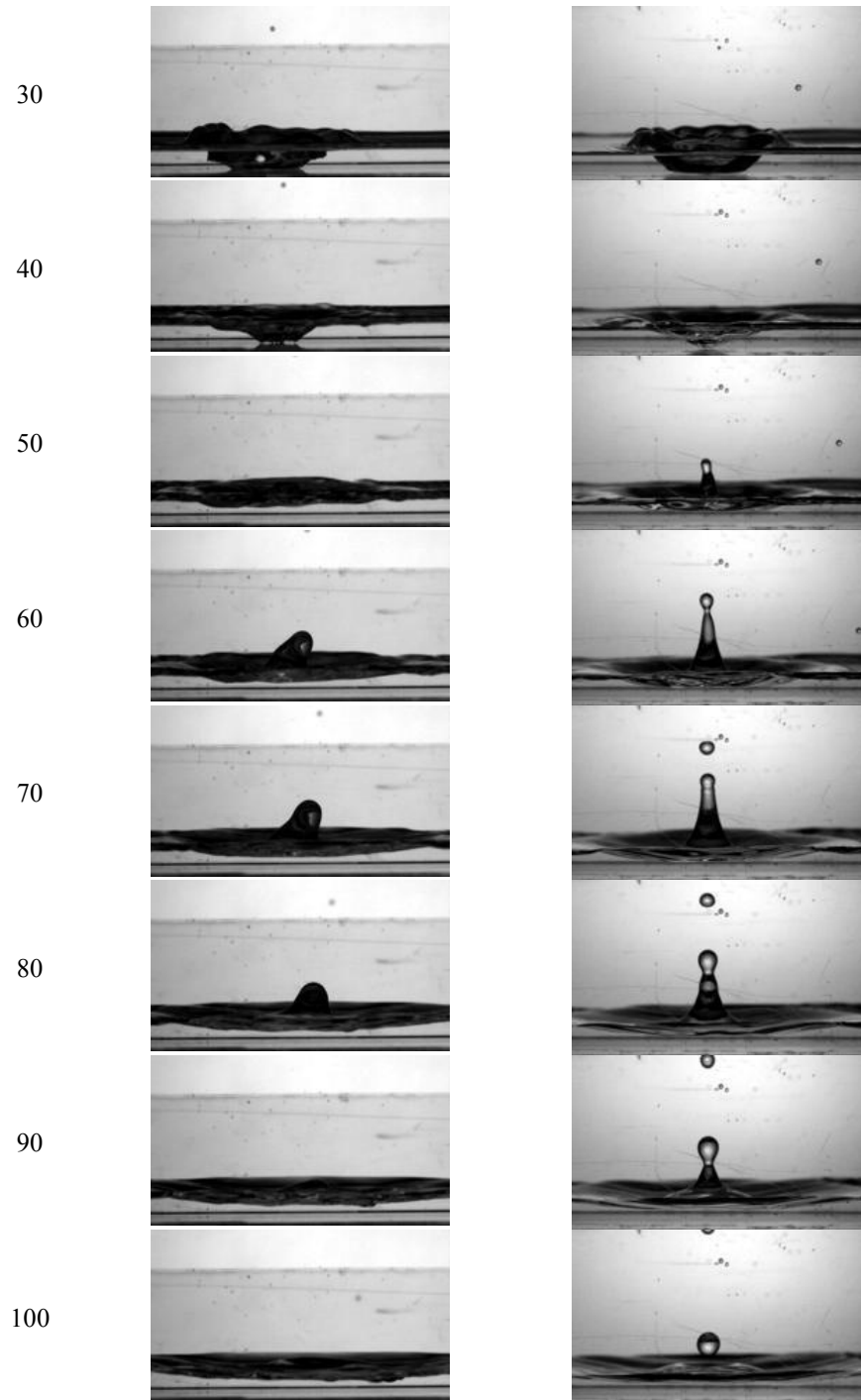


**Figure 3:** Comparison of jets produced from the impact onto static film (right) and moving film (left) at the same time sequence after the impact ( $D=3.8\text{mm}$ ,  $h_f=4.3\text{mm}$ ,  $We=459$ ,  $Ref=300$  for left images only)

The other case which is represented in Figure 4 is for the impact of 2.4mm water droplet ( $We=188$ ) onto 5.9mm thick water film. In this case the impact does not show the crown that is shown in the previous case due to the lower value of the impact Weber number. As a result the outcome of this case is *jet formation*. The differences between the outcomes of the impact for static and moving films can be seen much more directly in Figure 4. Similar behaviour to that shown at late stage in Figure 3 is found where the impact onto static films results in a break up of large secondary droplets while the impact onto moving films results only in jet formation.

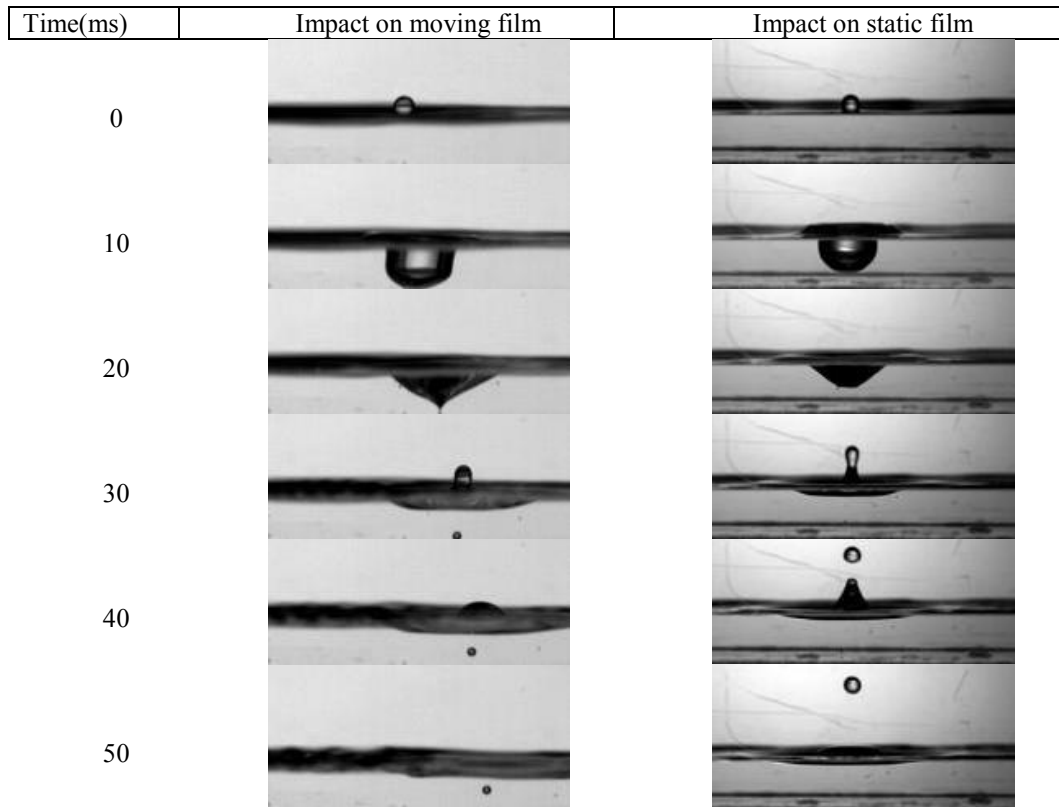


**Figure 4:** Comparison of jets produced from the impact onto static film (right) and moving film (left) at the same time sequence after the impact ( $D=2.4\text{mm}$ ,  $h_f=5.9\text{mm}$ ,  $We = 188$ ,  $Ref=674$  for left images only)

Having looked at the images of the outcomes of the impact on static and moving films, the differences seen in those images are now explored in more detail by analysing the jet height and the secondary droplets produced from jet break up.

### Jet height

Figure 5 shows a comparison of the jet height for static and moving films for the 3.8mm and 2.4mm droplet impacts. The jet height is changed by increasing the droplet impact Weber number while the film thickness for all cases is constant (4.3mm) which leads to constant film velocity for moving impacts. For both droplets the jet height increases with increasing impact Weber number. At the same Weber number the larger droplet always produces a higher jet than the jet produced from the smaller droplet. The most important trend this figure shows is that the jets produced from the impact onto static films are much higher than those produced from the impact onto the moving films even for the relatively slow film velocity studied here.

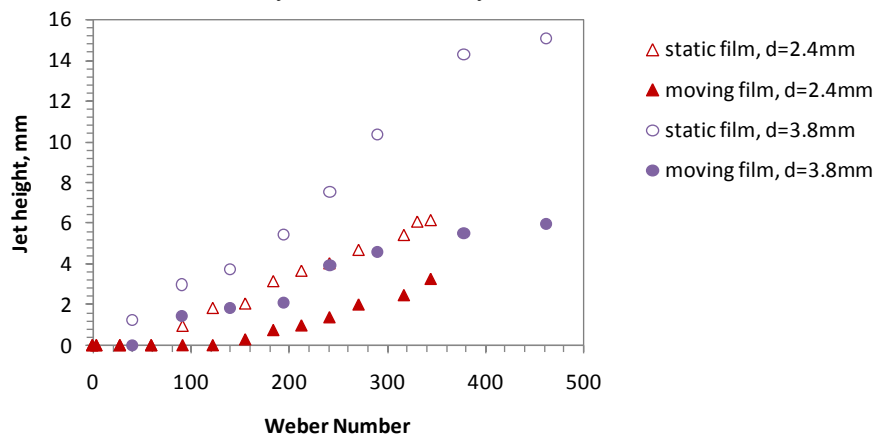


**Figure 5:** Comparison between jet height produced from the impact on 4.3 mm thick static and moving films.

The figure also shows that similar trends are shown for the same droplets but not for the same impact targets, i.e., the impact onto moving and static films showed similar trends for the same droplet.

In refrence (17) it has been reported that for normal impact on static films the jet height increases as the impact Weber number increases. The results in Figure 5 shows that, although jets produced from the impact on the moving films are inclined, the height and the lengths of the jets increase with increasing the impact Weber number. It should be noted that the jets produced from the normal impact on static films are normal to film surface as known in the literature and also as seen in Figure 3 and Figure 4.

Figure 6 shows the change of the jet height for the impact on moving films as a function of both the droplet Weber number and the film Reynolds number. As mentioned before increasing the droplet Weber number leads to an increase in the jet height. Figure 6 shows also that increasing the film Reynolds number leads to an increase in the jet height.

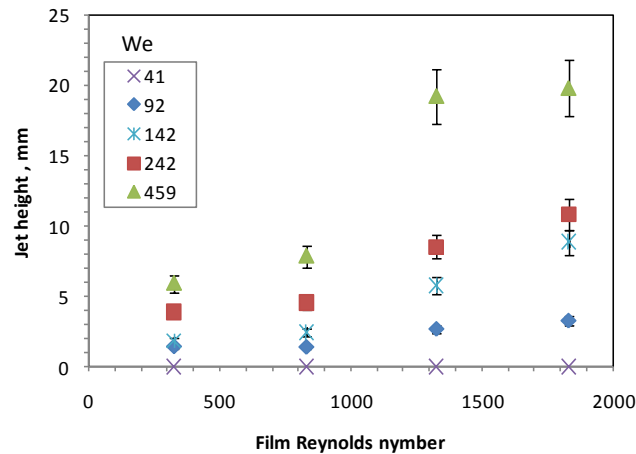


Figure 6: Measured jet height from the original free surface of the moving film.

### The mass of the secondary droplets

Figure 7 shows a comparison of the ratio of the secondary droplets (droplets detached from the tip of the jet) produced after the impact at different droplet impact Weber numbers. The ratio of the secondary droplets is defined as  $(m_s/m_p)$  where  $m_s$  is the secondary droplets mass and  $m_p$  is the primary droplet mass. The mass ratio is calculated from the secondary droplet diameters by assuming they have spherical shapes and in order to satisfy this assumption the diameters of the secondary droplets were measured from the images that show the closest shape to the sphere, i.e., tracking the secondary droplets in the records until it becomes spherical and then measuring the diameter.

The graph in Figure 7 clearly shows that the mass of the produced secondary droplets is much higher for the static case at the same experimental conditions. This was expected as the comparison of the jet height showed the jet height for static case is large which is the main reason for the jet to break up and produce secondary droplets (16).

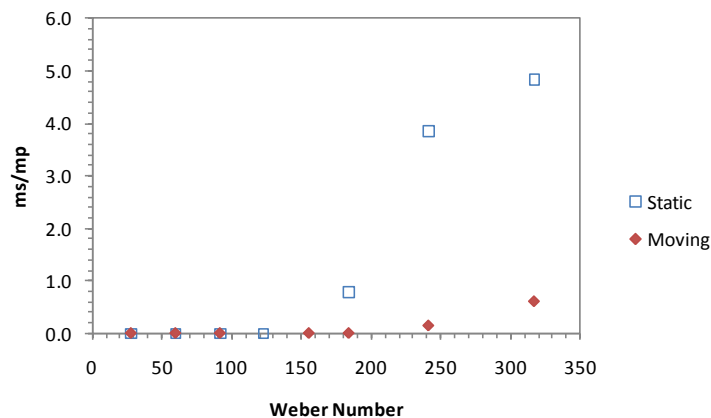


Figure 7 : Ratio of the secondary droplets for the impact of 2.4mm droplets on static (5.9mm) and moving (5.9mm,  $Re_f=675$ ).

## Conclusions

From the previous discussion, two main differences are identified as a result of comparing the outcomes from the impact on static and moving films. The first one is the lack of symmetry that is shown for impact onto moving film especially in the jet formation regime where the jets were always inclined in the direction of the film flow. The jet height is also shorter than that produced from the impact onto a static film as shown in Figure 3, Figure 4 and Figure 5.

The second main difference between the impact onto moving and static films is the mass of the secondary droplets produced after the impact. The film movement seems to enhance the coalescence between the droplet and the target film and as a result the amount of the mass of the secondary droplets produced after the impact is less than the amount produced from the impact onto static cases.

## References

- [1] M. Farrall, K. Simmons, S. Hibberd, P. Gorse, *Journal of Engineering for Gas Turbines and Power* 128, 111 (2006).
- [2] D. W. Stanton, C. J. Rutland, *International Journal of Heat and Mass Transfer* 41, 3037 (1998).
- [3] S. Alghoul, C. Eastwick, D. Hann, *Experiments in Fluids* 50, 1305 (2011).
- [4] S. Alghoul, C. Eastwick, D. Hann, in *ILASS – Europe 2010, 23rd Annual Conference on Liquid Atomization and Spray Systems*. (Brno, Czech Republic, 2010), pp. 10.
- [5] H. Zhao, R. Ecault, C. Dorao, S. Munkejord, paper presented at the Droplet impact phenomena and spray investigation Workshop, Bergamo, Italy, 2011.
- [6] M. Rein, *Fluid Dynamics Research* 12, 61 (1993).
- [7] M. Rein, *Journal of Fluid Mechanics* 306, 145 (1996).
- [8] G. E. Cossali, A. Coghe, M. Marengo, *Experiments in Fluids* 22, 463 (1997).
- [9] R. Rioboo, C. Bauthier, J. Conti, M. Voue, J. De Coninck, *Experiments in Fluids* 35, 648 (2003).
- [10] C. Mundo, M. Sommerfeld, C. Tropea, *International Journal of Multiphase Flow* 21, 151 (1995).
- [11] T. Okawa, T. Shiraishi, T. Mori, *Experiments in Fluids* 44, 331 (Feb, 2008).
- [12] T. Okawa, T. Shiraishi, T. Mori, *Experiments in Fluids* 41, 965 (2006).
- [13] R. L. Vander Wal, G. M. Berger, S. D. Mozes, *Experiments in Fluids* 40, 33 (2006).
- [14] R. L. Vander Wal, G. M. Berger, S. D. Mozes, *Experiments in Fluids* 40, 53 (Jan, 2006).
- [15] S. Alghoul, The University of Nottingham (2011).
- [16] S. L. Manzello, J. C. Yang, *Experiments in Fluids* 32, 580 (2002).
- [17] W. C. Macklin, P. V. Hobbs, *Science* 166, 107 (October 3, 1969, 1969).

## A Gibbs free Energy Relaxation Model for Cavitation Simulation in Diesel injectors

Chawki Habchi

IFP Energies nouvelles, 1 et 4 avenue de Bois-Préau, 92852 Reuil-Malmaison, France

### Abstract

In this paper, a comprehensive highly compressible and turbulent two-fluid multi-species model is presented. It involves an equation for the transport of the liquid volume fraction in addition to two different sets of partial differential equations for the gas and the liquid phase. The multicomponent gas species phase is governed by an ideal gas equation of state (EOS) while the stiffened gas EOS is specified to the single-component liquid phase. In this work, a Reynolds Averaged Navier-Stokes (RANS) formulation is adopted. For the turbulence, a standard  $k$ - $\epsilon$  model is used for the gas phase while a turbulent viscosity-based model is used the liquid phase. In addition, the model equations include different relaxation terms for mass, momentum and energy exchanges at the liquid-gas interfaces. For the present cavitation modelling, an instantaneous relaxation procedure is used for the velocity, pressure and temperature; while a slower procedure is adopted for the Gibbs free energy relaxation model (GERM) at the interfaces. These models have been applied for the simulation of the cavitation inside a transparent single-hole nozzle. The obtained cavitation pocket has a similar shape than the experiments. Moreover, two different cavitation regimes have been identified. A gaseous cavitation regime appears in region in which the static pressure is close to but above the liquid saturation pressure; and a second cavitation regime may happen when the static pressure goes below the liquid saturation pressure. In this case, the liquid become superheated and leads to a vaporous cavitation regime.

---

### 1. Introduction

With increasingly stricter emission regulations and greater demand on fuel economy, the injector has become one of the most critical components of modern diesel engines. Since the nozzle geometry influences the spray characteristics and the mixture preparation in the engine, the design of injector nozzles has become an important factor for the improvement of the combustion performance and pollutant reduction. In addition, the physical processes involved in direct injection engines are complex. Consequently, it is important to understand the effects of the nozzle geometry (sac, orifice ...) on the liquid injection, atomization and combustion behaviour, especially as the orifice size keeps getting smaller and the injection pressure higher. Moreover, the description of turbulent flow and its coupling with liquid atomization and dispersion is required, as well as the description of the mixing, the ignition and the combustion itself. An accurate prediction of liquid injection is then critical in this context, and has to be modelled from the in-nozzle region up to the dispersed evaporating spray region, where combustion takes place. A number of studies have been conducted on the effect of the nozzle characteristics on the internal and external spray characteristics [1], [2], [3]. Even if experiments of the complete process are a source of information and physical understanding, there is, at the present time, a growing willingness for the development of predictive numerical computations of such flows, which is particularly challenging for regions at the inner and near injector, as shown in [4], [5], [6]. Currently, most of cavitation models are based either on a single-fluid mixture approach using a homogeneous equilibrium model (HEM) [7] or a simplified Rayleigh-Plesset (RP) bubble dynamics equation [8]. On the one hand, in the HEM model, the cavitation is computed using a barotropic equation of state (EOS) derived from the Wood's speed of sound [9]. On the other hand, in the RP models, the cavitation is computed as the result of the pressure difference between the inner bubble and the surrounding liquid. Besides, it is usually assumed that cavitation should take place in regions in which the static pressure falls below the saturation pressure of the flowing liquid. Although, this condition is not necessary for the growing and collapse of cavitation bubbles, both of the HEM and RP models assume that cavitation bubbles or pockets are full of vapour and do not consider gaseous cavitation which is observed experimentally [10]. In addition, high velocity shears, pressure or temperature variations that one may encounter in two-phase flows formed inside and in the close vicinity of injectors cannot be resolved by such HEM models, as only momentum and energy equations for the mixture are accounted for. Moreover, both HEM and RP models ignore the thermodynamic processes happening at the liquid-gas interfaces during phase changes. In this work, a new cavitation model based on the equilibrium at liquid-gas interface of the Gibbs free energy of liquid and gas, is suggested in a general framework of highly compressible and turbulent two-fluid models. This paper is organized as follows: First, the comprehensive highly compressible and turbulent two-fluid model is presented in Section 2 along with the GERM cavitation model. Next, in Section 3, these models are applied for the simulation of the cavitation inside a transparent single-hole nozzle for which experimental cavitation results are available [11]. Present study also attempts to improve the understanding of the different cavitation regimes as discussed above by varying the temperature of the injected fuel from 300K to 450K. Finally, the conclusions of this work are reported with the future work.

## 2. Mathematical modelling

Flow regimes in internal and near injector regions can be handled through different Eulerian/Eulerian approaches [12], [13]. On the one hand, one may consider direct interface resolution using Navier-Stokes equations in each phase and jump conditions at the interfaces. The liquid jet atomization and the cavitation inception modelling are possible with sufficiently refined meshes and high order numerical schemes in order to be able to capture the interface position accurately. The minimum liquid or gas structure size that can be accounted for is directly related to the grid resolution. Direct interface resolution approaches can be used for understanding studies and validation purposes, limited to simple geometries. Yet, they are not appropriate for complex configurations such as internal combustion engines and multi-hole injector simulations. In addition, since these approaches are derived using an incompressible liquid assumption, they are not able to properly compute the cavitation inside the nozzle, where the liquid velocity may have a value as high as 700 ms<sup>-1</sup> and a Mach number greater than 0.5. In this paper, a comprehensive highly compressible and turbulent two-fluid multi-species model is presented. It is based on the Baer and Nunziato model [14] and previous work by Saurel and co-workers [15]. Their method is based on a compressible model involving seven partial differential equations, three for the gas phase and three for the liquid phase in addition to an equation for the liquid volume fraction transport. In this work, a multi-species model is proposed in the Reynolds Averaged Navier-Stokes (RANS) framework. The details of the averaging procedure may be found [16]. In addition, the specific internal energy equation is used instead of the total specific energy adopted in the work by Saurel and co-workers [17], [15]. Also, this two-fluid model is able to deal with liquid jet atomization as suggested by Devassy et al. [18]. In addition, phase change at the interface is considered in this paper. For two-phase flows, the model consists of the following governing equations:

$$\frac{\partial \alpha_p \bar{\rho}_{m,p}}{\partial t} + \frac{\partial \alpha_p \bar{\rho}_{m,p} V_{p,i}}{\partial x_i} = \frac{\partial}{\partial x_i} \left[ \bar{\rho}_p D_p \frac{\partial}{\partial x_j} \left( \frac{\bar{\rho}_{m,p}}{\bar{\rho}_p} \right) \right] + \psi (\tilde{g}_q - \tilde{g}_p) \delta_{mf} \quad (1)$$

$$\frac{\partial}{\partial t} (\alpha_p \bar{\rho}_p V_{p,i}) + \frac{\partial}{\partial x_i} (\alpha_p \bar{\rho}_p V_{p,i} V_{p,j}) = - \frac{\partial \alpha_p \bar{P}_p}{\partial x_i} + \bar{P}^I \frac{\partial \alpha_p}{\partial x_i} + \frac{\partial \alpha_p \bar{\tau}_{p,ij}^{L,T}}{\partial x_i} + \phi (V_{q,i} - V_{p,i}) \quad (2)$$

$$\begin{aligned} \frac{\partial}{\partial t} (\alpha_p \bar{\rho}_p e_p) + \frac{\partial}{\partial x_i} (\alpha_p \bar{\rho}_p V_{p,i} e_p) = & - \alpha_p \bar{P}_p \frac{\partial V_{p,i}}{\partial x_i} + \alpha_p \bar{\tau}_{p,ij}^{L,T} \frac{\partial V_{p,i}}{\partial x_j} - \frac{\partial \alpha_p \bar{q}_{p,i}^{L,T}}{\partial x_j} + \phi V^I (V_{q,i} - V_{p,i}) \\ & + \omega \bar{P}^I (\bar{P}_q - \bar{P}_p) + \theta (T_q - T_p) + \tilde{e}^I \psi (\tilde{g}_q - \tilde{g}_p) \end{aligned} \quad (3)$$

$$\frac{\partial \alpha_p}{\partial t} + V_i^I \frac{\partial \alpha_p}{\partial x_i} = \omega (\bar{P}_q - \bar{P}_p) + \frac{\theta}{\kappa} (T_q - T_p) + \frac{\psi}{\bar{\rho}^I} (\tilde{g}_q - \tilde{g}_p) \quad (4)$$

Here  $p=\{1,2\}$  and  $q=3-p$ ; say  $p=1$  for the liquid phase (index  $l$ ) and  $p=2$  for the gas phase (index  $g$ ). The over bar ( $\bar{\bullet}$ ) and tild ( $\tilde{\bullet}$ ) designate the Reynolds and Favre average operation, respectively. Equation (1) is the continuity equation for species  $m$ . The  $f^{\text{th}}$  species index designates the fuel vapour. For the gas, a Fick law with a single turbulent diffusion coefficient  $D_p$  is assumed; while the liquid is assumed single-component ( $D_l=0$ ). In Equations (2) and (3),  $\tau_{p,ij}^{L,T}$  is the shear stress tensor. It can be written as,  $\tau_{p,ij}^{L,T} = \tau_{p,ij}^L + \tau_{p,ij}^T$ , where the superscripts  $L$  and  $T$  stand for laminar and turbulent flow regimes, respectively. Its modelling is given below in Section 2.3. In the energy Equation (3),  $e_p$  is the Favre averaged specific internal energy and  $\bar{q}_{p,i}^{L,T}$  the heat flux which is modelled as follows:

$$\bar{q}_{p,i}^{L,T} = -\lambda_p \frac{\partial T_p}{\partial x_i} - \bar{\rho}_p D_p \sum_m h_{m,p} \frac{\partial}{\partial x_i} \left( \frac{\bar{\rho}_{m,p}}{\bar{\rho}_p} \right) \quad (5)$$

The first term in the right hand side (RHS) of Equation (5) is due to the conduction (Fourier's Law). For both phases, the turbulent contribution of the conductivity coefficient  $\lambda_p$  is computed from a specified turbulent Prandtl number taken equal to 0.9. However, only the liquid has a significant laminar conductivity coefficient contribution for  $\lambda_p$ . This contribution is computed using the Wilke and Lee correlation [19]. The second term in the RHS of Equation (5) represents the total flux of the enthalpy transported by the gaseous species due to turbulent advection. This term is not considered in the liquid since this phase is assumed single component. Equation (4) is solved only for  $p=1$  (i.e. for the liquid volume fraction,  $\alpha_l = \alpha_1$ ). The saturation constraint

$\alpha_1 + \alpha_2 = 1$  is then used for the calculation of the gas volume fraction,  $\alpha_g = \alpha_2$ . In the system of equations (1) to (4) also intervenes interfacial quantities denoted with a superscript “I”. The interfacial velocity,  $V^I$ , and the interfacial pressure,  $P^I$ , are assumed according to Baer and Nunziato model [14] ( $V^I = V_l$  and  $P^I = P_g$ ). In addition, the transport equations include different terms for the relaxation of the velocity, the pressure, the temperature and the Gibbs free energy at liquid-gas interfaces. Here, for the cavitation problem, the velocity and pressure are relaxed with an infinite rate by making  $\phi$  and  $\omega$ , respectively, tending to infinity. The description of these relaxation procedures can be found in Saurel and co-workers [17], [20]. Similarly, an infinite relaxation of the temperature at the interfaces is applied by tending the relaxation parameter  $\theta$  to infinity (see Zein et al. [21]). It is important to note that the pressure and temperature equilibrium are accomplished by computing the exact volume fraction variations (see the RHS of equation (4)). These volume fraction changes are happening without any phase change since they are absent from the RHS of the mass conservation Equation (1). Finally, the last terms in Equation (1) and (4) represent respectively, the mass flow rate and volume changes due to phase change at the interfaces. These processes are modelled using a finite relaxation numerical procedure for the Gibbs free energy equilibrium at the interfaces. This numerical iterative procedure will not be described in this paper for lack of space. A similar procedure may found in Zein et al. [21] along with the expression for the parameters  $\kappa$ ,  $\bar{\rho}^I$  and  $\tilde{e}^I$  appearing in the RHS of Equation (3) and Equation (4). As such, the suggested Gibbs free energy relaxation model (GERM) may simulate different cavitation regimes. Indeed, the two first terms,  $\omega(\bar{P}_q - \bar{P}_p) + \frac{\theta}{\kappa}(T_q - T_p)$ , in of equation (4) are dedicated for the modelling of the so-called “gaseous cavitation”. This first regime of cavitation may appear in regions in which the static pressure is close to but above the liquid saturation pressure. In this case, not only the disequilibrium of pressure but also the disequilibrium of temperature between the liquid and the gas are responsible of the growth or collapse of the bubbles without any phase change. In addition, a second cavitation regime may happen when the static pressure goes below the liquid saturation pressure. In this case, the liquid become superheated and leads to a “vaporous cavitation” regime. This vaporous regime is modelled by the last term,  $\dot{m}_p = \psi(\tilde{g}_q - \tilde{g}_p)$ , in Equation (1) and its corresponding energy flux and volume fraction in Equations (3) and (4), respectively.

## 2.1 Equations of State

Equations of state (EOS) are used to close the system of equations (1) - (4). In order to circumvent the difficulty of models having negative squared speed of sound in the two-phase region, the present study uses two EOS. Indeed, each fluid possesses separate EOS. In the present investigation, terms arising in the multi-species gas phase are closed by the perfect gas EOS where  $R$  is the universal constant:

$$P_g = \rho_g R T_g \quad (6)$$

In addition, the Stiffened Gas EOS (SG-EOS) is used in the single-species liquid phase. Two different expressions of the SG-EOS are given as follows:

$$P_l = \rho_l (\gamma_l - 1)(e_l - q_l) - \gamma_l P_{\infty,l} \quad , \quad T_l = \frac{P_l + P_{\infty,l}}{C_v \rho_l (\gamma_l - 1)} \quad (7)$$

Table 1 : SG-EOS parameters for the NF82BN18 fuel			
$P_{inf}$	$\gamma_l$	$C_v$	$q_l$
$5.3 \times 10^8$ Pa	3.48	761 J/kg/K	-1004 kJ

**Table 1** summarizes the values of the SG-EOS parameters for the NF82BN18 fuel. This fuel is a mixture of 82%vol Normafluid and 18%vol Bromonaphthalene used in the optical investigation by Blaisot et al. [11]. This mixture allows concealing the fluid-PMMA interface, especially in the orifice where the cavitation occurs. Details concerning the SG-EOS and its parameters may be found in Le Métayer et al. [22].

## 2.2 Stress Tensors and turbulence modelling

The stress tensor  $\tau_{p,ij}^{L,T} = \tau_{p,ij}^L + \tau_{p,ij}^T$  requires modelling in order to close the equations system (1) - (4). A standard Boussinesq approximation is used for the modelling of the Reynolds stress tensor ( $\tau_{p,ij}^T = -\bar{\rho}_p V_{p,i}'' V_{p,j}''$ ). As such, the total shear stress tensor can be written as,

$$\overline{\tau_{p,ij}^{L,T}} = \mu_p \left( \frac{\partial V_{p,i}}{\partial x_j} + \frac{\partial V_{p,j}}{\partial x_i} \right) - \frac{2}{3} \left( \mu_p \frac{\partial V_{p,i}}{\partial x_i} - \bar{\rho} k_p \right) \delta_{ij} \quad (8)$$



where  $\mu_p$  is the sum of the laminar and turbulent dynamic viscosities ( $\mu_p = \mu_p^L + \mu_p^T$ ). On the one hand, the laminar viscosity of gas phase,  $\mu_g^L$ , is calculated according to Sutherland's formula, a function of the gas temperature. On the other hand, the laminar viscosity of liquid phase,  $\mu_l^L$ , is given in a table as a function of the liquid temperature. The turbulent contribution,  $\mu_g^T$  is given using a standard  $k_g - \varepsilon_g$  model [23] by,

$$\mu_g^T = \bar{\rho}_g C_\mu \frac{k_g^2}{\varepsilon_g} \quad (8)$$

with  $C_\mu = 0.09$ , while for the liquid phase, a simple algebraic  $k_l - l$  model is used with  $k_l$  is modelled according to the following expression:

$$k_l = C_k l^2 |S|^2 \quad (9)$$

with  $C_k = 0.006$ . The characteristic length scale  $l$  is taken of the order of the of grid cell ( $l = (\text{Vol}_{\text{cell}})^{\frac{1}{3}}$ ) and

$|S|^2 = 2\tilde{S}_{ij} : \tilde{S}_{ij}$  where  $\tilde{S}_{ij} = \frac{1}{2} \left( \frac{\partial V_{p,i}}{\partial x_j} + \frac{\partial V_{p,j}}{\partial x_i} \right)$ . Finally,  $\mu_l^T$  is modelled according to the following relation:

$$\mu_l^T = \bar{\rho}_l (C_s l)^2 |S| \quad (10)$$

with  $C_s = 0.2$ .

### 3. Computational configuration

The GERM cavitation model described in the previous sections has been implemented in the software, IFP-C3D (Velghe et al. [24]). In this work, this new model is applied to the simulation of the cavitation inside a single-hole nozzle for which experimental cavitation results are available Blaisot et al. [11]. The main features of this optical nozzle used in this work are given in Table 2 and **Figure 1**.

Table 2 : Nozzle geometric features		
Sac Diameter du sac	μm	1200
Orifice Diameter	μm	200 ± 3
Orifice Length	μm	800
Sac to orifice axis offset	μm	50 ± 3
Radius of curvature between the sac and the hole	μm	50 ± 7

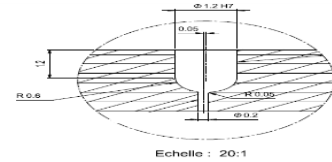


**Figure 1 : Sac and orifice offset**

In addition, the transport equations in IFP-C3D are written in the arbitrary Lagrangian Eulerian (ALE) formalism in order to allow the description of moving components such as the injector needle. Here, a simple linear interpolation of the vertices' coordinate between two grids is used for needle movement. The grids correspond to the maximum and minimum needle lifts. A minimum needle lift of 10 μm is used as shown in **Figure 2**. The mesh shown in **Figure 3** includes the nozzle and the combustion chamber. On the one hand, in order to make easier the specification of the inlet pressure boundary condition, the mesh of the nozzle has been extended to reach the inlet command chamber of the injector. On the other hand, a relatively rough mesh in the combustion is used in order to avoid possible flows with recirculation at outlet boundaries. Only the half of the nozzle has been meshed with 600000 hexahedron cells. It is worth to note that the needle lift region is initially meshed by ten hexahedron cells with a thickness lower than one micron. Furthermore, the cell size in the hole is taken relatively small (10 μm). And they are even smaller at the orifice wall (3 to 4 μm) in order to resolve possible secondary flows in the cavitation inception regions. The initial and boundary conditions are also given in **Figure 3**. Initially, the whole injector is full of liquid while the combustion chamber is full of gas (Nitrogen). Also, due to the two-fluid modelling, each phase contains a weak volume fraction  $\alpha_e$  of the other phase. For the cavitation modelling,  $\alpha_e$  of gas in the liquid is taken of the order of the dissolved gas value in typical fuels ( $\alpha_{eg} = 10^{-2}$ ). However, a much smaller value of  $\alpha_{el}$  in the gas is necessary and a value  $\alpha_{el} = 10^{-6}$  is adopted from previous works [20], [21]. The injection pressure is 25 MPa. This value is also the initial liquid pressure in the injector above the needle seat region. However, the liquid filling the sac and the hole is set to 0.1 MPa, which is the same pressure than the gas phase in the combustion chamber. The temperature of the gas in the combustion chamber is set to 300K; while the injected fuel has been varied from 300K to 450K. Also, the computations are assumed to start with a zero velocity and very small values of turbulent kinetic energy  $k_g$  and dissipation rate  $\varepsilon_g$ .

in the computational domain. In addition, weak turbulent kinetic energy and dissipation rate values have been specified at the inlet. Finally, all the walls are considered with a slip condition.

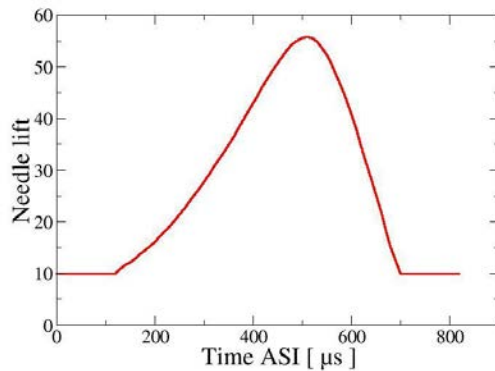


**Figure 2 :** Needle lift

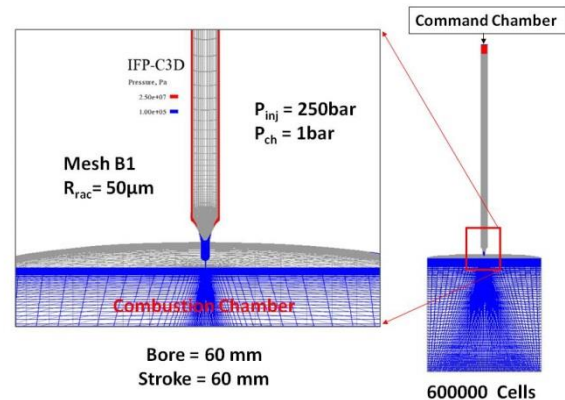


**Figure 3 :** Mesh, initial and boundary conditions

#### 4. Results and Discussion

Two computations have been carried out using two different injected liquid temperatures: 300K and 450K. For the low temperature case, shadow-images are available from the NADIA-BIO project [11]

**Figure 4** presents a fairly good qualitative agreement between the numerical and the experimental cavitation regions inside the optical nozzle.



**Figure 4 :** Qualitative comparison of the numerical and experimental cavitation regions. (a) Shadow-image obtained in the framework of NADIA-BIO project. (b) A volume fraction iso-value equal to 0.5 is used for delimiting cavitation region

In **Figure 5**, the numerical results of the two computations are compared in terms of cavitation regimes. On the one hand, for the 450K-case, the cavitation has appeared faster than in the 300K-case. In addition, there is no phase change for the 300K-case due to the extremely low saturation pressure (less than 10Pa) of the fuel at 300K. However, since the static pressure at the inlet edge of the orifice has decreased to a value close to but above the liquid saturation pressure, a gaseous cavitation regime has appeared during the injection period. On the other hand, since the saturation pressure is significant at 450K (greater than 10000Pa), a vaporous cavitation regime has appeared during the opening of the needle until 330μs. In this case, the fuel vapour mass fraction (shown in **Figure 5** by iso-lines) is up to 0.5 inside the cavitation pockets.

#### 5. Conclusions

This paper has presented a new cavitation (GERM) model which is based on a highly compressible and turbulent two-fluid multi-species formulation. First comparison of the numerical results with experimental shadow-images of the cavitation are very encouraging. Two regimes of cavitation have been identified and simulated by the GERM model. Future works will attempt to improve the understanding of the different cavitation regimes and their effects on atomizing liquid jets.

## Acknowledgements

The author would like to thank the support of the French ANR agency for its support to this work in the framework of the NADIA-BIO project (Contract N° 143886). The author is indebted to Prof. E. Daniel from Aix-Marseille University for his valuable advices, and to Mr. B. Reveillé (IFPEN) for providing the grid used in this article. Also, the author would like to thank Mr. R. Kumar (IFPEN) for his help about grid generation.

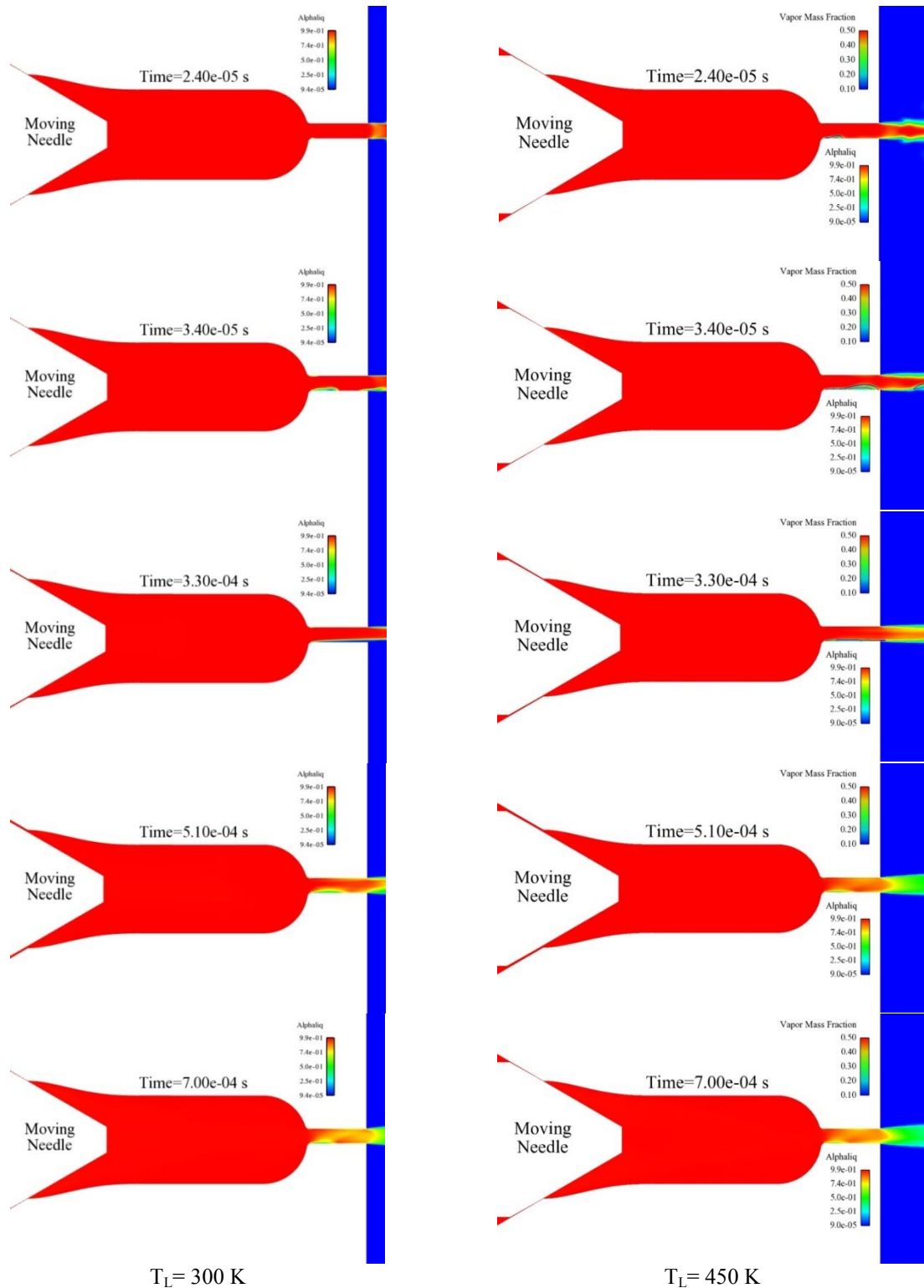


**Figure 5 :** (color Online) Liquid volume fraction and vapor mass fraction distributions. Identification of the gaseous and vaporous cavitation regimes. The presence of vapor inside the cavitation regions is depicted by its mass fraction iso-lines.

## References

- [1] C. Soteriou, R. Andrews, and M. Smith, “Direct injection Diesel Sprays and the Effect of Cavitation and Hydraulic flip on Atomization,” *SAE Technical Paper 950080*, vol. 950080, 1995.
- [2] M. Blessing, G. König, C. Krüger, U. Michels, and V. Schwarz, “Analysis of flow and cavitation phenomena in diesel injection Nozzles and its effects on spray and mixture formation,” *SAE Technical Paper 2003-01-1358*, vol. 2003-01-1358, 2003.
- [3] A. Andriotis and M. Gavaises, “influence of vortex flow and cavitation on near-nozzle diesel spray dispersion angle,” *ATOMIZATION AND SPRAYS*, vol. 19, no. 3, pp. 247–261, 2009.
- [4] N. Dumont, O. Simonin, and C. Habchi, “Cavitating flow in Diesel injectors and atomization : a bibliographical review,” in *8th International ICLASS, Pasadena, California, USA*, 2000, pp. 314–323.
- [5] J. B. Moreau and C. Habchi, “A numerical study of cavitation influence on diesel jet atomisation,” in *Proceedings of ILASS-EUROPE, Nottingham, 6-8 September*, no. P27, 2004.
- [6] C. Habchi. (2006, Juin) Modélisation Tridimensionnelle de l’injection et de la préparation du mélange gaz/carburant dans les moteurs à combustion interne. Personal Communication. France. [Online]. Available: [https://www.researchgate.net/profile/Chawki\\_Habchi/](https://www.researchgate.net/profile/Chawki_Habchi/)
- [7] C. Habchi, N. Dumont, and O. Simonin, “Multidimensional Simulation of Cavitating Flows in Diesel Injectors by a Homogeneous Mixture Modeling Approach,” *Atomization and Sprays*, vol. 18, no. 2, pp. 129–162, 2008.
- [8] E. Giannadakis, M. Gavaises, and C. Arcoumanis, “Modelling of cavitation in diesel injector nozzles,” *JOURNAL OF FLUID MECHANICS*, vol. 616, pp. 153–193, DEC 10 2008.
- [9] A. B. Wood, *A textbook of sound*. G. Bell and Sons Ltd., London, 1930.
- [10] P. F. Dunn, F. O. Thomas, M. P. Davis, and I. E. Dorofeeva, “Experimental characterization of aviation-fuel cavitation,” *PHYSICS OF FLUIDS*, vol. 22, no. 11, NOV 2010.
- [11] J. Blaisot, J. Daridon, C. Garsiand, P. Gastaldi, J. Grolier, S. Honnet, B. Loyer, P. Manuelli, L. Mèès, I. Mokbel, B. Réveillè, R. Saliba, and M. Zellat, in *Proceedings of the SLA, INSA Rouen, France, June 5-6*, 2012.
- [12] R. Lebas, T. Menard, P. Beau, A. Berlemont, and F. Demoulin, “Numerical simulation of primary break-up and atomization: DNS and modelling study,” *International Journal of Multiphase Flow*, vol. 35, no. 3, pp. 247 – 260, 2009.
- [13] M. Herrmann, “A parallel Eulerian interface tracking/Lagrangian point particle multi-scale coupling procedure,” *Journal of Computational Physics*, vol. 229, no. 3, pp. 745 – 759, 2010.
- [14] M. Baer, M. R. and J. Nunziato, “A 2-phase mixture theory for the deflagration-to-detonation transition (DDT) in reactive antigranulocytes-materials,” *International Journal of Multiphase Flow*, vol. 12, no. 6, pp. 861–889, NOV-DEC 1986.
- [15] R. Saurel, F. Petitpas, and R. Abgrall, “Modelling phase transition in metastable liquids: application to cavitating and flashing flows,” *JOURNAL OF FLUID MECHANICS*, vol. 607, pp. 313–350, JUL 25 2008.
- [16] B. Mandumpala Devassy, “Atomization Modeling of Liquid Jets using an Eulerian-Eulerian Model and a Surface Density Approach,” Ph.D. dissertation, Université Aix-Marseille/IFP Energies nouvelles, Technical report 62824, 2013.
- [17] R. Saurel and R. Abgrall, “A multiphase Godunov Method for Compressible multifluid and multiphase flow,” *Journal of Computational Physics*, vol. 150, pp. 425–467, 1999.
- [18] B. M. Devassy, C. Habchi, and E. Daniel, “A New Atomization Model for High Speed Liquid Jets using a Turbulent, Compressible, Two-Phase Flow Model and a Surface Density Approach,” in *Proceedings ILASS - Europe 2013, 25th European Conference on Liquid Atomization and Spray Systems, Chania, Greece, 1-4 September*, 2013.
- [19] R. REID, J. PRAUSNITZ, and B. POLING, *The properties of gases and liquids*, 4th ed. McGraw-Hill Inc., 1987.
- [20] R. Saurel and O. Le Métayer, “A multiphase model for compressible flows with interfaces, shocks, detonation waves and cavitation,” *Journal of Fluid Mechanics*, vol. 431, pp. 239–271, 2001.
- [21] A. Zein, M. Hantke, and G. Warnecke, “Modeling phase transition for compressible two-phase flows applied to metastable liquids,” *Journal of Computational Physics*, vol. 229, no. 8, pp. 2964 – 2998, 2010.
- [22] O. Le Métayer, J. Massono, and R. Saurel, “Elaborating equations of state of a liquid and its vapor for two-phase flow models,” *Journal of Computational Physics*, vol. 43, pp. 265–276, 2004.
- [23] A. Amsden, P. O’Rourke, and T. Butler, “A computer program for chemically reactive flows with sprays,” Los Alamos National Laboratory, Tech. Rep. LA–11560–MS, 1989.
- [24] A. Velghe, N. Gillet, and J. Bohbot, “A high efficiency parallel unstructured solver dedicated to internal combustion engine simulation,” *Computers & Fluids*, vol. 45, no. 1, pp. 116 – 121, 2011.

## Diesel Spray Breakup at Pressure

Zachary Falgout<sup>1</sup>, Mattias Rahm<sup>1</sup>, Zhenkan Wang<sup>1</sup>, Eugenio di Benito Sienes<sup>1</sup>, Mark Linne<sup>1</sup>,  
Megan Paciaroni<sup>2</sup>, Johan Hult<sup>3</sup> and Simon Matlok<sup>3</sup>

1: Applied Mechanics, Chalmers University, Sweden

2: Department of Engineering Technology, Metro State University of Denver, United States

3: MAN Diesel and Turbo, Denmark

### Abstract

Ballistic Imaging has been used to study the primary breakup region of a fuel spray produced by a full-size injector geometry similar to that found in heavy-duty marine diesel engines. The geometry was designed with a transparent nozzle to allow visualization of the interior orifice flow for correlation with primary break-up. The injection system was composed of a Scania XPI injector body with the transparent nozzle tip, a pneumatically-actuated valve outside the injector body for injection timing control, and a piston accumulator that supplied the injection pressure of approximately 110 bar using pressurized air. The injector was installed in a high-pressure/high-temperature flow rig, which allowed a back pressure of 10 bar to be used for the visualization experiments, which were all performed at room temperature. The momentum coefficient for the flow in both orifices across a range of cavitation numbers was measured with a spray impingement force measurement. The results of the momentum coefficient measurement reinforce the observation from the orifice flow visualizations that cavitation was present in both orifices. The spray's behaviour in the primary break-up region shows a marked transition with the end of orifice cavitation.

### Introduction

In 1997, a series of regulations limiting the air pollution from ship engines was added to the International Convention for the Prevention of Pollution from Ships (MARPOL). Annex VI sets target limits, known as Tier I, for ozone-depleting substances (ODS), volatile organic compounds (VOC), nitrogen oxides (NO<sub>x</sub>), and sulphur oxides (SO<sub>x</sub>). In 2008 Annex VI was revised and two new emissions limit targets were added, Tier II and III, which decreased the emissions limits for marine engines manufactured after 2010 and 2015, respectively. The deadline for newly manufactured ship engines to meet the emissions limits in Tier II has already passed, and Tier III will come into force in 2016. For NO<sub>x</sub> emissions, Tier III limits are 75-80% lower than Tier II limits, depending on the engine's rated speed. Also, starting this year, The first legally binding set of energy efficiency targets for ships, implemented as an Energy Efficiency Design Index (EEDI), has come into force. The manufacturers of heavy-duty marine engines are required to acknowledge and enforce the emissions and efficiency goals set by Annex VI for each engine model family they manufacture.

While SO<sub>x</sub> emissions can be limited by controlling the fuel quality usable by ships adhering to the regulations in MARPOL Annex VI, NO<sub>x</sub> emissions and efficiency are controlled by the characteristics of the combustion inside the engine. When it is impossible to meet NO<sub>x</sub> emissions requirements via engine tuning alone, exhaust after-treatment, exhaust gas recirculation (EGR), or some combination of both is often used to bridge the gap. In order to reduce engine-out pollutant emissions and the need for an exhaust after-treatment system or EGR, combustion in heavy-duty diesel engines used on ships needs to be well understood. In direct-injection diesel engines, emissions formation is dependent upon the fuel-air mixing, which is heavily dependent on the characteristics of the fuel spray (1, 2). The characteristics of any fuel spray are determined to a large extent by the flow inside the injector that produces the spray (3–7). There are still knowledge gaps in spray physics, one being the details of the liquid atomization occurring just after the exit of the injector orifice, known as primary break-up, under realistic operating conditions for a diesel engine, owing to the fact that the primary break-up region is very optically dense under these conditions. As a result, there have been few experimental observations in this region (8). While the primary breakup of non-cavitating turbulent liquid jets into still gases has been well characterized conceptually (9–13), hydrodynamic or geometric cavitation is often present in diesel engines, and the effect of this phenomenon on primary breakup has not been studied in detail in the primary breakup region itself, again due to the optical density of the spray formation region under these conditions.

Ballistic imaging provides unique access to the spray formation region (14–16). By taking advantage of the nature of the interaction between diesel droplets and light, ballistic imaging is able to separate light that has been scattered many times by the droplet cloud surrounding the primary break-up region from light that has been scattered only very few times or not at all. The latter provides optical access to the large liquid structures in the spray formation region, such as large ligaments, primary droplets, and liquid core. This diagnostic is still under

development, but it has been developed to the point where investigations of realistic diesel fuel sprays are possible (14).

A unique challenge in studying the fuel sprays in heavy-duty diesel marine engines is the size and cost of a test engine. The largest engines manufactured by MAN Diesel and Turbo can produce 85 MW and stand 15 m high. MAN Diesel and Turbo has a 4-cylinder mid-size test engine with a bore of 0.5 m in Copenhagen, Denmark. Unfortunately, mechanical vibrations of the engine make performing advanced laser diagnostics on spray physics and combustion in-situ difficult.

In order to better understand the primary break-up of sprays in heavy-duty diesel engines, a specialized injector with a transparent nozzle geometry resembling that found in these engines has been studied in a high-pressure flow rig at Chalmers. Cavitation has been found in similar geometries in previous studies, both experimental and computational (17, 18). The interior flow of the nozzle has been captured with front-light illumination imaging, and ballistic imaging has been used to capture the primary breakup region of the fuel spray produced by this geometry. The injection pressure and back pressure were scaled to produce a cavitation number for the interior nozzle flow relevant to real engine operation, since the transparent optical tip could not withstand the real injection pressure. The orifice flow visualizations have been correlated with the ballistic images in an effort to better understand the influence of cavitation on primary breakup of this fuel spray.

### Experimental test-rig

The heavy-duty diesel injectors in MAN engines are markedly different from the injectors found in diesel engines for road vehicles. These are two-stroke marine engines, and the center of the cylinder ceiling is occupied by a large exhaust valve. The injector, therefore cannot be mounted in the center of the cylinder as it commonly is in four-stroke road vehicle engines. The locations of the injector orifices are not cylindrically symmetric to avoid cylinder wall wetting, and the orifices often have a wide separation angle from the central axis of the injector body to avoid piston wetting. The spray plumes from these injectors are targeted in the direction of the swirling air flow inside the cylinder to maximize air utilization. The geometry investigated in this study is also different from most diesel injectors in the manner it controls flow to the orifices. Instead of a needle valve, this geometry has a cylindrical “cut-off shaft” that covers the entrance of the orifices to stop injection. Another interesting feature of this geometry is that the fuel flows through the center of this shaft, and during transient operation the fuel must flow around the bottom edge of the shaft before it reaches the orifice holes. The transparent geometry used in this study, shown in Figure 1, is a simplified version of the real injector geometry with only two orifices and a cut-off shaft fixed at maximum lift. The orifices are positioned so that there is no overlap when viewed from the side. Orifice 1 in Figure 1 is 780  $\mu\text{m}$  in diameter and is separated from the injector axis by 78°. Orifice 2 is 750  $\mu\text{m}$  in diameter and is 58° from the injector axis.

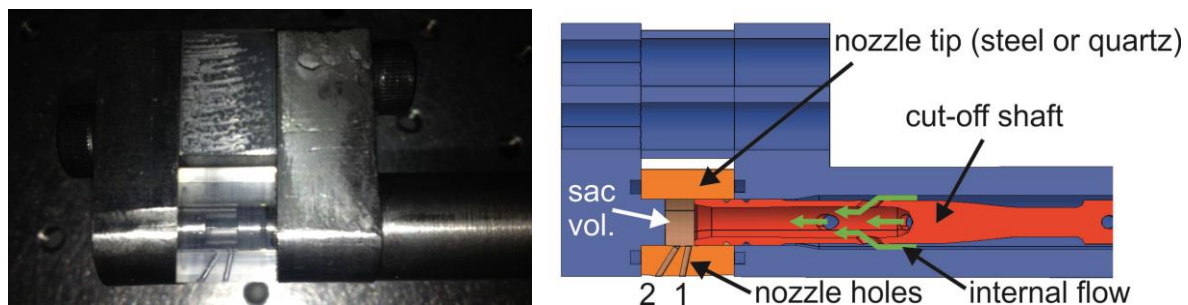


**Figure 1:** Picture(*left*) and solid model(*right*) of the transparent injector geometry.

A large hydraulic actuator controls injection by changing the lift of the stop shaft in the real engine, which would be difficult to mount in the vessel at Chalmers. Instead, a solenoid air valve is used to control a high-pressure piston valve that directly controls the supply of pressurized diesel fuel to the injector, and the stop shaft geometry in this injector remains fixed in position. The injection command duration was 250ms. If the injection duration were any longer, the large spray produced by this injector would begin to rebound off of bottom of the vessel interior and wet the vessel windows, even with a specially-designed spray diffuser placed in the bottom of the vessel. An early prototype of the injector can be seen mounted in the vessel with the spray diffuser beneath it in Figure 2. Since the flow rate of fuel through this injector is significantly larger than most reciprocating high-pressure piston pumps can handle, a piston accumulator with an internal volume of 6 liters was used to transfer pressure from compressed air to the injection system. The injection pressure outside the injector was 110 bar, limited by the strength of the transparent quartz nozzle tip.





**Figure 2:** Early prototype of experimental injector mounted in high pressure/high temperature vessel.

In the real engine, the injection pressure is approximately 800 bar, and so in order to achieve similarity between the engine injector flow and this experimental injector flow, the orifice flow cavitation number was matched by lowering the back pressure at the orifice exit relative to real engine operating conditions. All measurements were performed at room temperature, and the maximum back pressure used in this study was 20 bar. Due to the complex internal flow of this injector, there was a significant head loss from the accumulator to the sac volume, and the “real” injection pressure in the sac volume was measured during impingement force measurements to be approximately 80 bar.

For ballistic imaging, a mode-locked Ti-Sapphire laser (Spectra-Physics MaiTai) in series with a chirped-pulse regenerative amplifier (Spectra-Physics) was used to provide 130-150 fs, 4 mJ pulses at 1 kHz at 800 nm wavelength. An optical Kerr-effect (OKE) time gate was used as an ultra-fast shutter (gating time of approximately 1.8 ps) to allow only ballistic or quasi-ballistic photons to compose the final image (14). The heart of the OKE time gate is a chemical cell filled with CS<sub>2</sub>, which turns birefringent when exposed to a switching beam that is split from the main beam. When combined with crossed polarizers, this chemical cell forms a simple yet ultra-fast shutter. A retro-reflector on a translation stage is used to adjust the time alignment between the switching and imaging beams as they pass through the chemical cell, since the imaging beam passes through the vessel and the switching beam does not. A CCD camera is used to capture the ballistic image carried by the imaging beam. A schematic of this set up is shown in Figure 3.

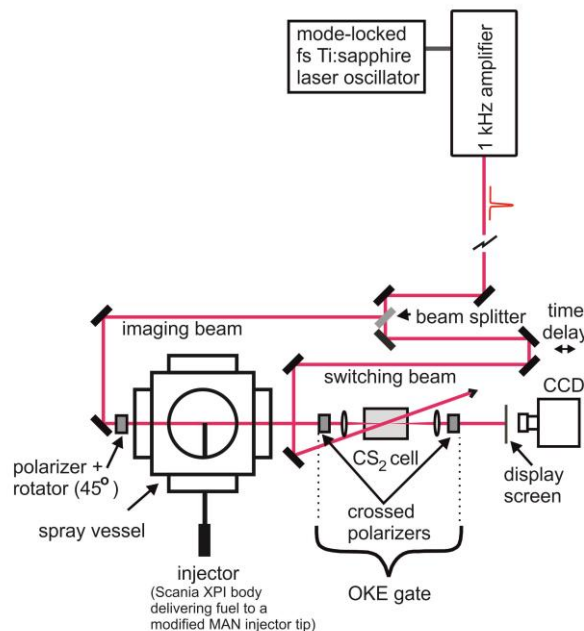


**Figure 3:** Ballistic Imaging setup on the high-pressure/high-temperature vessel.



The impingement force of each spray from the experimental injector was measured with a piezo-electric force transducer (Kistler 9215) in order to calculate the momentum coefficient of the orifice flow in support of the orifice flow visualizations. The momentum coefficient was measured with the same injection pressure as the visualization experiments, but at varied back pressures to cover a range of cavitation numbers. The cavitation number was calculated using Nurick's definition, shown in Equation 1(19). The back pressure was varied between 7 and 20 bar, resulting in a  $C_N$  range of roughly 1.07 to 1.32. There were 5 back pressure targets, with 50 measurements at each.

$$C_N = \frac{(P_{inj} - P_v)}{(P_{inj} - P_b)} \quad [1]$$

The injection pressure in the sac volume was also measured during the impingement force measurements using a piezo-resistive pressure transducer mounted in a special injector end with a pressure tap. The momentum coefficient is formulated from the maximum momentum flux through the orifice predicted by Bernoulli's equation and the impingement force measurement using Equation 2(20). For each injection, the momentum coefficient was calculated using the average impingement force and injection pressure measured between the start and end of injection, which were determined by detecting the sharp rise and fall in the data that correspond to the beginning and end of injection.

$$C_m = \frac{F_{imp}}{2 * A_o * (P_{inj} - P_b)} \quad [2]$$

## Results and Discussion

Since the steady injection period was approximately 280 ms, and the camera was able to capture one image roughly every 35 ms, 8 ballistic images were taken during each injection. During the steady period, the spray formed a thick cone of what the authors believe to be large primary ligaments or droplets, the images of which stack along the optical axis, and therefore not even ballistic imaging can probe inside. This cannot be a cloud of small droplets because some light would still pass through a droplet cloud, which is the light used to compose the image in ballistic imaging. The outer edge of this superposition of large liquid structures was still resolved. This seems to indicate that the diesel spray is no longer breaking up like turbulent liquid jets or diesel sprays in past experiments, with ligaments and primary droplets shedding from an intact liquid core. When cavitation exists in the orifice, it seems as if the bulk liquid flow disintegrates completely into large primary droplets as soon as the fuel leaves the injector orifice. This is similar to the break-up behaviour seen in past ballistic imaging studies of effervescent sprays with high gas-to-liquid ratios (21). As the sac volume pressure dropped at the end of injection, the orifice flow visualizations showed a decrease in cavitation, and the ballistic images began to resemble those taken in past studies of a non-cavitating diesel spray (14). A representative ballistic image of both break-up regimes is shown in Figure 4. There is still room for improvement in these measurements, and additional studies will be conducted on the same spray in the near future.

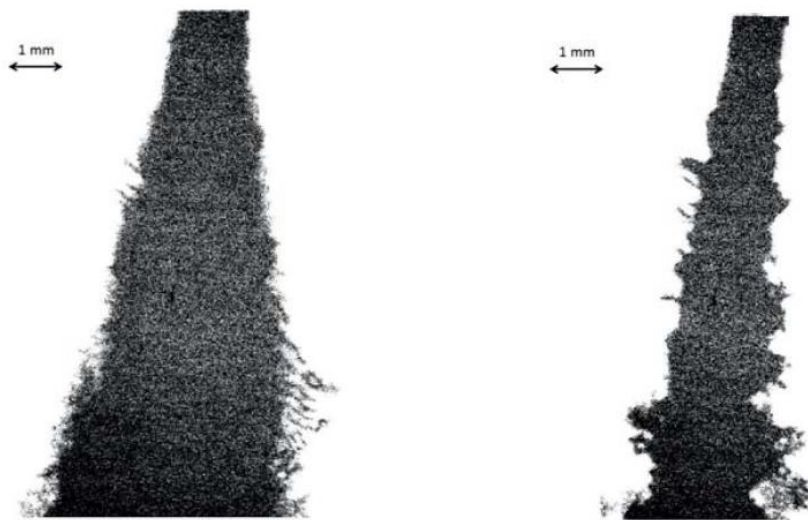


**Figure 4:** Ballistic images of the fuel spray from orifice 2 during the steady(left, 135 ms aSOI) and final transient(right, 337 ms aSOI) periods of injection.

The initial injection period is dominated by a large oscillation in injection pressure. The 50 injection pressure measurements taken at 20 bar back pressure are shown in Figure 5, where the pressure oscillation can be seen clearly. This phenomenon is likely due to the fact that the injection control valve is outside of the injector body, and the liquid fuel therefore has a long distance to build up momentum before it reaches the sac volume after the start of injection. When the fuel hits the sac volume and decelerates, this momentum is converted into static pressure, and this pressure wave travels up and down the injection system and is eventually dissipated. It is very likely that these observed oscillations are physical because several of the first quartz optical nozzles cracked, which was predicted by an FEA analysis to happen near the highest injection pressure reached during these oscillations. These oscillations also appeared in the impingement force measurements. This phenomenon appeared in the injection pressure signal of every injection; however, it did not affect the steady average of injection pressure used in calculations of the momentum coefficient.

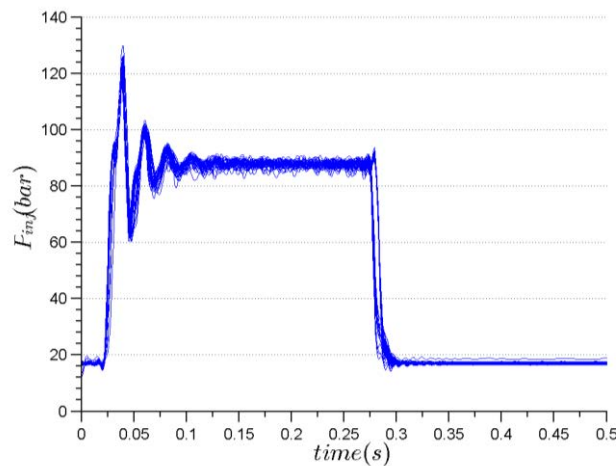


**Figure 5:** Sac volume pressure traces for  $P_b = 20$  bar.

When orifice flow is cavitating, the momentum coefficient measured at the orifice exit has been found to remain constant or increase slightly as the cavitation number increases (20). All momentum coefficient measurements are shown for both orifices in Figure 6. The measurements for each orifice are in 5 clusters centered roughly at the cavitation number targets for the measurement. There is some drift in cavitation number among measurements at the same back pressure due to the imprecision of the manual pressure regulator on the compressed air bottle used to supply pressure to the high-pressure accumulator. As a result, there were additional measurements that covered the range of cavitation numbers more evenly. The momentum coefficient is roughly steady or rises slowly with cavitation number for both orifices, indicating that the flow in both orifices was cavitating. This reinforces the observations from the orifice flow visualizations. The momentum coefficient for orifice 2 is significantly higher than that of orifice 1. This can be explained by the fact that the angle between the mean flow inside the injector and orifice 2 is 20 degrees lower than for orifice 1.

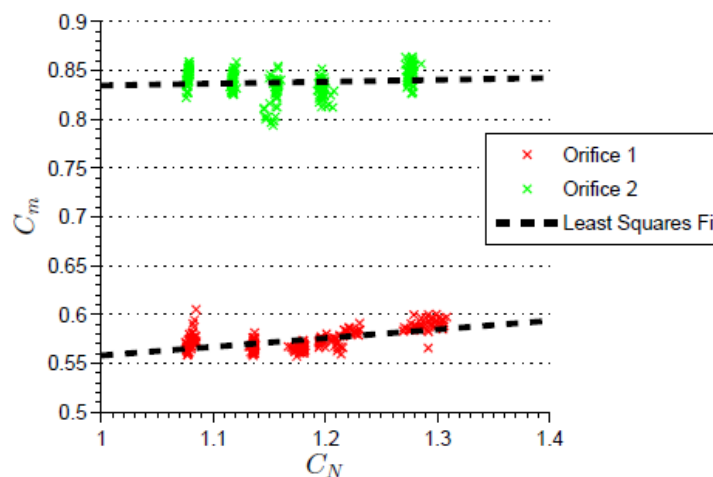


**Figure 6:** Results of the impingement force measurements for both orifices of the experimental injector.

## Conclusions

The results of this study indicate that primary break-up of fuel sprays is affected by the presence of cavitation in the nozzle orifice. For this case, the presence of cavitation seems to cause primary break-up similar to that of effervescent sprays with high gas-to-liquid ratios, where the authors believe the spray is breaking up so aggressively that the liquid core no longer exists outside the injector body. Once cavitation ceases, the spray breaks up according to previous studies of a diesel spray. These results are preliminary, and additional studies in the near future will provide additional insight into the observations made here.

## Acknowledgements

The authors would like to acknowledge the technical staff that assisted in the conduction and preparation of these experiments. Among them, Eugenio di Benito Sienes' contributions and dedication were exceptional. The research leading to these results has received funding from the European Union Seventh Framework Programme (FP7/2007-2011) under grant agreement no.284354. The ballistic imaging system was funded by the Swedish Research Council and the Swedish Energy Agency.

## References

- [1] J. E. Dec, A Conceptual Model of DI Diesel Combustion Based on Laser-Sheet Imaging, *Combustion*.
- [2] M. Arai, Physics behind Diesel Sprays, *ICLASS*, 1–18 (2012).
- [3] S. Som, A. I. Ramirez, D. E. Longman, S. K. Aggarwal, Effect of nozzle orifice geometry on spray, combustion, and emission characteristics under diesel engine conditions, *Fuel* **90**, 1267–1276 (2011).
- [4] J. Desantes, R. Payri, F. Salvador, J. D. la Morena, Influence of cavitation phenomenon on primary break-up and spray behavior at stationary conditions, *Fuel* (2010) (available at <http://www.sciencedirect.com/science/article/pii/S0016236110002863>).
- [5] C. Baumgarten, *Mixture formation in internal combustion engines* (2006; [http://203.158.253.140/media/e-Book/Engineer/Automotive/Mixture Formation in Internal Combustion Engine.pdf](http://203.158.253.140/media/e-Book/Engineer/Automotive/Mixture%20Formation%20in%20Internal%20Combustion%20Engine.pdf)).
- [6] R. D. Reitz, Mechanism of atomization of a liquid jet, *Physics of Fluids* **25**, 1730 (1982).
- [7] C. Arcoumanis, M. Gavaises, Linking nozzle flow with spray characteristics in a diesel fuel injection system, *Atomization and Sprays* (1998) (available at <http://www.theric.org/research/tech/periodicals/view.php?seq=24980>).
- [8] A. Coghe, G. Cossali, Quantitative optical techniques for dense sprays investigation: A survey, *Optics and Lasers in Engineering* (2012) (available at <http://www.sciencedirect.com/science/article/pii/S0143816611002351>).
- [9] K. Sallam, Z. Dai, G. Faeth, Liquid breakup at the surface of turbulent round liquid jets in still gases, *International journal of multiphase flow* (2002) (available at <http://www.sciencedirect.com/science/article/pii/S0301932201000672>).
- [10] G. Faeth, S. L. Bernal, G. Ruff, Structure of the near-injector region of nonevaporating pressure-atomized sprays, *Journal of Propulsion and ...* (1991) (available at <http://dspace.imech.ac.cn/hf/handle/3110071/10209>).
- [11] G. Faeth, L. Hsiang, P. Wu, Structure and breakup properties of sprays, *International Journal of Multiphase Flow* (1995) (available at <http://www.sciencedirect.com/science/article/pii/0301932295000597>).
- [12] P.-K. Wu, G. M. Faeth, Onset and end of drop formation along the surface of turbulent liquid jets in still gases, *Physics of Fluids* **7**, 2915 (1995).
- [13] S. P. Lin, R. D. Reitz, Drop and Spray Formation From a Liquid Jet, *Annual Review of Fluid Mechanics* **30**, 85–105 (1998).
- [14] M. Linne, M. Paciaroni, T. Hall, T. Parker, Ballistic imaging of the near field in a diesel spray, *Experiments in Fluids* **40**, 836–846 (2006).
- [15] M. a. Linne, M. Paciaroni, E. Berrocal, D. Sedarsky, Ballistic imaging of liquid breakup processes in dense sprays, *Proceedings of the Combustion Institute* **32**, 2147–2161 (2009).
- [16] M. Paciaroni, M. Linne, Single-shot, two-dimensional ballistic imaging through scattering media, *Applied optics* (2004) (available at <http://www.opticsinfobase.org/abstract.cfm?id=81110>).
- [17] a. Andriotis, M. Gavaises, C. Arcoumanis, Vortex flow and cavitation in diesel injector nozzles, *Journal of Fluid Mechanics* **610**, 195–215 (2008).

- [18] B. Dam, S. Sorenson, K. Meyer, S. Mayer, Experimental and numerical investigation of sprays in two stroke diesel Engines, (2007) (available at <http://forskningsbasen.deff.dk/Share.external?sp=S351aeb6a-c5e1-459d-98c3-ac7c00718b68&sp=Sdtu>).
- [19] W. Nurick, Orifice cavitation and its effect on spray mixing, *ASME Transactions Journal of Fluids Engineering* (1976) (available at <http://adsabs.harvard.edu/abs/1976ATJFE..98..681N>).
- [20] R. Payri, J. Garcia, F. Salvador, J. Gimeno, Using spray momentum flux measurements to understand the influence of diesel nozzle geometry on spray characteristics, *Fuel* **84**, 551–561 (2005).
- [21] M. Linne, D. Sedarsky, T. Meyer, J. Gord, C. Carter, Ballistic imaging in the near-field of an effervescent spray, *Experiments in Fluids* **49**, 911–923 (2010).

## Image-Based Analysis of Evaporating Diesel Sprays in the Near-Nozzle Region

C. Crua<sup>1</sup>, G. de Sercey<sup>1</sup>, M. Gold<sup>2</sup>, M. R. Heikal<sup>1</sup>

1: Centre for Automotive Engineering, University of Brighton, UK

2: BP Formulated Products Technology, Pangbourne, UK

### Abstract

Detailed measurements of near-nozzle spray formation is essential to better understand and predict the processes involved in diesel fuel atomisation. We previously showed that direct imaging with sub-micron resolution could yield droplet size measurements in the near-nozzle region under non-evaporative conditions, without an arbitrary requirement for droplet sphericity. We now report on progress made with ongoing experimental investigations at elevated pressure and temperature conditions. We conducted tests on a reciprocating rapid compression machine to produce high-resolution panoramas of the liquid spray interface, compared them with high-speed video frames, and measured droplet sizes at key locations. We also studied the size and shape of liquid structures formed during the end of injection, which were found to be significantly larger and slower than those recorded during injection.

### Introduction

Microscopic imaging experiments of diesel sprays have been reported in the literature (e.g. [1-6]), although with varying degrees in the quality of the images produced. Due to recent technological developments, microscopic imaging is now able to provide new information on the liquid and gaseous structures in the near-nozzle region of diesel sprays at elevated pressure and temperature conditions [7-9]. We recently showed that shadowgraphic micrographs could yield droplet size measurements in the near-nozzle region under non-evaporative conditions [10], without an arbitrary requirement for droplet sphericity, but challenges remain to apply this diagnostic to droplet sizing in high pressure and temperature environments. Potential sources of image degradation include motion blurring of fast-moving droplets, the relative motion between the optical chamber and the microscope, as well as the presence of density gradients within the in-cylinder gas, which will result in refractive index fluctuations. Such refractive index gradients have a detrimental effect on both the quality of the back-illumination, and the capability of the optical system to form a focused image of the liquid spray. At the same time, the droplet/gas interface is expected to become distinctly less clear as the droplets evaporate and approach supercritical conditions. Hence, whilst direct imaging has potential for resolving both spherical and arbitrary-shaped droplets in the near-nozzle region of diesel sprays, challenges remain to accurately measure microscopic droplets at evaporating conditions. In this publication we report on progress made with ongoing experimental investigations of the atomisation of diesel fuel at elevated pressure and temperature conditions. We conducted tests on a reciprocating rapid compression machine using high-resolution microscopic imaging and macroscopic high-speed video. We used microscopy to track the periphery of the dense spray and build a panoramic view of the spray interface from the nozzle orifice to 27 mm. We compared the liquid structures with the high-speed video, and measured droplet sizes and velocities at key locations. We then studied the end of injection, and report on the size, velocity and shape of liquid structures observed at the orifice outlet.

### Experimental test-rig

The experiment was conducted on a reciprocating rapid compression machine (RCM) based around a Ricardo Proteus single cylinder engine converted to liner ported, 2 stroke cycle operation. The fuel was delivered by a Delphi common-rail system, comprising a DFP-3 high-pressure pump rated at 200 MPa, and a seven-hole DFI-1.3 injector with a VCO type nozzle. The nozzle's orifices were cylindrical with a diameter of 135  $\mu\text{m}$  and a length/diameter ratio of 8. The nozzle had an equivalent cone angle of 154°, and the injector was mounted orthogonal relative to the cameras. The duration of the injection trigger pulse was constant at 700  $\mu\text{s}$ . A detailed description of the test rig is covered by Crua [11].

The fuel used for all results presented in this paper was an ultra-low sulphur fossil diesel fuel, which contained no bio components. Its physical properties are listed in Table 1..

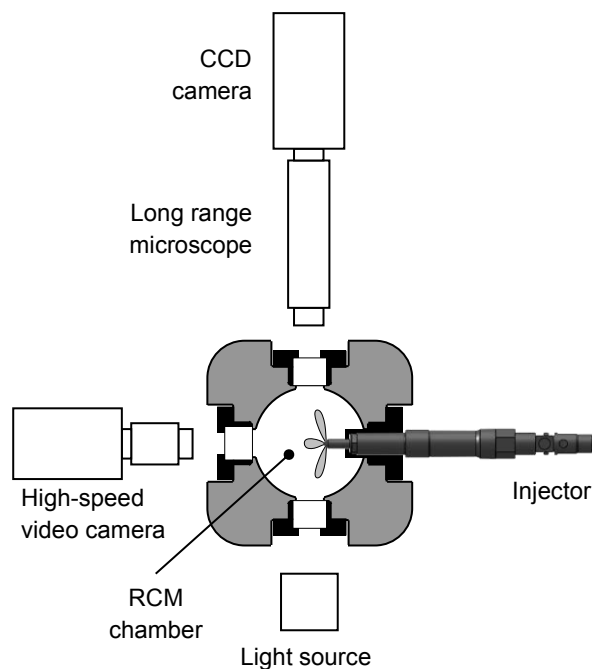
Property	Diesel
Density at 15°C ( $\text{kg.m}^{-3}$ )	837
Kinematic viscosity ( $\text{mm}^2.\text{s}^{-1}$ )	3.3
Surface tension ( $\text{dyn.cm}^{-1}$ )	29.8

Table 1. Physical properties of the fuel tested

The optical setup was covered in detail by the authors in [7], hence only the main features are included here. The light source was a frequency-doubled Nd:YAG laser, with a pulse duration of 7 ns. The light pulse was spectrally diffused and spatially expanded from 8 mm to 100 mm to provide homogeneous illumination over a sufficiently large area. A high performance dual-frame camera with a Peltier-cooled 12 bit CCD sensor was fitted with a long range microscope. The optical setup was adjusted to optimise both the spatial resolution and the viewing region. This was achieved with a magnification factor of 9.6 at the CCD sensor plane, giving a spatial scale factor of  $0.671 \mu\text{m}$  per pixel and a viewing region of  $923 \times 697 \mu\text{m}$ . The spatial resolution of the optical system was then measured as  $1.27 \mu\text{m}$  for a 3% contrast level. The main experimental conditions for the images presented in this paper are listed in Table 2. The use of a double-pulsed light source combined with a dual-frame camera and an interframe time of 500 ns allowed capturing the velocity of the fuel, as well as the droplet size distribution.

<b>Table 2.</b> Experimental conditions for the microscopic imaging experiments. Timings are relative to start of injection (SOI) trigger.	Injection pressures	40 MPa
	Nozzle orifice diameter	135 $\mu\text{m}$
	Gas pressure	3.2 MPa
	Gas temperature	700 K
	Axial distance from nozzle	0 to 27 mm
	Radial distance from axis	0 to 2 mm
	Acquisition timing	1 ms after SOI
	Image size	1376x1040 pixels
	Field of view	$923 \times 697 \mu\text{m}$
	Spatial scale factor	$0.671 \mu\text{m}/\text{pixel}$
	Spatial resolution (3% contrast)	$1.27 \mu\text{m}$

In order to obtain information on the overall structure of the sprays, a Phantom v12.1 high speed camera was used to record the macroscopic evolution of the complete spray. The camera was operated at 41,667 fps with a frame resolution of  $256 \times 512$  pixels and a spatial scale factor of  $83 \mu\text{m}$  per pixel. In order to avoid motion blur, a copper vapour laser with a 25 ns pulse duration was used to illuminate the sprays at the same frequency as the high-speed camera. The optical setups for microscopy and high-speed video are shown in Figure 1.



**Figure 1.** Optical setup for microscopic imaging and macroscopic high-speed video. For the high-speed video experiment the light source was a copper vapour laser pulsing at a frequency of 41,667 Hz.

## Results and Discussion

### *Spray interface*

Figure 3 shows a comparison of the shadowgraphs with a high speed video frame taken at the same timing of 1 ms after the start of injection. At this timing the spray is well developed and the fuel delivery rate is steady. Figure 2 shows the mean penetration versus time for a set of 101 individual videos. Figure 3a consists of a panorama of 54 full resolution shadowgraphs tracking the spray interface. Since the maximum repetition rate of the CCD camera is 8 Hz, the images composing this panorama are taken from different sprays. The images marked a1, a2, a3 and a4 are magnified images from the panorama, at position 1, 2, 3 and 4 respectively. Figure 3b shows a high speed video frame from a different cycle, with the position of the panorama outlined. Whilst the video frame captures the overall structure of a single spray, microscopic details are inevitably beyond the spatial resolution of the instrument. In contrast, long-range microscopy can give detailed information about a portion of the spray but at the expense of an understanding of what lies beyond that small region.

Shadowgraphy is sensitive to density gradients, which can be caused by temperature gradients in the gas phase or changes in fuel concentration in the air-fuel mixture. This sensitivity to gas temperature gradients contributes to the distortion of the optical path and often results in defocused shadowgraphs [10]. However, when the images are in focus, this sensitivity allows the capture of the air-fuel mixing (Figure 3a3). It is also possible to observe trails in the wake of some droplets (Figure 3a4; Figure 4), although it is not possible to establish whether they are caused by fuel vapour gradients or temperature gradients.

Near the nozzle (Figure 3a1, 900  $\mu\text{m}$  from the nozzle) and up to 10 mm away, the spray is optically dense with a well-defined interface between ambient gas and liquid spray. Droplets can be seen on the periphery of the dense region, with diameters of the order of 3  $\mu\text{m}$ . Cycle-to-cycle variations in the general appearance of this near-nozzle region are relatively small.

For the first 10 mm of the spray the liquid interface has a markedly conical shape with few signs of vaporised fuel. The boundary of the liquid spray can be tracked without difficulty as it is contained within the width of one or two frames. Beyond 10 mm from the orifice the liquid interface becomes progressively more difficult to identify as cycle-to-cycle variations become larger than the width of a frame. This is expected to be due to small scale recirculation zones caused by air entrainment. Density gradients in the gas phase start to appear, in agreement with the expectation that entrainment of hot gas into the spray promotes evaporation.

Beyond 20 mm from the orifice, the spray becomes dispersed as large clusters of droplets detach ahead of the main liquid jet. Strong density gradients are visible in the gas phase (Figure 3a3; Figure 3a4) most likely due to turbulent mixing of vaporised fuel. As a result the cycle-to-cycle variation of the number density of droplets is significant, with some images containing no liquid drops and others showing dispersed droplets. The droplets contained in these detached clusters can have relatively large diameters and less spherical shapes (Figure 4) than droplets found at the periphery of the near-nozzle region (e.g. Figure 3a1,a2). These clusters are composed of droplets with velocities of 30–40 m/s and diameters up to 20  $\mu\text{m}$  (Figure 4), which could be an indication of droplet coalescence and low relative velocities within the dense spray region.

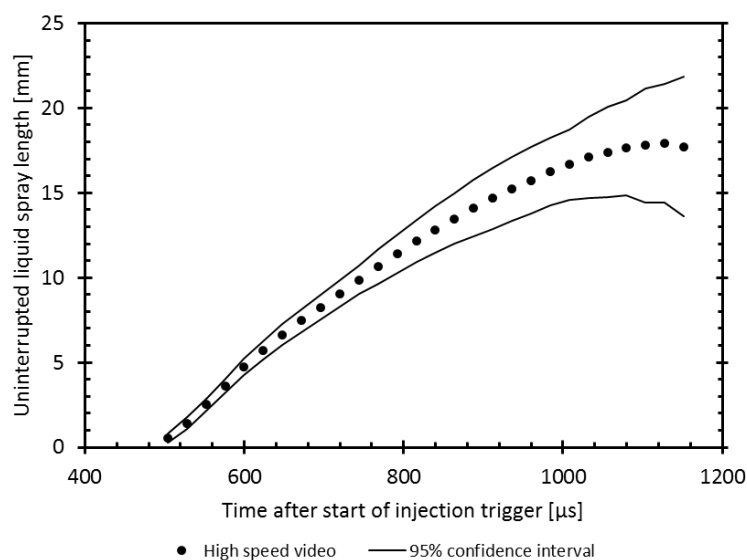


**Figure 2.** Uninterrupted liquid spray length versus time (mean of 101 videos) and 95% confidence interval ( $\pm 2$  standard deviations of the set).



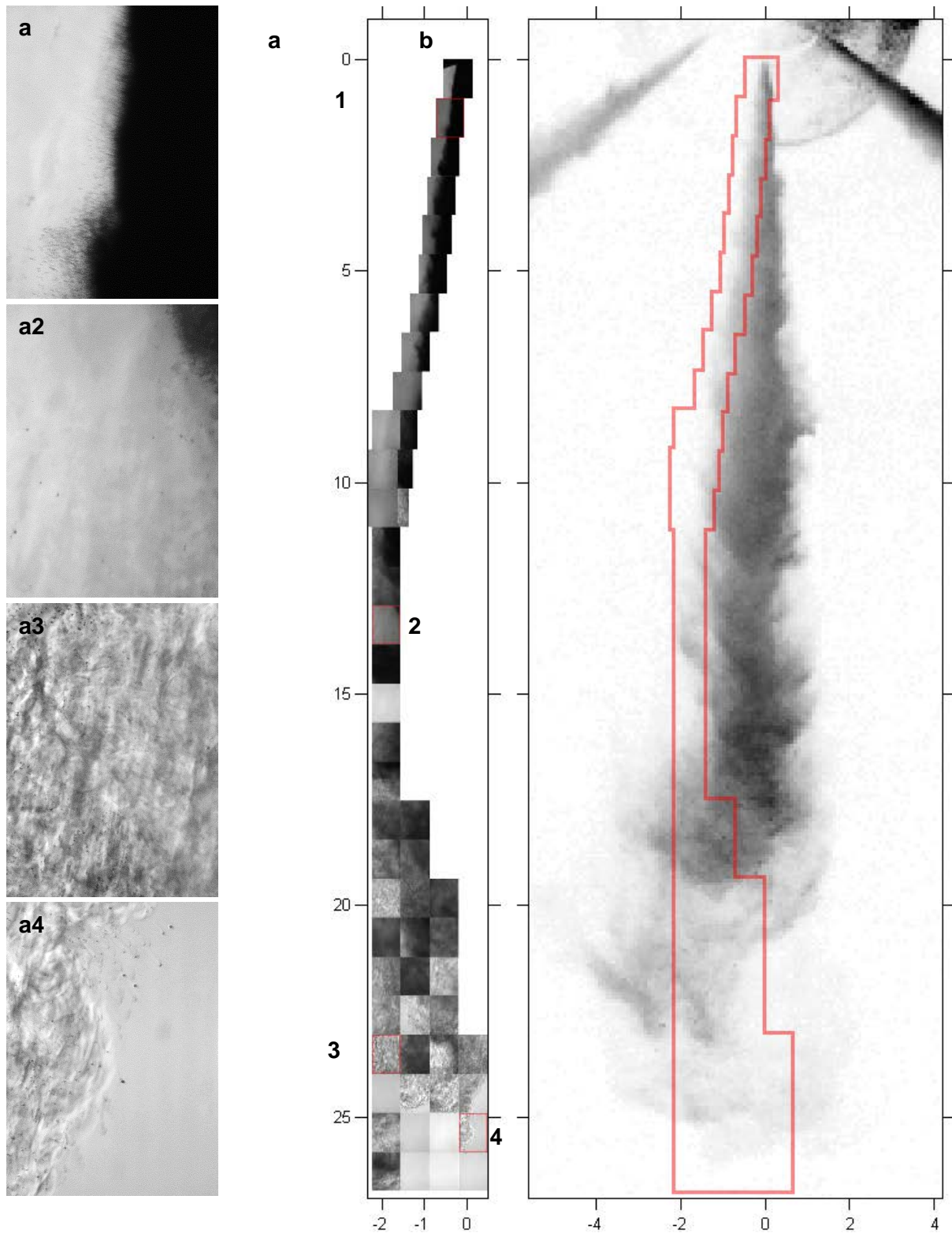


**Figure 3.** (a) Panorama composed of 54 microscopic shadowgraphs tracking the spray interface. (b) Frame from a high-speed video (intensities inverted for clarity) recorded 1ms after SOI. Scales are in mm from nozzle exit.

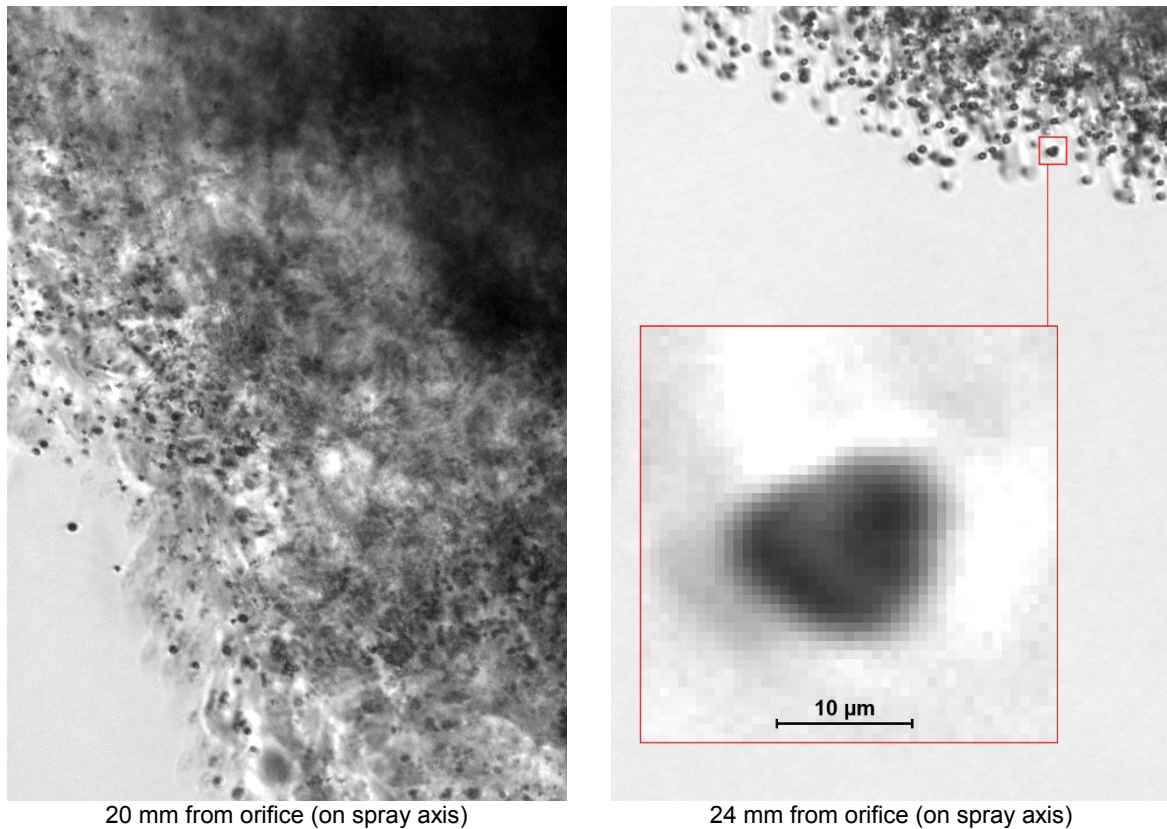


**Figure 4.** Examples of shadowgraphic micrographs recorded for non-additised fossil diesel fuel injected at 40 MPa into gas at 3.2 MPa pressure and 700 K bulk temperature.

### ***End of injection***

In order to characterise the end of injection we recorded shadowgraphs at the nozzle exit from 1 ms to 2.15 ms after the start of injection trigger, with 50  $\mu$ s time steps and 50 images recorded per time step. Due to the highly transient nature of the end of injection, it is particularly difficult to define quantitative criteria that can be used to support an objective description of the processes involved. Hence we conduct a descriptive analysis of the series of images captured over the end of injection phase.

As previously discussed, at 1 ms (Figure 5a) the spray is optically dense with little cycle-to-cycle variations in the position of the liquid interface. The droplets that are located at the periphery of the liquid jet have diameters smaller than 5  $\mu$ m and velocities between 15 and 30 m/s. As the nozzle closes (Figure 5b) the width of the spray increases in the near-nozzle region and droplet velocities drop to less than 10 m/s. As the fuel mass flow reduces, the spray seems to turn into a liquid sheet structure originating from the nozzle (Figure 5d,e). Within a short distance the sheet appears to break into ligaments with diameters between 10 and 25  $\mu$ m. Some dense regions larger than 100  $\mu$ m are also present along the spray axis, although it is not clear whether these contain ligaments, droplets or both. The ligaments that are clearly identifiable are surrounded by droplets with equivalent diameters up to 25  $\mu$ m. The velocities of liquid structures shown in Figure 5d,e are below 10 m/s, with many being below the lower limit of our system (2.6 m/s). At this transient stage the cycle-to-cycle variation naturally increases but the majority of images appear similar to Figure 5d with some resembling Figure 5f. At 1.5 ms after SOI large deformed ligaments appear (Figure 5f) with widths of 20 to 50  $\mu$ m and length of more than 600  $\mu$ m. In agreement with other studies [9], these liquid structures are much larger than those found during the steady state part of injection. The ligament in that figure appears to be undergoing breakup into relatively large droplets. Again, velocities are low, suggesting that some of these droplets may re-coalesce into larger ones. This could contribute to the formation of large droplets that were observed 2 ms after the start of injection (Figure 5h), some big droplets are sometimes visible. The presence of such large liquid structures when combustion would normally occur may have an effect on emissions, and warrants further investigations into the processes involved.

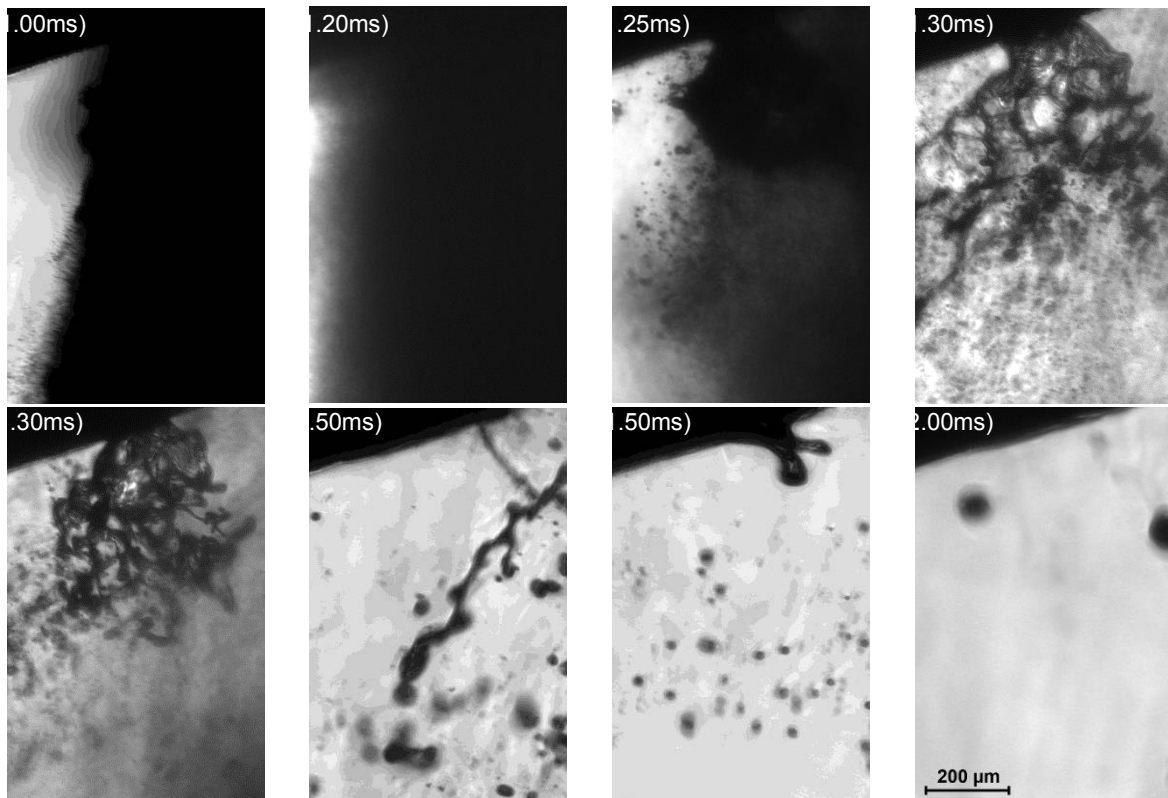


**Figure 5.** Evolution of the end of injection, timings relative to SOI trigger.

## Conclusions

We conducted tests on a reciprocating rapid compression machine using high-resolution microscopic imaging and macroscopic high-speed video. We used microscopy to track the periphery of the dense spray and build a panoramic view of the spray interface from the nozzle orifice to 27 mm. We compared the liquid structures with the high-speed video, and measured droplet sizes and velocities at key locations.

Beyond 20 mm from the orifice, the spray was relatively dispersed as large clusters of droplets detach ahead of the main liquid jet. Strong density gradients were visible in the gas phase, most likely due to turbulent mixing of vaporised fuel. The droplets contained in these detached clusters were found to have diameters up to 20  $\mu\text{m}$ , velocities in the region of 30-40 m/s, and some droplets had non-spherical shapes. These could be an indication of droplet coalescence and low relative velocities within the dense spray region.

We studied the end of injection and observed significantly larger and slower liquid structures than those recorded during injection. The volume of liquid contained in these large deformed structures, at a time when combustion would normally occur, could have a non-negligible effect on emissions which warrants further investigations into the processes involved.

## Acknowledgements

This work received financial and technical supported from BP International Ltd; and financial support from the European Regional Development Fund [INTERREG IVa project 'E3C3', grant number 4274].

## References

- [1] Heimgärtner, C. and A. Leipertz, *Investigation of Primary Diesel Spray Breakup Close to the Nozzle of a Common Rail High Pressure Injection System*, in *8th ICLASS*. 2000: Pasadena, USA. p. 1235-1241.
- [2] Bae, C., et al., *Effect on nozzle geometry on the common-rail diesel spray*. SAE 2002-01-1625, 2002.
- [3] Badock, C., et al., *Investigation of Cavitation in Real Size Diesel Injection Nozzles*. International Journal of Heat and Fluid Flow, 1999. **20**(5): p. 538-544.
- [4] Lai, M., et al., *Microscopic Characterization of Diesel Sprays at VCO Nozzle Exit*. SAE transactions, 1998. **107**: p. 1283-1293.

- [5] Sjöberg, H., G. Manneberg, and A. Cronhjort, *Long-working-distance microscope used for diesel injection spray imaging*. Optical Engineering, 1996. **35**: p. 3591.
- [6] Badock, C., et al., *Investigation of Cavitation in Real Size Diesel Injection Nozzles*. International Journal of Heat and Fluid Flow 20(5), 1999: p. 538-544.
- [7] Crua, C., et al., *High-Speed Microscopic Imaging of the Initial Stage of Diesel Spray Formation and Primary Breakup*, in *SAE paper 2010-01-2247*. 2010.
- [8] Shoba, T., et al., *Optical Characterisation of Diesel, RME and Kerosene Sprays by Microscopic Imaging*, in *24th ILASS-Europe*. 2011: Estoril, Portugal.
- [9] Manin, J., A. Kastengren, and R. Payri *Understanding the acoustic oscillations observed in the injection rate of a common-rail direct injection diesel injector*. Journal of Engineering for Gas Turbines and Power, 2012. DOI: 10.1115/1.4007276.
- [10] Crua, C., G. de Sercey, and M.R. Heikal, *Dropsizing of Near-Nozzle Diesel and RME Sprays by Microscopic Imaging*, in *12th ICLASS*. 2012: Heidelberg, Germany.
- [11] Crua, C., *Combustion Processes in a Diesel Engine*, in *School of Engineering*. 2002, University of Brighton: Brighton.

## Zooming into the primary breakup region of engine-related sprays

Manuel A. Reddemann, Florian Mathieu and Reinhold Kneer

Institute of Heat and Mass Transfer, RWTH Aachen University, Germany

### Abstract

The fundamental understanding of primary breakup close to a nozzle is an essential prerequisite for the prediction of the spray behavior further downstream. Therefore, primary breakup of liquid jets has been in focus of spray research for a long time. Unfortunately, there is still a lack of understanding, especially for Diesel engine sprays. The reason for this fact is substantially the lack of well-founded and comprehensive experimental data from the near-nozzle region, comprising data on sizes, shapes and velocities of primary ligaments and droplets. To fill this gap, a transmitted light microscopy technique is developed and applied by the authors for investigation of primary breakup especially for real Diesel nozzle configurations, using a state of the art Diesel nozzle with an orifice diameter of 109  $\mu\text{m}$ . This microscopy technique is optimized for high spatial resolution and high temporal discretization, respectively. Additionally, a double-frame imaging ability (frame separation time: 1  $\mu\text{s}$ ) allows the determination of velocities of resolved liquid structures at the same time. The breakup phenomenon is exemplarily studied for 1-Butanol at room temperature and 30 MPa injection pressure. Special attention is paid to a quantitative characterization of the primary droplets relative to size, numbers and velocities.

### Introduction

For decades the primary breakup of liquid jets has been in focus of spray research and detailed experimental visualizations of the primary breakup region have been performed by many authors. However, most of those experimental investigations use jet diameters above 1 mm, one order of magnitude larger than jet diameters found for engine-relevant Diesel nozzles, see e.g. [1], [2], [3], [4], [5], [6], [7] and [8]. Transferability to diesel engine nozzles is highly questionable. There are only few studies investigating the primary breakup for engine relevant nozzle types with sufficient spatial resolution, see [9], [10], [11] and [12]. However, all those studies use long working distance microscopes for magnification of the object. In the view of the authors' the image quality could be significantly increased by reducing the working distance to the object. For this reason a short distance transmitted light microscope is adapted for primary breakup investigations and used in this work for a qualitative and quantitative analysis of droplet and ligament behavior. This method was primarily introduced by Reddemann et al. 2013 (manuscript submitted for publication in March 2013 to Experiment in Fluids).

### Experimental test-rig

In Fig. 1 the experimental setup is shown. The microscopy system consists of an incoherent double-pulse light source (Cavilux Smart, 670 nm, 10 ns pulse duration, 1  $\mu\text{s}$  time delay), a self-made microscope with a working distance of approximately 8.7 mm and a simple double-frame CCD camera (1024 x 1280 pixels) for detection of the resulting shadowgraph images. The microscope can be applied using various magnification factors. In this work two setups are chosen: Setup-A with 607 nm / pixel and Setup-B with 995 nm / pixel, see also Fig. 2. By using a double-illumination system information about the velocity of liquid structures can be extracted from the images.

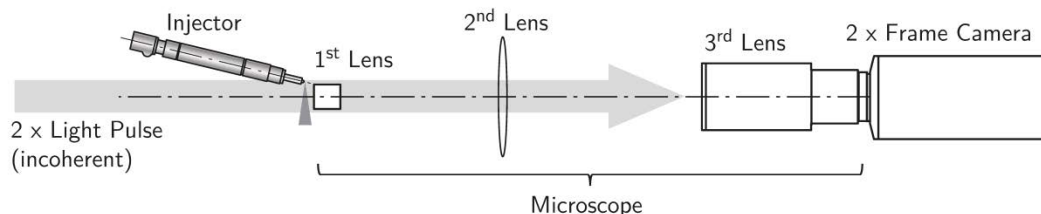


**Figure 1.** Experimental setup of the transmitted light microscope.

A state of the art Diesel nozzle from Bosch is used with 8 holes and a nozzle orifice diameter of 109  $\mu\text{m}$ . The injector is orientated in such a way that one spray cone penetrates in vertical direction, see Fig. 1. As fuel 1-Butanol is chosen (density: 804 kg/m<sup>3</sup>, viscosity: 2.4 mPa·s, surface tension: 24 mN/m).



## Results and Discussion

Considering a spray on a global macroscopic level, it seems to be a coherent, spatially discriminated structure with a clearly defined contour, propagating through the ambience, see Fig. 2 (i) [13]. However, this view of a spray results from an insufficient spatial resolution of imaging techniques, which cannot simultaneously capture both, the overall spray and its small-sized individual structures. However, information about sizes, shapes, numbers and velocities of single liquid spray structures is inevitable for a fundamental understanding of local spray phenomena, such as primary breakup in the near-nozzle region. Therefore, highly resolved microscopic measurement techniques are inevitable.

The conventional far-field microscopy method is typically used in literature for a more detailed view on the spray in this primary breakup region; see also Fig. 2 (ii) [14]. Unfortunately, due to an insufficient image quality this method cannot provide any information about the smallest primary liquid structures (droplets and ligaments) for engine relevant conditions.

It is well known, that a reduced working distance of the optics leads to a significant increase of the image quality. For this reason a short distance transmitted light microscope is used in this work for investigation of primary liquid structures, see Fig. 2 (iii). This microscope is used with two different magnifications, leading to spatial resolutions of 604 nm / pixel (Setup-A) and 995 nm / pixel (Setup-B).

The steady-state of injection is of special interest in research because it is characterized by a constant, reproducible and clearly defined outlet condition. However, any optical investigation of primary breakup in this steady-state is particularly complicated as liquid structures reach their maximum velocity and their minimum size. For this reason, in this study, the transmitted liquid microscopy is applied to this case. Below, in Fig. 3 an exemplary microscopic image of the steady-state of injection of 1-Butanol at 30 MPa injection pressure based on Setup-B is shown. Different characteristic structures can be distinguished:

- i. **jet core:** the inner region of the jet is quite cylindrical for the given injection pressure case; however, the cylindrical structure is characterized by inclusions of varying optical density.
- ii. **films and ligaments:** thin sheets can be detected at the spray edge collapsing into ligaments which are orientated parallel to the inner jet core and with a length much larger than the jet diameter.
- iii. **droplets:** the surroundings of the jet is governed by a large number of droplets of various sizes resulting from breakup of the jet and its films and ligaments at its edge. Both large and small droplets are detectable. This work will focus on a quantitative analysis of these final products of primary breakup. In a first step the droplets will be characterized with respect to their number, velocity and size. In a second step the reason for different droplet characteristics will be evaluated.

To illustrate the advantages of those highly resolved transmitted light microscopy, in the following, an image processing routine based on MATLAB's image processing tool box will be roughly introduced, which offers the potential for a fully automated analysis of droplet sizes and velocities.

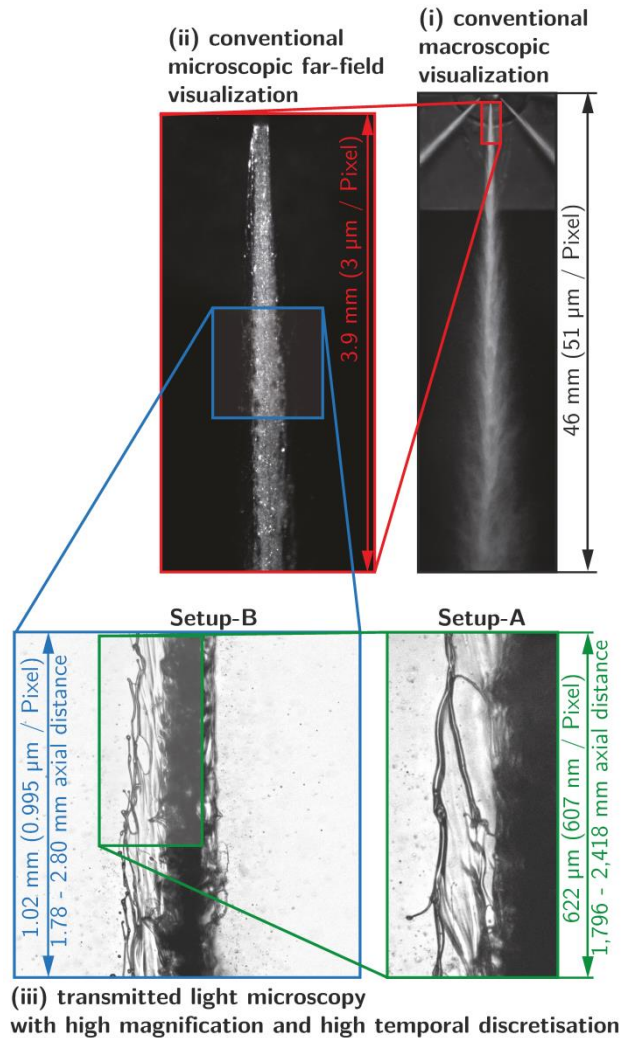


**Figure 2.** Zooming into the primary breakup region of an engine-related spray, 1-Butanol at 30 MPa injection pressure in the steady-state of injection.

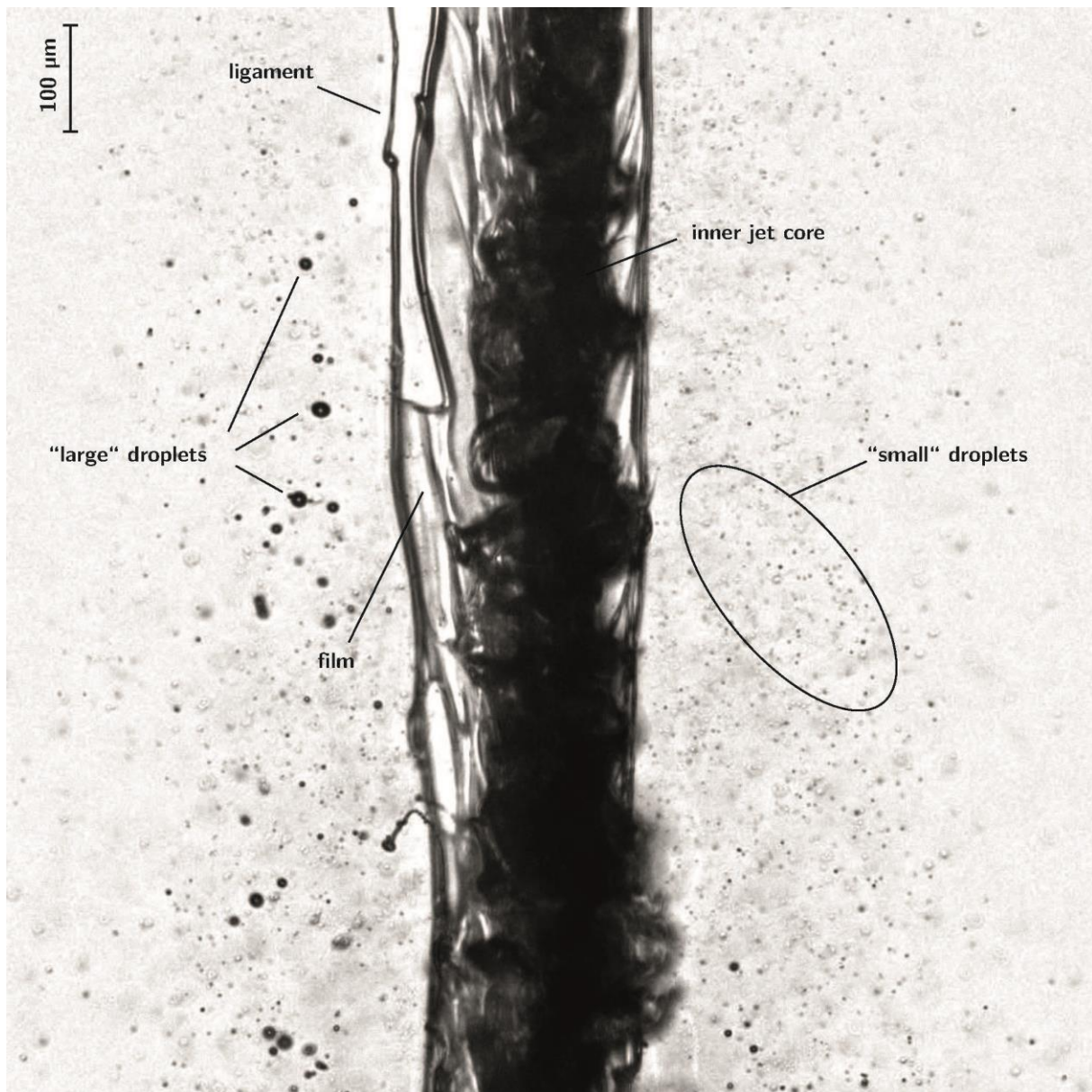


**Figure 3.** Raw image of the steady-state of injection of 1-Butanol at 30 MPa injection pressure based on Setup-B

In a first step, circular structures are automatically identified inside the grey scale image. In detail, the position and the radius of almost each droplet lying inside the depth of field can be determined. In Fig. 4 the resulting droplet size distribution is shown, i.e. the frequency of droplets as a function of droplet diameter. The majority of droplets (almost 60%) are found inside a diameter-range between 3 and 5  $\mu\text{m}$ , whereas the percentage of droplets below 3  $\mu\text{m}$  diameter is relatively low. It is assumed that the amount of those smallest droplets is bound to rise with increasing injection pressure. However, it cannot be ruled out in the present work that the sizes of the smallest droplets are slightly overestimated as a decreasing droplet size leads to a decreasing probability for droplet detection on the one hand and to an increasing influence of aberration effects resulting in a more diffuse droplet image on a camera chip on the other hand. Furthermore, droplets could be slightly out of focus. For clarification whether the smallest droplets are detected or overlooked on the basis of Fig. 3, a validation with improved spatial resolution is needed. Therefore in Fig. 5 Setup-A (607 nm / pixel) is used for visualizing the same operation point as already found in Fig. 3 (steady-state of injection of 1-Butanol at 30 MPa).



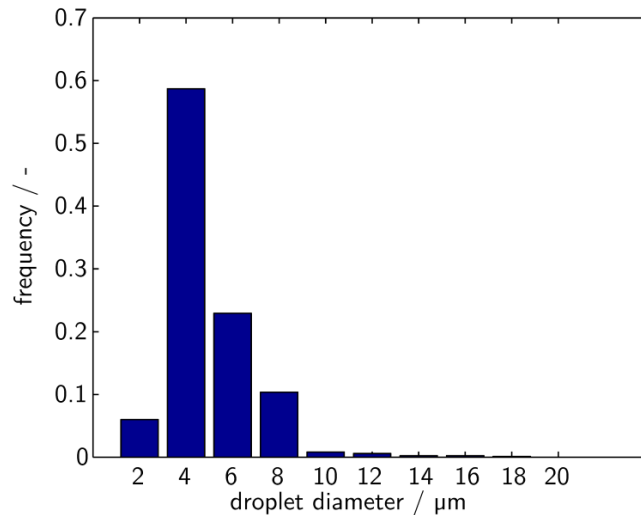


**Figure 4.** Droplet size distribution inside the greyscale image of Fig. 3.

A zoom on single structures in Fig. 5 reveals that even the smallest droplets consist of more than 4-5 Pixels in diameter, thus they should be detectable, even on the basis of Setup-B (995 nm / pixel). However, as a result of aberration effects the droplets are not sharply visualized.

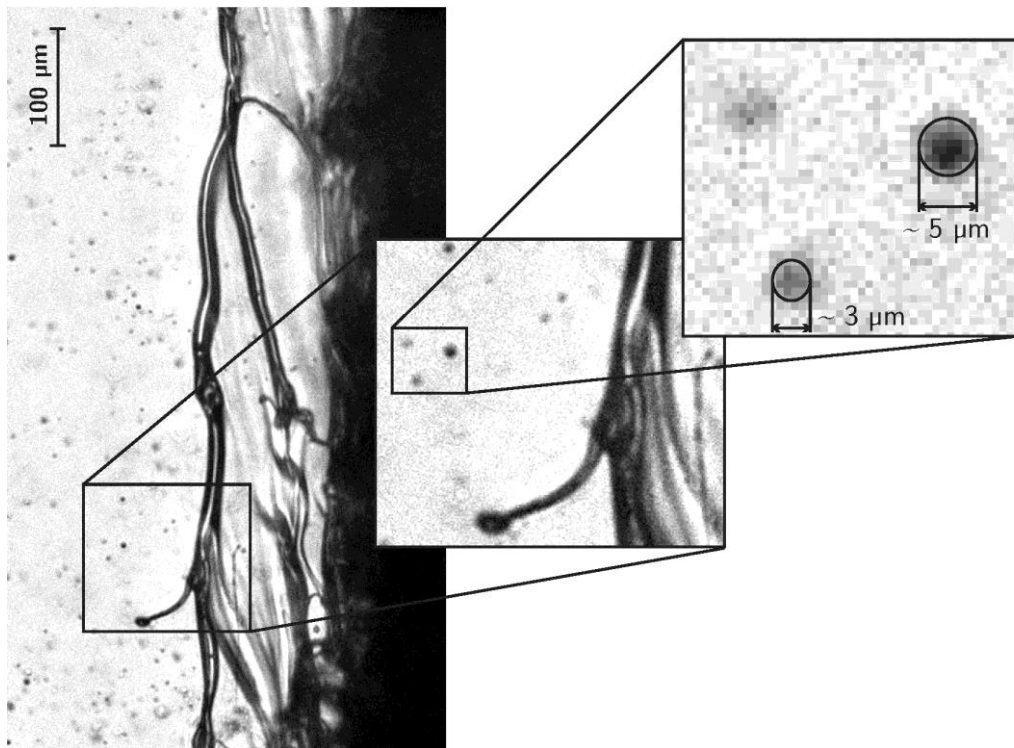


**Figure 5.** Zoom into a raw image which is based on Setup-A visualizing the primary breakup region for the steady-state of injection for 1-Butanol at 30 MPa injection pressure.

Based on Fig. 3 not only the sizes but also the **velocities of droplets** can be determined. For that purpose the droplets are subdivided into two different regimes, see Fig. 6 on the left. “Small” droplets are marked in red, “large” droplets are marked in blue. **“Large” droplets** are considered as those which are clearly identifiable in a given image section based on their radius, only - i.e. there is solely one single droplet of a given size. The algorithm is found to be robust for droplet sizes with a radius larger than 4 pixels and thus a diameter above 9  $\mu\text{m}$ . Due to their uniqueness for both time steps it is possible to track them over time and, thus to determine their local displacement and their velocity. „**Small“ droplets** (< 9  $\mu\text{m}$  in diameter) are not suitable for any tracking algorithm due to the fact that they consist of only a few pixels and can be found in great quantities

surrounding the jet, i.e. they are not clearly identifiable. However, the Particle Image Velocimetry (PIV) method could be an appropriate tool for velocity determination, instead. Using this method, the droplet velocity is not any longer determined for single droplets but based on a cross-correlation of the given grey scale image inside selected interrogation windows. There are several preconditions for a meaningful application of PIV: The tracer particles should have equal size and a similar velocity inside each interrogation window and in addition should be homogeneously distributed over the entire region of interest. In the present case the majority of the “small”

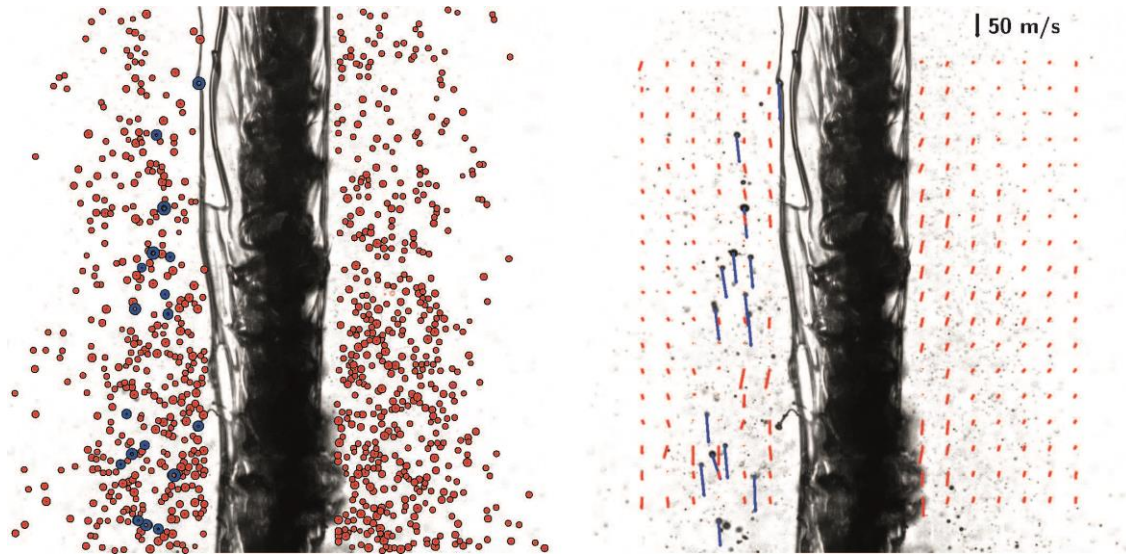


**Figure 6.** Results of the automatic evaluation method. Left: Detected droplets (blue: large, red: small). Right: Superimposed velocity field (blue: large tracked droplets, red: cross correlated small droplets).

droplets - serving as tracer particles - are supposed to follow the surrounding air stream almost slip-free. Therefore, the velocity variation inside single interrogation windows is expected to be small. Furthermore, the droplets are approximately homogeneously distributed over a wide image section. However, especially in regions close the inner jet and in the presence of large droplets a promising cross-correlation is not available and the PIV algorithm is expected to fail. Therefore, in this work instead of the raw image shown Fig. 3 an adapted image should provide the basis for the cross-correlation. In that adapted image large structures (inner jet, ligaments, films and “large” droplets) should be erased, i.e. their greyscale intensity distribution should be replaced by background noise. To decide whether a structure should disappear or not, in this work all coherent structures inside the image on Fig. 3 are searched and classified with respect to their pixel quantity on a binarized image. Consecutively, all liquid structures larger than 20 pixels are eliminated. The final contrast-adapted and inverted grey scale image is shown in Fig. 7, constituting the basis for the following PIV algorithm and allowing a determination of velocities even close to the spray core. The PIV algorithm is performed using the open source MATLAB PIV system *PIVLab*. The image is subdivided into interrogation windows of 192 x 192 pixels and a pixel shift of 48 pixels resulting in a great overlap. Due to this parameter choice the spatial resolution of the velocity field is reduced, but there are always enough droplets for a cross-correlation, even at the spray edge. However, a maximum spatial resolution is not in focus of this work, but rather the determination of the velocity field over wide image sections in a correct order of magnitude. Taking both the “large” (blue) and the “small” (red) droplets into account a superimposed velocity field is obtained, shown on the right hand side of Fig. 6. By comparing the velocity values it is found that the “large” droplets are faster than the “small” ones by at least a factor of two. One reason for this fact is that smaller droplets are decelerated stronger due to aerodynamic drag. The velocity of the “small” droplets slightly increases with decreasing radial distance to the inner spray region. However, the velocity of the inner core can never be reached. This is maybe due to the fact that the PIV algorithm is performed using large interrogation windows. However, following the no-slip condition



**Figure 7.** Adapted image prepared for PIV based on Fig. 3.

between liquid inner spray-core and surrounding air there must be a large radial velocity gradient inside the gaseous phase in the vicinity of the inner core. This velocity gradient results in shear effects leading single films and ligaments to move into radial direction where they finally break up. Additionally it can be found that all droplets (blue and red) slightly move towards the spray core (the radial velocity component is always negative) most likely due to a pressure drop close to the spray core. Questions arise: Where do the small and the large droplets come from and which mechanisms are relevant for their creation? To answer these questions it must be noted that Fig. 3 is one single snap-shot of the overall injection process, only. Even though Fig. 3 shows the primary breakup in the steady-state of injection, which is characterized by a constant and reproducible outlet and ambient conditions, it is important to be aware of the fact that the jet shape in that time region is not constant but a function of time. Consequently, the “large” and “small” droplets found in Fig. 3 result from primary breakup phenomena which have already occurred during steady-state but are not visible any more. Instead, the breakup processes are either completed or their educts and residual products have already left the image section downstream. Therefore information about relevant breakup phenomena can only be achieved on the basis of additional images for the same time after injector energizing and for identical operation conditions. In Fig. 8 two exemplary images are chosen by the authors showing various breakup types.

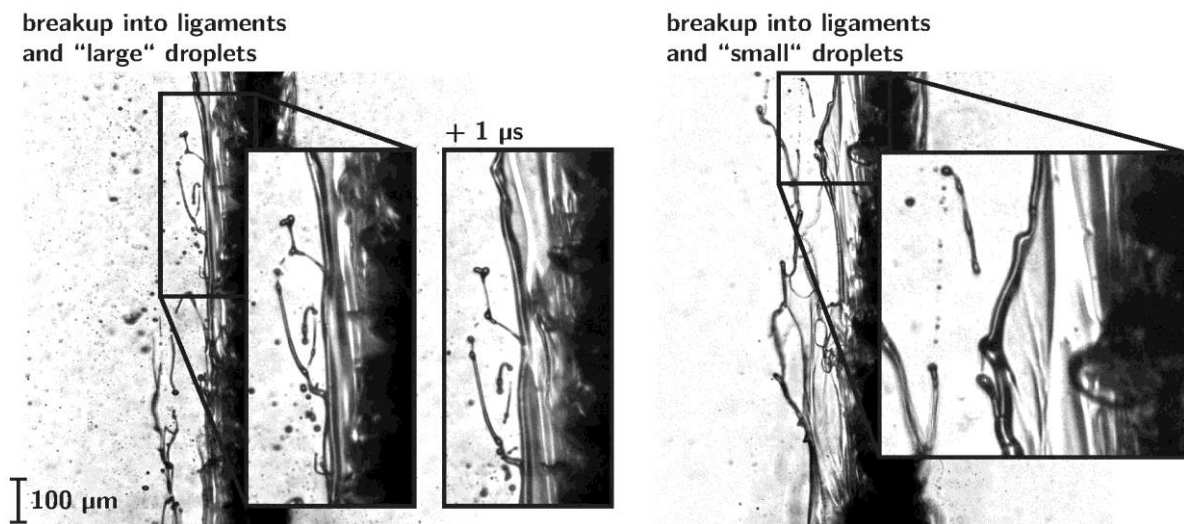


**Figure 8.** Raw images of the steady-state of injection of 1-Butanol at 30 MPa injection pressure based on Setup-B showing different ligament breakup types resulting in various droplet sizes.

On the left hand of Fig. 8 a ligament connected to the inner spray core is shown in a detailed view for two different time steps. Most likely due to acceleration it breaks up into large droplets, long ligaments and some isolated small droplets. On the right hand side of Fig. 8 a breakup of such a long detached ligament into plenty of small droplets is shown, most likely due to surface instabilities. From this, it can be concluded: Droplets can be classified in large and small droplets as a consequence of different breakup mechanisms.

## Conclusions

A self-made transmitted light microscope primarily introduced by Reddemann et al. 2013 (manuscript submitted for publication in March 2013 to *Experiment in Fluids*) is applied in this work for a quantitative analysis of the primary breakup region of a technically relevant jet (109  $\mu\text{m}$  nozzle diameter). In this work particular attention is paid to the steady-state of injection. In this time-regime any optical investigation is particularly difficult as the liquid structures reach their maximum speed and therefore their minimum size. The transmitted light microscope is applied for two different configurations (Setup-A with 607 nm / pixel and Setup-B with 995 nm / pixel) exemplarily for 1-Butanol at 30 MPa injection pressure.

Based on Setup-B the jet shape in the steady-state of injection can be subdivided in different parts: i) the inner spray core, ii) films and ligaments parallel to the edge of the inner spray part with lengths much longer than the orifice diameter and iii) primary droplets of various size. An automatic evaluation method based on MATLAB for analyzing the behavior of the primary droplets is implemented and used in this work. The number, the size and the velocity of primary droplets are quantitatively studied using different evaluation methods. Spherical structures are identified on the image for determination of droplet size, number and position. The velocity field around the inner spray core is determined by tracking the “large” droplets over time and by cross-correlating the homogeneously distributed “small” droplets using PIV. A correlation between droplet size and droplet velocity is

identified. Furthermore, the different droplet sizes are correlated to different breakup mechanisms. Large droplets result from the edges and small droplets result from the residual part of long detached ligaments. In the near future, the developed evaluation method should be applied to further cases: different injection pressures, different times after injector energizing and different fuels.

## Acknowledgements

This work was performed as part of the Cluster of Excellence "Tailor-Made Fuels from Biomass", which is funded by the Excellence Initiative of the German federal and state governments to promote science and research at German universities.

## References

- [1] P.K. Wu, L.K. Tseng, G.M. Faeth, Primary breakup in gas/liquid mixing layers for turbulent liquids, *Atomization Spray*, Volume 2, Number 3, 1992.
- [2] P.K. Wu, G.M. Faeth, Onset and end of drop formation along the surface of turbulent liquid jets in still gases, *Phys Fluids*, Volume 7, Number 11, 1995.
- [3] P.K. Wu, R.F. Miranda, G.M. Faeth, Effects of initial flow conditions on primary breakup of nonturbulent and turbulent round jets, *Atomization Spray*, Volume 5, Number 2, 1995.
- [4] K.A. Sallam, Z. Dai, G.M. Faeth, Liquid breakup at the surface of turbulent round liquid jets in still gases, *Int J Heat Mass Tran*, Volume 28, Number 3, 2002.
- [5] K.A. Sallam, G.M. Faeth, Surface properties during primary breakup of turbulent liquid jets in still air, *AIAA J*, Volume 41, Number 8, 2003.
- [6] H. Hiroyasu, Spray breakup mechanism from the hole-type nozzle and its applications, *Atomization Spray*, Volume 10, Number 3-5, 2000.
- [7] P. Mormontant, E. Villiermaux, On spray formation, *J Fluid Mech*, Volume 498, Number 1, 2004.
- [8] B. Balewski, B. Heine, C. Tropea, Experimental investigation of the correlation between nozzle flow and spray using laser doppler velocimeter, phase doppler system, high-speed photography, and x-ray radiography, *Atomization Spray*, Volume 20, Number 1, 2010.
- [9] M.G. Sjoeborg, H., A. Cronhjort, Long-Working-Distance Microscope Used for Diesel Injection Spray Imaging, *Optical Engineering*, Volume 35, Number 12, 1996.
- [10] M. Lai, T. Wang, X. Xie, J. Han, N. Henein, E. Schwarz, W. Bryzik, Microscopic Characterization of Diesel Sprays at VCO Nozzle Exit, *SAE Technical Paper*, 982542, 1998.
- [11] C. Bae, J. Kang, The structure of a break-up zone in the transient diesel spray of a valve-overed orifice nozzle, *Int. J. Engine Res.*, Volume 7, Number 4, 2006.
- [12] C. Crua, T. Shoba, M. Heikal, M. Gold, C. Higham, High-speed microscopic imaging of the initial stage of diesel spray formation and primary breakup, *SAE Technical Paper*, 2010-01-2247, 2010.
- [13] M.A. Reddemann, F. Mathieu, D. Cordes, R. Kneer, Parametric Study of Fuel Impact on Spray Behavior using High-Speed-Visualization, *ICLASS 2012*.
- [14] M.A. Reddemann, F. Mathieu, D. Cordes, R. Kneer, Impact of physical properties on primary breakup for a diesel nozzle configuration, *Atomization Spray*, Volume 21, Number, 2011, pp. 221–235.

## On the use of 3D spray impulse topography for analyzing the effects of nozzle geometry on spray break-up

Fabian Pinkert, Alexander Gerds, Ibrahim Najar, Christian Fink and Horst Harndorf

Institute for Piston Machines and Combustion Engines, University of Rostock, Germany

### Abstract

This publication covers the measurement of spray momentum of a diesel injector with high resolution regarding time and space. The object of the study are two nozzles, one with cylindrical and one with conical spray hole geometry. The Scope of the project is a detailed investigation of the impact of different nozzle geometries in order to reduce emissions of medium speed marine diesel engines. For this purpose a small pitot tube probe was designed and manufactured. The spray was analyzed by using the pitot tube to measure a grid perpendicular to the spray axis at varying injection pressure, ambient gas density and distance from the nozzle. The sensor was calibrated using an impact plate measurement and the injection rate of the injector. The results obtained are evaluated regarding their plausibility and differences between the two nozzles. There are significant differences in the momentum density profiles which are interpreted using experimental results from high speed spray imaging and simulative results of the inner nozzle flow. Correlations between the results suggest that the spray characteristics of different types of nozzles can be identified and studied using the proposed measurement system.

---

### Introduction

The Introduction of the IMO-TIER III Emission legislation in 2016 within the Emission control areas (ECA) demands a reduction in NO<sub>x</sub>-Emissions compared to IMO-TIER II by about 75% [1]. The high potential of EGR to lower the NO<sub>x</sub>-emissions is known especially from land based applications of high speed engines. Studies on medium speed ship engines [2] have shown that IMO-TIER III limits can be reached by the application of EGR. At the same time, however, a strong increase in soot emissions is observed. According to common perception this increase can be controlled by raising the injection pressure and applying a post injection strategy [2, 3]. The HFO capability complicates the development of appropriate injection systems, so that geometric variations of the injection nozzle as a means to influence the emission generation will become more important in the future.

No extensive research has been conducted so far concerning the influence of spray hole geometry on mixture formation in corresponding engines due to the comparatively low requirements for ship diesel engines by the emission legislation. Now, however, potential for in-engine reduction of emissions is expected from these options as well. Therefore, an experimental and numerical analysis of the injection and mixture formation for varying nozzle and hole geometries is an important basis for the development of future generations of large engines.

Within in the scope of the BMWi (German Federal Ministry of Economics and Technology) founded joined research project FAME (Fuel and Air Management for Emission reduction) the partners AVL Deutschland GmbH, Caterpillar Motoren GmbH und CO. KG, L'Orange GmbH, WTZ Roßlau gGmbH and the LKV of the University of Rostock study different nozzle geometries systematically using an injection chamber, a single cylinder research engine and 3D-CFD-calculations.

In this paper a newly developed measurement technique has been applied to the subject. The technique makes it possible to analyze the breakup behavior in the near nozzle region. The need for this kind of investigation arose from previous measurement campaigns where the macroscopic spray properties were measured using high speed imaging under non evaporative and evaporative condition. The spray of two different nozzles showed no apparent differences in a cold environment, however the liquid penetration length under evaporative conditions was significantly different. This leads to the conclusion that the microscopic spray properties cannot sufficiently be evaluated under cold conditions. The breakup behavior in the near nozzle region is expected to give hints as to the reasons for the changes in liquid penetration length.

Research on this field is further motivated by the numerical analysis of the processes, which is growing ever more important. While for a long time spray was mainly simulated using a Lagrangian approach and a discrete parcel model, in the future a Eulerian two phase flow simulation is expected to yield better results, especially in the primary breakup region. An analysis of the flow in the near nozzle region is apt to help improve the understanding of the processes involved and serve as a base for validation. At the current level of the investigation the results are used to link the findings from an internal nozzle flow simulation and an experimental measurement of the macroscopic spray properties as will be shown.

## Theoretical Background

The velocity and distribution of the liquid after exiting the nozzle are amongst the key components influencing the atomization of jet injectors as they are used in diesel engines. The measurement of these quantities presents a demanding task. Many approaches have been taken in the past to visualize the near nozzle region and the liquid core of the spray. Due to the high optical density of the spray, laser based techniques like PhaseDoppler anemometry are almost impossible to apply. Other approaches have been made using X-rays [11]. Here the attenuation of the radiation within the spray is analyzed for obtaining information about the density of the spray. The inability of evaluating the spray velocity and the very costly technical resources however make this technique impractical to use. A similar result can be achieved with ballistic imaging. This technique allows the temporal filtration of photons crossing the spray. This way the contrast of the spray and the liquid core is increased by only using the fastest and therefore least refracted photons for imaging. The drawbacks are similar to the X-ray techniques.

A different group of measurement systems involve probes inserted into the spray. These techniques are thus intrusive and bear the potential of influencing the propagation of the spray. One example is the measurement of the electrical conductivity between two points in the spray. The conductivity allows conclusions about the spray density between the electrodes. The subject of this publication is a measurement of the spray momentum flow or spray force. The analysis of the spray force is a common practice for evaluating the injection behavior of nozzles [4,5]. Most often an integral method is used in which the whole spray impinges on a plate and thus exerts a force on the plate which can be measured. In combination with a measurement of the mass flow rate information about the velocity of the spray can be gained. Furthermore cavitation effects within the nozzle can be evaluated [5]. The system employed here aims at resolving the spray force locally, in other words measuring the spray pressure, momentum flux or momentum flow density. Similar measurements have been used to measure momentum or velocity in one and two phase flows [6, 7]. The application to diesel sprays was realized by [8]. In this campaign the local momentum density was measured using a different kind of sensor. The results were validated using CFD simulation and used to study differences between the spray holes of an injector.

Regarding the ensemble of spray droplets, ligaments and entrained air as a continuum with averaged density  $\rho$  and averaged speed  $v$ , the momentum flow density becomes

$$\frac{d\dot{I}}{dA} = \dot{I}_A = \rho u^2 \quad [\text{eq.1}]$$

In an integral measurement using a plate the whole momentum flowing through a perpendicular cut through the spray is redirected therefore the Force on the plate corresponds to the momentum flow.

In order to measure the momentum flow locally a pitot tube was used. A pitot tube measures the total pressure comprised of dynamic and static pressure. The momentum flow density can thus be calculated as

$$\dot{I}_A = 2(p_{tot} - p_{st}) \quad [\text{eq.2}]$$

Since the spray is a free jet with air flowing into the jet, the static pressure must be smaller than the atmospheric pressure. The surrounding air flows into the jet with little obstruction so the pressure difference between static pressure within the spray and environmental pressure is assumed to be small. Therefore the contribution of static pressure to the momentum flow density was neglected.

The geometry of the sensor influences the measurement and the liquid and gas phase have different momentum transfer factors [7], therefore equation 2 must be regarded as a model only and the introduction of an experimentally determined constant is necessary,

$$\dot{I}_A = c_{exp} p_{tot} \quad [\text{eq.3}]$$

A calibration using the injection rate has shown a factor of 1.13 to yield the best agreement. The high deviation of this value from the theoretical value of 2 has to be seen critically and will be the subject of further studies. The emphasis of this investigation however is on comparing the differences between different nozzles rather than evaluating the absolute velocity or mass flow within the spray. If an error was made it is assumed to have no impact on the comparison of the nozzles.

## Experimental Setup

The object of the study is the single-circuit common rail injector by L'Orange GmbH. It is being deployed in a medium speed diesel engine with 320mm bore and a rated cylinder power of 500 kW. In the present case the injection rate has been adapted to fit a single cylinder research engine with 240mm bore. The injector was fitted with two different nozzles: a conical nozzle with a conicity factor  $k=6$  and a cylindrical nozzle. Both nozzles have a similar outlet diameter of  $\approx 0.35$  mm. The 8 bores of both nozzles were to a small degree hydro erosively rounded. The sprays were measured in a high-pressure/ high-temperature chamber. The chamber allows the analysis of sprays at gas pressures up to 50 bar and gas temperatures up to 900K.

The pitot tube used as probe consists of a capillary of 0.5 mm inner and 1.5 mm outer diameter leading into a small cavity where a Kistler 6041A piezo electric pressure sensor is mounted. The tip of the capillary is



rounded as is shown in Figure 1. During the measurement the cavity and capillary get filled with injected fuel which should act as good and fast pressure guide due to its incompressibility. The sensor is moved within the spray using a three axis traverse. A CAD-model of the complete measurement system is shown in Figure 1.

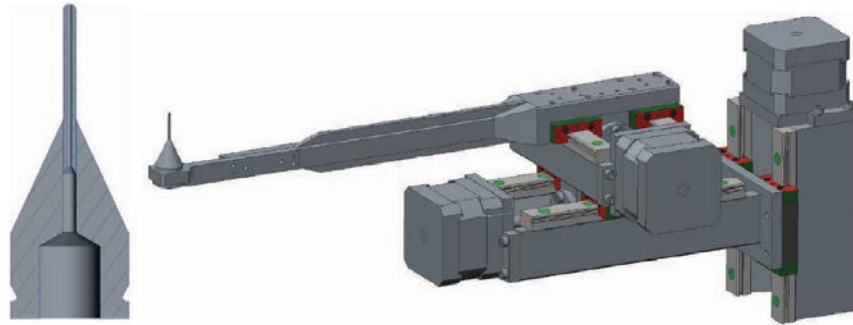


**Figure 1.** Geometry of pitot tube sensor and traverse

The measurements of the two nozzles were carried out at varying rail and gas pressure. Three planes perpendicular to the nozzle axis were measured. The spatial resolution was chosen as rectangular grid with a spacing of 0,25 mm. This way the round measurement areas of 0.5 mm diameter overlap. A complete overview of the measurement conditions and parameters is given in Table 1. Spatial plots shown in the results chapter are oriented so the x-Axis lies within the plane spanned by the injector axis and the nozzle axis.

The nozzles were also measured using a high speed camera in order to evaluate the breakup and penetration behaviour. These tests were conducted using 130mm quartz windows within the high pressure chamber under the same ambient and injection conditions given in Table 1. A scatter light technique is applied to visualize the spray. A suite of Matlab scripts was used to analyze the spray regarding its macroscopic properties. Further details regarding the test rig, measurement equipment and analysis procedures can be found in [9].

**Table 1.** Overview of Measurement points and conditions

Fuel	DIN EN 590 Diesel Fuel
Rail pressure	800; 1600 bar
Ambient pressure	8,4; 16,8 bar
Ambient density	10; 20 kg/m <sup>3</sup>
Duration of actuation	4ms @ 800 bar; 3ms @ 1600 bar
Distance to injector	10; 20; 30 mm
Number of Measurement points	121 @ 10 mm; 277 @ 20 mm; 405 @ 30 mm
Grid spacing	0.25 mm
Averaged events per grid point	10

## Results and Discussion

For validating the measurements conducted with the pitot tube the results were compared to measurements using an impact plate as well as the theoretical momentum within the orifice calculated from injection rates assuming no cavitation. For the impact measurement a 10 mm diameter and a 20 mm diameter plate were applied. The bigger plate is only applied at the longest distance from the nozzle. The construction of the sensor is based on the pitot tube sensor. For this reason the same piezo electric pressure transducer was used instead of a dedicated force sensor. The pressure transducer with impact plate was calibrated with weights. The impact plate measurement yields the impact force, corresponding to the momentum flow. A third reference value for the validation was calculated using the mass flow rate of the injector. It was simulated by means of a well calibrated hydraulic model of the injector described in [10]. The model itself was validated using measurements carried out on an injection rate analyzer. Assuming a homogenous velocity distribution and no cavitation in the orifice, the theoretical momentum can be calculated using the fuel density and the orifice area.

Figure 2 shows the validation. On the left the data were integrated spatially and temporally to obtain the total Momentum, on the right the spray force is shown. As can be seen, the pitot tube measurement was adjusted to fit the injection rate using the total spray momentum. The values obtained from the impact plate lie higher than the other measurements. The injection rate was used here for calibration since it is considered to be more accurate than the impact plate measurement.



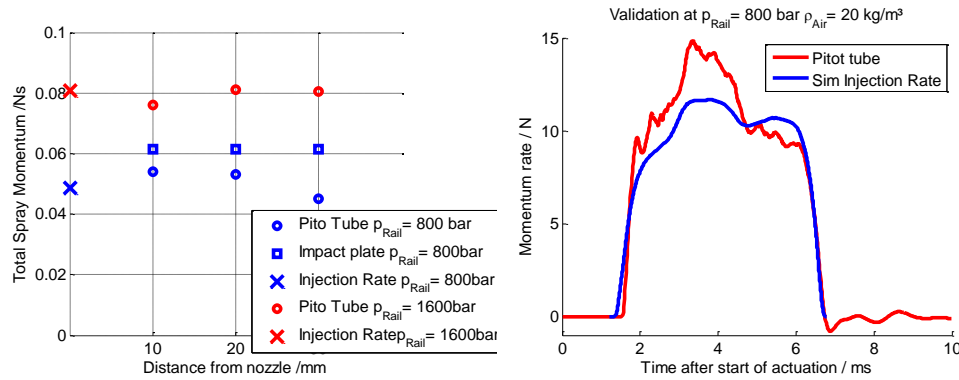


**Figure 2.** Validation of pitot tube measurement using impact plate measurement and simulated injection rate of the conical nozzle

A general impression of the kind of results that can be expected from the spray pressure sensor is given in Figure 3. Here the dependency of the spray profile on the nominal injection pressure and the counter pressure at a distance of 30 mm from the nozzle is shown. As in most other graphs presented here, the data was integrated over the time of the injection to obtain the momentum density. As can be seen from the cuts through the profile, the changing of rail pressure or ambient density have distinct effects on the profile. While a doubling of the rail pressure mainly amplifies the momentum density, a doubling of the ambient density significantly alters the shape of the profile. This behaviour is in agreement to the macroscopic spray properties, as the ambient density changes the spray angle whereas the rail pressure typically does not.

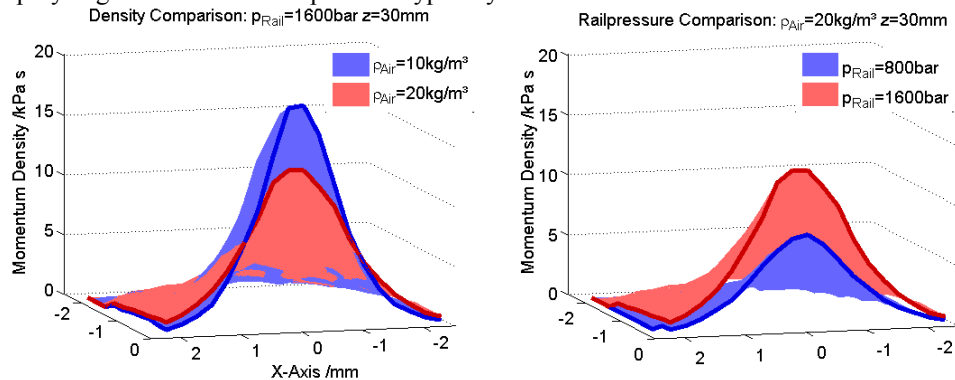


**Figure 3.** Plausibility of measured momentum density profile regarding general dependencies on rail pressure and air density

Figure 4 shows the comparison of the spray profiles of nozzles  $k=0$  and  $k=6$ . In the plots the momentum density profile was cut along the x and the y axis. For better comparison the positions of the graphs were adjusted. The top four graphs contain the momentum density for all ambient conditions at a distance of 10 mm from the nozzle. The bottom four graphs correspond to a distance of 20 mm.

The first characteristic to notice is the  $k=6$  nozzle having a higher maximum momentum density at a rail pressure of 800 bar and the  $k=0$  nozzle having a higher peak at 1600 bar. This is consistent throughout all measurement distances and gas densities. This behaviour is also illustrated in the left graph in Figure 5. The total momentum, obtained by integrating the momentum density over the area, however is higher for the conical nozzle at all measurement points. An explanation for the higher total momentum of the  $k=6$  nozzle is the higher discharge coefficient generally associated with a conical spray hole geometry. At higher injection pressures however, this effect is super compensated by the increased occurrence of cavitation within the cylindrical nozzle. The cavitation leads to a change in the velocity profile in the orifice. At the centre of the hole the velocity is increased, while at the circumference a decrease can be observed. This phenomenon was shown in [10] as can be seen in Figure 6. In these simulations the conical nozzle showed an almost constant rotational symmetric profile, while the cylindrical nozzle revealed a clearly asymmetric transient profile. The conical nozzle also exhibits a more flat velocity profile with a thinner boundary layer compared to the cylindrical nozzle. This leads to higher shear stresses between the spray and the air which in turn results in stronger break up forces.

Secondly the broader base of the momentum profile of the conical nozzle is to be pointed out. In all plots except at the highest rail pressure and 20 mm distance from the nozzle the red curve lies clearly above the blue in the outer region. An explanation for this behaviour can also be given from the above shown simulated velocity profile at the nozzle exit, as the cavitation leads to an artificially reduced orifice diameter (vena contracta).

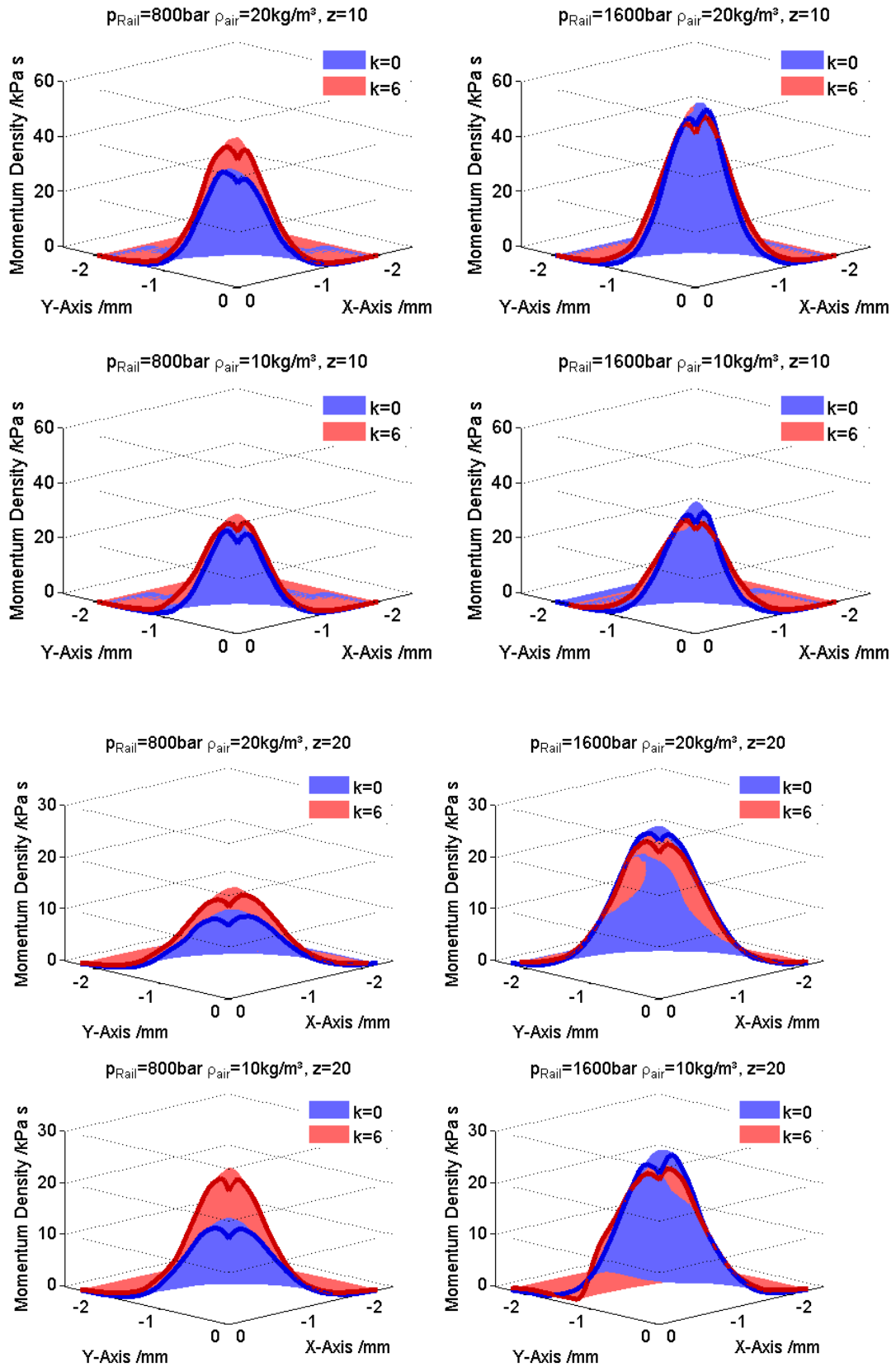
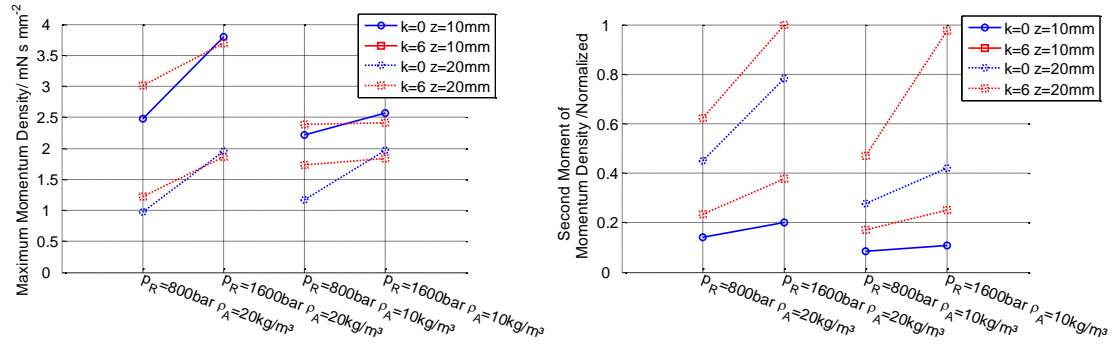
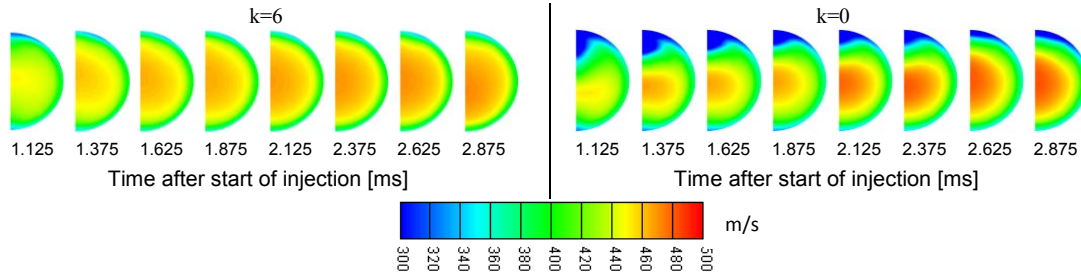


Figure 4. Comparison of momentum density profiles of cylindrical  $k=0$  and conical  $k=6$  nozzle



**Figure 5.** Comparison of nozzles by means of the maximum momentum density and the second moment of the momentum density



**Figure 6.** Explanation of phenomena using simulated velocity profile [m/s] at the nozzle outlet [10]

In order to be able to judge the implications of the above described characteristics of the spray force profile on the spray, the nozzles were also analyzed by high speed imaging, a method that is widely accepted and used for rating the break up behaviour of the diesel injectors. Between the penetration curves at 1600 bar rail pressure presented in Figure 7 little difference can be made out. The small differences in maximum momentum density shown in Figure 4 apparently do not affect the penetration. At 800 bar rail pressure a peculiarity of the injector was observed. Shortly after the start of injection the spray holds and continues. This leads to a step in the penetration curve that delays the spray of the  $k=0$  nozzle. This delay comes along with a lower spray velocity and should therefore be reflected in the spray momentum. The difference in the momentum density observed at 800 bar rail pressure is likely to be caused by this behaviour. The evolution of the cone angle over the time in Figure 4 shows that the conical nozzle causes a stronger break up at all measurement points. For the analyzed nozzles, both, rail pressure and gas density cause a widening of the cone angle.

This behaviour is also reflected in the momentum density. For better visualization of the spread of the profile the momentum density was weighted using the squared distance to the spray centre, also called second moment or variance of the momentum density

$$J_z = \int \dot{I}_A(x, y) \cdot (x^2 + y^2) dA \quad [\text{eq.4}]$$

This derived quantity is a measure of the shape of the profiles. The results of this analysis, shown in Figure 5, suggest that the spread of the momentum density profile tends to correlate with the spread of the cone angle. A thorough investigation regarding this correlation however requires a larger data base.

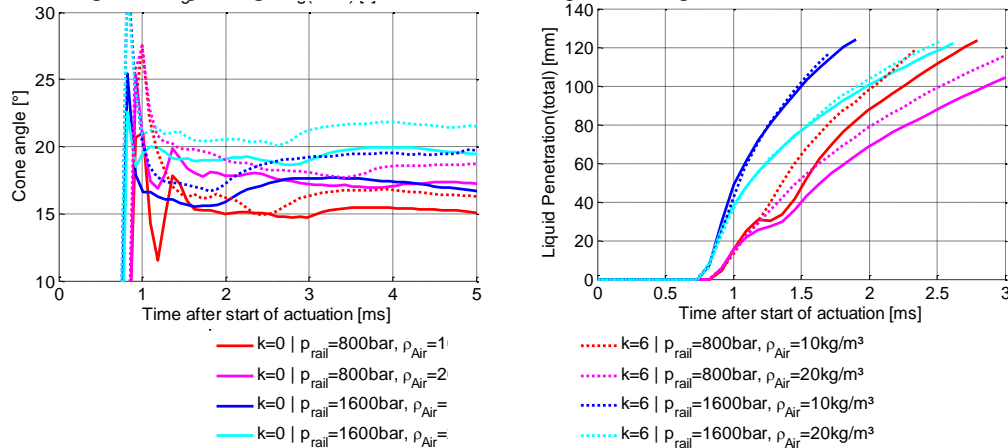


**Figure 7.** Comparison of macroscopic spray properties of the nozzles using high speed imaging

## Conclusions

The measurement technique presented gives insights into the spray structure of high pressure jets that are very hard to obtain using other techniques, especially when considering the simple design and operation of the sensor. In the paper the calibration of the sensor is discussed and the results obtained are proven to be plausible regarding the dependency of the spray momentum density on injection pressure and ambient gas density. A comparison of a conical and a cylindrical nozzle manufactured for the use in medium speed diesel engines is conducted with the measured spray momentum. It turns out that although the total spray momentum is higher for the conical nozzle in all measurement conditions, the cylindrical nozzle produces a higher maximum spray momentum and steeper rise of the momentum density profile at high injection pressures. This behaviour is explained by the occurrence of cavitation in the nozzle hole and the contraction of the effective orifice diameter caused by this flow regime. This interpretation is substantiated by internal nozzle flow simulations. Furthermore parallels are drawn between the momentum results and an analysis of high speed scatter light images. The visual cone angle is shown to correlate to the spread of the momentum density profile caused by an increased ambient gas density and the nozzle geometry. The lower penetration speed of the cylindrical nozzle at 800 bar rail pressure is explained by the significantly lower momentum density.

With this investigation a basis has been laid for further studies regarding the spatial and temporal distribution of the spray momentum, its implications on other macroscopic and microscopic spray properties and its usefulness in evaluating the effects of modified nozzle geometries on the spray. This task involves the further investigation and development of the pitot tube sensor regarding the effect of different sensor geometries, the temporal development of the spray momentum and above all the correlation of the momentum results with other spray measurement techniques and the performance of the nozzles in the engine. The project FAME provides the possibilities for this by combining resources and experience of injection system and engine manufactures, a CFD code developer and two research institutes.

## Acknowledgements

The authors would like to express their gratitude to the German Federal Ministry of Economics and Technology (BMWi) for funding the project FAME.

## References

- [1] International Maritime Organisation, MEPC 58/23/Add.1, ANNEX 13, "Amendments to the annex of the protocol of 1997 ...", 10/2008
- [2] Püschel M., Drescher M., Buchholz B., Schlemmer-Kelling U., Harndorf H., 2011. Abgasrückführung am mittelschnelllaufenden Common-Rail-Schiffsdieselmotor zur Erreichung der IMO Tier III. 13. Tagung Der Arbeitsprozess des Verbrennungsmotors, Graz,
- [3] Gärtner U., Werner P., Koch T., 2007. Wohin mit dem Ruß? – Grundlagen der passiven und thermischen Regeneration von Dieselpartikelfiltern im Nutzfahrzeug. FAD-Conference, Dresden, 10/2007
- [4] Husberg, T., Manente, V., Ehleskog, R., Andersson, S., 2006. Fuel Flow Impingement Measurements on Multi-Orifice Diesel Nozzles (SAE Technical Paper No. 2006-01-1552). SAE International, Warrendale, PA.
- [5] Desantes, J.M., Payri, R., Salvador, F.J., Gimeno, J., 2003. Measurements of Spray Momentum for the Study of Cavitation in Diesel Injection Nozzles (SAE Technical Paper No. 2003-01-0703). SAE International, Warrendale, PA.
- [6] Raghunathan, K., Mori, H., Whiting, W.B., 1988. A technique for measurement of jet penetration in hot fluidized beds with a modified Pitot-tube probe. Ind. Eng. Chem. Res. 27, 1011–1016.
- [7] Hau, K.F., Banerjee, S., 1981. Measurement of mass flux in two phase flow using combinations of pitot tubes and gamma densitometers. AIChE Journal 27, 177–184.
- [8] Postrioti, L., Battistoni, M., Ungaro, C., Mariani, A., 2011. Analysis of Diesel Spray Momentum Flux Spatial Distribution (SAE Technical Paper No. 2011-01-0682). SAE International, Warrendale, PA.
- [9] Fink, C., Pinkert, F., Harndorf, H., 2011. Experimental Characterization of Injection Sprays of Medium Speed Diesel Engines. ILASS 2011
- [10] Pinkert, F., Najar, I., Schmalhorst, C., Frobenius, M., Fink, C., Harndorf, H., 2013. Impact of nozzle and spray-hole design on mixture formation at medium-speed diesel engines. CIMAC Congress 2013, Shanghai.
- [11] Kastengren, A.L., Powell, C.F., Wang, Y., Im, K.-S., Wang, J., 2009. X-ray radiography measurements of diesel spray structure at engine-like ambient density. Atomization and Sprays 19, 1031.

## Influence of nozzle hole eccentricity on spray morphology

Andreas Schmid<sup>1</sup>, Beat von Rotz<sup>1</sup>, Reiner Schulz<sup>1</sup>, Kai Herrmann<sup>1</sup>, German Weisser<sup>1</sup> and Rolf Bombach<sup>2</sup>

1: Wärtsilä Switzerland Ltd., Winterthur, Switzerland

2: Paul Scherrer Institute, Villigen PSI, Switzerland

### Abstract

Large marine two-stroke diesel engines have an injector geometry, which differs substantially from the configurations used in most other diesel engine applications, as the injector orifices are distributed in a highly non-symmetric fashion. In order to experimentally assess the impact of key features of such orifice arrangements on spray morphology, orifice eccentricity relative to the injector axis in particular, a dedicated test setup has been realised, including the development and application of tailor-made data processing routines. The high-speed camera recordings of the Mie-scattering data obtained simultaneously for two perpendicular views of single sample sprays have been analysed in terms of spray tip penetration and spray angle as well as with respect to the orientation of the spray. These analyses confirm the complex three-dimensional structure of sprays at such conditions: They are in fact far from rotationally symmetric – specifically when high levels of eccentricity apply – and the actual orientation of their axis in such cases clearly deviates from the nominal one, normally assumed to be in line with the orifice axis. These deflections are in the range of 10° and they apply not only in the direction of the eccentricity but also perpendicular to it. Additional effects arise from the geometric configuration of the central bore of the injector, upstream of the orifice, and when varying the injection pressure. In the case of high eccentricity, moreover, a clear pattern can be discerned in the initial evolution of the spray deflection: Starting from a slight deflection in the direction of the eccentricity, the spray axis moves first to its nominal direction and then gradually changes orientation again towards the level of stabilisation.

### Introduction

In contrast to other diesel engine applications, large two-stroke marine diesel engines are equipped with at least two injectors, which are protruding from the side of the cylinder head into the combustion chamber. The fuel is injected into a cylinder charge characterised by significant swirl levels, via typically five orifices per injector. As a consequence, the injectors are highly non-symmetric, in contrast to the designs typically used in all other types of diesel engines. Figure 1 shows a sample design of the tip of such injector.

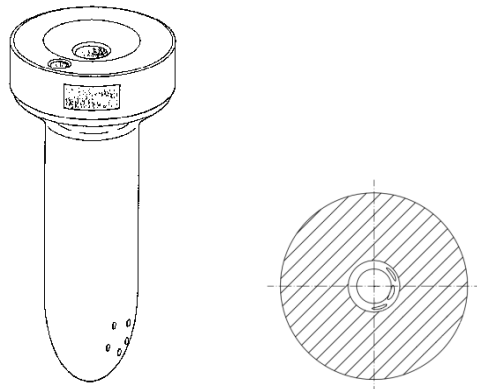


**Figure 1.** Sample design of typical fuel injector tip (left), cross-section through orifice region (right).

In order to achieve an optimum distribution of the fuel in the combustion chamber, the individual orifices are normally sized differently and covering only a relatively small range of angles on a plane perpendicular to the axis of the injector. This small range of angles of the orifices requires the suitable selection of their arrangement without unnecessarily prolonging the injector tip as this would result in excessive heating of the (uncooled) injectors, thus reducing their lifetime. On the other hand, fundamental mechanical stability requirements dictate a minimum distance between the orifices. In order to meet those requirements, the design of individual orifices involves non-negligible levels of eccentricity of the orifice axis relative to the injector axis.

Preliminary investigations by means of LES simulations [1] showed that the liquid core is no longer symmetrical in case of eccentric arrangements of the nozzle hole with respect to the central bore of the injector. First pre-tests [2] verified experimentally that nozzle hole eccentricity has a non-negligible effect on spray morphology. Based on these findings, the present, more extensive study was initiated.

### Experimental setup

The investigations were performed making use of the Spray Combustion Chamber (SCC), an optically accessible constant volume chamber of dimensions representative of smaller two-stroke as well as larger four-stroke marine diesel engines (Ø500x150mm) [3] and validated at conditions typical of those engines [4].

Figure 2 shows a schematic of the test facility, illustrating the working principle of the experimental setup: A pressure vessel equipped with fast opening valves feeds process gas via a heater, the so-called regenerator, into the SCC. Pressure and temperature levels as well as swirl in the spray combustion chamber are adjustable by changing accumulator pressure and/or duration of the blow down process and heater core temperature. By starting the injection with sufficient delay after the end of the blow-down process, due to the continuous decay of the swirl, quasi-quiet conditions can also be realised.

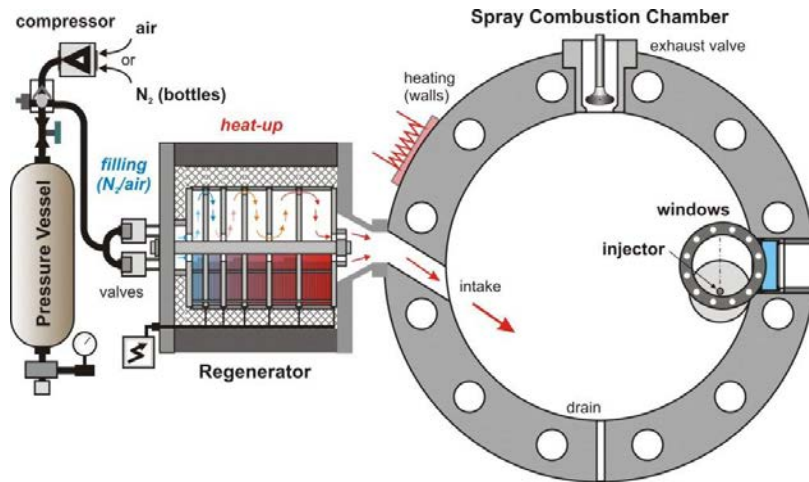


**Figure 2.** Spray Combustion Chamber schematics.

where the morphology of sprays has been analysed from a perspective perpendicular to the injector axis, the current experiments specifically target the observation of the spray in a direction parallel to the axis of the injector. Hence, whereas the earlier tests made use of an improved shadow-imaging technique [5], which is relying on the availability of optical access options in front and in the back of the item under investigation, the Mie scattering technique had to be applied in this context. However, in order to obtain additional information on the three-dimensional behaviour of the spray, the spray was simultaneously observed from the side by means of a second window and high-speed camera. A Nd:YLF-Laser was used for illuminating the liquid phase of the spray. The scattered light was then captured with two high speed cameras operated at 20 kHz, which were located in front and on the side of the spray.

Figure 3 shows the optical setup, with the injector mounted on the back side of the SCC and the two cameras in the front and on the side of the chamber. Camera one was flanked by the two illumination beams: With the help of a beam splitting cube, the laser light was separated into two part-beams which were then guided past both sides of the front camera. Using such setup resulted in a more homogenous illumination of the spray and therefore an easier detection of possible asymmetry in the spray pattern.

In order to enable the investigation of the isolated effect of orifice eccentricity on spray morphology, a special injector configuration has been developed, shown in Figure 4 (right photograph): The theoretical direction of the spray originating from the single orifice located at a certain eccentricity with respect to the axis of the injector is indicated by the red arrow. In order to realise the same flow conditions at the inlet of the injector as in a five-hole injector, a second orifice with correspondingly enlarged flow area is located at sufficiently large distance downstream of the first orifice for avoiding any disturbance of the flow into the latter. Any potential impact of this second orifice on the processes inside the SCC is avoided by redirecting the fuel flowing past it into a plenum outside the SCC (black arrows in right photograph of Figure 4). The injector was positioned in the back cover, via an adapted dummy device, which was mounted instead of a window. The left photograph in Figure 4 gives an impression of the complete assembly of this “injector in dummy” configuration, including the mounted injector, the nozzle with the eccentric single-hole and the fuel discharge system.

Figure 4 additionally illustrates the main design parameters varied in this investigation: A frontal cut of the nozzle (view A-A) visualizes the eccentricity  $e$ , the nozzle hole diameter  $d$  and the diameter  $D$  of the main bore through the injector tip. Sectional view B-B shows the inner geometry of the nozzle tip. Two types of designs were tested, in consideration of the expected different conditions for the flow approaching the nozzle hole: Whereas Type 1 was designed such that the fuel flows towards the orifice in a more or less undisturbed way

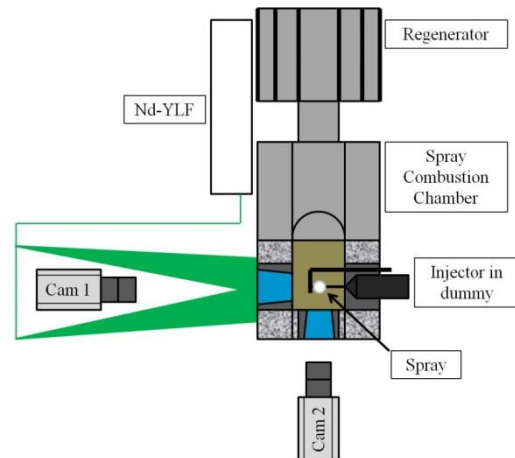


**Figure 3.** Optical setup at the Spray Combustion Chamber (SCC).



almost perpendicular to its axis, Type 2 is characterised by a backward facing step upstream of the nozzle hole. The intention was to generate strong turbulence at the entrance to the nozzle hole.

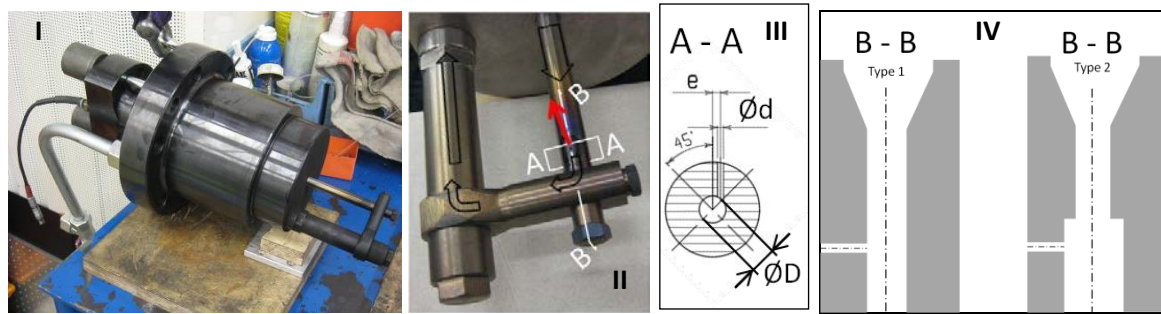


**Figure 4.** Injector design: Complete “injector in dummy” assembly (I), close-up view of injector arrangement including flow directions (II), injector frontal sectional view (III) and transversal sectional view (IV)

## Results and Discussion

The present investigations were applied with air as the process gas at chamber conditions of 4 MPa and 400 K in the absence of swirl. Table 1 gives an overview on the different measurement points. Beginning with the reference case (Case # 1: Type 1 nozzle, injection pressure 80 MPa, eccentricity  $e = 0$ ) the pressure of the light fuel oil in the rail has been varied from 60 to 100 MPa. The eccentricities  $e$  have been normalised to  $e = e_{real} / (D/2 - d/2)$  and have been varied from 0 up to 0.8.

Case #	1	2	3	4	5	6	7	8	9	10	11	12	13	14	15
Normalised eccentricity	0	0	0	0.80	0.80	0.80	0.40	0.40	0.40	0.59	0.59	0.59	0.29	0.29	0.29
Rail pressure [MPa]	80	100	60	60	80	100	100	80	60	100	60	80	80	100	60
Nozzle type	1	1	1	1	1	1	1	1	1	2	2	2	2	2	2

**Table 1.** Overview of measurement conditions

### Qualitative spray behaviour

The qualitative impact of the eccentric arrangement of an orifice with respect to the axis of the central bore of the injector on the fully established spray is illustrated in Figure 5: Whereas, in the absence of eccentricity, the actual axis of the spray coincides with the theoretical one, the spray is significantly deflected from the orifice axis with high eccentricity. The deflection is in the range of 10°, in the direction of the eccentricity.

An interesting effect can be observed during the initial phase of injection, before the spray is fully developed, specifically at high eccentricity (see Figure 6): Initially, a small portion of the fuel seems to leave the orifice at low velocity in a direction opposite of the direction of the eccentricity and the later stabilisation of the spray. In the course of the further development, the spray then first seems to follow the theoretical axis defined by the orifice direction and is then gradually more and more deflected towards the direction of the eccentricity, before it finally stabilises.

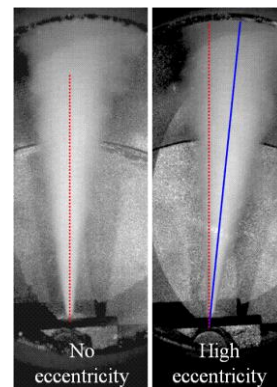


**Figure 5.** Spray deflection due to eccentricity.



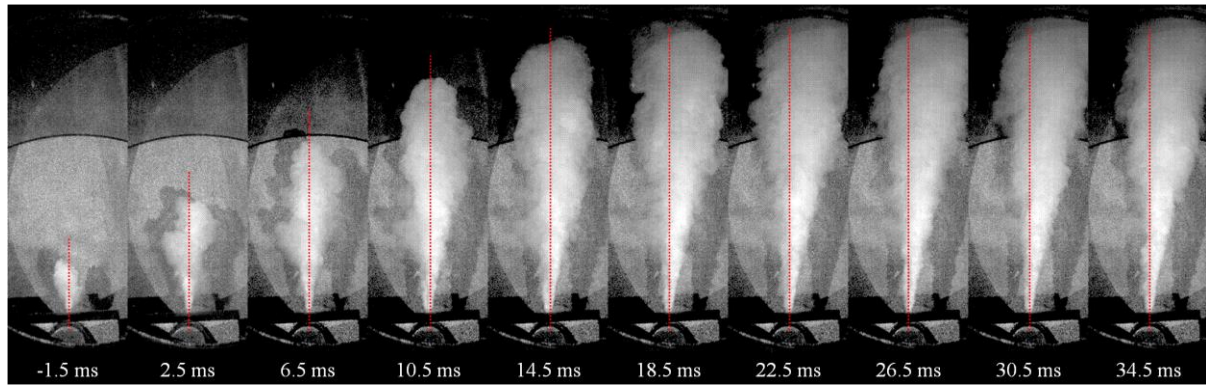


**Figure 6.** Temporal evolution of spray at maximum eccentricity.

#### Data processing for quantitative analyses

The presence of a metallic surface on the back of the cell poses significant challenges to the automation of image processing: The strong reflections made it virtually impossible to distinguish between spray and background merely on the basis of intensity differences. Therefore, a sophisticated filtering method had to be devised, which was subsequently applied to all individual images. Figure 7 gives an overview of the different steps:

The raw image (a) was first filtered with a so called range-filter. Due to the optically rough metal surface, the background showed different frequency behaviour compared to the much smoother surface of the illuminated spray (b). In order to amplify these differences the image was then divided by an average-smoothed version of the image. This led to a distinct separation between the spray plume and the background (c), which could then easily be filtered via a threshold (d). With the help of this image, both the spray penetration and the spray angle have been determined. This image was then defined as the region of interest, which was applied again to the raw image, resulting in the spray plume without any disturbances (e). This image was finally processed with a strong average filter. At a distance of 40 times the nozzle-hole diameter ( $40 \cdot d_0$ ), the angle between the nozzle hole symmetry axis (nominal spray axis) and the deflected spray plume axis was determined. For this purpose, the intensity distribution across the spray plume was taken. The maximum of this distribution was then defined as the spray axis.

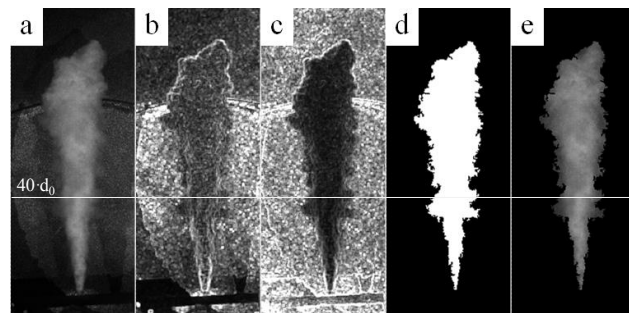


**Figure 7** Image processing steps.

This analysis was performed for each image of each measurement series of each realisation of each individual case. Note that, per case, ten high speed recordings were acquired. As an example, Figure 8 shows the spray

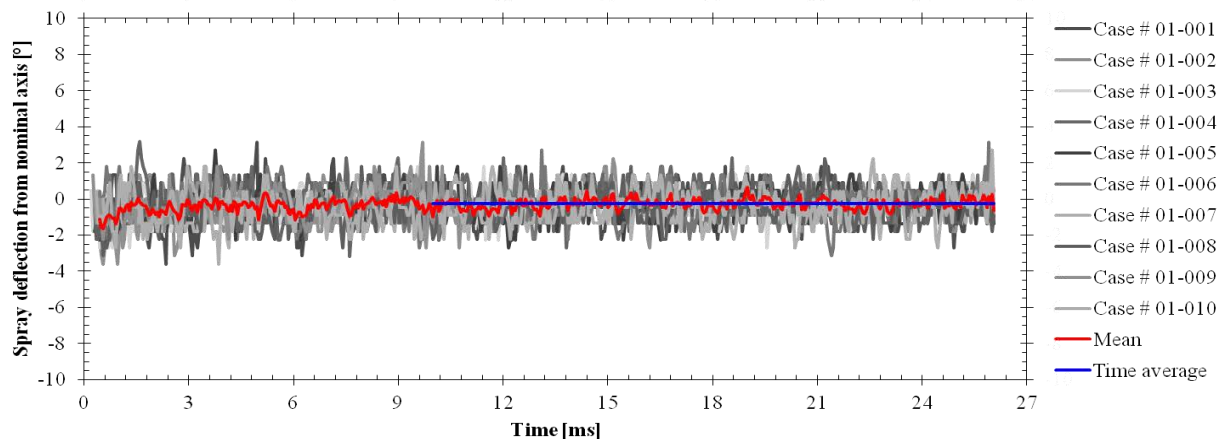


**Figure 8.** Spray deflection from nominal spray direction for the reference case with the mean value on top and the single value calculated from 10 to 26 ms. Time is set to zero for the arrival of the spray at  $40 \cdot d_0$ .

deflection from the nominal spray axis for the ten realisations of the reference case over a time period of 26 ms, with the start time defined as the timing of the arrival of the spray at the measuring location.

The curve of the averaged values over all ten measurements is plotted on top of the individual experiments (red curve). With the help of this mean value data plot two phases can be determined: During a first phase, up to about ten milliseconds, the axis of the spray is varying quite significantly. After that period, the spray axis has been established at a stable position, around which it continues fluctuating until the end of injection. The range for this fluctuation is within the standard deviation of all ten measurements, which is about  $0.82^\circ$  for the reference case during this second (stabilised) phase. The time average of the mean value data of all ten measurements for the period after stabilisation (at about 10 ms – blue line) is then used for comparing the results of different cases. For the reference case shown here, this single value characterising the spray deflection from the nozzle axis is about zero.

### Spray tip penetration

The penetration of the spray tip as a function of time for different levels of eccentricity (and nozzle types) at otherwise identical conditions (chamber pressure and temperature, rail pressure = 80 MPa) is shown in Figure 9. Note that the region below ca 10 mm from the orifice exit had to be excluded from the analysis for two reasons: Firstly, this region is partly shielded from the observation by the specific setup associated with the redirection of

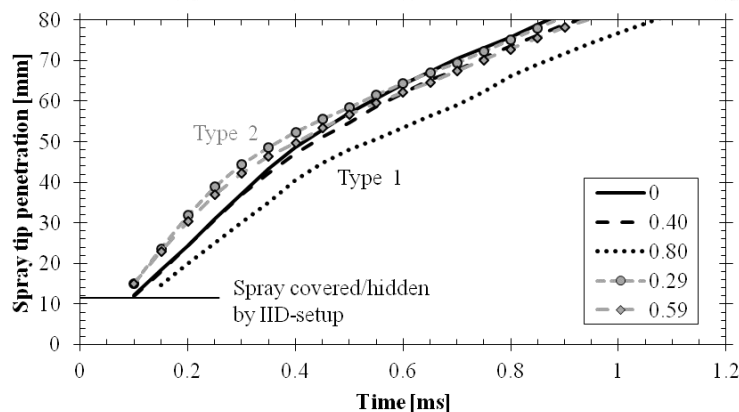


**Figure 9.** Spray tip penetration for the two nozzle types (Type 1 in black, Type 2 in grey) at different eccentricities.

the velocity during the linear phase and slows down spray tip penetration around the break-up length and during the second phase. In the large eccentricity case, the linear velocity is already clearly reduced. Whereas the break-up length is not influenced by different degrees of eccentricity, the second phase of the penetration shows an unsteady behaviour with higher eccentricity and also the shape is different: The second phase becomes more linear instead of the root shape as in the reference case. The reason for this particular behaviour is at present not fully understood.

The grey curves in Figure 9 show that the nozzle design (and the associated flow conditions at the inlet of the orifice), have a strong effect on spray penetration. Compared to the reference case, with Type 2 nozzles, the fuel exits the orifice at higher velocity until it reaches the break-up length. Apparently, it then undergoes a stronger reduction of spray tip velocity. The reason for all this is suspected in the reduced velocity due to the sudden increase in flow area within the nozzle (backwards facing step before the orifice, compare Figure 4 on the right side). This reduction in flow velocity (about 60%) increases the static pressure in the region of the orifice compared to the level of Type 1 nozzles, which, together with the different turbulence levels at the orifice inlet must be expected to have an impact on the formation and propagation of the spray. Unfortunately, the data available do not allow a conclusive statement on any potential effect of eccentricity.

### Spray angle

Figure 10 shows the time averaged spray angles for both nozzle types as a function of eccentricity. The upper data plot shows the “front view” spray angle (observed with camera 1) and the lower shows the “side view” spray angle (observed with camera 2).

For the reference case, the values of the “front view” and “side view” angles are at  $20.5^\circ$  and  $21.9^\circ$ , respectively, which clearly indicates that the spray is not rotationally symmetric with respect to its axis, but rather characterised by an elliptic shape. This had to be expected as a consequence of the change of direction of the flow by  $90^\circ$  at the inlet of the orifice, which is resulting in a significantly more pronounced distribution of all key parameters in direction of the injector axis compared to the transversal direction.

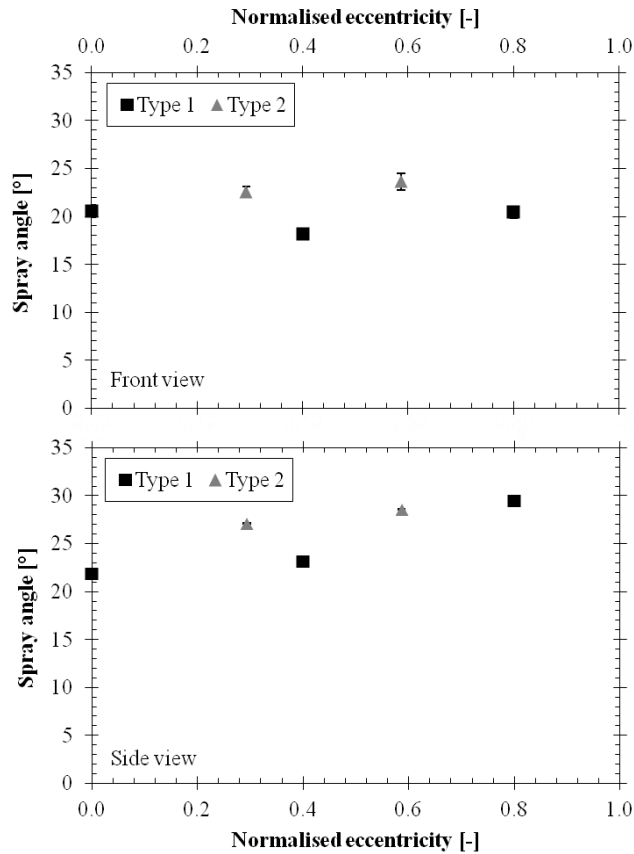


**Figure 10.** Spray angles in front (top) and side (bottom) views as a function of eccentricity.

It is worthwhile noting that, with Type 1 nozzles, the “front view” spray angle does not vary much as a function of eccentricity: Whereas the angle at intermediate eccentricity appears to be slightly lower than the one in the reference case, it is virtually back at the same level with the maximum eccentricity case.

In contrast, the “side view” angle shows a clear trend towards higher values with increasing eccentricity. Whilst the increase at intermediate eccentricity can be considered as sort of balancing the moderate decrease of the corresponding “front view” value, the level achieved at maximum eccentricity is significantly higher. Note that the elliptic structure of the spray is becoming clearly more pronounced with increasing eccentricity: Starting from a level of 1.07, the ratio of the angles observed in side and front views, respectively, increases to 1.28 at intermediate and 1.44 at high eccentricity level.

In the maximum eccentricity case, the average spray angle is clearly increased when compared to the reference and intermediate eccentricity cases, which is sort of consistent with the reduced penetration observed in this case (compare Figure 9).

For Type 2 nozzles, largely similar considerations apply; though, trendwise, the spray angles with those nozzles are generally higher than with the Type 1 variants. This was basically expected as a consequence of the

anticipated higher turbulence level at the inlet of the orifice. The sprays are also clearly non-symmetric and both the “front view” and “side view” angles seem to increase linearly as a function of eccentricity.

### ***Spray deflection (stabilised spray)***

In Figure 11, the spray deflection from the nominal axis is plotted as a function of eccentricity for Type 1 and Type 2 nozzles. The data have been normalised by referencing them to the maximum deviation measured at reference conditions (Type 1 nozzle, rail pressure 80 MPa). The upper diagram shows the radial deflection determined from the front view images (camera 1), whereas the lower diagram includes similar data for the “axial” deflection obtained from the side view images (camera 2). Note that the analysis procedure in this case has been slightly different, due to the fact that the spray was illuminated only from the front (compare Figure 20) such that the intensity distribution analysis might have lead to erroneous results. Instead, the spray axis is set at the middle of the contour of the spray. The subsequent identification of the stabilised spray angle from the data obtained from the individual images of the individual realisations of the respective cases then followed again the procedure outlined above.

Whereas the deviation of the actual from the nominal spray axis is close to zero in the reference case, sprays originating from Type 1 nozzles at increasing levels of eccentricity are characterised by progressively rising radial deflection  $s$ , in direction of the eccentricity  $e$ , a behaviour, which can be approximated by the function:  $s = (1.25 \cdot e)^{2.5}$ . With Type 2 nozzles, the effect seems to be less pronounced – in this case, the radial deflection rather follows a linear relationship with eccentricity:  $s = 0.9 \cdot e$ .

It is interesting to note that the deflection is not limited to the direction of the eccentricity (see axial deflection graph in Figure 11): Whereas the actual spray orientation in the reference case again coincides well with the nominal one (no deviation from the orifice axis), we observe a non-negligible deflection of the spray in direction of the flow in the central bore of the injector, specifically with the Type 2 nozzle cases and at high eccentricity with the Type 1 nozzle. In the case of the Type 2 nozzles, there seems to be no significant impact of eccentricity, at least not within the range considered here. The fact that the deflection with this type of nozzle is more pronounced than with the Type 1 variants at similar eccentricity could be attributed to the fact that the flow conditions at the inlet of the orifice are expected to be substantially different due to the effect of the recirculation region establishing at the backward facing step upstream of the orifice. The axial deflection of the spray at

maximum eccentricity with the Type 1 nozzle is at almost 30% of the radial deflection at the same conditions, which is again a strong indication of the pronounced three-dimensional character of sprays generated at such conditions.

For each of the presented cases, a rail pressure variation has been performed. Whereas the general spray behaviour in terms of penetration and angle has been in accordance with expectations (not discussed here in detail for the sake of brevity), there is an additional effect on the deflection of the spray. Figure 12 shows the nominal deflection in radial direction for both nozzle types obtained in tests at their respective maximum eccentricity (0.8 for Type 1, 0.59 for Type 2) as a function of rail pressure, which has been varied between 60 and 100 MPa.

Both nozzle types show similar behaviour: The spray deflection is clearly reduced with increased rail pressure, with the effect being relatively more pronounced in the case of the Type 2 nozzles. One can assume that the higher momentum of the spray outweighs the effects responsible for the deflection of the spray such as non-symmetric flow characteristics at the orifice inlet and non-uniform friction distribution inside the orifice due to the larger surface area on the side of the eccentricity. As the latter is of lower relevance in the Type 2 nozzle case, the flow distribution effects can be suspected to be dominant.

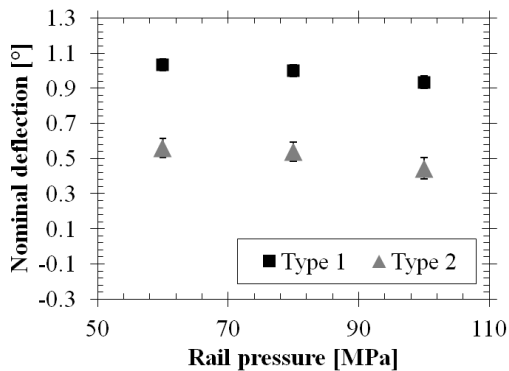


**Figure 12.** Influence of rail pressure on radial spray deflection at the respective maximum eccentricity.

behaviour: The right diagram in Figure 13 compares the evolution of the spray axis orientation during the same first four milliseconds for the 60, 80 and 100 MPa rail pressure cases. The general pattern is similar in all the cases; however, there are differences in the minimum deflection levels observed and also in the speed at which the orientation approaches the stable deflection level: On the one hand, with high injection pressure, the spray axis is no longer reaching its nominal direction. On the other hand, with reduced injection pressure, the stabilisation process takes considerably longer.

The background for this particular behaviour is at present not well understood. It requires further and more in-depth investigations, specifically into the transient fluid-dynamic effects governing the flow inside the injector in general and inside the orifice in particular.

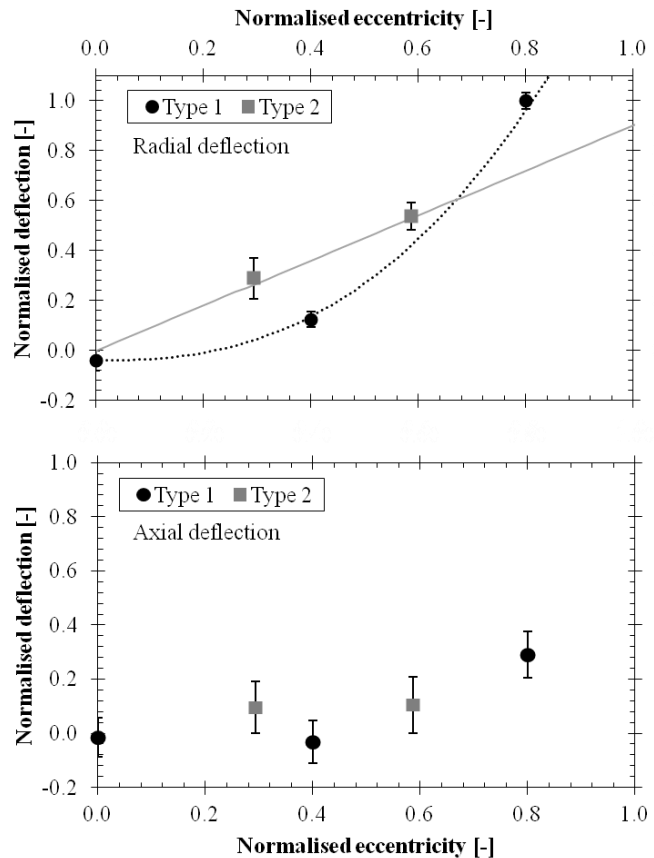


**Figure 11.** Axial (top) and radial (bottom) deflection of stabilised sprays from their nominal axis as a function of eccentricity.

### Transient spray deflection behaviour

The highly transient evolution of the spray deflection during the initial phase illustrated in Figure 6 has also been analysed quantitatively. The left diagram in Figure 6 shows the deviation of the actual spray axis orientation from the nominal axis as a function of time for three levels of eccentricity with Type 1 nozzles, during the first four milliseconds.

With the reference and intermediate eccentricity cases, we observe quite some fluctuations; however, no clear pattern can be recognised. This is different in the high eccentricity case, where, starting from a slight deflection in the direction of the eccentricity, the spray axis moves first to its nominal direction and then gradually changes orientation again towards the level of stabilisation.

Injection pressure also has an impact on this initial

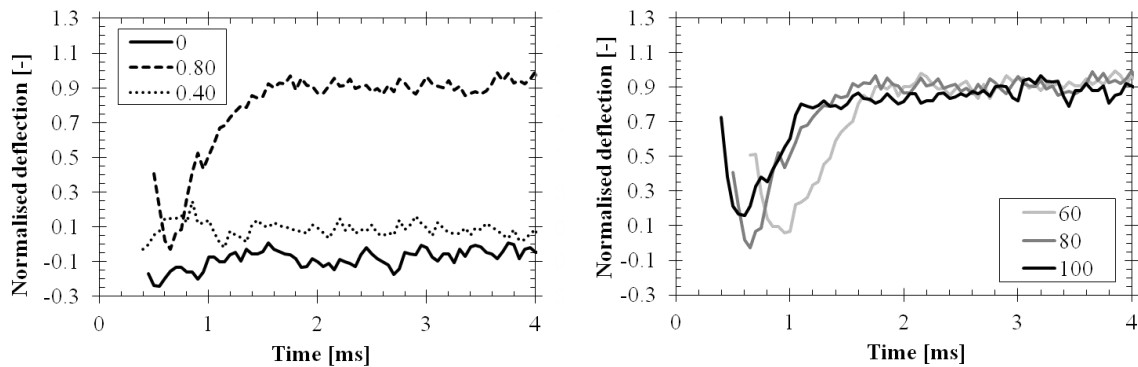


**Figure 13.** Transient behaviour of the spray axis for three different eccentricities (left) and at maximum eccentricity for three different rail pressures (right).

## Conclusions

The investigations confirm the findings of earlier pre-tests, in that the arrangement of the orifice relative to the central bore of the injector has a non-negligible impact on spray morphology; specifically, if non-negligible eccentricity levels are applied. In order to quantitatively assess such effects, a dedicated test setup has been realised, including the development and application of tailor-made data processing routines.

The key results of the present study can be summarised as follows:

- Fuel sprays in large diesel engines are basically non-symmetric. The rather elliptic shape of their cross-section is becoming even more pronounced with increased eccentricity.
- The eccentric arrangement of an orifice results in a deflection of the axis of a fully established spray from its nominal orientation, not only in the direction of the eccentricity but also in the direction perpendicular to it, with maximum deflection levels in the range of 10°. This is an additional confirmation of the complex three-dimensional structure of sprays at such conditions.
- The deflection increases as a function of eccentricity of the nozzle hole and is trendwise reduced with increasing injection pressure. The geometry of the central bore of the injector has an additional impact on the morphology of the spray.
- With high levels of eccentricity, a clear pattern can be discerned in the initial evolution of the spray deflection: Starting from a slight deflection in the direction of the eccentricity, the spray axis moves first to its nominal direction and then gradually changes orientation again towards the level of stabilisation.

The present results already provide an excellent basis for the better understanding of phenomena observed in large diesel engine combustion systems; however, further investigations are needed in order to explain in more detail and appropriately model the effects associated with injector geometry and injection parameter variations. For this purpose, both more in-depth experimental studies and computational investigations of the fluid dynamic aspects of injection systems are required.

## Acknowledgements

The present work has been conducted as part of the HERCULES-C project within EC's 7th Framework Program, Contract SCP1-GA-2011-284354. Additional financial support by the Swiss Federal Government (SFOE Contract 154269, Project 103241) is gratefully acknowledged. The authors thank Mr. Aleš Srna for his valuable support during the measurement campaign.

## References

- [1] Hensel S., Herrmann K., Schulz R. and Weisser G., COMODIA 2012, Fukuoka, Japan.
- [2] Schulz R., Hensel S., von Rotz B., Schmid A., Herrmann K. and Weisser G., CIMAC 2013, Paper No. 259, Shanghai, China, 2013.
- [3] Herrmann K., Schulz R. and Weisser G., CIMAC 2007, Vienna, Austria, 2007.
- [4] Herrmann K., Kyrtatos A., Schulz R. and Weisser G., ICLASS 2009, Vail, Colorado, 2009.
- [5] Herrmann K., von Rotz B., Schulz R., Weisser G., Boulouchos K. and Schneider B., ILASS 2010, Brno, Czech Republic, 2010.
- [6] Hiroyasu H. and Arai M., SAE 900475 (1990).
- [7] Naber J.D. and Siebers D.L., SAE 960034 (1996).
- [8] von Rotz B., Herrmann K., Weisser G., Cattin M., Bolla M. and Boulouchos K., ILASS 2011, Estoril, Portugal, 2011.

## Effects of the Nozzle Geometry on Fuel Dispersion in Non-Evaporative and Evaporative Conditions for a Diesel Injector

Allocca L.<sup>1</sup>, Lee S.Y.<sup>2</sup>, Marchitto L.<sup>1</sup>, Montanaro A.<sup>1</sup>, Naber J.<sup>2</sup>, Zhang A.<sup>2</sup>

1: Istituto Motori – CNR, Napoli 80125, Italy

2: Michigan Technological University, Houghton, MI, 49931, USA

### Abstract

Schlieren - Mie-scattering combined technique for image acquisition were built-up to study the liquid and vapor phases of a diesel fuel at engine-like conditions. The sprays were generated by a Common Rail injection system fuelling two axially-disposed single-hole injectors with k-factors 0 and 1.5. Three injection pressures were explored, 70, 120, and 180 MPa, while the sprays developed in a quiescent vessel filled with inert gas. The gas temperature varied from 373 to 900 K realizing both non-vaporizing and vaporizing conditions at back-densities typical of a diesel engine. Spray contours and penetrations of the liquid and vapor phase were extracted by processing the images of the spray acquired by a high-speed camera (40,000 fps) and enlightened by two pulsed LED light sources. The images were analyzed by digital processing software for distinguishing fuel spray from ambient gas. Mie-scattering for liquid phase and schlieren imaging visualization techniques for fuel evaporation were applied and the effects of the nozzle shapes on the fuel dispersion will be discussed.

### Introduction

The atomization of the fuel and the mixing with the air are factors that strongly influence the diesel engine mainly in terms of performances and emissions. Spray fluid dynamics are controlled by the fuel dispersion and the atomization processes in the combustion chambers. Typically, modern diesel engines use high injection pressures and micro-orifice ducts to feed the fuel and optimize the droplet rupture and vaporization. The nozzle hole geometry k-factor plays a non-negligible role in the fuel atomization and dispersion in the combustion chamber [1]. It is determined by elements like length, inlet/outlet diameter (conicity), roughness of the internal surface and roundness of inlet edges. Nozzles with different grade of conicity were compared in literature and interest on regions very close to the nozzle tip was developed by high magnifications of images and use of microscope-type collecting lenses. Different penetrations for conical nozzles were found with respect to the cylindrical ones reaching values up to 10%, depending on the k-value, such as different shapes in the fuel injection rate were related to the conicity [2,3]. The geometric factor influences the flow distribution downstream the hole exit determining the liquid core length. Several analytical relationships on the penetration were adopted to correlate the k-factor to the fuel dispersion and fuel velocity typically in a nearly constant level of the injection rate [1,4,5]. Aim of this paper is to study the effects of the nozzle geometry on the diesel spray using visualization techniques in the contest of collaboration between the Michigan Technological University and the Istituto Motori-CNR (Italy). Mie-scattering for liquid phase and schlieren imaging visualization techniques for fuel evaporation were applied. Measurements were carried out both in a high-pressure non-evaporating constant volume vessel at IM for the liquid phase and in a high pressure and temperature chamber at the MTU for the evaporative phase at 900 K, representative of advanced engine conditions. The work discusses the peculiarities of the two experimental set-ups, displays the results obtained with different facilities and provides a useful set of experimental data on non-vaporizing and vaporizing diesel spray at typical diesel engine condition for simulation applications and modelling approaches.

### Experimental test-rig

The fuel spray injection processes were characterized under both non-vaporizing and vaporizing environments to explore the effect of the nozzle geometry on liquid and vapor phase distributions at engine-like conditions. Two single-hole axial-disposed injectors (0.100 mm in diameter and 10 L/d ratio) with different k-factor (0 and 1.5) were studied. At Istituto Motori (IM) the non-vaporizing conditions were investigated in an optically-accessible vessel well controlled in temperature and pressure. At Michigan Technological University (MTU) the vaporizing conditions were studied by using a preburn-type combustion vessel to realize high-temperature and high-pressure gases in the volume. Moreover, the non-evaporative conditions were replicated at MTU too in order to compare the results with those obtained in IM. Finally, fuel injection rate measurements were carried out at IM by an AVL flow rate meter working on Bosch tube principle.

Three different fuel injection pressures (70, 120, and 180 MPa) were tested with a single pulse mode. A total injection duration of approximately 2.0 ms was used by setting the energizing solenoid current at 1 ms for all the tested cases. A summary of the test carried out at IM and MTU laboratories are reported in table 1. For IM tests a commercial diesel fuel was used while the MTU ones were conducted with the ultra-low sulfur diesel (ULSD).

The fuels have similar chemical-physical characteristics except for the cetane rating of 40 (MTU) and 46 (IM), respectively.

**Table 1.** Summary of the tests performed in this study

	IM	MTU	
k0/k1.5	$p_{inj}$ : 70-120-180 MPa $T_{ch}$ : 298-373-453K $\rho$ : 23.9 kg/m <sup>3</sup>	$p_{inj}$ : 70-120-180 MPa $T_{ch}$ : 373-453K $\rho$ : 23.9 kg/m <sup>3</sup>	0% O <sub>2</sub> $p_{inj}$ : 70-120-180 MPa $T_{ch}$ : 900K $\rho$ : 23.9 kg/m <sup>3</sup>
Diagnostic techniques	Mie Scattering	Mie Scattering Schlieren	Mie Scattering Schlieren

### IM-Experimental setup

At Istituto Motori, measurements of instantaneous fuel injection rates and spatial-temporal evolution of the jets sprayed from the nozzle in a spray bomb under non-evaporative conditions were conducted. The fuel injection rate was measured by an AVL fuel injection gauge rate system fitted on the Bosch tube inlet [6]. For the liquid spray evolution analysis, the test rig employed is a high temperature and high pressure test chamber where the thermodynamic conditions realized in a diesel engine at the injection time can be simulated in terms of density with a maximum ambient temperature of 600 K and pressure up to 6.0 MPa (N<sub>2</sub>). The chamber, 3L internal volume, has three large optical accesses (80 mm diameter) placed orthogonally in order to have a complete view of the injection event. The spatial and temporal evolution of the fuel was measured by analysing spray image captured at different times from the start of injection (SOI). SF<sub>6</sub> (specific density 6.2 kg/m<sup>3</sup>) was used in the vessel at the temperatures ( $T_{ch}$ ) of 296, 373, and 453 K realizing the desired gas densities ( $\rho$ ) at pressures lower than in air. SF<sub>6</sub> pressures of 0.39, 0.51, and 0.62 MPa was set in order to achieve gas densities of 23.9 kg/m<sup>3</sup> at temperatures of 296, 373, and 453 K, respectively. The images of evolving jets was captured by a Photron (FASTCAM SA4) high speed camera (14400fps@192x1024 pixels, 8.46  $\mu$ s shutter time) synchronized with both the injection system and a set of high intensity flashes disposed in an orthogonal configuration. A 90 mm macro-focal lens was used for the acquisition of images with a field of view capable to cover the complete penetration of the sprays with a spatial resolution of 12.4 pixel/mm. Five images of consecutive injections were acquired for each time-step at a fixed condition. The stability and uniformity of the evolving sprays made this repetition condition confident with the need of dispersion bars on the measuring parameters. Analysis of the liquid fuel spray images was carried out by processing in-house software to extract the main characteristics: edges determination, tip penetration, and cone angle. A sketch of experimental apparatus operating in IM for tests under non-vaporizing conditions and further details on the analysis procedure were reported in [7].

### MTU-Experimental setup

At Michigan Technological University the fuel spray was studied by delivering within a combustion vessel (CV) which is a constant volume visualization facility capable of withstanding high pressure (up to 345 bar) and high temperature (up to 2000 K). The CV features a cubical internal chamber with a 1 L internal volume. The six surfaces of the cube are made as removable windows and can be configured differently. For the current setup, the top window consists of two spark plugs and one mixing fan to generate homogeneous temperature environment with a pre-combustion. The fuel injector was mounted on one of the side windows and the other three sides of the cube are sapphire windows for optical access. The bottom of the cube is a stainless steel blank port. An intake valve, an exhaust valve and a pressure transducer have taken three corners of the cubic CV. A high-speed data acquisition system with 100 kHz sampling rate is available for recording CV pressure history. The Michigan Tech. CV facility was selected in Engine Combustion Network (ECN) as one of the facilities to provide “an open forum for international collaboration among experimental and computational researchers in engine combustion”. See the website (<http://www.sandia.gov/ecn/index.php>).

Modified Z-type schlieren imaging system was set up for this study. As shown in figure 1, the extended parallel beam was generated utilizing two schlieren mirrors ( $f_l = 750$  mm, 152 mm diameter with f-stop of 5) and a reflector. A high-intensity pulsed LED with a pin-hole aperture was used as a light source. The negative bi-convex focusing lens ( $f_l = 200$  mm) placed in front of camera was to adjust the field of view on the camera detector. The knife-edge was placed in a vertical position to generate density gradient along the injector axis. The final percentage cut off was adjusted based on the optimization between the schlieren sensitivity and intensity level obtained on the camera CCD at various exposure timing.



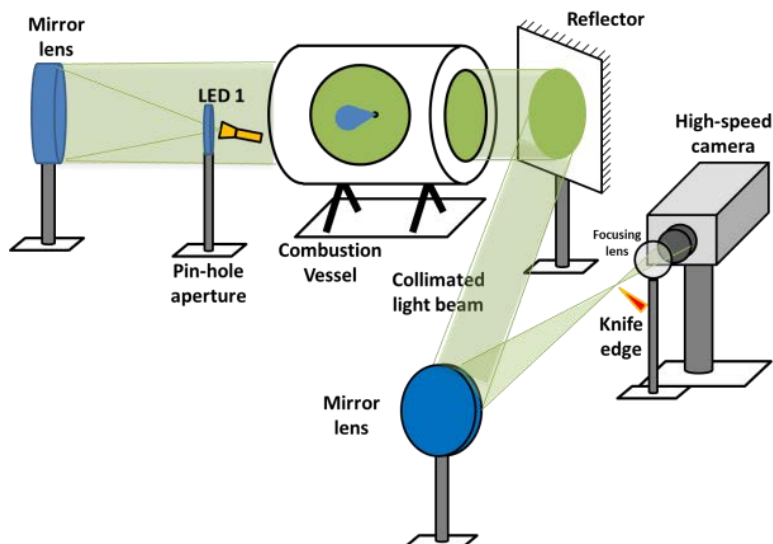


**Figure 1.** Optical setup of schlieren system in the Michigan Tech combustion vessel.

Illumination for Mie-scattering was provided by a second pulsed LED placed backside the top (non-vaporizing tests) or side (vaporizing tests) optical access of the CV. A cylindrical lens was located just downstream this LED to better focus the light along the spray axis. The resulting Mie-scattering images were collected along the same optical path utilized for the schlieren imaging. A Photron (FASTCAM SA1.1) camera was used. Two sets of camera settings were applied to non-vaporizing cases (40,000fps@704x192 pixel, 8.65  $\mu$ s shutter time) and vaporizing cases (25,000fps@768x288 pixel, 8.65  $\mu$ s shutter time) respectively. Mie-scattering and schlieren images were acquired alternatively starting from the Mie one. Moreover, the camera was equipped with a manual focus Nikon Nikkor lens focal length 85 mm and maximum aperture f-stop 1.8, obtaining a spatial resolution of 8.65 pixel/mm. The time resolved pair of schlieren and Mie-scattering images identifies the instantaneous position of both the vapor and liquid phases of the fuel spray, respectively.

Auto ignition of diesel spray requires relatively high temperature and pressure, which is similar to the condition of the end of compression stroke in a diesel engine. To generate such high temperature and pressure inside the combustion vessel, a pre-combustion procedure was designed and performed. A flammable preburn mixture of  $C_2H_2$ ,  $H_2$ ,  $O_2$  and  $N_2$  was mixed according to the volume fraction of 3.2%  $C_2H_2$ , 0.5%  $H_2$ , 8.2%  $O_2$  and 88.1%  $N_2$  in order to obtain inert conditions (0%  $O_2$ ) at the injection time. The 1-liter CV was filled with this mixture to 3.39 MPa, that corresponds to a gas density of 23.9 kg/m<sup>3</sup>. Once the desired density was reached, the intake and exhaust valves were closed to make the CV a constant volume closed system, thus the gas density was able to keep the same value during combustion process. Electrical spark was then triggered inside the CV to ignite the combustible mixture and the mixing fan starts to generate turbulence in order to make temperature distribution more homogeneous. Gas temperature rose to about 2000 K. After the combustion event, the CV temperature and pressure gradually decreased undergoing the cool down phase due to the heat transfer to the relatively cold CV walls.

Fuel injection was triggered when the desired target temperature (900 K) was reached during the cooling down process. Note that the initial  $O_2$  in the preburn mixture was consumed by the combustion of  $C_2H_2$  and  $H_2$  and therefore, the residual  $O_2$  mole fraction was about 0%. At these conditions the injected spray vaporizes only and doesn't auto ignite because of the zero oxygen level.

### Flow Rate Measurements

Figure 2 reports the fuel injection rate profiles for both injector types, k0 and k1.5, at all the investigated injection pressures. Each profile was the averaged result for one hundred shots to reduce the noise of the single measurement. The injected quantities are the integrals of each profile along the pulse durations. These measured values were compared with the weighted fuel collected at the discharge pipe; accordance in a range of 2% was found. The initial rise times of the signals are perfectly overlapping indicative of the reliability of the injectors. The close time and the stationary phase level increase with the injection pressure for both injectors. The different k-factor aspects didn't produce effects on the shapes rendering the graphs similar at the same injection pressure. Moreover, a delay of 0.34 ms of the injection rate profiles, respect to the start of energizing currents, was measured due to the hydraulic delay.

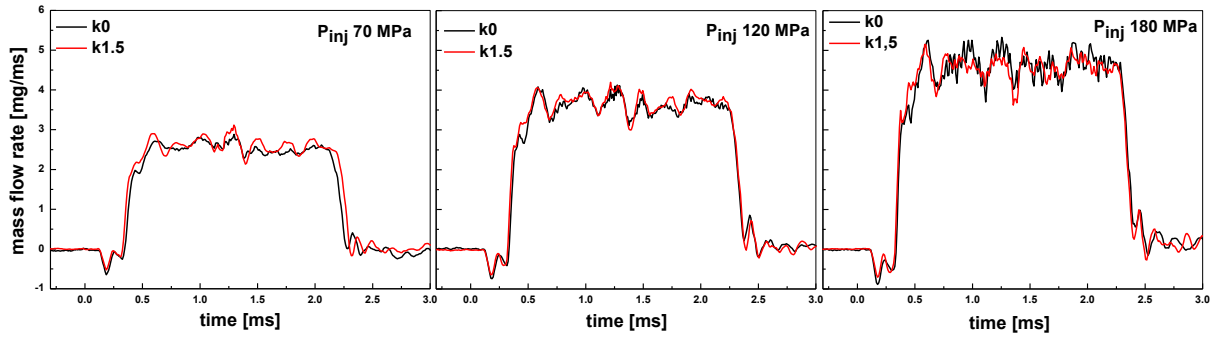


Figure 2. Mass flow rate profiles: k0 vs k1.5

In the table 2 the total amount of injected fuel per stroke ( $q_{inj}$ ) is reported for all the investigated injection pressures and both nozzle types. The k1.5 injects quantity slightly greater than k0 but this difference cancels out at increasing injection pressure.

Table 2. Injected fuel per stroke for the different injection pressures

Nozzle type / $Q_{inj}$	$P_{inj}$ 70 MPa	$P_{inj}$ 120 MPa	$P_{inj}$ 180 MPa
k0 / [mg/str]	4.35	6.88	9.07
k1.5 / [mg/str]	4.84	7.28	9.10

### Liquid spray penetration

The liquid spray penetration measures were carried out by Mie-scattering in IM and by Mie-scattering/schlieren optical techniques in MTU. Mie-scattering imaging sequences from single events, acquired at IM and MTU, are shown at equivalent time after SOI in figure 3a) for the k1.5 nozzle. The injection pressure is 120 MPa, the ambient temperature 453 K, and the gas density 23.9 kg/m<sup>3</sup>. The sprays develop in rather regular mode reaching equal penetration lengths at the same time indicating a good agreement between the two setups. However, slight spray shape differences are imputable both to differences in the light intensities and gas nature used to realize the backpressure in the vessel (SF<sub>6</sub> for IM and N<sub>2</sub> for MTU) [4,8]. Although the images from IM, left side, appear saturated, no influence on the penetration precision was registered.

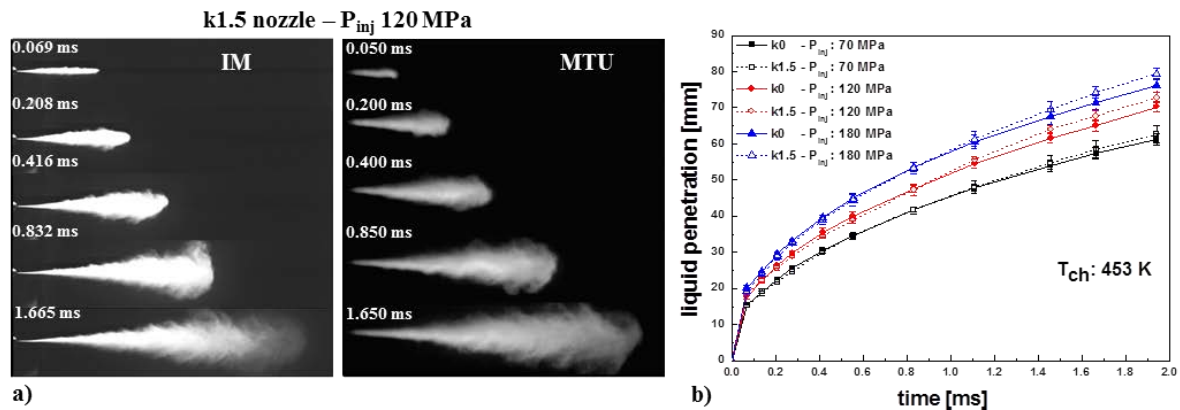
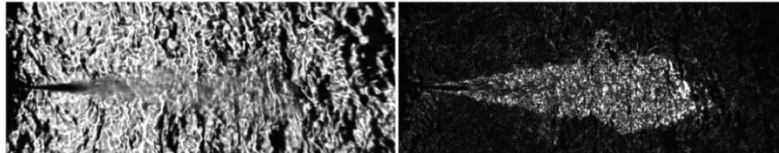


Figure 3. a) IM and MTU Mie-scattering imaging sequence; b) k0 vs k1.5 liquid penetration carried out at IM

Figure 3b) shows the comparison between k0 and k1.5 liquid penetration profiles versus time, at  $T_{ch}$ : 453 K and for the three injection pressures. The error bar displays the standard deviation due to shot-by-shot variation calculated on five images of consecutive injections. No significant differences in penetration appear until 1.2 ms after SOI. Later, a light prevalence of the k1.5 nozzle profiles appears mainly for the injection pressures of 120 and 180 MPa. It is hard to impute these prevalence to the greater amount of fuel injected by k1.5 nozzle, because the measured penetration is that of the “atomized fuel-entrained gas” mixture rather than pure liquid. In addition, the longer penetration at 180 MPa where equivalent mass was injected by the two nozzles indicates that the nozzle geometry has more significant effect on spray penetration.

### Liquid and vapor distribution

The liquid and vapor phase distribution of the sprays acquired at MTU laboratory was studied under non-reacting conditions spraying in the combustion vessel where the pre-burning of the gas generated high-temperature and high-pressure environment. The spray images from k0 and k1.5 injectors were processed to highlight the liquid and vapor phases, by using Mie-scattering and schlieren techniques, respectively. An anomaly in the background disturbed the images. It was caused by the time-varying refractive index of the hot combustion related to the fluid dynamic of the combustion products inside the CV. The early part of the spray shows a solid dark jet, mainly identified as the liquid phase of the emerging spray characterized by a high momentum and density. The schlieren spray images was processed by a background correction procedure,  $C*(I_n - I_{n-1}) + C*(I_{n-1} - I_n)$ , where  $C$  is a scale factor, in order to better determine the spray boundary by removing the differences between successive images [9,10]. Figure 4 displays a spray image without (left) and with (right) background correction.



**Figure 4.** Spray image without (left) and with (right) background correction.

Figure 5 shows a sequence of images, at different time after SOI, for k0 (left) and k1.5 nozzle (right), with boundaries of the vapor phase as emerges from the computer processing just described. By comparing each of the images it can be seen that the background doesn't change significantly between successive frames. The vapor area increases in regular mode for both nozzles and it seems to be more penetrating and thinner for the k1.5 with respect the k0 configuration. Similar trend was carried out for the other investigated conditions and both nozzle types.

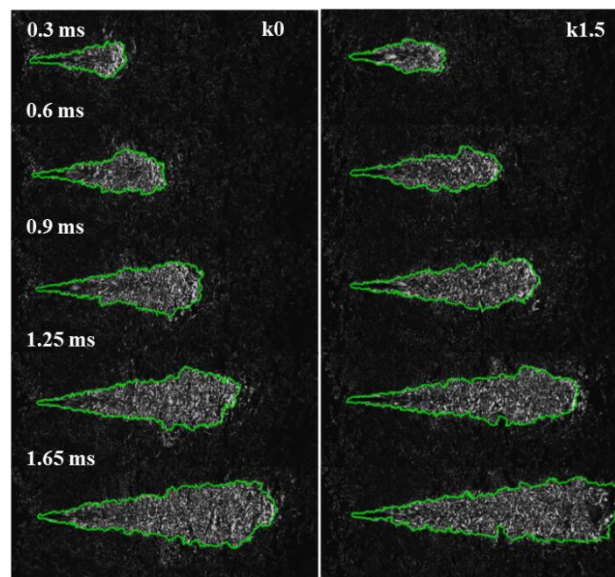


**Figure 5.** Schlieren images sequence with vapour boundary for k0 (left) and k1.5 (right) nozzles.  $P_{inj}$ : 120 MPa,  $T_{ch}$ : 900 K and gas density  $23.9 \text{ kg/m}^3$

The liquid as well as the vapor penetration lengths in non-reacting conditions (0%  $O_2$ ) are reported in figure 6 for both nozzles and the three injection pressures. Mie-scattering and schlieren images were used to extract the liquid and vapor measure, respectively. The spray forms and develops as follows: the liquid phase atomizes and penetrates up to a point where enough energy is entrained to heat up and vaporize the fuel. At this point liquid penetration stops while vapor phase still progresses downstream [11]. In all the conditions, the penetration of the liquid phase increases up to a value of 14 mm in about 0.1 ms. Then, it remains constant for all the injection duration. The liquid column length for the k0 configuration ranges between 13.89 and 14.39 mm at 70 and 180 MPa, respectively, while values slightly higher are registered for k1.5, at 15.26 and 14.67 mm under the same injection pressures. As regards the vapor phase, longer distances are reached at higher injection pressures because of the highest momentum impressed to the fluid. Differences appear in the penetration values between the k0 and k1.5 nozzle configurations with a prevalence of the vapor elongations for the k1.5 nozzle at all injection pressures.

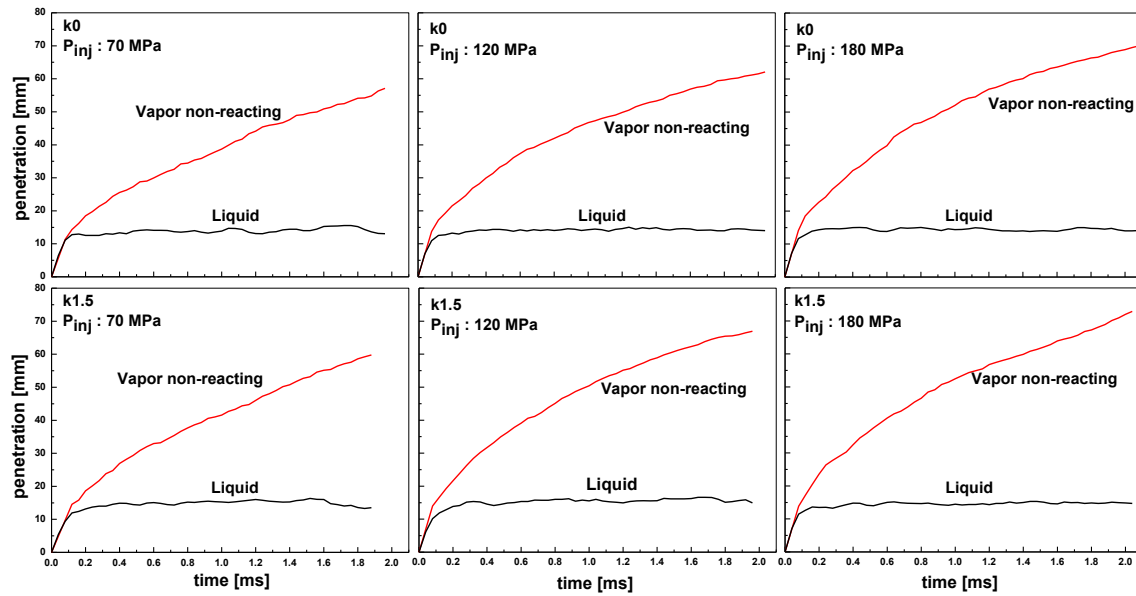


Figure 6. Liquid and vapor penetrations for k0 and k1.5 nozzles at all investigated injection pressures

Moreover, an important parameter for the engine combustion is to estimate the spatial distribution of the fuel. It was measured starting from the 2-dimensional images of figure 5. Under the hypothesis of an axial symmetry of the jets, the semi-surface of each image with respect to the spray axis was rotated on  $2\pi$  angle to obtain the total volume. The hypothesis of the jet symmetry is not always true but the discrepancies are randomly distributed around the jet axis and the average on a large number of shots, like in an engine, produces a substantial negligible error in the determination of the total volume. In figure 7, the volume of the vapor with respect to the total volume, is plotted versus the time from the SOI for k0 and k1.5 nozzles at injection pressures of 70 and 180 MPa. The profiles show similar behavior for both nozzles and injection pressures. At the injection pressure of 180 MPa, the vapor volume fraction reaches rapidly values of 90% at 0.25 ms and increases up to 96% at 0.45 ms. Small differences were registered for the 70 MPa condition with light delays in reaching analogous values. No substantial differences appear for k0 and k1.5 nozzles at 120 MPa.

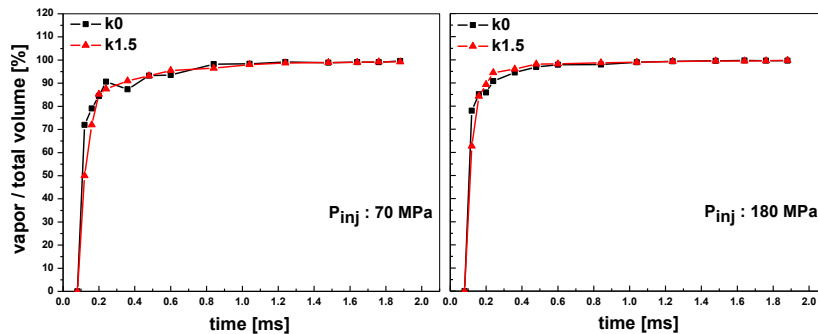


Figure 7. Vapor/total volume behavior for k0 and k1.5 nozzles at two injection pressures

## Conclusions

The fuel distribution generated by two single-hole diesel injectors ( $\Phi=0.100$  mm) with different k-factor (0 and 1.5) was studied in a constant volume combustion vessel simulating diesel engine conditions. The activity was carried out at Michigan Technological University for non-vaporizing and vaporizing conditions and, in parallel, at Istituto Motori for the non-vaporizing phase. Three injection pressures (70, 120, and 180 MPa), gas density of  $23.9 \text{ kg/m}^3$ , and gas temperature varied from 373 to 900 K were tested. Schlieren technique with high-speed camera permitted to acquire the evolution of the fuel vapor phase, while the liquid one was studied by using the Mie-scattering images.

The liquid penetration for k1.5 has an increasing trend with the injection pressure with respect to k0, resulting less penetrating at the lowest pressure and showing an increasing rate at growing pressures. At mounting temperature of the gas, the liquid lengths emerging from the two nozzles are equivalent with slight increasing values for k1.5 at longer time after the SOI.

The vapor phase, instead, penetrates continuously along the vessel with increasing values at the growing pressures; k1.5 configuration shows highest penetrations. The vapor volume, with respect to the total volume of the spray, reaches values of 90% at 0.25 ms and 96% at 0.45 ms after the SOI, respectively. No substantial differences appear in terms of vapor/total volume for k0 and k1.5 factors.

### Acknowledgements

The authors are grateful to Mr. Piersalvo Patanè for the support in carrying out the data analysis.

### Nomenclature

ULSD	Ultra Low Sulfur Diesel
SOI	Start Of Injection
CV	Combustion Vessel
CCD	Charge Coupled Device
fps	frames per second
$P_{inj}$	Injection pressure
str	stroke
$T_{ch}$	Chamber temperature
$Q_{inj}$	Injected fuel per stroke
$\rho$	Gas densities

### References

- [1] Kong, J., Bae, C., “Effect of Nozzle Hole Geometry on Non-Evaporating Diesel Spray Characteristics at High-Pressure Injection”, *Atomization and Sprays*, 22 (1): 1-21 (2012)
- [2] Payri, F., Bermúdez, V., Payri, R., Salvador, F.J., “The Influence of Cavitation on Internal Flow and Spray Characteristics in Diesel Injection Nozzle”, *Fuel*, vol. 83 no 4-5, pp. 419-431, 2004
- [3] Payri, R., Salvador, F.J., Gimeno, J., de la Morena, J., “Macroscopic Behavior of Diesel Sprays in the Near-Nozzle Field”, *SAE Int. J. Engines*, vol.1, no 1, pp. 528-536, 2008
- [4] Hiroyasu, H., “Spray Breakup Mechanism from the Hole-Type nozzle and its Applications”, *Atomization and Sprays*, vol. 10, no 3-5, pp. 511-527, 2000
- [5] Naber, J.D., Siebers, D.L., “Effect of Gas Density and Vaporization on Penetration and Dispersion of Diesel Sprays”, *SAE Trans, J. Engines*, vol. 105, no. 3, pp. 82-111, 1996
- [6] Bosch, W. “The Fuel Rate Indicator: a New Measuring Instrument for Display of the Characteristics of Individual Injection”, *SAE Paper 6607496*, 1966
- [7] Allocca L., Mancaruso E., Montanaro A., Vaglieco B. M. “Use of Mineral Diesel, 1st and 2nd Generation Biodiesels in Modern Common Rail Injection System under Non Evaporative and Evaporative Conditions”, *Atomization and Sprays 2012*, Vol.22 - n. 2, DOI: 10.1615/AtomizSpr.2012004362, ISSN: 1044-5110
- [8] di Stasio S., Alfuso, S., Allocca, L., Corcione F.E.: “Experimental Study on the Atomization Mechanism for Fuel Sprays Evolving in Atmospheres of Different Nature and Density” - *ImechE Seminar Publication 1999-17*, pp.241-255
- [9] Pickett, L., Genzale, C., Bruneaux, G., Malbec, L., Christiansen C., Schramm J. "Comparison of Diesel Spray Combustion in Different High-Temperature, High-Pressure Facilities," *SAE Int. J. Engines* 3(2):156-181, 2010, doi:10.4271/2010-01-2106
- [10] Pickett, L.M., Kook, S., and Williams, T.C., "Visualization of diesel spray penetration, cool-flame, ignition, high-temperature combustion, and soot formation using high-speed imaging," *SAE Int. J. Engines* 2(1):439-459, 2009, doi:10.4271/2009-01-0658
- [11] Pastor J.V., Payri R., Garcia-Oliver J.M., Nerva J.-G., “Schlieren Measurements of the ECN-Spray A Penetration under Inert and Reacting Condition” *SAE Paper*, doi:10.4271/2012-01-0456

## Optical Analysis of High-pressure Injections in Transparent Diesel Engine

Dragomirov P.<sup>1</sup>, Sauerhering J.<sup>1</sup>, Schmidt J.<sup>1</sup>, Rottengruber H.<sup>2</sup>, Tschöke H.<sup>2</sup>, Hadler J.<sup>3</sup>  
and Backofen D.<sup>2</sup>

1: Institute of Fluid Dynamics and Thermodynamics, University of Magdeburg “Otto von Guericke”, Germany

2: Institute of Mobile Systems, University of Magdeburg “Otto von Guericke”, Germany

3: Institute of automotive expertise, University of Magdeburg “Otto von Guericke”, Germany

### Abstract

The growing consumption of fossil fuels and the strict exhaust emissions regulations leads to the necessity to find clean, environmentally friendly and renewable alternative fuels. Even though alternative fuels have resemblance with the diesel fuel, they possess slightly different physical and chemical properties, which could lead to diverse spray development, fuel-air mixture formation and other combustion and exhaust emissions. Those differences evoke the need to examine closely their atomization characteristics.

In order to achieve that objective, high-speed visualisation experiments were carried out on an optically accessible single cylinder diesel engine. The atomisation of conventional diesel, rapeseed methyl ester (RME), and gas to liquid (GTL) was studied with recording rate of 63 kf/s and in addition the injection pressure was varied up to 1900 bar. To automate the processing a *Mallab* routine was developed to enable the extraction of the spray projections from the pictures and made possible the calculation of the spray cone angle and the penetration. The radiation of the soot particles was also detected with 32 kf/s at  $700 \pm 10$  nm wave length. The injection strategies for the different fuels were developed so that the break mean effective pressure and the point of 50 % heat release remain constant at respectively 4 bar and  $10^\circ$  after top dead centre (ATDC). The results at one operating condition, 2000 rpm and pressure charging at 1.6 bar, are presented in this paper.

The increase of the injection pressure caused an increase of the spray penetration and decrease of the cone angle by all examined fuels. RME showed the strongest penetration growth. The low-viscosity fuel GTL featured larger cone angle as RME. Increasing the injection pressure caused a weaker soot particle radiation and RME showed lower soot intensity than diesel.

---

### Introduction

Humanity's growing awareness of earth pollution on the one hand, and the pressing concerns of depletion of the petrol resources on the other hand, raises a constantly growing interest on alternative, cleaner fuels. Therefore it is mandatory nowadays to blend a certain volume fraction of bio fuel to the petrol diesel in order to cut down CO<sub>2</sub> emissions and reduce the dependence on crude oil.

The most well-known diesel fuel replacements are alternative fuels of the first and second generation. The high density and viscosity of the raw fuels makes necessary slight engine changes [1] and therefore - higher costs, making them rather unattractive. Biodiesels are typically methyl esters of acids with long chains derived from vegetable oils through transesterification [2]. Fuels of the first generation like rapeseed methyl ester (RME) are showing great potential for reducing the soot particle emissions because of the absence of aromatics and sulphur in them and their high oxygen content [1]. They, as well as the raw vegetable oil fuel, cannot be produced in sufficient quantities and also interfere with the human food supply chain. Great expectations have been laid upon the second generation fuels since they have relatively low viscosity and density [3], and despite the complex production methods could supply a considerable portion of mankind's fuel demand. Those alternative fuels have generally different chemical and physical properties, which may lead to different atomisation performance, air fuel mixture and emissions. For this reason rapeseed methyl ester (RME) and gas to liquid (GTL) fall into the scope of this work.

Most of the works in the literature providing information about the spray characteristics of diesel and its alternatives has been often achieved through investigations on constant volume vessels under engine-like conditions [4]. In this work optical techniques with high temporal resolution were applied on a transparent diesel engine to closely analyse the spray evolution for RME, GTL and diesel with 10% bio fraction as reference at different injection pressures up to 1900 bar. In addition, the natural soot incandescence of diesel and RME was analysed at high frame rate to assess its potential for further investigations and to contribute to the better understanding of the combustion behaviour of alternative fuels.



## Experimental apparatus and procedures

### Single-cylinder engine

The experiments discussed in this article were conducted in an optically accessible four-stroke engine, in a diesel engine set-up, provided by the institute of automotive expertise at the university in Magdeburg. The single-cylinder optical research engine's characteristics are: 81 mm bore and 95.5 mm stroke. The transparent engine has a compression ratio of 1:13 and can be operated at maximally 3000 rpm. It has been designed to withstand cylinder pressures and break mean effective pressures (BMEP) respectively up to 80 and 6 bar. Optical accesses to the combustion chamber is ensured through the UV-grade fused silica glass mounted in the bottom of the piston bowl and a 25 mm high ring positioned directly under the cylinder head, see Figure 1. The test bed is equipped with a supercharger capable of delivering air pressures up to 2.4 bar. Also a fuel conditioning system is available allowing temperature control over the fuel as well as the use of alternative fuels.

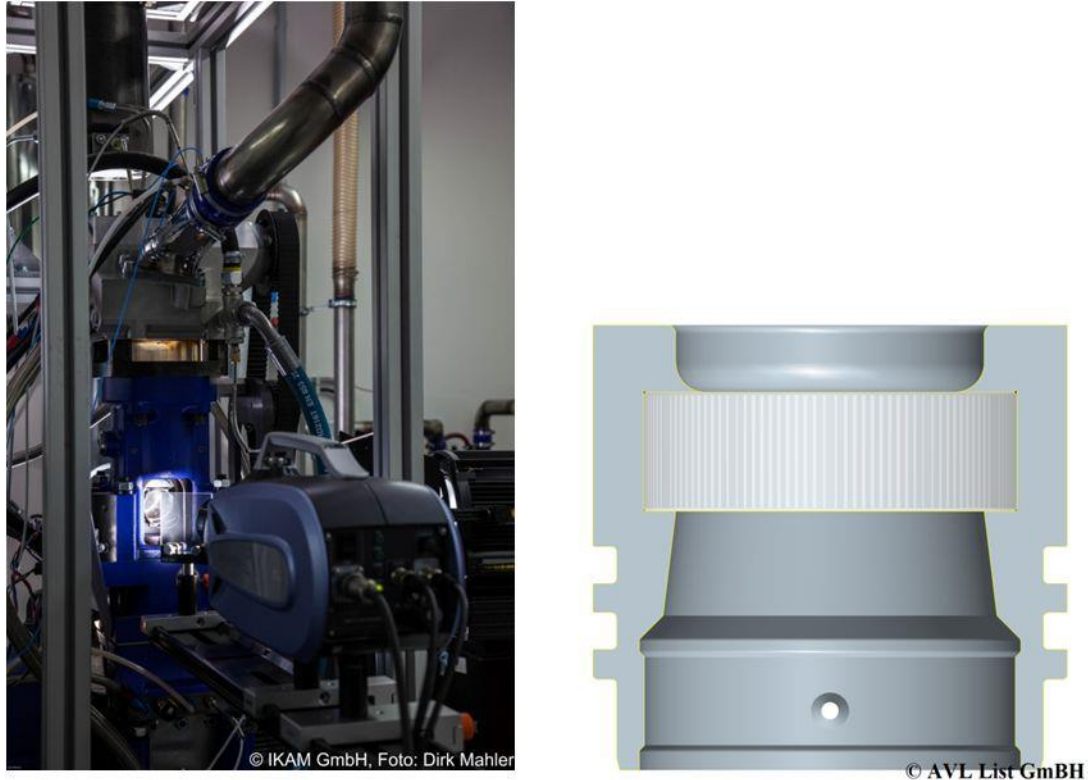


**Figure 1.** Transparent engine (left) and glass piston (right)

The test bed is equipped with a standard common-rail system plus an additional rail with a volume of 400 cm<sup>3</sup>. The solenoid-driven injector, previously introduced in [5], has the feature to internally double the injection pressure. The injector has a nozzle of type mini-sac with seven holes. A more detailed specification of the nozzle can be found in Table 1. The needed rail pressures were achieved with a CP3 pump. In order to implement different injection strategies, a fully flexible control unit was used to actuate the injector.

Description	nozzle 119
Nozzle type	Mini-sac
Nozzle hole diameter [ $\mu\text{m}$ ]	119
Number of holes [-]	7
Needle lift [mm]	0,25
Cone angle [ $^\circ$ ]	156
Flow rate [ $\text{cm}^3/30\text{s}/100\text{ bar}$ ]	390
k-/ks factor [-]	1,5 (ks)

**Table 1.** Nozzle specifications [5]



**Engine operating points and analysed fuels**

For the experiments to be presented in this work a constant engine speed of 2000 rpm was selected. The implemented injection strategies consisted of a single main injection and the energising time (ET) and the start of energising (SOE) were carefully chosen so that for each operating condition the BMEP and the point of 50 % heat release remain constant at respectively 4 bar and 10° after top dead centre (ATDC).

Two alternative fuels are presented in this work and compared to diesel fuel with 10% bio fraction to be referred as diesel in this paper. Alternative fuels of the first (rapeseed methyl ester (RME)), and second generation (gas to liquid (GTL)), have been analysed. Their physical properties are being compared in Table 2.

Description	unit	B10-Diesel	RME	GTL
Density (at 15°C)	kg/m <sup>3</sup>	820÷845 <sup>1</sup>	883	779,4
Viscosity ( at 40°C)	mm <sup>2</sup> /s	2÷4,5 <sup>1</sup>	4,5	2,74
Surface tension (at 25°C)	mN/m		31	26,04
Cetane number	-	>51 <sup>1</sup>	53	74
Low heating value	MJ/kg		37,2	44,2
Boiling range	° C		330-360	207-344
C/H ratio	%kg/%kg		6,28	5,6
Oxygen concentration	%kg/%kg		10,8	<0,03
Aromatics concentration	%kg/%kg		0	0
Flash point	° C	>55 <sup>1</sup>	>101	93
Ester concentration	%		>99,0	0

<sup>1</sup> DIN EN 590:2011-10

**Table 2.** Fuel specifications [5]

Furthermore, the injection pressure was increased in three steps to closely investigate its impact on the spray development by showing its influence upon the spray penetration and spray cone angle under evaporative real engine conditions (how the spray penetration and cone angle react to the pressure change under those conditions) – see Table 3.

As previously mentioned, the injector used in this paper has a hydraulic valve doubling the rail pressure provided the necessary energising time. Due to the relatively low loads the required time has not been reached and the actual injection pressures are shown in Table 3.

Rail pressure [bar]	560	830	1100	1380	
diesel	900	1200	1500	1800	max. nozzle pressure [bar]
RME	900	1200	1500	1900	max. nozzle pressure [bar]
GTL	800	1100	1400	1800	max. nozzle pressure [bar]

**Table 3.** Operating points

**Mie-scattering technique**

The single-cylinder optical engine was used to investigate the spray propagation (development) of the fuels in question under different injection pressures using the Mie-scattering technique. For the illumination of the spray, the combustion chamber was fitted with a 400 W focusable metal halide lamp. The macroscopic fuel atomisation characteristics were captured with a 10 bit high speed camera (*Shimadzu* HPV-2) capable of reaching frame rates up to 1 million fps and a Nikkor 135 mm f/2.8 lens. The special InSitu-Storage-CCD-chip, consisting of 1 plane of sensitive pixels and 100 non-sensitive directly behind them storing and passing the information to the next one, makes possible keeping a constant resolution of 312 x 260 pixels in the highest frequency. The camera was aligned with the 45° mirror in the elongated cylinder to provide a direct view of the combustion chamber. On the path of the cameras visual axis a beam splitter (50/50) was mounted coupling the camera with the light source and guiding them through the piston bowl in the combustion chamber, see Figure 2. This technique made it possible to achieve a relatively even distributed illumination, see Figure 2.

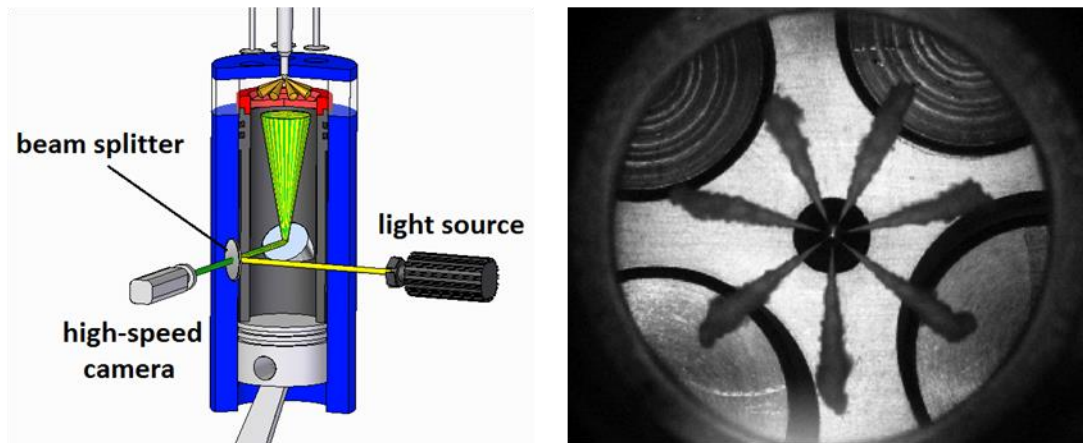


**Figure 2.** Experimental test-rig for spray visualisation (left) and spray picture (right)

### ***Spray data analysis***

The recorded spray pictures by the use of the scattering technique were imported in *Matlab* for processing because of the need to strip them from all pixels containing background information in order to separate the sprays from the cylinder head. To every spray sequence taken was also acquired a previous to that background sequence without an utilisation of injection in motored condition. The routine compares the two sequences and searches for differences between them larger than the predetermined threshold. By this technique the spray cones are being recognised and separated from the recorded pictures, see Figure 3b. While doing so, the software deletes also valuable spray pixels, which are afterwards restored, Figure 3c. After that the routine seeks all pixels not belonging to the spray jets and resets them to zero Figure 3d.

The *Matlab* processing is followed by an analysis in LaVision geometry software package, which enables the estimation of the spray cone angle and penetration. The cone angle was determined at a distance from 2 to 9 mm from the nozzle tip. For the estimation of the spray angle, the so called “count max” mode was used. The software starts with a small angle and opens it slowly until a given percentage (95% in this work) of the spray falls into the area formed by the measured angle. The fuel is being injected under an angle of  $156^\circ$ , see Table 3, causing a projected plain of the spray to appear on the recorded frames. That brought the necessity to account for those discrepancies as previously described by [6]. To ensure a relatively high statistical certainty all operating points were repeated 20 times and the average is shown for discussion in this paper.

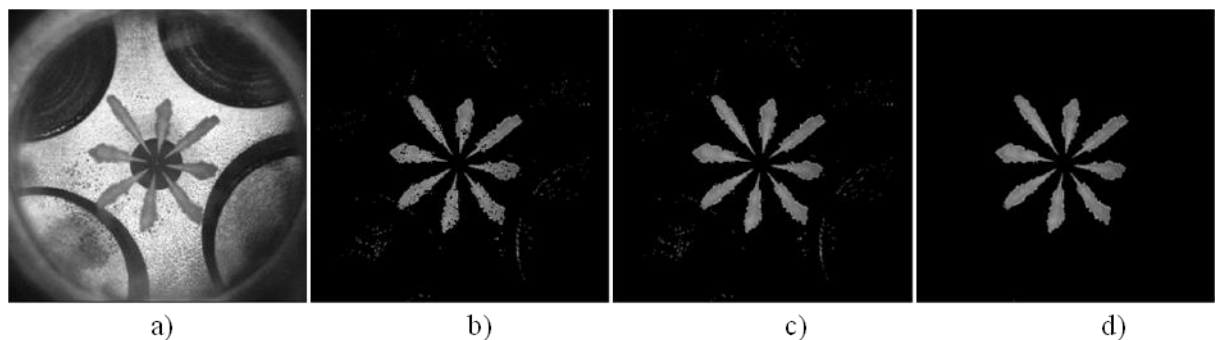


**Figure 3.** Spray processing

### **Results and Discussion of the macroscopic spray characteristics**

The injection pressure has always been a huge matter for the diesel engine, because of its great potential to improve the air-fuel mixture, hence leading to a better combustion.

After the visible start of injection (vSOI) the spray penetration increases vastly and almost linearly, which is often interpreted as the primary spray breakup. The injection pressure is the dominant phenomenon governing the spray propagation [7]. Afterwards the penetration is curved because the secondary spray breakup is taking place and the air entrainment process is controlling the spray penetration [7]. The higher injection pressure generates spray particles with higher kinetic energy. Their larger impulse diminishes the influence of the high density surrounding air and causes them to penetrate further for a given time, see Figure 4. This trend can be clearly seen in Figure 5. The spray penetration meets its maximum value at approximately 22 mm reaching the piston wall.

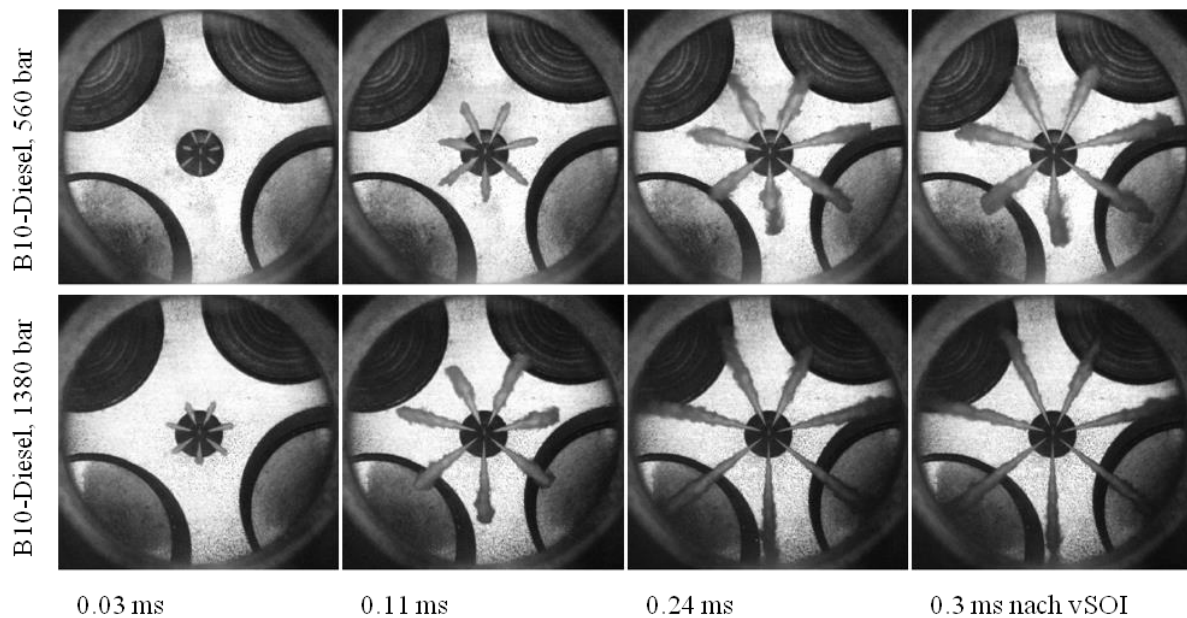


Figure 4. Spray propagation for diesel

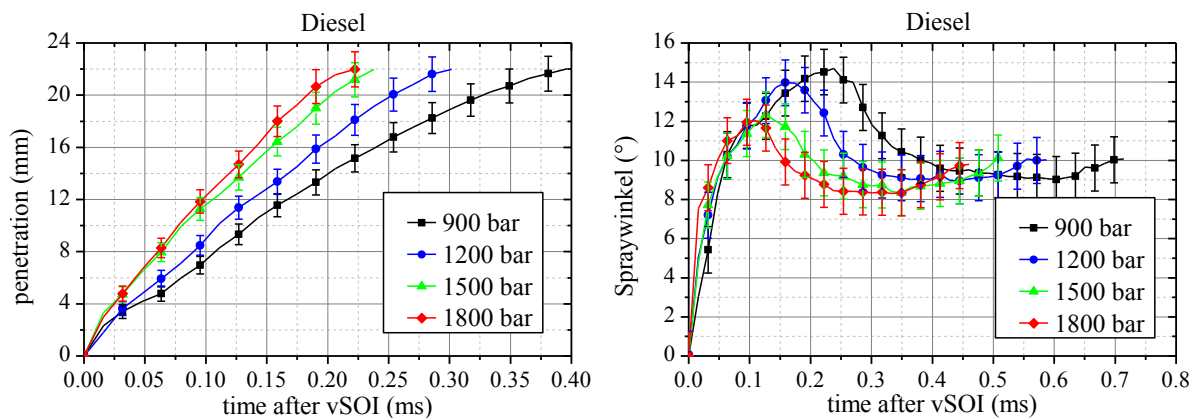


Figure 5. Spray penetration (left) and spray cone angle (right) as function of the visible start of injection (vSOI)

The measured spray angle increases rapidly after the nozzle needle starts lifting, see Figure 5. During this stage of the injection the spray development occurs, see Figure 4. At approximately 260  $\mu$ s after the vSOI a decrease in the spray cone angle was detected. This turning point takes place earlier with rising injection pressure. That first stage from SOI till the quasi-stationary phase is highly influenced by the needle liftoff and is typical for common-rail systems. This phase of the spray propagation is considerably shorter for the higher pressures, see Figure 5.

Furthermore, smaller spray angle was detected when the injection pressure was increased, see Figure 5. The higher spray impulse helps the spray to overcome the high density surrounding air and thereby results in a narrower spread of the fuel particles. In addition the better atomisation generally associated with the higher injection pressure brings forth smaller fuel drops, which can more easily evaporate and leads to a narrower spray cone angle. Such trends were previously reported by [8], [9] and [5]. At the end of the injection the measured angle increases again because of the pressure drop, while the nozzle holes are closing.

The increase of the injection pressure had a similar effect on the macroscopic characteristics of all investigated fuels. They feature quite similar values concerning the spray penetration. RME exhibits a slightly higher penetration growth compared to diesel and GTL favoured due to its high density directly resulting in a greater impulse of the spray particles, see Figure 6, as previously reported by [4] and [5]. For the lowest pressure a slightly larger penetration at the SOI could be noticed for the GTL.

At the start of injection (SOI) GTL exhibits marginally wider spray cone angle which complicates to overcome the air resistance because of its lower density and viscosity, see Figure 6. After the maximal spray angle is reached the characteristics are turned for the case of the minimal nozzle pressure and GTL has the

smallest angle. At the quasi-stationary region and during the closing of the nozzle holes Diesel and RME show again somewhat narrower spray cone angle because of their higher density compared to GTL.

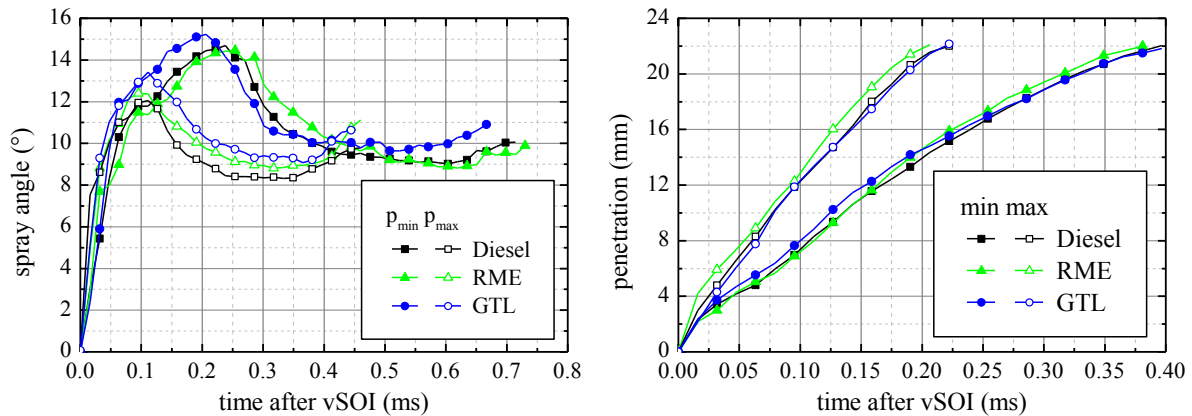


Figure 6. Spray cone angle (left) and penetration (right) for all investigated fuels

### Soot formation and flame luminosity

The analysis of the macroscopic spray characteristics showed that with GTL and RME comparable sprays to diesel can be achieved with negligible differences in the measured parameters. To aid the evaluation of the different fuels a second measurement method was put to use allowing us to take a closer look at the combustion process and in particular the soot formation.

The flame luminosity of a direct injection diesel engine is dominated by the radiation from the incandescent soot particles and therefore can be used to a certain extent as a qualitative indicator of the in-cylinder soot formation [10]. With the straight-forward analysis of the soot incandescence, the uncertainty coming from the temperature dependence of the thermal radiation from the soot particles must be considered. The influence of the temperature on the intensity of the detected light should be though smaller than that of the soot particle concentration, see Figure 7. The black body radiation emitted by the soot particles was captured by the high speed camera at a frame rate of 32 kf/s using the same alignment to the engine as before. Instead of the beam splitter, a 700 nm ( $\pm 10$ nm) band pass filter was put on the path of the camera's lens. This optical filter was used to avoid the light emitted in the visible and near ultraviolet regions by radicals, such as OH, CH, C<sub>2</sub>, HCO, NH and NH<sub>2</sub>, that could be formed in the flame reaction zones, as advised by [11]. The filter also blocks emissions coming from the infrared region (H<sub>2</sub>O, CO<sub>2</sub>, N<sub>2</sub>O and others). Azimov et. al [12] reported, that according to [13] the maximum emission intensity of the incandescent soot particles occurs at a wave length of 700 nm. He used such a filter himself to investigate the combustion behaviour of jets in a high pressure and temperature vessel.

The same operating conditions discussed in the previous chapter were used also for the investigation of the natural flame luminosity. Each operating point consists of 20 repetitions and noise filtering techniques was applied upon each of them. Experiments with diesel and RME were conducted and will be briefly discussed in this work in order to evaluate the potential of this measuring technique for further investigations.

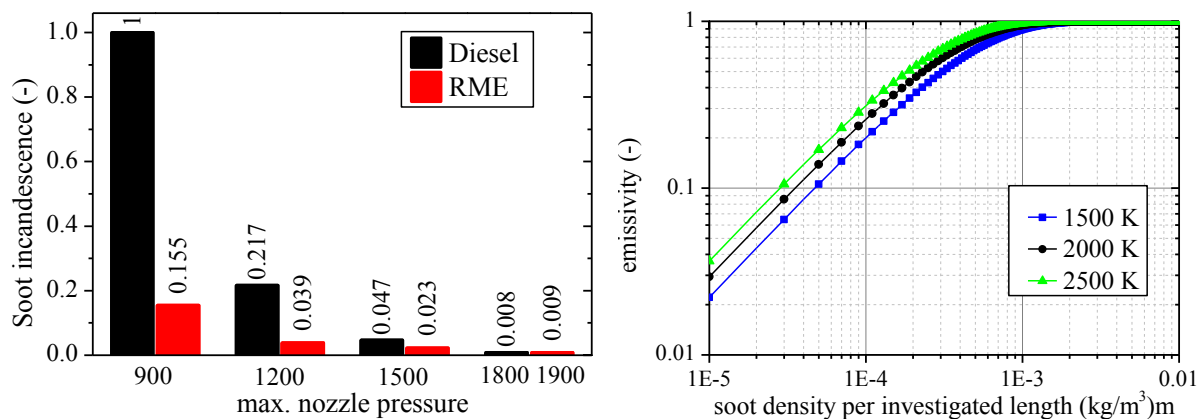
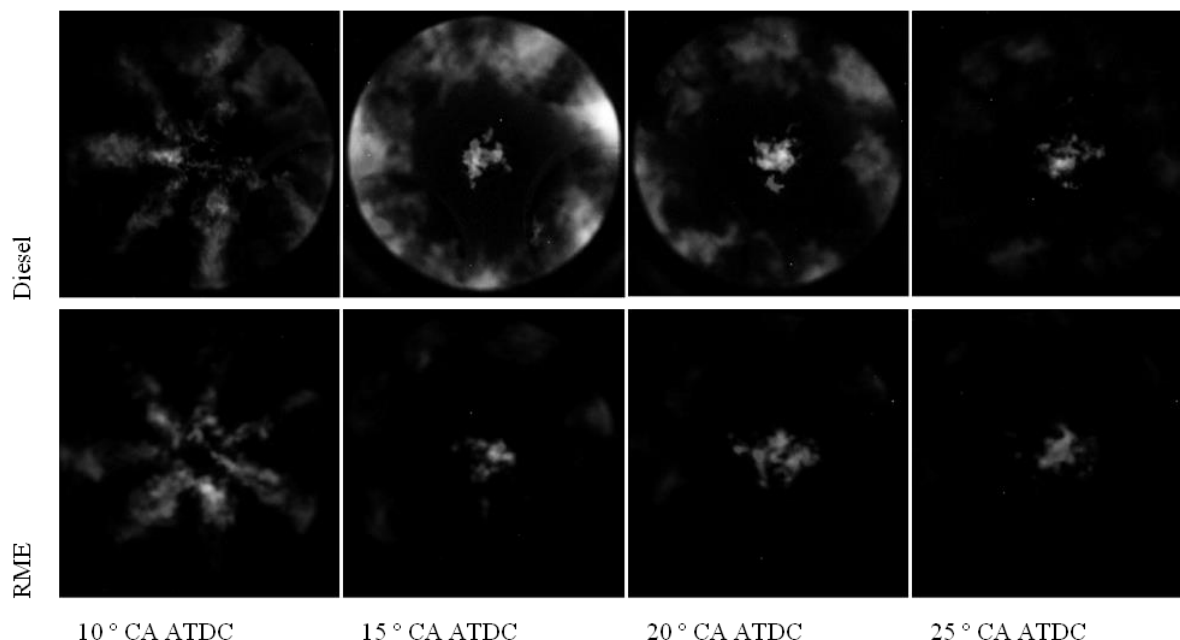


Figure 7. Cumulative soot incandescence for the whole combustion cycle (left) and soot emissivity as function of the soot density per length of interest according to [14] (right)

In Figure 7 the measured light intensity for the whole combustion cycle is shown and two apparent trends are easily noticeable.

First the increase of the injection pressure has a positive influence on the measured soot incandescence for both fuels. Second, although both of the analysed fuels exhibited quite similar macroscopic spray characteristics, for RME far lower soot incandescence was detected, even though RME atomises poorly and RME's jet breaks up in larger drops [15], due to its higher surface tension and viscosity preventing them for falling apart. Despite those facts other researchers also reported lower soot particle emissions for RME mainly due to its high oxygen content leading to a better combustion, see Figure 8. The stronger light intensity from the soot particles near the piston wall can be clearly seen in the case of diesel at 15° and 20° CA ATDC. Increasing the injection pressure from 900 bar to 1200 bar brought forth by both fuels a nearly 80% decrease in the detected soot incandescence. While diesel kept this rate for the other two increases, RME showed a lower decrease of approximately 42% and 63%.



**Figure 8.** Diesel and RME's soot incandescence by 900 bar max. nozzle pressure

## Conclusions

High speed visualisation technique was applied on an optically accessible diesel engine in order to investigate the macroscopic spray characteristics of two alternative fuels, RME and GTL, and compare them to diesel. In addition, four injection pressures were used to investigate their influence on the spray propagation at real diesel engine conditions. In order to achieve that goal, a new method for spray data analysis was introduced for separation of the spray jet from the cylinder head. Thereby a good estimation of the macroscopic spray parameters was achieved.

The analysis of the penetration curves revealed a significant influence of the injection pressure. The higher the pressure, the greater is the momentum of spray drops causing to penetrate further for a given time. A slightly higher penetration for RME could be detected due to its higher density. The increase of the injection pressure aided the jet at overcoming the air resistance and resulted in a narrower spray cone angle. At higher injection pressures the fuel is being atomised finer, resulting in smaller drops, which can easily evaporate at the spray edge, causing the spray angle to appear smaller. The low-viscous GTL showed a wider spray angle during the quasi-stationary region, the closing of the nozzle holes and right after the SOI. In comparison to RME and diesel GTL's spray front showed a higher deceleration rate due to its lower density and viscosity causing the jets to spread wider.

In all investigated fuels quite similar spray development was observed, which raises the question, whether they combustion behaviour is also like this. Therefore a second measurement method was utilised to examine their flame luminosity and in particular the soot incandescence. Experiments were conducted with diesel and RME - in order to assess the potential of the measuring technique for further investigations.

The analysis of the soot incandescences revealed that, although the two fuels possess quite similar physical properties and macroscopic spray characteristics, their combustion behaviour still has differences. In RME far lower intensities of the soot incandescence were detected, mainly due to its higher oxygen content. On account

of this result it may be concluded, that the investigation of the natural soot incandescence holds potential for analysis of alternative fuels.

## Acknowledgements

I would like to thank the land “Sachsen-Anhalt” for funding my research and the institute of automotive expertise for providing the opportunity to work on their state-of-the-art single-cylinder test bed.

## Nomenclature

abbreviation	definition
ATDC	after top dead centre
BMEP	break mean effective pressure
BTDC	before top dead centre
CA	crank angle
ET	energising time
GTL	gas to liquid
RME	rapeseed methyl ester
SOE	start of energising
SOI	start of injection
TDC	top dead centre
UV	ultra-violet
vSOI	visible start of injection

## References

- [1] Murugesan, A., Umarani, C., Subramanian, R., Nedunchezian, N., Bio-diesel as an alternative fuel for diesel engines-A review. *Renewable and Sustainable Energy Reviews*, 2009. 13: p. 653-662.
- [2] Valentino, G., Allocca, L., Iannuzzi, S., Montanaro, A., Biodiesel/mineral diesel fuel mixtures: Spray evolution and engine performance and emission characterization. *Energy and Buildings*, 2011. 36: p. 3924-3932.
- [3] Pastor, J.V., Garcia-Oliver, J. M., Nerva, J.G., Gimenez, Fuel effect on the liquid-phase penetration of an evaporating spray under transient diesel-like conditions. *Fuel*, 2011. 90: p. 3369-3381.
- [4] Mancaruso, E., Sequino, L. und Vaglieco, B. M., First and second generation biodiesels spray characterization in a diesel engine. *Fuel*, 2011. 90(2870-2883).
- [5] Backofen, D.u.T., H., Könnig, M., Schmidt, J. Extreme Hochdruckeinspritzung alternativer Dieselkraftstoffe - Von der Kraftstoffeinbringung bis zur Emissionsbildung. in *Diesel- und Benzindirekteinspritzung*. 2012. Berlin: Haus der Technik.
- [6] Delacourt, E., Desmet, B. und Besson, B., Characterisation of very high pressure diesel sprays using digital imaging techniques. *Fuel*, 2005. 84: p. 859-867.
- [7] Hiroyasu, H., Kodata, T., Arai, M., ed. Supplementary comments: fuel spray characterization in diesel engines. *Combustion modeling in reciprocating engines*, ed. J.N. Mattavi, Amann, Charles A., 1980. 369-408.
- [8] Blessing, M., Untersuchung und Charakterisierung von Zerstäubung, Strahlausbreitung und Gemischbildung aktueller Dieseldirekteinspritzsysteme, in *Institut für Verbrennungsmotoren und Kraftfahrwesen*. 2004, Universität Stuttgart: Stuttgart.
- [9] Lefebvre, A.H., Atomization and Sprays. *Combustion: An International Series*, ed. N. Chigier. 1989, New York: Hemisphere.
- [10] Siebers, D., Higgins, B. and Picket, L, Flame lift-off on direct-injection diesel fuel jets: Oxygen concentration effects. *SAE Technical Paper*, 2002. 2002-01-0890.
- [11] Zhao, H.L., N, Optical diagnostics for soot and temperature measurement in diesel engines. *Prog. Energy Combust. Sci.*, 1998. 24: p. 221-225.
- [12] Azimov, U.B., et al., Instantaneous 2-D visualization of spray combustion and flame luminosity of GTL and GTL-biodiesel fuel blend under quiescent ambient conditions. *International Journal of Automotive Technology*, 2011. 12(2): p. 159-171.
- [13] Vattulainen, J., Hernberg, R., and Kytölä, J, Experimental Determination of Spontaneous Diesel Flame Emission Spectra in a Large Diesel Engine Operated with Different Diesel Fuel Qualities. *SAE Technical Paper*, 1998. 981380.

- [14] Richter, W., Görner K., ed. Wärmestrahlung in Brennräumen. VDI-Wärmeatlas, ed. V.D. Ingenieure. 1997, Springer: Berlin Heidelberg.
- [15] Som, S., Longman, A.I., Aggarwal, S.K., A comparison of injector flow and spray characteristics of biodiesel with petrodiesel. *Fuel*, 2010. 98: p. 4014-4024.



## Effect of Geometric Shapes of Nozzle Hole for Direct Injection Diesel Engine on Spray Characteristics

Nobushige Tamaki<sup>1</sup>, Kazuma Nishikawa<sup>2</sup>, Shohei Fukamichi<sup>3</sup>

1: Faculty of Engineering, Department of Mechanical Engineering, Kinki University, Japan

2: Graduate School, Major in Systems Engineering, Kinki University, Japan

3: Undergraduate School, Department of Mechanical Engineering, Kinki University, Japan

### Abstract

Diesel engine is lifted in terms of high thermal efficiency, improvement and reduction of exhaust gas emission, and it is very economical on gas. In order to reduce NO<sub>x</sub> and soot emission, injection pressure of Diesel engine tends to increase over 200 MPa (2000 bar) and small hole diameter of 0.01 mm order. The purpose of this study is to improve spray and flow characteristics of a direct injection Diesel nozzle under low injection pressure. The final objects of this study are improvement of combustion characteristics, reduction of soot emission and progress of fuel consumption rate of a direct injection Diesel engine by improvement of spray characteristics.

---

### Introduction

Diesel engine in internal combustion engine has the highest thermal efficiency and it leads to reduce carbon dioxide caused by global warming. In order to improve combustion efficiency, exhaust gas characteristics and progress of fuel consumption rate by improvement of spray characteristics of fuel spray. It is a matter of great urgency to reduce carbon dioxide, which is caused by global warming. The final objects of this study are improvement of combustion characteristics of a direct injection Diesel engine, reduction of soot emission and progress of thermal efficiency by improvement over the injection nozzle and spray characteristics. In the previous studies included of this study, it was cleared that cavitation phenomena in the nozzle hole is considerably affected to atomization of spray, and it is effective to make aggressively use of cavitation in the nozzle hole, that is, disturbance of liquid flow due to collapse of cavitation bubbles [1]-[5]. Moreover, it was developed the atomization enhancement nozzle, which excellent spray characteristics with large spread angle, short breakup length, that is, liquid core length for a direct injection Diesel engine and small droplet diameters, are obtained at a standstill injection pressure or relatively low-injection pressure.

At the previous the author's studies, design of the atomization enhancement nozzle, which high-dispersion and high-efficiency spray are obtained at engine combustion, and improvement of spray and flow characteristics have been done by using the multi-hole nozzle separated one nozzle hole to four nozzle holes [6], [7].

The purpose of this study is to improve spray and flow characteristics of the direct injection Diesel nozzle from the point of view of only changing the part of the nozzle hole. The hole nozzle for the direct injection Diesel engine is dressed with round inlet cutting at the inlet of the nozzle hole in order to improve flow characteristics. This leads to become large of discharge coefficient.

Generally, it is well known that when the nozzle, which was dressed with round inlet cutting at the inlet of the nozzle hole, although discharge coefficient becomes large, spray characteristics becomes wrong and the high-injection pressure is needed to obtain spray characteristics which is fit for spray combustion. Recently, although injection pressure tend to high-injection pressure near of 300 MPa and small hole diameter of 0.01 mm order or smaller hole diameter, it is demanded from automobile makers that excellent spray characteristics is obtained at present injection pressure or relatively low-injection pressure and the same hole diameter as a general type Diesel injection nozzle of about 0.2 mm order.

In this study, on the basis of the previous the author's studies and results concerning design of the atomization enhancement nozzle, it was designed that the gathered multi-hole spray, which the same spray like that the actual Diesel injection nozzle as the sprays injected from the actual multi-hole nozzle, is obtained by dividing one nozzle hole in four small nozzle holes.

In this paper, the atomization enhancement nozzles, which were dressed with round inlet cutting and with inclined angle from vicinity of center of the injection nozzle to outside of one, was developed in order to improve both spray characteristics and flow characteristics and in order to simplify construction of the actual Diesel injection nozzle.

As a result, it was clarified that when the atomization enhancement nozzle with round inlet cutting was used, breakup length, that is, liquid core length becomes short about 20 p.c. and spray angle becomes large about two times, compared with the sharp inlet shapes of the nozzle hole. Moreover, when the nozzle, which inclined the nozzle holes of the multi-hole nozzle from vicinity of center of the injection nozzle to outside of one, was used, breakup length becomes considerably short about 2 mm for hole number of 4 and hole diameter of 0.3 mm

per one nozzle hole, spread of spray becomes dramatically large and spray angle becomes considerably large about over 100 deg., Sauter mean diameter was obtained about 20  $\mu\text{m}$  and spray characteristics was improved significantly compared with the previous actual multi-hole nozzle.

### Experimental test-rig

Schematic of experimental apparatus for steady state injection is shown in Fig.1. Equipment consists of a high-pressure pump worked by an air compressor, two spark light sources for taking photographs of spray and apparatus for measurement of droplet size and its distributions LDSA. Estimation of measure of atomization of spray was used breakup length of liquid core, spray angle, Sauter mean diameter and droplet size distributions. Water at room temperature pressurized by the high-pressure pump was continuously injected under atmospheric pressure condition. Maximum injection pressure is  $P_1 = 8 \text{ MPa}$  for total sectional area of the multi-hole nozzle which is corresponded to sectional area of one nozzle hole by restriction of the continuous injection system, and experimental data is discussed at spray region that even though the injection pressure is increased, breakup length and spray angle are almost constant.

Disintegration behavior of spray was photographed by scattered light, using two stroboscopes. Breakup length of a liquid core, which is defined as distance from the nozzle exit to breakup point of the liquid core, was measured by electrical resistance method [1] in which a screen detector was used. Breakup length was defined as the liquid core length, which was injected from four nozzle holes. Measurement method of breakup length of the multi-hole nozzle, which is injected vertically to injection direction, is shown in Fig. 2, and definition of breakup length, which is injected with inclination angle of 45 deg. is shown in Fig.3.

In case of the multi-hole nozzle, which is injected vertically and is injected from each four nozzle holes with inclination angle of 45 deg., it is necessary to measure the liquid core length of each sprays injected from each nozzle holes. The multi-hole nozzle, which is injected vertically, sprays injected from each four nozzle holes are generated one spray.

To the contrary, since the multi-hole nozzle with inclination angle of 45 deg. is injected from each four nozzle holes with inclination angle of about 45 deg., breakup length of the multi-hole nozzle with inclination angle of 45 deg. was measured along the spray injected with inclination angle. The disintegration behaviour of spray was photographed by scattering light illumination method. Spray angle was defined as spray boundary, and it was measured by images of photographed sprays.

Droplet size and droplet size distributions were measured by a narrow angle forward scattering type LDSA particle analyser at 120 mm downstream from the nozzle exit. It gives Sauter mean diameter that is spatially averaged along a line through the spray.

Schematic of test nozzles are shown in Fig. 4. The test nozzles are the multi-hole nozzle, which is separated four nozzle holes to one nozzle hole at outlet of nozzle hole. Figure 4 (a) shows test nozzle with

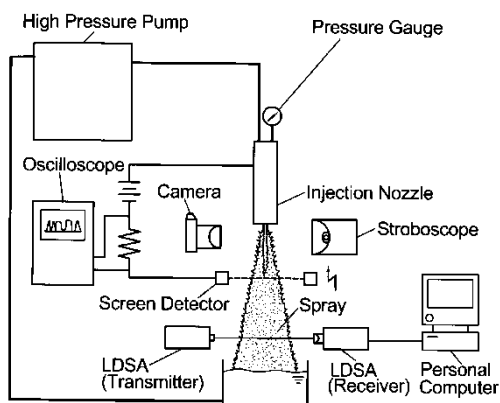


Figure 1. Schematic of experimental apparatus

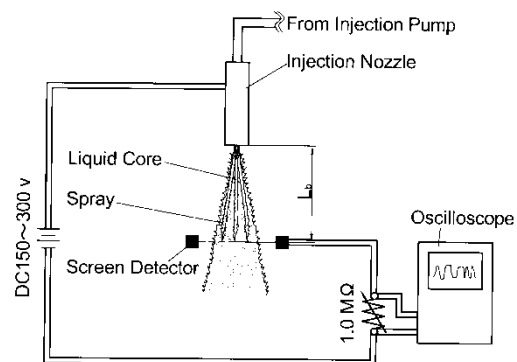
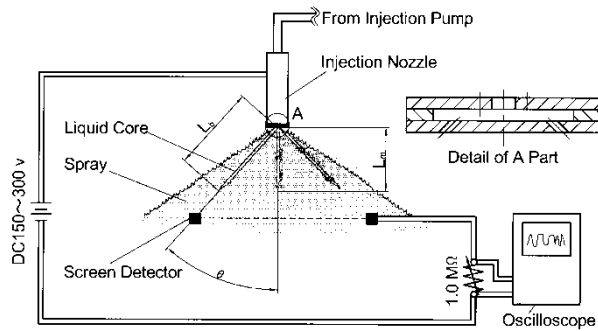
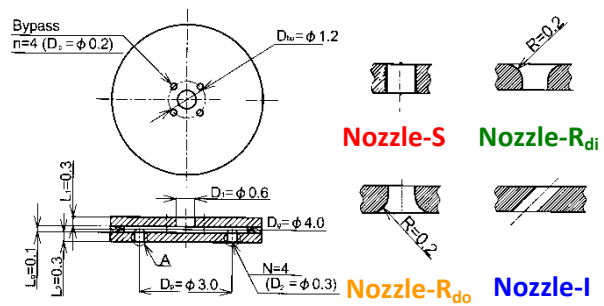


Figure 2. Definition of breakup length for straight injection<sup>(1)</sup>



**Figure 3.** Definition of breakup length for spray with inclination angle



**Figure 4.** Test nozzles and details of inlet and outlet of nozzle holes

sharp inlet shape nozzle (called Nozzle-S) used frequently by an actual Diesel injection nozzle. Figure 4 (b) shows the nozzle, which was dressed with round inlet cutting at inlet or outlet of the multi-hole nozzle (called Nozzle-R<sub>di</sub>, R<sub>do</sub>, respectively), which was inclined angle of 45 deg. at the nozzle holes to injection direction (Nozzle-I).

Structure of the atomization enhancement nozzle invented in the previous study is that the bypass, which is connected between the upstream chamber correspond to the sac chamber of the actual Diesel injector, and the gap which is installed at middle of the nozzle hole. The swirling flow occurs in the gap incoming from the bypass. Role of the bypass is that increasing the pressure in the gap in order to occur collapse of cavitation bubbles.

Total sectional area of the nozzle holes at the outlet of the nozzle hole is same values independent of geometric shapes of inlet and outlet of the nozzle hole. The test nozzles were used sectional area of the nozzle hole upstream from the gap equals total sectional areas of the nozzle holes downstream from the gap  $A_2 \text{ mm}^2$  ( $A_1 = A_2 \text{ mm}^2$ ), and total sectional areas of the nozzle holes downstream from the gap  $A_2$  is larger than sectional area of the nozzle hole upstream from the gap  $A_1 \text{ mm}^2$  ( $A_2 > A_1 \text{ mm}^2$ ).

## Results and Discussion

### Effects of Inlet and Outlet Shapes of Nozzle Hole Downstream from Gap on Atomization and Flow Characteristics

The effects of inlet and outlet shapes of nozzle hole downstream from gap on spread of spray and disintegration behavior of spray are shown in Fig.5. As shown in Fig.5, spread of spray of Nozzle-R<sub>di</sub>, that is, the nozzle, which is dressed with round inlet cutting at inlet of the multi-hole nozzle, becomes largest compared with spread of sprays of Nozzle-S and Nozzle-R<sub>do</sub>.

The effects of inlet and outlet shapes of the nozzle hole downstream from the gap on breakup length and spray angle are shown in Figs.6 and 7, respectively. As shown in Fig.6, breakup length becomes short with an increase in the injection pressure  $P_i$  until about  $P_i = 6 \text{ MPa}$ , independent of inlet and outlet shapes of the nozzle hole. When  $P_i$  is over about  $P_i = 6 \text{ MPa}$ , breakup length keep almost constant length with an increase in  $P_i$  independent of inlet and outlet shapes of the nozzle hole. Breakup length of Nozzle-R<sub>di</sub> becomes shortest compared with Nozzle-S and Nozzle-R<sub>do</sub> at all injection pressure. As shown in Fig.7, spray angle becomes large gradually with an increasing in the injection pressure. When spray angle was compared at maximum injection pressure of  $P_i = 8 \text{ MPa}$ , spray angle of Nozzle-R<sub>di</sub> becomes large about 60 p.c. compared with one of Nozzle-S.

Variations of the injection pressure on Sauter mean diameter at 120 mm downstream from the nozzle is shown in Fig.8. Sauter mean diameter becomes small monotonically with an increasing in the injection pressure. Sauter mean diameter is almost same values at arbitrary injection pressure independent of inlet and outlet shapes of the nozzle hole. Moreover, Sauter mean diameter of 20  $\mu\text{m}$  order are obtained at maximum injection pressure of  $P_i = 8 \text{ MPa}$  independent of inlet and outlet shapes of the nozzle hole.

Droplet size distribution at 120 mm downstream from the nozzle is shown in Fig.9. As shown in Fig.9, droplet size distribution, frequency of arbitrary droplet size and frequency of minimum and maximum size droplet diameter of each nozzles are almost same values.

Thus, since breakup length and spray angle of Nozzle-R<sub>di</sub> are obtained excellent atomization characteristics, Sauter mean diameter and droplet size distribution are obtained almost same characteristics. It is guessed that measurement point of Sauter mean diameter separates from nozzle exit 120 mm, atomization of spray droplets are completed at measurement point independent of inlet and outlet of the nozzle holes.

The effects of inlet and outlet shapes of the nozzle hole downstream from the gap on flow characteristics are

shown in Fig.10. As shown in Fig.10, volumetric flow rate increases monotonically with an increasing in the injection pressure and almost same volumetric flow rate compared with arbitrary injection pressure independent of inlet and outlet shapes of the nozzle hole. Volumetric flow rate of Nozzle-R<sub>di</sub> are largest at all injection pressure regions compared with Nozzle-S and Nozzle-R<sub>do</sub>.

Moreover, volumetric flow rate of Nozzle-R<sub>di</sub> is obtained about 20 p.c. larger than Nozzle-S at all injection pressure regions. In case of Nozzle-R<sub>di</sub>, volumetric flow rate of Nozzle-S at maximum injection pressure of  $P_i = 8$  MPa is obtained at about half injection pressure of  $P_i = 4$  MPa, and flow characteristics is improved significantly. In general, when the nozzle, which was dressed with round inlet cutting at inlet of the nozzle hole, was used, it is well known that although volumetric flow rate is improved, atomization characteristics are getting

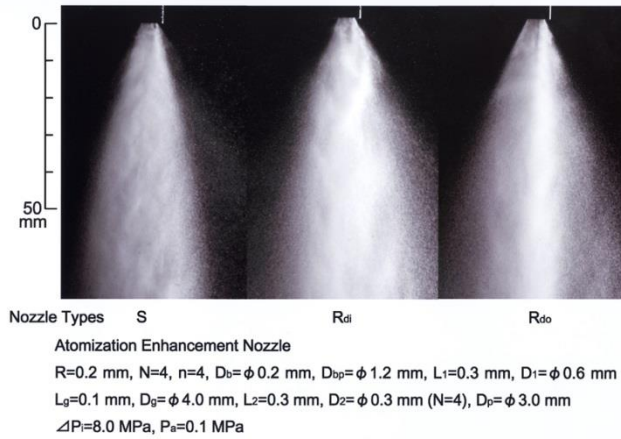


Figure 5. Effects of inlet and outlet shapes of nozzle hole

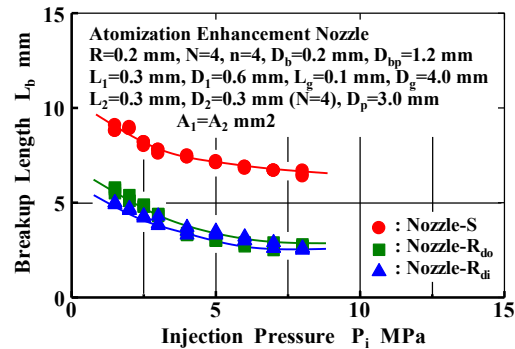


Figure 6. Effect of inlet and outlet shapes of nozzle hole downstream from gap

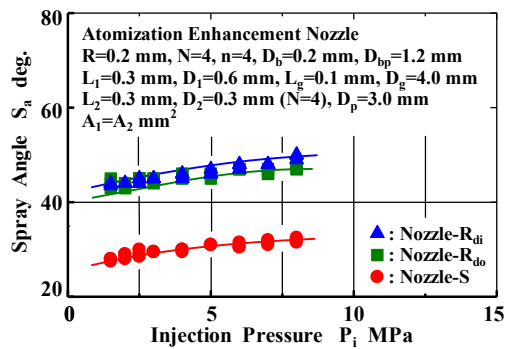


Figure 7. Effect of inlet and outlet shapes of nozzle hole downstream from gap on spray angle

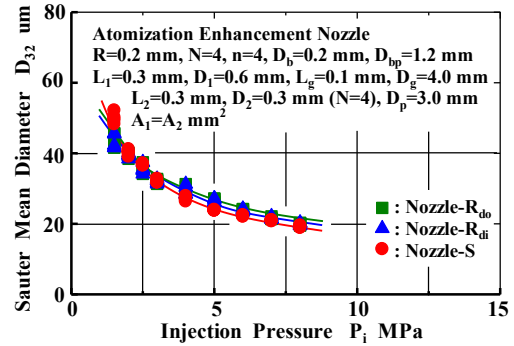
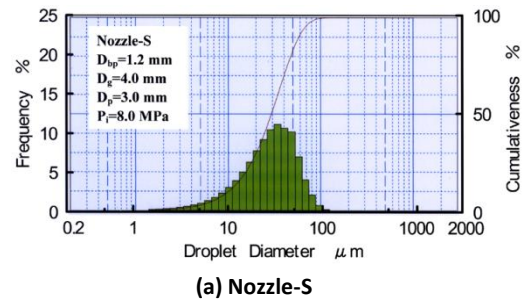
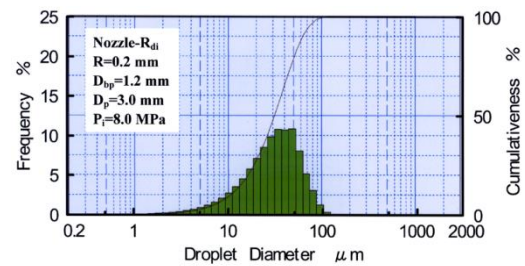


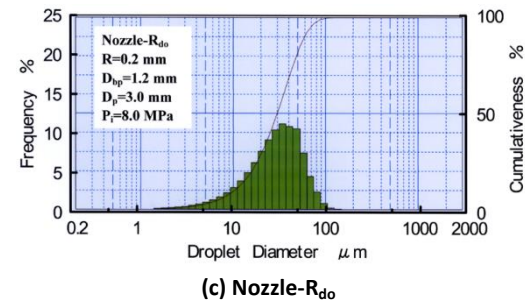
Figure 8. Effects of inlet and outlet shapes of nozzle hole downstream from gap



(a) Nozzle-S



(b) Nozzle-R<sub>di</sub>



(c) Nozzle-R<sub>do</sub>

Figure 9. Droplet size distribution at 120 mm downstream from nozzle

worse with an increase in volumetric flow rate. Moreover, it is expected that although excellent atomization characteristics is obtained at low-injection pressure, volumetric flow rate at low-injection pressure becomes less than one of high-injection pressure.

However, from these results, it can be seen that the nozzle, which was dressed with round inlet cutting at inlet of the nozzle hole, both atomization characteristics and flow characteristics are improved significantly.

From these results, it was cleared that Nozzle- $R_{di}$ , which was dressed with round inlet cutting at inlet of the nozzle hole, was used, both spray characteristics and flow characteristics are improved.

### Effects of Pitch Circle Diameter of Bypass on Atomization Characteristics

Atomization enhancement nozzle invented in this study is consisted of the gap installed at middle of the nozzle hole and the bypass, which was connected between the gap and upstream chamber correspond to the sac chamber of the actual Diesel injector. The gap and the bypass are strongly affected to atomization enhancement, as mentioned before. Measurement of the gap is decided the optimum conditions from previous in this study.

The bypass is one of these factors toward atomization enhancement of spray, increasing pressure in the gap needs to collapse of cavitation bubble and swirling flow due to influx from upstream chamber. It is expected that pitch circle diameter of the bypass  $D_{bp}$  affects to force of swirling flow within the gap. The effect of pitch circle diameter of the bypass, that is, force of swirling flow within the gap, which is influx from upstream chamber, on atomization of spray is shown in Fig.11. The atomization enhancement nozzle Nozzle- $R_{di}$ , which was obtained excellent spray characteristics as mentioned before, was used. As shown in Fig.11, spread of the spray of the nozzle with the smallest pitch circle diameter of  $D_{bp}=1.2$  mm, spread of spray is the largest and the nozzle with the largest pitch circle diameter of  $D_{bp}=3.0$  mm, it is the smallest.

Moreover, variation of atomization characteristics as a function of the injection pressure and the effect of pitch circle diameter of the bypass  $D_{bp}$  on atomization characteristics is shown in Fig.12. As shown in Fig.12, breakup length becomes short gradually and spray angle becomes large gradually with an increase in the injection pressure  $P_i$ , independent of pitch circle diameter of the bypass  $D_{bp}$ . In case the smallest pitch circle diameter of bypass  $D_{bp}=1.2$  mm, breakup length becomes short gradually and spray angle becomes large

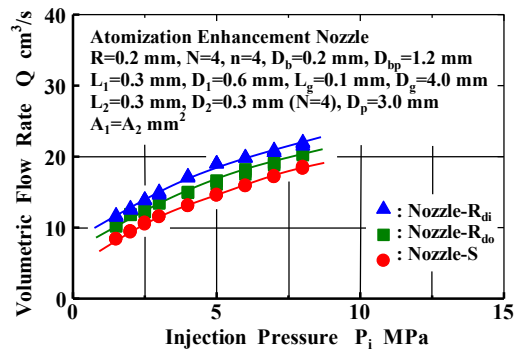


Figure 10. Effect of inlet and outlet shapes of nozzlehole downstream from gap

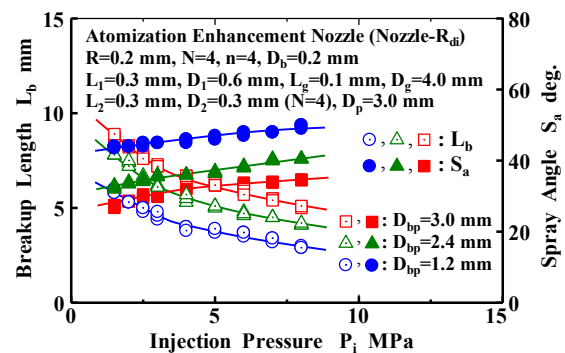


Figure 12. Effect of pitch circle diameter of bypass on atomization

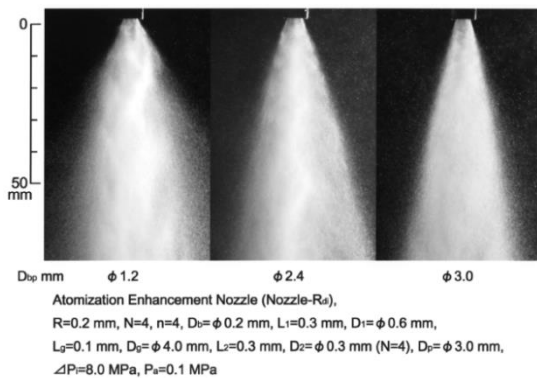


Figure 11. Effect of pitch circle diameter of bypass on atomization of spray

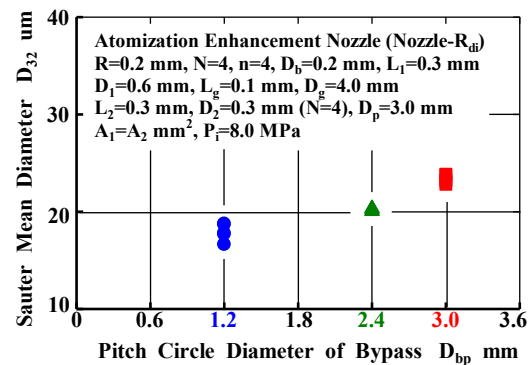


Figure 13. Effect of pitch circle diameter of bypass on Sauter mean diameter



gradually with an increase in the injection pressure  $P_i$ , independent of pitch circle diameter of the bypass  $D_{bp}$ . In case the smallest pitch circle diameter of the bypass  $D_{bp}=1.2$  mm, breakup length are the shortest and spray angle are the largest at all injection pressure regions. To the centrally, in case the largest pitch circle diameter of  $D_{bp}=3.0$  mm, breakup length is the longest and spray angle is the smallest at all injection pressure regions.

When atomization characteristics was compared at maximum injection pressure of  $P_i = 8$  MPa, breakup length of  $D_{bp}=1.2$  mm becomes short about half-length compared with one of  $D_{bp}=3.0$  mm, spray angle of  $D_{bp}=1.2$  mm becomes large about quarter dimension compared with one of  $D_{bp}=3.0$  mm.

The effect of pitch circle diameter of the bypass on Sauter mean diameter at maximum injection pressure of  $P_i = 8$  MPa is shown in Fig.13. Sauter mean diameter at the smallest pitch circle diameter of  $D_{bp}=1.2$  mm becomes smallest, and with an increase in pitch circle diameter increase with Sauter mean diameter.

It can be seen that when Nozzle- $R_{di}$  (nozzle with round inlet cutting at the inlet of the nozzle hole) which pitch circle diameter is the smallest of  $D_{bp}=1.2$  mm toward pitch circle diameter of multi-hole nozzle downstream from the gap of  $D_{bp}=3.0$  mm, was used, spread of spray becomes large toward radial direction of spray, excellent spray characteristics was obtained.

### Effect of Existence of Inclination Angle of Nozzle Hole Downstream from Gap on Spray Characteristics

In order to more disperse droplet of spray, the nozzle, which was inclined angle of 45 deg. at the nozzle hole to injection direction (Nozzle-I) and had atomization enhancement element, was used. In case of Nozzle-I, considerably excellent spray characteristics were obtained comparing with ones of Nozzle- $R_{di}$  that excellent spray characteristics were obtained as the facts above-mentioned. The effect of existence of inclination angle on disintegration behaviour of spray and dispersion of spray is shown in Fig.14.

As shown in Fig.14, although spray of Nozzle-I exists a few of heterogeneous regions, spread of spray becomes large dramatically. In spite sprays are injected from the nozzle hole, which is divided one nozzle hole into four small nozzle holes, the spray like that an actual multi-hole Diesel injection nozzle, for instance, hole numbers of 4 is obtained.

The effect of existence of inclination angle of nozzle hole downstream from gap on atomization characteristics is shown in Fig.15. As shown in Fig.15, breakup length becomes short gradually until about the injection pressure of about  $P_i = 6$  MPa at Nozzle- $R_{di}$  and Nozzle-I. When the injection pressure increases over about  $P_i = 6$  MPa, breakup length becomes almost constant length with an increase in the injection pressure until maximum injection pressure of  $P_i = 8$  MPa. Moreover, when breakup length was compared at maximum injection pressure of  $P_i = 8$  MPa, differences between breakup of Nozzle- $R_{di}$  and one of Nozzle-I is only about 0.2 mm, breakup length of Nozzle- $R_{di}$  becomes slightly short.

Spray angle becomes slightly large until about the injection pressure of about  $P_i = 6$  MPa at Nozzle- $R_{di}$  and Nozzle-I. When injection pressure increases over about  $P_i = 6$  MPa, variations of spray angle are almost the same tendency as variation of breakup length, and spray angle becomes almost constant with an increase in the injection pressure until maximum injection pressure of  $P_i = 8$  MPa. When spray angle was compared at maximum injection pressure of  $P_i = 8$  MPa, spray angle of Nozzle-I becomes large dramatically and it becomes large about 3 times latter than one of Nozzle- $R_{di}$ .

The developed nozzle in this study of Nozzle-I, which was separated one nozzle hole from four small nozzle holes at the same sectional area of the nozzle holes, considerably large spray angle was obtained compared with the actual multi-hole Diesel injection nozzle.

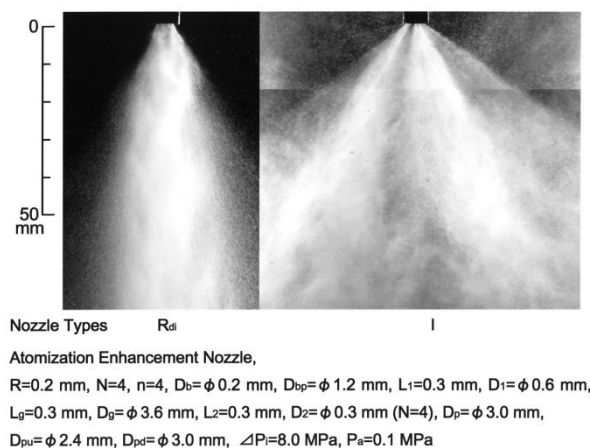


**Figure 14.** Effect of existence of inclination angle on disintegration behaviour of spray and dispersion of spray

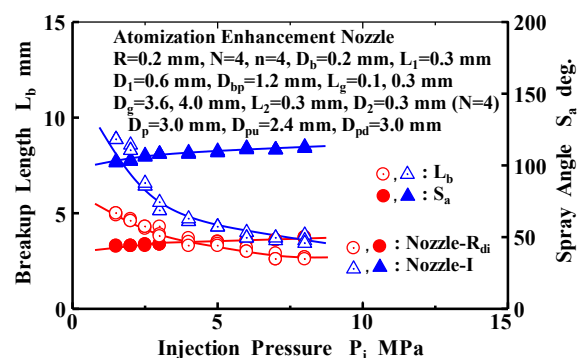


**Figure 15.** Effect of existence of inclination

## Conclusions

- (1) Spread of spray of Nozzle-R<sub>di</sub> (with round inlet cutting of the multi-hole nozzle) becomes largest compared with Nozzle-S (sharp inlet shape) and Nozzle-R<sub>do</sub> (with round outlet cutting of the multi-hole nozzle).
- (2) Breakup length of Nozzle-R<sub>di</sub> is the shortest compared with Nozzle-S and Nozzle-R<sub>do</sub>, spray angle of Nozzle-R<sub>di</sub> becomes large about 60 p.c. compared with one of Nozzle-S.
- (3) Sauter mean diameter is obtained almost same values of 20  $\mu\text{m}$  order, and droplet size distribution, frequency of arbitrary droplet size and frequency of minimum and maximum size droplet diameter are almost same values at maximum injection pressure of  $P_i=8$  MPa independent of inlet and outlet shapes of nozzle hole.
- (4) Volumetric flow rate of Nozzle-R<sub>di</sub> are largest at all injection pressure regions compared with Nozzle-S and Nozzle-R<sub>do</sub>.
- (5) Nozzle-R<sub>di</sub> is able to improve spray characteristics and flow characteristics.
- (6) Nozzle-R<sub>di</sub> with the smallest pitch circle diameter of the bypass of  $D_{bp}=1.2$  mm toward pitch circle diameter of multi-hole nozzle downstream from gap of  $D_{bp}=3.0$  mm is obtained excellent spray characteristics.
- (7) When spray angle was compared at maximum injection pressure of  $P_i=8$  MPa, spray angle of Nozzle-I becomes large dramatically and it becomes large about 3 times compared with Nozzle-R<sub>di</sub>.

## Acknowledgements

This work was partly supported by Japan Society for the Promotion of Science (JSPS) KAKENHI (C) Grant Number 19560217. Moreover, this research was partly supported by the Ministry of Education, Culture, Sports, Science and Technology (MEWT) MEXT-Supported Program for the Strategic Research Foundation at Private Universities. The authors wish to express their thanks for supporting this research.

## Nomenclature

$A_1$ mm <sup>2</sup>	: Sectional area of nozzle hole upstream from gap
$A_2$ mm <sup>2</sup>	: Total sectional area of nozzle hole downstream from gap
$D_1, D_2$ mm	: Hole diameter upstream from gap ( $D_1$ ), downstream from gap ( $D_2$ )
$D_{32}$ $\mu\text{m}$	: Sauter mean diameter
$D_b, D_{bp}$ mm	: Bypass diameter, Pitch circle diameter of bypass
$D_g, L_g$ mm	: Gap diameter ( $D_g$ ), Gap length ( $L_g$ )
$D_p$ mm	: Pitch circle diameter of nozzle hole downstream from gap
$D_{bd}$ mm	: Outlet pitch circle diameter of nozzle hole downstream from gap
$D_{pu}$ mm	: Inlet pitch circle diameter of nozzle hole downstream from gap
$L_1, L_2$ mm	: Hole length upstream from gap ( $L_1$ ), downstream from gap ( $L_2$ )
$L_b$ mm	: Breakup length
$n, N$	: Bypass number, Hole number
$P_i$ MPa	: Injection pressure
$Q$ m <sup>3</sup> /s	: Volumetric flow rate
$S_a$ deg.	: Spray angle

## References

- [1] Hiroyasu, H., Arai, M. and Shimizu, M., Break-up Length of a Liquid Jet and Internal Flow in a Nozzle, *Proc. Fifth International Conference on Liquid Atomization and Spray Systems*, (1991), pp.275-282.
- [2] Chaves, H., Knapp, M., Kubitzek, A., Obermeier, F. and Schneider, T., Experimental Study of Cavitation in the Nozzle Hole of Diesel Injectors Using Transparent Nozzles, *SAE Technical Paper*, No. 950290, (1995), pp. 645-657.
- [3] Tamaki, N., Nishida, K., Shimizu, M. and Hiroyasu, H., Effects of Cavitation and Internal Flow on Atomization of a Liquid Jet, *Atomization and Sprays*, Vol. 8, No. 2, pp. 179-197, 1998.
- [4] Arcoumanis, C. and Gavaises, M., Cavitation in Diesel Injectors: Modeling and Experiment, *Proc. Fourteenth Institute for Liquid Atomization and Spray Systems-Europe*, pp. 248-255, 1998.
- [5] Tamaki, N., Shimizu, M. and Hiroyasu, H., Enhancement of the Atomization of a Liquid Jet by Cavitation in a Nozzle Hole, *Atomization and Sprays*, Vol. 11, No.2, (2001), pp. 125-137.
- [6] Tamaki, N., Effects of Cavitation in a Nozzle Hole on Atomization of Spray and Development of High-Efficiency Atomization Enhancement Nozzle, *Proc. 11th Internal Conference on Liquid Atomization and Spray Systems ICLASS 2009*, CD-R, 6 pages, 2009.
- [7] Tamaki, N., Kato, A., Kato, K. and Imano, K., Improvement of Atomization Characteristics of Spray by Multi-Hole Nozzle for Pressure Atomized Type Injector, *Proc. 23rd Institute for Liquid Atomization and Spray Systems-Europe*, CD-R, 7 pages, 2010.



## Analysis of spray evolution from both piezo and solenoid injectors in single cylinder research engine

Agnese Magno<sup>1, 2</sup>, Ezio Mancaruso<sup>1</sup>, Luigi Sequino<sup>1</sup> and Bianca Maria Vaglieco<sup>1</sup>

1: Istituto Motori – Consiglio Nazionale delle Ricerche, Italy

2: Università di Napoli Federico II, Italy

### Abstract

The continuous requests for the improvement of performance and the fulfilment of strict emission legislation have required the use of advanced technologies in modern diesel engines. A primary role has been played by the injection system development. Two main technologies have been used so far for the control of the needle lift: the solenoid driven injectors and the piezoelectric injectors. For the first, the movement is due to a magnetic field induced by a current circulating in a coil; for the latter, it is a piezoelectric material that elongates when a voltage signal is applied between its opposite surfaces.

Investigations on the injection process by using solenoid and piezo injectors have been the objective of this paper. The experiments have been carried out in a single cylinder transparent engine operating in premixed mode. The head of a Euro 5 production engine has been mounted on an elongated cylinder and the production Common Rail injection system has been used. A sapphire window has been set in the piston head in order to observe the phenomena occurring in the combustion chamber. Engine has been fed with commercial diesel fuel. High speed camera has been used for the acquisition of spray evolution images. Information about the behaviour of the two injector types has been obtained. It has been observed that the two injector technologies show a different behaviour in terms of spray distribution in the combustion chamber. It has been found that piezoelectric injectors offer the advantage of a shorter injection delay than the traditional solenoid ones.

---

### Introduction

Nowadays, diesel engines have a dominant role in the improvement of combustion performances. The optimization of both the injection and combustion processes has been favoured by the introduction of new technologies. Since, an important role in the efficiency of the combustion process in diesel engines is played by the mixing between air and injected fuel, a lot of studies have been performed in order to understand the mechanism of the mixture formation [1-3]. A strong contribution in improving the efficiency of the mixture formation has been given by innovative injection [3, 4] systems. In particular, the injector characteristics as nozzle flow number, K factor and dimension, but also the principles governing the actuator of the injector needle have been considered.

Besides solenoid driven injectors commonly used in the Common Rail (CR) injection systems configuration, where the electric actuation is activated by a current circulating in a solenoid actuator valve, another technology based on piezo actuated injector has been used. In this case, it is a piezo actuator mechanically coupled with the injector needle that controls its position.

While CR injection systems equipped with solenoid-driven injectors have limitations in opening force and response in transient conditions, the piezo-driven injectors have a fast and precise control of the fuel flow through the injector nozzle [5].

Several authors have studied the spray behaviour using experimental [1] and computational tools [6, 7], as a result, some main macroscopic parameters of the spray have been identified as liquid length, vapour penetration, and cone angle. These spray parameters have been widely investigated, in both evaporative [8-10] and non-evaporative [11, 12] conditions, and correlations between the nozzle geometry, injector needle actuator and flow characteristics have been elaborated [3, 4, 13, 14]. Despite of many previous studies, it is still of great interest to investigate the effects of the injector driven type on spray characteristics, in particular, in engine-like conditions. In this work a study on the behaviour of a diesel spray from both an indirect-acting piezo and a solenoid driven injector in a transparent engine has been performed.

The optically accessible single cylinder diesel engine has been equipped with the latest-generation Euro 5 production engine head and a CR injection system. The comparison has been made in two engine operating points typical of the new European driving cycle NEDC, they are the points at 1500 rpm and 2 bar of brake mean effective pressure (BMEP) and at 2000 rpm and 5 bar of BMEP. Commercial diesel fuel has been used.

A high speed charge coupled device (CCD) camera has been used to investigate the injection evolution inside the cylinder through a sapphire window located in the top of an elongated piston. Images of injection have been processed to evaluate jets parameters such as the penetration and the cone angle. A statistical analysis of the standard deviation of the jets parameters has been made. From penetration data, the jets velocity has been calculated.

## Experimental test-rig

The optical single-cylinder engine used for combustion diagnostics has been equipped with the combustion system architecture and injection system of a four-cylinder commercial engine. The bowl wall shape and the combustion volume are the same as the production engine. A scheme of the experimental apparatus is shown in Figure 1. Moreover, the engine specifications have been reported in Table 1.

The optical engine utilizes a conventionally extended piston with a piston crown sapphire window of 46 mm diameter which provides full view of the combustion bowl by locating an appropriate 45° fixed mirror inside the extended piston. In Figure 1, the head of the engine reflected by the mirror is shown. The seats of the 4 valves appear as the dark curves while the injector tip is in the centre; finally, the dark circle in the top of the images is the pressure transducer seat.

The engine has been equipped with a Common Rail injection system managed by a fully opened electronic control unit (ECU). The used ECU has been designed to control solenoid injectors that are driven by a current signal and it has been modified in order to manage also piezoelectric injectors that are driven by a voltage signal. For this purpose, the ECU has been equipped with a power device capable to convert the current signal in a voltage one equal for start and duration. The current signal has been detected by a Hall-effect sensor and it was monitored with the voltage one. Two injector drivers have been tested; in particular, a solenoid driven and an indirect-acting piezo driven injectors have been compared. The piezo injector has been supplied by a voltage signal of 110 V corresponding to a partial needle lift. The geometry of the orifices is slightly different, for the first one the diameter is 107  $\mu\text{m}$  while for the latter is 111  $\mu\text{m}$ . Moreover, the solenoid injector has 8 holes versus the 6 holes of the piezo driven one. The nozzles have been chosen so that the exit area is the same for both the two tested injection technologies; the geometry of the orifices is slightly different: in particular, the nozzle for the solenoid injector has smaller outlet diameter and a greater number of holes. All the specifications about the injection system are reported in Table 2.

To obtain the in-cylinder conditions of the multi-cylinder engine tests, an external air compressor has been used to supply pressurized intake air that has been well filtered, dehumidified, and preheated.

The exhaust gas recirculation (EGR) and variable swirl actuator (VSA) have been managed by external devices; in order to achieve the correct amount of EGR, a back pressure valve has been fitted in the exhaust duct.

A piezoelectric pressure transducer (AVL GH13P) has been set in the glow plug seat of the engine head to record the in-cylinder pressure in motored and fired conditions.

For each operating condition, the in-cylinder pressure has been digitized and recorded at 0.1 crank angle degree (°CA) increments, and ensemble-averaged over 150 consecutive combustion cycles. The heat release rate has been calculated from the ensemble-averaged pressure data using the first law of thermodynamics and the perfect gas model [14]. The cyclic variation has been measured and it resulted less than 1% with respect to the maximum pressure and less than 3% with respect to the indicated mean effective pressure (IMEP).

All the data presented in this paper have been taken with the transparent engine operating in continuous mode. The intake air temperature has been set at 323 K. The intake pressure has been fixed at 1.21 and 1.32 bar for engine speeds of 1500 and 2000 rpm, respectively. At motored condition, temperature and density at Top Dead Centre (TDC) have been estimated assuming a polytropic coefficient of 1.36 [14]. They are 820 K and 18.6  $\text{kg/m}^3$  at 1500 rpm and 855 K and 22.3  $\text{kg/m}^3$  at 2000 rpm. The engine operating conditions investigated are representative of the engine behaviour on NEDC when installed on a D-class vehicle. They correspond to the engine calibration points at 1500 rpm with 2 bar of BMEP and 2000 rpm with 5 bar of BMEP. In the following they will be referred to as 1500x2 and 2000x5, respectively. Two injections per cycle have been performed, pilot and main, with injection pressure around 600 bar and 900 bar at 1500x2 and 2000x5, respectively. For both injectors investigated it has been used diesel fuel provided at the refill pump.

Digital imaging analysis has been performed by a CCD camera through the 45° mirror. The CCD camera with 640 x 480 pixels (pixel dimensions of 9.9 x 9.9  $\mu\text{m}^2$ ) and a high sensitivity over a wide visible range has been used in order to take images during the injection processes. A visible objective, Nikkor 55 mm f/3.5, has been used. With this optical configuration each pixel of the combustion chamber corresponds to an area of 0.1 x 0.1  $\text{mm}^2$ . Due to speed limitation of CCD camera, only one image has been recorded in a single cycle. Two halogen continuous lamps have been used to light the jets in the bowl via the 45° mirror. Five repetitions have been performed in order to carry out statistical analysis of the spray parameters. The synchronization of the CCD camera with the engine has been obtained by a delay unit connected with the signal coming from the engine shaft encoder. In particular, the images have been recorded with an exposure time of 55  $\mu\text{s}$  and 41  $\mu\text{s}$  that correspond at 0.5°CA of the shaft encoder at 1500 rpm and 2000 rpm, respectively.

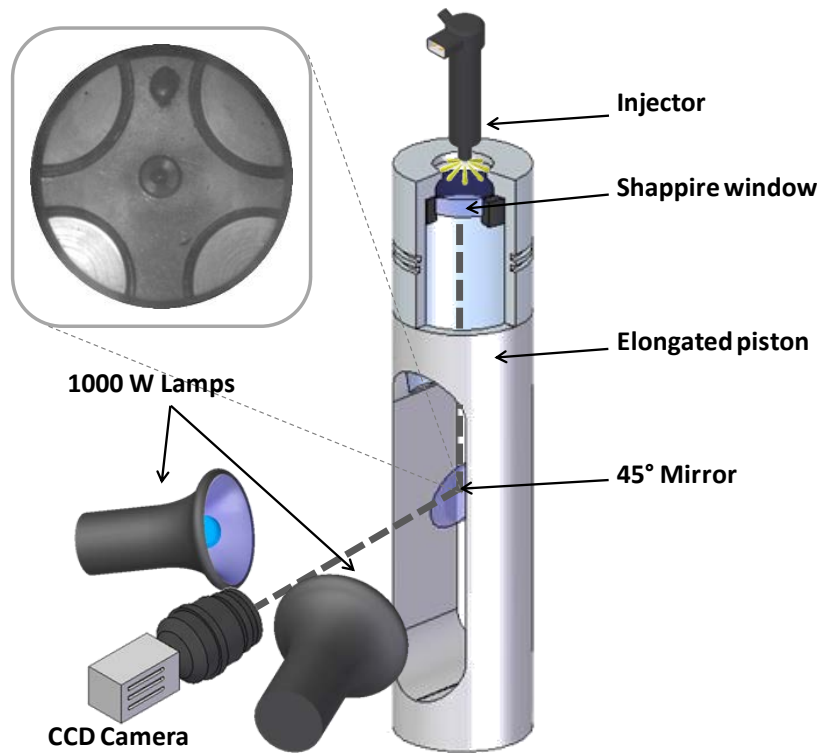


Figure 1. Single cylinder engine optical setup

Engine type	4-stroke single cylinder
Bore	8.5 cm
Stroke	9.2 cm
Swept volume	522 cm <sup>3</sup>
Combustion bowl	19.7 cm <sup>3</sup>
Vol. compression ratio	16.5:1

Table 1. Engine specifications

Injection system	Common Rail	
Injector driver	Solenoid	Piezo
Number of holes	8	6
Hole diameter [mm]	0.107	0.111

Table 2. Injection system specifications

## Results and Discussion

The investigation has concerned the comparison between two different injection technologies; the spray characteristics of a piezo and a solenoid driven injectors have been studied by means of optical diagnostics in a transparent engine. The effects of the injector driver on the jet distribution in the combustion chamber in terms of liquid penetration, jet velocity, cone angle, jet area have been analysed. Special attention has been given to the statistical repetition of the measured parameters.

In Figure 2, images of the main injection in the condition 1500x2 have been shown for both the piezo and solenoid injectors. Images are reported with respect to the crank angles after the start of main injection (ASOI). On the other hand, images of the pilot injection have not been reported because the short duration of this event does not allow to appreciate the principal differences between the two injectors.

By following the process from the start of injection, it is possible to observe the evolution of the jets in the combustion chamber, the jet shape is clearly discernible until the start of visible combustion, where the flames cover part of the spray. However, the measurements of the jet parameters have been made over five repetitions. The detection of visible injection in the bowl volume has allowed the determination of the response delay of the two nozzles. As it is known in literature [15, 16], piezo injectors are characterized by a faster response with respect to solenoid driven injectors; it has been measured a delay of about 0.1 ms for the first and 0.25 ms for the latter, in both engine speeds analysed. Therefore, the main characteristic of the piezo-driven injectors is the faster dynamic response. It is due to the capability of the piezo stack to generate forces of 800 N instead of the conventional solenoid system that has force values lower than 100 N [17].

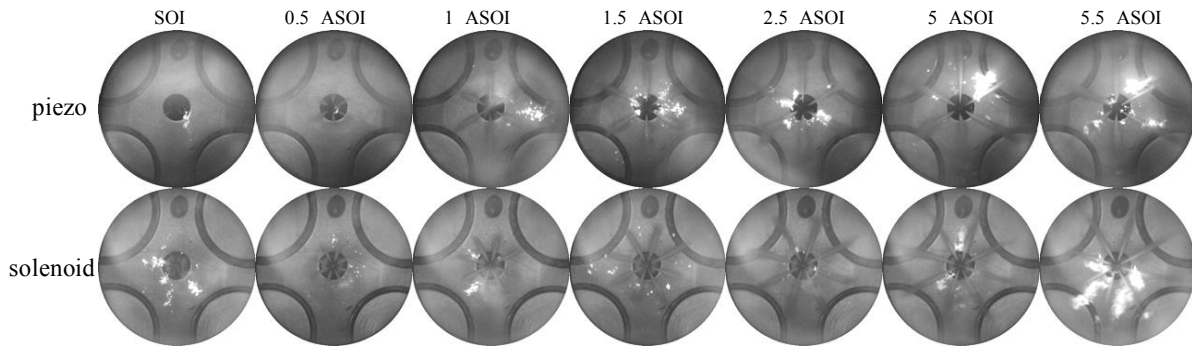


**Figure 2.** Main injection phase images of both the piezo and the solenoid injectors in the conditions 1500x2.

In Figure 3, a comparison of the average jets penetration for both the piezo and the solenoid injectors has been reported. The two graphs refer to the conditions 1500x2 (top) and 2000x5 (bottom). It has been firstly measured the length of the single jets from the images in Figure 2. For each jet, the average on 5 repetitions has been calculated to reduce the uncertainty due to the engine cycle variation. After that, a final penetration has been determined as the average value of the single jets measurements. Observing the slope of the penetration histograms, two different parts can be identified; the transition occurs at about 1.5°CA ASOI for both the engine speed. The first one has a linear dependence of the penetration on time and the phenomenon is dominated by the injected liquid; the second one shows a dependence of the penetration on the square root of time and it is dominated by the entrained gas effect [18, 19].

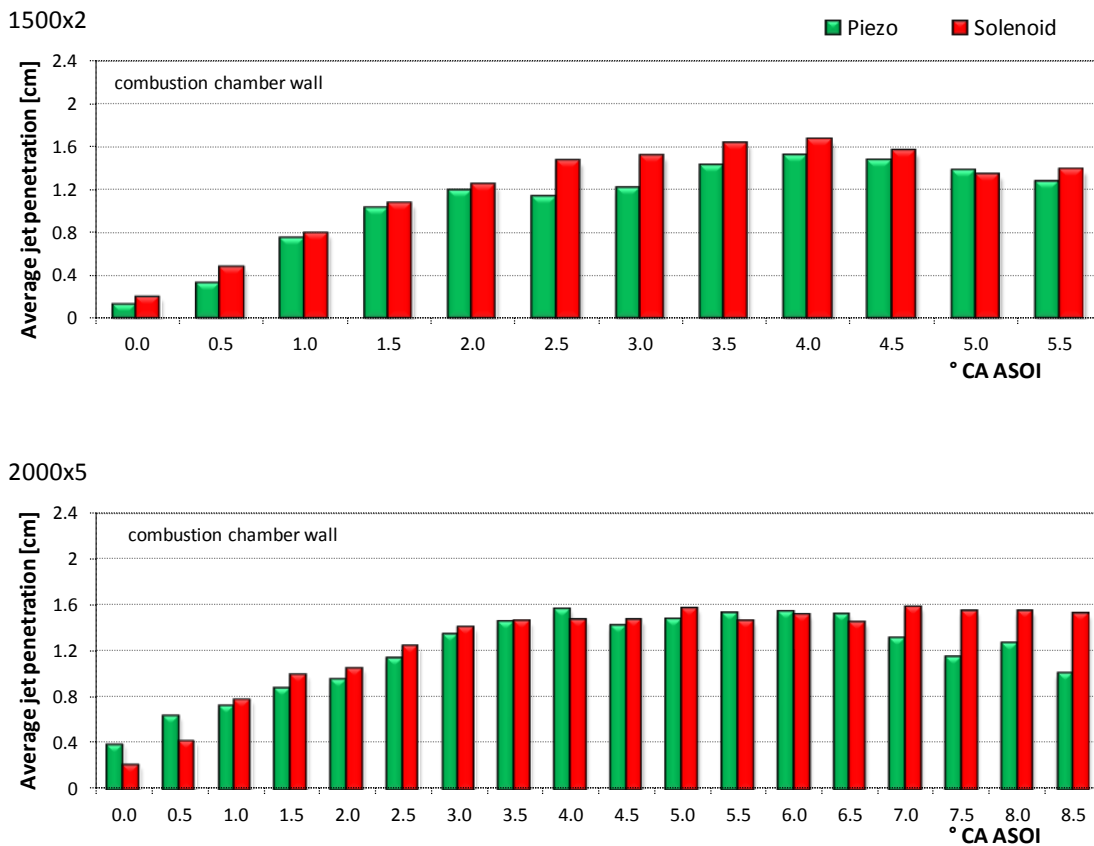


**Figure 3.** Average jets penetration of both the piezo and the solenoid injectors in the conditions 1500x2 and 2000x5, respectively.

It is evident that the injection process is longer in term of crank angle degree for the condition 2000x5 because of the longer duration of the injection at this engine speed. Higher penetration values have been detected for the solenoid injector during almost the whole evolution of the spray in both the tested conditions. This result could be justified by the high jet fluctuation for the piezo injector that affects the calculation of the average penetration over five repetitions. In order to emphasize the different jets behaviour in the combustion chamber between the two injector driver technologies, the standard deviation of the penetration measurements has been calculated. It has been evaluated for each jet over five repetitions. Similar trends have been found for all the jets. In Figure 4, the standard deviation of a single jet is shown as an example for both investigated conditions. At the condition 1500x2 the standard deviation of the piezo injector is very high with respect to the solenoid one. The hole to hole dispersion of the piezo injector is more evident because it has been supplied by low voltage corresponding to a partial needle lift. In this case, the interaction between the fuel flow and the needle causes a vibration of needle itself and so an irregular spray distribution [8]. On the contrary, these differences disappear at the condition 2000x5 because of the stabilizing effect of higher pressure gradients in the needle seat.

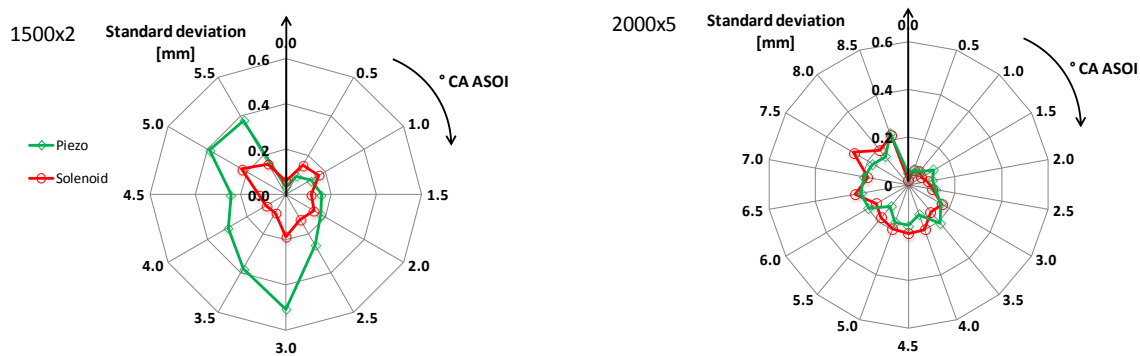


**Figure 4.** Standard deviation of jets penetration for both the piezo and the solenoid injectors in the conditions 1500x2 and 2000x5, respectively.

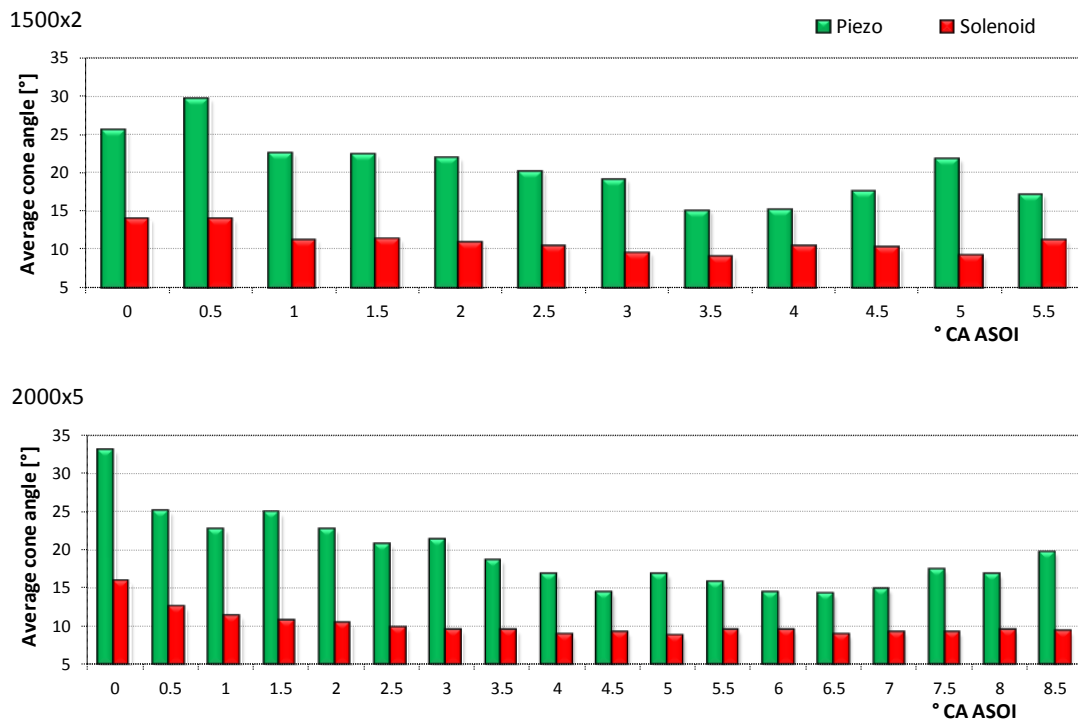


**Figure 5.** Average cone angle of both the piezo and the solenoid injectors in the conditions 1500x2 and 2000x5, respectively.

Beside the penetration, the cone angle of the spray dispersion has been measured. It has been evaluated as the vertex angle of an isosceles triangle which has been assumed as the shape of the jet [19]. In Figure 5, the cone angle evolution for both the piezo and the solenoid injectors in the conditions 1500x2 (top) and 2000x5 (bottom) have been reported. In both the tested conditions, larger cone angle values have been detected for the piezo injector. As it is reported in literature [13], this behaviour has been ascribed to the fast response of the injector in terms of mass flow rate that produces a higher fuel delivery in the first instants of injection. By comparing the cone angle evolution in the two investigated conditions, 1500x2 and 2000x5, almost the same values of cone angle have been measured; for the piezo injector, a starting value of 25°-30° gives way to smaller values until a stabilization around 15°. On the contrary, for the solenoid injector, the maximum value is 15° at the start of injection and then it quickly reaches and keeps a value of 10°.

Also in this case, the analysis of the standard deviation has revealed a good instrument for the evaluation of the statistical distribution of the jets. In Figure 6, the standard deviation of the cone angle for a single jet, over 5 repetitions has been reported. The piezoelectric injector shows higher standard deviation than the solenoid one. The fluctuating behaviour of the spray angle could be caused by the partial needle lift [20].

Whereas before, the higher standard deviation detected for the piezo injector at 1500x2 was not confirmed at 2000x5, for the cone angle, the dispersion between the jets seems not to be influenced by the operating condition, in particular injection pressure. The piezo injector has shown values of standard deviation of about four times larger than the solenoid one. Finally, although piezo injector is characterized by an irregular spray distribution it has a larger cone angle that enhances the air entrainment and hence the air/fuel mixing.

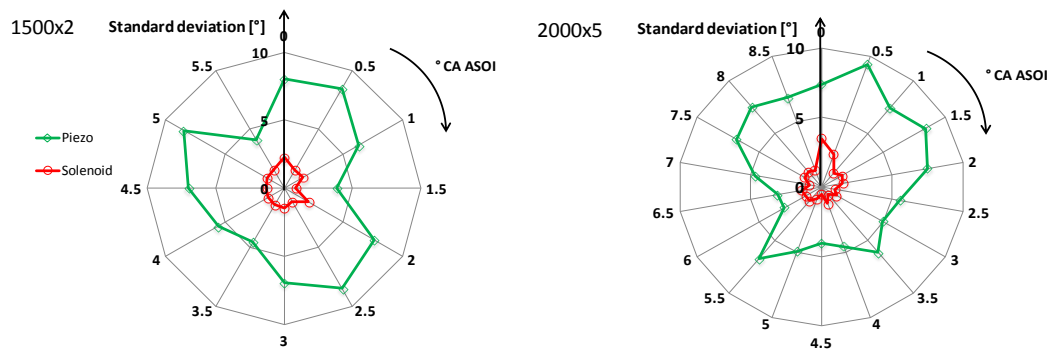


**Figure 6.** Standard deviation of cone angle for both the piezo and the solenoid injectors in the conditions 1500x2 and 2000x5, respectively.

On the other hand, solenoid injector has shown a uniform evolution of the jets but a more narrow spray angle that could affect in a negative way the charge mixing.

The effects of the injector driver have been studied also in terms of jet velocity. It has been obtained approximating the penetration of each jet with a four-order polynomial and differentiating it with respect to the time. The calculation range goes from the start of the injection to the crank angle where the penetration starts decreasing because of the fuel evaporation that is 3.5° CA and 5° CA at the conditions 1500x2 and 2000x5, respectively. As an example, in Figure 7, the curves of velocity of a single jet have been reported in the tested conditions 1500x2 and 2000x5. The jet velocity shows the typical decreasing trend with the maximum value at the start of injection. In the condition with injection pressure of around 600 bar (Fig. 7, left), the piezo injector shows the highest velocity, it is almost twice the value obtained for solenoid driven injector, 78 m/s versus 45 m/s. Moreover, while the first reaches faster the maximum injection rate [16], the latter needs more time, this behaviour is detectable from the shape of the velocity curves.

In fact, the piezo injector velocity quickly falls towards lower values; on the contrary, in order to reach the maximum injection rate, the solenoid injector keeps the initial velocity for a few crank angles later. This is maybe due to the longer stabilization time required by the solenoid actuator.

It was found in literature [13] that the higher spray velocity of the piezo injector at the beginning of injection could be responsible of a better fuel atomization than the solenoid one. Moreover, because of the higher velocity, the piezo injector could cause a better fuel penetration in the combustion chamber and, hence, a better fuel-air mixing since the early injection phase.

A different behaviour has been observed in the condition 2000x5 (Fig. 7, right) where both the injectors reach the maximum velocity at the beginning of the injection because of the reduction of the stabilization time. This can be due to higher injection pressure (around 900 bar) with respect the previous case. In fact, as Payri et al. [15] noted, the fast opening slope of mass flow rate for piezo injector is more prominent at low injection pressures.

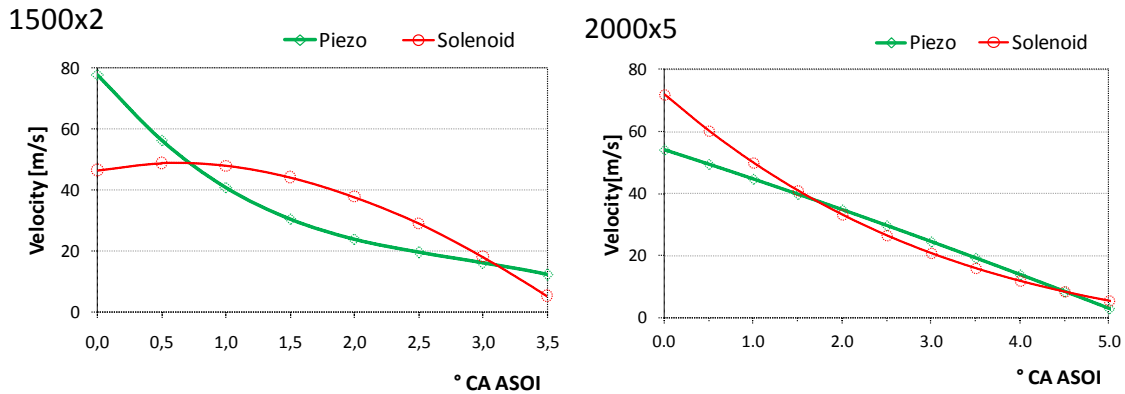


**Figure 7.** Jets velocity of both the piezo and the solenoid injectors in the conditions 1500x2 and 2000x5, respectively.

## Conclusions

In this work a study on the behaviour of a diesel spray from a piezo and a solenoid driven injectors has been performed. A transparent diesel engine equipped with the head of production engine has been used for the investigation by means of imaging technique. The analysis has been made in two engine operating points typical of the standard driving cycle NEDC.

Experiments have shown that:

- The piezo injectors are characterized by a faster response with respect to solenoid driven ones detected by the visible start of injection.
- Tests in engine-like conditions have revealed that the piezo injector has non-uniformly distributed jets; it has lower average jets penetration and larger cone angle than the solenoid one.
- The standard deviation of the piezo injector is very high with respect to solenoid one for both the penetration and cone angle measurements.
- The piezo injectors have the highest jet velocity at the start of injection. This behaviour is less evident at higher tested engine speed due to the higher injection pressure.

## Acknowledgements

The authors would like to thank Mr. Carlo Rossi and Mr. Bruno Sgammato for the engine assessment and for the support in the experimental activity.

## Nomenclature

• <b>ASOI</b>	After Start of main Injection	<b>ECU</b>	Electronic Control Unit
• <b>BMEP</b>	Brake Mean Effective Pressure	<b>IMEP</b>	Indicated Mean Effective Pressure
• <b>CA</b>	Crank Angle	<b>NEDC</b>	New European Driving Cycle
• <b>CCD</b>	Charge Coupled Device	<b>TDC</b>	Top Dead Centre
• <b>CR</b>	Common Rail	<b>VSA</b>	Variable Swirl Actuator
• <b>EGR</b>	Exhaust Gas Recirculation		

## References

- [1] Soid, S.N. and Z.A. Zainal, *Spray and combustion characterization for internal combustion engines using optical measuring techniques - A review*. Energy, 2011. **36**: p. 724-741.
- [2] Benajes, J., et al., *The role of in-cylinder gas density and oxygen concentration on late spray mixing and soot oxidation processes*. Energy, 2011. **36**: p. 1599-1611.
- [3] Bae, C., et al., *Effect of Nozzle Geometry on the Common-Rail Diesel Spray*, in SAE. 2002.
- [4] Soma, S., et al., *Effect of nozzle orifice geometry on spray, combustion, and emission characteristics under diesel engine conditions*. Fuel, 2011. **90**: p. 1267-1276.



- [5] Lee, J. and K. Min, *Effects of needle response on spray characteristics in high pressure injector driven by piezo actuator for common rail injection system*. Journal of mechanical science and technology, 2005. **19** (5): p. 1194-1205.
- [6] Abani, N. and R.D. Reitz, *A Model to Predict Spray-tip Penetration for Time-varying Injection Profiles*, in *ILASS Americas, 20<sup>th</sup> Annual Conference on Liquid Atomization and Spray Systems*. 2007: Chicago, IL.
- [7] Schmidt, D.P. and M.L. Corradini, *The internal flow of diesel fuel injector nozzles: A review*. International Journal of Engine Research, 2001. **2**: p. 1-22.
- [8] Payri, R., et al., *Study liquid length penetration results obtained with a direct acting piezo electric injector*. Applied Energy, 2013. **106**: p. 152-162.
- [9] Payri, R., et al., *Effect of Partial Needle Lift on the Hydraulic and Evaporative Performance Characteristics of a Common rail Diesel Fuel Injector*, in *THIESEL 2012 Conference on Thermo- and Fluid Dynamic Processes in Direct Injection Engines*. 2012: Valencia, Spain.
- [10] Desantes, J.M., et al., *Experimental Characterization of Internal Nozzle Flow and Diesel Spray Behavior. Part II: Evaporative Conditions* Atomization and Sprays, 2005. **15**: p. 517-544.
- [11] Desantes, J.M., et al., *Experimental Study of Biodiesel Blends' Effect on Diesel Injection Process*. Energy & Fuels, 2009. **23**: p. 3227-3235.
- [12] Desantes, J.M., et al., *Experimental Characterization of Internal Nozzle Flow and Diesel Spray Behavior. Part I: Nonevaporative Conditions*. Atomization and Spray, 2005. **15**: p. 489-516.
- [13] Suh, H.K., S.W. Park, and C.S. Lee, *Effect of piezo-driven injection system on the macroscopic and microscopic atomization of diesel fuel spray*. Fuel, 2007. **86**: p. 2833-2845.
- [14] Heywood, J.B., *Internal Combustion Engine Fundamentals*. 1988, New York: McGraw-Hill.
- [15] Payri, R., et al., *Influence of injector technology on injection and combustion development - Part I: Hydraulic characterizatio*. Applied Energy, 2011. **88**: p. 1068-1074.
- [16] Park, H.-b., et al., *Injection rate and spray characteristics of a piezo injector for multiple injection*, in *The Eighth International Conference on Modeling and Diagnostics for Advanced Engine Systems (COMODIA 2012)*. 2012: Fukuoka, Japan.
- [17] Ferrari, A., A. Mittica, and E. Spessa, *Benefits of hydraulic layout over driving system in piezo-injectors and proposal of a new-concept CR injector with an integrated Minirail*. Applied Energy, 2012. <http://dx.doi.org/10.1016/j.apenergy.2012.09.039>.
- [18] Naber, J.D. and D.L. Siebers, *Effects of gas density and vaporization on penetration and dispersion of diesel sprays*, in *SAE*. 1996.
- [19] Hiroyasu, H. and M. Arai, *Fuel Spray Penetration and Spray Angle in Diesel Engines*. Trans. JSME, 1980: p. 44-385, 3208-3220.
- [20] Stegemann, J., et al., *Influence of throttle effects at the needle seat on the spray characteristics of a multihole injection nozzle*, in *18th Annual Conference on Liquid Atomization & Spray Systems (ILASS 2002)*. 2002: Zaragoza, Spain.

## Boundary condition and fuel composition effects on injection processes of diesel sprays at the microscopic level

Julien Manin<sup>1</sup>, Michele Bardi<sup>2</sup>, Lyle M. Pickett<sup>1</sup> and Raul Payri<sup>2</sup>

1: Sandia National Laboratories, USA

2: CMT - Motores Térmicos, Universidad Politécnica de Valencia, Spain

### Abstract

In this work, we performed high-speed imaging in the near-nozzle field of DI n-dodecane and ethanol sprays injected into a constant-flow, high-pressure, high-temperature vessel equipped with large optical accesses. The imaging system consists of a long-distance microscopic objective backlit by a short-pulse LED to resolve the spray structure.

The effect of injection pressure, ambient pressure, fuel temperature and fuel composition have been studied through measurements of the hydraulic delay, penetration rate, and spreading angle. For a given condition, the transient stages of spray development are highlighted by lower penetration velocities and wider spreading angles than during the quasi-steady period of injection. The effects were relatively different depending on the variable: injection pressure had the most significant change and fuel composition had a more subtle impact. A decrease in fuel temperature produced up to a 30 % increase in initial penetration velocity. Lower injection pressure conditions produced a two-stage slope of the penetration rate, demonstrating the need for a better description of the rate of injection during injector-opening transients.

### Introduction

Liquid sprays are widely used to introduce fuel into the combustion chamber in most transportation engines. For the latest generation engines, particularly with the latest diesel injection strategies that utilize multiple injections, there are numerous transient processes (beginning or end of injection) during a single cycle. These transients present challenges for CFD models to be predictive, whether their goal is to predict apparently simple parameters such as penetration rate or more difficult ones like the mixing of liquid structures (i.e. liquid breakup and droplet size). Accurate boundary conditions such as actual injection pressure or fuel temperature in the nozzle sac are often lacking, which adds uncertainty to the true rate of injection during transients. As a result, injection and spray processes may be inaccurately estimated, and blame placed on the CFD methodology rather than the accuracy of the rate of injection input boundary conditions (e.g. [1]). The parameters mentioned above are important to the injection process, but the rapid variations undergone through an injection event make their quantification very difficult. Indeed, Pickett et al. [2] recently based their prediction for the actual rate of injection on highly resolved measurements of spray penetration since measurements of the actual rate of injection were too uncertain during injection startup.

The near-nozzle region has attracted the interest of many researchers as it represents the initiation of the spray and the first stage of the atomization process. The flow in this region is believed to be key to understand and potentially predict distribution of the flow in the far-field. Most CFD models make the assumption to treat the spray as Lagrangian particles in this first region by injecting liquid blobs through the orifice, instead of resolving the primary breakup process [3]. This approach requires assumptions about droplet size distribution and velocity profile (spatial and temporal). Issues may arise because potentially inaccurate initial parameters lead to errors downstream. Typically there is a lack of information in this region as probing the spray near the exit of the nozzle is very difficult mainly because of its optical density but also because of the high velocities and the turbulent behavior of the flow.

Information about diesel spray droplet size in the core (interior of the spray) have been obtained using phase Doppler interferometry [4] or combining extinction and scattering of light [5] for example, but they mainly concern more dilute regions downstream of what is generally considered the near-nozzle (note that there is no standard definition for near-nozzle, but in this work, we consider this region to be contained within 10 to 50 nozzle diameters). Experiments have been carried out in the near-nozzle region by many groups using long-distance microscopy to record the development and instabilities of diesel sprays in this region [6, 7, 8, 9]. The more recent iterations applying optical microscopy under engine-like conditions (high-pressure and temperature) used diffused and pulsed illumination in a line-of-sight arrangement to overcome the crippling effects of beam steering and freeze the motion [10, 11]. Crua et al. [12] used optical microscopy to measure the droplet size distribution in the near-field (although slightly farther than the limits indicated above) on the edges of the spray for two fuels under atmospheric conditions. They observed little differences between fuels and concluded that the fuel physical properties only have small influences on droplet size. Even though the shear forces must be

dominant during the quasi-steady period of the injection due to the high injection velocities and density differences, fluid properties might have larger impact during transients, when injection velocities are reduced as pointed out by Manin et al. [11]. To date, the near-field microscopic research has not systematically addressed the effect of fuel injection pressure, fuel temperature, or ambient pressure on the initial spray structure and penetration.

The aim of this work is to investigate the effects of boundary conditions such as injection and ambient pressures as well as fuel temperature and composition on the development of sprays in the near nozzle region (up to approximately 7 mm or 75 nozzle diameters). Quantification of the injection processes is necessary to understand whether the potential shortcomings in modeling results are coming from variations in boundary conditions or the code itself. High speed imaging of penetrating sprays using long-distance microscopy has been implemented to resolve the macroscopic parameters of the spray both spatially and temporally with high accuracy. The sprays were injected into pressurized and slightly heated ambient conditions to prevent large temperature gradients and thus optical distortions due to beam steering.

## Experimental apparatus and testing procedures

### *Spray vessels and injection system*

The sprays have been injected in a constant flow test rig with maximum ambient temperature of 1000 K and maximum pressure of 150 bar. The installation is composed of four parts: gas compressors, gas heaters, a test vessel and a control system. The gas, initially stored in high pressure reservoirs, is continuously flowed through the test chamber by volumetric compressors. Electrical heaters, placed upstream the test chamber, increase the temperature of the flowing gas up to the selected temperature. The main advantage of this installation over pre-burn type vessels is the repetition rate at which the experiments can be performed (one injection every few seconds). For these tests, the test rig has been run in a closed-loop configuration to circulate pure nitrogen and to prevent combustion of the injected fuel. The injected fuel is carried by the gas flow and is retained by a series of low-pressure filters downstream of the testing section. Both the pressure and temperature in the testing section are adjusted by a closed-loop PID control which, in order to reach and hold the temperature at or around the set-point, regulates the power to the heaters. To improve the temperature homogeneity within the test chamber, the vessel has a double wall configuration. The external shell's function is to hold pressure of the ambient gases, while the internal liner actually is an additional heater covered with insulating material on the outside to reduce heat transfer to the external wall. The testing section is relatively large (200 mm diameter) and is equipped with three fused-silica windows (128 mm in diameter) placed orthogonally to offer multi-view of the injection event. Further information on the design and operation of this combustion vessel are provided in Ref. [13].

Even though the temperature has been varied from 300 to 900 K for these experiments, the results presented thereafter only concern the measurements performed with a slightly heated environment of 440 K. As the purpose of these tests is to vary injection and ambient pressures as well as fuel type and coolant temperature, keeping the vessel well below the maximum capabilities offers much better control on all the parameters (especially to control injector temperature). In addition, for temperatures typical of diesel engines closer to top-dead-center when injection normally occurs, larger density gradients are expected, which severely degrade the optical quality because of beam steering. However, as observed by Manin et al. [11], the development (penetration rate) of sprays in the near-field is not significantly affected by changes in ambient temperature (from 440 to 900 K). The ambient pressure has been varied from 5 to 29 bar, corresponding to ambient densities of approximately 3.8 and 22.8 kg/m<sup>3</sup>, respectively. Note that the 22.8 kg/m<sup>3</sup> point is the target ambient density used in the Engine Combustion Network (ECN) for the Spray A condition.

Two different fuels have been used in this study: n-dodecane and ethanol. Table 1 provides specifications for both fuels relevant to this study. The sprays have been injected via a solenoid-driven common-rail injector belonging to the family of the Spray A ECN injectors (Serial # 201675). The nominal outlet diameter of the injector is 0.090 mm and the shape of the orifice is conical (K-factor = 1.5), hydro-grinding has been performed to round the edges and improve discharge. Extensive measurements have been performed for the ECN injector set and the results of these measurements, as well as other information relevant to the present study are available in Ref. [14, 15]. The nozzle is oriented with an angle of  $\theta = -60^\circ$  ( $\pm 30^\circ$ ) according to the conventions from the ECN (available at <http://www.sandia.gov/ecn/>). Injection pressure has been varied between 30 and 150 MPa. Although not relevant for spray penetration because of the short period of the analysis, the results of the spreading angle with respect to time are affected by the injection duration. In this study, we set the electronic duration to a constant value (790  $\mu$ s) equivalent to a 1.5 ms injection duration under the Spray A condition (150 MPa injection pressure, 60 bar ambient pressure). When injection and/or ambient pressure is varied, injection duration changes widely as shown in the results presented further in this manuscript, where this phenomenon is detailed and discussed.

As mentioned in the introduction, the temperature of the fuel could play an important role on the injection processes by affecting fuel properties. For that reason, the spray facility is equipped with a temperature-controlled injector holder in which a liquid coolant is flowed through to ensure that the injector body is at the desired temperature. The temperature of the injector body has been varied from 30 to 80°C (303 to 353 K, respectively). Note that the actual temperature of the fuel to be injected has been measured thanks to a thermocouple probe mounted into a dummy injector measuring the temperature of the liquid in the nozzle sac; the results of these measurements are detailed in Refs. [13, 16]. Because the vessel is only slightly heated, the temperature of the fuel is expected to be very close to that of the coolant; if not exactly matching, the fuel temperature is within 5°C above the coolant temperature set-point. When coolant temperature is not varied to investigate the effect of fuel temperature on injection processes, the liquid is running at 40°C around the injector, the fuel in the sac being at 42°C (315 K). The results presented later are related to coolant temperature as this is the controlled parameter.

Table 1. Relevant fuel properties at 40°C, 1 atm.

Parameters	N-dodecane	Ethanol
Chemical formula	C <sub>12</sub> H <sub>26</sub>	C <sub>2</sub> H <sub>6</sub> O
Density [kg/m <sup>3</sup> ]	734	773
Viscosity [mPa.s]	1.06	0.82
Surface tension [mN/m]	24.3	20.6
Boiling temperature [K]	489	352
Enthalpy of vaporization* [kJ/kg]	256	846

\*Measured at the boiling temperature for each fluid

### ***Illumination and acquisition systems***

The sprays have been visualized employing a line-of-sight arrangement based on diffuse lighting similar to the one described by Ghandhi and Heim [17]. Diffused back-illumination has been utilized here to provide an efficient and uniform illumination as well as to reduce beam steering blurring of the images when light goes through density gradients as those observed under high pressure environments [11]. As remarked by others [11, 12], performing detailed imaging of the spray in the near-nozzle field is very challenging as the spray exits the nozzle at speeds of several hundred meters per second (flow velocity is on excess of 600 m/s with a 150 MPa injection pressure). Therefore the image duration must be kept small to record the spray so that the image appears motionless. In this work, we relied on short illumination to acquire the fast-moving sprays in a motionless manner. The lighting was therefore provided by an ultra-fast LED system developed at Sandia National Laboratories that is capable of generating light bursts of light as short as 20 ns at high repetition rates (several MHz). The LED system is equipped with a quad-die LED chip and the pulse duration was set to 50 ns to provide powerful yet short illumination. The illumination's spectrum is centered around 450 nm with a 20 nm bandwidth. A 20° engineered diffuser is mounted in front of the LED (at approximately 15 mm from the emitter) to collect and direct the light from the LED in a quasi Lambertian way toward a 70 mm focal length Fresnel lens with an effective diameter of 125 mm.

The images have been recorded by a high-speed camera equipped with a 12-bit CMOS sensor with 20 µm pixel size. The images were recorded from the position corresponding to  $\theta = 90^\circ$  based on the nozzle orientation convention mentioned earlier. A long-distance microscope lens was mounted to the camera to offer detailed optical access of the near-nozzle region. Further information concerning the specifications and limitations of the optical system described above are available in Ref. [11]. Different frame rates, image resolution and magnifications have been used throughout the experiments depending on the parameter of interest: the resolution, for example, ranged from 7.8 to 16.9 µm per pixel while the frame rate has been varied from 50 thousand frames-per-second (kfps) to up to 263 kfps. The schematic representation shown in Fig. 1 presents the testing section of the combustion vessel in the center surrounded by the illumination system on the right side and the high-speed camera plus microscope lens on the other side as arranged for the experiments performed in this work. Note that as mentioned earlier, the optical system has been arranged such that the negative effects of beam steering are reduced, this has been achieved on the acquisition side by maximizing the collection angle by placing the microscope lens at approximately 250 mm from the spray, which offered a collection angle in excess of 300 mrad.

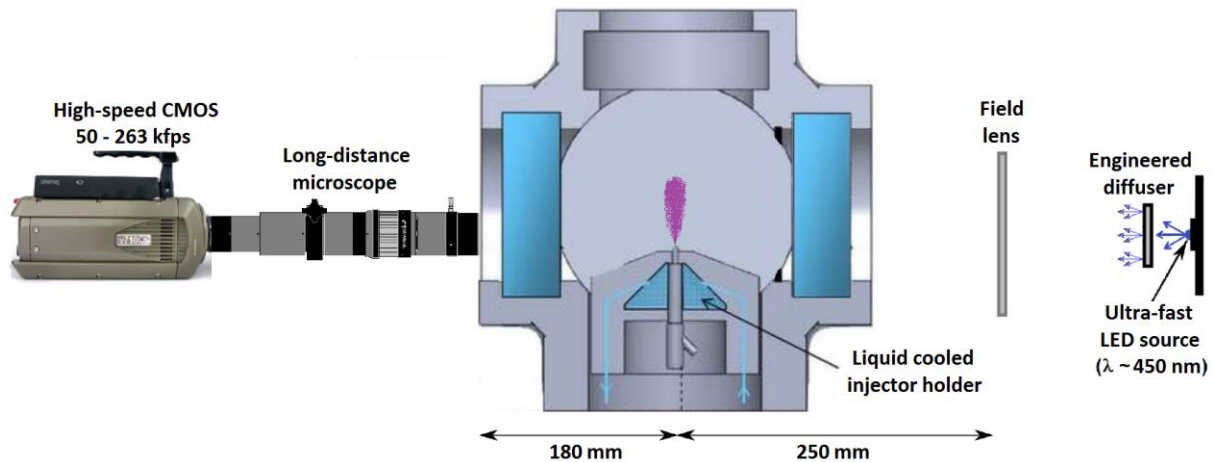


Figure 1. Schematic of the combustion vessel in the center, the long-distance microscope imaging system on the left and the illumination setup used for these tests

### Image processing

The images background correction scheme included dividing the images of the injection event ( $I$ ) by the initial intensity ( $I_0$ ) as a normalization procedure to overcome non-homogeneities in lighting distribution (due to beam steering or other optical artifacts). The initial intensity is taken from an average of several images immediately before injection. The result is a shadowgraph image with the imaging system being sensitive to the attenuation of light produced by the spray mainly due to Mie scattering (molecular absorption is negligible and beam steering is significantly reduced thanks to the optical system in place). Figure 2 represents a near-field penetration sequence of an n-dodecane spray injected at 50 MPa into relatively low ambient density ( $3.8 \text{ kg/m}^3$ ). Note that the camera frame rate for the penetration tests was 263 kfps (time step =  $3.8 \mu\text{s}$ ), but this sequence only represents every other image, or every  $7.6 \mu\text{s}$ , highlighting the detailed time-resolution of the penetration data considering the velocity of the flow and the relatively small visualization window.

The image quality is essential in such work, especially when focusing on spray edges as the relatively low fuel concentration might be below the detection limit of the system. Image blurring (or lack of focus) is another issue when performing optical microscopy as the edges of the spray would lack sharpness (particularly when measuring spreading angle). Attention has been paid by Manin et al. [11] to analyze the image quality and make the link between experiments with different focus quality. They found that the full-width at half-maximum (FWHM) criterion (considering a fixed level taken on the jet centerline) provided the highest level of robustness to repeatedly identify the edges of the spray under different levels of image quality (focus). It is important to note that as the tests have been performed under slightly heated environment (and as a result of the diffused back-illumination scheme employed), the negative effects of beam steering were very mild. Also, because evaporation is limited in these experiments, the gradients in light attenuation observed on the edges of the spray are steep, thus making the FWHM a robust measure of the spray boundaries. Previous works have successfully used this criterion to refer to spreading angle when a robust metric was needed [18, 19]. We decided to use the FWHM on the normalized images ( $I/I_0$ ) instead of on the optical depth ( $\tau = -\log(I/I_0)$ ) because the normalized FWHM corresponds to relatively low concentration of fuel (the slopes on the edges of the spray are steeper on the normalized images). Mie-scattering calculations have been performed and assuming mean droplet diameters between 10 and  $20 \mu\text{m}$  for instance, the averaged liquid fuel volume fraction over a 1 mm path length is on the order of 0.5 % on the edges of the spray corresponding to the FWHM threshold location. Because the liquid volume fraction is dependent upon the axial distance due to different path length through the spray, the total mass integrated along the path through the spray at the FWHM location might represent a better metric. By making the same assumptions used to compute the liquid volume fraction, it appears that the path-integrated projected mass at the FWHM radial location is approximately  $4 \mu\text{g/mm}^2$ , which again corresponds to a relatively low fuel concentration based on comparison with x-ray radiography measurements [18].

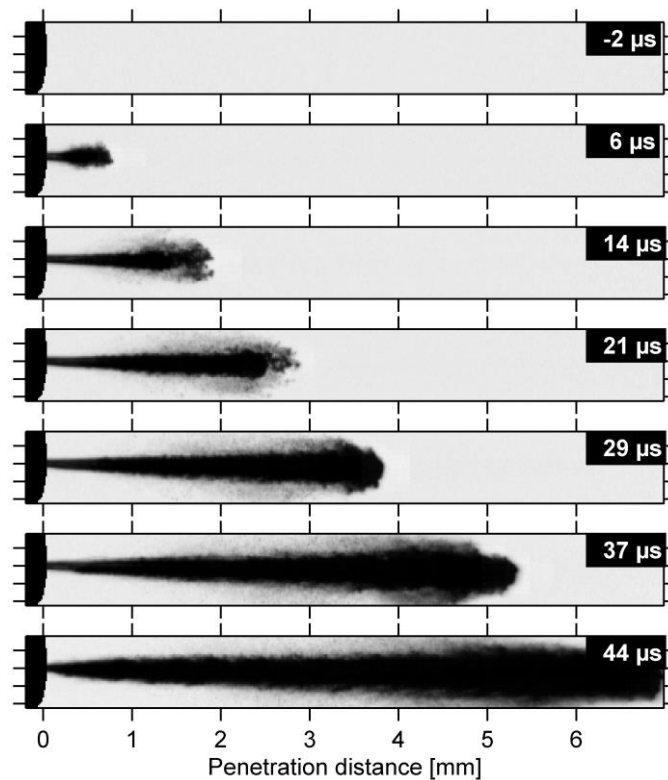


Figure 2. Normalized image sequence showing the penetration of an n-dodecane spray injected at 50 MPa into an ambient density of  $3.8 \text{ kg/m}^3$ .

The two main parameters directly extracted from the images were spray penetration and spreading angle. There are many definitions for these two parameters and the approach employed in this work is similar to the one used in [11].

- **Spray tip penetration:** The penetration rates of the sprays have been measured analyzing the attenuation of light produced by the spray in the axial direction of the background corrected image at every instant (image). The penetration was obtained as the furthest axial distance from the nozzle exit where the spray was detected with an attenuation level carefully chosen to be conservatively over the detection threshold.
- **Spreading angle:** The spreading angle of the sprays has been computed to get a time-resolved description of the spray radial growth employing the method described by Naber and Siebers [20]. The images are first binarized to extract the area of the spray applying the FWHM criterion on the time-resolved data. The spreading angle is then computed from an equivalent triangular area within the spray between the injector tip and half the penetration distance (up to 5 mm to give a measure of the near-field spreading angle and because the spray later exits the visualization window).

From the two macroscopic parameters detailed above, two additional variables have been extracted:

- **Spray penetration velocity:** The velocity of the spray in the first instants of the injection has been calculated to better quantify the differences in spray penetration when varying boundary conditions. A fifth degree polynomial fit of the experimental penetration data has been performed to get a smooth yet representative penetration curve. Time derivative of the fitted penetration curves provided the penetration velocities with respect to time. To present the results in a summarized way, the penetration velocities have been taken from an average between 5.2 and 6.3 mm away from the orifice exit (called penetration velocity at 5 mm in the figures). This region downstream of the orifice has been chosen because it seems to consistently be the maximum penetration velocity under the different conditions tested in this study, and therefore offers fair comparison between testing conditions. The velocities extracted to investigate the effect of fuel temperature were taken between 1.5 and 2.8 mm from the orifice (called penetration velocity at 2 mm) due to a different visualization window and magnification configuration. A 30 % decrease in penetration velocity is expected at the shorter distance downstream of the nozzle exit (1.5-2.8 vs. 5.2-6.3 mm); however, the trends and relative quantities of the results are expected to be fairly representative of the differences due to variations in boundary conditions.



- Hydraulic delay: The hydraulic delay corresponds to the time delay between energizing of the solenoid actuator driving the injector's needle (injector command) and actual injection of fuel through the nozzle outlet (called start of injection: SOI). Note that spray penetration and spreading angle are generally corrected for this delay and presented with respect to the time after start of injection (ASOI).

The high velocities of the flow in the observed phenomenon make the time measurement accuracy a primary issue. In the tests performed, we observed small jitter from the electronics employed (coming from the camera or the timing system for example) and/or from the mechanical actuation of the injector. As changing the conditions impacts the hydraulic delay, the system requires a certain time to adjust and be repeatable (to minimize shot-to-shot variations). Sufficient time has been taken between experiments to allow the system to stabilize, however, small variations in boundary conditions such as injection pressure (generally within 1 MPa) or coolant temperature (regulated to  $\pm 2^\circ\text{C}$ ), are beyond our control and their effect on hydraulic delay would be interpreted as jittering. Whether the jittering comes from fluctuations in the boundary conditions or slight deviations from the electronic timing system, this increases the uncertainty in the quantification of the hydraulic delay and a fortiori on spray penetration.

The results are all compiled from several injection events, from 5 to 20 high-speed recordings (injections), depending on the conditions and test performed. A statistically based estimation of the uncertainty (jitter) in the measurements of the hydraulic delay can be obtained from the standard deviation during one set of experiments. According to the calculations of the standard mean error [21] for these experiments, the uncertainty in hydraulic delay is below 9  $\mu\text{s}$  in the worst case scenario, corresponding to the lower injection pressure condition. This is expected to be well below the identified differences observed during the variations in boundary conditions as presented in the next section.

## Results and Discussions

This section presents results on tip penetration, penetration velocity and spreading angle in the near-field of diesel-like sprays as well as results on hydraulic delay to investigate the influence of boundary conditions on injection processes.

Figure 3 shows the influence of injection pressure on the penetration rate of n-dodecane sprays in the near-field (up to 7 mm) injected into an ambient temperature of 440 K and a density of  $22.8 \text{ kg/m}^3$ . The penetration rates are plotted as point data for the several experiments performed (10 repetitions), which after measurement of the hydraulic delay and time alignment, show very repeatable slopes across the different repetitions.

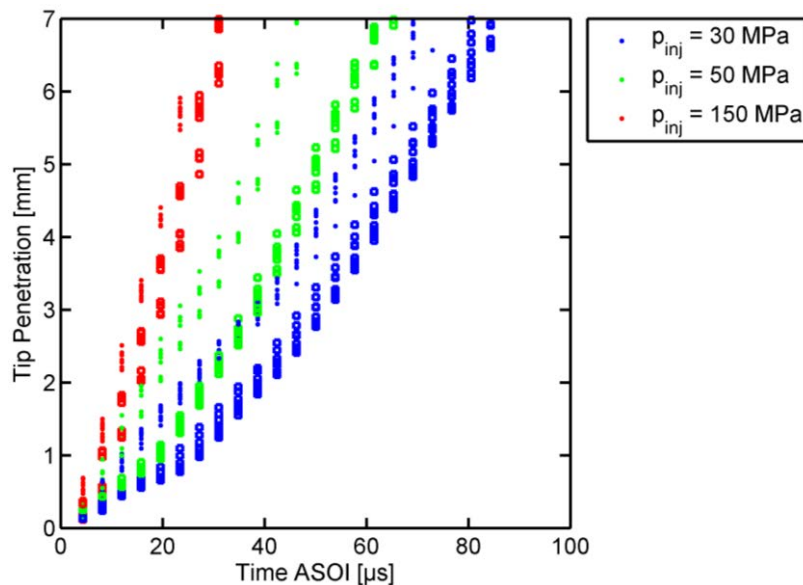


Figure 3. Spray tip penetration in the near-field as a function of time for n-dodecane at different injection pressures. The different repetitions are plotted as scattered points to show the repeatability and global deviation. The dots are for an ambient density of  $3.8 \text{ kg/m}^3$  while the squares are for  $22.8 \text{ kg/m}^3$ .

As expected, the penetration rates in Fig. 3 increase with the value set for the injection pressure. The time resolution employed during these experiments shows that the penetration rates are not linear with time unlike



reports in previous works using longer time steps or smaller field of view [9, 11]. The penetration rates for the intermediate injection pressure lies somewhat in the middle of the two other measurements, while the set-point is closer to the lower injection pressure case. This is expected as based on Bernoulli's equations, the velocity of the fluid through the orifice scales with the square root of the pressure difference (which is roughly equivalent to injection pressure due to the large difference between injection and ambient pressures). The effect of ambient density represented by the different symbols is also as expected as lower ambient pressure produces faster penetrating sprays due to a slower entrainment rate of ambient gases in the stream [20].

It appears on Fig. 3 that the sprays are accelerating in the first instants of the injection process (especially obvious for the lower injection pressure), which suggests that the pressure of the fluid is increasing upstream of the orifice. This acceleration of the sprays in the first part can be observed with more clarity in Fig. 4 presenting the time-derivative of the tip penetration (i.e., the penetration velocity) shown in Fig. 3 for the 22.8 kg/m<sup>3</sup> density case. The theoretical velocities at the orifice exit ( $u_B$ ), based on Bernoulli's expressions assuming the common-rail pressure as injection pressure, are indicated above each curve in the left plot of Fig. 4 as reference.

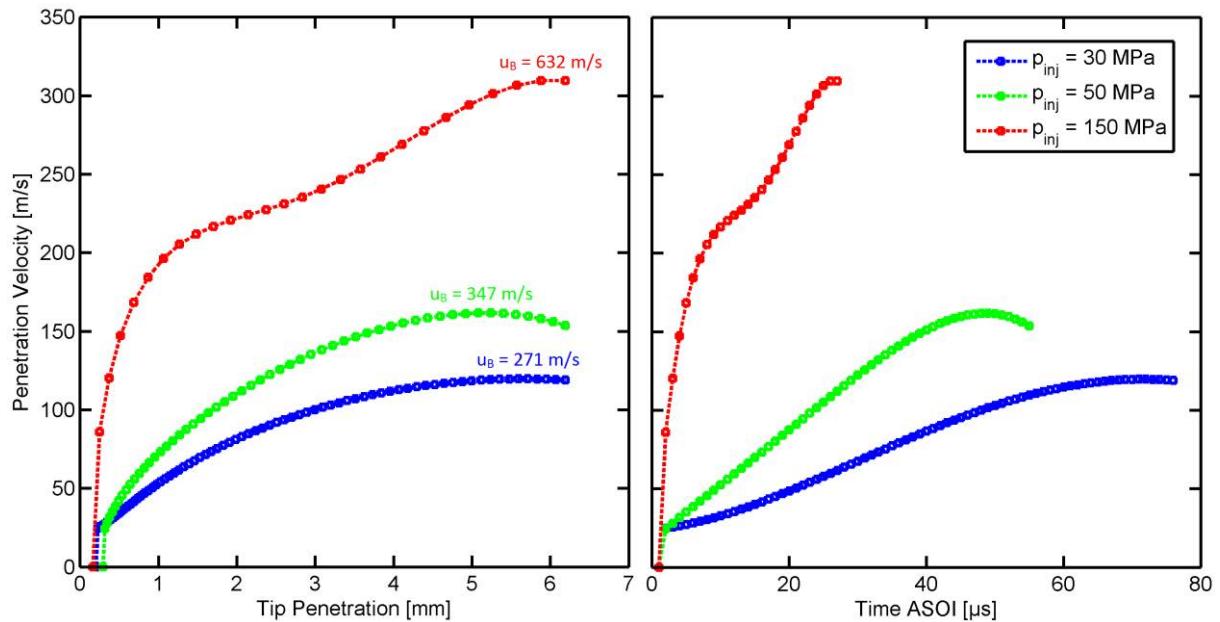


Figure 4. Velocity of the tip penetration in the near-field as a function of penetration distance (left) and time (right) for different injection pressures into an ambient density of 22.8 kg/m<sup>3</sup>.

Figure 4 confirms the observations about spray acceleration made in Fig. 3: the penetration rates increase as sprays progress as far as 5-6 mm into the chamber. After this quick ramp up, the penetration velocities reach maximum values (on the edge of the end of the visualization window for the higher injection pressure condition). Such information is paramount as it shows that the fluid is initially injected through the orifice into the chamber at much lower speed than the maximum value. This means that there is lower pressure across the orifice in the first instants of the injection process, and that there is a pressure “build-up” process that takes between 25 and 70 μs for the conditions represented in Fig. 4, which results in a ramping rate of injection [2]. It can also be appreciated that the maximum penetration velocity is less than half the Bernoulli velocity for the three cases presented in Fig. 4.

The penetration rates (or velocities) in the near-field can be used to extract information about rate of injection (ramp up) as detailed by Pickett et al. [2]. Not shown in this plot is the later behavior (downstream of 7 mm), which shows a decrease in spray velocity as the sprays mix more with the ambient gases. In addition to highlighting the increase and maximum value in tip penetration velocity, the left plot of Fig. 4 shows that the maximum velocity is reached roughly around the same distance from the nozzle for the three injection pressures presented here. Plotting the penetration velocity as a function of time (Fig. 4, right) shows that the peak velocity is reached earlier as injection pressure goes up. This is due to the faster lift of the injector's needle for higher injection pressure as observed by Kastengren et al. [22] using x-ray phase-contrast on the ECN injectors. As the needle leaves the seat, it opens a gap through which the fluid can flow to the sac and orifice. If the needle opens faster, a greater amount of fuel is expected to flow toward the sac of the injector and through the orifice to the

chamber, and vice versa. The impact of the needle position on spray development during the transients will be discussed in more detail later in this manuscript.

Figure 5 shows that the effects of fuel properties on the near-field penetration are minimal, with nearly identical spray developments whether ethanol or n-dodecane is injected. These observations agree with the fact that spray penetration is mainly momentum driven, while physical fluid properties have limited or no effects on spray momentum. For instance, Desantes et al. [23] investigated the influence of fluid properties on spray penetration from a macroscopic point of view (up to 40 mm downstream of the injector) by comparing diesel and biodiesel fuels; they also observed that the effect of fluid properties on global penetration was negligible. In addition, the differences in physical fluid properties for the two fuels compared in Fig. 5 are relatively small, giving more confidence that similar tip penetration rates are expected.

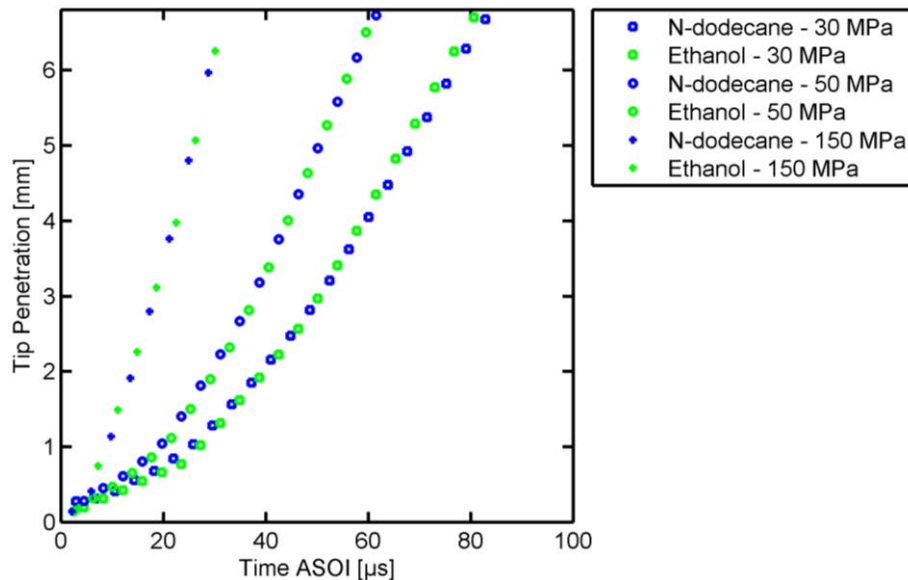


Figure 5. Spray tip penetration for n-dodecane and ethanol as a function of time for three injection pressures. Ambient density is  $22.8 \text{ kg/m}^3$ .

To provide a more global perspective of the effects of the different parameters varied in this study on penetration rate, the penetration velocity has been computed between 5.2 and 6.3 mm, which corresponds to the maximum penetration velocity of the Spray A case as shown in Fig. 4. The time ASOI corresponding to sprays reaching the region used for the calculation is around 20 to 25  $\mu\text{s}$  for Spray A; this is time necessary for the injection rate to reach the quasi-steady value as shown by Pickett et al. [2]. Figure 6 shows the penetration velocity as a function of injection pressure measured in the near-field for ethanol and n-dodecane at two ambient densities.

As seen on the previous figures, the penetration velocity in Fig. 6 increases as injection pressure gets higher; likewise, sprays injected into lower ambient density penetrate faster. Also observed earlier is the fact that the penetration velocity (as measured between 5.2 and 6.3 mm) is only a fraction of the velocity of the flow exiting the nozzle, based on Bernoulli's expression for the steady-state pressure difference. The penetration velocity varies between 45 and 75 % of the Bernoulli velocity across the different testing conditions represented in Fig. 6. It has to be noted that because of the effects of rate of injection ramp-up or ambient density for example, measuring the velocity at a fixed location might not be representative of the maximum tip penetration velocity, even though Fig. 4 showed fair agreement between injection pressures. The uncertainty increases with penetration velocity as one would expect; we estimate the maximum error to be comprised between 20 and 30 m/s for the data plotted in Fig. 6. Nevertheless, the results show reasonable consistency and it can be concluded that whether n-dodecane or ethanol is injected, the sprays are penetrating at roughly the same velocity in the measurement region.

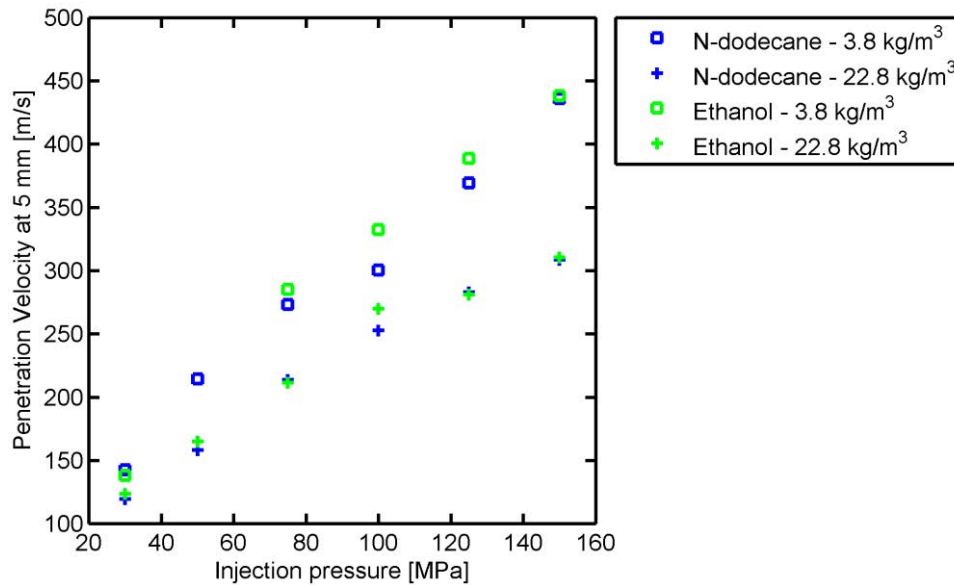


Figure 6. Spray penetration velocity measured between 5.2 and 6.3 mm from the nozzle outlet as a function of injection pressure for n-dodecane and ethanol into two ambient densities.

The effect of fuel temperature on penetration has also been studied through calculation of the penetration velocity at a certain distance. As mentioned earlier, due to a different optical configuration (smaller field-of-view), the penetration velocities for these tests have been measured between 1.5 and 2.8 mm downstream of the nozzle exit. Slower velocities are expected as the penetration rates are still increasing at such distances, but the velocities in the 1.5 to 2.8 mm range extracted from the penetration data measured with the larger optical configuration matched those measured with the smaller visualization window (at 40°C coolant temperature). Figure 7 presents the penetration velocity of sprays injected into two ambient densities while varying coolant temperature from 30 to 80°C (303 to 353 K). A relatively low injection pressure of 50 MPa has been chosen for this plot as it offers a higher level of confidence for the reasons mentioned above. Note that we estimate the uncertainty to be within approximately 7 m/s in the worst case scenario presented in Fig. 7.

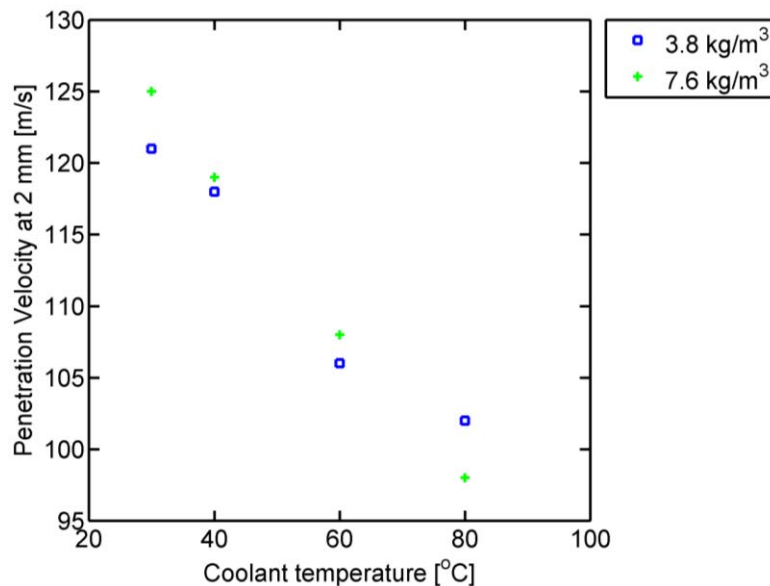


Figure 7. Spray penetration velocity measured between 1.5 and 2.8 mm from the nozzle outlet as a function of coolant temperature for n-dodecane into two ambient densities. Injection pressure is 50 MPa.

From Fig. 7, the effect of fuel temperature on penetration rate is evident as the sprays penetrate faster in the chamber as coolant temperature (fuel temperature) is lower. This is an interesting observation as fuel density

decreases when temperature rises. Based on the Bernoulli velocity on the outlet of the orifice, lower fuel density translates into higher flow velocity. For instance, the measurements performed by Caudwell et al. [24] for n-dodecane at 50 MPa showed a reduction in density from 774 to 745 kg/m<sup>3</sup> when fluid temperature varies from 30 to 80°C, in that order.

Viscosity is another parameter known to affect internal flow and injection processes; the viscosity for n-dodecane at 50 MPa goes from 2.17 to 1.05 mPa.s when temperature varies from 30 to 80°C [24], respectively. One possible explanation for the penetration dependence upon fuel temperature concerns the status of the sac and the presence of liquid or gas in it; as the fuel flows to the sac, the amount of gas is expected to change how the sac is pressurized and thus impact the injection of liquid. Another explanation can be found in the control volume as this is where lower fluid viscosity is going to reduce the pressure in the control volume faster as fuel flows out when the valve opens, inducing earlier movement of the needle. In fact, detailed measurements of the needle lift for this injector by Kastengren et al. [14] showed that the needle first moves a few micrometers, corresponding to the opening of the control volume valve; then, about a hundred microseconds later, the needle starts lifting and the fuel is injected. There are currently no studies on highly-resolved needle lift varying fuel or injector temperature to support this hypothesis, though, the measurements of hydraulic delay presented next certainly present valuable information in that regard.

The effects of fuel temperature on the start of injection (hydraulic delay) are shown in Fig. 8. Two ambient densities are displayed to show the consistency of the data when changing coolant temperature. An injection pressure of 50 MPa has been chosen as it exhibits relatively low uncertainty but larger variations in hydraulic delay than the higher injection pressures more typical of diesel engines running at high load conditions.

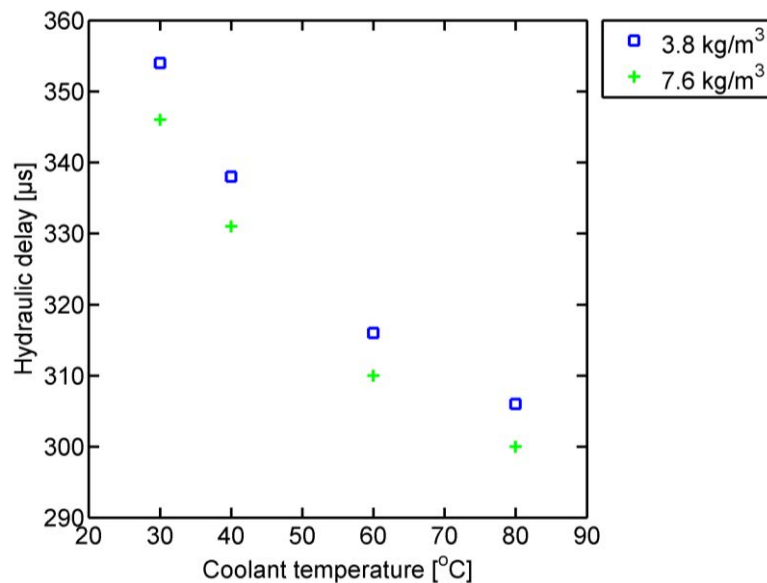


Figure 8. Hydraulic delay as a function of coolant temperature for n-dodecane into two ambient densities. Injection pressure is 50 MPa.

The plot in Fig. 8 demonstrated the influence of fuel temperature on hydraulic delay, as sprays exit the nozzle earlier after the command for higher coolant temperature, which therefore validates the hypothesis made after Fig. 7. This behavior is believed to be attributed mainly to the viscosity of the fuel for the reasons developed earlier. In addition to fluid flowing at higher rate through the seat and needle within the nozzle region, another impact of viscosity may come from the working principle of the injector as it is electro-hydraulically driven by the pressure difference in the control volume located above the needle assembly. The fluid has to go through a calibrated orifice in order to lower the pressure at the top of the needle and initiate the motion (opening of the injector). Higher viscosity is expected to reduce the flow through the orifice to the control volume, which would delay the balancing of pressures and thus the needle lift. Lower viscosity (for higher coolant temperature) is also going to reduce the contact friction between moving which could also make the needle lift faster. Fluid density is, on the other hand, not believed to significantly affect hydraulic delay because of the relatively small forces due to gravity, in addition to the random orientation of the injector. It can be noted that the fact that higher ambient density reduces hydraulic delay is expected as higher pressure in the chamber would result in a reduction of the relative cracking pressure to initiate the lift of the needle.

The effects of both fuel and ambient density on hydraulic delay are plotted in Fig. 9 as a function of injection pressure. As a general trend, it appears that the hydraulic delay gets shorter as injection pressure increases. This seems reasonable because higher forces would be applied to the needle in the nozzle region, thus helping the needle to lift. The first lift of the needle described earlier is believed to allow liquid to flow to the sac and pressurize it up to the cracking pressure of the injector (roughly 20 MPa). Once the sac is pressurized, the needle lifts and opens the gap to allow the flow to circulate downstream to the sac and the fuel to be injected through the orifice. It seems logical that higher flow rate would pressurize the sac more quickly during the slight initial lift of the needle, thus producing a faster response of the needle to lift.

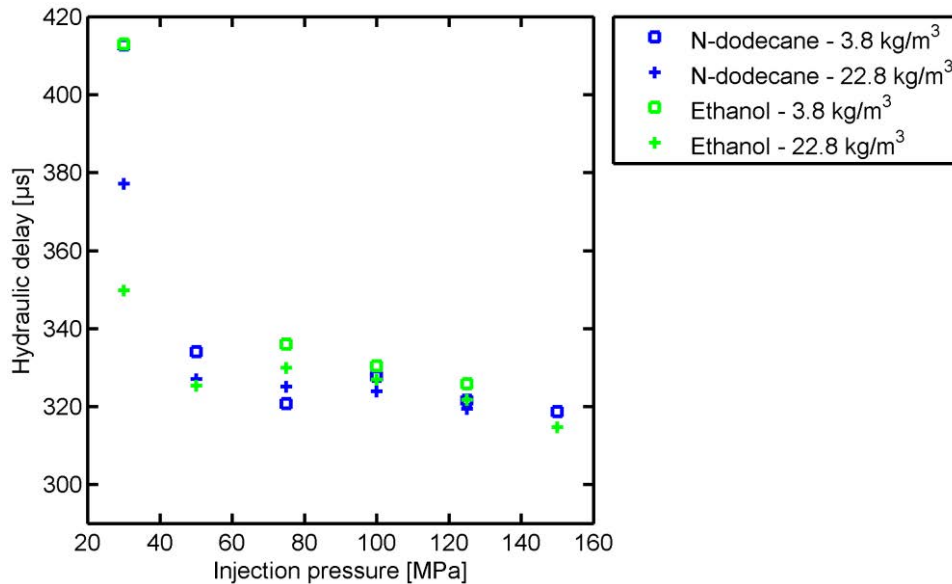


Figure 9. Hydraulic delay as a function of injection pressure for n-dodecane and ethanol into two ambient densities.

The differences observed between fuels are too small and/or the results of large dispersion in hydraulic delay when operating the injection system at low injection pressures (e.g.: 30 MPa) to be conclusive. The effect of viscosity (or fuel properties) on hydraulic delay has been seen in Fig. 8 by varying coolant (fuel) temperature. But looking at Table 1, it can be observed that the variation in viscosity between ethanol and n-dodecane is relatively small and hence, limited effect should be expected. Note that other fuels commonly used in thermal engines may present larger variations in physical properties, particularly viscosity (e.g. biofuels). For instance, Desantes et al. [23] measured longer hydraulic delay for biodiesel fuel (higher viscosity) when comparing the injection rate of rape methyl ester and regular diesel fuels.

Spreading angle is an important parameter as it describes the mixing of sprays in the near-field. Wider sprays, or larger spreading angles, are expected to entrain more air as they develop [19]. Figure 10 plots the spreading angle with respect to time for n-dodecane and ethanol at two injection pressures injected into a 22.8 kg/m³ ambient density. The standard mean error for the time-resolved measurements of spreading angle has been found to be below 1.2° in the worst case scenario. This uncertainty drops down to 0.2° when only the quasi-steady period of the injection event is considered.

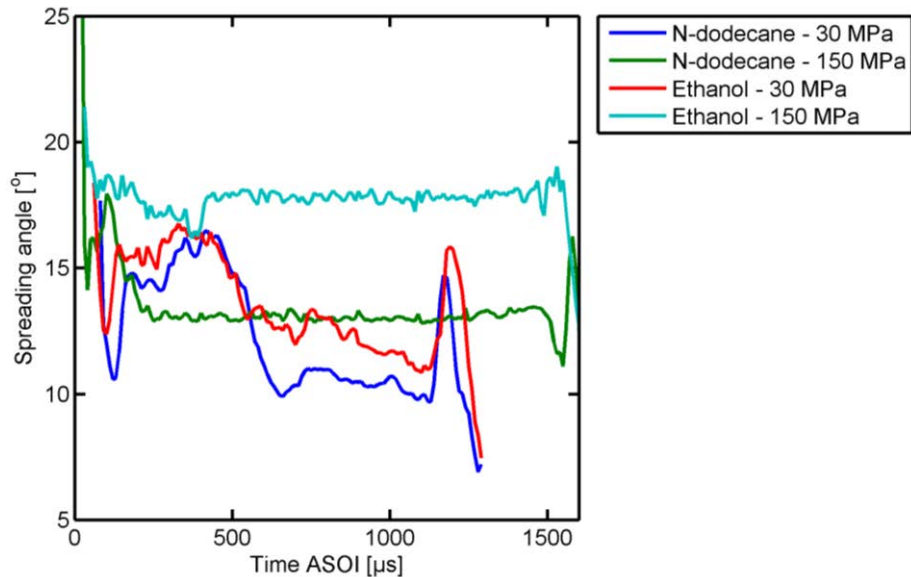


Figure 10. Spray spreading angle as a function of time for n-dodecane and ethanol at two injection pressures. Ambient density is  $22.8 \text{ kg/m}^3$ .

The effect of needle lift can also be observed on the spreading angle of the sprays with respect to time, as shown in Fig. 10. The variation in injection pressure plotted in this figure shows significant differences in spreading angle, with changes in transient and quasi-steady periods. Focusing on the transient period corresponding to the start of injection first, the sprays are several degrees wider than during the quasi-steady period. The difference between injection pressures is manifested through the duration of this transient start of injection; shorter transient is seen when high injection pressure is applied, while it is more than twice as long for a low injection pressure. This behavior is believed to come from a needle effect as it throttles the passage of the fuel to the sac and orifice as it has been experimentally observed by Payri et al [25]. Injection pressure changes the speed at which the needle lifts from the seat with higher injection pressures increasing the lift speed, as measured by Kastengren et al. [22]. As it has been commented earlier based on the different slopes in penetration and velocity with respect to time (Fig. 3 and 4, right), the spreading angle measurements shown in Fig. 10 seem to confirm the effect of needle position on spray development as mentioned earlier after Fig. 4.

During the quasi-steady period of the event, the difference in spreading angle is obvious, with higher injection pressure producing wider sprays. The change in spreading angle in the near-field between the two injection pressures is suspected to be slightly higher than that measured in the far-field under similar conditions [20].

The transient period corresponding to the end of injection shows that injection ends earlier for the low injection pressure case. In fact, while the electronic signal to control the injection duration has been kept constant (Energizing time =  $790 \text{ } \mu\text{s}$ ), the actual injection duration is longer when injection pressure goes up as observed by Kastengren et al. for the same family of injectors [22]. This comes from the faster needle lift at higher injection pressure, making the needle to reach a higher position (farther from its seat) at the time the command signal ends, and while needle closing is faster at higher injection pressure (but not as fast as opening), it does not allow the needle to come back to its seat at the same time.

Although the transient periods at the start and end of injection behave similarly for n-dodecane and ethanol, it is not the case for the quasi-steady period with ethanol producing wider sprays for both injection pressures represented in Fig. 10. It is clearer for the higher injection pressure case as a difference of approximately  $4^\circ$  remains quite constant during the quasi-steady period. Based on the similar penetration rates observed for these two fuels in Fig. 5 and the strong relationship between penetration rate and spreading angle found by Pickett et al. [19], such differences in spreading angle are rather surprising. However, the penetration rates correspond to the very beginning of the injection, which are necessarily related to the quasi-steady spreading angles, as shown in Fig. 10. In order to verify that the way the spreading angles are extracted is appropriate, the attenuation of light on the images has been averaged over the quasi-steady period, and the radial profiles (along the axial direction) have been examined. The analysis showed that the radial distribution of light attenuation is consistently wider for ethanol sprays, while maximum attenuation, normally found on the centerline, is very similar. The radial profiles confirmed that the FWHM criterion used to process spreading angle was appropriate



for the purpose of this study. It still remains though that the cause for wider sprays with ethanol is unclear and requires further investigation; reasons to explain such behavior might involve cavitation in the nozzle when ethanol is injected. Based on previous experiments with this injector, no cavitation has been observed when n-dodecane is injected, but cavitation has been seen to be affected by fluid properties as well [23]. Hydraulic measurements or comparison of the tip penetrations in the far-field might provide valuable information in that respect.

Fuel properties being similar for n-dodecane and ethanol, their impact cannot be successfully quantified here by changing fuel. However, changing fuel temperature has an impact on fuel physical characteristics, as demonstrated earlier through the variations in hydraulic delay shown in Fig. 8. Figure 11 represents the spreading angle with respect to time in the near-field for different coolant temperatures (from 30 to 80°C).

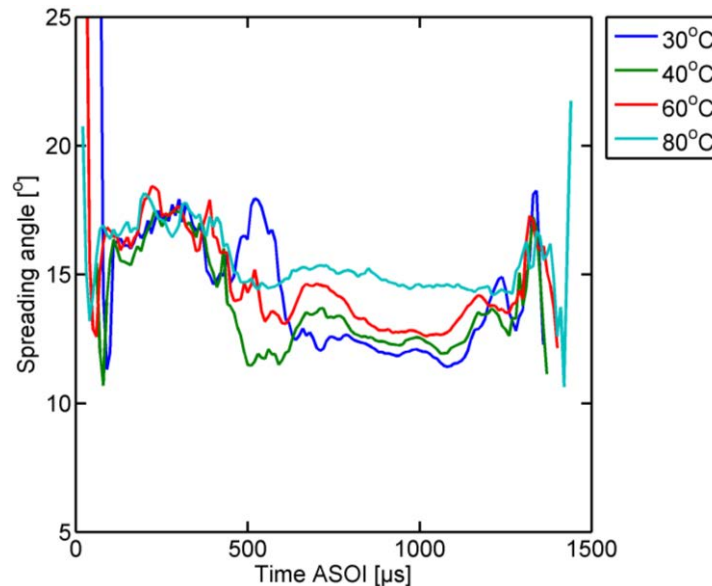


Figure 11. Spreading angle of the sprays as a function of time for n-dodecane when varying coolant temperature from 30 to 80°C. Injection pressure is 50 MPa and ambient density is 3.8 kg/m<sup>3</sup>.

Although the transients at the beginning and end of injection are inconclusive, a general trend can be observed during the quasi-steady period of the injection, with the spreading angle increasing with fuel temperature. Even though it can be argued the lack of relationship between initial penetration and quasi-steady spreading angle, following a similar path as the discussion developed above about differences in spreading angle between fuels support that such trend is expected because the penetration velocity results presented in Fig. 7 show a decrease in penetration rate in the near-field as fuel temperature increases. It is interesting to notice that the larger spreading angle observed during the transient periods are somewhat similar, while large differences are measured during the quasi-steady period of the injection. This demonstrates the large influence of fuel physical properties on the injection process as the mixing field downstream is expected to be widely affected by such results. Here, the fuel properties have been varied by changing the coolant temperature surrounding the injector, which highlights even further the necessity for researchers to control the temperature of the fuel in an accurate and precise way to get repeatable and useful measurements, or simply to make any comparison possible, as one of the objectives of the ECN working group for instance.

## Conclusions

Highly spatially and temporally resolved experiments have been performed in the near-field of diesel sprays injected into slightly heated environments with ambient pressure conditions corresponding to densities found in current diesel engines. Two different fuels have been injected in this study aiming at understanding the effects of varying boundary conditions, such as ambient and injection pressures or fuel temperature, on injection process and spray development in the first millimeters. The experiments have been performed in an optically accessible high-pressure, high-temperature capable flow rig. The images have been acquired by a high-speed camera equipped with a long-distance microscope lens and the illumination was provided by purposely-designed LEDs capable of nanosecond pulses at mega Hertz repetition rates.



The measurements showed a ramp up in penetration rate at the very beginning of the injection, also confirmed by an increase in penetration velocity, which suggests that there is a ramp up in injection pressure across the orifice which can be assimilated to the transient ramp up typically observed in rate of injection. No differences have been registered between n-dodecane and ethanol in penetration rate and velocity as the fluid properties under similar conditions are very similar. On the other hand, significant differences have been measured in penetration rates (velocities) when fuel temperature was changed; this is believed to come from variation in fluid viscosity which impacts the functioning of the injector by changing needle lift. The measurement of the spreading angle of the sprays demonstrated the impact of needle lift and position on spray development. Differences in spreading angle have been observed between n-dodecane and ethanol with the latter producing wider sprays in the near-field. Consistent with the penetration rate and velocity measurements while varying fuel temperature, wider spreading angles have been recorded when fuel temperature is higher. It is important to note that the differences registered during these experiments are expected to have large impacts on further spray developments. This demonstrates the need to associate measurements of the injection processes with accurate and controlled boundary conditions such that the data can be used with confidence for model validation.

### Acknowledgements

The authors wish to thank Chris Carlen from Sandia National Laboratories for designing and manufacturing specific ultra-fast LEDs, as well as Jose Enrique del Rey and Juan Pablo Viera from CMT–Motores Termicos for their support during the experiments. Support for the research carried out by Julien Manin at CMT–Motores Termicos was provided by the U.S. Department of Energy, Office of Vehicle Technologies. Sandia is a multi-program laboratory operated by Sandia Corporation, a Lockheed Martin Company for the United States Department of Energy's National Nuclear Security Administration under contract DE-AC04-94AL85000.

### References

- [1] V. Vuorinen, E. Antila, O. Kaario, M. Larmi, E. El-Hannouny, and S. Gupta. Near nozzle diesel spray modelling and x-ray measurements. *SAE Paper 2006-01-1390*, 2006.
- [2] L. M. Pickett, J. Manin, R. Payri, M. Bardi, and J. Gimeno. Transient rate of injection effects on spray development. *SAE Paper 2013-24-0001*, 2013.
- [3] S. V. Apte, M. Gorokhovski, and P. Moin. LES of atomizing spray with stochastic modeling of secondary breakup. *International Journal of Multiphase Flow*, 29(9):1503–1522, 2003.
- [4] H. Chaves, C. Kirmse, and F. Obermeier. Velocity measurements of dense Diesel fuel sprays in dense air. *Atomization and sprays*, 14(6):589–609, 2004.
- [5] J. Labs and T. Parker. Two-dimensional droplet size and volume fraction distributions from the near-injector region of high-pressure diesel sprays. *Atomization and Sprays*, 16(7):843–855, 2006.
- [6] M. C. Lai, T. C. Wang, X. B. Xie, J. S. Han, N. Henein, E. Schwarz, and W. Bryzik. Microscopic characterization of diesel sprays at VCO nozzle exit. *SAE transactions*, 107(4):1284–1292, 1998.
- [7] C. Heimgartner. Investigation of the primary spray breakup close to the nozzle of a common-rail high-pressure Diesel injection system. *SAE Paper 2000-01-1799*, 2000.
- [8] C. Bae and J. Kang. The structure of a break-up zone in the transient diesel spray of a valve-covered orifice nozzle. *International Journal of Engine Research*, 7(4):319–334, 2006.
- [9] R. Payri, F. J. Salvador, J. Gimeno, and J. De la Morena. Macroscopic behavior of diesel sprays in the near-nozzle field. *SAE Paper 2008-01-0929*, 2008.
- [10] T. Shoba, C. Crua, M.R. Heikal, and M. Gold. Optical characterisation of diesel, RME and kerosene sprays by microscopic imaging. *ILASS-Europe 2011, Estoril, Portugal*, 2011.
- [11] J. Manin, M. Bardi, L. M. Pickett, R. N. Dahms, and J. C. Oefelein. Development and mixing of diesel sprays at the microscopic level from low to high temperature and pressure conditions. *THIESEL 2012 Conference on Thermo and Fluid-dynamic Processes in Diesel Engines, Valencia, Spain*, 2012.
- [12] C. Crua, G. de Sercey, M. R. Heikal, and Gold M. Dropsizing of near-nozzle Diesel and RME sprays by microscopic imaging. *ICLASS 2012, Heidelberg, Germany*, 2012.
- [13] R. Payri, J. M. Garcia-Oliver, M. Bardi, and J. Manin. Fuel temperature influence on Diesel sprays in inert and reacting conditions. *Applied Thermal Engineering*, 35:185–195, 2012.
- [14] A. L. Kastengren, F. Z. Tilocco, C. F. Powell, J. Manin, L. M. Pickett, R. Payri, and T. Bazin. Engine Combustion Network (ECN): Measurements of nozzle diameter and hydraulic behavior. *Atomization And Sprays*, 22(12):1011–1052, 2013.
- [15] M. Bardi, R. Payri, L-M. Malbec, G. Bruneaux, L. M. Pickett, J. Manin, T. Bazyn, and C. L. Genzale. Engine Combustion Network (ECN): Comparison of spray development, vaporization and combustion in different combustion vessels. *Atomization And Sprays*, 22(10):807–842, 2012.

- [16] M. Meijer, B. Somers, J. Johnson, J. Naber, S.-Y. Lee, L.-M. Malbec, G. Bruneaux, L. M. Pickett, M. Bardi, R. Payri, and T. Bazyn. Engine Combustion Network (ECN): characterization and comparison of boundary conditions for different combustion vessels. *Atomization and Sprays*, 22(9):777–806, 2012.
- [17] J. B. Ghandhi and D. M. Heim. An optimized optical system for backlit imaging. *Review of Scientific Instruments*, 80:056105, 2009.
- [18] A. L. Kastengren, C. F. Powell, Y. Wang, K. S. Im, and J. Wang. X-ray radiography measurements of diesel spray structure at engine-like ambient density. *Atomization and Sprays*, 19(11):1031–1044, 2009.
- [19] L. M. Pickett, J. Manin, C. L. Genzale, D. L. Siebers, M. P. M. Musculus, and C. A. Idicheria. Relationship between diesel fuel spray vapor penetration/dispersion and local fuel mixture fraction. *SAE Int. J. Engines (SAE Paper 2011-01-0686)*, 4:764–799, 2011.
- [20] J. D. Naber and D. L. Siebers. Effects of gas density and vaporization on penetration and dispersion of diesel sprays. *SAE Paper 960034*, 1996.
- [21] R. J. Moffat. Describing the uncertainties in experimental results. *Experimental thermal and fluid science*, 1(1):3–17, 1988.
- [22] A. Kastengren, Z. Tilocco, and P. Powell. Initial evaluation of engine combustion network injectors with X-Ray diagnostics. *ILASS-Americas 2011, Ventura, CA*, 2011.
- [23] J. M. Desantes, R. Payri, A. Garcia, and J. Manin. Experimental study of biodiesel blends effects on Diesel injection processes. *Energy & Fuels*, 23:3227–3235, 2009.
- [24] D. R. Caudwell, J. P. M. Trusler, V. Vesovic, and W. A. Wakeham. The viscosity and density of n-dodecane and n-octadecane at pressures up to 200 MPa and temperatures up to 473 K. *International Journal of Thermophysics*, 25(5):1339–1352, 2004.
- [25] R. Payri, J. Gimeno, M. Bardi, and A. H. Plazas. Study liquid length penetration results obtained with a direct acting piezo electric injector. *Applied Energy*, 106:152–162, 2013.

## **Evaluation of high speed measurements on the spray/wall interaction for diesel injections**

K. Seel, D. Cordes, M. Cardena and R. Kneer

Institute of Heat and Mass Transfer, RWTH Aachen University, Germany

### **Abstract**

In down-sized direct injecting diesel engines, spray impingement on to the cylinder liner during pre- or post-injection is very likely to occur. Therefore the spray behavior before and during the interaction with the wall is of great interest. The goal of the present experiments is to determine the spray behavior for a wide combination of parameters (similar to those of a pre- or post-injection) when interacting with a flat wall. The parameters varied include injection parameters such as injection pressure and timing, as well as in-cylinder parameters such as gas phase pressure, temperature and injector-wall-distance. For these experimental conditions, high speed visualization measurements are performed at about 15 kHz, giving a good impression on the global spray behavior when interacting with a wall. Close to the wall, light-sheet measurements are carried out, which give information on the inner structure of the spray, such as wall vortices and spray detachment. Due to the smaller measurement area, these measurements could be carried out at an increased frame rate of 120 kHz.

Analyzing the spray behavior, a multitude of spray characteristics are evaluated: The free flow velocity, the spray width close to the wall, the temporal evolution of the area of impact, the height of the newly generated spray at the wall and the detachment of the spray from the wall.

---

### **Introduction**

To date, internal combustion engines play a major role in transportation and individual mobility. Therefore, fuel efficiency is a significant factor in engine development. For this, one approach is to reduce the engine displacement and to increase the charging pressure at the same time, commonly known as downsizing.

Through the application of pre- and post-injections the engine smoothness can be improved and the production of pollutants, such as soot and nitrogen oxides ( $\text{NO}_x$ ) can be significantly reduced. During these pre- and post-injections, spray impingement on to the cylinder liner in down-sized direct injecting engines is very likely to occur, leading to fuel deposits on the liner. At the same time oil from the cylinder liner is transported into the combustion chamber due to the impact of the impinging spray, which may lead to an increased production of pollutants. Due to the movement of the piston, the fuel contaminates the engine's oil-circuit, leading to undesired effects such as the reduction of viscosity and lubricity. Thus, further engine development requires a comprehensive understanding of the effects of spray/wall interaction.

Through the evaluation of high speed visualization measurements, this paper describes the temporal properties of a direct injecting diesel spray as it interacts with a flat wall. For various nozzle-wall distances, representing different piston sizes, the wall influence on the penetration length and width of the spray close to the wall are analyzed (before impact). Furthermore, through the application of high speed light-sheet measurements, the height of the newly formed spray at the wall as well as the area of impact on the wall are evaluated. Also the temporal detachment of the spray from the wall (leading to a decreasing width directly at the wall) is processed.

In the past, there have already been several visualization investigations on the spray/wall interaction for diesel engines, providing in general information on the spray structure. Major spray parameters in these studies were the temporal evolution of the maximum width [1,2,3,4,5,6] and the height of the spray close to the wall [2,3,4,6]. In the mentioned publications, these parameters were derived from single shot images of CCD Cameras or analog cameras [3,5]. However, a consistent time series of spray/wall dynamics is not available.

### **Experimental setup**

The spray behavior was investigated experimentally in a pressurized and heated chamber. To ensure the same boundary conditions for each injection, the chamber was continuously provided with an air flow of about  $25 \text{ m}^3/\text{h}$ . The air flow was delivered by a compressor and heated electrically to the desired temperature before entering the chamber. For these studies the ambient temperature ( $T_{\text{air}}$ ) was varied from 400 K to 500 K, as the ambient chamber pressure ( $p_{\text{air}}$ ) was changed from 10 bar to 20 bar, representing conditions similar to those of a pre- and post-injection. The injection pressure ( $p_{\text{inj}}$ ) is altered from 800 bar to 1400 bar. The duration of injection ( $t_{\text{inj}}$ ) is set through a programmable timing unit between 200  $\mu\text{s}$  and 600  $\mu\text{s}$ , which was also used to synchronize the injection with the measuring devices. Measurements on all combinations of the named injection and chamber air parameters were performed, leading to a total of 16 operating conditions. Each combination of experimental

settings was measured for up to 4 ms, with the time count starting at the beginning of the injection signal. In spray/wall measurements, the temperature of the flat wall is assumed to be the same as the temperature of the ambient air. The employed injector holds a three-hole nozzle, which is derived from an eight-hole Bosch Crip 3 nozzle with a 109  $\mu\text{m}$  sized diameter and a cone angle of 153°.

Through its four circumferentially arranged windows, the pressurized chamber allows optical access from different perspectives. In this case, the spray was first injected upward into the chamber, whilst being illuminated and recorded from the front (Figure 1). These measurements could be performed at a frame rate of about 15 kHz. This provides a good overview on the behavior of the entire spray in free flow conditions and also serves as a reference for the influence of the flat wall on the spray behavior. For the spray/wall investigation, the injector was turned 180° and the fuel was injected downward onto a solid flat wall (Figure 2). Again high speed visualization measurements were performed at about 15 kHz, giving a good overview on the global behavior of the spray when interacting with a wall.

Close to the wall high speed light-sheet measurements were carried out to gather detailed information about the inner structure of the spray. With the light-sheet oriented perpendicular to the viewing position of the camera, a measuring area of approximately  $7 \times 22.5 \text{ mm}^2$  at the wall was established, enabling the observation of one half of the impinging spray. Due to the smaller measurement area, the temporal resolution could be increased to 120 kHz. Through a pneumatic system inside the pressurized chamber, the nozzle-wall distance was set to 37.5 mm, 40.0 mm and 42.5 mm, allowing the study of the spray behavior for different piston diameters (Figure 3). 50 injections were recorded for each combination of parameters and automatically analyzed for determination of the spray characteristics.

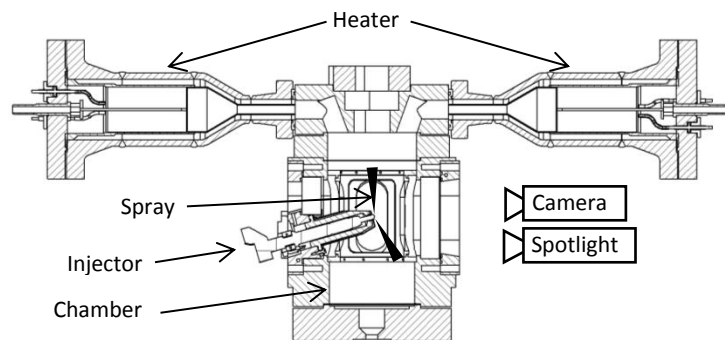


**Figure 1.** Experimental setup for visualization measurements of the spray in free flow, injected upward into the pressurized chamber.

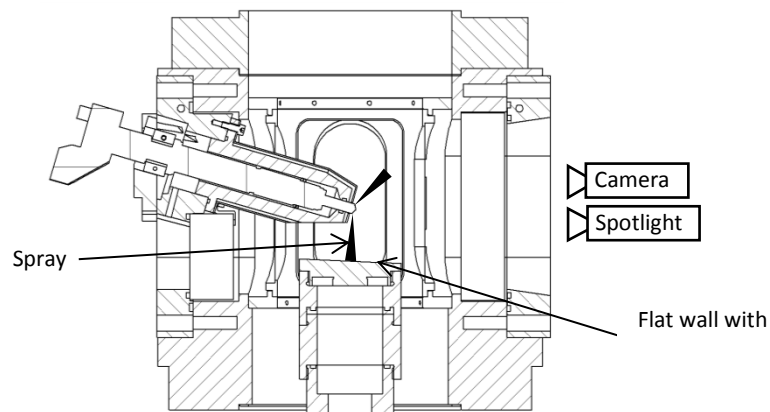


**Figure 2.** Experimental setup for spray/wall interaction visualization measurements with the spray injected downward on to the flat wall. For light-sheet measurements the spotlight was removed and the light-sheet comes underneath the injector at the wall, perpendicular to the camera. The position of the camera remains the same.

As the injector clamp was made for a nozzle with 148° cone angle, the spray is injected with an angle of 2.5° towards the plumb line (Figure 1 and Figure 2). To ensure a vertical impingement on to the wall, the wall also has an inclination of 2.5° (Figure 2).

For the visualization measurements with and without wall, the penetration length before impact and the spray width at a fixed distance of 35 mm away from the nozzle are evaluated (Figure 3). From the light-sheet measurements, the height of the spray at the wall, the width of the spray close to the wall and the width directly on the wall are analyzed (Figure 4). Radial symmetry is assumed when evaluating the spray at the wall.

The experimental setup shown in Figure 2 is similar to the experimental setup used by Meingast [1], who also performed measurements on a diesel spray interacting with a flat wall. Also the behavior of a gasoline spray

impinging on a inclined wall was measured with a phase-doppler anemometer in the pressurized chamber shown in Figure 2 by Stratmann et al. [7,8].

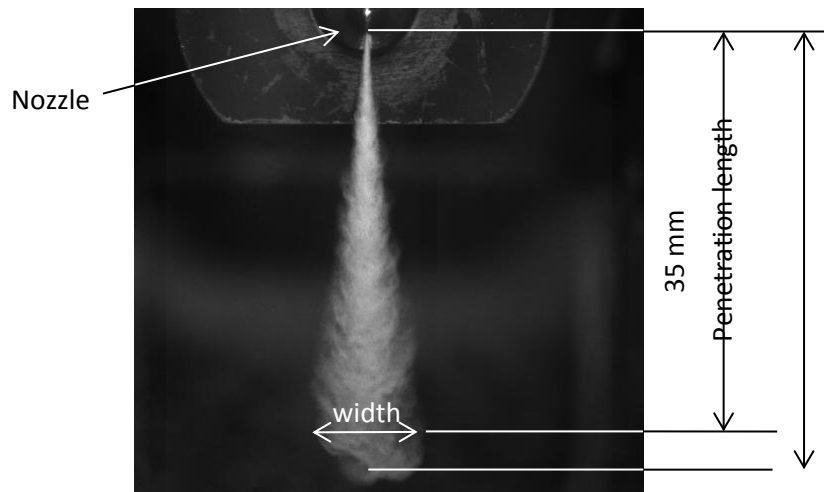


**Figure 3.** Overview of the evaluated parameters in visualization measurements: Penetration length and spray width at a fixed distance of 35 mm from the nozzle

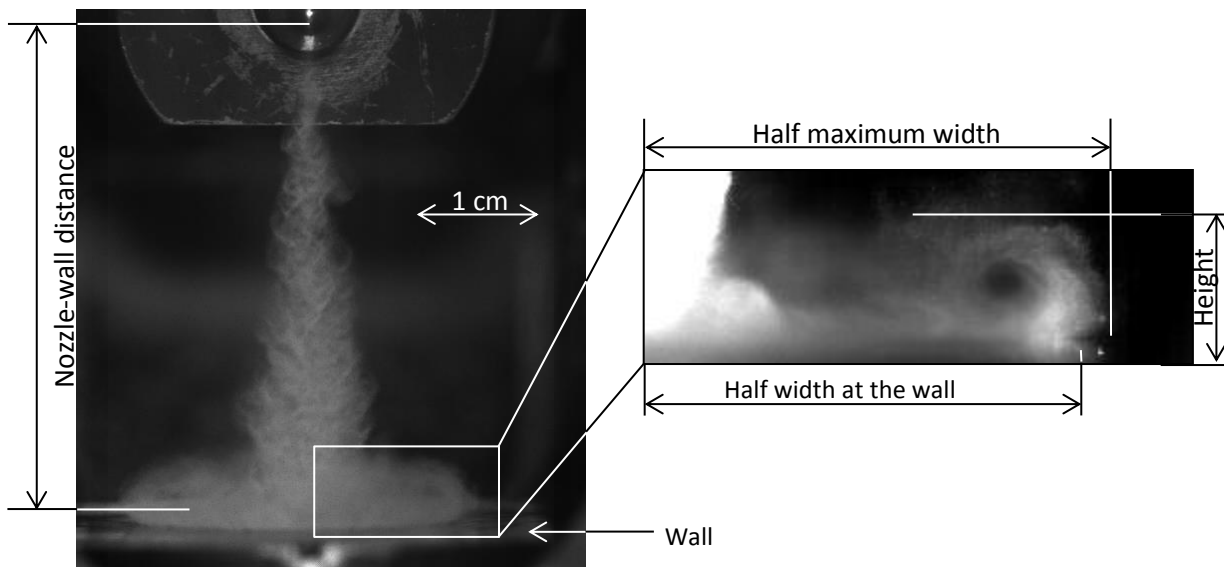


**Figure 4.** Definition of the nozzle-wall distance and parameters evaluated from the light-sheet measurements in the impingement configuration: The height of the spray, maximum width and the width on the wall. At the wall radial symmetry is assumed.

## Results and Discussion

To study the influence of the wall on the spray before impingement, visualization measurements of the spray with and without a wall were carried out. The measurements have been performed according to the experimental setups shown in Figures 1 and 2. The comparison of both measurements reveals the influence of the wall on the spray. The penetration of the spray in free flow can only be evaluated up to a length of about 47 mm, limited by the windows of the pressurized chamber. To demonstrate the wall influence on the spray before impingement, one set of injection parameters is chosen. For all three nozzle-wall distances the penetration and width of the spray (at a fixed distance of 35 mm from the nozzle) are compared. Due to a small difference in contrast between spray and wall, the penetration can be analyzed up to 2.5 mm close to the wall.

With a moderate chamber air density ( $p_{\text{air}}$  10 bar,  $T_{\text{air}}$  500 K) the injection is carried out with an injection pressure of 1400 bar and a short injection duration of 200  $\mu\text{s}$  (Figure 5). When interacting with the wall, all sprays show a comparable temporal development regarding their penetration length until they eventually hit the wall. In comparison to a freely propagating spray, they develop similar, but identical nozzle distances are reached at a later time. An explanation for this behavior could lie in the air between the spray and the wall, decelerating the

first injected spray through its higher inertia. Due to the different nozzle-wall-distances there is a temporal displacement until impingement occurs. Comparing the spray width, all measurements show a comparable behavior before impingement. After the sprays hit the wall, it takes up to one microsecond until the spray width (at a distance of 35 mm away from the nozzle) increases.

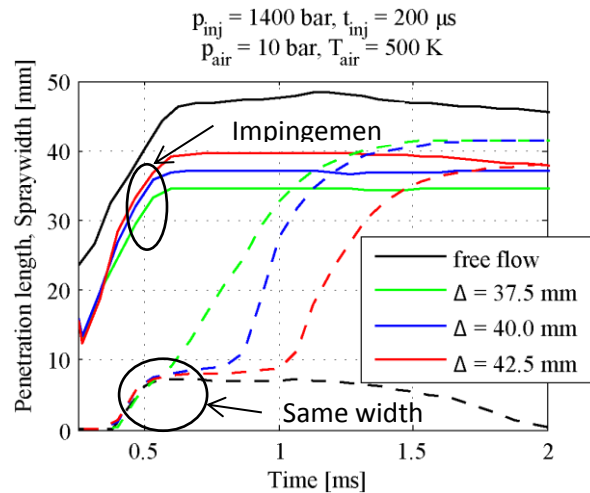


**Figure 5.** The wall reduces the penetration length of the spray before impingement (continuous curve). There seems to be no macroscopic influence on the width of the spray before impingement (dashed curve).

Light-sheet measurements close to the flat wall allow a detailed structural and temporal evaluation of the spray/wall interaction. These measurements were performed with the experimental setup shown in Figure 2. Figure 6 exemplarily shows the initial temporal evolution of the impinging spray. While the spray impinges on to the wall, it alters its direction and starts to move in radial direction. At the tip of the spray a toroidal vortex is formed, which moves along the wall and grows over time, as also described by Stratmann et al. [8]

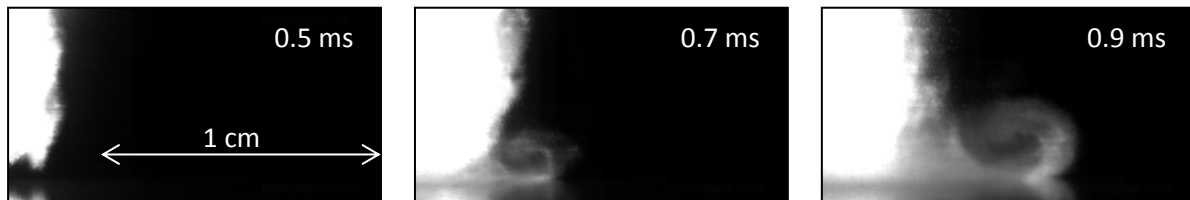


**Figure 6.** Light-sheet measurements performed at the wall, showing the temporal evolution of a spray impinging on a flat wall and the development of a toroidal vortex ( $p_{inj} = 800$  bar,  $t_{inj} = 600$   $\mu$ s,  $p_{air} = 10$  bar,  $T_{air} = 400$  K)

By evaluating the experimental data, the following conclusions can be made for the **height of the spray**:

For most settings, altering the injection duration does not influence the height of the spray at the beginning of impingement. In the later propagation of the spray a gain in the height can be observed (Figure 7, left). This is because the injection with higher injection duration possesses a higher overall momentum.

If the ambient density is high, the height of the spray benefits already shortly after impingement from an increased injection duration and the height clearly grows stronger (Figure 7, right).

The injection pressure shows the strongest influence on the height of the spray. By increasing the injection pressure from 800 bar to 1400 bar, impingement on the one hand occurs earlier through the increased exit velocity from the nozzle. On the other hand, the height of the spray grows stronger than it could be achieved through variation of any other parameter. All injections with an injection pressure of 1400 bar gain a height larger than the maximum accessible height of the measuring area (7 mm). However for injections with an pressure of 800 bar this only applies to the injection with the lowest ambient density and the longest injection duration (Figure 8, left).

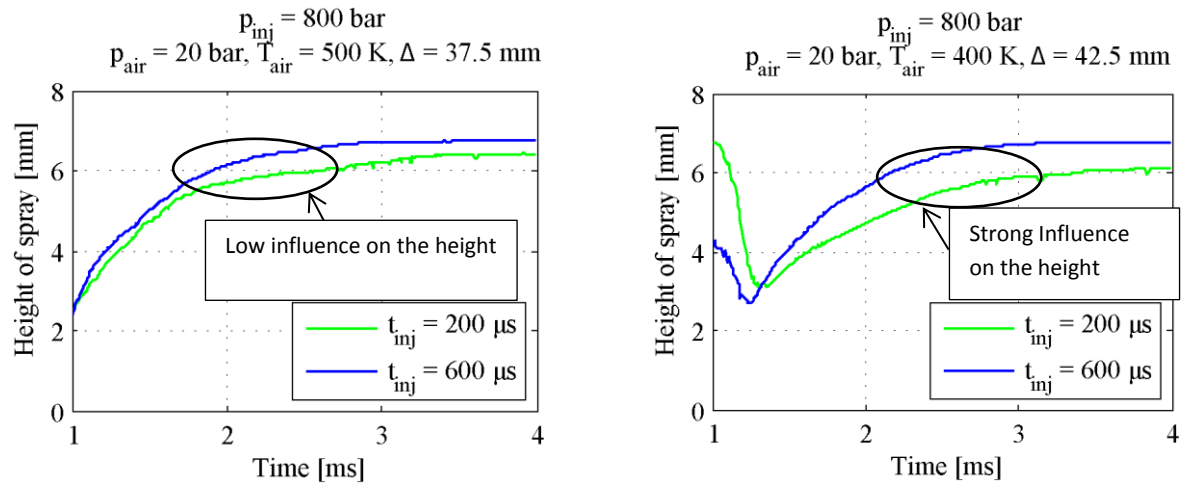


**Figure 7.** At low ambient densities the injection duration hardly influences the height of the spray (left). At high densities, its influence is more pronounced (right).

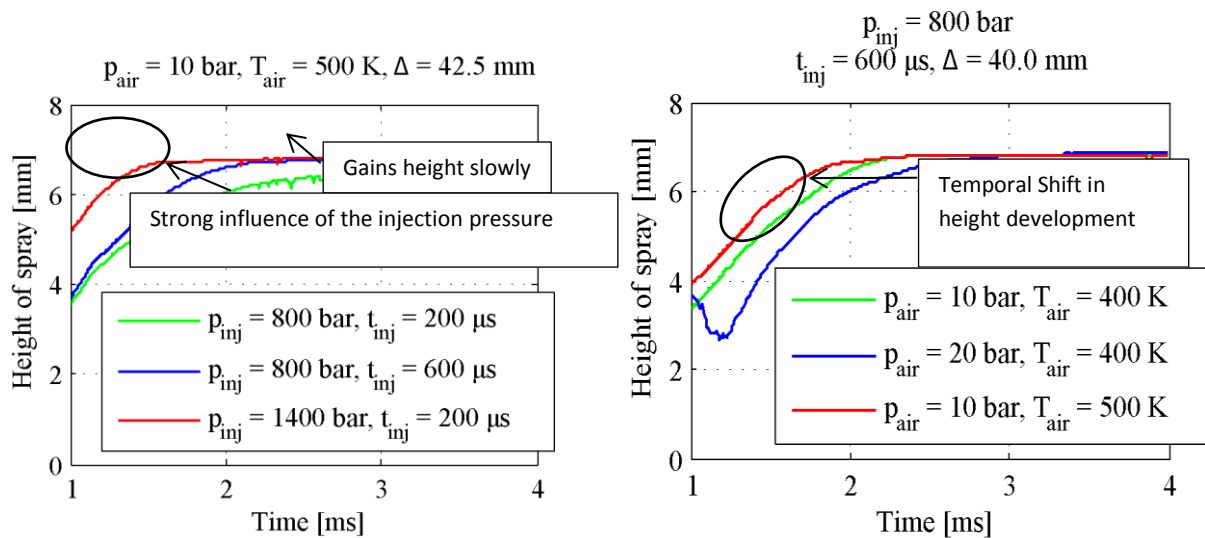


**Figure 8.** The injection pressure has a dominating influence on the height of the spray (left). Changes in the ambient density show a smaller influence on the height of the spray (right).

Decreasing the ambient density leads to an earlier spray impingement on the wall. This corresponds to the situation when increasing the injection pressure. Doubling the ambient pressure decreases the height growth rate more than a moderate decrease of 100 K in the ambient temperature. Reducing the ambient temperature practically only leads to a shift of temporal height development to a later time (Figure 8, right).

For the **maximum width of the spray** the following conclusions can be made:

Generally, all prior findings for the height of the spray also apply to its maximum width. An increase in the ambient density always leads to a slower growth in the maximum width, as well as the injection pressure again significantly determines the gain of maximum spray width.

Concerning the injection duration, there is always an influence on the maximum width. Even at lowest air densities and with an injection pressure of 1400 bar, there clearly is a small influence from the injection duration (Figure 9, left). At high ambient densities and low injection pressures, the influence of the injection duration on the maximum spray width is strong (Figure 9, right).

In the beginning of the impingement process, the spray width at the wall is almost equal to the maximum width of the spray (Figure 7). In the subsequent process the toroidal vortex grows, leading to a larger width close to the wall than at the wall itself (Figure 7). In some settings of experimental parameters, the spray detaches from the wall (Figure 10), leading to a decreasing width at the wall and yet an increasing maximum width. For most settings, the spray aligns again with the wall, but the width at the wall then always remains below the maximum width (Figure 11, left).



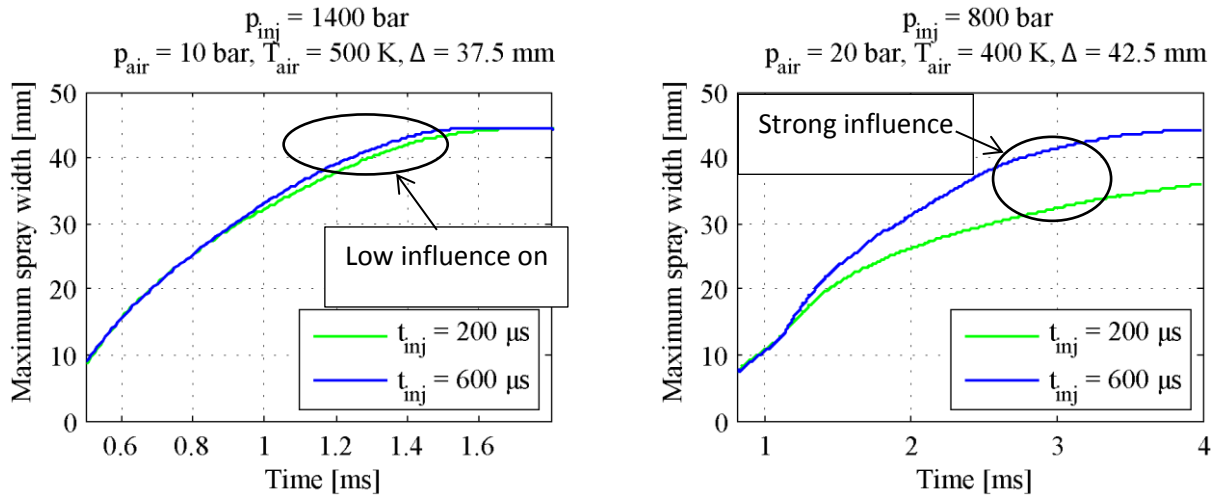


**Figure 9.** The injection duration shows a small influence on the maximum width of the spray at moderate ambient densities (left). At high ambient densities the influence increases strongly (right).

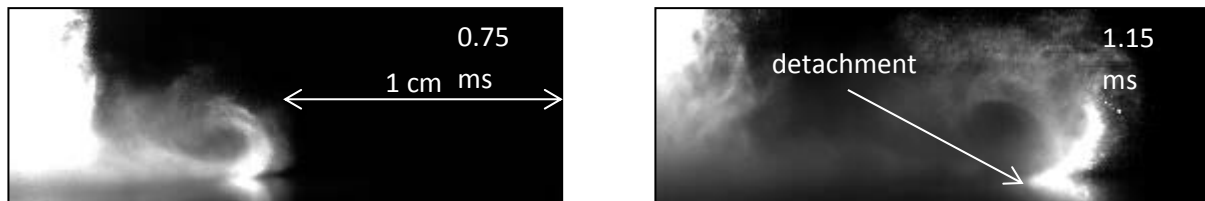


**Figure 10.** Later temporal propagation of an impinging spray at  $p_{inj} = 1400$  bar,  $t_{inj} = 200$   $\mu$ s,  $p_{air} = 10$  bar,  $T_{air} = 500$  K,  $\Delta = 37.5$  mm. In the later movement the torus vortex leads to a detachment of spray from the wall.

For the spray **width at the wall** the following conclusions can be made:

The evaluation of the light-sheet measurements shows that spray detachment always occurs if the overall injection momentum is high (achieved either through a high injection pressure or a long injection duration). If the overall injection momentum is low, spray detachment depends on ambient density. A high ambient density reduces the amount of spray detachment (Figure 11, right).

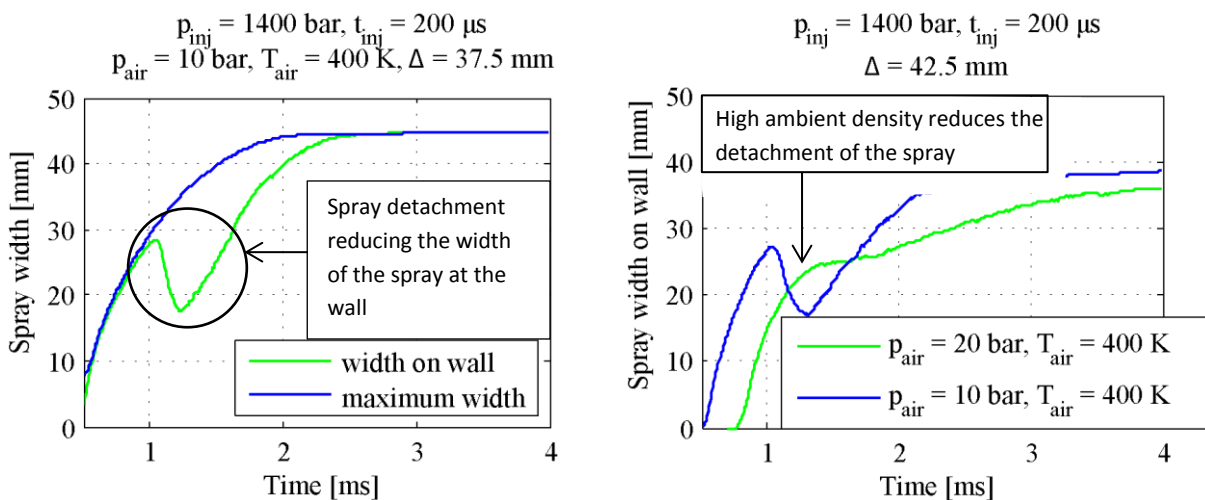


**Figure 11.** Spray detachment leading to a reduced width at the wall, while the maximum width increases (left). Ambient density hinders the detachment of the spray (right).

Regarding the growth rate of the spray width at the wall, the injections with a duration of 200  $\mu$ s always show an earlier decrease in spray width than the injections with a duration of 600  $\mu$ s, because of the lower momentum. If

detachment occurs, the injection with a duration of 600  $\mu\text{s}$  detaches later at about 0.2 ms to 0.5 ms. An explanation for this behavior could be the higher mass flow with its larger momentum.

The time until detachment occurs decreases when there is a higher injection pressure. Typical values of delay lie between about 0.1 - 0.3 ms (Figure 12).

Furthermore the scale in width reduction at the wall depends on the injection pressure. Increasing the injection pressure results in a more pronounced width decreasing at the wall (Figure 12).

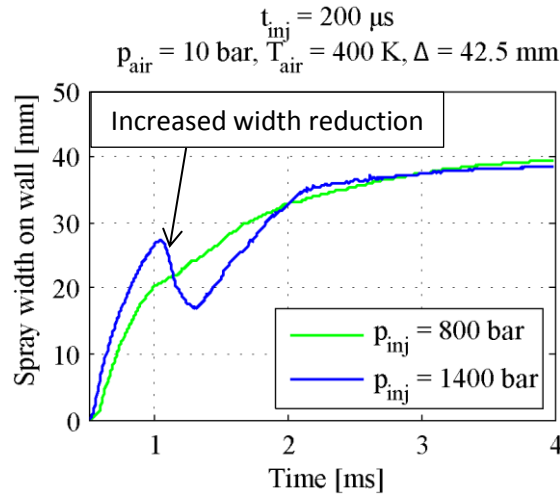


**Figure 12.** An increasing injection pressure increases the scale of width reduction when detachment occurs.

## Conclusions

The spray from a Bosch Crip 3 nozzle has been investigated when interacting with a flat wall, applying high-speed visualization and light-sheet measurements. Regarding the penetration before impact, the wall shows a strong influence on the spray. Initially the penetration is reduced, but not in the later propagation, leading to a temporal shift of the penetration, probably because of the air between the spray and the wall, decelerating the first injected spray through its higher inertia. The width of the spray in free flow at a fixed distance from the nozzle was not influenced through the presence of the flat wall before impingement.

At the wall, the height and the maximum width of the spray is mostly dependent on the injection pressure and therefore on the kinetic energy of the spray. An increased ambient density hinders the development of larger heights and widths, probably because of its higher inertia. Because of its larger momentum, a longer injection duration mainly influences the last part of the injection.

In a final step the detachment of the spray from the wall was discussed. At a high overall momentum, the spray always detaches from the wall, leading to a decreasing width at the wall and a yet increasing maximum width. Again, high ambient densities hinder the development of wall detachment and the spray remains at the wall.

## Acknowledgements

The authors thank the “Deutsche Forschungsgemeinschaft” (DFG), “Arbeitsgemeinschaft industrieller Forschungsvereinigungen” (AiF) and “Forschungsvereinigung Verbrennungskraftmaschinen e.V.” (FVV) for funding the cluster “Fuel in Oil”.

## Nomenclature

$p_{inj}$	Injection pressure
$t_{inj}$	Injection duration
$p_{air}$	Ambient air density inside the pressurized chamber
$T_{air}$	Ambient air temperature inside the pressurized chamber
$\Delta$	Nozzle-wall distance

## References

- [1] U. Meingast, Spray/Wand-Wechselwirkung bei der dieselmotorischen Direkteinspritzung, Shaker Verlag, 2002.
- [2] H. K. Suh, S. W. Park, C. S. Lee, A Study of the Flow and Atomization Characteristics of Impinged Diesel Spray on a Chamber Wall, Atomization and Sprays, 2007.
- [3] H. Fujimoto, J. Senda, M. Nagae, A. Hashimoto, Characteristics of a Diesel Spray Impinging on a Flat Wall, International Symposium COMODIA, 1990.
- [4] S. W. Park, C. S. Lee, Macroscopic and microscopic characteristics of a fuel spray impinged on the wall, Experiments in Fluid, 2004.
- [5] T. Ebara, K. Amagai, M. Arai, Image Analysis of a Diesel Spray Impinging on a Wall, International Journal of Fluid Mechanics Research, 1997.
- [6] S. Hohmann, P. Mattes, U. Renz, A. Schneemann and R. Wirth, Measurements of Droplet Size and Velocity in a DI-Diesel Spray Impinging on a Wall, ILASS, 1997.
- [7] J. Stratmann, Droplet-Wall and Spray-Wall Interaction at Increased Ambient Pressure and Wall Temperature, Shaker Verlag, 2009.
- [8] J. Stratmann, D. Martin, P. Unterlechner, R. Kneer, Near-Wall Characteristics of an Impinging Gasoline Spray at Increased Ambient Pressure and Wall Temperature, Atomization and Sprays, 2009.

## Study on Cyclic Variation in near-Nozzle Region of Diesel Spray by L2F

Keisuke KOMADA<sup>1</sup>, Takashi YAMADA<sup>1</sup>, Hiroshi TAJIMA<sup>2</sup>, Daisaku SAKAGUCHI<sup>1</sup>  
Hironobu UEKI<sup>1</sup> and Masahiro ISHIDA<sup>1</sup>

1: Graduate School of Engineering, Nagasaki University, Japan

2: Interdisciplinary Graduate School of Engineering Sciences, Kyushu University, Japan

### Abstract

A laser 2-focus velocimeter (L2F) was used for measurements of velocity and size of droplets in diesel sprays. The L2F has a micro-scale probe which consists of two foci. Diesel fuel was injected intermittently into the atmosphere by using a 5-hole injector nozzle. The diameter of the nozzle orifice was 0.113mm. The injection pressure was set at 40MPa. Measurement positions were located at 5, 12, 15, 20 and 25mm from the nozzle exit. At the spray periphery, the cyclic variation was small near the nozzle exit, and was large in the downstream region. It is understood that the cyclic variation was caused by the vortex at the spray periphery, and the vortex generated within each injection is not always the same. The correlation coefficient between the cyclic variations of velocity and size of droplets was small at the spray center near the nozzle exit, because the droplets with a high velocity decreased its size due to breakup.

### Introduction

Appropriate control of the combustion in the diesel engine is necessary for the improvement of thermal efficiency and reduction of exhaust emissions. It is important to understand the characteristic of cyclic variation in the combustion. The prime cause of cyclic variation in the combustion process may be broadly divided into two reasons: namely the gas flow in the cylinder and the characteristics of diesel sprays. The cyclic variation of gas flow affects the soot formation [1], and the indicated mean effective pressure [2]. The injection pressure and the ambient pressure affect the cyclic variations [3], and the behavior of the needle affects the unstable sprays [4]. However, there are few studies of the behavior of the droplets near the nozzle exit due to the high velocity and the high number density of droplets.

The L2F can measure the time-of-flight when a droplet flies between two foci and gives us the velocity. The L2F has the high optical signal to noise ratio, so the influence of multiple scattering on the spray measurement is small. Because the L2F has the micro-scale measurement volume, droplets can be measured in high number density sprays. It is reported by Chaves [5] and Shugger [6] that measurement systems similar to the L2F were successfully applied to measure droplets which were located inside the breakup length. Authors showed that the simultaneous measurements of the velocity and size of droplets could be conducted by adding the function of measurement of time-of-scattering to the L2F [7]. The measurement results have been reported about the velocity and size of droplets at 0.5 mm downstream from the nozzle orifice by the developed L2F [8]. Distributions of mass flow rate were evaluated based on the velocity and size of droplets between 5 and 25mm from the nozzle exit [9]. In the present study, the spray injected intermittently from a common rail injector into the atmosphere. The velocity and size of droplets in the spray have been measured by the L2F at 5, 12, 15, 20 and 25mm from the nozzle exit. The cyclic variation of diesel fuel spray has been evaluated by the standard deviation of velocity and size. And the cross correlation coefficient was evaluated in order to presume the region where the droplets broke up.

### Experimental setup

#### Fuel spray measurement system

The light probe of the L2F consists of highly focused two laser beams as shown in Fig.1. The diameter  $F$  of the focus is about 3 $\mu$ m, the distance  $S$  between two foci is 20 $\mu$ m, and the length  $L$  of the focus is about 20 $\mu$ m in the direction of optical axis. It can be mentioned that the L2F used in the present study has a micro-scale probe.

The measurements of time-of-flight and time-of-scattering are shown in Fig.2. The upper half of Fig.2 shows the cross-section of the L2F probe. When a droplet flies through both upstream and downstream foci, time-of-flight  $t_1$ , time-of-scattering  $t_2$  on the upstream focus and time-of-scattering  $t_3$  on the downstream focus are measured by a digital counter. The droplet velocity can be easily calculated by dividing the distance between two foci  $S$  with the measured time-of-flight  $t_1$ , that is

$$u = \frac{S}{t_1} \quad (1)$$

The relation used for the estimation of droplet size is that the ratio of the time-of-flight and the time-of-scattering corresponds to the ratio of the distance between two foci  $S$  and the droplet size  $d_p$  plus the focus size  $F$ . The time-of-scattering is estimated by averaging two time-of-scattering. The droplet size  $d_p$  can be estimated by

$$d_p = u \cdot \frac{t_2 + t_3}{2} - F \quad (2)$$

The L2F selects a droplet which passes through the upstream focus and downstream focus sequentially. When the number density of droplet is high, the local distance between droplets is sometimes shorter than the distance between two foci. In such a case, a droplet different from the droplet which passed the upstream focus will pass the downstream focus. Then, the time-of-flight is not measured correctly. When the flight direction of a droplet is fluctuating, the droplet which passes the upstream focus sometimes differs from the droplet which passes the downstream focus. The velocity obtained by such a pair of different droplets should not be correct. The clock signal with a frequency of 6MHz was used for recording the time when a droplet passed through the upstream focus. This means that the minimum time window for each data is 0.17μs.

Figure 3 is the measurement system of fuel sprays using the L2F. The light source is a semiconductor laser which has a maximum power of 100mW and a wave length of 830nm. A non-spherical lens which has a focal length of 8 mm and a numerical aperture of 0.5 is adopted as the condenser lens. By the optical system with a length of 350mm including the light source, the backscattering light of a droplet at the focus is guided to a Si - APD (Silicon Avalanche Photo Diode), and the guided light is converted into an electrical signal. The time-of-flight and time-of-scattering are measured by the digital counter which is mainly constituted by a FPGA (Field Programmable Gateway Array) with a clock of 480MHz. The maximum data sampling rate of the L2F system is 15MHz. Diesel fuel pressurized by the high pressure pump was stored in the common rail. The common rail was

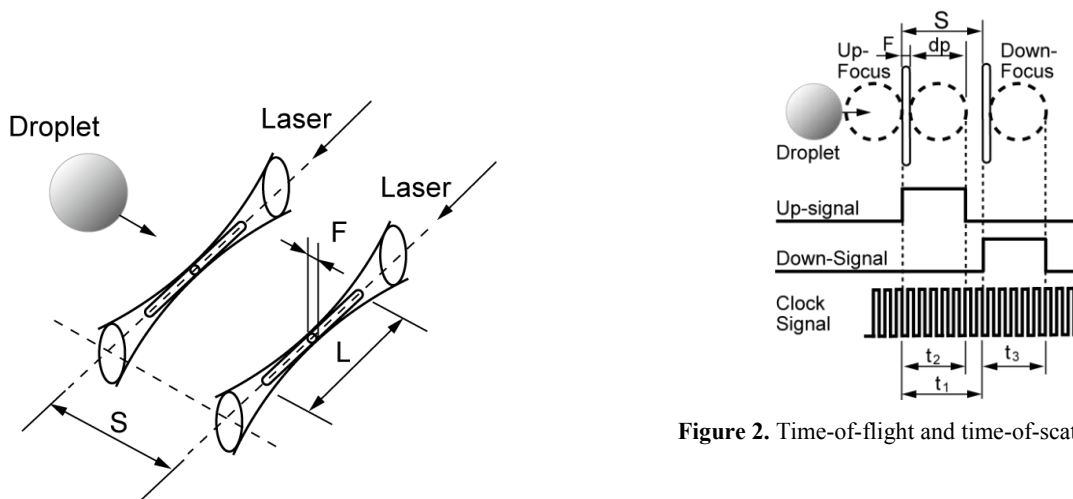


Figure 1. Light probe of L2F

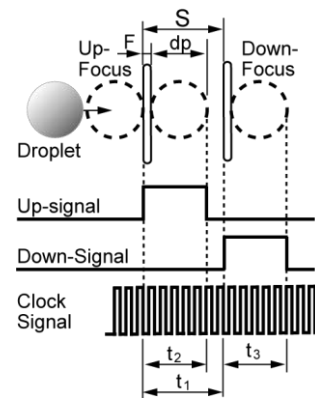
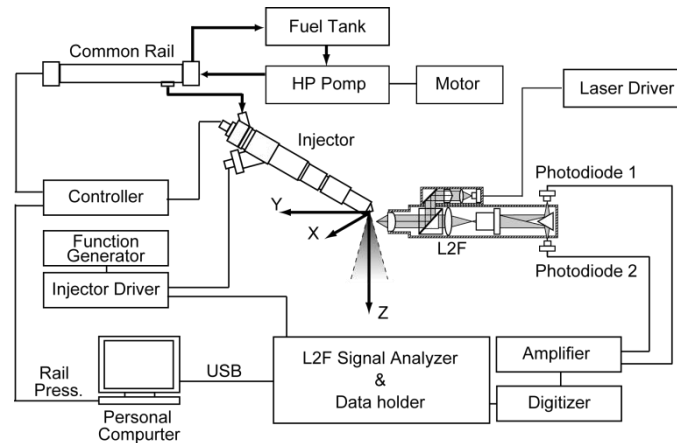


Figure 2. Time-of-flight and time-of-scattering



**Figure 3.** Fuel spray measurement system

used to control the injection pressure. Injection conditions such as the injection timing and the injection duration were controlled by the injector driver. The coordinate  $z$  is the distance along the spray axis from the nozzle exit, the coordinate  $y$  is the distance along the laser axis from the spray center, and the coordinate  $x$  is perpendicular to  $y$   $z$ -axis. The  $x$ -axis indicates the radius from the spray center in the plane where  $y$  is zero. Two foci of the L2F probe were set in such a way that the direction from the upstream focus to the downstream focus was adjusted to the spray axis.

The experimental conditions are shown in Table 1. The measurement of the spray was conducted on one of 5 spray plumes while the remaining 4 plumes were shielded and sucked out through small pipes. The measurement was conducted during 30 injections.

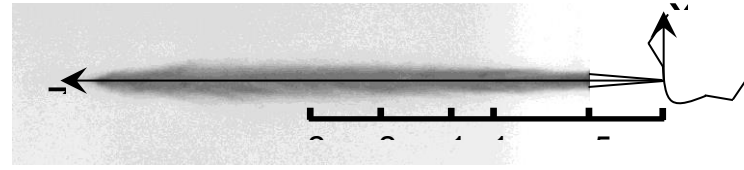
The image of spray was taken by a camera with the image sensor of 6-million-pixel CCD. A stroboscope with  $2.4\mu\text{s}$  lighting was used. Figure 4 shows the distance from the nozzle exit to measurement planes by L2F.

Simultaneous measurements of velocity and size of droplets were conducted in planes, which were perpendicular to  $z$ -axis, 5, 12, 15, 20 and 25mm downstream from the nozzle exit. In each plane where  $z$  is constant, the point closest to the spray axis corresponds to the spray center, and the measurement position at the outside edge of spray is called the periphery position.

Measurement positions were called with their signs of  $x$ -coordinate. For example, the periphery position with positive sign on the  $x$ -axis is called the plus-periphery  $PP$ . Table 2 shows the  $x$ -coordinate of measurement positions in each  $z$  plane. The  $y$ -coordinate of the measurement positions were fixed to zero.

**Table 1.** Experimental condition

Injector Specification		
Hole diameter	0.113	(mm)
Number of holes	5	
Test Condition		
Rail pressure	40	(MPa)
Ambient pressure	0.1	(MPa)
Injection interval	330	(ms)
Injection duration	0.87	(ms)
Ambient temperature	296	(K)



Measurement positions [mm]

**Figure 4.** Spray image and measurement positions

**Table 2.** Spray image and measurement positions

z(mm)	x(mm)				
	Minus Periphery (MP)	Minus Middle (MH)	Center (C)	Plus Middle (PH)	Plus Periphery (PP)
5	-0.8	-0.4	0	0.4	0.8
12	-1.0	-0.6	0	0.6	1.0
15	-1.2	-0.6	0	0.6	1.2
20	-1.4	-1.0	0.2	1.0	1.4
25	-2.0	-1.0	0	1.0	2.0

### Evaluation of cyclic variation

The mean velocity of droplets in each cycle  $u_i$  and the mean size of droplets in each cycle  $dp_i$  were calculated by

$$u_i = \frac{\sum u}{n} \quad (3a)$$

$$dp_i = \frac{\sum dp}{n} \quad (3b)$$

where  $u$  is the velocity of droplets in the one cycle, and  $dp$  is the size of droplets in the one cycle, and  $n$  is 30. The mean velocity of droplets of 30 injections  $\bar{u}$ , and the mean size of droplets of 30 injections  $\bar{dp}$  was calculated by

$$\bar{u} = \frac{\sum_{i=1}^n u_i}{n} \quad (4a)$$

$$\bar{dp} = \frac{\sum_{i=1}^n dp_i}{n} \quad (4b)$$

As an index of cyclic variation, the standard deviation of velocity  $s_u$ , and the standard deviation of velocity  $s_{dp}$  was calculated by

$$s_u = \sqrt{\frac{\sum_{i=1}^n (u_i - \bar{u})^2}{n-1}} \quad (5a)$$

$$s_{dp} = \sqrt{\frac{\sum_{i=1}^n (dp_i - \bar{dp})^2}{n-1}} \quad (5b)$$

In order to investigate the relation between the cyclic variations of velocity and size of droplets, the cross correlation coefficient was calculated by



$$r = \frac{\sum_{i=1}^n (u_i - \bar{u})(dp_i - \bar{dp})}{\sqrt{\sum_{i=1}^n (u_i - \bar{u})^2} \sqrt{\sum_{i=1}^n (dp_i - \bar{dp})^2}} \quad (6)$$

## Results and Discussions

Velocity and size of droplets are found by using the valid data obtained by the droplet which passed through both upstream and downstream foci. Figure 5 shows the mean velocity profiles at five positions on the plane  $z = 25\text{mm}$  from the nozzle exit. The horizontal axis is the time after the start of energizing the injector solenoid. The mean velocity of droplets was calculated within a time window of 0.1ms. It was confirmed that no droplet was observed by the L2F before the spray tip passed the measurement position. This means that floating droplets did not disturb the measurement of sprays injected sequentially. The injection duration is indicated by the arrow at the upper part of Fig. 5. The injection duration means the period when the fuel injected from injector nozzle. The injection started at 0.77ms, and injection duration was 0.87ms. The mean velocity of droplets increased in a period from 1.0 to 1.2ms at the center position  $C$ , and increased in a period from 1.0 to 1.1ms at the middle position. At the center position  $C$  and both middle positions, the mean velocities of droplets decreased after 1.6ms.

The arithmetic mean values of velocity and size in each measurement position were calculated by using the data in the period from when the spray front reached the measurement position to when the velocity began to decrease, for example, in the period from 1.0 to 1.5ms on the center 25mm downstream from the nozzle exit. Figure 6(a) shows the distributions of mean velocity along the spray axis. The horizontal axis is the distance from the nozzle exit. The mean velocities varied a little because the measurement was conducted on the near-nozzle region. The mean velocity at periphery position was lower than the one at center position within a distance from  $z = 5$  to 25mm. It is understood that the mean velocity monotonously decreased in radial direction.

Figure 6(b) shows the distributions of mean size along the spray axis. The mean sizes at periphery position changed a little with the distance from the nozzle exit. At the center position  $C$ , the mean size of droplets decreased with the distance from the nozzle exit. It is understood that the breakup of droplets occurred at the center position  $C$ .

Figure 7(a) shows the standard deviations of mean velocity. The standard deviation is taken as an index of the cyclic variation in this paper. At the center position  $C$ , the cyclic variation near the nozzle exit was larger than that in the downstream region. The Weber number, which was calculated by using the mean velocity and size, was about 16.5 at the center position on the plane  $z = 5\text{mm}$ . This value is nearly 12, which is the lowest value for the bag breakup [10]. It is thought that the breakup of droplets is occurred possibly. The velocity of droplets sometimes decreased under the breakup condition because broken up droplets had lower inertia force. On the other hand, the droplets kept its velocity under the no-breakup condition. Therefore the velocity is different at each cycle, and the standard deviation of mean velocity becomes larger.

At the periphery position, the cyclic variation in the downstream region was larger than that in the near-nozzle region, although the mean velocity itself varied a little in both regions as shown in Fig. 6(a). It is thought that the cyclic variation is caused by the vortex at the periphery position in the downstream region, and

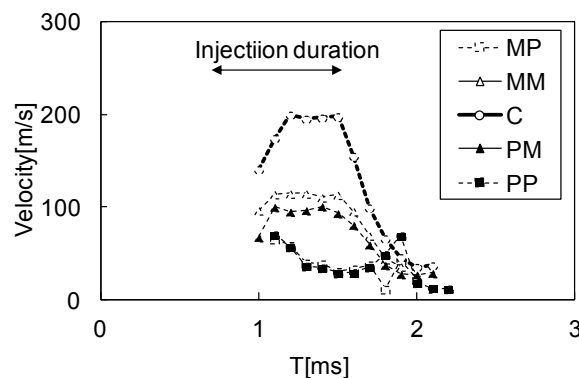
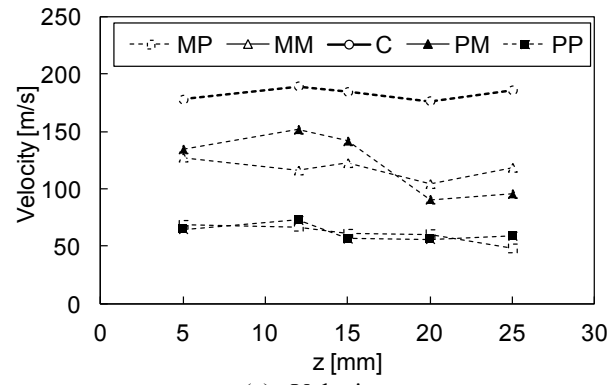
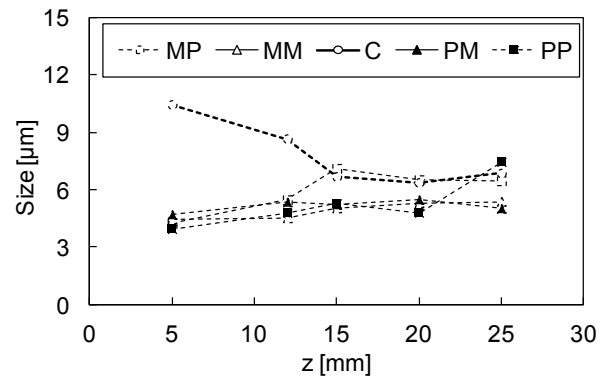


Figure 5. Time variation of mean velocity at  $z = 25\text{mm}$

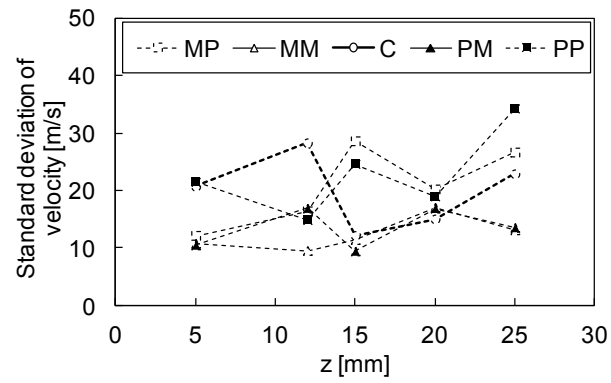


(a) Velocity

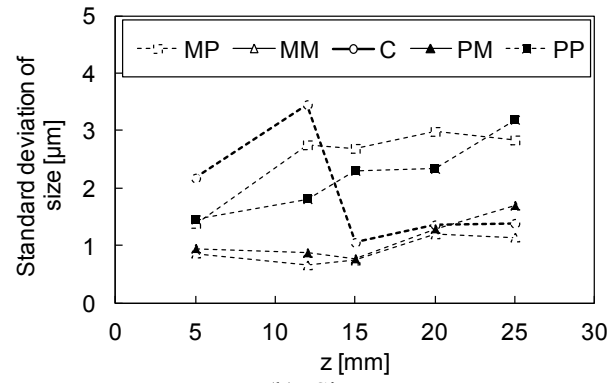


(b) Size

Figure 6. Spatial distributions of mean velocity and mean size



(a) Velocity



(b) Size

Figure 7. Spatial distributions of standard deviation

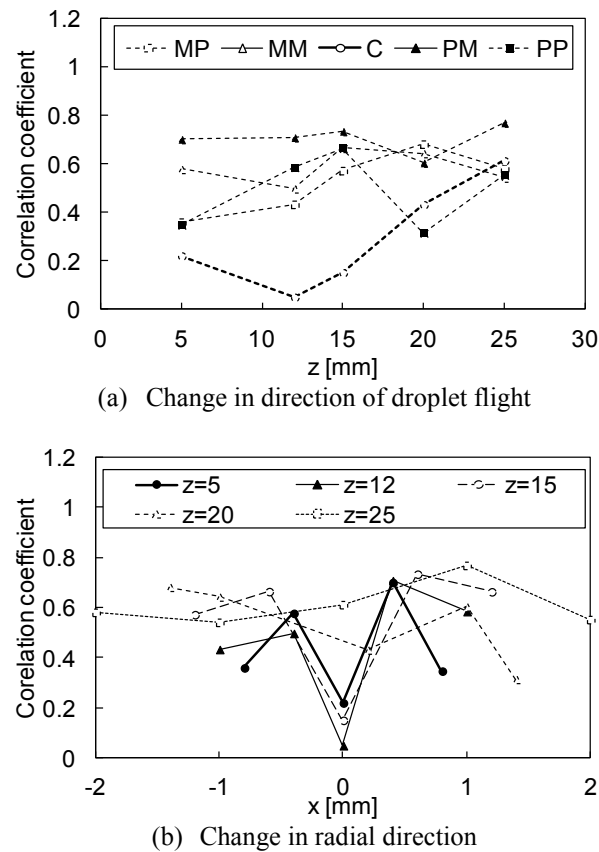


**Figure 8.** Correlation coefficient between velocity and size

that the condition of vortex generated within each injection is not always the same.

Figure 7(b) shows the standard deviations of mean size. At the center position  $C$ , the cyclic variation near the nozzle exit was larger than that in the downstream region. On the contrary, at the periphery position, the cyclic variation in the downstream region was large than that near the nozzle exit. It is thought that the vortex at periphery region affects the cyclic variations of the velocity and size of droplets.

The breakup of droplets hardly occurred at the periphery position, because the size of droplets at the periphery position did not decrease in the distance from  $z = 5$  to 25mm as shown in Fig. 6(b). Considering the relation between velocity and size under the no-breakup condition, larger droplets are easy to keep their velocities because of larger momentum, and smaller droplets are easy to decrease their velocities because of smaller momentum. In this condition, the correlation coefficient between velocity and size becomes higher. Figure 8(a) shows the spatial distribution of the cross correlation coefficient between the cyclic variations of velocity and size of droplets. The horizontal axis is the distance from the nozzle exit. At the periphery position, the correlation coefficient was higher than 0.3. It is confirmed that the correlation coefficient became higher at the no-breakup region.

At the center position  $C$ , the correlation coefficient near the nozzle exit was lower than that in the downstream region, and was lower than 0.2. The droplets at the center position  $C$  were broken up in the distance from  $z = 5$  to 25mm as shown in Fig. 6(b). The correlation coefficient decreased under the breakup condition because the droplet size was reduced.

Figure 8(b) shows the radial distribution of the cross correlation coefficient between the cyclic variations of velocity and size of droplets. The correlation coefficient was quite low at the spray center near the nozzle exit. It is understood that the breakup of droplets occurred within a narrow region.

## Conclusions

A L2F has been utilized for measurements of the velocity and size of droplets in diesel fuel sprays injected from a common rail injector under the rail pressure of 40MPa. Measurements were conducted on near-nozzle planes 5, 12, 15, 20 and 25mm from the nozzle exit. Experimental results are as follows.

1. At the spray periphery, the effect of cyclic variation was small near the nozzle exit, and was large in the downstream region. It is understood that the cyclic variation was caused by the vortex at the spray periphery, and the vortex generated within each injection is not always the same.

2. The correlation coefficient between the cyclic variations of velocity and size of droplets was small at the spray center near the nozzle exit, because the droplets with a high velocity decreased its size due to breakup.

## References

- [1] A.E.Greis, G.Grünefeld, M.Becker, S.Pischinger, Quantitative measurements of the soot distribution in a realistic common rail D.I. Diesel engine. 11th International Symposium on Application of Laser Techniques to Fluid Mechanics(2002)
- [2] W.B.Santoso, R.A.Bakar, S.Ariyono, and N.Cholis, Study of cyclic variability in diesel-hydrogen dual fuel engine combustion, International Journal of Mechanical & Mechatronics Engineering IJMME, Vol,12, No.04(2012)
- [3] J.Deppe, S.Wissel, C.Pauls and G.Grünefeld, Gaseous and liquid phase velocity measurements in dense sprays by means of laser flow tagging, Proceedings of ICLASS2006, ICLASS06-152(2006)
- [4] T.Shoji, Effect of cycle-to-cycle variations in spray characteristics on hydrocarbon emission in DI diesel engines, JSME International Journal Series B, 40(2):312-319(1997)
- [5] H.Chaves, C.Kirmse and F.Obermeier, Velocity Measurements of Dense Diesel Sprays in Pressurized Air, Proceedings of Spray 2001, TU Hamburg-Harburg, pp.II.2-1-II.2-8 (2001)
- [6] C.Schugger, U.Meingast and U.Renz, Time-Resolved Velocity Measurements in the Primary Breakup Zone of a High Pressure Diesel Injection Nozzle, Proceedings of ILASS-Europe 2000, pp.1-5 (2000)
- [7] H.Ueki, M.Ishida and D.Sakaguchi, Simultaneous Measurement of Particle Size and Velocity by Laser 2-Focus Particle Analyzer, Proceedings of ICLASS94, pp.483-490 (1994)
- [8] H.Ueki, M.Ishida, D.Sakaguchi and M.Naganuma, Simultaneous Measurements of Velocity and Size of Diesel Fuel Droplet near Nozzle Orifice by Laser 2-Focus Velocimeter with Micro-Scale Probe Volume, Proceedings of Thiesel2004, pp.369-380 (2004)
- [9] K.Komada, N.Kawaharada, D.Sakaguchi, H.Ueki and M.Ishida, Evaluation of Mass Flow Rate Distribution in Diesel Fuel Spray by L2F, Proceedings of the ASME 2011, CD-ROM pp.1-10(2011)
- [10] G.M.Faeth, L.-P.Hsiang and P.-K.Wu, Structure and Breakup Properties of Sprays Int. J. Multiphase Flow, Vol. 21, Suppl. pp. 99-127(1995)

## Transition of Fuel Components into Supercritical State under Diesel Process Conditions

Thomas Vogel<sup>1,2</sup>, Gudrun Götz<sup>1</sup>, and Michael Wensing<sup>1,2</sup>

1: Institute of Engineering Thermodynamics (LTT), FAU Erlangen-Nuremberg, Germany

2: Erlangen Graduate School in advanced optical Technologies (SAOT), Erlangen, Germany

### Abstract

The classic understanding of the mixture formation inside diesel engines consist of droplet breakup and evaporation models although the critical pressure and temperature for a high amount of the fuel components is exceeded. Research in other fields showed that the mixture formation changes when super critical conditions are reached.

In this study the behavior of single component hydrocarbon fuels, binary mixtures and multi-component fuels were simulated and experimentally investigated under present diesel engine conditions. The theoretical calculations used enhanced equation of state in terms of vapor liquid equilibrium and critical point of mixtures. In the experimental part of the work the phase transition behavior of these substances was observed in a flask which was put inside a high-pressure/high-temperature vessel. When the ambient pressure applied was above the critical pressure of the fluid and the temperature was varied from values below critical temperatures to values above, a transition into a super critical state without any boiling was observed.

Additionally injection experiments, using Mie-scattering and shadowgraph imaging, were compared to the results of investigations of injection processes under super-critical conditions from non-automotive applications. In shadowgraph images Schlieren patterns were found indicating a transition into super-critical state rather than an evaporation of the fuel.

### Introduction

Although, the compression ratio of direct injection compression ignition engines (DICI) has been decreased in the last years, pressures and temperatures during injection at high engine loads have been increased due to increased turbocharging. With charging pressures above 10 MPa and temperatures above 1000 K are reached at top dead center (TDC). Since diesel fuel consists of mostly alkanes, alkenes, allenes, alkynes and aromatics from approx. 10-22 C-atoms almost all critical values of both, temperature and pressure are exceeded. Furthermore, the critical values of oxygen and nitrogen are also exceeded. In most Diesel process investigations found in literature it is assumed that the fuel, after the droplet breakup, evaporates [1-3]. But in other, non-automotive applications, experiments carried out show that under strongly elevated conditions the injected fuel behavior changes significantly, showing a transition into super-critical state [4, 5]. However, automotive fuels are not single component fluids and therefore the critical point for the mixture changes. The new critical is strongly depended on the mixture.

### Thermodynamical background

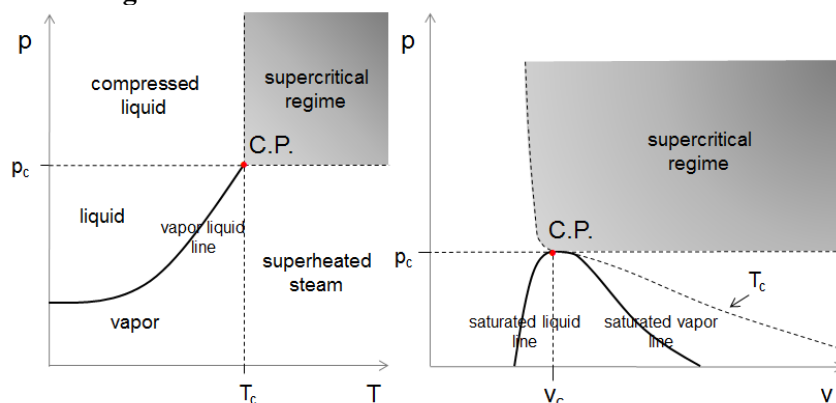
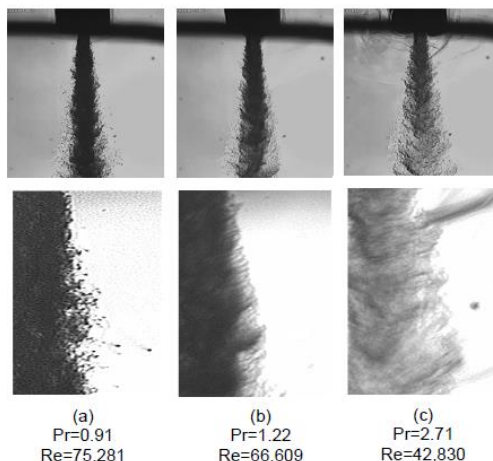


Figure 1. graphical representation of the supercritical regime

A fluid exceeding its critical temperature and pressure shows characteristics of a liquid, such as the density, and also characteristics of gas, such as diffusivity and no visible phase border. At the critical point the density of the liquid is equal to the density of the gas. In Figure 1 the supercritical regime is presented in dependency of the pressure, temperature and the specific volume. One key characteristic of the transition into supercritical state is

the complete absence of enthalpy of evaporation. Furthermore, surface tension is extremely decreased compared to liquid fuels. Transferring this knowledge to the in-cylinder situation, evaporation cooling is negligible and the mixture formation itself is highly depended on momentum input by the spray itself and moreover diffusion instead of evaporation controlled. Although, this situation has not been proofed completely for the internal combustion engines there exist results for different application investigating sprays or single droplets under super-critical conditions.

#### State of the art – resent research



**Figure 2.**  $\text{LN}_2$  ( $T_c = 126.2 \text{ K}$ ,  $p_c = 3.39 \text{ MPa}$ ) injected at an initial temperature of 99-110 K into ambient temperature  $\text{gN}_2$  ( $T = 300 \text{ K}$ ) at different reduced pressures, Chehroudi et al.[4]

In Figure 2 a jet of liquid nitrogen ( $\text{LN}_2$ ) injected in gaseous nitrogen ( $\text{gN}_2$ ) is presented. The research was performed by Chehroudi et. al. in a cooperation between the Air Force Research Laboratory (AFRL) and the German Aerospace Center (DLR) [4]. This experiment eliminates the effect of critical point shifting through a mixture of different gases since no other substance is present than  $\text{N}_2$ . It is clearly carried out that the formation of the spray changes from sub- to supercritical conditions. While the ambient temperature has been kept constant above the critical temperature the ambient pressure was varied from a reduced value of  $p_r$  of 0.91 to 2.71 (with  $p_r = p/p_c$ ). The temperature of the injected  $\text{LN}_2$  was below the critical temperature. At the reduced pressure of 0.91 a classical spray formed by droplets is visible. Single droplets can clearly be identified at the outer region of the spray structure while the middle structure has a high absorption for the installed background illumination. At a reduced ambient pressure of 1.22 the core shows nearly the same optical density but at the outside spray regions no droplets can be found. The jet shows a Schlieren-like structure on the outside. Increasing the ambient pressure to a reduced value of 2.71 the nitrogen jet is changed drastically. The optical density in the nozzle far region is significantly decreased and the whole jet shows a Schlieren pattern. Also, no droplets can be observed. The work of Weckenmann et al. [5, 6] and Dahms et al. [7] show similar results for acetone respectively n-dodecane injected into a supercritical environment.

#### Simulation of the vapor liquid equilibrium of a binary mixture of fuel and nitrogen

**Table 1.** critical data and molar mass of pure components [8]

	n-Heptane	n-Dodecane	n-Hexadecane	Nitrogen
$T_c \text{ [K]}$	540.2	658.3	717	126.2
$p_c \text{ [MPa]}$	2.73	1.82	1.42	3.39
$v_c \text{ [kg/m}^3\text{]}$	234	238	240	314
$M \text{ [g/mol]}$	100.21	170.34	226.45	28.01

In advance to the experimental part three alkanes with increasing chain length, representing typical diesel and gasoline fuel components, in combination with nitrogen were simulated in order to identify the critical points of the mixtures and the vapor pressure lines. The nitrogen was taken into account representing the air since it represents with ~78% the major fraction. In Table 1 the thermo-physical properties of the three fuel components and the nitrogen are given.

The simulation itself was performed with the software ‘ASPEN’ [9] using several equation of state (EOS). Two cubic EOS (Peng-Robinson [10], Soave-Redlich-Kwong [11]) and one viral (Lee-Kesler-Plöcker [12]) were compared. For the binary mixture of alkanes and nitrogen the Lee-Kesler-Plöcker is a standard EOS.

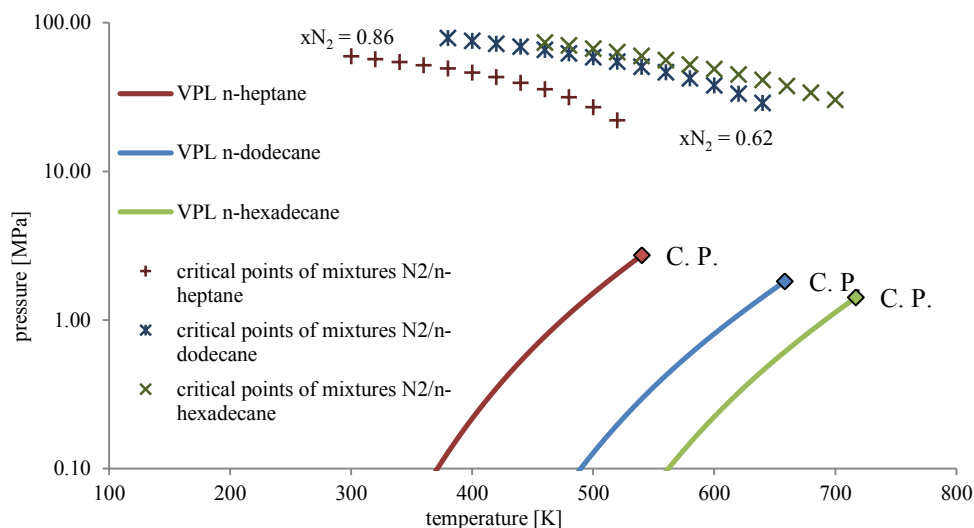


**Figure 3.** vapor-liquid equilibrium (VLE) of binary nitrogen/n-alkane-mixtures of pure substances and critical points of mixtures ( $x_{N_2} = 0.62 - 0.86$ )

In Figure 3 it becomes clear that the mixing of alkanes and nitrogen shifts the critical point dramatically. While the critical temperature is decreased with an increasing mole fraction of nitrogen moderately the critical pressure is dramatically increased. Starting from the smallest mole fraction of nitrogen the critical temperature is lowered from 717 K to 700 K for n-hexadecane, from 658 K to 640 K for n-dodecane and from 540 K to 520 K for n-heptane. The critical pressure is raised from 1.42 MPa to 30.3 MPa for n-hexadecane (1.82 MPa to 28.7 MPa for n-dodecane; 2.73 MPa to 21.9 MPa for n-hexadecane). Especially for long chain alkanes the critical pressure raises significantly when mixed with nitrogen to values even above the pressures found at TDC. Taking this into account, the presence of nitrogen inside the combustion chamber could prevent the fluid from a transition into a super-critical state. The curve of the critical points of the mixture calculated with ASPEN is in good accordance with the van Konynenburg type III curve [13].

#### *Simulation of the vapour liquid equilibrium of a binary mixture of two alkanes*

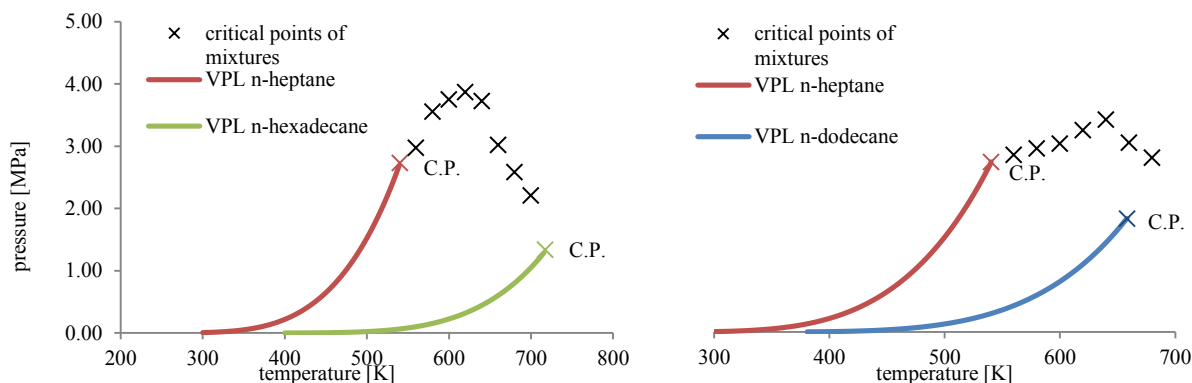


**Figure 4.** VLE of binary mixtures, including critical points and VPL (n-heptane/n-dodecane,  $x_{n\text{-heptane}} = 0.95 - 0.3$ ; n-heptane/n-hexadecane,  $x_{n\text{-heptane}} = 0.9 - 0.1$ )

Since fuels for automotive usage consist of a multi-component mixture of hydrocarbons the mixing of these fuel components has to be simulated as well. The equation of state of Soave-Redlich-Kwong, which is a standard EOS for alkane mixtures, was used to simulate the critical points of the mixture and the vapor pressure curve of the binary fuel mixtures. Figure 4 shows the calculation of a n-heptane/n-hexadecane mixture and a n-heptane/n-dodecane mixture. The behavior for the two mixtures as well as that of n-dodecane/n-hexadecane mixtures (calculated but not presented in this paper) is similar and also in good accordance with a curve of van Konynenburg, this time type I. In contrast to the n-alkane/nitrogen mixture the critical pressure is only raised moderately and does not exceed 40 MPa for all mixtures hence it is within the pressure ranges during injection in modern DIC engines. The critical temperature of the mixtures is mostly within the range of the critical temperature of the pure substances.



## Investigation of the transition into supercritical state

### The injection chamber



gas pressure	30 kPa to 10 MPa
maximum temperature	1000 K
Inner vessel volume	10 liters
maximum scavenging flow	110 m <sup>3</sup> N·h <sup>-1</sup>
scavenging medium	N <sub>2</sub> , air or mixtures
clearance of the optical	125 mm
maximum fuel pressure	250 MPa/28 MPa (diesel/gasoline)
fuel temperature	243 K to 383 K
injection repetition rate	0.1 Hz to 3 Hz

**Figure 5.** High-pressure and high-temperature injection chamber OptiVeP

All experiments were conducted in the high-pressure/high-temperature vessel “OptiVeP” from which a detailed description can be found in previous articles [14]. With a maximum pressure of 10 MPa and a maximum temperature 1000 K the cell simulates today’s DICI engine conditions, while pressures and temperatures are constant and (nearly) no charge motion is present. The cell itself is scavenged permanently with air, nitrogen or mixtures of these. Hence the simulation of EGR and the total suppression of the combustion are possible. The chamber base cube is optically accessible from five of the six cube sides while the sixth side provides the injector mounting.

In order to investigate the transition into super-critical state the tested fluids were filled into flasks (25ml) and put on a platform inside the vessel. The flask itself was not sealed and therefore the investigated fluid had contact with the ambient gas, here nitrogen. A normal video camera recorded the fuels while the experiment was performed. The temperature near the flask has been monitored with two thermocouples. No thermocouple had contact with the fluid in order to prevent heat transfer via the thermocouple body thus the measured temperature does not represent the temperature of the liquid directly, but all heating processes performed were done very slow so that the ambient gas temperatures measured are very close to the temperature of the fluid investigated.

Secondly, for comparing the spray behavior results found in literature for non-automotive applications a special 3-hole research injector has been mounted in the investigation vessel. The difference from this injector to an automotive production injector is just the number of holes and the elevation angle (45°) while the nozzle bore geometry and the injector body itself remains the same. The chosen placement of the fuel jets provides a good optical accessibility of a single fuel jet. The spray investigation itself has been obtained with Mie-scattering and shadowgraph imaging technique. In both cases the spray images were acquired via a CCD-camera at the same position. For Mie-scattering three flash lamps illuminated the spray rectangular to the line of sight, for shadowgraph imaging one flash lamp was installed behind an opaque glass on the line of sight.

### Experimental conditions

The first focus was set on the single component fuels. For these, the values of critical pressure and temperature are well known (see Table 1) [8]. In order to provide good comparability all fluids were tested with the same reduced values of pressure and temperature. The sequence of the measurements was as follows: In the beginning a reduced pressure  $p_1$  of factor two of the critical pressure was installed. This prevented the fluid from boiling while heating up. With rising temperature the investigation was started at 90% of the critical temperature and preceded until 120% of the critical temperature. Then the temperature has been decreased back to 90% of the critical temperature. The procedure has been repeated with the next lower value for the reduced pressure. In the end of a single measurement series a pressure of 90% of the critical pressure was installed hence boiling behavior has also been recorded therefore a transition into super-critical state is clearly identified. The values for the reduced pressures and temperatures are given in Table 2. The same procedure was repeated with the binary mixtures and the pure alkane diesel fuel.

**Table 2.** Measurement points for single components

		n-Heptane	n-Dodecane	n-Hexadecane
	reduced value		temperature [K]	
T <sub>1</sub>	0.90	486.18	592.47	504.00
T <sub>2</sub>	1.20	648.24	789.96	860.40
		pressure [MPa]		
p <sub>1</sub>	2.00	5.46	3.64	2.84
p <sub>2</sub>	1.50	4.10	2.73	2.13
p <sub>3</sub>	1.20	3.28	2.18	1.70
p <sub>4</sub>	1.05	2.87	1.91	1.49
p <sub>5</sub>	0.9	2.46	1.64	1.28

## Results and discussion

### Open flask investigation

As an example for a single component fluid transferred into super-critical state, the behavior of n-dodecane is presented in the following (see Figure 6). A reduced pressure of 1.5 at 2.73 MPa was chosen while the starting temperature in the ambient gas was 721 K which is above the critical temperature of n-dodecane. In the first image shown in Figure 6 the liquid is still colder than the gas, so that a phase boarder is clearly visible. As the fluid is heated up the volume starts to expand (s. 722 K). At the same time the phase border is contracted and does not touch the glass of the flask anymore (723 K). In the next step density fluctuation can be observed by means of the mesh pattern installed on the backside. During the heating process the phase boundary is contracted more and more until in the top right image (726 K) it has completely disappeared -- but strong density gradients are still visible. In the image on the bottom left of Figure 6 on the top of the flask Schlieren patterns can be observed indicating a high density super-critical phase exiting the glass vessel. With decreasing temperature the strong density gradients are re-entering the flask and descending down the neck until a phase boundary starts to reappear. Lowering the temperature further, the phase boundary is completely re-established but slightly lower than in the beginning due to the loss of fuel during the experiment.

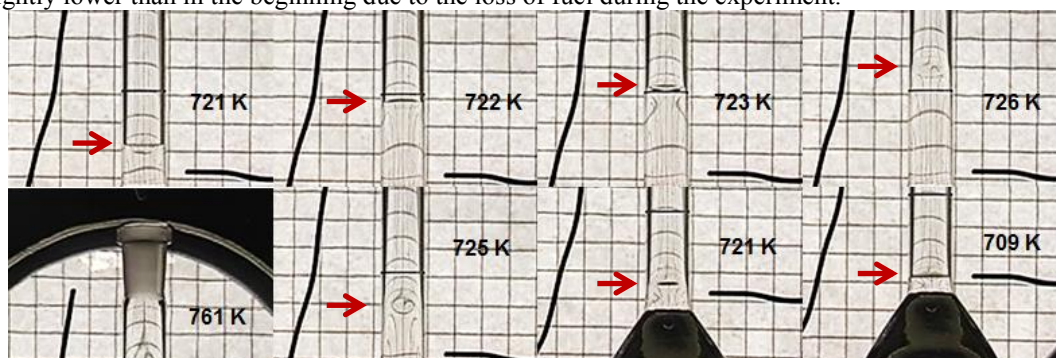


**Figure 6.** Transition into supercritical state of a single component in a high pressure nitrogen environment with the arrow marking the phase boundary (n-dodecane;  $p = 2.73$  MPa)

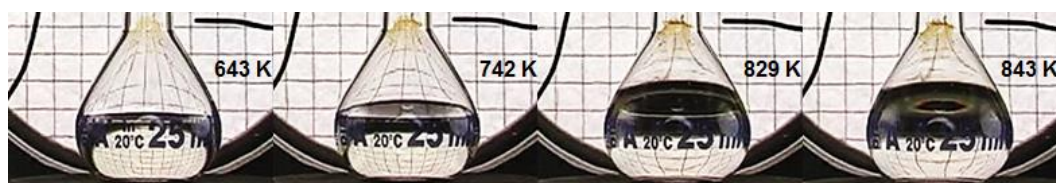


**Figure 7.** Transition into supercritical state of a GtL-diesel fuel ( $p = 8.0$  MPa;  $T \approx 643$  K – 873 K)

The results for the binary mixtures are similar to the results of the single components and are therefore not presented in this paper. The determined critical points for the mixture were within a certain tolerance comparable to the values simulated in advance.

The last investigated fuel was the multi-component diesel fuel produced by Fischer Tropsch synthesis which consists mainly of n-alkanes of the middle-distillates group. It is furthermore free from sulfur, oxygen components and aromatics. It is also fully transparent, colorless and odorless.

The behavior of the multi-component fuel was found to be very similar to that of n-dodecane presented in Figure 7. Since the flask was hard to access during the experiments the filling level varied. A critical pressure

could not be determined in advanced therefore it was done in this experiment. In this series the ambient pressure has been set to 8 MPa and the temperature has been varied in a range from 643 K to 873 K.

In the first image at 643 K a clear boundary, separating the fluid from the ambient nitrogen, is visible. With rising temperature the fluid volume starts to expand. At 829 K the phase boundary starts to contract. Due to the geometrical shape of the flask in the bottom region and therefore the strong diffraction the mesh pattern is not visible here. At 843 K the phase boundary is vanished completely. Unlike the single-component and the binary-mixtures the temperature range from start to the complete transition into the super-critical states covers a bigger temperature range of 250 K in total. Due to the high temperature and a small amount of remaining oxygen in the ambient gas the fuel starts to decompose and the remaining residues are chemically different from the starting fuel.

### ***Spray investigation***

In this part of the experiment the research injector has been mounted into the chamber and the operating point determined for the GtL-fuel transition was installed. Additionally a second operating point with decreased temperature of 473 K and pressure of 1 MPa has been acquired in order to provide results for both, sub-critical and super-critical conditions. For both operating points the same fuel was injected at 80 MPa with an initial temperature of 323 K. The total injection duration was set at 1 ms.



**Figure 8.** Injection of a GtL-fuel ( $p_{inj.} = 80$  MPa;  $T_{inj.} = 323$  K;  $t_{vSOI} = 1000$   $\mu$ s) into a low-pressure, low-temperature environment ( $p_{chamber} = 1$  MPa;  $T_{chamber} = 473$  K)

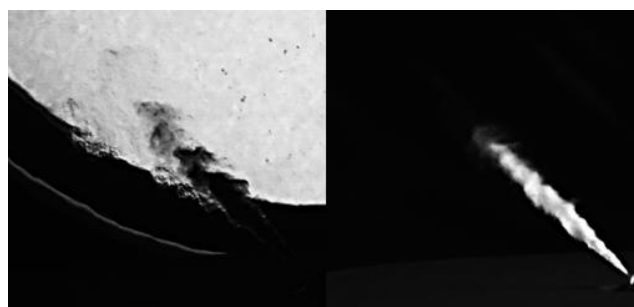


**Figure 9.** Injection of a GtL-fuel ( $p_{inj.} = 80$  MPa;  $T_{inj.} = 323$  K;  $t_{vSOI} = 1000$   $\mu$ s) into a high-pressure, high-temperature environment ( $p_{chamber} = 8$  MPa;  $T_{chamber} = 773$  K)

At the sub-critical operating point (Figure 8) both measurement techniques show a typical fuel spray jet, well known in engine application with a nearly constant spray angle over the whole spray cone and a round tip. The optical density, which can be observed at the shadowgraph images, indicates a decrease from the nozzle to the spray tip as well as from the inside to the outside of the spray. Although single droplets are not recorded due to the resolution, the spray shows signs for small droplets, areas with low but visible intensity and clear spray structures at both measurement techniques, in the outside regions at the tip.

At super-critical conditions (Figure 9) the Mie-scattering image (right) probably indicates an evaporating spray under elevated temperature conditions. No proof for a high density gas or super-critical phase is found here. The Shadowgraph image draws a different picture. While the optical density is decreasing with increasing distance the nozzle which also could indicate an evaporation Schlieren structures start to appear first on the side then strongly on the tip of the spray. In contrast to the low-pressure low-temperature conditions the penetration depth is decreased not only due to the increased gas density but also because of the gasification. The Schlieren structures indicate strong density gradients.

### **Conclusions**

The experiments performed indicate that a fuel injected under high-temperature/high-pressure conditions, found in today's DICI engines, does not evaporate but transitions into a super-critical state. A first set of measurement,

using pure alkanes, carried out that the presence of nitrogen in the ambient gas has negligible effect on the transition of the hydrocarbons into super-critical state. Instead, the mixing of different hydrocarbons has major effect on the critical properties of the mixtures. This is important since automotive fuels are in general mixtures of many species. For three binary mixtures of alkanes the critical values predicted from theory have been proven within tolerances of 50 K due to delayed heat transfer into the fluid which was necessary to avoid decomposition of the fuel.

The investigation of the GtL-diesel carried out that a multi-component fuel can show elevated values for the critical point, especially for the critical pressure. Nevertheless, a transition into super-critical state was also observed here. Due to the high residence time of the fuel in the hot ambient gas cracking processes were also observed in this experiment.

In addition to the results of the single- and multi-component fuels that were acquired using constant pressure and slow temperature changes the investigation of the spray of a research injector showed an investigation using realistic automotive time scales. The spray showed a super-critical transition instead of evaporation. While the Mie-scattering technique showed no noticeable proof under elevated pressure and temperature, the shadowgraph images carried out strong Schlieren structures indicating high density gradients. These structures are comparable to those Chehroudi et. al. conducted [4]. Compared to spray images acquired under sub-critical conditions the spray formation changes drastically. Structures with low optical density indicating small droplets are not present taking the shadowgraph image into account. Thus, the classical understanding of an evaporating fuel does not apply under elevated diesel conditions.

### Acknowledgements

The authors gratefully acknowledge funding of the Erlangen Graduate School in Advanced Optical Technologies (SAOT) by the German National Science Foundation (DFG) in the framework of the excellence initiative.

Furthermore the authors gratefully acknowledge the financial support of the European Community and the Federal State of Bavaria for the project “Optical high pressure combustion bench test”

### References

- [1] J.D. Naber, D.L. Siebers, *SAE Paper*, 960034 (1996).
- [2] P.F. Flynn, G.L. Hunter, A.O.z. Loye, O.C. Akinyemi, J.E. Dec, C.K. Westbrook, *SAE Technical Paper*, 1999-01-0509 (1999).
- [3] S.S. Sazhin, S.B. Martynov, T. Kristyadi, C. Crua, M.R. Heikal, *International Journal of Engineering Systems Modelling and Simulation*, 1 (2008) 1-19.
- [4] B. Chehroudi, D. Talley, *5th International Conference on Liquid Rocket Propellant*, Chattanooga, 2003.
- [5] F. Weckenmann, 2012.
- [6] F. Weckenmann, B. Bork, E. Oldenhof, G. Lamanna, B. Weigand, B. Böhm, A. Dreizler, *Zeitschrift für Physikalische Chemie*, 225 (2011) 1417-1431.
- [7] R.N. Dahms, J. Manin, L.M. Pickett, J.C. Oefelein, *Proceedings of the Combustion Institute*, 34 (2013) 1667-1675.
- [8] VDI, Springer-Verlag, Berlin.
- [9] AspenTech, Cambridge, 2003.
- [10] D.-Y. Peng, D.B. Robinson, *Industrial & Engineering Chemistry Fundamentals*, 15 (1976) 59-64.
- [11] S. Giorgio, *Chem Eng Sci*, 27 (1972) 1197-1203.
- [12] B.I. Lee, M.G. Kesler, *AIChE Journal*, 21 (1975) 510-527.
- [13] P.H.V. Konynenburg, R.L. Scott, *Philosophical Transactions of the Royal Society of London. Series A, Mathematical and Physical Sciences*, 298 (1980) 495-540.
- [14] T. Vogel, et al., *23rd International Conference on Liquid Atomization and Spray Systems*, Brno, Czech Republic, 2010.

## **Diesel spray interaction with porous structure: space- and time-dependent analysis of fuel distribution in space and its vaporization**

M. Weclas<sup>1</sup> and J. Cypris<sup>2</sup>

1: Georg Simon Ohm University of Applied Sciences Nuremberg, Department of Mechanical Engineering, IFZN, Kesslerplatz 12, D-90489 Nuremberg, Germany

2: Fraunhofer Institute for Building Physics IBP, Combustion Systems, Nobelstrasse 12, D-70569 Stuttgart, Germany

### **Abstract**

Future IC engines have to be environmentally clean, which means that the engine has to achieve a clean (homogeneous) combustion process. This process requires the mixture to be homogeneous prior to simultaneous volumetric ignition. One of possibility for realizing of such a process would be a combination of late injection strategy (control of ignition timing) along with an enhanced fuel vaporization and mixture homogenization. A significant support for realizing of this method could be utilization of spray interaction with porous structures. When a diesel spray impinges onto porous structure it penetrates into and interacts with inner structure, distributes throughout the structure volume, and finally may leave the porous medium (PM) volume in the form of multiple secondary jets. As a result the following effects are discussed: significant spatial spreading of the spray, reduced axial penetration length, significantly increased spray surface area, reduced propagating velocity after interaction with porous structure and enhanced vaporization if the porous structure is hot. There are two characteristic cases of diesel spray interaction with PM: interaction with thin PM = process performs and is observed outside the structure; interaction with thick PM = process performs in PM volume and may be observed directly inside PM or outside its volume.

---

### **Introduction**

Future internal combustion engines have to be environmentally clean, which means that the engine has to achieve a clean (homogeneous) combustion process. This process requires the charge to be homogeneous prior to simultaneous volumetric ignition. One of possibility would be complete temporal and spatial decoupling of the combustion process from fuel injection and mixture formation. Another possibility would be a combination of late injection strategy (advantageous for control of ignition timing) along with an enhanced fuel vaporization and mixture homogenization. A significant support for realizing of the latter method could be given by utilization of spray interaction with porous structures. When a diesel spray impinges onto porous structure it penetrates into and interacts with inner structure, distributes throughout the structure volume, and finally may leave the porous medium volume in the form of multiple secondary jets [1-5]. As a result of such an interaction the following effects are observed: significant spatial spreading of the spray, reduced axial penetration length, significantly increase spray surface area, reduced propagating velocity after interaction with porous structure and enhanced vaporization if the porous structure is hot. There are two characteristic cases of diesel spray interaction with porous medium (PM): interaction with thin PM - resulting process performs and is observed outside the structure; interaction with thick PM – the resulting process performs in PM volume and may be observed directly inside PM or outside its volume. In the latter case a limited insight into volume of a non-transparent medium limits process observation inside the volume. One of characteristic case of spray interaction with thin PM is represented by a combination of Diesel nozzle and a thin porous ring positioned in proximity to the nozzle outlet [3,4]. One of the critical factors that limit the possibility of direct insight into the mechanism of the process taken place within the porous structure volume is its non-transparency and the very limited application of optical measurement techniques. An initial application of micro-endoscopic visualization technique for process analysis inside the PM volume is also discussed in the paper.

### **Characterization of porous structures and conditions for spray interaction with PM**

Spray interaction with highly porous, three-dimensional structures occurs under conditions to be significantly different from spray formation and penetration in a free volume system. The most important factors influencing spray interaction with PM and specific test conditions in PM are selected in fig.1.

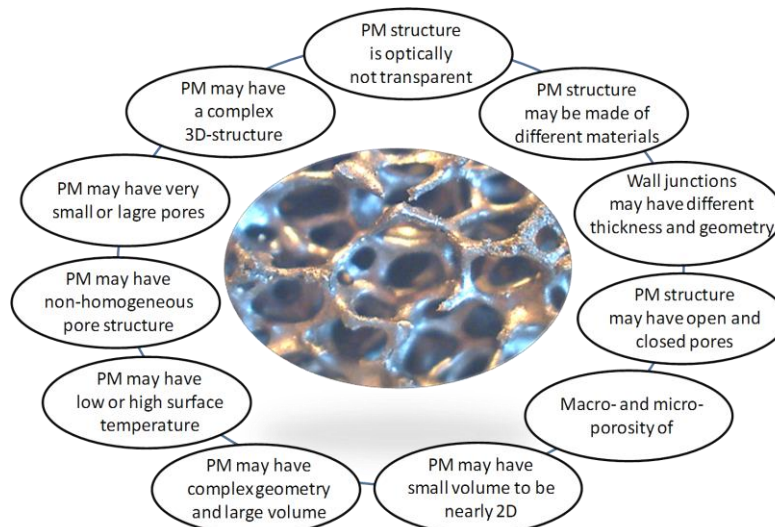


**Figure 1:** Specific features of porous structure important for investigation of spray interaction with porous medium

Specific process conditions of spray interaction with porous structure together with variable injection parameters characterize the process to be investigated (see Fig.2).

The following influencing factors and characteristic process (test) conditions may be selected:

- *Distance between nozzle and PM surface: small and large.* For nozzles positioned in proximity to the PM impingement surface there is no space available for diesel spray development and its atomization; if nozzle is positioned far away from PM the spray may (partly or fully) develop and atomize before colliding with PM
- *Pore size (as compared to spray diameter): small and large.* For nozzles positioned in proximity to the PM impingement surface the spray diameter is mostly much smaller than pore size; if nozzle is positioned far away from PM the developed spray may have much larger impingement cross section as the pore size of PM
- *Geometrical thickness of PM defines together with pore size and their structure the number of wall junctions for interaction with diesel spray: thin* (low number of wall junctions) and *thick* (large number of wall junctions). This parameter also defines if the resulting process may only be observed inside PM volume, or if the process may also be investigated outside the PM volume
- *Pore structure (with respect to spray impingement direction): irregular* (complex) with a number of wall junctions positioned along the spray propagation (impingement) direction; *regular* along the spray propagation direction with low number of wall junctions for interaction with PM
- *Spray impingement velocity (being a direct function of injection pressure):* together with pore size and spray geometry defines the conditions of spray impingement on to porous structure and penetration inside PM. This factor directly influences all parameter describing result of spray impingement on to individual wall junction
- *Temperature of PM:* in the case of cold PM the spray-PM interaction process is described by multi-jet splitting being result of spray collision with an individual wall junction of PM; in the case of hot PM the spray-PM interaction process is described by superposition of multi-jet splitting and fuel vaporization processes.





**Figure 2:** The most important features of injection process and spray interaction with PM

The combination of different factors influencing spray interaction with porous structure and possible test conditions (for different injection conditions) allow selection of characteristic configurations of diesel spray interaction with PM (fig.3):

- Case 1. Thin and cold PM with diesel nozzle positioned far away from the porous impingement surface. The process is characterized by a multi-jet splitting as a result of spray interaction with wall junctions of PM and the resulting spray-PM interaction process may mostly be observed outside the PM volume. In this case a diesel spray may fully develop in a free space before impinging on to PM. Spray tip impinging surface is large and in consequence spray interaction with PM in impingement area corresponds more to solid wall impingement process (strongly depends on the pore size, pore structure and wall junction thickness).
- Case 2. Thin and hot PM with diesel nozzle positioned far away from the porous impingement surface. The process is characterized by a multi-jet splitting superimposed with fuel vaporization as a result of spray interaction with hot wall junctions of PM and the resulting spray-PM interaction process may mostly be observed outside the PM volume. In this case a diesel spray may fully develop in a free space before impinging on to PM. Spray tip impinging surface is large and in consequence spray interaction with PM in impingement area corresponds more to solid wall impingement process (strongly depends on the pore size, pore structure, wall junction thickness and PM temperature).
- Case 3. Thin and cold PM with diesel nozzle positioned in proximity to porous impingement surface. The process is characterized by a multi-jet splitting as a result of spray interaction with wall junctions of PM and the resulting spray-PM interaction process may mostly be observed outside the PM volume. In this case a diesel spray may not well develop in a free space before impinging on to PM (depends on injection parameters and gap between nozzle and PM). Spray tip impinging surface is small and in consequence spray interaction with PM in impingement area corresponds to porous surface impingement process (strongly depends on the pore size, pore structure and wall junction thickness).
- Case 4. Thin and hot PM with diesel nozzle positioned in proximity to porous impingement surface. The process is characterized by a multi-jet splitting with fuel vaporization as a result of spray interaction with hot wall junctions of PM and the resulting spray-PM interaction process may mostly be observed outside the PM volume. In this case a diesel spray may not well develop in a free space before impinging on to PM (depends on injection parameters and gap between nozzle and PM). Spray tip impinging surface is small and in consequence spray interaction with PM in impingement area corresponds to porous surface impingement process (strongly depends on the pore size, pore structure and wall junction thickness and PM temperature).



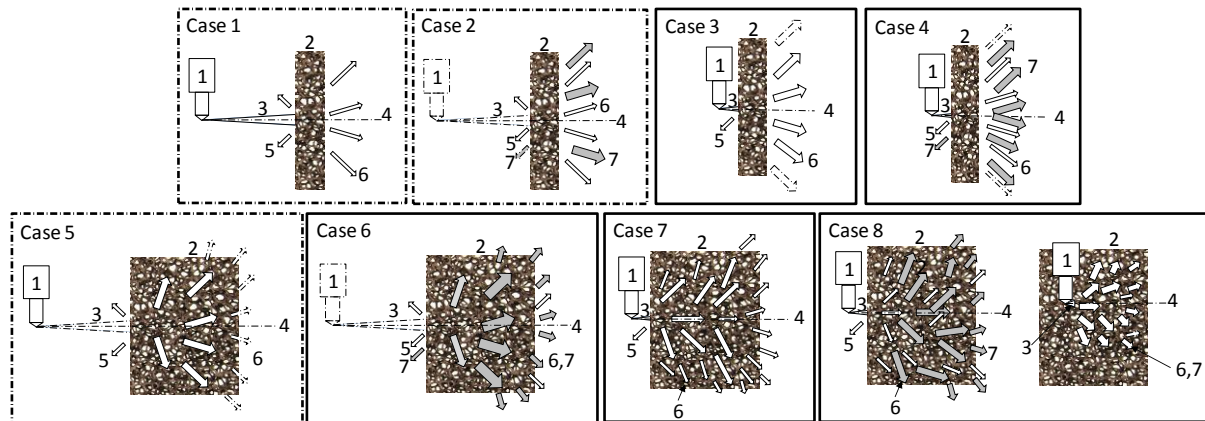


**Figure 3:** Characteristic configurations for diesel spray interaction with porous structure: 1-injector; 2-porous structure; 3-diesel spray (jet); 4-initial spray axis (from the nozzle); 5-fuel reflecting from the impingement surface of PM; 6-secondary jet as a result of multi-jet splitting; 7-fuel vapours

- Case 5. Thick and cold PM with diesel nozzle positioned far away from the porous impingement surface. The process is characterized by a multi-jet splitting as a result of spray interaction with wall junctions of PM and the resulting spray-PM interaction process may mostly be observed inside the PM volume. In this case a diesel spray may fully develop in a free space before impinging on to PM. Spray tip impinging surface is large and in consequence spray interaction with PM in impingement area corresponds more to solid wall impingement process (strongly depends on the pore size, pore structure and wall junction thickness).
- Case 6. Thick and hot PM with diesel nozzle positioned far away from the porous impingement surface. The process is characterized by a multi-jet splitting superimposed with fuel vaporization as a result of spray interaction with hot wall junctions of PM and the resulting spray-PM interaction process may mostly be observed inside the PM volume. In this case a diesel spray may fully develop in a free space before impinging on to PM. Spray tip impinging surface is large and in consequence spray interaction with PM in impingement area corresponds more to solid wall impingement process (strongly depends on the pore size, pore structure, wall junction thickness and PM temperature).
- Case 7. Thick and cold PM with diesel nozzle positioned in proximity to porous impingement surface. The process is characterized by a multi-jet splitting as a result of spray interaction with wall junctions of PM and the resulting spray-PM interaction process may mostly be observed inside the PM volume. In this case a diesel spray may not well develop in a free space before impinging on to PM. Spray tip impinging surface is small and in consequence spray interaction with PM in impingement area corresponds to porous surface impingement process (strongly depends on the pore size, pore structure and wall junction thickness).
- Case 8. Thick and hot PM with diesel nozzle positioned in proximity to porous impingement surface. The process is characterized by a multi-jet splitting superimposed with fuel vaporization as a result of spray interaction with hot wall junctions of PM and the resulting spray-PM interaction process may mostly be observed inside the PM volume. In this case a diesel spray may not well develop in a free space before impinging on to PM. Spray tip impinging surface is small and in consequence spray interaction with PM in impingement area corresponds more to porous surface impingement process (strongly depends on the pore size, pore structure, wall junction thickness and PM temperature).

### Experimental test-rig

Above selection of characteristic test and process conditions indicates two basis measurement configurations: process observation outside PM and process visualization inside PM. These conditions give different requirements on the test conditions and measurement technique. The spray interaction with porous structure, for both considered conditions, has been investigated in a special test chamber equipped with common-rail diesel injection system and multi-hole nozzle [2-4]. Highly time-and space resolved visualization technique with CCD and high-speed cameras have been used. For process investigation inside PM volume a micro-endoscopic visualization technique has been applied and first results are presented in the paper.

### Results and Discussion

In this section a few examples of different experimental investigation on diesel spray interaction with PM are discussed. The fundamental process of spray interaction with highly porous, open cell structures has been described in [1,2] and is shown in Fig.4.

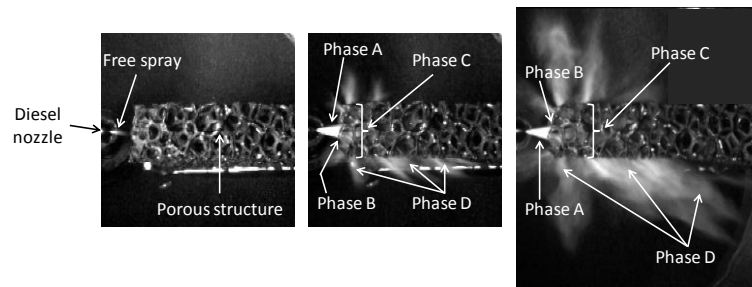


**Figure 4:** The most important phases of diesel spray interaction with PM

- Phase A* In a free space between nozzle outlet and porous-medium surface, a free jet penetrates throughout the available space defined by the distance between nozzle and PM until impinging onto the PM surface.
- Phase B* The jet impingement onto the PM surface may be divided into two parts: jet reflection from the interface (phase B) and jet propagation throughout (inside) the PM volume (phase C). This depends on the injection parameters, nozzle geometry, distance from the nozzle outlet, pore size, its density and the wall thickness of the pore junctions.
- Phase C* In this phase the jet is distributed and propagates throughout the PM volume, and this process is characterized by wide jet spreading and is related to a multi-jet splitting.
- Phase D* Depending on jet momentum, impingement velocity, PM geometry, pore size and density, the injected fuel is completely trapped inside the porous medium volume or part of the liquid may leave the PM volume (*Phase D*). This effect may be utilized for different applications in internal-combustion engines.

The porous structure may be created in the form of very thin ring inside which a diesel nozzle is positioned (fig.5).

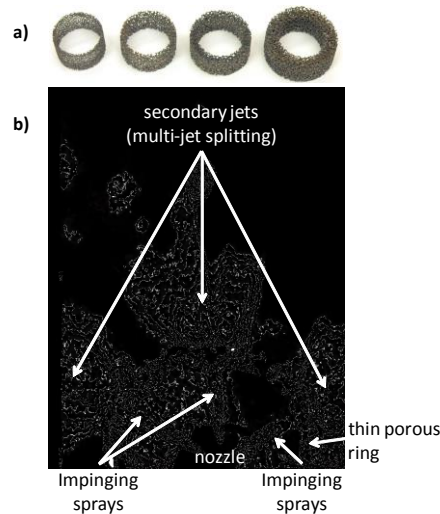


**Figure 5:** a- thin porous rings; b-Diesel spray interaction with thin PM-ring (cold conditions)

A rapid radial spreading of the Diesel jet by interaction with a porous structure is a result of multi-jet splitting. The effect of a multi-jet splitting is observed as a “radiant sun”-like structure and is three-dimensional in nature. This process is time and PM-ring geometry and structure dependent, as shown in Fig.6. Configuration 1 is characterized by a larger PM-ring diameter and its lower thickness. Configuration 2 uses thicker ring with no gap between inner ring surface and diesel nozzle. Both are made of metal foam structures.

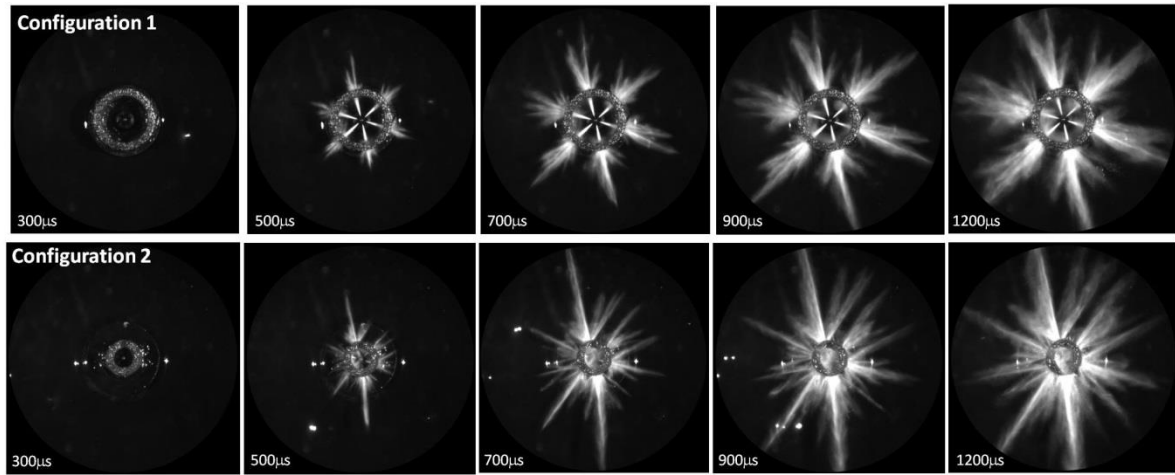


**Figure 6:** Diesel spray interaction with thin PM-ring for two different configurations (cold conditions)

If the porous ring is hot (e.g. in the case when positioned in the combustion chamber of engine) an enhanced fuel vaporization together with a multi-jet splitting may be observed (see Fig.7).

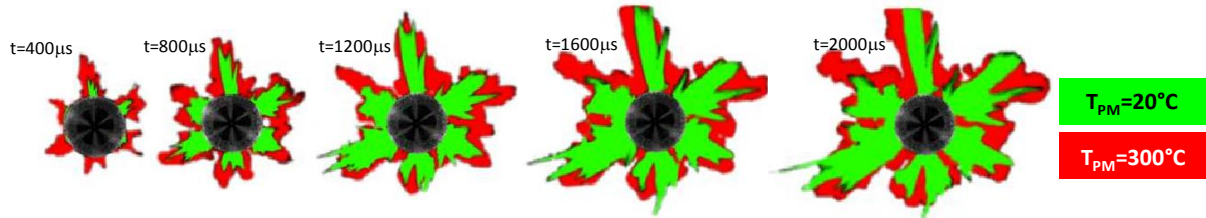


**Figure 7:** Diesel spray interaction with cold (20°C) and hot (300°C) PM-ring at different time instances after triggering of injector

There is a superposition of multi-jet splitting effect with fuel vaporization process. A multi-jet splitting results in significantly increased spray surface area (after interacting with PM-ring) and in reduced spray penetration length, as shown in Fig.8. These effects are more PM-ring structure and geometry dependent, and less influenced by ring temperature and injection conditions.

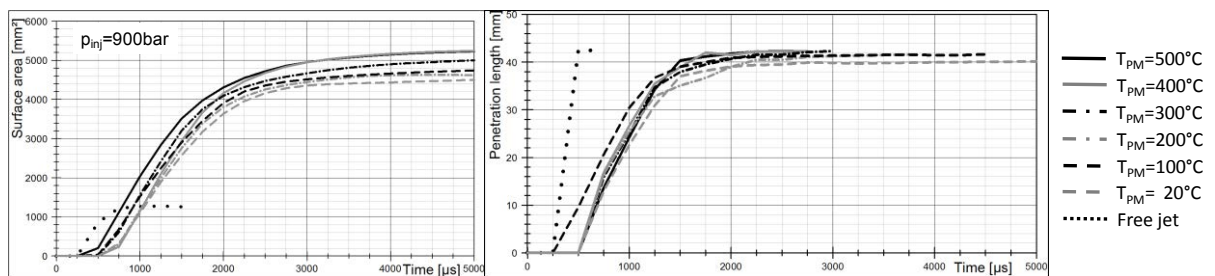


**Figure 8:** Example of surface area and penetration length of spray after interacting with PM-ring for different PM-ring temperatures (data for a free spray under cold conditions are also plotted)

For process investigation inside PM volume the authors starts initial experiments with using of micro-endoscopic visualization technique as shown in Fig.9. Example of process view using a micro-endoscopic visualization system is shown in Fig.10.

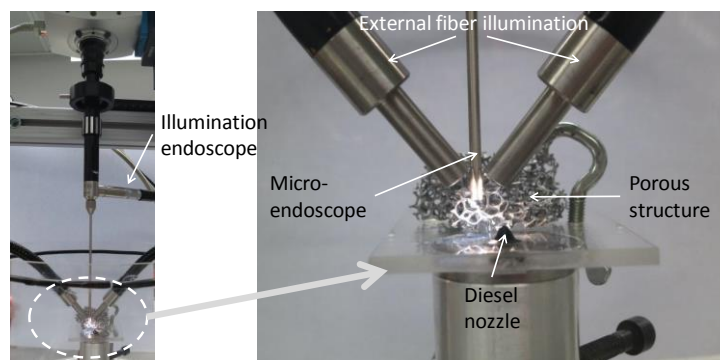


**Figure 9:** Setup with micro-endoscopic system equipped with a high-speed CCD camera for direct visualization of spray penetration inside porous structure

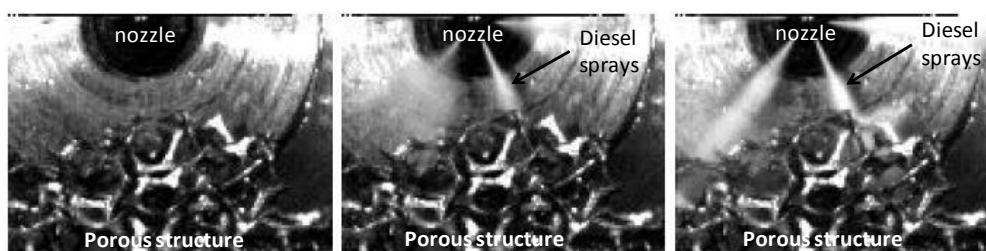


**Figure 10:** Examples of process view using a micro-endoscopic system equipped with a high-speed CCD camera

## Conclusions

Different aspects of Diesel spray interaction with highly porous structures for mixture homogenization and even for combustion in porous reactors have been presented. There is a number of important parameters influencing this process: porosity, pore size, thickness of PM, wall junction thickness, injection pressure, impingement velocity, gap between nozzle outlet and PM inner surface, as well PM temperature and time after spray impingement on PM surface. Spray interaction with PM results in significant spatial spreading of the spray, reduced axial penetration length, significantly increase spray surface area, reduced propagating velocity after interaction with PM and enhanced vaporization if the porous structure is hot. There are two characteristic cases of diesel spray interaction with PM: interaction with thin PM- process performs and is observed outside the structure; interaction with thick PM – process performs in PM volume and may be observed directly inside PM or outside its volume. For process observation inside PM volume the using of micro-endoscopic system has been proposed.

## References

- [1] [1] Weclas, M., Some fundamental observations on the Diesel jet “destruction” and spatial distribution in highly porous structures, *Journal of Porous Media*, vol. 11, iss.2, 2008, pp.125-145.
- [2] [2] Weclas, M., Homogenization of liquid distribution in space by Diesel jet interaction with porous structures and small obstacles, 22nd European Conference on Liquid Atomization and Spray Systems, Como, Italy, September 2008, Paper no. ID ILASS08-A003
- [3] [3] Weclas, M., Cypris, J. Characterization of distribution nozzle operation for mixture homogenization by late diesel injection strategy, *Proc. IMechE Vol. 226 Part D: J. Automobile Engineering*, 2012, pp.529-546, DOI: 10.1177/0954407011420499
- [4] [4] Weclas, M., Cypris, J., Maksoud, T.M.A, Diesel spray interaction with highly porous structures for supporting of liquid distribution in space and its vaporization, *Proceedings (CD) of the 4th International Conference on Porous Media and its Applications in Science and Engineering ICPM4*, June 17-22, 2012, Potsdam, Germany
- [5] [5] Shahangian, N. Ghojel, J. Investigation of the interaction between diesel spray and porous medium, in *Proceedings of the 17th Australasian Fluid Mechanics Conference*, Auckland, New Zealand, December 2010

## Combustion of diesel spray in 3D-highly porous reactors under CR-Diesel injection conditions

M. Weclas<sup>1</sup> and J. Cypris<sup>2</sup>

1: Georg Simon Ohm University of Applied Sciences Nuremberg, Department of Mechanical Engineering, IFZN, Kesslerplatz 12, D-90489 Nuremberg, Germany

2: Fraunhofer Institute for Building Physics IBP, Combustion Systems, Nobelstrasse 12, D-70569 Stuttgart, Germany

### Abstract

The combustion in porous reactors (PR) offers potential for high cycle efficiency under nearly zero-emissions level. Diesel engine-like conditions are simulated in a special combustion chamber with a common-rail injection system (free-volume combustion is also analyzed). The presence of porous reactor changes not only the conditions for mixture formation but significantly influences the thermodynamic conditions of the process. Owing to high heat capacity of porous structure, heat release in PR results in significantly reduced pressure peaks and lowered combustion temperature allowing reduction of thermal NO<sub>x</sub> formation. One of critical factors concerning applicability of the combustion in porous reactor to engine conditions is the time scale and dynamics (rate) of the process under lowered temperature. Even at lower initial temperatures the process is accelerated in porous reactors and heat release rate increases with initial pressure and initial temperature, and significantly depends on the amount of heat accumulated in the reactor. Also ignition delay time is significantly dependent on initial pressure and initial temperature, and, on the whole, decreases with increasing pressure and with increasing temperature. A qualitative similarity of the heat release process in a free volume and in porous reactors indicates applicability of combustion in porous reactors to engines.

---

### Introduction

Future development of internal combustion engines goes toward realization of clean combustion process, i.e. homogeneous combustion. For realizing of homogeneous combustion under variable load and speed engine conditions especially critical is control of: ignition timing, combustion duration, heat release rate and corresponding pressure gradient and pressure peak, combustion temperature and completeness of the process [1]. A novel kind of engine in which a free volume combustion chamber is replaced with highly porous three-dimensional reactor would satisfy the above conditions. Especially a combination of high cycle efficiency with a nearly-zero emission level is of great interest. In this concept the mixture formation, ignition and combustion processes are performed inside porous combustion reactor having significantly different features as compared to free volume combustion chamber conditions [2].

Very specific features of porous combustion reactor significantly influencing fuel injection, mixture preparation and combustion conditions, not relevant to free volume combustion chamber, are: porosity, heat capacity, pore structure and their size. One of crucial feature of combustion in porous reactor is heat transfer between the solid phase of the reactor and the fluid phase inside the porous medium volume. These results in simultaneous heat release process and heat accumulation in reactor structure making thermodynamic conditions significantly different from the free volume combustion chamber. One of critical questions concerns time-scale and the rate of oxidation processes in porous reactors and their applicability to internal combustion engine cycle conditions. These aspects are discussed in the present paper, and the attention is paid to particular processes of mixture formation and combustion realized in a porous reactor volume. Processes performed inside porous reactor can be divided into two groups: direct fuel injection into a porous reactor with corresponding mixture formation and low- and high-temperature oxidation processes.

### Experimental test-rig

#### Short description of engine concept with combustion in porous reactor

Durst and Weclas [2] proposed engine concept with mixture formation and combustion processes in porous reactor. Application of a combustion porous reactor to engine allows realization of homogeneous and flameless combustion process characterized by a near-zero emissions level. Heat recuperation in porous reactor allows increase of engine-cycle efficiency resulting in reduction of CO<sub>2</sub> emissions. Heat accumulation in porous reactor results in significantly lowered combustion temperature permitting nearly-zero NO<sub>x</sub> level. This is the most important difference between the combustion processes in conventional Diesel engine and in engine with combustion in porous reactor. The latter kind of engine may be realized as an engine in which the PM reactor has permanent contact with the cylinder content (open chamber fig.1a), and as an engine in which the PM

reactor has periodic contact with the cylinder content (closed chamber fig.1b) [2]. In the open-chamber system, as considered in the present paper, the porous reactor has permanent contact with the cylinder content (gas) and the most important are processes occurring close to the TDC of compression in a constant volume of porous reactor. These processes are: fuel injection into reactor, fuel distribution throughout reactor volume, fuel vaporization and mixing with air as well as thermal ignition and heat release. First of all the fuel must directly be injected into porous reactor and distributed throughout reactor volume [3,4].

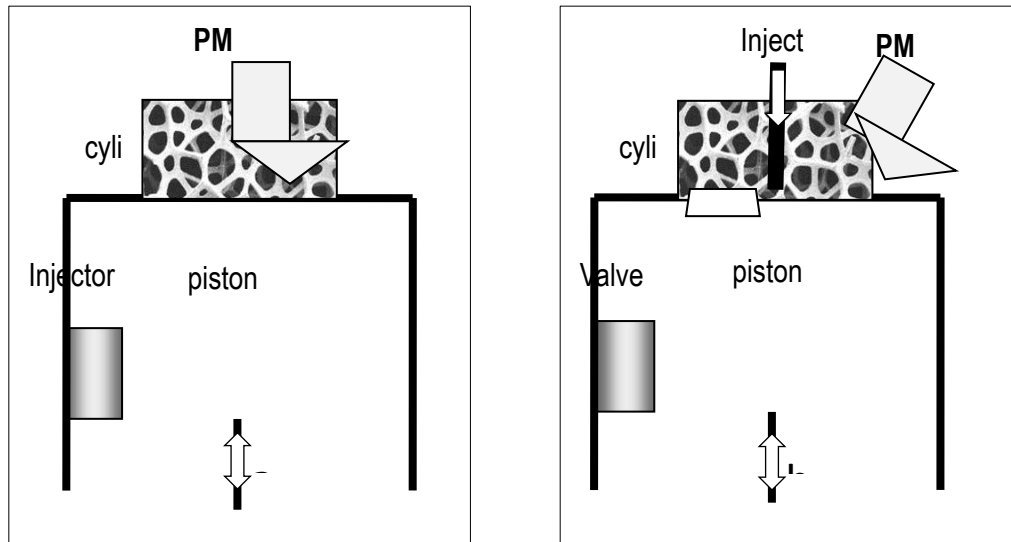


**Figure 1:** Principle of internal combustion engine with mixture formation and combustion in porous reactor [2]: a- combustion reactor with permanent contact with cylinder content; b- combustion reactor with periodic contact with cylinder content

### Simulation of engine concept using special combustion chamber

For experimental investigation of mixture formation and combustion processes in porous reactors under engine-like conditions with wide flexibility in setting the test conditions, a special high-pressure, high-temperature, constant volume and adiabatic combustion chamber has been built and equipped with a Diesel common-rail injection system [5,6] – see fig.2. The system simulates the thermodynamic conditions at the time instance corresponding to the nearly TDC of compression in a real engine equipped with porous reactor [5-7]. Initial gas pressure (corresponding to the time instant when fuel injection starts) and reactor temperature at this moment can be chosen independently of one another. The reactor is heated electrically, and it is assumed that at the moment of fuel injection start the gas trapped in the reactor has reactor temperature. The pressure in the chamber is measured with a piezoelectric pressure transducer which is able to switch between static pressure measurement and highly dynamic pressure change measurement. A synthetic dry air is used as combustion air and is supplied with variable pressure. The temperature inside the chamber is measured with a thermocouple and static conditions are preset prior start of experiment (fuel injection).



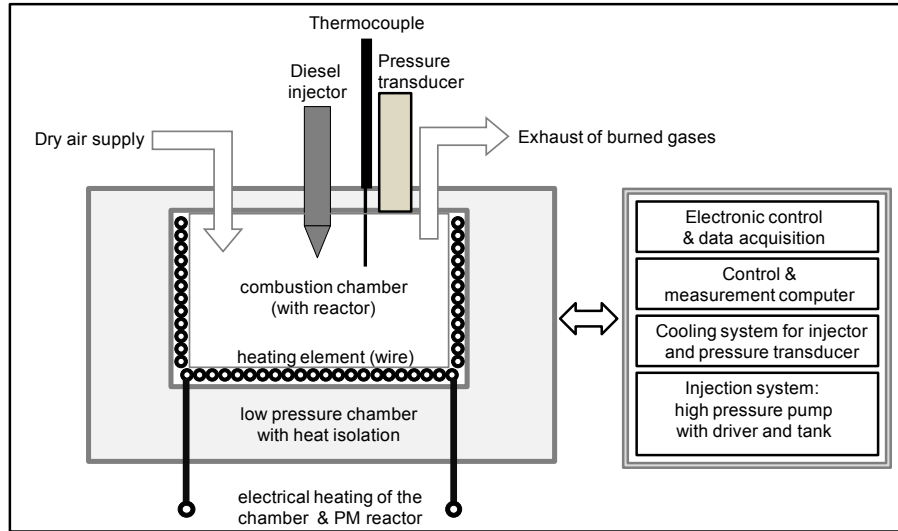


**Figure 2:** Basic components of combustion chamber used as a simulator of Diesel engine conditions for time instances closed to TDC of compression

### Thermodynamics of the system

For thermodynamic analysis of engine with combustion in porous reactor there are three systems to be considered in Fig.3 [5]:

Fig.3a: Free volume system - at the moment of fuel injection, the system consists of mass of air trapped in the combustion chamber volume;

Fig.3b: Ideal porous reactor - at the moment of fuel injection, the system consists of mass of air trapped in the porous reactor volume having mass  $m_{PM}$ ; it is assumed that at any instant of time the gas temperature is equal to porous reactor temperature  $T_{G(IR)} = T_{PM}$ ;

Fig.3c: Real porous reactor - at the moment of fuel injection consists of mass of air trapped in the porous reactor volume having mass  $m_{PM}$ ; it is assumed that at any instant of time after fuel injection starts the gas temperature is not (necessary) equal to porous reactor temperature  $T_{G(RR)} \neq T_{PM}$ .

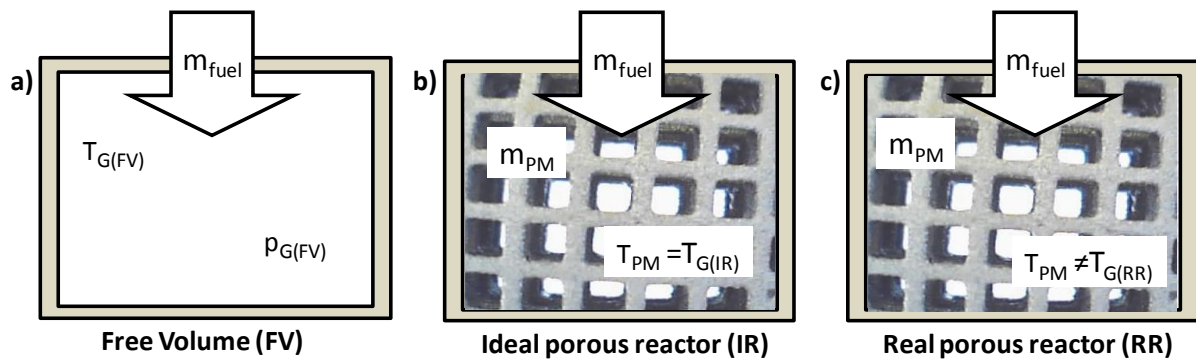


**Figure 3:** a-model of free volume combustion chamber; b-model of ideal reactor; c-model of real reactor



Both porous reactors are made of a highly porous structure having porosity higher than 90%. In all considered cases the fuel is directly supplied into the combustion chamber/reactor using a common-rail Diesel injection system with electronically controlled injector. The mass of injected fuel results from the combination of injection pressure and injection duration. For both models with porous reactor (PM), it is assumed that the mass of reactor is much higher than the mass of gas trapped in the reactor volume  $m_{PM} \gg m_{G(IR),(RR)}$ .

## Results and Discussion

Examples of pressure history and corresponding temperature for free volume combustion chamber and porous reactor systems are shown in figure 4. Data are plotted for initial gas temperature 500°C at different initial pressures.

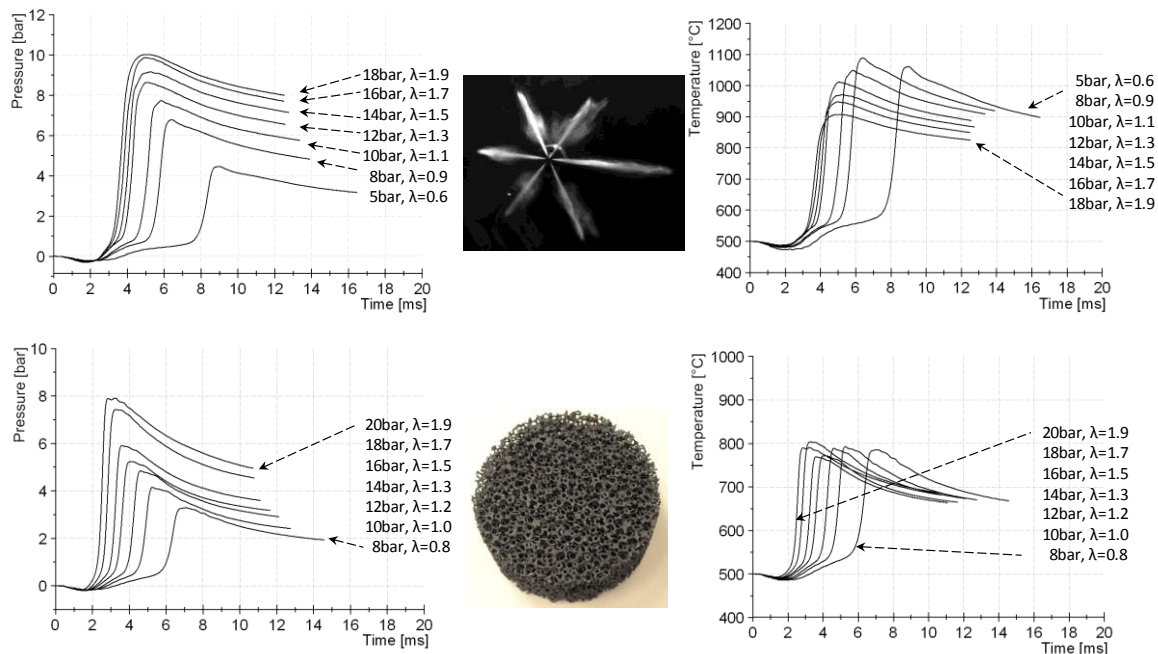


**Figure 4:** Pressure distribution (left) and temperature history (right) of the heat release process in time after Diesel injection starts at initial temperature 500°C and different initial pressures (mass of injected fuel is constant 23.8mg): top- in a free volume combustion chamber; bottom- in a SiC foam porous reactor with pore density 8ppi

The pressure history in a free volume combustion chamber shows a strong dependence of the heat release process on the initial pressure: the higher the initial chamber pressure the faster is the heat release process and the shorter ignition delay period. Also the corresponding pressure peak level increases with initial pressure. This is not the case for combustion temperature which does not directly scales with increasing pressure (in reporting experiments with increasing initial pressure air excess ratio also increases). Similar analysis is performed for porous reactor (see fig.4). The data are plotted at  $T_{PM}=500^{\circ}\text{C}$  for different initial pressures (real reactor conditions). Pressure history shows reduced pressure peaks as compared to free volume system, and heat release process is qualitatively similar to free volume heat combustion. Reduced pressure peaks correspond to the heat accumulated in the porous reactor, and the corresponding combustion temperatures are also reduced. The maximum temperature peaks in the porous reactor are much less dependent on air excess ratio than in a free volume system (reactor heat capacity and heat transfer to the reactor solid phase).

For reactors having higher pore density and larger specific surface area the heat transfer to the reactor should increase resulting in increased heat accumulation in the solid phase of porous reactor. This effect can be observed in fig.5 showing distribution of maximum combustion temperature after fuel injection in the case of free volume system and maximum gas temperature in foam porous reactors having different pore densities (8ppi and 30ppi).

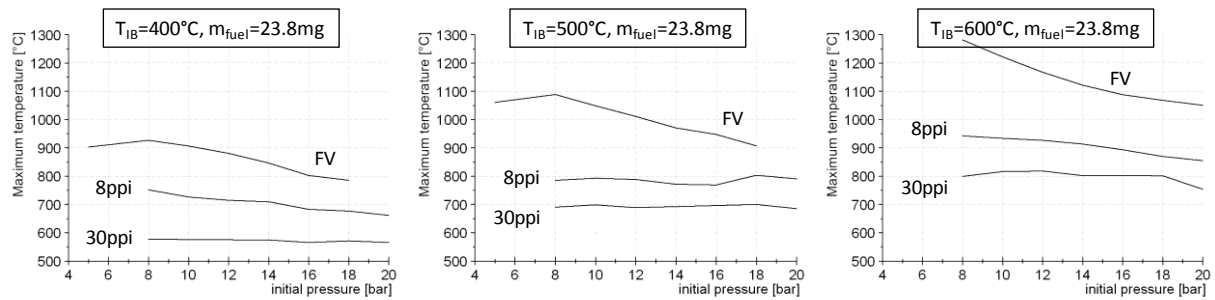


**Figure 5:** Distribution of maximum combustion temperature versus initial pressure in free volume system (FV) and in two porous reactors (8ppi and 30ppi) at three initial temperatures 400°C, 500°C and 600°C for a constant mass of injected fuel.

For reactor of higher pore density the maximum temperature is significantly reduced at all investigated initial pressures. Almost constant temperature recorded in real porous reactors independently of initial pressure indicates the role of heat capacity and heat transfer conditions defining amount of heat accumulated in the porous reactors. This effect is observed for all investigated initial temperatures. Distribution of ignition delay time is plotted in Figure 6 versus initial chamber pressure for free volume and porous reactor systems. Data are analysed for three initial temperatures 400°C, 500°C, and 600°C. Generally, the delay time decreases with increasing initial chamber pressure and initial chamber temperature. The combustion process in porous reactor shows qualitative behaviour similar to that in a free volume system. The delay time is reduced, especially at lower initial temperatures. Similarly to free volume combustion, the delay times at higher reactor temperatures are similar and much longer at 400°C.

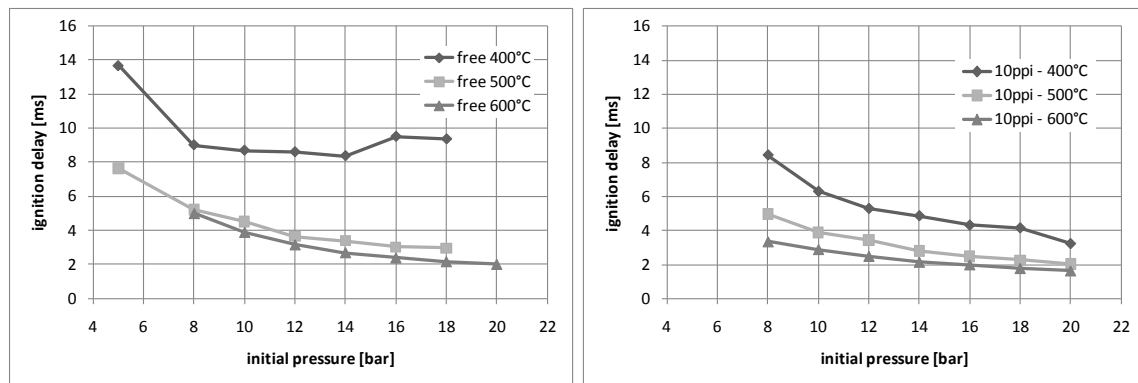


**Figure 6:** Comparison of delay time for heat release in free volume and in porous reactor (SiC foam of 8ppi pore density) as a function of initial pressure for three initial temperatures 400°C, 500°C, and 600°C (mass of injected fuel is 23.7 mg).

Reaction rate represented by pressure gradients after fuel injection begin, significantly depends on the porous reactor's heat capacity and pore density as compared to the free-volume process (fig.7). Generally, the reaction rate increases with increasing initial chamber pressure and with increasing initial temperature, but the latter dependence may be reactor configuration specific. Higher initial reactor temperature means more energy accumulated in the reactor and less influence of the gas temperature on the reaction rate. The maximum combustion temperature increases with increasing initial chamber pressure and results in increasing reaction rate. For reactors having large heat capacity and small pores (high density foam reactors) the heat release rate is lowered due to the large amount of heat transferred to the reactor. It must be noted that different pore densities and pore structures give different conditions for fuel injection into the reactor. This results in different mixture

formation conditions. These conditions, however, are very complex and it is still very difficult to describe them.

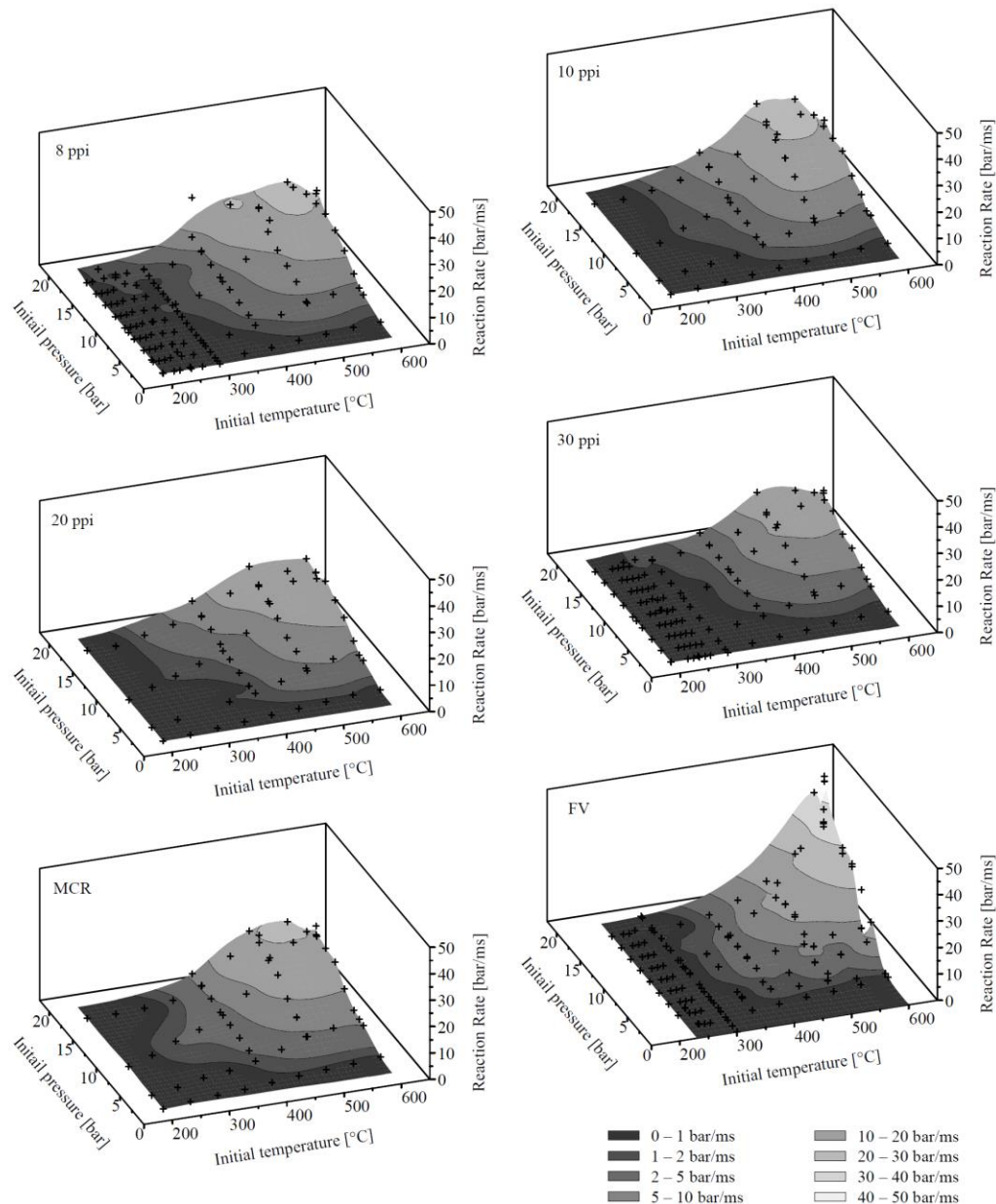


**Figure 7:** Reaction rate under porous reactor conditions and free volume in range over initial pressure and temperature; FV- free volume system; 8,10,20 and 30ppi-SiC foam reactors; MCR-SiC macro-cellular non-foam reactor

Under all investigated conditions the reaction rate is the highest in the range of high initial pressures and high initial temperatures. However, the maximum rates differ in case of investigated porous reactors and under free volume conditions. It is clearly visible, that the highest reaction rates are measured under free volume conditions with values up to 50 bar/ms. The lower values in case of porous reactors correlate with the heat transfer and accumulation in the porous reactor's solid phase. The highest reaction rate in reactors with high pore density (20ppi and 30 ppi) is lower than in porous reactors with lower pore density (8 ppi and 10 ppi). The reaction rate in macro-cellular reactor (MCR) [7] is similar to both low density foam reactors (8ppi and 10ppi).

## Conclusions

Despite of significantly changed thermodynamic conditions in porous reactors (lowered maximum temperature), the heat release process is very similar to that observed under free volume conditions, while the reaction rate is limited by the porous reactor at high initial pressures and temperatures. This indicates the applicability of this combustion technology to real IC engine conditions and its potential to realise a homogeneous combustion process even at high loads, which is not feasible with current HCCI concepts. Moreover, the great potential of combustion in porous reactors for achieving a near zero emission level makes its application to IC engines very

promising. Due to the improved mixture formation and vaporisation of the fuel and due to the heat accumulation in the porous reactor solid phase, the formation of soot can be avoided and complete oxidation of HC and CO may be realised by homogeneous combustion in porous reactors. Summarizing their process analysis, the authors constructed fields representing characteristic combustion modes in porous reactors as compared to free-volume Diesel injection conditions. These fields consider two kinds of parameters: distribution of characteristic reaction behavior represented by a single- and multi-step oxidation and time scale of the process. The data have been grouped according to number of slopes in the reaction curve and duration of delay time. There are three characteristic regions representing three different characteristic modes of the oxidation process: Region 1 is characterized by single-step reactions and is located at lower initial temperatures for all initial pressures; Region 2 is characterized by multi-step reactions with two slopes recognizable in the reaction curve and is located in the range of middle-high initial temperatures at middle-high initial pressures; Region 3 is characterized by multi-step reactions with three slopes recognizable in the reaction curve and is located in the range of higher initial temperatures at low-to-middle initial pressures. Analysis of delay time distribution in these two-dimensional fields allowed selection of five characteristic ranges. Region A is characterized by delay times  $t > 20\text{ms}$  and is located at lower initial temperatures at all initial pressures investigated. Region B is characterized by delay times  $10\text{ms} < t \leq 20\text{ms}$  and is located at higher initial temperatures and lower initial pressures as well as in a small region of high initial pressures. Region C is characterized by delay times  $5\text{ms} < t \leq 10\text{ms}$  and is located at higher initial temperatures and lower-to-middle initial pressures as well as in a small region of high initial pressures. Region D is characterized by delay times  $2\text{ms} < t \leq 5\text{ms}$  and is located at higher initial temperatures and middle-to-high initial pressures. Region E is characterized by delay times  $t \leq 2\text{ms}$  and is located at high initial temperatures and high initial pressures. Qualitative similarity of characteristic modes of the heat release process in a free volume and in porous reactors as performed under Diesel engine-like conditions indicates high probability of applicability of the combustion in porous reactor to engines.

## References

- [1] [1] Tanaka, S., Ayala, F., Keck, J. C., Heywood, J. B. Two-stage ignition in HCCI combustion and HCCI control by fuels and additives,” *Combustion and Flame*, vol. 132, no. 1-2, pp. 219–239, 2003.
- [2] [2] Durst, F., Weclas, M., A new type of internal combustion engine based on the porous-medium combustion technique, *J. Automobile Engineering, IMechE*, part D, Vol. 215, 2001, 63-81.
- [3] [3] Weclas, M., Homogenization of liquid distribution in space by Diesel jet interaction with porous structures and small obstacles, 22nd European Conference on Liquid Atomization and Spray Systems, Como (Italy), September 2008, Paper no. ID ILASS08-A003,
- [4] [4] Weclas, M., Cypris, J., “Distribution-nozzle” concept: a method for Diesel spray distribution in space for charge homogenization by late injection strategy, ILASS – Europe 2010, 23rd Annual Conference on Liquid Atomization and Spray Systems, Brno, Czech Republic, September 2010, Paper no.ID ILASS10-39
- [5] [5] Weclas, M., Cypris, J., Maksoud, T.M.A., Thermodynamic properties of real porous combustion reactor under Diesel engine-like conditions, *Journal of Thermodynamics*, Volume 2012, Article ID 798104, doi:10.1155/2012/798104
- [6] [6] Weclas, M., Cypris, J., Maksoud, T.M.A. Combustion of Diesel sprays under real-engine like conditions: analysis of low- and high-temperature oxidation processes, ILASS – Europe 2010, 23rd Annual Conference on Liquid Atomization and Spray Systems, Brno, Czech Republic, September 2010, Paper no.ID ILASS10-40.
- [7] [7] Cypris, J., Schlier, L., Travitzky, N., Greil, P., Weclas, M., Heat release process in three-dimensional macro-cellular SiC reactor under Diesel engine-like conditions, *FUEL*, 102 (2012) 115–128 doi.org/10.1016/j.fuel.2012.05.038

## Comparison of the Spray Evaporation and Inflammation of Alternative Fuels for Late Injection Timing Mode

Tobias Knorsch<sup>1,2</sup>, Michael Storch<sup>1,2</sup>, Lars Zigan<sup>1,2</sup> and Michael Wensing<sup>1,2</sup>

1: Department of Engineering Thermodynamics, FAU Erlangen-Nuremberg, Germany

2: Erlangen Graduate School in Advanced Optical Technologies, FAU Erlangen-Nuremberg, Germany

### Abstract

The complete engine reaction chain of modern direct-injection spark-ignition (DISI) engines from spray atomization, evaporation, inflammation and combustion mechanisms is depending on the spray quality. Effects of differing fuel properties – of both fossil fuels and novel fuel components – are still not completely understood. This paper addresses the effects of different fuel components on evaporation, ignition and inflammation as a first link between the single phenomena. The influence of the properties boiling point and heat of vaporization on vapor distribution, ignitability and spray combustion is examined in a spray chamber. The boundary conditions model a late injection timing mode and thus combustion of fuel-rich regions in the droplet cloud. It is found that the inflammation delay is besides the evaporation rate, driven by properties such as the laminar flame velocity.

### Introduction

The key advantage of direct-injection is the possibility to reduce throttle losses and thus increase the efficiency at part load conditions [1]. Results of previous studies [1-3] showed that the physiochemical fuel properties heat of vaporization and boiling point influence the spray evaporation at conditions which are applied at late injection timing mode in regions where the secondary breakup and momentum exchange with the surrounding gas is largely progressed [1,2]. The fuel effect on ignitability and spray combustion is still a research topic. Thus, this study addresses the evaporation and inflammation behavior of different single fuels and a blend.

Up to now the research octane number (RON) is the standard parameter which is commonly used to describe the ignitability of gasoline and gasoline alternative fuels comparing the knocking behavior to isooctane which has a RON of 100 by definition. However, the RON test procedures may be less relevant for modern DISI boundary conditions with novel ignition timing (e.g. fuel stratification at the spark plug). The importance of the RON and further parameters based on the previous findings of liquid and gas phase fuel distribution measurements is analyzed. For fuel stratification conditions or injection during catalysator heating with late injection timing an inhomogeneous temperature distribution throughout the cylinder and the spray occurs. This determines local inhomogeneities in the evaporation rates and, therefore, mixture formation and ignitability. Spatially-resolved information of the temperature and droplet size during and after injection is required to locally determine the evaporation rate and evaporation cooling in the spray as well as the affinity to pre-ignition or soot formation. In general the spray plumes of DISI injectors cool off the surrounding gas whereby the spray cone centers are typically expected to show lower temperatures due to the higher droplet density whereas in outer regions the concentration is lower due to stronger air entrainment. The spatial distribution of this cooling depends on the specific initial fuel temperature, the fuel amount per injection, pressure, heat of vaporization, and local concentrations.

First a study using two-line planar laser-induced fluorescence (2line-PLIF) is carried out. In this way, a vapor distribution and local temperature after the injection end can be calculated. This information is required to locally estimate the evaporation rate and cooling inside the spray plumes. Planar laser-induced fluorescence (PLIF) based on fuel tracers is commonly used to characterize the mixture formation for engine combustion or technical combustion processes [4] and is capable to determine the temperature distribution in the gas phase. Up to now, there are very few measurements with optical techniques to determine the temperature fields in sprays at engine conditions [5]. Due to the temperature dependency of the fluorescence signal, simultaneous measurements of fuel vapor concentration and temperature are possible. For thermometry, the tracer 3-pentanone, which already presented a high suitability in other publications [1,2], is applied.

Within this study the techniques of PLIF imaging and high-speed flame luminescence are both utilized. In this way, a distribution of the local spray vapor density during different ignition timing modes can be investigated and correlated to the post inflammation phase. The high-speed flame luminescence technique is used to find correlations between the results of quantitative spray vapor distribution measurements. Furthermore, correlations of the respective fuel mixture and direct impact on the inflammation and early flame propagation are possible. This information is required to estimate the local inflammation delay as well as fuel ignitability and misfire tendencies at stratified charge conditions. The complexity of the spray processes of ordinary gasoline fuels is most often simplified by using single-component surrogate fuels. However, multi-

component model fuels represent the spray behavior of gasoline in a better way [3,6]. The evaporation of multi-component fuels in turn can show demixing of fuel components in the droplet under DISI conditions with injection into a high-pressure atmosphere [3,7,8]. Due to this, both single- and multi-component fuels are analyzed within this study.

### Experimental test-rig

Pure biofuels n-butanol, iso-butanol and ethanol are examined and compared with both isooctane as a standard model fuel as well as 3-component mixtures. High boiling point fuels strongly influence the spray behavior, which has been verified in previous measurements [1-3,6].

The composition is chosen according to the boiling point diagram to cover the main fuel components for a more realistic spray behavior compared to single component fuels (table 1). The fuels, mixtures and boundary condition (table 3) sets were chosen in order to focus on the influences of physiochemical properties on the inflammation behavior based on spray vapor temperature measurements. Table 1 presents the investigated fuels with the respective physiochemical properties at ambient boundary conditions. At higher boundary conditions the trends of the physiochemical properties remain. Although the kinematic viscosity also represents an important parameter, it is more relevant for injection conditions with low evaporation rate, as is demonstrated in references [3,6,9] is not focus of this work. The multi-component mixture ‘3K’ consist of a low-boiling point fuel (n-hexane 35% by volume), middle (45% by vol. of isooctane) and a high-boiling point fuel component (20% by vol. of n-decane). This mixture has an average RON of 46. By this, the inflammation behavior for a multi-component fuel can be studied and compared to its main component isooctane. As a tracer for the laser-induced fluorescence measurements 3-pentanone (20% vol.) is added to non-fluorescent surrogate fuel mixtures. Table 1 presents the investigated fuels with their physiochemical properties at ambient conditions.

**Table 1.** Investigated fuel mixtures and fuel components with key physiochemical parameters at ambient conditions (20°C / 1 bar) [10-12]

fuel	boiling point / °C	heat of vaporization / kJ/kg	density / g·cm <sup>-3</sup>	kinematic viscosity / 10 <sup>-6</sup> m <sup>2</sup> /s	RON
isooctane	99	305	0.70	2.95	100
n-decane	174	278	0.73	1.9	- 40
‘3K’	69-174	~322	~0.69	-	~46
3-pentanone	102	441	0.73	0.62	-

**Table 2.** Composition of fuel mixture ‘3K’. **Table 3.** Applied chamber boundary conditions for both liquid and vapor phase investigations.

fuel ‘3K’	% vol.
n-hexane	25
isooctane	45
n-decane	20

OP	p <sub>Gas</sub> / MPa	T <sub>Gas</sub> /K	p <sub>Fuel</sub> /MPa	T <sub>Fuel</sub> /K	t <sub>inj</sub> /ms
#1	0.56	473	20	353	1
#2	0.80	473	20	353	1
#3	0.80	673	20	353	1

In order to obtain accurate measurement data, reproducible conditions have to be set up. Therefore, an optically accessible, high-temperature / high-pressure spray chamber was used for all measurements. This combustion test facility was designed for spray investigations at conditions up to 700 K and 5 MPa. The investigated 6-hole nozzle injector (Bosch HDEV 5.2) has a geometric spray cone angle of ~55° and a spray bend angle of ~10°. The fuel and the injector are conditioned to 353 K to simulate the engine wall temperature and the injection duration is set to 1 ms. Each single injection has a mass of ~12 mg/pulse at 20 MPa injection pressure [13]. The chamber pressure and temperature are set to different operating points (table 1), respectively, to model late injection timing. The measurement plane of the spray vapor temperatures is set to the spark plug position of the inflammation measurements which is 30 mm distance to the nozzle tip. To measure the temperature distribution under engine-relevant conditions laser-induced fluorescence is applied. The fuel spray is excited by two different excimer lasers (248 nm KrF, ‘Radiant Dyes EXC-400’ / 308 nm XeCl, ‘Lambda Physik LPX110’). The fluorescence signals were recorded by a double-shutter ICCD camera (PCO DiCam pro). Spray vapor temperature distribution is calculated from the signal intensity ratio S308/S248 which has been calibrated depending on temperature, pressure and mixture composition in a flow cell in advance [5]. The average temperatures show a systematic error less than 5%; more details of the accuracy and evaluation strategy can be found in references [5].

The subsequent flame luminescence measurements are conducted at the same optical spray chamber using the same boundary conditions, injector and fuels. For the inflammation of the spray, a spark plug (NGK R5, single electrode) is mounted at side of the chamber. The ICCD camera is replaced by a high-speed camera

(Vision Research Phantom V711 @ 10 kHz, 1280x800 pixel) facing the spark plug and thus mounted at the opposite chamber side. The injector is mounted on the rear side of the chamber. The spray plume of interest is turned 30° towards the spark plug so that the spray plume is directly impinging the spark plug (see figure 2).

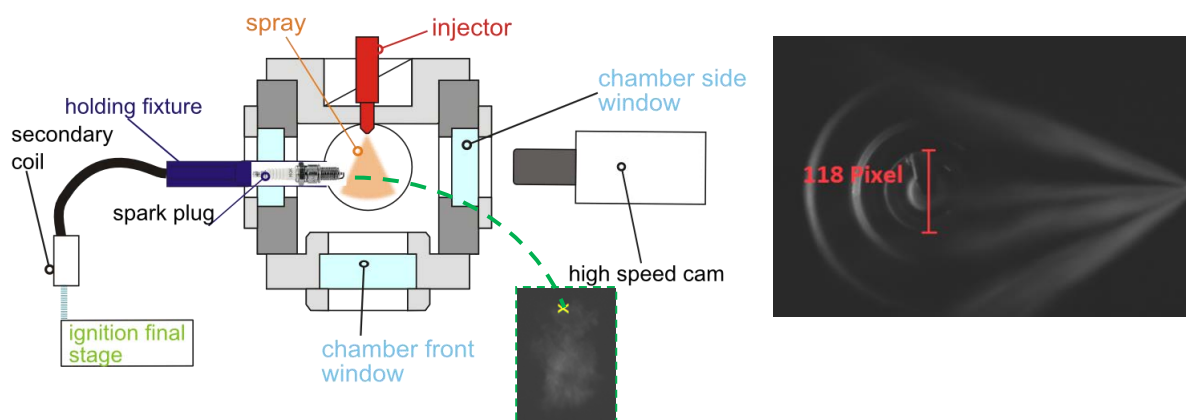


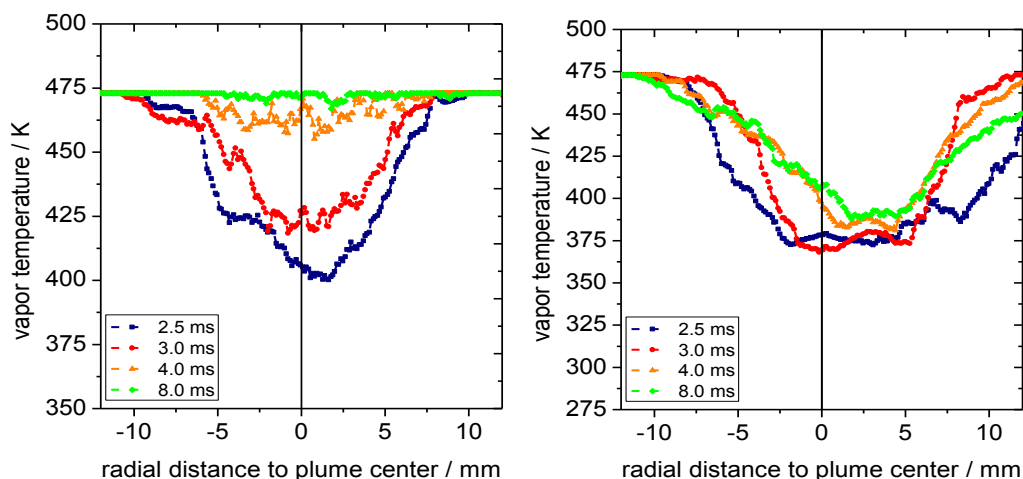
**Figure 2.** Setup for high-speed flame luminescence measurements (left) and Mie scattering image of the spray plume of interest centrally impinging on the spark plug before ignition (right)

The high-speed camera records the inflammation and early flame propagation till the flame is quite progressed (~3 ms after ignition). Five different ignition timings are observed at constant ignition energy (~50 mJ). For achieving constant and reliable ignition energy the spark plug is supplied by an ignition power amplifier (Genotec) combined with a secondary coil (Beru). Due to the applied ignition timings and geometrical setup of one single spray plume penetrating directly towards the spark plug just one spray plume inflames. The 2D images are evaluated by a threshold as burned pixel or unburned pixel in order to reduce soot influence with very high signal strength.

## Results and Discussion

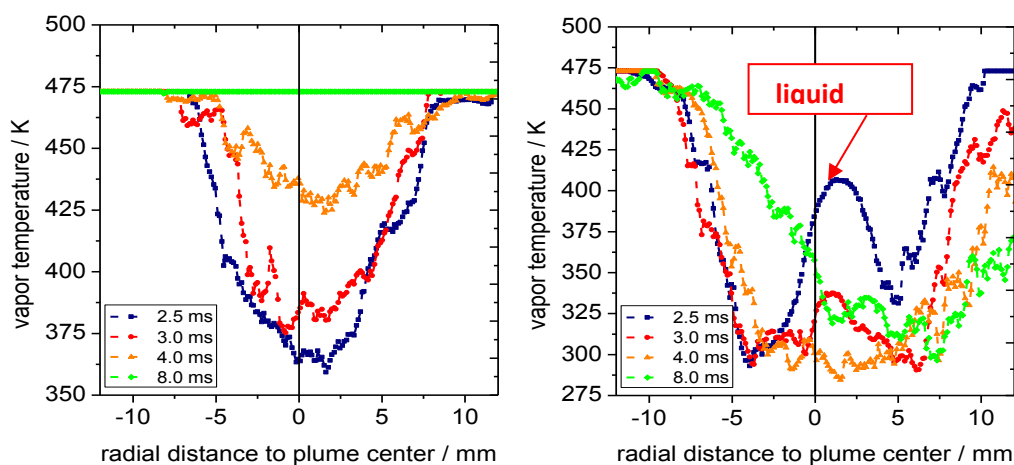
In this paper the influence of the fuel component on the evaporation and inflammation is investigated. Previous measurements of biofuels focusing on the droplet size and subsequent spray vapor phase temperature and concentration showed that for fuels owing a high value of heat of vaporization; the environment is cooled-off much higher than for fuels with lower values [1,2]. Some selected fuels are being investigated by PLIF imaging prior to the inflammation luminescence measurements. As gasoline surrogate fuel the multi-component fuel '3K' is measured and compared to its main component isooctane which is commonly used as a surrogate fuel. The heat of vaporization value of '3K' and isooctane is quite similar but boiling points strongly differ due to the high boiling point component n-decane of '3K' (20% by volume). Figures 3 to 5 present spray vapor phase temperature distributions achieved by average images of 32 single images. In the diagrams the position where the 'radial distance to the plume center' is 0, the subsequent measurement's spark plug will be mounted. In figure 3 the results of moderate boundary conditions (OP#1) are presented.





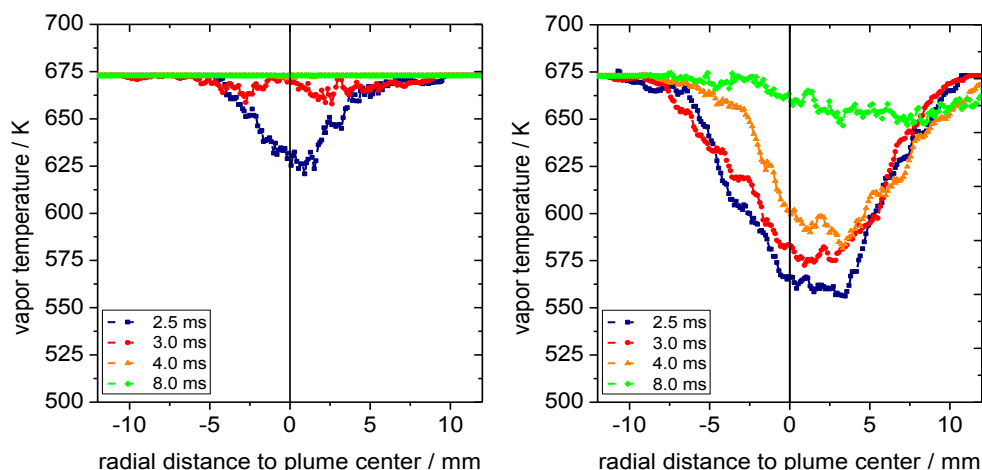
**Figure 3.** Absolute spray vapor temperature distributions at a nozzle tip distance of 30 mm for various points in time for pure isooctane (left) and the 3-component fuel 3K (right) at 0.56 MPa / 473 K

The record timing evaluations from 2.5 ms to 8 ms show very different results for the vapor temperature of both isooctane (fig. 3 left) and '3K' (right). Isooctane as a single component fuel with moderate boiling point and moderate heat of vaporization value presents an average gas cooling of  $\sim 75$  K at 2.5 ms after visible start of injection. Already at 4 ms after vSOI the temperature difference to the ambience decreases down to  $\sim 10$  K even in the spray cone center where the vapor concentration is higher than at the spray plume borders. At later points in time the cooling is quite low at this measurement location. The multi-component fuel '3K', in contrary, presents ambient gas cooling of up to 100 K. The boiling point of the high boiling point fraction n-decane is simply not reached and thus limits the evaporation rate. Thus, even 8  $\mu$ s after vSOI a cooling can be measured.



**Figure 4.** Absolute spray vapor temperature distributions at a nozzle tip distance of 30 mm for various points in time for pure isooctane (left) and the 3-component fuel 3K (right) at 0.8 MPa / 473 K

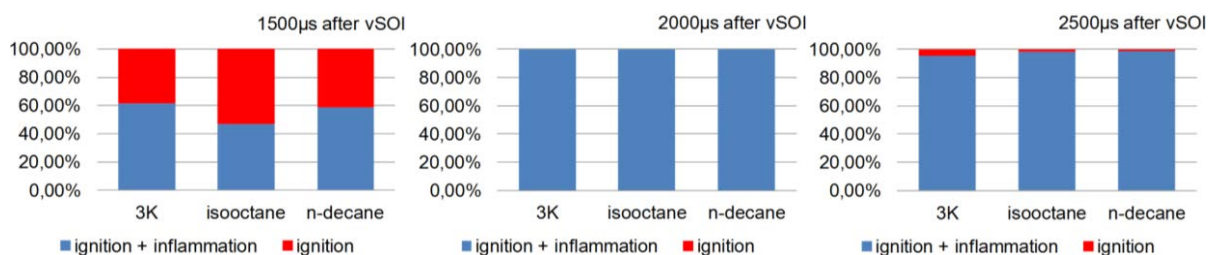
For higher gas pressure (0.8 MPa) at constant gas temperature (473 K) the boiling points of all fuels are reduced (figure 4). Figure 4 thus shows that for '3K' the calculated temperature distribution cannot be determined in the region around the spray axis due to liquid fuel at 2.5 ms and 3.0 ms for '3K'. Isooctane evaporates quite well and presents high evaporation rates. At 8 ms after vSOI the vapor cloud already passed the measurement line. If the gas temperature is increased to 673 K fast evaporation can be assumed. This is confirmed by the PLIF measurements. Figure 5 thus shows a very fast evaporation for the single component isooctane in case of OP#3. The cooling of  $\sim 50$  K at 2.5 ms after vSOI is lower compared to the other boundary condition sets due to the entrainment of hot ambient gas. Already 0.5 ms later, at 4.0 ms after vSOI, the vapor temperature is found to strongly decrease for isooctane. For '3K' the vapor temperature is lower at this time point due to the delayed evaporation. Thus, it can be stated that at very high boundary conditions, high boiling point fractions strongly limit the evaporation even if their content in a multi-component fuel is low. The slowest evaporating component is found to have a high influence on the overall evaporation rate of the mixture.



**Figure 5.** Absolute spray vapor temperature distributions at a nozzle tip distance of 30 mm for various points in time for pure isooctane (left) and the 3-component fuel 3K (right) at 0.8 MPa / 673 K

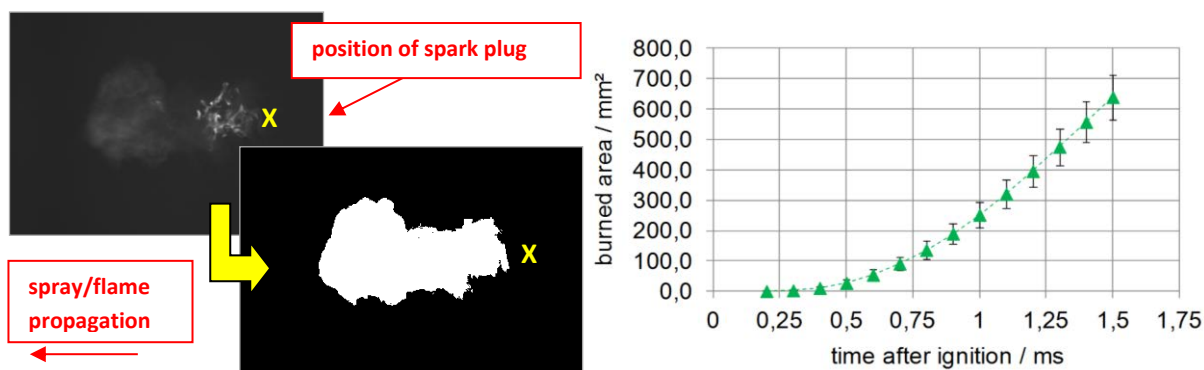
The boundary condition set with the highest pressure and temperature (OP#3, 0.8 MPa / 673 K) was found to present the highest evaporation rate due to strong air-fuel mixing potential. Thus, the inflammation measurements will be operated at OP#3 boundary conditions. In the following the high-speed chemiluminescence setup presented in figure 2 is used in order to characterize the inflammation behavior of the same fuels.

One specific spray plume center (see figure 2, right) is analyzed in terms of occurring inflammation or misfire (spark  $\sim 50 \text{ mJ} = \text{const.}$ ). The red part of the bar plots in figure 6 show the probability of misfires, the blue ones successful inflammation and flame propagation. The ignition timing, early ignition (1,500  $\mu\text{s}$  after vSOI) to late ignition (2,500  $\mu\text{s}$  after vSOI), were investigated. The timings represent both limited (early timing) or enhanced evaporation and fuel-air mixing (late timing). For the earliest ignition point in time (ignition 1,500  $\mu\text{s}$  after vSOI) isooctane shows the highest number of misfires with more than 50% of 100 spray ignitions. The high boiling point component n-decane (RON = -46) shows a higher ignition probability. '3K' is found to show the same misfire tendency like n-decane. For later ignition points in time the misfire tendency strongly decreases and slightly starts again at 2,500  $\mu\text{s}$  after vSOI.



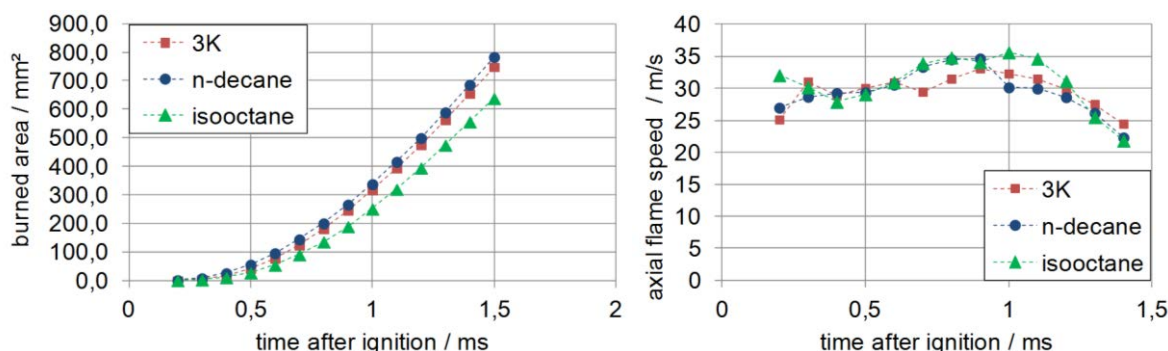
**Figure 6.** Misfire comparison for '3K' and single fuels, ignition timing 1,500  $\mu\text{s}$  – 2,500  $\mu\text{s}$  after vSOI

Figure 7 (right) presents a flame single shot image of one exemplarily point in time with corresponding binary image. The binary images are averaged over all successful inflammation series for all points in time. The inflammation and flame propagation of the high-speed images with a time delay of 100  $\mu\text{s}$  between two time steps are evaluated with respect to burned area (i.e. flame area) over time. The investigated burned area increases with time whereby the maximum values and slopes in the diagrams differ for variable fuels. In order to estimate the statistical reliability figure 7 presents exemplarily assessed mean value deviation of the burned area in the line of sight images at an ignition timing of 1,500  $\mu\text{s}$  after vSOI and thus very high burned area images. Images with misfire are not considered. The deviation increases with time after ignition and thus progressed flame. The calculated highest mean value deviation is below 10%. For readability reasons the deviations are neglected in the following as various samples did not show higher deviations.



**Figure 7.** Exemplarily flame image with corresponding binary evaluated image (left) and exemplary plot of burned area over time with assessed mean value deviation, ignition timing 1,500  $\mu$ s after vSOI (left) and

The flame growth and axial flame speed for the first ignition point in time (1,500  $\mu$ s after vSOI) for '3K', isooctane and n-decane is presented in figure 8. As it was already the case for the misfire comparison, pure n-decane and '3K' present similar combustion behavior indicated by almost equal burned area over. Isooctane which is the main component of '3K' shows a slower flame spread. This behavior can be explained by the laminar burning velocity which is lower for isooctane than for the remaining fuels. Isooctane thus shows an inflammation delay of  $\sim 100$   $\mu$ s. Isooctane with cross-shaped molecule structure is harder to crack and thus presents a limited reactivity. However, the estimated axial flame speed (figure 8, right) for this early ignition timing mode is similar for all fuels due to the turbulent spray environment. The droplet / gas velocity measured by phase Doppler anemometry is about  $\sim 5$ -10 m/s and in contrary to the droplet sizes quite similar for all fuels of this work [14].



**Figure 8.** Inflammation and flame propagation for 3K and single fuel, burned area (left) and axial velocity (right), ignition timing for both diagrams = 1,500  $\mu$ s after vSOI

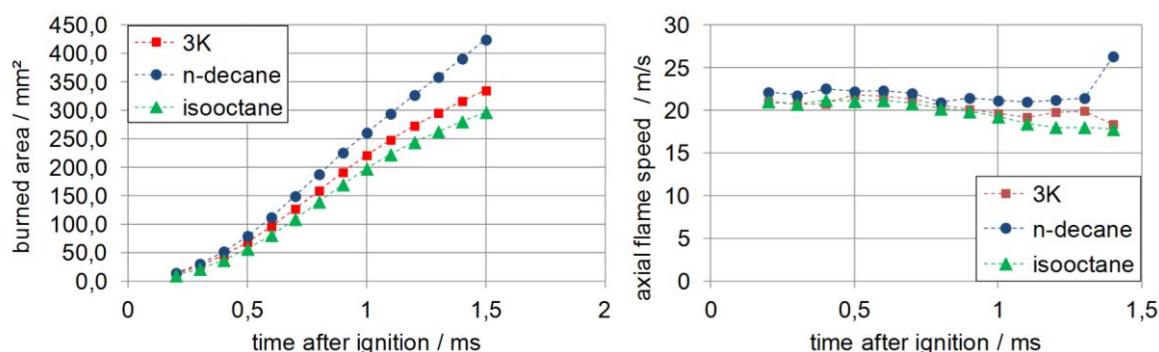


**Figure 9.** Inflammation and flame propagation for 3K and single fuels, burned area (left) and axial velocity (right), ignition timing for both diagrams = 2,000  $\mu$ s after vSO

For later ignition time points the temporal behavior of the burned areas over time as well as the axial flame propagation separate. N-decane owing the lowest RON and the highest laminar burning velocity value burns

faster than the other fuels (figures 9-10) even though the evaporation is limited and partially a diffusion flame can be detected.

For OP#3 (0.8 MPa / 673 K) the gas cooling of '3K' was higher than for isooctane at later time points due to the low evaporation rate. It can be assumed that for pure n-decane this would have been the case, too. Thus, it can be stated that the gas cooling temperature does further limit the evaporation and determines the momentum of successive droplets in the spray as well as the flame velocity. At late ignition timings the droplet and vapor velocity is quite low for this operating point [14]. The later the ignition takes place, the more the fuels separate in terms of flame growth and the slower the axial flame propagates in spray injection direction. Local vapor detachments limit the maximal flame size and thus heat release in this injection chamber environment.

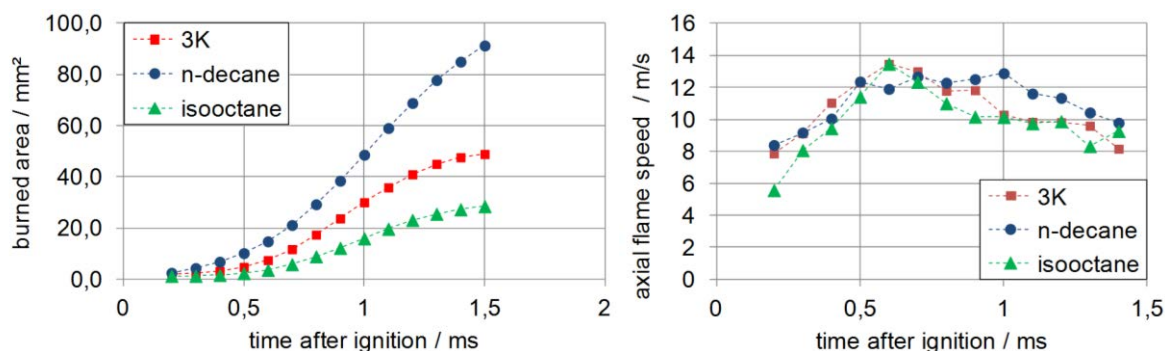


**Figure 10.** Inflammation and flame propagation for 3K and single fuels, burned area (left) and axial velocity (right), ignition timing for both diagrams = 2,500 μs after vSOI

## Conclusions

In this study a variety of single- and multi-component fuels was analyzed by planar Laser-induced fluorescence imaging and high-speed flame luminescence to identify the most significant effects on the evaporation and inflammation behavior and links between the phenomena. The inflammation measurements of some selected fuels were compared to local spray vapor measurements. Depending on the boundary conditions the high-boiling point component influenced the complete spray evaporation of the multi-component fuel. Only for very high boundary conditions the evaporation rate is high enough for generating well-premixed conditions. Depending on the ignition timing – early ignition (1,500 μs after vSOI) to late ignition (2,500 μs after vSOI) – and thus limited or enhanced fuel-air mixing and evaporation rate, different inflammation behavior are found for the analyzed fuels and mixtures. The later the ignition takes place, the more the inflammation behavior differs for the tested fuels. The results show that fuel properties are more important than the RON number. The flame growth after ignition depends also on the fuel's ignition delay and the laminar burning velocity even though different evaporation rates are found to be present before the ignition. With this example it can be seen that the inflammation behavior for modern engines using complex fuels and fuel mixtures cannot be described with one single number as different physiochemical properties and boundary conditions dominate the spray inflammation and combustion behavior. General links between the complex spray evaporation and inflammation behavior which are valid for all fuels could not be observed. The data is applicable for spray combustion model development and validation within CFD. As a next step, further 2D measurements investigating the radical distribution of the fuels are in preparation.

## Acknowledgements

This work and setup was supported by the Bavarian Research Foundation (BFS) in the framework of the project 'AZ-932-10: WiDiKO'. We also like to thank Dr. Oliver Hausner, Dr. Sebastian Grasreiner and Lukas Schäfer (BMW Group Munich) as well as Prof. Dr. Christian Hasse and Peter Keller (TU Freiberg) for the technical support and cooperation within this project and our colleague Johannes Trost for the development of the PLIF setup and evaluation support. Furthermore, the authors gratefully acknowledge the financial support for parts of this work from the Erlangen Graduate School in Advanced Optical Technologies (SAOT) within the framework of the German Excellence Initiative by the German Research Foundation (DFG).

## References

- [1] [1] Knorsch, T., Zigan, L., Trost, J., Wensing, M. and Leipertz, A., Biofuel Droplet Evaporation Rate of a DISI Spray by Laser-induced Fluorescence and Phase Doppler Anemometry, 12<sup>th</sup> Triennial Int. Conference on Liquid Atomization and Spray Systems (ICLASS), Heidelberg, Germany, September 2-6, 2012.
- [2] [2] Knorsch, T., Trost, J., Zigan, L., Wensing, M., and Leipertz, A. Quantitative DISI Spray Vapor Temperature
- [3] Study for Different Biofuels by Two-Line Excitation Laser-Induced Fluorescence, SAE Technical Paper 2012-01-1658, 2012, doi:10.4271/2012-01-1658.
- [4] [3] Zigan, L., Schmitz, I., Flügel, A., Knorsch, T., Wensing, M., and Leipertz, A., Energy Fuels 24: 4341-4350, 2010.
- [5] [4] Sick, V., Schulz, C., Tracer-LIF diagnostics: quantitative measurement of fuel concentration, temperature and fuel/air ratio in practical combustion systems, Progress in Energy and Comb. Science 31 (2005) 75-121.
- [6] [5] Trost, J., Zigan, L., Leipertz, A., Quantitative vapor temperature imaging in DISI-sprays at elevated pressures and temperatures using two-line excitation laser-induced fluorescence, Proceedings of the Combustion Institute Volume 34, Issue 2, 2013, Pages 3645-3652.
- [7] [6] Zigan, L., Schmitz, I., Flügel, A., Wensing, M., and Leipertz, A., Fuel 90: 348-363, 2011.
- [8] [7] Makino, A., and Law, C.K., Combust. Flame 73-3: 331-336, 1988.
- [9] [8] Zigan, L., Ammon, M., Gupta, V., Wensing, M., and Leipertz, A., SAE Int. J. Fuels Lubr. 5-1: 254-264, 2012.
- [10] [9] Heldmann, M., Knorsch, T., Wensing, M., Investigation of Fuel Atomization and Evaporation of a DISI Injector Spray Under Homogeneous Charge Conditions, SAE Int. J. Engines 6(2):2013.
- [11] [10] Institut für Arbeitsschutz der Deutschen Gesetzlichen Unfallversicherung: GESTIS-Stoffdatenbank. website: <http://gestis.itrust.de>, Sept. 2011.
- [12] [11] Bronkhorst High-Tech B.V.: FLUIDAT on the web. website: <http://www.fluidat.com>, pageview 12/19/2011
- [13] [12] VDI, Gesellschaft Verfahrenstechnik und Chemieingenieurwesen, Wärmeatlas, 10<sup>th</sup> edition, Springer Verlag Berlin Heidelberg, 2006.
- [14] [13] Knorsch, T., Heldmann, M., Zigan, L., Wensing, M., and Leipertz, A., On the role of physiochemical properties on evaporation behavior of DISI biofuel sprays, Exp. Fluids (2013):54-1522, 2013.
- [15] [14] Knorsch, T., Heldmann, M., Hagedorn, T., Wensing, M., and Leipertz, A., Influence of Key Biofuels on the DISI Spray Evaporation Rate by Phase Doppler Anemometry, 16<sup>th</sup> Int. Symposium on Applications of Laser Techniques to Fluid Mechanics, 9-12.07.2012, Lisbon, Portugal, 2012.

## Tomographical Reconstruction of the Radial Fuel Distribution of a DISI Gasoline Spray using Mie-Scattering and Laser Induced Fluorescence

M. Heldmann<sup>1,2</sup>, S. Fuchs<sup>1</sup> and M. Wensing<sup>1,2</sup>

1: Dept. Engineering Thermodynamics (LTT), FAU Erlangen-Nuremberg, Germany

2: Erlangen Graduate School in Advanced Optical Technologies (SAOT), FAU Erlangen-Nuremberg, Germany

### Abstract

In the first part of this work a tomographical reconstruction of a spray plume of a three hole DISI injector was done using averaged lightsheet illumination images. Therefore the spray was scanned by the laser lightsheet at different distances parallel to the injector axis. The measurement signal – on the one hand the Mie-scattering signal of scattered light, on the other hand the laser induced fluorescence signal (LIF signal) of the dye Rhodamine 6G, which was added to the used fuel ethanol – was detected by two cameras in order to get information about the extinction effects in the spray mostly resulting from multiple scattering. The cameras were placed in an angle of 180 degrees.

By a post-processing algorithm developed in MATLAB® it was possible to conclude to an averaged three dimensional model of the spray plume. Thus it was also possible to get information of the radial fuel distribution (perpendicular to the injector axis) of the spray plume.

The radial fuel distribution in sprays is often determined by laser lightsheet illumination perpendicular to the injector axis. Especially in dense sprays this method is affected by extinction effects due to multiple scattering.

The second part of this work shows these extinction effects in a dense region of the spray plume (distance to nozzle tip: 12.5mm) for a lightsheet illumination perpendicular to the injector axis.

Comparing the two methods for the detection of the radial fuel distribution a clear advantage for the tomographical reconstruction method, which is less affected by extinction effects, is worked out in this paper. Furthermore it is possible to compensate parts of the extinction effects using a two camera setup.

---

### Introduction

The global spray structure of multi-hole injectors is often investigated by shadowgraphy or Mie-scattering. Using these imaging techniques it is often impossible to give information about single spray plumes or give three dimensional information of the spray. Therefore for shadowgraphy imaging the object is investigated by different angles of observation. Based on the results of the investigations and with complex mathematical post-processing it is possible to conclude to a three dimensional structure. This technique is often used by the visualisation of three dimensional flows (tomographic particle image velocimetry) [1, 2], but was also used for spray visualisation [3]. In high dense sprays this method fails because of high signal extinction, especially for information about the radial intensity distribution of the spray. In order to handle this problem, e.g. time resolved X-ray tomography is used for investigation [4, 5].

The radial fuel distribution in sprays is often determined by laser lightsheet illumination perpendicular to the injector axis. Especially in dense sprays this method is affected by extinction effects due to multiple scattering.

In a first part of this work one spray plume of a 3-hole DISI injector was investigated by lightsheet illumination at different distances parallel to the spray axis. The measurement signal of the liquid spray (Mie-Scattering and Laser Induced Fluorescence) was used to collect the three dimensional information for a three-dimensional reconstruction of the spray plume. Therefore it is also possible to conclude to a radial fuel or even a three-dimensional fuel distribution using a tomographical post-processing algorithm. The advantage of this method is the possibility to compensate a part of the extinction effects – especially in dense sprays – by using a two camera setup.

The second part of this work deals with the comparison of the radial fuel distribution – on the one hand the fuel distribution evaluated from the tomographical post-processing algorithm, on the other hand results from the lightsheet illumination perpendicular to the injector axis.

### Experimental setup

In the first measurement setup one spray plume of a solenoid driven three-hole injector for gasoline injection – mounted in an optical accessible pressure chamber – was investigated using Mie-scattering and Laser



Induced Fluorescence. Therefore the spray plume was illuminated parallel to the spray axis at different measurement layers by a laser lightsheet (height: about 80mm / width: about 0.5mm), which was formed by telescope lenses out of the laser beam of a frequency doubled pulsed Nd:YAG laser (wave length: 532nm / pulse width: about 10ns).

In order not to affect the sensitive lightsheet setup, not the lightsheet, but the pressure chamber was moved. Therefore the pressure chamber was set on a traverse system with a high accuracy to adjust the distance between the lightsheet and the spray plume centre. The scanning of the spray was done in steps of 1mm.

In a first experiment using this setup the Mie-scattering signal of the injected liquid fuel (ethanol) was detected, in a second one the fluorescence signal of the dye Rhodamine 6G (absorption peak at about 530nm), which was added to ethanol (10mg Rhodamine/ 1.5 liter ethanol). The measurement signal was detected from two sides (compare Figure 1a) in order to get information about the signal extinction inside the spray plume, which results for example from multiple-scattering and absorption due to Beer-Lambert law.

In order to block the Mie-Scattering signal for the detection of the fluorescence a RazerEdge long pass filter was put in front of each camera. These filters have a very steep edge and block the elastic Mie-Scattering signal with an optical density of seven. For both experiments the signal was detected simultaneously from two sides perpendicular to the illumination with two CCD-cameras (PCO SensiCam) in order to get information about the extinction of the signal perpendicular to the spray axis for further post-processing (compare Figure 1).

With a tomography post processing algorithm, developed in MATLAB®, it was possible to calculate a three dimensional, averaged model, which was calculated out of 32 single shot images in each of about 15 scanning layers. This way it is possible to extract information about the radial fuel distribution.

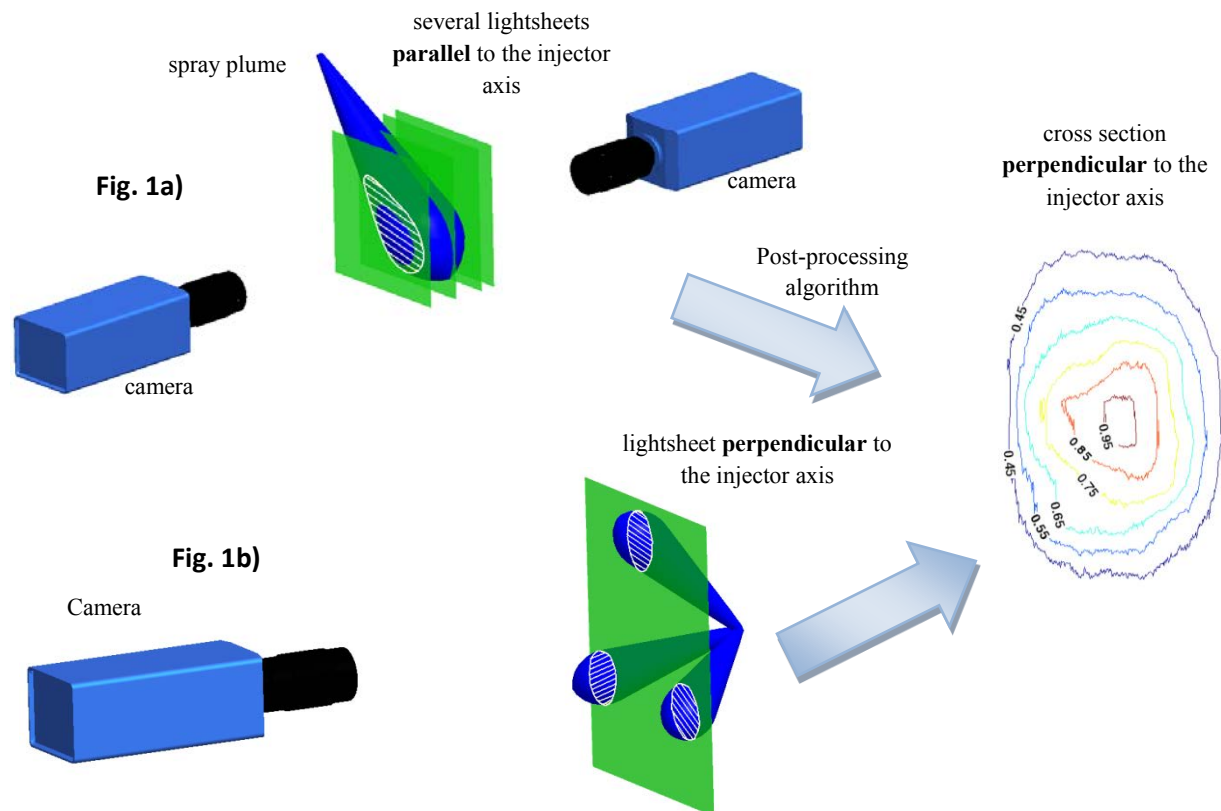


**Figure 1.** Experimental setup for the tomographical reconstruction of the radial fuel distribution: signal detection from two sides for lightsheet illumination parallel to the injector axis (*top*); experimental setup for lightsheet illumination perpendicular to the injector axis to get information about the radial fuel distribution (*bottom*)

In a second measurement setup (compare Figure 1b) the spray plume was illuminated by the laser lightsheet perpendicular to the injector axis in order to directly get information about the radial fuel distribution.

The ambient condition in the pressure chamber was set to a pressure of 0.1MPa and a temperature of 298K. The injection pressure of the fuel (temperature of 298K) was set to 15MPa.



## Results and Discussion

In a first step the post-processing of the axial laser lightsheet measurements (compare Figure 1a) is demonstrated in order to conclude to a three dimensional, averaged reconstruction of the spray investigated plume. Afterwards the results of the tomographical reconstruction of one radial cross-section of the investigated spray plume are compared to the measurements with laser lightsheet illumination perpendicular to the injector axis (compare Fig. 1b).

### *Post-processing the detected images (measurement setup Fig. 1a)*

In order to get information about the signal extinction as a function of radial distance to the spray axis, a region of interest was chosen at the broadest spray section. In a second step the intensity ratio of the associated images of the two cameras were calculated out of the ratio of the summed gray scale values detected in a region of interest. In Figure 2a the intensity ratios are plotted as a function of radial distance calculated out of the 32 image pairs of 32 injections. The region of interest was set in an image section (height: about 5mm / width: about 10mm) indicated with the red rectangle in Figure 2b in the region of maximal spray expansion. The detected intensity ratio can be approximated with a linear function, whereupon the coefficient of determination  $R^2$  was calculated to 0.982.

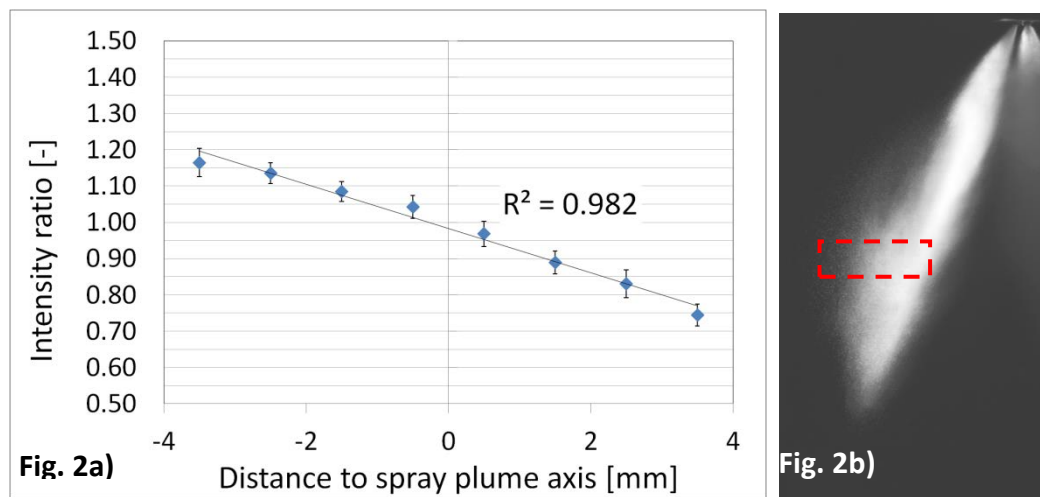


**Figure 2.** Intensity Ratio (Figure 2a) of the detected gray scale values in the particular image section (indicated with a red rectangle in Fig. 2b; position: maximal spray expansion / height: about 5mm / width: about 10mm) of the images taken from the two cameras

With the knowledge of a linear extinction function, the average images of the illuminated spray in each distance to the spray axis was calculated out of average images of the two cameras. For five different spray sections the averaged images are shown in Figure 3 for an injection pressure of 15MPa and an ambient pressure of 0.1MPa in a false color style.

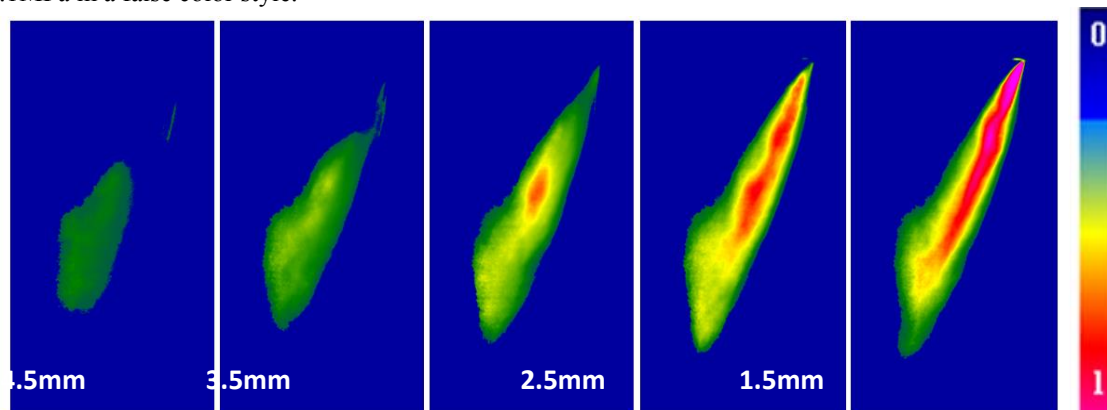


**Figure 3.** Averaged lightsheet illumination images of the spray plume of the investigated injector parallel to the injector axis in different distances (4.5mm – 0.5mm) to the spray plume center;

Out of the averaged images shown in Figure 3 a three dimensional model of the spray plume was calculated for an observation time of 800 $\mu$ s after visible start of injection (vSOI), whereby the total activation time of the injector was set to 1500 $\mu$ s. Therefore the two-dimensional spray information shown in the images in Figure 3 are put in a three-dimensional matrix. Subsequently the fuel distribution between the respective layers was reconstructed using a linear interpolation algorithm.

In Figure 4 the reconstructed three-dimensional model is indicated with the illustration of the calculated radial fuel distribution, whereby every cross section was normalized. The normalization was necessary because of the intensity profile of the laser along the axial laser lightsheet, which was not compensated yet.

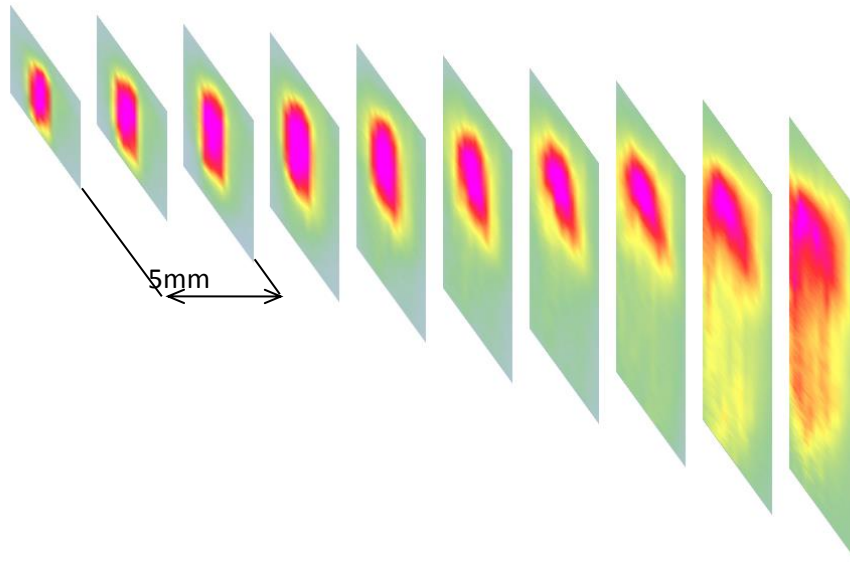


**Figure 4.** Tomographical reconstruction of the spray plume demonstrated with several radial cross sections of the spray plume (basis: LIF measurements);  
(parameter: injection pressure= 15MPa; images taken 800 $\mu$ s after vSOI; total activation time: 1500 $\mu$ s)

Comparison of the results of both measurement setups (Figure 1a / Figure 1b)

A reconstructed radial fuel distribution for an injection pressure of 15MPa is shown in Figure 5 for a distance to nozzle tip of 12.5mm. The observation time was chosen to 800 $\mu$ s by a total activation time of 1500 $\mu$ s. In the left part of the figure 5 the fuel distribution was reconstructed by the LIF measurements, in the right part by the Mie-scattering measurements. Comparing the results for the two measurement techniques, it can be observed, that the intensity profile of the LIF-signal through the cross section of the spray is steeper than the MIE-scattering signal, especially in the centre of the spray plume.

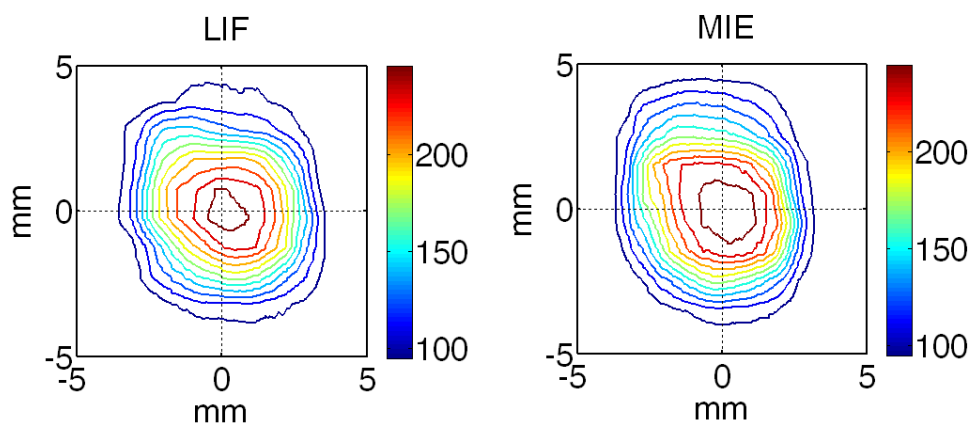


**Figure 5.** Reconstruction of the radial fuel distribution with LIF (left) and Mie-Scattering (right) in a distance of 12.5mm tip perpendicular to the injector axis (compare measurement setup in Figure 1a)  
(parameter: injection pressure= 15MPa; images taken 800 $\mu$ s after vSOI; total activation time: 1500 $\mu$ s)

In Figure 6 averaged images of 32 single shot Mie-scattering images are shown, which were detected with the radial lightsheet setup (compare Figure 1b), for four different points in time (225 $\mu$ s – 700 $\mu$ s) after visible start of injection. At 250 $\mu$ s after vSOI, when the spray has just fully developed in this investigated cross section of 12.5mm distance to nozzle tip, first extinction effects can be realized.

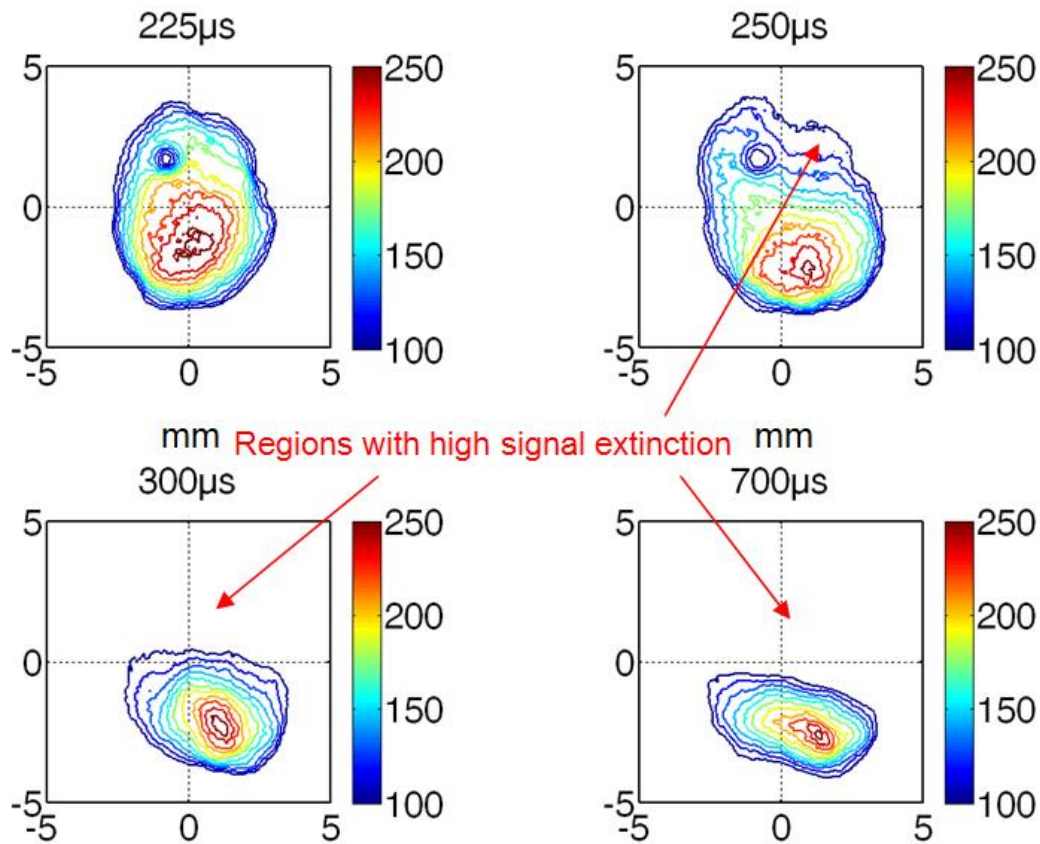


**Figure 6.** Intensity profiles of the cross section of the investigated spray plume illuminated by a laser lightsheet perpendicular to the injector axis in a distance of 12.5mm to the nozzle tip (compare measurement setup in Figure 1b) (images taken from 225 $\mu$ s (top left) until 700 $\mu$ s (bottom right) after visible start of injection)

This extinction effects grow until at 700 $\mu$ s after vSOI most parts of the scattered light are absorbed by the spray, which already has penetrated further in the pressure chamber. Hence the detected Mie-scattering signal leads to a misinterpretation of the radial fuel distribution. The length of the optical pathway of the signal through dense spray varies a lot: On the one hand the length is a function of detection time, on the other hand a function of the location in the illuminated cross section of the spray plume. This makes it impossible to give quantitative or even qualitative information of the radial fuel distribution with the measurements setup in Figure 1b – especially in dense spray regions. Deposits at the chamber windows resulting from injected fuel, which influence the measurement results (compare top images in Figure 6), are another problem of this measurement setup. Comparing the results of the two presented measurement setups, it gets clear, that the location of the maximum intensity varies. The maximum intensities in Figure 6 are obviously shifted to the lower edge of the spray plume. In Figure 7 a sketch of different paths of scattered light in a spray plume gives an explanation for the observed extinction phenomenon. Looking at the two light paths a and b, which represent the way of the measurement signal to the camera, the different path length through spray, gets clear for two different locations in a spray plume. The extinction effects for path a is more pronounced due to the longer path length through spray.

Furthermore light path c shows clearly on the one hand – in a comparison to path a and b – the influence of the orientation of the spray plume and on the other hand the dependency of penetration depth on the length of the measurement signal through spray.

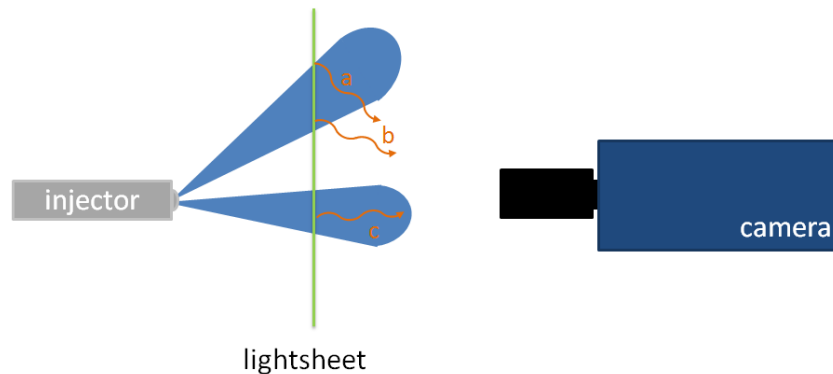


**Figure 7.** Sketch of the path of the scattered light through spray for different locations in a spray plume (compare path a and b) and for two different orientations of the spray plume (compare path a and c )

## Conclusions

A tomographical method was applied for the reconstruction of the three dimensional information of the fuel distribution in a spray plume of a three hole gasoline injector. Therefore it was also possible to conclude to the radial fuel distribution in the investigated spray plume. The obtained results describe the fuel distribution in a much better way compared to the commonly used illumination technique, like it was shown in the second measurements setup. A detection of the measurement signal from two sides makes it possible to give information about extinction in the spray and to correct a part of the effect.

For future work the scanning of a complete gasoline spray is planned. Furthermore investigations which consider and compensate the laser intensity profile along the cross section of the lightsheet are planned.

## Acknowledgements

The author gratefully acknowledges the financial support for parts of his work from the Erlangen Graduate School in Advanced Optical Technologies (SAOT) within the framework of the German Excellence Initiative by the German Research Foundation (DFG). Additionally, this work and setup was supported by the Bavarian Research Foundation (BFS) in the framework of the project 'AZ-1004-11: Twin-Jet'.

## References

- [1] Cao, L., Pan, G., de Jong, J., Woodward, S., Meng, H., "Hybrid digital holographic imaging system for three-dimensional dense particle field measurement, *Applied Optics*: Vol. 47, Issue 25, pp. 4501-4508 (2008)
- [2] Pu, Y., Meng, H., "Four-dimensional dynamic flow measurements by holographic particle image velocimetry", *Applied Optics*: Vol. 44, Issue 36, pp. 7697-7708 (2005)
- [3] Klinner, J., Willert, C., "Tomographic shadowgraphy for spray diagnostics", *24th ILASS- Europe 2011, Estoril, Portugal*
- [4] Meyer, T. R., Schmidt, J. B., Nelson, S. M., Drake, J. B., Janvrin, D. M., Heindel, T. J., "Three-Dimensional Spray Visualization using X-ray Computed Tomography", *21st ILASS Americas 2008, Orlando, Florida*
- [5] Kastengren, A. L., Powell, C. F., Arms, D., Dufresne, E. M., Wang, J., "Spray Diagnostics at the Advanced Photon Source 7-BM Beamline", *22nd ILASS Americas 2010, Cincinnati, Ohio*

## High-speed imaging of the sooting combustion of ethanol-gasoline blended fuel sprays under DISI cold start conditions

Michael Storch, Tobias Knorsch, Lars Zigan, Michael Wensing, Stefan Will

Lehrstuhl für Technische Thermodynamik and Erlangen Graduate School in Advanced Optical Technologies, Universität Erlangen-Nürnberg, Germany

### Abstract

The paper presents a spray combustion investigation within an optically accessible high temperature/ high pressure injection chamber at cold start, stratified engine operation conditions. The study focuses on the influence of ignition time variation on the combustion process. Therefore, three different ignition timings were analysed. The combustion behaviour of E20 and E85 sprays is studied by high-speed visualization. An image stereoscope setup was applied in order to visualize the combustion process in two different wavelength regions simultaneously. The temporal resolution of the measurement technique allows to analyse the combustion event and to identify premixed and non-premixed combustion regions. The results can be used to better understand the influence of ignition timing on soot formation and oxidation processes of ethanol blended fuels inside a DISI engine.

---

### Introduction

The use of biofuels in automotive engines may form an essential contribution for the reduction of CO<sub>2</sub>-emission. Especially for spark-ignition (SI) engines, ethanol is well established fuel, which is commonly used in European gasoline blends. Considering engine exhaust emission, soot formation is much more complex in modern direct-injection spark-ignition (DISI) IC engines compared to conventional port fuel injection, particularly when using biofuels. Besides this, it is important to note that the particulate matter emission limit for vehicles will become more stringent within the European emission standard (EURO6) in 2014. The formation of soot must be addressed in this context.

In common DISI engines, different sources for particulate matter (PM) and soot emission are known. Typical origins are fuel films and pool fires [1] which are ascribed to piston and wall wetting events. Especially in the stratified operation mode local fuel rich mixture zones are important for soot formation [2]. Furthermore, engine operation at cold start and warm up phase is a major source for increased PM emissions [3]. Besides this, the fuel composition may have an important impact on soot and PM emission, especially when using ethanol blended fuels.

Previous research studies have yielded contradictory results regarding the use of ethanol blended gasoline fuels for IC engine applications. Some report increasing [4] and others report decreasing [5] particulate matter emissions for higher ethanol contents. Ethanol has high enthalpy of evaporation, which increases engine charge cooling effects. This gives a potential for higher engine compression ratios. However, due to the liquid fuel injection process, insufficient atomization and evaporation can lead to mixture inhomogeneities [4] i.e., locally rich fuel-air mixture regions, which may alter the ignitability as well as the combustion effectiveness. Especially at cold start conditions the impact of these effects is even more significant.

Recent publications [6, 7] deal with stratified charge combustion of E85 in an optically accessible DISI engine. By optimization of the injection and ignition timing an ultra-low emission of NO and soot was achieved using E85. In this study, both the combustion efficiency as well as combustion stability remained relatively high. The results indicate that the injection timing and the ambient conditions during the compression stroke are mainly determining the spray behavior, mixture formation and pollutant emission. However, the underlying mechanisms are not fully understood, and further fundamental research is necessary.

In this study the variation of the ignition time of E85 and E20 blended fuels is analyzed inside a high-pressure, high-temperature spray chamber under cold start stratified engine conditions. The alignment represents a spray-guided combustion concept where the spark plug is mounted close to the injection valve. The chamber setup allows spray formation which is not influenced by additional charge motion and turbulence. Compared to an engine, in the injection chamber the spray combustion is studied at simplified conditions allowing a deeper insight into sub-processes. The use of the high-speed imaging technique allows resolving the complete cycle of the combustion process and therefore, the sources of soot formation can be identified.

An insufficient mixing of fuel and surrounding air leads to a diffusion flame. For hydrocarbon combustion the diffusion flame is characterized by an intensive yellow, orange visible radiation produced by soot particles. In contrast a blue flame luminescence indicates a more premixed combustion [8]. In this study the high-speed camera is equipped with an image stereoscope which contains an optical longpass and an optical shortpass filter (filter cut-off wavelength at 525 nm) allowing a simultaneous visualization of these two flame types. The

premixed region is identified by the shortpass filter and a diffusion flame region by the longpass filter. Thus, sooting combustion can be visualized.

### Experimental setup

In this work an optical accessible high temperature, high pressure injection chamber equipped with a spark ignition system was used. The chamber was operated at a pressure of 0.8 MPa and at a temperature of 473 K. This operation condition represents a typical direct injection engine condition at stratified operation [9]. Figure 1 (left) shows the experimental set-up.

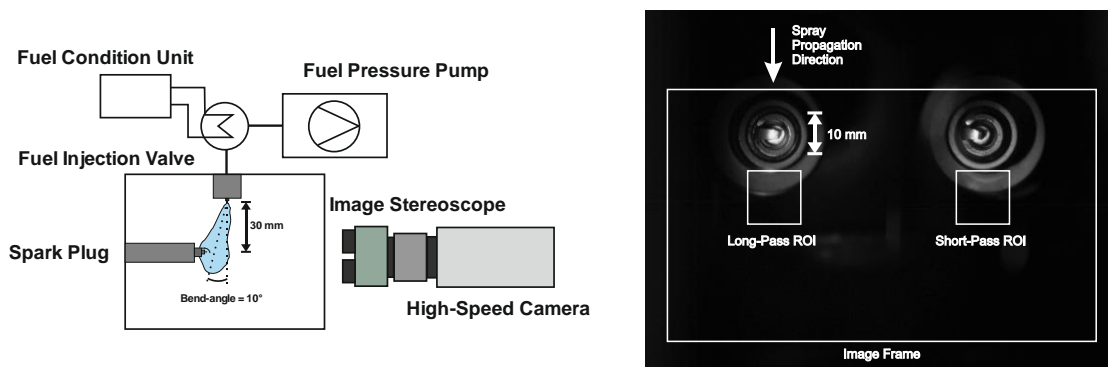


**Figure 1.** Left: Experimental setup of the spray chamber with high-speed stereoscope imaging system. Right: Exemplary image without injection using the stereoscope and two different filters. The injection valve is located outside visible area. The spray formation is from the top of the image towards the spark plug.

The spark plug was placed perpendicular to the fuel injection valve. The distance in between the injection valve and the spark plug was 30 mm. A BOSCH multihole injector (HDEV 5) was used with a bend-angle of 10°. For all the experiments the injection time of 1 ms was kept constant. The fuel pressure for this experiment was set to 15 MPa. The fuel pipes and the valve mounting were pre-conditioned at a mean fuel temperature of 266 K. This condition represents a cold start engine operating point [10]. The fuel blends used in this study were E85 (85vol% of ethanol in isooctane) and E20 (20vol% of ethanol in isooctane). The spark ignition system consisted of a spark plug with a single side electrode and an ignition power amplifier. For this experiment the spark duration was held constant at 1 ms. Ignition timing was varied between 1.4 ms, 1.6 ms and 1.8 ms after visible start of injection (VSOI).

For combustion luminosity imaging a high-speed camera (Vision Research Phantom v711), equipped with a Nikon 24 – 85 mm lens (f/2.8), was used. The camera was driven at a constant frequency of 10 kHz. In front of the camera an image stereoscope, with a set of two different optical filters was mounted. The first filter was a shortpass filter (525 nm cut-off wavelength) which was used to detect the main flame chemiluminescence species which are OH\*, CH\*, C<sub>2</sub>. These species are good indicators for the heat release rate in a premixed flame [11]. The second stereoscope filter was a longpass filter (525 nm cut-off wavelength). It was used in order to investigate the black body radiation originating from a sooting combustion [8]. An exemplary stereoscope image without injection is shown in Figure 1 (right). The ROI frames (Region Of Interest) display the area where the spatial average of the pixel intensity was calculated. Thus, a comparison of the two stereoscope channels (longpass, shortpass) can be performed.

Additionally, a shadowgraphy setup was used in order to perform a highly resolved spray formation analysis. For back illumination of the spray the left flange of the chamber containing the ignition unit is substituted by a continuous light source. This setup modification allows imaging of the spray formation at the same condition as it was in the combustion experiment. Here the high-speed camera was driven at 10 kHz, without the image stereoscope. For all experiments the image read-out and post processing was conducted by an inhouse MATLAB<sup>®</sup> code. At each operating point several cycles were taken and averaged later on. Misfire cycles were sorted out.

### Results and Discussion

First, the spray formation behaviour is illustrated by a typical cycle of the spray injection of E85. Afterwards an averaged spray series applying shadowgraphy imaging is presented for a more detailed spray investigation. Finally, a comparison of E20 and E85 spray combustion using the stereoscope setup is shown.



Figure 2 shows an exemplary high-speed series of an injection event for an E85 spray at 1.4 ms, 1.6 ms and 1.8 ms after VSOI. These three time points represent the three different ignition timings. The location of the spark plug is marked by the white circle.

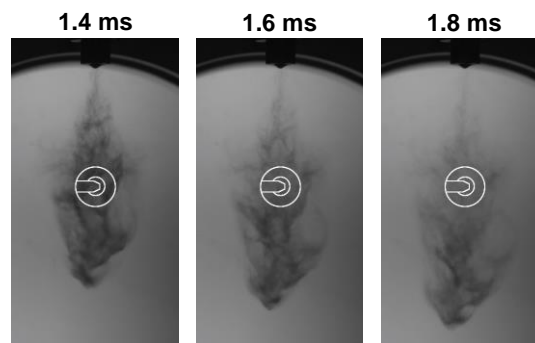


**Figure 2.** Single shot series of E85 spray formation at three different timings after VSOI, Spark plug is marked by white circle.

The fuel spray appears to be rather compact and no single jet generated by the 7-hole injector can be distinguished. This is because of an interaction of the different spray plumes at the beginning of the injection process due to the small spray cone angle. Dense spray regions indicate the inhomogeneous fuel distribution around the spark plug at all three ignition timings. At 1.4 ms after VSOI the highest liquid fuel concentration is centred at the spark plug. At 1.6 ms after VSOI a reduced liquid fuel concentration appears in the spark plug region. This is because of the axial and radial spray propagation as well as the enhanced evaporation and air entrainment. At 1.8 ms after VSOI, the main spray cloud passed the spark plug and the spray tail is positioned in the ignition region.

Besides the single shot images a series of averaged spray images is presented in Figure 3 for E20 and E85 at each of the three ignition times.

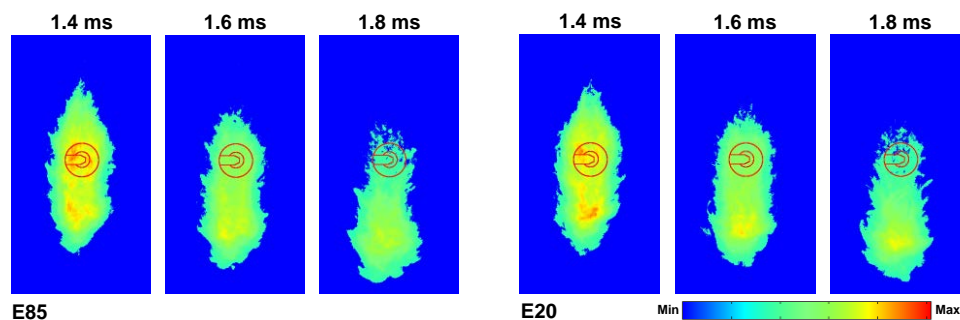


**Figure 3.** Averaged shadowgraphy images of E85 and E20 fuel spray at 1.4 ms, 1.6 ms and 1.8 ms after VSOI, Spark plug is marked by red circle; colours show minimum and maximum light attenuation.

The results show that still liquid fuel is positioned around the spark plug for all three ignition points in time and for both fuels. The spray shape is very similar for both fuels, but the signal intensity at the spray front is slightly higher for E20 indicating a higher fuel concentration, due to slower evaporation. This may be attributed to the lower boiling point of ethanol (normal boiling point is 78°C) compared to that of isooctane (99.2°C) [12]. In the course of time the dense spray core is moving further away from the spark plug. In addition the light attenuation as well as the total spray area decrease with time indicating the progressing evaporation and mixing with air.

The following paragraph covers the high-speed combustion luminosity results of the spray combustion event. First a study of a single shot series was done. It compares the two ethanol blended fuels E85 and E20 at 3 different ignition times. In Figure 4 these results are displayed in false colours.



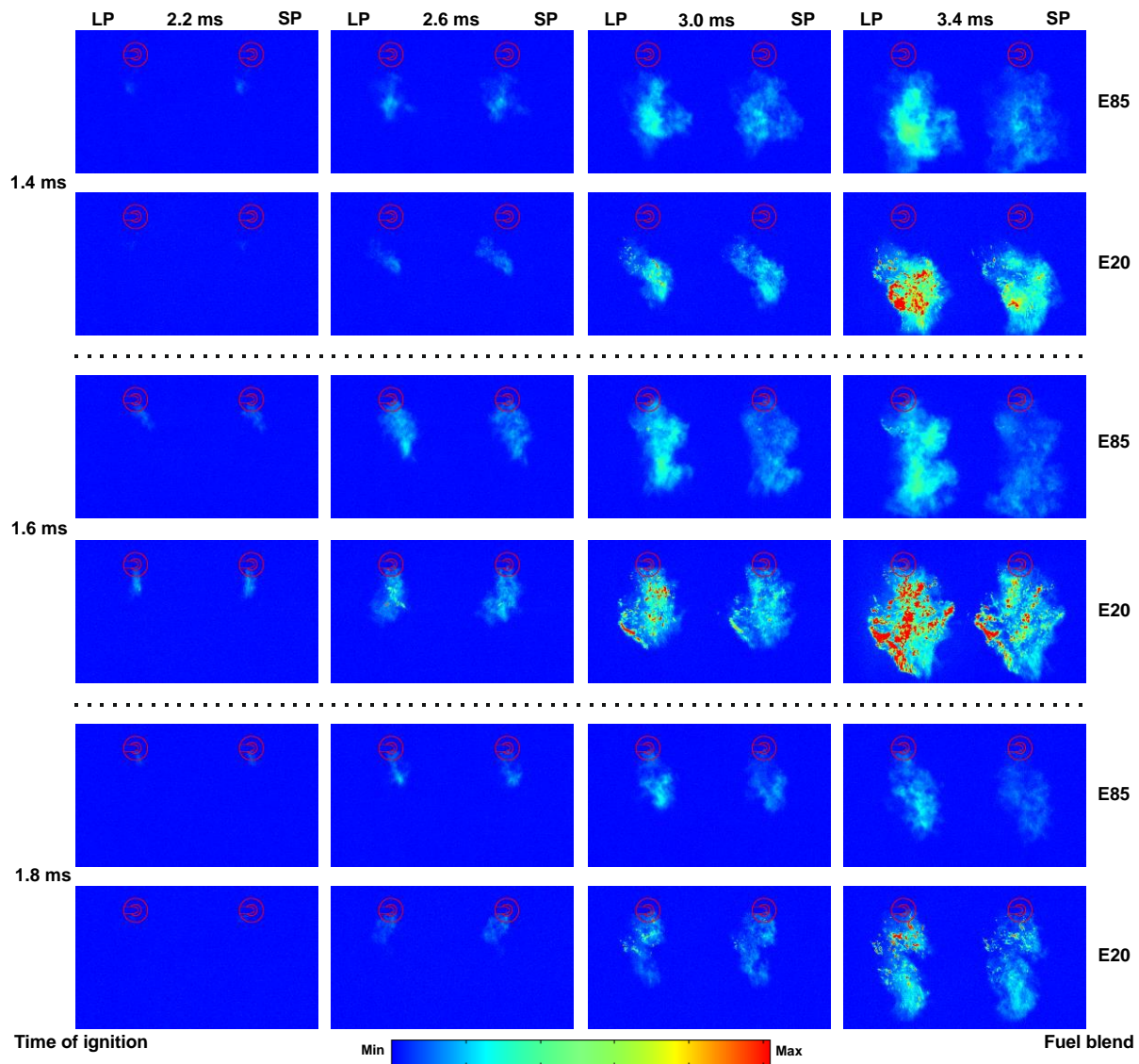


**Figure 4.** Representative single shot combustion luminosity series with stereoscope setup, comparing the two different fuels at 3 ignition times, left half image: combustion luminosity through the longpass filter (upper spectral range, LP), right half image: combustion luminosity through the shortpass filter (lower spectral range, SP).

In general, by observation with the human eye the E85 spray combustion shows a more bluish and less intense combustion luminosity than the E20 fuel. Furthermore, E20 exhibits higher combustion inhomogeneity with regions of intense droplet burning and sooting combustion at all ignition timings investigated. This is in agreement with earlier observations presented in [13] and can be seen within the results shown in Figure 4 as well. For both fuels and all three ignition times one can see from Figure 3 that the spray is not fully evaporated at the point of ignition. Consequently, droplet combustion occurs which is visible in form of a diffusion flame. This combustion behavior can clearly be seen from the strong longpass filter signal levels in Figure 4. Moreover, the intensity of some bright spots is too strong to be blocked by the shortpass filter. Considering the ignition timing at 1.4 ms after VSOI, Figure 4 shows that the initial flame kernel is not connected to the spark plug for either fuel. In addition, the main combustion region is located further downstream from the spark plug. This behavior could be caused by a higher spray momentum at earlier times of spray formation. The droplet cloud at earlier injection stages is more dense and compact and has a higher spray velocity. Accordingly, the ignition causes an early flame kernel which is moving in the spray direction. Thereafter, this flame kernel is growing and finally the whole spray cloud is ignited. This high momentum theory also fits with a higher misfire ratio, compared to the later ignition timings.

A comparison of the two wavelength signals shows nearly the same intensity at the beginning of the combustion process. At 2.6 ms after VSOI, Figure 4 the lower spectral range exhibits a higher intensity than the upper spectral range, although the total transmission of the shortpass filter is about a factor of 3 lower than the total transmission of the longpass filter. This shows that in the early stages of combustion the premixed combustion mode is dominant.

Especially for E85 the lower spectral range shows more sharp flame structures at the edges of the combustion zone. In the upper spectral range these structures are not visible or overexposed by the diffusion flame luminescence of different view field depths. Since the flame is propagating at the edges of the combustion zone, these structures could state the flame front. There the flame travels from the rich fuel regions into the leaner fuel regions of the surrounding air. Thus, the flame front movement can be visualized by the shortpass filter.

For E85 at 1.4 ms after VSOI ignition timing the high-speed series shows that the lower spectral range intensity is decreasing at later points in time (e.g. 3.4 ms after VSOI). This can be interpreted by a dominating non-premixed combustion mode at later times. The remaining combustion is mainly assigned to a diffusion flame caused by residual droplets in the core of the spray. This assumption is supported by the decrease of the total flame area at later points in time as shown in [13]. The later ignition time point at 1.6 ms after VSOI shows in total a larger combustion luminosity area for both fuels. (Figure 4) This is because the fuel-air mixing is more efficient at larger residence time. This assumption is supported by a less compact droplet cloud due to longer evaporation time as shown in Figure 2. At 1.8 ms after VSOI the mixing time relative to the ignition is the largest. So it is expected that mixing is most efficient and the premixed combustion prevails. Consequently, the diffusion flame appearance is supposed to be lowest. Figure 4 displays exactly this behavior. The combustion intensity of both fuels is lower than for the other ignition timings. Furthermore, E20 shows a decreased combustion inhomogeneity with less droplet and diffusion flame regions. Along with that, the sooting tendency of the fuels is lower. Especially for E20 (at the latest ignition timing) the stereoscope image series shows brighter and more defined flame edges at the spray front comparing the lower and upper spectral range. This investigation fits with the theory of advanced mixing and hence a stronger pre-mixed flame propagation.

The next section covers the time dependent ratio of the two color channels from the stereoscope high-speed imaging. For the calculation of this ratio, the ROI average of the shortpass signal was divided by the ROI of the longpass signal for an averaged image series as displayed in Figure 1 (right). High resulting stereoscope intensity ratios indicate the dominance of the premixed combustion mode over the diffusive combustion mode. Figure 5 displays the temporal trend of the stereoscope intensity ratio for the two fuels and two ignition times. All operating points in Figure 5 show a high premixed combustion amount at the beginning of the flame propagation. At around 3.5 ms after VSOI the diffusive combustion prevails. For advanced ignition timing, the combustion of both fuels tends to be more premixed. E20 shows a reduced intensity ratio at early ignition times compared to the later ones. This goes along with the theory of advanced mixing of fuel and air at late ignition timing. E85 shows a steep decline of premixed combustion for all the ignition time settings in the initial phase. Furthermore, the E85 intensity ratio curve for 1.6 ms after VSOI ignition time does not show the increasing behavior of E20 at the beginning of combustion. So premixing of the E85 fuel and air must proceed faster than for the E20 fuel. As the shadowgraphy study has revealed that the spray evaporation of the two fuels shows no significant difference (Figure 3), the chemical properties of the fuel (e.g. oxygen content) must have greater influence on the premixed combustion process as the physical ones (e.g. heat of evaporation, boiling point). However, further investigation is necessary in order to confirm that statement.

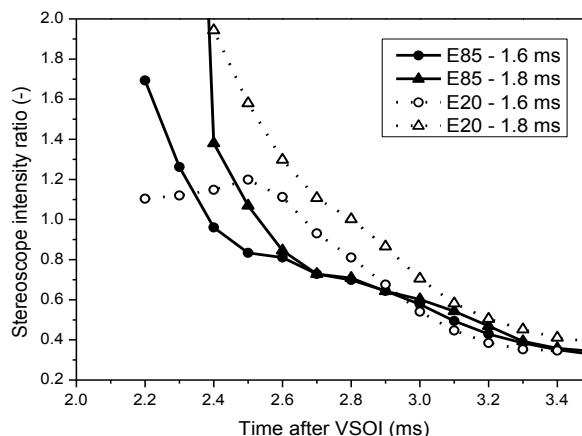


**Figure 5.** Stereoscope intensity ratio of an averaged high-speed image series for the fuels E85 and E20 at two different ignition timings. The intensity ratio is derived by dividing the pixel intensity of the shortpass through the pixel intensity of the longpass channel.

## Conclusion

In this study high-speed imaging was applied to investigate spray formation and spray combustion inside a spray-chamber under cold start, stratified spark ignition engine conditions. Two different mixtures of ethanol and isooctane fuels (E85, E20) were compared. The image stereoscope measurement technique allowed the investigation of premixed combustion zones and flame fronts during the spray combustion at different ignition times. Together with the spray formation images at the same conditions the study revealed the following conclusions.

- The spray formation study revealed that at the ignition time point E20 and E85 show nearly no differences in spray shape and liquid fuel distribution. However, some small differences were observed in fuel evaporation showing a slightly advanced evaporation for E85 compared to E20.
- The combustion luminosity study turned out that at early ignition times the flame was blown away from the spark plug because of higher spray momentum and spray velocities. This may also be a cause for higher misfire rates at these times.
- The stereoscope measurement technique is able to visualize flame front and premixed flame propagation structures at the edges of the spray where strong air entrainment occurs. The time resolved high-speed imaging allows observing the evolution of these structures.
- By comparing the two fuels, the stereoscope intensity ratio revealed that the premixing of fuel and air does not only depend on the ignition time. Here the influence of chemical fuel properties, mainly oxygen content, is assumed to be significant, especially at the initial stage of the spray combustion. This supports the theory of the small differences in spray attenuation signal (revealed in the shadowgraphy study) and the strong differences in the total combustion luminosity and combustion homogeneity.
- In general, the study showed that late ignition times cause lower soot and inhomogeneity levels because of advanced mixing, especially for the E20 fuel. The E85 sooting combustion level was lower than for E20 for all the different ignition times.

In further work additional spray investigations are planned. Furthermore, an extended fuel mixture and fuel pressure study is in preparation. This also involves a cycle-to-cycle analysis in order to compare the statistical variation of the spray and its combustion. The image stereoscope technique will be extended by a high-speed intensifier and an OH-chemiluminescence filter.

## Acknowledgements

The authors gratefully acknowledge the financial support by the German Federal Ministry of Food, Agriculture and Consumer Protection (BMELV) through the Agency for Renewable Resources (FNR), FKZ: 22026711. We also like to thank our project partners Prof. Christian Hasse (NTFD), Prof. Dimosthenis Trimis (GWA) and Prof. Sven Kureti (RT) at TU Bergakademie Freiberg. Furthermore, we acknowledge funding of the Erlangen Graduate School in Advanced Optical Technologies (SAOT) by the German Research Foundation (DFG) in the framework of the German excellence initiative.

## References

- [1] E. Stevens, R. R. Steeper, SAE Technical Paper 2001-01-1203 (2001).
- [2] M. Rossbach, A. Velji, U. Wagner, U. Spicher, R. Suntz, H. Bockhorn. The spark ignition engine of the future, Strasbourg INSA, December 2009.
- [3] W. Piock, G. Hoffmann, A. Berndorfer, P. Salemi, B. Fusschoeller, SAE Int. J. Engines 4 (2011) 1455–1468.
- [4] L. Chen, R. Stone, Energy Fuels 25 (2011) 1254–1259.
- [5] J. Lee, R. Patel, A. Schönborn, N. Ladommatos, C. Bae, Energy Fuels 23 (2009) 4363–4369.
- [6] M. Sjöberg, D. L. Reuss, Proceedings of the Combustion Institute 34 (2012) 2933–2940.
- [7] A. Krisman, E. R. Hawkes, S. Kook, M. Sjöberg, J. E. Dec, Fuel 99 (2012) 45–54.
- [8] I. Glassman, R. A. Yetter, Combustion, Academic Press, Amsterdam, Boston, 2008.
- [9] T. Knorsch, J. Trost, L. Zigan, M. Wensing, A. Leipertz, SAE Technical Paper 2012-01-1658 (2012).
- [10] M. Clairotte, T. Adam, A. Zardini, U. Manfredi, G. Martini, A. Krasenbrink, A. Vicet, E. Tournié, C. Astorga, Applied Energy 102 (2013) 44–54.
- [11] P. Aleiferis, Y. Hardalupas, A. Taylor, K. Ishii, Y. Urata, Combustion and Flame 136 (2004) 72–90.
- [12] Institut für Arbeitsschutz der Deutschen Gesetzlichen Unfallversicherung, GESTIS Stoffdatenbank, <http://gestis.itrust.de>, pageview 04 June 2013.
- [13] M. Storch, T. Knorsch, L. Zigan, M. Wensing, S. Will, Proceedings of the 6th European Combustion Symposium, Lund, Sweden (2013).

## Near-Nozzle Instabilities in Gasoline Direct Injection Sprays

Z. Rewse-Davies, J. Nouri, M. Gavaises and C. Arcoumanis

School of Engineering and Mathematical Sciences, City University London, UK

### Abstract

Nozzle flow of multi-hole GDI injectors can lead to undesirable and uncontrolled spray instabilities. In this study, two different injectors were utilised in order to observe the near-nozzle spray using high magnification optics and a high speed camera; a symmetrical multi-hole injector and an asymmetric, stepped nozzle injector. It was found that the symmetric injector exhibited a number of different spray instabilities, including flapping of the spray cone from an individual nozzle, flapping across all nozzles and rapid flapping along a single spray axis. The typical time scale of the phenomena was in the order of a hundredth of a millisecond. On the other hand, the stepped nozzle injector was found to exhibit fewer spray structures associated with spray instability. The results also suggest the nozzle step plays an important role in the primary breakup of the spray and that most of this breakup occurs before the exit of the step.

---

### Introduction

Since GDI was reintroduced to the mass market in 1996 with the advent of the Mitsubishi 4G93 it has demonstrated its potential advantages over the conventional PFI engine configuration. The main benefit of GDI is that it allows an engine to operate with the throttle plate fully open during part load operation by controlling the engine output through mixture control rather than induction throttling, as with a diesel engine [6, 14]. This is achieved by creating a stratified heterogeneous mixture so that while the overall induction mixture is lean, the region in the vicinity of the spark plug is close to stoichiometric ratio and combustible. To create this heterogeneous mixture the fuel needs to be injected directly into the combustion chamber. To run in stratified mode the fuel is injected late in the compression stroke so that the combustible fuel-air mixture remains in the region of the spark plug and is not transported throughout the rest of the combustion chamber by mass air motion present in the cylinder, such as swirl and tumble [13, 16]. This is in contrast to high load operation where the fuel is injected during the induction stroke so as to achieve high mixing and create a uniform homogeneous fuel-air mixture in the combustion chamber, as achieved by PFI [14]. However, injecting fuel directly into the combustion chamber poses two serious problems that need to be overcome. Firstly in both stratified late injection and pre-mixed early injection strategies the fuel has significantly less time to evaporate than it would in PFI where the fuel is usually injected onto the back of a hot intake valve before the air is even drawn into the cylinder. This is overcome by increasing the atomisation level of the fuel droplets leaving the injector by raising the rail pressure of the fuel to significantly higher levels than found in a PFI system; typically around 200 bar in modern GDI systems [15, 17, 20]. The other problem that needs to be addressed focuses on the stratified range of operation and is a result of the need to create an ignitable mixture directly in the region of the spark plug. So as to have a mixture that is reliably in the same region at the SOC, the injector needs to be able to produce a very stable and predictable spray.

Inside the injection nozzle and just after the exit of the nozzle the fuel first undergoes primary breakup where instabilities in the liquid core cause it to break up into large droplets and ligaments. These large droplets and ligaments then immediately undergo a secondary breakup process [3, 12, 24]. By promoting rapid primary and secondary breakup, the whole process is accelerated. It is generally accepted that cavitation structures present within the injection nozzle result in more rapid and complete primary breakup of the fuel so that secondary breakup can further reduce the size of the droplets and ligaments. However despite the benefits to atomisation of the fuel that cavitation can provide, it can have the unwanted effect of causing instabilities in the spray. This is a result of the different types of cavitation that can occur within a GDI injector. The two types concerned with in this paper are geometric and string cavitation. Geometric cavitation is the result of the working fluid being forced around a sharp feature or corner, such as the entrance of nozzle hole from the sac volume [5, 7, 22]. Studies of large scale and real size optical injectors have shown this to be a relatively stable form of cavitation that promotes atomisation with little increase in the instability of the spray [4, 19]. This can take different forms such as film cavitation or supercavitation and once established, especially the former, has been observed to be stable in microsecond timescales [11]. However, string cavitation being the result of the low pressure region in the centre of a rotating fluid body, has been observed to be very unstable and can fluctuate within very short time scales [1, 2, 9]. Further to this, when a string structure reaches the exit of a nozzle hole, this can cause relatively large changes to spray parameters such as overall cone angle while also manifesting in very localised spray flapping where spray on one side of the main cone can be ejected at an angle much greater than the average cone angle of the rest of the spray. These phenomena are known as spray

flapping and can result in both fuel outside of the ignitable region of the spark plug and the ignitable fuel-air region missing the spark plug entirely when operating in stratified mode.

In this paper, a high speed video camera has been utilised to observe the near-nozzle spray instabilities caused by two different types of commercially available GDI injectors which feature different exit shapes. The first one is a 'conventional' symmetric-spray GDI injector while the second one features a step-exit nozzle with an asymmetrical spray shape. This geometric feature is affecting the atomisation process of the injected spray and seems to suppress the influence of the internal flow on the near-nozzle instabilities observed with the other injector. The next section of the paper describes the experimental test-rig, followed by presentation of representative spray images; the main conclusions are summarised at the end.

## Experimental test-rig

Previous high-speed video studies of the near-nozzle region have all used shadowgraphy technique due to the inherent difficulties of providing enough light for high magnification imaging when using a continuous light source. However, despite the associated difficulties, Mie scattering was chosen as the preferred technique because it provides much clearer details of the spray structure which is important when identifying and following subtle structures within the spray. A Photron SA1.1 high speed camera operating at 100,000 fps was used for image acquisition so as to follow structures within the fast moving spray. The image size for all injection imaging was 192x192 pixels which resulted in a 2.4mm x 2.4mm image. The images were post processed to scale the pixel intensities from 0-255 using Matlab software which also allowed standard deviation images to be calculated during the steady state portion of the injection event. To achieve the required magnification a 135mm Nikon lens was used in conjunction with an in-house designed telescopic extension tube variable from 200mm to 1000mm depending on the configuration used. Continuous white light illumination was provided by an Arri 575W HMI lamp with the beam controlled by custom infra-red removal and three-stage focusing optics. The light was initially collimated using a 200mm diameter primary lens before being focused by a second 200mm diameter lens and a final focus lens of 50mm diameter. Heat removal consisted of a pair of hot-mirrors after the collimating lens followed by a pair of infra red filters between the final two focusing lenses.

The gasoline fuel injection system that provided the injectors with pressurised fuel consisted of a water cooled, two stage pump rig using a low pressure Bosch lift pump followed by a high pressure, three piston pump with a maximum pressure of 180 bar. The injectors were driven using an injector driver controlled by an in-house LabView control and monitoring program that allowed the injection duration and fuel pressure to be set. Two different injectors were chosen for the experiment to represent either end of the current market in terms of technology. Injector 1 was a 6-hole symmetrical multi-hole injector typical of the second generation spray guided injection systems found in the early 2000's was used to provide a bench mark. This is a commonly used injector in the automotive market, has a maximum working pressure of 120 bar, a nozzle hole diameter of 140µm and an L/D of 2.14. Injector 2 was a new 6-hole, asymmetric injector that is typical of the new generation of side-mount injectors with nozzles designed specifically to match a particular combustion chamber. The injector is tailored specifically to the 2.0 ltr TSI VW Golf which is a modern straight four engine utilising both supercharging and turbo charging for low and high rpm operation respectively [23]. The side mount configuration is used to reduce impingement of the fuel on the cylinder walls during heterogeneous operation and impingement on the piston crown during late injection when operating in stratified injection mode [16, 18]. The main nozzle section has a diameter of 180µm and a length to diameter ratio of unity where as the step has a diameter of 400µm and a varying length depending on the particular hole, though typically around 400-500µm. The injector also has an unusual internal configuration in that the internal upstream flow profile does not reach the needle seat from above, following the path of the needle as with most injectors. In fact it enters the needle seat area from the side, following four evenly spaced channels.

During this investigation the duration of all injection events was set at 2ms so as to provide a realistic spray duration as might be found within an operational engine that also allows a significant proportion of the spray to be within a steady state, full needle lift phase. Fuel temperature was set to around 20°C though its exact temperature within the injector body was not determined for this investigation. The single component fuel used was 2,2,4 trimethyl-pentane as this has very similar phase change characteristics and viscosity to high octane gasoline typically used by modern passenger vehicles.

## Results and Discussion

During the course of the investigation, batches of images for a range of typical GDI working pressures were analysed to record spray instabilities that occurred in both injectors. Events were categorised into two separate types; firstly a phenomenon that will be referred to as spray flapping, and secondly a phenomenon referred to as spray ejection, though both are a flapping type event. Spray flapping was defined as a spray instability that caused an individual spray cone angle to fluctuate significantly, either symmetrically along its axis or resulting in the spray to shift off axis. Included in this is the visible change in instantaneous mass flow

rate of an injection nozzle. This was usually found to occur in just one nozzle at a time though some flapping events occurred across multiple nozzles at the same time. The time scales for these events recorded ranged from a minimum of 30 $\mu$ s to a maximum of 150 $\mu$ s though typically the events lasted between 50 $\mu$ s and 100 $\mu$ s. An example of such an event can be seen occurring at the maximum working pressure of 120 bar in the central nozzle of injector 1 in Figure 1. Two features of the spray flapping in this instance can be distinguished. Firstly there is a 'flattening' of the spray evident in Figure 1c, while from Figure 1e onwards it can be seen that the central spray cone is shifted to the right. The likely cause of this is film cavitation extending further down the nozzle and blocking part of the hole, hence changing the axis of the spray.

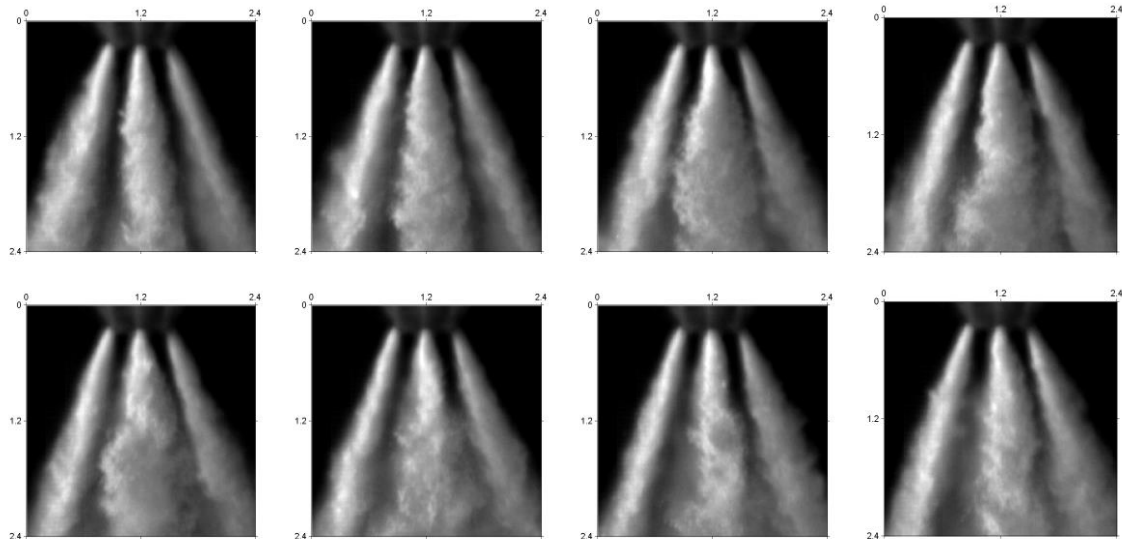


**Figure 1.** a-h. Spray flapping event occurring in the central nozzle of injector 1 at its maximum working pressure of 120 bar, in time steps of 10 $\mu$ s.

Spray ejection, the second type of instability that occurred, was defined as a small ejection of droplets from the main spray cone that did not alter the individual cone angle or structure of the parent spray, as documented by [11] and [21]. For such an event the droplets are ejected at an angle greater than 7.5° from the main spray and in this study, occur in timescales no more than 20 $\mu$ s, though it was found that the actual ejection from the nozzle occurred in timescales less than 10 $\mu$ s almost exclusively. Figure 2 shows such an ejection event occurring in the left hand nozzle of the Bosch injector at 60 bar rail pressure.

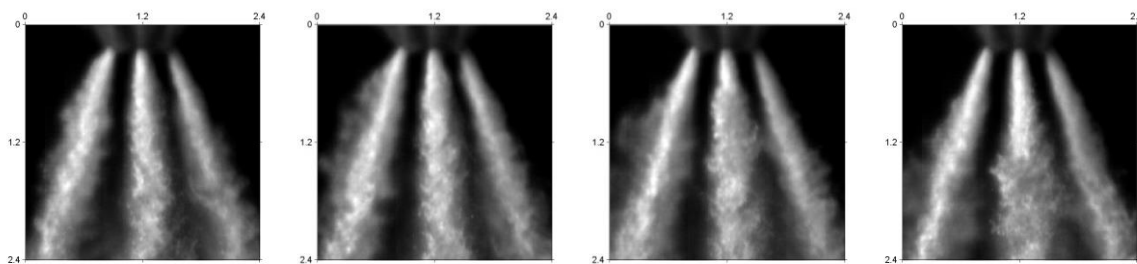


**Figure 2.** a-d. Spray ejection visible from the left hand nozzle of injector 1 at 60 bar rail pressure and time steps of 10 $\mu$ s.

A more significant, though statistically much less frequent, flapping event can be seen Figure 4. Here a change in the quantity of fuel can be observed across all visible nozzles and suggests that an internal event has occurred to temporarily choke the nozzles. Despite these usually minor spray flapping events, injector 2 was shown to exhibit good spray stability and uniformity across individual spray cones. Other than dribbling at the EOI, no visible ligaments or large droplets were detected at any of the pressures investigated and the spray is observed as a fine mist of small droplets from the SOI right though the whole injection duration. For this study five different rail pressures were chosen to represent typical injection pressures at which a GDi injector would be operated at during the course of normal engine running. A maximum pressure of 120 bar was used with lower pressures investigated in increments of 20 bar down to a minimum of 40 bar; the lowest pressure that might be used [23]. The average number of ejection and flapping events per injection are shown for both injectors in Figure 3. Firstly it can be seen the number of both ejection and flapping events for all pressures was



significantly higher for injector 1 than injector 2, save for spray flapping at the maximum pressure of 120 bar. However, it should be noted that the flapping events that occurred in injector 1 were of significantly higher intensity with a greater change in spray cone angles and disruption to the typical conical spray shape than in injector 2. Nearly all of the spray flapping events that occurred in the latter were very minor with very little change in the aforementioned parameters, though often distinguished by a visible change in the normally uniform spray distribution with some locally higher concentration of spray to one side of the cone.

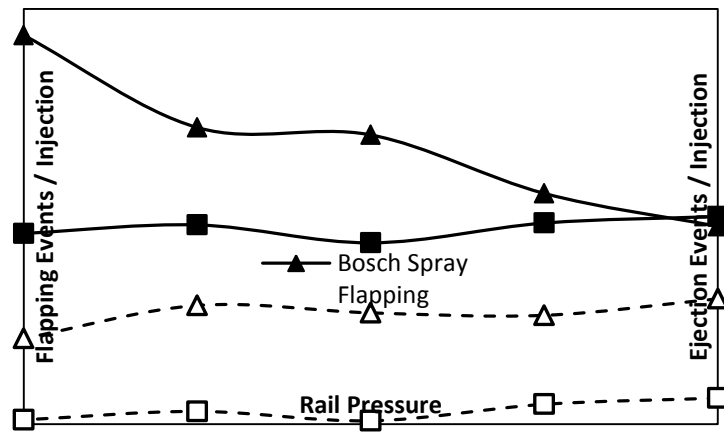


**Figure 3.** Graph showing the average number of both types of recorded spray instability for each injector.

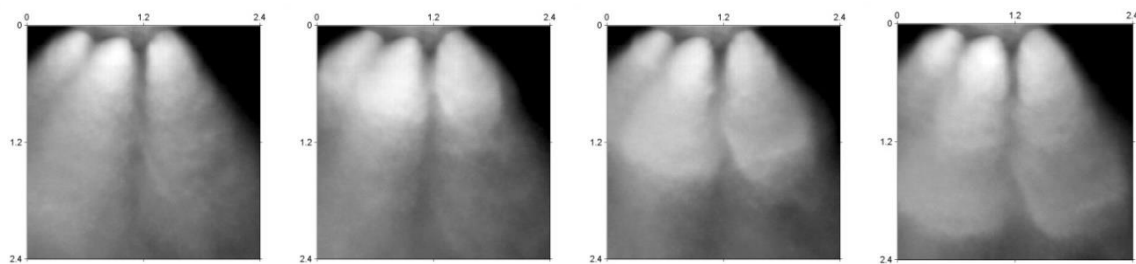


**Figure 4.** a-d. A rare spray flapping event across all visible nozzles of injector 2 at its lowest likely working pressure of 40 bar, shown in time steps of 10μs.

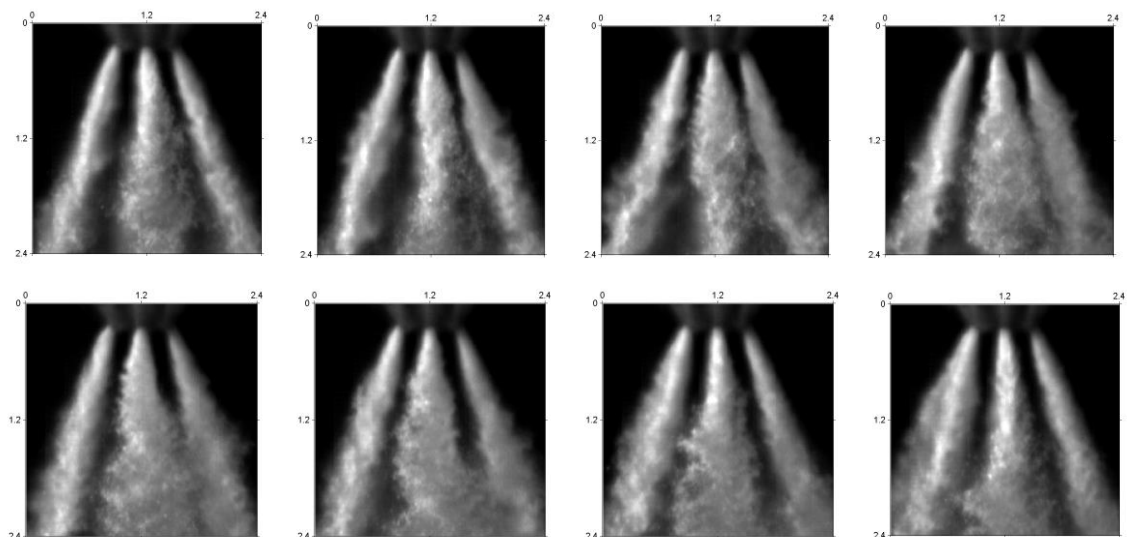


**Figure 5.** a-h. Spray flapping occurring across all three visible nozzles to different degrees, starting with the central nozzle, in injector 2 when operating at 60 bar rail pressure, shown in time steps of 10μs.

In comparison to the injector 2, injector 1 shows a noticeably less uniform spray with large droplets and ligaments present throughout the spray even during the middle of the injection phase at the maximum working pressure. While no liquid spray core can be visualised using the Mie technique in this experiment, it is likely that at these pressures most of the primary breakup takes place inside or just at the exit of the nozzle hole.

However it is clear that a significant amount of the primary breakup of the resulting ligaments and droplets takes place in the near nozzle region, and to some extent, further along the spray path. This is typical behaviour of a cylindrical nozzle and confirmed by other studies in the near nozzle region [8, 11, 21]. At the lower end of the range of pressures investigated the spray uniformity of injector 1 decreases further. A flapping event in the central nozzle of injector 1 operating at 60 bar is shown in Figure 5 and the decrease of uniformity of the spray compared to Figure 4 can be observed. Also visible is the effect of the flapping of the central nozzle on the two outer nozzles, particularly in the second half of the images. The cavitation structures inside the nozzle responsible for this phenomenon either occur across all holes simultaneously, though to different extents, or the appearance of the structures in one nozzle induces further flapping effects, slightly delayed, in the other nozzles. [11] and [21] showed that spray ejection like events, when operating at the low pressures (40 bar and below) required for the single hole optical nozzles used in the investigations, occurred in reasonably long timescales of at least  $100\mu\text{s}$  and the in nozzle imaging suggested that geometric cavitation was the cause. This is reasonable given the stability of geometric cavitation. As shown in Figure 2, the ejection events occurred in much shorter timescales of less than  $10\mu\text{s}$  and as such it is unlikely that the same mechanisms are occurring in the real 6 hole injector. [10] and [2] have shown that the emergence of string cavitation is a much more rapid process generally and thus it is thought that the extension of a cavitation string to the nozzle exit is the likely cause for these ejection events.

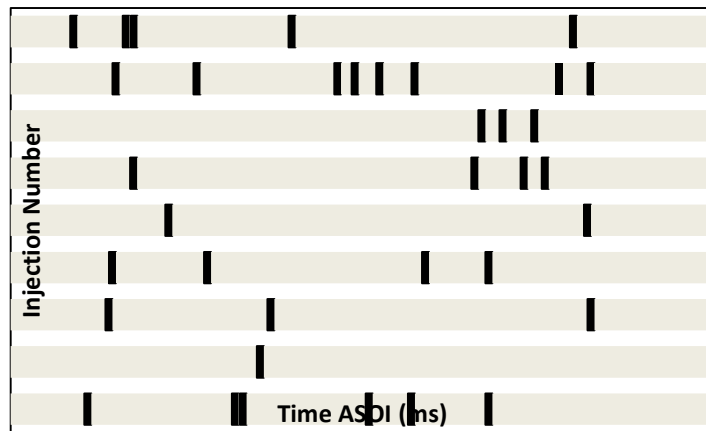


Figure 6. Spray ejection events occurring at 60 bar rail pressure in injector 1.

Recording the ejection events for a batch of 9 sequential injections using nozzle 1 and a rail pressure of 60 bar shows that the events are reasonably randomly distributed throughout an individual injection and the frequency at which they occur during an injection is reasonably widespread, as seen in Figure 8. However, it can be seen that there is some tendency for the events to group together. This could imply that either the same cavitation string is responsible for a group of events, its penetration along the nozzle hole varying, or that the flow field that creates these cavitation strings is able to occur in a reasonably stable fashion for such time periods and is responsible for a number of strings.

In injector 1, Figure 3 shows they occur reasonably frequently where as they are a much rarer occurrence in the spray of injector 2. Not only this, as seen in the left hand nozzle of Figure 7 the ejection events occurring in injector 2 are almost always smaller with respect to their ejection angle relative to that of the main spray. However this does not mean that string cavitation, at least the extension of it to the nozzle exit, is less frequent in injector 2. Due to the large step in the nozzle of the injector it is possible that such ejection events are 'captured' by the outer walls of the step and thus contained. It is also thought that the combination of the L/D ratio of 1 and the nozzle step is responsible for the increased atomisation and stability of injector 2, something that will be investigated in further studies. Another point of interest in the sequence in Figure 7 is that the fraction of the step exit that the fuel occupies as it leaves the central nozzle is not complete and in fact fluctuates.

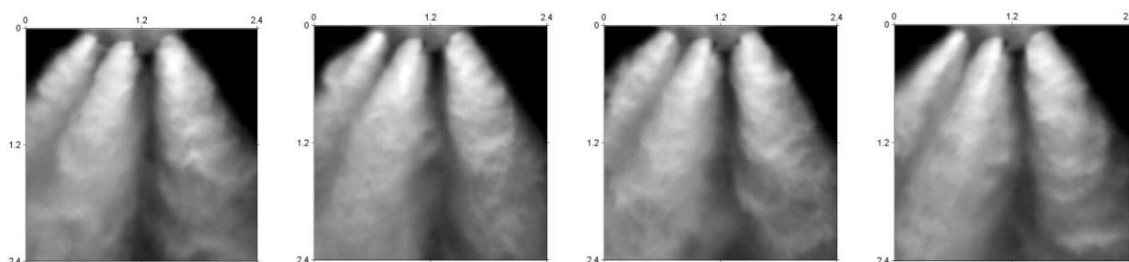
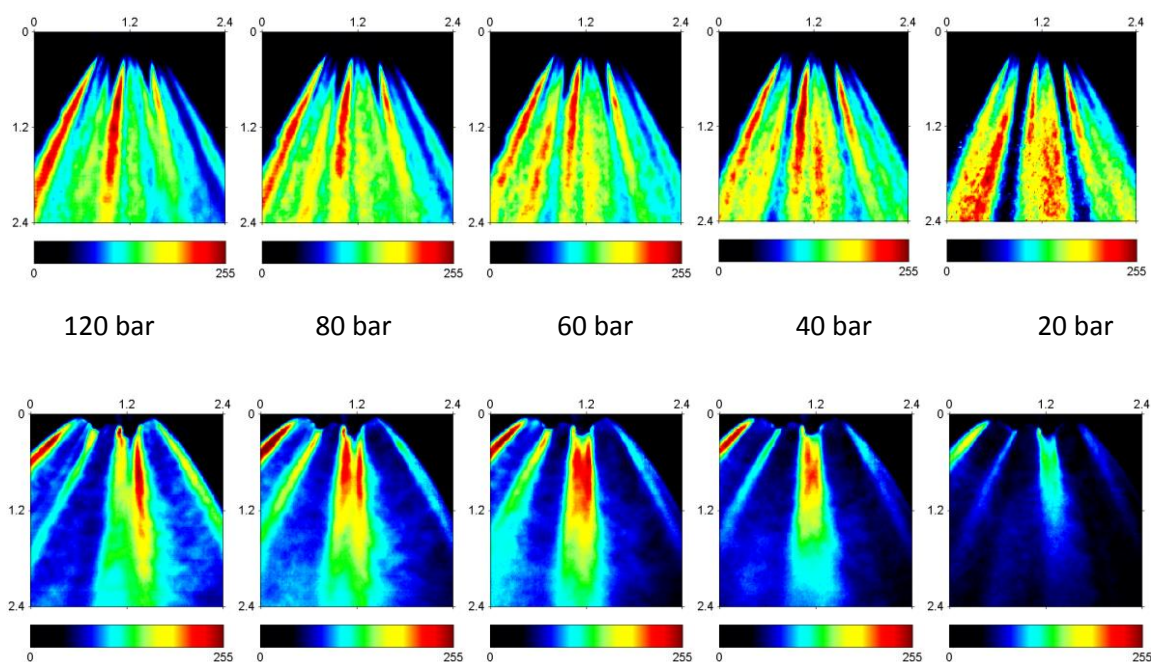


Figure 7. a-d. A small spray ejection occurring in the left hand visible nozzle of injector 2 at 120 bar rail pressure, shown in time steps of  $10\mu\text{s}$ .

To further investigate the effect of rail pressure on the stability of the two injectors, standard deviation images were produced using Matlab software from batches of 90 injections, as shown in Figure 8 with the top row produced from injector 1 and the bottom row from injector 2. Only the main injection phase (i.e. not the needle opening or closing phases) were used for the calculations and all images are scaled by the same factor resulting in a 0-255 colormap of image intensity. Included for interest is a 20 bar rail pressure case, although this is not a condition used in modern multi-hole GDI injectors under working conditions. It is immediately clear that in the centre of the spray cones there is less deviation in the results from injector 2 while both injectors appear to exhibit similar levels of variation in at the peripherals of the spray, partly due to low frequency cone angle fluctuation. It can also be noticed, as expected, for injector 1 that on the whole as rail pressure increases the stability of the spray increases. This data is reflected in Figure 3 where an increase in pressure resulted in fewer average spray flapping events per injection.

The story is different for injector 2 though as on the whole, deviation from mean, especially in the centre of the spray cone, is increased as the pressure rises. The 20 bar case shows very little deviation and the raw data shows that at such low pressures the stability of the spray is very good. Even at pressures as low as 10 bar, injector 2 shows no evidence of ligaments exiting the nozzle step, though the droplet sizes are visibly larger than at higher pressures. This provides evidence that the effect of the step has a dramatic effect in the secondary breakup characteristics of the emerging spray. It is believed that the majority of the secondary breakup of the fuel occurs within the very small region of the nozzle step. To allow this to happen within such a small region and with very little time for air interaction, it is believed that the level of primary atomisation occurring in the short nozzle prior to the step must be substantially greater than injector 1. However at this time it is not known whether it is the unity L/D responsible or an increase in frequency or size of cavitation structures inside the nozzle due to the different flow profile within the injector that are responsible.



**Figure 8.** a-j. Standard deviation false colormap images for both injectors at different rail pressures on an image intensity scale of 0-255. Top row is injector 1 and bottom row injector 2.

## Conclusions

An investigation into the near-nozzle flapping phenomena in gasoline direct injection sprays was undertaken on two different injectors. The two injectors were operated at a range of pressures typically found during normal operating conditions in a GDI engine; 120, 100, 80, 60 and 40 bar. The number of flapping type instabilities was recorded for each injector during the course of a number of injections and designated into two categories; spray flapping that effects one or more entire spray cones and spray ejection where a small quantity of fuel was ejected from the main spray at an angle greater than  $7.5^\circ$  and had no effect on the rest of the spray structure. The standard deviation images for the spray during the main phase of injection were calculated for each of the investigated pressures, as well as at a lower pressure of 20 bar for reference.

## Acknowledgements

The authors would like to thank R. Cattell for her selfless help with programming, Dr. N. Mitroglou for his experimental advice and also G. Clow and R. Cherry for always finding time to manufacture parts.

## Nomenclature

GDI	- Gasoline Direct Injection
PFI	- Port Fuel Injection
PM	- Particulate Matter
SOI	- Start of Injection
ASOI	- After Start of Injection
SOC	- Start of Combustion
CCD	- Charge Coupled Device
HMI	- Hydrargyrum Medium-Arc Iodide
L/D	- Length to Diameter Ratio

## References

- [1] Andriotis, A., M. Gavaises, and C. Arcoumanis. Vortex flow and Cavitation in Diesel Injector Nozzles. *Journal of Fluid Mechanics* , 2008, 610, 195-215.
- [2] 2 Andriotis, A. and M. Gavaises. Influence of vortex flow and cavitation on near-nozzle diesel spray dispersion angle. *Atomization and Sprays* , 2009, 19, 247.
- [3] 3 Arai, M. Physics behind Diesel Sprays. In *International Conference on Liquid Atomisation and Spray Systems*, Heidelberg, Germany, 02/09/2012.
- [4] 4 Arcoumanis, C., H. Flora, M. Gavaises, N. Kampanis, and R. Horrocks. Investigation of cavitation in a vertical multi-hole injector. *Transactions Journal of Engines*, SAE paper 1999-01-0524, SAE Transactions , 1999, 108, 661-678.
- [5] 5 Arcoumanis, C., M. Gavaises, and J. M. Nouri. The role of cavitation in fuel injection systems. In *AVL 8th International Symposium on Internal Combustion Diagnostics*, Invited Paper, Kurhaus Baden-Baden, 10-11th June.
- [6] 6 Breitbach, H., P. Luckert, A. Waltner, and J. Beiler. Fuel economy and emission potential of spray-guided combustion in gasoline engines. In *CAV 2012*, Berkley, USA, 07/07/2012, pp. 239.
- [7] 7 Brennen, C. E. *Cavitation and Bubble Dynamics*. , 1995, , 294.
- [8] 8 Crua, C., T. Shoba, M. Heikal, M. Gold, and C. Higham. High-Speed Microscopic Imaging of the Initial Stage of Diesel Spray Formation and Primary Breakup. *SAE International Journal of Engines* , 2010, .
- [9] 9 Gavaises, M., A. Andriotis, D. Papoulias, N. Mitroglou, and A. Theodorakakos. Characterization of string cavitation in large-scale Diesel nozzles with tapered holes. *Physics of Fluids* , 2009, 21.
- [10] 10 Gavaises, M., A. Andriotis, D. Papoulias, N. Mitroglou, and A. Theodorakakos. Characterization of string cavitation in large-scale Diesel nozzles with tapered holes. *Physics of Fluids* , 2009, 21, 052107.
- [11] 11 Gilles-Birth, I., M. Rechs, U. Spicher, and S. Bernhardt. Experimental investigation of the in-nozzle flow of valve covered orifice nozzles for gasoline direct injection. In *7th International Symposium on Internal Combustion Diagnostics*, Baden-Baden, Germany, 2006, pp. 59-78.
- [12] 12 Khare, P., D. Ma, X. Chen, and V. Yang. Breakup of Liquid Droplets. In *International Conference on Liquid Atomisation and Spray Systems*, Heidelberg, Germany, 02/09/2012.
- [13] 13 Kim, S., J. M. Nouri, Y. Yan, and C. Arcoumanis. Effects of intake swirl and coolant temperature on spray structure of a high pressure multi-hole injector in a direct-injection gasoline engine. *Journal of Physics: Conference Series* , 2007, 85.
- [14] 14 Kume, T., Y. Iwamoto, K. Iida, M. Murakami, K. Akishino, and H. Ando. *Combustion Technologies for Direct Injection SI Engine*. SAE technical paper , 1996, .
- [15] 15 Lee, J., A. Saha, A. Basu, and A. Kumar. Effects of Injection Pressure on Spray Atomization Characteristics with Measurement<br />Technique Cross-Validation. In *International Conference on Liquid Atomisation and Spray Systems*, Heidelberg, Germany, 02/09/2012.
- [16] 16 Mitroglou, N., C. Arcoumanis, K. Mori, and Y. Motoyama. Mixture distribution in a multi-valve twin-spark ignition engine equipped with high-pressure multi-hole injectors. *Journal of Physics: Conference Series* , 2006, 45, 46.

- [17] 17 Mitroglou, N., J. M. Nouri, M. Gavaises, and C. Arcoumanis. Spray characteristics of a multi-hole injector for direct-injection gasoline engines. *International Journal of Engine Research* , 2005, 7, 255.
- [18] 18 Mitroglou, N., C. Arcoumanis, K. Mori, and Y. Motoyama. Mixture distribution in a multi-valve twin-spark ignition engine equipped with high-pressure multi-hole injectors. *Journal of Physics: Conference Series* , 2006, 45, 46-58.
- [19] 19 Papoulias, D., E. Giannadakis, N. Mitroglou, M. Gavaises, and A. Theodorakakos. Cavitation in Fuel Injection Systems for Spray-Guided Direct Injection Gasoline Engines. SAE SP, 2007-01-1418 , 2007, 2084, 199.
- [20] 20 Sens, M., J. Maass, S. Wirths, and R. Marohn. Effects of highly heated fuel and/or high injection pressures on the spray formation of gasoline direct injection injectors. In CAV 2012, Berkley, USA, 07/07/2012, pp. 215.
- [21] 21 Serras-Pereira, J., Z. van Romunde, P. G. Aleiferis, D. Richardson, S. Wallace, and R. F. Cracknell. Cavitation, primary break-up and flash boiling of gasoline, iso-octane and n-pentane with a real-size optical direct-injection nozzle. *Fuel* , 2010, 89, 2592.
- [22] 22 Sou, A., R. Pratama, T. Tomisaka, and Y. Kibayashi. Cavitation Flow in Nozzle of Liquid Injector. In International Conference on Liquid Atomisation and Spray Systems, Heidelberg, Germany, 02/09/2012.
- [23] 23 Szengel, R., H. Middendorf, E. Pott, J. Theobald, T. Etzrodt, and R. Krebs. The TSI with 90 kW – the expansion of the Volkswagen family of fuelefficient<br />gasoline engines. In Internationales Wiener Motorensymposium 2007, 2007.
- [24] 24 Weickgenannt, C., I. Roisman, and C. Tropea. Experimental investigation of liquid ligament fragmentation. In International Conference on Liquid Atomisation and Spray Systems, Heidelberg, Germany, 02/09/2012.

## **Investigation of the interaction of in-cylinder flow and fuel injection in an optically accessible direct injection gasoline engine**

R. Stiehl<sup>1\*</sup>, J. Schorr<sup>2</sup>, C. Krüger<sup>2</sup>, A. Dreizler<sup>1</sup>, B. Böhm<sup>3</sup>

1: Fachgebiet Reaktive Strömungen und Messtechnik, Technische Universität Darmstadt, Petersenstrasse 32, D – 64287 Darmstadt, Germany

2: Daimler AG, RD/RPE, Mercedesstrasse 143, 70546 Stuttgart, Germany

3: Fachgebiet Energie- und Kraftwerkstechnik, Technische Universität Darmstadt, Petersenstrasse 32, D – 64287 Darmstadt, Germany

### **Abstract**

Stratified combustion in spray-guided direct injection spark-ignition engines offers high potential for improved efficiency. A stratified mixture is provided by multiple injections late in the compression stroke. Due to large spatial and temporal gradients in fuel vapor concentration, the reproducibility of mixture formation is crucial for reliable ignition. Cycle-to-cycle variations (ccv) of mixture formation can lead to delayed combustion and misfire. The interaction of in-cylinder flow and the injected fuel is one possible reason for ccv. Time resolved particle image velocimetry and Mie scattering of fuel droplets at 16 kHz was used to simultaneously measure the temporal evolution of in-cylinder flow and spray formation. The first injection was found to be very reproducible in its shape while the subsequent second injection exhibited severe fluctuations. The tumble flow was significantly perturbed by the first injection. Fluctuations of the resulting flow structures correlated with the spray shape of the second injection. These fluctuations were traced back in time prior to the first injection, indicating that ccv in the compression flow are the origin of spray shape fluctuations of the second injection.

---

### **Introduction**

One of the primary goals for the development of modern internal combustion engines is the reduction of fuel consumption and exhaust emissions. A very promising approach for mid- and part-load operation in direct injection spark-ignition (DISI) engines is stratified combustion (1). It is realized by the injection of fuel late in the compression stroke directly followed by ignition. With the proper injection timing, the fuel is only mixed with parts of the air, creating a stratified mixture. This enables de-throttled operation and qualitative load control, leading to reduced pumping losses and increased efficiency. However, stable combustion requires an ignitable air/fuel mixture at the spark plug at the time of ignition. Therefore, with stratified combustion, cycle-to-cycle variations (ccv) of the in-cylinder flow and the mixture formation can lead to partial burns or even misfires (2).

For future engine development, the understanding of the physical and chemical processes governing mixture formation and combustion is essential. Conventional diagnostic techniques that provide global values, for example in-cylinder pressure, equivalence ratio or exhaust gas composition are able to detect misfires, but do not provide insights into their origin. Laser diagnostics enable a more detailed investigation by providing higher spatial and temporal resolution. Time-resolved measurements are required for the analysis of individual engine cycles, due to fluctuations from cycle to cycle. Combined time-resolved flow and scalar measurements providing information on the mutual interaction of the underlying flow field with mixture formation or flame development are reviewed within (3). Peterson and Sick (4) for example combined high-speed particle image velocimetry (PIV) and planar laser induced fluorescence of biacetyl in a DISI engine with stratified charge operation to monitor in-cylinder flow fields and fuel concentrations simultaneously.

The fuel injection event is of primary importance for the preparation of a stratified in-cylinder mixture. Outwards opening piezo-injectors allow for very short energizing times below 100  $\mu$ s and thus for realizing several injections per cycle. The hollow cone spray forms toroidal vortices in the inner and outer shear layer entraining ambient air into the vortices, providing rapid air-fuel mixing. Due to the key role of the vortex for mixture preparation, its reliable occurrence at any engine operation point must be ensured. Spray stability is therefore mandatory. Sprays are generally characterized in constant volume chambers at high-pressure providing gas densities similar to those inside an engine at spray timing (5) or heated pressure chambers for more realistic fuel evaporation rates (6). To identify the significance of in-cylinder flow in addition to the thermodynamic conditions, Marchi et al. (7) performed similar experiments within an optical engine investigating the spray angle. For stratified engine conditions spray instabilities were found to increase with engine speed. In case of double injection the first injection remained unchanged compared to the case of single injection, but the second injection revealed significant cycle-to-cycle fluctuations. Measurements of the flow field simultaneously with the spray structure as performed in this study are thus of primary importance to understand the coupling between multiple injections.

In a previous work (8) by the authors time-resolved PIV at 16 kHz and Mie scattering of fuel droplets was used to simultaneously measure the temporal evolution of the in-cylinder flow and spray formation. The data revealed significant spray-induced vortices perturbing the tumble flow. Sprays from subsequent injections were disturbed and showed greatly enhanced ccv compared to the first injection. In the present study this analysis is extended to the flow prior to the first injection. A backward analysis in time is performed to investigate the cause-and-effect chain.

## Experimental setup

### Engine

The experiments were performed in an optically accessible research single-cylinder DISI engine (83 mm bore, 92 mm stroke, compression ratio 9.5). The four valve cylinder head was equipped with a centrally mounted outwards opening piezo-actuated injector and a spark plug located between the exhaust valves. A piston window, quartz glass liner and pent-roof windows provided optical access to the combustion chamber. The engine was operated at 2000 rpm using gasoline E10. Injection pressure was 200 bar pressurized by gaseous nitrogen to avoid oscillations of the fuel supply. For subsequent injections slight fuel pressure fluctuations were observed in the rail system but were excluded as origin for substantial spray shape variations (8).

To generate a stratified mixture at the instant of ignition triple injection was utilized late in the compression stroke. The electrical voltage trace applied to the injector is given in Figure 1. Note that due to the injector's internal delays and the field of view, first droplets are recorded approximately 1°CA after Start of Injection (SoI). The mixture was ignited by the spark plug in-between second and third injection. Therefore the focus of this study lies on the stability of the 2<sup>nd</sup> injection. A total of 273 consecutive cycles were recorded to provide a base for statistical analysis.

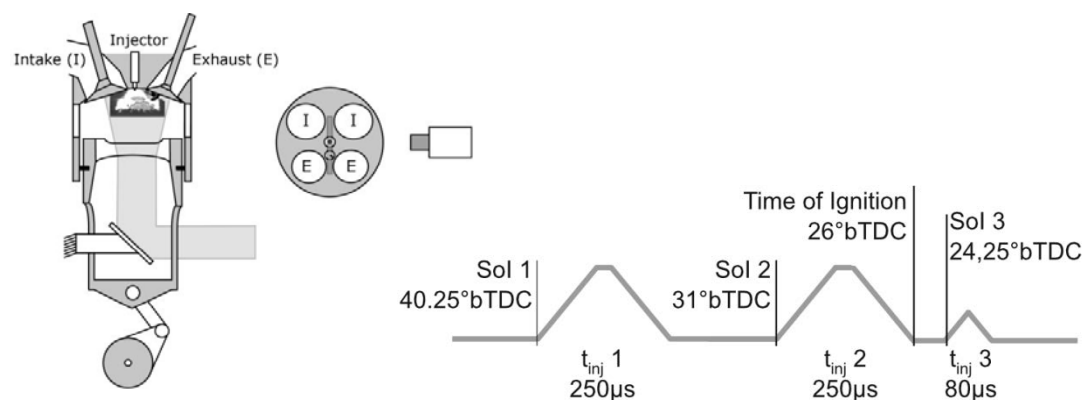


Figure 1: Experimental set-up and injection scheme.



*High-speed particle image velocimetry (PIV) and Mie scattering*

A frequency-doubled dual cavity Nd:YLF (Litron 304 PIV) laser operated at 527 nm was used for PIV. The repetition rate was set to 16 kHz. The laser beam was formed into a light sheet with a thickness of 1.5 mm and guided through the piston window to illuminate the central tumble plane (Figure 1). Silicone oil droplets ( $\sim 0.5 \mu\text{m}$  mean diameter) were seeded to the intake air 700 mm upstream of the intake valves, ensuring a homogeneous particle distribution. Mie scattering off the particles and the spray was captured by a 12-bit CMOS camera (Phantom v1610) equipped with an 85 mm Nikon lens. Time separation ( $\Delta t$ ) between the two PIV images was optimized resulting in two different  $\Delta t$  of 7 and 10  $\mu\text{s}$  (“variable  $\Delta t$ ”) within an individual cycle. PIV data processing was based on commercial software (LaVision DaVis 8.1). Prior to calculating PIV correlations, a dark image and a sliding Gaussian average (4x4 px) were subtracted from the raw images. The correlation map was calculated with decreasing interrogation window size from 64x64 px to 32x32 px (75% overlap) corresponding to a vector spacing of approximately 0.4 mm.

To ensure that the PIV data reliably represented the gas phase velocity, regions of high intensities stemming from the spray were masked out first. Since the scattered light intensity of particles approximately increases with the diameter squared, this already excludes droplets larger than 3  $\mu\text{m}$  (compared to seeding particles of 0.5  $\mu\text{m}$ ). The response time of fuel droplets with a diameter of 3  $\mu\text{m}$  was estimated (9) to be less than 0.5°CA. Towards end of injection, high intensity was observed within the spray vortex regions only, as expected for hollow cone sprays. Fuel droplets that were convected by the gas flow into the central region of the hollow cone within 2°CA after end of injection showed only slightly increased intensity compared to the seeding. Their time response in respect to changes of the gas phase flow can therefore be assumed to be the similar.

In order to evaluate the spray shape, scattered light at high intensity level was used to identify the spray contour in the central tumble plane. A robust automated analysis based on Matlab was used focusing primarily on the area between the injector and spark plug (termed “right” wing of the hollow cone spray) due to its relevance for the subsequent ignition. In a first step the spray was identified using a global threshold. Subsequently two vertical stripes (grey shaded area in Figure 2a) were selected corresponding to the onset of the spray vortex regions. Within this region the averaged distance between all pixels located at the outer contour of the spray and the cylinder head was calculated. Within a sensitivity analysis the image timing after SOI as well as the location and width of these stripes were varied but did not significantly influence the findings (not shown). In the following distance of the upper spray contour to the cylinder head is termed “spray height” (SH).

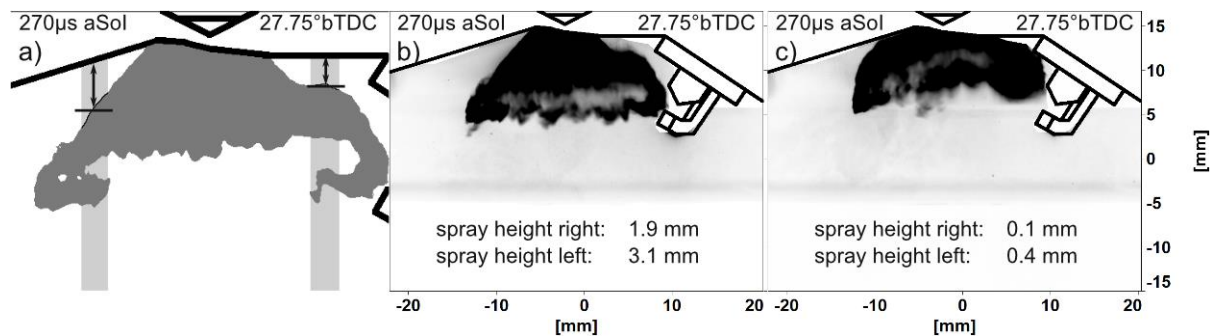


**Figure 2:** Spray height (SH) detection (a) and individual snapshots of the spray (b, c).

## Results and Discussion

Figure 2b presents a cross section of an individual snapshot for the second injection at 270  $\mu\text{s}$  after SOI. Toroidal vortices are formed in the shear layers of the hollow cone spray. The outer vortex is visible as an expansion of the cone midway between the nozzle exit and the spray tip. On the right spray side an ignitable air/fuel mixture is generated. The spark plug is located within the path of the outer vortex, interrupting the right wing of the spray. Figure 2b shows a typical desirable spray event where the spray points directly onto the spark plug gap as it is needed for a reliable ignition. The spray height for this individual event was 1.9 mm which is the average of all recorded cycles. Figure 2c in contrast shows an example of a very low SH for the right spray wing. Notice that the spray is attached to the cylinder head. This highlights the importance of an accurately designed spray targeting and a reliably reproducible spray pattern.

A statistical analysis of SH of the right spray wing was performed for 1<sup>st</sup> and 2<sup>nd</sup> injection. For both injections the injector is energized for 250  $\mu$ s, injecting 48% of the total injected fuel mass each. The frequency of occurrence for SH is presented in Figure 3. The 1<sup>st</sup> injection is very stable and repeatable in its shape, resulting in a narrow SH distribution between 2.3 and 3.5 mm and a standard deviation of 0.2 mm. In contrast to this, the SH of the 2<sup>nd</sup> injection fluctuates much more (std. 0.8 mm) with a mean value of 1.9 mm compared to 2.9 mm in the 1<sup>st</sup> injection.

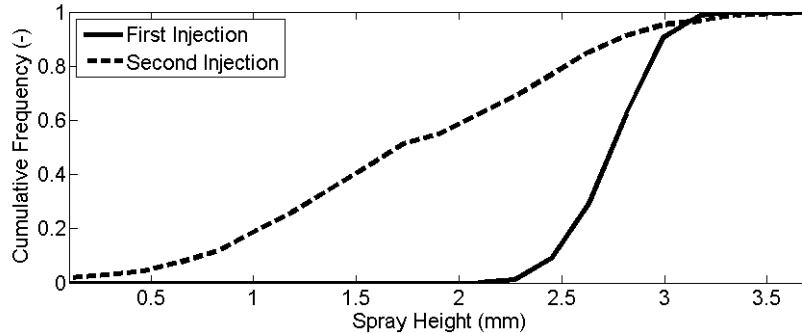


**Figure 3:** Spray height distribution for 1<sup>st</sup> and 2<sup>nd</sup> injection.

For a comparable injector the spray shape was observed to be very reproducible within constant volume chamber experiments, where the spray is injected into quiescent air (10). This even holds for short energizing times ( $t_{inj}=100 \mu$ s) and multiple injections. In the present experiment, however, the fuel is injected into a turbulent flow field. The 1<sup>st</sup> injection already faces a turbulent flow that differs from cycle-to-cycle. The injector is fully open for a period of time adding substantial momentum to the gaseous flow. Shear forces between spray and surrounding air generate local vortices that contribute significantly to the local turbulence field. Turbulence levels are increased and length scales are locally modified (spray-induced turbulence (11)). Thus the subsequent 2<sup>nd</sup> injection faces a modified enhanced turbulence field.

This spray-flow interaction is presented in Figure 4 exemplarily by the phase-averaged flow field during compression prior to 1<sup>st</sup> (40.5° bTDC) and 2<sup>nd</sup> injection (30.75° bTDC). The large scale tumble vortex is visible at 40.5° bTDC (Figure 4a). Mean flow velocities are  $\sim 14$  m/s in the vicinity of the injector. Rms values (not shown) are within 2.5-3 m/s. Without any injection the tumble vortex is further compressed at 30.75° bTDC and the velocity at the injector increases towards 25 m/s (Figure 4b). With injection, the 1<sup>st</sup> injection heavily modifies the flow field (Figure 4c). The large scale tumble flow is interrupted by several vortical structures. Ambient air is accelerated towards the high velocity spray flow, redirected at the spray and entrained into the spray. A low pressure region (12) is generated within the hollow cone in the vicinity of the injector inducing an upwards directed “funnel” flow.

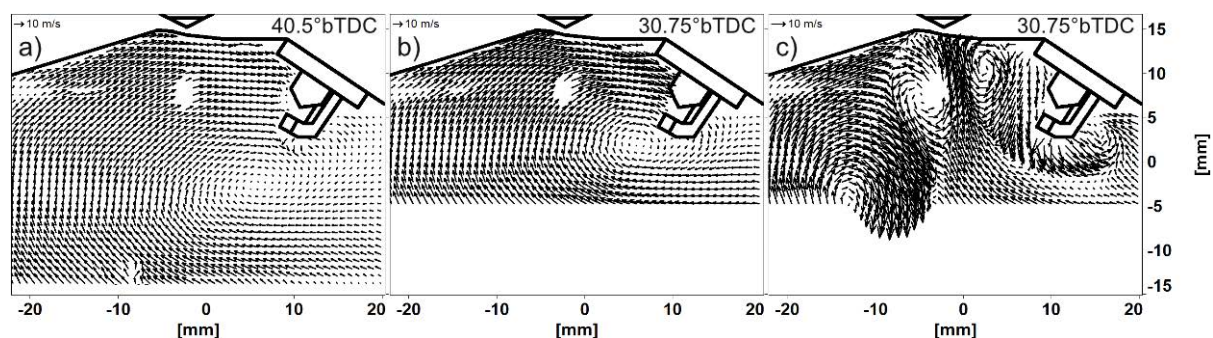


**Figure 4:** Phase-average flow field before (a) and at a CAD after 1<sup>st</sup> injection without (b) and with injection (c). Every 2<sup>nd</sup> vector shown.

The modified turbulent flow seems to play an important role for the increased fluctuations present at the onset of the 2<sup>nd</sup> injection. Therefore a more detailed investigation of the flow field is performed. The acquired data set gives access to the temporal evolution of the flow field prior to injection and thus allows a backward analysis in time. To identify different flow structures correlating with different spray heights recorded cycles were sorted by SH of the 2<sup>nd</sup> injection. Phase averaging was performed for the 25 cycles with smallest ( $0.6 \pm 0.5$  mm) and largest ( $3.2 \pm 0.5$  mm) spray height corresponding to “high” and “low” sprays.

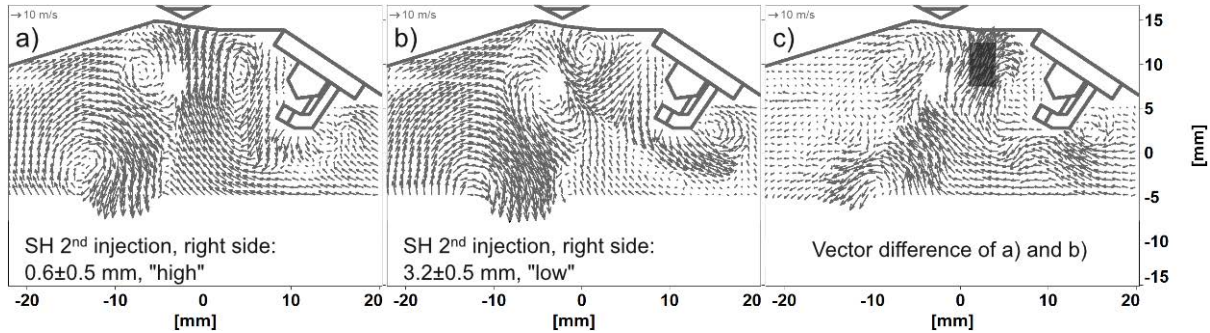


**Figure 5:** Conditionally averaged flow field at 30.75°bTDC for cycles with high (a) and low (b) SH for the right wing of the 2<sup>nd</sup> injection. (c) shows the vector difference of (a) and (b). Every 2<sup>nd</sup> vector shown.

The conditionally averaged flow fields prior to 2<sup>nd</sup> injection (30.75°bTDC) are shown in Figure 5 together with the vector difference of the two. Different flow patterns are observed for both groups, especially for the funnel flow shown in Figure 4c. Cycles with “high” sprays show an upwards directed high velocity funnel flow. The superimposition of the global tumble flow transports this flow structure to the right towards the spark plug. This leads to a slight offset of this flow pattern to the right with respect to the injector’s axis. For the “low” spray the funnel flow is slower (18 m/s compared to 25 m/s) and tilted to the left. In contrast to the “high” spray, it targets the injector axis and does therefore not interact directly with the right spray’s wing of the 2<sup>nd</sup> injection. As a result the difference vector field between “low” and “high” shows large deviations on the right side of the injector marked by the grey box in Figure 5c. Similar observations were made for other injection timings (not shown here) (8), indicating a correlation between the flow field prior to the 2<sup>nd</sup> injection and the spray height of the 2<sup>nd</sup> injection. This seems surprising considering the high initial velocity of droplets due to the injection pressure of 200 bar. However, because of their size (below 20 µm for primary droplets under these conditions (13)) the response time of the fuel droplets is short. As a result, their momentum is rapidly transferred to the ambient air. It therefore seems plausible that the in-cylinder flow can influence the entrainment and thus the spray.

Since the flow between injections is dominated by the 1<sup>st</sup> injection, it appears that cycle-to-cycle variations of the 2<sup>nd</sup> injection are dominated by the 1<sup>st</sup> injection. However, the 1<sup>st</sup> injection is comparably stable and therefore the injection itself is unlikely to be the initial cause. To verify this, the analysis is continued back in time prior to the 1<sup>st</sup> injection.

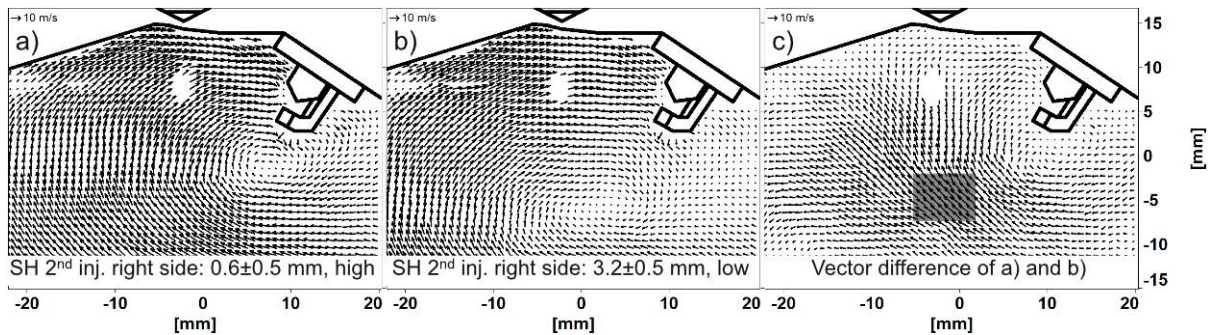


**Figure 6:** Conditionally averaged flow field at 40.5°bTDC for cycles with high (a) and low (b) SH for the right wing of the 2<sup>nd</sup> injection. (c) shows the vector difference of (a) and (b). Every 2<sup>nd</sup> vector shown.

Figure 6 shows the conditionally averaged flow fields prior to the first injection (40.5°bTDC) for the same groups of 25 cycles presented in Figure 5. Similarly a significant difference of the conditionally averaged flow fields is observed for both groups. For “high” SH the center of the large scale tumble vortex is located directly below the spark plug at [7.5 mm, -1.2 mm]. For the “low” case it is located closer to the cylinder axis at a larger distance from the cylinder head at [2.5 mm, -6 mm]. The difference between both (Figure 5c) shows the largest variation in the center of the cylinder marked by the grey box. This region is centered ~20 mm below the injector. The velocity difference is approximately 15 m/s.

The observations from the conditionally averaged flow fields as discussed in Figure 5 and 6 were based on two sets of 25 cycles each. For improved statistical significance a further analysis was performed including all 273 cycles to ensure that results are not biased by either the number of cycles selected for the conditional analysis or the criteria used for classification. Therefore the regions of largest differences between the “high” and “low” sprays were closer examined for all cycles. The spatially averaged velocity was calculated for all individual cycles from the regions marked by the grey box in Figure 5c (30.75°bTDC) and 6c (40.5°bTDC), respectively. Figure 7 shows the vertical component of this spatially averaged velocity versus the spray height of the right wing of the 2<sup>nd</sup> injection in the respective cycle for 30.75° bTDC (prior to the 2<sup>nd</sup> injection). In cycles with a strong upwards directed flow within this area, the sprays are closer to the cylinder head and vice versa. This correlation is not sensitive regarding slight changes in the size of the investigated area. The correlation coefficient  $r$  was -0.74 calculated by

$$r_{xy} = \frac{\sum_{i=1}^n (x_i - \bar{x})(y_i - \bar{y})}{\sqrt{\sum_{i=1}^n (x_i - \bar{x})^2 \cdot \sum_{i=1}^n (y_i - \bar{y})^2}}$$

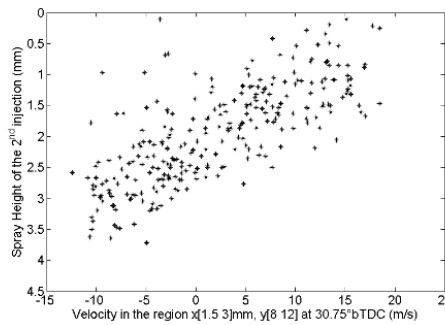


**Figure 7:** Velocity before 2<sup>nd</sup> injection (30.75°bTDC) versus SH of the 2<sup>nd</sup> injection.

The same analysis was performed for the flow prior to the 1<sup>st</sup> injection at 40.5°bTDC. In order to include the magnitude and the direction of the flow, the average direction from the flow in the marked box in Figure 6c was calculated. In a second step, the spatial average of each individual cycle was projected onto this direction as illustrated in Figure 8a.

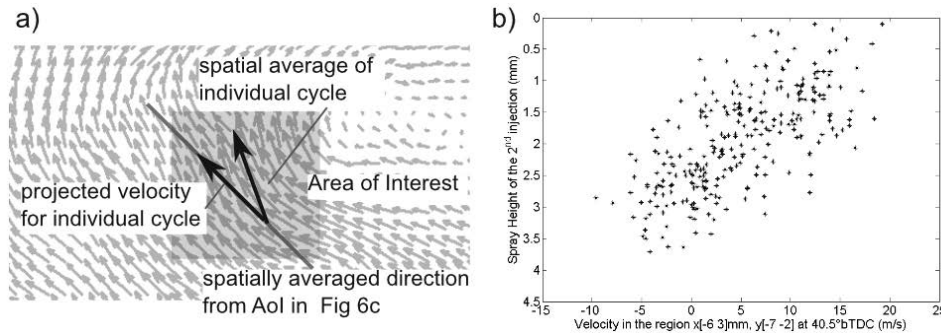


**Figure 8:** Velocity before 1<sup>st</sup> injection (40.5°bTDC) versus SH of the 2<sup>nd</sup> injection.

Figure 8b shows the velocity plotted versus spray height of the right wing of the 2<sup>nd</sup> injection in the respective cycle. For cycles with a high velocity, the sprays are closer to the cylinder head and vice versa. The correlation coefficient decreases to -0.68. A further analysis back in time with a correspondingly shifted area of interest reveals a further decreasing correlation coefficient of -0.52 at 63°bTDC and -0.41 at 73.5°bTDC.



The correlation shown here is remarkable as it only contains data from the tumble plane, thus not taking into account the 3<sup>rd</sup> dimension of the highly three-dimensional flow. It reveals an impact of cycle-to-cycle fluctuations of the in-cylinder flow prior to injection and spray formation. Large scale in-cylinder flow fluctuations which are already present before any injection are carried on beyond the 1<sup>st</sup> injection event. The 1<sup>st</sup> injection modifies the local flow field in the vicinity of the injector and thereby transfers fluctuations to the flow field after the injection. For the investigated configuration it amplifies the influence of the flow on the 2<sup>nd</sup> injection leading to a strongly fluctuating spray pattern. A reduction of large scale cycle-to-cycle flow fluctuations during intake and compression therefore is a promising strategy in reducing the fluctuations of the 2<sup>nd</sup> injection's spray shape.

## Conclusions

In this work High-Speed PIV and Mie scattering off fuel droplets has been applied to a direct injection spark-ignition engine to study the interaction between in-cylinder flow and fuel spray. A triple injection scheme was used to create a stratified mixture late in the compression stroke. The first two injections were investigated, as they provide the mixture at time of ignition. While the shape of the 1<sup>st</sup> injection was very reproducible, the shape of the 2<sup>nd</sup> injection was subject to strong fluctuations. The focus of the present work was on potential causes of these fluctuations. Flow field statistics conditioned on the spray shape of the 2<sup>nd</sup> injection revealed regions with macroscopic cycle-to-cycle flow variations, correlating well with the spray shape for all recorded cycles. This correlation was tracked back in time even beyond the first injection. It revealed that cycle-to-cycle fluctuations of the large scale in-cylinder flow structures had a strong impact on the spray shape of the second injection whereas the first injection remained unaffected. The turbulence generated by the 1<sup>st</sup> injection amplified the impact of the flow ccv on the subsequent 2<sup>nd</sup> injection. This indicates that the origin of the 2<sup>nd</sup> injection spray's fluctuation may already be formed during intake. For further improvement of engine performance minimizing large scale flow ccv in the compression stroke is a potential mean for a more robust stratified mixture formation. For a more detailed analysis, three dimensional data are needed, i.e. from tomographic PIV, simultaneous multi-plane PIV or large eddy simulation.

## Acknowledgements

The authors gratefully acknowledge the discussion with and information provided by Dr. Nils Laudenbach, Dr. Uwe Schaupp and Dr. Werner Sauter. Fruitful discussion with Dr. Brian Peterson and M.Sc. Elias Baum are also gratefully acknowledged.

## References

1. A. C. Alkidas, *Energy Conversion and Management* **48**, 2751 (2007).
2. H. Baecker, A. Kaufmann, *SAE Technical Paper*, 2007-01-1407 (2007).
3. B. Böhm, C. Heeger, R. Gordon, A. Dreizler, *Flow, Turbulence and Combustion* **86**, 313-341 (2011).
4. B. Peterson, V. Sick, *Applied Physics B* **97**, 887 (2009).
5. W. Sauter *et al.*, *SAE Technical Paper*, 2006-01-3377 (2006).
6. D. Martin, J. Stratmann, P. Pischke, R. Kneer, M.-C. Lai, *SAE International Journal of Engines* **3**, 372 (2010).
7. A. Marchi, J. Nouri, Y. Yan, C. Arcoumanis, *International Journal of Engine Research* **11**, 413 (2010).
8. R. Stiehl, B. Böhm, J. Schorr, C. Krüger, A. Dreizler, *Submitted to Flow, Turbulence and Combustion*.
9. M. Raffel, *Particle image velocimetry, A practical guide* (Heidelberg, Berlin, ed. 2, 2007).
10. Werner Sauter, personal communication.
11. J. Moreau, J. Boree, R. Bazile, G. Charnay, *Experiments in Fluids* **37**, 856-871 (2004).
12. A. Hermann *et al.*, *Proceedings of the 9th international symposium on internal combustion diagnostics. Baden-Baden (2008)*.
13. Franck Nicollet, personal communication.

## Experimental Study on Characteristics of Laser-induced Ignition in Liquid Fuel Spray

Takehiko SEO, Yasuhiro HISATOMI, Yuki ISHIMURA and Masato MIKAMI

Dept. of Mechanical Engineering, Yamaguchi University, Japan

### Abstract

To ignite fuel spray with a laser beam directly, it is necessary to investigate the characteristics of laser-induced breakdown in fuel spray. In this present study, the effects of incident energy and spray characteristics on the breakdown and ignition characteristics were investigated experimentally. Laser-induced breakdown ignition experiments were conducted in ethanol spray by using the third harmonic of the Q-switched Nd:YAG laser (wavelength  $\lambda=355$  nm, pulse width is about 6 ns and maximum output energy is about 375 mJ/pulse) as a laser source. Probability of breakdown occurrence and ignition for different incident energy and equivalence ratio were obtained. And to clarify the ignition mechanism, the Schlieren images of the plasma and flame propagation process were taken. It found that there is a large gap between the required incident energy for breakdown and ignition in ethanol spray. And plasma is generated by the multiple points in ethanol spray. In case of ignition success, flame kernels were formed around each plasma.

### Introduction

Internal combustion engine plays a dominant role in energy production. To protect the resources and to reduce CO<sub>2</sub> emissions, which have the greenhouse effect, require a lowering of the fuel consumption of IC engine. Many researches had been conducted to reduce its pollutant emissions and improve its efficiency.

The early stages of combustion have strong effects on formation of pollutant, flame propagation and quenching. In spark ignition engine (SI engine), flame kernel development is disturbed by the loss of heat to the electrode and wall. Moreover, the heated electrode may cause the abnormal combustion (Pre-ignition). To reduce SI engine's pollutant emissions and to improve its efficiency, it is necessary to develop a new ignition method of the replacement to the spark plug.

Laser-induced ignition [1]-[4] that is the non-contact ignition method is a promising technology. A lot of researches about laser-induced ignition and breakdown had been conducted. However, these researches are for the gas fuel cases. Considering an application to the SI engine, it is important to clarify the characteristics of ignition of liquid fuel spray and its mechanisms. In this present study, the characteristics of laser-induced ignition of ethanol spray were investigated experimentally.

### Experimental apparatus and procedure

Figure 1 shows the schematic of experimental apparatus used in the present study. The third harmonic of the Q-switched Nd:YAG laser (wavelength  $\lambda=355$  nm, pulse width is about 6 ns and maximum output energy is about

Table 1 Experimental conditions of premixed spray

Air flow rate [L/min]	10	6	4
Equivalence ratio	1.59	2.38	3.06
Sauter Mean Diameter [ $\mu\text{m}$ ]	12.8	13.7	14.1

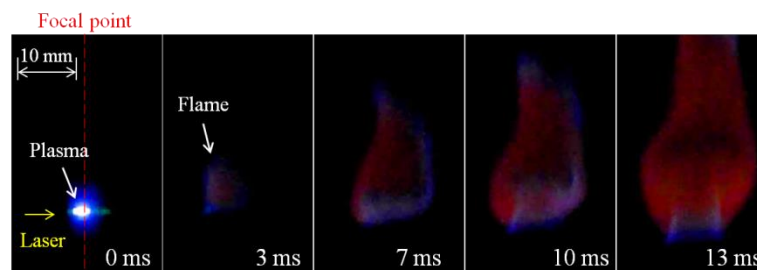


Figure 1. Typical time-series images of success of ignition in ethanol spray (Incident energy: 5 mJ, Equivalence ratio: 2.38)

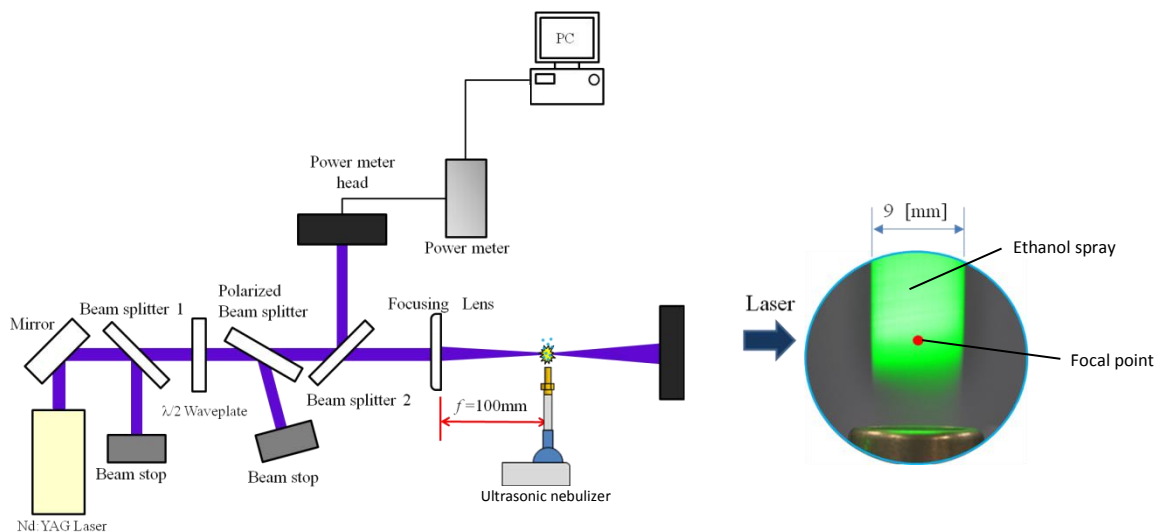


Figure 2. Schematic of experimental apparatus and shape of ethanol spray

375 mJ/pulse) was used as a laser source. The pulse energy was adjusted by using 1/2 wave plates and the polarization beam splitter not to change the spatial intensity profile of laser beam. The laser beam was converged by the planoconvex lens (focal length  $f=100$  mm and lens diameter 40mm). The energy of incident pulse was measured with power meter.

Ethanol spray generated with the ultrasonic nebulizer was carried by air flowed into the ultrasonic nebulizer and supplied around the focal position. Equivalence ratio of premixed spray was controlled by changing air flow rate. The experimental conditions of premixed spray were shown in Table 1.

Schlieren image of flame kernels and plasma were taken by high-speed CMOS camera. The probabilities of the breakdown and ignition occurrence are defined as number of successful ignition and breakdown events divided by number of attempts. In this study, the determination of the generation of plasma and the success or failure of the ignition were carried out by checking the generation of plasma and propagation of flame by time-series images taken in the vicinity of the focal point with a digital camera. Typical time-series images of success of ignition in ethanol spray were shown in Figure 1. For each pulse energies investigated, laser beam was pulsed 100 times.

## Results and Discussion

### Relationship between incident energy and probability of breakdown occurrence and ignition

In the case of equivalent ratio 2.38, the relationship between incident energy and probability of breakdown occurrence and ignition is shown in Figure 3. Incident energy breakdown occurs absolutely is about 5 mJ. Compared with gas target case, this energy is much smaller. This is the same tendency as previous reports [5] [6].

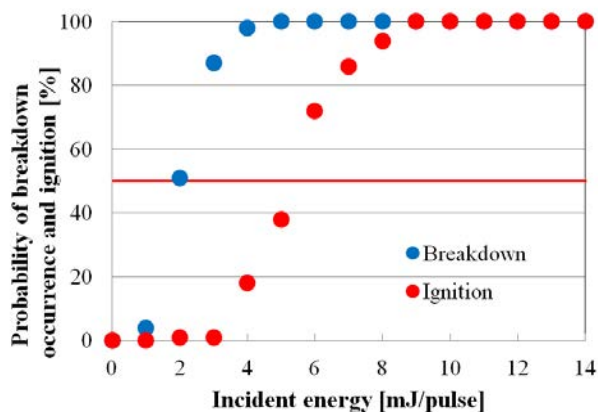




Figure 3. Probability of breakdown occurrence and ignition for different incident energy

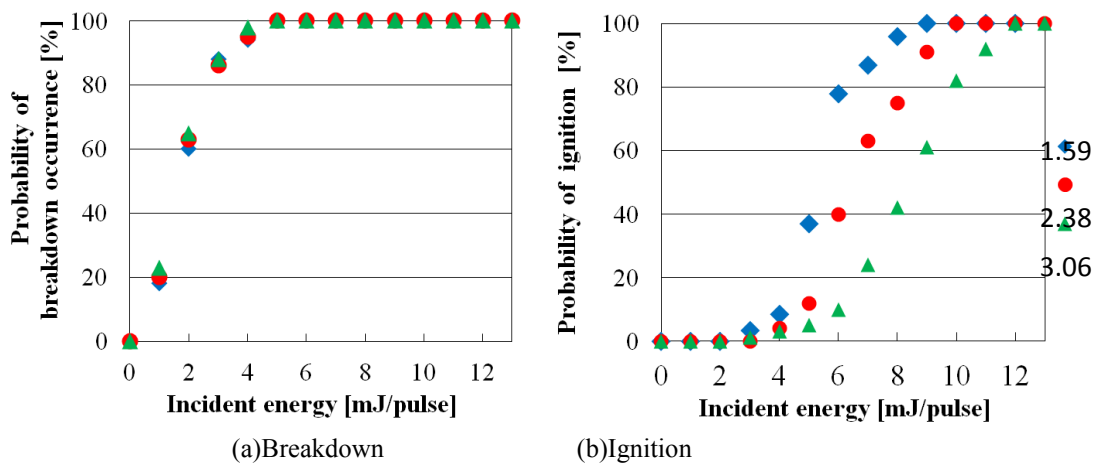


Figure 4. The relationship between equivalence ratio of premixed spray and probability of breakdown occurrence and ignition

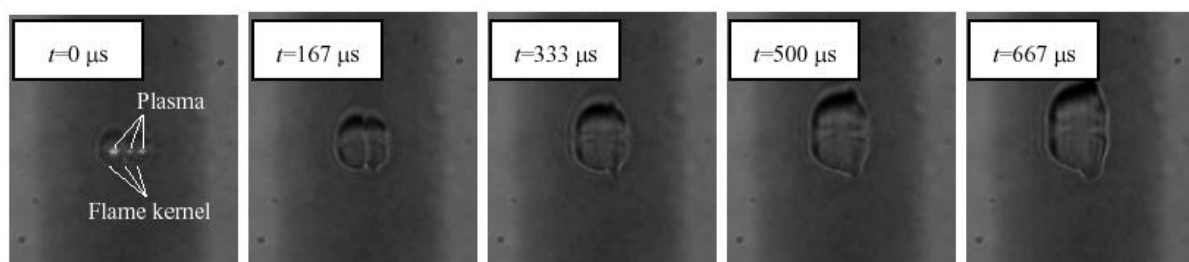
However, energy ignition always occurs is about 10 mJ, it found that there is a large gap between the required incident energy.

#### Dependence of equivalence ratio on probability of breakdown occurrence and ignition

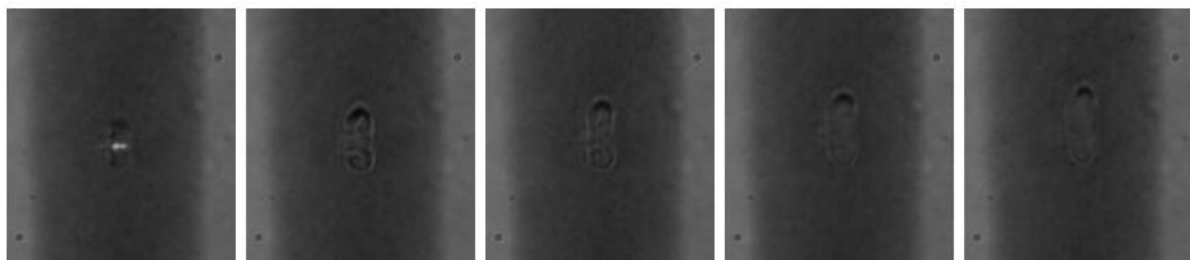
The relationship between equivalence ratio of premixed spray and probability of breakdown occurrence and ignition is shown in Figure 4. In Figure 4 (a), even though the equivalent ratio is increased, there was no change in the breakdown probability. In this study, the equivalent ratio was adjusted by changing the air flow rate, the number density of the spray also changed when the equivalent ratio was changed. It was considered that the fuel spray was supplied in a region with sufficient energy density to generate the plasma. In Figure 4 (b), it found that the ignition was likely to occur in the premixed spray of  $\phi=1.59$  which was most lean conditions in this study and energy ignition always occur was about 9 mJ. Further, with increasing equivalence ratio, ignition probability was decreased.

#### Flame propagation process

Figure 5 shows the time-series Schlieren images of plasma and flame propagation process in case of (a) ignition



(a) Ignition success



(b) Ignition failure

Figure 5. Typical Schlieren images of plasma and flame propagation process

success and (b) ignition failure. Incident energy was 5 mJ, the time when the plasma appeared in the image was defined as 0 ms. Ethanol spray flowed from the bottom to the top and laser beam was irradiated from the left side of images. At  $t=0$   $\mu$ s, it can be seen that plasma is generated by the multiple points. Around each plasma, the regions there are differences in the density of the ambient premixed spray are formed. Then, each regions are combined and continued to expand as one flame after 167  $\mu$ s. These regions seem to be formed by combustion of the premixture around fuel droplets, it is considered to be flame kernels. On the other hand, in the case of ignition failure of Figure 5(b), the plasma is generated by the multiple points as in the case of successful ignition can be seen in the image of  $t=0$  ms. However, the regions have differences in the density of the ambient premixed spray are extended in the longitudinal and are not formed around each plasma. Then, flame is not formed. In order to clarify the mechanism of ignition in fuel spray, it is necessary to fully understand the characteristics of the plasma generated in the vicinity of the droplet.

## Conclusions

This study experimentally investigated the effects of incident energy and spray characteristics on the breakdown and ignition characteristics. Conclusions of the experiment results are as follow:

1. There is a large gap between the required incident energy for breakdown and ignition in ethanol spray.
2. With increasing equivalence ratio, ignition probability was decreased in this study.
3. Plasma is generated by the multiple points in ethanol spray. In case of ignition success, flame kernels were formed around each plasma.

## References

- [1] P. D. Ronney, "Laser versus conventional ignition of flames," *Optical Engineering*, 33, 510-521, 1994.
- [2] M. H. Morsy, Y. S. Ko, and S. H. Chung, "Laser-induced ignition using a conical cavity in CH<sub>4</sub>-air mixtures," *Combustion and Flame*, 119, 473-482, 1995.
- [3] Jian X. Ma, Dennis R. Alexander, Dana E. Poulain., "Laser spark ignition and combustion characteristics of methane-air mixtures," *Combustion and Flame*, 112, 492-506, 1998.
- [4] J.-L. Beduneau, B. Kim, L. Zimmer, Y. Ikeda, "Measurements of minimum ignition energy in premixed laminar methane/air flow by using laser induced spark," *Combustion and Flame*, 132, 653-665, 2003.
- [5] Ronald G. Pinnick, Petr Chylek, M. Jarzembski, E. Creegan, V. Srivastava, Gilbert Fernandez, J. D. Pendleton, and A. Biswas, *Appl. Opt.*, 27(1988), pp. 987-996.
- [6] T. Seo, Y. Hisatomi, M. Mikami, "Study on characteristics of laser-induced breakdown in liquid spray," 24th European Conference on Liquid Atomization and Spray Systems, 2011.

# Session:

## **Wall Impingement**

## Experimental study of evaporating sessile liquid droplets on a heated horizontal surface

N. Giraldo<sup>1\*</sup>, S. Harmand<sup>2,3</sup>, C. Morin<sup>2,3</sup>, J. I. Huertas<sup>1</sup>

1: Automotive Mechatronic Research Center (CIMA), Tecnológico de Monterrey (ITESM) - Toluca Campus,  
C.P. 50110 Toluca, México

2: Université Lille Nord de France, 59000 Lille, France

3: UVHC, TEMPO, Le Mont Houy, 59313 Valenciennes Cedex 9, France

### Abstract

In this work it is studied the physical and thermal processes involved in the vaporization of sessile droplets. Small droplets, made of 0%, 25% and 50% aqueous solutions of acetone, were evaporated over silicon and quartz substrates at 60°C under ambient temperature and atmospheric pressure. The evolution of the vaporization process was followed through simultaneous measurements: a gravimetric measurement with the mass evolution, a droplet shape analysis which allows measurements of the dynamic contact angle, the droplet volume and the contact diameter as a function of time, and a measurement by infrared thermography of the droplet surface temperature, axial and radial profiles, triple line evolution, buoyancy and convective internal flows. It was observed that droplets deposited over silicon surfaces exhibit higher evaporation rates than those of similar composition deposited over quartz and that evaporation rate increase with acetone concentration. Water droplets show a constant evaporation rate while aqueous acetone droplets exhibit two vaporization stages. The first stage influenced largely by the most volatile substance. It was also observed that the initial contact angle decrease with the acetone concentration and that during the vaporization process the contact angle decreases while the base diameter remains nearly constant. Finally, temperature distribution within the droplet suggests that the vaporization process occurs mainly in the triple line and that the internal buoyancy is not axysymmetrical.

### Introduction

Droplet evaporation is a fundamental mechanism in several industrial and technological applications, such as in Diesel and propulsion engines [1-3], in caloduc systems [4], in rapid cooling in heat exchangers [1]. The study of the droplet evaporation on a heated support is also interesting in the case of engine downsizing, developed to decrease the fuel consumption. But in this configuration, the droplet can impact the combustion chamber walls, due to the low engine displacement and can modify the subsequent wetting, heating, vaporization and combustion phenomena that occur after the droplet hits the surface.

The influence of different parameters on the droplet evaporation has been studied: the droplet size or the capillary length [3], the droplet geometry (spherical symmetry or not) [5], the gravity and Brownian motion [6], the liquid nature (thermodynamics properties, volatility) [1], the temperature and pressure [1, 6] and several types of substances and surfaces [7]. Concerning the studies of evaporation on heated surfaces, according to the substrate (nature, roughness), thermal properties of the system droplet-substrate-gas and heat transfers have been established [5, 8], by underlining the effects of the surface tension gradients, the free convection and the buoyancy [1].

Different measurement techniques have been investigated: gravimetric measurement, ADSA (Axisymmetric drop shape analysis) and infrared thermography to characterize and study the vaporization process of sessile droplets. In gravimetric studies, the main parameter studied is the evolution of the droplet mass during the time of vaporization. In several studies [5, 9, 10] the droplet mass has been monitored to establish the influence of different air velocities over the substrate surface. Another technique widely developed to study the vaporization process is ADSA. This technique can monitor contact angle, base width, height of the droplet, and from images processing it can establish the sessile volume evolution during evaporation.[5, 6]

Infrared thermography is also used in the study of vaporization, it allows the observation of infrared heat transfer, triple line dynamics, thermal motions inside the drop. Brutin et al. [8], Saha et al. [11] have used infrared thermography, the first to study one substrate and several substances, and the second to study vaporization of pure and blended biofuels.

Acetone studied in this work is a good solvent and cleaner, intermediate reactant in the chemical production of explosives, polymers and epoxy resins. It has physical and chemical characteristics that are comparable to other fuels like ethanol and propanol, some particular characteristics like light absorption and volatility, that explains its use to perform fundamental studies of mass and heat transfer. Moreover, radiative properties of acetone allow to measure the droplet surface temperature by infra-red thermography [8]. Fundamental studies on droplet evaporation can then be easily investigated, to a better understanding of the phenomena.

The objective of this paper is to understand and underline the physical and thermal processes involved in the evaporation of sessile droplets. The evolution of the evaporation rate, the dynamic contact angle, base diameter and volume of sessile droplets of water and mixtures acetone-water and the evolution of the surface temperature of the droplet on two heated substrates (silicon, quartz) are presented and discussed.

### Experimental set-up and measurement techniques

The experimental set-up is described in Figure 1. Via a 10 cm<sup>3</sup> syringe with a needle of 650µm diameter and piloted by a pump with a volume rate between 1.28pl/min to 88.28 mL/min, a droplet with a controlled volume is deposited on a heated support by electric resistance (16.9 Ω) connected to a power supply (0 – 4 V and 0 – 0.25 A). The evolution of the droplet mass versus time is realized by a very sensitive balance (Sartorius) with a precision of 0.01 mg. As soon as the droplet is deposited on the solid surface, the temporal evolution of the droplet shape is recorded using a CCD camera (640x480 pixels, 30 fps) obtaining images for analysis with a horizontal resolution of 0.0804 mm/pixel (2.08 % uncertainty), vertical resolution 0.0619 mm/pixel (6.08 % uncertainty). For each experiment test, a minimum of 5400 images are recorded to have a good resolution. A minimum of three experiments were performed for every test condition. An infrared camera (FLIR SC7650, 640x512 pixels<sup>2</sup>) is used to measure the droplet surface temperature. A Plexiglas chamber protects the experimental set-up from convective currents of the ambient air at 21 °C. Two different surfaces heated to 60 °C are used: the first one is in silicon (roughness of 0.1-1.5 nm rms, thermal conductivity of 1 W/m.K), the second one is in quartz (roughness of 3-4 nm rms, thermal conductivity of 0.8 W/m.K).

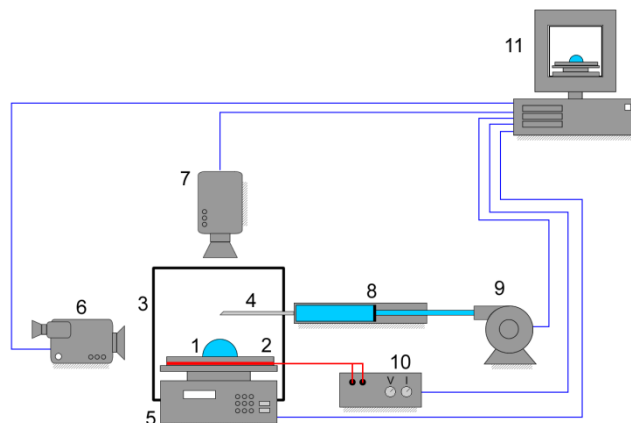


**Figure 1:** Experimental set-up with the measurement techniques. 1: droplet, 2: heated surface, 3: protective chamber, 4: needle, 5: analytic balance, 6: CCD camera, 7: IR camera, 8: syringe, 9: syringe pump, 10: power supply, 11: acquisition system

The experimental conditions are an ambient temperature of 21 °C, the atmospheric pressure, a 91% relative humidity and motionless air. The physical and chemical properties of acetone and water are presented in Table 1.

**Table 1:** Physical and chemical properties of acetone and water at 1 atm and 25°C.

Properties	Acetone (CH <sub>3</sub> COCH <sub>3</sub> )	Water (H <sub>2</sub> O)
Molecular weight (g/mol)	58	18
Density (kg/m <sup>3</sup> @ 298K)	784	997
Dynamic viscosity (10 <sup>-2</sup> Po @ 298K)	0.303	0.895
Surface tension (10 <sup>-3</sup> N.m @ 293K)	23	72
Latent heat of vaporization (kJ/mol @ 298K)	31.21	43.94
Boiling temperature (°C)	56.2	100
Vapor pressure (kPa @ 298K)	24.26	2.2

The post processing of sequences of images were done using ADSA technique. One of the methodologies of this technique is to use images of the droplet to fit a mathematical expression to the drop boundary and then, calculate several related variables for example the contact angle, the surface tension [12]. The main assumptions are that the drop is symmetric according to a central vertical axis and the drop is not in motion.. For this study,

the software for image analysis created by FTA [13] is applied, by using the thermodynamic properties and surface tension of the substances, the following liquids: water, acetone and their mixtures [14]. Concerning the post processing of infrared images, from the emissivity of the liquid, the surface temperature is deduced giving a previous calibration of the camera.

The experiments are done for pure water and two mixtures (25% vol. acetone – 75% vol. water and 50% vol. acetone – 50% vol. water).

## Results and discussion

### Gravimetric analysis

Figure 2 shows the results obtained from gravimetric tests for aqueous solutions of acetone (ACE) at 0%, 25% and 50% volume concentrations over silicon surface at 60°C. The reproducibility of the vaporization process was verified with water droplets of a specific volume (13.82  $\mu$ l) over surface at 60°C. There is a reproducibility of 98% related to the vaporization rate.

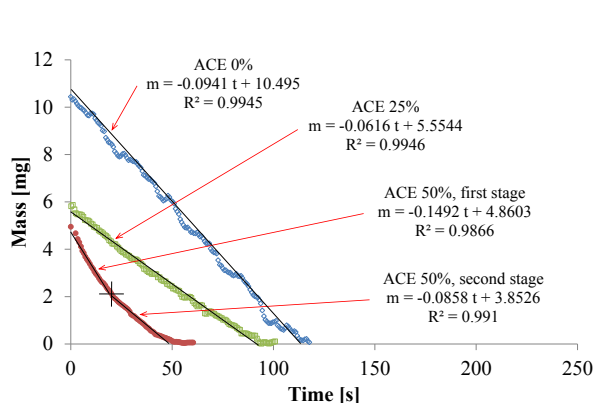


**Figure 2:** Mass evolution of sessile acetone-water droplets over silicon surfaces at 60 °C.

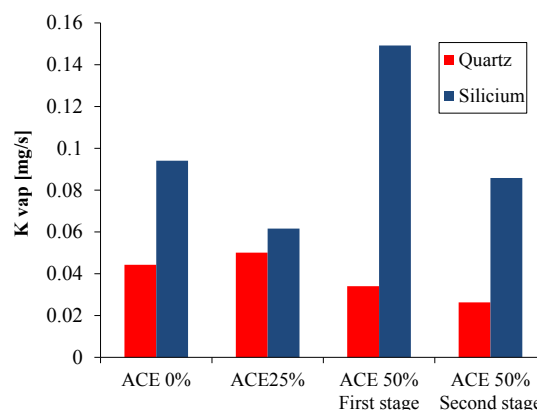


**Figure 3:** Average vaporization rates of sessile acetone-water droplets over quartz and silicon surfaces at 60 °C.

The mass decreases linearly versus time for the different mixtures. The linear evolution is in agreement with the quasi-steady model developed in the 1950's by Godsave [15] and Spalding [16] for an isolated, one component droplet, vaporizing in a oxidizing and stagnant environment. In the present study, it was also verified a linear decrease of the droplet mass (from the gravimetric analysis) and droplet diameter (from the image analysis presented later) versus time during the vaporization time for all the experimental conditions. Vaporization rates are calculated by a linear least square fit from the evolution of the droplet mass versus time. For a mixture of 50% water – 50% acetone, the mass evolution presents two linear stages, the first linear stage allows to determine the first average vaporization rate and the second linear stage a second average vaporization rate. For silicon surface it is found that the rates of vaporization are 0.096±0.012, 0.058±0.007, 0.1492±0.015 and 0.085±0.009 mg/s for acetone concentrations of 0%, 25%, 50% first stage and 50% second stage, respectively. Over quartz surface the vaporization rates are 0.044±0.011, 0.050±0.006, 0.034±0.009 and 0.0263±0.013 mg/s for acetone concentration of 0%, 25%, 50% first stage and 50% second stage, respectively. These results are summarized in Figure 3.

In the case of mixtures of 50% acetone – 50% water the vaporization presents two phases [6, 17]. In the first stage, the most volatile substance vaporizes firstly and in the second stage the less volatile one vaporizes. The volatility of the acetone at 60°C is 5.7 higher than of the water, the vapor pressure of acetone is 113.73 kPa in equilibrium while the vapor pressure of water is 19.85 kPa. In these experiments, it can be observed that this behavior is influenced by the concentration of acetone in water. That is, the more concentration of acetone, the more differs from the behavior of pure water. However, in Figure 2 it can be seen that for 25% concentration of acetone, the two different vaporization linear stages are not quite distinguishable, that means, the vaporization rate is different from pure water but the behavior is almost linear and can be fitted very well with a determination coefficient R<sup>2</sup> of 0.994. On the other hand, for the mixture of 50%, it can be easily divided in two intervals with the corresponding vaporization rate, the behavior linear in each case with R<sup>2</sup> of 0.98 and 0.99, respectively. The latter analysis shows that there is an influence of the concentration of acetone in the aqueous solution over the vaporization rate. In Figure 3, by comparing the K<sub>vap</sub> of pure water and K<sub>vap</sub> of the second stage of the mixture of 50% acetone, in the case of silicon surface, the difference between the both rates is of 10%, and in the case of quartz surface is 40%. In Figure 2, there is a difference in the K<sub>vap</sub> of pure water and acetone mixtures depending on the surface, with higher vaporization rates for silicon surfaces. It is related to roughness of the silicon surface which is lower than of the quartz surface and thermal conductivity of the silicon

surface that is higher than that of the quartz surface, improving the heat transfer to the droplet and in consequence the vaporization process.

### Image analysis

The image sequences were processed with ADSA (Axisymmetrical Drop Shape Analysis), for the purposes of the present document, the analysis of sessile volume, contact angle and base diameter only for silicon are presented. Figure 4 shows the evolution of the droplet sessile volume for different dilutions of acetone-water over silicon surface at 60 °C. The behavior is similar to that obtained by Sefiane et al. [6] with ethanol-water mixtures. The vaporization rate depends on the concentration of the most volatile substance of the mixture. As previously mentioned from gravimetric analysis, a linear evolution of the droplet sessile volume versus time is observed and the two stages for a mixture of 50% acetone-50% water. For silicon surface, the vaporization rates are  $0.12 \pm 0.010$ ,  $0.0766 \pm 0.003$ ,  $0.1634 \pm 0.012$  and  $0.1148 \pm 0.004$   $\mu\text{L/s}$  for acetone concentrations of 0%, 25%, 50% first stage and 50% second stage, respectively. As in the case of gravimetric analysis, the assumption of two linear stages in the case of 50% of acetone concentration was assumed. Figure 4 also shows a similar behavior to that observed in gravimetric tests.

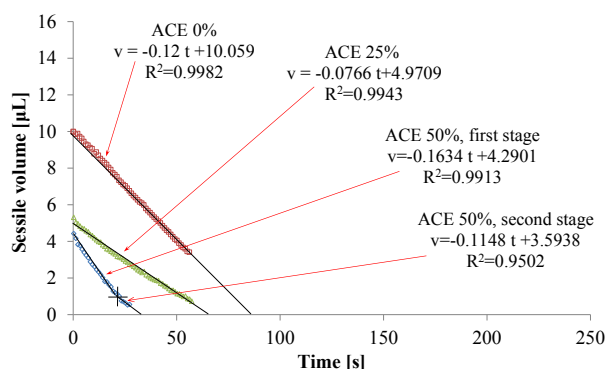


**Figure 4:** Evolution of the sessile volume of acetone-water droplets over silicon surface at 60 °C.

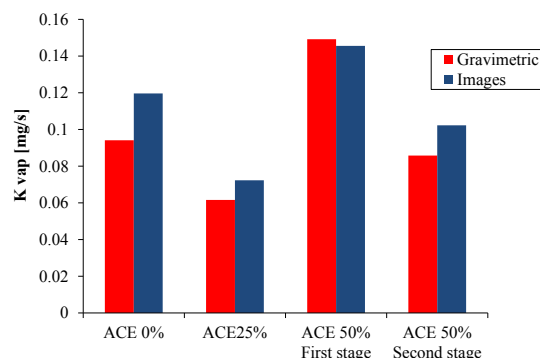


**Figure 5:** Comparison between the vaporization rate obtained through two techniques: Gravimetric analysis and images sequences for silicon surface.

From Figure 4 and assuming the density of every liquid and the mixture correspondingly constant, the vaporization rate in  $\mu\text{L/s}$  was converted into  $\text{mg/s}$ , obtaining the results showed in Figure 5. In this figure, the vaporization rates obtained from gravimetric analysis and the image analysis were compared. The differences between the vaporization rates measured from the two techniques were 25%, 15%, 5% and 16% for acetone concentrations of 0%, 25%, 50% first stage and 50% second stage, respectively.

The differences are due to experimental error of measurements. Additionally, image analysis could have errors when the droplet density variations are observed, given that the density used to convert the vaporization rate in the case of the mixture water-acetone is supposed constant during all the vaporization. The vaporization mechanism is modified by factors like i) the droplet dilatation when it heats over the heated surface, ii) the contraction due to cooling caused by the phase change (vaporization) and iii) the composition change to the extent that the most volatile substance vaporizes first.

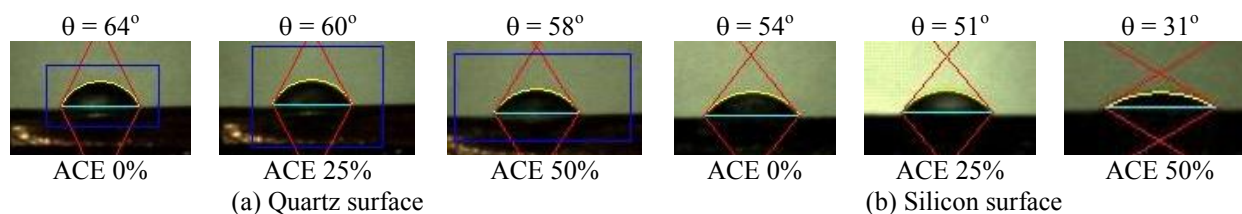
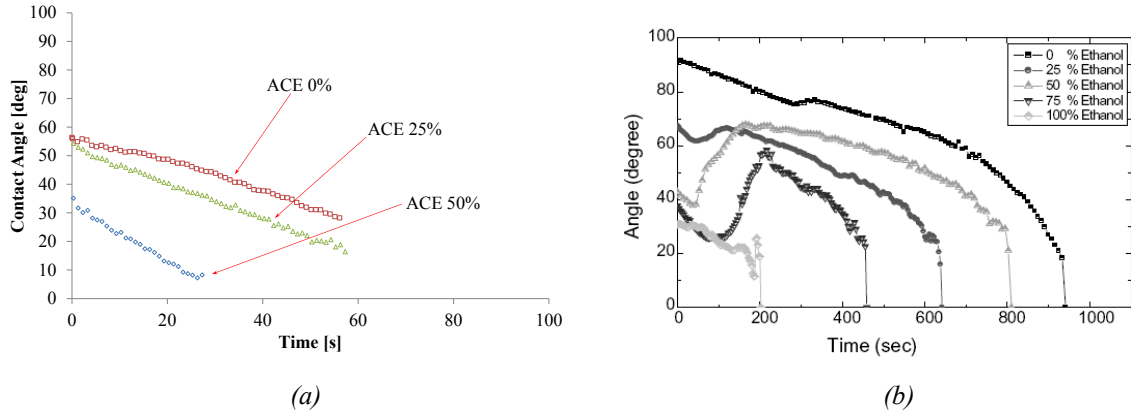


**Figure 6:** Initial contact angles of sessile droplets over (a) Quartz surface and (b) Silicon surface at 60°C.

Figure 6 shows the initial contact angle formed by pure water and acetone-water mixtures of sessile droplets at the initial stage of the evaporation process under the same conditions. The behavior of the initial contact angle is related to the surface tension at the triple line which depends on the substance, the surface and the gas phase, and the surface energy, which is related to the roughness [18]. In this case it is observed that the rougher is the surface (Quartz surface) the higher is the initial contact angle for the corresponding mixture compared to the other surface (Silicon surface). It is also observed that the concentration of acetone has also an influence, that is, the more diluted the solution the higher is the initial contact angle.

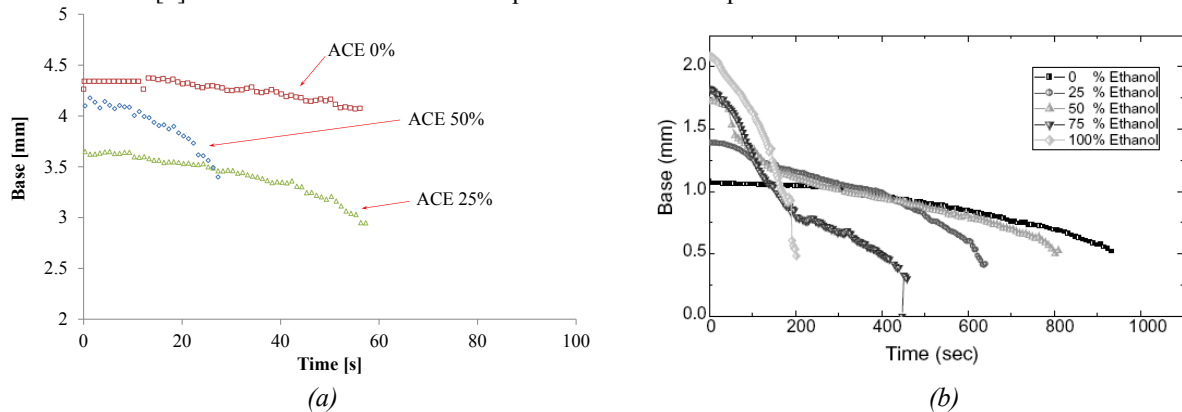


Figure 7 shows the evolution of the contact angle formed by the acetone-water sessile droplets on silicon surfaces at 60°C. These results are compared with those obtained by Sefiane et al. [6] with water-ethanol mixtures on PTFE (Polytetrafluoroethylene) surface at ambient temperature. For all the liquids, the contact angle has a slight continuous decrease versus time when the concentration of water increases in the mixture, this decrease becomes higher. Similar evolutions are obtained with water-ethanol mixtures. In this case, the contact angle for pure water droplets presents a slight decrease versus time and then at the end of the lifetime of the droplet a sharp decrease. Similar behavior is found for pure ethanol droplets with slight differences. However, at the end of the droplet lifetime, a sudden jump in the contact angle is observed, according to Sefiane et al. [6] this is related to the depinning of the triple line. The initial contact angle for different droplet concentrations ranges between the initial contact angle of the pure substances (water and ethanol). The contact angle decreases as the concentration of ethanol is increased.



**Figure 7:** Evolution of the contact angle formed by the acetone-water sessile droplets on (a) Silicon surface at 60°C. (b) Results of Sefiane et al. [6] with water-ethanol mixtures on PTFE surface at ambient temperature.

Figure 8 shows the evolution of base width of the acetone-water sessile droplets on silicon surface at 60°C, and are compared with the results obtained by Sefiane et al. [6] with water-ethanol mixtures on PTFE surface at ambient temperature. The base diameter reduces monotonically and slowly with time. At 50% of the vaporization time, the base diameter is still more than 80% of the initial value. Additionally, the rate of decrement increases with the acetone content in the mixture. These observations agree with the ones obtained by Sefiane et al. [6] with ethanol-water sessile droplets at ambient temperature.

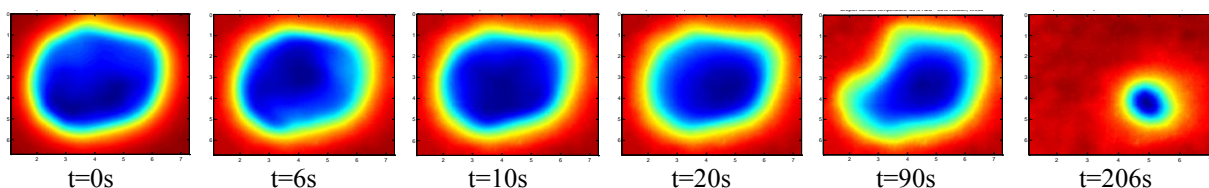


**Figure 8:** Evolution of the base width formed by the acetone-water sessile droplets on (a) Silicon surface at 60°C. (b) Results of Sefiane et al. [6] with water-ethanol mixtures on PTFE surface at ambient temperature.

### Infrared imaging

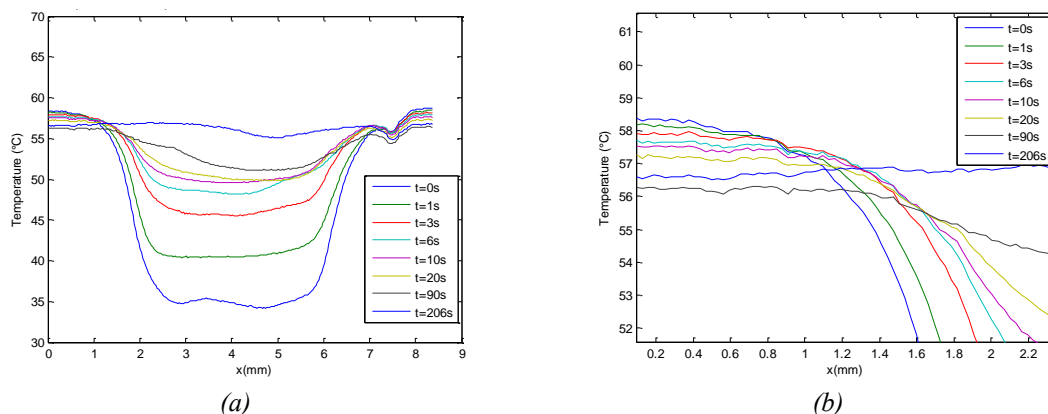
The results for the mixture 50% acetone - 50% water over quartz surface at 60°C are presented in this work. The surface temperature of the support is uniform, as observed in initial verification sequences of all the tests. In the test, after depositing the drop over the surface, the infrared sequences are recorded until the end of the vaporization process.

Figure 9 presents the droplet surface temperature during the vaporization for the mixture 50% acetone-50% water over a quartz surface at 60°C. The surface temperature of the droplet is not uniform. The vaporization mechanism is not axisymmetric: at 206s, the droplet surface temperature is visualized in the lower right part of the IR image, that means a first sequence of vaporization of the more volatile liquid took place in the higher left part of the IR image.



**Figure 9:** Droplet surface temperature for different times for the mixture 50% acetone-50% water over a quartz surface at 60°C. Higher temperature red (60°C), lower temperature dark blue (36°C).

Figure 10 shows the axial superficial temperature, the initial temperature of the droplet surface at the center is 36°C, then given the heat flux and the warming of the droplet this temperature increases.



**Figure 10:** Evolution of (a) the axial superficial temperature and (b) superficial temperature at the contact line of the mixture 50% acetone-50% water sessile droplets on quartz surface at 60°C.

At the same time, the vaporization process takes place, and according to the profile temperatures of the Figure 10 (a) and (b), the temperature in the triple line maintains higher than 56°C, which is the boiling temperature of acetone. During all the vaporization time, the low temperature at the center of the droplet surface and the high temperature at the triple line, suggest that the vaporization process takes place in the triple line, starting from the most volatile substance, in this case acetone, by means of internal buoyancy movements flows towards the triple line. The sequences show also, that there is not formation of patterns over some axis of the droplet or the formation of micro convection cells nor convective instabilities like underlined by Brutin et al. [8] for pure substances. There is no formation of a phase separation between the water and acetone, at least, at the level of accuracy of the infrared system. It is important to note, that the internal movements of fluid observed are not axisymmetric.

## Conclusions

An experimental work was performed to understand and underline the physical and thermal processes involved in the vaporization of sessile droplets of different binary mixtures acetone-water (0%, 25% and 50% vol.) and over two different surfaces, silicon and quartz at 60°C from gravimetric measurements, a droplet shape analysis and infrared thermography..

It was shown that the rate of vaporization of the binary mixtures is influenced by the kind of substrate where the droplets are deposited. Vaporization rates over silicon surface are higher compared to those on quartz surface. They are also influenced by the concentrations of the substances in the binary mixture. The higher the concentration of acetone, the higher the vaporization rate and the behavior of the vaporization differs substantially from vaporization of pure water, showing two different vaporization stages each one with the corresponding vaporization rate.

Image analysis suggests for all cases that the vaporization process is given by a decreasing of the contact angle and the base diameter nearly constant over all the vaporization time. The higher the concentration of acetone, the more the rate of decrease of the contact angle. Surface temperature of the droplet shows that the vaporization process occurs in the triple line and the internal buoyancy are not axisymmetric.

## Acknowledgements

Authors would like to thanks Mexican Government CONACYT – *Consejo Nacional de Ciencia y Tecnología*, the Laboratory TEMPO of the UVHC and the CIMA of the ITESM – Campus Toluca for supporting this research.

## References

- [1] Erbil, H.Y., *Evaporation of pure liquid sessile and spherical suspended drops: A review*. Advances in Colloid and Interface Science, 2012. **170**(1-2): p. 67-86.
- [2] Sefiane, K., M.E.R. Shanahan, and M. Antoni, *Wetting and phase change: Opportunities and challenges*. Current Opinion in Colloid & Interface Science, 2011. **16**(4): p. 317-325.
- [3] Semenov, S., et al., *Evaporation of sessile water droplets: Universal behaviour in presence of contact angle hysteresis*. Colloids and Surfaces A: Physicochemical and Engineering Aspects, 2011. **391**(1-3): p. 135-144.
- [4] Harmand, S., et al., *Transient cooling of electronic components by flat heat pipes*. Applied Thermal Engineering, 2011. **31**(11-12): p. 1877-1885.
- [5] Bin, L., R. Bennacer, and A. Bouvet, *Evaporation of methanol droplet on the Teflon surface under different air velocities*. Applied Thermal Engineering, 2011. **31**(17-18): p. 3792-3798.
- [6] Sefiane, K., L. Tadrist, and M. Douglas, *Experimental study of evaporating water-ethanol mixture sessile drop: influence of concentration*. International Journal of Heat and Mass Transfer, 2003. **46**(23): p. 4527-4534.
- [7] Fang, X., et al., *Factors Controlling the Drop Evaporation Constant*. The Journal of Physical Chemistry B, 2005. **109**(43): p. 20554-20557.
- [8] Brutin, D., et al., *Infrared visualization of thermal motion inside a sessile drop deposited onto a heated surface*. Experimental Thermal and Fluid Science, 2011. **35**(3): p. 521-530.
- [9] Lu, G., et al., *Internal flow in evaporating droplet on heated solid surface*. International Journal of Heat and Mass Transfer, 2011. **54**(19-20): p. 4437-4447.
- [10] Chan, K.B. and S.M. Pierce, *Sessile droplet de-pinning: New life for gravimetric data*. Journal of Colloid and Interface Science, 2007. **306**(1): p. 187-191.
- [11] Saha, A., R. Kumar, and S. Basu, *Infrared thermography and numerical study of vaporization characteristics of pure and blended bio-fuel droplets*. International Journal of Heat and Mass Transfer, 2010. **53**(19-20): p. 3862-3873.
- [12] Hoorfar, M. and A.W. Neumann, *Recent progress in Axisymmetric Drop Shape Analysis (ADSA)*. Advances in Colloid and Interface Science, 2006. **121**(1-3): p. 25-49.
- [13] Woodward, R.P., *Contact angle measurements using the drop shape method*. 2000, First Ten Angstroms, Inc: Portsmouth, VA, US. p. 1-8.
- [14] Poling, B.E., J.M. Prausnitz, and J.P. O'Connell, *The properties of gases and liquids*. Fifth ed. 2001, New York: McGraw-Hill. 803.
- [15] Godsave, G.A.E., *Studies of the combustion of drops in a fuel spray - The burning of single drops of fuel*. Symposium (International) on Combustion, 1953. **4**(1): p. 818-830.
- [16] Spalding, D.B., *The combustion of liquid fuels*. Symposium (International) on Combustion, 1953. **4**(1): p. 847-864.
- [17] Morin, C., et al., *Vaporization and oxidation of liquid fuel droplets at high temperature and high pressure: Application to n-alkanes and vegetable oil methyl esters*. Combustion science and technology, 2004. **176**(4): p. 499-529.
- [18] Sefiane, K. and L. Tadrist, *Experimental investigation of the de-pinning phenomenon on rough surfaces of volatile drops*. International Communications in Heat and Mass Transfer, 2006. **33**(4): p. 482-490.

## Mapping Drop Impact Regimes on a Heated Surface

C. Lakhanpal, K. Black and V. Bertola

1: School of Engineering, University of Liverpool, UK

### Abstract

A 2-D impact regime map has been developed based upon a comprehensive set of investigations carried out on the impact dynamics resulting from orthogonal impact of a water drop on a heated polished aluminium surface. High-speed photographic records reveal different regimes on the basis of the final impact outcomes: secondary atomization, splashing with secondary atomization, rebound with secondary atomization, rebound and splashing. Some characteristics of transition boundaries are discussed. Finally, comparison with data of previous researchers shows significant differences due to a flaw identified in their experimental procedure.

---

### Introduction

The dynamics of liquid drops impacting a heated surface is a phenomenon of interest in many areas of engineering, including: spray cooling, inkjet printing for advanced manufacturing applications, quenching of alloys in the steel industry and nuclear reactor safety. Despite several decades of research, this phenomenon still attracts further work. Specifically, the development of impact regime maps (IRMs) is of interest because they provide a consolidated understanding of the impact behaviour and represent a tool of practical use in the design of nozzles, printheads etc. A quantitative and comprehensive IRM also presents an important test case for the development and validation of theoretical models describing specific features of impact.

When a drop impacts a heated surface, the final impact outcome is a function of two key parameters, namely, the Weber number and the surface temperature. The realised physical mechanisms can be classified relative to the boiling curve. At surface temperatures below the boiling point of the liquid, the morphology of drop impact is essentially single phase in nature and only some very small-scale isolate bubble formation is observed. At surface temperatures above the boiling point of the liquid, different regimes are realised; these include nucleate boiling, transitional boiling and subsequently, film boiling where the drop is separated by a vapour film, stable enough to allow drop levitation.

Bai & Gosman [1] were the first in producing an IRM, even though vaguely qualitative in nature. Although, the map identified some of the impact regimes, there was no clear quantitative description on the initiation and extent of these regimes.

This work was soon followed by a detailed investigation carried out by Bernardin et al. [2] who produced three distinct IRMs corresponding to Weber numbers of 20, 60 and 220 and for surface temperatures ranging from 100° to 300°C. Although their work included substantial information on the spreading behaviour of a drop and its heat transfer characteristics, the IRMs were far from being fully comprehensive, particularly lacking information on all possible impact regimes that can be realised as well as the transitional boundaries between these. This was partly because of the limitations in photographic techniques available for analysis at the time. Moreover, their photographic results were not based on studying the lifetime of a single drop but rather based upon an ensemble principle of several drops; with one photograph taken per drop.

A recent review by Moreira et al [3] also reported IRMs developed by Rein [4] and Lee & Ryu [5]. The comparison between these maps shows significant clear differences. These differences have been associated to the fact that both these investigations lacked a thorough understanding of the boundary temperatures [3]. Although, this is partly the case, close examination of these maps reveals that the differences are most likely due to following different and most likely, rather non-robust experimental protocols. This argument can additionally be sustained because the map produced by Lee & Ryu [5], which is remarkably similar to that produced by Bai & Gosman [1], shows an additional intermediate rebound regime between the ‘stick’ and ‘spread’ regimes identified by them. Our concern arises because they have shown this regime to exist at surface temperatures below the boiling point of the liquid. This should not be the expected outcome because rebound regime can only be realised when the drop is separated from the surface by a vapour film which plays a critical role in inducing the rebound phenomena; and this only occurs at temperatures above the Leidenfrost point of the liquid. Since, no additional explanation has been provided by them, it’s difficult for us to ascertain as to why they observed rebound at lower temperatures. Moreover, both these IRMs, as produced by Rein and Lee & Ryu are only, partially, qualitative in nature as again, they lack information on the initiation and extent of the identified regimes and location of the transitional boundaries.

Black & Bertola [6] have considered the drop impact morphology on heated surfaces and provided a quantitative and comprehensive 2-d impact regime map based upon the final impact outcomes. This work has considered characteristics of transition boundaries besides proposing more accurate empirical correlations to predict the Leidenfrost temperature and the onset of splashing. Moreover, this work also recognizes the

importance of precision control in calculating Weber numbers due to its significance in the achieved impact outcomes.

Castanet & Lemoine [7] have investigated in detail, both the heat transfer characteristics and drop impact regimes for a water drop impacting on a nickel surface. Apart from Weber number and the surface temperature, they also considered drop incidence angle and size. The impact regime map, produced with Mundo, K number (combination of Weber and Ohnesorge numbers) and dimensionless temperature (as prescribed in earlier literature) as its coordinates provided information on the three impact regimes, namely, rebound, splashing and deposition of a liquid film. This work specifically provided comprehensive information on the transition boundary between the deposition and splashing regimes.

More recently, Tran et al [8] have also published an IRM developed by them for surface temperatures between 200° and 600°C and Weber numbers between 0.5 and 600. They considered two different liquid drops (milliQ water & Fluorinert liquid FC-72) and two different impact surfaces (silicon plate & sapphire) to reflect different surface roughness values. Their impact regime map includes information on the impact behaviour and is separated into three regimes: contact boiling, film boiling and spray film boiling. However, a key shortcoming of this work has been their experimental protocol and set up, which causes some serious discrepancies in the calculated Weber numbers.

Most of the previous studies subject to accurate investigations concerned individual transitions, for example, [7, 9]. The drop dynamics are influenced by Weber number, accurate consideration of which, has received rather less attention. Our study therefore aims at revisiting the investigation of drop impact dynamics and focusing on the production of a fully comprehensive and quantitative impact regime map based on the final outcomes.

### Experimental test-rig

The experimental work was carried out using the set-up as shown in Figure 1 below. The drop generation system employed was designed to control the temperature of the liquid drops. Deionised water, obtained using the Barnstead Easypure II system was supplied to a gauge 18 (internal diameter 0.838 mm) hypodermic needle via a syringe. The temperature of the released drops was controlled using a PID controller to  $85^\circ \pm 5^\circ \text{C}$ .

Drop weight measurements made with a precision balance (Mettler Toledo MT100) allowed calculation of the drop diameter at equilibrium,  $D_0 = \sqrt[3]{6m/\pi\rho}$ : the average value, calculated over 50 samples, was  $3.15 \pm 0.1$  mm. The drop equilibrium radius,  $D_0/2$ , being smaller than the capillary length,  $a = \sqrt{\sigma/\rho g}$  indicates the competition between surface forces and gravity: thus, surface forces prevail ensuring that the equilibrium shape of drops is spherical.

The height of the released drops and hence the impact Weber number (assuming all other conditions kept constant) was controlled using a digital vernier calliper. The impact velocity,  $u$ , is calculated using the relation  $\sqrt{2g(H - D_0)}$  where  $D_0$  is the equilibrium drop diameter, while the Weber number is defined as  $We = \rho D_0 u^2 / \sigma$ .

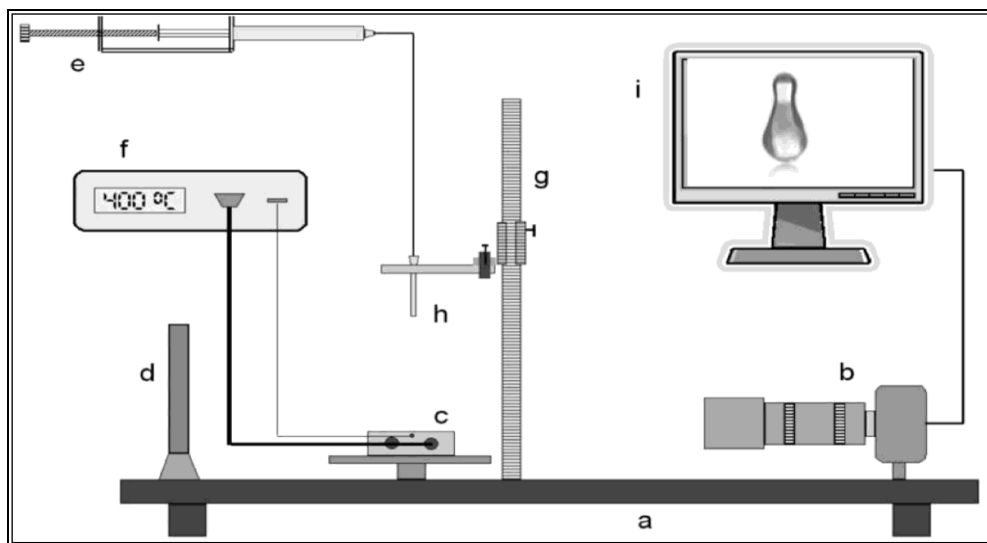


**Figure 1:** Schematic of experimental setup (image incorporated from Black & Bertola, [6]): a) optical breadboard; b) high-speed camera; c) heated aluminium block; d) LED backlight; e) temperature controlled drop dispensing system; f) temperature controller; g) digital vernier callipers; h) needle; i) computer

The drop surface tension, an important physical property affecting the impact process is embedded in the Weber number. Previous investigations (as explained in the introduction section) have used drops released at room temperature. The temperature boundary, for all test cases considered is significantly higher. So, from release to impact, the temperature of the drop is set to rise thereby influencing the fluid surface tension and hence the impact Weber number. For example, when the fluid temperature changes from 20°C to 99°C, the corresponding change in Weber number is +20%. With the current set-up, the temperature of the released drops is controlled close to the boiling point and allows us to better control the impact Weber number.

The released drops impacted upon a heated and polished aluminium surface which was electrically heated using two 100W cartridge heaters and the temperature controlled by a PID controller. The temperature was kept constant near the transition boundaries and administered to an accuracy of  $\pm 2^\circ\text{C}$  elsewhere. The impacts of single drops were recorded using a high-speed CMOS camera (Mikrotron MC1310) at the rate of 1000 frames per second, with back-to-front illumination. For each set of experimental parameters and for the sake of statistical analysis, the impact experiment was repeated three times and near the transition boundaries, was repeated ten times. For all the surface temperatures and Weber numbers considered, a total of approximately 10,000 impact experiment runs were carried out and analysed.

## Results and Discussion

The impact dynamics considered in this work are a function of two key parameters, namely the Weber number and the surface temperature. When the temperature of the surface is below the fluid boiling point, the drop impacts the surface, spreads on it to a maximum diameter, retracts back and demonstrates an up-down oscillation before eventually simply ‘sitting’ on the surface. This is a single phase only regime where the drop provides maximum surface wetting. The complete evaporation of the drop occurs as a result of convection heat transfer, the only primary mode of heat transfer in this regime. Figure 2a shows the impact outcome obtained for the *direct deposition on the surface* regime.

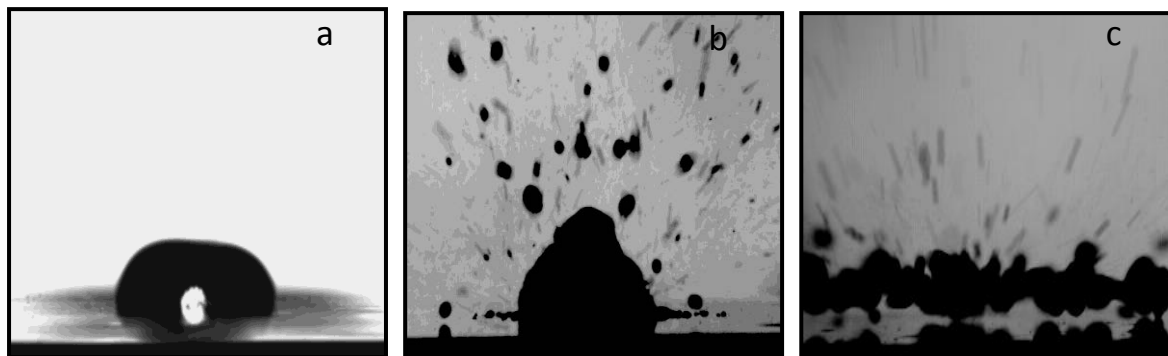


**Figure 2:** (a) Drop deposition on the surface ( $We = 40$ ;  $T = 100^\circ\text{C}$ ). (b) Secondary atomization ( $We = 100$ ;  $T = 150^\circ\text{C}$ ). (c) Breakup with secondary atomization ( $We = 100$ ;  $ST = 200^\circ\text{C}$ ).

When the surface temperature is above the boiling point of the liquid, vapour bubbles produced by heat transfer on the surface rise by buoyancy and burst on the free surface of the drop, thereby scattering a number of satellite droplets. This regime, known as the *secondary atomization*, relates to the nucleate boiling heat transfer regime and only partially wets the surface. The size distribution of the secondary drops is observed to be bimodal in nature. Figure 2b shows the impact outcome for the Secondary Atomization regime.

When the temperature of the surface is increased further, two intermediate regimes, namely *breakup with secondary atomization* (Figure 2c) and *rebound with secondary atomization* (Figure 3a) are observed; these relate to the transitional boiling regime on the boiling curve, thereby signifying an unstable vapour layer. The splashing with secondary atomization regime is observed within the mid-high Weber number range whilst the rebound with secondary atomization is observed within the low-mid Weber number range. Within both these regimes, the drops make partial contact with the heated surface thereby leading to the generation of vapour bubbles on a relatively smaller scale as compared to the neat secondary atomization regime. As a result, only a very small-scale secondary atomization is observed within these regimes.

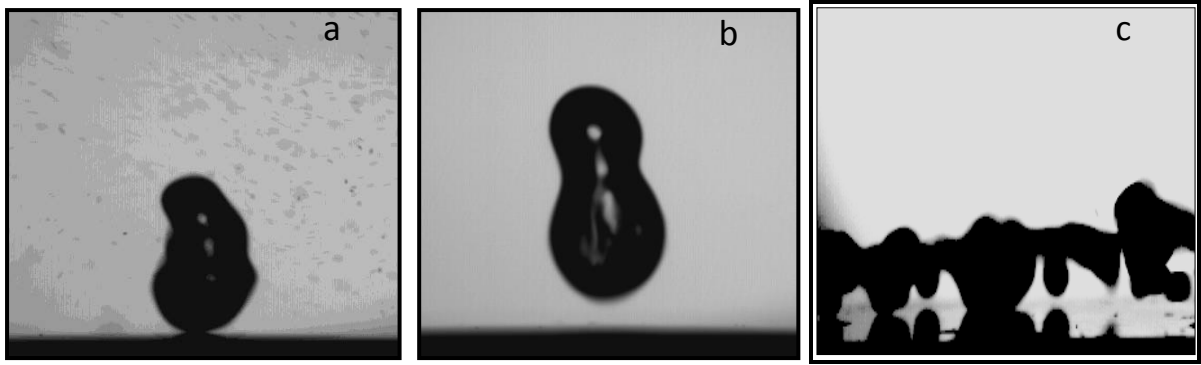


**Figure 3:** (a) Rebound with secondary atomization ( $We = 100$ ;  $T = 250^\circ\text{C}$ ). (b) Dry rebound ( $We = 40$ ;  $T = 400^\circ\text{C}$ ). (c) Breakup ( $We = 150$ ;  $T = 400^\circ\text{C}$ ).

When the temperature of the surface is increased even further, i.e. at temperatures above the Leidenfrost point, one can either observe a complete drop rebound (Figure 3b) or breakup (Figure 3c); these regimes relate to the film boiling regime on the boiling curve, with no occurrence of surface wetting. The rebound regime is observed within the low-mid Weber number range whilst breakup is observed at higher Weber numbers.

The observed impact outcomes can be displayed on a two-dimensional impact regime map, shown in Figure 4, where the coordinates are the Weber number and the surface temperature. A key characteristic of the transition boundaries is their probabilistic nature [6]. For example, repeating an impact experiment several times close to the transition boundaries, it is possible to observe outcomes on either side of the boundary.

In a given point of the map, near a transition boundary, the probability of observing a particular outcome was calculated as the number of times the outcome was actually observed divided by the total number of impacts considered. Three examples of such probability curves are shown in Figure 5, respectively for the transitions between rebound and rebound with secondary atomization (Figure 5a), the transition between rebound with secondary atomization and breakup with secondary atomization (Figure 5b), and the transition between rebound and breakup (Figure 5c).

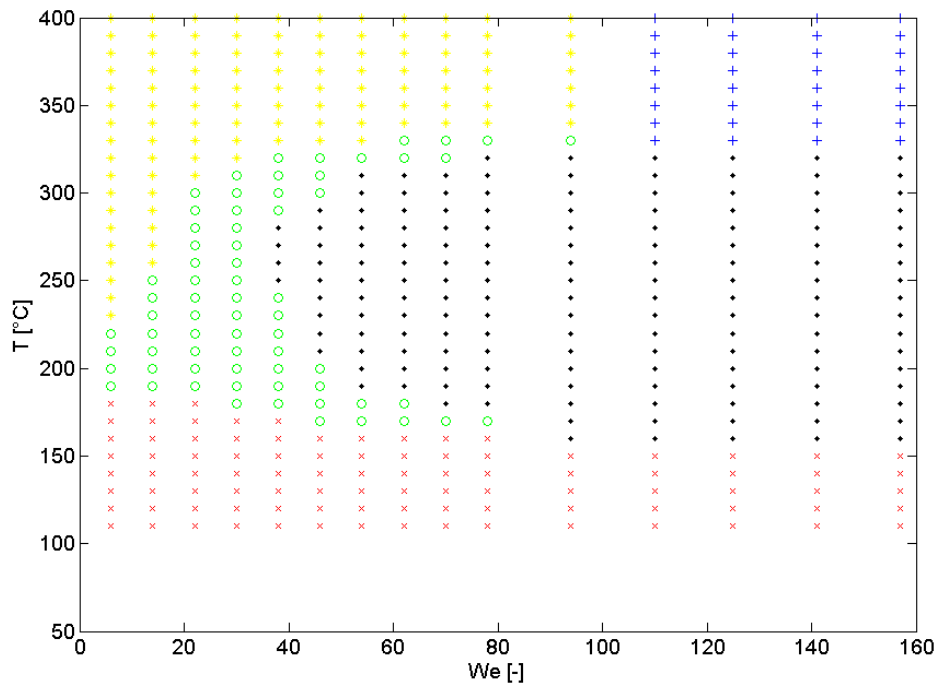


**Figure 4:** Impact regime map for water drops impacting a heated, polished aluminium surface. (x) Secondary atomization; (o) Rebound with secondary atomization; (d) Breakup with secondary atomization; (\*) Dry rebound; (+) Breakup.



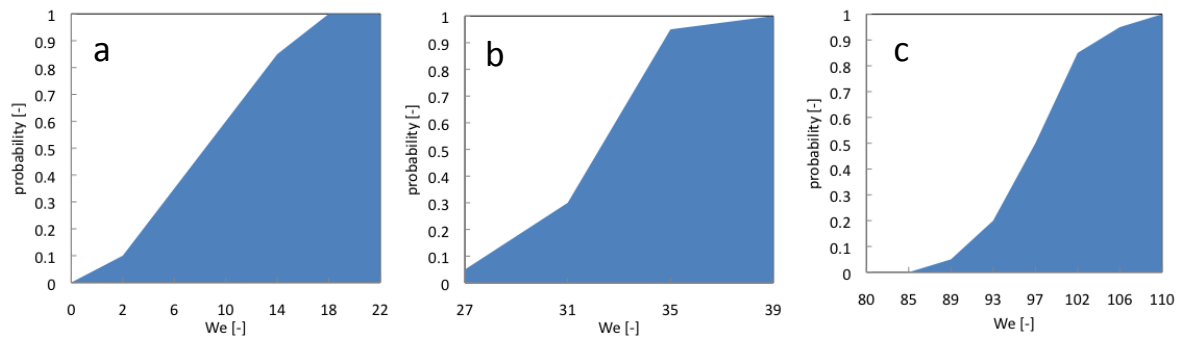


**Figure 5:** Probabilistic nature of impact regime transitions. (a) Rebound – rebound with secondary atomization (T=250°C); (b) Rebound with secondary atomization – breakup with secondary atomization (T=250°C); Rebound – breakup (T=350°C).

In a recent work, Tran et al. [8] proposed an impact regimes map for water drops impacting on a heated silicon wafer. The map shows three separate regions, corresponding to different impact regimes, named “contact boiling regime” (i.e., nucleate boiling), “gentle film boiling regime” (usually referred to as “Leidenfrost impact” or “dry rebound” in the literature), and “spraying film boiling regime”, where secondary atomization is observed. Drop breakup/splashing was not observed for Weber numbers up to 500, and rebound with secondary atomization (“spraying film boiling”) was observed for temperatures above the dry rebound regime (“gentle film boiling”).

The absence of a breakup regime might be related to the different surface roughness of the impact surfaces: in fact, while silicon wafers can be considered perfectly smooth, polished aluminium has an average surface roughness  $R_a \sim 100$  nm. It is well known that reducing the average surface roughness moves the onset of drop breakup upon impact towards higher Ohnesorge numbers (or, in cases where only one fluid is considered, higher Weber numbers) [10]. However, the effect of surface roughness on the breakup threshold should be less noticeable in the case of Leidenfrost impact, where the surface and the liquid droplet are kept separated by the vapor cushion.

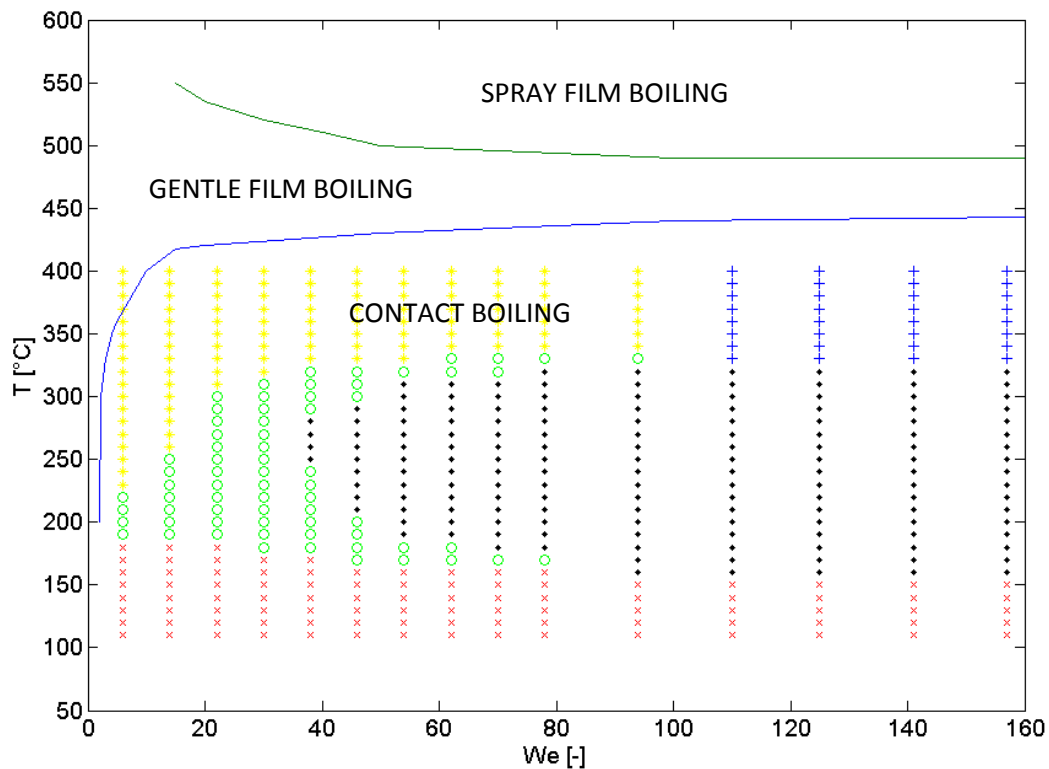


**Figure 6:** Comparison between the results of the present work and the impact regime map proposed by Tran et al. [8]. Reducing the surface roughness is also expected to improve the stability of the vapor layer, therefore dry rebound (or “gentle film boiling”) should be observed at slightly lower temperatures than in the case of rough

surfaces, in contrast with the results presented in Ref. [8], as shown in Figure 6. We argue this large discrepancy between our results and those of Ref. [8] is due to an erroneous estimation of the impact surface temperature. In fact, in the experimental setup used by these Authors the impact surfaces (silicon wafers and sapphire plates) are placed on a hollow, stainless steel cylindrical holder, with a 2 cm i.d. hole to allow visualization from below. However, the surface temperature was approximated as the holder temperature, based on the assumption that sapphire and silicon both have high thermal conductivity, therefore the temperature difference between the holder and the test surface can be neglected in the explored temperature range (from 200 °C to 600 °C). This assumption is not correct, because it neglects the contact thermal resistance between the holder and the surface, and, more importantly, free convection heat transfer on the top and bottom sides of the surface, which can reduce significantly the temperature at the point of impact.

To prove this argument, we have measured, using a surface thermocouple, the temperature in the centre of a 2-inches diameter silicon wafer placed on a similar hollow, stainless steel cylindrical holder with a 2-cm i.d. bore, and compared it with the temperature measured by a thermocouple placed inside the holder. The results, displayed in Figure 7, show that, as expected, the holder temperature significantly overestimates the surface temperature.

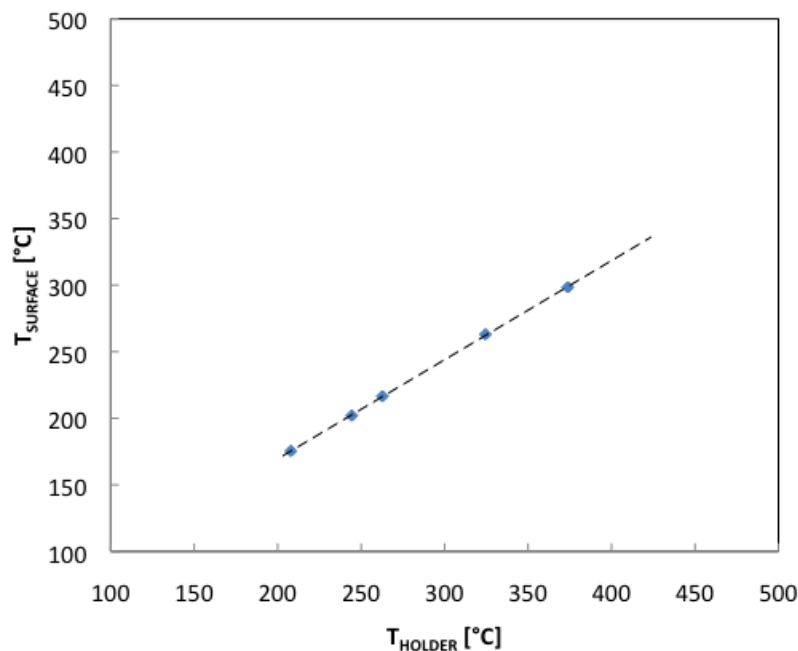


**Figure 7:** Comparison between the holder temperature and the impact surface temperature in the experimental setup used in Ref [8].

## Conclusions

An extensive set of experiments to investigate the impact dynamics has been carried out leading to the production of a quantitative impact regime map. Data based on the final impact outcomes reveal five different regimes, namely, secondary atomization, breakup with secondary atomization, rebound with secondary atomization, dry rebound, and breakup. The transition boundaries between such impact regimes have a probabilistic nature, which means that these boundaries do not represent a sharp transition, but instead are smoothed over a certain area. The comparison of the present results with a recent work shows significant differences, which can be attributed to an erroneous estimation of the surface temperature.

## Nomenclature

$a$	Capillary length	$\rho$	Density
$D_0$	Drop diameter	$\sigma$	Surface Tension
$g$	Acceleration due to gravity	IRM	Impact Regime Map
$H$	Impact height	DDS	Direct deposition on the surface
$m$	Mass	SA	Secondary Atomization
$T$	Surface Temperature	RSA	Rebound with secondary atomization

$u$	Velocity	SSA	Splashing with secondary atomization
$We$	Weber Number	R	Rebound
$\eta$	Viscosity	S	Splashing

## References

- [1] BAI, C., 1995. Development of methodology for spray impingement simulation. *SAE Tech paper* 950283.
- [2] BERNARDIN, J.D., STEBBINS, C.J. and MUDAWAR, I., 1997. Mapping of impact and heat transfer regimes of water drops impinging on a polished surface. *International Journal of Heat and Mass Transfer*, **40**(2), pp. 247-267.
- [3] MOREIRA, A.L.N., MOITA, A.S. and PANAO, M.R., 2010. Advances and challenges in explaining fuel spray impingement: How much of single droplet impact research is useful? *Progress in Energy and Combustion Science*, **36**(5), pp. 554-580.
- [4] REIN, M., 2002. Interactions between drops and hot surfaces. *Courses and Lectures-International Centre for Mechanical Sciences, No. 456*, pp. 185-218.
- [5] LEE, S.Y. and RYU, S.U., 2006. Recent progress of spray-wall interaction research. *Journal of mechanical science and technology*, **20**(8), pp. 1101-1117.
- [6] BLACK, K. and BERTOLA, V., 2012. Drop impact morphology on heated surfaces. *Proceedings of the DIPSI workshop 2012: Droplet Impact Phenomena & Spray Investigations*, University of Bergamo, pp. 6-10.
- [7] CASTANET, G., LIÉNART, T. and LEMOINE, F., 2009. Dynamics and temperature of droplets impacting onto a heated wall. *International Journal of Heat and Mass Transfer*, **52**(3), pp. 670-679.
- [8] TRAN, T., STAAT, H.J.J., PROSPERETTI, A., SUN, C. and LOHSE, D., 2012. Drop impact on superheated surfaces. *Physical Review Letters*, **108**(3), 036101.
- [9] COSSALI, G.E., MARENGO, M. and SANTINI, M., 2005. Secondary atomisation produced by single drop vertical impacts onto heated surfaces. *Experimental Thermal and Fluid Science*, **29**(8), pp. 937-946.
- [10] COSSALI, G.E., COGHE, A., and MARENGO, M., 1997. The impact of a single drop on a wetted solid surface. *Experiments in Fluids*, **22**, pp. 463-472.

## Wetting Dynamics of Dilute Polymer Solution Drops Impacting on Hydrophobic Surfaces

D. Biolè and V. Bertola

School of Engineering, University of Liverpool, UK

### Abstract

The dynamic wetting of dilute polymer solutions after drop impact is studied through the contact line and the contact angle. The experimental results, collected in the range of impact speeds between 0.6 and 1.6 m/s for two different hydrophobic surfaces (Parafilm-M film – surface energy 25 mJ/m<sup>2</sup> - and FluoroPEL coating – surface energy 10 mJ/m<sup>2</sup>), in the form of high resolution movies, were compared with the behaviour of pure water on the same surfaces. Finally, images taken with 400x magnification from below the substrate, reveal the dilute polymer solution forms liquid filaments on the substrate slowing down the recoiling phase and leading to the formation of secondary droplets having diameter size comparable to the filaments width (15 µm).

---

### Introduction

The study of the dynamical problem of a fluid droplet impacting a solid substrate (in air environment) and consequently its control, finds a large number of applications in industry such as agro-chemistry, ink-jet printing, spray coating and micro-fluidics of biological fluids. Depending upon the fluid kind, the surface characteristics and on the impact speed, several different impact morphologies can be observed which explains the high research appeal of this topic during the last century [1, 2].

Still today, indeed, the behavior of non-Newtonian fluids drops impacting on hydrophobic substrates (e.g. a pesticide on the waxy leaf of a plant) is poorly understood. Recent experiments [3, 4, 5] show that drops containing small amounts of poly-(ethylene oxide) in a Newtonian solvent (e.g. water) do not bounce on the hydrophobic substrate, whereas water drops do, even if the measured shear viscosity and surface tension of such drops are almost identical. A possible application of these drops is found in agro-chemistry field, as additive to reduce the wasted pesticide amount: in fact the suppression of the rebound of the drops on the leaves represents the crucial point to achieve this goal.

Other works show that in the early stages of the drop impact (where the drop is interested by a strong elongational flow which determines its shape to spread out from spherical into a liquid circular lamella and then recoil into a semi-spherical drop), dilute polymer solutions cannot be characterized as fluids with an increased extensional viscosity because this should affect their results both in spreading and in retraction, and they are only in the second phase; this points out the possibility that the contact line has a stronger role in the case of dilute polymer-solutions.

This work aims to give a deeper understanding of the reasons behind such differences are noticeable during the investigation of dilute PEO solution/pure water drops impacting in the same experimental conditions (impact speed, substrate type), through the analysis of the contact line, the contact angle and by showing high resolution images of the contact line area.

### Experimental test-rig

#### *Fluid and Surfaces*

The water solutions used for this study were made with poly(ethylene oxide) supplied by ALDRICH Chemistry in powder form, having the average molecular weight of  $M_v = 4.000.000$ ; we considered dilutions of 200 ppm, 100 ppm, 60 ppm, 40 ppm and 0 ppm (pure water). The water was de-ionized by a Berustead Easy-pure machine.

The two substrates used in this study were both hydrophobic and prepared by coating laboratory slides; the first surface was obtained by wrapping the Parafilm-M film on the glass (final expected surface energy of 25 mJ/m<sup>2</sup>), the second by immersing the glass in a bath of (Cytonix) FluoroPEL (dip-coating technique) and then drying the coated glass slide for few hours in a laboratory oven at 25°C (final expected surface energy of 10 mJ/m<sup>2</sup>). From the optical point of view the Parafilm-M substrate is semi-transparent and the FluoroPEL is transparent.

In the experiments (all carried out at the average room temperature of 22°C) we assumed that the heat transfer between the different materials involved (the fluid, the surface and the air) could be considered as negligible since every component has been stored, prepared and used at the same temperature.

### Experimental apparatus

The drops were released from a blunt hypodermic needle (equilibrium diameter  $D_0=2,8\text{mm}$ ) suspended above the substrates. The release heights were 20 mm, 60 mm, 100 mm and 140 mm, with corresponding average impact speeds of 0,58 m/s, 1,06 m/s, 1,38 m/s and 1,64 m/s.

The early stages of the drop impact (80 ms after impact) were been recorded with a high speed camera (Vision Research Phantom V9.1), at the speed of 5,000 fps and the resolution of 576x576 pixels for the case of the contact line and 480x480 for the contact angle. In the case of the contact line perimeter measurement, the camera and the lens were disposed vertically under the drop target looking up from under (Fig. 1 / Pict. a2 and b2); in the case of the contact angle amplitude measurement, the setup (camera and lens) was horizontal (Fig. 1 col. c).

The camera was equipped with three different lenses accordingly to the type of measurement; a Sony TV Zoom Lens was used to get images of the overall contact line perimeter from beneath (magnification range of 1x-2.5x) (Fig. 1 col. a), a Keyence VH-100ZR zoom lens (magnification range of 100x-1000x) (Fig. 1 col. b) to collect the detail of the contact line during the receding phase and a Edmund Optics VZM 450 (magnification range 0.7x-4.5x) for the contact angle (Fig. 1 col. c).

### Image Processing Technique

The images collected from the camera were then processed by an application developed on Mathworks MATLAB platform, to find the perimeter of the wetted area and to measure the contact angle.

In both cases images were first converted to binary through an algorithm which computed the background removal (the division technique was used in the case of the contact line, the subtraction technique for the contact angle), then noise reduction (holes filling in the case of dark pixels noise, morphological erosion in the case of bright pixels noise) and finally cleaned the borders from the neighbouring pixels with connection to the nearer stronger edge smaller than a threshold value.

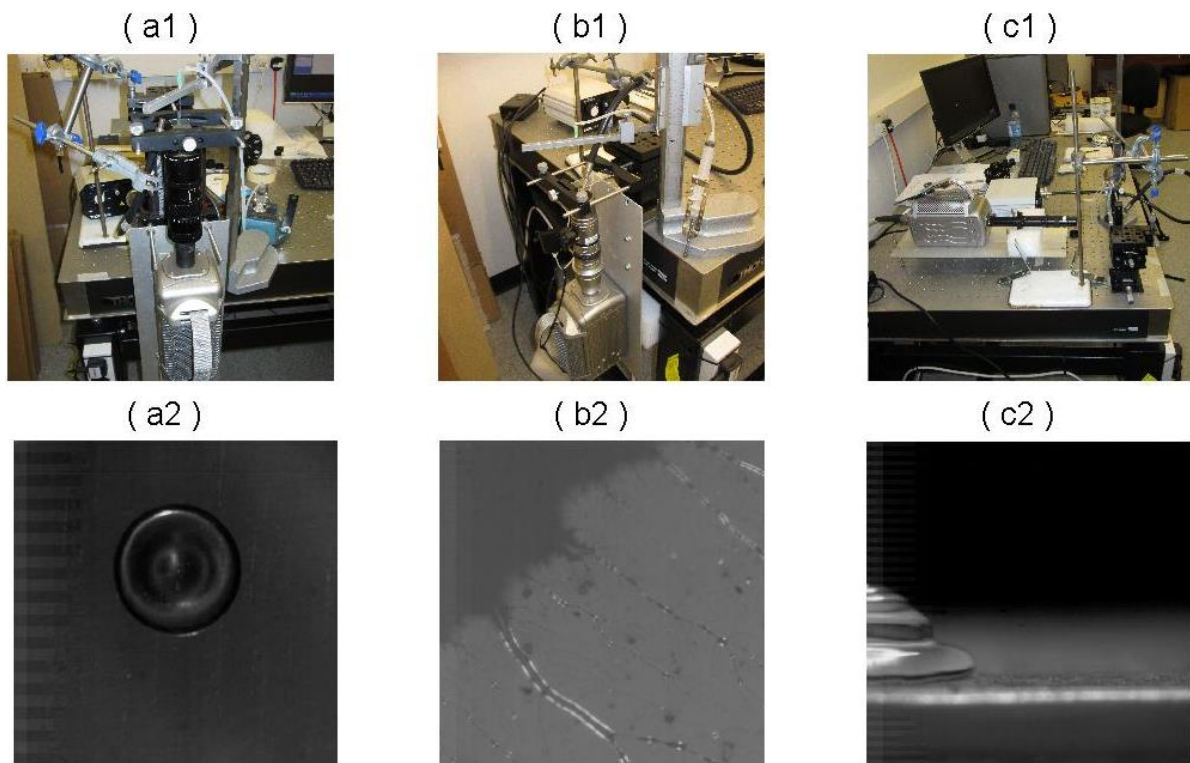


**Figure 1.** View of the three experimental setups used for the investigation: a Vision Research Phantom V9.1 camera is combined with **(a1)** a Sony TV Zoom lens to record the (full) contact line perimeter (vertical setup), **(b1)** a Keyence VH-Z100R lens to record the detail of the receding contact line (vertical setup) and **(c1)** an Edmund Optics VZM 450 to record the dynamic contact angle (horizontal setup – view from the side). **(row 2)** Preview of the output of the listed configurations.

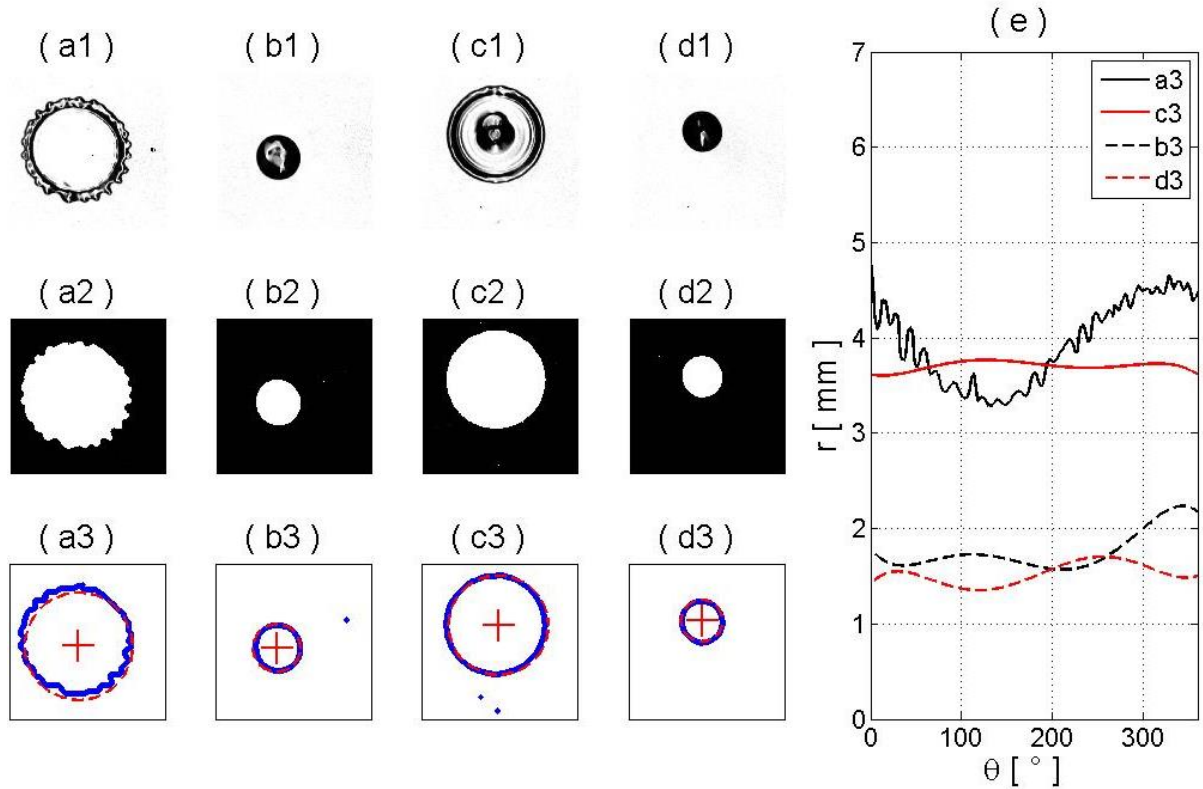


**Figure 2.** Example of the contact line perimeter measurement routine: (**row 1**) the background is subtracted from the frames of the droplets (**row 2**) the frames are converted to logical images (**row 3**) the center and the radius of the white object are detected through the LSF of circles method, the edges through Sobel algorithm (**a col.**) water  $t=5\text{ms}$  (**b col.**) water  $t=350\text{ms}$  (**c col.**) 100 ppm PEO solution  $t=5\text{ms}$  (**d col.**) 100 ppm PEO solution  $t=350\text{ms}$  (**e**) angular plot of the distance between the edge points of the third set of images and their respective centres – all the droplet are impacting on laboratory glass coated with Cytonix FluoroPEL with impact speed of 1,64 m/s

In this binary representation of the contact line the pixels in correspondence of the area the drop wets are set to 1 (bright) otherwise to 0 (dark background) (Fig. 2). The perimeter of the target is then computed by numerical integration of the distance  $r = r(\theta)$  measured in the polar coordinate system. The origin is estimated through the application of the Least Squares Fitting method [7] for circular shapes to the edges [8] of the target (the Sobel detection algorithm [9] was used for this purpose). Thus, the distance  $r$  represents the Euclidean length of the segment intercepted by the axis origin and the target contour. In this study we adopted an angular discretization step of  $\Delta\theta \approx 0.5^\circ$ , which corresponds to the approximate value of 720 points on the full circle, numbering the interval clockwise from a horizontal reference (Equation 1).

$$L = \int_0^{2\pi} d\theta r(\theta) \approx \Delta\theta \sum_{i=1}^N r_i \quad (1)$$

In the case of the contact angle, the binary representation is built at the reverse of the contact line case: the pixels where the drop is are set to 0 and the background is set to 1. The height of the impacting surface was estimated through the detection of the stronger edge of the image taken as background reference, then the contact angle was calculated as inverse of the tangent of a fixed vertical step (the end point was defined as the interception between the binary representation contour and a parallel line to the impact surface level).

## Results and Discussion

### Contact Line Perimeter

In comparison with pure water, the dilute polymer solutions show a contraction of the contact line perimeter length when the drop spreads out (1-2 mm contraction across the first 20 ms after time zero reference); furthermore the dilute polymer solutions reach the respective peak lengths earlier in time (0,5-1 ms in advance) (Fig. 3 and 4). After this phase, when the drop starts to recoil, their contact line length become comparable.



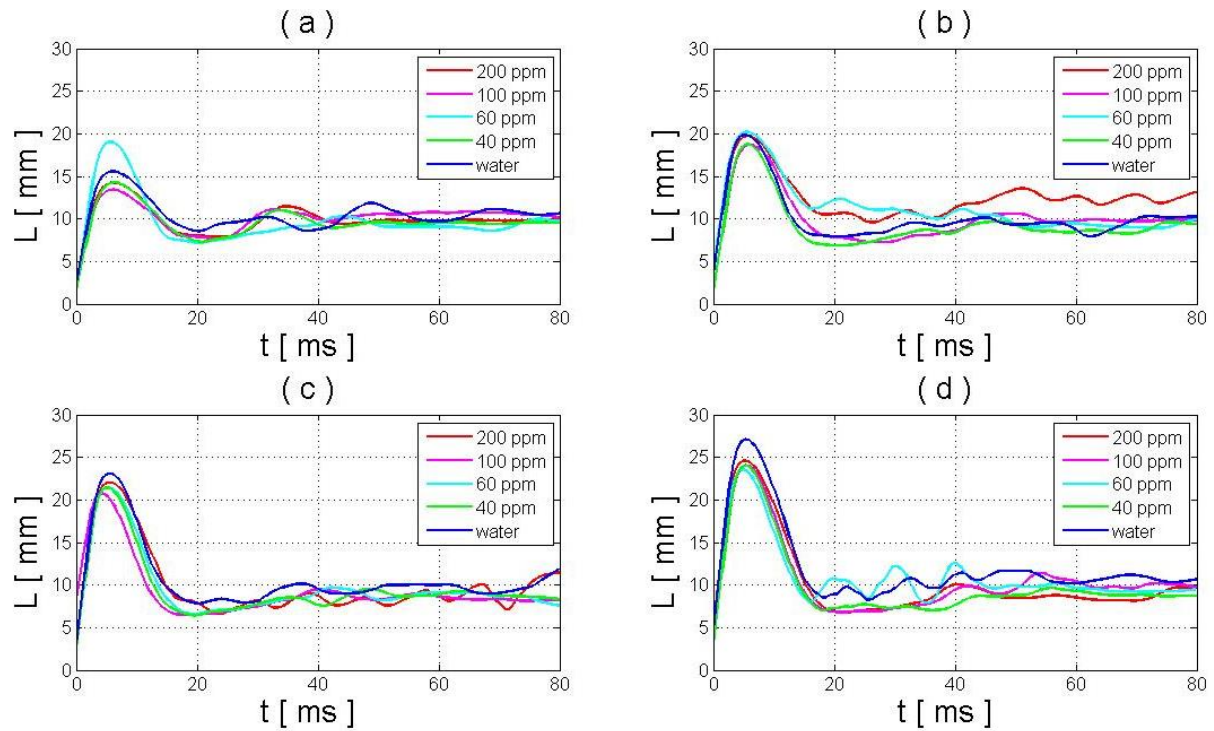


**Figure 3.** Temporal evolution of the contact line perimeter  $L$  for pure water and different poly(ethylene oxide) solutions (refer to legend for concentrations) impacting on laboratory glass wrapped with Parafilm-M film and same impact speed (a) 0,58 m/s (b) 1,06 m/s (c) 1,38 m/s (d) 1,64 m/s

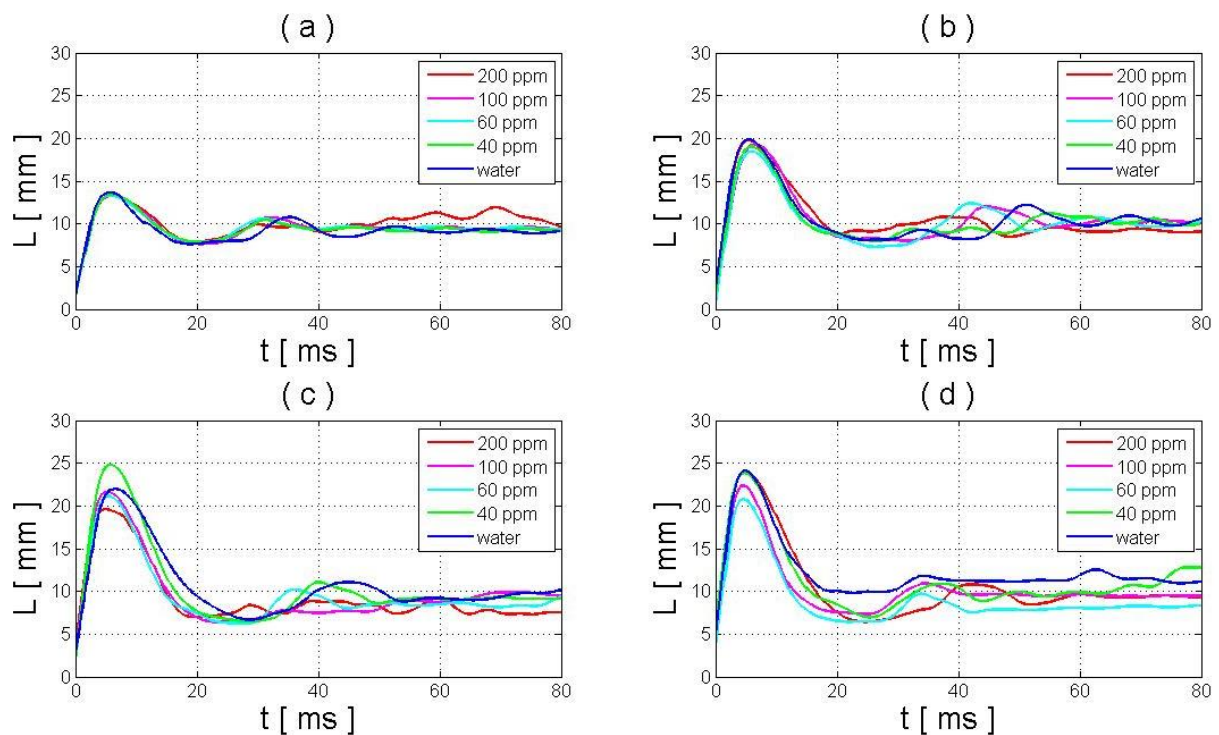


**Figure 4.** Temporal evolution of the contact line perimeter  $L$  for pure water and different poly(ethylene oxide) solutions (refer to legend for concentrations) impacting on laboratory glass coated with FluoroPEL and same impact speed (a) 0,58 m/s (b) 1,06 m/s (c) 1,38 m/s (d) 1,64 m/s



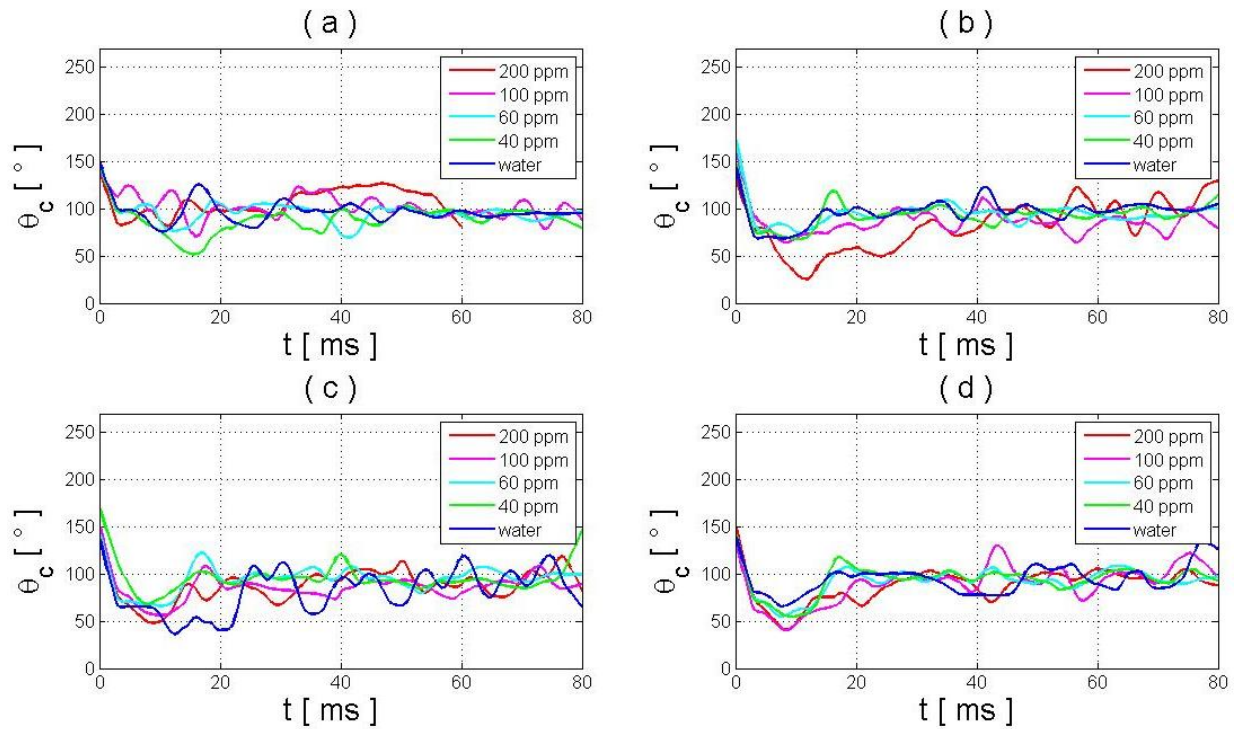


**Figure 5.** Temporal evolution of the contact angle  $\theta_c$  for pure water and different poly(ethylene oxide) solutions (refer to legend for concentrations) impacting on laboratory glass wrapped with Parafilm-M film and same impact speed (a) 0,58 m/s (b) 1,06 m/s (c) 1,38 m/s (d) 1,64 m/s

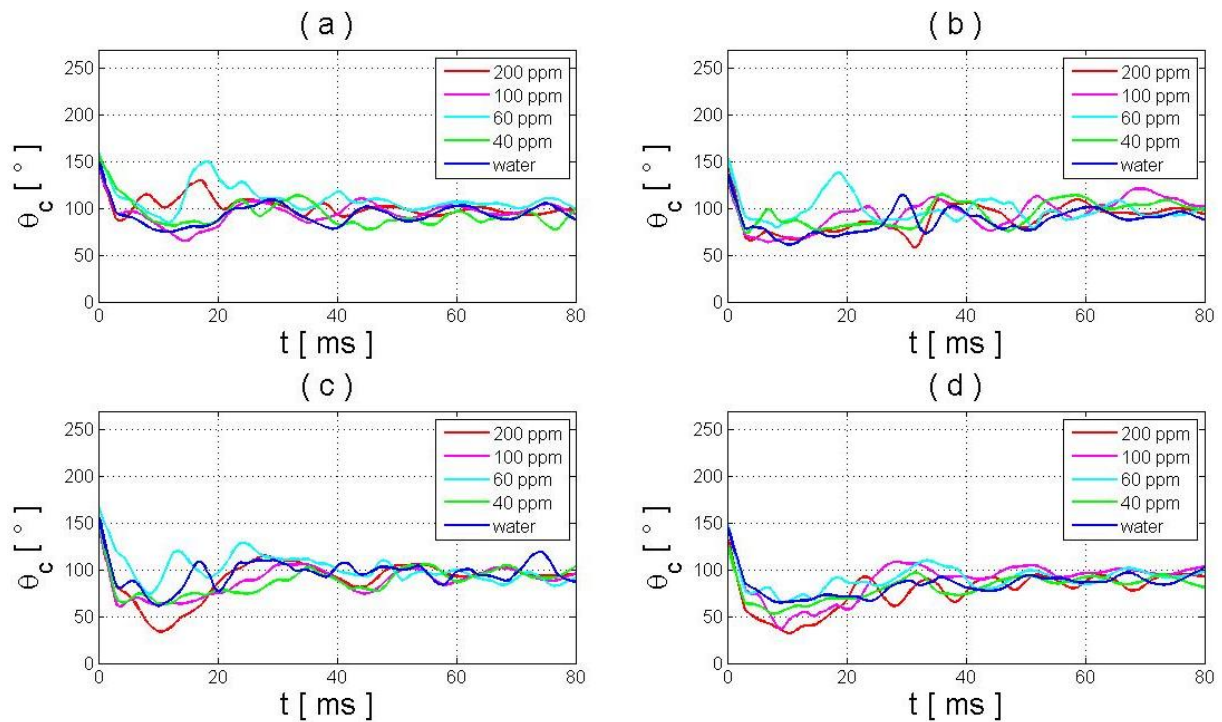


**Figure 6.** Temporal evolution of the contact angle  $\theta_c$  for pure water and different poly(ethylene oxide) solutions (refer to legend for concentrations) impacting on laboratory glass coated with FluoroPEL and same impact speed (a) 0,58 m/s (b) 1,06 m/s (c) 1,38 m/s (d) 1,64 m/s

However the presence of the polymer in the fluid is noticeable during the receding phase (the last 60 ms) where the contact line perimeter length tends to oscillate less than water (in terms both of amplitude and

frequency) around its steady state value. The only exception is represented by the solution with PEO concentration of 60 ppm in Fig. 3/d). From the point of view of the contact line perimeter, for the analysed sample, the surface energy difference between the substrates plays only a little role giving comparable results (Figure 2 Parafilm-M film, Figure 3 FluoroPEL). Finally, the mean wet diameter value, calculated by the relation  $D_w = L/\pi$ , (where  $L$  is the perimeter of the wetted area – the contact line length) confirms numerically the results of previous investigations [4, 5, 6] where the measured maximum value of the ratio  $D_w/D_0 \approx 3$  (maximum spreading point).

### Contact Angle

In the first half of the time domain considered, the contact angle of the polymer solution drop is characterized by having amplitudes smaller than  $90^\circ$  and as the inertial energy of the drop grows (impact speed increases), this contact angle decreases, as in the case of the pure water. The graphs of Figs. 5 and 6 confirm that under certain constraints (high impact speeds between all), the contact angle of the polymer can reach also values significantly different from those of water (e.g. Figure 6 / Pic. b - the 200 ppm PEO solution reaches a minimum of  $25^\circ$ ).

Moreover, as for the contact line length, when the liquid drop recedes after impact, the contact angle first starts growing again from its minimum value and then oscillating around the steady state condition. The polymer solutions show comparable values to those of water in terms of steady state values, but the frequency of the oscillations and their amplitude is slightly smaller. The cause of this behaviour is likely the drop pinning to the surface all along the receding phase.

### Contact Line Detail

More interesting results are shown increasing the magnification factor up to 400x zoom (Fig. 7): the study revealed that, when the polymer solution drop recedes after impacting the target, it leaves behind microscopic liquid fingers, or filaments, on the impacting surface.

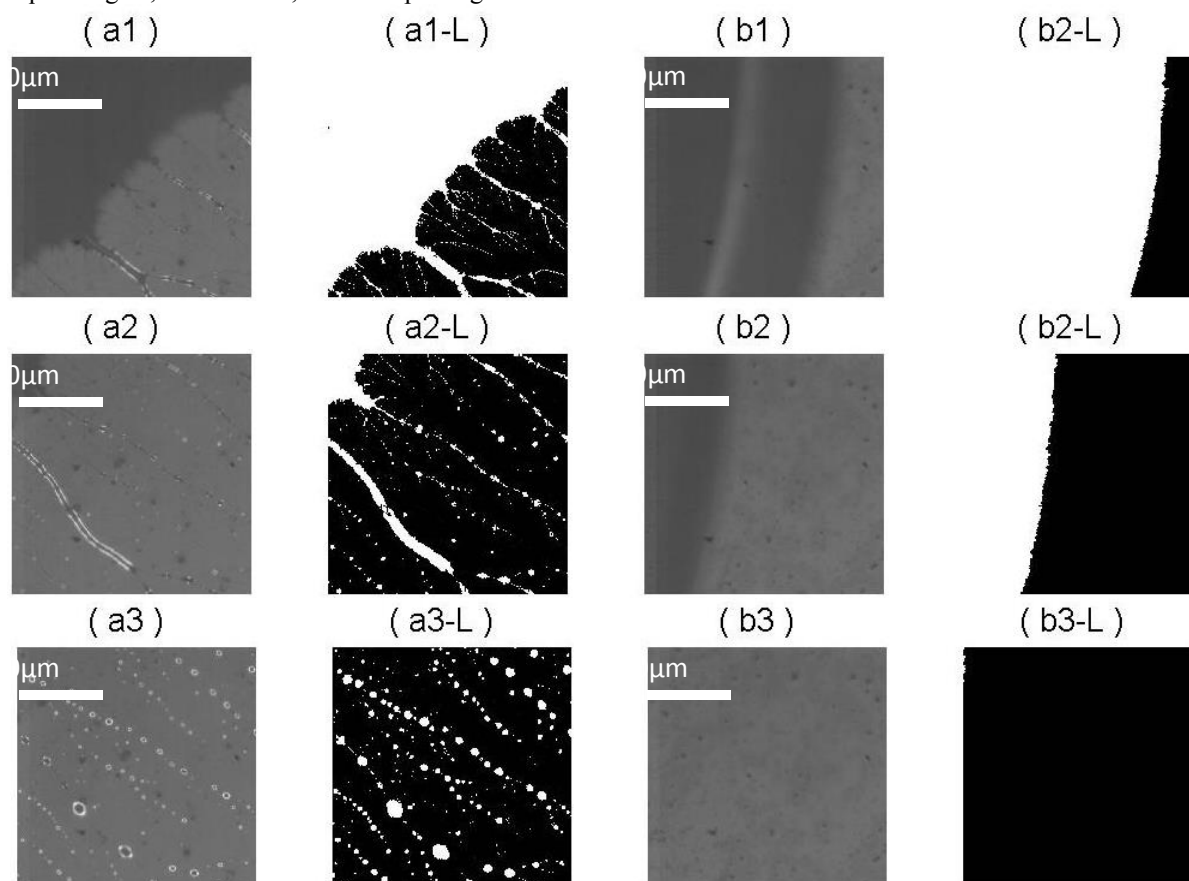


**Figure 7.** Receding contact line for **(a col.s)** 200 ppm PEO solution and **(b col.s)** water, impacting on laboratory glass coated with FluoroPEL at 1,66 m/s speed: the polymer solution left visible filaments on the surface (10  $\mu\text{m}$ ) which recoil in secondary droplets (mean diam. 5-15  $\mu\text{m}$ ) (**row 1**) ref. time (**row 2**) +2 ms (**row 3**) +10 ms

The size of these filaments, which measured is approximately 10  $\mu\text{m}$  in width, decreases in time (the filaments tend to disappear) and the fluid locally breaks up into secondary microscopic droplets. Furthermore, the complexity of these filaments, in terms of spatial displacement, orientation and size, grows with the impact

speed and the polymer concentration in the fluid; in fact reducing the polymer concentration from 200 ppm to 40 ppm we observed the liquid filaments to become less noticeable (2  $\mu\text{m}$  width), and disappear when the impact speed is lower than 1 m/s. The mean diameter of the secondary droplets formed after the liquid filaments have broken up is 5-15  $\mu\text{m}$  in the case of 200 ppm polymer solution impacting with speed of 1,66 m/s, but tends to smaller values for decreasing impact speeds / polymer concentrations. We analysed in detail also the case of pure water but we have not noticed the formation of analogue liquid patterns on the surface.

## Conclusions

The results of the present study shows the behaviour of dilute polymer solutions is reasonably near to those of pure water both in terms of contact line length and of contact angle amplitude, with exception of the receding phase where drop re-bounce on the impacting surface is inhibited; as consequence of this different behaviour dilute polymer solutions develop slightly smaller contact line length and contact angle values. Then, in the 50 ms that follows the completion of the receding phase, the dissipation of the initial inertial energy of the drop is still active causing the contact angle to oscillate around the equilibrium conditions; these oscillations for the solution drops are smaller than those of water.

Once observing directly the contact line morphology at microscopic scale (zoom 400x), polymer solution drops exhibit a more irregular contact line, whereas the water drop has a very smooth edge; in particular one can notice the generation of liquid filaments which affect the inertial forces – surface tension energy balance, leading to a reduction in the contact line speed and in a small loose of mass (due to the local recoil of the filaments). The time needed for these filaments to disappear is around 20 ms and for the secondary drops to reach their equilibrium around 35-40 ms.

## Acknowledgements

This work is supported by the University of Liverpool – A\*STAR (Singapore) partnership.

## Nomenclature

$t$	Time, ms	$\theta$	Angle, $^{\circ}$
$L$	Contact line length, mm	$D_0$	Equilibrium diameter of the drop, mm
$r$	Distance between the estimated drop centre and the drop edge, mm	$D_w$	Mean diameter of the wetted area, mm
		$\theta_c$	Contact angle, $^{\circ}$

## References

- [1] M. Rein, Phenomena of liquid drop impact on solid and liquid surfaces. *Fluid Dyn* **12**, 61-93 (1993).
- [2] Yarin AL., Drop impact dynamics: splashing, spreading, receding, bouncing. *Annu Rev Fluid Mech* **38**, 112-24 (2006).
- [3] V. Bergeron, D. Bonn, J.Y. Martin, L. Vovelle, Controlling droplet deposition with polymer additives. *Nature* **405**, 772-775 (2000).
- [4] V. Bertola, Effect of polymer additives on the apparent dynamic contact angle of impacting drops. *Colloids and Surfaces A: Physicochemical and Engineering Aspects* **363**, 135 (2010).
- [5] V. Bertola, Dynamic wetting of dilute polymer solutions: The case of impacting droplets. *Advances in Colloid and Interface Science* (2013).
- [6] M. I. Smith, V. Bertola, Effect of polymer additives on the wetting of impacting droplets. *Physical Review Letters* **104**, (2010).
- [7] N. Chernov, C. Lesort, Least squares fitting of circles. *Journal of Mathematical Imaging and Vision* **23**, 239 (2005).
- [8] D. Marr, E. Hildreth, Theory of Edge Detection. *Proceedings of the Royal Society of London. Series B. Biological Sciences* **207**, 187 (February 29, 1980, 1980).
- [9] I. Sobel, An isotropic 3 x3 image gradient operator. *Academic Press*, **376** (//, 1990).
- [10] I. S. Bayer, C. M. Megaridis, Contact angle dynamics in droplets impacting on flat surfaces with different wetting characteristics. *Journal of Fluid Mechanics* **558**, 415 (2006).
- [11] S. ikalo, C. Tropea, E. N. Ganic., Dynamic Wetting Angle of a Spreading Droplet. *Experimental Thermal and Fluid Science* **29**, pp. 795-802 (2005).
- [12] N. Milman, J. K. Yoon, A. J. Hickey, D. J. Burgess, Comparison of contact angle measurements by three methods. *Colloids and Surfaces B: Biointerfaces* **1**, 315 (1993).
- [13] M. Versluis, High-speed imaging in fluids. *Experiments in Fluids* **54**, (2013).

## **A study of liquid spray, droplet impingement and heat transfer**

Thomas. D, Lees. A.W, and Gethin. D

College of Engineering, Swansea University, United Kingdom

### **Abstract**

Liquid spray impingement and surface heat transfer receive great interest from researches in many different areas of study partly due to its ability to remove large heat fluxes, use of small fluid volumes and provides optimum control for the regulation of system temperature. A theoretical model was developed to study the characteristics of droplets formed by a full cone pressure swirl nozzle, followed by the impingement and heat transfer relating to a single droplet impacting a target surface. The aim of the model was to create a basic method of obtaining the rate of heat transfer into a sprayed target material, based entirely from first principles. Experimental tests were carried out consisting of a heated pumped water supply fed to a full cone type nozzle, directed at a target material containing thermocouples. Spray droplet size and droplet velocity were controlled through adjustment of liquid flow rate to the nozzle and nozzle orifice diameter. Comparisons of the data obtained from the experiments with the results of the analytical model indicate the model to be sufficient at providing a rapid estimate for heat transfer into a sprayed target material as a function of nozzle inlet flow rate and nozzle orifice diameter.

---

### **Introduction**

Liquid sprays provide a unique method of achieving controlled conditions for many different applications from fire suppression systems to spray deposition processes. Almost all applications involving liquid sprays take advantage of the ability to accurately control parameters such as droplet size, droplet velocity and spray flux distribution through atomizer design. The fluid dynamics and heat transfer phenomena associated with the impingement of sprayed liquid droplets has gained much attention from several different areas of study. Detailed theoretical models have been developed to evaluate the spreading and receding stages of droplet impingement with a substrate [1], successfully validated against physical test data. Studies into liquid spray for surface cooling have indicated that decreasing droplet Sauter mean diameter (SMD) tends to lead to an increase in heat transfer coefficient between droplet and surface [2]. For increased cooling efficiency, making use of small fluid volumes, Chen et al. [3] found that droplet SMD should be small and droplet impact velocity high. Moving on from the simplified approach of a single droplet impinging a substrate, a spray of droplets will over time produce a thin liquid film. If the velocity of the impacting droplets is high enough, the film breaks up into secondary droplets [4]. To model theoretically the complete process of a polydisperse spray of droplets impinging a substrate over time exceeds theoretical capabilities, which is where numerical modelling comes into play. Computational fluid dynamics (CFD) extends capabilities in spray modelling to include features such as droplet breakup, coalescence, droplet size and velocity distributions and liquid film momentum [5]. CFD is without doubt the preferred method of choice when computational capacity, simulation expertise and time are unconstrained. On the other hand if it is possible to produce results which will help to guide spray characteristics towards an optimum very quickly with little computational expense and relative ease of use, this could be highly useful for any spray systems user interested in heat transfer.

Literature including studies of liquid spray for applications such as surface cooling and removal of heat from a pre heated surface is available and research on-going. However, spray as a method of supplying heat to a surface body has not received any attention up until now. This paper introduces a study into the effects of droplet size and droplet velocity on the associated heat transfer from a heated liquid spray into a target solid body by a combined experimental and mathematical approach.

A theoretical model has been developed with its aim to serve as a guide to the interested user. Inputs for which the model requires are restricted to liquid flow rate into the spray nozzle, nozzle dimensions, and the geometry and thermodynamic properties of the domain, including the target solid material. An experimental spray test rig was constructed in attempt to provide control over the mean droplet size, velocity and spray temperature. A rectangular block of mild steel incorporating nine thermocouples was positioned normal to the centre axis of the spray. Spray droplet size and velocity were controlled through use of different size full cone type nozzles, along with adjustment of liquid flow rate to the nozzle.

## Experimental test-rig

The spray test rig as illustrated in Figure 1 was made up of the following main components:

- 1) Spray boom with Lurmark nozzle body fitted, positioned inside of aluminium container.
- 2) Mild steel block with nine probe K-type thermocouples internally fixed.
- 3) National instruments Nlc DAQ-9172 data logging unit connected to a Laptop running LabVIEW software, used to record temperature data.
- 4) 12V 3 bar diaphragm pump.
- 5) Diaphragm pressure relief/regulating valve with flow return back to water bath and 3 bar pressure gauge.
- 6) Turbine flow meter.
- 7) Clinton unstirred water bath to heat and maintain water temperature.

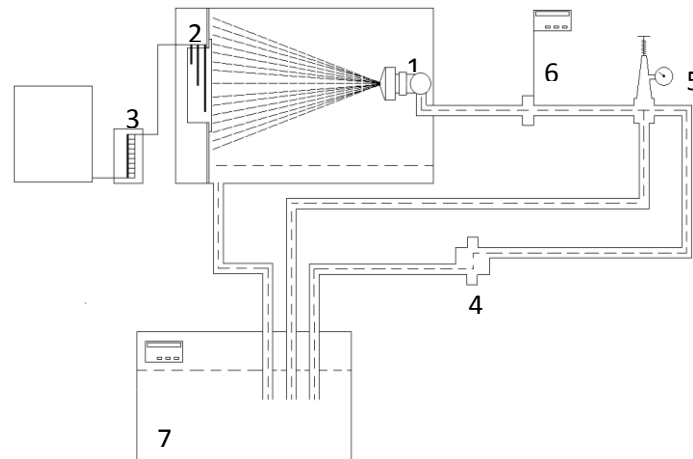


**Figure 1.** Schematic diagram of the experimental setup.

Hypro FCX pressure swirl nozzles were used for their low operating pressure and liquid flow rate. The FCX nozzle provides a full cone spray pattern with uniform distribution across the sprayed area [6]. Four nozzles were used during the tests, operating at pressures of between, 0.3 to 2.8 bar, equating to flow rates of 1 to 3.5 litres per minute (lpm).

Nine 3 mm holes were drilled into the top face of the mild steel block as shown in figure 2 (dimensions in mm), to accommodate the thermocouple probes. A small amount of silicon heat transfer compound was injected into each hole prior to inserting the thermocouples so as to ensure contact between probe tip and inner steel surface.

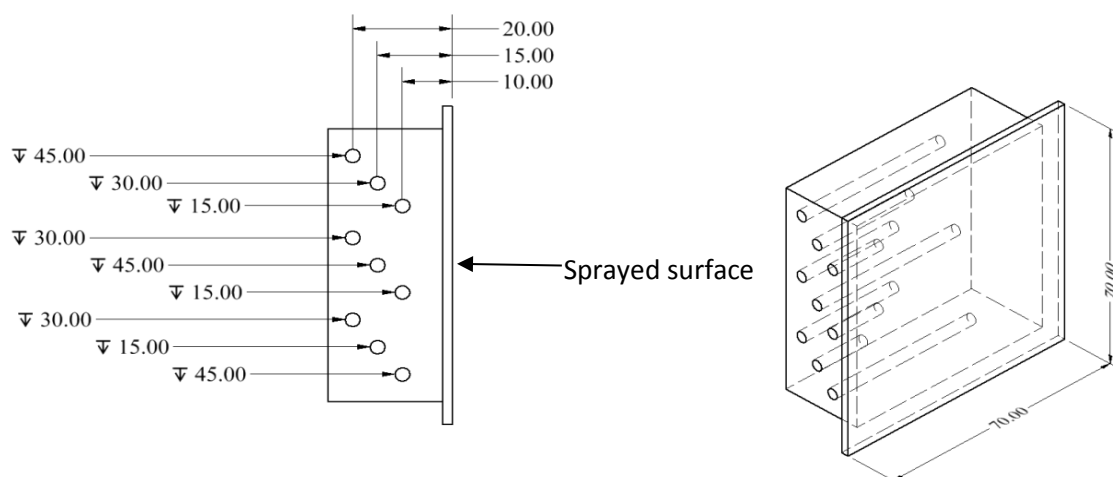


**Figure 2.** Diagram to illustrate geometry of mild steel block (spray target) and position of thermocouple probes.

### Mathematical modelling

A simple one-dimensional theoretical model was developed as a basic design tool to provide instant estimates for the rate of heat transfer through a sprayed target solid body, based on the impingement of a single droplet formed by a full cone spray nozzle. A calculation for the SMD, as formulated by Mudawar and Estes [7] was used to represent an average droplet size for the entire spray based on the nozzle orifice diameter and liquid velocity at the orifice,

$$\frac{d_{32}}{d_o} = 3.67 [We_{d_o}^{0.5} Re_{d_o}]^{-0.259}. \quad (1)$$

The Reynolds and Weber number based on the nozzle orifice conditions were defined, respectively, as follows,

$$Re_{d_o} = \frac{\rho_l (2\Delta p / \rho_l)^{0.5} d_o}{\mu_l} \text{ and } We_{d_o} = \frac{\rho_a (2\Delta p / \rho_l) d_o}{\sigma}. \quad (2)$$

$\Delta p$  in the above represents the pressure differential across the nozzle, calculated using Bernoulli's equation, assuming the fluid to be of incompressible and inviscid flow. At the point of droplet impact with solid surface, the droplet deforms rapidly, resulting in a thin film between the solid and surrounding liquid [2]. The principal effect of increasing the droplet impact velocity is the increase in drop spread and the resultant spread area. By increasing the wetted area of a single droplet in contact with solid, provides greater surface area for heat transfer between droplet and solid to take place. Droplet spread area can be quantified by measuring the diameter of surface in contact with the droplet and normalising it with the initial droplet diameter to give the spread factor ( $\xi$ ). A simple expression for the maximum spread factor was formulated by Pasandideh-Fard et al. [8] based on a conservation model for droplet impact,

$$\xi_{max} = \frac{d_{max}}{d_o} = \sqrt{\frac{We + 12}{3(1 - \cos\theta_a) + 4(We/Re^{0.5})}}. \quad (3)$$

The advancing liquid to solid contact angle ( $\theta_a$ ) in the above was taken to be 110° for all calculations [9]. Pasandideh-Fard et al. [8] showed that the maximum spread factor increased up to a certain impact velocity at which point above this velocity the liquid film recoiled resulting in a decrease in contact spread area. Time taken for the impinging droplet to reach its maximum spread area was estimated using the following expression [8],

$$t_c = \frac{8d_{32}}{3v_d}. \quad (4)$$

The rate of heat transfer between the liquid film of the impinging droplet and solid surface is controlled by the heat conduction within the droplet and convection between droplet film and solid surface. Heat transfer through the droplet liquid film is calculated based on the maximum spread area of the impinging droplet and the thermal boundary layer thickness of the liquid film [9],

$$q = k_l \frac{\Delta T}{\delta_T} \frac{\pi d_{max}^2}{4}. \quad (5)$$

$\Delta T$  equals the initial temperature difference between droplet liquid film and contacting solid surface and thermal boundary layer thickness,  $\delta_T$  is formulated from the droplet Prandtl number and the velocity boundary layer thickness ( $\delta_u$ ) [9], as follows,

$$\delta_T = \frac{\delta_u}{Pr^{0.4}}, \quad \text{where } \delta_u = \frac{2D_o}{Re^{0.5} Pr^{0.4}}. \quad (6)$$

Through rearrangement of Newton's law of cooling and by substitution of the rate of heat transfer from equation 5 leads to the following derivation for the convective heat transfer coefficient,

$$h = \frac{k_l (\Delta T / \delta_T) (\pi d_{max}^2 / 4)}{(\pi d_{max}^2 / 4) \Delta T} = \frac{k_l}{\delta_T}. \quad (7)$$

Transient one-dimensional conductive heat transfer through the target body is calculated assuming that the height and width of the body are large relative to its thickness [10]. The body has thickness  $L$ , initially at uniform temperature  $T_i$  throughout. The transient one-dimensional heat conduction equation in its non-dimensional form is represented as follows,

$$\frac{\partial^2 \theta}{\partial X^2} = \frac{\partial \theta}{\partial \tau}, \quad (8)$$

with dimensionless boundary conditions,  $\partial\theta/\partial X(0, \tau) = 0$  and  $\partial\theta(1, \tau)/\partial X = -Bi\theta(1, \tau)$  and dimensionless initial condition,  $\theta(X, 0) = 1$ .  $\theta, X, \tau$  and  $Bi$  represent dimensionless expressions for temperature, distance from sprayed surface, time (Fourier number) and heat transfer coefficient (Biot number), respectively, as shown below,

$$\theta(x, t) = \frac{[T(x, t) - T_\infty]}{[T_i - T_\infty]}, \quad X = \frac{x}{L}, \quad \tau = Fo = \frac{\alpha t}{L^2}, \quad Bi = \frac{hL}{k}. \quad (9)$$

From the dimensional terms above,  $x$  is the actual distance from sprayed surface and  $\alpha$  is the thermal diffusivity of the solid material, given by,  $\alpha = k/(\rho c_p)$ .

The non-dimensional partial differential equation (equation 8) together with its boundary and initial conditions (equations 9) were solved by separation of variables technique. In its final form the solution to this heat conduction problem is given by [10],

$$\theta = \sum_{n=1}^{\infty} A_n e^{-\lambda_n^2 \tau} \cos(\lambda_n X). \quad (10)$$

From which the constants  $\lambda_n$  and  $A_n$  were calculated from the characteristic equation,  $\lambda_n \tan \lambda_n = Bi$  and  $A_n = 4 \sin \lambda_n / (2\lambda_n + \sin(2\lambda_n))$ . Because of the exponential decay function  $e^{-\lambda_n^2 \tau}$ , the terms in the summation decline rapidly as  $n$  and thus  $\lambda_n$  increase. Therefore, only the first four terms of the infinite series have been evaluated to determine the dimensionless temperature.

Heat and mass transfer between the droplet surface and surrounding air during the time the droplet exits the nozzle up until impact with solid surface, due to convection and diffusion are calculated assuming the droplet and surrounding air are of spherical symmetry [11]. If the droplet atomises from the nozzle at time  $t$ , and time taken to reach solid substrate equals  $\Delta t$ , then the temperature of the droplet at  $t + \Delta t$  can be shown by,

$$T_{d(t+\Delta t)} = T_{dt} + \frac{\Delta t \times \left( \frac{\phi_{conv}}{(h_{cv} S_d (T_a - T_d))} + \left( \frac{\phi_{lat}}{\Delta m_d L_v / \Delta t} \right) \right)}{m_d C_{p_d}}. \quad (11)$$

Derivations for heat exchange by convection and latent heat as included above, assume the droplet and its environment to form an isolated system, with uniform droplet and air temperature,  $T_d$  and  $T_a$ , respectively [11]. The coefficient of thermal heat exchange is given by,  $h_{cv} = Nu \cdot k_a / D_d$ , from which the Nusselt number for the case of forced convection ( $v_d \neq v_a$ ), as derived by Ranz and Marshal [12], is given by,  $Nu = 2 + 0.6 Re_d^{0.5} Pr^{0.33}$ . While the surrounding air of the droplet is not saturated, evaporation occurs naturally and the change in droplet mass can be shown by,  $\Delta m_d = -\Delta t S_d \phi_{evap}$ , from which  $\phi_{evap} = Df_{mass} \Delta C_{mass}$ , equates from the product of the coefficient of mass diffusion and the difference between mass concentrations of water vapour between droplet air interface and air. Assuming air to be a perfect gas, the coefficient of mass diffusion and difference between mass concentrations are represented, respectively, as follows,

$$\begin{aligned} Df_{mass} &= \frac{Sh Df_a}{d_{32}} \quad \text{and} \quad \Delta C_{mass} = C_{mass_d} - C_{mass_a} \\ &= \frac{M}{R} \left( \frac{P_{v_d}}{T_d} - \frac{P_{vap}}{T_a} \right). \end{aligned} \quad (12)$$

The Sherwood number for forced mass transfer is given by [12],  $Sh = 2 + 0.6 Re_d^{0.5} Sc^{0.33}$ , from which the Schmidt number is given by [12],  $Sc = \mu_a / (\rho_a Df_a)$ . The coefficient of mass diffusion is given by [11],  $Df_a = 2.26 \times 10^{-5} \cdot (101325/P_a) \cdot (T_a/273.15)$ . Total pressure of air ( $P_a$ ) is dependent of the temperature of air, given by [11],  $P_a = e^{77.3417 - 8.2 \times \ln(T_a - 0.15) + 5.7114 \times 10^{-3} \times T_a - \frac{7235.46}{T_a - 0.15}}$ .

Derivations above were embodied into a Microsoft Excel spread sheet in order to predict thermal transients and to include mass transport from droplet during its time of flight. The model was compared with experimental data and this comparison is set out below.

## Results and Discussion

A minimum of three tests were performed for each nozzle at each predetermined flow rate, to ensure consistent results. Water spray temperature was set to 39°C ( $\pm 0.5^\circ\text{C}$ ), and the mild steel block was left to cool to 21.5°C



( $\pm 0.5^\circ\text{C}$ ), before the start of each test. Nozzle orifice diameter ( $\phi$ ) and the range of flow rates tested (restricted by operating range), for each nozzle are included in the relevant keys in each of the plots in Figure 3.

Figure 3 represents tests for each of the four nozzles at three chosen flow rates so to help to provide some visual comparison between each. Data produced by the model to represent maximum and minimum tested flow rates for each nozzle are also included. The key within each of the plots in Figure 3 includes the time taken for the target block to reach spray temperature, according to flow rate for each nozzle (1 - 4). Time taken for the target block to reach temperature of the spray was determined by fitting a 4<sup>th</sup> order polynomial trend to the temperature differentials calculated between each recorded time step. The 4<sup>th</sup> order polynomial equation for this trend was then made equal to a prescribed change in temperature that would satisfy the target temperature reached. Taking a reasonable initial guess at the time taken for the block to reach spray temperature, Newton Raphson technique was used to solve the polynomial equation, and determine the ‘actual time taken for the block to reach the temperature of the spray’.

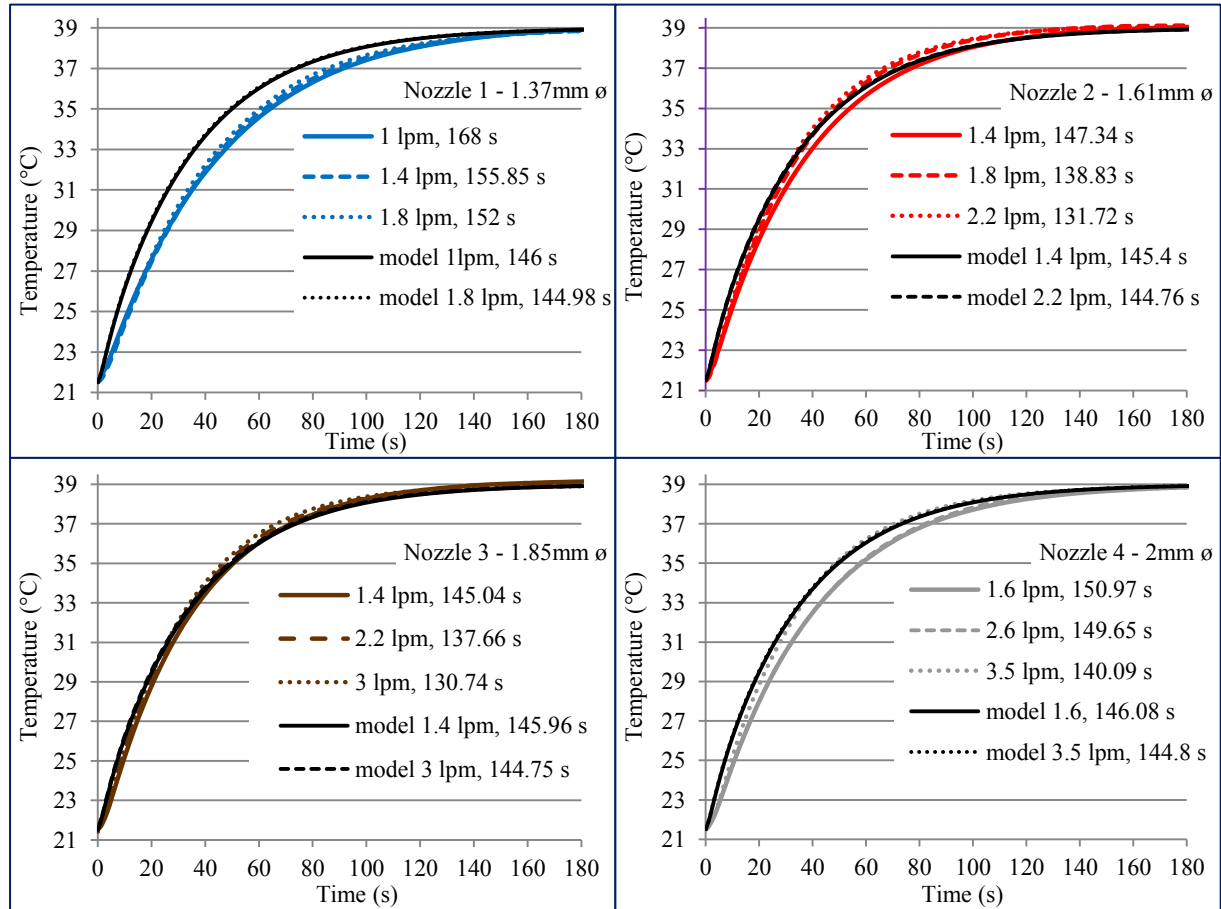


**Figure 3.** Plots to Illustrate rate of heat transfer through sprayed block, comparing results of experiments with results produced by the model.

Table 1 lists droplet SMD (equation 1), droplet impact velocity (equation 13) and dimensionless Biot number ( $Bi$ , equation 9), for nozzles 1 to 4 at flow rates given in figure 3. Assuming the fluid to be of inviscid, incompressible flow, droplet impact velocity ( $v_d$ ) was calculated based on the nozzle liquid flow rate ( $q$ ) and orifice diameter ( $d_0$ ),

$$v_d = \frac{q}{\pi d_0^2 / 4} \quad (13)$$

Nozzle	Flow rate (lpm)	Droplet SMD ( $\mu\text{m}$ )	Droplet velocity (m/s)	Biot number
1. $\phi = 1.61 \text{ mm}$	1	422.8	8.1	63.6
	1.4	355.2	11.4	82.1
	1.8	311.8	14.7	99.3
2. $\phi = 1.63 \text{ mm}$	1.4	361.8	11.2	80.4
	1.8	317.7	14.3	97.3
	2.2	286.3	17.5	113.3
3. $\phi = 1.85 \text{ mm}$	1.4	444.9	8.7	64.0
	2.2	352	13.6	90.1
	3	299.8	18.6	114.1
4. $\phi = 2.00 \text{ mm}$	1.6	472.3	8.5	61.4
	2.6	367.2	13.8	88.8
	3.5	314.8	18.6	111.2

**Table 1.** Output data provided by the model, including droplet SMD, droplet velocity and dimensionless heat transfer coefficient.

For each nozzle, increasing liquid flow rate and hence pressure differential across the nozzle, equates to an increase in Biot number (Table 1), resulting in greater rate of heat transfer into the target solid body, as shown in Figure 3. Based on equations 1 and 13, by increasing flow rate to the nozzle, reduces droplet SMD and increases droplet impact velocity. Table 1 illustrates that nozzles 2 and 3 operating at maximum flow (2.2 and 3 lpm, respectively), produce smallest droplet SMD, highest impact velocity, and result in highest Biot number and greatest rate of heat transfer from spray to target solid body (Figure 3). Spray produced by nozzle 1 has shown to be the least effective at transferring heat into the target material. Although the calculated droplet SMD (equation 1) for nozzle 1, shows to be slightly finer than that calculated for nozzle 4, droplet impact velocity as calculated by equation 13 for nozzle 1, indicates the average droplet velocity within the spray produced by nozzle 1 is the lowest of the four nozzles.

Plots for nozzles 2 and 3 in Figure 3, demonstrate the model to provide a relatively good overall prediction for the rate of heat transfer from water spray into the target material. Time taken for the block to reach the temperature of the spray (model) was calculated using the same method as applied to the experimental results.

Comparing the results of the model with the results of the experiments (as provided within each key in Figure 3), the average (mean) difference between the two is just 8 seconds. At set flow rate of 1.4 lpm, the difference between experimental and modelled results for nozzles 2 and 3 is within 1.9 seconds.

A reduction in droplet SMD results in greater surface area to volume ratio of liquid, which in turn increases the available surface area for heat transfer between liquid droplet and solid surface. Droplet SMD and impact velocity are related by pressure differential across the nozzle, a reduction in either leads to an increase in the other. An increase in droplet impact velocity causes a direct increase in droplet Reynolds number and an increase to the power of  $v_d^2$  to the droplet Weber number, resulting in a higher droplet spread factor  $\xi_{max}$  (equation 3). In a similar way to reducing droplet SMD, by increasing droplet  $\xi_{max}$  results in an increase in available surface area for heat transfer between liquid droplet and solid surface.

## Conclusions

Water spray as a method of transferring heat into a target solid body has been studied through both experimental and theoretical methods. The aim of this piece of work was to form an introduction to what will be a rigorous study of the underlying physics involved when a spray of water droplets impinge and transfer heat into a solid material. Four, full-cone, pressure swirl type nozzles of varying orifice diameter were selected to provide a range of droplet size and droplet velocity.

Through a combination of results of the experimental tests and outputs provided by the model, it has been shown that rate of heat transfer from a heated liquid spray into a target solid body is improved by reduction in droplet SMD and increase in droplet impact velocity.

Output data produced by the simple one-dimensional model has shown to match reasonably well with results of experiments (Figure 3), proving the model to be an efficient, easy to use method of obtaining rates of heat transfer, which requires very little user input.

## Acknowledgements

Thank you to my supervisors, Professor Arthur W Lees and Professor David Gethin for their enthusiasm, continued support, and for sharing with me their expertise in the subject of spray systems and heat transfer.

## Nomenclature

$C_{mass}$	Mass concentration	$R$	Universal gas constant
$C_p$	Specific heat	$Re$	Reynolds number ( $= \rho_l v_d d_{32} / \mu_l$ )
$d_{max}$	Maximum droplet spread diameter	$Sc$	Schmidt number
$d_0$	Nozzle orifice diameter	$S_d$	Droplet surface area
$d_{32}$	Droplet Sauter mean diameter (SMD)	$Sh$	Sherwood number
$Df$	Coefficient of mass diffusion	$t$	Time
$h$	Convective heat transfer coefficient (W/m <sup>2</sup> .K)	$T$	Temperature
$k$	Thermal conductivity (W/m.K)	$v_d$	Droplet velocity
$m$	Mass	$We$	Webber number ( $= \rho_a v_d d_{32} / \sigma$ )
$M$	Molar mass	$X$	Dimensionless space variable
$P$	Total pressure	$\theta_a$	Advancing liquid to solid contact angle
$P_{vap}$	Vapour pressure of air	$\theta$	Dimensionless temperature
$P_{v_d}$	Pressure of vapour/droplet interface	$\mu$	Dynamic viscosity
$Pr$	Prandtl number ( $= \mu_l C_p / k_a$ )	$\rho$	Density
$q$	Liquid flow rate	$\lambda_n$	Characteristic root
$\sigma$	Surface tension of dispersed phase in air		

## Subscripts

$a$	Air
$d$	Droplet
$l$	Liquid
$t$	Time
$T$	Temperature

## References

- [1] Roisman, I.V., R. Rioboo, and C. Tropea, *Normal impact of a liquid drop on a dry surface: model for spreading and receding*. Proceedings of the Royal Society A: Mathematical, Physical and Engineering Sciences, 2002. **458**(2022): p. 1411-1430.
- [2] Briones, A.M., et al., *Micrometer-Sized Water Droplet Impingement Dynamics and Evaporation on a Flat Dry Surface*. Langmuir, 2010. **26**(16): p. 13272-13286.
- [3] Chen, R.H., L.C. Chow, and J.E. Navedo, *Optimal spray characteristics in water spray cooling*. International Journal of Heat and Mass Transfer, 2004. **47**(23): p. 5095-5099.
- [4] Roisman, I.V., et al., *Multiple Drop Impact onto a Dry Solid Substrate*. Journal of Colloid and Interface Science, 2002. **256**(2): p. 396-410.
- [5] Sirignano, W.A., *Fluid dynamics and transport of droplets and sprays*. 2nd ed. 2010, New York: Cambridge University Press. xviii, 462 p.
- [6] Hypro. [http://www.hypro-ind.co.uk/Full\\_Cone\\_Spray.htm](http://www.hypro-ind.co.uk/Full_Cone_Spray.htm). 2013 [cited 2013 28 May]; 18-20].
- [7] Estes, K.A. and I. Mudawar, *CORRELATION OF SAUTER MEAN DIAMETER AND CRITICAL HEAT-FLUX FOR SPRAY COOLING OF SMALL SURFACES*. International Journal of Heat and Mass Transfer, 1995. **38**(16): p. 2985-2996.
- [8] PasandidehFard, M., et al., *Capillary effects during droplet impact on a solid surface*. Physics of Fluids, 1996. **8**(3): p. 650-659.
- [9] Pasandideh-Fard, M., et al., *Cooling effectiveness of a water drop impinging on a hot surface*. International Journal of Heat and Fluid Flow, 2001. **22**(2): p. 201-210.
- [10] Carslaw, H., S. and J. Jaeger, C., *Conduction of Heat In Solids*, ed. Oxford. 1959.
- [11] Chaker, M., C.B. Meher-Homji, and T. Mee, *Inlet fogging of gas turbine engines - Part I: Fog droplet thermodynamics, heat transfer, and practical considerations*. Journal of Engineering for Gas Turbines and Power-Transactions of the Asme, 2004. **126**(3): p. 545-558.
- [12] Ranz, W.E. and W.R. Marshall, *Evaporation from drops. Parts I & II*. Chem. Eng, 1952. **48**: p. 141-6;173-80.

## Phenomenology of Two-Component Droplet-Wall Film-Interaction

A. Geppert, F. Greif<sup>1</sup>, G. Lamanna and B. Weigand

Institute of Aerospace Thermodynamics, Universität Stuttgart,  
Pfaffenwaldring 31, 70569 Stuttgart, Germany

### Abstract

In the present paper a first insight in the impact phenomenology of Hyspin droplets impacting on Hexadecane wall films is presented. The results of this study will be used to improve the carbon footprint of Diesel engines by the development of a model predicting the impact outcome. A comparative study is performed to highlight differences (formation of holes in crown wall and crown rip off) and similarities (crown shape and ejection direction of secondary droplets) between one- and two-component splashing. Further, we try to identify the most plausible parameters to explain these discrepancies. The therefore used experimental setup, a two-perspective high-speed shadowgraphy imaging system, is presented too. We suppose that the duration of the impact process is too short for the development of a homogeneous mixture of liquids. The resulting surface tension gradients in the crown wall trigger the Marangoni-effect, which is responsible for the formation of holes. In our opinion the impact phenomenology is dominated by the properties of the wall film liquid.

### Introduction

The reducing of emissions in Diesel engines is still a topic of high importance these days. An efficient strategy for achieving this goal is to increase the exhaust gas temperature by means of one or multiple post-injections. The major issue of this strategy is the oil dilution in the combustion chamber. During the post-injection, the piston moves downwards leaving the chamber's wall, with its lubricating oil film, exposed to the injected Diesel. The Diesel droplets impact onto the oil film. This leads to its dilution and hence to a significant reduction of its lubrication performance. Furthermore, if the impact energy is sufficient, secondary droplets, consisting of Diesel and oil, are ejected into the combustion zone, increasing the engine emission. Hence, the development of a model, predicting the conditions under which secondary droplets are produced and what properties they have, is necessary for improving the carbon footprint of Diesel engines. To date the understanding and modeling of one-component splashing is relatively well advanced. Cossali et al. [1], for example, described in detail the splash morphology and the splashing/deposition limit for water/glycerin solutions. For various alcohols and alkanes, Vander Wal et al. [2] compared the splash morphology and proposed an alternative correlation for the splashing threshold [3]. For two-component interactions, in the contrary, only little research is done. The only contribution can be found in Thoroddsen et al. [4]. The authors investigated the impact of water/glycerin droplets on thin ethanol films and focused mostly on the mechanism of formation of the crown, which differs significantly from the one-component counterpart.

The main objective of this paper is to give a first insight in the phenomenology of the two-component interaction at conditions representative for Diesel engine operations. For this purpose, a precise rationale is followed. As a first step, we chose a miscible liquid combination with liquid properties at ambient conditions that are similar to the liquid properties of Diesel and engine oil at combustion chamber conditions. The fluids of choice are: Hyspin, hydraulic oil, as surrogate fluid for the Diesel droplet and Hexadecane as surrogate for the oil wall film. Second, a comparative study is performed between two- and one-component splashing, using Hyspin and Hexadecane under the same conditions. The objective is twofold: 1) to highlight differences and similarities between one- and two-component splashing; 2) to identify the most plausible parameters to explain the observed discrepancies. The experiments are conducted for two film thicknesses ( $h = 0.25 \text{ mm}$  and  $h = 0.5 \text{ mm}$ ) and two impact velocities ( $v = 4.5 \text{ m/s}$  and  $v = 2.6 \text{ m/s}$ ). The present paper presents the preliminary findings of this comparative study. Similarly to one-component splashing, we found that the two-component interaction can be classified into two categories, deposition and splashing, depending upon the initial kinetic energy of the droplet. Hereafter, we focus on the splashing behavior. Known splashing phenomena like the evolution of crown, liquid fingers along the crown rim and ensuing secondary droplets were also observed. However, some new phenomena were found: During the evolution of crown holes appeared randomly

distributed in the crown wall. We supposed that due to an inhomogeneous mixture of the two liquids local surface tension gradients are existent. These gradients trigger the Marangoni-effect that caused the formation of holes. During the droplet impact onto thin wall films the formation of holes resulted in a crown rip off at the wall film. On the contrary, the formation of holes was not observed during the one-component interaction. The comparison between the two- and one-component interactions yielded that the impact phenomena are dominated by the properties of the wall film liquid.

## Experimental Setup and Method

The experimental setup is presented schematically in Figure 1. Its distinctive feature is that the droplet impact is observed from two perspectives in order to verify the symmetry of two-component splashing.

The setup mainly consists of three parts: the droplet generation system, the impact area and the imaging system. For the droplet generation, the so called dropper is employed. The liquid is conveyed by a peristaltic pump from the reservoir to the dropper exit, where it drips off as soon as the critical droplet mass is reached. The droplet diameter depends on the dropper exit diameter and the properties of the liquid. In this study the dropper exit diameter is 2 mm. The resulting droplet diameter is about 2.5 mm. The droplet impact velocity depends on the fall height between dropper exit and impact surface. The maximum adjustable fall height in our experiments is

1.5 m. As a consequence the maximum droplet impact velocity is 4.5 m/s.

The impact area consists of a smooth glass plate on which a thin metallic ring is glued. The resulting basin is filled with a small amount of liquid, so that a wall film of defined thickness is generated. The wall film thickness is determined with a micrometer screw. For this purpose, the dry tip of the screw is lowered until it touches the liquid surface. Due to adhesion between liquid and screw tip, the contact between both is clearly visible. Subsequently, the screw tip is lowered until it touches the glass plate. The difference of these two measurements is equivalent to the wall film thickness.

After detaching from the dropper exit the droplet passes a light barrier, located close to the impact area. The obscuration of the light barrier is detected by a photodiode and used to trigger the imaging system. With it the droplet impact was observed and recorded from two different viewing angles and one high-speed camera (Photron Fastcam SA1.1 675K-M1). The frame rate of the camera was adjusted to 20000 fps and the shutter speed to 1/16100 s. The resulting sensor size was 896 x 320 pixels. The impact area was illuminated constantly with light emitting diodes from two directions. The shadow images of the front and side

view of the impact area are redirected by several mirrors and focused by the prime lens ( $f = 50$  mm) so that both images are projected next to each other on the camera sensor. The optical paths of both views are depicted in Figure 1. The blue dotted line represents the optical path of the front view and the red dashed line represents the optical path of the side view. Figure 2 shows a two-perspective image of a Lego manikin, which is placed at the impact area with its rear side facing the reader, with its right hand up. The blue surrounded section of the image in Figure 2 shows the front view of the Lego manikin. Due to the redirection of the corresponding optical path by only one mirror the front view is projected mirror-inverted onto the camera sensor. The lateral view of the Lego manikin is shown in the red surrounded section in Figure 2. For the transformation of the views into each other the left image section needs to be mirrored on its vertical axis and the right image section needs to be rotated 90 ° clockwise. The droplet diameter and droplet impact velocity were determined out of the shadow images immediately prior to the impact. Therefore, an image analysis program written in MATLAB is used.

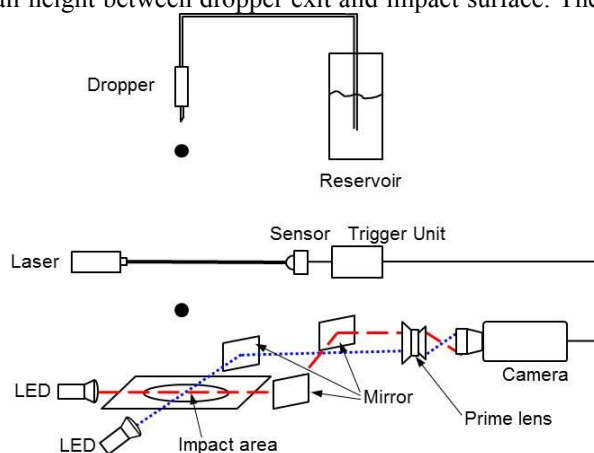


Figure 1. Schematic view of the experimental setup

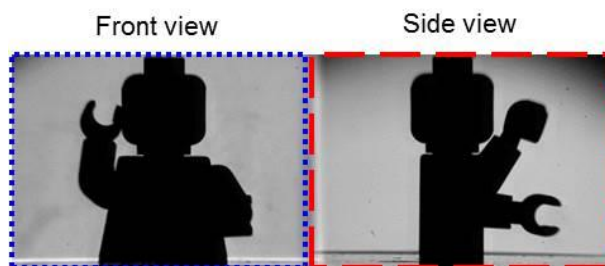


Figure 2. Two perspective image of Lego manikin

view of the impact area are redirected by several mirrors and focused by the prime lens ( $f = 50$  mm) so that both images are projected next to each other on the camera sensor. The optical paths of both views are depicted in Figure 1. The blue dotted line represents the optical path of the front view and the red dashed line represents the optical path of the side view. Figure 2 shows a two-perspective image of a Lego manikin, which is placed at the impact area with its rear side facing the reader, with its right hand up. The blue surrounded section of the image in Figure 2 shows the front view of the Lego manikin. Due to the redirection of the corresponding optical path by only one mirror the front view is projected mirror-inverted onto the camera sensor. The lateral view of the Lego manikin is shown in the red surrounded section in Figure 2. For the transformation of the views into each other the left image section needs to be mirrored on its vertical axis and the right image section needs to be rotated 90 ° clockwise. The droplet diameter and droplet impact velocity were determined out of the shadow images immediately prior to the impact. Therefore, an image analysis program written in MATLAB is used.

After several post processing steps the droplet diameter and velocity are calculated from consecutive images. The analysis program further allows the counting of secondary droplets as well as the determination of the size distribution of them.

	Kin. viscosity $\nu$ $10^{-6} [m^2/s]$	Surface tension $\sigma$ $[mN/m]$	Density $\rho$ $[kg/m^3]$
Castrol Hyspin AWS 10	18.000	28.65	878
n-Hexadecane	4.109	27.60	773

**Table 1.** Physical properties of the used fluids

The experimental results of a hydraulic oil (Castrol Hyspin AWS 10) droplet impacting on n-Hexadecane wall film are presented. The physical properties of both liquids at ambient conditions are summarized in Table 1. For the comparison of the experimental results five non-dimensional numbers were used: the dimensionless wall film thickness  $\delta = h/D$ , the Weber number of the droplet  $We_{drop} = \rho v^2 D / \sigma$ , the Ohnesorge number of the droplet  $Oh_{drop} = \eta / \sqrt{\rho D \sigma}$  and the wall film  $Oh_{film} = \eta / \sqrt{\rho h \sigma}$ . The non-dimensional time  $T = tv/D$  starts at the time of impact of the droplet onto the film. The experimental parameters for cases one to four of the two-component experiments are summarized in Table 2 in terms of non-dimensional numbers. In addition one-component droplet-wall film-interaction experiments with Hyspin and Hexadecane for similar impact conditions are performed.

Case	Droplet	Wall film	$\delta [-]$	$We_{drop} [-]$	$Oh_{drop} [-]$	$Oh_{film} [-]$
1	Hyspin	Hexadecane	0.1	1524	0.0635	0.0453
2	Hyspin	Hexadecane	0.2	1666	0.0623	0.0332
3	Hyspin	Hexadecane	0.1	548	0.0611	0.0435
4	Hyspin	Hexadecane	0.2	534	0.0612	0.0308

**Table 2.** Non-dimensional numbers of the four experimental cases

## Results and Discussion

### Impact symmetry

The two-perspective high-speed shadowgraphy imaging system enabled to evaluate the symmetry of the droplet impact process. The upper picture in Figure 3 showed a symmetric crown evolution. Liquid fingers are formed all-over the crown rim. It further enhanced the visualization of the spatial arrangement of the observed phenomena. For example, the left part of the image in Figure 3 indicated that the two red marked holes close to the crown rim are placed next to each other. But on the right image it gets obvious that the holes are on opposite sides of the crown. The lower picture in Figure 3 showed an unsymmetrical crown break up. Due to the two-perspective imaging system, it is easy to judge the impact symmetry. For the experiments conducted here the symmetry for a vertically impacting droplet is ensured. In the following only the front view of the droplet impact will be used.

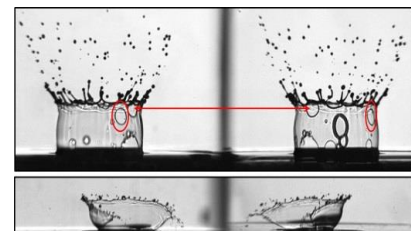


**Figure 3.** Example for symmetric and asymmetric droplet impact

### Case 1: Thin film ( $\delta = 0.1$ ) and high impact velocity ( $We = 1524$ )

The impact of a Hyspin droplet into a thin Hexadecane wall film is depicted in the first column of Figure 4. The evolution of crown, fingers and secondary droplets out of them, proceeds as described for the one-component interaction by Cossali et al. [1]. But, during the growing of the crown its wall is not transparent. A rippled horizontal line and Schlieren occurred (Fig. 4, col. 1,  $T = 5.6$ ), which led us to the assumption that wall film liquid is transported into the crown. In addition, the rippled horizontal line seemed to be the border between droplet and wall film liquid. After reaching a maximum height, crown receding started (Fig. 4, col. 1,  $T = 10.2$ ) and holes appeared in the crown wall. Thoroddsen et al. [4] reported a similar phenomenon for water/glycerin droplets impacting on thin ethanol films. They concluded that the generation of holes is driven by the Marangoni instability, hence by large surface tension gradients. It is triggered by the impact of small spray droplets onto the crown wall. In our experiments the global surface tension gradient of Hyspin and Hexadecane

is close to one and we did not observe any droplet impact on the crown wall. But we assumed that at various local spots in the crown a heterogeneous mixture of droplet and wall film liquid may exist. Around these spots high concentration gradients and therefore high surface tension gradients may develop. Due to the Marangoni-driven flows, the crown wall is thinned out until the wall film ruptures. The emerging holes grow, driven by the imbalance of surface tension along their rims. The holes grow until they meet adjacent holes or the crown rim transforming the crown wall into a filament like structure. The evolution of holes takes place at the contact line between crown base and wall film (Fig. 4, col. 1,  $T = 12.1$ ), too. The flow induced by the kinetic energy of the impacting droplet forwarded the growing of the holes, since it stretched the crown wall. The less viscous parts (local Hexadecane areas) of the crown get punctured and opening of holes started. The holes shorten the contact

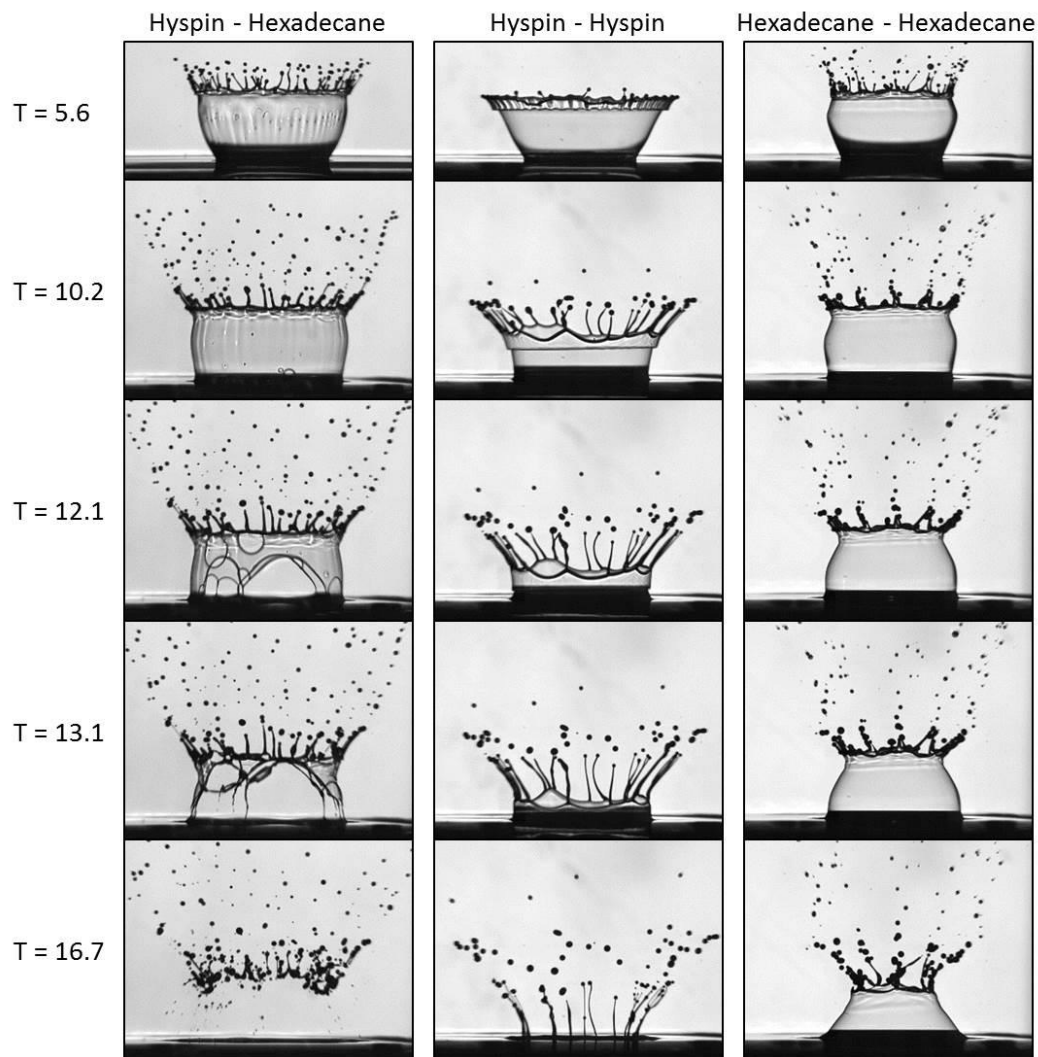


**Figure 4.** A 2.5 mm droplet of the first named liquid impacts at 4.5 m/s on 0.25 mm wall film of the second named liquid

line between crown and wall film until only thin liquid columns remain (Fig. 4, col. 1,  $T = 13.1$ ). Finally, these columns rip off the wall film and resolve into small secondary droplets. Due to the lower viscosity of the thin Hexadecane wall film, not enough of the droplets kinetic energy is dissipated by viscous forces to prevent the crown rip off. The lower rim of the crown moves upwards and collides with the upper crown rim (Fig. 4, col. 1,  $T = 16.7$ ), producing more secondary droplets.

The one-component interaction of Hyspin is shown in the second column of Figure 4. The crown is V-shaped and two clearly separated parts are formed (Fig. 4, col. 2,  $T = 5.6$ ). Only the upper part disintegrates into long thin fingers, while the lower part of the crown fall down into the wall film (Fig. 4, col. 2,  $T = 10.2$ ). At the fingertips secondary droplets are detached, which slowly moved upwards. During the breakup of the crown, the



fingers are prolonged. They remain until the crown breakup has finished (Fig. 4, col. 2,  $T = 16.7$ ). Not till then, the fingers fall down and disintegrate into further secondary droplets, falling down onto the wall film.

In the third column of Figure 4 the one-component interaction of Hexadecane is depicted. It shows well-known crown and finger formation. From the upper end of the fingers secondary droplets are ejected. The increasing crown had a convex shape (Fig. 4, col. 3,  $T = 10.2$ ), with the largest diameter at medium height. During the receding of the crown, its rim contracts faster than it fell down, what causes a turn in crown shape from convex to concave (Fig. 4, col. 3,  $T = 16.7$ ). Due to the contraction, the liquid fingers melt together and disintegrated into large bundles of liquid.

A comparison of the Hexadecane phenomenology to the two-component interaction yielded that both crown shapes during the increase of the crown are similar to each other. Furthermore, the ejection direction of the

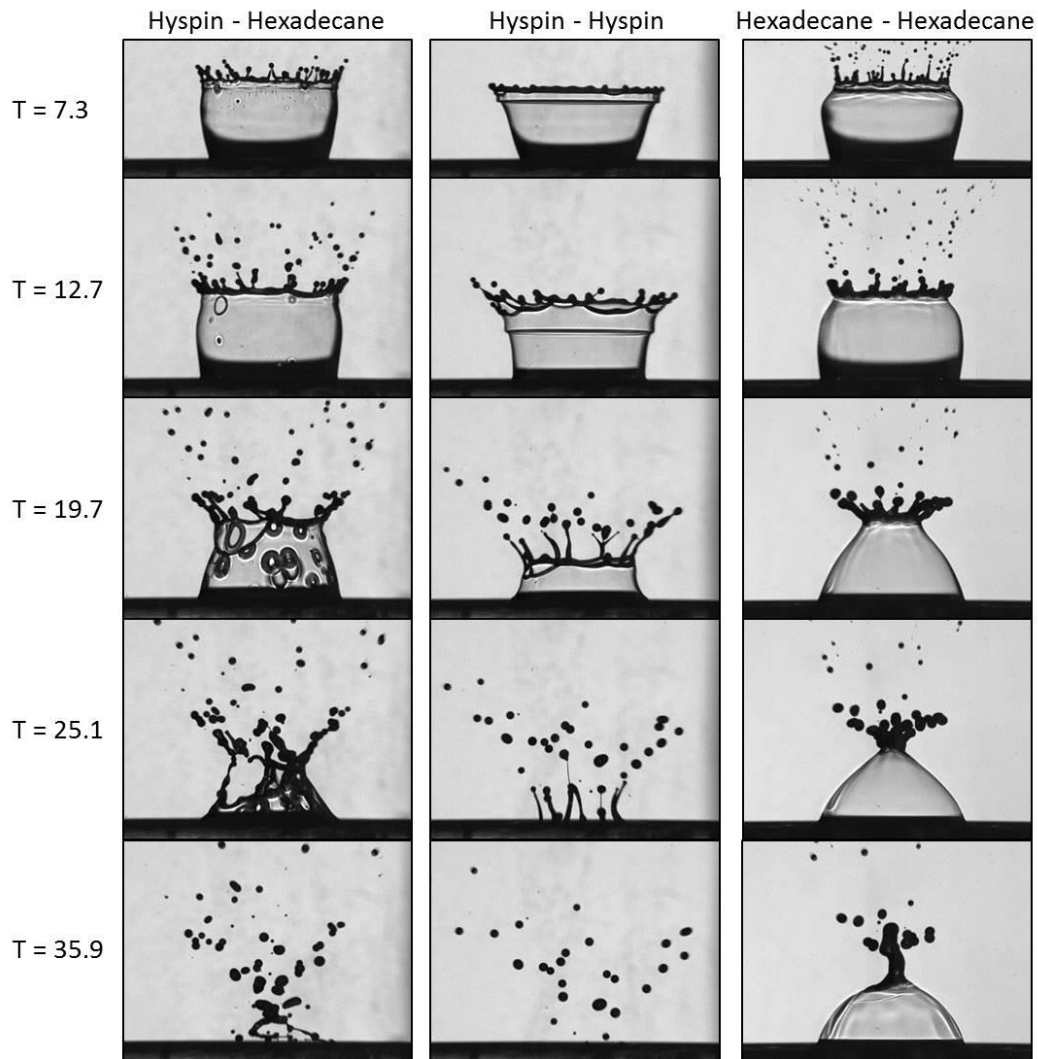


**Figure 5.** A 2.5 mm droplet of the first named liquid impacts at 4.5 m/s on 0.5 mm wall film of the second named liquid

secondary droplets is the same. A comparison of the Hyspin phenomenology to the two-component one yielded that only the prolonged liquid fingers emerging at the crown rim are shared. The kinetic energy of the droplets seemed to affect the crown height and characteristic of the secondary droplets. This leads to the conclusion, that the film properties (thickness and viscosity) dominate the impact phenomenology. Furthermore, the evolution of holes in the crown wall, as well as the crown rip off, indicate that after impact an inhomogeneous mixture of the two liquids is existent. The duration of the impact process is too short for development of a homogeneous mixture of liquids.

**Case 2: Thick film ( $\delta = 0.2$ ) and high impact velocity ( $We = 1666$ )**

In the experiments of case two the wall film thickness is doubled compared to case one. The Hypsin-Hexadecane interaction is again shown in the first column of Figure 5. As expected the crown formation proceeded more slowly, but in a similar manner. The number of fingers and secondary droplets decreased, while their size increased. The evolution of holes already started during the growing of the crown. The holes moved upwards and collided with the crown rim, demolishing it (Fig. 5, col. 1,  $T = 19.7$ ). The holes that are formed during the receding of the crown had a thicker edge. Furthermore, the crown rim contraction was faster than the receding of the crown or evolution of the holes. The crown is disintegrated by hole evolution, rim contraction and break off and breakup into the wall film (Fig. 5, col. 1,  $T = 25.1$ ). During this process large secondary droplets are created (Fig. 5, col. 1,  $T = 35.9$ ). There was no crown rip off at the wall film observed. Again we assumed that concentration gradients were responsible for the formation of holes. Hence, the liquid mixture was inhomogeneous, too. The one-component interactions of Hypsin and Hexadecane are depicted in column two and three of Figure 5. The impact phenomenology for the one-component interaction of Hypsin for  $\delta = 0.2$  was almost identical to the one described in the previous section for  $\delta = 0.1$ . As a consequence of the thicker wall film the number of fingers and secondary droplets decreased but their size increased. The phenomenology had no similarities with the two-component interaction. The one-component interaction of Hexadecane for  $\delta = 0.2$  is depicted in the third column of Figure 5. Until  $T = 12.7$  the crown formation is similar to the one described for  $\delta = 0.1$ . The receding of the crown proceeded more slowly, whereas the contraction of the crown rim proceeded undamped. The contraction stopped when the crown rim is closed and a bubble is formed (Fig. 5, col. 3,  $T = 35.9$ ). The liquid fingers on the crown rim are melted together forming a slowly turning bundle of liquid above the bubble. Later on the bubble will be destroyed by the downwards moving bundle of liquid or by a rip off at the wall film. A comparison to the two-component phenomenology revealed some similarities: The contraction of the crown rim and the melting of the liquid fingers. In the case of two-component interaction the formation of holes tore the crown apart before the rim is contracted completely. The observed impact phenomena confirm the assumption that the properties of the wall film dominate the impact phenomenology. Furthermore, the formation of holes leads to the assumption that the fluids after impact are not mixed homogeneous.

**Case 3: Thin film ( $\delta = 0.1$ ) and low impact velocity ( $We = 548$ )**

For the experimental results presented in the following the impact velocity of the droplet is reduced to 2.6 m/s, while all further parameters are kept constant. The Hypsin-Hexadecane interaction is depicted in the first

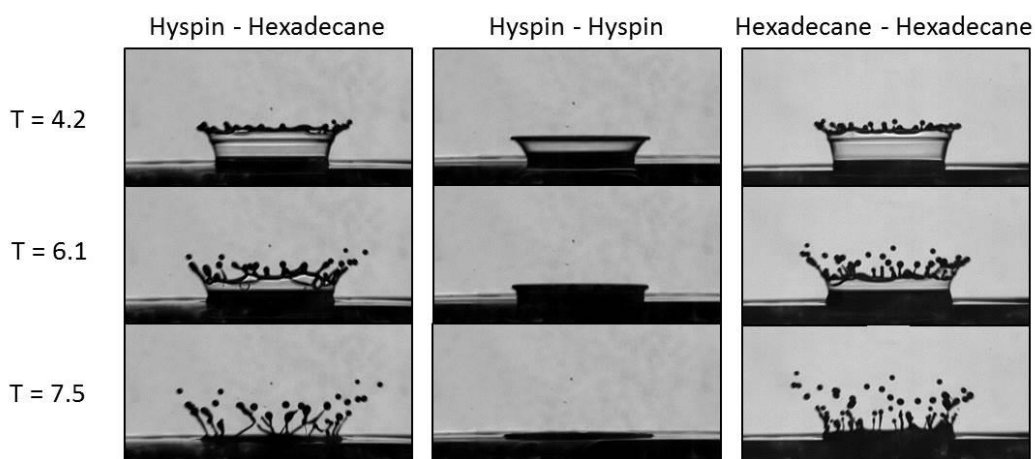


**Figure 6.** A 2.5 mm droplet of the first named liquid impacts at 2.6 m/s on 0.2 mm wall film of the second named liquid

column of Figure 6. The lower droplet impact velocity resulted in a lower crown height and a decreased number of fingers and secondary droplets. The formation of holes was still observed (Fig. 6, col. 1,  $T = 6.1$ ), but the growing of the holes proceeds simultaneously to the crown breakup. For the Hypsin interaction already deposition occurred (Fig. 6, col. 2). For the higher viscosity of Hypsin the droplet impact energy is too small to create splash. The impact process was already finished (Fig. 6, col. 2,  $T = 7.5$ ), while for the two other

interactions the crown breakup is still incomplete. In this case the discrepancy to the two-component interaction was highly visible, since the impact outcome is completely different. The impact phenomenology of the Hexadecane interaction (Fig. 6, col. 3) is very similar to the Hypsin-Hexadecane one, except for the absent formation of holes in the crown wall. These results seem to indicate that, for two-component interactions, the onset of splashing is mostly dominated by the wall film viscosity rather than by the liquid drop viscosity.

#### Case 4: Thick film ( $\delta = 0.2$ ) and low impact velocity ( $We = 534$ )

The impact phenomena occurring for this case are less remarkable compared to the previous presented. For all three liquid combinations deposition occurred. But at the Hypsin-Hexadecane and the Hexadecane-Hexadecane experiments a Worthington-jet and thereof large secondary droplets were formed after the crown breakup. The jet forming at the Hypsin-Hexadecane impact is thicker and climbs less high compared to the jet of the Hexadecane interaction. We interpreted this as an indicator that the jet formation is a droplet driven process, because only the droplet liquid differs in both experiments. The higher viscosity of the Hypsin droplet drags the jet formation process. In the Hypsin-Hypsin experiments the impact process is already finished, when the jet formation in the other experiments started.

#### Conclusion

The necessity for the development of a model describing the two-component droplet-wall film interaction originates from the issue of lubricating oil dilution in Diesel engines. In this paper a first inside in the impact phenomenology of two-component droplet-wall film-interaction, using the example of a Hypsin droplet impacting on a Hexadecane wall film, is presented. Therefore, the experimental setup for a two-perspective high-speed shadowgraphy imaging system is used. This experimental setup allowed further to verify the symmetry of the two-component splashing. The latter, however, refers only to the shape of the crown. Experimental observations, in fact, yielded some new phenomena, namely the formation of holes in the crown wall and the crown rip off at thin wall films. No symmetrical or regular pattern could be observed concerning the distribution of holes and the inception of crown detachment. This led to the assumption that the liquids did not have enough time to form a homogeneous mixture. Consequently, local concentration gradients trigger the Marangoni-effect, which in our opinion is responsible for the formation of holes. The comparison to the one-component experiments revealed that the impact phenomenology is dominated by the properties of the wall film liquid. The kinetic energy of the droplet influenced the characteristic of the observed phenomenology. In future work, improvements of the measurement technique for the wall film thickness will be made. The focus of the future investigations will then be the determination of the splashing threshold and the detailed analysis of the properties of secondary droplets. Later on the visualization of the crown composition employing e. g. LIF will be a further work package. Another focus will be on the study of impact phenomenology of further two-component systems.

#### Acknowledgements

The authors kindly acknowledge the financial support of this work by the Deutsche Forschungsgemeinschaft (DFG).

#### References

- [1] Cossali, G. E., Coghe, A., & Marengo, M. (1997). The impact of a single drop on wetted solid surface. *Experiments in Fluids* 22, pp. 463-742.
- [2] Vander Wal, R. L., Berger, G. M., & Mozes, S. D. (2006). Droplet splashing upon films of the same fluid of various depths. *Experiments in Fluids* 40, pp. 33-52.
- [3] Vander Wal, R. L., Berger, G. M., & Mozes, S. D. (2006). The splash/non-splash boundary upon dry surface and thin fluid film. *Experiments in Fluids* 40, pp. 53-59.
- [4] Thoroddsen, S. T., Etoh, T. G., & Takehara, K. (2006). Crown breakup by Marangoni instability. *Journal of Fluid Mechanics* vol. 557, pp. 63-72.

## Local heat flux investigation during single drop impingement onto a heated wall

Sebastian Fischer<sup>1</sup>, Stefan Herbert<sup>1</sup>, Tatiana Gambaryan-Roisman<sup>1,2</sup> and Peter Stephan<sup>1,2</sup>

1: Institute of Technical Thermodynamics, Technische Universität Darmstadt, Petersenstr. 17, 64287 Darmstadt, Germany

2: Center of Smart Interfaces, Technische Universität Darmstadt, Petersenstr. 17, 64287 Darmstadt, Germany

### Abstract

In the present work the local heat flux distribution at a heated wall during single drop impingement is investigated experimentally with high spatial and temporal resolution. As heated wall an infrared transparent heater design is used. A droplet is created by re-condensation at the tip of a slightly sub-cooled syringe needle. The drop grows in size until it detaches and falls due to gravity. By changing the height of the syringe above the heater target three different impact velocities of  $u_i = 0.24$  m/s, 0.44 m/s and 0.58 m/s are realized, corresponding to Weber numbers of 11, 37 and 65 and Reynolds numbers of 870, 1530 and 2040, respectively. The transient temperature field during the drop impingement event on the heater is recorded by high-speed infrared thermography and from this the local heat flux distribution is calculated numerically. It is found that at early stages of drop impingement the process is dominated by transient single phase heat transfer to the liquid with only a slight influence of contact line heat transfer, whereas during later stages of drop impingement and for sessile droplets contact line evaporation becomes the dominating heat transfer mode.

---

### Introduction

Heat transfer during drop impingement onto heated walls is of high importance in many technical applications, e.g. in jet engine combustion chambers, internal combustion engines or spray cooling technology. An important precondition for establishing a physically correct model of single droplet evaporation is to understand the different heat transfer paths between solid heated wall, the liquid of the droplet and the surrounding air or vapour and their contribution to the overall heat transfer.

It is known that heat transfer close to the three-phase contact line can be of tremendous importance in systems incorporating evaporation [1], e.g. in heat pipes or nucleate boiling [2,3]. When approaching the apparent three-phase contact line from the liquid phase, the liquid film thickness gradually decreases, resulting in a decreasing thermal resistance between hot wall and liquid/vapour interface. However, with decreasing liquid film thickness the adhesion forces exerted onto the interface from the heater wall increase, finally resulting in an adsorbed liquid layer that cannot be evaporated [4]. In order to analyse the contribution of contact line heat transfer to the overall heat transfer during drop impingement, a high resolution measurement technique is necessary to resolve the local phenomena. In literature nevertheless, experiments devoted to local analysis are rarely found.

Chandra and Avedisian conducted experiments on the influence of heater surface temperature by measuring the evolution of the global heater temperature during single drop impingement above and below Leidenfrost temperature [5]. A strong wall temperature drop was found as soon as the droplet wetted the surface. However, as no local measurements were conducted, no distinction between the contributions of contact line heat transfer and single phase convective heat transfer combined with evaporation at the droplet surface was possible. Bhardwaj et al. have carried out local temperature measurements at the centre of the solid/liquid interface of single isopropanol droplets during drop impact using a laser thermorefectance technique [6]. It was found that a temperature drop of about 2 K occurs within 6-8 ms after impact. As no temperature data was recorded at the wetting front of the droplet, no distinction between the different heat transfer paths was possible. The strong cooldown of the surface temperature at the droplet centre however suggests a strong contribution of single phase convective heat transfer during the very early stages of impingement. Chatzikyriakou et al. measured the transient local temperature distribution at the surface of a hot wall using IR-thermography and calculated the local heat flux distributions numerically in the Leidenfrost regime of water droplets impinging onto an inclined plate [7]. They reported local temperature drops as high as 50 K accompanied by local heat flux peaks during the early stages of impact. An interesting approach was pursued by Lee et al. [8]. By using a feedback loop controlled microheater array developed by Kim and Co-Workers [9,10], they kept the surface temperature constant during drop impact and measured the local heat flux distribution with high temporal resolution. The overall heat flow was found to have a maximum during spreading of the droplet and a second smaller maximum during receding of the droplet.

## Experiment setup and measurement principle

In contrast to most experimental investigations found in literature, where impinging droplets are evaporated into air, in the frame of this work droplets were evaporated into a saturated vapour atmosphere. This allows comparability to numerical simulations of the impingement process without the necessity to account for vapour diffusion in the gas phase. In Figure 1 a schematic of the experiment test cell is depicted. As experiment fluid the refrigerant FC-72 is used. The vapour temperature is measured using eight type K thermocouples, calibrated to an absolute accuracy of  $\pm 0.3$  K. To create a saturated vapour atmosphere, the test cell is filled with the fluid prior to the experiments and the test cell walls are set slightly above the saturation temperature at ambient pressure of  $t_{\text{sat}} = 56.6$  °C, to initiate boiling of the fluid. The resulting vapour/air mixture is removed from the test cell and new liquid is added until the temperature in the gas phase corresponded to the saturation temperature at the given pressure and the boiling process within the bulk fluid stopped. At the non-heated regions of the bottom of the test cell, some liquid remains at a constant volume, indicating thermodynamic equilibrium between liquid and vapour phases and therefore absence of non-condensable gases in the atmosphere. The pressure inside the cell is kept at ambient with the help of a pressure equalization membrane connected to the cell. As heater element an infrared transparent Calcium fluoride ( $\text{CaF}_2$ ) glass with a thickness of 2 mm is used, onto which a two-layer coating is deposited by High Power Impulse Magnetron Sputtering (HiPIMS). The first layer is a chromium based black layer with a thickness of approx. 400 nm to improve the surface emissivity and thereby enhance signal-to-noise-ratio for infrared thermography [11]. The second layer is a pure chromium layer, which acts as electrical resistance heater. The thickness of the pure chromium layer is 400 nm as well to allow convenient voltage and current settings. A closer description of the heater design is given in [12].

Above the heater a syringe is placed which is slightly subcooled towards saturation temperature. At the syringe a droplet is formed due to condensation of the vapour, which detaches as soon as the gravity forces exceed the surface tension forces, resulting in highly reproducible droplet diameters of  $d_D = 0.965$  mm - 1.008 mm. The droplet detaches from the syringe and is accelerated due to gravity towards the heater surface. The droplet impact velocity is varied in the range of  $u_i = 0.27$  m/s - 0.58 m/s by adjusting the height of the syringe.

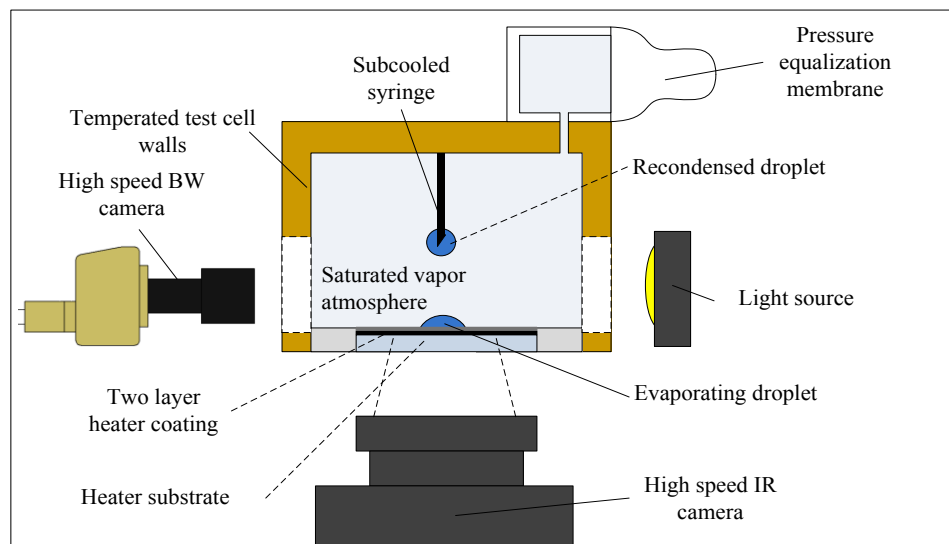


**Figure 1:** Schematic of the experimental setup

Droplet contour, velocity and impact behaviour are recorded using a high speed black and white (BW) camera at a framerate of 1000 Hz and a spatial resolution of 37.11  $\mu\text{m}/\text{pixel}$  through an optical access in the test cell. The droplets are illuminated through a second optical access by a LED backlight, to achieve high contrast at the liquid/vapor interface. From the black and white camera frames, the droplet diameter and impact velocity are derived with a contour detection algorithm implemented in MATLAB®.

The temperature distribution at the heater/fluid interface is measured using high speed infrared (IR) thermography. As the heater substrate is IR transparent (a transmissivity of 99.9% at the given substrate thickness of 2 mm was calculated), the temperature measured by the IR camera is the temperature of the black layer approximately 800 nm away from the heater/fluid interface. Due to its extremely small thickness, the temperature difference across the thickness of the two layer coating and heat storage within the coating are negligible, making the measured temperature effectively the heater/fluid interface temperature. The IR camera is synchronized with the high speed BW camera and records at the same framerate of 1000 Hz with a spatial resolution of 29.27  $\mu\text{m}/\text{pixel}$  and a field of view of 4.68 x 4.68 mm. A pixel-wise in-situ calibration of the IR camera is performed after the measurements by pressing a copper block with a homogeneous temperature on top of the heater and adjusting several constant temperature points to cover the whole measurement range. The raw data of each pixel is then fitted to the reference temperature measured inside the copper block.

From the temperature fields, the transient two-dimensional heat flux distribution is calculated using a three-dimensional energy balance for the heater substrate material:

$$\frac{\partial t}{\partial \tau} = \nabla \cdot (\alpha_{\text{CaF}} \nabla t) \quad (1)$$

The  $\text{CaF}_2$  substrate below the field of view of the IR camera is discretized and equation (1) is solved in this domain using the CFD toolbox OpenFOAM. The measured temperature fields are preconditioned by applying a two-dimensional Gaussian filter to eliminate high frequency measurement noise of the IR camera and patched into the calculation as transient boundary condition at the upper surface of the computation domain. All other boundaries are assumed to be adiabatic. This is not exactly true, but as the area of interest is far away from those boundaries, their influence can be assumed to be low. The output of the calculation are the transient heat flux fields between the  $\text{CaF}_2$  substrate and the chromium based black layer with the same spatial and temporal resolution as the temperature fields. As explained earlier, thermal gradients and heat storage in the sputtered layers are negligible. Therefore the heat flux at the heater/fluid interface is calculated by adding the uniformly distributed heat flux generated by joule heating of the pure chromium layer to the numerically calculated heat flux. An evaluation of the accuracy of this method is given in [13].

## Results and Discussion

In the studied range, no influence of the droplet impact velocity  $u_i$  onto the evolution of temperature and heat flux distributions could be determined. This was to be expected, as the droplet diameter was kept relatively constant by the droplet generation technique and the impact velocity was only varied in a narrow range. Since the droplet Reynolds and droplet Weber numbers, as well as the mean surface superheat, in this study are rather low ( $Re_D = 931 - 2090$ ,  $We_D = 13.6 - 65.6$ ,  $\Delta T_w < 25^\circ\text{C}$ ), the drop impact was always in the non-Leidenfrost regime and splashing was never observed. The droplets always spread after impact, then retracted again and reached sessile state after a short oscillation of the spreading radius around the sessile equilibrium shape. Decay of the oscillation took around 40 ms. In Figures 2 and 3 the results of a typical drop impingement event is shown from 1 ms after impact (Figure 2 a) until the stage of sessile droplet evaporation is reached at 39 ms after impact (Figure 3 d). In the left column of Figures 2 and 3 frames from the high speed BW camera, in the central column the temperature distributions measured by IR thermography and in the right column the calculated heat flux fields are shown. It is evident that directly after impact high heat fluxes occur in the whole wetted region (Figure 2 a), indicating that this stage is governed by single phase convective heat transfer to the droplet. However at 3 ms after impact (Figure 2 b), the heat flux maximum can already be found close to the three-phase contact and is accompanied by a local temperature minimum, indicating the increasing importance of contact line heat transfer. In the high speed frames the formation of a liquid rim at the outer radius of the droplet can be observed. At 6 ms after impact a second high heat flux plateau in the central droplet region arises (Figure 2 c), which decays over time, as the liquid of the rim flows back inwards and the spreading radius decreases. Even though evaporation from the thin liquid layer, caused by the formation of the rim, could be held responsible for this high heat flux, one should keep in mind that the liquid forming the thin layer originates from the former tip of the droplet and is far colder than the wall, so the high heat fluxes can also be caused by transient heat storage in the liquid and must not be caused by immediate evaporation.

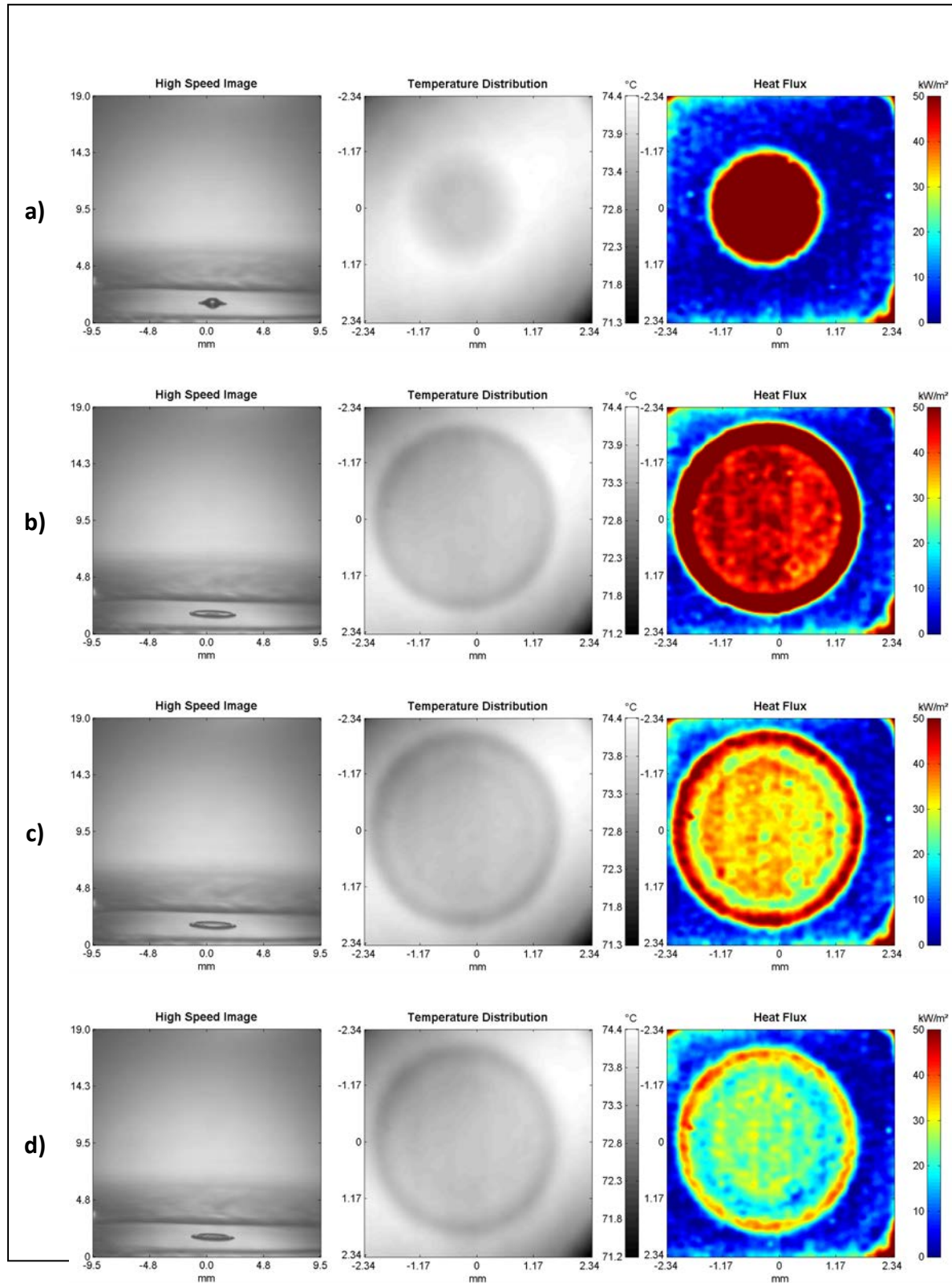
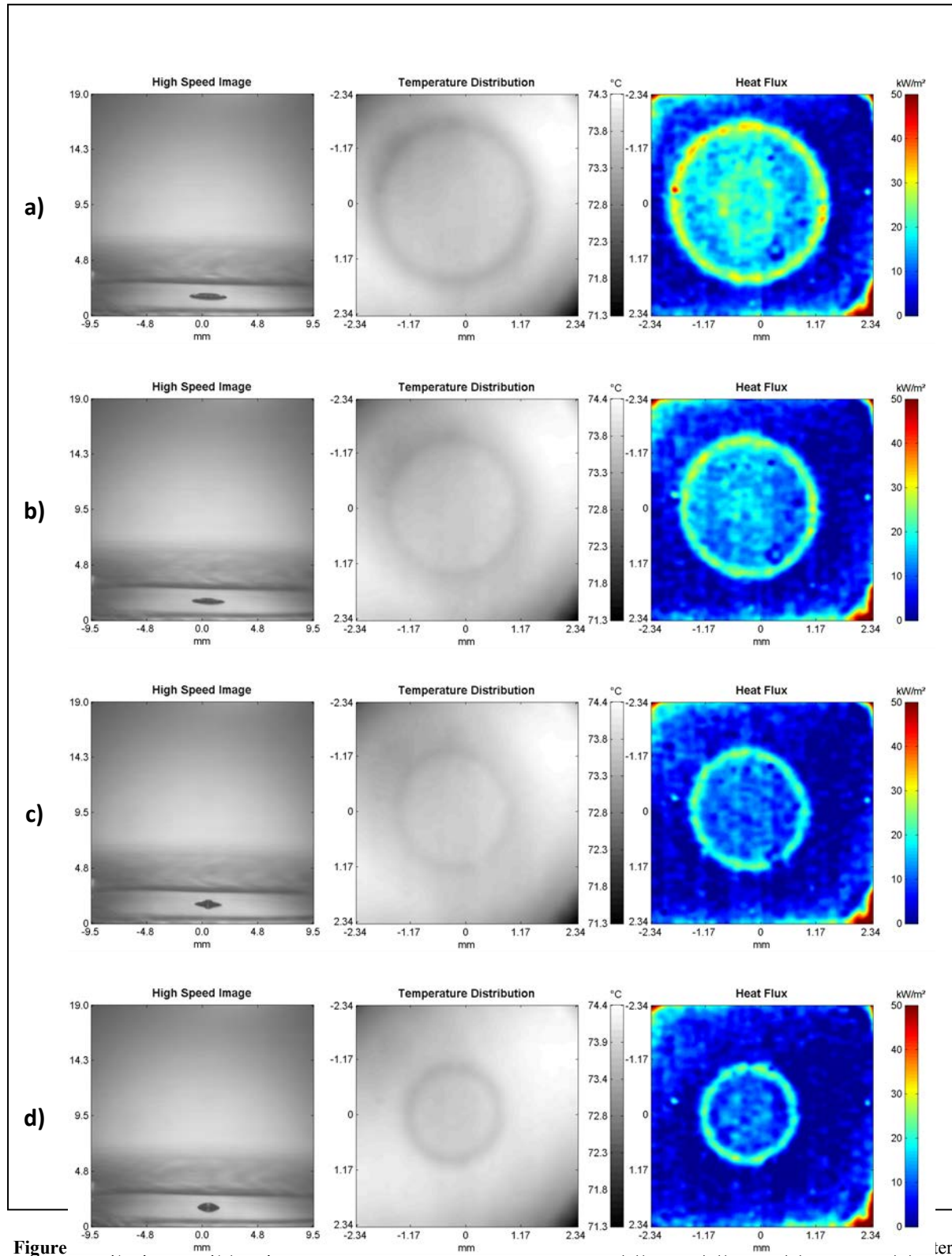


**Figure 2:** High speed image, temperature field and heat flux distribution 1 ms (a), 4 ms (b), 7 ms (c) and 10 ms (d) after drop impact ( $t_{\text{sat}} = 56.14$  °C,  $t_{\text{vapor}} = 56.29$  °C,  $Re_D = 2040$ ,  $We_D = 65$ )





Figure

drop impact (  $t_{\text{sat}} = 56.14$  °C,  $t_{\text{vapor}} = 56.29$  °C,  $Re_D = 2040$ ,  $We_D = 65$ )

ier

During reduction of the droplet radius shown in Figure 3, the overall heat flux gradually decreases. Nevertheless the ratio of heat transferred close to the contact line to overall heat transferred to the droplet steadily increases and is clearly the dominant heat transfer mechanism for a sessile droplet (Figure 3 d).

## Summary and Conclusion

With the experimental method presented it was possible to qualitatively evaluate the importance of different heat transfer paths from heated wall to a single droplet during different stages of drop impact in a low Reynolds and Weber number regime.

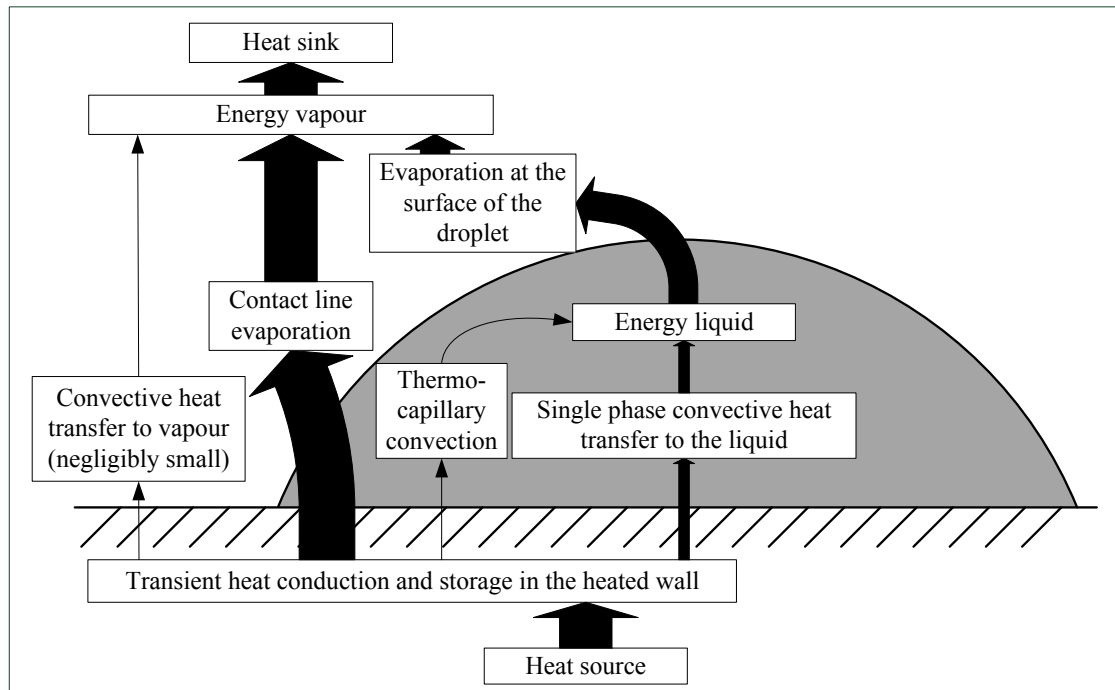


**Figure 4:** Heat transfer paths for drop impact and sessile droplet evaporation

In Figure 4 the different heat transfer paths are illustrated. The arrow thickness indicates the contribution of the different paths for the sessile case. Thermocapillary convection is included for completeness and may play an important role for evaporation into an inert gas atmosphere. In case of this work it can be neglected, as the droplets were evaporated into a pure vapour atmosphere at saturation temperature. While during the early stages of drop impact, most heat is transferred to the energy of the liquid through single phase convection, contact line heat transfer gains more and more importance with advancing time until it is the dominant heat transfer mechanism when the sessile state is reached. Heat transfer to the droplet bulk fluid on the other hand is almost negligibly small for a sessile droplet. The energy temporarily stored in the sensible heat of the liquid is transferred to the vapour energy through evaporation at the droplet surface.

A comparison of the experimental results to numerical simulations of the droplet impingement process with the same boundary conditions yielded excellent qualitative agreement [14]. The distinctive global heat flux peak caused by single phase convective heat transfer directly after drop impact, shows, that the impact process itself must be considered in droplet evaporation models, to capture the physics of the process correctly.

## Acknowledgements

The authors kindly thank the German science foundation DFG for financial support in the frame of the Transregio SFB-TRR 75: “Droplet Dynamics Under Extreme Ambient Conditions”.

## Nomenclature

$d_D$	Droplet diameter	[m]
$t$	temperature	[°C]
$t_{\text{sat}}$	saturation temperature	[°C]
$u_i$	Droplet impact velocity	[ms <sup>-1</sup> ]
$\alpha_{\text{CaF}}$	thermal diffusivity of CaF <sub>2</sub>	[m <sup>2</sup> s <sup>-1</sup> ]
$\nu_l$	liquid kinematic viscosity	[m <sup>2</sup> s <sup>-1</sup> ]
$\rho_l$	thermal diffusivity of CaF <sub>2</sub>	[m <sup>2</sup> s <sup>-1</sup> ]
$\sigma$	surface tension	[Nm <sup>-1</sup> ]
$\tau$	time	[s]
$\Delta T_w$	mean wall superheat	[°C]
$Re_D = \frac{u_i d_D}{\nu_l}$	Droplet Reynolds number	[ ]
$We_D = \frac{\rho_l u_i^2 d_D}{\sigma}$	Droplet Weber number	[ ]

## References

- [1] Wayner, P. C., Kao, Y. K. and LaCroix, L. V.: *The interline heat-transfer coefficient of an evaporating wetting film*, International Journal of Heat and Mass Transfer, 19: pp. 487–492, 1976.
- [2] Stephan, P. C. and Busse, C. A.: *Analysis of the heat transfer coefficient of grooved heat pipe evaporator walls*, International Journal of Heat and Mass Transfer, 35: pp. 383–391, 1992.
- [3] Stephan, P. and Hammer, J.: *A new model for nucleate boiling heat transfer*. Heat and Mass Transfer, 30: pp. 119–125, 1994.
- [4] DasGupta, S., Kim, I.Y., and Wayner, P. C.: *Use of the kelvin-clapeyron equation to model an evaporating curved microfilm*, Journal of Heat Transfer, 116: pp. 1007–1015, 1994.
- [5] Chandra, S. and Avedisian, C.T.: *On the Collision of a Droplet with a Solid Surface*, Proceedings: Mathematical and Physical Sciences 432, pp. 13–41, 1991.
- [6] Bhardwaj, R., Longtin, J. P. and Attinger, D.: *Interfacial temperature measurements, high-speed visualization and finite-element simulations of droplet impact and evaporation on a solid surface*, International Journal of Heat and Mass Transfer 53: pp. 3733–3744, 2010.
- [7] Chatzikyriakou, D., Walker, S.P, Hale, C.P and Hewitt, G.F: *The measurement of heat transfer from hot surfaces to non-wetting droplets*, International Journal of Heat and Mass Transfer 54, pp. 1432–1440, 2011.
- [8] Lee, J., Kim, J. and Kiger, K.: *Time- and space-resolved heat transfer characteristics of single droplet cooling using microscale heater arrays*. International Journal of Heat and Fluid Flow 22: pp. 188–200, 2001.
- [9] Kim, J, Benton, J. F. and Wisniewski, D.: *Pool boiling heat transfer on small heaters: effect of gravity and subcooling*, International Journal of Heat and Mass Transfer 45: pp. 3919–3932, 2002.
- [10] Myers, J. G., Yerramilli, V. K., Hussey, S. W., Yee, Glenda F. and Kim, J.: *Time and space resolved wall temperature and heat flux measurements during nucleate boiling with constant heat flux boundary conditions*, International Journal of Heat and Mass Transfer 48, pp. 2429–2442, 2005
- [11] Slomski, E. M., Scheerer, H., Trossmann, T. and Berger, C.: *Effect of PVD process parameters on nucleation and structure of CrN layers*, Material Science and Engineering Technology 41, pp. 161 – 165, 2010.
- [12] Fischer, S., Herbert, S., Sielaff, A., Slomski, E. M., Stephan, P. and Oechsner, M.: *Experimental Investigation of Nucleate Boiling on a Thermal Capacitive Heater Under Variable Gravity Conditions*, Microgravity Science and Technology 24, pp. 139–146, 2012.
- [13] Fischer, S., Herbert, S., Slomski, E. M., Stephan, P. and Oechsner, M.: *Local heat flux investigation during pool boiling single bubble cycles under reduced gravity*, Proceeding of the 8<sup>th</sup> ECI International Conference on Boiling and Condensation Heat Transfer, Lausanne, Switzerland, June 2012.
- [14] Herbert, S., Fischer, S., Gambaryan-Roisman, T. and Stephan, P.: *Local heat transfer and phase change phenomena during single drop impingement on a hot surface*, International Journal of Heat and Mass Transfer 61, pp. 605–614, 2013

## Droplet impacts of non-Newtonian fluids for bioengineering applications

A. S. Moita<sup>1</sup>, D. Hermann<sup>1</sup> and A. L. N. Moreira<sup>1</sup>

1: Laboratory of Thermofluids, Combustion and Energy Systems, IN+, Dep. Mechanical Eng., Instituto Superior Técnico, Univ. Técnica de Lisboa, Portugal

### Abstract

The present paper is part of a broader project addressing the experimental and theoretical description of the dynamic behaviour of non-Newtonian droplets impacting on cold and heated surfaces. Main focus is put in the description of power-law fluids, particularly shear-thinning, for bioengineering applications. In this context, a parametric study is performed to evaluate the post-impact behaviour of Newtonian and shear-thinning droplets, within a wide range of impact conditions ( $28 < We < 448$ ). Several models devised for Newtonian droplet impacts are adapted and their accuracy is compared for the shear-thinning. The results evidence the increase of the consistency coefficient  $K$  with the mass concentration of the shear-thinning element and stress the dominant role of this parameter in describing droplet's spreading and receding motions. This effect can be well described by the Cross constitutive model and is significantly enhanced when the surface is heated. The Cross model was successfully used to determine the equivalent dimensionless numbers that were required to adapt the energy conservation approach, to estimate the spreading diameter of the shear-thinning droplets. Additional research is however required to fully integrate the dependence of the viscosity of these complex fluids with the temperature.

### Introduction

Unlike Newtonian fluids, for which the stress tensor is a linear function of the velocity gradient and therefore the viscosity remains constant regardless of the shear rate, in non-Newtonian (or complex) fluids, the stress tensor is a generic function of the velocity gradient and of its derivatives [1]. When a droplet impacts a solid surface, large spatial and temporal gradients are observed, so the dynamic behaviour of a non-Newtonian droplet can be significantly different from that of a Newtonian one. Despite most of the studies on droplet impacts focus on Newtonian fluids, many applications deal in fact with non-Newtonian liquids. There are different classes on non-Newtonian fluids, namely power-law-fluids, viscoelastic and yield-stress (or Bingham plastic) [1], whose viscosity-shear rate dependence is governed by different constitutive models. Although significant breakthrough has been achieved to experimentally describe the spreading and the rebound behaviour of viscoelastic, yield-stress and shear-thinning fluids (*e.g.* [2-6]), the results are sometimes contradicting as the physical description of the phenomena is mostly based on a pure empirical description. In fact, several constitutive models are based on empirically fitting parameters, but the effect of each parameter is not understood, either is their relation with the composition of the fluids. For instance, the simplest non-Newtonian fluids are probably the so-called power-law-fluids. For these, the viscosity is not constant, but is a polynomial function of the shear velocity gradient, described as:

$$\tau = K \left( \frac{u}{y} \right)^n \quad (1)$$

being  $\tau$  the shear stress and  $u/y$  the velocity gradient. Here,  $K$  is the consistency coefficient and  $n$  the power law index. For  $n < 1$ , one obtains the so-called shear-thinning (or pseudoplastic) fluids, while for  $n > 1$  one has the shear (thickening) or dilatant fluids. For  $n = 0$ , equation (1) describes the behaviour of Newtonian fluids, so that the consistency coefficient coincides with the Newtonian viscosity. Recently, German and Bertola [7] have discussed on the role of  $K$  and of  $n$  in the spreading behaviour reporting a non-intuitive result: as the concentration of a shear thinning component increases,  $n$  increases, so one should expect lower spreading diameters, since there should be a larger viscosity at high velocity gradients (at the beginning of spreading), which would promote energy dissipation. However, the opposite trend is observed. The  $n$  and  $K$  parameters cannot be independently observed because changing the mass concentration also affects  $K$  in the opposite trend of  $n$ . So, larger concentration leads to thicker fluids (large “zero” viscosity) but more shear-thinning (low “infinite” viscosity). This variation of the viscosity between a minimum and a maximum, for low and high shear rates is quantitatively described by a number of constitutive models [8, 9], whose validation and fitting are still dependent from appropriate experimental data. Additionally, it is not clear yet how the constitutive models change with different parameters such as the liquid/surface temperature, despite the fact that, for many of the aforementioned applications, the surface temperature is an important variable.

Since many coating and painting solutions are shear-thinning, describing accurately the post-impinging behaviour and particularly, being able to accurately predict the spreading and receding diameters of this class of fluids is of major importance. Another particular reason to focus on this class of non-Newtonian fluids is in the

creation of new interfaces and biomaterials, using the so-called cell printing method. Here, the cells or organic preparations are printed on demand on “bio-papers”, so that they can grow with customized direction/organization (*e.g.* [10]). Only recently the deposition process was modelled by Bioengineers based on impacts of Newtonian droplets (*e.g.* [11]), in order to try to predict the desired cell disposition. On the other hand, when living cells are used, they are extremely sensitive to shear stress, so that the velocity rates inside the droplet during the spreading must be accurately quantified. Ultimately, the appropriate impact conditions are chosen to assure the desired deposition process while keeping the cells viable. Many of these preparations also have shear-thinning characteristics, so, also here, description of the post impingement spreading and receding motions is of vital importance.

In line with this, the present work addresses the description of the effect of the mixture concentration on the parameters governing the constitutive models of shear-thinning fluids. These are then used to derive equivalent dimensionless numbers, which are required to devise the spreading models equivalent to those available for Newtonian drops, as in [12, 13]. A parametric study is performed to evaluate the post-impact behaviour of Newtonian and shear-thinning droplets, within a wide range of impact conditions ( $28 < We < 448$ ). Several models devised for Newtonian droplet impacts are adapted and their accuracy is compared for the shear-thinning liquids, as a function of the impact conditions, mixture composition and surface temperature. Surface topography and wettability will be explored as a way to play with the parcel of the dissipated energy.

## Experimental Procedure

The experiments encompass the impact of droplets within a wide range of diameters ( $80\mu\text{m} < D_0 < 3.3\text{mm}$ ) impacting on solid and dry surfaces, surfaces with velocities  $U_0$  ranging from 0.88 to 7m/s. For this paper, only the results obtained with the millimetric droplets are discussed.

The surfaces are accommodated on a copper base in which a 264 W cartridge heater is inserted and are heated from room temperatures up to 140°C. Surface temperature of the targets is acquired using fast response type K thermocouples “Medtherm”. The thermocouples are 3mm apart, taking from the reference the thermocouple that is placed in the center of the droplet impact region ( $r=0\text{mm}$ ). They are aligned with the top of the surface where the impact occurs. Another embedded thermocouple is used to control the cartridge heaters, using a PMA KS20-I controller. Care is taken to assure that the surface is dry and recovers the initial temperature before the impact of the droplet. The liquid is kept at the droplet generator at room temperature and atmospheric pressure. Ambient temperature and relative humidity were measured through the experiments to ensure that their variation did not produce relevant changes in the results.

The signal of the thermocouples is sampled with a National Instruments DAQ board associated with a BNC2120 and amplified with a gain of 300 before processing. Different acquisition frequencies were used to characterize the temporal variation of the instantaneous temperature. Hence, to capture the entire variation along droplet deformation process, a relatively low frequency must be used (of the order of 2Hz). Then to refine the measures to particular instants a larger frequency was considered, of the order of 10kHz.

Droplet impacts are recorded using a high-speed camera (Phantom v4.2 from Vision Research Inc., with  $512 \times 512 \text{ pixels} @ 2100 \text{ fps}$  and a maximum frame rate of 90kfps). To record the impact history of the millimetric droplets, the frame rate was set to 2200fps. For the micrometric droplet streams the frame rate was increased up to 6300 fps ( $208 \times 400 \text{ pixels}$ ). For the set-up used here, the resolution is 25pixel/mm.

The behaviour of non-Newtonian liquid droplets is compared with that of water and water-glycerine mixtures. The non-Newtonian liquid drops are made of different water+xanthan gum (G1253, Sigma-Aldrich) solutions at levels of 0.05%, 0.1%, 0.2% and 0.35% wt%. Shear viscosities were measured using capillary viscometer and rotational rheometer. Specific mass and surface tension of all the xanthan gum solutions are very close of those of water, as depicted in Table 1. Although, different concentrations, namely 0.05, 0.1, 0.15, 0.20, 0.25, 0.30 and 0.35wt% are being tested, due to paper length constrains, most of the results discussed here were obtained for the extreme limits of xanthan mass fraction, 0.05% and 0.35%, which are presented in the table.

**Table 1.** Thermophysical properties of the working liquids taken at 20°C.

Liquid	Specific mass $\rho$ [kg/m <sup>3</sup> ]	Surface tension $\sigma_{lv}$ [mN/m]	Dynamic viscosity $\eta_0$ [Pa.s]	Dynamic viscosity $\eta_\infty$ [Pa.s]
Water	998	72.75	$8.9 \times 10^{-4}$	$8.9 \times 10^{-4}$
X0.05 (Xanthan gum 0.05wt%)	999	73.0	0.12	$1.2 \times 10^{-3}$
X0.05 (Xanthan gum 0.35wt%)	999	72.95	12.5	$2.0 \times 10^{-3}$

### Characterization of the test surfaces

The surfaces used here are made from a silicon wafer and are micro-patterned using square structural, with side size  $l$  and height  $h$ . The pillars are apart within a distance  $\lambda_R$ , as defined in Figure 1. The patterns are printed on the silicon wafer by lithography and processed by plasma etching. To reach higher pillars, the wafer surfaces were coated with aluminum, before the lithography. So, besides plasma etching, wet chemical etching is required for the aluminum coating. The micro-patterns are controlled to have known, precise values, using a profilometer, with a measurement precision of  $\pm 100$  Angstroms. An example of a roughness profile is depicted in Figure 1. Finally, the surfaces are checked by SEM/EDS analysis. Heterogeneity of the patterns was found to be lower than 3%. The wettability of the surfaces was also characterized, based on the static and dynamic contact angles, measured at room temperatures using an optical tensiometer THETA from Attension.

An average value is considered for each pair liquid-surface which is determined from at least eight measurements taken at different regions of the surface. The time evolution of the average contact angles is obtained by curve fitting and the final values are determined by extrapolation. The detailed measurement procedure has been described in previous works (e.g. Moita and Moreira [14]).

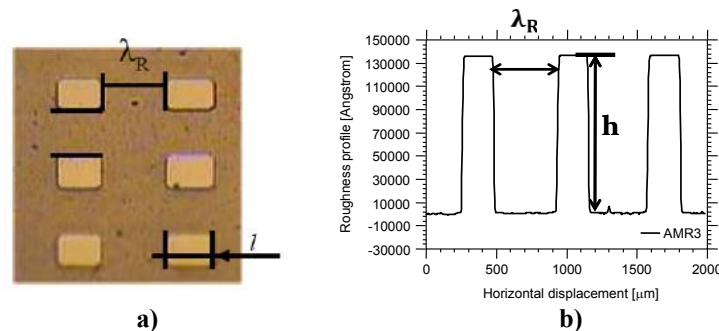
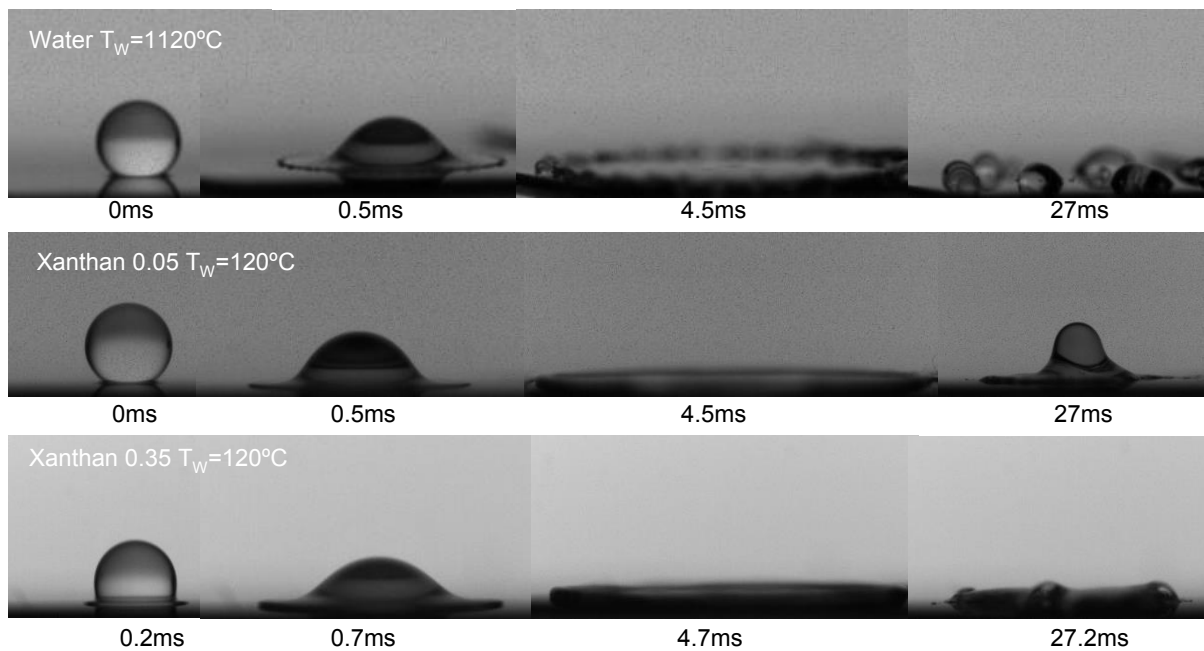


**Figure 1.** a) Detail of a micro-structured surface, showing the definition of the dimensions  $a$ ,  $h$ , and  $\lambda_R$  characterizing its topography. b) Sample 1-D roughness profile of the surface.

### Results and Discussion

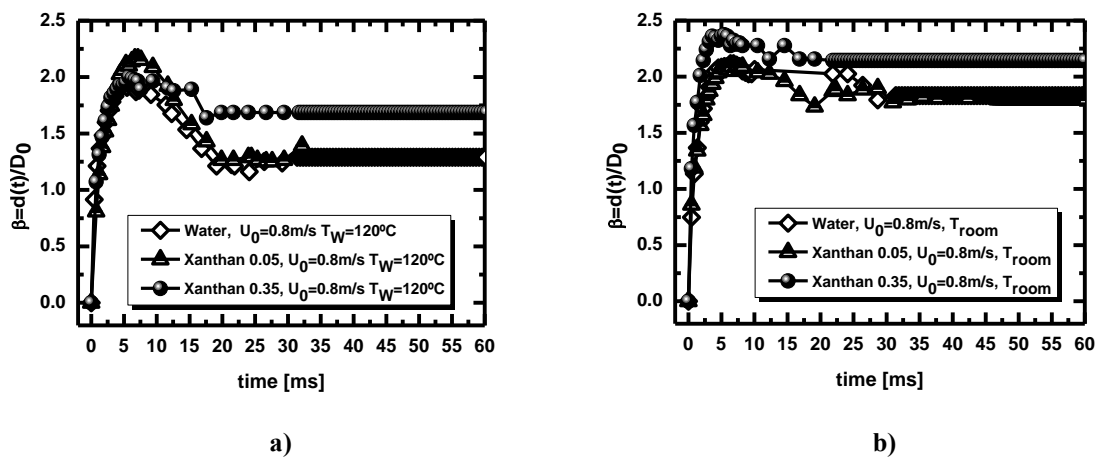
The qualitative analysis of droplet impact taken from high-speed visualization of its post-impingement morphology shows that the dynamic behaviour of the shear-thinning droplets does not depict any particular morphology, when compared to that of Newtonian droplets, but the impact outcomes can be significantly different. Hence, a fast expansion of the lamella is observed for the xanthan mixture with 0.35 wt%, which is followed by a slow spreading with a moderately low expansion diameter. Compared with water, the fast expansion, which occurs right after the impact is related to the shear thinning effect, but then, as the shear rate quickly decreases, as the lamella approaches its maximum diameter, the zero viscosity tends to increase, thus limiting the value of the spreading diameter. This is not very clear in the illustrative images shown in Figure 2, but is obvious in the plots in Figure 3, which depict the temporal evolution of the spreading ratio  $\beta = d(t)/D_0$ , where  $d(t)$  is the spreading diameter of the lamella and  $D_0$  is the initial droplet diameter. A similar trend is observed for higher impact velocities, since although the shear rates at the beginning of the expansion of the lamella are higher, thus decreasing the viscosity, the dissipation associated to these large velocity gradients is actually larger. Then, the viscosity tends to increase at the end of the expansion of the lamella. Consequently, the receding motion is very slow for these high concentrations of xanthan, so the spreading and equilibrium diameters remain larger than those of water, both for cold and heated surfaces, even though its zero shear rate viscosity is significantly higher than that of water.

A different trend is nevertheless observed for the xanthan mixture with the lowest concentration (0.05wt%): in this case, the spreading behaviour is similar to that observed for the 0.35wt% concentration. However, very fast recoil is instead observed for the liquid with the smallest concentration, which can be even slightly faster than that observed for water droplets. This is particularly evident at the highest impact velocity and when the surface is heated. Indeed, augmenting the surface temperature seems to stress this fast recoiling motion for the xanthan mixture with 0.05wt%, which actually results in a partial rebound for the impact at the highest velocity (Figure 3d). Similar rebound phenomenon is reported in [13], for impacts onto hydrophobic surfaces, for which the energy dissipation is lower. Hence, one may speculate that the temperature is acting on the  $K$  and  $n$  factors in a way that, overall the entire spreading and receding process, a smaller parcel of the surface energy is dissipated.



**Figure 2.** Impact of water and water-xanthan gum mixtures impacting a smooth silicon wafer, heated at  $T_W=120^\circ\text{C}$ . For all the droplets  $D_0=3.2\text{mm}$  and  $U_0=3.2\text{m/s}$ .

A wider view of how the maximum spreading ratio are varying, for different wt% of xanthan gum and for various surface temperatures, as a function of the impact velocity (quantified here as the Weber number) is further presented in Figure 4. Our results are depicted here together with those reported by [13] for comparative proposes and to allow a more general analysis, covering a wider range of data.





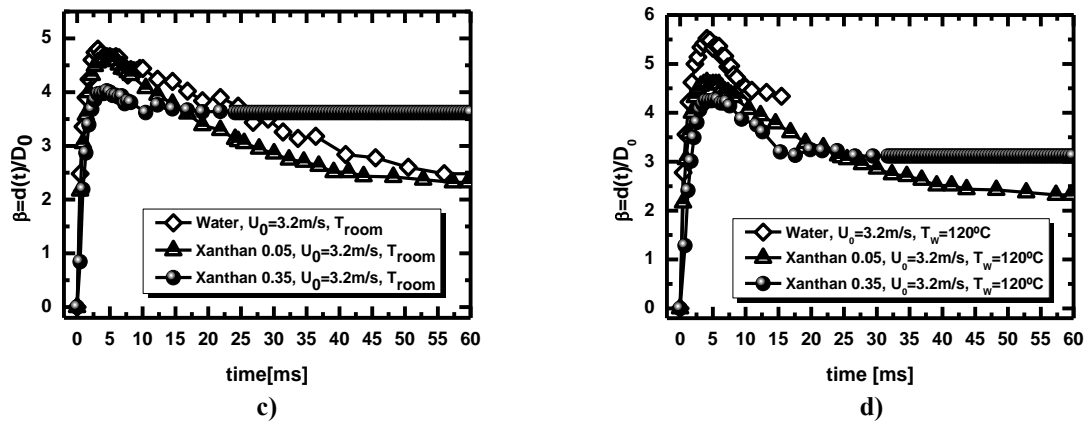


**Figure 3.** Spreading ratio for water and xanthan gum mixtures impacting onto a smooth silicon surface at: a)  $U_0 = 0.8 \text{ m/s}$ , room temperature; b)  $U_0 = 0.8 \text{ m/s}$ , surface temperature  $T_w = 120^\circ\text{C}$ ; c)  $U_0 = 3.2 \text{ m/s}$ , room temperature; d)  $U_0 = 3.2 \text{ m/s}$ , surface temperature  $T_w = 120^\circ\text{C}$ .

The results depicted here, can be explained as follows. As the mass fraction of the shear-thinning element increases,  $K$  in equation (1) increases, while  $n$  decreases [7]. According to the behaviour described above,  $K$  seems to play the dominant role, and represents the maximum viscosity that the fluid may exhibit. These findings are in agreement with those reported in [7]. The fact that the surface temperature enhances this behaviour is not yet clear and deserves further investigation. This behaviour should be carefully taken into account for applications dealing with heat transfer such as for cooling purposes. Lower concentrations of the shear thinning element actually result in expanding spreading diameters, for higher temperatures, but also lead to fast recoiling motion, which can significantly reduce the contact time and contact area of the liquid over the surface to cool, within a temporal range which is still relevant for the heat transfer characteristic times. A way to compensate this enhanced recoiling motion can be by playing with the surface wettability, at the expense of altering its topography. At this stage it is still yet to soon to withdrawn any conclusion, but preliminary results, suggest that an average well controlled spreading diameter can be achieved for non-Newtonian droplets, impacting onto micro-patterned surfaces, which are actually quite similar to those obtained for Newtonian droplets, as previously reported in [15]. Although speculative, this result is contrasting with previous findings, *e.g.* [7] who report a minor role of the surface wettability on the dynamic behaviour of shear-thinning droplets, and can be explained by the fact that in the present work the wettability is mainly varied at the expense of changing the surface topography, not only affecting the usual energy dissipation occurring at the contact line, due to contact angle hysteresis, but is also possibly influencing the viscous dissipation.

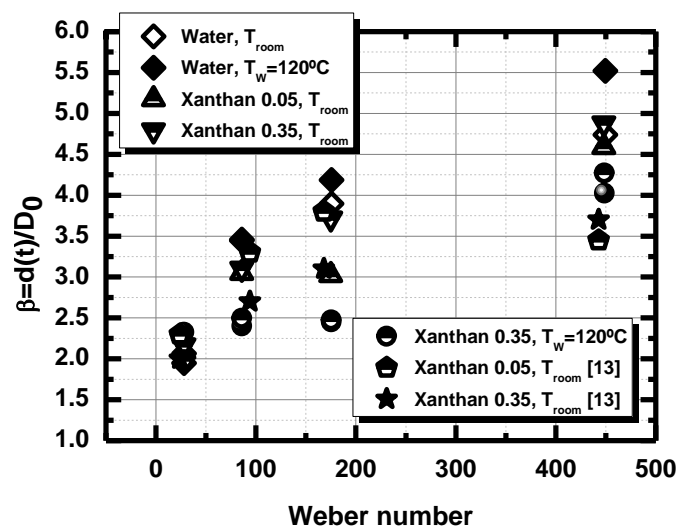


**Figure 4.** Spreading ratio as a function of the impact Weber number for different wt% of the Xanthan gum, for diverse surface temperatures.

Regarding to the prediction of the spreading diameter, the variation of the viscosity between zero and infinite shear during the entire deformation process is well related to the Cross model:

$$\frac{\eta_{eff} - \eta_{\infty}}{\eta_0 - \eta_{\infty}} = \frac{1}{1 + \left( k.C \frac{3\beta_{max}^2 U_0}{2D_0} \right)^m}. \text{ At this stage of the work, a semi-empirical approach is still required to be}$$

followed to determine the parameters  $k$ ,  $C$  and  $m$ , as in [14]. Here, the shear rate is scaled, following a similar approach to that of [14], based on mass conservation principles. This procedure allows determining equivalent

viscosities which were used to compute equivalent Ohnesorge  $Oh_{eff} = \frac{\eta_{eff}}{(\rho D_0 \sigma_{lv})^{1/2}}$  and Reynolds

$Re_{eff} = \frac{\rho U_0 D_0}{\eta_{eff}}$  numbers, which in turn are used to evaluate the equivalent model following that of Scheller

and Bousfield [16], in the general form:  $\beta_{max, predicted} = C_1 (Re_{eff}^2 Oh)^n$ . The results show an acceptable good agreement between the experimental data and the predicted values, although the enhanced effect of the surface temperature is not completely well captured. Additionally, a more complex scaling of the shear rate is required, to be consistent with the non-uniform thickness of the rim, as suggested for instance by Roisman [17].

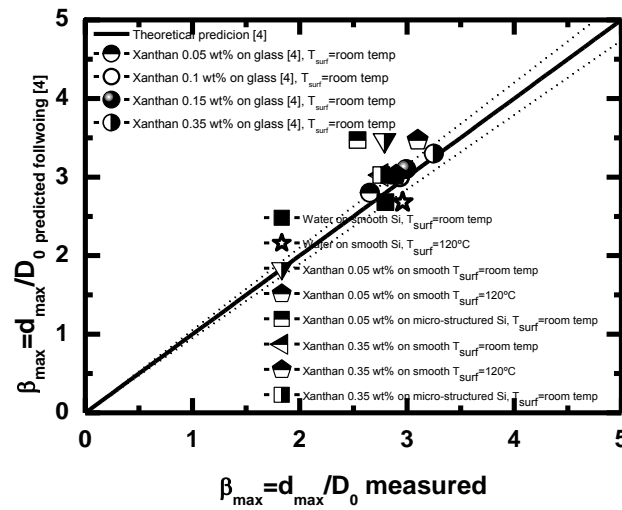


**Figure 5.** Comparison between our experimental results and the predicted values of the maximum spreading diameter made dimensionless by droplet initial diameter  $\beta_{max, predicted}$ , following the approach of [14].

## Final Remarks

The present paper is part of a broader project addressing the experimental and theoretical description of the dynamic behaviour of non-Newtonian droplets impacting on cold and heated surfaces. Main focus is put in the description of power-law fluids, particularly shear-thinning, for bioengineering applications. In this context, a parametric study is performed to evaluate the post-impact behaviour of Newtonian and shear-thinning droplets, within a wide range of impact conditions ( $28 < We < 448$ ). Several models devised for Newtonian droplet impacts are adapted and their accuracy is compared for the shear-thinning liquids. The results evidence the increase of the consistency coefficient  $K$  with the mass concentration of the shear-thinning element and stress the dominant role of this parameter in describing droplet's spreading and receding motions. This effect can be well described by the Cross constitutive model. Hence, larger mass concentrations of the shear thinning element lead to smaller viscosities at high shear rates and larger viscosities occur at low shear rates. Consequently, significant energy dissipation occurs at the earliest spreading stages, when the shear rates are higher, for the largest mass concentration drops. On the other hand, larger viscosity is obtained as the spreading lamella reaches the maximum expanding diameter and decelerates. Therefore the lowest maximum spreading diameters generally occur for the largest mass concentrations of the shear-thinning element, for which the receding motion is almost inexistent. This behaviour contrasts with the large and fast spreading, recoiling and even rebound, which are observed for the impact of the droplets with the lowest concentration of the shear-thinning element. This effect is significantly enhanced when the surface is heated.

The Cross model was successfully used to determine the equivalent dimensionless numbers that were necessary, in order to adapt the energy conservation approach, to estimate the spreading diameter of the shear-thinning droplets. Additional research is however required to fully integrate the dependence of the viscosity of

these complex fluids with the temperature.

### Acknowledgements

The authors are grateful to Fundação para a Ciência e a Tecnologia (FCT) for partially financing the research under the framework of the project PTDC/EME-MFE/109933/2009 and for supporting A.S. Moita with a Fellowship (Ref: SFRH/BPD/63788/2009).

### References

- [1] V. Bertola, M. Marengo, Koninklijke Brill NV, Leiden (2012).
- [2] R. Crooks, D.V. Boeger., *J. Rheol.*, 44:973-996 (2000).
- [3] A. Rozhkov, B. Prunet-Foch, M. Vignes-Adler, *Phys. Fluids*, 15:2006-2019 (2003).
- [4] V. Bertola, *Exp. Fluids*, 37:653-664 (2004).
- [5] D. Bartolo, A. Boudaoud, G. Narcy, D. Bonn, *Phys. Rev. Lett.*, 99:174502 (2007).
- [6] M. Smith, V. Bertola, in: *Proc. 23<sup>rd</sup> Annual Conf. Liquid Atom. Spray Syst. – ILASS Europe-2010*, p.124 (2010).
- [7] G. German, V. Bertola, *J. Phys. Condens. Matter*, 21:16pp (2009).
- [8] M. M. Cross, *J. Coll. Sci.*, 20:417-437 (1965).
- [9] P. J. Carreau, *PhD Thesis*, University of Wisconsin, Madison, USA (1968).
- [10] S. Tasoglu, G. Kaynak, A. J. Szeri, U. Demirci, M. Muradoglu, *Phys. Fluids*, 22:082013 (2010).
- [11] T. Xu, J. Jin, C. Gregory, J. J. Hickman, T. Boland, *Biomaterials*, 26:93-99 (2008).
- [12] S. M. An, S. Y. Lee, *Exp. Thermal Fluid Sci.*, 37:37-45 (2012).
- [13] S. M. An, S. Y. Lee, *Exp. Thermal Fluid Sci.*, 38:140-148 (2012).
- [14] A. S. Moita, A. L. N. Moreira, *Exp. Fluids*, 52:679:695 (2012).
- [15] A. S. Moita, A. L. N. Moreira, in: *Proc. 12<sup>th</sup> Triennial Int. Conf. Liquid Atom. Spray Syst. – ICLASS 2012*.
- [16] B. L. Scheller, D.W. Bousfield, *AIChE J.*, 41:1357-1365 (1995).
- [17] I.V. Roisman, *Phys. Fluids*, 21:052104 (2009).

## Numerical study on air entrapment in droplets under impact onto a solid surface

Qiaoyan Ye, Oliver Tiedje

Fraunhofer Institute for Manufacturing Engineering and Automation  
Nobelstr. 12, 70569 Stuttgart, Germany

### Abstract

Air entrapment in droplets under impact onto a dry smooth solid surface was numerically investigated using three-dimensional computational domain with high-resolution grid. The study was focused on the drop spreading phase without splash and break-up. We present detailed numerical observations of the velocity and pressure distributions, as well as the initial air disc formed at the impact point. Results of numerical simulations indicate that the initial size of the air disc is independent of the drop properties and the impact velocity. However, the maximal size of the enlarged air disc during the first advancing scenario depends on the  $Oh$  and  $Re$  numbers, especially for viscous droplets. The air disc contracts into micro bubbles. The simulations also show the bubble release processes. The effects of the bubble release from the liquid film were discussed.

---

### Introduction

Droplet impingement and spreading on a solid surface are phenomena that happen frequently in many industrial applications, such as coating processes using liquid sprays. The paint film quality of such coating processes is affected by the entrapment of air bubbles in the liquid film which release later in the drying process, resulting in pinholes in the dry paint film. In general, there are two presumptions on where air bubbles come from. One is the air entrapment resulting from the impact of the liquid drops, which has been observed by many researchers using different liquid materials and impact velocities. The other is the air inclusion in the droplets after the atomisation processes, probably due to the release of dissolved air in the liquid, which is however quite difficult to be experimentally observed.

Experimental observations of the impact of liquid drops onto dry solid surfaces at room temperature with the analysis of air entrapment have been reported extensively [1-5]. By using flash photographic methods and high speed cameras, as well as different light settings, such as back, or oblique lighting, with and without light diffuser, the authors observed bubble formation at the stagnation point and assumed bubble formation because of a dimple created at the drop surface at impact point (Chandra and Avedisian (1991), Thoroddsen and Sakakibara (1998)). In investigations using viscous drops, Thoroddsen et al. (2010) found much more bubble entrapment during the drop spreading process, resulting from the localised contacts of the levitated lamella with the solid substrate, especially for intermediate values of the Reynolds number ( $Re \sim 250-350$ ). Similar researches [6] have also been carried out recently by Palacios et al. (2012). Besides myriad of air bubbles at the interface between liquid and solid, they also observed two rings of micro-bubbles under the impact of glycerol/water drops onto a dry glass surface at Reynolds and Weber numbers around the splashing/deposition threshold and analysed the dependency of the behaviour of the two rings of micro-bubbles on the drop impact velocity and the ranges of the relevant dimensionless numbers.

There are not so many numerical studies that focus on the air entrapment under drop impact. Mehdi-Nejad, Mostaghimi and Chandra ([7], 2003) simulated the impact of water, n-heptane, and molten nickel droplets on a solid surface using two-dimensional computational domains. They included the effect of the gas around the droplets and predicted the formation of air bubbles at the solid-liquid interface.

Although the air entrapment phenomenon under drop impact onto a solid surface is well known experimentally, the knowledge on the detailed process and on the mechanisms underlying air bubble entrainment as well as air bubble release from the liquid film is still limited, especially for high-viscous and non-Newtonian liquids. In this work, we present numerical studies on viscous drops ( $0.04 - 1 \text{ Pa s}$ ) impacting onto a dry smooth solid surface, aiming to observe the air entrainment and release at relatively low impact Reynolds numbers ( $Re < 300$ ).

## Simulation methods

### Governing equations

The Droplet impact and spreading on a surface is an example of an interfacial flow problem that can be calculated using the Volume of Fluid (VOF) method, a surface tracing technique, with which two or more immiscible fluids can be modelled by solving a single set of momentum equations and tracking the volume fraction of each of the fluids throughout the domain. The numerical simulations in this work were carried out with the commercial CFD code ANSYS-FLUENT based on the finite-volume approach. The flow field and the liquid-gas interfaces during the droplet impact process are solved by the volume fraction equation and single momentum equations:

$$\frac{1}{\rho_q} \left[ \frac{\partial}{\partial t} (\alpha_q \rho_q) + \nabla \cdot (\alpha_q \rho_q \vec{v}_q) \right] = 0 \quad (1)$$

$$\frac{\partial}{\partial t} (\rho \vec{v}) + \nabla \cdot (\rho \vec{v} \vec{v}) = -\nabla p + \nabla \cdot \left[ \mu (\nabla \vec{v} + \nabla \vec{v}^T) \right] + \rho \vec{g} + \vec{F} \quad (2)$$

where  $\vec{v}$  denotes the velocity vector,  $t$  the time,  $\rho$  the density,  $\mu$  the dynamic viscosity,  $p$  the pressure and  $\alpha_q$  the  $q^{\text{th}}$  volume fraction of the fluid in the cell. The resulting velocity field is shared among the phases. Time-dependent VOF calculations were carried out using an explicit scheme. At the beginning of the calculations, a constant time step size of 0.1  $\mu\text{s}$  was used, later after droplet impact, variable time step size from 0.01 to 10  $\mu\text{s}$  for drop spreading. A geometric reconstruction scheme for the volume fraction discretization [8] was used, ensuring a sharp interface between liquid and gas phase. PRESTO scheme was applied for the pressure discretization. For the momentum equation we used QUICK scheme that is based on a weighted average of second-order-upwind and central interpolation of the variable. This discretization scheme will be typically more accurate on quadrilateral and hexahedral meshes aligned with the flow direction.

Additional user defined functions were coded for catching the detailed time-resolved quantities for droplet impact dynamics, for instance, spread factors and the volume summation of air bubbles, etc.

### Computational domain, mesh and boundary conditions

By experimental investigation of the droplet impact, droplet diameters of 1 – 4 mm were usually applied, which makes the experimental observation of drop impact dynamics with large range of the Weber and Reynolds number, especially the air entrapment processes, easier and more accurate. In contrast to mentioned experiments, which used large droplets, the present numerical study uses a 300  $\mu\text{m}$  drop, corresponding to the droplet size in coating processes. The smaller droplet diameter will also save computational capacity, if micro-sized bubbles produced by a drop impacting on a solid surface should be observed. Thereby, a computational domain of  $1400 \times 1400 \times 380 \mu\text{m}^3$  with Cartesian grid (cut cell) was created. A uniform structured grid with cell volume  $2 \times 2 \times 2 \mu\text{m}^3$  in the region around the droplet and liquid film on the substrate was found to be necessary to avoid grid effects and get accurate results. Far away from the liquid-air interface coarse hexahedral meshes were used to reduce the total number of the cells.

Based on common spray painting conditions, droplet impact velocities that are smaller than 10 m/s were applied. The numerical initial drop injection position was 30  $\mu\text{m}$  away from the wall surface, so that the surrounding gas field can be calculated, which is absolutely necessary in order to study the mechanism of air bubble entrapment under droplet impact. Initial pressure inside the drop because of surface tension of the liquid was calculated. Atmosphere pressure was set on the boundaries of the computational domain. A dry smooth wall with no-slip boundary condition was used.

For the parameter study, model viscous liquids with variant Newtonian viscosity were used in the present numerical simulation. Static contact angles (SCA) have to be specified on the wall, although experimental investigations [9] show that dynamic contact angle (DCA) differs appreciably from both the static advancing and receding value. The comparison of the evolution of drop shapes obtained using SCA and DCA in the numerical study carried out by Lunkad et al. [10] showed that the difference in drop spreading is not so significant, especially for the large SCA and in the early impact stage. The objective of the present study is mainly to report the mechanism of air entrapment under drop impact, which does not, as shown later, depend on wettability. However, the speed of bubble formation and bubble release from the liquid will be influenced by wettability. We include therefore the SCA as parameter in our numerical study. SCA-values of 60° are quite close to practical applications in painting processes, whereas 30° corresponds to well wettable systems, such as a liquid on some glass target.

Table 1 summarizes the parameters used in this study. The corresponding dimensionless numbers are Reynolds number  $Re = \rho Du/\mu$ , Weber number  $We = \rho u^2 D/\sigma$ , Ohnesorge number  $Oh = \mu/\sqrt{\rho\sigma D}$ , where  $D$ ,  $\rho$ ,  $\mu$ ,  $\sigma$  are the diameter, density, viscosity and surface tension of the drop, respectively;  $u$  is the drop impact velocity. For viscous liquids we have,  $Re < 75$ ,  $We < 1200$  and  $Oh = 0.271 \sim 11.55$ . Considering the shear-thinning behaviour of most paint liquids, where the viscosity decreases with increasing shear rate, a high and a relative low viscosity, e.g. 1 and 0.04 Pa s, were respectively applied. For comparison we also carried out drop impact simulations of water drops with  $Re = 300 \sim 3000$ . Clearly, the regime of drop impact presented in this study is mainly the droplet spreading on the wall without breakup, especially for viscous liquids.

**Table 1** Parameters and fluid properties used in the simulation

Case name	Liquid	$\rho$ (kg/m <sup>3</sup> )	$\mu$ (Pa s)	$\sigma$ (N/m)	U (m/s)	SCA (°)	$Re$	$We$	$Oh$
/h2o_1	Water	1000	0.001	0.0725	1	60	300	4.14	0.00678
/h2o_2	Water	1000	0.001	0.0725	10	60	3000	414	0.00678
/1a	A	1000	0.04	0.0725	1	60	7.5	4.14	0.271
/1b	B	1000	0.04	0.025	1	60	7.5	12	0.462
/1c	C	1000	1.0	0.025	1	60	0.3	12	11.55
/2b	B	1000	0.04	0.025	10	60	75	1200	0.462
/2c	C	1000	1.0	0.025	10	60	3	1200	11.55
/3b	B	1000	0.04	0.025	1	30	7.5	12	0.462

## Results and Discussion

The parallel calculations with at least 60 CPUs were carried out using supercomputing facilities at the Höchstleistungsrechenzentrum (HLRS) in Stuttgart. The computational model consists of approx. 18 million cell elements. The images created in the centre cross-section of the drop and on the substrate bottom were applied to analyse the drop impact dynamics. Unless stated otherwise,  $t = 0$  represents the time when the droplet comes into contact with the solid wall. Simulation results are summarized and discussed in the following sections.

### Air entrapment under a water droplet impacting on a solid surface

Water liquid has been widely used in the investigation of droplet impact on solid surfaces. At a first stage our numerical study was also carried out using water droplets, in order to compare with results from literature. Figure 1 shows the early stage of a water drop impact on the wall. The clear interface contour lines were obtained by showing contours of the air volume fractions scaled from 0.01 to 0.8 in a centre cross-section. Just before impacting, a slight flattening at the bottom of the drop (Fig. 1a) can be observed. In none of our simulations did we observe a dimple created at the drop surface at impact point assumed by Chandra and Avedisian (1991). The experimental observations made by Thoroddsen et al. [4] have shown different flatness of bottom curvature of water drops before the impact, which results in different sizes of the entrapped air disc under water drops at the initial contact. The droplet shape, however, could be unstable because of the surrounding experimental conditions in a droplet free-fall. The large droplet usually used in experimental research makes its shape change easily.

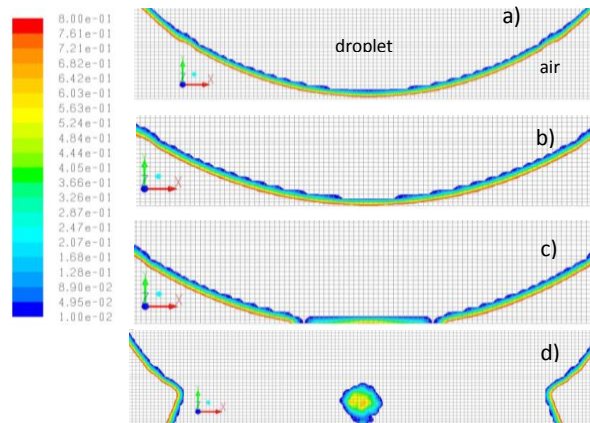


**Figure 1.** Detailed view of contours of air volume fractions scaled from 0.01 to 0.8 for the impact of a water drop (case:  $h_{2o\_1}$  from table 1:  $D = 300 \mu\text{m}$ , impact velocity = 1 m/s, corresponding to  $Re = 300$ ,  $We = 4$ ). The time interval from a) to d) is about 20  $\mu\text{s}$ , a): 1  $\mu\text{s}$  before impact, b): droplet contacts just with the wall, c): maximal air disc on the wall ( $t = 3 \mu\text{s}$ ), d): air bubble under the bottom centre of the drop.

An initial air disc (Fig. 1b) with a radius of 11  $\mu\text{m}$  was obtained. The air disc is enlarged continuously during the drop spreading until a fully wetted contact line is created. The subsequent spreading is driven by the contact line movement. Such wetting process can be seen more clearly in the following section. The maximal radius of the captured air disc, as shown in Fig. 1c, is about 32  $\mu\text{m}$  with the thickness  $< 1 \mu\text{m}$ . This air disc contracts into a bubble whose equivalent diameter is about 13  $\mu\text{m}$  under the bottom centre of the drop. The time interval of the contraction is ca. 20  $\mu\text{s}$ .

Figure 2 shows the evolution of the water drop impact with the focus particularly on the droplet shape, air bubble formation and release. The bubble created by the air disc could not drift up at once and is located under the centre of the drop because of the symmetrical down flow inside the droplet. With the decreasing of the apex height of the drop, the bubble leaves the liquid film (Fig. 2c). In this case, inertia force is lower than the large surface tension and high SCA, namely worse wettability, yielding a strong contraction of the liquid film, which in turn results in droplet breakup (Fig. 2d). Formation of new small bubbles during the coalescence of drops on the solid surface was observed (Fig. 2e). During the advance and recoil of the droplet, the bubbles drift up. An air-bubble-free condition was observed after approx. 2 ms by examining the 3D-region of the liquid phase.

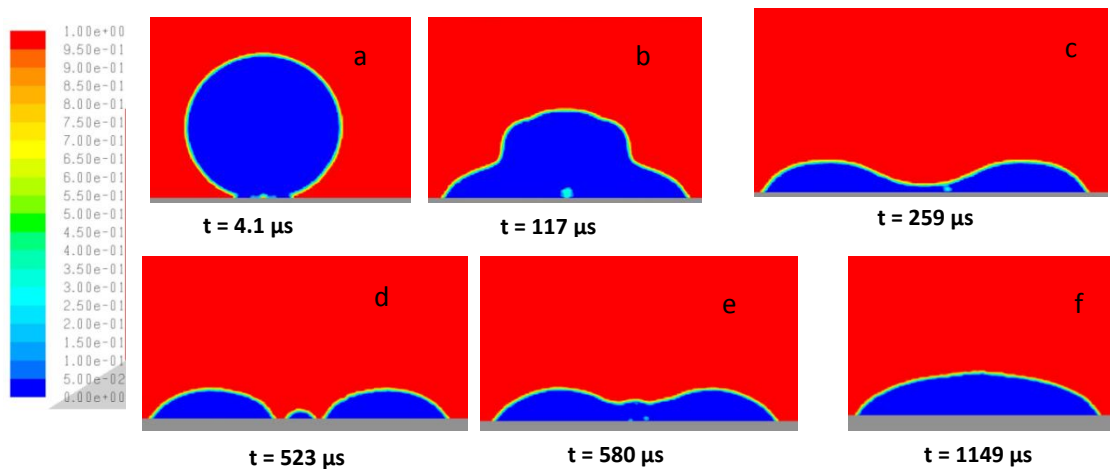


**Figure 2.** Contours of volume fractions (1: air, 0: water liquid), impact of a water drop ( $D = 300 \mu\text{m}$ , impact velocity = 1 m/s, corresponding to  $Re = 300$ ,  $We = 4$ ),  $t$  is the real impact time.



### Air entrapment under a viscous droplet impacting on a solid surface

The simulation results using a viscous fluid listed in the case /1b in table 1 are presented in this section. Air volume fractions scaled from 0.01 to 0.8 are shown in figure 3 with the focus on the phase contours close to the solid wall. Compared to the water drop, a slightly weaker flatness and smoothness of the curvature around the impact point can be observed in figure 3 at  $t = 0$ . The initial air disc radius is about  $9\ \mu\text{m}$  and is enlarged continuously, as shown in figure 3 at  $t = 0.022\ \text{ms}$ . The air contracts into bubbles during the spread process, resulting in a partly wetted region. The maximal air disc on the wall (strictly speaking, the region with bubbles and partly wetted area) was observed at  $t = 0.23\ \text{ms}$  to have a radial size of  $253\ \mu\text{m}$  (figure 3). A more detailed view of the evolution of the entrapped air on the solid surface will be shown later.

In order to understand the formation of the air disc under a droplet impacting on a solid surface, it is necessary to analyse the velocity and pressure distribution around the impact point. Figure 4 shows contour lines of the velocity magnitude for the both water and viscous drops. The maximal pinch-off air velocities from the impact region are  $4.17\ \text{m/s}$  for water drop and  $3.97\ \text{m/s}$  for viscous drop, since the gap between the solid wall and the water surface contour is smaller. This is due to the flatness of the bottom curvature of water drops. A less uniform velocity distribution in the liquid phase close to the impact point can be observed for viscous drops. Significant differences between water and viscous drops at the initial impact are found to be the pressure distribution, as shown in figure 5. The maximal stagnation pressure is  $1.33 \times 10^4$  and  $4.04 \times 10^4\ \text{Pa}$  for water drops and viscous drops, respectively. In the figure the pressure contours larger than 10% of the maximum values are blanked out. Clearly, a significant pressure fluctuation near the impact point and along the interface between liquid and air can be observed for viscous drops. This initial disturbance promotes the wave propagation in the interface, which also can be observed in figure 3 at  $t = 0$ . However, figuring out the quantitative wave length is impossible in the present study because of the grid resolution.

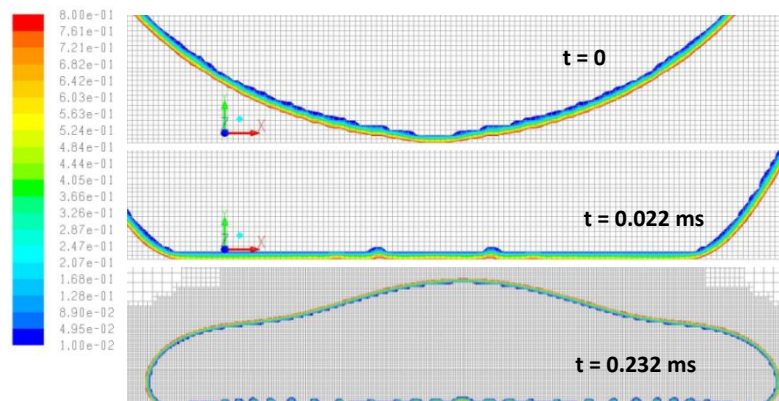


**Figure 3.** Viscous droplet: Detailed view of contours of air volume fractions scaled from 0.01 to 0.8 (case: /1b:  $D = 300\ \mu\text{m}$ , impact velocity =  $1\ \text{m/s}$ , corresponding to  $Re = 7.5$ ,  $We = 12$ ).

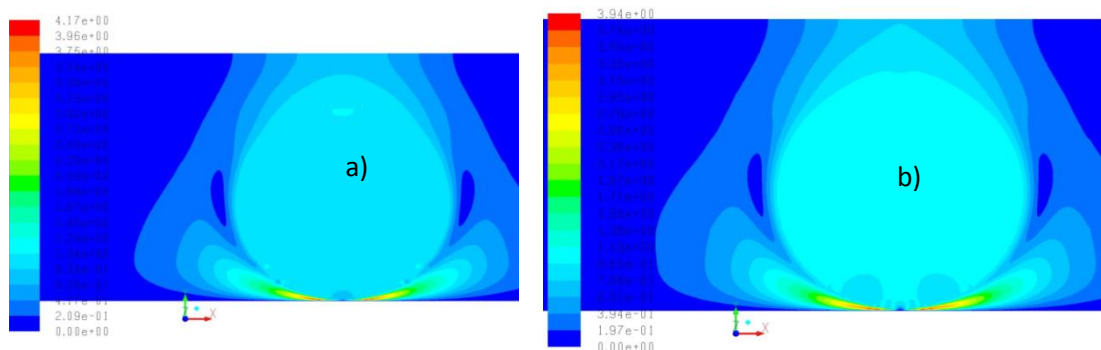


**Figure 4.** Contours of velocity magnitude (m/s) at  $t = 0$ . a): Water drop (case: /h2o\_1,  $Re = 300$ ,  $We = 4$ ); b): Viscous drop (case: /b1,  $Re = 7.5$ ,  $We = 12$ )

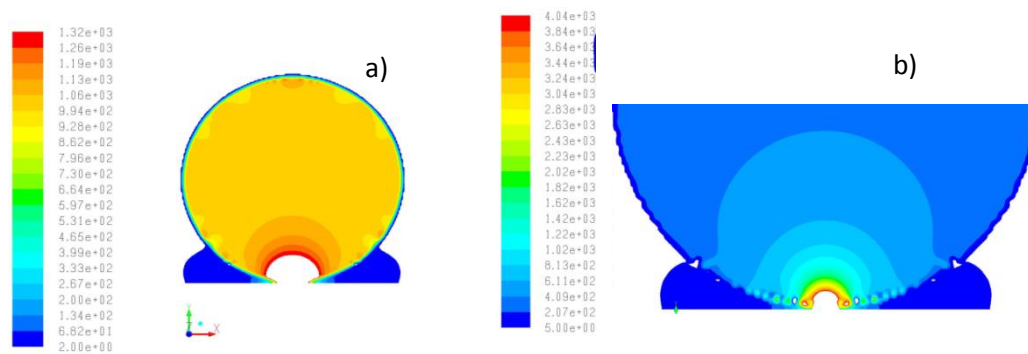


**Figure 5.** Contours of static pressure in [Pa] at  $t = 0$ . a): Water droplet scaled from 2 to 1320 (case: lh2o\_1,  $Re = 7.5$ ,  $We = 12$ ); b): Viscous drop scaled from 5 to 4040 (case: lb1,  $Re = 7.5$ ,  $We = 12$ )

Figure 6 and 7 show numerous impact sequences from the centre cross-section and corresponding bottom view. Much more air bubbles are entrapped in the liquid-solid interface for the viscous drop, which is in accordance with experimental observations [5, 6]. During the advance and recoil processes micro-bubbles combine and some of them are able to leave the liquid film if the height of the film decreases sufficiently. During the first advance scenario, the lowest apex height of drop in the centre is reached, resulting in the escape of large bubbles located in the centre at first (figure 6 at  $t = 0.972$  ms). The remaining bubbles move radially outward by the oscillation of the drop spreading and drift up as soon as the drift forces are strong enough to overcome the adhesion force. Figure 7 shows detailed air bubble formation on the solid surface. Automatic scaling of air volume fraction was applied, 0.62 to 1 for the sequence at  $t = 0.022$  ms, 0 to 1 for the rest of sequences. Some air bubble patterns, e. g. centre bubble rings and cartwheel patterns in Fig. 7 at  $t = 0.022$  ms, can be observed, which is similar to the experimental observations reported by Palacios et al. [6]. At  $t = 0.743$  s, a quasi-equilibrium phase, there are still fairly large air bubbles on the substrate, the release of such bubbles becomes more slowly and more difficult.

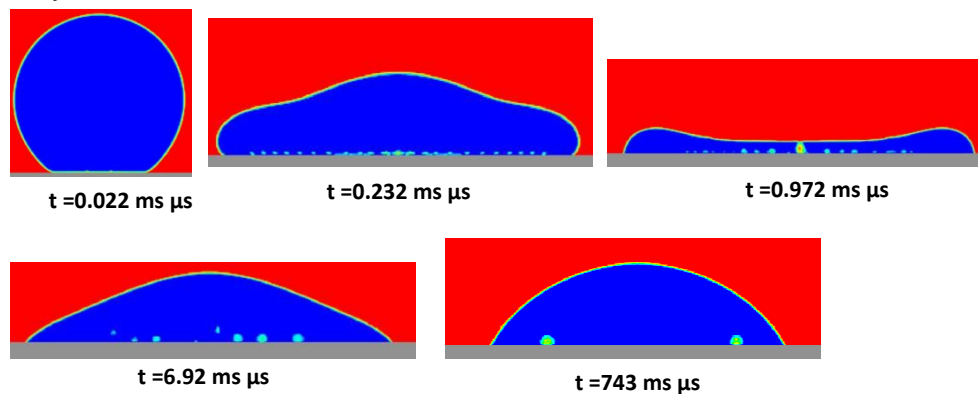


**Figure 6.** Contour lines of air volume fraction (1: air, 0: water liquid), impact of a viscous drop ( $D = 300 \mu\text{m}$ , impact velocity = 1 m/s, corresponding to  $Re = 7.5$ ,  $We = 12$ ),  $t$  is the real impact time.

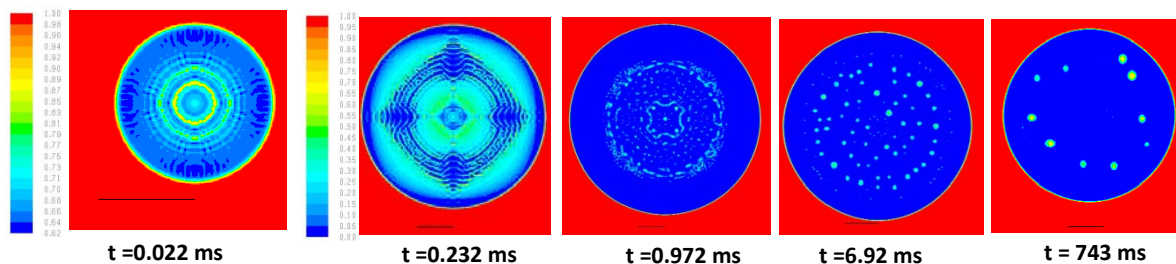


**Figure 7.** Contour lines of air volume fraction (1: air, 0: water liquid), impact of a viscous drop ( $D = 300 \mu\text{m}$ , impact velocity = 1 m/s, corresponding to  $Re = 7.5$ ,  $We = 12$ ). Scale line is  $100 \mu\text{m}$ .

### Effect of liquid property and impact velocity on the air entrapment

Based on the present simulation results, it was found that the initial radius of the air disc at the impact point for the 300  $\mu\text{m}$  droplet is  $10 \pm 2 \mu\text{m}$  for all the test cases, due to the (nearly spherical) shape of the original drop in the simulation. However, the maximal air disc caught under the droplet depends on the droplet properties, the impact velocity, as well as the wettability, namely the substrate properties and resulted in a myriad of micro-bubbles at the interface between the liquid and the substrate. The size of such air discs, or air regions, is plotted against Ohnesorge number and Reynolds number with a relationship of  $Oh \times Re^{0.8}$  in figure 8. In general, the size of the air region is inversely proportional to the surface tension of the fluid and increases with impact velocity and liquid viscosity, except for the water droplet, in which the maximal air disc does not change by increasing the impact velocity.

The effect of static contact angle SCA was also investigated in the present study. With decreasing SCA, i. e. improving wettability, the maximal air disc reduces from 253  $\mu\text{m}$  in case /1b to 238  $\mu\text{m}$  in case /3b. Figure 9 and 10 show the entrapped air bubbles under the drop at  $t = 0.18 \text{ s}$  in detail. On the substrate there are only two visible small bubbles for the case with  $SCA = 30^\circ$ , whereas many more large bubbles can be observed for the case with  $SCA = 60^\circ$ . The small SCA helps the bubbles to break the adhesion force and leave the solid surface much easier. The decreasing height of the droplet film (small SCA) also makes bubbles drift up quickly.

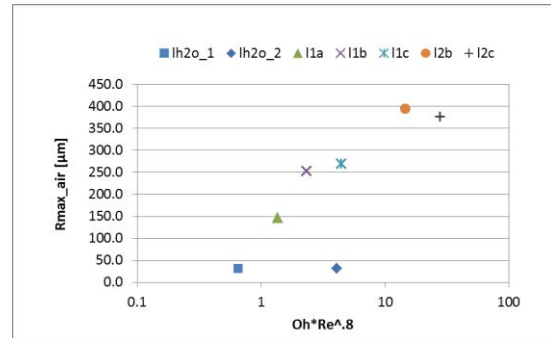


**Figure 8.** The maximal radius of the air disc vs.  $Oh \times Re^{0.8}$

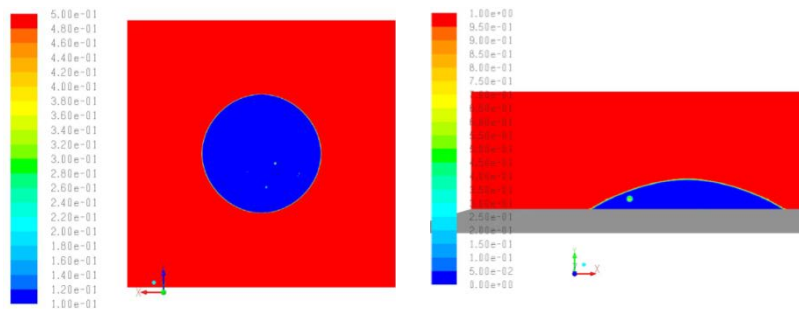


**Figure 9.** Contours of air volume fractions for the viscous drop with  $SCA = 30^\circ$  at  $t = 0.18 \text{ s}$  (case /3b).

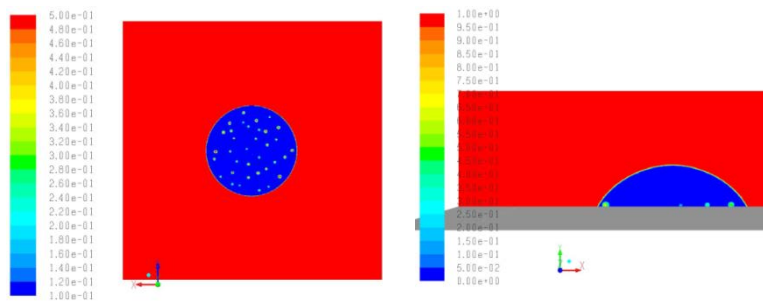


**Figure 10.** Contours of air volume fractions for the viscous drop with  $SCA = 60^\circ$  at  $t = 0.18 \text{ s}$  (case /1b).

### Conclusions

For the first time, a numerical simulation on the time-resolved imaging of the entrapment of air bubbles under a drop impact onto a dry solid surface was carried out. We focused only on the drop spreading phase without splash and break-up. The droplets used in the present study have the original spherical shape and there were no

significant shape changes during the drop free-fall. Therefore, we did not observe the variation of the initial air disc size formed at the impact point, as experimental observations obtained by Thoroddsen et al. [4]. Simulations show that there are significant pressure fluctuations in the liquid-air interface close to the impact point, especially for the viscous drop, which results in a wave propagation along the interface. At the early stage of the drop spreading, the initial air region, or air disc, contracts slowly for the viscous drop. Actually there is no wetted contact line at that time, instead, the drop interface with slight wave contacts with the solid surface, which results in a continuous air entrapment, an enlarged air disc or air region under the drop. The maximal air disc was reached when the drop spreading is driven by the movement of the fully wetted contact line.

The effects of the drop properties and impact velocity, as well as static contact angles on the maximal air disc and on the air bubble release from the droplet film were studied. More detailed quantitative analysis of the drop spreading process with air entrapment and bubble release can be carried out based on the present simulation results, which is an on-going project.

## References

- [1] S. Chandra and C. T. Avedisian, On the collision of a droplet with a solid surface, *Proc. R. Soc. London, Ser. A* 432, 13 (1991).
- [2] H. Fujimoto, H. Shiraishi and N. Hatta, Evolution of liquid/solid contact area of drop impinging on a solid surface, *Int. J. of Heat and Mass Transfer* 43, 1673-1677 (2000).
- [3] S. T. Thoroddsen and J. Sakakibara, Evolution of the fingering pattern of an impacting drop, *Phys. Fluids* 10(6):1359–1374 (1998).
- [4] S. T. Thoroddsen, T. G. Etoh, K. Takehara, N. Ootsuka and Y. Hatsuki, The air bubble entrapped under a drop impacting on a solid surface, *J. Fluid Mech.* 545, 203 – 212 (2005).
- [5] S. T. Thoroddsen, K. Takehara and T. G. Etoh, Bubble entrapment through topological change, *Phys. Fluids* 22(051701):1–4 (2010).
- [6] J. Palacios, J. Hernandez, P. Gómez, C. Zanzi and J. Lopez, Experimental study on the splash/deposition limit in drop impact onto solid surfaces, *Exp. Fluids* 52:1449-1463 (2012).
- [7] V. Mehdi-Nejad, J. Mostaghimi and S. Chandra, Air bubble entrapment under an impacting droplet, *Phys. Fluids* 15(1):173–183 (2003).
- [8] Fluent 14.0 User Manual.
- [9] Š. Šikalo, C. Tropea, E.N. Ganić, Dynamic wetting angle of a spreading droplet, *Experimental Thermal and Fluid Science* 29, 795-802 (2005)
- [10] S.F. Lunkad, V.V. Buwa, K.D.P. Nigam, Numerical simulations of drop impact and spreading on horizontal and inclined surfaces, *Chemical Engineering Science* 62 7214-7224 (2007)

## Numerical Investigation of Drop Impact onto Hot Surfaces

Ali H. Dawi<sup>1</sup>, Stefan Herbert<sup>1</sup>, Ilia V. Roisman<sup>2,3</sup>,  
Tatiana Gambaryan-Roisman<sup>1,3</sup>, Peter Stephan<sup>1,3</sup> and Cameron Tropea<sup>2,3</sup>

1: Institute of Technical Thermodynamics, Technische Universität Darmstadt, Germany

2: Institute for Fluid Dynamics and Aerodynamics, Technische Universität Darmstadt, Germany

3: Center of Smart Interfaces, Technische Universität Darmstadt, Germany

### Abstract

This study focuses on the numerical analysis of drop impact onto hot surfaces in the Leidenfrost regime for varying impact Weber numbers. A two-phase incompressible solver combined with a phase change model is used. The Volume-Of-Fluid method with a smooth calculation of the interface curvature is utilized to track the liquid-vapor interface. The maximum spreading diameter is evaluated and related to the Weber number. Moreover, the temporal evolution of the vapor layer thickness and the effect of the initial velocity of the droplet on the minimal film thickness occurring during the impact process are analyzed.

The flow underneath the droplet in the initial stage of the impact differs substantially from the static Leidenfrost phenomenon during the initial stage of the impact process. A vapor flow towards the droplet center is observed during this phase due to a tremendous decrease of the minimal thickness of the vapor layer.

---

### Introduction

Drop impact onto hot surfaces plays a crucial role in internal combustion engines or gas turbines. If the surface temperature is high enough, a vapor layer forming underneath the droplet due to the intense evaporation prevents wetting. This phenomenon is known as the Leidenfrost effect. High impact velocities (corresponding to high Weber numbers) require a dynamic description of the Leidenfrost phenomenon rather than a static one, often encompassing the lubrication approximation for the vapor flow.

Several experimental investigations were performed, aiming at a better understanding of the dynamic Leidenfrost effect. Different boiling regimes were studied by Tran et al. [1] for a varying target temperature and a range of  $We$  between 0.5 and 600. A universal relation between the dimensionless maximum spreading diameter  $S$  and the Weber number ( $S \sim We^{0.39}$ ) was observed for  $We > 10$ , independent of the target temperature. A qualitative analysis of the vapor layer thickness has also been performed and a relation between different boiling regimes (including Leidenfrost) and the Weber number has been observed. Chandra and Avedisian [2] showed experimentally a temperature dependency of the dynamics during the early period of impact, which was attributed to very low surface tension and viscous effects. Neglecting those effects allows a simple prediction of the maximum spreading diameter using energy conservation, such that the sum of initial kinetic energy and surface energy remains constant during deformation. This energy balance leads to a scaling  $S \sim We^{0.5}$  which contradicts the experimental data of Tran et al. [1]. Moreover, the high impact velocity produces a dynamic pressure ( $\rho U^2$ ) which is large compared to the hydrostatic pressure; hence the predicted vapor layer thickness in the dynamic Leidenfrost phenomenon is an order of magnitude smaller than the thickness in the static Leidenfrost phenomenon [1]. Buchmüller et al. [3] showed that an increasing ambient pressure results in a shift of the boundaries between different boiling regimes towards higher temperatures. A review paper of Quéré [4] is devoted to the Leidenfrost effect including the Leidenfrost dynamics.

Important phenomena, such as the temporal evolution of vapor layer thickness and the temporal evolution of evaporation rate, occur on a microscopic scale. Therefore, experimental investigations are not always able to quantitatively analyze these processes, whereas numerical simulations are able to provide more detailed information. In this work the impact of droplets onto hot surfaces in the Leidenfrost regime is studied numerically. In order to validate the numerical simulations, the simulated maximum spreading ratio for different Weber numbers is compared with experimental results. Furthermore, the evolution of the vapor layer thickness with time during the impact process is evaluated. The numerical simulation allows a quantitative analysis of the phase change rate.

## Numerical method

The numerical model employed for the present simulations of the Leidenfrost phenomenon has originally been developed by Kunkelmann and Stephan [5] for the simulation of pool boiling heat transfer. It is implemented utilizing the finite volume method within the open source toolbox OpenFOAM. The flow is described by the incompressible Navier-Stokes equations

$$\rho \nabla \cdot \vec{u} = \dot{\rho} \quad (1)$$

$$\frac{\partial(\rho \vec{u})}{\partial t} + \nabla \cdot (\vec{u} \otimes \rho \vec{u}) = -\nabla p + \nabla \cdot [\mu (\nabla \vec{u} + (\nabla \vec{u})^T)] + \vec{f}_g + \vec{f}_\sigma, \quad (2)$$

where the term on the right hand side of the continuity equation represents the phase change and the source terms  $f_i$  in the momentum equation account for gravity and surface tension forces, respectively. In addition the energy equation

$$\frac{\partial(\rho c T)}{\partial t} + \nabla \cdot (\rho c \vec{u} T) = \nabla \cdot (k \nabla T) + \dot{h} \quad (3)$$

is solved. Herein the source term represents the heat removal through evaporation of the liquid. The evaporation rate is determined according to the evaporation model by Hardt and Wondra [6] based on the local interfacial temperature. The two-phase flow is tracked utilizing the Volume of Fluid (VOF) method. The continuous surface force model as proposed by Brackbill et al. [7] is employed to incorporate surface tension effects. The curvature of the liquid-vapor interface is obtained using a contour based interface reconstruction. More details on this methodology can be found in [8].

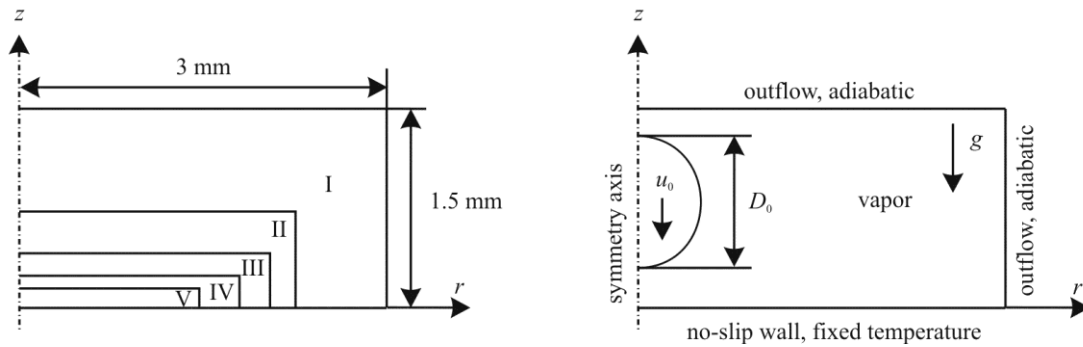


**Figure 1:** Mesh topology (left) and boundary conditions (right) of the computational domain

The numerical simulation is performed in an axisymmetric domain, since no three-dimensional structures during drop impact are expected in the range of  $We$  investigated. In order to resolve the flow and the heat transfer within the vapor layer close to the wall, the mesh has to be extremely fine in this region. Far from the wall the mesh can be coarser, as the gradients are expected to be much smaller. To maintain an aspect ratio of the cells close to unity in the entire mesh, a hierarchically structured, locally refined numerical grid is employed. The structure of the computational grid is shown in Figure 1. The overall size of the domain is chosen according to the initial droplet diameter and the expected spreading ratio, respectively. The cell size in the distinct regions is summarized in Table 1.

**Table 1:** Cell size distribution of the numerical grid, the cell size is equal in  $r$ - and  $z$ -direction

region	range of radial coordinate $r$	range of axial coordinate $z$	cell size $\Delta x$
I	$r > 2 \text{ mm}$	$z > 0.5 \text{ mm}$	$5 \text{ }\mu\text{m}$
II	$r < 2 \text{ mm}$	$z < 0.5 \text{ mm}$	$2.5 \text{ }\mu\text{m}$
III	$r < 1.8 \text{ mm}$	$z < 0.1 \text{ mm}$	$1.25 \text{ }\mu\text{m}$
IV	$r < 1.7 \text{ mm}$	$z < 50 \text{ }\mu\text{m}$	$0.625 \text{ }\mu\text{m}$
V	$r < 1.65 \text{ mm}$	$z < 10 \text{ }\mu\text{m}$	$0.3125 \text{ }\mu\text{m}$
VI (for $We \geq 20$ )	$r < 1.6 \text{ mm}$	$z < 5 \text{ }\mu\text{m}$	$0.15625 \text{ }\mu\text{m}$

The boundary conditions of the numerical simulation can also be found in Figure 1. The temperature of the wall is set to a constant value of  $T_w = 350^\circ\text{C}$ , which is  $250^\circ\text{C}$  superheated against the saturation temperature of water at atmospheric pressure. A numerical test, including the transient heat conduction inside a solid domain consisting of steel with a thickness of 0.1 mm, has shown a maximum temperature change of approx.  $1^\circ\text{C}$ , which is less than 0.5 % of the total superheat. Therefore, a constant wall temperature boundary condition is employed in order to reduce the computational effort.

The simulations are performed using the fluid properties of water under saturation conditions at atmospheric pressure. Even though most of the experimental investigations are performed in an air atmosphere, underneath the droplet pure vapor can be found due to the intense evaporation in the interaction zone. The initial droplet size is fixed to  $D_0 = 1$  mm and the droplet is initialized 0.1 mm above the solid surface. The liquid and vapor temperature is initially set to be at saturation temperature. The Weber number is varied by varying the initial velocity  $u_0$  of the droplet in the range between 0.24 – 1.36 m/s. As the initial droplet diameter and the fluid properties maintain unchanged, the Bond number is kept constant.

## Results and Discussion

The maximum Weber number investigated in the present study is  $We = 30$ . As will be shown later, the minimal thickness of the vapor layer in the early stage of the impact decreases towards extremely small length scales with increasing Weber number. Since the flow within the vapor layer always has to be resolved by some numerical cells in order to properly predict the pressure field underneath the droplet, the simulation of larger Weber numbers would require an even finer mesh resolution. At the same time the maximal velocity in the vapor layer will increase drastically. Both will enforce a much smaller numerical time step in order to maintain the Courant number to be smaller than unity. Hence, simulating larger Weber numbers would result in a tremendous increase of computational costs.

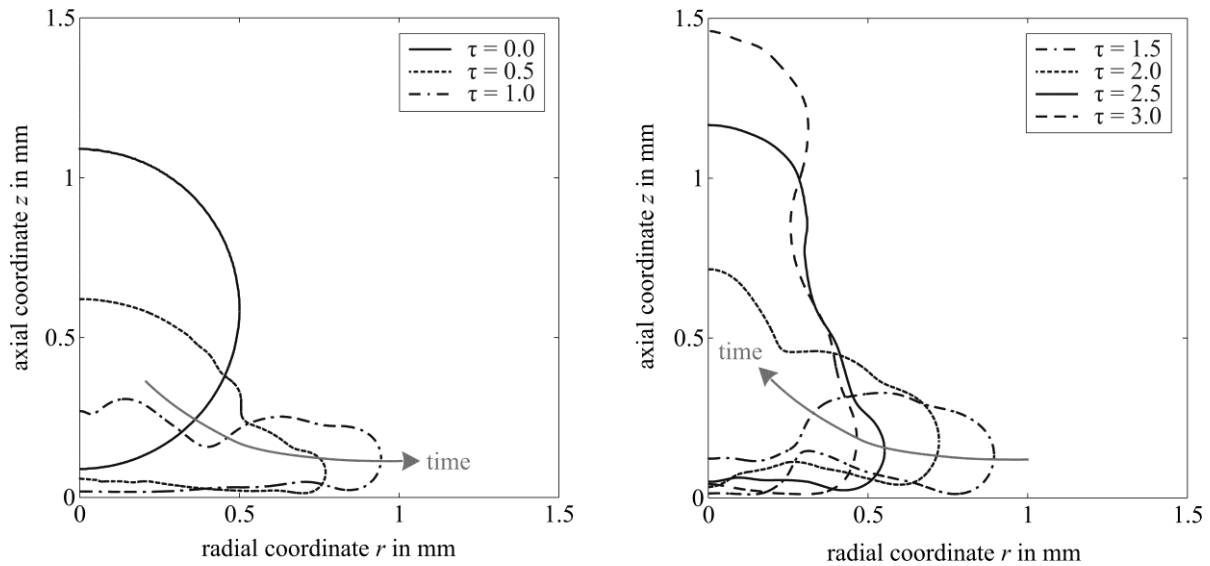


**Figure 2:** Droplet shape during the spreading phase (left) and the receding/bouncing phase (right) for  $We = 20$ . The initial droplet diameter is  $D_0 = 1$  mm and the initial velocity is  $u_0 = 1.109$  m/s.

The droplet shape obtained from the numerical simulation at different time instants is depicted in Figure 2 for a Weber number of  $We = 20$ . The dimensionless time is defined as

$$\tau = \frac{tu_0}{D_0} \quad (5)$$

While the droplet approaches the wall, it flattens, and the kinetic energy of the droplet is converted to surface energy. Due to the intense evaporation underneath the droplet, a thin vapor layer is formed separating the



droplet from the wall. During the spreading several capillary waves travel along the surface. At  $\tau \approx 1$  the droplet reaches its maximum diameter. Afterwards, the droplet starts to contract and the surface energy is converted back to kinetic energy. A part of the vapor layer is trapped under the droplet and thereby the thickness of the vapor layer increases, as can be seen from the droplet shape at  $\tau = 2$  in the right part of Figure 2. At  $\tau \approx 4$  the droplet leaves the surface and bounces. After the bounce the droplet would re-impact on the surface and would reach a steady state after a certain number of bouncing cycles. However, the simulations performed in this study are terminated as soon as the droplet leaves the surface for the first time, since the emphasis of this study is placed on the initial impact of the droplet.

A characteristic quantity of the hydrodynamic behavior of the liquid droplet during the impact process is the spreading ratio

$$S = \frac{D_{\max}}{D_0}, \quad (4)$$

where  $D_{\max}$  denotes the maximal extend of the droplet in the radial direction. The temporal evolution of the spreading ratio for a Weber number of  $We = 20$  versus the dimensionless time is presented in Figure 3. The spreading and receding phase of the impact can clearly be detected. At the transition between these phases the maximum spreading ratio  $S_{\max}$  is reached. This value is frequently reported in experimental studies allowing for a quantitative comparison of the numerical results with experiments.

In Figure 4, the maximal spreading ratio obtained from the simulations for a varying Weber number is compared to the experimental results of Tran et al. [1]. A variation of the target temperature between 350°C and 700°C showed no influence on the spreading ratio in the investigated range of impact velocities, which has also been reported in [1]. The scaling of  $S_{\max} \sim We^{0.39}$  proposed by Tran et al. in the range  $We > 10$  and indicated in the figure compares well to the trend observed in the numerical data. However, the range of the numerical data is too small to derive a precise scaling law.

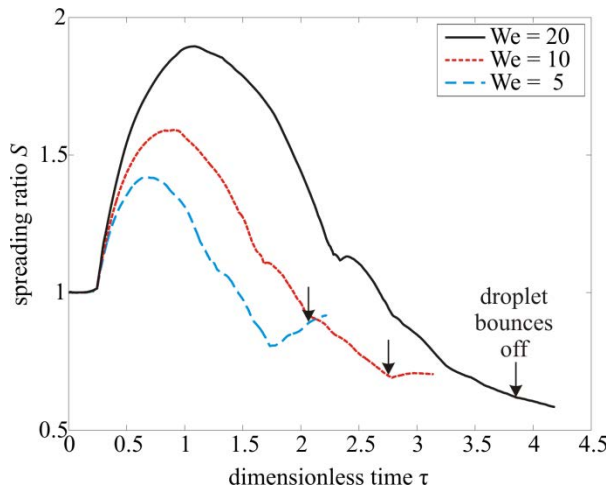


**Figure 3:** Temporal evolution of the spreading ratio during drop impingement

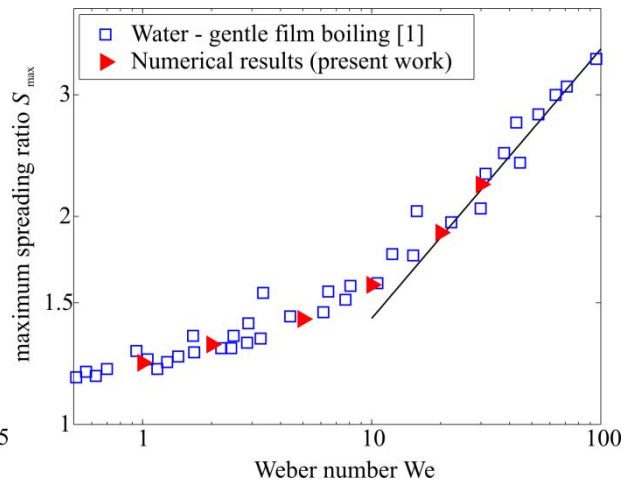


**Figure 4:** Log-log plot of the maximal spreading ratio versus the Weber number

In contrast to the spreading ratio, the vapor layer thickness is hard to measure in experiments, since optical access to the very thin vapor layer is limited. Especially in the dynamic Leidenfrost phenomenon the vapor film can become extremely thin in the initial stage of the impact. As reported by Tran et al. [1], who measured the vapor layer thickness using interferometry, even for comparably small Weber number the thickness is significantly smaller than in the case of static Leidenfrost drops.

A typical evolution of the minimal thickness  $h$  of the vapor layer is depicted in Figure 4. The droplet approaches the wall, and the film thickness exhibits a significant minimum of less than one micrometer during the initial stage of the impact process. After this minimum the layer thickness increases and stabilizes at approx. 10  $\mu\text{m}$ . Due to the capillary waves travelling along the interface in the spreading and bouncing phase, small oscillations can be detected in the minimal layer thickness. During the contraction of the droplet, two additional significant

minima can be observed in the layer thickness. At  $\tau \approx 4$  the layer thickness increases sharply indicating that the droplet leaves the solid surface.

The first minimum of the layer thickness, referred to as  $h_0$ , is shown in Figure 6 as a function of the Weber number. As expected, the minimal layer thickness decreases with increasing  $We$ . For  $We < 10$  the data show the approximate trend of  $h_0 \sim We^{-0.7}$ , while for larger Weber numbers the film thickness follows  $h_0 \sim We^{-3.5}$ . It should be noted that this change of the trend occurs at approximately the same Weber number at which a transition in the dependency of the maximal spreading ratio on  $We$  is observed (cf. Figure 4).

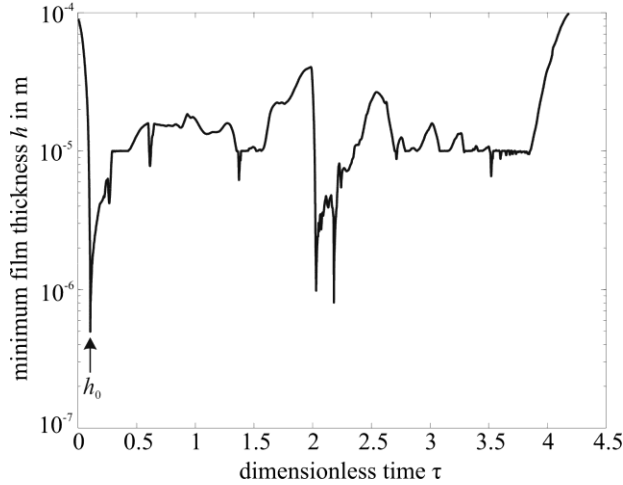


**Figure 5:** Temporal evolution of the minimal vapor layer thickness for  $We = 20$

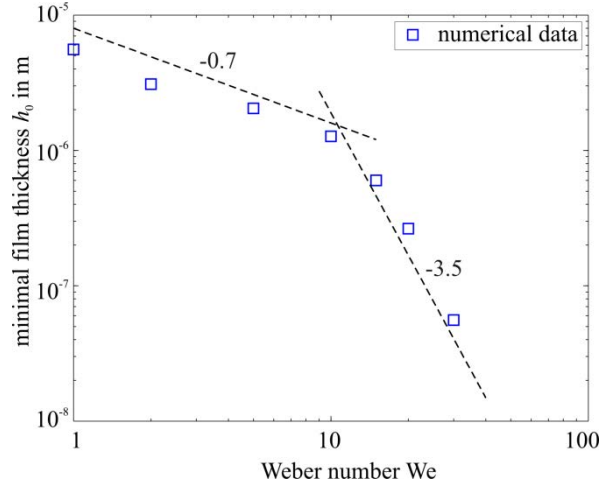


**Figure 6:** Minimal vapor film thickness in the initial stage of the impact

The tremendous decrease of the minimal vapor layer thickness in the early stage of the impact with increasing Weber number also has a substantial influence on the flow within the vapor layer. Figure 7 shows the shape of the interface 15  $\mu$ s after the film thickness exhibits its minimum. In contrast to the typical situation observed for a static droplet in the Leidenfrost regime, the vapor flow is not directed radially outwards everywhere. Instead, the large mass flow following from the massive evaporation due to the very thin vapor layer cannot escape completely through the thin gap formed by the liquid-vapor interface and the wall.

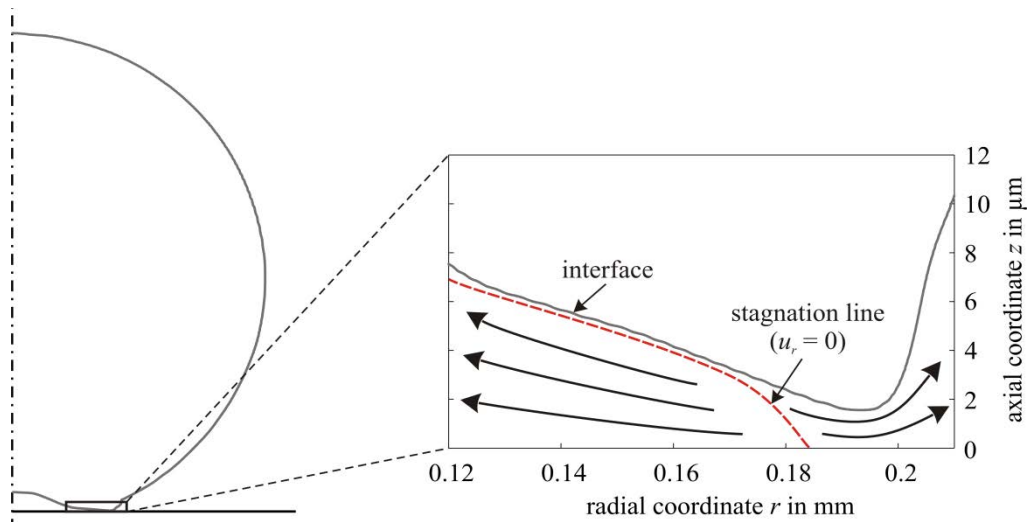


**Figure 7:** Shape of the liquid-vapor interface and flow direction in the vapor layer in the early stage of the impact ( $We = 20$ ,  $\tau = 0.122$ ), axes are not shown to scale in the blow-up.

A stagnation line can be detected, and a part of the vapor flows towards the centerline where it accumulates underneath the droplet. As soon as the vapor layer thickness increases, the stagnation line travels towards the centerline and approx. 0.2 ms after reaching the minimal thickness, i.e. at  $\tau = 0.31$ , the flow is directed outwards

in the complete vapor layer similar to the situation of static Leidenfrost. Thereby the previously accumulated vapor near the center of the drop is pushed out towards the atmosphere and the layer thickness near the center of the droplet decreases rapidly.

The global evaporation rate of the droplet is shown in Figure 8 for  $We = 20$ . Even though some small oscillations arising from the capillary waves travelling along the interface can be observed, the phase change rate follows the spreading ratio of the droplet shown in Figure 3 for  $\tau < 2$ . At  $\tau = 2.2$  a sharp peak of the evaporation rate can be observed which goes along with the secondary minima in the vapor layer thickness presented in Figure 5.

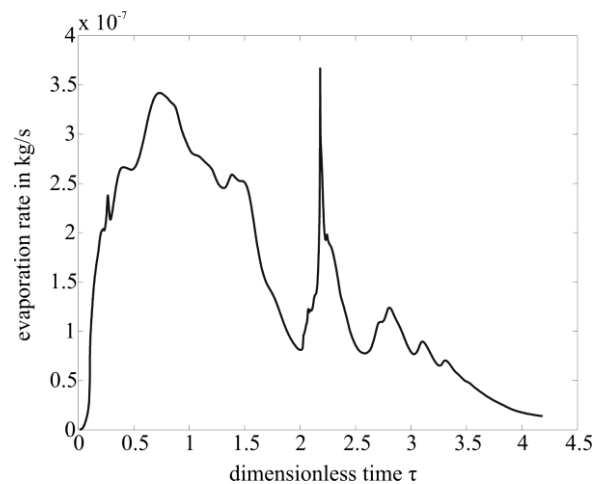


**Figure 8:** Evaporation rate of the droplet for  $We = 20$

## Conclusions

Results of numerical simulations of the drop impact at high Weber numbers in the Leidenfrost regime are presented. The global hydrodynamic behavior of the droplet was found to be in agreement with data from the literature. In addition, the development of the vapor layer underneath the droplet is discussed and an approximate scaling law of the minimal film thickness to the Weber number is proposed. Moreover, the flow field within the vapor layer for large impact velocities is analyzed and found to substantially differ from the flow field underneath a static Leidenfrost droplet. In the early stage of the impact a vapor flow towards the center of the droplet is observed.

## Acknowledgements

The authors kindly acknowledge the German Science Foundation (DFG) for financial support within the Transregio project SFB-TRR 75.

## Nomenclature

$c$	specific heat capacity	J/(kg K)
$D$	droplet diameter	m
$h$	vapor layer thickness	m
$k$	thermal conductivity	W/(m K)
$p$	pressure	Pa
$r$	radial coordinate	m
$S$	spreading ratio	-
$T$	temperature	K
$t$	time	s
$u$	velocity	m/s
$z$	axial coordinate	m
$\mu$	dynamic viscosity	kg/(m s)
$\rho$	density	kg/m <sup>3</sup>
$\sigma$	surface tension	N/m
$\tau$	dimensionless time	-
We	Weber number = $\rho_l D_0 u_0^2 / \sigma$	-

## References

- [1] Tran, T., Staat, H.J.J., Prosperetti, A., Sun, C. and Lohse, D., *Drop Impact on Superheated Surfaces*. Physical Review Letters, 2012. **108**(3): p. 036101.
- [2] Chandra, S. and Avedisian, C.T., *On the Collision of a Droplet with a Solid Surface*. Proc. R. Soc. Lond., 1991. **432**.
- [3] Buchmüller, I., Roisman, I.V. and Tropea, C., *Influence of Elevated Pressure on Impingement of a Droplet Upon a Hot Surface*, in *12th Triennial International Conference on Liquid Atomization and Spray Systems, Heidelberg*. 2012.
- [4] Quéré, D., *Leidenfrost Dynamics*. Annual Review of Fluid Mechanics, 2013. **45**(1): p. 197-215.
- [5] Kunkelmann, C. and Stephan, P., *CFD Simulation of Boiling Flows Using the Volume-of-Fluid Method within OpenFOAM*. Numerical Heat Transfer, Part A: Applications, 2009. **56**(8): p. 631-646.
- [6] Hardt, S. and Wondra, F., *Evaporation model for interfacial flows based on a continuum-field representation of the source terms*. Journal of Computational Physics, 2008. **227**(11): p. 5871-5895.
- [7] Brackbill, J.U., Kothe, D.B. and Zemach, C., *A continuum method for modeling surface tension*. Journal of Computational Physics, 1992. **100**(2): p. 335-354.
- [8] Kunkelmann, C., *Numerical modeling and investigation of boiling phenomena*, Ph.D. Thesis, Technische Universität Darmstadt. 2011.

## **A new model for droplet – solid surface interaction. Impingement onto hydrophilic and superhydrophobic surfaces**

I. Malgarinos<sup>1,\*</sup>, M. Marengo<sup>2</sup>, C. Antonini<sup>3</sup>, N. Nikolopoulos<sup>1</sup>, G. Strotos<sup>1</sup>, and M. Gavaises<sup>1</sup>

1: School of Engineering and Mathematical Sciences, City University London, Northampton Square, EC1V 0HB London, UK, \*Corresp. Author – e-mail: Ilias.Malgarinos.1@city.ac.uk

2: Department of Engineering, University of Bergamo, viale Marconi 5, 24044 Dalmine, Italy

3: Laboratory of Thermodynamics in Emerging Technologies, Mechanical and Process Engineering Department, ETH Zurich, Sonneggstrasse 3, 8092 Zurich, Switzerland

### **Abstract**

In this study, a new model for the wetting interaction between a liquid droplet and a solid surface is presented. Based on this model, a force which acts on the contact line is incorporated as a source term in the Navier-Stokes momentum equation. The advantage of the new model in comparison with the widely-used Brackbill's model is that the contact angle is not inserted as a boundary condition, but is derived by the induced fluid flow and the adhesion physics of the liquid-surface combination. For the interface tracking, the Volume of Fluid (V.O.F) method is used, accompanied by an automatic local grid refinement technique in order to minimize the arithmetic diffusion of volume fraction and thus acquire more representative physical results. The new model is validated against experimental data for low and moderate We numbers both for hydrophilic and superhydrophobic surfaces. Results of the model are also compared against the standard Brackbill's model for the implementation of the wetting force. The apparent contact angle during droplet spreading and recoiling is plotted in order to gain insight on the dynamic angle temporal evolution during the impingement process.

### **Introduction**

Droplet impingement is an area of fluid mechanics that concerns a vast number of technological applications varying from spray cooling and spray coating to combustion in internal combustion engines. Most recently, hydrophobic and super-hydrophobic surfaces have attracted the interest of many researchers due to their ability to repel water droplets, which in turn gives them the most significant advantage, among other surfaces, of self-cleaning (like lotus leaves). Many researchers have fabricated new materials using different ways (chemically, or mechanically treated surfaces) with varying surface roughness that show different behavior in terms of their interaction with liquid droplets [1]. The main focus of researcher's interest is to predict either qualitatively or quantitatively the interaction of liquid droplets with a solid surface, and finally achieve to control the contact time of the droplet onto this surface. In this way, the main advantages of large contact times can be exploited in cases of spray cooling for example, while for surfaces, which need to be self-cleaned, (as airfoils – avoid solidification, or photovoltaic panels) the minimum contact time is requested to be achieved.

So far, a vast number of experimental studies [2-6] have focused on the temporal evolution of a droplet spreading on a solid substrate in relation to the droplet's properties (surface tension, impact velocity, initial radius), as well as the properties of the solid surface (wettability, roughness). Most recently, due to the great advancements in photography, researchers can focus on more microscopic details of the process, such as the dynamic contact angle and the velocity of the rim throughout the evolution of the phenomenon [6-8]. Based on these experiments, it is proved that the contact angle between the droplet and the solid surface changes throughout the advancing and receding phases of droplet spreading. In order to account for this change, many dynamic contact angle models concerning CFD simulations can be found in literature, a review of which is given in [9]. However, as Yokoi et al. [10] suggest, the change in contact angle values which are implemented in a CFD simulation can affect the outcome of the impingement process. In all cases mentioned, the contact angle is not derived based on the induced flow, but is implemented in the momentum equation as a boundary condition. Therefore, a new model needs to be developed that can dynamically alter the contact angle based on the fluid flow and operating conditions, rather than insert it as a boundary condition.

### **Mathematical modelling**

For solving the two-phase flow of a liquid droplet impinging on a flat surface, the Volume of Fluid Method (V.O.F) [11] is used, using the CSF model for the surface tension force term in the momentum equation (see Brackbill et al. [12]). The solution of V.O.F equations is executed in ANSYS FLUENT solver, where the axis-symmetric approach is adopted (along the mass centre of the droplet) for minimization of the computational cost. In order to keep the interface as sharp as possible and avoid numerical diffusion, an automatic adaptive grid refinement technique is used, similar to the one proposed by Theodorakakos et al [13]. This method has

been successfully applied by Nikolopoulos et al. [14], Strotos et al. [15, 16] in cases concerning droplet impingement, collision and splashing onto a liquid film, with and/or without heat transfer, making it a reliable way to save computational time and retain a fine level of accuracy. The model for adaptive local grid refinement was implemented in ANSYS/FLUENT commercial software via User Defined Function (UDF). For the discretization of the advection term in the volume fraction equation, the high-resolution HRIC scheme [17] is used. At the end of every time-step, an additional equation, which was proposed by Olsson et al. [18] and used in Level-Set, is solved in order to keep interface thickness constant to approximately 3 cells. This equation is:

$$\frac{\partial \alpha}{\partial \tau} + \beta \nabla \cdot \alpha (1 - \alpha) = \beta \varepsilon \nabla \cdot (\nabla \alpha) \quad (8)$$

Equation (8) is solved once (for one  $\Delta \tau$ ) in pseudo-time with time-step equal to the advection time-step, while  $\varepsilon$  takes the value of  $\Delta x/2$  (where  $\Delta x$  is the grid cell edge, as proposed in [19]). The additional variable  $\beta$  is proposed by Sato et al. [19] in order to avoid deformation in droplet shape and it is reported to take values in the range from 0.01 to 1. In this study,  $\beta$  is set equal to 0.25 throughout the domain, which by a number of numerical tests undertaken, is proven to be both compressive, as well as enough for the mass conservation of the volume fraction field. Pressure – Velocity coupling is achieved by adopting a coupled approach [20], for which momentum and pressure-based continuity equations are solved together, while the Rhie-Chow pressure dissipation terms are included in the face mass fluxes. The time-step of the calculations, is varying for all simulations, so that the Courant number can be kept constant at around 0.25. The solution of equation (8) was implemented in FLUENT through a user-defined scalar, while its solution was implemented via UDFs.

### Wetting Force

The wetting angle of the droplet with the solid surface is a matter of great interest. The interaction between liquid and solid surface molecules in the three-phase contact line of the drop is what determines microscopically the angle which is formed, and macroscopically the maximum spread of the droplet, as well the contact time on the surface, which are the main areas of interest that concern industrial applications. So far, the most widely-used model in VOF, for the implementation of the wetting angle, is the approximation proposed by Brackbill et al. [12]. In this paper, a new model is proposed for contact angle implementation, in which contact angle is derived from the induced fluid flow. Based on this model, it is assumed that a force acts on the contact line, as proposed in [21]. If energy is assumed to be conserved in the 3-phase contact line, as proposed by Young, for a static droplet, then the force acting on the rim is tangent to the liquid-gas interface (Figures 1a,b).

In relation to the typical friction force, the adhesion force, is assumed to be higher when the droplet is static and is lower when the droplet is moving (in case of sliding, for example Figure 1a). As the contact line moves (Figure 1b), its value is equal to:

$$\begin{aligned} f_{\sigma mar} &= \sigma [\cos(\theta_{eq}) - \cos(\theta_{app})] r \quad \text{if } v_{conline} > 0 \quad \text{or} \quad v_{conline} < 0 \\ f_{\sigma mar} &= \sigma [\cos(\theta_{eq})] r \quad \text{if } v_{conline} = 0 \end{aligned} \quad [N] \quad (9)$$

where:

$$\begin{cases} \theta_{eq} = \theta_{adv} & \text{if } v_{conline} \geq 0 \\ \theta_{eq} = \theta_{rec} & \text{if } v_{conline} < 0 \end{cases} \quad (10)$$

$\theta_{adv}$  and  $\theta_{rec}$  are the advancing and receding contact angle, respectively, measured using the standard sessile drop method, i.e. while expanding and retracting a drop quasi-statically on a horizontal surface; their difference,  $\Delta \theta = \theta_{adv} - \theta_{rec}$ , is the contact angle hysteresis. During the spreading/receding phase, if the apparent contact angle is higher than the equilibrium, the force would be positive, trying to accelerate the rim and reach  $\theta_{eq}$ , while if it is lower, then the force would take negative value. This force is higher for large differences between the equilibrium and the apparent contact angle. For the time instant when the velocity of the contact line approaches zero, the value of the force is higher, and results in the deformation of the rim, so that it can reach its receding shape beginning from its advancing one. This “contact line stress” (equation 9) is incorporated in the momentum equation as a source term only on the interface-contact line cells, namely the boundary wall cells where volume fraction is neither 0 nor 1. As for the model expression (equation 9), the part which concerns the force when the rim velocity is equal to zero (mainly during the “hysteresis” time), was not used in the scope of the present study due to the high uncertainty to define the time instant when  $v_{conline} = 0$ . For the remainder of this paper, the wetting force model will be referred as Marengo’s Force Model.

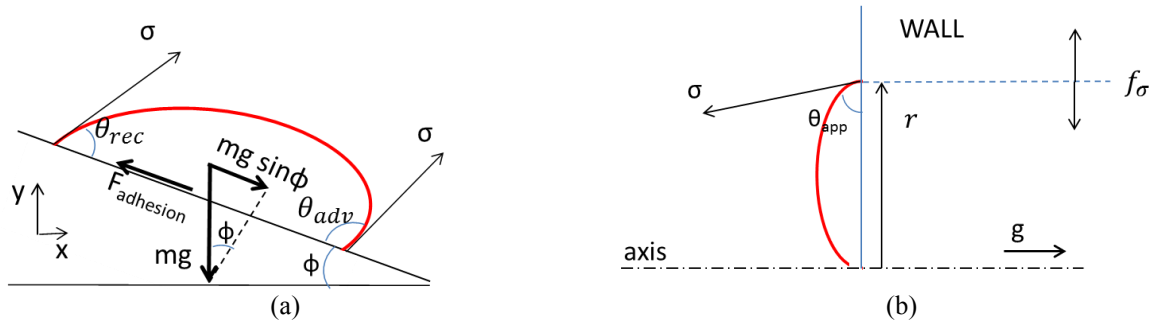


**Figure 1.** (a) Adhesion force for a liquid droplet sliding down an incline, (b) Direction of the wetting force (Marengo's Force Model) on a typical time instant of a droplet spreading on a wall (axisymmetric case)

An advantage of using this approach instead of the typical Brackbill's model would be the dynamic tracking of the apparent contact angle, which could shed light in the impinging process from the contact angle viewpoint.

Four cases are used for the validation of the new model, which are summarized in Table1 and concern the impingement of a water droplet on a hydrophilic and a Super-Hydrophobic surface, at low and moderate We numbers. For the numerical validation of the new methodology, results of the Marengo's Force Model are compared against the ones derived using the Brackbill's approach.

	$R_0(\text{mm})$	We	$\theta_{adv}$	$\theta_{rec}$	$\xi_{max}$ Exper	$\xi_{max}$ Theoret [22]	$\xi_{max}$ Brackbill	$\xi_{max}$ Marengo's Force Model	Reference
Case1	1.43	30	48	5	2.60	3.51	3.61	3.55	[2]
Case2	1.43	92	48	5	3.60	3.98	4.20	4.16	[2]
Case3	1.43	29	162	154	1.75	2.24	1.81	1.72	[2]
Case4	1.43	93	162	154	3.06	3.02	2.52	2.58	[2]

**Table1.** Test cases used for the validation of the methodology.

## Results and Discussion

In Figure2, the dimensionless maximum droplet spreading radius is plotted against We number for the four cases listed in Table1, as it is derived from the two models described above (Brackbill, Marengo's Force Model) together with the experimental values gathered from the work of Antonini et al. [2]. In this Figure, it is deemed necessary to include the maximum droplet spreading as it results based on the theoretical equation of Pasandideh-et al. [22]:

$$\frac{D_{max}}{D_0} = \sqrt{\frac{We + 12}{3(1 - \cos \theta) + 4(We / \sqrt{Re})}} \quad (12)$$

because of the overprediction of droplet spreading from the simulation. This equation has resulted from the energy balance of kinetic and surface energy, before impact and at maximum spreading, where the work loss due to viscous dissipation is accounted for, while the droplet is assumed to take the shape of a cylinder with height as much as its splat thickness at maximum spreading. Results of the simulation are much closer to this equation, as expected, due to the fact that the exact experimental conditions (e.g. oscillations of the droplet just before its impact) or crucial operating conditions such as surface roughness cannot be included in the CFD model. Therefore, simulation results can be compared with better certainty with these theoretical values. However, the comparison between the experimental values together with the theoretical and the simulation results can give insights as to what can be missing based on the aforementioned assumptions.

## Low We number

For the super-hydrophobic surface, results for both models (Brackbill – Marengo's Force Model) seem to be in very good agreement with the experimental values as well as with the theoretical  $\xi_{max}$  from equation (12).

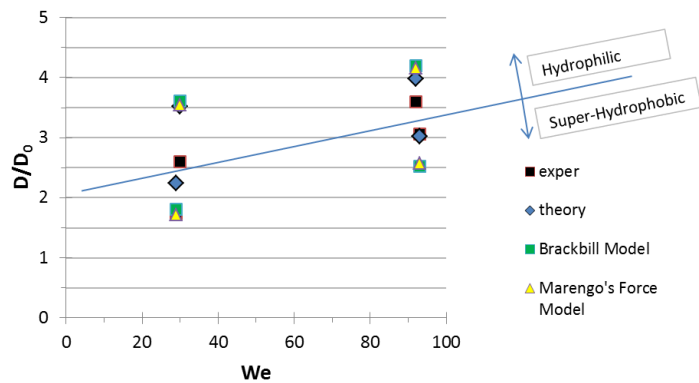


**Figure 2.** Comparison of dimensionless maximum spreading ( $D/D_0$ ), predicted by the different numerical models and the experimental data.



This means that the force that is assumed to act on the rim is very close to the one which appeared during the experiment. As for the hydrophilic glass surface, maximum spreading is highly overestimated, when it is compared to the experimental data. However, it is much closer to the theoretical  $\xi_{\max}$ , given by Pasandideh's simple equation. As this equation results from a simple energy conservation, and this theoretical value is in very good accordance with the results of the simulation, this means that the net force, assumed to exert on the rim, is not enough for the CFD simulations to reach the experimentally measured maximum spreading. Therefore, it is believed, that an adhesion force, counteracting the free movement of the droplet onto the solid surface as it spreads on it, is believed to be missing from the implementation of the momentum equation near the boundary cells. To sum up, for low We number, where the effect of inertia in relation to surface tension is small, two different behaviors are observed. For a hydrophilic surface, where small values of contact angle are apparent, a significant over prediction of maximum spreading is observed, while in comparison to the case of a hydrophobic surface the results are more promising. This disagreement between the numerical simulations and the experimental data may be as well attributed to experimental uncertainties in terms of contact angle measurement, which are of high importance for the validation and the right implementation of a numerical model, in all cases.

### Moderate We number

Turning now to the cases with moderate We number, different behaviours are observed. For hydrophilic surfaces the maximum spread is again overestimated, however the deviation is lower than the corresponding one of the low We number impact. On the other hand, for the superhydrophobic surface, the increase of the We number resulted in the further underestimation of maximum spreading. This means that by increasing the effect of inertia while keeping surface tension effects constant, the net force that is applied on the rim in the CFD simulation is closer to the experiment for the hydrophilic surface than that for the hydrophobic surface. This, in turn, means that inertia plays an important role to the evolution of the phenomenon, and that the wetting forces exerted in real life (as well as the experiment) change according to the initial kinetic energy and impingement conditions. For a hydrophilic surface and for a low We number impact, stronger forces, than the one predicted by the numerical models, dominate. As the We number is increasing, these forces become more insignificant. For a hydrophobic surface, on the other hand, it seems that as the We number increases the wetting forces of the simulation are much stronger than the ones the experiment suggest, implying that the forces that act on the rim are more significant in the case of a superhydrophobic surface than the hydrophilic one. However, again uncertainties in terms of contact angle measurements are of importance. Figures 3 and 4 depict the temporal evolution of the dimensionless spreading radius, as a function of the maximum spreading value,  $D_{\max}$ .

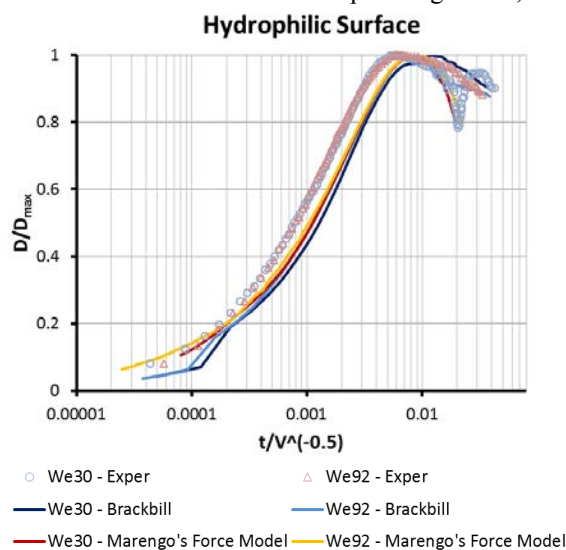


**Figure 3.** Comparison of the time that droplet reaches its maximum radius for Brackbill's Model, Marengo's Force Model and experiment. X axis is logarithmic.

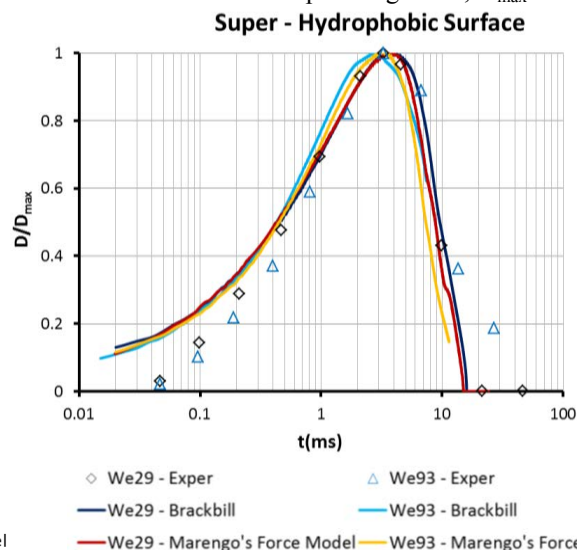


**Figure 4.** Comparison of the time that droplet reaches its maximum radius for Brackbill's Model, Marengo's Force Model and experiment. X axis is logarithmic.

The numerical results after the implementation of both models against the measured values are given. For the hydrophilic surface, time is divided by  $U_0^{-0.5}$ , in accordance with the work of Antonini et al. [2], who suggest that for a hydrophilic surface, the time that a droplet reaches its maximum radius, is constant, if divided by this value. This is obvious for the simulation results too. It is also clear that although in the case of  $We = 30$ , where maximum spread is greatly overestimated, its time derivative, until this maximum is reached is much closer to the experiment, showing that the simulation results agree qualitatively very well with the experiment. For both

cases, however, this characteristic time, as predicted, is a little higher than the one measured, suggesting that this adhesion-like force should exist. For the hydrophobic surfaces, the actual time of the impingement is plotted, while the numerical results are in good agreement with the experimental values, depicting again that although maximum spread from the simulation may deviate from the experiment, the temporal evolution of the phenomenon is described accurately enough.

### Effect of adhesion force

The implementation of the new model (Marengo's Force Model) does not seem to affect the macroscopic results (maximum spreading) of all four cases examined, when compared to the Brackbill's model. Nevertheless, the Marengo's Force Model, during the receding phase of the droplet impacting onto the hydrophilic surface, induces a smaller hysteresis time and thus faster receding phase. This is clearly shown in Figure 5, where the slope for the receding phase is much steeper.

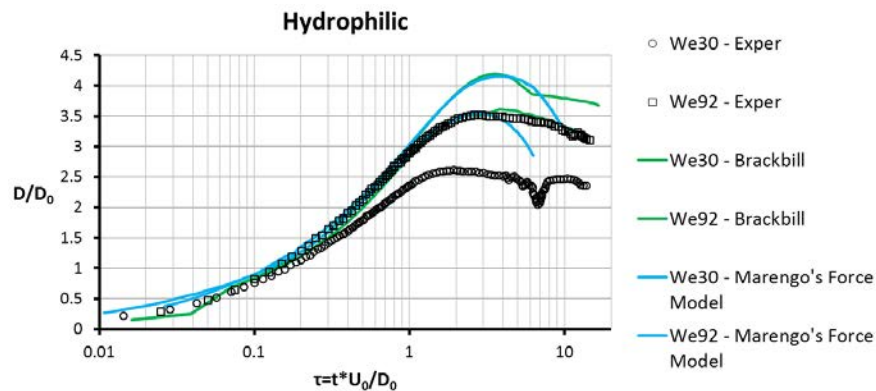


**Figure 5.** Dimensionless spread factor plotted against dimensionless time for a hydrophilic surface.

For the super-hydrophobic surface, although the maximum spreading results are similar for both models, the temporal evolution of the phenomenon is predicted more accurately by the Marengo's Force Model, as depicted in Figure 6. As discussed above, for the superhydrophobic surface, for low We numbers, where the effect of inertia is smaller, the Marengo's Force Model predicts more accurately the wetting effects during the impingement process. Further increase of the We number, results in a significant divergence between the experimental data and the simulation results, despite the fact that the trend of the line is similar to the one measured, showing that at least qualitatively, the temporal evolution of the impingement process is accurately described.

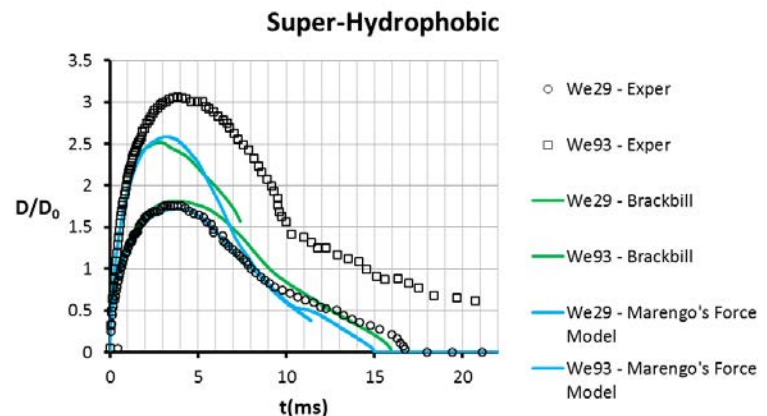


**Figure 6.** Dimensionless spread factor plotted against real time (in ms) for a superhydrophobic surface.

Figure 7 shows the temporal evolution of the impingement process for Case3. The similarities between the two models are obvious. Marengo's Force Model predicts a quicker receding phase, which is closer to the experiments. Furthermore, the angle which is observed for both the advancing and receding phases is bigger for Marengo's Model.

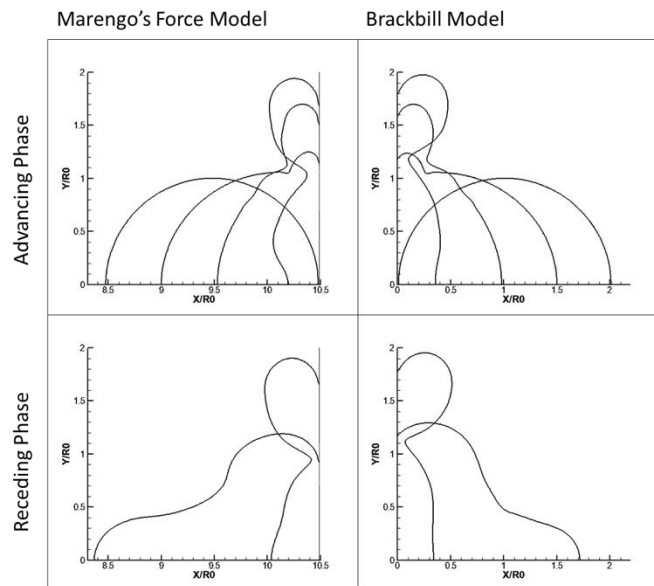


**Figure 7.** Temporal evolution of the impingement process for Case 3 of Table 1. Results of the isoline of  $VOF = 0.5$  are depicted for  $t=0, 0.9, 1.9, 3.9$ ms (advancing phase), and  $t=4.7, 8.4$ ms (receding phase).

Finally, Figure 8 depicts the temporal evolution of the apparent contact angle for Case 3 ( $We = 29$  - impingement on superhydrophobic surface), which is a novel information, not previously presented in CFD calculations.

This information is of high added value for the further validation of the model as well as for the experiments to comment on in future works. From this Figure, it is clear that the apparent contact angle increases during the first stage of impingement, then it remains approximately constant at around 155 degrees, while during the receding phase it reduces rapidly to 145 and then fluctuates around this value. The noise in the graph can be attributed to the choice of the contact line cell, where this velocity is measured. For the scope of this study, the contact line cell is supposed to be the cell where the isoline of volume fraction 0.5 lies on. The apparent contact angle is derived from the gradient of volume fraction in this cell.

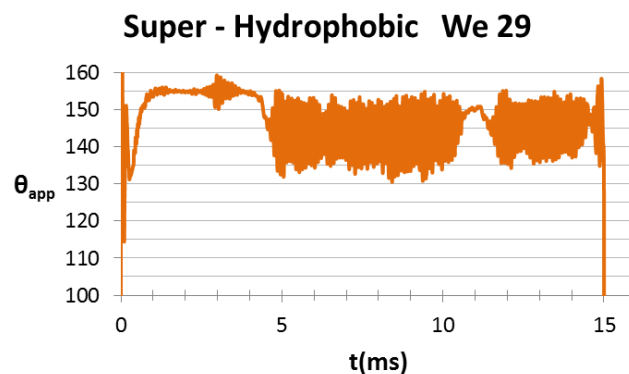


**Figure 8.** Temporal evolution of the apparent contact angle for Case 3 of Table 1.

## Conclusions

In this study, a new model for the interaction between a liquid droplet and a solid surface is presented. Based on this model, a force is assumed to act on the contact line as the droplet moves along the surface, but without assuming a constant angle of triple-phase formation, as the conventional one proposed by Brackbill. For hydrophilic surfaces, significant over prediction of maximum radius is observed, for both models, which can be attributed to either the absence of a viscous-friction term in the momentum equation or to the uncertainty which lies on the measurement of the contact angle. For the super-hydrophobic surface, on the other hand, results are much closer to the experimental values, which suggest that as the effect of the solid surface increases (higher contact angle), the contact angle models show a better behavior. For low  $We$  number, Marengo's Force Model exhibited almost the same results with those of Brackbill's model, in terms of the temporal evolution of the impingement process. Marengo's Force Model has the significant advantage over all previous methods for the implementation of wettability effects, that the apparent contact angle of the droplet comes as a result of the net force exerted on droplet's rim, rather than inserted as a boundary condition. Therefore, this new model offers a way of observing the impingement phenomenon from a more macroscopic point of view, as the contact angle is a result of the induced flow and force field. This model needs to be further developed, in order to be more

universal and be applicable for a large range of operating conditions. Up to now, results are very promising, so the next step would be to validate the new methodology against measurements of the dynamic contact angle values.

## Acknowledgements

The present work was funded by the Marie Curie Fellowship (FP7-PEOPLE-2012-IEF) with Grant Agreement number 329500 funded by the European Commission entitled as “Non Flat Impingement— Droplet Impingement on Non-flat Surfaces”. CA acknowledges funding by the Marie Curie Intra-European Fellowship ICE<sup>2</sup> with Grant Agreement 301174.

## References

- [1] Marengo, M., et al., *Drop collisions with simple and complex surfaces*. Current Opinion in Colloid & Interface Science, 2011. **16**(4): p. 292-302.
- [2] Antonini, C., A. Amirfazli, and M. Marengo, *Drop impact and wettability: From hydrophilic to superhydrophobic surfaces*. Physics of Fluids, 2012. **24**(10): p. 102104-13.
- [3] Kim, H.Y. and J.H. Chun, *The recoiling of liquid droplets upon collision with solid surfaces*. Physics of Fluids, 2001. **13**(3): p. 643-659.
- [4] Rioboo, R., M. Marengo, and C. Tropea, *Time evolution of liquid drop impact onto solid, dry surfaces*. Experiments in Fluids, 2002. **33**(1): p. 112-124.
- [5] Šikalo, Š., et al., *Analysis of impact of droplets on horizontal surfaces*. Experimental Thermal and Fluid Science, 2002. **25**(7): p. 503-510.
- [6] Sikalo, S., et al., *Dynamic contact angle of spreading droplets: Experiments and simulations*. Physics of Fluids, 2005. **17**(6): p. 062103-13.
- [7] Hung, Y.-L., et al., *Initial wetting velocity of droplet impact and spreading: Water on glass and parafilm*. Colloids and Surfaces A: Physicochemical and Engineering Aspects, 2011. **384**(1-3): p. 172-179.
- [8] Vadillo, D.C., et al., *Dynamic contact angle effects onto the maximum drop impact spreading on solid surfaces*. Physics of Fluids, 2009. **21**(12): p. 122002-8.
- [9] Ashish Saha, A. and S.K. Mitra, *Effect of dynamic contact angle in a volume of fluid (VOF) model for a microfluidic capillary flow*. Journal of Colloid and Interface Science, 2009. **339**(2): p. 461-480.
- [10] Yokoi, K., et al., *Numerical studies of the influence of the dynamic contact angle on a droplet impacting on a dry surface*. Physics of Fluids, 2009. **21**(7): p. 072102-12.
- [11] Hirt, C.W. and B.D. Nichols, *Volume of fluid (VOF) method for the dynamics of free boundaries*. Journal of Computational Physics, 1981. **39**(1): p. 201-225.
- [12] Brackbill, J.U., D.B. Kothe, and C. Zemach, *A continuum method for modeling surface tension*. J. Comput. Phys., 1992. **100**(2): p. 335-354.
- [13] Theodorakakos, A. and G. Bergeles, *Simulation of sharp gas-liquid interface using VOF method and adaptive grid local refinement around the interface*. International Journal for Numerical Methods in Fluids, 2004. **45**(4): p. 421-439.
- [14] Nikolopoulos, N., K.S. Nikas, and G. Bergeles, *A numerical investigation of central binary collision of droplets*. Computers & Fluids, 2009. **38**(6): p. 1191-1202.
- [15] Strotos, G., et al., *Non-dimensionalisation parameters for predicting the cooling effectiveness of droplets impinging on moderate temperature solid surfaces*. International Journal of Thermal Sciences, 2011. **50**(5): p. 698-711.
- [16] Strotos, G., et al., *Numerical investigation on the evaporation of droplets depositing on heated surfaces at low Weber numbers*. International Journal of Heat and Mass Transfer, 2008. **51**(7-8): p. 1516-1529.
- [17] Muzafferija, S., et al., *A Two-Fluid Navier-Stokes Solver to Simulate Water Entry*. Proc 22nd Symposium on Naval Hydrodynamics, Washington, DC, 1998: p. 277-289.
- [18] Olsson, E. and G. Kreiss, *A conservative level set method for two phase flow*. Journal of Computational Physics, 2005. **210**(1): p. 225-246.
- [19] Sato, Y. and B. Ničeno, *A conservative local interface sharpening scheme for the constrained interpolation profile method*. International Journal for Numerical Methods in Fluids, 2012. **70**(4): p. 441-467.

- [20] FLUENT 14.5, Theory Guide, 2011.
- [21] Antonini, C., et al., *General Methodology for Evaluating the Adhesion Force of Drops and Bubbles on Solid Surfaces*. Langmuir, 2009. **25**(11): p. 6143-6154.
- [22] Pasandideh-Fard, M., et al., *Capillary effects during droplet impact on a solid surface*. Physics of Fluids, 1996. **8**(3): p. 650-659.

## **Selected Results of the Collaborative Research Center: Droplet Dynamics under Extreme Boundary Conditions SFB-TRR/75**

Cameron Tropea<sup>1</sup>, Bernhard Weigand<sup>2</sup> and Andreas Birkefeld<sup>2</sup>

1: Institute of Fluid Mechanics and Aerodynamics, Center of Smart Interfaces, Technische Universität Darmstadt, Germany

2: Institute of Aerospace Thermodynamics, University of Stuttgart, Germany

### **Abstract**

The Collaborative Research Center (CRC) SFB-TRR 75 was established in January 2010 to focus on the dynamics of very basic drop processes, and in particular on processes involving extreme boundary conditions, for example, near thermodynamic critical conditions, very low temperatures, under strong electric fields or in situations involving extremely large gradients of boundary conditions. The CRC is a joint initiative of the University of Stuttgart, the Technische Universität Darmstadt and the DLR in Lampoldshausen, operating with 16 projects structured into three main areas

- A: Methods and Fundamentals
- B: Free Droplets
- C: Droplets with Wall Interaction

and involving researchers from numerous faculties: Mathematics, Chemistry, Electrical Engineering, Mechanical Engineering and Computer Sciences. After a brief introduction into the structure of the CRC, this contribution will present selected results after the first three years of the center, with emphasis on highly interacting projects

---

### **Introduction**

Drops and drop dynamics are ubiquitous, in nature, e.g. in clouds, fog, rain, or spindrift, and in many engineering systems e.g. in gasoline or Diesel engines, gas turbines, aero-engines, rocket engines, spray cooling processes, chemical reactors, or agricultural sprays. Despite the fact that interest and research into the behaviour of droplets has begun very early, e.g. (Plateau, 1873) (Rayleigh, 1878) many fundamental aspects of droplet behaviour and drop dynamics remain unclear, especially under extreme boundary conditions. In this context, extreme boundary conditions are considered to include:

- Drops near the thermodynamic critical point or at very high pressures
- Drops in strong force fields, e.g. Lorentz forces
- Drops exposed to extreme temperatures (high or low) and/or in thermodynamic non-equilibrium
- Drops exhibiting extreme gradients, e.g. at the three-phase contact line

Under such extreme boundary conditions, the prediction and simulation of drop behaviour is often unreliable, moreover, standard literature on the topic of drop dynamics, e.g. (Lefebvre, 1989) (Pruppacher & Klett, 1978) (Frohn & Roth, 2000) often treat drops under only moderate ambient conditions. Therefore, in the particular area of drops under extreme boundary conditions a need was identified for further basic research, with the aim to improve our understanding and predictive capabilities of both naturally occurring and engineering systems involving droplets. It is clear that the scope of such an undertaking goes far beyond the capabilities of a single research group or research discipline and this has led to the establishment of the Collaborative Research Center (CRC) SFB-TRR 75 ‘Droplet Dynamics under Extreme Boundary Conditions’. This ‘Transregio’ funding instrument from the German Deutsche Forschungsgemeinschaft allows several research groups at different institutions to collaborate in a complementary manner over an extended period of time towards a common goal. The SFB-TRR 75 was first funded in January 2010 and involves 14 research groups at the three institutions: University of Stuttgart, Technische Universität Darmstadt and Deutsche Zentrum für Luft- und Raumfahrt (DLR) Lampoldshausen.

The SFB-TRR75 is structured into three many research areas comprising a total of 15 sub-projects, listed below together with the responsible researcher(s):

### **Research Area A: Methods and Fundamentals**

- TP-A1: Interactive Visualization of Droplet Dynamics (T. Ertl, F. Sadlo)
- TP-A2: Development of Numerical Methods for the Simulation of Compressible Droplet Dynamics under Extreme Ambient Conditions (C.D. Munz)

- TP-A3: Analysis and Numerics of Front- and Phase Field Methods for Droplet Dynamics (C. Rohde)
- TP-A4: Molecular Dynamics Simulations of Droplet Evaporation in the Non-linear Response Regime (F. Müller-Plathe, N. van der Vegt)
- TP-A5: Simulation of the Mechanical Deformation and Movement of Droplets on Polymer Insulation Surfaces with Strong Electric Fields (T. Weiland, E. Gjonaj)
- TP-A6: Non-equilibrium Thermodynamics of Boundaries: Application of the Density Functional Theory to Mixtures of Polar Substances (J. Groß)

#### Research Area B: Free Droplets

- TP-B1: Investigation of the Behavior of Super-cooled Droplets Concerning Evaporation, Condensation and Solidification for Different Boundary Conditions (B. Weigand, N. Roth)
- TP-B2: Experimental Investigations of Droplet Evaporation under Extreme Conditions with high Resolution Laser Diagnostic Methods (G. Lamanna, A. Dreizler)
- TP-B3: Modelling and Simulation of Droplet Evaporation in Foreign-Gas Environment under Transcritical Conditions (A. Sadiki, J. Janicka)
- TP-BX (Associated Project): Experimental Investigation of Transient Injection Phenomena in Rocket Combustion Chambers under High Altitude Conditions with Special Focus on Flash-Evaporation (C. Manfretti, M. Oswald)

#### Research Area C: Droplets with Wall-Interactions

- TP-C1: Numerical Simulation of the Transport Phenomena for Droplet-Wall Interaction on Hot Walls with special Focus on the Three-Phase Contact Line (T. Gambaryan-Roisman, P. Stephan)
- TP-C2: High Resolution Measurements for the Heat Transfer during Droplet-Wall-Interactions with special Focus on the Three-Phase Contact Line (P. Stephan, T. Gambaryan-Roisman)
- TP-C3: Droplet-Wall Interactions of Super-cooled Droplets on Cold Surfaces (S. Jakirlic, C. Tropea)
- TP-C4: Droplet-Wall Interactions for Hot Surfaces and High Ambient Pressures (I. Roisman, C. Tropea)
- TP-C5: Mechanical and electrical phenomena of water drops under the influence of high electric fields (V. Hinrichsen, M.H. Nazemi)
- TP-Z: Administration of the SFB-TRR 75 (B. Weigand)

In **Research Area A** numerical and analytical methods are developed which are pre-requisites for conducting the work in the other research areas. Methods for visualization are developed in TP-A1. TP-A2 and TP-A3 are concerned with the development of numerical methods. In TP-A4 basic droplet dynamic processes are investigated by molecular thermodynamics. In TP-A5 simulations of the mechanical deformation and movement of droplets on polymer insulation surfaces with strong electric fields are investigated. TP-A6 investigates the non-equilibrium thermodynamics of interfaces. Here the classical density functional theory is applied to mixtures of polar substances. All projects in **Research Area A** contribute fundamental results to **Research Area B** and **Research Area C**. In **Research Area B** droplets free of solid boundaries are investigated. In TP-B1 droplet dynamics problems involving sub-cooled droplets in clouds and the formation of ice crystals in clouds are investigated. TP-B2 investigates experimentally the evaporation of droplets under extreme thermodynamic conditions. The modelling and simulation of droplet evaporation in a foreign-gas environment under transcritical conditions is investigated in TP-B3, whereas the associated project TP-B4 investigates flash evaporation for the transient injection of propellant in a rocket combustion chamber. In **Research Area C** droplet-wall interactions are investigated. In TP-C1 and TP-C2 special focus is set on the three-phase contact line during droplet-wall interaction. In TP-C3 droplet-wall interactions are investigated for sub-cooled droplets on cold surfaces and in TP-C4 droplet-wall interaction is investigated for hot surfaces under high ambient pressures. The administration of the CRC is embedded in TP-Z and within this project a vigorous guest scientist program involving a large number of invited speakers from all over the world is organized.

In order to foster cooperation and interaction among the individual research groups, several lead applications and experiments have been identified, each involving several groups. These include:

- Phase change in supercooled and electrically charged drops in clouds
- Impact of supercooled liquid drops (SLD) on aircraft components
- Behavior of water drops on insulator surfaces on high-voltage installations
- Behavior of drops in rocket engines (cryogenic conditions)
- Behavior of drops in future combustion systems

Wherever possible, comparisons between theoretical, experimental and numerical simulations are to be drawn for these particular systems.

In summary, the main goals of the SFB-TRR-75 are as follows:

- To gain physical insight into drop processes at non-equilibrium and/or (super) critical conditions
- Mathematical and numerical modeling of these processes; description and analysis



- Development of appropriate experimental methods to validate analytic and numerical formulation of models
- Establishment of reference experimental data and mathematical fundamentals, use of modern visualization techniques to illustrate results
- Application of these developments to the lead applications given above.

First results from this CRC have been reported in (Weigand & Tropea, 2012); the present contribution reviews briefly the organization and goals of the CRC and presents further selected results.

## Research Area A: Methods and Fundamentals

### A2, A3: DNS of compressible multi-phase flow

(C.-D. Munz\*, C. Rohde\*\*, S. Fechter\*, V. Schleper\*\*, \* Institute of Aerodynamics and Gas Dynamics, \*\* Institute for Applied Analysis and Numerical Simulation, University of Stuttgart)

At extreme ambient conditions near the critical point the typically used assumption of an incompressible flow field is no longer valid. Therefore, a main objective is to develop numerical methods for the simulation of compressible multi-phase flow. This flow regime is of technical interest as modern fuel injection systems (e.g. in Diesel engines) operate at such conditions. In open literature only limited data for the near-critical conditions are available and many phenomena are not totally understood yet.

The compressible simulation of multi-phase flows introduces three major difficulties: The first is an accurate method to describe the temporal evolution of the phase boundary. The second is an efficient method to resolve the physics at the phase interface and the third is an accurate thermodynamic model to describe the fluid properties within the range of interest. To tackle the first challenge, we track the phase boundary by a method based on the level-set approach. Concerning the second and third difficulty described above, the presented scheme is designed such that arbitrary equations of state can be used in the bulk phases, while the physics at the interface are included as micro-models that can be chosen specifically for the problem at hand.

In the compressible case thermodynamics and hydrodynamic are closely linked and a decomposition of the equations is not possible any more. Typically, an equation of state that is valid in the investigated near-critical range is complex and consequently costly to evaluate. The discretization of the flow as well as the interface tracking is done using a high-order Discontinuous Galerkin (DG) approximation to allow for an efficient discretization of the flow field. The high-order discretization is especially advantageous for the level-set equation because of the good dissipation and dispersion properties of the DG scheme.

At the interface we use ideas of the Ghost-Fluid method that allow for a complete separation of both bulk phases. Numerically the phase interface is shifted to the nearest grid boundary. At the phase interface, the micro-model consists of special Riemann solvers which provide the necessary jump conditions at the interface and resolve the related interface physics. These interface Riemann solvers (see e.g. (Fechter, Jaegle, & Schleper, 2013) (Jaegle, Rohde, & Zeiler, 2012)) allow for a straightforward inclusion of interface physics like surface tension forces, coupling of dissimilar equations of state and phase transition. Within the bulk phases well-known single-phase Riemann solvers as e.g. described by (Toro, 2009) are used.

Exemplary, we present here one micro-model that does not include phase changes, but is able to treat arbitrary surface forces such as surface tension at the place where they occur – namely directly at the phase boundary. For more details and other micro-models, we refer e.g. to (Fechter, Jaegle, & Schleper, 2013) and (Jaegle, Rohde, & Zeiler, 2012). As typical equations of state near the critical point are very complex, micro-models based on iterative solutions of nonlinear systems of equations are very costly. However, the exact resolution of the interface behaviour requires not only the solution of such a nonlinear system, but also the knowledge and evaluation of associated quantities such as the sound speed. To avoid this, a local linearization of the characteristic shock-rarefaction curves (called Lax-curves) is used to derive a system of two linear equations that can be solved directly and allow a cheap but accurate approximation of the interface behaviour.

The multi-phase solver has been validated with several test cases including three-dimensional compressible shock-droplet interactions similar to the two-dimensional test case of (Hu, Adams, & Iaccarino, 2009). In this test case a simple equation of state is chosen for both bulk phases, in the gaseous phase the ideal gas law and the Tait equation in the liquid phase. In Figure 1, a Schlieren type visualization of the numerical results for the density gradient in the droplet median plane is shown at different time levels. The impinging shock wave is partially reflected at the droplet surface; the other part enters the droplet and travels at a much higher speed. The main features of the simulations appear as physical and resemble the (higher resolved but 2D) results shown by (Hu, Adams, & Iaccarino, 2009).

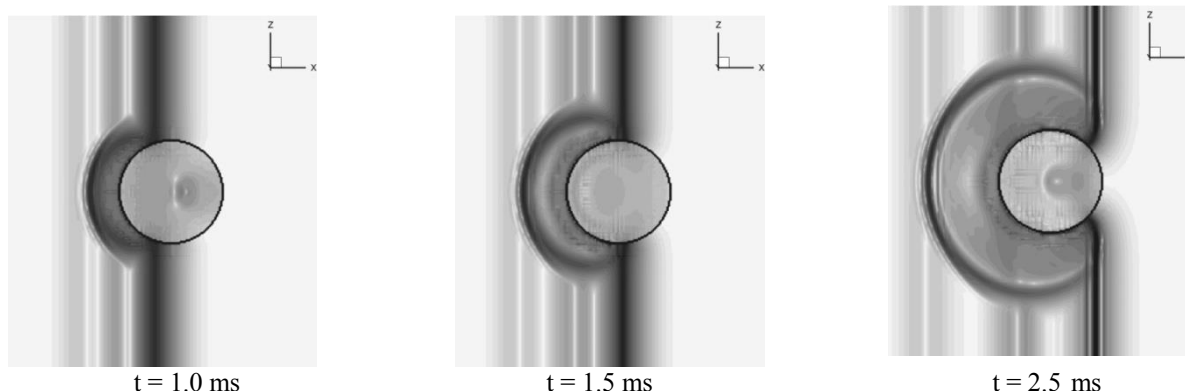


**Figure 1:** Three-dimensional shock-droplet interaction using the linearized wave curve Riemann solver at the interface and a fourth order scheme in time and space ( $60^3$  grid cells). The plot shows the logarithmic density derivative ( $s=\log(\text{grad}(p)+1)$ ) at three different simulation times.

#### A4: Steady state evaporation of droplets using non-equilibrium molecular dynamics

(Jianguo Zhang, Frédéric Leroy, Florian Müller-Plathe, Theoretical Physical Chemistry, TU Darmstadt)

The evaporation behaviour of droplets under extreme conditions doesn't usually follow the model developed for subcritical conditions. Under extreme conditions, e.g. extreme temperature gradients, a droplet can't keep its spherical shape due to the loss of surface tension, and evaporates at very high rates. Consequently, it is difficult to study the evaporation properties of interest, such as the mass flux and the heat flux. One solution to this problem is artificially creating steady state evaporation through reinsertion of molecules into the droplet. In this case, the droplet size and evaporation rate are maintained constant during the evaporation. Two approaches, namely the *bubble* and *splitting* methods, based on RNEMD have been programmed and tested on an ethanol molecular system. For the bubble method, a bubble is created and centered at the centre of mass of the droplet, then a gas molecule was selected and reinserted into bubble, finally, the inserted molecule was released gradually from the bubble. As to the splitting method, a molecule at the center of droplet was chosen and then splitted into two gradually. These two approaches are illustrated schematically in Figure 2

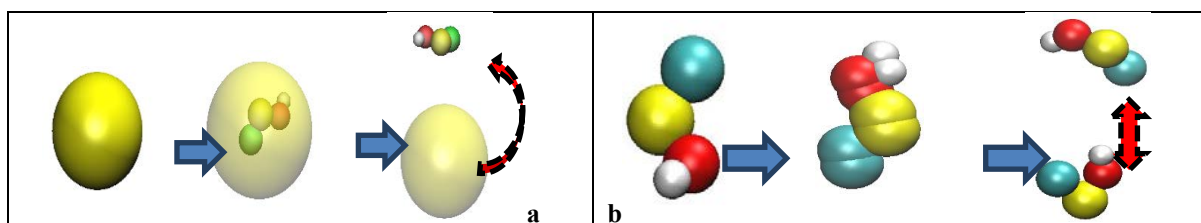


**Figure 2:** Two insertion approaches: a) bubble method; b) splitting method

For the bubble method, after the molecules were released from the bubble, they moved around the bubble for a while rather than migrating directly to the droplet surface, thus, the long distance effect of insertion was reduced. For the splitting method the droplet size remains constants once the insertion starts at a threshold of droplet size of 24320 atoms. The average number of atoms for each insertion is 16. Some preliminary results of these techniques are illustrated in Figure 3. Both methods achieve steady state evaporation

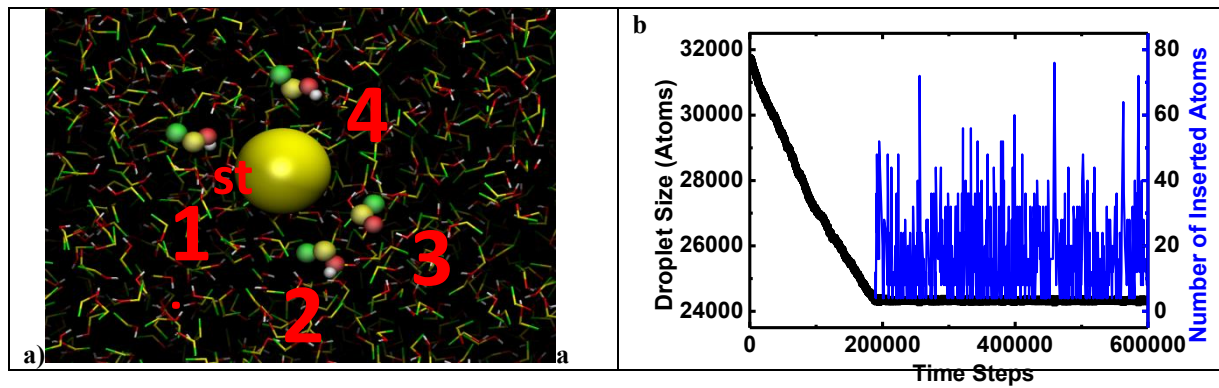


**Figure 3:** a) Snapshot for the successive insertions of four molecules using the bubble method; b) Number of atoms inside the droplet (black line) and the number of atoms for each insertion (blue line) using the splitting method.

## Research Area B: Free Droplets

### TP-B4: Experimental Investigation of Transient Injection Phenomena in Rocket Combustion Chambers under High Altitude Conditions with special Focus on Flash-Evaporation

(C. Manfretti, M. Oswald, DLR, Institute of Rocket Propulsion, Lampoldshausen)

Liquid rocket space propulsion applications cover a wide range of initial combustion chamber conditions varying from sea level pressures to near-vacuum pressures. In addition, propellants used vary from hypergolic propellants, which are liquid at sea-level ambient temperatures to propellants which are liquid at cryogenic temperatures. Upper stage liquid rocket engines as well as RCS (Reaction and Control System) and OMS (Orbital Manoeuvring System) engines are such engines which operate in extremely low pressure (high altitude) ambient conditions and pressures in the combustion chamber prior to the start-up of the engine (opening of the main propellant valves) are near vacuum. Depending on the engine cycle and propellant types and cycling of the engine, its start-up varies greatly. A phenomenon which is invariably encountered during this phase is flashing or flash-evaporation of the liquid propellant. This evaporation is due to the fact that the injection temperature of the liquid is above its ambient saturation temperature. The difference between these two temperatures is defined as the level of superheat (Lecourt, Barricau, & Steelant, 2009):  $\Delta T_{\text{sup}} = T_{\text{inj}} - T_{\text{sat},a}$ . The level of superheat defines the quality of flashing that will occur. It is important to note that flashing is not limited in occurrence to the combustion chamber but may occur as far upstream as the main propellant valves.

Using the experimental set-up which was already in use in the first phase of the project and which includes a battleship thruster complete with a feed and vacuum system which allows feed and vacuum pressures to be varied, additional flash injection experiments were conducted using liquid oxygen (LOx). Two injector configurations with different diameters, 2.4 mm and 0.3 mm, were tested for a range of pressure ratios,  $R_p$ ,  $R_p = \frac{p_{\text{sat}}(T_{\text{inj}})}{p_{\infty}}$ , defined as the ratio between the saturation pressure at the fuel injection temperature and the backpressure, with the aim of examining variations in injection angle as a function of  $R_p$ . The shadowgraphy images in Figure 4 illustrate the dependency of the spray angle on  $R_p$  for the 0.3 mm configuration.

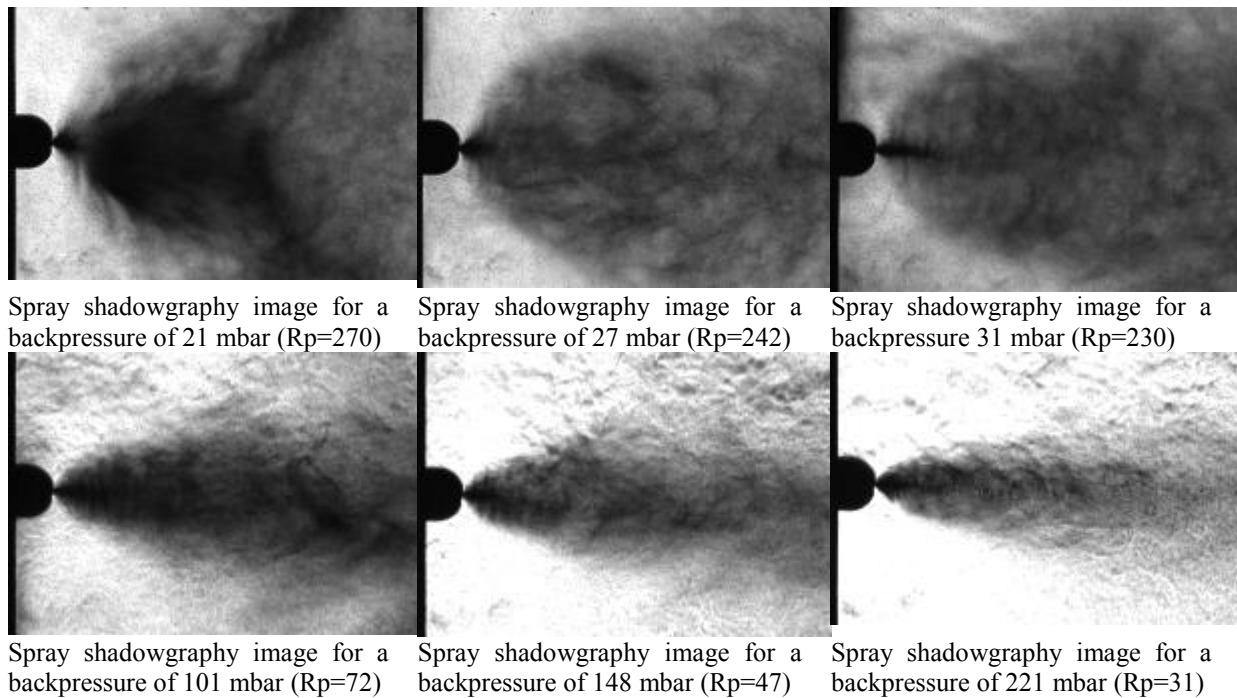


**Figure 4:** Schadowgraph images illustrating the dependency of spray angle on  $R_p$  for the 0.3mm configuration.

Figure 5 shows that, as postulated by (Kamoun, Lamanna, & Weigand, 2010) the injection angle reaches an asymptotic maximum value. The physical motivation behind this behaviour is discussed in detail in (Kamoun H., et al., 2013).

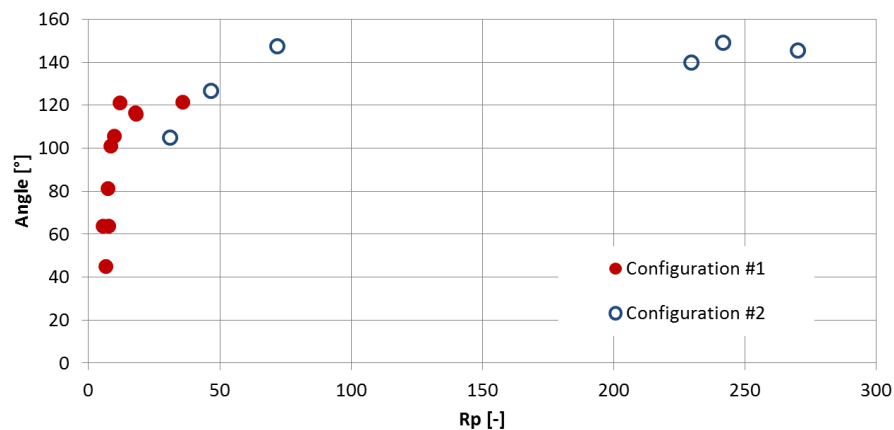


**Figure 5:** Spray angle as a function of  $R_p$  for configuration #1 (2.4 mm) and configuration #2 (0.3 mm) at  $L/D=6$

To overcome the limitations of the current experimental set-up which does not allow a regulation of the temperature of the injected liquid oxygen, a new set-up is necessary. For this purpose, a parameter analysis has been performed based on the correlation developed by (Cleary, Bowen, & Witlox, 2007) which characterizes the onset of flash evaporation, i.e. the transition from aerodynamic jet disintegration to flash evaporation, as well as the conditions for a full flashing of the jet as a function of Jacob and Weber numbers and of the density ratio,  $\Phi$ , between liquid and vapour conditions. This analysis has helped determine the range of injection temperatures, 70-120 K, injection pressures, 0-3 MPa, chamber pressures, 0.001-0.1 MPa, nozzle diameters, 0.1 - 2 mm, and jet velocities, 10-40 m/s, for which flashing of liquid oxygen will be observed. According to these parameters a new feed and injection system is currently being designed.

## Research Area C: Droplets with Wall-Interactions

### TP-C5: Mechanical and electrical phenomena of water drops under the influence of high electric fields

(V. Hinrichsen, M.H. Nazemi, *High-Voltage Laboratory, Department of Electrical Engineering and Information Technology, Technische Universität Darmstadt*) In this subproject the behaviour of water droplets on hydrophobic surfaces of polymeric high-voltage insulators (e.g. those of high-voltage overhead transmission lines) under the influence of the continuously applied electric field is investigated. Under these conditions, the droplets, which are typically deposited either by rain or by condensation, will experience periodically changing deformations, synchronized with the frequency of the applied electric field. The deformation increases local electric field stress at the triple zones (three-phase contact line), leading to reduced electric partial discharge inception voltages and, in the long term, to electro-chemical deterioration of the insulator surface even under normal continuous operating stress (e.g. total loss of hydrophobicity, electrical tracking and erosion). The laboratory investigations are performed under variation of a large set of parameters such as water droplet volume, frequency of the applied electric field, electrical conductivity of the water droplets as well as the insulator's surface inclination. The aim is to develop, in close cooperation with TP-A5, a simulation tool that is able to predict the mechanical deformations, to determine field enhancement factors at the triple zones and to finally calculate the partial discharge inception voltage (and thus the maximum permissible voltage per insulator length) of an insulator under real service conditions.

Standard flat test insulator specimens are used for the experiments, made up from silicone rubber with two embedded high-voltage electrodes. When voltage is applied, a virtually homogeneous tangential electrical field develops on the specimen's surface. Individual (or several) water droplets of defined volume, conductivity etc. are placed in this area with the help of a pipette. A high-speed video camera is then used to capture the periodical deformations, and a daylight UV camera takes pictures of the electrical partial discharges, which are additionally evaluated by sensitive electrical measurements. Thus, oscillation modes dependant on droplet volume and frequency of the applied electric field, the degree of deformation and the exact location and intensity of electric partial discharges can be determined. Figure 6 shows examples of typical oscillation modes under applied alternating field stress, and Figure 7 gives an example for typical locations of electrical partial discharges in case of one individual droplet or a triplet of droplets.



**Figure 6:** Typical oscillation modes of water droplets under the impact of an alternating electrical field

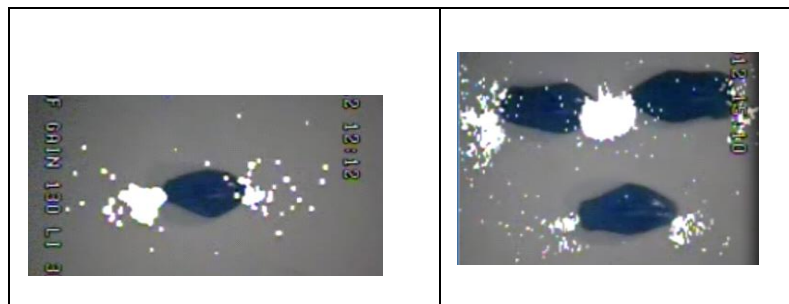


**Figure 7:** Locations of electric partial discharges for one droplet (left) and a triplet of droplets (right)

The experimental results are used as input for the development of the simulation tool in TP-A5 as well as for validation of the tool.

## Conclusions

In 2010, the Collaborative Research Center SFB-TRR75 was started, including 15 subprojects carried out at the University of Stuttgart, Technische Universität Darmstadt and DLR Lampoldshausen. The main goal of the CRC is the investigation of droplet dynamics under extreme ambient conditions. The nature of the investigated problems leads to strong interactions between the individual sub-projects. Exemplary results from this CRC demonstrate the progress achieved over the last three years. Further information and current information regarding research at the CRC can be found under [www.sfbtrr75.de](http://www.sfbtrr75.de).

## Acknowledgements

The members of the SFB-TRR 75 would like to thank the Deutsche Forschungsgemeinschaft (DFG) for the funding of the SFB-TRR 75.

## References

- [1] Cleary, V., Bowen, P., & Witlox, H. (2007). Flashing liquid jets and two-phase droplet dispersion I: Experiments for derivation of droplet atomization correlations. *J Hazardous Material*, S. 786-796.
- [2] Criscione, A., Kintea, D., Roisman, I. V., Jakirlic, S., & Tropea, C. (2013). A new approach for water crystallization in the kinetics-limited growth region. *8th Int Conf on Multiphase Flow*. Jeju, Korea: ICMF.
- [3] Frohn, A., & Roth, N. (2000). *Dynamics of Droplets*. Heidelberg: Springer Verlag.
- [4] Kamoun, H., Lamanna, G., & Weigand, B. (2010). High-speed shadowgraphy investigations of superheated liquid jet atomisation. *22nd ILASS-Americas*. ILASS.
- [5] Kamoun, H., Lamanna, G., Weigand, B., Manfretti, C., Rees, A., Oswald, M., & Steeland, J. (2013). Flashing behaviour of rocket engine propellants. *ILASS-Europe*. Chania: ILASS-Europe.
- [6] Lecourt, R., Barricau, P., & Steelant, J. (2009). *Atomization and Sprays*, S. 103-133.
- [7] Lefebvre, A. (1989). *Atomization and Sprays*. New York: Hemisphere Publishing Corporation.
- [8] Plateau, J. (1873). *Statique Expérimentale et Théorique des Liquides Soumis aux Seules Forces Moléculaires*. Paris: Gauthier & Villars.
- [9] Pruppacher, H., & Klett, J. (1978). *Microphysics of Clouds and Precipitation*. Dordrecht: Reidel Publishing.
- [10] Rauschenberg, R., Criscione, A., Eisenschmidt, K., Kintea, D., Jakirlic, S., Tukovic, Z., . . . Tropea, C. (Vol. 79 2013). Comparative assessment of volume-of-fluid and level-set methods by relevance to dendritic ice growth in supercooled water. *Computers and Fluids*, S. 44-52.
- [11] Rayleigh, L. J. (1878). On the instability of jets. *Proc. London Math. Soc.*, S. 4-13.
- [12] Weigand, B., & Tropea, C. (2012). Droplet dynamics under extreme boundary conditions: The collaborative research center SFB-TRR 75. *ICLASS 2012*. Heidelberg, Germany: ICLASS.

# Session:

## **CFD & LES Simulations**



## Liquid-Fuel Ejector Pump under Multi-Phase Flow Conditions

Carsten Mehring

Central Engineering, Parker Aerospace, Irvine, CA, USA

### Abstract

The present paper summarizes the numerical analysis of an aerospace liquid-fuel ejector pump subject to air desorption from the fuel. The analysis has been carried out using the commercial flow solver CFX v13.0 by ANSYS Inc. To simulate the evolution/desorption of air from the fuel, the so-called “Full Cavitation Model” by Singhal et al. has been deployed. In addition to gas desorption (i.e., gas cavitation) and absorption, vapour cavitation has been modelled based on the Rayleigh-Plesset equation for bubble dynamics. Analysis results predicting the effect of air desorption on ejector pump performance and its performance limit are compared with experimental data obtained for an ejector pump operating at sea level and altitude conditions.

### Introduction

Ejector pumps are frequently used for fuel handling and delivery in aircraft fuel systems. Under design flow conditions these pumps operate in a single-phase mode, i.e., only liquid fuel is delivered through the pump; even though some contaminants might be present in the suction flow for the case where these pumps are used to scavenge fuel from remote corners or the bottom of fuel tanks; see Figure 1.

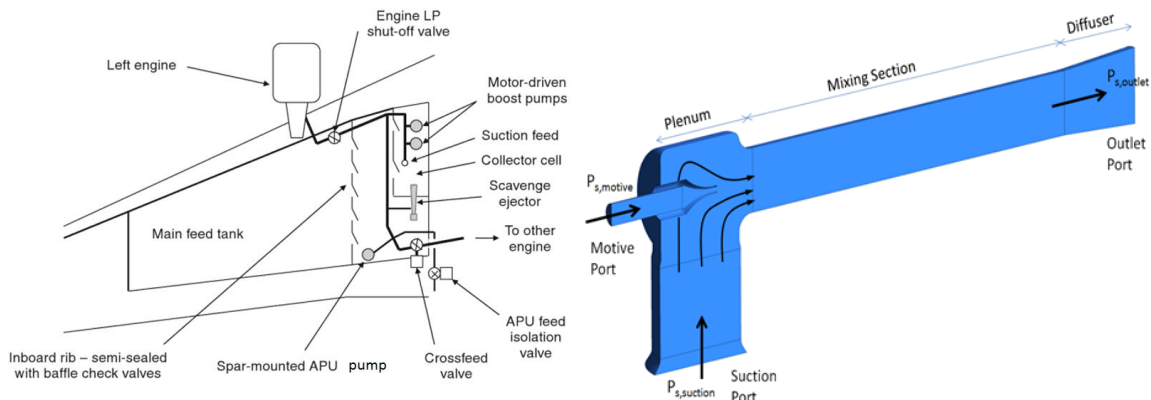


**Figure 1:** Left: Schematic of aircraft fuel system including ejector pump for fuel scavenging, see Ref. (1). Right: Typical ejector pump geometry, including inlet and exit flow boundaries.

Ejector or jet pumps operate on a very simple principle (see Figure 1): A driving fluid is expanded through a nozzle (motive flow), converting its pressure energy into kinetic energy thereby reducing its static pressure according to Bernoulli's Principle. The low pressure high-speed fluid zone downstream of the motive nozzle draws in and entrains the surrounding suction fluid fed from a separate inlet. Motive and suction fluids mix as the static pressure of the mixture increases further downstream when kinetic head is transformed back into pressure head. The fact that ejector pumps do not have any moving parts makes them not only reliable but allows also the pumping of suction fluids that cannot be delivered by other pumps, e.g., due to impurities such as particle loading, for example. For the prescribed reasons, ejector pumps have found significant applications in slurry pumping and in nuclear applications.

Suction and motive fluids can be of the same type or they can be different and the fluids themselves can be mixtures of gases, liquids and/or solids. For the prescribed fuel delivery application in aircraft, ejector pumps are to deliver/pump liquid fuel or to some extent a mixture of liquid fuel and small amounts of liquid water entering the fuel tank through the vent-lines or via condensation. However, under certain conditions, air (and/or fuel vapour) can be present in a liquid-liquid ejector pump. One such condition is being investigated in this paper, i.e., where air originally dissolved within the fuel is evolving from the suction flow of the pump.

## Modelling Approach and Implementation

### Dissolved Air / Equilibrium Condition

When an aircraft climbs to its cruising altitude, the reduction in ambient pressure or the pressure in the ullage space of the fuel tank will cause gases dissolved within the liquid fuel to evolve such that the amount of gas remaining dissolved within the fuel is in equilibrium with the partial pressure of the gas in the ullage space. The equilibrium condition is given by Henry's Law (2) which relates the partial pressure of the gas above the liquid phase to the mole fraction of the gas in solution within the liquid phase under equilibrium conditions, i.e.,

$$P_G = H_{DA} X_{DA} \quad (1)$$

where  $P_G$  is the partial pressure of the dissolved gas species (G) above the liquid surface,  $X_{DA}$  denotes the mole fraction of dissolved gas/air (DA) ([moles of dissolved gas]/[moles of liquid phase]) and  $H_{DA}$  represents Henry's Law constant expressed in units of pressure. Note that, there are various different definitions or units of measure for the Henry's Law constant  $H$  and care needs to be taking when selecting the proper values/units of measure from the open literature; see Ref. (3).

The prescribed evolution of gases (i.e., air) from the liquid phase, in order to reach the equilibrium condition given by Eqn.(1), can take place in the fuel tank as well as during delivery of the fuel into and through the suction port of the ejector pump. In fact, further pressure drop of the suction flow from suction inlet port to the ejector throat will enhance the outgassing or the evolution of air from the fuel. The objective of the present analysis is to identify in how far the evolution of air from the liquid fuel impacts ejector pump performance, and specifically the ejector pump performance limit. Note that, for the subsequent analysis, the fuel flow through the motive nozzle was assumed to contain no dissolved air.

### Models for Vapour and Gas Cavitation

The performance of fuel ejector pumps is limited by vapour and/or gas cavitation. The appearance of fuel vapour in the case of vapour cavitation which effectively determines the performance limit of some pumps has already been discussed in Ref. (4). Similarly, to this prior work, the present steady-state analysis was carried out by employing ANSYS CFX v. 13.0 with constant fluid properties and the SST (Shear Stress Transport) turbulence model of Menter (5). Cavitation was modelled by the homogeneous multiphase model together with the Rayleigh-Plesset Cavitation Model assuming a nucleation site diameter of  $2\mu\text{m}$ . No changes have been made to the other cavitation model parameters, i.e., cavitation condensation/vaporization coefficients = 0.01 and 50, respectively; and a nuclei volume fraction of 0.0005. A correction to account for the effect of (laminar) viscous stresses on the critical pressure for the onset of cavitation as originally proposed by Joseph (6) (7) and employed by the author in Ref. (4) has not been included here.

While phase-change phenomena between the liquid fuel and its vapour phase have been modelled based on the Rayleigh-Plesset equation for (vapour) bubble dynamics, desorption and absorption of non-condensable gases out-of and into the liquid phase have been captured by deploying the Full Cavitation Model proposed by Singhal et al. (8) and Yang et al. (9). Within both models, driving force for the mass transfer is the pressure difference between the local pressure field in the liquid and a critical pressure. In the case of vapour cavitation that critical pressure is the liquid fuel vapour pressure (neglecting the prescribed viscous normal stress effect), in the case of gas cavitation the relevant critical pressure is the equilibrium pressure given by the liquid vapour pressure augmented by the partial pressure  $P_G$  of the dissolved gas phase species under equilibrium conditions, see Eqn.(1).

For a detailed review of the prescribed Rayleigh-Plesset Cavitation Model and the Full Cavitation Model, the reader is referred to Ref. (10), which describes the implementation and benchmarking of these models in context of the CFX flow solver. Both models are only coupled via their joint velocity and pressure fields. The impact of dissolved non-condensable gases on vapour bubble growth and onset of cavitation, as discussed in Refs. (11), (12), (13), is not captured by the two models.

In order to verify and validate our set-up of the prescribed mass-transfer models, the analysis of a sudden contraction of a pipe with sharp edges and water as the operating medium described in Ref. (10) has been repeated for a variety of cavitation numbers  $\sigma = (P_1 - P_v)/(P_1 - P_2) = 1.009, 1.45, 1.871$  and using the 'Grid 3'

mesh (with 44800 nodes) according to Refs. (10) and (14). See also Figure 2 in this context. Note that, for this test case, the flow exhibits vapour cavitation for  $\sigma < 1.7$  whereas air evolution from water takes place even at higher  $\sigma$ -values. Present analysis results showed excellent agreement with the reported references for both phenomena, i.e., vapour cavitation and gas cavitation (gas desorption and absorption). Figure 3 shows analysis results for the prescribed test case with  $\sigma = 1.9$  together with results for the similar case but Jet-A as the working fluid.

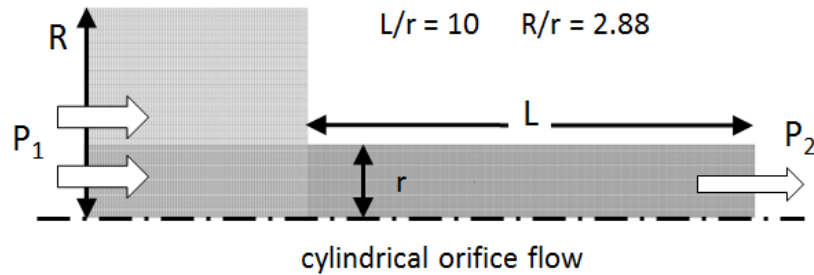


**Figure 2:** Test case set-up from Ref. (10) to validate implementation of gas and vapour cavitation models for water.

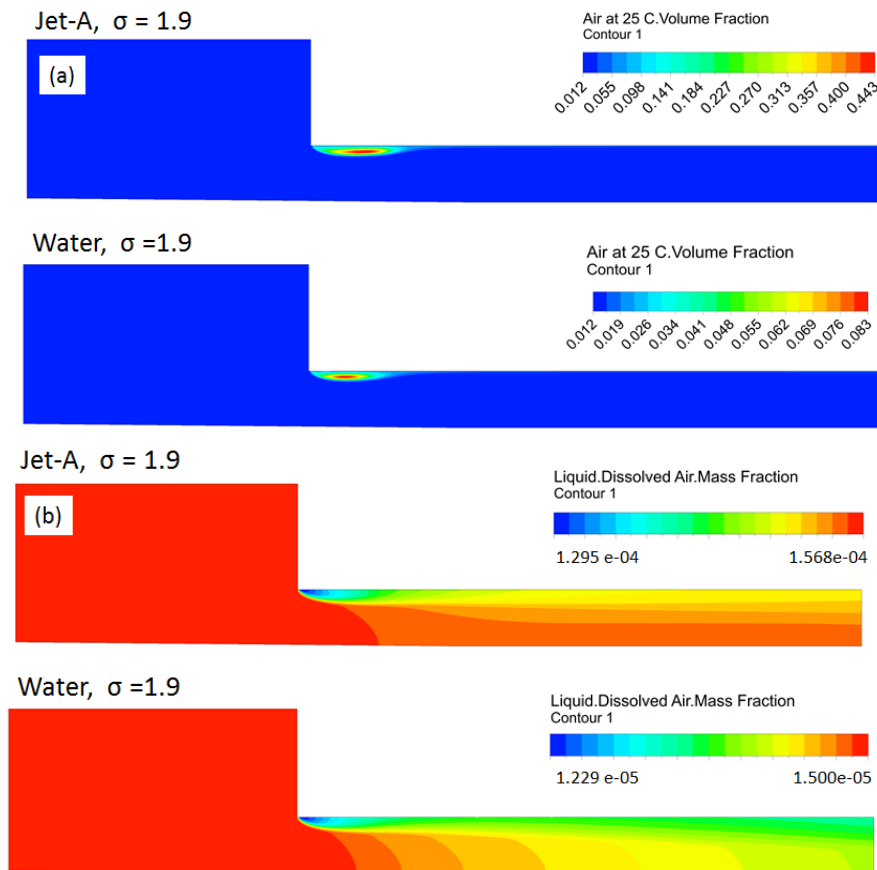


**Figure 3:** Contour lines of air volume fraction (a) and dissolved air mass fraction (b) for the test case set-up depicted in Figure 2 and water or Jet-A as the working fluid.

For both cases, the downstream static pressure was  $P_2=0.95$  bar and the upstream pressure  $P_1=2$  bar. Fluid densities and dynamic viscosities for the different phases were specified according to Table 1 with vapour pressures for water and Jet-A at  $T=25^\circ\text{C}$ , i.e.,  $P_v=3540$  and  $330$  Pa, respectively. Henry's law constant for Jet-A has been computed following the procedure detailed in Ref. (15) and utilizing Ostwald coefficient information from Refs. (15) and (16). Values of Henry's Law constant for other configurations and operating conditions considered within this paper have been computed in the same way. Also, the same values for absorption and desorption coefficient have been used throughout.

Figure 3 illustrates that, the two-orders of magnitude smaller value of the Henry's Law constant for Jet-A versus that of water (see Table 1) results in a significant larger dissolved air mass fraction at the same inlet pressure (see Figure 3 (b)) and a significant larger amount of air evolving from Jet-A upon flow acceleration and pressure drop through the contraction; see Figure 3 (a) . However, in the case of Jet-A air evolution/desorption is limited to the entrance region of the contraction while the evolution of air continues further downstream in the case of water.

The prescribed example is a good illustration of how significant gas evolution can be in the delivery of fuel in aerospace applications. Evolution of air in the delivery of liquid fuel to small turbo-jet engines as used in cruise missiles and reconnaissance drones can lead to engine flame out and equipment loss. In the case of fuel delivery via ejector pumps, it can have a significant impact on pump performance, as discussed below.

Full Cavitation Model Parameters		Fluid Properties	Density	Dyn. Viscosity
Absorption Coefficient	0.1 ms/kg		kg/m <sup>3</sup>	kg/(ms)
Desorption Coefficient	2 ms/kg	Water	997	8.90E-04
Maximum Solubility	0.01	Jet-A	804	1.56E-03
Henry's Constant, H <sub>2</sub> O	8.17E+09 Pa	Water Vapour	0.023	9.86E-06
Henry's Constant, Jet-A	9.69E+07 Pa	Jet-A Vapour	5.4	1.20E-05
		Air at 25 deg C	1.185	1.83E-05

**Table 1:** Fluid properties (right) and parameter selection for the 'Full Cavitation Model' used for the test-case shown in Figure 3.

## Ejector Pump Performance with Evolved/ Evolving Air

After verification and validation of the analysis setup via the prescribed test case, the Rayleigh-Plesset Cavitation Model and the Full Cavitation Model were deployed to study the effect of air evolution on the performance of liquid fuel ejector pumps.

Figure 4 shows a cross-section of the fluid inverse generated from the ejector pump geometry considered for this study together with the employed computational mesh. The total number of mesh nodes for this analysis was 3.3 million and great care was taken in order to properly resolve wall shear layers and free shear layers of the discharging motive jet. Planar symmetry conditions were employed, i.e., only one half of the ejector was analyzed (see Figure 1). Due to additional pressure recovery beyond the diffuser end and in order to reflect the experimental set-up, the analysis domain was extended to include a pipe section downstream of the diffuser (see Figure 4). Various operating points of the ejector pump were analyzed. Each analysis was carried out by specifying motive, suction and downstream static pressures at the respective boundaries (see Figure 1). Motive and suction static pressures were held constant and the outlet static pressure was adjusted in order to generate pump performance curves (pressure vs. flow) at sea level and altitude (41,000 feet) conditions. Pumping fluid was Jet A with a vapour pressure of 0.468 psia corresponding to a fuel temperature of 161°F. Note that, due to the use of aircraft fuel as heat sink, fuel temperatures of an aircraft in flight can be significantly higher than the local ambient air temperature.

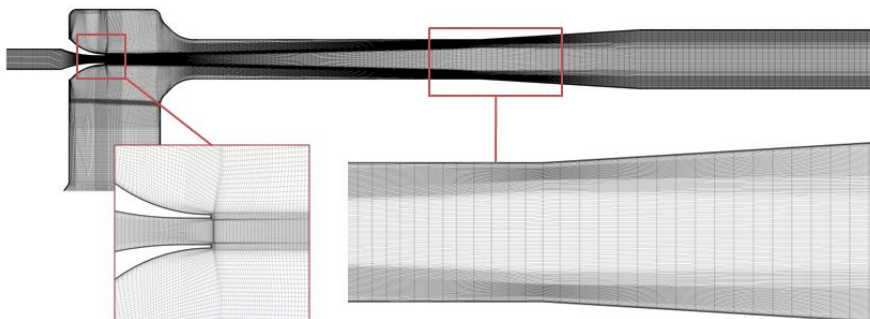


**Figure 4:** Hexahedral mesh (3.3 million nodes). Top: mesh in ejector pump symmetry plane; bottom: mesh detail near motive nozzle and in diffuser entrance region.

## Sea Level Performance

Figure 5 shows analysis results together with test data for the ‘Sea Level’ (SL) case. Analysis results in red indicate the case where the ‘Full Cavitation Model’ (FCM) has *not* been employed and evolution of air is *not* considered. Results in green reflect the case where the FCM has been deployed with proper specification of the Henry’s Law constant as described earlier and with the remaining model parameters identical to the test case.

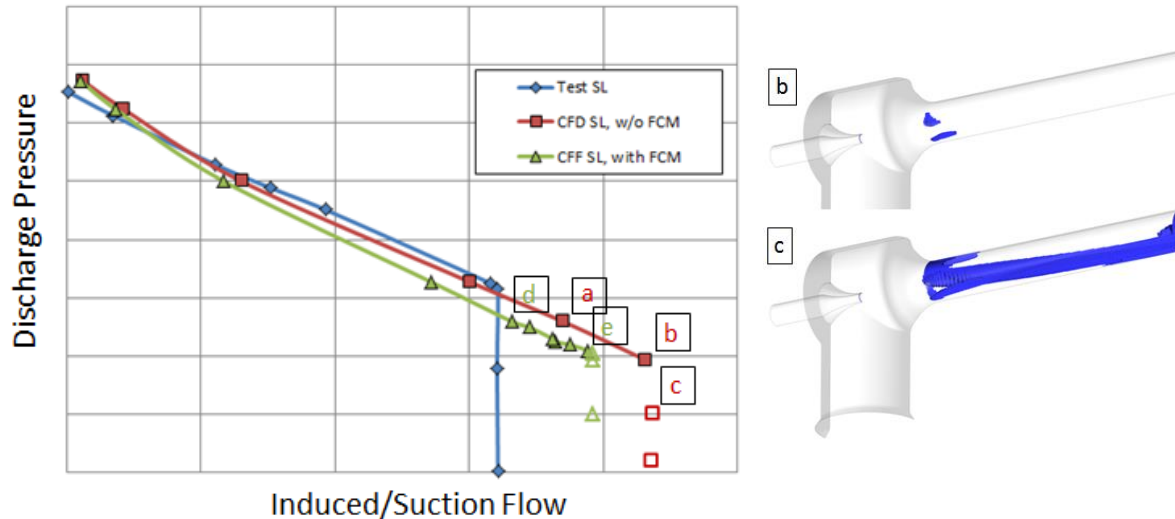


**Figure 5:** Left: Ejector pump performance curves at sea level (SL) as tested (blue) and from CFD without (red) and with (green) Full Cavitation Model (FCM). (Open markers indicate non-converging CFD cases). Right: Iso-surfaces of Jet-A vapour volume fraction ( $=0.01$ ) indicative of vapour cavitation limit.

The dissolved air mass fraction at the suction inlet was assumed to reflect that of a fully saturated fuel at sea level. The dissolved air content for the motive flow was assumed to be zero.

The performance limit indicated by Cases [b] and [c] (obtained without the consideration of air evolution) is a result of vapour cavitation and has been discussed in Ref. (4). See also the corresponding iso-surfaces of vapour volume fraction ( $=0.01$ ) in Figure 5. In contrast, Case [e] indicates the observed performance limit for the configuration where air evolution has been considered via the FCM model. As shown in Figure 6, at that condition, a large amount of air evolves from the fuel near the throat and in the upstream mixing region of the ejector pump. Note however that, the onset of air evolution is found at considerably higher downstream pressures (and in the ejector throat) as indicated by Case [d]. Considering a virtual stream tube and conservation of mass, the reduction in mixture density due to outgassing causes an increased flow velocity and a decrease in static pressure (see right side of Figure 6 where cases [d] and [a] are compared). As a result, the vapour pressure of the fuel is reached earlier, leading to the observed shift in performance limit and improved agreement between the predicted and the experimentally observed limits. Even better agreement can be expected with an increased value of the desorption coefficient, although recent analysis has shown that convergence is rendered difficult with increasing magnitude of mass-transfer source terms.

Note that, the analysis points indicated in Figure 5 (and Figure 7) by non-filled markers represent (steady-state) solutions which failed to converge due to the presence of large amounts of evolved air and/or fuel vapour. For the purpose of assessing pump performance limits, these points are considered to reflect said limits. Transient analysis is underway to establish flow behaviour under these conditions.

#### Altitude Performance

Air already evolved from the fuel and present in the suction port flow of an ejector pump is of importance during aircraft climb. Its effect on ejector pump performance (and specifically shift in performance limit) has already been described in Refs. (17) and (18). However, these one-dimensional analyses of mixed flow pumps did not account for the additional evolution of gas/air as the static pressure of the suction flow drops from the suction inlet to the ejector throat.

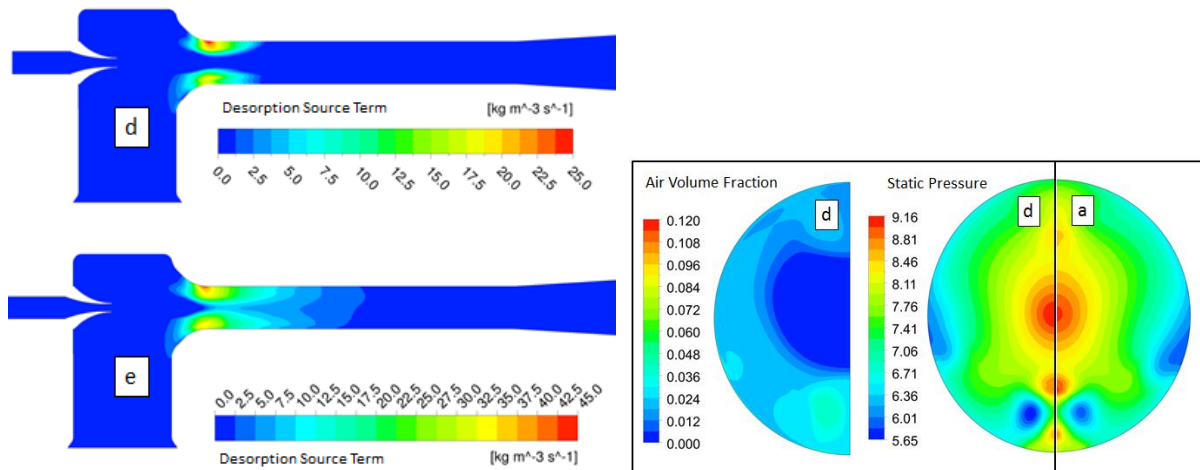


**Figure 6:** Ejector pump performance limit due to air evolution. Left: Contour plots of desorption source term in pump symmetry plane for onset of air evolution [d] and at performance limit [e]. Right: Contour plots of air volume fraction and static pressure in ejector throat plane for analysis with [d] and without [a] Full Cavitation Model at same discharge pressure.

Figure 7 illustrates the shift in pump performance limit with changes in the amount of (evolved) air present at the suction port inlet, i.e., 0% (grey), 25% (orange), and 50% (red) air volume fraction, whereby the latter corresponds to the amount of air evolving out of the fuel, if the fuel is taken from sea level (at fully saturated condition) instantly to 41,000 feet altitude and assuming the fuel (with its dissolved air content) instantly takes the fully saturated equilibrium state at that altitude. Note that, the prescribed cases did not include the Full Cavitation Model in the analysis and, accordingly, did not consider the additional evolution of air within the jet pump itself. Figure 7 shows that, at identical pressure conditions, the induced/suction flow is significantly reduced as the air volume fraction at the suction port increases. This is in part due to the reduced suction flow density, as well as due to the reduced entrainment effectiveness of the motive flow. Figure 7 also illustrates that, as the air volume fraction in the suction port increases, the pump performance limit is reduced considerably. However, the predicted performance limit remains well above the experimentally observed value. Improved agreement between predicted and measured limits is found if air evolution within the pump is considered (via the FCM); more specifically, for the case with 50% air volume fraction in the suction flow, the induced flow limit is reduced by 10%. However, even that value remains about 34% above the experimentally observed induced-flow limit.

Clearly, while ejector performance is reasonably well predicted at low flow conditions, discrepancies between test data and analysis results increase as suction flow rate increases. Note that, the present test data reflects a condition with approximately 50% air volume fraction in the suction port of the pump. Similar to the sea level case, an increase of the desorption coefficient is expected to improve performance limit predictions.

## Conclusions

The Full Cavitation Model by Singhal et al. (8) with standard values for absorption and desorption coefficients was applied to a fuel ejector pump operating under conditions where air evolves from the fuel. The analysis was carried out using ANSYS CFX v.13.0. Relevant Henry's Law constants have been determined according to ASME Standards. It was shown that both, air evolved from the fuel prior to entering the pump as well as evolution of air during the flow through the pump have a significant impact on pump performance and performance limit, the latter via influencing the on-set of vapour cavitation. Differences between test data and analysis results were considerable. An improvement w.r.t. performance limit prediction can be expected, however, with changes in the desorption-coefficient model parameter. In other words, if the ejector pump performance limit is induced by gas evolution, that limit might serve to identify suitable desorption-coefficient values within the deployed Full Cavitation Model, prior to utilizing the model for design purposes.



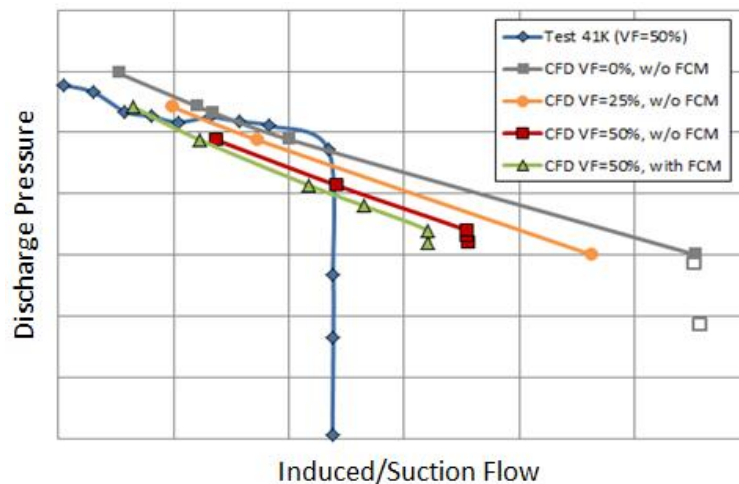


**Figure 7:** Ejector pump performance curves at altitude (41k feet) as tested (blue) and from CFD without Full Cavitation Model at various percentages of air volume fraction (VF) in the suction flow and with Full Cavitation Model at VF=50%.

## References

- [1] R Langton, C. Clark, M. Hewitt, and L. Richards. *Aircraft Fuel Systems*. s.l. : Wiley & Sons, 2009.
- [2] *The Solubility of Gases in Liquids*. R. Battino, L. Clever. 1966, Chemical Reviews, pp. 395-463.
- [3] Harvey, F. Smith and A. Avoid Common Pitfalls When Using Henry's Law. *Chemical Engineering Progress*. September 2007, pp. 33-39
- [4] *Evaluation of Cavitation in a Liquid-Liquid Ejector*. Mehring, C. San Antonio, TX : s.n., 2012. ILASS Americas, 24th Annual Conference on Liquid Atomization and Spray Systems.
- [5] F. Menter, M. Kuntz, and R. Langty. Ten Years of Industrial Experience with the SST Turbulence Model. *Turbulence, Heat and Mass Transfer 4*. ed: K. Hanjalic, Y. Nagano, and M. Tummers, 2003, pp. 625-632.
- [6] *Cavitation and the state of stress in a flowing liquid*. Joseph, D. 1998, J. Fluid Mechanics, pp. 367-378.
- [7] *Cavitation in a flowing liquid*. Joseph, D. 1995, Physical Review E, pp. 1649-1650.
- [8] *Mathematical Basis and Validation of the Full Cavitation Model*. A. Singhal, M. Athavale, H. Li, and Y. Jiang. 2002, Journal of Fluids Engineering, pp. 617-624.
- [9] H. Yang, A. Singhal and M. Megahed. *The Full Cavitation Model*. Brussels : Von Karman Institute for Fluid Dynamics, 2005. Lecture Series 2005-04.
- [10] C. Lifante, T. Frank. *Investigation of higher order pressure fluctuations and its influence on ship stern, taking into account cavitation at the propeller blades*. Otterfing, Germany : ANSYS Germany GmbH, 2008.
- [11] Brennen, C. *Cavitation and Bubble Dynamics*. s.l. : Oxford University Press, 1995. ISBN-10: 0195094093
- [12] *Effects of Dissolved Gas on Cavitation Inception in Free Surface Flows*. T. Baur, J. Koengeter, R. Leucker. Grenoble, France : Third Int. Symp. on Cavitation, 1998.
- [13] *Cavitation in Control Valves*. Frankfurt, Germany : Samson Technical Information. SAMSON AG, V74/Training.
- [14] ANSYS Presentation: *Non condensable gas cavitation. Full cavitation model*. s.l. : ANSYS, Inc., 2006.
- [15] Standard, ASTM. *ASTM D2779-92(2002)*. West Conshohocken, PA : ASTM International, 2002. DOI: 10.1520/D2779-92R02.
- [16] Coordinating Research Council, Inc. *Handbook of Aviation Fuel Properties*. Alpharetta, GA : Coordinating Research Council, Inc., 2004. CRC Report No. 635.
- [17] Cunningham, R. Jet Pump Theory. [book auth.] J. Messina, P. Cooper, and C. Heald I. Karassik. *Pump Handbook, 4th Edition*. s.l. : McGraw-Hill Professional, 2008.
- [18] *The Jet Pump as a Lubrication Oil Scavenge Pump for Aircraft Engines*. Dayton, OH : Wright Air Development Center, 1954. WADC TR 55-143.



## **Gasoline direct injection internal injector flow CFD simulations for various bioethanol blends**

Charalambos A. Chasos, George N. Karagiorgis and Chris N. Christodoulou

Department of Mechanical Engineering, Frederick University, Cyprus

### **Abstract**

In direct-injection spark-ignition (DISI) engines, the quality of the air-fuel mixture is highly affected by the characteristics of the injected spray, which affects the performance of the engine. The bioethanol fuel properties, as well as the bioethanol blending percentage in gasoline fuel affect the injector nozzle flow and the emerging spray atomisation and spray characteristics. The objective of the present study is to model the full geometry of a typical high-pressure swirl injector employed in DISI engines and carry out computational fluid dynamics (CFD) simulations of the internal injector flow for increasing blending percentage of bioethanol fuel in gasoline fuel. Five test fuels were examined, namely pure gasoline fuel, 10 % by volume of bioethanol blending in gasoline fuel, 20 % by volume of bioethanol blending in gasoline fuel, 50 % by volume of bioethanol blending in gasoline fuel and pure bioethanol, denoted E0, E10, E20, E50 and E100, respectively. The fuels physical properties were determined from literature and the European standard for bioethanol fuels. The Eulerian single-phase modelling methodology was used for the simulation of the internal fuel flow in a gasoline direct injection (GDI) injector with an inwardly opening needle at full open position. A computer aided design (CAD) software was employed for the design of the three-dimensional geometry of the injector and the geometry was used for the setup of the computational domain in the commercial CFD code STAR-CD, which was employed for the investigations. From the injector internal flow simulations of the three test fuels, the nozzle exit velocity was determined along with the emerging liquid sheet thickness at the nozzle exit. From the predicted velocity profiles at the nozzle exit, the emerging spray angle was calculated with an empirical expression adopted from literature. From the injector simulations and comparisons between the test fuels results, discussion is carried out for the connection of the spray injection characteristics at the nozzle exit with the quality of spray atomisation. Recommendations are also provided regarding the engine spray injection strategy for utilising increasing percentages of bioethanol blends in gasoline fuel.

---

### **Introduction**

DISI engines have been developed during the last two decades and are nowadays widely used. The main strategy of the fuel preparation system is to inject the fuel early during the engine induction stroke for high load engine operation, and alternatively and more efficiently to inject the fuel late during the compression stroke in order to achieve a lean stratified air fuel mixture. With recent interest in the utilisation of biofuels which are regulated by the European Union, it is important to understand the effect of bioethanol blends which can fuel DISI engines at various percentages. It is the objective of the present study to investigate the effects of bioethanol blends on the internal flow of gasoline direct injector (GDI) which is employed in DISI engine.

The methodology for modelling and simulations has been employed by [2] and [3] among others. The spray atomisation models and CFD simulation methodology for DISI engines has been widely reviewed by [1]. In the literature, various types of GDI injectors have been investigated and the dominant type is the high-pressure swirl-injector with inwardly opening needle. A typical injector of this type is designed and modelled in the present study. The visualisation of the internal flow of GDI injectors is almost impossible because of the small dimensional scales, thus validation of internal injector flow simulations is not possible. However, flow simulations can provide insightful and useful results.

### **Numerical methods and simulations setup**

In the present section, first the modelling methodology for the simulation of the GDI injector internal flow is described. Then, the modelling approach which was used and was based on the GDI injector internal flow simulations to calculate the characteristics of emerging liquid film from the nozzle exit is described. The computational mesh along with the boundary conditions which were employed for the investigations of the effect of the bioethanol blending percentage on the internal flow field and the liquid film characteristics are presented. Furthermore, three computational meshes with increasing number of cells, which were employed for investigation of the dependence of the simulations on the cell number are illustrated. Finally the details of the properties of the test fuels are provided.

The GDI injector internal flow simulations were carried out with the Eulerian single-phase modelling methodology, which was utilised with the commercial CFD code STAR-CD. For the injector internal flow,

steady state simulations were performed for the full three-dimensional geometry of the GDI injector operating with the needle at fully open position. The  $k$ - $\epsilon$  RNG turbulence model [21] was used for turbulence modelling of the internal injector flow. The differencing scheme MARS was employed and the conjugate gradient algorithm was utilised.

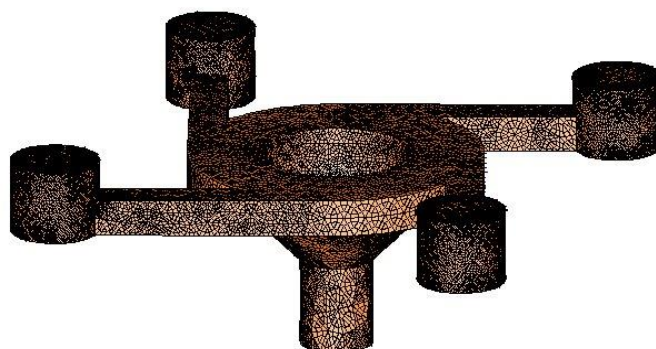


**Figure 1.** Injector mesh (M3) perspective view.

A computer aided design software was employed for the design of the three-dimensional geometry of a typical GDI injector. The geometry was used for the setup of the computational domain in the commercial CFD code STAR-CD utilising the automatic meshing tool of the code. The computational mesh which was created and was employed for the simulation of the different test fuels is shown in Figure 1 and it is denoted as M3. The M3 is an unstructured mesh with tetrahedral cells, which consists of 21321 cells. Figure 1 shows the part of the fluid included in the injector passages. It can be seen that the geometry of the injector is comprised of four tangential slots where cylindrical inlet are at top from where the fuel passes through into the tangential slots. The needle tip is assumed spherical and the fuel cells surrounding the needle can be seen at the void centre of the mesh. The fuel which passes through the tangential slots enters the swirl gallery where a swirling motion is to be established before the fuel will emerge from the injector nozzle. For the geometry shown in Figure 1, the nozzle diameter is that of a typical GDI injector and it is equal to 0.5 mm.

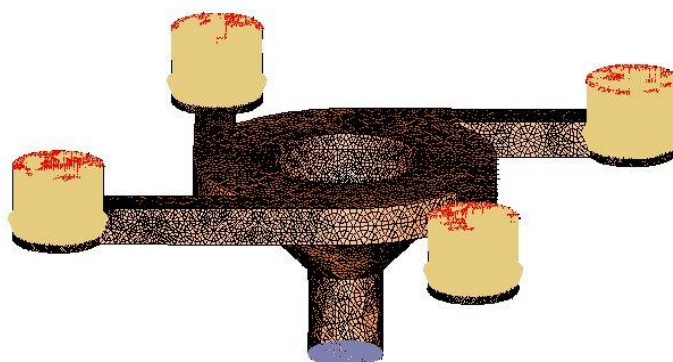


**Figure 2.** Boundary conditions on the injector mesh (M3).

The boundary conditions for the simulations are indicated with colour in Figure 2. At the entrance of the slots the inlet boundary conditions were applied shown in dark yellow velocity vectors. At the exit of the nozzle pressure boundary condition was set, shown in blue colour. The pressure at the pressure boundary was selected to be equal to atmospheric pressure, which is representative of the early spray injection in DISI engine cylinder.

For the purposes of mesh independent solution, a mesh sensitivity study was performed. Three computational meshes were constructed with unstructured mesh consisting of tetrahedral cells. The three computational meshes are illustrated in Figure 3. The first mesh denoted M1, included around 21000 cells. The second mesh denoted M2 was composed of around 54000 cells and the third mesh M1 consisted of around 151000 cells.

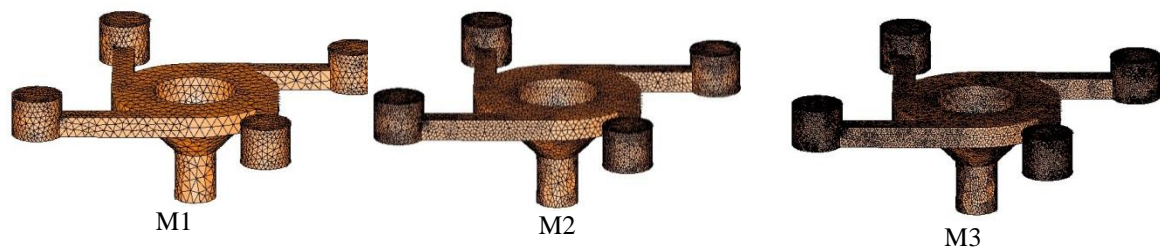


**Figure 3.** Injector mesh for increasing number of cells (M1, M2, M3 and M4).

The same amount of mass of fuel of 15 mg was assumed to be injected for an injection duration of 1.5 ms, corresponding to typical injection characteristics of a GDI injector. The resulting mass flow rate of fuel was 0.01 Kg/s and it was assumed constant. For the test fuels at atmospheric conditions, the fuel density of E0, E10, E20, E50 and E100 were set to 696, 705, 714, 741 and 785 Kg/m<sup>3</sup>, respectively. The molecular viscosity was assumed 0.00215, 0.002376, 0.00324 and 0.0045 Kg/ms for of E0, E10, E20, E50 and E100, respectively.

## Results and discussion

First, the results of the simulations with fuel E0 for the three different computational meshes, M1, M2 and M3 are presented. Then, the comparison between the flow simulations with the test fuels are presented and discussed. Based on the predicted velocity fields for the five test fuels, the spray cone angle is estimated for each fuel. The predicted fuel film at the nozzle exit is to be exiting the injector producing an emerging liquid sheet resulting to the spray full cone angle.

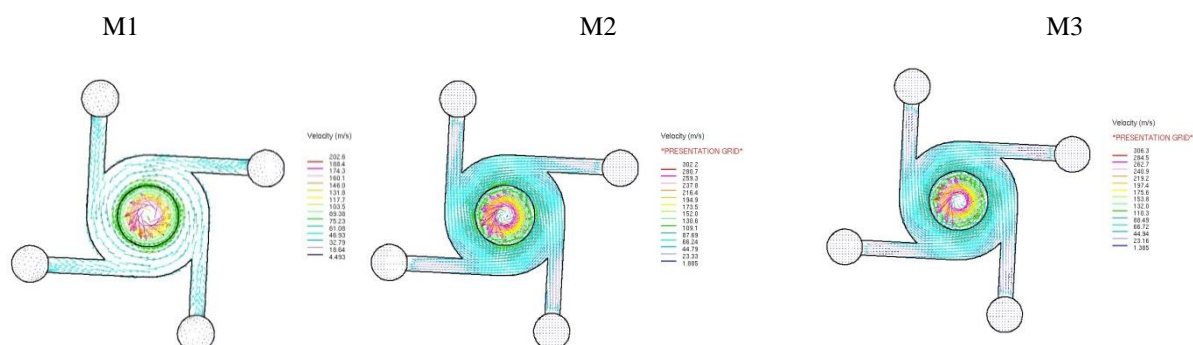


**Figure 4.** Predicted velocity field top view for mesh M1, M2 and M3.

Figure 4 shows the predicted velocity field top view for mesh M1, M2 and M3. It can be seen that the flow pattern is similar and that the velocity magnitude increase by almost 50 % when the number of cells were increased from 21000 of M1 to 54000 cells of M2. However, when the number of cells increased by a factor of 3 from M2 to M3 the changes of the velocity magnitude were negligible, as shown in Figure 4. Thus the finest mesh M3 was selected for the investigations with the test fuels which follow.

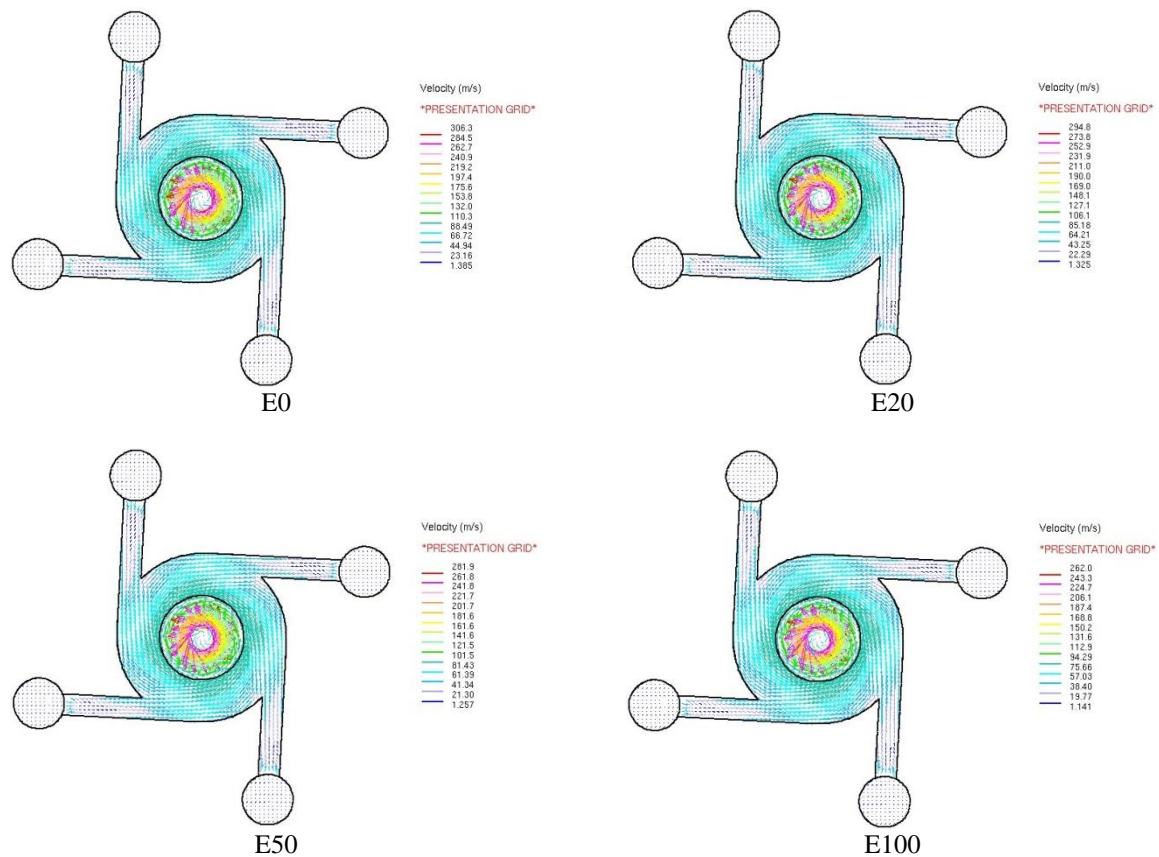


**Figure 5.** Predicted velocity field top view for test fuels E0, E20, E50 and E100

The predicted velocity fields top view for test fuels E0, E20, E50 and E100 are shown in Figure 5. The test fuels result in similar flow patterns where a swirling motion can be observed with low fuel velocity at the central area around the axis of the nozzle. From Figure 5, it can be observed that the maximum fuel velocities are located close to the nozzle edge. Also, the maximum velocity is decreasing from around 300 m/s to 260 m/s when the fuel was pure gasoline E0 and became pure bioethanol E100.

For the test fuels E0, E20, E50 and E100, the field of the axial and radial velocity components shown as velocity vectors at the x-y plane (where x is along the radius of the nozzle and y is from the centre in the upward direction which is the axis of symmetry of the needle) are illustrated in Figure 6. It can be seen that a backflow of the fuel is present and that the maximum velocity is around the axis of the nozzle. For the fuel which flows towards the exit of the nozzle it can be observed that the maximum velocity is close to the nozzle edge. Also two regions of very low velocities are located around the nozzle axis and a recirculation at the middle of the nozzle returns the fuel in the area of the liquid film that is created around the edge of the nozzle. Along the nozzle the observed flow structure, considered as the liquid film does not have a constant thickness. However, the thickness of the film will be seen as smallest at the nozzle exit according to the velocity field. The flow pattern of the test fuels is similar as shown in Figure 6, however the velocity magnitude is decreasing with increasing blending percentage.

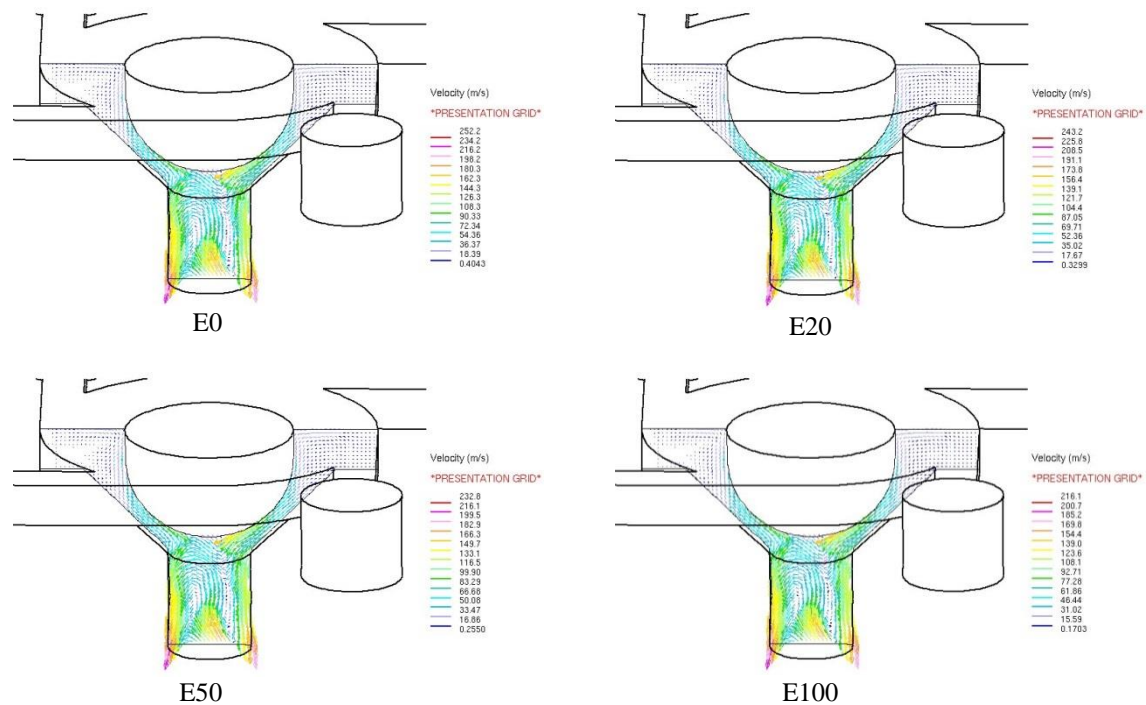


**Figure 6.** Predicted velocity field at the section plane for test fuels E0, E20, E50 and E100

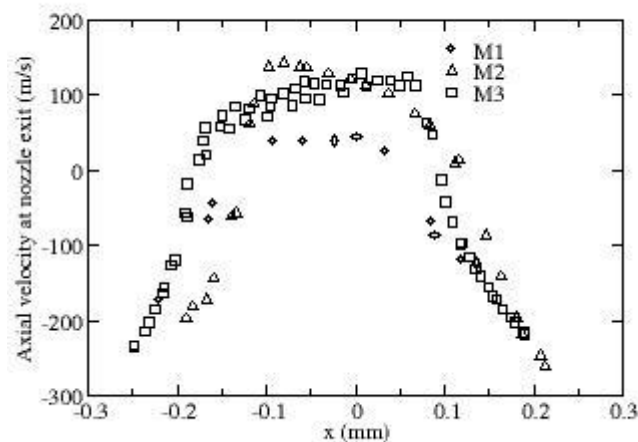


**Figure 7.** Window averaged axial velocity versus radius at nozzle exit, for E0, E10, E20, E50 and E100

Figure 7 includes the axial velocity profiles which were volume averaged at 10 radial rings accounting the cells residing therein at the nozzle exit surface. The fuel film is assumed to be at the negative axial velocity, while the positive axial velocity indicates the backflow of the fuel where an air-core would be created. The maximum axial velocity is close to the nozzle edge, and it can be seen that the differences between E0, E10, E20, E50 and E100 are more obvious close to the nozzle edge. However, the differences between axial velocities at the windows are small and the average axial velocity, as well as the average radial and tangential velocity components were calculated for each test fuel and are presented in Figure 8.

The area where the film is created is annular and it can be defined by the negative velocities observed in Figures 6 and 7. For the cells at the nozzle exit surface the residing in the annular area, the axial tangential and radial velocities were volume averaged and their absolute values are plotted in Figure 8 as function of the bioethanol blending percentage for the test fuels E0, E10, E20, E50 and E100. All the velocity components are decreasing with increasing blending percentage by around 10 to 20 %.

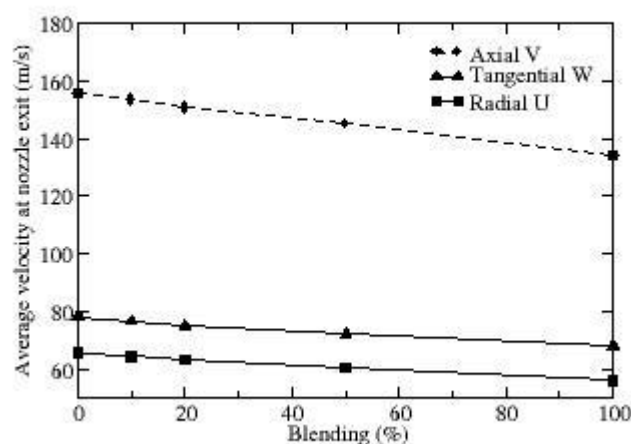


**Figure 8.** Predicted average axial, tangential and radial velocity components of the liquid film at the nozzle exit as function of bioethanol blending percentage (fuels E0, E10, E20, E50 and E100)

The locations at the nozzle exit surface where along the radial direction from the nozzle centre to the nozzle edge the velocity sign changes from negative to positive provide the boundary of the liquid film, which was averaged for each simulation and provided the liquid film thickness. The calculated film thickness is shown in Figure 9, where it can be seen that the film thickness slightly increasing by almost 2 % from E0 to E20 fuel and then linearly decreases by around 5 % from E20 to E100. However, the variations of the liquid film thickness are small and the main observation is that the liquid sheet thickness tends to decrease with increasing blending percentage.

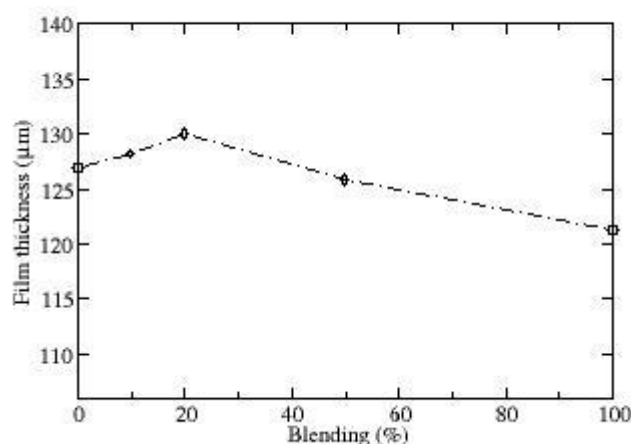


**Figure 9.** Predicted film thickness at the nozzle exit as function of bioethanol blending percentage (fuels E0, E10, E20, E50 and E100)

The average tangential W and axial V velocity components of the liquid film at the nozzle exit, which are plotted in Figure 8, were used for the estimation of the spray cone angle at the nozzle exit. For each of the test fuels E0, E10, E20, E50 and E100, the spray cone angle  $\theta$  is estimated by the equation  $\theta = 0.79 \arctan(W/V)$  from [2]. The estimated spray cone angle is presented in Figure 10, where it can be seen that the differences are very small between 1 to 2 %. However, detailed measurements of the spray cone angle at the nozzle exit are required in order to validate the results.

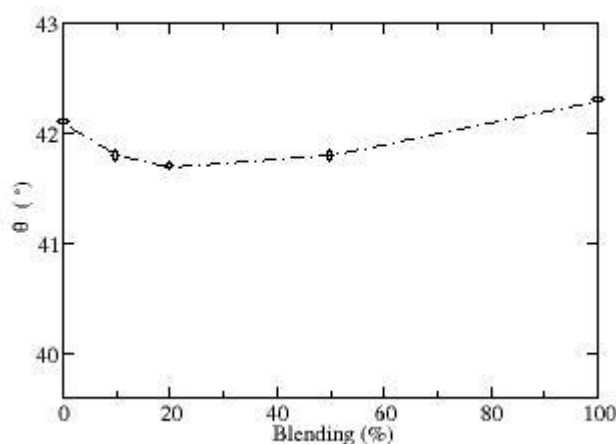


**Figure 10.** Estimated spray cone angle at the nozzle exit as function of bioethanol blending percentage (fuels E0, E10, E20, E50 and E100)

### Summary and conclusions

In the present study, the CFD methodology was used to simulate the internal flow in a typical GDI injector for test fuels at increasing bioethanol blending percentage in gasoline fuel. The Eulerian single phase modelling methodology was used for the simulation of the steady state fuel flow in an inwardly opening GDI injector where the three dimensional geometry was modelled. Three computational meshes with increasing number of cells were examined and the finest mesh was used for the simulations with the E0, E10, E20, E50 and E100 test fuels. It was found that the flow pattern internally in the injector is similar for the tests fuels and that velocity components are decreasing by around 10 – 20 % when the blending percentage is increasing. The fuel film thickness at the nozzle exit was estimated and the variations in the liquid film thickness are small and a trend for decreased film thickness when the blending percentage substantially increased. The spray cone angle was estimated by an empirical expression and it was found that the effects of blending percentage are negligible on the spray angle. However, it remains to examine the spray development with the predicted film characteristics as input into special spray atomisation models

For future work, detailed internal geometry of GDI injectors, the injector needle lift history, experimental measurements of the fuel mass flow rate history and detailed data of gasoline and bioethanol fuel properties should be used. Validation studies should be performed, including comparisons with detailed experimental data of liquid film thickness and spray angle at the nozzle exit. Modelling and simulation transient state internal injector flow should be carried out with other modelling methodologies including the volume of fluid method for transient internal and external two-phase flow simulation of GDI injectors.

### Acknowledgements

The provision of computer facilities by Frederick University is acknowledged.

### References

- [1] Chasos, C.A., *CFD simulation of direct injection gasoline sprays*, PhD in Mechanical Engineering, 2006, Imperial College.
- [2] Ren, W.M. and J.F. Nally, *Computations of Hollow-Cone Sprays from a Pressure-Swirl Injector*. SAE Technical Paper Series, 1998. **982610**.
- [3] Azhar, A.A. and F.A. Mas, *Numerical investigation on the needle-shape of hollow-cone pressure-swirl type gasoline direct injector*. SAE Technical Paper Series, 2006(2006-01-1002).



## Towards More Realistic Fuel Injector Simulations

Padmesh Mandloi, Sourabh Shrivastava, Rohit Kumar

Ansys Inc, India

### Abstract

Fuel injectors display extreme complexity of physics due to their very small size, intricate geometrical details and extremely high operating pressure. CFD simulations are used at design engineering level to analyze several designs and segregate the bad ones from good. More importantly CFD simulations can be used to understand effect of various factors like change in fuel, temperature dependency of fuel properties, backflow conditions and compressibility of liquid and vapor phase on fuel injector performance, especially due to cavitation. The present work attempts at performing more realistic fuel injector simulations by including as many real-life effects as possible.

*Keywords: Fuel Injector, Cavitation, CFD, Multiphase*

---

### Introduction

Fuel injector plays an important role in the overall performance of an IC engine. It affects fuel efficiency, combustion process, pollutant formation, start ability, acceleration and combustion noise of an IC engine. Simulations are now extensively used by designers as well as analysts to understand and improve the performance of fuel injector systems. The most important physics to capture accurately in a fuel injector is cavitation and although the focus has been, over years to develop accurate, fast and robust cavitation models, it is also important to account for all the different factors in a simulation that can affect cavitation.

Many researchers have investigated cavitating flows inside injectors by numerical simulations. Ming [1] investigated through numerical simulations that cavitation inside the conical nozzle significantly influences the conical spray characteristics. He observed that spray velocity loss is increased through the choked cavitation flow, and liquid spray angle and drop size is reduced by cavitation. Hagar [2] numerically evaluated the inception of fuel cavitation inside the actual diesel injector nozzle for a steady state condition and validated with experimental measurements of total vapor mass flow rate. Som [3] compared the propensity of cavitation for different on-fleet diesel fuels with that for n-dodecane through computational investigation. Results indicated that the cavitation characteristics of n-dodecane were significantly different from those of the other three fuels considered. He also investigated the effect of needle movement on cavitation by performing simulations at different needle lift positions. Franzoni [4] also analyzed cavitation and aeration phenomena using different fuel mixtures i.e. ethanol, gasoline and an ethanol/gasoline blend. The analysis of the cavitating regions within the nozzle demonstrated that in case of gasoline wider high vapor fraction areas was formed due to the larger vapor pressure. Michele [5] compared the injection process with different fuels, i.e. standard diesel fuel and pure biodiesel by means of transient simulations from needle opening to closure with different nozzle designs. He concluded that cylindrical orifice with low values of edge rounding and biodiesel result in fully cavitating flow which gives significantly higher mass flow.

There are numerous other CFD studies on cavitation in fuel injectors which consider effects of injector geometry, type of fuel and injection pressure but not much information is available on modeling fuel injector cavitation under more realistic operating situations like temperature dependency of fuel properties, backflow conditions, compressibility of phases etc.

The purpose of this work is to attempt addition of more realistic conditions in fuel injector simulations. The paper also talks about overall improvement in accuracy of CFD simulations by smartly improving mesh resolution in key regions of a fuel injector and by improving numeric.

### Problem Description

In order to show the effect of different realistic factors on cavitation prediction a consistent CFD model is chosen. A twelve hole diesel engine fuel injector model is considered in the current study. Due to geometrical symmetry, only a 1/12<sup>th</sup> section model is used for simulation. Fig. 1 shows the sector model. Simulation cycle consists of plunger motion from minimum lift position to maximum lift position. The plunger profile is shown in Fig. 2. Decane (C<sub>10</sub>H<sub>22</sub>) is assumed as the working fluid with base density as 730 kg/m<sup>3</sup> and dynamic viscosity as 0.0024 kg/m-s.

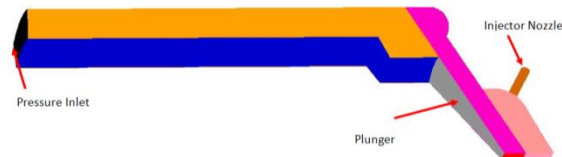


**Figure 1.** Sector model of fuel injector

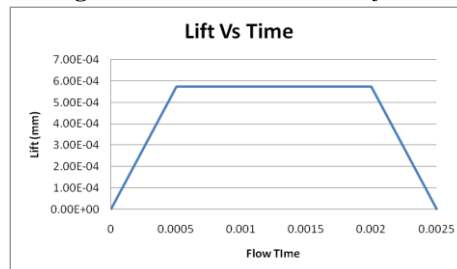


**Figure 2.** Lift profile of the plunger

### CFD Setup

Commercial CFD code ANSYS Fluent is used for the present study. The 1/12<sup>th</sup> model for transient simulation geometry is properly decomposed to accommodate plunger motion. Wall motion in a system is handled using Dynamic Mesh model. This model has three different approaches to perform mesh motion due to boundary movement. These approaches are termed as Smoothing, Layering and Remeshing. Layering and Smoothing takes comparatively lesser computational time than Remeshing. For this reason usually it is justified to put some efforts to decompose a model such that the motion can be handled using Layering or Smoothing approach. Since Layering approach needs structure mesh aligned to boundary motion, given injector model is first decomposed into sections, as shown in Fig 3.

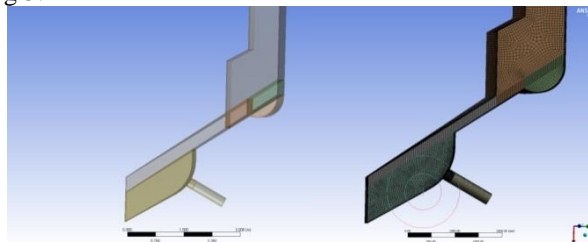


**Figure 3.** Geometry decomposition for transient analysis

### Case Studies

Description of simulations performed to understand factors like mesh resolution, temperature dependence of properties and effect of back pressure on performance of fuel injectors are as follows:-

#### Effect of mesh resolution on fuel injector simulations

To check the effect of mesh resolution on flow behavior of fuel injector three different meshes were created that have one, four and ten layer of cells between plunger and plunger seat, at the minimum lift position of plunger, as shown in Fig.4. (Note: Dynamic mesh models do not allow simulating complete closure of plunger, i.e. surface to surface contact between plunger and plunger seat, and hence it requires at least one layer of cells in this region. Closure and opening of plunger is modeled by making and breaking mesh interface that connects top and bottom portion of fuel injectors). To optimize the overall mesh count of simulation, these different sets of mesh resolutions were simulated using different techniques of dynamic mesh models. Mesh with one layers of cell at minimum gap position was modeled using pure 'Layering' approach because of initial large cell size. Mesh with four layers of cells was modeled using Smoothing-Layering approach, which includes pure smoothing till cell sizes become large enough and then Layering approach was used. With ten layers of cells, full 'Smoothing' approach was used, which made sure that no addition of cell layers takes place on plunger motion from closed to open position. In this approach only elongation and contraction of cells were allowed to perform the plunger motion.

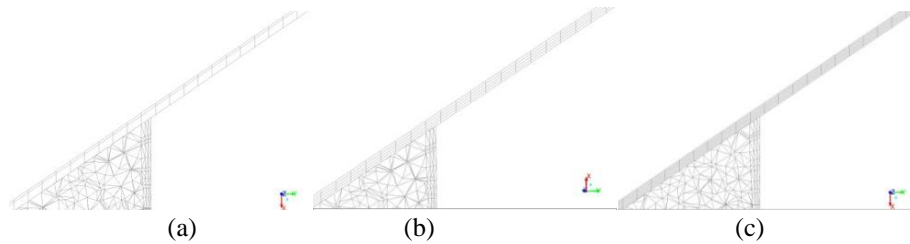


**Figure 4.** Different levels of mesh refinement tested (a) 1-cell layer (b) 4-cell layers (c) 10-cell layers

## Results and Discussions

Fig.5 shows the diesel vapor fraction for (a) Layering (1 layer) (b) Layering-Smoothing (4 layers) and (c) Smoothing (10 layers) approaches at low valve lift. It can be observed that at lower plunger lift, Smoothing & Layering-Smoothing approaches (meshes b and c) predicts lower cavitation in the nozzle section compared to Layering-only approach (mesh a).

At high plunger lifts all the three approaches give similar results. This difference in cavitation behavior can be attributed to the fact that mesh resolution is fine in case of Smoothing & Layering-Smoothing at lower plunger lift compared to Layering-only approach. This refinement in mesh results in different velocity prediction in the thin region near plunger seat as shown in Fig.-6. Fine mesh cases (b) and (c) predicts higher velocity in this gap, which results in lower pressure in the sac region. And hence reduces the pressure drop between sac region and injector outlet for these two cases compare to pure layering case. All this therefore results in lower cavitation in the nozzle section of fine mesh cases compare to coarser mesh (mesh with single layer of cells at closed position) which is modeled using pure Layering approach setup-a.

This study concludes that it is advisable to put fine mesh near the plunger and plunger-seat region, and then use ‘Smoothing’ or ‘Layering-Smoothing’ dynamic mesh approach to perform fuel injector simulations.

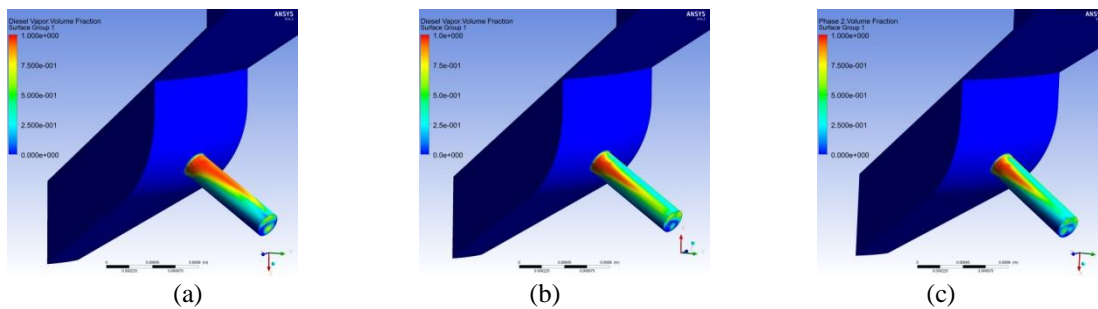


**Figure 5.** Contours of vapor volume fraction for different meshes (a) 1-cell layer (b) 4-cell layers (c) 10-cell layers

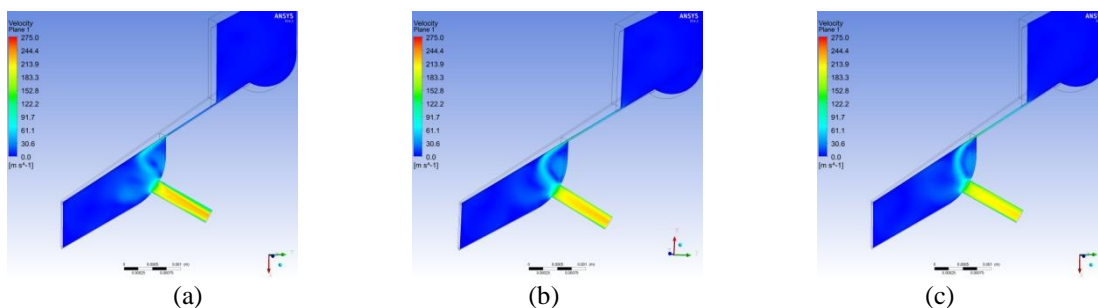


**Figure 6.** Velocity contours for different meshes (a) 1-cell layer (b) 4-cell layers (c) 10-cell layers

## Effect of temperature dependence of fluid properties

Viscous heating is important in fuel injectors due to high velocity and high shear. This can lead to local rise in temperature. Vapor Pressure is strongly dependent upon temperature (as shown in Fig. 7), so it is important to consider the change of vapor pressure with temperature to accurately predict cavitation. But to simplify system complications many times people consider constant properties for fuel in a fuel injector simulation. To understand significance of error that gets introduced due to such assumption, one simulation was performed with temperature dependent vapor pressure to compare the results with baseline case that did not considered temperature dependent vapor pressure. Proper mesh resolution was included in thin regions to capture viscous heating properly.

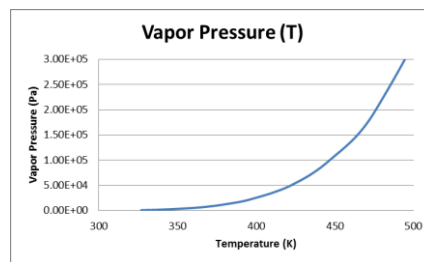


**Figure 7.** Vapor Pressure as a function of Temperature

## Results and Discussions

Fig.-8a and 8b show distribution of diesel vapor for simulations performed with constant vapor pressure and vapor pressure as a function of temperature, respectively for low valve lift position. Similarly, Fig-9 (a) and (b) shows results for high valve lift. Results indicate that cavitation is more for variable vapor pressure case.

This behavior can be described by considering the fact that saturated vapor pressure increase with increase in temperature as shown in Fig. 7. Fig.-10 shows temperature distribution in the domain. It can be seen that there is temperature rise in plunger-seat and nozzle area. The increase in temperature is due to viscous heating, which is prominent at a) lower lifts, in the smallest gap between plunger and seat b) higher lifts, in the nozzle due to high shear. This rise in temperature thus leads to higher cavitation rate for simulation that includes change in vapor pressure as a function of temperature.

This change in results conclude that it is always advisable to include temperature dependent properties to capture cavitation zones accurately.

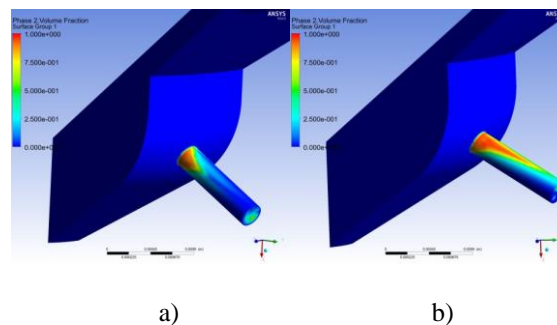


**Figure 8.** Vapor volume fraction for low. lift, (a) constant, (b) temperature dependent vapor pressure

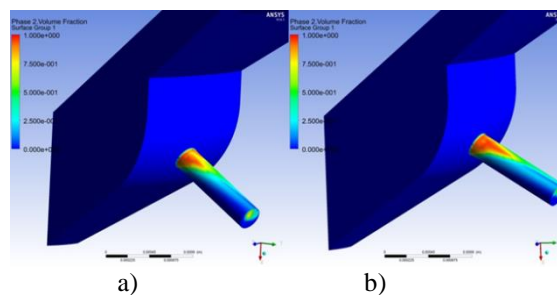


**Figure 9.** Vapor volume fraction for max. lift, (a) constant, (b) temperature dependent vapor pressure

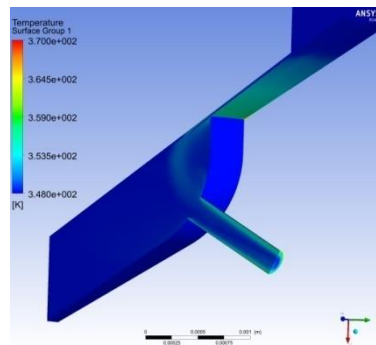


**Figure 10.**Temperature contour, temperature rise due to viscous heating

### Effect of liquid and vapor compressibility

Under high pressure condition within fuel injector system, change in density of liquid and vapor is possible. To understand how significantly this changes the flow behavior, simulation were performed by modeling liquid compressibility using 'Tait equation' and vapor compressibility using 'ideal gas law', and then results were compared with constant density vapor system

### Results and Discussions

Fig.-11 shows diesel vapor volume fraction for i) Considering diesel vapor density as constant and diesel liquid compressible (fig. a and c), ii) Considering diesel vapor density and diesel liquid as compressible (fig. b and d). It is observed that volume covered by vapor is comparatively less for compressible vapor case.

This can be attributed to following factors:-

Even with the same cavitation rate, the case with vapor compressibility will have lesser volume fraction for vapor, because compressibility will allow rise in density in high pressure region and hence smaller volume.

Cavitation in case of compressible vapor is comparatively less. This can be concluded from the fact that when vapor phase is incompressible, liquid has smaller volume to move and therefore it has higher velocity, lower pressure and higher cavitation

This change in distribution of vapor volume fraction concludes that it is always advisable to include compressibility effect of fuel liquid and vapor to calculate proper cavitation regions.

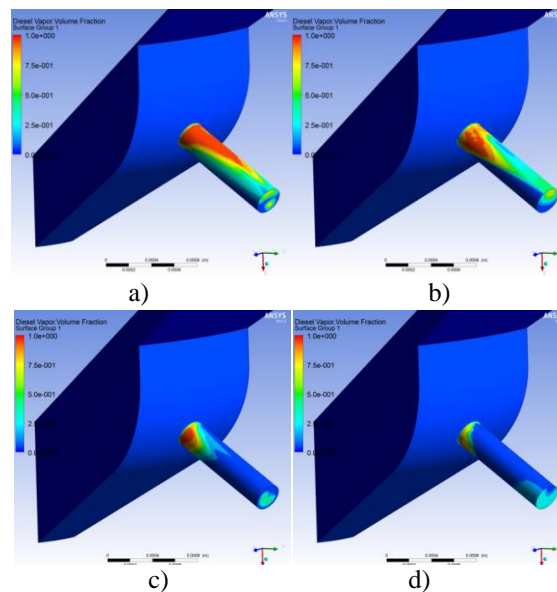


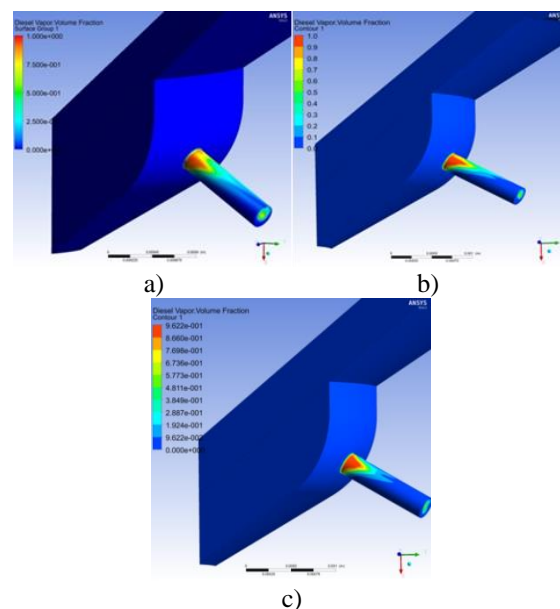
**Figure 11.**Vapor volume fraction for:-incompressible vapor (a & c), compressible vapor (b & d) at low and high lift positions respectively.

## Effect of including back pressure from the combustion chamber

In real operating conditions, outlet of fuel injector is exposed to cylinder chamber. Also there is a possibility of cylinder chamber gases going inside the fuel injector. To understand how significantly these can affect fuel injector flow behavior test runs were made by including these effects and then results were compared with baseline case of constant back pressure condition. Comparisons were done between 2-phase flows (diesel liquid and vapor) with and without variable back pressure and 3-phase flow (fuel liquid, fuel vapor and exhaust-gas) with variable back pressure.

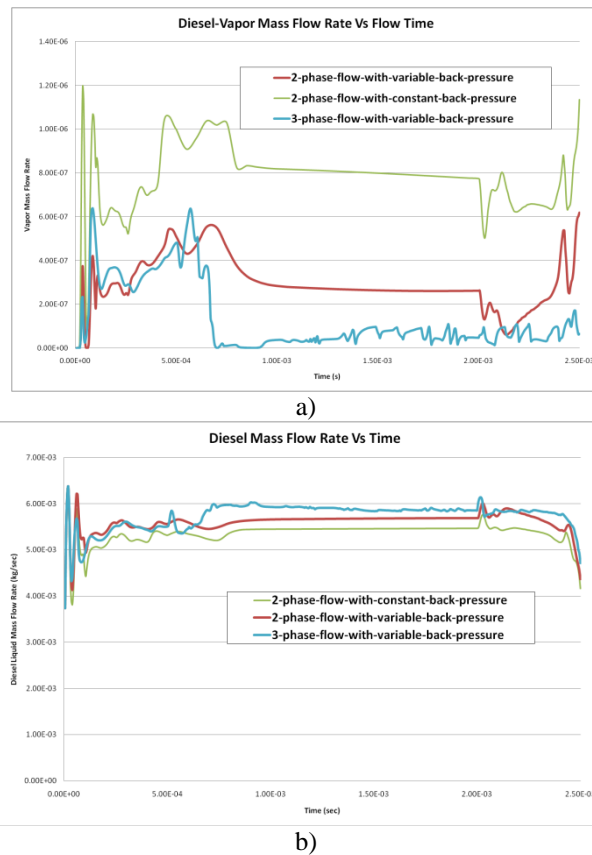
## Results and Discussions

Fig.-12 shows comparison of vapor volume fraction for simulations: - (i) considering constant back pressure (Fig. 12-a), (ii) with variable back pressure (Fig. 12-b), (iii) Considering third phase of exhaust-gas (modeled as air) with variable back pressure (Fig 12-c). As shown in Fig. 13-a, vapor phase mass flow rate is reduced for variable back pressure case. This can be understood from the fact that due to reduced pressure drop across the nozzle for variable back pressure case, it shows lesser cavitation, therefore lesser vapor flow rate. This ultimately leads to overall increase of liquid flow rate in case of variable back pressure as shown in Fig. 13-b.



**Figure 12.** Vapor volume fraction for: - (i) constant back pressure, (ii) variable back pressure, (iii) variable back pressure with air as third phase (to replicate exhaust-gas)

Figure 13-a also shows vapor mass flow rate for simulation with exhaust-gas, which is included in the system as third phase. For this simulation back flow at injector outlet is defined as flow that only consists of air (to model exhaust-gas). Cavitation rate drops further for this case compare to two-phase variable back pressure case. This can be understood by considering the fact that air phase occupies some of the volume which liquid or vapor could otherwise have occupied and hence reduces the cavitation sites. This phenomenon becomes predominant during the maximum lift position.



**Figure 13.** Mass flow rate of diesel vapor and liquid at outlet

## Conclusions

Current study indicates that factors like, mesh refinement in gap region, temperature dependent vapor pressure, vapor compressibility and exhaust-gas back flow, plays an important role in overall prediction of cavitation and hence flow characteristics of fuel injector. For this reason fuel injector simulations should not overlook these factors. It is further recommended to benchmark a CFD simulation process with some standard experimental results before applying it to design improvements process.

## Acknowledgement

Authors would like to thank Dr. Aleksandra Egelja-Maruszewski for providing guidance in optimizing solver settings. Also Authors would like to thank Dr. Saeed Jahangirian of ANSYS Inc. for valuable inputs.

## References

- [1] Jia, M., Hou, D., Li, J., Xie, M., A Micro-Variable Circular Orifice Fuel Injector for HCCI-Conventional Engine Combustion - Part I Numerical Simulation of Cavitation, SAE Technical Paper 2007-01-0249, 2007,
- [2] Bastawissi, H. and Elkelawy, M., Computational Evaluation of Nozzle Flow and Cavitation Characteristics in a Diesel Injector, SAE Int. J. Engines, 5 (4) (2012) 1605-1616
- [3] S. Som, S.K Aggarwal, El-Hannouny, D.E Longman, "Investigation of Nozzle Flow and Cavitation Characteristics in a Diesel Injector", Journal of Engineering for Gas Turbines and Power, 132 (4) (2010)
- [4] Franzoni, F., Milani, M., and Montorsi, L., The Influence of Cavitation and Aeration in a Multi-Fuel Injector, SAE Technical Paper 2008-01-2390, 2008
- [5] Michele Battistoni and Carlo Nazareno Grimaldi, Analysis of Transient Cavitating Flows in Diesel Injectors Using Diesel and Biodiesel Fuels", SAE International Journal of Fuels and Lubricants, 03 (2) (2010) 879-900



## CFD Simulation of a Tapered Swirl Injector Spray in Cross Air-Flow

F.Abdl-Aziz<sup>1</sup>, H. Kayed<sup>1</sup>, M. Hassan<sup>1</sup>, and E. Abo-Serie<sup>2</sup>

1: Mechanical Power Department, Cairo University, Egypt

2: Mechatronics Department, Mevlana University, Turkey

### Abstract

Injecting atomized liquid inside a gas pipe flow and achieving a uniform mixture within a short distance from a surface mounted injector is a challenging problem. The swirl injector with a taper cut nozzle produces a spray with a crescent cross section. It has the advantage of achieving a better spatial distribution and atomization with lower injection pressure compare to the single/multi hole pressure injectors. However to achieve a uniform spatial distribution of liquid-gas mixture within a short distance from the injector, the nozzle cut angle, installation inclination angle and gas and injection velocities has to be optimized. In this study an atomization model has been developed and implemented to carry out a three-dimensional computational fluid dynamics CFD to study the mutual interaction between cold air and the injected spray droplets. The structure of the spray and uniformity of the mixture at different sections from the injector locations have been investigated for various injector installation angles and injector orientation relative to air flow. The final results provide overview on the effect of the above mentioned parameters on achieving a uniform mass distribution.

### Introduction

Swirl injectors have the advantage of producing low penetration and well atomized spray at lower injection pressure compared to pressure type multi-hole injectors. It is therefore suitable in industrial application where liquids have to be injected in a gas that is flowing in a pipe. However, when the injector is installed on the surface of a pipe some droplets impinges on the internal pipe surface leading to liquid film and poor mixing, consequently, droplets uniformity decreases on gas flow pipe. Moreover previous studies showed that swirling spray structure is sensitive to airflow conditions that cause change in its geometry and the microscopic structure; velocity and droplet size distribution [1]. One major factor for this change is the static air pressure inside the spray which has a smaller value compared to the ambient pressure due to the rotational motion of the air inside the liquid spray cone. The temperature of the gas or liquid provides also significant variation in the spray geometry and structure [2]. The liquid is injected by the swirl injector through tangential holes or slots into a conical passage. The tangential velocity component leads to a formation of a thin hollow cylindrical film at the nozzle exit with an air core in the center [3]. The liquid film thickness created inside the nozzle of the swirl injector has been measured using high resolution CCD camera with magnified lenses and using PIV system by many authors [3,4].

Several studies [5, 6] provide guideline to control swirl spray particularly to optimize the combustion of gasoline direct injection. The tilted cut nozzle has been tested to achieve a robust spray that is less sensitive to gas physical properties. Having a large tilt nozzle cut leads to a crescent cross section spray and as a result the pressure difference across the spray envelop becomes very small and accordingly contributing on having a more robust spray. However it leads to a non-uniform spatial mass distribution of the injected liquid and therefore an asymmetrical spray geometry [7].

In this study an atomization model has been developed and implement in Computational Fluid Dynamics software to identify the droplet size distribution for different nozzle cut angles, installation inclination angles injection pressures and gas velocities. The mass distribution from the nozzle has initially been identified using geometrical analysis and using previous published studies. The initial droplet size distribution and velocity have been identified to match experimental Phase Doppler Anemometer data for plane nozzle swirl injector. Further, the Lagrangian-Eulerian spray model has been applied to track the droplets inside the pipe. It is worth mentioning that this study has been performed for cold gas without taking into account droplet evaporation and having high temperature gas can lead to different distribution.

## Mathematical Model

### Gas flow modelling

The governing equations for the gas (air) flowing inside the pipe are given as follow:

Continuity equation:

$$\frac{\partial \alpha_g}{\partial t} + \frac{\partial}{\partial x} (\alpha_g u_i^g) = 0 \quad (1)$$

Momentum equation:

$$\frac{\partial \alpha_g u_i^g}{\partial t} + u_j^g \frac{\partial \alpha_g u_i^g}{\partial x_j} = - \frac{\alpha_g}{\rho_g} \frac{\partial p_g}{\partial x_i} + \frac{\partial}{\partial x_j} [\alpha_g (\nu + \nu_T) (\frac{\partial u_i^g}{\partial x_j} + \frac{\partial u_j^g}{\partial x_i})] + \frac{1}{\alpha_g \rho_g} M_p \quad (2)$$

The standard  $k$ - $\varepsilon$  turbulence is adopted as viscous model to simulate the behavior of turbulence as follow;

Turbulent Kinetic Energy, ( $k$  equation):

$$\frac{\partial (\rho k)}{\partial t} + \nabla \cdot (\rho U k) = \nabla \cdot \left[ \left( \mu + \frac{\mu_t}{\sigma_g} \right) \nabla k \right] + P_k - \rho \varepsilon \quad (3)$$

Turbulence Dissipation Rate Equation, ( $\varepsilon$  equation):

$$\frac{\partial (\rho \varepsilon)}{\partial t} + \nabla \cdot (\rho U \varepsilon) = \nabla \cdot \left[ \left( \mu + \frac{\mu_t}{\sigma_g} \right) \nabla \varepsilon \right] + \frac{\varepsilon}{k} (C_{\varepsilon 1} P_k - C_{\varepsilon 2} \rho \varepsilon) \quad (4)$$

### Particle trajectory modelling

Lagrangian approach is adopted for the disperse phase (spray particles). Trajectory of liquid droplets is tracked using a two-way coupling with the fluid phase. The scheme is performed by integrating the force balance equations for individual particles [8].

$$\frac{dx_p}{dt} = u_p \quad (5)$$

$$m_p \frac{du_p}{dt} = \frac{1}{8} \pi \rho_p d_p^2 C_D (u_g - u_p) |u_g - u_p| \quad (6)$$

The interphase drag term is determined by [9] drag model

$$C_D = \frac{24}{\text{Re}_m} (1 + 0.15 \text{Re}_m^{0.687}) \quad \text{for } \text{Re} < 1000 \quad (7)$$

When the droplets are in the viscous regime, the drag coefficient is identical to the Schiller Naumann correlation [10] and the shape of droplet is assumed to be spherical.  $\text{Re}_m$  is the mixture Reynolds number which is defined as

$$\text{Re}_m = \frac{\rho_m d_p |u_p - u_g|}{\mu_m} \quad (8)$$

In the distorted fluid particle regime, there is increased drag on fluid particles, due to the wake characteristics of turbulent eddies and particle motions. The Drag coefficient becomes:

$$C_d = \frac{4}{3} r_p \sqrt{\frac{g \Delta \rho}{\sigma}} \left\{ \frac{1 + 17.67 [f(\alpha_d)]^{6/7}}{18.67 f(\alpha_d)} \right\}^2 \quad (9)$$

Where

$$f(\alpha_d) = (1 - \alpha_d)^{1/2} \mu_g / \mu_m \quad (10)$$

An additional correction formula is used to determine the dynamic drag coefficient of deformed droplets [11].

$$C_{D, \text{droplet}} = C_d (1 + 2.63y)^{0 < y < 1} \quad (11)$$

where  $y = 1$  when the particle is maximally distorted

## Primary breakup model

The primary breakup was calculated by the Linear Instability Sheet Atomization (LISA) model. This model assumes that a two-dimensional, viscous, incompressible liquid sheet of thickness  $2h$  moving with a relative velocity  $U$  through an in viscid, incompressible gas medium. A spectrum of infinitesimal disturbance of the form

## Numerical Model

The physical domain is a cylinder of 100 mm diameter and 550 mm length. A grid independence test is employed to mesh the grids to 305536 quad and hexa elements, this test was physically based on spray penetration. (see Figure 1), since the difference in penetration depth of models of finer mesh is not significant. The injector is modeled in Fluent as solid cone injector and the injection takes place in a cross direction to the main air flowing inside the pipe. The nozzle consists of 36 solid cone injectors and the net mass flow rate equals to real mass flow rate from 5 MPa swirl injector [3].

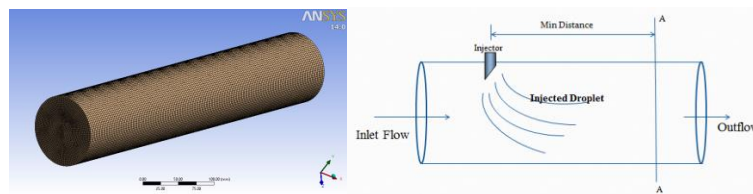


**Figure 1:** Geometry mesh and boundary conditions.

**Table 1:** properties of liquid and gas phase and injection conditions are based on previous research [3]

Properties of spray		Properties of Air	
Density	720 kg/m <sup>3</sup> (Iso-Octane)	Density	1.225 kg/m <sup>3</sup>
Viscosity	0.0135 kg/m.s	Viscosity	1.789e-5 kg/m.s
Surface Tension	0.0212 N/m	Temperature	298.15 K
Injection pressure	5 bar		
Mass Flow Rate	0.00145 kg/s		
Spray Cone Angle	25°		
Nozzle Radius	0.1 mm		
Spread parameter	3.5		

## Results and Discussion

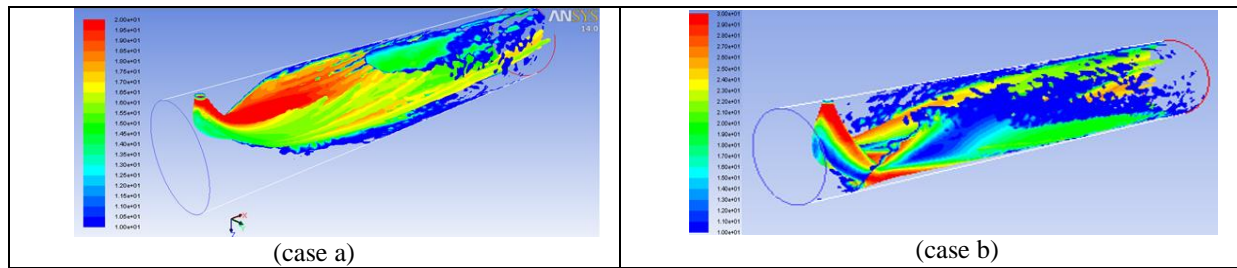
### a) Effect of injector orientation

The effect of directing the taper cut position in two extreme cases has been examined. In the first case, the taper cut is positioned in the opposite direction to air flow while in the second case the taper cut is positioned in the same direction to air flow as illustrated in Figure 2.



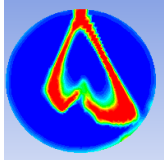
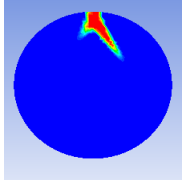
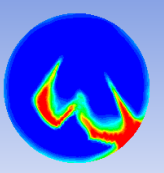
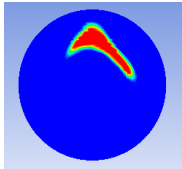
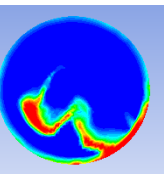
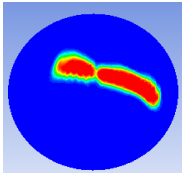
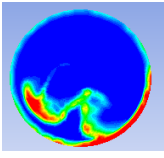
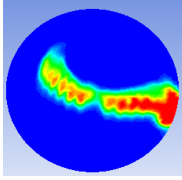
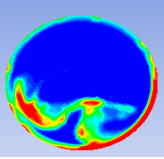
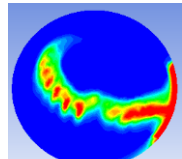
**Figure 2:** the taper injector position relative to air flow; Case (a): Taper cut in opposite direction to air flow, Case (b): Taper cut in same direction to air flow

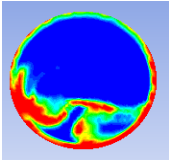
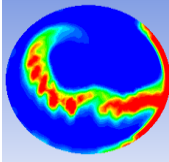
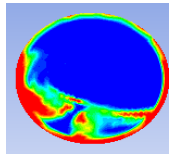
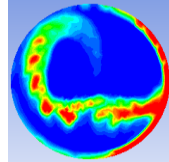
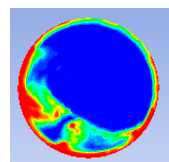
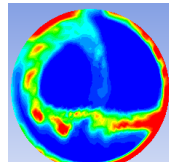
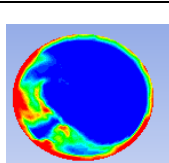
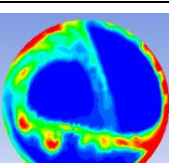
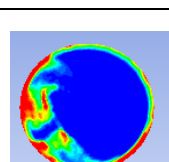
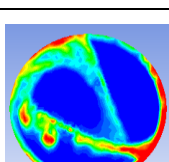
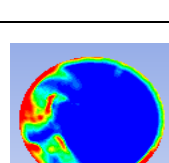
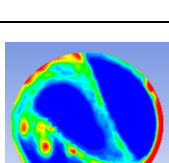
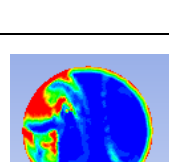
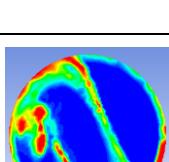
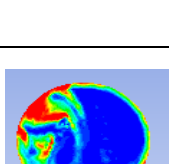
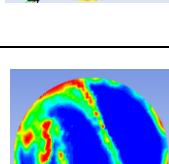
The velocity contours for the two studied cases are depicted in figure 3. It is obvious that in the vicinity of injector, the mixing distribution for case (b) is better than case (a) but this is no longer to last for far distance from injector. At the distant planes, case (a) enhances its mixing distribution and gives better uniformity factor than case (b) as illustrated in table 2.



**Figure 3:** Velocity contours in case of taper cut position in the opposite direction to air flow (case a), and in case of taper cut position in the same direction to air flow (case b)

**Table 2:** Comparison of spray patterns at different pipe sections for cases (a) and case (b) injectors

Distance of cross-sectional plane from injector	Tapper cut position in the same direction of airflow (case b)	Tapper cut position in the opposite direction of airflow (case a)
Distance 0 mm Color Range (1:0) $\text{kg/m}^3$		
Distance 10 mm Color Range (1:0) $\text{kg/m}^3$		
Distance 25 mm Color Range (0.8:0) $\text{kg/m}^3$		
Distance 50 mm Color Range (0.6:0) $\text{kg/m}^3$		
Distance 75 mm Color Range (0.6:0) $\text{kg/m}^3$		

Distance 100 mm Color Range (0.4:0) $\text{kg/m}^3$		
Distance 150 mm Color Range (0.4:0) $\text{kg/m}^3$		
Distance 200 mm Color Range (0.4:0) $\text{kg/m}^3$		
Distance 250 mm Color Range (0.4:0) $\text{kg/m}^3$		
Distance 300 mm Color Range (0.4:0) $\text{kg/m}^3$		
Distance 350 mm Color Range (0.4:0) $\text{kg/m}^3$		
Distance 400 mm Color Range (0.3:0) $\text{kg/m}^3$		
Distance 500 mm Color Range (0.3:0) $\text{kg/m}^3$		

To be able to represent the data more efficiently the mass-weighted uniformity index has been calculated across various sections from the nozzle exit. The uniformity index  $\gamma_a$  is calculated based on the following equation [12]

$$\gamma_a = 1 - \frac{\sum_{i=1}^n \left[ \left( \left| \phi_i - \bar{\phi}_a \right| \right) A_i \right]}{2 \left| \bar{\phi}_a \right| \sum_{i=1}^n A_i}$$

where the value of

Figure 4 summarizes all results illustrated in table 2. It presents the uniformity factor distribution for different types of injector (normal injector, tapered injector in the opposite direction to air flow (a), and tapered injector in the same direction to air flow (b)). It also confirms the fact of increasing the uniformity factor with increasing pipe distance for all injector types due to existence of sufficient time of diffusion. Case (a) gives better uniformity than case (b) for distant sections which is suitable for high distance mixing applications however, case (b) is better than case (a) for low distance mixing applications.

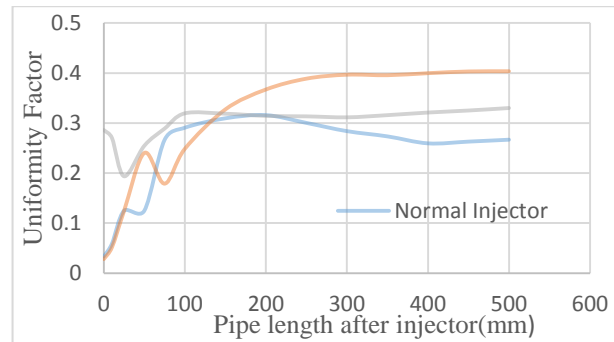


**Figure 4:** comparison between Uniformity factor distribution for normal injector without taper cut, tapered injector in the opposite direction to air flow (a), and tapered injector in the same direction to air flow (b).

#### b) Effect of injector inclination angle

Studying the effect of changing the tilting angle of the injector of case (b) on spray pattern and mass concentration is illustrated in table 3. By tilting the injector in counter clockwise direction as shown in Figure 5, the penetration length decreases. Also the relative velocity between air and droplets increases. This enhances more recirculation in the region after the injector and minimizes the number of droplets reflect from pipe wall. Those factors enhance the spray pattern distribution in the vicinity of injection point. A typical mass distribution of droplets inside the pipe is show in table 3 and the uniformity factor is shown in figure 6.

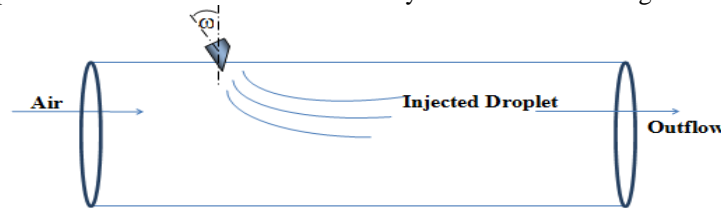
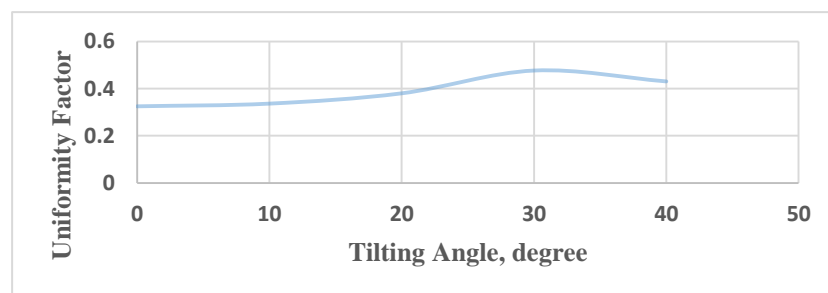
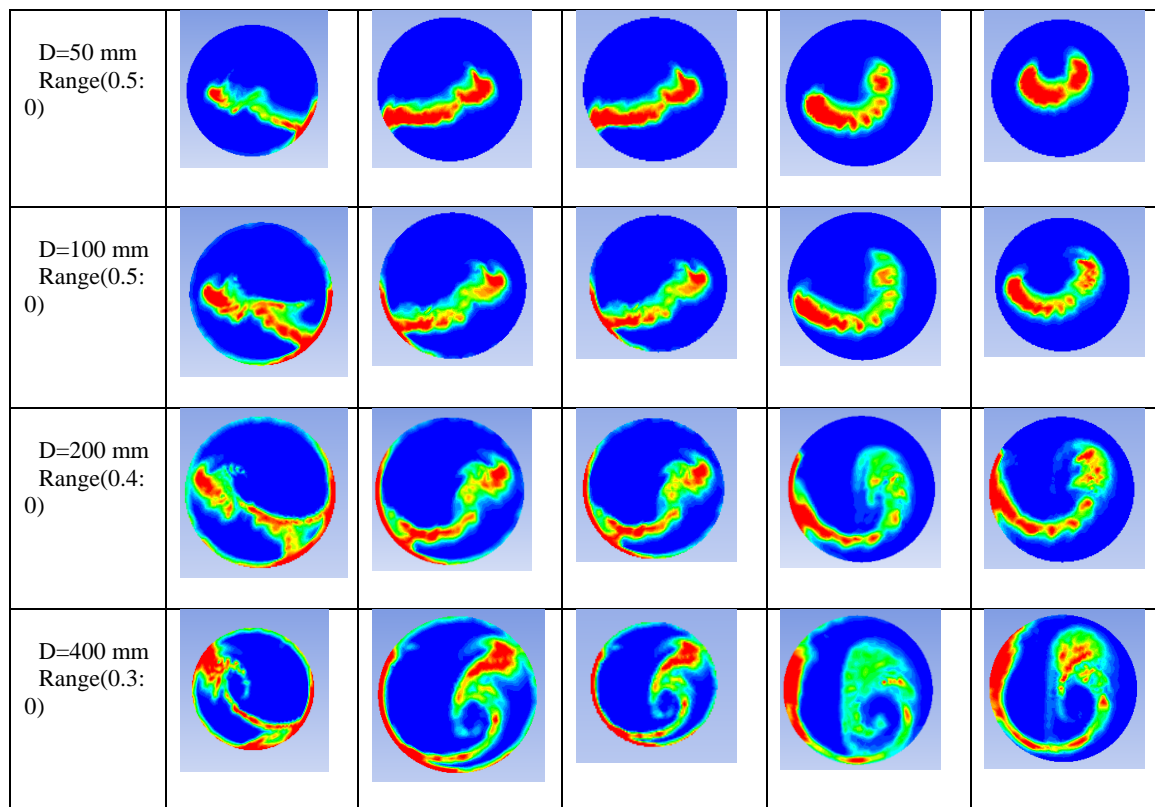


Figure 5: titling the injector of case (b)

Table 3: spray pattern at different pipe sections for different tilting angles of injector of case (b)

(mm) Range	Angle 0	Angle 10	Angle 20	Angle 30	Angle 40
D=0 mm Range(0.5: 0)					



**Figure 6:** Uniformity factor variation with titling the injector of case (b).

### c) Effect of air velocities

Figure 7 shows that the uniformity factors for three different air velocities, 7.5, 15 and 22.5 m/s. The air velocity 15m/s achieve the highest uniformity factor. Decreasing air velocity leads to a decrease in the mixing rate, causing droplets to acquire higher momentum than air, and therefore uniformity factor decreases and more time or longer distance is needed to achieve reasonable distribution. On the other hand increasing air velocity leads to higher air momentum which scavenges relatively smaller droplets away which can lead to lower uniformity factor. There is therefore an optimum air velocity that can achieve best distribution.

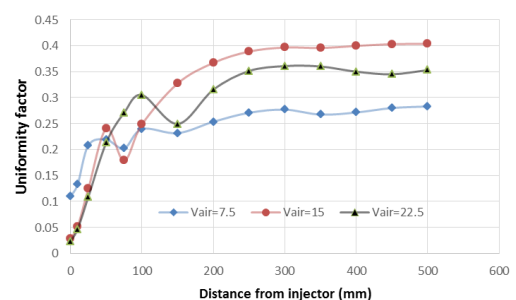


**Figure 7.** Uniformity versus distances for various air flow velocities



The model has been validated using the spray images and the PDA measurements under no air flow conditions of a previous study [13]. A good agreement between CFD model and experiment spray images as shown in Figure 8. Moreover there is a acceptable compliance for the Rosin Rammler distribution at section 40 mm away from the injection point although the experimental data is showing higher volume percentage of larger droplets. The deviation between CFD and experiment is acceptable and can be justified due to modelling assumptions invoked, specifying exact boundary conditions and some experimental imperfectness matters. The taper injector adopted for the CFD model has the same configuration of the experimental injector with a 70 degree taper cut.

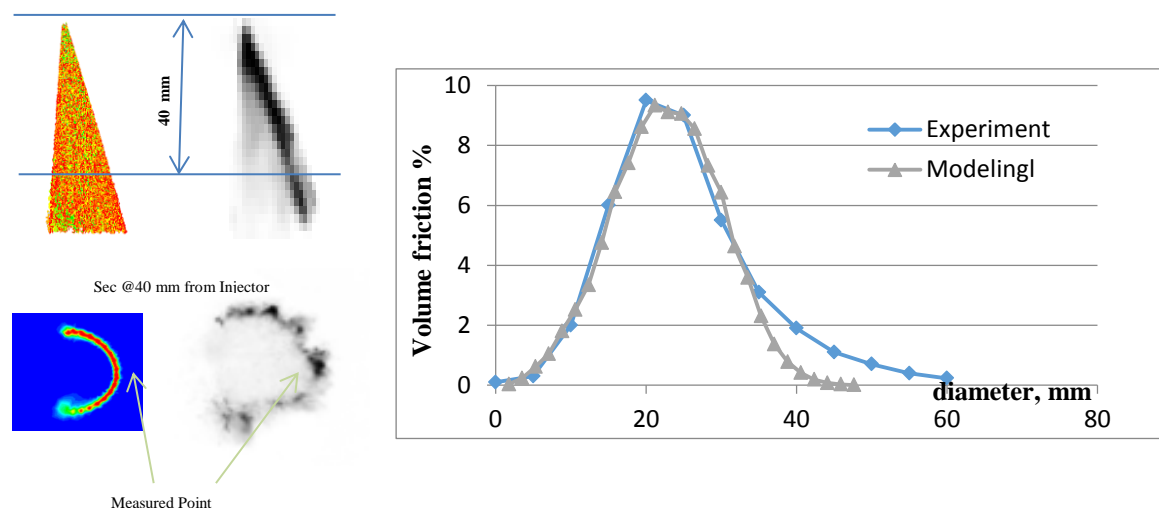


**Figure 8:** Validation of CFD model with spray images and droplet size distribution measurements at a section of 40 mm downstream the injector of a taper cut angle 70°.

## Conclusions

The study provides a CFD analysis for the liquid mass distribution at different sections from the injector locations. The results showed that the distribution defined by a uniformity index can be improved by tilting the injector and orientation of the injector. Although the injecting opposite to gas direction can produce better uniformity however further downstream results showed that injecting in the direction of the flow can have better distribution. The effect of increasing air velocity has shown that the location of smaller droplets depends on the relative momentum of the air and spray. If the spray momentum is getting higher the smaller droplets lose their momentum early and are likely to be located behind the main spray. However, if the airflow momentum is higher than spray momentum the smaller droplets lead the spray. Accordingly, the cross airflow always acts in such a way as to push smaller droplets away from the main spray in the same direction of the airflow pattern. Therefore there is always an optimum value for air velocity to achieve the highest uniformity at a specific section downstream the injector.

## References

1. E. Abo-Serie, C. Arcoumanis, M. Gavaises, Spray characteristics of swirl pressure atomizers for GDI engines: Phase Doppler measurements, ILASS Europe, 11-13 September, Darmstadt, Germany, (2000).
2. S. Moon, J. Choi, E. Abo-Serie, C. Bae, The effect of temperature on spray and combustion characteristics in a single cylinder DISI engine, SAE Paper 2005-01-0101, (2005)
3. M.R. Halder, S.K. Dash, S.K. Som, Initiation of air core in a simplex nozzle and the effects of operating and geometrical parameters on its shape and size, Experimental Thermal and Fluid Science 26, pp 871–878, (2002)
4. Y. C. Khoo, G. K. Hargrave, Real-sized pressure swirl GDI injector investigation with HSFV and FPIV, Journal of Physics: Conference Series 45, pp 77– 84, (2006).
5. A. Miyajima, Y. Okamoto, Y. Kadomukai, S. Togashi, M. Kashiwaya, M., A study on fuel spray pattern control of fuel injector of gasoline direct injection engines. SAE Trans. 109, 1242–1251, (2000).
6. M. Abe, Y. Okamoto, Y. Kadomukai, Fuel spray pattern control using L-step nozzle for swirl-type injector. SAE Trans. 1832, 233–238, (2004)
7. E. Abo-Serie, F. Abdl-Aziz, M. Afify, H. Kayed, Swirl injector nozzle profile for different spatial mass distribution and spray dispersion, 24th ILASS Europe, Estoril, Portugal, September, (2011)

8. H. Hshi, C. Kleinstreuer, Simulation and analysis of high-speed droplet spray dynamics, *Journal of Fluids Engineering*, 129, 621-633, (2007)
9. M. Ishii, N. Zuber Drag coefficient and relative velocity in bubbly, droplet or particulate flow, *AIChE Journal*, 25, 843-855, (1979) .
10. R. Clift, J. R. Grace, M. E. Weber, Bubbles, drops, and particles, New York, Academic Press, (1978).
11. B. Liu, D. Mather, R. D. Reitz, Effects of drop drag and breakup on fuel sprays. SAE Technical Paper, (1993).
12. ANSYS, Inc. Release 14.0, ANSYS FLUENT Theory Guide, South pointe November, (2011)

## Coupled Simulation of Spray Process for Metal Matrix Composite Powder Production

Li, Xinggang<sup>1</sup>, Sander, Sören<sup>2</sup>, Ellendt, Nils<sup>1</sup>, Achelis, Lydia<sup>2</sup>  
and Fritsching, Udo<sup>1,2</sup>

1: Foundation Institute of Materials Science (IWT), Germany

2: Department of Particles and Process Engineering, Bremen University, Germany

### Abstract

Metal matrix composite particles can be produced through spray atomization process. Here ceramic particles are co-injected with atomization gas to be impacted with the liquid metal droplets in flight. Thus, a three-phase spray flow is formed. Euler-Lagrange-Lagrange method is employed to simulate the mixing of metallic droplet spray and ceramic particle jets. The atomization of liquid sheet, droplet breakup and in-flight spray phenomena are considered. The simulation results, such as gas flow field, spray evolution and droplet size distribution, are compared with experimental results. The influence of operation conditions on particle/droplet mixing configurations is analysed. Based on numerical simulations, optimum flow and spray configurations can be derived for maximum generation efficiency of metal matrix composite particles.

### Introduction

Metal matrix composite (MMC) particles can be used in powder processes to generate composite parts or for thermal spraying applications. A viable route for the preparation of MMC particles is based on the mixture of ceramic particulate reinforcements and metallic droplets in spray atomization and co-injection process. In this paper, a two-stage atomization technique named pressure-gas-atomization (PGA) has been employed to fabricate MMC particles. The principle is illustrated in **Fig. 1**. This atomization technique combines pressure-swirl-atomization and gas atomization. In the upper part the molten metal enters a pressure-swirl-nozzle and leaves the nozzle exit as a hollow cone due to the rotation and centrifugal forces. The diameter of nozzle exit is between 1-2 mm. Initially the thickness of the lamella is 200 to 300  $\mu\text{m}$  when the melt leaves the nozzle. With increasing distance from the nozzle the thickness of the lamella declines until break-up starts and results in the formation of droplets of several hundred micrometers in diameter (primary atomization). Those droplets are still fully liquid and then atomized by discrete high velocity gas streams from a ring gas nozzle which surrounds the lamella (secondary atomization). Simultaneously, solid particles, continuously supplied by a particle pump and conveyed by atomization gas, are co-injected and impacted with liquid droplets in the secondary atomization zone (A.Z.). The tiny solid particles can penetrate into the liquid droplets, or adhere on or reflected by the droplet surface. Finally, the atomized metal droplets incorporated with solid particles are frozen, forming metal-matrix-composite (MMC) particles.

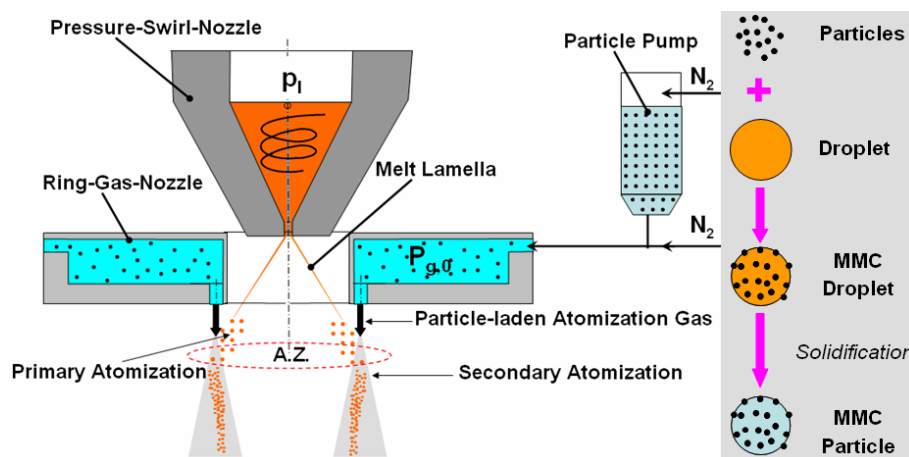


**Figure 1.** Schematic of generation of metal-matrix-composite (MMC) particles in pressure-gas-atomization

The objective of this paper is to develop an integrated model taking into account liquid sheet breakup, droplet breakup and other in-flight spray phenomena in atomization and spray process. With the model, the three-phase flow, comprising atomization gas, ceramic particulate reinforcements and metallic droplets, can be simulated. The model is developed based on Eulerian-Lagrangian approach and implemented in open source CFD code openFOAM.

## Model description

### Eulerian phase

The atomization gas is compressible ( $Ma \sim 1$  at nozzle exit) and turbulent ( $Re \sim 10^5$ ). Thus compressible, viscous gas flow solvers are employed together with Reynolds-averaged Navier-Stokes (RANS) based turbulence models such as standard  $k-\epsilon$  model and  $k-\omega$  SST (shear stress transport) model in the present work. One way coupling is considered between continuous phase and dispersed phase. The calculated gas flow field is applied as background for liquid droplet sprays and solid particle jets.

### Lagrangian phase

In the atomization process the molten metal leaves the pressure-swirl-nozzle exit as a swirling conical sheet which, due to the perturbations on the sheet surface, is subsequently disintegrated into ligaments and large droplets. The primary element may then undergo many physical phenomena during its flight, including secondary breakup, drag, dispersion, heat transfer, solidification and collision. The Lagrangian approach describes the spray by integrating different physical sub-models for different spray phenomena.

#### • Spray formation and initial conditions

The primary breakup of liquid metal sheet was experimentally investigated in Achelis (2009, 2010) and Uhlenwinkel (2010). Two kinds of metals, pure tin (Sn) and its alloy SnCu30, were atomized using pressure-gas-atomization technique. By analyzing the high speed video pictures, the spray characteristics such as liquid sheet breakup length ( $L_b$ ), spray angle ( $\alpha$ ), primary droplet size ( $d_d$ ) and primary droplet velocity ( $u_d$ ) can be quantitatively evaluated. For pure tin, the dominant breakup mechanism is wave disintegration. Ligaments are firstly formed and subsequently disintegrate into droplets. For SnCu30 alloy, the sheet breakup is mainly initiated by perforations. The primary breakup process is greatly influenced by liquid metal mass flow and atomization gas mass flow, with the former determined by the overpressure ( $\Delta P_t$ , the difference between  $P_t$  and the ambient pressure  $P_a$ ) on the liquid in pressure-swirl-nozzle while the latter by the atomization pressure ( $P_{g,0}$ ) in ring-gas-nozzle (see Fig. 1). In this paper metal tin (Sn) is selected. As indicated in Achelis (2010), the breakup length of liquid tin sheet is mainly around 20 mm without gas flow despite an increasing melt mass flow from 120 kg/h to 180 kg/h. With gas flow (gas mass flow above 40 kg/h) the liquid sheet disintegrates immediately after leaving pressure-swirl-nozzle, and after ring-gas-nozzle mainly metallic droplets are observed. The spray angle ( $\alpha$ ) was investigated by varying melt mass flow and gas mass flow in Achelis (2009). In the experiments a ring-gas-nozzle containing 20 circular inlets was employed and the diameter of each inlet is 1.1 mm. The diameter is 1.3 mm at pressure-swirl-nozzle exit. For a constant gas mass flow, with increasing melt mass flow and thereby increasing melt swirling velocity at pressure-swirl-nozzle exit, the spray angle ( $\alpha$ ) increases in a nearly linear trend. For a constant melt mass flow, with increasing GMR (gas to melt mass flow ratio) and thereby increasing gas mass flow, the variation of spray angle ( $\alpha$ ) also exhibits a nearly linear increase. As described in Uhlenwinkel (2010), at melt mass flow  $\sim 180$  kg/h, primary droplet size mainly ranges between 400 and 600  $\mu\text{m}$  without gas flow and between 300 and 400  $\mu\text{m}$  with gas flow; primary droplet velocity is in a range between 7 and 13 m/s but correlates slightly with increasing gas flow. Since the present work is based on the same atomizer and spray tower the experimental data from Achelis (2009, 2010) and Uhlenwinkel (2010) are taken to model primary breakup coupled with the assumption that the droplets created by sheet disintegration follows a root normal distribution (Gjesing, 2009) as:

$$f(d_d) = \frac{x}{2\sqrt{2\pi}\sigma d_d} \exp\left\{-\frac{1}{2}\left[\frac{x-\mu}{\sigma}\right]^2\right\}, \text{ with } x = \sqrt{\frac{d_d}{d_{0.5}}}, \mu = 1, \text{ and } \sigma = 0.25 \quad (1)$$

#### • Secondary atomization

In secondary atomization the aerodynamic force deforms a drop causing it to fragment. This deformation is resisted by the surface tension ( $\sigma$ ) and drop viscosity ( $\mu$ ). Therefore, two important dimensionless parameters, Weber number ( $We$ ) and Ohnesorge number ( $Oh$ ), are defined when describing secondary atomization as:

$$We = \frac{\rho_g U_{rel}^2 d_d}{\sigma} \text{ and } Oh = \frac{\mu_d}{\sqrt{\rho_d d_d \sigma}} \quad (2)$$

The former is the ratio of the disrupting aerodynamic force to the restorative surface tension force and the latter represents the ratio of drop the viscous force to the surface tension force. A larger  $We$  indicates a higher tendency toward fragmentation while a higher  $Oh$  indicates a lower tendency toward fragmentation. Different

flow conditions lead to different breakup modes, and the transitions are functions of initial  $We$  and  $Oh$ . For  $Oh < 0.1$ , the transition  $We$  is essentially constant, whereas  $Oh$  becomes important for  $Oh > 0.1$  (Hiang and Faeth, 1995).

Semi-empirical model developed in Schmehl (2000) and Gjessing (2009) is employed in the present work. The time it takes to deform and disrupt a droplet is described by the characteristic breakup time:

$$t^* = \frac{d_d}{u_{rel}} \sqrt{\frac{\rho_d}{\rho_g}} \quad (3)$$

The initial deformation of the droplet into disc shape is similar for all breakup modes. The duration of this initial phase is estimated as

$$t_{def} / t^* = 1.6 \quad (4)$$

Thereafter, the droplet will fragment depending on the breakup modes. The breakup time  $t_b$  is used to describe the time where no fragmentation occurs. Since  $Oh < 0.1$  for most of metallic droplets in experiments, the following correlation for  $t_b$  is given (Gjessing, 2009):

$$t_b / t^* = \begin{cases} 6, & 3 \leq We < 12 \\ 6(We - 12)^{-0.25}, & 12 \leq We < 18 \\ 2.45(We - 12)^{0.25}, & 18 \leq We < 45 \\ 14.1(We - 12)^{-0.25}, & 45 \leq We < 351 \\ 0.766(We - 12)^{0.25}, & 351 \leq We < 2670 \\ 5.5, & We \geq 2670 \end{cases} \quad (5)$$

And then the total break-up time is

$$t_{total} = t_{def} + t_b \quad (6)$$

When a droplet breaks up it results in a group of new droplets with a certain distribution and mean diameter. For vibrational breakup two equal sized droplets are created. The Sauter mean diameter  $d_{32}$  (SMD) is computed for bag breakup and multimode breakup from the following relation:

$$d_{32} / d_d = 1.5Oh^{0.2}We^{-0.25} \quad (7)$$

where  $d_d$  is the initial droplet diameter. The volume distribution of the droplet fragments is described by a root normal distribution as in **Eq. (1)** but with  $\sigma = 0.238$ . The mass median diameter ( $d_{0.5}$ ) and SMD are related by:

$$d_{0.5} / d_{32} = 1.2 \quad (8)$$

Sheet stripping is characterized by continuous film stripping leaving a larger core droplet at the end of the break-up process. In the computational model, the maximum stable diameter ( $d_s$ ) of this droplet is evaluated by:

$$d_s = 12\sigma / \rho_g u_{rel}^2 \quad (9)$$

The fine fraction of the droplet fragments is distributed according to a root normal distribution based on a reduced SMD  $d_{32,red}$  which is derived from the Sauter mean diameter  $d_{32}$  given by **Eq. (7)** and the maximum stable diameter  $d_s$  by **Eq. (9)**:

$$d_{32,red} = \frac{4d_{32}d_c}{5d_c - d_{32}} \quad (10)$$

Other common droplet breakup models include Taylor Analogy Breakup (TAB) model (O'Rourke and Amsden, 1987) and Wave breakup model (Reitz, 1987). TAB model is based on the droplet deformation dynamics and has a critical deformation as breakup criterion while Wave model is based on the instability growth on droplet surface. It is known that TAB model works better in bag and multimode breakup (usually  $12 < We < 40-100$ ) while Wave model gives good agreement with experimental data in stripping and catastrophic breakup (usually  $We > 80$ ). Since  $We < 50$  is for most of liquid droplets, TAB model and its extension are tested in the present work.

**Taylor Analogy Breakup (TAB) model:** This model treats the oscillation of a distorting droplet with the analogy of a spring-mass system. The restoring force of the spring is represented by the surface tension, while the external force by aerodynamic force. The liquid viscosity represents the damping force. To model droplet breakup, TAB model first determines the amplitude  $A$  for an undamped oscillation for each droplet at time step  $n$  using the following expression:

$$A = \sqrt{\left(y_n - \frac{We}{12}\right)^2 + \left(\frac{dy/dt}{\omega}\right)_n^2} \quad (11)$$

where  $y$  is the normalized droplet distortion parameter and  $\omega$  the droplet oscillation frequency. Breakup is possible only if the following condition is satisfied:

$$We/12 + A > 1 \quad (12)$$

The breakup time  $t_b$  is estimated assuming the droplet oscillation is undamped for its first period and is the smallest root greater than  $t_n$  of the equation:

$$We_g/12 + A \cos(\omega(t - t_n) + \phi) = 1 \quad (13)$$

where

$$\cos \phi = \frac{y_n - We_g/12}{A} \quad \text{and} \quad \sin \phi = -\frac{(dy/dt)_n}{A\omega} \quad (14)$$

The expression of Sauter mean radius ( $r_{32}$ ) of the child droplets after breakup can be derived:

$$r_{32} = \frac{r_{old}}{1 + \frac{4y^2}{3} + \frac{\rho_d r_{old}^3 (dy/dt)^2}{8\sigma}} \quad (15)$$

The diameter of each child droplet is sampled from a root-normal distribution as in semi-empirical model.

**Enhanced Taylor Analogy Breakup (ETAB) model:** ETAB model (Tanner, 1997) is based on the droplet dynamics of TAB model, but the change rate of the droplet diameter is computed from:

$$r_{new} / r_{old} = e^{-K_{br} t} \quad (16)$$

The breakup constant  $K_{br}$  depends on the breakup regime (bag or stripping breakup) according to the Weber number as follows:

$$K_{br} = \begin{cases} k_1 \omega, & We_g \leq We_{trans} \\ k_2 \omega \sqrt{We_g}, & We_g > We_{trans} \end{cases} \quad (17)$$

with  $k_1 = 2/9$ ,  $k_2 = 4/9$  and  $We_{trans} = 80$ .

### • Momentum and drag model

Since the density ratio between the discrete and continuous phases is of the order  $10^3$ , the main forces acting on the particles or droplets are aerodynamic drag and gravity. The momentum equation for a particle or droplet is thus:

$$m_{p/d} \frac{d\vec{u}_{p/d}}{dt} = \frac{\pi d_{p/d}^2}{8} \rho_g C_D (\vec{u} - \vec{u}_{p/d}) |\vec{u} - \vec{u}_{p/d}| + m_{p/d} \vec{g} \quad (18)$$

Since the shape of the ceramic particles is irregular, standard drag model is employed for simplicity. Accordingly, the drag coefficient  $C_D$  is calculated using the standard empirical correlations for a rigid sphere:

$$C_D = \begin{cases} \frac{24}{Re} (1 + \frac{1}{6} Re^{2/3}), & Re \leq 1000 \\ 0.44, & Re > 1000 \end{cases} \quad (19)$$

in which the Reynolds number ( $Re$ ) is in the form:

$$Re = \frac{\rho_g |\vec{u}_g - \vec{u}_{p/d}| d_{p/d}}{\mu_g} \quad (20)$$

For the liquid droplets the distortion parameter  $y$  as defined in TAB model can be used to modify the drag coefficient to account for the drop deformation. This can be done using the relation:

$$C_{D,y} = C_D (1 + 2.63y) \quad (21)$$

proposed by Liu et al. (1993) where  $C_{D,y}$  is the drag coefficient for the deformed drop and  $C_D$  is that of the initially spherical drop.

### • Heat transfer model

A classical Newtonian cooling model is employed in the following form:

$$m_d c_p \frac{dT_d}{dt} = Nu \kappa \pi d_d (T_g - T_d) \quad (22)$$

with  $c_p$  liquid specific heat capacity,  $T$  temperature,  $\kappa$  gas thermal conductivity and  $Nu$  Nusselt number. Nusselt number  $Nu$  is taken from the conventional Ranz-Marshall correlation (Fritsching, 2004):

$$Nu = 2 + 0.6 Re^{1/2} Pr^{1/3} \quad (23)$$

with  $Pr$  representing Prandtl number.

### • Dispersion model

Here a stochastic dispersion model by Sommerfeld (1996) is applied, in which the velocity is perturbed in random direction, with a Gaussian random number distribution with variance of  $\sqrt{2k/3}$ , which characterizes an isotropic turbulence. The interaction time between a particulate and an eddy ( $\tau_I$ ) can be defined as the minimum of the eddy life time ( $\tau_E$ ) and the residence time of the particulate in the eddy ( $\tau_r$ ). The eddy life time is given as:

$$\tau_E = C_E \frac{k}{\varepsilon} \quad (24)$$

where  $C_E$  is a constant (preferred 0.3),  $k$  the turbulence energy and  $\varepsilon$  the dissipation rate. The residence time of a particulate in an eddy is expressed as:

$$\tau_r = \frac{L_e}{|\vec{u} - \vec{u}_{p/d}|}, \text{ with } L_e = \tau_E \sqrt{\frac{2k}{3}} \quad (25)$$



During the interaction time, a fluctuation velocity is selected by the Gaussian random number generator and added to the mean gas velocity. The modified velocity holds until either the eddy has dissipated or the particulate has left the eddy.

### Case Setup

Discrete jet nozzle is employed as gas atomization nozzle, which consists of 20/24 circular inlets in annular configuration with the melt stream in its centre. These circular inlets are straight bored holes with 1.1/3 mm in diameter. As recommended in OpenFOAM, for a single gas jet, the simulation is conducted in a 2D axis-symmetric computational domain (see **Fig. 2(a)**) by creating a wedge shaped block of one cell thickness and a 5° angle at the centre. The axis-symmetric planes are specified as ‘wedge’ type patches. The computational domain is of 200 mm in axial direction and 40 mm in radial direction, and consists of 50 000 cells. For the simulation of the whole atomizer, the circumferential symmetry of the flow field is considered by creating a three-dimensional wedge through the atomizer with ‘cyclic’ boundary condition imposed on front and back sides of the wedge for all variables (see **Fig. 2(b)**). The 3D computational domain contains two inlets and the dimensions are 200 mm in axial direction and 50 mm in radial direction. For a good compromise between accuracy and computational effort, the 3D domain is discretized using 100 000~170 000 cells.

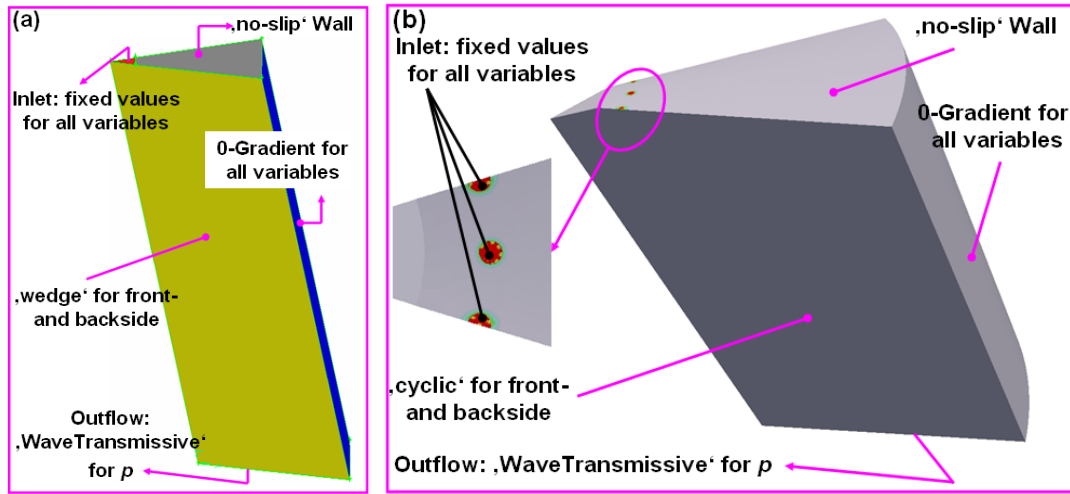


**Figure 2.** Computational domain and boundary conditions: (a) 2D axis-symmetric computational domain; (b) 3D computational domain

The gas flow (nitrogen  $N_2$ ) through conventional straight bored holes or apertures during expansion of gas from an atomizer nozzle is that of under-expanded jets if the pressure ratio is above a critical value:

$$p_{g,0} / p_a > 1.893 \quad (26)$$

where the subscript ‘0’ represents the stagnation conditions in the plenum and the subscript ‘a’ represents the ambient conditions in the spray chamber. Here the pressure value is absolute, and the ambient pressure is 1 bar ( $10^5$  Pa) in spray chamber. In this case the gas exits the nozzle at a Mach number  $Ma = u_e/c_e = 1$  where the subscript ‘e’ denotes the state of gas at the nozzle exit (‘Inlet’ in **Fig. 2(a)** and **Fig. 2(b)**) which is determined by the stagnation conditions in the plenum as follows (Markus, 2006):

$$c_e = 0.913c_0, \quad p_e = 0.528p_{g,0}, \quad \rho_e = 0.634\rho_0, \quad T_e = 0.833T_0 \quad (27)$$

The speed of sound  $c$  in atomization gas is defined as:

$$c = \sqrt{\gamma RT / M} \quad (28)$$

where  $R$  is ideal gas constant ( $R = 8.314 \text{ J} \cdot \text{mol}^{-1} \cdot \text{K}^{-1}$ ) and  $M$  is gas molar mass (for nitrogen  $N_2$ ,  $M = 0.02802 \text{ kg/mol}$ ). The turbulence intensity is set to 5% in the inlets.

A cone nozzle injector (see **Fig. 3**) is employed to mimic the initial hollow cone spray. The information about liquid conical sheet disintegration is incorporated into the injector model. The liquid droplets are injected from the coloured circular ring. The outer radius ( $R_{outer}$ ) is determined by the radius of the pressure-swirl-nozzle exit, the droplet injection position from the origin of the lamella and the spray angle ( $\alpha$ ). Since few ligaments are observed after ring-gas-nozzle in tin (Sn) atomization, the injection position is selected at the same horizontal level as ring gas nozzle. The inner radius ( $R_{inner}$ ) is determined by the difference of the outer radius and the maximum size of primary droplets. The cone outer and inner angles are determined by the spray angle ( $\alpha$ ). The ceramic particles are directly injected together with gas from inlets (see **Fig. 2(b)**). The diameter of the particulates is smaller compared to the grid scale of the computational cell to ensure the validity of Lagrangian approach.

For liquid tin, temperature dependent physical properties, like density, viscosity and surface tension, are used (Sharafat and Ghoniem, 2000).

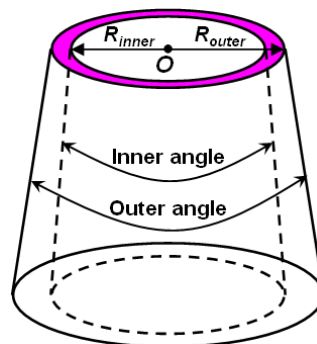


**Figure 3.** Cone nozzle injector for injection of liquid droplets

## Results and Discussion

### Gas flow dynamics

Up to a critical pressure ratio of  $P_{g,0}/P_a = 1.893$ , the pressure in a straight nozzle or simple converging nozzle decreases monotonically until the ambient pressure is achieved. If the pressure ratio exceeds the critical value, the gas pressure at the nozzle exit is above the ambient pressure. The gas exits the nozzle in this case at  $Ma = 1$  and further expansion occurs outside of the nozzle. The remaining pressure potentials in the gas are decomposed by the Prandtl-Meyer expansion waves that start at the edges of the nozzle exit. The expansion waves are reflected from the free-jet boundaries and combine in front of the nozzle to form oblique or straight shocks. The left in **Fig. 4** exhibits the calculated gas flow field from an individual gas jet at atomization pressure  $P_{g,0} = 0.5$  MPa ( $P_{g,0}/P_a = 5$ ). The diameter at the nozzle exit is 3 mm. The simulation is conducted based on the 2D axisymmetric geometry (see **Fig. 2(a)**) and the results are mirrored on the plane through the axis but normal to the radial direction. Five cells with shocks can be found after the nozzle exit. The right in **Fig. 4** exhibits the velocity distribution at the centre line of the jet where experimental data was obtained by laser Doppler anemometry (LDA). A good agreement is achieved between experimental data and numerical simulation results, e.g., in the location and number of shock cells, the calculated length of the supersonic core of the jet and the decay rate of the gas velocity in the subsonic region. Only the amplitudes of the velocity fluctuation differ between experiment and simulation: the peak in velocity values behind the shock is more intense than those measured in experiment. The experimental deviation may be caused by the behaviour of the tracer particles used for LDA measurements. These small but still inertial tracer particles cannot follow the steep velocity gradients across a shock exactly. The  $k-\omega$  SST model indicates a better performance than standard  $k-\epsilon$  model. The left in **Fig. 5** exhibits the calculated gas flow field from discrete jet ring nozzle at atomization pressure  $P_{g,0} = 0.5$  MPa, which consists of 24 inclined straight bored holes with a 3mm diameter at nozzle exit (incline angle  $10^\circ$ ). The simulation is conducted in a 3D computational domain (see **Fig. 2(b)**) and the results are also mirrored on the plane through the axis but normal to the radial direction. The 3D mesh near nozzle exit is not as dense as in 2D mesh and only two shock cells are observed. However, as the right in **Fig. 5** indicates, the calculated gas velocity distribution behind the recirculation region exhibits a good agreement with the experimental data. At  $z=0$  the velocity is positive because the primary gas velocity (0~50 m/s) is considered here. The location of the entrainment differs between experiment and simulation, possibly due to the unresolved complicated nozzle arrangement and the lack of accurate information on primary gas flow in simulation.

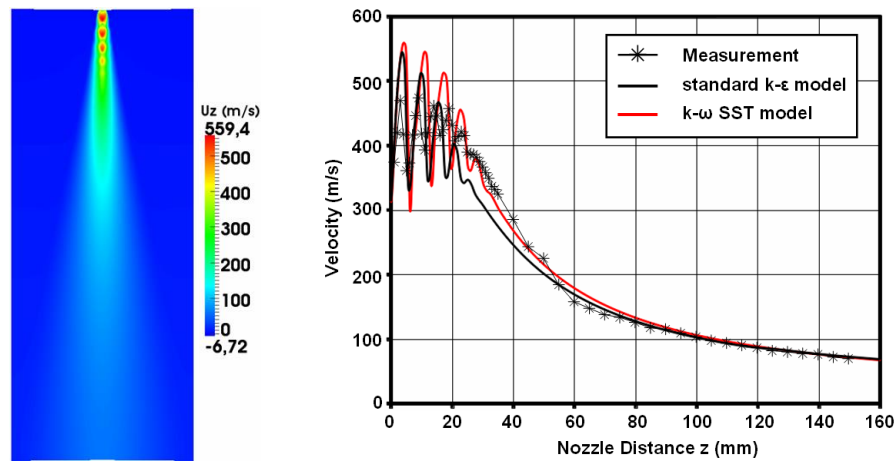


**Figure 4.** Left: Numerical simulation of the flow field near the nozzle for an under-expanded jet (slice),  $P_{g,0} = 0.5$  MPa; Right: Axial velocity component distribution at the centre-line of the jet, comparison between simulation and experiment (Heck, 1998)

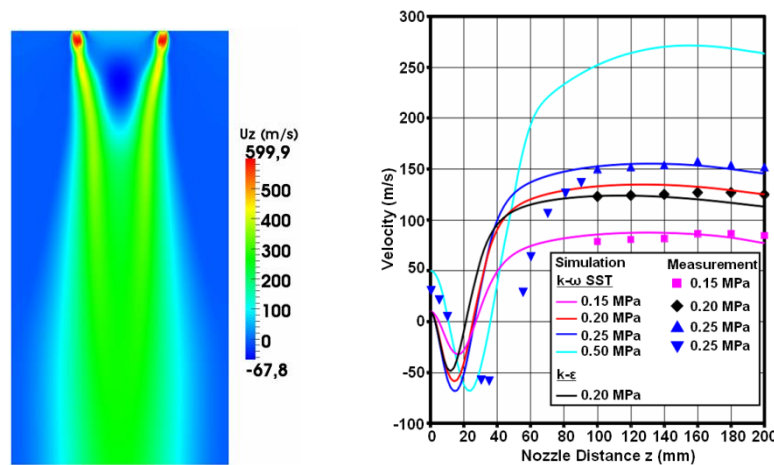


**Figure 5.** Left: Numerical simulation of the flow field near the nozzle for under-expanded jets (slice); Right: Axial velocity component distribution at the centre-line of the atomizer, comparison between simulation and experiment (Uhlenwinkel, 1992)

For the generation of MMC particles, the discrete jet nozzle, composed of 20 circular inlets, is employed. The diameter of each inlet in nozzle exit area is 1.1 mm. **Fig. 6** presents the calculated gas velocity distributions under different atomization pressures ( $P_{g,0}$ ). As shown in **Fig. 6(a)**, an entrainment zone occurs just under the pressure-swirl-atomizer and enclosed by the gas jets from gas atomizer. The gas jets are bended towards the centre-line of the atomizer despite the jets from vertical straight bored holes. **Fig. 6(b)** exhibits the axial gas velocity distributions along the centre axis. The entrainment is limited within 20 mm from the pressure-swirl-atomizer and becomes stronger with increasing gas atomization pressure. The axial velocity on the centre axis achieves the maximum value around  $z = 60$  mm and then decays smoothly. Secondary atomization mainly occurs in the region between  $z = 20$  and  $40$  mm. **Fig. 6(c)** and **Fig. 6(d)** show the radial profiles of the axial velocity component at  $z = 20$  mm and  $z = 40$  mm, respectively. In this region the maximum velocity in the radial direction occurs at 5-10 mm away from the centre axis for different atomization pressures and then the velocity decreases greatly.

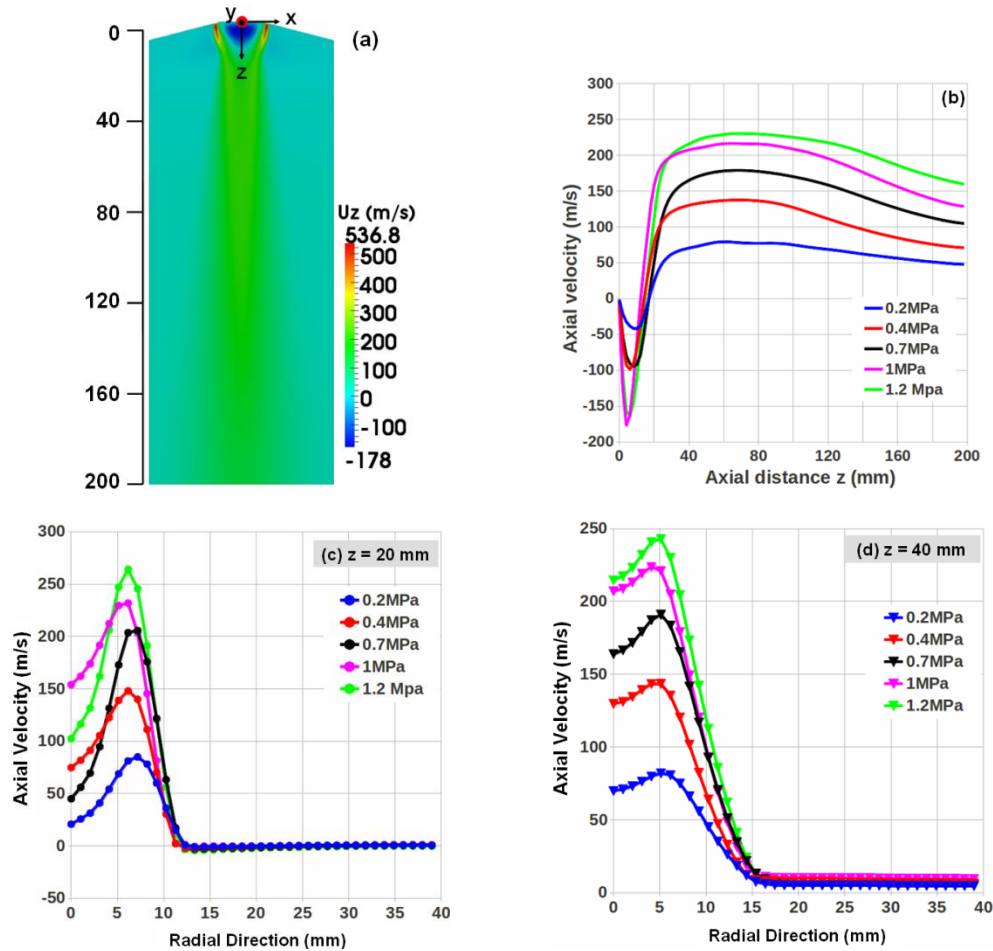


**Figure 6.** Gas velocity: (a) Calculated gas velocity field at atomization pressure  $P_{g,0} = 1$  MPa; (b) Axial velocity component distribution along the centre axis; (c) Axial velocity component distribution in radial direction at  $z = 20$  mm; (d) Axial velocity component distribution in radial direction at  $z = 40$  mm

### Atomization and spray

**Fig. 7** shows the comparison of spray shapes between experiment and simulation. The main features of the spray evolution are captured by all of the three breakup models: at the point where the metallic droplet spray meets the secondary gas flow (see **Fig. 6(a)**), intense droplet breakup occurs, leading to a mass of tiny droplets which follow the main gas stream, and thus the spray is bended towards the atomizer centre-line; the large droplets tend to gather outside the spray due to the large inertia. The primary droplets disintegrate later in semi-empirical model than in another two models, which can be ascribed to the different criteria for determining droplet breakup. In semi-empirical model, the droplet breakup time is determined from empirical correlations which are derived based on the observations of temporal evolution of droplet breakup in experiment; whereas in TAB and ETAB model the breakup occurs when the critical droplet deformation is reached. In TAB and ETAB model the secondary atomization has happened in the entrainment region. In TAB model, the child droplets' diameter follows a root-normal distribution, resulting in a mass of tiny droplets circulating in this region. **Fig. 8** shows the particle size cumulative mass distributions. In simulation the droplets with temperatures below 505K (liquidus temperature) are collected, assuming such droplets don't experience breakup any more. The mass median diameter can be predicted but the models perform differently at different conditions, e.g., for the first case ( $P_{g,0} = 1$  MPa and  $\Delta P_l = 0.8$  MPa), the mass median diameter ( $d_{50,3}$ ) is  $\sim 42$   $\mu\text{m}$  in experiment (Achelis, 2009),  $\sim 27$   $\mu\text{m}$  in semi-empirical simulation,  $\sim 40$   $\mu\text{m}$  in TAB simulation, and  $\sim 33$   $\mu\text{m}$  in ETAB simulation; and for the second case ( $P_{g,0} = 0.4$  MPa and  $P_l = 0.6$  MPa), the mass median diameter ( $d_{50,3}$ ) is  $\sim 97$   $\mu\text{m}$  in experiment (Uhlenwinkel, 2010),  $\sim 101$   $\mu\text{m}$  in semi-empirical simulation,  $\sim 88$   $\mu\text{m}$  in TAB simulation and  $\sim 91$   $\mu\text{m}$  in ETAB simulation. The distribution is not well captured, especially at the extreme regions. Generally speaking, TAB model exhibits a constant performance.

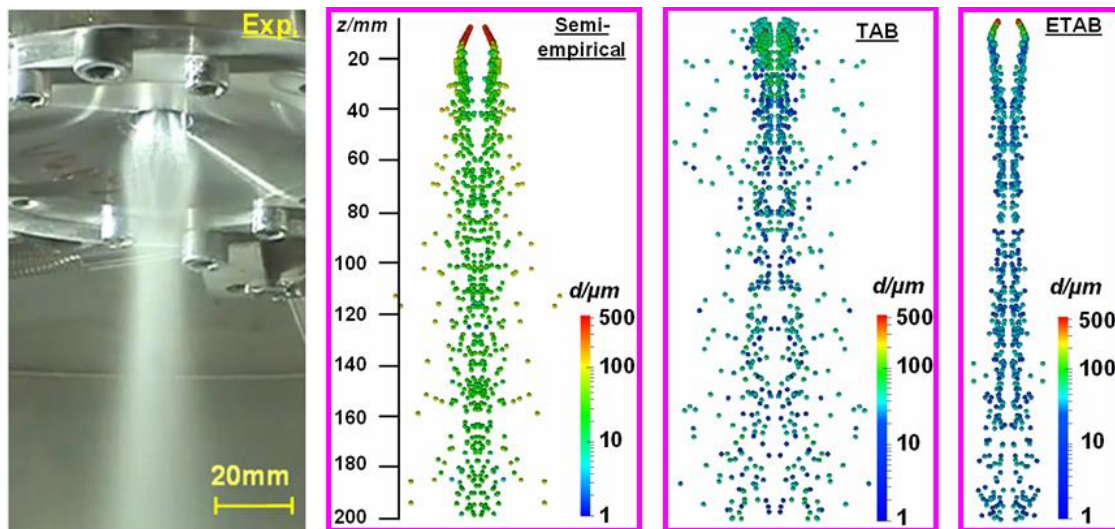


**Figure 7.** Comparison of spray configurations between experiment (Achelis, 2009) and numerical simulations: liquid mass flow 186 kg/h,  $\Delta P_l \sim 0.8$  MPa; gas mass flow 111 kg/h,  $P_{g,0} \sim 1.0$  MPa

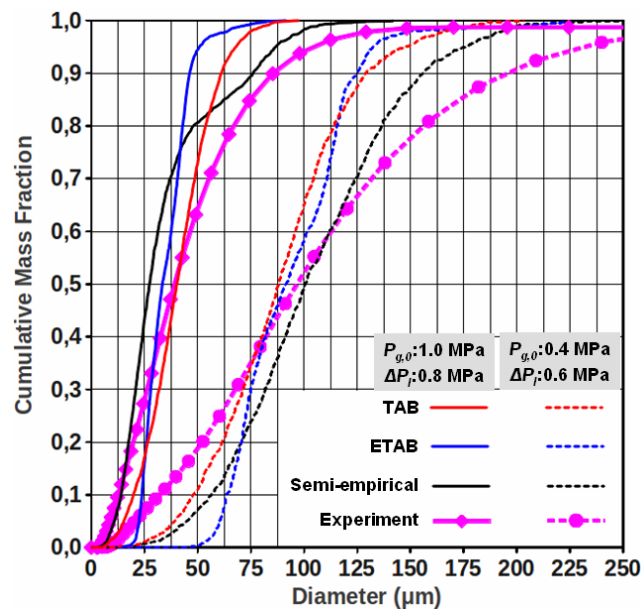


**Figure 8.** Particle size distributions, comparison between experiments (Achelis, 2009; Uhlenwinkel, 2010) and different breakup models

### Mixing of metallic sprays and ceramic particle jets

A fully mixed flow of dispersed phases is preferred in generation of metal matrix composite (MMC) particles, which means more interactions between liquid metallic droplets and ceramic particles. **Fig. 9** presents the mixing configurations of metallic droplet sprays and ceramic particle jets at different gas atomization pressures ( $P_{g,0}$ ) and liquid overpressures ( $\Delta P_l$ ). The ceramic particles (SiC) are injected by atomization gas. For ceramic particles, the mass flow is 6.4 kg/h and the mass median diameter ( $d_{50,3}$ ) is  $\sim 6.1$   $\mu\text{m}$ . The tiny ceramic particles always follow the main gas flow. The mixing of dispersed phases covers two aspects: mixing of primary metallic droplets and ceramic particles, and mixing of secondary metallic droplets and ceramic particles. As shown in **Fig. 9**, the mixing configuration is greatly influenced by the gas atomization pressure. At low atomization pressure (e.g., at  $P_{g,0} = 0.2$  MPa or 0.4 MPa), the primary droplet spray can meet ceramic particle jets at between  $z = 20\sim 40$  mm. However, if the gas flow is not strong enough (e.g., at  $P_{g,0} = 0.2$  MPa), the primary droplets will experience slight or even no secondary breakup, and penetrate the ceramic particle jets due to the large inertia, resulting in no mixing of droplets and particles downstream. At high atomization pressure (e.g., at 1 MPa), the strong entrainment (see **Fig. 6**) can disintegrate the primary droplets in the recirculation



region, resulting in tiny secondary droplets of small inertia which then mix with ceramic particles fully in the main gas flow downstream, but also leads to slight or no mixing of primary droplets with ceramic particles. It seems thus applying moderate gas atomization pressure is a reasonable choice to get a fully mixing of metallic droplets and ceramic particles. However, the following issues should also be considered:

- Small droplet/particle size ratio leads to low particle/droplet impact frequency ( $q$ ) which can be approximated by the following correlation (Li et al., 2011):

$$q = \frac{\pi(d_p + d_d)^2}{4} u_{rel} N_p \quad (29)$$

where  $N_p$  is the local particle number concentration ( $/m^3$ ). For tiny liquid droplets, the impact frequency ( $q$ ) decreases due to the reduction in impact area (the first term in **Eq. (29)**) and the reduced relative velocity.

- Tiny metallic droplet has a high solidification rate, reducing the time for particles to penetrate into droplets. Moreover, for a smaller droplet/particle size ratio, a particle needs more kinetic energy to penetrate into a droplet (Li et al., 2013).

The mixing of primary droplets and ceramic particles in secondary atomization region becomes important since much tinier droplets are generated after secondary atomization. The atomization pressure, which can lead to a full particle/droplet mixing but an optimal droplet/particle size ratio, is necessary for a high incorporation rate of ceramic particles in metallic droplets. Based on the numerical simulations, the recommended gas atomization pressure is between 0.4 MPa and 0.7 MPa for maximum generation efficiency of metal matrix composite particles.

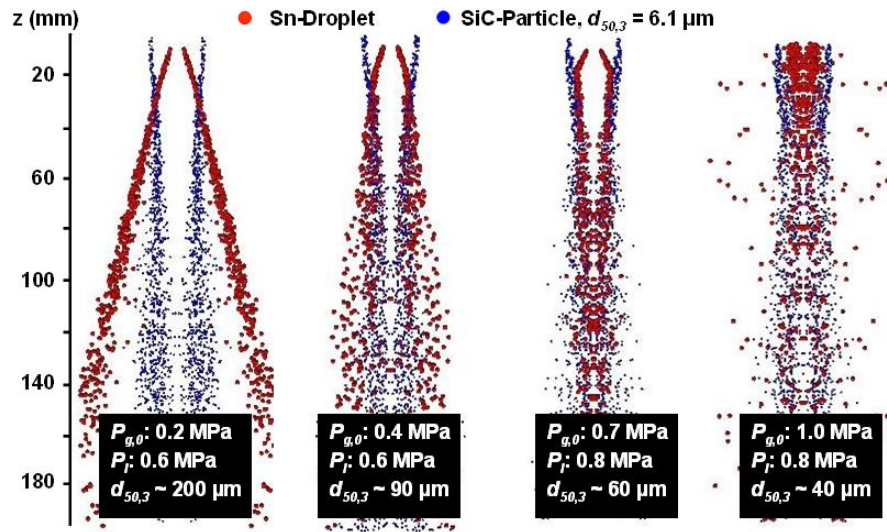


**Figure 9.** Mixing configurations of metallic droplet sprays and ceramic particle jets under different working conditions, droplet mass median diameter ( $d_{50,3}$ ) predicted by TAB model

## Conclusions

An integrated CFD model is developed to simulate the generation of metal-matrix-composite (MMC) particles in spray process. The model is based on Eulerian-Lagrangian approach, which describes the spray by integrating different physical sub-models for different spray phenomena like liquid sheet breakup, droplet breakup and other in-flight spray phenomena in atomization and spray process. The comparison between experimental data and simulation results, e.g., in gas velocity distribution, spray evolution and metal particle size distribution, indicates an acceptable agreement. The secondary atomization gas flow imposes a great influence on the mixing of metallic droplet sprays and ceramic particle jets. By taking into account the full particle/droplet mixing configuration and the optimal droplet/particle size ratio, the gas atomization pressure is suggested between 0.4 MPa and 0.7 MPa for the production of MMC particles based on the present spray atomization system. In the present work, the information on liquid sheet breakup is mainly from experiments, which limits the application of the model in other material systems. In future, interface tracking/capturing methods, like volume of fluid

(VOF) method and level set (LS) method, will be coupled with Eulerian-Lagrangian approach, providing the information on the primary breakup of liquid sheets or jets.

## Acknowledgements

We gratefully acknowledge the support of this project provided by the German Research Foundation (DFG) within the scope of SPP 1423 “Process-Spray” as well as from the China Scholarship Council (CSC).

## References

- [1] Achelis, L., Kombinierte Drall-Druck-Gas-Zerstäubung von Metallschmelzen, Shaker Verlag GmbH, Aachen, Germany (2009).
- [2] Achelis, L., Sulatycki, K., Uhlenwinkel, V., Mädler, L. Lamellenzerfall von Metallschmelzen im Düsenbereich eines Druck-Gas-Zerstäubers zur Erzeugung von Kompositpartikeln, Spray 2010 Proceedings (2010).
- [3] Fritsching, U., Spray Simulation-Modeling and Numerical Simulation of Sprayforming Metals, Cambridge University Press, New York, USA (2004).
- [4] Gjesing, R., Hattel, J., Fritsching U., Coupled Atomization and Spray Modelling in the Spray Forming Process using openFOAM, Engineering Applications of Computational Fluid Mechanics, 3(4), pp. 471-486 (2009).
- [5] Heck, U., Zur Zerstäubung in Freifalldüsen, VDI-Verlag GmbH, Düsseldorf, Germany (1998).
- [6] Hsiang, L.P., Faeth, G.M., Drop Deformation and Breakup due to Shock Wave and Steady Disturbance, Int. J. Multiphase Flow, 21(4), pp. 545-560 (1995).
- [7] Li, X.G., Heisterüber, L., Achelis, L., Uhlenwinkel, V., Fritsching, U., Spray Process Modelling in Metal Matrix Composites Powder Production, Atomization and Sprays 21 (11), pp. 933–948 (2011).
- [8] Li, X.G., Achelis, L., Fritsching, U., Interaction of Solid Particles and Liquid Droplets in Sprays, Proceedings of 8th International Conference on Multiphase Flow, Paper No. ICMF2013-622 (2013).
- [9] Liu, A.B., Mather, D., Reitz, R.D., Modeling the Effects of Drop Drag and Breakup on Fuel Sprays, SAE Paper 930072 (1993).
- [10] Markus, J.S., Zerstäubung von Metallschmelzen beim Sprühkompaktieren, VDI Verlag GmbH, Düsseldorf, Germany (2006).
- [11] O'Rourke, P.J., Amsden, A.A., The TAB Method for Numerical Calculation of Spray Droplet Breakup, SAE International, SAE paper 872089 (1987).
- [12] Reitz, R.D., Modeling Atomization Processes in High-Pressure Vaporizing Sprays, Atomisation and Spray Technology 3, pp. 309-337 (1987).
- [13] Schmehl, R., Maier, G., Wittig, S., CFD Analysis of Fuel Atomization, Secondary Droplet Breakup and Spray Dispersion in the Üremix Duct of a LPP Combuster, Proceedings of 8th International Conference on Liquid Atomization and Spray Systems (2000).
- [14] Sharafat, S., Ghoniem, N., Summary of Thermo-Physical Properties of Sn, and Compounds of Sn-H, Sn-O, Sn-C, Sn-Li, and Sn-Si, and Comparison of Properties of Sn, Sn-Li, Li, and Pb-Li, Apex Study, University of California Los Angeles (2000).
- [15] Sommerfeld, M., Modellierung und numerische Berechnung von partikelbeladenen turbulenten Strömungen mit Hilfe des Euler/Lagrange Verfahrens, Verlag Shaker, Aachen, Germany (1996).
- [16] Tanner, F.X., Liquid Jet Atomization and Droplet Breakup Modeling of Non-Evaporating Diesel Fuel Sprays, SAE International, SAE paper 970050 (1997).
- [17] Uhlenwinkel, V., Zum Ausbreitungsverhalten der Partikeln bei der Sprühkompaktierung von Metallschmelzen, VDI-Verlag GmbH, Düsseldorf, Germany (1992).
- [18] Uhlenwinkel, V., Achelis, L., Sulatycki, K., Mädler, L., New Approach To Generate Composite Particles, PMTEC 2010 Proceedings, Paper No. 2010-01-0039 (2010).



## Numerical computation of ice particle accretion in aircraft engines or on heated surfaces

D. M. Kintea<sup>1</sup>, I. V. Roisman<sup>1,2</sup> and C. Tropea<sup>1,2</sup>

1: Institute for Fluid Mechanics and Aerodynamics,

2: Center of Smart Interfaces, Technische Universität Darmstadt, Germany

### Abstract

A numerical algorithm for the computation of heat and mass fluxes within and over the system boundaries of a porous ice/water layer is presented. Such a porous layer builds up on hot surfaces in aircraft engines or on heated probes and eventually leads to their malfunction. The described thermal solver is capable of accounting for phase transitions between the solid, liquid and gaseous state. Heat fluxes in the substrate on which the ice accretes and in the porous ice/water layer are accounted for. A verification of the developed solver is carried out using three simple test cases for which analytical or experimental data are available. These cases encompass all the physical mechanisms which eventually lead to the ice accretion and shedding. The numerical results show excellent agreement to available data in all of the three test cases.

### Introduction

Icing is a severe problem for aviation as it can significantly affect airworthiness; hence the aerospace industry has a great interest in understanding the physical mechanisms which lead to ice accretion in order to better evaluate potential dangers and especially to support the certification process of new aircrafts. In the past, ice particles have been considered as benign to aircraft icing, because solid particles bounce off the cold airframe and do not accumulate. More recent investigations (1-3) have shown that such ice particles accrete on hotter surfaces with a temperature above the melting point. This is due to a partial melting of the ice crystals, resulting in the formation of a thin liquid film to which the particles adhere (1). Such hot surfaces can be found in the engine or on probes, which are heated in order to prevent icing caused by supercooled droplets or ice particles. The growing porous ice layer on engine parts leads to a loss of power and efficiency and can lead to a shutdown. Also, a thick ice layer is susceptible for shedding of ice fragments, which then pose a danger for the engine in the form of mechanical damage, increased wear or induced combustion instabilities. Heated measuring probes exposed to such icing conditions can also malfunction. Present algorithms for the computation of icing are based on the Messinger model. In this simple model, the ice layer is accounted for as a black box and the icing is assumed to be due to supercooled droplets. Because there are no clearly defined models for crystal accretion, we think this approach should be revisited and improved.

Growth and shedding of the ice layer is determined by the impact behaviour of the crystals and its composition, which strongly depends on the local temperature. The composition influences the collection efficiency of impacting particles, i.e. how much of the impinging mass accretes. Therefore a thermal model is developed which is capable of predicting the temperature within the layer and, as a result, its composition. Setting up a thermal model for the porous ice/water layer is the first step towards a better understanding of ice particle accretion.

### Numerical approach

The temperature in the porous ice/water layer and thus its composition depend on several physical mechanisms taking place within the layer and across its system boundaries. Figure 1 (a) shows a sketch of the layer's system boundaries and the heat and mass fluxes across them. Thermal fluxes are shown as solid arrows, whereas the dashed arrows denote mass fluxes. Also, the processes taking place within the system boundaries are depicted. Each of the mechanisms has to be accounted for in the numerical algorithm in order to represent the layer's thermal behaviour correctly. The temperature is dominated by unsteady heat fluxes, convection, conduction and heat sources due to phase changes. Therefore, the basis for the numerical considerations is given by the energy equation (4), which reads

$$\frac{\partial(\rho c_p T)}{\partial t} + \nabla \cdot (\rho c_p T \vec{u}) = \nabla \cdot (k \nabla T), \quad (1)$$

where  $\rho$  is the density,  $T$  the temperature and  $t$  stands for time. The vector field  $\vec{u}$  represents the fluid's velocity,  $k$  the thermal conductivity of the material and  $c_p$  its heat capacity at constant pressure. The heat which

arises or is absorbed by the phase change is accounted for in the numerical algorithm as a source term, which is only present at an interface where a phase change occurs.

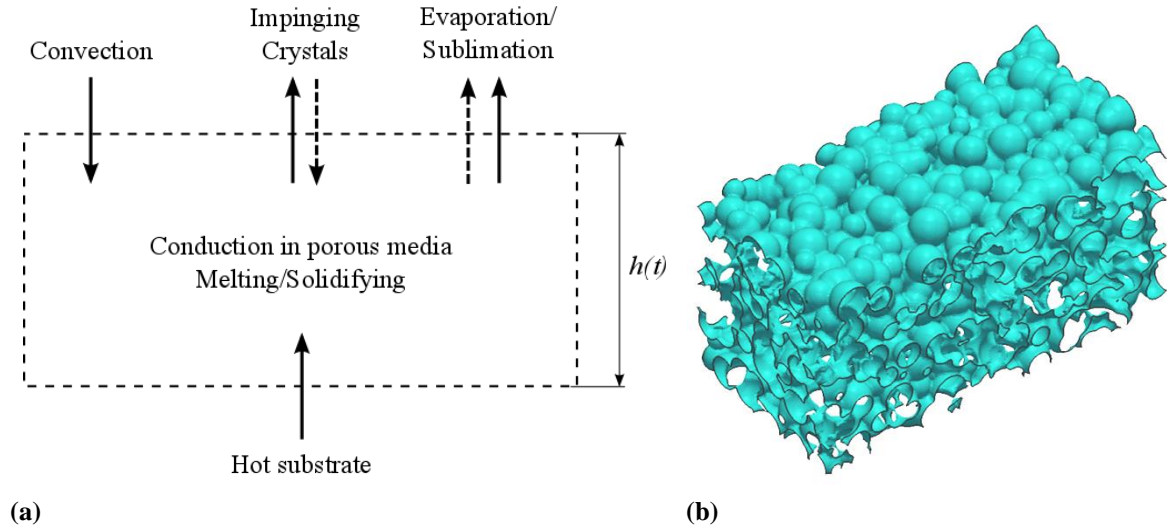


**Figure 1.** Sketch of the system (a); Numerical model of the porous layer (b).

The distribution of the phases is accounted for using a Volume-of-Fluid (VOF) method (5), which is extended to fit our needs and implemented into the open source software OpenFOAM. A colour-function  $\alpha_i$  for each phase  $i$  ( $W$ : Wall/Substrate,  $S$ : Solid water/Ice,  $L$ : Liquid water,  $A$ : Air) is introduced, which takes values between zero and one. The value gives the volume fraction of the considered phase for each cell of the finite volume discretization. Thus, the sum of the four colour-functions is unity at all times. An averaging of the material properties according to these volume fractions  $\alpha_i$  is given by equation 2

$$\beta = \sum_i \alpha_i \beta_i, \quad (2)$$

yielding the averaged field of the arbitrary property  $\beta$ . By means of such averaged property fields it is possible to solve equation 1 for the entire numerical domain. The crystals are assumed to be spherical and to have a random diameter ranging from 5  $\mu\text{m}$  up to 320  $\mu\text{m}$  (6). The particles of the initial layer are allowed to overlap each other and are randomly distributed, resulting in a layer as shown in Figure 1 (b). The small size of the particles results in cavities of minor dimensions between them. Since the Grashof number is a function of those dimensions raised to the power of three, it becomes very small for the cavities inside of the layer. As the natural convection depends directly on that Grashof number, it is neglected in the numerical algorithm. The forced convective heat and mass transfer from the surface of the porous ice/water layer to the airflow is accounted for via similarity theory. As a model case the flow over a flat plate is used, assuming a turbulent boundary layer and the surface area of the flat plate. The resulting heat and mass fluxes are spread evenly over the rough surface of the ice/water layer and accounted for in the energy equation as source terms. This yields an altered partial differential equation:

$$\frac{\partial(\rho c_p T)}{\partial t} - \nabla \cdot (k \nabla T) = \underbrace{\left[ \frac{\partial \alpha_L}{\partial t} \right]_{LS} \rho_L L_{LS}}_{\text{MELTING / SOLIDIFYING}} + \underbrace{\left[ \frac{\partial \alpha_L}{\partial t} \right]_{LG} \rho_L L_{LG}}_{\text{EVAPORATION / CONDENSATION}} + \underbrace{\left[ \frac{\partial \alpha_S}{\partial t} \right]_{SG} \rho_S L_{SG}}_{\text{SUBLIMATION / RE-SUBLIMATION}} + \text{sgn}(|\nabla \alpha_A|) \cdot \dot{q}_C, \quad (3)$$

where the  $\dot{q}_C$  represents the convective heat flux determined by means of the similarity theory. A multiplication of that value with the signum function  $\text{sgn}(|\nabla \alpha_A|)$  ensures, that the convective heat flux is only applied at the interface of the layer to the airflow. The evaporative and sublimative derivatives of the volume fraction with respect to time are also obtained from the similarity to a flat plate.  $L$  represents the latent heat of the phase change combined with an index denoting which phase change is considered. The index  $LS$  denotes a phase

change from liquid to solid or vice versa, *LG* represents the evaporation or condensation and *SG* stands for the solid-gaseous phase transitions. Accounting for the convection this way renders the algorithm highly efficient by avoiding the need for the iterative solution of the velocity and pressure field.

An enthalpy formulation, similar to the ones described in (7-10), is employed to account for the melting and solidifying taking place within the layer. The first step is to compute the temperature field by solving equation 3. In a next step the enthalpy, which is stored in the  $H_2O$ , i.e. in the solid and the liquid water, is calculated according to

$$h_{H_2O} = \underbrace{\alpha_S c_{P,S} T}_{\text{Sensible heat of ice}} + \underbrace{\alpha_L [c_{P,S} T_m + c_{P,L} (T - T_m)]}_{\text{Sensible heat of liquid water}} + \underbrace{\alpha_L L_{LS}}_{\text{Latent heat of water}} \quad (4)$$

In this equation  $T_m$  represents the melting temperature. The enthalpies at which the onset of melting occurs and at which the melting is complete are called  $h_{Low}$  and  $h_{High}$ , respectively. They are defined for each cell as follows:

$$h_{Low} = c_S T_m \gamma, \quad (5)$$

$$h_{High} = [c_S T_m + L_{LS}] \cdot \gamma. \quad (6)$$

The water content  $\gamma$  of the considered cell is the sum of  $\alpha_L$  and  $\alpha_S$ . The amount of solid and liquid water in a cell is then calculated from the following rule:

$$\alpha_S = \begin{cases} \gamma & h_{H_2O} < h_{Low} \\ \frac{h_{H_2O} - h_{Low}}{h_{Low} - h_{High}} \gamma + \gamma & h_{Low} \leq h_{H_2O} \leq h_{High} \\ 0 & h_{H_2O} > h_{High} \end{cases} \quad (7)$$

and accordingly

$$\alpha_L = \gamma - \alpha_S. \quad (8)$$

This results in an altered  $\alpha_S$  and  $\alpha_L$  field which in the next time step of the computation releases or absorbs the latent heat of melting according to equation 3. Another modelled heat and mass transfer are the impinging ice particles. They are in a first step assumed to have a constant temperature and simply attach on top of the layer in a random manner at a given impingement rate.

## Verification

The developed numerical algorithm is verified using three simple cases for which analytical or experimental data is available. The three test cases cover all the mentioned physical mechanisms. Thus, every implemented process is verified by means of these cases. Before comparing the numerical results with analytical solutions or measurements, the applicable theory is briefly depicted.

### Effective Conductivity of porous media

Several theoretical approaches towards the computation of the effective conductivity of porous media are available. Figure 2 shows schematically the three most common models (11). The Composite-Layer-Model (CLM) assumes that the porous medium consists of two layers. Their thickness depends on the volume fraction of each phase, i.e. the porosity. An effective conductivity is calculated analytically for a heat flux perpendicular and parallel to the layer orientation. It must be noted, that the effective conductivity obtained from the parallel CLM poses the maximum possible value for two given materials and a given porosity, while the perpendicular CLM yields the minimum. Thus, the CLM poses the limits within which every solution must lie. The model by Zehner and Schlünder (ZSM) assumes the porous medium to be a packed sphere bed. Two spheres touch each other only in a single point; denoted in Figure 2 (b) as black dots. A sketch of the Area-Contact-Model (ACM) is shown in Figure 2 (c). It also assumes a packed sphere bed, but they touch each other over a contact area depicted as black ellipses. The size of that contact area is an adjustable parameter in this theory.

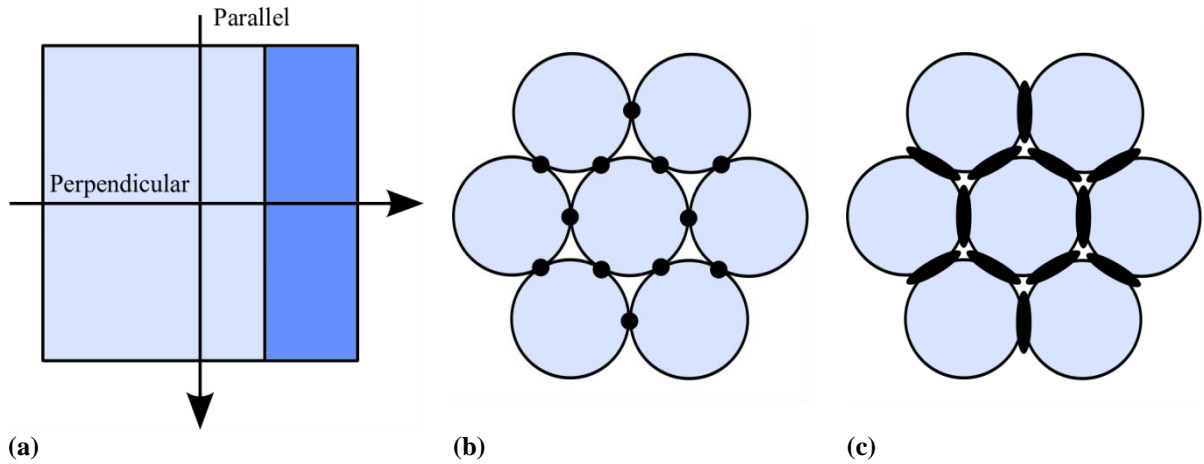


**Figure 2.** Theoretical approaches: (a) Composite-Layer-Model, (b) Zehner and Schlünder approach, (c) Area-Contact-Model.

Figure 3 (a) shows the dimensionless effective conductivity  $k_e/k_L$  over the ratio of the thermal conductivities  $\zeta$ . The diagram applies for a constant porosity  $\epsilon = 0.38$ . Every numerically or analytically computed value should lie within the limits the CLM poses. For  $\zeta < 1$  the numerical solutions exhibit excellent agreement with the ZSM and the ACM. Within this range of  $\zeta$  the conduction in the liquid dominates, thus the two packed sphere models yield nearly the same result. In the range of  $1 < \zeta < 50$  the numerical approximation exhibits good agreement with the Area-Contact-Model, but deviates from the Zehner and Schlünder model. This is because the solid's conductivity and thus the contact area between the spheres prevail. For  $\zeta = 3.97$  (water) the numerical algorithm yields results in good agreement with the ACM and is also in fair agreement with the ZSM as seen in Figure 3 (b). This diagram shows the effective thermal diffusivity over the porosity for water.

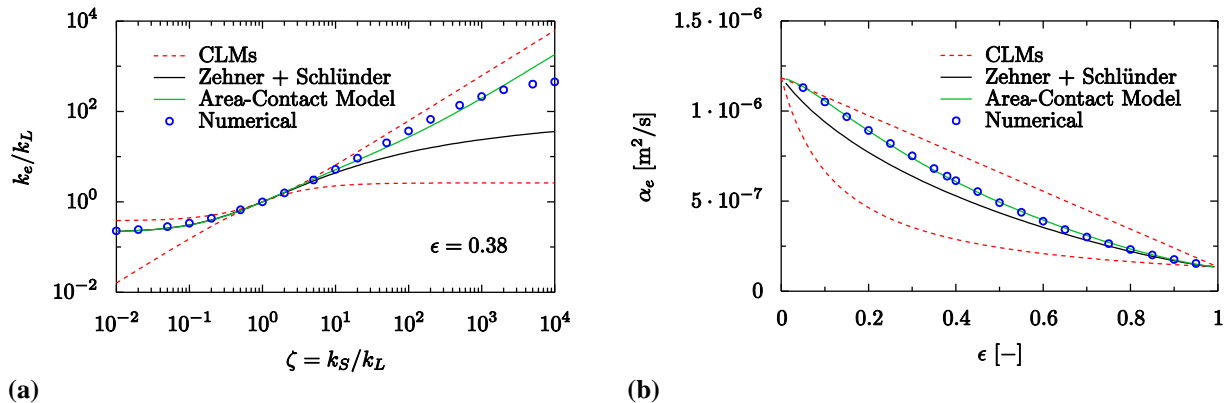


**Figure 3.** Comparison of the numerical results with analytical theories for the effective values for conductivity (a) and diffusivity (b).

The agreement and deviation between the different theories and the numerical results confirms the algorithm's ability to compute heat fluxes in multiple phases correctly and based on plausible physical models. Thus, the computation of heat conduction in porous media and the heat flux through the substrate are verified.

### Planar Solidification (Stefan-Problem)

The Stefan Problem describes a one-dimensional phase change where the interface which separates the two phases poses a moving boundary. Mathematically, it describes the position of the interface and the temperature field arising from the diffusion of the latent heat in the solid and the liquid phase (12). This latent heat is released or absorbed by the phase change taking place at the interface. Figure 4 shows the position of the solidification front over time for a one-dimensional solidification in a semi-infinite slab. At  $t = 0$ , the water has an initial temperature of 273.15 K and the boundary condition at  $x = 0$  is a constant temperature of 250 K. The

diagram shows the analytical solution of the Stefan-Problem and three numerical approximations for different grid resolutions. The solution obtained by means of the developed numerical algorithm converges with increasing grid density towards the analytical solution in a first-order manner. This behaviour confirms the implementation of the phase change using the enthalpy formulation.

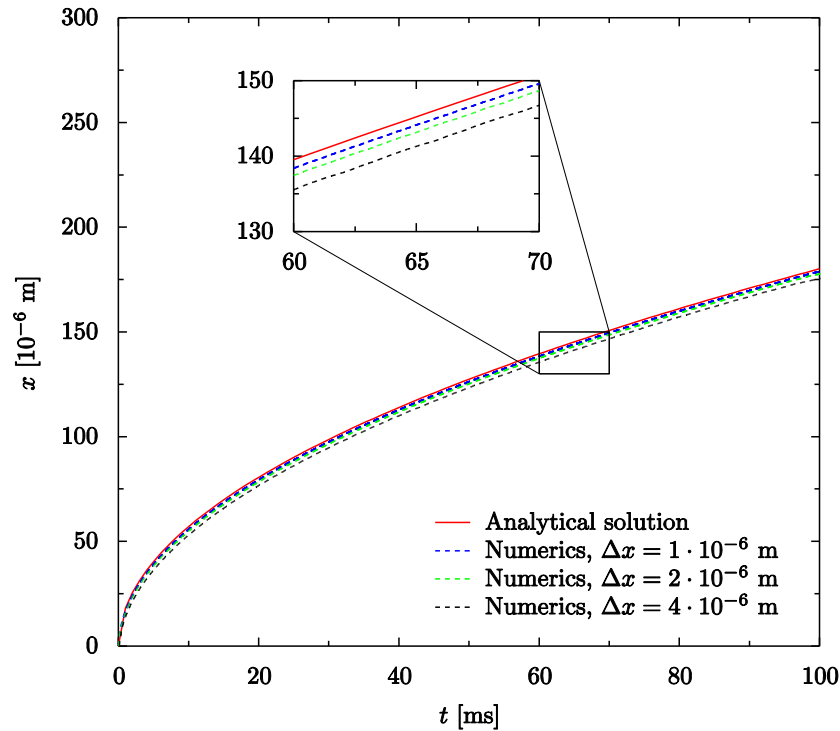


**Figure 4.** One-dimensional Stefan-Problem: Position of the interface over time.

### **Wet-bulb temperature**

If a water surface is exposed to a flow of non-saturated air, convection and evaporation occur. The wet-bulb temperature  $\vartheta_{wb}$  is the temperature which emerges at the surface if equilibrium between convective heat flux and the heat flux due to evaporation is reached and no other thermal fluxes are present. It only depends on the state of the incident flow (13) and can be obtained from the  $h_{1+x}, x$ -Diagram. Figure 5 compares the results obtained from the numerical algorithm with the values given by the diagram for three incident air temperatures  $\vartheta_l$  over the relative humidity  $\phi$ . The numerical values are obtained by exposing a thin liquid layer to a flow of the shown properties, while keeping the rest of the domain adiabatic. The liquid's surface temperature approaches the temperatures shown in Figure 5 as the time advances.

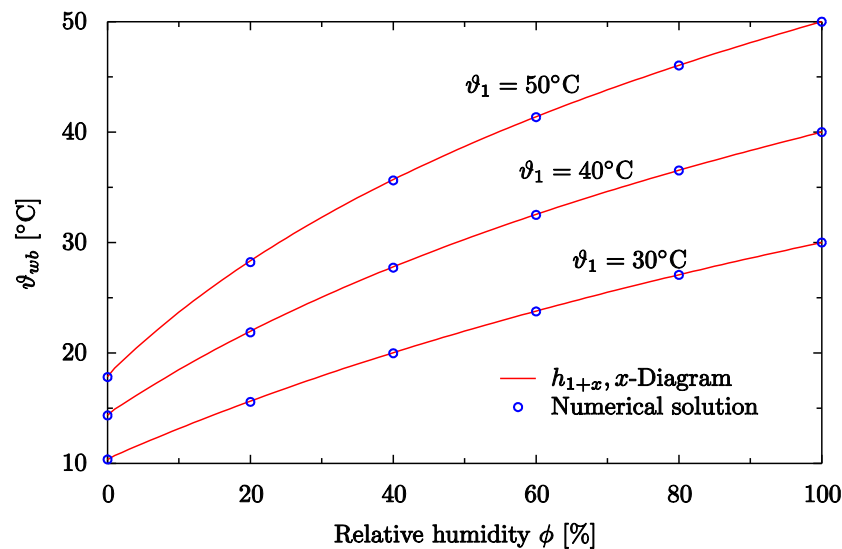


**Figure 5.** Wet-bulb temperature for different temperatures and humidities of the incident flow at an ambient pressure of 1 bar.

The rate of the convective heat flux is verified using a saturated incident flow. No evaporation is possible if the incoming air is saturated before interacting with the surface of the liquid. Therefore the surface adopts in that case the temperature of the incoming flow at a rate consistent with the one obtained by means of the similarity theory. For non-saturated air the evaporative cooling of the surface reduces the wet-bulb temperature. The excellent agreement between the numerical results and the values obtained from the  $h_{1+x}, x$ -Diagram verifies this treatment of the convective heat flux and the evaporation or sublimation of water to the airflow.

## Conclusions and Outlook

A numerical algorithm for the computation of heat and mass transfer in a porous ice/water layer, which accretes on a hot substrate, has been developed and implemented. It has been verified by computing multiphase heat conduction in the substrate and in the porous ice particle accretion. Also, the computation of the phase changes taking place, such as melting, evaporation and sublimation have been verified. Thus, the numerical algorithm is considered to be verified in its ability to account for each relevant physical mechanism, which eventually leads to the accretion of particles. In the future we plan to use this algorithm for the computation of the impact of single solid particles (ice crystals), the accretion of those particles and the shedding of the ice. This allows the prediction of the growth of a porous ice/water layer and the phenomena taking place inside of it and thus improves our understanding of the ice particle accretion on hot surfaces.

## Acknowledgement

The research leading to these results has received funding from the European Union Seventh Framework Programme FP7/2007-2013 under grant agreement n°ACP2-GA-2012-314314 (HAIC – High Altitude Ice Crystals).

## References

- [1] J. G. Mason, J. Walter Strapp, Philip Chow, The Ice Particle Threat to Engines in Flight. *44th AIAA Aerospace Sciences Meeting and Exhibit*. 2006.
- [2] J. G. Mason, Philip Chow, Understanding Ice Crystal Accretion and Shedding Phenomenon in Jet Engines Using a Rig Test. *Journal of Engineering for Gas Turbines and Power* **133**, (2011)10.1115/1.4002020).
- [3] P. M. Struk, Tom Currie, Andy P. Broeren, Jen-Ching Tsao, Mario Vargas, William B. Wright, Danny Knezevici, Dan Fuleki, Fundamental Ice Crystal Accretion Physics Studies. *International Conference on Aircraft and Engine Icing and Ground Deicing*. 2010.
- [4] J. H. Lienhard IV, John H. Lienhard V, *A Heat Transfer Textbook*. (Phlogiston Press, Cambridge, Massachusetts, U.S.A., 2008).
- [5] C. W. Hirt, B. D. Nichols, Volume of Fluid (VOF) Method for the Dynamics of Free Boundaries. *Journal of Computational Physics* **39**, 201-225 (1981).

- [6] G. Vidaurre, John Hallett, Particle Impact and Breakup in Aircraft Measurement. *Journal of Atmospheric and Oceanic Technology* **26**, 972-983 (2009).
- [7] V. R. Voller, C. R. Swaminathan, Fixed grid Techniques for phase change Problems: A Review. *International Journal for Numerical Methods in Engineering* **30**, 875-898 (1990).
- [8] V. R. Voller, Implicit Finite-difference Solutions of the Enthalpy Formulation of Stefan Problems. *IMA Journal of Numerical Analysis* **5**, 201-514 (1985).
- [9] Q. Duan, F. L. Tan, K. C. Leong, A numerical study of solidification of n-hexadecane on the enthalpy formulation. *Journal of Materials Processing Technology*, 249-258 (2002).
- [10] K.-H. Tacke, Discretization of the explicit Enthalpy Method for planar phase change. *International Journal for Numerical Methods in Engineering* **21**, 543-554 (1985).
- [11] D. B. Ingham, Ioan Pop, *Transport phenomena in porous media*. (Elsevier Science Ltd., 1998).
- [12] V. Alexiades, Alan D. Solomon, *Mathematical Modeling of Melting and Freezing Processes*. (Hemisphere Publishing Corporation, 1993).
- [13] E. Schmidt, *Einführung in die Technische Thermodynamik*. (Springer Verlag Berlin/Göttingen/Heidelberg, 1963).



## Numerical Analysis of a Partially Pre-Vaporized Turbulent Spray Flame using LES and FGM

F. L. Sacomano Filho<sup>1</sup>, M. Chrigui<sup>2</sup>, A. Sadiki<sup>1</sup> and J. Janicka<sup>1</sup>

1: Institute for Energy and Power Plant Technology, TU-Darmstadt, Germany

2: National Engineering School of Gabes, University of Gabes, Tunisia

### Abstract

The focus of this paper is to assess the ability of a spray combustion modeling technique based on the Euler-Lagrangian approach to compute droplet evaporation and dispersion close to the reaction zone of a lean partially premixed flame. To achieve this objective the turbulent motion of the carrier phase is computed with the Large Eddy Simulation, where the subgrid scale stresses are closed by means of the dynamic procedure of the Smagorinsky-model proposed by Germano et al. [1], while subgrid scalar flux vectors are closed by means of the eddy diffusivity approach. The Flamelet Generated Manifold tabulated chemistry coupled with the presumed  $\beta$ -PDF is used to model the turbulent combustion. The modeling includes the two-way coupling between the phases. The phase transition of droplets is captured using a non-equilibrium evaporation model. The evaporating droplets are tracked using a Lagrangian procedure. They are injected in a polydisperse manner and generated in time dependent boundary condition mode. Comparisons of numerical simulation results and experimental data in terms of mean droplets diameters, velocities and volumetric flux are presented. An overall good agreement is achieved.

### Introduction

Spray flames are attractive as a combustion process in industrial devices. The interest on this combustion process is related to economical and environmental issues. The fuel in liquid state offers easily storage, transportation and distribution when compared with the found in gas state. The injection of fuel into a combustion chamber increases more control on the fuel distribution in the flow field. For instance, this requirement stands out in the development of direct injection engines with stratified charge. Furthermore, the evaporative cooling, a consequence of fuel evaporation into the chamber, contributes to the reduction of NO<sub>x</sub> emissions, which contributes the attendance of the emission requirements of many commercial applications. All of these economical and environmental questions are strongly connected with the main issues in the modelling of spray flames, which are: atomization, droplets inter-particle interactions (breakup, collision and coalescence), dispersion, turbulence modification, evaporation and multiphase combustion. These phenomena are strongly interacting and develop in an unsteady way, which illustrate the high complexity inherent to this kind of reactive flow. A correct understanding of these interactions and all the other underneath phenomena is prerequisite for accurate simulations of combustion processes, that in turn, are essential procedures to support design of practical application devices.

Modeling issues of Large Eddy Simulation (LES) in two-phase flows have been addressed by Bellan et al. [2]. Rutland [3] and James et al. [4] focused especially on LES in IC-engines and aircraft combustion chambers, respectively. Since for engineering applications it is not realistic to solve transport equations for all species occurring in the chemical reaction process, reduction techniques are often employed. One trend is formed by the flamelet based tabulated chemistry along with the Flamelet Generated Manifold (FGM) (see e.g., Van Oijen and De Goey [5] and Vreman et al. [6]) or the Flamelet extended ILDM (Fiorina et al. [7], Franzeli et al., [8]). Though a considerable work has been carried out, except the contribution by Chrigui et al. [9], to our knowledge, applications of FGM reduction technique coupled to LES to model spray combustion have not yet been reported in the literature.

The main objective of this work is therefore to appraise the ability of an Eulerian-Lagrangian spray module including LES coupled to FGM and to a non-equilibrium based evaporation model in predicting the droplets dispersion and evaporation in a lean partially premixed spray combustion.

This paper is structured as follows. In the next section, an introduction of the modeling method is done. Then, a description of the experimental configuration and computational setup is presented. Comparisons of the numerical results with the experimental data are presented and discussed. A subsequent analysis is then provided while conclusions are summarized in the final section.

## Mathematical modelling

The computations are performed following the Eulerian-Lagrangian approach, in which carrier phase quantities are transported using an Eulerian fluid flow representation while the droplets are tracked in a Lagrangian framework. The coupling of the disperse phase in the carrier phase is done by computing transported quantities in droplets positions, while the reverse is done through source terms in every coupling time step along with a full two-way coupling. The turbulence is described by LES equations expressed in a variable-density low Mach number formulation.

Within the FGM framework, the filtered transport equations for mass and momentum conservation and also for control variables, namely the mixture fraction and one reaction progress variable (RPV), form the set of equations that models the carrier phase dynamics.

The sub-grid scale stresses are closed by means of the Smagorinsky-model with the dynamic procedure proposed by Germano et al. [1]. Over this model, two modifications are applied: the modification proposed by Sagaut [10] to stabilize the model and a clipping to reset negative Germano coefficient to zero to avoid destabilizing values. No special wall-treatment is included in the SGS model relying on the ability of the dynamic procedure to capture the correct asymptotic behavior of the turbulent flow velocities when approaching to the wall (see e.g., Wegner [11]).

To model droplets displacement only the drag, gravitation and buoyancy forces are considered to act on them, since the ratio between the specific mass of liquid n-heptane and that of the gas phase mixture has a value around 103. To describe the evaporation process, the Uniform Temperature (UT) evaporation model following Abramzon and Sirignano [12] is applied where non-equilibrium aspects are included (see [9]). Since the droplets carried by the gas phase have diameter smaller than 50  $\mu\text{m}$ , the uniform temperature assumption is reasonable.

In the present paper the control variables used to describe the detailed chemistry through the FGM method are the mixture fraction and one reaction progress variable (RPV). The choice of the species defining the RPV depends on the problem being solved. In case of partially premixed spray combustion, the three major species ( $\text{H}_2\text{O}$ ,  $\text{CO}_2$ ,  $\text{H}_2$ ) are considered to properly capture the reaction zone.

The generation of the chemistry tables is achieved using the steady and unsteady flamelet approaches. A combination of both approaches is used to improve the properties determination in the extinction zone [9]. Thereby a detailed chemical reaction mechanism for n-heptane developed and validated by Yoo et al. [13] is used. It involves 88 species and 387 reactions.

However, before using the table, a statistical treatment is necessary. As usually made in turbulent combustion, the filtered reaction variables are retrieved by integrating over a presumed joint PDF of the mixture fraction and the RPV. It is considered a conditional PDF on RPV, which is modelled with a Dirac delta function, while a presumed  $\beta$ -PDF is used for mixture fraction.

## Numerical Procedure

The governing equations of the carrier gas phase are solved using the code FASTEST3D, which is based on a variable density, low-Mach number formulation. This computational program is able to compute 3D complex geometries by using flexible, block structured and boundary fitted grids [15]. The code uses a finite volume method with the co-located cell arrangement. For spatial discretization, specialized central differencing schemes that hold the second order for arbitrary grid cells are used [16]. The convective term in the scalar transport equations is discretized using a non-oscillatory, bounded TVD scheme. For the time stepping multiple stage, Runge–Kutta schemes with second order accuracy are used. A fractional step formulation is applied and at each stage a momentum correction is carried out in order to satisfy the continuity. The continuity equation is fulfilled by the solution of the Poisson equation and solved iteratively with the Strongly Implicit Procedure (SIP) [17] that uses the successive-over relaxation method (SOR).

The parcels are tracked using the LAG3D code [18] in which the equation of motion, the temperature evolution and the evaporation rate are discretized using Euler first/second order schemes and solved explicitly.

The tracking of the droplets is not done in every time-step used to compute the carrier phase in the present simulations, i.e. the distinct phases are computed with distinct time steps. This is employed to save computational time. For that reason a coupling time step is necessary to be defined in a form to ensure the capture of the interaction of the turbulent motions of the carrier phase on droplets trajectories. The same procedure adopted by Chrigui et al. [9] is used in this work, which set this coupling time step to  $3.0 \times 10^{-4}$  s. As in [9], this value tends toward the Kolmogorov micro-scale that varies between  $4.0 \times 10^{-5}$  s and  $10^{-3}$  s in the flame region. Test cases were performed with lower coupling time steps showing no significant improvement in the results.

The simulations were initiated from a stagnated flow, where the carrier phase was computed with a constant time step of  $4.0 \times 10^{-6}$  s. As a consequence, the time averaging was started after 0.18s, when the injection volume of gas could cross 3 times the computational domain of interest, until 0.6s ensuring converged statistical results.

## Experimental Configuration and Simulations Setup

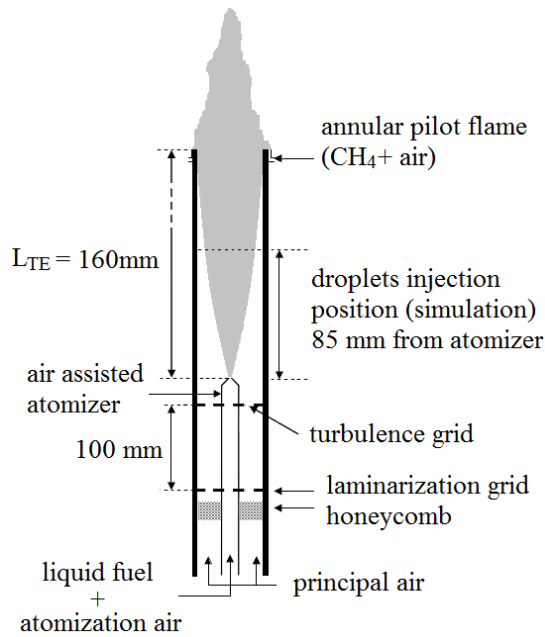


**Figure 1:** Scheme of the geometry of the experiment. Adapted from Pichard [19].

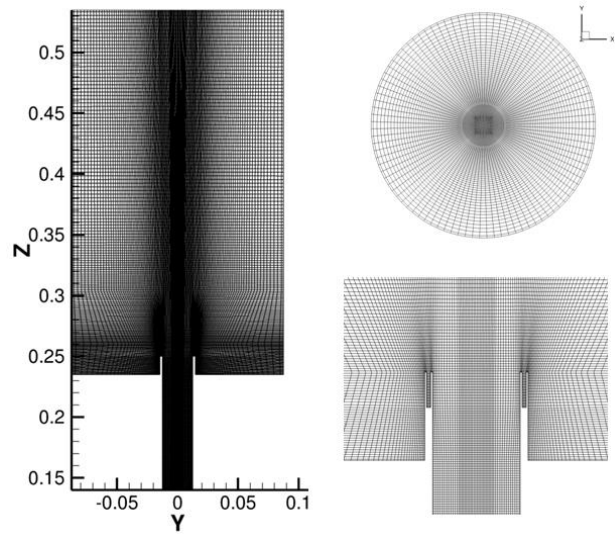


**Figure 2:** Computational domain of the spray burner. Left: cut plane in a longitudinal cross section. Right top: top view. Right bottom: detail of the burner exit and pilot flame.

The configuration investigated experimentally in this work was the measured by Pichard [19]. This is one of the spray flame databases listed by Jenny et al. [20] and accepted as one of target spray flames at the workshop on turbulent spray combustion (TCS). As illustrated in Fig. 1, the configuration consists of a spray jet flame of n-heptane stabilized by a pilot flame. The spray jet is produced by an air-assisted atomizer evolved by a co-flowing bulk of air (principal air) under controlled temperature conditions. The air stream, indicated as "atomization air" in Fig. 1, assists the fuel atomization. It is worth to notice that before the flow reaches the flame zone, droplets traverse a pre-evaporation distance and release a great part of their mass. Consequently, this turns the combustion regime from diffusion to partially premixed. The experimental operating conditions are summarized in Tab. 1 for the analysed flame ( $\phi=0.72$ ) and a reference flame ( $\phi=0.79$ ) used in this work to analyse the volumetric fluxes (see Fig. 11).

**Table 2:** Experimental operating conditions

$\phi$	$m_{IA}$ (g/s)	T (K)	$m_{PA}$ (g/s)	$m_{fuel}$ (g/s)
0.72	0.115	303	1.69	0.086
0.79	0.115	303	1.69	0.094

In Table 1,  $m_{IA}$  corresponds to the injection (or atomization) air, T temperature of the coflowing air,  $m_{PA}$  is related to the principal air and  $m_{fuel}$  to the mass rate of injected fuel.

In the present simulations, atomization and dense spray zone are not computed. Focussed on the diluted spray region, the boundary conditions for the disperse phase are defined at the first plane from the atomizer, where experimental data are available. This plane is indicated with a dashed line in Fig. 1 at a distance of 85 mm from the atomizer nozzle.

The computational domain along with the grid used in the simulation is represented in Fig. 2. It amounts 1,283,040 cells and 117 blocks beginning at 40 mm from the nozzle exit. This was so determined to ensure a well-developed flow at the plane where droplets are injected while enabling to resolve at least 80% of the instantaneous carrier phase turbulence.

To define the droplets boundary conditions for an Euler-Lagrangian approach the droplet size distributions are necessary in the injection region. However, these data are not provided in [19]. In order to gain the needed information, log normal functions were used to reconstruct the droplet size distribution curves. This reconstruction was based on the moments achieved with the measured profiles of number of droplets, D10, D20 and D30. In the reconstruction 30 curves of droplets size distribution were reconstructed along the radii at the

injection plane, although only a half are used to define the boundary conditions in this work, as it is shown in Fig. 3. Notice that the measured profiles are extrapolated to the burner center-line at a distance of  $r/D=0.39$ , where  $r$  is the radial distance from the center-line in mm and  $D$  the diameter of the burner (25 mm).

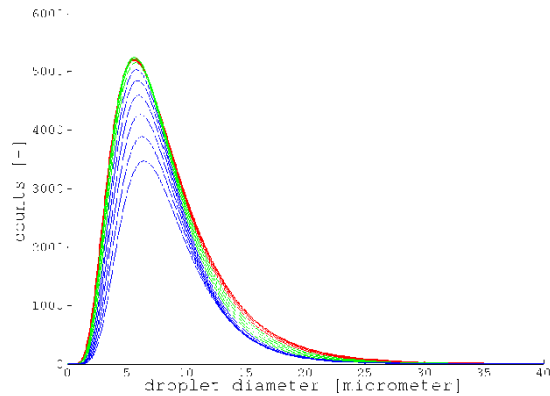


**Figure 3:** Droplets size distributions reconstructed from the boundary conditions.

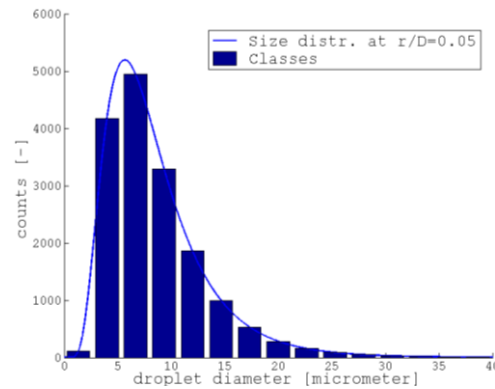


**Figure 4:** Classes achieved from the curve  $r/D=0.05$ .

For every droplet size distribution curve, 20 different classes are used. In this way, a detailed description of the boundary conditions could be achieved. Fig. 3 presents the extracted size bands for the curve at  $r/D=0.05$ . The number of parcels injected within one coupling time step is 105,000. The disperse phase properties are statistically independent and not conditioned on the number of parcels tracked on coupling time steps. The boundary condition for the RPV is set to zero in the entire domain except at the pilot flame inlet, which is set to the maximum absolute value. The total number of numerical tracked parcels exceeded  $10^6$  within one coupling-iteration.

## Results and Discussion

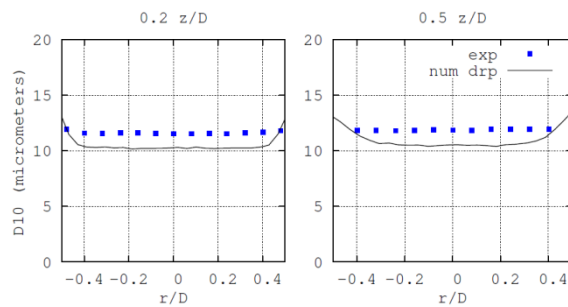


**Figure 5:** Radial profiles of D10.

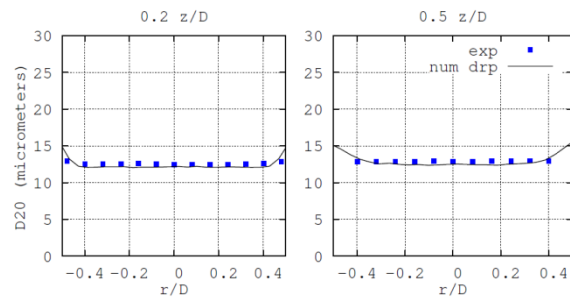


**Figure 6:** Radial profiles of D20.

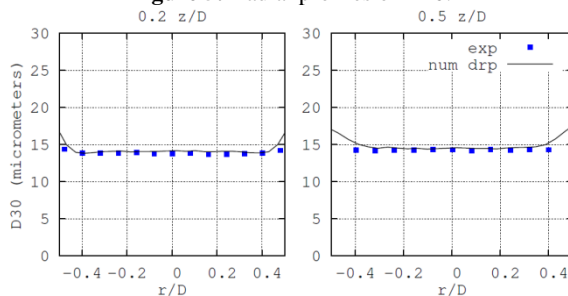


**Figure 7:** Radial profiles of D30.

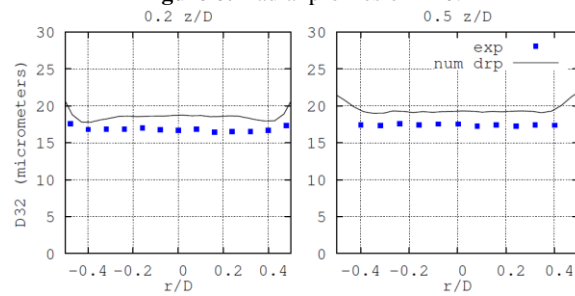


**Figure 8:** Radial profiles of D32.

Figs. 5 - 8 show the comparisons radial profiles of the characteristic diameters of the droplets size distributions in two flame positions (0.2 and 0.5  $z/D$ , where  $z$  is the coordinate along the flame center line starting from the pilot flame). A good agreement can be noticed. The slight deviations observed are within the experimental error as presented by Pichard [19].

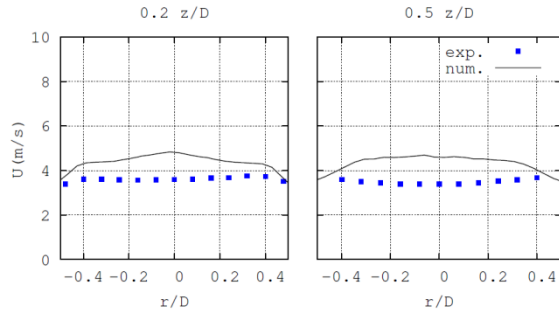


**Figure 9:** Radial profiles of the longitudinal component of mean droplets velocity.

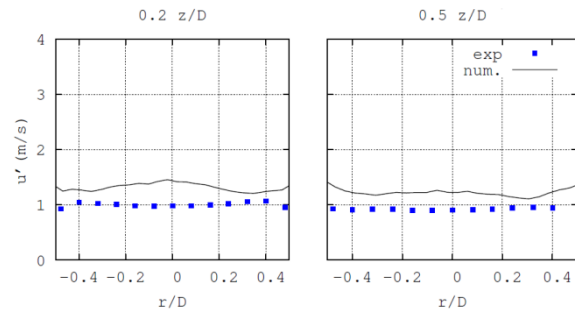


**Figure 10:** Radial profiles of the longitudinal component of droplets velocity fluctuations.

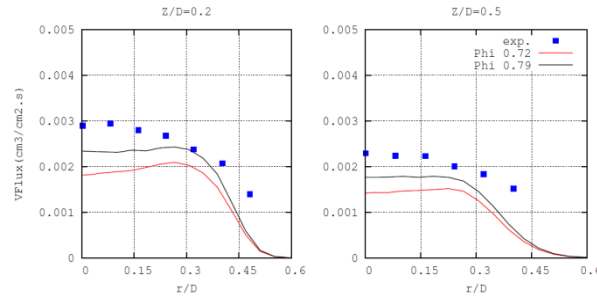


**Figure 11:** Radial profiles of volumetric flux.

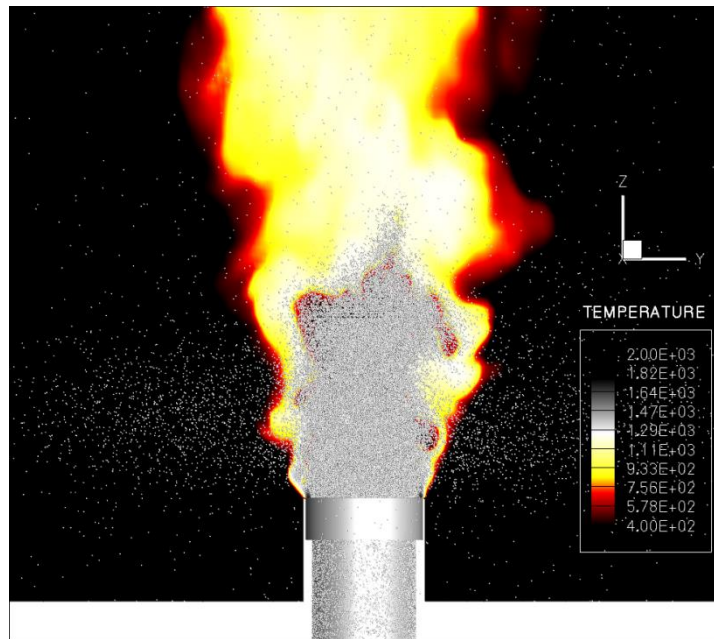


**Figure 12:** Interaction between the disperse phase with the flame.

Figs. 9 and 10 present the comparisons of the longitudinal component of mean droplets velocities and its fluctuations, respectively. The deviations of the numerical results with respect to the experimental data can be linked to the injection velocity of the droplets. No information about the correlation between droplets diameters and velocity is provided in [19], such as the mean value of the droplets velocities is used at the injection plane for all droplets sizes. This assumption surely increases the velocity of the biggest particles, which have higher relaxation time and can increase penetration of the spray.

This lack of knowledge about the correlation between droplets diameters and velocity may also explain the deviations observed in the liquid volumetric fluxes shown in Fig. 11. The results of a simulation with a the equivalence ratio  $\phi = 0.79$  was added since the experimental reefers to this value of  $\phi$ . Obviously, differences appear between both simulations.

From these results, it can be observed that, the droplets dispersion is well captured along with the unsteady behavior of the large scale turbulent fluctuations captured by the LES approach. Even though a SGS dispersion

model was not included, well prediction of droplets moments is achieved despite the slight deviation in droplet volume flux due to the homogeneous distribution of droplet size in the comparison positions.

Fig. 12 shows the vanishment of droplets when they reach the reaction zone. It is to notice that the majority of droplets evaporates before they reach the high temperature zone, just a few can be found in regions where the RPV is not zero. This implies that for this configuration the neglect of the influence of the evaporative cooling on the reaction development is an acceptable hypothesis.

## Conclusions

The simulation of a lean partially pre-vaporized spray flame are presented. The carrier phase turbulence was modelled in the LES framework together with the reduction of the chemistry by means of the FGM method to capture the combustion. The disperse phase was described using a Lagrangian formulation where non-equilibrium approach for the evaporation modelling was applied.

An overall good agreement between the achieved numerical results with the experimental data is observed. Droplets dispersion, evaporation and dynamics are well predicted.

## Acknowledgements

The authors acknowledge the financial support from German Council of Research (DFG). The first author specially acknowledges the financial support (scholarship) by the CNPq (Brazil) and DAAD (Germany).

## References

- [1] Germano, M., Piomelli, U., Moin, P., and Cabot, W. H., "A dynamic subgrid-scale eddy viscosity model", *Phys. Fluids A* 3. 7: 1760–1765 (1991)
- [2] Bellan, J., Radhakrishnan, S., "Explicitly Filtered Large Eddy Simulation of Two-Phase Flows with Evaporating Drops for Separating Numerical and Modelling Aspects" 12th ICLASS (2012)
- [3] Rutland, C. J., "Large-eddy simulations for internal combustion engines-A review" *Int. J. of Engine Res.* 12: 421-451(2012)
- [4] James, S., Zhu, J., Anand, M. S., "Large Eddy Simulations of Bluff-Body Stabilized Turbulent Flames and Gas Turbine Combustors" *AIAA J.* 44: 674-686 (2006)
- [5] J. A. Van Oijen, L. P. H. De Goey, "A numerical study of confined triple flames using a flamelet-generated manifold" *Comb. Theory Modell.* 8: 141–163 (2004)
- [6] Vreman, A. W., Albrecht, B. A., Van Oijen, J. A., Goey, De L. P. H., Bastiaans, R. J. M., "Premixed and non-premixed generated manifolds in large-eddy simulation of Sandia flame D and F", *Comb. Flame* 153: 394–416 (2008)
- [7] Fiorina, B., Gicquel, O., Vervisch, L., Carpentier, S., Darabiha, N., "Premixed turbulent combustion modeling using tabulated detailed chemistry and PDF" *Proc. Comb. Inst.* 30: 867–874 (2005)
- [8] Franzelli, B. G., Fiorina, B., Darabiha, N. "Modeling the chemical structure of spray flames using tabulated chemistry method", ICLASS 2012, Heidelberg, Germany, (2012).
- [9] Chrigui, M., Gounder, J., Sadiki, A., Masri, A. R., Janicka, J., "Partially premixed reacting acetone spray using LES and FGM tabulated chemistry", *Comb. Flame* 159: 2718-2741 (2012)
- [10] Sagaut P., *Large Eddy Simulation for Incompressible Flows*, Springer, Berlin (2001).
- [11] Wegner, B. A *Large-Eddy Simulation Technique for the Prediction of Flow, Mixing and Combustion in Gas Turbine Combustors*, PhD Thesis, Technische Universität Darmstadt (2007)
- [12] Abramzon, B., Sirignano, W. A., "Droplet vaporization model for spray combustion calculations" *Int. J. of Heat and Mass Transfer.* 32: 1606-1618 (1989)
- [13] Yuen, M. C., Chen, L. W., "On Drag of Evaporating Liquid Droplets", *Comb. Sci. & Tech.* 14: 147-154 (1976)
- [14] Yoo, C. S., Lu, T. F., Chen, J. H., Law, C. K., "Direct numerical simulations of ignition of a lean n-heptane/air mixture with temperature inhomogeneities at constant volume: Parametric study" *Comb. Flame* 159: 1727-1741 (2011)
- [15] Olbricht, C., Ketelheun, A., Hahn, F., Janicka, J., "Assessing the predictive capabilities of Combustion LES as applied to the Sydney flame series." *Flow Turb. Comb.* 83: 513-547 (2011)
- [16] Lehnhäuser, T., Schäfer, M., "Improved Linear Interpolation Practice for Finite-Volume Schemes on Complex Grids" *Int. J. Numer. Meth. Fluids.* 38: 625–645 (2002)
- [17] FASTEST - User Manual. Fachgebiet für Numerische Berechnungsverfahren im Maschinenbau - TU Darmstadt. (2006).

- [18] Kohnen, G., Rüger, M., Sommerfeld, M., FED-Vol. 185, ASME (1994).
- [19] Pichard, C., Thèse présentée à l'université d'Orléans pour obtenir le grade de docteur de l'université d'Orléans (2003).
- [20] Jenny, P., Roekaerts, D., Beishuizen, N., "Modeling of turbulent dilute spray combustion" *Prog. Energy Combust. Sci.* 38: 846-887 (2012)



## Large Eddy Simulation of a lab-scale spray burner

PAULHIAC Damien<sup>1,2</sup>, RIBER Eléonore<sup>1</sup> and CUENOT Bénédicte<sup>1</sup>

1: CERFACS, 42, av Gaspard Coriolis, 31057 Toulouse Cedex 1, France

2: TURBOMECA, av Joseph Szydlowski, 64511 Bordes Cedex, France

### Abstract

The numerical study of an academic lab-scale spray burner using Large Eddy Simulation coupled with a Discrete Particle Simulation is presented. The objectives are first to validate current turbulent combustion modelling approaches, then to bring new insight on two-phase flame structure. In comparison with the experiment, the non-reacting case shows a good quantitative prediction of the velocity field. Experimental and numerical images of the spray flame are also in good agreement. Numerical results allow a detailed study of the interaction between the flame front and the droplets, in both single droplet and group combustion regimes that occur in the present configuration. It is shown that the presence of liquid fuel has a strong impact on the flame structure, due to the modification of the fuel vapour distribution in the chamber that tends to enhance non-premixed combustion.

---

### Introduction

Accurate modelling of spray combustion is currently one of the key issues for the simulation of gas turbines. The interaction between fuel droplets and the heat released by their combustion has been shown to deeply influence the flow and flame structure, the emission of pollutants [1] [2] or the flame ignition [3]. Two-phase combustion has been extensively studied in the literature [4]. One particularity is the existence of various combustion modes, as described analytically by Chiu [5] or Annamalai and Ryan [6], due to the strong coupling between the droplet evaporation and the combustion of the evaporated fuel. These modes range from single droplet combustion [7], where a flame stabilizes around and close to one droplet, to group combustion, where the flame stabilizes around a cloud of droplets. In the latter case, evaporation may decrease or even stop inside the droplet cloud due to over-saturation of the surrounding gaseous mixture, while the flame, mainly fed by frontier droplets, maintains a non-saturated environment around the droplet cloud. The various two-phase combustion regimes lead therefore to different burner performances, in terms of flame length, stabilisation, maximum temperature or emissions.

Many experimental works have been undertaken on sprays and spray flames, ranging from the simplest configuration of a single droplet combustion to more complex spray burners [8]. They all observe the various spray flame regimes mentioned above. They also observe either flame speed increase or decrease compared to gaseous flames, depending on the operating conditions, which again illustrates the complexity of the flame-droplets interaction. Unfortunately, the presence of droplets makes most classical measurement techniques very difficult, even impossible for some of them, and quantitative data on spray flames is still rare and most often incomplete.

In this context, numerical simulation, if accurate, is of particular interest to understand the physics of spray flames. Simple flow simulations including evaporating and burning single droplets or small groups of droplets [9], or one-dimensional flames fed by droplets [10], showed some of the typical features of spray flames such as droplet-droplet interaction, flame propagation through the inter-droplet space, or hysteresis behaviour of single droplet combustion... Particle dispersion and evaporation were investigated in Homogeneous Isotropic Turbulence (HIT) in square boxes, using Direct Numerical Simulation (DNS) for the turbulent flow and a Discrete Particle Simulation (DPS) approach for the liquid phase [11]. It was shown that particle segregation, which occurs due to turbulence, may lead to large heterogeneities of the fuel vapour distribution. This is an important difference from gaseous flows, where turbulence is known to enhance mixing. DNS-DPS of HIT flow was also used by Reveillon and Vervisch [12] to study reacting turbulent spray combustion and more precisely the impact of several parameters on the droplet/gas interaction. They constructed a diagram of two-phase combustion regimes, and analysed for each regime the influence of the liquid fuel on the flame structure, flame length and heat release.

The use of DNS-DPS for realistic flows being not yet affordable in terms of CPU cost, Large Eddy Simulation (LES) coupled with DPS is preferred. In such approach, the explicit resolution of the turbulent large scales, combined to a Lagrangian tracking of droplets, shows a good potential to take into account the subtle interactions between the spray, turbulence and combustion. Complex two-phase spray flames have already been computed in LES-DPS ([13], [14], [15]) with encouraging results. It is proposed in this paper to use LES-DPS to simulate an experimental spray burner, to evaluate the capacity of the models to reproduce observed physical behaviours and to understand the droplet-flame interaction in complex flows. The chosen configuration was

selected for its capacity to focus on two-phase combustion phenomena, while keeping realistic burner features, such as strongly swirled flow.

### Experimental setup

The experimental test rig was designed by the university of Cambridge in order to obtain a swirl-stabilized flame with large possibilities of measurements [16]. The geometry consists of a 350 mm-long circular vertical duct in which a conical bluff body is fitted (sketch in Figure 1), and leading to a rectangular chamber made of synthetic optical-quality quartz. A swirler placed in the duct gives a precessing motion to the incoming flow. The chamber exits directly into the atmosphere. The pressure-swirl liquid injector is imbedded in the bluff body and injects a hollow-cone spray directly inside the chamber. The liquid fuel is n-heptane, chosen for its fast evaporation, which allows the spray flame to stabilise without air preheating. The characteristics of the operating point are summarized in Table 1. It is important to note that the diameter distribution of the fully atomized spray at injection is not known precisely and had to be supposed *a priori* in the simulation.

**Table 1:** Chosen operating conditions for the spray burner (case SWH1 in [16]).

<b>Liquid injection</b>	<b>Diameter of the injector</b>	0.15 mm
	<b>Angle of hollow cone</b>	80°
	<b>n-heptane flow-rate</b>	0.12 g/s
	<b>Sauter Mean Diameter</b>	40 $\mu\text{m}$
<b>Air Inlet</b>	<b>Air flow-rate</b>	500 L/s
	<b>Temperature</b>	298 K
	<b>Pressure</b>	1 bar
	<b>Global equivalence ratio</b>	0.17

Several measurements are available. OH\* chemiluminescence and OH-PLIF were used to monitor the flame-shape and flame sheet structure. Mie Scattering was used to monitor the spray location. Velocity measurements were made along several perpendicular lines using PLIF (Figure 4). Species emission data were obtained along the gray dotted line in Figure 2 at the chamber exit.

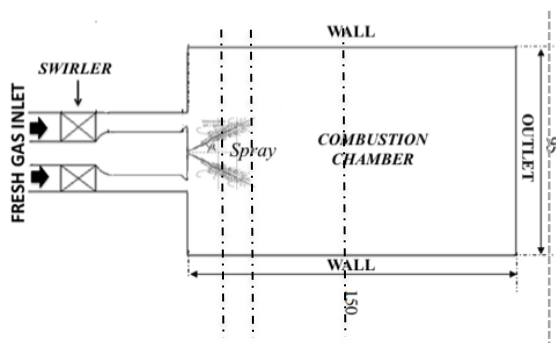


**Figure 2.** Sketch of the n-heptane spray burner by Cambridge University [16]. Dimensions are in mm.

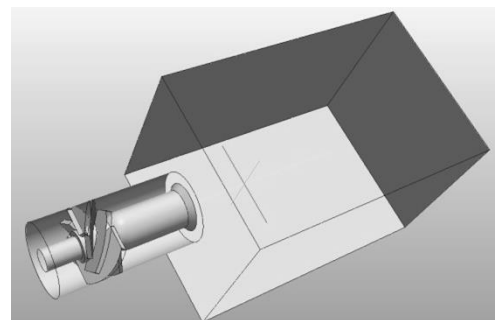


**Figure 1:** Geometry of the simulated

## Numerical setup

The simulated geometry includes the swirler, in order to let the turbulence develop in the duct, and to avoid imposing a guessed value of the turbulence intensity at the chamber inlet. A large spherical atmospheric plenum was added to the chamber exit to minimize the influence of outlet boundary conditions. The LES refinement is evaluated looking at the ratio  $\Delta$  between a local Kolmogorov turbulent length scale and a local mesh cell size. DNS is obtained for a ratio greater than unity. Classical LES is of the order of  $10^{-1}$ . To correctly develop and transport turbulence inside the duct, the cell size in this zone was kept homogeneous, and sufficiently small ( $\Delta \approx 0.7$ ). In the chamber, the mesh is coarsened from the injection point to the outlet ( $\Delta \approx 0.4$ ). The primary zone where the spray is located and where the flame stabilizes is refined in order to resolve the flame front, leading to a  $\Delta$  ratio of 0.7, which corresponds to cell size of 0.2 mm for a flame thickness of approximately 2 mm.

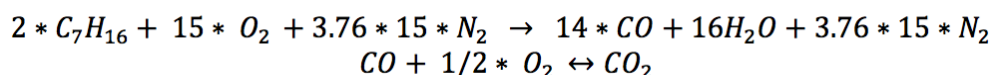
The simulation was performed with the code AVBP developed by CERFACS/IFP-EN [17]. The liquid phase is modelled using a Lagrangian formalism, where a point source approximation is made: the droplets are considered isolated from others, and are seen as points by the gaseous phase. The coupling between the liquid and the gaseous phase is ensured by a first order interpolation between the droplet location and the grid nodes, and is two-way. As the mesh size in the flame zone is of the order of magnitude of some droplet size, the point source approximation in this first order two-way coupling may be questionable for these droplets [18] and is the subject of further research.

Droplets are subjected to the Stokes drag force, other forces being negligible in this case. The drag coefficient is obtained by the Schiller-Neumann correlation [19]. The evaporation model is the one proposed by Abramzon and Sirignano [20], with corrected Prandtl and Schmidt numbers to better match the mixture properties in the gaseous layer close to the droplet surface [21]. Corrections are obtained from a 0D simulation of an evaporating droplet using complex transport, performed with the open-source code CANtera [22].

The liquid injection procedure follows the FIMUR method [23], which considers a fully atomized spray with a Rosin-Rammler size-distribution, typical for this kind of injector, and a hollow cone spray shape of given angle, evaluated from the MIE scattering data (Figure 6). It is noted that the injected spray shape and drop-size distribution may have an important impact on the structure and position of the flame, and further characterization of injection conditions are currently on-going.

Chemical kinetics are described with a reduced two-steps scheme, called 2S\_C7H16\_BFER, built on the idea proposed by Franzelli et al. for kerosene-air flames [24]. This scheme accurately reproduces the adiabatic flame temperature, the flame speed, and the composition of burnt gas, for equivalence ratio ranging from 0.7 to 1.4, at atmospheric pressure and ambient temperature. In rich mixtures, a correction of the pre-exponential factor with equivalence ratio (PEA methodology) is necessary to recover the correct flame behaviour. The correction function is calculated *a priori* to match the flame speed curve.

The two reactions retained for n-heptane/air combustion write:



The behaviour of 2S\_C7H16\_BFER is displayed in Figure 3. Reference values of flame speeds are issued from [25] while the adiabatic temperature and concentrations of products come from a detailed mechanism calculation (with CANtera), with 2540 reactions among 556 species [26]. The agreement is very good and justifies the use of the two-steps scheme. No sub-grid scale modelling is applied to the combustion reaction source terms, as the flame front is close to be resolved on the grid.

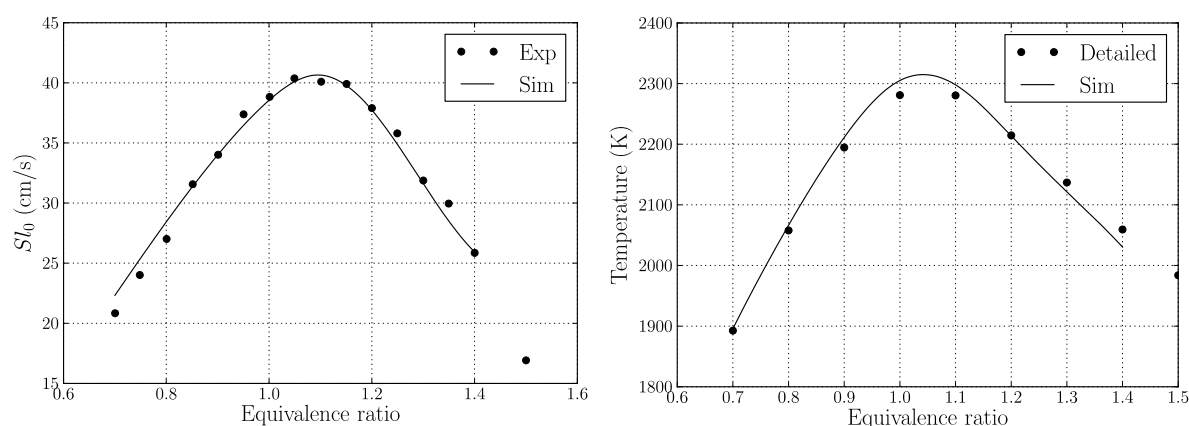


**Figure 3:** Two-steps reaction scheme 2S\_C7H16\_BFER results vs. experimental data or detailed chemistry simulation data. Left: flame speed (exp. values from [25]), right: adiabatic temperature (ref. values from [26]).

## Results and Discussion

The ability of LES to reproduce the main features of the experiment was checked for the non-reacting purely gaseous case. Very good agreement is found for the mean and RMS velocities along several lines through the chamber (Figure 4). A large and long Inner Recirculation Zone (IRZ) appears in the middle of the chamber, accompanied by two smaller Corner Recirculation Zones (CRZ). The swirled jet of fresh air impinges on the sidewalls of the chamber and flows along the walls downstream to the outlet (velocity field in Figure 5). The simulation correctly reproduces the jet opening and the location and size of the recirculation zones. Moreover, LES allows to capture the correct velocity fluctuations, in terms of both level and profile shape. This validates the LES methodology for the present configuration and allows the reacting case simulation and analysis.

In the reacting case, a quasi-axisymmetric, M-shape flame is obtained behind the bluff body (Figure 6). It is attached to the edge of the bluff body and stabilizes at the central axis due to the presence of the large IRZ (Figure 5). Fuel is emitted from the spray and is confined inside this M-flame, while oxidizer is only present outside, which yields the equivalence ratio field of Figure 5. Main rotating and recirculating motions in the chamber are illustrated in Figure 5.

When compared with experimental data in Figure 6, the overall agreement is qualitatively good. Mean spray and flame shapes are very similar, in terms of angle of spray, dispersion of droplets, and stabilisation of the flame. Moreover, on both simulation and experiment, some droplets manage to go through the main reactive zone. However several differences are observed. First, the simulated flame is directly attached to the bluff body and the flame front seems more intense in terms of heat release in this zone. In the experience, the flame front stabilises at a lift-off distance from the wall and the maximum heat release seems higher downstream. This is probably due to the adiabatic wall assumption in the simulation, which neglects heat loss at the walls. The second difference is related to the axial position of the flame center, very close to the wall in the experiment.

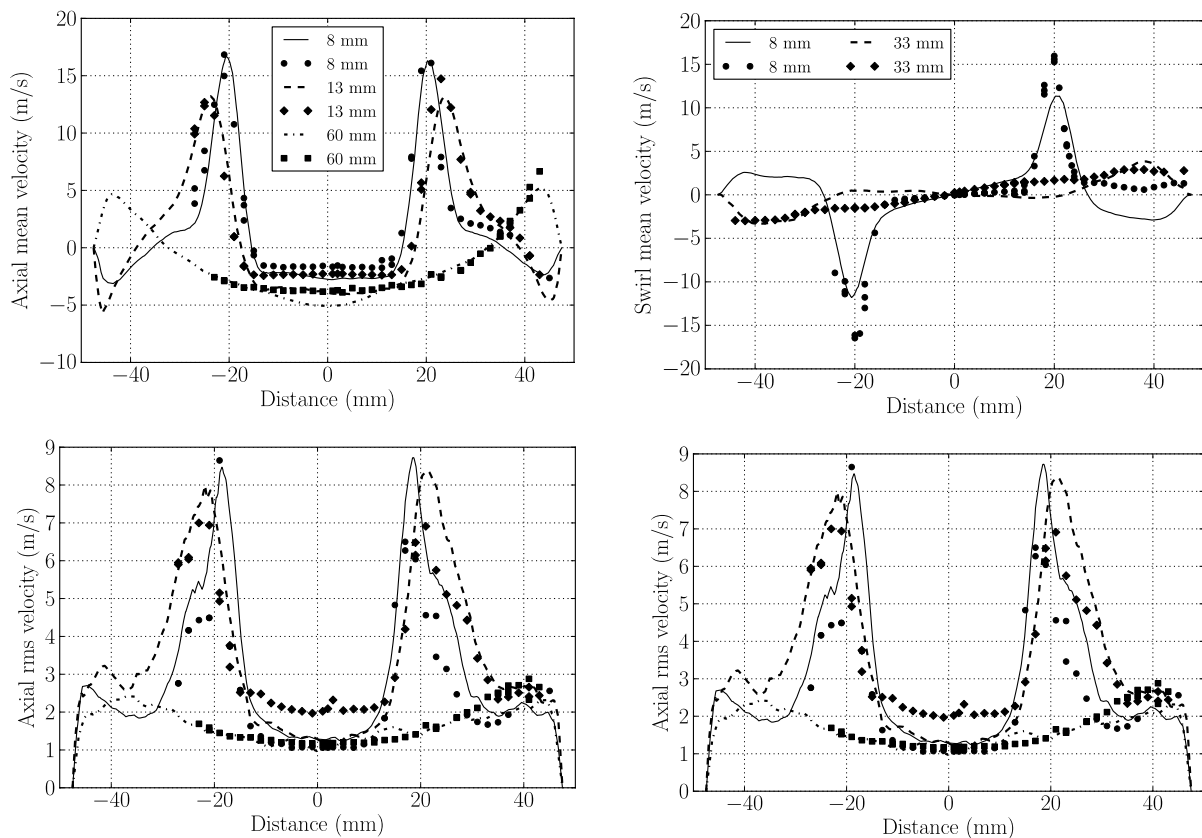


**Figure 4:** Non-reacting case. Comparison of the mean and rms axial velocity between experiment and simulation for the non-reactive case, at different sections in the chamber along a line in the X- plane (black dotted line on **Figure 1**). Lines: Simulation; Symbols : Experiment.

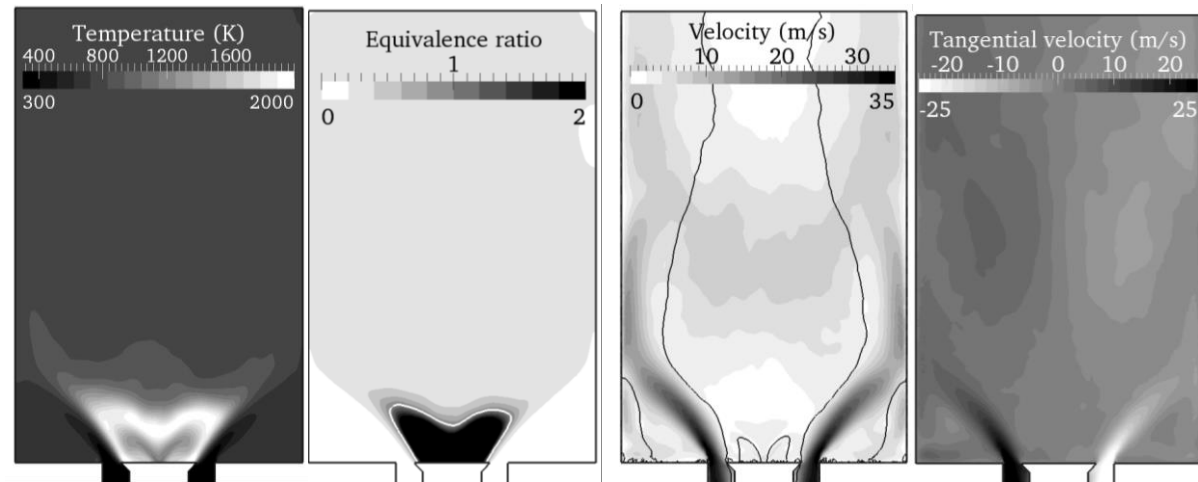


**Figure 5 :** Reacting case SWH1. Numerical mean fields in the vertical cut plane at  $X = 0$  from the simulation: temperature, equivalence ratio (with the stoichiometric line), velocity magnitude (with the zero-velocity iso-contour) and tangential velocity.

The time-averaged total heat released in the simulated chamber is around 5.26 kJ/s, which corresponds to a burning efficiency of 97% if compared to the 5.4 kJ/s that would be released by the complete burning of the injected fuel. This is consistent with the amount of unburned hydrocarbons (UHC) exiting the chamber in both experiment and simulation. These UHC were measured at 2546 ppm along the grey line near the exit of the chamber in Figure 2. This value can be compared to the 1346 ppm found in the simulation at the same location, showing that slightly more fuel is burned in the simulation. It is noted that this configuration is particularly discriminating for modeling because the amount of UHC in the simulation is directly linked to the accuracy of the two-phase flame resolution. The good overall agreement validates the current methodology and enables to analyse in more detail the simulated two-phase flame.

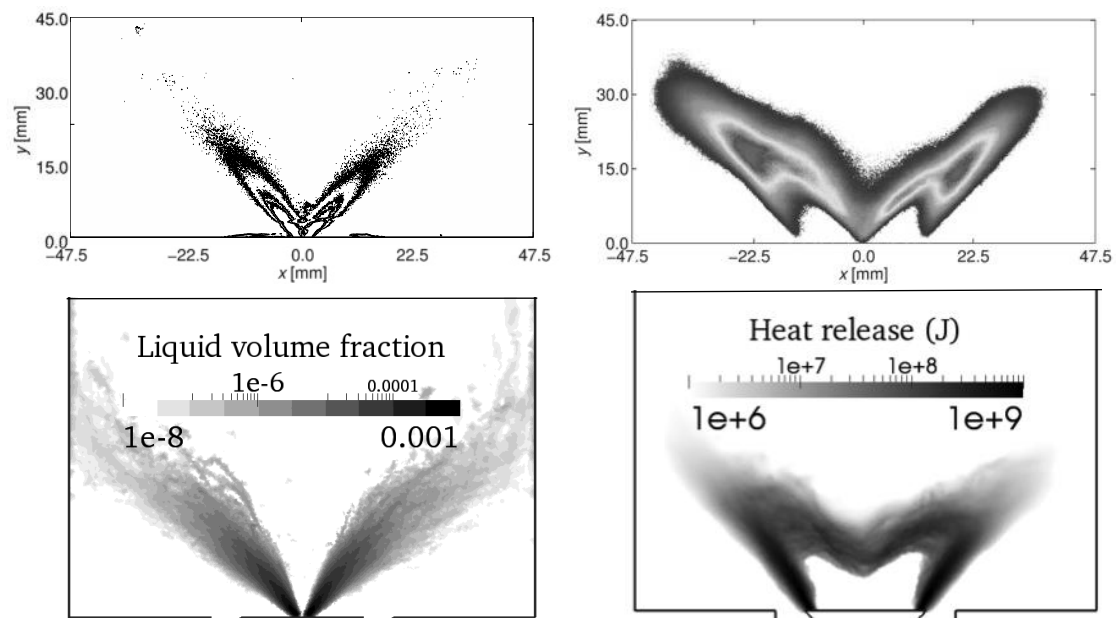


**Figure 6 :** Reacting case SWH1, Comparison between experiment (top) [16] [27], and simulation (bottom). Left : mean spray visualisation, right : mean flame visualization.

The simulated instantaneous field, displayed in Figure 7 (left), shows the same characteristic M-shape flame. It is highly wrinkled by turbulence and is anchored at the lips of the bluff-body. The M-flame engulfs the liquid spray, which mainly evaporates before crossing the flame front. The oxygen initially present above the bluff-body is consumed during the flame development and stabilization, so that no oxygen is left behind the M-flame. As a consequence the region limited by the bluff-body and the flame contains only fuel (gas and liquid) and hot

products. Outside this region, high dilution by the turbulent cold air injection enhances mixing, dilutes the products and decreases the temperature (Figure 5). The resulting flame is a purely non-premixed flame.

The M-flame can be split into three relatively distinct parts, identified in Figure 7. The side conical branch of the M-shape, numbered 1, consists of a highly wrinkled diffusion flame, attached to the adiabatic wall. The flame features large Kelvin-Helmholtz instabilities, triggered by the very high shear generated at the frontier of the swirled air jet. The heat release is maximum along this branch, as it is much strained and purely gaseous. It is fed by gaseous fuel convected from the injection zone. The intensity of the local reaction rate along this flame front is heterogeneous and highly unsteady. Some large decreases in reaction rate on several points of the flame front are encountered. However, no extinction due to strain occurs. Scatterplots of temperature vs. mixture are displayed on Figure 8. A typical diffusion flame structure is observed, as most points are close to the equilibrium lines [28]. However, some points located far below the equilibrium line represent local pre-mixing between fuel and oxygen that appears from time to time due to high turbulence intensity.

The middle V-shaped part of the M-shaped flame, numbered 2 in Figure 7, is also a diffusion flame similar to the side branches (zone 1 in Figure 7), with however some differences. It is stabilized at the bottom of the IRZ, and has a very slow motion, following the motion of the tip of the IRZ. It is little wrinkled, due to lower turbulent intensity in this area, and less intense in terms of heat-release. The scatterplot of temperature versus equivalence ratio (Figure 8) also shows a typical diffusion flame, with very low dispersion of the scatter points along the equilibrium line.

The junction between zones 1 and 2, numbered 3 in Figure 7, features a complex flame structure, where the spray highly interacts with the reacting zone. The presence of liquid droplets, which locally generate fuel by evaporation inside the reaction zone, strongly alters the flame structure. Some droplets do not fully evaporate inside the reaction zone and manage to go through the diffusion flame front, resulting in either group combustion or simultaneous local evaporation and combustion. In the group combustion regime, the flame stabilizes around a small group of droplets without penetrating it. This flame vanishes after full evaporation and consumption of the droplet cloud. Such events are however rare because the spray is not dense enough in this zone. The simultaneous evaporation and combustion mode that is seen in Figure 7 may correspond to single droplet combustion, i.e. where individual flames stabilize around each droplet, or to single droplet evaporation, surrounded by premixed combustion (wake flames [29]). The current modelling approach does not allow to distinguish between these two phenomena and further model developments are required. The temperature scatterplot of Figure 8 also shows a diffusion-like flame structure. The small number of droplets that manages to survive across the flame are so diluted by fresh air that evaporation is dramatically slowed down. Some of the fuel that still evaporates from these droplets is too cold and diluted to burn, and is convected downstream to the outlet, trapped in the IRZ or in the CRZ, leading to the UHC emissions at the outlet.

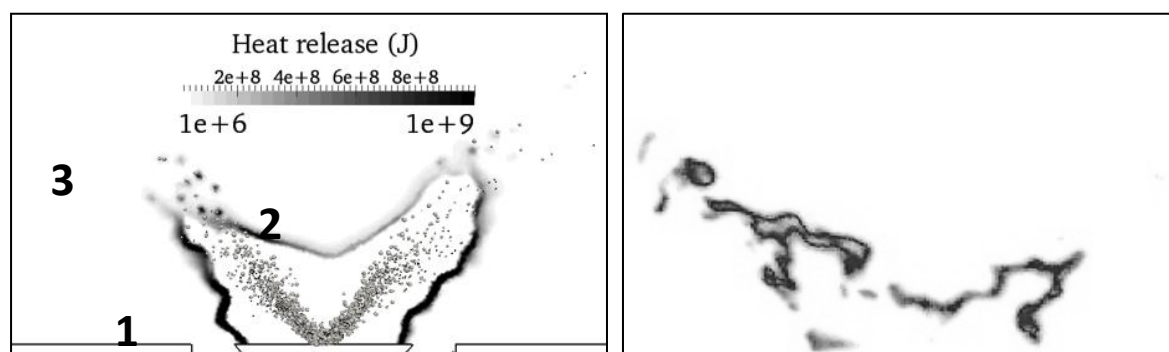


**Figure 7 :** Reacting case SWH1. Visualisation of the spray flame in a vertical cut. Left: field of the oxidation reaction rate obtained by the simulation with a Lagrangian droplet visualisation; Right: Instantaneous OH-PLIF image.

When comparing the instantaneous simulation with the experimental OH-PLIF picture in Figure 7, which represents the reactive zones, a very similar instantaneous flame structure is found. Especially, the interaction of the spray with the reaction zone is qualitatively similar. Like in the simulation, some pockets of reactive gas eject from the tip of the M, engulfing surviving droplets. Group combustion and single droplet combustion are also both encountered on several instantaneous images. The flame is attached to the wall and stabilized by the IRZ. Some differences however appear. The branch 2 in the experiment seems to stabilize lower and is more wrinkled in the experiment. Moreover, the OH-PLIF intensity, which is related to the reaction rate, is lower in zone 1 than in zone 3 of the flame, while the simulation presents more intense combustion in zone 1. This is maybe due to the fact that, in the simulation, the mesh refinement is not sufficient to solve the correct wrinkling of the flame, which increases the flame surface and thus the local reaction rate. Applying a sub-grid scale (SGS)

model such as proposed in [30] is a possible improvement. However, it will be necessary to adapt such model to two-phase combustion. Third, the experimental flame front shows numerous extinction zones along the reaction line. The fact that this feature is not seen on the simulation is maybe due to the oversimplified two-step reaction mechanism, which was not designed for this particular purpose. Its ability to recover correct extinction limits under high strain should be checked.

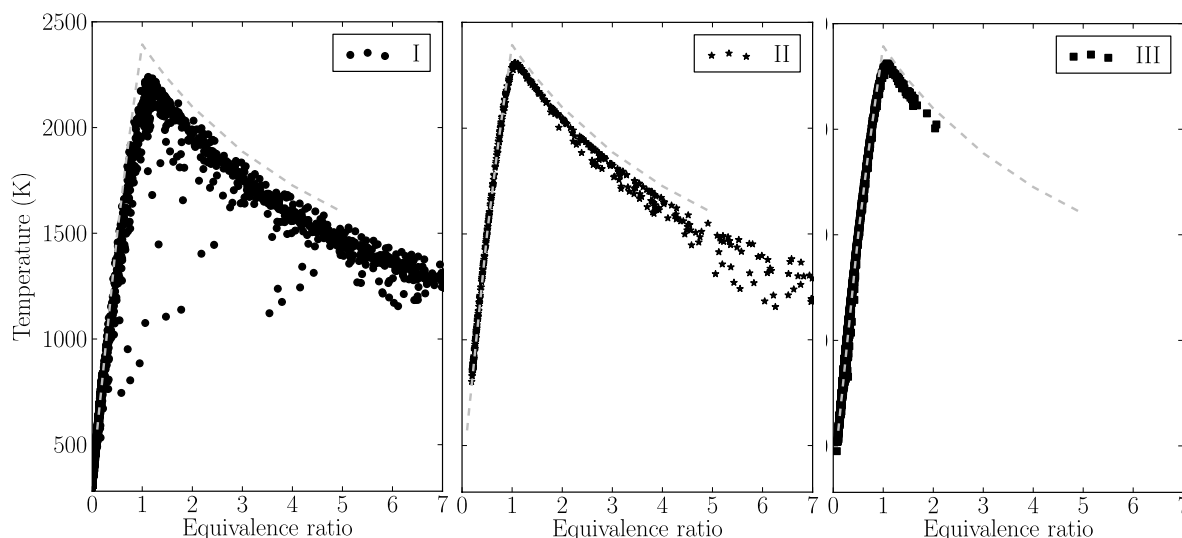


**Figure 8 :** Reacting case SWH1. Scatter plots of temperature versus equivalence ratio for the three flame zones identified in Figure 7, along with the equilibrium line (dashed line).

## Conclusions

A lab-scale swirl-stabilized spray burner has been simulated by mean of LES-DPS. As a first validation, a quantitative comparison of velocity field in a non-reacting case has been made, showing very good agreement for both mean and fluctuating values. The spray flame was simulated using a reduced two-steps n-heptane chemistry. The qualitative comparison with experimental images shows that the simulation is able to recover the correct flame shape and flame structure. The spray flame has a M-shape, and is anchored at the lips of the bluff body. Flame branches open as they follow the swirl flow. The flame is highly wrinkled by turbulence, and is mainly of the non-premixed type. The flame features various spray combustion regimes, from pre-vaporized to simultaneous evaporation and burning, this latter regime being either in group or isolated droplet combustion mode. The simulation is however not able to capture the local extinctions observed in the experiment, which may be a direct consequence of the turbulent combustion model.

Measurements allowing quantitative comparison with the simulation are currently undergoing in the reacting case. In parallel, work to improve the turbulent combustion model for two-phase combustion is on-going.

## Acknowledgements

This work was made possible thanks to the fruitful collaboration with D.E Cavaliere, A. Tyliczszak and Pr. E. Mastorakos from the University of Cambridge. This work was also performed using HPC resources from GENCI-CCRT (Grant 2013- **x20132b5031**).

## References

- [1] Beck, C. H., Koch, R., & Bauer, H.-J., *Proceedings of the Combustion Institute* 32, 2195--2203, (2009).
- [2] Beck, C., Koch, R., & Bauer, H. J., *Flow, turbulence and combustion* 82, 571--598, (2009).
- [3] A. Eyssartier, B. Cuenot, L. Y. M. G. & T.Poinsot, *Combustion and Flame* , (Submitted in June 2011)
- [4] Jenny, P., Roekaerts, D., & Beishuizen, N., *Progress in Energy and Combustion Science* , , ()
- [5] Chiu, H. H., *Progress in Energy and Combustion Science* 26, 381-416, (2000).
- [6] Annamalai, K. & Ryan, W., *Progress in Energy and Combustion Science* 18, 221--295, (1992).
- [7] Kuo, K. K., *Principle of Combustion*, (2005 Second Edition).
- [8] Marchione, T., Ahmed, S. F., & Mastorakos, E., *Combustion and Flame* 156, 166--180, (2009).
- [9] Wu, G., Sirignano, W. A., & Williams, F. A., *Combustion and Flame* 158, 1171--1180, (2011).



- [10] Neophytou, A. & Mastorakos, E., *Combustion and Flame* 156, 1627--1640, (2009).
- [11] Boivin, M., Simonin, O., & Squires, K. D., *Journal of Fluid Mechanics* 375, 235-263, (1998).
- [12] Réveillon, J. & Vervisch, L., *Journal of Fluid Mechanics* 537, 317-347, (2005).
- [13] Sankaran, V. & Menon, S., *Journal of Turbulence* 3, 011, (2002).
- [14] Li, K., Zhou, L. X., & Chan, C. K., *Cleaner Combustion and Sustainable World*, Springer Berlin Heidelberg, 105--109, (2013).
- [15] Jones, W. P., Lettieri, C., Marquis, A. J., & Navarro-Martinez, S., *International Journal of Heat and Fluid Flow* 38, 145-158, (2012).
- [16] J. Kariuki, D. E. Cavaliere, C. L. E. M., *50th AIAA Aerospace Sciences Meeting AIAA 2012-0505*, , (2012).
- [17] CERFACS, AVBP Handbook - [http://cerfacs.fr/\\$\sim\\$ avbp/AVBP\\\_V5.X/HANDBOOK](http://cerfacs.fr/$\sim$ avbp/AVBP\_V5.X/HANDBOOK), (2009).
- [18] Rangel, R. H. & Sirignano, W. A., *Newspaper of Heat Transfer* 16, 37--57, (1989).
- [19] Schiller, L. & Nauman, A., *VDI Zeitung* 77, 318-320, (1935).
- [20] Abramzon, B. & Sirignano, W. A., *Journal of Heat and Mass transfer* 9, 1605-1618, (1989).
- [21] Hannebique G., Sierra P., Riber E., Cuenot B., *Flow, Turbulence and Combustion*, 90(2):449-469, (2012).
- [22] Goodwin, D. G., CANTERA, handbook, <http://code.google.com/p/cantera/>, (2009).
- [23] Jaegle, F., Senoner, J. M., Garcia, M., Bismes, F., Lecourt, R., Cuenot, B., & Poinso, T., *Proceedings of the Combustion Institute* 33, 2099--2107, (2011).
- [24] Franzelli, B., Riber, E., Sanjosè, M., & Poinso, T., *Combustion and Flame* 157, 1364-1373, (2010).
- [25] Smallbone, A. J., Liu, W., Law, C. K., You, X. Q., & Wang, H., *Proceedings of the Combustion Institute* 32, 1245--1252, (2009).
- [26] [https://www-pls.llnl.gov/?url=science\\_and\\_technology-chemistry-combustion-n\\_heptane\\_version\\_3](https://www-pls.llnl.gov/?url=science_and_technology-chemistry-combustion-n_heptane_version_3)
- [27] Cavaliere, D. A., University of Cambridge, PhD Thesis, in preparation, (2013).
- [28] Poinso, T. & Veynante, D., *Theoretical and Numerical Combustion*, (2005).
- [29] Chiu, H.-H. & Huang, J.-S., *Atomization and Sprays* 6, , (1996).
- [30] Colin, O. & Rudyard, M., *Journal of Computational Physics*, 162, 338-371, (2000).

## **A new model for marine Heavy Fuel Oil thermophysical properties: validation in a constant volume spray chamber**

Panagiotis Kontoulis, Dimitris Kazangas<sup>1</sup>, and Lambros Kaiktsis<sup>1</sup>

1:Division of Marine Engineering  
Department of Naval Architecture and Marine Engineering  
National Technical University of Athens, Greece

### **Abstract**

Heavy Fuel Oil (HFO) is widely used in marine propulsion. Marine HFOs are blending products of residue and light fractions, and are commonly referred to as Intermediate Fuel Oils (IFOs). In Computational Fluid Dynamics (CFD) studies, physical model performance depends critically on the accuracy of fuel property values. In this context, a new detailed model for calculating IFO thermophysical properties has been developed in the present work. The new model considers IFO as an equivalent one-component heavy petroleum fraction with undefined composition, while the required input is four values of fuel properties, commonly measured at fuel bunkering, namely: (a) density at 288.15 K, (b-c) kinematic viscosity values at 288.15 K and 323.15 K, (d) sulphur weight content. Here, the thermophysical properties of four widely used marine heavy fuel grades, namely IFO 700/RMK, IFO 500/RMK, IFO 380/RMK and IFO 180/RMG, as prescribed by the ISO 8217:2010, are calculated, validating the new model. Further, the model is tested with CFD simulations of non-reactive spray flow in a large constant volume chamber; the results are in good agreement with recent experiments. The present results are deemed very promising, yielding a solid basis for CFD studies of HFO combustion in marine Diesel engines.

### **Introduction**

Marine Heavy Fuel Oil (HFO) is produced by blending visbroken residue, light petroleum products and performance additives, at the refinery. Thus, marine HFOs are widely known as Intermediate Fuel Oils (IFOs) and characterized by high molecular weight, as well as high density and kinematic viscosity values at ambient temperature. The main IFO content, the visbroken residue, consists of heavy hydrocarbon structures, referred to as asphaltenes and resins, sulphur (S) and metals, such as sodium (Na) and vanadium (V). Partially due to storage requirements, refineries offer a limited number of IFO grades, commonly named by the value of kinematic viscosity at a temperature of 323.15 K (50 °C). For instance, IFO 380 has a kinematic viscosity of 380 cSt at 323.15 K.

IFO is the predominant fuel used in marine Diesel engines, since it is cost effective with respect to its Lower Heating Value (LHV). However, the quality of IFO delivered by refineries is constantly deteriorating, due to the increasing demand for light products. Thus, the overall performance of marine propulsion systems is affected, in terms of increased pollutant emissions, possible Specific Fuel Oil Consumption (SFOC) penalties, as well as casualties in auxiliary machinery. The existing specifications of IFOs delivered onboard vessels are included in the ISO 8217:2010, accommodating developments in marine engine technology, crude oil refining processes, as well as in pollutant emission regulations.

Currently, Computational Fluid Dynamics (CFD) studies can substantially contribute to understand and optimize engine aerothermochemistry. Main in-cylinder processes include the spray breakup, evaporation, fuel-air mixing, ignition and combustion. The effectiveness of CFD modeling depends crucially on the precision of fuel thermophysical properties utilized. In this context, Lin et al. [1] developed an approach for calculating constant (temperature-independent) values of marine fuel properties, and applied it to a double film combustion model of a single liquid droplet. Kyriakides et al. [2] proposed a thermophysical properties model of a given residual fuel, utilizing refinery data and literature studies. The proposed residual fuel properties were adopted in the HFO CFD studies of Chrysosakis et al. [3] for constant volume chambers, the results of which have been compared against experiments. Recent computational studies utilizing a simple representation of HFO composition have considered a two-component approach, with the two components representing a residual (heavy) and a cutter (light) part, both characterized by vapor pressures which are increasing with temperature, and constant or temperature-dependent values for dynamic viscosity, density, latent heat, specific heat capacity and surface tension [4], [5]; the approach has resulted in an adequate representation of HFO combustion in constant volume chambers. A more complex representation of HFO composition is in the context of SARA modeling [6], which considers Saturates, Aromatics, Resins and Asphaltenes as the HFO content. Very recently, Bolla et al. [7] performed non-reactive CFD spray simulations of HFO utilizing a five-component approach, and obtained good agreement against experimental data in a large Spray Combustion Chamber (SCC), presented in [8].

The present study aims at developing a general calculation model of marine HFO thermophysical properties, accounting for different IFO qualities, for engineering CFD studies in marine engines. To this end, the present model builds on the assumption that marine HFO is a heavy petroleum fraction of undefined composition. The model input consists of four thermophysical property values commonly provided at fuel bunkering, while its output is the temperature dependence of the thermophysical properties required in engine CFD simulations. Thus, the model may account for any IFO quality stored onboard a vessel. The present model predictions are compared against literature data. Further, the model performance in the context of non-reactive CFD spray simulations is tested against recent experimental measurements reported in [8], [9], [10]. The results are deemed very promising for CFD studies in marine Diesel engines operating with marine HFO.

### Marine HFO thermophysical properties model and results

In the present work, a new detailed model of marine HFO thermophysical properties is developed, for CFD studies in marine engines. The model is implemented in the fuel library of the CFD code KIVA-3 [11]. The model builds on different experimental and theoretical investigations of heavy petroleum fractions, and considers marine HFO as an equivalent one-component heavy fraction of undefined composition; the model thus follows an approach widely adopted in literature CFD studies for distillate fuels (e.g. approximation of Marine Diesel Oil (MDO) properties with those of n-tetradecane –  $C_{14}H_{30}$ ). CFD modeling of fuel spray breakup, evaporation, ignition and combustion processes in internal combustion engines requires values of the following thermophysical properties: density, viscosity, molecular weight, critical properties, vapor pressure, heat of evaporation, sensible enthalpy, enthalpy of formation, carbon-to-hydrogen atomic ratio and surface tension. The present model accounts for all of the above properties, yielding temperature-dependent values.

In the present section, the new model is briefly described, and applied to the calculation of thermophysical properties of fuel qualities IFO 700/RMK, IFO 500/RMK, IFO 380/RMK and IFO 180/RMG, widely used in the marine industry. Four thermophysical property values, commonly available at bunkering, constitute the model input. Table I shows the values utilized in the present study; the density and sulphur weight content correspond to the upper limits set by ISO 8217:2010 and the International Maritime Organization (IMO), respectively. Further, fuel properties of the HFO utilized in the experiments reported in [10] are calculated. The corresponding input values are given in Table II.

Property	IFO 180/RMG	IFO 380/RMK	IFO 500/RMK	IFO 700/RMK	Remarks
Density at 288.15 K, 1 atm	991 kg/m <sup>3</sup>	1008.5 kg/m <sup>3</sup>	1010 kg/m <sup>3</sup>	1010 kg/m <sup>3</sup>	ISO 8217:2010 (upper limit)
Kinematic viscosity at 323.15 K	180 cSt	380 cSt	500 cSt	700 cSt	
Kinematic viscosity at 288.15 K	2250 cSt	7164.5 cSt	10769.6 cSt	17791.7 cSt	
Sulphur weight content	3.5%	3.5%	3.5%	3.5%	IMO MARPOL ANEX VI (global)

**Table I:** Properties of fuel qualities IFO 700/RMK, IFO 500/RMK, IFO 380/RMK and IFO 180/RMG according to ISO 8217:2010. The corresponding values form the input data set, as required by the present model.

Property	HFO of [10]	Remarks
Density at 288.15 K, 1 atm	1001.1 kg/m <sup>3</sup>	
Kinematic viscosity at 323.15 K	1255 cSt	
Kinematic viscosity at 288.15 K	42504.5 cSt	
Sulphur weight content	0.806%	Low Sulphur HFO

**Table II:** Properties of the HFO utilized in the experimental SCC study of [10]. The corresponding values form the input data set, as required by the present model.

### Density

The dependence of density on temperature is characterized by a negative gradient. The following equation proposed by Denis et al. [12] can be effective in calculating the density of a heavy petroleum fraction, if the value of liquid density at a certain temperature of fuel is known:

$$\frac{\Delta\rho}{\Delta T} = -10^{-3} \cdot (2.34 - 1.9 \cdot \rho_T) \quad (1) \quad \text{where } \rho_T \text{ is the fuel density at temperature } T, \text{ in } gr/cm^3; T \text{ is the}$$

temperature. Figure 1 presents the computed density of the different HFO qualities versus temperature. The corresponding curve of n-tetradecane is also included.

### Kinematic viscosity

The validated correlation of Walther [13], known to be accurate over the wide viscosity range of  $2 \div 2 \cdot 10^7$  cSt, is used for the calculation of kinematic viscosity versus temperature:

$\log[\log(v_T + 0.7)] = A + B \cdot \log(T)$  (2) where  $v_T$  is the kinematic viscosity of fuel at temperature  $T$ , in cSt;  $T$  is the temperature, in degrees Kelvin;  $A$  and  $B$  are constants. Figure 2 shows the computed temperature variation of kinematic viscosity of the present HFO qualities.

### Dynamic viscosity

The dynamic viscosity can be readily calculated via its definition:

$$[\mu = \nu \cdot \rho]_T \quad (3)$$

Figure 3 shows the calculated HFO dynamic viscosity curves. The n-tetradecane curve of Figure 3 is based on the Thermodynamic Research Center (TRC) database [11].

### Molecular weight

The calculation of molecular weight of heavy petroleum fractions, in  $gr/mole$ , can be based on the correlation based on the American Petroleum Institute (API) procedure 2B2.3, known to be valid for molecular weight values up to 700  $gr/mole$  [14]:

$$MW = 223.56 \cdot v_{311.15K}^{(-1.2435+1.1228 \cdot SG_{60F/60F})} \cdot v_{372.15K}^{(3.4758-3.038 \cdot SG_{60F/60F})} \cdot SG_{60F/60F}^{-0.6665} \quad (4) \quad \text{where } v_{311.15K} \text{ and } v_{372.15K}$$

are known values of kinematic viscosity at the given temperatures, in cSt;  $SG_{60F/60F}$  is the specific gravity 60F/60F of the fuel, and is readily calculated through the given density input. The calculated values of HFO molecular weight are listed in Table III.

### Watson characterization factor and normal boiling point

The Watson characterization factor is an indication of a fuel fraction paraffinicity, with values lower than 12 corresponding to heavy fuels [14]. It is defined as follows:

$$K_w = \frac{(1.8 \cdot T_b)^{1/3}}{SG_{60F/60F}} \quad (5) \quad \text{where, } T_b \text{ is the fuel normal boiling point (temperature at which the vapor pressure is}$$

equal to 1 atm), in degrees Kelvin. The property values in the RHS of the above definition may not be known; nonetheless, the Watson characterization factor can still be determined, if the fuel molecular weight and API gravity (other expression of density) are known, according to the API figure 2B2.2 [14]. Once the Watson characterization factor value is known, utilizing its definition, the fuel normal boiling point is readily determined. It is noted that here the normal boiling point of heavy petroleum fractions is considered as an average boiling point of the individual fuel components. The computed values of Watson characterization factor and normal boiling point are presented in Table III.

### Pseudo-critical temperature and pressure

The critical properties of heavy petroleum fractions are hardly determined with experiments. As a result, the pseudo-critical properties are adopted and calculated by empirical equations. Here, the pseudo-critical temperature and pressure (in degrees Kelvin and bar, respectively) are estimated by the validated correlation of Lee and Kesler [12]:

$$T_{pc} = 189.8 + 450.6 \cdot SG_{60F/60F} + (0.4244 + 0.1174 \cdot SG_{60F/60F}) \cdot T_b + (0.1441 - 1.0069 \cdot SG_{60F/60F} \cdot 10^5) / T_b \quad (6)$$

$$P_{pc} = \exp(5.689 - 0.0566 / SG_{60F/60F} - (0.43639 + 4.1216 / SG_{60F/60F} + 0.21343 / SG_{60F/60F}^2) \cdot 10^{-3} \cdot T_b + (0.47579 + 1.182 / SG_{60F/60F} + 0.15302 / SG_{60F/60F}^2) \cdot 10^{-6} \cdot T_b^2 - (2.4505 + 9.9099 / SG_{60F/60F}^2) \cdot 10^{-10} \cdot T_b^3) \quad (7)$$

The calculated values of pseudo-critical properties are listed in Table III, and also identified in Figure 4.

### Acentric factor and vapor pressure

The acentric factor represents the eccentricity (non-sphericity) of a molecule, and can be calculated as follows [15]:  $\omega = -\log P_r^* - 1$  (8) where,  $P_r^*$  is the reduced vapor pressure corresponding to a reduced temperature of 0.7. (A reduced value corresponds to normalization with the critical value). Utilizing the computed value of acentric factor, the vapor pressure can be calculated using a formula suggested in [15], which is valid for values of reduced temperature higher than 0.7. An extension has been suggested by Twu et al. [16], applicable for reduced temperatures higher than 0.5, and is adopted in the present implementation. The computed values of acentric factor are presented in Table III, while the corresponding HFO vapor pressure curves are presented in Figure 4, which also includes an n-tetradecane curve [11].

### Heat of evaporation

The heat of evaporation of a petroleum fraction, in  $KJ/kg$ , is predicted by implementing the equation proposed by Carruth and Kobayaski [17], which correlates the heat of evaporation to the pseudo-critical temperature, the reduced temperature,  $T_r$ , and the acentric factor, and is valid over the range  $0.6 \leq Tr \leq 1.0$ :

$$\Delta h_v = R \cdot T_{pc} \cdot 7.08(1 - T_r)^{0.354} + 10.95 \cdot \omega \cdot (1 - T_r)^{0.456} \quad (9) \text{ where, } R \text{ is the specific gas constant, in } KJ/kg \cdot K.$$

The calculated heat of evaporation curves for the HFO qualities considered are presented in Figure 5; a corresponding curve for n-tetradecane, based on the API procedure 7C1.1, is also included [14]. The present results for HFO are consistent with those obtained in [18], based on an improved generalized equation proposed therein, as well as experimental values reported in [17].

### Enthalpy (sensible)

In the present model, the difference in enthalpy, in  $J/mole$ , is calculated from the following relation:

$$\Delta h = \int_{T_{ref}}^{T_2} c_p(T) \cdot dT \quad (10) \text{ where, } c_p = f(K_w, \omega, T) \text{ is the specific heat capacity, in } J/mole \cdot K, \text{ calculated}$$

as a function of the Watson characterization factor, the acentric factor and temperature, according to the equation proposed for heavy petroleum fractions by Lee and Kesler [12]. Table III includes the computed specific heat of the HFO qualities considered at 288.15 K. Further, Figure 6 presents the full temperature dependence; corresponding curves for n-eicosane and n-tetradecane are also included, based on the API procedure 7A1.1 [14].

### Enthalpy of formation

The enthalpy of formation of a hydrocarbon,  $C_xH_y$ , is defined as follows:

$$[\Delta h_f = \Delta h_f^{liq} + \Delta h_v]_{298.15K}^{1atm} \quad (11) \text{ where, } \Delta h_f \text{ is the enthalpy of formation, } \Delta h_f^{liq} \text{ is the enthalpy of}$$

formation in the liquid state, and  $\Delta h_v$  is the heat of evaporation, in  $KJ/kg$ .

The liquid heat of formation at 298.15 K and 1 atm is derived from the net heat of combustion, and is computed according to the following equation, which neglects pressure corrections [14]:

$$\left[ \Delta h_f^{liq} = \Delta h_c + x \cdot \frac{MW_{CO_2}}{MW_{C_xH_y}} \cdot \Delta h_{f,CO_2} + \frac{y}{2} \cdot \frac{MW_{H_2O}}{MW_{C_xH_y}} \cdot \Delta h_{f,H_2O} \right]_{298.15K}^{1atm} \quad (12) \text{ where, } \Delta h_c \text{ is the net heat of}$$

combustion, in  $KJ/kg$ ;  $\Delta h_{f,CO_2}, \Delta h_{f,H_2O}$  are the enthalpies of formation of carbon dioxide and water, respectively, in  $KJ/kg$ ;  $MW_{C_xH_y}, MW_{CO_2}, MW_{H_2O}$  are the molecular weights of fuel, carbon dioxide and

water, respectively, in  $gr/mole$ ;  $x$  and  $y$  are the numbers of carbon and hydrogen atoms in the equivalent fuel molecule, respectively.

The calculation of net enthalpy of combustion at 298.15 K and 1 atm (in  $KJ/kg$ ), which coincides with the fuel LHV, utilizes a formula that correlates the net enthalpy of combustion with the fuel density and sulphur weight content, suggested for marine heavy fuels in [19]:

$$\Delta h_c = 55500 - 14.4 \cdot \rho - 320 \cdot S\% \quad (13)$$

It is noted that determination of the number of carbon and hydrogen atoms in the equivalent fuel molecule utilizes the calculated molecular weight and the carbon-to-hydrogen ratio. Here, the formula suggested in [12] is utilized:

$$CH_{weight} = 8.7743 \cdot 10^{-10} \cdot \left[ \exp(7.176 \cdot 10^{-3} \cdot T_b + 30.06242 \cdot SG_{60F/60F} - 7.35 \cdot 10^{-3} \cdot T_b \cdot SG_{60F/60F}) \right] \cdot T_b^{-0.98445} \cdot SG_{60F/60F}^{-18.2753} \quad (14)$$

Following [12], carbon-to-hydrogen atomic ratio (the ratio of total carbon atoms to the total hydrogen atoms) is calculated as follows:

$CH_{atomic} = (A_H / A_C) \cdot CH_{weight}$  (15) where,  $A_H$  and  $A_C$  are the atomic weights of hydrogen and carbon, respectively. The calculated values of enthalpy of formation, LHV and  $CH_{atomic}$  ratio are presented in Table III.

#### Surface tension

The surface tension of a heavy petroleum fraction of unknown composition, in mN/m, is calculated based on the API procedure 10A3.2, as follows [14]:

$$\sigma = 673.7 \cdot \left[ \frac{(T_{pc} - T)}{T_{pc}} \right]^{1.232} \cdot K_w^{-1} \quad (16)$$

Figure 7 presents the computed surface tension variation of the different HFO qualities with temperature. The corresponding curve for n-tetradecane, based on the API procedure 7A3.2 [14], is also included. The present results are very similar to experimental ones, reported in [20].

Thermophysical properties	IFO 180/RMG	IFO 380/RMK	IFO 500/RMK	IFO 700/RMK	HFO of [10]
Molecular weight	450 gr/mole	460 gr/mole	474 gr/mole	494 gr/mole	555 gr/mole
Watson / Acentric factors	11.3 / 1.13	11.1 / 1.09	11.1 / 1.10	11.2 / 1.17	11.4 / 1.27
Boiling point at 1 atm	782.27 K	781.51 K	784.94 K	806.34 K	828.03 K
Pseudo-critical temperature	950.59 K	957.33 K	960.28 K	974.86 K	985.68 K
Pseudo-critical pressure	10.87 bar	11.63 bar	11.53 bar	10.54 bar	9.29 bar
Specific heat at 288.15 K	1.351 KJ/Kg	1.312 KJ/Kg	1.312 KJ/Kg	1.331 KJ/Kg	1.369 KJ/Kg
Enthalpy of formation at 298.15 K	167 KJ/Kg	457 KJ/Kg	742 KJ/Kg	844 KJ/Kg	783 KJ/Kg
LHV	40110 KJ/Kg	39857 KJ/Kg	39836 KJ/Kg	39836 KJ/Kg	40826.2 KJ/Kg
Carbon-to-hydrogen atomic ratio	1.0	1.09	1.12	1.06	0.98

**Table III:** Calculated thermophysical properties of fuel qualities IFO 700/RMK, IFO 500/RMK, IFO 380/RMK and IFO 180/RMG according to ISO 8217:2010, as well as the HFO utilized in [10].

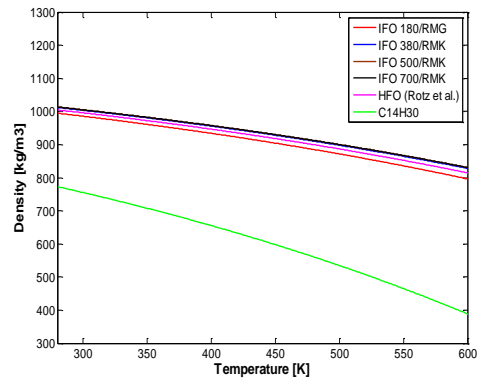


**Figure 1:** Computed density of HFO qualities versus temperature. A corresponding curve for  $C_{14}H_{30}$  is also included.

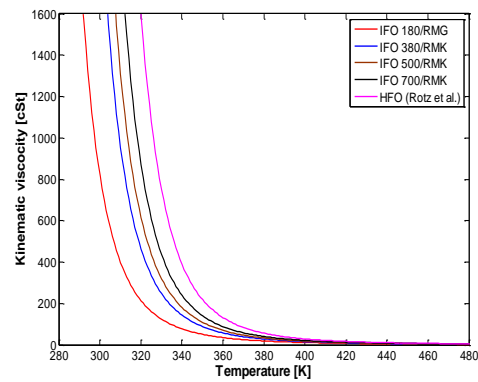


**Figure 2:** Computed kinematic viscosity of HFO qualities versus temperature.

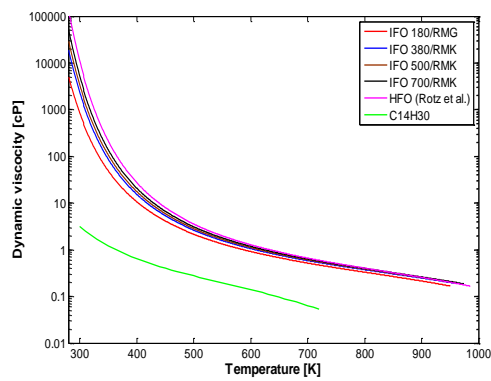


**Figure 3:** Computed dynamic viscosity of HFO qualities versus temperature. A corresponding curve for  $C_{14}H_{30}$  is also included.

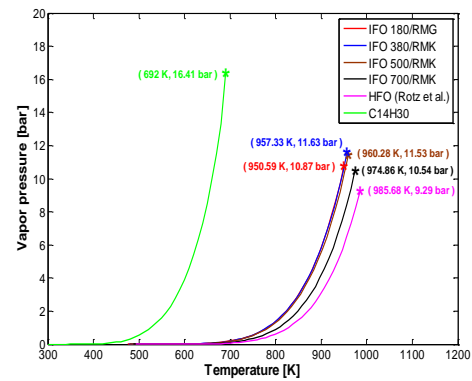


**Figure 4:** Computed vapor pressure of HFO qualities versus temperature. A corresponding curve for  $C_{14}H_{30}$  is also included.

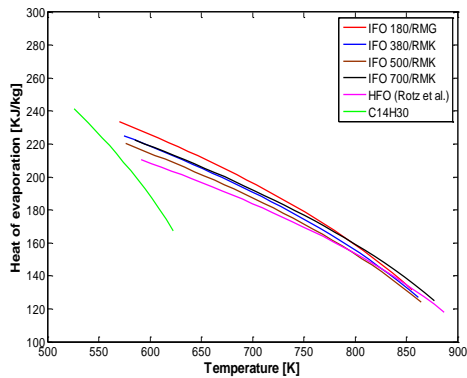


**Figure 5:** Computed heat of evaporation of HFO qualities versus temperature. A corresponding curve for  $C_{14}H_{30}$  is also included.

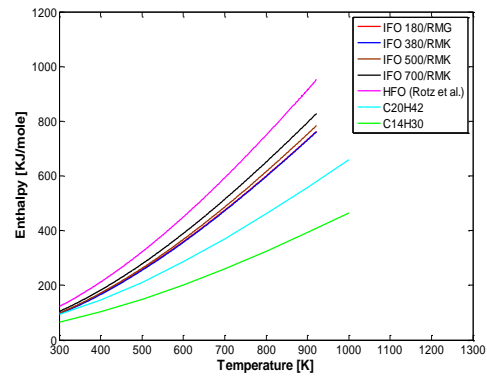


**Figure 6:** Computed sensible enthalpy of HFO qualities versus temperature. Corresponding curves for  $C_{14}H_{30}$  and  $C_{20}H_{42}$  are also included.



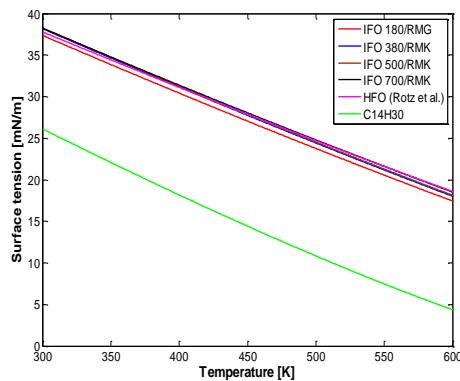


**Figure 7:** Computed surface tension of HFO qualities versus temperature. A corresponding curve for  $C_{14}H_{30}$  is also included.

### Model validation: CFD results in a constant volume spray chamber

The HFO thermophysical properties model presented in the previous section is tested by performing CFD simulations of non-reactive spray flow in a constant volume chamber. Here, the KIVA-3 code is utilized to predict HFO spray development in the large SCC device described in [8], [9], [10]; the chamber size and operating conditions are representative of large marine Diesel engines. The chamber has a size of  $\varnothing 500 \times 150$  mm, and is operated with injection from a single-hole injector of  $\varnothing 0.875$  mm. The present simulations utilize the ETAB spray model [21], [22]. Extensive resolution studies have confirmed the grid and time step independence of the results presented subsequently. Details of the present simulations, including values of the ETAB model constants, are presented in Table IV.

Spray propagation can be characterized by the development of penetration tip with time after the Start Of Injection (SOI) [23]. In the present simulations, the effect of injected fuel temperature is investigated by considering five temperature values, in particular 353.15K, 373.15K, 393.15 K, 413.15 K and 433.15 K; the high end range is representative of fuel preheating in large marine engines. The computational results for penetration tip are presented in Figure 8, which also includes the experimental results of [10], obtained for a fuel temperature of 393.15 K. In all cases, the calculated penetration tip follows the well-known progressive behavior of spray propagation, and is in qualitative agreement with the correlations of [24], [25], which are based on extensive experimental data. The computational results illustrate a marked difference between the spray development of “cold” ( $T=353.15K$ ) and sufficiently heated fuel, with the “cold” spray characterized by substantially higher penetration, due to its minimal breakup. It is worth noting that, in all cases, the initial stage of linear development is similar for all temperatures, while the CFD predictions are in good agreement with the experiment of [10]. In the subsequent stage, spray development is found to depend on fuel temperature: interestingly enough, the penetration tip is initially decreasing with fuel initial temperature, while the trend reverses in the high end of fuel temperatures prescribed in the present computations. Finally, the spray distribution, including Sauter Mean Diameter (SMD) values, is presented in Figure 9 for two representative time instants, for different values of initial temperature, illustrating a minimal breakup and evaporation of the “cold” spray.

<b>Computation case: Non-reactive conditions (N<sub>2</sub>)</b>	
Gas pressure [bar]	30
Gas temperature [K]	900
Injector nozzle hole [mm]	0.875
Injection pressure [bar]	1000
Injection duration [ms]	25
Injector nozzle orientation	co-swirl
Swirl angular velocity [rad/s]	125
Structured grid (Ø500x150 mm)	200,000 cells
<b>ETAB model constants</b>	
Initial spray angle [deg.]	16
Jet breakup length (C)	20
Time scale parameter for 'bag breakup' (k <sub>1</sub> )	0.05
Time scale parameter for 'stripping breakup' (k <sub>2</sub> )	0.222
Initial deformation velocity: $\dot{\gamma}(0) / \omega$	-810
Exponent for initial droplet size distribution (n)	0.5

**Table IV:** SCC simulation parameters and corresponding ETAB model constants.

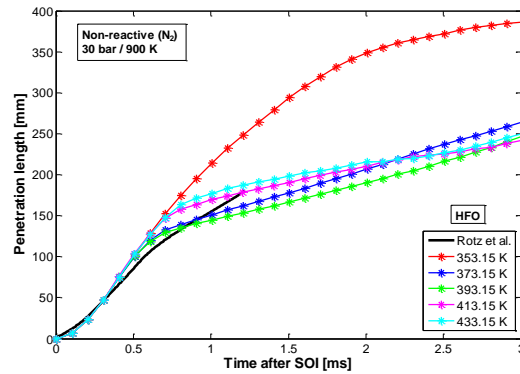


**Figure 8:** Computed HFO spray penetration tip versus time, for different values of preheating temperature. The experimental results of [10] are also included.

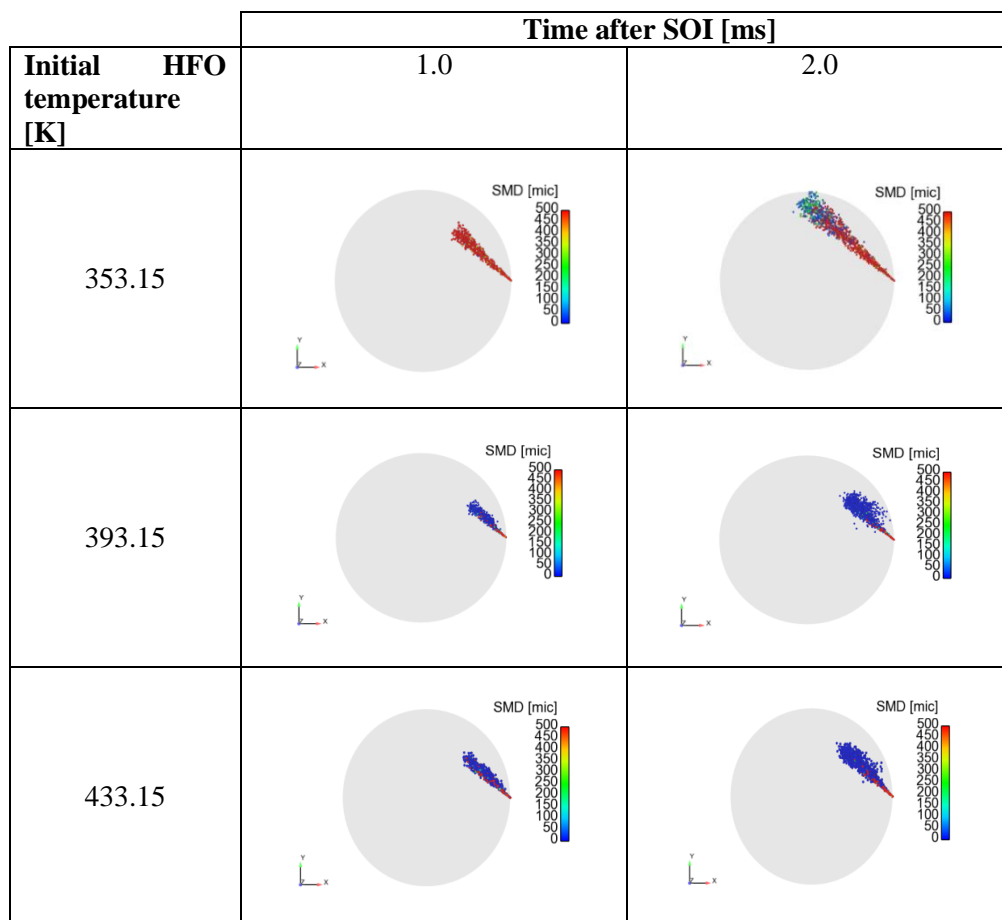


**Figure 9:** HFO droplet SMD distribution for initial fuel temperatures of 353.15 K, 393.15 K and 433.15 K, at 1.0 ms and 2.0 ms after SOI.

## Conclusions

In the present study, a detailed calculation model of marine HFO thermophysical properties was developed. The model assumes that marine HFO is a blended heavy petroleum fraction of undefined composition (IFO). The required model input includes four values of thermophysical properties: (a) density at 288.15 K, (b-c) kinematic viscosity values at 288.15 K and 323.15 K, and (d) sulphur weight content. The choice of the input setting has been intentional, since the required values are provided during bunkering, and characterize the quality of IFO. As a result, the present model can predict the thermophysical properties of any IFO stored onboard a vessel.

Applying the new model, the thermophysical properties of four representative marine HFO qualities, prescribed by the ISO 8217:2010, namely IFO 700/RMK, IFO 500/RMK, IFO 380/RMK and IFO 180/RMG, have been computed. Further, the properties of an HFO utilized in a recent experimental study in a large SCC device were also computed. For the same SCC device, CFD calculations of non-reactive spray flow were performed utilizing the present model, and good agreement with experiments was found for the spray penetration tip. While further testing of the new model, especially for reactive flow, is essential, it appears that the present development may constitute a substantial step towards reliable engineering CFD studies in marine Diesel engines.

## Acknowledgements

The authors would like to thank Dr. G. Weisser, Dr. K. Herrmann and Mr. B. von Rotz of Wrtsil Switzerland, for their valuable support and fruitful discussions. The first author would also like to thank the Norwegian Classification Society (DNV), for financing his doctoral thesis project.

## References

- [1] Lin C.Y., Pan T.C., Chen C.S., *Journal of Marine Science and Technology*, Vol. 3, No. 1, pp. 29-34 (1995).
- [2] Kyriakides N., Chryssakis C., Kaiktsis L., *SAE 2009-01-1858* (2009).
- [3] Chryssakis C., Pantazis K., Kaiktsis L., *CIMAC Congress*, Bergen, Norway, Jun 2010, Paper No. 236.
- [4] Goldsworthy L., *International Journal of Engine Research*, 7: pp. 181-199 (2006).
- [5] Struckmeier D., *Ph.D. Thesis*, Kyushu University, Japan (2010).
- [6] Garaniya B. V., *Ph.D. Thesis*, University of Tasmania, Australia (2009).
- [7] Bolla M., Cattin M.A., Wright Y.M., Boulouchos K., Schulz R., *Proceedings of the ASME 2012 Internal Combustion Engine Division Spring Technical Conference*, ICES2012-81016, Piemonte, Torino, Italy, May 2012.
- [8] Herrmann K., Kyrtatos A., Schulz R., Weisser G., von Rotz B., Schneider B., Boulouchos K., *ICLASS 2009, 11<sup>th</sup> Triennial International Annual Conference on Liquid Atomization and Spray Systems*, Paper No 005, Vail, Colorado USA, July 2009.
- [9] Herrmann K., von Rotz B., Schulz R., Weisser G., Boulouchos K., Schneider B., *ILASS-Europe 2010, 23<sup>rd</sup> Annual Conference on Liquid Atomization and Spray Systems*, Paper No 139, Brno, Czech Republic, September 2010.
- [10] von Rotz B., Herrmann K., Weisser G., Cattin M., Bolla M., Boulouchos K., *ILASS-Europe 2011, 24<sup>th</sup> European Conference on Liquid Atomization and Spray Systems*, Estoril, Portugal, September 2011.
- [11] Amsden A.A., “*KIVA-3: A KIVA program with block-structured mesh for complex geometries*”, fuel library, Los Alamos National Laboratory, LA-12503-MS (1993).
- [12] Riazi M.R., “*Characterization and properties of petroleum fractions*”, ASTM USA (2005).
- [13] Walther C., *Erdöl und Teer*, 7: pp. 382-384 (1931).
- [14] Refining dep't, “*Technical data book, petroleum refining*”, American Petroleum Institute (API), 6<sup>th</sup> edition (1997).
- [15] Pitzer K.S., Lippmann D.Z., Curl R.F., Huggins C.M., Persen D.E., *Journal of the American Chemical Society*, 3433: pp. 77 (1955).
- [16] Twu C.H., Coon J.E., Cunningham J.R., *Fluid Phase Equilibria*, 96: pp. 19-31 (1994).
- [17] Gray J.A., Holder G.D., Brady C.J., Cunningham J.R., Freeman J.R., Wilson G.M., *Industrial & Engineering Chemistry Process Design and Development*, Vol. 24, No. 1, pp 97-107 (1985).
- [18] Zhong X., *Chemical Engineering Communications*, 29: 1-6, pp 257-269 (1984).
- [19] Wauquier J.P., “*Petroleum refining, crude oil, petroleum products, process flowsheets*”, Institute Francais Du Petrole Publications (IFP) (1995).
- [20] Fink C., Buchholz B., Niendorf M., Harndorf H., *ILASS, European Conference on Liquid Atomization and Spray Systems*, Paper ID ILASS08-6-9, Como Lake, Italy, September 2008.
- [21] Tanner F.X., *SAE 970050* (1997).
- [22] Tanner F.X., Weisser G.A., *SAE 980808* (1998).
- [23] Arcoumanis C., Gavaises M., French B., *SAE 970799* (1997).
- [24] Hiroyasu H., Arai M., *SAE 900475* (1990).
- [25] Naber J.D., Siebers D.L., *SAE 960034* (1996).

## Investigation of Fuel Injection Strategies for Partially Premixed Compression Ignition Combustion in Two-Stroke Marine Diesel Engines

Emmanouil Pananakis<sup>1</sup>, Panagiotis Kontoulis<sup>1</sup>, Christos Chrysakakis<sup>2</sup>  
and Lambros Kaiktsis<sup>1</sup>

1: Division of Marine Engineering, Department of Naval Architecture and Marine Engineering, National Technical University of Athens, Greece

2: Maritime Transportation, Research and Innovation Department, DNV, Norway

### Abstract

The implementation of multiple-injection strategies in marine Diesel engines may partially contribute to compliance with emission regulations, while also maintaining a high engine performance. The present computational study investigates the possibility of implementing Partially Premixed Compression Ignition (PPCI) combustion in two-stroke marine Diesel engines. In particular, the concept is implemented in terms of pilot fuel injection with proper orientation of the spray jets, and tested by Computational Fluid Dynamics (CFD) simulations in a large two-stroke marine Diesel engine operating at full load. An early fuel injection is accompanied by long ignition delay, thus allowing fuel-air premixing.

In the present study, a different orientation of fuel injection is considered for pilot and main injection, which can be implemented in practice in terms of twin needle injectors. A CFD parametric study of spray pilot injection angles is first performed, aiming at a proper fuel-air mixing, while also avoiding spray wall impingement. Next, the entire spray injection profile (pilot and main injection) is optimized, by coupling the KIVA-3 CFD code with an optimization code based on evolutionary algorithms. Here, multi-objective optimization is performed, aiming at minimizing simultaneously the engine nitric oxides (NOx) emissions and Specific Fuel Oil Consumption (SFOC). Solutions are evaluated against a reference operation mode, characterized by continuous injection. Both an unconstrained and a constrained optimization problem are considered, the latter complying with the engine maximum pressure limit, while also maintaining the work output of the reference mode. The algorithm converges to Pareto optimal solutions. For the unconstrained problem, several solutions are characterized by NOx reduction slightly higher than 20% and SFOC reduction of the order of 3%. For the constrained problem, reductions up to 18% in NOx emissions are attained, without a SFOC penalty. Optimal solutions are further characterized by visualizations of the computed reactive flow fields and assessment of the associated engine thermal loads.

---

### Introduction

The environmentally friendly and efficient operation of two-stroke marine Diesel engines is dependent on air charging, fuel-air mixing, ignition and combustion processes. Engine optimization is associated with minimizing Specific Fuel Oil Consumption (SFOC), emissions and thermal loads. To this end, understanding of in-cylinder flow and combustion processes is essential.

Among different approaches, the concept of Partially Premixed Compression Ignition (PPCI) appears as a promising candidate for the reduction of pollutant emissions from large marine engines. PPCI is associated with the use of multiple injection events (e.g. pilot and main injection) within an engine cycle; a precise shaping of injection profile is enabled by common rail injection systems. In the context of PPCI, the timing of pilot injection is well advanced before Top Dead Center (TDC), allowing enough time for fuel-air premixing. This contributes to minimization of pollutant emissions formation, due to the low levels achieved for the local values of both equivalence ratio and temperature.

PPCI has been investigated mostly for engines of the automotive industry. In particular, Lechner et al. [1] employed PPCI by implementing early pilot injection in a four-stroke high speed Diesel engine, in conjunction with heavy Exhaust Gas Recirculation (EGR) rates. Their study, including both experiments and CFD analysis, has demonstrated that a substantial reduction in both nitric oxides (NOx) and soot emissions is feasible, at the expense of increased SFOC. Motivated by its longer ignition delay times, Struckmeier et al. [2] utilized Light Cycle Oil (LCO) in an experimental two-stroke medium size Diesel engine operated with split injection, thus attaining a PPCI mode with reduced NOx emissions.

Engine optimization can utilize the advances in both CFD and optimization methods, in particular evolutionary algorithms. Engine optimization studies coupling CFD and optimization tools are nowadays feasible, both for the small (automotive) [3] and the large (marine) engines [4]. In particular, the study of [4] has shown that, in a large two-stroke marine engine operating at full load, optimization of the injection profile consisting of pilot and main injection can result in gains in SFOC of the order of 2% accompanied by NOx

reductions of the order of 15%. Nonetheless, several of the optimal solutions identified in [4], characterized by an early pilot injection, resulted in significant wall wetting, which is associated with increased formation of unburned hydrocarbons and soot, as well as elevated engine thermal loads. Following the study of [4], the present work addresses the problem of optimizing the injection profile of the same large two-stroke marine Diesel engine, while simultaneously surpassing the above disadvantages. To this end, the PPCI concept is utilized for pilot injection, by implementing separate injection orientation for the pilot and main injection. This can be nowadays readily implemented in terms of twin needle fuel injectors [5]. The present study utilizes a coupling between a CFD code and an optimization code based on evolutionary algorithms, and aims at simultaneously minimizing SFOC and NOx emissions.

### Engine parameters and computational set-up

The engine geometry corresponds to the RT-flex58T-B engine of Wärtsilä Switzerland. The main engine characteristics are given in Table I. Each cylinder head is equipped with three identical injectors, located symmetrically on its periphery; each injector has one needle with five orifices of different diameter, to enhance dispersion of the liquid fuel into the cylinder. The injection direction is defined in terms of angles  $\alpha$  and  $\beta$ , shown in Figure 1. In the reference design, the injection direction generally coincides with that of air swirl (positive values of angle  $\alpha$ , see Table II), while the values of angle  $\beta$  correspond to injection directions which do not deviate significantly from a horizontal one.

Bore Diameter [m]	0.58
Stroke [m]	2.416
Injection System	Common Rail
Exhaust Valve Closing, EVC [°CA ATDC]	-96
Exhaust Valve Opening, EVO [°CA ATDC]	120
Full Load Speed [RPM]	105

**Table I:** Main engine characteristics.

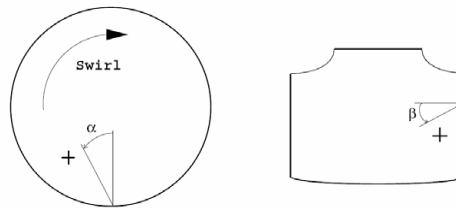


**Figure 1:** Definition of injection angles  $\alpha$  and  $\beta$ .

hole nr.	1	2	3	4	5
angle $\alpha$	-	+	+	+	+
angle $\beta$	+	+	+	+	+

**Table II:** Reference engine design: signs of injection angles  $\alpha$  and  $\beta$ , defined in Figure 1.

The present CFD study utilizes the KIVA-3 code [6, 7], modified in terms of physical models appropriate for large two-stroke marine Diesel engine conditions. These modifications concern spray atomization, ignition, combustion and NOx formation models [8, 9, 10, 11]. The engine has been tested experimentally with Marine Diesel Oil (MDO) as fuel; in the present implementation, the fuel thermophysical properties are approximated with those of n-tetradecane ( $C_{14}H_{30}$ ). The closed part of the engine cycle is simulated; the swirl (tangential) velocity profile is initialized in terms of a Bessel function, and corresponds to a proper value of the swirl number ( $\omega_{swirl}/\omega_{engine}$ ). CFD results have been validated against experimental data corresponding to operation of the engine at full load with continuous injection; good agreement has been demonstrated [4]. In the present study, the validated discretization parameters of [4] are maintained.

As indicated above, in the present work the PPCI concept is implemented by considering different injection orientation between the pilot and main injection, enabled by twin needle injectors. Lift of each needle results in the fuel exit from five holes - different for the pilot and main injection events. In both cases, the diameter values of the reference design are maintained. For a given injector, the exit points of all spray jets are considered identical.

### Parametric variation of spray injection angles for pilot injection

As noted above, in the present work PPCI is implemented in the context of split injection from twin needle injectors. Thus, injection angles are different for the pilot and main injection. To avoid cylinder liner wetting, relatively high values of the angle  $\beta$  should be considered for pilot injection (injection towards the piston), for a proper range of angle  $\alpha$ , which should be also identified. An early pilot injection may thus allow for extensive fuel-air mixing and a PPCI combustion mode of the pilot injected fuel, without wall wetting. To this end, proper values of angles  $\alpha$  and  $\beta$  should be identified for pilot injection. For main injection, the  $\alpha$  and  $\beta$  values of the reference design are maintained.

An extensive variation of angles  $\alpha$  and  $\beta$  for pilot injection was therefore performed, and CFD results were evaluated in terms of the final NO<sub>x</sub> concentration and net cycle work output. It was realized that a pilot injection pattern characterized by (i) small negative values of angle  $\alpha$ , and (ii) values of  $\beta$  covering a wide range was appropriate for the present engine (see Table III). Thus, a proper “pilot injector” was identified, and was subsequently used in optimization studies of the injection profile.

hole nr.	1	2	3	4	5
angle $\alpha$	-	-	-	-	-
angle $\beta$	+	+	+	+	+

**Table III:** Signs of injection angles  $\alpha$  and  $\beta$  for pilot injection, defined in Figure 1, as identified in the present parametric studies.

### Optimization results

In the present engine optimization studies, the KIVA-3 CFD code has been coupled with the EASY optimization code [12], which is based on Evolutionary Algorithms (EAs). EAs are semi-stochastic methods, based on an analogy with Darwin’s laws of natural selection. In the context of EAs, a candidate solution (search point) is called an *individual* or *chromosome*. Individuals are composed of genes, which are the problem design variables, encoded using a floating-point representation in the form of bit strings. EAs evolve an initial population (first generation) of individuals, and finally converge to the optimal solution(s). In multi-objective optimization, the final set of optimal solutions forms the Pareto front [13].

In the present implementation, each generation is composed of 72 individuals, which are evaluated simultaneously by KIVA-3 simulations. Utilizing the evaluator results, solutions are ranked, and a number of them are selected as parents. The new generation (offspring), also consisting of 72 individuals, is evaluated, and the procedure terminates after evaluation of a total of 16 generations (over 1000 individuals).

A generic injection profile, consisting of a pilot and a main injection event is considered (see Figure 2). This shape is readily determined in terms of four parameters, which form the present problem’s design variables: (a) Start Of Pilot Injection (SOPI), (b) Start Of Main Injection (SOMI), (c) Pilot Mass Fraction (PMF), as percentage of the total fuel mass, and (d) Mass Reduction (MR), as percentage of the reduction in total injected fuel mass with respect to the reference case. The opening and closing of injection valves follows the dynamics of the actual engine injector.

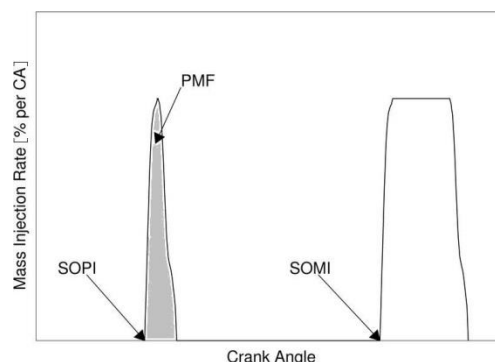


**Figure 2:** Sketch of injection profile, consisting in pilot and main injection, with three design variables identified. Considering a fourth design variable, related to the total injection fuel mass, fully identifies the injection velocity variation.



The specification of each design variable search space was guided by corresponding studies for the same engine, reported in Kontoulis et al. [14] and Andreadis et al. [4], and also takes into account trends identified in the present studies of pilot injection angles variation. For instance, the variation of SOPI was limited to the range  $[-40^\circ, -30^\circ]$  CA ATDC, which is a marked difference to the corresponding range in [4] ( $[-40^\circ, -5^\circ]$  CA ATDC). The present choice regarding SOPI values is thus consistent with the requirement of avoiding wall wetting. The selected range of all four design variables is given in Table IV.

Design Variable	Range	
	Min	Max
Start Of Pilot Injection, SOPI ( $^\circ$ CA ATDC)	-40	-30
Start Of Main Injection, SOMI ( $^\circ$ CA ATDC)	1	4
Pilot Mass Fraction, PMF (% of total injected mass)	2	17
Mass Reduction, MR (% of reference case)	0	10

**Table IV:** Range of the optimization problems design variables.

The objective functions of the present optimization problems are: (a) the final NO<sub>x</sub> concentration, normalized with the reference case value, and (b) an estimated value of SFOC, normalized with the corresponding value of the reference case. Here, the SFOC estimate is the ratio of the injected total fuel mass to the work integral,  $\int p dV$ , of the closed part of the cycle.

Both an unconstrained and a constrained optimization problem have been considered. The latter has taken into account real limitations imposed, namely: (i) a limit of 150 bar for the maximum cylinder pressure, to avoid excess component loading, and (ii) a limit of minimum work output per cycle equal to that of the reference case.

In Figure 3, the final Pareto fronts of both the unconstrained and constrained optimization problems are presented; the corresponding results of Andreadis et al. [4] are also included. The results demonstrate that the present implementation of the PPCI concept improves both performance and NO<sub>x</sub> emissions of the engine, in comparison to using the same orientation of the spray jets for pilot and main injection. In particular, for the unconstrained problem, a number of solutions are characterized by NO<sub>x</sub> reduction of the order of 20% and SFOC reduction of the order of 3%, with respect to the reference case.

For the constrained problem, NO<sub>x</sub> reduction up to 18% is attained, without a SFOC penalty (Figure 3). In both cases, the present results consist a significant improvement over the ones reported in Andreadis et al. [4]. In Table V, the values of injection profile parameters, the resulting objective functions and the values of constrained variables for cases H, I, J, K and the reference case are presented. These results indicate a nearly zero reduction in injected fuel mass. The pilot injected mass is close to 10% of the total fuel mass. Values for SOPI are close to  $-35^\circ$  ATDC, while the SOMI values are slightly higher than  $3.5^\circ$  ATDC. Among the optimal constrained solutions, case H is most attractive, characterized by NO<sub>x</sub> reduction of 18%, at no SFOC penalty. Thus, case H is further analyzed.

The injection profile of Case H is presented in Figure 4, in which the (continuous) profile of the reference case is also included. Pilot injection initiates around  $-35^\circ$  ATDC and lasts about  $3^\circ$  CA, while main injection starts at  $4^\circ$  ATDC ( $2^\circ$  CA delayed in comparison to the reference case), and its duration is nearly  $14^\circ$  CA. Visualizations of computed flow fields are presented in Figure 5, at representative values of engine crank angle. Figure 5 also presents visualizations of Case C reported in [4]; the pilot injection parameters of the two cases are very similar, but the injection angles are substantially different, since single-needle injectors were considered in [4]. The flow visualization illustrates that, in Case C, pilot injection is associated with wall wetting, with fuel still remaining in the near-wall region at TDC. This is avoided for injection from twin needle valves, due to the modified injection angles. Thus, in the present Case H, a PPCI mode is attained, characterized by increased fuel-air mixing, reduced temperatures and substantial reduction of thermal loads.

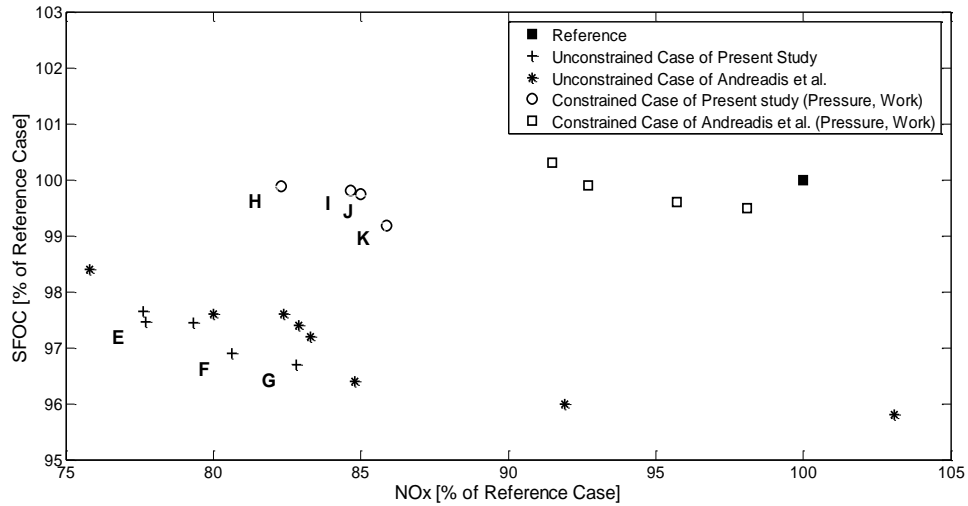


**Figure 3:** Final Pareto fronts (normalized values of exhaust NOx concentration and SFOC) of both unconstrained (cases E, F and G) and constrained (cases H, I, J and K) problems. The corresponding Pareto fronts of Andreadis et al. [4] are also presented.

Design Variables	Reference	H	I	J	K
SOPI (°CA ATDC)	-	-35.71	-36.53	-37.71	-34.26
PMF (% total injected mass)	-	9.93	8.98	8.35	10.09
SOMI (°CA ATDC)	2.00	3.98	3.65	3.59	3.67
MR (% of reference case)	-	0.06	0.24	0.50	0.89
<b>Objective Functions</b>					
NOx (% of reference case)	100	82.29	84.66	85.00	85.87
SFOC (% of reference case)	100	99.88	99.80	99.74	99.18
<b>Constrained Variables</b>					
Maximum cylinder pressure (bar)	149.80	147.74	149.54	148.66	149.46
Work output, W (% of reference case)	100	99.99	99.97	99.78	99.95

**Table V:** Series of computations with constrained maximum pressure and minimum work output: injection profile design variables, normalized values of the final NOx concentration and SFOC, values of constrained variables, for the reference case and the optimal cases H, I, J and K, identified in Figure 3.

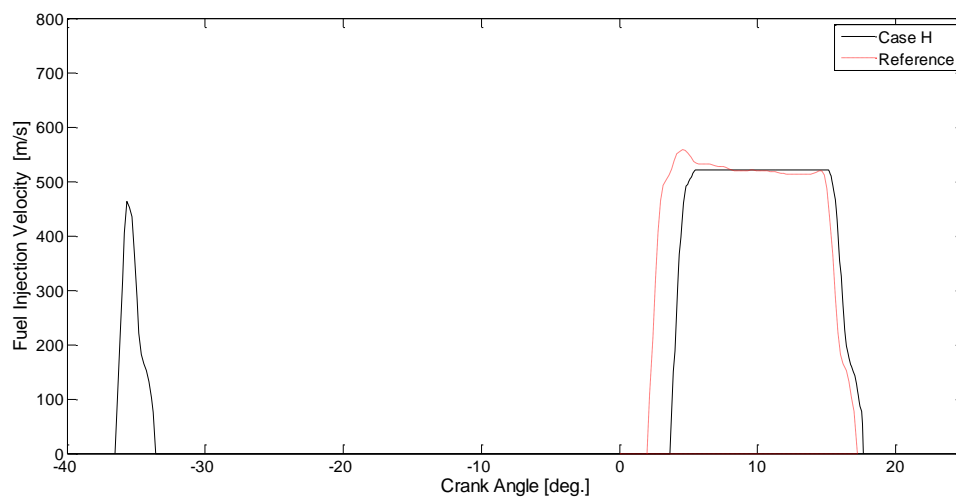


**Figure 4:** Fuel injection velocity profile for case H and for the reference case.

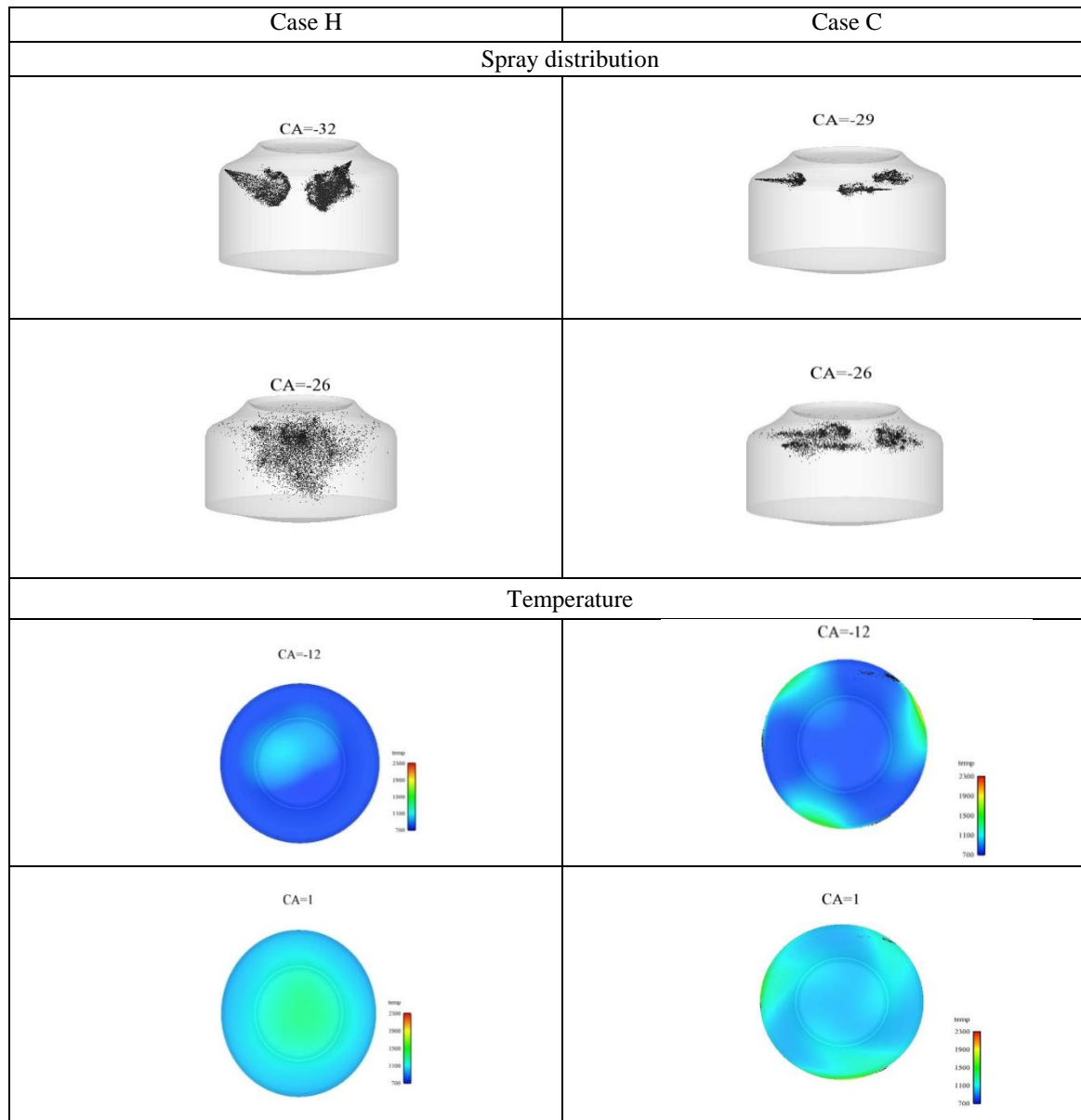


**Figure 5:** Visualization of computed flow fields, at representative engine crank angle values, for Case H, and for Case C reported in [4]: spray distribution and color-coded temperature contours at the injectors' plane.

## Conclusions

In the present study, alternative injection strategies were investigated in the context of split injection, including pilot and main injection, in order to implement PPCI combustion in a large two-stroke marine Diesel engine. With respect to the reference engine design, a major difference implemented is a pilot injection directed towards the piston, which can be implemented in terms of twin needle valves. This contributes to increased fuel-air mixing, while simultaneously avoiding wall wetting. A parametric study has identified a proper range of injection angles and injection profile parameters. Those were utilized in the frame of multi-objective optimization studies, based on a coupling between the CFD code and an optimization code. Both an unconstrained and a constrained problem (in terms of maximum cylinder pressure and minimum cycle work output) were considered. For the unconstrained problem, substantial reductions in both NO<sub>x</sub> emissions and SFOC, in comparison to the reference case, were attained. For the constrained problem, a reduction of nearly 20% in NO<sub>x</sub> was achieved, while maintaining the reference case SFOC level. The present development yields a basis for more extensive optimization studies, including the addition of injection angles in the design variables, as well as of soot emissions in the objective functions.

## Acknowledgements

The authors would like to thank Professor K.C. Giannakoglou of the National Technical University of Athens, for providing the EASY optimization software, and for helpful discussions. They would also like to thank Dr. G. Weisser of Wärtsilä Switzerland, for fruitful discussions and for providing the engine data. This work has been partially supported by the EU project MARINELIVE, grant Nr. 264057. This support is gratefully acknowledged. The second author would also like to acknowledge the financial support by the Norwegian Classification Society (DNV).

## Nomenclature

$\omega_{\text{swirl}}$	swirl angular velocity
$\omega_{\text{engine}}$	crankshaft angular rotational speed
$p$	pressure
$V$	volume

## References

- [1] Lechner G.A., Jacobs T.J., Chryssakis C.A. and Assanis D.N., *SAE 2005-01-0167* (2005).
- [2] Struckmeier D., Tsuru D., Kawauchi S., Shinnosuke O. and Tajima H., *COMODIA 2008*, pp. 335-342, Sapporo, Japan, July 2008.
- [3] Shi Y., and Reitz R.D., *SAE 2008-01-0949* (2008).
- [4] Andreadis P., Zompanakis A., Chryssakis C. and Kaiktsis L., *International Journal of Engine Research*, pp. 14-29, Vol. 12, 2011.
- [5] Sillanpää H. and Åstrand U., *CIMAC Congress*, Bergen, 2010, Paper No. 95.
- [6] Amsden A.A., O'Rourke P.J. and Butler T.D., "*KIVA II – A Computer Program for Chemically Reactive Flows with Sprays*", Los Alamos National Laboratory LA-11560-MS, 1989.
- [7] Amsden A.A., "*KIVA-3: A KIVA Program with Block-structured Mesh for Complex Geometries*", Los Alamos National Laboratory, LA-12503-MS (1993).
- [8] Tanner F.X., *SAE 970050* (1997).
- [9] Tanner F.X., Weisser G.A., *SAE 980808* (1998).
- [10] Weisser G., Tanner F. and Boulouchos K., *SAE 981451* (1998).
- [11] Weisser G., *PhD Thesis*, ETH Zurich, Switzerland, 2001.
- [12] EASY, the evolutionary algorithms system, 2008, Home page available from <http://velos0.ltt.mech.ntua.gr/EASY/>.
- [13] Zitzler E., Laumanns M. and Thiele L., *Evolutionary Methods for Design, Optimization and Control*, Barcelona, Spain, 2002.
- [14] Kontoulis P., Chryssakis C. and Kaiktsis L., *COMODIA 2008*, pp. 1-8, Sapporo, Japan, July 2008.

## Detailed Investigation of Multi-Component Spray Model Capabilities for Diesel Engine Simulation

S. Möller<sup>1</sup>, G. Dutzler<sup>1</sup>, E.v. Berg<sup>2</sup>, P. Priesching<sup>2</sup>, W. Payer<sup>3</sup>,  
J.M. Garcia-Oliver<sup>4</sup> and J.V. Pastor<sup>4</sup>

1: Virtual Vehicle Research Center, 8042 Graz, Austria

2: AVL List GmbH, 8020 Graz, Austria

3: OMV Refining & Marketing GmbH, 2320 Schwechat, Austria

4: CMT Motores Térmicos, Universitat Politècnica de València, Spain

### Abstract

In order to improve the accuracy of the numerical prediction of soot and NO<sub>x</sub> formation in internal combustion engine simulations, it is possible that representative components of fuel are considered. This investigation aims to validate a methodology to represent Diesel fuel by a discrete number of chemical species. In the first step the spray and mixture formation is investigated. For this purpose a binary mixture of Decane and Hexadecane of varying percentages has been considered. Extensive measurements were conducted in an optically accessible test engine to characterize the inert spray behavior of these binary mixtures. Experimental data was obtained for the spray liquid-length as well as the spray vapor penetration and the plume shape. The experimental data was used extensively to adapt the free parameters of the multi-component CFD spray submodels. An optimization method was used combined with a quality function based on mean deviations of experimental and calculated liquid and vapor penetration curves. Results generally show a substantial improvement of the predicted spray liquid length and vapor penetration. The effect of different combustion chamber pressures and temperatures could be predicted well whereas the effect of varying injection pressures was overestimated.

### Introduction

Compared to the classical approach using a single compound fuel in CFD simulations multi-component (MC) modelling has the potential for significant improvements. The representation of spray behaviour depending on varying properties of different fuel mixtures is improved in terms of spray penetration, entrainment and fuel vapor distribution.

The aim of the work was an extensive experimental validation of the involved spray submodels in a range of boundary conditions typical for the combustion in diesel engines. The multi-component approach is applied for mixtures of the two components Decane and Hexadecane to reduce the fuel composition complexity and to analyse the effect of hydrocarbons with low and high volatility in most simple way. Further analysis with more realistic 6-component surrogate fuels will be done in future work.

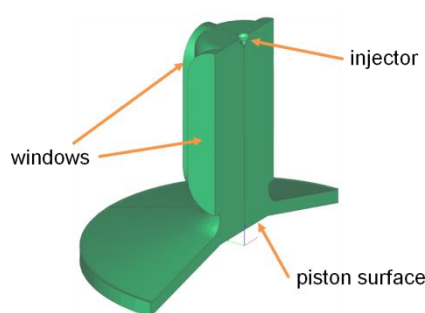


**Figure 1.** Cut through the inner volume of the combustion chamber of JW50 engine

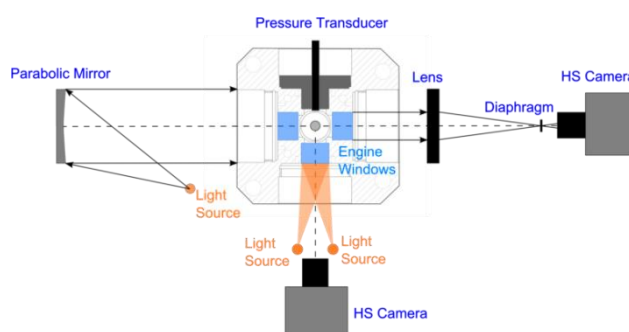


**Figure 2.** Experimental set-up for spray measurements

### Experimental facility

Experiments for spray characterization under inert conditions have been conducted in a hot spray test rig which is described in detail in [8]. This facility is based on a modified loop-scavenged single cylinder 2-stroke direct injection Diesel engine (Jenbacher JW50) with a displacement of 3 L and low rated rotational speed (500 rpm). This apparatus makes optical studies on free sprays under inert or reactive diesel-like thermodynamic conditions possible. Optical access to the high-pressure chamber can be easily achieved through the cylinder head which encloses a cylindrical combustion chamber large enough to avoid spray impingement against engine

walls. This chamber has an upper port where a single-hole injector is mounted, and four lateral orthogonal openings used for optical access and instrumentation purposes. Figure 1 features a cut through the inner volume of the combustion chamber in near top-dead-center (TDC) position.

During the course of this investigation the injection system and the two-component spray were characterized by measuring the spray liquid length (LL) and the spray vapor penetration (VP) by Mie scattering and Schlieren technique, respectively, see Figure 2. For the liquid phase, light scattered by liquid droplets is imaged by a digital high-speed camera. Further details on a similar arrangement can be found in [9]. For the vapor phase, a transmission Schlieren arrangement is used, see also [10].

### Fuels used in the investigation

In this investigation five binary mixtures of Decane and Hexadecane were considered. The mixture composition was varied from 0% (D0) to 30% (D30), 50% (D50), 70% (D70) and 100% (D100) Decane. The required physical properties data base for Decane and Hexadecane as well as the mixture rules to obtain mixture properties for viscosity, density, vapor pressure and surface tension were cross checked against measurement data provided by OMV. Good agreement in the temperature range covered by the measurements has been found, see Figure 3.

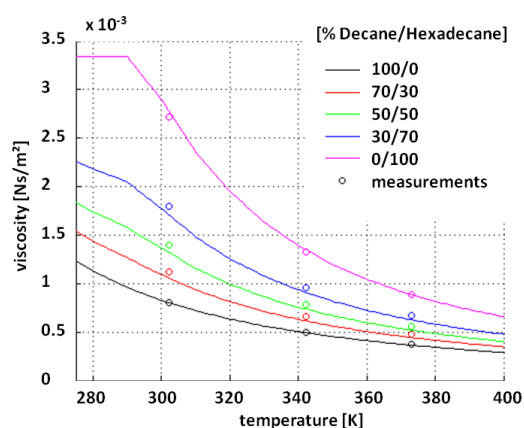


Figure 3. Comparison of measured fuel viscosity and data used in the simulation software

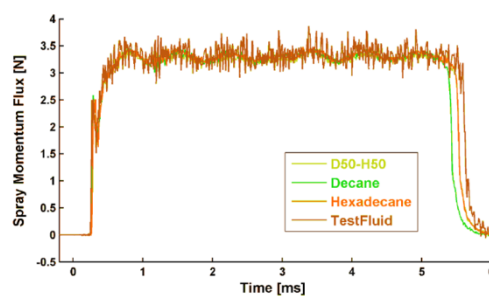


Figure 4. Spray momentum measurements for different fuels at a rail pressure of 1500 bar

### Injection system

The injection system in the JW50 engine consists of a single-hole injector and is akin to current designs used in common road car engines. The injector orifice diameter at the tip is nominally 0.14mm. The injection hole has a length of around 1mm and is of conical shape. The difference between the inlet and outlet diameter is around 0.014mm. The injector was processed by hydro-erosive grinding in order to avoid cavitation. To obtain valid data for setting up proper initial and boundary conditions for the simulation the injector was characterized through rate of injection (ROI) and spray momentum measurements before start of the tests in the research engine. Here generally no significant differences between different mixtures could be observed, see Figure 4.

### Test Matrix

A range of different injection conditions were simulated. These correspond with the tests carried out on the JW50 engine by CMT Motores Térmicos. The test matrix included a variation of the injection pressure from 500 to 1000 and 1500bar. The combustion chamber pressure was varied from 43 to 53 and 73bar. The test matrix was carried out for two different combustion chamber temperatures of 765K and 900K, respectively. Finally 90 different test points were considered in this study, see also scheme in Figure 7.

### Simulation Model setup

#### Computational Mesh

Based on test calculations with a detailed moving mesh taking into account the piston motion a simplified mesh with strongly reduced size has been derived to be used for spray simulations in the near injector region, see Figure 5. For this mesh the neglected features of piston motion and geometrical details of the chamber have been found to be small if the simulation period is limited to 0.6 ms after SOI, see Figure 6. In the final mesh hexahedral cells of a side length of 0.5 mm have been used and mesh expansion in radial direction was applied

to further reduce cell count. Finally the spray box mesh used for the optimization consists of 5.250 cells only which allows for acceptable simulation time despite performing numerous design variations during the optimization procedure.

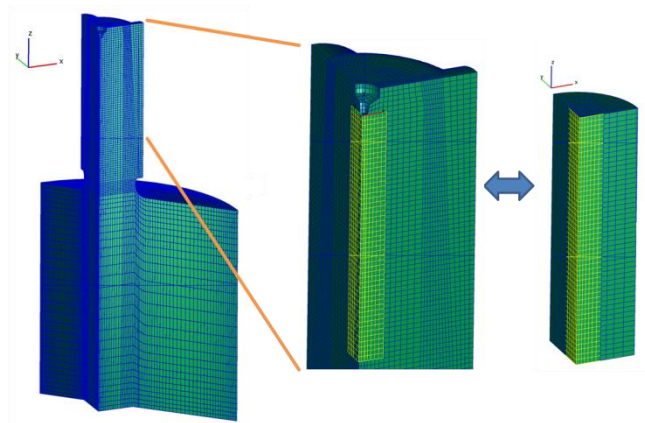


**Figure 5.** Derivation of mesh used in optimization

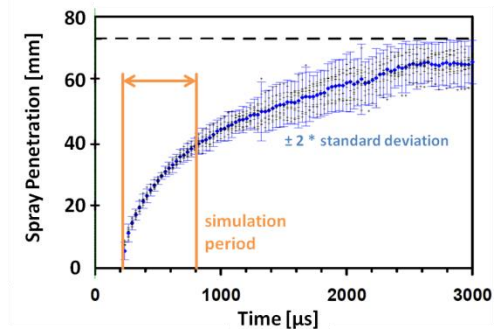


**Figure 6.** Scattering of measured penetration length depending on transient secondary flow structures

### Boundary and Initial Conditions

In-cylinder flow simulations with the detailed engine mesh were conducted to obtain initial conditions for the reduced simulation model used in the optimization. As a result the static pressure boundary condition was taken from the measured pressure trace and averaged over the simulation period. The initialization of the turbulence and temperature for the simplified simulation model was done by averaging corresponding simulation results from the detailed simulation. The initial mean velocity was set to zero in the entire calculation domain. The turbulence model utilized for all simulations was the  $k$ - $\zeta$ - $f$  model in combination with a hybrid wall treatment (see [7]).

### Spray Model

In general the Eulerian-Lagrangian approach was applied in order to carry out the spray simulations. The utilized spray model consisted of submodels for droplet break-up, evaporation and turbulent dispersion. In order to model the injection behaviour of the binary mixture of Decane and Hexadecane appropriate multi-component formulations of the above submodels were used.

The multi-component evaporation model in the AVL FIRE program is based on the model of Abramzon and Sirignano [1]. The model sets up mass balances for each of the vapor components as well as an overall enthalpy balance for the thermal and concentration boundary layers which are solved with an iterative method [2,3].

The break-up of the liquid jet is commonly divided in two distinct processes: the primary jet and secondary droplet break-up. In this study for both processes, the stripping break-up of large fuel droplets near the injector nozzle as well as the atomization process further away from the injector were simulated with the WAVE child break-up model [4,11]. This model combines the continuous reduction of droplet diameters with the production of child parcels mainly to improve spray evaporation near the injector nozzle. Turbulent dispersion is simulated based on the stochastic dispersion method by Gosman and Ioannidis [6] combined with a drag model based on a correlation by Schiller and Naumann [7].

### Optimization

The simulation model described above was applied to the whole test matrix. First results using standard settings for the spray submodels were reasonably good regarding trends of experimentally varied boundary conditions. However differences for the predicted absolute levels of LL and VP were observed. This served as the starting point for the following optimizations. Based on the experimental data the choice of model parameter settings should be improved by means of a numerical optimizer. Further critical regions for model improvement should be identified.

### Optimization strategy

The employed strategy was to vary certain parameters of the spray submodels to alter the break-up and evaporation behaviour. Through the definition of a quality function the deviations between experimental results and numerical prediction for the LL and VP should be minimized. For the optimization a genetic algorithm



(GA) method was used, see also [7]. As this is a stochastical global search method a GA method theoretically explores the whole parameter space but tends to converge to an optimum after a number of design evaluations. An advantage of such a method is its robustness against local optima, which can corrupt especially deterministic optimization methods. Starting with a certain number of start designs the principle of mutation and selection is used to find design variations which minimize the quality function. In the method used in this study new designs are built partly through recombination of settings from pairs of existing design points and partly through direct stochastical variation of single parameter values.

### Case selection

The simulations during the optimization were carried out for a selection of cases only to reduce the computational effort. The test cases were selected in such a manner that the selected points should represent the entire range of boundary conditions and weighting of a specific boundary condition should be avoided. Figure 7 shows the complete test matrix and highlights cases selected for the optimization.

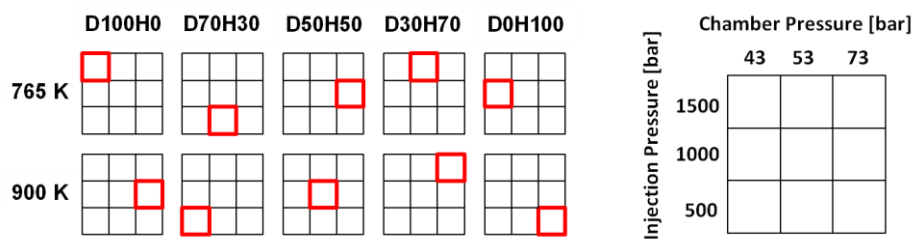


**Figure 7.** Full test matrix and selection of ten cases used in numerical optimization

After the optimization the entire test matrix was recalculated using the spray model with the improved parameter set to evaluate the quality of the optimization results.

### Optimized Parameters

In order to achieve the matching of the penetration curves with the numerical optimizer the spray model parameters listed in Table 1 were modified:

Break-up parameters		Evaporation parameters	
C1	Controls final stable droplet size	E1	Heat transfer correction
C2	Controls break-up time	E2	Mass transfer correction
C4	Controls number of child parcels		
C5	Controls mass in new child parcels		
C7	Pressure influence on droplet diameter reduction		
C8	Pressure influence on break-up time		

**Table 1.** Parameters modified during numerical optimization

The continuous reduction of the droplet diameter calculated by the break-up submodel is influenced by model parameters C1 and C2. The parameter C1 is given in the literature [4] as a fix value but is varied indirectly during the optimization by changing C7 which represents the influence of the static pressure on C1, according to Wakisaka [5]. The effective value of C2 is varied in a similar manner by changing C8. The production of child parcels by the break-up submodel is influenced by the parameters C4 and C5. More details about all model parameters can be found in the description of the submodels in reference [7].

### Quality Function

During the optimization the 10 selected test cases are calculated simultaneously to evaluate one single variation of the design parameters. As response 10 resulting liquid penetration curves as well as 10 vapor penetration curves were considered and compared against corresponding measurement results. A quality function was defined based on the time-averaged absolute deviation between simulated and measured curves. These averaged deviations are squared and summed up. This way the quality function includes a stronger weighting for cases with bigger deviations but avoids a strong weighting for temporal deviations resulting from scattered measurement data. Both the initial behaviour and the steady penetration level of the liquid spray should match the experimental findings. Considering this the length of the simulation period was chosen to equally cover the steady part of the liquid penetration curve as well as the initial transient part.

## Results

Typically the numerical optimizer performed approximately 1000 parameter variations until it reached an asymptotic optimum. As result Table 2 shows the optimized set of spray parameters and the parameter set “base” which represents previous best practice settings. In Table 3 additionally the effective values for the break-up parameters C1 and C2 are given resulting from the linear pressure dependency introduced in the optimized parameter set by the parameters C7 and C8 (Wakisaka submodel [5]).

	base	optimized
<b>E1</b>	1	1.76
<b>E2</b>	1	2.04
<b>C2</b>	15	12
<b>C4</b>	0.1	0.2
<b>C5</b>	0.3	0.073
<b>C7</b>	0	0.08
<b>C8</b>	0	-0.485

**Table 2.** Comparison of spray parameter settings

Chamber pressure	effective C1	effective C2
<b>43 bar</b>	0.946	14.04
<b>53 bar</b>	1.026	14.52
<b>73 bar</b>	1.186	15.49

**Table 3.** Effective break-up parameter values resulting from the optimized parameter set

The optimized spray submodel parameters alter the behaviour of the spray model. The heat and mass transfer in the evaporation submodel is significantly increased by the correction factors. Looking at the effective value of C2 the time period between the break-up events has not changed significantly compared to base settings whereas the value of C1 is finally increased from 0.61 in the base configuration to higher values in the optimized setting. This causes larger stable droplet diameters favouring deeper penetration while enhanced evaporation parameters E1, E2 have opposite effect. The child parcel model parameter C4 is increased compared to base settings. Therefore the frequency of the generation of child parcels with a stable diameter is reduced. The first child-parcel generation event is delayed and happens farther from the nozzle. Due to decreasing of the parameter C5 less mass is shed in a separate droplet parcel during a single child-parcel generation event. In summary, the child-parcel generation is decreased significantly which also reduces the strength of evaporation as well as the momentum transfer to the gas phase especially near to the nozzle. In the following selected results of measurements and simulations are shown in more detail.

### Effect of chamber pressure

In Figure 8 liquid and vapor penetration curves are shown for three sets of boundary conditions which differ only by chamber pressure. Here measured curves show decreased penetration with increased chamber pressure which results from the higher gas density.

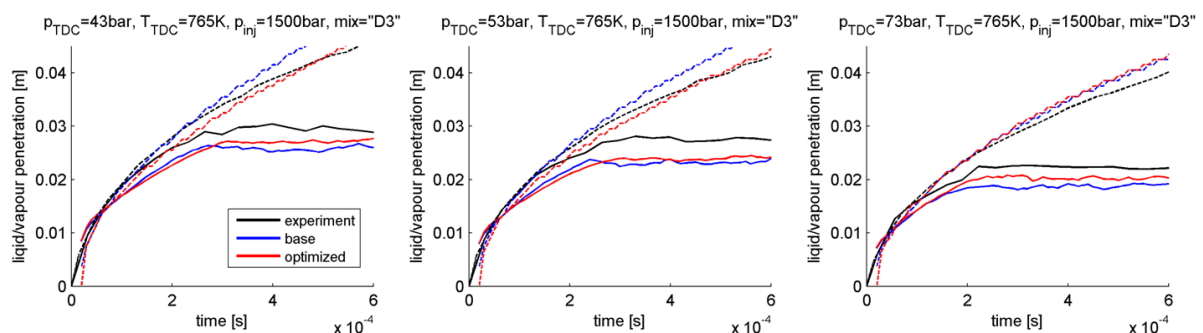


**Figure 8.** Comparison of simulated and measured penetration curves for different chamber pressures at a chamber temperature of 765 K and an injection pressure of 1500 bar with a 30% Decane mixture

The spray simulation model using the “base” parameter setting is predicting this trend quite well whereas the optimized settings lead to a significant quantitative improvement. In especially vapor penetration is improved for chamber pressures of 43 bar and 53 bar more than for 73 bar which might be explained by the introduced pressure dependency of the break-up behaviour.

### Effect of injection pressure

Only the injection pressure is varied in the boundary conditions of the cases compared in Figure 9. Here the rate of injection is increased with higher injection pressure. Combined with the increased spray momentum this leads to an increased vapor spray penetration in the experimental results. For measured liquid penetration this effect is not present which might be explained by enhanced break-up and entrainment effect.

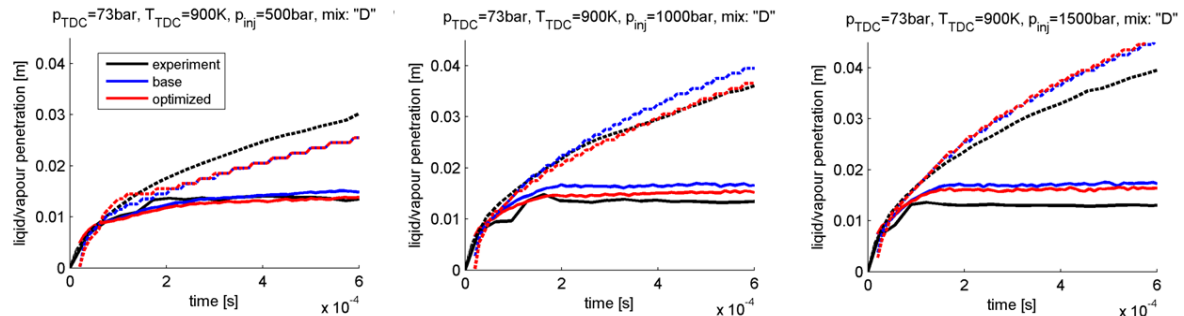


**Figure 9.** Comparison of simulated and measured penetration curves for different injection pressures

The vapor penetration trend is predicted by both simulation settings but overestimated quantitatively. This way vapor penetration is predicted too low for low injection pressure conditions and too high for high injection pressure conditions. Also an increased spray liquid length is predicted by both simulation settings. Both deviations could be assumed as resulting from the break-up model. Here a potential for model improvements is visible. However, in all cases shown the results obtained using optimized settings are closer to the experimental findings.

### Effect of mixture composition

To visualize the mixture composition dependency of the results the penetration curves were time averaged over the last third of the simulation period. Thus in most cases only the steady level of the liquid length is considered. This is illustrated on the left side of Figure 10.

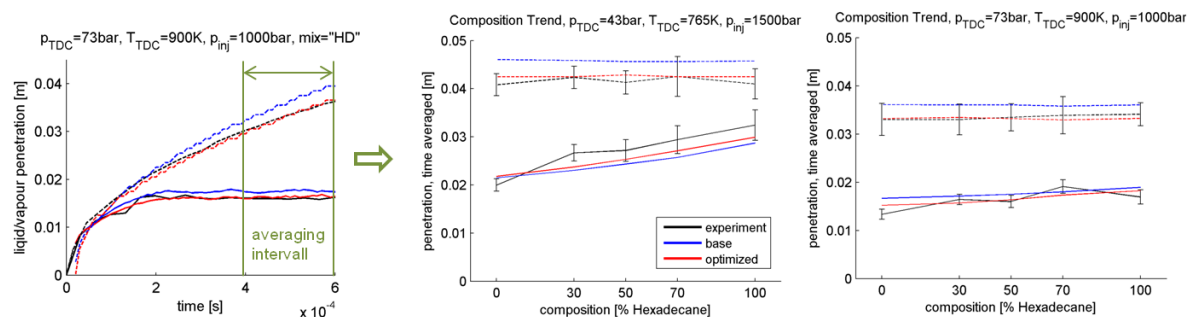


**Figure 10.** Comparison of trends of simulation results and experimental data in terms of mixture composition

On the right hand side of Figure 10 composition trends for both simulation settings are shown compared to corresponding experimental data. In the two diagrams the results from different combinations of boundary conditions are shown. Measured vapor penetration does not show a dependency on mixture composition in both cases. This is consistent to measurements of the rate of injection and spray momentum where no significant differences between different mixtures were observed, too. In the measured liquid penetration the effect of smaller fuel volatility and higher liquid density of the Hexadecane component is visible. Trends are predicted well by the simulation models for both vapor and liquid penetration. Also in Figure 10 we observe significant improvements through the optimization of the spray submodel parameters.

As Figure 10 shows exemplarily it can be stated generally that the remaining differences between measured and calculated penetration curves tend to be slightly bigger for lower chamber temperature and lower chamber pressure which is comparable to part load conditions in passenger car engines.

### Conclusions

Extensive spray measurements were conducted in a hot spray test rig using two-component fuel blends of varied percentages of Decane and Hexadecane to produce a validation basis for a multi-component spray

simulation. The spray simulation model investigated in this study has shown to be able to predict trends of spray behavior reasonably well with standard settings for the parameters of the spray submodels. Numerical optimization of these parameters additionally resulted generally in an improvement of the predicted spray liquid length and the spray vapor penetration. Especially the effect of the fuel composition could be matched well with the experimental findings. The effect of different combustion chamber pressures and temperatures also could be predicted well whereas the effect of varied injection pressures was overestimated.

Compared to the standard settings the optimized parameter set shows increased evaporation behavior as well as modified break-up characteristics including an additional pressure dependency. The break-up behavior especially for the part load injection pressure of 500 bar as well as the behavior of the MC evaporation model under low temperature and low pressure conditions were identified as regions where model improvements are indicated. This will be subject of further work.

## Acknowledgements

We would like to express our thanks to our supporting industrial project partners AVL List GmbH and OMV Refining & Marketing GmbH. The authors would like to acknowledge the financial support of the "COMET K2" Program of the Austrian Federal Ministry of Transport, Innovation and Technology (BMVIT), the Federal Ministry of Economy, Family and Youth (BMWFJ), the Austrian Research Promotion Agency (FFG) and the Styrian Business Promotion Agency (SFG).

## Nomenclature

<b>CFD</b>	Computational Fluid Dynamics
<b>GA</b>	Genetic Algorithm
<b>LL</b>	Liquid Length
<b>MC</b>	Multi Component
<b>ROI</b>	Rate Of Injection
<b>SOI</b>	Start Of Injection
<b>TDC</b>	Top Dead Centre
<b>VP</b>	Vapor Penetration

## References

- [1] Abramzon, B. and Sirignano, W.A., Droplet Vaporization Model for Spray and Combustion Calculations, *AIAA 26<sup>th</sup> Aerospace Sciences Meeting*, (1988).
- [2] Brenn, G., Deviprasath, L.J. and Durst, F. Computations and Experiments on the Evaporation of Multi-Component Droplets, *Proc. 9<sup>th</sup> Int. Conf. Liquid Atomiz. Spray Syst. (ICLASS)*, (2003)
- [3] Fink, C., A Multi-Component Evaporation Model for the 3D CFD Code FIRE 8 – Development and Validation with Experimental Data, *Diploma Thesis, TU-Graz*, (2005).
- [4] Lui, A.B. and Reitz, R.D., Modeling the Effects of Drop Drag and Break-up on Fuel Sprays, *SAE Paper*, 930072.
- [5] Wakisaka, T. et al. Numerical Prediction of Mixture Formation and Combustion Processes in Premixed Compression Ignition Engines, *COMODIA 2001*, (2001).
- [6] Gosman, A.D. and Ioannides, E., Effects of Computer Simulation of Liquid-Fueled Combustors, *AIAA*, 81-323, (1981).
- [7] AVL Advanced Simulation Technologies, AVL FIRE Version 2011, Main Program, Software Package with Integrated User Manual, Ver. 10/2011, Document No. AST.08.0201.2011, AVL List GmbH, Graz, Austria, (2011).
- [8] Bermúdez, V., García, J.M., Juliá, J.E. and Martínez, S., Engine with Optically Accessible Cylinder Head: A Research Tool for Injection and Combustion Processes, *SAE Paper*, 2003-01-1110, (2003).
- [9] Pastor, J.V., García-Oliver, J.M., Nerva, J.-G. and Giménez, B., Fuel effect on the liquid-phase penetration of an evaporating spray under transient diesel-like conditions, *Fuel* 90, (2011), pp. 3369–3381.
- [10] Pastor, J.V., Payri, R., García-Oliver, J.M. and Nerva, J.-G., Schlieren measurements of transient ECN-Spray: A penetration under inert and reacting conditions, *SAE Paper*, 2012-01-0456, (2012).
- [11] Reitz, Rolf D., Modeling atomization processes in high-pressure vaporizing sprays, *Atomisation and Spray Technology* (ISSN 0266-3481), vol. 3, no. 4, (1987), p. 309-337

## **Investigation of Spray Combustion with Fuel-Water Emulsification under Exhaust Gas Recirculation using Detailed Visualization and Spray Modelling**

Daisuke TSURU, Keisuke Komada, Ryosuke Ishibashi, and Hiroshi Tajima

Interdisciplinary Graduate School of Engineering Sciences, Kyushu University, Japan

### **Abstract**

The combination of Exhaust Gas Recirculation (EGR) to Fuel-Water Emulsification (FWE) is in the spotlight as a NO<sub>x</sub> reduction measure from vessels against the stringent regulation. Although FWE could partially offset the increase of pumping-loss in 2-stroke cycle engines with an EGR system, a lack of the collective view of the FWE effects makes its optimization difficult. In this study, a Rapid Compression-Expansion Machine (RCEM) was introduced to realize the equivalent in-cylinder conditions with larger engines. Artificial air of different oxygen concentrations was charged to reproduce the EGR running conditions and the effects of FWE were carefully examined through the experiments with various injection setups. Simulation of spray propagation and combustion processes were also carried out using three-dimensional CFD code: KIVA3V in order to evaluate the effect of water vapour distribution on cylinder temperature and NO<sub>x</sub> formation. Concentric water-in-oil type droplet had to be newly introduced as an outcome of oil and water droplet coalescence for the calculation of emulsion system. Concentric water-in-oil type droplets were injected as an emulsion fuel. And different treatments in calculating its breakup and evaporation processes were considered. It has been concluded that the effect of NO<sub>x</sub> reduction by FWE becomes small as engine load increases, especially in the case that injection pressure was increased to inject additional water amount. Through the comparison with simulation results, the clues for the effective NO<sub>x</sub> reduction measure were derived for the first time for large marine diesels.

---

### **Introduction**

Large two stroke marine diesel engines have a high efficiency and it relates that shipping has low fuel oil consumption and low emission of greenhouse gases compared to other transportation. However, they have demanded dramatically to reduce harmful regulated pollutants, especially Nitrogen Oxide emission. International Maritime Organization sets the limit of Nitric Oxides (NO<sub>x</sub>) emission from ship engines in global sea areas by the Tier II regulation since 2011. Especially in NO<sub>x</sub> Emission Control Areas (NECAs), a 75% of NO<sub>x</sub> reduction will be required by the Tier III from 2016, compared to the standard of the Tier II. Emissions from engine can be controlled either external reduction methods or internal methods. Various technologies such as Exhaust Gas Recirculation (EGR) [1] with a scrubber tank, Exhaust Gas Separation (EGS) [2] from MES Co., LTD and Selective Catalytic Reduction (SCR) [3] have been proposed as external reduction methods for marine diesel engines. Meanwhile, internal reduction methods focus on the combustion process and emission formation controlled by optimization of injection condition including injection pressure, timing and duration as well as technologies such as Water injection and charging gas condition of EGR. In those methods, the EGR has a potential to reduce NO<sub>x</sub> formation until regulation level. However, to achieve the intake air as 17% of oxygen for reduction needs huge amount of exhaust gas recirculation and it leads to less thermal efficiency by increase of pumping loss in the two stroke marine engines. Recently FWE system is attempted to use with EGR system to reduce the amount of exhaust gas recirculation. FWE system can reduce to NO<sub>x</sub> emission keeping the thermal efficiency by using emulsion instead of diesel fuel. Though various injection conditions, such as injection pressure, diameter of nozzle hole and injection duration, to inject the increasing fuel mass by additional water were reported, there is no result comparing effects of reduction under same engine condition and It is difficult to optimize the injection strategy for applying to EGR system.

The one objective of this paper is to observe the combustion phenomenon of FWE in EGR condition using Rapid Compression Expansion Machine (RCEM) which has a large combustion chamber and two windows in order to visualize spray propagation correspond to the free spray under the high in-cylinder pressure and intake air with different oxygen concentration to reproduce spray combustion of EGR condition. Other objective is to reveal differences of NO formation distribution in the combustion chamber between FWE and EGR. Simulations of FWE and EGR combustion were also carried out in order to evaluate the effect of water vapour distribution on cylinder temperature and NO<sub>x</sub> formation using three-dimensional CFD code:KIVA3V modified for droplet model to reproduce emulsion fuel.

## Experimental apparatus and procedure

To observe the combustion process, a RCEM was used in this experiment. Table 1 shows the basic specifications of the RCEM. Figure 1 shows the schematic of RCEM. The RCEM has a bore of 240 mm and a stroke of 260 mm. Combustion chamber is cubic shaped volume consisted of  $200 \times 66 \times 80$  and it has three quartz windows on the walls for objective of visualization. Geometrical compression ratio of RCEM is 9.08. An air tank with heats is connected to the intake port of RCEM. The pressure and the temperature of the initial intake air can be controlled respectively in the air tank so that the clearance volume is large enough to observe the behavior of spray and combustion in the actual engine condition. Procedures of its one-shot firing are as follows. First it starts up motoring with its intake valve kept close, and then it actuates the valve only once synchronously with its piston motion immediately after the rating speed is reached, and finally the pre-compressed-heated charge flows into the cylinder, so as to simulate the intake and compression stroke of a real engine. After combustion, CO, CO<sub>2</sub>, O<sub>2</sub>, THC and NO<sub>x</sub> in the burned gas are measured by using exhaust gas analyzer (HORIBA:MEXA-7100). The combustion processes were taken by photographs directly using high speed camera (Photoron: Fastcam SA-4). Temperature distribution of DWI combustion was obtained from Photographs analyzed by Two Color Method (TCM). Spatial resolution of photographs is  $832 \times 224$ . In addition, frame rate is 20,000fps and exposure time is 5.8us.

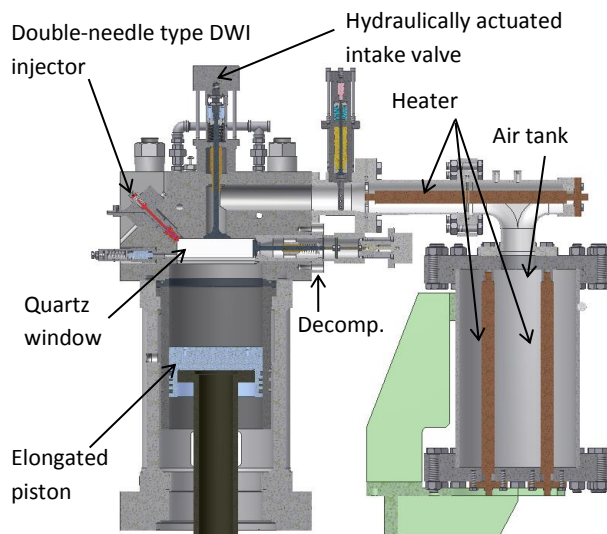


Figure 1. Schematic of RCEM

Table.1. Main specifications of RCEM

Bore × Stroke	φ240 mm × 260 mm
Clearance volume (upper, lower)	200 × 66 × 80 mm <sup>3</sup> φ240 mm × t5.4 mm
Compression ratio	9.08
Engine speed	320 rpm
Compression pressure	10MPa
Quartz window	200 × 50 × 100 mm <sup>3</sup>
Initial charging conditions	
Pressure	0.81 MPa
Temperature	353 K
Compression Pressure at TDC	10.0 MPa

## Injection system

Mass of water injection was set to almost 25% and 40% of fuel injection mass cause of more water injection mass give rise to the SFOC penalty. Refined water and gas oil were used for water injection and fuel injection respectively. In FWE case, fuel is premixed with 0.1% Glycerin while the water is premixed with 0.9% RHEODOL SP-L 10; whereas percentages refer to the total emulsion volume. The chosen emulsifier guarantees reversible emulsions that can be mixed again after sedimentation of the water. As shown in Fig. 2, the fuel is slowly mixed to the water before a pump starts circulating the emulsion through a homogenizer, where the emulsion is forced with high pressure to narrow channels, leading to a sharp increase in flow velocity while the pressure declines below the saturation steam pressure, followed by an expansion.

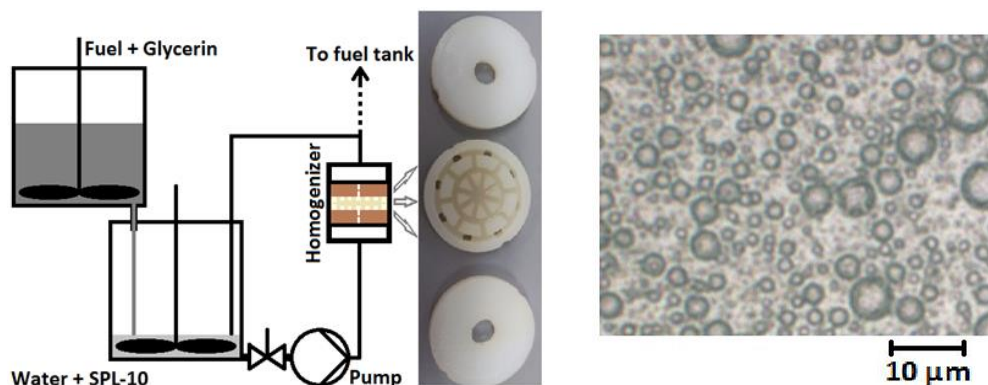


Figure 2. Formation of emulsion and Microscope photo of emulsified fuel



### Experimental Conditions of EGR and FWE

The experiments under the EGR or FWE conditions were carried out separately. The EGR experiments had the three cases in which initial Oxygen concentrations of intake air were 21.0, 18.3 and 16.3% on volume base with injection pressure set to 150MPa. The FWE experiments had the three cases in which ratios of water to fuel were 0, 25 and 40% on volume base. The 0% means that fuel was only gas oil. Because the total volume of emulsified fuel was larger than that of gas oil, the injection duration must have been increased from 20.3 to 25.1 or 28.9 degrees. That intake air was diluted by pure Nitrogen, and the values of Oxygen concentration were not able to be adjusted accurately due to dilution by residual air in the cylinder. The further FWE experiments were conducted. The injection time, injection pressure or diameter of nozzle hole was changed in the FWE case according to the ratio of additional water to fuel. Therefore, the FWE experiments with the three injection method were carried out in this study. The experimental conditions are listed on Table 2. Injection pressure of base case is set to 80MPa lower than that of EGR case due to increase injection pressure in case2.

**Table 2** Experimental conditions of FWE

	Base	Case 1		Case 2		Case 3
Initial Oxygen concentration [vol%]	21.0					
Fuel	Gas Oil	FWE 25	FWE 40	FWE 25	FWE 40	FWE 40
Ratio of water to fuel [vol%]	0	25	40	25	40	40
Injection duration [deg.]	26	33.5	37.5	29	29	26
Injecting pressure [MPa]	80	80		125	150	80
Diameter of nozzle hole [mm]	0.5	0.5		0.5		0.6

### Computation Method

A combustion process in the water injection system was calculated by improving the spray sub models of the KIVA3v code. [4] The submodels used in this study are listed in Table 3.

#### Spray model

Figure 3 shows the model for water-in-fuel droplets which are treated as two layer concentric sphere; the outer layer is consisted of fuel while an inner zone is consisted of water. This model describes the droplets of FEW to be injected from nozzle hole. With this change in a treatment of droplet in each water injection system, spray model was improved as described in following part.

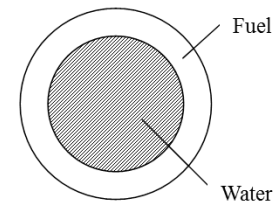


**Figure 3.** Model of FWE droplet

#### Breakup and evaporation model

The Kelvin-Helmholtz(KH) and Rayleigh-Taylor (RT) breakup model was used to predict spray atomization. In FEW case and DWI case after collision of coalescence and reflexive separation, droplets are dealt with combined droplets between fuel and water shaped in the form of water-in-oil concentric droplet. Breakup model was also modified with a different application manner. The coalesced drop behaves as a fuel droplet in KH breakup mode because surface properties of the relevant droplet have dominant effects there, while it behaves as a water droplet because RT breakup supposedly requires large drop deformation. Consequently, droplets stripped by KH breakup were composed of only fuel.

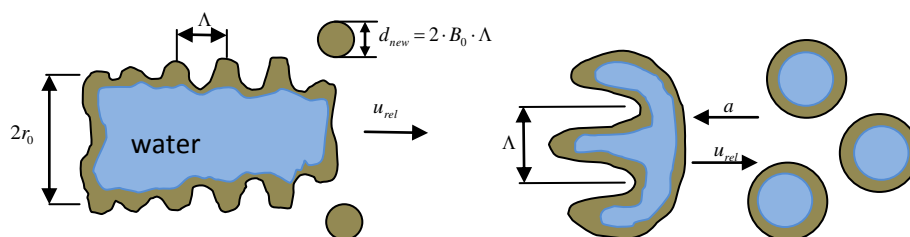


**Figure 4.** Schematic of KH model of combined drop and RT model of ombined drop



The evaporation process of a concentric sphere starts fuel at the equilibrium temperature after the coalescence. The concentric sphere evaporates from its fuel surface assuming the water core keeps the same temperature, which means the concentric water-in-oil droplet evaporates as an oil droplet of an expanded surface area. After the fuel layer is completely vaporized, the droplet continues to evaporate (and also to breakup) as a pure water droplet, so that phenomena like micro-explosion of the concentric droplet were not considered.

### Injection method of FWE

At the injection of FWE, droplets of FWE which formed two layers of fuel and water are injected, however, fuel droplets which do not contain water are also injected alternate with FEW droplets to represent the real condition of FEW fuel that not all droplets forms fuel-water merged condition seen in Figure 2.

### Computational grid and calculation condition

Figure 5 shows a computational grid shaped in the form of RCEM and used in this study. The computational mesh is composed of approximately 76000 at BDC. The calculation is performed from -124 deg.ATDC to 50 deg.ATDC. Injection timing and duration and pressure are the same as experimental results.

**Table 3.** Submodels adopted in KIVA3V

Phenomenon	Sub model
Primary breakup	Blob model
Secondary breakup	Modified KH-RT model
Collision and Coalescence	Model of O'Rourke (water, fuel)
Evaporation	Model of Amsden (water, fuel) + Two-step evap of coaxial drops of water(inner) and fuel (outer)
Turbulence	RNG k- $\epsilon$ model
Ignition	Shell model
Combustion	CTC model

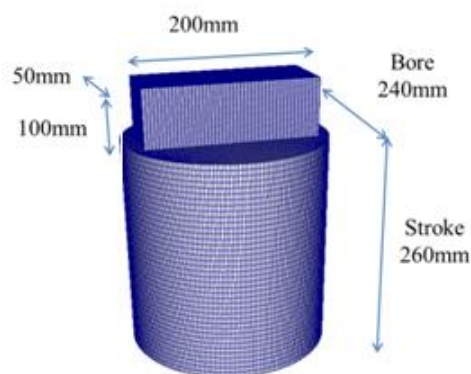


**Figure 5.** Computational grid at BDC

## Results and Discussion

### Experiments of EGR or FWE

Figure 6 shows the histories of heat release every crank angle in the combustion chamber. The heat release at late crank angle indicates afterburning, which decreases thermal efficiency. As can be seen in the graphs of Figure 6, the afterburning became longer as the Oxygen concentration of intake air decreased in the EGR cases, while the afterburning disappeared in the FWE cases even though the injection duration time of fuel was increased due to the additional water. The reason why longer afterburning happened under the EGR conditions is considered to be that the low Oxygen concentration made the chemical reaction rate of fuel and Oxygen slow, and some of the injected fuel was unburned and remained at the late crank angle, where cylinder temperature had already decreased, and that resulted the heat release had continued until the late crank angle. Because Mixing of fuel and air is improved by using FWE due to the increased momentum of emulsified fuel by additional water mass. The most amount of fuel was consumed effectively by the improved mixture of fuel and air, which resulted in the shorter afterburning with the FWE. These results suggest that both high NO<sub>x</sub> reduction ratio and the same thermal efficiency could be achieved simultaneously due to the improved mixture by the FWE, if the both FWE and EGR techniques were applied.

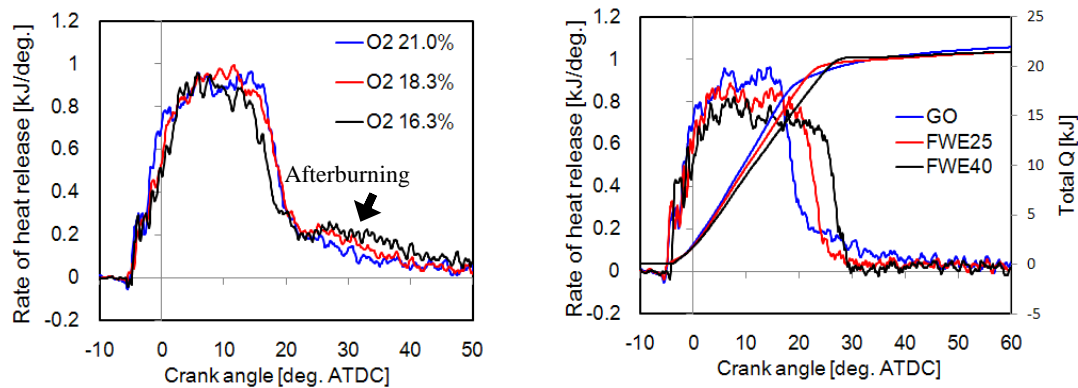


Figure 6. Histories of heat release in EGR cases (left) and FWE cases (right)

However, the amount of NO<sub>x</sub> emission and the improved thermal efficiency depend strongly on the injection conditions which are additional water ratio, injection time, injection pressure and diameter of nozzle hole. Those parameters were varied in the next FWE experiments in order to investigate how they affect the amount of NO<sub>x</sub> emission.

#### Further experiments of FWE

Figure 7 shows the NO<sub>x</sub> emission in the FWE experiments and NO formation in the calculations. The value on the mark in the graph means experiment data. The amount of NO<sub>x</sub> emission decreased as ratio of water to fuel increased in Case 1 of the changed injection duration time and Case 3 of the changed diameter of nozzle hole. It increased as the additional water ratio increased in Case 2 that changed injection pressure. According to the momentum theory, the momentum of fuel spray in the case that the injection pressure was changed is the largest among the three cases. And the more amount of air was entrained into fuel spray and a mixture of fuel and air was promoted by more increase of momentum due to increased injection pressure in the case that the injection pressure was changed, which resulted in the more amount of NO<sub>x</sub> emission in Case 2.

The amounts of NO<sub>x</sub> emission in the FWE cases were calculated by KIVA-3V with new spray model in good agreement with experiment results. And both trends of decreasing NO formation with FWE in Case 1 and 3 and of increasing in Case 2 were reproduced well.

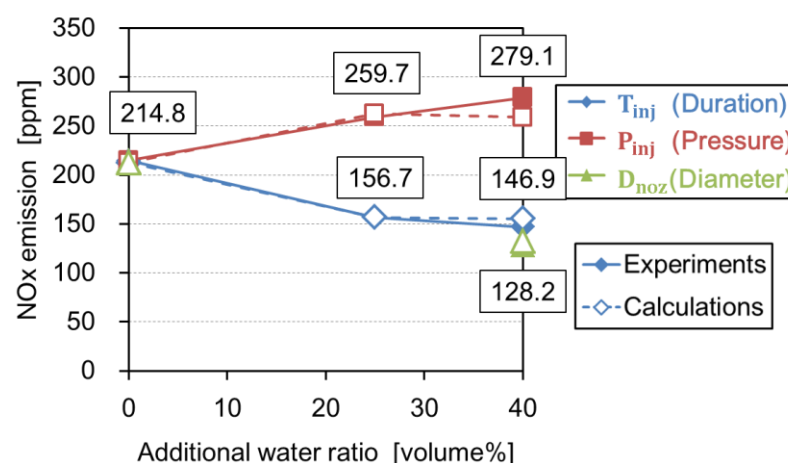
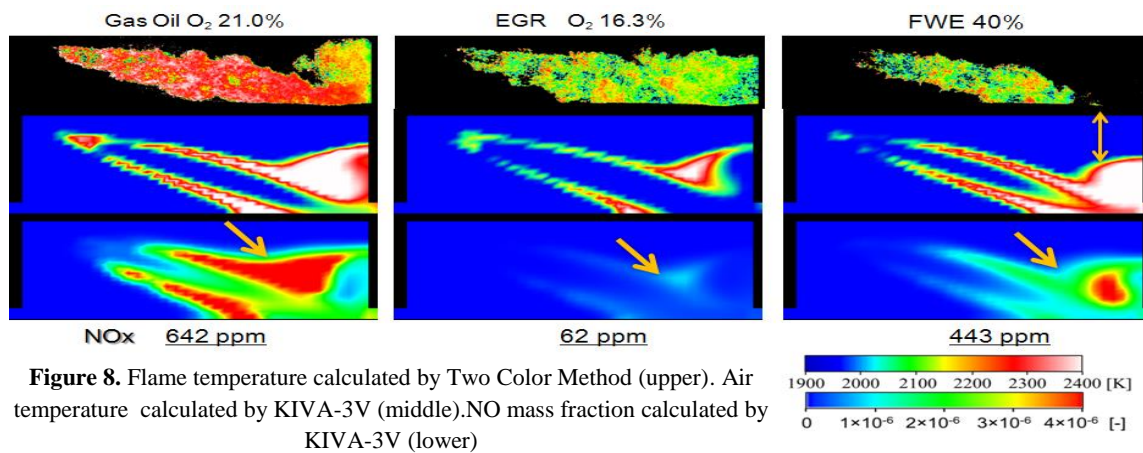


Figure 7. NO<sub>x</sub> emissions in FWE experiment on three injection methods

### Simulation results

At first, the differences of NO<sub>x</sub> reduction mechanism between EGR and FWE will be discussed, with comparing the calculation results to the Experiment results. Figure 8 shows the flame temperature distributions calculated by Two Color Method and the air temperature distribution and the NO mass fractions at the centre of flame calculated by KIVA-3V. The FWE case is the condition that the injection duration time was changed. Though Flame temperature in the upper pictures looks lower in the EGR and FWE cases than in the case that neither EGR nor FWE was applied, the amounts of NO emission were completely different between the EGR and FWE cases. The distributions of NO mass fraction calculated by KIVA-3V indicate that the much amount of NO was produced at the front edge of combustion flame where temperature looks lower in the upper distribution by Two Color Method, while the amount of NO product was reduced uniformly with the EGR.



**Figure 8.** Flame temperature calculated by Two Color Method (upper). Air temperature calculated by KIVA-3V (middle). NO mass fraction calculated by KIVA-3V (lower)

The temperatures in the calculations did not decrease as the additional water ratio increases in the FWE, even though the flame temperature calculated by Two Color Method decreased drastically. These results suggest that high temperature region exists in the area where combustion flame is not observed, and flame temperature in the FWE conditions could not be calculated accurately by Two Color Method due to decreasing soot particle. And burned gas without luminescence produced NO<sub>x</sub>. Therefore, NO<sub>x</sub> emission was not decreased drastically.

### Evaluation of EGR and FWE Combination

The calculations in the combination use of EGR and FWE were carried out. Table 4 shows the NO reduction ratios that were calculated from the amount of NO product in all the conditions that several initial Oxygen concentration, additional water ratio and injection method. The red boxes in Table 4 indicate the case that more than 75% of NO reduction, which is the standard of the Tier III, was achieved with EGR and/or FWE. The amount of NO product was reduced by 75% in all the cases that initial Oxygen concentration was less than 18.0% and in the cases that additional water ratio was 40% under the condition of 16.0% of Oxygen concentration.

**Table 4.** NO reduction ratios in calculations of EGR and FWE combination

		NO Reduction Ratio [%]								
Setup	None	T <sub>inj</sub>			P <sub>inj</sub>			D <sub>noz</sub>		
Water %	0	10	25	40	10	25	40	10	25	40
O <sub>2</sub> %										
21.0	0.00	14.15	19.57	38.96	2.80	-6.48	5.67	14.32	23.57	32.15
20.0	27.60	39.02	45.84	59.42	31.93	26.03	34.97	39.51	48.47	56.49
19.0	48.93	58.81	65.48	74.79	54.21	52.25	57.69	58.26	65.77	72.28
18.0	65.84	73.11	80.04	85.98	70.52	71.15	75.56	72.59	78.95	84.15
17.0	79.26	84.14	89.32	93.07	82.18	84.43	87.14	83.44	88.37	91.75
16.0	89.26	91.96	95.02	93.90	90.94	92.58	94.09	91.64	94.38	96.19

However, all the cases are not necessarily useful for diesel engines to meet the 75% of NO<sub>x</sub> reduction, because low Oxygen concentration deteriorates thermal efficiency and decreases the value of Pmi. Table 5 shows the ratio of Pmi to the reference Pmi, and the blue boxes indicate the case that the Pmi decreased by more than 5% and the red ones indicate the cases that the Pmi increased. Though the 75% of NO reduction was achieved by the EGR in which initial Oxygen concentration was less than 18.0%, the Pmi in the many cases decreased by more than 5%. The 5% of Pmi decrease demands much higher engine propulsion and fuel cost, and it should be avoided to apply. Therefore, the application of FWE under the condition of 18.0% of Oxygen concentration is favourable, especially with the Pinj setup. Looking at the case that the initial Oxygen concentration was 18.0%, the additional water ratio was 40% and the injection pressure was changed, the amount of NO product was reduced by 75.6% with the increase of Pmi by 6%. This case was the only one that has met both the 75% of NO reduction and the increased Pmi. Therefore, the most effective way to meet the Tier III regulation is the setup that initial Oxygen concentration with EGR is 18.0% and additional water ratio with FWE is 40%, with increasing injection pressure.

**Table 5.** Ratio of Pmi to reference Pmi

		Pmi / Reference Pmi [-]								
Setup	None	Tinj			Pinj			Dnoz		
Water % O <sub>2</sub> %	0	10	25	40	10	25	40	10	25	40
21.0	1.000	0.962	0.984	0.996	0.986	1.037	1.070	0.957	0.987	1.012
20.0	0.994	0.949	0.975	0.989	0.978	1.030	1.068	0.943	0.977	1.001
19.0	0.984	0.933	0.964	0.982	0.961	1.023	1.065	0.930	0.964	0.989
18.0	0.969	0.919	0.952	0.972	0.945	1.016	1.060	0.913	0.947	0.978
17.0	0.950	0.901	0.937	0.960	0.931	1.004	1.054	0.894	0.929	0.961
16.0	0.931	0.878	0.918	0.996	0.911	0.989	1.044	0.871	0.913	0.947

## Conclusions

Two methods of EGR and FWE were investigated in this study. For investigation of the effect of NO formation, combustion process of EGR and FWE system were observed and exhaust gas was measured using a RCEM. Simultaneously Simulation was carried out by using KIVA3V code. Conclusions of this study are follows.

- Lower Oxygen concentration in EGR has a problem of longer afterburning that deteriorates thermal efficiency. FWE has an effect to improve a mixture of fuel and air due to increased momentum by additional water mass, and leads better combustion and shorter afterburning. Therefore, a combination of EGR and FWE could achieve simultaneously high NO<sub>x</sub> reduction ratio and thermal efficiency.
- The calculation results by the 3D-CFD code, KIVA-3V, show that the amount of NO product was reduced uniformly in whole of combustion flame under the EGR condition, while the large amount of NO was produced at the front edge of combustion flame under the FWE condition. And increased momentum due to additional water led better mixture of fuel and air, and promoted NO formation at the front edge of flame.
- The application of FWE under the low Oxygen concentration with EGR is very effective not only for high NO reduction ratio but also for high thermal efficiency. The calculation result in the case that the initial Oxygen concentration was 18.0% and the additional water ratio was 40% with increasing injection pressure shows that the 75% of high NO reduction ratio and the 6% of the improved mean pressure (Pmi) were achieved simultaneously.

## Nomenclature

<i>EGR</i>	: Exhaust Gas Recirculation
<i>FWE</i>	: Fuel Water Emulsion
<i>RCEM</i>	: Rapid Compression Expansion Machine
<i>CA</i>	: Crank Angle [degree]
<i>TDC</i>	: Top Dead Center [degree]
<i>ATDC</i>	: After TDC[degree]
<i>BDC</i>	: Bottom Dead Center[degree]
<i>ROHR</i>	: Rate of Heat Release

## References

- [1]Pedersen,M., Andreasen,A. and Mayer,S., “Two-stroke Engine Emission Reduction Technology: State-of-the-art”, *CIMAC 2010* , Paper No. 85
- [2]Takahashi,M., Tanaka,I., and Ohtsu,M., “Study of Exhaust Gas Separation (EGS) System on 2-stroke Engine” *CIMAC 2010* , Paper No. 108
- [3]Niki,Y. et al., “SCR system for NOx reduction of Medium Speed Marine Diesel Engine”, *CIMAC 2010* , Paper No. 228
- [4]Amsden,A.A. “KIVA-3V: a block-structured KIVA program for engines with vertical or canted valves”, LA-13313-MS, 1997

## **A multi-coupled Eulerian-Lagrangian solver for airblast injectors including liquid film evolution and primary breakup – Numerical model**

A. Andreini<sup>1</sup>, C. Bianchini<sup>1</sup>, B. Facchini<sup>1</sup>, A. Giusti<sup>1</sup> and F. Turrini<sup>2</sup>

1: Department of Industrial Engineering, University of Florence, Italy

2: Combustion System Office, AVIO Group S.p.A., Italy

### **Abstract**

In order to reduce NO<sub>x</sub> emissions, modern aero-engines are often equipped with advanced prefilming injection systems. The combustion process is strongly influenced by the liquid fuel preparation, thus, in order to perform reliable predictions of engine emissions, it is important to develop proper tools aimed at predicting film evolution and its subsequent breakup. A multi-coupled Eulerian-Lagrangian solver for reactive sprays integrated with a film solver based on the thin film approximation has been developed in the framework of the open source code called OpenFOAM. Interactions between the different phases have been considered, with particular attention to the liquid film primary breakup which was modelled introducing a new phenomenological model. The computation of droplet population SMD is based on literature correlations starting from the solution of the gas-phase and liquid film. Different criteria to determine the breakup locations have been introduced as well as different strategies to accelerate solution towards steady-state. This work is divided into two different parts: the first one deeply describes the numerical model and its validation whereas in the second one an application to an industrial combustor is considered. In this paper the first part is presented; the companion paper reporting the application is also presented in this conference.

### **Introduction**

The more and more stringent regulations on pollutant emissions, in particular NO<sub>x</sub>, have led aero-engine manufacturers to adopt advanced combustion technologies in order to meet emission requirements and allow a heavy reduction of nitrogen oxides emission. Even though classical Rich-Quench-Lean (RQL) technology has still relevant improvement potentials, the expected future regulations concerning NO<sub>x</sub> emissions from civil aero-engines (ACARE Vision 2020 objectives and future ICAO-CAEP standards) have forced in the last ten years huge research investments from the main engine manufacturers to introduce lean burn combustion systems. In order to achieve lean combustion in liquid fuelled combustors, advanced injection systems able to guarantee rapid evaporation and mixing are required. The recently developed injectors are usually based on prefilming airblast atomizers which have several advantages including fine atomization, comparatively little change in performance over a wide range of fuel flow rates, and low pressure losses [4]. In prefilming airblast atomizers the fuel is spread out into a liquid film and then is driven along a surface by a co-flowing air. When the atomizing edge is reached, a second air flow interacts with the film leaving the edge and fine atomization is produced in a process that is often referred to as “primary breakup”. The combustion process and consequently the engine emissions are strongly influenced by the liquid fuel preparation and thus, in order to perform reliable predictions of the combustor behaviour, it is important to properly predict the characteristics of the droplet population injected in the gas flow.

The physics that regulates primary atomization in prefilming systems is very complex and not completely understood and very few numerical models for primary breakup can be found in literature. Dombrowski [6] presented a model for atomization of a high speed liquid sheet interacting with air on both its top and bottom surfaces. A linear stability analysis is used to calculate the most unstable wavelength for a given sheet thickness which leads to break up into streamwise ligaments. Finally, these ligaments are assumed to form drops following typical mechanisms of capillary instabilities. It is important to note that this model requires the mean film thickness to be known and according to the assessment performed in reference [6] it could lead to an uncertainty up to 20%. This model was also applied by Gepperth et al. [7] to predict the droplet population mean diameter in a prefilming airblast system finding a good agreement with downstream measurements of SMD. Gepperth et al. [7] developed a model based on the breakup frequency that does not require the film thickness as an input. Mass conservation and breakup frequency are used to calculate the ligament diameter and using the Rayleigh’s capillary instability analysis an expression for droplet diameter is found. Inamura et al. [8] use the same breakup mechanism but in this case the ligament dimension before capillary instability breakup is computed starting from the longitudinal and tangential wavelengths related to Kelvin-Helmholtz and Rayleigh-Taylor instabilities. However, it should be noted that in experimental condition similar to the ones of Inamura et al. [8], Gepperth et al. [4] observed that the atomization process and breakup frequency are completely uncorrelated with the development of film surface instabilities. Furthermore, they also pointed out that in the investigated operating conditions the mean diameter of the droplet population generated by the film primary breakup is not really influenced by the film thickness whereas the parameter that plays the main role in film

atomization is the atomizing edge thickness as a consequence of the liquid film accumulation phenomenon at the atomizing edge that makes the actual film thickness less important. In general, all the models that try to reproduce the physics of liquid film atomization suffer the lack of a comprehensive theory on the mechanisms of primary breakup (in prefilming airblast configurations). As a consequence, especially in an industrial context, experimental correlations are often preferred. In the past years, several studies aimed at determining the most important parameters affecting primary breakup have been performed considering both real atomizers and simplified planar injectors. Starting from experiments, correlations to predict droplet sizes in such atomizers were developed. A review of the main correlations can be found in reference [9]. Droplet population SMD mainly depends on air velocity, liquid surface tension and dynamic viscosity and a characteristic length which, depending on the correlation, could be the edge thickness, the film thickness or a representative dimension of the atomizer. Film properties at the atomizing edge are determined by liquid film evolution and its interaction with the prefilming wall and the surrounding gas.

In order to perform reliable simulations of combustors equipped with prefilming airblast atomizers, proper tools able to predict liquid film evolution and primary breakup are necessary. In this work a multi-coupled Eulerian-Lagrangian solver integrated with a film solver based on the approach of Bai and Gosman [1] has been developed in the framework of the open source code called OpenFOAM. A new phenomenological model for film primary breakup based on experimental correlations has been introduced. The Eulerian-Lagrangian solver without film solver was presented and validated in a previous work of the same authors [11], thus in the following, particular attention will be devoted to the analysis of the film solver whereas in the companion paper [16] the application to a combustion chamber is presented. The capabilities of the film solver and its interaction with the gas-phase solver have been assessed using two different test cases found in literature [5] with detailed measurements of film thickness whereas the newly implemented film primary breakup model has been assessed by numerically replicating the experiments used to derive one of the droplet size correlations inserted in the model [4]. Specific strategies to accelerate solution towards steady-state are also described due to their relevance in an industrial context.

## Numerical modelling

As introduced before, in order to perform numerical simulations of complex two-phase flows in modern aero-engine combustors, a fully coupled numerical solver able to compute gas phase fields, evaporating fuel spray and shear-driven wall film has been developed. The gas flow and wall-film flow are described in Eulerian coordinates whereas the fuel spray computation is based on the Lagrangian approach. The interaction between the different phases, that is gas flow, spray and liquid film, is taken into account by means of specific source terms in the conservation equations describing their dynamics. In the following the mathematical and numerical modelling will be described with particular attention to the interactions between the different phases.

### *Gas-phase field*

The mathematical model for the continuous gas phase is represented by the Reynolds-averaged Navier-Stokes equations, which state the laws of conservation of mass and species, momentum and energy, with further assumptions on fluid properties such as ideal gas equation of state, Newtonian modeling for viscous forces or constant transport properties and additional simplifications in the case of steady-state computations. The basic equations can be represented by the following general formulation for the flow variable  $\phi$  (it could be the one of the velocity components, a quantity related to energy, the mass fraction of species or the number 1 in the case of continuity equation):

$$\frac{\partial(\rho\phi)}{\partial t} + \text{div}(\rho\bar{u}\phi) = \text{div}(\Gamma_{\phi}\text{grad}\phi) + S_{\phi}$$

where  $\Gamma_{\phi}$  is an effective diffusion coefficient and  $S_{\phi}$  allows local source due to the presence of liquid film, spray or combustion to be considered in the gas-phase evolution. Additional transport equations are solved depending on the turbulence model used to evaluate the effects of turbulence on the mean flow. Unsteady computations are based on PIMPLE algorithm whereas steady-state computations exploit SIMPLE loop [10] to solve for the pressure velocity coupling. Energy, as well as specie and turbulence model equations, is solved segregated; furthermore viscous heating effects are neglected. Finite-volume discretization is achieved by means of Total Variation Diminishing schemes for the convective terms and central differencing for the diffusive terms whereas the Euler scheme is used for the evolutive terms.

### *Droplet motion*

A diluted spray is considered so the interaction between different droplets can be neglected. As a consequence, neither collision models nor specific treatments for dense spray region have been included in the formulation



and models developed for a single droplet can be used to describe the dynamics of each particle. The spray is numerically represented by a cloud of parcels, where a parcel is a group of droplets with the same physical characteristics. Particular attention must be paid in the choice of the number of parcels introduced in the simulation in order to have a statistically representative population. Both accuracy and computational cost increase with the number of parcels, thus a compromise between these two aspects has to be found.

The Lagrangian method consists in the tracking of individual parcels in the gas-phase flow field based on the time integration of their equation of motion simply represented by the Newton's second law which states the balance between forces acting upon a particle and its acceleration. In the implemented method only drag and buoyancy forces are considered so that the equation of motion can be written as:

$$\frac{d\vec{u}_p}{dt} = \frac{3}{4} \frac{\rho}{d_p \rho_p} C_D (\vec{u} - \vec{u}_p) \|\vec{u} - \vec{u}_p\| + \frac{\rho_p - \rho}{\rho_p} \vec{g}$$

Droplets are considered spherical, non-rotating with deformability accounted for by means of specific correction factors and secondary breakup models. An energy equation is also resolved in order to determine the variation of droplet temperature during the tracking. Specific models for evaporation, turbulent dispersion and secondary breakup are also included in the formulation. During the time integration, source terms for specie, energy and momentum conservation equations are passed to the gas-phase solver. Specific strategies for parcel tracking to be used in steady-state computations are described in reference [11].

### Liquid film

The film solver is based on the approach of Bai and Gosman [1]. Under the main assumption of thin film (boundary layer approximation) the Navier-Stokes equations have been simplified and integrated over the film thickness. This allows numerical solution to be performed in a two-dimensional framework and thus the film thickness is directly resolved together with depth-averaged velocity and enthalpy fields. Equations have the following general form:

$$\frac{\partial}{\partial t}(\phi\delta) + \frac{\partial}{\partial x}(g_\phi \phi \bar{u}_x \delta) + \frac{\partial}{\partial y}(f_\phi \phi \bar{u}_y \delta) = S_\phi$$

where  $\delta$  is the film thickness,  $f_\phi$  and  $g_\phi$  represents coefficient arising from integration and the over-bar denotes depth-averaged velocity values.

Figure 1 shows the main interactions between the liquid film solver and the other solvers. As in all shear-driven films, the fluid motion is mainly determined by the surface shear stress exerted by the gas phase flow with the additional contribution of pressure gradients (the pressure inside the film is equal to the sum of gas flow pressure, droplet impact pressure and pressure induced by surface tension), body forces and tangential momentum sources provided by impinging droplets. Thus, the gas-phase flow directly influences the film dynamics through the contribution of pressure gradients and surface shear stresses in the film momentum equation; furthermore heat transfer between film and gas flow is also accounted for in the energy equation whereas the condensation process is not included in the formulation. On the other hand, liquid film interacts with the gas phase solver through the evaporation and heat transfer processes which determine source terms in mass, species and energy conservation equations whereas the gas-phase momentum equation is influenced by the presence of the film through boundary conditions. Gas-phase velocity at the interface is imposed to be equal to the film surface velocity which, following reference [1], is computed using a cubic profile which allows mass flow and shear stresses on both wall and gas-phase interfaces to be conserved. As regards interactions with the spray Lagrangian solver, specific models for dripping, breakup or, more in general, film separation, provide parcels to be injected and thus added to the spray population. Wall/film-droplet interaction is accounted for by means of a particular impingement model derived from the work of Bai et al. [2].

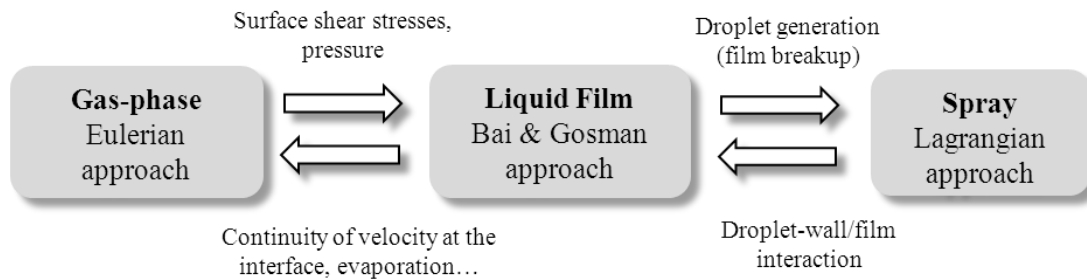


**Figure 1.** Main interactions between liquid film and the other phases.

The liquid film computational domain is basically a single layer prismatic mesh created by extrusion starting from the boundary mesh of patches where a wall-film is prescribed.

#### *Coupled solution of gas-phase, spray and liquid film*

As described above, the gas-phase, spray and liquid film interact with each other by means of mass, momentum and energy transfer. The different phases are solved following a segregated scheme. In the unsteady approach each phase is separately advanced in time and once the integration along the assigned time step is completed, source terms are updated and returned to the other phases. In steady-state calculation the coupling strategy is more complex due to the different nature of Lagrangian and Eulerian approaches. As described in references [11,12], a statistically representative population of parcel is tracked all over the domain until all of them have evaporated or exited the domain. The representative population of parcels also includes the particle injection due to film breakup with the film solver that assigns the injection point and the mass flow rate of droplet population generated at the atomizing edge. Also droplet impacts on the film surface are treated in a statistical way: after the parcel tracking source fields per unit time are assigned to the film equations and used in the subsequent integration. As regards film solver, two different approaches can be followed: solving the film with steady-state version of the governing equations as for the gas-phase or using artificial time integration with a given number of time steps. Because of the intense interdependence between the different phases and the intrinsic oscillatory behaviour of source terms derived from spray solution, relaxation strategies are largely used in the computation of source fields.

In the current implementation, first of all liquid film is solved, then the spray evolution is computed and finally the gas-phase with the all source terms is calculated.

#### **Primary breakup model for liquid film**

In order to consider droplet generated at the atomizing edge of a typical airblast atomizer, a new phenomenological model for film primary breakup has been introduced in the formulation. This is basically a correlative approach which uses literature correlations [9] for the computation of the SMD of droplet population generated by the film breakup. The use of correlations makes the model very flexible allowing new formulations to be easily included. Two different strategies were considered to determine the location of atomization as shown in Figure 2. The first one detects the presence of the atomizing edge using a criterion based on surface curvature [3]. In this case the injection point is not prescribed in advance and can vary during the simulation so it is important to extend the wall-film mesh around the atomizing edge. On the contrary, the second strategy consists in defining an outlet boundary for the film and computing the mass flow rate exiting the film domain which is used to determine the injected parcel mass. This approach, to be preferred in steady-state computations in order to make the solution much more stable, requires the definition of the location of atomization which in prefilming airblasts can be set at the atomizing edge.

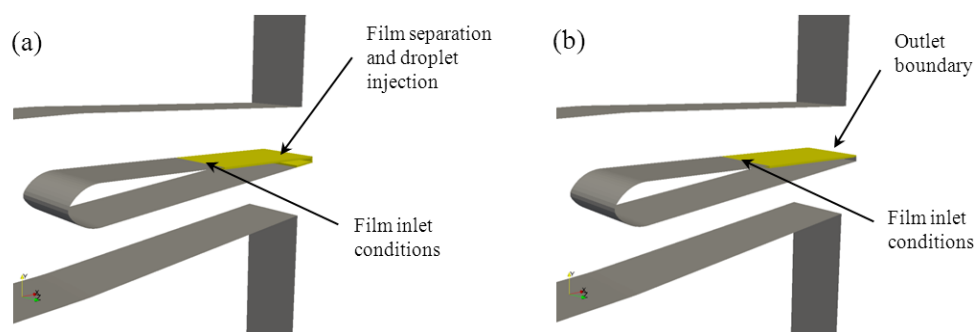


**Figure 2.** Different strategies for determining the breakup cells.

When the film reaches the edge, new droplets are injected and thus added to the parcel population of the Lagrangian solver. Droplet properties are derived starting from the local film and gas-phase fields computed with the respective solvers. In particular, droplet diameter is computed exploiting correlations for the SMD and a Rosin-Rammler distribution. Parameters required by correlations are given as external inputs or, in the case of thermo-fluid dynamic quantities, directly taken from gas-phase and liquid film solutions. The magnitude of particle velocity is taken equal to the film velocity at the atomization point with the possibility to use correlations also for this value. The direction of velocity can be set equal to the direction of the gas-phase velocity at the injection point (if the gas-phase solution is unsteady it might be possible to catch the atomization spreading angle) or equal to the direction of film velocity which is parallel to the prefilming surface. In the latter case the opportunity to define a spreading angle has been included in the formulation. Furthermore it is also

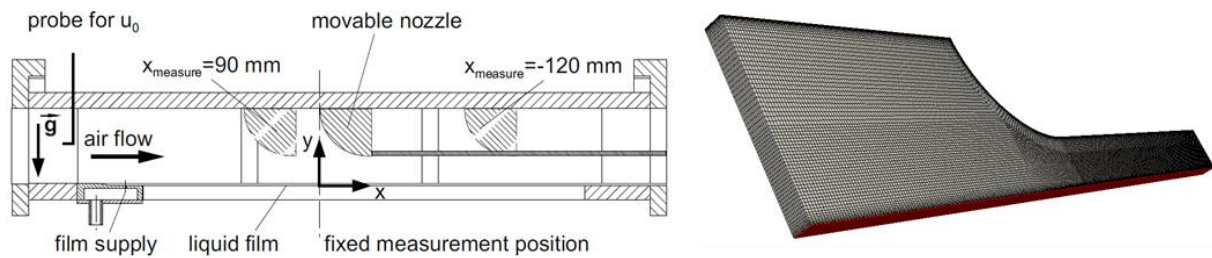
possible to define a breakup length: in this case the real injection point is placed downstream of the location defined by one of the two strategies of Figure 2.

### Film solver validation

In this section the solver capabilities to reproduce shear-driven films have been assessed by considering two different test cases [5] which allow us to simulate the main interactions between liquid film and gas-phase that could be found in typical airblast atomizers. Typical injector configurations are characterized by an acceleration of the surrounding air, thus, in the first test case, a liquid film undergoing a pressure gradient is considered. Additionally, airblast used in gas turbines usually have a conical shape and thus the film load  $\Lambda_f$  (volume flow rate per unit width) varies as a consequence of a different radius. The combined effect of pressure gradient and film load gradient is considered in the second test case. For the geometrical characteristics of these test cases the reader is addressed to reference [5].

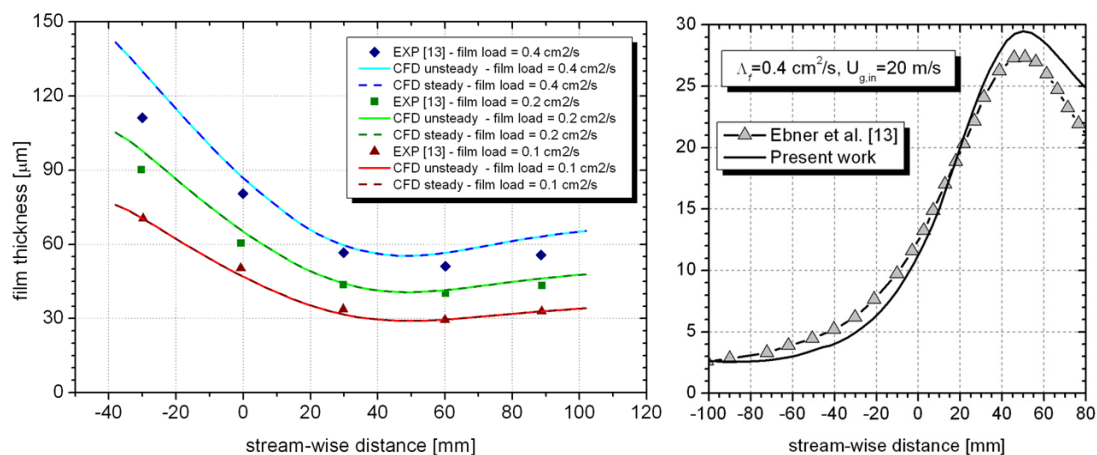
#### Test case 1

Figure 3 shows the test case geometry and the hexahedral computational mesh (the single layer mesh for the film solver is reported in red). The liquid film (a fluid with physical properties similar to those of kerosene at 80°C [5]) develops on the bottom surface whereas the air flow is accelerated by means of the nozzle opposite the film propagation surface. Different measurements were performed varying the inlet air velocity and the film loading. In the simulation a uniform velocity was imposed at the inlet boundary, atmospheric static pressure was assigned at the outlet boundary whereas a cyclic condition was assigned to the lateral faces. Solid walls have been modelled with a no-slip condition whereas a wall function with an equivalent sand-grain roughness was used at the interface between gas-phase and liquid film together with the  $k-\omega$  SST turbulence model.



**Figure 3.** Schematic representation of the test case geometry (taken from [5]) and computational mesh.

Figure 4 shows a comparison between experimental measurements (taken from reference [13]) and numerical results in the case of inlet air velocity magnitude equal to 20 m/s. A good agreement with experiments was found; the over-prediction of the film thickness at high film load is probably due to the equivalent sand-grain roughness expression which does not have an explicit dependence on film-thickness causing an under-estimation of the shear stress in the first part of the computational domain (compared to results of reference [13]). This leads to a lesser acceleration of the film and thus to a greater thickness. Results obtained with both unsteady and steady-state film solver are reported showing that the two approaches give very similar results.



**Figure 4.** Film thickness distribution as function of film load for inlet air velocity equal to 20 m/s and surface shear stress for the case  $\Lambda_f = 0.4 \text{ cm}^2/\text{s}$ .

### Test case 2

A representation of the second test case is reported in Figure 5 together with the computational domain representing a 6 degrees sector of the experimental rig (the film domain is represented by the red region). A liquid film with the same properties of the fluid used in the previous case is supplied around the circumference of the inner duct. Several measurements were performed varying the inlet air velocity and pressure and the film load. A computational setup similar to the one used in the previous case was also applied to this simulation which was performed using a fully steady approach (both gas-phase and liquid film solved with steady-state acceleration techniques).

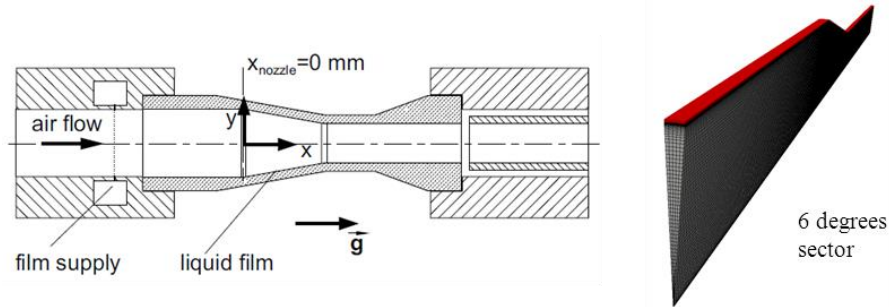


**Figure 5.** Schematic representation of the test case geometry (taken from [5]) and computational mesh.

In Figure 6 comparisons between numerical results and experimental measurements (taken from reference [14]) are reported for two selected conditions. A good agreement with experiments was found proving the capability of the code to correctly represent typical gas turbine airblast configuration where a pressure gradient and a film load gradient are present at the same time.

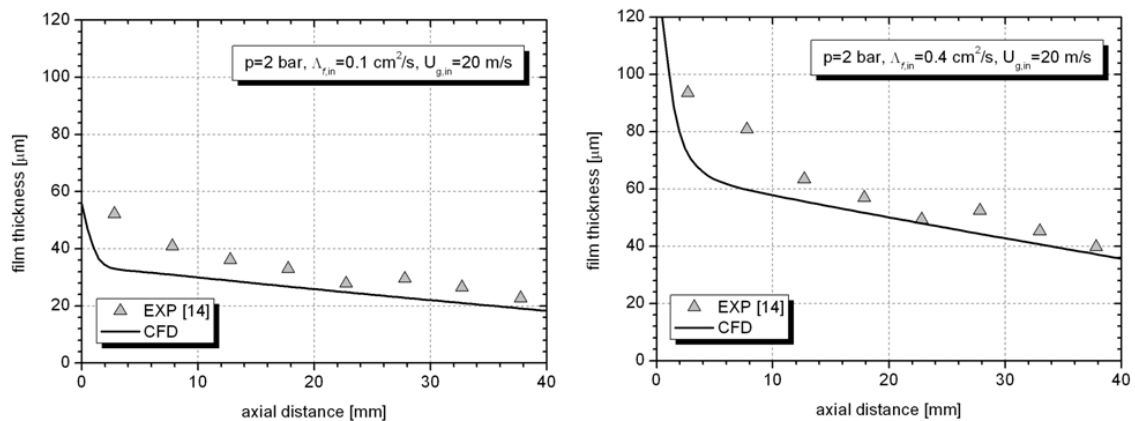


**Figure 6.** Comparison between numerical results and experimental measurements [14].

### Assessment of film breakup model

The capability of the implemented primary breakup model to reproduce the characteristics of droplet population after breakup strongly depends on the correlation chosen to compute the droplet SMD and on the ability of the film solver to compute the parameters required by the correlation (for example the film thickness). Film breakup model has been assessed by simulating a case reproducing the experimental setup [7] used by Gepperth et al. to find their correlation [4] and comparing measurements with numerical predictions performed with different correlations following the analysis of reference [9]. In particular, the Rizkalla and Lefebvre correlation [15] was considered. This formulation has an explicit dependence on film thickness and thus a proper prediction of liquid film evolution over the prefilming surface is necessary to properly predict the mean diameter. It is important to consider this kind of expressions because typical industrial correlations are often based on similar formulations with constants calibrated according to the given injector geometry. In Figure 7 the geometry is presented together with a comparison between experimental measurements and numerical results in terms of mean film thickness [7]. The case with Shellsol D70 liquid and mean air velocity equal to 60 m/s is considered. Numerical predictions are in good agreement with experiments and the SMD predictions follow the behaviour depicted in reference [9].

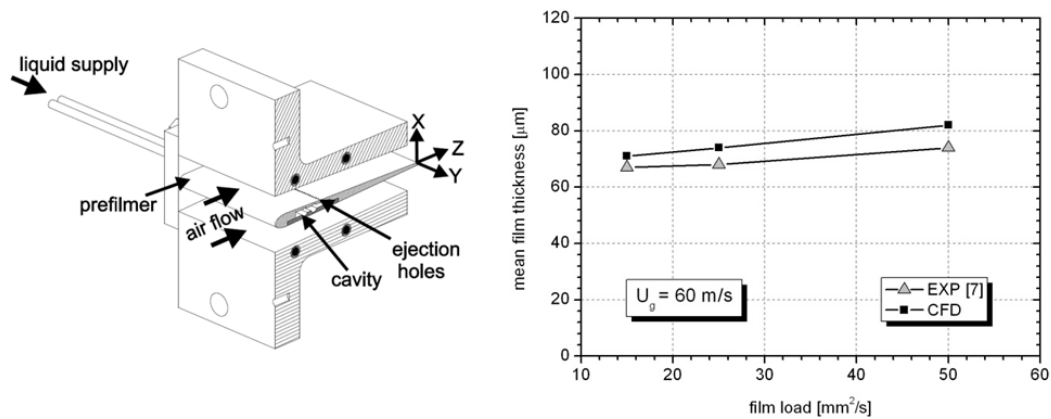


**Figure 7.** Schematic representation of the test case geometry (taken from [4]) and comparison between numerical results and experimental measurements.

## Conclusions

A multi-coupled solver for airblast injectors including film evolution and film primary breakup has been developed and successfully validated. Since the liquid film is directly solved, it is possible to reliably compute its thermodynamic properties before atomization which, in general, are very important for both the primary breakup and the subsequent droplet evolution, including evaporation and secondary breakup. Comparison with experiments showed that the solver is able to properly represent the interaction between gas-phase and liquid film in presence of both pressure gradients and film load gradients. For the success of shear-driven film simulations it should be pointed out the importance of the equivalent roughness of the film surface which highly enhances the surface shear stress. As regards the film primary breakup, a new phenomenological model has been introduced. It is important to highlight that this model is based on a correlative approach and so the success of spray population predictions after breakup require a well-calibrated correlation.

## Acknowledgements

The research leading to these results has received funding from the European Union Seventh Framework Programme (FP7/2007-2013) under grant agreement n°265848 and was conducted within the FIRST project. The permission for the publication is gratefully acknowledged by the authors.

## References

- [1] C.X. Bai and A.D. Gosman, *SAE Paper 960626* (1996).
- [2] C.X. Bai, H. Rusche and A.D. Gosman, *Atom. Sprays*, 12: 1-27 (2002).
- [3] I. Owen and D.J. Ryley, *Int. J. Multiphase Flow*, 11(1): 51-62 (1985).
- [4] S. Gepperth, A. Müller, R. Koch and H.-J. Bauer, *Proceedings of the ICLASS 2012* (2012).
- [5] P. Schober, J. Ebner, O. Schäfer and S. Wittig, *Proceedings of the ICLASS03* (2003).
- [6] Dombrowski, N., Johns, W. R., *Chemical Engineering Science* 18(3): 203-214 (1963).
- [7] S. Gepperth, D. Guildenbecher, R. Koch and H.-J. Bauer, *Proceedings of the ILASS-Europe 2010* (2010).
- [8] T. Inamura, M. Shirota, M. Tsushima, M. Kato, S. Hamajima and A. Sato, *Proceedings of the ICLASS 2012* (2012).
- [9] S. Gepperth, R. Koch and H.-J. Bauer, *Proceedings of the ASME Turbo Expo 2013*, GT2013-94033 (2013).
- [10] Patankar, S., *Numerical Heat Transfer and Fluid Flow*, Hemisphere Pub. Corp. McGraw-Hill (1980).
- [11] A. Andreini, C. Bianchini, B. Facchini and A. Giusti, *Proceedings of the ICLASS 2012* (2012).
- [12] A.D. Gosman and E. Ioannides, *J. Energy*, 7(6) (1983).

- [13] J. Ebner, P. Schober, O. Schäfer, R. Koch and S. Wittig, *Progress in Computational Fluid dynamics*, 4(3-5), (2004).
- [14] J. Ebner, P. Schober, O. Schäfer, and S. Wittig, *Proceedings of the ICLASS03* (2003).
- [15] A.A. Rizkalla and A.H. Lefebvre, *Journal of Fluids Engineering*, 97: 316-320, (1975).
- [16] A. Andreini, C. Bianchini, B. Facchini, A. Giusti and F. Turrini, *ILASS 2013* (2013).

## **A multi-coupled Eulerian-Lagrangian solver for airblast injectors including liquid film evolution and primary breakup – Application**

A. Andreini<sup>1</sup>, C. Bianchini<sup>1</sup>, B. Facchini<sup>1</sup>, A. Giusti<sup>1</sup> and F. Turrini<sup>2</sup>

1: Department of Industrial Engineering, University of Florence, Italy

2: Combustion System Office, AVIO Group S.p.A., Italy

### **Abstract**

In order to reduce NO<sub>x</sub> emissions, modern aero-engines are often equipped with lean burn combustion systems. The combustion process is strongly influenced by the liquid fuel preparation and advanced prefilming airblast injection systems are usually employed. Thus, in order to perform reliable predictions of engine emissions, it is important to develop proper tools aimed at predicting film evolution and its subsequent breakup. In this work a multi-coupled Eulerian-Lagrangian solver integrated with a film solver has been applied to the study of a tubular combustor equipped with a PERM (Partially Evaporating and Rapid Mixing) injection system developed by AVIO. Liquid fuel preparation has been analysed in detail with particular attention to liquid film evolution and droplet dynamics after primary breakup. This paper is the second part of a work aimed at developing a solver suitable for the analysis of lean-burn aero-engine combustors and presents an application of the numerical model to an industrial case. The companion paper reporting a detailed description of the numerical model is also presented in this conference.

### **Introduction**

The increasingly stringent regulations on pollutant emissions, in particular NO<sub>x</sub>, have led aero-engine manufactures to adopt advanced combustion technologies in order to meet emission requirements. Even though classical Rich-Quench-Lean (RQL) technology has still relevant improvement potentials, the expected future regulations concerning NO<sub>x</sub> emissions from civil aero-engines (ACARE Vision 2020 objectives and future ICAO-CAEP standards) have forced in the last ten years huge research investments from the main engine manufacturers to introduce lean burn combustion systems. The application of lean combustion in aero-engines requires the development of advanced injection systems aimed at guaranteeing a proper liquid fuel preparation. In particular, fine atomization and rapid mixing are desired so that the air fuel mixture can burn prevalently following the mechanisms of lean premixed flames.

Typical injector configurations are based on prefilming airblast atomizers and thus liquid film, droplets and gas-phase are present at the same time interacting with each other. As also pointed out by Schmehl et al. [5] who presented a multi-coupled numerical approach for the simulation of complex two-phase flows in gas turbine combustors, a reliable prediction of the performance of an aero-engine combustor requires numerical tools able to catch the most important interactions among the different phases together with a proper representation of primary breakup of liquid film since the combustion efficiency strongly depends on liquid fuel preparation. In this work a multi-coupled Eulerian-Lagrangian solver including liquid film evolution and primary breakup has been developed in the framework of the open source code OpenFOAM. A detailed description of the numerical approach is reported in reference [3]. In this paper the application of the solver to the analysis of an advanced lean burn injection system developed by AVIO in a tubular combustor configuration is presented with the main aim of showing the capabilities of the developed solver in the prediction of the complex phenomena characterizing lean burn aero-engines. First of all, a brief description of the combustor is given with particular attention to the characteristics of the injection system; then the computational setup is presented. Finally simulation results are presented and discussed.

### **Combustor and injection system geometry**

Figure 1 shows a schematic representation of the combustor geometry together with the injection system functioning concept. The combustor consists in a cylindrical flame tube with a length to diameter ratio  $L/D$  equal to 3.25. The injector, based on the PERM (Partially Evaporating and Rapid Mixing) concept, is basically a double swirler airblast atomizer developed in order to achieve partial evaporation inside the inner duct and rapid mixing within the combustor, optimising the location and the stability of the flame. A film of fuel is generated over the lip that separates the two swirled flows. As the film reaches the edge of the lip, primary atomization occurs: fine droplets and rapid mixing are promoted by the two co-rotating swirled flows generated by the double swirler configuration. Furthermore a hollow cone pressure atomizer (pilot injector) is located at centre of the primary swirler which, depending on the operating conditions, could generate a pilot flame to stabilize the combustion. The physics that characterizes this type of injector is very complex and as pointed out before, in



order to develop low emission engines, manufacturers need proper tools able to describe the liquid fuel preparation and droplet evolution inside the combustor.

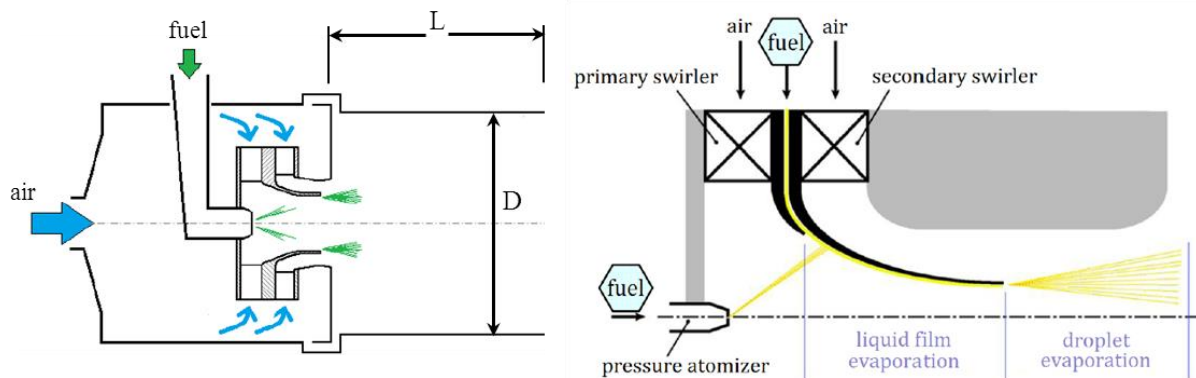


**Figure 1.** Tubular combustor and PERM injection system functioning concept.

### Computational setup

The numerical simulation of the tubular combustor has been performed considering a 9 degrees sector of the real geometry. Figure 2 reports a representation of the computational mesh (a hexahedral mesh of about 350000 cells was used) in the region near the injection system. The single layer mesh used by the film solver is also reported. Swirler blades have not been included in the computational domain and air inlet boundaries have been placed at blade exit plane. Swirled flows are reproduced by assigning to air flows a mass flow rate and the direction of velocity vectors. A static pressure has been imposed at the exit of the combustor whereas cyclic boundaries have been used for the lateral sides; furthermore no-slip and adiabatic conditions have been assigned to all the solid surfaces. Boundary conditions for the liquid film include a uniform thickness, temperature and velocity at the film inlet boundary and cyclic conditions on lateral edges. The pressure atomizer has been modelled by injecting a statistically representative population of parcels assigning the hollow cone angle and a proper Rosin-Rammler distribution. A diluted spray is considered so neither collision models nor specific treatments for dense spray region have been included in the numerical simulation. Wall/film-droplet interaction is accounted for by means of a particular impingement model derived from the work of Bai et al. [2] whereas a phenomenological model developed by the same authors of this work has been used for film primary breakup [3]. This model is basically a correlative approach which allows injection of new parcels in the Lagrangian solver as the film reaches the atomizing edge. The droplet injection location related to the film atomization has been defined by means of an outlet boundary for the film region. A breakup length and a spreading angle have also been defined in order to have a more physically realistic behaviour of the injection. As regards the correlation used to determine the droplet SMD, the formulation that gave the best fit with data given by the industrial partner was used. The model of Abramzon and Sirignano [4] has been used for droplet evaporation; turbulent dispersion has been accounted for using a stochastic model following the approach of Bai and Gosman [1]. Secondary breakup has been included using the TAB model [8] whereas gas-phase combustion has been modelled using a double step EDC model together with the  $k-\omega$  SST turbulence model.

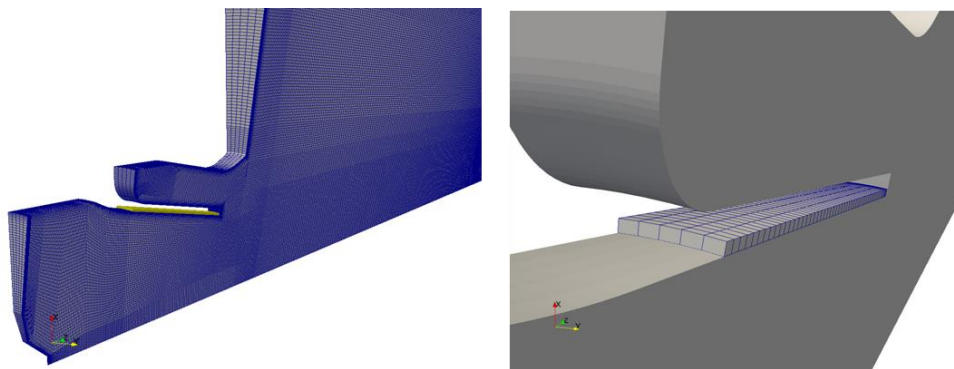


**Figure 2.** Computational mesh.

## Results and Discussion

In this section the main results obtained in the numerical investigation are presented. Several aspects were analysed ranging from liquid film evolution to dynamics of droplets derived from both pilot injector and liquid film atomization showing the highly coupled nature of interactions between the different phases.

### Flow field

Before describing liquid film and droplet dynamics, the most important features of the flow field are presented. Figure 3 shows the velocity field inside the combustion chamber generated by the two co-rotating swirlers. The presence of swirl in the flow allows the development of a strong vortex core along the axis with the typical vortex breakdown structure. The formation of a corner vortex in the region between the dome and the flame tube liner can also be noted. These structures, in particular the vortex breakdown, are very important for the combustion process allowing the formation of a stable flame. Furthermore the gas-phase velocity field has a great influence on the droplet tracking through the drag force. Droplets characterized by a very small dynamic relaxation time (for example particles generated by film breakup) basically follow the mean flow streamlines.

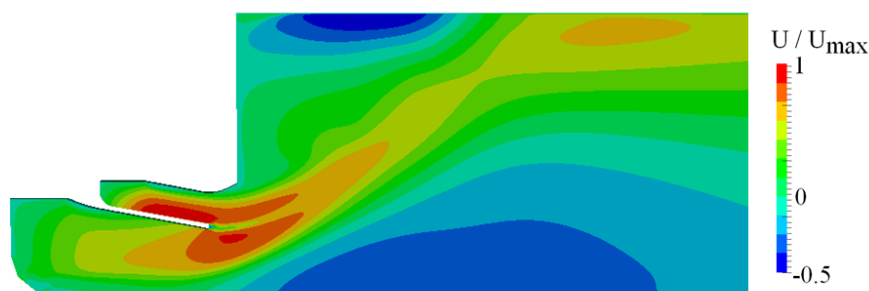


**Figure 3.** Mean axial velocity in the region near the injector.

### Pilot injector

The operating pressure and the fuel split between pilot injector and main injection appear the most important parameters influencing the combustor behaviour and droplet dynamics. In particular, at low pressure and high pilot/main fuel split droplets injected through the pressure atomizer could reach the lip promoting the formation of liquid film. In these cases the inclusion of a proper wall-film droplet impact model is fundamental in order to determine the amount of fuel added to liquid film or droplet generated as a consequence of the impact. Figure 4 compares parcel evolution at two different operating conditions obtained performing non-reactive simulations. The case in Figure 4(a) is representative of a low pressure operating condition with 20% of fuel injected through the pilot injector whereas in Figure 4(b) a high pressure case is reported with only the 5% of fuel supplied using the pilot injector. Different colours are used for droplets derived from the pressure atomizer (blue) and the ones generated by the film primary breakup (red). It is possible to observe that in the first case droplets are characterized by a much higher droplet residence time with the pilot injection that could impinge the lip depending on the injection angle and velocity.

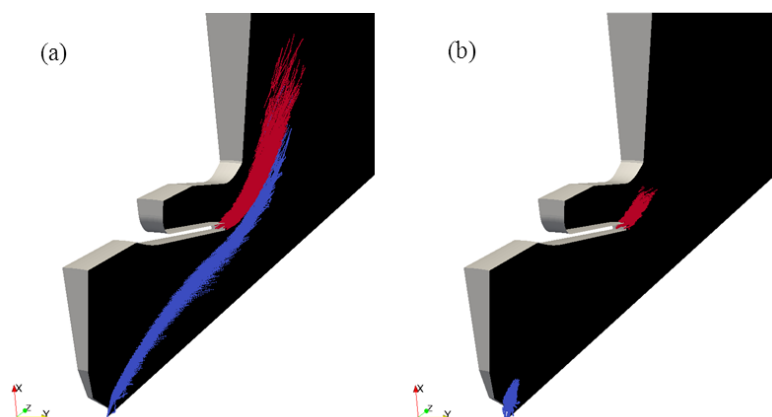


**Figure 4.** Droplet evolution at two different operating conditions. (a) Low-pressure and high pilot/main fuel split; (b) High-pressure and low pilot/main fuel split

*Liquid film*

The liquid fuel is supplied to the inner surface of the lip that separates the two swirlers through an array of holes and, thanks to the action of the air flow, it develops as a thin film until the atomizing edge is reached. Shear stresses acting on the liquid film surface due to the primary swirled flow give a tangential acceleration to the liquid film determining a centrifugal force. This force pushes the liquid against the wall contributing to make the film more stable. In the numerical simulation the film has been injected uniformly along the circumference. The film inlet boundary (see Figure 2) is placed at the same location of the injection holes, however film inlet conditions are not known as well as the location at which the film can actually be considered uniform. Thus, before performing a fully-coupled numerical simulation of the combustor, a sensitivity analysis to the most important film inlet conditions has been performed. In this analysis only the interaction of the gas-phase on the liquid film has been considered in a non-reactive simulation. Four different cases, differing by inlet normal and tangential velocity components, initial thickness and mass flow rate (see Table 1), have been evaluated with the main aim of determining the influence of inlet conditions on the quantities at the outlet boundary which are used by the film breakup model. Table 2 reports the liquid film characteristics at the outlet boundary for each case whereas Figure 5 shows film thickness (indicated with “delta”) and the axial velocity field over the lip. Film inlet conditions have a small influence on the velocity normal to the outlet boundary as well as on the film thickness which mainly depends on the film mass flow rate. On the contrary, different inlet tangential velocity components determine a different final tangential velocity and thus a different droplet injection velocity. However, as will be shown below, the dynamic relaxation time related to the droplets generated by the film primary breakup is quite small and parcels tend to follow the main stream in a short distance from the atomizing edge making the effect of the different velocity important only in the region near the edge.

**Table 1.** Liquid film inlet conditions.

Case	$U_n$ [m/s]	$U_t$ [m/s]	Film thickness [ $\mu\text{m}$ ]	$m/m_{nom}$ [-]
1	1.635	2.5	200	0.5
2	1.635	2.5	400	1.0
3	3.27	5.0	200	1.0
4	3.27	7.5	200	1.0

**Table 2.** Liquid film characteristics at the outlet.

Case	$U_n$ [m/s]	$U_t$ [m/s]	Film thickness [ $\mu\text{m}$ ]
1	12.8	2.3	30.3
2	15.5	3.8	50.3
3	15.5	5.2	50.3
4	15.4	6.8	50.4

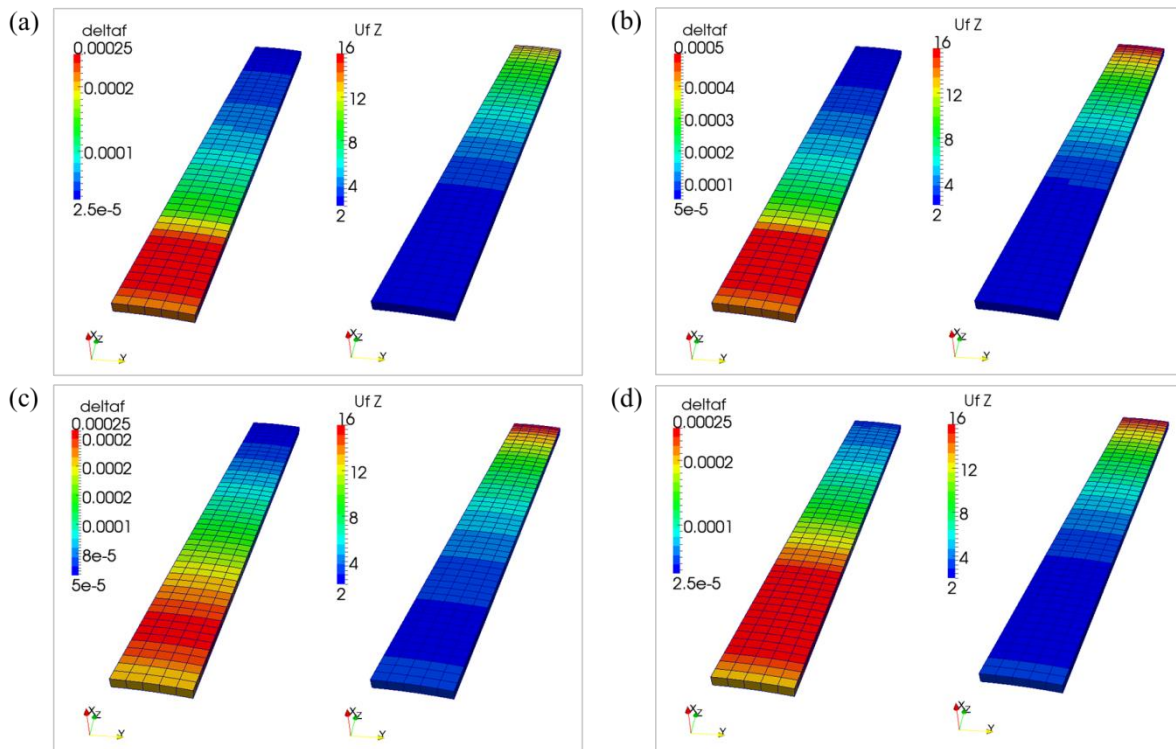


**Figure 5.** Analysis of liquid film evolution: (a) Case 1, (b) Case 2, (c) Case 3, (d) Case 4.

#### *Droplet dynamics after film primary breakup*

Using the setup of Case 3, droplet dynamics after primary breakup has been investigated. A high pressure with low pilot to main fuel split ratio operating condition is considered so that it is possible to neglect the influence of pilot injection on the film evolution. The main aim of this analysis is to show the influence on droplet dynamics of the most important physical interactions. Different non-reacting simulations were performed varying the models reproducing the coupling between gas-phase and dispersed phase (although combustion is not considered, the air inlet temperature is high enough to ensure droplet evaporation). Four cases were considered and Table 3 shows the models that have been activated in the different simulations.

**Table 3.** Cases considered in the droplet dynamics analysis.

Case	Turbulent dispersion model	Drag model	Evaporation model	Secondary breakup model
1	X	X	X	X
2	X	X	X	
3	X	X		
4	X			

Figure 6 shows the results obtained in unsteady simulations after 0.001 s from injection (note that the parcels are coloured with the tangential velocity). Comparing Case 1 with the others it is possible to point out the great influence exerted by the secondary breakup. Parcels fragment into smaller droplets near the atomizing edge promoting a rapid evaporation. Particles fully evaporate in a region very close to the atomizing edge allowing an efficient mixing between fuel and air. If the secondary breakup model is disabled (Figure 6(b)), the evaporation process is much slower and parcels follow a path similar to the one of Case 3, where only turbulent dispersion and drag models are enabled (Figure 6(c)). It is important to point out again that in these simulations the combustion is not activated, thus in reactive cases a higher evaporation rate due to higher temperatures could be generally expected. Finally, comparing Case 4 (where also the drag model is not activated, see Figure 6(d)) with the others it is possible to see that the injected parcels are accelerated by the main flow in a short distance from the atomizing edge.

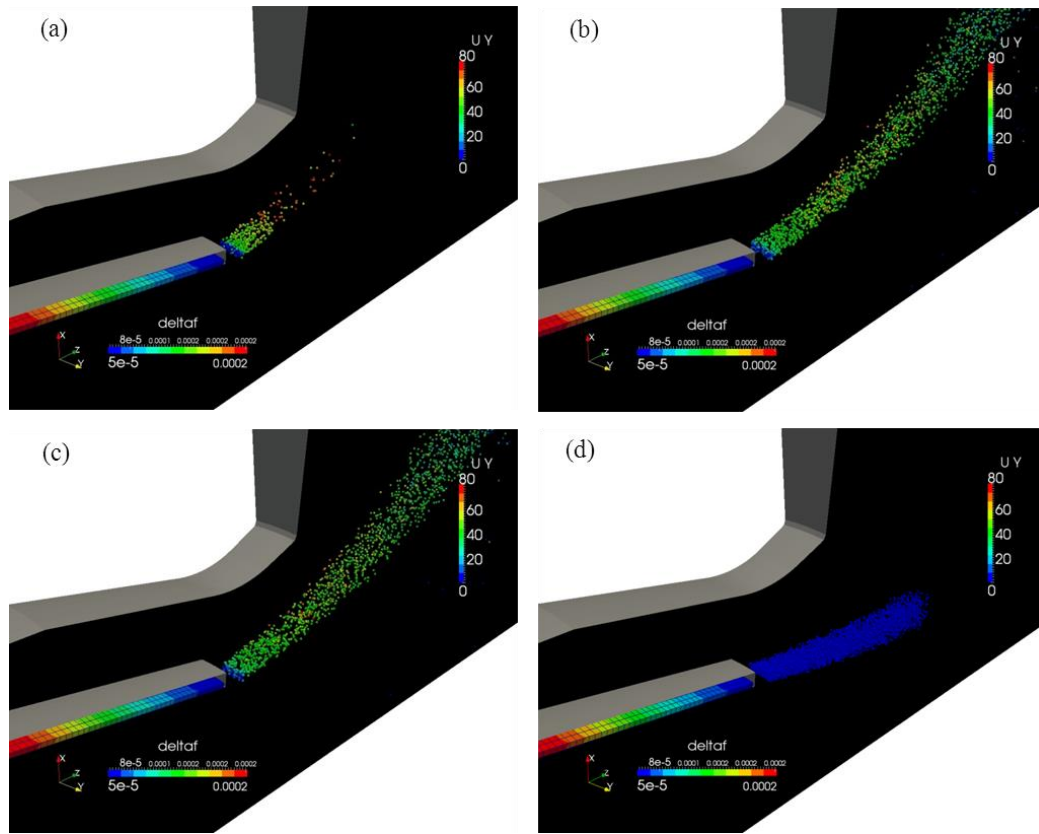


**Figure 6.** Analysis of the dynamics of droplet generated by the liquid film primary breakup: (a) Case 1, (b) Case 2, (c) Case 3, (d) Case 4.

#### Reacting case

In this section results obtained in a reactive simulation are reported. A high pressure case with low pilot/main fuel split has been simulated. When combustion is considered, source terms due to chemical reactions appear in species and energy conservation equations and a combustion model aimed at evaluating reaction rates is needed. In this work it is assumed that evaporating droplets simply behave as a source of fuel without considering formation of diffusion flames around the single droplet or groups of droplets. As mentioned before, a double step EDC model [7] has been used. In this model the reaction rate  $\omega_R$  is computed as:

$$\omega_R = \min(\omega_{ARR}, \omega_{EDC})$$

where  $\omega_{EDC}$  is the reaction rate of the standard EDC model [6], which assumes that the reactants are fast-burning and thus the overall reaction rate is controlled by the turbulent mixing, and  $\omega_{ARR}$  is the Arrhenius reaction rate. In practice, the Arrhenius rate acts as a kinetic limiter which delays the reaction near the injector exit where the turbulence is high.

In Figure 7 the mean temperature field near the injection system predicted by the simulation is reported. It is important to note that the combustion behaviour near the pilot injector characterized by high temperature values is not so representative of the real physics. This is mainly due to the  $k-\omega$  SST turbulence model which over-predicts the backflow and to the simple form of the combustion model that is not able to predict the quenching phenomena.

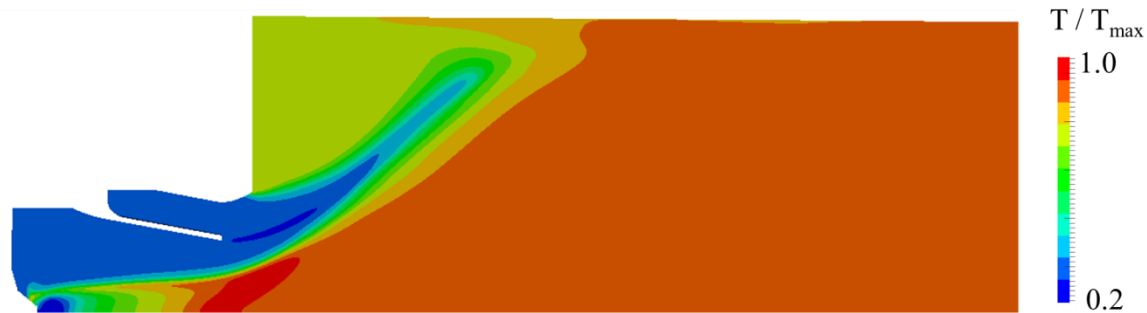


**Figure 7.** Mean temperature field near the injection system.

## Conclusions

In order to reproduce the complex physical phenomena that characterize the advanced airblast injection systems commonly used in lean burn aero-engines, a numerical solver able to describe the interactions among gas-phase, liquid film and fuel droplets is necessary. In this work a multi-coupled Eulerian-Lagrangian solver including liquid film evolution and primary breakup has been developed and applied to the study of a PERM injection system in a tubular combustor configuration with the main aim of showing the solver capabilities in the study of lean burn aero-engine combustors. The developed solver allows us to analyse a wide range of phenomena with a relative small computational cost typical of approaches based on averaged Navier-Stokes equations. The influence on spray evolution of the main injector parameters, such as the fuel split between pilot injector and main injection, has been investigated together with an analysis of the effect of film inlet boundary conditions on liquid film evolution and its characteristics at the atomizing edge. The film thickness at the atomizing edge as well as the velocity component normal to the outlet boundary seem to be influenced only by the film mass flow rate. On the other hand, droplet dynamics strongly depends on operating conditions. At high pressure the great influence exerted by secondary breakup on spray penetration and droplet residence time has been shown. Finally the results of a reactive simulation have also been reported. The combustion process is strongly influenced by the characteristics of droplet population generated by liquid film and pilot injector and the reliability of a numerical simulation requires an accurate reproduction of the basic phenomena regarding spray formation and evolution together with the choice of a suitable combustion model able to describe the most important features of the combustion process. This study proposes a computational setup, suitable for industrial calculations, able to account for all the main physical processes that characterize a combustor equipped with an advanced pre-filming injection system.

## Acknowledgements

The research leading to these results has received funding from the European Union Seventh Framework Programme (FP7/2007-2013) under grant agreement n°265848 and was conducted within the FIRST project. The permission for the publication is gratefully acknowledged by the authors.

## References

- [1] C.X. Bai and A.D. Gosman, *SAE Technical Paper* 960626 (1996).
- [2] C.X. Bai, H. Rusche and A.D. Gosman, *Atom. Sprays*, 12: 1-27 (2002).
- [3] A. Andreini, C. Bianchini, B. Facchini, A. Giusti and F. Turrini, *ILASS 2013* (2013).
- [4] B. Abramzon and W.A. Sirignano, *Int. J. Heat Mass Transfer*, 32(9): 1605-1618 (1989).
- [5] R. Schmehl, H. Roskamp, M. Willmann and S. Wittig, *International Journal of Heat and Fluid Flow*, 20: 520-529, (1999).
- [6] B.F. Magnussen, B.H. Hjertager, *Proc. Combust. Inst.*, 16: 719-729, (1976).
- [7] A. Andreini, A. Ceccherini, B. Facchini, F. Turrini and I. Vitale, *Proceedings of the ASME Turbo Expo*, GT2009-59539, (2009).
- [8] P.J.O'Rourke and A.A. Amsden, *SAE Technical Paper*, 872089 (1987).



## Validation of Eulerian-Eulerian Approach for Diesel Sprays, and 3D Coupling with Lagrangian Spray Approach

Zvonimir Petranović<sup>1</sup>, Wilfried Edelbauer<sup>2</sup>, Milan Vujanović<sup>1</sup> and Neven Duić<sup>1</sup>

1: Faculty of Mechanical Engineering and Naval Architecture, University of Zagreb, Zagreb, Croatia

2: AVL List GmbH, Graz, Austria

### Abstract

Spray process in Computational Fluid Dynamics (CFD) calculations is usually modelled by use of the wide spread Eulerian-Lagrangian multiphase method. Model for spray calculations based on this method is called Discrete Droplet Model (DDM), which is suitable for calculations of dilute spray in the region far away from the nozzle, but it has disadvantages for calculations in the near nozzle region. This region is also known as dense spray region where liquid phase occupies around 90 % of the entire cell volume. Drawback mentioned before is the result of a weak physical coupling between the gaseous and the liquid phase. Hence, the assumption of a single droplet surrounded by a gas field is not reasonable in a dense spray region. Use of the Eulerian-Eulerian multiphase model is one way how this can be avoided. This model divides the liquid phase into several phases with corresponding diameters and volume fractions. For such phase definition a model solves conservation equations and this result in better physical coupling of the mentioned phases. In this paper validation of the Eulerian-Eulerian spray model was done by running calculations of high pressure Diesel fuel injection into combustion chamber. Afterwards, the Eulerian-Eulerian model was used in combination with DDM model in real-case engine simulations. These two approaches were coupled by use of the AVL's Code Coupling Interface (ACCI). This procedure will be described inside section mathematical modelling. Fuel injection simulations were performed with commercial AVL's CFD code FIRE. The results shows penetration comparison of vaporized and liquid fuel, as also pressure and temperature curves in real-case engine simulations.

### Introduction

Diesel engine performance and emissions strongly depends on fuel atomization and spray processes [1]. Therefore an appropriate computer modelling of these processes is essential for optimization and development of modern diesel engines [2].

Different models currently exist for computational multiphase flows as DNS resolving the particles, Discrete Particle Model (DPM), Eulerian-Lagrangian Discrete Droplet Model (DDM), Eulerian-Eulerian etc. The Eulerian - Lagrangian DDM model has been applied for engineering calculations for many years and it is proven as a good simulation tool for prediction of a complex multiphase flows [3]. A well-known drawback of the DDM model is the limited use in the dense spray region due to the limited statistical convergence and the weak physical coupling between the gaseous and the liquid phase, as discussed in [4], [5]. Thus, for the dense spray the use of the Eulerian-Eulerian spray model is the more appropriate approach. In this model a cloud of droplets is regarded as polydispersed continuum, which is divided into a number of separate liquid phases depending on their sizes. Conservation equations are solved both, for the gaseous and for all liquid phases [6]. However, the main drawback of the Eulerian spray model is its higher computational effort because each phase requires its own set of conservation equations.

Overall, it can be said that the Eulerian-Eulerian and the Lagrangian DDM spray approaches are complementary. Thus, it is reasonable to combine the benefits of both approaches in a coupled simulation.

The Eulerian-Lagrangian model was first introduced by Dukowicz [7] and others and since then various improvements to the basic scheme have been proposed in [6], [8] and [9]. First calculations with Eulerian-Eulerian multiphase model were simulated by Gosman [10], Issa [11] and Lopez [12]. First coupling concept of Eulerian-Lagrangian and Eulerian-Eulerian approaches was proposed by Vallet and Borghi [13] and later extended by Lebas [14]. Such simulations are called coupled simulations and have been proven as efficient and practical approach for using the benefits of each model.

In the coupled simulations presented here the computational domain is divided into a dense and a diluted region. In the dense region the Eulerian-Eulerian model is used while in the diluted region the Eulerian-Lagrangian DDM model is used. For the first region conservation equations are solved for the gaseous and the liquid phases while in the diluted region parcels are introduced into the domain. The combination of the Eulerian-Eulerian and Eulerian-Lagrangian approach by use of the code coupling interface, called ACCI, is accomplished by running two separate simulations simultaneously - one on a highly resolved mesh for the Eulerian-Eulerian model and other on a coarser mesh where the Eulerian-Lagrangian model is applied, as discussed in [5], [15].

The focus of this work is on parameterization and validation of the Eulerian-Eulerian approach and afterwards its application for the high pressure IC diesel engines. The validated Eulerian-Eulerian multiphase



model is used in coupled simulations on the real case engine simulations. All simulations have been performed with the commercial AVL's CFD code FIRE.

The paper is organized as follows. Section experimental data briefly gives and overview of the available experimental data that is used for the model validation. Section mathematical modelling gives an overview of the spray models used in the simulations. Section Results and discussion outlines the differences before and after parameterization, simulation set-up on an experimental engine and discusses simulation results. Finally, the conclusions outline work done in this paper, mention necessary improvements and give overview about the future work.

### Available experimental data

The corresponding experiments have been performed at DaimlerChrysler Research [19] in the frame of the funded European I-LEVEL project. Six different operating points which differ in injection (50 and 80 and 120 MPa) and chamber (5.4 and 7.2 MPa) pressures were measured. Figure 1 represent experimental data for three different cases (Case 50/5.4, 80/5.4 and 120/5.4) where the numbers in brackets stand for injection and chamber pressure respectively.

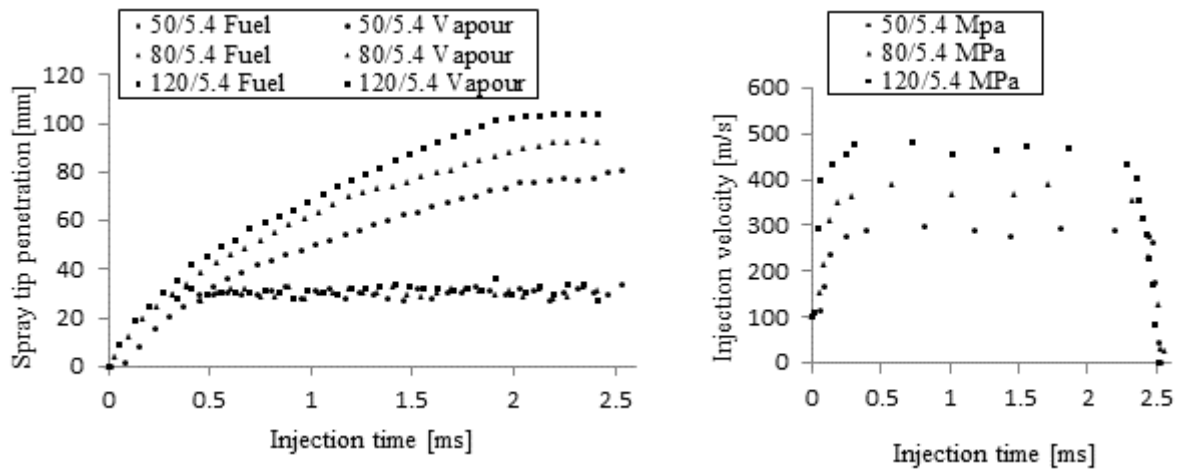


**Figure 1.** Fuel liquid and vapour penetration (left) and injection velocity (right)

From Figure 1 one can conclude that with higher injection pressure liquid jet velocity is higher and penetration of the vapour into the combustion chamber is stronger, while liquid fuel penetration stays at the same intensity. On Figure above it is not visible but it must be mentioned that increasing chamber pressure lowers the liquid penetration. As fuel jet velocity depends on injection pressure, on right hand side of the Figure 1 three different injection velocity profiles are shown. Maximum injection velocity values are 300, 400 and 500 m/s for injection pressures of 50, 80 and 120 MPa respectively. Increase of the chamber pressure from 5.4 to 7.2 MPa does not have any remarkable influence on injection velocity profile.

In the second part of the validation the experimental data for mean cylinder pressure and temperature of the EHVA LP7 engine are used for comparison. Those will be shown in the section Results and Discussion.

### Mathematical modelling

This section discusses the modelled processes of the liquid fuel atomisation during high pressure injection through small diameter nozzle. The first step of the atomisation process is fuel jet disintegration into ligaments and droplets, called primary breakup. Inside FIRE code there are several implemented primary breakup models (Prescribed breakup length, Diesel core injection and Diesel core injection + Nozzle file). The one used here is the Diesel core injection model which is originally developed by Huh et al. [16] and later adapted by Bianchi and Pelloni [16]. The main difference is that in the latter model the turbulence time and length scales are assumed to be constant while in the original model by Huh et al. [16] they vary with time. The average turbulence kinetic energy dissipation is calculated according to:

$$k_{avg} = \frac{u_{inj}^2 D_{noz}}{8L_{noz}} \left( \frac{1}{C_7^2} - C_4 - (1 - C_6^2) \right); \quad (1)$$

$$\varepsilon_{avg} = C_5 \frac{u_{inj}^3}{2L_{noz}} \left( \frac{1}{C_7^2} - C_4 - (1 - C_6^2) \right). \quad (2)$$

The diameter of newly created droplet is proportional to the turbulent length scale and it is modelled using expression:

$$D_d = 2L_T ; \quad (3)$$

where  $L_T$  stands for the turbulent length scale which is calculated according to:

$$L_T = C_2 C_\mu \frac{k_{avg}^{1.5}}{\varepsilon_{avg}} = L_A . \quad (4)$$

The atomization time scale which is originally modelled as linear combination of two time scales (aerodynamic and turbulent), is here calculated as harmonic mean value of two time scales. This means that the faster process dominates the primary breakup process [4].

$$\tau_A = \left[ \frac{1}{C_1 \cdot \tau_T + C_3 \cdot \tau_W} \right]^{-1} . \quad (5)$$

The next two expressions describe the calculation of the turbulent  $\tau_T$  and aerodynamic  $\tau_W$  time scales:

$$\tau_T = C_\mu \frac{k_{avg}}{\varepsilon_{avg}} ; \quad (6)$$

and

$$\tau_W = \frac{L_W}{\sqrt{\frac{\rho_{gas} \rho_{liq} |\mathbf{v}_{liq} - \mathbf{v}_{gas}|^2}{(\rho_{liq} + \rho_{gas})^2} - \frac{\sigma}{(\rho_{liq} + \rho_{gas}) L_W}}} . \quad (7)$$

In the Diesel Core Injection model coefficients  $C_1$ ,  $C_2$  and  $C_3$  have been varied to match experimental data. The mass source due to primary breakup is calculated by the equation:

$$\Gamma = 4\pi R_N^2 \rho_N \frac{d_R}{d_t} \text{ with } \frac{d_R}{d_t} = \frac{L_A}{\tau_A} . \quad (8)$$

Regarding the secondary break up process there are several existing models used in CFD simulations. The one of the implemented models into FIRE is the WAVE model modified for disintegration of the droplets. There, the radius reduction of the parent droplet is calculated according to:

$$\frac{dR_k}{dt} = \frac{R_k - R_{stable}}{\tau_a} ; \quad (9)$$

where  $R_k$  is the diameter of target droplet which is correlated to the wavelength of the fastest growth wave on the droplet surface and  $\tau_a$  is time scale of the secondary atomisation. Target diameter and time scale are calculated according to:

$$\tau_a = \frac{3.726 C_2 R_k}{\Lambda_k \Omega_k} ; \quad (10)$$

and

$$R_{stable} = C_2 \Lambda_k . \quad (11)$$

The WAVE model coefficients  $C_1$  and  $C_2$  have been varied to match experimental data.

In the second part of the paper the previously validated Eulerian-Eulerian multiphase model is coupled with the Lagrangian model by using the AVL ACCI approach. The main idea is to combine the advantages of both of the models. Figure 2 shows a schematic of the ACCI approach used for simultaneous simulations. Two simulations are running on separate clients, one for the Eulerian spray client and other for the Lagrangian engine

client. The clients exchange data via ACCI server that manages the exchange events, spatial mapping and data transfer. Simulation starts with initialization of the flow field of the engine client and data transfer to the spray client. To be precise, velocity, pressure, enthalpy, species mass fractions and quantities regarding turbulence are transferred to the spray client. Data exchange is done at every engine client time step. The computational mesh of the engine client must overlap the spray client so flow field boundaries can be transferred. This is done with 3D/2D mapping which is in detailed explained in [17]. Once on the Eulerian spray client the initial and boundary conditions are fully defined, simulation on spray client starts. Since Eulerian model requires smaller time steps then that used in the Lagrangian model several time steps must be calculated until next triggering of the ACCI data exchange. During this period momentum, mass and energy conservation equations and species transport equations are solved on the Eulerian spray client. Next step is to transfer data from spray to the engine client. Interaction of the gas and liquid phases is fully described in the overlapping region of the engine client (inside red boundaries inside engine mesh - Figure 2) despite there is no liquid phase existing in this part of the domain. Afterwards, calculation of the combustion and emission in the Lagrangian framework is applied. At next exchange event, heat and species mass sources from combustion and emission model which are calculated on the engine client are sent to the Eulerian spray client. This exchange is very important, since otherwise the Eulerian spray client would not recognize the rise of the temperature due to combustion. Details on the transition of the liquid phase from the Eulerian spray to the Lagrangian spray and details on the ACCI server can be found in [17] and [15].

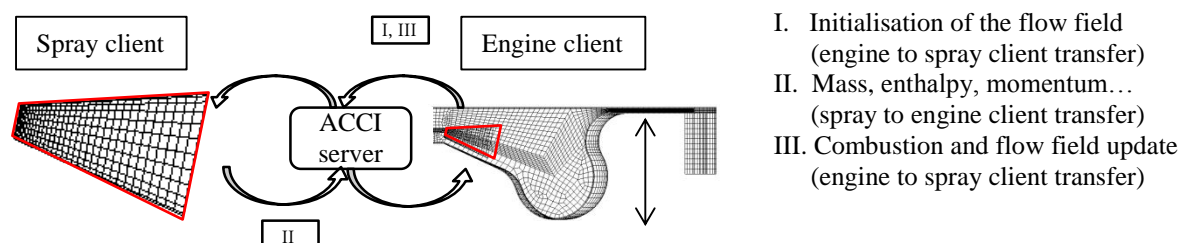


**Figure 2.** The concept of coupling Eulerian spray and Lagrangian engine calculation

## Results and Discussion

This section discusses the simulation set-up and the results of the Eulerian validation and its use in the ACCI coupled simulation. Validation was performed on the 2D cake mesh with 1400 control volumes which is shown in the Figure 3. Examined mesh is created with angle of 10° and only one cell in the  $x$  direction. Length of the domain in the  $-z$  direction is 120 mm. Inlet of the fuel is set as the normal velocity boundary condition with values taken from experimental measurements. The nozzle orifice diameter is 205  $\mu\text{m}$  and is resolved with 6 cells in diameter. The Diesel fuel is approximated by the species  $\text{C}_{13}\text{H}_{23}$  and total injection time length is 2.6 ms. At the orifice the fuel temperature is set to 373 K while inside the chamber temperature is set to 900 K. For the Eulerian model 6 phases are defined, where phases 2 to 5 are droplet phases and phase 6 is bulk liquid phase. Initial diameters are 5, 10, 20, 40 and 205  $\mu\text{m}$  for phase 2-6 respectively. The advanced multiphase model with variable droplet size classes (VDSC) is used. In this model additional transport equation for number density are solved to obtain the local class mean diameter of the droplets, as discussed in [2]. Pressure condition is set on the lateral boundary and as the initial condition inside the whole domain. For resolving turbulence,  $k-\epsilon$  model is used and for droplet evaporation Abramzon and Sirignano model [18].

Figure 4 shows penetration results before and after modification of the primary and secondary breakup for two different cases. Same conclusions are valid for all other cases. Changing of the coefficient influences the rate of fuel jet and droplets disintegration and also droplet target diameter. With fine tuning of the parameters, one can influence on droplet size distribution and lower or extent penetration curves.

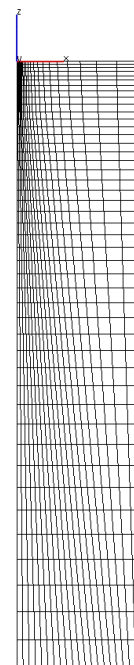


**Figure 3.** Spray mesh

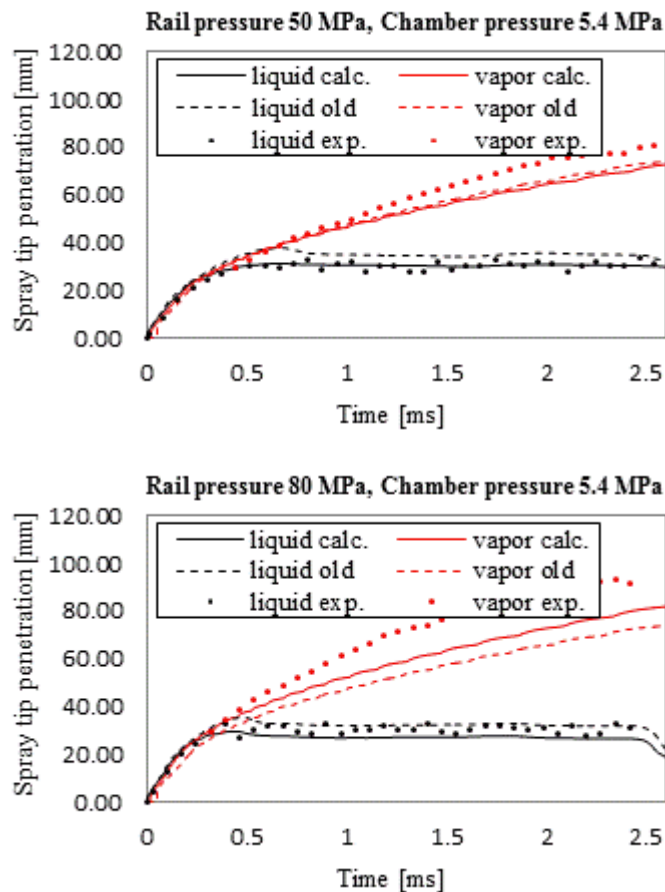


**Figure 4.** Spray tip penetration of vapour and fuel penetration

Figure 5 shows engine and spray (red) computational domain used for the ACCI calculation. The engine has a omega shaped geometry with a sector angle of 60 °, since injector is made with 6 holes. Spray mesh consists of 13440 control volumes, while moving engine mesh consists of 27000 cells in the UDP. Orifice diameter is 100 μm. Injection of the fuel with temperature of 320 K starts at 713.5 and ends at 734.8 deg. CA. Engine operates with 3000 min<sup>-1</sup> and inside chamber swirl of the residual gases is present. The same number of the droplet phases as for Eulerian validation is used with initial diameters of 5, 10, 20, 40 and 100 μm for phase 2-6 respectively. Engine client starts at 610 deg. CA with initial pressure 0.252 MPa and temperature 421.4 K.

For resolving turbulence, k-ε model is used and for droplet evaporation Abramzon and Sirignano model. Regarding primary and secondary breakup coefficients, the best parameter set from Eulerian validation is used. For DCI model:  $C_1=20(10)$ ,  $C_2=5(8)$ ,  $C_3=30(25)$ , and for WAVE model:  $C_1=0.61(10)$ ,  $C_2=60(30)$ .

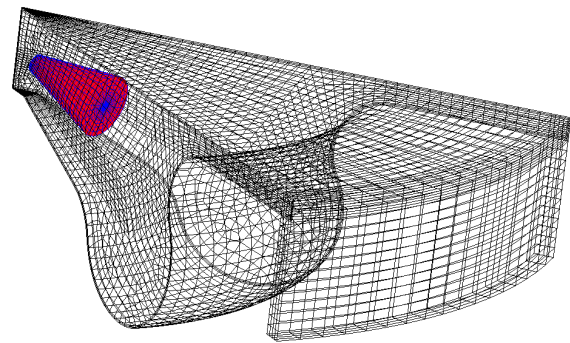


**Figure 5.** Engine and spray client control volume mesh

New (old) used primary breakup coefficients are:  $C_1=20(10)$ ,  $C_2=5(8)$ ,  $C_3=30(25)$  and secondary breakup:  $C_1=0.61(1)$ ,  $C_2=60(30)$ . Using new set of coefficients for fuel atomisation penetration curves correspond better to the experimental data.

Black and red colour represents fuel and vapour penetration respectively. Dots represent experimental data, solid lines stands for new results while dashed lines show results before modification of the model coefficients. Increase of the coefficients  $C_1$  and  $C_2$  in DCI model and  $C_2$  in the WAVE model results in faster disintegration of the liquid core and droplets. This leads to higher number of smaller droplets which are more influenced by the drag force. Thus penetration of the liquid fuel is reduced. From Figure 4 it is visible that new parameter set is more suitable for diesel injection for the investigated cases and this set is used in the ACCI simulations.

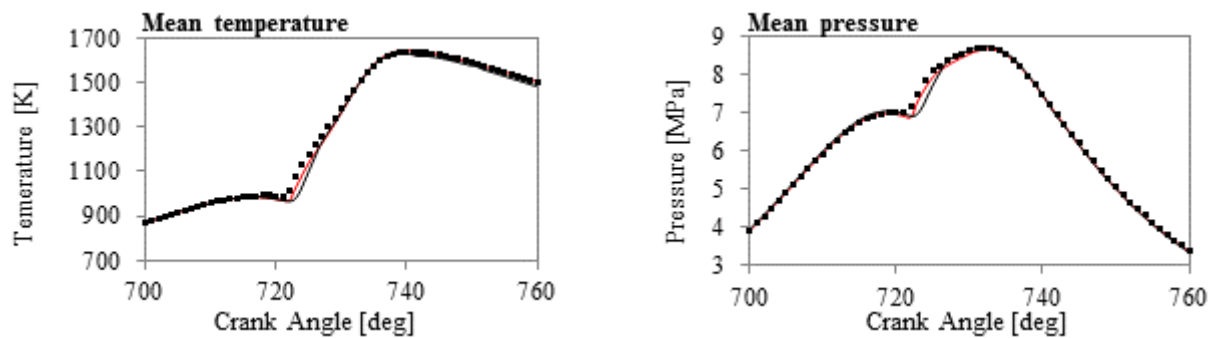


**Figure 7.** Mean pressure and temperature ( ■Exp. — ACCI — Lagrangian)

Figure 7 shows mean temperature and pressure curves for one of the available cases. It is visible that using the ACCI approach mean pressure and temperature curves are in even better agreement with the experimental data than ones using pure Lagrangian approach. On the left hand side of the Figure 8 temperature field for the ACCI simulation is shown, while on the right hand for the Lagrangian simulation. The small Figure enveloped with the solid black line represents spray client. The dashed black line represents its position inside the engine client domain. Using ACCI, the liquid fuel core existence is visible inside this region. On the right hand side, enveloped with the white solid line, is marked where spray client takes place in the ACCI simulation. ACCI simulation gives more physical results in term that higher amount of the liquid fuel is present in the near nozzle region. Because of higher number of bigger droplets, evaporation rate is smaller which leads to later combustion and lower temperatures.

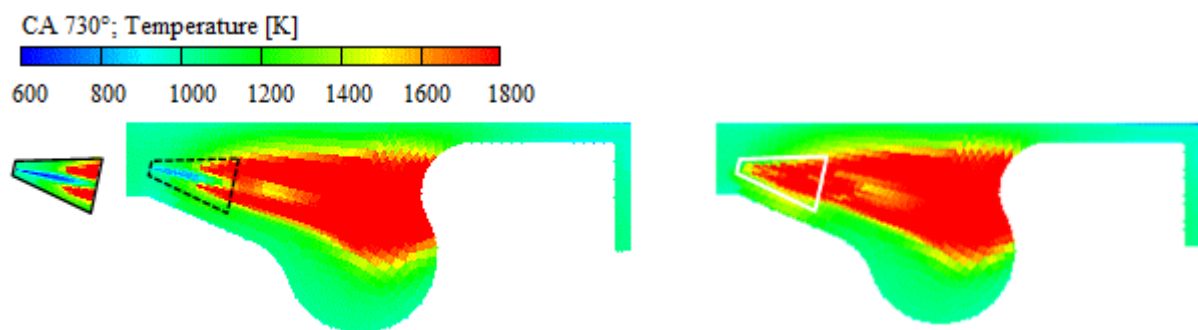


**Figure 8.** Temperature field at the 730 °CA, ACCI simulation (left) and Lagrangian (right)

## Conclusions

An Eulerian-Eulerian spray model has been presented and validated on the simplified 2D geometry. Results of the validation show that with the right set of model coefficients simulation results are in a good agreement with the experimental data. Six different cases that differ in rail pressure and chamber pressure were investigated. In the second part advanced ACCI coupling method was shown on the real case experimental engine. This methodology is a proven and useful simulation tool used for detailed spray atomisation and combustion process. Eulerian spray and DDM approaches are used in the regions where they are beneficial, as mentioned in the work. Coupled simulation results give better agreement with the available experimental data than those when only Lagrangian model is applied for the engine simulation.

For next step of the research experimental data on droplet size distribution and spray angle are validated. Droplet size distribution plays crucial role in the engine fuel efficiency and pollutant emissions and thus must be in detail investigated. Also, one additional model which influences the droplet size distribution will be implemented into the CFD code FIRE – collision model.

To summarize, validation of the Eulerian spray model is on-going work. Although shown results are sufficient and are in a good agreement with the experimental data, additional work is needed to conclude validation. For this reason, O'Rourke collision model [20] will be implemented and droplet size distribution will be investigated.



## Nomenclature

$k$	Turbulence kinetic energy	$\text{m}^2/\text{s}^2$	$u$	Velocity	
$D$	Droplet diameter	$\text{m}$	$L$	Length scale	$\text{m}$
$C$	Model constant		$\varepsilon$	Turbulent dissipation rate	$\text{m}^2/\text{s}^3$
$\tau$	Time scale	$\text{s}$	$R$	Droplet radius	$\text{m}$
$\rho$	Density	$\text{kg}/\text{m}^3$	$\Gamma$	Mass source	$\text{kg}/\text{s}$
$\Omega$	Wave growth rate		$\lambda$	Wavelength	

### Subscripts:

$avg$	Average	$inj$	Injection
$noz$	Nozzle	$d$	Droplet
$T$	Turbulent	$A$	Atomization
$gas$	Gas	$liq$	Liquid
$W$	Aerodynamic	$stable$	Droplet stable diameter
$k$	phase index		

### Abbreviations:

$CFD$	Computational Fluid dynamics	$WAVE$	Secondary break-up model
$DDM$	Discrete Droplet Model	$VDSC$	Variable droplet size model
$ACCI$	AVL code coupling interface	$UDP$	Upper dead point
$FIRE$	CFD computer program	$^\circ CA$	Degrees of crank angle
$DNS$	Direct Numerical Simulation	$IC$	Internal combustion
$DPM$	Discrete Particle Model	$EHVA$	Electro hydraulic valve actuation
$DCI$	Diesel Core Injection		

## References

- [1] S. Sibendu, A.I. Ramirez, D.E. Longman and S.K. Aggarwal, (2011) *Effect of Nozzle Orifice Geometry on Spray, Combustion and Emission Characteristics Under Diesel Engine Conditions*, Fuel.
- [2] M.Vujanović, W. Edelbauer, E.V. Berg, R. Tatschl and N. Duić, (2008) *Enhancement and Validation of an Eulerian-Eulerian Approach for Diesel Sprays*, European Conference on Liquid Atomization and Spray Systems ILASS, Como Lake, Italy, ILASS08-A087.
- [3] M. Sommerfeld, B.V. Wachema and R. Oliemans, (2008) *Best Practice Guidelines for Computational Fluid Dynamics of Dispersed Multiphase Flows*, Swedish Industrial Association for Multiphase Flows
- [4] AVL List GmbH, (2011) *Multiphase Flow, FIRE Version 2011 user manual*, Graz, Austria.
- [5] W. Edelbauer, (2011) *Coupling of 3D Eulerian and Lagrangian Spray Approaches in Industrial Combustion Engine Simulations*, 24<sup>th</sup> European Conference on Liquid Atomization and Spray Systems ILASS, Estoril, Portugal.
- [6] G. Gouesbet, A. Berlemont, (1999) *Eulerian and Lagrangian Approaches for Predicting the Behavior of Discrete Particles in Turbulent Flows*, Progress in Energy and Combustion Science 25 133-159.
- [7] J.K. Dukowicz, (1980) *A Particle-Fluid Numerical Model for Liquid Sprays*, J. Computational Physics 35, pp. 229-253.
- [8] E. Loth, (2000) *Numerical Approaches for Motion of Dispersed Particles, Droplets and Bubbles*, Progress in Energy and Combustion Science, 26, 3, pp. 161-223.
- [9] A.P. Watkins and H. Khaleghi, (1990) *Modelling Diesel Spray Evaporation Using a Noniterative Implicit Solution Scheme*, Applied Mathematical Modelling, 14, 9, pp. 468-474.
- [10] A.D. Gosman, C. Lekakou, S. Politis, R.I. Issa and M.K. Looney, (1992) *Aiche Journal* 38: p 1946-1956.
- [11] R.I. Issa and R.J. Oliveira, (1995) *Two Phase Flow Modelling and Experimentation*, p. 421-428.
- [12] M.A. Lopez de Bertodano, (1998) *Nuclear Engineering and Design* 179: p. 65-74.
- [13] A. Vallet, A.A. Burluka and R. Borghi, (2001) *Atomization and Sprays* 11: p. 619-642.
- [14] R. Lebas, G. Blokkeel, P.A. Beau, F.X. Demoulin, (2005) *SAE 2005-01-0213*.
- [15] W. Edelbauer, D. Suzzi, P. Sampl, R. Tatschl, C. Krueger and B. Weigand, (2006) *10<sup>th</sup> International Conference on Liquid Atomization and Spray Systems*, Kyoto, Japan.
- [16] Huh, K.Y. and Gosman, A.D. "A Phenomenological Model of Diesel Spray Atomization", Proceedings of the International Conference on Multiphase Flows, Sept. 24-27, 1991
- [17] AVL List GmbH, *Coupling Module CAE, FIRE Version 2013*, Graz, Austria, 2013
- [18] Abramzon, B., Sirignano, W.A., *International Journal of Heat Mass* 32: p. 1605-1618, 1989.
- [19] Koenig, G., *Private communication*, DaimlerChrysler Research, Stuttgart, Germany.
- [20] O'Rourke, P.J. and Bracco, F.V. *Modelling of Drop Interactions in Thick Sprays and a Comparison With Experiments*, IMECHE, 1980.

## Model of Two-Phase Flowfield around Shattering Drop

A. G. Girin

Odessa National Maritime University, Odessa, Ukraine,

### Abstract

Two-levelled mathematical model is developed in present paper which describes spatial aerodynamics of evaporating stripped mist around shattering drop in a uniform air stream. The model is based on the previous one-dimensional point-source model. The model utilizes the concept of quasi-continuous, high-frequency periodic dispersion from the unstable part of the parent drop surface caused by gradient instability in conjugated boundary layers. Torn-off droplets are considered as multi-velocity continuum and the equations of axisymmetric evaporating mist ballistics are composed in a dynamic 4-D space.

The following assumptions are made: air-velocity field around spherical drop is potential; the daughter droplets and their vapours do not influence on the air flowfield; the initial velocities of tearing-off droplets are proportional to the parameters of fastest unstable wave on the drop surface that produces them; Ranz – Marshall model is used to describe droplet evaporation.

The spatial distributions of the volume mass and number densities of torn-off droplets and of the vapour volume mass density are calculated and analysed. The large vapour concentrations are revealed which show a necessity of evaporation kinetics improving. The detailed fields of daughter droplets mean diameters and polydispersity in the spray are also obtained.

### Introduction

The liquid atomization is able to affect essentially on the high-speed gas-liquid flow dynamics. For instance, the feasibility of rapid detonative regime of liquid aerosol combustion is determined by the drop atomization into a cloud of tiny daughter droplets, which increases total liquid surface and thus the evaporation rate by 5–7 orders [1]. The secondary drop breakup after the fuel jet impinging in the engine combustor boosts up the preparation processes of evaporation and mixing. Thus, the engine efficiency rising and  $CO_2$  and NOx reducing are impossible without proper spray modelling [2].

The processes, which proceed in a shattering drop wake, are hidden by the mist and latent. The complexity of a drop spray modeling was reflected in [3]: spatial structure of a wake spray has a transient character since every droplet has its own velocity, radius and evaporation rate, and the droplets volume concentration varies due to a non-uniform two-dimensional acceleration field. However, the internal structure of a wake spray cannot be set up a priori but must be calculated as a dynamic process of spray formation. The model was built in [3] that reflected the evolution of the stripped droplets size distribution resulting from their acceleration and evaporation.

The drop or jet spray modelling is carrying out on the two levels: firstly, the lower level of elementary processes (mechanism and kinetics of droplet generation, acceleration, evaporation and heating) is a primary description; secondly, the upper level of general evaporating mist motion and mixing is a closing description for the transport processes. Subsequently, the presented here model consists of the two parts: 1) the parent drop atomization mechanics; 2) the aerodynamics of two-phase evaporating mist around shattering drop.

The atomization model is a core of spray dynamics investigation. In turn, such a model must be grounded on the daughter droplets tearing-off mechanism. The listed below atomization model utilizes the concept of quasi-continuous, high-frequency periodic dispersion from the unstable part of the parent drop surface due to the action of the gradient instability [1, 4]. Thus, the liquid-gas interface instability analysis with accounting for the gradient flow in conjugated boundary layers at drop surface [4] has justified the classic Kelvin – Helmholtz model application in inviscid instability treatment only when the liquid kinematic viscosity is greater than that of the gas one:  $\nu_l > \nu_g$ . But for the most of the liquid fuels used the inverse inequality takes place:  $\nu_l < \nu_g$ . The unstable root of dispersion relation of the boundary-value problem for disturbances in this case essentially differs from that of Kelvin – Helmholtz type. It defines the different type of hydrodynamic instability – gradient instability, which has the unstable mechanism working inside liquid boundary layer due to huge velocity gradient of the order  $(10^4 - 10^5) \text{sec}^{-1}$ .

Another base for presented model is the system of governing differential equations for the atomization process kinetics: equations for parent drop mass reduction and for torn-off droplets quantity have been derived in [1, 5]. Their integration provided all the necessary relations of the atomization process theory. The parent drop distribution function of stripped droplets by size  $f_{n,p}(r, t)$ , the ablating drop motion law  $x_p(t)$  and the



parent drop mass reduction  $m_p(t)$  (ablation law), obtained theoretically in [1, 5], present an opportunity to find out quantitatively further spray processes of rapid acceleration and evaporation of the stripped mist. The mathematical model of one-dimensional polydisperse spray, which was built on this basis and elementary results of evaporation ballistics of a wake spray were published in [3].

The previous model is extended here to the 2-D spatial case which considers the evaporating spray aerodynamics around atomizing spherical drop related with mechanics of dispersion process at the drop surface. The study contains a detailed calculation of the droplets generation and of the evaporating mist aerodynamic flowfield. The following assumptions are made: 1) air-velocity field around spherical drop is potential; 2) the daughter droplets and their vapours do not influence on the air flowfield; 3) the tearing-off droplet initial velocity is proportional to the parameters of fastest unstable wave on the drop surface that produces them; 4) droplet evaporation kinetics is simplified in accordance with Ranz – Marshall model. The varying in time spatial distributions of volume mass and number densities of torn-off droplets and of the vapour volume mass density are obtained as well as the detailed fields of daughter droplets mean diameters within the spray.

### Drop Atomization Mechanics

If we adopt the hypothesis regarded the high-frequency periodic dispersion due to the gradient instability action, then the parent drop surface ought to be considered as a quasi-continuous surface source of tearing-off daughter droplets. The main dispersion process parameters are varying in space and time and are distributed along drop surface. In order to implement the atomization mechanics into calculation algorithm we divide the drop surface onto a system of elementary grounds  $\Delta l_i = a \Delta \varphi_i$  and apply the results of instability analysis [4] to the locally-plane flow conditions at each ground (here  $a(t)$  is drop radius,  $\varphi$  is polar angle of the ground). In accordance with the main modeling hypothesis, the torn-off droplet radius  $r_i$  and the torn-off period  $t_{t.o.i}$  are proportional to the wavelength  $\lambda_m$  and increment  $t_m$  of the fastest unstable wave on a given  $i^{th}$  ground:

$$r_i = k_r \lambda_{mi}, \quad t_{t.o.i} = k_t t_{mi}. \quad (1)$$

The constant  $k_t$  is enlisted to account in some way for the delay time on non-linear stage of disturbance development; in present calculations the value  $k_t = 1.1$  was adopted [1, 5].

For every small time interval  $\Delta t$  while the flow parameters may be considered as invariable, the numerical algorithm requires  $\lambda_{mi}$  and  $t_{mi}$  current values calculation. For each  $\Delta t$  the algorithm has comprised the following steps at every ground (sub index  $i$  is omitted).

- 1). Gas – drop relative velocity  $V_\infty - W_p$  calculation; evaluation of parent drop Weber  $We_p$  and Reynolds  $Re_p$  numbers current values. The shattering parent drop motion law  $W_p = 1 - \exp(-H\tau)$ , obtained in [1], being used (here  $\tau = t/t_{ch}$  is dimensionless time,  $t_{ch} = 2a_0/\alpha^{0.5}V_\infty$ ,  $\alpha = \rho_\infty/\rho_l$  is gas-liquid density ratio).
- 2). Gas velocity  $V_g(\varphi)$  and liquid boundary layer thickness  $\delta_l(\varphi)$  evaluation at every ground. The formulae for potential gas flowfield around the drop in spherical coordinate system are used:

$$V_{gR} = V_\infty \left( 1 - \left( \frac{a(t)}{R} \right)^3 \right) \cos \theta; \quad V_{g\theta} = -V_\infty \left( 1 + \frac{1}{2} \left( \frac{a(t)}{R} \right)^3 \right) \sin \theta; \quad p = p_\infty - \frac{\rho_\infty}{2} (V_g^2 - V_\infty^2); \quad V_g^2 = V_{gR}^2 + V_{g\theta}^2, \quad (2)$$

as well as Ranger's relationship  $\delta_g(\varphi, t) = 2.2a(t)Re_p^{-0.5}(t)\Psi(\varphi)$  [6] for the gas boundary layer thickness on a sphere, where  $a(\tau) = a_0 \exp(-H\tau)$  is current parent drop radius,  $\Psi(\varphi) = ((6\varphi - 4\sin 2\varphi + 0.5\sin 4\varphi)/\sin^5 \varphi)^{0.5}$ ,  $V_\infty$  is gas stream velocity. Evaluation of "surface" Weber number  $We_s(\varphi) = \rho_g \delta_l V_s^2 / \sigma$  and calculation of fastest unstable wave parameters at every ground with the use of the relations  $\lambda_m(We_s)$ ,  $t_m(We_s)$  obtained in [4] (here  $V_s$  is liquid velocity on drop surface). It was shown in [1, 4] that for the conditions in the rocket combustor chambers and in detonation waves, when the gradient instability criterion is large enough,  $GI > 3.5$ , the fastest unstable wave parameters have the values  $\lambda_m = 1.64\pi\delta_l$ ,  $t_m = Im^{-1}(\omega_m) = 4.17\delta_l/V_s$ , and  $Re\omega_m \approx 1.5 Im\omega_m$ .

- 3). Checking up the tearing-off necessary condition, which consists in the sufficiency of unstable wave amplitude growth and takes the form of the requirement that the part of the induction time must be completed:

$$\int \frac{dt}{t_t(t)} \geq 1. \quad (3)$$

When inequality (3) is satisfied at some ground  $\varphi_i$ , it is suggested that the liquid toruses (due to axial symmetry) of number  $\Delta n_{\text{tori}} = \Delta l_i / \lambda_{mi}$  are torn off from that ground. They are breaking quickly into  $\Delta n_d = 2\pi a(t) \sin \varphi (k_r \lambda_m)^2 \cdot \Delta n_{\text{tor}}$  droplets of radius  $r_i = k_r \lambda_{mi}$ . In present work the value  $k_r = 0.2$  was adopted as calculations [1, 5] with this value showed an agreement with experiment.

5) The boundary conditions  $f_{n.d.}(\varphi_i) = \Delta n_d(\varphi_i) / \Delta r$  for the distribution function and the initial conditions  $R = a$ ,  $\theta_i = \pi - \varphi_i$ ,  $r(\varphi_i)$ ,  $w_{dR} = w_{\lambda n}(\varphi_i)$ ,  $w_{d\theta} = -w_{\lambda \tau}(\varphi_i)$  for each stripped droplet fraction  $\Delta r$  are assigned.

6) The stripped droplets are spaced into the gas flow near parent drop surface at  $R = a$ ,  $\theta_i = \pi - \varphi_i$  as spray's "liquid-phase" component and their velocities and trajectories begin to be calculated.

7). The dispersed liquid total amount and the new parent drop mass value  $M = \tilde{a}^3$ ,  $\tilde{a} = a/a_0$ , are determined.

The periodic instability gives rise to unstable wave amplitude growth in the normal direction with a speed  $w_{\lambda n}$  and simultaneous liquid motion in tangential direction along drop surface with a speed  $w_{\lambda \tau}$ . It is assumed in present paper that *the initial values of normal and tangential components of torn-off droplet velocity are proportional to the corresponding velocity components of the unstable wave's tip*:  $w_{dn} = w_{\lambda n}$ ,  $w_{d\tau} = w_{\lambda \tau}$  at the tearing moment. When the non-linear stage of the disturbance development begins, the ligament formation starts which radius is proportional to the fastest unstable wave length,  $r = k_r \lambda_m$ . The non-linear stage terminates at  $\tau_{ti} = k_t \tau_{mi}$  when the discreet droplet tears off the ligament tip (fig. 1). These daughter droplet parameters  $r$ ,  $\tau_t$ ,  $w_{dn}$ ,  $w_{d\tau}$  are definitive ones for further droplet motion, evaporation and thus the parent drop spray formation. But neither theoretical nor empirical data concerning the torn-off droplet velocity at the tearing-off

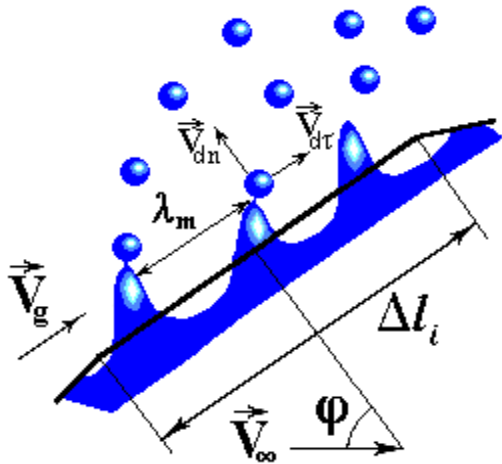


**Figure 1.** Scheme of dispersion on a ground

moment are known. Most likely, the ligament pulling out from the drop or jet surface is similar to that one in aperiodic instability case, which was investigated experimentally by Lewis [7]. Lewis has established two stages of the process: linear stage of the sinusoidal disturbance shape and exponential amplitude growth,  $E = E_0 \exp(ihx - i\omega t)$ , and non-linear one with the constant amplitude velocity increasing,  $w_{\lambda n} = 0.239(g\lambda_m)^{0.5}$ , when the disturbance's spike sharpens and air column widens (here  $\omega$  is complex wave frequency,  $h$  is wavenumber,  $g$  is acceleration). The stages are divided by the moment, when  $E = 0.4\lambda_m$ . Despite the different nature of the forces that produce the ligaments (inertial forces in the case of aperiodic instability and pressure difference in periodic one) the kinematics of their growth in normal to the surface direction can be similar. This analogy is used here, in the periodic instability case.

We have adopted here an assumption that *in the flow at infinite plane surface without characteristic size and time scales, any size, or time, or velocity value is defined by  $\lambda_m$ ,  $t_m$  or  $\lambda_m/t_m$ , respectively*. This assumption is being confirmed by the experimental data [7]. It follows from Lewis' results that  $w_{\lambda n}$  is proportional to  $\lambda_m/t_m$ . Indeed, according to Lewis, the normal velocity component is  $w_{\lambda n} = 0.239(g\lambda_m)^{0.5} = k_w (G/We_p)^{1/4} \alpha^{1/2} V_\infty$ ,  $k_w = 0.239 \cdot (3)^{1/4} (2\pi)^{1/2}$ , when rewriting in the parent drop criteria  $G$ ,  $We_p$ , where  $G = g2a_0/\alpha V_\infty^2$  – dimensionless drop acceleration. When we calculate the ratio  $\lambda_m/t_m$  with a help of the relations  $\lambda_m = 2\pi \cdot 2a_0 (GWe_p/3)^{-1/2}$ ,  $t_m = 2\pi (4G^3We_p/27)^{-1/4} 2a_0/\alpha^{1/2} V_\infty$ , inherent to Rayleigh – Taylor instability, we will have:  $\lambda_m/t_m = k_w (G/We_p)^{1/4} \alpha^{1/2} V_\infty$ ,  $k_w = 2\pi(4/3)^{1/4}$ .

From the other hand, the  $w_{\lambda n}$  value calculated at the moment when the linear stage terminated,  $E = 0.4\lambda_m$ , is similar:  $w_{\lambda n} = dE/dt = E \text{Im} \omega = 0.4\lambda_m \text{Im} \omega = 0.4\lambda_m/t_m = k_w (G/We_p)^{1/4} \alpha^{1/2} V_\infty$ ,  $k_w = 0.4 \cdot 2\pi(4/3)^{1/4}$ . The comparison gets evidence that the proportionality  $w_{\lambda n} \propto \lambda_m/t_m = k_w (G/We_p)^{1/4} \alpha^{1/2} V_\infty$  is true, as Lewis experiments show.

Thus, in the present case of periodic instability the tearing-off droplet velocity components may be calculated in accordance to the relations:  $w_{dn} = E_{\max} \operatorname{Im} \omega$ ,  $w_{d\tau} = E_{\max} \operatorname{Re} \omega$  (see also Lighthill [8]). Amplitude at the tearing-off moment,  $E_{\max}$ , is to be proportional to the wavelength, too:  $E_{\max} = k_{\text{amp}} \lambda_m$ , as the any other linear size is. Coefficient  $k_{\text{amp}}$  can be determined with a help of the additional assumption regarding the tearing

process stationarity: *when the flow conditions at a ground are steady, the steady are dispersion parameters*. Namely, the tearing act performs always at one and the same amplitude value  $E_{\max}$  and in one and the same time interval  $T = 1/\operatorname{Im} \omega$  passed. Just after the tearing-off, the residual amplitude  $E_{\max} - 2r$  every time has one and the same value too, which is the initial for the consequent disturbance:  $E_0 = E_{\max} - 2r$ . Gathering altogether, we will have  $E_{\max} = E_0 \exp(T \operatorname{Im} \omega) = E_0 \exp(1) = (E_{\max} - 2r) \exp(1) = k_{\text{amp}} \lambda_m$ . Hence,  $(k_{\text{amp}} \lambda_m - 2k_r \lambda_m) \exp(1) = k_{\text{amp}} \lambda_m$ , and finally,  $k_{\text{amp}} = 2k_r / (1 - \exp(-1))$ . So, with the value  $k_r = (0.18 - 0.20)$  adopted in [1, 5] as a result of comparison with experiment, we will have  $k_{\text{amp}} = 0.63$ . Hence,  $E_0 = (k_{\text{amp}} - 2k_r) \lambda_m = 0.23 \lambda_m$ , and  $E_{\max} = E_0 \exp(1) = 0.63 \lambda_m$  – the iterated value is returned.

Then  $w_{dn} = E_{\max} \operatorname{Im} \omega = k_{\text{amp}} \lambda_m \operatorname{Im} \omega_m = 0.18 \cdot 2\pi k_{\text{amp}} V_s$ . Similarly,  $w_{d\tau} = E_{\max} \operatorname{Re} \omega_m = E_{\max} \operatorname{Im} \omega_m \cdot \operatorname{Re} \omega_m / \operatorname{Im} \omega_m = 1.5 w_{dn}$ , as  $\operatorname{Re} \omega_m \approx 1.5 \operatorname{Im} \omega_m$ . Finally,

$$\begin{cases} w_{dn} = 0.18 \cdot 2\pi k_{\text{amp}} V_s = 0.18 \cdot 2\pi k_{\text{amp}} \frac{1.5(\alpha\mu)^{1/3}}{1 + (\alpha\mu)^{1/3}} (V_\infty - w(t)) \sin \varphi; \\ w_{d\tau} = 0.27 \cdot 2\pi k_{\text{amp}} \frac{1.5(\alpha\mu)^{1/3}}{1 + (\alpha\mu)^{1/3}} (V_\infty - w(t)) \sin \varphi, \end{cases} \quad (4)$$

– at any elementary ground  $(\Delta\varphi)_i$  on the parent drop surface, accounting for the value  $V_s = 1.5(\alpha\mu)^{1/3} (1 + (\alpha\mu)^{1/3})^{-1} (V_\infty - w(t)) \sin \varphi$  found in [5].

The differential equation for the number  $\Delta n_d$  of droplets stripped from an elementary ground  $\Delta\varphi$  by time interval  $\Delta\tau$  was theoretically derived in [5]:

$$\Delta n_d(\varphi, \tau) = \dot{n}'(\varphi, \tau) \Delta\varphi \Delta\tau = B_2 \sqrt{\tilde{a}(\tau) (1 - W_p(\tau))^5} \frac{\sin^2 \varphi}{\Psi^3(\varphi)} \Delta\varphi \Delta\tau, \quad \Delta n_d(\varphi, \tau) = f_{n,p} \Delta\tilde{r}, \quad (5)$$

$$\text{where } B_2 = \frac{0.075 \sqrt{2 \operatorname{Re}_{p0}^3} \mu^{7/3}}{\pi k_r k_t (1 + (\alpha\mu)^{1/3}) \alpha^{7/6}}; \quad \tilde{r}(\varphi, \tau) = B_1 T(\tau) \Psi(\varphi), \quad T(\tau) = \sqrt{\frac{\tilde{a}(\tau)}{(1 - W(\tau))}}, \quad B_1 = \frac{2.2 k_r \lambda_m}{\delta_l \sqrt{2 \operatorname{Re}_{p0}}} \frac{\alpha^{1/3}}{\mu^{2/3}}.$$

### Evaporating Mist Aerodynamics in around Atomizing Drop

The upper-scale modelling concept here follows that one of the paper [3]. Below we consider the phenomena in the meridian plane  $R, \theta$  of spherical coordinate system with regard to the flow axial symmetry. Polydispersity of the spray makes it necessary to regard the droplet size scale,  $r$ , as an independent variable for describing velocity fields and evaporation rates. To take into account all the peculiarities of evaporation ballistics, we introduce the transient size distribution function of daughter droplets  $f_{n,d}(R, \theta, r, t)$  as it exactly reflects the entire evolution of stripped droplets in time  $t$ , in space  $R, \theta$ , as well as in size,  $r$ . On the parent drop surface,  $R = a(t)$ , it coincides with the parent drop source distribution function:  $f_{n,d}(a, \theta, r, t) = f_{n,p}(a, \theta, r, t)$  given by (5).

Unlike the one-dimensional approximation [3], the source of daughter droplets here is distributed along parent drop surface. In order to obtain  $f_{n,p}(a, \theta, r, t)$ , the production-rate function  $\dot{n}'(\varphi, \tau)$  (eq. 5) must be integrated numerically in both  $\varphi$  and  $\tau$ . The daughter droplets are moving with a velocity  $\vec{w}_d(R, \theta, r, t)$  and each daughter droplet is a moving point source of vapor with a strength  $\dot{F}_v(R, \theta, r, t)$ . They altogether form the distribution of a vapor mass  $m_v(R, \theta, t)$  in the wake. To describe the evolution of  $f_{n,d}$  in the  $(R, \theta, r, t)$ -space, we enlist an equation of dispersed fuel, which was derived by Williams [9]. It describes the changing density of the daughter droplet distribution,  $f_{n,d}$ , in the radial direction, which proceeds with the velocity  $dR_d/dt = w_{dR}(R, \theta, r, t)$ , in transversal direction – with velocity  $R d\theta_d/dt = w_{d\theta}(R, \theta, r, t)$  due to droplet

acceleration by the gas flow, and in  $r$ -axis direction – due to evaporation, which proceeds with a rate  $u_d = dr/dt$ , determined by the evaporation law. The equation of evolution must be supplemented with the equation of motion of daughter droplets continuum and with the equation of vapor influx in a spray volume. Therefore, the droplet phase is considered as a continuum fluid in dynamic  $(R, \theta, r, t)$ -space.

Thus, two-phase aerodynamics in a wake spray of an atomizing drop is described by four dimensionless functions  $f_{n.d.}(\tilde{R}, \theta, \tilde{r}, \tau)$ ,  $W_{dR}(\tilde{R}, \theta, \tilde{r}, \tau)$ ,  $W_{d\theta}(\tilde{R}, \theta, \tilde{r}, \tau)$ ,  $M_v(\tilde{R}, \theta, \tau)$ , which are the solutions to a system of differential equations describing spray dynamics

$$\left\{ \begin{aligned} \frac{\partial f_{n.d.}}{\partial \tau} + \frac{\partial}{\partial \tilde{r}}(U_d f_{n.d.}) + \frac{\partial}{\partial \tilde{R}}(R^2 W_{dR} f_{n.d.} \sin \theta) + \frac{\partial}{\partial \theta}(R W_{d\theta} f_{n.d.} \sin \theta) &= 0; \end{aligned} \right. \quad (6)$$

$$\left\{ \begin{aligned} \frac{\partial W_{dR}}{\partial \tau} + W_{dR} \frac{\partial W_{dR}}{\partial \tilde{R}} + \frac{W_{d\theta}}{R} \frac{\partial W_{dR}}{\partial \theta} - \frac{W_{d\theta}^2}{R} &= \frac{3}{2} \frac{\sqrt{\alpha} C_{dr}}{B_1 \tilde{r}} \frac{(V_{gR} - W_{dR}) |V_{gR} - W_{dR}|}{2}, \end{aligned} \right. \quad (7)$$

$$\left\{ \begin{aligned} \frac{\partial W_{d\theta}}{\partial \tau} + W_{dR} \frac{\partial W_{d\theta}}{\partial \tilde{R}} + \frac{W_{d\theta}}{R} \frac{\partial W_{d\theta}}{\partial \theta} + \frac{W_{dR} W_{d\theta}}{R} &= \frac{3}{2} \frac{\sqrt{\alpha} C_{dr}}{B_1 \tilde{r}} \frac{(V_{g\theta} - W_{d\theta}) |V_{g\theta} - W_{d\theta}|}{2}, \end{aligned} \right. \quad (8)$$

$$\left\{ \begin{aligned} \frac{\partial M_v}{\partial \tau} + V_{gR} \frac{\partial M_v}{\partial \tilde{R}} + \frac{V_{g\theta}}{R} \frac{\partial M_v}{\partial \theta} &= \dot{F}_v f_{n.d.} \Delta \tilde{r}, \end{aligned} \right. \quad (9)$$

where  $\tilde{r} = r/(a_0 B_1)$ ,  $x' = x\alpha^{1/2}/2a_0$ ,  $W_d = w_d/V_\infty$ ,  $U_d = 2u_d/(B_1\alpha^{1/2}V_\infty) = -\Lambda \text{Nu}_d/16\tilde{r}$ ,  $M_v = m_v/m_{p0}$ ,  $\Lambda = 2\lambda/(\alpha^{1/2}B_1^2V_\infty a_0)$  is dimensionless evaporation constant,  $\tau = t/t_{ch}$ ,  $t_{ch} = 2a_0/\alpha^{1/2}V_\infty$  is characteristic time,  $B_1 = 0.51\pi\alpha^{1/3}\mu^{-2/3}\text{Re}_{p0}^{-1/2}$  has a sense of size scaling parameter for daughter droplets ( $r_{\min}, r_{\max} \in a_0 B_1$ ),  $\mu = \mu_\infty/\mu_l$  is the media viscosity ratio,  $\text{Nu}_d$  – Nusselt number for daughter droplet. It is assumed in (9), that vapors instantly accelerate to the gas velocity  $V_g$  due to negligible mechanical non-equilibrium of gas components, and it is neglected in (9) by the parent drop evaporation rate.

The dependence of the drag coefficient  $C_{dr}$  on droplet velocity and size was taken in the form  $C_{dr} = 24/\text{Re}_d + 6/\text{Re}_d^{1/2} + 0.28$ , which is valid for  $\text{Re}_d < 4 \cdot 10^3$ . For the reasons listed in [3] the enhancement of evaporation due to the high-speed flow past droplet was taken into account by using the evaporation law in Ranz – Marshall form

$$\frac{dr}{dt} = -\frac{\lambda \text{Nu}_d}{16r}, \quad \text{Nu}_d = 2 + 0.53 \text{Re}_d^{1/2} \quad (10)$$

where  $\text{Re}_d = \rho_g 2r W_{rel}/\mu_\infty$  is the daughter droplet Reynolds number,  $W_{rel} = \sqrt{(V_{gR} - W_{dR})^2 + (V_{g\theta} - W_{d\theta})^2}$ . The strength of vapor source in (9) is then  $\dot{F}_v = 0.1875 \tilde{r} \Lambda B_1^3 \text{Nu}_d$ . The strength of a spray source was set up as a boundary condition,  $\dot{f}_{n.d.}(\tilde{a}, \theta, \tilde{r}, \tau) = \dot{f}_{n.p.}(\tilde{a}, \theta, \tilde{r}, \tau)$ , at  $\tilde{R} = \tilde{a}$ , while  $M_v$  was set to zero. Initial values for droplet velocity components were set in accordance with (4).

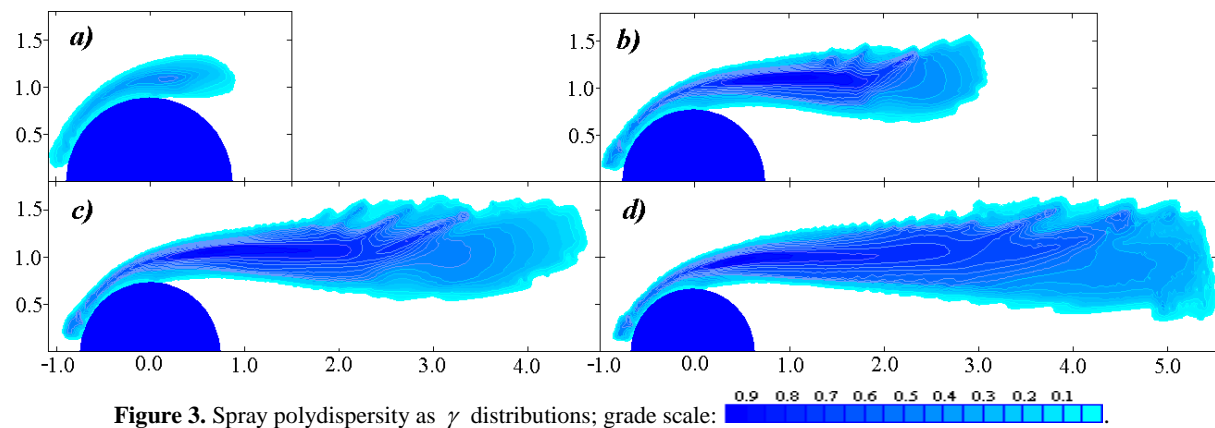
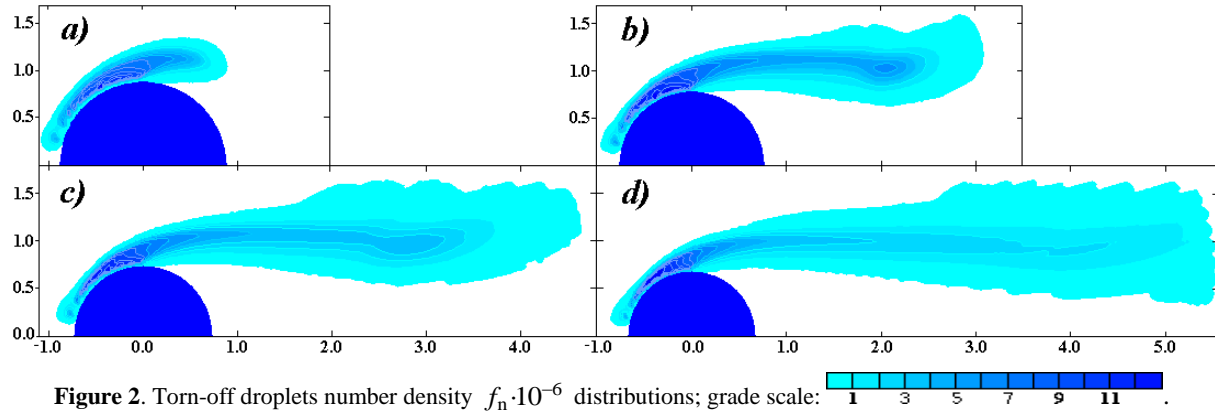
Formulated in this way problem for the system (6)–(10) is solved numerically. The same code in 3-D non-stationary modification is applied here that was used in [3], which is based on Lax–Vendroff finite-difference scheme of second-order accuracy. The following set of definitive input parameters is considered below:  $V_\infty = 10^3 \text{ m/sec}$ ,  $a_0 = 5 \cdot 10^{-4} \text{ m}$ ,  $t_{ch} = 14.4 \mu\text{sec}$ ,  $We_{p0} = 5.3 \cdot 10^4$ ,  $\text{Re}_{p0} = 9.2 \cdot 10^4$ ,  $B_1 = 5.1 \cdot 10^{-3}$ ,  $B_2 = 4.01 \cdot 10^6$ .

## Results and Discussion

The elaborated model allows investigating the formation dynamics of a two-phase wake of an atomizing drop, given the parent drop radius and the physical properties of the gas – liquid system. A vivid portrayal of drop atomization process is given in figs. 2-5 as a result of calculations in the form of the field toned pictures at time moments  $t_1 = 1.0 t_{ch}$  (a),  $t_2 = 2.0 t_{ch}$  (b),  $t_3 = 2.4 t_{ch}$  (c) and  $t_4 = 3.0 t_{ch}$  (d) when the parent drop radius has the consequent values  $\tilde{a}_1 = 0.87$ ,  $\tilde{a}_2 = 0.76$ ,  $\tilde{a}_3 = 0.72$  and  $\tilde{a}_4 = 0.66$ . The evaporation constant value  $\lambda = 2.7 \cdot 10^{-6} \text{ m}^2/\text{sec}$  corresponding to hot flow conditions [10] was used. Distances along Cartesian coordinate axes are in  $a_0$  units and uniform gas flow is coming from left to right. Dark blue semicircle is shattering parent drop silhouette.

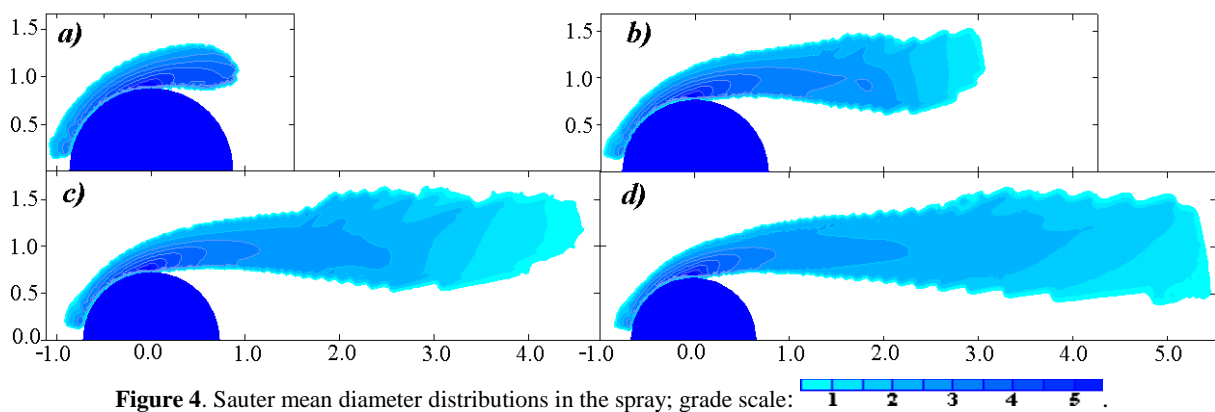
The essential non-uniformity of spray spatial structure is revealed. Almost straight dense jet of daughter droplets goes for a run past the atomizing drop edge, which contains the main part of stripped liquid (fig. 2). During the observed time the utmost  $f_n$  values locate above stripping area near the parent drop surface.

The important conclusion can be drawn after the fig. 2 examining that the visible in experiments lateral image size is significantly greater than the real drop diameter: the increase due to the dense mist above drop edge can reach 40%.



The entire spray has a significant degree of polydispersity. The spray polydispersity can be measured with a help of the parameter  $\gamma = (d_{43} - d_{10}) / 2a_0B_1$  which is formed by spray maximum,  $d_{43}$ , and minimum,  $d_{10}$ , mean diameters [3]. The  $\gamma$  distributions over the spray region are given in fig. 3. By comparing with fig. 2 we can see that polydispersity fills up all the spray volume, while the utmost values are located within liquid-phase jet along all its length.

In contradistinction to polydispersity, Sauter mean diameter values (fig. 4) are always greatest near the parent drop edges and then gradually diminish to the spray tip due to droplets entire evaporation.



The vapour cloud consists of two parts, as fig. 5 shows. That vapour which was generated just above parent drop surface has gone with a gas stream down into a region near axis of symmetry where the vapour

concentration is small. Another part is generated within the liquid-phase jet where the vapour is transported in the almost parallel to gas stream direction. Despite rarefaction due to general spreading, the vapour always remains very dense in the region of liquid spray jet, although with some weakening in time. The utmost  $M_v$

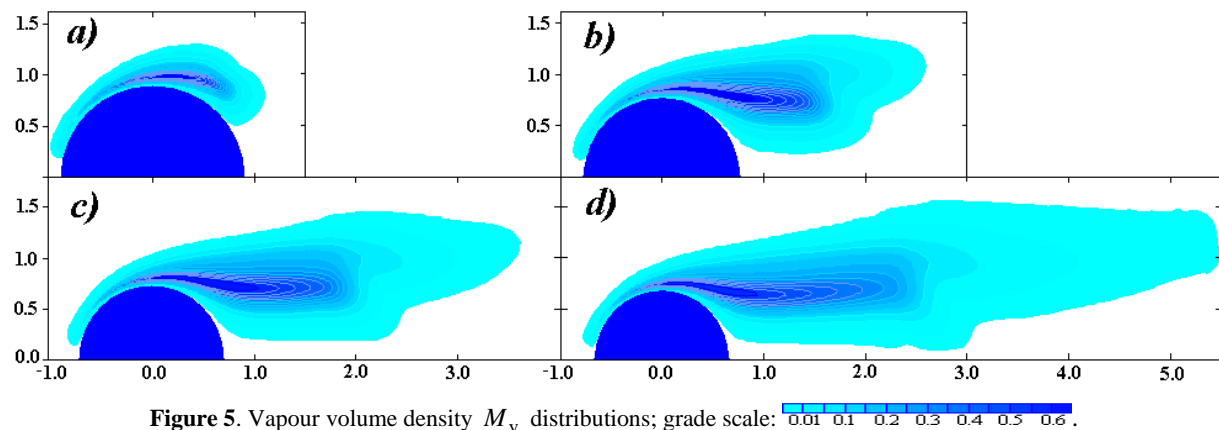


**Figure 5.** Vapour volume density  $M_v$  distributions; grade scale: 0.01 0.1 0.2 0.3 0.4 0.5 0.6.

values locate just behind the drop's edge with some elongation in the direction of the liquid jet which is the cause of these utmost values. Extremely high vapour volume density values are established in that domain. The utmost values exceed the average ones given by rough estimation in [3] more than by order. This conclusion means that this region is extremely inauspicious for fuel mixture igniting and burning since vapour concentration is far away from the limit value and chemical kinetics conditions are inappropriate here due to the large temperature dropping.

To evaluate the influence of evaporation rate the same calculation was performed with the value  $\lambda=10^{-6}m^2/sec$ . It resulted in the same flow structure, but with the elongated elements, showing that the evaporation rate decreasing delays the processes.

The obtained relationship  $\vec{W}_d(\vec{r})$  gets evidence about the droplet collision possibility. Inasmuch as fine fraction droplets are able to avoid collision due to light inertia while flowing past the coarse ones, for the middle fraction the collision effect with coarse one can be strong and must be taken into account at advanced modelling.

The spray edges erosion in figs. 3-4 seems to be realistic, but it is due not to a turbulence that is absent in the model. It rather caused by the flow or numerical instability, when the mist becomes less dense and decelerates at the spray edges, coupled with the rarefaction of numerical grid there.

## Conclusions

Two-dimensional problem regarding the evaporating mist aerodynamics in around atomizing drop is solved theoretically in closed form. The elaborated mathematical model of spray evaporation ballistics allows us to investigate the formation dynamics of a two-phase wake of an atomizing drop, given the parent drop radius and the physical properties of the gas – liquid system. The stripped droplet size-distribution function was obtained here as a numerical solution of a derived earlier differential equation and was used as a spray source function.

## References

1. Girin, A.G., *Journal of Engineering Physics & Thermophysics* **84**: 872–880 (2011).
2. Franzelli, B., Florina, B. and Darabiha N., *12<sup>th</sup> ICLASS-2012, Heidelberg, Germany, Sept. 2-6, 2012*, Book of abstracts, p. 50.
3. Girin, A.G., *Combustion Science & Technology* **184**: 1412–1426 (2012).
4. Girin, A.G., *Journal of Engineering Physics & Thermophysics* **48**: 560-564 (1985).
5. Girin, A. G., *Journal of Engineering Physics and Thermophysics* **84**: 262–269 (2011).
6. Ranger, A. A., *Astronautica Acta* **17**: 675–683 (1972).
7. Lewis, D.J., *Proceedings of Royal Society of London, Ser. A* **202**: 81-96 (1950).
8. Lighthill, J. *Waves in Fluids*, Cambridge: Cambridge Univ. Press. London, New York, Melbourne, 1978.
9. Williams, F.A. *Combustion theory*, Palo-Alto: Addison–Wesley Publ. Comp., 1964)
10. Lambiris, S. and Combs, L.P., Steady-state combustion measurements in a LOX/RP-1 rocket chamber. Eds. S.S. Penner, F.A. Williams. *Progr. Astron. Rocketry*, Acad. Press. New-York –London. P. 269-304 (1962).

## Primary Breakup Modelling Within the LES Framework

Z. Pavlovic<sup>1,2</sup>, S. Jakirlic<sup>2</sup>, B. Basara<sup>3</sup> and C. Tropea<sup>2</sup>

1: Advanced Simulation Technologies, AVL-AST, Maribor, Slovenia

2: Institute of Fluid Mechanics and Aerodynamics, Technical University Darmstadt, Germany

3: Advanced Simulation Technologies, AVL List GmbH, Graz, Austria

### Abstract

Although jet primary breakup plays important role in the initial spray formation, the detail nature of this phenomenon is still not fully understood. The governing idea of the present work is to investigate the possibilities for primary breakup modelling in the large eddy simulation (LES) framework. The results from LES simulations using Eulerian approach (based on Volume of Fluids method) should be exploited (together with the available experimental findings) to develop/improve existing primary breakup models in the Lagrangian (Discrete Droplet Model) framework, which is more suitable for practical engineering simulations. The performance of LES-VOF model was investigated on the simple injector case where the cases with flat and turbulent inlet profiles are compared. Turbulence at the nozzle outlet clearly triggers faster and more intensive disintegration of the liquid jet. Similar approach is also applied to exploit experimental data obtained from two cavitation-free nozzles with slightly different intensity and spatial distribution of turbulence field. Internal nozzle flow field is simulated with LES and obtained results could be used as the boundary conditions for spray investigations, both in Eulerian and Lagrangian framework.

### Introduction

Reliable numerical prediction of spray behaviour (spray angle, penetration, evaporation etc.) is of significant importance for the internal combustion engine analysis, since spray propagation and evaporation directly influence mixture formation, combustion process and consequently the level of emissions. Fuel is usually introduced in the combustion chamber (Diesel and Gasoline Direct Injection engines) or the intake port (Port Fuel Injection engines) in the form of liquid jet, which is then subjected to the breakup process. It can be distinguished between two breakup mechanisms: 1) primary breakup, which covers the phase of jet deformation and the creation of ligaments and the first droplets, and 2) secondary breakup, which is related to the subsequent breakup of the droplets generated during primary breakup.

Although primary breakup plays decisive role in the initial spray formation and therefore influences the final spray characteristics, the detail nature of this phenomenon is still not fully understood [1,2].

Experimental investigations of the primary breakup process are more difficult than measurements of secondary breakup, since the spray is very dense in the region of interest. In fact, we can speak about the liquid core surrounded by the great number of ligaments and droplets. So, the primary breakup zone is not accessible by optical means and more advanced measurement techniques have to be used.

Dumouchel [1] gave extensive overview of experimental work related to the primary atomization of different jet configurations. It is evident that there is no universal characterization of the atomization regimes (for all considered liquid stream configurations). The explanation for this could be the fact that some of the important parameters, which have influence on the breakup phenomena, are not taken into account in non-dimensional numbers which are usually used for the characterization of atomization regimes. For example, one of the most influencing parameter in the atomization regime is the internal nozzle design, i.e. internal nozzle flow. The mechanism through which nozzle design affects jet breakup is the cavitation. However, the impact of the cavitation is still not fully understood, since there are few processes which are triggered by the cavitation: the increase of turbulence, jet contraction, bubble collapse, which have different effect on the jet breakup. Also, even in the absence of the cavitation, different nozzle designs and operating conditions lead to different turbulence fields and this is then reflected in the final spray shape.

Also, it should be noted that there are certain discrepancies in the published results, like for example, the fact that some researchers [3,4] have reported the absence of liquid jet at the nozzle exit, i.e. an immediate atomization is detected, while the other works [5,6] indicate that non-atomized liquid jet is present in the short region near the nozzle exit.

The recent experimental work by Balewski [7,8] is especially interesting for the present work. High spatial resolution laser Doppler velocimetry (LDV) was used to measure 3D velocity and turbulence fields inside the nozzle. Dense spray region in the vicinity of the nozzle exit was accessed by X-ray system, which makes it possible to estimate 3D density distribution. Velocity and spray droplet diameter distribution at the boundary area of the spray near nozzle exit were measured by Dual Mode phase Doppler system (PDA). Visual observation of the spray formation was enabled by the high-speed videos taken during the entire spray.



Nozzles' shape and operating points were chosen in such a way to avoid the occurrence of cavitation in order to isolate solely the effect of turbulence. Experimental data reveal that the turbulence can be considered as the main cause of breakup. Turbulence has strong impact on the spray width and the number of droplets, but it has no effect on the droplet diameter. It was shown that higher turbulence level at the nozzle exit leads to wider spray angle. Also, it was found that the breakup of two different liquids at different Reynolds numbers (Shell Gravex 917 at  $Re = 2000$  and Shell V-Oil 1404 at  $Re = 15500$ ) is completely different, although both operating points are in the atomization region of Ohnesorge diagram. It was concluded that this difference can be explained only by different viscosity of two liquids. It seems that for lower viscosity the turbulent energy is high enough to cause jet-ligament formations at the liquid surface, which is not possible in the higher viscosity case.

The experimental work of Balewski was numerically investigated by Fischer [9,10] who used it to validate novel primary breakup model based on the calculation of spray core development.

### Mathematical modelling

The role of numerical simulations, more precisely Computational Fluid Dynamics (CFD), related to primary breakup phenomena can be seen in the two ways: 1) detailed simulation of the breakup process, which should provide deeper insight into the underlying mechanisms, since the experimental investigations are quite challenging and 2) primary breakup is represented by the simplified model in order to perform large scale simulations of e.g. internal combustion engines, where the spray is just one part of the complex simulation.

#### Volume of Fluid model

One of the available approaches for the first task is multiphase simulation in the Eulerian framework, based on the Volume of Fluid (VOF) method, where the sharp interface between the phases (liquid and gas) is accurately resolved. In VOF approach, the motion of the interface is tracked by the solution of a scalar transport equation (i.e. volume fraction equation) for a phase-indicator field that is discontinuous at the interface and uniform elsewhere [11,12]. Incompressible form of the governing equation for the volume fraction of tracked phase can be written as:

$$\frac{\partial \alpha}{\partial t} + \nabla \cdot \alpha \vec{v} = 0$$

where  $\alpha$  is the volume fraction of tracked phase and  $\vec{v}$  is the velocity of the flow. Volume fraction can take values between zero and one, where  $\alpha = 1$  indicates that the cell is fully occupied by the tracked phase. The different fluids (e.g. liquid and gas) are modelled as a single continuum with sharp gradients of fluid properties at the interface. The local density and viscosity of the fluid occupying the whole computational domain are defined as:

$$\rho = \alpha \rho_1 + (1 - \alpha) \rho_2, \quad \mu = \alpha \mu_1 + (1 - \alpha) \mu_2$$

where 1 and 2 denotes density/viscosity values of the first and second phase. The single set of momentum equations is solved for both phases with the mixture properties defined by the equations above.

Numerical scheme employed for the solution of volume fraction equation must be bounded (no over- and under-shooting), monotonic (without artificial oscillations near the interface) and the sharpness of the interface has to be maintained. Present implementation relies on the extended donor-acceptor concept using high resolution schemes [13]. Two differencing schemes are combined in the linear way: CBC scheme, as a bounded gradient-sharpening scheme, and ULTIMATE-QUICKEST scheme.

Surface tension force, which acts at the phase interface location, plays important role in the primary atomization and has to be accurately treated. In the present work, Continuum Surface Force (CSF) method is adopted [14]. In CSF, surface tension effect is taken into account as a body force:

$$\vec{F} = \int_V \sigma \kappa \nabla \alpha dV = \sigma \kappa_P (\nabla \alpha)_P V_P$$

where  $\sigma$  is surface tension coefficient, which is assumed to be constant, and  $\kappa_P$  is the curvature of the phase interface, defined as:

$$\kappa_P = -(\nabla \cdot \vec{n}) = -\left[ \nabla \cdot \left( \frac{\nabla \alpha}{|\nabla \alpha|} \right) \right]_P$$

where  $\vec{n}$  is unit vector normal to the surface. Subscript "P" indicates the values at the centre of the computational cell.

In the present work, VOF method is coupled with the LES approach. The governing LES equations are filtered Navier-Stokes equations, which can be written in the following form for the incompressible flows:

$$\frac{\partial \bar{u}_i}{\partial t} + \frac{\partial (\bar{u}_i \bar{u}_j)}{\partial x_j} = -\frac{1}{\rho} \frac{\partial \bar{p}}{\partial x_i} + \frac{\partial}{\partial x_j} \left( \nu \frac{\partial \bar{u}_i}{\partial x_j} - \tau_{ij} \right)$$

The influence of the sub-grid scales, through SGS tensor, is taken into account with the Smagorinsky [SMAG] model:

$$\tau_{ij} - \frac{\delta_{ij}}{3} \tau_{kk} = -2\nu_{sgs} S_{ij}$$

$$\nu_{sgs} = (C_s f \Delta)^2 |S|$$

where  $C_s = 0.1$ ,  $f$  is Van Driest damping function and the resolved strain-rate tensor is  $|S| = \sqrt{2S_{ij}S_{ij}}$ . The filter size  $\Delta$  is defined by the resolution of the computational mesh.

It should be noted that in the current implementation, SGS term which arises from the filtering of volume fraction equation is not included, i.e. it is assumed that it is negligible. This is valid assumption if instantaneous contribution is estimated, however cumulative effect may become important [15], especially if the mesh resolution is not very fine.

For the internal nozzle flow simulations, alternative SGS model is used – Coherent Structure Model [16]. In this model, parameter  $C_s$  is not constant, but is locally estimated according to the resolved coherent structures.

## Simulation setup

### LES-VOF test case

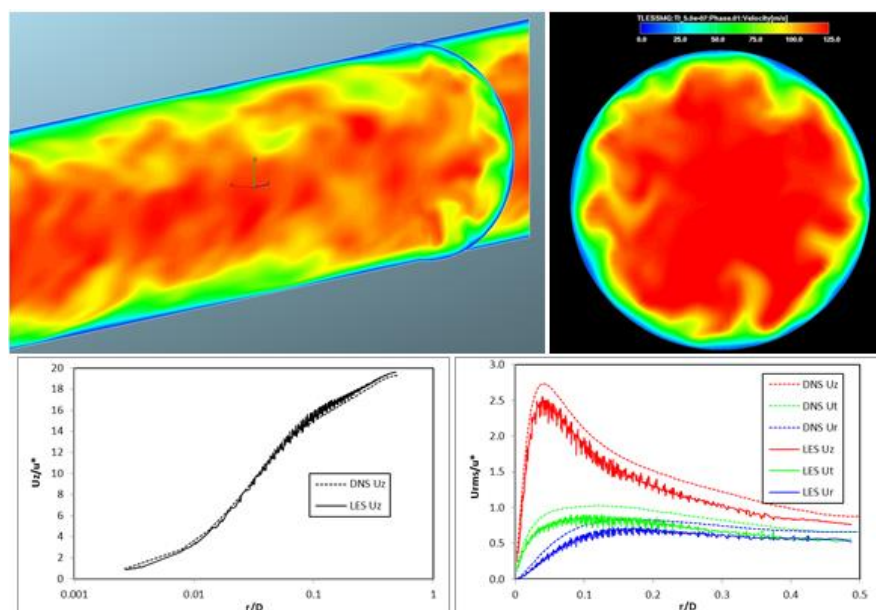
The performance of LES-VOF approach is investigated on the example of liquid jet injected in the quiescent chamber, where the conditions and dimensions are selected in such a way to achieve atomization regime. The main characteristics of the simulated system are given in the Table 1.

Table 1. Main characteristics of simulated system

Nozzle diameter [mm]	0.1
Injection velocity [m/s]	100
Reynolds number	5800
Weber number (liquid)	11600
Liquid density [kg/m <sup>3</sup> ]	696
Gas density [kg/m <sup>3</sup> ]	50
Liquid viscosity [kg/ms]	0.0012
Gas viscosity [kg/ms]	1.824e-5
Surface tension [N/m]	0.06

Cylindrical domain with the radius of 0.3mm and the length of 2.1mm was chosen for this simulation. The uniform cubic mesh size is used, where the cell size was selected to be 2.5μm, resulting in the total number of cells equal to cca. 9.5 million.

Gradient-free boundary condition is set at the outlet, while slip-wall boundary condition is used for the side walls. Velocity field is prescribed at inlet boundary. Two cases were investigated: 1) flat velocity profile, 2) transient turbulent velocity profile, where the velocity field is taken from LES pipe flow simulation (see Figure 1), performed at the similar Reynolds number. The spatial mapping from the pipe mesh to LES-VOF mesh is done using barycentric interpolation method.



**Figure 1.** LES of pipe flow: top figures – instantaneous velocity field; bottom left – normalized profile of average stream-wise velocity; bottom right – normalized profiles of mean RMS values. Profiles compared to DNS of THTLAB [17]

### Nozzle V4 and V5

The next step of the work was to exploit extensive experimental data obtained from Balewski to get deeper insight into the impact of turbulence on the primary breakup process. Two cases from the experimental base are selected: V4 and V5 nozzles, using Shell V-Oil as a working fluid. These particular cases were selected due to the fact that different level and spatial distribution of turbulence field induced by the nozzles V4 and V5 has clear impact on the final spray.

The following workflow is established: A) simulate internal nozzle flow using single phase LES approach; B) run LES-VOF jet simulation using the output of the simulation A) as an inlet condition; C) run the spray simulation in Lagrangian framework using the averaged output of simulation A) as an inlet condition in order to detect shortcomings of the present primary breakup model. The results from the third task are not fully completed at the moment of writing this paper, so they will be delivered in the near future.

Geometries of the V4 and V5 nozzles are shown in the figure 2. The main nozzle characteristics and fluid properties are given in Table 2. The length of the straight outlet portion/pipe is 10D.

The block structured meshes consisting of approximately 2.5 million hexahedron cells were created. LES simulation was run until the quasy-steady state is reached, that is, until the fluid flow is fully developed.

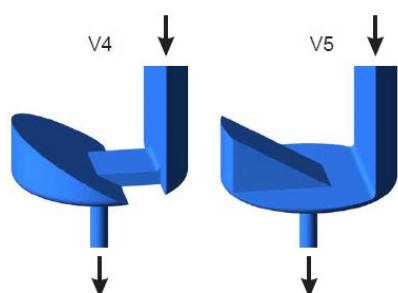


**Figure 2.** Geometry of test nozzles V4 and V5

**Table 2.** Test conditions

Nozzle diameter [mm]	1
Injection velocity [m/s]	42
Reynolds number	15500
Weber number	53000
Liquid density [kg/m <sup>3</sup> ]	826
Liquid viscosity [kg/ms]	0.00223
Surface tension [N/m]	0.028

The results collected at the nozzles' outlet are used to specify inlet conditions (velocity field) for the subsequent LES-VOF simulation. The dimensions of rectangular domain used for LES-VOF simulation are: 8x8x40mm (8Dx8Dx40D). Uniform mesh is generated with cca. 20 million cells. Due to the fact that diameter of experimental nozzle was quite large (1mm), the size of computational cells is also large – 50μm. With such cell dimensions it is unlikely to expect that small liquid structures (ligaments and droplets) could be resolved, however this kind of simulations might reveal, at least to the certain extent, the influence of different inlet flow conditions on the jet disintegration process. Slip-wall boundary condition is set at side wall, while gradient-free condition is used at the outlet boundary.

All simulations were performed with CFD code AVL FIRE which is based on the finite volumes method.

## Results and Discussion

### LES-VOF test case

Figure 3 shows the results from the first LES-VOF test simulation. Iso-surface of liquid volume fraction at two instances of time is displayed. The cases with flat and turbulent inlet velocity profiles are given in parallel. In both cases breakup is initiated at the rim of the mushroom shaped tip, but it is clear that jet disintegration is strongly enhanced if the turbulence is prescribed at the inlet boundary. This is confirmed on the Figure 4, where the liquid volume fraction along the jet is shown. The values of the volume fraction are extracted within the cylindrical volume with the diameter of 0.1mm, which corresponds to the diameter of the nozzle.

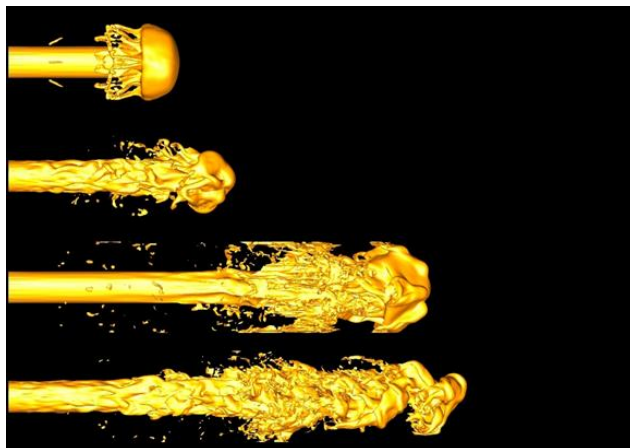


**Figure 3.** Iso-surface of the liquid volume fraction at the instances of time; 1<sup>st</sup> and 3<sup>rd</sup> row – case with flat inlet velocity profile, 2<sup>nd</sup> and 4<sup>th</sup> row – case with turbulent inlet velocity profile

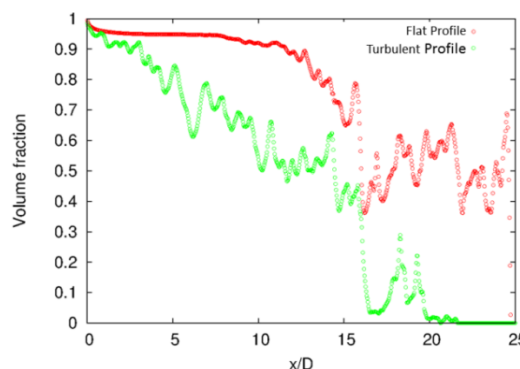


**Figure 4.** Liquid volume fraction as the function of axial distance from the nozzle exit

The quality of the obtained results is hard to precisely estimate, due to the lack of reliable experimental data. However, at least from the qualitative point of view, applied LES-VOF simulation seems to give reasonable results, which could be used as an auxiliary base for the improvement of the primary breakup model. But, one should always keep in mind the limitations and shortcomings [18] of the applied method, in the process of data analysis. Also, the proximity of slip-wall boundary (often used in such simulations [19,20]) has an impact on the final results through the effect of gas flow induced by the liquid jet, so the extension of the computational domain is desired for the future analysis.

### Nozzle V4 and V5

The results from internal nozzle flow, using LES method, are shown in the Figures 5 and 6 in comparison to experimentally obtained data. LES results are averaged over the period which covers cca. 100 run-through times related to the straight outlet portion of the nozzle.

Figure 5 displays velocity field at the nozzle exit for nozzles V4 (left side) and V5 (right side). Fairly good match with experimental data is achieved. Smaller differences can be observed in the location of the secondary vortices. It can be seen that the location of highest velocity is opposite for these two nozzles.

Turbulence field is displayed in Figure 6. The agreement between the simulation and the experiment is not as good as for the velocity field, but the spatial redistribution and the increase of mean turbulence intensity of nozzle V5 in comparison to nozzle V4 are captured. The turbulence level predicted by the simulation is higher than measured one. The explanation for this could be the fact that the maximum of turbulence kinetic energy is in the near wall region where the measurements are the most challenging. Also, as shown in Figure 7, quite complex turbulent structures are generated inside the nozzle, so the further mesh refinement might be necessary in the most important flow regions in order to eventually improve the results.

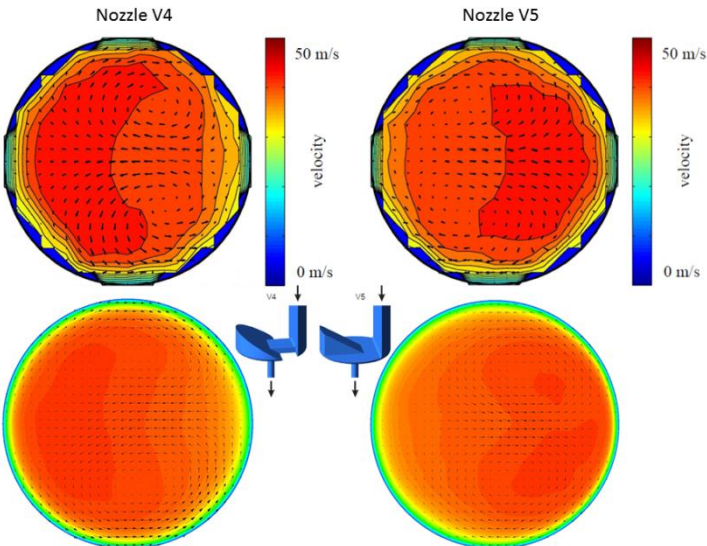


Figure 5. Velocity field at the nozzle exit; Top row – experiment; Bottom row - simulation

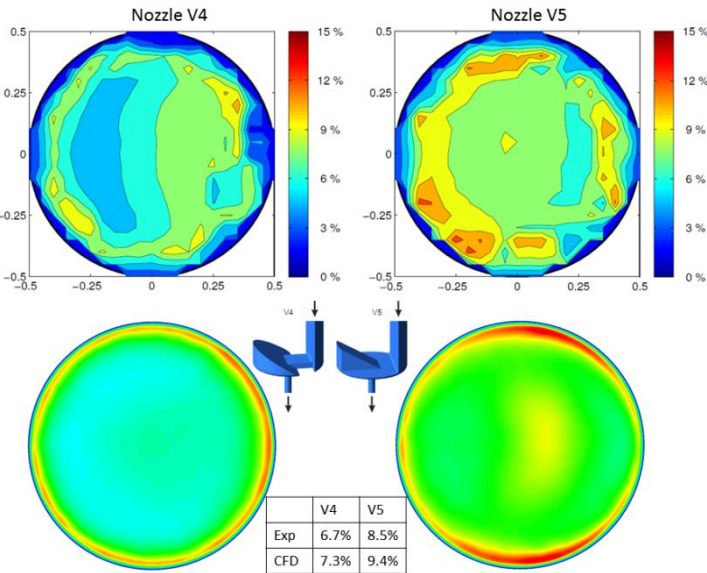


Figure 6. Turbulence intensity at the nozzle exit; Top row – experiment; Bottom row - simulation

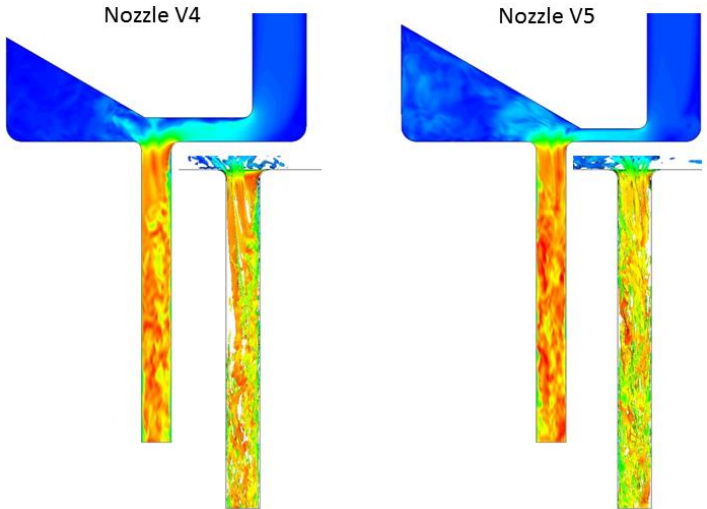
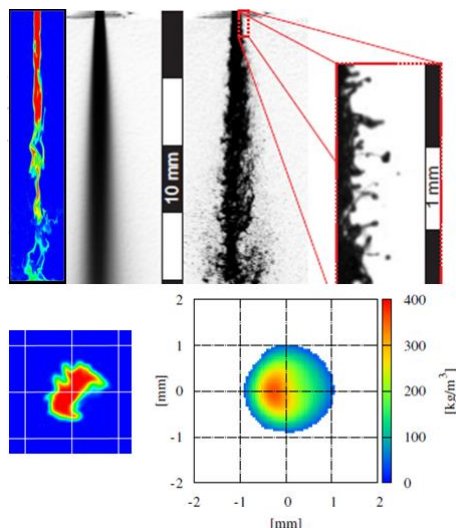


Figure 7. Instantaneous velocity field at the mid-plane cut and iso-surface of Q invariant

The results from LES-VOF simulation, where inlet conditions are taken from the calculated nozzle flow, reveals that the current mesh resolution is not fine enough for capturing all important features of the flow. As can be seen in Figure 8, ligaments and droplets are not resolved, while jet disintegration and liquid phase distribution are to certain extent captured, however intensity of disintegration/breakup is underestimated. It is expected that the suitable local mesh refinement (especially near the liquid-gas interface and at the nozzle exit) will significantly improve the results and give better insight into breakup process.



**Figure 8.** Top - Liquid volume fraction from the simulation vs. spray visualization for nozzle V5; Bottom – liquid volume fraction from the simulation vs. measured liquid density field 6mm from the exit of the nozzle V4

## Conclusions

Numerical simulation of primary breakup process still remains very challenging task. Nevertheless, the results obtained in the present study indicate that LES-VOF simulations, in the combination with detailed experimental data, could provide useful insight into the mechanisms of primary breakup.

It was shown that turbulence induced by the internal nozzle flow has strong impact on the primary atomization (jet disintegration) and consequently on the final spray shape. The jet introduced with turbulent profile is subjected to substantially more intensive disintegration in comparison to the jet introduced with flat velocity profile.

LES-VOF study of V4 nozzle indicates that imposed mesh resolution is insufficient to accurately capture behaviour observed by experiment, therefore additional effort is needed in order to extract more useful information from such simulation approach, which might be useful for the improvement of primary breakup model used in Lagrangian spray simulations.

It is strongly desired to provide the primary breakup model of good predictivity, which will contain as less fitting parameters as possible and also be applicable for LES framework. On-going work is aiming in this direction. In the next steps, numerical investigations of Balweski's experimental work will be completed and the improved primary breakup model will be proposed.

## Acknowledgements

The present work is done as the part of PhD work at the Department of Fluid Mechanics and Aerodynamics, Technical University Darmstadt, Germany, which is financially supported by AVL GmbH, Graz, Austria.

## Nomenclature

$\alpha$	Volume fraction	[-]
$\vec{v}$	Velocity vector	[m/s]
$\rho$	Density	[kg/m <sup>3</sup> ]
$\mu$	Dynamic viscosity	[kg/s · m]
$F$	Force	[N]
$\sigma$	Surface tension coefficient	[N/m]
$\kappa$	Curvature	[1/m]
$V$	Volume	[m <sup>3</sup> ]



$\vec{n}$	Unit vector normal to the surface	[-]
$u_i$	Velocity in i-th direction	[m/s]
$t$	Time	[s]
$x_i$	Coordinate in i-th direction	[m]
$p$	Pressure	[Pa]
$\tau_{ij}$	SGS stress tensor	[N/m <sup>2</sup> ]
$\nu_{SGS}$	SGS viscosity	[m <sup>2</sup> /s]
$C_S$	Smagorinsky constant	[-]
$S$	Strain-rate	[1/s]

## References

- [1] Dumouchel, C., On the experimental investigation on primary atomization. *Experiments in Fluids* 45:371-422, 2008.
- [2] Lin, S.P. and Reitz, R.D., Drop and spray formation from liquid jet. *Annual Review of Fluid Mechanics* 30:85-105, 1998.
- [3] Yue, Y., Powell, C.F., Poola, R., Wang, J., Schaller, J.K., Quantitative measurements of diesel fuel spray characteristics in the near nozzle region using X-ray absorption. *Atomization and Sprays* 11:471-490, 2001
- [4] Parker, T.E., Raimaldi, L.R., Rawlins, W.T., A comparative study of room-temperature and combustion fuel sprays near the injector tip using infrared laser diagnostics. *Atomization and Sprays* 8:565-600, 1998.
- [5] Hiroyasu, H., Spray breakup mechanism from the hole-type nozzle and its applications. *Atomization and Sprays* 10:511-527, 2000.
- [6] Paciaroni, M., Linne, M., Hall, T., Delplanque, J.P., Praker, T., Single-shot two-dimensional ballistic imaging of the liquid core in an atomizing spray. *Atomization and Sprays* 16:51-69, 2006.
- [7] Balewski, B., Heine, B. and Tropea, C., Influence of nozzle-flow turbulence on the primary spray breakup. In ICLASS 2009, *11th International Annual Conference on Liquid Atomization and Spray Systems-ICLASS*, July 2009.
- [8] Balewski, B.S., “Experimental investigation of the influence of nozzle-flow properties on the primary spray breakup”, PhD Thesis, TU Darmstadt, 2010.
- [9] Fischer, F., Heine, B. and Tropea, C., Primary Breakup Model Considering Spray Core Development, ILASS – Europe 2010, 23rd Annual Conference on Liquid Atomization and Spray Systems, 2010.
- [10] Fischer, F., “Primary breakup modeling considering the spray core development”, PhD Thesis, TU Darmstadt, 2011.
- [11] Hirt, C.W. and Nichols, B.D., Volume of fluid (VOF) method for the dynamics of free boundaries. *Journal of Computational Physics* 39:201-225, 1981.
- [12] Ubbink, O. and Issa, R.I., A Method for Capturing Sharp Fluid Interfaces on Arbitrary Meshes, *Journal of Computational Physics* 153:26-50, 1999.
- [13] AVL FIRE Multiphase Manual, 2011
- [14] Brackbill, J.U., Kothe, D.B. and Zemach, C., A continuum method for modeling surface tension, *Journal of Computational Physics* 100:335-354, 1992.
- [15] Chesnel, J., Menard, T., Reveillon, J., Berlemont, A. and Demoulin, F.X., A LES simulation of atomisation, *Proceedings of the ASME 2010 3rd Joint US-European Fluids Engineering Summer Meeting and 8th International Conference on Nanochannels, Microchannels and Minichannels*, 2010
- [16] Kobayashi, H., The subgrid-scale models based on coherent structures for rotating homogeneous turbulence and turbulent channel flow. *Physics of Fluids*, Vol. 17, 2005.
- [17] Eggels, J.G.M., Unger, F., Weiss, M.H., Westerweel, J., Adrian, R.J., Friedrich, R. & Nieuwstadt, F.T.M., Fully developed turbulent pipe flow: A comparison between direct numerical simulation and experiment. *Journal of Fluid Mechanics* 268:175-210, 1994
- [18] Gorokhovski, M. and Herrmann, M., Modelling primary atomization. *Annual Review of Fluid Mechanics*, 40:343-366, 2008.
- [19] Menard, T., Tanguy, S. and Berlemont, A., Coupling level set/VOF/ghost fluid methods: Validation and application to 3D simulation of the primary break-up of a liquid jet, *International Journal of Multiphase Flow* 33:510-524, 2007.
- [20] Shinjo, J. and Umemura, A., Simulation of liquid jet primary breakup: Dynamics of ligament and droplet formation, *International Journal of Multiphase Flow* 36:513-532, 2010.



## Mixing model effects on LES-PDF-PBE simulations of DBP droplets in a turbulent jet

N. Seubert<sup>1</sup>, A. Kronenburg<sup>1\*</sup>, O. T. Stein<sup>1</sup>, Y. Ge<sup>2</sup>, M.J. Cleary<sup>3</sup>

1: Institut für Technische Verbrennung, University of Stuttgart, Herdweg 51, 70174 Stuttgart, Germany

2: The University of Queensland, School of Mechanical and Mining Engineering, QLD 4072, Australia

3: The University of Sydney, School of Aerospace, Mechanical and Mechatronic Engineering, NSW 2006, Australia

### Abstract

Homogeneous nucleation and condensation of dibutyl phthalate (DBP) droplets in a turbulent jet are simulated using LES to model the turbulent flow and a probability density function/Monte Carlo (PDF/MC) method to capture the particle size distribution (PSD). LES resolves the largest turbulence structures and reverts to modelling of the small, universal scales. The information on the gas temperature and species mass fractions is represented by the MC particles. Furthermore the (virtual) MC particles hold discrete size bins representing the PSD of the (physical) DBP droplet ensemble. Given appropriate modelling of the sub-grid scalar mixing, the scalar information on the MC particles can be considered locally exact and no closure assumption for the non-linear nucleation and growth terms is required. Here, the effect of different scalar mixing models is assessed. Therefore the scalar fields and PSD obtained using the Interaction by Exchange with the Mean (IEM) and the modified Curl's mixing model are examined. Supersaturation, homogeneous nucleation and condensation, as well as the PSD and the zeroth moment show a considerable dependence on LES-filtering and the chosen mixing model.

### Introduction

Small scale particle formation and evolution are widespread in both industrial and natural energy- and material-conversion processes and the ability to predict the particle size distribution (PSD) is desired to optimise the production process, to minimise pollution or to assess the environmental influence. Natural particle sources such as volcano eruptions or large fires and their effect on the climate, the filtering of industrial combustion products or liquid phase reactors are just some examples of processes, where particle formation and evolution takes place and show the wide potential of predictive models for particle nucleation and growth. The insights gained from experiments provide an understanding of the physics of particle dynamics [1, 2, 3], but limitations arising from measurement techniques like possible interferences with reacting environments and the maximum possible resolution at the nano-scale level create the need for additional tools for detailed investigations. Furthermore, the high cost of clean room environments and restrictions due to health risks make numerical simulations a useful, cheap and risk-free tool to extend the range of analysis beyond the experimental capabilities. The evolution of the PSD in polydispersed flows can be predicted by the solution of the population balance equation (PBE). In turbulent flows a number of unknown terms arises in the PBE and various modelling techniques are available to obtain closure. A recent review on the major approaches such as analytical and perturbation methods, moment and approximate moment-based methods, discretisation and global approximation methods and the Monte-Carlo approach can be found in [4]. A brief selection of relevant numerical work in this field (based on [4]) is given in the following: Tsantilis et al. [16] employed a moving sectional model and simulated flame synthesis of titania nanoparticles. Morgan et al. [17] predicted coagulation, sintering, particle inception and surface growth of nanoparticles in a zero-dimensional system by means of a stochastic particle method. Mitchell & Frenklach [18] performed Monte Carlo simulations of particle aggregation and surface growth in the absence of fluid flow. Dang & Swihart [19] simulated the synthesis of silicon nanoparticles in 2D, including the effects of fluid flow, laser heating, chemical reactions and all relevant aerosol processes using both a moment- and section-based approach. Wang & Garrick [20] used a sectional approach for their 2D-DNS of TiO<sub>2</sub> nanoparticle formation in a transient mixing layer.

Numerical studies comparable to the present work have been conducted by Garmory & Mastorakos [5] and Di Veroli & Rigopoulos [7]. A Stochastic Fields transported Probability Density Function (SF-PDF) method was used by Garmory & Mastorakos [5], while Di Veroli & Rigopoulos [7] employed a Monte Carlo particle-PDF method [6]. The latter MC/PDF method was combined with a Reynolds Averaged Navier-Stokes (RANS)-based flow solver for the modelling of the PBE evolution in a turbulent flow. Lagrangian MC particles can provide information equivalent to the PDF transport equation, but at a cost which scales only linearly with the dimensionality of the joint-PDF, making it a suitable prediction approach even with current computer resources. Garmory & Mastorakos [5] and Di Veroli & Rigopoulos [7] applied their models to the turbulent round jet laden with dibutyl phthalate (DBP) of Lesniewski & Friedlander [1]. This experimental set-up allows for detailed model development and validation since the jet configuration provides a relatively simple flow field. Also, due

to the presence of the liquid DBP droplets, complex shapes of agglomerates (as in solid phase agglomeration) do not need to be considered. We combine the PDF/MC particle method with LES to model time-resolved droplet nucleation and condensation and apply our PDF/MC-LES model to the Lesniewski jet.

### Experimental test-rig

The experimental configuration used by Lesniewski & Friedlander [1] to investigate homogeneous nucleation and condensation features a hot ( $T_{\text{jet}}=413\text{K}$ ) nitrogen jet laden with DBP. Turbulent mixing of the heated jet with a co-flow at ambient temperature leads to rapid cooling of the central jet region, which triggers supersaturation and consequently homogeneous droplet nucleation and growth. The co-flow conditions were kept fix during the experimental campaign ( $u_{\text{co}}=0.18\text{ m/s}$ ,  $T_{\text{co}}=299\text{K}$ ), while the effect of various different jet conditions was investigated. The concentration (mole fraction) of DBP was varied within the range  $1.1 \cdot 10^{-4} < x_{\text{DBP,jet}} < 5.2 \cdot 10^{-4}$ . Two different nozzle diameters were used and the effect of various bulk jet velocities was examined. The experimental campaign comprised measurements of the zeroth moment (total concentration of particles), the PSD, the mean particle diameter, the particle formation rate and the vapour concentration of DBP as functions of the Reynolds number and of the inlet DBP mole fraction for various locations along the jet centreline. In this paper we study the experimental configuration specified in [15] as *trial 824*, where  $u_{\text{jet}}=51.55\text{ m/s}$ ,  $T_{\text{jet}}=413\text{K}$ ,  $x_{\text{DBP,jet}}=3.6 \cdot 10^{-4}$  and  $D_{\text{noz}}=0.00235\text{m}$ .

### LES-PDF-MC model for turbulent particulate flows

The Favre-filtered conservation equations of mass and momentum are solved and the Smagorinsky model is used to close the sub-grid stresses. The droplet phase is governed by the Population Balance Equation [8]

$$\frac{\partial N(d_p, \vec{x}, t)}{\partial t} + \nabla[\vec{u} \cdot N(d_p, \vec{x}, t)] + \frac{\partial}{\partial d_p}[G(d_p, \vec{Y}) \cdot N(d_p, \vec{x}, t)] = D_p \nabla^2 N(d_p, \vec{x}, t) + \dot{\omega}_N(\vec{Y}, N), \quad (1)$$

where  $d_p$ ,  $\vec{x}$ ,  $t$  and  $\vec{Y}$  denote the particle diameter, particle position, time and species mass fractions, respectively.  $N$  is the particle number density,  $\vec{u}$  the velocity vector,  $G$  the particle growth rate,  $D_p$  the particle diffusivity and  $\dot{\omega}_N$  denotes source terms to account for, e.g. droplet nucleation, aggregation and break-up. The high dimensionality of the joint-PDF of species, temperature and PSD prohibits a Eulerian solution of Eq. (1) with present day computational resources. Equivalently, a system of Langevin equations for a representative number of stochastic Monte-Carlo particles can be solved [9]

$$d\vec{x} = \vec{u}(\vec{x}, t) \cdot dt + (2 \cdot \Gamma(\vec{x}, t))^{\frac{1}{2}} \cdot d\vec{\omega}, \quad (2)$$

$$d\Phi_i = [M(\vec{x}, \Phi_i) + W_i(\Phi)]dt, \quad (3)$$

where Eq. (2) represents particle motion in turbulent flow,  $\Gamma$  denotes the effective diffusivity and  $d\vec{\omega}$  is the increment of a Wiener process with zero mean and variance  $\sqrt{\Delta t}$ . Equations (3) describe the rate of change of  $i=1\dots n$  transported scalars  $\Phi_i$ ,  $M$  is the mixing operator and  $W_i$  are the scalar source terms. The  $\Phi_i$  include temperature, the species mass fractions of DBP,  $\text{O}_2$  and  $\text{N}_2$  and 30 size bins to represent the discrete PSD. The mixing operator  $M$  requires modelling and we focus on the comparison of different mixing models in our results section. In contrast to Eulerian solution approaches for the PBE, where the sub-grid contribution is unknown, the information carried by the MC particles is locally exact and hence the source terms  $W_i$  are closed. The source terms for the discrete droplet size bins reflect droplet nucleation and growth. A source term in the temperature equation would represent the latent heat of phase change, but it is assumed to be small and neglected here, which leads to a unidirectional coupling of the gas-phase with the DPB droplets. Homogeneous nucleation requires a critical droplet diameter

$$d_{p,cr} = \frac{4\sigma v_m}{kT \ln(S)}, \quad (4)$$

Where  $\sigma$ ,  $v_m$ ,  $k$ ,  $T$  and  $S$  are the surface tension ( $\sigma=f(T)$ , [7]), molecular volume, Boltzmann constant, temperature and the saturation ratio, respectively. The saturation ratio  $S=P_{\text{DBP}}/P_{\text{sat}}$  relates the DBP partial pressure  $P_{\text{DBP}}$  to the saturation pressure  $P_{\text{sat}}$ , where the latter is modelled according to [5]. We use the equation by [11] to express the nucleation rate  $B$

$$B(S, \sigma, T) = \frac{N_v^2 v_m}{S} \left( \frac{2\sigma}{\pi m} \right)^{\frac{1}{2}} \exp \left( -\frac{16\pi\sigma^3 m^2}{3(kT)^3 \rho_l^2 (\ln(S))^2} \right) \exp \left( \frac{s_{\text{mon}}\sigma}{kT} \right), \quad (5)$$

with the vapour concentration  $N_v$  [molecules/ $\text{m}^3$ ], the mass of a monomer/molecule  $m$ , the liquid density  $\rho_l$  and the monomer surface area  $s_{\text{mon}}$ . According to [7] the experimental Knudsen number governing droplet growth

$Kn=2l_p/d_p$ , where  $l_p$  is the gas mean free path, ranges from very large numbers for nucleating particles to  $Kn \approx 1$  for the largest droplets and hence, condensation both in the free molecular and continuum regimes should be considered. We use the formula of Fuchs & Sutugin [14] for the full range of  $Kn$ , which modifies the growth rate for the continuum regime by a corrective coefficient  $\alpha(Kn)=(1+Kn) / (1+1.71*Kn + 1.333*Kn^2)$  to yield

$$G_{d_p} = \alpha(Kn) \cdot \frac{4Dv_m P_{sat}}{kTd_p} (S - 1), \quad (6)$$

with the molecular diffusivity  $D$ . Since [7] estimated the characteristic particle collision time scale for the highest experimental DBP mole fraction to be  $\tau_{coll}=100s$ , particle collision and aggregation are neglected here.

### Mixing Models

To account for turbulent mixing of the scalars transported on the MC particles two mixing models have been implemented. The Interaction by Exchange with the Mean (IEM) mixing model by Villermaux & Devillon [10] and the modified Curl's mixing model by Janicka et al. [22] have been chosen for comparison. Both models fulfil the mandatory requirements for a mixing model such as boundedness and conservation of mass [24]. Localisation is achieved by the limited spatial extent of the LES cell containing the particles which participate in the mixing process. The IEM mixing model relaxes the values of all particles within a cell to the weighted cell mean value  $\bar{\Phi}$ , whereas the modified Curl's model mixes randomly selected pairs of particles. Due to the high sensitivity of the homogeneous nucleation and condensation to changes in the governing quantities (i.e.  $T$  and  $Y_{DBP}$ ), the modelling of the mixing process in turbulent flows will have a large impact on supersaturation, homogeneous nucleation and condensation, as well as the PSD and its moments. Using IEM the new scalar value for the particle  $i$ ,  $\Phi_i^*$ , is calculated as

$$\Phi_i^* = \bar{\Phi} + (\Phi_i - \bar{\Phi}) * \exp\left(-\frac{C_\phi * \Delta t}{\tau_{mix}}\right), \quad (7)$$

where  $\tau_{mix}=C_z * \Delta^2 / (2*D_{eff})$  is the mixing time [27],  $D_{eff}$  the effective diffusivity obtained from the LES and  $C_\phi$  and  $C_z$  are model constants, which were set to equal values and therefore cancel out. The modified Curl's mixing model computes the new scalar values for the particle  $j$ , mixing with the particle  $i$ , for each time step according to

$$\Phi_i^* = \Phi_i - \frac{w_i}{w_i + w_j} \cdot (\Phi_i - \Phi_j) \cdot \Delta t, \quad (8)$$

where  $w_i$  and  $w_j$  are the weights of the MC particles and each particle represents a given fluid mass within an LES control volume.

### Computational Parameters and Implementation

The OpenFOAM toolbox, v2.1.x, was used and the existing particle class was modified to account for the needs of the LES-PDF simulation using MC particles. The simulation domain measures 53 nozzle diameters ( $D_{noz}=0.00235m$ ) in length and 23D in radial direction. The nozzle diameter  $D$  is resolved with 17 cells resulting in a grid size of 138  $\mu m$  at the nozzle exit and in the upstream shear layer. Mesh stretching is applied to ensure a sufficient resolution of the nozzle and the shear layer, but saving computational resources in the outer regions and further downstream. The bulk velocity at the nozzle is superimposed with a turbulent inflow generated using the method by Kempf et al. [13] and the pressure boundary condition is set to zero-gradient. Ambient pressure is specified as an outlet condition for the pressure and a zero-gradient condition is used as the standard boundary condition for all other quantities. Due to computational restrictions the number of MC particles per LES cell is kept relatively low ( $6 < N_{MC} < 10$ ). This can be justified by the stochastic nature of the MC particles and long sampling times using thousands of realisations in LES for temporal averaging, ensuring statistically independent results. Due to the decrease of the mean axial velocity and mesh stretching with increasing distance from the nozzle exit a significant number of MC particles needs to be deleted in the downstream region to keep the MC particle number per LES cell constant, which is achieved by a population control algorithm. Previous calculation results published in [26] were unduly influenced by spurious mixing effects from an early version of the MC particle number control algorithm. In this paper great care has been taken to ensure that the algorithm does not introduce artificial mixing when the scalar information is transferred from the deleted particle to the remaining ones. Several possible methods for particle control have been tested and the following algorithm was finally applied in this work: Since latent heat and mass loss due to condensation are neglected, temperature and the DBP mass fraction are passive scalars, the evolution of which can be expressed by a mixture fraction. The PSD

is an extensive path-independent property and needs to be treated with care. The implemented MC population control algorithm first selects the two MC particles closest in mixture fraction space to the particle to be deleted within an LES cell. The new particle weights are then calculated based on the requirement of conserving the mean value of the mixture fraction and the total weight. From the requirement of conserving the total particle number  $(1/\sum w_i) * \sum (w_i * N_i / \rho_i)$  and its variance  $(1/\sum w_i) * (\sum w_i * [N_i / \rho_i - \bar{N} / \bar{\rho}]^2)$  within each LES cell, equations for the new droplet populations of the two MC particles receiving the information from the deleted particle can be derived. The resulting PSDs are then assigned to the two receivers, before the donating particle is deleted.

## Results and Discussion

As discussed above, the focus of the present work is to evaluate mixing model effects on the results of our LES-PDF-MC simulations. We therefore present data obtained from the particle simulations using the IEM and modified Curl's model and compare them with each other, as well as results obtained by evaluating the PBE source terms from the LES-filtered values directly, i.e. without using an LES sub-grid model. Figure 1(a) shows the comparison of the normalised (time-)mean axial velocity from LES with experimental reference data along the jet centreline, and it can be seen that the experimental jet break-up is faithfully captured. Figure 1(b) shows the normalised, mean temperature along the jet centreline, where the particle information has been weight-averaged and mapped to the LES grid before temporal averaging. It can be seen that both MC simulations recover the results from the (pure) LES, as expected for temperature, which -in the absence of chemical reactions and ignoring latent heat- behaves as a passive scalar. It can also be observed that both mixing models equally leave the mean value unaltered as required. The slight differences in the predictions from LES and the MC simulations at  $z/D \approx 8$  are possibly a result from insufficient sub-grid turbulent transport by the Wiener term.

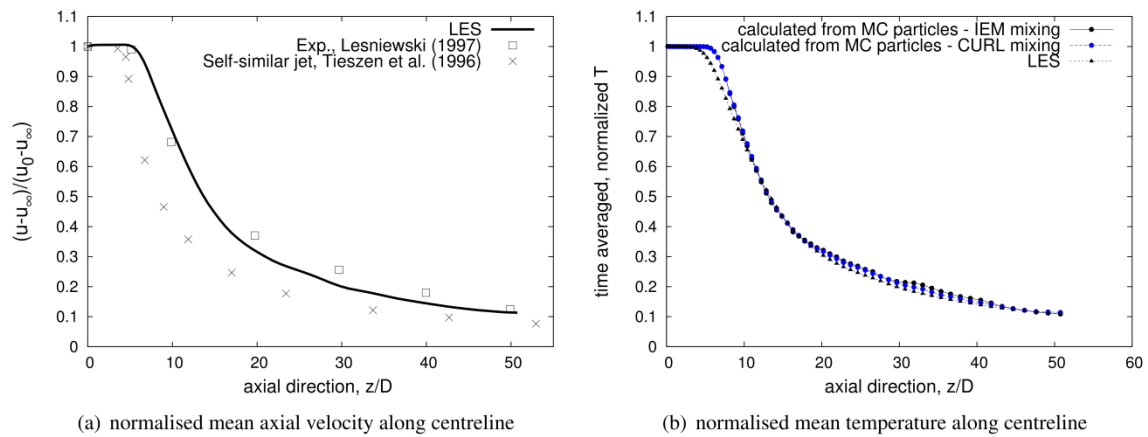


**Figure 1.** (a) Comparison of the mean axial velocity along the centreline, experiments by Lesniewski [15] and the self-similar jet profile of Tieszen et al. [21]. The velocity  $u$  is normalised with the free-stream (co-flow) velocity  $u_\infty$  and the inlet centreline velocity  $u_0$ . (b) Comparison of the normalised mean temperature obtained from the LES and the MC particles using IEM and the modified Curl's mixing model.

Figures 2(a) and 2(b) compare the mean saturation and nucleation rates from the different simulations along the jet centreline and the radius at  $z/D=20$ . It can be observed that the results obtained directly from the LES-filtered values differ greatly from the LES-PDF-MC particle data due to the non-linear source terms and the missing sub-grid model. This difference leads to a much delayed saturation and nucleation prediction by the (pure) LES along the centreline, Fig. 2(a), but considerably larger predictions of both quantities at large radii, Fig. 2(b). The cross-comparison of the results obtained from IEM and modified Curl's model shows a stronger increase of the mean saturation along the jet centreline from IEM compared with Curl in the upstream region and consequently an earlier increase of the nucleation rate predicted by the former model, Fig. 2(a). These trends are reversed downstream along the axis, Fig. 2(a), and at higher radii, Fig. 2(b), where the saturation and nucleation rate predictions by IEM fall below the corresponding values from Curl's model.

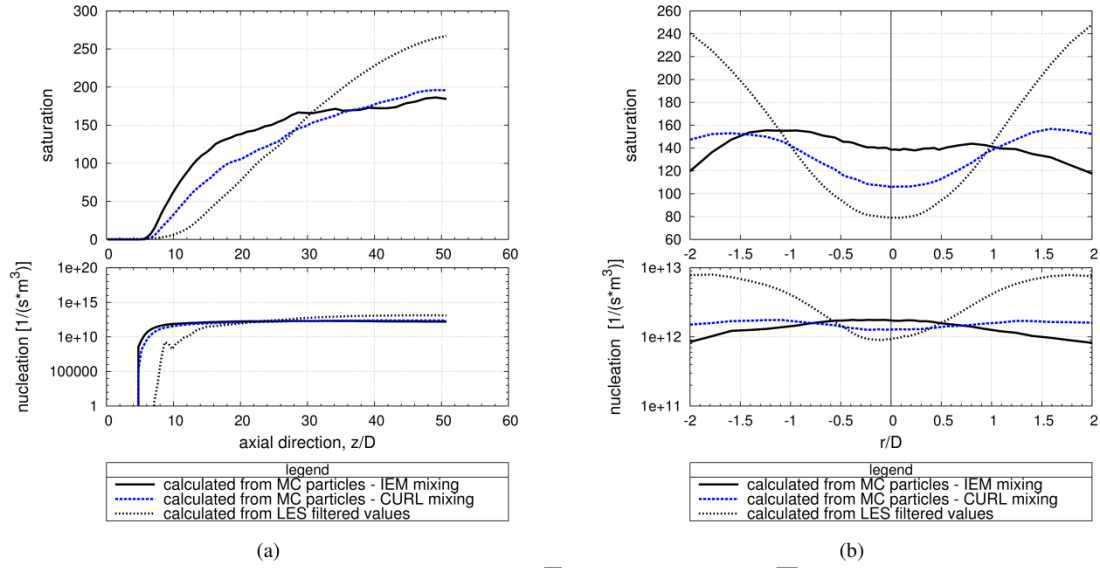


**Figure 2.** Comparison of the time-averaged saturation  $\bar{S}$  and nucleation rate  $\bar{B}$ , evaluated from the instantaneous, local particle information from IEM, modified Curl's model, and the LES-filtered values along (a) the jet centreline, (b) the radius at  $z/D = 20$ .

The condensation rates obtained from the different models plotted along the centreline in Fig. 3(a) and along the radius at  $z/D=20$  in Fig. 3(b) reveal the opposite behaviour as the (upstream) saturation and nucleation fields. The condensation rate obtained from calculations with the modified Curl's-mixing model exceeds the rate obtained from IEM by a factor of 2 along the centreline at  $z/D \approx 15$ . Comparing the rates along the radius for  $z/D=20$  the peak condensation rate obtained using Curl is three times the one from IEM.

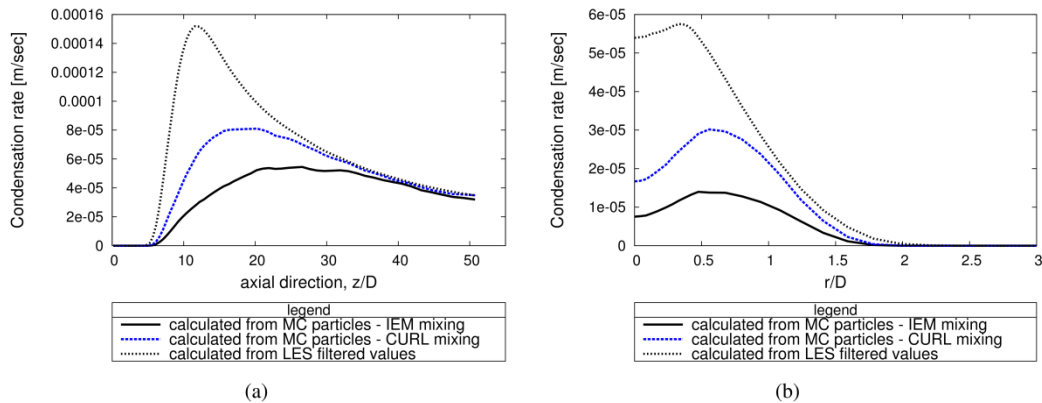


**Figure 3.** Comparison of the mean condensation rates along (a) the jet centreline, (b) the radius at  $z/D = 20$ .

Figures 4(a) and 4(b) present the particle number density  $N_i$  as a function of the particle diameter  $d_p$  extracted from the LES-PDF-MC simulations at axial locations  $z/D=10$  and  $z/D=50$ . It can be seen that in the upstream region ( $z/D=10$ , Fig. 4(a)) the number of small droplets predicted by IEM is larger than predicted by Curl, whereas the latter model produces slightly more larger droplets ( $d_p > 0.03 \mu m$ ). These trends are consistent with the larger nucleation rate in the upstream region and near the jet centreline from IEM and the generally higher condensation rate from Curl. At the downstream location  $z/D=50$ , Fig. 4(b), this trend is reversed and the number of droplets from Curl is larger across the entire diameter range, except from very large droplets ( $d_p > 0.09 \mu m$ ), which is readily explained by the larger centreline nucleation rate from Curl's model and comparable condensation rates from both models in the downstream region.

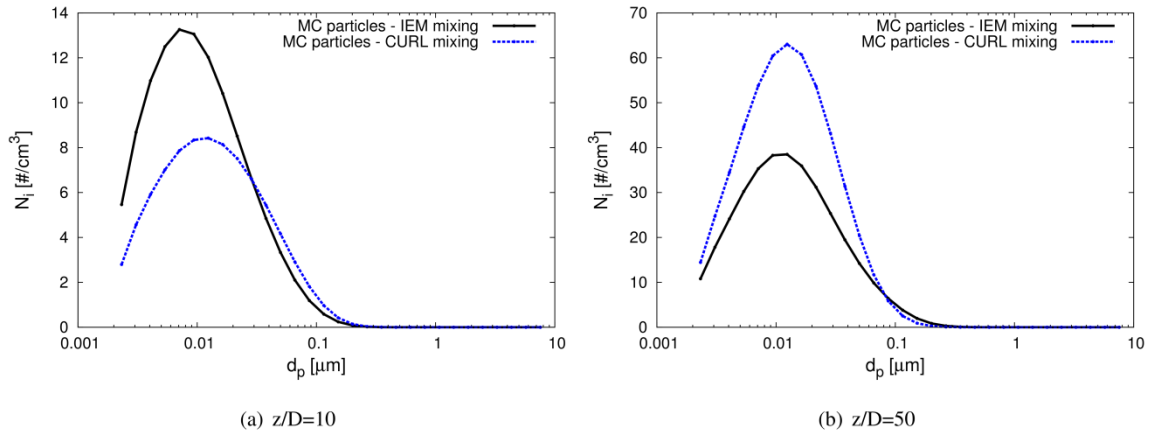


**Figure 4.** Comparison of the particle number density extracted from the simulations at (a)  $z/D=10$  and (b)  $z/D=50$ .

Figure 5(a) presents the time-averaged zeroth moment of the PSD (total number of particles per unit volume) along the jet centreline. As expected, the higher nucleation rate from IEM in the upstream region leads to a larger number of droplets compared with Curl, whereas the increased downstream nucleation rate from Curl leads to a higher prediction of the downstream  $m_0$ . This is presented more clearly in Fig. 5(b), where the percentage difference between  $m_0$  predicted using IEM and Curl is plotted and IEM predicts a roughly 90% higher  $m_0$  in the upstream jet core, but an approximately 50% lower  $m_0$  near the exit of the computational domain, with a sign change at  $z/D \approx 28$ . However, it is important to note that nucleation and condensation mainly occur in the mixing layer away from the jet centreline and that the overall trends of particle formation due to the different mixing models cannot be inferred from centreline data only. In fact, the evaluation of the global zeroth moment representing the entire domain reveals that the overall particle number density from Curl is about 2 times the  $m_0$  predicted by IEM, which is consistent with a series of plots of  $N_i=f(d_p)$  for  $z/D=10, 20, 30, 40, 50$ , of which only  $z/D=10$  and  $z/D=50$  were shown in Fig. 4 due to space limitations. It is also noted here that - irrespective of the employed mixing model- the predicted PSD (not shown) is considerably different from the measured one, with a significantly larger amount of small droplets in the simulations. These differences are expected to stem from the high sensitivity of the simulations to the chosen sub-models for surface tension, saturation pressure, nucleation and condensation, as well as experimental uncertainties like additional condensation within the measurement probe.

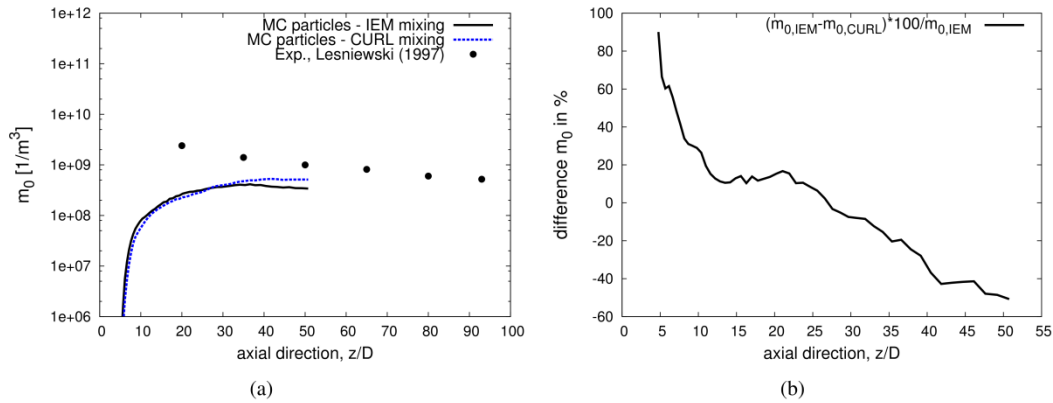


**Figure 5.** (a) Time-averaged zeroth moment  $m_0$  of the PSD along the jet centreline. (b) Percentage difference between  $m_0$  predicted by IEM and Curl.

## Conclusions

Results from the novel LES-MC/PDF approach used to simulate homogeneous nucleation and condensation of DBP droplets in a hot, turbulent nitrogen jet illustrate the high sensitivity of saturation, homogeneous nucleation, condensation and the resulting PSD to LES-filtering and mixing model effects. While evaluating the highly non-linear droplet source terms from LES-filtered values only yields considerably different predictions, the simulation results from the MC particle simulations are more similar. The differences between the mixing models amount to a factor of 2 for the global zeroth moment of the PSD, at least for the currently employed mixing models, where no tuning of the model parameters was attempted.

## References

- [1] T. K. Lesniewski and S. K. Friedlander, *Proc. Roy. Soc. Lond. A*, 454:2477-2504, 1998.
- [2] A. Gupta, P. Ifeacho, C. Schulz and H. Wiggers, *Proc. Combust. Inst.*, 33:1883-1890, 2011.
- [3] S.E Pratsinis, O. Arabi-Katbi, C.M. Megaridis, P.W. Morrison Jr., S. Tsantilis and H.K. Kammler *Mat. Sci. Forum*, 343-346:511-518, 2000.
- [4] S. Rigopoulos, *Progr. Energy Combust. Sci.*, 36:412-443, 2010.
- [5] A. Garmory and E. Mastorakos, *Chem. Eng. Sci.*, 63:4078-4089, 2008.
- [6] S. B. Pope, *Combust. Sci. Technol.*, 25(5-6):74-159, 1981.
- [7] G. Y. Di Veroli and S. Rigopoulos, *Phys. Fluids*, 23(4):043305, 2011.
- [8] G. Y. Di Veroli and S. Rigopoulos, *AIChE Journal*, 56(4):878-892, 2010.
- [9] C. W. Gardiner, *Handbook of Stochastic Methods*, 2nd Ed., Springer Verlag.
- [10] J. Villiermaux and J. C. Devillon, *2nd Int. Symp. Chem React. Eng.*, 1-13, 1972.
- [11] S. L. Girshick and C. Chiu, *J. Chem. Phys.*, 93:1273, 1990.
- [12] S. K. Friedlander, *Smoke, Dust, and Haze*, 2nd Ed., Oxford University Press.
- [13] A. Kempf, M. Klein, J. Janicka, *Flow Turbul. Combust.*, 74:67-84, 2005.
- [14] N. A. Fuchs, A. G. Sutugin, *Topics in Current Aerosol Research* 2:1-60, 1971.
- [15] T. K. Lesniewski, "Particle Nucleation and Growth in Turbulent Jets", *PhD thesis*, UCLA, USA, 1997.
- [16] S. Tsantilis, H.K. Kammler, S.E. Pratsinis, *Chem. Eng. Sci.*, 57:2139-2156, 2002.
- [17] N. Morgan, C. Wells, M. Kraft, W. Wagner, *Combust. Theo. Mod.*, 9(3):449-461, 2005.
- [18] P. Mitchell, M. Frenklach, *Phys. Rev. E*, 67:061407, 2003.
- [19] H. Dang, M.T. Swihart, *Aeros. Sci. Technol.*, 43(3):250-263, 2009.
- [20] G. Wang, S.C. Garrick, *J. Aeros. Sci.*, 37, 431-451, 2006.
- [21] S. R. Tieszen, D. W. Stamps and T. J. O'Hern, *Combust. Flame* 106:442-462, 1996.
- [22] J. Janicka, W. Kolbe, W. Kollmann *J. Non-Equilib. Thermodyn*, 4, 47, 1979.
- [23] R. L. Curl, *AIChE Journal*, 9, 175, 1963.
- [24] S.B. Pope, *Theor. Comput. Fluid Dyn.*, 2, 255, 1991.
- [25] S. Subramaniam, S. B. Pope, *Combustion and Flame*, 115, 487-514, 1998.
- [26] N. Seubert, A. Kronenburg, O. T. Stein, Y. Ge, M.J. Cleary *12th ICLASS conference*, Heidelberg, 2012.
- [27] V. Raman, H. Pitsch, *Proc. Combust. Inst.*, 31:1711-1719, 2007



## Large Eddy Simulation of a prefilming airblast atomizer

G. Chaussonnet, E. Riber<sup>1</sup>, O. Vermorel<sup>1</sup>, B. Cuenot<sup>1</sup>, S. Gepperth<sup>2</sup> and R. Koch<sup>2</sup>

1: CERFACS, France

2: Institut für Thermische Strömungsmaschinen (ITS),  
Karlsruhe Institut of Technology (KIT), Germany

### Abstract

A Large Eddy Simulation of an academic experiment is performed with an unstructured, explicit in time, gaseous flow solver (AVBP). The configuration is a planar prefilming atomizer designed and manufactured at KIT-ITS. Results of the simulation are compared to experiments in terms of air velocity profiles, film thickness, drop size distribution and spray angle. The different forms of the liquid phase (film and spray) are described by a Lagrangian approach. The film model is built upon a depth-averaged method and a new approach for primary atomization is presented, based on the parametrization of a Rosin-Rammler function to describe the drop size distribution. Preliminary results indicate a good agreement with measurements, with regards to the predicted drop size probability function and the predicted spray angle.

### Introduction

The increasing scarcity of fossil fuel and the strengthening of environmental constraints are strong motivations for the improvement of the combustion process in aeronautical gas turbines. One important prerequisite for a ‘more efficient’ combustion is the quality of the fuel spray that feeds the flame. Due to their thermal inertia, large droplets evaporate slowly. As a consequence, fuel-air mixing becomes insufficient and may be a significant source of unburned hydrocarbon emissions. On the contrary, fine droplets are rapidly evaporated and the fuel vapor better mixes with air before reaching the flame front, leading to a better-controlled combustion. A precise characterization of the drop size distribution in the spray is thus a necessary input to predict the flame structure and topology. This becomes even more critical for transient phenomena such as ignition or extinction.

Prefilming airblast atomizers are commonly used in aeronautical engines for their capacity to generate fine sprays. Moreover they exhibit stable performances for a wide range of fuel flow rates, and a low pressure loss [1]. In such devices, the liquid phase is subject to various phenomena that occur sequentially: injection, wall impact, filming, primary and secondary atomization (**Figure 1**). A peculiar aspect of this type of atomizer is the shearing of the liquid film by the gas flow. Film dynamics and the resulting atomization process directly depend on the flow configuration. For example, in swirled flows, the outbreak of a Precessing

Vortex Core can significantly alter the film shearing. Therefore, film modelling has to be taken into account to properly capture its fragmentation at the atomizing edge.

Recent developments in direct numerical simulation, where both the turbulence and the liquid – gas interface are explicitly resolved, allow to compute thin film flows [2] and primary atomization [3, 4] in academic configurations. Such techniques require a very high mesh resolution and advanced numerical methods, and are too CPU-time consuming to be applied to complex realistic configurations. As a consequence they are mostly dedicated to the understanding of the mechanisms of liquid fragmentation in simple configurations. The present work proposes to address the problem of liquid film flow and atomization in complex geometries using Large Eddy Simulation, coupled to a Lagrangian approach to describe the droplet trajectories. This approach has already demonstrated its ability to describe spray dynamics in industrial configurations [5, 6]. In order to improve the description of the liquid path from injection to spray, a Lagrangian film and atomization model is developed.

The paper starts by presenting the experimental test configuration and the general numerical set-up. Then details are given about both film and atomization models that have been implemented in the solver. Results are finally described and compared to measurements, to draw some first conclusions about the proposed approach.

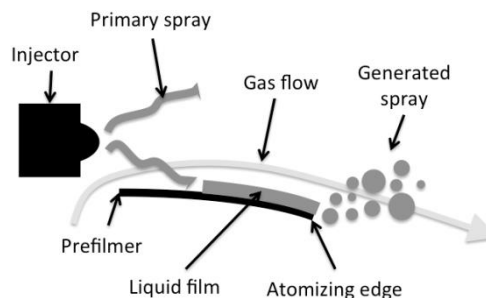


**Figure 1.** Schematic of the prefilming atomizing process

## Experimental investigations

The experimental rig designed at the ITS by Gepperth *et al.* [7, 8] has been chosen to test the model. It consists of a wing-shaped pre-filmer (Figure 2), placed in a channel. Liquid is injected at the surface of the pre-filmer via fifty equidistantly distributed holes, located 45 mm upstream the pre-filmer tip. To enhance accessibility for measurements, and to reduce the configuration complexity, the pre-filmer and the channel walls are planar, but still considered representative of the annular geometry encountered in real systems. The high gas velocity entrains the liquid towards the atomizing-edge of the pre-filmer, *i.e.* in the Z-direction, and induces high shear at the film surface. A thin film forms, that wets homogeneously the pre-filmer, before full atomization at the pre-filmer edge. No atomization is observed from the film surface before reaching the edge of the pre-filmer. Measurements combine particle and ligament tracking velocimetry, and backlight illumination. More details can be found in [7]. All experiments have been performed at ambient conditions, summarized in Table 1. The air and liquid flow rates were varied to study various regimes. Various liquids were also tested to measure the impact of their transport properties on the film and atomization behaviours.

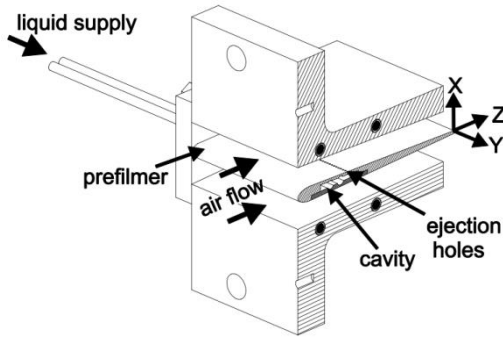


**Figure 2.** Schematic of the experimental configuration, from [8]

Mean air velocity	$\overline{u}_g$	20 – 70 m/s
Air temperature	$T$	298 K
Air density	$\rho_g$	1.21 kg/m <sup>3</sup>
Air kinematic viscosity	$\nu_g$	1.5 x 10 <sup>-5</sup> m <sup>2</sup> /s
Liquid density	$\rho_l$	770 <sup>*</sup> , 1008 <sup>**</sup> kg/m <sup>3</sup>
Liquid surface tension	$\sigma$	0.0275 <sup>*</sup> , 0.0466 <sup>**</sup> kg/s <sup>2</sup>
Surface liquid flow rate	$\dot{s}$	12.5 – 75 mm <sup>2</sup> /s

**Table 1.** Operating conditions, from [8]. <sup>\*</sup> Shellsol D70, <sup>\*\*</sup> a volume mixture of 50% of propanediol and 50% of water, labelled ‘1:1 W-P’ in the following

Measurements showed that the mean film thickness decreases as the gas velocity increases (due to a larger interface shear stress), and increases with liquid viscosity. Under the investigated conditions, the breakup process was observed to always follow three steps. First, a reservoir is formed at the atomizing edge, fed by the liquid coming from the film. Second, under the action of aerodynamics, bubbles and ligaments form out of this reservoir. When the bubble bursts (like a bag-breakup process in secondary atomization [9]), small droplets are produced. The rim of the bag remains attached to the reservoir and finally disintegrates into large droplets.

The drop size distribution of the generated spray has been measured in a series of test cases to evaluate the impact of several operating conditions. The pre-filmer length ( $L_p$ ), the film thickness ( $h_f$ ), the liquid viscosity ( $\mu_l$ ) and the surface liquid flow rate ( $\dot{s}$ ) have a minor effect on the drop-size distribution, even if the latter induces a significant increase in the number of fragmentation events [8]. The three main influencing parameters are: a) the momentum flux of the gas  $M = \rho_g u_g^2$  which sizes the quantity of momentum transferred from the gas to the liquid, b) the surface tension of the liquid  $\sigma$  which influences the volume of liquid accumulation at the pre-filmer edge as well as the ligament size and c) the atomizing edge thickness  $h_p$  which partly controls the volume of the accumulated liquid. Shadowgraphs and high-speed diagnostics allow to measure the diameter (or the equivalent diameter for near spherical structures) in the primary atomization zone. From this experiments, Gepperth *et al.* [8] provide a droplet number and volume probability density function for different gas velocities, liquid properties and atomizing edge thicknesses.

For every operating condition, the resulting PDF is compared to the Rosin-Rammler distribution [10]:

$$F_0(d) = 1 - \exp\left[-\left(\frac{d}{m}\right)^q\right] \Leftrightarrow f_0(d) = \frac{q d^{q-1}}{m^q} \exp\left[-\left(\frac{d}{m}\right)^q\right] \quad (1)$$

where  $f_0(d)$  is the probability density function and  $F_0(d)$  its cumulative density function. The volume probability density function is defined as  $f_3(d) = d^3 \times f_0(d)$  and agrees well with the experimental data (Figure 3) for all

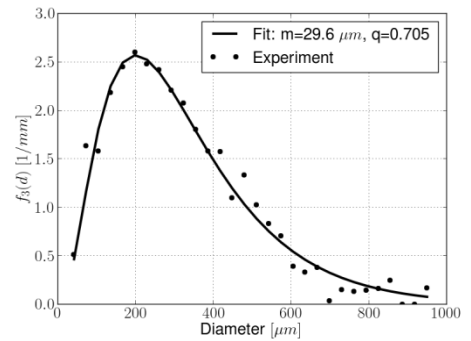


**Figure 3.** Volume PDF (Shellsol D70,  $h_p = 1$  mm,  $u_g = 50$  m/s)

investigated conditions. The Rosin-Rammler distribution depends on two parameters: the *shape*  $q$  and the *scale*  $m$ . However the set  $(q, m)$  ensuring the best experimental fitting is different for each condition.

## Models

In order to describe the targeted phenomena, it is necessary to take into account transfers between both phases, i.e. to couple the gas and liquid flow solvers. No thermal effects have been observed in the considered configuration so that the energy equation will be omitted in the following. In addition, droplet evaporation is neglected and the gas will be considered as a single-species mixture.

### Gaseous phase solver

The unstructured LES code AVBP explicitly solves the filtered compressible Navier–Stokes equations that are here simplified to the continuity and momentum equations [11]:

$$\begin{aligned} \frac{\overline{\rho}}{\overline{\rho}} + \frac{\overline{\rho} \tilde{u}_i}{\overline{\rho} x_j} &= 0 \quad \text{and} \\ \frac{\overline{\rho} \tilde{u}_i}{\overline{\rho}} + \frac{\overline{\rho} \tilde{u}_i \tilde{u}_j}{\overline{\rho} x_j} &= \frac{\overline{\rho}}{\overline{\rho} x_j} \left( \bar{p} d_{ij} - \bar{\tau}_{ij} - \bar{\tau}_{ij}^{sgs} \right) + \bar{s}_{mo,i} \end{aligned} \quad (2)$$

The symbol  $\overline{\cdot}$  states for spatial filtering and  $\tilde{\cdot}$  for mass-weighted Favre filtering. Einstein's summation convention is applied over repeated indices and  $d_{ij}$  denotes the Kronecker symbol. The inter-phase momentum exchange term  $\bar{s}_{mo,i}$  is detailed below.  $\bar{\tau}_{ij}$  stands for the laminar filtered stress tensor. The subgrid unclosed term is classically expressed by an eddy-viscosity approach and the turbulent viscosity is computed via the dynamic Smagorinsky model.

### Liquid phase solver

The liquid phase is assumed to be diluted, and heavier than the carrier phase. Droplet diameters are considered much lower than any other resolved flow characteristic scale, to allow point-source approximation. In these conditions, drag is the only significant momentum transfer type, and the Lagrangian governing equations of motion are:

$$\frac{dx_{p,i}}{dt} = u_{p,i} \quad \text{and} \quad \frac{du_{p,i}}{dt} = \frac{f_{p,i}}{m_{p,i}} \quad (3)$$

where the subscript  $p$  refers to the droplet and  $x_{p,i}$ ,  $u_{p,i}$  and  $m_p$  represent its position, velocity and mass, respectively. The force acting upon the droplet  $f_{p,i}$  is expressed by the Stokes drag extended by Schiller and Naumann's correlation [12]:

$$f_{p,i} = -\frac{m_p}{t_p} (u_{p,i} - \tilde{u}_{g@p,i}) \quad \text{with:} \quad t_p = \frac{r_p d^2}{18 m_g} \frac{1}{1 + 0.15 \text{Re}_p^{0.687}} \quad (4)$$

where  $\tilde{u}_{g@p,i}$  is the gaseous velocity seen by the droplet and is computed as a linear interpolation from the filtered gas field at the droplet position, without accounting for the subgrid scale contribution. The momentum transfer  $\bar{s}_{mo,i}$  is calculated at each node as the sum of the drag force of all particles located in all elements containing the considered node, weighted by the conservative projector  $w_{p@n}$ :

$$\bar{s}_{mo,i} = -\frac{1}{V} \sum_p \tilde{a}_p w_{p@n} \times f_{p,i} \quad (5)$$

### Lagrangian film model

Liquid thin film flows have been studied in various industrial contexts. In piston engines, Foucart *et al.* [13] used an Arbitrary Lagrangian Eulerian approach, while O'Rourke and Amsden [14] applied a Lagrangian Particle Model. In aeronautical burners, Elsässer *et al.* [15] and Ebner *et al.* [16] described the film flow with an Eulerian approach. The common denominator of these studies is the use of height-averaged film equations. The underlying idea is that the film thickness is negligible compared to all gaseous macroscopic length scales, and is usually referred to as *thin film hypothesis*. Most previous studies of liquid films were conducted in a RANS approach. In the present work, the model is embedded in a LES solver, resulting in a liquid film that undergoes turbulent fluctuations.

As the film is made of liquid fuel and its Reynolds number is about 100, the film flow is supposed laminar and incompressible. The characteristic time scale of the film flow is the momentum diffusion time along the film thickness. Since this time scale is lower than the film convective time, the flow is supposed steady, i.e. it follows instantaneously the shear stress variation imposed by the gas. Finally, because of the thin film

hypothesis, longitudinal gradients (except the pressure gradient) are neglectable compared to the wall normal ones.

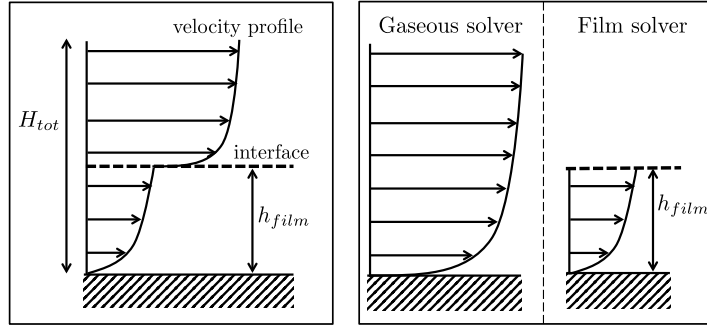


**Figure 4.** One-way coupling hypothesis on a flat interface. a) Real configuration. b) Modelled configuration.

In addition, and in the context of aeronautical combustors, the velocity ratio of the liquid film and the gas flow is supposed to stay below 100. The film may then be seen as stationary in comparison to the gas. Coupling of this assumption to the *thin film hypothesis* leads to a stationary boundary condition at the liquid-gas interface. The local shear stress can therefore be considered as equal to the wall

shear stress in the absence of a film. This may not be true if the film surface presents strong wrinkling and instabilities,

introducing some surface roughness or even deformation, but this assumption will be used here as a first attempt. The physical consequence is a one-way coupling approach, where the gas flow influences the film flow without feedback from the liquid to the gas. The resulting approach is depicted in Figure 4: the film flow profile is not solved, the “liquid film boundary condition” being derived from a model as described below. Compiling all assumptions leads to the depth-averaged film velocity magnitude:

$$\bar{u}_f = \frac{h_f}{2m_l} t_w - \frac{h_f^2}{3m_l} \frac{dp}{dx} \quad (6)$$

Equation (6) states that the film motion is a result of the film surface shear stress and the pressure gradient within the film. The shear term being proportional to the film thickness  $h_f$ , and the pressure gradient term to  $h_f^2$ , the pressure gradient impact is assumed to be negligible compared to the shear stress.

### Primary atomization model

In the present study, a new approach is proposed to model primary atomization in pre-filming configurations, called PAMELA (**P**rimary **A**tomization **M**odel for **p**re**E**filming **a**ir**L**ast injectors). It is based on the transverse instability prediction, initiated by Hong *et al.* [17] and Varga *et al.* [18]. It is calibrated to fit the experimental results of Geperth *et al.* [8]. The basic idea is to describe the drop size distribution of the generated spray by a Rosin-Rammler distribution whose parameters ( $q, m$ ) are expressed from the operating conditions. The main parts of the model are explained in the following.

#### Expression of $m$

In configurations of planar liquid sheets [19, 20] as well as axial jets [17, 21], experiments have shown that a transverse instability develops prior to the atomization, and that the Sauter mean diameter ( $D_{32}$ ) of the generated spray is proportional to this instability length scale  $\lambda_T$ :

$$D_{32}^{\text{exp}} = C \times l_T \quad (7)$$

The transverse instability is also visible in the present experiment and its length scale is estimated using Hong's approach. Liquid structures, which are immersed in the main flow stream, are accelerated by the gas flow through the drag force. This streamwise acceleration generates a Rayleigh-Taylor instability that propagates in the spanwise direction. In the present configuration where the liquid fragmentation occurs at the pre-filmer edge, the size of the accelerated liquid structure is supposed to be proportional to the edge thickness. This leads to a transverse instability wavelength estimated as:

$$l_{RT} = 2\rho \sqrt{\frac{6S \times (ah_p)}{C_d r_g (u_g - u_c)^2}} \quad (8)$$

where  $C_d$  is the drag coefficient of the liquid structure, reported to be close to one [20]. The constant  $a$  is between 0 and 1 and represents the characteristic length of accelerated liquid compared to the pre-filmer thickness. It is set to 0.67 from the observations of Müller *et al.* [22]. The interface velocity is denoted by  $u_c$ .

From the Rosin-Rammler distribution (Eq.(1)), the Sauter mean diameter ( $D_{32}^{RR}$ ) writes:

$$D_{32}^{RR} = m \frac{G(3/q + 1)}{G(2/q + 1)} \quad (9)$$

where  $G$  is the Gamma function. Combining Eqs. (7), (8) and (9) leads to the final expression of  $m$  that depends on the three parameters  $M = r_g u_g^2$ ,  $S$  and  $h_p$ :

$$m = 2\rho C \sqrt{\frac{6S \times (ah_p)}{C_d r_g (u_g - u_c)^2}} \times \frac{G(2/q+1)}{G(3/q+1)} \quad (10)$$

#### Expression of $q$

Experimental results indicate a dependency of the parameter  $q$  on the Weber number expressed with gaseous aerodynamic force:

$$We = \frac{r_g \gamma_{70} u_{70}^2}{S} \quad (11)$$

where  $u_{70}$  is equal to 70% of the free stream velocity and  $\gamma_{70}$  represents the height in the boundary layer where the local velocity is equal to  $u_{70}$ . Both values correspond to experimental observations, where the liquid is accelerated at a vertical position above the pre-filmer where the local gas velocity is approximately 70% of the free stream velocity, taken as the bulk velocity in the present experiment. The shape parameter  $q$  also depends on the pre-filmer thickness. Finally,  $q$  is expressed as:

$$q(We, h_p) = \frac{\kappa}{\sqrt{We}} + (ah_p + b) \quad (12)$$

where  $\kappa$ ,  $a$  and  $b$  are model constants. The linear form  $(ah_p + b)$  in Eq. (12) derives from the fact that only two different pre-filmer thicknesses have been investigated.

#### Model constants

The four model constants are fitted with a multi-variate optimization technique where the test values are the Sauter mean diameter and the  $q$  parameter. The varying parameters are the pre-filmer thickness (1 and 2.5 mm), the type of liquid (see Table 1) and the gas velocity  $u_g$ . The result is given in Table 2.

C, Eq. (7)	$\kappa$ , Eq. (12)	$a$ , Eq. (12)	$b$ , Eq. (12)
0.1166	1.76	112 m <sup>-1</sup>	-0.043

**Table 2.** Model constants of PAMELA

Results of PAMELA are shown in Figure 5, obtained for a pre-filmer thickness of 2.5mm and the liquid 1:1 W-P. Figure 5a) illustrates the influence of the gas velocity onto  $D_{32}$  and the mean volume diameters  $D_{V10}$  and  $D_{V90}$  (drop diameter such that 10% and 90% of the total spray volume is in droplets of smaller diameter).  $D_{V10}$  and  $D_{32}$  are well recovered while  $D_{V90}$  is overestimated for low velocities with a maximum deviation of 20%. Figure 5b) represents the volume PDF for a mean gas velocity  $u_g = 70$  m/s. The trend of the distribution is well recovered and presents an absolute surface deviation ( $\int_0^{\infty} |f_3^{\text{mod}}(d) - f_3^{\text{exp}}(d)| d(d)$ ) of 14.6%.

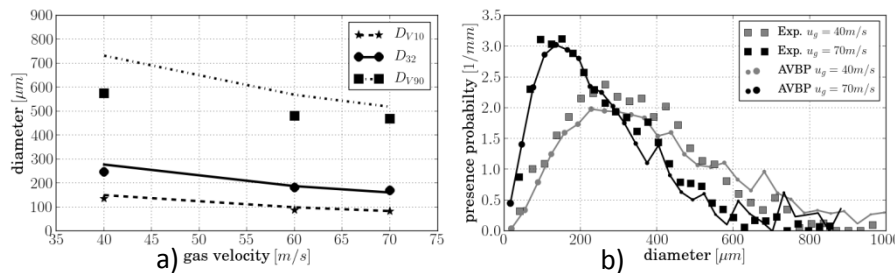


**Figure 5.** a) Mean diameters evolution with gas velocity. Lines: PAMELA, symbols: experiment b) Volume PDF for 1:1 W-P liquid,  $h_p = 2.5$  mm,  $u_g = 70$  m/s.

#### Numerical Set-up

Two-phase Large Eddy Simulations of the pre-filmer experiment have been performed with the code AVBP, an unstructured, compressible, explicit in time, flow solver [11], including a Lagrangian approach for the liquid phase [23]. The computational mesh contains 1.5 millions of tetrahedra, with a characteristic cell size in the atomization region of 0.1 mm. A mid-plane Y-cross section of the mesh, zoomed at the pre-filmer edge region, is shown in Figure 6. Boundary conditions consist in a turbulent gas velocity inlet with a turbulent intensity of 10%, an atmospheric pressure outflow and solid law-of-the-wall. In Figure 7, the mean gaseous velocity profiles on a vertical line located at 0.3 mm from the atomizing edge (dashed line in Figure 6) are compared for three bulk velocities. Both horizontal and vertical components agree well with the experimental data. However the predicted vertical velocity profiles show a slight discrepancy illustrated by additional inflexion points. Those are related to the counter rotating eddies that lie in the recirculation zone. These eddies

are small ( $\sim 0.5$  mm), and any uncertainty on the measurement device position ( $\sim 0.1$  mm) induces a large variation in the measured velocity profile.

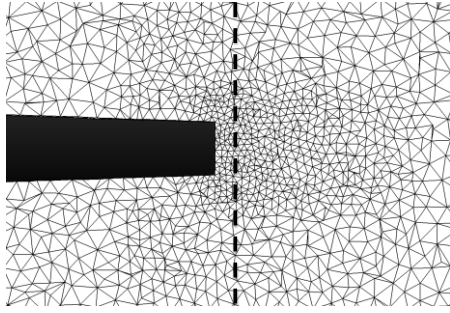


**Figure 6.** Mid-plane Y-cut of the computational mesh in the atomizing edge region

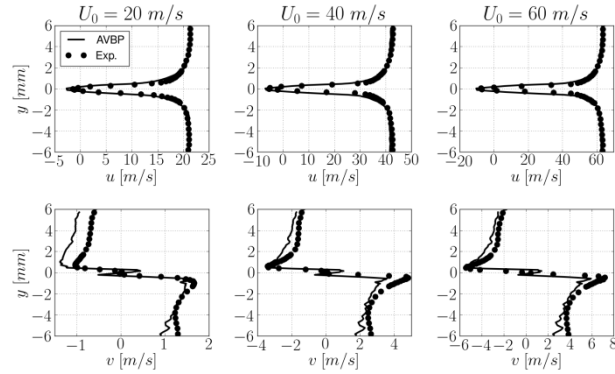


**Figure 7.** Comparison of experimental (symbols) and numerical (lines) results for single phase gas velocity profiles (0.3 mm downstream the atomizing edge)

The film thickness evolution with air velocity is shown in Figure 9. Although the film thickness is not well recovered, the film model succeeds to capture the correct dependence on air velocity and liquid viscosity. Note the factor 2 in film thickness between both liquids, to be related to the factor 4 between their viscosities. Indeed, from Eq. (6) it can be seen that the film thickness is proportional to the square root of the liquid viscosity. The large over-estimation of the film thickness results from the strong one-way coupling hypothesis: in reality the liquid surface is not flat and some waves can alter the gas boundary layer and the interface shearing. To account for this phenomenon, Elsäßer *et al.* [15] proposed a method to model the feedback from the film to the gas. Moreover, the wrong estimation of the wall shear stress may also be related to the weakness of LES to predict accurately shear stress and pressure loss [24]. However the film thickness has a minor influence on the spray population, so that the observed deviation is not an issue for the prediction of atomization.

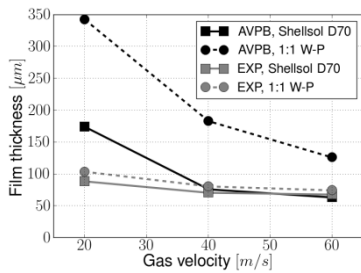


**Figure 8.** Film thickness evolution with air velocity

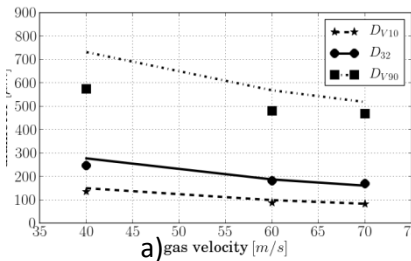


**Figure 9.** a) Mean diameters evolution with air velocity. Lines: PAMELA, symbols: experiment b) Volume PDF for Shellisol D70 on a 1 mm thick pre-filmer

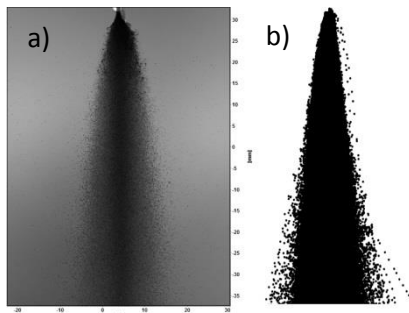
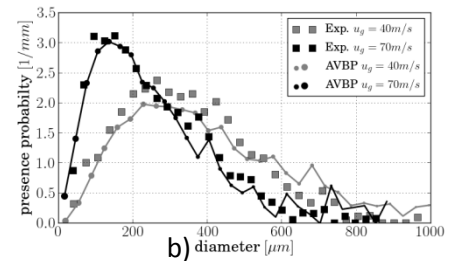


**Figure 10** Spray visualisation. a) Experiment. b) Simulation.

This is confirmed by the plots of  $D_{V10}$  and  $D_{32}$  in Figure 8a, showing good agreement with the experiment. Because of a lower statistical convergence, larger diameters ( $D_{V90}$ ) are less representative. The drop size PDF, depicted in Figure 8b is accurately reconstructed for two different gas velocities. Here again, the poor statistical convergence at high diameters is responsible for a noisy behaviour. Figure 10a presents a superposition of a series of experimental snapshots, to be compared to the numerical spray in Figure 10b). The spray angle is in good agreement with the experiment but the width of the spray just behind the atomizing edge region is slightly under-predicted. This is due to the flapping of the liquid accumulation at the edge, not described in PAMELA, that forms droplets with a zero velocity.

## Conclusions

An academic experiment devoted to the study of pre-filming atomization in the case of a planar geometry has been simulated with the use of Large Eddy Simulation and Lagrangian particle tracking. To describe pre-

filming atomization typical phenomena, a film model and an atomisation model have been developed and implemented in the solver AVBP.

The film model is capable to represent the trends in the film thickness evolution with regards to the interface shearing (depending on the gas velocity) and to the liquid viscosity. However the film thickness is not well reproduced, with a relative error that peaks to a factor 3. This is explained by first, the neglected retroaction of the liquid on the gas and second, the difficulty that LES faces to accurately predict wall shear stress and pressure loss.

The atomization model (PAMELA) is calibrated on the experimental results presented in Gepperth *et al.* [8] and allows to predict the correct distribution of droplet diameters in the generated spray. Simulations and experimental results are in good agreement for all tested conditions. As the fragmentation mechanism in real annular air-blast atomizers is expected to be similar to the one observed in the present configuration, the atomization model proposed in this work is believed to provide an accurate description of the spray topology in real combustors, which constitutes the next step of this study.

## Acknowledgements

The research leading to these results has received funding from the European Union Seventh Framework Programme (FP7/2007-2013) under grant agreements n°265848 and n° ACP8-GA-2009-234009; and was conducted within the FIRST and KIAI projects. This work was performed using HPC resources from GENCI-CINES (Grant 2013- x20132b5031).

## Nomenclature

Nomenclature					
Symbols					
$C_d$	drag coefficient [-]	$q$	shape parameter of the Rosin-Rammler function [-]	$\sigma$	surface tension [kg/s <sup>2</sup> ]
$d$	diameter [m]	$u$	velocity [m/s]	$\tau_{ij}$	stress tensor [N/m <sup>2</sup> ]
$D_{32}$	Sauter mean diameter [m]	$u_{70}$	70% velocity of the free stream	$\tau_p$	particle response time [s]
$D_{V10}$	drop diameter such that 10% total liquid volume is smaller droplets [m]		velocity [m/s]	$\tau_w$	wall shear stress [Pa]
$D_{V90}$	drop diameter such that 90% total liquid volume is smaller droplets [m]	$u_c$	convection velocity of the interface [m/s]	<b>Subscripts</b>	
$f$	volume force [N/m <sup>3</sup> ]	$\dot{s}$	surface film flow rate per unit length [mm <sup>2</sup> /s]	$f$	Film
$f_0, f_3$	number and volume dropsize PDF [1/m]	$y_{70}$	height such that local velocity is equal to $u_{70}$ [m]	$g$	Gas
$F_0$	number dropsize Cumulative Density Function [-]	$We$	Weber number [-]	$l$	Liquid
$h$	thickness [m]	$\delta_{ij}$	Kronecker symbol	$p$	Prefilmer
$L$	length [m]	$\lambda_T$	transverse instability wavelength [m]	<b>Superscripts</b>	
$m$	scale parameter of the Rosin-Rammler function [m]	$\lambda_{RT}$	Rayleigh-Taylor instability wavelength [m]	$exp$	Experience
$M$	momentum flux [N/m <sup>2</sup> ]	$\mu$	dynamic viscosity [Pa.s]	$mod$	Model
		$\nu$	kinematic viscosity [m <sup>2</sup> /s]	<b>Acronym</b>	
		$\rho$	density [kg/m <sup>3</sup> ]	PDF	Probability Density Function

## References

- [1] Lefebvre, A. H., (1989). *Atomization and Spray*, Ed. Norman Chigier.
- [2] Lan, H., Friedrich, M., Armaly, B. F., & Drallmeier, J. A. (2008). *International Journal of Heat and Fluid Flow* 29, 449 - 459.
- [3] Fuster, D., Bagué, A., Boeck, T., Le Moyne, L., Leboissetier, A., Popinet, S., Ray, P., Scardovelli, R., & Zaleski, S. (2009). *International Journal of Multiphase Flow* 35, 550--565.
- [4] Lebas, R., Menard, T., Beau, P., Berlemont, A., & Demoulin, F. X. (2009). *International Journal of Multiphase Flow* 35, 247--260.
- [5] Ham, F., Apte, S. V., Iaccarino, G., Wu, X., Herrmann, M., Constantinescu, G., Mahesh, K., & Moin, P. (2003). *Center for Turbulence Research Annual Briefs*, 139-160.
- [6] Jaegle, F., Senoner, J.-M., Garcia, M., Bismes, F., Lecourt, R., Cuenot, B., & Poinot, T. (2011). *Proc. of the Comb. Inst.* 33, 2099-2107.
- [7] Gepperth, S., Guildenbecher, D., Koch, R., & Bauer, H. (2010). *23rd Annual Conf. on Liq. Atomization and Spray Syst.*
- [8] Gepperth, S., Müller, A., Koch, R., & Bauer, H. (2012). *12th Triennial International Conf. on Liq. Atomization and Spray Syst.*
- [9] Rimbart, N. & Castanet, G. (2011). *Physical Review E* 84, 016318.
- [10] Babinsky, E. & Sojka, P. E. (2002). *Progress in Energy and Combustion Science* 28, 303-329.



- [11] Gourdain, N., Gicquel, L., Montagnac, M., Vermorel, O., Gazaix, M., Staffelbach, G., Garcia, M., Boussuge, J., & Poinot, T. (2009). *Computational Science & Discovery* 2, 015003.
- [12] Schiller, L. & Nauman, A., (1935). *VDI Zeitung* 77, 318-320.
- [13] Foucart, H., (1998). PhD thesis, *Université de Rouen*.
- [14] O'Rourke, P. & Amsden, A. A. (1996). *SAE Technical Paper*.
- [15] Elsässer, A. (1998). PhD thesis, *Department of Thermal Turbomachinery, Karlsruhe Institute of Technology*.
- [16] Ebner, J., Schafer, O., Schober, P., & Wittig, S. (2003). *Proc. of the 9th International Conf. on Liq. Atomization and Spray Syst.*
- [17] Hong, M., Cartellier, A., & Hopfinger, E. (2002). *Proc. 4th Int. Conf. on Launcher Technology" Space Launcher Liq. Prop."*, 3--6.
- [18] Varga, C., Lasheras, J. C., & Hopfinger, E. (2003). *Journal of Fluid Mechanics* 497, 405--434.
- [19] Raynal, L. (1997). PhD thesis, *Université de Grenoble 1*.
- [20] Rayana, F. B., Cartellier, A., & Hopfinger, E. (2006). *Proc. of the international conf. on Liq. Atomization and Spray Syst.* 27.
- [21] Marmottant, P. & Villermaux, E. (2001). *Actes du colloque de synthèse du groupe de recherche CNES/CNRS/ONERA/SENECMA*.
- [22] Müller, A., Meier, R., Schäfer, O., & Wittig, S. (2004). *DFG-Tagung - Atomization and Spray Processes*.
- [23] Garcia, M. (2009). PhD thesis, *Institut Polytechnique de Toulouse*.
- [24] Barré, D., Kraushaar, M., Staffelbach, G., Moureau, V., & Gicquel, L. Y. M. (2013). *Comptes Rendus de l'Académie des Sciences - Mécanique* 341, 277-287.

## **VoF-LES Studies of GDi Multi-Hole Nozzle Plume Primary Breakup and Comparison with Imaging Data**

Bizhan Befru<sup>1</sup>, Peter Spiekermann<sup>1</sup>, Mark A. Shost<sup>2</sup> and Ming-Chia Lai<sup>2</sup>

1: Delphi Customer Technology Center, Bascharage, G.-D. Luxembourg

2: Mechanical Engineering Department, Wayne State University, Michigan, USA

### **Abstract**

A combined VoF-LES computational and spray shadowgraphic imaging investigation of the primary atomization of a skew-angle plume from a gasoline direct injection (GDi) high-pressure multi-hole injector has been carried out. The objective is two-fold: (1) investigation of the plume breakup structure of the short length-to-diameter ratio (l/d) GDi nozzle holes, and (2) assessment of the predictive accuracy of the VoF-LES method. The study is carried out for three fuel pressures of 5, 10 and 20 MPa, in order to assess the jet breakup structure and VoF-LES capability for a representative fuel system pressure range. The spray plume imaging data reveal plume primary atomization in the vicinity of the nozzle near-field, almost immediately after the start of injection. The data shows insubstantial effect of fuel pressure on the plume primary breakup structure, notably the plume trajectory and cone angle. The VoF-LES predictions of the jet primary breakup structure, including insignificant influence of fuel pressure, are in good quantitative agreement with the spray imaging data.

---

### **Introduction**

The multi-hole GDi injector's spray macroscale and atomization characteristics (plume targeting, plume cone angle, plume penetration, droplet-size distribution, etc.) exert major influence on the mixture preparation process and, consequently, the engine combustion performance. Therefore, optimization of the GDi multi-hole spray pattern, penetration and atomization characteristics, within the constraints imposed by the engine geometry and performance targets is a critical component of the combustion system optimization process. The GDi multi-hole seat design and spray characteristics have been the subject of investigation over the past decade [1,2]. However, recent trends towards gasoline engine down-sizing and the stringent EU6C particulate emissions have spurred intensive R&D activities towards study of nozzle design with respect to the spray characteristics [3,4].

The multi-fluid LES method for analysis of the jet breakup process has been under development and verification over the past decade. The capability of the method has been broadly demonstrated [5-8], although with the exception of Ref.6, the injector internal flow domain was not included in the simulation, thus requiring prescription of the nozzle-exit velocity conditions (either a prescribed velocity distribution with superimposed turbulent disturbances, or from the LES of a stationary channel flow). This practice overlooks the influence of the seat-nozzle geometry on the nozzle-exit velocity condition and, thereof, the jet breakup process. This, in particular, is of paramount importance in the case of the GDi multi-hole nozzle due to its short l/d geometry.

This paper presents VoF-LES analyses of the seat-nozzle internal flow and plume near-field breakup structure of a GDi single plume, with the  $\beta=30^\circ$  nozzle skew (bend) angle. The simulation pertains to a single hole of a purpose-designed GDi multi-hole seat geometry, with three identical nozzle-holes per  $120^\circ$  seat circumferential segment. This seat geometry provides sufficient spray-to-spray spacing to enable optical investigation of a single plume without interference of the neighbouring plumes. The computational domain is comprised of 1/3 of the seat geometry and a segment of the downstream ambient space: hence it enables simultaneous simulation of the nozzle internal flow and the jet primary breakup process, with a single computational method. The shadowgraphic imaging technique is utilized to investigate the spray near-field primary atomization and its dependence on the fuel pressure in the range 5 – 20MPa.

### **Experimental Test-rig**

The objective of the experimental spray imaging is to study the nozzle near-field spray breakup morphology and macroscale parameters (e.g. spread angle, skew angle) of a GDi nozzle, with short nozzle l/d ratio, and to characterize their dependence on the fuel system pressure.

The experimental test-rig, shown in Figure 1, comprises of the injector fixture, the illumination system, the camera and auxiliary equipments and the fuel supply system. The synchronization of the injector operation, optical system and the data collection system is effected through Lavision software. The test-rig incorporates additional equipment that affords multi-functional capability for complementary laser diagnostic techniques.

### Shadowgraphic Optical Image Acquisition Instrumentation and Set-Up:

CCD-Camera:	LaVision Flow Master
Camera lens:	Nikon 50mm, f#1.8 (retro mounting)
Camera lens aperture:	4
Back light:	ND-YAG Laser combined with Dye Diffuser Plate
Fluorescence screen:	LaVision                      Dye                      Diffuser                      Plate
	[Light output pulse duration (@ 5 ns input): 20 ns, 580nm]
ND YAG Laser:	Quantel Big Sky Laser Twins Ultra (25mJ per cavity)
Image size:	9 x 8 mm (width x height)
Camera Orientation:	0° & 120° to Injector
Image acquisition:	single shot imaging (one spray image per injection)

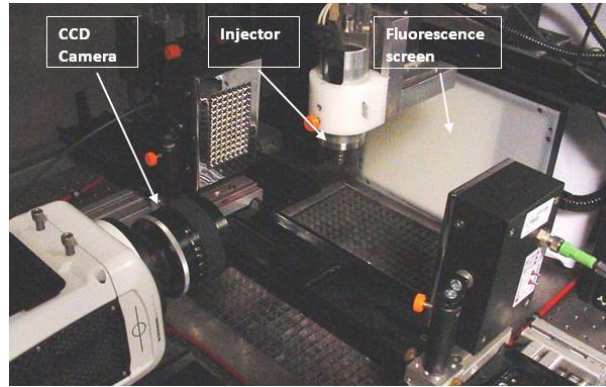


Figure 1. Shadowgraphic optical imaging instrumentation and experimental setup

### The Computational Method

A detailed description of the mathematical model and the numerical solution method is available in the literature [9] therefore, here, a brief summary of the methodology is provided.

#### Conservation Equations of Multi-Phase System

The mathematical model comprises of the governing equations for the conservation of mass and momentum of a two-phase flow system, comprised of two immiscible, incompressible Newtonian fluids, that includes the surface tension force. The set of conservation equations that describe the flow of the two-phase mixture are:

$$\frac{\partial \rho}{\partial t} + \nabla \cdot (\rho U) = 0 \quad (1)$$

$$\frac{\partial \rho U}{\partial t} + \nabla \cdot (\rho U \otimes U) = -\nabla P + \nabla \cdot \tau + \int_{S(t)} \sigma \kappa n \delta(x - x') ds$$

(2)

Where,  $U$  is the velocity,  $\rho$  is the density,  $\sigma$  is the surface tension coefficient,  $\tau$  is the stress tensor,  $\kappa$  is the curvature of the liquid surface, and  $n$  represents a unit vector normal to the liquid surface. The operators  $\Delta ( )$  and  $\Delta \cdot ( )$  denote the gradient and the divergence operations, respectively. The integral term in equation (2) represents the momentum source due to surface tension: it acts only at the interface - indicated by the Dirac function  $\delta(x)$  - over the entire liquid surface  $S(t)$ . This is an important term in the simulation of the liquid jet breakup process and is evaluated according to the Continuum Surface Force model of Brackbill et. al. [10].

### **Large Eddy Simulation Method**

The VoF-LES equations are derived from equations (1) to (3), through a process of volume averaging of the phase-weighted hydrodynamic variables. This entails decomposition of the dependent variables into resolvable and irresolvable (sub-grid) scales of turbulent fluctuations, and application of a filter that removes the sub-grid scale fluctuations from the direct numerical simulation. The filtering process, in conjunction with the non-linear term in equation (2), produces additional terms, involving correlations of the hydrodynamic variable fluctuations at sub-grid scales that require closure with the aid of mathematical models. The most notable of these terms is the Sub-Grid-Scale (SGS) stress tensor that represents the effect of unresolved scales of turbulence on the momentum transport process and its viscous dissipation. The Sub-Grid-Scale (SGS) stress is defined as:

$$\tau_{sgs} = \overline{U(t)U(t)} - \overline{U(t)}\overline{U(t)} \quad (5)$$

Where  $U(t)$  is the instantaneous resolved velocity field. The closure of the sub-grid-scale stresses is affected through a sub-grid-scale eddy-viscosity model [9].

### **VOF Interface Tracking Method**

The principle of the “Volume of Fluid” (VoF) approach is that a two- (or indeed multi-) phase system can be represented as a mixture of phases in which the phase-fraction distribution includes sharp, yet resolvable, transitions between the phases. Accordingly, the interface in a two-phase flow system is computed with the aid of the transport equation for the liquid volume fraction as the indicator function to locate the interface. The transport equation for the phase fraction  $\alpha$ , for two incompressible fluids, is:

$$\frac{\partial \rho \alpha}{\partial t} + \nabla \cdot (\rho U \alpha) = 0 \quad (7)$$

According to the definition of  $\alpha$ , the mixture thermo-physical properties are calculated as:

$$\rho = \alpha \rho_f + (1 - \alpha) \rho_g \quad (8)$$

$$\mu = \alpha \mu_f + (1 - \alpha) \mu_g \quad (9)$$

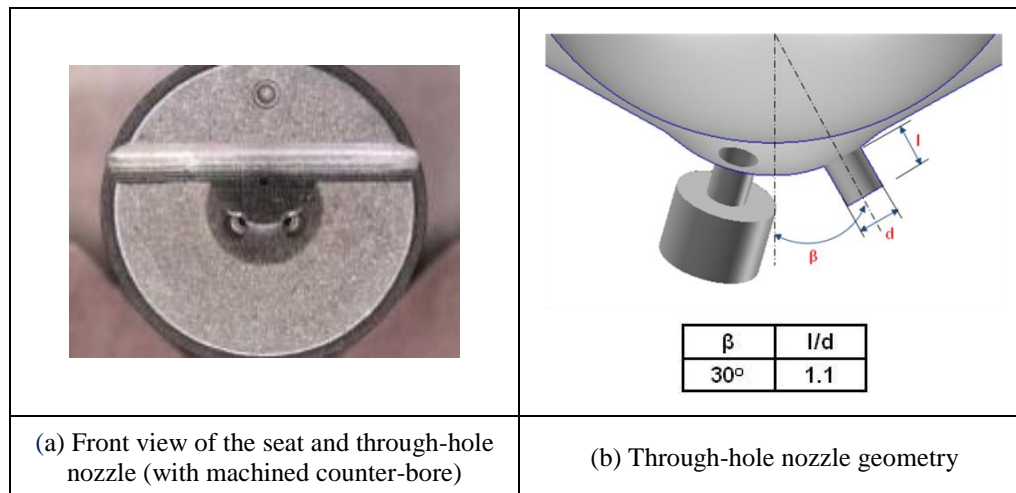
In the present simulations, an advanced method formulated in Open-FOAM [11] that adopts a two-fluid formulation of the conventional volume-of-fluid concept, within the frame-work of the finite-volume method, is used. The method employs a formulation of the phase transport equation that includes a “compression velocity” term [12] which acts to maintain a sharp interface resolution.

### **Numerical Solution Method**

The numerical solution of the VoF-LES conservation equations are performed using Open-FOAM [12], an open-source finite-volume CFD tool-box. The solution method employs a blend of central/upwind schemes for spatial discretization of the transport terms, and the Crank-Nicholson/Euler-implicit temporal integration schemes the primitive –variable conservation equations. This is intended to afford second-order spatial and temporal discretization / integration accuracy and to ensure the fluid dynamic variables are bounded. Numerical solution of the primitive-variable flow equations is obtained with PISO [13] algorithm.

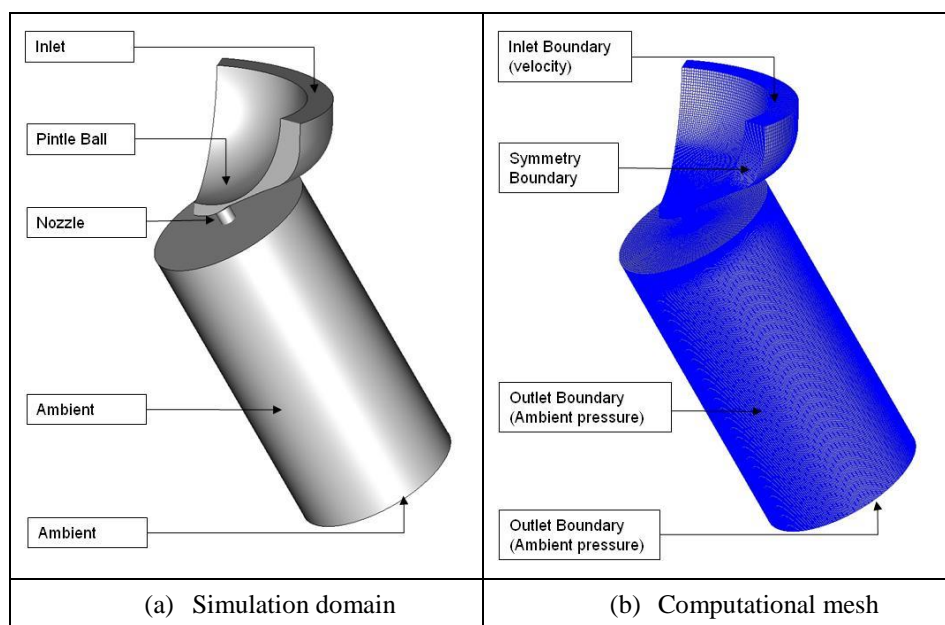
### **Geometry, Computational Mesh and Boundary Conditions**

Figure 2 presents views of the purpose-built 3-hole GDi seat geometry. The seat was fabricated to have 3 identical flow hole and counter-bore nozzles arranged at 120° circumferential spacing. A secondary process was then applied to precisely grind off the counter-bore of one nozzle, thus producing a GDi representative short length-to-diameter ratio ( $l/d$ ) through-hole with optical access to the plume at the nozzle exit.



**Figure 2.** Geometry of the 3-nozzle seat and the through-hole nozzle

Figure 3 presents the computational domain that comprises the injector seat and nozzle domain and its immediate near-field ambient. The computational mesh is of the order of 5 M cells (1 M cells within the injector domain and 4 M cells within the ambient) and affords a spatial resolution in the range 2-5  $\mu\text{m}$  (within the injector seat-nozzle) to 10  $\mu\text{m}$  (within the ambient domain). This mesh resolution is of the order of the Taylor (micro) length scale in the nozzle domain.



**Figure 3.** Computational domain, mesh and boundaries

The pintle motion is not included in the simulation, due to severe requirements of the VOF-LES method for mesh geometric quality which would not permit the required severe mesh deformation. Hence, the transient simulation of the seat-nozzle flow development is performed on a fixed geometry mesh with the pintle at the nominal stroke position. The simulation initial conditions are: (a) filled nozzle (from inlet to the pintle sealing band) with liquid at rest, (b) the remainder of the computational domain filled with stagnant air at ambient conditions.

In the present calculations, the liquid is n-Heptane at  $T=293^\circ\text{K}$  temperature. The following boundary conditions are applied:

- Inlet: Uniform inlet velocity, corresponding to the nozzle static flow for 5, 10 and 20 MPa fuel pressures (without imposition of artificial velocity disturbances),
- Outlets : Non-reflective, uniform static ambient pressure,
- Walls: zero-slip velocity condition, in conjunction with near-wall treatment of the shear stress

## Results and Discussion

### Test Conditions

The flow conditions pertinent to the nozzle dimension and 10MPa fuel pressure test are provided in Table 1.

$Re = \rho_{liquid}UL / \mu$	$We = \rho_{liquid}U^2L/\sigma$	$Oh = \mu / \sqrt{\rho\sigma L}$	$Ma = U/a$
38000	80000	0.007	0.33

**Table 1.** Flow conditions for fuel pressure of 10MPa

### Experimental Results

Figure 4 presents the temporal development of the spray plume near-field for the fuel system pressures of 5 and 10MPa. The images provide evidence of the spray primary atomization within close vicinity of the nozzle, almost concurrent with the injector opening and emergence of the spray plume ( $t = 20\mu s$  after start of fuelling (ASOF)). Remarkably, the development of jet interface instabilities and primary atomization is evident within the 2mm vicinity of the nozzle. The effect of pintle opening on the injection pressure – thus the plume propagation - is detectable during  $40\mu s$  ASOF; thenceforth, plume penetration correlates with the fuel pressure. A notable feature of the temporal-spatial plume development is the stream-wise intermittent jet breakup structure, evident in the pattern of spatial liquid mass distribution, that is caused by the high-frequency fuel pressure oscillations within the injector valve-group.

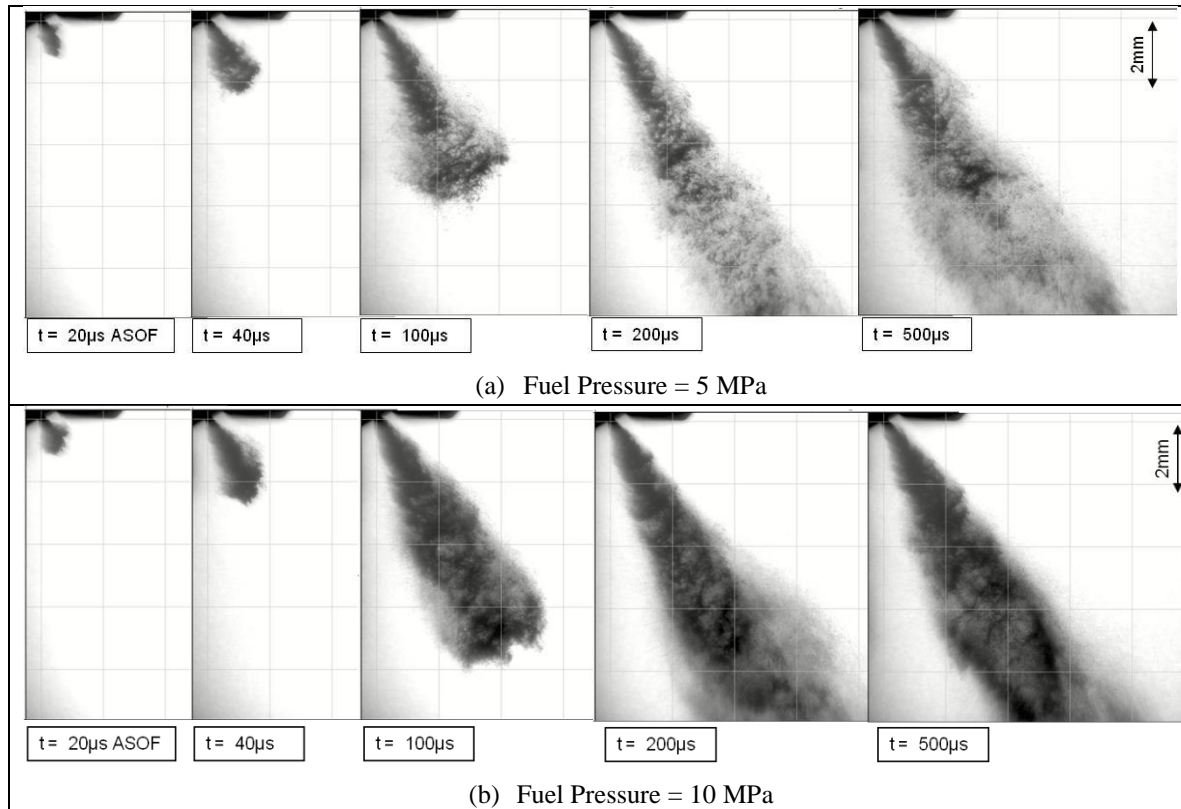


**Figure 4.** Shadowgraph images of the nozzle near-field plume primary breakup structure ( $t$  = time after start of fuelling (ASOF))

Figure 5 provides a comparison of the spray near-field structure for the fuel system pressures of 5, 10 and 20 MPa, with the aid of images of the spray plume liquid presence probability density function (pdf) from 5 injection events, at  $t = 500\mu s$  ASOF. The plume near-field cone angle is defined based on the plume lateral spread between  $z=1mm$  and  $z=8mm$  from the injector tip, along the injector axis. Remarkably, there is not a significant (and consistent) influence of the injection pressure on the spray plume macroscale, as evidenced by the plume trajectory and cone angle. Similar observation is reported in the literature on GDi spray atomization [2, 3]. This is notable, as it implies (1) absence of a nozzle flow regime change, (2) self-similarity (Reynolds number independence) of turbulent liquid jet issuing from the nozzle, and (3) that the known influence of fuel pressure on the spray atomization (i.e. deplete size distribution) is related to the secondary atomization process.



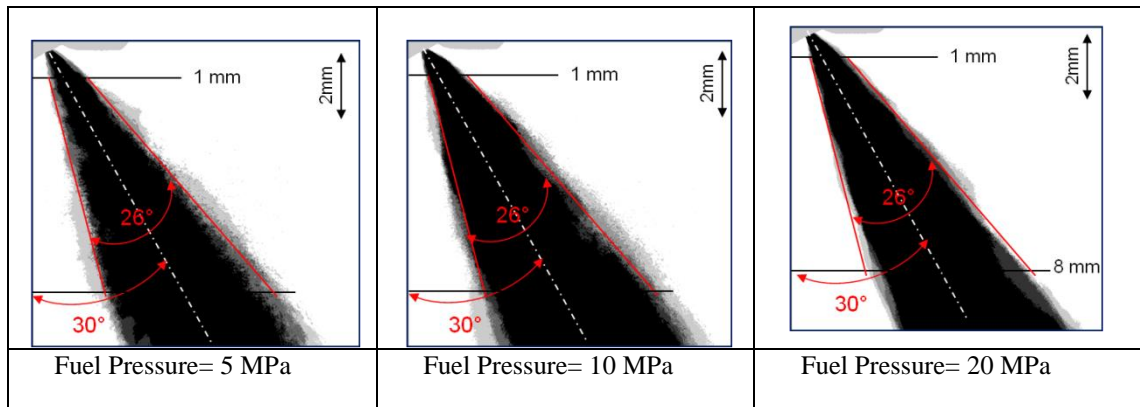


**Figure 5.** Effect of fuel pressure on the nozzle near-field plume primary breakup structure (Liquid presence pdf, fuel pressure =5, 10, 20MPa,  $t=500\mu s$  ASOF)

### ***VoF-LES Results***

Figure 6 illustrates the development of the nozzle flow and the near-field plume primary breakup for the fuel system pressure of 10 MPa, with the aid of contour plots of VoF on the nozzle symmetry plane. Accordingly, the initial stage of the transient nozzle flow is characterized by the scavenging of the entrapped air in the sac volume that transition to an attached nozzle flow, issuing a full-cone liquid jet. The nozzle flow attains a ‘stationary’ state at  $t = 40\mu s$  after start of simulation (ASOS). However, Figure 6 illustrates the unsteady jet primary breakup process, caused by the nozzle flow pressure and velocity turbulent disturbances (in addition to the inlet boundary pressure oscillations induced by the imposed impulsive flow boundary condition).

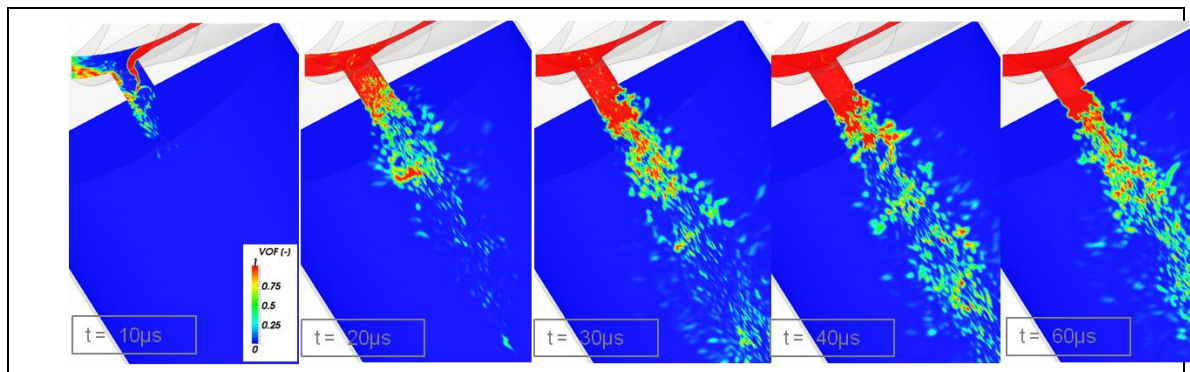


**Figure 6.** Development of nozzle flow and jet primary breakup depicted by VOF contour plots on the nozzle symmetry plane (fuel pressure =10 MPa)

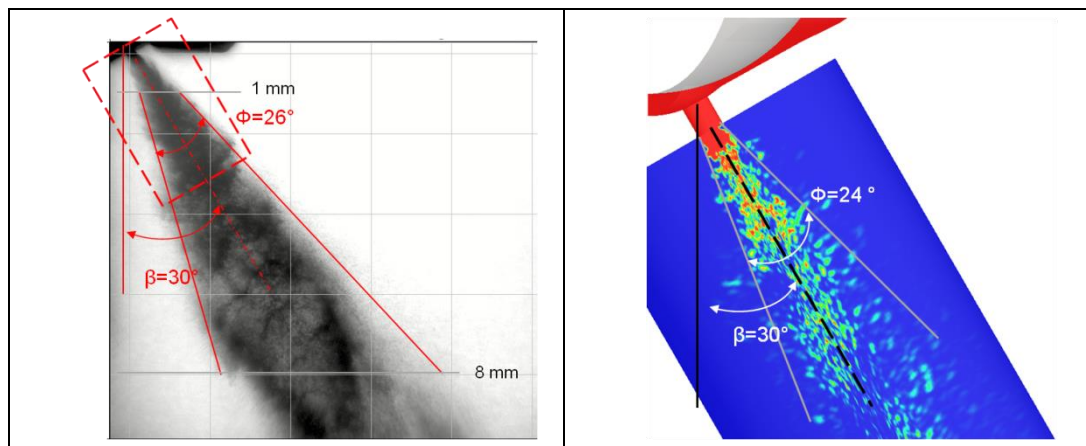


**Figure 7.** Comparison of plume single-event shadow image with VOF-LES simulation



### Comparison of VoF-LES with Imaging Data

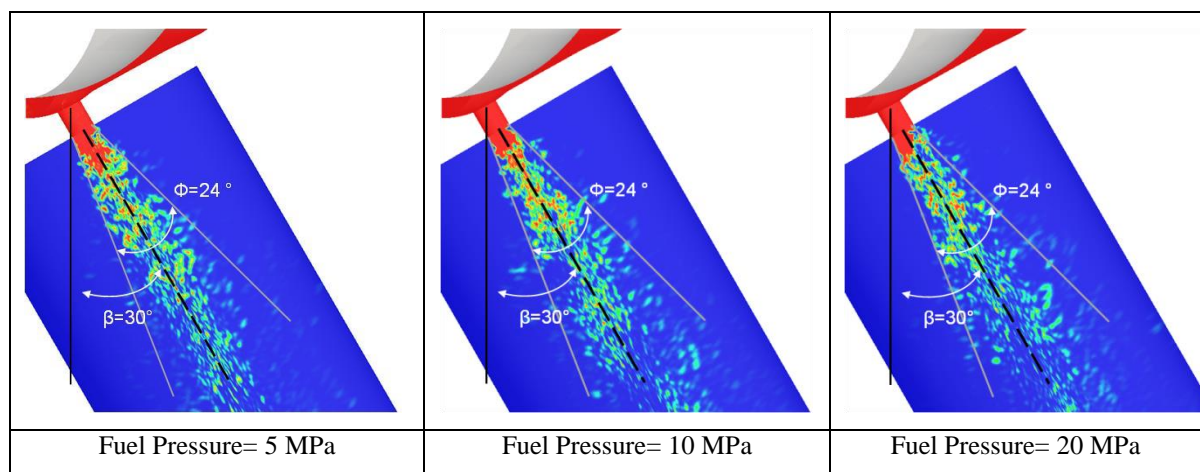
Figure 7 presents a comparison of the VoF-LES simulation of the ‘stationary’ jet primary breakup structure (at  $t=60\mu\text{s}$  ASOS) with the single-shot plume image (at  $t=500\mu\text{s}$  ASOF) for the fuel pressure of 10MPa. The computational domain for the VoF-LES simulation is indicated by the dashed-line rectangle. There is good agreement with respect to the (a) the jet primary breakup in the immediate vicinity of the nozzle exit, (b) the plume trajectory angle alignment with the nozzle axis, and (c) the near-field plume cone angle.

Figure 8 presents the VoF-LES predictions of the jet primary breakup for the fuel system pressures of 5, 10 and 20 MPa., which correspond to the spray imaging data in Figure 5. The simulations show insignificant effect of fuel pressure on the jet breakup structure and plume macroscale features, in agreement with the imaging data of Figure 5. The primary effect of the fuel pressure is increase of the jet velocity and reduction of transient time for development of a ‘stationary’ jet.

### Conclusions

The conclusions of this study can be summarized as:

- Nozzle near-field plume imaging data provides evidence of the jet breakup in the immediate downstream vicinity of the nozzle, at very early stage of injection.
- Evidence of insubstantial influence of fuel pressure on the plume primary breakup structure and near-field macroscale characteristics, for the fuel pressure range 5 – 20 MPa.
- Indication of intermittent jet breakup structure (that is expected to influence the jet atomization and air entrainment rate) caused by high-frequency hydraulic pressure oscillations.
- Excellent predictive capability of VoF-LES method for prediction of the jet primary breakup structure and the (insubstantial) effect of fuel pressure.



**Figure 8.** VoF-LES simulations of effect of fuel pressure on plume primary breakup ( $t = 60\mu\text{s}$  ASOS)

The absence of a substantial effect of fuel pressure on the jet primary breakup macro-structure (also observed in the literature [2,3]) is noteworthy and requires further investigation. Additional experimental investigations of the effect of GDI seat and nozzle geometry on the plume primary breakup and assessment of the predictive accuracy of VoF-LES method are in progress.

### References

- [1] Mitroglou, N., Multi-Hole Injectors for Direct Injection Gasoline Engines, PhD Thesis, City University London, UK, 2006.
- [2] Papoulias, D., Giannadakis, E., Mitroglou, N., Gavaises, M., Theodorakakos, A., Cavitation in Fuel Injection Systems for Spray-Guided Direct Injection Gasoline Engines, SAE 2007-01-1418, 2007.
- [3] Lai, M.C., Zheng, Y., Shost, M., Xie, A., Matsumoto, A., et. al., Characterization of Internal flow and Spray of Multihole DI Gasoline Spray using X-ray Imaging and CFD, SAE 2011-01-1881, 2011.
- [4] Befrui, B., Corbinelli, G., Spiekermann, P., Shost, M., Lai, M.C., et al., Large Eddy Simulation of GDI Single-Hole Flow and Near-Field Spray," *SAE Int. J. Fuels Lubr.* 5(2):2012, doi:10.4271/2012-01-0392.

- [5] De Villiers, E., Gosman, A. D., Weller, H. G., Large Eddy Simulation of Primary Diesel Atomization, SAE 2004-01-0100, 2004.
- [6] Klein, M., Direct Numerical Simulation of a Spatially Developing Water Sheet at Moderate Reynolds Number, *Int. J. Heat Fluid Flow*, 26, 722-731, 2005.
- [7] Befrui, B., Corbinelli, G., Reckers, W., Large Eddy Simulation and Optical Studies of the Primary Break-Up of a Thin Planar-Sheet Liquid Jet, *SAE Int. J. Fuels Lubr.* 3 (1) , 266-276, August 2010.
- [8] Hermann, M., On Simulating Primary Atomization using the Refined Level Set Grid Method, *J. Atom. Sprays*, 21 (4), 283-301, 2011
- [9] Befrui, B., Aye, A., Spiekermann, P., Varble, D. A., Shost, M.A., Lai, M.C., Wang, J., GDi Skew-Angled Nozzle Flow and Near-Field Spray Analysis Using Optical and X-ray Imaging and VOF-LES Computational Fluid Dynamics, SAE 2013-01-0255, 2013.
- [10] Brackbill, J. U., Kothe, D. B., Zemach, C., A Continuum Method for Modeling Surface Tension, *J. Comp. Phys.*, 100, 335-354, 1992.
- [11] OpenCFD Ltd., OpenFOAM – User Guide, <http://www.opencfd.com>
- [12] Weller, H., A New Approach to VOF-based Interface Capturing Methods for Incompressible and Compressible Flows, OpenCFD Ltd., Technical Report TR/HGW/04, 2008 (unpublished).
- [13] Issa, R.I., Solution of the Implicitly Discretized Fluid Flow Equations by Operator Splitting, *J. Comp. Phys.* 62, 40-65, 1986.

## Multi-Scale Analysis of Liquid Atomization Processes and Sprays

Christophe Dumouchel<sup>1</sup> and Jean-Bernard Blaisot<sup>1</sup>

1:CNRS UMR 6614 – CORIA, Université et INSA de Rouen, France

### Abstract

Atomization process designates the behaviour of liquid flow thrown out from an injector into a gaseous environment with the aim of producing a spray. Investigating and understanding such a process is important since it is the vital link between the injector and the spray. It is proposed here to achieve this by describing the temporal evolution of the shape of the liquid system. Since this shape is complex, a multi-scale description is performed: it provides the temporal evolution of the system scale distribution during the atomization process. This concept is applied here to investigate the behaviour of liquid jets issuing from triple-disk injectors. Such jets initially develop as liquid sheet and then reorganize as a ligament network that eventually breakup into liquid fragments and drops. First, the analysis of the temporal evolution of the scale-distribution characterizing the whole system is performed with the help of the scale entropy diffusion model. Second, the analysis of isolated ligaments of the network is conducted with the concept of Equivalent System introduced here. Besides new ways for atomization process characterization, the multi-scale analysis is found to provide physical information such as a clarification of surface tension effects on the jets produced by triple-disk injectors.

### Introduction

The most common technique to produce a liquid spray consists in throwing out a liquid flow in a gaseous environment. Being free of any parietal constraints, deformations appear on the liquid interface. Some of these deformations grow in space and time and eventually result in the ejection of liquid fragments and drops from the main flow. The initial flow deformation and the subsequent production of liquid fragments constitute the atomization process. Understanding the atomization process is of paramount importance since it is the vital link between the injector and the fully developed sprays [1]. During the atomization process, the amount of liquid gas interface continuously varies (it is actually expected to increase) by a continuous variation of the shape of the liquid flow. Thus, addressing the atomization process can be approached by investigating the temporal evolution of the liquid system shape. In most applications, the liquid system shape is so complex that it cannot be characterized by a single length scale and a multi-scale description is required. The concept of fractal developed in many fields of physics offers a multi-scale description [2]. Using this concept, the notion of scale distribution has been developed to describe systems of any shapes. Initially introduced for liquid sprays [3], the scale distribution can be applied to systems or parts of it of any shape. The technique to measure scale distribution from images has been derived from the Euclidean Distance Mapping technique used to determine fractal dimension [4].

This paper first reminds the definition of the scale distribution. Furthermore, the application of this concept to systems composed of simple objects will lead to the Equivalent System notion. Then, application of the multi-scale analysis is performed on liquid jets produced by triple-disk atomizers. These jets initially develop as liquid sheet and then reorganize as a ligament network that eventually breakup into liquid fragments and drops. First, the temporal evolution of the scale distribution characterizing the whole system is determined and analysed with the scale-entropy diffusion model. This model comes from the investigation of turbulent interfaces [5]. Second, the behaviour of some isolated liquid ligaments of the ligament network is described by the scale distribution and analysed with the help of the Equivalent System notion. The main parameter of this investigation is the liquid surface tension. We will see that the two parts of the application contribute to a better understanding of the role of surface tension forces in the present atomization process.

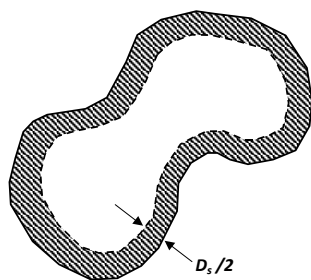


**Figure 1.** Description of an object at scale  $D_s$

### The scale distribution: definition and examples

A detail definition of the surface-based scale distribution is available in Dumouchel et al. (2008). Let us consider the 2D projection of a system of any shape as shown in Fig. 1. The cumulative surface-based scale distribution  $E_2(D_s)$  is the ratio of the area of the surface constituted of all points that are located at a distance less or equal to the scale  $D_s/2$  from the system boundary (grey surface in Fig. 1) on the total area of the system surface. For  $D_s = 0$ ,  $E_2(D_s) = 0$  and at scales allowing recovering the whole system  $E_2(D_s) = 1$ . Between these scales,  $E_2(D_s)$  monotonously increases from 0 to 1: it is a cumulative distribution. This concept can be easily applied to define the cumulative volume-based scale distribution:  $E_3(D_s)$  is the ratio of the volume made by the points that are located at a distance less

or equal to the scale  $D_s/2$  from the system boundary on the total volume of the system. Note that no assumption is made on the system: It may be of any shape, composed of several fragments or be a portion of a bigger system. For systems composed of simple objects such as spheres or cylinders, the mathematical expression of the scale distributions can be established. Cylinders are defined of having a unit height and a surface area limited to the lateral one: the upper and lower circular sections are not considered as boundary with the external medium. With these precisions, spheres and cylinders are fully characterized by their diameter  $D$ . It can be shown that the scale distributions of ensembles of spheres and cylinders with a diameter distributed according to a series of cumulative diameter distributions  $F_n(D)$  are equal to:

$$\begin{cases} E_n^S(D_s) = F_n(D_s) + \sum_{i=1}^n (-1)^{i-1} C_n^i \left( \frac{D_s}{D_{n,n-i}} \right)^i (1 - F_{n-i}(D_s)) \\ E_n^C(D_s) = F_n(D_s) + \sum_{i=1}^{n-1} (-1)^{i-1} C_{n-1}^i \left( \frac{D_s}{D_{n-1,n-1-i}} \right)^i (1 - F_{n-1-i}(D_s)) \end{cases} \quad n = 2, 3 \quad (1)$$

where the subscripts  $S$  and  $C$  refer to the sphere and cylinder system, respectively,  $D_{ab}$  is the classical mean diameter series and  $C_a^b = a!/(b!(a-b)!)$ . If the objects of the system all have the same diameter  $D'$  (mono-dispersed case),  $F_n(D) = 0$  if  $D < D'$  and is equal to 1 otherwise and Eq. (1) gives:

$$E_n^S(D_s) = 1 - \left( 1 - \frac{D_s}{D'} \right)^n \quad E_n^C(D_s) = 1 - \left( 1 - \frac{D_s}{D'} \right)^{n-1} \quad n = 2, 3 \quad (2)$$

If the diameter of the objects are equally distributed between 0 and  $D_{max}$  (equiprobable case), the cumulative diameter distributions of the systems can easily be established and Eq.(1) gives:

$$E_n^S(D_s) = 1 - \left( 1 - \frac{D_s}{D_{max}} \right)^{n+1} \quad E_n^C(D_s) = 1 - \left( 1 - \frac{D_s}{D_{max}} \right)^n \quad n = 2, 3 \quad (3)$$

Comparing Eq. (2) and (3) indicates that the scale distribution of an equiprobable ensemble of cylinders is the same as the scale distribution of a mono-dispersed ensemble of spheres. This observation introduces the notion of equivalent system: Equivalent systems are defined as system having the same scale distribution. On the basis of the observation made here, it can be demonstrated that any system of spheres admits an equivalent system of cylinders. The opposite is not true. For instance, there is no system of spheres that would have the same scale distribution as a mono-dispersed system of cylinders.

## Atomisation of liquid sheet produced by triple-disk injectors: the Scale Entropy Diffusion Model

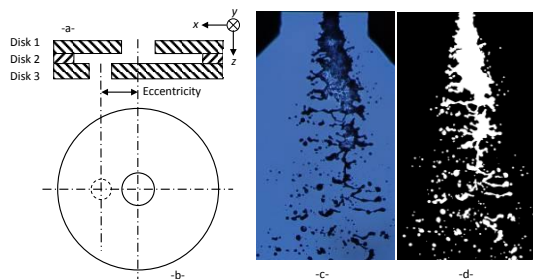


**Figure 2.** Atomizer side view (a) and top view (b), Visualization of the liquid sheet at the

This section shows an example of the use of the scale distribution to describe a liquid atomization process. (Parts of the results presented here are detailed in [6] and [7].) The atomization process is the one observed on the flow issuing from a triple-disk injector (Fig. 2-a and b). The liquid flow produced by this injector is a sheet of liquid which expands in the  $(0, x, z)$  plane (Fig. 2-c). Perturbations of small characteristic lengths (small ligaments) and of large characteristic lengths (waves) deform the liquid sheet as soon as it leaves the nozzle. These perturbations are imposed by the issuing liquid flow characteristics. The growth of some of the perturbations leads to the reorganisation of the system of a ligament network that eventually breaks into liquid fragments, which, to their turn,

break into smaller fragments. The injection conditions are characterized by a small discharge orifice diameter (180  $\mu\text{m}$ ) and small injection pressure (less than 0.5 MPa). Thus, the gaseous Weber numbers are small enough to exclude any aerodynamic effects on the liquid system deformation and breakup, this latter mechanism being mainly controlled by surface tension forces. During this process, the shape of the liquid system continuously evolves, which is characterized by the surface-based scale distribution. Using image treatment tools, images are

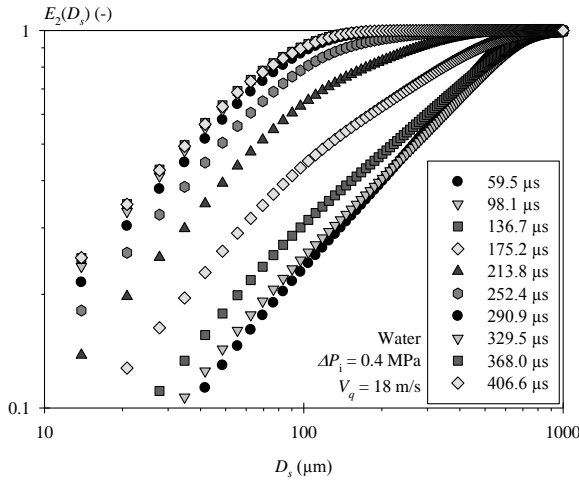


**Figure 3.** Temporal evolution of  $E_2(D_s)$  during an

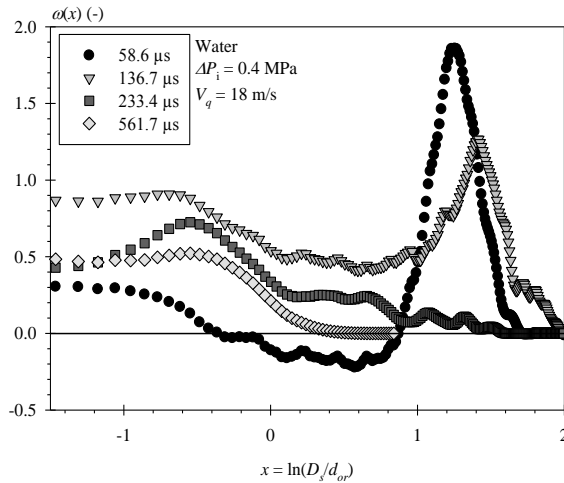


**Figure 4.** Temporal evolution of  $\omega(x, t)$

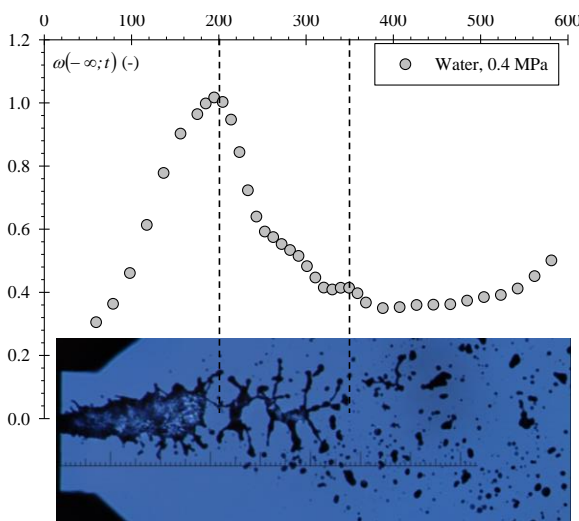


**Figure 5.** Temporal evolution of the quantity  $\omega(-\infty, t)$  during the atomization process

transformed as two-grey level images in which the liquid appears in white on a black background (Fig. 2-d).  $E_2(D_s)$  is measured in portions of the liquid system that is delimited by a 0.7 mm height rectangular analysing window, and the temporal evolution of  $E_2(D_s)$  is obtained by sliding this window from the nozzle exit (top of the image) down to the spray region (bottom of the image). The statistical propriety of the scale distribution is ensured by averaging the measurements performed on a series of 150 images. For every operating conditions, the time  $t$  is obtained by dividing the distance between the nozzle exit and the analysing window position by the measured average velocity  $V_q$  of the issuing flow. Figure 3 shows an example of the temporal evolution of the distribution  $E_2(D_s)$  during the atomization process (water, injection pressure  $\Delta P_i = 0.4$  MPa). The interesting aspect of this result is the continuous evolution of the distribution during the atomization process even in the breakup phase. Modelling the temporal evolution of  $E_2(D_s)$  constitutes a possible approach to model the atomization process. The scale entropy diffusion model developed to characterize turbulent interfaces [5] has been envisaged to perform this modelling [6].

The scale-entropy diffusion model is based on the following diffusion equation:

$$\frac{\partial^2 \Sigma(x, t)}{\partial x^2} - \omega(x, t) = \frac{1}{\chi} \frac{\partial \Sigma(x, t)}{\partial t} \quad (4)$$

where the scale entropy  $\Sigma(x, t) = -\ln(E_2(D_s))$ , the variable  $x = \ln(D_s/D_c)$  (where  $D_c$  is a characteristic scale of the problem taken here as the diameter of the discharge orifice, i.e.,  $d_{or} = 180 \mu\text{m}$ ),  $\chi$  is the scale diffusivity and  $\omega(x, t)$  characterizes the scale entropy flux density sink in the scale space. The scale entropy is a global quantity that offers a description of the shape of the system and decreases towards zero for the outer cutoff scale. Queiros-Conde [5] emphasizes the analogy between Eq. (4) and the one-dimensional heat conduction equation: the scale logarithm  $x$  would correspond to the position, the scale entropy to the temperature, the scale diffusivity to the thermal diffusivity and the function  $\omega$  to a quantity proportional to a volumetric heat sink that would be space dependent. The entropy flux  $\phi(x, t)$  defined as the first derivative in the  $x$ -space of the scale entropy  $\Sigma(x, t)$  is therefore equivalent to the heat flux.

Since Fig. 3 is presented in a logxlog coordinate system, it is an illustration of  $-\Sigma(x, t)$ . The analysis of such results obtained with the same injector and several liquids led to an analytical expression for the scale diffusivity  $\chi$  [7]:

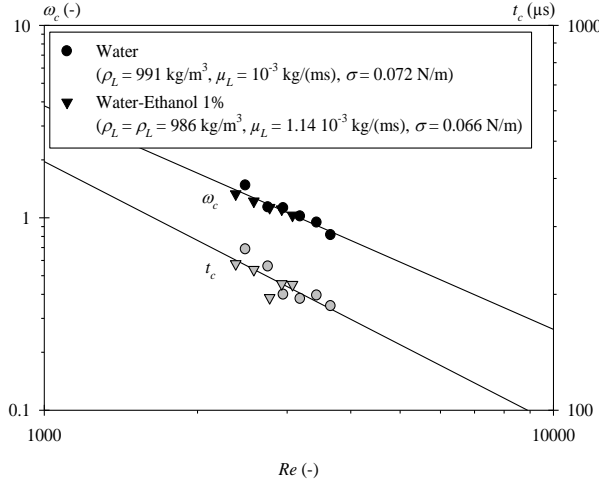


**Figure 6.** Coordinates ( $t_c$ ,  $\omega_c$ ) as a function of the Reynolds number  $Re$  of the issuing flow

$\Sigma(x,0) = -x$ . Furthermore, at initial time, the characteristics of the issuing flow that will impact the jet behaviour are described by the function  $\omega(x,0)$ . Furthermore, to be fully resolvable, the problem requires the knowledge of the function  $\omega(x,t)$  for each scale  $x$  and at each time  $t$ . Thoughts on this very function are presented here.

Figure 4 presents functions  $\omega(x,t)$  in the scale space at four specific times including the smallest and largest possible times. For the two smaller times,  $\omega(x,t)$  can be divided in two parts, i.e., in the small scale-region and in the large-scale region. These functions describe the liquid sheet for which the textural and structural tortuosities, representative of the interface and of the whole system respectively, imply disconnected characteristic scale intervals. For the two greater times,  $\omega(x,t)$  describes the ligament network and spray for which the whole system is characterized by a single representative scale interval. It can be noted in Fig. 4 that in the small scale range, the function  $\omega(x,t)$  is independent of the scale  $x$ . For these scales, the first condition expressed by Eq. (6) is satisfied and the variation of the scale entropy is due to a variation of the scale entropy flux density sink only. It can be shown that these scales are those for which the deformation of the system is felt as pure stretching. In other words, these scales are so small that the system boundary is always seen as a straight line. We see in Fig. 4 that the scale interval concerned by this behaviour varies with time. The value of the function  $\omega(x,t)$  for this scale interval is noted  $\omega(-\infty,t)$  and varies as a function of time as shown in Fig. 5. Three regions delimited by lines appear on this graph. Thanks to the locking of an image, the three regions appear related to specific phase of the atomization process. (The liquid system shown in the image selected here has the average breakup length otherwise measured.) The increase of  $\omega(-\infty,t)$  in the first region corresponds to the development of the liquid

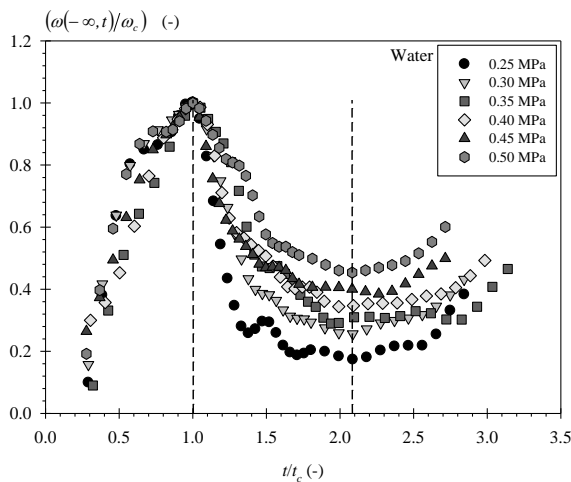


**Figure 7.** Non-dimensional representation of the  $\omega(-\infty, t)$

$$\chi = 0.4356 \ln^2 \left( \frac{We_L}{67} \right) We_L^{0.555} \sqrt{\frac{\sigma}{\rho_L \lambda_0^3}} \quad (5)$$

where  $We_L$  designates the liquid Weber number and  $\lambda_0$  is a length dependent on the surface tension.

The boundary conditions of the model expressed by Eq. (4) are flux conditions in the small and large scale region:

$$\begin{cases} \phi(x,t) = -1 & x \rightarrow -\infty \\ \phi(x,t) = 0 & x \rightarrow +\infty \end{cases} \quad (6)$$

For the large scale range, we can add that both functions  $\Sigma(x,t)$  and  $\omega(x,t)$  are equal to 0. At initial time,  $\Sigma(x,0)$  describes the shape of the flow at the nozzle exit section. In the absence of any liquid gas interface, this condition writes

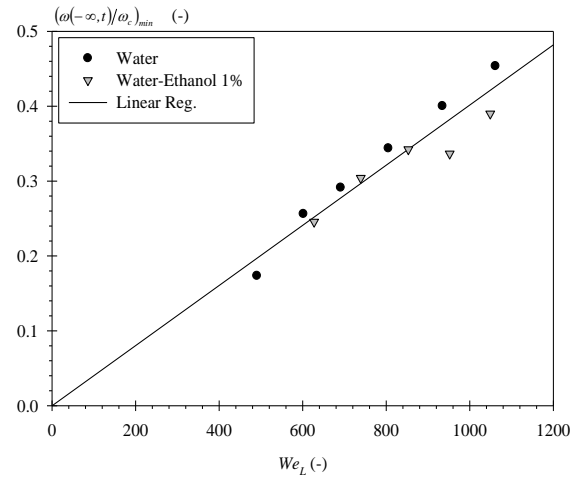


**Figure 8.** Correlation between  $(\omega(-\infty, t)/\omega_c)_{min}$  sheet down to the reorganization as a ligament



network; the decrease in the second region corresponds to the evolution of the ligament network down to the breakup in liquid fragments; and the slight increase in the third region corresponds to the deformation of the bigger liquid fragments that eventually will produce smaller fragments.

The maximum between regions 1 and 2 in Fig. 5 is a characteristic point whose coordinates  $(t_c, \omega_c)$  are shown in Fig. 6 for two liquids as a function of the issuing flow Reynolds number. Both  $t_c$  and  $\omega_c$  correlate with the Reynolds number in a way that is independent of the liquid. Thus, the characteristic point  $(t_c; \omega_c)$  depends on the flow issuing from the injector only. For water, Fig. 7 shows the non-dimensional temporal evolution of  $\omega(-\infty, t)$  using the coordinates  $(t_c, \omega_c)$ . (A similar results is found for water-ethanol 1%.) With this representation, we see in the first region ( $t/t_c < 1$ ) a behaviour almost independent of the injection pressure. Considering the results shown in Figs. 5 and 6, this says that the first-region behaviour, i.e., formation and evolution of the liquid sheet, is imposed by the issuing liquid flow characteristics only including the velocity distribution and turbulent intensity and that the surface tension effects have a limited influence in this region. Note that the characteristic time  $t_c$  that delimits the first and second regions ( $t/t_c = 1$ ) is also appropriate to delimit the second and the third regions ( $t/t_c = 2.2$ ). In the second ( $1 < t/t_c < 2.2$ ) and third ( $2.2 < t/t_c$ ) regions, the evolution of the ratio  $\omega(-\infty, t)/\omega_c$  shows a clear dependence with the injection pressure. The reason for this is that the formation and evolution of the ligament network and of the liquid fragments include the surface tension forces whose action depends on the liquid Weber number, i.e., on the injection pressure. To illustrate this, Fig. 8 presents the minimum value of the ratio  $\omega(-\infty, t)/\omega_c$  as a function of the liquid Weber number. This figure reports a strong correlation that appears independent of the liquid. Thus, the time  $t_c$  appears as the characteristic time of the appearance of the surface tension force effects. These results show that the scale entropy diffusion model applied to analyse the temporal evolution of the scale-distribution during an atomization process provides interesting physical information and characteristics of the process.

### Atomization of isolated liquid ligaments: the Equivalent System

In this section, we analyse the temporal evolution of atomizing liquid ligaments such as those present in the ligament network encountered in the second phase of the atomization process described in the previous section. The triple-disk atomizer used here is twice larger than the one used in the previous section ( $d_{or} = 400 \mu\text{m}$ ). A high-speed camera Phantom V12 set at 25,000 frames/s was used and the visualisation field was positioned in the ligament network region. A Cavilux HF laser source (500W Infra-Red Diode Laser) was used. This is a mono-chromatic and incoherent light source which is appropriate to perform high quality transmission images. The physical visualization field was 3.5 mm x 6.4 mm and the corresponding spatial resolution was equal to 10.36  $\mu\text{m}/\text{pixel}$ . Three liquids are used: water, a water-ethanol 10% mixture ( $\rho_L = 980 \text{ kg}/\text{m}^3$ ;  $\mu_L = 1.32 \cdot 10^{-3} \text{ kg}/(\text{ms})$ ;  $\sigma = 0.0442 \text{ N}/\text{m}$ ) and a water-ethanol 15% mixture ( $\rho_L = 967 \text{ kg}/\text{m}^3$ ;  $\mu_L = 1.57 \cdot 10^{-3} \text{ kg}/(\text{ms})$ ;  $\sigma = 0.0376 \text{ N}/\text{m}$ ). In order to ensure a good temporal resolution, the injection pressure was limited to 0.1 MPa. For every liquid, this corresponds to an average velocity of the order of 7 m/s.

The first duty consisted in identifying ligaments on the high speed films. Examples of such ligaments are presented in Fig. 9 to 11 for every liquid. At initial times the ligament is often attached to the main stream and it is necessary to perform an arbitrary cut on one end of the ligament. Being produced from an atomizing liquid sheet, the initial shapes of the ligaments is complex and different from one situation to another. Despite they are perturbed, some of the ligaments, such as those shown in Fig. 9 and 11, have an initial shape close to a traditional ligament. For others, such as the one shown in Fig. 10, the initial shape is more complex and looks

like the coalescence of several ligaments. These differences are important since they participate to the production of dispersed sprays in terms of drop size. We must add here that the variety of the initial shape is not particularly correlated with the liquid physical properties. Furthermore, the shape variety causes no problem as far as the use of the scale-distribution analysis is concerned. For every ligament, the surface-based scale distribution was

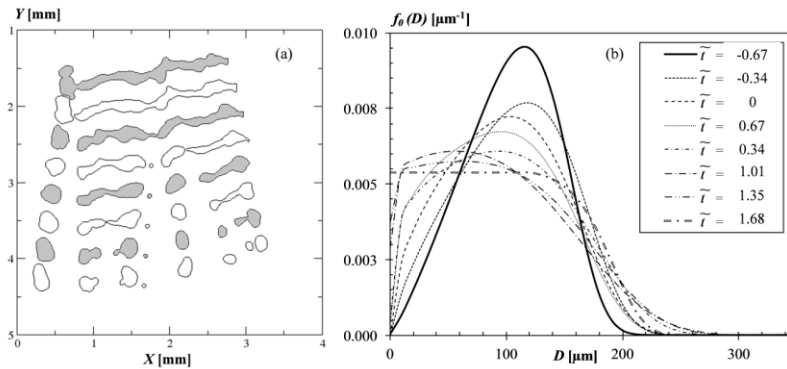


**Figure 9.** Left: Temporal evolution of a ligament of water; Right: Number-based diameter distribution of the corresponding Equivalent System of cylinders



measured as a function of time. The interesting aspect to be mentioned here is that the limited number of drops produced by each ligament (see Figs. 9 to 11) does not affect the quality of the scale distribution that, in every case, remains smooth. As for the situation presented in the previous section, the scale distribution shows here a continuous temporal evolution from the ligament formation down to the spray. As shown in the previous section, this temporal evolution is due to the action of the surface tension forces. In the present work, we suggest using the concept of equivalent system introduced in Section 2 to analyse this behaviour.

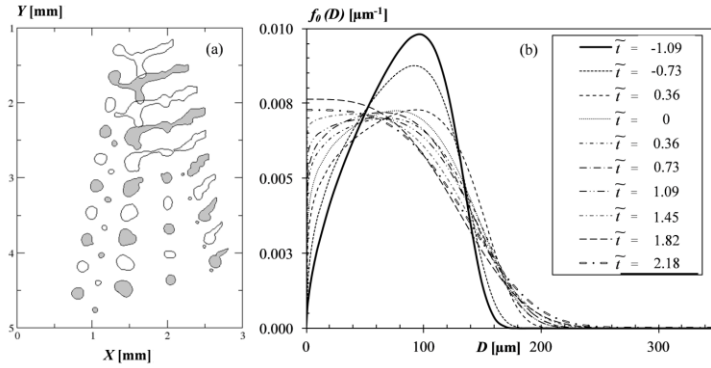


**Figure 10.** Left: Temporal evolution of a ligament of water-Ethanol 10%; Right: Number-based disiameter distribution of

given by:

$$F_0(D) = 1 - \frac{\Gamma\left(\frac{\alpha}{q}, X\right)}{\Gamma\left(\frac{\alpha}{q}\right)} \quad F_2(D) = 1 - \frac{\Gamma\left(\frac{\alpha+1}{q}, X\right)}{\Gamma\left(\frac{\alpha+1}{q}\right)} \quad (7)$$

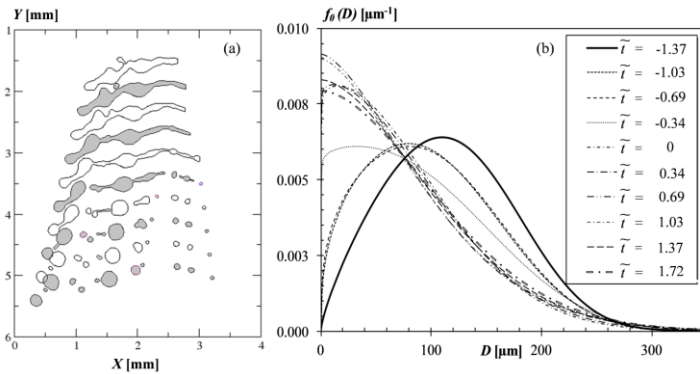


**Figure 11.** Left: Temporal evolution of a ligament of water-Ethanol 15%; Right: Number-based disiameter distribution of the corresponding Equivalent System of cylinders

system are shown in Figs. 9 to 11. (The time indicated in these figures is a non-dimensional time whose exact definition is not necessary within the context of this work.) The equivalent system and its evolution appear dependent on the liquid, i.e., on the surface tension. The result obtained for water (Fig. 9) shows a high distribution at initial time and a collapse of this distribution as time passes to end-up as a step distribution close the equiprobable case. As discussed in Section 2, an equiprobable set of cylinders is equivalent to a mono-dispersed system of spheres. In other words, the droplets produced by the ligaments of water have almost the same size. (This is confirmed by the image shown in Fig. 9.) On the other hand, we see that the ligament of water-ethanol 15% (Fig. 11) accepts a wide distribution at initial time and that the evolution of this distribution is very different than the one observed in Fig. 9. As time passes, the distribution is left shifted and finishes with

We consider equivalent systems of cylinders. The surface-based scale distribution of such system is given by Eq. (1) and is fully known provided that the cylinder diameter distribution is specified. In the present analysis, we use systems of cylinders whose diameters are distributed according to a 3-parameter Generalized-Gamma (3pGG) function. Often encountered to characterize size distribution of dispersed systems, this distribution is identical to the Nukiyama-Tanasawa distribution. The number-based and surface-based cumulative 3pGG diameter distributions of cylinders required by Eq. (1) are

where  $\Gamma$  designates the gamma function (either complete or incomplete),  $X = (\alpha/q)(D/D_{q0})^q$ , and  $q$ ,  $\alpha$  and  $D_{q0}$  are the three parameters of the distribution. The triplet of parameters allowing the best fit between the measured surface-scale distributions and  $E_2^C(D_s)$  given by Eqs. (1) and (7) are determined with the software Scilab. For every situation an excellent fit is obtained. This says that, at all times, the liquid systems can be represented by an equivalent system of cylinders, i.e., a system of cylinders having the same surface-based scale distribution as the actual system. The temporal evolutions of the number-based diameter distribution of the equivalent

a maximum at  $D = 0$ . This is representative of the production of droplets of varying sizes as shown in Fig. 11. In Fig. 10, we see that the liquid water-ethanol 10% adopts an intermediate behaviour. Note that, despite the initial distribution for this liquid has the same height as the one of water, it shows a fundamental difference in the small diameter region.

The analysis based on the equivalent system allows understanding that varying the surface tension influences the characteristic length scale as well as the scale interval dynamic of the atomization process. In other word, a decrease of the surface tension decreases the characteristic scales and promotes a cascade disintegration process which enhances the poly-dispersion of the final dispersed system. Decreasing the surface tension has therefore a double favourable effect.

## Conclusions

A multi-scale analysis is presented here as an interesting alternative to investigate liquid atomization processes. It allows following the shape of the liquid system during the atomization process by determining and analysing the scale-distribution of the system. One of the interesting aspects of the scale-distribution already mentioned in previous works ([6], [7]) is that it reports a continuous temporal evolution during the whole atomization process. This continuity has to be related to the continuous variation of the amount of interface which is a characteristic of each atomization process. The application of the multi-scale analysis presented in this contribution points out a new way of modelling atomization process from the temporal evolution of the scale distribution. As far as this point in concerned, the potential of the scale-entropy diffusion model already mentioned in previous approached ([6], [7]) is confirmed here from the analysis of characteristics of the function  $\alpha(x,t)$ . In the future, a part of our efforts must concentrate on the modelling of this function. Furthermore, the new concept of Equivalent System introduced here and applied to analyse individual liquid ligament is interesting since it provides a mathematical expression for the scale distribution. Beside these general comments, it is important to point out here that the multi-scale analysis performed here on the liquid jets produced by triple-disk injectors allows clarifying the role of the surface tension forces. It is found that surface tension forces play no role on the formation and development of the liquid sheet at the nozzle exit and that their first influence is to destroy the sheet as a ligament network. Furthermore, the surface tension has an important influence on the dynamic of the scale interval characterizing the atomization of ligaments: reducing the surface tension increases this dynamic and promotes the poly-dispersion in size of the drop produced and therefore enhances the production of small droplets.

## Nomenclature

$D$	diameter ( $\mu\text{m}$ )
$d_{or}$	discharge orifice diameter ( $\mu\text{m}$ )
$D_s$	scale ( $\mu\text{m}$ )
$E_n(D_s)$	cumulative scale distribution (-)
$F_n(D)$	cumulative diameter distribution (-)
$Re$	Reynolds number (-)
$We_L$	liquid Weber number (-)
$\mu_L$	liquid dynamic viscosity ( $\text{kg}/(\text{ms})$ )
$\rho_L$	liquid density ( $\text{kg}/\text{m}^3$ )
$\sigma$	surface tension ( $\text{N}/\text{m}$ )

## References

- [1] Chigier, N., The future of atomization and sprays. Proc. ILASS-Europe 2005, Orléans, France, 5-7 September 2005
- [2] Mandelbrot, B., The Fractal Geometry of Nature. WH Freeman & Co, New-York, 1982
- [3] Dumouchel, C., Cousin, J., Grout, S., Analysis of two-dimensional liquid spray images: the surface-based scale distribution. J. Flow Visu. & Image Proc., 2008. 15: p. 59-83.
- [4] Bérubé, J., Jébrak, M., 1999. High precision boundary fractal analysis for shape characterization. Comput. Geosci., 1999. 25: p. 1059-1071.
- [5] Queiros-Conde, D., A diffusion equation to describe scale and time-dependent dimensions of turbulent interfaces. R. Soc. Lon. A., 2003. 459: p. 3043-3059.
- [6] Dumouchel, C., Grout, S., Application of the scale entropy diffusion to describe a liquid atomization process. Int. Journ. Multiphase Flow, 2009. 35: p. 952-962.
- [7] Dumouchel, C., Grout, S., On the scale diffusivity of a 2-D liquid atomization process analysis. Physica A, 2011. 390: p. 1811-1825.

## Modelling of Unsteady Effects on Jet Breakup

E.O. Diemuodeke and I. Sher

School of Engineering, Cranfield University, Cranfield, Bedfordshire, UK

### Abstract

The theory of jet instabilities has been developed under several assumptions, which include the assumption that the jets are steady. The common-rail diesel fuel injection systems utilizing pulsed injection have drastically improved the ability to lower emissions, noise, and fuel consumption. However, with the application of the injection techniques in modern engines, the unsteady effects introduced by the pulsed injection are yet to be fully investigated. These unsteady effects may be attributed to some of the deviations observed in the literature between theoretical predictions and experimental data. The present paper has been able to demonstrate through analytical means that unsteady effects of liquid jet have significant impacts on the instability and breakup of liquid fuel. The model was developed from the Navier-Stokes equation with linear perturbations, which considers transient base flow parameters. Results obtained have good agreement with experimentally obtained data for penetration length and spray angle.

---

### Introduction

Fuel injector performance has a direct effect on the combustion efficiency, pollutant emissions and combustion instability of combustion systems[1]. Government legislations regarding emissions are becoming stringent. Therefore, there is a need for more effective design of fuel combustion systems. The effective design of combustion systems is a function of good understanding of fuel breakup processes. The aim is to introduce the liquid fuel in a high surface area to volume ratio for a stable combustion process. The process surrounding the injection of liquid through a small aperture and the subsequent breakup of the bulk liquid has proven to be very complex [2][3].

The atomization processes are mainly attributed to cavitation, turbulent and aerodynamic forces, but it is generally acknowledged that the aerodynamic forces are the major controlling factor of the atomization process[4][5]. The Kelvin-Helmholtz (KH) instability model for liquid breakup was suggested by Reitz and Bracco [6] on the basis of surface waves formation as a result of hydrodynamic and aerodynamic forces interactions. The model is constructed on the basis of a first order linear analysis of a KH instability growing on the surface of a cylindrical liquid jet that is penetrating into a quiescent incompressible gas with a relative velocity. Both the liquid and the gas are assumed to be incompressible, and the gas is assumed to be inviscid. The dynamic of the liquid jet and gas interaction are described by the linearization of Navier-Stokes equations for two-phase flow based on steady base flow parameters. The liquid phase is assumed as the disperse phase and the gas phase as the continuous phase. The detailed analysis, which can be found in [6], yields a dispersion equation relating the growth rate of a perturbation to its wavelength. The dispersion equation obtained is not amenable to analytical solution; however, numerical curve fit was sorted, which shows that there exists a single maximum in the wave growth rate curve and assumed that the maximum growth rate controls the liquid breakup.

The theory of jet instabilities has been developed under several assumptions, including an assumption that the jets are steady. However, in most practical engineering applications these jets are highly unsteady, and the transient effects are attributed to some of the inconsistencies between experimental data and theoretical data [4] [5][7][8][9]. The acceleration of the liquid during start-up of the convectional injectors is in the order of  $10^6$  [m/s<sup>2</sup>] at the orifice exit for high Reynolds numbers. This transient effect on the liquid breakup mechanisms would be more severe in the modern fuel injection techniques, e.g pulsed injection (illustrated in Figure. 1), which are intended to mitigate exhaust emission and to improve fuel economy. Sazhin et al [4] have stressed the importance of transient effects on jet instability and breakups by incorporating the jet acceleration into the classical KH instability model. The solution method was further advanced in Turner et al. [5]. In this paper we

present results of a reconstructed K-H model [10, 11], predicting the characteristic breakup and penetration lengths of an unsteady jet.

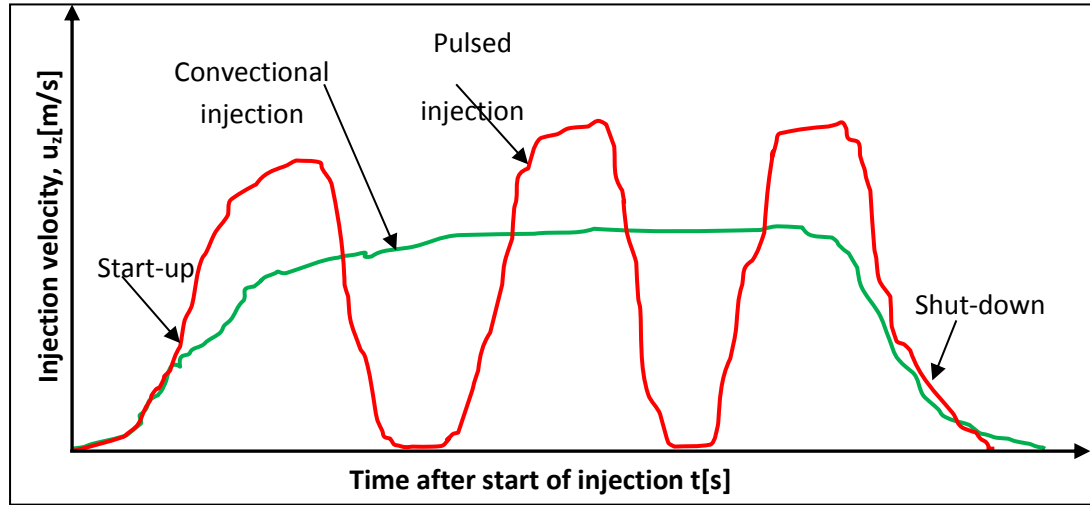


**Figure 1.** Velocity Evolution after Start of Injection

### Mathematical modelling

It is assumed that the interaction between aerodynamic forces and the jet hydrodynamic forces induce surface waves, as shear flow, because of relative velocity between the liquid and gas. Considering the assumptions made by Reitz and Bracco [6] and Egger and Villermaux [12], one proceeds with the reconstruction of the classical KH instability model for liquid breakups by modifying the linearization process of the Navier-Stokes equation. The free-surface shear of a liquid jet indicating the linearization parameters is shown in Figure 2.

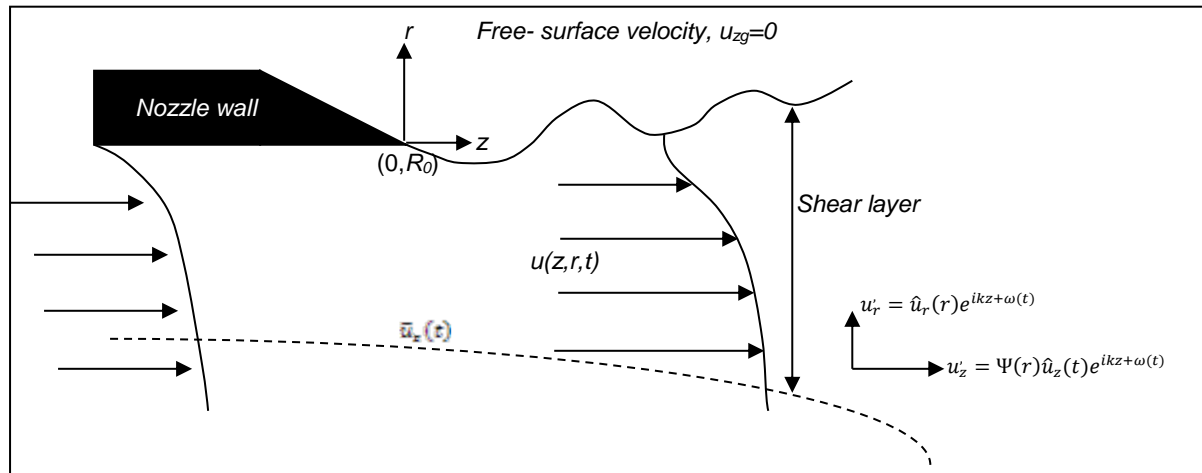


**Figure 2.** Cylindrical material coordinate system model for a liquid jet

The Navier-Stokes equations for the 2D cylindrical material coordinate system shown in Figure 2 can be written, as follows:

The continuity equation:

$$\frac{u_r}{r} + \frac{\partial u_r}{\partial r} + \frac{\partial u_z}{\partial z} = 0 \quad (1)$$

The momentum equation:

*r-direction momentum*

$$\frac{\partial u_r}{\partial t} + u_r \left( \frac{\partial u_r}{\partial r} \right) + u_z \left( \frac{\partial u_r}{\partial z} \right) = -\frac{1}{\rho} \left( \frac{\partial p}{\partial r} \right) \quad (2)$$

*z-direction momentum*

$$\frac{\partial u_z}{\partial t} + u_r \left( \frac{\partial u_z}{\partial r} \right) + u_z \left( \frac{\partial u_z}{\partial z} \right) = -\frac{1}{\rho} \left( \frac{\partial p}{\partial z} \right) \quad (3)$$

The transient effects of the fuel injection are incorporated in the linearization process by decomposing velocity and pressure as follows:

$$u_r = \bar{u}_r + u'_r; \quad u_z = \bar{u}_z(t) + u'_z \quad \text{and} \quad p = \bar{p}(t) + p' \quad (4)$$

It is postulated that the growth of perturbed parameters varies with time [10, 11], thus, the perturbed parameters have the following forms:

$$\delta = \delta_0 e^{ikz + \omega(t)}; u'_r = \hat{u}_r(r) e^{ikz + \omega(t)}; u'_z = \Psi(r) \hat{u}_z(t) e^{ikz + \omega(t)}; p' = \Psi(r) \hat{p}(t) e^{ikz + \omega(t)} \quad (5a,b,c,d)$$

The governing equations are subject to the following boundary conditions:

(1) The kinematic boundary condition

$$u'_{r=R_0} = \frac{\partial \delta}{\partial t} + \bar{u}_z(t) \frac{\partial \delta}{\partial z} \quad (6)$$

(2) The dynamic boundary condition at the interface of liquid and gas

$$p'_l - p'_g = \sigma K, \quad r = R_0 + \delta \quad (7)$$

With  $K = \text{div}(\nabla G/|\nabla G|)$  where  $G(r, z) = 0$  denotes the surface for which  $K$  has to be determined, it follows thus

$$K = \frac{1}{R_0} - \frac{\delta}{R_0^2} - \frac{\partial^2 \delta}{\partial z^2} \equiv \frac{1 - \delta/R_0}{R_0} - \frac{\partial^2 \delta}{\partial z^2} \quad (8)$$

(3) The axisymmetric assumption

$$\left. \frac{\partial u'_r}{\partial r} \right|_{r=0} = 0 \quad (9)$$

Solving this system with its boundary conditions for the dispersion relation, for a case of a quiescent gas phase  $\bar{u}_{zg}(t) = 0$  gives ([11]):

$$(\rho_l + \rho_g) \left[ \frac{d^2 \omega(t)}{dt^2} + \left( \frac{d\omega(t)}{dt} \right)^2 \right] + \rho_l \left[ 2ik\bar{u}_z(t) \frac{d\omega(t)}{dt} + ik \frac{d\bar{u}_z(t)}{dt} - k^2 \bar{u}_z^2(t) \right] + \sigma k \left( k^2 - \frac{1}{R_0^2} \right) = 0 \quad (10)$$

It is assumed that the disturbance growth rate is approximately constant,  $\frac{d\omega(t)}{dt} \approx \text{const}$ , and that the base velocity rate change is the jet acceleration, hence,  $\frac{d^2 \omega(t)}{dt^2} = 0$  and  $\frac{d\bar{u}_z(t)}{dt} = a$ . With these assumptions and considering the real part,  $\text{Re} \left( \frac{d\omega(t)}{dt} \right) \equiv \omega' [1/s]$ , in the frame of temporal analysis, Eq.(11) is obtained:

$$\omega' = \frac{(2^{-1}k)^{1/2}}{(\rho_l + \rho_g)} \left( \left( \left[ \rho_l \rho_g \bar{u}_z^2(t) - (\rho_l + \rho_g) \sigma \left( k^2 - \frac{1}{R_0^2} \right) \right]^2 + [(\rho_l + \rho_g) \rho_l a]^2 \right)^{1/2} + \rho_l \rho_g \bar{u}_z^2(t) - (\rho_l + \rho_g) \sigma \left( k^2 - \frac{1}{R_0^2} \right) \right)^{1/2} \quad (11)$$

The plot of Eq.(11), for constant axial velocity, shows that there exists a maximum (Figure 3). The dominant or the liquid breakup controlling wave number,  $k_{opt}$ , which corresponds to the maximum growth rate,  $\omega'_{max}$  [1/s], is expected to occur at  $\frac{dRe(\omega')}{dk} = 0$  [6].

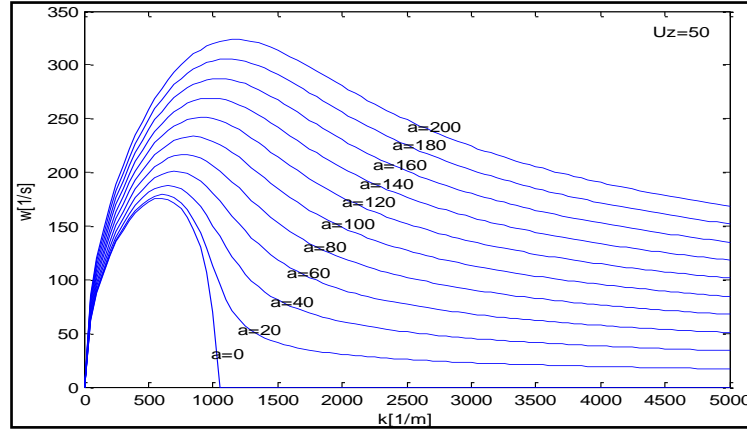


**Figure 3.** Variation of growth rate,  $\omega'$  [1/s], with wavenumber,  $k$  [1/m], and jet acceleration,  $a$  [m/s<sup>2</sup>] at constant velocity

The breakup controlling wavenumber and the corresponding growth rate are, therefore, respectively given as ([11]):

$$k_{opt} = \frac{\left( \left( 4 \left[ \rho_l \rho_g \bar{u}_z^2(t) + \frac{\sigma}{R_0^2} (\rho_l + \rho_g) \right]^2 + 3 [(\rho_l + \rho_g) \rho_l a]^2 \right)^{1/2} - \left[ \rho_l \rho_g \bar{u}_z^2(t) + \frac{\sigma}{R_0^2} (\rho_l + \rho_g) \right] \right)^{1/2}}{(3\sigma(\rho_l + \rho_g))^{1/2}} \quad (12)$$

and

$$\omega'_{max} = \frac{\left( \left( \left[ k_{opt} \rho_l \rho_g \bar{u}_z^2(t) - (\rho_l + \rho_g) \sigma k_{opt} \left( k_{opt}^2 - \frac{1}{R_0^2} \right) \right]^2 + [(\rho_l + \rho_g) \rho_l k_{opt} a]^2 \right)^{1/2} + k_{opt} \rho_l \rho_g \bar{u}_z^2(t) - (\rho_l + \rho_g) \sigma k_{opt} \left( k_{opt}^2 - \frac{1}{R_0^2} \right) \right)^{1/2}}{2^{1/2} (\rho_l + \rho_g)} \quad (13)$$

The unsteady jet breakup macro structure is obtained accordingly. The relation for the half spray angle,  $\theta/2$ , in Trinh and Chen (2006) as proposed by Reitz and Bracco (1982) [6] is used:

$$\tan \theta/2 = \Omega \frac{\Lambda \omega'_{max}}{\bar{u}_z} \quad (14)$$

where  $\Omega$  is a constant that accounts for the nozzle entrance shape, which must be fitted experimentally [6], and  $\Lambda = 2\pi/k_{opt}$  is the optimum wavelength.

The spray angle can be obtained by geometrical considerations - approximating the half of the spray as an isosceles triangle with the height being half the penetration length[13][14], as follows:

$$\tan \theta/2 = \frac{A}{(L_p/2)^2} \quad (15)$$

where  $A$  is the upstream half image projected spray area and  $L_p$  is the spray penetration length.

The penetration length is obtained as:

$$L_p = \gamma \sqrt{\frac{\bar{u}_z}{\Lambda \omega'_{max}}} \quad (16)$$

where  $\gamma \equiv 2(A/\Omega)^{1/2}$

## Results and Discussion

Transient experimental injection velocity,  $\bar{u}_z$ , presented in [8][9] for a 3 hole 0.2 mm diameter valve covered orifice (VCO) diesel injector at different injection pressures, were used for the validation of the developed transient KH instability model.

Figure 4 shows the model predicted spray angle and experimental spray angle data [8] for transient fuel injection. Figure 4 shows that there is a good agreement between model predicted results and the experimental data. The spray angle is observed to be very high at the initial start of injection and later settled for a value around  $17^\circ$ , which corresponds to the steady fuel injection region. It is observed that the 60 [MPa] injection pressure has a wider spray angle compared to higher injection pressures, this may be attributed to initial low penetration velocity into dense ambient and more time to adjust to the surrounding gases, which makes it less constrained to expand. The significant difference in the spray angle in the accelerating region, 0-0.5 [ms] after start of injection and the steady region shows that the unsteady effects have significant effects on the liquid fuel breakups.

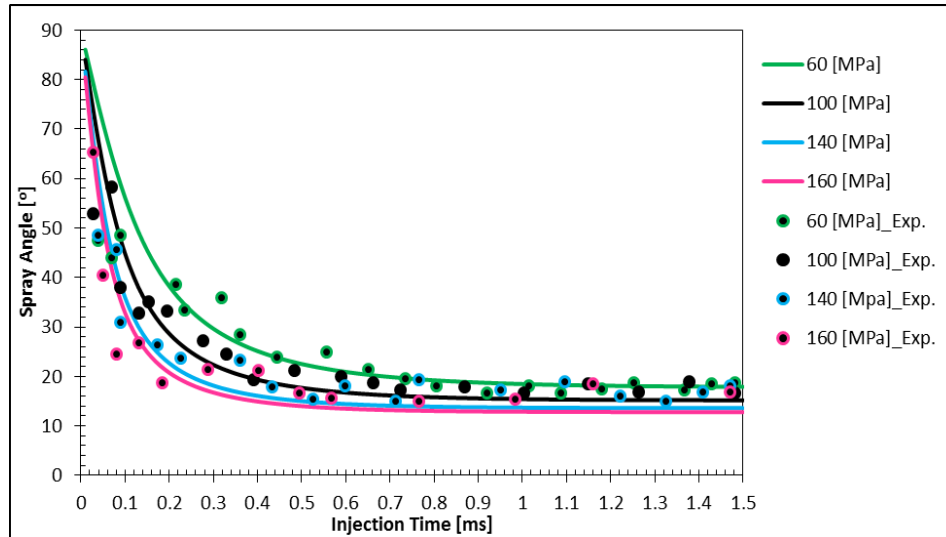


**Figure 4.** Spray Angle Variation with the Time after Start of Injection in an Ambient of Density 47 [kg/m<sup>3</sup>] at various Injection Pressures.

Figure 5 shows the penetration length variation with injection time at various injection pressures in an ambient density of 47 [kg/m<sup>3</sup>]. Figure 5 shows that there exists an agreement between unsteady KH instability model and the experimental penetration length [8]. Careful observation of Figure 5 reveals that there exists a maximum in



the predicted penetration length by the KH instability model. This observation is in conformity with majority of experimental data presented in the literature [15]. In terms of the injection pressure, it is observed that the liquid penetration reached the maximum value faster with elevated injection pressure due to the higher jet velocity, which induces instability and breakup more rapidly.

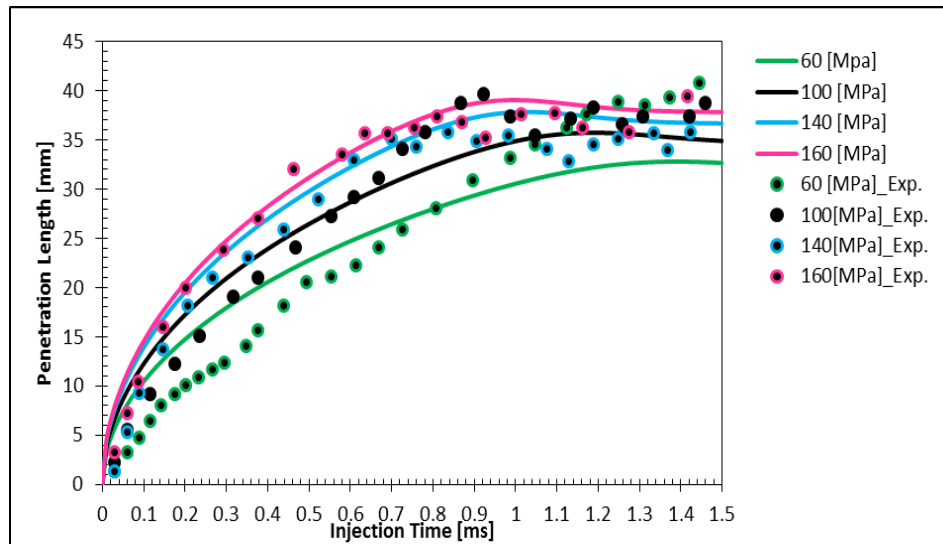


**Figure 5.** Evolution of Penetration Length after time of injection at various Injection Pressures in an ambient Density of 47 [kg/m<sup>3</sup>]

## Conclusions

The theory of jet instabilities has been developed under several assumptions, which include the assumption that the jets are steady. These assumptions may be attributed to some of the deviations observed in the literature between theoretical predictions and experimental data. The present work has been able to demonstrate through analytical means that unsteady effects of liquid jet have significant impacts on the instability and breakup of liquid fuel. Results obtained have good agreement with experimentally obtained data for penetration length and spray angle. Unsteady jets are particularly prevalent in modern fuel injection strategies, like pulsed injection.

## Nomenclature

Symbol	Quantity	Units
A	Area	m <sup>2</sup>
A	Acceleration	m/s <sup>2</sup>
I	Modified first-kind Bessel function	
K	Modified second-kind Bessel function	
L	Length	m
p	Pressure	N/m <sup>2</sup>
R <sub>0</sub>	Jet radius	m

<b>Re</b>	Real part	
t	Timescale	s
u	Velocity	m/s
k	wavenumber	1/m
<b>Greek letter</b>		
$\gamma$	Function parameter	m
$\theta$	Full spray angle	°
$\Lambda$	Wavelength	m
$\Psi$	Smooth function	
$\Omega$	Constant	-
$\delta$	Perturbed boundary	m
$\rho$	Density	kg/m <sup>3</sup>
$\sigma$	Surface tension	N/m
$\omega$	Growth rate	1/s
<b>Subscript</b>		
0	Zero-order	
1	First-order	
g	Gas	
l	Liquid	
max	Maximum parameter	
opt	Optimum parameter	
p	Penetration	
r	Radial direction	
z	Axial direction	
<b>Superscript</b>		
'	Perturbed parameter; derivative	

## References

- [1] Stiesch, G. *Modelling Engine Spray and Combustion Processes: Heat and Mass Transfer*. Berlin Heidelberg: Springer Verlag, 2010.
- [2] Gorokhovski, M.; Herrmann, M. "Modelling Primary Atomization," *Annual Review of Fluid Mechanics*, vol. 40, pp. 343–366, 2008.
- [3] Jiang, X.; Siamas, G.A.; Jagus, K.; Karayiannis, T. G. "Physical Modelling and Advanced Simulation of Gas-Liquid Two-phase Jet Flows in Atomization and Sprays," *Progress in Energy and Combustion Science*, vol. 36, pp. 131–167, 2010.
- [4] Sazhin, S.S.; Turner, M.R.; Healey, J.J.; Martynov, S. B. "Transient Diesel Fuel Jets and Spray: Mathematical Analysis and Application," in *ILASS-Europe, 24th European Conference on Liquid Atomization and Spray Systems, Sept. 2011*, 2011.
- [5] Turner, M.R.; Healey, J.J.; Sazhin, S.S.; Piazzesi, R. "Wave Packet Analysis and Breakup Length Calculations for an Accelerating Planar Liquid Jet," *Fluid Dynamics Research*, vol. 44, no. 1, p. 015503, 2012.
- [6] Reitz, R.D.; Bracco, F. V. "Mechanism of Atomization of Liquid Jet," *Physics of Fluids*, vol. 25, no. 10, pp. 1730–1742, 1982.
- [7] Bae, C.; Kang, J. "The Structure of a Break-up Zone in the Transient Diesel Spray of a Valve-Covered Orifice Nozzle," *International Journal of Engine Research*, vol. 7, no. 4, pp. 319–334, 2006.
- [8] Karimi, K. "Characterisation of Multiple-Injection Diesel Sprays at Elevated Pressures and Temperatures," PhD Thesis, School of Engineering, University of Brighton, 2007.
- [9] Karimi, K.; Sazhina, E. M.; Abdelghaffar, W. A.; Crua, C.; Cowell, T.; Heikal, M. R.; Gold, M. R. "Developments in Diesel Spray Characterisation and Modelling," in *THIESEL 2006 Conference on Thermo- and Fluid Dynamic Processes in Diesel Engines, 13-15 September*, 2006.
- [10] Sher, I. "Stability and Breakup of Transient Jets," in *ILASS-Europe, 6-8 September*, 2010.
- [11] Sher, I., E.O. Diemuodeke, "Transient Jet Breakup Modelling", to be published, 2013.
- [12] Eggers and E. Villermaux, J. "Physics of liquid jets," *Reports on Progress in Physics*, vol. 71, no. 3, p. 036601, 2008.
- [13] Naber, D.; Siebers, D. L. "Effects of Gas Density and Vaporization on Penetration and Dispensation of Diesel Spray," *SAE Paper*, p. 960034, 2006.
- [14] Payri, F.; Payri, R.; Salvador, F.J.; Bardi, M. "Effect of Gas Properties on Diesel Spray Penetration and Spreading Angle for the ECN Injectors," in *ICLASS-Europe, 2-6 September*, 2012.
- [15] Ming, H.; Shenlun, L.; Haifeng, L.; Chia-fon, F. L. "Investigation on Spray Characteristics of Water Emulsified Diesel with Different Injection Pressure and Ambient Temperature," in *Proc. of ICLASS-Europe, 2-6 September*, 2012.

## Numerical modelling of liquid jets atomization due to leakage of liquefied gas storage

Cedric LEMOFACK<sup>1,2</sup>, J. M. LACOME<sup>2</sup>, J. REVEILLON<sup>1</sup> and F. X. DEMOULIN<sup>1</sup>

1: CNRS, UMR6614-CORIA, Technopole du Madrillet, BP 12, Avenue de l'Université, 76801 Saint-Etienne-du-Rouvray Cedex, France

2: INERIS, Parc Technologique ALATA, B.P. N°2, 60550 Verneuil-en-Halatte, France

### Abstract

The objective of this work is to develop a numerical model with the aim of simulating a two phase jet resulting from a breach or leakage in a vessel or pipe containing liquefied gas. The work focuses especially on the effect of the vaporization and boiling process in the jet. To represent the flash boiling phenomena that occurs at the exit of the injector up to the end of expansion zone of the jet, the Homogeneous Equilibrium Model (HEM) have been used. Consequently, at the end of this expansion zone, gas and liquid velocities are identical and the spray is supposed to be at boiling temperature with a gas environment composed only by vapour. The velocity is considered to be driven mainly by the pressure drop, thus it is determined by the Bernoulli law at the end of expansion zone. After this zone, thanks to the thermal condition, any increase of temperature will promotes boiling. But if some air diffuses inside the spray, a non-classical vaporization process is expected. A thermodynamic equilibrium model for vaporization was thus developed. To test the model, an atmospheric two-phase jet of butane, emanating from a circular orifice is considered. The modelling results show that the calculated temperature behaviour in the spray jet by comparison with the observations is generally satisfactory. This result cannot be obtained with classical vaporization model.

### Introduction

Experiments were carried out by INERIS with the aim to study the two-phase releases of hazardous chemicals into the atmosphere. These experiments involve to measure the main characteristics of the jet and to increase the understanding of the behaviour of sub-cooled (non-flashing) and superheated (flashing) liquid jets. It is now necessary to develop a numeric model which will include all those phenomena and will help the prediction of jet expansion.

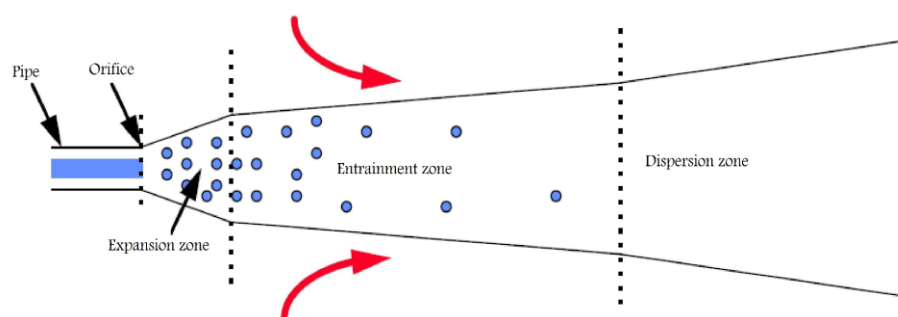


**Figure 1.** Schematic representation of the areas of the flashing jet

The objective of this work is to develop a numerical model with the aim of simulating a two phase flow resulting from a breach or leakage in a vessel containing liquefied gas. Basic principles of this kind of injection are summarized in **Figure 1**, the jet consists in 3 areas:

- The expansion zone (flash boiling, atomization): Here, the fluid expand from the vessel hole pressure to the atmospheric pressure. At the end of this zone, we assume that the jet consist only in gas phase and liquid phase. Both of them are at the boiling temperature. During the expansion, jet atomization occurs and the liquid jet ends here in droplets.
- The entrainment zone (eventual secondary break-up, droplets evaporation): the turbulent jet drives the ambient air. The energy brings by the air, of which the temperature is greater than that of the jet, is used for droplet vaporization and the two-phase jet heating. At the end of this zone, it is assumed that the velocity of the two-phase jet reaches the velocity of the ambient air atmosphere.

- The final dispersion zone: the ambient air velocity and turbulence is predominant compare to which of the two phase jet.

The first step of the work includes models used to describe the jet up to the end of expansion zone. These will be used as boundary conditions for the simulation of the jet from the beginning of the entrainment zone. In the second step, precisions are given on the new phenomena brought by the flashing liquid jet and the models suggested for it. Finally, results are given and discussed to see how to continue the work.

## Materials and Methods

To represent the flash boiling phenomenon that occurs at the exit of the injector up to the end of expansion zone, the isenthalpic Homogeneous Equilibrium Model (HEM) has been used. The model is used to determine the vapour mass fraction at the end of the zone.

The model supposes that the gas and liquid have the same velocity and the same saturation temperature due to the thermodynamic equilibrium assumption between the two phases. The mixture of the phases is homogeneous. These assumptions imply that:

- The two-phase flow is considered as a homogeneous fluid with properties at the middle of those of liquid and gas phase.
- The flow quickly tends to a thermodynamic equilibrium (no energy exchange between the liquid-gas system and the outside). So it is supposed to have this thermodynamic equilibrium during the expansion.
- Isenthalpic expansion: the enthalpy of the flow is constant while its entropy decreases.

There is another HEM model with isentropic expansion; the entropy of the flow is constant while its enthalpy decreases. This causes the fall in temperature of the system. Van den Akker [1983] showed that both of the assumptions are unrealistic but fewer errors are involved with the isenthalpic expansion.

In the case of this work, the HEM model presents the advantage of vapour/liquid mass fraction estimation. This will help to determine the mass flow of each phase from the total mass flow given by the experimental data.

## Isenthalpic HEM Model:

$$h(T_{\text{exp}}) = (1-X) * h_l(T_{\text{exp}}) + X * h_g(T_{\text{exp}}) \quad (1)$$

$$\int dh(T) = \int C_{pl} dT \quad (2)$$

From the equation (1) describing the enthalpy conservation, we introduce (2) After a derivation by X:

$$h_l(T_i) - h_g(T_i) = -\int C_{pl} dT + \int C_{pg} dT + \left( (1-X) + X * \frac{C_{pg}}{C_{pl}} \right) * C_{pl} * \frac{dT}{dX} \quad (3)$$

By supposing  $X \ll 1$  and  $C_{pl} > C_{pg}$ , we see that the term  $-(1-X) * C_{pl} * dT/dX$  in (3) is equal to latent heat vaporization:

$$Lv(T_{\text{exp}}) = -(1-X) * C_{pl} * \frac{dT}{dX} \quad (4)$$

The heat exchange due to vaporization is supposed greater than the heat due to warming:  $C_{pl} * dT \ll Lv$ . By taking account of this assumption after the integration of (4) between the internal vessel and the end of expansion zone, we finally have:

$$X_{\text{exp}} = C_{pl} \frac{T_i - T_{\text{exp}}}{Lv} \quad (5)$$

At the end of expansion zone, the jet is in atmospheric pressure. So the liquid, which is in thermodynamic equilibrium with its vapour, is at its boiling temperature ( $T_{\text{exp}} = T_{eb}$ ).

Another issue of this work is the determination of the velocity induced by the pressure drop inside the injector and by the flash effect. The maximum kinetic energy can be estimated by the pressure drop and the variation of thermodynamic energy in the flow. Here, the velocity is considered to be driven mainly by the pressure drop, thus it is determined by the Bernoulli law. Additional velocity could be considered due to the flow expansion (liquid to gas) however there is also a reduction of velocity due to pressure loss.

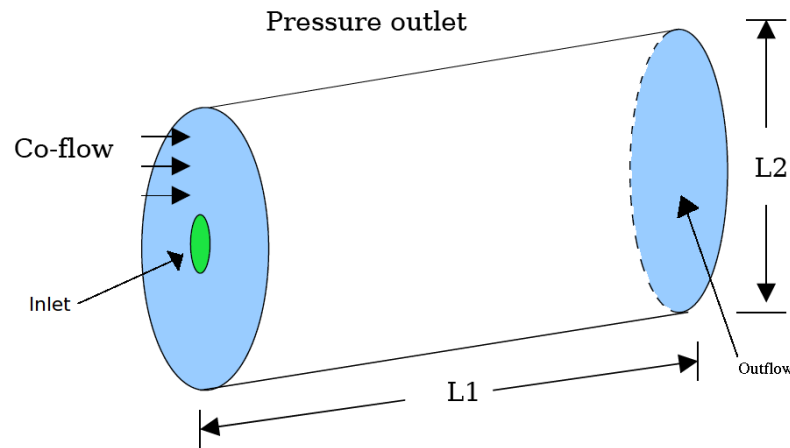


**Figure 2.** Computation area

Simulation presented in this paper starts at this point. The numerical software used for this study is numerical package FIRE V8.41 from AVL. An atmospheric two-phase jet of butane, emanating from a circular orifice with a diameter of  $D = 60.45$  mm is considered. It is now assumed that the flash-boiling has already taken place (in the expansion zone) and therefore, the simulation starts at the beginning of the entrainment zone. This means that for the liquid phase, only droplets are considered. The Euler-Lagrange approach has been used for this two-phase simulation. The numerical domain in which the butane is spreading is presented in **Figure 2**. It consists in a cylinder of 24 m in length and 4 m in diameter. To simulate a rejection of liquefied gas with wind effect, a co-flow of air surrounds the spray injection. The mass fraction of each phase is given by the HEM model. The boundary conditions are recapitulated in Table 1. Finally, the turbulence is modelled with the  $K-\epsilon$  model.

**Table 1.** Boundary layer conditions

Variable	Inlet	Coflow	Outlet, Outflow
Velocity (m/s)	60.45	1	-
Temperature (°K)	272.8	300.15	-
Mass flow (kg/s)	1.33	-	-
Vapour fraction	0.166 67	-	-
Droplets size (µm)	100	-	-
Turbulence intensity	10	1	-
Length scale	0.005	0.1	-
Pressure (Mpa)	-	-	0.1013

### Abramzon vaporization model:

Vaporization is based on Abramzon vaporization model [1989]. So, the mass transfer rate is given by (6) and (7):

$$\dot{m} = \pi \rho D a S h_c \ln(B_M + 1) \quad (6)$$

$$\dot{m} = \pi \frac{ak}{C_{pg}} Nu_c \ln(B_T + 1) \quad (7)$$

Usually, the mass Spalding number  $B_M$  (equation (8)) and the thermal Spalding number  $B_T$  (equation (9)) are supposed to be the same ( $B_M = B_T = B$ ). One part of the energy available in the gas phase goes for the evaporation of liquid phase. The other part goes for heating the droplet. This is described in equation (10) below.

$$B_M = \frac{Y_{F,s} - Y_{F,\infty}}{1 - Y_{F,s}} \quad (8)$$

$$Q_l = \pi a k \left( \frac{h_c a}{k} (T_\infty - T_s) - \frac{Lv}{C_{pg}} Nu_c \ln(B_T + 1) \right) \quad (11)$$

$$B_T = \frac{\rho_s v_s C_{pg}}{h_c} \quad (9)$$

$$h_c (T_\infty - T_s) = \rho_s v_s Lv + \frac{Q_l}{\pi a} \quad (10)$$

The introduction of the thermal Spalding number in (10) combined with equation (7) give the heat quantity necessary for droplet heating.

However thermodynamic conditions at the end of the expansion zone are very particular in the case of flashing jets. Thermodynamic equilibrium assumption imposes that the liquid and gas temperature are the same and equal to the boiling temperature. Additionally, near the inlet boundary conditions of the jet droplet, environment is composed of pure vapour ( $Y_{F,\infty} = Y_{F,s} = 1$ ). Thus, this is a limit case between boiling and vaporization. As seen in equation (9), with these conditions,  $B_M$  is uncertain. However, the security brought by putting the maximum value of the both vapour mass fraction at 0.99 is not sufficient. Thus, some simulation cases have shown that the classic Abramzon vaporization model is not suitable for post flashing two-phase jet. So there is a necessity to develop another model for vaporization.



### Thermodynamic Equilibrium Model (TEM):

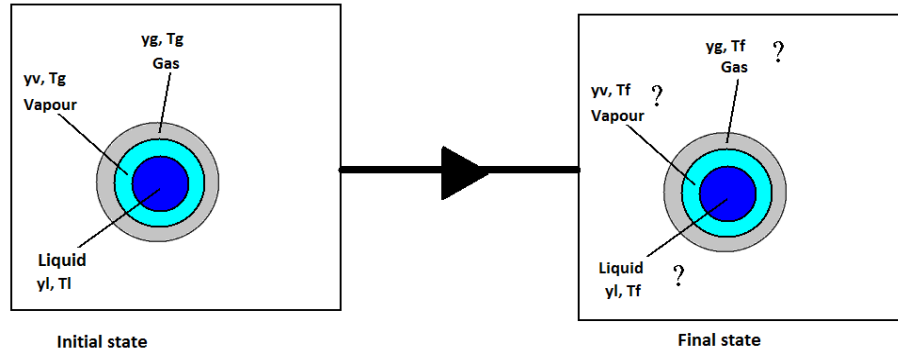


**Figure 3.** Initial and final state in the thermodynamic

We propose a special procedure to solve this problem. It is considered a thermodynamic system at its initial state with certain liquid mass fraction ( $y_l$ ) and vapour mass fraction ( $y_v$ ) in the presence of other gas like air ( $y_g$ ). The liquid temperature ( $T_l$ ) differs from vapour temperature ( $T_g$ ). Like in HEM model, we consider thermodynamic equilibrium model at the final state. The physics assumptions here are:

- Ideal gas.
- Mass conservation (12).
- Isolated system with constant pressure transformation: enthalpy conservation (13).

$$\sum_k y_k^{initial} = \sum_k y_k^{final} = 1 \quad (12)$$

$$h_t = \sum_k h_k(T_k^{initial}) * y_k^{initial} = \sum_k h_k(T_k^{final}) * y_k^{final} = Cte \quad (13)$$

The first step of this method is to find the enthalpy at the initial state with de quantities  $y$  and  $T$  in (13). Knowing that the enthalpy is constant, the second step consists in finding the new values of these quantities by applying a method for finding the zero of the function  $f(T^{final})$  (14). At the final state, thermodynamic equilibrium implies that the liquid and gas are at the same temperature.

$$f(T^{final}) = h^{initial}(T_l^{initial}, T_g^{initial}) - h^{final}(T^{final}) \quad (14)$$

This method can be more interesting than the Abramzon model, because not only it resolve the particular problem of flash-boiling, but also it integrates the condensation phenomenon, which is supposed to occurs during the jet spreading.

The test of this model is done with the butane properties. The purpose of the test is to see if it is consistent by varying the initial quantities of  $y$  and  $T$ . In this paper we show the test of the model by varying the initial liquid mass fraction, with the liquid and gas temperature at 272.5°K and 350°K respectively. The total pressure is equal to 0.1MPa.

The **Figure 4** shows the final temperature in the system and the **Figure 5** shows the final mass fractions of liquid and vapour in the system. The model is consistent with the physics. If the liquid initial amount is small, because of the great temperature in the gas compared to the liquid temperature, it evaporates completely. The temperature evolution in this case of total evaporation is linear, accordingly to the ideal gas law. But, the system come to a stage where the energy in the gas phase is not sufficient to completely evaporates the liquid. Thus, as we can see in **Figure 6**, which compare the vapour saturation pressure of butane at the final temperature and the butane vapour pressure in the system, there is an equilibrium between the two phases when liquid remain in the system.

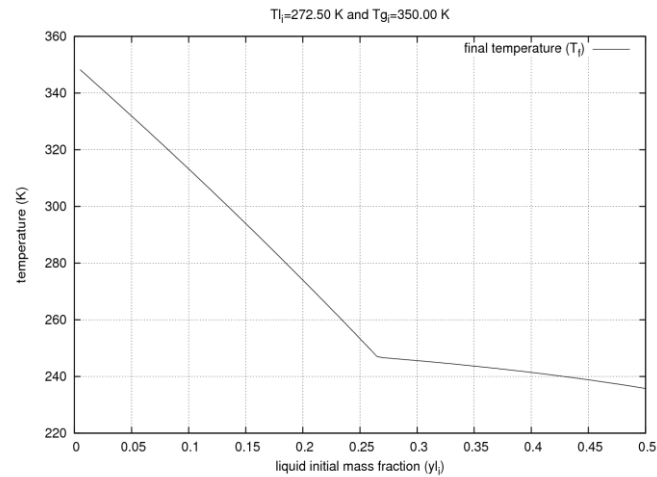


**Figure 4.** Test of TEM – final state temperature in the system by varying the initial liquid mass fraction of butane

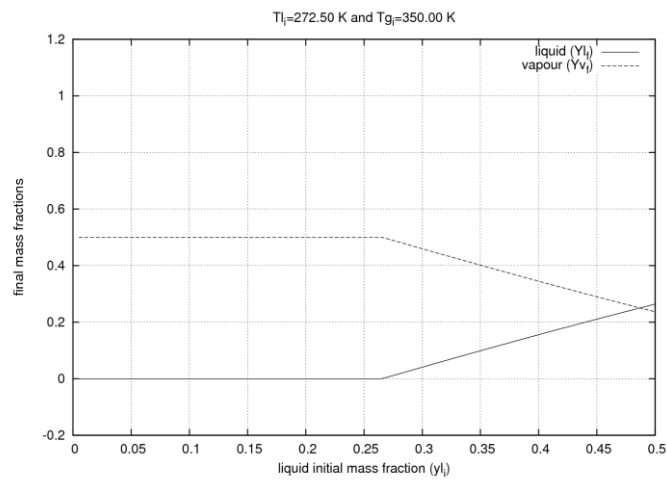


**Figure 5.** Test of TEM – final state liquid and vapour mass fraction in the system by varying the initial liquid mass fraction of butane

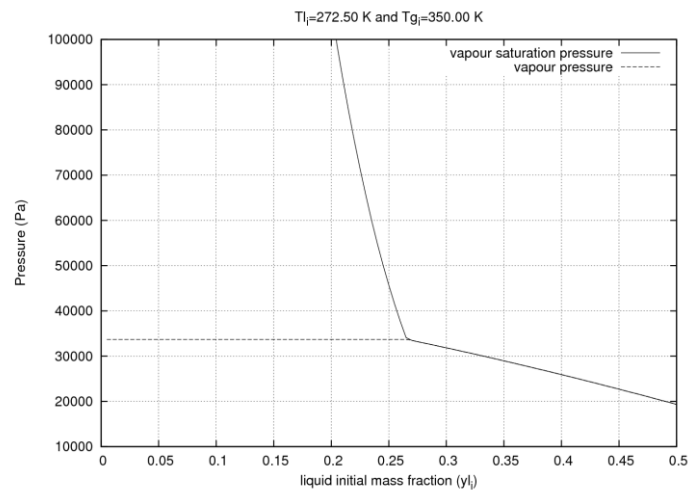


**Figure 6.** Test of TEM - comparison between the vapour saturation pressure and the butane final state vapour pressure in the system by varying the initial liquid mass fraction of butane

## Results and Discussion

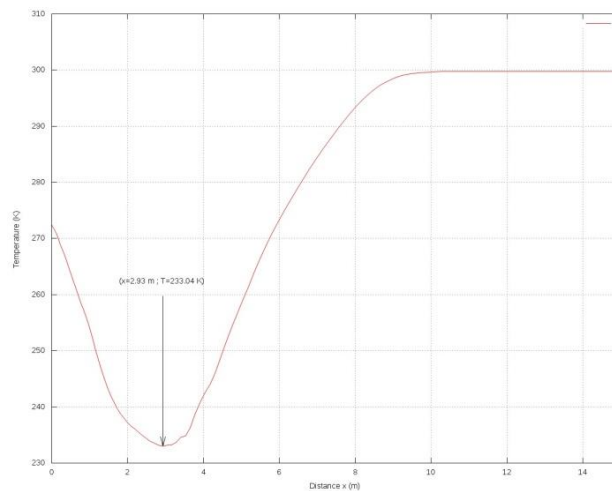


**Figure 7.** Temperature evolution in the jet axis

It is complicated to have experimental results on the types of jets described above. But the INERIS were able to have more reliable measurements in temperature. These measurements show the same behaviour as seen on Figure 7, showing the evolution of the temperature in the jet axis. The spray is surrounded by a hot gas environment. However, the temperature of the spray decreases up to a certain distance. Due to the initial droplet boiling temperature, close to the injection, the vaporization process dominates the flow. Since evaporation is an endothermic phenomenon, the spray jet cools down until there is no droplet enough. Thus the spray temperature rises only once the liquid vaporization does not have enough influence in the flow. So, the minimum temperature ( $T=233.04^{\circ}\text{K}$ ) in the axis.

INERIS has done experiments by placing thermocouples as seen in the **Figure 8** showing the position of these thermocouples in a vertical plane passing by the jet axis. There are three axes in these experiments: the up axis, the horizontal axis and the down axis. The comparison results between experiment and computation on these axes is show in **Figure 9**, **Figure 10** and **Figure 11**.

Despite the fact that the model of the expansion zone is very complex and or vaporization model is a first set, we see that the computation has a similar behaviour in the horizontal axis. And the differences aren't noticeable. The same is said for the up axis. Here the axis is at the top of the jet. So, from the third thermocouple it can be considered to be in the atmospheric conditions. For the down axis differences in evolution and values are noticed. We expect the influence in temperature of the rain out, a deposit in the soil of a mixture of liquid and solid crystals that occurs in actual experiments and that can be caused by the solidification of the water vapour in the atmosphere (humidity). This phenomenon due to the low temperature by vaporisation in the jet is not yet taken account in our model.

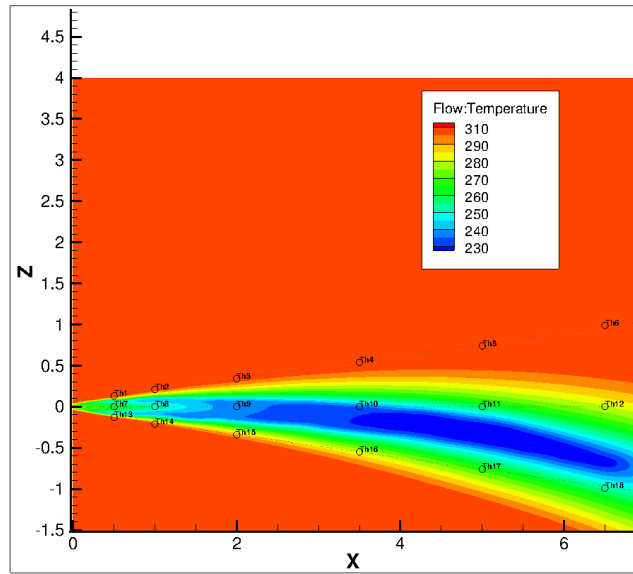


**Figure 8.** Gas temperature along a plane trough the jet axis with thermocouples position

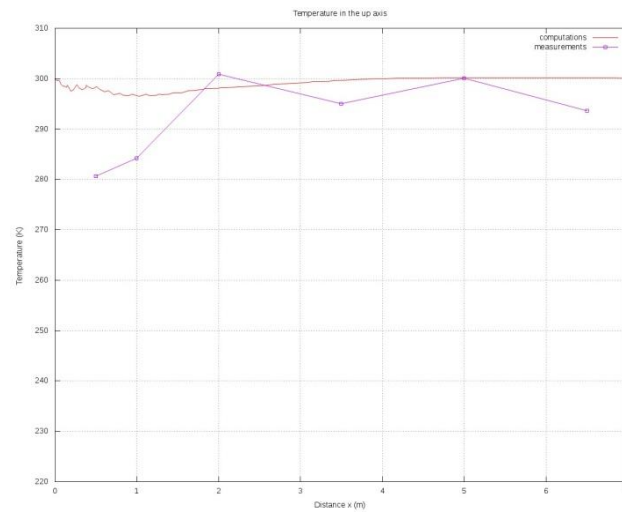


**Figure 9.** Gas temperature along the up jet axis, comparison between experimental and simulation results

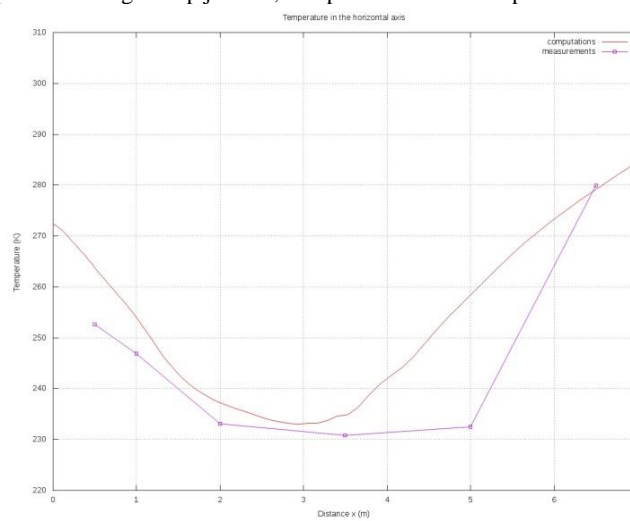


**Figure 10.** Gas temperature along the horizontal jet axis, comparison between experimental and simulation results

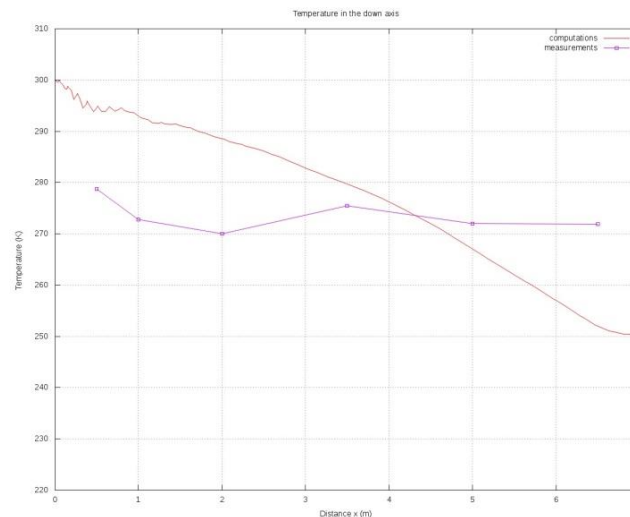


**Figure 11.** Gas temperature along the down jet axis, comparison between experimental and simulation results

It would be also useful to compare the HEM model of end of expansion zone with other models developed for the description of this expansion zone. The conditions with all these models are resumed in the Table 2.

The two other models are the ATEX (ATmospheric Expansion) models. They consider the difference in pressure between the interior and the exterior by assuming the energy conservation (ATEX-MME) or entropy conservation (ATEX-MEE). The flow is also considered as one-dimensional, homogeneous and also with the equilibrium between liquid and gas phases.

**Table 2.** Models conditions at the end of expansion zone

End of expansion zone model	$u_{\text{exp}}$ (m/s)	$\dot{m}_{\text{exp}}$ (kg/s)	$X_{\text{exp}}$	Diameter (mm)
HEM	29.5	1.33	$\frac{0.16}{7}$	60.45
ATEX-MME	38.3	1.33	0.17	53.69
ATEX-MEE	87.9	1.33	$\frac{0.16}{28}$	34.6

In the **Figure 12** showing the gas temperature in the horizontal jet axis and comparing results of HEM, ATEX-MME ATEX-MEE and the measurements, it is shown that the three models are sensibly the same until the region of minimum of temperature. These measurements are not very far from the measurements. But the closer model is ATEX-MME, still until the region of minimum in temperature. But after this region, the three models show some differences between them and with the measurements. This can be caused by the fact that the models are not accurate. And the noticeable differences between models if caused by the differences in velocity and jet diameter at the end of expansion zone given each model.

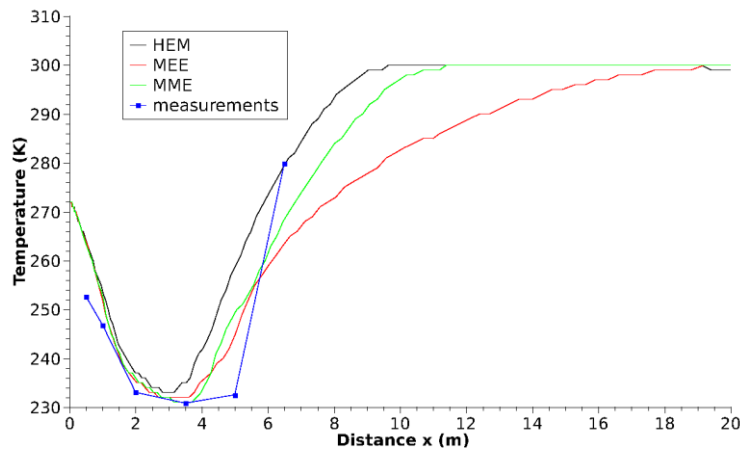


**Figure 12.** Comparison between expansion models computation results and experiment.

## Conclusion

The modelling results with the TEM model show that the calculated temperature behaviour in the spray jet by comparison with the observations is generally satisfactory. This result cannot be obtained with classical vaporization model. But the assumptions used to calculate the boundary conditions bring many lack of precisions. It would be desirable to do a CFD model of the material flow from inside the vessel to the end of expansion zone.

## Nomenclature

$a$	Droplet diameter (m)
$B_M$	Mass Spalding number (-)
$B_T$	Thermal Spalding number (-)
$C_p$	Specific heat capacity at constant pressure ( $\text{J kg}^{-1} \text{K}^{-1}$ )
$D$	Binary diffusion coefficient ( $\text{m}^2 \text{s}^{-1}$ )
$h$	Enthalpy ( $\text{J kg}^{-1}$ )
$h_c$	Convective heat transfer coefficient ( $\text{W m}^{-2} \text{K}^{-1}$ )
$k$	Thermal conductivity ( $\text{W m}^{-1} \text{K}^{-1}$ )
$L_v$	Latent heat ( $\text{J kg}^{-1}$ )
$\dot{m}$	Mass transfer rate ( $\text{kg s}^{-1}$ )
$Nu_c$	Convective Nusselt number (-)
$Sh_c$	Convective Sherwood number (-)
$\dot{Q}_l$	Droplet heating ( $\text{J s}^{-1}$ )
$T$	Temperature (T)
$X$	Vapour mass fraction between liquid and vapour of released product (-)
$y$	Mass fraction besides which of vapour, liquid and air (-)
$Y_F$	Vapour mass fraction besides which of vapour and air (-)

## Greek letters

$\rho$	Density ( $\text{kg m}^{-3}$ )
--------	--------------------------------

## Subscripts

eb	Ebullition
exp	Value at the end of expansion zone
g	Gas
i	Internal vessel value
l	Liquid

s      Value at droplet surface  
 $\infty$       Value far from droplet

## References

- [1] W. A. Abramzon, B. & Sirignano, Droplet vaporization model for spray combustion calculations, Int. J. Heat Mass Transfer.( 1989)
- [2] A.E. Holdo R.K. Calay, Modeling the dispersion of flashing jets using CFD, Journal of Hazardous Materials. (2007)
- [3] S. DUPLANTIER Y. MOUILLEAU D. GASTON, Analyse des conditions de dispersion d'un gaz liquéfié en champ proche en présence d'obstacles, Rapport d'Etudes INERIS. (2001)
- [4] SPOELSTRA H. VAN DEN AKKER H.E.A., SNOEY H., Discharges of pressurized liquefied gases through apertures and pipes, 4th International Symposium on Loss Prevention and Safety Promotion in the Process Industries, 33(1) :E23–E35.(1983)



## **A New Atomization Model for High Speed Liquid Jets using a Turbulent, Compressible, Two-Phase Flow Model and a Surface Density Approach**

B. Mandumpala Devassy<sup>1</sup>, C. Habchi<sup>1</sup> and E. Daniel<sup>2</sup>

1 : IFP Énergies nouvelles, 1-4 av. Bois-Préau - 92852 Rueil Malmaison, France

2 : Aix-Marseille Université, IUSTI, 5 rue E. Fermi 13453 Marseille cedex 13, France

### **Abstract**

Liquid jet atomization is an important process in engineering applications such as aerospace propulsion systems, automotive engines, food processing, and inkjet printing. For engine applications, the fuel spray characteristics are critical to determining the engine performance such as fuel consumption rate or exhaust gas cleanliness. The present work focuses on the liquid jet atomization phenomena under Diesel engine conditions. This study describes a new atomization model, for a high speed liquid jet, based on an Eulerian two-phase approach. The current trend to track the liquid-gas interface is done by defining surface density equations. The new atomization model studied in this work adopts this strategy by defining different surface density equations, for the liquid core and the spray droplets. This new model has been coupled with a turbulent two-phase system of equations of Baer-Nunziato type [2]. The primary and secondary breakup processes are modelled with respect to available experimental and numerical observations. The phenomenon of ligament growth is modelled with respect to the turbulent stretching of the interface from both liquid and gas sides. The model results are later compared with recent DNS results under typical Diesel engines conditions. It has been shown that turbulence in the liquid play a major role in the primary atomization process.

---

### **1 Introduction**

Atomization of a liquid jet generally refers to a process in which a bulk liquid is disintegrated into small drops or droplets by internal and/or external forces as a result of the interaction between the liquid and surrounding medium. This disintegration or breakup occurs when the disruptive forces exceed the liquid surface tension and viscous forces. The most important factor which affects the liquid flow and its atomization is the interaction with the gas in the combustion chamber. This interaction may be affected by the gas density and temperature, the injection velocity magnitude and turbulence. In addition, the effect of cavitation and the induced secondary flows inside the injector orifices are recognized among the important parameters which directly influence the process of liquid jet atomization [1].

The final droplet size formed greatly depends on the primary breakup process of the liquid jet. The breaking of ligaments into large primary droplets and its subsequent breakup into child droplets is a cascade process. The ligaments start growing from the liquid core due to several reasons. It can occur by the flow turbulence due to cavitation or due to collapse of the cavitation pockets. The flow of gas over the high speed liquid jet can introduce shearing at the gas-liquid interface which can also be a source of ligament generation. At a critical condition this ligaments can pinch off from its parent liquid core. The ligaments thus produced are unstable and undergo breakup producing droplets. This changeover from large liquid structures to small droplets is the issue addressed in this work.

Present study attempts to improve the understanding of the primary atomization process using RANS computations. An Eulerian formulation is used for both gas and liquid phases since it is well adapted to the liquid core region. This paper is organized as follows: Details of the two-phase system are explained in Section 2. Next, the new atomization models using two surface density equations are proposed in Section 3 along with its implementation into the professional two-phase flow software, IFP-C3D (Velghe et al. [13]). In Section 4, these comprehensive atomization models are then applied for the simulation of liquid jets injected under actual diesel engine conditions and the results are compared with the DNS observation of Herrmann [4]. Finally, the conclusions with future work are presented in Section 5.

### **2 Two-Phase Flow Governing Equations**

The starting point for the two-phase flow model proposed here is adopted directly from the work of Saurel and Abgrall [10]. Their method is based on a compressible model involving seven partial differential equations, three for the gas phase and three for the liquid phase in addition to an equation for the liquid volume fraction transport. In this work, these equations have been generalized for the RANS simulations of turbulent two-phase flows in a way similar to the averaging method of Drew and Passman [3]. In addition, the specific internal energy equation is used instead of the total specific energy adopted in the work of Saurel and Abgrall [10]. Also, phase change at the interface is not considered in this paper. For two-phase flows, the model consists of the following governing equations:

$$\frac{\partial \alpha_p \bar{\rho}_p}{\partial t} + \frac{\partial \alpha_p \bar{\rho}_p V_{p,i}}{\partial x_i} = 0 \quad (1)$$

$$\frac{\partial}{\partial t} (\alpha_p \bar{\rho}_p V_{p,i}) + \frac{\partial}{\partial x_i} (\alpha_p \bar{\rho}_p V_{p,i} V_{p,j}) = -\frac{\partial \alpha_p \bar{P}_p}{\partial x_i} + \bar{P}^I \frac{\partial \alpha_p}{\partial x_i} + \frac{\partial \alpha_p \bar{\tau}_{p,ij}^{L,T}}{\partial x_i} + \lambda (V_{q,i} - V_{p,i}) \quad (2)$$

$$\begin{aligned} \frac{\partial}{\partial t} (\alpha_p \bar{\rho}_p e_p) + \frac{\partial}{\partial x_i} (\alpha_p \bar{\rho}_p V_{p,i} e_p) = & -\alpha_p \bar{P}_p \frac{\partial V_{p,i}}{\partial x_i} + \alpha_p \bar{\tau}_{p,ij}^{L,T} \frac{\partial V_{p,i}}{\partial x_j} - \frac{\partial \alpha_p \bar{q}_{p,i}^{L,T}}{\partial x_i} + \lambda V^I (V_{q,i} - V_{p,i}) \\ & + \mu \bar{P}^I (\bar{P}_q - \bar{P}_p) + \theta (T_q - T_p) \end{aligned} \quad (3)$$

$$\frac{\partial \alpha_p}{\partial t} + V_i^I \frac{\partial \alpha_p}{\partial x_i} = \mu (\bar{P}_q - \bar{P}_p) + \frac{\theta}{\kappa} (T_q - T_p) \quad (4)$$

Here  $p=\{1,2\}$  and  $q=3-p$ ; say  $p=1$  for the liquid phase (index  $l$ ) and  $p=2$  for the gas phase (index  $g$ ). Equation (4) is solved only for  $p=1$  (i.e. for the liquid volume fraction,  $\alpha_l = \alpha_1$ ). The saturation constraint  $\alpha_2 = 1 - \alpha_1$  is then used for the calculation of the gas volume fraction,  $\alpha_g = \alpha_2$ . The  $(\bar{\bullet})$  and  $(\bar{\bullet})$  designate the Reynolds and Favre average operation, respectively.  $\tau_{p,ij}^{L,T}$  is the shear stress tensor which has the contribution from both the laminar and turbulent flow regimes. In the energy equation (Equation (3)),  $e_p$  is the Favre averaged specific internal energy and  $\bar{q}_{p,i}^{L,T}$  the heat flux. In the system of equations (1) to (4) also intervenes an interfacial velocity and an interfacial pressure. They are assumed according to Baer and Nunziato model [2] ( $V^I = V_l$  and  $P^I = P_g$ ). In addition, the model equations include relaxation terms to restore pressure, velocity and temperature at the interfaces. Here the velocities are relaxed at the interface with an infinite relaxation by making  $\lambda$  tending to infinity. This means that for any arbitrary small time increment, the velocities must be in equilibrium at the interfaces. Similar to the velocity relaxation, pressure at the interface is also relaxed by tending the pressure relaxation coefficient  $\mu$  to infinity. The description of this relaxation parameters and its calculation is carried out in Saurel and Abgrall [10]. Similarly, an infinite relaxation of the temperature at the interfaces is applied by tending the relaxation parameter,  $\theta$  to infinity (see Zein et al., [16]). It is important to note that the pressure and temperature equilibrium are accomplished by computing the exact volume fraction variations (see the right hand side (RHS) of equation (4)). These volume fraction changes are happening without any phase change since the RHS of the mass conservation Equation (1) is zero. Further analyses of each source term of the governing equations are available in Mandumpala Devassy [7].

### 3 The New Atomization Model

In the previous atomization models (Vallet et al. [12], Lebas et al. [5], Vessiller [14] etc.) using surface density approach, both the dispersed and separate phases are treated using one equation of liquid mass fraction and one surface density equation. But at the nozzle premises, the liquid jet comprises a region with a dense liquid core, ligaments and droplets. Lebas et al. [5] have already developed a model for the dense and dilute regions by employing one equation of surface density. But, the method followed here is more straightforward by distinguishing the primary and secondary atomization processes using separate equations of surface density: One for the separate phase and the other for the dispersed phase. The notations,  $s$  stands for the separate phase and  $d$  stands for the dispersed phase or droplets.

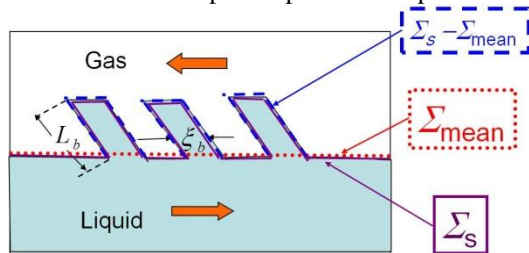


**Figure 1 :** Layout of the different surface density ( $\Sigma_{mean}$  and  $\Sigma_s$ ) used in the suggested atomization model.

The development of the proposed atomization model is carried out in different steps. Firstly, the liquid core surface is mapped as shown in Figure 1. On one hand, mean of surface area,  $\Sigma_{mean}$ , is considered at

undisturbed conditions. On the other hand,  $\Sigma_s$  is defined as the total separate phase surface. But, due to the effect of instabilities and underlying turbulent eddies at the gas-liquid interface,  $\Sigma_s$  surface begins deforming and producing irregularities, which later end up in the formation of ligaments as depicted in Figure 1. The quantity of surface,  $(\Sigma_s - \Sigma_{mean})$  thus accounts for the ligament surfaces. These ligaments later undergo breakup if they satisfy a critical breakup condition, which will be discussed later. This also shows the importance and the necessity of a transport equation for the mean surface density,  $\Sigma_{mean}$ .

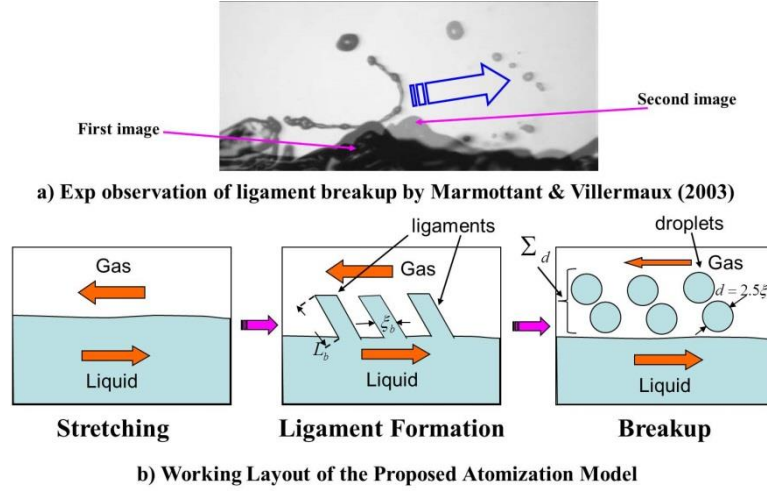


**Figure 2:** a) Experimental observation [8]. b) The working layout of the new atomization model and definition of the problem.

The second step mainly addresses the breaking of these matured ligaments from the liquid core surface. Figure 2 shows the diagrammatic representation of this ligament breakup process. In the figure, the ligament length at the breakup time is labelled as  $L_b$  and its diameter as  $\xi_b$ . At a critical breakup condition the matured ligaments will pinch off and the quantity of surface  $(\Sigma_s - \Sigma_{mean})$  will detach and move away from the separate phase surface. In the third and the final step, the ligaments thus detached from the liquid core become unstable and assumed to breakup as shown in Figure 2a, which is an experimental observation from Marmottant and Villermaux [8] of the breakup of detached ligaments. As such, under a critical ligament thickness, the ligament pinches off and at the same time it itself breaks up into droplets [15].

This analysis thus concludes the requirement of three surface density equations; one for separate phase, the second for the dispersed phase and the third for the reference mean area transport.

$$\frac{\partial \Sigma_{mean}}{\partial t} + \nabla \cdot (V_{l,i} \Sigma_{mean}) = 0 \quad (5)$$

Similarly, the transport equations of surface density for the separate and dispersed phase can be written respectively as follows:

$$\frac{\partial \Sigma_s}{\partial t} + \nabla \cdot (V_{l,i} \Sigma_s) = \left( \nabla \cdot V_{l,i} - \overline{n_{s,i} n_{s,j}} : \nabla V_{l,i} \right) \Sigma_s + \dot{\Sigma}_{s,prod} - \dot{\Sigma}_{s,d} + \frac{2}{3} \frac{\dot{\alpha}_{relax,l}}{\alpha_l} \Sigma_s \quad (6)$$

$$\frac{\partial \Sigma_d}{\partial t} + \frac{\partial (V_{l,i} \Sigma_d)}{\partial x_i} = \frac{2}{3} \frac{\partial \overline{V_{l,i}}}{\partial x_i} \Sigma_d + \dot{\Sigma}_{d,prod} + \dot{\Sigma}_{d,d} - \frac{2}{3} \frac{\dot{\alpha}_{relax,l}}{\alpha_l} \Sigma_d \quad (7)$$

The model is built in such a manner that  $\Sigma_{mean}$  represents the undisturbed surface density (at the initial condition we have  $\Sigma_{mean} = \Sigma_s$ ). The first term on the RHS of Equation (7) is the simplified stretch term [6] [9] for droplets compared to the similar term in Equation (6) by considering the isotropic behaviour of the normal  $\overline{n_d}$  on the droplet surface. The quantity  $\overline{n_s}$  in Equation (6) is the resolved normal acting at the separate phase interface, and can be modelled by  $\overline{n_s} = \frac{\nabla \alpha_s}{|\nabla \alpha_s|}$ , where  $\alpha_s$  is the volume fraction of separate phase surface and is

discussed in next subsection.  $\dot{\alpha}_{relax,l}$  in Equations (6) and (7) is the quantity associated with the change in the volume fraction occurring due to pressure and temperature relaxation [10][16] at the gas-liquid interface and is given as follows:

$$\dot{\alpha}_{relax,l} = \left[ \mu (\overline{P_g} - \overline{P_l}) + \frac{\theta}{\kappa} (T_g - T_l) \right] \quad (8)$$

Thus, Equation (6) represents the evolution of the surface due to primary atomization and Equation (7) the evolution of the surface due to secondary atomization.  $\dot{S}_{\Sigma_s} = \frac{(\Sigma_s - \Sigma_{mean})}{\Delta t}$  is the rate of surface which is detached from the separate phase, see Figure 1.  $\dot{S}_{\Sigma_d}$  is the rate of surface which is added to the dispersed phase due to the ligament breakup.  $\dot{\Sigma}_{s_{prod}}$  is the turbulent production term for the separate phase.  $\dot{\Sigma}_{d_{prod}}$  is the turbulent secondary atomization production source term for the dispersed phase. The models for  $\dot{S}_{\Sigma_d}$ ,  $\dot{\Sigma}_{s_{prod}}$  and  $\dot{\Sigma}_{d_{prod}}$  are described in the following sections.

### 3.1 Significance of Volume Fraction Equation

With respect to the modelling description in the last section, the transfer of ligaments surface must be accompanied by a volume fraction transfer. According to this principle one can write two equations for liquid volume fraction, one for the total liquid volume fraction ( $\alpha_l$ ) and the second for the separate phase liquid volume fraction ( $\alpha_s$ ).

$$\frac{\partial \alpha_l}{\partial t} + \frac{\partial \alpha_l V_{l,i}^I}{\partial x_i} = \alpha_l \frac{\partial V_{l,i}^I}{\partial x_i} + \dot{\alpha}_{relax,l} \quad (9)$$

$$\frac{\partial \alpha_s}{\partial t} + \frac{\partial \alpha_s V_{l,i}^I}{\partial x_i} = \alpha_s \frac{\partial V_{l,i}^I}{\partial x_i} - \dot{S}_\alpha + \left( \frac{\alpha_s}{\alpha_l} \right) \dot{\alpha}_{relax,l} \quad (10)$$

$$\alpha_d = \alpha_l - \alpha_s \quad (11)$$

where the two last terms on the RHS of Equation (9) and (10) represent the relaxation of pressure and temperature. Besides, in Equation (10) the relaxation parameter  $\dot{\alpha}_{relax,l}$  is multiplied by a factor  $\left( \frac{\alpha_s}{\alpha_l} \right)$  in order to ensure that only the separate phase liquid is relaxed. By computing  $\alpha_l$  and  $\alpha_s$ , the dispersed phase volume fraction,  $\alpha_d$ , can be computed from Equation (11).  $\dot{S}_\alpha$  is the transfer rate of liquid volume fraction due to the ligament(s) separation. Form Figure 2 this quantity can be found out by

$$\dot{S}_\alpha = \frac{\text{Volume of the ligaments}}{\text{Volume of the cell} \times \Delta t} = \frac{\text{Vol}_{lig}}{\text{Vol}_{cell} \times \Delta t} = \frac{N_{lig}}{\text{Vol}_{cell}} \frac{\pi}{4} \xi_b^2 L_b \quad (12)$$

Where  $\Delta t$  is the time step and,  $N_{lig}$  is the total number of ligaments under breakup in the sub-grid scale.

### 3.2 Primary breakup: Breakup of ligaments

This section describes the primary breakup process. Firstly the breakup of ligaments occurs at a critical Weber number,  $We_{\xi_b}$ , based on ligament diameter ( $\xi_b$ ) [8] as  $We_{\xi_b} = \frac{\rho_g V_{rel}^2 \xi_b}{\sigma}$ , where  $\sigma$  is the liquid surface tension and  $V_{rel}$  is the relative velocity between gas and liquid. The model considers that the ligament length at the time of breakup is directly proportional to the ligament diameter,  $\xi_b$ . This gives,  $L_b = C_{\xi_b} \times \xi_b$ . The value of  $C_{\xi_b}$  is found out to be 6 from the derived experimental correlations [8][15]. During the time of

ligament pinch off, the quantity of surface density  $\dot{S}_{\Sigma_s}$  leaving the separate phase surface density ( $\Sigma_s$ ) is computed as follows,

$$\dot{S}_{\Sigma_s} = \frac{\Sigma_s - \Sigma_{mean}}{\Delta t} = \frac{\text{Surface Area of ligaments}}{\text{Vol}_{cell} \times \Delta t} = \frac{N_{lig} \times \pi \xi_b \times L_b}{\text{Vol}_{cell} \times \Delta t} \quad (13)$$

Breakup will occur if  $N_{lig} \geq 1$ , and  $\dot{S}_{\alpha}$  can be rewritten from Equation (12).

The present study invokes the findings of Villiermaux and assumes that the ligaments are breaking into droplets with mean diameter's,  $d = 2.5\xi_b$  [8][15].  $N_{drop}$  can be calculated from Equation (12). Then, from  $N_{drop}$  and  $d$  the total surface of droplets added to the dispersed phase ( $\dot{S}_{\Sigma_d}$ ) can be calculated.

### 3.3 Secondary Breakup: Breakup of blobs/droplets into child droplets

The model for performing this secondary atomization has already been studied by Vessiller [14], according to the work of Vallet et al.[12]. The present investigation recalls this model for executing secondary atomization through the same surface production source term,  $\dot{\Sigma}_{d_{prod}}$  as follows;

$$\dot{\Sigma}_{d_{prod}} = \underbrace{C_5 \text{Re}_t^{1/2} \frac{\varepsilon_g}{k_g} \Sigma_d}_{\text{production}} - \underbrace{\frac{C_7 a \sigma_l}{\alpha_l \rho_g k_g} \Sigma_d^2}_{\text{destruction}} \quad (14)$$

Here the constants  $C_5$  and  $C_7$  are kept as 0.1 and 0.16 respectively.  $\text{Re}_t = (k_g^2 / \nu_g \varepsilon_g)$  and  $a = C_5 \text{Re}_t^{1/2} \frac{\varepsilon_g}{k_g}$ .

### 3.4 Modelling Turbulent Surface Production Source term, $\dot{\Sigma}_{s_{prod}}$

This production term accounts for the formation of SGS ligaments on the separate phase surface and is modelled as,

$$\dot{\Sigma}_{s_{prod}} = C_{prod_s} \frac{V_{p,i}'' V_{p,j}''}{k_p} \frac{\partial V_{p,i}}{\partial x_j} \Sigma_s \quad (15)$$

A numerical investigation of this production term is required and is carried out in Section 4 in order to check the turbulence of which phase (gas, liquid or both) plays a crucial role for surface production.

A preliminary analysis of the comprehensive atomization model described in Section 3 is carried out in the next section.

## 4 Results and Discussion

The model proposed in Section 3 is analysed here. The DNS results of Herrmann [4] are used for the assessments and calibration of the constants of the suggested atomization model. There are mainly two modelling constants which demand the inquiry. They are  $C_{prod_s}$  and  $We_{\xi_b}$ .

#### 4.1 Computational conditions.

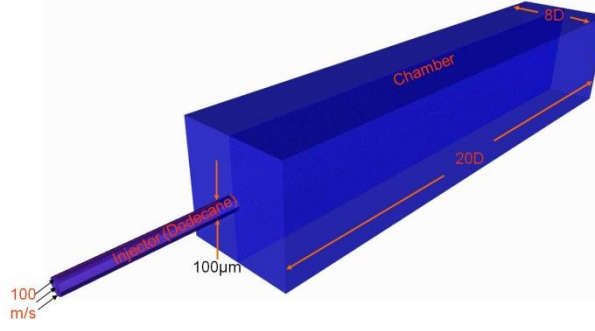


**Figure 3.** The working layout of the computational configuration and definition of the problem.

Gas density $\rho_g$	$24 \text{ kg/m}^3$
Liquid density $\rho_l$	$850 \text{ kg/m}^3$
Temperature of gas in the chamber $T_g$	$300 \text{ K}$
Temperature of liquid in the injector $T_l$	$325 \text{ K}$
Pressure of gas in the chamber $P_g$	$22.3 \text{ bar}$
Pressure of liquid in the nozzle $P_l$	$22.3 \text{ bar}$
Injector diameter $D$	$100 \text{ } \mu\text{m}$
Injection Velocity	$100 \text{ m/s}$
Computational Domain	$20D \times 8D \times 8D$

**Table 1:** Operating Conditions

A typical 3D finite volume hexahedron grid shown in Figure 3 has been generated. The configuration has an inflow boundary at the injector pipe inlet and an outflow at the right boundary. The diameter value of the inflow injector is  $100 \text{ } \mu\text{m}$ . The injector hole is filled by a liquid fuel (n-dodecane) and the chamber is initially filled by gas (nitrogen). The initial pressure and temperature in the liquid and gas phases are shown in the Table 1. For the initial conditions, all velocities inside the liquid (the injector pipe section) are set to  $(0,0,100)^T \text{ m/s}$ , whereas all velocities inside the gas phase are set to zero. All the wall boundary faces are considered with slip condition. The computations are carried out for  $20 \text{ } \mu\text{s}$  and the total computational CPU time required is 3.2hrs running in 8 AMD Barcelona 2.3Ghz processors.

#### 4.2 Numerical investigation of modelling constants

##### 4.2.1 Determination of the model constants $C_{prod_s}$ and $We_{\xi_b}$

The quantity  $\dot{m}_D / \dot{m}_{in}$  computed by Herrmann [4] is used for determining  $C_{prod_s}$ .  $\dot{m}_D$  is the rate of droplet mass generation due to primary atomization and  $\dot{m}_{in}$  is the total injected liquid mass flow rate.

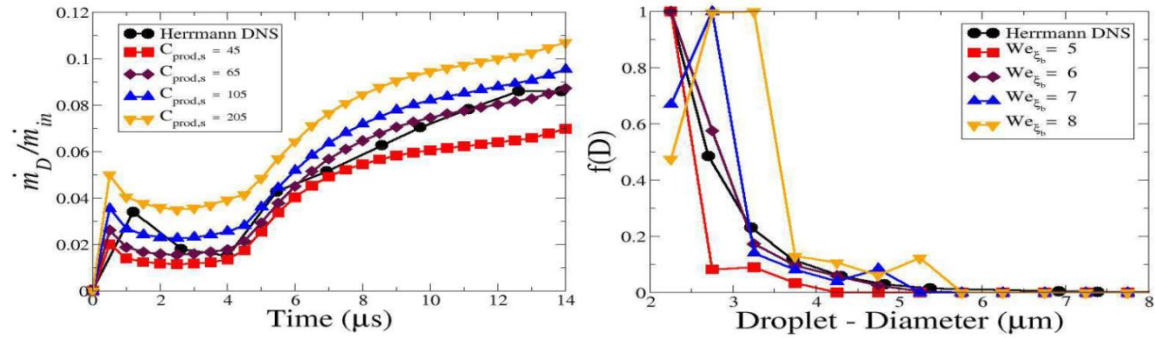


**Figure 4:** Effect of a)  $C_{prod_s}$  in the variation of  $\dot{m}_D / \dot{m}_{in}$  b)  $We_{\xi_b}$  in the final droplet distribution with time.

Figure 4a shows the comparison of  $\dot{m}_D / \dot{m}_{in}$  for different  $C_{prod_s}$  values from 45 to 205. From the figure it is clear that the sensitiveness of this parameter is small. Indeed, a slight increase in  $C_{prod_s}$  will not lead to a significant increased atomization. Besides, all the graphs in Figure 4a follow the same trend compared to the DNS results of Herrmann and out of which the value of  $C_{prod_s} = 65$  provides the best comparison. The Weber number  $We_{\xi_b}$  is an important parameter which determines the primary atomization mechanism. It is worth to

note that an increase in the  $We_{\xi_b}$  leads to an increase in the critical ligament diameter  $\xi_b$  which later corresponds to an increase in the droplet diameter formed from the ligament breakup. Figure 4b shows the  $We_{\xi_b}$  effect on droplet distribution.  $We_{\xi_b}$  is tested with four different values of 5, 6, 7, and 8. For this analysis the value of  $C_{prod_s}$  is considered with a value of 65 and  $C_{\xi_b} = 6$ . From the figure it is found that the behaviour of  $We_{\xi_b}$  is sensitive to this small change. For a higher value of  $We_{\xi_b}$  the trend is to shift towards the right by occupying the maximum number of droplets with higher diameters. Present investigation chooses the value 6 for  $We_{\xi_b}$  and rests near to the DNS results.

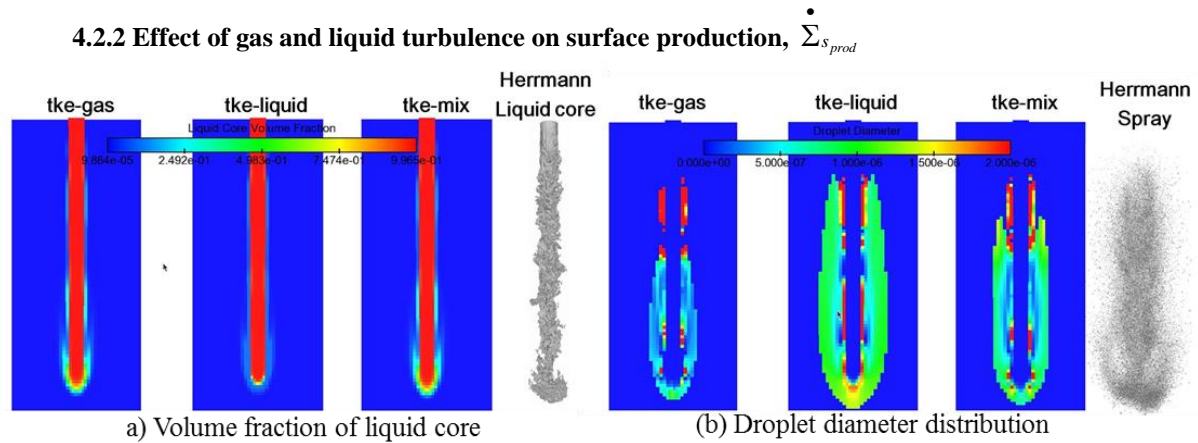


**Figure 5:** Distinguishing the effect of gas, liquid and mixture properties in the turbulent production of surface.

Present investigation uses the mixture turbulent properties for surface production. The reason is that from the above figure (Figure 5), it is found that liquid turbulence has an effect on the spray cap and gas turbulence involves the shearing of the liquid core surface. The mushroom-shape tip is created due to the lateral liquid spread by impingement against the stagnant gas and roll-up. This kind of phenomenon has already been studied extensively by Shinjo and Umemura [11]. This study thus considers these two factors important and thus takes the mixture turbulence as the right choice for the production of ligaments.

## 5 Conclusions

Present study has suggested a new atomization model using surface density approach within the framework of an Eulerian two-phase system. The new atomization model follows a breakup cascade process containing, first the formation of liquid core, then the production of liquid core surface due to gas and liquid turbulence forming ligament like structures, this later follows the breakup of the ligaments under critical breakup condition and at last the deformed ligaments undergo further breakup to form droplets of different sizes. The results also signify the formation of a spray cap at the jet tip where the disintegration seems to occur due to liquid turbulence in addition to the gas turbulence. For the turbulent production of surface, it has been shown that both the gas and liquid turbulence is necessary. Besides, in future, if new precise experimental observations from the near nozzle of the spray are obtained then the proposed atomization model can be further validated.

## Acknowledgements

The authors would like to acknowledge the financial support provided by AVL LIST GMBH, Graz-Austria for presenting this work in ILASS 2013 Conference.

## References

- [1] Habchi, C., Dumont, N., and Simonin, O., *Atomization and Sprays*, vol. 18, no. 2, pp. 129–162, 2008.
- [2] Baer, M.R. and Nunziato, J.W., *Int. J. Multiphase Flow.*, 12, 861-889, 1986.
- [3] Drew, D.A. and Passman, S.L., *Theory of multi component fluids*. In: *Applied Mathematical Sciences*, vol. 135. Springer, 1999.
- [4] Herrmann, M., *Atomization and Sprays.*, 21(4), 283-301, 2011.



- [5] Lebas, R., Ménard, T., Beau, P.A., Berlemont, A., Demoulin, F.X., *Int. J. Multiphase Flow.*, 35, 247-260, 2009.
- [6] Mandumpala Devassy, B., Habchi, C., Daniel, E., In: *Proceedings of the 24<sup>th</sup> Annual Conference ILASS-Europe*, 2011.
- [7] Mandumpala Devassy, B., Atomization modelling of liquid jets using an Eulerian-Eulerian model and a surface density approach. PhD Thesis, Aix-Marseille University, France, 2013.
- [8] Marmottant, P. and Villermaux, E., *J. Fluid Mech.*, 498, 73-111, 2004.
- [9] Morel, C., *Int. J. Multiphase Flow.*, 33, 1045-1073, 2007.
- [10] Saurel, R. and Abgrall, R., *J. Comp. Physics.*, 150, 425-467, 1999.
- [11] Shinjo, J. and Umemura, A., *Int. J. Multiphase Flow.*, 36, 513-532, 2010.
- [12] Vallet, A., Burluka, A.A., Borghi, R., *Atomization and Sprays.*, 11(6), 619-642, 2001.
- [13] Velghe, A., Gillet, N., Bohbot, J., *22nd International Conference on Parallel Computational Fluid Dynamics (ParCFD 2010)*.
- [14] Vessiller, C., Contribution à l'étude des bouillards denses et dilués par les approches Euleriennes et Lagrangiennes. PhD Thesis, Ecole Centrale Paris, France, 2008.
- [15] Villermaux, E., *New Journal of Physics.* 6:125, 2004.
- [16] Zein, A., Hantke, M., Warnecke, G., *J. Comp. Physics.*, 229, 2694-2998, 2010.

Session:

**Phase change,  
combustion and  
particle phenomena**

## Implementation and Calibration of the Icing and Contamination Research Facility (iCORE)

T. Hauk, T. Strobl and D. Raps

EADS Innovation Works, TCC2 - Metallic Technologies and Surface Engineering,  
81663 Munich, Germany

### Abstract

Research on fundamental physics of small ice particles, their trajectories around, and impact onto aerofoils, as well as ice accretion on surfaces now demands major attention by aircraft manufacturers and research institutions due to scheduled regulatory changes regarding the certification of airworthiness. Moreover, with regard to future laminar wing structures, the focus is also put on the development of innovative and viable solutions against insect contamination.

In order to be able to perform efficient and broad research on these topics, EADS Innovation Works has built a laboratory Icing and Contamination Research Facility (iCORE).

In this paper, an introduction to iCORE is given, with special focus on three configurations later referred to as the basic, the icing (with a spray bar system for cloud generation) and the contamination (with an ejection module for small particles) configuration together with calibration data. Results are presented which show the spatial and temporal distributions of the total temperature, the total pressure and the velocity for different operating parameters. Flow angularity data as well as turbulence measurements using a 1D hot-wire probe are shown. Furthermore, an exemplary liquid water content (LWC) distribution within the icing area and a droplet size histogram are provided using the icing blade method and the phase Doppler technique.

### Introduction - Overview of the iCORE

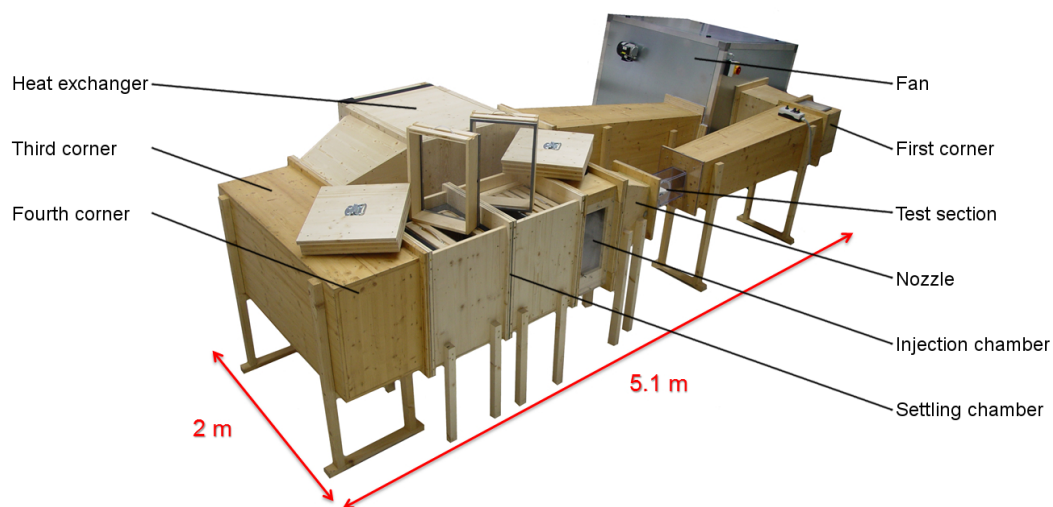


**Fig. 1** - Pictorial view of the iCORE facility

The iCORE facility (see **Fig. 1**) is a closed-circuit wind tunnel with a ground area of about 10 m<sup>2</sup>. Its walls are made out of up to three layers of spruce wood, partly containing insulation material. The inner surfaces are varnished to protect the wood from moisture. The wind tunnel atmosphere consists of ambient air which is accelerated by a radial fan with a maximum power of 22 kW, installed in a noise-reducing metal box in the second corner. The maximum achievable test section Mach number is 0.45. For icing experiments, the air can be cooled down to a minimum test section total temperature  $T_t$  of -40 °C by a cooling system with a cooling power of up to 17.5 kW. The cross section of the heat exchanger is 500 x 800 mm<sup>2</sup> and its internal area is about 118 m<sup>2</sup>. This results in the effect of a low pressure loss and a short response time to reach stable selected negative temperatures (usually within 15 minutes).

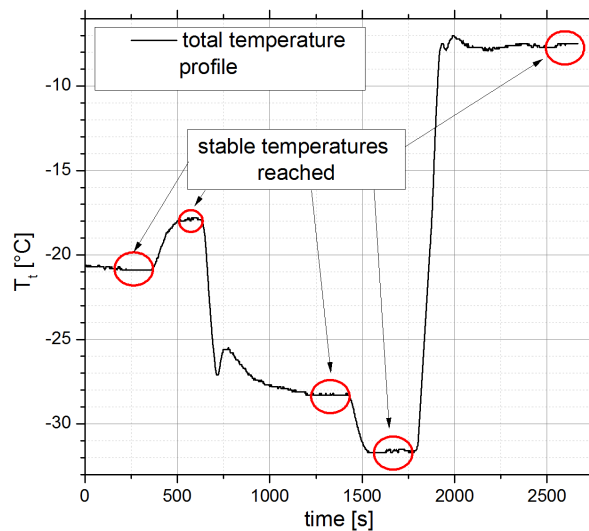


**Fig. 2** - Total temperature profile in the test section for five different selected temperature values in one single test run

An example is given in **Fig. 2**, where five different total temperatures in the geometric centre of the test section have been selected in a single test run. The graph shows that stable total temperatures are reached within minutes depending on the temperature difference between the actual and previously selected total temperature. Turning vanes are installed in the third and fourth corner behind the heat exchanger. In the middle of these two corners, in the centre of the cross section with the dimensions 300 x 450 mm<sup>2</sup>, a Prandtl probe with a total temperature sensor (K-type; uncertainty:  $\pm 1.1$  K) from United Sensor Corp. is installed. This cross section size is maintained throughout the 960 mm long settling and 300 mm long injection chamber. In the settling chamber, just behind the fourth corner, different screens, honeycomb structures and filter mats as well as the spray bar system can be placed. A relative humidity sensor is also situated in the settling chamber. In the injection chamber, which follows the settling chamber, an ejection module for small particles or a monodisperse droplet generator system can be installed. Using either the spray bar system or the monodisperse droplet generator system, a cloud of droplets with a median volume diameter (MVD) between 10  $\mu\text{m}$  and 40  $\mu\text{m}$  can be generated or a distinct stream of monodisperse droplets with a diameter ranging from 40  $\mu\text{m}$  up to 250  $\mu\text{m}$  can be injected. The side walls of the injection chamber are made out of plexiglass to provide optical access.

The nozzle has a contraction ratio of 9:1 and consists of glass fibre reinforced plastic. It is equipped with six static ports, three per entrance and exit cross section, to be able to set the Mach number in the test section without using an extra probe. Different test sections are available which are usually made out of polycarbonate and have a length of 450 mm and a cross section of 100 x 150 mm<sup>2</sup>. From the end of the test section up to the first corner, in which there are also turning vanes installed, the end diffuser with an half-angle of 1.8 ° spans.

Regarding the instrumentation, an 18-port pressure transducer array from Aerolab LLC (uncertainty:  $\pm 40$  Pa) as well as a Graphtec GL 220 10-channel data logger for the measurement of the temperature (uncertainty:  $\pm(0.05\% \text{ of value} + 1\text{ }^{\circ}\text{C})$ ) and the relative humidity (uncertainty: N/A) are used. The fan power and the cooling power can be controlled via two separate frequency drives.

The iCORE facility can achieve a wide range of total temperatures and air velocities. The envelope is presented in **Fig. 3**. Within the blue frame, all combinations of air velocity and total temperature in the test section are shown which can be achieved permanently using the cooling system. This is in contrast to the combinations which can be found in the black frame. Here, the cooling system is inactive during testing since a cooling power smaller than the minimum cooling power of about 6 kW would be required to maintain these states continuously. Within this frame the change of the total temperature with time  $|(dT_t/dt)|$  during tests is less than 1 K per minute. The combinations surrounded by the red frame can be achieved permanently with an open-loop configuration without an active cooling system. In this case, the total temperature is determined by the ambient temperature and the first corner is removed. The open-loop configuration is mainly used for contamination experiments in order to avoid the contamination of the fan blades and the heat exchanger.

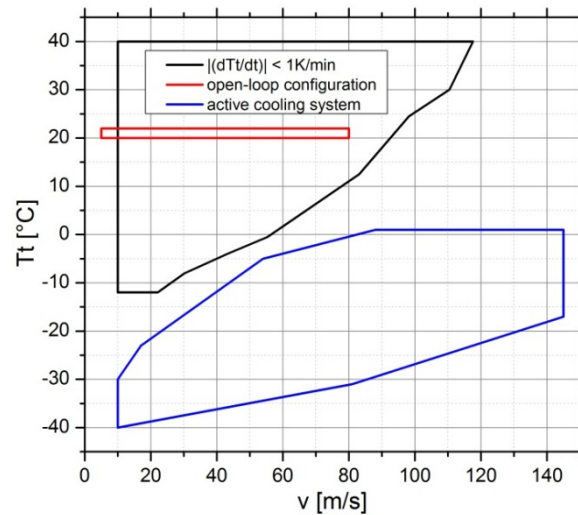


Fig. 3 - Air velocity and total temperature envelope of iCORE

## Experimental test-rig

Three different configurations of the settling and injection chamber, namely the basic, the icing and the contamination configuration are described in detail in this section. For tests, single wall and double wall test sections are available in which small aerofoils or flat plates can be placed. In this paper, only the calibration test section with a single wall design is presented.

### Basic configuration

The settling chamber consists of a honeycomb structure with about 15 000 hexagonal cells and a length to hydraulic diameter ratio of 8, placed at the beginning of the chamber. It is followed by eight almost equally positioned screens (distance: 111 mm each) with a mesh width of 3.15 mm, a wire diameter of 0.45 mm and a porosity of 0.766 (see Fig. 4 and Fig. 5). Optionally, the honeycomb structure and the screens can be easily replaced by empty frames. The injection chamber is empty.

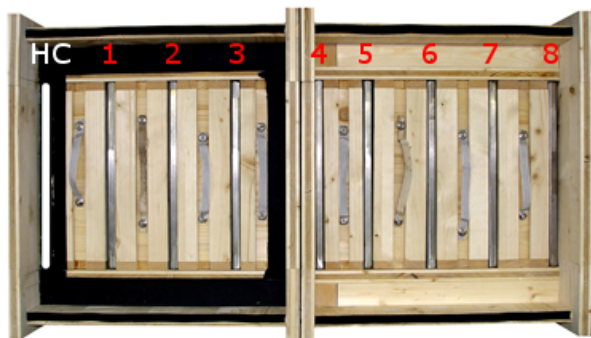


Fig. 4 - Top view of the settling chamber in basic configuration (one honeycomb structure (HC) and eight screens)

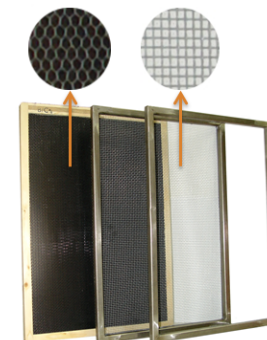


Fig. 5 - Detail view of a honeycomb structure, a screen and an empty frame

### Icing configuration

A spray bar system with three horizontally aligned pneumatic atomizing nozzles is placed behind the honeycomb structure and three closely placed screens in the first quarter of the settling chamber. The spray bar is vertically placed in the middle of the settling chamber and consists of a NACA 0030 which houses the nozzles (see Fig. 6 and Fig. 7). The water mass flow of each nozzle is regulated by three digital water mass flow controllers. The injection chamber is empty. An exemplary ice shape, generated by the described spray system, is shown in Fig. 8.



**Fig. 6** - Top view of the spray bar system with three nozzles

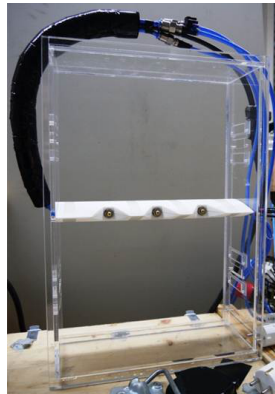


**Fig. 7** - Front view of the spray bar system rack



**Fig. 8** - Exemplary ice shape generated with the spray bar system on a NACA 0012 aerofoil

### Contamination configuration

An ejection module (see **Fig. 9**) is placed in the injection chamber (see **Fig. 10**) to accelerate small particles with pressure air, for example, fruit flies or ice particles for contamination and impact tests. The maximum achievable speed of the particles is approximately 90 m/s. The tube, in which the acceleration takes place, is located in the centre of the cross section and ends 80 mm ahead of the entrance of the test section. A honeycomb structure and eight screens are installed in the settling chamber in this configuration (see **Fig. 4**). An exemplary post-impact high speed camera image of a common fruit fly is shown in **Fig. 11** (see Kok et al., [1], for more information).

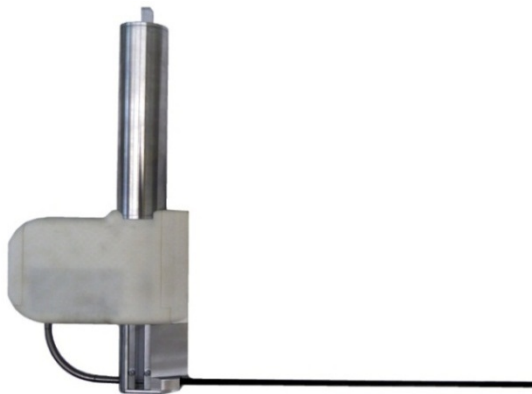


**Fig. 9** - Ejection module for the acceleration of small particles



**Fig. 10** - Ejection module placed in the injection chamber

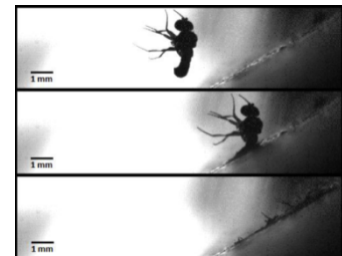


**Fig. 11** - Exemplary impact of a *Drosophila Melanogaster* on a flat plate; Kok et al. [1]

### Calibration test section

For the calibration and flow quality measurements, a test section is used on top of which a traverse unit for different probes (e.g. a Prandtl probe, a 3D directional probe or a hot-wire probe) is installed (see **Fig. 12**). The traverse unit can be moved arbitrarily horizontally, perpendicular to the flow. Moreover, the vertical position of the installed probe can be varied continuously and its exact position can be read from a calliper gauge (see **Fig. 13**). Furthermore, the position of the traverse unit including the probe can be changed in the flow direction when iCORE is in a non-operating state. Replacing the traverse unit, an icing blade (see **Fig. 14**) with a length of 145 mm and a width of 3.2 mm can be installed to measure the LWC using the icing blade technique according to Stallabrass, [2]. A movable shield protects the icing blade until a steady-state in the test section has been reached. The icing blade can also be moved horizontally, perpendicular to the flow.



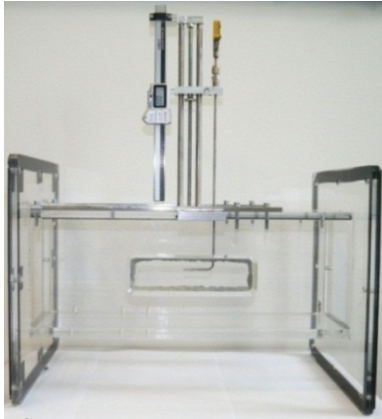


**Fig. 12** - Calibration test section with the traverse unit and a Prandtl probe



**Fig. 13** - Detail view of the traverse unit with a 3D probe

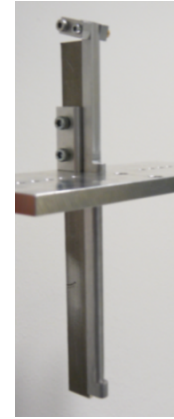


**Fig. 14** - Icing blade with movable shield

## Results and Discussion

The cross section which has been chosen for the flow quality and calibration measurements spans through the geometric centre of the test section and is perpendicular to the direction of the flow (X – axis). The flow quality plots, looking downstream, show the spatial deviation of the values measured in different positions (black dots) in relation to the values in the centre of the cross section. The respective physical quantities are the total temperature  $T_t$ , the total pressure  $p_t$  and the velocity  $v$ . Temporal stability measurements of the velocity and the total temperature in the geometric centre are shown for the basic configuration. Moreover, outcomes of the flow turbulence and the flow angularity investigations are presented. An exemplary liquid water content (LWC) distribution and a droplet size histogram for the icing configuration are shown as well. For the spatial uniformity and temporal measurements of the total temperature, of the total pressure and of the velocity, an airspeed of 90 m/s and a total temperature of -15 °C have been chosen. During these measurements, the spray bar system or, respectively, the ejection module were not active. The flow turbulence was determined at the same velocity at  $Z = 0$  mm using a 1D hot-wire probe with a sampling rate of 10 kHz. However, a positive total temperature of 25 °C has been chosen for all configurations to eliminate the risk of ice particle impacts on the sensitive wire. Due to calibration limits of the manufacturer of the 3D directional probe a velocity of 55 m/s and a total temperature of 25 °C have been chosen for the yaw angle measurements. The exemplary LWC distribution measurement with the icing blade has been done at a static temperature  $T_s$  of -18 °C and at a velocity of 90 m/s at  $Y = 0$  mm. The exemplary droplet size histogram was measured in the geometric centre with a PDI system at a velocity of 90 m/s and a total temperature of 0 °C (see **Fig. 24**).

### Basic configuration

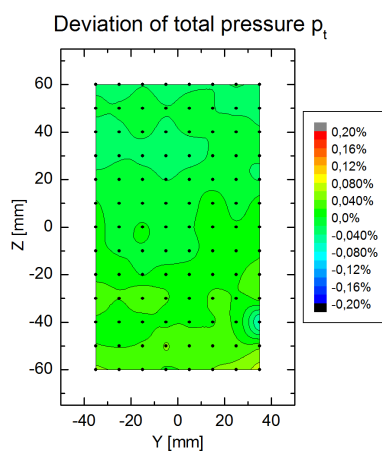


**Fig. 15** -  $v = 90$  m/s;  
 $T_t = -15$  °C

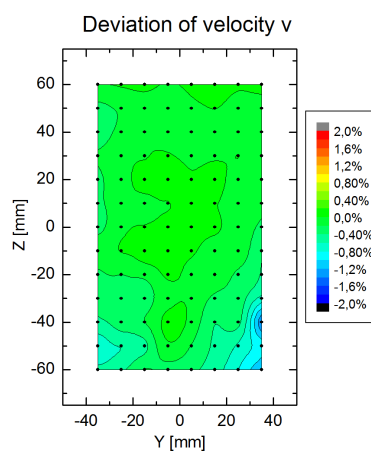


**Fig. 16** -  $v = 90$  m/s;  
 $T_t = -15$  °C

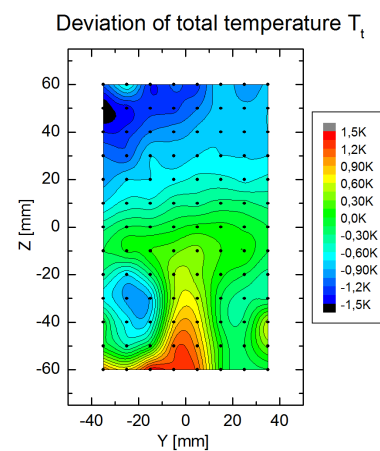


**Fig. 17** -  $v = 90$  m/s;  
 $T_t = -15$  °C



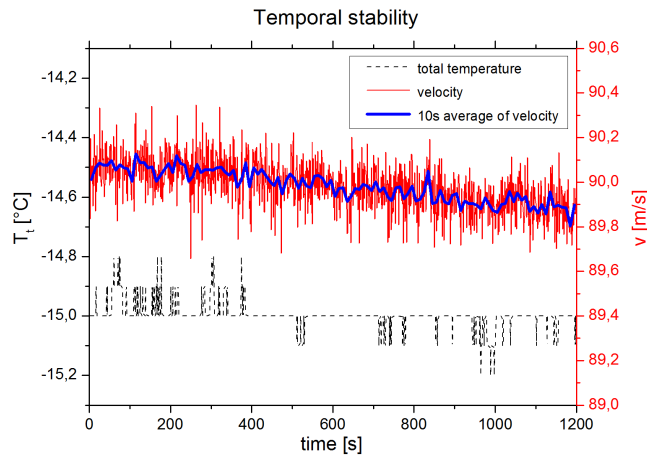


Fig. 18 -  $v = 90$  m/s;  $T_t = -15$  °C

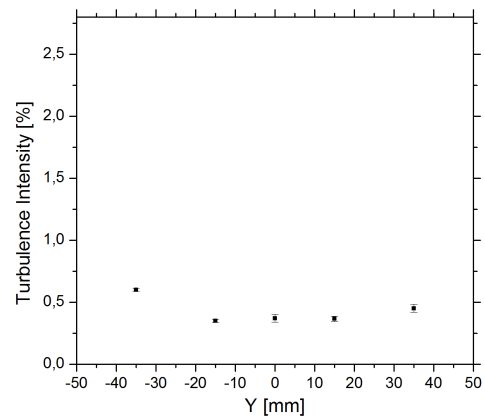


Fig. 19 - Turbulence intensity at  $Z = 0$  mm;  
 $v = 90$  m/s;  $T_t = 25$  °C

### Icing configuration

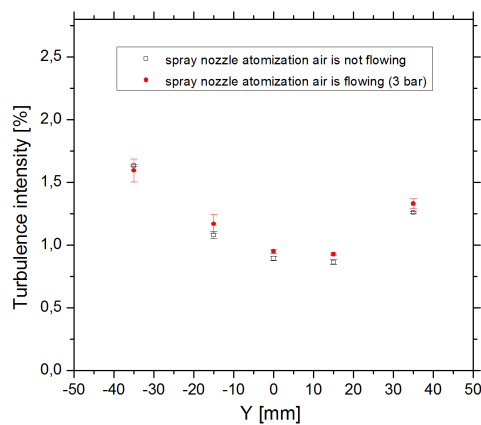


Fig. 20 - Turbulence intensity at  
 $Z = 0$  mm;  $v = 90$  m/s;  $T_t = 25$  °C



Fig. 21 - Icing  
blade with exemplary  
rime ice distribution  
at  $Y = 0$  mm

Z [mm]	LWC [g/m <sup>3</sup> ]
40	0.032
30	0.058
20	0.12
10	0.18
0	0.21
-10	0.17
-20	0.097
-30	0.036
-40	0.0081

Tab. 1 - LWC distribution at  $Y = 0$  mm  
measured with the icing blade technique  
(see Fig. 21; assumed collection  
efficiency  $e_b = 0.9$ ; ice density  $\rho_i =$   
880 kg/m<sup>3</sup>;  $v = 90$  m/s;  $T_s = -18$  °C)

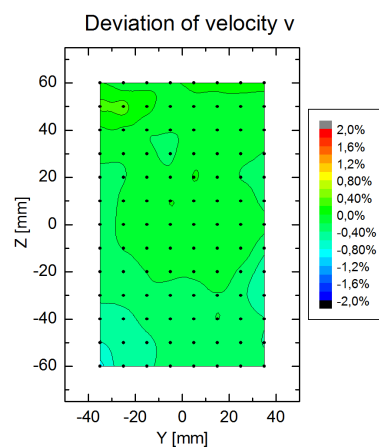


Fig. 22 -  $v = 90$  m/s;  
 $T_t = -15$  °C

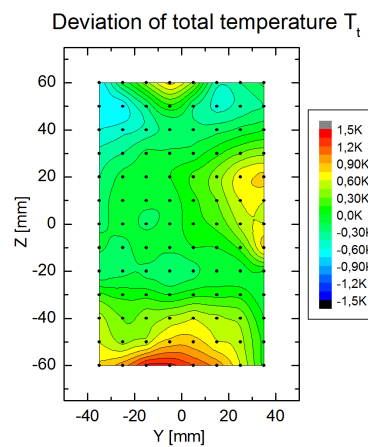
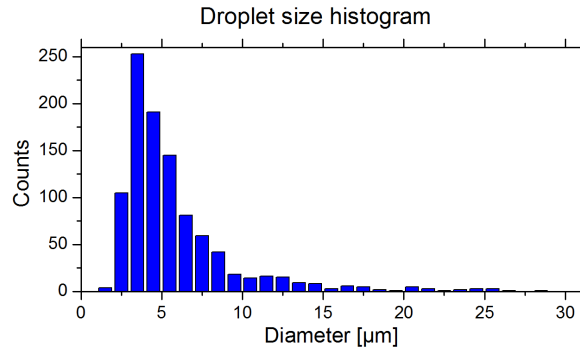
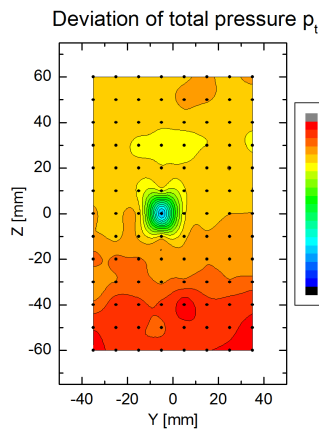


Fig. 23 -  $v = 90$  m/s;  
 $T_t = -15$  °C



**Fig. 24** - MVD = 16  $\mu\text{m}$ ;  $v = 90 \text{ m/s}$ ;  $T_t = 0 \text{ }^\circ\text{C}$

### Contamination configuration



**Fig. 25** -  $v = 90 \text{ m/s}$ ;  
 $T_t = -15 \text{ }^\circ\text{C}$

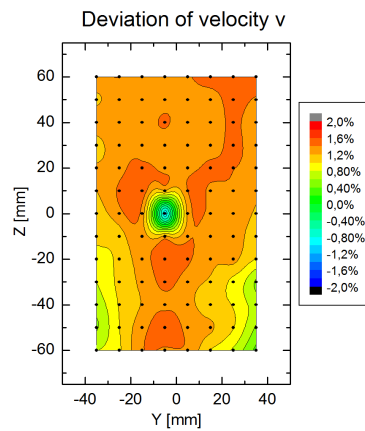


**Fig. 26** -  $v = 90 \text{ m/s}$ ;  
 $T_t = -15 \text{ }^\circ\text{C}$

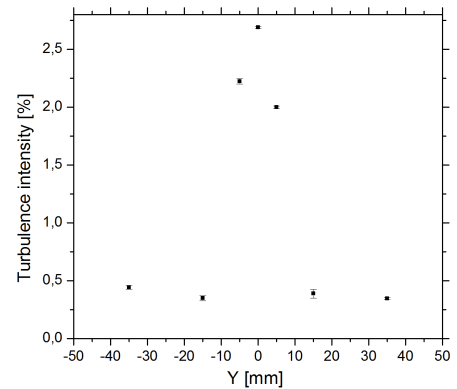


**Fig. 27** - Turbulence intensity at  
 $Z = 0 \text{ mm}$ ;  $v = 90 \text{ m/s}$ ;  $T_t = 25 \text{ }^\circ\text{C}$

### All configurations: Yaw angle measurement results

Negative angles refer to flow velocity vectors which point towards the negative Y – direction. The measurement uncertainty is  $\pm 0.5 \text{ }^\circ$ .

Configuration	Position (Y [mm] / Z [mm])								
	(-25/35)	(0/35)	(25/35)	(-25/0)	(0/0)	(25/0)	(-25/-35)	(0/-35)	(25/-35)
Basic	-0.5 $^\circ$	-1.0 $^\circ$	-1.0 $^\circ$	-1.0 $^\circ$	-1.0 $^\circ$	-1.3 $^\circ$	1.3 $^\circ$	-0.8 $^\circ$	-2.8 $^\circ$
Icing	0.5 $^\circ$	-0.3 $^\circ$	-0.3 $^\circ$	-1.2 $^\circ$	-1.7 $^\circ$	-2.0 $^\circ$	-2.0 $^\circ$	-2.7 $^\circ$	-2.5 $^\circ$
Contamination	-0.5 $^\circ$	-1.0 $^\circ$	-1.0 $^\circ$	-1.0 $^\circ$	-1.0 $^\circ$	-1.2 $^\circ$	1.2 $^\circ$	-1 $^\circ$	-2.5 $^\circ$

**Tab. 2** - Yaw angles of the flow at different positions for  $v = 55 \text{ m/s}$  and  $T_t = 25 \text{ }^\circ\text{C}$

Regarding the basic configuration, the spatial distributions of the total pressure (see **Fig. 15**) and the velocity (see **Fig. 16**) are within  $\pm 0.08 \text{ }^\circ$  and  $\pm 1.4 \text{ }^\circ$  respectively. The total temperature (see **Fig. 17**) varies within  $\pm 1.6 \text{ K}$ . The temporal stability measurements (see **Fig. 18**) of the total temperature and the velocity over a period of 20 minutes show minor changes of 0.4 K and of less than 0.4 m/s (in this case regarding a 10 second average value). The turbulence intensities (see **Fig. 19**) at five different positions (along a usually located leading edge of an aerofoil) stay below 0.6 %. The yaw angle does not exceed  $\pm 2.8 \text{ }^\circ$  (see **Tab. 2**).

With respect to the icing configuration, the activation of the atomization air, having a pressure of 3 bar, has no significant influence on the turbulence intensity which stays below 1.7 % at the selected positions (see **Fig. 20**). In **Fig. 21**, an exemplary rime ice distribution is shown. The accordant LWC distribution is presented in **Tab. 1**. The shape of the distributions can be traced back to the fact of using only one horizontal spray bar which is vertically placed in the middle of the settling chamber. The spatial distributions of the velocity and the total temperature are within  $\pm 0.06 \text{ }^\circ$  and  $\pm 1.5 \text{ K}$  respectively (see **Fig. 22** and **Fig. 23**). The yaw angle does not

exceed  $\pm 2.7^\circ$  (see **Tab. 2**). During the spatial distribution and yaw angle measurements, the atomization air was turned off.

Regarding the contamination configuration, the influence of the tube of the ejection module causing a loss in total pressure and in velocity as well as an increase of the turbulence intensity can be clearly seen in the respective figures (see **Fig. 25**, **Fig. 26** and **Fig. 27**). However, the deviations of the total pressure and the velocity still stay within the boundaries of  $\pm 0.2\%$  and  $\pm 1.6\%$ . The turbulence intensity close to the centreline is increased and has a maximum value of  $2.7\%$ . The slight off-centre location of the minimum total pressure and the minimum velocity is consistent with the yaw angle of the flow at the geometric centre of the test section (see **Tab. 2**). The yaw angle stays within  $\pm 2.5^\circ$ .

According to SAE ARP 5905, [3], regarding the calibration of icing wind tunnels (with an activated atomization air flow), the maximum values of the spatial uniformity of the velocity and the temperature in the relevant temperature range of icing tests should be  $\pm 2\%$  and  $\pm 1\text{ K}$  respectively. The tunnel centreline temporal stability of the velocity and the temperature should not exceed  $\pm 2\%$  and  $\pm 0.5\text{ K}$ . The limit value of the flow angularity is  $\pm 3^\circ$ . Regarding the flow turbulence, the limit value with an inactive spray bar system is  $2\%$  and with the atomization air turned on this value is  $5\%$ . The uniform icing cloud is defined as the area of the test section over which the LWC does not vary by more than  $\pm 20\%$  from the test section centreline LWC. As a result, the uniform icing cloud spans from about  $Z = -13\text{ mm}$  to about  $Z = 13\text{ mm}$  in case of the exemplary icing blade test for a selected LWC of  $0.18\text{ g/m}^3$  (see **Fig. 21** and **Tab. 1**).

The application of these standards on the presented calibration, under the assumption that the active pressure air would not change the results significantly, leads to the finding that the vast majority of the requirements are met. Requirements which are not completely met are the total temperature distributions where there are values near the boundaries of the grid exceeding  $\pm 1\text{ K}$ . However, the relevant icing area for a typical NACA 0012 aerofoil in iCORE spans vertically from  $Z = -11\text{ mm}$  to  $Z = 11\text{ mm}$  (see **Fig. 8**) and almost all contamination and impact tests are executed in the centre of the test section. That is why the total temperature deviations near the boundaries of the grid exceeding  $\pm 1\text{ K}$  can be neglected.

## Conclusions

The calibration measurements showed very satisfying results for all three presented configurations, namely the basic, the icing and the contamination configuration. Due to this fact, its flexible design and its short response times to reach stable temperatures, iCORE is a powerful multi-purpose and cost efficient tool to cope with the actual and future demands of aircraft manufacturers and research institutions.

## Acknowledgements

The authors would like to acknowledge the funding provided by the European Union's Seventh Framework Programme (FP7/2007-2013) under grant agreement n° AAT-2010-RTD-1-266029 (AEROMUCO project: "AERodynamic Surfaces by advanced Multifunctional COatings").

## References

- [1] Kok, M., Raps, D. and Young, T.M. "Effects of surface roughness and energy on insect residue adhesion to aircraft leading edge surfaces," Proceeding of the 36th Annual Meeting of The Adhesion Society, The Hilton, Daytona Beach, 3–6 March, 2013
- [2] Stallabrass, J.R., "An Appraisal of the Single Rotating Cylinder Method of Liquid Water Content Measurement," Canadian Research Council Report LTR-LT-92, Nov. 1978
- [3] "Calibration and Acceptance of Icing Wind Tunnels," SAE ARP 5905, SAE International, Warrendale, PA, Sept. 2003

## Assessing icephobicity of superhydrophobic surfaces as passive coating icing mitigation strategy on helicopter blades

Stefania Tarquini<sup>1</sup>, Carlo Antonini<sup>1,2</sup>, Alidad Amirfazli<sup>3</sup> and Jose Palacios<sup>4</sup> and Marco Marengo<sup>1</sup>

1: Department of Engineering, University of Bergamo, Dalmine, BG, Italy

2: Laboratory of Thermodynamics in Emerging Technologies, Mechanical and Process Engineering Department, ETH Zurich, 8092 Zurich, Switzerland

3: Department of Mechanical Engineering, York University, Toronto, ON, M3J13P, Canada

4: Department of Aerospace Engineering, The Pennsylvania State University, University Park, PA, 16802, United States

### Abstract

Ice accretion represents a major hazard for helicopter blades. The state-of-art of icing protection is based on electro-thermal de-icing systems, which require high power inputs and operate intermittently, allowing partial ice accretion. The present work aims to investigate the potential of a new coating strategy, based on the use of functionalized surfaces. Superhydrophobic surfaces, characterized by low water adhesion, were tested in different icing conditions inside the rotor ice chamber of the Pennsylvania State University, in order to verify if they also exhibit icephobic properties (low ice adhesion) and if they can be used to promote ice shedding. Results for SHS showed a decrease in ice adhesion load respect to common metals, but the entity of the reduction is affected by a complex variety of factor, such as environmental conditions and surface properties. Nonetheless, it was observed that SHS shorten the shedding time and decrease the ice shape thickness on the airfoil leading edge.

---

### Introduction

Helicopter icing, or better ice accretion on helicopter surfaces, can compromise flight safety and affect performance, stability and control of the helicopter. Flight into adverse icing conditions leads to potentially dangerous ice accretion phenomena on helicopter blades, which change the airfoil shape and increase the blade weight, inducing the helicopter to degrade its performances for the decreased lift, increased drag, torque on the main rotor and blade vibration. Further, ice shedding from blades due to centrifugal force creates large vibrations due to imbalanced rotors and poses a ballistics danger to the helicopter.

Electro-thermal devices are the state-of-the-art for ice protection systems. These de-icing systems melt the ice layer interface of accreted ice, allowing ice removal by centrifugal and aerodynamic forces. Furthermore, they require a high power input ( $3.9 \text{ W/cm}^2$  or  $25 \text{ W/in}^2$ ) [1], which leads to an increase of the overall weight of the helicopter related to power supplies unsuitable for smaller gross-weight helicopters [2,3] and lead these devices to work intermittently only on the leading edge of the blade (where most of ice accretes) in order to limit power consumption, but causing also the formation of “runback ice”, the ice obtained by freezing the water which travels in the aft direction. Nevertheless, these systems effectiveness rely on high thermal conductivity of leading edge materials, unsuitable for new generation erosion resistant polymer based leading edge materials [4].

Passive coating strategies might be helpful for icing mitigation: a first possible strategy is based on *icephobicity* (the property of a surface coating on where ice adhesion is low), which should lead to an ice adhesion reduction [7, 12, 13, 15]. However, materials with this characteristic have problems under erosion conditions inherent to rotor blade operations (rain, sand particles impact), degrading or losing their icephobic properties after few tests [1, 6, 11], concluding that the erosion resistance of the coatings is not sufficient to be considered for practical applications.

A second strategy is based on *superhydrophobicity* (the property of a surface coating on where liquid water adhesion is low), which aims to reduce or eliminate water accumulation on the surface before water freezes by letting droplets rebound off the aerodynamic surface, thanks also to the high mobility of the superhydrophobic surface (SHS) [18]. Antonini et al, during Icing Wind Tunnel tests on a fixed wing configuration, showed that a SHS can effectively mitigate ice accretion: SHS coatings reduced the heat power consumption to promote ice de-bonding from 20% to 80% (depending on icing conditions) and suppressed runback ice, if compared to a standard aluminum surface [5]. Further authors obtained performances improvements in reduced adhesion strength thanks to SHS surfaces [10, 12, 14]. In [15], the authors studied various advanced icephobic coatings,

explaining that the potential of SHS coatings for ice protection lies in the fact that SHS are normally porous materials that promote the presence of “tiny” air pockets at the ice/solid interface, reducing the real ice/coating surface area and disrupting bonding by creating stress concentrations. Nevertheless, the authors of [8] found that icephobic properties of superhydrophobic surfaces can be compromised in case of frost formation that occurs at below-zero temperatures (tested were performed at  $-5^{\circ}\text{C}$ , analyzing impact of millimetric water drops). Therefore, it may be important to study how to improve the icephobicity of materials using conditions close to real icing conditions.

The objective of the present paper is to study the icephobic qualities of SHS coatings with application to rotor blades, evaluating ice accretion, ice regime and ice adhesion load on different surfaces to see if the coatings might be effective in reducing ice adhesion. The presence of centrifugal forces makes icing tests on rotor blades a valuable test case, since ice accretion and shedding are studied in an environment that is able to simulate different natural atmospheric icing conditions, which can be obtained by changing icing parameter like temperature, Liquid Water Content (LWC) or Mean Volumetric Diameter (MVD) of the spray. By changing natural icing condition is also possible to obtain different ice regimes in the accreted ice, like *glaze* ice (obtained for temperatures from  $0^{\circ}\text{C}$  to around  $-12^{\circ}\text{C}$ , with a transparent color and trapezoidal or horns shapes) and *rime* ice (very difficult to detach, obtained for temperatures lower than  $-12^{\circ}\text{C}$ , with a milky color and a round and compact shape), to investigate the ice regime role in the ice adhesion phenomena.

### Experimental test-rig

At the Pennsylvania State University, the Adverse Environment Rotor Test Stand (AERTS) facility shown in **Figure 1** is formed of an industrial  $(6.1 \times 6.1 \times 6.1)\text{m}^3$  cold chamber with a 89.5 kW motor in its center that rotates the lower hub of a QH-50D DASH UAV vehicle. The chamber can generate temperatures between  $-25^{\circ}\text{C}$  and  $0^{\circ}\text{C}$ . The configuration has the capability to reach 1500 RPM with 1.37 m radius blades, reproducing full-scale helicopter tip speeds. The measurement apparatus is composed by a load cell, accelerometers and shaft torque sensor. 15 NASA standard icing nozzles are located in the chamber ceiling to generate the icing cloud. Nozzles inject inside the chamber a combination of water droplets of controllable MVD. The cloud LWC can also be controlled depending on the air pressure and on the number of nozzles selected [16].

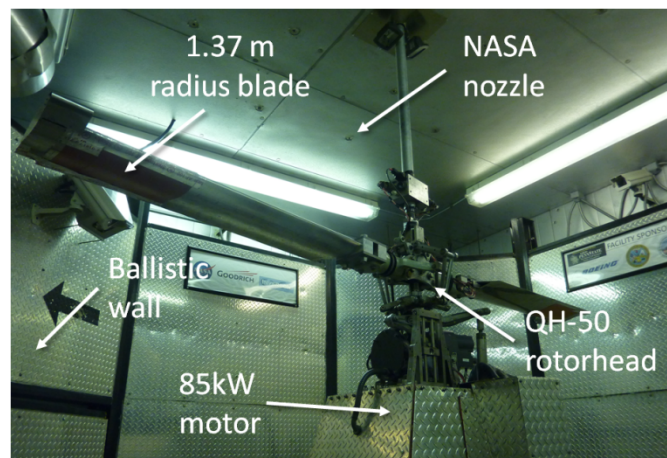


**Figure 1.** Photograph of the AERTS facility and detail of icing cloud. Test rotor has a diameter of 5.72m.

A fixed structure has been built on the tip of each blade, to support test coupons and to allow the measurement of the ice shedding force. In **Figure 2a** is shown the metallic fairing mounted on the tip of the blade together with the coupon, while in **Figure 2b** is shown the inner structure of the mounting, including a titanium beam (able to bend only along the spanwise direction) on which 4 strain gauges are mounted in a full bridge configuration plus amplifiers to measure the strain amount, while compensating for temperature and increasing the sensitivity of the measure. On the beam tip a metallic hardware is attached to support the inter-changeable coupons, which measure  $(9.14 \times 13.97)\text{cm}$ . Differently from [1], no heating mats were used on the blade or on the fixture because, during the experiments, it has been proved that thermal energy leakage from side heaters and traveling liquid water in the span direction influence the test results.

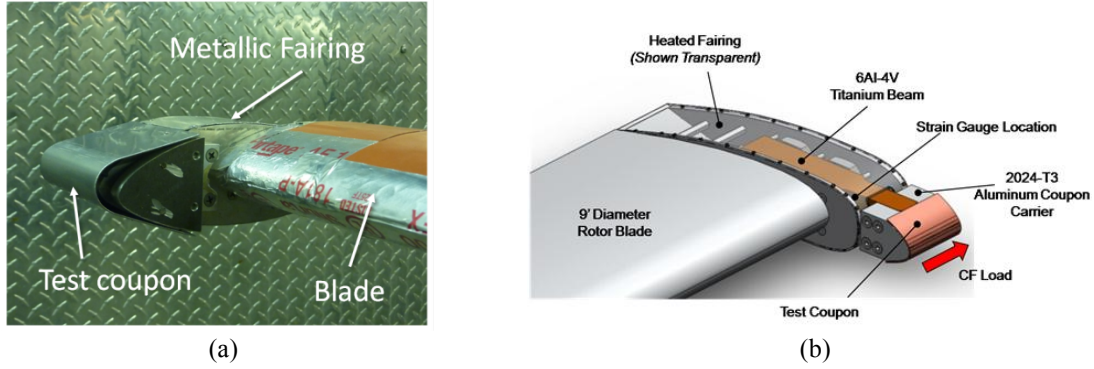


**Figure 2.** View of the the structure used to mount the test coupon onto the blade tip: a) metallic support attached on the tip of the blade with the test coupon mounted onto the fairing. b) CAD drawing showing the inside components of the supporting structure for the sample (red), highlighting the bending beam (dark orange), which is used to measure ice load. Image B taken from [1].

### Ice load measure

After the chamber temperature is cooled down to a desired temperature, both water spray MVD and LWC are set. In Figure 3 is shown the typical voltage trace obtained from the strain gauges of one blade during the test: starting from the left of the graph,  $V_0$  is the gauge voltage measured when the rotor is not spinning; then the gauge voltage starts to decrease while the rotor is spooled up to the test RPM value ( $V_{RPM}$ ), at which the trace stays stable until the cloud is turned on and the proper test begins. Small liquid water droplets exit from the nozzles on the ceiling and enter in the cold environment of the chamber, becoming sub-cooled. When subjected to this icing environment, ice starts to accrete on the samples and continues to accumulate until the centrifugal forces exceed ice adhesion forces and the ice sheds. During ice accretion, the gauge voltage further decreases due to the increasing ice centrifugal load from an initial value,  $V_{RPM}$ , to a value  $V_{in}$  (or  $V_{shed}$ ), when the ice sheds and the voltage jumps to the value  $V_{fin}$ . The mass of detached ice is then proportional to the difference of gauge voltage ( $V_{fin} - V_{in}$ ) and the ice load due to the adhesion force ( $L_{ice}$ ) can be calculated with the formulas:

$$L_{RPM} = m_{tip} r \Omega^2 \quad [1]$$

$$L_{ice} = (V_{shed} - V_{fin}) \cdot \frac{L_{RPM}}{V_{RPM} - V_0} \quad [2]$$

Where  $L_{RPM}$  is the ice load due to the RPM velocity;  $m_{tip}$  is the total mass of the carrier assembly and the test coupon;  $r$  is the radius of the test coupon center (fixed at 1.41m) and  $\Omega$  is the rotational velocity. After the end of the test, pictures of samples were taken with different views to record the detach area of ice and the ice shape.

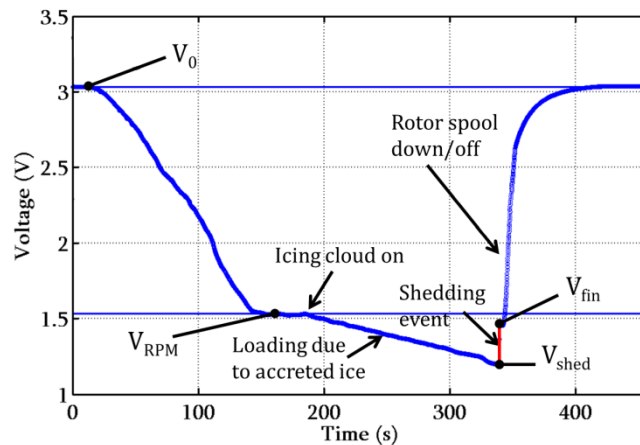


**Figure 3.** Test voltages trace recorded by the strain gauges with test time.

## Materials and Test Conditions

The test conditions are summarized in Table 1. Four surface materials were tested: two standard metals and two superhydrophobic surfaces, whose characteristics are reported in Table 2. Testing were conducted for three different temperatures and two conditions of LWC (see [16], for cloud calibration procedures) with the MVD of 30  $\mu\text{m}$  (to be representative conditions of the FAA icing envelope, ref. [17]) and with the objective to investigate the combined effect of temperature, LWC and, therefore, of ice regime. Rotor tip velocity was kept constant at  $\sim 60\text{m/s}$  (corresponding to 400RPM).

**Table 1.** Test conditions

Temperatures	LWCs	MVD	Rotor velocity
-8°C	0,5 g/m <sup>3</sup>	30 $\mu\text{m}$	400 rpm
-12°C	2 g/m <sup>3</sup>		( $\sim 60\text{ m/s}$ )
-16°C			

**Table 2.** List of surface material properties. CAH, or Contact Angle Hysteresis is quantified as the difference between the advancing and receding contact angles and it is a measure of droplet mobility: the lowest values of CAH indicates high droplet mobility.

Material	Weight [g]	Surface roughness [ $\mu\text{in}$ ]	Surface roughness [ $\mu\text{m}$ ]	Advancing angle [°]	Receding angle [°]	CAH [°]
Stainless steel 430	86.1	20	0.5	92	32	60
Inconel 625	85.3	20	0.5	95	58	37
SHS FAS	17.2	$\sim 40$	1.1	169	161	8
SHS Nanotech	14.8	$\sim 100$	2.42	159	157	2

## Results and Discussion

By analyzing the pictures taken during the shedding tests, it is possible to define a chart which correlates ice regime with LWC for both SHS and baseline materials. The accreted ice type (*rime* or *glaze*) was identified for every test conducted and, knowing temperature and LWC of the test, it was possible to classify the case in the chart, which is shown in **Figure 4**, valid for both metallic and SHS materials. In **Figure 5** are shown the ice shape pictures observed during the relevant test cases used in the chart.

From the chart it is possible to deduct that for the low LWC (0,5 g/m<sup>3</sup>), both glaze and rime ice regimes were observed, whereas for the high LWC (2 g/m<sup>3</sup>) only glaze ice was identified. For rime regimes (low LWC) the heat exchange process related to convection cooling is able to freeze the upcoming supercooled droplets on impact, while at higher LWC, the saturated cloud also saturates the heat exchange process on the airfoil surface, making more difficult to obtain rime ice at low temperatures.

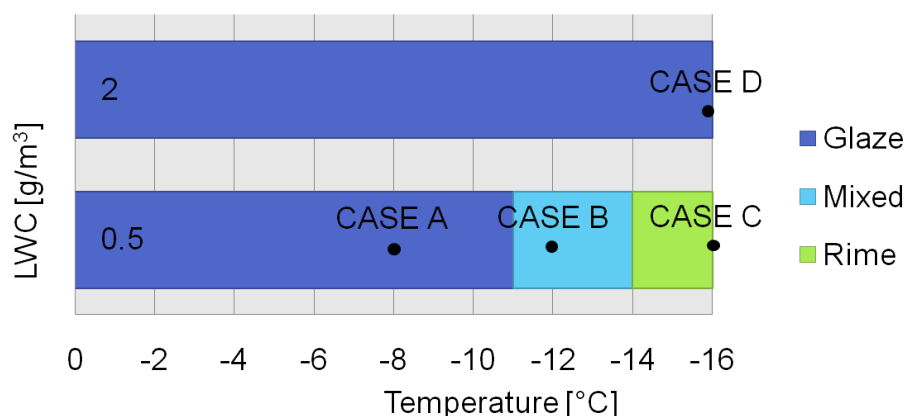


**Figure 4.** Ice regimes based on temperature and LWC for the relevant test cases. The chart is valid for all the tested materials.



For the temperatures and LWCs analyzed, there is no difference in terms of ice regime between a superhydrophobic surface and a common metal, in the way that the surface wetting does not affect the type of ice, as described also in [11]. However, looking at Figure 5, there is a difference in terms of ice thickness: the ice mass accreted on the leading edge is usually smaller for superhydrophobic rather than common materials. In all cases A, B, C and D, SHS are thinner than the baselines and the difference in thickness it is more relevant in cases C and D. This diversity is due to the difference in shedding time, smaller for superhydrophobic materials respect to the baselines, as it can be seen also from Table 3. Therefore ice accretion time is not the same for all the cases and this difference in time becomes a difference in ice thickness, leading the reader to expect also a difference in the adhesion load.

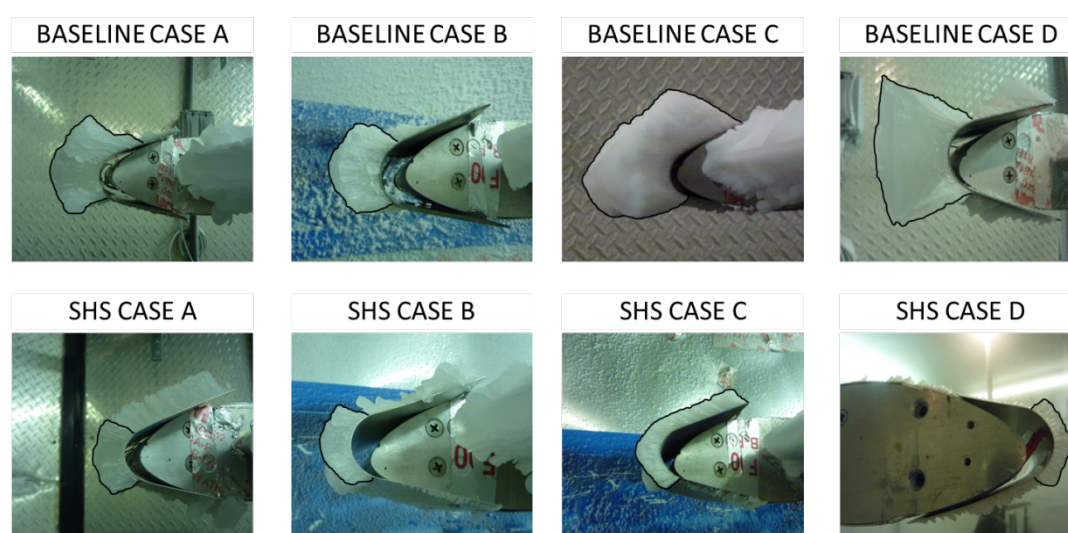


**Figure 5.** Ice shape pictures for both metallic (baseline) and SHS materials, taken before the shedding event. Case nomenclature is the same of Figure 4. Ice shape profile has been enhanced to ease visual comparisons. SHS case A seems having a lot of ice on the top surface not enhanced, but this is due to the upper part being made only of light ice feathers, that would have shed earlier and separately from the leading edge ice.

**Table 3.** Shedding time after the start of the test for the main cases (for both common metals and SHS materials).

	CASE A (-8°C; 0,5 g/m <sup>3</sup> )	CASE B (-12°C; 0,5 g/m <sup>3</sup> )	CASE C (-16°C; 0,5 g/m <sup>3</sup> )	CASE D (-16°C; 2 g/m <sup>3</sup> )
Me tal	25 min	30 min	50 min	9 min
SHS FAS	18 min	25 min	30 min	6 min

In **Figure 6** are shown the ice adhesion results obtained after the different shedding tests. In the graph, ice adhesion load is plotted versus chamber temperature for all four tested samples. A test point is calculated using at least three measures of three different tests for the same icing condition and the bar over the point represent the standard deviation of the average. **Figure 6a** illustrates data for  $LWC = 2.0 \text{ g/m}^3$ : ice shedding load on each sample remains constant in the temperature range from -8°C to -16°C on three of the four tested samples, and it even decreases for one superhydrophobic sample, the SHS-FAS.

By comparing the ice load of the Inconel 625 and SHS Nanotech it is possible to notice that that SHS surface allows a decrease in ice adhesion load of around 59% at -8°C and at -16°C, while SHS FAS allows a decrease of 26% at -8°C and 62% at -16°C, driving the reader to think that a SHS surface might be advantageous in facilitating the shedding event.

As it can be seen in **Figure 6 b**, for  $LWC = 0.5 \text{ g/m}^3$  the situation is different. At -8°C, all materials present similar shedding forces, while at -16°C the shedding load increases by a factor of 3 for SS 430 and by a factor of 4 for Inconel 625. Rather than an effect of temperature, this variation could be attributed to a change in ice type

(glaze ice  $-8^{\circ}\text{C}$ , and rime ice at  $-16^{\circ}$ ). Despite the change in ice regime the adhesion remains constant for SHS-FAS and, at  $-16^{\circ}\text{C}$ , it is 70% lower than on Inconel 625 sample.

The general behavior of SHS samples observed after these experiments is to reduce the ice adhesion load. This reduction has already been reported in references [7, 8, 9, 14, 15], where the ice adhesion strength was found to decrease with an increase of the contact angle. A possible explanation can probably be attributed to a reduced effective contact area in the case of high contact angle materials, thanks to vapor pockets that are present at the solid-ice interface characteristic of a SHS. However, the two SHS behave differently in rime ice regimes, despite having similar wetting parameters (similar contact angles). Therefore, contact angles are not sufficient to predict ice adhesion, since various phenomena could affect superhydrophobicity, like a partial or complete loss of superhydrophobicity when drops impact on a SHS at high speed, or the presence of frost due to cold temperatures might fill the gas pockets, increasing the contact between ice and solid surface, as shown in reference [8].

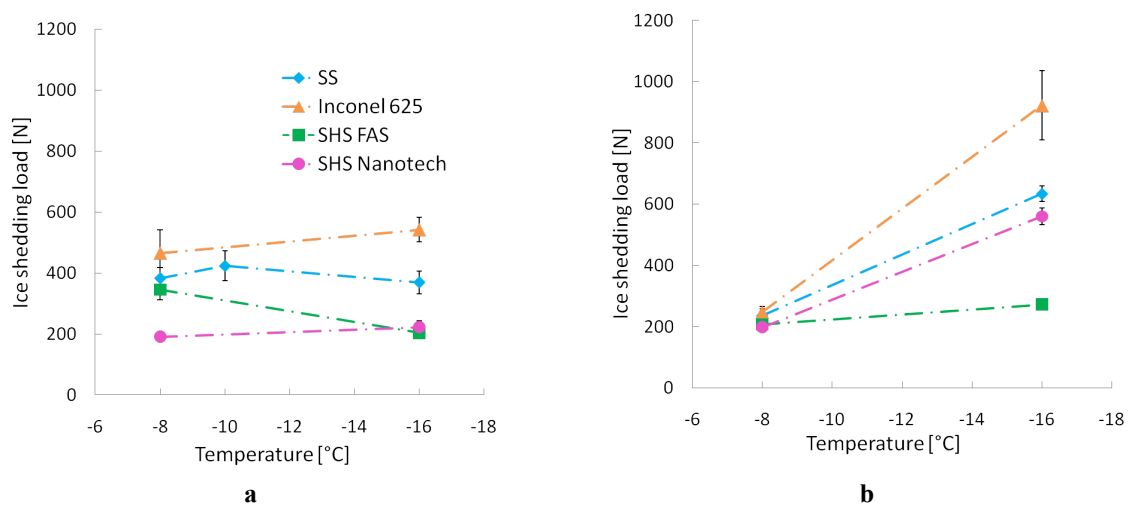


**Figure 6:** Ice shedding load vs. temperature for MVD=30 $\mu\text{m}$  on two hydrophilic and two superhydrophobic samples: a) LWC=2g/m<sup>3</sup>; b) LWC=0.5g/m<sup>3</sup>.

## Conclusions

The average ice adhesion load for different icing conditions was measured on airfoil samples made of four different surface materials, two uncoated metal surfaces and two superhydrophobic surfaces on aluminum substrates. Experimental tests were performed inside an icing chamber with a helicopter rotor, to test the icephobic properties of superhydrophobic coatings in icing environments representative of atmospheric icing conditions. It was found that the ice type formed for the same icing conditions is the same for both uncoated metals and SHS, even if there is a difference in the ice shape or, more precisely, in the thickness of the ice shape, reduced in the case of SHS materials due to the shorter time to shed. Comparing the ice adhesion load results for the different materials and the different icing conditions, it was found that the environment temperature has a behavior coherent with literature (i.e. ice adhesion increases with the environment temperature decrease) and that the ice regime has a strong effect: the ice adhesion load increases significantly in passing from glaze to rime ice. Further, the effect of the type of surface shows that wettability might not be the key parameter for a reduced ice adhesion load, since it can be easily modified by high velocity impacts of the water droplets onto the surface or by frost, meaning that, despite the improvement in the performances, these superhydrophobic material are not advisable for practical helicopter applications. However, the general trend is that SHS presents lower ice adhesion load than uncoated metals, phenomenon that might be explained saying that even if few air is entrapped inside the vapor pockets (due to high velocity impacts or to frost), the pressure build-up can be significant and can lead to crack initiation and propagation as well as ice de-bonding.

## Acknowledgements

ST, CA, and MM acknowledge funding from Regione Lombardia through the grant “Strumenti innovativi per il progetto di sistemi antighiaccio per l’aeronautica”. CA acknowledges funding by a Marie Curie Intra-European Fellowship, within the 7th European Community Framework Programme (ICE2, 301174). The authors are

thankful to Ilaria Bernagozzi (University of Bergamo), Alessandro Surpi and Alessandro Patelli (Veneto Nanotech) for superhydrophobic samples preparation.

## Nomenclature

LWC	Liquid Water Content
MVD	Mean Volumetric Diameter
SHS	Superhydrophobic surface

## References

1. Palacios, J. L., Brouwers, E. W., Han, Y., and Smith, E. C., “Ice Adhesion Strength Measurements for Rotor Blade Leading Edge Materials”. American Helicopter Society 67th Annual Forum, Virginia Beach, May 3-5, (2011).
2. Yaslik, A.D., De Witt, K.J., Keith, T.G., and Boronow, W., “Three-Dimensional Simulation Of Electrothermal Deicing Systems”. Journal of aircraft (0021-8669), 29 (6), p. 1035., (1992).
3. Coffman, H. J., "Helicopter Rotor Icing Protection Methods". Journal of the American Helicopter Society (0002-8711), 32 (2),p. 34, (1987).
4. Palacios, J., Smith, E., Rose, J., and Royer, R., “Ultrasonic De-Icing of Wind-Tunnel Impact Icing”. Journal of aircraft (0021-8669), 48 (3),p. 1020, (2011).
5. Antonini, C., Innocenti, M., Horn, T., Marengo, M., and Amirfazli, A., “Understanding The Effect of Superhydrophobic Coatings on Energy Reduction in Anti-icing Systems”. Cold Regions Science and Technology, vol.67, pp. 58–67, (2011).
6. Laforte, C. and Laforte, J.L., “How a Solid Coating Can Reduce Ice Adhesion on Structures”. Proceedings of the 10th International Workshop of Atmospheric Icing of Structures, Brno, Czech Republic, (2002).
7. Meuler, A.J., Smith, J. D., Varanasi, K.K., Mabry, J.M., McKinley, G.H., and Cohen, R.E., “Relationships between Water Wettability and Ice Adhesion”. Applied Material & interfaces, Vol.2, no.11, 3100-3110, (2010).
8. Varanasi, K.K., Deng, T., Smith, J. D., Hsu, M., and Bhate, N., “Frost formation and ice adhesion on superhydrophobic surfaces”. Applied Physics Letters, vol.97, 234102, (2010).
9. Zou, M., Beckford, S., Wei, R., Ellis, C., Hatton, G., and Miller, M.A., “Effects of surface roughness and energy on ice adhesion strength”. Applied Surface Science 257 3786–3792, (2011).
10. Kimura, S., Yamagishi, Y., Sakabe, A., Adachi, T. et al., “A new surface coating for prevention of icing on airfoils”. Proceedings of SAE Aircraft and Engine Icing International Conference, Sep. Seville, Spain, (2007).
11. Anderson, D., and Reich, A., “Tests of the performance of coatings for low ice adhesion”. AIAA-1997-303, Aerospace Sciences Meeting and Exhibit, 35th, Reno, NV, Jan. 6-9, (1997).
12. Karmouch, R.; Coude S., Abel G., and Ross G.G, “Icephobic PTFE coatings for wind turbines operating in cold climate conditions”. IEEE Electrical Power&Energy Conference (EPEC), ISBN 1424445086, pp. 1 - 6, (2009).
13. Raraty, L.E., and Tabor D., “The adhesion and strength properties of ice”. Proceedings of the Royal Society of London, series A, Mathematical and Physical Sciences, Vol.245, n°1241, pp.184-201, (1958).
14. Kulinich, S.A, and Farzaneh M., “Ice adhesion on super-hydrophobic surfaces”. Applied Surface Science 255, 8153–8157, (2009).
15. Menini, R.i, and Farzaneh M., “Advanced Icephobic Coatings”. Journal of Adhesion Science and Technology 25 971–992, (2011).
16. Palacios, J. L., Yiqiang, H., and Edward, W. B., “Icing Environment Rotor Test Stand Liquid Water Content Measurement Procedures and Ice Shape Correlation”. JAHS-1562-Jun-2010, (2010).
17. FAA Advisory Circular no 20-73A, “Aircraft Ice Protection”. 8/16/06, (2006).
18. Marengo, M., Antonini, C., Roisman, I.V., Tropea, C., “Drop collisions with simple and complex surfaces”. Current Opinion in Colloid & Interface Science, vol.16, pp.292–302, (2011).

## Biodiesel fuel droplets: transport and thermodynamic properties

Ruslana Kolodnytska<sup>1</sup>, Mansour Al Qubeissi<sup>2</sup> and Sergei S Sazhin<sup>2</sup>

1: Department of Mechanical Engineering, Zhytomyr State Technological University, Chernyakhovskogo, 103, Zhytomyr 10005, Ukraine, e-mail: ruslanakol@yahoo.com

2: Sir Harry Ricardo Laboratories, School of Computing, Engineering and Mathematics, University of Brighton, Brighton BN2 4GJ, UK

### Abstract

A detailed comparative analysis of transport and thermodynamic properties of biodiesel fuels and components of these fuels is presented. Five types of biodiesel fuels are considered: Palm Methyl Ester, produced from palm oil; Hemp Methyl Esters, produced from hemp oil in the Ukraine and European Union; Rapeseed oil Methyl Ester, produced from rapeseed oil in the Ukraine; and Soybean oil Methyl Ester, produced from soybean oil. Up to 16 components (methyl esters in most cases) of these fuels are considered. The results are applied to the analysis of biodiesel fuel droplet heating and evaporation in conditions relevant to internal combustion engines, using the model described elsewhere.

### Introduction

As an alternative to Diesel fuel biodiesel fuels have been developed (1). The dominant oils for production of these fuels are rapeseed oil in Europe, soybean oil in the USA, and palm oil in Asia (2). The 'second-generation biodiesels' have been produced from inedible oil or algae (3); hemp biodiesel has been produced from waste (4). Most studies of biodiesel fuels have focused on rapeseed, soybean and palm oil biodiesels (5). This paper concentrates upon the investigation of biodiesel transport and thermodynamic properties in view of the application of the results to the modelling of fuel droplet heating and evaporation.

### Biodiesel fuels

Five types of biodiesel fuel are considered: Palm Methyl Ester (PME), produced from palm oil (6); Hemp Methyl Esters, produced from hemp oil in the Ukraine (HME1) (4) and European Union (HME2) (7); Rapeseed oil Methyl Ester (RME), produced from rapeseed oil in the Ukraine (5); and Soybean oil Methyl Ester (SME), produced from soybean oil (8).

The Sauter Mean Diameters (SMD) of biodiesel and Diesel fuel droplets at temperature 80°C, as reported in (9, 10), are shown in Table 1.

**Table 1.** The Sauter Mean Diameters (SMD) of biodiesel and Diesel fuel droplets at temperature 80°C.

Reference	PME	HME1	HME2	RME	SME	Diesel
(9)	25.1 $\mu\text{m}$	-	-	28.8 $\mu\text{m}$	25.7 $\mu\text{m}$	17.7 $\mu\text{m}$
(10)	-	23.55 $\mu\text{m}$	23.55 $\mu\text{m}$	26.69 $\mu\text{m}$	23.87 $\mu\text{m}$	18.3 $\mu\text{m}$

The average values of SMD of biodiesel fuel droplets (25.32  $\mu\text{m}$ ) are larger than those of Diesel fuel droplets which can be attributed to the higher viscosity of biodiesel fuels (10).

Chemical formulae and molar fractions of components of biodiesel fuels (methyl esters) are shown in Table 2.

**Table 2.** Molar fraction and chemical formulae of components (pure methyl esters) for 5 biodiesel fuels.

Components	Chem. form.	PME	HME1	HME2	RME	SME
C12:0 M	C <sub>13</sub> H <sub>26</sub> O <sub>2</sub>	0.0026	0.0000	0.0000	0.0000	0.0000
C14:0 M	C <sub>15</sub> H <sub>30</sub> O <sub>2</sub>	0.0129	0.0000	0.0000	0.0000	0.0000
C16:0 M	C <sub>17</sub> H <sub>34</sub> O <sub>2</sub>	0.4513	0.0662	0.0651	0.0495	0.109
C17:0 M	C <sub>18</sub> H <sub>36</sub> O <sub>2</sub>	0.0000	0.0021	0.0000	0.0000	0.0000
C18:0 M	C <sub>19</sub> H <sub>38</sub> O <sub>2</sub>	0.0447	0.0206	0.0246	0.0167	0.044
C20:0 M	C <sub>21</sub> H <sub>42</sub> O <sub>2</sub>	0.0035	0.0045	0.0090	0.0056	0.004
C22:0 M	C <sub>23</sub> H <sub>46</sub> O <sub>2</sub>	0.0000	0.0025	0.0000	0.0000	0.0000
C24:0 M	C <sub>25</sub> H <sub>50</sub> O <sub>2</sub>	0.0000	0.0023	0.0000	0.0000	0.0000
C16:1 M	C <sub>17</sub> H <sub>32</sub> O <sub>2</sub>	0.0021	0.0033	0.0000	0.0000	0.0000
C18:1 M	C <sub>19</sub> H <sub>36</sub> O <sub>2</sub>	0.3839	0.1188	0.1188	0.2671	0.240
C20:1 M	C <sub>21</sub> H <sub>40</sub> O <sub>2</sub>	0.0017	0.0027	0.0090	0.0000	0.0000
C22:1 M	C <sub>23</sub> H <sub>44</sub> O <sub>2</sub>	0.0000	0.0017	0.0000	0.2204	0.003
C24:1 M	C <sub>25</sub> H <sub>48</sub> O <sub>2</sub>	0.0000	0.0015	0.0000	0.0077	0.0000
C18:2 M	C <sub>19</sub> H <sub>34</sub> O <sub>2</sub>	0.0916	0.5671	0.5482	0.2484	0.528
C18:3 M	C <sub>19</sub> H <sub>32</sub> O <sub>2</sub>	0.0019	0.2067	0.2007	0.0973	0.072
Other		0.0038	-	0.0246	0.0873	-

The numbers of carbons in fatty acids ( $n_{acid}$ ) and numbers of double bonds (DB) are shown by the numbers on the left and on the right of ‘:’ respectively in the expressions for the components. For example, C18:2 M has  $n_{acid} = 18$  and DB = 2. The total number of carbon atoms in methyl esters is equal to  $n_{acid} + 1$ .

### Transport and thermodynamic properties of liquid components

The methyl ester density shown in Table 2 is estimated based on the following formula which is valid in the temperature range  $288.15 \leq T \leq T_{cr}$  (11):

$$\rho_l = \rho_{l0} - \alpha_T (T - 288.15), \quad (1)$$

where

$$\rho_{l0} = 851.471 + \frac{250.718DB + 280.899}{1.214 + n_{acid}}, \quad \alpha_T = \frac{7.536}{\ln(n_{acid}) + 3.584} - 0.446.$$

The methyl esters’ kinematic viscosity in the temperature range  $T \leq 0.7 T_{cr}$  in the case of saturated molecules (DB=0) is estimated as (12):

$$\ln[\nu_l \times 10^6] = -2.177 - 0.202n_{acid} + \frac{403.66}{T} + \frac{109.77n_{acid}}{T}; \quad (2)$$

in the case of unsaturated molecules (DB>0), it is estimated using the Orrick and Erbar method (13):

$$\ln \frac{\nu_l \rho_l 10^6}{\rho_{l(20)} M} = A_k + \frac{B_k}{T}, \quad (3)$$

where  $\rho_{l(20)}$  is liquid density at  $T = 293.15$  K.

The molar latent heat of evaporation of components is estimated as (14):

$$L = (a_L + b_L M) \Phi_L, \quad (4)$$

where

$$T_{cr} = a_{cr} + b_{cr} M, \quad T_b = a_b + b_b M, \quad (5)$$

$$\Phi_L = \left( \frac{T_{cr} - T}{T_{cr} - T_b} \right)^{0.38}. \quad (6)$$

Eq. (4) gives good agreement with experimental data (15) for saturated molecules as shown in Fig. 1.

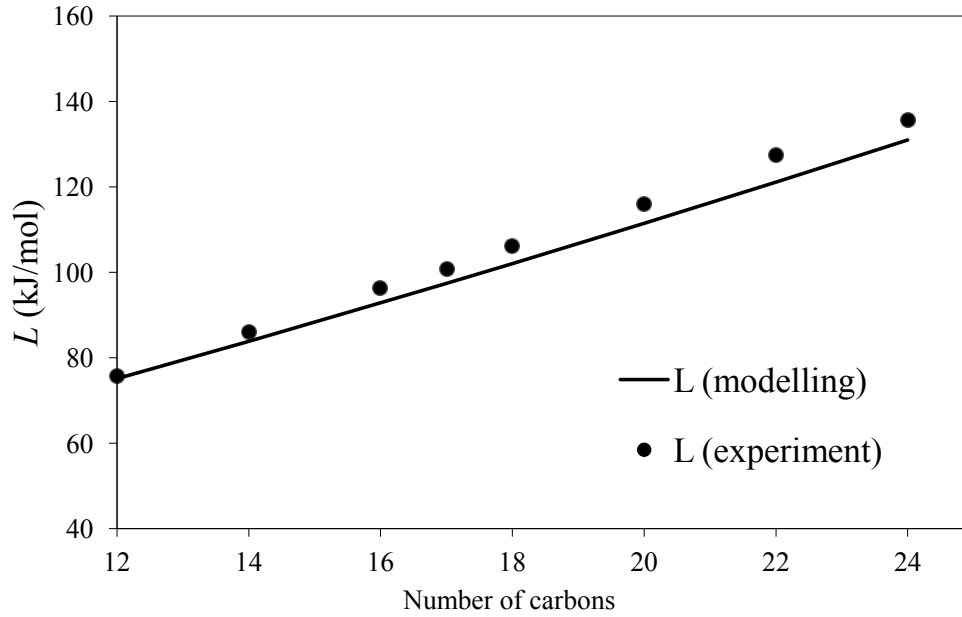


**Figure 1.** Latent heat of evaporation at 298.15 K for saturated methyl esters against experimental data (15).

The liquid heat capacity and liquid thermal conductivity of components are estimated as (14,13):

$$c_l = (a_{pl} + b_{pl}T + c_{pl}T^2)10^3, \quad (7)$$

$$k_l = \frac{A^* T_b^{1.2} (1 - T_r)^{0.38}}{MT_{cr}^{0.167} T_r^{1/6}}, \quad (8)$$

$$\text{where } T_r = \frac{T}{T_{cr}}.$$

Eqs. (4), (7), (8) are used in our analysis for temperatures from 300 K up to the critical temperature. The coefficient  $A^*$  in Eq. (8) was set at  $A^* = 0.0713$  which is different from  $A^* = 0.0415$  suggested by Latini (13). The values of coefficients in Eqs. (3), (4), (5), (6), (7) are given in Table 3 (16, 17). The values for C18:3M in Eqs. (4), (7) have been obtained via the linear extrapolation of the values of coefficients for C18:1M and C18:2 M.

**Table 3.** The values of coefficients used in Eqs. (3) - (7).

Coefficients	C12:0 M – C24:0 M	C16:1 M – C24:1 M	C18:2 M	C18:3 M
$A_k$	-	-10.83	-9.93	-9.03
$B_k$	-	2099	1721	1343
$a_b$	348.7	350.4	352.1	353.82
$b_b$	0.8478	0.8463	0.8463	0.8472
$a_{cr}$	534.3	538.5	542.6	546.8
$b_{cr}$	0.784	0.777	0.772	0.7711
$a_L$	$1.506 \times 10^7$	$1.389 \times 10^7$	$1.270 \times 10^7$	$1.154 \times 10^7$
$b_L$	$1.814 \times 10^5$	$1.822 \times 10^5$	$1.834 \times 10^5$	$1.843 \times 10^5$
$(T_{cr} - T_b)^{0.38}$	7.027	7.047	7.067	7.087
$a_{pl}$	1.816	1.915	2.018	2.115
$b_{pl}$	$-1.462 \times 10^{-3}$	$-2.163 \times 10^{-3}$	$-2.878 \times 10^{-3}$	$-3.580 \times 10^{-3}$
$c_{pl}$	$7.51 \times 10^{-6}$	$8.29 \times 10^{-6}$	$9.09 \times 10^{-6}$	$9.92 \times 10^{-6}$

The liquid diffusivity of biodiesel  $D_l$  is estimated using the Wilke-Chang approximation (13) assuming that liquid diffusivity is the same for all components:

$$D_l = \frac{7.4 \times 10^{-15} \sqrt{\bar{M}_v} T}{\mu_l V_v^{0.6}}, \quad (9)$$

where  $\bar{M}_v$  is the average molar mass of components,  $\mu_l$  is the liquid dynamic viscosity,  $\text{kg m}^{-1} \text{s}^{-1}$ .

Molar volume  $V_v$  at the normal boiling point and Lennard-Jones length  $\sigma_v$  for individual components is estimated as (18,19):

$$V_v = (\sigma_v / 1.18)^3, \quad (10)$$

$$\sigma_v = 1.486 M^{0.297}. \quad (11)$$

The plots of liquid diffusivity for PME, SME and HME2 calculated based on Eq. (9) are shown in Fig. 2.

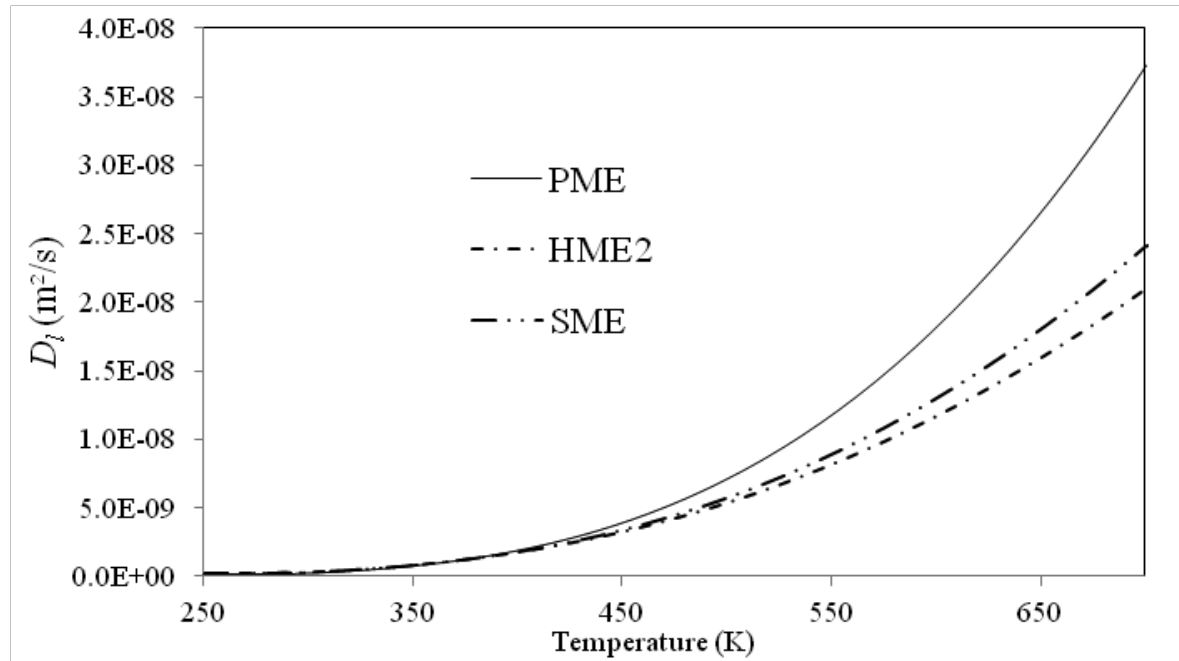


**Figure 2.** The liquid diffusivity  $D_l$  for PME, SME, and HME2 calculated based on Eq. (9).

As one can see from Fig. 2 the highest liquid diffusivity is for PME, the diffusivities for SME and RME are close to each other, the liquid diffusivity for HME2 is very close to the diffusivity for HME1 (plots are not presented). An alternative approximation for liquid diffusivity of components was suggested by Hayduk and Minhas (13):

$$D_{AB}^0 = 15.5 \times 10^{-12} \left( \frac{P_B^{0.5}}{P_A^{0.42}} \right) \frac{T^{1.29}}{V_B^{0.23} \mu_B^{0.92}}, \quad (12)$$

where  $\mu_B$  is the dynamic viscosity of solvent B, cP;  $P_A$  and  $P_B$  are Parahors (see (10,13) for the details) for the solute and solvent.

The following approximation was derived for liquid diffusivity of saturated molecules (C12:0 M - C24:0 M) at the temperature 293.15K using Eqs. (12), (10) and (11):

$$D_{AB}^0 = A_D \times 10^{-8} e^{(-0.142 n_{acid})}, \quad (13)$$

where  $A_D = 2$  for methyl esters C12:0 M – C24:0 M.



### Transport and thermodynamic property of methyl esters vapour

The saturated vapour pressure (in Pa) of pure liquid methyl esters is estimated based on the following general formula which is valid in the temperature range (260 K < T < 610 K) (20):

$$p_v = 10^3 a_{CN,0} \left[ a_{uc}(DB+1) + b_{uc} + \frac{c_{uc}}{DB+1} \right] \exp(a_{CN,1} n_{acid}), \quad (14)$$

where

$$a_{CN,0} = 1.908 \exp[0.01715T].$$

$$a_{CN,1} = -5.656 + 0.02649T - 4.5417 \times 10^{-5} T^2 + 2.6571 \times 10^{-8} T^3,$$

for  $DB = 0$  or  $T > 323$  K,  $a_{uc} = 0$ ,  $b_{uc} = 1$ ,  $c_{uc} = 0$ , otherwise,

$$a_{uc} = 4.62 \times 10^{-5} T^2 - 3.06 \times 10^{-2} T + 5.05, \quad b_{uc} = 3.39 \times 10^{-2} T - 9.93, \quad c_{uc} = -2.97 \times 10^{-2} T + 9.62.$$

Using data provided in (21), the following approximation for the vapour heat capacities of the components of biodiesel fuels in the range of temperatures 300 K < T < 1500 K has been derived:

$$c_{pv} = 4184 C_{pv,0} C_{pv,1} M^{-1} (J \text{ kg}^{-1} K^{-1}) \quad (15)$$

where  $C_{pv,0} = (6.37561 \times n_{acid} + 6.6472) \ln(T) - 31.361 \times n_{acid} - 26.118$ ,

$$C_{pv,1} = \exp[(0.01105 \ln(T) - 0.0425) DB].$$

Vapour diffusion coefficients were approximated as (17, 22):

$$D_v = \frac{2 \times 10^{-10} T^{1.75}}{p},$$

where  $p$  is ambient pressure in bars.

### Transport and thermodynamic properties of biodiesel fuels

Data presented earlier allow us to calculate average values of liquid density, specific heat capacity, dynamic viscosity and thermal conductivity for all 5 biodiesel fuels using the mixture rules (23, 24).

Table 3 shows the values of calculated/estimated (27) density and viscosity for RME and calculated/estimated (28) values of thermal conductivity for RME.

**Table 4.** The values of calculated liquid density and viscosity versus experimental data (27); and calculated/ estimated thermal conductivity (28) for RME.

Temperature	Dynamic viscosity	Density	Temperature	Thermal conductivity
	Measured/Calculated	Measured/Calculated		Estimated/Calculated
293.15 K	0.0063413/0.0058339	879.6/878.823	300 K	0.17696/0.16423
303.15 K	0.0048825/0.0046859	872.9/871.729	350 K	0.16860/0.15349
313.15 K	0.0038665/0.0038166	865.7/864.634	400 K	0.15991/0.14320
323.15 K	0.0031336/0.0031482	858.3/857.540	450 K	0.15083/0.13306
333.15 K	0.0025883/0.0026269	851.0/850.445	500 K	0.14125/0.12280
343.15 K	0.0021724/0.0022151	843.7/843.350	550 K	0.13104/0.11415
353.15 K	0.0018320/0.0018860	836.4/836.256	600 K	0.11997/0.11317
363.15 K	0.0015837/0.0016198	829.1/829.161		
373.15 K	0.0013923/0.0014026	821.7/822.066		

As one can see from Table 4, the calculated and experimental data for density and dynamic viscosity are very close and the agreement between the predicted values of thermal conductivity for both approaches is reasonably good. The thermal conductivity of biodiesel is higher than that of Diesel fuel (25). Biodiesel produced from rapeseed oil has a thermal conductivity of  $0.153 \pm 0.002 \text{ Wm}^{-1}\text{K}^{-1}$  (25) (or  $0.17 \text{ W} \cdot \text{m}^{-1} \cdot \text{K}^{-1}$  (26)) at 298 K compared to Diesel fuels, for which the respective value is  $0.115 \pm 0.002 \text{ Wm}^{-1}\text{K}^{-1}$  (25).

### Biodiesel droplet evaporation modelling

The above results were applied to the analysis of biodiesel fuel droplet heating and evaporation in conditions relevant to Diesel engines, using the Effective Thermal Conductivity/Effective Diffusivity (ETC/ED) model (23, 24). Our analysis is focused on the following values of parameters (assuming that the ideal gas law is valid):  $\rho_a = 11.9 \text{ kg/m}^3$ ,  $T_a = 880\text{K}$ ,  $p_a = 30 \text{ bar}$  and assuming that droplets have a velocity of 10 m/s. Fig. 3 shows the results of calculations using the multi-component evaporation model taking into account the contribution of some or all of the 16 components shown in Table A2 for SME and HME1. Our results show that HME1 droplets

take slightly longer to evaporate than SME droplets and the surface temperatures of HME1 droplets at the final stage of droplet evaporation are slightly higher than the ones predicted for the SME droplets or HME2 droplets (plots for HME2 are very close to SME and are not presented in Fig. 3). The difference in evaporation between HME1 and HME2 can be attributed to the presence or absence of the heaviest components (C22:1 and C24:1 M) in HME2 and HME1 (see Table 2). A more detailed analysis of biodiesel fuel droplet heating and evaporation is presented in our parallel paper (29).

## Conclusion

A detailed comparative analysis of transport and thermodynamic properties of biodiesel fuels and components of these fuels (methyl esters) is presented. The analysis has been focused on five types of biodiesel fuels: Palm Methyl Ester (PME); Hemp Methyl Esters, produced from hempseed oil in the Ukraine (HME1) and European Union (HME2); Rapeseed oil Methyl Ester (RME), produced from rapeseed oil in the Ukraine; and Soybean oil Methyl Ester (SME), produced from soybean oil. Up to 16 components of these fuels are considered. The results are applied to the analysis of biodiesel fuel droplet heating and evaporation in Diesel engine-like conditions using the previously suggested model that takes into account temperature gradient and recirculation inside droplets and species diffusion within them. Our results show that the evaporation time for Hemp Methyl Esters is very close to that of Soybean oil Methyl Esters.

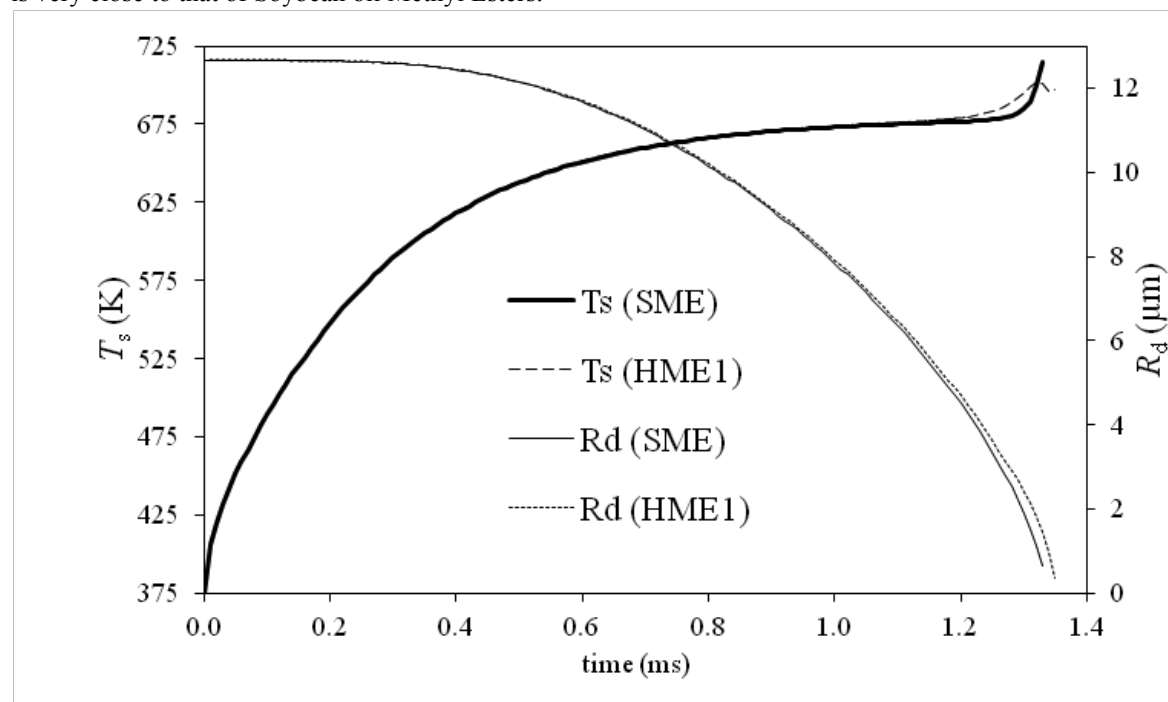


**Figure 3.** The plots of SME and HME1 droplet surface temperatures ( $T_s$ ) and radii ( $R_d$ ) versus time predicted by the multi-component model. Gas temperature and pressure are assumed to be equal to 880 K and 30 bar respectively. The initial droplet radius is assumed to be equal to 12.66  $\mu\text{m}$ . The droplet is assumed to be moving with a constant velocity equal to 10 m/s.

## Acknowledgements

The authors are grateful to the Ministry of Education of the Ukraine, Zhytomyr State Technological University (Ukraine) and INTERREG IVa (Project E3C3, Reference 4274) for their financial support.

## Nomenclature

Symbol	Description	Unit	Subscripts	Description
$c$	specific heat capacity	$\text{J} \cdot \text{kg}^{-1} \cdot \text{K}^{-1}$		
$D$	diffusion coefficient	$\text{m}^2 \cdot \text{s}^{-1}$	$A$	Solute
$DB$	number of double bonds	-	$a$	air
$k$	thermal conductivity	$\text{W} \cdot \text{m}^{-1} \cdot \text{K}^{-1}$	$B$	solvent
$L$	latent heat of evaporation	$\text{J} \cdot \text{kmol}^{-1}$	$cr$	critical
$M$	molar mass	$\text{kg kmol}^{-1}$	$b$	boiling
$n_{acid}$	number of carbon atoms in acid	-	$l$	liquid
$p$	pressure	$\text{Pa/bar}$	$p$	constant pressure
$T$	temperature	$\text{K}$	$r$	reduced

$T$	molar volume at boiling temperature	$\text{m}^3 \text{mol}^{-1}$	$v$	vapour
$V$	kinematic viscosity	$\text{m}^2 \cdot \text{s}^{-1}$	$0$	initial
$\nu$	density	$\text{kg} \cdot \text{m}^{-3}$		
$\rho$	dynamic viscosity	$\text{kg m}^{-1} \text{s}^{-1} / \text{cP}$		
$\mu$	Lennard-Jones length	$\text{\AA}$		
$\sigma_v$				

## References

1. M. Lapuerta, O. Armas, Effect of biodiesel fuels on diesel engine emissions. *Progress in Energy and Combustion Science* **34**, 198-223 (2008).
2. S.K. Hoekman, A. Broch, Review of biodiesel composition, properties, and specifications. *Renewable and Sustainable Energy Reviews* **16**, 143-169 (2012).
3. G. Knothe, Biodiesel and renewable diesel: a comparison. *Progress in Energy and Combustion Science* **36**, 364-73 (2010).
4. M. Su, R. Yang, Biodiesel production from hempseed oil using alkaline earth metal oxides supporting copper oxide as bi-functional catalysts for transesterification and selective hydrogenation. *Fuel* **103**, 398-407 (2013).
5. I.G. Grabar, R.V. Kolodnytska, Biofuels Based on Oil for Diesel Engines. (ZDTU, Zhytomyr, 2011) (In Ukrainian).
6. A. Schonborn, N. Ladommatos, The influence of molecular structure of fatty acid monoalkyl esters on diesel combustion. *Combustion and Flame* **156**, 1396-412 (2000).
7. P. Emberger, K. Thuneke, Examination of hemp oil with regard to its suitability as fuel for engines adapted to pure plant oil use. (<http://www.nova-institut.de>) (2007).
8. L.F. Ramirez-Verduzco, J.E. Rodriguez-Rodriguez, Predicting cetane number, kinematic viscosity, density and higher heating value of biodiesel from its fatty acid methyl ester composition. *Fuel* **91**, 102-11 (2012).
9. C.E. Ejim, B.A. Fleck, Analytical study for atomization of biodiesels and their blends in a typical injector: Surface tension and viscosity effects. *Fuel* **86**, 1534-44 (2007).
10. R.V. Kolodnytska, Analytical study for atomization of hemp oil biodiesel. *Visnik Shydnio-Ukrainskogo Natsionalnogo Universitetu imeni Volodymyra Dalya* **6 (148)**, 41-46 (2010) (In Ukrainian).
11. M. Lapuerta, J. Rodriguez-Fernandez, Correlation for the estimation of the density of fatty acid esters fuels and its implications. A proposed Biodiesel Cetane Index. *Chemistry and Physics of Lipids* **163**, 720-7 (2010).
12. K. Krisnangkura, T. Yimsuwan, An empirical approach in predicting biodiesel viscosity at various temperatures. *Fuel* **85**, 107-13 (2006).
13. B.E. Poling, J.M. Prausnitz, The Properties of Gases and Liquids. (McGraw-Hill, New York, ed. 5, 2000).
14. W.L.H. Hallett, N.A. Clark. A model for the evaporation of biomass pyrolysis oil droplets. *Fuel* **85**, 532-44 (2006).
15. D. Lipkind, Y. Kapustin, The vaporization enthalpies and vapor pressures of a series of unsaturated fatty acid methyl esters by correlation gas chromatography. *Thermochimica Acta*. **456**, 94-101(2007).
16. W.H.L. Hallett, N.V. Legault, Modelling biodiesel droplet evaporation using continuous thermodynamics. *Fuel* **90**, 1221-28 (2011).
17. H. An, W.M. Yang, Detailed physical properties prediction of pure methyl esters for biodiesel combustion modeling. *Appl Energy* **102** 647-56 (2013).
18. R.B. Bird, E.W. Stewart, *Transport Phenomena* (Wiley & Sons. New York, ed. 2, (2002).
19. S. Dooley, M. Uddi, Methyl butanoate inhibition of n-heptane diffusion flames through an evaluation of transport and chemical kinetics, *Combustion and Flame* **159**, 1371-84 (2012).
20. O.C. Diaz, F. Schoeggl, Modelling the vapour pressure of biodiesel fuels. *World Academy of Science, Engineering and Technology (WASET)* **65**, 876-86 (2012).
21. A. Osmont, L. Catoire, Thermochemistry of Methyl and Ethyl Esters from Vegetable Oils. *International Journal of Chemical Kinetics* 481-491 (2007), doi: 10.1002/kin.20264.
22. B. Abramzon, S.S. Sazhin, Convective vaporization of fuel droplets with thermal radiation absorption. *Fuel* **85**, 32-46 (2006).
23. S.S. Sazhin, A. Elwardany, A simplified model for bi-component droplet heating and evaporation. *Int. J of Heat and Mass Transfer*, **53**, 4495-505 (2010).

24. S.S. Sazhin, A. Elwardany, Multi-component droplet heating and evaporation, numerical simulation versus experimental data. *Int. J of Thermal Science* **50**, 1164-80 (2011).
25. F.A.L. Machado, E.B. Zanelato, Thermal properties of biodiesel and their corresponding precursor vegetable oils obtained by photopyroelectric methodology. *Int J Thermophys* **33**, 1848-55. 2012DOI 10.1007/s10765-012-1245-6.
26. A. Anand, R.P. Sharma, A comprehensive approach for estimating thermo-physical properties of biodiesel fuels. *App. Therm. Eng.* **31**, 235-42 (2011).
27. K. Mauer, N.N. Cordos, Researches of the viscosity and density of the fuels based on rape oil. *AMMA 2002. Editura U.T. Pres Cluj-Napoca. Conferinta Nationala cu participare Internationala* **2**, 13-16 (2002).
28. J. McCrady, A. Hansen, Physical property measurement of biodiesel fuels for low temperature combustion modelling. An ASABE Meeting Presentation. UIIU 2006 -7020. Paper Number, 066146.
29. M. Al Qubeissi, R. Kolodnytska, Biodiesel fuel droplets: modelling of heating and evaporation processes. Proceedings of ILASS-Europe 201, Chania, Greece (2013) (in press).

## Biodiesel Fuel Droplets: Modelling of Heating and Evaporation Processes

Mansour Al Qubeissi<sup>1</sup>, Ruslana Kolodnytska<sup>2</sup> and Sergei S Sazhin<sup>1</sup>

1: Sir Harry Ricardo Laboratories, School of Computing, Engineering and Mathematics,  
University of Brighton, Brighton BN2 4GJ, UK

2: Zhytomyr State Technological University, Chernyakhovskogo, 103, Zhytomyr, 10005, Ukraine

### Abstract

A recently developed model for heating and evaporation of multi-component droplets, taking into account the effects of temperature gradient, recirculation and species diffusion inside them is described. The model is applied to the analysis of biodiesel droplets. The predictions of this model are compared with the predictions of the model based on the approximation of biodiesel fuel by a single component. Five types of biodiesel fuels are considered: Palm Methyl Ester, produced from palm seed oil; Hemp Methyl Esters, produced from hemp seed oil in the Ukraine and the European Union; Rapeseed oil Methyl Ester, produced from rapeseed oil in the Ukraine; and Soybean oil Methyl Ester, produced from soybean oil. It is shown that a simplistic model, based on the approximation of biodiesel by one component, leads to errors in predicted droplet evaporation times and surface temperatures of up to 5.5% and 2.4%, respectively.

### Introduction

The term ‘biodiesel’ typically refers to fuels comprised of mono-alkyl esters of long-chain fatty acids derived from vegetable oils or animal fats (1). Some researchers (2) describe it as “fatty acid methyl or ethyl esters made from vegetable oils or animal fats, whose property is suitable to be used in diesel engines”. This paper is focused on modelling biodiesel fuel droplet heating and evaporation. Modelling of these processes is very important for understanding the combustion processes in Diesel engines. A number of models of biodiesel fuel heating and evaporation of various complexities have been suggested (3,4). Most of these models, however, either ignored temperature gradient and species diffusion inside droplets or took them into account based on the numerical solutions of the underlying partial differential equations. An alternative approach to modelling these processes, based on the implementation of analytical solutions to these equations into numerical codes, was suggested in (5,6). The model used in our analysis is based on the latter approach.

### Basic Equations and Approximations

The model of heating and evaporation, used in this study, is described in (6). The main ideas of the model are briefly summarised in this section. As in (3)-(13), the processes in the droplet are assumed to be spherically symmetric. The model takes into account the following processes inside the droplet: 1) diffusion of various species; 2) finite thermal conductivity; and 3) internal recirculation (vortices) due to relative velocity between ambient gas and droplets. The effects of droplets on gas are ignored. The heating of the droplet is described by the transient heat conduction equation:

$$\frac{\partial T}{\partial t} = \kappa \left( \frac{\partial^2 T}{\partial R^2} + \frac{2}{R} \frac{\partial T}{\partial R} \right), \quad (1)$$

where  $t$  is the time,  $R$  is the distance from the centre of the droplet,  $T$  is the temperature and  $\kappa$  is the effective thermal diffusivity defined as (11):

$$\kappa = k_{eff} / C_l \rho_l, \quad (2)$$

$k_{eff}$  is the effective thermal conductivity,  $C_l$  is the specific heat capacity of liquid and  $\rho_l$  is the density of liquid.  $k_{eff}$  is defined by the following expression:

$$k_{eff} = \chi k_l, \quad (3)$$

where  $\chi$  takes into account the effect of recirculation inside droplets (7,8).  $\chi$  varies between 1 (when Peclet number  $Pe_{d(l)} = Re_{d(l)} Pr_l < 10$ ) and 2.72 (for  $Pe_{d(l)} > 500$ ). The model based on Approximation (3) is known as the Effective Thermal Conductivity (ETC) model. The initial and boundary conditions are introduced as:

$$\left. \begin{aligned} T(t=0) &= T_{d0}(R) \\ h(T_g - T_s) &= k_{eff} \left. \frac{\partial T}{\partial R} \right|_{R=R_d-0} \end{aligned} \right\}, \quad (4)$$

where  $T_s = T_s(t)$  is the droplet surface temperature,  $R_d$  is the droplet radius,  $T_g = T_g(t)$  is the ambient gas temperature,  $h = h(t)$  is the convective heat transfer coefficient, linked with the Nusselt number  $Nu$  by the following expression:

$$Nu = 2R_d h/k_g, \quad (5)$$

$k_g$  is the gas thermal conductivity. To take into account the effect of evaporation, the gas temperature  $T_g$  is replaced by the so-called effective temperature  $T_{eff}$  (5):

$$T_{eff} = T_g + \frac{\rho_l L \dot{R}_{de}}{h}, \quad (6)$$

where  $L$  is the latent heat of evaporation and  $\dot{R}_{de}$  is the rate of change of droplet radius due to evaporation.

Assuming that  $h = \text{const}$ , the analytical solution to Equation (1), applied for the time step  $\Delta t = t_1 - t_0$ , gives the following expression for the temperature at the end of each time step  $t_1$  (7):

$$T(R, t_1) = \frac{1}{R} \sum_{n=1}^{\infty} \left\{ q_n \exp[-\kappa_R \lambda_n^2 t_1] - \frac{R_d^2 \sin \lambda_n}{\|v_n\|^2 \lambda_n^2} \mu_0(0) \exp[-\kappa_R \lambda_n^2 t] - \frac{R_d^2 \sin \lambda_n}{\|v_n\|^2 \lambda_n^4} \int_0^t \frac{d\mu_0(\tau)}{d\tau} \exp[-\kappa_R \lambda_n^2 (t - \tau)] d\tau \right\} \sin\left(\lambda_n \frac{R}{R_d}\right) + T_g(t_1), \quad (7)$$

where

$$\|v_n\|^2 = \frac{R_d}{2} \left(1 - \frac{\sin 2\lambda_n}{2\lambda_n}\right) = \frac{R_d}{2} \left(1 + \frac{h_{0T}}{h_{0T}^2 + \lambda_n^2}\right), \quad q_n = \frac{1}{\|v_n\|^2} \int_0^{R_d} R T_{d0}(R) \sin\left(\lambda_n \frac{R}{R_d}\right) dR, \\ k_R = \frac{k_l}{c_l \rho_l R_d^2}, \quad \mu_0(t) = \frac{h T_g(t) R_d}{k_l}, \quad h_{0T} = \left(\frac{h R_d}{k_{eff}}\right) - 1, \quad \mu'_0 \equiv \frac{d\mu_0(t)}{dt}.$$

A set of positive eigenvalues  $\lambda_n, n > 0$  (the trivial solution  $\lambda = 0$  is not considered), is found from the solution to the following equation:

$$\lambda \cos \lambda + h_{0T} \sin \lambda = 0. \quad (8)$$

The effect of thermal swelling is taken into account alongside the evaporation. The droplet radius  $R_d$  is updated at the end of each time step  $\Delta t$  as (7-9):

$$R_{d(new)} = R_{d(old)} + \dot{R}_d \Delta t; \quad \dot{R}_d = \frac{\dot{m}_d}{4\pi R_d^2 \rho_l} + \frac{R_d(\bar{T}_0)}{\Delta t} \left[ \left( \frac{\rho(\bar{T}_0)}{\rho(\bar{T}_1)} \right)^{1/3} - 1 \right], \quad (9)$$

where  $\dot{R}_d$  is the rate of change in radius due to evaporation and swelling,  $\bar{T}_0$  and  $\bar{T}_1$  are average droplet temperatures at the beginning  $t = t_0$  and the end of the time step  $t = t_1$ ,  $\Delta t = t_1 - t_0$  and  $\dot{m}_d$  is the droplet evaporation rate (9):

$$\dot{m}_d = -2\pi R_d D_v \rho_g B_M \text{Sh}_{iso}, \quad (10)$$

$\rho_g$  is the ambient gas density,  $D_v$  is the binary diffusion coefficient of biodiesel vapour in air,  $B_M = (Y_{vs} - Y_{v\infty})/(1 - Y_{vs})$  is the Spalding mass transfer number,  $Y_{vs}$  and  $Y_{v\infty}$  are the mass fractions of vapour near the droplet surface and in the ambient gas, respectively, and  $\text{Sh}_{iso}$  is the Sherwood number for an isolated evaporating droplet.  $\text{Sh}_{iso}$  and the corresponding Nusselt number for isolated droplets  $Nu_{iso}$  are determined as in the Abramzon and Sirignano model (8).

The Spalding heat transfer number  $B_T$ , which is used to determine  $Nu_{iso}$ , is linked with  $B_M$  by the following equation (8):

$$B_T = (1 + B_M)^\varphi - 1, \quad (11)$$

where

$$\varphi = \left( \frac{C_{pv}}{C_{pa}} \right) \left( \frac{Sh^*}{Nu^*} \right) \frac{1}{L}, \quad (12)$$

$C_{pv}$  and  $C_{pa}$  are specific heat capacities of biodiesel vapour and air, respectively, and  $Sh^*$  and  $Nu^*$  are defined in (8). Since  $\varphi$  is a function of  $B_T$ , Equation (11) is solved using the iteration procedure. In the previously used version of this model (7,11,12), the effect of the parameter  $\frac{Sh^*}{Nu^*}$  was ignored by assuming that  $\frac{Sh^*}{Nu^*} = 1$ .

In the case when the droplet contains several components, the effect of species diffusion inside the droplet needs to be taken into account. The time evolution of species mass fractions at any  $R$  is described by the following equation (6,7):

$$\frac{\partial Y_{li}}{\partial t} = D_{eff} \left( \frac{\partial^2 Y_{li}}{\partial R^2} + \frac{2}{R} \frac{\partial Y_{li}}{\partial R} \right), \quad (13)$$

where  $i > 1$ ,  $D_{eff}$  is the effective liquid species diffusivity,  $D_{eff} = \chi_Y D_l$ ,  $D_l$  is the liquid diffusivity and  $\chi_Y$  is a coefficient that varies between 1 and 2.72 (7,10).  $\chi_Y$  takes into account the recirculation inside droplets and is approximated as:

$$\chi_Y = 1.86 + 0.86 \tanh[2.225 \log_{10}(Re_{d(l)} Sc_l / 30)], \quad (14)$$

where  $Re_{d(l)}$  is the Reynolds number generated from the liquid internal recirculation and  $Sc_l = \frac{\nu_l}{D_l}$  is the liquid Schmidt number and  $\nu_l$  is the liquid kinematic viscosity. The model based on the introduction of  $D_{eff}$  is known as the Effective Diffusivity (ED) model.

In most previously used approaches to the analysis of biodiesel droplet heating and evaporation, the Infinite Thermal Conductivity (ITC) and Infinite Diffusivity (ID) models have been used. In these models, it is assumed that  $k_{eff} = \infty$  and  $D_{eff} = \infty$ . Equation (13) is solved subject to the following initial and boundary conditions:

$$\left. \begin{aligned} Y_{li}(t=0) &= Y_{li0}(R) \\ \alpha(\epsilon_i - Y_{lis}) &= -D_{eff} \left. \frac{\partial Y_{li}}{\partial R} \right|_{R=R_d-0} \end{aligned} \right\}, \quad (15)$$

where  $Y_{lis} = Y_{lis}(t)$  are the mass fractions of components at the droplet surface,  $\epsilon_i$  is the evaporation rate of each component, defined as  $\epsilon_i = Y_{vis} / \sum_i Y_{vis}$ , and  $\alpha$  is defined as  $\alpha = |\dot{m}_d| / (4\pi\rho_l R_d^2)$ .

Assuming that  $D_{eff}$  and  $\alpha$  are constant and the same for all components, the analytical solution to Equation (13) can be presented as (6):

$$Y_{li} = \epsilon_i + \frac{1}{R} \left\{ \left[ \exp \left[ D_{eff} \left( \frac{\lambda_0}{R_d} \right)^2 t \right] [q_{i0} - \epsilon_i Q_0] \sinh \left( \lambda_0 \frac{R}{R_d} \right) + \sum_{n=1}^{\infty} \left[ \exp \left[ -D_{eff} \left( \frac{\lambda_n}{R_d} \right)^2 t \right] [q_{in} - \epsilon_i Q_n] \sin \left( \lambda_n \frac{R}{R_d} \right) \right] \right\}, \quad (16)$$

where  $\lambda_0$  and  $\lambda_n$  are determined from the solutions to equations  $\tanh \lambda_0 = -\lambda_0 / h_{0Y}$  and  $\tanh \lambda_n = -\lambda_n / h_{0Y}$  ( $n \geq 1$ ), respectively,  $h_{0Y} = -\left(1 + \frac{\alpha R_d}{D_{eff}}\right)$ ,



$$Q_n = \begin{cases} -\frac{1}{\|v_0\|^2} \left(\frac{R_d}{\lambda_0}\right)^2 (1 + h_{0Y}) \sinh \lambda_0 & \text{when } n = 0 \\ \frac{1}{\|v_n\|^2} \left(\frac{R_d}{\lambda_n}\right)^2 (1 + h_{0Y}) \sin \lambda_n & \text{when } n \geq 1 \end{cases},$$

$\|v_n\|^2$  is obtained from Equation (7), replacing  $h_{0T}$  with  $h_{0Y}$ , and:

$$q_{in} = \begin{cases} \frac{1}{\|v_0\|^2} \int_0^{R_d} R Y_{li0}(R) \sinh\left(\lambda_0 \frac{R}{R_d}\right) dR & \text{when } n = 0 \\ \frac{1}{\|v_n\|^2} \int_0^{R_d} R Y_{li0}(R) \sin\left(\lambda_n \frac{R}{R_d}\right) dR & \text{when } n \geq 1 \end{cases},$$

$D_{eff}$  is estimated as an average parameter of the biodiesel fuel based on the mass fractional contribution of each component. In the mono-component model, Equation (16) is not used.

## Results and Analysis

Using the following values of input parameters:  $R_{d0} = 12.66 \mu\text{m}$ ,  $T_{s0} = 375 \text{ K}$ ,  $T_g = 880 \text{ K}$  and  $p_g = 30 \text{ bar}$ , for a droplet moving at constant velocity ( $10 \text{ m s}^{-1}$ ), the calculations have been performed for all above mentioned types of biodiesel. These calculations have been performed: 1) taking into account the contribution of up to 16 components (multi-component models), using the ETC/ED model; 2) replacing these components with a single component with average transport and thermodynamic properties, using the ETC model (10); and 3) taking into account the contribution of all components using the ITC/ID model.

The plots of the surface temperature and radii versus time for Rapeseed oil Methyl Ester (RME), as a typical example of biodiesels, are shown in Fig. 1. As one can see from the figure, the multi-component model predicts up to 2.4% higher maximal droplet surface temperatures and 5.5% longer evaporation times compared with the single component model. These trends are consistent with the ones reported earlier in (6,9-13) for Diesel and gasoline fuel droplets. This behaviour of the multi-component droplet surface temperature and radius is related to the fact that the mass fractions of species with larger carbon numbers increase at the expense of species with smaller carbon numbers. This phenomenon is illustrated in Fig. 2, where the time evolution of surface mass fractions of 6 dominant RME components (C16:0, C18:1, C22:1, C24:1, C18:2, C18:3) is shown.

The plots of temperatures in RME droplets versus normalised distance from the centre of the droplet  $R/R_d$  at three time instants (0.02 ms, 0.3 ms and 0.5 ms) predicted by the ETC/ED model are shown in Fig. 3. As one can see from this figure, the temperature gradient inside the droplet is noticeable at the very early stage ( $t = 0.02 \text{ ms}$ ). The plots of species mass fractions versus  $R/R_d$  predicted by the ETC/ED model at three time instants (0.3 ms, 0.5 ms and 1 ms) are shown in Fig. 4.

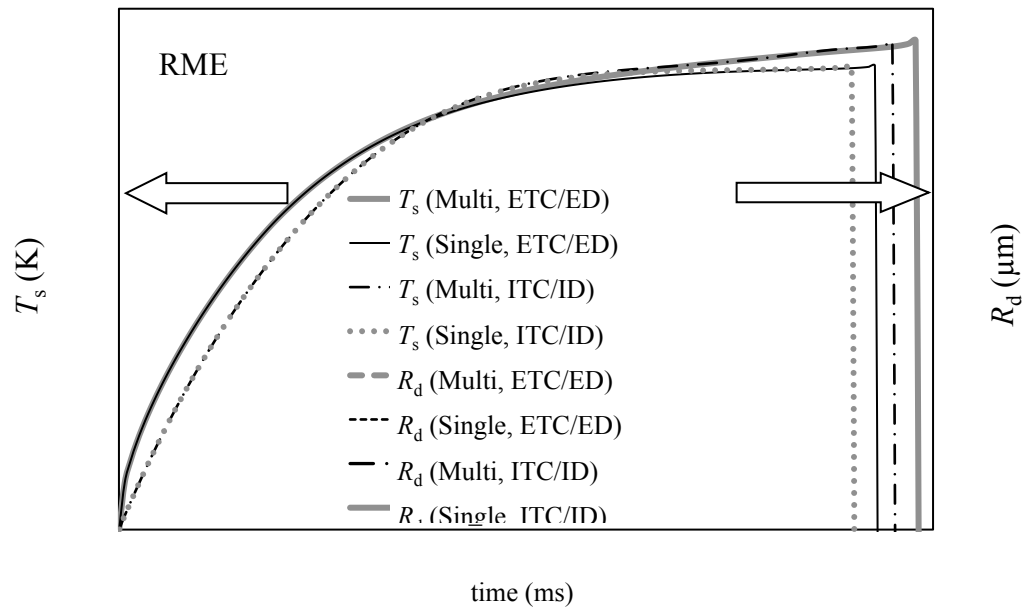


**Figure 1.** The time evolution of RME droplet surface temperatures ( $T_s$ ) and radii ( $R_d$ ) predicted by the four models. Initial droplet radius and temperature are assumed equal to 12.66  $\mu\text{m}$  and 375 K, respectively. The ambient gas pressure and temperature are equal to 30 bar and 880 K, respectively. The droplet is moving at a constant velocity of 10 m/s.

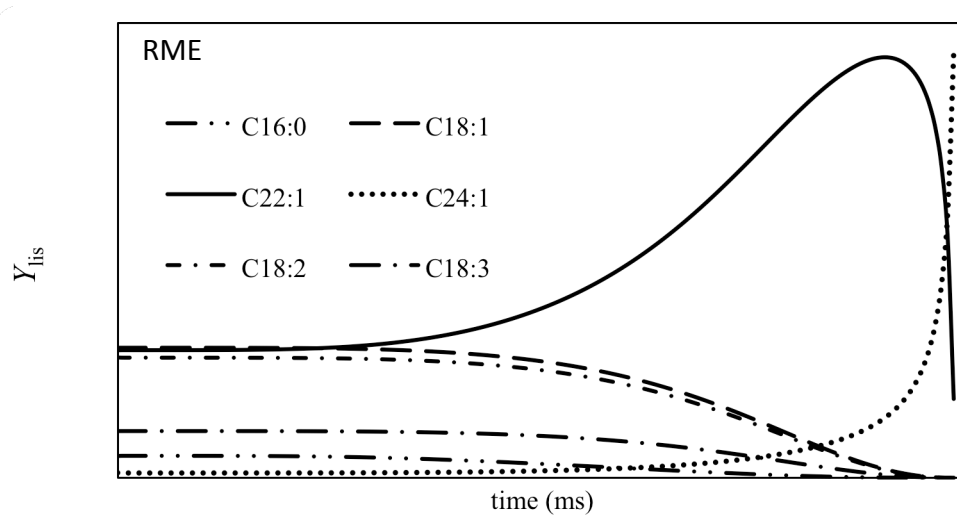


**Figure 2.** Liquid species mass fractions at the droplet surface  $Y_{\text{lis}}$ , for six RME dominant components versus time (ms), for the same parameters as in Fig. 1.

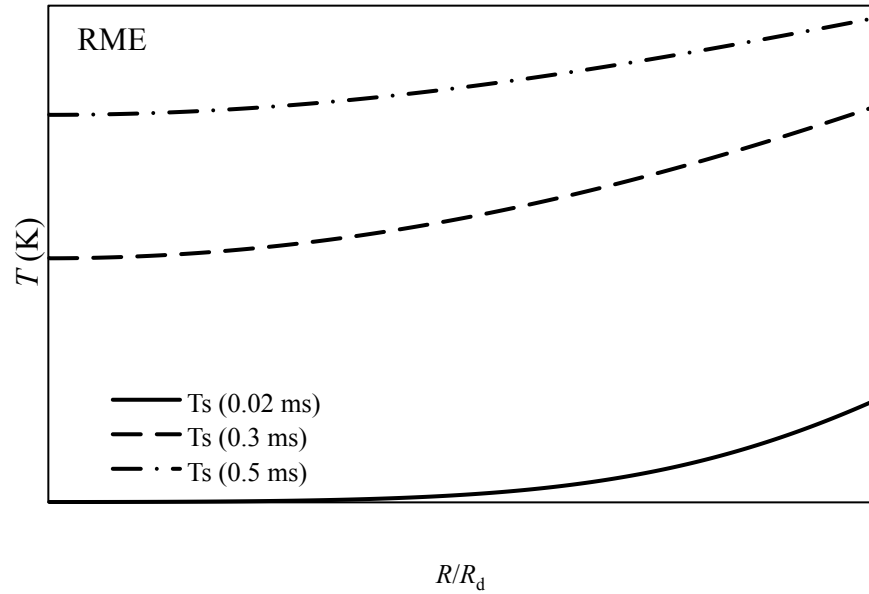


**Figure 3.** The temperature  $T$  versus  $R/R_d$  at 3 time instants, 0.02 ms, 0.3 ms and 0.5 ms, predicted by the ETC/ED model, for the same parameters as in Fig. 1.

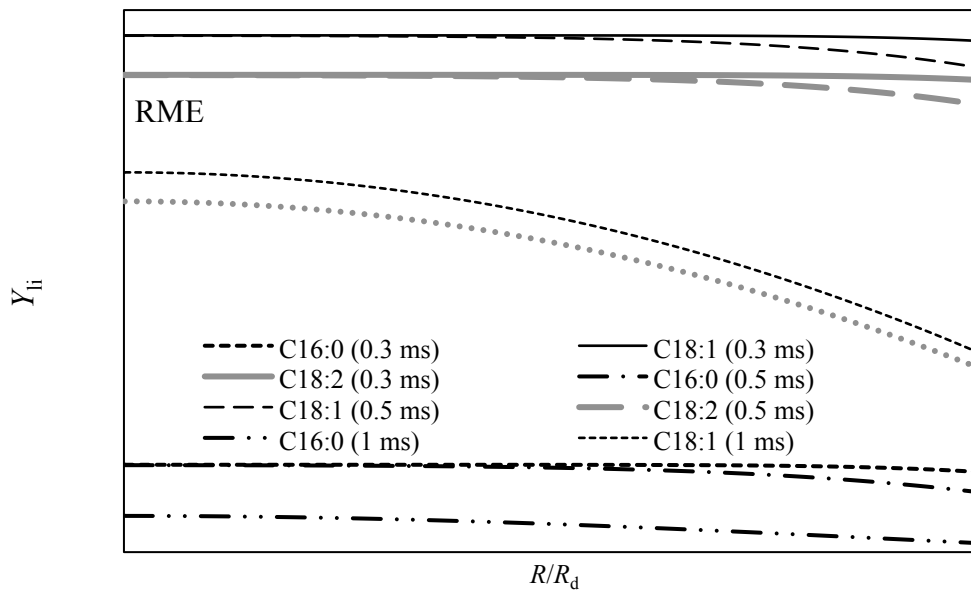


**Figure 4.** The liquid species mass fraction  $Y_{li}$  versus  $R/R_d$  at 3 time instants, 0.3 ms, 0.5 ms and 1 ms, predicted by the ETC/ED model for the same parameters as in Fig. 1.

The difference between time evolutions of liquid species mass fractions is noticeable in Fig. 2. This difference can be related to the time delay in the evaporation of heavier components in comparison to the lighter ones. This is consistent with the results shown in Fig. 4. These two figures indicate the importance of taking into account the diffusions of species inside droplets alongside the effects of temperature gradient within them (see Fig. 3). It can be concluded that ignoring the effects of species diffusion, temperature gradient and recirculation inside droplets, which is common practice in modelling the heating and evaporation of biodiesel fuel droplets in engineering applications, can lead to noticeable errors in the predictions of droplet surface temperatures and evaporation times.

## Acknowledgements

The authors are grateful to INTERREG IVa (Project E3C3, Reference 4274) and Zhytomyr State Technological University for their financial support.

## Nomenclatures

$B_M$	Spalding mass transfer number
$B_T$	Spalding heat transfer number
$C$	specific heat capacity [ $\text{J} \cdot \text{kg}^{-1} \cdot \text{K}^{-1}$ ]
$D$	diffusion coefficient [ $\text{m}^2 \cdot \text{s}^{-1}$ ]
$h$	heat transfer coefficient [ $\text{W} \cdot \text{m}^{-2} \cdot \text{K}^{-1}$ ]
$k$	thermal conductivity [ $\text{W} \cdot \text{m}^{-1} \cdot \text{K}^{-1}$ ]
$L$	latent heat of evaporation [ $\text{J} \cdot \text{kg}^{-1}$ ]
$P$	pressure
$Pe$	Peclet number
$q_{in}$	parameter introduced by Equation (14)
$q_n$	parameter introduced in Equation (7)
$Q_n$	parameter introduced by Equation (14)
$R$	distance from the droplet centre [m]
$R_d$	droplet radius [m]
$Re$	Reynolds number
$Sc$	Schmidt number
$Sh$	Sherwood number
$t$	time [s]
$T$	temperature [K]
$Y$	mass fraction
$\kappa$	thermal diffusivity
$\varepsilon$	evaporation rate
$\lambda$	eigenvalues
$\mu$	dynamic viscosity [ $\text{Pa} \cdot \text{s}$ ]
$\mu_0$	parameter introduced in Equation (7)
$\rho$	density [ $\text{kg} \cdot \text{m}^{-3}$ ]

### Subscripts

$d$	droplet
$eff$	effective
$g$	gas
$i$	index for species
$iso$	isolated
$l$	liquid
$s$	surface
$T$	temperature
$v$	vapour
$Y$	species

### Abbreviations

ED	Effective Diffusivity
ETC	Effective Thermal Conductivity
ID	Infinite Diffusivity
ITC	Infinite Thermal Conductivity
RME	Rapeseed Methyl Ester

## References

1. S.K. Hoekman, A. Broch, Review of biodiesel composition, properties, and specifications. *Renewable and Sustainable Energy Reviews* **16**, 143169 (2012).
2. M. Lapuerta, O. Armas, Effect of biodiesel fuels on diesel engine emissions. *Progress in Energy and Combustion Science* **34**, 198-223 (2008).

3. W.H.L. Hallett, N.V. Legault, Modelling biodiesel droplet evaporation using continuous thermodynamics. *Fuel* **90**, 1221-8 (2011).
4. K. Saha, E. Abu-Ramadan, Multicomponent evaporation model for pure and blended biodiesel droplets in high temperature convective environment. *Applied Energy* **93**, 71-79 (2012).
5. S.S. Sazhin, T. Kristyadi, [Models for fuel droplet heating and evaporation: comparative analysis](#). *Fuel* **85**:1613–1630 (2006).
6. S.S. Sazhin, Advanced models of fuel droplet heating and evaporation. *Progress in Energy and Combustion Science* **32**, 162-214 (2006).
7. S.S. Sazhin, A.E. Elwardany, A simplified model for bi-component droplet heating and evaporation. *Int. J of Heat and Mass Transfer* **53**, 4495-4505 (2010).
8. B. Abramzon, W.A. Sirignano, Droplet vaporization model for spray combustion calculations. *Int. J of Heat and Mass Transfer* **32**, 1605-1618 (1989).
9. I.G. Gusev, P.A. Krutitskii, A study of the species diffusion equation in the presence of the moving boundary. *Int. J of Heat and Mass Transfer* **55**, 2014-2021 (2012).
10. A.E. Elwardany, I.G. Gusev, Mono- and multi-component droplet cooling/heating and evaporation: comparative analysis of numerical models. *Atomization and Sprays* **21**, 907-931 (2011).
11. S.S. Sazhin, A. Elwardany, A quasi-discrete model for heating and evaporation of complex multicomponent hydrocarbon fuel droplets. *Int. J of Heat and Mass Transfer* **54**, 4325-4332 (2011).
12. A.E. Elwardany, S.S. Sazhin, A quasi-discrete model for droplet heating and evaporation: application to Diesel and gasoline fuels. *Fuel* **97**, 685-694 (2012).
13. S.S. Sazhin, A.E. Elwardany, Multi-component droplet heating and evaporation: numerical simulation versus experimental data. *Int. J of Thermal Science* **50**, 1164-1180 (2011).

## Modelling of Heating and Evaporation of Gasoline Fuel: Effects of Input Parameters

Elwardany A E<sup>1</sup>, Sazhin S S<sup>2</sup> and Farooq A<sup>1</sup>

1: Clean Combustion Research Centre, Division of Physical Sciences and Engineering, King Abdullah University of Science and Technology, Thuwal 23955-6900, Saudi Arabia

2: Sir Harry Ricardo Laboratories, Centre for Automotive Engineering, School of Computing, Engineering and Mathematics, Faculty of Science and Engineering, University of Brighton, Brighton, BN2 4GJ, UK

### Abstract

A sensitivity study of the model predictions of droplet surface temperatures and radii for various values of input parameters (droplet initial radius, temperature and velocity, ambient gas temperature and pressure) has been carried out under the assumption that gasoline fuel is approximated by three quasi-components used in the quasi-discrete model.

### Introduction

Models for heating and evaporation of fuel droplets can be classified based on fuel composition: models based on the assumption that fuel is mono-component and those taking into account the multi-component composition of the fuel. Models taking into account the multi-component composition of fuel are very important and relevant for practical applications and our analysis will be focused upon them. This group of models can be further subdivided into two subgroups: those applicable for a small number of components (Discrete Component Model (DCM)) [1-8] and those applicable for large numbers of components (e.g. Continuous Thermodynamics approach [9-12] and the Distillation Curve Model [13]). In the first subgroup, the choice of discrete components could be based on either the pseudo-components or the key components approach [10]. The pseudo-components approach is based on replacing the continuous distribution of the mixture with a discrete one. The key components approach is based on replacing the continuous mixture with components with thermodynamics properties similar to those of the continuous mixture [10]. In the second subgroup a number of additional simplifying assumptions are used including the assumption that species mix infinitely quickly inside the droplet or do not mix at all.

In [14, 15], it was pointed out that the effects of finite thermal conductivity and recirculation inside the droplets need to be taken into account in modelling droplet heating and evaporation. The simplest approach to doing this can be based on the application of the Effective Thermal Conductivity (ETC) model [16, 17]. Also, in [6, 18], which focused on the modelling of heating and evaporation of bi-component droplets, it was demonstrated that the effect of finite diffusivity and recirculation of liquid species cannot be ignored. These effects were taken into account based on the Effective Diffusivity (ED) model.

A quasi-discrete model for heating and evaporation of complex mixtures with large numbers of components was suggested in [19]. This model is based on replacing a large number of actual components with a small number of quasi-components to approximate complex mixtures. The version of this model developed in [19] is based on the assumption that fuel consists only of alkanes ( $C_nH_{2n+2}$ ). These quasi-components are then treated as actual components with averaged values of the carbon number  $n$ , taking into account the effect of finite thermal conductivity and species diffusivities within the liquid droplet. It was assumed that the liquid density, viscosity, heat capacity and thermal conductivity of all quasi-components are the same as those for  $n$ -dodecane, while the values of latent heat of evaporation and saturated vapour pressure take into account the effect of the number of carbon atoms as suggested in [12]. This model was applied for the analysis of heating and evaporation of Diesel fuel approximated by 21 components. These correspond to a maximum of 20 quasi-components, having average properties between those for neighbouring alkanes with the difference between carbon numbers equal to 1. It was demonstrated that the predictions of the model with 5 quasi-components are very close to the predictions of the model that includes contributions from all 20 quasi-components.

In [20], the original quasi-discrete model was generalised to take into account the dependence of liquid density, viscosity, heat capacity and thermal conductivity on the number of carbon atoms. The new model was applied to the analysis of heating and evaporation of both Diesel (approximated by 21 components or maximum 20 quasi-components) and gasoline (approximated by 14 components or maximum 13 quasi-components) fuels. As in [19], it was demonstrated that in the case of Diesel fuel the results predicted using 5 quasi-components are almost indistinguishable from the results predicted by the model taking into account the contribution of all 20 quasi-components. In the case of gasoline fuel the results predicted using 3 quasi-components were very close to the results predicted by the model taking into account the contribution of 13 quasi-components. This

demonstrates the potential usefulness of the quasi-discrete model for the analysis of heating and evaporation of droplets consisting of many components.

## Models

### Heat transfer equation

The heat conduction equation inside spherically-symmetric droplets can be presented as [25,28]:

$$\frac{\partial T}{\partial t} = \kappa \left( \frac{\partial^2 T}{\partial R^2} + \frac{2}{R} \frac{\partial T}{\partial R} \right), \quad (1)$$

where  $\kappa = \frac{k_l}{c_l \rho_l}$  is the liquid thermal diffusivity,  $k_l$ ,  $c_l$ , and  $\rho_l$  are the liquid thermal conductivity, specific heat capacity and density respectively. Ignoring the effect of evaporation, the boundary and initial conditions for Eq. (1) can be presented as [15, 16]:

$$\left. \begin{aligned} h(T_g - T_s) &= k_l \frac{\partial T}{\partial R} \Big|_{R=R_d-0} \\ T(t=0) &= T_{d0}(R) \end{aligned} \right\}, \quad (2)$$

where  $T_s = T_s(t)$  is the droplet's surface temperature,  $T_g = T_g(t)$  is the ambient gas temperature,  $h$  is the convective heat transfer coefficient. The solutions to Eq. (1) with the above-mentioned boundary and initial conditions are discussed in [15].

### Species diffusion equations

The species diffusion equations inside spherically-symmetric droplets can be presented as [15]:

$$\frac{\partial Y_{li}}{\partial t} = D_l \left( \frac{\partial^2 Y_{li}}{\partial R^2} + \frac{2}{R} \frac{\partial Y_{li}}{\partial R} \right), \quad (3)$$

where  $Y_{li} \equiv Y_{li}(t, R)$  is the mass fraction of the species  $i$  and  $D_l$  is the liquid mass diffusivity (assumed to be the same for all species). The boundary condition for this equation can be written as:

$$\alpha(\epsilon_i - Y_{lis}) = -D_l \frac{\partial Y_{li}}{\partial R} \Big|_{R=R_d-0}, \quad (4)$$

where

$$\alpha = \frac{|\dot{m}_d|}{4\pi\rho_l R_d^2}, \quad (5)$$

$$\dot{m}_d = -2\pi R_d D_v \rho_g B_M Sh, \quad (6)$$

$\rho_g$  is the gas density,  $D_v$  is the diffusion coefficient of all vapour species in air,  $B_M$  is the Spalding mass transfer number and  $Sh$  is the Sherwood number. Both Sherwood and Nusselt numbers are calculated based on Abramzon and Sirignano correlations [17].

The evaporation rate,  $\epsilon_i$ , of species  $i$  is presented as:

$$\epsilon_i = \frac{Y_{vis}}{\sum_i Y_{vis}}, \quad (7)$$

where  $Y_{vis}$  is the species mass fraction at the droplet surface.

The solutions to Eq. (3) at the end of the timestep with the corresponding boundary conditions are described in [6].

### The effect of recirculation

The effect of recirculation inside the droplet, due to its motion relative to the ambient gas, is taken into account by replacing the liquid thermal conductivity and liquid diffusivity with the so-called effective thermal conductivity and effective liquid diffusivity, respectively:

$$\left. \begin{aligned} k_{eff} &= \chi k_l \\ D_{eff} &= \chi_Y D_l \end{aligned} \right\}, \quad (8)$$

where the coefficients  $\chi$  and  $\chi_Y$  vary from 1 to 2.72 and can be approximated as [6]:

$$\left. \begin{aligned} \chi &= 1.86 + 0.86 \tanh[2.225 \log_{10}(Pe_{d(l)}/30)] \\ \chi_Y &= 1.86 + 0.86 \tanh[2.225 \log_{10}(Re_{d(l)} Sc_{d(l)}/30)] \end{aligned} \right\}, \quad (9)$$

$Pe_{d(l)} = Re_{d(l)} Pr_{d(l)}$  is the droplet Peclet number, in which the liquid transport properties were used.  $Sc_{d(l)} = \frac{\nu_l}{D_l}$  is the liquid Schmidt number,  $\nu_l$  is the liquid kinematic viscosity,  $Re_{d(l)}$  is the droplet Reynolds number, based on the maximal liquid velocity near the surface of the droplets [8, 17] and  $Pr_{d(l)}$  is the droplet Prandtl number.

The model based on Eqs. (1) and (8) is called the Effective Thermal Conductivity (ETC) model, while the model, based on Eqs. (3) and (8), is called the Effective Diffusivity (ED) model. The model that combines both of these will be referred to as the ETC/ED model. In contrast to the ETC/ED model, the ITC/ID model is based



on the assumption that the droplet is well-mixed and there are no temperature or species gradients inside the droplet.

The effects of coupling between the droplet and the surrounding gas and the effects of thermal radiation are ignored at this stage.

#### *Quasi-discrete model*

Following [19-21], the molar mass is used to describe the continuous distribution of gasoline fuel which is assumed to consist only of n-alkanes  $C_nH_{2n+2}$  ( $n \geq 5$  for liquid fuels). The molar mass (kg/kmole) of n-alkane components is related to the number of carbon atoms  $n$  as:

$$M(n) = 14n + 2. \quad (10)$$

The distribution function was taken as:

$$f_m(n) = C_m(n_0, n_f) \frac{(M(n)-\gamma)^{\alpha-1}}{\beta^{\alpha}\Gamma(\alpha)} \exp\left[-\left(\frac{M(n)-\gamma}{\beta}\right)\right], \quad (11)$$

where  $n_0 = 5 \leq n \leq n_f = 18$ , subscripts 0 and  $f$  stand for initial and final values of  $n$ ,  $\Gamma(\alpha)$  is the Gamma function,  $\alpha$  and  $\beta$  are parameters that determine the shape of the distribution (they are taken to be the same as in [21]),  $\gamma$  determines the original shift (assumed to be zero) and  $C_m$  is the normalisation constant and it is calculated based on Eq. (4) of [20]. The distribution function was chosen to reproduce the distillation for ASTM D439 [9].

The dependence of the latent heat of evaporation, vapour pressure, liquid density, viscosity, specific heat capacity and thermal conductivity on the number of carbon atoms are taken into account using the same approximations as in [27].

Following [19, 20], the continuous distribution (11) is replaced with a discrete one, consisting of  $N_f$  quasi-components with carbon numbers:

$$\bar{n}_j = \frac{\int_{n_{j-1}}^{n_j} n f_m(n) dn}{\int_{n_{j-1}}^{n_j} f_m(n) dn}. \quad (12)$$

The corresponding molar and mass fractions are found as

$$X_j = \int_{n_{j-1}}^{n_j} f_m(n) dn, \quad (13)$$

$$Y_j = \frac{M(\bar{n}_j)X_j}{\sum_{j=1}^{j=N_f} [M(\bar{n}_j)X_j]}, \quad (14)$$

where  $j$  is an integer in the range  $1 \leq j \leq N_f$ .

Equations (12-14) are applied to each quasi-component using relevant values of  $n_j$  and  $n_{j-1}$ .

## **Results and Discussion**

### *Effect of initial droplet parameters and ambient temperature and pressure*

Three initial droplet temperatures were considered in the analysis of heating and evaporation of gasoline fuel droplets using 3 quasi-components in the quasi-discrete model: 300, 320 and 350 K. The initial droplet radii and is assumed equal to 10  $\mu\text{m}$  in all cases; the droplet velocities are assumed to be constant and equal to 10 m/s, while gas temperature and pressure are assumed equal to 450 K and 0.3 MPa respectively. The calculations were performed using the ETC/ED model. The temporal variations of droplet surface temperatures and radii are shown in Fig. 1. The results are shown for both ETC/ED and ITC/ID models.

It can be seen from Fig. 1 that increasing the initial droplet temperature from 300 to 320 K leads to a decrease in the evaporation time by approximately 4%. Increasing the initial droplet temperature from 320 K to 350 K leads to a further decrease in the evaporation time by approximately 6%. These trends are observed for both ETC/ED and ITC/ID models. For the case of 350 K, the droplet surface temperature initially decreases slightly, and then it increases until the evaporation process has been completed. This behaviour was not observed for initial droplet temperatures of 300 and 320 K. This can be attributed to the higher initial evaporation rate for hotter droplets compared with the cooler ones. The droplet lifetimes predicted by the ETC/ED model are shorter than those predicted by the ITC/ID model for all initial droplet temperatures under consideration by approximately 15%. Hence, the effects of the finite thermal conductivity and species diffusivities and recirculation inside the droplets need to be taken into account when modelling heating and evaporation of multi-component fuel droplets for both low and high initial droplet temperatures.

It is well-known that fuel spray that supplied to the combustion chamber, consists of a large number of droplets with different radii. In this section, the sensitivity of the predictions of the quasi-discrete model with 3 quasi-components to the choice of the initial droplet radii is investigated. Three initial droplet radii are considered: 5, 10 and 15  $\mu\text{m}$ . All other input parameters are kept the same as in Fig. 1. The plots of droplet surface temperatures and radii for these initial droplet radii, predicted by the ETC/ED and ITC/ID models, are shown in

Fig. 2. It can be noticed from this figure that increasing the droplet radius from 5  $\mu\text{m}$  to 10  $\mu\text{m}$  increases the droplet lifetime by approximately 200% and increasing the radius from 10  $\mu\text{m}$  to 15  $\mu\text{m}$  increases the droplet lifetime further by approximately 100%. For the case of 5  $\mu\text{m}$ , the droplet lifetime predicted by the ETC/ED model is shorter than the one predicted by the ITC/ID model by about 2%. This difference increases to about 4% and 10% for the cases of initial droplet radii of 10 and 15  $\mu\text{m}$  respectively.

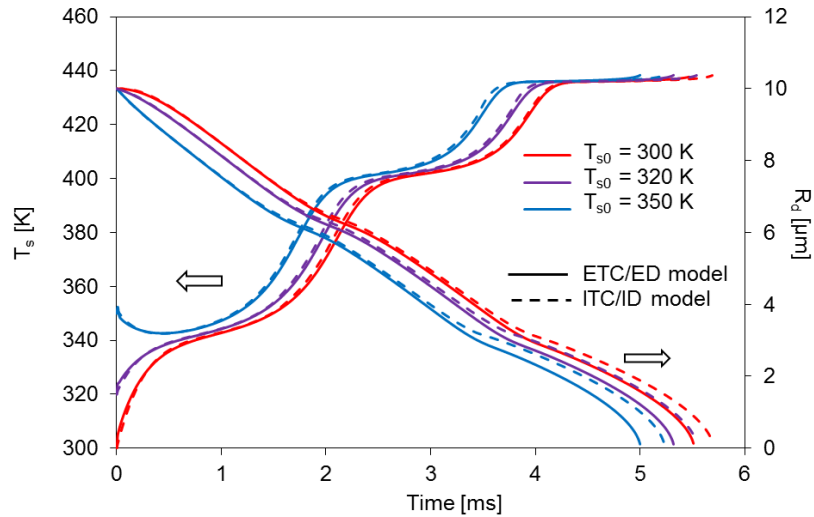


**Figure 1.** Plots of droplet surface temperatures  $T_s$  and radii  $R_d$  versus time predicted for the approximation of gasoline fuel with 3 quasi-components for three initial droplet temperatures (300, 320, 350 K). The plots are presented for both ETC/ED (solid) and ITC/ID (dashed) models.

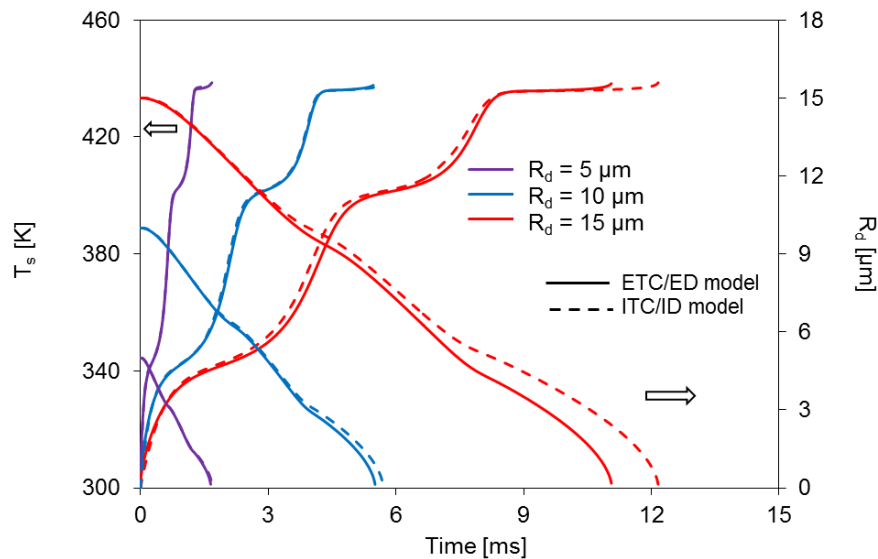


**Figure 2.** The same as Fig. 1 but for three initial droplet radii (5, 10, 15  $\mu\text{m}$ ).

Droplet surface temperatures and radii versus time are presented for three droplet velocities (5, 10 and 15 m/s) in Fig. 3. As in the cases shown in the previous figures, these velocities are assumed to be constant during droplet heating and evaporation. All other input parameters are the same as in Fig. 1. Increasing the droplet velocity from 5 m/s to 15 m/s decreases its evaporation time by approximately 40%. This can be attributed to the increase in the convective heat transfer coefficient with droplet velocity which leads to an increase in droplet surface temperatures and evaporation rates. Also, it can be noticed that the evaporation times predicted by the ETC/ED model are shorter by approximately 20% than those predicted by the ITC/ID model for the droplet velocities under consideration.

Three different ambient temperatures (450, 500 and 600 K) are used for the analysis of the sensitivity of the droplet surface temperatures and radii to the choice of this temperature. All other input parameters are assumed to be the same as in Fig. 1. The results are shown in Fig. 4. It is seen from this figure that increasing the ambient temperature from 450 K to 600 K leads to a decrease in the evaporation time by approximately 200% and to an increase in the droplet surface temperature by approximately 15%. This is related to the fact that as the ambient

temperature increases, the energy available for heating the droplet increases. It is also noticeable that the ETC/ED model predicts evaporation times shorter than those predicted by the ITC/ID model by approximately 10% at all temperatures. This result is different from the one reported in [22] for mono-component droplets, where it was shown that taking into account the finite liquid thermal conductivity affects mainly the droplet surface temperature at the initial state of droplet heating and evaporation, but not the evaporation time.

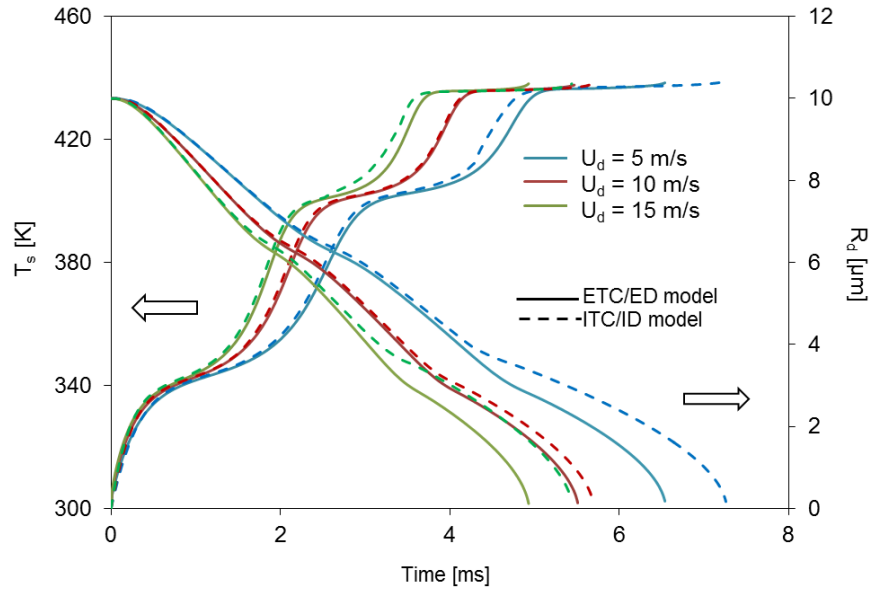


**Figure 3.** The same as Fig. 1 but for three initial droplet velocities (5, 10, 15 m/s).

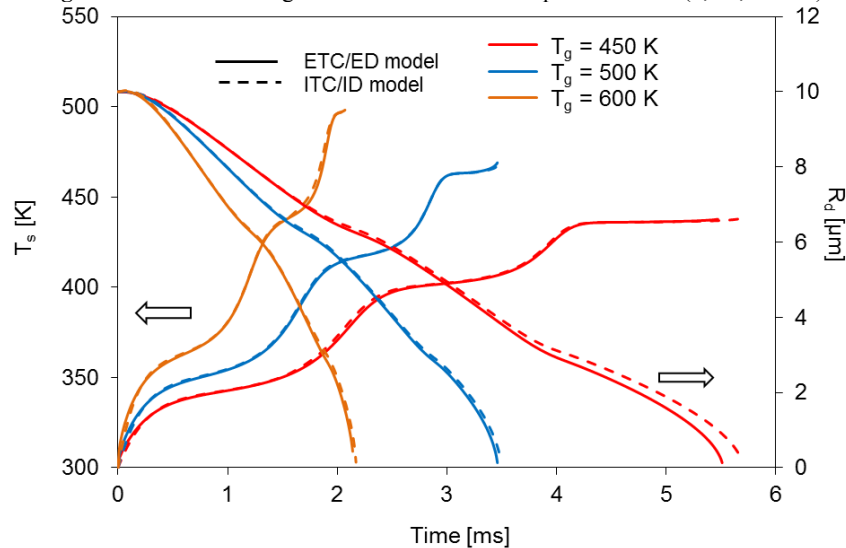


**Figure 4.** The same as Fig. 1 but for three ambient gas temperatures (450, 500, 600 K).

The plots of droplet surface temperatures and radii versus time for three ambient pressures (0.15, 0.3 and 0.45 MPa), all other input parameters being the same as in Fig. 1, are shown in Fig. 5. As can be seen from this figure, the increase in gas pressure from 0.15 MPa to 0.45 MPa leads to an increase in the evaporation time by approximately 5% for both ETC/ED and ITC/ID models. This can be attributed to a decrease in the vapour diffusion coefficient (see Eq. (42) in [6]) with ambient gas pressure as shown in Fig. 9. As in the cases shown in the previous figures, the ETC/ED model predicts evaporation times shorter than those predicted by the ITC/ID model by approximately 10% at all pressures.

The dependence of the droplet mass evaporation rate versus time for the same parameters as in Fig. 8 is shown in Fig. 6. The general shape of the curves is similar to that reported earlier in a number of papers for mono-component droplets, including [23]. In contrast to the curves presented in [23], one can clearly see three stages of droplet evaporation. The dependence of the mass flow rate on pressure turns out to be rather complex. During

some periods, the evaporation rate increases with increasing pressure, while during other periods it decreases with increasing pressure.

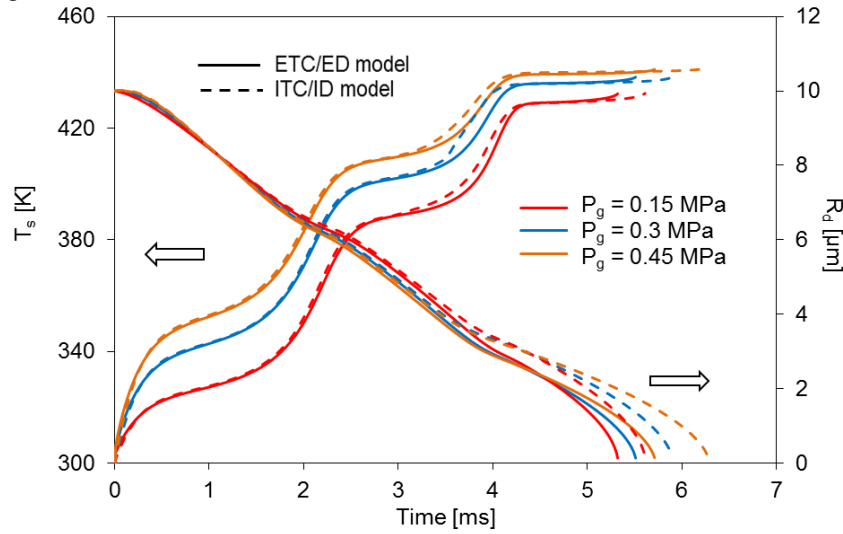


**Figure 5.** The same as Fig. 1 but for three ambient gas pressures (0.15, 0.3, 0.45 MPa).

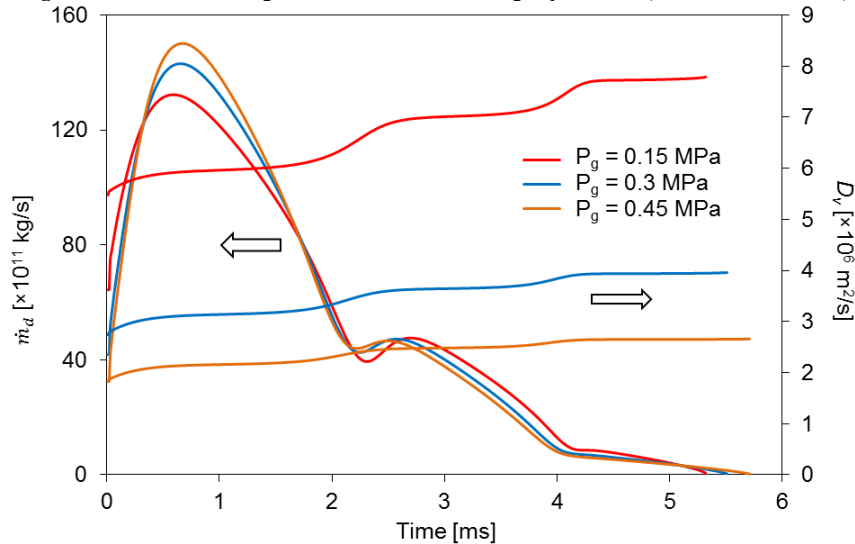


**Figure 6.** Plots of total mass evaporation rate  $\dot{m}_d$  and the vapour diffusion coefficient  $D_v$  for the same cases as shown in Fig. 5, except that only the ETC/ED model is used.

## Conclusions

The sensitivity of the model predictions to the values of input parameters is investigated for the quasi-discrete model in which the gasoline fuel is approximated by three quasi-components. It has been demonstrated that the ETC/ED model predicts shorter droplet evaporation times than the ITC/ID model. The increase in the initial droplet temperature from 300 K to 350 K, the decrease in the initial droplet radius from 15  $\mu\text{m}$  to 5  $\mu\text{m}$ , the increase in the droplet velocity from 5 m/s to 15 m/s, increase in ambient gas temperature from 450 K to 600 K and increase in ambient gas pressure from 0.45 MPa to 0.15 MPa, lead to a decrease in droplet evaporation times by approximately 10%, 300%, 40%, 200% and 5% respectively

## Acknowledgements

The authors acknowledge EPSRC in the UK (grants EP/H001603/1 and EP/J006793/1) and the Clean Combustion Center of King Abdullah University of Science and Technology for financial support.

## References

1. Abraham, J. and V. Magi, *Model for multicomponent droplet vaporization in sprays*. 1998.
2. Aggarwal, S. and H. Mongia, *Multicomponent and high-pressure effects on droplet vaporization*. TRANSACTIONS-AMERICAN SOCIETY OF MECHANICAL ENGINEERS JOURNAL OF ENGINEERING FOR GAS TURBINES AND POWER, 2002. **124**(2): p. 248-255.
3. Sirignano, W.A. and G. Wu, *Multicomponent-liquid-fuel vaporization with complex configuration*. International Journal of Heat and Mass Transfer, 2008. **51**(19): p. 4759-4774.
4. Strotos, G., et al., *Influence of species concentration on the evaporation of suspended multicomponent droplets*. ILASS, Como Lake, Italy, 2008.
5. Ra, Y. and R.D. Reitz, *A vaporization model for discrete multi-component fuel sprays*. International Journal of Multiphase Flow, 2009. **35**(2): p. 101-117.
6. Sazhin, S., et al., *A simplified model for bi-component droplet heating and evaporation*. International Journal of Heat and Mass Transfer, 2010. **53**(21): p. 4495-4505.
7. Elwardany, A., et al., *The Modelling of Heating and Evaporation of Mono-component, Bi-component and Multi-component Droplets*, in *ILASS - Europe 2011* 2011: Lisbon, Portugal.
8. Elwardany, A., et al., *Mono-and multi-component droplet cooling/heating and evaporation: Comparative analysis of numerical models*. Atomization and Sprays, 2011. **21**(11).
9. Tamim, J. and W.L. Hallett, *A continuous thermodynamics model for multicomponent droplet vaporization*. Chemical Engineering Science, 1995. **50**(18): p. 2933-2942.
10. Ratzsch, M.T., *Continuous thermodynamics*. Pure and Applied Chemistry, 1989. **61**(6): p. 1105-1114.
11. Zhu, G.-S. and R.D. Reitz, *A model for high-pressure vaporization of droplets of complex liquid mixtures using continuous thermodynamics*. International journal of heat and mass transfer, 2002. **45**(3): p. 495-507.
12. Arias-Zugasti, M. and D.E. Rosner, *Multicomponent fuel droplet vaporization and combustion using spectral theory for a continuous mixture*. Combustion and Flame, 2003. **135**(3): p. 271-284.
13. Burger, M., et al., *Droplet evaporation modeling by the distillation curve model: accounting for kerosene fuel and elevated pressures*. International journal of heat and mass transfer, 2003. **46**(23): p. 4403-4412.
14. Sazhina, E.M., et al., *A Detailed Modelling of the Spray Ignition Process in Diesel Engines*. Combustion Science and Technology, 2000. **160**(1): p. 317-344.
15. Sazhin, S.S., *Advanced models of fuel droplet heating and evaporation*. Progress in energy and combustion science, 2006. **32**(2): p. 162-214.
16. Sazhin, S., et al., *Transient heating of diesel fuel droplets*. International Journal of Heat and Mass Transfer, 2004. **47**(14): p. 3327-3340.
17. Abramzon, B. and W. Sirignano, *Droplet vaporization model for spray combustion calculations*. International journal of heat and mass transfer, 1989. **32**(9): p. 1605-1618.
18. Sazhin, S.S., et al., *Multi-component droplet heating and evaporation: Numerical simulation versus experimental data*. International Journal of Thermal Sciences, 2011. **50**(7): p. 1164-1180.
19. Sazhin, S.S., et al., *A quasi-discrete model for heating and evaporation of complex multicomponent hydrocarbon fuel droplets*. International Journal of Heat and Mass Transfer, 2011. **54**(19-20): p. 4325-4332.
20. Elwardany, A.E. and S.S. Sazhin, *A quasi-discrete model for droplet heating and evaporation: Application to Diesel and gasoline fuels*. Fuel, 2012. **97**(0): p. 685-694.
21. Elwardany, A., S. Sazhin, and A. Farooq, *Modelling of heating and evaporation of gasoline fuel droplets: A comparative analysis of approximations*. Fuel, 2013.
22. Sazhin, S., et al., *Models for fuel droplet heating and evaporation: comparative analysis*. Fuel, 2006. **85**(12): p. 1613-1630.
23. Abramzon, B. and S. Sazhin, *Convective vaporization of a fuel droplet with thermal radiation absorption*. Fuel, 2006. **85**(1): p. 32-46.

## Experimental study on the regimes of W/O interface in the presence of vertical electric field

Behnam Sadri<sup>1</sup>, Pejman Tabatabaee-Hosseini<sup>2</sup>, Babak Vajdi Hokmabad<sup>2</sup>, Mehdi Rezayati Charan<sup>2</sup> and Esmail Esmaeilzadeh<sup>3</sup>

1: Department of Mechanical Engineering, University of Alberta, Canada

2: Heat and Fluid Flow Research Laboratory, University of Tabriz, Tabriz, Iran

3: Science and Research branch, Islamic Azad University, Tabriz, Iran

### Abstract

Electrified interfaces have been used to produce fine particles. Here, we investigate the behaviour of planar electrified interface in the presence of vertical electric field. Corn oil and four KCl aqueous solutions with different concentrations are employed. During the experiments, for the first time, four distinct behaviours of electrified interfaces were disclosed and named as: Hump figure of interface, Taylor cone appearance and its rotary motion on the interface, intermittent jetting and thorough ascending of the interface. Taylor cones' mean droplet diameter and their angles, discharging velocity at the tip of the cone, the frequency of Taylor cones appearance and their merging to each other are studied in this paper. Additionally, the circumstances of interface levitation affected by electric field are some of the major results of this study to gain some insight into the electrified interfaces issue.

### Introduction

Producing fine particles via electrical forces has been attracting great attention in the last century. Mixing of two immiscible fluids, increasing interfacial area between two fluids and producing stable emulsion are the significant contributions of electric fields in fluids media (1). Electrical forces promise a stable way to manipulate fluids in wide range of applications including electrospraying (2), electrified flow focusing (3), pumping of fluids via EHD body forces (4), EHD mixing (5) and aggregation of droplets in emulsions (6). Interface experiences different regimes when it is exposed to different applied electric fields. Taylor cone is one of the so-called regimes. Eow and Ghadiri measured the electric current of two immiscible fluids exposed to vertical applied electric field. They reported a turning point in electric current which implies existence of Taylor cone on the two fluids' interface (7). De la Mora, extensively, reviewed Taylor-cone jetting and produced droplets (8). The singularity of electrohydrodynamic spout in which the interface levitates to the oppositely charged electrode is studied by Oddershede and Nagel (9). Based on their experiments, the interface experiences a logarithmic levitation in respect of time which implies the critical dynamics underlying the electrified interface discharging. Interface responds to applied electric field in different regimes. The rotary motion on the interface which is one of these regimes is introduced by Uemera and his co-workers in which they just introduce the existence of this regime when electric field is applied to the interface (10).

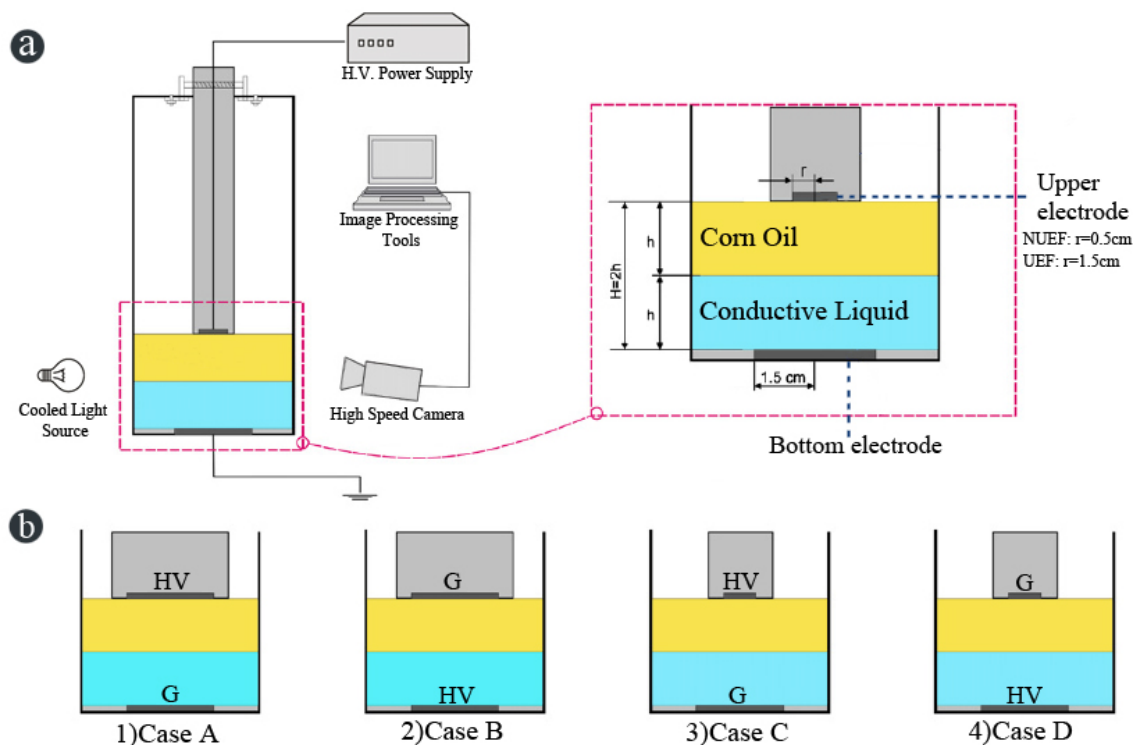
The study of all regimes in the electrified interface is still a subtle area in the literature. To date, there is no work that reports comprehensively the regimes of W/O interface in wide range of applied electric field. In this paper, we study the different regimes of W/O interface in which the authors try to present a thorough portrait of the behaviour of electrified interface for the first time.

### Experimental test-rig

A cell was made of Plexiglas to facilitate visualization. The figure 1 illustrates the schematic view of experimental setup. As shown in this figure, two different electrodes ( $D=15, 30$  mm) which pertains to produce non-uniform electric field (NUEF) and uniform electric field (UEF) have been installed horizontally to produce vertical electric field into W/O interface. Corn oil and 4 different aqueous KCl solutions, having apparently different electrical conductivities, are employed in this work. Table 1 presents the electrical and physical properties of these working fluids. In this table, the interfacial tension between the two phases is calculated by a well-known equation (11):

$$\gamma_{c-d} = \gamma_c + \gamma_d - 2\sqrt{\gamma_c\gamma_d} = (\sqrt{\gamma_c} - \sqrt{\gamma_d})^2$$

	Electrical conductivity (s/m)	Conductivity Ratio ( $\sigma/\sigma_{\text{Cornoil}}$ )	Relative permittivity	Interfacial tension (mN/m)	Density (kg/m <sup>3</sup> )
Distilled water	0.048E-3	0.96E6	72.9	6.71	1000
0.01 M KCl solution	1.634E-3	3.27E7	72.9	6.73	1000.7
0.1 M KCl solution	11.82E-3	2.36E8	72.9	6.87	1001.7
1 M KCl solution	108.62E-3	2.17E9	72.9	7.37	1041.5
Corn oil	5E-11	1	3.1	0	918

**Table1.** The properties of employed fluids.

**Figure 1.** The schematic view of the experimental setup

## Results and Discussion

To help with better interpretation of experimental observations, a finite element code was developed to solve electric potential,  $V$ , and provide electric field lines at initial moment (Assuming no deformation in the interface and no surface charges on the interface). This simplified solution is presented to show the differences between the two geometries utilized in this work, for instance uniformity of the electric field and changes in the quantity of tangential to normal electrical stresses ratios are elucidated. Knowing that the electric field is zero inside the conductive phase, Laplace Equation is solved only for the dielectric fluid assuming perfect dielectric model (12). Figure 2 depicts the electric field lines in both non uniform and uniform electric field. As depicted in this figure, the surface contours represent electric potential and stream lines show electric field lines. With this in mind that the charge relaxation time is very short in comparison with other hydrodynamic times we can assume that the liquid bulk is free of charges except on the interface (13).

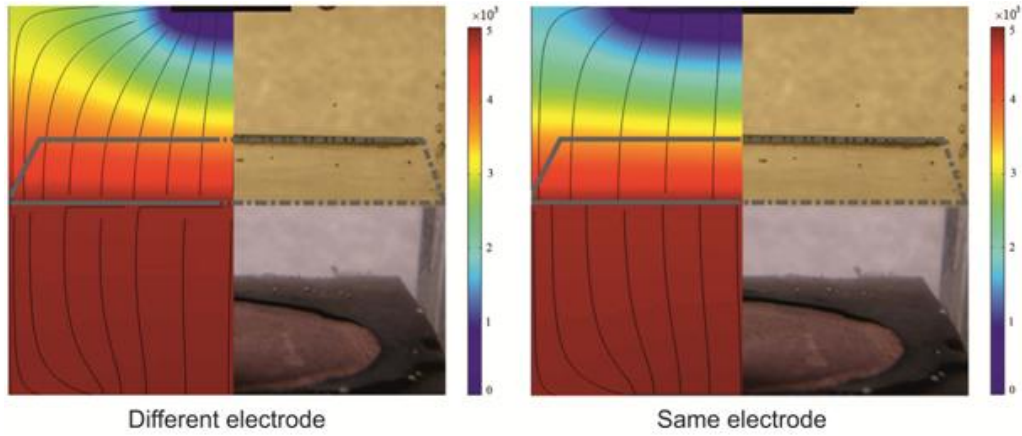




**Figure 2.** Electric potential distributions and electric field lines in two different electrode geometry

Figure 3 illustrates the overall behaviour of planar interface in the presence of electric field. In rather low electric fields, planar interface do not show any significant change, as expected. The augmentation of applied voltage and consequently more charge transportation leads to the gradient of electric field strength in the interface. The instabilities with rotary motion are the first response of interface to electric field gradients. Applying more electric field triggers the hump figure of interface (figure 3-b). In addition, the instabilities on the interface appear before the manifestation of hump figure (figure 3-a). Taylor cones appear on the interface in higher applied voltages (figure 3-b). As shown in figure 3-c, the normal electric stresses are large enough to make droplets emerge from the cone shape instabilities. Besides, these normal forces up rises the height of the water as mentioned before.

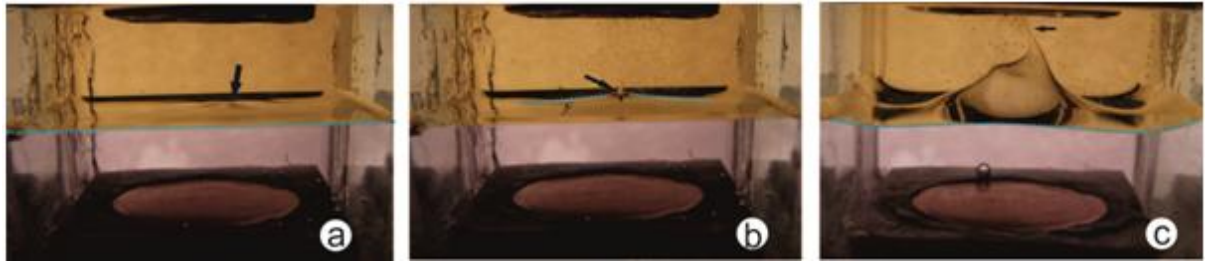


**Figure 3.** a-the instabilities on the interface (V=4.1 KV), b- The Taylor cone in the interface (V=5.1 KV), c- discharging phenomenon (V=6.8 KV); electrode diameter= 3cm

The tiny droplets which detach from these cone tips are of great importance. As shown in figure 4, the mean discharged droplet diameters diminish with increasing the electric Bond number. This procedure illustrates the paramount role of applied voltage in the producing tiny droplets. Increasing applied voltage leads to producing more fine particles. Tangential electrical stresses augmentations which are consequences of electric field increasing lead to extracting more fine drops from the cone tip. It is worthy that the minimum droplet radius that was observed during the experiments is about 10 micrometer. The droplets precipitate during the pinch off from Taylor cones. Figure 5 represents the overall behaviour of pinch off velocity of tiny droplets from the cone tip. As shown in this figure, the velocity of droplets decreases in higher concentration of KCl in water. To figure out the circumstances of this trend, the equation of motion for an incompressible Newtonian fluid is helpful in which is (14):

$$\rho \frac{Du}{Dt} = -\frac{1}{2} \epsilon_0 E \cdot E \nabla \epsilon + \rho^e E + \mu \nabla^2 U$$

It is considerable that  $E$ ,  $\rho^e$  and  $U$  are Electric field (Kg.m/s<sup>3</sup>.A), Local free charge density(C/m<sup>2</sup>) and Velocity (m/s) respectively. Here, the first term in the right hand side of equation is dipole force per unit volume. The second term represents Columbic force per unit volume and the last term is the viscous force per unit volume for uniform viscosity fluid.

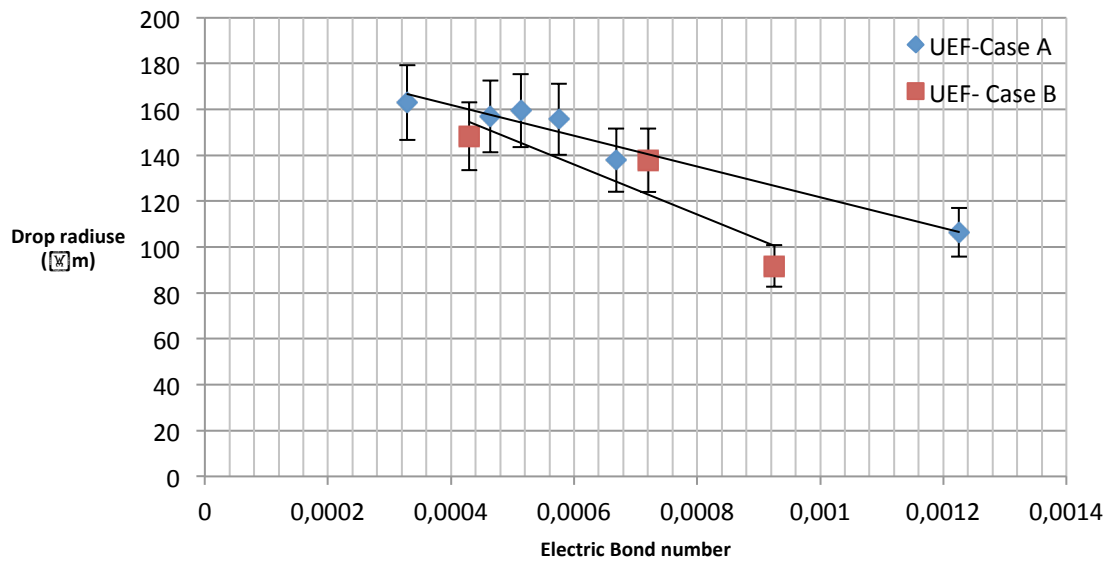


Figure 4. droplet radiuses fluctuation versus electric bond number

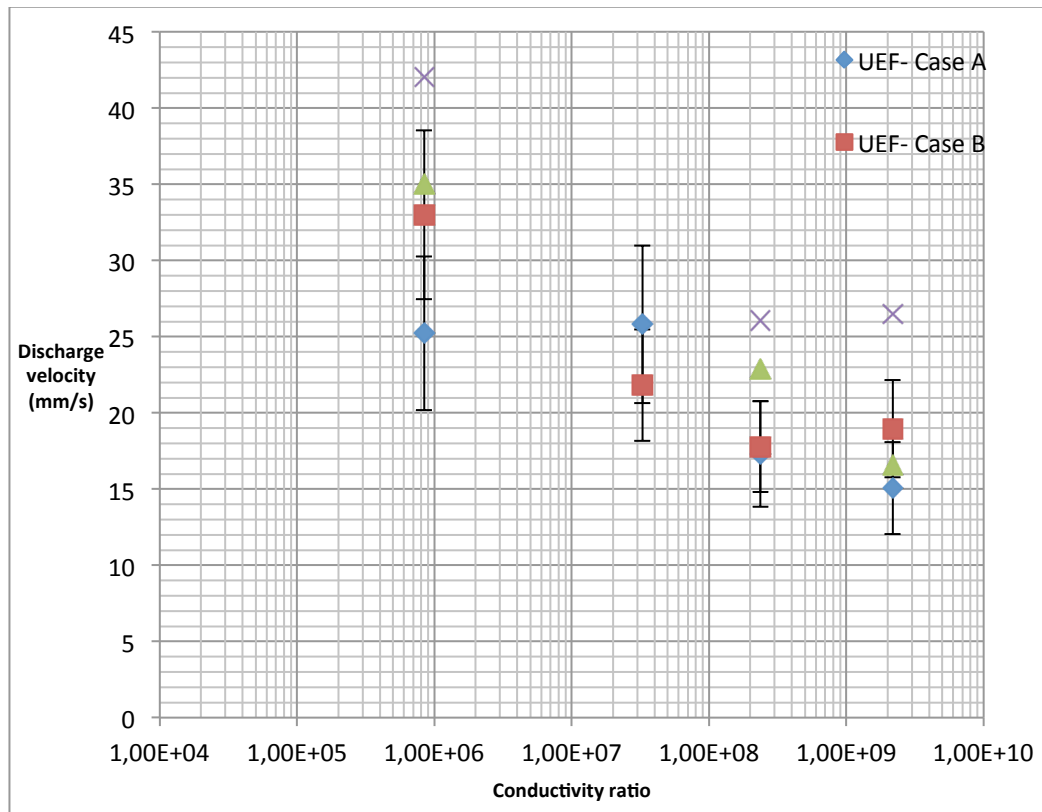


Figure 5. discharge velocity of droplets changes with conductivity ratio

As can be seen in figure 6, there is a string of water drops or ligament that acts like a wire after contact with electrode. In fact, the water drops transport the charge of interface like a wire. Figure 7 depicts the different pattern of these ligaments and strings. In lower electric fields, one ligament transfers the charges of interface to the upper electrode. With electric field augmentation, the normal electrical stresses raise so that the ligaments distort completely. As shown in figure 7-b, drops contact with each other and transfer the charges. In some of the cases, Taylor cones appear on the ends of drops and starts to electrospray fine particles which is obvious in the figure 7. In stronger electric fields, drops distort faster and the small drops produce the string of water. These small droplets contact frequently to each other and vacate the charges on the interface like a wire. These

drops still remain until the electric field strength becomes zero. They do not merge and act like a wire, by frequent contacts with each other, to release the charges from electrified interface.



**Figure 6.** The procedure of discharging distilled water into oppositely charged electrode ( $E=219.88$  V/mm, scale bar= 5mm)

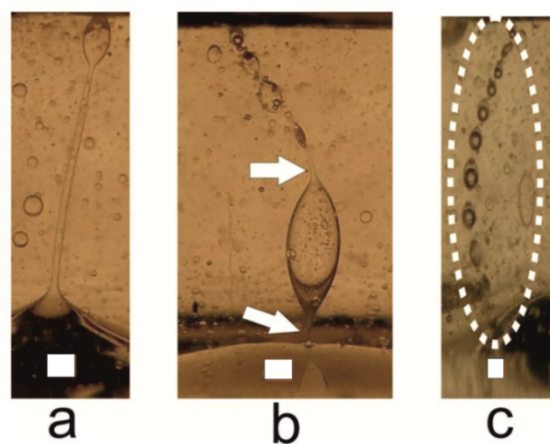


**Figure 7.** The string of water drops in the different electric field for different electrode sizes (a:  $E=219.88$  V/mm, b:  $E=301.2$  V/mm, c:  $E=335.84$  V/mm, Scale bar=0.1 mm)

On the other hand, when these strings of water disappeared, the interface levitates and contact with the electrode (Fig 6).

The more applied voltage is, the more height of the interface is. Owing to the fact that increasing the applied electric field strength has a direct effect on the rate of charges on the interface and subsequently this procedure leads to more electrostatic normal stresses, therefore the ascending velocity of interface in higher voltages is more than lower voltages. This story is also valid for similar electrodes in which the augmented normal electrical stresses levitate the interface. The upward velocity also increases with voltage rising which also illustrates the paramount role of charges rate and normal electrical stresses in the overall behaviour of the interface.

The tangential electrical stresses rise with electric field augmentation and these stresses lead to the phenomenon which we call it “intermittent cone jetting”. Figure 8 shows this phenomenon in 1/60 s intervals.

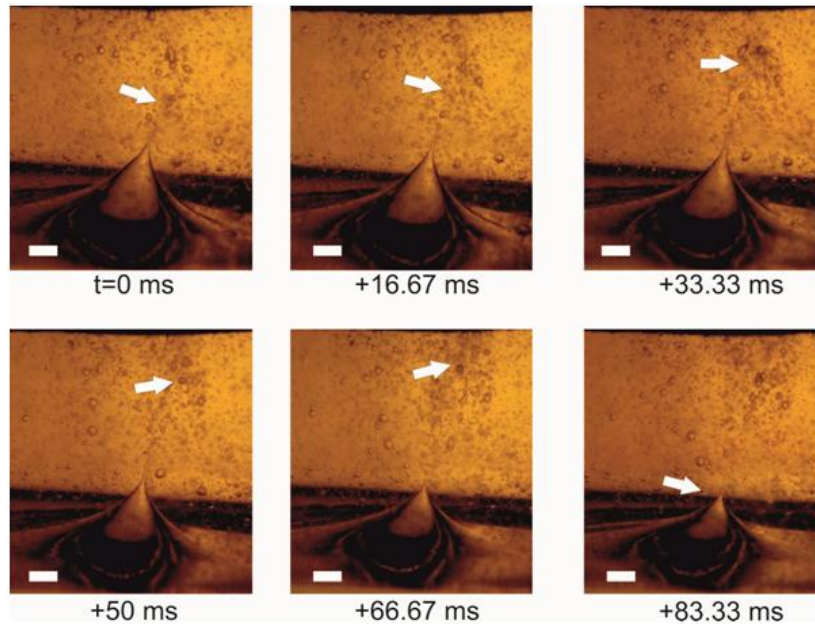


**Figure 8.** Intermittent jetting and the behaviour of W/O interface (Scale bar=0.5 mm)

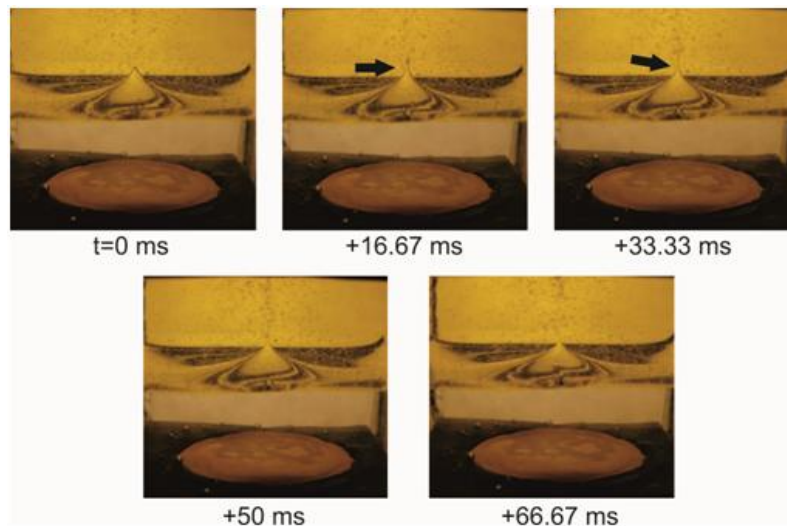


**Figure 9.** The illustration of intermittent Taylor cone frequency (E=112.16 V/mm, non-uniform electric field)

This Figure 9 shows that the oscillation frequency of cone-jet in the pulsed mode grows with liquid conductivity. It is noteworthy that liquid conductivity increment due to KCl addition will reduce the charge relaxation time. So, formed Taylor cone cannot go further and after sharpening in the conic cusping form returns to equilibrium state to replenish its charge. Owing to the higher conductivity rate, charge transport rate is rather instantaneous in both giving and getting. As a matter of fact, the conical meniscus can oscillate for much more

times in a definite period. This is not the case with lower conductivity solutions. Here, charges cannot be brought to the meniscus fast enough and streaming as a conical meniscus takes more time. Also, Charge relaxation time increases with conductivity descendant. This makes an opportunity for the meniscus tip to soar farther with the stretching effect of electrical stress on the fluid charges. These are the two reasons which decrease the pulsation frequency of cone in lower conductivities.

## Conclusion

In the present work, we study the behaviour of planar electrified interface and its responses to the vertical electric field. The significant results of this study are listed below:

- Four specific regimes of W/O interface responses to electric field have been disclosed for the first time in this work which are hump figure of the interface, Taylor cone appearance on the interface and its rotary motion, Intermittent jetting and thorough ascending of W/O interface.
- During the experiments, we concluded that the convection charge transport is the predominant regime of charge transfer into the interface while when the conductive liquid contacts with oppositely charged electrode, the Ohmic charge transport precedes.
- For the first time, the merging of Taylor cones on the interface is reported in this study.
- The rotary motion of the interface and the circumstances of Taylor cone emerging on the interface are investigated.
- The produced mean droplet diameter, the discharge velocity, the cone angle and the frequency of the Taylor cones are studied in this paper.
- The circumstances of interface ascending in rather higher applied electric fields are discussed in the present work.

## References

- 1- Jong-Wook Ha and Seung-Man Yang, Fluid dynamics of a double emulsion droplet in an electric field, *Physics of Fluids* **1995**, 11 (5), 1029-1041
- 2- B. Sadri, B. Vajdi Hokmabad, E. Esmaeilzadeh, R. Gharraei, Experimental investigation of electrosprayed droplets behaviour of water and KCl aqueous solutions in Silicone oil, *Exp. Therm. Fluid Sci.* **2012**, 36, 249-255
- 3- A. M. Gañán-Calvo, J. M. López-Herrera, y P. Riesco-Chueca, The combination of electrospray and flow focusing, *J. Fluid Mech.* **2006**, 566, 421-445
- 4- M. Hojjati, E. Esmaeilzadeh, B. Sadri, R. Gharraei, Electrohydrodynamic conduction pumps with cylindrical electrodes for pumping of dielectric liquid film in an open channel, *J. Coll. Surfaces A: Phys. & Eng. Aspects* **2011**, 392 (1), 294-299
- 1- El Moctar AO, Aubry N, Batton J, Electro-hydrodynamic micro-fluidic mixer, *Lab Chip* **2003**, 3 (4), 273-280
- 2- C. R. Vigo and W. D. Ristenpart, Aggregation and Coalescence of Oil Droplets in Water via Electrohydrodynamic Flows, *Langmuir* **2010**, 26 (13), 10703-10707
- 3- John S. Eow, M. Ghadiri, The behaviour of a liquid/liquid interface and drop-interface coalescence under the influence of an electric field, *Journal of Col. surfaces A* **2003**, 215(1-3), 101-123
- 4- J. F. De la Mora, Fluid dynamics of Taylor cones, *Annual Rev. Fluid Mech.* **2007**, 39, 217-243
- 5- Lene Oddershede, Sidney R. Nagel, Singularity during the Onset of an Electrohydrodynamic Spout, *Phys. Rev. Lett.* **2000**, 85, 1234-1237
- 6- T. Uemura, Y. Ueda, M. Iguchi, Behavior of an oppositely charged oil–water interface, *J. of Vis.* **2010**, 13, 85-87
- 7- B. Khorshidi, M. Jalaal , E. Esmaeilzadeh, F. Mohammadi, Characteristics of deformation and electrical charging of large water drops immersed in an insulating liquid on the electrode surface, *J. Colloid Interface Sci.* **2010**, 352, 211–220.
- 8- H. Paknemat, A. R. Pishevar and P. Pournaderi, Numerical simulation of drop deformations and breakup modes caused by direct current electric fields, *PHYSICS OF FLUIDS* **2012**, 24, 102101-26.
- 9- M. A. Herrada et al., Numerical simulation of electrosprays in cone-jet mode, *Physical review E* **2012**, 86: 0263905
- 10- D.A. Saville, *ELECTROHYDRODYNAMICS: The Taylor-Melcher leaky dielectric model*, *Annu. Rev. Fluid Mech.* **1997**. 29, 27-64.



## Experimental studies on internal circulation during droplet evaporation

Soma Sundaram .S, Anand T N C and Shamit Bakshi

Department of Mechanical Engineering, IIT Madras, India

### Abstract

Experiments conducted on single droplet evaporation are useful in characterising fuels and also help in developing evaporation models. In an earlier work experiments in a closed chamber were conducted and it was observed that the diffusion driven evaporation rate is much smaller than the experimental evaporation rate [1]. It was suggested that the increase in evaporation rate may be due to the presence of internal circulation inside the droplet. There is, however no internal circulation in slow evaporating droplets like water [1]. Oscillatory internal circulation was observed in multi-component droplets [2]. In the present work an effort is made to characterize evaporating droplets further by measuring the velocity field of internal circulation. Experimental results from the study indicate that the velocities are higher for methanol droplet than in case of ethanol droplets.

### Introduction

Droplet evaporation has been an important area of research for its practical and fundamental significance. Evaporation of droplets plays a significant role in cooling applications. It is also an important process in mixing of sprays in internal combustion engines and gas turbines. In the present study, internal circulation in different evaporating droplets and its influence on evaporation rate is measured with an objective of characterizing it in detail. In the literature, internal circulation in evaporating droplets has been observed in sessile, suspended and levitated droplets [1, 3, 4]. It has been observed that the velocity of internal circulation is more for fast evaporating droplets. In the present work, the velocity of internal circulation is found by particle tracking velocimetry method in a pendant droplet. The optical distortion effect occurring in the droplet while calculating the velocity due to the change in refractive index is corrected using ray tracing method [3, 5]. Ray tracing equations are used for the pendant droplet and the distortion effect is corrected and the velocities are determined.

### Experimental Setup

The experimental setup for the present study is shown in Figures 1 and 2. It consists of a test rig, syringe pump, a CCD camera with a data acquisition system, a continuous wave laser, nitrogen cylinder, cylindrical lens and a backlight. All parts of the experimental setup are placed over an optical bread board. The test rig is a cubic air tight chamber made of mild steel closed with glass on five sides. The top of the test rig is fitted with an acrylic plate which has a provision for passing nitrogen gas in and out and for inserting a needle. Nitrogen gas which is 99.5% pure is used to purge the chamber, and the evaporation of the droplet takes place in a nitrogen filled chamber. A needle of outer diameter 2.7 mm whose tip is made flat, is used in order to suspend the droplet. The needle is inserted at the centre of the cubical test rig. The syringe pump is fitted with a 20 ml syringe which in turn is connected to the needle through a tube. The syringe pump whose flow rate can be adjusted to as little as 900 nl/min helps to suspend known diameter droplet repeatedly. A continuous wave laser of 532 nm is used to form a sheet by passing it through cylindrical lenses. Two lenses one of 20 mm focal length and another of 250 mm focal length are being used to form a thin laser sheet. A LED light is used as a backlight for capturing shadow images of the droplet. A CCD camera with 640 x 480 pixel resolution is used to capture these images.

The sample liquid is mixed with seeding particles made up of Poly Methyl Meta Acrylate (PMMA) whose size ranges from 1  $\mu\text{m}$  to 20  $\mu\text{m}$ . The fluid is then taken in a syringe and it is fixed in the syringe pump. Nitrogen gas is purged inside the chamber, and allowing the gas velocity to subside, the droplet is introduced inside the chamber and it is suspended from the needle. The laser sheet is passed at the centre of the droplet and scattering images are taken using the camera. Images are taken keeping the exposure time around 80  $\mu\text{s}$  and the frame rate at 60 frames per second. The backlight is switched on and off at regular intervals to take the shadow images in order to find the outer profile of the droplet with the same camera. The time between two images will be 1/60 s.

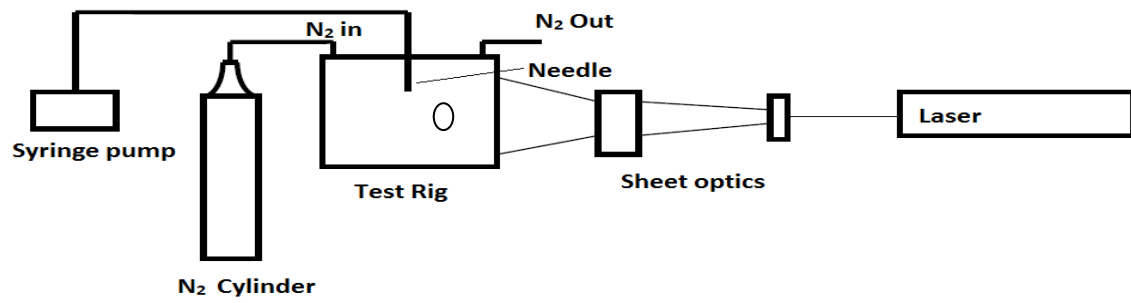


**Figure 1:** Front view of the experimental setup

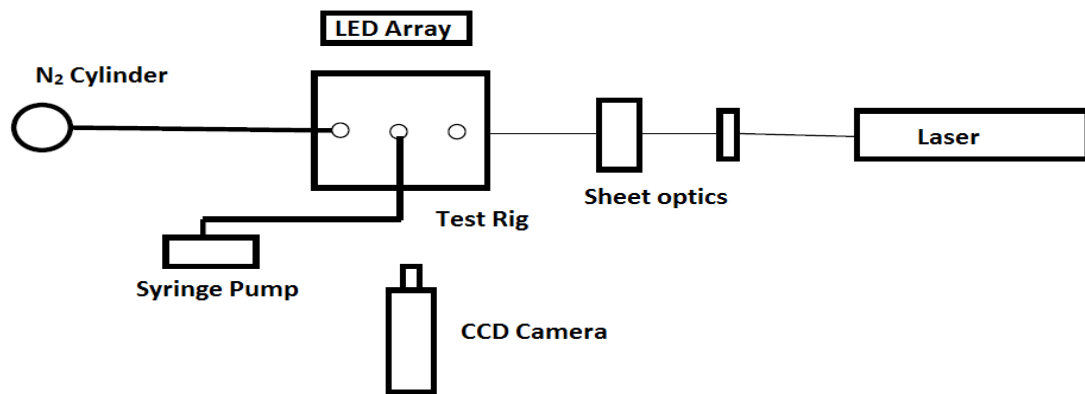


**Figure 2:** Top view of the experimental setup.

Particle tracking velocimetry is used to find the velocity of internal circulation. The velocity of internal circulation by scattering technique is not accurate because of refraction of light at the surface of the droplet. Since the light ray has to travel two media, i.e., the liquid and the air, there is bending of light rays because of a difference in refractive indices. In this experiment the velocity of internal circulation is found for an evaporating pendant droplet in nitrogen atmosphere. The distortion effect is eliminated by using ray tracing method [3]. A shadow image of the pendant droplet is taken and the outer boundary profile of the droplet is found. The profile is fitted using the following equation

$$F(\theta) = R + b \cdot \cos\theta, \text{ where } F \text{ is the profile of the droplet}$$

Least square fit method is used and the constants  $R$  and  $b$  values are found. A code is developed in Matlab to process the images and velocities are found. Figure 3 shows the geometry of the droplet in Cartesian co ordinate. The point  $P$  on the surface of the droplet is in polar co-ordinates with radius  $r$ , polar angle  $\theta$  and azimuthal angle  $\phi$ . The droplet profile in any  $x$ - $y$  plane is given by the shape function  $F(\theta)$ .



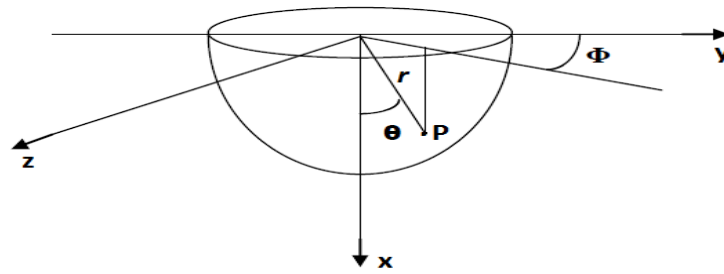


**Figure 3:** Geometry of the droplet.

In order to validate the code, a hemisphere made of Perspex is placed over a graph sheet. The line on the graph sheet gets displaced because of change in refractive index as shown in the Figure 4. The code is used to process the image and the lines are restored which can be seen inside the white circle.

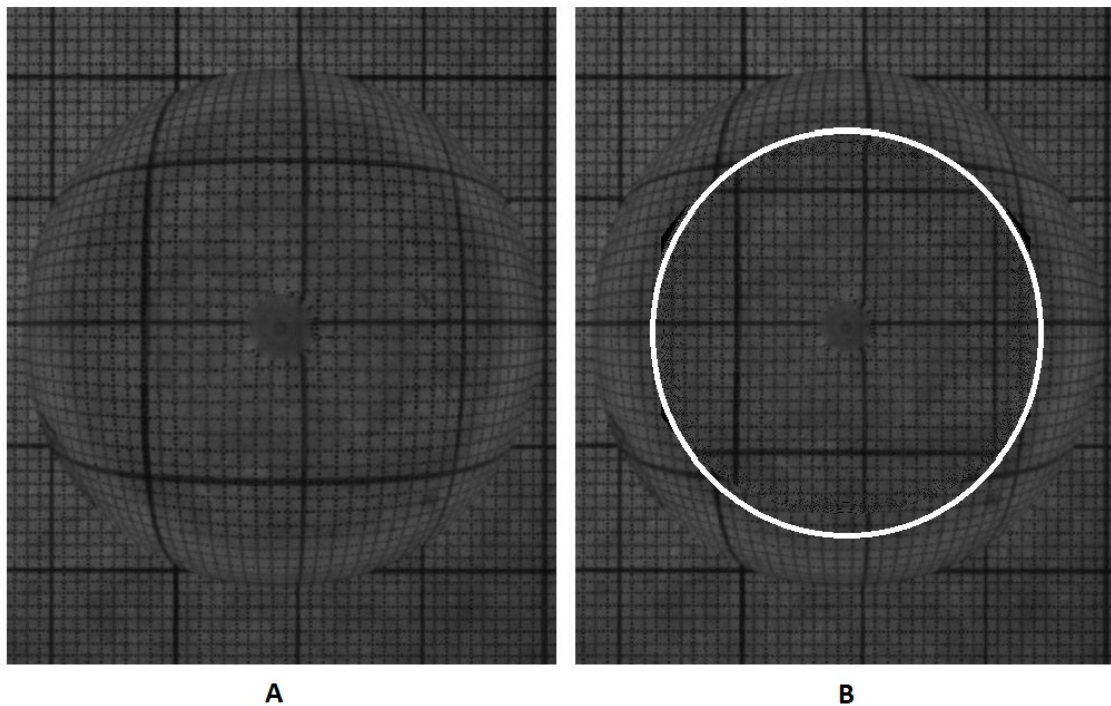


**Figure 4:** (a) The image taken by placing a hemispherical lens over a graph paper (b) The restored image after processing and the lines are restored in image B which is shown inside the white circle.

### Results and discussion

The velocity inside evaporating droplet of methanol and ethanol are found and the maximum, minimum and average velocities are reported. It can be observed from Figure 5, that the maximum velocity for methanol is around 1.1 cm/s, the minimum velocity is around 0.2 cm/s and the average velocity is around 0.6 cm/s. From Figure 6, it can be observed that the maximum velocity for ethanol is around 1 cm/s, the minimum velocity is around 0.1 cm/s and the average velocity is around 0.5 cm/s. Figure 7, shows a selected region inside the droplet and a velocity vector plot for ethanol droplet. A particular region is selected in the middle portion and the velocities are calculated. From the vector plot it can be seen that the flow is upwards in the middle part of the droplet and it is downwards along the boundary of the droplet. It is found from the experiments that the evaporation time for methanol droplet with an initial diameter of 2.8 mm is 2 minutes and 45 seconds and with the same initial diameter it takes 3minutes 30 seconds for the ethanol droplet to evaporate. Thus, it indicates that the velocity of internal circulation is high for fast evaporating droplets and it reduces gradually towards slow evaporating droplets.

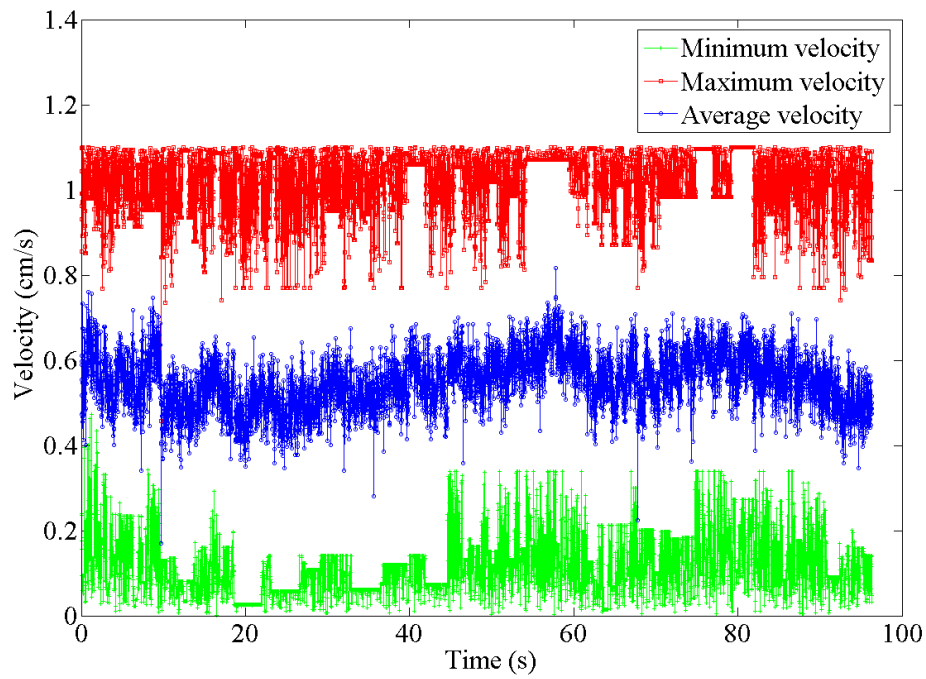


**Figure 5:** Variation of maximum, minimum and average velocities for methanol droplet

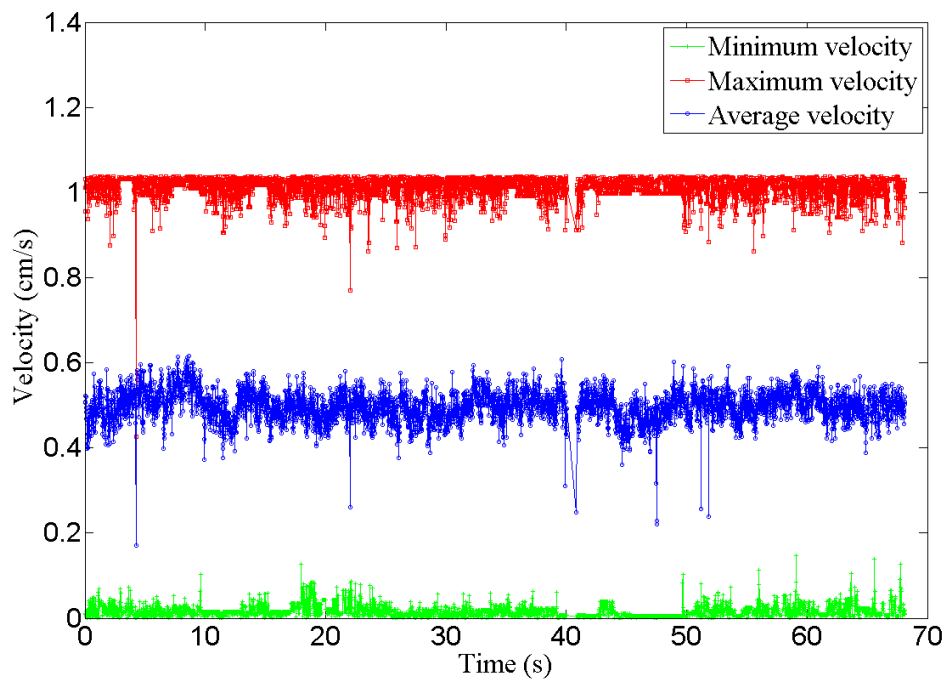


**Figure 6:** Variation of maximum minimum and average velocities for ethanol droplet.

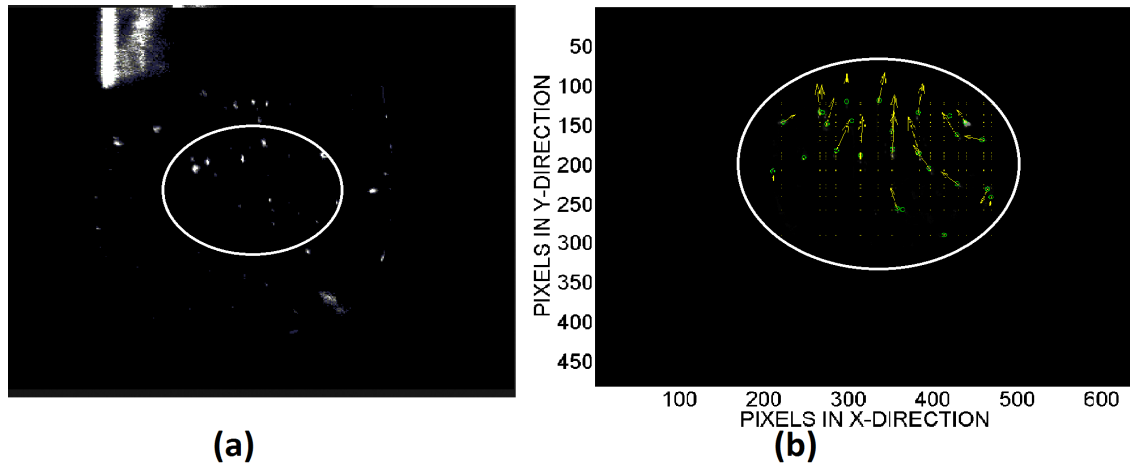


**Figure 7:** (a) Selected region inside the evaporating droplet (b) Vector plot of the particles inside the selected region.

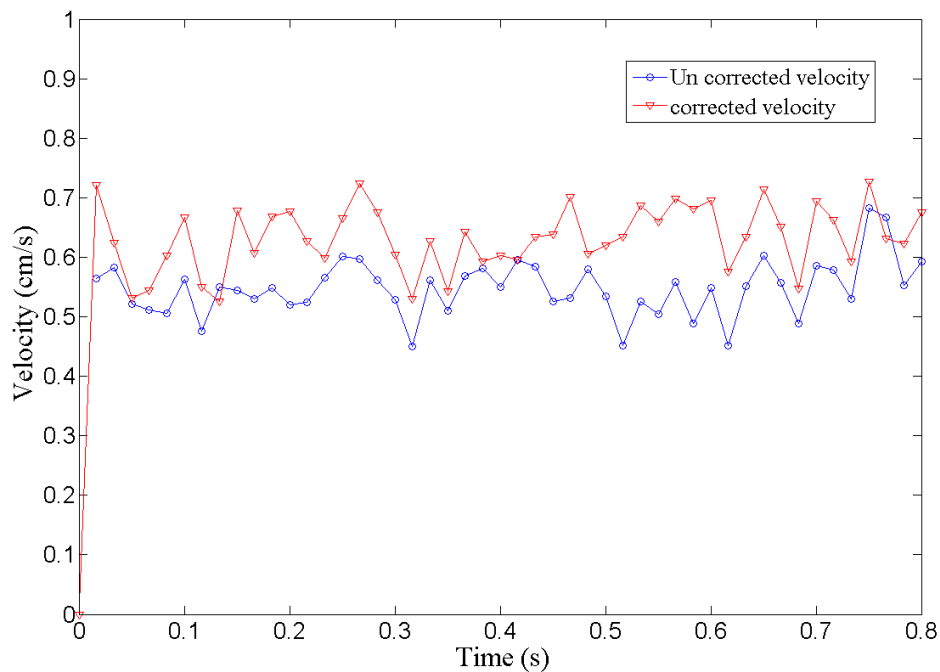


**Figure 8:** Corrected and un-corrected mean velocity variation for methanol droplet.

Figure 8, shows the variation of mean velocity of methanol droplet for corrected image and also for un-corrected image. It can be observed that there is some difference in velocity between the corrected and uncorrected images.

## Conclusion

The velocity of internal circulation in evaporating droplets is measured. The velocity of internal circulation is observed to be higher for fast evaporating droplets. The internal circulation velocity of methanol is greater than that in ethanol. There is a slight change in velocity due to the lens effect at the surface of the droplet. The corrected velocities will help to model evaporation in more accurate manner.

## References

1. Mandal, D.K. and S. Bakshi, Internal circulation in a single droplet evaporating in a closed chamber. *International Journal of Multiphase Flow*, 2012. 42: p. 42-51.
2. Mandal, D.K. and S. Bakshi, Evidence of oscillatory convection inside an evaporating multicomponent droplet in a closed chamber. *J Colloid Interface Sci*, 2012. 378(1): p. 260-2.
3. Kang, K.H., et al., Quantitative visualization of flow inside an evaporating droplet using the ray tracing method. *Measurement Science and Technology*, 2004. 15(6): p. 1104-1112.
4. Yamamoto, Y., et al., Internal Flow of Acoustically Levitated Droplet. *Microgravity Science and Technology*, 2008. 20(3-4): p. 277-280.
5. Minor, G., P. Oshkai, and N. Djilali, Optical distortion correction for liquid droplet visualization using the ray tracing method: further considerations. *Measurement Science and Technology*, 2007. 18(11): p. L23-L28.

## Turbulence Induced Droplet Breakup

E.O. Diemuodeke and I. Sher

School of Engineering, Cranfield University, Cranfield, Bedfordshire, UK

### Abstract

A simplified mathematical model is developed for breakup criterion of a turbulence induced droplet breakup. The understanding of the mechanisms of liquid-fuel droplet breakup is critical to liquid-fuel combustion in internal combustion engines, where the efficiency and stability of the engine depend on the atomization process. The atomization process is aimed at presenting the bulk liquid fuel in smaller spray droplet sizes, which increase the specific surface area of the fuel, and thereby achieve high rates of mixing and evaporation. Atomization processes are classified as primary and secondary. The primary atomization involves the liquid jet breakup into parent droplets, while these further break in secondary breakup caused by aerodynamic drag force. Droplet breakup limits are mostly characterized in We-Oh representation. The utilisation of high-injection-pressure (HIP) fuel system in direct diesel injection (DDI) requires liquid fuel been injected at a very high pressure, which is later converted to a corresponding high velocity by the injector nozzle, which gives rise to a turbulent flowfield around droplets. Experimental work has shown the importance of flowfield characteristics on droplet breakup. Further experimental results, for low Oh values, have shown that turbulence flow has a remarkable influence on the droplet breakup process in gaseous flowfield. Therefore, We-Oh droplet breakup criterion models for turbulence induced droplet breakup are required for modern DDI engines. In developing the mathematical model the energy criterion for a disturbed parent droplet to disintegrate and the dual-timescale for turbulent energy transfer in droplet dispersion were considered.

---

### Introduction

The understanding of the mechanisms of liquid-fuel droplet breakup is critical to liquid-fuel combustion in internal combustion engines, where the efficiency and stability of the engine depend on atomization processes [1][2]. Atomization processes are classified as primary and secondary. The primary atomization involves the liquid jet breakup into parent droplets, while these further break in secondary breakup caused by aerodynamic drag force. The droplet breakup occurs first by deformation as a result of aerodynamic forces exerted on a droplet overcoming the forces due to surface tension. Breakup actually occurs if the droplet deformation goes beyond a certain limit. Droplet breakup is characterised, in the context of laminar flow, by five distinct breakup mechanisms: vibration, bag, transition, stripping and catastrophic; but a fundamentally different mechanism occurred for a turbulence flowfield, which has been termed as bulgy. Droplet breakup mechanisms limits are mostly characterized in Weber number (We)-Ohnesorge number (Oh) representation [3]. According to the We-Oh representation, the critical Weber number found for low-viscosity liquids ranges from 7.2 to 16.8 [3]. Sher and Sher [4] proposed a single We-Oh analytical criterion for the minimum essential conditions for a droplet to breakup. The total dependence on the We-Oh droplet breakup presentation might be constrained for non-entirely inertially-driven flowfield, for example, effect of turbulence flowfield.

One of the recent developments in diesel direct injection (DDI) engines is the utilization of electronically controlled high-injection-pressure (HIP) fuel system, which is aimed at achieving high-power-density low-emission DDI engine[5]. In the HIP fuel system liquid fuel is injected at a very high pressure, as high as near 200MPa and is expected to increase progressively [9]; which is later converted to a corresponding high velocity, at near sonic speed, by the injector nozzle, which gives rise to a turbulent flow field around droplets. Experimental work has shown the importance of flow-field characteristics on droplet breakup [6]. Further experimental results, for low Oh values, have shown that turbulence flow has a remarkable influence on the droplet breakup process in gaseous flowfield [7]. It suffices, therefore, to say that existing We-Oh droplet breakup criterion models are inherently handicap for turbulence induce droplet breakup, which is expected in the contemporary DDI engines.

The prevalence of turbulent flow on droplet breakup has long been noted by Clift et al [8] but recognised the inherent experimental difficulty to establish the relationship between droplet breakup and turbulence flowfield. They, however, noted two basic established conditions used in investigating droplet breakup in turbulence flowfield: 1. Breakup occurs when local shear stress imposed by the continuous-phase exceeds the surface tension and the disperse-phase dissipative viscous force; 2. breakup occurs only when the energy carried by

eddies is smaller than droplet diameter. However, an order of magnitude analysis conducted to determine effects of different time and length scales on the breakup of droplet in turbulent flowfields shows that eddies in an order of magnitude larger than the droplet diameter are most significant and influential in droplet breakup [7].

There is inherent difficulty to analytically capture all the phenomena of droplet breakup in turbulence flowfield. This difficulty and some other inherent advantages have necessitated many researchers in the field to resort to CFD applications. However, there is ambiguity in droplet breakup criterion from CFD simulations of spray flows, especially in turbulent flowfields. Some important, specific details of the atomization process can be achievable through the use of simplified basic mathematical models. Therefore, in this paper, a simplified mathematical model for the critical Weber number, which accounts for the turbulent effects, is developed.

### Mathematical modelling

This study builds on previous study [4], by incorporating turbulent effects into the breakup mechanism, as shown in Figure 1. The droplet breakup depends on the droplet velocity, on the droplet thermo-physical properties, and on the ambient properties, through the time scales of the droplet's trajectory deceleration and droplet breakup (a balance of deformed surface energy and breakup dissipation).

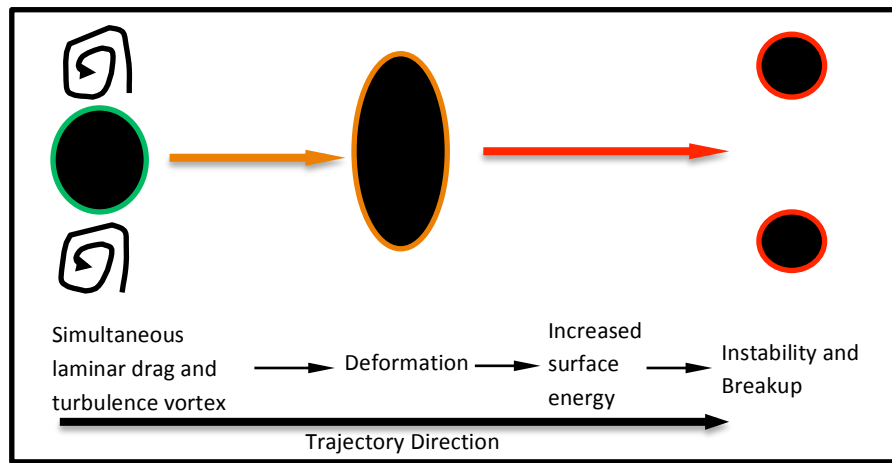


Figure 1. Droplet Breakup Processes

The energy criterion, according to [4], for a disturbed parent droplet to disintegrate can be written, for a symmetrical breakup process, as

$$E_s = ne_s + E_{diss} \quad (1)$$

where  $E_s$  is the deformed droplet extended surface energy;  $n$  is the number of daughter droplets;  $e_s$  is the surface energy of a drop and  $E_{diss}$  is the dissipative energy, which accounts for viscous effect.

Substituting the deformed droplet extended surface energy, product droplet surface energy and the dissipative energy, according to [4], into Eq.(1) to obtain

$$\sigma \pi r_e^2 \left( \frac{3^2}{2^{6.5}} We^2 + 4 \right) = 4n^{1/3} \sigma \pi r_e^2 + \frac{4}{3} \pi r_e^3 \mu_l \frac{1}{t} \quad (2)$$

where  $\sigma [N/m]$  is the surface tension,  $r_e$  is the radius of a spherical droplet of the same volume as the deformed droplet,  $We = \frac{\rho_l U^2 r_e}{\sigma}$  is the dispersed phase Weber number,  $\mu_l$  and  $t$  is the dissipation timescale.

In the current work, it is argued that the droplet breakup is due to the simultaneous mechanisms of drag induced deformation (laminar drag breakup) and turbulence vortex induced breakup, the faster breakup mechanism being the relatively dominant. The breakup time is proposed, in a similar way to the dual-timescale for turbulent energy transfer in droplet dispersion [10], as follows:

$$\frac{1}{t} \sim \frac{1}{t'} + \frac{1}{t_{bu}} \quad (3)$$

The laminar drag breakup timescale,  $t_{bu}$ , and the turbulence breakup timescale,  $t'$ , are coupled to the dissipation timescale in the breaking droplet, which is the timescale in the energy balance for droplet breakup.

The turbulence time scale,  $t' [s]$ , is generally given as [2]

$$t' = \frac{l}{u'} \equiv \frac{l}{I_{rt}U} \quad (4)$$

where  $l$  is the turbulence length scale,  $u'$  is the fluctuating velocity and  $I_{rt} = u'/U$  is the relative turbulence intensity.

It is expected that for a droplet fragmentation to occur the turbulence lengthscale should be of the order of the droplet size, which supports some researchers' submissions that eddy close to droplet size or order of magnitude larger than the droplet diameter has the most contributing factor in its disintegration process [11].

The trajectory of the droplet in the continuous phase of the two-phase flow field is readily described by the particle's equation of motion, which relates acceleration and drag force on the bases of momentum balance, given as [2]

$$\rho_l V_p \frac{dU}{dt} = -\frac{1}{2} \rho_g C_D A_p U^2 \quad (5)$$

where  $V_p$  is the droplet volume,  $C_D$  is the drag coefficient,  $A_p$  is the frontal area of the particle, which is  $A_p = \pi r_e^2$  for spherical droplet and  $U$  is the mean flow velocity.

Integration of Eq.(5), between  $U_0$  at zero time – initial droplet velocity, and an arbitrary point in time,  $t$ , where the velocity is  $U$ , gives:

$$\frac{1}{t_{bu}} = \frac{3}{2^3} C_D \frac{\sqrt{\rho_g r_e \sigma}}{\rho_l r_e^2} \frac{\sqrt{We_0} \sqrt{We}}{\sqrt{We_0} - \sqrt{We}} \quad (6)$$

Where  $We_0$  is the initial Weber number and  $We$  is the local Weber number.

Substituting Eqs.(6) and (5) into Eq.(3) gives

$$\frac{3^2}{2^{8.5}} We_{bu}^2 = (n^{1/3} - 1) + \frac{1}{2^3} C_D Oh \sqrt{\frac{\rho_g}{\rho_l} \frac{\sqrt{We_0} \sqrt{We_{bu}}}{\sqrt{We_0} - \sqrt{We_{bu}}}} + \frac{1}{3\phi} Oh I_{rt} \sqrt{We_{bu}} \quad (7)$$

where  $Oh$  is the Ohnesorge number.

It is assumed that the parent droplet is approximately broken into two new daughter droplets, which supports [2] claim for low Weber number near the critical value, hence  $n=2$  is adopted. It is evident that Eq.11, from Figure 2, has two extrema (minimum and maximum). It should be noted that for a decelerating droplet, which is the case under investigation, the physical region is where the minimum occurred in the figure, because it is expected that  $We_0 > We_{bu}$ . The figure supports the theory that turbulence effects enhance droplet breakup mechanisms since the critical initial Weber number decreases with increasing relative turbulence intensity [12].

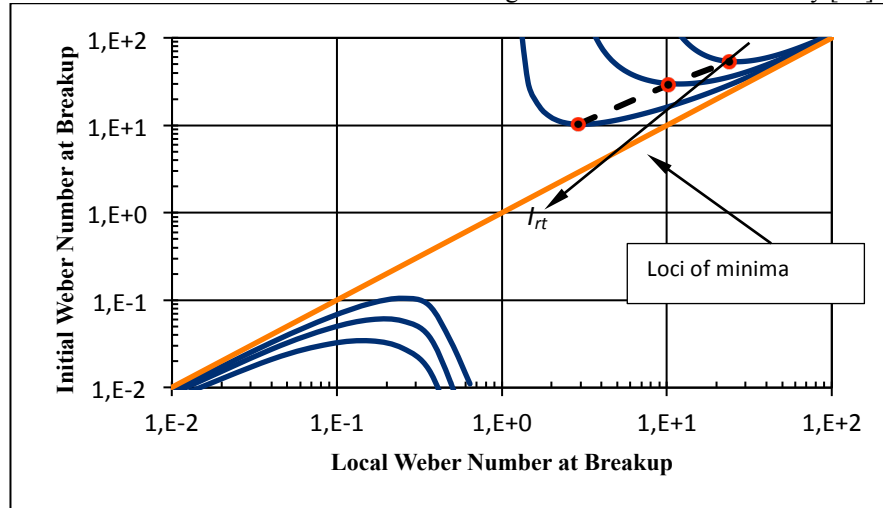


Figure 2. Initial Weber number,  $We_0$ , vs. local Weber number at breakup,  $We_{bu}$



The critical breakup conditions correspond to the minimum values, can be obtained at  $\left. \frac{d\sqrt{We_0}}{d\sqrt{We_{bu}}} \right| = 0$ .

The critical Weber number (which is the critical initial Weber number) is therefore obtained (see [13]):

$$We_{0,cr} = \left\{ 3.45(n^{1/3} - 1)^{1/4} + 5.52 \left( C_D Oh \sqrt{\frac{\rho_g}{\rho_l}} \right)^{1/3} - 0.92 \left( \frac{1}{\phi} \right) Oh^{1/3} \left( C_D \sqrt{\frac{\rho_g}{\rho_l}} \right)^{-2/3} I_{rt} \right\}^2 \quad (8)$$

## Results and Discussion

Although drop drag coefficients vary with droplet deformation and turbulence intensity of the flowfield [14], but use of constant average coefficients have been effective for earlier considerations of drop motion[4]. Two base cases for the drag coefficient are used for the model, Eq.(8), and validation (as shown in Figures 3 and 4) for n-heptane and methanol fuel droplets in turbulent flowfield are presented (with parameters shown in Table 1).

**Table 1.** Input Parameters [7]

Fuel	$\frac{\rho_g}{\rho_l}$	$Oh$
n-Heptane	0.0087	0.0064
Methanol	0.0076	0.0082

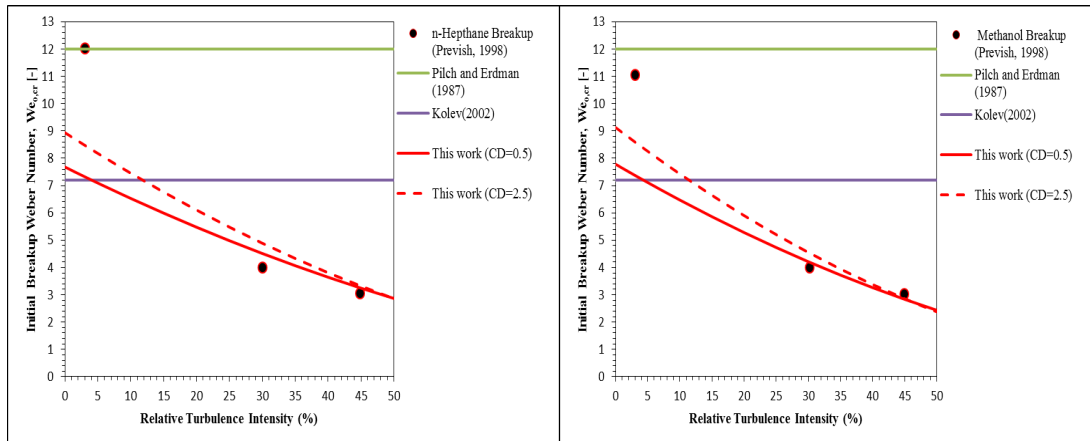


**Figure 3.** Theoretical Prediction vs Experimental Data for n-Heptane Critical Weber Number

**Figure 4.** Theoretical Prediction vs Experimental Data for n-Heptane Critical Weber Number

The critical Weber number in Previsi experimental work [7], circle markers in Figures 3 and 4, was established at the flowrate where about 5% of droplets experienced breakup. For the two fuel types, the critical Weber number of droplet breakup decreases with increasing turbulence intensity whereas two popular empirical criteria for droplet breakup [15, 16] predict constant values for the critical Weber number for the droplet breakup, Figures 3 and 4. Kolev [16] empirical criterion under-predicts the critical Weber number at low turbulence intensities and over-predicts same at high turbulence intensities. Pilch and Erdman [15] criterion, however, over-predicts the critical Weber number of droplet breakup in turbulent flowfield. The ambiguity in the empirical models predictions may be attributed to the non-consideration of turbulence effects. It is evident from Figures 3 and 4 that the analytical model, Eq.(8), gives an improved prediction of the experimental data. However, the analytical model has poor prediction at moderate low turbulence intensities. Transition from laminar to turbulent flowfield is accompanied with rapid  $C_D$  rise well above the standard value, which is often referred to as the drag crisis [14]. Also, the figures show that the analytical model predicts higher critical Weber number for corresponding higher  $C_D$ . Therefore, the deviation of the model predictions from the experimental data, at moderate low turbulence intensities, may be attributed to the “drag crisis”, since constant  $C_D$  is used in the model.

## Conclusions

The utilisation of high-injection-pressure (HIP) fuel system in direct diesel injection (DDI) requires liquid fuel to be injected at a very high pressure, which is later converted to a corresponding high velocity by the injector nozzle, which gives rise to a turbulent flowfield around droplets. Experimental work has shown the importance of flowfield characteristics on droplet breakup. Further experimental results, for low  $Oh$  values, have shown that turbulence flow has a remarkable influence on the droplet breakup process in gaseous flowfield. Two popular empirical criteria for droplet breakup[15][16] do not consider turbulent effects in their formulation, and exhibit large discrepancies in their predictions for turbulent flowfields. Therefore, a simplified mathematical model for

the critical Weber number, which accounts for the turbulent effects, is developed. The developed model offers better prediction performance when compared with turbulent experimental data.

## Nomenclature

Symbol	Quantity	Units
$C_D$	Drag coefficient	-
$E, e$	Energy	Nm
$l$	Lengthscale	m
$n$	Number of daughter droplet	-
$r_e$	Droplet radius	m
$t$	Timescale	s
$U$	Mean velocity	m/s
$V$	Volume	m <sup>3</sup>
$Oh = \frac{\mu}{\sqrt{\rho r_e \sigma}} \equiv \frac{\sqrt{We}}{Re}$	Ohnesorge number	-
$We = \frac{\rho_l U^2 r_e}{\sigma}$	Weber number	-
<b>Greek letter</b>		
$\beta$	Parameter	1/m
$\mu$	Viscosity	Nm <sup>-2</sup> s
$\rho$	Density	kg/m <sup>3</sup>
$\sigma$	Surface tension	N/m
$\varphi$	Empirical fit	-
<b>Subscript</b>		
0	Initial	
bu	breakup	
diss	Dissipative	
g	Gas	
l	Liquid	
p	Particle	
s	Deformed droplet surface	
<b>Superscript</b>		
'	turbulent attributed parameter	

## References

- [1] Liang, P.Y., Eastes, T.N. and Gharakhari, A. "Computer Simulations of Drop Deformation and Drop Breakup," in *24th Joint Propulsion Conference*, 1988, pp. 88–3142.
- [2] Stiesch, G. *Modelling Engine Spray and Combustion Processes: Heat and Mass Transfer*. Berlin Heidelberg: Springer Verlag, 2010.
- [3] Reitz, R.D.; Diwakar, R. "Effect of Drop Breakup on Fuel Sprays," 1986.
- [4] Sher, I., Sher, E., "Analytical Criterion for Droplet Breakup," *Atomization and Sprays*, vol. 21, no. 12, pp. 1059–1063, 2012.
- [5] Themel, T.; Jansons, M.; Campbell, S.; Rhee, K. "Diesel Engine Response to High Fuel-Injection Pressures," 1998.
- [6] Wierzbna, A. "Deformation and Breakup of Liquid Drops in a Gas Stream at Nearly Critical Weber Numbers," *Experiments Fluids*, vol. 9, pp. 59–64, 1990.
- [7] Prevish, T.D. "Secondary Droplet Breakup in Highly Turbulent Flowfield," Pennsylvania State University, 1998.
- [8] Clift, R.; Grace, J.R.; Weber, M. E. *Bubbles, Drops and Particles*. New York: Academic Press, 1978.
- [9] Mahr, B. "Future and Potential of Diesel Injection System," in *THIESEL Conference on Thermo-and Fluid-Dynamic Processes in Diesel Engine*, 2002.
- [10] Pai, M. G., Subramaniam, S. "Modeling droplet dispersion and interphase turbulent kinetic energy transfer using a new dual-timescale Langevin model," *International Journal of Multiphase Flow*, vol. 33, no. 3, pp. 252–281, Mar. 2007.
- [11] Andersson, R.; Andersson, B. "Modelling the Breakup of Fluid Particles in Turbulent Flows," *AIChE J.*, vol. 52, no. 11, pp. 2031–2038, 2006.

- [12] Trinh, H. P.; Chen, C. P. “Modelling of Turbulence Effects on Liquid Jet Atomization and Breakup,” *Atomization and Sprays*, vol. 16, pp. 907–932, 2006.
- [13] Diemuodeke, E.O., Sher. I., "Droplet breakup in turbulent flow fields", to be published, 2013.
- [14] Snyder, M.R; Knio, O.M.; Katz, J.; Maitre, O. L. “Numerical Study on the Motion of Microscopic Oil Droplets in High Intensity Isotropic Turbulence,” *Physics of Fluids*, vol. 20, p. 073301, 2006.
- [15] Pilch, M.; Erdman, C. A. “Use of Breakup Time Data and Velocity History Data to Predict the Maximum Size of Stable Fragments for Acceleration-Induced Breakup of Liquid Droplet,” *International Journal of Multiphase Flow*, vol. 13, pp. 741–757, 1987.
- [16] Kolev, N. I. *Multiphase Flow Dynamics I. Fundamental*. Berlin: Springer-Verlag, 2002.

## Droplet entrainment from a single wave propagating in a stratified air-water pipe flow

A. Audouin, P. Ern and F. Charru

Institut de Mécanique des Fluides de Toulouse,  
Université de Toulouse and CNRS, Allée C. Soula, 31400 Toulouse, France

### Abstract

We investigate the distribution of sizes and velocities of droplets detached from a single roll wave propagating in a pipe. The wave is induced by a pulse in liquid flowrate in a stratified air-water flow. Due to the shear applied on the crest of the wave by the faster gas stream, droplets are formed and entrained by the gas. Detection and tracking of the droplets is performed by image processing. The distributions of sizes and velocities of the droplets are determined in the center of the pipe for various distances to the roll wave and compared to those measured for higher gas flowrate when droplets are produced from all the roll waves formed naturally at the gas-liquid interface without external forcing.

### Introduction

In this paper, we investigate the atomization and redeposition of droplets in a horizontal stratified air-water flow in a pipe. Due to the shear applied on the liquid layer by the faster gas flow, waves appear at the interface and propagate on the liquid surface. For sufficiently high velocities of the gas, large-amplitude waves arise and droplets detach from the crest of these waves. It has recently been shown that primary atomization mainly occurs through two mechanisms: bag- and ligament-breakup, as illustrated in Figure 1. Since the characteristic sizes of the ligaments and bags vary from a few millimeters to a few centimeters, the range of sizes of the droplets produced is large [1]. Moreover, it turns out that the droplets size distributions are more peaked and have heavier tails than the lognormal distribution usually used to account for these distributions. Notably, the distribution of droplets sizes presents a heavy tail at large drop diameters ( $> 0.5$  mm), which gives the predominant contribution to the mass of entrained droplets. Analysis of the joint distributions of sizes and horizontal velocities also revealed that the most numerous droplets (diameters about 0.1 mm) travel at a velocity close to the gas speed, while larger drops travel at much lower velocities. Furthermore, the associated distribution of vertical velocities is non-Gaussian (displaying exponential power tail-off), large-size droplets being responsible for the larger weight of positive vertical velocities. However, most droplets present negative vertical velocities. As discussed in [1], the following sketch then emerged concerning the contributions to the dispersed phase provided by the various roll waves upstream the volume of measure: drops that are still accelerating and in particular larger drops that are still not redeposited are provided by roll waves closer to the measurement volume, while smaller drops also originate from further away waves, since they rapidly reach their terminal velocity and are carried by the gas stream over longer distances before they redeposit. A better understanding of the effect of acceleration and transport by the gas and the effect of sedimentation by gravity on the droplets detaching from a roll wave is therefore needed. The aim of this work is thus to focus on the contribution provided by a single wave and to determine the size and velocity distributions of the droplets according to the distance between the measurement volume and the isolated wave.

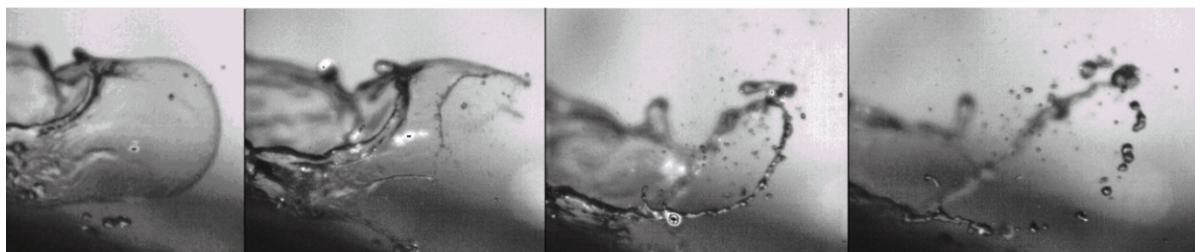


Figure 1. Example of bag-breakup at the crest of a roll wave.

## Experimental set-up

The experiments were performed for an air-water flow in a horizontal pipe of diameter 5 cm and length 5 m. The configuration considered here corresponds to the superficial gas velocity  $U_{gs} = 10$  m/s and the superficial liquid velocity  $U_{ls} = 0.07$  m/s. The roll wave is induced by increasing the liquid flowrate by a factor 2.4 during about 1s. The passage of the wave in a tube section is detected with a differential pressure transducer measuring the pressure loss between two sections of the pipe located 3.75 m-apart and is used as trigger for image recording. The characteristics of the droplets produced from the wave were investigated in the center of the pipe for two distances from the volume of observation to the wave. The shortest one  $d_s$  is 35 cm and the largest one  $d_l$  is 80 cm. We used a high-speed camera (5000 fps) and a 20ns flash lamp to get motion-blur-free images (especially for the smaller droplets). The field of view was set to a length of 12.47 mm, a height of 6.50 mm, along with a depth of field 1.9 mm and a resolution of  $9.28 \mu\text{m}/\text{pix}$ . This enabled us to detect droplets as small as  $30 \mu\text{m}$  and as large as 2 mm in diameter. Image calibration and processing were used to discriminate the droplets present in the volume of observation from those which were out-of-focus thanks to a gradient-based method [2] and to retrieve their equivalent diameter from their area in the image. Together with the droplet detection program, a tracking routine employing a multi-hypothesis method [3] was used to follow the droplets along a sequence of images and to determine their vertical and horizontal velocities. All programs were implemented using Matlab and its Image Processing Toolbox.

## Celerity of the roll wave

It is generally assumed that roll waves propagate on the liquid surface with a constant celerity unlike the capillary-gravity ripples [4]. To confirm this, we recorded the passage of sixty isolated roll waves at two different locations of the pipe. We used two high-speed cameras (500 fps) situated 1.1 m apart to record the position of the air-liquid interface using a field of view of length about 58 mm and height 46 mm. Image processing then provided an estimation of the liquid layer thickness as well as the celerity of the wave by cross-correlating the temporal signals of the liquid-layer thickness obtained at two points (located 5 cm apart) of an image of a given camera and between two points of each camera. The celerity of the roll wave  $U_w$  is then defined by the ratio between the distance separating the two points of reference used in the cross-correlation and the time delay corresponding to its maximum value. For a given roll wave, three different estimations were thus obtained, yielding the celerity  $U_w = 1.5 \pm 0.25$  m/s. No acceleration of the roll wave was observed along the pipe, but the differences in the measured values indicate that the wave celerity fluctuates as the wave propagates in the pipe, as do the structure and shape of the wave.

## Size distributions

The probability density functions (*pdf*) of droplets sizes and velocities were obtained for a total number of 16.000 droplets for each distance to the wave. In order to compare the different results, all the *pdf* are normalized, so that their integral is equal to 1. For both distances to the wave, the measured distributions are large, with droplets diameters ranging from about  $40 \mu\text{m}$  to 3 mm with a predominance of small droplets.

**Figure 2.** Distributions of droplets diameters for two distances to the isolated wave (with  $U_{ls} = 0.07$  m/s and  $U_{gs} = 10$  m/s) and for a wavy-stratified regime with natural atomization (with  $U_{ls} = 0.07$  m/s and  $U_{gs} = 16.9$  m/s).

Nevertheless, the contribution to the liquid volume in the dispersed phase provided by larger droplets is considerable. It also appears that larger drops disappear when increasing the distance between the wave and the measurement volume as a consequence of deposition while the amount of small drops is kept almost constant (Figure 2). The size and velocity distributions were investigated in a previous work [1] for a wavy-stratified regime characterized by nearly the same superficial liquid velocity  $U_{ls} = 0.067$  m/s and a higher superficial gas velocity  $U_{gs} = 16.9$  m/s. In this regime, roll waves are formed naturally at the gas-liquid interface without external forcing of the liquid flow rate. Comparison of the distributions measured in the present work to those obtained in the wavy-stratified regime with natural atomization indicates that the relative weight in the distributions of smaller drops and of larger drops is stronger in the latter regime, which supports the idea of an accumulation in the dispersed phase of smaller droplets originating from a large range of roll waves.

**Figure 3 .** Comparison between the experimental pdf of droplets diameters (dotted blue) and a lognormal fit (dashed red) and a Fréchet fit (solid black), for (a) the isolated wave at the distance  $d_s$  and (b) the wavy-stratified regime (with  $U_{ls} = 0.067$  m/s and  $U_{gs} = 16.9$  m/s).

For the wavy-stratified flow and for the isolated wave, figure 3 shows the comparison between the experimental distributions of droplets sizes and the *Fréchet* law (Fr) and the *lognormal* law (LN), which is commonly used in this context, e.g. [5]. The expressions of these laws are

$$v_{Fr}(d) = \frac{k d^{-k-1}}{\bar{d}^{-k}} e^{\left(\frac{d}{\bar{d}}\right)^{-k}} \quad \text{and} \quad v_{LN}(d) = \frac{1}{\sigma d \sqrt{2\pi}} e^{-\frac{1}{2\sigma^2} \left(\ln \frac{d}{\bar{d}}\right)^2}$$

where  $d$  is the droplet diameter,  $\bar{d}$  the mean diameter of the droplets,  $\sigma$  the standard deviation, and  $k$  an adjustable parameter. It turns out that the droplets sizes distributions for the wavy-stratified flow are clearly better fitted by the Fréchet law (figure 3.b), as shown in [1], whereas the lognormal law is more appropriate in the case of the isolated wave it for both distances  $d_s$  and  $d_l$  (figure 3.a).

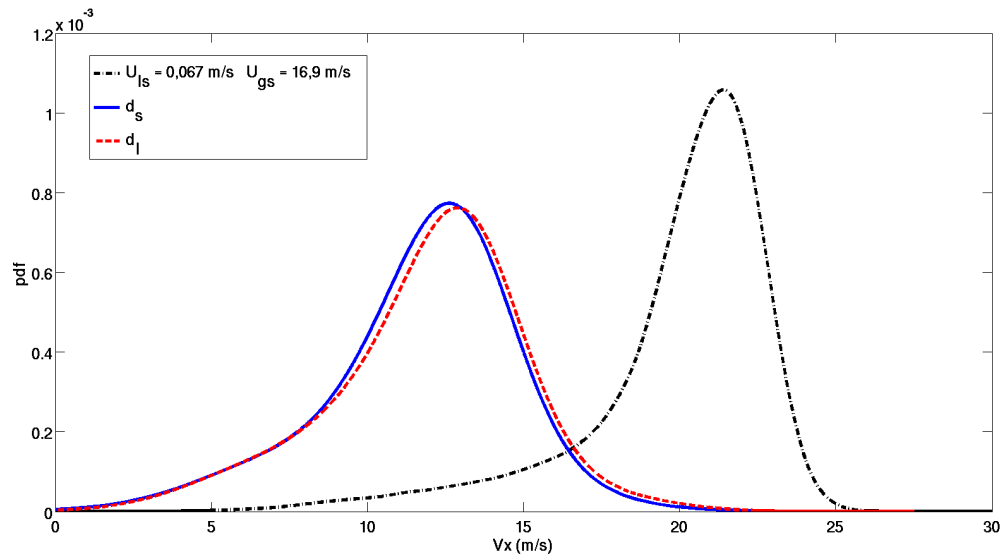


**Figure 4.** Horizontal velocity distribution of droplets for both distances to the isolated wave ( $U_{ls} = 0.07$  m/s and  $U_{gs} = 10$  m/s) and for the wavy-stratified regime (with  $U_{ls} = 0.067$  m/s and  $U_{gs} = 16.9$  m/s).

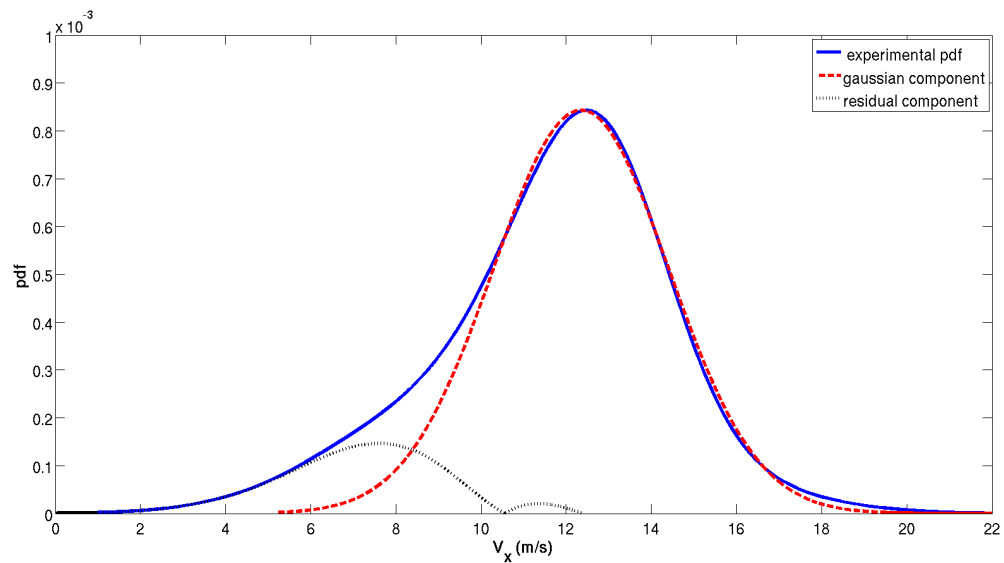


**Figure 5.** Horizontal velocity distribution for the short distance to the wave  $d_s$  compared to a gaussian fit (dashed red line); the dotted black line is the residual component; ( $U_{ls} = 0.07$  m/s and  $U_{gs} = 10$  m/s).

### Horizontal and vertical velocities distributions

We now consider the distributions of horizontal and vertical velocities associated to the size distributions of the droplets. Figure 4 presents the distributions of horizontal velocities  $V_x$  of the droplets for both distances to the isolated wave and for the wavy-stratified regime investigated in [1]. The distributions display a similar shape, with a long tail for lower horizontal velocities. It also appears that the pdf for the largest distance to the wave is slightly shifted towards the higher velocities. This result is consistent with an acceleration of the droplets by the gas stream. As shown in Figure 5, two different contributions can be distinguished in the distributions. The first is a gaussian contribution which includes smaller droplets whose horizontal velocities are distributed around the mean gas velocity  $U_g$  (determined by considering the mean liquid-layer thickness) because of the turbulent velocity fluctuations of the gas and of the variations in liquid layer thickness. The second component of the distribution which corresponds mainly to the lower velocities



includes both large and small droplets that are still accelerating. This result is more clearly seen in Figure 6, which displays the distributions of droplets diameters by classes of horizontal velocities (for  $V_x < 10$  m/s,  $10 < V_x < 14$  m/s,  $14 < V_x < 25$  m/s): only small droplets reach high horizontal velocities ( $14 < V_x < 25$  m/s), while droplets with low horizontal velocities ( $V_x < 10$  m/s) present a broad range of diameters. Note that the lognormal law also suits to these distributions.

**Figure 7.** Distributions of droplets diameters by classes of horizontal velocities, for the short distance  $d_s$  and for  $U_{ls} = 0.07$  m/s and  $U_{gs} = 10$  m/s.

**Figure 6.** Vertical velocity distributions of droplets for both distances to the isolated wave ( $U_{ls} = 0.07$  m/s and  $U_{gs} = 10$  m/s) and for the wavy-stratified regime ( $U_{ls} = 0.067$  m/s and  $U_{gs} = 16.9$  m/s).

The distributions of vertical velocities  $V_y$  of the droplets display a non-gaussian behavior (Figure 7). Owing to the gravity, most of the droplets are settling (around 65%) and in particular the largest ones. Comparison of the distributions measured in this work to those obtained for the wavy-stratified with natural atomization (with  $U_{ls} = 0.067$  m/s and  $U_{gs} = 16.9$  m/s) indicates that the peak of the distributions as well as the mean vertical velocity are negative, with a more negative peak for the wavy-stratified flow with natural atomization. Nevertheless, the

distributions are asymmetric with heavier tails for the positive velocities. As can be seen in Figure 8, most droplets with horizontal velocities close to the gas velocity have a negative vertical velocity while droplets with positive vertical velocities have lower horizontal velocities and can be considered to be still under the inertia of their ejection from the liquid layer.

**Figure 8.** Distributions of droplets horizontal velocities for positive (dashed red) and negative (solid blue) vertical velocities, for the short distance  $d_s$ ,  $U_{ls} = 0.07$  m/s and  $U_{gs} = 10$  m/s.

## Conclusions

Digital image processing was used to investigate the probability density functions of the sizes and velocities of the droplets detached from an isolated roll wave in a horizontal stratified air-water flow. For the two distances to the wave that were investigated, the size and velocity distributions of the droplets are large. However, we observed that larger drops are present in the vicinity of the isolated wave and disappear when increasing the distance between the measurement volume and the wave, as a consequence of redeposition. On the other hand, the amount of small drops is kept almost constant for both distances to the wave. Furthermore, it turns out that the droplets size distribution can be satisfactorily fitted by a lognormal law in both cases. Comparison of the distributions measured in this work to those obtained for a wavy-stratified regime with natural atomization [1] indicates that the relative weight in these distributions of smaller drops and of larger drops is stronger in the latter regime, which supports the idea of an accumulation in the dispersed phase of smaller droplets originating from a large range of roll waves. Analysis of the distribution of horizontal velocities also revealed that the droplets have a lower speed for the smallest distance to the wave, confirming the acceleration effect of the gas on the droplets. Our goal is now to obtain a better description of the atomization and deposition distributions that could be used in the closure models for the momentum conservation equations in the liquid and gas phases.

## Acknowledgements

This work was supported by TOTAL Exploration & Production and Scientific Development Division. We would like to thank in particular D. Larrey, F. Luck and J.M. Munoz for their involvement in the project. We also thank S. Cazin, G. Ehses, H. Ayroles and M. Marchal from IMFT for the technical support.

## Nomenclature

$d$	diameter of droplets [ $\mu\text{m}$ ]
$\bar{d}$	Mean diameter of the droplets [ $\mu\text{m}$ ]
$d_s$	short distance to the wave [m]
$d_l$	long distance to the wave [m]
$t$	delay [s]
$U_g$	mean gas bulk velocity [m/s]
$U_{gs}$	gas superficial velocity [m/s]
$U_{ls}$	liquid superficial velocity [m/s]
$U_w$	roll wave celerity [m/s]
$\sigma$	Standard deviation [ $\mu\text{m}$ ]

## References

1. Boulesteix S., Ern P., Charru F. and Luck F., *Size and velocity distributions of droplets in an air-water horizontal pipe flow*. ILASS, Brno, Czech Republic (2010).
2. Marmottant P. and Villermaux E., *On spray formation*. J. Fluid Mech **498**:73-111 (2004).
3. Reid D., *An algorithm for tracking multiple targets*. IEEE Transactions on Automatic Control, **AC-24**:843-854 (1979).
4. Belt R.J., *On the liquid film in inclined annular flow*. Technical university of Delft (2007).
5. Azzopardi B.J., *Drops in annular two-phase flow*. Int. J. Multiphase Flow **23**:1-53 (1997).

## The Effect of Superheat on the Performance Characteristics of a Flash Atomized Spray

Kevin M. Breton, David S. Nobes and Brian A. Fleck

Department of Mechanical Engineering, University of Alberta, Canada

### Abstract

The operating characteristics of a flash atomized spray were measured using long exposure images and phase Doppler particle analyzer (PDPA) measurements. The spray was tested with an operating pressure ratio of 13.6 and with degrees of superheat ranging from 20-80°C. It was found that the operating regime of the spray transitioned from a partially shattering, to a flare flashing regime as the degree of superheat was increased. In the partially shattering regime, an intact liquid core remained along the jet centreline, resulting in increased droplet diameters in this region. In the flare flashing regime, the atomization was increasingly consistent and droplet diameters along the centreline were minimized. An abundance of relatively large particles were located along the spray periphery primarily related to the entrainment of ambient air into the jet.

### Introduction

Flash atomization is a thermodynamic process by which a dispersed spray of droplets is produced [1]. This process occurs when a liquid, maintained at a temperature and pressure which renders it super-heated relative to the ambient, is introduced rapidly into ambient conditions. The liquid in this state is in a thermodynamically unstable condition because the liquid temperature exceeds the saturation temperature at ambient conditions. The system returns to a thermodynamically stable state as a portion of the liquid boils rapidly and the latent heat of the phase change process removes excess energy from the remaining liquid state [1]. This rapid expansion creates large shear forces on the remaining liquid, resulting in the atomization of the liquid component. Given the large density ratios between liquid and vapour phases ( $\rho_l / \rho_g \approx 1600$ ), even for low mass fractions of vapour, the void fraction is large.

There are many different measurement techniques used in the study of flash atomized sprays. There are also many difficulties in gathering measurements in the dense spray environment produced by many ash atomization systems. The nature of the desired data will often dictate the type of measurement system used.

An early, yet persisting method of measuring dispersed sprays is the use of shadowgraphy. A short exposure photograph is taken of a back-lit spray. This method can be used to measure aggregate spray characteristics and works well even in dense sprays. Kamoun *et al.* [2] used high speed shadowgraphy with a 1  $\mu$ s camera exposure in order to measure the effect of reservoir conditions on the spray angle and lateral spreading of a ash atomized spray. Kim *et al.* [3] used a similar type of system with a 7 - 10 ns exposure with a high intensity back light. A 1,000 frame per second high speed video camera was used by Zhifu *et al.* [4] in order to characterise the spray produced by a flashing R134a jet.

The use of optical measurement systems in flash atomizing systems can be complicated by the nature of the spray. A high spray density can limit the optical transparency of the spray. In these cases, the data rate from most optical systems diminishes. Higher laser power and tuned optics can be used to mitigate these problems, but the issue persists. This problem was encountered by Hervieu and Veneau [5] whose research necessitated the use of protections to limit the spray density in the measurement region. In order for the phase Doppler particle analyser (PDPA) to provide sufficient signal, obstructions were placed that blocked the majority of the flow and introduced errors of up to 40% in velocity measurements and 20% in diameter measurements. Yildiz *et al.* [6] studied the feasibility of various laser based measurement techniques in flash atomization research and found that, while useful, PDPA measurements are subject to some limitations. First, spray measurements in the near field of the nozzle outlet were complicated by the relatively high concentration of large, non-spherical ligaments in the flow. These ligaments are rejected by the PDPA system and the data rate declines.

An important parameter in many sprays is the spray angle and width of the spray envelope. These parameters influence the degree to which the spray mixes with the ambient fluid. This is of considerable importance in combustion applications where sufficient mixing with the ambient air is required for optimal performance. Kamoun *et al.* [2] tested the effect of the degree of superheat on the spray angle in flash atomized sprays. It was found that when the liquid is not super-heated, or only super-heated to low levels, the spray formation is dominated by mechanical breakup. Once the onset of flashing begins, the spray angle increases rapidly and exhibits a positive correlation with the degree of super-heat. This effect was also observed by Kim *et al.* [3] in studying the effect of flash boiling in emulsified heavy oils. These results indicated that increasing temperatures results in increased spray angles, but only for a certain temperature range. Beyond a certain temperature, the spray angle remains relatively constant or decreases. This effect is explained as being a

balance of enhanced atomization at high temperatures, resulting in smaller droplets with larger radial velocities, and with the increased effect of air entrainment on small droplets.

The velocity profiles of flashing sprays have also been studied in detail. In studying a flashing R134a spray, Zhifu *et al.* [4] measured the velocity profiles a variety of axial distances from the nozzle outlet. It was found that the velocity profiles were Gaussian in shape and that the centreline velocity decreased at larger axial distances. As the spray envelope increased in the downstream direction, the velocity profile became increasingly uniform. Yildiz *et al.* [7] found that, as in single phase jets, the maximum velocity at a given axial location is located on the jet centreline. It was also noted that while the droplet velocities decreased in the radial direction, the root-mean-squared (RMS) of the velocities increased, indicating increased fluctuations.

Another important parameter in the measurement of spray systems is the droplet diameter produced by the spray. In reactive flows, this parameter is of vital importance. In studying dimethyl ether (DME) blended diesel fuel, Li *et al.* [8] found that as the mass percentage of DME in the fuel increased resulted in decreased droplet diameters. The authors attributed this decrease in diameter to the flash boiling of the DME in the injector system. Lecourt and Barricau [9] studied the flashing phenomenon in a single fluid spray. Their work found negative correlations between the Sauter mean diameter and the degree of super-heat. These correlations were consistent across a variety of nozzles and the general effect of upstream super-heat on the diameter distribution was posited to be independent of nozzle type. Sher *et al.* [10] state that a flash atomized spray can be used in fuel injectors in order to achieve comparable fuel atomization with lower injector pressures.

This study aims to investigate the performance characteristics of a flash atomized jet over a broad range of degrees of superheat. The overall spray shape, velocity field and generated droplet size will be investigated. This will allow for the evaluation of the evolving influence of the degree of superheat,  $\Delta T_{SH}$ , on the spray characteristics.  $\Delta T_{SH}$  is defined as the difference between the liquid temperature prior to release and the saturation temperature of the liquid at the ambient pressure.

### Experimental test-rig

A schematic of the experimental setup used can be found in Figure 1. This image depicts the flash atomization system used, as well as the important auxiliaries used. A high pressure N<sub>2</sub> gas supply was used in order to pressurize the liquid water in a cylindrical pressure vessel. Heat was supplied to the liquid water by means of three 200 W band heaters placed around the pressure vessel. The liquid water temperature was monitored using a Type J thermocouple probe immersed in the pressure vessel, and the reservoir pressure was monitored using a diaphragm pressure transducer. The experiments were performed with degrees of superheat ranging from 20 - 80°C and with a constant pressure ratio,  $p_r$ , of 13.6

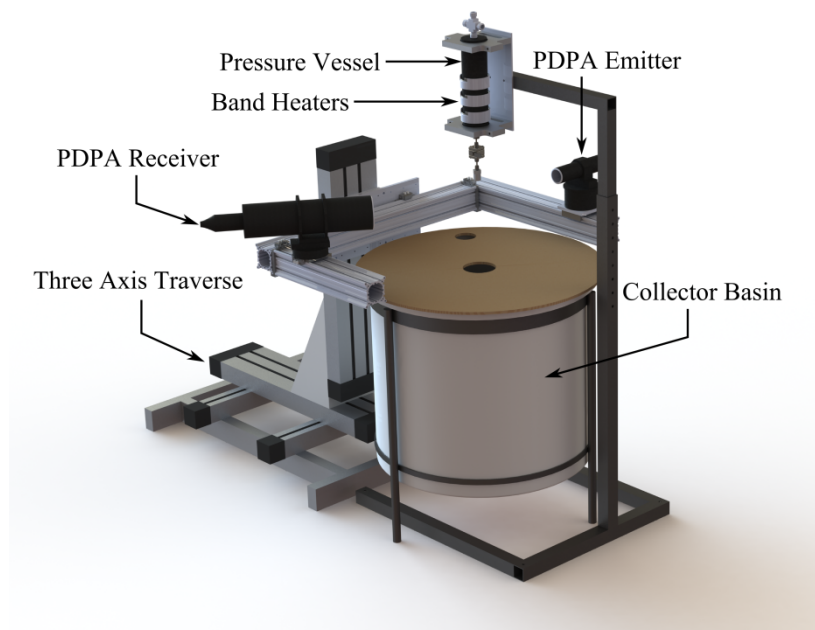


**Figure 1.** A rendered image of the experimental facility

In this experiment, the release of the liquid was designed to be adiabatic. In order to limit the heat loss of the fluid as it passes through the nozzle assembly, the valve, nozzle, and pipe downstream of the cylindrical pressure vessel were pre-heated with a 120 W flexible band heater. Three surface mounted Type T thermocouples were used in order to measure the temperature along the nozzle assembly. During experiments, a maximum allowable deviation of 10°C from the reservoir temperature was used for the nozzle assembly. By minimizing the temperature gradients along the flow direction, the heat transfer of the fluid is minimized. The nozzle used is a conical converging diverging nozzle with a throat diameter of  $D_t=0.8$  mm, an outlet diameter of  $D_o=1.6$  mm and an aspect ratio of  $L/D_o=16$ . It was stated by Lee and Park [11] that flash boiling systems with aspect ratios above 7 undergo internal flashing, with the boiling of the liquid occurring prior to the nozzle outlet.

The flash atomized spray was characterized using long exposure images. These images were collected using a commercial CCD camera (Rebel XTi, Canon) and an incandescent light source in a back scatter configuration. A number of 30s exposures of the spray operating at various inlet conditions were collected. The images collected were then post-processed using custom scripts in a commercial software package (MATLAB 2012a). These images were used in order to quantitatively measure the jet spreading angle as well as to qualify the operating regime of the flashing jet. The image analysis process is outlined in Figure 2. The raw image was first binarized based on the light intensity measured by the CCD camera in order to produce a measureable contour of the spray periphery. It was noted in preliminary observation of the spray that the spreading angle of the jet varies along the axial direction. It was therefore decided to quantify the jet spreading angle using both the near-field spreading angle,  $\theta_n$ , and the far-field spreading angle,  $\theta_f$ . The near-field spreading angle, was measured in the region of  $z = 3.4 - 10.2$  mm and the far-field spreading angle was measured in the region of  $z = 45 - 190$  mm.

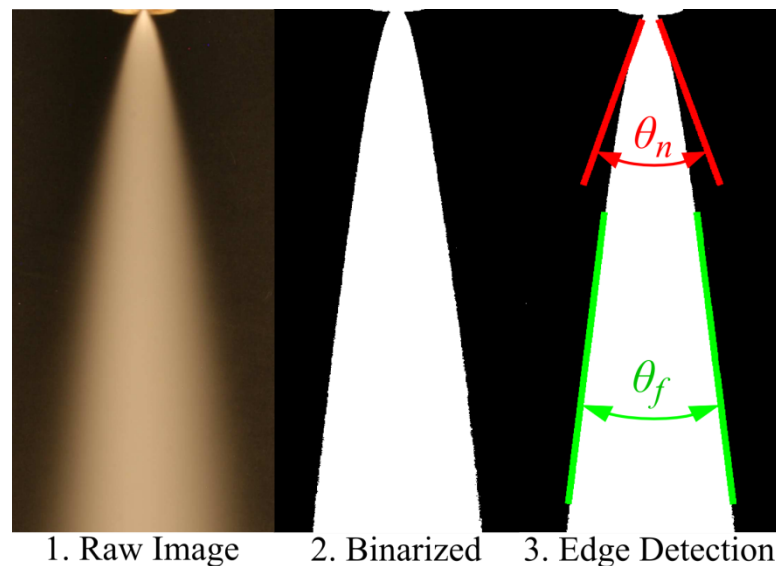


Figure 2. Image analysis procedure

PDPA measurements were also used in order to characterize the operation of the spray at a variety of inlet conditions. A commercial PDPA system (FlowLite 2D, Dantec) was used in order to measure both the velocities and diameters of the droplets produced. Measurements were made along a radial plane located at an axial distance of  $z = 150$  mm downstream of the nozzle outlet. Due to the high spray density near the nozzle outlet, PDPA measurements were made along a plane an axial distance of  $z = 150$  mm.

## Results and Discussion

### Characterising spray shape:

Long exposure images were used in order to assess the qualitative operation of the flash atomized spray at various degrees of superheat. Example images are shown in Figure 3. From Figure 3, a change in the operating regime of the jet is apparent at  $\Delta T_{SH} = 20^\circ\text{C}$ . In this case, there exists an intact liquid core observable along the jet centreline. At low temperature, the spray appears to operate in the partially shattering regime, as defined by Peter *et al.* [12]. At all higher temperatures, the jet appears to operate in the flare shattering regime.

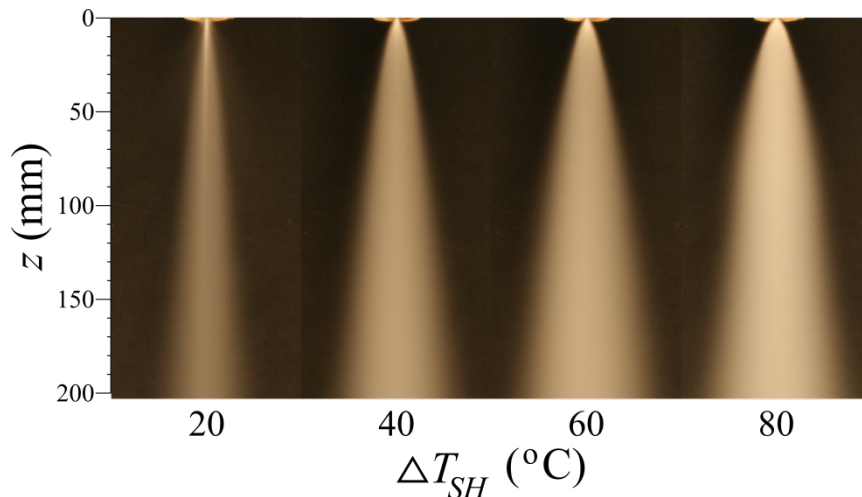


**Figure 3.** Effect of superheat,  $\Delta T_{SH}$  on the general shape of the flash atomized spray

The spreading angles in for the near-field and far-field were also measured using the long exposure images. For the spray operating with  $p_r = 13.6$  and at various values of  $\Delta T_{SH}$ , the near-field spreading angle  $\theta_n$  and the far-field spreading angle,  $\theta_f$  are shown in Figure 4.

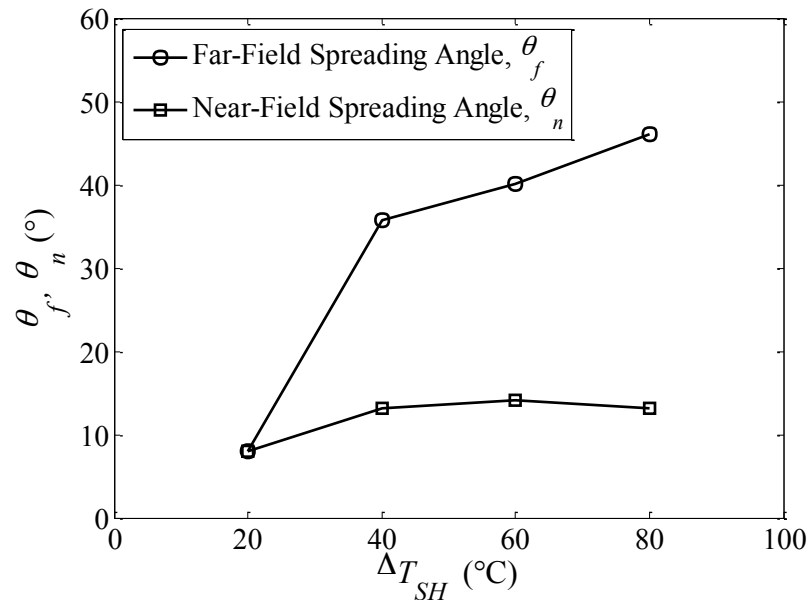


**Figure 4.** Effect of  $\Delta T_{SH}$  on near and far-field spreading angles with  $p_r = 13.6$



From Figure 4, it is clear that the near-field spreading angle increases significantly as  $\Delta T_{SH}$  is increased. In general, it can be seen that the near-field spreading angle is larger than the far-field spreading angle. This indicates a curvature in the jet, as the rapid spreading in the near-field lessens downstream. For  $\Delta T_{SH} = 20^\circ\text{C}$ , however,  $\theta_n$  and  $\theta_f$  are approximately equal.

### Velocity Profiles:

The PDPA system was used in order to concurrently measure the droplet velocity and diameter. By using the three axis traverse system shown in Figure 1, the measurements were made across the spray profile. The velocity profiles represent the average droplet velocity,  $U_z$  at various radial locations for an axial location of  $z = 150$  mm. The measurements were made from the jet centerline towards the jet periphery. Due to declining data rates near the periphery of the spray, PDPA measurements could not be collected beyond  $r = 30$  mm. Beyond this point, the low droplet velocity and low spray density resulted in prohibitively low data rates.

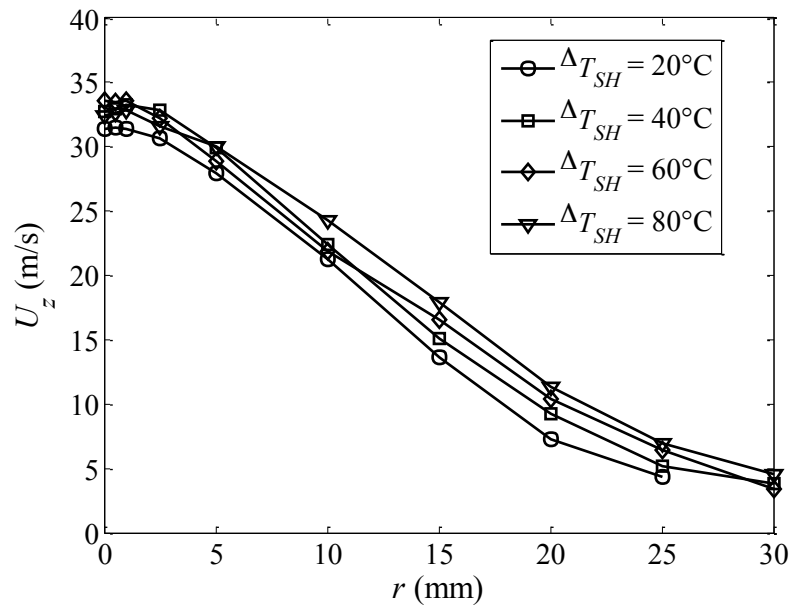


Figure 5. Radial profiles of droplet axial velocity with  $p_r = 13.6$ .

Figure 5 represents the radial profiles of droplet diameter at a variety of degrees of superheat for a given pressure ratio of  $p_r = 13.6$ . From Figure 5, it can be noted that, in general, the droplet velocity profiles exhibit an expected Gaussian distribution. This is the type of velocity profile expected of single-phase jets and is consistent with the findings reported by Wilcox and Bowen [13]. The maximum spray velocity occurs at or in the near vicinity of the jet centreline. At increasing radial positions, the droplet velocities decrease monotonically, in general, towards a minimum at the spray periphery. The radial profiles of droplet velocity appear relatively unaffected by changes in the degree of superheat.

### Diameter Measurements

Using the PDPA system and the three axis traverse, the average droplet diameters across the radial profiles of the spray at an axial distance of  $z = 150$  mm were measured. The measured droplet diameters are characterized using the Sauter mean diameter,  $D_{32}$ , which is defined as:

The value of  $D_{32}$  is a measure of the ratio of the total volume to surface area of the spray passing through the measurement volume. This value is equal to the diameter of a droplet possessing the same volume to surface area ratio as the aggregate spray in the measured location. Radial profiles of  $D_{32}$  collected with  $p_r = 13.6$  and at various values of  $\Delta T_{SH}$  are shown in Figure 6.

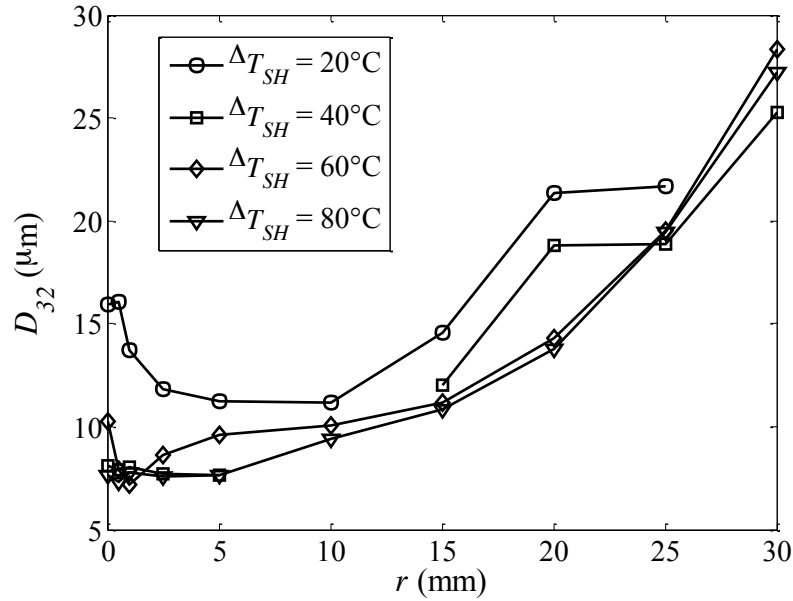


Figure 6. Radial profiles of  $D_{32}$  with  $p_r = 13.6$ .

From Figure 6 it can be noted that, in general, the value of  $D_{32}$  increases in the radial direction. Given that PDPA measurements were made 150 mm downstream of the nozzle outlet, the entrainment of ambient air will impact the measurements. The drag force per unit mass is larger for small diameter droplets. Therefore, as air is entrained into the jet, the small diameter droplets are disproportionately affected and migrate towards the jet centreline. This results in a relative abundance of larger diameter droplets along the jet periphery. A notable exception to this trend occurs at  $\Delta T_{SH} = 20^\circ\text{C}$ , where a local maximum of the measured  $D_{32}$  values occurs along the jet centreline. As was noted in analysing the long exposure images, at low degrees of superheat, the jet operates in the partially-shattering mode, and an intact liquid core persists some distance downstream. The influence of this intact liquid core results in relatively large diameter droplets along the centreline when the spray operates at low degrees of superheat.

## Conclusions

The operating regime of the flash atomized spray was found to be a function of the degree of superheat. As the temperature was increased, the spray transitioned from the partially shattering regime to the flare shattering regime. The spreading angle in the nozzle near-field also increased significantly as the degree of superheat was increased, resulting in increased dispersion of the spray. The droplets velocities were found to be relatively independent of changes in the degree of superheat, and the radial profile of droplet velocities was relatively unaffected by the degree of superheat.

The droplet diameters were also measured using the PDPA system. It was found that in general, large diameter droplets were located towards the spray periphery. This is due to the effect of entrained ambient air causing relatively small droplets to migrate towards the jet centreline. At low degrees of superheat, when the spray is operating in the partially shattering regime, the Sauter mean diameter along the jet centreline exhibits a local maximum. This is the result of incomplete flashing, resulting in an intact liquid core along the jet centreline. Further experimentation will examine the operating characteristics of the flash atomized spray under a variety of pressure ratios as well as degrees of superheat.

## Nomenclature

$p_r$	pressure ratio	[-]
$\Delta T_{SH}$	degree of superheat	[°C]
$D_p$	droplet diameter	[m]
$D_{32}$	Sauter mean diameter	[m]
$\theta_n$	near-field spreading angle	[°]
$\theta_f$	far-field spreading angle	[°]
$z$	axial position	[m]
$r$	radial position	[m]

## References

1. M. R. Vetrano, A. Simonini, J. Steelant, and P. Rambaud, “Flashing jet characterization by non intrusive laser based measurement technique,” in *16th Int Symp on Applications of Laser Techniques to Fluid Mechanics*, 2012, pp. 9–12.
2. H. Kamoun, G. Lamanna, B. Weingand, and J. Steelant, “High-Speed Shadowgraphy Investigations of Superheated Liquid Jet Atomisation H. Kamoun, G. Lamanna, B. Weigand Institute of Aerospace Thermodynamics,” in *ILASS-Americas 22nd Annual Conference on Liquid Atomization and Spray Systems*, 2010, no. May.
3. W. Kim, T. Yu, and W. Yoon, “Atomization characteristics of emulsified fuel oil by instant emulsification,” *Journal of Mechanical Science and Technology*, vol. 26, no. 6, pp. 1781–1791, Jun. 2012.
4. Z. Zhifu, W. Weitao, C. Bin, W. Guoxiang, and G. Liejin, “An experimental study on the spray and thermal characteristics of R134a two-phase flashing spray,” *International Journal of Heat and Mass Transfer*, vol. 55, no. 15–16, pp. 4460–4468, Jul. 2012.
5. E. Hervieu and T. Veneau, “Experimental determination of the droplet size and velocity distributions at the exit of the bottom discharge pipe of a liquefied propane storage tank during a sudden blowdown,” *J. Loss Prev. Process Ind.*, vol. 9, no. 6, pp. 413–425, 1996.
6. D. Yildiz, J. Van Beeck, and M. Riethmuller, “Feasibility Exploration of Laser-based Techniques for Characterization of a Flashing Jet,” *Particle & Particle Systems Characterization*, vol. 21, no. 5, pp. 390–402, Dec. 2004.
7. D. Yildiz, P. Rambaud, J. Van Beeck, and J. Buchlin, “Characterization of superheated liquid jet atomisation with phase Doppler anemometer (PDA) and high-speed imaging,” *Proceedings of FEDSM2006 2006 ASME Joint U.S. - European Fluids Engineering Summer Meeting*, pp. 1–10, 2006.
8. G. Li, J. Cao, M. Li, Y. Quan, and Z. Chen, “Experimental study on the size distribution characteristics of spray droplets of DME/diesel blended fuels,” *Fuel Processing Technology*, vol. 104, pp. 352–355, Dec. 2012.
9. R. Lecourt and B. Philippe, “Spray Velocity and Drop Size Measurements in Flashing Conditions,” *Atomization and Sprays*, vol. 19, no. 2, pp. 103–133, 2009.
10. E. Sher and M. Zeigerson-Katz, “Spray formation by flashing of a binary mixture: An energy balance approach,” *Atomization and Sprays*, vol. 6, pp. 447–459, 1996.
11. S. Y. Suh Park, Byung; Lee, “An experimental investigation of the flash atomization mechanism,” *Atomization and Sprays*, vol. 4, pp. 159–179, 1994.
12. E. Peter, A. Takimoto, and Y. Hayashi, “Flashing and shattering phenomena of superheated liquid jets,” *JSME International Journal*, vol. 37, no. 2, 1994.
13. W. Wilcox and P. Bowen, “Flashing liquid jets and two-phase dispersion A review,” in *Health and Safety Executive*, 2002.

## Acetone Photophysics Investigations for the Application of PLIFP to Droplet Evaporation Measurements under Supercritical Conditions

B. Bork<sup>1</sup>, F. Stritzke<sup>1</sup>, F. Weckenmann<sup>2</sup>, G. Lamanna<sup>2</sup>, B. Weigand<sup>2</sup>, A. Dreizler<sup>1</sup>

1: Fachgebiet Reaktive Strömungen und Messtechnik, Center of Smart Interfaces,  
Technische Universität Darmstadt, Germany, bork@csi.tu-darmstadt.de

2: Institut für Thermodynamik der Luft- und Raumfahrt, University of Stuttgart, Germany

### Abstract

In modern internal combustion engines and gas turbine combustors pressure and temperature during fuel injection approach and in some cases exceed the critical conditions of the initially liquid fuel. To investigate droplet evaporation for trans- and supercritical conditions in detail, experimental methods are needed to distinguish between highly concentrated vapour and liquid fuels. For the model-fuel acetone one promising approach is to measure laser induced fluorescence and phosphorescence (PLIFP) simultaneously. It is based on the emission of light by acetone molecules following excitation by a uv laser.

In this work the photophysics of liquid and gaseous acetone in nitrogen/oxygen mixtures were investigated as a prerequisite for subsequent droplet experiments. Mixture fractions and thermodynamic conditions were varied in a wide range from sub- to supercritical. The acetone light emission was resolved spectrally, temporally and spatially along the laser beam propagation. The results indicate a remarkably high sensitivity of the acetone phosphorescence signal intensity to even small amounts of oxygen added to the mixture. Additionally a correlation between liquid acetone temperature and the phosphorescence-to-fluorescence signal ratio was discovered that does have potential for droplet temperature measurements.

---

### Introduction

Downsizing of internal combustion engines and efficiency considerations for gas turbines lead to increasing pressures and temperatures during fuel injection. In some cases the critical temperature or pressure of the initially liquid fuel is exceeded [1,2]. Furthermore in some rocket engines the liquid fuel injection takes place in a supercritical environment [3]. Established modelling approaches for spray evaporation and mixture formation are not applicable at these conditions and have to be revised [4]. However, experimental data for droplet evaporation are rare in these conditions. Almost all experimental data is based on shadowgraphy and Mie scattering [5–7]. Those methods are well established in atmospheric conditions but might yield misleading results under near critical conditions as the difference in refractive index between liquid and gas phase is decreased. Furthermore, light gets redirected not only by the droplet's surface but also by the strong density gradients in the dense vapour surrounding the droplet.

Methods based on the interaction of light and matter on a molecular level such as Raman spectroscopy [8] and fluorescence/phosphorescence methods have the potential to overcome the aforementioned issues. Planar laser induced fluorescence and phosphorescence (PLIFP) of acetone was proposed as a method to distinguish between liquid fuel and dense fuel vapour regions by Ritchie and Seitzman [9]. It is based on the characteristic of acetone to absorb uv light followed by emission of fluorescence (lifetime of a few nanoseconds) and phosphorescence (lifetime in the microsecond regime). If the gas surrounding the droplet contains oxygen it will quench the phosphorescence but not the fluorescence of the acetone vapour due to significant difference in lifetimes. The phosphorescence inside droplets of oxygen free acetone will not be quenched as the liquid-vapour interface inhibits a fast transport of oxygen into the droplet. Hence, the phosphorescence signal will only appear in liquid acetone. This method was further investigated and applied to liquid jets in air by Tran [10]. Weckenmann et al. [11] showed that phosphorescence is effectively quenched even by oxygen concentrations below 5%.

Recently Charogiannis and Beyrau [12] showed that phosphorescence of acetone can be more suitable for vapour mixture fraction measurements close to the droplet than fluorescence. Fluorescence measurements of the vapour phase suffer from halation effects due to the strong signal produced by the droplet. The intensity ratio between liquid and vapour phase signals from acetone is in the order of ten times lower for phosphorescence compared to fluorescence signals. For aforementioned reasons this method is limited to oxygen free environments.

In the current project a droplet generator has been developed that injects single droplets at near critical temperature into an environment that is supercritical considering the critical properties of the droplet liquid [13]. Acetone is used as droplet liquid ( $p_c = 47$  bar,  $T_c = 508$  K). The droplet is falling freely in gravity and can be observed through fused silica windows. Droplet size, vapour mixture fraction around the droplet and droplet temperature are of special interest when investigating the droplet evolution. PLIFP aims to measure the temporal

evolution of mixture fraction and droplet size. For quantitative measurements of the mixture fraction and for the investigation of the phosphorescence characteristics it is necessary to quantitatively characterise this technique with regard to mixtures of acetone, nitrogen and oxygen at well controlled conditions. The detailed investigation of acetone photophysics under well-defined conditions is the scope of this work.

There is also a need for non-intrusive droplet temperature measurement techniques. Since the thermodynamic behaviour in the vicinity of the critical point is sensitive to additives, techniques that do not require additional fluorescent dyes are favoured. Therefore the data is searched for sensitive dependencies of fluorescence and phosphorescence signals on the liquid acetone temperature.

The acetone photophysics for gaseous mixtures with air were investigated in detail by Thurber et al. [14] who proposed an empirical modelling approach for the acetone fluorescence yield. Thurber also measured the absorption cross section for acetone vapour at different temperatures at atmospheric pressure. Koch et al. [15] modified the model to fit the absolute fluorescence yields that were measured with a Rayleigh scattering calibrated setup. Later the “Thurber-model” was modified by Braeuer et al. [16] to be consistent with fluorescence yield measurement results at pressures towards 20 bar with an excitation wavelength of 248 nm. The absorption of acetone in mixtures with air and nitrogen is well documented in literature [14,17,18] whereas the only absorption data for pure liquid acetone found in literature was measured by Renge et al. [19] and reported relative to the absorption maximum. In turn there is a need for advanced measurements of the acetone absorption cross section that are equally addressed in this study.

### Theoretical background

To derive mixture fractions from acetone fluorescence signals in practice it is necessary to perform calibration measurements. If the detection system used for calibration is identical to the final measurement setup the fluorescence signal  $S_f$  depends on the laser pulse energy for excitation of acetone  $E$ , the excitation wavelength  $\lambda$ , the absorber molecule number density  $n_{abs}$ , the absorption cross section  $\sigma$  and the fluorescence yield  $\Phi$ :

$$S_f = C_{calib} \cdot E \cdot \lambda \cdot n_{abs} \cdot \sigma \cdot \Phi \quad (1)$$

All characteristics of the detection system are included in the calibration constant  $C_{calib}$  that is obtained by calibration measurements in well-defined conditions. The above relationship is applicable for linear fluorescence processes and is usually applied to measurements with rather low acetone concentrations in air or nitrogen. For gases it is common to define the absorption cross section as used in the Lambert Beer law:

$$\frac{I}{I_0} = e^{-\sigma \cdot l \cdot n_{abs}}, \quad (2)$$

where  $I_0$  is the initial intensity and  $I$  is the intensity of light after having travelled the path length  $l$ . For the absorption in liquids commonly the molar absorptivity is used. This distinction between liquid and gas is impracticable for the current study that extends into the supercritical regime. Above the critical point a substance is neither a gas nor a liquid and can be transferred to a gas or a liquid continuously without a phase change. Hence a consistent formulation for the absorption process for the entire regime has to be found. The authors decided to use the absorption cross section for gas, liquid and supercritical fluid.

For acetone the absorption cross section is a function of wavelength and temperature and is usually treated as independent from pressure. While this seems to be a solid assumption for gaseous mixtures with acetone partial pressures below 0.25 atm it has to be revised for the current study where partial pressures of acetone exceed 50 bar. This pressure dependency of the acetone absorption cross section is supported additionally by the fact that it differs for acetone vapour in bath gas and for liquid acetone at the same temperature. Thus, not only fluorescence yield but also the absorption cross section depends on temperature and pressure. On the other hand, the other parameters laser pulse energy and excitation wavelength are easily monitored.

To obtain the absorption cross section from absorbance measurements the absorber number density has to be known. A substance in the vicinity of the two phase region and the critical point can obviously not be treated as an ideal gas. One of the most widely used real gas equation of state (EOS) is the cubic Peng-Robinson EOS. It is a valuable tool for many applications but its errors average 38% in the prediction of the liquid phase density of acetone [20]. This issue is tackled by using a quartic EOS proposed by Yun et al. [21] that predicts the liquid phase density of acetone with an error of about 2% [20,21].

### Experimental setup

The pressure chamber that is used for the photophysics investigations (see Figure 1) is identical in construction to that one used for the droplet experiments by Oldenhof et al. [11,13]. The cell is electrically heated and has four windows for optical access whereas one window is exchanged by a specially designed window that extends almost to the middle of the cell. This is necessary to avoid significant absorption of the uv laser light before entering the probe volume. The droplet generator is exchanged by a lid with a connection that is used either as inflow or outflow (see below). The cell is continuously purged. The acetone is supplied directly to the cell or to

the evaporator by a pump that is controlled by a Coriolis flow meter. For all measurements acetone of high purity for spectroscopy (Merck UVASOL) is used.

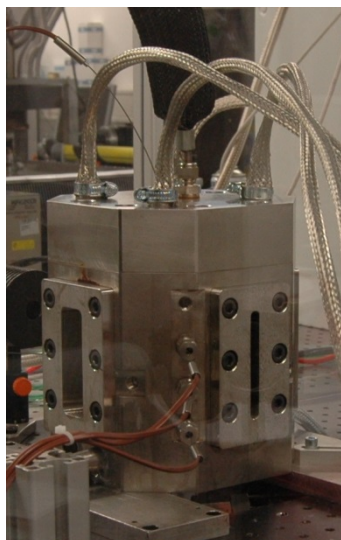


**Figure 1.** Photograph of the pressure chamber

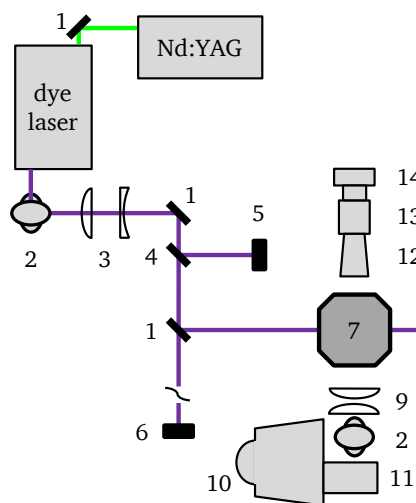


**Figure 2.** Experimental setup: 1 – mirror, 2 – periscope, 3 – telescope, 4 – glass plate, 5 – energy meter, 6 – beam monitor, 7 – pressure chamber, 8 – beam dump, 9 – achromatic lenses, 10 – spectroscope, 11 – ICCD camera, 12 – macro lens, 13 – image intensifier, 14 – CCD camera

Gaseous mixtures are supplied to the top of the cell and leave it through the bottom to avoid any accumulation of potential condensate when operated close to the dew point of the particular mixture. Acetone is transferred to its gaseous state by an evaporator that is operated without carrier gas. Subsequently it is mixed with the preheated gas mixture (nitrogen/oxygen) and led to the pressure chamber through a temperature controlled hose to avoid condensation.

For measurements of pure acetone the bottom connector is used as the inlet and the connector in the lid as the outlet. This is necessary as pure acetone is supplied as a liquid and has to displace the nitrogen used to purge the cell before filling it with acetone. For pure acetone the flow rate is set to less than 2 g/min which allows the direct supply of acetone to the cell without preheating as it gets heated on its way through the 40 mm thick stainless steel bottom of the pressure chamber.

A dye laser (Radiant Dyes) operated with DCM is pumped by the second harmonic of a Nd:YAG laser (Spectra Physics Quanta Ray Pro 270) to provide 10 ns pulses with wavelengths tuneable from 308 to 325 nm as depicted in Figure 2. The dye laser, equipped with a Bethune-cell, delivers a circular beam profile with a diameter of about 3 mm diameter (FWHM). For spectral measurements the laser's diameter is reduced to a non-converging beam of 1.5 mm intersecting the pressure cell. About 15% of the laser's pulse energy is split off by a fused silica plate and sent on an Energy Sensor (Coherent EnergyMax) to monitor the laser's single pulse energy. An ICCD camera (Princeton Instruments PI-MAX) mounted on a Horiba Triax 320 spectrometer with a 150 lines/mm grating is used for collecting fluorescence and phosphorescence spectra. The signal is focused on the spectrometer entrance slit by a combination of two achromatic lenses with focal lengths of 200 and 360 mm. For all spectrally unresolved measurements an Andor Clara CCD camera is used, equipped with a lens coupled Hamamatsu image intensifier for gating in the nanosecond regime. The image is produced by a 105 mm, f/2.8 macro lens (Sigma).

The absorption cross section of pure acetone was measured by two different methods. The first method is based on the excitation of pure acetone in the pressure chamber by the uv laser and the fluorescence signal detection spatially resolved along the laser beam propagation. Figure 3 shows such a 2D sample (left hand side) with laser propagation from left to right and the same signal as a plot along the beam propagating path (right hand side). At the end of the laser window in the measurement volume the signal rises, followed by mono-exponential signal decay from left to right. An exponential function is fitted to this curve in the interval from 80% to 10% of the signal maximum. The fit exponent yields the absorption coefficient  $\alpha$  that relates to the absorption cross section as follows:

$$\sigma = \alpha / n_{\text{abs}} \quad (3)$$

The described method allows the measurement of absorption cross sections of pure acetone under thermodynamic conditions from ambient to supercritical. The second method is limited to ambient conditions and therefore liquid acetone. It makes use of an uv-vis spectrometer (Shimadzu uv-2450). Fused silica cuvettes with sheet thicknesses of 20, 10, 2 and 1 mm are filled with acetone and used for absorbance measurements. The absorbance data is corrected for reflection at the cuvette walls by the absorbance data for wavelengths detuned

from any molecular acetone absorption. As mentioned above the absorption cross section data for liquid acetone presented by Renge [19] are reported relative to the absorption maximum and cannot be used to derive absolute values since the maximum cross section is not provided. Receiving the spectrometer measurement data from Renge (Indrek Renge, personal communication, May 13, 2013) made it possible to process the data in exactly the same way as it is done with the data measured with the spectrometer in this work.

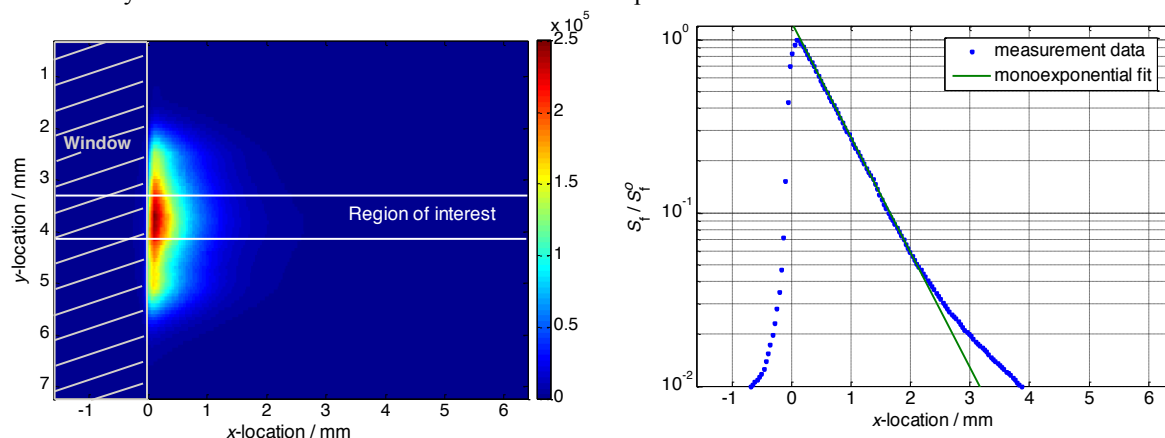


**Figure 3.** Absorption cross section determination, left – exemplary fluorescence image, pure acetone at 320 nm, 295 K, 55 bar, right – corresponding 1D projection in the region of interest with monoexponential fit

## Results and discussion

### Pure acetone

The results of pure liquid acetone absorption cross section measurements at 295 K including the data obtained from Renge are presented in Figure 4 in comparison to the data for gaseous mixtures with dilute acetone concentrations by Thurber [14] and Yujing [18]. Renge et al. [19] used a cell with a sheet thickness of  $0.01 \text{ mm} \pm 0.002 \text{ mm}$  specified by the manufacturer (Starna). The resulting absorption cross sections exceed the values measured in this work in the overlapping regime ( $\lambda \geq 308 \text{ nm}$ ). This could be due to the limited manufacturing accuracy of the cuvettes, which is 20% of the cuvette's thickness and limits the accuracy of the measured absorption cross section to about 20%. This effect is much less pronounced for cuvettes used in this work as their manufacturing accuracy is  $\pm 0.01 \text{ mm}$ , which is  $\pm 1\%$  at maximum for the 1 mm cuvette's thickness. More important is the uncertainty in temperature of  $\pm 2 \text{ K}$  as it was not measured inside the cuvette and that leads to an uncertainty of 3% for the absorption cross section. The uncertainties are shown by error bars in figure 4 at 316 nm on Renge's data and at 318 nm on the spectrometer data of this work. The vapour acetone absorption cross section extends further towards longer wavelengths than for liquid acetone. At 330 nm this results in a difference of factor 4.

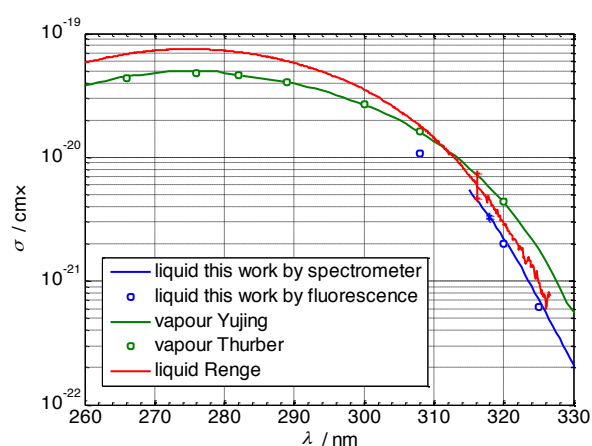


**Figure 4.** Absorption cross section of liquid acetone in comparison with data for acetone vapour

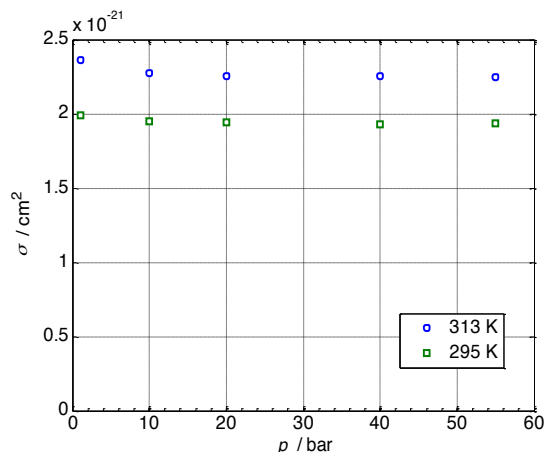


**Figure 5.** Pressure dependence of pure acetone absorption cross section at 320 nm

The pressure dependence of the absorption cross section for liquid acetone at 295 K at 320 nm is shown in Figure 5. From 1 to 10 bar the absorption cross section decreases by 3% which is only slightly more than the error in number density prediction of 2%. Hence no significant dependence of the absorption cross section on pressure is observed. The influence of temperature on the absorption cross section of pure acetone at a constant



pressure of 55 bar is displayed in Figure 6 in comparison to the temperature dependence of vapour acetone at atmospheric pressure published by Thurber et al. [14].

The fluorescence and phosphorescence spectra for pure acetone at 1 bar and 295 K at 320 nm excitation are shown in Figure 7. The fluorescence spectrum is plotted with and without spectral intensity correction. For the spectral intensity correction an Ulbricht sphere with a known spectrum is used to correct for non-uniform spectral sensitivity of the detection system. The corrected fluorescence spectrum is in good agreement with published data [10,22]. The small peak at 368 nm is also visible in the data of Pischel and Nau [22] but is not discussed any further due to space restrictions. The phosphorescence spectra are shown as uncorrected data, since the decreasing signal to noise ratio of the phosphorescence spectra at short wavelengths lead to unphysical results when corrected. Hence the presented spectra can only be compared to each other and at wavelengths longer than 425 nm. The red shift reported by Tran [10] for 266 nm excitation is also visible in this data. In contrast, the also reported blue shift of early phosphorescence is not visible.

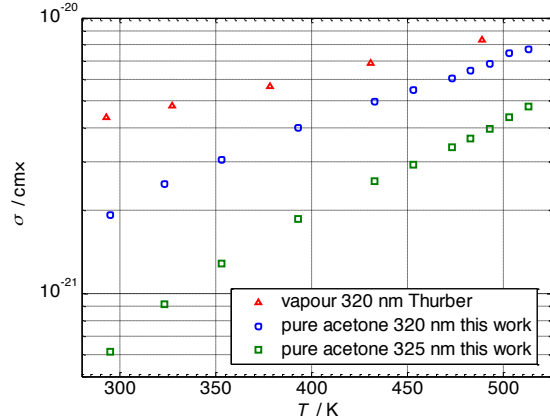


**Figure 6.** Acetone absorption cross section versus Temperature at 55 bar (liq.) / 1 atm (vap.)

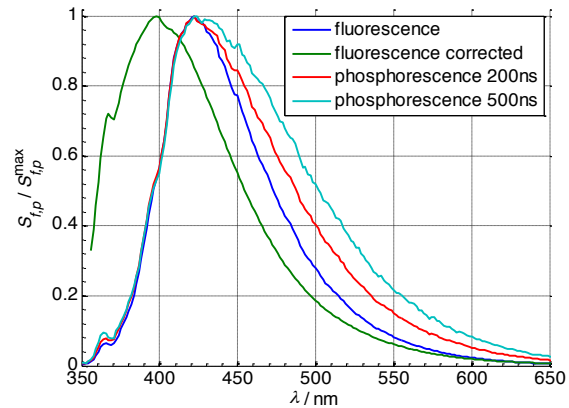


**Figure 7.** Fluorescence and phosphorescence spectra of pure acetone at 1 bar, 295 K and 320 nm excitation

To investigate the linearity of fluorescence and phosphorescence the laser energy density is varied from 0.5 mJ/cm² to 58 mJ/cm² averaged over the 3 mm diameter beam profile. Results for 320 nm excitation in Figure 8 show that the fluorescence is linear whereas the phosphorescence is strongly non-linear. The linear regime ranges up to approximately 2 mJ/cm². For the application of the PLIFP method as marker of the liquid phase a linear dependence of phosphorescence on laser energy is not necessary. For quantitative measurement techniques, however, the non-linearity has to be considered.

Figure 9 displays the luminescence decay of pure acetone at high temporal resolution. This is achieved by setting the intensifier gate to 20 ns and increasing the intensifier delay to the laser pulse in small steps, starting with 10 ns. On the x-axis the time delay between the fluorescence peak and the centre of each gate interval is plotted.

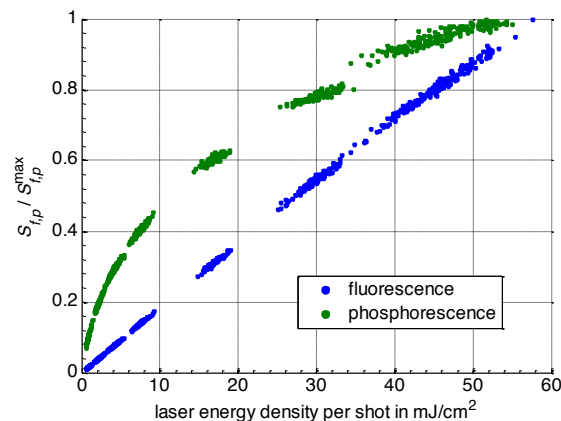


**Figure 8.** Fluorescence/phosphorescence signal, laser energy density dependence at 295 K, 55 bar, 320 nm

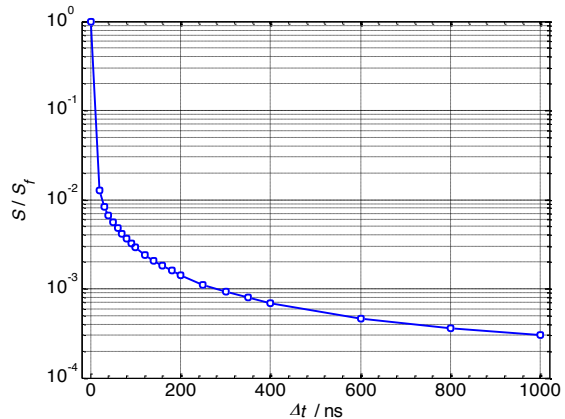


**Figure 9.** Temporal luminescence decay, pure acetone at 295 K, 55 bar, 320 nm, 20 ns gate time

The influence of temperature on the luminescence decay for pure acetone at 55 bar and excitation with 320 nm is shown in Figure 10. The intensifier gate is set to 100 ns. The first phosphorescence signal at 75 ns strongly depends on temperature. Starting from 300 ns all phosphorescence curves reveal a similar slope.

A ratio of phosphorescence and fluorescence is built by taking the 10  $\mu$ s integral phosphorescence signal starting 100 ns after the fluorescence peak. This ratio is plotted versus temperature in Figure 11. The signal ratio decreases with increasing temperature. Tran et al. [23] reported an exponential decrease of the phosphorescence signal with increasing temperature with 266 nm excitation of pure liquid acetone. Highest sensitivity is observed between 323 and 433 K. Especially in this range this ratio should be applicable for liquid acetone temperature measurements.

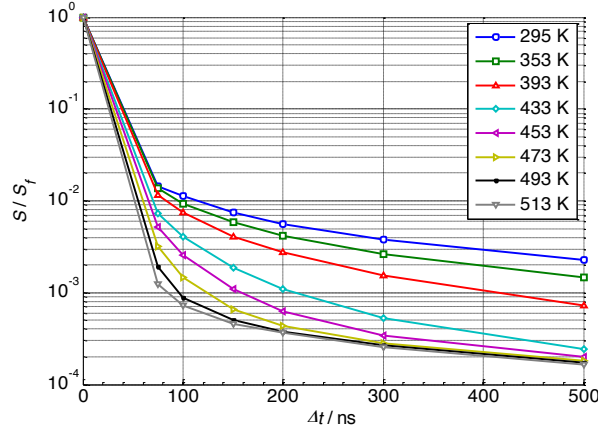


**Figure 10.** Temporal luminescence decay, pure acetone at different temperatures, 55 bar, 320 nm

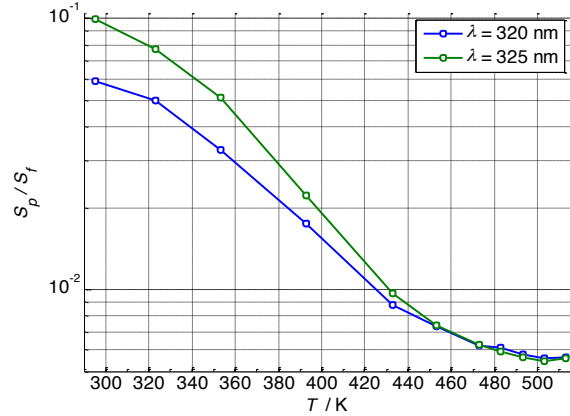


**Figure 11.** Phosphorescence/fluorescence ratio, temperature dependence, pure acetone at 55 bar

#### *Gaseous mixtures of acetone, nitrogen and oxygen*

Oxygen quenching of acetone vapour phosphorescence forms the basis for the distinction between liquid and vapour phase by the PLIFP method. For the experiments presented here, the acetone concentration is set to 20%. In accordance to a droplet setup, the oxygen concentration is given as per cent of the nitrogen/oxygen mixture. In the current study the quenching effect of oxygen on the vapour phosphorescence of acetone is investigated for three different conditions as presented in Figure 12. The acetone fluorescence decays significantly faster with increasing oxygen concentration. Figure 13 displays the phosphorescence/fluorescence signal ratio for three different thermodynamic conditions. Even small amounts of oxygen efficiently quench the phosphorescence. Contrary to data published previously [11] there is no plateau at oxygen concentrations below 0.5%. Quenching is reproducibly evident starting at oxygen concentration of 0.1%. It is speculated that our earlier measurement results suffered from technical problems concerning the determination of the oxygen concentration. Quenching efficiency increases with increasing pressure and temperature which seems reasonable as both parameters lead to increasing molecular collision rates.

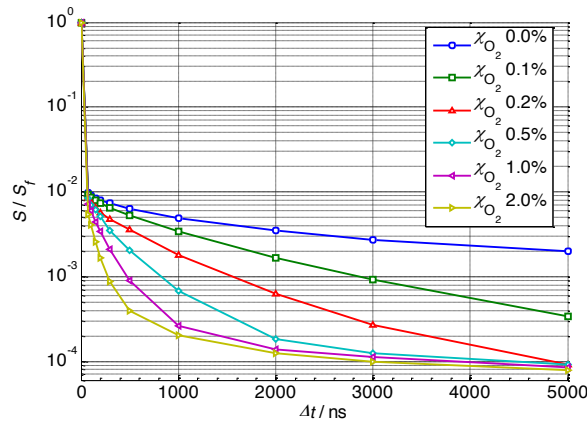


**Figure 12.** Temporal luminescence decay, gaseous mixtures at 2 bar, 313 K, 320 nm,  $\chi_{ac} = 0.2$

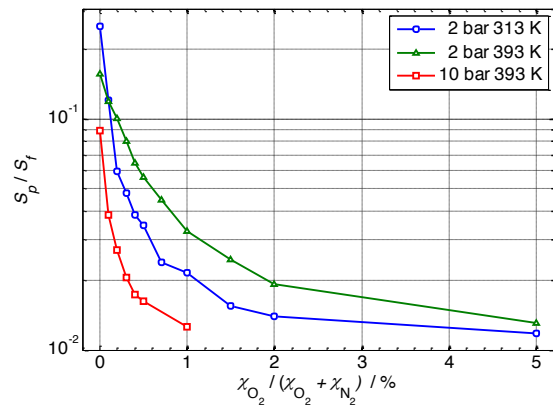


**Figure 13.** Phosphorescence/fluorescence ratio, gaseous mixtures at 320 nm,  $\chi_{ac} = 0.2$

## Conclusions

The absorption cross section of pure acetone shows a temperature dependence which is comparable to that of acetone vapour at the same excitation wavelength. The absorption cross section of pure acetone at 295 K

showed no significant dependence on pressure up to 55 bar. The phosphorescence spectrum was red-shifted compared to fluorescence at excitation between 308 and 325 nm as reported before for 266 nm excitation. No significant difference of the fluorescence and phosphorescence spectra for excitation wavelengths between 308 and 325 nm was found when compared to measurements with excitation at 266 nm.

The temperature dependence of the phosphorescence/fluorescence signal ratio for pure acetone shows potential for droplet temperature measurements, although the sensitivity above 450 K is quite low. Anyhow, for this purpose the non-linearity of the phosphorescence signal has to be solved. One approach is to use laser pulse energy densities of less than 2 mJ/cm<sup>2</sup> at 320 nm. This rather low laser excitation might suffer from low signal intensities but might be sufficient for measuring a representative temperature for the entire droplet.

The oxygen quenching efficiency was found to be even stronger than reported before, especially with increasing temperature and pressure. Thus, it is not necessary to use oxygen concentrations of more than 5%. Oxygen concentrations below 5% do not significantly alter the thermodynamic interaction of acetone droplets and gas atmosphere (nitrogen/oxygen).

## Acknowledgements

We kindly acknowledge the financial support by Deutsche Forschungsgemeinschaft through SFB-TRR 75.

## Nomenclature

$C_{calib}$	Calibration constant	$\alpha$	Absorption coefficient
$E$	Laser single pulse energy	$\lambda$	Wavelength
$I$	Intensity	$\sigma$	Absorption cross section
$n_{abs}$	Absorber molecule number density	$\Phi$	Fluorescence yield
$S_f$	Fluorescence signal	$\chi$	Molar fraction
$S_p$	Phosphorescence signal		

## References

- [1] Oefelein, J., Dahms, R. N. U., Lacaze, G., Manin, J. L., Pickett, L. M., Effects of Pressure on the Fundamental Physics of Fuel Injection in Diesel Engines, *12<sup>th</sup> International Conference on Liquid Atomization and Spray Systems*, Heidelberg, Germany (2012).
- [2] Amaya, J. A., Hunt, A. T., Colby, J. A., Menon, S., Thermal Effects on Fuel Injection in a Swirl-Stabilized Gas Turbine Combustor, *42<sup>nd</sup> Joint Propulsion Conference & Exhibit*, Sacramento, California, USA (2006).
- [3] Yang, V., *Proc. Combust. Inst.* 28:925–942, (2000).
- [4] Bellan, J., *Prog. Energ. Combust.* 26: 329–366 (2000).
- [5] Nomura, H., Ujiie, Y., Rath, H. J., Sato, J., Kono, M., *Proc. Combust. Inst.* 26:1267–1273 (1996).
- [6] Ghassemi, H., Baek, S. W., & Khan, Q. S., *Combust. Sci. Technol.* 178:1031–1053 (2006).
- [7] Lamanna, G., Oldenhof, E., Baab, S., Stotz, I., Weigand, B., Disintegration Regimes Near the Critical Point, *18<sup>th</sup> International Space Planes and Hypersonic Systems and Technologies Conference*, Tours, France (2012).
- [8] Braeuer, A., Knauer, O. S., Quiño, J., Leipertz, A., *Int. J. Heat Mass Transfer* 62:729–740 (2013).
- [9] Ritchie, B. D., Seitzman, J., Simultaneous imaging of vapor and liquid spray concentration using combined acetone fluorescence and phosphorescence, *42<sup>nd</sup> Aerospace Sciences Meeting and Exhibit*, Reno, NV, USA (2004).
- [10] Tran, T., “Acetone Planar Laser-Induced Fluorescence and Phosphorescence for Mixing Studies of Multiphase Flows at High Pressure and Temperature”, Ph.D. Thesis, Georgia Institute of Technology, USA (2008).
- [11] Weckenmann, F., Bork, B., Oldenhof, E., Lamanna, G., Weigand, B., Böhm, B., Dreizler, A., *Z. Phys. Chem.* 225:1417–1431 (2011).
- [12] Charogiannis, A., Beyrau, F., *Exp. Fluids* 54:1518–1532 (2013).
- [13] Oldenhof, E., Weckenmann, F., Lamanna, G., Weigand, B., Bork, B., Dreizler, A., *Prog. Propul. Phys.* 4:257–270 (2013).
- [14] Thurber M., Grisich F., Kirby, B., Votsmeier, M., Hanson, R., *Appl. Opt.* 37, 4963–4978 (1998).
- [15] Koch, J. D., Hanson, R. K., Koban, W., Schulz, C., *Appl. Opt.* 43:5901–5910 (2004).
- [16] Braeuer, A., Beyrau, F., Leipertz, A., *Appl. Opt.* 45:4982–4989 (2006).
- [17] Martinez, R. D., Buitrago, A. A., Howell, N. W., Hearn, C. H., Joens, J. A., *Atmos. Environ.* 26:785–792 (1992).

- [18] Yujing, M., Mellouki, A. *J. Photochem. Photobiol., A*, 134:31–36 (2000).
- [19] Renge, I., *J. Phys. Chem. A* 113:10678–10686 (2009).
- [20] Wang, Y., Huang, G., Ge, C., *Bull. Chem. Soc. Ethiop.* 25:287–294 (2011).
- [21] Yun, Z., Shi, M., Shi, J., Lee, H., *Fluid Phase Equilib.* 187–188: 275–298 (2001).
- [22] Pischel, U., Nau, W. M., *J. Am. Chem. Soc.* 123: 9727–9737 (2001).
- [23] Tran, T., Kochar, Y., Seitzman, J., Acetone Photophysics at Near Critical to Supercritical Conditions, 46<sup>nd</sup> *Aerospace Sciences Meeting and Exhibit*, Reno, NV, USA (2008).

## Influence of fluid media on flow pattern and spray break-up applying cylindrical nozzles for the atomization of superheated liquids

Astrid Günther<sup>1</sup>, Benedikt Köninger<sup>1</sup>, Karl-Ernst Wirth<sup>1</sup>

1: Institute of Particle Technology, University Erlangen - Nuremberg, Germany

### Abstract

In the process of superheated atomization, heat is used as additional energy source for the disintegration of fluid jets. Evaporation phenomena inside the nozzle capillary induce the generation of a two-phase flow. Bubbles contained in the mass flux exiting the nozzle, feature an inner pressure higher than the ambient pressure. Accordingly, the bubbles burst, by this disintegrating the fluid jet. In addition, the heating of the fluid media lowers the viscosity of the fluid. This is advantageous for vapour formation inside the nozzle capillary, as well as for the disintegration of the fluid outside the nozzle. Another way to alter the flow pattern and spray morphology is the addition of particles to the fluid media. Effects of viscosity changes as well as the influence of particle addition will be analysed in this work.

### Introduction

Superheating of a fluid can be achieved in two ways: Either by lowering the ambient pressure beneath the vapour pressure or by heating the media above the saturation temperature with regard to ambient conditions [1, 2, 3, 4, 5]. In this work the latter is of importance. After initiating the spraying process, evaporation occurs in the nozzle capillary. A two-phase flow inside the nozzle is generated. An inner bubble pressure corresponding to the respective vapour pressure can be assumed. When those bubbles get into contact with the ambient atmosphere they burst, by this shattering the fluid jet [5, 6]. Depending on geometrical features of the nozzle like L/D-ratio or roughness of the capillary, process conditions like pressure or fluid temperature and fluid properties like viscosity or surface tension, different spray morphologies are achieved. In state of the art spraying processes an enhancement of fluid viscosity hampers the breakup of the spray [7]. This also applies for flash atomization, but in this process a lowering of the viscosity is achieved by the heating of the fluid. This is advantageous for the disintegration of the jet exiting the nozzle capillary. In order to analyse the influence of viscosity on superheated atomization Polyvinylpyrrolidone (PVP) solutions of different concentrations are used. Another factor influencing flow pattern inside the nozzle capillary, as well as the spray morphology is the addition of particular matter. A suspension of glass beads mixed with deionised water is used to analyse the behaviour triggered by a suspension flowing through the nozzle capillary.

### Experimental test-rig

The applied test rig is presented in Figure 1. The fluid is heated inside a pressure vessel. This vessel is surrounded by heating jackets that allow a heating of the fluid up to a maximum temperature of  $T_0 = 150^\circ\text{C}$ . During the heating period a stirrer is constantly mixing the fluid in order to allow a homogenous temperature distribution inside the pressure vessel. The pressure level is set by pressurized air, up to a maximum value of  $p_0 = 7$  bar. The vessel is attached to a movable framework by a load cell. This load cell constantly measures the total weight of the vessel. During a spraying event this weighing method allows the measuring of the mass flux exiting the nozzle. The nozzle applied in this work is depicted in Figure 2. A simple cylindrical nozzle is applied for the measurements in this work. It has an L/D-ratio of 20 and a diameter  $D = 1.8$  mm. The capillary was fabricated by drilling; hence a rather rough surface inside the capillary is to be expected.

The outlet of the nozzle is pointed. Accordingly, the contact between spray

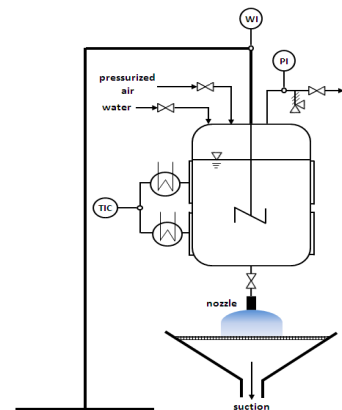


Figure 1: Test-rig

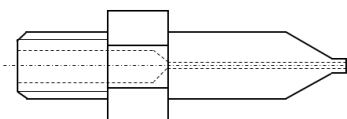


Figure 2: Cylindrical nozzle

and nozzle is minimized. A formation of a liquid sheet at the nozzle outlet is thereby hindered. This induces a lowered generation of coarse droplets originating at a liquid sheet that would disturb the spray. Beneath the nozzle, and hence spray (Figure 1), a suction system is applied in order to prevent disturbance of the process by recirculating vapour. The suction system is constructed in a way that the spray in the measuring zone is not altered in

any way.

Other measurement techniques are of an optical nature. These techniques are non-invasive, allowing an analysis of the spray without disturbing it. The morphology of the spray is monitored by a simple shadowgraphic set-up. Opposite to each other a CCD – camera (PCO, 2048 x 2048 Pixel) and a pulsing LED are located. The spray is in between. The LED pulsing and image taking are synchronized by a synchronizer. Images are taken in a frequency of 10 Hz. The size of the images is 40 mm x 35 mm. Furthermore, droplet size measurements with a laser diffraction system (Malvern, SprayTec) are conducted. The laser beam passes the spray at its centre, in 15 cm distance to the nozzle outlet. A lens with a focal length of 100 mm is used, allowing a measurement range of droplet sizes between 0.5  $\mu\text{m}$  and 200  $\mu\text{m}$ . The sample rate is set to 2500 Hz. Furthermore a PIV system is applied to measure the velocities of the droplets. PIV measurements were only conducted for water in the vicinity of the nozzle outlet, since for PVP – solutions the spray was too dense to determine reliable values.

As test fluids deionized water, PVP – solutions of varying PVP content, and suspensions of glass beads with different solid matter contents are used. The polymer is Luvitec® K30 with a molecular weight  $M_w \approx 50$  kDa. Applied concentrations in weight percent wt % are: 20 wt %, 30 wt % and 40 wt %. For the employed polymer concentrations the density  $\rho_f$  and surface tension  $\sigma_f$  of the fluid remains nearly constant. Hence, the influence of these material parameters on the generated spray can be neglected. The shear viscosity  $\eta_f$  of the fluid is a function of the PVP concentration. The maximum shear viscosity applied is 514 mPas, as can be seen in Table 1. In the same table, values for the viscosity at 80°C for 20 wt % and 40 wt % (maximum temperature possible for the viscosity measurement with the given measurement device) are shown. An enhancement of fluid temperature, even below 100°C, results in a quite remarkable reduction of the viscosity. In the case of a low polymer concentration (20 wt %) the viscosity at 80°C is 80 % lower than the value at 25°C. This behavior is more pronounced for a high PVP concentration (90 % reduction of shear viscosity value). In order to prevent thermal degradation, the upper temperature limit for experiments with PVP was set to 120°C.

**Table 1:** Viscosity of PVP solutions

	20 wt %	30 wt %	40 wt %
$\eta_{f,25^\circ\text{C}} / \text{mPas}$	25	103	514
$\eta_{f,80^\circ\text{C}} / \text{mPas}$	5		55

The employed suspensions consist of deionized water and glass beads. Solids concentrations of 5 wt%, 15 wt % and 25 wt % are used. The pH – value of the mixture rises slightly with bead content (5 wt % = 9.1, 15 wt % = 9.7, 25 wt % = 10). The primary particles have a Sauter mean diameter  $x_{32} = 3$   $\mu\text{m}$ .

## Results and Discussion

The morphologies of the generated sprays are depicted in Figure 3. In the case of subcooled (25°C) deionized water, a fluid jet exits the nozzle (Figure 3a)). Enhancing the temperature, above the boiling temperature, induces the generation of a disintegrated spray that is even more disintegrated for 120°C. For a higher temperature the growth of vapour bubbles in the nozzle capillary is intensified according to equation (1) (Rayleigh – Plesset – equation) [6]:

$$R\ddot{R} + \frac{2}{3}\dot{R} = \frac{1}{\rho_f} \left( (p_v - p_x) - 2\frac{\sigma_f}{R} - 4\frac{\eta_f}{R}\dot{R} \right) \quad (1)$$

The driving force for evaporation is the pressure difference  $p_v - p_x$  (vapor pressure minus the pressure at a certain location). Hence, the higher the vapour pressure (and accordingly fluid temperature), the higher is the ability of the fluid to evaporate. A higher evaporation rate results in higher vapour content. More bubbles yield a more dispersed spray. The same effect is true for the morphologies of the suspension spray depicted in Figure 3 b). In comparison to water no great differences of the spray morphology can be detected. A rise of particle concentration seems to hamper the breakup slightly. An addition of PVP greatly changes the spray morphology. For 25°C (subcooled) a smooth fluid jet exits the nozzle. For higher superheating of the media, an intensified breakup can be observed. The higher the concentration of the polymer in the solution, and hence the higher the viscosity of the fluid, the weaker breakup is observed. In the case of 40 wt % PVP (514 mPas) a superheating of 110°C is not sufficient to induce disintegration. This effect can be explained with equation (1). While a rising vapour pressure intensifies bubble growth, a rise of fluid viscosity  $\eta_f$  lowers it. Accordingly, a lower vapour content is to be expected, which results in a less distinct breakup. In addition, the fluid breakup itself is hampered by rising viscosity.

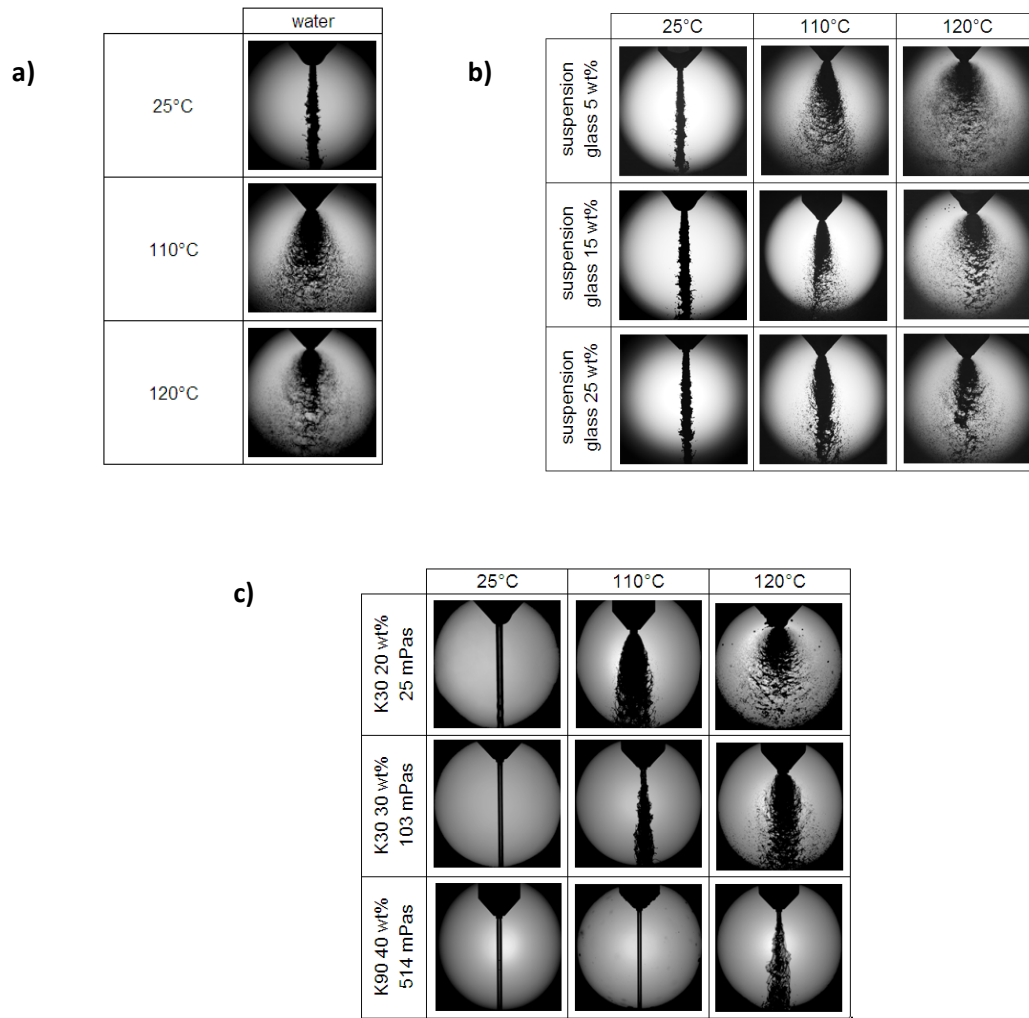


**Figure 3:** Spray morphology ( $p_0 = 5$  bar)

a) Deionized water b) Glass bead suspension c) PVP - solution

The results for the conducted mass flux measurements are depicted in Figure 4. The mass flux for deionized water is shown in Figure 4 a). One can see that the mass flux is lowered for higher superheat. This can be explained by an increase of evaporation inside the nozzle capillary. The biphasic mixture passing the nozzle has a reduced density in comparison to a fluid. This induces a lower mass flux. As was explained before, a higher temperature means an intensified driving force for evaporation, according to equation (1). The same behavior is measured for the glass bead suspensions. The mass flux is lowered with rising superheating. The higher the glass bead content, the lower is the achievable mass flux. The friction of the glass beads with the nozzle capillary, or with each other, may reduce the maximum possible mass flux. The most pronounced difference in regard to deionized water is achieved for the polymer solutions. Applying superheating first yields an enhancement of the measured mass flux. By heating the fluid, the viscosity of the media is greatly lowered, as has been shown before (Table 1). A decrease of viscosity lowers the inner friction, and hence the resistance to the flow of the fluid. This leads to an enhancement of the mass flux with a temperature rise. This enhancement is higher, the higher the basic viscosity at 25°C, since the temperature dependent lowering of shear viscosity is more pronounced. For higher fluid temperature, a lowering of mass flux can be observed for some of the curves. For higher temperatures evaporation phenomena are intensified, which in turn reduces the mass flux. This behavior exceeds the influence of viscosity in the case of a decreasing mass flux.



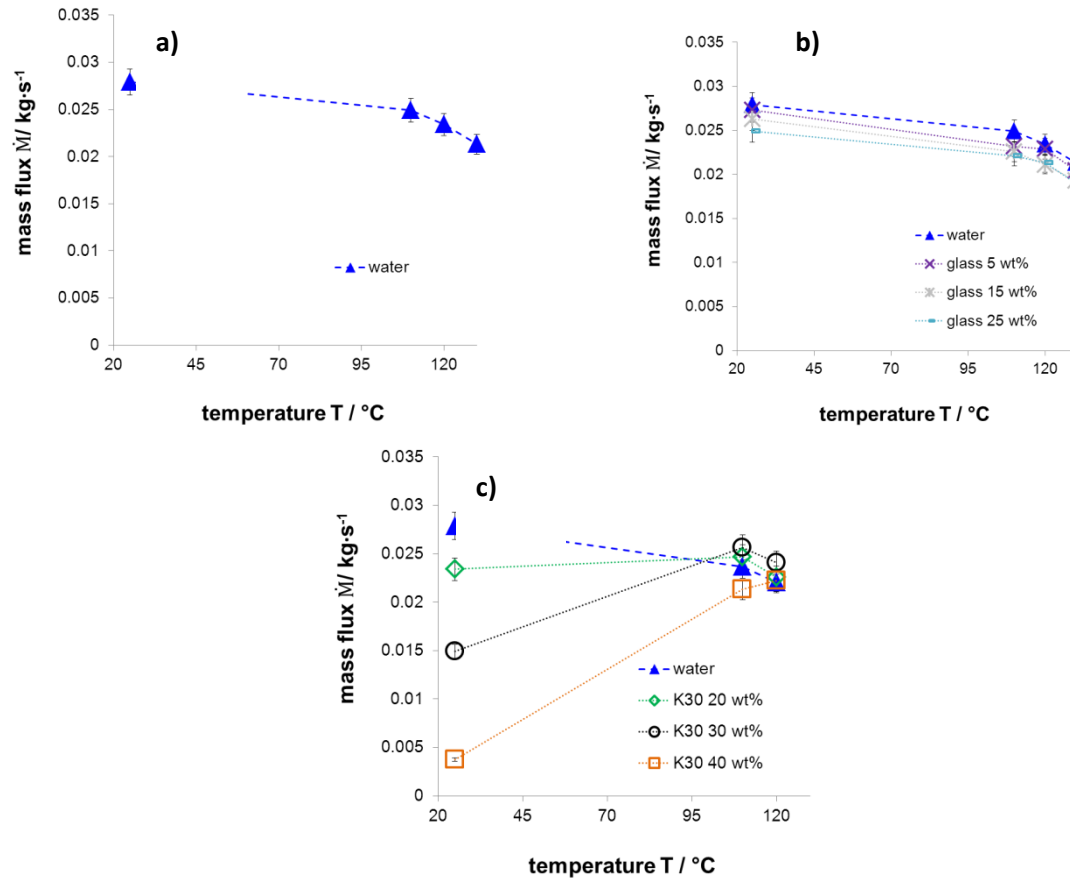


**Figure 4:** Mass flux ( $p_0 = 5$  bar)  
 a) Deionized water    b) Glass bead suspension    c) PVP - solution

The results for laser diffraction measurements are depicted in Figure 5. The results for water are shown in Figure 5 a). For rising superheating a decrease of the Sauer mean diameter is observed. This can again be attributed to the fact that an enhanced evaporation is triggered by rising vapour pressure. The bubbles dispersing the spray in addition offer a higher inner pressure. This leads to a comparably higher energy for disintegration. The Sauter mean diameter decreases for all applied glass bead concentrations. The same explanation as before is of importance. Regarding the trend for glass bead concentrations one can see that bigger droplets are generated for higher concentrations up to 15 wt %. Bigger droplets can occur if the primary particles form agglomerates. The change in behaviour for 25 wt % ( $\approx 45$  vol. %), can be forwarded to the fact that the suspension was not stabilized for the experiments. In the case of 25 wt % a separation of fluid and solid phase in a comparably short time was observed. This could lead to a non-homogeneity of particle concentration that disturbs the results. Measurements for PVP solutions were only conducted at 120°C, since for lower temperatures the spray was not dispersed for all polymer concentrations. In Figure 5 c) one can see that the droplet size rises for 20 wt % to 30 wt % as was expected. Higher viscosities accordingly reduce the spray breakup. On the other hand a lowering of the droplet size is observed for 40 wt %. This behaviour can be explained taking into account the images shown in the same figure. For 30 wt % a fine dispersed spray is achieved in a distance of 15 cm to the nozzle outlet. In the case of 40 wt %, the breakup is still incomplete with a majority of coarse droplets in the centre of the spray. The major part of these particles does not offer a spherical morphology. Those droplets and droplets bigger than 200  $\mu\text{m}$  are not measured. Accordingly only satellite droplets are considered and not the whole particle size range.

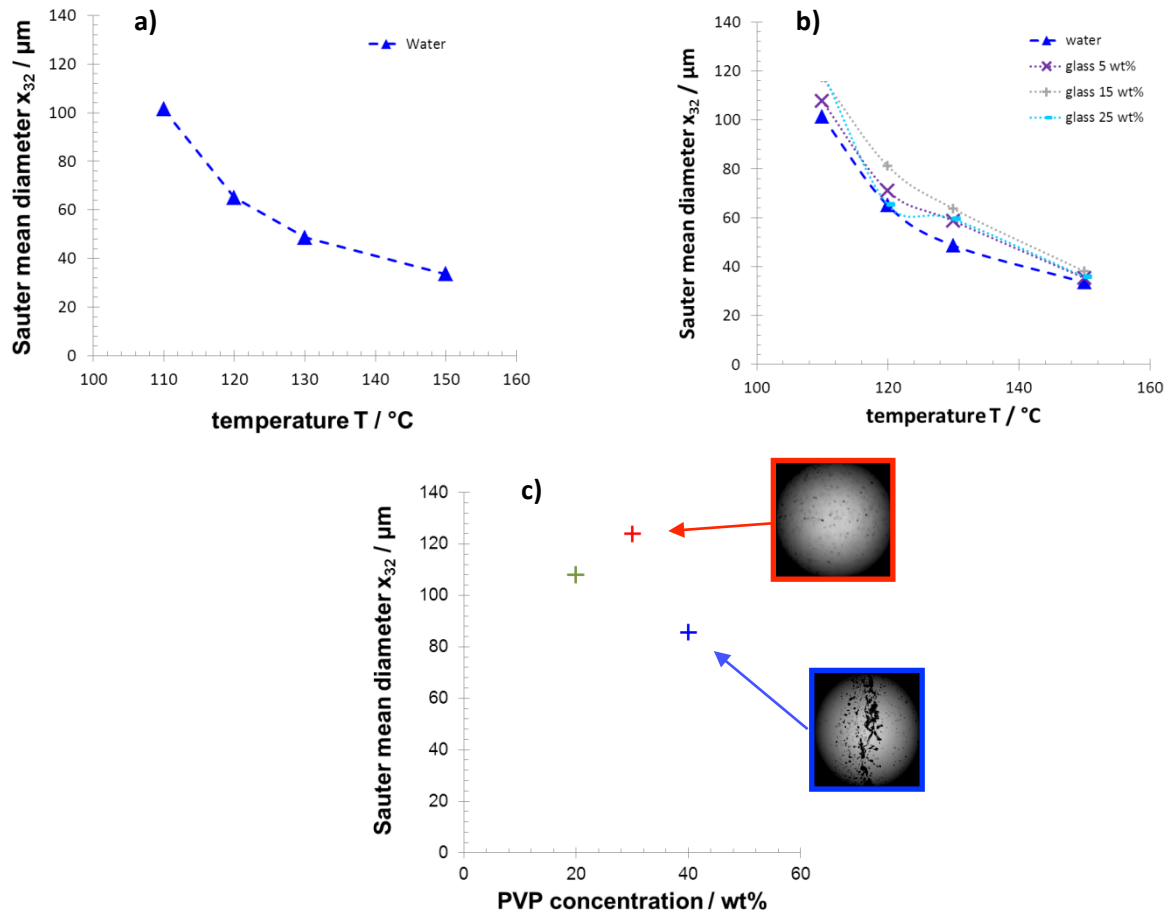


**Figure 5:** Droplet Sauter mean diameter ( $p_0 = 5$  bar)  
a) Deionized water    b) Glass bead suspension    c) PVP – solution

The velocity for water droplets is measured in a distance of 1 cm to the nozzle outlet for a pressure  $p_0 = 5$  bar at a temperature of 120°C. The measurements yielded a medium velocity of 30 ms<sup>-1</sup>. It can be assumed that the values for the suspension droplets are in the same range. Since the droplet velocities for PVP solutions were not accessible by PIV measurements, a simple calculation ( $v = \dot{M} \cdot A^{-1} \cdot \rho_f^{-1}$ ) yielded velocities between 3 ms<sup>-1</sup> (40 wt %) and 18 ms<sup>-1</sup> (20 wt %). Comparing the resulting velocities, one can deduce that in addition to a lowered breakup (decrease evaporation), a hampered disintegration results based upon smaller aerodynamic interactions between fluid and gas phase.

## Conclusions

It has been shown that the disintegration of fluids with high viscosities up to 514 mPas is possible with flash atomization. The breakup is less intense for lower temperatures and higher shear viscosities (polymer concentration). The mass flux can be enhanced for higher fluid temperatures because of a shear viscosity lowering with temperature. With the applied simple cylindrical nozzle a complete breakup was not achieved for the highest PVP concentration. More complex nozzle geometries like hollow cone nozzles will be applied in further measurements, in order to generate a finely dispersed spray. With respect to the spraying of the glass bead suspension, it has been shown that the observed behaviour does not differ greatly from the behaviour of deionised water. Further measurements will be conducted in order to analyse the amount of water that can be evaporated from within. This could lead to reduced energy consumption for particle drying.

## Acknowledgements

The authors would like to thank the Deutschen Forschungsgesellschaft (DFG) for the financial support of the research project within the priority program 1423 “Process sprays”.

## Nomenclature

### *Roman symbols*

A	Nozzle capillary cross section area
CCD	charge coupled device
D	nozzle diameter / mm
L	length / mm
L/D – ratio	length – to – diameter – ratio / -
LED	light emitting diode
$\dot{M}$	mass flux / $\text{kg s}^{-1}$
p	pressure / bar
PIV	particle image Velocimetry
R	vapor bubble diameter / $\mu\text{m}$
$x_{32}$	Sauter mean diameter / $\mu\text{m}$
T	temperature / $^{\circ}\text{C}$

### *Greek symbols*

$\rho$	density / $\text{kg m}^{-3}$
$\sigma$	surface tension / $\text{Nm}^{-1}$
$\eta$	shear viscosity / Pas

### *Subscripts*

<i>f</i>	<i>fluid</i>
<i>v</i>	<i>vapor</i>
<i>x</i>	<i>at at certain location</i>

## References

- [1] A. Günther, M. Rossmeissl, K. - E. Wirth, Atomization of superheated liquids – Discharge characteristics , ILASS – Europe 23rd Annual Conference on Liquid Atomization and Spray Systems, Brno, Czech Republic, September 2010.
- [2] M. Razzaghi, Droplet size estimation of two – phase flashing jets, Nuclear Engineering and Design 114 (1989) 115 - 124.
- [3] A. Günther, K. –E. Wirth, Einfluss der Düsengeometrie auf Massenstrom und Spraycharakteristik bei überhitzter Zerstäubung, Chemie Ingenieur Technik 1-2 (2012) 149 - 153.
- [4] A. Günther, K. - E. Wirth, Influence of the geometry of cylindrical nozzles on superheated atomization , ILASS – Europe 24rd Annual Conference on Liquid Atomization and Spray Systems, Estoril, Portugal, September 2011.
- [5] B. S. Park, S. Y. Lee, An experimental investigation of the flash atomization mechanism, Atomization and Sprays 4 (1994) 159 - 179.
- [6] E. Sher, T. Bar-Kohany, A. Rashkovan, Flash-boiling atomization, Progress in Energy and Combustion Science 34 (2008) 417-439.
- [7] Lefebvre A. H.; Atomization and Sprays; Hemisphere Publishing Corporation; New York 1989.

## Phase Doppler characterization of burning sprays from an auxiliary emission control fuel nozzle of a lean two-stage low-NO<sub>x</sub> combustor for an aero-engine at a simulated aircraft approach condition

Kazuaki Matsuura<sup>1</sup>, Kousei Ide<sup>2</sup>, Yasutaro Yoshiura<sup>3</sup>, Sunao Ohori<sup>3</sup>, Yoji Kurosawa<sup>1</sup>, Hideshi Yamada<sup>1</sup>, Kazuo Shimodaira<sup>1</sup>, Takeshi Yamamoto<sup>1</sup>, Yutaka Ohta<sup>2</sup> and Shigeru Hayashi<sup>3</sup>

1: Aviation Program Group, Japan Aerospace Exploration Agency, Japan

2: Department of Mechanical Engineering, Waseda University, Japan

3: Department of Mechanical Engineering, Hosei University, Japan

### Abstract

Phase Doppler measurements were performed to understand the spray combustion field in a lean two-stage low-NO<sub>x</sub> combustor for an aero-engine, at a condition simulating a flight phase of approach to airport for landing. The combustor was equipped with a coaxial staging fuel nozzle (pilot and main) on the combustor dome and an auxiliary emission control fuel nozzle (ECF) on its liner wall. At the approach condition, the pilot and ECF are to be in operation without the main. The purpose of this study is to understand the burning spray characteristics from the ECF and to obtain a clue for improvement of combustion efficiency. Two operating conditions in terms of fuel split ( $S_E = 36$  and  $64\%$ ) were studied, where  $S_E$  is defined by the ratio of the fuel flow rate of the ECF to that in total. At a location around 65mm downstream from the ECF exit (along the ECF jet) after which the heat support from the pilot is no longer expected, a fast evaporation rate was still observed for  $S_E = 64\%$ , whereas the evaporation rate got slower than upstream for  $S_E = 36\%$ . The result was consistent with the higher combustion efficiency for  $S_E = 64\%$ , suggesting that the self-heat release of the ECF flame has more positive impact as a heat source on combustion efficiency, than the heat support of the hot gas from the pilot, for the conditions tested.

### Introduction

A low-NO<sub>x</sub> character of aero-engine combustors is essential for modern and future civil aircrafts, as the regulations of aircraft emissions, especially those for NO<sub>x</sub>, are getting stringent. A lean-burn technology is a promising candidate for this purpose. However, it must be accompanied by fuel staging technology to obtain full combustor operability, covering wide turn-down ratios from low power to high power [1]. Yamamoto et al. [2] have recently developed a research combustor equipped with a high-performance coaxial staging lean burn fuel nozzle, with its pilot nozzle at the centre and its main nozzle surrounding the pilot, and achieved drastic NO<sub>x</sub> reductions. They have further improved its low-NO<sub>x</sub> performance by employing an auxiliary emission control fuel nozzle (ECF) mounted on the liner wall of the combustor to achieve lean two-stage combustion at high power [3]. However, at a condition corresponding to aircraft approach to airport for landing (relatively low power rating), the obtained combustion efficiency is not satisfactory because of the incomplete combustion of fuel from the ECF. Thus, there is a need to characterize the combustion field at the simulated approach condition to find a way to improve the combustion efficiency. For this purpose, preliminary flame visualization and PIV measurements have been performed so far, whose results were partially reported by Yoshiura et al. [4]. The target of the present study is, as a second step, to characterize the burning ECF sprays for further understanding of the combustion field. In this paper, our discussions mainly focus on the results of the phase Doppler measurements. It should be noted that the ECF was found to be operating in a spray combustion mode at the approach condition, though at high power it is designed and supposed to operate at a partially, but reasonably premixed and pre-vaporized mode. The evaporation characteristic of the spray is of our interest as it is expected to have influence on the resulting combustion efficiency. The results of the two different fuel split cases,  $S_E = 36$  and  $64\%$ , at a fixed overall air-to-fuel mass flow rate ratio ( $AFR = 68$ ) are discussed, where  $S_E$  is defined by the ratio of the fuel flow rate of the ECF to that in total (pilot + ECF). Within the range of  $S_E$  tested in our previous exhaust gas analysis experiments (from 36 to 75%), the combustion efficiency is minimum for  $S_E = 36\%$ , whereas it is close to its maximum value at  $S_E = 64\%$ . Therefore, understanding the cause of different combustion efficiency between the two cases could be a good clue for its improvement. As expected, the difference of the evaporation characteristics of the two cases obtained by the experiments turns out to be consistent with the difference of their combustion efficiency. The results support the interpretation that, at the present experimental conditions, the self-heat release of the ECF flame has more positive impact as a heat source on combustion efficiency than the heat support of the hot gas from the upstream pilot.

### Experimental setup and test conditions

The lean two-stage combustor used in our experiments is shown in Fig.1, together with the definition of the coordinate system. It was equipped with the coaxial staging fuel nozzle on the combustor dome and the

auxiliary emission control fuel nozzle (ECF) on the combustor liner wall. At high power, the burnt gas from the staging burner, with both the pilot and main nozzles operating, provides heat to the lean premixed ECF flame to achieve complete combustion. On the other hand, at the approach condition, only the pilot flame is responsible to sustain the ECF flame, as no fuel is supplied to the main nozzle. Further details on the combustor design and emission characteristics are found in Ref.[3].

For optical measurements, three optical accesses from top and sides were provided through quartz windows installed on the walls of the combustor liner and outer casing. The laser ignition was employed, which realized better optical access as it saved the space for a spark ignitor. A 35mm spacer was inserted for the phase Doppler measurements as in Fig.1, to shift the relative positions between the combustor liner and the outer casing to let the PDA optics access the ECF spray, which was not used in our previous experiments with other techniques such as visualization and planar measurements with laser sheets. The system of the phase Doppler anemometry (PDA) in the present study is mostly described in Ref. [5], but the employed laser power (about 60mW for the green beams at the probe volume) and the scattering angle (30 degrees) were different from the reference. The PDA optics was set up so that the scattering plane was normal to the  $y$ -axis. The PDA measurements were performed on the cross-sectional planes of  $y=-15.5$ ,  $-5.5$ ,  $4.5$ ,  $14.5$  and  $24.5$ mm. The spacing between adjacent measurement locations (traverse points) in  $z$  and  $x$  directions is 2mm for  $y=-15.5$ mm and 4mm for the other four planes.

The experiments were conducted at the high temperature and high pressure combustion test facility at Japan Aerospace Exploration Agency. The combustor inlet pressure and temperature were 0.8MPa and 609K, respectively. The combustor pressure loss was 4%, in which condition the air flow rate was around 527g/s (typically  $\pm 8$ g/s). Kerosene was used as the liquid fuel. The overall air-to-fuel mass flow rate ratio ( $AFR$ ) was fixed at  $68 (\pm 1)$ . The fuel split, in terms of  $S_E$  defined by the ratio of the fuel flow rate of the ECF to that in total (pilot + ECF), was varied between 36% and 75% for the exhaust gas analysis and between 36% to 64% for optical measurements[4] in our previous study. In the present PDA measurements, we focused on two cases corresponding to the ends of the latter range,  $S_E = 36\%$  and  $64\%$ .

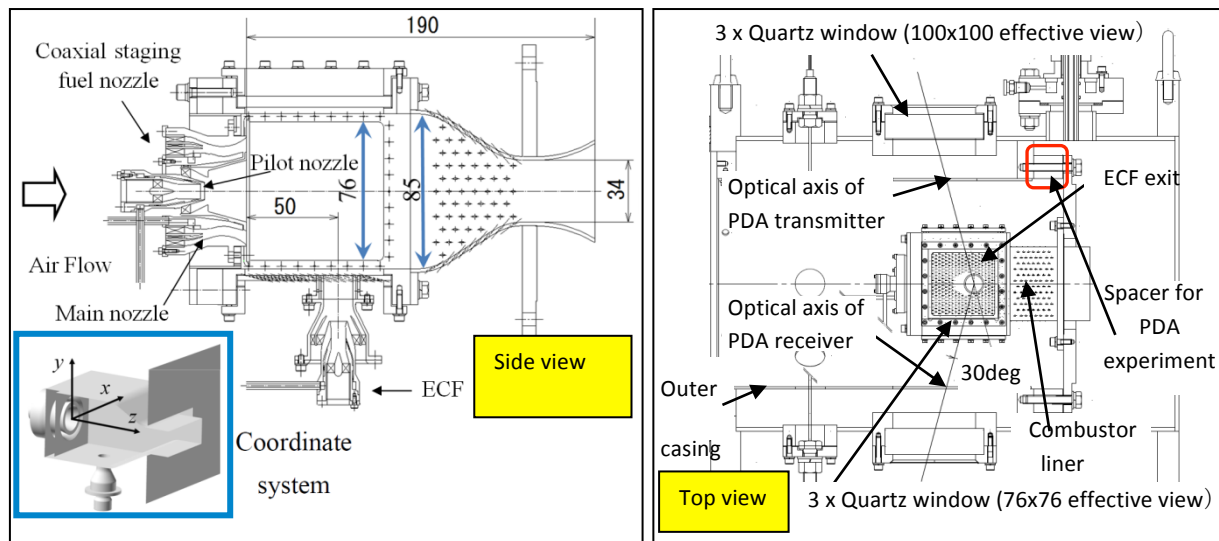


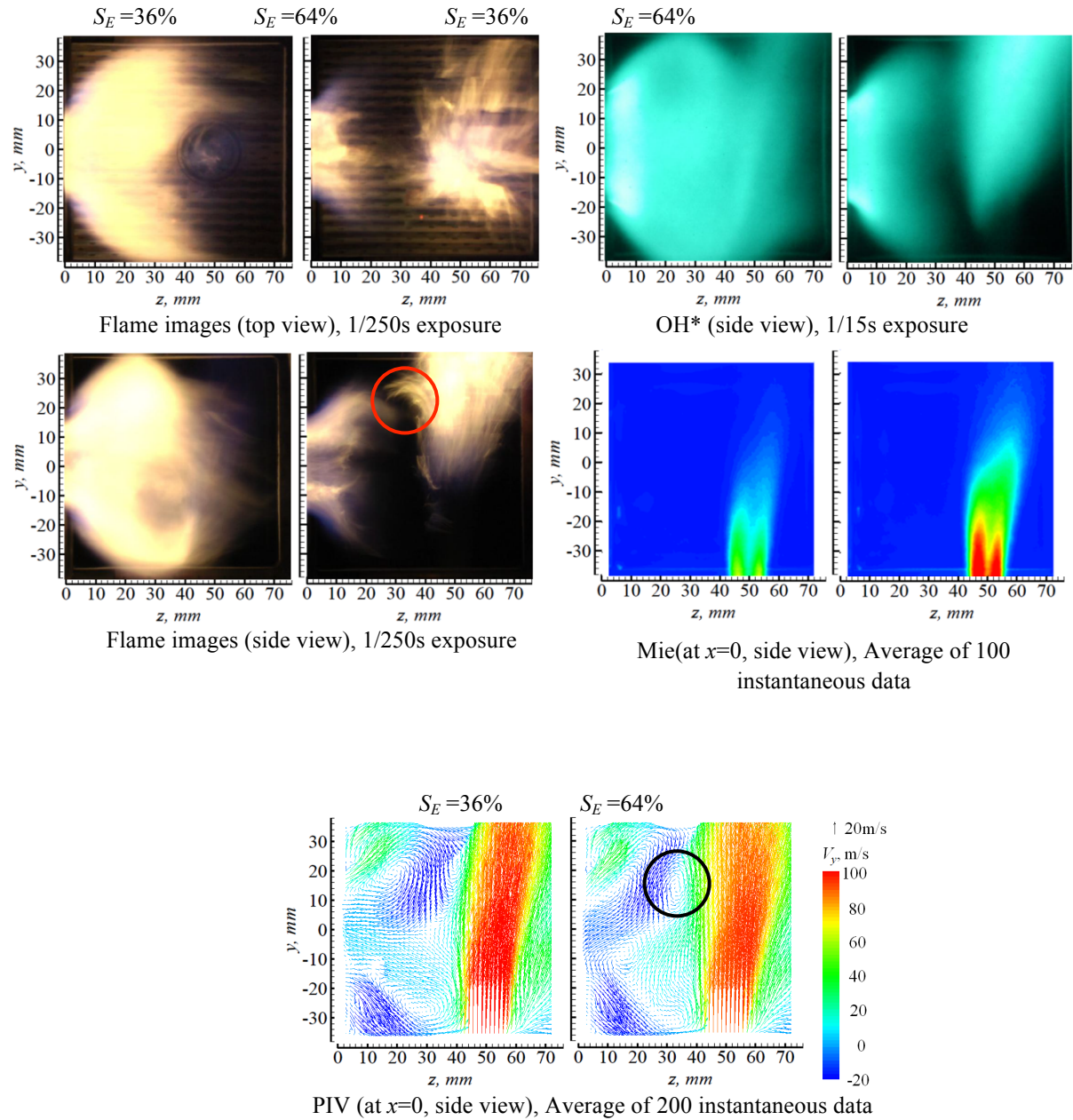
**Figure 1.** Schematic drawing of lean two-stage combustor and experimental setup.

## Results and Discussion

Before the discussions on the PDA results, our previous study is briefly summarized, which is partially published in Ref. [4]. Flame images, OH\* chemiluminescence, laser sheet Mie scattering and PIV results for  $S_E = 36\%$  and  $64\%$  are presented in Fig.2. For  $S_E = 36\%$ , the pilot flame is characterized by its strong luminosity, and its OH\* chemiluminescence extends to the downstream side of the window edge. The ECF flame is not clearly observed in the simple flame image, but its weak OH\* emissions are detected. On the other hand, for  $S_E = 64\%$ , visible light emissions as well as those of OH\* from the ECF flame are enhanced. The PIV results show how the fuel split modifies the flow field structure. For  $S_E = 64\%$ , the region where the flow field characteristics are governed by the ECF jet is wider and that governed by the staging nozzle is more shrunk due to the enhanced reactions of the ECF flame than for  $S_E = 36\%$ .

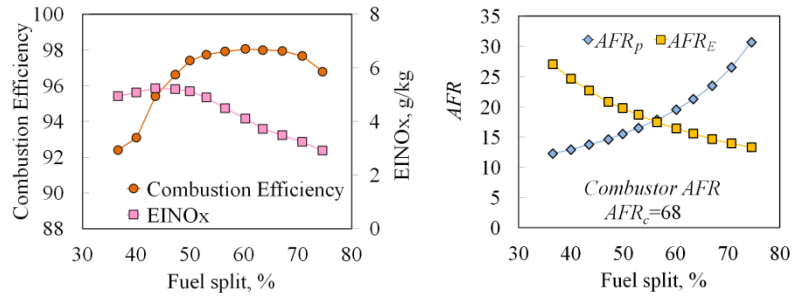
The results of exhaust gas analysis in terms of combustion efficiency and NO<sub>x</sub> emission index (EINO<sub>x</sub>) are presented in Fig.3. The estimated local  $AFR$ s for the pilot ( $AFR_p$ ) and ECF ( $AFR_E$ ) are also shown. It should be noted that the emission performance of the present optical combustor is not identical to the combustor used for emission evaluation tests [3] because of the existence of the optical windows for example. However, the

tendency of its dependence on  $S_E$  was similar between the combustors. The combustion efficiency increases monotonically as  $S_E$  increases from 36% to around 60% and stays close to its maximum value up to 70%. Considering the trade-off among emissions, stability of the ECF flame (also see discussion below) and liner wall temperature, the best fuel split at the approach condition for the current combustor is around 65% and the emission values at this condition were referred to when evaluating overall LTO (Landing and Take-off cycle) emissions for ICAO (International Civil Aviation Organization) regulations [3].



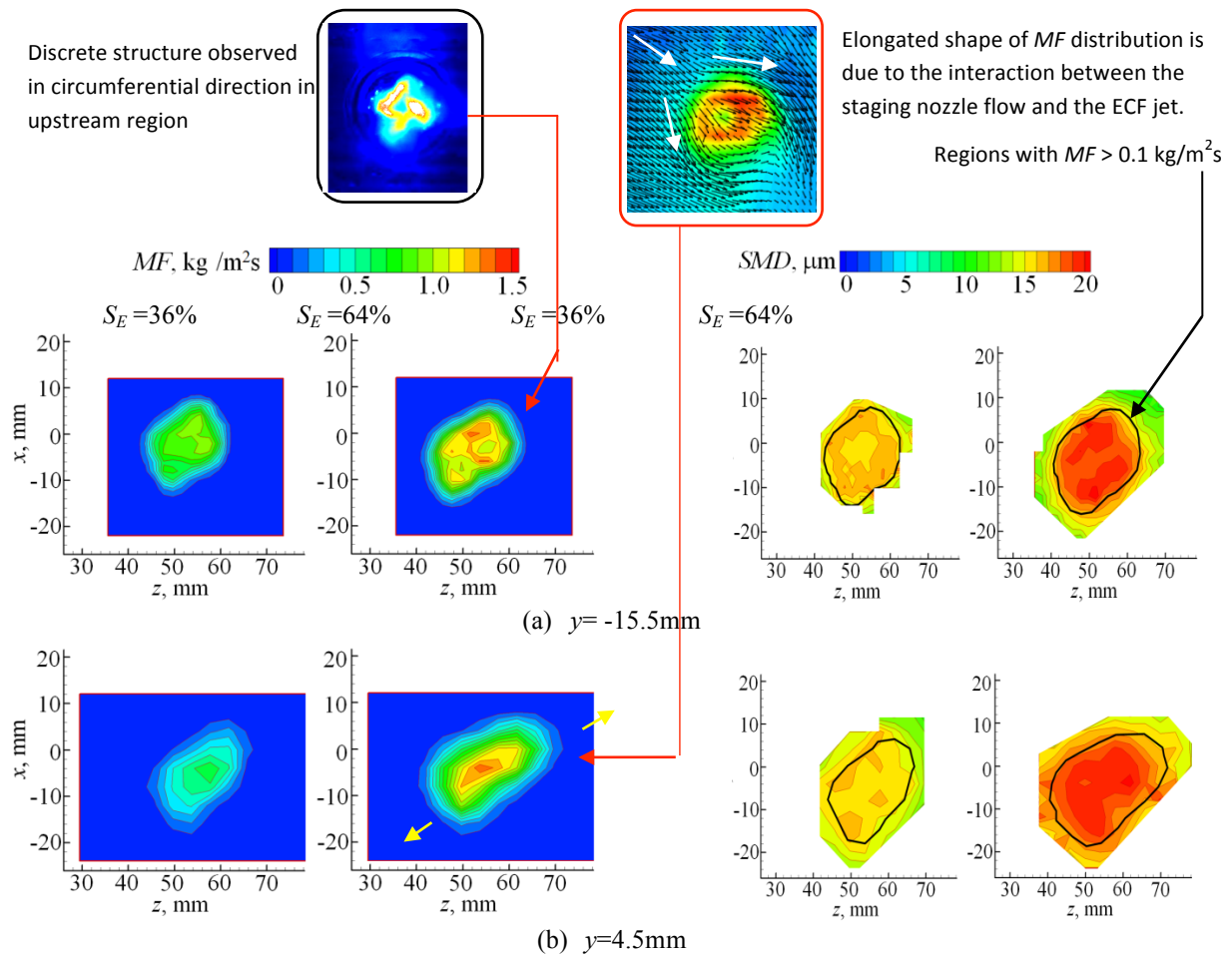
**Figure 2.** Flame images, OH\* chemiluminescence, Laser sheet Mie scattering and PIV results for  $S_E = 36$  and 64%.





**Figure 3.** Dependence of combustion efficiency and NOx emission index on the fuel split. (Corresponding Local  $AFR$  for the pilot and ECF are also shown on the right.)

The results of the phase Doppler measurements are discussed in the following. The spatial distributions of the mass flux density ( $MF$ ) and Sauter mean diameter ( $SMD$ ) at three cross sections,  $y=-15.5$ ,  $4.5$ , and  $24.5$ mm, are presented in Fig.4. The central axis of the ECF corresponds to  $(z,x)=(50,0)$ . In the results of  $SMD$ , the regions with  $MF > 0.1$  kg/m<sup>2</sup>s are enclosed by the black lines, for easier comparison of the both spatial distributions. The  $MF$  distributions give a qualitative idea on where the liquid phase fuel exists. However, a care is needed for quantitative interpretation due to relatively poor reliability of the PDA data close to the ECF exit as the sprays are dense in such regions. The  $MF$  distributions are elongated in the direction of the yellow allows shown in the figure as the spray develops along the ECF jet. This is because of the interaction of the flow from the staging fuel nozzle with the ECF jet. The PIV result inserted in Fig 4 highlighted in the red box shows the flow of the same combustor at  $y=-32$ mm. It is for iso-thermal flow, but still helps understand its qualitative flow structure. The airflow from the staging fuel nozzle, with its overall swirl finally dominated by the outermost swirl of the main nozzle (clockwise when viewed from downstream), approaches from top left of the figure and is split into two streams. The two streams stretch the ECF jet towards each flow direction and eventually elongate the cross-sectional shape of the jet and the spray. Because of the nature of the ECF design, a discrete structure of the spray in the circumferential direction is observed in both results ( $MF$  and  $SMD$ ) and in the laser-sheet Mie scattering





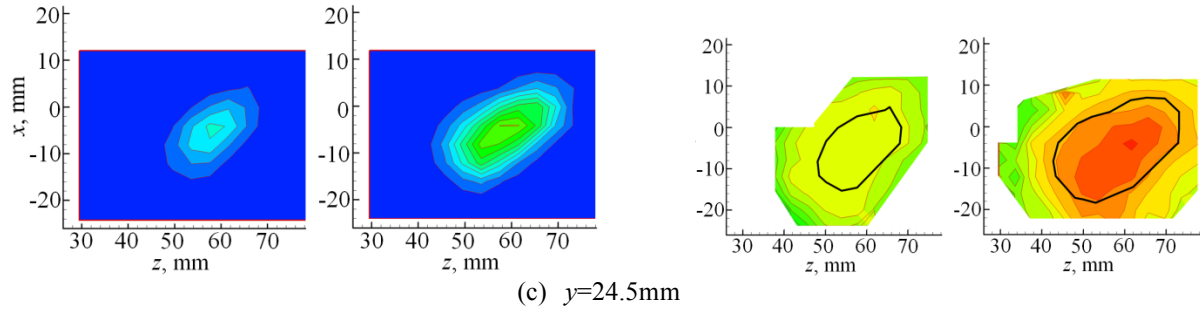


**Figure 4.** Spatial distributions of mass flux density ( $MF$ ) and Sauter mean diameter ( $SMD$ ) at three different horizontal cross sections ( $y = -15.5, 4.5$  and  $24.5$ mm).

image also presented in Fig.4 (highlighted in the black box). This structure disappears as it goes far from the ECF exit. In general, the  $SMD$  is larger in denser regions because of the high mass loading. Similarly, the  $SMD$  is larger for  $S_E = 64\%$  as its spray is denser than for  $S_E = 36\%$ . The  $SMD$  at  $y = 24.5$ mm seems smaller than the other two upstream locations, which will be discussed later with the results of other representative diameters.

Spatial distributions of the mean vertical droplet velocity  $v_y$  for two different size classes ( $0-5\mu\text{m}$  and  $15-25\mu\text{m}$ ) are presented in Fig. 5 at two horizontal cross sections,  $y = -15.5$  and  $24.5$ mm. The regions with  $MF > 0.1\text{ kg/m}^2\text{s}$  are again enclosed by the black lines similar to Fig. 4. The results show that  $v_y$  is higher for the droplets in the larger size class. This is because the ECF jet is decelerating towards its downstream. Therefore, the larger droplets with longer relaxation time against the decelerating carrier phase flow show higher  $v_y$ . On the other hand, for the same size classes,  $v_y$  is lower for  $S_E = 64\%$  than for  $S_E = 36\%$ . This is because of the higher mass loading. More kinetic energy of the carrier phase is converted to the kinetic energy of the dispersed phase for the higher mass loading case, which causes the deceleration of the carrier phase flow and then eventually slower droplet velocity. This also reduces the amount of energy which can be used for the production of the liquid surface area, causing the poorer atomization performance as discussed above for  $SMD$ .

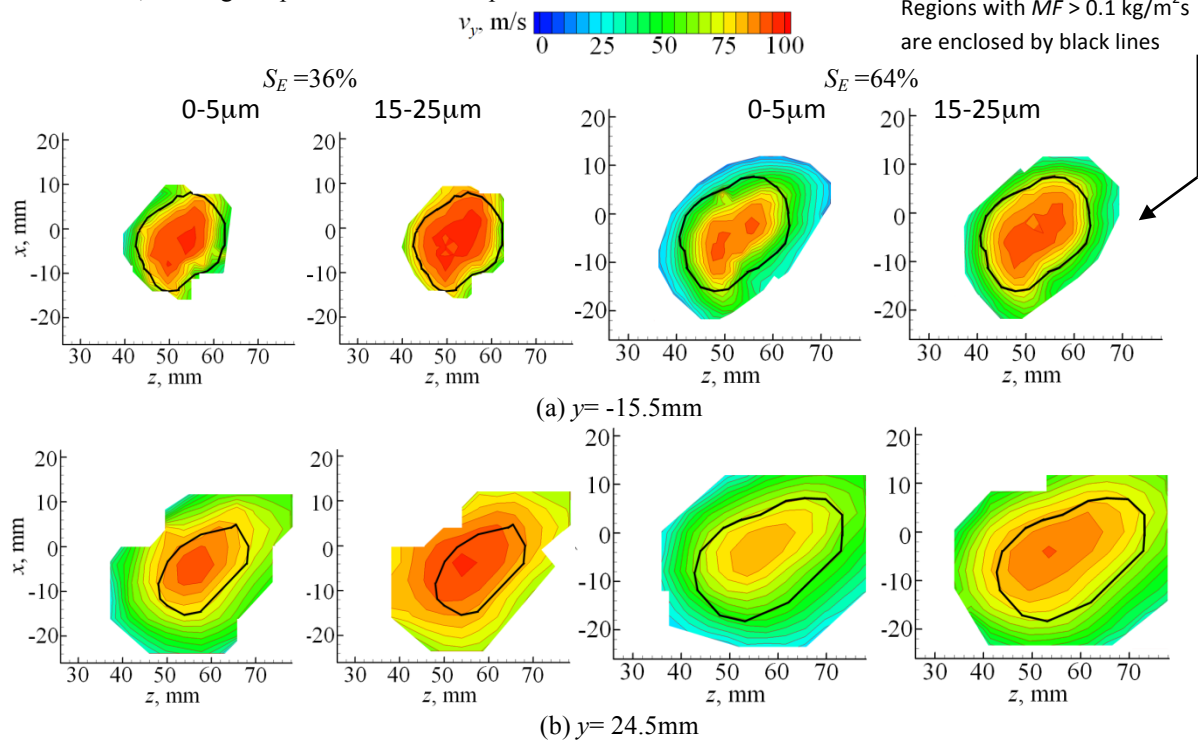


**Figure 5.** Spatial distributions of mean vertical droplet velocity ( $v_y$ ) for two different size classes ( $0-5\mu\text{m}$  and  $15-25\mu\text{m}$ ) at horizontal cross sections  $y = -15.5$  and  $24.5$ mm.

The mass flow rates of the liquid phase fuel passing through five different horizontal ( $y = \text{const.}$ ) cross-sectional planes captured by the PDA are presented in Fig. 6. These values are normalized by the mass flow rates of the ECF measured by a liquid flow meter. Again, careful interpretation is required for the measured data as the sprays are dense near the ECF exit. In the present experiments, the maximum data rate obtained by the PDA system was 65kHz and further dense spray resulted in its artificial decrease. Thus, the data enclosed in either blue or red ellipse, which include measurement locations with the data rate close to 65kHz (for example more

than 60kHz) and/or exhibit a higher mass flow rate than the adjacent upstream location, meaning negative evaporation rate (thus unrealistic), should be excluded from even qualitative or semi-quantitative interpretation because of the possibility of excessive number flux. Nevertheless, an interesting feature is captured from the rest of the data, that is, the amount of loss of liquid phase due to evaporation between  $y=14.5$  and  $24.5$ mm, in terms of both normalized (in Fig.6) and absolute values, is much smaller for  $S_E=36\%$  than for  $S_E=64\%$ . This is probably explained by the heat source for evaporation. For  $S_E=36\%$ , the richer pilot flame is the main heat provider, and the interaction of the ECF jet flow with the hot gas from the pilot flame occurs mainly in front of the ECF jet region (around  $z=40\sim 50$ mm). The effective heat exchange between the two probably ceases at a location around  $65$ mm downstream from the ECF exit (along the ECF jet), or in other words, around  $y=20\sim 25$ mm, because after that, the jet starts to interact with the relatively cool flow of the main nozzle (Note that no main fuel is provided.). On the other hand, for  $S_E=64\%$ , the main heat provider is the ECF flame itself, and the contribution of the pilot flame is relatively small though its contribution to the initiation of the ECF flame is still important. As expected by the luminous flame in Fig.2, even at high horizontal location ( $y=24.5$ mm) where the ECF jet is about to facing the cool flow from the main nozzle, the temperature is kept relatively high compared with  $S_E=36\%$  and thus the high evaporation rate is observed in Fig.6. Though the downstream phenomena have not been investigated, no further significant source to re-enhance the evaporation and chemical reaction for  $S_E=36\%$  is expected, whereas the self-heat release of the ECF would support further evaporation and reaction for  $S_E=64\%$ . This is probably the reason of the higher combustion efficiency for  $S_E=64\%$ . It should be noted that too high  $S_E$ , meaning far leaner pilot operation, is not preferable as it causes the lift-off and unstable behaviour of the ECF flame due to the less contribution of the pilot flame.

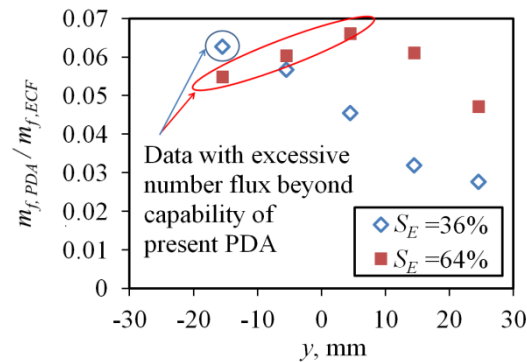


**Figure 6.** Mass flow rates of the liquid phase captured by PDA at different horizontal cross-sectional planes, normalized by those of the ECF measured by the liquid flow meter.

The global representative diameters,  $SMD$ ,  $D10$ ,  $D50$  and  $D90$  ( $Dx$  means  $x\%$  volume undersize diameter), and the global number-based size PDFs normalized at their peak values are shown in Fig.7 for five different horizontal ( $y=\text{const.}$ ) cross-sectional planes. For  $S_E=36\%$ , the representative diameters decrease as the spray develops towards downstream along the ECF jet. More than 8% decrease of them is observed between  $y=-14.5$  and  $24.5$ mm. On the other hand, for  $S_E=64\%$ , the similar tendency for  $y>4.5$ mm is observed but it is not as clear as for  $S_E=36\%$ . Especially,  $D90$  shows only modest decrease compared to  $S_E=36\%$ . The size PDF for  $S_E=36\%$  shifts to the left (towards smaller diameters) as the spray develops towards downstream, whereas the shapes of the size PDFs for  $S_E=64\%$  hardly change (or change slightly but not in a consistent manner) except for  $y=24.5$ mm, where the relative population of the larger droplets decrease compared to the other four PDFs.

The decrease of representative diameters towards downstream is not easy to interpret. This may be attributed to evaporation and/or combustion of droplets. The decrease of them due to evaporation might be seen at its early

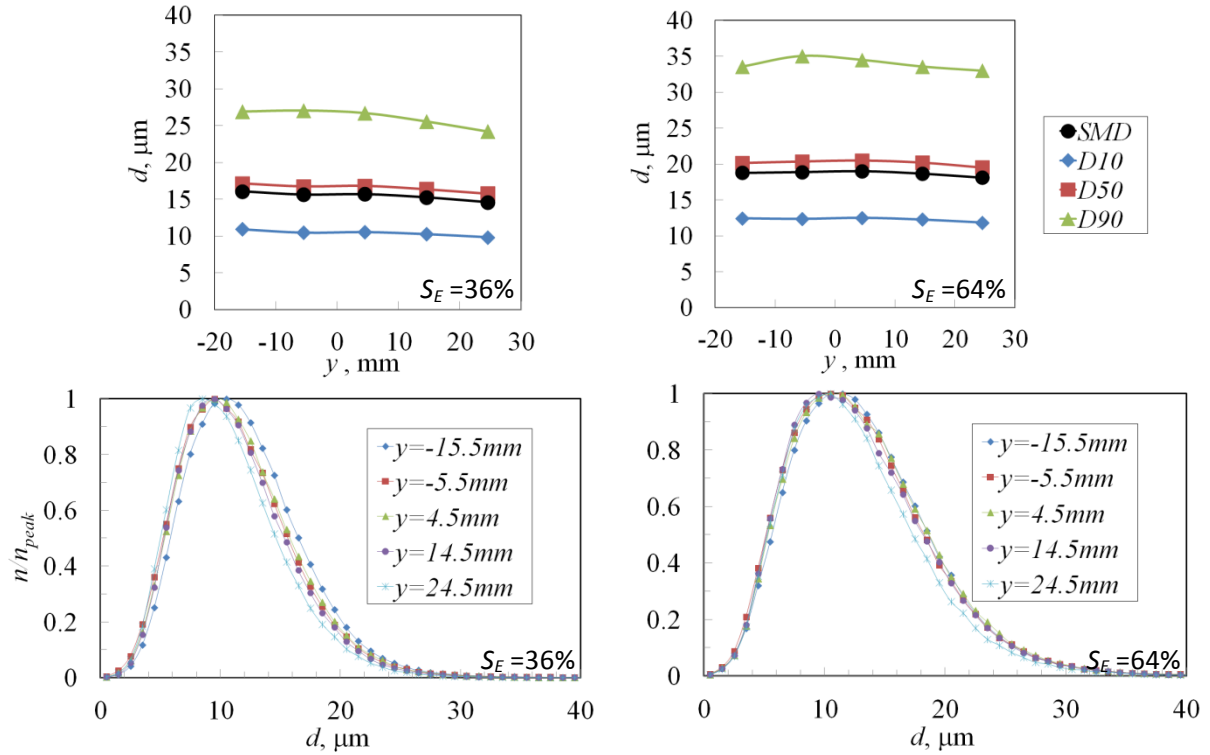


**Figure 7.** Global representative diameters ( $SMD$ ,  $D10$ ,  $D50$  and  $D90$ ) and global number-based size PDFs at five different horizontal ( $y=\text{const.}$ ) cross-sectional planes.

stage, as found in the example of Chin et al. [6] for Rosin-Rammler distributions with their large “distribution parameters” (narrow size distributions). Another possible explanation would be the progress of atomization process such as the secondary atomization.

Finally, it is interesting to investigate the intermediate zone between two regions, one mainly occupied by the flow from the staging fuel nozzle and the other dominated by the ECF jet. In Fig. 2, the trace of the luminous flame highlighted by the red circle shows interaction of the two regions via the vortex, as seen in the PIV result at  $x=0\text{mm}$  plane highlighted by the black circle. In order to investigate the role of the vortex on the interaction, the size/velocity correlation of the droplets at the position P ( $x,y,z$ )= $(-6, 14.5, 31.6)$  for  $S_E=64\%$  is presented in Fig.8. The PIV result for  $x=-6\text{mm}$  plane which includes the position P is also shown, where the lower part of the vortical structure is no longer clear but the upper part still remains. The correlation plot shows the existence of the small droplets with negative vertical velocity ( $v_y < 0$ ), reflecting the direction of the mean flow of the vortical structure at the position P. For  $S_E=64\%$ , it is unlikely that the droplets from the pilot nozzle can survive up to this region through the hot environment. Therefore, there is a possibility that unburned fuel from the ECF can either penetrate in a ballistic manner ( $v_y > 0$ ) or enter by following the vortical fluid motion ( $v_y < 0$ ), into the region of the staging lean burn nozzle flow through this intermediate zone, and that such fuel could affect its combustion performance if its amount is not negligible.

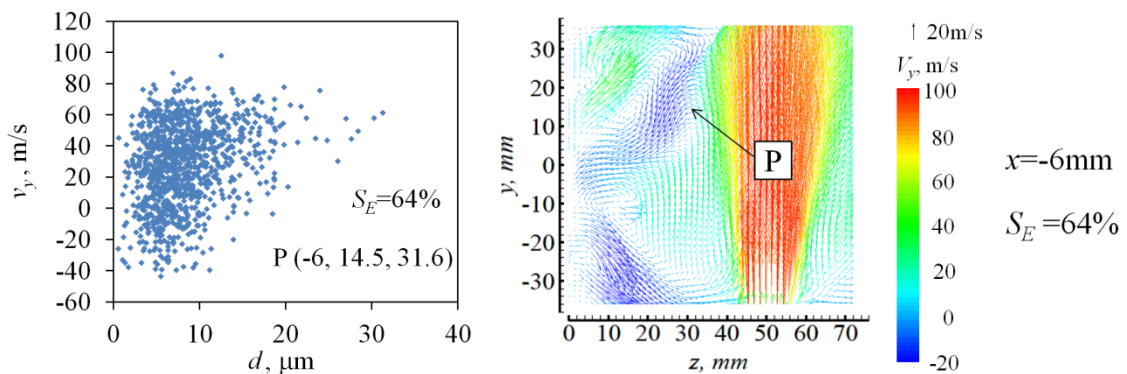


**Figure 8.** Size/velocity correlation of the droplets at the position P ( $x,y,z$ )= $(-6, 14.5, 31.6)$  for  $S_E=64\%$  (PIV result at  $x=-6\text{mm}$  including the position P is also shown.)

## Conclusions

The Phase Doppler measurements were performed to understand the spray combustion field in a lean two-stage low-NO<sub>x</sub> combustor for an aero-engine, at a condition simulating a flight phase of approach to airport for landing. The combustor was equipped with a coaxial staging fuel nozzle (pilot and main) on the combustor dome and an auxiliary emission control fuel nozzle (ECF) on its liner wall. At the approach condition, the pilot and ECF are to be in operation without the main. The purpose of this study is to understand the burning spray characteristics from the ECF and to obtain a clue for improvement of combustion efficiency. Two operating conditions in terms of fuel split ( $S_E=36$  and  $64\%$ ) were studied, where  $S_E$  is defined by the ratio of the fuel flow rate of the ECF to that in total. At a location around 65mm downstream from the ECF exit (along the ECF jet) after which the heat support from the pilot is no longer expected, a fast evaporation rate was still observed for  $S_E=64\%$ , whereas the evaporation rate got slower than upstream for  $S_E=36\%$ . The result was consistent with the higher combustion efficiency for  $S_E=64\%$ , suggesting that the self-heat release of the ECF flame has more positive impact as a heat source on combustion efficiency, than the heat support of the hot gas from the pilot, for the conditions tested.

## References

1. Doerr, T. *The Significance of Fuel Preparation for Low Emissions Aero-Engine Combustion Technology*. in *Proc. 12th ICLASS*. 2012.
2. Yamamoto, T., et al. *Combustion Characteristics of Fuel Staged combustor for Aero Engines at LTO Cycle Conditions*. ASME GT2011-46133.
3. Yamamoto, T., et al. *Emission Reduction of Fuel Staged Aircraft Engine Combustor using an Additional Premixed Fuel Nozzle*. ASME GT2012- 68590.
4. Yoshiura, Y., et al. *PIV Measurement of Flow Field in a Two-Stage Premixed Combustor at High Temperature and High Pressure Conditions*. in *Proc. Gas Turbine Society of Japan*. 2012.
5. Yoshida, K., et al. *Airblast Spray Characteristics of Planar Liquid Films in Longitudinal Gas-Phase Shear Layers at Various Ambient Pressure Conditions*. in *Proc. 12th ICLASS*. 2012.
6. Chin, J. S., et al, *The Interdependence of Spray Characteristics and Evaporation History of Fuel Sprays*. J. Eng. Gas Turbines Power, 1984. **106**(3): p. 639-644.

## Experimental Study on Flame Spread of Droplet-cloud Elements with Two-droplet Interaction in Microgravity

Masato MIKAMI<sup>1</sup>, Tsutomu HIROSE<sup>1</sup>, Hidetaka WATARI<sup>1</sup>, Takehiko SEO<sup>1</sup>,  
Osamu MORIUE<sup>2</sup> and Masao KIKUCHI<sup>3</sup>

1: Department of Mechanical Engineering, Yamaguchi University, Japan

2: Department of Mechanical Engineering, Kyushu University, Japan

3: ISS Science Project Office, Japan Aerospace Exploration Agency, Japan

### Abstract

This research conducted microgravity experiments to investigate flame-spread characteristics of two-dimensional fuel-droplet-cloud element with uneven droplet spacing, which is a basic element of randomly-distributed droplet cloud at the critical condition. Flame spread to a droplet followed by burning with two-droplet interaction was observed to investigate the effect of flame-spread direction and local interactive effect. The results show that the flame spread rate to the droplet in the perpendicular direction to the axis of interacting two droplets was greater than that to the droplet in the same direction as the axis of two droplets. Temperature distribution around burning droplets was measured by Thin Filament Pyrometry (TFP) method based on radiation from SiC fibers suspending droplets at their intersections. The local flame-spread-limit distance also increased with two droplet interaction in both flame-spread directions. It also shows the dependence of flame-spread direction. The flame spreads after two droplet interaction in two different directions were discussed considering the temperature distribution development.

### Introduction

Spray combustion is utilized in many liquid-fueled combustors. Flame spread in fuel spray occurs immediately after ignition in diesel engines and also near the flame base in gas turbine engines. Flame spread plays an important role in heat release in the initial stage in the former case and in the stability of group combustion of fuel spray in the latter case. In order to elucidate basic flame spread mechanisms, many researchers have investigated flame spread along fuel droplet arrays in microgravity [1-6]. However, the findings from such basic researches have not been well utilized for elucidation of spray combustion. In order to bridge theoretically between the droplet combustion and the spray combustion, some researchers have developed percolation models which predict that a transition occurs at the critical droplet-number density between partial combustion and group combustion of fuel sprays in flame spreading over randomly-distributed droplet clouds [7, 8, 9] (Fig. 1). The percolation theory shows that near-field connection rule determines macroscopic behavior of randomly distributed particle cloud. If it is applied to spray combustion, we can say that near-field flame-spread rule determines macroscopic group combustion behavior of droplet cloud. Oyagi et al. [9] employs simple flame-spread rule considering the flame-spread limit  $(S/d_0)_{\text{limit}}$  in terms of the dimensionless droplet separation distance, below which the leading flame can spread to the next droplet, but over which it cannot spread. At the critical condition of group combustion appearance, there are locally dense regions and sparse regions. If the local droplet spacing is small enough, droplet interaction occurs. Oyagi et al. [9] experimentally investigated the flame-spread-limit distance of unevenly-spaced droplet arrays in microgravity and showed that the flame-spread-limit distance increases with droplet interaction.

This research extended the previous research and conducted microgravity experiments to investigate flame-spread characteristics of two-dimensional fuel-droplet-cloud element with uneven droplet spacing, which is a basic element of randomly-distributed droplet cloud at the critical condition. A schematic of droplet-cloud element is shown in Fig. 2. Flame spread to a droplet followed by burning with two-droplet interaction was observed to investigate the effect of flame-spread direction and local interactive effect.

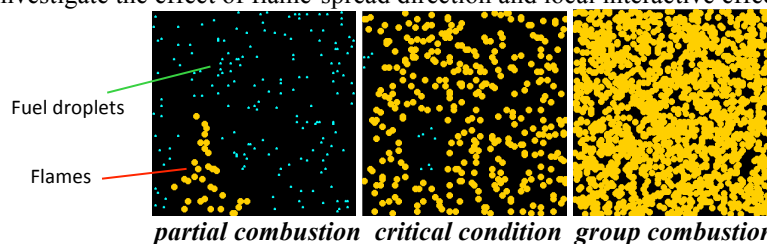


**Figure 1.** Flame patterns of randomly distributed droplet clouds with different droplet-number densities.

## Experimental Apparatus and Procedure

Figure 2 shows a schematic of two-dimensional droplet-cloud element. The droplet-cloud element consists of five droplets. Droplet I is the droplet for ignition. Droplets A and B are interactive droplets with the droplet spacing  $S_{BA}/d_0$ . Droplets L is the droplet to investigate the flame spread in  $\theta$  direction from interactive burning Droplets B and A. The droplet spacing between Droplets A and L is expressed  $S_{AL}/d_0$ . The droplet spacing between Droplets I and B was  $S_{IB}/d_0=10$  or 12. The initial droplet diameter  $d_0$  was 0.5 mm with less than 5 % uncertainty.

Figure 3 shows a schematic of the experimental apparatus. Each droplet was generated at a designated cross point of 14  $\mu\text{m}$  SiC fibers (Nippon Carbon, Hi-Nicalon) by supplying the fuel, n-decane, through a glass tubes whose tip inner diameter was about 40  $\mu\text{m}$ . Each glass tube was connected to a stepping-motor-driven micro-syringe through Teflon tube to supply fuel. The position of the glass tube tip was controlled by a three-axis traverse system. After generating all the droplets, a digital video camera (SANYO, DMX-FH11) was moved over the droplets. The first droplet was ignited by a hot-wire igniter in microgravity. Flame-spread behavior was recorded by a digital video camera with the framing rate of 240 fps. All the experiments were performed at atmospheric pressure and at room temperature (292 - 303 K). The microgravity experiments were performed at the drop facility of Yamaguchi University, Japan. The microgravity duration is 0.95 s.

Temperature distribution around burning droplets was measured by Thin Filament Pyrometry (TFP) method based on radiation from SiC fibers suspending droplets. Since the response time of the 14  $\mu\text{m}$  SiC fiber is about 1 ms, the temperature of SiC fiber will well follow the gas temperature change. In order to know the relation between luminosity from the fiber and temperature, both SiC fiber and 25  $\mu\text{m}$  Pt-Pt/13%Rd thermocouple were simultaneously heated by butane/O<sub>2</sub> burner and image was taken by the digital video camera (SANYO, DMX-FH11). The thermocouple wire was coated by silica to prevent surface reaction on Pt. R values of pixels in heated SiC fiber image are plotted against temperature. Considering the temperature dependence of radiation energy density in Plank's radiation law, we used a fitting function as  $R=A\exp(-B/T)$ , where  $T$  is temperature and A and B are constants. Figure 4 suggests that the present TFP method is valid for 980 K <  $T$  < 1500 K. We focus on the development of 1000 K region during flame spread, especially the spatial distribution of such a high-temperature region.

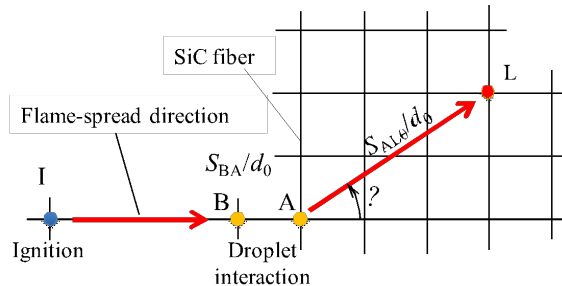


Figure 2. Droplet-cloud element

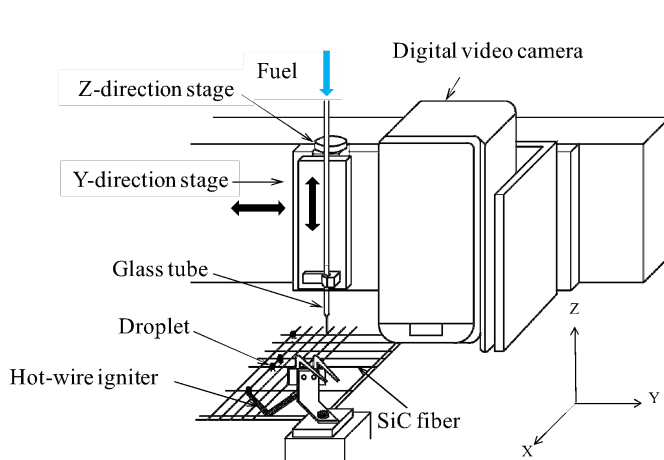


Figure 3. Apparatus of droplet-cloud element generation.

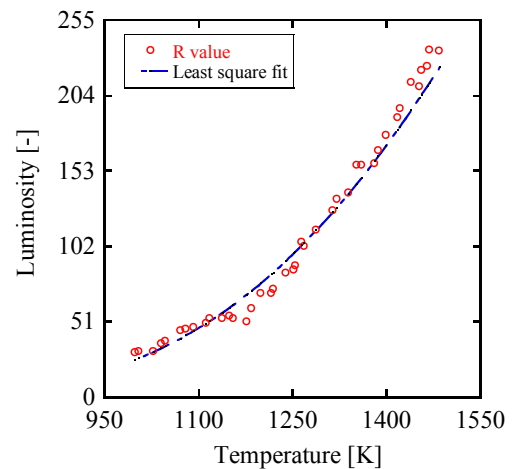


Figure 4. Relation between R value of heated SiC fiber image and temperature.

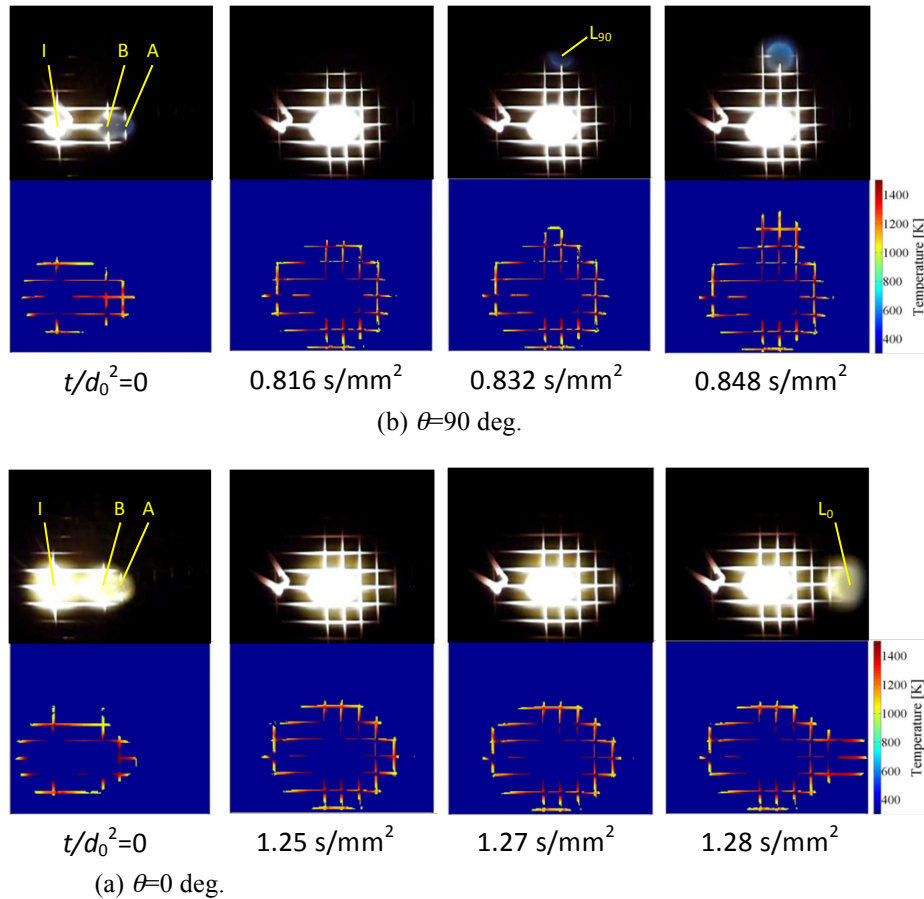


## Results and Discussion

Figure 5 displays flame spreading behavior of a droplet-cloud element with  $S_{BA}/d_0=4$  and  $S_{AL}/d_0=16$  for different Droplet L positions,  $\theta=0$  deg. and  $90$  deg. Time  $t$  starts from the moment of ignition of Droplet A. The temperature distributions on SiC fibers measured by TFP method in microgravity are also displayed. Although the color bar in Fig. 5 ranges from  $300$  to  $1500$  K, the present TFP method is valid within the temperature range  $980\text{ K} < T < 1500\text{ K}$ , as mentioned in the previous section. Therefore, the color map only shows the region with higher temperature than  $980$  K.

When Droplet A is ignited by spreading flame from Droplet B ( $t/d_0^2=0$ ), the outer edge of thermal layer ( $T>980$  K) around Droplet A is close to the outer edge of the yellow luminous flame. After a certain time from ignition of Droplet A, the thermal layer develops largely and the outer edge of it is far from the outer edge of the yellow luminous flame. The initial flame was observed around Droplet L at  $t/d_0^2=1.28\text{ s/mm}^2$  for the direction of Droplet L  $\theta=0$  deg. and at  $t/d_0^2=0.832\text{ s/mm}^2$  for the direction of Droplet L  $\theta=90$  deg. Since both  $S_{AL0}/d_0$  and  $S_{AL90}/d_0$  are  $16$ , the flame spread rate for  $\theta=90$  deg. is greater than that for  $\theta=0$  deg.

When the initial flame appears around Droplet L in Fig. 5, a blue flame with a half circle shape is observed around Droplet L for each direction  $\theta$  of Droplet L. This type of flame was observed by Mikami et al. [10] and is explained as the propagating premixed flame in the flammable mixture layer around Droplet L [3]. According to Mikami et al. [3], the flame-spread mechanism from Droplet A to Droplet L is as follows: an unburned Droplet L is heated by thermal conduction from the leading flame around Droplet A, a flammable-mixture layer forms around Droplet L, ignition occurs in the mixture layer, the premixed flame propagates in the mixture layer, and an envelope diffusion flame forms around Droplet L. As can be seen in Fig. 5, the outer edge of thermal layer ( $T>980$  K) in the direction of Droplet L reaches the rear edge of the initial flame around Droplet L. This fact suggests that the temperature of ignition point in the flammable-mixture layer around Droplet L is around  $1000$  K.



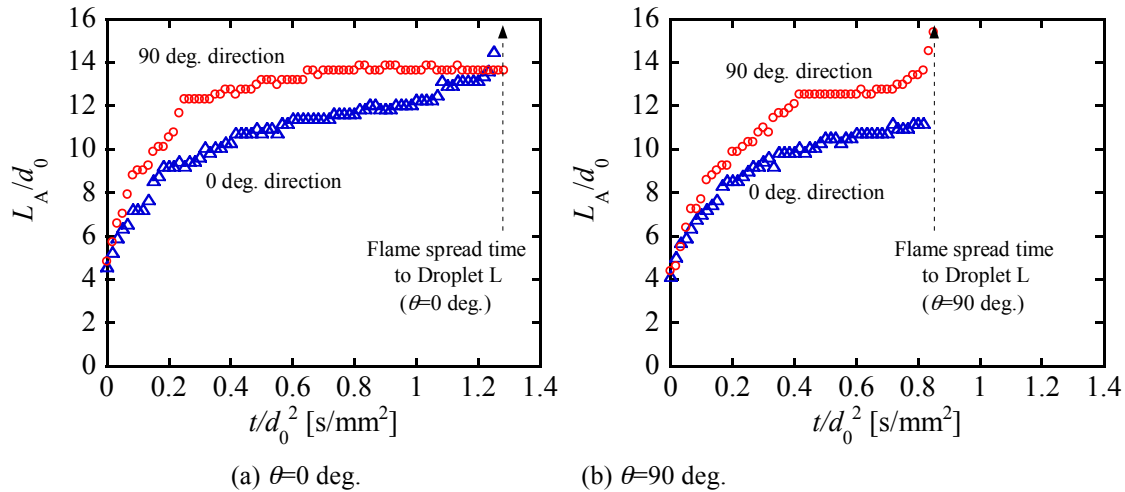
**Figure 5.** Flame spreading behavior of a droplet-cloud element with  $S_{BA}/d_0=4$  and  $S_{AL}/d_0=16$  for different Droplet L positions and temperature distribution on SiC fibers measured by TFP method in microgravity. Time  $t$  starts from the moment of ignition of Droplet A.



Figure 6 shows temporal variation of 1000 K positions of thermal layer measured from Droplet A in different directions for different Droplet L positions. In the case of Droplet L direction  $\theta=0$  deg. (Fig. 6a), the size of 1000 K positions of thermal layer in 90 deg. direction is greater than that in 0 deg. direction. This is the same in the case of Droplet L direction  $\theta=90$  deg. (Fig. 6b). Therefore, if Droplet L exists in the direction of larger thermal layer, i.e.,  $\theta=90$  deg., the flame spread rate becomes greater.

It is interesting that there is an inflection point in the size of 1000 K positions of thermal layer in 0 deg. direction for  $\theta=0$  deg. (Fig. 6a) and in 90 deg. direction for  $\theta=90$  deg. (Fig. 6b). This means that the developing speed of the thermal layer in the direction of Droplet L decreases with time first but then increases again before ignition of the flammable-mixture layer around Droplet L. The real time from the inflection point to the moment of the initial flame around Droplet L is about 0.03 s for  $\theta=90$  deg. and about 0.05 s for  $\theta=90$  deg. These times are much greater than the premixed-flame propagation time in the flammable-mixture layer around 0.5 mm droplet, about 0.001 s. Therefore, the increase of the developing speed of the thermal layer in the direction of Droplet L after the inflection point is not caused by the heat from the premixed flame initially appearing around Droplet L. A possible explanation is that cool flame might occur near the rear edge of the flammable-mixture layer around Droplet L and assist the thermal layer development in the direction of Droplet L.

Figure 7 shows the flame-spread limit distribution around Droplet A for  $S_{BA}/d_0=4$ . The experiment was repeated at least three times at the same position of Droplet L to check if the flame spread occurred to Droplet L, or not. The flame spread results were not always same even for the same position of Droplet L near the flame-spread limit distance, probably due to uncertainty associated with relatively small initial droplet diameter  $d_0$  of 0.5 mm. We use different symbols depending on the flame-spread probability  $P_f$  as shown in Fig. 7. The flame-spread limit exists around  $P_f$  of 0.5.



**Figure 6.** Temporal variation of 1000 K positions of thermal layer measured from Droplet A in different directions for different Droplet L positions ( $S_{BA}/d_0=4$  and  $S_{AL}/d_0=16$ ). Time  $t$  starts from the moment of ignition of Droplet A.

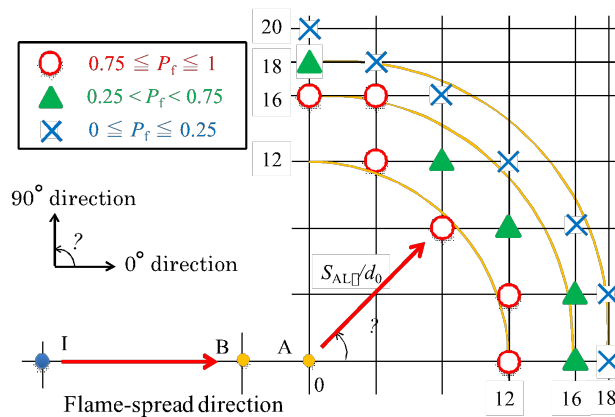


**Figure 7.** Flame-spread limit distribution for  $S_{BA}/d_0=4$ .

Figure 7 shows that the flame-spread-limit distance from Droplet A,  $(S_{AL}/d_0)_{\text{limit}}$  is about 16 in 0 deg. direction. Oyagi et al. [9] experimentally investigated the flame-spread-limit distance of unevenly-spaced droplet arrays in microgravity and showed that the flame-spread-limit distance increases with droplet interaction and about 16 after two droplet interaction with  $S/d_0=4$ . The present result corresponds to the result of Oyagi et al. [9].

The flame-spread-limit distance from Droplet A,  $(S_{AL}/d_0)_{\text{limit}}$  is larger in 90 deg. direction than that in 0 deg. direction. The difference between them is about 2. As can be seen in Fig. 6, the size of 1000 K positions of thermal layer  $L_A/d_0$  in 90 deg. direction is initially same as that in 0 deg. direction, but the difference between two direction sizes increases up to 2 with time before the inflection point. Right after the ignition of Droplet A, the development of thermal layer is affected only by Droplet A burning and thus there is almost no dependence of the size of thermal layer on the direction. As time goes, the interactive burning effect becomes significant between Droplets B and A and causes the difference in development of thermal layer depending on the direction relative to the axis of Droplets B and A.

If Droplets B and A are seen from far field, two droplets can be approximated as a point source of one droplet with twice volume ( $2^{1/3}$  times diameter) at the center position between Droplets B and A. The flame-spread limit distance from the imaginary droplet at the center between Droplets B and A is considered spherical. Mikami et al. [3] reported that the flame-spread-limit distance  $(S/d_0)_{\text{limit}}$  in the linear droplet array is about 14. The flame-spread-limit distance from the droplet with  $2^{1/3}$  times diameter is estimated as 17.6 based on  $(S/d_0)_{\text{limit}}=14$ . Since the distance from Droplet A to the center between Droplets B and A is 2 in dimensionless form, the flame-spread limit distance from Droplet A in the same direction as the axis of Droplets B and A is 15.6, which is close to the result in Fig. 7 and Oyagi et al. The flame-spread limit distance from Droplet A in the perpendicular direction to the axis of Droplets B and A is estimated as 17.5. The difference between two values is about 2. Therefore, the flame-spread-limit distance from interactive burning two droplets can be understood approximately based on that from a point source of a burning droplet with twice volume.

## Conclusions

This research conducted microgravity experiments to investigate flame-spread characteristics of two-dimensional droplet-cloud element with uneven droplet spacing, which is a basic element of randomly-distributed droplet cloud at the critical condition. Flame spread to a droplet followed by burning with two-droplet interaction was observed to investigate the effect of flame-spread direction and local interactive effect. The results show that the flame spread rate to the droplet in the perpendicular direction to the axis of interacting two droplets was greater than that to the droplet in the same direction as the axis of two droplets. The local flame-spread-limit distance increased with two droplet interaction in both flame-spread directions. These findings can be understood approximately based on that from a point source of a burning droplet with twice volume.

## Acknowledgements

This research was partly subsidized by Grant-in-Aid for Scientific Research (B) (24360350) and a research WG of JAXA.

## References

- [1] Kato, S., Mizuno, H., Kobayashi, H., Niioka, T., *JSME Int. J. B* 41 (1998) 322-330.
- [2] Kobayashi, H., Park, J., Niioka, T., *Proc. Combust Inst.* 29 (2002) 2603-2610.
- [3] Mikami, M., Oyagi, H., Kojima, N., Wakashima, Y., Kikuchi, M., Yoda, S., *Combust. Flame* 146 (2006) 391-406.
- [4] Nomura, H., Takahashi, M., Ujiie, Y., Hara, H., *Proc. Combust. Inst.* 30 (2005) 1991-1995.
- [5] Umemura, A., *JSME Trans. B* (in Japanese) 68 (2002) 2442-2428.
- [6] Kikuchi, M., Wakashima, Y., Yoda, S., Mikami, M., *Proc. Combust Inst.* 30 (2005) 2001-2009.
- [7] Umemura, A., Takamori, S., *Combust. Flame* 141 (2005) 336-349.
- [8] Shigeno, H., Oyagi, H., Mikami, M., Kojima, N., *Twenty-Fifth International Symposium on Space Technology and Science (ISTS2006)*, 2006-h-24.
- [9] Oyagi, H., Shigeno, H., Mikami, M., Kojima, N., *Combust. Flame* 156 (2009) 763-770.
- [10] Mikami, M., Oyagi, H., Kojima, N., Kikuchi, M., Wakashima, Y., Yoda, S., *Combust. Flame* 141 (2005) 241-252.

## Study of reactive spray using global rainbow refractometry

M. Ouboukhlik<sup>1,2</sup>, S. Saengkaew<sup>2</sup>, M-C. Fournier-Salaün<sup>1</sup>, L. Estel<sup>1</sup> and G. Gréhan<sup>2</sup>

1: LSPC EA 4704, INSA de Rouen, Avenue de l'Université 76800 St Étienne du Rouvray, France.

2: UMR 6614 CORIA, Avenue de l'Université 76800 St Étienne du Rouvray, France.

### Abstract

As carbon dioxide is one of the main greenhouse gases produced by human activity, many current studies are related to the processes of CO<sub>2</sub> capture and storage from industrial effluents. CO<sub>2</sub> capture in economic conditions is still a challenge. Among numerous existing technologies, amine based solvents are widely used to reach this aim at the industrial scale. To date, all commercial CO<sub>2</sub> capture plants use processes based on chemical absorption with a monoethanolamine (MEA) solvent. The key point is the exchange between the gas phase carrying the CO<sub>2</sub> and the liquid phase carrying the amine. The actual processes are closed-loop absorption/desorption with two packed columns. The first packed column for absorption is the main concern of this study, its pressure drop, size and packing material are the reduction in cost and energy targets. In the latter case, using energy generates more CO<sub>2</sub> emissions, which is precisely what we want to avoid. Therefore, capturing CO<sub>2</sub> requires more emphasis on reducing energy inputs than traditional commercial process. The purpose of this work is to characterize the mass transfer in a spray contactor during a CO<sub>2</sub> absorption using MEA as a solvent. An interesting way to investigate this mass transfer is to measure the refractive index during the reactive absorption. The concentration and temperature evolution inside the droplet during the absorption induces a modification of the refractive index. By using the rainbow refractometry technique (GRT), the CO<sub>2</sub> absorbed is measured at different partial pressures of CO<sub>2</sub> in the inlet gas stream. The measured profile is then compared to a model one.

### Introduction

CO<sub>2</sub> emissions from fossil fuel combustion represent 57% of greenhouse gases causing global warming and the analysis of greenhouse gas emissions shows the increase of CO<sub>2</sub> from a combustion process, with 56.6 % eq-CO<sub>2</sub> of emissions in 2004 [1]. In addition to the use of renewable energy and energy consumption efficiency, it is important to reduce CO<sub>2</sub> emissions from power plants after combustion. Therefore, many authors have studied the sustainability of CO<sub>2</sub> post combustion capture. Khol and Nielsen [2] have provided a comprehensive summary of this process. A standard unit consists of an absorption column where the CO<sub>2</sub> is captured and a desorption column to regenerate the solvent. Aqueous solutions of alkanolamines are widely used as solvents for acid gases capture [3]. MEA high reaction rate with acid gas and its capability of removing even trace of carbon dioxide makes this chemical absorption one of the most promising technologies [4]. Packed columns are the most used contactors for CO<sub>2</sub> capture. Many authors have evaluated the sustainability of carbon dioxide capture by MEA from incinerator flue gas, using packed columns [5]. It appears obvious that a significant improvement in separation technology is required, with high efficiency, compactness, and operationally flexible contactors. Sprays columns are widely used for SO<sub>2</sub> capture and have been studied in term of capture efficiency [6]. The main advantages of this technology are to optimize the exchange area between the two phases and to reduce gas head loss in the contactor. Kuntz et al. [7] have studied the spray column performance and shown that the spray column offers a better performance comparing to the packed column.

The aim of this study is to characterize the mass transfer flux (CO<sub>2</sub> absorbed) using a spray column. A non-intrusive optical technique is used: global rainbow refractometry. The refractive index is measured during the CO<sub>2</sub> absorption with chemical reaction. Rainbow refractometry relies on the sensitivity of the rainbow location during the chemical absorption with respect to the refractive index value. An evolution of droplets refractive index in the spray is due to a change of density, which represents a temperature and/or a composition evolution. With a calibration refractive index as function of temperature and CO<sub>2</sub> absorbed [8], the measurement of refractive index provides a measurement of composition at a known temperature. Global rainbow refractometry has been used as a thermometry technique in many studies to measure droplets temperature when the concentration is known and without any reaction. Saengkaew et al. [9] measured temperature of water droplets with an accuracy of 0.0001 on the refractive index. However, the problem becomes more complex when a chemical reaction occurs. The dependence of the refractive index with concentration (CO<sub>2</sub> absorbed in aqueous MEA) is significantly higher than its dependence with temperature. In this paper, the CO<sub>2</sub> absorbed concentration is measured during the absorption inside a spray column, for different CO<sub>2</sub> concentrations in flue gas. The experimental results are compared to a model which predicts the evolution of CO<sub>2</sub> absorbed regarding the CO<sub>2</sub> partial pressure.

### Mass transfer model

The reaction between CO<sub>2</sub> and MEA (HO-CH<sub>2</sub>-CH<sub>2</sub>-NH<sub>2</sub>) has been described in many studies. According to Satori and Savage [10], the carbamate formation is considered to be the main reaction between CO<sub>2</sub> and MEA. The reversible reaction is neglected in the absorption column. The reaction can be expressed as follows, with a rate constant k:



(1)

The reaction is first order for both CO<sub>2</sub> and MEA [11] and the reaction rate is:

$$V = k C [\text{MEA}] \quad (2)$$

The aim of this model is to obtain the CO<sub>2</sub> absorbed into a rigid spherical droplet. During the absorption, CO<sub>2</sub> dissolves into the droplet and diffuses while it reacts. Three phenomena are then taken into account:

- CO<sub>2</sub> Solubility modelled by Henry's law
- CO<sub>2</sub> Diffusion modelled by Fick's law
- Kinetic of CO<sub>2</sub> and MEA reaction

Table 1 shows transfer parameters at a temperature of 30°C.

CO <sub>2</sub> diffusivity : D <sub>CO2</sub> (m <sup>2</sup> /s)	1.48 10 <sup>-09</sup>	[12]
CO <sub>2</sub> Henry constant : He <sub>CO2</sub> (mol/m <sup>3</sup> /bar)	23.07	[12]
Rate constant k (m <sup>3</sup> /mol/s)	7.78	[4]

**Table 1.** Mass transfer parameters for CO<sub>2</sub> capture by 30 % (w,w) aqueous MEA at 30°C

The mass balance on CO<sub>2</sub> inside the droplet in spherical coordinates is processed with the following assumptions:

- The mass balance is done in steady-state (no accumulation).
- The droplet is spherical and rigid, with a diameter (2R).
- The mass balance is done in spherical coordinates with only radius (r) dependence (axisymmetric droplet).
- The transfer parameters are taken at a steady temperature.
- CO<sub>2</sub> is neglected comparing to MEA concentration. Therefore the reaction rate in equation 2 becomes :  
 $V = k' C$   
 (3)  
 And  
 $k' = k [\text{MEA}]$  (4)
- At the droplet interface (r=R), gas is in equilibrium with liquid (Henry's law) and at the droplet center (bulk), CO<sub>2</sub> concentration doesn't change.

According to the assumptions mentioned above, the CO<sub>2</sub> mass transfer equation is:

$$D_{\text{CO}_2} \left( \frac{\partial^2 C}{\partial r^2} + \frac{2}{r} \frac{\partial C}{\partial r} \right) = V = k' C \quad (5)$$

The solution to differential equation 5 is obtained by variable substitution:

$$C = \frac{1}{r} \left( A \exp \left\{ \sqrt{\frac{k'}{D_{\text{CO}_2}}} r \right\} + B \exp \left\{ -\sqrt{\frac{k'}{D_{\text{CO}_2}}} r \right\} \right) \quad (6)$$

A and B are obtained with the following boundary conditions:

$$\text{At the droplet bulk: } \left\{ \frac{\partial C}{\partial r} \right\}_{r=0} = 0 \quad (7)$$

$$\text{At the gas liquid interface: } C_{(r=R)} = \text{He}_{\text{CO}_2} P_{\text{CO}_2} \quad (8)$$

CO<sub>2</sub> evolution inside the droplet is:

$$C = \text{He}_{\text{CO}_2} P_{\text{CO}_2} \frac{R}{r} \frac{\sinh \left\{ \sqrt{\frac{k'}{D_{\text{CO}_2}}} r \right\}}{\sinh \left\{ \sqrt{\frac{k'}{D_{\text{CO}_2}}} R \right\}} \quad (9)$$

$\text{CO}_2$  mass flux  $N_{\text{CO}_2}$  represents the quantity of  $\text{CO}_2$  crossing the gas/liquid interface during a time through a surface:

$$N_{\text{CO}_2 r=R} = D_{\text{CO}_2} \left\{ \frac{\partial C}{\partial r} \right\}_{r=R} = \frac{D_{\text{CO}_2}}{R} \text{He}_{\text{CO}_2} P_{\text{CO}_2} \left( \frac{\sqrt{\frac{k'}{D_{\text{CO}_2}}} R}{\tanh \left\{ \sqrt{\frac{k'}{D_{\text{CO}_2}}} R \right\}} - 1 \right) \quad (10)$$

And the  $\text{CO}_2$  absorbed during a contact time between the droplet and the gas ( $t_c$ ) is:

$$[C\text{O}_2]_{\text{abs}} = a t_c N_{\text{CO}_2 r=R} = a t_c \frac{D_{\text{CO}_2}}{R} \text{He}_{\text{CO}_2} P_{\text{CO}_2} \left( \frac{\sqrt{\frac{k'}{D_{\text{CO}_2}}} R}{\tanh \left\{ \sqrt{\frac{k'}{D_{\text{CO}_2}}} R \right\}} - 1 \right) \quad (11)$$

### Global rainbow technique (GRT)

In ray optics, a rainbow corresponds to a minimum of deviation [13]. It is characterized by a local peak of intensity. Furthermore, its angular location is only a function of the real part refractive of the index value. In wave optics, interference and diffraction will be taken into account. Therefore the rainbow shape and the angular location of the maximum of intensity depend not only on the refractive index value but also on the droplet size. By using the Lorenz-Mie theory, the light distribution is rigorously predicted. In figure 1, three ‘rainbows’ are plotted. The straight line, located at about 138°, corresponds to the ray optics rainbow. The narrow line corresponds to the rainbow created only by the onetime internally reflected light (Airy’s or Debye’s ( $p=2$ ) theory) while the large line corresponds to the rainbow predicted by the rigorous Lorenz-Mie theory when all kinds of interaction are taken into account. The use of the rainbow to measure droplet refractive index has been proposed by Roth et al. [14] for standard rainbow thermometry. To bypass difficulties due to non sphericity and ripple structure, Van Beeck et al. [15] have introduced the GRT. In this technique, the rainbows created by droplets crossing the measurement volume during a time interval are added together, creating a global rainbow. This global rainbow is characterized by a smooth behavior (ripple is suppressed) and robustness to non-sphericity [16, 17]. Such a normalized rainbow is displayed in figure 2.

The rainbow location is a function of the refractive index value and its shape depends on the size distribution of the droplets. To extract information from GRT signals, Van Beek et al. [15] have proposed different inversion algorithms based on Airy theory with the assumption that the size distribution is a lognormal function.

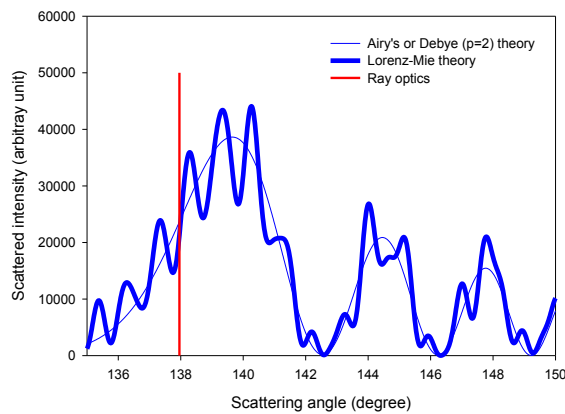


**Figure 1.** Comparison of the rainbow predicted by: Geometrical optics, Debye theory and Lorenz-Mie theory.

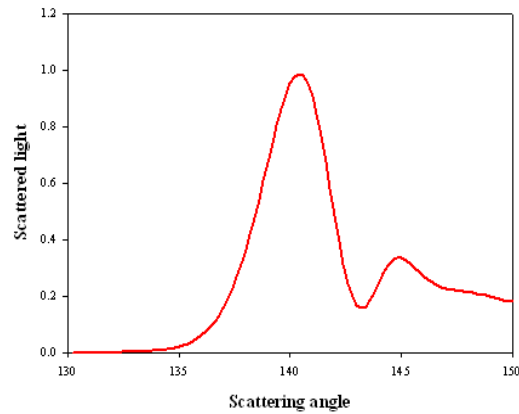


**Figure 2.** A typical global rainbow.

As previously said, Lorentz-Mie theory is the most rigorous theory but it is also the most time consuming. A code has been developed by Saengkaew [18], which is based on the Nussenzveig's theory combined with Non Negative Least Square (NNLS) and minimization. Nussenzveig's theory takes into account the interference between first internal reflected light ( $p=2$ ) and the ripple structure (interference with the external reflected light). NNLS researches the best size distribution for a given refractive index and the refractive index is extracted by minimizing the distance between the computed intensity profile by using NNLS and the measured intensity. This inversion algorithm is used in this work to measure the average refractive index value and the associated size distribution.

### Experimental setup: Optical setup

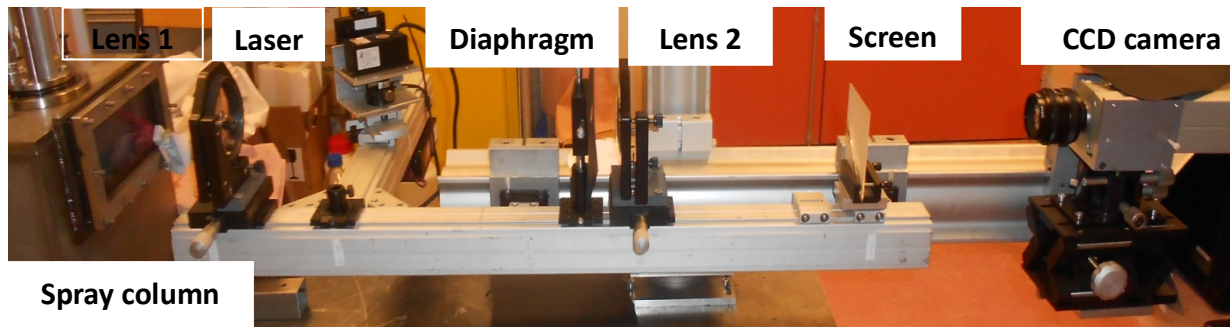


**Figure 3.** A view of the global rainbow setup.

The optical setup is displayed in figure 3. It consists of a continuous laser (wavelength: 532 nm). The laser emits a beam of 1mm of diameter towards the spray through an optical window (figure 4). A first collecting lens (diameter: 80 mm, focal length: 160 mm) creates the image of the measurement volume on a spatial filter. The diaphragm (spacial filter) is placed to select scattered light on a semi-transparent screen. The second lens (diameter: 80 mm, focal length: 200 mm) which is placed between the screen and the diaphragm, creates an image of the first lens image focal plane on the screen. This optical setup allows collecting only the light scattered by the particles located in the control volume ( $1 \text{ mm}^3$ ) and organized by scattering angle. A CCD camera with an integration time equal to about 100ms collects images for the following light scattered processing. The absolute rainbow location requires an absolute angular location of each pixel of the camera. Therefore, calibration angles/pixels are done using a rotating mirror placed at exactly the same position as the measurement volume in the spray. By rotating the mirror, the laser beam is reflected on the screen. The angular location is obtained by reading the position on the mirror rotation stage, while the pixel is extracted from the pictures recorded.

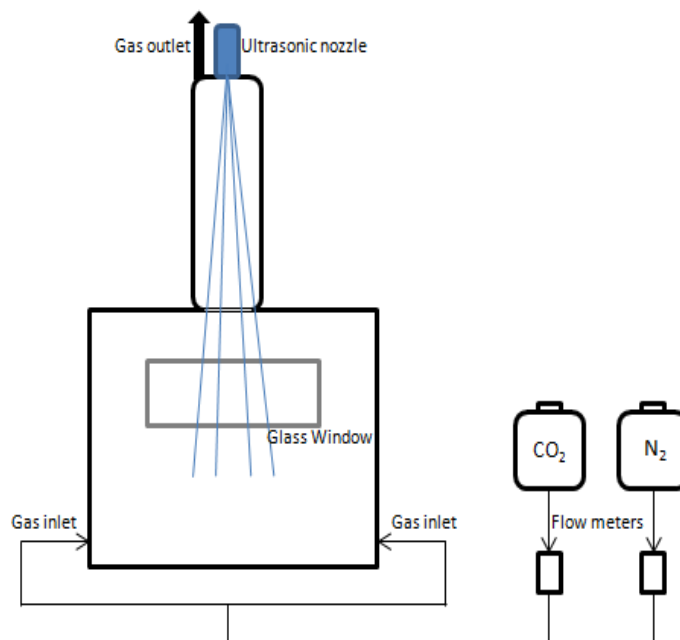


**Figure 4.** Flow chart of the experimental setup.

### Experimental setup: Spray column

The gas absorption setup (figures 4) consists of a stainless steel cylinder (inside diameter =9 cm) on top of a stainless steel chamber (13.5L). The chamber is fitted with an optical window on the front. An ultrasonic nozzle (40 kHz) is placed on the top of the column, which creates droplets with an average diameter equal to 30  $\mu\text{m}$  and a mean velocity equal to about 1 m/s (for a flow rate of 20 mL.min<sup>-1</sup>). The spray nozzle is connected to the feed bottle with 30% (w,w) aqueous MEA. The gas inlet is located at the bottom of both sides of the chamber. This brings the gas and the liquid into counter current exchange. The gas, after CO<sub>2</sub> absorption is carried out through the top of the column while the rich solution is sent to the liquid receiver located at the bottom of the column. The measurement volume is located at 25.5cm from the spray nozzle.

### Experimental procedure

The experiment begins by introducing a mixture of N<sub>2</sub> and CO<sub>2</sub> at the desired flow rate and CO<sub>2</sub> partial pressure. The gas composition is controlled with flow meters for each gas. To make sure that the gas concentrations are uniform inside the column, the solvent is injected after four times the time needed to fill up the column. Once the system reached steady-state, the laser is beamed on the measurement volume. The same method is done to measure temperature with a probe in the plane with the measurement volume.

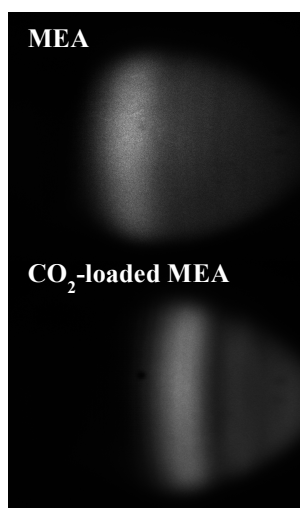
Column height	25.5 cm
Droplets velocity	1 m.s <sup>-1</sup>
Time contact with gas (tc)	255 ms
Droplets average diameter	30 $\mu\text{m}$

**Table2.** Test conditions.

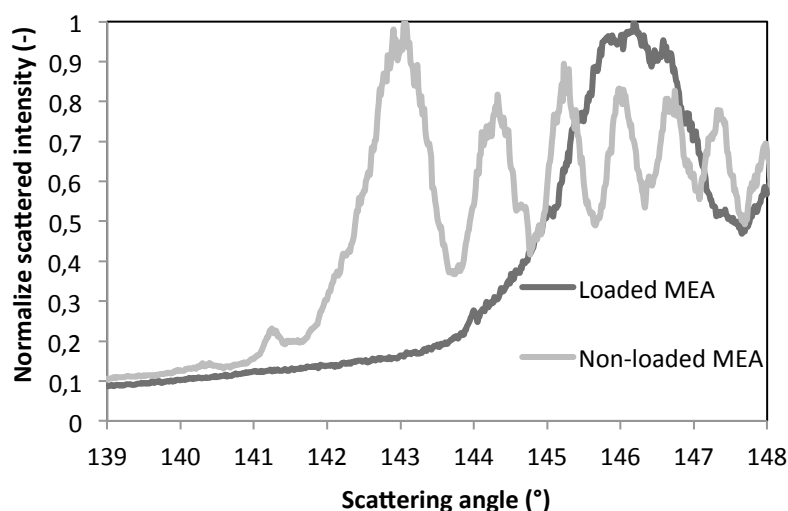
### Results and Discussion

Figure 5 shows the rainbow pictures obtained for a 30% (w,w) aqueous MEA solution with and without CO<sub>2</sub>. The main rainbow translates to the right after CO<sub>2</sub> absorption. By using a pixel/angle calibration, the normalized scattered intensity is plotted versus the scattering angle for the CO<sub>2</sub> loaded MEA (figure 6).

It shows that the rainbow angle goes from 142.5° for non-loaded MEA to 145.5 for loaded MEA for absorption at a CO<sub>2</sub> partial pressure of 0.6.



**Figure 5.** Rainbows for MEA



**Figure 6.** Intensity VS scattering angle extracted as displayed in figure

7

before and after absorption.

By using the Nussenzweig's theory [18], the average refractive index is extracted from the scattered intensity and the scattering angle at different CO<sub>2</sub> partial pressure. A correlation between the refractive index, the loaded CO<sub>2</sub> and the temperature [8] is used to obtain the CO<sub>2</sub> absorbed in the droplets at the temperature absorption. The refractive index increases with density, which increases with concentration but decreases with temperature. Table 3 shows the evolution of refractive index and the CO<sub>2</sub> absorbed versus CO<sub>2</sub> partial pressure in flue gas. The refractive index increases when CO<sub>2</sub> concentration in inlet gas stream increases. Its slow evolution is due to the temperature increase in the spray by the exothermic reaction.



P <sub>CO2</sub> (bar)	T <sub>measurement volume</sub> (°C)	Refractive index (-)	CO <sub>2</sub> absorbed (mol/L)
0.3	23	1.3912	1.6
0.5	26	1.3919	1.7
0.6	30	1.3927	1.9
0.7	33	1.3930	2

**Table 3.** Refractive index and CO<sub>2</sub> loaded VS CO<sub>2</sub> partial pressure.

The measured CO<sub>2</sub> absorbed during the absorption is plotted versus CO<sub>2</sub> partial pressure in figure 7 to compare it with the modeled one in equation 11. It shows that, according to the model, the CO<sub>2</sub> absorbed should reach about 2.5 mol.L<sup>-1</sup> at a CO<sub>2</sub> partial pressure of 0.3. However in the experiment, aqueous MEA under the test conditions mentioned above, absorbs 2 mol.L<sup>-1</sup> at the highest experimental partial pressure (0.7 bar).

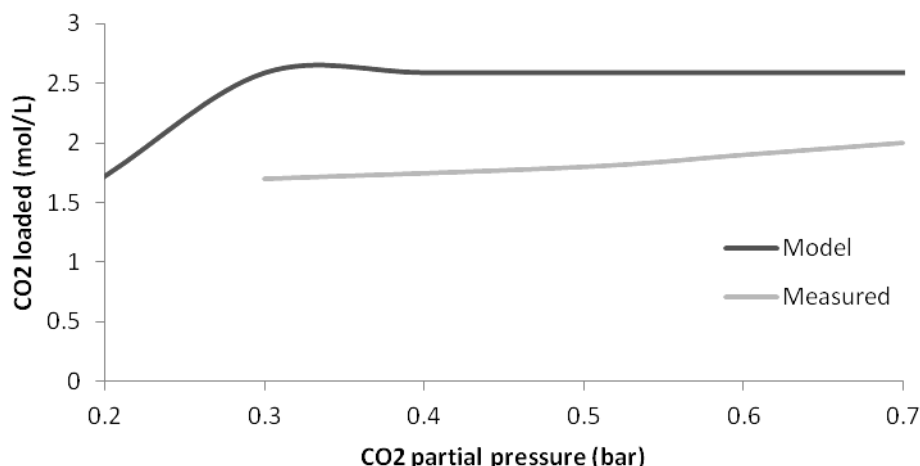


**Figure 7.** CO<sub>2</sub> loaded vs CO<sub>2</sub> concentration in flue gas.

The deviation between the prediction and the experiment could be due to :

- The droplets in the measurement volume are not in contact with the same CO<sub>2</sub> concentration.
- Solvent volatility, which could create a change of MEA concentration inside the droplets. Indeed, the bigger exchange area provided by sprays could increase in addition to CO<sub>2</sub> transfer, solvent volatility comparing to packed columns.
- The effect of concentration gradient in the droplets.

### Conclusions and perspectives

Global rainbow technique (GRT) has been successfully used to measure CO<sub>2</sub> absorbed in a 30% aqueous MEA during a CO<sub>2</sub> reactive absorption in a spray.

By changing CO<sub>2</sub> concentration in the inlet gas stream, the temperature and the CO<sub>2</sub> loaded in the spray increases making the refractive index change. By comparing the measured CO<sub>2</sub> loaded into the spray to a model, experiment shows that CO<sub>2</sub> is not absorbed as predicted.

In the future experiment, research should consider having more information about the measurement volume. Indeed, the density of the spray is a key point to model the heat transfer inside the measurement volume knowing CO<sub>2</sub> enthalpy of reaction (-85 kJ/mol of CO<sub>2</sub> absorbed). Imagery, in addition to the density, also gives information about average droplets diameter to compare with the ones extracted by global rainbow refractometry.

### Acknowledgements

Authors gratefully acknowledge the financial support received from “La Haute Normandie” and “Grand Réseaux de Recherche Sciences de l’environnement, analyse et gestion des risques - Maitrise des Emissions et Rejets”.

Authors thank also INTERREG E3C3 project.

## Nomenclature

<i>Symbol</i>	<i>Corresponds to</i>
CO <sub>2</sub>	Carbon dioxide
MEA	Monoethanolamine
MEACCO <sup>-</sup>	Carbamate
MEA <sup>+</sup>	Protonated MEA

<i>Symbol</i>	<i>Corresponds to</i>	<i>SI unit</i>
a	Interfacial area (Droplet area/droplet volume = 3/R)	m <sup>-1</sup>
C	CO <sub>2</sub> concentration inside the droplet	mol.m <sup>-3</sup>
[CO <sub>2</sub> ] <sub>abs</sub>	CO <sub>2</sub> absorbed (or loaded) in the droplet	mol.m <sup>-3</sup>
D <sub>CO2</sub>	CO <sub>2</sub> diffusion coefficient in 30% MEA	m <sup>2</sup> .s <sup>-1</sup>
He <sub>CO2</sub>	CO <sub>2</sub> Henry constant in 30% MEA	mol.m <sup>-3</sup> .Pa <sup>-1</sup>
k	Reaction rate coefficient	m <sup>3</sup> .mol <sup>-1</sup> .s <sup>-1</sup>
k'	First order reaction rate coefficient	s <sup>-1</sup>
[MEA]	MEA concentration	mol.m <sup>-3</sup>
N <sub>CO2</sub>	CO <sub>2</sub> mass flux	mol.m <sup>-2</sup> .s <sup>-1</sup>
P <sub>CO2</sub>	CO <sub>2</sub> partial pressure	Pa
r	Radius	m
R	Droplet radius	m
T	Temperature	K
V	Reaction rate	mol.m <sup>-3</sup> .s <sup>-1</sup>

## References

1. Intergovernmental Panel on Climate Change 2007.
2. Kohl A and R. Nielsen, 1997, Gas purification, 5<sup>th</sup> ed. Houston: Gulf Publishing Company.
3. Lecomte F., P. Broutin and E. Lebas, 2010, Le captage de CO<sub>2</sub>. Technip, Paris.
4. Hikita H., H. Asai, H. Ishikawa and M. Honda, 1977, Chemical Engineering Journal, 13, p 7-12.
5. DeMontigny D., P. Tontiwachwuthikul and A. Chakma, 2005, Industrial and Engineering Chemistry Research. 44(15) 5726-5732.
6. Bandyopadhyay A. and M.N. Biswas, Scrubbing of sulphur dioxide in a dual-flow scrubber, 1998, Journal of Indian for Environment Management, 26:113-133.
7. Kuntz J. and A. Aroonwilas, Mass transfer efficiency of a spray column for CO<sub>2</sub> capture by MEA, 2009, Energy procedia 1, p. 205-209.
8. Tagutcho J.P., S. Saengkaew, G. Gréhan, L. Estel, GPE 2011, Kuala Lumpur, Malaysia.
9. Saengkaew S., Charinpanikul T., Laurent C., Biscos Y., Lavergne G., Gouesbet G. and Grehan G., (2010) Processing of individual rainbow signal to study droplets evaporation, Experiments in Fluids, pp. 111-119.
10. Satori J.G. and D.W.Savage, 1983, Industrial Engineering Chemistry Fundamentals, 22 p 239.
11. Danckwerts P.V., 1970, Gas liquid reactions; McGraw-Hill Book Company.
12. Versteeg G. F. and W. P. M van Swaaij, 1988, Solubility and Diffusivity of Acid Gases (CO<sub>2</sub>, H<sub>2</sub>S) in Aqueous Alkanolamine Solutions. J.Chem. Eng. Data, 33, 29-34.
13. Adam J., 2002, The mathematical physics of rainbows and glories, Physics report, 356, pp. 229-365.
14. Roth N., K.Anders and A. Frohn, 1990, Simultaneous measurement of temperature and size of droplets in the micrometer range, J. of Laser Applications, pp. 37-42.
15. Van Beeck J., D. Giannoulis, L. Zimmer and M. Riethmuller, 1999, Global rainbow refractometry for droplet temperature measurement, Optics Letters, Vol. 24, 1696-1698.
16. Saengkaew S., G. Godard, J.B. Blaisot and G. Grehan, 2009, Experimental analysis of global rainbow technique: sensitivity of temperature and size distribution measurements to non-spherical droplets, experiments in fluids, 47, 839-848.

17. Wang J.J., Grehan G., Han Y.P., Saengkaew S., (2011) Numerical study of global rainbow technique: sensitivity to non sphericity of droplets, DOI 10.1007/s00348-010-1036-4.
18. Saengkaew S., 2006, Development of noval global rainbow technique for characterizing spray generated by ultrasonic nozzle: PhD Thesis, University of Chulalongkorn (Thailand) and Université de Rouen (France).

## Generation of Fine Particles with Specified Characteristics

A.N. Ishmatov<sup>1</sup>, V.V. Elesin<sup>2</sup>, A.A. Trubnikov<sup>1</sup>, S.P. Ogorodnikov<sup>2</sup>

1: Institute for Problems of Chemical & Energetic Technologies  
of the Siberian Branch of the Russian Academy of Sciences (IPCET SB RAS), Russia

2: Join Stock Company Federal Research & Production Center ALTAI, Russia

### Abstract

The research is devoted to the generation of fine particles (particles size below 5  $\mu\text{m}$ ) and gas-droplet flows with specified characteristics for a wide range of scientific problems. The aspects of aerodynamic fine atomization and the effects of atomizing gas density, gas velocity and mass flow rate, and liquid film thickness on the droplet formation are investigated. The hypothesis of highly efficient utilization of secondary droplets from a coarse polydisperse flow to produce fine particles is suggested and experimentally confirmed. A prototype device to implement the idea of separating the desired droplets' fraction from a primary polydisperse flow was developed. In the case of fine liquid atomization, the developed spraying system enabled an increase in the gas-droplet flow concentration. The possibility of producing particles with different dispersiveness and morphology by employing the methods of spray separation and dilute solution atomization is demonstrated. The criteria of the system settings to generate the droplet flow with specified characteristics were determined. A Laval nozzle design is suggested for liquid atomization. A series of numerical experiments showed that a significant decrease in gas pressure (density) at the nozzle outlet provides an increase in the gas flow rate up to 734 m/s. The numerical estimation showed that the Laval nozzle proposed can improve the fine atomization efficiency by ~ 36%.

### Introduction

Fine particles are widely used in the modern world. The special attention is paid to the generation of particles and gas-droplet flows with a high surface activity (high surface area of particles). The high surface area of particles ensures highly effective neutralization of toxic aerosols, gases, and smoke, and reduces the negative environmental impact when agricultural chemicals are used.

Ultrafine particles have found their widespread application in medicine for pulmonary drug delivery as a noninvasive administration of drugs. Features of the pulmonary drug delivery application are characterized by the depth of penetration and deposition of ultrafine drug particles in the lungs. The introduction of new drug delivery technologies requires the development of effective methods and tools to generate preparations with desired characteristics, as well as the study of delivery principles and mechanisms. The elaboration of new approaches for the production of substances having particles with specified morphology as well as the investigation of properties and kinetics of such particles is promising.

There is a major problem in the industry associated with improving the manufacture efficiency of ultrafine materials to design new types of energetic constituents for fuels and of electric power sources.

Current trends in the ecologization and reduction of pollutions caused by the sources of smoke and gas emissions make it important to study the interaction between ultrafine particles and the environment.

The problem we deal with is the generation of fine particles with specified characteristics (dispersion, concentration, flow rate) for a broad range of scientific problems.

### Research problem formulation

To produce submicron nanosized particles, the method of dispersing dilute solutions containing volatile solvents (spray drying) has widely been used. The effectiveness of this approach is due to the efficiency of liquid atomization. For the generation of ultrafine droplets, the most widely applied method is aerodynamic atomization [1, 2].

The fine and ultrafine liquid atomization is due to the complex influencing factors such as strong turbulence, air resistance, cavitation, etc. [1, 3]. The liquid disintegration occurs in the near-nozzle region chaotically and highly irregularly [1, 4, 5]. At the first stage, there is formed a conical liquid film on the nozzle edge. The aerodynamic gas flow exposure causes formation of unstable surface waves, which leads to the liquid film sheet breakup and spray formation [1, 4, 6]. Schematically, the liquid disintegration can be represented as shown in fig. 1. Dombrowski and Johns [7], on the basis of analytical relations, the analysis of aerodynamic instability, and disintegration of viscous liquid films, suggested the following expression for estimating the diameter of ligaments formed upon the breakup of a planar liquid film:

$$d_L = 2 \left( \frac{4}{3f} \right) \left( \frac{K_N^2 \sigma^2}{\rho_g \rho_L U_f^4} \right)^{1/6} \cdot \left( 1 + 2.6 \mu_L \left( \frac{K_N \rho_g^4 U_f^8}{72 \rho_L^2 \sigma^5} \right)^{1/3} \right)^{1/5}, \quad (1)$$

where  $d_L$  is the diameter of ligaments;  $f$  is the constant (for large Weber Numbers,  $We \gg 1$ ,  $f=12$  [8];  $K_N$  is the “nozzle parameter”;  $\sigma$  is the liquid surface tension;  $\rho_g$  and  $\rho_L$  are the gas and liquid densities, respectively;  $U_f$  is the velocity of gas flowing around the liquid film;  $\mu_L$  is the liquid viscosity. The “nozzle parameter” is determined by the design of the nozzle and, in a general case, can be expressed as [8]:  $K_N \approx t_s h$ , where  $t_s$  is the time required for disintegration of the liquid film;  $h$  is the film thickness. For an incompressible flow [9, 10], the following relation is suggested to estimate parameter  $K$ :

$$K_N = h^2 \cos^3 \theta / U_L, \quad (2)$$

where  $\theta$  is the cone semi-angle of the liquid flow;  $U_L$  is the liquid velocity at the atomizer tip. For an aerodynamic atomizer,  $U_L = U_f$ . Thus, for large Weber Numbers and substituting relations (1) and (2), we will have:

$$d_L = 0.9614 \cos \theta \left( \frac{h^4 \sigma^2}{\rho_g \rho_L U_f^4} \right)^{1/6} \cdot \left( 1 + 2.6 \mu_L \cos \theta \left( \frac{h^2 \rho_g^4 U_f^7}{72 \rho_L^2 \sigma^5} \right)^{1/3} \right)^{1/5}. \quad (3)$$

According to expression (3), the dispersiveness can be altered by changing the liquid film thickness ( $h$ ), the gas velocity ( $U_f$ ), and the gas density ( $\rho_g$ ). The estimation of the influence of these parameters on the liquid atomization is given below.

### Mathematical model

For the experimental study, we chose a standard aerodynamic nozzle shown in fig. 2.

To estimate the flow characteristic, we built a mathematical model of the intra-chamber channel with a variable cross-section. For building the model, we used non-stationary differential equations of gas dynamics in a one-dimensional case, expressing the law of mass conservation (4), momentum (5), energy (6), and equation of state (7) written for the internal energy.

$$\partial \rho_g S / \partial t + \partial \rho_g S U / \partial x = 0, \quad (4)$$

$$\partial \rho_g S U / \partial t + \partial (\rho_g U^2 + P) / \partial x = 0, \quad (5)$$

$$\partial \rho_g S (e + U^2/2) / \partial t + \partial [\rho_g U (e + P/\rho_g + U^2/2)] / \partial x = 0, \quad (6)$$

$$e = P / [\rho_g (k-1)], \quad (7)$$

where  $U$ ,  $P$ ,  $e$  are the velocity, the pressure, and the energy of the gas flow;  $S$  is the cross-section area of the channel;  $t$  is the time;  $x$  is

the coordinate;  $k$  is the adiabatic exponent. The inlet boundary conditions for a given inlet gas pressure,  $P_{in}$ , are calculated by the relations:

$$\rho_{in} = P_{in} / (R_v T), \quad G = S \cdot P \cdot \sqrt{(R_v T / k)^{-1} \cdot ((k+1)/2)^{-\frac{k+1}{k-1}}}, \quad U_{in} = G / (\rho_{in} \cdot S_{in}),$$

where  $R_v$  is the gas constant;  $T$  is the gas temperature;  $G$  is the gas mass flow rate through the nozzle;  $S_{in}$  is the inlet cross-sectional area.

The outlet boundary conditions are calculated for known drag parameters on one of the preceding nodes (because drag parameters characterize the gas state in this node for any process) [11].

$$P_{out} = P_{I1} \cdot ((k+1)/2)^{-\frac{k}{k-1}}, \quad \rho_{out} = \rho_{I1} \cdot ((k+1)/2)^{-\frac{1}{k-1}}, \quad U_{out} = G / (\rho_{I1} S_{out}),$$

where  $I1$  is the penultimate node.

To implement the calculation of equations (4-6), a grid was built and a finite-difference scheme (8-10) suggested by S. Godunov [12] was employed that is robust and stable when solving similar problems.

$$(\rho_g \cdot S)_i^{j+1} = (\rho_g \cdot S)_i^j - (\tau/l) \cdot (M_i^j - M_{i-1}^j), \quad (8)$$

$$(\rho_g \cdot U \cdot S)_i^{j+1} = (\rho_g \cdot U \cdot S)_i^j - (\tau/l) \cdot (I_i^j - I_{i-1}^j) - (\tau P_i^j / l) \cdot (S_i^j - S_{i-1}^j), \quad (9)$$

$$\left[ S \cdot \rho_g \cdot \left( \frac{P}{(k-1) \cdot \rho_g} \right) + \frac{U^2}{2} \right]_i^{j+1} = \left[ S \cdot \rho_g \cdot \left( \frac{P}{(k-1) \cdot \rho_g} \right) + \frac{U^2}{2} \right]_i^j - \frac{\tau}{l} \cdot (E_i^j - E_{i-1}^j), \quad (10)$$

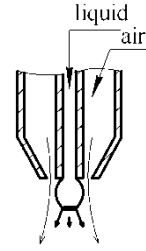


**Figure 1.** A schematic showing liquid film sheet breakup mode in aerodynamic atomization

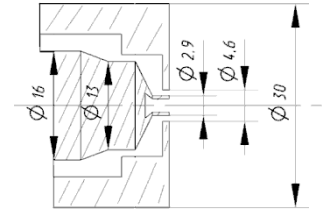


**Figure 2.** A nozzle drawing

where  $i$  is the node number along the axis of the nozzle;  $j$  is the number of the time iteration;  $l$  is the step size (length divided by the number of nodes);  $\tau$  is the time step, which is calculated according to the Courant condition ( $\tau = K \cdot l / c$ , where  $K$  is the Courant number,  $c$  is the sound speed in the gas);  $S$  is the cross-sectional area in the node  $i$ ;  $M$ ,  $J$ ,  $E$  are the flows of mass, momentum, and energy calculated by the formulae:

$$M = S \cdot \rho'_g \cdot P', \quad J = S \cdot (P' + \rho'_g \cdot (U')^2), \quad E = S \cdot \left[ \rho'_g \cdot U' \cdot P' / ((k-1) \cdot \rho'_g) + U'^2 / 2 \right],$$

where  $\rho'_g$ ,  $P'$ ,  $U'$  are the density, pressure, and velocity at the contact discontinuity between two adjacent grid nodes, which are calculated according to the method proposed by S. Godunov [12].

Using the above methods, the dependence of the gas density at the outlet orifice on the inlet gas pressure was numerically investigated (fig. 3).

It was also found that, for the chosen nozzle and steady flow, the inlet gas pressure had almost no effect on the gas flow velocity and the volume flow rate. The outlet flow velocity is limited to 350 m/s; the volume flow rate is  $2.46 \cdot 10^{-3} \text{ m}^3/\text{s}$ .

This phenomenon can be explained as follows: with increasing gas pressure, the density and the mass flow increase at the same time by a proportional value, thus giving  $G_V = G / \rho_{out} = \text{const}$ .

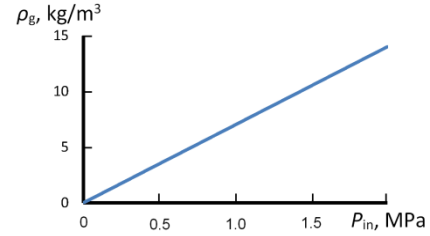


**Figure 3.** Influence of the inlet gas pressure on the gas density at the outlet orifice

### Influence of the gas jet density on liquid atomization

In this work, the following parameters were used: distilled water for spraying, liquid flow rate  $\sim 0.003 \text{ kg/s}$ , operating gas pressures from 0.2 MPa to 2.0 MPa, which corresponded to the change in the outlet gas density from  $1.4 \text{ kg/m}^3$  to  $14 \text{ kg/m}^3$  (calculation results).

For the numerical experiment, the thickness of the liquid film was estimated using (11) [10] and reverse numerical calculations of (3) for a known Sauter mean diameter (SMD).

$$h = 0.5 \left[ d_0 - \left( d_0^2 - 4m_L / (\pi \rho_L U_L) \right)^{1/2} \right], \quad (11)$$

where  $d_0$  is the final discharge orifice diameter;  $m_L$  is the mass flow rate of the liquid.

For measurements of the spray characteristics, a Malvern Spraytec laser analyzer (Malvern Instruments, Malvern, UK) [13] was employed. The calculation results and experimental data are presented in fig. 4.

The results of numerical and experimental studies showed that the influence of the gas density (from  $3 \text{ kg/m}^3$  to  $14 \text{ kg/m}^3$ ) on the dispersiveness was insignificant. The experiment showed that the mean droplet size decreased with increasing gas density up to  $3 \text{ kg/m}^3$ . This phenomenon can be attributed to a non-stationary nozzle injection mode. Further increase in the gas density leads to no variation in the dispersiveness, which is in agreement with the calculations.

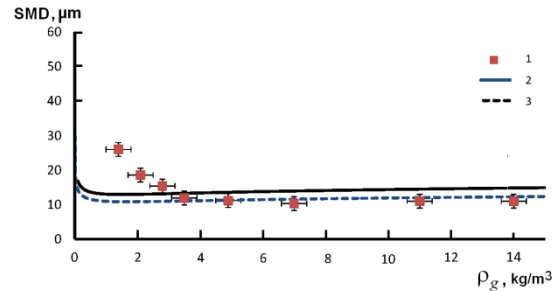


**Figure 4.** Influence of the gas density on the mean droplet size: 1 – experiment; 2 – calculation,  $h=190 \text{ μm}$  (Eq.(11)); 2 – calculation,  $h=150 \text{ μm}$  (Eq. (3))

### Influence of the gas velocity on liquid atomization

A numerical estimation was performed to study the possibility of improving the efficiency of liquid atomization. The thickness of the liquid film is considered to be  $150 \text{ μm}$  and gas density –  $4 \text{ kg/m}^3$ , which corresponds to the given nozzle and the experimental conditions. The calculation results are given in fig. 5.

The above analysis of the atomizer showed that the outlet gas velocity did not depend on the inlet gas pressure and was limited to the value of  $\sim 350 \text{ m/s}$ . The numerical estimation of the gas velocity effect on the mean droplet size demonstrated that an increase in the gas velocity (above 350 m/s) led to a decrease in the mean droplet size. To optimize the atomization (increasing gas velocity), we propose a simple design of the Laval nozzle (fig. 6).

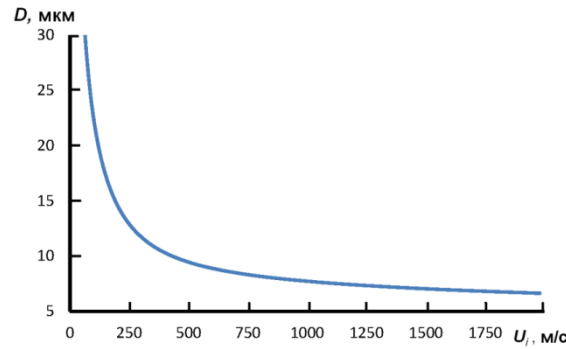


**Figure 5.** The gas velocity versus the mean droplet size ( $h=150 \mu\text{m}$ )

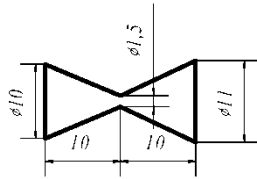


**Figure 6.** A schematic of the Laval nozzle

The Laval nozzle has a high efficiency of the conversion of compressed gas energy to the flow velocity. Considering the following parameters, i.e. volume gas flow rate from  $2.5 \cdot 10^{-3} \text{ m}^3/\text{s}$  to  $5.0 \cdot 10^{-3} \text{ m}^3/\text{s}$  and the inlet gas pressure of 0.5 MPa, we performed a series of numerical experiments. The numerical calculation revealed that the simple nozzle of Laval type gave an increment in the outlet gas velocity from 354 m/s to 734 m/s owing to a significant pressure decrease in the nozzle throat ( $\sim 0.01 \text{ MPa}$ ). The numerical estimation showed that the Laval nozzle used would allow an improvement in the ultrafine atomization performance by  $\sim 36\%$  (the average SMD decreased from  $11.26 \mu\text{m}$  to  $8.24 \mu\text{m}$ ).

### Influence of the film thickness on liquid atomization

Theoretical and experimental results of the estimation of the film thickness influence on atomization are presented in fig. 7. The theoretical estimation was performed by numerical computation of expression (3). The experimental estimation was performed for the following conditions:  $m_L \sim 0.003 \text{ kg/s}$ , inlet gas pressure ( $P_{\text{in}}$ )  $\sim 0.5\text{-}0.7 \text{ MPa}$ ,  $h=150 \mu\text{m}$ . In the experiments, the film thickness was varied by changing the liquid mass flow rate. The comparison between the film thickness and the mass flow rate of the liquid was made in accordance with relation (11) for the assumption that the liquid velocity at the atomizer tip is independent of the liquid mass flow rate and equal to the outlet gas velocity ( $\sim 350 \text{ m/s}$ ). Thus, fig. 7 shows that the decrease in the film thickness leads to a decrement in the average droplet size in the spray.

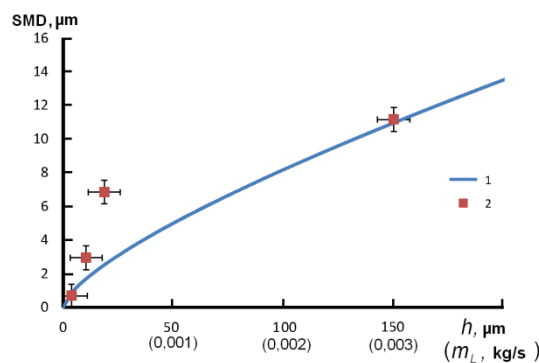


**Figure 7.** The film thickness as a function of the mean droplet size: 1 – calculation; 2 – experiment



Obviously, there is a restriction on the film thickness value, caused by surface tension, viscosity, as well as surface wettability of the atomizer tip. In the experiments, the reduction of the flow rate allowed us to increase the amount of the fine droplet fraction in the gas-droplet flow (results are also shown in fig. 8):

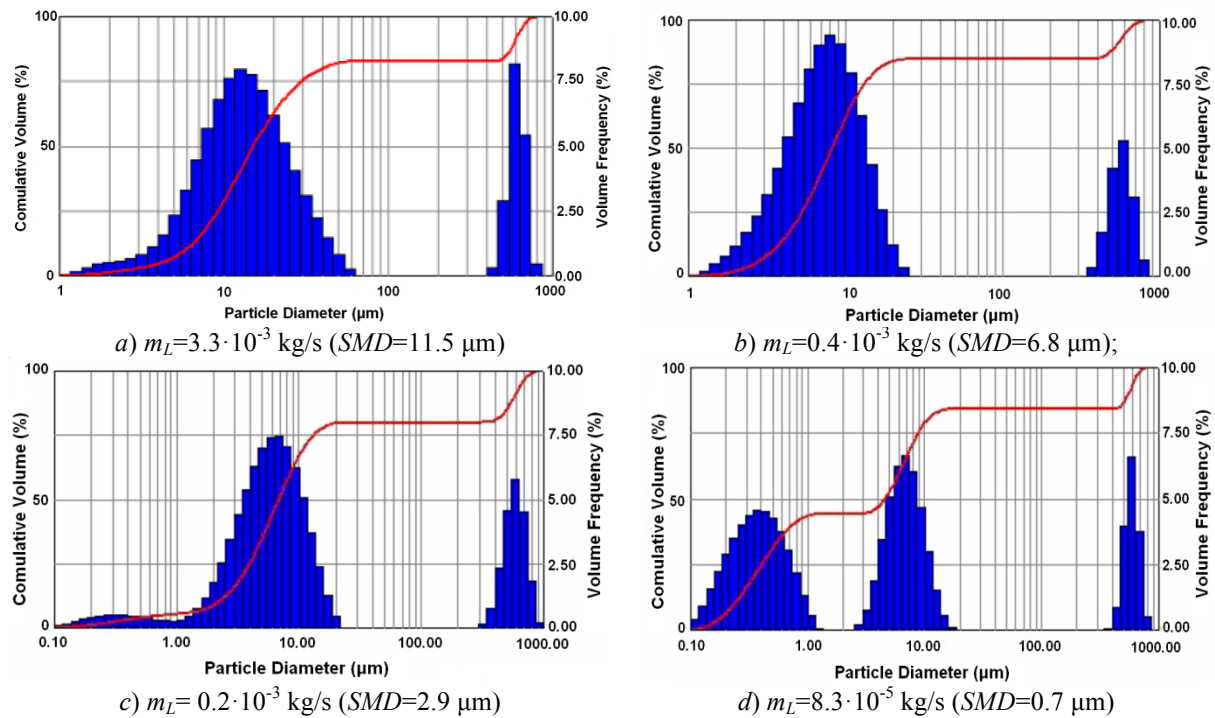


**Figure 8.** The droplet mass distribution function for different liquid flow rates at the atomizer tip

Fig.8d illustrates the possibility of generating submicron droplets using the atomizer with a minimized liquid flow rate at the atomizer tip. At this point, to atomize 100 g of liquid into droplets with SMD=6.8  $\mu\text{m}$  (fig.8b), the gas volume of  $\sim 1.3 \text{ m}^3$  is required; for SMD=2.9  $\mu\text{m}$ , the gas volume of  $\sim 2.5 \text{ m}^3$  is necessary. The droplet concentration in the gas flow was  $\sim 0.077 \text{ kg/m}^3$  (SMD=6.8  $\mu\text{m}$ ) and  $\sim 0.038 \text{ kg/m}^3$  (SMD=2.9  $\mu\text{m}$ ), respectively (here, we mean the droplet concentration in the gas flow at atmospheric pressure).

It was noted that, for the maximum liquid flow rate ( $m_L = 3.3 \cdot 10^{-3} \text{ kg/s}$ ), the percentage by volume of droplets below 10  $\mu\text{m}$  in the main flow was  $\sim 30\%$ ; the percentage by volume of droplets below 6  $\mu\text{m}$  was  $\sim 12\%$ .

Thus, to produce 100 g of droplets less than 10  $\mu\text{m}$  in size, it is required to atomize 303 g of liquid into droplets with SMD=11.5  $\mu\text{m}$ ; the required gas volume is  $0.5 \text{ m}^3$  (the mass of all droplets is 303 g and 100 g (30 %) is the mass of droplets less than 10  $\mu\text{m}$  in size); to produce 100 g of droplets less than 6  $\mu\text{m}$ , it is needed to atomize 833 g of liquid into droplets with SMD=11.5  $\mu\text{m}$  and the required gas volume is  $\sim 0.9 \text{ m}^3$  (the mass of all droplets is 833 g and 100 g (12 %) is the mass of droplets less than 6  $\mu\text{m}$ ).

Thus, it can be assumed that the utilization of secondary fine and ultrafine droplets from the coarse polydisperse flow to generate fine droplets is more effective than primary fine liquid atomization.

### Spray separation

The method of spray separation is widely used to produce fine droplets [14-17]. In this paper, to implement the idea of separating the desired droplet fraction, a primary polydisperse flow is passed into a separator as a spirally rolled-up pipe (fig. 9). The separation occurs in the field of centrifugal forces when droplets move into the pipe.

The separation is adjusted by changing the parameters: flow rate, number of turns, and pipe radius. Experimentally, by using a flexible corrugated pipe, we determined the parameters of the separator. Further, on the basis of the obtained data, we designed a separator system from polyvinyl chloride.

The experimental study revealed the restriction on the use of the separator in the performance mode (operating gas pressures above 0.4 MPa)—this is due to the increase in the flow rate in the pipe and the decrease in the separation quality. Results of the study devoted to solving this problem will be published in the nearest future.

In terms of maximum efficiency, the following parameters were chosen: operating gas pressure – 0.4 MPa, liquid flow rate  $\sim 0.003$  kg/s, pipe diameter – 0.1 m, diameter of the rolling-up is about 0.3 m, the number of turns – 1; height – 0.5 m. To stabilize the evaporation of the droplets in the flow, we used a 10% aqueous solution of glycerol. The designed system allows generating the droplet flow with  $SMD=2.7$   $\mu\text{m}$ , droplet concentration –  $0.055$  kg/m<sup>3</sup>, and production capacity  $\sim 0.167 \cdot 10^{-3}$  kg/s (the data are shown in fig. 10).

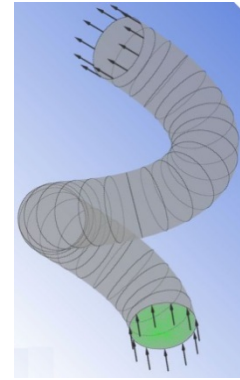


**Figure 9.** A schematic of the separator

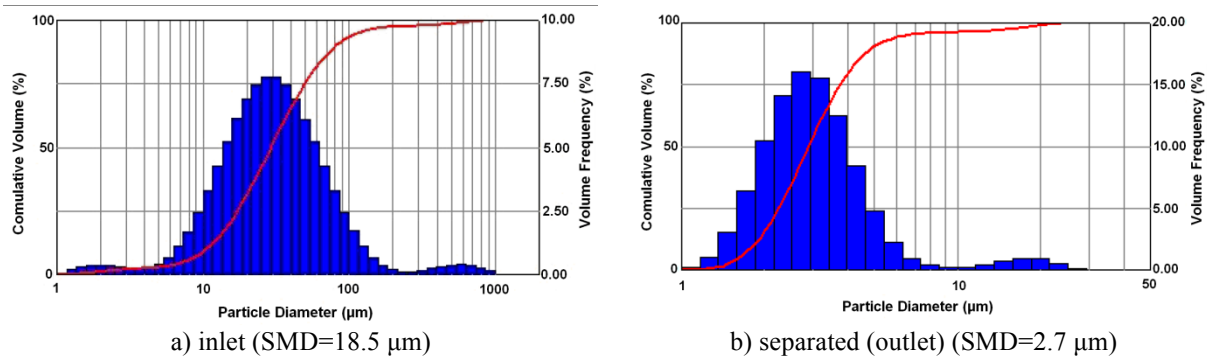


**Figure 10.** The droplet mass distribution function

The experimental results showed that the aerodynamic atomization method combined with the method of spray separation, in contrast to the "direct" setting of the aerodynamic atomizer, allows producing an ultrafine gas-droplet flow with a single-mode droplet mass distribution function close to the gamma function. The designed system enabled an increase in the gas-droplet flow concentration in the case of fine liquid atomization ( $SMD \sim 2.7$   $\mu\text{m}$ ) from  $0.038$  kg/m<sup>3</sup>—for a single aerodynamic atomizer – to  $0.055$  kg/m<sup>3</sup>—for the separator mode. The obtained experimental results confirm the hypothesis of highly efficient utilization of secondary droplets from the polydisperse flow to generate fine droplets.

The possibility of producing a fraction of fine droplets with certain dispersiveness is shown in fig. 11b.

Obviously, to obtain submicron droplets at the outlet of the separator, they must be contained in the droplet flow at the inlet. The content of desired fine droplets in the inlet flow results in their concentration at the outlet. To produce ultrafine particles, one may use the method of dispersing dilute solutions containing volatile solvents (spray drying). By changing the concentration of the solutions, particles with specified sizes can be produced [2, 18].

Also, by controlling the evaporation and crystallization processes, particles with different morphologies can be achieved [19]. As an example, one can consider the morphology of the particles formed as a result of the droplets evolution in a high-speed, impulse dispersed flow (fig. 12) [20-22].

The non-stationary conditions and high evaporation rate of droplets lead to the formation of particles with different morphologies [19].

Thus, the possibility of generating particles with different dispersiveness and morphology by using the spray separation method and the method of dispersing dilute solutions have been demonstrated.

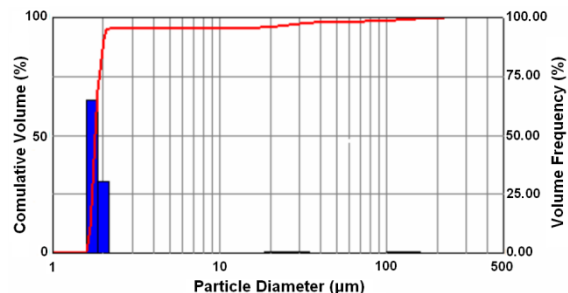


**Figure 11.** The monodisperse droplet flow generation

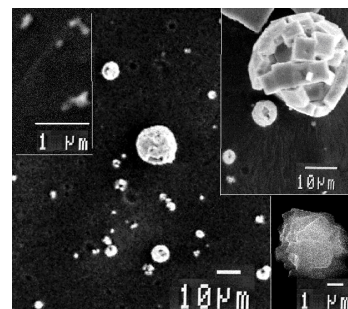


**Figure 12.** The morphology of the particles formed in a high-speed, impulse dispersed flow [21]

## Conclusions

As a consequence, the generation of fine particles and gas-droplet flows with specified characteristics for a wide range of scientific problems has been investigated. The aspects of aerodynamic fine atomization and the effects of atomizing gas density, gas velocity and mass flow rate, and liquid film thickness on the droplet formation have been studied.

As a result of gas-dynamic calculations, we have found that the standard atomizer is low efficient because of the limitation of the outlet gas velocity (less than 350 m/s). For further investigation, we proposed a design in the form of a Laval nozzle. A series of numerical experiments have shown that a significant decrease in the gas pressure (density) at the nozzle outlet provides an increase in the gas flow rate up to 734 m/s. The numerical estimation has shown that the Laval nozzle utilization will allow an improvement in the ultrafine atomization efficiency by  $\sim 36\%$ .

The hypothesis of high efficient utilization of secondary droplets from the polydisperse flow to generate fine particles have been suggested and experimentally confirmed. A prototype device implementing the idea of separating the desired droplet fraction from the primary polydisperse flow has been developed. The experimental results showed that the aerodynamic atomization method, coupled with the method of spray separation, in contrast to the "direct" setting of the aerodynamic atomizer, makes it possible to produce an fine gas-droplet flow with a single-mode droplet mass distribution function close to the gamma function.

In the case of fine liquid atomization, the designed spray system enabled the increase in the gas-droplet flow concentration. The possibility of efficiently generating the fine fraction of droplets with certain dispersiveness has been demonstrated. The criteria of the system settings for the generation of a droplet flow with specified characteristics have been determined.

The research results have many technological and scientific applications, e.g., the urgent task of improving the productivity and efficiency of technologies for the synthesis of ultrafine materials.

## Acknowledgements

The research was partially supported by the RFBR, research project No. 12-08-31282 mol\_a.

## Nomenclature

$c$  is the speed of sound in the gas;  
 $d_L$  is the diameter of ligaments;  
 $d_0$  is the final discharge orifice diameter;  
 $E$  is the flows of energy;  
 $e$  is the energy of the gas flow;  
 $G$  is the gas mass flow rate;  
 $G_V$  is the gas volume flow rate;  
 $h$  is the film thickness;  
 $l_1$  is the penultimate node  
 $J$  is the flows of momentum;  
 $K$  is the Courant number;  
 $K_N$  – is the “nozzle parameter”;  
 $k$  is the adiabatic exponent.  
 $l$  is the step size (length divided by the number of nodes);  
 $M$  is the flows of mass;  
 $m_L$  is the mass flow rate of liquid;  
 $P$  is the gas pressure;  
 $P_{in}, P_{out}$  are the inlet and outlet gas pressure;  
 $R_v$  is the gas constant;  
 $S$  is the cross section area;  $S_{in}$  is the inlet sectional area.  
 $T$  is the gas temperature;  
 $t_s$  is the time required for disintegrated of the liquid film;  
 $U$  is the gas velocity;  
 $U_f$  is velocity of gas flowing the liquid film;  
 $U_L$  is the liquid velocity at the atomizer tip;  
 $x$  is the coordinate;

$\theta$  is the cone semi-angle of liquid flow

$\mu_L$  is the liquid viscosity.

$\rho_g$  and  $\rho_L$  are the gas densities and liquid, respectively;

$\sigma$  is the liquid surface tension;

$\tau$  is the time step, which is calculated according to the Courant condition ( $\tau = K \cdot l / c$ );

## References

- [1] Liu H., Science and Engineering of Droplets: Fundamentals and Applications. New York: William Andrew Publishing: Noyes 508, 1999.
- [2] Salisbury, L., Tuncel, G., Ondov, J.M., *Aerosol Science and Technology* 15: 156-169 (1991).
- [3] Lienemann, H., Shrimpton, J., Fernandes, E., *Experiments in fluids* 42: 241-258 (2007).
- [4] Lefebvre, A.H., *Atomization and sprays*. New York: Hemisphere 417, 1989.
- [5] Yule, A.J., Widger, I.R., *International Journal of Mechanical Sciences* 38: 981-999 (1996).
- [6] Jazayeri, S.A., Li X., *Journal of Fluid Mechanics* 408: 281-308 (2000).
- [7] Dombrowski, N., Johns, W.R., *Chemical Engineering Science* 18: 203-214 (1963).
- [8] Dombrowski, N., Hooper, P.C., *Chemical Engineering Science* 17: 291-305 (1962).
- [9] Couto, H.S., Bastos-Netto D., *Journal of Thermal Science* 9: 265-270 (2000).
- [10] Lefebvre, A.H., Wang, X.F., *J. Prop. Power* 3: 11-18 (1987).
- [11] Sorokin, R.E., The theory of intrachamber processes in missile systems for solid fuels: internal ballistics. M:Nauka (in Russian) 288, 1983.
- [12] Godunov, S.K., Zabrodin, A.V., Ivanov, M.Y., Krayko, A.N., Prokopov, G.P., The numerical solution of multi-dimensional tasks of gas dynamics. M:Nauka (in Russian) 400, 1976.
- [13] Swithenbank, J., Beer, J.M., Taylor, D.S., *AIAA, Aerospace* 53: 421-447 (1976).
- [14] Gibb, F.R., Utell, M.J., Morrow, P.E., *Aerosol science and technology* 12: 376-385 (1990).
- [15] Tillery, M.I., Wood, G.O., Ettinger, H.J., *Environ. Health Perspect* 16: 25-40 (1976).
- [16] Kulkarni, P., Baron, P.A., Willeke, K., *Aerosol measurement: principles, techniques, and applications*. Hoboken, NJ, USA: John Wiley & Sons, Inc 904, 2011.
- [17] Clark, A.R., *Aerosol science and technology* 22: 374-391 (1995).
- [18] Sheth, P., Sandhu, H., Singhal, D., Malick, W., Shah, N., Kislalioglu, M.S., *Curr Drug Deliv* 9: 269-84 (2012).
- [19] Zhukov, A.S., *Izvestia VUZov. Physics* (in Russian) 53(11/3): 104-108 (2010).
- [20] Vorozhtsov, B.I., Kudryashova, O.B., Ishmatov, A.N., Akhmadeev, I.R., Sakovich, G.V., *Journal of Engineering Physics and Thermophysics* 83-6: 1149-1169 (2010).
- [21] Ishmatov, A.N., Vorozhtsov, B.I., Proc. 12th Triennial International Conference on Liquid Atomization and Spray Systems, Heidelberg, Germany, Sept. 2-6, 2012 # 1112.
- [22] Ishmatov, A.N., Vorozhtsov, B.I. 2013. Atmospheric and Oceanic Optics 26: 74-77 (2013).

## Spray drying of particles with narrow PSD by LAMROT atomizer and optimized gas distributor

Axel Mescher, Jens Kamplade and Peter Walzel

Particle Technology Lab, TU Dortmund, Germany

### Abstract

In laminar operated rotary atomization spiralling liquid threads are breaking up to droplets with narrow drop size distribution (DSD). However, the aerodynamic interaction of the spiralling liquid threads and the ambient gas leads to a distinctively broader DSD compared to the case without aerodynamic disturbance. In spray drying, the drying-gas-flow leads to even higher gas-relative-velocities of the liquid threads and to stronger disturbances of the thread break-up. Spray dried particles show a broader particle size distribution (PSD) due to the aerodynamic disturbance of thread break-up. After quantification of the gas-influence on the break-up of spiralling liquid threads in similarity trials, an optimization strategy was developed allowing for narrow distributed particles in spray drying processes with laminar operated rotary atomization. A new type of drying gas-distributor was designed by numerical flow simulation and tested with downscaled models of rotary atomizer and drying-gas-distributor. It could be shown that the apparatus allows for less intense aerodynamic interaction of liquid threads and drying-gas. The present work deals with a review on the development of the new gas-distributor and with drop and particle size data from atomization and spray drying experiments. Low *span*-values according to narrow distributed drop and particle sizes were obtained.

### Introduction – Spray drying demands on the DSD of the spraying system

In spray drying processes particles can be formulated directly from sprays [1]. The drops are dried by a drying gas that is contacted with the spray in a spraying tower. Due to the typically gentle drying conditions sensitive products can be dried. In Figure 1 a spray drying process is illustrated. Here, it contains a rotary atomizer for spray generation and the drying gas is supplied from the top of the spray drying tower. However, also pressure nozzles and pneumatic atomizers are frequently used for spray drying purposes, depending on the desired DSD and on the properties of the liquid feed. Concurrent and countercurrent flows of spray and drying gas are possible [1]. Another advantage of spray drying is the production of typically spherical particles, leading to highly flowable products.

One example for a spray dried product is shown in Figure 2. D-Mannitol particles spray dried from aqueous solution are shown. Depending on the drying conditions, the particles show completely different morphologies. While low drying rates, according to low dryer outlet temperatures, lead to rough particle surfaces, higher drying rates, high outlet temperatures respectively, lead to smoother particle surfaces [2, 3].

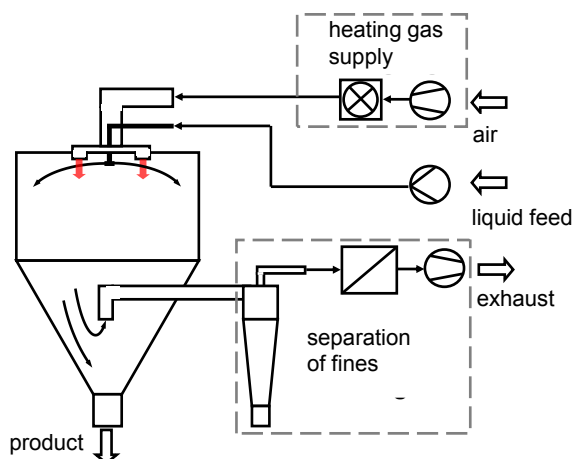


**Figure 1:** Flowsheet of a spray drying process with rotary atomization and ring-slit drying gas distributor. Larger particles can be collected directly at the cone of the spray dryer, while fines have to be separated from the drying gas by cyclone and/or filter.

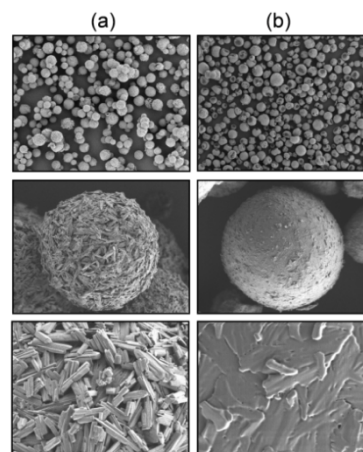


**Figure 2:** Exemplary images of spray dried D-Mannitol particles. Depending on the drying conditions the particles show a smooth or a rough morphology. The dryer outlet temperature in a) was 77 °C, and 111 °C in b).

The morphology of the particles shown in Figure 2 is crucial for their functionality as carrier for active pharmaceutical ingredients (API). See [2, 3] for further information regarding the spray drying of D-Mannitol as carrier particle for APIs. For the application of these powders, it is necessary to achieve homogeneous single particle properties, with high selectivity to the desired superficial morphology.

An important aspect for spray drying of powders with homogeneous particle morphologies is the width of the drop size distribution of the atomizer [4]. By usage of an atomizer dealing with a narrow DSD, homogeneous and worthy products can be obtained. The width of the DSD or PSD can be expressed in terms of the *span*, defined as:

$$span = \frac{d_{90,3} - d_{10,3}}{d_{50,3}} \quad (1)$$

### Rotary atomizers for narrow DSD and specific challenges in spray drying

Atomization with low *span* can be obtained with laminar operated rotary atomizers (LAMROT). In LAMROT atomization, the liquid feed is distributed into multiple laminar open-channel-flows [5], see Figure 3, left. After detachment, the liquid forms thin threads, elongated and attenuated by centrifugal acceleration, see Figure 3, center. The open channel flows in the atomizer bores exhibit small hydraulic diameters compared to the bore diameters. Additional attenuation of the threads leads to small drop size  $d_{50,3}$  compared to the detachment diameter. Thereby small drops can be achieved even by atomizers with large bores. Thread break-up is caused by capillary instability (Rayleigh-break-up), leading to narrow distributed droplets.

However, the spiralling liquid threads are subjected to relative movement to the gaseous ambience, causing a gas-relative-velocity  $v_{rel}$  of the threads. In spray drying  $v_{rel}$  is even higher due to the drying-gas-flow. Most often ring-slit drying-gas-distributors are used and the drying-gas is introduced with high axial momentum, in order to deflect the spray from the atomization plane and to prevent drops or wet particles from deposition at the dryer wall, compare Figure 1. The impact of the liquid/gas-interaction on the break-up of spiralling threads and on the *span*, especially in spray drying, has not been investigated yet.

Our research focusses on the development of an optimization strategy for spiralling thread break-up and LAMROT atomization in spray drying. In [6] the strategy to carry out similarity trials in the field of gravity was firstly introduced, compare Figure 3, right. In the similarity experiments the break-up of liquid threads, attenuated by gravity and under gas-crossflow was investigated. The experimental setup and operating conditions of the similarity trials were chosen with respect to typical liquid properties and operating conditions of LAMROT atomizers in spray drying. Empirical correlations for the mean drop size, the break-up length and the width of the DSD could be formulated from the similarity experiments. For further information see [7, 8]. In [9] it was shown, that the empirical correlations formulated from the similarity trials can be used for the design of rotary atomizers operated in the regime of spiralling thread break-up.

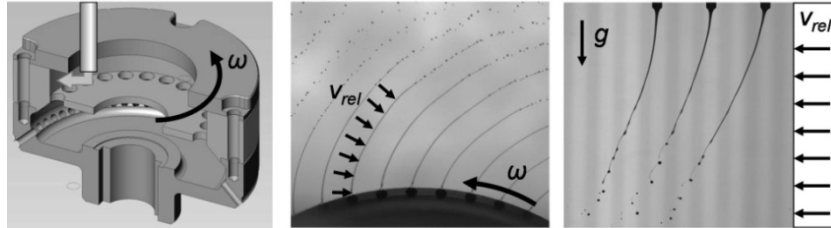


**Figure 3:** Left: Sketch/Cut-plane of a LAMROT atomizer [5]. Center: Backlight photograph of spiralling thread break-up. Threads are undergoing a gas-relative-velocity  $v_{rel} = R\omega$ . Right: Similarity experiments: Break-up of liquid threads, stretched by gravity and under gas crossflow. The system exhibits similar behaviour to spiralling thread break-up.

Experimental results can be transferred by usage of nondimensional numbers.

According to the similarity trials the width of the DSD (*span*) can be described as [9]:

$$span = [1,61 - \exp(-5,44We_g - 0,605)] \cdot [0,099\mu^{*0,364}We_g + 0,183\mu^{*-0,128}] \quad (2)$$

With the viscosity parameter  $\mu^* = (\alpha/\rho_l \sigma_{lg}^3)^{0,25}$ . The influence of the ambient air and its interaction with the threads is characterized by the gas-Weber-number  $We_g = v_{rel}^2 L_c \rho_g / \sigma_{lg}$ , defined as the ratio of dynamic gas pressure, caused by the gas-relative-velocity ( $v_{rel}$ ), and the capillary pressure. The capillary length  $L_c = (\sigma/\rho_l g)^{0,5}$  was found to be a suitable characteristic length scaling the break-up process of stretched liquid threads [10, 11], as it relates capillary forces to the field forces responsible for thread acceleration.

The similarity trials gave rise to the theory that the liquid/gas-interaction leads to distinctly higher *span*-values from laminar thread break-up. According to eq. 2 lowest gas-Weber-numbers, e.g. by realizing low  $v_{rel}$ , have to be targeted in order to achieve a low *span*-value of the spray. Regarding the application of LAMROT



atomizers in spray drying the desired low  $v_{rel}$  can be obtained by using an optimized drying-gas-distributor. The design of the apparatus was optimized to achieve the lowest possible gas-relative-velocity of the liquid threads.

### Development of the optimized drying-gas-distributor

In Figure 4 the optimized drying-gas-distributor is shown. The left figure shows the gas-distributor with installed LAMROT atomizer [12]. The right figure shows a sketch of atomizer, drying-gas-distributor and the intended flow-profile. The apparatus consists of two flow-chambers and two ring-slits for gas-supply. The flow-chambers are separated by an enclosed chamber, in order to achieve thermal insulation of the two separated gas-flows. The innermost flow-chamber contains of tangential inlets to apply a swirl-flow. The swirl-flow detaches from the inner ring-slit, delimited by a Coanda-opening of the drying-gas-distributor and the rotary atomizer itself. The geometry of the swirl-chamber as well as the swirl-intensity of the gas-flow were optimized in order to achieve a minimum gas-relative-velocity of the liquid threads close to the atomizer. Gas-flow-direction and velocity were optimized in order to realize a coincident movement of gas and liquid threads and a low  $v_{rel}$ .

At larger radii and after thread break-up has occurred, the second gas-flow detaches from the outermost flow-chamber. This flow consists of high axial momentum and high  $v_{rel}$  between gas and spray, in order to prevent the drops or wet particles from getting deposited at the wall of the spray dryer. However, the second gas-flow is supplied at radii large enough to not disturb the break-up of the liquid threads in the zone of drop formation. The correlation for break-up length of the threads gained from the similarity experiments [7, 8] was used to estimate the optimum position of the outer ring-slit. The outermost flow-chamber also consists of tangential inlets. This feature allows for circumferential flow homogenization across the outer ring-slit. The swirl-flow is transformed into an axial flow by blades installed just above the ring-slit.

Due to the design of the drying-gas-distributor with separated flow-chambers, it is possible to separately adjust the initial temperature or humidity of the gas-flows in spray drying. By using colder or humidified air for the inner swirl-flow atomizer, crusting can be avoided, while the axial gas-flow can be supplied with higher temperature to obtain the needed drying capacity of the process.

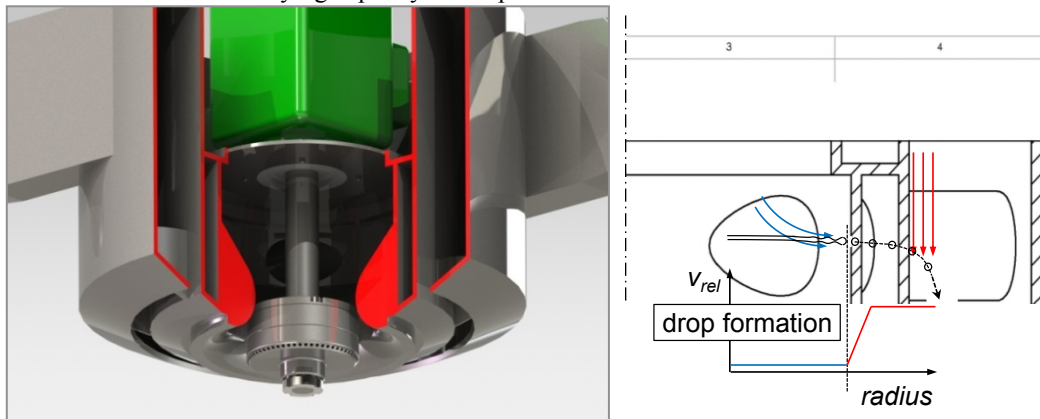


**Figure 4:** Optimized drying-gas-distributor for low aerodynamic influence on spiralling thread break-up. Due to the implementation of a swirl-flow close to the rotary atomizer, the liquid threads are subjected to low  $v_{rel}$ . Narrow distributed droplets, dry particles respectively, can be expected from such system. At larger radii and after drop formation the drying gas is supplied from a second ring-slit to deflect the spray and to avoid wall deposition of drops or wet particles. Swirl-gas-flow and axial drying gas-flow can be conditioned separately to prevent atomizer crusting, e.g by decreased temperatures or increased humidity of the swirl-gas-flow.

The geometry of the drying-gas-distributor was optimized regarding  $v_{rel}$  of the liquid threads. The calculation was carried out by numerical simulation (Ansys CFX 12) of the gas-flow inside and outside the drying-gas-distributor. Even though the atomizer and its rotation was included in the simulations, no interaction between gas and liquid threads were considered directly. The interaction between simulated gas-flow and liquid threads was calculated by an external routine including the analytical equations of motion of liquid threads as suggested in [6]. By superimposition of the velocity profiles of the liquid threads (analytical) and of the gas-velocity-profile in the atomization plane (numerical simulation), the relative-velocity profile of the liquid threads could be approximated.

In Figure 5 calculated profiles of the gas-relative-velocity of the liquid threads are shown. The figure illustrates qualitatively the decrease of  $v_{rel}$  due to the application of the swirl-flow from the optimized drying-gas-distributor. In Figure 5 a) the case without superimposed swirl-flow is shown. Assuming stagnant gaseous ambience and by neglecting air-drag,  $v_{rel}$  along the threads is given by the circumferential velocity of the atomizer. In Figure 5 b) the resulting relative-velocity-profile of the liquid threads is shown for a case with superimposed gas-flow from the drying-gas-distributor. The contour plot shows the axial velocity component of  $v_{rel}$  caused by the gas supply from above the atomization plane. In Figure 5 c) a calculation result with an even



higher swirl-gas-flowrate is shown. According to the circumferential speed of the rotary atomizer and the related initial velocity of the liquid threads respectively, the swirl-gas-flowrate can be optimized regarding a low  $v_{rel}$ .

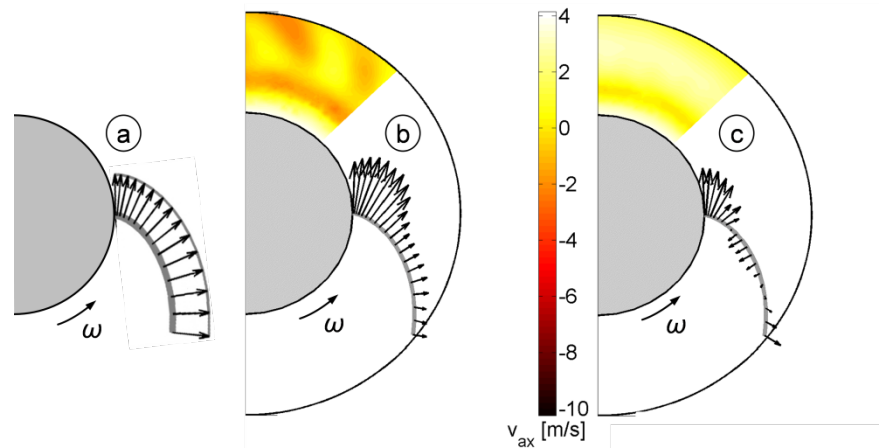


**Figure 5:** a) Gas-relative-velocity of a spiralling thread. Assuming stagnant gaseous ambience and by neglecting air-drag along the threads,  $v_{rel}$  is given by the circumferential velocity of the atomizer. b) By increasing the flowrate of the swirl-gas-flow  $v_{rel}$  of the threads is decreased. The contour plot illustrates the axial velocity component  $v_{ax}$ , caused by the gas-supply from above the atomization plane. c) By further increasing the flowrate of the swirl-flow, the gas-relative-velocity decreases towards a minimum value.

Prior to the implementation of the optimized gas-distributor to a spray drying process, the calculations were validated by a flow model. A downscaled PMMA-model (scale 2:3) of the drying-gas-distributor was fabricated. Additionally, a downscaled rotary atomizer was installed (Diameter: 66 mm). Figure 6 shows the test-rig. It consists of the PMMA-model and the downscaled rotary atomizer, both installed in a cylindrical housing. The housing contains an opening for spray characterization via laser-diffraction (Malvern Spraytec). Due to the transparency of the model, also qualitative observations of the liquid thread break-up are possible by using a strobe-light. The gas-distributor-model is connected to a blower, in order to supply the swirl-gas-flow around the rotary atomizer. For material conservation reasons, the experiments at the flow-model were carried out with cold air ( $\sim 40^\circ\text{C}$  blower outlet temperature) exclusively. However, in order to achieve comparable flow behaviour, the Reynolds-number of the gas-flow  $Re = \dot{V}_g \rho_g / (L \mu_g)$ , with the characteristic length scale  $L$  of the apparatus, was kept constant with respect to the simulations of the drying-gas-distributor.

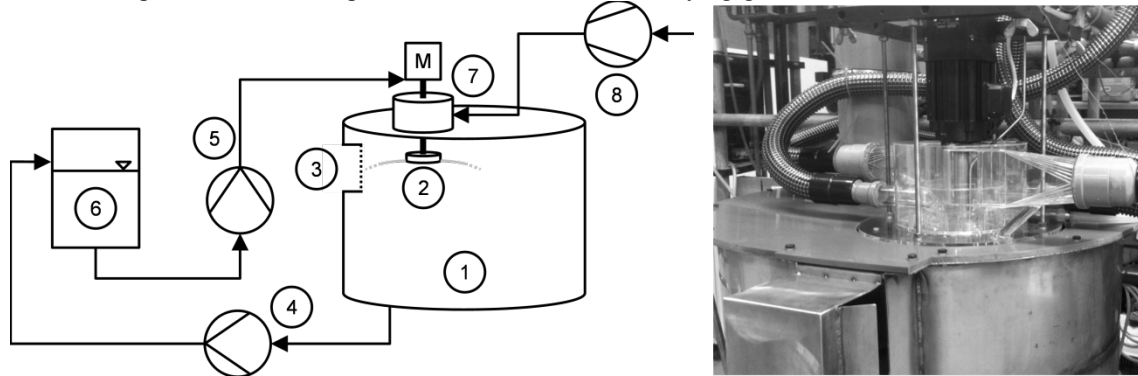


**Figure 6:** Test-rig for characterization of the optimized drying-gas-distributor. 1) Cylindrical housing. 2) rotary atomizer. 3) Opening for laser-diffraction-measurements. 4) Reflux-pump. 5) Feed-pump. 6) hold-up. 7) PMMA-model of the optimized drying-gas-distributor. 8) Blower for air supply to the PMMA-model.

### Characterization of the gas-flow-profiles of the optimized gas-distributor

Before the atomization experiments at model scale were carried out, the gas-velocity-profiles generated by the gas-distributor model were measured. A hot-wire-anemometer was used at 30 angular positions and at 4 radial positions within the atomization plane. The gas-distributor-model was operated at different swirl-gas-flowrates  $\dot{V}_{gas}$ . Even at low  $\dot{V}_{gas}$ , the swirl-gas-flow detached almost tangentially from the inner ring-slit, due to the high swirl-intensity. Furthermore, the swirl-gas-flow spread in a planar manner into the atomization plane of the rotary atomizer. From these observations, it can be assumed that the coincident movement of gas-flow and liquid threads is given during spiralling thread disintegration. Figure 7 shows the measured gas-velocities. From

the figure, it can be seen that the gas-velocity  $v_g$  decreases at larger radii. However, closer to the atomizer sufficient values of  $v_g$  can be obtained in order to influence the liquid thread break-up in a positive manner. The circumferential distribution of the gas-velocity is comparably homogenous, as shown in the right figure.

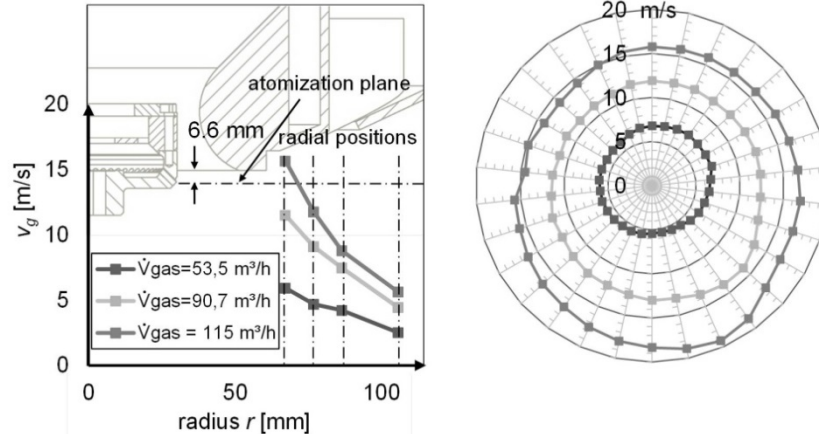


**Figure 7:** Gas-velocity-profile at the gas-distributor-model. The gas-velocity was measured with a hot-wire-anemometer at 30 angular positions and at 4 radial positions in the atomization plane. Left: Radial gas-velocity-profiles for different swirl-gas-flowrates and radial measurement positions (angular average). Right: Circumferential gas-velocity-profiles for different swirl-gas-flowrates at the inner radial measurement position.

### Results of atomization experiments with downscaled models of atomizer and gas-distributor

Atomization experiments were carried out after the characterization of the gas-velocity profile of the gas-distributor-model. According to the characterization of the gas-velocity-profile the gas-distributor-model was operated at different swirl-gas-flowrates  $\dot{V}_{gas}$ . Additionally different atomizer revolution rates were considered. Thereby, the influence of the coincident gas-flow on the spiralling thread break-up could be investigated for different gas-relative-velocities  $v_{rel} = R\omega - v_g$ .  $v_{rel}$  is given by the atomizer circumferential velocity  $R\omega$ , i.e. the initial velocity of the threads, and the measured gas-velocity  $v_g$ , see Figure 7.

In Figure 8 the course of the nondimensional mean drop size is shown as a function of the gas-Weber-number  $We_g$ . Results for a Newtonian water-glycerol-solution (24 mPas) are shown. The atomizer-revolution rate was varied between 3000 and 8000 rpm and  $\dot{V}_{gas}$  was varied between 0 and  $\sim 120 \text{ m}^3/\text{h}$ . The experimental results from rotary atomization (laser-diffraction measurements, see Figure 6) are plotted as marks and compared to the nondimensional correlations (lines) formulated from the similarity experiments in the field gravity [7, 8]. Figure 8 demonstrates that the mean drop size under gas-influence from the gas-distributor-model shows the behaviour expected from the similarity experiments. Larger drops are found at increased  $We_g$ .

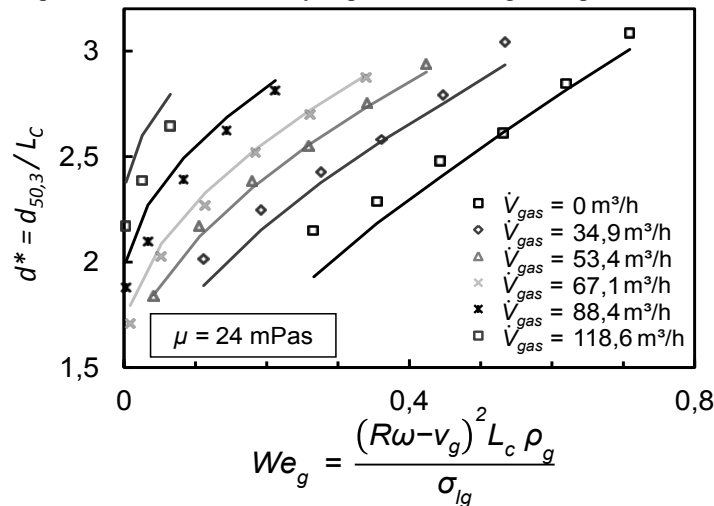


**Figure 8:** Comparison of the similarity experiments (lines) to rotary atomization experiments with PMMA-model of the optimized drying-gas-distributor for different  $\dot{V}_{gas}$  and atomizer revolution rates. The course of the nondimensional drop size as function of the effective gas-weber-number of the liquid threads shows comparable behaviour of rotary atomization and similarity experiments.

In Figure 9 the influence of the swirl-gas-flow from the gas-distributor-model on the *span* is shown. These experiments were, again, carried out at different swirl-gas-flowrates  $\dot{V}_{gas}$  and atomizer-revolution rates with a water-glycerol-solution. The results from rotary atomization experiments are compared to eq. 2, see also [7, 8]. From Figure 9 it can be seen that the *span* is low by usage of the optimized gas-distributor. On the other hand, Figure 9 shows that the *span* does not decrease at low  $We_g$  as expected from the similarity experiments. Though the *span* does not decrease towards the minimum value, it should be stated that the width of the DSD can be kept at least constant, even though a gas-flow is supplied. Regarding spray drying application of the gas-distributor, this observation is of major importance as gas must to be supplied in spray drying.

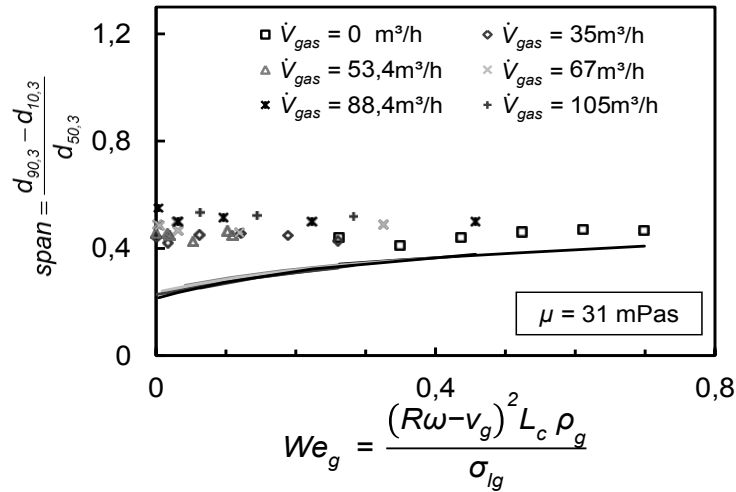


**Figure 9:** *span* of the drop size distribution. Rotary atomization experiments with PMMA-model of the optimized drying-gas-distributor are compared to the similarity trials (lines). Different gas throughputs and atomizer revolution rates were investigated.

In additional tests of the gas-distributor-model with axial gas-supply through the outer ring-slit (Figure 4), no impact of the additional gas-flow on the liquid threads or on the spray could be observed. Thereby, the feasibility of spray generation from LAMROT atomizer with the optimized gas-distributor could be demonstrated and the implementation of the system in spray drying could be approached.

### Results of spray drying experiments with optimized drying-gas-distributor

The study of the spray formation at the downscaled model of LAMROT atomizer with optimized drying-gas-distributor led to the implementation of the system in a pilot-scale spray drying plant, see Figure 1. The gas-distributor was fabricated from stainless steel according to the results of the geometry optimisation, see Figure 4. A 100 mm LAMROT atomizer was used (Figure 3, left) and spray drying experiments with aqueous solutions of D-Mannitol were carried out, compare Figure 2. Figure 10 shows first results of spray drying experiments with optimized drying-gas-distributor. Typical operating conditions regarding the atomizer revolution rate, the liquid feed rate  $\dot{V}_{Feed}$  as well as the drying conditions, i.e. heating gas throughput and inlet temperature, were chosen [2] and kept constant during all experiments. Only the swirl-gas-flowrate  $\dot{V}_{gas}$  was varied in order to quantify its impact on the spray drying process and on the width of the dry powder's PSD. The swirl-gas-flow was supplied at  $\sim 40^\circ\text{C}$  (blower outlet temperature) in order to prevent any atomizer crusting.

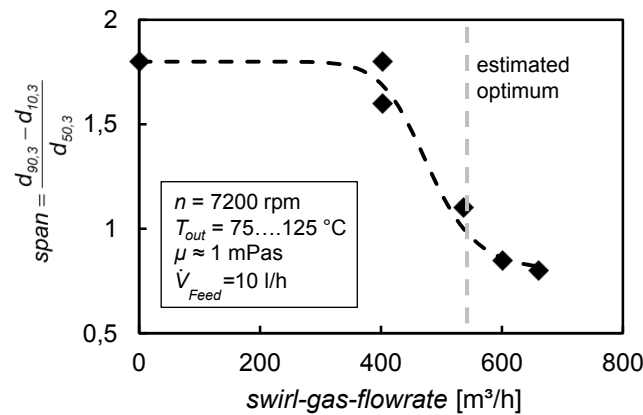


**Figure 10:** *span* of the particle size distribution from several spray drying experiments with optimized drying gas distributor. D-Mannitol was spray dried at constant atomizer revolution rate and liquid feed rate. The different dryer outlet temperatures  $T_{out}$  are caused by the different swirl-gas-flowrates  $\dot{V}_{gas}$ . The swirl-gas-flow was supplied at about 40 °C, while the heating gas temperature and flowrate were constant.

Figure 10 demonstrates the positive effect of the optimized drying-gas-distributor on the *span* of the dry powder. The *span* was measured via laser-diffraction (Malvern Spraytec) with a liquid dispersion system. Low swirl-gas-flowrates  $\dot{V}_{gas}$  according to low gas velocities  $v_g$  lead to high *span* values due to high gas-relative-velocity  $v_{rel} = R\omega - v_g$  and intense aerodynamic interaction with high  $We_g$ . By increasing  $\dot{V}_{gas}$ , lower values of  $v_{rel}$  and a less intense aerodynamic interaction with lower  $We_g$  can be obtained and a lower *span* of the PSD is achieved. The dashed line in Figure 10 indicates the “estimated optimum” calculated from flow velocity measurements within the spray dryer ( $v_g$ ) and from eq. 2. Even though the *span* still decreases slightly for even higher  $\dot{V}_{gas}$ , no spray drying experiments were carried out at higher swirl-gas-flowrates yet. The drying process itself is increasingly disturbed by the increasing amount of comparatively cold gas. In the future experiments will be carried out with a slightly heated swirl-gas-flow in order to not disturb the drying process. However, this may be disadvantageous for the handling of products with a strong tendency to atomizer crusting.

## Conclusions

The present work reviews the development of an optimized drying-gas-distributor for spray drying application of rotary atomizers operated in the regime of laminar thread disintegration. In similarity experiments, the aerodynamic interaction of liquid threads and ambient gas could be identified to disturb the break-up process and to lead to higher *span*-values of the DSD and PSD in spray drying. Therefore, the aim was to develop a spraying system allowing for a less intense aerodynamic interaction in spray drying. A coincident motion of liquid threads and drying gas was targeted in order to obtain a low gas-relative-velocity and a less disturbed break-up process. Therefore, a gas-distributor allowing for a low gas-relative-velocity was designed and optimized by numerical flow simulation. A downscaled model of gas-distributor and rotary atomizer were fabricated and investigated under conditions comparable to the spray drying application. In rotary atomization experiments with optimized gas-distributor, the desired behaviour with low *span* could be observed. First spray drying results also confirmed the positive effect of the optimized drying-gas-distributor on the dry powder *span*.

## Acknowledgements

The authors want to thank the German Research Foundation (DFG, SPP 1423) for the financial support.

## References

1. Masters, K., *Spray Drying Handbook*. 4th ed. 1985, London: George Godwin Ltd.
2. Littringer, E.M., et al., *Spray Drying of Mannitol as a Drug Carrier - The Impact of Process Parameters on Product Properties*. Drying Technology, 2011. **30**(1): p. 114-124.
3. Littringer, E.M., et al. *Tailoring particle morphology of spray dried mannitol carrier particles by variation of the outlet temperature*. in *ILASS - Europe 2010, 23rd Annual Conference on Liquid Atomization and Spray Systems*. 2010. Brno, Czech Republic.
4. Walzel, P., *Influence of Spray Method on Product Quality and Morphology in Spray Drying*. Chem. Eng. Technol., 2011. **34**(7): p. 1039-1048.
5. Schröder, T. and P. Walzel, *Design of Laminar Operating Rotary Atomizers under Consideration of the Detachment Geometry*. Chem. Eng. Technol., 1998. **21**(4): p. 349-354.

6. Mescher, A. and P. Walzel. *Breakup of stretched liquid threads at low gas relative velocities - Comparison of the laminar rotary atomization to the gravity condition*. in *ILASS - Europe 2010, 23rd Annual Conference on Liquid Atomization and Spray Systems*. 2010. Brno, Czech Republic.
7. Mescher, A., et al., *Gravity affected break-up of laminar threads at low gas-relative-velocities*. Chem. Eng. Sci., 2012. **69**(1): p. 181-192.
8. Mescher, A., A. Möller, and P. Walzel. *Influence of slow gas-crossflows on the drop size from stretched liquid threads*. in *ILASS - Europe 2011, 24rd Annual Conference on Liquid Atomization and Spray Systems*. 2011. Estoril (P).
9. Mescher, A. and P. Walzel. *Designing thread forming rotary atomizers by similarity trials*. in *ICLASS - International Conference on liquid atomization and spraying systems* 2012. Heidelberg.
10. Bär, P., *Über die physikalischen Grundlagen der Zerstäubungstrocknung*. 1935, TU Karlsruhe: Karlsruhe.
11. Eggers, J. and T.F. Dupont, *Drop formation in a one-dimensional approximation of the Navier-Stokes equation*. J. Fluid Mech., 1994. **262**: p. 205 - 21.
12. Mescher, A., *Einfluss der Gasführung in Sprühtrocknern auf den Fadenzerfall an Rotationszerstäubern - Analyse und Optimierung*, in *Fakultät Bio- und Chemieingenieurwesen*. 2012, TU Dortmund: Dortmund.

## **Influence of particles on ligament stretching and fragmentation of suspensions**

Christina M. Weickgenannt<sup>1</sup>, Ilia V. Roisman<sup>1</sup> and Cameron Tropea<sup>1</sup>

1: Institut for Fluid Mechanics and Aerodynamics, Technische Universität Darmstadt,  
D-64287 Darmstadt, Germany

### **Abstract**

This experimental study is devoted to fast stretching of suspension liquid bridges. The work is aimed at obtaining a better understanding of the behavior of particles in strong elongation flow. Suspensions of different particle geometries, sizes and concentrations are used. The elongation flow is generated by stretching a liquid bridge at a constant high acceleration. It is found that suspensions of a low particle concentration behave like Newtonian fluids irrespective of the particle form. The highest particle concentration up to which a Newtonian flow behavior is observed, is found for small spherical particles. Whenever the dimension of the diameter of the stretched liquid bridge equals the dimension of the particles, the particles tend to accumulate and force the bridge break-up.

An asymptotic similarity solution for the pinching of the quasi plastic liquids, corresponding to dense suspensions is obtained. It is shown that such liquids can break up faster than the Newtonian liquids.

---

### **Introduction**

Various industrial processes work with fluids that are enriched by particles like for example paints, cosmetics or sprays. In order to predict and control the suspension behavior during the melding process it is of great importance to understand their rheology. One of the pioneering works that deals with the viscosity of suspensions was developed by Einstein [1] and is related to the theoretical prediction of the shear viscosity of dilute suspensions. Numerous works have been published which refer to the measurement or calculation of the viscosity of suspensions under shear stress; in particular the work of Hoffman [2] deserves mention. While most of the existing studies try to find a correlation between particle volume fraction, or particle size and viscosity, Hoffman was the first who was able to visualize interaction between the particles in a shear flow.

Even if great efforts have been expended to understand the rheological behavior of suspensions, the existing knowledge is still insufficient to control and optimize industrial processes adequately. The main reason for that is that most of the published works are focused on the suspension behavior under shear stress. Regarding processes where suspension flow often occurs, it is obvious that their behavior under elongation also needs to be investigated. For example the mechanism of liquid transfer in printing is based on stretching and fragmentation of a tiny liquid bridge that forms between the gaps inside the gravure roll and the substrate. The basic mechanism of spray generation, for example for spray drying applications, consists also of the elongation of small liquid ligaments until they fragment into multiple droplets.

Some works are aimed at determining the elongational viscosity of suspensions using popular existing techniques [3,4,5]. Also there exist some investigations which are related to the microstructure and formation of particles inside the flow [6]. It is well known that the uniaxial flow of complex fluids, like suspensions, is determined by the interplay between the microstructure and macroscopic flow phenomena. One of the parameters that strongly increase the interaction between the particles, and therewith the rheological behavior, is the elongation rate. Although an understanding of the phenomena of fast stretching elongation flow would be of great importance for industrial processes like printing or spraying, less work is done on this topic.

The aim of the present work is therefore to identify effects that particles can have on a strong elongational flow based on experimental data. A standard experimental configuration is used in which a liquid bridge that is initially held between two parallel plates is stretched by increasing the distance between the plates. The contour evolution has been recorded by a high-speed camera. The device allows us to accurately control constant acceleration of a moving plate.

### **Experimental**

In order to investigate the influence of particles on elongational flow an experimental setup shown schematically in Fig. 1 is used. A liquid bridge, which is initially formed between two parallel plates, is stretched by moving the plates apart from each other. The setup is built in such a way that the top plate is mounted at a fixed position while the lower one is connected with a linear drive system in order to achieve the maximal possible acceleration downwards. The plates are aligned perfectly parallel to each other. A displacement pipette was used for metering, which allows dosing both low viscous and highly viscous liquids. A high speed camera is positioned horizontal to the gap and records the stretching and break-up processes.

To measure the force during stretching of liquid bridge a force transducer is fixed at the top plate and is directly in contact with the liquid bridge. To be able to compensate the noise produced by the linear drive, a

second force sensor is mounted similar to the first right next to it, as a reference. A National Instruments USB-6210 measurement system was used and the data was processed in Labview. The signal is sampled at 100 kHz in differential mode, and after that numerically integrated. The difference between the integral of the sensor and the integral of the reference is proportional to the force induced by the liquid filament.

Four different types of particles have been used in the experiments. In order to ensure a stable suspension, the bulk fluid is a 50% Glycerin-Water mixture whose densities equals the particle density. This means the particles can be transported easily by the flow and only the interactions between the particles affect the outcome of the stretching flow. Suspensions of different volume concentrations of particles have been prepared. All experiments are performed at constant plate acceleration of  $120 \text{ m/s}^2$ , the liquid bridge volume is always  $5 \mu\text{l}$ .

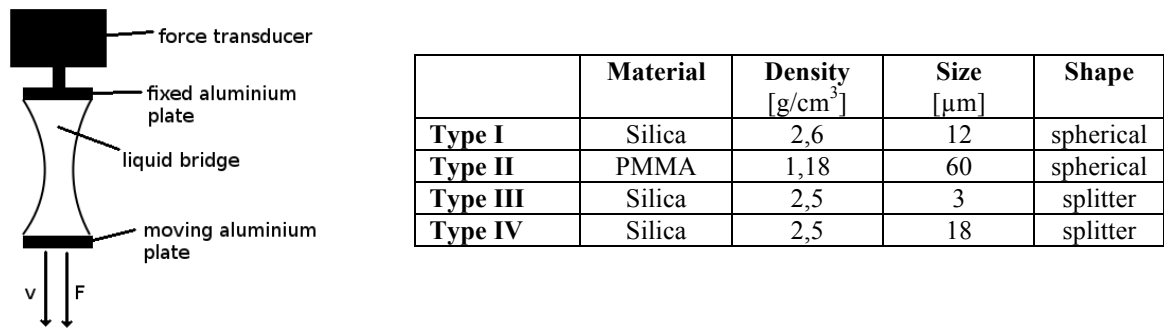


Fig. 1: Left: experiment setup, right: suspension properties.

## Results and Discussion

### Characteristics of Newtonian liquid bridge stretching

A liquid bridge forms between two plates, when the liquid tends to wet the surface. When such a bridge is stretched by increasing the distance between the two plates it is elongated in its axial direction while it contracts in its middle part. Above a critical bridge length the variation of curvature accounts for a variation of capillary pressure along the bridge, which introduces a second internal flow inside the bridge. The liquid from the middle flows towards the edge. In the region of the largest pressure difference which is the transition region between the cylindrical part and the liquid bridge head, the ligament finally detaches and breaks up into multiple droplets. If the stretching speed is very high and the moving plate is accelerated, as in this work, the detachment is not symmetrical. Because of the fast stretching, the part of the liquid bridge that is fixed at the moving plate is stretched more than the bottom part. This leads to a difference in the contour which results in different intensities of the capillary driven flow. The ligament first detaches at the fixed plate.

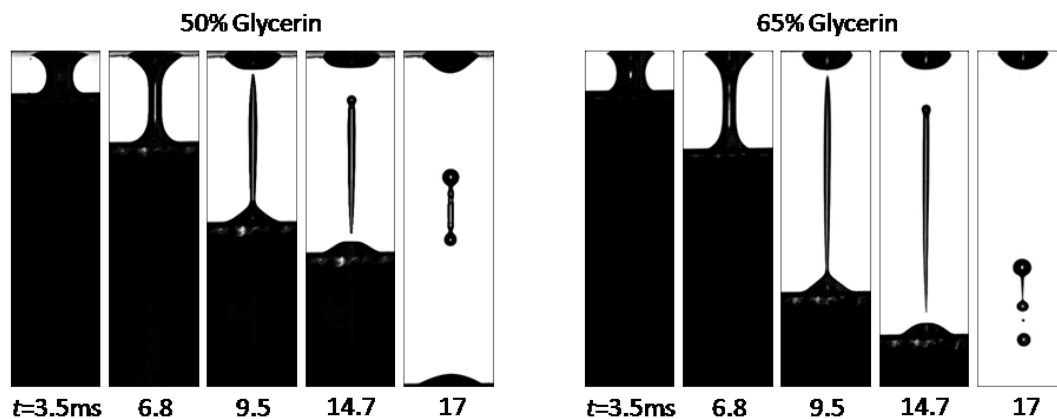


Fig. 2 Liquid bridge stretching. Left: 50% glycerin-water-mixture, right: 65% glycerin-water mixture.

The two images in Fig. 2 demonstrate the influence of liquid viscosity on the stretching behavior. One can see that during the stretching phase, the contour of the bridge seems to be unaffected by the liquid viscosity. On contrary, viscosity slows down the detachment process, which can be seen by the increase of the time and length of the ligament in the moment of the first detachment.

The evolution of the mid-point diameter does not show distinct differences for the two glycerine mixtures plotted in Fig. 3. More revealing insights are visualized by regarding the evolution of the force at the fixed plate over time during the stretching process. It can be noted that the liquid volume that has been used to



perform the force measurements is 50  $\mu\text{l}$ . At the beginning of the stretching process the force increases because the plate accelerates and the velocity gradients (and thus the viscous stresses) increase. The maximum in the evolution indicates the onset of detachment of the ligament middle part from the head. It can be seen that higher viscosities, corresponding to higher concentration of glycerine, lead to a higher maximum force, because the resistance to flow is higher. The maximum is reached nearly after the same time, because the onset of detachment of the jet in our case mainly depends on the geometrical parameters.

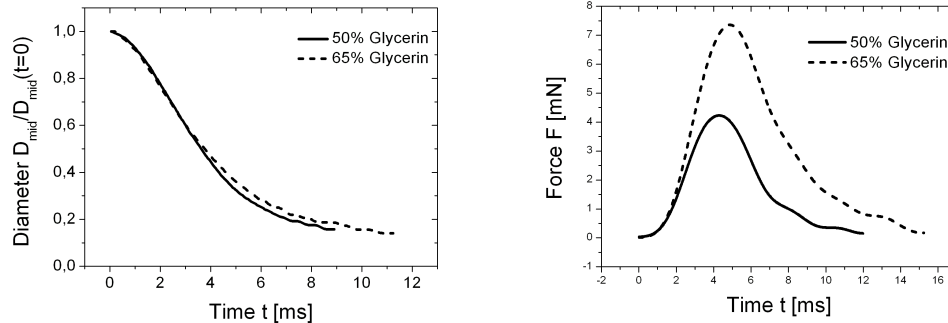


**Fig. 3** Left: Evolution of the mid-point diameter over time, right: evolution of force over time.

#### *Characteristics of dilute suspensions*

If the concentration of particles in the fluid is lower than 10% of the total volume the suspension behaves like a Newtonian fluid independent of the form of the particles. This is shown in the left diagram in Fig. 4 where 10% of particle type II is suspended in the 50% glycerine- mixture. No changes in comparison to the contour evolution of the pure glycerine-mixture as shown in Fig.3 are visible. If the concentration is very low the particles have enough space to freely follow the flow and no noticeable interactions occur.

For the case of very small spherical particles, type I, Newtonian flow behavior can be observed until a particle concentration of 20%. The viscosity of this suspension equals the one of a 65% glycerine-mixture, as it can be seen by comparing the contour evolution in Fig. 2 and 4. Small spherical particles can easily go round each other because they only touch each other at one point when they clash.

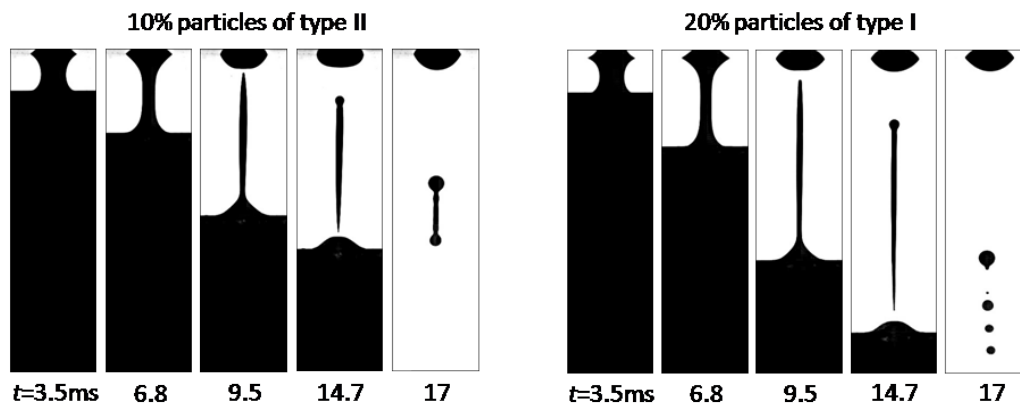


**Fig. 4** Suspensions behave like Newtonian liquids.

#### *Characteristics of dilute and semi dilute suspensions, up to 20% of particles*

Newtonian flow behavior is also revealed for suspensions of higher concentrations of large spherical and complex particles. But regarding the contour evolution of the suspension, unexpected phenomena are observable. In contrast to the small spherical particles it is more difficult for larger spherical particles to go round each other, since the space they need for an evasive maneuver is greater. Such evasive maneuver is necessary when the capillary driven flow sets in. Particles from the middle part will be moved towards the head. On their way they will clash with other particles. If the diameter of the liquid bridge in that region is too thin, the particles cannot pass each other and will accumulate. This happens for particles of type II at a concentration of 20%. Since their diameter is 60  $\mu\text{m}$  while the mid-point diameter is around several hundred accumulations forms along the middle part of the liquid bridge as it is shown in the left diagram of Fig. 4. The observation that the particles accumulate during the stretching in the ligament middle part is also the reason why the viscosity

could not have been measured with a standard rheological device like FiSer. There the evolution of the diameter is needed to determine the axial stress and thereby the fluid's extension viscosity.

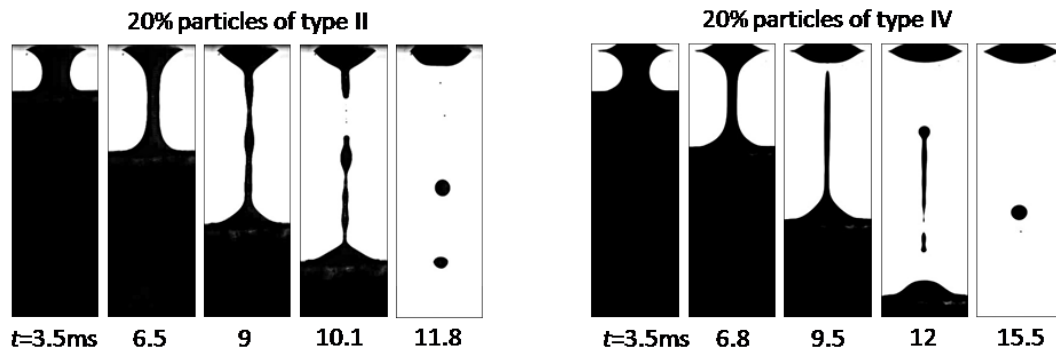


Fig. 5 Particle accumulation during stretching

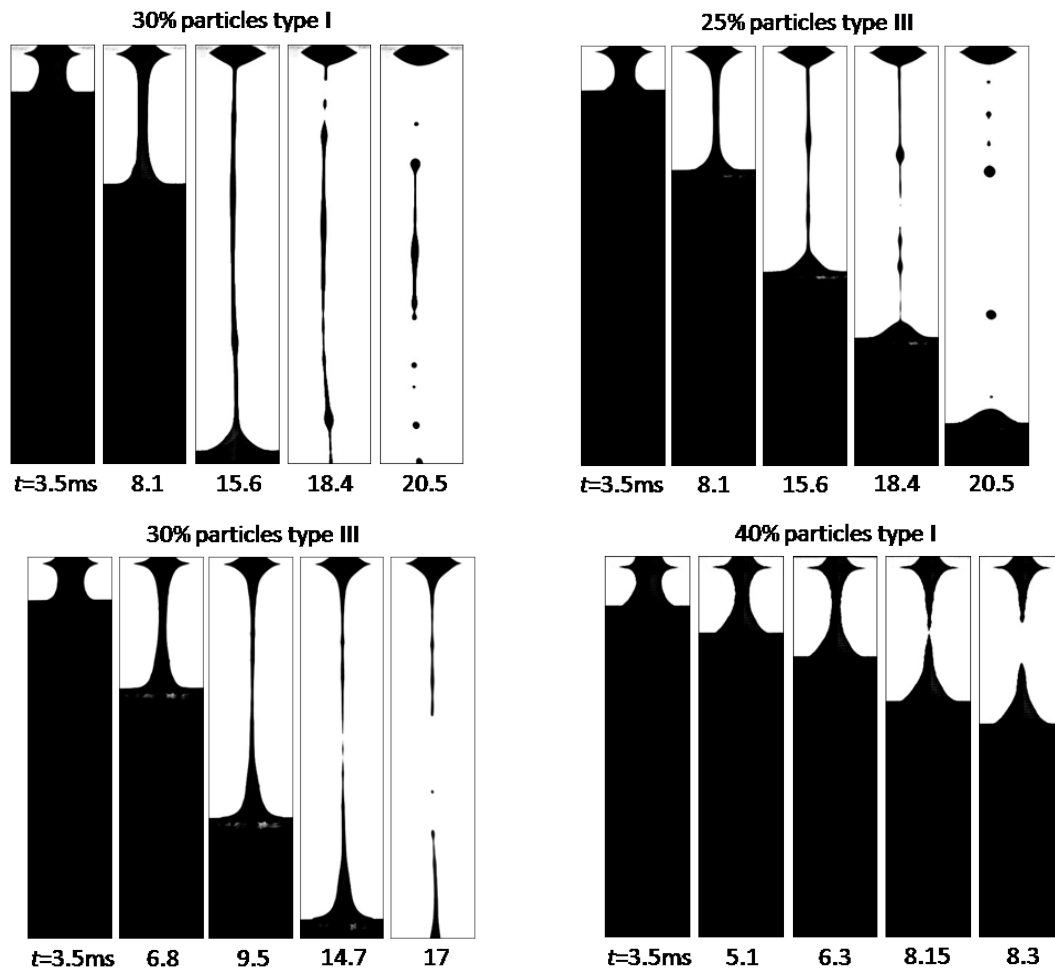


Fig. 6 Stretching of dense suspensions

Another phenomenon occurs for the case of complex, non-spherical particles. The main difference in comparison with spherical particles is that they have multiple points and areas of contact when they clash, instead of only one. Therefore the number of interactions as well as the possibility and strength of accumulations increase. The results of this can be seen in the right diagram in Fig. 5. The suspension used in that case consists of 20% of particles of type IV. The main difference to the other example is that the ligament appears to be thinner than in the previous examples. The reason for that can be explained as follows. When the

movable plate sets into motion the liquid bridge head that is connected to the plate will contract. This happens because the stretching velocity is faster than the velocity of a capillary wave for the chosen acceleration of  $120\text{m/s}^2$ . The contraction of the head means that the distance between the particles decreases. While this process does not lead to a noticeable change in the flow behavior for low particle concentrations it affects the flow of higher concentrated suspensions. Because of compression the particles in the liquid bridge head form a network and are therefore unable to follow the flow. On the other hand this means that less fluid is available in the middle part during elongation and therefore the diameter of the middle regions is thinner.

#### Characteristics of dense suspensions, particle concentration from 20% to 40%

With further increasing of the particle concentration the intensity of the described phenomena increases. If the amount of small spherical particles, type I, is increased up to 30% one can see the formation of very long ligaments as visualized in Fig. 6. The additional amount of particles leads to a further increase of the suspension viscosity. This leads to a slowdown of the capillary driven flow and therewith to a longer and thinner ligament. Now that the ligament is becoming thinner the effect of particle accumulation in the middle part of the liquid bridge during stretching that is described for big spherical particles in the previous section also occurs for the smaller particles. From this observation it can be concluded that whenever the geometrical dimension of the flow field reaches the dimension of suspended particles they tend to accumulate, since they are not able to move round each other.

#### Break-up characteristics

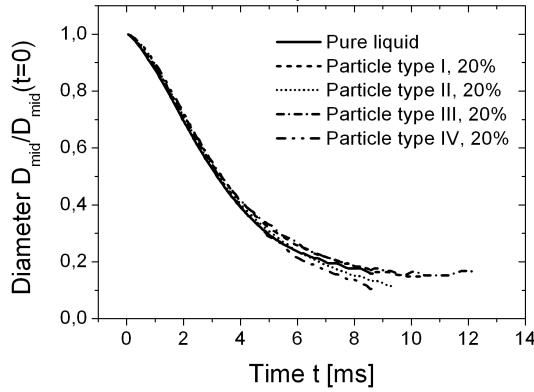


Fig. 7. Evolution of the jet diameter for various suspensions

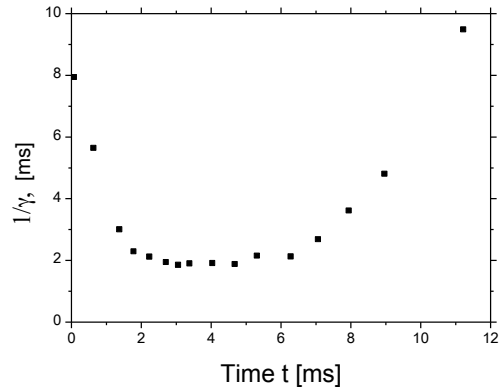


Fig. 8. Evolution of the typical stretching time  $1/\gamma$ .

The evolutions of the jet diameter in time are shown in Fig. 7 for various types of the particles, listed in the table in Fig. 1. The typical characteristic stretching time, defined as

$$\gamma = -\frac{D_{mid}}{2} \left[ \frac{dD_{mid}}{dt} \right]^{-1} \quad (1)$$

It can be seen, that at times  $t > 6$  ms, the value of  $\gamma$  increases linearly in time (see Fig. 8). This means that the jet is stretched in the inertial regime, corresponding to the approximately uniform diameter and linear distribution of the axial velocity.

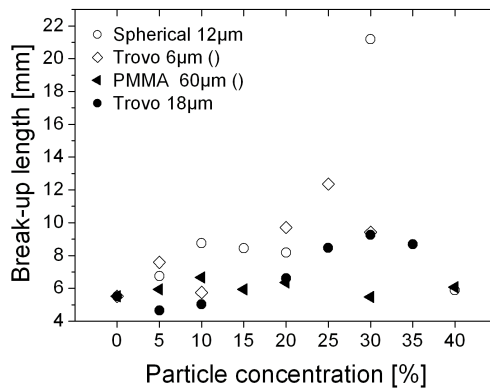


Fig. 9. Breakup length as a function of the suspension concentration for various particle types.

The variation of the breakup lengths for various particle concentrations and times is shown in Fig. 9. The breakup length of dilute suspensions increases with concentration, since the effective viscosity increases. The suspension viscosity in a wide range of concentrations can be described by numerous theoretical [1] and empirical correlations [4], [5]. However, the flow of the dense suspensions is much more complicated, since such suspensions have non-Newtonian properties. The decrease of the breakup length can be explained by the consideration of the jet necking.

The rheology of dense suspensions can be described by those as pseudo-plastic. In this case the axial stress in the suspension jet can be expressed as [6]

$$\Sigma_{xx} = -\sigma \kappa + 3^{\frac{n+1}{2}} K |u_x|^n \text{sign}(u_x) \quad (2)$$

where  $\sigma$  is the surface tension,  $\kappa$  is the curvature,  $u_x$  denotes the partial differentiating of the axial velocity  $u$  on the axial coordinate  $x$ .

The mass and momentum conservation equations can be thus written in the following form, taking into account only the leading terms

$$a_t + u a_x + \frac{u_x a}{2} = 0 \quad (3)$$

$$\rho(u_t + u u_x) = \sigma \frac{a_x}{a^2} + 3^{\frac{n+1}{2}} \frac{K}{a^2} \partial_x (a^2 u_x) \quad (4)$$

when the jet radius  $a$  approaches zero.

Denote now the time  $\tau = t - t_{\text{breakup}}$ . The similarity solution in the proximity to the breakup point can be found defining the similarity variable

$$\zeta = \sqrt{\frac{\rho}{K}} t^{-1+\frac{n}{2}} x \quad (5)$$

The jet radius and velocity are expressed through

$$a = \frac{\sigma t^n f(\zeta)}{K}, \quad u = \frac{\sqrt{K} t^{-n/2} g(\zeta)}{\sqrt{\rho}} \quad (6)$$

where the functions  $f(\zeta)$  and  $g(\zeta)$  can be obtained by integration of the following system of ordinary differential equations

$$f(2n + g') = 2(\zeta - \frac{n\zeta}{2} - g)f', \quad (7)$$

$$\sqrt{3}g'[-2f' + f^2(((-2+n)\zeta + 2g)g' - ng)] + 2 \cdot 3^{1+\frac{n}{2}} f g'^n (2f'g' + n f g'') \quad (8)$$

obtained by substitution of (5)-(6) in (3)-(4).

At the neck,  $\zeta = 0$ , the jet radius reduces as a power function,  $a \sim t^n$ , whereas for the viscous jet [7] it reduces linearly in time,  $a \sim t$ .

Since for the shear thickening liquids, like dense suspensions,  $n > 1$ , breakup can occur much faster. It should be noted, however, that the total breakup time of the stretching ligaments in our experiments consists of the time required for the reaching the jet length corresponding of the cut length of the Rayleigh instability, development and growth of small perturbations and only then, neck formation and breakup. We considered theoretically only the last stage of the break up process.

## Conclusions

Stretching of suspensions by an accelerated plate is investigated experimentally. It is shown, that jets of dilute suspensions behave similarly to the Newtonian jets, whereas breakup of dense suspensions show clear non-Newtonian effects. The breakup length of Newtonian and dilute suspensions increases monotonously with the effective viscosity. This length for dense suspensions in some cases reduces with the concentration of the particulate phase.

A similarity solution for the pinching of shear thickening liquid is obtained. The solution shows that the jet radius reduces as  $a \sim t^n$ , which can be much faster than the pinching of Newtonian jets.

## Acknowledgements

The financial support of C.M.W. from the Center of Smart Interfaces (Technische Universität Darmstadt) is appreciated as is the support from the DFG Research Training Group 1114 and DFG-Priority Programme (SPP) 1423. Furthermore the authors would like to thank Prof. Edgar Doersam and Dr. Hans-Martin Sauer from the Institute for Printing Science Technology at the TU Darmstadt for his encouraging discussions about the application of these investigations.

## References

- [1] Einstein, A., *Investigations on the theory of the Brownian movement*, Dover, New York (1956).
- [2] Hoffman, R.L., *Discontinuous and dilatant viscosity behaviour in concentrated suspension. I. Observation of a Flow instability*, Trans. Soc. Rheol., 1972. **16**, pp. 155-173.
- [3] Sinha-Ray, S., Fezzaa, K., Yarin A.L., *The internal structure of suspensions in uniaxial elongation*, J. Appl. Phys. 2013. **113**, 044906.
- [4] Pabst, W. *Fundamental considerations on suspension rheology*, Ceramics – Silikáty 2004. **48**(1), pp. 6-13.
- [5] Boyer, F., Guazzelli, E. and Pouliquen, O. *Unifying suspension and granular rheology*, PRL 2011. **107**, 188301.
- [6] Yarin, A. *Free liquid jets and films: hydrodynamics and rheology*, Longman Scientific & Technical, Harlow, John Wiley & Sons, Inc., New York (1993).
- [7] Eggers, J. *Universal pinching of 3D axisymmetric free-surface flow*, PRL 1993. 71, pp. 3458-3460.

## Atomization and spray formation for PVP powder production

A. Lampa and U. Fritsching

Particles and Process Engineering, University of Bremen,  
Badgasteiner Str. 3, Bremen, Germany

### Abstract

In a specific powder production process liquid feed materials of complex rheology are atomized with heated air to enhance the liquid breakup performance. The hot atomizer air is also used to dry the feedmaterial. A multiscale process design has been carried to predict the drying kinetics within the spray tower. The atomization of liquids with high viscosity and complex rheological behaviour (e.g. viscoelastic behavior) is of high industrial relevance. Higher concentrated feed solutions can be dried with less solvent content, thus saving energy. With conventional atomizers (especially pressure nozzles) process stability cannot be guaranteed or atomization of complex liquids is incomplete. The advantages of hot-gas atomization are investigated by atomizing polymer solutions with complex-rheology (Polyvinylpyrrolidon; Luvitec® PVP). Two different molecular weight classes of the polymer and different concentration of the polymer-water solutions are sprayed. Especially the polymers with high molecular weight (PVP Luvitec® K90) tend to form ligaments which stretch to filaments and finally form fibers. The difference between cold and hot atomizer gas on the breakup of the liquid is analyzed with shadowgraphy in the liquid breakup zone. The effect of high gas temperatures on the particle morphology in the pilot plant spray process is analyzed for differently concentrated feed solutions.

---

### Introduction

In this contribution the influence of hot atomizer gas on the disintegration of complex fluids has been investigated. The process design includes the experimental analysis of the disintegration of complex liquids, a multiscale process analysis with CFD-models and the powder production in pilot plant scale. The atomization of fluids with complex rheology (e.g. viscoelastic fluid) is of great importance in industrial applications. When using conventional atomizers, e.g. pressure nozzles, only an incomplete atomization can be achieved. The target of this project is the improved atomization of high viscous fluids with complex rheology with hot gas as assisting gas. The atomization of high viscous media (dynamical viscosity higher than 1 Pas) imposes great challenges in spraying processes. The fluid imposes a great resistance towards the disintegration in the first and secondary atomization step [1,2]. A strategy to improve the atomization is to increase the gas-liquid interface by e.g. prefilming nozzle (closed-coupled twin-fluid atomizer), where a liquid sheet is produced before the actual atomization takes place.

Several Processes for the fragmentation of complex rheological system are analysed and discussed in [4]. Several other nozzle design studies can be found in the literature. For the atomization of very viscous liquids through an internal mixing atomizer is conducted by Campanile and Azzopardi [6]. Fluids with newtonian rheology and dynamical viscosities up to 50 Pas can be atomized with air. Depending on the fluid properties and atomizer design and parameters strongly stretched ligaments can be detected, which result in a high fiber fraction in the dried spray product.

The increase in atomizer efficiency through the use of hot atomizer gas could be shown theoretically and in experiments [7, 8]. The increase of performance is due to the increase of the energy transfer into the atomization process through the heated gas. The shear and elongational processes are intensified by the increase of the dynamical viscosity of the gas and the rise of the sonic gas velocity. Especially the influence of elongational stresses on the ligaments during the atomization is of importance. Fluids with high elongational viscosities are generally difficult to atomize since stretching is the dominant disintegration mechanism after the ligaments are produced (see e.g. [10]).

### Materials and Methods

#### Materials

Polyvinylpyrrolidon (PVP) is a model substance used for the experimental runs. The properties, e.g. rheological data, for PVP- water solutions have been investigated. The polymers Luvitec K30 and K90 differ essentially in the mean molecular weight. The mean molecular weight of Luvitec K30 is about 50 kDa, whereas the molecular weight of the K90 polymer is 30 times higher (1400 kDa).

The rheology of K30 - water solutions are characterized by measurements with rotational and capillary viscometers. Also measurements concerning the elongation viscosity of the fluid are presented. The measurements (e.g. Fig. 1) have been conducted by Schröder et. al. [9].

Newtonian behavior can be obtained at low shear rates (Fig. 1 left), while higher concentrated PVP K30 solutions, e.g. 45 m%, show shear thinning behavior at shear rate high than 1000 1/s. The extensional viscosities of K30 are also depicted in Figure 1. The plateau value for higher strain rates can be characterized by the Trouton factor for newtonian fluids. That means that the extensional viscosity (plateau value) linearly depends on the average shear viscosity. The theoretical values which are typically about three times the value of the average shear viscosity are represented by dashed lines (Fig. 1 right).

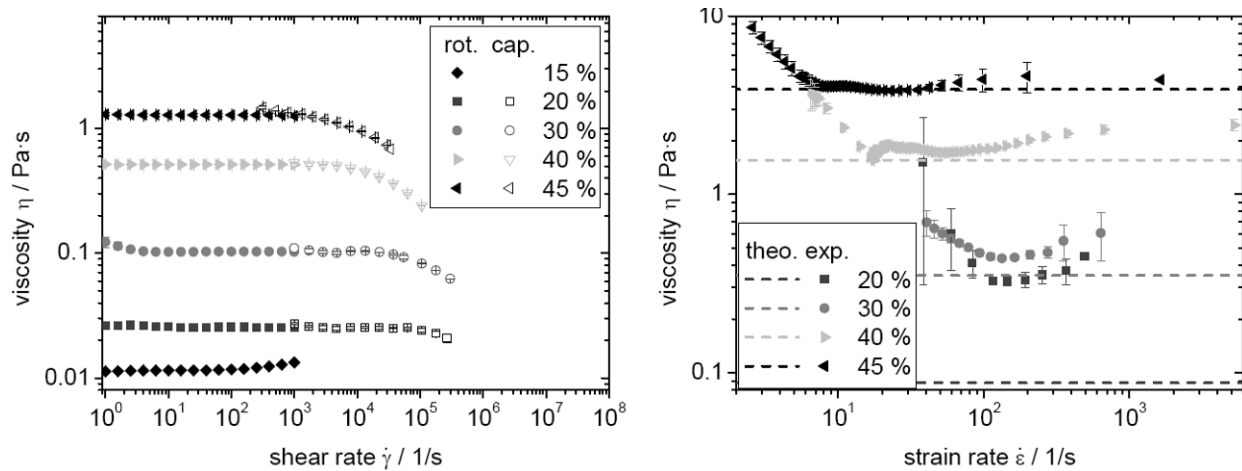


**Figure 1.** Shear- (left) and elongational - (right) rheological data for Polyvinylpyrrolidone (PVP K30)-solutions with different polymer contents (from [8])

For K90 with a polymer content of 5% for shear rates up to 1000 1/s Newtonian behavior with a mean viscosity of 0.047 Pas. Information about the extensional viscosity are not available (see [9]). Further information about the polymer Luvitec PVP can be found under [11].

## Methods

The pilot plant consists of a spray tower with a height of 4.5 m. At the top of the tower the hot gas atomizer is installed for the atomization and the drying of the polymer solution. Due to the high ratio of height and diameter ( $d = 1\text{ m}$ ) this spray dryer type is called Tall-Form-Dryer (e.g. [12]). Figure 2 shows a simplified depiction of the pilot plant. Through the instationary heat exchanger („Cowper“) pressurized air or nitrogen can be heated up to 700°C at a maximum absolute pressure of 6.5 bar. The volumetric flow rate at standard condition is 250 m<sup>3</sup>/h. The temperature range is between 300-600°C. The gas expands outside the nozzle, resulting in a decrease of temperature (Joule-Thomson effect). For an ideal expansion a preset temperature of 500°C will cool down to about 300°. If the temperature is set to 400°C before the nozzle the static temperature of the expanded gas is about 240°C.



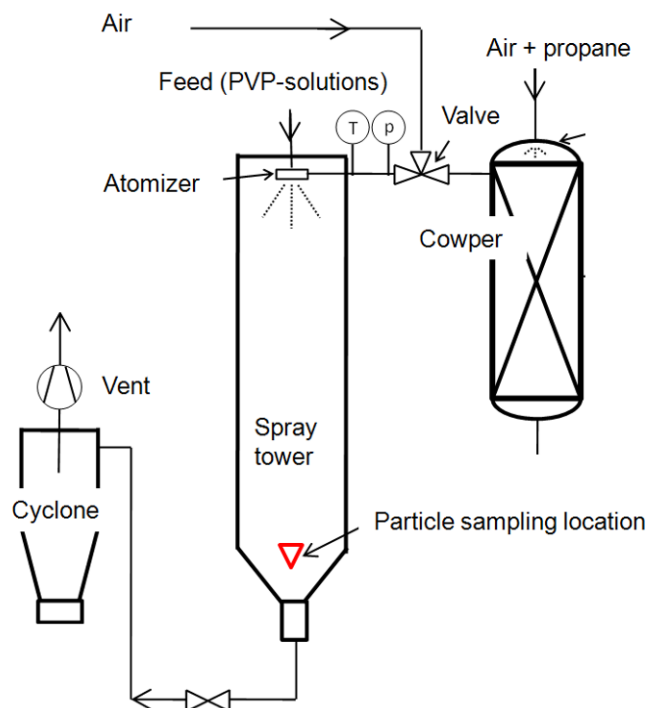


**Figure 2.** Flow sheet diagram of hot gas atomization plant

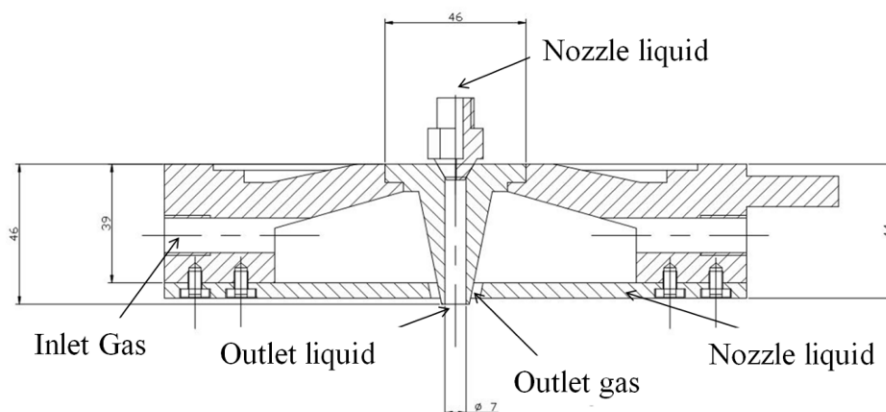


**Figure 3.** Hot gas nozzle

The Atomizer gas nozzle has a concentric slit (Fig. 3). The angle between the axis of the spray and the exiting gas ring jet is  $7^\circ$ . A liquid jet is going through the nozzle body. To avoid pre-filming at the gas exit, the liquid jet velocity has to be sufficiently high. Further downstream the liquid jet is disrupted by the sub pressure in the gas. Thus, an increase of the effective surface area of the liquid is achieved. The atomizer gas also serves the purpose of drying the polymer solution. Thus, the Air-liquid-rat-ion (ALR) is considerably high. In order achieve well dried powder the ALR is set to 60. The powder product is probed at the conical part of the spray tower. Thermo-couples inside the pilot plant are used to determine the temperature distribution. In the pilot-plant scale the spray morphology was not investigated. Therefore, measurements using shadowgraphy were conducted with a lab-scale nozzle under similar conditions.

The two atomizers under investigation mainly differ in their pre-filming mechanism and in the value of the air-liquid ratio. Table 1 provides a brief overview of the atomizer parameters. The key parameter in this study is the atomizer gas temperature. All other parameters are kept constant during the experiments.

**Table 1.** Parameters for lab-scale atomizer (closed coupled twin-fluid atomizer) and for the hot gas nozzle (pilot plant scale)

Atomizer parameters	Lab-scale atomizer	Pilot plant hot gas atomizer
Liquid feed [kg/h]	6	6
ALR [-]	0.624	60
Temperature after expansion [°C]	15	240-300
Atomizer gas pressure [bar absolute]	5	6

The shadowgraphy method is an optical measurement technique, in which the objects in front of a screen can be identified by their shadows (Fig. 4 left). A CCD camera records two shadow pictures with a temporal delay of minimum 1 $\mu$ s. Thus, also velocity information can be derived from the shadowgraphy pictures.

The fluid mass flow of the external mixing atomizer (Fig. 4 right) is the same as in the hot gas atomization runs. The lab-scale nozzle runs at standard atomizer conditions at an ALR of 0.624.

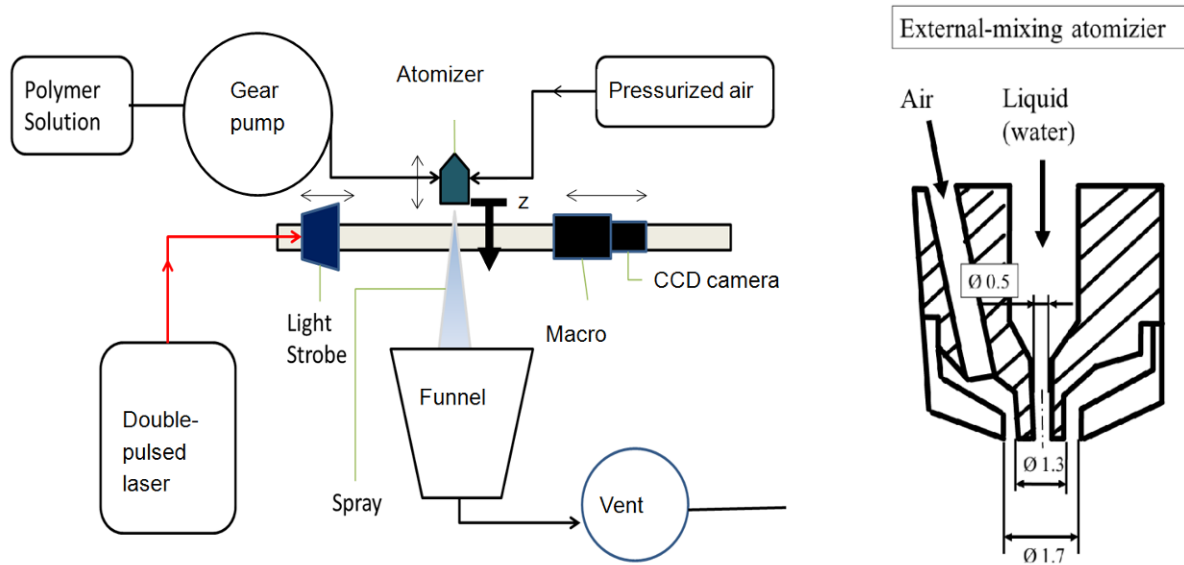


**Figure 4.** Shadowgraphy setup with double pulsed background light (left) and schematic depiction of external mixing atomizer (lab-scale)

## Results and Discussion

### Atomization under isothermal conditions

To analyze the breakup of the PVP-water-solutions shadowgraphy measurements have been performed with an external-mixing atomizer in a lab-scale environment. PVP K90 solutions are difficult to atomize in contrast to K30 solutions at comparable shear viscosities (Fig. 5, Fig.6). The shadowgraphy measurements of PVP show an increase of ligament thickness after primary atomization with increasing polymer content (Fig. 5). For K30 the ligaments break up into droplets more easily. For K90 with a polymer content above 4% the ligaments do not breakup into droplets even at positions further away from the nozzle. Fine ligaments are produced which would result in fine filaments after the drying process.

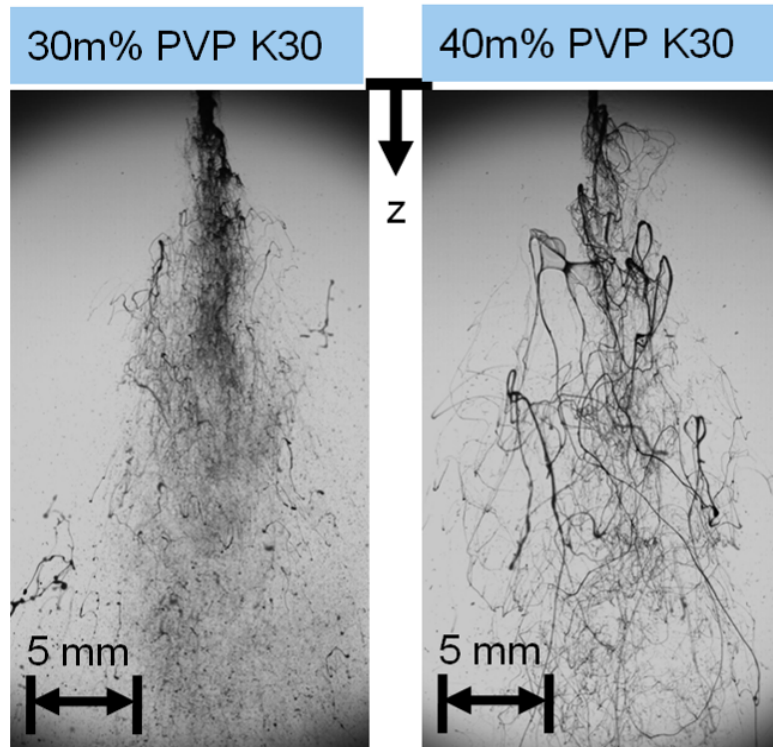


**Figure 5.** Atomization of PVP K30 solution with different polymer content.  
 $P_{\text{Atomizer}} = 4 \text{ bar}$ , 30 m%:  $\eta = 0.1 \text{ Pas}$ ; 40 m%:  $\eta = 0.5 \text{ Pas}$  ( $ALR \approx 0.6$ )

For a concurrent spray dryer and especially for the hot gas atomization process the fine ligaments are dried rapidly. The evaporation of solvent from the elongated ligaments increases the shear and extensional viscosity locally. Thus, breakup might be hindered. Also skin formation might take place. Nevertheless it has to be considered that the time scales for the atomization are much smaller than the time scales for the evaporation. Thus the energy transfer into the liquid is beneficial. In own rheometric measurements it has been found for PVP K90, that the shear viscosity decreases with increasing temperature. A raise in temperature inside the liquid by 50 K decreases the average shear viscosity at low shear rates by over the half of the value at room temperature. Nevertheless, it has to be considered that the flow and breakup behavior of a complex liquid cannot be reduced to its shear viscosity value (at low shear rates) only.

Concerning the ligament breakup in secondary atomization step it is postulated that the breakup into droplets should be completed after some distance from the nozzle since the aero-dynamical forces become smaller. The spray morphology is tendentially inhomogeneous (e.g. Fig. 5 left).

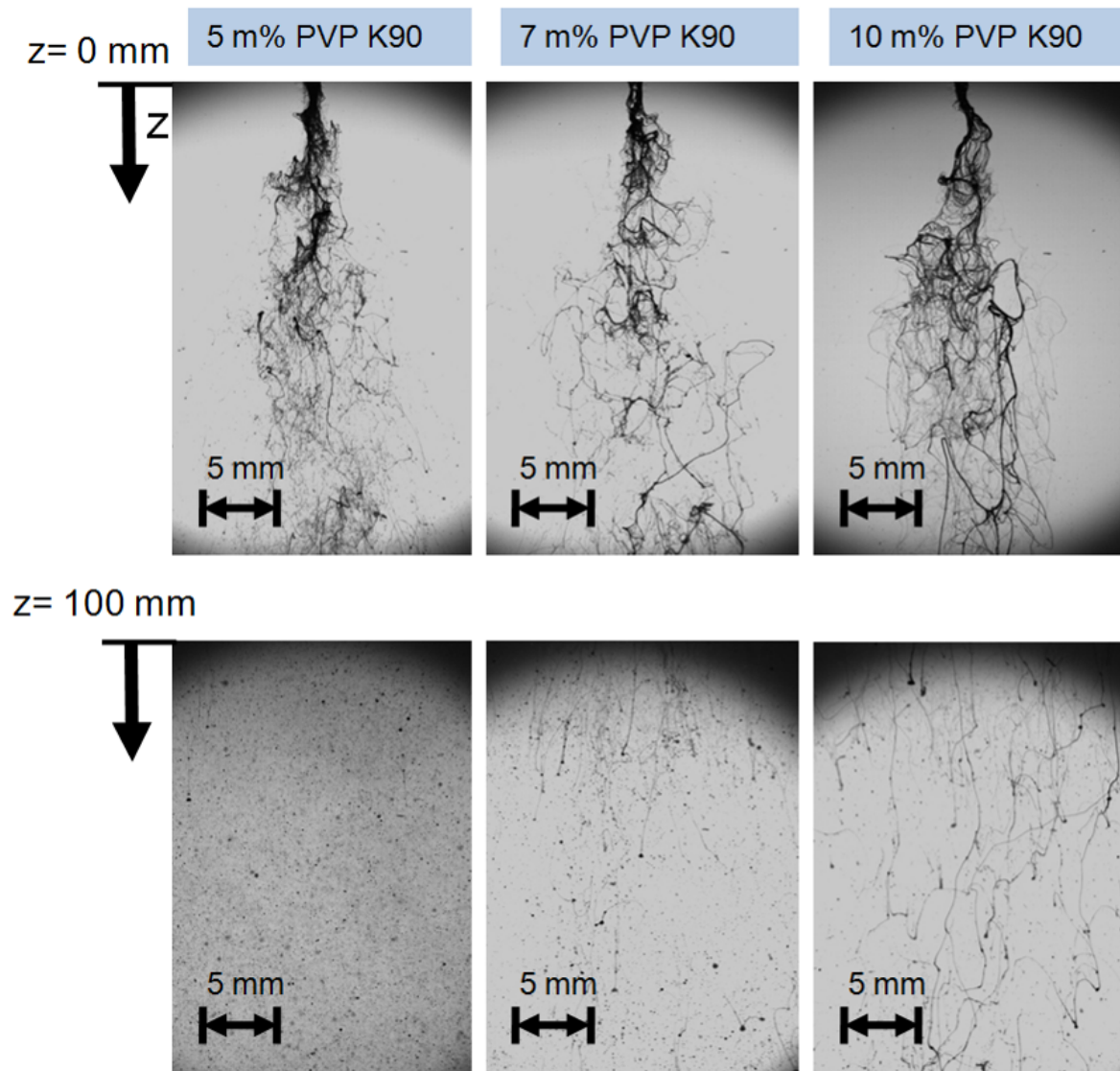


**Figure 6.** Atomization of PVP K90 solutions with different polymer content.  
(5 m%:  $\eta = 0.047$  Pas; 7 m%:  $\eta = 0.15$  Pas; 10 m%:  $\eta = 0.4$  Pas),  $p_{\text{Atomizer}} = 4$  bar ( $ALR \approx 0.6$ )

For K90 solutions with a polymer content above 4 m% and standard atomizer settings a formation of thick elongated ligaments can be seen (Fig. 6). Further downstream most of the ligaments still exist, but they are stretched in the streamwise direction and become very thin. In close up photo shoots for a 5 m% K90 solution these thin ligaments can be seen (Fig. 7). Also a lot of fine droplets and a number of bigger droplets can be detected. This circumstance was also found under similar atomization and drying conditions in [13].

A tracking of the ligaments can be performed on two subsequent pictures. The stretching of ligaments is detectable. At the same time the fast translation movement of the ligaments makes it difficult to differentiate shear and elongation strain within liquid from the dynamical motion of the ligament.

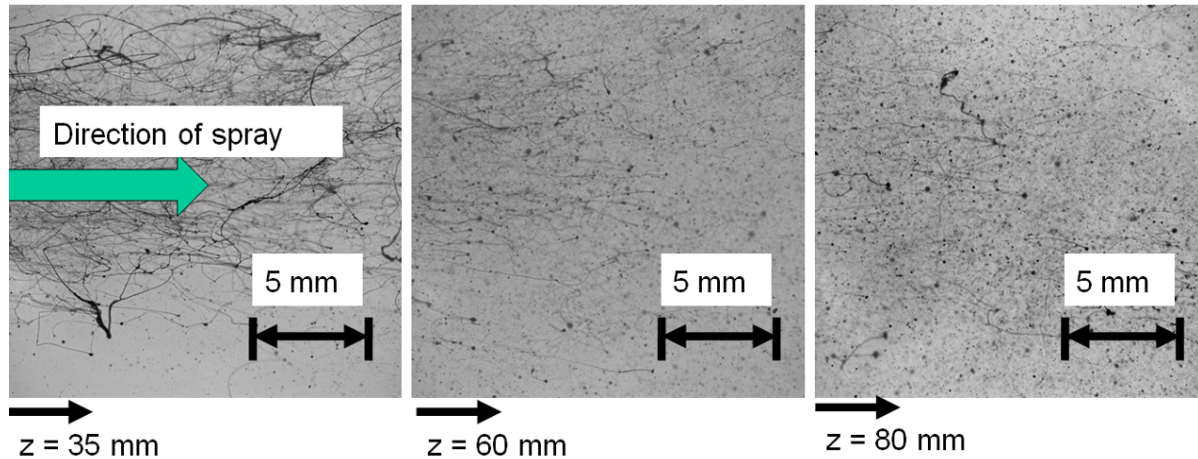


**Figure 7.** Shadow pictures of PVP K90 solution (5 m%) in different distances from the nozzle

The high fiber fraction within the Spray makes it difficult to characterize the particle size distribution with the laser diffraction method [10]. The detection and the quantification of the droplets and ligaments is part of the ongoing investigations.

#### Flow behavior in spray dryer

In Reynolds-Averaged-Navier-Stokes-(RANS) – simulation the velocity and temperature field within the spray tower and close to the nozzle has been computed for the gas flow.

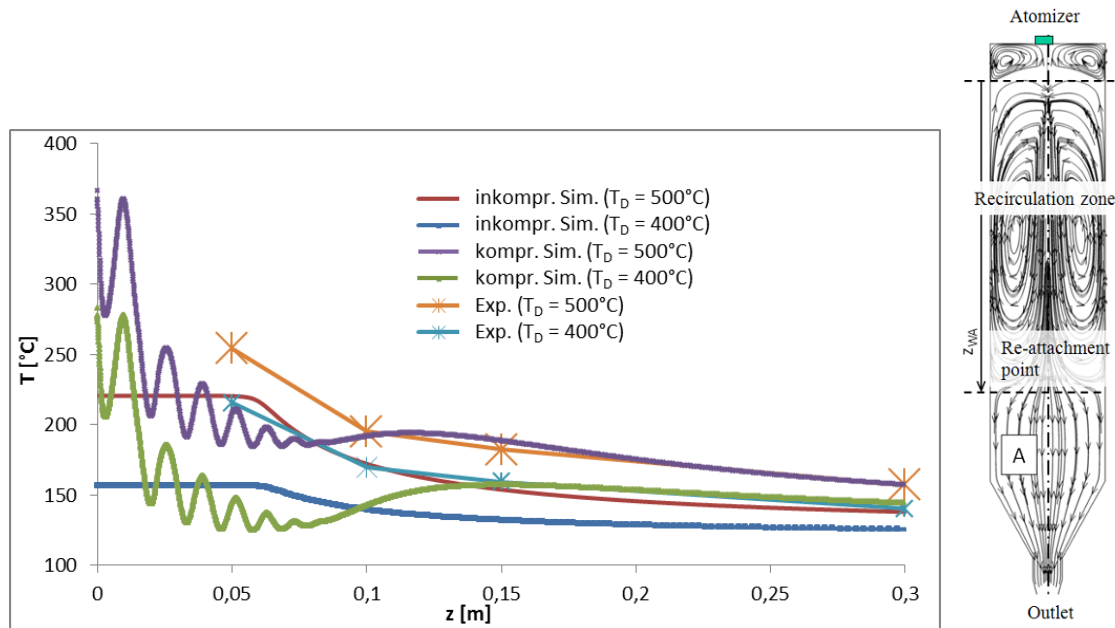


**Figure 8.** Left: Gas temperature profiles from numerical simulation and measurements (single phase)

Right: Integral spray structures within the spray tower (num. simulation)

The axial profile of the gas temperature was compared to experimental results (Fig. 8 left). In the compressible simulation model pressure shocks are given up to 10 cm away from the nozzle. Outside the nozzle the gas is under-expanded. That means that the pressure of the gas is higher than the ambient pressure and energy stored in the fluid as pressure is used for acceleration of the gas outside the nozzle. The static temperature measured on the spray axis shows good agreement with the simulated results.

The results coming from the incompressible simulation with simplified boundary conditions (round jet) show no temperature peaks near the nozzle. For stability and convergence reason the global spray simulation has been performed only with the incompressible RANS simulation. The flow inside the spray tower is characterized by a



high recirculation rate ( $(\dot{V}_{\text{recirculation}}/\dot{V}_{\text{atomizer}})_{\text{max}} \approx 100$ ) in the center of the recirculation zone (s. Fig. 8 right; cf. [14]). Through the entrainment/recirculation of gas and particles large-scale mixing within the spray process takes place. Strong temperature gradients can only be found near the nozzle. The position of the re-attachment point (Fig. 8 right:  $z_{\text{WA}}$ ) could be verified in the experiments qualitatively.

#### Powder production in hot-gas plant

Two different polymer solutions (K30 with 30%, K90 with 5% concentration) at two different atomizer gas temperatures ( $T_{\text{Gas}} = 400^\circ\text{C}$  and  $500^\circ\text{C}$ ) have been sprayed. For the K30 solution with a mass content of 30% some thin fibers can be found in the dried product (Fig. 9). The particles's shape is spherical though the surface of most particles shows dimples. The morphology of the droplets is similar for all specimen. Fibers reduce the powder flow ability. Since the full shape of the fibers is not visible only qualitative statements about the fiber fraction can be made. In the investigated range of the atomizer gas temperatures there is no qualitative change for the fibers in the final product.

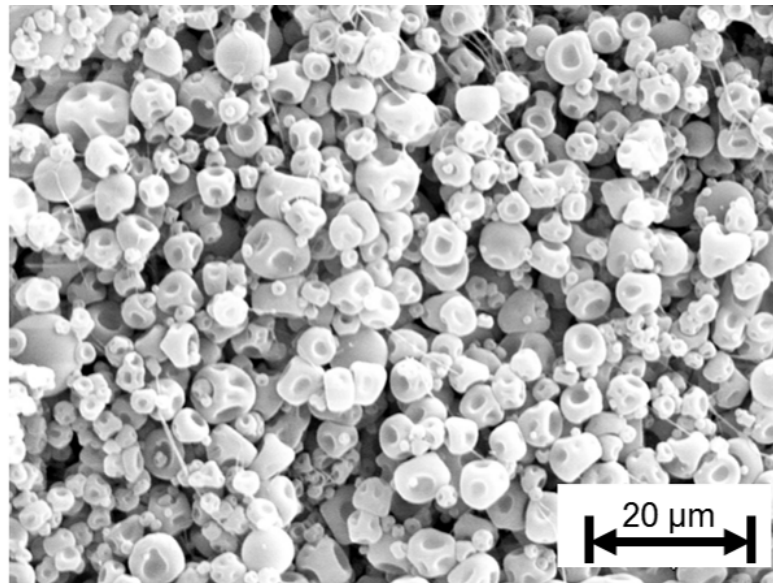


**Figure 9.** Particles from spray drying of PVP-K30 – water – solution (30m%) in hot gas ( $T_{\text{Gas}}=400^\circ\text{C}$ )

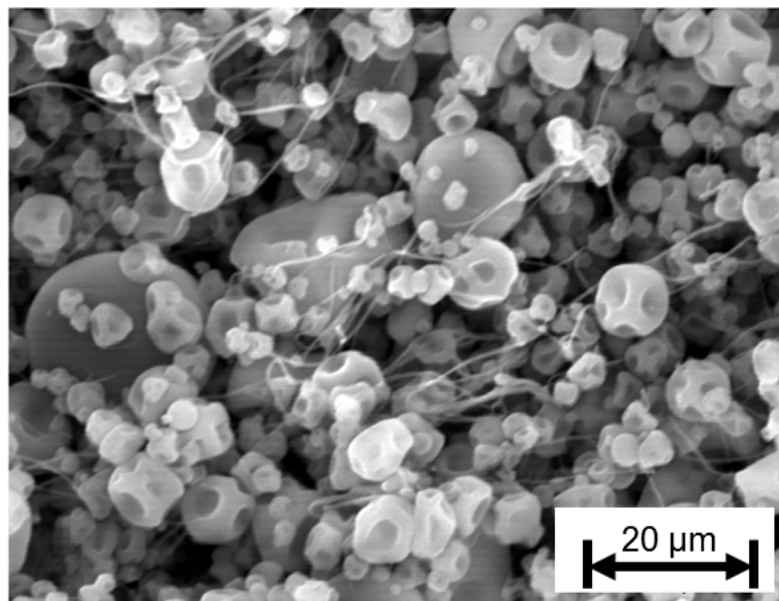


**Figure 10.** Particles from spray drying of PVP-K90 – water – solution (5m%) in hot gas ( $T_{\text{Gas}} = 400^\circ\text{C}$ )

The same can be found for the K90 at 5% solution (Fig. 10). Here the amount of fibers in the product is substantially increased. This fact can also be deduced from the shadowgraphy results, where the ligaments of K30 break up more easily, while the ligaments of the K90 solutions breakup at positions further downstream. The shape of the K90 particles is similar to the dried K30 product. To quantify the product properties the particle size distribution from REM pictures was determined (Fig. 11). A minimum of 8 pictures from one spray run was evaluated manually for each particle size distribution.

The  $d_{50,3}$  of the particles increases slightly with temperature (Fig. 12). The difference between the polymer solutions is minimal. For the characterization of the droplets that are much bigger than the median particle size still more samples have to be evaluated.

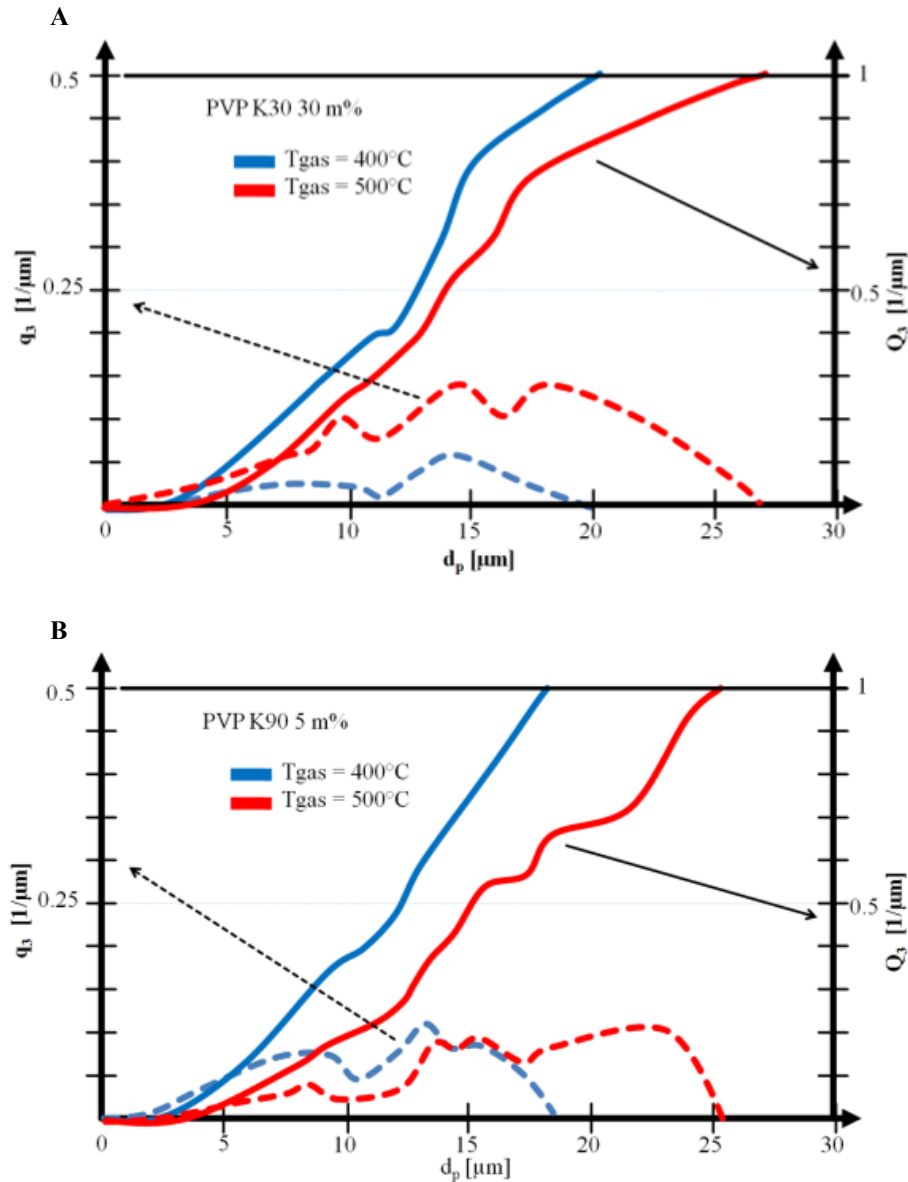


**Figure 11.** Particle size distribution PVP K30 (A) and PVP K90 (B) for different gas temperatures



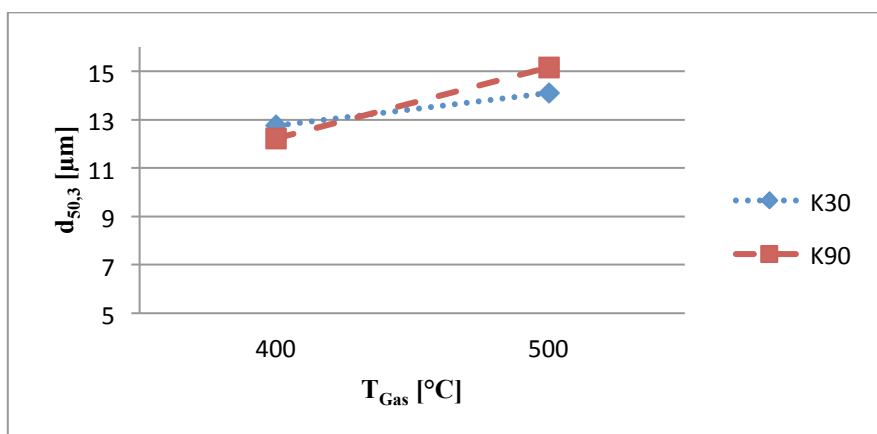


**Figure 12.** Median particle size

In ongoing experiments the direct influence of the hot atomizer gas on the primary and secondary atomization is quantified. Therefore, larger gas temperatures will be applied to intensify the momentum, heat and mass transfer. The influence of the fluid's rheology on the sensitivity towards the atomizer gas temperature is investigated in detail. A rheological question is how efficient fluids like polymer solutions with low complexity, but high shear viscosities, are atomized using hot atomizer gas. Additionally the drying kinetics for the hot-gas spray drying process are determined.

## Conclusions

The method of using hot atomizer gas for the atomization of complex liquids has been applied in this work. In the hot gas atomization process the momentum exchange between the liquid phase and the gas phase is intensified by the use of hot gas. The properties of the feed material and the atomizer performance have been investigated for two polymer solutions. Therefore, Polyvinylpyrrolidon – water solutions characterized by different molecular weights have been prepared and sprayed with different atomizer gas temperatures. In shadowgraphy results it can be observed that for K30 the ligaments break up more easily while some of the ligaments for K90 solutions are elongated to very thin ligaments. These thin ligaments are dried and result in a higher fiber fraction in the final product. For the polymer solutions used in the experiments the influence of the applied atomizer gas temperature on the final product is rather low.

## Acknowledgements

The funding of the german research foundation (DFG) within the priority program SPP 1423 Process-Spray is gratefully acknowledged.

## References

- [1] G.G. Nasr, A.J. Yule, L. Bendig, *Industrial Sprays and Atomization - Design, Analysis and Applications*, Springer-Verlag Heidelberg, 2002.
- [2] A.H. Lefebvre, *Atomization and Sprays*, Hemisphere Publ. Corp., New York, 1989.
- [3] A. Lampa, U. Fritsching, *Spray structure analysis in atomization processes in enclosures for powder production*, *Atomization and Sprays*, 2011, vol 21, pp. 737-752.
- [4] U. Fritsching, *Droplets and particles in sprays: tailoring particle properties within spray processes*, *China Particuology*, 2005, vol 3, pp. 125-133.
- [5] G. Schulz: *Rapid Solidified Materials Made by Wideflow Melt Film Gas Atomization*, *Adv. Powder Met. Part. Mat.*, 2002, vol. 3, pp. 227-234.
- [6] F. Campanile, B.J. Azzopardi, *Atomisation of very viscous liquids*, in: *Conf. Liquid Atomization and Spray Systems ICLASS 2003*, Sorrento, Italy, 2003.
- [7] H. Lohner, C. Czisch, U. Fritsching, K. Bauckhage, *Granulation viskoser Mineralschmelzen mittels Heißgaszerstäubung*, *Chemie Ingenieur Technik*, 2002, vol. 74 pp. 1270-1272.
- [8] J. Dunkley, *Hot Gas Atomisation - Economic and Engineering Aspects*, PM2005 World PM Congress, Vienna, 2005.
- [9] J. Schroeder, M.-L. Lederer, V. Gaukel, H.P. Schuchmann, *Effect of atomizer geometry and rheological properties on effervescent atomization of aqueous polyvinylpyrrolidone solutions*, in: *ILASS 2011*, Estoril, Portugal, 2011.

- [10] J. Schroeder, *Charakteristika der "effervescent atomization" rheologisch komplexer und mehrphasiger Flüssigkeiten*, Dissertation Karlsruher Institut für Technologie (KIT), 2012.
- [11] BASF SE, *PVP and more - LUVITEC; LUVICROSS UND COLLACRAL VAL Spezialpolymere für technische Anwendungen*, 2013.
- [12] R. Kuriakose, C. Anandharamakrishnan, *Computational fluid dynamics (CFD) applications in spray drying of food products*, Trends in Food Science & Technology, 2010, vol. 21 pp. 383-398.
- [13] M. Tewes, U.A. Peuker, *Zerstäuben von Polymerlösungen unterschiedlicher Viskosität und Molekülmasse bei konditioniertem Zerstäubergas*, SPRAY 2010 - 9. Workshop über Sprays, Techniken der Fluidzerstäubung und Untersuchungen von Sprühvorgängen, Heidelberg, 2010.
- [14] D.J.E. Harvie, T.A.G. Langrish, D.F. Fletcher, *A Computational Fluid Dynamics Study of a Tall-Form Spray Dryer*, Food and Bioproducts Processing, 2002, vol. 80 pp. 163-175.



# AUTHOR INDEX

Abbas A.J.	145	Chaussonnet G.	870
Abdl-Aziz1 F.	751	Chrigui M.	779
Abo-Serie E.	751	Christodoulou C.N.	737
Achelis L.	321, 760	Chrysakis C.	802
Al Qubeissi M.	936, 944	Cleary M.J.	863
Alghoul S.K.	475	Colinet P.	91
Allocca L.	525	Cordes D.	571
Amirfazli A.	929	Cousin J.	151
Anand T.N.C.	966	Crua C.	496
Andreini A.	826, 834	Cuenot B.	786
Aniszewski W.	219	Cuenot B.	870
Antonini C.	713, 929	Cypris J.	594, 601
Arcoumanis C.	158, 629	Daaboul M.	387
Asmuin N.	351	Daniel E.	912
Audouin A.	978	Dawi A.H.	706
Backofen D.	532	de Sercey G.	496
Baillot F. 3	67	Déjean B.	337
Bakshi S.	141	Demoulin F.X.	209, 246, 901
Balcaen J.	314	di Benito Sienes E.	489
Balzan M.	394	Di Martino P.	329
Bardi M.	556	Diemuodeke E.O.	893, 972
Baroud Y.	115	Dinkelacker F.	462
Basara B.	855	Domnick J.	374
Befrui B.	878	Dragomirov P.	532
Bereaux Y.	314	Dreizler A.	637, 992
Berrocal E.	173	Drusch S.	115
Berthoumieu P.	337	Duić N.	841
Bertola V.	656, 663	Dumouchel C.	886
Bianchini C.	826, 834	Duret B.	209
Biolo D.	663	Durox D.	415
Birkefeld A.	721	Dutzler G.	811
Bitner K.	462	Edelbauer W.	841
Black K.	656	Eisenschmidt K.	39
Blaisot J.-B.	108, 136, 367, 886	Elesin V.V.	1027
Blanchard G.	254, 261	Ellendt N.	760
Blond A.	314	Elwardany A.E.	952
Böhm B.	637	Enyi G.C.	145
Bombach R.	517	Ern P.	978
Bork B.	992	Ertl M.	76, 188
Bothe D.	225	Ertl T.	122
Bouali Z.	246	Esmaeilzadeh E.	959
Brenn G.	76	Estel L.	1019
Breton K.M.	985	Estivalezes J.-L.	202, 218
Burby M.	351	Facchini B.	826, 834
Caltagirone J.-P.	215	Falgout Z.	489
Cardena M.	571	Farooq A.	952
Charneau J.Y.	314	Fink C.	510
Charru F.	978	Fischer S.	684
Chasos A.	737	Fleck B.A.	394, 985
Chatterjee D.	141	Focke C.	225

Fournier-Salaün M.-C.	1019	Horváth I.T.	91
Fritsching U.	321, 760, 1050	Hu Y.	10
Fuchs S.	616	Huertas J.I.	649
Fukamichi S.	541	Hult J.	489
Furuichi H.	167	Ide K.	1006
Gajan P.	337	Idlahcen S.	136
Galle J.	296	Idlahcen S.	108
Gambaryan-Roisman	684, 706	Inamura T.	344
Garcia-Oliver G.M.	811	Ishibashi R.	818
Gaukel V.	381, 408	Ishida M.	579
Gavaises. M.	629, 713	Ishimura Y.	644
Ge Y.	863	Ishmatov A.N.	1027
Gebretsadik M.	329	Jakirlic S.	855
Geppert A.	677	Janicka J.	195, 239, 779
Gepperth S.	870	Jedelsky J.	446
Gerds A.	510	Jicha M.	446
Gethin. D.	670	Jollet S.	462
Giraldo N.	649	Kaario O.	98
Girin A.G.	55, 848	Kaiktsis L.	794, 802
Giusti A.	826, 834	Kalmbach T.	31
Gjonaj E.	122	Kamoun H.	269, 277
Gold M.	496	Kamplade J.	430, 1035
Gomaa H.	76, 225	Karagiorgis G.N.	737
Gopireddy S.R.	17, 47	Karch G.K.	122
Götz G.	587	Kayed H.	751
Grehan G.	277, 1019	Kazangas D.	794
Greifl F.	677	Keskinen K.	98
Gröhn A.	321	Kibayashi Y.	469
Gumprich W.	24	Kikuchi M.	1014
Gun'ko V.M.	62	Kintea D.M.	772
Günther A.	1000	Klaiber M.	115
Gutheil E.	10, 17, 47, 69	Kleinhans A.	381
Habchi C.	482, 912	Klostermann M.	423
Hadler J.	532	Kneer R.	438, 503, 568
Harmand S.	649	Knorsch T.	608, 622
Harndorf H.	510	Koch R.	870
Hassan M.	751	Koester M.	47
Hauber M.	31	Kolodnytska R.	936, 944
Hauk T.	921	Komada K.	579, 818
Hayashi S.	1006	Köninger B.	1000
Hecht N.	246	Kontoulis P.	794, 802
Heikal M.R.	496	Kristensson E.	173, 180
Heilig A.	462	Kronenburg A.	863
Heldmann M.	616	Krüger C.	637
Hélie J.	151	Kumar R.	744
Herbert S.	684, 706	Kurosawa Y.	1006
Hermann D.	691	Lacome J.M.	901
Herrmann K.	517	Lacroix T.	108
Hirose T.	1014	Lai M.-C.	878
Hisatomi Y.	644	Lakhanpal C.	656

Lamanna G.	269, 277, 677, 992	Niemeyer D.	462
Lampa A.	1050	Nikolopoulos N.	713
Lee S.Y.	525	Nishikawa K.	541
Lees. A.W.	670	Nobes D.S.	394, 985
Lemofack C.	901	Nouri J.M.	158, 629
Levy M.	291	Nourian A.	145
Levy Y.	291	Nuri Sara O.	329
Li X.	321, 760	Ogorodnikov S.P.	1027
Liebing M.	31	Ohori S.	1006
Linder N.	232	Ohta Y.	1006
Linne M.	489	Olguin H.	69
Littringer E.	47	Opfer L.	423
Louste C.	387	Oschwald M.	269
Magno A.	548	Osmar L	218
Makhlouf S.	151	Ouboukhlik M.	1019
Malgarinos I.	713	Paciaroni M.	489
Mancaruso E.	548	Palaciiios J.	929
Mandloi P.	744	Palmer J.	438
Mandumpala Devassy	912	Paloposki T.	344
Manfletti C.	269	Pananakis E.	802
Manin J.	556	Pastor J.V.	811
Marchi A.	158	Paulhiac D.	786
Marchitto L.	525	Pavlovic Z.	855
Marengo M.	713, 929	Payer W.	811
Marschall H.	232	Payri R.	556
Mathieu F.	435, 503	Petranović Z.	841
Matlok S.	489	Pettersson S.G.	173
Matsuura K.	1006	Peuker U.A.	304
Mehring C.	730	Pickett L.M.	556
Meierhofer F.	321	Piesche M.	31
Menard T.	209, 218, 246	Pinkert F.	510
Mercadé C.	225	Prasad. C.	141
Mescher A.	47, 1035	Pratama R.H.	469
Mescher A.	400	Priesching P.	811
Mikami M.	643, 1014	Rahm M.	489
Mirat C.	415	Raps D.	921
Mishra Y.N.	173	Rauschenberger P.	39
Mizushima Y.	84	Reddemann M.A.	438, 503
Moita A.S.	691	Rees A.	269
Möller S.	811	Reveillon J.	209, 246, 901
Montanaro A.	525	Rewse-Davies Z.	629
Moreira A.L.N	691	Rezayati Charan M.	959
Morin C.	649	Riber E.	786, 869
Moriue O.	1014	Richard C.	367
Musemic E.	430	Rohde C.	39
Naber J.	525	Roisman I.V.	225, 232, 419, 706,772, 1043
Najar I.	510	Roth N.	76, 225
Najmabadi M.	115	Rottengruber H.	532
Nasiri R.	62	Rozé C.	108 , 136
Nasr G.G	145, 351		

Sacomano Filho F.L.	779	Stritzke F.	992
Sadiki A.	24, 195, 239, 779	Strobl T.	921
Sadlo F.	122	Strotos G.	713
Sadri B.	959	Tabatabaee-Hosseini	959
Saengkaew S.	277	Tajima H.	579, 818
Saengkaew S.	1019	Tamaki N.	541
Saito T.	84, 167	Tamm F.	115
Sakaguchi D.	579	Tarquini S.	929
Sander S.	760	Tewes M.	304
Sauer B.	195	Theron M.	367
Sauerhering J.	532	Thomas D.	670
Sazhin S.S.	62, 936, 944, 952	Tiejde O.	698
Schäfer W.	130	Traore P.	387
Scheibe A.	374	Tropea C.	130, 232, 423, 706, 721, 772, 855, 1043
Schmid A.	517	Trubnikov A.A.	1027
Schmidt J.	532	Tschöke H.	532
Schorr J.	637	Tsuru D.	818
Schreiner M.	321	Turrini F.	329
Schröder J.	381	Turrini F.	826, 834
Schuchmann H.P.	381, 408	Ueki H.	579
Schulz R.	517	Urbanetz N.	47
Sculler T.	415	Uzol O.	454
Sedarsky D.	136	v. Berg E.	811
Seel K.	571	Vaglieco B.M.	548
Sen D.	394	Vajdi Hokmabad B.	959
Sender J.	269	Venzmer J.	423
Seo T.	644, 1014	Verhelst S.	296
Sequino L.	548	Vermorel O.	870
Seubert N.	863	Vetrano M.R.	91
Shamit B.	966	Villedieu P.	254, 261
Sharief R.A.	358	Vincent S.	202, 218
Sher E.	291	Vogel T.	587
Sher I.	893, 972	von Rotz B.	517
Shevchuk I.	339	Vujanović M.	841
Shimodaira K.	1006	Walzel P.	47, 1035
Shost M.A.	878	Walzel P.	400, 430
Shrivastava S.	744	Wang Z.	489
Simon S.	115	Watari H.	1014
Soma Sundaram S.	966	Weckenman F.	992
Songoro H.	122	Weclas M.	594, 601
Sou A.	469	Wegner K.	321
Spiekermann P.	878	Weickgenannt C.M.	1043
Stähle P.	381, 408	Weigand B.	39, 76, 188, 225, 269, 277, 677, 721, 992
Steelant J.	269, 277	Weiland T.	122
Stein O.T.	863	Weisser G.	517
Stephan P.	684, 706	Wensing M.	587, 608, 616, 622
Stevenin C.	314	Wigley G.	284
Stiehl R.	637		
Storch M.	608, 622		
Stratmann A	400		



Will S.	622
Wirth K.-E.	1000
Wollgarten J.C.	329
Wood A.	284
Yamada H.	1006
Yamada T.	579
Yamamoto T.	1006
Yan Y.	158
Yazici B.	454
Ye Q.	374, 698
Yoshiura Y.	1006
Yule A.	351
Zarzalís N.	329
Zhang A.	525
Zhu C.	188
Zigan L.	608, 622
Zuzio D.	254, 261